OHBM 2024
JUNE 23~27, SEOUL, KOREA

ABSTRACTS

Sunday, June 23 – Thursday, June 27
COEX CONVENTION & EXHIBITION CENTER | SEOUL

30TH ANNUAL MEETING OF THE
ORGANIZATION FOR HUMAN BRAIN MAPPING

Poster No 1037

Harry Potter meets Markov: Detecting event boundaries in narrative reading by a data-driven model

Huidong Xue[1], Filipp Dokienko[2], Giovanni Menon[1], Francesco Gentile[1], Bernadette Jansma[1]

[1]Maastricht University, Maastricht, Limburg, [2]Imperial College London, London, Greater London

Introduction: In narrative reading, we integrate a series of words into meaningful mental representations, so-called events. Recent neuroimaging studies applying data-driven analysis have shown a temporal cortical hierarchy of event structure during movie watching and story listening[1,2]. How event segmentation takes place within the neural reading network remains elusive. A Hidden Markov model-based event segmentation technique allows inferring unobserved temporal event structure from neuroimaging data without annotations[1]. We applied this data-driven model to fMRI data acquired during reading of a Harry Potter story to detect the event boundaries within the neural reading network, and compared the obtained event structure with the human annotation.

Methods: We used public-release fMRI data of eight volunteers reading chapter nine of the book "Harry Potter and the Sorcerer's Stone"[3] (Figure 1). Around 5200 words were presented in four runs by rapid serial visual presentation with 0.5s presentation duration per word. Imaging data was acquired using a T2*-weighted echo planar imaging pulse sequence with repetition time (TR) of 2 seconds. Wehbe et al. preprocessed the data in SPM8 with slice-time and motion correction, 3 × 3 × 3mm isotropic spherical Gaussian kernel smoothing, and detrending[3]. We extracted fMRI data from six ROIs, namely the Angular Gyrus (AG), Posterior temporal lobe (PTL), Anterior temporal lobe (ATL), Middle frontal gyrus (MFG), Inferior frontal gyrus (IFG), Inferior frontal gyrus orbital (IFGorb) according to the reading network mask[4] in subject space. To reduce data dimensions and align the fMRI data across subjects, we used the shared response model to project all subject's space data into shared 90-dimensional space for each ROI[5]. We obtained the human annotations by asking five independent volunteers to read the chapter and to mark boundaries of scenes with shifts in topic, location, time, or other crucial elements. In order to detect the event boundaries for each ROI, we applied a HMM-based event segmentation model in BrainIAK software[6]. We evaluated the model using the leave-one-subject-out method. The optimal number of events for each region was determined by computing the maximum t-distance (t-value), defined as difference in distributions between within-event and across-event correlations[7]. We investigated the temporal alignment of the event boundaries across regions using optimal number of events. The alignment of HMM boundaries and human annotations were tested using the human annotations as upper limit in the model. Significance of alignment was computed by means of permutation testing.

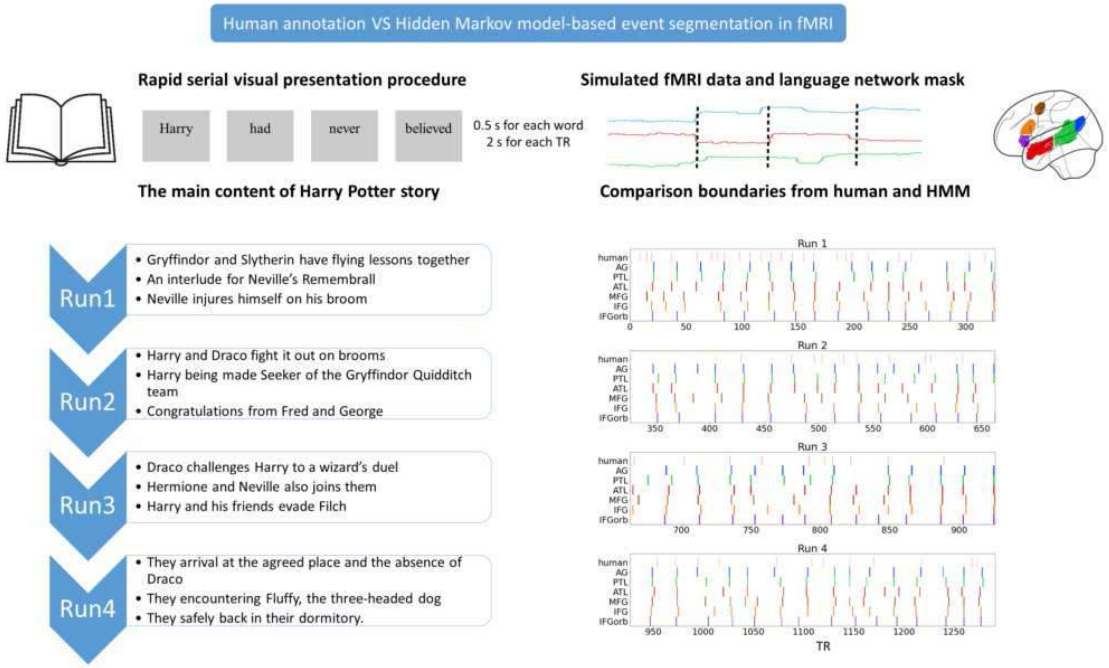

Figure 1. Overview of the fMRI reading experiment and HMM results. The left part shows the words presented using rapid serial visual presentation with two words per second presentation rate, and the main content of the Harry Potter story in the 4 runs. The right panel (top row) illustrates the HMM-based event segmentation of simulated fMRI time course. The boxes represent detected event boundaries separated per run for human annotation and ROIs of the reading mask (displayed in the brain icon).

Results: Human annotation unveiled 58 events on average, with 31 events being common across individuals. The HMM detected 37 (MFG) to 67 (AG) events across ROIs (Figure 2A). Their boundaries were significantly aligned with eachother (Figure 2B). ATL (p=0.013) and AG (p=0.042) boundaries were aligned with human annotation (Figure 2C&D). Interestingly, in the first run, all regions showed a higher alignment with human annotation (p value for each: AG=0.009, PTL=0.087, ATL=0.016, MFG=0.022, IFG=0.015, IFGorb=0.044), and only the AG (p=0.015) showed significantly aligned in the fourth run (Figure 2D).

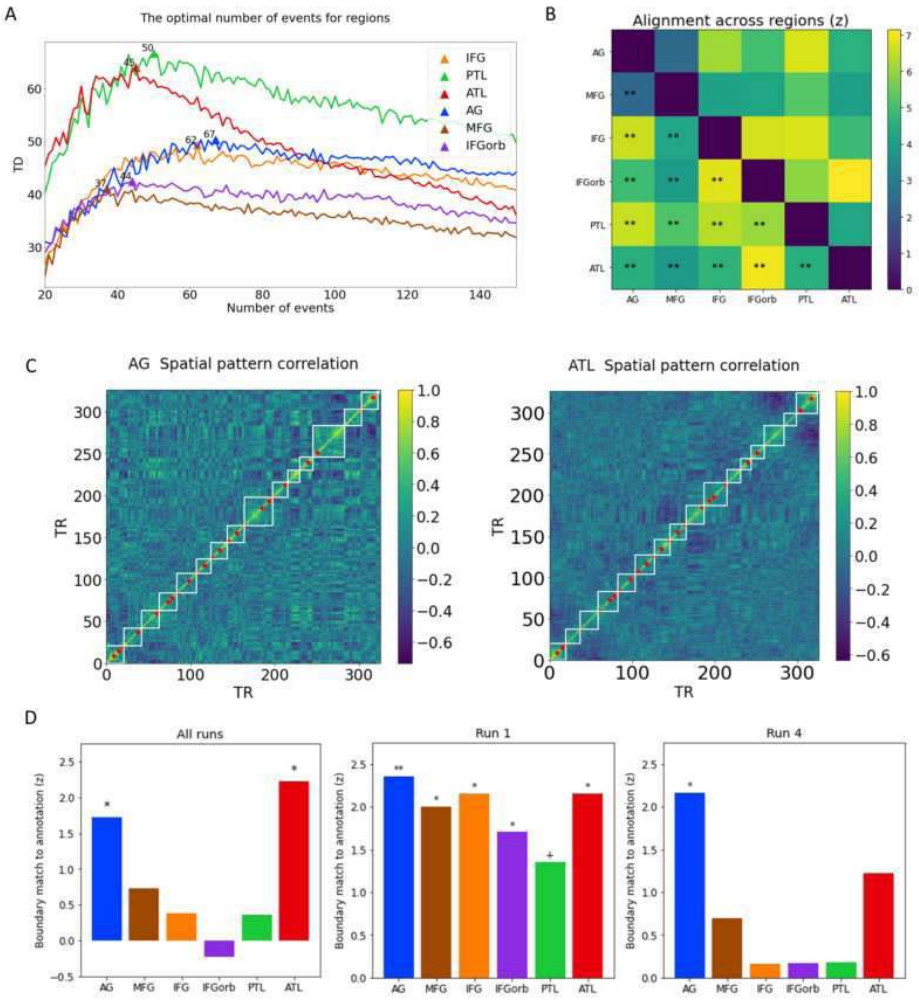

*Figure 2. Alignment of HMM and human-labeled boundaries. (A) Optimal number of events for each region, (B) Comparison of HMM boundaries across regions, (C) TR-TR correlation matrix overlayed with the HMM-predicted event boundaries (white box) and human annotation (red dots) for AG and ATL, (D) permutation test results for comparison of HMM-predicted event boundaries to human annotations for all runs, and run 1 and 4, respectively. (+ = 0.087, *p < 0.05, **p < 0.01).*

Conclusions: The present results show a nested event structure in the narrative reading network with shorter events in AG and longer events in frontal and temporal areas, and high-frequent boundaries partially nested in low-frequency boundaries. Results of ATL and AG support their role in conceptual representation[8,9], Their event boundaries were aligned with human annotation, suggesting a link between conceptual relevance and event structure. The AG shows good tracking with human annotation along the entire reading time, suggesting an involvement in context integration over time[10]. These findings provide neuroscientific insight into event segmentation in narrative reading.

References

1. Baldassano, C. (2017). “Discovering Event Structure in Continuous Narrative Perception and Memory.” Neuron 95(3): 709-721 e705.
2. Soares, A. D. (2023). “Top-down attention shifts behavioral and neural event boundaries in narratives with overlapping event scripts.” bioRxiv: 2023.08.08.552465.
3. Wehbe, L. (2014). “Simultaneously uncovering the patterns of brain regions involved in different story reading subprocesses.” PLoS One 9(11)
4. Fedorenko, E. (2010). “New method for fMRI investigations of language: defining ROIs functionally in individual subjects.” J Neurophysiol 104(2): 1177-1194.
5. Chen, P. H. (2015). “A Reduced-Dimension fMRI Shared Response Model.” Advances in Neural Information Processing Systems 28 (Nips 2015) 28.
6. Kumar, M. (2021). “BrainIAK: The Brain Imaging Analysis Kit.” Apert Neuro 1(4).

7. Geerligs, L. (2021). “Detecting neural state transitions underlying event segmentation.” Neuroimage 236: 118085.
8. Correia, J. (2014). “Brain-based translation: fMRI decoding of spoken words in bilinguals reveals language-independent semantic representations in anterior temporal lobe.” Journal of Neuroscience 34(1): 332-338.
9. Acunzo, D. J. (2022). “Deep neural networks reveal topic-level representations of sentences in medial prefrontal cortex, lateral anterior temporal lobe, precuneus, and angular gyrus.” Neuroimage 251: 119005.
10. Branzi, F. M. (2021). “The left angular gyrus is causally involved in context-dependent integration and associative encoding during narrative reading.” Journal of cognitive neuroscience 33(6): 1082-1095.

Poster No 1038

The Representational Dynamics of Speech Prosody: An MEG Study

Seung-Cheol Baek[1], Seung-Goo Kim[1], Burkhard Maess[2], Maren Grigutsch[2], Daniela Sammler[1]

[1]Max Planck Institute for Empirical Aesthetics, Frankfurt am Main, Hesse, [2]Max Planck Institute for Human Cognitive and Brain Sciences, Leipzig, Saxony

Introduction: Speech prosody is crucial for communication as it conveys meaning, such as intentions, beyond the propositions. Prosody is processed in a bilateral frontotemporal network (Belyk & Brown, 2014), and is thought to involve multiple steps along the ventral auditory stream (Schirmer & Kotz, 2006). These steps are likely to include the sensory analysis in bilateral posterior temporal areas, the identification and evaluation of prosodic forms in right anterior temporal and frontal areas. Additionally, right premotor cortex (PMC) as part of the dorsal auditory-motor stream was found to play a causal role in prosody categorization (Sammler et al., 2015). However, it remains to be shown where and when speech prosody is actually represented in its acoustic and/or abstract categorical form, and if prosodic representations are dominant in the right hemisphere.

Methods: We collected magnetoencephalogram (MEG) data from 29 native Germans while they listened to single words that gradually varied in prosody and word-initial phoneme along orthogonal continua generated by audio morphing (Fig. 1A). Participants categorized these words into either prosody (statement vs. question) or phoneme (/b/ vs. /p/) in alternating blocks (Fig. 1B). The MEG data were analyzed in source space (eLORETA) by time-resolved representational similarity analysis to explore the dynamics of prosodic representations (Kriegeskorte et al., 2008). We first defined ten regions of interest (ROI) based on a multimodal cortical parcellation (Glasser et al., 2016; Fig. 2A), including the bilateral primary auditory (PAC), anterior and posterior superior temporal (a/pSTC) cortices, PMC and inferior frontal gyri (IFG). Per ROI, time-varying neural dissimilarity patterns (window size/step = 24/4ms, Crossnobis distance) were computed over different morphing levels of prosody and compared with dissimilarity models of their acoustic forms and perceived categories (behavior; Fig. 1C). Then, we estimated the variance of neural dissimilarity patterns explained by a non-negative linear combination of acoustic and categorical models, and the unique variance explained by each model. Fisher-Z-transformed variance explained was inferred against baseline (-0.2-0s) by cluster permutation tests. The same analysis was carried out for phoneme representations. In case representations were significant in only one of the homologous ROIs, the difference between these ROIs was tested to examine hemispheric lateralization.

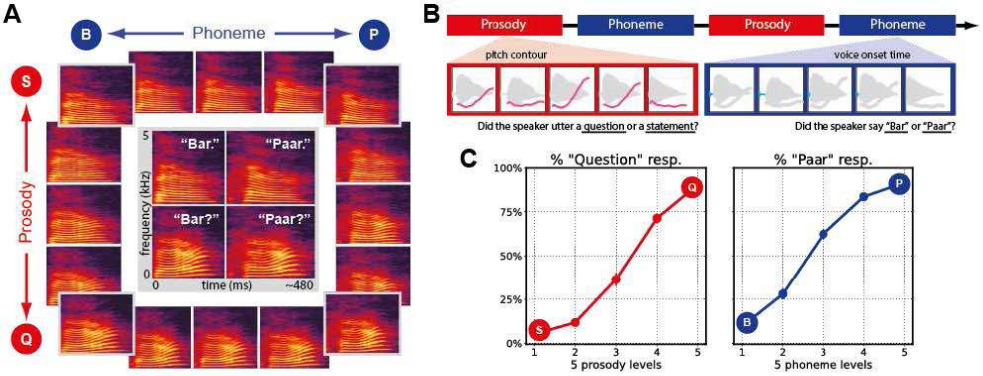

Fig. 1. (A) Spectrograms of the original single word recordings (“Bar” [bar], “Paar” [pair], in the middle) and examples of the experimental stimuli (480ms on average, outside) morphed in five steps in terms of pitch contour (statement – question) or voice-onset time (/b/ – /p/). **(B)** Schematic illustration of one experimental run. Prosody and phoneme identification tasks alternated over six experimental runs, and the identical set of stimuli was repeated in both tasks. **(C)** Behavioral results of the prosody (red) and phoneme (blue) categorization tasks along the five morph steps of a relevant feature. Individual behavioral respones were used to model perceptual dissimilarity patterns that encoded abstract categories of speech prosody or phonemes.

Results: Combined acoustic and categorical representations of prosody emerged first in bilateral PAC and a/pSTC around 300ms after word onset, followed by left IFG and right PMC. Phoneme representations emerged earlier (from 70ms) and only in the bilateral temporal areas. The unique variance analysis showed that acoustic representations of prosody emerged earlier (340ms; Fig. 2B) than categorical representations (480ms) in bilateral PAC and pSTC (Fig. 2C), followed by the right aSTC (420ms) and left IFG (464ms), both significantly lateralized (Fig. 2B). Notably, PMC exhibited additional categorical representations which were right-lateralized during word presentation (384ms) and bilateral after word offset (532ms; Fig. 2C). These temporal and interhemispheric dynamics substantiate the representational abstraction of prosodic pitch contours along the ventral auditory stream (Schirmer & Kotz, 2006), and a two-staged role of PMC in the perceptual categorization of prosody and motor-based decision-making (Liebenthal & Möttönen, 2018). While early auditory and late decision-making processes were bilateral, intermediate perceptual processes in aSTC and PMC showed right-hemispheric predominance, in line with cue-dependent models of prosody perception (van Lancker & Sidtis, 1992).

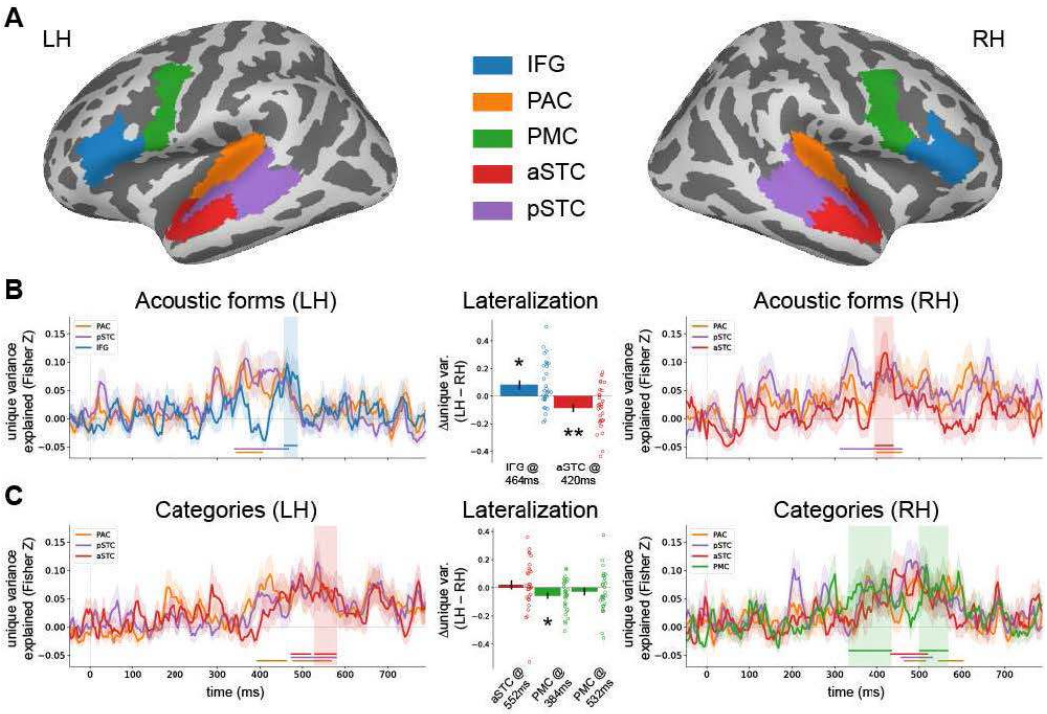

Fig. 2. (A) Ten bilateral regions of interest (ROIs). **(B-C)** Time-varying acoustic **(B)** and categorical **(C)** representation of speech prosody in the left (left panels) and right (right panels) ROIs. Shaded areas show s.e.m. Significant time intervals are indicated by horizontal lines (one-sided *t*-test, cluster-forming threshold $p < 0.05$, ROI-wise FDR-corrected $p < 0.05$). Middle panels show the differences in prosodic representations between the homologous ROIs (two-sided *t*-test, Bonferroni-corrected $p < 0.05$, *; $p < 0.01$, **) during the intervals of unilateral representations (highlighted by shaded rectangles). Error bars indicate s.e.m. Empty circles denote individuals. IFG, inferior frontal gyrus; PAC, primary auditory cortex; PMC, premotor cortex; a/pSTC, anterior/posterior superior temporal cortex.

Conclusions: This study draws a comprehensive picture of the dynamic frontotemporal representations of speech prosody. At the network level, the representational transfer will be further investigated by a directed information transfer analysis.

References

1. Belyk, M., & Brown, S. (2014). Perception of affective and linguistic prosody: an ALE meta-analysis of neuroimaging studies. Social cognitive and affective neuroscience, 9(9), 1395-1403.
2. Glasser, M. F., Coalson, T. S., Robinson, E. C., Hacker, C. D., Harwell, J., Yacoub, E., ... & Van Essen, D. C. (2016). A multi-modal parcellation of human cerebral cortex. Nature, 536(7615), 171-178.
3. Liebenthal, E., & Möttönen, R. (2018). An interactive model of auditory-motor speech perception. Brain and Language, 187, 33-40.
4. Kriegeskorte, N., Mur, M., & Bandettini, P. A. (2008). Representational similarity analysis-connecting the branches of systems neuroscience. Frontiers in systems neuroscience, 4.
5. Schirmer, A., & Kotz, S. A. (2006). Beyond the right hemisphere: brain mechanisms mediating vocal emotional processing. Trends in cognitive sciences, 10(1), 24-30.
6. Sammler, D., Grosbras, M. H., Anwander, A., Bestelmeyer, P. E., & Belin, P. (2015). Dorsal and ventral pathways for prosody. Current Biology, 25(23), 3079-3085.
7. Van Lancker, D., & Sidtis, J. J. (1992). The identification of affective-prosodic stimuli by left- and right-hemisphere-damaged subjects: All errors are not created equal. Journal of Speech and Hearing Research, 35, 963-970.

Poster No 1040

Microstructural asymmetry of the planum temporale guides lateralization of speech processing

Peipei Qin[1], Qiuhui Bi[2], Gaolang Gong[3]

[1]BeijIng Normal University, BeijIng, Hiadian,Beijing, [2]Beijing Normal University, Beijing, Beijing, [3]State Key Laboratory of Cognitive Neuroscience and Learning & IDG/McGovern Institute for Brain Resea, Beijing, Beijing

Introduction: A classic neuroscience hypothesis posits a fundamental role of structural asymmetries in functional lateralization[1], but the empirical evidence remains scarce. As a well-known structurally asymmetric region[2], the planum temporal (PT) is involved in speech processing[3], a lateralized function. Thus, this region has been much studied to elucidate the relationship between structural and functional asymmetries, but the results are mixed[4,5]. The present study aims to revisit this important issue using both macrostructural and microstructural imaging approach with a large cohort of healthy young adults.

Methods: We included 907 right-handed subjects from HCP S1200 release (Mean age ± SD: 28.8 ± 3.7 years, 507 females and 398 males)[6]. The study manually outlined the PT and manually determined the type of the Heschl's gyrus (HG) (single or duplicated) by two trained raters[7]. Functional activation was assessed for three contrasts ('story – baseline,' 'math – baseline,' and 'story - math') in a story-telling task, which were then factor-analyzed into two components: speech perception and speech comprehension. The modified LI-toolbox[8] was then used to calculate the functional activation and its asymmetry index (AI). Structural metrics of PT, including macrostructural (surface area, thickness) and microstructural metrics (myelin content, neurite density index(NDI), and orientation dispersion index(ODI)[9]), were calculated. Structural AIs were defined as (Left - Right) / (Left + Right). We tested the correlation between the 5 structural and 2 functional AIs using 5*2 general linear models (GLM), with the functional AI as the response variable and structural AI as the fixed effect in the model. Furthermore, intra-hemispheric structural-functional correlations were examined by another 2*5*2 GLMs, with the functional activation as the response variable and structural metric as the fixed effect in the model. Covariates included age, sex, brain size, and HG type in each GLM. Significance levels were Bonferroni-corrected $P < 0.05$.

Results: As shown in Figure 1, the functional AI for speech perception was positively correlated with the AI of myelin (R=0.26, PFWE <10-12), NDI (R=0.13, PFWE<10-2), and ODI (R=0.22, PFWE<10-9). On the other hand, the functional AI for speech comprehension was significantly correlated with the AI for surface area (R=0.21, PFWE<10-9), myelin (R=0.20, PFWE<10-8), and NDI (R=0.11, PFWE<0.01). As shown, the significant correlations were mainly observed the AI of micro- metrics (myelin, NDI, ODI). The correlations between PT functional activation and structural metrics for each hemisphere are shown in Figure 2. For the activation of speech perception, significant correlations were observed for the myelin (R=0.16, PFWE <10-4) and ODI (R=0.17, PFWE <10-5) in the left PT, and for the surface area (R=-0.11, PFWE <0.02), myelin (R=0.20, PFWE <10-6), NDI (R=0.14, PFWE <0.01) and ODI (R=0.18, PFWE <10-6) in the right PT. For speech comprehension, functional activation was significantly correlated with the NDI (R=-0.12, PFWE <0.02) in the left PT, and with the myelin (R=0.16, PFWE <10-5) in the right PT.

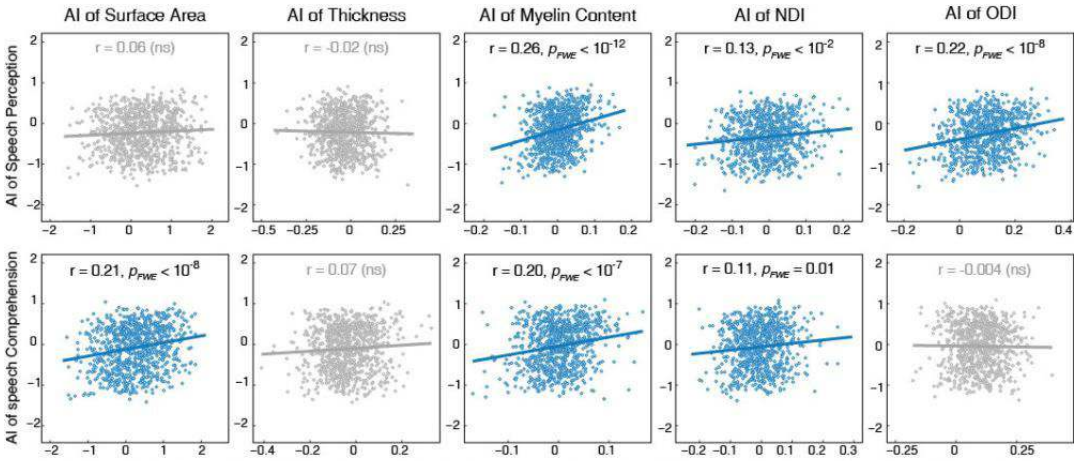

Fig 1. Interindividual correlation of PT functional and structural asymmetries. The scatter plots for nonsignificant correlations ($P_{FWE} > 0.05$) are colored gray. AI, asymmetry index; NDI, neurite density index; ODI, orientation dispersion index; ns, non-significant.

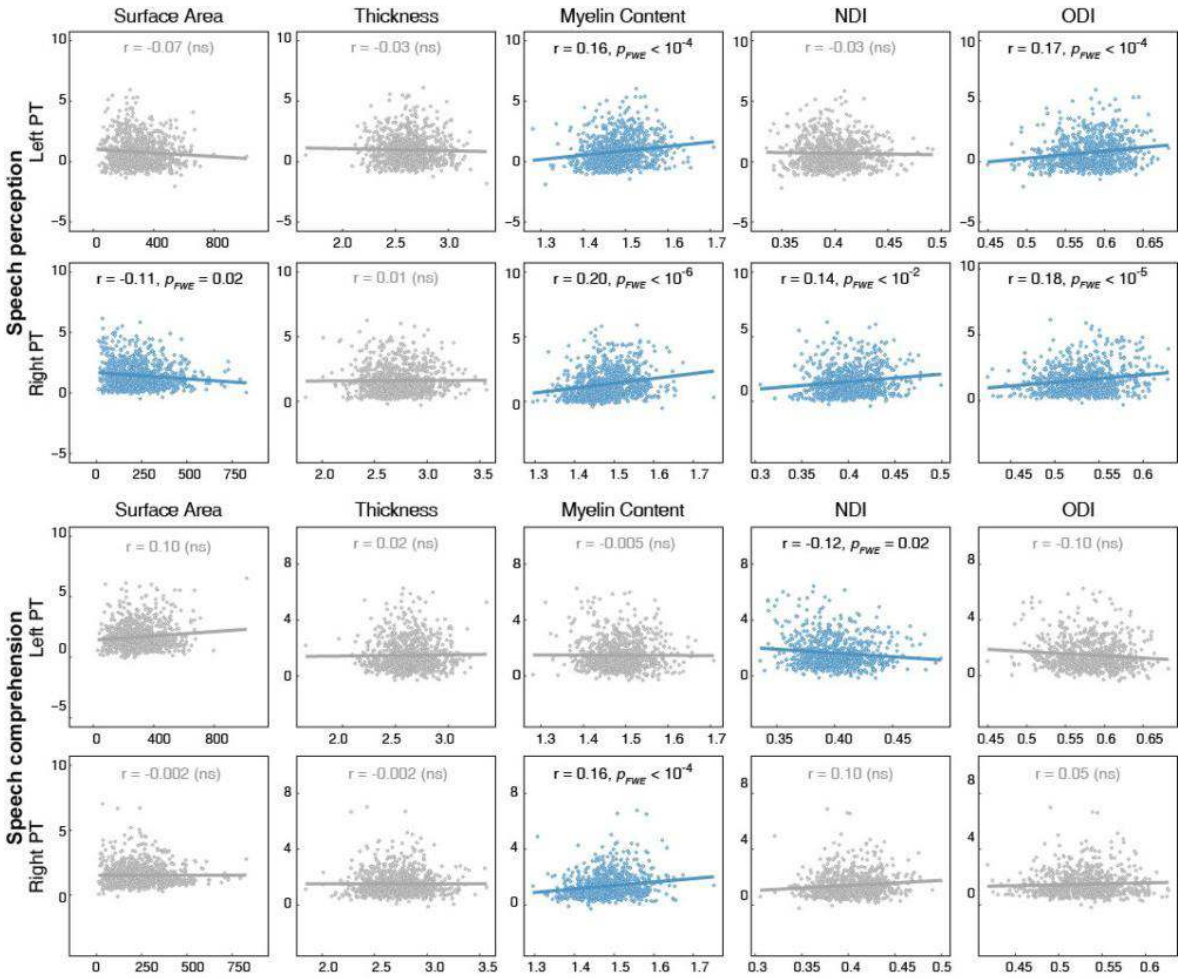

Fig 2. Interindividual functional-structural correlations of the left and right PT. The scatter plots for nonsignificant correlations ($P_{FWE} > 0.05$) are colored gray. NDI, neurite density index; ODI, orientation dispersion index; ns, non-significant.

Conclusions: Our results revealed significant association of functional PT asymmetries with several microstructural asymmetries, such as intracortical myelin content, neurite density, and neurite orientation dispersion. The PT microstructure per se also showed hemispheric-specific coupling with PT functional activity. These results suggest that microstructural asymmetry guides functional lateralization of the same brain area and highlight a critical role of microstructural PT asymmetries in auditory-language processing.

References

1. Wada, J. A. (2009), "Is functional hemispheric lateralization guided by structural cerebral asymmetry?," The Canadian Journal of Neurological Sciences. Le Journal Canadien Des Sciences Neurologiques, vol. 36 Suppl 2, pp. S25-31
2. Galaburda, A. M. et al. (1978), "Right-left asymmetrics in the brain," Science, vol. 199, no. 4331, pp. 852–856
3. Sajid, N. et al. (2023), "Degeneracy in the neurological model of auditory speech repetition," Communications Biology, vol. 6, no. 1, Art. number 1
4. Trimmel, K. et al. (2021), "Decoupling of functional and structural language networks in temporal lobe epilepsy," Epilepsia, vol. 62, no. 12, pp. 2941–2954
5. Tzourio, N. et al. (1998), "Left planum temporale surface correlates with functional dominance during story listening," Neuroreport, vol. 9, no. 5, pp. 829–833
6. Van Essen, D. C. et al. (2013), "The WU-Minn Human Connectome Project: An overview," NeuroImage, vol. 80, pp. 62–79
7. Abdul-Kareem, I. A. et al. (2008), "Heschl gyrus and its included primary auditory cortex: Structural MRI studies in healthy and diseased subjects," Journal of Magnetic Resonance Imaging, vol. 28, no. 2, pp. 287–299
8. Wilke, M. et al. (2007), "LI-tool: A new toolbox to assess lateralization in functional MR-data," Journal of Neuroscience Methods, vol. 163, no. 1, pp. 128–136
9. Zhang, H. et al. (2012), "NODDI: Practical in vivo neurite orientation dispersion and density imaging of the human brain," NeuroImage, vol. 61, no. 4, pp. 1000–1016

Poster No 1041

Speech processing around the auditory cortex: the distinct contribution of gray and white matter

Qiuhui Bi[1,2], Peipei Qin[1], Gaolang Gong[1]

[1]State Key Laboratory of Cognitive Neuroscience and Learning & IDG/McGovern Institute for Brain Resea, BeijIng, China, [2]School of Artificial Intelligence, Beijing Normal University, BeijIng, China

Introduction: Understanding the structural substrates of functional activity is one of the major challenges in neuroscience. Putatively, the microcircuit within gray matter (GM) serves as the basis of local neural activity, and axons within white matter (WM) supports rapid transfer of information across remote brain regions. Previous studies have revealed distinct contribution of GM/WM structural properties to specific functional activation, depending on brain regions and hemispheres[1,2,3]. In this study, we aim to ascertain how the underlying GM/WM contribute to functional activity of the planum temporale (PT) and Heschl's gyrus (HG) during auditory speech tasks, with respect to different hemispheres and speech processing component.

Methods: Subjects. 782 right-handed participants with high-quality T1w structural MRI, diffusion MRI and language fMRI from the human connectome project (S1200 release) were included. ROI delineation. The ROIs of PT/HG (Fig 1A) were manually delineated following a well-established procedure by Altarelli et al[4]. Functional measures. We applied a widely-used LI toolbox[5] approach to quantify functional activation of left and right ROIs and the asymmetry indexes (AIs). For three contrasts in the language processing task, factor analysis was performed on the PT/HG activation left, right, and AI across the three contrasts, separately, resulting two main factors: speech perception and comprehension. Structure measures. For GM, the total surface area, average thickness, myelin content, neurite density index (NDI) and orientation dispersion index (ODI) across all vertices were calculated for each ROI. For WM, tractography of the long and posterior segments of the arcuate fasciculus (AF) was conducted using MRtrix3[6] with multiple ROIs (Fig 1B, C), separately for PT and HG. Average fibre length, NDI and ODI were calculated for each tract. The AI of structural measure was computed as (L – R) / (L + R) Statistical analysis. General linear models were applied to each functional activation of PT/HG, with left/right activation and functional AI as the dependent variable, and structural left/right measures and AIs as the independent variables. Dominance analyses were performed to evaluate the contribution (general dominance weight, GDW) of structural measures to the variance of functional measures. To determine whether the degree of GM/WM measures' contribution to functional measure differ between the left and right hemisphere, as well as between the ipsilateral PT and HG, permutation tests were then performed.

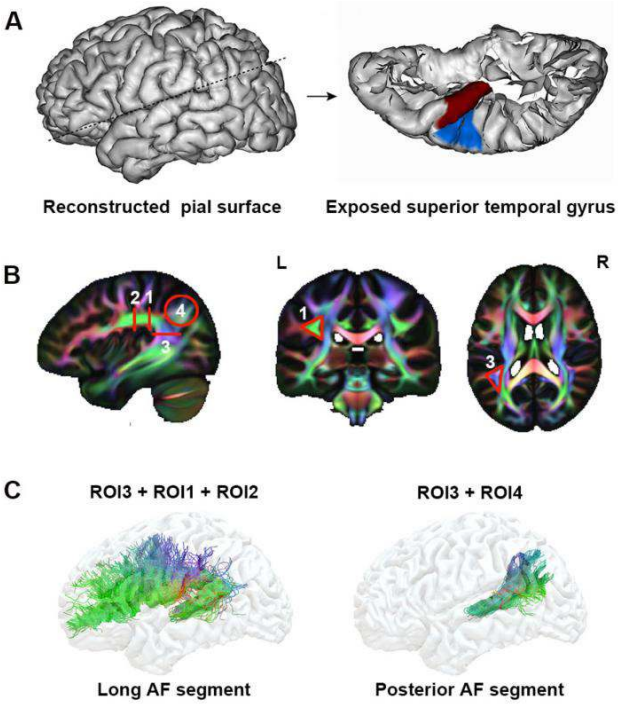

Fig 1. (A) The manual delineation of planum temporale (PT) and Heschl's gyrus (HG) on individual pial surface. **(B)** The location of inclusion ROIs used for the tractography of arcuate fasciculus (AF) on HCP-1065 standard FA image. **(C)** The tractography initiated from the PT/HG ROIs, only streamlines traversing the inclusion ROIs in the specified sequence were accepted. Specifically, streamlines originating from PT/HG ROI and sequentially travelling through ROI3 – ROI1 – ROI2 were identified as long AF segment. Streamlines travelling through ROI3 – ROI4 were included as posterior AF segment.

Results: The explained variance for each structural measure is illustrated in Figure 2A. As shown, GM measures of the left ROIs consistently explained a larger proportion of the variance for the speech perception, but a less proportion of the variance for the speech comprehension. Particularly, the model of speech comprehension was dominated by the fibre length of long AF segment in both left PT and HG, accounting for 41.9% and 47.6% of the all explained variance separately. In contrast, GM and WM measures of the right ROIs explained similar amount of variance for both speech perception and comprehension. For the speech comprehension, WM measures explained significantly greater proportion of variance of the left ROI than the right ROI (Fig 2B): PT, L-R=0.07, P<0.001; HG, L-R=0.03, P<0.01. The premutation test further revealed greater explained variance of WM measures in the left PT, compared with the left HG for both speech perception (PT-HG=0.04, P=0.01) and comprehension (PT-HG=0.05, P=0.01). In addition, PT WM asymmetric measures captured a higher proportion of the variance of speech comprehension lateralization (PT-HG=0.03, P=0.03), compared with the HG (Fig 2B).

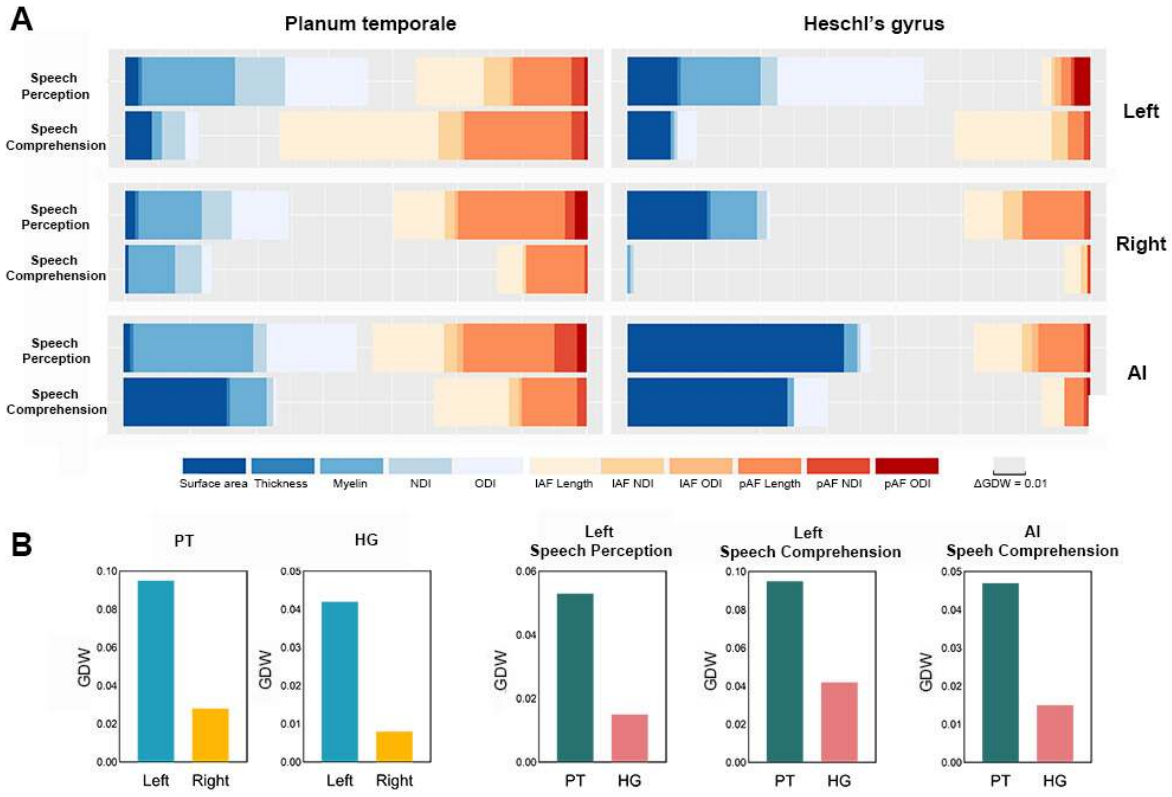

Fig 2. (A) Dominance analyses were applied to assess the contribution of each structural to the fitted models, done separately for speech perception and comprehension component of left, right and asymmetric measures of PT and HG. The width of each bar segment indicates the GDW(R^2) value of the structural measure. **(B)** White matter measures accounted for a higher portion of variance in the speech comprehension models of the left PT/HG when compared to those of the right, and in the left speech perception, left comprehension, and comprehension AI models of PT in contrast to those of HG. PT, planum temporale; HG, Heschl's gyrus; AI, asymmetry index; GDW, general dominance weight.

Conclusions: The present study demonstrated distinct contribution of GM and WM structural measures to speech processing activity around the auditory cortex, depending on the selected region of interest, hemisphere, and functional components.

References

1. Vazquez-Rodriguez, B. et al. (2019), 'Gradients of structure-function tethering across neocortex', Proceedings of the National Academy of Sciences of the United States of America, vol. 116, no. 42, pp. 21219–21227
2. Ocklenburg, S. et al. (2018), 'Neurite architecture of the planum temporale predicts neurophysiological processing of auditory speech', Science Advances, vol. 4, no. 7, Art. number 7
3. Hickok, G. et al. (2007), 'The cortical organization of speech processing', Nature Reviews Neuroscience, vol. 8, no. 5, pp. 393-402
4. Altarelli, I. et al. (2014), 'Planum Temporale Asymmetry in Developmental Dyslexia: Revisiting an Old Question', Human Brain Mapping, vol. 35, no. 12, pp. 5717–5735
5. Wilke, M. et al. (2007), 'LI-tool: A new toolbox to assess lateralization in functional MR-data', Journal of Neuroscience Methods, vol. 163, no. 1, pp. 128–136
6. Tournier, J.-D. et al. (2019), 'MRtrix3: A fast, flexible and open software framework for medical image processing and visualisation', NeuroImage, vol. 202, pp. 116137

Poster No 1042

Involvement of Auditory Dorsal Stream in Processing of Spectrally Degraded Speech Examined with iEEG

Kirill Nourski[1], Mitchell Steinschneider[1], Ariane Rhone[1], Joel Berger[1], Emily Dappen[1], Hiroto Kawasaki[1], Matthew Howard[1]

[1]*The University of Iowa, Iowa City, IA*

Introduction: Cochlear implants (CIs) are the treatment choice for severe to profound hearing loss. Despite the tremendous progress in CI technology, including hardware and processing strategies, there remains a considerable variability in speech perception outcomes following implantation (Geers, 2006; Pisoni et al., 2017; Carlyon and Goehring, 2021). The function and plasticity of central auditory pathways are major contributing factors to this variability (Moberly et al., 2016; Glennon et al., 2020; Pavani & Bottari, 2022). Assessing auditory processing at the cortical level in CI users is methodologically difficult. However, spectrally degraded sounds presented to normal-hearing individuals can approximate the input to the central auditory system provided by the CI (Shannon et al., 1995). This study used intracranial electroencephalography (iEEG) to investigate cortical processing of spectrally degraded speech.

Methods: Participants were 15 adult neurosurgical epilepsy patients. Stimuli were utterances /aba/ and /ada/, spectrally degraded using a noise vocoder (1-4 bands) or presented without vocoding (Fig. 1a; Nourski et al., 2019). The stimuli were presented in a two-alternative forced choice task. Cortical activity was recorded using depth and subdural iEEG electrodes (2051 contacts). Electrode coverage included Heschl's gyrus (HG), superior temporal gyrus (STG), dorsal and ventral auditory-related areas, prefrontal and sensorimotor cortex. Analysis focused on high gamma (70-150 Hz) power augmentation and alpha (8-14 Hz) suppression, measured at 250-500 and 500-750 ms after stimulus onset, respectively.

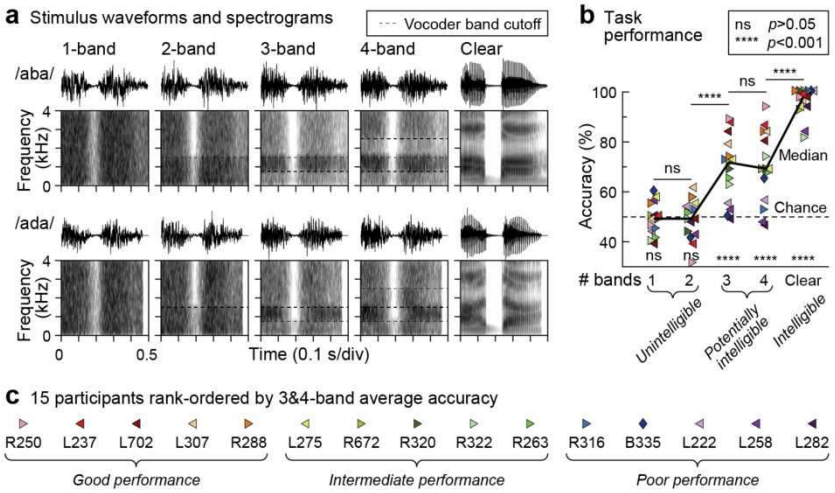

Figure 1. Experimental stimuli and task performance. **a:** Experimental stimuli. Vocoder band cutoff frequencies (0.8, 1.5, 2.5 kHz) are denoted by dashed lines. **b:** Two-alternative (aba/ada) forced choice task performance accuracy, plotted for vocoded (1-4 bands) and clear stimuli. Data from the 15 participants and median values are plotted as symbols and solid lines, respectively. Left- and right-pointing arrowheads represent participants with mainly left- and right hemisphere electrode coverage, respectively; participant B335 with bilateral electrode coverage is denoted by a diamond. Significance (Wilcoxon signed rank tests) of task accuracy relative to chance (dashed line) is indicated on the bottom. Pairwise comparisons between adjacent stimulus conditions were performed using Wilcoxon rank sum tests. **c:** Participants are rank-ordered based on their 3&4-band accuracy, from best (R250) to worst (L282).

Results: Chance task performance occurred with 1-2 spectral bands and was near-ceiling for clear stimuli (Fig. 1b). Performance was variable with 3-4 bands, permitting segregation of good from poor performers Fig. 1c). There was no relationship between task performance and participants' demographic, audiometric, neuropsychological, or clinical profiles. Several patterns were identified based on high gamma response magnitude and differences between stimulus conditions (Fig. 2a). Within HG, responses were typically strong to all stimuli, while more diverse patterns emerged on the lateral STG. Good performers typically had strong responses to all stimuli along the dorsal auditory processing stream, including posterior STG, supramarginal, and precentral gyrus (Fig. 2b). Additional recruitment of the dorsal stream for the difficult (vocoded) stimuli manifested as vocoded-preferred responses. In poor performers, clear-specific responses in the dorsal stream were more common, suggesting that within the dorsal stream, vocoded stimuli were not processed as speech. In contrast, poor performers engaged the ventral stream (posterior middle temporal gyrus, MTGP) to a greater extent than good performers. Patterns of alpha suppression were generally less diverse than high gamma augmentation; differences between good and poor performers paralleled those seen in high gamma responses.

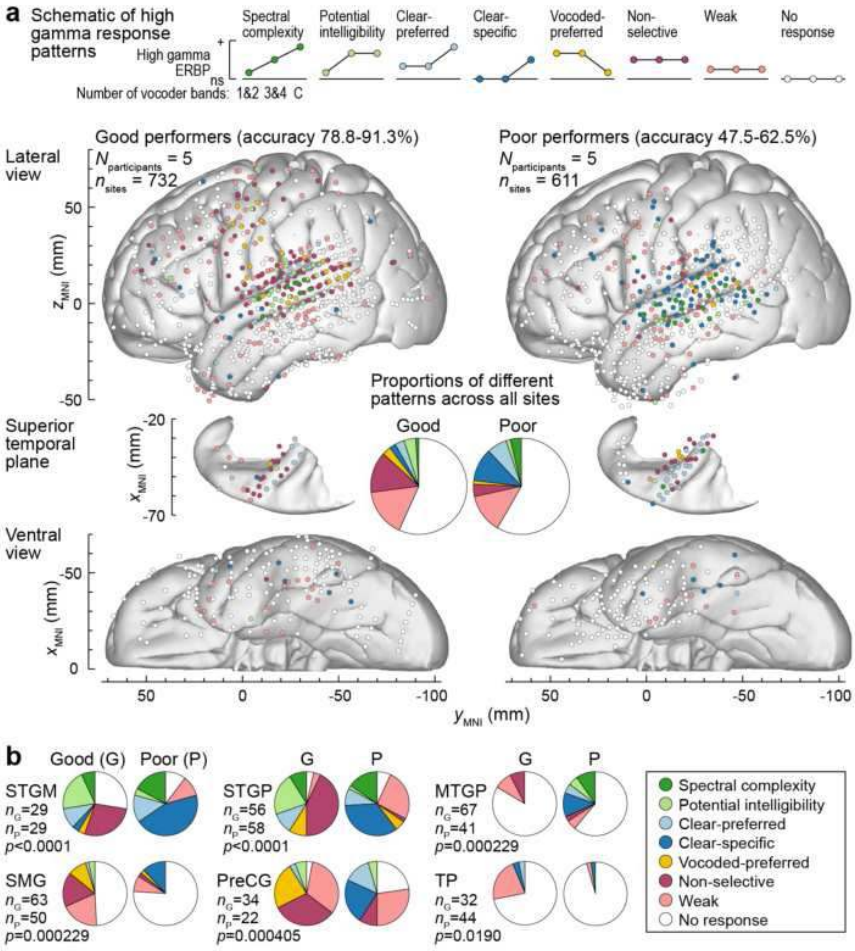

Figure 2. High gamma response patterns in participants who exhibited good and poor task performance. **a:** Summary of data plotted in MNI coordinate space and projected onto the left hemisphere of the Freesurfer average template brain for spatial reference. Right hemisphere MNI *x*-axis coordinates (x_{MNI}) were multiplied by –1 to map them onto the left-hemisphere common space. Schematics of the eight high gamma response patterns are shown on top. ERBP, event-related band power. **b:** Proportions of different high gamma response patterns in areas with significant (p<0.05, Fisher exact tests, false discovery rate-corrected) differences between good and poor performers. STGM, middle superior temporal gyrus; STGP, posterior superior temporal gyrus; MTGP, posterior middle temporal gyrus; SMG; supramarginal gyrus; PreCG, precentral gyrus; TP, temporal pole.

Conclusions: Responses to noise-vocoded speech provide insights into potential factors underlying CI outcome variability. The results emphasize differences between good and poor performers in the balance of neural processing along the dorsal and ventral stream, identify specific cortical regions that may have diagnostic and prognostic utility, and suggest potential targets for neuromodulation-based CI rehabilitation strategies.

References

1. Carlyon, R.P., Goehring, T. (2021), 'Cochlear Implant Research and Development in the Twenty-first Century: A Critical Update', Journal of the Association for Research Otolaryngology, vol. 22, no. 5, pp. 481-508.
2. Geers, .AE. (2006), 'Factors influencing spoken language outcomes in children following early cochlear implantation', Advances in Otorhinolaryngology, vol. 64, pp. 50-65.
3. Glennon, E., Svirsky, M.A., Froemke, R.C. (2020), 'Auditory cortical plasticity in cochlear implant users' Current Opinion in Neurobiology, vol. 60, pp. 108-114.
4. Moberly, A.C., Bates, C., Harris, M.S., Pisoni, D.B. (2016), 'The Enigma of Poor Performance by Adults With Cochlear Implants', Otology and Neurotology, vol. 37, no. 10, pp. 1522-1528.
5. Nourski, K.V., Steinschneider, M., Rhone, A.E., Kovach, C.K., Kawasaki, H., Howard, M.A. 3rd. (2019), 'Differential responses to spectrally degraded speech within human auditory cortex: An intracranial electrophysiology study', Hearing Research, vol. 371, pp. 53-65.
6. Pavani, F., Bottari, D. (2022), 'Neuroplasticity following cochlear implants', Handbook of Clinical Neurology, vol. 187, pp. 89-108.
7. Pisoni, D.B., Kronenberger, W.G., Harris, M.S., Moberly, A.C. (2018), 'Three challenges for future research on cochlear implants', World Journal of Otorhinolaryngology - Head and Neck Surgery, vol. 3, no. 4, pp. 240-254.
8. Shannon, R.V., Zeng, F.G., Kamath, V., Wygonski, J., Ekelid, M. (1995), 'Speech recognition with primarily temporal cues', Science vol. 270, no. 5234, pp. 303-304.

Poster No 1043

Decoding the 'silent' neural symphony: unraveling the intricacies of lip-reading in the brain

Joanna Beck[1,2], Jakub Wojciechowski[1,2], Hanna Cygan[1], Martyna Bryłka[1], Tomasz Wolak[1]

[1]Bioimaging Research Center, Institute of Physiology and Pathology of Hearing, Kajetany, Poland, Warsaw, Poland, [2]Nencki Institute of Experimental Biology PAS, Warsaw, Poland

Introduction: Lipreading (LR) is the ability to extract speech information from the movements of a speaker's lips and face. It is an essential skill for individuals with hearing loss (Bernstein et al., 2022) and those who work in noisy or distracting environments (e.g., Erber, 1969; Middelweerd & Plomp, 1987). Visual information from the talker's face helps fill in the missing auditory information. Articulatory lip movements enable it to recognize visemes (the visual equivalent of phonemes), and supplement degraded auditory information during speech perception. Despite its practical importance, the neural and cognitive mechanisms underlying lipreading still need to be better understood. Neuroimaging studies have shown that the brain regions involved in LR overlap with those involved in auditory speech processing, suggesting that lipreading relies on neural mechanisms similar to those involved in normal hearing (Calvert, 2001; Skipper et al., 2007). Generally, studies on the correlates of LR point to different areas relevant to this skill; these differences may be due to the different fMRI paradigms used in each study. The goal of our study was to examine G1. Aspects of language processing during LR in a robust manner G2. Mechanisms involved in learning LR

Methods: To answer question G1, we tested 51 right-handed subjects using a lip-reading task during fMRI. The task used 20-second clips of an actor speaking on various topics (cuisine, style, sports, weather). The paradigm included four conditions: clips with sound, clips without sound, clips backward, and a static face without sound. Half of the blocks presented entire sentences, and the other half presented only words. In the G2 study, 60 healthy right-handed subjects underwent a month-long lip reading course, with three 45-minute sessions of fMRI neurofeedback or sham neurofeedback, with scanning before and after the course. To assess the influence of the factors, a rmANOVA was conducted.

Results: Both G1 and G2 results showed that the lexical vs. non-lexical factor revealed the presence of numerous language-related regions (e.g., STG, MTG, TP). The "words" vs. "sentences" factor produced clusters in the left ATL and bilateral pMTG/TPJ. The effects found in the anterior and inferior temporal poles indicate a differential role for semantic information retrieval (Binder et al., 2011) in reading word and sentence text, likely due to the complexity and difficulty of the linguistic material. Additionally, ATL plays a central role in integrating semantic and syntactic information and is particularly sensitive to meaningful sentences (Visser et al., 2010). In contrast, the TPJ's differential involvement in reading words and sentences may be due to the high cognitive demands during sentence recognition and the involvement of extensive attentional resources in analyzing lip movements. The results also showed that during lip reading (vs. observation of non-linguistic lip movements), participants were actively engaged in phoneme and lexical encoding. They were also involved in the retrieval of the semantic lexicon. Form G2, longitudinal, pre- and post-scanning analysis showed changes in the mentioned areas, and the pattern of differences was driven by the baseline level of lip-reading ability.

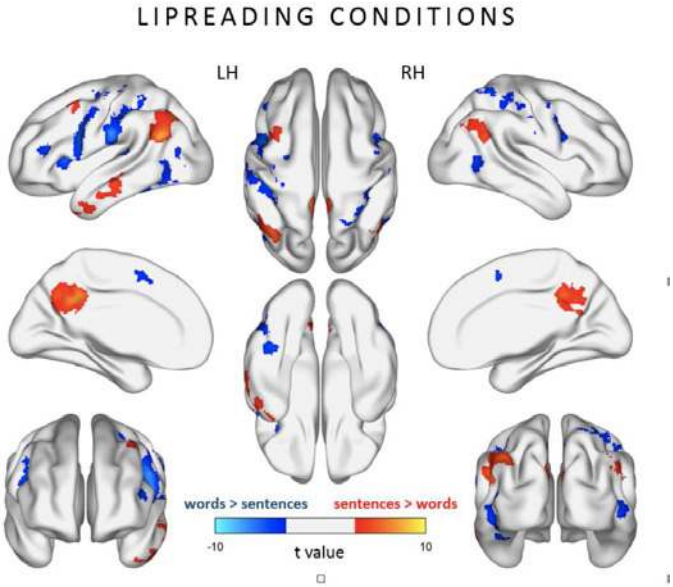

Figure 1. Whole-brain results for lip-reading sentences vs. words effect

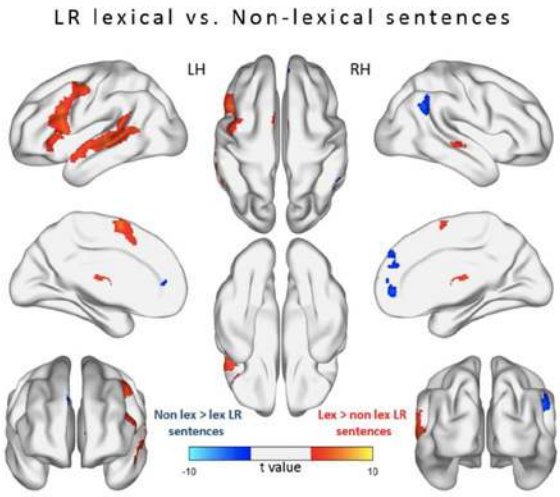

Figure 2. Whole-brain results for lip-reading lexical sentences vs non-lexical sentences effect

Conclusions: Our study identifies shared and unique neural activity patterns in lip reading, expanding on existing literature. Uncovering task-specific activations that have not previously been reported contributes to a more nuanced understanding of lipreading mechanisms. The cortical regions revealed in our analysis suggest that both cognitive abilities related to language comprehension and language production are engaged in lip reading. This insight holds promise for enhancing support for individuals with hearing disabilities or undergoing cochlear implantation, paving the way for targeted interventions and improved accessibility.

References

1. Bernstein, LE., Jordan, N, Auer, ET., & Eberhardt, SP. (2022). Lipreading: A review of its continuing importance for speech recognition with an acquired hearing loss and possibilities for effective training. American Journal of Audiology, 1-17.
2. Binder, JR, Gross, WL., Allendorfer, JB., ... & Weaver, KE. (2011). Mapping anterior temporal lobe language areas with fMRI: a multicenter normative study. Neuroimage, 54(2), 1465-1475.
3. Calvert, G. A. (2001). Crossmodal processing in the human brain: Insights from functional neuroimaging studies. Cerebral Cortex, 11(12), 1110–1123. https://doi.org/10.1093/cercor/11.12.1110
4. Erber, N. P. (1969). Interaction of audition and vision in the recognition of oral speech stimuli. Journal of speech and hearing research, 12(2), 423-425.
5. Skipper, J. I., Van Wassenhove, V., Nusbaum, H. C., & Small, S. L. (2007). Hearing lips and seeing voices: how cortical areas supporting speech production mediate audiovisual speech perception. Cerebral Cortex, 17(10), 2387-2399.
6. Visser M, Jefferies E, Lambon Ralph MA. Semantic processing in the anterior temporal lobes: A meta- analysis of the functional neuroimaging literature. Journal of Cognitive Neuroscience. 2010;22:1083–1094

Poster No 1044

Prosodic Pitch Perception in Right Premotor Cortex: A Transcranial Magnetic Stimulation Study

Daniela Sammler[1], Gesa Hartwigsen[2]

[1]Max Planck Institute for Empirical Aesthetics, Frankfurt am Main, Hesse, [2]Leipzig University, Leipzig, Saxony

Introduction: Speech perception is believed to recruit (pre)motor cortex (PMC) in the left dorsal auditory stream (Liebenthal & Möttönen, 2018). Articulator-specific involvement of left PMC has been found for the perception of phonemes (D'Ausilio et al., 2009) and lexical tones (Liang et al., 2023). However, PMC's role for prosody-the melody of speech-still lacks investigation. Motor control of prosodic pitch contours is anchored in the right (and left) PMC (Dichter et al., 2018). This kindles questions of hemispheric lateralization, reminiscent of auditory asymmetries (Zatorre et al., 2002). Moreover, the role of PMC in supporting either perceptual or response-related processes is still a matter of debate (Hickok, 2010). The present study used repetitive transcranial magnetic stimulation (rTMS) and behavioral drift diffusion modelling to (i) assess the causal role of right PMC in prosodic pitch categorization, compared to left PMC and a non-prosodic pitch control task (speaker gender categorization), and to (ii) disentangle the weighting of perceptual vs. response-related biases in PMC contributions.

Methods: In two separate sessions, 24 listeners (M ± SD = 27 ± 3.4 years) categorized prosodic pitch contours (question vs. statement) and speaker gender (male vs. female) of monosyllabic words while receiving neuronavigated inhibitory or sham rTMS of left or right PMC (MNI: ±45, 5, 40 mm, based on Sammler et al., 2015) using co-registered individual T1-weighted

images. A 5-pulse train of 10 Hz rTMS at an intensity of 100% individual resting motor threshold was delivered in each trial, time-locked to word onset, using a focal figure-of-eight-shaped coil (CB-60, 7.5 cm outer diameter) connected to a MagPro X100 stimulator. Sham rTMS was delivered by a second coil placed in a 90° angle over the first coil. The order of sessions (left/right PMC) and blocks (prosody/gender task, sham/effective rTMS) was counterbalanced across subjects (Fig 1A). Single trial response times and accuracies were analyzed with the drift diffusion model (DDM; Ratcliff, 1978; fast-dm: Voss & Voss, 2007) to decompose latent processes that lead to a decision. Parameters v (drift rate; rate of evidence accumulation), a (threshold separation; indicating response biases), and t0 (non-decision time; decision-independent time for stimulus encoding and button press) were compared between tasks (prosody/gender), stimulation (effective/sham), and hemispheres (left/right) using rmANOVAs. Multiple regressions were used to predict Δv (effective–sham) in both tasks from individual ratings of (i) perceptual focus on prosodic contour, (ii) on mean pitch, (iii) amount of subvocal rehearsal, and (iv) stimulated hemisphere, controlled for (v) years of musical training and (vi) perceived task difficulty.

Results: Drift rate v in the prosody task dropped after effective compared to sham stimulation of right (but not left) PMC, and more strongly in participants who were biased to focus on the prosodic contours (Fig 1B). No such effects were found for parameters a and t0 or the categorization of speaker gender. Neither amount of subvocal rehearsal, nor years of musical training or perceived task difficulty influenced Δv.

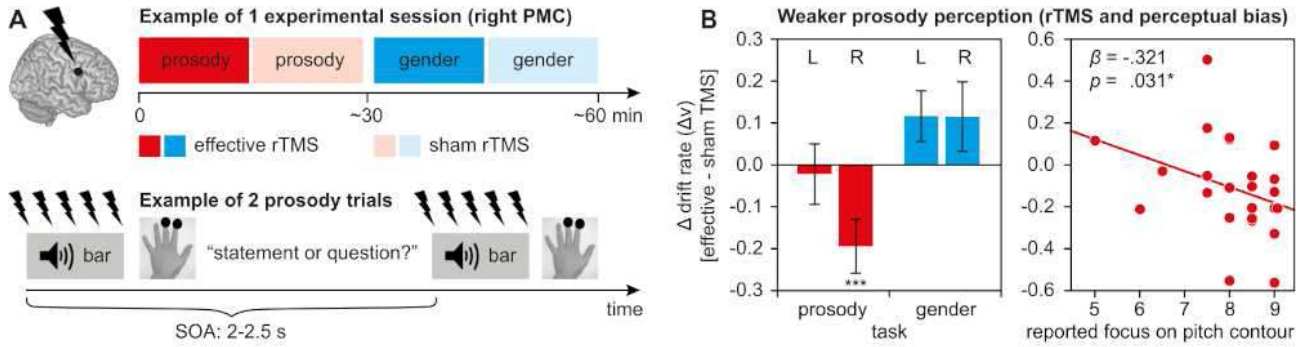

Fig 1. (A) Top: Example of one experimental session with effective and sham rTMS of right PMC during blocks with prosody and gender task. Left PMC was stimulated in a separate session. Bottom: Example of 2 prosody trials with 5-pulse trains at 10 Hz time-locked to word onset. SOA: stimulus onset asynchrony. **(B)** Left: Mean rTMS-induced drift rate change (Δv) in the prosody (red) or gender task (blue). The drift rate v indicates the rate of evidence accumulation that leads to a decision and is affected by rTMS-induced noise (Hartwigsen et al., 2015). Error bars denote ±1 *SEM*. ***: $p < .001$ L: left, R: right hemisphere. Right: Relationship between rTMS-induced drift rate changes in prosody categorization and participants' reported focus on pitch contour.

Conclusions: The combined findings extend the modulatory role of PMC in speech perception from phonemes and tones to speech prosody. In particular, the results highlight the causal role of right PMC in pitch contour categorization, in line with auditory cortical asymmetries (Zatorre et al., 2002). The absence of rTMS effects on parameter a denoting response biases, and the stronger modulation of performance in case of a stronger perceptual bias towards pitch contour suggests a role of PMC in perceptual rather than solely response-related processes. Future studies should investigate the time-course of PMC involvement during prosody processing using chronometric protocols to substantiate this conclusion.

References

1. D'Ausilio, A., Pulvermüller, F., Salmas, P., Bufalari, I., Begliomini, C., & Fadiga, L. (2009). The motor somatotopy of speech perception. Current Biology, 19(5), 381–385. doi:10.1016/j.cub.2009.01.017
2. Dichter, B. K., Breshears, J. D., Leonard, M. K., & Chang, E. F. (2018). The control of vocal pitch in human laryngeal motor cortex. Cell, 174, 21–31. doi:10.1016/j.cell.2018.05.016
3. Hartwigsen, G., Bergmann, T. O., Herz, D. M., Angstmann, S., Karabanov, A., Raffin, E., Thielscher, A., & Siebner, H. R. (2015). Modelling the effects of noninvasive transcranial brain stimulation at the biophysical, network and cognitive level. Progress in Brain Research, 222, 261–287. doi:10.1016/bs.pbr.2015.06.014
4. Hickok, G. (2010). The role of mirror neurons in speech perception and action word semantics. Language and Cognitive Processes, 25(6), 749–776. doi:10.1080/01690961003595572
5. Liang, B., Li, Y., Zhao, W., & Du, Y. (2023). Bilateral human laryngeal motor cortex in perceptual decision of lexical tone and voicing of consonants. Nature Communications, 14, 4710. doi:10.1038/s41467-023-40445-0
6. Liebenthal, E., & Möttönen, R. (2018). An interactive model of auditory-motor speech perception. Brain and Language, 187, 33–40. doi:10.1016/j.bandl.2017.12.004
7. Ratcliff, R. (1978). A theory of memory retrieval. Psychological Review, 85, 59–108. Doi:10.1037/0033-295X.85.2.59
8. Sammler, D., Grosbras, M.-H., Anwander, A., Bestelmeyer, P. E. G., Belin, P. (2015). Dorsal and ventral pathways for prosody. Current Biology, 25(23), 3079–3085. doi:10.1016/j.cub.2015.10.009
9. Voss, A., & Voss, J. (2007). Fast-dm: A free program for efficient diffusion model analysis. Behavior Research Methods, 39(4), 267–275. doi:10.3758/bf03192967
10. Zatorre, R. J., Belin, P., & Penhune, V. B. (2002). Structure and function of auditory cortex: Music and speech. Trends in Cognitive Sciences, 6(1), 37–46. doi:10.1016/S1364-6613(00)01816-7

Poster No 1046

Cortical tracking of the speech and music acoustic signals under naturalistic conditions

Sergio Osorio[1,2,3], M. Florencia Assaneo[4]

[1]Departamento de Psiquiatría, Escuela de Medicina, Pontificia Universidad Católica de Chile, Santiago de Chile, Chile, [2]Department of Neurology, Harvard Medical School, Massachusetts General Hospital, Boston, MA, [3]Athinoula A. Martinos Center for Biomedical Imaging, Massachusetts General Hospital, Boston, MA, [4]Instituto de Neurobiología, Universidad Nacional Autónoma de México, Santiago de Queretaro, Mexico

Introduction: Music and speech are quasi-rhythmic acoustic signals that not only encode hierarchically organized structural complexity, but also convey emotional and semantic expressiveness in human communication. These signals are also characterized by temporal modulations around 2Hz and 4Hz correspondingly, reflecting their mean note and syllabic rates (Assaneo et al., 2018; Ding et al., 2017; van Noorden et al., 1999). Studies using both non-invasive and invasive electrophysiological techniques in humans have shown that brain signals within the Slow Frequency Band range (SFB, 1-8Hz) and the High Frequency Gamma Band (HFB, > 70hz) align with such temporal modulations in the incoming acoustic input (Harding et al., 2019; Doelling et al., 2015; Nozaradan, 2014; Herff et al., 2020). However, whether cortical tracking of acoustic signals in the SFB and HFB is modulated by stimulus type, or whether this effect can be mapped to distinct cortical areas remains poorly understood.

Methods: Here, we present data from a subset of 30 individuals (mean age = 27.33, SD=15.28; n elecs = 1,858, mean = 61.93) within a publicly available Electrocorticography (EcoG) dataset (Berezutskaya et al., 2022) who passively watched a film with interleaved segments of naturalistic music-only or speech-only auditory stimuli. Electrode locations were transformed to the MNI space and plotted in the ICBM-152 cortical template using the Brainstorm toolbox. Electrophysiological data was bandpass-filtered between 1-8Hz (SFB) and 70-120Hz (HFB), re-referenced, and epoched into music and speech segments using the fieldtrip toolbox. The cross-correlation was estimated for each electrode between the cochlear envelopes (Chi et al., 2005) of music and speech and the brain signals in the SFB and the power of the HFB. Significant correlation values and their corresponding temporal lags were identified via permutations along with density-based clustering analysis (Ester et al., 1996).

Results: Results showed a higher number of electrodes tracking speech compared to music in both frequency bands. In the SFB, electrodes tracking music and speech concentrate around middle and superior temporal gyri (MTG/STG), and lower portions of the sensorimotor cortices (music: mean r = 0.09, SD = 0.006; speech: mean r = 0.11, SD = 0.001). For the HFB, electrodes tracking music converge in middle and posterior portions of the MTG and STG, inferior parietal, and prefrontal areas (mean r = 0.096, SD = 0.013). In contrast, tracking of speech in the same frequency band concentrates in parabelt regions and inferior frontal gyrus, IFG (mean r = 0.10, SD = 0.023). Interestingly, while temporal lags for music in the SFB and HFB, and speech in the HFB concentrate around zero, thus suggesting time locked brain responses to the acoustic stream, temporal lags for speech in the HFB shows positive lags (mean lag = 87 ms, SD = 120 ms), suggesting that brain responses follow the speech signal with a delay of ~100 ms. Mixed effect modeling showed that HFB activity predicted higher correlation values ($F(1, 161.81) = 7.406$, $p = 0.0072$) for music. For speech, significantly higher r values were found for SFB in IFG ($p < 0.0001$), MTG ($p = 0.022$) and somatomotor regions ($p < 0.0001$) and for HFB in the STG ($p = 0.016$). For speech, delays in cortical tracking in the HFB were higher in STG (mean = 135.30ms, $p < 0.0001$), somatosensory cortex (mean 85.50ms, $p = 0.004$), MTG (mean = 80.7ms, $p < 0.0001$) and somatomotor cortex (mean = 48ms, ($p = 0.004$) compared against the same regions in SFB range. HFB tracking was also statistically higher in STG compared to all other identified cortical regions within the same frequency band.

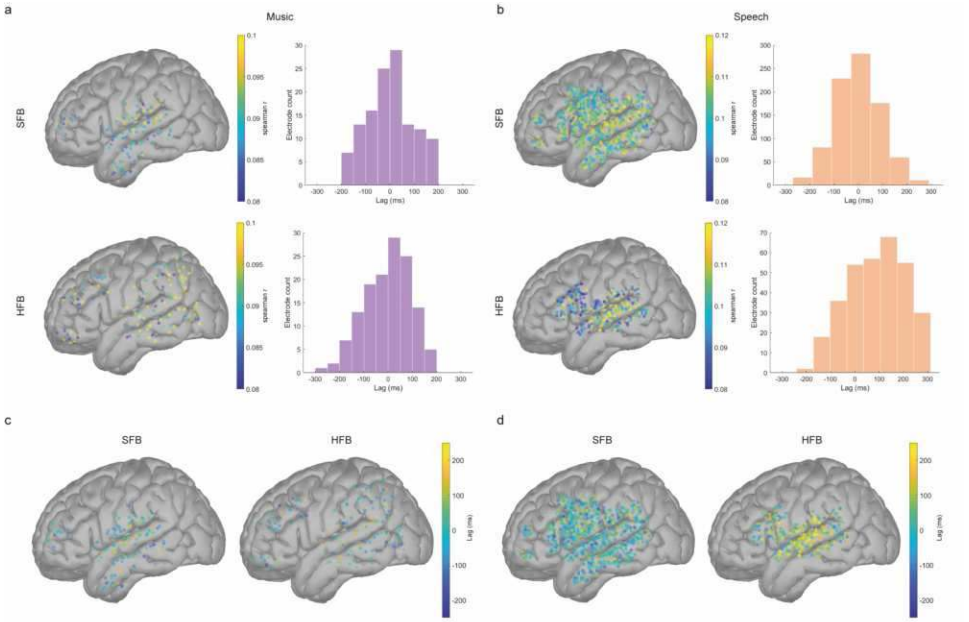

Figure 1. Cortical tracking of naturalistic music and speech stimuli. **a**. Statistically significant electrodes plotted in a common cortical template and their corresponding maximum correlation values for SFB and HFB. Histograms show the distribution of their corresponding temporal lags. **b.** as in **a**, but data shows the effect of cortical tracking for speech stimuli. **c** and **d**. Temporal gradients of temporal lags for music (**c**) and speech (**d**).

Conclusions: Early and late delays across conditions and frequency bands potentially reflect both predictive processes, responses driven by acoustic features and, potentially, information retrieval processes. We discuss our findings in the context of the affordances and limitations inherent to the use of uncontrolled naturalistic stimuli.

References

1. Assaneo, M. F., & Poeppel, D. (2018). The coupling between auditory and motor cortices is rate-restricted: Evidence for an intrinsic speech-motor rhythm. Science Advances, 4(2), 1–10.
2. Berezutskaya, J., Vansteensel, M. J., Aarnoutse, E. J., Freudenburg, Z. V., Piantoni, G., Branco, M. P., & Ramsey, N. F. (2022). Open multimodal iEEG-fMRI dataset from naturalistic stimulation with a short audiovisual film. Scientific Data, 9(1), 1–13.
3. Chi, T., Ru, P., & Shamma, S. A. (2005). Multiresolution spectrotemporal analysis of complex sounds. The Journal of the Acoustical Society of America, 118(2), 887-906.
4. Ding, N., Patel, A. D., Chen, L., Butler, H., Luo, C., & Poeppel, D. (2017). Temporal modulations in speech and music. Neuroscience and Biobehavioral Reviews, 81, 181–187.
5. Doelling, K. B., & Poeppel, D. (2015). Cortical entrainment to music and its modulation by expertise. Proceedings of the National Academy of Sciences of the United States of America, 112(45), E6233–E6242.
6. Ester, M., Kriegel, H.-P., Sander, J., Xu, X., & others. (1996). A density-based algorithm for discovering clusters in large spatial databases with noise. In kdd (Vol. 96, pp. 226–231).

Poster No 1047

A dissociated neural index of speech perception and understanding in background noise

Qingqing Meng[1], Angela Wong[1], Jennifer Clemesha[1,2], Jorge Mejia[1]

[1]National Acoustic Laboratories, Sydney, NSW, Australia, [2]Cochlear Limited, Sydney, NSW, Australia

Introduction: Human brain activity measured with magnetoencephalography (MEG) has been shown to track the hierarchical linguistic units embedded in connected speech (Ding et al., 2016). In addition, the responses at hierarchical levels that are dissociated from any acoustic cues to them, such as phrase and sentence level, can be directly modulated by changes in speech intelligibility caused by spectral degradation or immediate prior knowledge on speech signal (Meng et al., 2021, 2022).

Methods: In the current study, we introduce background noise and manipulate its sound level relative to the target speech to reduce the Signal-to-Noise Ratio (SNR) and speech intelligibility. We hypothesis that the tracking responses can be simultaneously but differently modulated by the variations in SNR and associated changes in speech intelligibility. Continuous Electroencephalography (EEG) responses to isochronous speech sentences presented alone and together with a multi-talker babble noise at three different levels were measured in nineteen normal hearing participants. Subjective ratings of speech understanding were also collected from individual participant after each stream of sentences presentation, across all

background noise conditions. Sensor level coherence between the EEG recordings and the temporal regularities of multi-level linguistic units were calculated and mapped back to the cerebral cortex using a whole-brain frequency domain beamforming technique (Gross et al., 2001).

Results: Results showed that concurrent brain responses to hierarchically nested linguistic structure in connected speech can be reliably measured using EEG, even in the presence of background noise. Driven by the reduction in speech intelligibility, cortical activities coherent to "abstract" linguistic units with no accompanying acoustic cues (phrases and sentences) were reduced relative to the "no noise" condition, and lateralized to single cerebral hemisphere. In contrast, brain response tracking word units that are aligned with syllable/acoustic onsets, were bilateral and exhibited a systematic reduction as the noise level increased (SNR decreased) across conditions.

Conclusions: This dissociated result suggests that brain processes of encoding linguistic information during speech perception are directly affected by speech intelligibility, which in turn are powerfully shaped by acoustic properties of the speech signal. Subjective rating scores on speech understanding differed significantly across all conditions and correlated with the magnitude of EEG tracking responses at all linguistic levels. These results provide an objective and sensitive neural level index of speech intelligibility and speech perception which has the potential to be further developed into clinical applications for the assessment of speech-in-noise performance among hearing impaired population, such as hearing aid users and cochlear implant recipients.

References

1. Ding, N., Melloni, L., Zhang, H., Tian, X., & Poeppel, D. (2016). Cortical tracking of hierarchical linguistic structures in connected speech. Nature Neuroscience, 19(1), 158.
2. Gross, J., Kujala, J., Hämäläinen, M., Timmermann, L., Schnitzler, A., & Salmelin, R. (2001). Dynamic imaging of coherent sources: Studying neural interactions in the human brain. Proceedings of the National Academy of Sciences, 98(2), 694–699.
3. Meng, Q., Hegner, Y. L., Giblin, I., McMahon, C., & Johnson, B. W. (2021). Lateralized cerebral processing of abstract linguistic structure in clear and degraded speech. Cerebral Cortex, 31(1), 591–602.
4. Meng, Q., Hegner, Y. L., Giblin, I., McMahon, C., & Johnson, B. W. (2022). Prior exposure to speech rapidly modulates cortical processing of high-level linguistic structure (p. 2022.01.25.477669). bioRxiv. https://doi.org/10.1101/2022.01.25.477669

Poster No 1048

ECoG Gamma-band Modulations Induced by Cognitive-linguistic Tasks during Awake Craniotomy

Sujit Prabhu[1], Israt Tasnim[2], Priscella Asman[1], Matthew Hall[2], Chandra Prakash Swamy[3], Giuseppe Pellizzer[4], Kyle Noll[1], Sudhakar Tummala[1], Nuri Firat Ince[3]

[1]The University of Texas MD Anderson Cancer Center, Houston, TX, [2]University of Houston, Houston, TX, [3]Mayo Clinic, Rochester, MN, [4]University of Minnesota, Minneapolis, MN

Introduction: Intraoperative functional language mapping using Direct Cortical Stimulation (DCS), the gold standard for defining eloquent language areas, has uncertainty in predicting language functions and post-surgical outcomes[1]. Moreover, DCS mapping can potentially induce seizure with prolonged usage. Here, we study the feasibility of intraoperative functional mapping using gamma-band modulations of electrocorticogram (ECoG) induced by linguistic tasks having different complexity levels during awake craniotomy.

Methods: Seven subjects with left temporal lobe glioma underwent resection surgeries involving awake language mapping using a 4x8 ECoG electrode grid (2.3mm contact exposure and 10mm pitch). A MATLAB/Simulink based real-time software system running on a portable laptop computer was used to map task-induced gamma-band modulations as 2D heat maps (Fig. 1)[2]. Tasks included verbally responding to individual words versus tones categorization, picture naming (object/nouns, action/verbs), written descriptive and auditory naming (AN) respectively[3]. Auditory stimuli were provided during word versus tone categorization (duration 300~500ms) and auditory naming tasks (> 1s). Other naming tasks provided visual stimuli (line drawings or written phrases). Bipolar DCS (2/4/6 mA, 60Hz, 2s) was applied at different electrode pairs while repeating the naming tasks.

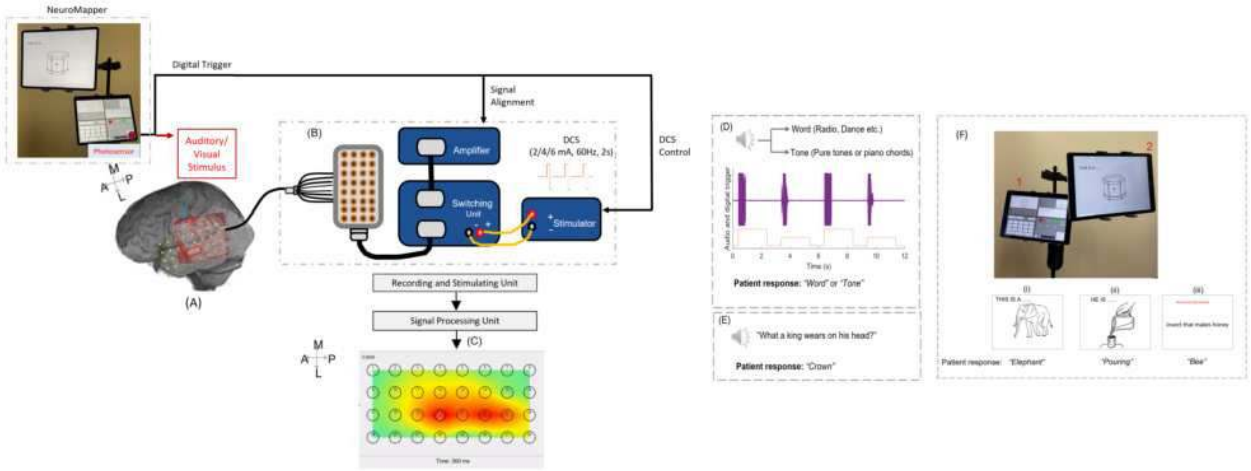

Figure 1: Functional language mapping pipeline; (A) 3D cortical rendering from pre-operative MRI scans, overlapped with intra-op photo to localize ECoG grid contacts (yellow circles), CS (cyan) are marked. (B) Recording unit: ECoG grid connected with bio-amplifier for recording. Digital trigger (D I/O) obtained from audio/photosensor system is used for aligning neural data with audio onset. (C) Signal processing unit: MATLAB/Simulink based task-specific 2D heat map is generated for AN task (ECoG frequency: 50~300Hz, 300ms post-stimulus onset). (D) Sample audio (purple), digital trigger (orange) waveforms and task paradigm from "word vs tone categorization" task. (E) AN task example stimulus, (F) NeuroMapper device and task paradigms, Device includes control screen (1) and patient view screen (2), Example visual stimuli for different tasks: (i) object naming, (ii) action naming, (iii) written descriptive naming.

Results: The electrodes having strongest gamma-band modulations (ERS power> 2dB for >=200ms) were distinct for different tasks across subjects (Fig. 2). Cortical regions activated by word stimuli and the AN task were similar; superior and middle temporal gyri (STG, MTG). Gamma band modulations with tone stimuli were observed early (<200ms post stimuli onset) in the STG. Whereas with word and AN stimuli additional late activated (>200ms) contacts were observed. Visual naming tasks modulated posterior MTG (pMTG), written naming induced additional long latency activations (>500ms) around STG, indicating STG involvement in higher level cognitive-linguistic processing. DCS induced reproducible speech arrests occurred during different naming tasks while stimulating specific electrode pairs, responsive electrodes were not necessarily those with strong task-specific gamma-band activations. Considerable inter-personal variability of language areas identified with DCS was observed, despite the similarity of task-specific gamma-band modulated regions across subjects.

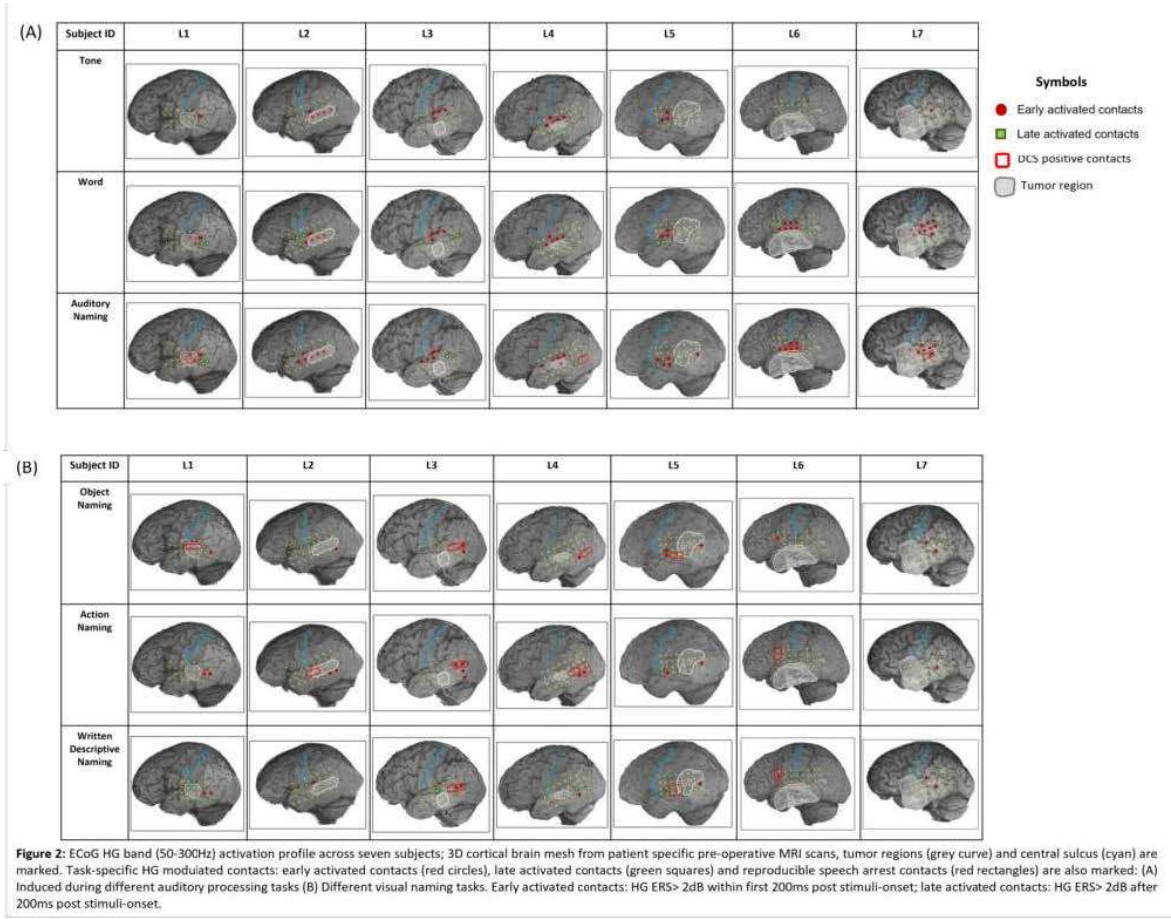

Figure 2: ECoG HG band (50-300Hz) activation profile across seven subjects; 3D cortical brain mesh from patient specific pre-operative MRI scans, tumor regions (grey curve) and central sulcus (cyan) are marked. Task-specific HG modulated contacts: early activated contacts (red circles), late activated contacts (green squares) and reproducible speech arrest contacts (red rectangles) are also marked: (A) Induced during different auditory processing tasks (B) Different visual naming tasks. Early activated contacts: HG ERS> 2dB within first 200ms post stimuli-onset; late activated contacts: HG ERS> 2dB after 200ms post stimuli-onset.

Conclusions: Intraoperative language mapping guided by gamma-band ECoG modulations induced by simple word versus tone categorization task exhibited similar patterns to more complex naming tasks, suggesting this task may be a viable approach to localize functional cortex, especially in patients unable to reliably perform more difficult paradigms. With this task-based activations in conjunction with DCS mapping guided by visual naming tasks, eloquent cortical language areas may be better preserved, thereby reducing post-operative language deficits.

References

1. Hamberger, Marla J., William T. Seidel, Guy M. Mckhann, Kenneth Perrine, and Robert R. Goodman. "Brain stimulation reveals critical auditory naming cortex." Brain 128, no. 11 (2005): 2742-2749.
2. Tasnim, Israt, Priscella Asman, Chandra Prakash Swamy, Sudhakar Tummala, Sujit Prabhu, and Nuri Firat Ince. "Microcontroller-Based Low Latency Audio System to Study Cortical Auditory Evoked Potentials: Applications with Intraoperative Language Mapping." In 2023 11th International IEEE/EMBS Conference on Neural Engineering (NER), pp. 01-04. IEEE, 2023.
3. Israt Tasnim, Nuri Ince, Sujit Prabhu, Kyle Noll, Chandra Swamy, Katherine Connelly, Priscella Asman, Tummala Sudhakar, Sarah Prinsloo, Chibawanye Ene, Roxana Grasu, Ho-Ling Liu, Matthew Muir, Shreyas Bhavsar, Vinodh Kumar, NIMG-64. INTRAOPERATIVE LANGUAGE MAPPING USING GAMMA-BAND MODULATIONS OF ELECTROCORTICOGRAM (ECOG) INDUCED BY WORD/SOUND CATEGORIZATION TASK: VALIDATION WITH REPRODUCIBLE SPEECH ARRESTS DURING LINGUISTIC TASKS, Neuro-Oncology, Volume 24, Issue Supplement_7, November 2022, Pages vii178–vii179,

Poster No 1049

Language Switching Training Reveals an Adaptive Cerebellar Network for Bilingual Language Control

Qianwen Chang[1], Taomei Guo[2]

[1]Beijing Normal University, China, Beijing, [2]Beijing Normal University, Beijing, Beijing

Introduction: When bilinguals speak in one of their two languages, both languages are activated. Language control is recruited to select the appropriate language and inhibit interference from the other language. Previous studies have revealed that the cerebellum, especially the posterior cerebellum, plays an important role in bilingual language control. According to the Adaptive Control Hypothesis[1], neural correlates underlying bilingual language control exhibit adaptive changes to meet the demands in different language contexts. However, most past work has focused on the plasticity of the cerebral regions. In the present study, we examined the involvement of the cerebellum in bilingual language control and the plasticity of the intracerebellar network using short-term language-switching training.

Methods: Two groups of Chinese-English bilinguals performed language switching task in the pre-test and post-test sessions during functional magnetic resonance imaging (fMRI) scanning. After the pre-test, only the training group received an 8-day training in language switching. MRI data were collected by a 3T Siemens Trio Tim MRI scanner. Functional scanning with a T2-weighted gradient EPI sequence was acquired. After functional scanning, a high-resolution T1-weighted anatomical scanning was obtained. Whole-brain images were preprocessed using the DPABI toolbox[2]. We used the SUIT toolbox to isolate the cerebellum from the whole-brain image[3]. At the group level, a paired-sample t-test was performed to compare the cerebellum activation patterns between the pre-test and post-test in both groups with FDR correction. To further investigate the network-level changes after training, we constructed the networks in the pre-test and post-test using the euSEM method[4]. The seven cerebellar sub-regions obtained in the activation analysis were selected as ROIs. Network measures including global efficiency, local efficiency, transitivity and betweenness centrality were calculated using the Brain Connectivity Toolbox[5]. We performed specification curve analysis (SCA) with a 1000-time bootstrapping to further reveal the influence of network plastic changes on language control performance[6].

Results: For the training group, a significant increase in language control performance (switch cost) was observed after training, $t = 3.388$, $p = 0.003$. For the control group, there was no significant change after training, $t = 1.832$, $p = 0.082$. Activation analysis showed reduced activation in the bilateral lobules IV-V and VI, vermis IV-V, the right Crus I and VIIB after training for the training group. In contrast, there was no significant change for the control group. Intra-cerebellar language control networks in the pre-test and post-test for the training group are shown in Fig 1. Paired sample t-tests showed a significant increase in global efficiency, mean local efficiency, transitivity and betweenness centrality after training, $ps < 0.001$. Furthermore, SCA showed a significant negative relationship between the change of betweenness centrality of the hub node (right lobule IV-V) and the switch cost in the post-test (Fig 2).

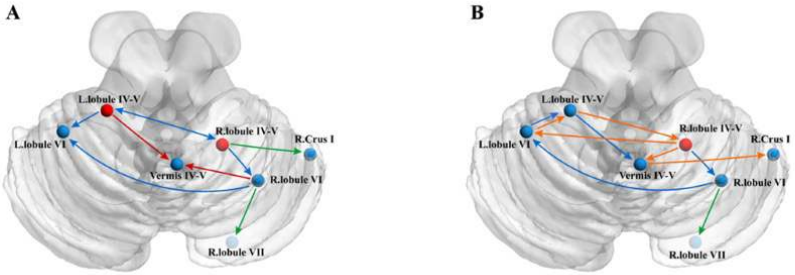

Fig. 1. Cerebellar connectivity for the training group in the pre-test and post-test.

A) the connectivity map in the pre-test. B) the connectivity map in the post-test. Hubs are marked in red.

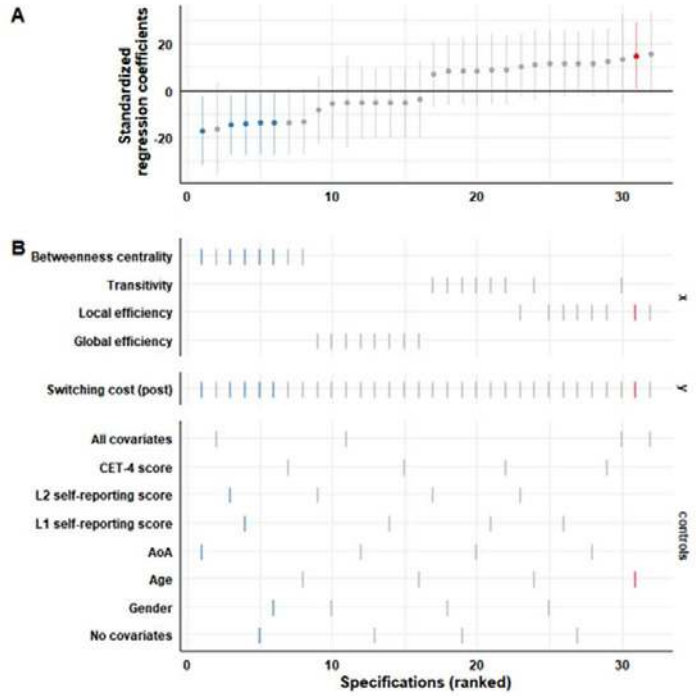

Fig. 2. Specification curve analysis

Conclusions: Bilingual language control activates an intra-cerebellar network including multiple posterior cerebellar sub-regions as well as the anterior cerebellum (i.e. lobules IV-V). Furthermore, the intra-cerebellar network exhibited adaptive changes by enhancing local neural efficiency and network connectivity after training. The reorganization of the intra-cerebellar network in the present study might be associated with better coordination in speech production[7]. Global and local properties of the network were also modulated by training. For the first time, our study revealed the plasticity of the intra-cerebellar network in bilingual language control.

References

1. Green, D. W., & Abutalebi, J. (2013). Language control in bilinguals: The adaptive control hypothesis. Journal of Cognitive Psychology, 25(5), 515–530.
2. Yan, C.-G., Wang, X.-D., Zuo, X.-N., & Zang, Y.-F. (2016). DPABI: Data Processing & Analysis for (Resting-State) Brain Imaging. Neuroinformatics, 14(3), 339–351.
3. Diedrichsen, J. (2006). A spatially unbiased atlas template of the human cerebellum. NeuroImage, 33(1), 127–138.
4. Duffy, K. A., Fisher, Z. F., Arizmendi, C. A., Molenaar, P. C. M., Hopfinger, J., Cohen, J. R., Beltz, A. M., Lindquist, M. A., Hallquist, M. N., & Gates, K. M. (2021). Detecting Task-Dependent Functional Connectivity in Group Iterative Multiple Model Estimation with Person-Specific Hemodynamic Response Functions. Brain Connectivity, 11(6), 418–429.
5. Rubinov, M., & Sporns, O. (2010). Complex network measures of brain connectivity: Uses and interpretations. NeuroImage, 52(3), 1059–1069.
6. Simonsohn, U., Simmons, J. P., & Nelson, L. D. (2020). Specification curve analysis. Nature Human Behaviour, 4(11), 1208–1214.
7. Moberget, T., & Ivry, R. B. (2016). Cerebellar contributions to motor control and language comprehension: Searching for common computational principles. Annals of the New York Academy of Sciences, 1369(1), 154–171.

Poster No 1050

Rhythmic Cues Influence Neural Oscillations Differently in Adults and Children

Yanni Liu[1], Amanda Hampton Wray[2], Shanley Treleaven[1], Valeria Caruso[1], Erica Lescht[1], Emily Garnett[1], Soo-Eun Chang[1]

[1]University of Michigan, Ann Arbor, MI, [2]University of Pittsburgh, Pittsburgh, PA

Introduction: Understanding neural dynamics in speech processing is crucial for uncovering speech and language production mechanisms. Beta frequency (13-30 Hz) neural oscillations are key in sensorimotor processing and speech preparation, showing reduced power (i.e., more desynchronization) before movement, reflecting motor planning and intended speech output (Gehrig et al., 2012; Pfurtscheller & Lopes, 1999). Beta power modulation changes with age, increasing from childhood to early adulthood and further during the transition to late adulthood (Gaetz et al., 2010; Rossiter et al., 2014). Beyond coordinating sensorimotor systems, beta oscillations encode temporal predictions, decreasing after rhythmic tone onsets but not in non-rhythmic sequences (Fujioka et al., 2012; Chang et al., 2019). This study explores beta power patterns preceding speech onset, examining age-related differences across brain regions in response to rhythmic and non-rhythmic cues during word production tasks.

Methods: 29 adults (mean age=27.8 ± 8.6) and 40 children (mean age=10.3±1.7) with no neurological conditions participated in a spoken word task (Fig.1) while EEG data were recorded. They heard rhythmic (presented with a constant 400 ms interval) or non-rhythmic (variable 200-600 ms interval) auditory tones, followed by word prompts and a speech cue to repeat the word. EEG data were recorded using 64 electrodes. Analysis of beta power (low beta,13-20 Hz; high beta,21-30 Hz) focused on the time periods immediately before [-400 0 ms] and after [0 400 ms] the speech cue. We assessed rhythm effects (rhythmic vs. non-rhythmic) and developmental differences (Adult vs. Child) in speech preparation (before and after speech cue) using repeated-measures ANOVAs. Speech latency, defined as the duration between the cue to speak and the onset of speech, was also assessed using an ANOVA. Post-hoc analyses were conducted following any observed significant ($p<0.05$) main effects or interactions.

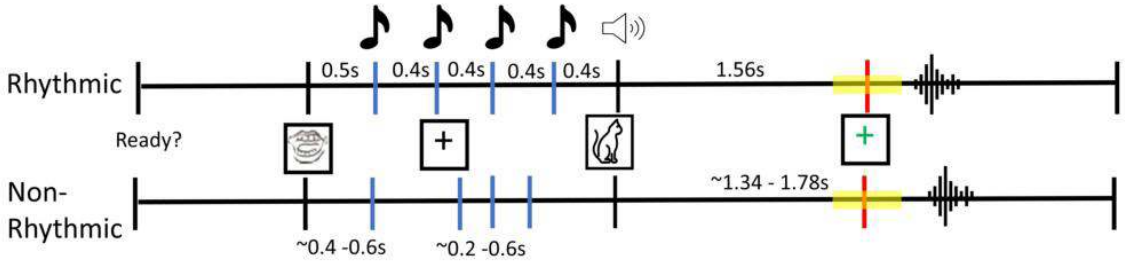

Fig. 1: Experimental paradigm. Each trial began with a visual cue indicating the specific block condition (e.g., speech), followed by the presentation of four pure tones at a fixed rhythmic interval (400 ms) or a variable non-rhythmic interval (ranging from 200 to 600 ms). Subsequently, a target object (e.g., a picture of a cat) appeared on the screen, accompanied by the auditory presentation of the corresponding word. Following a delay (1560 ms for rhythmic trials and varying between 1340 ms and 1780 ms for non-rhythmic trials), a speech cue (green cross) prompted participants to reproduce the heard word within 1500 ms.

Results: Findings revealed a significant reduction in speech latency in the rhythmic compared to the non-rhythmic condition (544 ms vs. 475 ms, $p<0.001$), indicating faster speech initiation times across all age groups. Regarding beta power (See Fig. 2), before the speech cue, there was noticeable low-beta desynchronization, particularly in the frontal areas compared to central and parietal regions ($p<0.05$), and the left hemisphere showed more desynchronization than the right ($p<0.05$). Rhythm effects were seen in frontal and central areas but not in parietal regions. The two age groups showed rhythm effects in distinct brain regions: left frontal and right central regions for adults, and bilateral central regions for children (Fig. 2). After the speech cue, parietal regions exhibited larger desynchronization compared to central and frontal regions ($p<0.05$), and the left hemisphere showed more desynchronization than the right ($p<0.05$). Adults consistently had higher low-beta desynchronization than children ($p<0.001$). Rhythm effects were only seen in adults, with increased low-beta desynchronization in the rhythmic condition compared to the non-rhythmic condition ($p<0.01$); children did not show this difference. For high-beta desynchronization, effects were similar before and after speech cues with no significant regional differences. Adults consistently showed higher desynchronization than children ($p<0.001$), with rhythm effects only observed in adults, particularly in the right hemisphere ($p<0.01$) (Fig. 2).

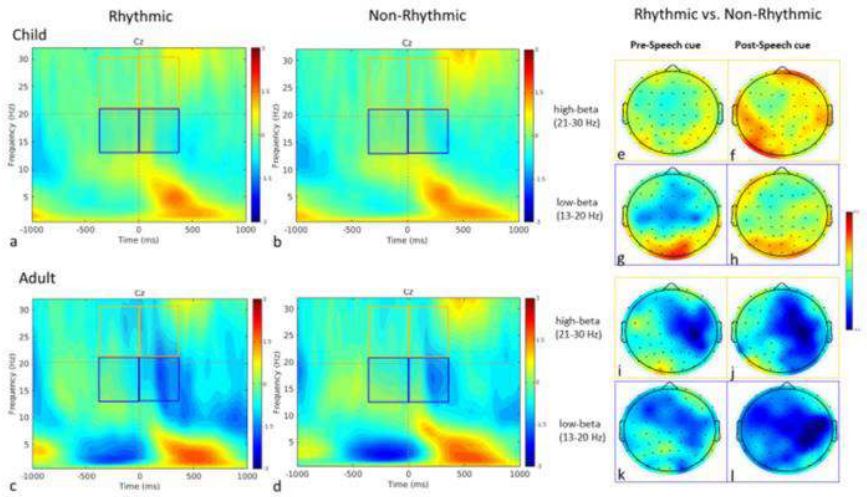

Fig. 2: Time-frequency decomposition (TFD) time-locked to the onset of speech cues in Rhythmic conditions (a, c) and Non-Rhythmic conditions (b, d) at a representative electrode (Cz), along with the topography of rhythmic effects (Rhythmic vs. Non-Rhythmic) in high-beta (21-30 Hz) and low-beta (13-30 Hz) frequencies before (-400 to 0 ms) and after (0 to 400 ms) the speech cue (e-l). Specifically, panels (a) and (b) present TFD for child participants in the rhythmic and the non-rhythmic conditions, respectively. Similarly, panels (c) and (d) display TFD for adult participants in the rhythmic and non-rhythmic conditions. The topography of rhythmic effects for children is illustrated in panels (e) and (f) for high-beta frequencies before and after the speech cue, and in panels (g) and (h) for low-beta frequencies before and after the speech cue. For adults, the topography of rhythmic effects is shown in panels (i) and (j) for high-beta frequencies before and after the speech cue, and in panels (k) and (l) for low-beta frequencies before and after the speech cue.

Conclusions: These results underscore the influence of rhythmic auditory cues on speech latency and beta oscillation dynamics across participants of different ages. The distinct neural responses between adults and children highlight the developmental disparities in processing rhythmic cues during speech tasks. These findings hold potential implications for understanding the neural bases of speech development and of clinical disorders associated with speech timing deficits (e.g., stuttering).

Poster No 1051

Degeneracy in the neurological model of auditory speech repetition

Noor Sajid[1], Andrea Gajardo-Vidal[2], Justyna Ekert[1], Diego Lorca-Puls[3], Thomas Hope[1], David Green[4], Karl Friston[1], Cathy Price[1]

[1]Wellcome Centre for Human Neuroimaging, University College London, London, London, [2]CICS Centro de Investigación en Complejidad Social, Universidad del Desarrollo, Concepción, N/A, [3]Sección de Neurología, Departamento de Especialidades, Universidad de Concepción, Concepción, N/A, [4]Experimental Psychology, University College London, London, London

Introduction: The neurological language model[1] posits that auditory speech repetition engages four left hemisphere brain regions sequentially: primary auditory cortex (A1), Wernicke's area (WA), Broca's area (BA), and primary motor cortex (M1), with the arcuate fasciculus mediating information relay. Recent studies challenge this, emphasising the importance of areas near WA and BA (2). Here, we investigate the bilateral interaction amongst these and their involvement with A1 and M1 during auditory speech repetition. Using previously identified activations[2] we estimate effective connectivity (i.e., directed interactions) across these areas using Dynamic Causal Modelling (DCM)[3]. Our findings reveal variable effective connectivity across word or pseudoword repetition, indicative of functional degeneracy.

Methods: We studied 59 right-handed native English speakers during auditory speech repetition using 3T fMRI scanning runs with 40 stimuli in 4 blocks. The stimuli had an average syllable count of 1.68 (words) and 1.5 (pseudowords) and pre-scan training ensured accuracy. Data processing included spatial realignment, unwarping, normalisation, and smoothing. Activation timeseries were extracted from peak responses ($p<0.05$ FWE-corrected) in anatomical constrained regions (Figure 1A): Te1.0 & Te1.2 for A1, rostro-posterior superior temporal sulcus (pSTS) for WA, dorsal and ventral pars opercularis for BA, and face and tongue & larynx subregion for M1 (M1-f & M1-tl). Effective connectivity amongst these was estimated using participant[3] and group-level[6] DCM hypothesising input from A1, A1's connections to all regions barring M1, connection from pSTS to pOp, and M1 as the output region (Figure 1B). The winning group-level model quantified estimated connection strengths (posterior probability>0.75) after Bayesian model comparison over 256 models.

Results: The winning models revealed excitatory connectivity from A1 to pSTS, pSTS to M1, A1 to pOp, and pOp to M1 (Figure 1C-D); positive extrinsic connections were excitatory & inhibitory if negative). There were inhibitory connections from M1 to A1,

pSTS to A1, and surprisingly, between pSTS and pOp. The results were consistent across task and subregional configurations. To investigate the unanticipated effective connectivity from pSTS to M1, we evaluated individual models (Figure 2A). Each model was assigned given estimated connectivity from pOp or pSTS to M1: A had excitatory connections from both to M1; B only from pSTS to M1; C only from pOp to M1; and D had an absence of significant connections. More than half the models were assigned to Group A, 20% to Group B and D and <5% in Group C (Figure 2C). Importantly, only 2% of models were consistent with the neurological model (pSTS->pOp->M1). We measured degeneracy via high intra-subject variability in how M1 was influenced by pSTS and/or pOp (Figure 2B). Connectivity variability was quantified by assigning participants to groups A-D. Entropy measurement, reflecting functional degeneracy[7], showed an average entropy in individual group membership of 0.49 (word) and 0.55 (pseudoword). 73% were assigned to ≥2 groups, indicating the ability to execute auditory speech repetition in diverse ways, exemplifying degeneracy.

Conclusions: We used fMRI DCM to evaluate the effective connectivity between pSTS and pOp, and with A1 and M1. Contrary to the neurological model, we show that pSTS drives M1 independently of pOp, there is bilateral inhibitory connectivity between pOp and pSTS, and participants vary in the degree to which M1 activity is driven by pSTS or pOp. This demonstrates a distributed, functional architecture between pSTS and pOp, implying alternative pathways for auditory speech repetition (degeneracy), and serve to generate hypotheses about how auditory speech repetition can be maintained or recovered after brain damage.

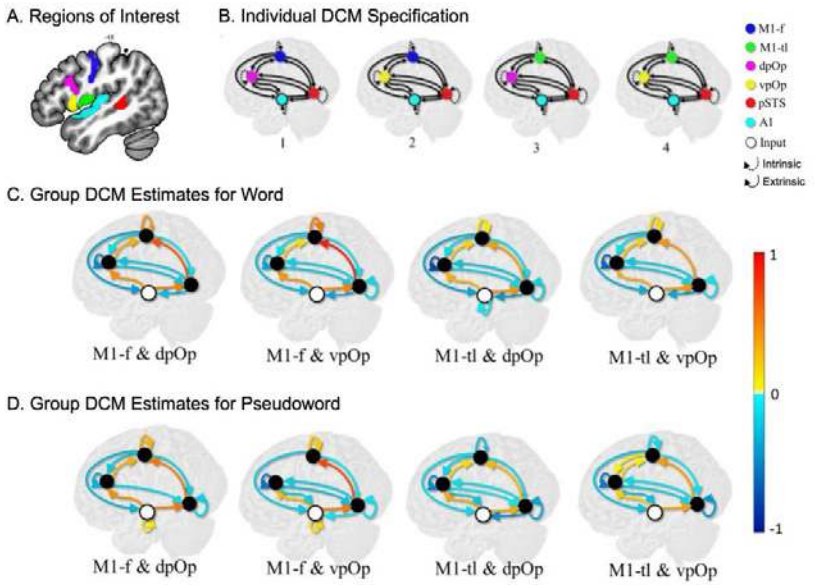

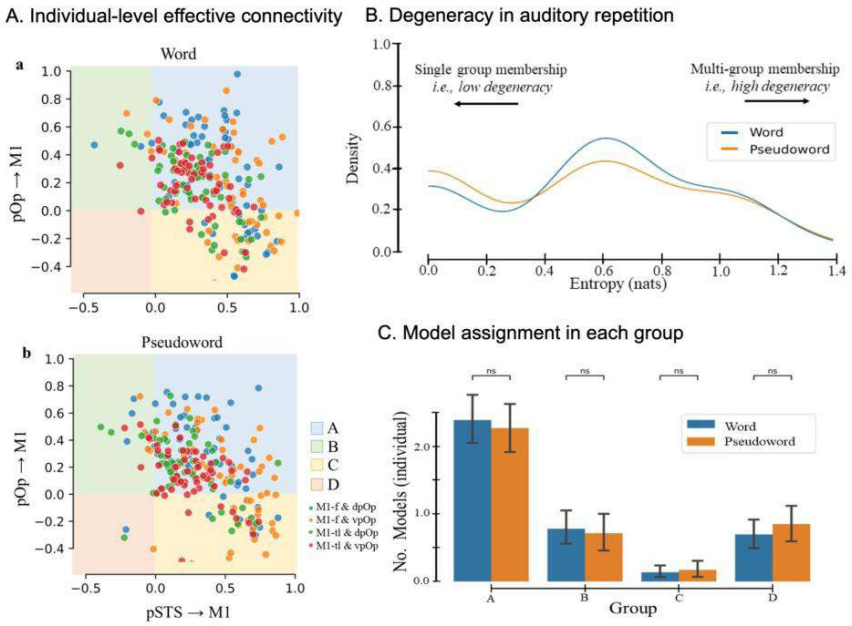

References
1. Lichtheim L. (1885), On Aphasia.
2. Hope TMH, et al. (2014), Dissecting the functional anatomy of auditory word repetition. Frontiers in human neuroscience 8, 246-246.
3. Friston KJ, et al. (2003), Dynamic causal modelling. NeuroImage 19, 1273-1302.
4. Price CJ, et al. (2002), Degeneracy and cognitive anatomy. Trends in cognitive sciences 6, 416-421.
5. Fan L, et al. (2016), The Human Brainnetome Atlas: A New Brain Atlas Based on Connectional Architecture. Cerebral cortex, 26, 3508-3526
6. Zeidman P, et al. (2019), A tutorial on group effective connectivity analysis, part 2 : second level analysis with PEB, Neuroimage. 200,12-25.
7. Sajid N, et al. (2020), Degeneracy and Redundancy in Active Inference. Cerebral Cortex, 30(11), 5750-5766.

Poster No 1052

Mapping individual and shared cortical language representations during real-time natural dialogues

Zaid Zada[1], Samuel Nastase[1], Sebastian Speer[1], Laetitia Mwilambwe-Tshilobo[1], Lily Tsoi[2], Shannon Burns[3], Uri Hasson[1], Diana Tamir[1]

[1]Princeton University, Princeton, NJ, [2]Caldwell University, Caldwell, NJ, [3]Pomona College, Claremont, CA

Introduction: How is language encoded in the brain during everyday conversations, and how is that linguistic encoding shared across interlocutors? Typical studies of the neural basis of language present subjects with predetermined, isolated words or sentences (Price, 2010), and do not consider the role of spontaneous language production nor linguistic neural coupling (Garrod & Pickering, 2004). Here, we aim to address both gaps and map brain areas involved in both speech production and comprehension during natural dialogue.

Methods: We developed a hyperscanning paradigm to collect simultaneous fMRI data in 30 dyads (60 subjects, 41F) as they freely discussed 10 topics across 5 runs (Fig 1A) (Speer et al., 2023). Topics were presented as a starting point, but each dyad was free to pursue the discussion in different ways. Our goal was to characterize the linguistic content encoded in the brain within subjects. To that end, we estimated voxel-wise encoding models to predict held-out BOLD signals during speech production or comprehension from 6 feature spaces: nuisance task structure regressors, mel-spectral features, phonetic articulatory features, head motion parameters, and word embeddings extracted from the GPT-2 language model (Fig 1B) (la Tour et al., 2022). To account for turn-taking during natural conversations, we split all regressors into separate sets for speaking and listening, and fit both submodels jointly using banded ridge regression; this allows the model to learn different weights for each process, and allows us to quantify the relative contribution of each submodel. Then, we correlated the actual and predicted BOLD activity for left-out runs in each voxel only from the language model word embedding, quantifying the extent of linguistic content in the signal for production or comprehension time points separately (Fig 1C).

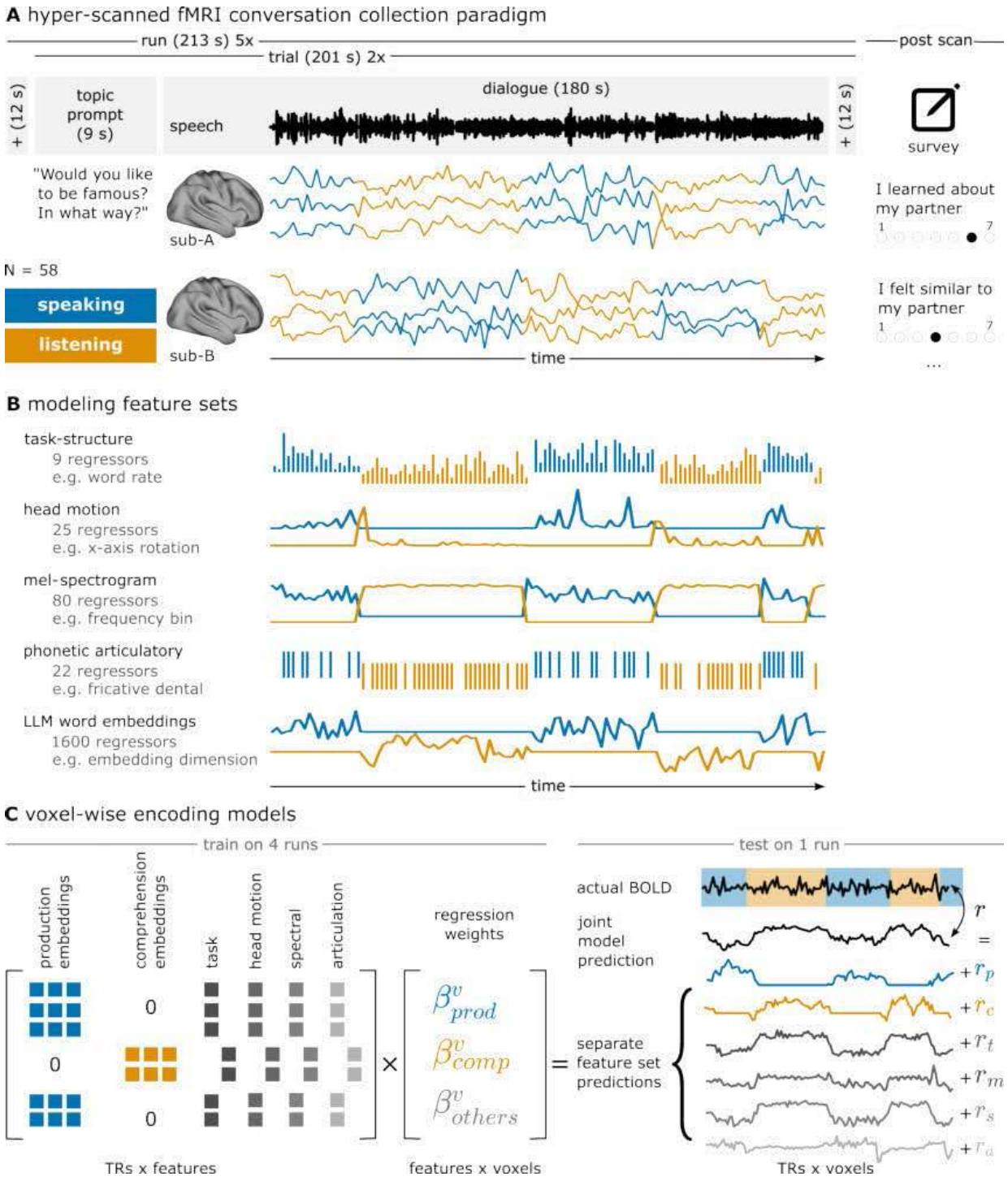

Results: We found strong encoding performance bilaterally throughout the language network-superior temporal cortex, middle frontal gyrus, inferior frontal gyrus, and angular gyrus-as well as somatomotor and precuneus areas. When evaluating the feature sets separately, we found that the task structure, spectral, and articulation features all recruited the somatomotor cortex during speech production, while speech comprehension more strongly recruited the superior temporal cortex (Fig 2C). While head motion features predicted a typical halo in the superior area. With that variance accounted for, the language model embeddings predicted posterior temporal cortex and middle frontal regions the most (Fig 1A). Surprisingly, we found better overall accuracy in the right hemisphere than left, and the right angular gyrus is heavily recruited for production. The superior temporal region depicted a ventral accuracy gradient for comprehension only (orange), to joint processing (white), and then only production (blue). In order to test for linguistic coupling across dyads, we developed a model-based coupling method where we correlate the production/comprehension model predictions of one subject to the comprehension/production responses of their partner. We found that model-based predictions can generalize between subjects in several hubs across the language network from the early auditory cortex, to temporal regions, and to precuneus (Fig 2B).

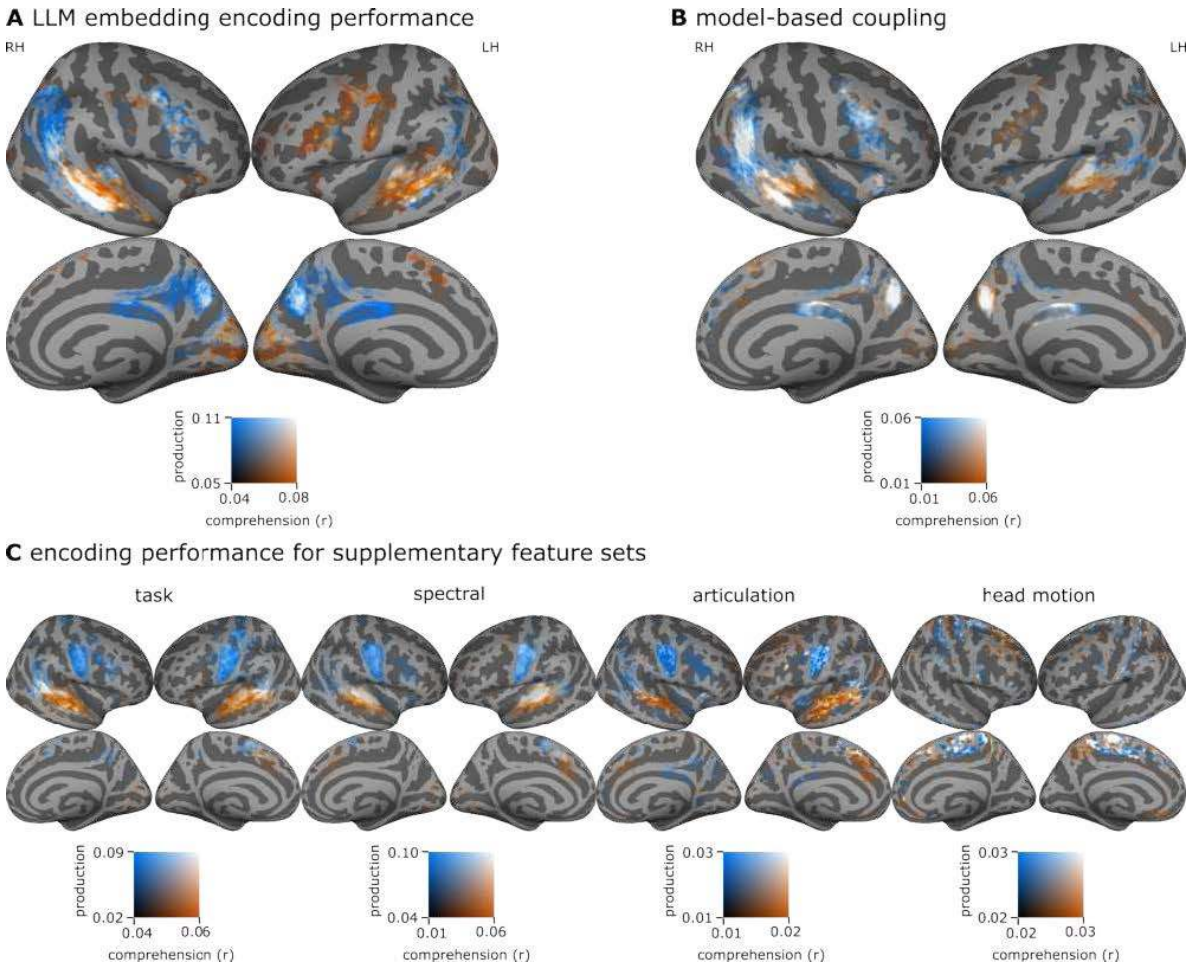

Conclusions: Our findings lay the foundation for assessing model-based, brain-to-brian coupling between speakers and listeners. We showed that cortical language representations during interactive natural dialogues can be predicted by language model embeddings, revealing both shared and selective encoding for speaking and listening. While this concurs with existing literature for language comprehension (Caucheteux & King, 2022; Schrimpf et al., 2021), we also show this in production during dialogue (Goldstein et al., 2023; Yamashita et al., 2023). We further extend the production–perception relationship by formally modeling the shared speaker–listener alignment on linguistic features (Zada et al., 2023).

References

1. Caucheteux, C., & King, J.-R. (2022). Brains and algorithms partially converge in natural language processing. Communications Biology, 5(1), 134.
2. Garrod, S., & Pickering, M. J. (2004). Why is conversation so easy? Trends in Cognitive Sciences, 8(1), 8–11.
3. Goldstein, A., Wang, H., Niekerken, L., Zada, Z., Aubrey, B., Sheffer, T., Nastase, S. A., Gazula, H., Schain, M., Singh, A., Rao, A., Choe, G., Kim, C., Doyle, W., Friedman, D., Devore, S., Dugan, P., Hassidim, A., Brenner, M., … Hasson, U. (2023). Deep speech-to-text models capture the neural basis of spontaneous speech in everyday conversations. In bioRxiv. https://doi.org/10.1101/2023.06.26.546557
4. la Tour, T. D., Eickenberg, M., Nunez-Elizalde, A. O., & Gallant, J. L. (2022). Feature-space selection with banded ridge regression. In bioRxiv. https://doi.org/10.1101/2022.05.05.490831
5. Price, C. J. (2010). The anatomy of language: a review of 100 fMRI studies published in 2009. Annals of the New York Academy of Sciences, 1191, 62–88.
6. Schrimpf, M., Blank, I. A., Tuckute, G., Kauf, C., Hosseini, E. A., Kanwisher, N., Tenenbaum, J.
7. B., & Fedorenko, E. (2021). The neural architecture of language: Integrative modeling converges on predictive processing. Proceedings of the National Academy of Sciences of the United States of America, 118(45). https://doi.org/10.1073/pnas.2105646118
8. Speer, S., Mwilambwe-Tshilobo, L., Tsoi, L., Burns, S., Falk, E. B., & Tamir, D. (2023). What makes a good conversation? fMRI-hyperscanning shows friends explore and strangers converge. In PsyArXiv. https://doi.org/10.31234/osf.io/jfvpx
9. Yamashita, M., Kubo, R., & Nishimoto, S. (2023). Cortical representations of languages during natural dialogue. In bioRxiv. https://doi.org/10.1101/2023.08.21.553821
10. Zada, Z., Goldstein, A., Michelmann, S., Simony, E., Price, A., Hasenfratz, L., Barham, E., Zadbood, A., Doyle, W., Friedman, D., Dugan, P., Melloni, L., Devore, S., Flinker, A., Devinsky, O., Nastase, S. A., & Hasson, U. (2023). A shared linguistic space for transmitting our thoughts from brain to brain in natural conversations. bioRxiv : The Preprint Server for Biology. https://doi.org/10.1101/2023.06.27.546708

Poster No 1053

Deep Speech-to-Text Models Capture the Neural Basis of Spontaneous Speech in Everyday Conversations

Ariel Goldstein[1], Haocheng Wang[2], Leonard Niekerken[2], Zaid Zada[2], Bobbi Aubrey[2], Tom Sheffer[3], Samuel Nastase[2], Mariano Schain[3], Harshvardhan Gazula[2], Aditi Singh[2], Aditi Rao[2], Gina Choe[2], Catherine Kim[2], Werner Doyle[4], Daniel Friedman[4], Sasha Devore[4], Patricia Dugan[4], Avinatan Hassidim[3], Michael Brenner[3], Yossi Matias[3], Orrin Devinsky[4], Adeen Flinker[4], Uri Hasson[2]

[1]Hebrew University, Jerusalem, Israel, [2]Princeton University, Princeton, NJ, [3]Google Research, Mountain View, CA, [4]New York University School of Medicine, New York, NY

Introduction: One of the most distinctively human behaviors is our ability to use language for communication during spontaneous conversations. Here, we collected continuous speech recordings and concurrent neural signals recorded from epilepsy patients during their week-long stay in the hospital, resulting in a uniquely large ECoG dataset of 100 hours of speech recordings during spontaneous, open-ended conversations. Deep learning provides a novel computational framework that embraces the multidimensional and context-dependent nature of language (Goldstein et al., 2022; Schrimpf et al., 2021). Here, we use Whisper, a deep multimodal speech-to-text model (Radford et al., 2022) to investigate the neural basis of speech processing.

Methods: We separately extracted "speech embeddings" from the Whisper encoder network based on continuous speech inputs and "language embeddings" from the decoder network based on transcript inputs. To test whether embeddings extracted from Whisper can capture neural activity during natural conversations, we developed linear encoding models based on speech and language embeddings separately. We built electrode-wise encoding models for each lag ranging from -2000 ms to +2000 ms relative to word onset. To evaluate encoding model performance, we calculated the correlation between predicted and actual neural signal for held-out test words using ten-fold cross-validation.

Results: We observed encoding patterns indicating a distributed cortical hierarchy of speech processing (Fig 1A, 1B): Electrodes in superior temporal gyrus (STG) and somatomotor areas (SM) demonstrated higher correlations with speech embeddings, whereas higher-level language areas like inferior frontal gyrus (IFG), posterior medial temporal gyrus (pMTG) and angular gyrus (AG) were better correlated with language embeddings. Furthermore, we observed a spatial distribution of electrodes preferentially engaged in speech production versus speech comprehension. High-level language areas showed a mixed selectivity, indicating a shared neural mechanism between speech production and comprehension (Fig 1C). During speech production, we observed double encoding peaks occurring before and after word onset for some electrodes. We trained encoding models on comprehension data and tested prediction performance on production data. The 'flipped' encoding models learned a comprehension-specific mapping and successfully predicted the neural signal after word onset for speech production (Fig. 1D). Evaluating encoding models at each lag relative to word onset allows us to trace the temporal flow of linguistic information across speech-related ROIs. We observed a temporal encoding pattern where language encoding in IFG peaks significantly earlier than speech encoding in STG during speech production (Fig. 2A), and vice versa during speech comprehension (Fig. 2B).

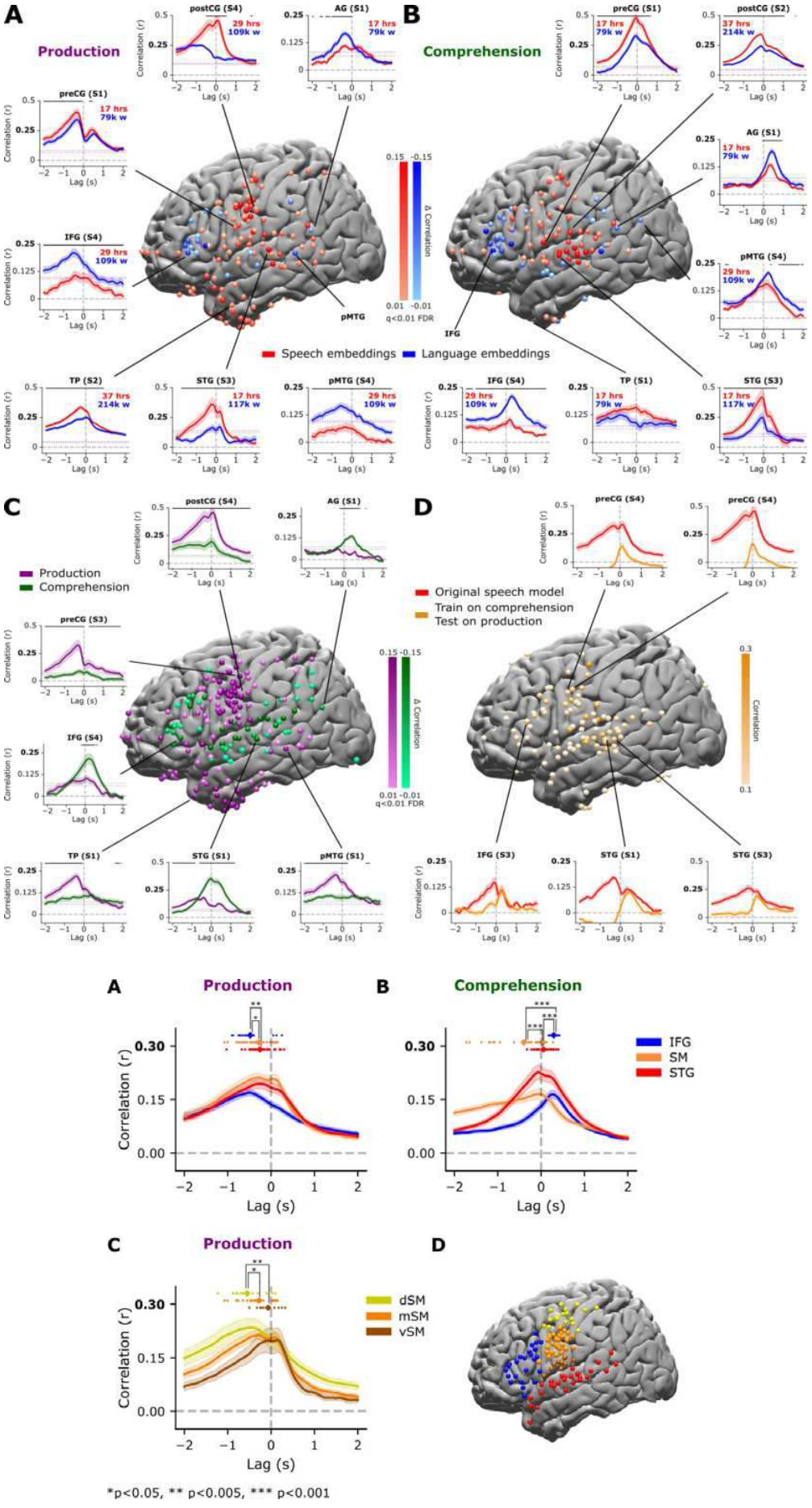
A
Production
B
Comprehension
Speech embeddings
Language embeddings
C
Production
Comprehension
D
Original speech model
Train on comprehension
Test on production
Correlation (r)
Lag (s)
Δ Correlation
q<0.01 FDR
IFG
SM
STG
dSM
mSM
vSM
*p<0.05, ** p<0.005, *** p<0.001

Conclusions: Our encoding models identify a distributed cortical hierarchy where auditory and sensorimotor areas in the brain were better aligned with speech embeddings and high-level frontal and parietal language areas were better aligned with language embeddings (Fig. 1). These findings are in line with established theories about the cortical hierarchy of language processing (Hickok & Poeppel, 2007). At the same time, electrode-wise selectivity for speech or linguistic information was mixed across most brain areas. This mixed selectivity is common in both biological and artificial learning systems that are "directly" fit to the complex structure of their inputs (Hasson, Nastase, & Goldstein, 2020). We identified shared mechanisms between speech production and comprehension (Fig. 1C, 1D) and mapped the temporal flow of information during spontaneous speech production and comprehension (Fig 2A, 2B). This study demonstrates that deep language models are a powerful computational tool to build comprehensive models of speech processing in the brain, without compromising the rich dynamic and contextual qualities inherent in everyday language.

References

1. Goldstein, A., Zada, Z., Buchnik, E., Schain, M., Price, A., Aubrey, B., . . . Cohen, A. (2022). Shared computational principles for language processing in humans and deep language models. Nature neuroscience, 25(3), 369-380.
2. Hasson, U., Nastase, S. A., & Goldstein, A. (2020). Direct fit to nature: An evolutionary perspective on biological and artificial neural networks. Neuron, 105(3), 416-434.
3. Hickok, G., & Poeppel, D. (2007). The cortical organization of speech processing. Nature reviews neuroscience, 8(5), 393-402.
4. Radford, A., Kim, J. W., Xu, T., Brockman, G., McLeavey, C., & Sutskever, I. (2022). Robust speech recognition via large-scale weak supervision. arXiv preprint arXiv:2212.04356.
5. Schrimpf, M., Blank, I. A., Tuckute, G., Kauf, C., Hosseini, E. A., Kanwisher, N., . . . Fedorenko, E. (2021). The neural architecture of language: Integrative modeling converges on predictive processing. Proceedings of the National Academy of Sciences, 118(45), e2105646118.

Poster No 1054

Distinct subgroup-level functional connectivity in stuttering and non-stuttering children

Soo-Eun Chang[1], Yanni Liu[1], Fiona Höbler[1], Hannah Becker[1], Valeria Caruso[1], Michael Angstadt[1], Adriene Beltz[1]

[1]University of Michigan, Ann Arbor, MI

Introduction: Developmental stuttering (DS) emerges during a heightened period of speech motor skill development, manifesting as blocks, prolongations, or repetitions on the initiation of speech sequences. DS has been modelled as a systems-level impairment[1,2], with structural and functional anomalies identified in the basal ganglia-thalamo-cortical (BGTC) circuits that support planning and execution of speech motor sequences[3,4,5]. Yet, past studies have predominantly focused on select brain areas or connections through research with adult participants[6,7], without leveraging analytical advances of network-based approaches. The aim of this study was to test hypothesized impairments in the speech network's motor and planning circuits among children who stutter, using the Group Iterative Multiple Model Estimation (GIMME)[8] that allows deriving of group- as well as individual-level connectivity measures. We hypothesized that functional connectivity patterns detected with GIMME would show distinct subgroup-level network differences between stuttering and control groups in the (i) planning loop (ii) motor loop (iii) broader network defined in an established neurocomputational model of speech production (Gradient Order Directions Into Velocities of Articulators, GODIVA)[9,10], encompassing feedback and feedforward structures.

Methods: We used confirmatory subgrouping (CS-GIMME)11,12, a recent extension of GIMME, to estimate subgroup-level connections for priori known groups (stuttering, control). Connectivity results are derived at the group as well as at individual level, which allows examining subject-specific heterogeneity in connectivity. CS-GIMME can detect paths between nodes ("edges") that are consistently present for individuals within stuttering and control groups, thus facilitating our interpretation of the heterogeneous connectivity maps and allowing for subgroup-specific inferences. Resting state fMRI (rsfMRI) data were acquired from 73 children who stutter (CWS) and 76 age- and gender-matched children who do not stutter (CNS) (mean age=72 ± 22 months, age range from 38-129 months, 34 CWS girls, 40 CNS girls). Stuttering severity (SSI) range was 2-37 (17.8±6.3) (very mild~very severe). Data were processed using standard methods in SPM12. Subjects were eligible to be included if they had at least 4 minutes of useable data (after motion censoring at FD>0.5mm) and a usable T1 image. Participant-specific time series (164 functional volumes) from 17 regions of interest (ROIs) were extracted. The ROIs and their locations were selected according to regions defined in the DIVA model (Tourville & Guenther, 2011). CS-GIMME was run using a threshold of 75% for group-level edges and 50% for subgroup-level edges.

Results: Group differences in network density were observed in the posterior inferior frontal sulcus (pIFS) within the Planning loop (Fig 1): 1) control group showed greater connectivity between the left pIFS and the caudate; 2) CWS showed greater connectivity of the left pIFS with the ventral later thalamus (VL) within the Motor Loop. Overall, there was a greater number of

connections within the planning loop structures for controls relative to CWS (Fig 2). No group differences were observed in network connectivity found for motor loop or among DIVA structures.

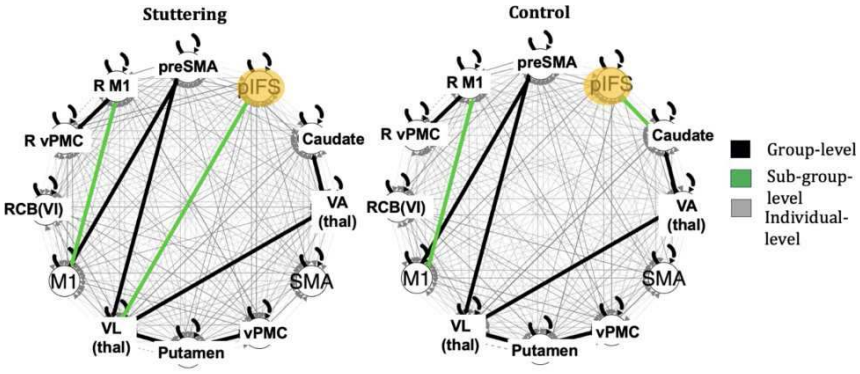

Figure 1. **Subgroup-specific connection increases differentiate stuttering children from controls.** The group level connections common across the two groups are shown in black, while subgroup-specific increased connections are shown in green. The stuttering group showed heightened connection between planning loop structure pIFS with motor loop structure ventral lateral thalamus (VL), while the control group showed heightened connections between pIFS with the caudate, both within the planning loop.

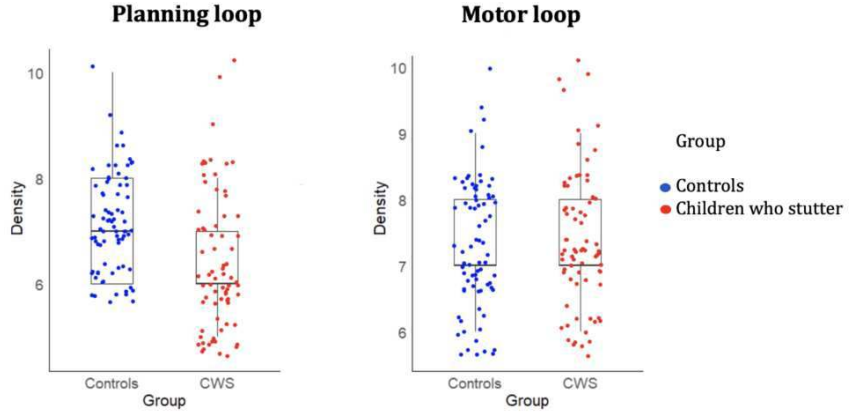

Figure 2. **Network density plots by loop (planning, motor) and group (children who stutter [CWS], controls).** Network density counts of connections occurring among ROIs within planning and motor loops were derived from each individual's connectivity maps. The density was significantly greater for controls relative to children who stutter in the connectivity among planning loop structures. The groups did not differ significantly in network density involving the motor loop structures.

Conclusions: These results show that CS-GIMME can derive functional connectivity results that differentiate stuttering from non-stuttering groups in pathways predicted by a neurocomputational model of speech processing (GODIVA, DIVA). The current findings suggest that stuttering may be associated with impaired planning of speech sounds in their sequential order. We plan to further apply CS-GIMME to examine persistent vs. recovered groups within the stuttering group. In future research, we will further apply GIMME to derive data-driven subgroups within the group of children who stutter to examine whether this method can help predict specific subtypes, or eventual persistence and recovery in developmental stuttering.

References

1. Beal, D.S. (2015), 'The trajectory of gray matter development in Broca's area is abnormal in people who stutter', Frontiers in human neuroscience, vol. 9, no. 89, pp. 1-9.
2. Bohland, J.W. (2010), 'Neural representations and mechanisms for the performance of simple speech sequences', Journal of cognitive neuroscience, vol. 22, no. 7, pp. 1504-1529.
3. Cai, S. (2014), 'Diffusion imaging of cerebral white matter in persons who stutter: evidence for network-level anomalies', Frontiers in human neuroscience, vol. 8, no. 54, pp. 1-18.
4. Chang, S.E. (2020), 'Involvement of the cortico-basal ganglia-thalamocortical loop in developmental stuttering', Frontiers in Psychology, vol. 10, no. 3088, pp. 1-15.
5. Chow, H.M. (2023), 'Brain developmental trajectories associated with childhood stuttering persistence and recovery', Developmental Cognitive Neuroscience, vol. 60, no. 101224, pp. 1-14.
6. Gates, K.M. (2012), 'Group search algorithm recovers effective connectivity maps for individuals in homogeneous and heterogeneous samples', NeuroImage, vol. 63, no. 1, pp. 310-319.
7. Gates, K.M. (2017), 'Unsupervised classification during time-series model building', Multivariate behavioral research, vol. 52, no. 2, pp. 129-148.

8. Guenther, F.H. (2016), 'Neural Control of Speech', Cambridge, MA: MIT Press.
9. Henry, T.R. (2019), 'Comparing directed functional connectivity between groups with confirmatory subgrouping GIMME', NeuroImage, vol. 188, pp. 642-653.
10. Lu, C. (2010), 'Altered effective connectivity and anomalous anatomy in the basal ganglia-thalamocortical circuit of stuttering speakers', Cortex, vol. 46, no. 1, pp. 49-67.
11. Masapollo, M. (2021), 'Behavioral and neural correlates of speech motor sequence learning in stuttering and neurotypical speakers: an fMRI investigation', Neurobiology of Language, vol. 2, no. 1, pp. 106-137.
12. Tourville, J.A. (2019), 'Functional parcellation of the speech production cortex', Journal of Speech, Language, and Hearing Research, vol. 62, no. 8S, pp. 3055-3070.
13. Tourville, J.A. (2011), "The DIVA model: A neural theory of speech acquisition and production', Language and cognitive processes, vol. 26, no. 7, pp. 952-981.

Poster No 1055

Internal production reveals the spatiotemporal neural dynamics of speech

Joan Orpella[1,2], Francesco Mantegna[1], M. Florencia Assaneo[3], David Poeppel[1,4]

[1]New York University, New York, NY, [2]Georgetown University, Washington D.C., DC, [3]Universidad Nacional Autónoma de México, Santiago de Queretaro, Mexico, [4]Ernst Strüngmann Institute, Frankfurt, Germany

Introduction: Speech production models converge on a sequence of necessary stages (e.g., phonological retrieval, phonetic encoding)[1,2]. Establishing the neural substrates for these stages has proven surprisingly challenging, primarily due to the correlational nature of most experiments. While recent ECoG studies[3,4] overcome this limitation by using machine-learning to decode speech from neural data, their spatial coverage remains limited. Here, we used MEG with its excellent temporal resolution and whole-brain coverage along with a decoding approach to track participants' sequence of speech representations over time and brain space. To avoid data artifacts from muscle activity during the preparation and execution of speech, we used internal speech, which closely mirrors overt speech[5,6].

Methods: 31 subjects participated; 22 (mean age=28.19(6.57)) were tested on syllables pa-ta-ka and 9 (mean age=23(7.94)) on ta-tu-ti. Participants either internally produced or passively viewed one of three visually presented syllables (Fig 1A). We estimated the onset of subjects' internal productions based on their productions in an overt version of the task. To determine whether/when each internally produced syllable can be decoded from the noninvasive neural data, we trained and tested a linear classifier at each millisecond for each of the possible pairwise syllable contrasts and for each participant/condition. The average time course of decoding performance for these contrasts per participant was subjected to a permutation test to determine the times of significant decoding (Fig 1B). To establish the neural sources of syllable decoding, we projected each participant's sensor data to source space and performed a decoding analysis for each source and pairwise syllable contrast, taking as input features the times corresponding to each identified peak (trough to trough; Fig 1B). The averages within participant of the pairwise syllable decoding results for each source were morphed to a standard source space and subjected to a permutation test to determine spatial clusters of significant syllable decoding for each peak (Fig 1C). We acquired electromyographic data from participants' upper lip and jaw to confirm that the MEG signals were not contaminated by micromovements.

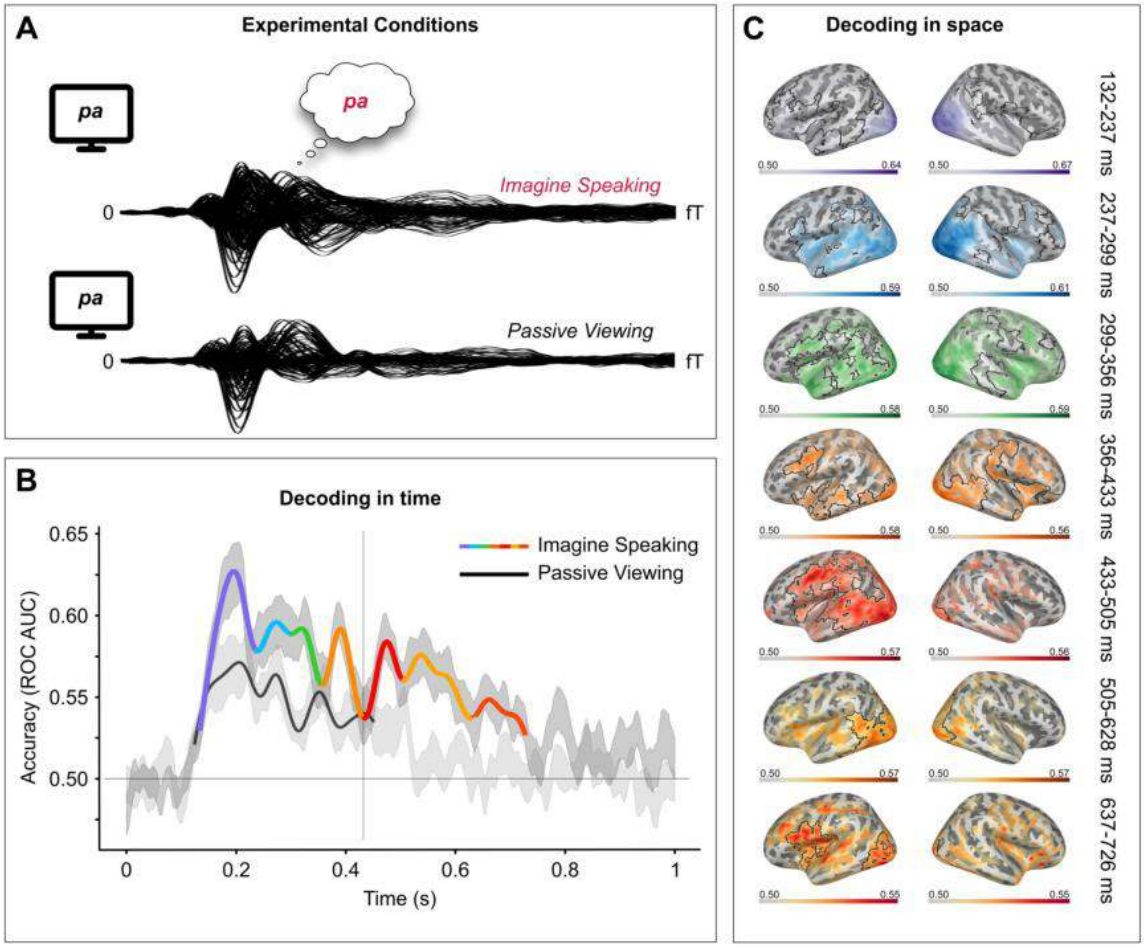

Figure. 1. Spatiotemporal dynamics of internal speech representations. A. Task and experimental conditions. Imagine Speaking: Participants internally produced one of three syllables (/pa/, /ta/, /ka/) in each trial as soon as it appeared on the screen (time 0). Passive Viewing: Participants passively viewed one of three syllables (/pa/, /ta/, /ka/) in each trial. We recorded MEG data of participants during 4 blocks of Imagine Speaking and 4 blocks of Passive Viewing (counterbalanced; total of 960 trials per condition). A representative participant's grand average MEG data (157 channels) is shown for each experimental condition. These data were decoded for each participant. B. Decoding syllables in time: The plot shows the decoding performance over the experimental trial using all MEG sensors and averaged across participants and pairwise contrasts (/pa/ vs. /ka/, /pa/ vs. /ta/, /ta/ vs. /ka/). Results are shown for the Imagine Speaking condition (solid multicolored line) and for the Passive Viewing condition (solid black line) at the times when decoding is statistically significant [one-sample cluster-based permutation test against chance across participants (N = 22; 10,000 permutations; two-tailed)]. ROC AUC = Receiver Operating Characteristic Area Under the Curve (chance level = 0.5). Grey shadings = standard error of the mean. The vertical dotted line at 432 ms indicates the median sound onset for all syllables produced by participants in an overt version of the same task. For the Imagine Speaking condition, we identified a series of decoding peaks in the decoding accuracy time series. Each peak is shown in a different color. C. Decoding syllables in brain space: Clusters indicate a significant contribution to syllable decoding of the corresponding neural sources at the times comprised by each of the peaks (trough to trough times) identified in the Imagine Speaking condition (panel B). Clusters are color-coded, each color corresponding to a different peak in panel B.

Results: Fig 1B shows that the identity of syllables –differing only by the onset stop consonant and internally planned/produced by participants– can be robustly recovered from the MEG data with high temporal resolution. The succession of decoding peaks suggests that a sequence of distinct neural representations underlies internal syllable production. This succession is markedly different from that obtained from passively viewing the syllables (Fig 1B). We sought to determine the neural sources of syllable decoding corresponding to the identified peaks. Fig 1C shows the resulting sequence of neural speech representations decoded from the planning and internal production of speech. The sequence, which includes robust decoding from left speech motor/auditory areas immediately preceding/following the expected syllable onset time (based on subjects' overt productions), adheres to current processing models. Data from the ta-tu-ti cohort validated these results and extended them by revealing a greater presence of auditory (vs motor) representations for this set.

Conclusions: Subtle phonemic contrasts can be recovered from the neural substrates identified by current models for each stage of the speech production process. These results resolve longstanding questions regarding the informational content of previously reported dynamic brain activity patterns for speech production. The data also provide direct evidence for the generation of precise sensory predictions during speech production, so far only inferred from speaking induced suppression[7,8] or responses to altered feedback[9,10] and supports the close parallels between core processes for internal and overt speech.

References
1. Levelt, W. J. M. (1989), "Speaking: From intention to articulation". The MIT Press.
2. Guenther, F. H. (2016), "Neural Control of Speech". The MIT Press.
3. Metzger, S. L. et al. (2023), "A high-performance neuroprosthesis for speech decoding and avatar control". Nature, vol. 620, pp. 1037–1046.
4. Wang, R. et al. (2023), "Distributed feedforward and feedback cortical processing supports human speech production". Proc. Natl. Acad. Sci., vol. 120, pp. 1–12.
5. Tian, X. & Poeppel, D. (2010), "Mental imagery of speech and movement implicates the dynamics of internal forward models". Front. Psychol., vol. 1, pp. 1–23.
6. Soroush, P. Z. et al. (2022), "The Nested Hierarchy of Overt, Mouthed, and Imagined Speech Activity Evident in Intracranial Recordings". Neuroimage, vol. 269, pp. 1–26.
7. Flinker, A. et al. (2010), "Single-trial speech suppression of auditory cortex activity in humans". J. Neurosci., vol. 30, pp. 16643–16650.
8. Numminen, J., Salmelin, R. & Hari, R. (1999), "Subject's own speech reduces reactivity of the human auditory cortex". Neurosci. Lett., vol. 265, pp. 119–122.
9. Houde, J. F. & Jordan, M. I. (1998), "Sensorimotor adaptation in speech production". Science, vol. 279, pp. 1213–1216.
10. Tremblay, S., Shiller, D. M. & Ostry, D. J. (2003), "Somatosensory basis of speech production". Nature, vol. 423, pp. 866–869.

Poster No 1056

Premotor-hippocampal connectivity and sense of agency during encoding predicts reliving of events

Nathalie Heidi Meyer[1], Baptiste Gauthier[1], Lucas Burget[1], Jevita Potheegadoo[1], Juliette Boscheron[1], Elizabeth Franc[1], Florian Lance[1], Olaf Blanke[1]

[1]EPFL, Geneva, Switzerland

Introduction: Autonoetic consciousness (ANC), the ability to re-experience a personal past event has been theorized to link episodic memory and self-consciousness in the act of remembering (Klein and Nichols, 2012; Tulving, 1985). Although the sensory and the self-conscious aspects of ANC have been investigated separately, multiple pieces of evidence point towards an association of self-consciousness and sensory information when modulating ANC. Bodily self-consciousness (BSC), defined as a unitary sense of self within the bodily boundaries, has been shown to arise from multisensory and sensorimotor perceptual mechanisms of specific bodily signals (Blanke et al., 2015), and has been argued to be the missing link joining sensorimotor and self-conscious context during encoding with later re-living of the encoded event and ANC (Bréchet et al., 2019). However, how BSC and its related subjective experience at encoding affect ANC remains unknown. In this study, we addressed this question by modulating sensorimotor context and sense of agency (SoA) of participants during the encoding of virtual scenes while simultaneously recording brain activity using fMRI.

Methods: We tested 73 young healthy right-handed participants, of which 24 participated to the experiment in the MR scanner during encoding. Participants encoded three different scenes in immersive virtual reality. Each scene was associated with a different BSC condition with a different level of visuomotor and perspectival congruency to modulate the SoA (1PP synchronous -SYNCH1PP, 1PP asynchronous – ASYNCH1PP, 3PP asynchronous – ASYNCH3PP). We assessed ANC one week later using a 28 items questionnaire. We applied a linear mixed model to investigate whether we could explain the ANC by the interaction between the experimental conditions and the SoA score. We then computed a generalized psychophysiological interaction analysis (gPPI;using the CONN toolbox v20b) to investigate whether the encoding functional connectivity between the left hippocampus and left dorsal premotor cortex (dPMC), two regions previously found to be sensitive to our BSC manipulation (Meyer et al., 2023), differ between conditions. Finally, we investigated whether ANC could be explained by the functional connectivity between left dPMC and left hippocampus and its interaction with SoA using a linear mixed model. To control that the effect was specific to our experimental condition, we applied the same analysis using the regions reversed on the right hemisphere (using ImCalc from SPM12).

Results: At the behavioral level we found that the SoA during encoding predicted ANC score at 1 week (significant interaction between SYNCH1PP and ASYNCH3PP with SoA; estimate = -0.15, t = -3, p = 0.003). Post-hoc analysis applied separately on SYNCH1PP and ASYNCH3PP revealed a significant correlation between SoA and the ANC score, but only with preserved-normal visuomotor and perspectival congruency (SYNCH1PP: estimate = 0.13, t = 2.05, p = 0.04, ASYNCH3PP: estimate = -0.06, t = -1.27, p = 0.21). Compatible with the behavioral results, we found that the functional connectivity between the left hippocampus and left dPMC during encoding significantly differed between the SYNCH1PP and the ASYNCH3PP condition (Figure 1B, estimate = -0.099, t = -2.47, p = 0.02). Finally, we found a significant interaction between SoA and the functional connectivity of the left hippocampus and dPMC when we applied it to explain ANC scores (estimate = 4.8, t = 2.39, p = 0.02). Posthoc analysis of the interaction revealed that the positive relationship between SoA and ANC only holds when the functional connectivity is strong. We found no significant relationship between SoA and ANC when applying the same models with the functional connectivity of the right dPMC and hippocampus (estimate = 0.31, t = 0.55, p = 0.58).

Conclusions: These results link the self in the present (BSC) with self in the past (ANC), through premotor-hippocampal functional connectivity at encoding.

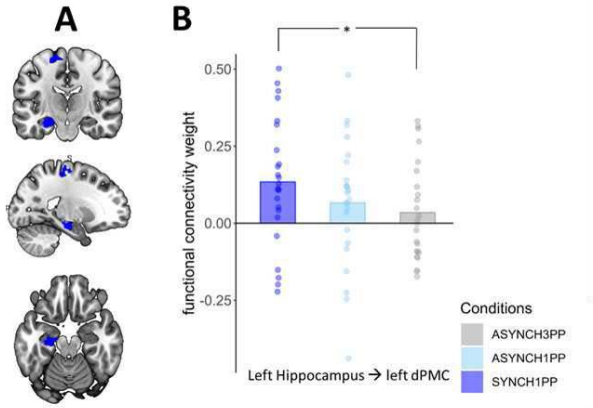

*Figure 1 : **A.** Apriori region of interest (left hippocampus and dorsal premotor cortex- dPMC) identified in previous study (Meyer& Gauthier et al., 2023). **B.** Functional connectivity weight between the left hippocampus and the left dPMC when applying a generalized psychophysiological interaction analysis (gPPI) on the experimental encoding condition.*

References

1. E. Tulving, Memory and consciousness. Canadian Psychology / Psychologie canadienne 26, 1–12 (1985)
2. S. B. Klein, S. Nichols, Memory and the Sense of Personal Identity. Mind 121, 677–702 (2012)
3. N. H. Meyer, B. Gauthier, S. Stampacchia, J. Boscheron, M. Babo Rebelo, J. Potheegadoo, B. Herbelin, F. Lance, V. Alvarez, E. Franc, F. Esposito, M. Morais Lacerda, O. Blanke, "Embodiment in episodic memory through premotor-hippocampal coupling" (preprint, 2023); https://doi.org/10.1101/2023.09.23.559108.

Poster No 1057

Common regularities between different memory types link motor network excitability to word learning

Alberto Failla[1], Martina Bracco[2], Edwin Robertson[1]

[1]Institute of Neuroscience and Psychology, Centre for Cognitive Neuroimaging, Glasgow, United Kingdom, [2]Sorbonne Université, Paris Brain Institute, Inserm, CNRS, APHP, Hôpital de la Pitié Salpêtrière, Paris, Ile de France

Introduction: A common regularity can structure different types of information (actions vs. words). These common features allow information to be shared between otherwise segregated memory systems (Robertson, 2022). We sought to understand how common regularities alter brain networks to allow information to be shared between different memory types (actions vs. words). Network excitability has been linked to memory processing, for example, it is critical in determining the allocation of memories to particular circuits (Cai et al., 2016, Rashid et al., 2016).

Methods: We measured motor network excitability by applying single pulses of transcranial magnetic stimulation to the right motor cortex, and measuring the amplitude of the elicited motor evoked potentials (with electromyography - EMG; Figure). Excitability was measured at baseline prior to the motor sequence learning task, throughout word-list learning (after each iteration of the list; t1 to t5), and at subsequent free recall (t6; Figure). Along with excitability, we also measured the performance on both memory tasks. Both tasks had a repeating serial structure (sequences) of either actions (skill learning) or words (word-list learning), each of 12 items. The motor sequence consisted of four different finger movements (1,2,3,4) and the word-list of four different semantic categories (transport, vegetable, furniture, clothing) with three words from each category (to give a 12-item word list). The movement sequence constrained the subsequent word-list through a simple mapping between the four elements within the motor sequence and the four semantic categories within the word-list (Figure). When this mapping was maintained the sequences with different content had a common abstract structure (same, n=25) whereas, when this mapping was violated, the sequences had different structures (different, n=25).

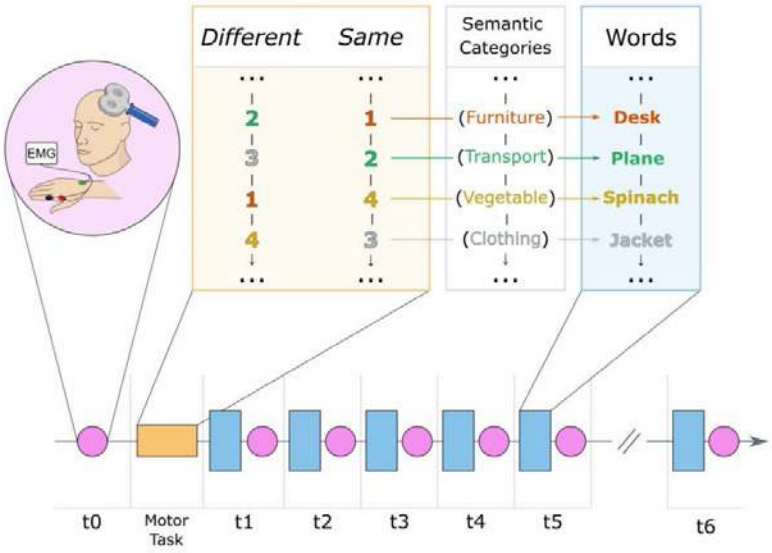

Figure 1, *Experimental Design.* Participants initially learnt a sequence of movements (orange bar), which either did (*same*) or did not (*different*) share the same structure with a word-list learning task (t1 to t5, blue bars). Over the five word-list task iterations, all participants were presented with the same list of words just before motor-network excitability was measured (pink circles). Finally, following the fifth iteration, participants had a free recall test (t6), and excitability was once again measured.

Results: We found that both serial word recall and excitability during word-list learning was significantly affected by the memory tasks having the same or different structures. The change in serial recall performance during word-list learning was greater when the memory tasks had the same rather than different structures (unpaired t-test with estimated marginal means: t2 to t5, $p<0.05$). This difference between the groups was maintained at the subsequent free recall (t6; same vs. different; unpaired t-test: t6, $t(49)= 2.91$, $p=0.005$). Similarly, motor network excitability during word-list learning was significantly greater when the memory tasks had the same rather than different serial structures (unpaired t-test with estimated marginal means: t1 to t5, $p<0.05$). Not only did excitability increase when the memory tasks had the same structure, it was significantly correlated with the enhanced serial recall during word-list learning (repeated measure correlation: $r=0.25$, $p=0.01$). By contrast, when the tasks had different structures there was no significant correlation between excitability and serial recall during word-list learning ($r=0.15$, $p=0.12$). Excitability was specifically linked to learning. We found no increase in excitability during the free recall of the word-list (same vs. different; unpaired t-test: $p=0.23$), and no correlation between the excitability and free recall (Spearmann correlation; Same: $r=-0.01$, $p=0.96$; Different: $r=-0.01$, $p=0.96$).

Conclusions: A common task structure caused an increase in motor network excitability, which was linked to enhanced serial recall. The network became embedded within the declarative learning of a list of words when it had previously experienced the same abstract serial regularity. This allowed previous experience of the serial regularity within the context of actions to enhance learning within a new context (words). These results provide insight into how the segregation between memory systems breaks down and supports the generalization of knowledge across different contexts (actions vs. words).

References

1. Cai, D. J., Aharoni, D., Shuman, T., Shobe, J., Biane, J., Song, W., Wei, B., Veshkini, M., La-Vu, M., Lou, J., Flores, S. E., Kim, I., Sano, Y., Zhou, M., Baumgaertel, K., Lavi, A., Kamata, M., Tuszynski, M., Mayford, M., … Silva, A. J. (2016). A shared neural ensemble links distinct contextual memories encoded close in time. Nature, 534(7605), 115–118. https://doi.org/10.1038/nature17955
2. Rashid, A. J., Yan, C., Mercaldo, V., Hsiang, H.-L., Park, S., Cole, C. J., De Cristofaro, A., Yu, J., Ramakrishnan, C., Yeun Lee, S., Deisseroth, K., Frankland, P. W., & Josselyn, S. A. (2016). Competition between engrams influences fear memory formation and recall (Vol. 353). https://www.science.org
3. Robertson, E. M. (2022). Leaky Memories. Trends in Cognitive Sciences, 1–249.

Poster No 1058

Hippocampal Morphology and Stress Levels in Medical and Non-Medical Students: Implications for Learn

Ashwag Alruwaili[1], Sumyah Alnajashi[1], Afnan Alwasedi[2], Sara Albraihi[2], Ross Keenan[3], Tracy Melzer[3], Mustafa Almuqbel[4]

[1]King Saud University, Riyadh, Ryiadh, [2]King Saud University, Riyadh, Riyadh, [3]New Zealand Brain Research Institute, Christchurch, Christchurch, [4]Pacific Radiology Group, Christchurch, Christchurch

Introduction: The presence of hippocampal atrophy has been consistently identified in studies involving stress imaging. Maintaining overall mental health is crucial for sustaining this ability. Even seemingly trivial factors such as apprehensive thoughts regarding potential threats or anxieties about the future have the potential to disrupt our well-being (WHO, 2004). In this study, we investigate the impact of academic stress on hippocampal volume. This study aimed to investigate the role of stress on academic students.

Methods: A cohort of 20 medical and 20 non-medical female students underwent assessment for stress and anxiety levels during the examination period using the Kessler Psychological Distress Questionnaire (K10). Following this assessment, magnetic resonance imaging (MRI) scans of the brain were conducted on our 3-Tesla (Siemens Spectra) MRI scanner (Iselin, NJ). For each participant, we acquired a three-dimensional T1-weighted MPRAGE dataset. The data were collected in sagittal plane with a FOV=256mm, voxel size = 1.0x1.0x1.0mm, TR=1900ms, TE=2.42ms, TI=900ms, rBW=220Hz, FA=90, and an acquisition time of 04:23 minutes. Hippocampal segmentation and volumetric quantification were assessed using the FreeSurfer software package. All participants' T1-weighted MR images were processed using the freely available FreeSurfer 7.1.0 (http://surfer.nmr.mgh.harvard.edu) standard cross-sectional processing pipeline. Following that, the dedicated FreeSurfer hippocampal subfields pipeline was employed on all data sets. Briefly, the algorithm for segmentation of individual sub-regions uses Bayesian inference based on observed image intensities and a probabilistic atlas built from a library of in vivo manual segmentations and ultra-high resolution (~0.1 mm isotropic) ex-vivo labelled MRI data. Details of these steps are described by Iglesias and colleagues (Lee et al. 2009, Iglesias et al. 2015, Brown et al. 2020). The hippocampal subfield segmentation module resulted in volumetric estimation of the hippocampal head, body, and tail for each hemisphere. Estimated total intracranial volume (eTIV) generated by FreeSurfer was used as an estimate for intracranial volume (ICV) in this study. All the processed data were visually inspected for artifacts; no manual editing was performed on the data. The estimated right and left volumes of the hippocampal head, body, and tail were used in the statistical analysis. Figure 1 demonstrates the hippocampal subfields segmentation in one of the study subjects. Demographic data and imaging metrics were subjected to rigorous statistical analysis using the R software°

Results: Our findings revealed a notable disparity in stress levels between medical and non-medical students, with the former experiencing significantly higher stress level. Contrary to expectations, medical students had larger hippocampal head volumes, with no significant differences in hippocampal body and tail volumes between the two groups. Discussion: Medical students' rich learning environment and cognitive demands may have contributed to larger hippocampal volumes, as head region plays a vital role in encoding information and building associations based on learning and memorization. The hippocampal head region has been associated with declarative memory, learning, and visual associations, which are highly relevant to medical students who constantly face novel information and body organ imagery. The lack of a significant correlation between hippocampal volume and stress may be due to a shorter duration of stress exposure, as chronic stress may require an extended period to induce structural changes.

Conclusions: This research underscores the potential role of learning over stress on brain morphology and, subsequently, the overall well-being of students. As a result, educators should consider implementing strategies to equip students with effective stress-coping mechanisms to mitigate the risk of enduring long-term and potentially irreversible consequences.

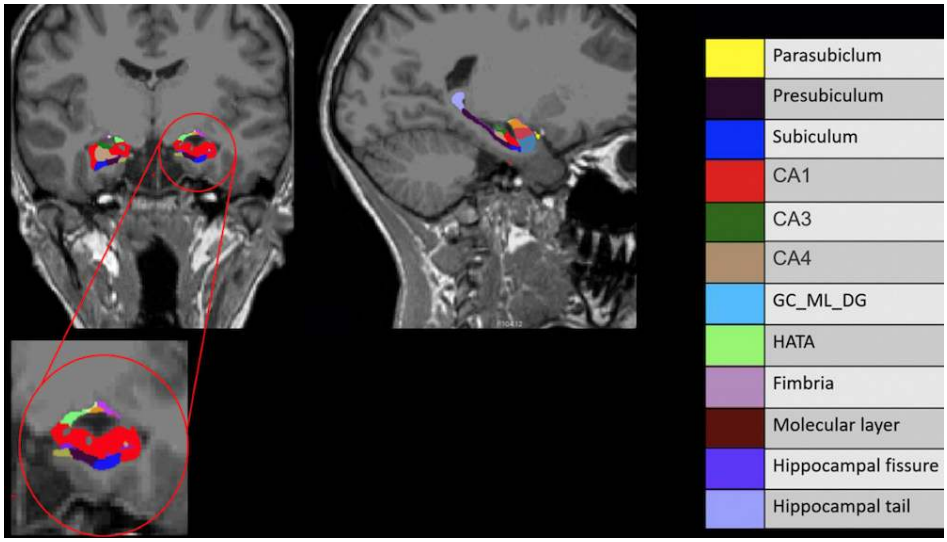

References

1. Brown, E. M., M. E. Pierce, D. C. Clark, B. R. Fischl, J. E. Iglesias, W. P. Milberg, R. E. McGlinchey and D. H. Salat (2020). "Test-retest reliability of FreeSurfer automated hippocampal subfield segmentation within and across scanners." Neuroimage 210: 116563.
2. Iglesias, J. E., J. C. Augustinack, K. Nguyen, C. M. Player, A. Player, M. Wright, N. Roy, M. P. Frosch, A. C. McKee, L. L. Wald, B. Fischl and K. Van Leemput (2015). "A computational atlas of the hippocampal formation using ex vivo, ultra-high resolution MRI: Application to adaptive segmentation of in vivo MRI." NeuroImage 115: 117-137.
3. Kessler, R. and D. Mroczek (1992). "An update of the development of mental health screening scales for the US national health interview study." Ann Arbor: University of Michigan, Survey Research Center of the Institute for Social Research: 31115-31118.
4. Lee, T., T. Jarome, S.-J. Li, J. J. Kim and F. J. Helmstetter (2009). "Chronic stress selectively reduces hippocampal volume in rats: a longitudinal magnetic resonance imaging study." Neuroreport 20(17): 1554-1558.
5. Reuter, M., Schmansky, N.J., Rosas, H.D., Fischl, B. 2012. Within-Subject Template Estimation for Unbiased Longitudinal Image Analysis. Neuroimage 61 (4), 1402-1418. http://reuter.mit.edu/papers/reuter-long12.pdf
6. WHO, W. H. O. (2004). The International Statistical Classification of Diseases and Health Related Problems World Health Organization.

Poster No 1059

10-Hz Flicker Boosts Early Consolidation of Visual Perceptual Learning via Augmented Glx/GABA Ratio

Xin-Yue Yang[1,2,3,4], Qing He[5], Chuyue Zhao[6,7], Zhentao Zuo[6,7,8], Fang Fang[1,2,3,4]

[1]School of Psychological and Cognitive Sciences and Beijing Key Laboratory of Behavior and Mental Health, Peking University, Beijing, China, [2]Key Laboratory of Machine Perception, Ministry of Education, Peking University, Beijing, China, [3]IDG/McGovern Institute for Brain Research, Peking University, Beijing, China, [4]Peking-Tsinghua Center for Life Sciences, Peking University, Beijing, China, [5]State Key Laboratory of Brain and Cognitive Science, Institute of Biophysics, Chinese Academy of Sciences, Beijing, China, [6]Institute of Biophysics, Chinese Academy of Sciences, Beijing, China, [7]University of Chinese Academy of Sciences, Sino-Danish College, Beijing, China, [8]Institute of Artificial Intelligence, Hefei Comprehensive National Science Center, Hefei, China

Introduction: Visual perceptual learning (VPL) refers to the phenomenon where certain aspects of vision obtain sustainable enhancement after extensive training, constituting an important form of neural plasticity in the visual system[1]. VPL consists of multiple stages with different neural substrates[2], among which the stage of early consolidation immediately after training, though documented to be active and plastic[3,4], remains largely elusive. Multiple means of intervention have been used to interfere with early consolidation (disruption[4], facilitation[5]). Repetitive visual stimulation (RVS), as a means of behavioral intervention, was found to evoke LTP-like activities when administrated at alpha (8-12 Hz) frequencies and LTD at 1 Hz[6,7]. Little is known as to how RVS acts on neuronal activation/inhibition and whether it can be harnessed to influence early consolidation of VPL in a directed manner. To probe the neural mechanisms underpinning early consolidation, we implemented RVS immediately after training on a parafoveal orientation discrimination task (ODT). We used 3T functional magnetic resonance imaging (fMRI) to map out the activated area and used 3T magnetic resonance spectroscopy (MRS) to measure the concentrations of excitatory neurotransmitter glutamate (Glx: glutamate and glutamine) and inhibitory neurotransmitter γ-aminobutyric acid (GABA) in this area during VPL.

Methods: We conducted a between-subject, single-blind study where 30 healthy volunteers with normal or corrected-to-normal vision were allocated to a 10-Hz (H), 1-Hz (L), or non-frequency (S) flicker group and went over 10 blocks of ODT training

(session 1) and 25 minutes of RVS, took a break of 4 hours, and then finished 6 blocks of ODT post-test (session 2). In ODT, two embedded-in-noise gabor patterns with different orientations appeared in succession in the peripheral. Participants answered whether the rotation between gabors was clockwise or counter-clockwise by pressing keys placed under index fingers. In RVS, a sinusoidal grating was flashed in the same location as the gabors at the frequency of each group. Before sessions 1 and 2, we presented a localizer and acquired fMRI data to determine the activation locale corresponding to the gabor location, based on which we defined the field of view (2×2.5×2.5 cm3) in MRS. MRS was acquired using the MEGA PRESS sequence[8] throughout sessions 1 and 2. Data were analyzed using R, a customized Gannet[9] toolbox, and SPSS 24.

Results: Repeated measures ANOVA of behavioral results showed that group and session had significant interaction ($F_{interaction}(2,26) = 6.364$, $p = 0.006$). 10-Hz flicker in the RVS session resulted in improved orientation discrimination in the post-test, while 1-Hz RVS resulted in detriments to task performance (simple main effect of session with Bonferroni adjustment: $p_H = 0.009$, $p_L = 0.034$, $p_S = 0.936$. Fig. 1). We subsequently analyzed the E/I ratio, calculated as Glx/GABA, using linear mixed effect (LME) models. E/I decreased along VPL training ($F_{batch}(4,51) = 0.322$, $p = 0.024$), indicating that the excitation-inhibition balance shifted to the inhibition side with training participation. Lastly, we found that E/I ratio increased after 10-Hz but not 1-Hz RVS or S-RVS (simple main effect of session: $p_H = 0.022$, $p_L = 0.426$, $p_S = 0.893$. Fig. 2).

Conclusions: Training-involved neural circuits and newly founded/strengthened neural connections remain plastic for at least 25 minutes after initial encoding in VPL training. The plastic stage of early consolidation opens the opportunity for intervention. 10-Hz RVS upscaled excitatory activities in the task-recruited areas and facilitated early consolidation, while 1-Hz RVS disrupted consolidation. At last, training alone shifted the E/I balance in the inhibitory direction, possibly through sensory adaptation.

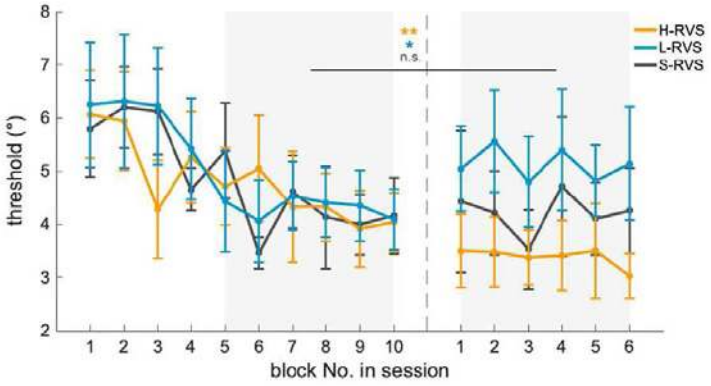

Figure 1. Learning curves of VPL training and post-test. Thresholds of orientation discrimination were measured using Quest. Data from the last six blocks of training and the six blocks of post-test (shadowed areas) were used in statistical analysis. Orange, blue, and black lines denote the H, L, and S groups respectively. Error bar is MSE. ** $p < 0.01$, * $p < 0.05$.

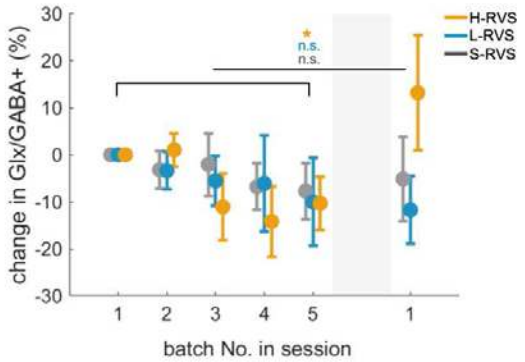

Figure 2. Dynamics of E/I balance in training and post-test. MRS data from 10 training blocks were batch-analyzed with sliding windows of the length of 6 blocks. The training session consists of 5 batches and the post-test 1. Each participant's ratios of Glx/GABA were normalized to the first batch. E/I ratio declined during training. Only the H group has increased E/I ratio in the post-test. Shaded area denotes the time interval between sessions 1 and 2 (i.e., the RVS session and the 4-h break). Error bar is MSE. * $p < 0.05$.

References
1. Sasaki, Y., J. E. Nanez and T. Watanabe (2010). "Advances in visual perceptual learning and plasticity." Nature Reviews Neuroscience 11(1): 53-60.
2. Censor, N., H. Harris and D. Sagi (2016). "A dissociation between consolidated perceptual learning and sensory adaptation in vision." Scientific Reports 6(1): 1-5.
3. Vilsten, J. and M. Mundy (2014). "Imaging early consolidation of perceptual learning with face stimuli during rest." Brain and Cognition 85: 170-179.
4. Seitz, A. R., N. Yamagishi, B. Werner, N. Goda, M. Kawato and T. Watanabe (2005). "Task-specific disruption of perceptual learning." Proceedings of the National Academy of Sciences 102(41): 14895-14900.
5. Yang, X.-Y., Q. He and F. Fang (2022). "Transcranial direct current stimulation over the visual cortex facilitates awake consolidation of visual perceptual learning." Brain Stimulation: Basic, Translational, and Clinical Research in Neuromodulation 15(2): 380-382.
6. Hamilton, H. K. and D. H. Mathalon (2023). "Probing long-term potentiation-like visual cortical plasticity in humans using repeated visual stimulation: effects on visual evoked potentials." Neuropsychopharmacology 48(1): 217-218.
7. Marzoll, A., T. Saygi and H. R. Dinse (2018). "The effect of LTP-and LTD-like visual stimulation on modulation of human orientation discrimination." Scientific Reports 8(1): 1-12.
8. Tremblay, S., V. Beaulé, S. Proulx, L. P. Lafleur, J. Doyon, M. Marjańska and H. Théoret (2014). "The use of magnetic resonance spectroscopy as a tool for the measurement of bi-hemispheric transcranial electric stimulation effects on primary motor cortex metabolism." J Vis Exp(93): e51631.
9. Edden, R. A., N. A. Puts, A. D. Harris, P. B. Barker and C. J. Evans (2014). "Gannet: A batch-processing tool for the quantitative analysis of gamma-aminobutyric acid–edited MR spectroscopy spectra." J Magn Reson Imaging 40(6): 1445-1452.

Poster No 1060

Hippocampal Theta-based Alarm Enhances Associative Memory: Human intracranial EEG Study

Seong Jin Lee[1], Chun Kee Chung[2]

[1]Seoul National University, Seoul, Korea, Republic of, [2]Seoul National University Hospital, Seoul, Korea, Republic of

Introduction: This study focuses on the role of hippocampal theta oscillation in memory formation, particularly in associative memory encoding. We use real-time monitoring of hippocampal activity through intracranial EEG (iEEG) in pharmaco-resistant epilepsy patients with hippocampal depth electrodes. Employing neurofeedback with audio signals, the study aims to investigate the impact of modulating hippocampal theta power in real-time on associative memory performance. The hypothesis is that a decrease in hippocampal theta power during encoding may lead to decreased memory performance, and preventing this decrease could enhance memory performance.

Methods: This study involved 7 patients with pharmaco-resistant epilepsy who underwent intracranial electrode implantation to identify the seizure onset zone, with all patients having hippocampal depth electrodes inserted. The experimental session included Practice Encoding and Retrieval, Encoding, Distraction, and Retrieval blocks. In the Encoding block, participants faced No alarm, Random alarm, and Theta-based alarm conditions, tasked with encoding 20 word-pairs of Korean nouns in each. Real-time monitoring of the hippocampal target electrode's theta power determined alarm conditions. The Distraction block involved solving 12 math problems, and in the Retrieval block, participants responded to 80 word-pairs (including 60 from Encoding: 20 intact, 20 rearranged, 20 new). The experiment comprised two sessions, varying the order of conditions between sessions. No word-pair was presented more than once.

Results: This study analyzed band power during a 3-second encoding period, finding significant differences in Theta, Alpha, and Gamma bands between successful and failed memory trials across all conditions ($p < 0.05$). Notably, significant differences were observed only in the No alarm condition, emphasizing the importance of hippocampal theta oscillations in successful encoding. When examining the impact of alarms on encoding, band power during the 1.8-second interval post-alarm revealed significant differences in mean theta power between successful and failed trials for all conditions. Alarms were triggered when average theta power during an 800ms interval fell below a threshold, demonstrating significant differences in Theta and Beta band power for all conditions. Using theta band power for alarm triggering significantly enhanced memory accuracy, particularly in the Theta-based alarm condition compared to No alarm and Random alarm conditions ($p < 0.05$). These findings robustly support the hypothesis that alarms based on hippocampal theta power lead to improved memory performance.

Conclusions: This study introduces a groundbreaking use of intracranial electroencephalography (iEEG) to target the human hippocampus and enhance real-time hippocampal theta power for the purpose of improving memory performance. Unlike previous neurofeedback studies primarily relying on non-invasive methods like EEG, this study presents novel real-time neurofeedback specifically based on hippocampal theta power. We employed the Hjorth activity method to compute hippocampal theta power in real-time, delivering alarms in case of a decrease, with the goal of improving memory performance. The study confirmed the hypothesis by showing that hippocampal theta power was not decreased in response

to theta-based alarms compared to no alarm or random alarm conditions. Simultaneously, associative memory has been shown to improve. This novel approach is expected to significantly contribute to our understanding and improvement of human memory mechanisms, offering potential strategies for preventing memory-related neurological and mental health disorders.

References

1. Kota, S., M.D. Rugg, and B.C. Lega, Hippocampal theta oscillations support successful associative memory formation. Journal of Neuroscience, 2020. 40(49): p. 9507-9518.
2. Addante, R.J., et al., Prestimulus theta activity predicts correct source memory retrieval. Proceedings of the National Academy of Sciences, 2011. 108(26): p. 10702-10707.
3. Jun, S., J.S. Kim, and C.K. Chung, Direct stimulation of human hippocampus during verbal associative encoding enhances subsequent memory recollection. Frontiers in human neuroscience, 2019. 13: p. 23.
4. Lin, J.J., et al., Theta band power increases in the posterior hippocampus predict successful episodic memory encoding in humans. Hippocampus, 2017. 27(10): p. 1040-1053.
5. Wang, J.-R. and S. Hsieh, Neurofeedback training improves attention and working memory performance. Clinical Neurophysiology, 2013. 124(12): p. 2406-2420.
6. Nan, W., et al., Individual alpha neurofeedback training effect on short term memory. International journal of psychophysiology, 2012. 86(1): p. 83-87.
7. Hsueh, J.J., et al., Neurofeedback training of EEG alpha rhythm enhances episodic and working memory. Human brain mapping, 2016. 37(7): p. 2662-2675.
8. Escolano, C., M. Aguilar, and J. Minguez. EEG-based upper alpha neurofeedback training improves working memory performance. in 2011 annual international conference of the IEEE engineering in medicine and biology society. 2011. IEEE.
9. Friedman, D. and R. Johnson Jr, Event-related potential (ERP) studies of memory encoding and retrieval: A selective review. Microscopy research and technique, 2000. 51(1): p. 6-28.
10. Koizumi, K., et al., Paving the Way for Memory Enhancement: Development and Examination of a Neurofeedback System Targeting the Medial Temporal Lobe. 2023.
11. Khader, P.H., et al., Theta and alpha oscillations during working-memory maintenance predict successful long-term memory encoding. Neuroscience letters, 2010. 468(3): p. 339-343.
12. Jun, S., J.S. Kim, and C.K. Chung, Prediction of successful memory encoding based on lateral temporal cortical gamma power. Frontiers in Neuroscience, 2021. 15: p. 517316.
13. Hjorth, B., EEG analysis based on time domain properties. Electroencephalography and clinical neurophysiology, 1970. 29(3): p. 306-310.
14. Oh, S.-H., Y.-R. Lee, and H.-N. Kim, A novel EEG feature extraction method using Hjorth parameter. International Journal of Electronics and Electrical Engineering, 2014. 2(2): p. 106-110

Poster No 1061

Role of M1 in schema-mediated motor memory consolidation assessed with fMRI and disruptive TMS

Serena Reverberi[1], Nina Dolfen[2], Mareike Gann[3], Koen Cuypers[4], Bradley King[5], Genevieve Albouy[1]

[1]Department of Movement Sciences, Movement Control and Neuroplasticity Research Group, KU Leuven, Leuven, Belgium, [2]Department of Psychology, Columbia University, New York, NY, [3]Department of Neurophysiology and Pathophysiology, University Medical Center Hamburg-Eppendorf, Hamburg, Germany, [4]Neurologic Rehabilitation research group, Hasselt University, Diepenbeek, Limburg, [5]Department of Health and Kinesiology, College of Health, University of Utah, Salt Lake City, UT

Introduction: New information is rapidly learned when it is compatible with previous knowledge[1-3]: this memory effect, termed the "schema effect", has been widely studied in the declarative memory domain, and recently demonstrated in the motor memory domain[4]. However, its underlying neural substrates remain unknown. In this study, we first investigated the neural substrates of schema-mediated motor memory consolidation with fMRI (Experiment 1, E1); then, we aimed to provide causal evidence for the involvement of the identified substrates in this process using disruptive TMS (Experiment 2, E2). Given the critical role of striatal-cortical networks in motor memory[5], we hypothesized that these regions would be involved in schema-mediated motor memory consolidation, and that their disruption via TMS would affect the integration of new motor information into available motor schema.

Methods: E1 - 60 young healthy participants performed 2 experimental sessions, approximately 24 hours apart. During Session 1 (S1), all participants learned a bimanual, eight-element motor sequence through repeated practice. During Session 2 (S2), participants learned a novel sequence whose structure (i.e., schema) was either highly compatible (COMP group) or highly incompatible (INCOMP) with that learned in S1 (see Fig.1). Eight runs of fMRI data were collected during S2 task practice (TR=2s, TE=30ms, voxel size= 2.5x2.5x2.5mm; Philips Achieva 3T MR scanner) and processed with SPM12. Brain activity related to task practice was extracted and contrasted between experimental groups using two-sample t-tests. E2 – 48 young healthy participants performed 2 experimental sessions, approximately 24 hours apart. The task was identical to that of E1,

but during S2 all participants performed the compatible (COMP) sequence. Prior to task performance in S2, disruptive TMS (COMP STIM group) or sham stimulation (COMP SHAM group) was applied to the left primary motor cortex (M1), as identified in E1. Disruptive TMS was performed using continuous theta-burst stimulation consisting of 3 pulses at 50 Hz repeated every 200ms for 40s, delivered at an intensity of 80% of the resting motor threshold. Motor-evoked potentials (MEPs) were collected from the right first dorsal interosseous muscle prior to and post-task learning in S1, and prior to and post-TMS in S2.

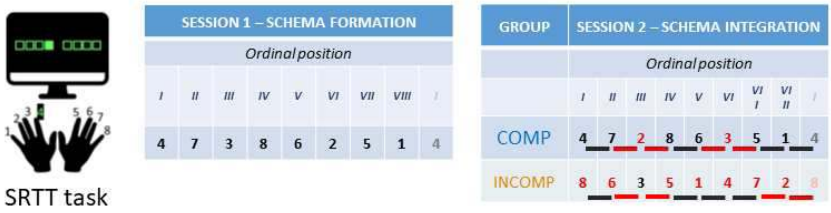

***Figure 1**: Task and schema manipulation. Participants are instructed to press the key shown on-screen with the corresponding finger as fast as possible. All participants learn the same sequence in Session 1 (S1). In Session 2 (S2), they can learn a highly compatible or incompatible sequence. Ordinal position columns provide the serial order (I to VIII) of the keys/fingers to be pressed in the sequence (1 to 8: left to right little finger). Both the compatible and incompatible sequences contain identical movement transitions and differ exclusively based on their starting point and thus their ordinal compatibility with S1 sequence. Keys highlighted in red are presented in a new ordinal position in S2 compared with S1. Moreover, sequences in S2 contain 4 movement transitions that were already learned as part of S1 sequence (underlined in black) and 4 transitions that are novel to S2 sequence (underlined in red), allowing us to investigate the effects of schema-compatibility on the retention of previously learned transitions as well as the integration of novel transitions into memory.*
In Experiment 1, in S2 half of participants performed the compatible sequence (COMP group) and the other half the incompatible (INCOMP).
In Experiment 2, in S2 all participants performed the compatible sequence. Half of participants received disruptive TMS prior to performance (COMP STIM group), and the other half received sham stimulation (COMP SHAM group).

Results: E1 - The COMP group displayed enhanced performance during S2 compared to the INCOMP group (i.e. lower response time during pre-scan test; group effect p=0.03, Fig. 2A) suggesting a beneficial effect of schema compatibility on overall performance. FMRI analysis showed that this effect was supported by greater activity in the left M1 in the COMP – as compared to the INCOMP – group during task practice (Fig. 2B). E2 – Performance of the COMP STIM and COMP SHAM groups did not differ in either S1 or S2 (see Fig. 2C), suggesting that TMS did not disrupt memory integration at the group level. In S1, we detected a significant decrease in corticospinal excitability post explicit SRTT learning across both groups (p=0.02), as in previous research6. Within the COMP STIM group, although no overall significant MEP suppression was detected post-TMS, greater MEP suppression significantly correlated with decreased accuracy at S2 training (r2=0.2, p=0.03, Fig. 2D). In the COMP STIM group, greater MEP suppression in S1 was also correlated with greater suppression in S2 (r2=0.25, p=0.01) and with decreased accuracy at S2 training for learned movement transitions (r2=0.16, p=0.05).

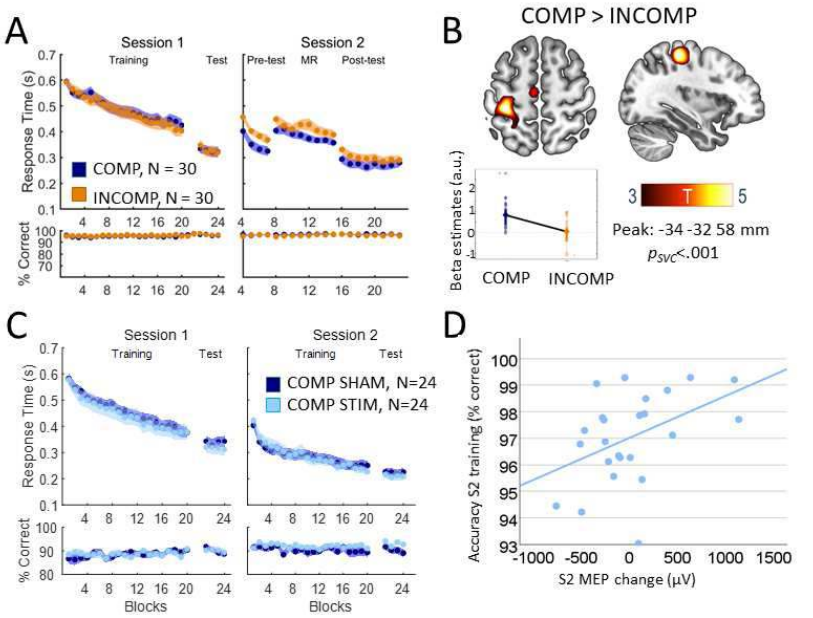

***Figure 2**: **A.** Experiment 1: Response time and Accuracy per group, per Session. S1 is divided into training and test runs. S2 consists of 8 runs of task performed in the MR scanner flanked by pre- and post-tests performed outside the scanner. **B.** Experiment 1: Regions of significantly higher neural activity in COMP versus INCOMP group, for the contrast Practice > Rest. **C.** Experiment 2: Response time and Accuracy per group, per Session, divided into training and test runs. **D.** Experiment 2: Correlation of S2 MEP change with Accuracy at S2 training (fit line: linear) within the COMP STIM group.*

Conclusions: Overall, our results suggest that the left primary motor cortex supports schema-mediated motor memory consolidation. The data show that the greater the TMS-induced decrease in cortico-spinal excitability, the greater the decrease in movement accuracy during schema-compatible practice. Our findings therefore provide novel insights into the role of M1 in schema-mediated integration of new movements into memory.

References

1. Tse, D. (2007). Schemas and memory consolidation. Science, 316(5821), 76-82.
2. Tse, D. (2011). Schema-dependent gene activation and memory encoding in neocortex. Science, 333(6044), 891-895.
3. Lewis, P. A. (2011). Overlapping memory replay during sleep builds cognitive schemata. Trends in cognitive sciences, 15(8), 343-351.
4. King, B. R. (2019). Schema and motor-memory consolidation. Psychological science, 30(7), 963-978.
5. Albouy, G. (2015). Maintaining vs. enhancing motor sequence memories: respective roles of striatal and hippocampal systems. Neuroimage, 108, 423-434.
6. Tunovic, S., Press, D. Z., & Robertson, E. M. (2014). A physiological signal that prevents motor skill improvements during consolidation. Journal of neuroscience, 34(15), 5302-5310.

Poster No 1062

Passive Spatial Learning in Humans: Neural Alignment during Naturalistic Navigation

Xinyu Liang[1], Joern Alexander Quent[1], Liangyue Song[1], Yueting Su[1], Deniz Vatansever[1]

[1]Institute of Science and Technology for Brain-inspired Intelligence (ISTBI), Fudan University, Shanghai, China

Introduction: Learning of spatial environments plays a vital role in the survival of both animal and human species. Emerging evidence has highlighted a “navigational neural network” in supporting the encoding and internal representation of a cognitive map of our environments during active navigation[1]. However, the contribution of this network to passive encoding (i.e. observer effect) of spatial environments remains unclear[2]. Recent work has shown that passive learning from lecture recordings could evoke shared neural representations across participants, with greater alignment to experts’ responses linked to better learning outcomes[3]. Here, we conducted a virtual reality experiment using 3T fMRI with a naturalistic navigation video to investigate the neural underpinnings of passive spatial learning.

Methods: A total of 48 participants (mean age = 23.69 years, SD = 2.15, F/M ratio = 30/18) underwent 3T fMRI scanning (TR = 0.8 s, TE = 37 ms, 2 mm iso voxels). Participants were asked to learn the locations of 6 different objects while watching a video of an agent navigating within a circular virtual arena (Fig. 1a). Subsequently, participants performed an Object Location Memory (OLM) task within the same arena, in which they actively searched and retrieved the hidden objects. We assessed participants’ passive learning outcomes by analyzing their performance during the initial presentation of all objects, focusing specifically on the accuracy and placement error (Fig. 1b). Based on performance, we defined a fast-learner group comprising of four participants with high accuracy (≥3 trials) and low placement error (<30 vm), categorizing the remaining participants as part of the slow-learner group. The HCP style fMRI data was minimally preprocessed using HCP pipelines (Qunex)[4]. To calculate the shared neural activity patterns across slow and fast-learners during video watching, we employed an inter-subject pattern correlation framework[3,5]. In total, 360 cortical regions from multi-model parcellation[6] and 16 subcortical regions from Desikan-Killiany atlas were included. For each region, we derived a neural alignment score to fast-learners by correlating the shared response model (SRM) pattern in each slow-learner with the mean pattern across fast-learners in each time point, and then temporally averaged within each individual (Fig. 1c). To test if the neural alignment could predict learning outcomes, we calculated correlation between alignment scores and average placement error. Statistical significance was assessed using a one-side non-parametric permutation testing.

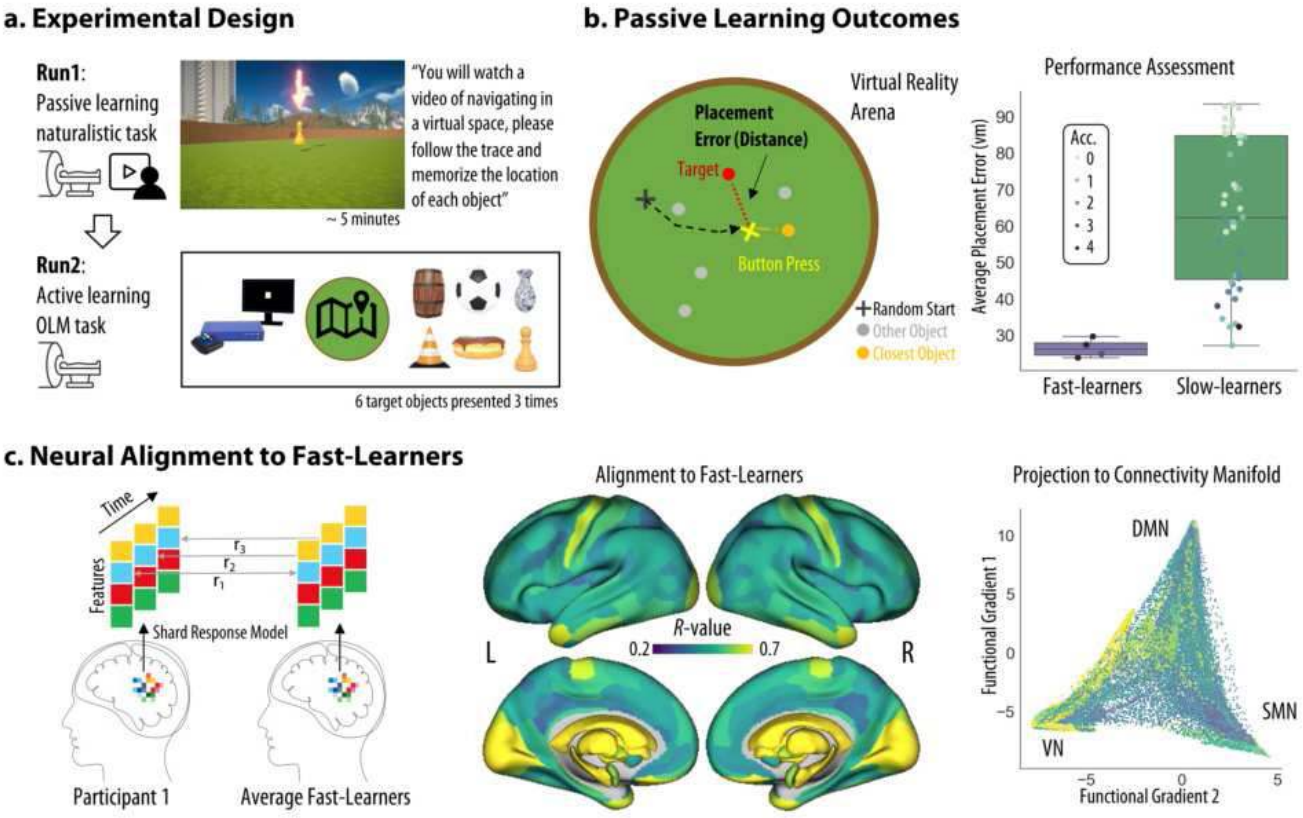

Figure 1. Neural alignment during passive naturalistic navigation. a) Participants passively learned the locations of 6 different objects through a naturalistic navigation task. Subsequently, they actively searched and retrieved the hidden objects within the same circular arena during the object location memory (OLM) task. **b)** The initial trials of all object from OLM task were utilized for assessing participants learning outcomes, including the accuracy determined by counting if the closest object to retrieved location was correct and the placement error measured as Euclidean distance. We defined the fast and slow-learner group according to their learning outcomes. The distribution of average placement error within each group was shown in boxplot. **c)** We derived regional alignment scores to fast-learners by correlating the spatial pattern from shared response model (SRM, 30 features) in each slow-learner with the mean pattern across fast-learners in each time point, then they were temporally averaged. Group-averaged alignment scores were shown across whole cerebrum. The alignment scores were projected to the connectivity gradient space from Margulies et, al. 2016. (DMN: default mode network, VN: visual network; SMN: somatomotor network)

Results: The neural alignment results revealed shared neural activity patterns centered within the occipital visual, motor, medial orbital frontal and anterior temporal cortices as well as subcortical regions such as the bilateral hippocampus and thalamus (Fig. 1c). When projected onto the cortical connectivity gradient space[7], the effects highlighted the distribution of the neural alignment scores both at the intermediate zones and at the endpoints of the unimodal-to-transmodal gradient. The alignment scores from the bilateral visual pathway, visual motion area, attention and navigation related regions could significantly predict average placement error, indicating better performance (FDRp < .05) (Fig. 2a). Moreover, neural alignment in the hippocampus, amygdala, and other cortical regions involved in cognitive control and navigation also displayed association with improved learning outcomes.

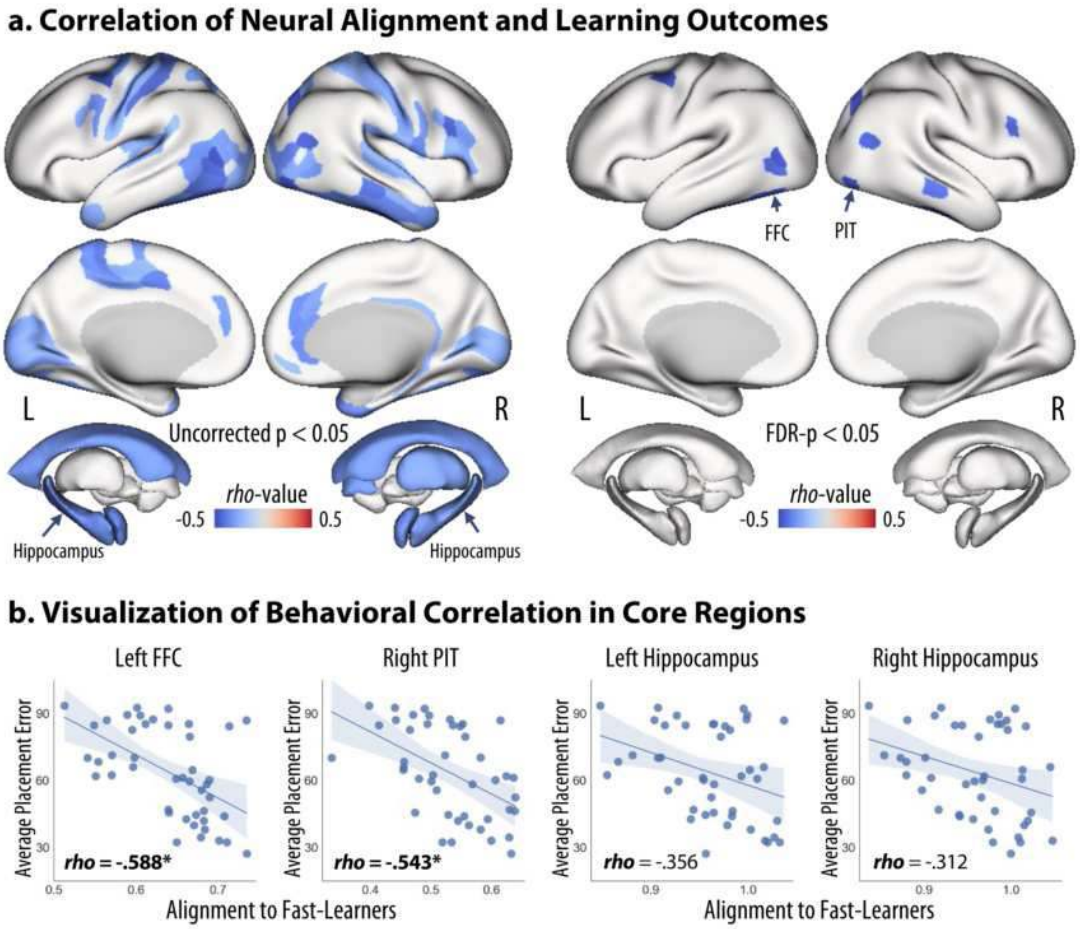

Figure 2. Neural alignment to fast-learners during naturalistic navigation task predicts subsequent learning outcomes. a) The correlation analyses revealed neural alignment within the visual pathway, attention and control regions as well as navigation network regions are negatively correlation with the average placement error (one-sided permutation test with 10,000 times, uncorrected $p < .05$). After FDR correction, the significant regions include FFC, MST, TF, FEF, and FST in left hemispheres, and PIT, TPOJ3, TF, IPS1, TE1m, and IFJa in right hemisphere. **b)** We demonstrated the scatterplot between alignment score and learning outcomes for left FFC, right PIT, and bilateral hippocampus. (FFC: fusiform face cortex; MST: medial superior temporal area; FEF: Frontal Eye Fields; FST: fundus of superior temporal sulcus; PIT: posterior inferior temporal cortex; TPOJ3: temporo-parieto-occipital junction area 3; IPS1: intraparietal sulcus area 1; TE1m: middle of temporal area 1; and IFJa: anterior of inferior frontal gyrus; * FDR-corrected $p < .05$)

Conclusions: Our results revealed that neural alignment to fast-learners within the hippocampus and visual regions during passive spatial learning could predict subsequent memory performance. Collectively, our findings not only highlight the potential value of using naturalistic navigation in investigating spatial learning and memory, but also provide vital evidence for the neural mechanisms underlying passive learning of spatial environments.

References

1. Epstein, R. A., Patai, E. Z., Julian, J. B. & Spiers, H. J. The cognitive map in humans: spatial navigation and beyond. Nat Neurosci 20, 1504–1513 (2017).
2. Chrastil, E. R. & Warren, W. H. Active and passive contributions to spatial learning. Psychon Bull Rev 19, 1–23 (2012).
3. Meshulam, M. et al. Neural alignment predicts learning outcomes in students taking an introduction to computer science course. Nat Commun 12, 1922 (2021).
4. Ji, J. L. et al. QuNex—An integrative platform for reproducible neuroimaging analytics. Frontiers in Neuroinformatics 17, (2023).
5. Chen, J. et al. Shared memories reveal shared structure in neural activity across individuals. Nat Neurosci 20, 115–125 (2017).
6. Glasser, M. F. et al. A multi-modal parcellation of human cerebral cortex. Nature 536, 171–178 (2016).
7. Margulies, D. S. et al. Situating the default-mode network along a principal gradient of macroscale cortical organization. Proc Natl Acad Sci USA 113, 12574–12579 (2016).

Poster No 1063

Decoding visual predictions in stimulus sequences: concurrent EEG/fMRI study

Ryszard Auksztulewicz[1]

[1]*Freie Universität Berlin, Berlin, Berlin*

Introduction: Mounting evidence suggests that neural processing of the present (perception) is informed by the past (memory) and aimed at the future (prediction). This notion has been formalised in the predictive processing framework [Friston, 2010]. Canonical models posit that predictions are grounded in memories [Baldeweg, 2006], and evidence from animal models suggests that mnemonic and predictive representations co-occur in the sensory neocortex [Cappotto et al., 2022]. However, recent studies in humans suggest that predictive processing may actually interfere with memory formation, and that the same neural structures may switch from encoding prediction errors to predictions at different stages of memory formation [Aitken & Kok, 2022]. Together with colleagues, we have formulated a hypothesis that memory and prediction are simultaneously implemented via distinctive interactions between sensory neocortex and the hippocampus [Barron et al., 2020]. This study is an attempt to replicate and extend our previous findings in animal models [Cappotto et al., 2022], where sensory memory traces could be decoded from sensory (auditory) cortical activity. Crucially, we could simultaneously decode sensory predictions related to upcoming stimuli. Here, we have translated the study from anaesthetised rodents to awake human volunteers; from the auditory modality to the visual modality; and from direct electrophysiological recordings to simultaneous EEG/fMRI. The aim of the study was to test whether we can decode predictions based on EEG and fMRI recordings in healthy human volunteers, and whether fMRI-based prediction decoding relies on the multivariate activity patterns in the sensory neocortex and/or the hippocampus.

Methods: N=24 healthy human volunteers were exposed to visual sequences comprising repeated triplets of images (Faces, Houses, Tools). A subset of 10% images was replaced with a visual "impulse" stimulus (concentric grating), aimed at reactivating memory/prediction traces for subsequent decoding [Stokes, 2015]. As a control condition, we presented the same stimuli in a random order (Figure panel A). While participants were exposed to sequences, their brain activity was recorded using simultaneous EEG/fMRI. In the analysis, first we used multivariate decoding techniques based on cross-validated Mahalanobis distance and representational similarity analysis (RSA) [Cappotto et al., 2022] to decode prediction traces from EEG signals. Second, we used the same techniques to decode prediction traces from fMRI data. Finally, we correlated single-trial EEG-based decoding estimates with fMRI BOLD amplitudes. In the latter analysis, single-trial EEG-based decoding estimates were treated as a regressor in a mass-univariate analysis based on the general linear model. Correction for multiple comparisons across voxels was based on family-wise error rate.

Results: EEG-based decoding showed that predictions of sequence elements replaced by "impulse" stimuli could be decoded in the predictable blocks (based on repeated stimulus triplets) but not in the control/random blocks (paired t-test, $p<.05$, corrected across time points). This result was linked to EEG latencies approx. 250 ms after impulse onset (Figure panel B, left). fMRI-based decoding showed the same pattern of results (significant prediction decoding in predictable but not in random blocks; paired t-test, $p<.05$, cluster-level corrected across voxels). Here, decoding was linked to early visual regions (Figure panel C). Finally, single-trial EEG-based decoding was found to significantly correlate with BOLD activity in the right hippocampus (Figure panel B, right).

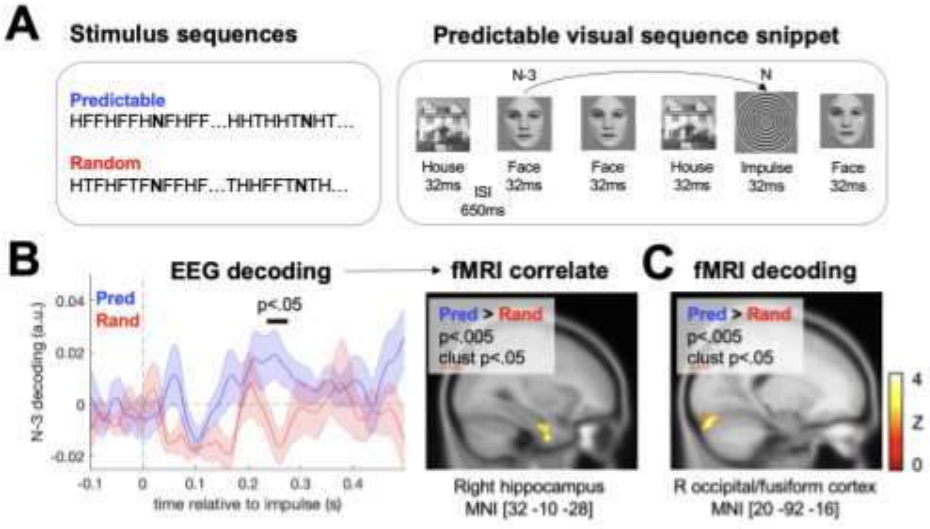

Conclusions: In conclusion, while fMRI-based prediction decoding was linked to early visual regions, EEG-based decoding correlated across trials with BOLD amplitude in the hippocampus. These results provide evidence for a neocortical-hippocampal network subserving predictive processing in stimulus sequences.

References
1. Aitken et al. (2022) Nature Communications, doi: 10.1038/s41467-022-31040-w
2. Baldeweg (2006) Trends in Cognitive Sciences, doi: 10.1016/j.tics.2006.01.010
3. Barron et al. (2020) Progress in Neurobiology, doi: 10.1016/j.pneurobio.2020.101821
4. Cappotto et al. (2022) Current Biology, doi: 10.1016/j.cub.2022.04.022
5. Friston (2010) Nature Reviews Neuroscience, doi: 10.1038/nrn2787
6. Stokes (2015) Trends in Cognitive Sciences, doi:10.1016/j.tics.2015.05.004

Poster No 1064

Charting neural representations behind human spatial learning

Liangyue Song[1,1], Joern Alexander Quent[2], Xinyu Liang[3], Yueting Su[3], Deniz Vatansever[3]

[1]Fudan University, Shanghai, China, [2]Fudan University, Shanghai, [3]Fudan University, Shanghai, Shanghai

Introduction: Spatial navigation is a core cognitive process that relies on the coordinated activity of a complex and widespread neural circuitry[1]. Notably, a set of brain regions centered on the medial temporal, parietal and prefrontal cortices are now suggested to exhibit grid-like activity patterns during spatial navigation[2], providing mechanistic insights into the use of cognitive maps in the navigation of learned spatial environments. However, there is notable scarcity of research on the encoding of spatial memory and thus the learning process itself. Here, using an ecologically valid virtual reality environment, we aimed to map the neural mechanism underlying the naturalistic encoding of spatial memory in humans.

Methods: A group of 55 participants (mean age = 23.70, SD = 2.21, F/M ratio = 34/21) were scanned at 3T MRI via HCP style data acquisition protocols, while performing two runs of an Object Location Memory (OLM) paradigm. In this task, participants were asked to navigate in a virtual arena in order to learn and memorize the locations of six hidden objects through multiple cycles of memory retrieval and update (Fig. 1a). Memory performance and learning in each trial was measured via placement error i.e. the the Euclidean distance between the estimated and correct object location (Fig. 1b), which was subsequently employed as a parametric modulator in a GLM-based analysis of the task fMRI data. Our main analysis of interest was to investigate brain regions which showed greater activity with a reduction in placement error, indicating the onging learning process. Results were further interrogated to unveil their distribution across the cortical and subcortical organization of the human brain.

Results: Behavioral results revealed a significant reduction in the placement error within and between runs, demonstrating a learning effect in the memorization of object locations. Using placement error as the parametric modulator, we identified a host of regions responsive to improved memory performance, suggesting their involvement in spatial learning. These results encompassed regions that are highly connected to learning such as the hippocampus, as well as regions associated with grid-like activity patterns during navigation, such as the entorhinal cortex (EC), orbital prefrontal cortex (OFC) and temporal cortex (Fig. 1c). Network partitioning revealed that regions belonging to the Default Mode (DMN) and Somatomotor Networks (SMN) contributed most to the significant clusters (FDRp < 0.05, Fig. 2ai). This was further supported by cortical gradient projection, where significant clusters were positioned along transmodal and somatomotor endpoints of the principal connectivity gradients (Fig. 2aii). In a between-subject analysis, the role that the DMN plays in spatial learning was further highlighted by the significant correlation between modulation of regions within this network and task performance ($p<0.05$, Fig. 2aiii). While at the subcortical level, the results revealed that the learning related modulation was localized in the bilateral anterior hippocampus, left amygdala, and the ventral striatum (Fig. 2bi). The modulation effect from the left hippocampus positively correlated with performance improvement from Run 1 to Run 2 (cor=0.27, p=0.04), indicating its contribution to spatial learning (Fig. 2bii).

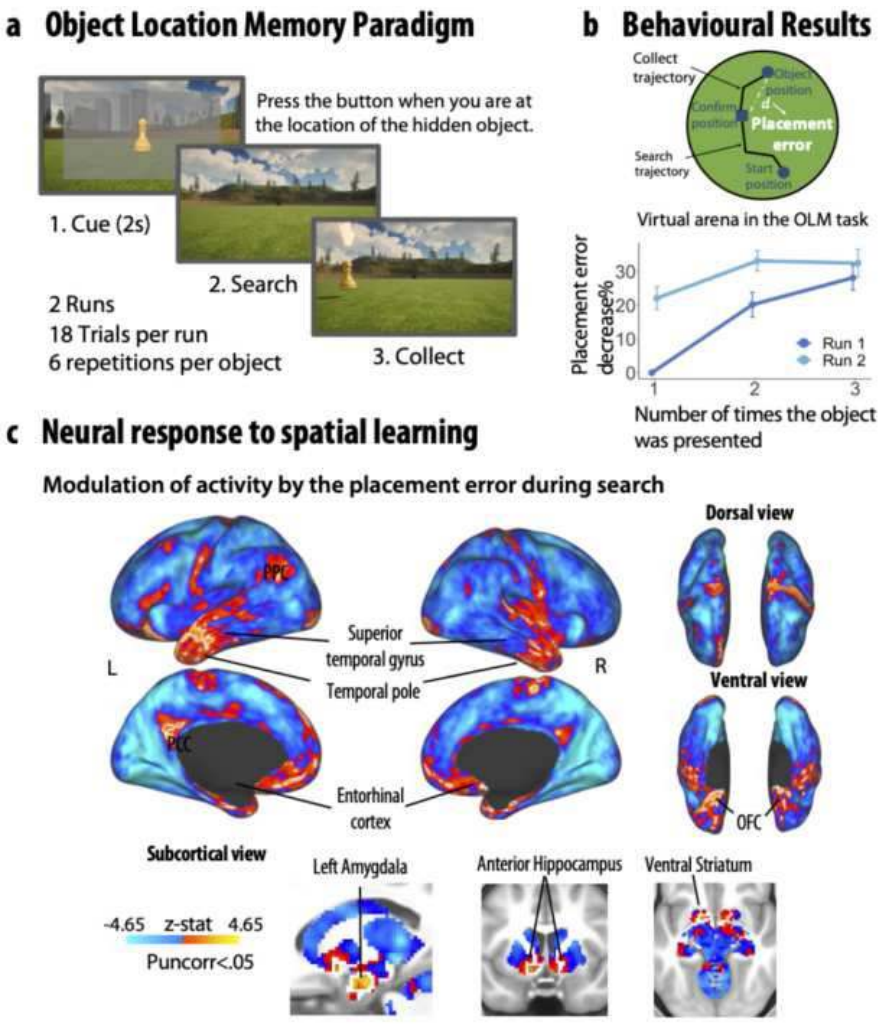

Figure. 1. Neural activity patterns underlying spatial learning. a. An Object Location Memory (OLM) virtual reality paradigm was designed with three distinct phases: cue, search and collection. **b.** Behavioral results revealed improvement in task performance as indicated by a decrease within and between runs. **c.** The brain activity modulated by placement error during the search period. Regions with positive z-stat values show increased activity when participants perform better. Imaging data was minimally preprocessed using Qunex containerized versions of the HCP preprocessing pipelines and statistically modelled using FSL FEAT routines [3] . Significance was estimated using non-parametric permutation testing via PALM and corrected for gender, age and the button control ability score tested by a pre-scan training. The clusters at the significance level of 0.05(uncorrected) are distributed across orbital prefrontal cortex (OFC), posterior cingulate cortex (PCC), motor cortex, temporal cortex, entorhinal cortex, posterior parietal cortex (PPC) and visual cortexes. These are regions associated with learning and memory and grid-like activity patterns from a cognitive perspective and the DMN for a cortical organization perspective. Regions also involve hippocampus, amygdala and ventral striatum in subcortical areas.

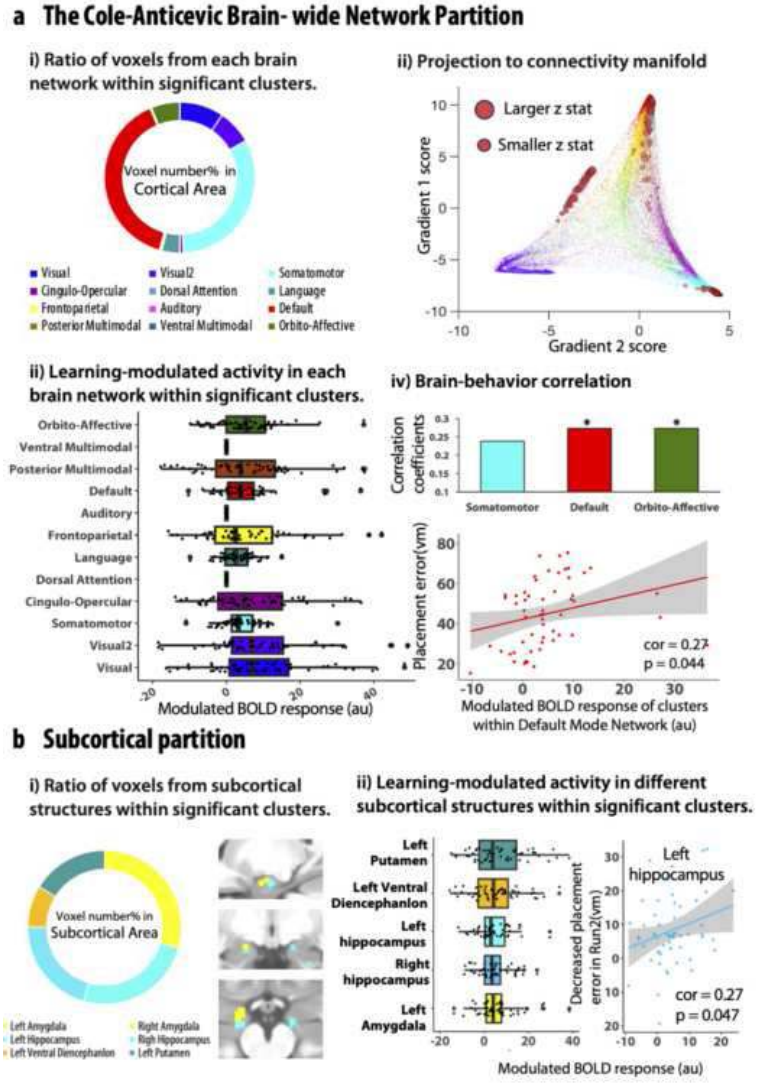

Figure. 2. Partition analysis for significantly highlighted clusters in spatial learning. a. We employed the Cole-Anticevic brain-wide network partition on FDR-corrected significant cortical regions and computed the voxel percentage of each brain network. i) The prominent clusters are primarily associated with the Default Mode Network and Somatomotor Network and display a noticeable distribution in the Visual, Orbito-Affective, and Dorsal Attention Networks as well. ii) The z-stats of significant clusters were projected to Gradient 1 and Gradient 2 using Toolbox BrainSpace [4], and the results indicate that significant learning-modulated clusters are situated along the edge and endpoints of the gradient graph. iii) Extracted beta values for these clusters within each network reveal that subjects exhibit the most concentrated brain modulation in the Somatomotor and Default Mode Networks. In the between-subject analysis, only the Somatomotor, Default, and Orbito-affective networks achieve significance at the 0.1 level, indicating a positive correlation between learning-modulated activity and placement error, and consequently, a negative correlation with performance at the between subject level. **b.** The similar partition analysis was also done for the subcortical structures and the most substantial contributions to the significant learning modulation in subcortical regions come from the left amygdala and bilateral anterior hippocampus. And only the modulation of significant clusters in left hippocampus shows a significant correlation with the decreased placement error in Run2, indicating a positive correlation between modulation and learning at the between-subject level.

Conclusions: Our findings indicate that spatial learning in a virtual reality environment engages medial temporal lobe regions that often exhibit grid-like activity patterns, suggesting a potential role for cognitive map dynamics in this encoding process. Moreover, the additional involvement of regions within the Default Mode Network adds an intriguing layer to our findings, highlighting the active contribution of this transmodal network to spatial learning.

References

1. Epstein RA, Patai EZ, Julian JB, Spiers HJ (2017), 'The cognitive map in humans: spatial navigation and beyond'. Nature Neuroscience, 20(11):1504-1513.
2. Doeller CF, Barry C, Burgess N (2010), 'Evidence for grid cells in a human memory network.' Nature, 463(7281):657-61.
3. Glasser MF et al. (2016), 'The Human Connectome Project's neuroimaging approach', Nature Neuroscience, 19:1175–1187.
4. Worsley KJ et al. (2009), 'A Matlab toolbox for the statistical analysis of univariate and multivariate surface and volumetric data using linear mixed effects models and random field theory.' NeuroImage, 47(S1):S39-S41.

Poster No 1065

Emergence and reconfiguration of modular structure for synaptic neural networks during learning

Shi Gu[1]

[1]*University of Electronic Science and Technology of China, Chengdu*

Introduction: To study the learning dynamics of HebbFF, we developed a multi-pronged approach examining the dynamic reconfiguration of the networks from different perspectives. We begin with an analysis of the modularity over temporal scales and its relationship to variations in task accuracy and distribution entropy across diverse learning paradigms. We then explored the synchronicity of states during the training phase and its subsequent correlation with accuracy. We show that network modularization enhances with learning, and that network flexibility serves as a robust metric encapsulating model performance, in line with results from neuroscience in biological organisms. We hope that our findings will shed light on the interplay between network modularity, accuracy, and learning dynamics, and ultimately advance our understanding of artificial neural networks and their biological counterparts.

Methods: The method section refers to an external link https://arxiv.org/abs/2311.05862 due to the format issue.

Results: We explored the dynamic reconfiguration of artificial neural networks, focusing on a class of recurrent (RNNs) called Hebbian Feed Forward Network (HebbFF). This network determines the familiarity of a stimulus based on whether it matches a stimulus encountered at a prior time-step. We use a neural network with 120 units in the hidden layer to provide sufficient representation power for encoding the input. A more detailed result can be found at https://arxiv.org/abs/2311.05862.

Conclusions: In sum, our discoveries contribute significantly to the broader aim of intersection between AI and Neuroscience - using AI not only to replicate but also to understand and learn from the intricate workings of the brain. The tools and methods we developed present new opportunities to study learning dynamics in both artificial and biological neural networks. Such cross-fertilization of ideas can potentially lead to more efficient, adaptable, and robust AI systems while providing insights into the neuroscience of learning and memory. We note that our research so far focused on memory tasks, which are well-suited for Hebbian feedforward networks that are inherently amenable to descriptions based on modularization. Future work should expand our approach to other cognitive tasks like multimodal matching, value decision, and perception tasks, as well as to other types of ANNs including RNN and deep feedforward networks. We hope that multimodal continual tasks learned through complex networks could serve as a digital analogue of the brain in terms of cognitive execution and may provide novel insights into how functional modules reconfigure to support complex tasks.

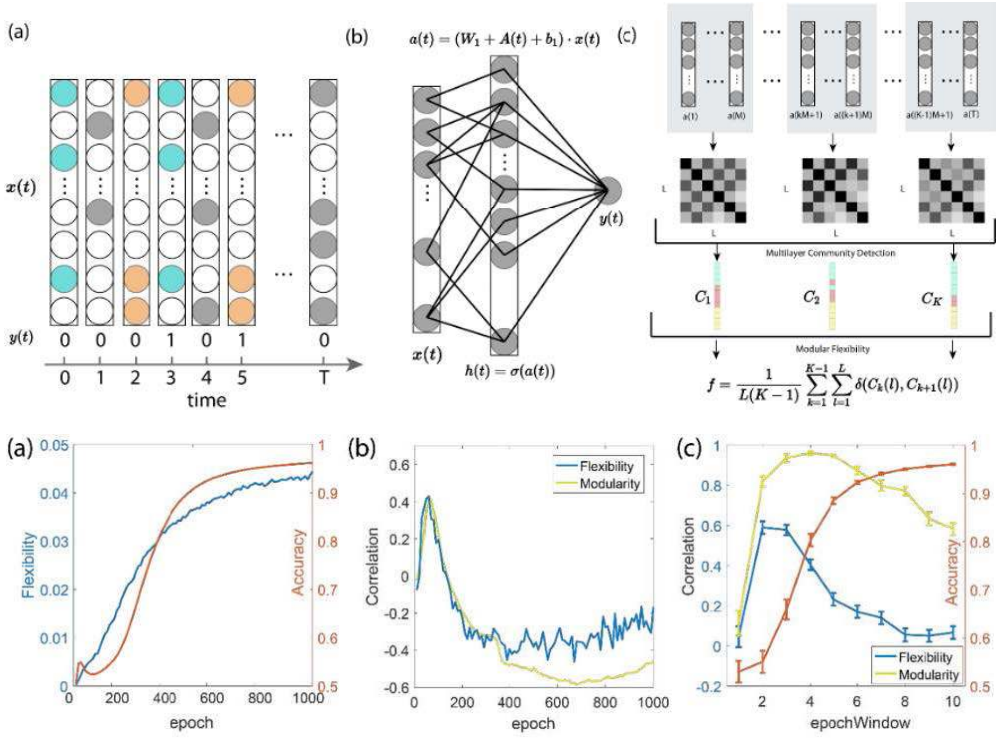

References

1. Gu, Shi, et al. “Emergence and reconfiguration of modular structure for synaptic neural networks during continual familiarity detection.” arXiv preprint arXiv:2311.05862 (2023).

Poster No 1067

Gamma-band sensory stimulation enhances episodic memory retrieval

Benjamin Griffiths[1], Katharina Duecker[1], Daniel Weinert[2], Ole Jensen[1], Tobias Staudigl[2]

[1]University of Birmingham, Birmingham, West Midlands, [2]Ludwig-Maximilians-Universität München, Munich, Bavaria

Introduction: Enhanced gamma activity (30-100Hz) coincides with successful episodic memory retrieval, but it remains unknown whether this oscillatory activity is a cause or a consequence of the retrieval process. We aim to address this question of causality.

Methods: 32 human participants completed a paired associates memory task whilst undergoing visual sensory stimulation (at 65Hz, 43.3Hz and 32.5Hz) during episodic memory retrieval. MEG activity was simultaneously recorded. The impact of sensory stimulation on memory performance was quantified using multi-level logistic regression models. The MEG data was preprocessed to attenuate noise and analysed using two approaches: (i) a standard time-frequency decomposition using wavelets, and (ii) a time-series average computed by locking the MEG data to each light pulse delivered during sensory stimulation. Non-parametric permutation tests were used to assess statistical significance and correct for multiple comparisons.

Results: In the behavioural data, both 68Hz and 34Hz sensory stimulation enhanced memory recall above a baseline condition where no sensory stimulation was applied. Only a small proportion of participants (~10%) could perceive the 65Hz visual flicker, suggesting 65Hz sensory stimulation is imperceptible. In the time-frequency analysis, 68Hz and 44Hz stimulation produced narrowband increases in spectral power within their respective bands over occipital sensors. In contrast, 34Hz stimulation produced narrowband increases in power at both 34Hz and 68Hz over occipital sensors. In the analysis of the peak-locked time-series data, the 34Hz condition produced two oscillations superimposed over one another: a 34Hz oscillation that principally arose over occipital sensors, and a spatially- and statistically distinct 68Hz oscillation over parietal sensors.

Conclusions: These results suggest imperceptible sensory stimulation enhances recall, providing a novel and entirely unintrusive means of tackling mnemonic issues. This appears to be achieved by 34Hz and 68Hz stimulation both enhancing an endogenous 68Hz gamma oscillation, suggesting that this gamma activity plays a causal role in episodic memory retrieval. Furthermore, the observation that subharmonic frequencies can modulate endogenous gamma activity suggests that non-linear interactions exist between endogenous brain activity and exogenous stimulation, opening new avenues for future neuro-stimulation interventions.

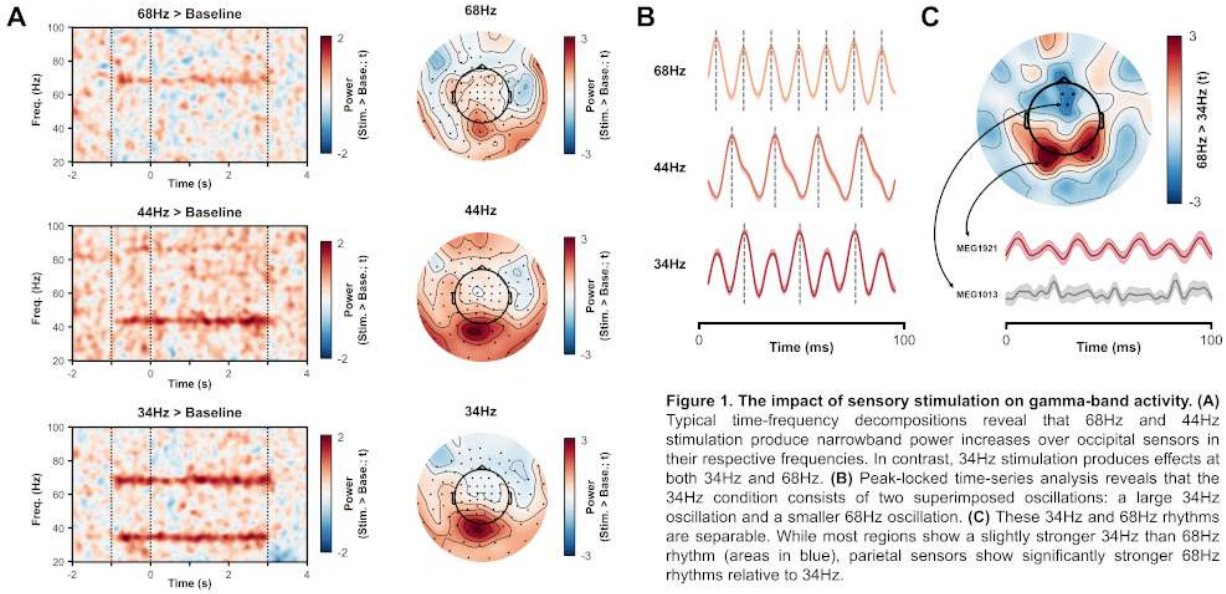

Figure 1. The impact of sensory stimulation on gamma-band activity. (A) Typical time-frequency decompositions reveal that 68Hz and 44Hz stimulation produce narrowband power increases over occipital sensors in their respective frequencies. In contrast, 34Hz stimulation produces effects at both 34Hz and 68Hz. **(B)** Peak-locked time-series analysis reveals that the 34Hz condition consists of two superimposed oscillations: a large 34Hz oscillation and a smaller 68Hz oscillation. **(C)** These 34Hz and 68Hz rhythms are separable. While most regions show a slightly stronger 34Hz than 68Hz rhythm (areas in blue), parietal sensors show significantly stronger 68Hz rhythms relative to 34Hz.

Poster No 1068

Own-Body Perception in the Encoding and Retrieval of Memories for Naturalistic Events

Heather Iriye[1], H. Henrik Ehrsson[2]

[1]Karolinska Institutet, Solna, Select a State, [2]Karolinska Institutet, Stockholm, Select a State

Introduction: The vivid, coherent perception of one's own body (i.e., body ownership) during memory encoding facilitates retrieval (Bergouignan, Nyberg, & Ehrsson, 2014; Iriye, Chancel & Ehrsson, In Press; Iriye & Ehrsson, 2022). Yet, the underlying mechanism explaining how perception of our bodies contributes to memory is unclear. Body ownership may act as a contextual memory cue since it is typically a constant feature of both encoding and retrieval. Alternatively, body ownership may be a privileged type of information that supports memory beyond contextual memory effects, given its high self-relevance.

Methods: Here we measured patterns of activity in core brain areas involved in contextual memory (i.e., the angular gyrus, parahippocampus, hippocampus, and medial prefrontal cortex; Preston & Eichenbaum, 2013) as we manipulated body ownership during the encoding and retrieval of immersive videos (Figure 1). We predicted that consistent strong body ownership between encoding and retrieval would impact the strength of a memory trace in the medial prefrontal cortex, as this region uses contextual information to bias the selection of memory details during retrieval5. We immersed healthy participants (N = 25) within videos seen through virtual reality glasses, which depicted lifelike events that included a first-person view of a mannequin's reclining body aligned with participants' real bodies during fMRI scanning. Participants saw an object touch the mannequin and synchronously felt touches on the corresponding location of their real body, which created an illusory sense of ownership over the mannequin. As a control condition, we disrupted the illusion by delivering seen and felt touches asynchronously in half of the videos. 1 week later, participants were re-immersed within videos depicting the mannequin receiving dynamic visuotactile stimulation overlaid on still-frames of the previously seen videos during fMRI scanning. We again manipulated feelings of ownership over the mannequin, which was either congruent or incongruent with how a video was encoded, while participants retrieved memories for the videos. Participants completed ratings of emotional intensity, vividness, reliving and belief in memory accuracy to assess subjective remembering.

Results: Peak skin conductance response magnitudes to bodily threats directed towards the mannequin were greater in the synchronous versus asynchronous condition ($p = .006$), demonstrating greater ownership over the mannequin's body. Using a multivariate classifier and region-of-interest approach, we found that patterns of activity during memory retrieval in the angular gyrus, parahippocampal cortex, hippocampus, and medial prefrontal cortex predicted current body ownership perception in the context of body ownership perception during encoding (p's $< .003$). Next, we used encoding-retrieval pattern similarity to test whether patterns of activity during encoding were reinstated more at retrieval for memories formed and recalled with strong body ownership perception, considering subjective remembering measures of emotional intensity, vividness, reliving, and belief in memory accuracy. We compared patterns of neural activity in the medial prefrontal cortex to a target dissimilarity matrix weighted for congruent strong body ownership perception at encoding and retrieval and increasing levels of subjective remembering measures (Figure 2A). Consistent strong body ownership perception at encoding and retrieval combined with increasing levels of emotional intensity led to stronger memory reinstatement (i.e., higher encoding-retrieval pattern similarity) in the medial prefrontal cortex ($p = .008$).

Conclusions: Together, our results suggest that the influence of own-body perception on our ability to remember past events cannot be solely attributed to contextual memory effects. Rather, strong consistent body ownership perception during encoding and retrieval may calibrate patterns of activity in medial prefrontal regions to support remembering.

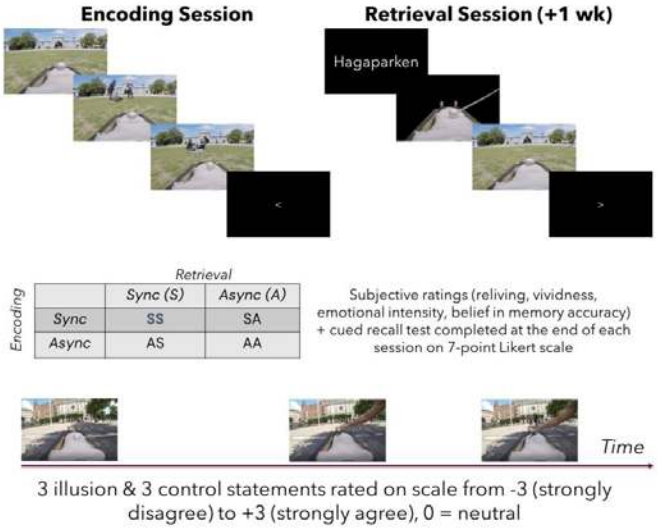

Figure 1. Experimental protocol. Participants watched videos of naturalistic events (6 per condition) while receiving either synchronous visuotactile stimulation to induce strong body ownership over the mannequin, or asynchronous visuotactile stimulation to reduce it. 1 week later, they retrieved memories for the videos while receiving visuotactile stimulation that was either congruent or incongruent encoding. We then tested the strength of the full-body illusion induction. Subjective memory ratings and a cued recall test were completed after each session. $N = 25$.

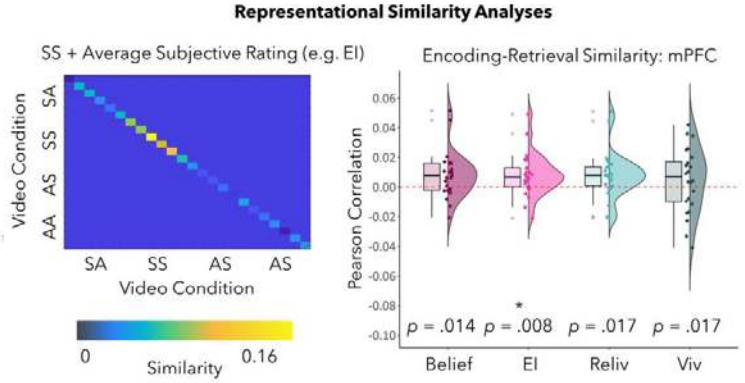

Figure 2. Encoding-Retrieval Pattern Similarity Analysis. We compared patterns of neural activity in the medial prefrontal cortex to a target dissimilarity matrix weighted for memories encoded and retrieved with synchronous visuotactile stimulation and increasing levels of subjective remembering measures. Memory reinstatement in the medial prefrontal cortex was greater for memories encoded with congruent strong body ownership during encoding and retrieval and high emotional intensity. SS = Synchronous Encoding - Synchronous Retrieval; SA = Synchronous Encoding - Asynchronous Retrieval; AS = Asynchronous Encoding – Synchronous Retrieval; AA = Asynchronous Encoding - Asynchronous Retrieval; Belief = belief in memory accuracy EI = emotional intensity, Reliv = reliving, Viv = vividness.

References

1. Bergouignan, L., Nyberg, L., & Ehrsson, H. H. (2014). Out-of-body–induced hippocampal amnesia. Proceedings of the National Academy of
2. Sciences, 111(12), 4421-4426.
3. Iriye, H., Chancel, M., Ehrsson, H.H. (In Press). Sense of Own Body Shapes Neural Processes of Memory Encoding and Reinstatement. Cerebral Cortex
4. Iriye, H., & Ehrsson, H. H. (2022). Perceptual illusion of body-ownership within an immersive realistic environment enhances memory accuracy and re-experiencing. Iscience, 25(1)
5. Preston, A. R., & Eichenbaum, H. (2013). Interplay of hippocampus and prefrontal cortex in memory. Current biology, 23(17), R764-R773.

Poster No 1069

Memory Ability Following Brain Stimulation and Lesions Reveals Potential Neuromodulation Targets

Simon Kwon[1], Joshua Siegel[2], Melissa Hebscher[3], Molly Hermiller[4], Eyre Ye[5], Joel Voss[3], Jordan Grafman[6], Maurizio Corbetta[7], Shan Siddiqi[8]

[1]Brigham and Women's Hospital, Boston, USA, [2]Washington University St Louis, St Louis, USA, [3]University of Chicago, Chicago, USA, [4]Florida State University, Tallahassee, USA, [5]Beijing Normal University, Beijing, China, [6]Northwestern University, Chicago, USA, [7]University of Padova, Padova, Italy, [8]Harvard Medical School/Brigham and Women's Hospital, Boston, USA

Introduction: The key aim in memory research is to enhance memory ability in healthy individuals and patients with neurocognitive deficits. Previous research involving transcranial magnetic stimulation revealed memory performance to be enhanced following stimulation of the key brain network target, parietal-hippocampal network (Wang et al., 2014). Those neuromodulation studies nevertheless involve only healthy volunteers, providing little insight to potential brain stimulation target with which to facilitate neurocognitive recovery in patients with brain lesions. We sought to find those potential neuromodulation targets.

Methods: Lesion-symptom mapping analysis approach often reveals brain regions essential for neurocognitive functions (Fox 2018). We adapted this analysis approach by including brain-behavior data stemming from three groups of people (total N = 570). The first dataset consists of neuropsychological scores from 179 patients with penetrating head injury, whose lesions are primarily in prefrontal cortex (Grafman 1986a). We also included 113 patients with lesions primarily in medial region, following stroke, aiming to detect key brain regions important for memory function in medial regions as well (Corbetta et al., 2015). We sought to assess if lesion-symptom maps stemming from patients resemble those stemming from healthy volunteers following a virtual lesion or 'brain stimulation'. We therefore included data from 278 healthy volunteers following stimulation of the parietal-hippocampal network target stimulation (Wang et al., 2014 and subsequent replication studies).

Results: The lesion-symptom mapping analysis revealed brain-memory maps in health and brain lesions. Those neurocognitive maps tend to resemble each other ($n = 570$, $r = 0.625$, $p < 0.001$). Those maps converge at the potential neuromodulation target, inferior temporal gyrus (MNI = -53, -63, -19). Stimulation of this target might come to facilitate neurocognitive recovery in patients with brain lesions. Sometimes, however, those lesion locations might include inferior temporal gyrus and therefore yield no meaningful neuromodulation effect. In such cases patients may recover by adapting to draw on functioning of neurocognitively similar contralateral regions. Direct comparison between brain-memory relationships in the ipsilateral and contralateral regions of interests did indeed reveal neurocognitive symmetry between the regions ($r > 0.246$, $p < 0.05$).

Conclusions: Current findings point to potential neuromodulation targets, inferior temporal gyrus and contralateral regions of interest. Neuromodulation of those targets might come to facilitate memory ability recovery in patients with brain lesions.

References

1. Corbetta, M., Ramsey, L., Callejas, A., Baldassarre, A., Hacker, C. D., Siegel, J. S., Astafiev, S. V., Rengachary, J., Zinn, K., Lang, C. E., Connor, L. T., Fucetola, R., Strube, M., Carter, A. R., & Shulman, G. L. (2015). Common behavioral clusters and subcortical anatomy in stroke. Neuron, 85(5), 927–941. https://doi.org/10.1016/j.neuron.2015.02.027
2. Fox, M. (2018). Mapping Symptoms to Brain Networks with the Human Connectome. The New England Journal of Medicine, 379(23), 2237–2245. https://doi.org/10.1056/nejmra1706158
3. Grafman, J., Salazar, A. M., Weingartner, H., Vance, S. C., & Amin, D. (1986). The relationship of brain-tissue loss volume and lesion location to cognitive deficit. The Journal of Neuroscience, 6(2), 301–307. https://doi.org/10.1523/jneurosci.06-02-00301.1986
4. Wang, J. X., Rogers, L. M., Gross, E. Z., Ryals, A. J., Dokucu, M. E., Brandstatt, K. L., Hermiller, M. S., & Voss, J. L. (2014). Targeted enhancement of cortical-hippocampal brain networks and associative memory. Science, 345(6200), 1054–1057. https://doi.org/10.1126/science.1252900

Poster No 1070

Learning from quantified episodic prediction errors: On the neural basis of gist revision

Nina Liedtke[1,2], Marius Boeltzig[1,2], Ricarda Schubotz[1,2]

[1]University of Muenster, Muenster, NRW, [2]Otto Creutzfeldt Center for Cognitive and Behavioral Neuroscience, University of Muenster, Muenster, Germany

Introduction: Episodic memories do not always accurately reflect our past experiences, but can be changed through new input. It is hypothesized that such changes are driven by mnemonic prediction errors which arise when an expectation based on memory representations does not match the actual experience (Sinclair & Barense, 2019). Further research suggests that

there might be a qualitative difference in brain responses and memory performance after prediction errors that affect the gist of an episode (gist modifications) compared to ones that leave the gist intact (surface modifications; Siestrup & Schubotz, 2023). However, it remains unknown whether the magnitude of prediction errors is related to the likelihood of memory updating. It has been suggested, that especially prediction errors of medium strength might lead to changes in memory (Ritvo, 2019). Therefore, we elicited surface and gist prediction errors of different strengths to investigate their distinct effects on brain activity and memory.

Methods: The sample consisted of forty-three healthy, right-handed participants (36 women, age 18-32 years, M= 22.66 years). The study used short dialogues as highly naturalistic and meaningful stimuli and it was designed as a five day paradigm. Day one to three were functional Magnetic Resonance Imaging (fMRI) sessions, day four and five took place on the computer. On the first day, 30 dialogues were presented for the first time in the MR scanner and a second time outside of the scanner. On day two, 24 of the presented dialogues were partly modified, while six remained unchanged. The modification was either on the surface level (i.e., synonyms or different phrasings) or on the gist level (i.e., changing the meaning of the utterance) and designed to be either low or high in degree. For each dialogue, each participant listened to only one modification. On day three, the fMRI session from day one was repeated. Imaging on the first three days was conducted on a 3T Siemens Prisma MR tomograph (TR/TE= 2000/30ms, FOV= 192x192mm2, 33 slices, slice thickness= 3mm). Recognition tests and cued recall were conducted on day four to assess memory for both the original versions and the heard modifications. On day five, participants rated to what extent the original and modified versions differed. FMRI data were preprocessed (slice time correction, realignment, co-registration of functional to structural scans, normalization, and smoothing) and analyzed with SPM12 using a general linear model.

Results: For surface modifications compared to non-modified dialogues we found activation in the inferior frontal gyrus, left dorsal premotor cortex, left (pre-) supplementary motor area and in the right anterior as well as left middle superior temporal sulcus ($p<.005$, FDR corrected). Gist modifications also caused activations in these regions, but compared to surface modifications we found additional brain responses in medial frontal areas, the ventral precuneus, the posterior cingular cortex and the temporo-parietal junction ($p<.005$, FDR corrected). In the recognition test, participants recognized low gist modifications less confidently than other modification types ($F(1,1050) = 5.02$, $p = .025$). In accordance with that, modeling the BOLD response with participant-rated degree of difference revealed brain activation in both parahippocampal gyri for lower compared to stronger gist changes ($p<.001$, uncorrected).

Conclusions: We demonstrated that gist modifications differ from surface modifications not only quantitatively but also qualitatively. While there were no effects for the strength of surface modifications, we found a behavioral effect of low gist modifications on new learning and the original memory. This could possibly reflect the postulated particular effect of medium-strength prediction errors, which was also associated with specific parahippocampal activity.

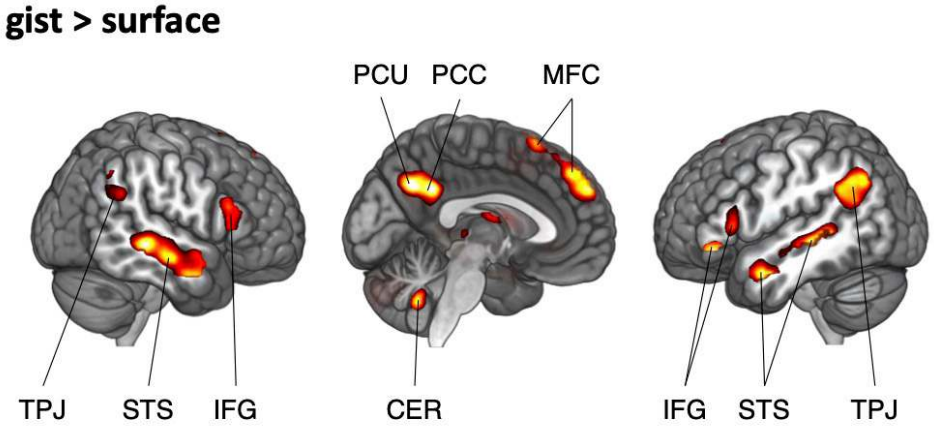

Note. FDR-corrected ($p < .005$) *t*-map for the gist > surface contrast. Activations were found in the ventral precuneus (PCU), posterior cingular cortex (PCC), medial frontal cortex (MFC), temporo-parietal junction (TPJ), superior temporal sulcus (STS), inferior frontal gyrus (IFG) and in the cerebellum (CER). Saggital cuts were made at x = 57 (left), x = -4 (middle) and x = -50 (right).

References

1. Ritvo, V. J. (2019), 'Nonmonotonic plasticity: how memory retrieval drives learning', Trends in cognitive sciences, vol. 23, no. 9, pp. 726-742
2. Siestrup, S. (2023), 'Minor Changes Change Memories: Functional Magnetic Resonance Imaging and Behavioral Reflections of Episodic Prediction Errors', Journal of Cognitive Neuroscience, vol. 35, no. 11, pp. 1823-1845

3. Sinclair, A.H. (2019), 'Prediction Error and Memory Reactivation: How incomplete Reminders Drive Reconsolidation', Trends in Neurosciences, vol. 42, no. 10, pp. 727-739

Poster No 1071

The neural correlates of different sources of surprise: Evidence from two naturalistic fMRI studies

Dominika Varga[1], Petar Raykov[2], Elizabeth Jefferies[3], Aya Ben-Yakov[4], Chris Bird[1]

[1]University of Sussex, Brighton, United Kingdom, [2]MRC CBU, Cambridge, United Kingdom, [3]University of York, York, United Kingdom, [4]The Edmond and Lily Safra Center for Brain Sciences (ELSC), Jerusalem, Israel

Introduction: In general, we experience surprise when an observation contradicts expectations based on our past experiences. However, we can be surprised for different reasons, depending on the source of our expectations. Expectations can be flexibly drawn from either our general knowledge about how the world works or memories of specific episodes in the past. Because current leading theories on how surprising events are processed do not account for this complexity in sources of predictions, it is unclear if surprise based on different sources of expectations engage the same or distinct neural processes. A currently prominent view is that the hippocampus acts as a comparator between prior experience and incoming information, and plays an important role in detecting events that mismatch our expectations (e.g. Kumaran & Maguire, 2007; Barron, Auksztulewicz, Friston, 2020). However, this idea stems from work in which participants learned arbitrary associations which were violated after minimal delay. For example, violating the temporal order or spatial arrangement of recently experienced items (e.g. Kumaran & Maguire, 2006; Duncan et al., 2012). In short, these studies have demonstrated a role of the hippocampus in processing surprise based on episodic-like memories. However, outside of the laboratory we often rely on our general semantic or schematic knowledge to predict what is likely to happen in a given situation (Elman & McRae, 2019). While some theories predict increased hippocampal engagement when there is a mismatch between prior schematic knowledge and current experience (e.g. SLIMM framework, van Kesteren et al., 2012), there is no direct evidence to support this idea.

Methods: Across two fMRI experiments (Experiment 1 N=36; Experiment 2 N=33; Fig. 1), we tested the hippocampus' role in processing unexpected events based on general knowledge or episodic memory-based predictions. We created 34 pairs of custom made video clips that showed actors carrying out sequences of actions in a range of everyday situations. Each pair of clip included an Unexpected version, where the actor carried out an unexpected sequence of actions (e.g., putting flowers into a washing machine), and a corresponding Expected version, where the unexpected action was replaced by an expected, context-congruent action (e.g., putting clothes into a washing machine). In both experiments we showed 17 Unexpected and 17 Expected clips in the scanner. Crucially, we manipulated participants' pre-scan exposure to the clips, either having no pre-exposure and only showing clips inside the scanner (Expt 1), or showing all clips in the Expected version before scanning (Expt 2). This meant that Experiment 1 participants could be surprised only based on their general knowledge of everyday situations, while Experiment 2 participants could also be surprised based on their memory for the specific clips.

Figure 1

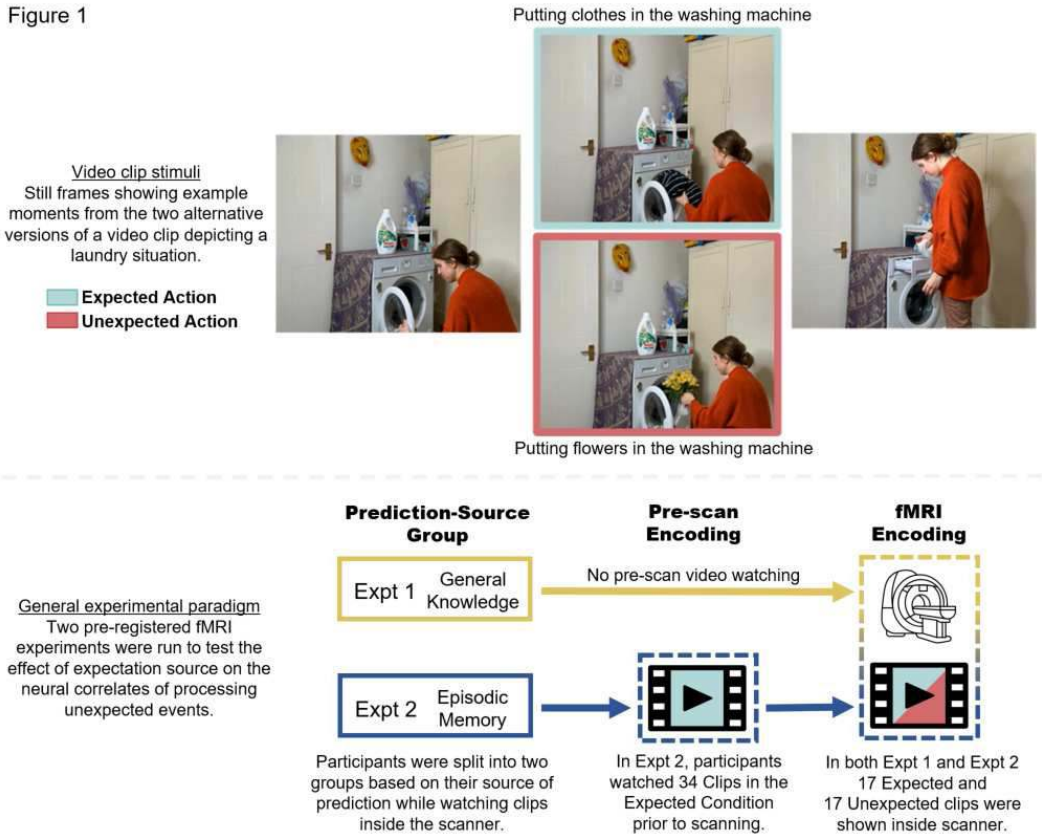

Results: A significant action-expectedness by prediction-source interaction showed that hippocampal univariate activity increased to Unexpected relative to Expected actions when predictions relied on memory for specific clips (Expt 2), but not when predictions relied on general knowledge (Expt 1), suggesting that this region does not have a general role in processing unexpected events. Exploratory network analyses showed increased response to Unexpected actions in the Semantic Control and Multiple Demand Network in both experiments, suggesting that these networks have a role in processing information incongruent with the general context. Conversely, activity in the Default Mode Network increased to Unexpected actions only in Experiment 2, suggesting that this network is involved when input violates internally stored representations of specific contexts. See Fig. 2.

Figure 2

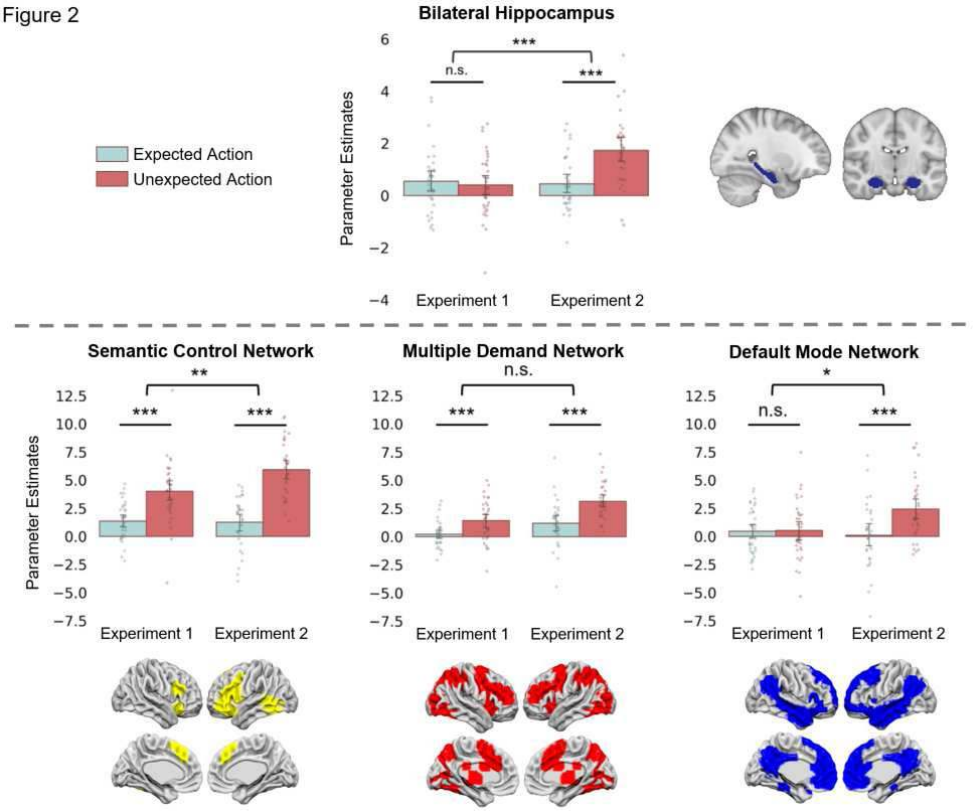

Conclusions: We show that differentiating expectation sources is crucial in studying neural responses to surprise. Our results contradict a general role for the hippocampus in processing unexpected events, informing updates to models of mismatch detection.

References

1. Barron, H.C. et al. (2020). Prediction and memory: A predictive coding account. Progress in neurobiology, vol. 192, p.101821.
2. Duncan, K. et al. (2012). Evidence for area CA1 as a match/mismatch detector: a high-resolution fMRI study of the human hippocampus. Hippocampus, vol. 22, no. 3, pp.389-398.
3. Elman, J.L. et al. (2019). A model of event knowledge. Psychological Review, vol. 126, no. 2, p.252.
4. Kumaran, D. et al. (2007). Which computational mechanisms operate in the hippocampus during novelty detection?. Hippocampus, vol. 17, no. 9, pp.735-748.
5. Kumaran, D. et al. (2006_. An unexpected sequence of events: mismatch detection in the human hippocampus. PLoS biology, vol. 4, no. 12, p.e424.
6. Van Kesteren, M.T. et al. (2012). How schema and novelty augment memory formation. Trends in neurosciences, vol. 35, no. 4, pp.211-219.

Poster No 1072

Decoding personal mental images with an fMRI model of general semantic features

Andrew Anderson[1], Leonardo Fernandino[1], Lisa Conant[1], Bill Gross[1], Hernan Rey[1], Jeffrey Binder[1]

[1]Medical College of Wisconsin, Milwaukee, WI

Introduction: People simulate their own personal experiences through imagination and understand descriptions of others' experiences via language. Although both processes are anchored in experience, it remains unclear whether autobiographical simulations and language comprehension are encoded in common brain systems. For instance, automated meta-analyses[1] and popular renditions of the brain's language[2] or semantic[3] network exclude medial cortical zones that underpin autobiographical simulations, whereas other fMRI studies have implicated these medial cortices in encoding semantic features of language[4-7]. However, demonstrating feature encoding in medial cortices does not entail that the same features underlie the content of autobiographical imagery. We hypothesized that this would be the case and that the encoding of autobiographical-imagery and sentence semantics would overlap in a shared neural feature space. To test this, we evaluated whether the content of autobiographical imagery could be decoded from corresponding fMRI activity using a pre-trained decoder built from

a separate fMRI data set in which participants read sentences. Such decoding would not be possible if autobiographical imagery and sentence semantics were encoded in separate neural systems or different feature spaces.

Methods: See Fig 1. (1) Mental imagery data from 50 participants were reanalyzed[8]. 20 generic scenario cues (e.g. party, exercising, wedding) were read to each participant, who vividly imagined themselves experiencing each scenario. Participants rated each mental image on 20 sensory, motor, affective, social, cognitive and spatiotemporal features[9] of experience (0-6 scale). Participants then underwent fMRI as they re-imagined the same scenarios in random order on written prompt. Preprocessing produced a single fMRI volume for each mental image per person that was standardized in Schaefer atlas space[10]. (2-3). A semantic feature fMRI decoder was built from a sentence reading dataset scanned as 14 other participants read 240 sentences[6]. Sentences were third person and 3-9 words long, e.g. “The child broke the glass at the shop”. Sentence semantics were modeled via crowd-sourced ratings of the same 20 features above. A cross-participant decoder was built using ridge regression to map the entire sentence fMRI dataset onto the 20 crowdsourced feature ratings. (4) To test whether the personal content could be reconstructed from the fMRI data, we applied the pretrained semantic feature decoder to reconstruct participants’ feature ratings. To establish that the reconstructed features reflected personal content rather than general semantics of the stimuli, we ran an individual-differences analysis. This selected 2 participants at a time, and cross-correlated the reconstructed rating matrices with the genuine ratings. Discrimination was scored a success if the sum of the two congruent coefficients exceeded the sum of the two incongruent coefficients. This was repeated for all participant pairs. Statistical significance was evaluated with permutation testing.

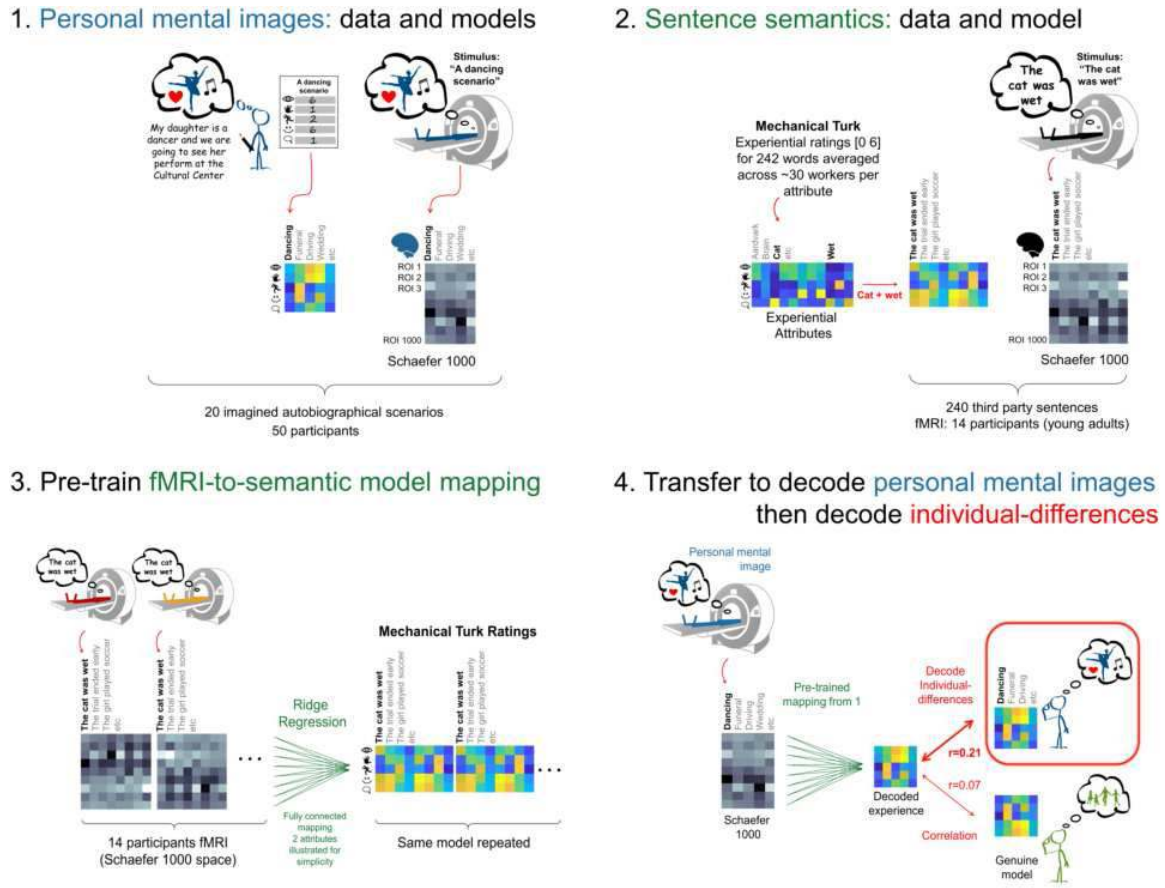

Results: See Fig 2. Top: The individual-differences analysis revealed that autobiographical simulations from different participants were discriminated with 70% accuracy, p<1e-4. To evaluate which features contributed most to discrimination, we repeated the individual-differences analysis with individual feature vectors, which revealed that social- and speech-related features contributed the most. Bottom: To test whether the encoding of mental images and sentence semantics overlapped in medial cortices we used ridge regression to fit a model-to-fMRI encoder on the sentence data. We then used it to predict mental image fMRI data from participants’ feature ratings. fMRI data were accurately predicted in medial cortices.

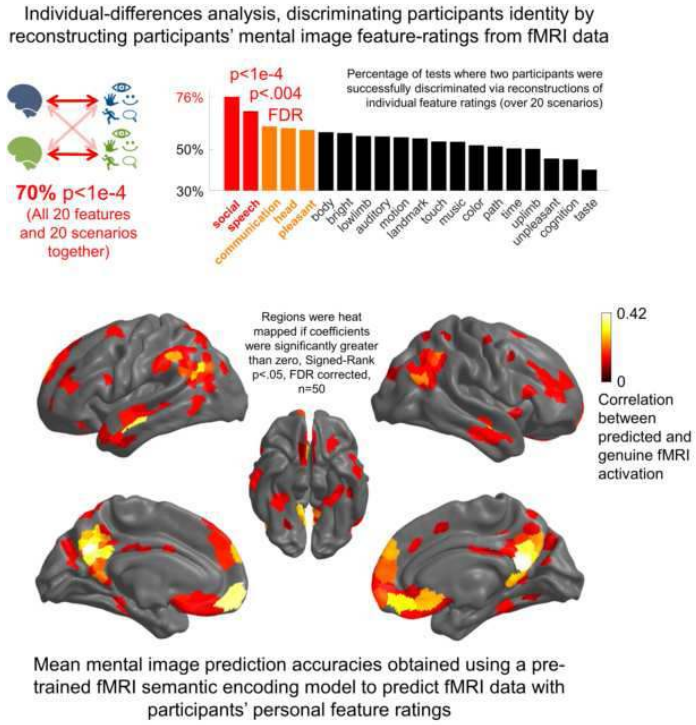

Conclusions: 1. Autobiographical simulations and third-person sentence semantics overlap in a shared neural feature space. 2. Personal mental states can be discriminated from fMRI data with a pre-trained decoder.

References

1. Yarkoni T, Poldrack RA, Nichols TE, Van Essen DC, Wager TD. (2011). Large-scale automated synthesis of human functional neuroimaging data. Nature MNethods. 8(8):665-70.
2. Fedorenko E, Hsieh PJ, Nieto-Castañón A, Whitfield-Gabrieli S, Kanwisher N (2010). New method for fMRI investigations of language: defining ROIs functionally in individual subjects. Journal of Neurophysiology 104:1177–1194.
3. Lambon Ralph MA, Jefferies E, Patterson K, Rogers TT. (2017). The neural and computational bases of semantic cognition. Nature Reviews Neuroscience. 18(1):42-55.
4. Binder JR, Desai RH, Graves WW, Conant LL. (2009). Where is the semantic system? A critical review and meta-analysis of 120 functional neuroimaging studies. Cerebral Cortex. 19(12):2767-96.
5. Huth AG, de Heer WA, Griffiths TL, Theunissen FE, Gallant JL (2016). Natural speech reveals the semantic maps that tile human cerebral cortex. Nature 532:453–458.
6. Anderson AJ, Binder JR, Fernandino L, Humphries CJ, Conant LL, Aguilar M, Wang X, Doko D, Raizada RD (2017). Predicting neural activity patterns associated with sentences using a neurobiologically motivated model of semantic representation. Cerebral Cortex 27:4379–4395.
7. Fernandino L, Tong JQ, Conant LL, Humphries CJ, Binder JR. (2022). Decoding the information structure underlying the neural representation of concepts. Proceedings of the National Academy of Sciences. 119(6):e2108091119.
8. Anderson AJ, McDermott K, Rooks B, Heffner KL, Dodell-Feder D, Lin FV. (2020). Decoding individual identity from brain activity elicited in imagining common experiences. Nature Communications. 20;11(1):1-4.
9. Binder JR, Conant LL, Humphries CJ, Fernandino L, Simons S, Aguilar M, Desai R. (2016). Toward a brain-based componential semantic representation. Cognitive Neuropsychology 33 (3-4), 130-174.
10. Schaefer A, Kong R, Gordon EM, Laumann TO, Zuo XN, Holmes AJ, Eickhoff SB, Yeo BTT. Local-Global parcellation of the human cerebral cortex from intrinsic functional connectivity MRI. 2018. Cerebral Cortex, 29:3095-3114.

Poster No 1073

Cerebral reflections of memory modification following episodic prediction errors

Sophie Siestrup[1,2], Ricarda Schubotz[1,2], Benjamin Jainta[1], Sen Cheng[3]

[1]University of Münster, Münster, Germany, [2]Otto Creutzfeldt Center for Cognitive and Behavioral Neuroscience, Münster, Germany, [3]Ruhr University Bochum, Bochum, Germany

Introduction: Episodic memories do not always accurately reflect our experiences, but can be modified in favor of new information. Such changes are potentially fueled by mnemonic prediction errors which arise when there is a mismatch between what was expected based on memories and what is experienced in a new situation[1,2]. While it is believed that such

memory changes allow us to maintain valid predictions in a dynamic environment[2,3], little is known about how the brain adapts existing memories in response to such prediction errors. Therefore, the aim of the present study was to identify brain regions which are involved in the establishment of updated episodic representation.

Methods: Thirty-six healthy female participants (age: 22 ± 2.78 years), all right-handed, took part in the study. First, participants encoded 24 different episodes by playing short toy stories in the laboratory. During two further sessions, one day and one week after the encoding, participants went through further video-based retrieval sessions to aid memory consolidation. Another week later, participants returned for a functional Magnetic Resonance Imaging (fMRI) session, during which episodic retrieval was cued by videos showing the original episodes or slightly modified versions thereof to induce prediction errors. Modified videos deviated from originally encoded ones by a single aspect which was either the order of action steps or an individual object. Imaging was conducted on a 3T Siemens Prisma MR tomograph (TR/TE= 2000/30 ms, FA= 90°, FOV= 192 x 192 mm^2, 33 slices, slice thickness= 3 mm). Lastly, participants completed a post-fMRI memory test during which each video was presented in the original and one modified version in pseudo-randomized order. Participants were asked to indicate on a four-point Likert scale (with 1= yes to 4= no) whether or not each video showed an episode that had been originally encoded. FMRI data were preprocessed (slice time correction, realignment, co-registration of functional to structural scans, normalization, and smoothing) and analyzed with SPM12 using a general linear model. Behavioral data were analyzed using R Studio.

Results: In the post-fMRI memory test, participants were significantly more prone to falsely accept modified episodes as truly encoded when they had experienced prediction errors during the fMRI session ($p = .001$). Additionally, they also had an increased tendency to reject originally encoded episodes as such ($p < .001$). Together, these behavioral findings demonstrate that as expected, memories were modified in response to prediction errors. To investigate the neural effects of memory modification, we analyzed the parametric increase in brain activation to modified episodes that later elicited false alarms in the post-fMRI memory test. On the whole-brain level, increasing activation was detected in several areas, including ventrolateral prefrontal cortex, precuneus, anterior and posterior cingulate cortex, and middle temporal cortex ($p < .01$, FDR corrected). Further, we performed region of interest analyses in areas which are involved in memory formation, hippocampus and parahippocampal gyrus. In hippocampus, a significant increase of activation was detected for later false alarms ($p = .01$). In parahippocampal gyrus, we detected a significant decrease in activation for later correct rejections in the post-fMRI memory test ($p = .04$) and additionally found that contrast estimates were significantly higher for later false alarms compared to later correct rejections ($p = .034$).

Conclusions: The findings of the current study support the idea that episodic memories can be modified in response to prediction errors. For the first time, we demonstrated that false alarms in an episodic memory test were preceded by parametric increases in brain activation during the processing of prediction errors. Consequently, we suggest that this activation might be reflective of the establishment of updated episodic representations.

References

1. Sinclair, A. H. (2019), 'Prediction Error and Memory Reactivation: How Incomplete Reminders Drive Reconsolidation', Trends in Neurosciences, vol. 42, no. 10, pp. 727–739.
2. Siestrup, S. (2022), 'What Happened When? Cerebral Processing of Modified Structure and Content in Episodic Cueing', Journal of Cognitive Neuroscience, vol. 34, no. 7, pp. 1287–1305.
3. Exton-McGuinness, M. T. J. (2015), 'Updating memories-The role of prediction errors in memory reconsolidation', Behavioural Brain Research, vol. 278, pp. 375–384.
4. Fernández, R. S. (2016), 'The fate of memory: Reconsolidation and the case of Prediction Error', Neuroscience and Biobehavioral Reviews, vol. 68, pp. 423–441.

Poster No 1074

Task-based functional connectivity during mnemonic discrimination and cognitive training effects

Panagiotis Iliopoulos[1], Jeremie Güsten[1], Eoin Molloy[2,3], Anne Maass[2], Emrah Düzel[1,2]

[1]Institute of Cognitive Neurology and Dementia Research, Otto-von-Guericke University, Magdeburg, Germany, [2]German Center of Neurodegenerative Diseases (DZNE), Magdeburg, Germany, [3]Division of Nuclear Medicine, Department of Radiology & Nuclear Medicine, Faculty of Medicine, Otto von Guericke University, Magdeburg, Germany

Introduction: Successful memory relies on the process of mnemonic discrimination (MD) to establish distinct representations[1,4,5,9]. Despite extensive research on the role of medial temporal lobe (MTL) areas in MD[2,4,9], little is known about MTL interactions with prefrontal (PFC) and visual (VIS) areas and the impact of cognitive training on functional communication

and MD performance. Here, we investigated the task-based functional connectivity underlying MD, focusing on major MTL-PFC-VIS areas, in addition to the effects of a 2-week cognitive training intervention on connectivity and behavior.

Methods: In a longitudinal study, 54 young adults (M = 23.76 years, SD = 3.35, 61.11% female) underwent a cognitive task differentiating similar objects and scenes ('lures'; correct response: 'new') from repeated items ('repeats', correct response: 'old'). Stimuli were presented in 12-item sequences with the first six being new images, while each of the subsequent six could be either a lure or a repeat trial (Fig.1). Data were acquired on a 3T-MRI Siemens scanner, using a BOLD-EPI (2 runs x 12 min; resolution 2 mm isotropic, TR= 2.2 secs) and MPRAGE sequence (1 mm isotropic), pre- and post- a 2-week web-based cognitive training intervention (three 45-minute sessions per week). Participants were divided into an experimental group (n=26) that underwent training using a web-based version of the task, and an active control group (n=27) that was presented with the same set of stimuli but performed a psychomotor task clicking on moving icons on top of the images. Data were preprocessed using the fMRIPrep pipeline3, denoised and modeled with generalized psychophysiological interaction (gPPI) analysis[6,8].All fMRI analyses focused on the MD contrast (correct lures versus repeats). First, we performed a hypothesis-driven region of interest (ROI)-to-ROI analysis on the whole-sample pre-training data. Major MTL, PFC, VIS regions were used as ROIs. Time x Group interaction analyses (ANOVA) assessed cognitive training effects on memory performance and the task-based functional connections identified in the previous step. Gender and age were used as covariates.

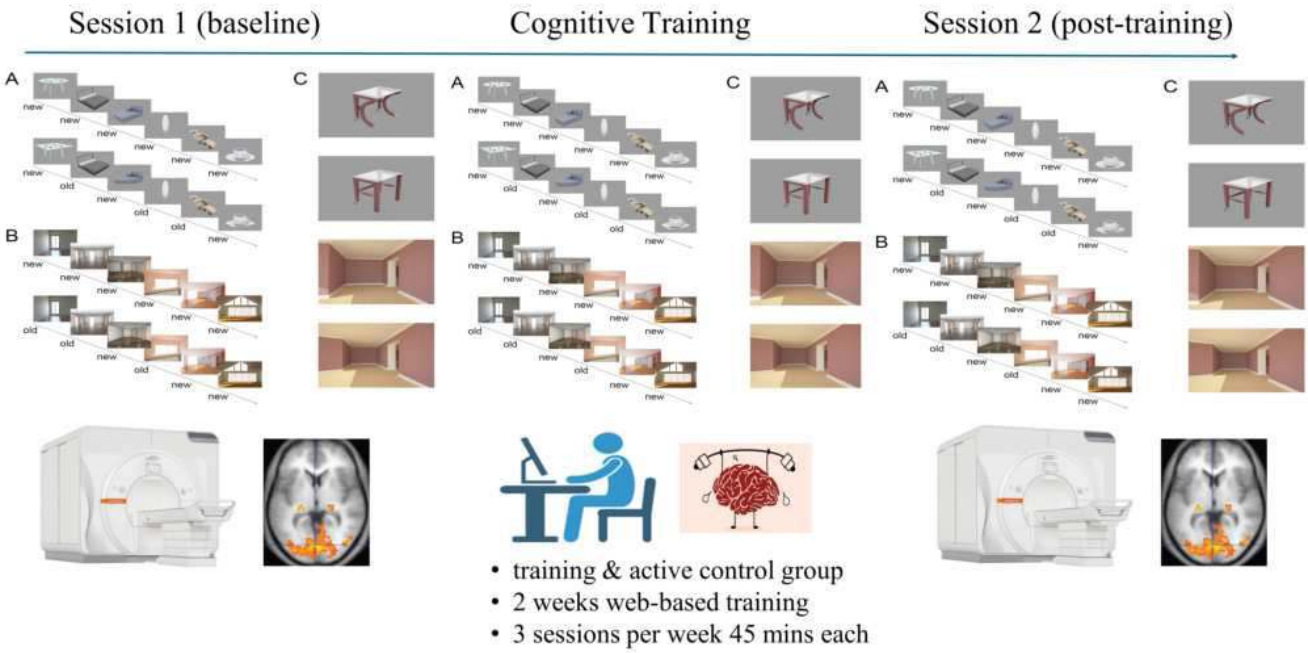

Figure 1. Experimental design. Mnemonic discrimination task performed in a 3T scanner (fMRI). Stimuli were presented in sequences of 12 items (6 encoding followed by 6 test phase images). Subjects had to discriminate similar stimuli ('lures') from identically repeated items ('repeats'). Each sequence consisted of either objects (A) or scenes (B) only. Lure and repeat stimuli only differed in shape or geometry (C). Each stimulus was presented for 3 secs. The subjects were scanned pre- and post- a 2-week web-based cognitive training intervention that included three 45-minute sessions per week. One group (n=26) trained using a web-based version of the above task, whereas a control group (n=27) was presented with the same images but was instructed to click on moving neurons shown on top of the images.

Results: In the whole-sample pre-training analysis, we identified three significant connectivity clusters during successful MD (cluster-based inference $p < .05$ p-FDR): 1) reduced VIS-to-VIS and VIS-MTL connectivity, and increased 2) VIS-PFC and 3) hippocampal-PFC connectivity (Fig.2A). Focusing on the individual connections within these three clusters, we found a significant training effect (MD contrast, Time x Group interaction: $F(1,49)=10.00$, $\eta 2p = .170$, p-FDR=.016) observing post-training increase in task connectivity specifically from the lateral occipital cortex (LOC) to the occipital pole (OP) (Fig.2B, 2C). Notably, Time x Group interaction analyses indicated that the training group exhibited improved memory performance after training, reflected in higher discriminability (A') ($F(1,49) = 9.34$, $\eta 2p = .160$, $p=.004$) and improved correct lure performance ($F(1,49) = 15.73$, $\eta 2p = .243$, $p<.001$) compared to the control group (Fig.2D).

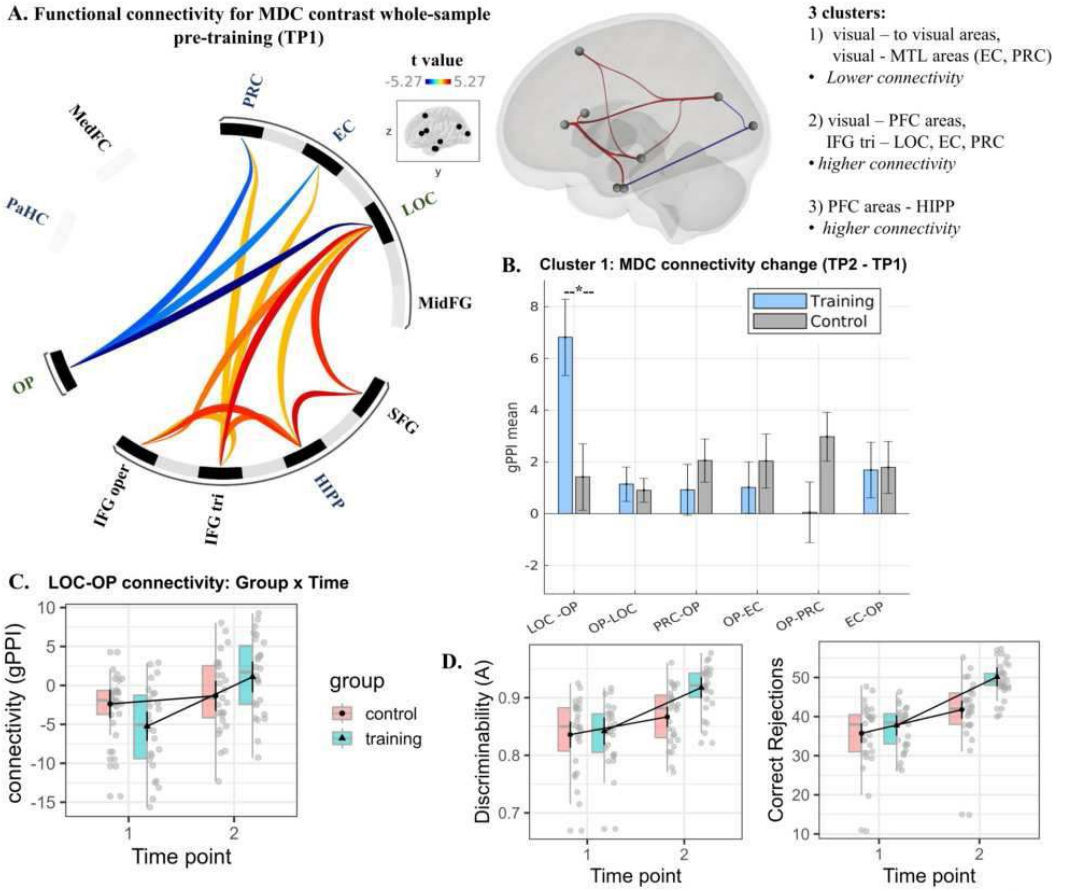

Figure 2. Task functional connectivity for mnemonic discrimination and cognitive training effects on connectivity and behavior. A: Functional connectivity for the mnemonic discrimination contrast (MDC: correct lures minus repeat trials). Visualization of 3 significant clusters found shown in a ring plot, brain template, and a summary of the connections in each cluster. **B**: Visualization of the significant cognitive training effect on the LOC-OP connection from cluster 1 (connectivity change: post-training minus pre-training) for the training versus the control group. **C:** Visualization of the significant cognitive training effects (Group x Time interaction) on LOP-OP connectivity, and **(D)** behavioral performance (Discriminability A' index, and correct rejections/lures). Comparisons marked * are significant at $p < .05$ level. **TP**= time point, **PaHC**: parahippocampal cortex, **MedFC**: medial frontal cortex, **PRC**: perirhinal cortex, **EC**: enthorhinal cortex, **LOC**: lateral occipital cortex, **MidFG**: mid-frontal gyrus, **SFG**: superior frontal gyrus, **HIPP**: hippocampus, **IFG**: inferior frontal gyrus; **tri**: triangularis, **oper**: opercularis. **OP**: occipital pole.

Conclusions: Our results highlight the role of VIS-to-VIS, VIS-MTL, VIS-PFC, and PFC-hippocampal connectivity during successful MD. They extend previous findings that involve wider networks in MD1,7, suggesting a role of MTL-PFC-VIS connectivity. A brief 2-week cognitive training not only enhanced MD performance but also increased LOC-OP task-based functional connectivity. This suggests improved functional communication from higher to lower-order visual areas, indicating a potential enhancement in neural visual processing. Our findings demonstrate that even a short-duration intervention can induce neural changes, boosting memory performance. Future investigations may test whether more prolonged training yields broader functional alterations in MD.

References

1. Amer, T., & Davachi, L. (2023). Extra-hippocampal contributions to pattern separation. ELife, 12, 1–23. https://doi.org/10.7554/elife.82250
2. Berron, D., Schütze, H., Maass, A., Cardenas-Blanco, A., Kuijf, H. J., Kumaran, D., & Düzel, E. (2016). Strong evidence for pattern separation in human dentate gyrus. Journal of Neuroscience, 36(29), 7569–7579. https://doi.org/10.1523/JNEUROSCI.0518-16.2016
3. Esteban, O., Markiewicz, C. J., Blair, R. W., Moodie, C. A., Isik, A. I., Erramuzpe, A., Kent, J. D., Goncalves, M., DuPre, E., Snyder, M., Oya, H., Ghosh, S. S., Wright, J., Durnez, J., Poldrack, R. A., & Gorgolewski, K. J. (2019). fMRIPrep: a robust preprocessing pipeline for functional MRI. Nature Methods, 16(1), 111–116. https://doi.org/10.1038/s41592-018-0235-4
4. Kirwan, C. B., & Stark, C. E. L. (2007). Overcoming interference: An fMRI investigation of pattern separation in the medial temporal lobe. Learning and Memory, 14(9), 625–633. https://doi.org/10.1101/lm.663507
5. Leal, S. L., & Yassa, M. A. (2018). Integrating new findings and examining clinical applications of pattern separation. Nature Neuroscience, 21(2), 163–173. https://doi.org/10.1038/s41593-017-0065-1
6. McLaren, D. G., Ries, M. L., Xu, G., & Johnson, S. C. (2012). A generalized form of context-dependent psychophysiological interactions (gPPI): A comparison to standard approaches. NeuroImage, 61(4), 1277–1286. https://doi.org/10.1016/j.neuroimage.2012.03.068
7. Pidgeon, L. M., & Morcom, A. M. (2016). Cortical pattern separation and item-specific memory encoding. Neuropsychologia, 85, 256–271. https://doi.org/10.1016/j.neuropsychologia.2016.03.026
8. Whitfield-Gabrieli, S., & Nieto-Castanon, A. (2012). Conn: A Functional Connectivity Toolbox for Correlated and Anticorrelated Brain Networks. Brain Connectivity, 2(3), 125–141. https://doi.org/10.1089/brain.2012.0073
9. Yassa, M. A., & Stark, C. E. L. (2011). Pattern separation in the hippocampus. Trends in Neurosciences, 34(10), 515–525. https://doi.org/10.1016/j.tins.2011.06.006

Poster No 1075

The extraction and application of temporal structures: a fMRI study

Linda Sempf[1], Peter Vavra[1], Toemme Noesselt[1,2]

[1]Institute of Psychology, Otto-von-Guericke-University, Magdeburg, Saxony-Anhalt, [2]Center for Behavioral Brain Sciences, Magdeburg, Saxony-Anhalt, Germany

Introduction: The comprehension of recurrent temporal structures in our environment allows us to recognize causal relationships between events and build expectations about the timing of future ones. Previous studies on temporal attention have often used symbolic cues to indicate the probability of a target to appear at a particular moment in time. However, temporal expectations can also be based on unconsciously perceived probability distributions - for instance, a recurrent temporal interval between two stimuli. After statistical learning, the first of two stimuli can then be used as a meaningful cue to predict the moment when the second stimulus will occur. While this memory-based predictive mechanism is often used to optimize everyday behaviour and has been studied behaviorally, it is not fully understood, how the brain recognizes, extracts, and neuronally represents temporal relationships and utilizes them to guide attention to specific points in time. Here, we characterized the neural underpinnings of statistical learning and utilizing temporal structures with functional magnetic resonance imaging (fMRI).

Methods: In a longitudinal fMRI study participants (n=36) were exposed to audiovisual cue-target combinations. Targets appeared either at early (500ms) or late (1500 ms) time points after the cue and the probability of the two cue-target intervals was manipulated block-wise (1:4 or 4:1, early : late ratio). The two blocks alternated and each consisted of a likely and an unlikely interval (e.g. early likely and late unlikely). On day 1 participants passively observed the AV-combinations inside the scanner (4 runs), on day 2 and 3 they were trained on visual target detection outside the scanner and on day 4 they first passively observed the parings (4 runs) before they actively detected targets again inside the scanner (4 runs). fMRI-data (voxel size: 2.2 mm3, 66 slices, 250 volumes/run) was collected on a 3T Prisma scanner. After preprocessing (slice timing, realignment, normalization, smoothing) and first level modelling (with hemodynamic response function plus derivatives for all experimental conditions (early/ late & likely/ unlikely)) and realignment parameters) second level models (flexible factorial designs) were used for population level inferences.

Results: Behaviorally, participants responded faster to early targets when they were more likely confirming that temporal expectations were formed to guide behaviour. Neurally, targets in the early-likely context elicited enhanced responses in the left hippocampus (CA1 region) already during passive viewing on day 1. During the active task left inferior parietal lobule (IPL), bilateral prefrontal gyrus and retrosplenial cortex (RSC) showed enhanced fMRI-responses for likely>unlikely trials. In IPL this effect was more pronounced for likely early than likely late targets. In addition, the fMRI response in this area correlates significantly with subject-specific mean response times. In contrast, unlikely>likely events modulated visual areas and right temporoparietal junction, in accord with previous findings on prediction-error processing.

Conclusions: Our results indicate that the processing of temporal context and potentially the extraction of temporal structures is initially associated with activity within the CA1 hippocampal subregion, even during passive observation. In keeping with this, neurophysiological animal studies have reported that the CA1 region contains time-sensitive neurons. When temporal expectations have been established, IPL and RSC are more engaged during likely trials, reflecting the use of temporal expectancies during active task performance. Similar activation patterns have also been observed during episodic memory processing, as confirmed by an association test (Yarkoni et al., 2011). These results conform with the notion of an engagement of episodic memory when learning and using temporal information (Frings et al., 2020).

References

1. Refs: Frings C, et al. (2020) Binding and Retrieval in Action Control (BRAC). Trends in Cognitive Sciences 24:375–387.
2. Yarkoni T, et al. (2011) Large-scale automated synthesis of human functional neuroimaging data. Nat Methods 8:665–670.

Poster No 1076

Organizational principles of semantic control in the human brain

Kaixiang Zhuang[1], Xinyu Liang[1], Cheng Liu[2], Theodoros Karapanagiotidis[3], Jonathan Smallwood[4], Elizabeth Jefferies[5], Deniz Vatansever[1]

[1]Fudan University, Shanghai, Shanghai, [2]Southwest University, Chongqing, Chongqing, [3]University of Sussex, Sussex, Sussex, [4]Queen's University, Ontario, Canada, [5]University of York, York, United Kingdom

Introduction: The human semantic system affords a multi-dimensional conceptual space through which we ascribe meaning to various words and objects around us. Notably, accessing concepts that are more remotely connected in this space is suggested to require higher levels of demand for semantic control[1]. However, the precise neural signature of semantic control, and its distributed organization within the cortical hierarchy remains unclear. By combining an fMRI-based semantic retrieval task[2], a natural language processing model[3] and multivoxel pattern analysis (MVPA)[4], here we captured a neural signature associated with varying demands for semantic control and charted its distribution within the cortical connectivity gradients[5]. We demonstrate that semantic control requires the engagement of multiple brain networks, dispersed along two principal gradients relevant to different aspects of semantic processing. This offers new insights into how the brain's functional networks are architecturally specialized to support semantic cognition.

Methods: A group of 46 healthy young adults (mean = 21.31 years old, 21/25 Word List A to B ratio) completed a 3-alternative forced choice semantic retrieval fMRI task, in which they were probed with a cue word and asked to select the most conceptually associated target word amongst two other distractors across 80 trials. Crucially in each trial, semantic distance between word pairs, defined by the cosine distance within 300-dimensional GloVe vectors, were used to systematically manipulate the demand for semantic control (Fig. 1a-b). Next, we employed thresholded partial least squares T-PLS[6] and GLMsingle derived single-trial beta maps[7] to identify a whole-brain multivariate signature of semantic control (Fig. 1c), which served as a predictive model for semantic distance during semantic retrieval. After a series of rigorous assessments, the feature weights of semantic control signature were projected onto a continuous 2D space of functional connectivity gradients in order to characterize its organizational principles within the large-scale cortical hierarchy.

Results: The identified neural signature of semantic control spanned areas sensitive to both high and low-demand semantic decisions (e.g. left IFG, pMTG, mPFC, PCC), as well as bilateral anterior insula and primary visual cortices (Fig. 1c). In addition to demonstrating high accuracy and generalizability (Fig. 1d-e), the semantic control signature distinguished subtle differences between word pairs (Fig. 1f), and accurately captured the response speed of participants during semantic retrieval (Fig. 1g). Furthermore, the identified semantic control signature exhibited spatial correlations with two out of 10 principal gradients (Fig. 2a). Specifically, we observed clear boundaries in the 2D space constituted by Gradients 6 and 10, which demarcated positive and negative feature weights of the neural signature (Fig. 2b). Based on the NeuroSynth meta-analytic decoding, we further revealed that both gradients were closely related to semantic cognition (Fig. 2c). While Gradient 6 arranged brain regions in a cognitive continuum from "low to high demand semantic cognition", Gradient 10 arranged brain regions from "verbal to visual semantic cognition".

Conclusions: Based on a semantic retrieval task and machine learning approach, we revealed a robust and generalizable neural signature sensitive to varying levels of semantic control demands. Notably, the identified signature was constrained by two functional connectivity gradients, both of which related to different aspects of semantic cognition. Together, our findings demonstrate how disparate regions within the cortical organization unite within a lower dimensional space to facilitate the control of semantic cognition.

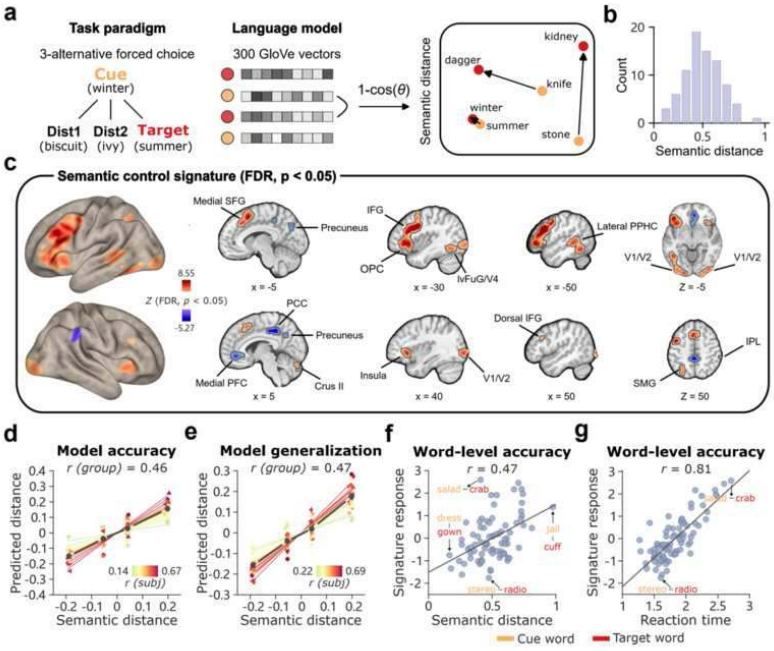

Figure 1. Experimental procedure and model evaluation. (a) Experimental procedure. A group of healthy young adult participants took part in an fMRI session designed to probe semantic memory retrieval utilizing a 3-alternative forced choice (3-AFC) paradigm. T-PLS was employed to identify a whole-brain neural signature of semantic control. **(b)** Distribution of semantic distance. 300 dimensional GloVe word vectors were employed to quantify semantic distance between the cue and target word pairs. **(c)** Semantic control signature. The maps was thresholded using a 5,000-sample bootstrap procedure at FDR $p < 0.05$. **(d)** Evaluation of model accuracy. Subject-level prediction-outcome correlation: $r = 0.46 \pm 0.12$ SE; group-level prediction-outcome correlation: $r = 0.46$. **(e)** Evaluation of model generalizability. Subject-level prediction-outcome correlation: $r = 0.48 \pm 0.09$ SE in the generalization of A-to-B; group-level prediction-outcome correlation: $r = 0.47$ in A-to-B. **(f)** Word level prediction for semantic distance. The identified neural signature was used to predict semantic distance between word pairs. The beta maps corresponding to each word pair were averaged across all trials. Correlation between signature response and semantic distance: $r = 0.47$. **(g)** Word level prediction of reaction time (RT). The identified neural signature was used to distinguish the differences in RT between word pairs. The beta maps and RTs corresponding to each word pair were averaged across all trials. Correlation between signature response and RTs: $r = 0.81$.

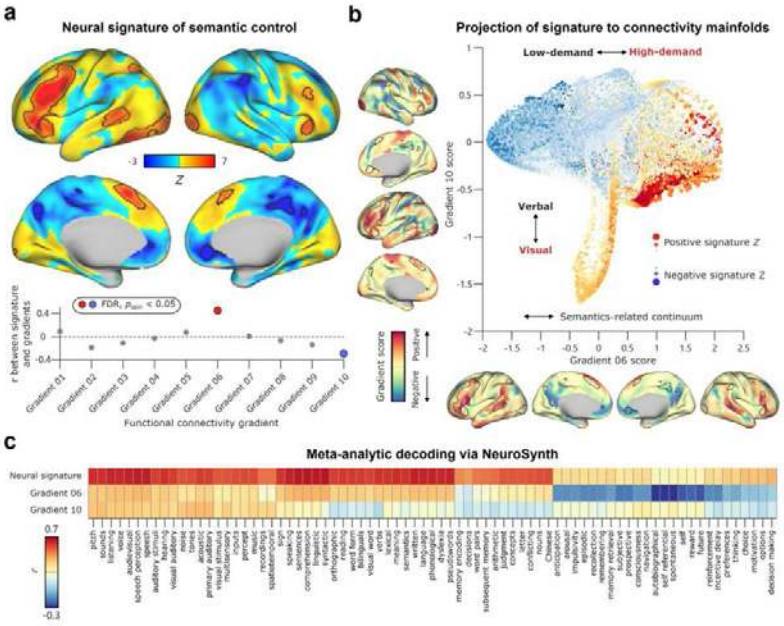

Figure 2. Semantic control signature within low-dimensional cortical connectivity gradients. (a) Relationship between semantic control signature and functional connectivity gradients. The 'spin'-based method was used to correct the p values for potential confounding effects of spatial autocorrelation. $r = 0.45$ for gradient 6, $r = -0.29$ for gradient 10, FDR, p-spin < 0.001. **(b)** Projection of semantic control signature onto the specific 2D gradient space. Gradient scores were adjusted according to the correlation direction of each gradient with the semantic control signature. **(c)** Distribution of correlation coefficients for the three brain patterns of interest in the NeuroSynth feature matrix. Top 30 cognitive terms (features) from the NeuroSynth database are displayed for both the positive and negative extrema of each brain pattern.

References

1. Ralph, M. A. L., Jefferies, E., Patterson, K., & Rogers, T. T. (2017). The neural and computational bases of semantic cognition. Nature reviews neuroscience, 18(1), 42-55.
2. Vatansever, D., Smallwood, J., & Jefferies, E. (2021). Varying demands for cognitive control reveals shared neural processes supporting semantic and episodic memory retrieval. Nature communications, 12(1), 2134.
3. Pennington, J., Socher, R., & Manning, C. D. (2014). Glove: Global vectors for word representation. In Proceedings of the 2014 conference on empirical methods in natural language processing (EMNLP)
4. Spisak, T., Bingel, U., & Wager, T. D. (2023). Multivariate BWAS can be replicable with moderate sample sizes. Nature, 615(7951), E4-E7.
5. Citation: Lee, S., Bradlow, E. T., & Kable, J. W. (2022). Fast construction of interpretable whole-brain decoders. Cell Reports Methods, 100227.
6. Mars, R. B., Passingham, R. E., & Jbabdi, S. (2018). Connectivity fingerprints: from areal descriptions to abstract spaces. Trends in cognitive sciences, 22(11), 1026-1037.
7. Prince, J. S., Charest, I., Kurzawski, J. W., Pyles, J. A., Tarr, M. J., & Kay, K. N. (2022). Improving the accuracy of single-trial fMRI response estimates using GLMsingle. Elife, 11, e77599.

Poster No 1077

Verbal memory outcomes after temporal lobe resection in pediatric epilepsy

Freya Prentice[1,2], Maria Eriksson[1,2], Sara Shavel-Jessop[1,2], Patricia Martin-SanFilippo[1,2], Frederique Liegeois[1,2], Torsten Baldeweg[1,2]

[1]University College London, London, UK, [2]Great Ormond Street Hospital, London, UK

Introduction: Verbal memory deficits are consistently documented in adults after left temporal lobe resection (TLR) for intractable epilepsy (Lee et al., 2002) but not in children. This may reflect less lateralized memory networks in the developing brain as well heterogeneity in the use of neuropsychological measures of verbal memory across pediatric studies. The task specificity model (Saling, 2009) suggests that tests which involve the delayed recall of unrelated word pairs are more sensitive to hippocampal functioning due to the specific role of the hippocampus in binding unrelated information. It would, therefore, be expected that decline on this measure would be greatest after left TLR including hippocampal removal (TLR+H). In this retrospective study, we aimed to replicate previous findings (Law et al. 2017; Danguecan & Smith, 2019) that declines in word pair recall in children are more likely after left TLR with hippocampectomy (TLR+H) compared to without and right TLR. Secondly, we sought to identify additional clinical and neuroimaging predictors of word pair decline.

Methods: We included 44 children who underwent TLR for intractable epilepsy at Great Ormond Street Hospital between 2000-2022 and had pre- and postoperative assessments on the Children's Memory Scale (CMS). Change scores were calculated from the difference between pre- and postoperative scores and decline was defined based on published Reliable Change Indices (Busch et al., 2015). The extent of TLR was coded based on surgical reports and confirmed by the visual inspection of the MRI scan by an experienced neuroanatomist. Where patients had a preoperative language fMRI, a laterality index was calculated in a frontal region of interest for a verb generation task.

Results: Rates of RCI-defined declines on the word pairs subtest of the CMS differed between all four groups (see Table 1; X2=9.14, p=.027), with decline only demonstrated in those who underwent left TLR+H. Within the left TLR+H group, greater postoperative decline in word pairs was associated with higher preoperative word pair scores (r=-0.48, p=.039) and an older age at surgery (r=-0.66, p=.002), but not postoperative seizure freedom (t(1.17)=0.14, p=.909; see Figure 1). Preoperative left language lateralization was significantly correlated with an older age at surgery (r=0.61, p=.026, N=13), but not word pair decline (r=-0.52, p=.069, N=13). A final linear regression model including preoperative word pair scores and age at surgery explained 46% of the variance in word pair decline (adjusted r2=0.46, p=.003).

Table 1. Epilepsy characteristics and neuropsychological scores in TLR groups

	Left TLR		Right TLR	
	Hippocampus resected (N=19)	Hippocampus spared (N=11)	Hippocampus resected (N=8)	Hippocampus spared (N=6)
Age at seizure onset (years)	5.1 (3.3)	7.2 (3.9)	4.8 (3.5)	9.4 (2.6)
Age at surgery (years)	11.8 (2.9)	12.3 (3.0)	12.6 (1.9)	13.5 (2.6)
Language lateralisation (typical/atypical/unknown)	13/0/6	9/2/0	4/1/3	0/1/5
Seizure free (Y/N/unknown)	16/2/1	7/4/0	5/3/0	5/1/0
Delayed word pair recall score • Preoperative • Postoperative	 8.6 (3.7) 7.6 (3.8)	 9.1 (4.7) 10 (4.7)	 7.5 (3.4) 8.9 (5.1)	 9.2 (5.5) 10.3 (3.9)
Proportion demonstrating decline in word pair recall (%)	32	0	0	0

Figure 1. Potential predictors of word pair decline after left TLR with hippocampal resection

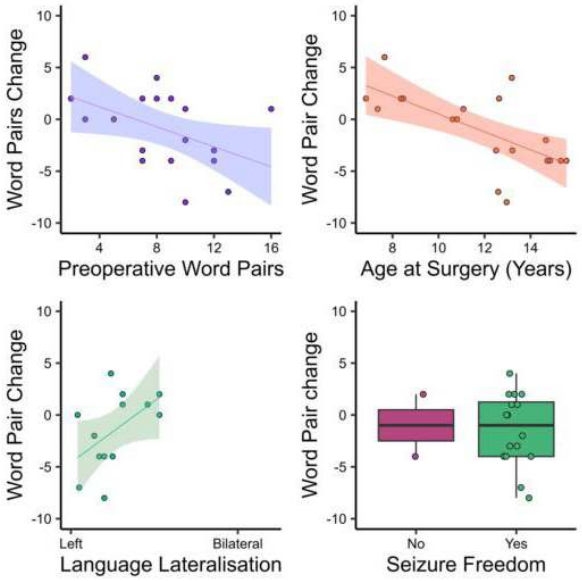

Conclusions: We replicated previous findings that decline on the delayed word pairs subtest was specific to patients with a left TLR+H, with 32% of this group experiencing a clinically meaningful decline. Within the left TLR+H group, all patients who experienced a decline had surgery after 12 years of age and an older age at surgery was associated with decline. This may reflect increasingly lateralized verbal memory functions with age, resulting in greater verbal memory deficits after left TLR+H, similar to those observed in adults. Left language lateralisation was associated with an older age at epilepsy surgery, however, language lateralisation was not predictive of word pair decline. The power of this analysis was likely limited by a small and entirely left-lateralized group. Larger fMRI samples are needed to examine whether the greater word pair declines seen with an increasing age at surgery partially reflect increasing left lateralisation of language and memory networks over development.

References

1. Busch, R.M. (2015), 'Reliable Change Indices and Standardized Regression-Based Change Score Norms for Evaluating Neuropsychological Change in Children with Epilepsy', Epilepsy & Behavior, vol. 47, pp. 45-54.
2. Danguecan, A.N. (2019), 'Verbal associative memory outcomes in pediatric surgical temporal lobe
3. epilepsy: Exploring the impact of mesial structures', Epilepsy & Behavior, vol. 101, 106529.
4. Law, N. (2017), 'Verbal memory after temporal lobe epilepsy surgery in children: Do only mesial structures matter?', Epilepsia, vol. 58, pp. 291-299.
5. Lee, T.M.C (2002), 'Memory deficits after resection from left or right anterior temporal lobe in humans: a meta-analytic review', Epilepsia, vol. 43, pp. 283-291.
6. Saling (2009). 'Verbal memory in mesial temporal lobe epilepsy: beyond material specificity', Brain, vol. 132, pp. 570-582.

Poster No 1078

A gradient of spatial novelty and familiarity along the hippocampal long axis

Joern Alexander Quent[1], Xinyu Liang[1], Liangyue Song[1], Yueting Su[1], Kaixiang Zhuang[1], Deniz Vatansever[1]

[1]Fudan University, Shanghai, China

Introduction: Recognition of novelty constitutes a vital aspect of our ability to encode and navigate our surroundings. Though extensively studied e.g. in the context of item novelty[1], human neuroimaging studies of spatial novelty and its impact on long-term memory formation remains relatively scarce. Limited reports show that spatial novelty can boost long-term memory [e.g. 2] and is associated with distinct responses along the cortical surface and hippocampal long axis[3,4], which requires further investigation. Here, we assessed participants during navigation of a virtual reality environment using ultra-high field 7T fMRI to chart the neural representation of spatial novelty.

Methods: A group of 56 healthy participants (20 - 37 years, M = 24 years, SD = 2.8 years, F/M ratio: 35/21) were scanned at 7T MRI (MB-BOLD, TR = 1.0 s, TE = 22.2 ms, 1.6 mm isotropic voxels) while navigating within a grassy circular environment enclosed by a wall and surrounded by landmarks (e.g. trees, buildings, mountains). Across two runs of an object location memory task, participants were asked to navigate to the locations of 6 cued objects in order to collect them and memorise

their location for subsequent retrieval. To analyse spatial novelty, the environment was divided into hexagonal sectors. Events were defined as time points that the participants spent in those sectors, which were weighted by a novelty score based on a) the number of times the sectors were visited and b) how much time passed since the last visit of the sector. The HCP-style fMRI data was pre-processed and analysed[5,6] as a GLM-based parametric modulation of events by spatial novelty using FSL FEAT routines. Statistical significance was assessed via non-parametric permutation testing based on PALM (voxel-wise cFDRp < .05). Results were projected onto cortical connectivity-based gradient space for interpretation purposes[7]. A spatial gradient analysis was also performed to further interrogate effects within the hippocampal long axis. Each voxel was assigned a value between 1 and 6 based on the novelty response[8], which were then projected on to the average shape of the hippocampi (Fig. 2a). A slope was calculated for predicting the classification based on the projection, which was finally compared to a permutation-derived null distribution.

Results: Behaviourally, novelty scores displayed an expected decrease over time due to exploration: Run 1 β = -0.48 (95 % CI [-0.56, -0.41]) and Run 2 β = -0.71 (95 % CI [-0.75, -0.66]). At the neural level, fMRI analyses across the cortical surface revealed positive modulation (greater activity for novelty) mainly centred on regions distributed across the visual and frontoparietal networks. On the other hand, negative modulation (greater activity for familiarity) was observed within somatosensory/motor and default mode areas (Fig. 1b). We also found significant negative modulation effects within the bilateral amygdala and anterior hippocampus. Notably, a significant spatial novelty-familiarity gradient was observed along the hippocampal long axis, where the posterior to anterior portions of the right hippocampus preferred to process novel to familiar sectors respectively, p < 2e-06. However, no significant spatial novelty gradient was present in the left hippocampus, p = .53 (Fig. 2a).

Conclusions: Collectively, our results highlight an extensive set of cortical and subcortical brain regions contributing to the neural representation of spatial novelty, including a novelty-familiarity gradient along the hippocampal long axis. Further work will be required to provide a more detailed mapping of the functional roles played by these regions, which will be crucial to further advance our mechanistic understanding of the novelty signature and spatial cognition in humans.

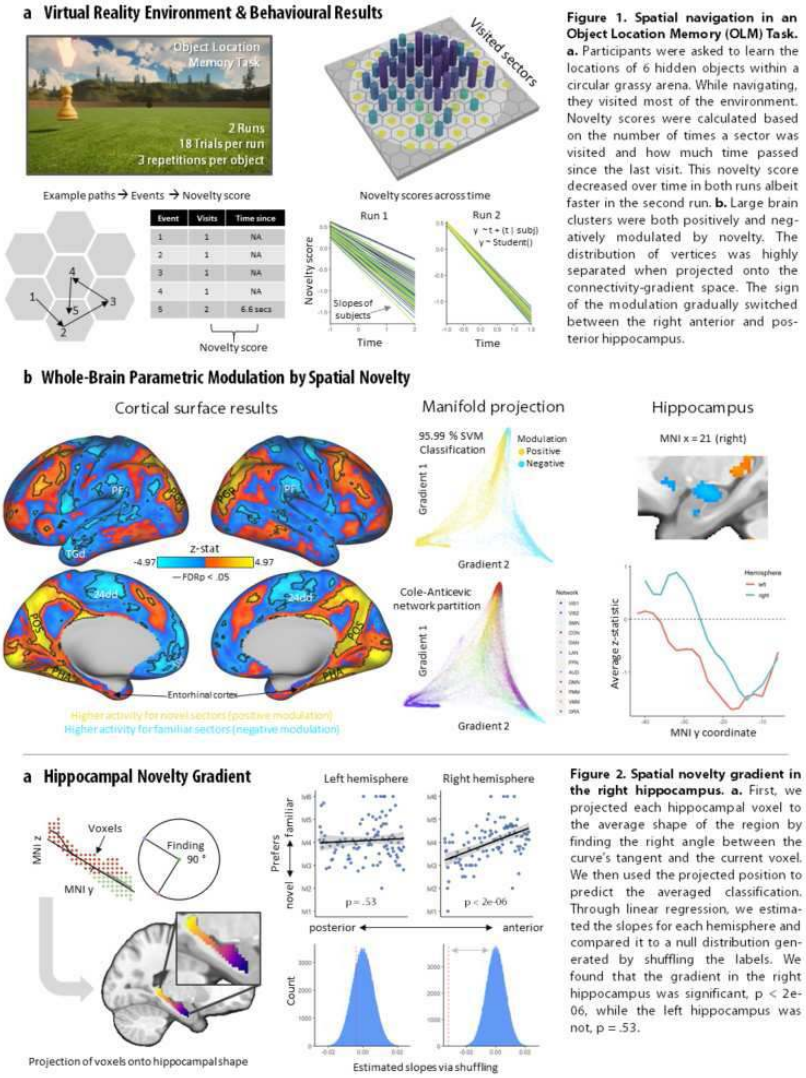

Figure 1. Spatial navigation in an Object Location Memory (OLM) Task. a. Participants were asked to learn the locations of 6 hidden objects within a circular grassy arena. While navigating, they visited most of the environment. Novelty scores were calculated based on the number of times a sector was visited and how much time passed since the last visit. This novelty score decreased over time in both runs albeit faster in the second run. **b.** Large brain clusters were both positively and negatively modulated by novelty. The distribution of vertices was highly separated when projected onto the connectivity-gradient space. The sign of the modulation gradually switched between the right anterior and posterior hippocampus.

Figure 2. Spatial novelty gradient in the right hippocampus. a. First, we projected each hippocampal voxel to the average shape of the region by finding the right angle between the curve's tangent and the current voxel. We then used the projected position to predict the averaged classification. Through linear regression, we estimated the slopes for each hemisphere and compared it to a null distribution generated by shuffling the labels. We found that the gradient in the right hippocampus was significant, p < 2e-06, while the left hippocampus was not, p = .53.

References
1. Quent, J. A., Henson, R. N. & Greve, A. A predictive account of how novelty influences declarative memory. Neurobiology of Learning and Memory 179, 107382–107382 (2021).
2. Schomaker, J., van Bronkhorst, M. L. V. & Meeter, M. Exploring a novel environment improves motivation and promotes recall of words. Frontiers in Psychology 5, 1–6 (2014).
3. Poppenk, J., Evensmoen, H. R., Moscovitch, M. & Nadel, L. Long-axis specialization of the human hippocampus. Trends in Cognitive Sciences 17, 230–240 (2013).
4. Strange, B. A., Fletcher, P. C., Henson, R. N. A., Friston, K. J. & Dolan, R. J. Segregating the functions of human hippocampus. Proc. Natl. Acad. Sci. U.S.A. 96, 4034–4039 (1999).
5. Glasser, M. F. et al. The Human Connectome Project's neuroimaging approach. Nat Neurosci 19, 1175–1187 (2016).
6. Ji, J. L. et al. QuNex—An integrative platform for reproducible neuroimaging analytics. Front. Neuroinform. 17, 1104508 (2023).
7. Margulies, D. S. et al. Situating the default-mode network along a principal gradient of macroscale cortical organization. Proc. Natl. Acad. Sci. U.S.A. 113, 12574–12579 (2016).
8. Peer, M., Ron, Y., Monsa, R. & Arzy, S. Processing of different spatial scales in the human brain. eLife 8, e47492 (2019).

Poster No 1079

Coordinated sleep oscillations between human hippocampal subfields

Zhipeng Li[1], Xia Liang[1]

[1]Harbin Institute of Technology, Harbin, Heilongjiang

Introduction: The hippocampus is a heterogeneous brain structure, comprising histologically distinguishable subfields including the dentate gyrus (DG), CA3, CA1, subiculum (SUB). Interactions between these hippocampal subfields play a critical role in memory consolidation[1,2]. During non-rapid eye movement (NREM) sleep, multiple brain oscillations (e.g., slow wave, spindle and ripple) have been shown to be involved in the computation and distribution of hippocampal information[3,4]. However, it remains elusive how these oscillations interact to regulate information routing within the local hippocampal circuit. Here, using human intracranial recordings (iEEG), we found that DG/CA3 displays strong cross-frequency coupling (CFC) with CA1 and SUB, but CA1 and SUB show a more precise event-based coupling. We also showed that hippocampal synaptic plasticity, as indexed by delta slope, is modulated by spindle and ripple.

Methods: We obtained iEEG data from 25 epilepsy patients writing the informed consent, and used pre-MRI and post-CT to locate electrode contacts[5]. NREM was identified by low delta (<2 Hz), spindle (12-16Hz) and high frequency band (70-200Hz) power[6]. Power spectral density (PSD) was calculated by 4 s window Welch method[7], and was normalized. Phase-amplitude coupling (PAC) calculated by mean vector length method was z-standardized to a shuffled distribution[4]. We extracted spindle and ripple events, and used preferred PAC phases to measure the event-based coupling[3]. Then, ripple power was grouped according to the SO-spindle coupling phase to measure the triple coupling of delta-spindle-ripple[8]. Correlation between spindle/ripple and delta slope was calculated by spearman correlations.

Results: The PSD results revealed high delta and spindle power in all hippocampal subfields (Fig.1A). PAC analysis revealed that DG/CA3 not only exhibited robust within-region delta-ripple and delta-theta coupling (Fig.1B), but also showed strong delta-ripple coupling with the CA1 and SUB (Fig.1C). During PAC analysis, we did not identify any significant delta-spindle or spindle-ripple coupling in any of the four hippocampal subfields[3,9]. We thus proceeded to examine event-based coupling between the subfields. Interestingly, we found that both delta-spindle and spindle-ripple coupling were evident in CA1 and SUB regions (Fig. 1D and E). Furthermore, our assessment of the relationship between delta-spindle coupling phase and ripple power indicated that the ripple power was significantly modulated by the coupling phase between delta and spindle in the CA1 (Fig. 1F), suggesting triple coordination among the delta, spindle and ripple oscillations in this subfield. Prior studies have demonstrated that synaptic plasticity could be reflected in the alteration of slow wave slope[10]. We therefore measured the delta slope in each hippocampal subfield (Fig1G) and evaluated its changes as a function of the spindle or ripple power. The results demonstrated a significant correlation between delta slope and spindle power across all hippocampal subfields (Fig1.H). In contrast, ripple affects the delta slope only at the maximum power (Fig1.I, top), which is where the ripple event occurs (Fig1.I, bottom).

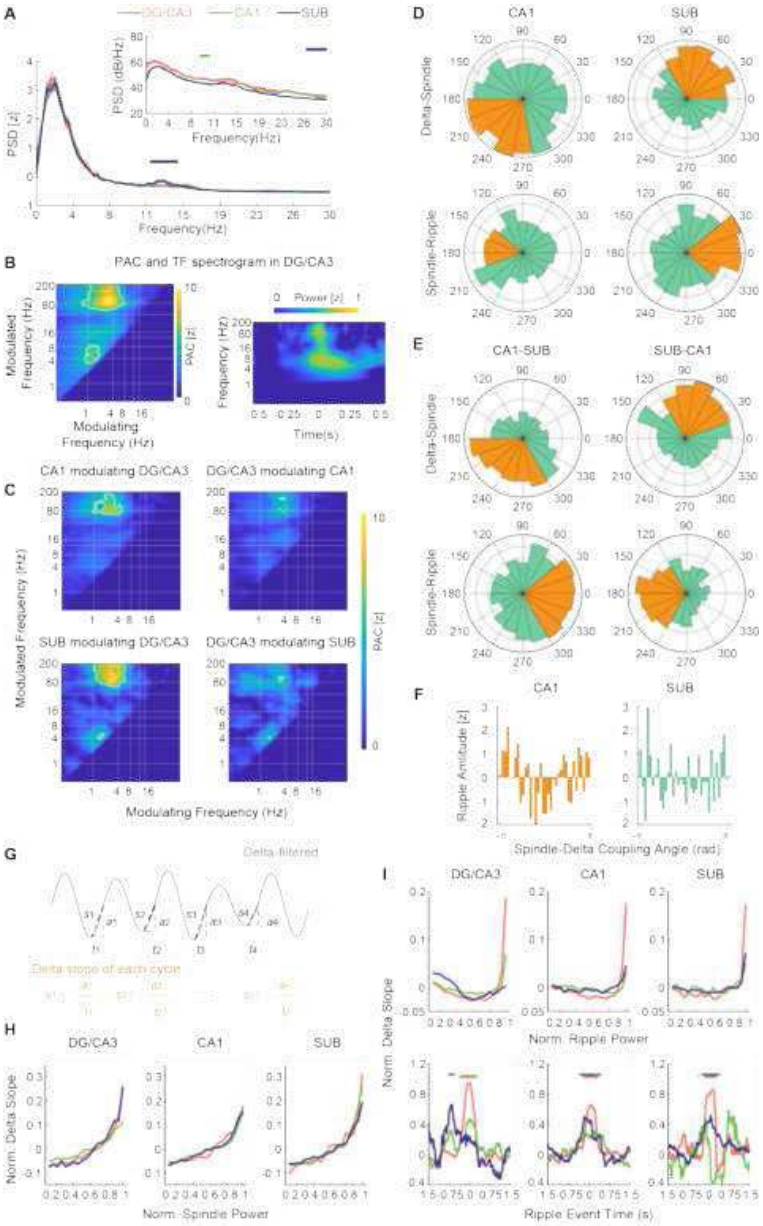

Fig.1 (A) Pairwise comparisons of the normalized spectra in the four subfields (cluster test: $p < 0.05$; purple represents SUB > CA3: spindle band, 12-15 Hz). Inset: Pairwise comparisons of the raw spectra in all subfields (cluster test: $p < 0.05$; green represents DG/CA3 > CA1: 10-11 Hz; purple represents DG/CA3 > SUB: 27-30 Hz). **(B)** Left: Phase-amplitude coupling (PAC) in DG/CA3 (white curves within range represent significant; cluster test: $p < 0.05$). The core of the significant range is delta-ripple and delta-theta (1.3-3.8 Hz). Right: Ripple-locked grand average time-frequency spectrogram in DG/CA3. **(C)** Phase-amplitude coupling between various hippocampal subfields. DG/CA1 exhibited significant coupling with CA1 and SUB, with the frequency range primarily concentrated in the delta-ripple (cluster test: $p < 0.05$). **(D)** Top: Normalized histogram (18 bins, 20° each) of preferred SO-spindle modulation phases across all detected spindle events in CA1 and SUB (yellow bars represent significant coupling angle ranges; V-test: $p < 0.05$, Bonferroni correction. CA1: -180–-80°, SUB: 0–120°). Bottom: Normalized histogram of preferred spindle-ripple modulation phases across all detected spindle events (CA1: 140–200°, SUB: -40–40°). **(E)** Top: Normalized histogram (18 bins, 20° each) of preferred SO-spindle modulation phases between CA1 and SUB (yellow bars represent significant coupling angle ranges; V-test: $p < 0.05$, Bonferroni correction. CA1-SUB: -180–-60°, SUB-CA1: 20–120°). Bottom: Normalized histogram of preferred spindle-ripple modulation phases between CA1 and SUB (CA1-SUB: -60–40°, SUB-CA1: 120–240°). **(F)** Ripple power as a function of the precise SO-spindle phase in CA1 and SUB. CA1 showed a significant correlation (correlation between one circular and one linear random variable. CA1: $r = 0.5575$, $p = 0.0017$). **(G)** Calculation method for the delta slope. The slow-wave slope was defined as the amplitude over time calculated by the straight line connecting the most negative peak of the signal with the following zero crossing. We calculated both the ascending and descending slopes, but since they yielded similar results, this paper only reports the results for the ascending slope. **(H)** Relationships between spindle power in each hippocampal subfield and delta slope in all subfields (Spearman's correlation; Bonferroni correction; All subfields showed a significant positive correlation with delta slope, $p < 0.05$). **(I)** Top: Relationships between ripple power in each hippocampal subfield and delta slope in all subfield s(Spearman's correlation; Bonferroni correction. Only a few lines showed significant associations). Ripple modulation exhibits a "binary" modulation pattern, only affecting the delta slope when ripple power at maximum. Bottom: Time-resolved delta slope relative to the ripple event (-1.5 s). We detected enhanced delta slope around time zero (cluster test: $p < 0.05$).

Conclusions: Our findings suggest that the different hippocampal subfields may play different but complementing role in regulating information during NREM sleep. Specifically, DG/CA3 region communicated globally with CA1 and SUB through delta-ripple coupling, while CA1 and SUB exhibited local event-based coupling, presumably to enable further processing and transmission of critical information. Furthermore, the spindle and ripple functioned at different temporal scales to regulate the delta slope, which could reflect important synaptic changes within hippocampus. Overall, these findings provide valuable insights into the circuitry of the hippocampus during NREM sleep and enhance our understanding of how it facilitates memory consolidation.

References
1. Mizuseki, K. and T. Kitanishi (2022), 'Oscillation-coordinated, noise-resistant information distribution via the subiculum', Curr Opin Neurobiol, vol. 75, no. pp. 102556.
2. Hainmueller, T. and M. Bartos (2020), 'Dentate gyrus circuits for encoding, retrieval and discrimination of episodic memories', Nature reviews. Neuroscience, vol. 21, no. 3, pp. 153-168.
3. Staresina, B. P., et al. (2015), 'Hierarchical nesting of slow oscillations, spindles and ripples in the human hippocampus during sleep', Nat Neurosci, vol. 18, no. 11, pp. 1679-1686.
4. Cox, R., et al. (2019), 'Heterogeneous profiles of coupled sleep oscillations in human hippocampus', Neuroimage, vol. 202, no. pp. 116178.
5. Stolk, A., et al. (2018), 'Integrated analysis of anatomical and electrophysiological human intracranial data', Nat Protoc, vol. 13, no. 7, pp. 1699-1723.
6. Jiang, X., et al. (2017), 'Replay of large-scale spatio-temporal patterns from waking during subsequent NREM sleep in human cortex', Sci Rep, vol. 7, no. 1, pp. 17380.
7. Vijayan, S., et al. (2017), 'Frontal beta-theta network during REM sleep', Elife, vol. 6, no. pp.
8. Helfrich, R. F., et al. (2019), 'Bidirectional prefrontal-hippocampal dynamics organize information transfer during sleep in humans', Nat Commun, vol. 10, no. 1, pp. 3572.
9. Girardeau, G. and V. Lopes-Dos-Santos (2021), 'Brain neural patterns and the memory function of sleep', Science, vol. 374, no. 6567, pp. 560-564.
10. Kurth, S., et al. (2010), 'Characteristics of sleep slow waves in children and adolescents', Sleep, vol. 33, no. 4, pp. 475-480.

Poster No 1080

Predicting Medial Temporal Lobe Integrity and Memory from Thalamic Microstructure Using Radiomics

Rowan Lawrence[1], Daniela Montaldi[1], Alex Kafkas[1]

[1]University of Manchester, Manchester, Greater Manchester

Introduction: Dual-process episodic memory models posit separation of recall (recognition with additional retrieval) and familiarity (simple recognition without further recall) in the medial temporal lobes (MTL). The MTL is functionally connected to other structures including nuclei of the thalamus (Aggleton et al., 2023), together supporting episodic memory. FMRI evidence suggests anterior nuclei support recall, while the medial / mediodorsal nuclei support familiarity (Kafkas et al., 2019). Radiomics, a recently-developed image analysis method, posits that images such as MRI contain microstructure and disease process information which can be extracted by mathematical transforms, providing high-dimensional datasets of quantitative features (Lambin et al., 2017). Features include shape, such as elongation and sphericity; features derived from the voxel intensity histogram; and higher-order features which quantify texture, reflecting spatial relationships of voxels in a region (Li et al., 2023). We used radiomics to establish relationships between thalamic integrity, episodic memory, and MTL damage in a large sample of patients with selective memory deficit.

Methods: T1 images (0.83mm isotropic) were used to produce volumes of MTL structures using stereology, following a custom protocol based upon histological evidence (Insausti et al.,1998; Kivisaari et al., 2020). Patient volumes were compared to age-matched controls. Resulting Z-scores categorised patients as either hippocampal (HC N = 8), MTL cortical (MTLc N = 19), or both (MTL+ N = 43). T1 images were processed with FreeSurfer 7.2.0, and thalamic nuclei segmented with segmentThalamicNuclei (Iglesias et al., 2018). In-house Python scripts extracted radiomics features with the PyRadiomics library (van Griethuysen et al., 2017). Feature selection for each outcome variable was conducted with LASSO regression, with lambda hyperparameter tuned using leave-one-out cross-validation (LOOCV). Model fit was assessed with assess.glmnet (glmnet 4.7-1).

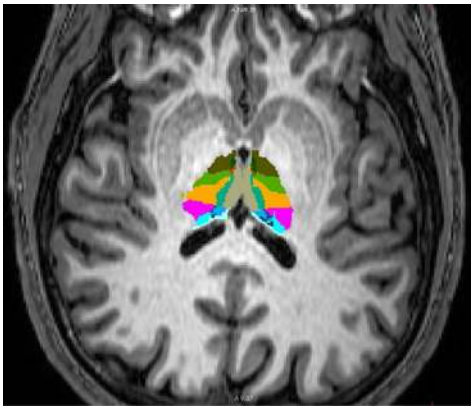

Fig. Transverse slice through T1 of a Control subject showing thalamic nuclei ROIs following segmentation via FreeSurfer. Masks were collapsed into their respective nuclei groups before feature extraction.

Results: Patients did not differ on tests of executive (Brixton; H(3) = 0.84, p = .840), semantic (Pyramids & Palm Trees; H(3) = 4.87, p = .182), or visuospatial (VOSP; H(3) = 2.95, p = .400) function, suggesting selective memory deficit. LASSO identified 35 features with non-zero coefficients which classified controls from patients, with accuracy of 87% (Fig. 2). A model fit to classify patient subtype (HC, MTLc, MTL+) showed prediction accuracy of 51%. 9 features with non-zero coefficients were related to recall memory. The model was overall significant F(9, 141) = 3.89, p <.001, Adj. R2 = .148 - two anterior thalamic features were significantly predictive of recall (both p <.05). 11 features were related to familiarity memory. The model was overall significant F(11, 101) = 6.53, p <.001, Adj. R2 = .352. An anterior thalamic texture feature was significantly predictive of familiarity (p = .040). 12 features were identified related to hippocampal volume, with a significant linear regression model F(12, 138) = 6.61, p <.001, Adj. R2 = .310. Multiple anterior and medial thalamic nuclei features were individually significant, including sphericity, elongation, size zone nonuniformity, and coarseness (anterior); and surface-volume ratio and elongation (medial).

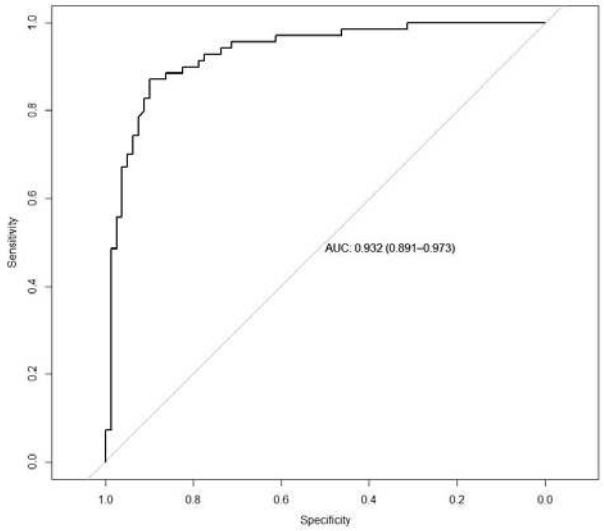

Fig. ROC of Control - Patient binomial classification using first-order and textural thalamic radiomics features

Conclusions: We used radiomics-derived thalamic shape and texture information to characterise relationships between thalamus integrity, recall, familiarity, and upstream hippocampal atrophy in a dual-process episodic memory context. Despite primarily MTL damage and normal cognitive profile, patients could be classified based upon thalamic features suggesting downstream microstructural changes, which were additionally related to episodic memory performance. Future work will investigate microstructural bases of features using diffusion imaging, and attempt to improve subgroup classification with the use of image filters prior to feature extraction.

References

1. Aggleton, J.P. (2022), “Time to retire the serial Papez circuit: Implications for space, memory, and attention”, Neuroscience & Biobehavioural Reviews, vol. 140, 104813
2. Griethuysen, J.J.M. (2017), “Computational radiomics system to decode the radiographic phenotype”, Cancer Research, vol. 77, no. 21, pp. 104-107
3. Iglesias, J.E. (2018), “A probabilistic atlas of the human thalamic nuceli combining ex vivo MRI and histology”, NeuroImage, vol. 183, pp. 314-326
4. Insausti, R. (1998), “MR volumetric analysis of the human entorhinal, perirhinal, and temporopolar cortices”, American Journal of Neuroradiology, vol. 189, pp. 659-671
5. Kafkas, A. (2020), “Thalamic-medial temporal lobe connectivity underpins familiarity memory”, Cerebral Cortex, vol. 30, no. 6, pp. 3827-3837
6. Kivisaari, S.L. (2020), “The Perirhinal, Entorhinal, and Parahippocampal Cortices and Hippocampus: An Overview of Functional Anatomy and Protocol for Their Segmentation in MR Images”, fMRI - Basics and Clinical Applications (eds.), Springer-Verlag, Berlin Heidelberg
7. Lambin, P. (2017), “Radiomics: the bridge between medical imaging and personalized medicine”, Nature Reviews Clinical Oncology, vol. 6, no. 5, pp. 749-762
8. Li, M. (2023), “The radiomics features of the temporal lobe region related to menopause based on MR-T2WI can be used as potential biomarkers for AD”, Cerebral Cortex, vol. 33, no. 14, pp. 9067-9078

Poster No 1081

Characterizing hippocampal activation with magnetoencephalography using the Mnemonic Similarity Task

Pei Robins[1], Jessica Gilbert[2], Zhi-De Deng[1]

[1]National Institutes of Health, Bethesda, MD, [2]NIMH/NIH, Bethesda, MD

Introduction: The hippocampus is crucial for memory formation and consolidation, and aspects of emotion regulation in psychiatric disorders such as depression. The Mnemonic Similarity Task (MST) is a pattern separation task that can be used to measure hippocampal function. This study aims to determine the feasibility of magnetoencephalography (MEG) to characterize hippocampal activation during the MST in a cohort of healthy participants.

Methods: Sixteen healthy participants completed the MST, comprising of two phases. In the encoding phase, 120 pictures of everyday objects were presented. In the retrieval phase, 360 pictures comprised of 120 each of repeated, new, and similar pictures were presented, and participants were asked to categorize them. Pattern separation performance was measured by the Lure Discrimination Index (LDI) and Recognition (REC) score. MEG data was recorded on a 275-channels CTF system. The data was filtered and artifacted using Independent Component Analysis (ICA) to remove cardiac, blinking, and movement artifacts. Source reconstruction was performed using the linearly constrained minimum variance beamformer method.

Results: The mean LDI was 0.35±0.20. The mean REC was 0.61±0.12. Participants were significantly faster in recognizing old objects compared to identifying similar objects ($t=-5.6$, $p<.001$). MEG revealed peak hippocampal activation approximately 200ms post-stimulus onset during both encoding and retrieval phases. The peak activation is observed in anterior hippocampus.

Conclusions: Our results demonstrate that MEG during the pattern separation task can detect hippocampal activation during the memory encoding and retrieval phases. Future directions include using this task to assess hippocampal function in depressed patients receiving electroconvulsive therapy.

References

1. Stark, S. M. (2019), 'Mnemonic Similarity Task: A Tool for Assessing Hippocampal Integrity', Trends in Cognitive Sciences, vol. 23, no. 11, pp. 938-951

Poster No 1082

Hippocampal Development during Adolescence in Episodic Memory and Its Interaction with Anxiety

Kahyun Choi[1], Jiook Cha[1], Dongil Chung[2], Grace Chung[1], Jae Won Kim[3,4], Sang Ah Lee[1]

[1]Seoul National University, Gwanak-gu, Seoul, [2]UNIST, Ulsan, NA, [3]Seoul National University College of Medicine, Jongno-gu, Seoul, [4]Seoul National University Hospital, Jongno-gu, Seoul

Introduction: Adolescence is a period of transition from childhood to adulthood, marked by the development of biological and higher-order cognitive function[4]. Hippocampus, which is critically involved in cognitive abilities such as episodic memory, develops rapidly from infancy, with distinct trajectories along the anterior-posterior axis[1,3], with protracted development in its connections with cortical regions across adolescence[2,5]. However, mixed results have been reported regarding the effects of cortico-hippocampal functional maturation on spatiotemporal episodic memory, and the effects of mental health measures in adolescence. In the present study, we aimed to investigate the interaction between developmental changes in the hippocampal memory network during adolescence, their influences on episodic memory, and the individual differences that may be explained by measures of depression and anxiety.

Methods: A total of ninety-eight adolescents, ranging from 10 to 17 years of age (mean = 14.62, std = 1.63, 57 females), were recruited for the study. Activation and functional connectivity of the hippocampus were measured through fMRI scans while performing an episodic memory task. In the task, participants watched a 12-second video featuring animal characters emerging from holes in the ground (encoding phase). They were instructed to remember what animals (what) appeared at which locations (where) in what order (when). After a short interference task, participants were instructed to recall the previous events (retrieval phase), and then to re-enact the events using a button box (re-enactment phase). Each trial consisted of a sequence of four animals appearing from various locations in the ground and participants completed 4 runs, each consisting of 2 trials. Additionally, questionnaires, including STAI and CES-D, were collected to assess the adolescents' mental health.

Results: We observed a general age-related trend in episodic memory accuracy and found development-related correlates of hippocampal engagement in episodic memory. During memory encoding, activation in the hippocampal tail was greater than in hippocampal head, and this tail-head difference increased with age ($r=0.34$, $p<0.001$). Specifically, we found that the posterior dominance in activity in the left hippocampus mediates the relationship between age and episodic memory accuracy. Developmental changes and memory-related correlates in connectivity patterns were observed with the anterior hippocampus as a seed region. In particular, functional connectivity with the temporal lobe, including the superior temporal gyrus, decreased with age ($T(95)>3.17$, $p<0.001$, unc.), revealing a maturing episodic memory network across adolescence. In general, anterior hippocampal connectivity with temporal, parietal and frontal regions was correlated with memory accuracy; however, better memory performance in early adolescents (age 11-14) was associated with higher connectivity with temporal regions ($T(49)>3.26$, $p<0.001$, unc.). In terms of differences in neural activation correlated with anxiety scores, greater activation was observed in the right hippocampus compared to the left hippocampus, particularly in the anterior hippocampus. This was also observed in the amygdala. Functional connectivity between the amygdala and medial prefrontal cortex increased with anxiety, notably in middle adolescence (age 15-17), suggesting that the development of the fronto-amygdala circuit is reflected in the hippocampal network through its connection with the amygdala.

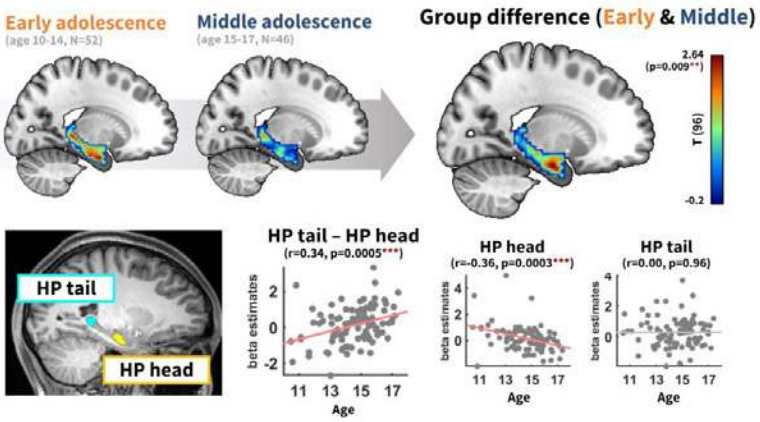

Hippocampal activation along the anterior-posterior axis

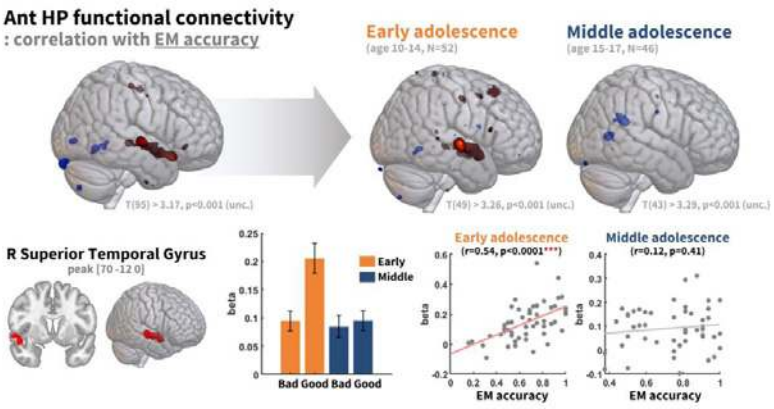

Age-specific memory-related connection with anterior hippocampus

Conclusions: We investigated the developmental aspects of hippocampal engagement and its functional connections during episodic memory encoding in adolescents. These findings suggest that the functional specialization of the hippocampus along the anterior-posterior axis and the development of the cortico-hippocampal network may explain higher cognitive development during adolescence and that this process may interact with adolescents' mental health.

References

1. DeMaster, D. (2014). Structural development of the hippocampus and episodic memory: developmental differences along the anterior/posterior axis. Cerebral cortex, 24(11), 3036-3045.
2. Gogtay, N. (2004). Dynamic mapping of human cortical development during childhood through early adulthood. Proceedings of the National Academy of Sciences, 101(21), 8174-8179.
3. Gogtay, N. (2006). Dynamic mapping of normal human hippocampal development. Hippocampus, 16(8), 664-672.
4. Larsen, B. (2018). Adolescence as a neurobiological critical period for the development of higher-order cognition. Neuroscience & Biobehavioral Reviews, 94, 179-195.
5. Tang, L. (2020). Differential functional connectivity in anterior and posterior hippocampus supporting the development of memory formation. Frontiers in Human Neuroscience, 14, 204.

Poster No 1083

Brain activity at event boundaries during movie watching in ageing and its association with memory

Helena Gellersen[1], Yannik Lottes[1], Merle Hinz[1], David Berron[1]

[1]German Center for Neurodegenerative Diseases (DZNE), Magdeburg, Germany

Introduction: The brain organizes the continuous stream of information we experience through a process termed “event segmentation” where the hippocampus and regions in the posterior-medial network (PMN) show increased activity when changes in a narrative occur[1,2]. In younger adults, such a boundary-evoked response observed during movie watching correlates with memory recall for movie content[3,4]. Ageing results in a reduction of these hippocampal boundary responses[5], but whether such changes can explain inter-individual differences in memory performance in older adults is unclear. Prior studies also did not investigate boundary responses outside regions in the PMN to test for content-specific associations between boundary responses and memory performance. Here, we examine this relationship between ageing, event segmentation and memory using functional MRI during naturalistic movie watching.

Methods: The study included 18 cognitively unimpaired older adults aged 63 to 84 years in the MRI cohort and 33 older and 18 younger adults aged 18 to 35 in the behavioural cohort. The behavioural cohort watched a 12-minute movie while marking event boundaries. The MRI cohort watched the same movie in a 3T scanner without indicating boundaries for more natural viewing conditions. After watching the movie, all participants answered memory questions about event order, perceptual details, actions, characters and locations in the narrative. High- and low-salience event boundaries were defined based on 50% and 30% agreement across participants, respectively. We contrasted brain activity at event boundaries with activity around the middle of an event (6s windows for sufficient separation of events). We conducted a whole-brain voxel-wise analysis (uncorrected p<.001) and a region of interest analysis in native subject space, extracting beta values from MTL (anterior, posterior hippocampus; entorhinal and parahippocampal cortices), posterior-medial parietal regions (precuneus; posterior cingulate) and the visual ventral stream as a control.

Results: For high-salience boundaries, the whole-brain analysis revealed boundary-related activity in the PMN, including the precuneus and posterior cingulate, retrosplenial, and parahippocampal cortices. Bilateral posterior hippocampal boundary effects were also observed. Anterior hippocampus activity was restricted to the right hemisphere. Ventral temporopolar cortex in the anterior-temporal network and regions in the visual ventral stream also increased their activity at event boundaries. Low-salience boundary responses were only observed in occipital cortex, precuneus, and posterior cingulate, not the hippocampus. Older and younger adults did not differ in terms of the number of boundaries placed but in boundary position (t=3.16, p=.002). Younger adults’ responses were less variable and more tightly clustered around boundaries. An ANOVA showed that older adults had poorer memory for information for specific actions (t=-2.18, p=.037), characters (t=-2.35, p=.026) and perceptual details (t=-2.18, p=.037) but not for the general order of events or locations in the narrative. There was no association between the magnitude of neural boundary responses in MTL, parietal PMN, anterior-temporal network or visual ventral stream regions and memory performance.

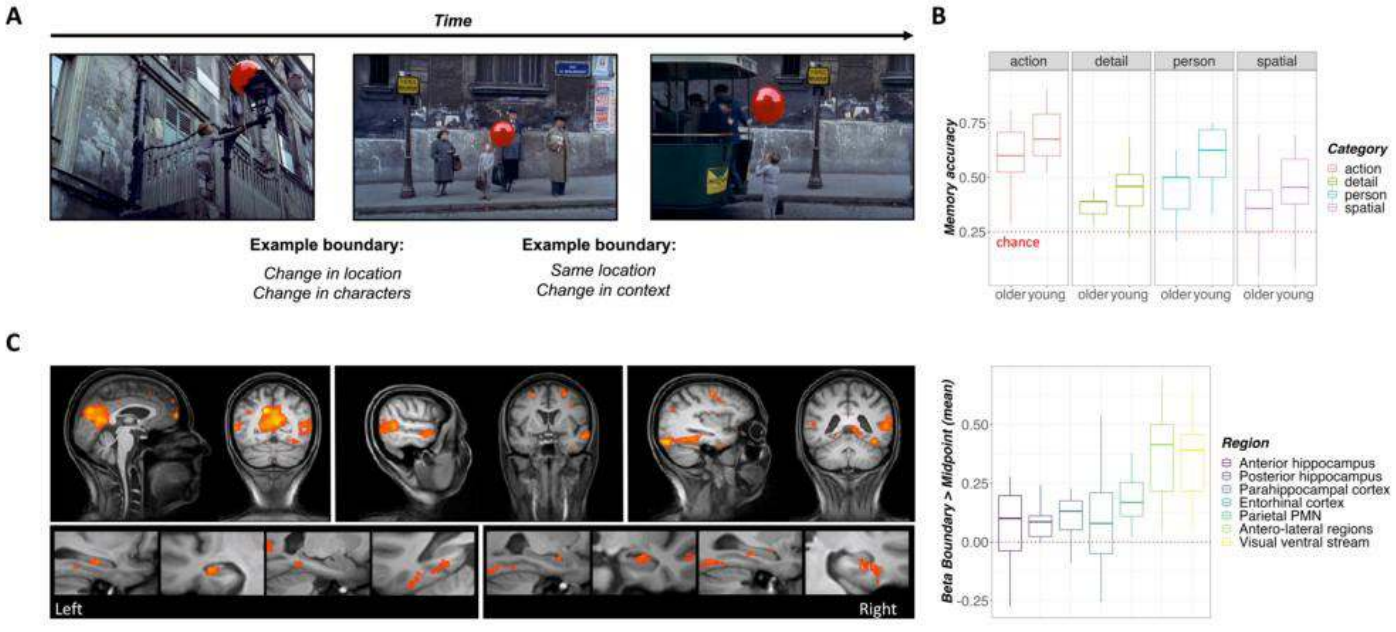

Conclusions: The pattern of activation in PMN regions and the hippocampus in older adults aligns with that in younger adults in prior studies, suggesting preserved neural responses to event segmentation[3,4]. Increased hippocampal activity was not seen with low boundary salience, while occipito-parietal activity increases remained. Ageing is associated with more variability in boundary placement and content-specific memory decline with more forgetting of narrative details. Although no relationships were found between boundary-evoked brain activity and memory, this may be due to our relatively small sample size and will be investigated in a larger lifespan cohort going forward.

References

1. Baldassano et al. (2017). Neuron, 95(3).
2. Ben-Yakov & Henson (2018). JoN, 38(47).
3. Ben-Yakov et al. (2013). JEPG, 142(4).
4. Ben-Yakov & Dudai (2011). J Neurosci, 31(24).
5. Reagh et al. (2020). Nat Comms, 11:3980.

Poster No 1084

Neural mechanisms of insight during narrative comprehension

Hayoung Song[1], Jin Ke[1], Yuan Chang Leong[2], Monica Rosenberg[1]

[1]University of Chicago, Chicago, IL, [2]The University of Chicago, Chicago, IL

Introduction: How do we experience insight, or a feeling of "aha"? Behavioral evidence suggests that we experience insight as we comprehend causal structures of events[1]. A block-design study showed that insight leads to changes in representation patterns in the hippocampus and the medial prefrontal cortex (mPFC)[2]. Despite initial evidence, however, the cognitive and neural mechanisms of insight during naturalistic and continuous narrative comprehension remain to be studied. This study introduces a novel experimental design to ask how memory retrieval and causal reasoning guide insight during an unfolding narrative.

Methods: We collected fMRI data as human participants (N=36) watched an episode of a TV show, This is Us (41m 40s). To elicit multiple "aha" moments, the episode was segmented into 48 events (each ~50 secs) and scrambled in temporal order. Scrambled events were grouped into 10 fMRI runs (~5 min each). Participants were randomly assigned to three scrambled-order groups, such that one-third of the participants watched the episode in the same scrambled order (Fig 1A). Participants were instructed to press an "aha" button whenever they understood something new about the show's events and characters. After watching a set of events, participants were shown screenshots taken whenever they pressed the aha button and were asked to verbally explain their insight at these moments (Fig 1B).

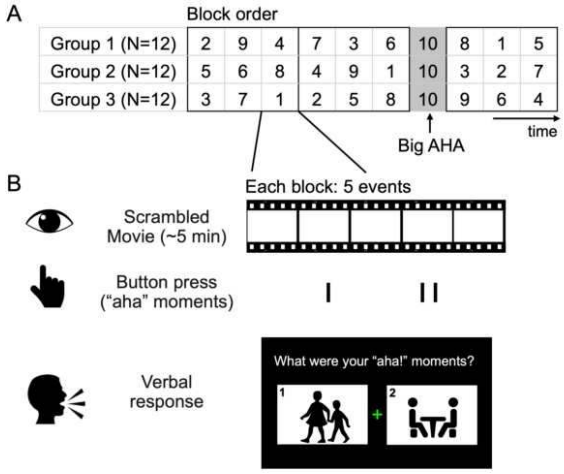

Figure 1. Stimulus and experimental design. **(A)** Block order for the three stimulus groups. The episode was segmented into 48 scenes and assigned to one of the 10 blocks (blocks 1-9: 5 scenes in scrambled order, block 10: last 3 consecutive scenes of the episode which contain the big reveal). Twelve participants in each group watched the episode in the same scrambled order. **(B)** Experimental design of one fMRI run (out of 10 runs in total). Participants pressed the aha button as they watched ~5 min of scrambled episode. Then, they were asked to verbally recall why they had pressed the button as they watched the screenshots of all the moments they pressed.

Results: The frequency of aha button presses varied across participants, ranging from roughly 4 presses per minute to one press every 3 minutes. Despite such variability, aha button presses were synchronous across participants (dice coefficient

compared to chance distribution; z = 37.0, p < 0.001). Coding of verbal responses found that 55.05% (SD 23.52%) of participants' explanations of aha moments mentioned past events, which suggests that insight occurs by retrieving causally related past events in memory.To identify brain areas that represent the causal structure of events, we correlated an event-by-event causal relationship matrix with an event-by-event voxel pattern similarity matrix that was extracted from each of the 100 cortical parcels[3] (Fig 2B). The causal relationship matrix was created based on participants' verbal responses; if a past event was recalled at an aha moment, a causal relationship between the pair of events was scored. Voxel activity patterns in the mPFC, retrosplenial cortex, and early visual cortices represented causally related events to be similar to one another and causally unrelated events as dissimilar, when controlling for semantic similarity between events (Fig 2A). Next, we hypothesized that activity patterns in these brain regions would shift at aha moments due to a change in event representation. To test this, we applied a hidden Markov model (HMM)[4] on the voxel activity pattern time series of each parcel. Sudden shifts in representation patterns were observed ~2s prior to aha button presses. The effect was observed throughout the cortex, including bilateral mPFC, where the likelihood of the HMM boundaries significantly increased ~2s prior to button presses (Fig 2C, D). Furthermore, cortico-hippocampal cofluctuation time series[5] showed that representation pattern shifts were accompanied by a transient decoupling between the hippocampus and mPFC[6], again at ~2s prior to button presses (Fig 2E, F). This indicates that moments of insight are characterized by a transient change of event representation in the mPFC, in coordination with the hippocampus.

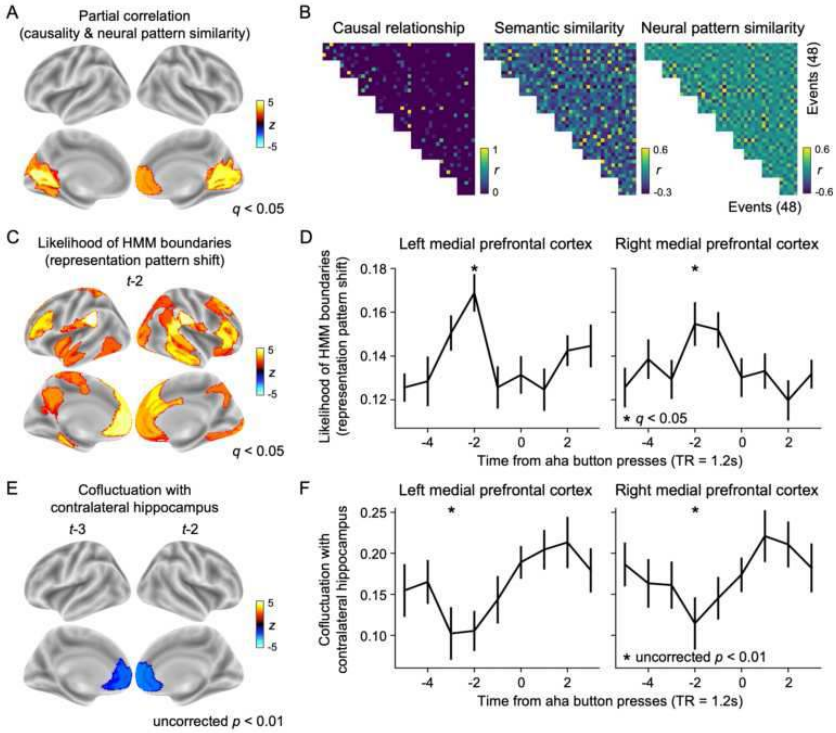

Figure 2. FMRI results. **(A)** Regions that show significant partial correlations between causal relationship and neural pattern similarity, while controlling for semantic similarity. A non-parametric permutation test was used to compute significance; the aha moments were randomly shuffled (1,000 iterations) and compared with the actual *r* value of each parcel (*z* statistics). The significance was corrected for 100 tests across cortical areas. **(B)** Three types of exemplar matrices that were used in the analysis. Causal relationships of 48 events were calculated by aggregating all participants' verbal responses, respectively for the three scrambled-order groups. The semantic similarity matrix was calculated from the last-layer embeddings of a pre-trained GPT2 model [7] applied to annotations and dialogues of the events. A multivariate voxel pattern similarity matrix was computed for each participant's each parcel. **(C)** Regions that show significant differences in the likelihood of hidden Markov model (HMM) boundaries at 2 TRs prior to the aha button presses. **(D)** Likelihood of HMM boundaries in bilateral medial prefrontal cortex, from 5 TRs prior to and 3 TRs after the aha button presses. **(E)** Regions that show significant differences in the degree of cofluctuation with the contralateral hippocampus at 3 TRs (left hemisphere) and 2 TRs (right hemisphere) prior to the aha button presses. No region other than mPFC showed significant change in cofluctuation near aha moments. **(F)** Degree of cofluctuation with the hippocampus in the bilateral medial prefrontal cortex, from 5 TRs prior to and 3 TRs after the aha button presses.

Conclusions: Insight occurs by retrieving causally related past events in memory. The mPFC represents causal event structures, and shows a shift in representation patterns at moments of insight with dynamic interaction with the hippocampus. The study demonstrates that insight during narrative comprehension involves memory retrieval and causal reasoning as well as dynamic reconfiguration and representational changes in the hippocampal-default mode network circuit.

References

1. Song, H., Park, B. -Y., Park, H., Shim, W. M. (2021). 'Cognitive and neural state dynamics of narrative comprehension', Journal of Neuroscience, 41 (43), 8972-8990.
2. Milivojevic, B., Vincente-Grabovetsky, A., Doeller, C. F. (2015). 'Insight reconfigures hippocampal-prefrontal memories', Current Biolology, 25 (7), 821-830.
3. Schaefer, A., Kong, R., Gordon, E. M. et al. (2018). 'Local-global parcellation of the human cerebral cortex from intrinsic functional connectivity MRI', Cerebral Cortex, 28 (9), 3095-3114.
4. Baldassano, C., Chen, J., Zadbood, A., Pillow, J. W., Hasson, U., Norman, K. A. (2017). 'Discovering event structure in continuous narrative perception and memory', Neuron, 95 (3), 709-721.
5. Zamani Esfahlani, F., Jo, Y., Faskowitz, J., Betzel, R. F. (2020). 'High-amplitude cofluctuations in cortical activity drive functional connectivity', The Proceedings of the National Academy of Sciences, 117 (45), 28393-28401.
6. Van Kesteren, M. T. R., Ruiter, D. J., Fernandez, G., Henson, R. N. (2012) 'How schema and novelty augment memory formation', Trends in Neuroscience, 35 (4), 211-9.
7. Radford, A., Wu, J., Child, R., Luan, D., Amodei, D., Sutskever, I. (2019). 'Language models are unsupervised multitask learners', OpenAI Blog.

Poster No 1085

The neural correlates of attending to external (semantic) and internal (episodic) stimuli

Chen Chen[1], Katya Krieger-Redwood[1], Elizabeth Jefferies[1]

[1]Department of Psychology, University of York, York, United Kingdom

Introduction: Semantic cognition supports different thoughts and behaviours, e.g., making sense of information from the external world, such as comprehension of what we are reading or listening to[1,2], but also generating thoughts and memories that are independent of the external environment[3]. Using functional MRI, the current study explores how activation changes when participants (i) attend to external information, (ii) generate internally or (iii) ignore external semantic inputs for internally-focused autobiographical recall.

Methods: This study occurred across two consecutive days. On day 1, participants generated personal memories linked to cue words (e.g., gift) outside the scanner. On day 2, participants recalled these memories from the cue word in the scanner, and also read and listened to factual sentences in a comprehension task. The experiment consisted of the following conditions (1) sentence reading; (2) sentence listening; (3) personal memory retrieval ignoring written sentences or (4) spoken sentences; (5) personal memory retrieval (no conflicting sentence presented). After each trial, task focus ratings on a scale of 1 (i.e., not at all focused) to 4 (i.e., highly focused) were collected to index the extent to which participants were able to focus on the current task. 30 participants were recruited (18-23 Years, 24 females, 4 excluded). We performed a univariate analysis using a general linear model (GLM) to identify neural differences across these tasks and parametric effects of task focus.

Results: Behaviorally, the task focus ratings showed that participants were more focused in the comprehension than the recall task and that ignoring auditory input was harder than ignoring visual sentences during recall. Neurally, when participants attended to external information, activation spread along STG for auditory inputs, and along the ventral visual stream for visual inputs. These meaning pathways were activated automatically, even when participants focused their attention internally to recall personal memories, whilst ignoring the external input. When participants did not have to ignore external inputs, activation was higher in medial prefrontal and posterior cingulate cortex. The parametric effects of focus revealed differential engagement of default mode network (DMN) subsystems and control/salience networks. Greater task focus for external auditory or visual information was associated with greater activation in the dorsomedial DMN subsystem, previously been shown to be involved in semantic cognition[4] and auditory network and increased deactivation in the core DMN, salience and control-B networks. In contrast, greater task focus for internal memory generation, ignoring external information, correlated with increased activation in medial temporal and some core DMN, as well as somatomotor networks, and deactivation in dorsomedial and other aspects of core DMN. In this way, core DMN showed a functional split between task-positive and negative responses. Greater focus on internal generation, regardless of external distractions or not, was correlated with increased deactivation in salience and control-B networks. Compared to internal memory generation, dorsomedial DMN showed a stronger effect of task focus for comprehension of external inputs, while core DMN showed a stronger effect of task focus for recall, relative to comprehension.

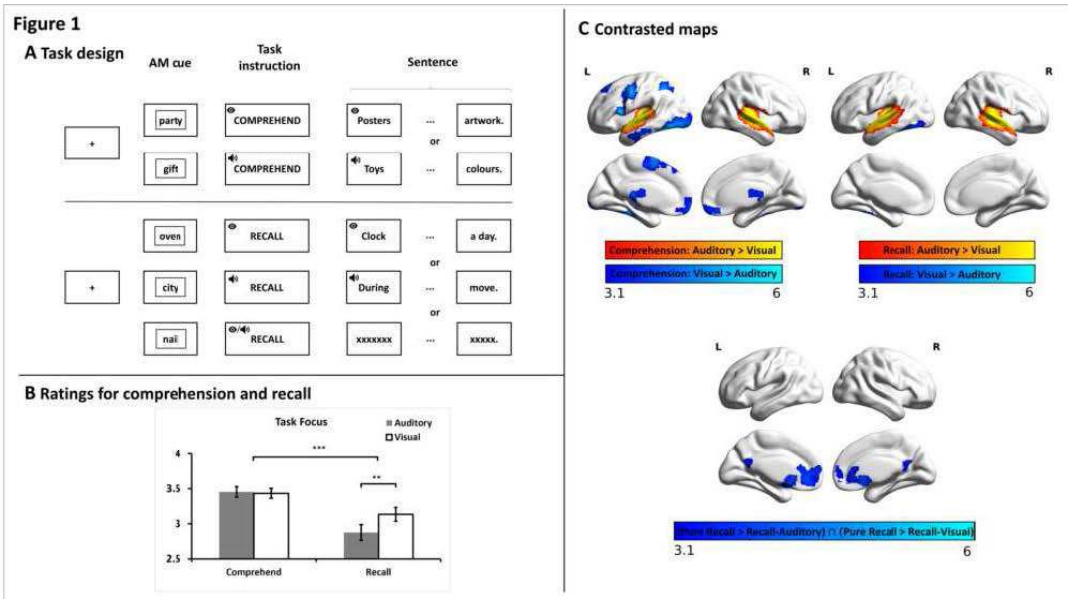

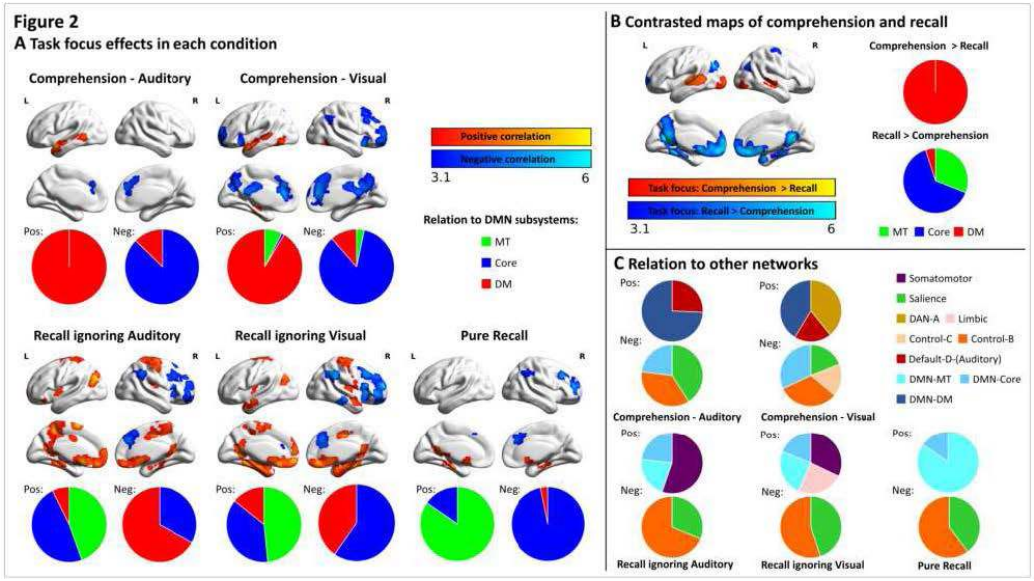

Conclusions: Focus on external semantic information is associated with activation in dorsomedial DMN, while activation of core and medial temporal DMN regions is linked to focus on internal memory generation. When participants ignore semantic inputs and increase focus internally, activation increases in medial temporal and core DMN and somatomotor networks, and decreases across control networks. This study finds differential activation and deactivation of DMN subsystems, as opposed to recruitment of control systems, are aligned to our capacity to flexibly focus on internal memory generation and external semantic processing.

References

1. Keidel, J. L., C. S. H. Oedekoven, A. C. Tut and C. M. Bird (2018). "Multiscale Integration of Contextual Information During a Naturalistic Task." Cereb Cortex 28(10): 3531-3539.
2. Spitsyna, G., J. E. Warren, S. K. Scott, F. E. Turkheimer and R. J. Wise (2006). "Converging language streams in the human temporal lobe." J Neurosci 26(28): 7328-7336.
3. Smallwood, J. and J. W. Schooler (2015). "The science of mind wandering: empirically navigating the stream of consciousness." Annu Rev Psychol 66: 487-518.
4. Zhang, M., B. C. Bernhardt, X. Wang, D. Varga, K. Krieger-Redwood, J. Royer, R. Rodriguez-Cruces, R. Vos de Wael, D. S. Margulies, J. Smallwood and E. Jefferies (2022). "Perceptual coupling and decoupling of the default mode network during mind-wandering and reading." Elife 11.

Poster No 1086

False Recall is Associated with Larger Caudate in Males but not in Females

Xuhao Shao[1], Ao Li[1], Bi Zhu[1]

[1]Beijing Normal University, Beijing, Beijing

Introduction: After learning semantically related words, some individuals are more likely than others to incorrectly recall unstudied but semantically related lures (i.e., Deese-Roediger-McDermott [DRM] false recall). Previous studies have suggested that neural activity in subcortical regions (e.g., the caudate) is involved in false memory (Kurkela & Dennis, 2016). Moreover, there are sex differences in the neural basis of false memories (Slotnick, 2021; Spets, Karanian, & Slotnick, 2021; Spets & Slotnick, 2021; Zhu et al., 2016). However, the sex-specific association between subcortical volume and false memory remains unclear. The current study examined whether sex modulates the relationship between caudate volume and DRM false recall. We tested two hypotheses. First, females should have higher true and false recall than males. Second, sex should moderate the relationship between caudate volume and false recall. To test these two hypotheses, this study measured individual differences in DRM false recall in healthy young adults and then acquired their structural imaging data to measure the volume of subcortical regions.

Methods: The current study recruited 400 Chinese college students (mean age: 21.33 ± 1.97 years [M ± SD]; 211 females and 189 males). In the DRM recall task (Roediger & McDermott, 1995), participants studied 12 lists of 8 semantically related Chinese words (e.g., apple, vegetable, lychee, melon, banana, grape, cherry and pear) during encoding. After a 10-minute filler task (i.e., an anti-saccade task), participants were asked to write down as many words as they could remember on a piece of paper within the next 10 minutes. The raw scores for true, false, and foil recall were the number of recalled targets (studied words), lures (unstudied but semantically related words), and foils (unstudied and unrelated words). To examine the relationship between subcortical volume and memory performance, we used FreeSurfer (version 7.1.1) to obtain subcortical segmentation (i.e., caudate, accumbens, amygdala, hippocampus, pallidum, putamen and thalamus) and total intracranial volume (ICV). In the current study, we used repeated-measures ANOVA to examine sex differences in memory performance, and linear regression models to examine whether sex moderates the relationship between memory performance and subcortical volumes. The Bonferroni method was used to control for multiple comparisons when calculating separate tests for seven subcortical regions.

Results: In terms of sex differences in recall performance, we found that males had lower levels of both true and false recall compared to females. In terms of sex differences in subcortical volumes, the caudate, accumbens, amygdala, hippocampus, pallidum, putamen and thalamus were larger in males compared to females. Importantly, sex moderated the relationship between caudate volume and false memory after controlling for age and ICV. Specifically, larger caudate volume was associated with higher false recall in males, but not in females. This correlation was significant in males after controlling for age and ICV. Except for the caudate, the volumes of the other six subcortical regions were not associated with false recall in males or females. Furthermore, individual differences in true recall were not associated with the volumes of the seven subcortical regions, nor did sex moderate their relationships.

Conclusions: This study found that sex modulates the relationship between caudate volumes and DRM false recall, suggesting that males and females produce false recall in different ways. Specifically, caudate volume was positively associated with false recall in males but not in females. This association was significant both before and after controlling for age and intracranial volume. This study emphasizes the importance of including sex as a moderator when investigating the neural correlates of human memory.

References

1. Kurkela, K. A., & Dennis, N. A. (2016). Event-related fMRI studies of false memory: An activation likelihood estimation meta-analysis. Neuropsychologia, 81, 149-167. https://doi.org/10.1016/j.neuropsychologia.2015.12.006
2. Roediger, H. L., & McDermott, K. B. (1995). Creating false memories: Remembering words not presented in lists. Journal of Experimental Psychology: Learning, Memory, and Cognition, 21, 803-814. https://doi.org/10.1037/0278-7393.21.4.803
3. Slotnick, S. D. (2021). Sex differences in the brain. Cognitive Neuroscience, 12(3-4), 103-105. https://doi.org/10.1080/17588928.2021.1957808
4. Spets, D. S., Karanian, J. M., & Slotnick, S. D. (2021). False memories activate distinct brain regions in females and males. Neuroimage: Reports, 1(4), 100043. https://doi.org/10.1016/j.ynirp.2021.100043
5. Spets, D. S., & Slotnick, S. D. (2021). Are there sex differences in brain activity during long-term memory? A systematic review and fMRI activation likelihood estimation meta-analysis. Cognitive Neuroscience, 12(3-4), 163-173. https://doi.org/10.1080/17588928.2020.1806810
6. Zhu, B., Chen, C., Loftus, E. F., He, Q., Lei, X., Dong, Q., & Lin, C. (2016). Hippocampal size is related to short-term true and false memory, and right fusiform size is related to long-term true and false memory. Brain Structure and Function, 221(8), 4045-4057. https://doi.org/10.1007/s00429-015-1145-1

Poster No 1087

Longitudinal association between structural brain change and episodic memory change

Marie Strømstad[1], Didac Vidal-Piñeiro[1], Øystein Sørensen[1], Anders Fjell[1], Kristine Beate Walhovd[1]

[1]Department of Psychology, Center for Lifespan Changes in Brain and Cognition, University of Oslo, Oslo, Norway

Introduction: Longitudinal studies are crucial for understanding the intra-individual variability in structural brain changes and their associations with cognitive functions. While correlations between episodic memory decline and gray-matter atrophy have been found (Gorbach et al., 2020, Sele et al., 2021, Oschwald et al., 2019), extensive investigation into these associations are limited, with studies often focusing on specific regions (e.g. hippocampus) and relying on relatively small sample sizes. Hence, here we have harmonized several longitudinal datasets to study the relationship between age-related episodic memory change and regional structural brain changes (cortical thickness and subcortical volumes). We use a mega-analytical to aggregate the different datasets and maintain statistical power (Eisenhauer, 2021). The main aim of the study is to explore the regional brain-memory change associations and their interaction with age.

Methods: Longitudinal neuroimaging and cognitive data from 13 datasets (Lifebrain cohorts and open-sharing datasets, see Figure 1), including 3,763 cognitively healthy participants (1,744 females; mean age = 62.5, age range 16.8-93 years), were analyzed. To harmonize cognitive data, we fitted – in each dataset - memory scores with age, sex, and retest effects as covariates using generalized additive mixed models (GAMM). Structural MRI data was processed with longitudinal FreeSurfer (version 7.1.0, http://surfer.nmr.mgh.harvard.edu), parcellated using the Destrieux and aseg atlases, and fed into a normative modeling pipeline (Rutherford et al., 2022). The slopes of change for both memory and brain data were estimated using linear models per subject using follow-up time as a predictor. The mega-analysis included linear mixed-effects models on each ROI, with memory change as a function of brain change. To account for varying reliability of measurements across datasets, weights derived from squared intraclass correlation coefficient were used in the models (longitudinal reliability estimated as in Fitzmaurice et al., 2012). For the age interaction we applied a GAMM with a tensor interaction of brain change and age on memory change. We also conducted a supplementary analysis with a meta-analytical approach, using the R metafor package (Viechtbauer, 2010). All models were corrected for multiple comparisons using False Discovery Rate (FDR).

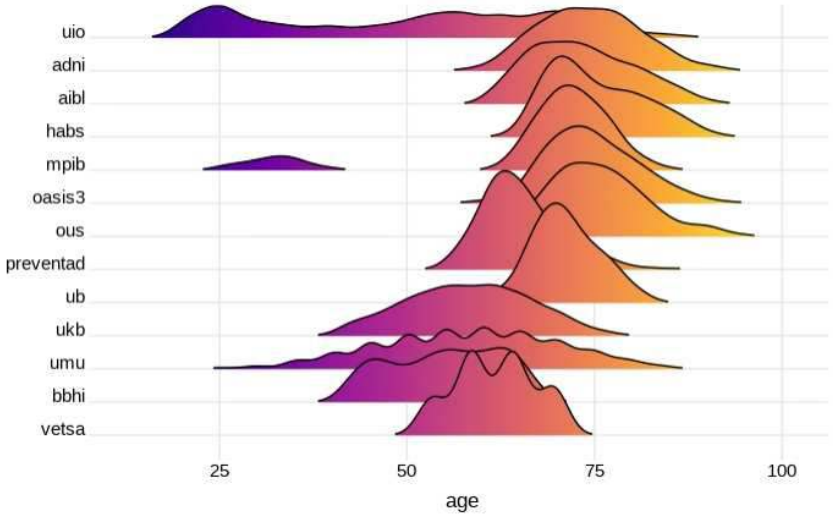

Figure 1. Density plot of age distribution across all datasets

Results: 57 memory - brain change associations were significant across several regions ($p < 0.05$, FDR corrected, see Figure 2a). Specifically, positive associations were found in the medial temporal regions, including the hippocampus, amygdala and parahippocampal gyrus, as well as the medial frontal sulcus, posterior cingulate gyrus, inferior frontal gyrus, and precentral sulcus. We also found significant age interaction effects in many of these regions, including the left hippocampus, amygdala and parahippocampal gyrus, where the effect increased with higher age (see Figure 2b). The meta-analysis results were similar, with highly correlated estimates across regions between the methods ($r = .72$), although fewer regions survived multiple comparison corrections due to higher error estimates.

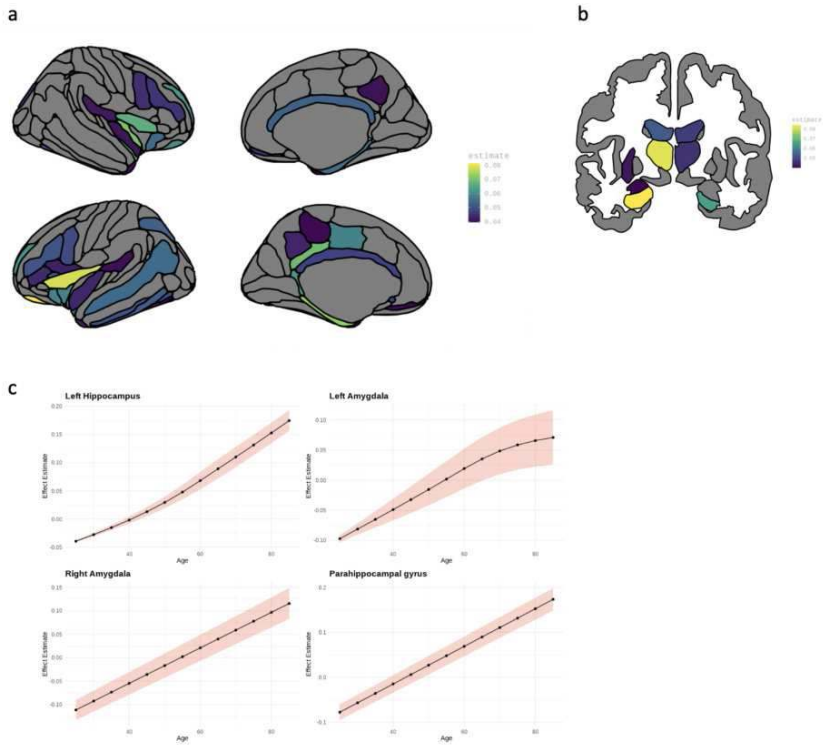

Figure 2. Memory-brain change associations. A) Estimates for FDR-significant cortical regions. B) Estimates for FDR-significant subcortical regions. C) Age interaction effects for significant regions.

Conclusions: The results reveal significant change-change correlations between brain and episodic memory in distributed cortical and subcortical regions with known links to memory processing. The strength of these relationships tended to increase with age.

References

1. Eisenhauer, J. G. (2021). Meta-analysis and mega-analysis: A simple introduction. Teaching Statistics, 43(1), 21-27.
2. Fitzmaurice, G. M., Laird, N. M., & Ware, J. H. (2012). Applied longitudinal analysis. John Wiley & Sons.
3. Gorbach, T., Pudas, S., Bartrés-Faz, D., Brandmaier, A. M., Düzel, S., Henson, R. N., ... & Nyberg, L. (2020). Longitudinal association between hippocampus atrophy and episodic-memory decline in non-demented APOE ε4 carriers. Alzheimer's & Dementia: Diagnosis, Assessment & Disease Monitoring, 12(1), e12110.
4. Oschwald, J., Guye, S., Liem, F., Rast, P., Willis, S., Röcke, C., ... & Mérillat, S. (2019). Brain structure and cognitive ability in healthy aging: a review on longitudinal correlated change. Reviews in the Neurosciences, 31(1), 1-57.
5. Rutherford, S., Fraza, C., Dinga, R., Kia, S. M., Wolfers, T., Zabihi, M., ... & Marquand, A. F. (2022). Charting brain growth and aging at high spatial precision. elife, 11, e72904.
6. Sele, S., Liem, F., Mérillat, S., & Jäncke, L. (2021). Age-related decline in the brain: a longitudinal study on inter-individual variability of cortical thickness, area, volume, and cognition. NeuroImage, 240, 118370.
7. Viechtbauer W (2010). "Conducting meta-analyses in R with the metafor package." Journal of Statistical Software, 36(3), 1–48.

Poster No 1088

The Effect of Auditory Misinformation on Eyewitness Memory and its Neural Basis

Ao Li[1], Xuhao Shao[1], Bi Zhu[1]

[1]*State Key Laboratory of Cognitive Neuroscience and Learning & IDG/McGovern Institute for Brain Research, Beijing Normal University, Beijing, China*

Introduction: The misinformation effect refers to changes in an eyewitness's memory of an original event due to exposure to post-event misinformation (Loftus et al., 1974; Loftus, 2005). It involves three stages. A witness first saw an event, then read or heard narratives about this event (including some misinformation), and finally underwent a memory test based on what he or she saw in the original event. False memory from misinformation refers to the report of misinformation during the memory test of the original event. Previous research has investigated the impact of visually presented text-based misinformation on eyewitness memory of the original event and its cross-stage neural pattern similarity (Okado & Stark, 2005; Shao et al., 2023).

However, it is unclear about the neural representations of the original event when hearing misinformation. Using functional magnetic resonance imaging (fMRI) and neural pattern similarity analysis, the current study investigated the cross-stage neural pattern similarity between the original-event image and the post-event auditory misinformation, and then compares the neural representations between true and false memories.

Methods: In this study, 30 college students viewed 6 events with 300 original-event images (e.g., an image depicting a man taking a blue candy box) and then listened to 300 post-event narratives (e.g., an AI-generated auditory misinformation "the man took a red candy box") in the fMRI scanner. Finally, they completed the memory test for the original event containing 156 questions (e.g., "What color of candy box did the man take in the original event?"). True memory, false memory, and foil memory refer to trials in which participants selected the original information (blue), misinformation (red), and unpresented information (white), respectively. MRI scans were performed on a 3.0T Siemens Prisma scanner with a 20-channel head-neck coil. The fMRIPrep and FSL were used for image preprocessing and analysis. Using the representational similarity analysis, the neural pattern similarity between the original-event and post-event stages (OP), were calculated for each of two memory types (i.e., true memory and false memory), for the corresponding items and the non-corresponding items in the same event, separately. We conducted the whole-brain searchlight analysis to identify brain regions that show differences in neural representations between true and false memories.

Results: The behavioral results showed that the false memory rate was higher than the foil memory rate, indicating a significant misinformation effect. For true memory, neural pattern similarity between the original-event image and the post-event misinformation for the corresponding items was higher than that for the non-corresponding items in the left inferior frontal gyrus and left inferior parietal lobe, whereas the neural pattern similarity for the corresponding items was lower than that for the non-corresponding items in bilateral occipital cortex. However, no such differences were found for false memory.

Conclusions: When a person hears misinformation, if he or she can reinstate the original event with gist representations in the frontoparietal cortex (i.e., a semantic match: "the man took a candy box") and verbatim representations in sensory cortex (i.e., a visual mismatch: hearing "a red candy box" and reactivating an image of "a blue candy box"), then he or she will be more likely to resist the misinformation. This study supports and extends the sensory reactivation and fuzzy-trace theories. It may contribute to the understanding of the reconstructive nature of human memory and its application in the legal system.

References

1. Loftus, E. F. (1974). Reconstruction of automobile destruction: an example of the interaction between language and memory. Journal of Verbal Learning and Verbal Behavior, 13(5), 585-589.
2. Loftus, E. F. (2005). Planting misinformation in the human mind: A 30-year investigation of the malleability of memory. Learning & Memory, 12(4), 361-366.
3. Okado, Y. (2005). Neural activity during encoding predicts false memories created by misinformation. Learning & Memory, 12(1), 3-11.
4. Shao, X. (2023). Cross-stage neural pattern similarity in the hippocampus predicts false memory derived from post-event inaccurate information. Nature Communications, 14(1), 2299.

Poster No 1089

Shared cortical activation dynamics across individuals during virtual navigation

Jaeseob Lim[1], Sang-Eon Park[1], Sang-Hun Lee[1], Sang Ah Lee[1]

[1]*Seoul National University, Seoul, Korea, Republic of*

Introduction: During exploration of a new environment, visual information, navigation events, and their importance for spatial memory are unevenly distributed across space and time. Consequently, various brain regions are likely to exhibit dynamic activities corresponding to the different demands of processing and encoding across time. Our study aims to identify the brain regions displaying such dynamic activity through inter-subject correlation analysis of fMRI data and use them to better understand how the human brain processes information as complex events unfold in our day to day experiences. We hypothesized that to efficiently encode and structure navigational episodes under limited cognitive capacity, the brain heavily allocates resources for visual processing and memory encoding during the occurrence of crucial portions of the episode such as turning or the emergence of a landmark, but not as much at other points in time. If this process fails, and the brain follows a sub-optimal pattern of encoding, it may lead to a decrease in performance, reflected in the memory accuracy of the navigational episode.

Methods: 44 healthy adults (mean age = 23.2, 25 female) performed a task involving the viewing of first-person navigational episodes through virtual environments and later identifying the correct route or destination on a map. Participants watched 24 different 1-minute episodes in the MRI scanner. Following each movie, participants answered a navigation-related question, choosing a map retracing the correct navigational path or a map marked with the destination location. 33 segmented cortical

regions were analyzed using an intersubject correlation (ISC) method, measuring the correlation between one person's activity dynamics and the mean activity dynamics of all other participants.

Results: With 3 exceptions, all regions exhibited a significant ISC larger than 0 (FDR-adjusted $p < 0.05$). The occipital regions showed high ISC compared to the other regions. In a subset of the brain regions (occipital regions, parahippocampal gyrus, and precuneus, adjusted $p < 0.05$), navigation episodes with landmarks showed greater ISC than navigation episodes without landmarks. Notably, these regions did not show a significant increase in average activation during navigation. ISC in the visual cortex in correct trials exceeded that of incorrect trials (adjusted $p < 0.05$), while average activation was not related to memory performance. Other brain regions showed no significant differences between correct and incorrect trials.

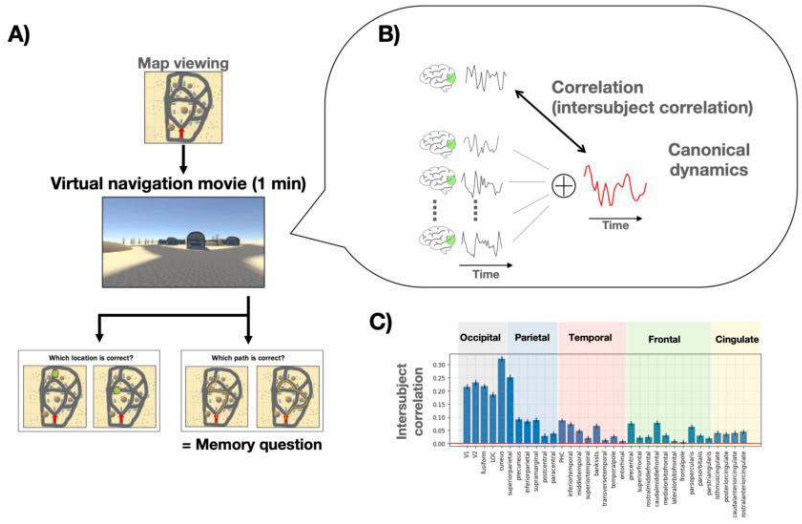

A) Task design. **B)** Calculation of intersubject correlation. **C)** Mean intersubject correlation of 33 cortical regions.

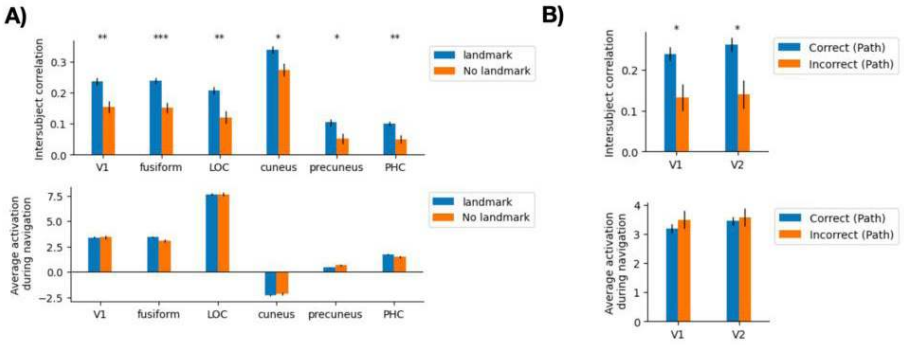

A) High intersubject correlation was observed in navigation episodes with landmarks. Six cortical regions exhibited significantly greater intersubject correlation during navigation episodes with landmarks than those without landmarks (Top). However, in those regions, the average activation during navigation episodes with landmarks was not significantly greater than the average activation during navigation episodes without landmarks (Bottom).

B) The early visual cortex (V1 and V2) exhibited greater intersubject correlation during navigation episodes that were successfully memorized (correct trials) compared to episodes that failed to be memorized (incorrect trials). However, the average activation during navigation episodes did not differ between the two conditions (correct vs. incorrect).

Stars indicate statistical significance: * denotes FDR-adjusted $p < 0.05$, ** $p < 0.01$, *** $p < 0.001$
LOC: Lateral occipital cortex; PHC: parahippocampal cortex

Conclusions: During navigation, various brain regions displayed shared dynamic processing. Sensory processing regions in the occipital lobe had the highest ISC, while frontal regions associated with higher-level cognitive functions exhibited smaller yet significant ISC. One factor contributing to ISC was the presence of distinguishable landmarks in the environment. This suggests that events related to landmarks act as temporal anchors, with most individuals similarly encoding them at those moments in the episode. Memory performance was found to be related to the dynamic activities, rather than the overall activation level, in the visual cortex. Given that the visual cortex reflects visual attention and memory, we suggest that inadequate control of such processes may, in part, explain why some individuals fail to encode the entire navigational event in memory. These results demonstrate that utilizing ISC as a neural marker of spatiotemporal encoding may provide further insight into the role of various brain regions in the formation of episodic memory, and provide new interpretations which may not be revealed through analyzing average activation level alone.

References
1. Harrison, S. A. (2009). Decoding reveals the contents of visual working memory in early visual areas. Nature, 458(7238), 632–635. https://doi.org/10.1038/nature07832
2. Hasson, U.(2004). Intersubject Synchronization of Cortical Activity During Natural Vision. Science, 303(5664), 1634–1640. https://doi.org/10.1126/science.1089506
3. Hasson, U.(2008). Enhanced Intersubject Correlations during Movie Viewing Correlate with Successful Episodic Encoding. Neuron, 57(3), 452–462. https://doi.org/10.1016/j.neuron.2007.12.009
4. Sheng, J. (2023). Intersubject similarity in neural representations underlies shared episodic memory content. Proceedings of the National Academy of Sciences, 120(35), e2308951120. https://doi.org/10.1073/pnas.2308951120
5. Watanabe, T. (1998). Attention-Regulated Activity in Human Primary Visual Cortex. Journal of Neurophysiology, 79(4), 2218–2221. https://doi.org/10.1152/jn.1998.79.4.2218

Poster No 1090

Memory reactivation during rest is coupled with fluctuations in ongoing brain states

Arielle Tambini[1], Ting Xu[2], Karl-Heinz Nenning[1], Mark D'esposito[3], Stanley Colcombe[1], Michael Milham[2]

[1]Nathan Kline Institute, Orangeburg, NY, [2]Child Mind Institute, New York, NY, [3]University of California, Berkeley, CA

Introduction: A rich repertoire of neural dynamics is present during rest periods. One example is the reactivation of representations of past experience, a key mechanism supporting memory consolidation[1]. Although memory-related reactivation has been measured during rest (and sleep)[2,3], it is unclear which awake brain states preferentially support reactivation. Prior work suggests a trade-off between internally-oriented brain states that promote reactivation, versus externally-focused states[4-7]. Recent findings support this idea, such that reactivation and related electrophysiological events coincide with default network activity, which is linked with internal processing[8,9]. A separate literature has characterized distinct brain states during rest via coactivation pattern (CAP) analysis[10,11], which typically isolates a state reflecting internal vs. external processing (differentially weighting default vs. task-positive networks)[12]. Moreover, the recurring nature of CAPs is linked with slow fluctuations in global brain-wide activity (global fMRI signal, GS)[13]. Here, we sought to better understand which brain states support consolidation by characterizing relationships between reactivation events, brain states (i.e. CAPs), and GS fluctuations during rest.

Methods: We analyzed an fMRI dataset (n=52), in which the reactivation of incidentally encoded object-face stimuli has been reported14. We first isolated brain states (i.e. CAPs) from the baseline (pre-encoding) rest scans (see design in Fig. 1A)[10,11]. To classify brain states during post-encoding rest (three 9-minute scans), the correlation between each CAP and post-encoding time point was measured and each time point was assigned to the most similar CAP. Reactivation events were defined as time points of high similarity between the encoding and post-encoding rest patterns concurrently in the hippocampus and lateral occipital cortex (LOC)[14,15]. Although here we characterize brain states during reactivation, the primary goal of this dataset was to test the causal role of visual cortical activity in memory consolidation, such that inhibitory Transcranial Magnetic Stimulation (TMS) was applied to LOC or a Control site after learning. As LOC TMS reduced reactivation in LOC and memory retention vs. Control conditions, here, we also tested whether TMS influenced the coupling between reactivation and CAPs.

Results: We identified four distinct pairs of brain states (Fig. 1B). CAPs 1A and 1B captured modes of internal vs. external processing (differentially weighted default vs. dorsal attention networks). Other CAPs weighted the visual network (2A/B), the sensorimotor-association axis (3A/B), and somatomotor and ventral attention networks (4A/B). Reactivation was not uniformly distributed across CAPs (Fig. 2; $F=14.5$, $P<10\text{-}9$), but occurred preferentially during CAPs 1A and 2A, and was less likely during 1B and 3B. TMS influenced coupling between reactivation and CAPs ($F=2.2$, $P=0.04$); after LOC TMS, reactivation occurred more often during CAP 3A, and less during 2A. Moreover, reactivation tended to occur during the peak or zero phase of the GS ($P<10\text{-}9$, not affected by TMS). To ensure that the results were not an artifact of reactivation detection, we verified that parallel analysis of the encoding data revealed distinct coupling with CAPs.

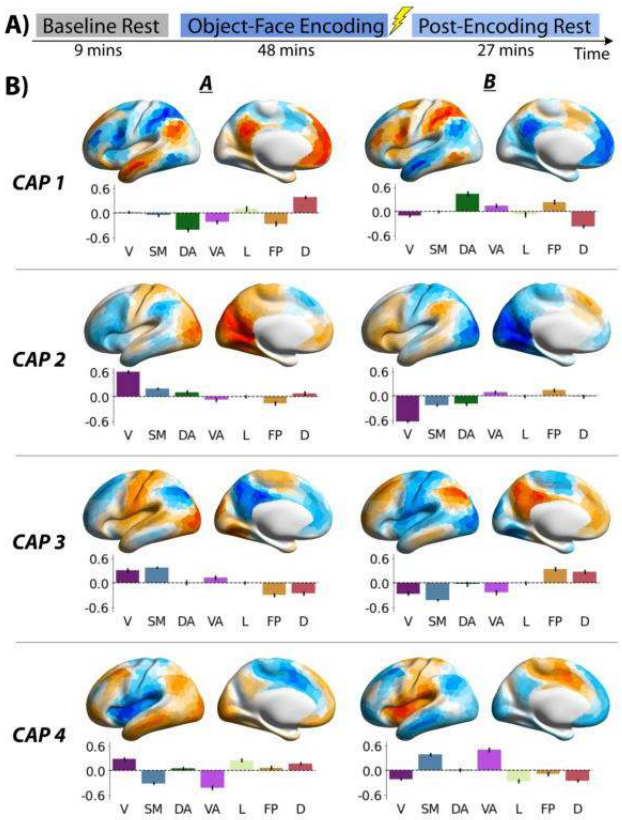

Figure 1. A) Experimental Design. **B)** CAP pairs (A, B) shown on the cortical surface (top row) and their weighting of seven cortical networks defined by Yeo et al., 2011 (bottom row). V: Visual, SM: Somato-motor, DA: Dorsal Attention, VA: Ventral Attention, L: Limbic, FP: Fronto-parietal, D: Default

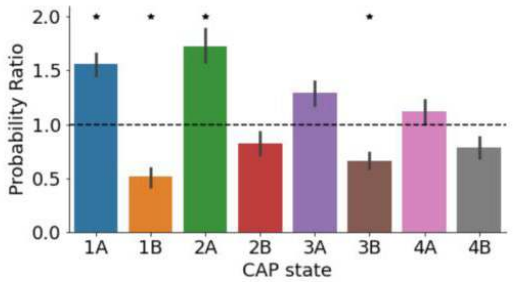

Figure 2. The occurrence probability of each brain state (CAP) during reactivation events. The probability of each CAP was divided by its total occurrence during rest, such that values of 1 indicate that CAPs occur as often as expected by chance, and values > or < 1 indicate that reactivation occurs more or less frequently than expected during a given CAP. *P < .05 (multiple comparison corrected)

Conclusions: Memory reactivation preferentially occurred during brain states reflecting internal vs. external processing and visual activation, suggesting that promoting these brain states may facilitate (visual) memory consolidation. Modulation of these dynamics by TMS suggests that this coupling may be functionally relevant for consolidation. Our results highlight that memory reactivation is coupled with ongoing, slow fluctuations in brain states and brain-wide activity, which may reflect slow changes in other factors (e.g. arousal) that shape memory consolidation.

References

1. Klinzing, J. G., Niethard, N. & Born, J. Mechanisms of systems memory consolidation during sleep. Nat. Neurosci. 22, 1598–1610 (2019).
2. Liu, Y., Nour, M. M., Schuck, N. W., Behrens, T. E. J. & Dolan, R. J. Decoding cognition from spontaneous neural activity. Nat. Rev. Neurosci. 23, 204–214 (2022).
3. Tambini, A. & Davachi, L. Awake Reactivation of Prior Experiences Consolidates Memories and Biases Cognition. Trends Cogn. Sci. 23, 876–890 (2019).

4. Hasselmo, M. E. & McGaughy, J. High acetylcholine levels set circuit dynamics for attention and encoding and low acetylcholine levels set dynamics for consolidation. Prog. Brain Res. 145, 207–231 (2004).
5. Fox, M. D. et al. The human brain is intrinsically organized into dynamic, anticorrelated functional networks. Proceedings of the National Academy of Sciences 102, 9673–9678 (2005).
6. Mednick, S. C., Cai, D. J., Shuman, T., Anagnostaras, S. & Wixted, J. T. An opportunistic theory of cellular and systems consolidation. Trends Neurosci. 34, 504–514 (2011).
7. Wamsley, E. J. Offline memory consolidation during waking rest. Nature Reviews Psychology 1, 441–453 (2022).
8. Higgins, C. et al. Replay bursts in humans coincide with activation of the default mode and parietal alpha networks. Neuron 109, 882–893.e7 (2021).
9. Kaplan, R. et al. Hippocampal sharp-wave ripples influence selective activation of the default mode network. Curr. Biol. 26, 686–691 (2016).
10. Liu, X., Chang, C. & Duyn, J. H. Decomposition of spontaneous brain activity into distinct fMRI co-activation patterns. Front. Syst. Neurosci. 7, 101 (2013).
11. Yang, H. et al. Reproducible coactivation patterns of functional brain networks reveal the aberrant dynamic state transition in schizophrenia. Neuroimage 237, 118193 (2021).
12. Gutierrez-Barragan, D., Basson, M. A., Panzeri, S. & Gozzi, A. Infraslow State Fluctuations Govern Spontaneous fMRI Network Dynamics. Curr. Biol. 29, 2295–2306.e5 (2019).
13. Tambini, A. & D'Esposito, M. Causal Contribution of Awake Post-encoding Processes to Episodic Memory Consolidation. Curr. Biol. 30, 3533–3543.e7 (2020).
14. Liu, X., Zhang, N., Chang, C. & Duyn, J. H. Co-activation patterns in resting-state fMRI signals. Neuroimage 180, 485–494 (2018).
15. Tanrıverdi, B. et al. Awake Hippocampal-Cortical Co-reactivation Is Associated with Forgetting. J. Cogn. Neurosci. 35, 1446–1462 (2023).

Poster No 1091

Structural connectivity of the anterior temporal lobe impacts semantic retrieval efficiency

Nicolas Deom[1], Omar Khalil[2], Irene Giannoylis[2], Mary Pat McAndrews[2]

[1]University of Toronto, Toronto, MT, [2]Krembil Research Institute, Toronto, Ontario

Introduction: Semantic memory is the term usually used to describe the sum of all conceptual knowledge an individual possesses. Knowledge about unique entities, usually denoted with proper nouns, is thought to involve integration of many specific bits of information, and accessing these unique concepts is thought to rely on a network of ventrotemporal regions with a key hub in the left anterior temporal lobe (ATL). Individuals with left temporal lobe epilepsy (TLE) have particular difficulty with proper name retrieval, but the unique contribution of white-matter tracts, which connect this hub to the rest of the network, to this impairment remains an open question. Here, we examine the hypothesis that abnormalities in key tracts in TLE patients will impact successful retrieval of these concepts.

Methods: We recruited a sample of 26 left TLE patients being investigated for surgery and 17 healthy controls. Participants performed a semantic decision task where they were presented with a cue word (e.g., Jennifer Aniston) and two target words (e.g.,Brad Pitt and George Clooney) and had to select which of the two targets was more closely related to the cue (Brad Pitt being the expected answer here). Diffusion-weighted images were acquired on a 3T Signa MR system. Standard preprocessing operations were applied on the collected data, using the fMRIPrep pipeline. Tract reconstruction of the left and right uncinate fasciculus (UF) and inferior longitudinal fasciculus (ILF), as well as all analyses were performed using TRACULA, running on Freesurfer 7.4.1. We compared mean fractional anisotropy (FA) and FA voxel-by-voxel along the tract between patients and controls. We also examined the relationship between mean FA and performance on the semantic task. Significant clusters in the along-the-tract analysis were considered significant at $p<0.05$ FWE-corrected. Mean FA comparisons of whole tracts were considered significant at $p<0.05$.

Results: Patients overall showed worse performance on the behavioral task than the healthy controls, suggesting they have more difficulty retrieving information about unique entities. Comparing mean FA values between the groups showed greater asymmetry in the ILF in left TLE group compared to healthy controls, where the left TLE group had significantly lower FA in their left ILF compared to their right while the controls showed no asymmetry. There was no significant difference for the UF. In the voxel-wise analyses, there was a significant cluster in the frontal-lobe section of the left UF, where patients had significantly lower FA than controls. No cluster reached significance in the other three tracts considered. In patients, reduced mean FA in the left ILF was associated with poorer task performance, while reduced mean FA in the left UF was associated with a less cautious approach (faster reaction time, but poorer accuracy).

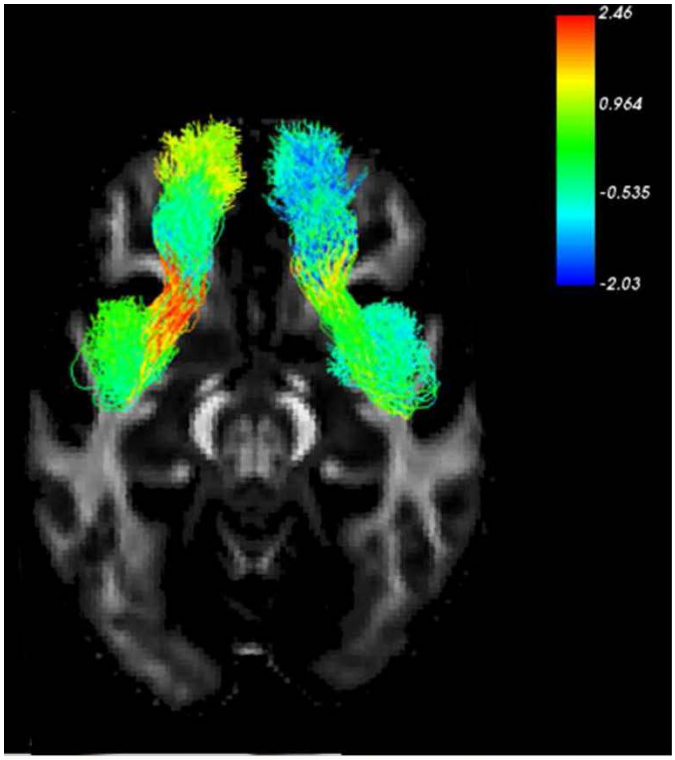

Figure 1: Map of voxel-by-voxel differences in FA between left temporal lobe epilepsy patients and healthy controls in left and right uncinate fasciculus (UF). Cluster in red is significant at p<0.05, FWE-corrected, showing higher FA in controls than patients in the left UF.

Conclusions: We found that FA in the left ILF and UF, as a measure of white-matter tract integrity, was reduced in TLE. For TLE patients, having lower FA in the left ILF was also related to a reduced ability to retrieve semantic information about unique entities. The impact of structural damage or dysfunction in the anterior temporal hub on this process is well-established in the literature. Our findings add to the newer literature indicating that retrieval of information about unique semantic entities is also related to the integrity of long-ranging temporooccipital connections.

References

1. Esteban, O. (2019). fMRIPrep: A robust preprocessing pipeline for functional MRI. Nature Methods, 16(1), Article 1. https://doi.org/10.1038/s41592-018-0235-4
2. Gonzalez Alam, T. R. J. (2021). Intrinsic connectivity of anterior temporal lobe relates to individual differences in semantic retrieval for landmarks. Cortex: A Journal Devoted to the Study of the Nervous System and Behavior, 134, 76–91. https://doi.org/10.1016/j.cortex.2020.10.007
3. Kreilkamp, B. A. K. (2017). Automated tractography in patients with temporal lobe epilepsy using TRActs Constrained by UnderLying Anatomy (TRACULA). NeuroImage: Clinical, 14, 67–76. https://doi.org/10.1016/j.nicl.2017.01.003
4. Patterson, K. (2007). Where do you know what you know? The representation of semantic knowledge in the human brain. Nature Reviews Neuroscience, 8(12), Article 12. https://doi.org/10.1038/nrn2277
5. Tranel, D. (2009). The left temporal pole is important for retrieving words for unique concrete entities. Aphasiology, 23(7–8), 867–884. https://doi.org/10.1080/02687030802586498
6. Viskontas, I. V. (2002). Memory for famous people in patients with unilateral temporal lobe epilepsy and excisions. Neuropsychology, 16(4), 472–480.

Poster No 1092

Aberrant brain network reorganization underlies emotional memory suppression under long-term stress

Tan Wenlong[1], Shaozheng Qin[2]

[1]Beijjing Normal University, Beijing City, Beijing, [2]Beijing Normal University, Beijing, Beiijng

Introduction: Long-term stress (LTS) is believed to result in a tendency to be more sensitive and unforgettable to emotional information (e.g, threat or adversity) as seen in various stress-related mental disorders (Joels,2006; McGaugh,2015), which could be maladaptive for mental health (Anderson,2021). Memory suppression, specifically through voluntarily impeding

the retrieval of unwanted memories (Anderson, 2001), holds the potential to serve as a strategy to alleviate this tendency. However, the extent to which memory suppression can alleviate the over persistence of aversive memories caused by long-term stress, as well as its underlying neural mechanisms, remains elusive. We conducted a fMRI study to investigate neural pattern reorganization associated with the influence of suppression on emotional memories before and after overnight under long-term stress.

Methods: Sixty-one young male college students participated in this experiment: 40 of them who were in a long-term high academic stress environment (all were preparing for the Chinese National Postgraduate Entrance Exam (CNPEE) for at least 6 months) were assigned to the Long-term stress group, the other 21 participants, who had not been exposured to other any major stressors in past 6 months, were the healthy control group. (Fig. 1A). The experiment consisted of four phases, including two training sessions which were conducted two days respectively, “Think/NoThink” paradigm, post-scan memory test and questionnaire (Fig. 1B). Brain images were acquired on a 3T Siemens scanner using an echo-planar imaging sequence. Imaging data were preprocessed and analyzed by using SPM12. We employed several analytical techniques, including univariate general linear models (GLM), representational similarity analysis (RSA), functional connectivity analysis, and network topology analysis, to analyze the brain data.

Results: Behaviorally, Exposure to long-term stress increases the SCL90 scores (Fig. 1 C). Long-term stress group showed less decay of emotional memories over time, and this trend could be intercepted by memory suppression(Fig. 1 D,E). The decay of memories under baseline conditions mediated the difference in inhibition scores between the two groups in the remote condition(Fig. 1 G). Neurally, at network level, the increase of communication efficiency in suppression-related brain network over time was attenuated under long-term stress(Fig. 2 B,C), and the most affected node was the left amygadala, which had an enhanced hubness in control from recent to remote and an abnormal decreased hubness over time in long-term stress(Fig. 2 D,E). The correlation patterns of brain connnectivity and suppression efficiency are distinct during suppression before and after overnight, indicated that consolidation reconfigures brain system involved in suppression, however, these is no similar reconfiguration under long-term stress. The long-term stress group showed change of suppression network communication over time was negatively associated with suppression efficiency of remote memories(Fig. 2 F,H).

Conclusions: Participants under long-term stress exhibited less aversive memories loss from 30 minutes to 24 hours delay, indicated altered consolidation and forgetting process. Neurally, consolidation is manifested by significant reorganization of neural activity patterns during suppression at different time points, However, in the long-term stress group, these corresponding reorganization patterns are altered or even reversed, especially in the left amygadala. Due to the insufficient consolidation and forgetting of emotional memories, the long-term stress group demonstrated a higher efficiency in suppressing remote memories, which was characterized by the extent of reorganization of neural activity patterns was negatively associated with more effective suppression of remote memories. Our findings have significant implications for the application of memory suppression strategies in the treatment of stress-related disorders.

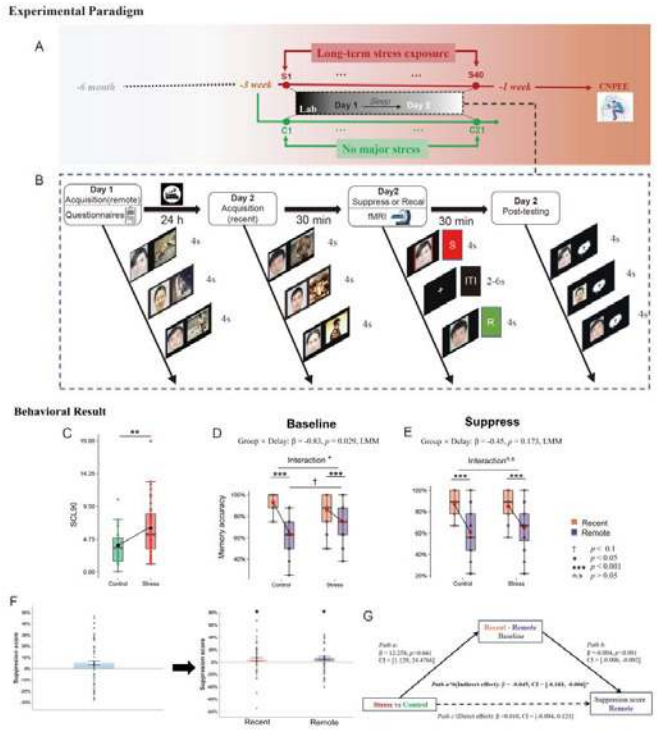

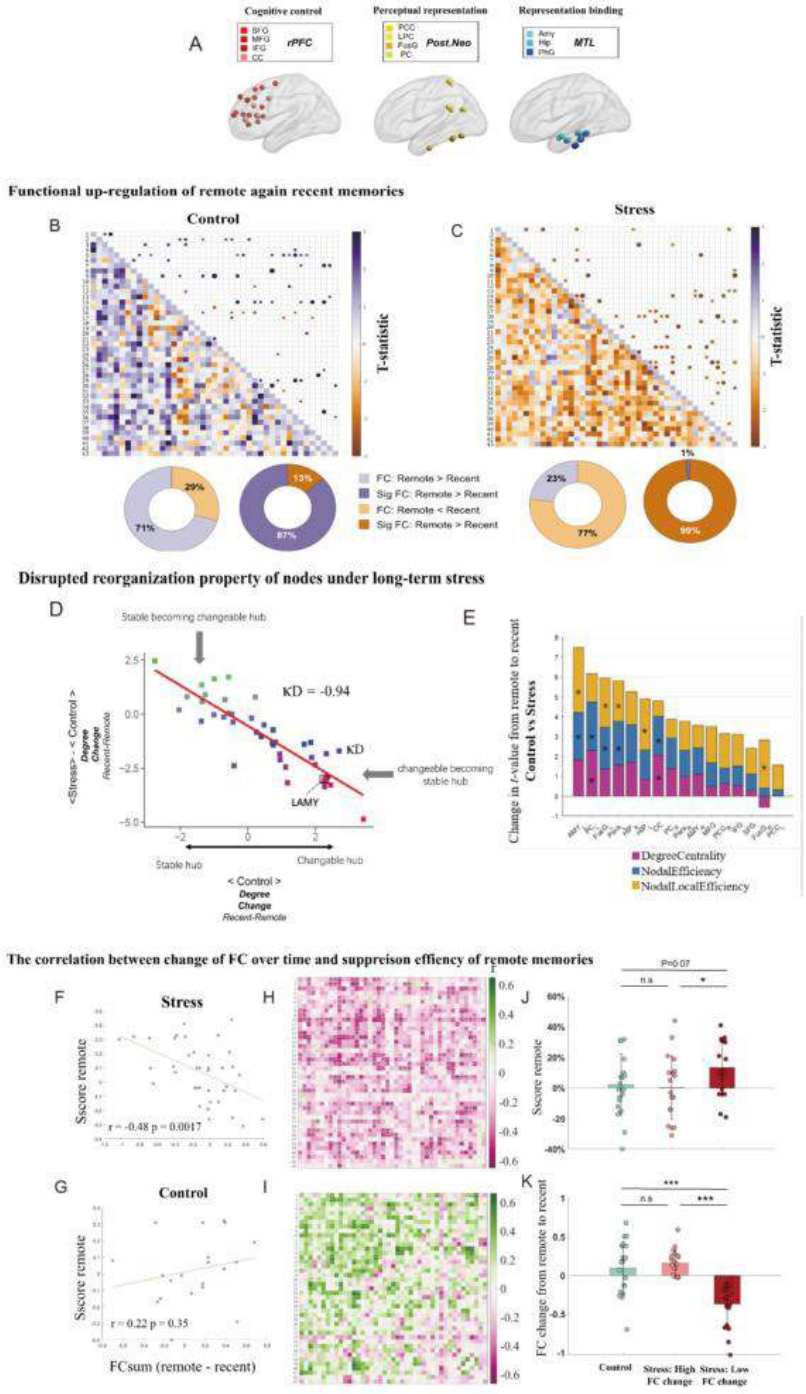

References

1. Anderson, Michael C.(2021) “Active forgetting: Adaptation of memory by prefrontal control.” annual review of psychology 72 : 1-36.
2. Anderson, Michael C.(2001), “Suppressing unwanted memories by executive control.” Nature 410.6826 : 366-369.
3. Joëls, Marian.(2021), “Learning under stress: how does it work?.” Trends in cognitive sciences 10.4 : 152-158.
4. McGaugh, James L. (2015),”Consolidating memories.” Annual review of psychology 66 : 1-24.

Poster No 1093

Influences of long-term memory systems on individual neural differences in early language processing

Analia Marzoratti[1], Anna Youngkin[1], Ian Lyons[2], Michael Ullman[2], Tanya Evans[1]

[1]University of Virginia, Charlottesville, VA, [2]Georgetown University, Washington, DC, DC

Introduction: Long-term memory (LTM) is typically divided into distinct interacting subsystems: declarative (DM) and procedural memory (PM). The declarative-procedural (DP) model of language learning posits a shift from reliance upon explicit DM retrieval to more efficient, automated PM retrieval for language processing.[1] This is thought to be particularly relevant for processing rule-based grammatical content, which has been shown to strongly rely on implicit retrieval of linguistic patterns from PM.1,2 Semantic processing has conversely been associated with explicit DM retrieval of acquired knowledge (e.g., vocabulary) from memory.[2] However, individual differences in the developmental timing, extent, and adaptive value of this DM/PM shift posed by the DP model are poorly understood.

Methods: This study uses open source functional magnetic resonance imaging data from children (n = 159) aged 7 years (M = 7.60, SD = 0.78).[3] By studying same-aged children, we could isolate individual differences from effects of typical, age-related shifts in function such as those posed by the DP model. We estimated mean hemodynamic response across voxels within bilateral regions linked with LTM in the literature (DM: caudate, putamen; PM: hippocampus, parahippocampal gyrus; Fig. 1) while children performed a semantic and a grammatical auditory language task.[1] Through multilevel modeling, we used random slope terms to quantify the influence of individual differences on group-level effects of language demand on neural response.[4] We tested predictions based on the DP model that PM engagement would (1) predict improved task accuracy, and (2) show stronger activity and effects for the grammatical task. We also expected (3) stronger effects of individual differences in PM activity effects given its emergent role across development.

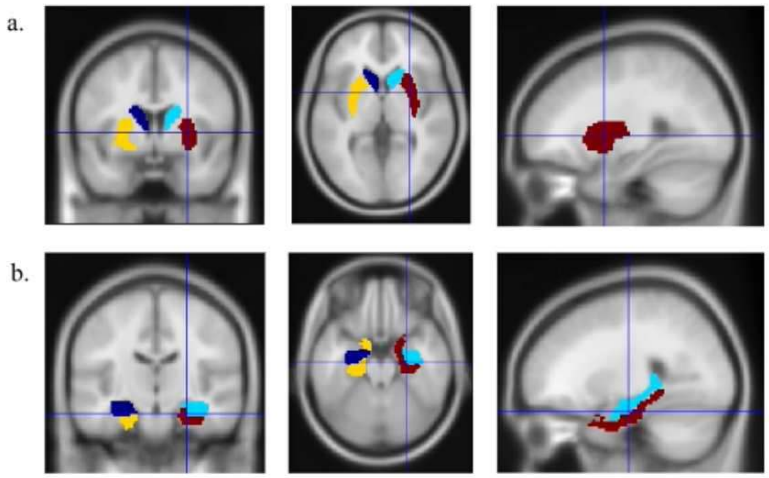

Note. PM-related regions shown in (a) include the left and right caudate in yellow and red, and the left and right putamen in dark and light blue. DM-related regions shown in (b) include the left and right hippocampus in yellow and red and the left and right parahippocampal gyri in dark and light blue.

Results: We found reduced activation during the grammatical task compared with the semantic task in bilateral DM and PM brain network-related structures (Fig. 2). This average fixed task effect was larger for bilateral PM (B = -0.47) vs. DM ROIs (B = -0.31). Based on the DP model, we predicted this negative effect in DM but not in PM regions. Both the fixed negative effect and random effects were largest in models of PM ROI activity, suggesting that the PM system may be particularly influenced by language processing demand and individual differences in neural response. Contrary to our predictions, accuracy showed a significant negative association with left PM activity (B = -4.04, p = .041), with no other significant neural effects on performance. This suggests that our findings of significantly reduced activity in left PM ROIs during the grammatical task may have exerted some benefit for their accuracy. As random slope terms were smaller in accuracy models with PM ROIs relative to DM ROIs, this negative effect appears relatively consistent across members of this sample. These findings suggests that the benefits ascribed to PM retrieval by the DP model of language processing may not extend to grammar at this age.

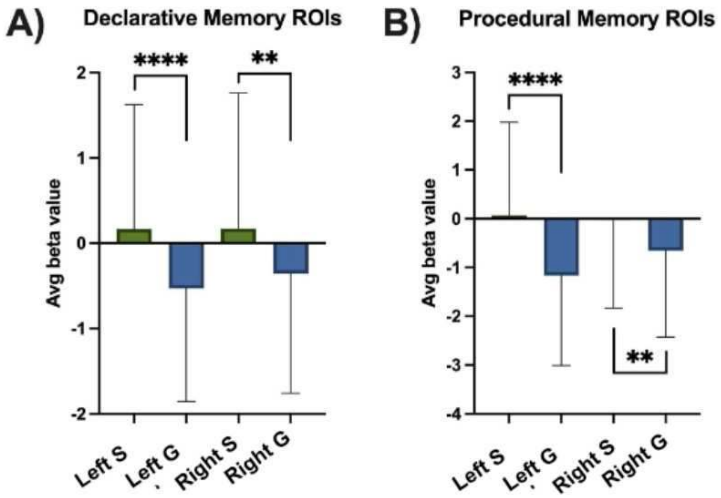

Note. 'S' refers to the sentence-level semantic task and 'G' refers to the grammatical task. A) Within Declarative memory ROIs (i.e., the hippocampus and parahippocampal gyrus), there was significantly higher activity during semantic task than during grammatical tasks for both hemispheres. B) Procedural memory ROIs (i.e., the caudate nucleus and putamen) also showed significantly lower activity during the grammatical task than the semantic task.

Conclusions: Our results suggest that the DP model may not wholly explain the relative roles of LTM systems for language processing at this stage of development, demonstrating complex individual differences in the links between neural activation, and behavioral outcomes. Even at the same age and stage of development, typically developing children may rely on differential degrees of DM and PM retrieval to perform identical cognitive tasks. Therefore, quantifying subject-level variability may be crucial for understanding the scope and stability of patterns of neurocognitive function, even patterns linked to purportedly consistent and generalizable developmental trends. The framework leveraged for this study serves as one example of how future work may similarly account for individual differences in their analyses to better characterize the diversity of neural mechanisms for children's learning.

References

1. Ullman, M. T. (2016). Chapter 76 - The Declarative/Procedural Model: A Neurobiological Model of Language Learning, Knowledge, and Use. In G. Hickok & S. L. Small (Eds.), Neurobiology of Language (pp. 953–968). Academic Press.
2. Clark, G. M., & Lum, J. A. G. (2017). Procedural memory and speed of grammatical processing: Comparison between typically developing children and language impaired children. Research in Developmental Disabilities, vol. 71, pp. 237–247.
3. Wang, J., Lytle, M. N., Weiss, Y., Yamasaki, B. L., & Booth, J. R. (2022). A longitudinal neuroimaging dataset on language processing in children ages 5, 7, and 9 years old. Scientific Data, vol. 9. no. 1.
4. Beckmann, C. F., Jenkinson, M., & Smith, S. M. (2003). General multilevel linear modeling for group analysis in FMRI. NeuroImage, vol. 20. no. 2, pp. 1052–1063.

Poster No 1094

Four-month aerobic exercise training improves hippocampal volume in older adults at metabolic risk

Svenja Schwarck[1,2], Jose Bernal[2], David Berron[2], Hannah Baumeister[2], Helena Gellersen[2], Marcel Daamen[3], Anne Maass[2], Gabriel Ziegler[1,2], Henning Boecker[3], Emrah Düzel[1,2]

[1]Institute of Cognitive Neurology and Dementia Research, Magdeburg, Germany, [2]German Center of Neurodegenerative Diseases (DZNE), Magdeburg, Germany, [3]German Center of Neurodegenerative Diseases (DZNE), Bonn, Germany

Introduction: Higher metabolic risk is associated with poor cardiovascular health and greater risk of developing dementia (Duzel et al., 2016). Even though aerobic exercise training has been shown to improve cardiovascular and metabolic health, memory performance, and hippocampal volume in older healthy adults (Aghjayan et al., 2021), evidence of such effects in older adults with metabolic risk remains limited and conflicting. Here, we conducted a combined physical and cognitive training in older adults with metabolic risk to analyze the cumulative and analytically challenging immediate training effects.

Methods: Materials. We recruited thirty-five sedentary older adults (age: 67.77 ± 2.60 years; 12 female) with at least one metabolic risk factor and monitored them for four months, as they engaged in either aerobic exercise and cognitive training (n=17, 40 training sessions) or none (n = 18; pseudo-random allocation). At baseline and after four months, we assessed

pre and post-intervention changes in neuropsychological tests, metabolic health, biomarkers (inter alia, Cathepsin-B), spiroergometric and structural MRI-based brain morphological features. The training regime comprised physical performance (PP, ratio Watt and heart rate) and subsequent memory picture recognition performance (MEM, reaction time corrected for error). MRI features. We estimated whole hippocampal volumes (wHCV) from T2w MRI scans (3T TSE, 0.39x0.39x2.0 mm) with the T2-ASHS longitudinal segmentation algorithm (manual correction of 19 hemispheres); total gray matter volumes with CAT12 in SPM12; and white matter hyperintensities from their T1w MRI images (3T MPRAGE, 1.0x1.0x1.0 mm) with the SAMSEG longitudinal pipeline. We corrected all volumes for intracranial volume. Statistical analysis. We tested for potential time x group interaction effects on each of the outcomes with linear mixed effects models with random intercepts (a model per outcome, age and sex as covariates). To overcome limitations of conventional longitudinal modelling approaches, we analyzed training effects using a hierarchical continuous-time dynamic model with two fully connected state variables, enabling bidirectional effects between PP and MEM over 40 measurement occasions.

Results: Linear mixed effects. During the four-month intervention, the control group showed a decrease in left wHCV, while the volumes in the training group increased (time x group interaction: β = 161.70, 95%-CI[12.80, 310.26]). The training group also maintained their levels of Cathepsin-B and physical fitness over time, whereas the control group experienced a decline in both (physical fitness, maximal Wat: β = 11.45, 95%-CI[0.74, 21.79]; Cathepsin-B levels: β = 39.53, 95%-CI[6.71, 72.22]). Dynamic modeling. In the training group only, PP improved MEM in subsequent dual-task session (-1.11, 95%-BCI[-1.22, -0.99]). Such effect lasted for up to 15 days. Higher baseline wHCV was associated with a stronger coupling-effect of PP on MEM (-0.15, 95%-BCI[-0.18, -0.11]) and lower persistence of MEM (-0.145, 95-BCI[-0.21, -0.08]).

Conclusions: Four months of combined physical and cognitive training has a neuroprotective effect in older adults with metabolic risk factors. Specifically, training, as opposed to a sedentary lifestyle, helped to maintain Cathepsin-B levels and increase left hippocampal volume. Cognitive changes were nonetheless not evident within such a short time period. Using a sophisticated dynamic modelling approach, we demonstrated that exercise training is dynamically linked to cognition in a day-by-day manner, with higher levels of physical fitness improving memory performance in subsequent sessions. The observed benefits were midterm, i.e., lasting for up to 15 days after training session. Interestingly, this interaction was most pronounced in individuals with higher baseline hippocampal volume. Taken together, our data show some evidence for exercise-induced effects on brain health and plasticity in older adults at metabolic risk.

References

1. Aghjayan, SL (2021), 'Aerobic exercise, cardiorespiratory fitness, and the human hippocampus', Hippocampus, vol. 31, no. 8, pp. 817-844. doi: 10.1002/hipo.23337.
2. Duzel, E, (2016), 'Can physical exercise in old age improve memory and hippocampal function?', Brain, vol. 139, no. 3, pp. 662-73. doi: 10.1093/brain/awv407.

Poster No 1095

Using LTP to investigate the Neurosteroid Withdrawal Hypothesis of Perimenstrual Catamenial Epilepsy

Malak Alshakhouri[1], Rachael Sumner[1], Farheen Kothiwala[1], Suresh Muthukumaraswamy[1], Khalid Hamandi[2], Paul Hofman[3], Peter Bergin[4], Cynthia Sharpe[5]

[1]The University of Auckland, Auckland, New Zealand, [2]CUBRIC, University Hospital of Wales and Cardiff University, Cardiff, Wales., [3]Liggins Institute, The University of Auckland, Auckland, New Zealand, [4]Neurology Auckland Hospital, Te Whatu Ora, Auckland, New Zealand, [5]Starship Hospital, Auckland District Health Board, Auckland, New Zealand

Introduction: Catamenial epilepsy refers to seizure exacerbations during certain phases of the menstrual cycle, a condition affecting 40% of women with epilepsy (WWE) that is often treatment-resistant (Herzog, 2015). Perimenstrual catamenial epilepsy (PCE) is the most common pattern, exemplified by a two-fold increase in seizure frequency around menstruation (Herzog, 2004). Female sex steroids are involved in modulating cortical excitability. Very broadly, oestradiol enhances glutamatergic excitation, while progesterone enhances GABAergic inhibition via its neuroactive metabolite, allopregnanolone (ALLO) (Reddy, 2016). The current hypothesis, which has only been tested in rodents, suggests PCE could be a withdrawal symptom caused by the rapid premenstrual decline of ALLO following prolonged exposure during the luteal phase (Reddy, 2016). Long-term potentiation (LTP) is a model of neural plasticity that allow us to non-invasively investigate changes in cortical excitability (Sumner, 2020b). This study utilised an established visual LTP and electroencephalography (EEG) paradigm to investigate the effect of ALLO withdrawal directly in humans.

Methods: This study used a within-subject, repeated-measures, counterbalanced, observational design. Twenty-one WWE with uncontrolled seizers and 25 healthy controls attended 3 sessions timed to their perimenstrual (day -3 to +2), mid-follicular

(day 5 to 8), and mid-luteal (day -5 to -9) phases, with day 1 being the first day of menstrual bleeding. Cycle timing was confirmed using ovulation and blood tests. Blood will be analysed for changes in progesterone, oestradiol, ALLO and GABAA receptor (GABAAR) mRNA. At each session, participants were presented with repetitive sine gratings at low frequency (1Hz) for 4 minutes, preceding a 2-minute high-frequency photic tetanus (9Hz) to induce LTP (Fig 1). The low-frequency condition was repeated at 2- and 40-minutes post-tetanus to record early and sustained LTP changes, respectively. EEG was recorded using a 64-channel actiCAP system. Data was pre-processed using Fieldtrip and analysed using SPM12 in MATLAB. LTP was assessed as changes in visual evoked potential (VEP) amplitude between pre-tetanus and post-tetanus recordings.

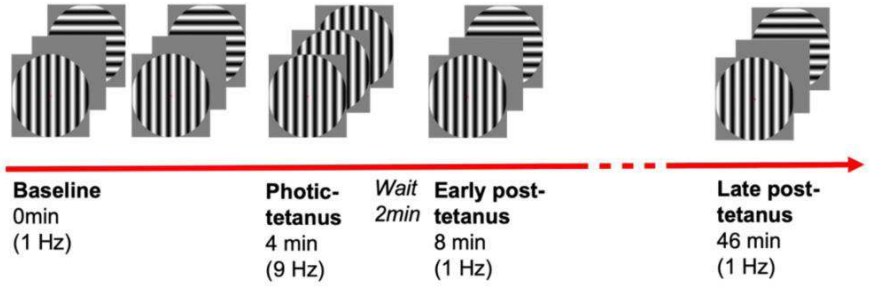

Fig 1. Diagram of the LTP paradigm timing and sequence. Adapted from Sumner, et al., (2020a).

Results: The data from the entire control cohort and the first nine WWE were included in the analysis. Initial analysis revealed a significant enhancement of the P2 peak of the VEP in the late post-tetanus condition at 183ms in the control cohort ($F(1,288) = 76.8$, $p < 0.05$ FWE-c) and at 215ms in the epilepsy cohort ($F(1,96) = 73.3$, $p < 0.05$ FWE-c). The timing of these peaks was used to inform the main within-subject analysis of menstrual cycle phase effect. A significant effect of menstrual cycle phase on visual LTP was found in the control cohort ($F(2, 288) = 12.1$, $p < 0.05$ FWE-c). P2 enhancement was significantly greater during the mid-follicular phase than the perimenstrual phase ($t(48) = 4.41$, $p < 0.05$ FWE-c) (Fig 2a). In the epilepsy cohort, exploratory analyses revealed a trend in the opposite direction. P2 enhancement was greater during the perimenstrual phase than the mid-follicular phase ($t(16) = 3.23$, $p < 0.01$ unc) (Fig 2b).

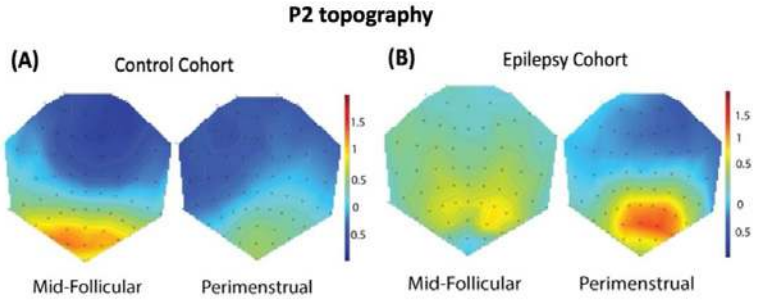

Fig. 2. Topographies of the P2 peak during the perimenstrual and mid-follicular phases for (A) the healthy control cohort and (B) the epilepsy cohort.

Conclusions: We found greater LTP enhancement during the mid-follicular phase compared to the perimenstrual phase in healthy females, although both phases are associated with low serum hormone levels. The latter is however associated with higher progesterone to oestradiol ratio, potentially leading to dominating effects of GABAergic inhibition and thus reduced cortical excitation (Reddy, 2004). It is too early to interpret the epilepsy findings, given the small sample size at the time of analysis. Yet, our preliminary finding shows some promise as it appears to align with rodent findings of increased cortical excitation during the perimenstrual phase (Reddy, 2007). This could reflect heightened sensitivity of women with PCE to ALLO withdrawal, possibly underlined by dysregulation of GABAAR as the current hypothesis suggests.

References

1. Herzog, A. G. (2015), 'Catamenial epilepsy: Update on prevalence, pathophysiology and treatment from the findings of the NIH Progesterone Treatment Trial', Seizure, vol. 28, pp. 18-25.
2. Herzog, A. G. (2004), 'Frequency of catamenial seizure exacerbation in women with localization-related epilepsy', Ann Neurol, vol 56, no. 3, pp. 431-4.
3. Reddy, D. S. (2016), 'Catamenial Epilepsy: Discovery of an Extrasynaptic Molecular Mechanism for Targeted Therapy', Front Cell Neurosci, vol 10, pp. 101.
4. Sumner, L. R. (2020a). 'Ketamine enhances visual sensory evoked potential long-term potentiation in patients with major depressive disorder', Biological Psychiatry: Cognitive Neuroscience and Neuroimaging, vol 5, pp. 45-55.
5. Sumner, L. R. (2020b). 'The role of Hebbian learning in human perception: a methodological and theoretical review of the human Visual Long-Term Potentiation paradigm', Neuroscience & Biobehavioral Reviews, vol 115, pp. 220-37

Poster No 1096

Neuroplasticity related to sound localization in single-sided deafness patients: an fMRI study

Leeseul Shim[1,2], Ja Hee Kim[1,3], Gibbeum Kim[1], Hyo-Jeong Lee[1,2,3]

[1]Laboratory of Brain & Cognitive Sciences for Convergence Medicine, Hallym University College of Medi, Anyang, Korea, Republic of, [2]Ear and Interaction Center, Doheun Institute for Digital Innovation in Medicine (D.I.D.I.M.), Hallym University Medical Center, Anyang, Korea, Republic of, [3]Department of Otorhinolaryngology-Head and Neck Surgery, Hallym University College of Medici, Chuncheon, Korea, Republic of

Introduction: In patients with bilateral deafness, cortical plasticity related to behavioral outcomes has been explored in the auditory/visual sensory domain and the modality-independent cognitive domain. However, neuroplastic change in patients with single-sided deafness (SSD) is still largely unknown and associated with a specific binaural process such as sound localization is scarce. In this fMRI study, neural activity while performing sound localization tasks was explored in patients with single-sided deafness compared to the binaural or monaural hearing controls.

Methods: A total of 35 patients with severe to profound SSD and 13 normal-hearing controls (NC, n=13, age = 45.2±11.9) participated in the study. The patients with SSD were comprised into two groups: the left SSD (Lt SSD, n=17, age=43.9±15.2) and the right SSD group (Rt SSD, n=18, age=52.6±7.2). All participants performed two fMRI sessions of 14 blocks, each with an auditory localization task. The NC group have conducted the same experiment in three conditions: binaural, right ear-only, and left ear-only. All participants. verbally responded the source direction among the left, front, and right sides. The correct response rate and the RMS error were also acquired during the scan. Imaging analysis was performed using the SPM12 package. Aside from whole-brain analysis of group comparison and correlation, cortical laterality was explored in three auditory ROIs that are cytoarchitectonically defined, accounting for both cluster size and activity strength (WLI: weighted laterality index).

Results: The NC group in the binaural condition revealed significant activation in the bilateral auditory cortices, regions in the frontal cortex, and the cingulo-opercular network. As expected, the NC group with one ear plugged showed a completely biased response to the side of the open ear. The auditory cortical response is shifted to the hemisphere contralateral to the open ear regardless of the source direction. Similar to the NC group in the binaural state and different from them in monaural conditions, the SSD groups revealed activity in the bilateral STG to all stimuli directions, suggesting that abnormal aural preference has developed in the ipsilateral auditory cortex to the intact ear. Localization-related activity in the right Heschl's gyrus changes as a function of the duration of single-sided deafness, leading to a decreased interhemispheric asymmetry in both SSD groups. In the SSD groups, activity in the posterior STG contralateral to the intact ear and in the cingulo-opercular network was related to the better localization performance in the scanner. Analysis of WLI revealed that a time-related decrease in auditory cortical asymmetry is significant in the earlier auditory areas when the source is in the direction of the impaired ear.

Conclusions: With an extended duration of the asymmetric hearing, auditory cortical plasticity occurs to respond to the direction of the sound source, regardless of the side of hearing. The functional change seems to occur rapidly in the non-primary areas, while it changes slowly in the core area in a time-varying fashion. The result suggests compensatory neuroplasticity in the dorsal auditory pathway and areas for attentional control is essential to overcome the distorted auditory spatial information for sound localization in patients with SSD.

References

1. Derey, K. (2016), 'Opponent Coding of Sound Location (Azimuth) in Planum Temporale is Robust to Sound-Level Variations', Cerebral Cortex, vol.26(1), pp. 450-464
2. Gordon, K.A. (2013), 'Bilateral input protects the cortex from unilaterally driven reorganization in children who are deaf', Brain, vol.136, pp.1609-1625
3. Callan, A. (2015), 'An fMRI Study of the Ventriloquism Effect', Cerebral Cortex, vol.25, pp. 4248-4258
4. Kumpik D.P., King A.J. (2019), 'A review of the effects of unilateral hearing loss on spatial hearing', Hearing research. vol.372, pp.17-28.
5. Heijden K.V.D, Rauschecker J.P, Formisano E., Valente G., Gelder B.D. (2018), 'Active Sound Localization Sharpens Spatial Tuning in Human Primary Auditory Cortex', Journal of Neuroscience, vol.38, pp.8574-8587.
6. Zhang GY, Yang M, Liu B, Huang ZC, Li J, Chen JY, Chen H, Zhang PP, Liu LJ, Wang J, Teng GJ. (2016), 'Changes of the directional brain networks related with brain plasticity in patients with long-term unilateral sensorineural hearing loss', Neuroscience, vol.28, pp.149-161.
7. Reeder RM, Cadieux J, Firszt JB. (2015), 'Quantification of Speech-in-Noise and Sound Localisation Abilities in Children with Unilateral Hearing Loss and Comparison to Normal Hearing Peers', Audiology & neuro-otology, vol.20, pp. 31–37.
8. Slattery WH, Middlebrooks JC. (1994), 'Monaural sound localization: acute versus chronic unilateral impairment', Hearing research, vol.75, pp. 38-46.

Poster No 1097

Swing Dance Induced Brain Plasticity: Morphometry and Quantitative Study

Chengyi Yuan[1], Weishun Dong[1], Qian Wang[1], Xiao Wang[1], Yanlin Yu[1], Chu-Chung Huang[1]

[1]*East China Normal University, Shanghai, China*

Introduction: Dancing has been regarded as an effective approach for improving cognitive and psychological health, in either older or young adults (Mitterová et al., 2021). To investigate the brain plasticity effect of dancing, traditional neuroimaging research has mostly focused on functional or gray matter morphological changes. However, the structural basis of brain functional change may not be linked with morphological information derived from non-quantitative image, such as T1w, which may be insensitive to short-term intervention, especially in young adults (Broessner et al., 2021). In contrast, quantitative MRI (qMRI) allows a more constant and specific measurement of tissue microstructure, which provide a new view to link structural and cognitive functional changes (Weiskopf et al., 2021) To better understand the structural reorganization underlying functional performance improvements, we conducted an interventional study on healthy adults to investigate the neural plasticity effect after partner dancing training, both traditional grey matter morphometry and qMRI indices were used.

Methods: Seventeen healthy adults (9 females; mean age: 19.8 ± 1.3 years) with no prior dancing experience were included in the study. They underwent MRI scans before (Scan 1) and after (Scan 2) a five-week swing dance workshop lasting two-hours per week. Gray matter volume (GMV) was extracted following optimized voxel-based morphometry approach using T1w. MTsat map and R2* map were acquired using the multi-parameter mapping (MPM) approach (Tabelow et al., 2019) and co-registered to T1w image for further spatial normalization. T1w images from both scans were segmented by a within-subject template and warped to MNI space separately. For each time point, the same deformation was applied to the quantitative maps without modulation. A combined weighting/smoothing approach procedure was implemented on the quantitative maps (Draganski et al., 2011). The statistical threshold for each voxel was defined as uncorrected $p < 0.005$, with a minimum cluster size requirement of 100, 170, and 140 voxels for GMV, MTsat, and R2* maps, respectively. Further exploration on the correlation between brain structural alterations and cognitive functional changes was conducted on clusters showing significant difference in voxel-based analysis.

Results: After 5 weeks of swing dancing training, participants demonstrated regional GMV increase in left superior temporal gyrus (STG), left cerebellar lobule VIII (CER3), right cerebellar lobule IV-V (CER4_5) and GMV decrease in bilateral middle cingulate & paracingulate gyri (ACG). We observed larger MTsat value in brain regions including left superior frontal gyrus-medial (SFGmedial), left middle frontal gyrus (MFG), left middle temporal gyrus (MTG), right anterior orbital gyrus (OFCant) and bilateral crus I of cerebellar hemisphere (CERCRU1). R2* demonstrated higher values in Right IFG pars orbitalis (IFGorb). A positive correlation emerged between the change of MTsat value in the left CERCRU1 and the change in Self-Acceptance Scale (SAQ) score ($R2 = 0.37$, $p = 0.0124$) while a negative correlation was found between the change of MTsat value in the left SFG-medial and the change in Susceptibility to Embarrassment Scale (SES) score ($R2 = 0.291$, $p = 0.031$).

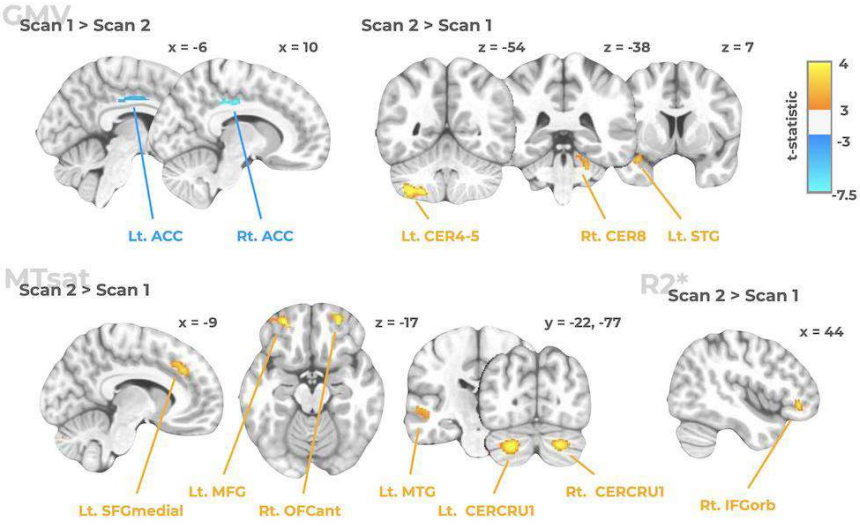

Fig. 1. Brain regions with structural alterations between two scans. The warm color maps show significantly larger value. The cool color maps show trends toward smaller values. Lt, left; Rt, Right; ACC, anterior cingulate & paracingulate gyri; CER4-5, lobule IV, V of cerebellar hemisphere; CER8, lobule VIII of cerebellar hemisphere; CERCRU1, crus I of cerebellar hemisphere; IFGorb, IFG pars orbitalis; MFG, middle frontal gyrus; MTG, middle temporal gyrus; OFCant, anterior orbital gyrus; SFGmedial, superior frontal gyrus, medial; STG, superior temporal gyrus.

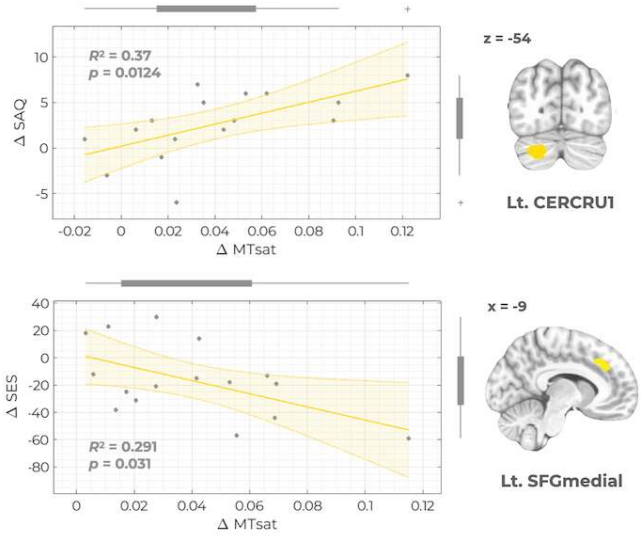

Fig. 2. Correlations between regional brain structural alteration and change of cognitive variables. The confidence interval is established at 95%. The boxplots represent changes in the corresponding variable. On each box, the edges of the box represent the 25th and 75th percentiles, respectively. Whiskers extend to the furthest data point that is not an outlier, and outliers are individually plotted with a '+' symbol. SES , Susceptibility to Embarrassment Scale score; SAQ, Self Acceptance Scale score; Lt, left; CERCRU1, Crus I of cerebellar hemisphere; SFGmedial, Superior frontal gyrus, medial.

Conclusions: Our analysis demonstrates that partner dancing training can induce significant microstructural differences in the brain areas responsible for motor skill learning, action planning, task execution and social cognition. Additionally, we observed correlations between brain microstructural alterations and social cognition changes regarding mental health and interpersonal relationships. Our findings demonstrated that partner dancing may induce myelination in specific brain regions, suggesting the neural basis of social cognition improvement. These findings support the potential of partner dancing as a comprehensive intervention, integrating both exercise and social attributes.

References

1. Broessner, G., Ellerbrock, I., Menz, M. M., Frank, F., Verius, M., Gaser, C., & May, A. (2021). Repetitive T1 imaging influences gray matter volume estimations in structural brain imaging. Frontiers in Neurology, 12. https://doi.org/10.3389/fneur.2021.755749
2. Draganski, B., Ashburner, J., Hutton, C., Kherif, F., Frackowiak, R. S., Helms, G., & Weiskopf, N. (2011). Regional specificity of MRI contrast parameter changes in normal ageing revealed by voxel-based quantification (VBQ). NeuroImage, 55(4), 1423–1434. https://doi.org/10.1016/j.neuroimage.2011.01.052
3. Mitterová, K., Klobušiaková, P., Šejnoha Minsterová, A., Kropáčová, S., Balážová, Z., Točík, J., Vaculíková, P., Skotáková, A., Grmela, R., & Rektorová, I. (2021). Impact of cognitive reserve on dance intervention-induced changes in brain plasticity. Scientific reports, 11(1), 18527. https://doi.org/10.1038/s41598-021-97323-2
4. Tabelow, K., Balteau, E., Ashburner, J., Callaghan, M. F., Draganski, B., Helms, G., Kherif, F., Leutritz, T., Lutti, A., Phillips, C., Reimer, E., Ruthotto, L., Seif, M., Weiskopf, N., Ziegler, G., & Mohammadi, S. (2019). hMRI - A toolbox for quantitative MRI in neuroscience and clinical research. NeuroImage, 194, 191–210. https://doi.org/10.1016/j.neuroimage.2019.01.029
5. Weiskopf, N., Edwards, L. J., Helms, G., et al. (2021). Quantitative magnetic resonance imaging of brain anatomy and in vivo histology. Nature Reviews Physics, 3, 570–588. https://doi.org/10.1038/s42254-021-00326-1

Poster No 1098

Prehabilitation before neurosurgery modifies cognitive brain networks preserving function

Alba Roca-Ventura[1], Leonardo Boccuni[1], David Leno-Colorado[1], Edgar Buloz-Osorio[1], Selma Delgado-Gallen[1], María Cabello-Toscano[2], David Bartrés-Faz[2], Alvaro Pascual-Leone[3], Jose M. Tormos[4], Kilian Abellaneda-Pérez[1]

[1]Institut Guttmann, Barcelona, Spain, [2]University of Barcelona, Barcelona, Spain, [3]Harvard Medical School, Boston, MA, [4]Universidad Católica de Valencia, Valencia, Spain

Introduction: Optimizing tumor excision while limiting harm to healthy brain tissue is the main objective of brain tumor surgery. However, the use of invasive prehabilitation techniques come with a higher risk of consequences. Recent research has demonstrated the brain's ability for change plastically, allowing functional activity to be transferred between different brain regions. However, it remains unclear whether this externally-triggered reorganization of cognitive brain networks could temporarily and adversely affect cognitive functioning in patients awaiting brain surgery.

Methods: Twelve patients (4 women, 8 men; mean age: 52.67 ± 13.4) diagnosed with brain tumors were admitted for prehabilitation. Patients were categorized into two equivalent groups based on the tumor's location and its potential risk to either language or motor functionality. Pre- and post-prehabilitation assessments encompassed functional magnetic resonance imaging (fMRI) and a comprehensive neuropsychological assessment. Prehabilitation involved non-invasive brain

stimulation targeting networks relevant to the function at-risk, combined with intensive language or motor training, tailored to each individual's specific case. Language performance and fMRI-derived language brain networks were explored as the main variables, with their metrics compared to those of the motor group, employed as a control. Two Way Repeated Measures Anova, post hocs and Wilcoxon test were used for the statistical analyses.

Results: A significant interaction between groups (language vs. motor) and time (pre vs. post-PRH) was found for the fMRI language brain networks modulation ($F = 5.007$; $p = 0.049$). Pairwise post-hoc analyses revealed a significant decrease in the language group ($p= 0.047$) but not in the motor control group ($p= 0.495$). These statistically significant changes in brain network arrangement were not associated with language performance in any of the groups (all p-values > 0.05).

Conclusions: Non-invasive prehabilitation induced distinct brain network changes for language and motor groups and these changes showed no association with cognitive impact, and hence, without generating an impact on cognitive function. Therefore, the relocation of brain activity from its initial site does not seem to result in any potential crowding effects. In this context, these results suggests that non-invasive prehabilitation before brain tumor surgery opens a safe neuroplasticity window where brain configuration is temporarily modified, but cognitive performance is preserved. Notwithstanding, more research is necessary to confirm and explore deeper into these findings, which lies on the horizon (ClinicalTrials.gov: NCT05844605).

References

1. Boccuni, L. (2023). 'Neuromodulation-induced prehabilitation to leverage neuroplasticity before brain tumor surgery: a single-cohort feasibility trial protocol', Frontiers in neurology vol. 14 1243857.
2. Barcia, J. (2012b). 'rTMS stimulation to induce plastic changes at the language motor area in a patient with a left recidivant brain tumor affecting Broca's area', Neurocase vol. 18,2, pp. 132-138.
3. François, C (2019). Right Structural and Functional Reorganization in Four-Year-Old Children with Perinatal Arterial Ischemic Stroke Predict Language Production. eNeuro vol. 6,4

Poster No 1099

Detecting motor plasticity in the human thalamus and putamen with precision functional mapping

Roselyne Chauvin[1], Dillan Newbold[2], Ashley Nielsen[1], Samuel Krimmel[1], Athanasia Metoki[1], Benjamin Kay[1], Timothy Laumann[3], Evan Gordon[4], Nico Dosenbach[1,5,3,6]

[1]Department of Neurology, Washington University School of Medicine, Saint Louis, MO, [2]Department of Neurology, New York University Grossman School of Medicine, New York, NY, [3]Department of Psychiatry, Washington University School of Medicine, Saint Louis, MO, [4]Mallinckrodt Institute of Radiology, Washington University School of Medicine, Saint Louis, MO, [5]Department of Biomedical Engineering, Washington University in St. Louis, Saint Louis, MO, [6]Department of Pediatrics, Washington University School of Medicine, Saint Louis, MO

Introduction: Cortico-striato-thalamo-cortical loops have been studied to better understand motor adaptation. Plasticity has been observed in these circuits using invasive electrophysiology in patients[1], and animals[2]. Human plasticity studies, using fMRI, have been limited by low signal-to-noise ratios in subcortex, differences in sensitivity between cortical and subcortical brain measures and plasticity paradigms that induce only small effects[3,4]. To overcome these limitations, our study paired arm immobilization by casting, with repeated functional imaging in three individuals (Precision Functional Mapping; PFM[5]) to address low signal-to-noise ratio in the subcortex. Daily resting-state functional connectivity (FC) and motor task fMRI[6,7] were used to measure functional systems pre, during, and post, 2 weeks of casting. Previously, we identified increased FC between the disused somatomotor cortex hand region and the cingulo-opercular network (CON), an executive control system. We also observed large, spontaneous pulses during casting involving the cortical component of the disused motor circuit. We recently discovered the previously unrecognized Somato-Cognitive Action network (SCAN)[8], which is inter-digitated with effector-specific motor regions in the central sulcus and connects the CON and motor networks within the primary motor cortex. Thus, to capture disuse-driven plasticity effects in human cortex and subcortex, and integrate them with our new understanding of motor circuit, we expanded our prior investigation of the cast dataset to include analysis adapted to the signal characteristic of subcortical regions.

Methods: We analyzed the casting dataset (3 subjects, daily 30min rest+10min HCP motor task fMRI over 6 weeks). For each subject, we employed two complementary methods to measure motor plasticity. First, we quantified disuse-related changes in FC. We computed seed-based voxel correlation maps of FC with somatomotor hand region for each rest session and quantified the change between pre and during casting sessions using within-anatomical structure cluster-based correction, against randomized label null distribution. Second, we performed a detection of disuse pulse presence using a novel HRF-based local modeling method. Finally, we compared resulting subcortical plasticity maps (FC changes, disuse pulses) to

conventional motor execution maps generated from pre casting task fMRI. Similarities between subcortical maps were tested against spatial null distribution using Moran algorithms[9].

Results: While the SCAN regions in the cortex did not show involvement in disuse-driven plasticity, subcortical nodes of SCAN, particularly the central thalamus and posterior putamen, exhibited strengthened FC during disuse and presence of spontaneous activity pulses, that partially overlapped anatomically (Fig. 1). Motor task fMRI validated that subcortical disuse-driven plasticity effects spatially correspond to the upper extremity movement execution circuitry (Fig. 2).

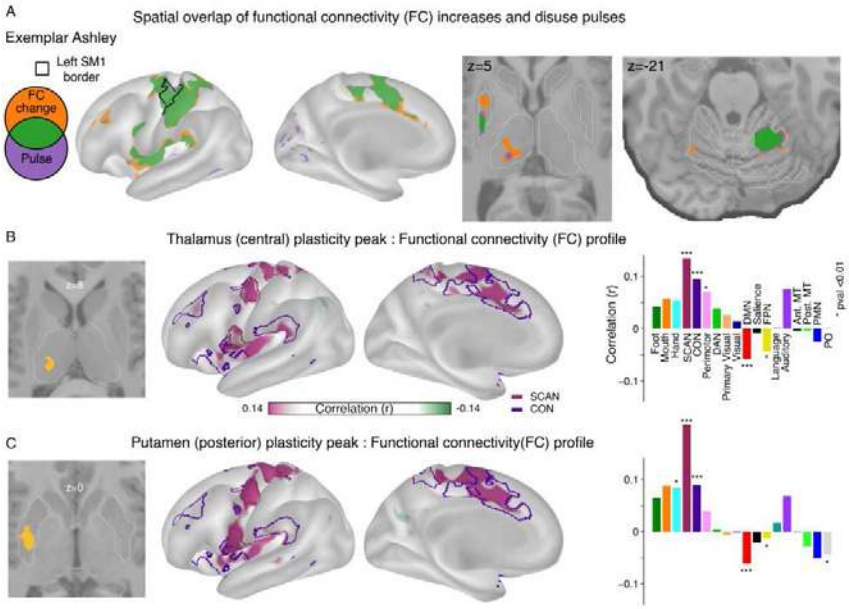

Figure 1: Plasticity effects in cortex and subcortical nodes for an exemplar subject (A)Spatial overlap of functional connectivity (FC) increases and disuse pulses. The strongest disuse-driven FC increases (orange, Cast>Pre, cluster corrected) and disuse pulses (purple, top 20% threshold), as well as their overlap (green) are shown on the cortical surface (left), in the thalamus and putamen (middle) and the cerebellum (right). Results are displayed on the lateral left hemisphere surface, medial left hemisphere surface, and two horizontal slices (MNI z = 5 and -21). White borders on horizontal slices defined individual specific freesurfer based anatomical structures (z = 5: putamen, globus pallidus, caudate, thalamus; z = -21: cerebellum, hippocampus). (B/C) Baseline FC for the 10 voxels (yellow) that showed the greatest FC changes during casting in Thalamus (B) and putamen (C). (left) Seed voxels are displayed on the T1 image. (center) The seed correlation map is shown on the inflated cortical surface with borders of the Cingulo-Opercular (CON; purple) and Somato-cognitive action (SCAN; maroon) networks. (right) Quantification of average seed FC to each cortical network (Gordon parcellation) is provided in the bar plots (* indicate significance at FDR(p) < 0.01 against saptial null distribution, *** indicate significance common across participants).

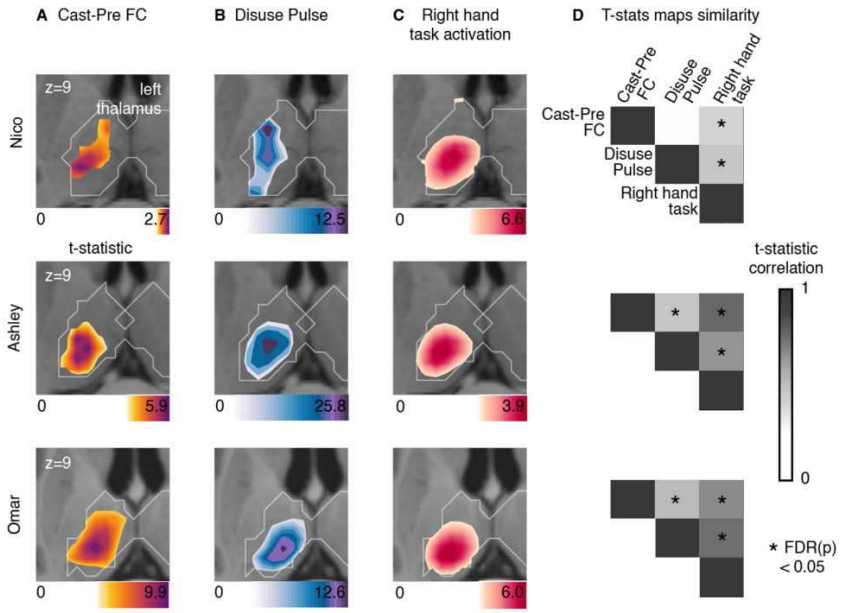

Figure 2: Thalamus representations of disuse-driven FC changes, pulses and hand movement task fMRI activations. (A) Map of disuse-driven increases in FC with left SM1ue ROI (top 30th percentile t statistics). (B) Map of disuse pulses (top 30th percentile t statistics). (C) Map of right hand movement vs baseline task fMRI (HCP motor task; pre-cast; top 30th percentile t statistics). For all three maps, color scales are represented at the bottom of the map with maximum value at 99.5th percentile. (D) Correlation between left thalamic t statistic maps for disuse-driven FC increases, pulse and activation during hand movement (right hand vs baseline). Correlations between unthresholded t statistics maps were tested against individual-specific null distribution effects for each participant (top to bottom : Nico, Ashley, Omar). Reported significant p < 0.05 corrected for FDR (black *).

Conclusions: Our study highlights the significance of subcortical motor circuits in human motor plasticity and a potential role for information integration across networks in motor adaptation. Indeed, the SCAN seems to serve as its downstream actuator, turning more abstract plans into integrated whole-body actions[8]. While cortical SCAN regions might implement whole-body motor commands and do not show large plasticity effects, SCAN subcortical nodes could mediate the disuse-induced FC change between CON and motor effector regions. This subcortical plasticity role is supported by knowledge of thalamic involvement in memory consolidation and homeostasis during sleep[10].

References

1. Opri E, Cernera S, Okun MS, Foote KD, Gunduz A. (2019) The Functional Role of Thalamocortical Coupling in the Human Motor Network. J Neurosci.;39(41):8124-8134. doi:10.1523/JNEUROSCI.1153-19.2019
2. Bonelli RM, Cummings JL. (2007) Frontal-subcortical circuitry and behavior. Dialogues Clin Neurosci.;9(2):141-151.
3. Appelbaum LG, Shenasa MA, Stolz L, Daskalakis Z. (2023) Synaptic plasticity and mental health: methods, challenges and opportunities. Neuropsychopharmacology.;48(1):113-120. doi:10.1038/s41386-022-01370-w
4. Gordon EM, Laumann TO, Gilmore AW, et al. (2017) Precision Functional Mapping of Individual Human Brains. Neuron.;95(4):791-807.e7. doi:10.1016/j.neuron.2017.07.011
5. Mateos-Aparicio P, Rodríguez-Moreno A. (2019) The Impact of Studying Brain Plasticity. Front Cell Neurosci.;13. https://www.frontiersin.org/articles/10.3389/fncel.2019.00066
6. Newbold DJ, Gordon EM, Laumann TO, et al. (2021) Cingulo-opercular control network and disused motor circuits joined in standby mode. Proc Natl Acad Sci.;118(13):e2019128118. doi:10.1073/pnas.2019128118
7. Newbold DJ, Laumann TO, Hoyt CR, et al. Plasticity and Spontaneous Activity Pulses in Disused Human Brain Circuits. Neuron. 2020;107(3):580-589.e6. doi:10.1016/j.neuron.2020.05.007
8. Gordon EM, Chauvin RJ, Van AN, et al. (2023) A somato-cognitive action network alternates with effector regions in motor cortex. Nature.;617(7960):351-359. doi:10.1038/s41586-023-05964-2
9. Alexander-Bloch, A. F., Shou, H., Liu, S., Satterthwaite, T. D., Glahn, D. C., Shinohara, R. T., Vandekar, S. N., & Raznahan, A. (2018). On testing for spatial correspondence between maps of human brain structure and function. NeuroImage, 178, 540–551. https://doi.org/10.1016/j.neuroimage.2018.05.070
10. Latchoumane CFV, Ngo HVV, Born J, Shin HS. (2017) Thalamic Spindles Promote Memory Formation during Sleep through Triple Phase-Locking of Cortical, Thalamic, and Hippocampal Rhythms. Neuron.;95(2):424-435.e6. doi:10.1016/j.neuron.2017.06.025

Poster No 1100

Latent connectivity-behavior dimensions following stroke

Ke Wu[1], Gong Gaolang[1]

[1]State Key Laboratory of Cognitive Neuroscience and Learning & IDG/McGovern,Beijing Normal University, Beijing, China

Introduction: Understanding neurobiological mechanisms behind behavioral deficits is crucial for prognosing and treating stroke patients[1,2]. To address this issue, previous neuroimaging studies on stroke patients largely applied univariate correlation or machine learning approaches to predict each single behavioral score with single or multiple brain features[3,4]. These approaches, however, ignore the highly correlation nature of post-stroke deficits across behavioral domains and possible latent dimensions of heterogeneous behavioral phenotypes in stroke patients[4,5]. The present study applied a multivariate data-driven method to explore the latent dimensional associations between post-stroke behavioral measures of multiple domains and distributed functional connectivity of the entire brain.

Methods: Dataset A public shared longitudinal stroke dataset from the Corbetta's group was used[1,2,4]. This dataset includes a battery of neuropsychological tests and multi-modal MRI scanning at three poststroke time points: ~2 weeks, ~3 months, and ~12 months. For each time point, the patients with all behavioral assessments and qualified resting-state functional MRI scans were entered into our analysis (~2 weeks: 57 patients; ~3 months: 63 patients; ~12 months: 63 patients; 31 healthy controls). Data processing For each of the 5 neuropsychological domains (motor, language, spatial attention, verbal memory, and spatial memory), principal component analysis (PCA) was applied to all within-domain tests, resulting in 5 component scores. For each patient, stroke lesions have been manually outlined by the Corbetta's group. Resting-state functional data was minimally preprocessed using FSL[4]. We then applied the Gordon 333 cortical parcellation and Pearson correlation to estimate a 333×333 functional connectivity (FC) matrix[5]. Here, lesion voxels within each parcel were masked out, and the functional connectivity from the parcel with more than 50% lesion voxels were excluded from the FC matrix[6]. Statistical analysis The partial least squares correlation (PLSC) was applied to identify significant latent components (LC) between the multi-domain neurological scores and FC measures within the matrix. Each identified LC accompanies with a whole-brain weighted matrix pattern (i.e., FC salience) and behavioral profile (i.e., behavioral salience), and a FC composite score and a behavioral composite score then can be yielded for each individual. Pearson correlations between the original data and resultant LC composite scores was used to quantify the contribution of each raw variable to the LCs, referred to as LC loading.

Results: As shown in Figure 1, PLSC analysis consistently revealed one significant LC for poststroke three time points, as well as for the healthy controls. The loadings of the original features (i.e., 5 behavioral domain scores and 55278 functional connectivity) were illustrated in Figure 1B-C. Interestingly, both FC saliences and loadings exhibited overall similar pattern among the three poststroke time points by showing significant correlations between each other (Fig.2). However, their correlation with health controls was gradually increased along the poststroke time, suggesting a reorganization of the behavior-connectivity relationship following the gradual poststroke recovery.

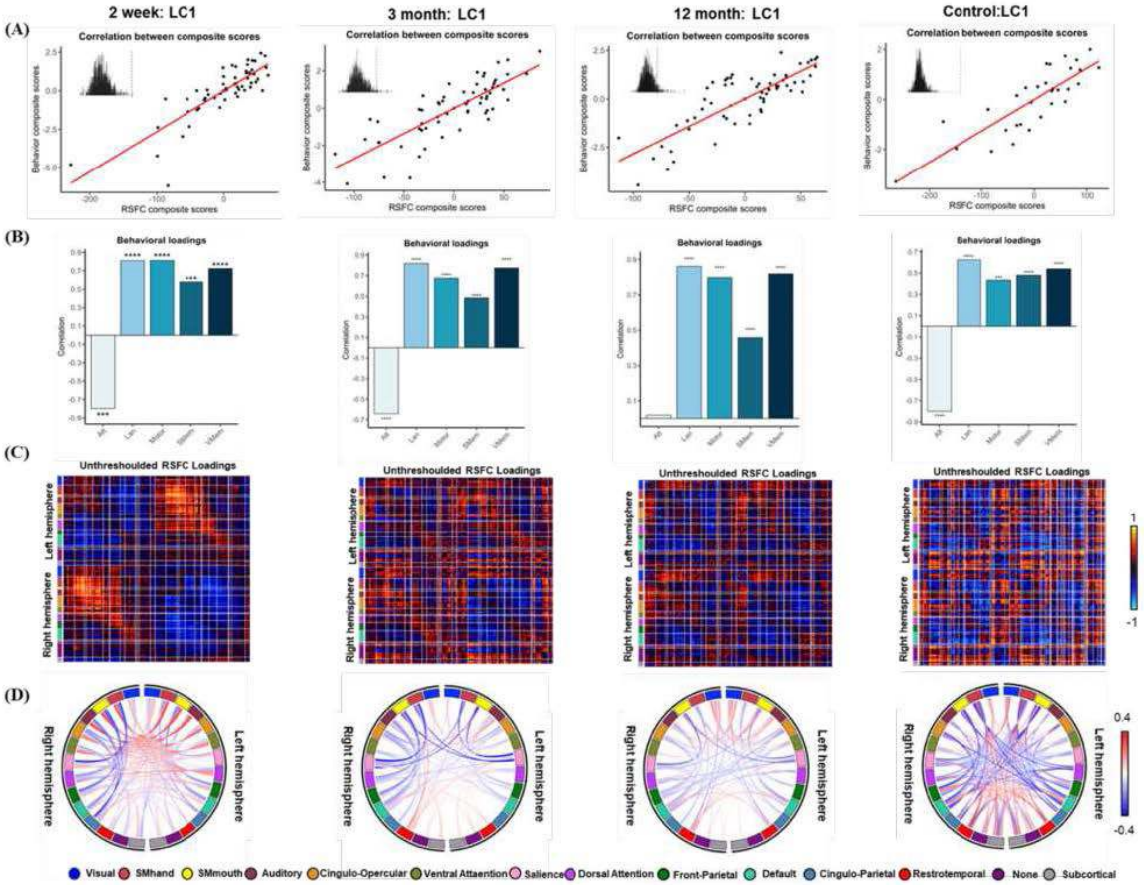

Figure1. (A) Latent dimension in 2-week, 3-month, 12-month strokes and control. Each scatterplot shows the brain and behavioural composite scores. Inset shows null distribution obtained by permutation testing. (B) Correlations between participants' behavioral measures and their behavioral composite scores strokes and controls. Greater loading on LC1 was associated with better performance across behavioral domains. Significant symbols indicate behavioral loadings with significant bootstrapped Z scores. (C) Correlations between participants' RSFC data and LC1's RSFC composite scores stokes and controls. Red (or blue) color indicates that greater RSFC is positively (or negatively) associated with LC1. (D) Correlation between RSFC data and their RSFC composite scores, averaged within and between networks with significant bootstrapped Z scores.

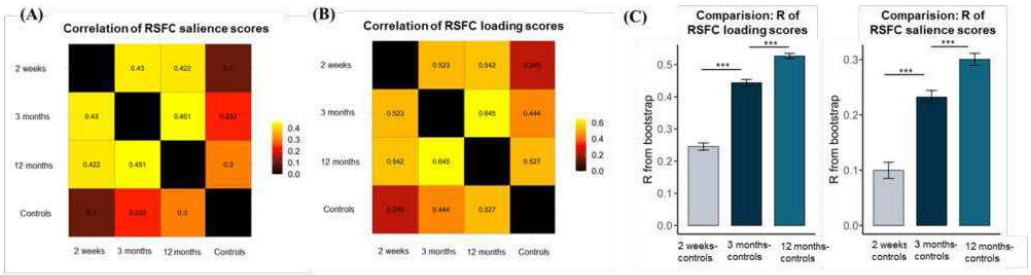

Figure 2. The correlation of the obtained LC1 across strokes and healthy controls. (A) Correlation of RSFC salience among 2-week, 3-month, 12-month strokes and healthy controls. (B) Correlation of RSFC loadings among the four groups. (C) Comparision of correlation coefficient between strokes and controls RSFC loadings/saliences.

Conclusions: Using a multivariate data-driven approach, the present study revealed a robust latent connectivity-behavior component/association in both stroke patients and healthy controls. Particularly, the poststroke FC pattern underlying such association is gradually changed toward the pattern in healthy controls, supporting a dynamic reorganization of functional connectivity networks after the stroke.

References
1. Corbetta, M. et al. (2015), 'Common behavioral clusters and subcortical anatomy in stroke', Neuron, vol. 85, no. 5, pp. 927-941.
2. Ramsey, L. E.et al. (2017), 'Behavioural clusters and predictors of performance during recovery from stroke', Nature human behaviour, vol. 1, no. 3, pp. 0038.
3. Baldassarre, A.et al. (2014). 'Large-scale changes in network interactions as a physiological signature of spatial neglect'. Brain, vol. 137, no. 12, pp. 3267-3283.
4. Siegel, J. S. et al. (2016), 'Disruptions of network connectivity predict impairment in multiple behavioral domains after stroke', Proceedings of the National Academy of Sciences, vol. 113, no. 30, pp. E4367-E4376.
5. Genon, S. et al. (2022), 'Linking interindividual variability in brain structure to behaviour', Nature Reviews Neuroscience, vol. 23, no. 5, pp. 307-318.
6. Gordon EM, et al. (2016), 'Generation and evaluation of a cortical area parcellation from resting-state correlations', Cerebral Cortex, vol. 26, no. 1, pp. 288–303
7. Siegel, J. S. et al. (2018). 'Re-emergence of modular brain networks in stroke recovery', Cortex, vol. 101, pp. 44-59.

Poster No 1101

Ultrafast resting state fMRI unveils layer-specific feedforward and feedback interactions

Joana Carvalho[1], Francisca Fernandes[1], Mafalda Valente[1], Koen Haak[2], Noam Shemesh[1]

[1]Champalimaud Foundation, Lisbon, Lisbon, [2]Radboud University Medical Centre, Donders Institute for Brain, Cognition and Behaviour, Nijmegen, Gelderland

Introduction: Decoding the intricate directionality of information flow within cortical circuits is crucial for deciphering brain dynamics and understanding the driving forces behind learning, sensory training and neuroplasticity following brain damage. Despite its scientific and clinical relevance, a model describing layer-specific feedforward and feedback interactions in health and disease is still lacking. Here, we applied a layer based connective field (lCF) model[1] to ultrafast fMRI and diffusion (d)fMRI resting-state (RS) data to reveal the feedback vs feedback layer specific fingerprints in healthy controls and brain damage animals.

Methods: All experiments were preapproved by the competent authorities. N=15 adult Long Evan rats were scanned on a 9.4T Biospec scanner, under medetomidine sedation. Two different acquisitions were performed: BOLD (N=9) and dfMRI (N=6). BOLD: 6 healthy controls and 3 cortical blind (CB, V1 lesioned), animals were scanned in two scanning sessions: retinotopic mapping and ultrafast RS (3 RS datasets were obtained using GE-EPI acquisitions from: a multislice set; a visual cortex and visual pathway slice sets). V1 Lesioning: Bilateral V1 lesions were performed in 3 animals using a 1% solution of ibotenic acid, Fig2A. The CB animals were scanned 2 weeks post-lesioning. Diffusion fMRI: One scanning session with a visual stimulation and RS paradigms (b= 1.2 ms/µm2 and b=0.05 ms/µm2.) Preprocessing: Images were NORDIC denoised, slice-timing and motion corrected, coregistered, normalized to the SIGMA atlas. Population receptive field mapping and lCF models were implemented in in-house python scripts and build on the work of[1,3].

Results: The lCF position maps estimated from ultrafast RS data show retinotopic organization, Fig1A. LCF size, which reflects the source layer sampling extent, revealed that deeper layers have larger lCF sizes than superficial layers, Fig.1B. This is in agreement with the idea that deeper layers receive feedback information from higher visual areas. Furthermore intracortical lCF between layers of VC showed two different lCF size profiles: feedforward (L4 projecting to all the other layers of the cortex) with inverse U shape with the larger lCF sizes at layer 5 and feedback with a U shape with the larger CF sizes at superficial (L1) and deeper layers (L6), Fig1C. Similar lCF size profiles were also found between V1 and V2 Fig1D. To confirm that larger CF sizes are associated with feedback signals, we computed CFs during visual stimulation and RS. LCFs estimated during visual stimulation (reflecting predominantly feedforward connections) have significantly smaller size than lCFs estimated during RS (spontaneous activity is thought to be feedback dominated) Fig 1F. Fig 1E shows the reliability of the CF model, CF estimated from functionally linked areas (i,.e V1 to other visual areas) have a higher variance explained than areas that are not connected. LCF when applied to CB animals shows increased V2 sampling from visual areas that provide direct input to V1 (LGN and LP) but not to visual areas indirectly connected with V1 (SC), consistent with idea that residual vision is mediated by V1-bypassing circuits[4], Fig2D. Furthermore, also in CB animals deep layers of V2 have the larger lCFs, Fig2C. In addition, lCF estimates obtained from the RS ADC signal show smaller lCF size than the ones obtained form BOLD, and they seem to be more layer specific, Fig2 E,F.

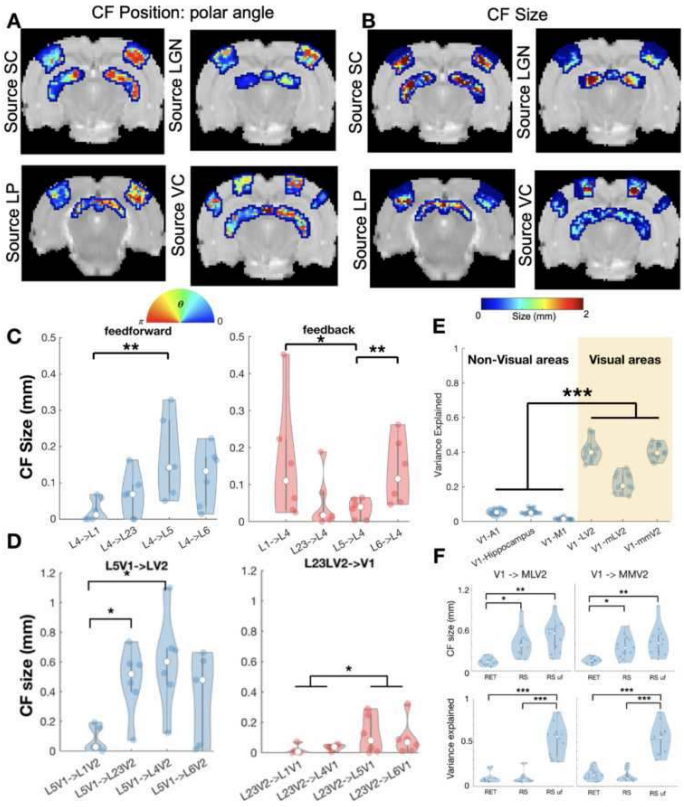

Figure 1: **LCF disentangles feedforward and feedback information.** A.Visualization of the ICF maps averaged over animals, polar angle (Panel A) and size (PanelB), obtained from multislice RS data for inter-areal CF. C. Violin plot of the ICF size estimated for the projections between L4 and all other layers of V1 (feedforward connections) and between all other layers to L4 (feedback connections). D: Layer CF size obtained between V1 and V2. E: Variance explained of the CF estimated between visual areas (V1-> other visual areas) and between V1 and non visual areas. F: CF size and Variance explained obtained for the retinotopy stimulus and RS (1.5 s TR) and ultrafast resting state (350ms) between multiple functionally linked visual areas.

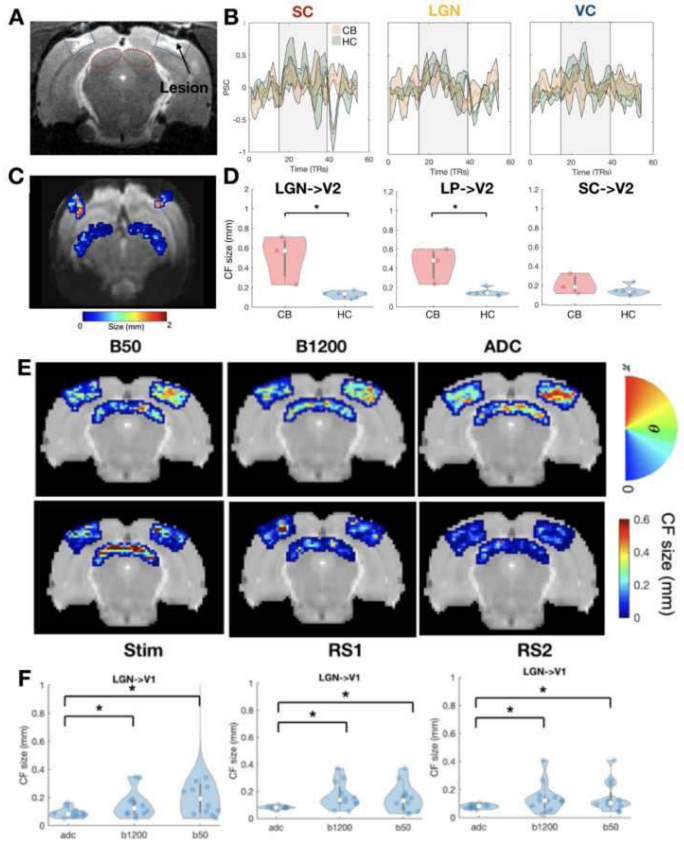

Figure 2. V1-bypassing circuits in Cortical Blindness. A: Anatomical image of an animal with V1 bilateral lesions. B: Superior colliculus (SC), LGN and Visual cortex (VC) time series in response to the retinotopic stimulus for cortical blind and healthy controls. C: LCF size estimates in CB. D:Violin plot of the CF size for CB and HC estimated for the connections LGN->V2, LP->V2 and SC->V2. E: CF maps (position and size) estimated from the ADC, b50 and B1200 signals during RS. F: Violin plot of the CF size obtained from ADC, b50 and B1200 signals for visual stimulation, and RS.

Conclusions: The application of ICF model to ultrafast RS and dfMRI data shows: 1) A bypass of V1 in CB animals mediated by feedback to deep layers of V2; 2) functional connectivity reflects visuotopic organization in the absence of visual input; 3) the size profiles of ICFs enable to disentangle feedback and feedforward signals. Our findings align with the idea that in the visual system layers 5 and 6 carry the feedback information to layer 4, and with the underlying neural architecture[5,6].

References

1. Haak, K. V. et al. Connective field modeling. Neuroimage 66, 376–384 (2013).
2. Barrière, D. A. et al. The SIGMA rat brain templates and atlases for multimodal MRI data analysis and visualization. Nat. Commun. 10, 5699 (2019).
3. Dumoulin, S. O. & Wandell, B. A. Population receptive field estimates in human visual cortex. Neuroimage 39, 647–660 (2008).
4. Rima, S. & Christoph Schmid, M. V1-bypassing thalamo-cortical visual circuits in blindsight and developmental dyslexia. Current Opinion in Physiology 16, 14–20 (2020).
5. Semedo, J. D. et al. Feedforward and feedback interactions between visual cortical areas use different population activity patterns. Nat. Commun. 13, 1099 (2022).
6. Kok, P., Bains, L. J., van Mourik, T., Norris, D. G. & de Lange, F. P. Selective Activation of the Deep Layers of the Human Primary Visual Cortex by Top-Down Feedback. Curr. Biol. 26, 371–376 (2016).

Poster No 1102

Neuroplasticity following auditory working memory training post-stroke: A case study

Ada Leung[1], Winnie Chow[1]

[1]University of Alberta, Edmonton, Alberta

Introduction: Recovering from a stroke is a challenging process. Working memory is one of the cognitive functions that is impacted in a stroke involving the dorsolateral prefrontal cortex. Prior studies have found that improvement in working memory abilities post-stroke is predictive of functional gains (Vallat et al., 2005). Thus, studying how working memory training induces neuroplasticity may shed light on strategies for improving everyday functions. This pilot study aimed to examine the neuroplastic effects of working memory training in a patient with an ischemic stroke resulting in damage of the frontal regions. Our goal was to examine whether auditory working memory training led to changes in auditory and visual working memory abilities, as well as self-perceived cognitive and daily living abilities.

Methods: A woman, aged 56, sustained a right cerebral infarction involving the right middle cerebral arteries six months before the experiment. In the experiment, the patient completed auditory working training that consisted of 1-back, 2-back, and 3-back tasks using spoken digits and letters as stimuli. The training lasted six weeks, five days a week, and 40 minutes a day, with increasing task difficulties across weeks. Before and after the training, the patient underwent functional magnetic resonance imaging (fMRI) on auditory 1-back and 2-back tasks and visual 1-back and 2-back tasks. Also, the patient rated her performance and satisfaction in functional activity engagement using the Canadian Occupational Performance Measures (COPM) and the Cognitive Failure Questionnaire (CFQ). These subjective ratings reflected how well the patient felt herself performing highly prioritized daily activities. The fMRI scanning was conducted at the Peter S. Allen MR Research Center at the University of Alberta. A 3T MRI system (Siemens) with a standard birdcage head coil was used. Structural T1 weighted anatomical volumes were obtained (axial orientation, TR=2080 ms, TE=4.38 ms, FOV=256 mm, slice thickness=1 mm). The T2* weighted echo planar image sequence acquisition parameters were: TR=2000 ms, TE=30 ms, flip angle=80°, FOV=256 mm, and effective acquisition matrix=64×64 mm. Each functional sequence consisted of 36 4-mm thick axial slices, positioned to image the whole brain. The functional run began with a 30-second rest block followed by 8 blocks alternating between task and rest. A whole brain analysis was conducted using SPM12. The design matrix was modelled with blocks of 2-back, 1-back and rest for the auditory and visual tasks in the pre- and post-training scans. Contrasts were extracted with multiple comparisons controlled at $p < 0.05$ corrected.

Results: The patient completed the training. In the post-training scans (compared to pre-training) there was increased neural activation in the left superior frontal gyus, the bilateral inferior parietal lobe, and multiple cerebellar regions in the 2-back > 1-back contrast for both the auditory and visual 2-back tasks. There was also increased striatal activation in the 2-back > rest contrast for the auditory 2-back task. Hit rate and reaction time increased by about 12% and 21% respectively for all the n-back tasks (averaged scores). The ratings on the COPM and the CFQ also improved.

Conclusions: Neuroimaging findings suggest positive learning effects, with increased frontoparietal activations and striatal activations, together with improved behavioral performance. The former is the core network for working memory (Klingberg, 2010) while the striatum is related to learning (Salminen et al., 2016; Dahlin et al., 2008). Although transfer effects of working memory training have been inconclusive (Melby-Lervåg et al., 2016), this study showed transfer effects across tasks of similar

task structures. Also, the patient found daily activities slightly easier after the training. The results suggest that working memory training may be beneficial for stroke recovery. A larger sample is needed to verify the training effects.

References
1. Dahlin, E. (2008), Transfer of learning after updating training mediated by the striatum, Science, 320, 1510-1512.
2. Klingberg, T. (2010), Training and plasticity of working memory, Trends in Cognitive Science, 14(7), 317-324.
3. Melby-Lervåg, M. (2016), Working memory training does not improve performance on measures of intelligence or other measures of "far transfer": Evidence from a meta-analytic review, Perspectives on Psychological Science, 11(4), 512-534.
4. Salminen, T. (2016), Transfer after dual n-back training depends on striatal activation change, Journal of Neuroscience, 36(39), 10198-10213.
5. Vallat, C. (2005), Rehabilitation of verbal working memory after left hemisphere stroke, Brain Injury, 19(13), 1157-1164.

Poster No 1104

Neurochemical Alterations in Bilateral DLPFC after Structure Learning Training in Healthy Adults

Deepika Shukla[1,2], Chia-Lun Liu[1,2], Xiaoqin Cheng[1,2,3], Chie Takahashi[4], SH Annabel Chen[1,2,5,6,7], John Suckling[8,2], Zoe Kourtzi[4,2], Balazs Gulyas[1,5,2], Eleanor Koo[1,2], Wei Ler Koo[1,2], Jia Yuan Janet Tan[1,2], Marisha Ubrani[1,2], Boon Linn Choo[1,2], Min Hong[1,2], CLIC Consortium[2]

[1]Centre for Research and Development in Learning (CRADLE), Nanyang Technological University, Singapore, Singapore, [2]Centre for Lifelong Learning and Individualised Cognition (CLIC), Cambridge Centre for Advanced Research and Education in Singapore(CARES), Singapore, Singapore, [3]Department of Psychology, University of Innsbruck, Innsbruck, Austria, [4]Department of Psychology, University of Cambridge, Cambridge, CB2 3EB, United Kingdom, [5]Lee Kong Chian School of Medicine, Nanyang Technological University, Singapore, Singapore, [6]School of Social Sciences, Nanyang Technological University, Singapore, Singapore, [7]National Institute of Education, Nanyang Technological University, Singapore, Singapore, [8]Department of Psychiatry, University of Cambridge, Cambridge, CB2 0SZ, United Kingdom

Introduction: Structural learning (SL) integrates "Learning to learn" approach of individual's abilities to extract underlying pattern and develop rules to adapt new changes through cognitive flexibility (CF). Homeostatic plasticity in neuronal circuits is crucial for critical learning and depends upon coordinated modulation of synaptic excitation and inhibition through Glutamate and GABA interactions[1]. Disruption in this coordinated neurotransmitter's interplay triggers cognitive deficits[2], while adaptive modulation contributes to relearning capacity[3-4]. Studies reported associative interaction with learning and cognitive skills development with neurotransmitters[5], but the underlying neuro-cognitive model of these interactions is illusive. Using controlled SL training intervention, we aim to investigate the effect of learning in both the neuronal and behavioral levels to assess its transferability to other cognitive abilities.

Methods: 113 healthy volunteers aged between 18-55 years were pseudo-randomized to control (C) (55) and training (T) (58) groups matching with age (mean±SD: 28.21±7.89), gender: (65-F, 48-M) and intelligence (IQ) (109±16.30). T-group underwent 2-week SL training[6]. Out of the 113, 106 (C:53, T:53) participants completed with post-session magnetic resonance (MR) imaging, of which 7 (C:2, T:5) withdrew/dropped out of the study. All MR scans were performed in 3T Siemens MAGNETOM Prisma MRI scanner with a 64-channel head coil. All participants consented to Cognitive testing and MRI sessions with ethics approval from NTU-IRB. MR spectroscopy (MRS) for GABA quantitation in bilateral (left (L)- and right(R)-dorsolateral prefrontal cortex (DLPFC) were performed at two different time points of pre- and post- SL training sessions along with cognitive assessments. Each MR session included 3D T1-MPRAGE (TR=2000ms; TE=22.6ms; TI=800ms; flip-angle=8°; FOV=256×256; slices=176; voxel-size=1×1×1mm3) and 1H-MEGA-PRESS MRS (voi: 30x15x30 mm3, TR=2000ms, TE=68ms, ON=1.98ppm, OFF=7.5ppm, Navg:128) with one unsuppressed water spectra of Navg=4. Voxels were placed close to middle frontal gyrus maximizing gray matter. Manual shimming resulted linewidth < 16 Hz. MRS data in BIDS structure was applied for pre-processing and Osprey[7] was used for quantitation of GABA+ (GABA + macromolecule) and Glx (Glutamate+ glutamine). Quality check for MRS data included visual artefacts, head movements, broad Creatine (Cr) linewidth in the OFF-spectra, and poor fitting.

Results: Tissue corrected GABA+ and Glx levels in both L- & R-DLPFC of study groups did not differ at pre-training stage. After training, the T-group showed significant reduction in R-DLPFC Glx ($p = 0.007$, mean-diff: -2.479) compared to C-group (Fig.1a). Paired comparison between sessions showed significant decrease in post-training R-DLPFC GABA+ in T-group ($p = 0.03$, mean-diff: 0.656) but not in C-group ($p= 0.12$) (Fig. 1d). No significant difference was observed for L-DLPFC GABA+, Glx and GABA+/Glx ratio across groups and sessions. MRS measures did not relate to SL test-scores. However, R-DLPFC Glx in the T-group correlated positively with switch-cost reaction time ($r = 0.3247$, $p = 0.0409$) between shift-repeat trials of color-shape task, indicating reduced Glx levels in the R-DLPFC relates to short reaction time in the T-group (Fig. 2b). GABA+/Glx ratio in

T-group showed significant positive relation (r = 0.317, p < 0.05) with probability shift measure levels in contrast to negative relation (r = -0.093) observed in C-group. A strategy shifting ability in the T-group is observed in CF, and other cognitive domains (i.e. working memory, inhibition, and non-verbal intelligence) in contrast to C-group (Fig. 2a).

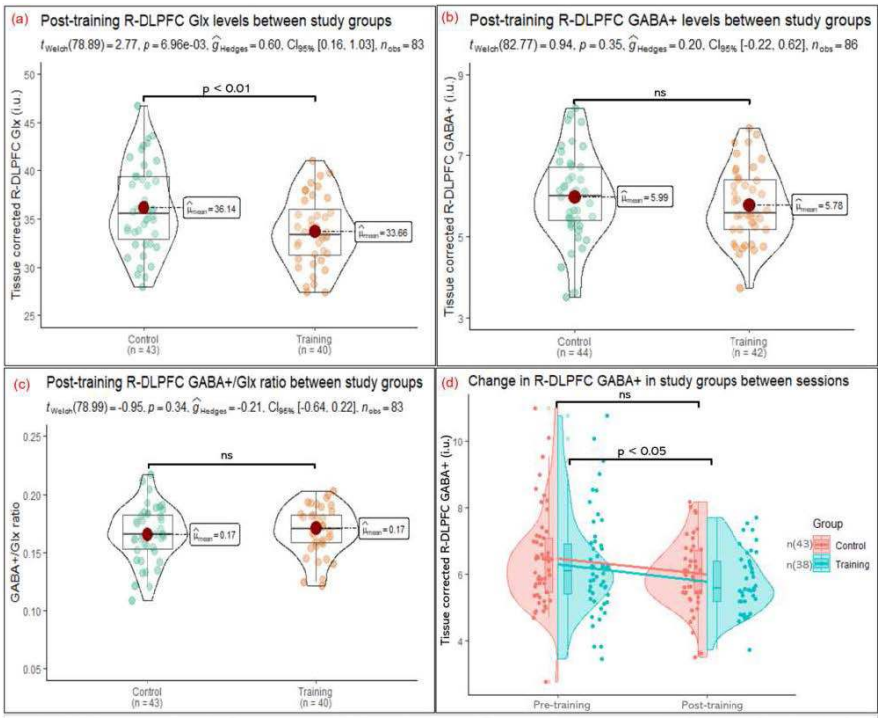

Fig. 1. Violin-box comparing alteration in neurometabolic levels among study groups illustrates the effect of structure learning training. Independent test analysis of post-training (a) R-DLPFC Glx level shows significant reduction in training group as compared to control group. No significant changes observed in (b) R-DLPFC GABA+ and, (c) R-GABA+/Glx ratio between control and training groups. R-DLPFC GABA+ depletes significantly in training group as shown in (d) paired comparison of R-DLPFC GABA+ in study groups between pre- and post-training sessions. (Note: All p-values reported above are adjusted using Bonferroni method.)

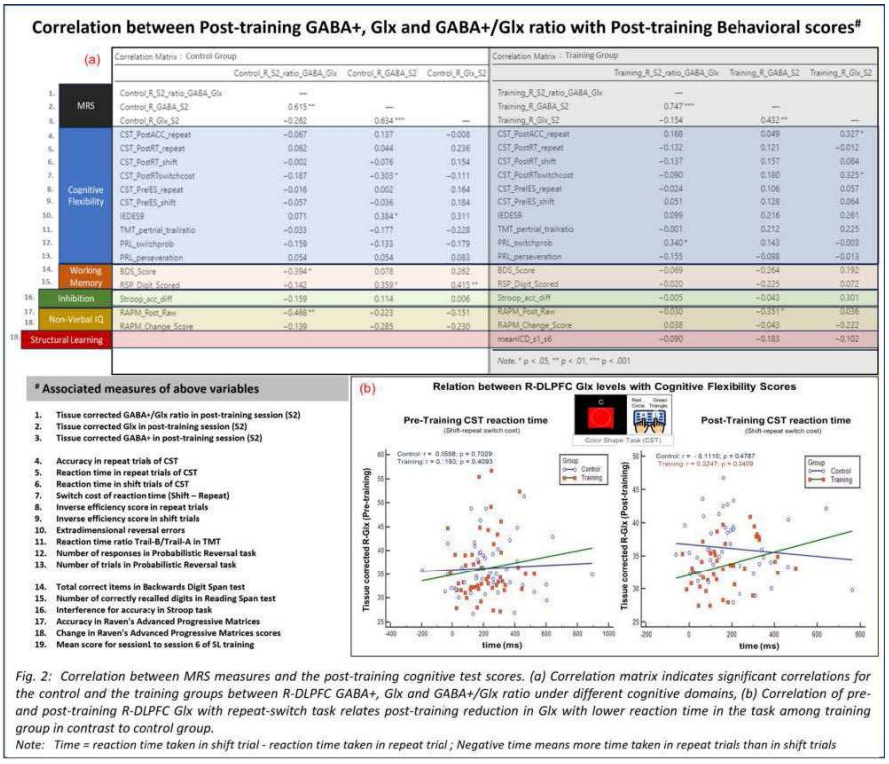

Fig. 2: Correlation between MRS measures and the post-training cognitive test scores. (a) Correlation matrix indicates significant correlations for the control and the training groups between R-DLPFC GABA+, Glx and GABA+/Glx ratio under different cognitive domains, (b) Correlation of pre- and post-training R-DLPFC Glx with repeat-switch task relates post-training reduction in Glx with lower reaction time in the task among training group in contrast to control group.
Note: Time = reaction time taken in shift trial - reaction time taken in repeat trial ; Negative time means more time taken in repeat trials than in shift trials

Conclusions: SL training evidenced significant modulation in neurochemicals after training and associates to response time and accuracy measure in CF. We also observed potential transfer of SL training to selective cognitive domains of working memory and Inhibition and fluid intelligence.

References

1. Wen, Y., Dong, Z., Liu, J., Axerio-Cilies, P., Du, Y., Li, J., Chen, L., Zhang, L., Liu, L., Lu, J., Zhou, N., Chuan Wu, D., & Wang, Y. T. (2022). Glutamate and GABAA receptor crosstalk mediates homeostatic regulation of neuronal excitation in the mammalian brain. Signal transduction and targeted therapy, 7(1), 340.
2. Li, H., Heise, K. F., Chalavi, S., Puts, N. A. J., Edden, R. A. E., & Swinnen, S. P. (2022). The role of MRS-assessed GABA in human behavioral performance. Progress in neurobiology, 212, 102247.
3. Cohen Kadosh, K., Krause, B., King, A. J., Near, J., & Cohen Kadosh, R. (2015). Linking GABA and glutamate levels to cognitive skill acquisition during development. Human brain mapping, 36(11), 4334–4345.
4. Spurny, B., Vanicek, T., Seiger, R., Reed, M. B., Klöbl, M., Ritter, V., Unterholzner, J., Godbersen, G. M., Silberbauer, L. R., Pacher, D., Klug, S., Konadu, M. E., Gryglewski, G., Trattnig, S., Bogner, W., & Lanzenberger, R. (2021). Effects of SSRI treatment on GABA and glutamate levels in an associative relearning paradigm. NeuroImage, 232, 117913.
5. Zacharopoulos, G., Sella, F., Cohen Kadosh, K., Hartwright, C., Emir, U., & Cohen Kadosh, R. (2021). Predicting learning and achievement using GABA and glutamate concentrations in human development. PLoS biology, 19(7), e3001325.
6. Liu, C. L., Cheng, X., Choo, B. L., Hong, M., Teo, J. L., Koo, W. L., Tan, J. Y. J., Ubrani, M. B., Suckling, J., Gulyás, B., Leong, V., Kourtzi, Z., Sahakian, B., Robbins, T., & Chen, A. S. (2023). Potential cognitive and neural benefits of a computerised cognitive training programme based on Structure Learning in healthy adults: study protocol for a randomised controlled trial. Trials, 24(1), 517.
7. Oeltzschner, G., Zöllner, H. J., Hui, S. C. N., Mikkelsen, M., Saleh, M. G., Tapper, S., & Edden, R. A. E. (2020). Osprey: Open-source processing, reconstruction & estimation of magnetic resonance spectroscopy data. Journal of neuroscience methods, 343, 108827.

Poster No 1105

Music Training Increased thalamus connectivity in sensorimotor information bottom-up processing

Gujing Li[1,2,3], Kexin Gao[1,2,3], Hui He[1,2,3], Yayun Liu[1,2,3], Yuanyuan Yu[1,2,3], Cheng Luo[1,2,3], Dezhong Yao[1,2,3]

[1]School of life Science and technology, University of Electronic Science and Technology of China, Chengdu, Sichuan, China, [2]MOE Key Lab for Neuroinformation, Center for Information in Medicine, Chengdu, Sichuan, China, [3]The Clinical Hospital of Chengdu Brain Science Institute, Chengdu, Sichuan, China

Introduction: Music training is well known to improve sensorimotor skills. However, it is still not clear its influence on sensorimotor information bottom-up processing in the brain. The thalamus is an obligatory station through which nearly all sensory information must pass before reaching the cerebral cortex (McCormick and Bal 1994). Our previous study has proven that music training results in structural adaptations of the thalamus (Gujing et al. 2018). Thus, we selected thalamus subregions as regions of interest (ROI) and utilized stepwise function connectivity (SFC) (Sepulcre et al. 2012) to map the connectivity patterns of ROIs at different step distances, to represent the sensorimotor information bottom-up processing pattern in music participants.

Methods: 28 proficient musicians, 33 dancers, and 33 matched controls were recruited in this study. Dancers were recruited to detect the similarities and differences between dance and music training. Then, 510s resting-state functional images (TR=2s, TE=30ms) of all subjects were collected on a 3T MRI scanner. After preprocessing, stepwise function connectivity (SFC) analysis was performed. The coordinate of eight thalamus subregion ROI (radius=4 mm) was defined by the human brainnetome atlas. FC matrices were constructed and only positive correlations of the FC matrix above the threshold (r=0.6) served as input data for the following calculation. The SFC value of a voxel j for a given step distance l and a seed area i is computed from the count of all paths that connect voxel j and any voxel in seed area i, and have an exact length of l. Therefore, SFC value of a brain voxel represents the sum of the number of pathways that connect to any one of the voxels in the seed region. We explored a wide range of link-step distances, from 1 to 8, to characterize the progression of the derived maps. Finally, one-way ANOVA was performed to determine differences among the three groups. The multiple compare correction took the form of GRF (voxel p value=0.001, cluster p value =0.05) was performed. Post-hoc analysis was performed on each significant cluster.

Results: Statistical analysis of SFC results gave the information that compared with the dance and control group, the SFC value of lateral pre-frontal thalamus at step 2 in the music group were significantly higher in right temporal pole: superior temporal gyrus, right inferior frontal gyrus opercular part and right precentral gyrus.

(A) Demographics of the participants

	Dance group	Music group	Control group	*p*
Gender (F/M)	21/11	14/14	21/12	0.412[c]
Age	19.4 (2.5)	19.6 (1.4)	19.5 (1.03)	0.88[d]
Education years	13.1 (2.4)[a]	13.5 (1.7)[b]	-	0.31[e]

(B) Statistic results of lateral pre-frontal thalamus (lPFtha) SFC value at step 2

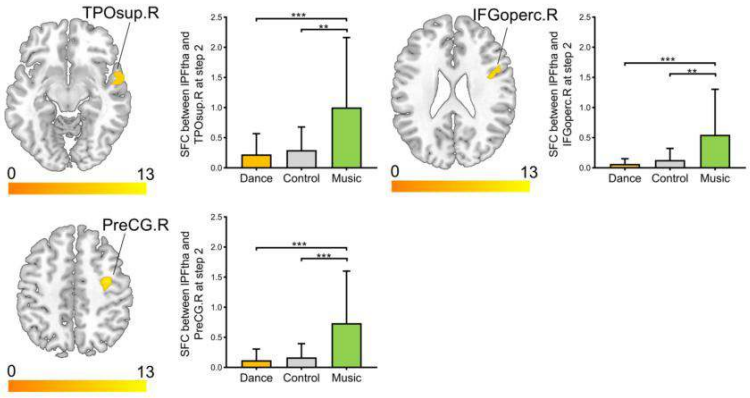

Figure 1 Statistic results

(A) Demographics of the participants Indicated values are shown as mean (standard deviation). [a] data of 27 participants available; [b] data of 27 participants available; [c] Indicates the p-values from the comparison analysis (chi-square test); [d] Indicates the p-values from the comparison analysis (ANOVA); [e] Indicates the p-values from the comparison analysis (two-sample t-test) **(B) Statistic results of lateral pre-frontal thalamus (lPFtha) SFC value at step 2** The brain maps are ANOVA results of lPFtha SFC pattern at step 2 among three group. And the bar graphs show the post-hoc results. lPFtha: lateral pre-frontal thalamus; TPOsup.R: right temporal pole: superior temporal gyrus; IFGoperc.R: right inferior frontal gyrus opercular part; PreCG.R: right precentral gyrus.*p<0.05, **p<0.01 and ***p<0.001.

Conclusions: Our study deepens understanding of music and dance training effects on sensorimotor information bottom-up processing. Music training enhanced connectivity between thalamus and primary sensorimotor areas, which is the early phrase of sensorimotor information bottom-up processing.

References

1. Gujing et al. (2018), 'Modern dance training and string instrument training have different effects on grey matter architecture', Advances in Psychological Science, 26: 1165.
2. McCormick and Bal (1994), 'Sensory gating mechanisms of the thalamus', Current Opinion in Neurobiology, 4: 550-56.
3. Sepulcre et al. (2012), 'Stepwise Connectivity of the Modal Cortex Reveals the Multimodal Organization of the Human Brain', Journal of Neuroscience, 32: 10649-61.

Poster No 1107

Effects of Development and Cognitive Training on Brain Signal Variability

Fan Liu[1], Feiyan Chen[1]

[1]Bio-X Laboratory, School of Physics, Zhejiang University, HangZhou, China

Introduction: Previous works on both fMRI(Grady and Garrett 2014) and EEG(Mcintosh, Kovacevic, and Itier 2008) suggested that the variability in brain signal is necessary for individuals to adapt to the changing environment. Moreover, the brain signal variability shows an "inverted U-shaped"(Grady and Garrett 2014) dynamic trajectory, where young adults with better cognitive abilities have the greatest brain signal variability(Mcintosh et al. 2010). Therefore, the metric could be a potential biomarker of aging and changing of cognitive abilities. However, previous studies were based on task-fMRI(Boylan et al. 2021; Grady and Garrett 2014) or defined the fixation before tasks as the resting data(Garrett et al. 2011), while the fixation is more likely to be influenced by the preceding and following tasks. In addition, previous studies have focused on aging adults or younger adults (20-30 years old)(Garrett et al. 2011) to explore the changes in aging. Finally, there was a large age span of subjects in the same study, which may confound some of the underlying changes. Therefore, our study used the resting-state fMRI and select first, fourth, and sixth graders in primary school to delineate these developmental changes in brain signal variability through school years. Additionally, abacus-based mental calculation training (AMC) has been used as a cognitive training to study the effects of training intervention on variability.

Methods: We recruited a group of children of whom resting-state fMRI (rs-fMRI) were collected in Grade 1, Grade 4 (three years' AMC training) and Grade 6 (five years' AMC training), as well as the matched control group. Preprocessing steps included discarding the first five images, slice-timing, and head-motion correction. Then the functional images were aligned to the corresponding T1-weighted images, and were normalized to the MNI space with a resampling voxel size of 3 × 3 × 3 mm3. The spatial smoothing was skipped to reduce the impact of signals from other voxels(Garrett et al. 2010). The scans with excessive head motion (3 mm and 3°) were excluded. Some nuisance variables were removed in multiple linear regression analysis, including 24 Friston body-motion parameters and average white matter, cerebrospinal fluid. And a band-pass (0.01–0.1 Hz) filter was applied to reduce the effects of physiological noise. Then we extracted the time series for ROIs defined by the BN-246 template(Fan et al. 2016). MSE (multiscale sample entropy) were computed for the variability of signals.

Results: We found that brain signal variability presented an "U-shaped" dynamic trajectory during school years, which is different from the previous studies. The trend of variability was firstly decrease and then an increase occurred after the fourth grade, which could be accelerated by AMC training (see Fig 1). In the ROI-level analysis, we observed that after three years of AMC training, the AMC group already showed a significant decrease in brain signal variability in the orbital gyrus, inferior temporal gyrus, basal ganglia, and thalamus compared to that of first year. The variability then shifted to an elevated trend with continued training. In addition, more brain regions in the control group remained in a state of reduced variability at grade 6 compared to AMC group. In grade 4, the AMC group showed lower variability compared to the control group, while in grade 6, the AMC group had higher brain signal variability. Thus, these results revealed that training accelerated the dynamical change of brain signal variability. The AMC group achieves the transition from lower to higher brain signal variability earlier than children in the control group.

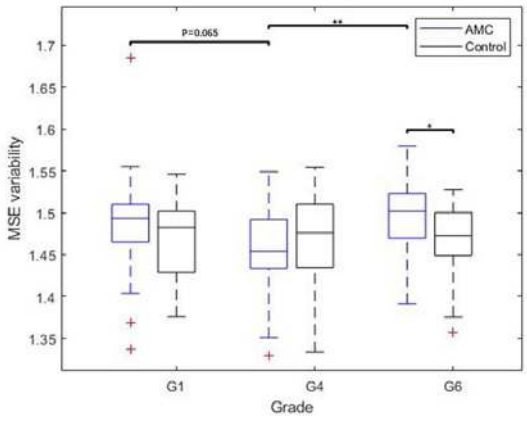

Fig 1. The MSE results of the brain signal variability.

Conclusions: Brain signal variability can be used as a biomarker of children's development and training. It exhibited an "U-shaped" dynamic trajectory among the school-aged children. Notably, the intervention of AMC training accelerates this dynamic process, making the metric reach a minimum more quickly and then return to increasing.

References

1. Boylan.(2021), "Greater BOLD Variability Is Associated With Poorer Cognitive Function in an Adult Lifespan Sample." Cerebral Cortex 31(1): 562.
2. Fan, Lingzhong.(2016), "The Human Brainnetome Atlas: A New Brain Atlas Based on Connectional Architecture." Cerebral Cortex 26(8): 3508–26.
3. Garrett. (2010), "Blood Oxygen Level-Dependent Signal Variability Is More than Just Noise." The Journal of Neuroscience 30(14): 4914.
4. Garrett. (2011). "The Importance of Being Variable." The Journal of Neuroscience 31(12): 4496-503.
5. Grady. (2014). "Understanding Variability in the BOLD Signal and Why It Matters for Aging." Brain Imaging and Behavior pages274–283.
6. Mcintosh, A R. (2010), "The Development of a Noisy Brain." Archives Italiennes de Biologie 148(3): 323–37.
7. Mcintosh, A R. (2008), "Increased Brain Signal Variability Accompanies Lower Behavioral Variability in Development." PLoS Comput Biol 4(7): 1000106.

Poster No 1109

Long-Term Abacus Training Reshapes Substrates of Executive Function and Mathematics among Children

Tianyong Xu[1], Xinyang Liu[2], Andrea Hildebrandt[3], Changsong Zhou[1,4], Feiyan Chen[1]

[1]School of Physics, Zhejiang University, Hangzhou, China, [2]School of Psychology and Cognitive Science, East China Normal University, Shanghai, China, [3]Department of Psychology, Carl von Ossietzky University of Oldenburg, Oldenburg, Germany, [4]Department of Physics, Hong Kong Baptist University, Kowloon, Hong Kong

Introduction: Domain-general executive functions (EFs) serve critically for mathematical skills (Cragg et al., 2014), which relationship of these two closely-related abilities show a variable role among cohorts with individual difference (Best et al., 2011; Cragg et al., 2017; Spiegel et al., 2021; Dong et al., 2022). However, little is known about whether the plasticity of this relationship between EF and math as well as their individual difference during childhood can be affected by cognitive training and the neural underpinnings. By analyzing behavioral performances and brain functional neuroimaging of children with and without five-year abacus mental calculation (AMC) study, we investigated the training effect on the association and individual difference of EF and mathematics, together with relevant changes in neural substrates.

Methods: A total of 142 children were recruited in this experiment, whom were randomly assigned to the training group (n = 72) and the control group (n = 70). Children in the training group received a two-hour AMC training per week for five school years, while children in the control group did not have any prior experience in AMC. In the post-training session, all of them participated in the EF- and mathematics-associated behavioral tests. Among them, 66 children completed resting-state fMRI scanning performed on a 1.5T Philips MRI scanner. We made following investigations. First, we applied multiple group structural equation modeling (SEM) analysis to test group difference of EF-math relationship. Then, we calculated similarity of EF-math FC patterns for the overlap size of shared neural circuits. Further, we computed the inter-subject similarity of FC (ISFC) patterns in frontal-parietal regions. Finally, we explored the role of ISFC on the relationship between EF and mathematics by performing mediation analysis.

Results: By demonstrating that training promoted EF and mathematical abilities (Fig. 1A), we also observed long-term abacus training reduced individual variability and enhanced the relationship between EF and mathematics (Fig. 1B, C). Using different constraint strategies, step-wise comparisons were made based on the SEM model, and all results in model comparisons were shown in the table (Fig. 1B). It revealed higher EF-math relationship (r = 0.856, p = 0.008) in the AMC group relative to the controls (r = 0.468, p = 0.060, Fig. 1C). These results demonstrated significantly decreased individual variances of mathematics and EF, as well as their enhanced relationship. Focusing on the relevant frontal-parietal regions from meta-analytic maps with EF/math-related terms in Neurosynth, we found that long-term training modulated FCs within these regions (Fig. 2A). Moreover, the AMC group presented higher overlapping circuits in EF-math FC patterns, which might support the enhanced EF-math transfer (Fig. 2B). Notably, training enhanced ISFC in frontal-parietal regions significantly (Fig. 2C), which partially mediated EF-related improvement in mathematical ability in the AMC group but not in the control group (Fig. 2D).

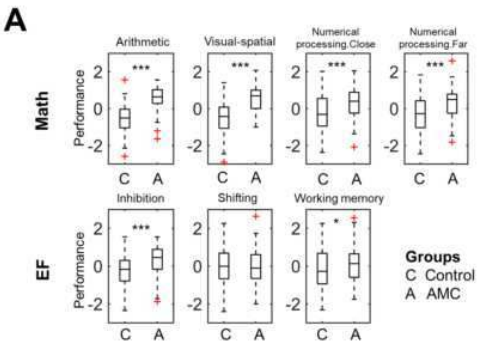

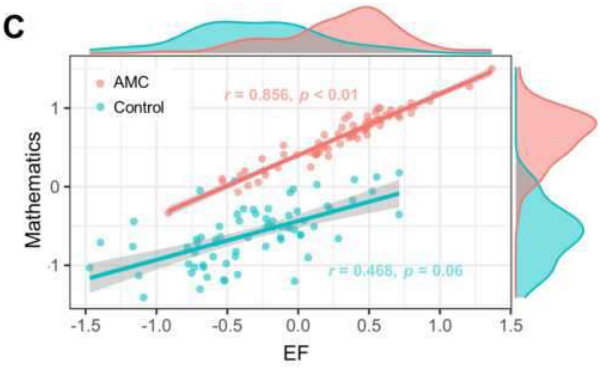

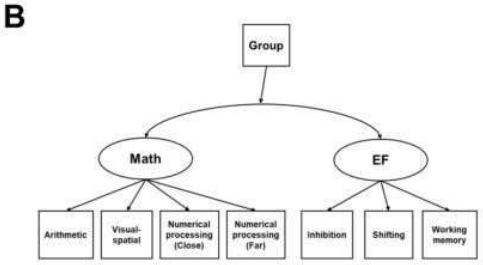

Model	Df	AIC	BIC	Chisq	Chisq diff	Df diff	Pr(>Chisq)
model1	24	2100.1	2235.8	54.242			
model2	29	2094.7	2215.6	58.787	4.545	5	0.474
model3	31	2097.6	2212.6	65.693	6.906	2	0.032*
model4	32	2102.9	2215.0	73.033	7.340	1	0.007**

Model 1: Unconstrained model.
Model 2: The factor loadings is constrained to be equal across groups.
Model 3: The factor loadings and variances of latent variables are constrained to be equal across groups.
Model 4: The factor loadings, variances and covariances of latent variables are constrained to be equal across groups.

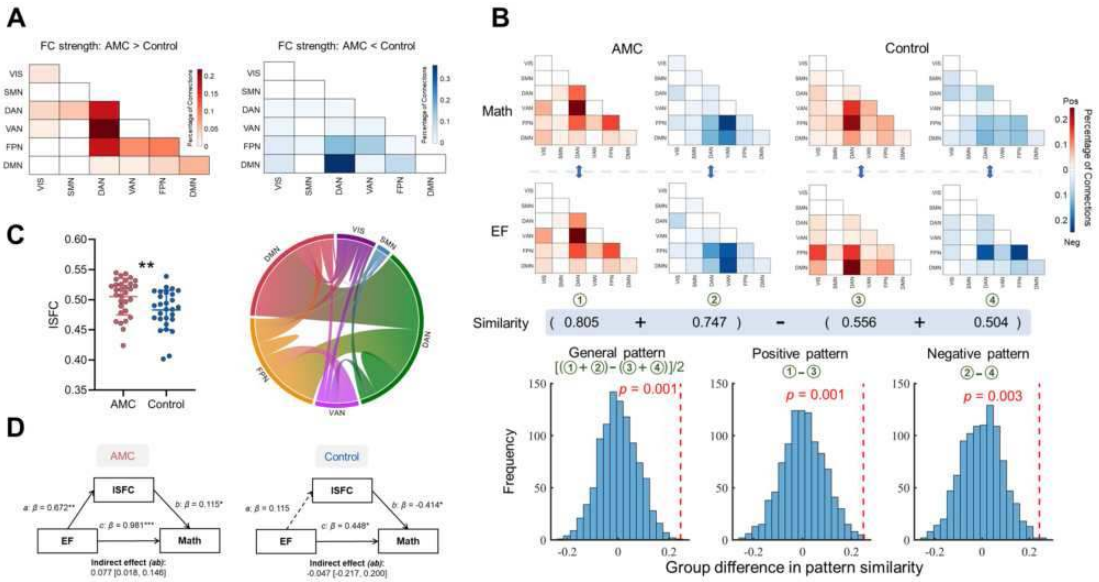

Conclusions: Our current study revealed the plasticity of transfer effect and individual difference affected by cognitive training. Long-term abacus training with visuospatial strategy can modulate FCs within frontal-parietal systems. Therefore, EF and mathematical abilities depending on the common neural substrates of frontal-parietal circuits could be improved and their relationship becomes strengthened. Besides, sustained training over multiple years with same strategy should reduce individual variability especially in the relevant neural networks. These different dimensions of training/learning as demonstrated here for EF and math is expected to be generalizable to other transferable abilities.

References

1. Best, J.R. (2011), 'Relations between executive function and academic achievement from ages 5 to 17 in a large', representative national sample, Learning and Individual Differences, vol. 21, no. 4, pp. 327–336
2. Cragg, L. (2014), 'Skills underlying mathematics: The role of executive function in the development of mathematics proficiency', Trends in Neuroscience and Education, vol. 3, no. 2, pp. 63–68
3. Cragg, L. (2017),'Direct and indirect influences of executive functions on mathematics achievement', Cognition, vol. 162, pp. 12–26
4. Dong, Y. (2022), 'Mathematics and executive function competencies in the context of interventions: A quantile regression analysis', The Journal of Experimental Education, vol. 90, no. 2, pp. 297–318
5. Spiegel, J.A. (2021), 'Relations between executive functions and academic outcomes in elementary school children: A meta-analysis', Psychological Bulletin, vol. 147, no. 2, pp.329

Poster No 1110

Abacus Training Affects Brain Hemispheric Asymmetry of Connectivity Gradients during Childhood

Jiali Mu[1], Feiyan Chen[1]

[1]*Bio-X Laboratory, School of Physics, Zhejiang University, Hangzhou, China*

Introduction: Hemispheric asymmetries are influenced by various factors, among which development and cognitive training are the most influencing ones (Toga et al. 2003). However, it remains largely unknown the impact of these factors on the children's hemispheric asymmetry of functional hierarchical topology. Previous study has adopted a framework to identify whole-brain functional gradients that capture the similarity of connectivity patterns in different cortical regions (Margulies et al. 2016). The current study extended such framework to explore the effect of abacus-based mental calculation (AMC) training on brain asymmetry during child development.

Methods: 2.1 Participants This study recruited a total of 283 children who were randomly assigned into AMC and control groups at the beginning of primary school. The AMC group received 2 h per week of training from the 1st to the 6th grade, while the control group did not receive any physical or mental abacus instructions throughout this experiment. Four resting fMRI sessions were administered in the longitudinal study, including 1st, 2nd, 4th, and 6th grade. 2.2 Functional connectome gradients We calculated within-hemispheric functional connectivity (FC) in voxel-level. Specifically, the atlas of intrinsic connectivity of homotopic areas (AICHA, 4mm) was used to parcellate the brain regions, yielding 9316 voxels in the left hemisphere and 9198 voxels in the right hemisphere. For each hemisphere, we utilized the BrainSpace toolbox to estimate functional gradients (Vos et al. 2020). Notably, the current study focused on the unimodal-transmodal gradient. 2.3 Statistical

analysis To quantify hemisphere asymmetry, we chose left-right as the asymmetry index (AI) (Wan et al. 2022). A positive AI-score meant the hemispheric leftwards, while a negative AI-score dominated rightwards. To test group and development effects on the AI of the unimodal-transmodal gradient, we applied a linear mixed model. Then we examined hemispheric differences across Yeo's seven network computing their network's gradient average. Temperament was assessed through scale, with two main levels of exuberance and BI.

Results: 3.1 Group and grade effects on the AI of the hemispheric gradient The linear mixed linear model revealed a significant group × grade interaction effect of the unimodal-transmodal gradient AI (p=0.027). In 1st grade, there was no significant difference between the AMC group and the control group; In 6th grade, the two groups had a significant difference (p = 0.003). From a developmental perspective, in 1st grade, there was no significant hemispheres asymmetry both the two group. However, the control group showed significant leftward asymmetry in following 2nd, 4th and 6th grade (p < 0.001), while the AMC group always showed no significant lateralization in these time points. 3.2 Frontoparietal network asymmetry and temperament From 1st grade to 6th grade, both groups of children showed significantly rightward asymmetry in the frontoparietal network. There was a positive correlation between the AI of frontoparietal network in the 1st grade and their 3rd grade exuberance in the control group (r = 0.489, p = 0.008), but not in the AMC group. In addition, there was a positive correlation between the asymmetry in the 1st grade and their 3rd grade another temperament BI in the AMC group (r = 0.406, p = 0.009).

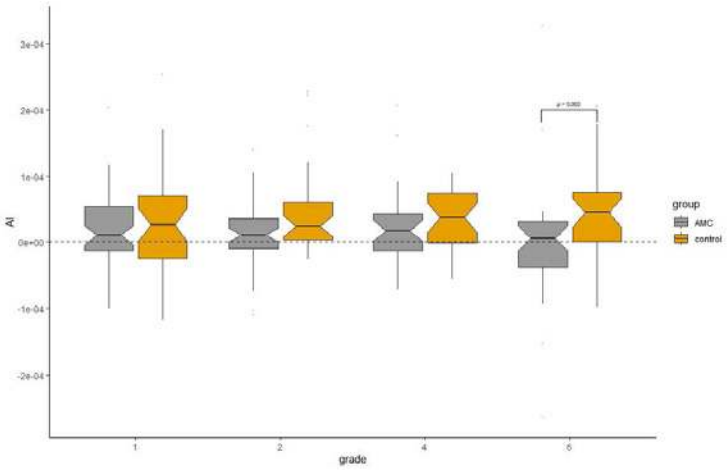

Fig 1. Group and grade effects on the AI of the hemispheric gradient

Conclusions: In current study, we investigated the effects of developmental and cognitive training on the hemispheric asymmetry of connectivity gradient. Our study showed that both the development and cognitive training play important roles in hemispheric asymmetry of connectivity gradient. Additionally there was a significant correlation between the asymmetry of the frontoparietal network and temperament, which was distinct across these two groups. These findings provide novel insights of the impact of long-term cognitive training on hemispheric asymmetry of connectivity gradients.

References

1. Margulies D S. (2016), 'Situating the Default-Mode Network along a Principal Gradient of Macroscale Cortical Organization', Proceedings of the National Academy of Sciences, vol. 113, no. 44, pp. 12574–12579.
2. Toga A W. (2003), 'Mapping Brain Asymmetry', Nature Reviews Neuroscience, vol. 4, no. 1, pp. 37–48.
3. Vos de Wael R. (2020), 'BrainSpace: A Toolbox for the Analysis of Macroscale Gradients in Neuroimaging and Connectomics Datasets', Communications Biology, vol. 3, no. 1, pp. 103.
4. Wan B. (2022), 'Heritability and cross-species comparisons of human cortical functional organization asymmetry', eLife, vol. 11, pp. e77215.

Poster No 1111

The modulation of neurotransmitters in sensory areas during motor learning: an MRS study

Hong Li[1], Sima Chalavi[1], Amirhossein Rasooli[1], Geraldine Rodríguez-Nieto[1], Stephan Swinnen[1]

[1]KU Leuven, Leuven, Vlaams Brabant

Introduction: Gamma-aminobutyric acid (GABA) and glutamate (Glu), as the primary inhibitory and excitatory neurometabolites in the human central nervous system, play pivotal roles in human learning[1,2]. Numerous studies using animal models have shown that the administration of drugs that facilitate or hinder GABAergic transmission can modulate learning outcomes[3] and

the formation of memories[4,5]. These findings further highlight the critical role of the GABAergic system and the inhibitory-excitatory balance in learning. Considering that static resting-state neurometabolite levels, measured at a single time point, may not provide a comprehensive picture of the dynamics of inhibitory and excitatory processes and their role in behavioral performance[6], the repeated measurements of neurometabolites may provide complementary insight into the relationships between the modulation of neurometabolits and behavior. However, evidence on how neurometabolites are modulated to facilitate learning is scarce[7]. Therefore, the aim of this study was to investigate whether feedback types and phases of learning affect the modulation of neurometabolites in specific sensory processing brain areas. Additionally, we aimed to investigate whether the modulation of neurometabolites is associated with behavioral progress.

Methods: We used magnetic resonance spectroscopy (MRS) to measure the modulation of neurometabolites during a motor learning task under two different feedback conditions. Fifty healthy young participants were trained on a bimanual tracking task over five days (Day 1 – Day 5) while receiving either concurrent augmented visual feedback (CA-VFB group, N=25) or terminal intrinsic visual feedback (TA-VFB group, N=25) of their performance. Additionally, GABA+ (GABA + macromolecules) and Glx (Glu + glutamine) levels in two sensory-processing brain areas were determined: primary somatosensory cortex (S1) and medial temporal cortex (MT/V5). We used three time points for MRS measurement, i.e., before (baseline), during and after task training on Day 1 (initial learning phase) and Day 5 (late learning phase).

Results: Behaviorally, the behavioral progress was more pronounced on the first training day than on the last training day and worse initial performance was associated with larger behavioral progress. From all samples, MT/V5 GABA+ levels increased from baseline to during the task and it reduced back to baseline following the end of behavioral task training on Day 1. S1 Glx levels were reduced from baseline to after the behavioral training on Day 1. Additionally, S1 GABA+ levels were reduced from baseline to during the task and remained at this level after the end of behavioral task training during the late learning phase (Day 5). Furthermore, we found that higher baseline GABA+ levels in either the S1 or MT/V5 area were associated with larger reduction of GABA+ levels along with behavioral training. However, the behavioral progress achieved under either feedback or feedback withdrawal conditions was not correlated with the modulation of neurometabolites during motor training.

Conclusions: Our findings suggest that the modulation of neurometabolites in task-related brain areas constitutes one of the mechanisms driving motor learning. Furthermore, the modulatory capacity of the neurometabolites is linked to its baseline concentration.

References

1. Hebb, D.O. (1949), The organization of behavior; a neuropsychological theory.Wiley.
2. Rioult-Pedotti M.S. (2000), Learning-induced LTP in neocortex. Science. 290(5491), 533–536.
3. Ishikawa K. (1978), Effect of intraventricular gamma-aminobutyric acid (GABA) on discrimination learning in rats. Psychopharmacology. 56(2), 127–132.
4. Brioni J.D. (1988), Post-training administration of GABAergic antagonists enhances retention of aversively motivated tasks. Psychopharmacology. 96(4), 505–510.
5. Makkar S.R., (2010). Behavioral and neural analysis of GABA in the acquisition, consolidation, reconsolidation, and extinction of fear memory. Neuropsychopharmacology. 35(8), 1625–1652.
6. Li H. (2022), The role of MRS-assessed GABA in human behavioral performance. Prog Neurobiol. 2022;212, 102247.
7. Maes C. (2022), Task-Related Modulation of Sensorimotor GABA+ Levels in Association with Brain Activity and Motor Performance: A Multimodal MRS-fMRI Study in Young and Older Adults. J Neurosci. 42(6), 1119–1130.

Poster No 1112

Alpha Traveling Waves: Coexistence of Idling and Active Inhibition in Selective Working Memory

Yifan Zeng[1], Paul Sauseng[1], Andrea Alamia[2,3]

[1]University of Zurich, Zurich, Switzerland, [2]CNRS Université de Toulouse, Toulouse, France, [3]Artificial and Natural Intelligence Toulouse Institute, Toulouse, France

Introduction: The functional role of alpha waves (8-12 Hz) has been the subject of debate. However, much attention has been focused on investigating alpha amplitude, leaving the functional significance of its temporo-spatial dynamics, particularly traveling waves, relatively unexplored. Importantly, previous studies have shown that alpha waves traveling in different directions may serve distinct functional roles (Alamia et al., 2023; Alamia & VanRullen, 2019; Pang et al., 2020). During visual stimulation, forward waves (propagating from posterior to anterior sites) convey bottom-up information, while backward waves (anterior to posterior sites) reflect top-down regulation (Pang et al., 2020). Here, we extended the understanding of the functional spectrum of alpha waves by investigating their traveling direction during selective working memory processes.

Methods: We re-analyzed two pre-existing, open-access EEG datasets (dataset 1: Feldmann-Wüstefeld & Vogel, 2019; dataset 2: Adam et al., 2018). In both datasets, participants performed similar lateralized delayed match-to-sample working memory

tasks, where they were required to memorize the color of the targets in the presence of distractors. Following a brief retention phase, participants reported whether the probe matched the target (dataset 1, Figure 1A) or all the colors of the target (dataset 2, Figure 1B). In the first dataset, the distractor load (2, 4, or 6 distractors) was manipulated. In the second dataset, both the memory span and the distractor load varied synchronously between 1, 3, and 6 items. We focused our analysis on the amount of forward and backward alpha waves during the retention phase. We quantified the amount of alpha traveling waves using a two-dimensional fast Fourier transform-based algorithm inspired by the work of Alamia and VanRullen (2019; Figure 1C).

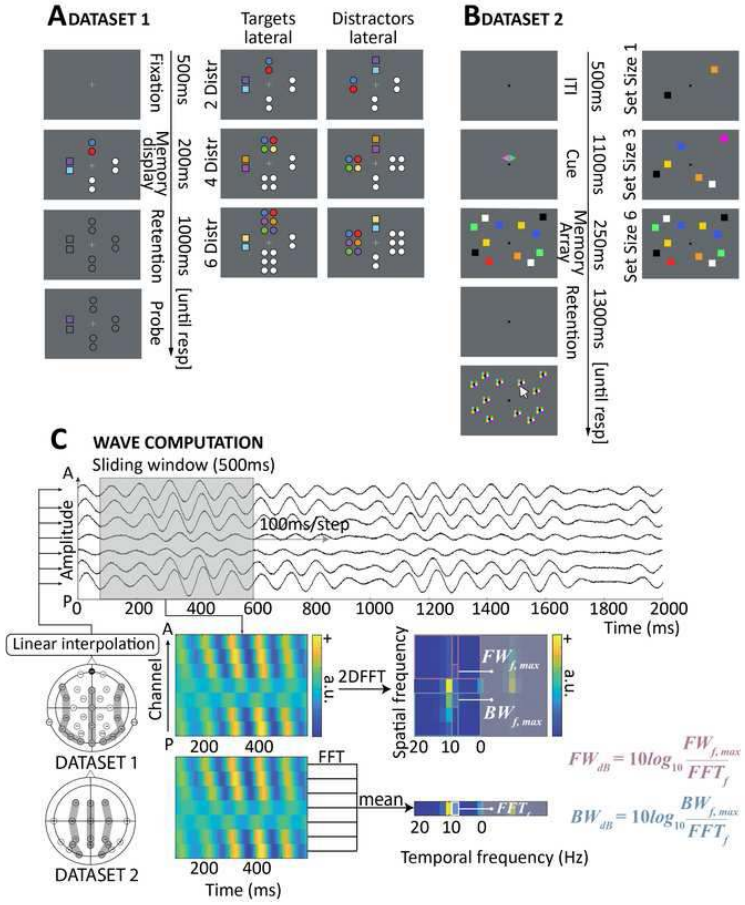

Figure 1| The experimental design and wave quantification. (A) the task of dataset 1 (Feldmann-Wüstefeld & Vogel, 2019) included a memory display consisting of three types of stimuli: colored squares (targets), colored circles (salient distractors), and grey circles (neutral distractors). In half of the trials, the target cluster was presented in the left or right position, and the salient distractor cluster was presented at the top or bottom (target lateral). In the rest of the trials, the positions of targets and distractors were reversed (distractor lateral). Distractor load varied between 2, 4, and 6, while the number of targets was kept constant. Participants were asked to report where the probe was the same as the target presented at the same location before the retention phase. (B) Dataset 2 (Adam et al., 2018) employed a lateralized whole report task. Before the memory display, a diamond-shaped cue was presented and was composed of a green and a pink triangle. Participants were instructed to pay attention to half of the stimuli (targets) in the hemifield cued by the green triangle while ignoring the rest (distractors). The set size of targets and the distractor load varied simultaneously between 1, 3, and 6. After the retention period, participants reported the colors of targets by clicking the color within the matrix corresponding to the items previously presented. (C) To quantify the traveling waves, we selected three electrode axes; midline, left and right hemisphere. The channels within each axis were linearly interpolated into seven channels and were sorted according to their spatial location (from posterior to anterior). We employed a 500-ms sliding window at the step of 100ms, and the resulting segments were fed into two-dimensional fast Fourier Transform. In the power spectrum, the power of forward waves falls into the top-left (or down-right) quarter, whereas that of the backward waves falls into down-left (or top-right) quarter. For a given temporal frequency and traveling direction, we defined the power as the maximum value in the corresponding column of the respective quarter, normalized by the averaged fast Fourier Transform power of the same temporal frequency. A: anterior, P: posterior, 2DFFT: two-dimensional fast Fourier Transform, FFT: fast Fourier Transform, FW: forward waves, BW: backward waves.

Results: Figure 2 shows alpha traveling waves observed during the retention phase. In dataset 1, we found an increase in the power of alpha forward waves as the distractor load increased. In dataset 2, increased distractors/memory set size led to an increase in forward waves and a decrease in backward waves. Notably, the effect interacted with hemisphere. Alpha forward waves exhibited a more pronounced increase in the hemisphere contralateral to the distractors. Conversely, the reduction in backward waves was stronger in the hemisphere contralateral to the targets. In both datasets, the forward waves were lateralized contralateral to distractors, while backward waves displayed lateralization towards the hemisphere ipsilateral to targets.

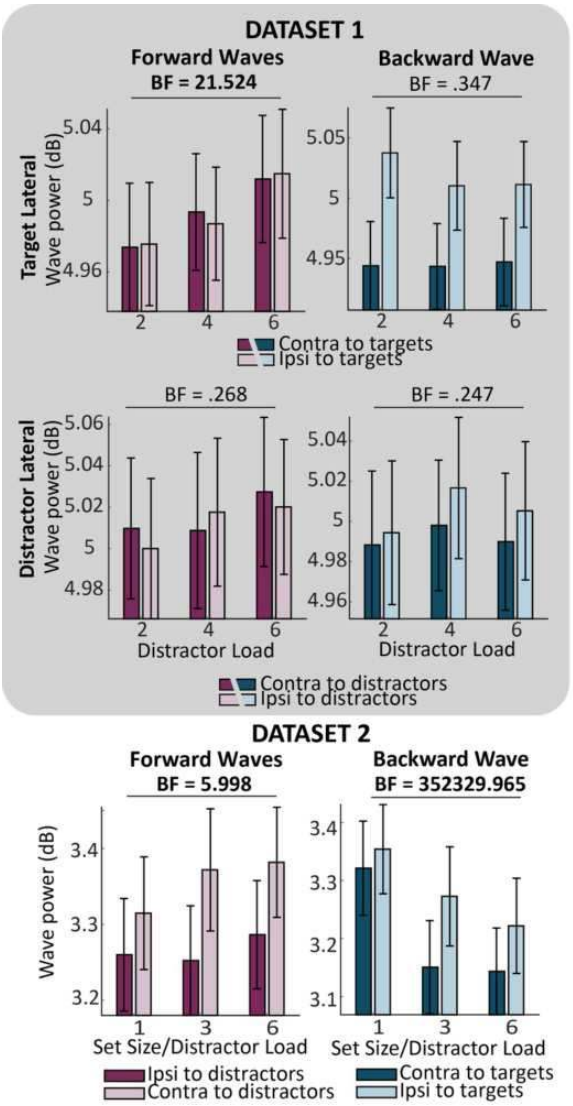

Figure 2| Effects of distractor load or (and) set size on alpha traveling waves during the retention phase. Upper panel: in dataset 1, increased distractor load resulted in elevated alpha forward waves but not backward waves. Under the "target lateral" condition, backward waves were lateralized to the hemisphere ipsilateral to the targets.- No effect was found for "distractor lateral" condition. Lower panel: for dataset 2, we found increased forward and decreased backward waves with increased set size/distractor load. More waves were observed on the axis ipsilateral to targets (contralateral to distractors), irrespective of the traveling direction. Importantly, we found strong evidence for the interaction between set size/distractor load effect and hemisphere for both forward and backward waves (all effects not reported in the figure have BF > 16.855; BF, inclusion Bayes Factor)

Conclusions: Our results demonstrated that the distractor load regulated the amount of alpha forward waves during working memory retention. This observation suggests that the forward waves may serve as active inhibition of distracting information, superimposing on the bottom-up visual stream. In contrast, increasing memory set size led to a reduction in backward alpha waves. This might indicate a reduction of cortical idling when more information needs to be kept in working memory.

References

1. Adam, K. C. S. (2018). 'Contralateral Delay Activity Tracks Fluctuations in Working Memory Performance', Journal of Cognitive Neuroscience, vol. 30, no. 9, pp. 1229–1240.
2. Alamia, A. (2023). 'Distinct roles of forward and backward alpha-band waves in spatial visual attention'. eLife, vol. 12, pp. e85035.
3. Alamia, A. (2019). 'Alpha oscillations and traveling waves: Signatures of predictive coding?' PLOS Biology, vol. 17, no. 10, pp. e3000487.
4. Feldmann-Wüstefeld, T. (2019). 'Neural Evidence for the Contribution of Active Suppression During Working Memory Filtering'. Cerebral Cortex, vol. 29, no. 2, pp. 529–543.
5. Pang, Z. (2020). 'Turning the Stimulus On and Off Changes the Direction of α Traveling Waves'. eNeuro, vol. 7, no. 6, pp. ENEURO.0218-20.2020.

Poster No 1113

Dynamics of Decision-Consistent Bias in Human Visual Working Memory

Hyunwoo Gu[1,2], Joonwon Lee[3], Sungje Kim[3], Jaeseob Lim[3], Hyang-Jung Lee[3], Heeseung Lee[3], Minjin Choe[3], Dong-Gyu Yoo[3], Jun Hwan (Joshua) Ryu[1,2], Sukbin Lim[4,5,6], Sang-Hun Lee[3]

[1]Stanford University, Stanford, CA, [2]Wu Tsai Neurosciences Institute, Stanford, CA, [3]Seoul National University, Seoul, Korea, Republic of, [4]NYU Shanghai, Shanghai, China, [5]Shanghai Frontiers Science Center of Artificial Intelligence and Deep Learning, Shanghai, China, [6]NYU-ECNU Institute of Brain and Cognitive Science, Shanghai, China

Introduction: Humans tend to bias their ongoing actions toward their past decisions, a phenomenon dubbed decision-consistent bias[3,4]. Efforts to explain this seemingly irrational bias have been limited to the sensory level, despite the evidence that it is affected by post-perceptual processes[2,9]. Here, by combining psychophysical and cortical measurements with a class of dynamical models, we uncover a previously unidentified source of the decision-consistent bias: the interplay of decision-making with the drift dynamics of working memory.

Methods: In a scanner, participants were asked to memorize the orientation of a briefly (1.5s) presented grating and estimate it after a prolonged (15s) delay, intervened by a discrimination task (1.5s) (Fig. 1a-b). In the discrimination task, upon the appearance of a reference, participants had to decide, whether the remembered orientation was tilted clockwise or counter-clockwise relative to the reference. We quantified the decision-consistent bias as the difference between choice-conditioned mean errors (Fig. 1c). To characterize the dynamics of decision-consistent bias, we considered a model class of the memory process with or without drift dynamics (Fig. 1e-f). In these models, the initial point at the sensory encoding stage is constrained by the efficient encoding scheme[8], and the encoding and drift functions are constrained by the stimulus-specific bias inferred from the estimation errors (Fig. 1d) using the von Mises basis functions. To probe the working memory dynamics during delay, we performed linear decoding from the early visual cortex, V1, V2, and V3, considering the availability of working memory information there[6,7]. We used the inverted encoding model[1] and projected the reconstructed responses onto the polar space to readout the orientation. To compare the BOLD decoding trajectories and the model predictions, we convolved the canonical hemodynamic response functions with the model predictions and the boxcar-modeled visual drives during the stimulus and reference epochs.

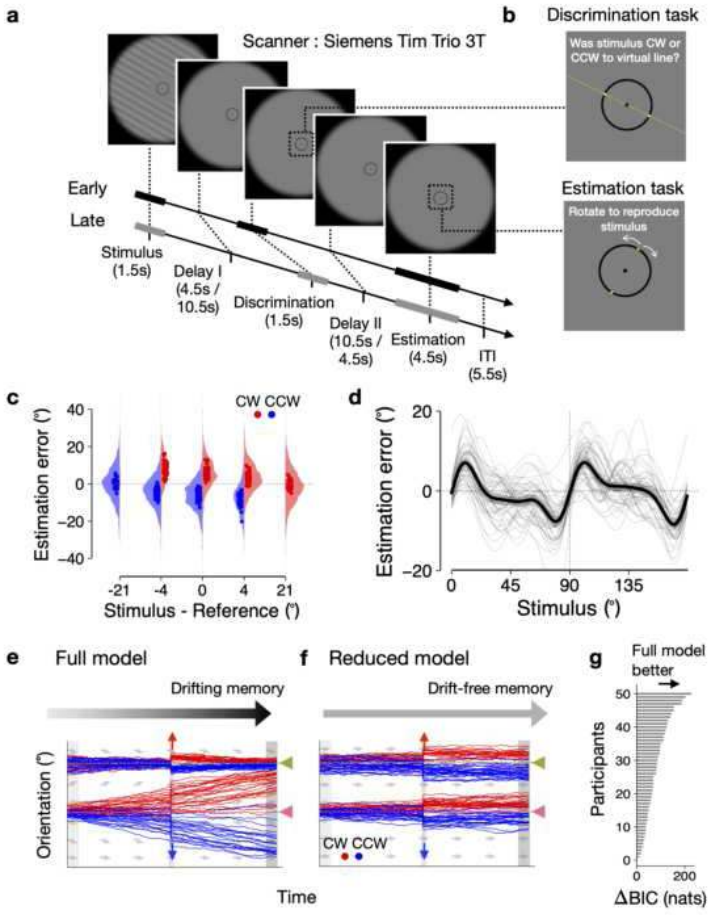

Fig. 1 | Decision-consistent bias dynamics in discrimination and estimation tasks with intervening delays. a-b, Task paradigm. Participants remembered the target orientation, followed by discrimination and estimation tasks about the same target. **c,** Decision-consistent bias, the conditional mean estimation errors under CW or CCW discrimination, separately shown for stimulus-reference differences. Dots represent the data from individual participants. **d**, Stimulus-specific bias, the mean estimation errors under each stimulus orientation. Transparent lines represent the stimulus-conditioned errors from individual participants. **e-f,** Dynamical models of decision-consistent bias, $m_t = m_0 + \int_0^t K(m_s)ds + \int_0^t D(m_s)dB_s + \beta(m_{t_{DM}}, r) \cdot \mathbf{1}_{t \geq t_{DM}}$ where $K(m_s)$, $D(m_s)$ denote the drift and diffusion functions of the memory process m_s, $\beta(m, r)$ the memory updating at discrimination time induced by the binary decision, and B_s the Brownian motion. While both accounting for the efficient coding bias at m_0, the full model includes both memory drift and diffusion terms, whereas the reduced model only includes diffusion. **g**, Goodness of fit of models based on the Bayesian information criterion (BIC). Participants were sorted according to ΔBIC, whose positive values indicate the evidence in favor of the full model. All participants showed a better fit for the full model.

Results: First, the drifting dynamics of the decision-consistent bias well explained behavioral responses. Across all participants, the full model with both drift and diffusion terms was superior to the reduced model without drift when the Bayesian information criterion was compared (Fig. 1g). Next, the working memory signals in the visual cortex were consistent with the drifting dynamics. When conditioned on the discrimination decisions, the decoded trajectories showed a bifurcation away from the target orientation towards the direction consistent with the decision (Fig. 2b). Trajectories predicted by the full model closely resembled those observed in the BOLD signals, compared to the diffusion-only reduced model (Fig. 2c). As predicted in the drifint time course (Fig. 2a), the post-decision component (b_post) decreases in late trials, whereas the pre-decision component (b_pre) increases. To quantify these delay-dependent changes, we estimated their differences in early and late trials, namely, Δb_pre and Δb_post, by inferring the conditional means during the discrimination and estimation tasks both from behavior (Fig. 2d) and BOLD signals (Fig. 2f). These results matched the full model prediction (Fig. 2h), both in the signs of Δb_post and in their negative correlation, while the reduced model failed to capture these signatures (Fig. 2j). Furthermore, when conditioned on the converging (zero-crossing points in drift functions with negative slopes) and diverging (positive slopes) stimuli characterized for each participant, the full model correctly captured the larger absolute amounts of Δb_pre and Δb_post in diverging stimuli, whereas the reduced model could not (Fig. 2e,g,i,k).

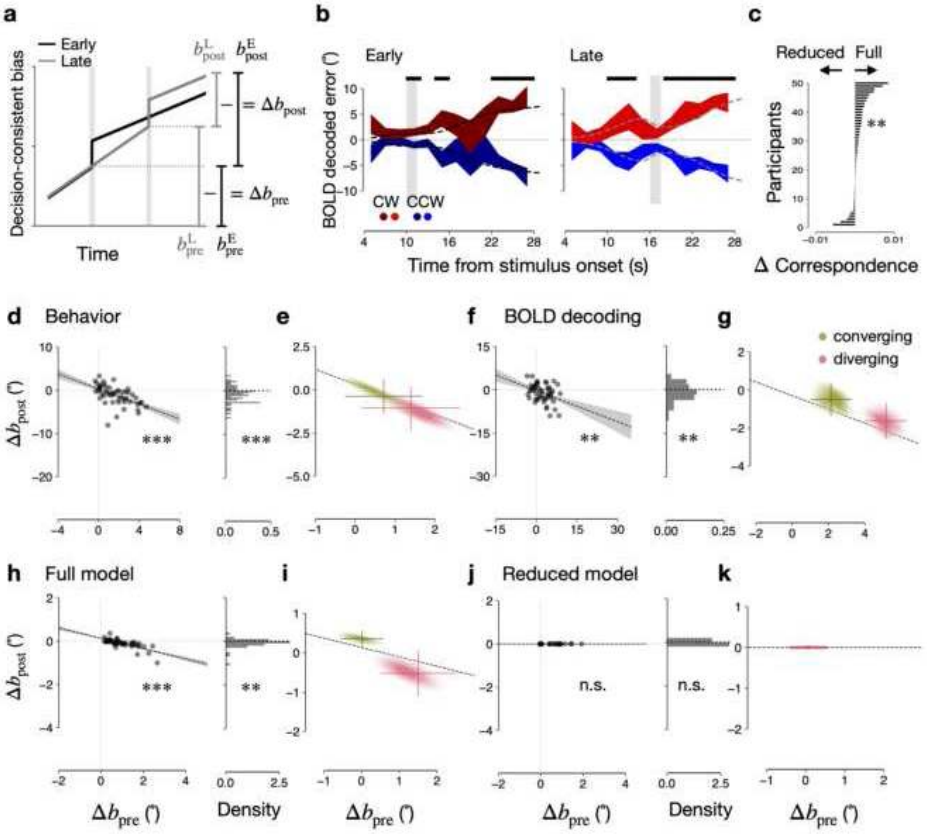

Fig. 2 | Behavior and BOLD signatures supporting the drifting dynamics of decision-consistent bias. a, Predicted time courses of the decision-consistent bias under the full model in early and late trials. b_{pre}, b_{post} are defined as the pre-decision and post-decision components of the decision-consistent bias, and Δb_{pre}, Δb_{post} are their differences in early and late trials. As suggested in Fig. 1e-f, b_{post} depends on the post-decision time in the full model, whereas the reduced model predicts b_{post} is unaffected by time. **b,** Evolution of decision consistent bias in the signals of orientation decoded from the BOLD responses of the early visual cortex (V1, V2, and V3). Dashed lines are the fits of the piecewise linear function, $(\alpha_0 + \beta_0 \cdot t)\,\mathbf{1}_{t \le t_{DM}} + (\alpha_1 + \beta_1 \cdot (t - t_{DM}))\,\mathbf{1}_{t > t_{DM}}$, accounting for the hemodynamic response filter and the impact of visual drives. **c**, Correspondence scores, a lower bound of the cosine distance between the model predictions (also accounting for the hemodynamic filter and visual drives) and the observed BOLD decoding trajectory. Across participants, the full model better resembled the trajectories ($p = 0.006$). **d-k**, Dynamic signatures of decision-consistent bias across the behavior and BOLD responses. **d**, Relation between Δb_{pre} and Δb_{post} (left) and the distribution of Δb_{post} (right) in the behavioral estimates (inferred from psychometric functions of discrimination tasks and estimation conditional means) across participants. Line and shade denote the linear regression fit. **e**, Relation between Δb_{pre} and Δb_{post}, conditioned on the converging (zero-crossing points in drift functions with negative slopes) and diverging (with positive slopes) stimuli characterized from each participant. Density estimates at half-maximum, with error bars denoting ± S.E.M. (colors corresponding to Fig. 1e-f). **f-g**, Same with d-f, but with the estimates inferred from the piecewise linear fit to BOLD decoding. **h-k**, Same with d-e, but for the best-fit predictions of dynamical models. ***, $p < 0.001$, **, $p < 0.01$.

Conclusions: Our findings provide empirical support for the drifting working memory and its interplay with decision-consistent bias in humans, accounting for how the working memory representations can continuously develop in a decision-consistent manner.

References
1. Brouwer, G.J. (2009), 'Decoding and Reconstructing Color from Responses in Human Visual Cortex', Journal of Neuroscience 29, 13992–14003.
2. Fritsche, M. (2019), 'Reference repulsion is not a perceptual illusion', Cognition 184, 107–118.
3. Jazayeri, M. (2007), 'A new perceptual illusion reveals mechanisms of sensory decoding', Nature 446, 912–915
4. Luu, L. (2018), 'Post-decision biases reveal a self-consistency principle in perceptual inference', Elife 7, 1–24
5. Panichello, M.F. (2019), 'Error-correcting dynamics in visual working memory', Nature Communications 10, 1–11
6. Rademaker, R.L. (2019), 'Coexisting representations of sensory and mnemonic information in human visual cortex', Nature Neuroscience 22, 1336–1344.
7. Serences, J.T. (2009), 'Stimulus-specific delay activity in human primary visual cortex', Psychological Science 20, 207–214.
8. Wei, X.X. (2015), 'A Bayesian observer model constrained by efficient coding can explain 'anti-Bayesian' percepts', Nature Neuroscience 18, 1509–1517
9. Zamboni, E. (2016), 'Do perceptual biases emerge early or late in visual processing? Decision-biases in motion perception', Proceedings of the Royal Society B: Biological Sciences 283.

Poster No 1114

Exploring the Behavioral and Neural Mechanisms of Mindfulness in Enhancing Spatial Working Memory

Yuwen He[1], Seng-Hang Lei[1], Wenyue Gao[1], Anqi Gu[1], Jieting Chen[1], Jiaze Li[1], Mek Wong[1], Kuai Long Sou[1], Zhen Yuan[1]

[1]University of Macau, Macau, China

Introduction: Mindfulness practice has been shown to enhance various cognitive functions, including memory (Creswell, 2017; Tang et al., 2015). Although several studies have demonstrated the positive impact of mindfulness on working memory (Jha et al., 2010; Stein et al., 2022), its effects on spatial working memory in college students remain largely unexplored. Furthermore, the neural mechanisms underlying the regulation effects of mindfulness on spatial working memory remain poorly understood. To address these gaps, we conducted a brief mindfulness intervention study.

Methods: In the initial phase of the study, we recruited 15 participants with no prior mindfulness experience for the experimental group, which underwent a 4-week mindfulness workshop. Additionally, we recruited 10 matched participants for the control group, who did not engage in mindfulness practice. Both groups performed a spatial working memory task during an fMRI scan on two occasions: first upon recruitment and again three months later. For further analysis, 11 participants from the experimental group and 9 participants from the control group met the eligibility criteria.

Results: Preliminary results revealed that the brief mindfulness intervention significantly reduced dysfunctional metacognition in individuals who practiced mindfulness (Figure 1, group*time interaction p=0.02), suggesting the effectiveness of our intervention. As depicted in Figure 2A, participants in the mindfulness group demonstrated improved spatial working memory performance after three months, whereas the control group showed decreased performance, although the group*time interaction was not significant in the current sample (p = 0.2). Neuroimaging findings indicated a significant group*time interaction effect in the right frontal eye field (Figure 2 B, uncorrected p < 0.001), a crucial brain region involved in attentional control.

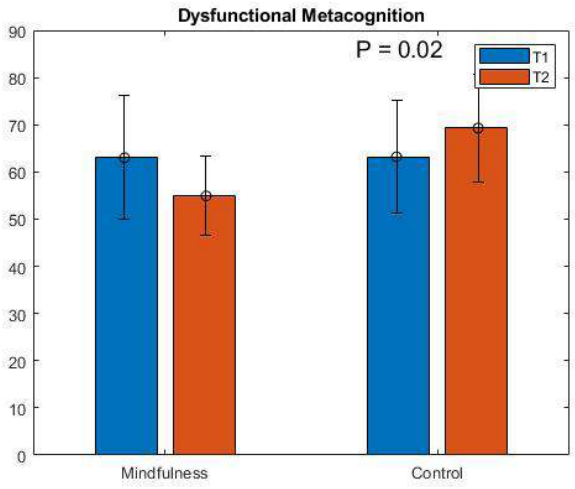

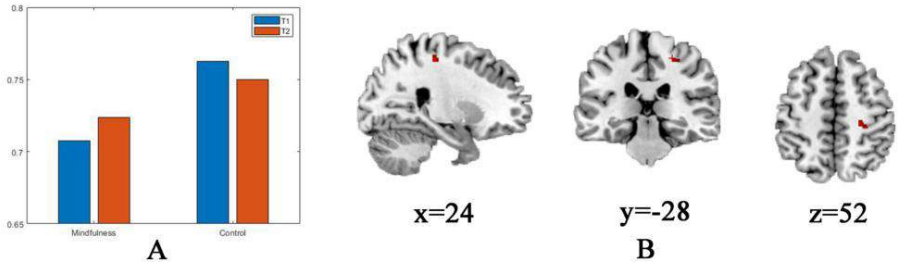

Conclusions: In summary, our preliminary results suggest that the brief mindfulness intervention holds the potential for enhancing spatial working memory in individuals. Furthermore, the observed modulated brain activations in the right frontal eye field, resulting from mindfulness practice, may underlie the improvements in spatial working memory performance.

References

1. Creswell, J. D. (2017). Mindfulness interventions. Annual review of psychology, 68, 491-516.
2. Jha, A. P., Stanley, E. A., Kiyonaga, A., Wong, L., & Gelfand, L. (2010). Examining the protective effects of mindfulness training on working memory capacity and affective experience. Emotion, 10(1), 54-64. https://doi.org/10.1037/a0018438
3. Stein, J. A., Bray, S., MacMaster, F. P., Tomfohr-Madsen, L., & Kopala-Sibley, D. C. (2022). Adolescents with High Dispositional Mindfulness Show Altered Right Ventrolateral Prefrontal Cortex Activity During a Working Memory Task. Mindfulness, 13(1), 198-210. https://doi.org/10.1007/s12671-021-01785-4
4. Tang, Y. Y., Holzel, B. K., & Posner, M. I. (2015). The neuroscience of mindfulness meditation. Nat Rev Neurosci, 16(4), 213-225. https://doi.org/10.1038/nrn3916

Poster No 1115

Volitional Breathing Alerts Brain for Faster Reaction in Emotionally Distracted Working Memory Task

Seulgi Eun[1], Phan Nguyen[1], Kyungmo Park[1]

[1]Department of Biomedical Engineering, Kyung Hee University, Yongin, South Korea

Introduction: Emotion, as a comprehensive psychophysiological response to internal or external environment, plays a crucial role in survival mechanisms. Emotion sometimes enhances our cognitive function, while it often disturbs even it leads to failure [Dolcos, 2011]. When it comes to the detrimental effect of emotion is somewhat retrogressive response to survival, investigating strategy to reduce the effect could be an attractive research topic. Here, considering neurobehavioral association between breathing and emotion, which the volitional breathing (VB) could rebalance and regulate emotional states [Ashhad, 2022], we applied simple breathing strategy (i.e., slow and deep breathing) to emotionally distracted working memory task to investigate brain mechanisms of VB in emotional processing.

Methods: Twenty-eight healthy young females participated in our fMRI experiment. Participants performed three different delayed match to sample working memory (WM) tasks depending on types of breathing strategy and visual distraction during memory maintenance phase (Maintenance) (i.e., scrambled image distraction for control, Scram; negative emotional image, Emo; and volitional breathing with emotional image, EmoVB) (Fig 1A). In EmoVB, participants were instructed to breathe deep and slow, while they were given instruction to concentrate on performing WM task without any instruction on breathing in Scram and Emo. Acquired functional images for each task were preprocessed and used in the ROI-based GLM analysis. ROIs were chosen from Human Brainconnetome Atlas [Fan, 2016], and we extracted representative ROI time series within each ROI by calculating 1st principal component of principal component analysis. Then, considering brain regional heterogeneity of hemodynamic response function (HRF) [Bright, 2009], we calculated optimal HRF delays for each ROI using ROI-based GLM with time shifted stimulus HRFs (Fig 1B). Finally, we extracted ROI brain responses including BOLD activity (beta) and latency (optimal delay), and those of Maintenance were compared between Scram and Emo to investigate effect of emotional arousal, and between Emo and EmoVB to investigate effect of VB on the emotional processing. During experiment, we also measured breathing patterns and WM performance (i.e., accuracy, AC; and reaction time, RT).

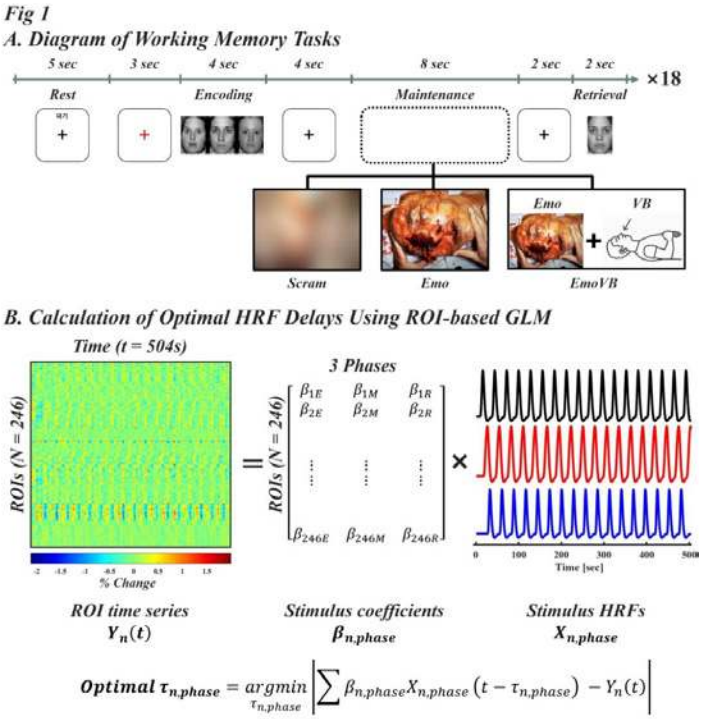

Results: As we instructed, participants' breathing pattern showed deeper in breathing depth and slower in rate in EmoVB than Emo. We found that the Emo impaired RT but not AC compared to Scram. Interestingly, VB restored the impaired RT to almost the same level of Scram, but it did not change in AC. As results of contrasted brain responses between Emo and Scram, the Emo decreased activity in the motor control and cognitive processing regions, and increased in the emotional processing regions, while it simultaneously prolonged latency in the emotional processing regions and shortened in the motor control regions. Also, our correlation analysis between brain responses and WM performance showed brain responses related to coping mechanisms both in the cognitive (i.e., dorsolateral prefrontal cortex) and emotional processing (i.e., parahippocampal gyrus and visual cortex) regions as well as to detrimental mechanisms in the emotional processing (i.e., amygdala) region. On the other hand, from results of brain contrast between EmoVB and Emo, the VB decreased activity in the motor control as well as in the emotional processing regions, and shortened latency in most of brain regions. Interestingly, the improved RT by the VB was associated with the decreased activity and shortened latency in the motor control regions, and more consistent breathing of the VB caused more improvement in the RT (Fig 2).

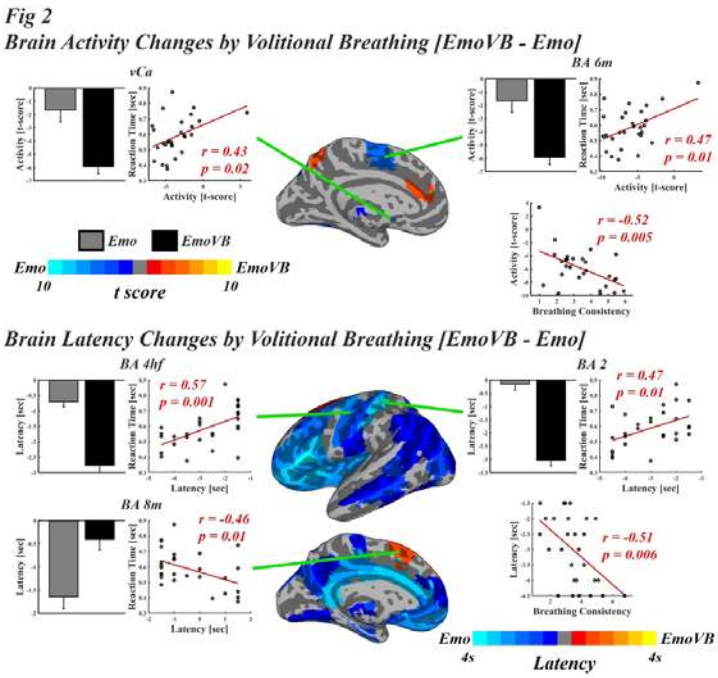

Conclusions: Collectively from our results, it seems that the VB not only regulates the excessive brain responses in the emotional processing network induced by the emotional distraction but also makes brain in alert state for faster response by recruiting motor control networks.

References
1. Ashhad, S. (2022), 'Breathing Rhythm and Pattern and Their Influence on Emotion', Annual Review of Neuroscience, vol. 45, pp. 223-247
2. Bright, M.G. (2009), 'Characterization of Regional Heterogeneity in Cerebrovascular Reactivity Dynamics Using Novel Hypocapnia Task and BOLD fMRI', NeuroImage, vol. 48, no. 1, pp. 166-175
3. Dolcos, F. (2011), 'Neural Correlates of Emotion-cognition Interactions: A Review of Evidence from Brain Imaging Investigations', Journal of Cognitive Psychology, vol. 23, no. 6, pp. 669-694
4. Fan, L. (2016), 'The Human Brainconnetome Atlas: A New Brain Atlas Based on Connectional Architecture', Cerebral Cortex, vol. 26, no. 8, pp. 3508-3526

Poster No 1116

Cortico-cerebellar patterns differentiate maintenance and manipulation in working memory tasks

Joshua Tan[1], Eli Müller[1], Claire O'Callaghan[1], James Shine[1]

[1]*University of Sydney, Sydney, NSW*

Introduction: Working memory involves the temporary storage and manipulation of information. It plays an important part of our day-to-day lives, such as when organising your daily schedule and engaging in conversations. However, the mechanisms of working memory are poorly understood, due in part to largely cortical explanations for the phenomenon. Intriguingly, working memory has previously been associated with regions of the dorsolateral prefrontal cortex that share extensive connections with the cerebellum, and rodent studies have implicated this circuit in working memory tasks. We hypothesised that working memory mechanisms are facilitated by cerebellar engagement, which may provide a parsimonious understanding for the neural mechanisms of working memory.

Methods: Twenty-four right-handed individuals (mean age = 23.8, SD = 2.6, 16 women) participated in the study and completed both a working memory spatial map and mental rotation task (King et al., 2019). Participants underwent three days of training before the first scanning session. Each participant completed 16 imaging runs (10 min per run) spread across two days. Each task consisted of an instruction period (5 s) and a response period (30 s). For the mental rotation task, there were 9 trials per run (duration = 3 s; ITI = 300 ms), with three difficulties with different degrees of rotation (easy = 0°, medium = 50°, hard = 150°). For the spatial map task, there were 6 trials per run (duration = 4.8 s; ITI = 200 ms) with three difficulties with differing number of digits to memorise (easy = 1, medium = 4, hard = 7). fMRI scans were pre-processed using fMRIprep, denoising and a high-pass filter (0.01) was applied using python scripts. Time-series signal was extracted and z-scored from a parcellation of 502 regions (400 cortical regions; Schaefer et al., 2018, 28 cerebellar regions; Diedrichsen, 2006, 74 subcortical regions; Tian et al., 2020). General linear models were fitted to the subject ROI time-series, comparing the effect of task difficulty on the BOLD response. Linear discriminant analysis (LDA) was used to find a low-dimensional manifold that separated both the spatial map and mental rotation tasks. Time-varying functional connectivity was estimated using the multiplication of temporal derivatives, a windowed approach (Shine et al., 2015). Edge connectivity across the whole brain was compared across tasks using permutation testing.

Results: General linear models were constructed comparing the effect of task difficulty on regional BOLD response. From these models, increased difficulty in the mental rotation task was associated with increased BOLD in the dorsolateral prefrontal, parietal cortices, and cerebellar lobules V and VIII ($p < 0.05$). The spatial map task was associated with increased BOLD response in the dorsolateral prefrontal, premotor, parietal, cortices, as well as lobule VI, Crus I and Crus II of the cerebellum ($p < 0.05$). The beta coefficients from these models were then compared using LDA and the principal eigenvector was analysed. The principal eigenvector described a gradient separating the middle lobe from the anterior and flocculonodular lobes of the cerebellum. Where the middle cerebellar lobe was related to maintenance in the spatial map task, and the anterior and flocculonodular lobes were related to manipulation in the mental rotation task. At the cortical level, there were minimal differences between the two tasks. Time-varying analyses revealed increased connectivity over time between dorsolateral regions with Crus I and Crus II of the cerebellum during spatial mapping. During mental rotation there was a decoupling between dorsolateral regions and Crus I and Crus II of the cerebellum.

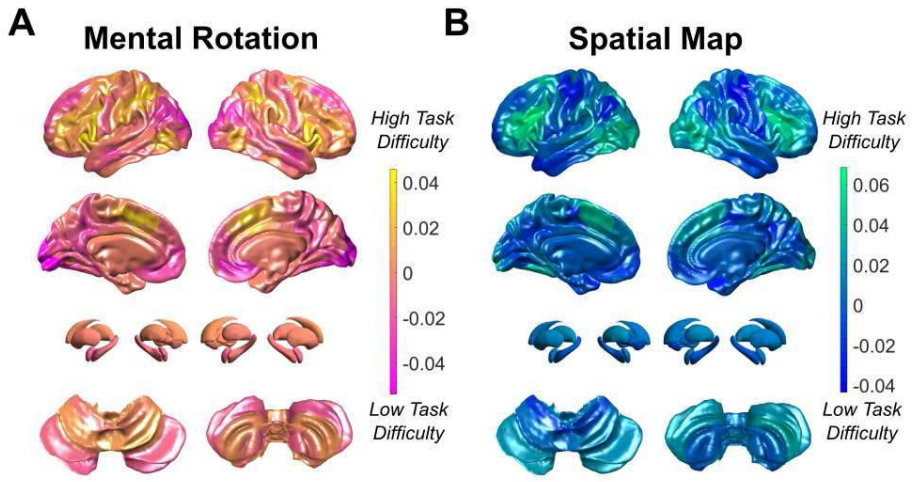

Figure 1 Brain maps comparing levels of difficulty in mental rotation and spatial map tasks

Conclusions: These results provide evidence that task demands of different working memory processes are differentiated in the cerebellum. By going beyond cortico-cortical interactions, we find distinct differences in neural patterns that differentiate processes of working memory.

References

1. Diedrichsen, J., 2006. A spatially unbiased atlas template of the human cerebellum. NeuroImage 33, 127–138. https://doi.org/10.1016/j.neuroimage.2006.05.056
2. King, M., Hernandez-Castillo, C.R., Poldrack, R.A., Ivry, R.B., Diedrichsen, J., 2019. Functional boundaries in the human cerebellum revealed by a multi-domain task battery. Nat Neurosci 22, 1371–1378. https://doi.org/10.1038/s41593-019-0436-x
3. Schaefer, A., Kong, R., Gordon, E.M., Laumann, T.O., Zuo, X.-N., Holmes, A.J., Eickhoff, S.B., Yeo, B.T.T., 2018. Local-Global Parcellation of the Human Cerebral Cortex from Intrinsic Functional Connectivity MRI. Cerebral Cortex 28, 3095–3114. https://doi.org/10.1093/cercor/bhx179
4. Shine, J.M., Koyejo, O., Bell, P.T., Gorgolewski, K.J., Gilat, M., Poldrack, R.A., 2015. Estimation of dynamic functional connectivity using Multiplication of Temporal Derivatives. NeuroImage 122, 399–407. https://doi.org/10.1016/j.neuroimage.2015.07.064
5. Tian, Y., Margulies, D.S., Breakspear, M., Zalesky, A., 2020. Topographic organization of the human subcortex unveiled with functional connectivity gradients. Nat Neurosci 23, 1421–1432. https://doi.org/10.1038/s41593-020-00711-6

Poster No 1117

Dynamic neural representations in the prefrontal and parietal cortex during selective retrieval

Jisu Park[1], Sue-Hyun Lee[1]

[1]Department of Psychology, College of Social Sciences, Seoul National University (SNU), Seoul, Korea, Republic of

Introduction: The retrieval of selectively relevant information from stored memory is an essential process guiding goal-directed behaviors. State-based models of working memory propose that the selective reactivation of goal-related memory traces, facilitated by attentional focus, brings memorized information into working memory (D'Esposito and Postle, 2015). However, while prior studies of working memory have predominantly examined the neural processing of just-experienced information (Lepsien and Nobre, 2007; Harrison and Tong, 2009; Lee, Kravitz and Baker, 2013), the specific neural mechanisms underlying the activation of goal-dependent information and the suppression of irrelevant information from long-term memory in the brain still remain elusive.

Methods: To elucidate the specific neural mechanisms underlying goal-dependent selective retrieval, we conducted an event-related functional magnetic resonance imaging (fMRI) experiment, consisting of separate sessions for learning and selective retrieval. During the learning session, participants memorized scenes in which multiple objects are naturally placed. On the following day, the participants were instructed to selectively retrieve a cued object from the memorized scene inside the scanner, followed by independent scans of object and scene perception. To investigate neural representations of goal-relevant object information selectively retrieved from original scenes, we directly compared neural response patterns during selective retrieval with those elicited by perception of objects or scenes. Simultaneously, we examined retrieval cue-specific representations during selective retrieval by comparing neural response patterns elicited by the same retrieval cue and those

elicited by different cue. Additionally, we tracked temporal changes in neural representations by comparing pattern similarities between adjacent time points.

Results: The direct comparison between retrieval and perception patterns revealed dissociable information processing in the dorsolateral prefrontal cortex (dlPFC) and angular gyrus (AG) during selective retrieval. The dlPFC and AG commonly represented the goal-related original scene information during the early phase of selective retrieval. On the other hand, the AG primarily represented the targeted object, whereas the dlPFC showed prominent representations of non-targeted objects. During the later phase of retrieval, shared representations between retrieval and perception were not observed in either area. In parallel, we found a persistent retrieval cue-specific representation during this later phase in both the dlPFC and AG. By comparing pattern similarities between adjacent time points, we confirmed distinct neural representations between the early and later phases of retrieval. Specifically, while dynamic changes in neural representation were observed during the early phase, consistently similar representations across time points were observed during the later phase.

Conclusions: These findings suggest that goal-dependent retrieval of selective information involves dissociable information processing in the prefrontal and parietal cortex, along with dynamic temporal changes in neural representations in both areas.

References

1. D'Esposito, M. and Postle, B.R. (2015) 'The cognitive neuroscience of working memory', Annual Review of Psychology, 66, pp. 115–142. Available at: https://doi.org/10.1146/annurev-psych-010814-015031.
2. Harrison, S.A. and Tong, F. (2009) 'Decoding reveals the contents of visual working memory in early visual areas', Nature, 458(7238). Available at: https://doi.org/10.1038/nature07832.
3. Lee, S.H., Kravitz, D.J. and Baker, C.I. (2013) 'Goal-dependent dissociation of visual and prefrontal cortices during working memory', Nature Neuroscience, 16(8). Available at: https://doi.org/10.1038/nn.3452.
4. Lepsien, J. and Nobre, A.C. (2007) 'Attentional modulation of object representations in working memory', Cerebral Cortex, 17(9). Available at: https://doi.org/10.1093/cercor/bhl116.

Poster No 1118

Contingency representations in prefrontal cortex unify goal-directed planning and working memory

Jacob Miller[1,2], Daniel Ehrlich[3], Yvette Afriyie-Agyemang[4], Nicole Santamauro[1], Zailyn Tamayo[1], Alan Anticevic[1], John D. Murray[5,1]

[1]Yale University School of Medicine, New Haven, CT, [2]Wu Tsai Institute, Yale University, New Haven, CT, [3]University of California, Berkeley, Berkeley, CA, [4]University of Pittsburgh, Pittsburgh, PA, [5]Dartmouth College, Hanover, NH

Introduction: Working memory (WM) is critical in guiding our adaptive behavior based on immediate and future demands (van Ede & Nobre, 2023). The prefrontal cortex (PFC) and a connected network of areas are consistently active during WM (Sreenivasan & D'Esposito, 2019). But, it remains difficult to parse out the differential contributions of brain areas to WM function, especially when the maintenance and usage of WM content is often intertwined. How do representations for stimuli, task rules, and future behavior all contribute to WM, and what is their brain circuit organization? A recently developed computational framework and task paradigm helps unify the representational geometry for goal-directed planning and WM (Ehrlich & Murray, 2022). In this WM task, patterns of human behavior and activity in neural networks suggest the emergence of combined representations of stimuli and task rules into response contingencies. Here, we tested for differential neural substrates of stimulus, rule, and response information, and newly predicted contingency representations to clarify the role of PFC during WM.

Methods: During functional magnetic resonance imaging (fMRI), human participants completed 4 runs (32 trials each) of a conditional delayed logic WM task (Fig. 1a). On each trial, participants were shown a rule cue (colored box), then a gabor filter stimulus (vertical/horizontal), followed by a jittered delay period, and then a second gabor (vertical/horizontal), after which participants responded with a left or right hand button. The correct response on each trial was determined based on the rule and the first and second stimulus (Fig. 1b-c). fMRI data was acquired via 8x multi-band sequence with 2mm isotropic voxels, along with field maps and T1w/T2w anatomical scans. Functional data were minimally pre-processed in native anatomical space for each participant using fMRIprep (Esteban et al., 2019). We then used a general linear modeling framework in Nilearn (Abraham et al., 2014) with separate regressors for each combination of cue 1 stimulus and rule, modeling the initial cue period (1.6 s) and delay (3.2-8.0 s). Separate F-test contrasts were constructed to test for voxels that responded highly to different levels of stimulus, rule, response, and contingency information (Fig. 1b). Contrast maps were passed through probabilistic Threshold-Free Cluster Enhancement (pTFCE) to incorporate cluster information into voxel inference (Spisák et al., 2019) and corrected at FWE level or an arbitrary threshold for visualization.

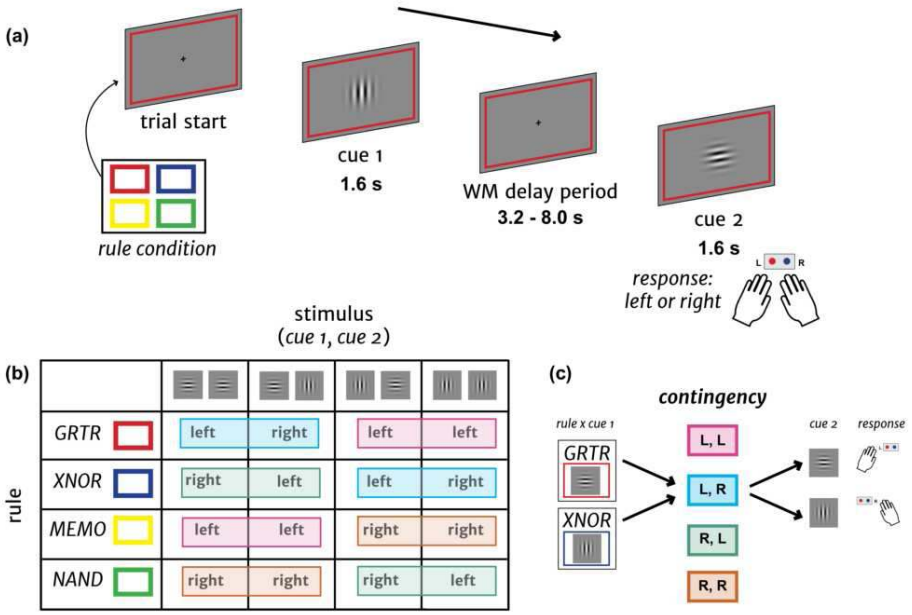

Figure 1. (a) Example trial timing of the conditional delayed logic (CDL) WM task using the "GRTR" rule, indicated by the red square, which was on the screen for the duration of the trial. The rule was randomly assigned on every trial and counterbalanced during the experiment for each participant. **(b)** Table of possible rule (row) and stimuli (column) information on each trial, determining the correct response and response contingencies (haded colors). **(c)** Schematic of contingencies as a central framework for translating rule and stimulus information on trials into a central framework, showing how different WM stimuli and rules may lead to a shared contingency [L, R].

Results: During the cue period, stimulus (orientation: horizontal vs. vertical) and rule (GRTR vs. XNOR vs. MEMO vs. NAND) information was present across voxels in early and high-level visual areas, extending into the lateral occipital complex and intraparietal sulcus. During the WM delay, a distributed set of voxels in frontal, parietal, and temporal cortex responded highly to different levels of contingency across trials (LL vs. LR vs. RL vs. RR), but most strongly in lateral frontal cortex (pFWE < 0.05, Fig. 2a). Maps of contingency representations often overlapped with rule representations, however, contingency sensitive voxels showed specific, non-overlapping territory in more anterior PFC areas (Fig. 2b), extending ventrally beyond the inferior frontal sulcus and dorsally along superior frontal sulcus/gyrus (Miller et al., 2021), or even wrapping around the frontal pole onto the medial PFC surface.

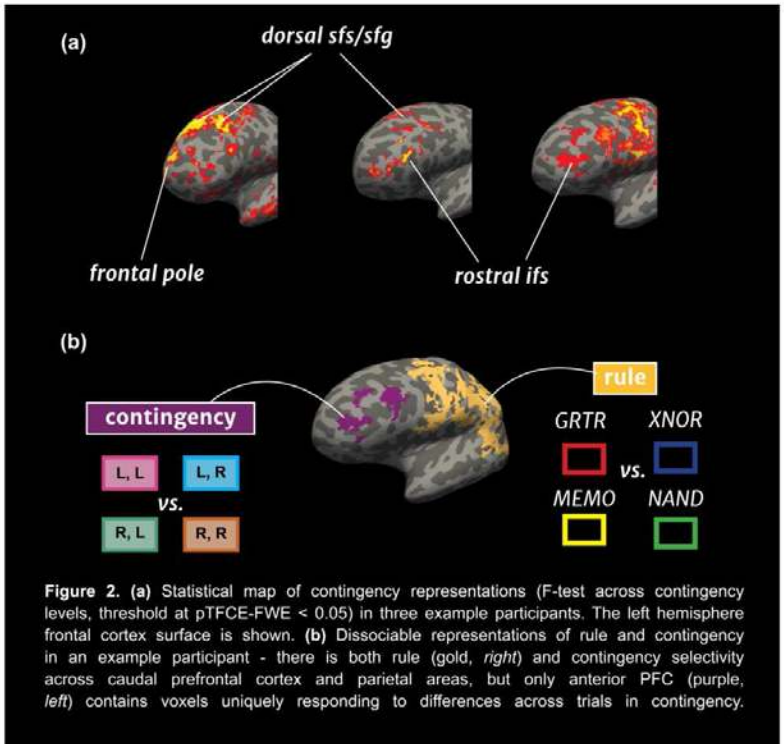

Figure 2. (a) Statistical map of contingency representations (F-test across contingency levels, threshold at pTFCE-FWE < 0.05) in three example participants. The left hemisphere frontal cortex surface is shown. **(b)** Dissociable representations of rule and contingency in an example participant - there is both rule (gold, *right*) and contingency selectivity across caudal prefrontal cortex and parietal areas, but only anterior PFC (purple, *left*) contains voxels uniquely responding to differences across trials in contingency.

Conclusions: Building on classic and modern studies of rule coding in PFC (Milner, 1963; Vallentin et al., 2012), we show that the most anterior PFC areas in the human brain display unique representations of task contingencies in WM by transforming stimulus and rule information to future responses. Tying in perspectives of hierarchical cognitive control in PFC (Badre & Nee, 2018), these results suggest anterior PFC subserves WM by integrating different task information to plan future behavior.

References

1. Abraham, A., Pedregosa, F., Eickenberg, M., Gervais, P., Mueller, A., Kossaifi, J., Gramfort, A., Thirion, B., & Varoquaux, G. (2014). Machine learning for neuroimaging with scikit-learn. Frontiers in Neuroinformatics, 8, 14.
2. Badre, D., & Nee, D. E. (2018). Frontal Cortex and the Hierarchical Control of Behavior. Trends in Cognitive Sciences, 22(2), 170–188.
3. Ehrlich, D. B., & Murray, J. D. (2022). Geometry of neural computation unifies working memory and planning. Proceedings of the National Academy of Sciences of the United States of America, 119(37), e2115610119.
4. Esteban, O., Markiewicz, C. J., Blair, R. W., Moodie, C. A., Isik, A. I., Erramuzpe, A., Kent, J. D., Goncalves, M., DuPre, E., Snyder, M., Oya, H., Ghosh, S. S., Wright, J., Durnez, J., Poldrack, R. A., & Gorgolewski, K. J. (2019). fMRIPrep: a robust preprocessing pipeline for functional MRI. Nature Methods, 16(1), 111–116.
5. Miller, J. A., Voorhies, W. I., Lurie, D. J., D'Esposito, M., & Weiner, K. S. (2021). Overlooked Tertiary Sulci Serve as a Meso-Scale Link between Microstructural and Functional Properties of Human Lateral Prefrontal Cortex. The Journal of Neuroscience: The Official Journal of the Society for Neuroscience, 41(10), 2229–2244.
6. Milner, B. (1963). Effects of Different Brain Lesions on Card Sorting: The Role of the Frontal Lobes. Archives of Neurology, 9(1), 90–100.
7. Spisák, T., Spisák, Z., Zunhammer, M., Bingel, U., Smith, S., Nichols, T., & Kincses, T. (2019). Probabilistic TFCE: A generalized combination of cluster size and voxel intensity to increase statistical power. NeuroImage, 185, 12–26.
8. Sreenivasan, K. K., & D'Esposito, M. (2019). The what, where and how of delay activity. Nature Reviews. Neuroscience, 2019/05/16. https://doi.org/10.1038/s41583-019-0176-7
9. Vallentin, D., Bongard, S., & Nieder, A. (2012). Numerical rule coding in the prefrontal, premotor, and posterior parietal cortices of macaques. The Journal of Neuroscience: The Official Journal of the Society for Neuroscience, 32(19), 6621–6630.
10. van Ede, F., & Nobre, A. C. (2023). Turning Attention Inside Out: How Working Memory Serves Behavior. Annual Review of Psychology, 74, 137–165.

Poster No 1120

Decoding Replay during Working Memory Manipulation and Retention in Humans

Shiva Sedghi[1,2]

[1]Université Laval, QC, Canada, [2]CERVO Brain Research Center, QC, Canada

Introduction: Working memory, known as the ability of the human brain to temporarily hold and manipulate sequential items, is at the critical juncture between memory, attention, and perception, and is central to a range of cognitive functions and goal-directed behaviors[3,4]. Load-dependent increase of brain activity and brain rhythmic activity in the theta frequency range in fronto-parietal networks have been associated with working memory performance[1,2]. In parallel, recent studies have suggested that internally generated sequences of neural representations can be reactivated or 'replayed' to support memory consolidation and learning. Replay has also been proposed as a mechanism that enables planning and action preparation based on past experiences [5-10]. However, the potential relationship between replay and active working memory retention and manipulation remains unexplored.

Methods: In this study, we utilized magnetoencephalography (MEG) to measure neural activity before, during after associative learning and during the working memory processes. We recruited 30 young participants in 2 consecutive MEG sessions with pre-learning exposure, associated learning, post-learning evaluation, and working memory tasks. During the working memory task, participants had to mentally recall, and regenerate the previously learned sounds based on given instructions. We used multivariate classification techniques to identify neural patterns associated with memorized items and investigate the dynamics of these patterns during working memory retention and manipulation periods. In addition, we explored the neural mechanisms associated with associative learning in humans by using a combination of behavioral, MEG, and machine learning approaches.

Results: Our analysis demonstrated sustained theta activity within a distributed network, indicating the temporal cooperation of brain regions during and after learning. ERF and Hilbert transform analysis also revealed a learning-associated beta desynchronization over fronto-temporal and parietal lobes, regions known to be involved in working memory functions. Furthermore, we detected evidence of backward replay during the manipulation and retention phases of working memory processes.

Conclusions: We observed sustained theta activity in the defined regions of interest after a memory-related task, which may be attributed to the role of theta oscillation in facilitating long-range communication between distant brain regions and can serve as a marker for the formation and retention of memory associations. These findings provide further support for the involvement of theta activity in cognitive processes. We also observed functional changes in the beta range (12–30 Hz)

across several brain regions after the learning task. Notably, these alterations encompassed a decrease in beta power. The desynchronization was observed over a distributed network, which may be related to flexible processing and integration of information between different brain regions. Our results align with previous studies that have shown beta desynchronization during memory tasks and suggest a learning-associated beta desynchronization. While our study provides valuable insights into the neural mechanisms underlying working memory and proposes that the fast-backward replay may play a crucial role in strengthening memory traces, it is important to note that our analyses on the sequenceness of the backward and forward replay during working memory retention and manipulation are still ongoing. Our findings of fast-backward replay during working memory phases are an exciting development but need to be validated. Further research is needed to elucidate the exact functions and mechanisms of backward replay during the manipulation phase of working memory and to determine the implications of this finding for our understanding of the neural basis of working memory processes.

References

1. Here are the citations arranged in alphabetical order by the first author's last name, with journal names given in full:
2. Albouy, P. (2017). 'Selective entrainment of theta oscillations in the dorsal stream causally enhances auditory working memory performance', Neuron, vol. 94, no. 1, pp. 193-206.
3. Albouy, P. (2018). 'Driving working memory with frequency-tuned noninvasive brain stimulation', Annals of the New York Academy of Sciences, vol. 1423, no. 1, pp. 126-137.
4. Baddeley, A. (1992). 'Working memory', Science, vol. 255, no. 5044, pp. 556-559.
5. Baddeley, A. (2010). 'Working memory', Current Biology, vol. 20, no. 4, R136-R140.
6. Eldar, E. (2020). 'The roles of online and offline replay in planning', eLife, vol. 9, e56911.
7. Liu, Y. (2019). 'Human replay spontaneously reorganizes experience', Cell, vol. 178, no. 3, pp. 640-652.
8. Liu, Y. (2020). 'Temporally delayed linear modelling (TDLM) measures replay in both animals and humans', eLife, vol. 10.
9. Nour, M. M. (2021). 'Impaired neural replay of inferred relationships in schizophrenia', Cell, vol. 184, no. 16, pp. 4315-4328.
10. Wimmer, G. E. (2020). 'Episodic memory retrieval success is associated with rapid replay of episode content', Nature Neuroscience, vol. 23, no. 8, pp. 1025-1033.
11. Wittkuhn, L. (2021). 'Dynamics of fMRI patterns reflect sub-second activation sequences and reveal replay in human visual cortex'.

Poster No 1121

Alpha oscillations protect auditory working memory against different distractors

Chia-An Tu[1], Yi-Fang Hsu[1]

[1]National Taiwan Normal University, Taipei, Taiwan

Introduction: Alpha oscillations are proposed to serve the function of pulsed inhibition to protect items in working memory from irrelevant information (Klimesch, 1999; Jensen & Mazaheri, 2010). Previous visual research showed that occipital alpha activity increased at the anticipation of strong distractors (Bonnefond & Jensen, 2012; Sghirripa et al., 2021). However, in the auditory modality, it was found that strong distractors were associated with pre-distractor decrease of alpha power in the left superior temporal gyrus (Weisz et al., 2020), which might be due to the involuntary direction of attention to strong distractors or the prioritisation of memorised information in anticipation of strong distractors. It remains unclear whether and how auditory distractors are inhibited by alpha oscillations.

Methods: We used a modified Sternberg paradigm where we manipulated the strength of distractors (strong vs weak distractors) and the amount of distractors (more vs fewer distractors) in a block design. A total of 22 participants were presented with six primes of spoken digits (where distractors were sandwiched between targets) with an SOA of 1100 ms (i.e., encoding), a silent interval of 2200 ms (i.e., retention), and a probe of a spoken digit to which participants had to press a key to indicate whether it was one of the targets presented earlier (i.e., retrieval). While 50% of the probes called for a yes response, 50% of the probes called for a no response. Participants' response was followed by a jittered ITI of 900-1300 ms. EEG was recorded from 32 active electrodes on a Brain Products actiCAP snap according to the extended 10-20 system.

Results: Pairwise comparisons of the ERSP suggested that distractor strength and distractor amount modulated alpha activity differently. On the one hand, alpha power increased by distractor strength (i.e., strong vs weak distractors) at the encoding phase both before and after the presentation of distractors as well as at the retention phase over right centroparietal area. On the other hand, alpha power increased by distractor amount (i.e., more vs fewer distractors) at the encoding phase before but not after the presentation of distractors beyond right centroparietal area.

Conclusions: Strong vs weak auditory distractors seem to be inhibited by increased alpha activity in a similar way to visual distractors. Moreover, the increased alpha activity is both proactive and reactive. More vs fewer auditory distractors seem to be inhibited by increased alpha activity proactively but not reactively, which likely involves a broad network of cortical regions.

References
1. Klimesch, W. (1999) EEG alpha and theta oscillations reflect cognitive and memory performance: a review and analysis. Brain Research Reviews, 29(2-3), 169-195.
2. Jensen, O., & Mazaheri, A. (2010) Shaping functional architecture by oscillatory alpha activity: gating by inhibition. Frontiers in Human Neuroscience, 4:186.
3. Bonnefond, M., & Jensen, O. (2012) Alpha oscillations serve to protect working memory maintenance against anticipated distracters. Current Biology, 22(20), 1969-1974.
4. Sghirripa, S., Graetz, L., Merkin, A., Rogasch, N. C., Ridding, M. C., Semmler, J. G., & Goldsworthy, M. R. (2021) The role of alpha power in the suppression of anticipated distractors during verbal working memory. Brain Topography, 34(1), 102-109.
5. Weisz, N., Kraft, N. G., & Demarchi, G. (2020) Auditory cortical alpha/beta desynchronization prioritizes the representation of memory items during a retention period. eLife, 9:e55508.

Poster No 1122

Distinct neural patterns for working memory and sensory representations in the early visual cortex

Sungje Kim[1], Joonwon Lee[1], Hyunwoo Gu[2], Dong-Gyu Yoo[1], Heeseung Lee[1], Hyang-Jung Lee[1], Jaeseob Lim[1], Minjin Choe[1], Sang-Hun Lee[1]

[1]Seoul National University, Seoul, Korea, Republic of, [2]Stanford University, Stanford, CA

Introduction: Numerous studies have demonstrated the presence of working memory (WM) representations within the early visual cortex (EVC) (Harrison and Tong, 2009; Serences et al., 2009; Ester et al., 2013). The sensory recruitment hypothesis proposes that the EVC utilizes the same neural code for both WM and sensory representations (referred to as the 'sensory code'), enabling WM to benefit from the high fidelity of sensory coding (Adam et al., 2022; D'Esposito and Postle, 2015). However, a recent study challenges this view, suggesting that the population activity patterns in the EVC during sensory encoding differ from those observed during WM maintenance (Kwak and Curtis, 2022). In this study, we investigate whether the EVC uses a shared code for sensory and working memory information by designing a paradigm that sensory and mnemonic representations are sufficiently separated in time and compared them using several measures of neural codes.

Methods: In a magnetic resonance imaging (MRI) scanner, 50 human observers participated in a task where they briefly viewed an oriented grating and later reproduced its orientation after a substantial delay period (16.5 s), which is long enough for the blood-oxygen-level-dependent (BOLD) responses to the grating to dissipate. During the delay period, there was a decision period where the subjects was asked whether the remembered orientation was clockwise or counter-clockwise than the presented stimulus orientation. Sensory codes were defined based on BOLD responses during the period of peak univariate BOLD activity, while working memory codes were defined using responses during the last moment of the delay period.

Results: Both sensory code and working memory code could successfully read out the information in the EVC, but their informative period were different. Decoding performance by sensory code was peaked after the stimulus onset, decreased during delay and disappeared at the last period of delay. Conversely, the working memory code exhibited lower decoding performance than the sensory code during stimulus onset, but maintained higher performance in entire delay period. During the decision period, where the physical stimulus was present, the sensory code accurately decoded the orientation of the physical stimulus, while the working memory code successfully retrieved the remembered orientation. These findings underscore the differential temporal characteristics of sensory and working memory codes in the EVC, highlighting a unique representation of working memory distinct from sensory representation. Several measures were employed to compare sensory and working memory representations. First, when projected onto a low-dimensional state space (Panicello and Buschman, 2021), sensory and working memory orientations formed in two separate planes orthogonal to each other. Second, using the inverted encoding model (Brouwer and Heeger, 2009), decoding stimulus orientation revealed that working memory information could not be decoded using voxel weights trained on sensory representations, and vice versa. Third, voxel-level analysis demonstrated that the differences in codes were derived from distinct distributions of orientation preferences. Lastly, examination of retinotopic properties showed that orientation preferences in the sensory representation were correlated with radial positions in retinotopic space (Ryu and Lee, 2018; Lee and Ryu; 2023), while such correlation was absent in the working memory representation.

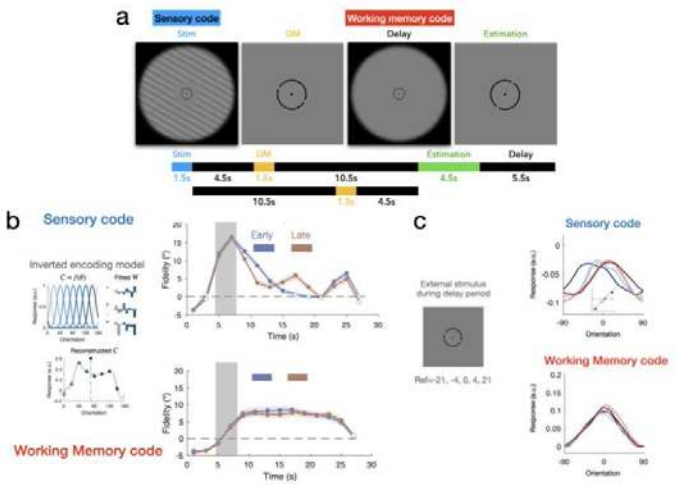

Figure. (a) Task Structure. DM: Decision Making. There were two conditions(Early and Late) by when DM task was provided, and subject couldn't know which condition will be presented. (b) By using inverted encoding model, multivariate decoding was performed. Decoding fidelity by sensory code (Top-right) and by working memory code (Bottom-right). (c) In DM task, sensory code read out the presented orientation(reference was presented near memorized orientation), and working memory read out the memorized orientation.

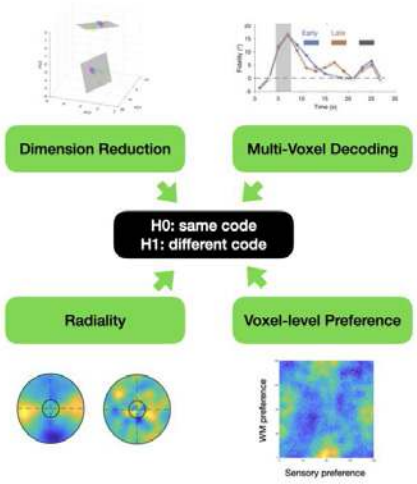

Figure. There were four approaches for testing the difference of two codes.

Conclusions: Our findings suggest that EVC employs distinct neural codes for representing sensory and mnemonic orientations. This differentiation may enable the brain to perform tasks involving the comparison of both types of representations with less distraction from external interference. The observed separation in coding mechanisms supports the idea that EVC adapts to the unique demands of sensory and working memory processes, providing insights into the neural underpinnings of working memory within the early visual cortex.

References

1. Harrison, S. A., & Tong, F. (2009). Decoding reveals the contents of visual working memory in early visual areas. Nature, 458(7238), 632-635.
2. Serences, J. T., Ester, E. F., Vogel, E. K., & Awh, E. (2009). Stimulus-specific delay activity in human primary visual cortex. Psychological science, 20(2), 207-214.
3. Ester, E. F., Anderson, D. E., Serences, J. T., & Awh, E. (2013). A neural measure of precision in visual working memory. Journal of cognitive neuroscience, 25(5), 754-761.
4. Adam, K. C., Rademaker, R. L., & Serences, J. T. (2022). Evidence for, and challenges to, sensory recruitment models of visual working memory. Visual memory, 5-25.
5. D'Esposito, M., & Postle, B. R. (2015). The cognitive neuroscience of working memory. Annual review of psychology, 66, 115-142.
6. Kwak, Y., & Curtis, C. E. (2022). Unveiling the abstract format of mnemonic representations. Neuron, 110(11), 1822-1828.
7. Panichello, M. F., & Buschman, T. J. (2021). Shared mechanisms underlie the control of working memory and attention. Nature, 592(7855), 601-605.
8. Brouwer, G. J., & Heeger, D. J. (2009). Decoding and reconstructing color from responses in human visual cortex. Journal of Neuroscience, 29(44), 13992-14003.
9. Ryu, J., & Lee, S. H. (2018). Stimulus-tuned structure of correlated fMRI activity in human visual cortex. Cerebral Cortex, 28(2), 693-712.
10. Lee, S. H., & Ryu, J. (2023). A mismatch between human early visual cortex and perception in spatial extent representation: Radial bias shapes cortical representation while co-axial bias shapes perception. bioRxiv, 2023-02.

Poster No 1123

Brain activity during working memory in autoimmune Addison's disease

Annelies van't Westeinde[1], Olle Kämpe[1], Sophie Bensing[1], Svetlana Lajic[1]

[1]Karolinska Institute, Stockholm, Stockholm's Län

Introduction: Individuals with autoimmune Addison's disease (AAD) lack production of adrenal hormones and therefore need to take daily oral replacement for cortisol and aldosterone (Husebye, Pearce et al. 2021). This replacement in its current form is sub-optimal, and frequently results in supra- and infra-physiological cortisol levels that might negatively affect the brain and cognitive functioning. Research has begun mapping the effects of having AAD on cognition, neuro-structure and neuro-function, in an effort to understand if the brain needs to be better protected in this patient group (Schultebraucks, Wingenfeld et al. 2015, Russell, Kalafatakis et al. 2023). Our group has found some indication of reduced total brain volume and changes in resting-state connectivity in individuals with AAD (Van't Westeinde, Padilla et al. 2022, Van't Westeinde, Padilla et al. 2023). Most notably, women with AAD report to be mentally fatigued, which impairs their daily functioning (van't Westeinde, Ström et al. 2022). The present study aims to further our understanding of brain function in AAD by investigating brain activity during verbal and visuo-spatial working memory in a cohort of young adults with AAD, compared to healthy controls. In addition, we investigate the modulating role of mental fatigue.

Methods: All participants (56 with AAD (33 females) and 62 controls (39 females), aged 19-43 years), underwent MRI scanning of the brain while performing a visuo-spatial and verbal working memory task. FSL was used to compare task-related BOLD-signal between patients and controls, for the encoding and decoding phases of both tasks. In addition, we estimated the temporal standard deviation of the BOLD-signal in certain regions of interest where a significant group difference or interaction was found. Estimates of working memory performance included reaction time, variability in reaction time (coefficient of variation) and accuracy. Self-reported mental fatigue in the two days prior to testing was estimated with the multidimensional fatigue inventory (MFI), which was used in an analysis testing if the relationship between fatigue and brain activity during the task differed between patients and controls.

Results: No difference in mean accuracy, reaction time or brain activity during the working memory tasks were found between the groups, and there were no interactions with sex. Patients did have more variable reaction times during the control conditions of both tasks. In addition, a differential association between mental fatigue and brain activity during the visuo-spatial task was found in a cluster in the right occipital pole (80 voxels, peak MNI 32, -94, -6), and three in the cerebellum, specifically a cluster covering Vermis VI; Left V and Bilateral VI, (117 voxels, peak MNI -4, -68, -10), a cluster in Right I-IV (67 voxels, peak MNI 8, -50, -20) and a cluster in Right Crus I (67 voxels, peak MNI 40, -82, -30), where patients with more mental fatigue had stronger activity in these clusters. Stronger activity in the right occipital pole was associated with slower reaction times in patients, and a greater temporal standard deviation in the bilateral cerebellum region VI was associated with more mental fatigue in patients, but not controls.

Conclusions: These findings suggest that while patients perform at the same level as controls on this specific task, mental fatigue is affecting their brain activity, in particular in the cerebellum and primary visual areas. Our findings suggest that the cerebellum is involved in fatigue and performance regulation in patients with AAD, which is in line with a recent study showing the involvement of cerebellar excitability in fatigue regulation (7). Future studies are needed to better understand fatigue in patients with AAD, how to improve this and how to best protect their brains on the long term. In particular, the development of a pump to deliver cortisol might help improve brain function in AAD and should be further investigated (3).

References

1. Casamento-Moran, A. (2023). "Cerebellar Excitability Regulates Physical Fatigue Perception." J Neurosci 43(17): 3094-3106.
2. Husebye, E. S. (2021). "Adrenal insufficiency." Lancet 397(10274): 613-629.
3. Russell, G. (2023). "Ultradian hydrocortisone replacement alters neuronal processing, emotional ambiguity, affect and fatigue in adrenal insufficiency: The PULSES trial." J Intern Med.
4. Schultebraucks, K. (2015). "Cognitive function in patients with primary adrenal insufficiency (Addison's disease)." Psychoneuroendocrinology 55: 1-7.
5. Van't Westeinde, A. (2023). "Increased resting-state functional connectivity in patients with autoimmune Addison's disease." J Clin Endocrinol Metab.
6. Van't Westeinde, A. (2022). "Brain structure in autoimmune Addison's disease." Cereb Cortex.
7. van't Westeinde, A. (2022). "Young adult Swedish patients with autoimmune Addison's disease report difficulties with executive functions in daily life despite overall good cognitive performance." Psychoneuroendocrinology. 140: 105714.

Poster No 1124

Integrating Multimodal Neuroimaging Features to Predict Working Memory and Psychiatric Disability

Catherine Walsh[1,2], Jean-Baptiste Pochon[1], Agatha Lenartowicz[1], Sandra Loo[1], Catherine Sugar[1], Carrie Bearden[1], Robert Bilder[1], Jesse Rissman[1]

[1]University of California, Los Angeles, Los Angeles, CA, [2]National Institute of Mental Health, Bethesda, MD

Introduction: Individual differences in working memory (WM) capacity have been linked to variation in higher order cognition and psychiatric disability. One goal of the NIH Research Domain Criteria (RDoC) paradigm is to formally characterize this relationship and relate neurocognitive markers of WM to psychopathology across broad diagnostic categories[1]. Although a variety of structural and functional brain measures have been shown to account for variance in WM capacity, recent work integrating distinct modalities of brain structure and function explain more variance than can any single modality on its own[2,3]. The present investigation sought to leverage machine learning to characterize the relative importance of different functional and structural neuroimaging measures for predicting WM task performance, trait-level WM capacity, and overall psychiatric disability.

Methods: Data from 169 participants (106 females, age 21-40) were collected as a part of a project recruiting adults with a wide range of mental health concerns, as well as non-care-seeking adults. Participants underwent behavioral testing to measure cognitive ability and self-reported clinical symptomatology, as measured by the WHO Disability Assessment Scale (WHODAS) and the Brief Psychiatric Rating Scale (BPRS). Indices of WM were submitted to an exploratory factor analysis, producing visual and verbal WM capacity factor scores. All participants underwent whole-brain imaging using a Siemens 3.0T MRI scanner. Functional data collection (multiband EPI, TR=1.5s, TE=34.2ms, voxel resolution = 2 mm3) included a resting state scan, a face localizer[4], and a delayed facial recognition WM task (DFR;[5]). Structural data collection included a high-resolution (1 mm3) T1-weighted scan and a diffusion-weighted scan. We identified 3 modalities of neuroimaging features to use as predictors in our models: task-based fMRI from the DFR task (univariate BOLD parameter estimates and representational similarity-based indices of face-specific representational content and encoding-to-delay pattern stability), resting state fMRI (mean connectivity across networks; global and local graph theoretical measures), and structural measures (cortical thickness and subcortical volume). Separate ElasticNet models were built for each modality, in addition to models for each task-fMRI measure and a full model including predictors from all modalities. Model were trained and tested with a 10-fold cross-validation framework. Spearman correlation was used to index explained variance, and permutation testing was used to determine statistical significance for overall models and individual predictors.

Results: Different patterns of modalities were able to predict each outcome measure (Fig 1a). Task fMRI models significantly predicted task performance, visual WM capacity, and BPRS. Resting state fMRI models predicted task performance and WHODAS, while structural MRI models could only predict WHODAS. Decomposing task fMRI models into individual measures revealed a striking dissociation, where task performance was most predicted by univariate BOLD and encoding to delay pattern stability measures, while visual WM capacity was best predicted by the strength of face-specific representational content (Fig 1b). Combined multimodal models were able to predict a significant variance in most measures, especially for WHODAS where the multimodal modal model outperformed the unimodal models (Fig 1c).

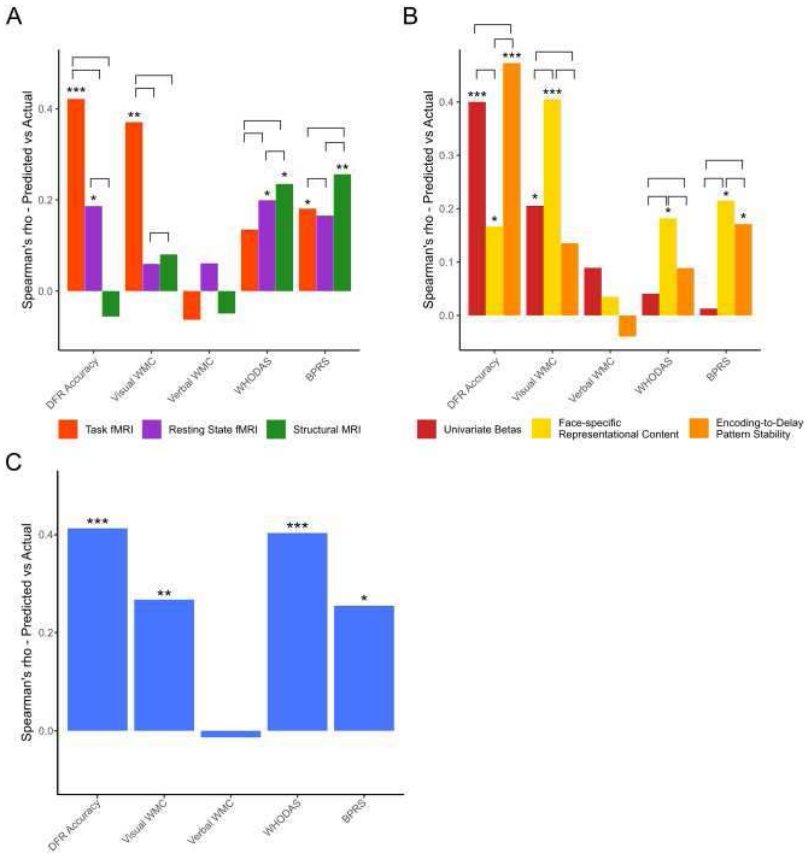

Figure 1: Predictive ability of models. Models using A. individual modalities, B. task fMRI measures, and C. all features. Each model was run in a 10-fold cross validation framework, where nine folds were used to train the models and one fold was held out as an independent testing set to ensure that the model generalized to new data. This cross-validation was repeated 100 times. Values depicted are the median Spearman's rho between the predicted and actual values across runs. Correlation values are calculated on data from all N = 168 participants concatenated across folds. Symbols reflect statistical significance derived from permutation testing, where the response variables were permuted 25 times per run to break the relationship between features and outcomes (* $p < 0.05$, ** $p < 0.01$, *** $p < 0.001$). Brackets reflect significant differences across 5,000 bootstrapped iterations.

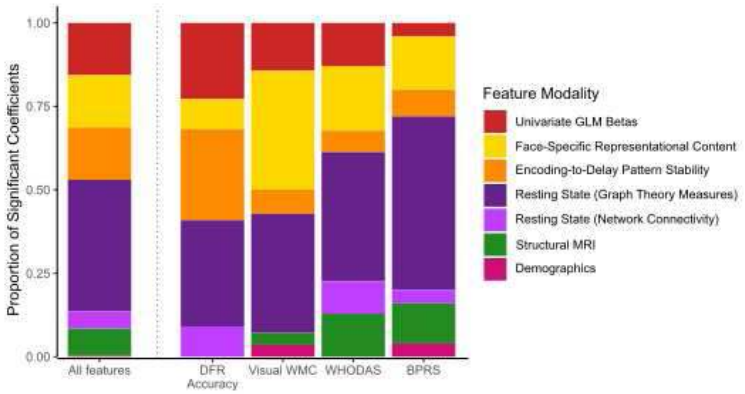

Figure 2: Distribution of feature modalities in full models. Proportion of significant features from full models for each outcome measure belonging to each feature modality. Statistical significance determined through permutation testing. Proportions relative to number of features for each individual model. Bar to left of dotted line depicts distribution of feature modalities across all potential features. Colors represent feature modality - red: univariate GLM activity, orange: encoding-to-delay pattern stability, yellow: face-specific representational content, dark purple: resting state graph theory measures, light purple: resting state network-average functional connectivity, green: structural MRI measures, pink: demographic measures.

Conclusions: Predictive modeling revealed unique contributions of structural and functional MRI in predicting WM task performance, trait-level WM capacity, and psychiatric disability. Better trait visual WM capacity was associated with high-fidelity representation of task-relevant features during maintenance, while WM task performance was predicted by neural persistence of encoding processes. Psychiatric disability was predicted by task-related functional activity measures. These potential neural biomarkers could inspire novel targeted interventions.

References
1. Bilder, R.M. (2013), "Multilevel models from biology to psychology: Mission impossible?", Journal of Abnormal Psychology, vol., 122, no.3, pp. 917-927
2. Dhamala, E. (2021), "Distinct functional and structural connections predict crystallised and fluid cognition in healthy adults", Human Brain Mapping, vol. 42, no. 10, pp. 3102-3118
3. Tetereva, A. (2022), "Capturing brain-cognition relationship: Integrating task-based fMRI across tasks markedly boosts prediction and test-retest reliability", NeuroImage, vol. 263
4. Saxe, R. (2006), "Divide and Conquer: A defense of functional localizers", NeuroImage, vol. 30, no. 4, pp. 1088-1096
5. Druzgal, T.J. (2003), "Dissecting Contributions of Prefrontal Cortex and Fusiform Face Area to Face Working Memory", Journal of Cognitive Neuroscience, vol.15, no. 6, pp. 771-784
6. Schaefer, A. (2018), "Local-Global Parcellation of the Human Cerebral Cortex from Intrinsic Functional Connectivity MRI", Cerebral Cortex, vol. 28, no.9, pp. 3095-3114

Poster No 1125

Task-Dependent Reconfiguration of Global Functional Connectivity and Complexity

Maren Wehrheim[1], Joshua Faskowitz[2], Christian Fiebach[1]

[1]Goethe University Frankfurt, Frankfurt am Main, Hesse, [2]Indiana University Bloomington, Bloomington, IN

Introduction: Brain activity continuously fluctuates over time, even if the brain is in controlled (e.g., experimentally induced) states. Recent years have seen an increasing interest in understanding the complexity of these temporal variations, particularly also with respect to between-person differences in brain function. Here, we study how the variability and complexity of task-elicited BOLD activation, as well as global functional network properties, adjust to increasing cognitive demands and how these dynamic reconfigurations relate to individual differences in task performance.

Methods: We use data from the Human Connectome Project (van Essen et al., 2013) from the working memory task (N-back). We select a subset of unrelated low-motion individuals (see Ito et al., 2020) for whom complete scan protocols were available (N=330). We compute time-resolved global functional connectivity across the complete scan following Esfhalani et al. (2020). We then measure the temporal variability of global connectivity (standard deviation and mean squared successive difference) within each task block. Additionally, we measure the complexity of the BOLD activation time series as the extrinsic (linear) dimensionality and intrinsic (non-linear) dimensionality of the signal within each block. To determine reliability of the derived measures of neural variability and complexity used in the present study, we compute reliability across consecutive runs (within-session Spearman-Brown-corrected split-half correlations).

Results: As cognitive load increases, brain-wide functional connectivity is reduced (global functional decoupling). While this result may appear unexpected at first glance (under the assumption that higher cognitive load requires increased functional integration), we observed that load-dependent functional decoupling is directly associated with an increase in complexity (non-linear dimensionality) of the BOLD signal across all brain networks, reflecting a fundamental reconfiguration of the whole functional connectome. Both components of reconfiguration, functional decoupling and dimensionality increase, are directly associated ($r = -.77$) and directly behaviorally relevant, as indicated by significant across-participant correlations with working memory performance ($r = .29$ and $r = -.24$, respectively). Thus, better performance goes hand in hand with greater functional decoupling and increased network complexity. We furthermore observed that functional decoupling evolves over the course of task blocks and that better performance is associated with less variable connectivity dynamics over the course of the task ($r = -.26$). Lastly, we demonstrate that intrinsic BOLD dimensionality and the variability of global functional connectivity strength have good split-half reliability ($r > .76$), thus supporting the use as robust markers of individual differences at the neuro-functional level.

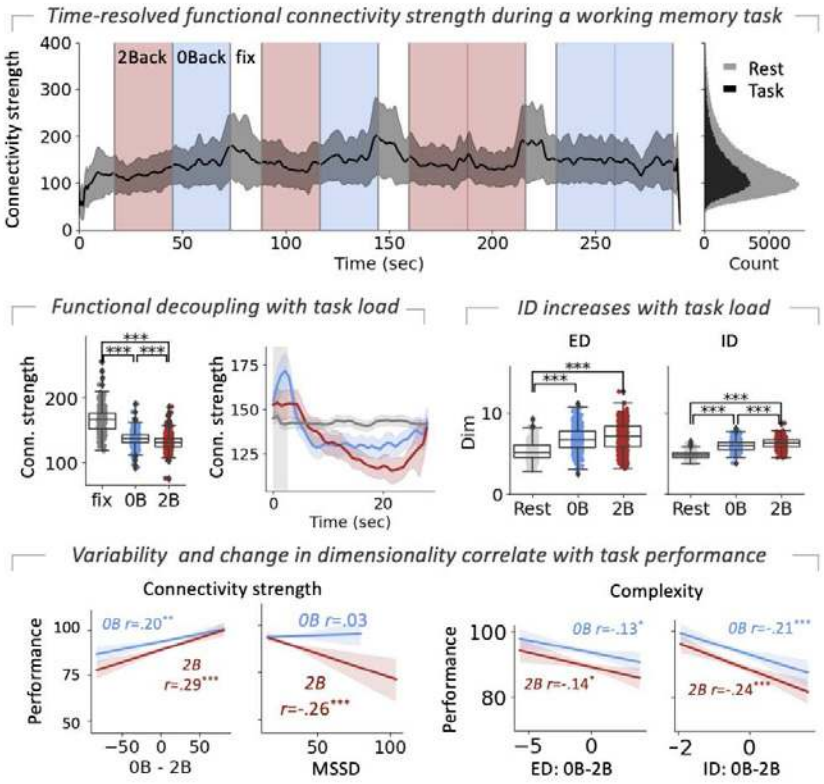

Conclusions: Our results demonstrate the dynamic reconfiguration of brain networks in response to varying cognitive task demands. Whereas previous literature showed heterogeneous results with respect to how functional connectivity is adjusted under increasing working memory demands, our results indicate that global connectivity is reduced because the brain is reconfigured dynamically in a task-dependent manner. Interestingly, reconfiguration is on the one hand more pronounced in persons with better working memory performance (and thus 'more dynamic'), while at the same time more consistent (i.e., less variable over time). More generally, our results demonstrate that variability and complexity in the brain are reliable measures with high behavioral relevance, which will contribute important insights into understanding the nature of individual differences in cognitive abilities.

References

1. Esfahlani, Z. F., Jo, Y., Faskowitz, J., Byrge, L., Kennedy, D. P., Sporns, O., & Betzel, R. F. (2020). High-amplitude cofluctuations in cortical activity drive functional connectivity. Proceedings of the National Academy of Sciences, 117(45), 28393-28401.
2. Ito, T., Brincat, S. L., Siegel, M., Mill, R. D., He, B. J., Miller, E. K., ... & Cole, M. W. (2020). Task-evoked activity quenches neural correlations and variability across cortical areas. PLoS computational biology, 16(8), e1007983.
3. Van Essen, D. C., Smith, S. M., Barch, D. M., Behrens, T. E., Yacoub, E., Ugurbil, K., & Wu-Minn HCP Consortium. (2013). The WU-Minn human connectome project: an overview. Neuroimage, 80, 62-79.

Poster No 1126

Neuroanatomical basis of working memory in fibromyalgia and the moderating influence of depression

Irene Peláez[1], Ana Belén del Pino[1], María Luisa Fernández[1], María Eugenia de la Hoz[1], Diego Galán[1], Dino Soldic[1]

[1]Rey Juan Carlos University, Madrid, Spain

Introduction: Fibromyalgia (FM) is a chronic pain syndrome characterized by persistent chronic pain, fatigue, sleep problems, anxiety, depression and cognitive impairments in various domains. In particular, poor working memory performance has been consistently observed in patients with FM compared to healthy control subjects (HC). This dysfunction has been specifically linked to the abnormal functioning of frontoparietal networks. However, studies investigating brain morphology have yielded inconclusive results, with contradictory evidence emerging regarding potential differences between individuals with FM and HC. With this in mind, the main of this research was to investigate potential differences in brain volume within frontoparietal regions between patients with FM and HC, examining their relationship with performance in working memory tasks. In addition, the study analyzed depression and anxiety levels as potential modulating variables between working memory task

performance and brain volume, given that elevated levels of these socio-affective variables have previously been associated with cognitive impairment.

Methods: The study included 30 patients with FM and 27 HC. Voxel-Based Morphometry analyses were used to examine brain morphology, and working memory was assessed using various neuropsychological tests from the WAIS-III and WMS-III scales. Psychological variables, including depression and anxiety, were also measured.

Results: As expected, FM patients demonstrated lower scores in arithmetic, letter-number sequencing, and the working memory index. However, no significant differences in grey matter volume were observed between the two groups. Simple regression analyses between brain volume and neuropsychological tests revealed that, in the HC group, lower brain volume in the studied areas was associated with poorer performance in most working memory tests. Conversely, in the FM group, a minimal relationship was observed between these two variables, and the few significant effects that emerged were contradictory. Moderation analyses revealed that, in the FM group, depression affected the relationship between brain volume and performance on working memory tests, while anxiety did not yield significant results.

Conclusions: These results offer valuable insights into the intricate relationship between working memory deficits in FM, their neural substrate, and the moderating effect of socio-affective variables such as depression. This information could contribute to the development of intervention strategies better tailored to this patient population. This research was funded by the project PID2020-115463RB-I00; 2021-2025 of the Ministry of Science and Culture and from the Rey Juan Carlos University: A515 'Proyectos Impulso' young PhD researchers–URJC–INEMODOL2023.

References

1. Castel, A., Cascón-Pereira, R., & Boada, S. (2021). Memory complaints and cognitive performance in fibromyalgia and chronic pain: The key role of depression. Scandinavian Journal of Psychology, 62(3), 328–338.
2. Luerding, R., Weigand, T., Bogdahn, U., & Schmidt-Wilcke, T. (2008). Working memory performance is correlated with local brain morphology in the medial frontal and anterior cingulate cortex in fibromyalgia patients: structural correlates of pain–cognition interaction. Brain, 131(12), 3222–3231.
3. Seo, J., Kim, S.-H., Kim, Y.-T., Song, H., Lee, J., Kim, S.-H., Han, S. W., Nam, E. J., Kim, S.-K., Lee, H. J., Lee, S.-J., & Chang, Y. (2012). Working Memory Impairment in Fibromyalgia Patients Associated with Altered Frontoparietal Memory Network. PLoS ONE, 7(6), 1–10.

Poster No 1127

Neural correlates of auditory working memory precision: an intracranial EEG study

Joel Berger[1], Alexander Billig[2], Phillip Gander[3], Meher Lad[4], Sukhbinder Kumar[5], Kirill Nourski[1], Christopher Kovach[6], Ariane Rhone[1], Christopher Garcia[5], Hiroto Kawasaki[1], Brian Dlouhy[5], Matthew Howard[1], Timothy Griffiths[4]

[1]The University of Iowa, Iowa City, IA, [2]University College London, London, United Kingdom, [3]University of Iowa, Iowa City, IA, [4]Biosciences Institute, Newcastle, United Kingdom, [5]University of Iowa, IOWA CITY, IA, [6]University of Nebraska, Omaha, NE

Introduction: Working memory is the capacity to hold and manipulate behaviorally relevant information in mind in the absence of ongoing sensory input. Utilizing intracranial EEG in a recent paper (Kumar et al., 2021), we demonstrated oscillatory correlates of auditory working memory (AWM) during maintenance of a tone in various structures, including the hippocampus. Here, we extend this work further by developing a paradigm that accounts for a precision model of working memory, allowing for measurement of error on a single trial basis and enabling a clear distinction of the retrieval period from the maintenance period, whilst simultaneously recording single units and local field potentials (LFPs).

Methods: We simultaneously recorded behavioral responses to the task and LFPs from the hippocampi of five human subjects undergoing invasive monitoring for presurgical localization of epileptic foci [wherein the hippocampus was subsequently found to be not a seizure focus]; in three patients, single units were also recorded in the hippocampus and Heschl's gyrus. For the AWM task (Figure 1), participants were presented with a short tone, followed by a 3-second retention period. They were instructed that they then had 5 seconds to alter a repeated tone to match it as close in frequency as they could to the target tone ("tuning/retrieval" period), for a total of 60 trials. We carried out time-frequency analysis using wavelet transforms for the LFP data, whilst single units were isolated with an automated spike sorting procedure and examined with trial raster plots and peri-stimulus time histograms. Behaviorally, working memory precision was calculated as the reciprocal of the standard deviation of response error.

Results: Patients performed the task similarly to previously observed non-epileptic populations. Across all hippocampal contacts, we observed low frequency activity (< 8 Hz) that was persistent throughout the retention period and was particularly striking at the onset of the tuning period, as well as following the offset of this period, concurrent with high gamma suppression (70-150 Hz). Trials were concluded with a significant desynchronization of theta-alpha (4-15 Hz) hippocampal activity (for all time-frequency data, see Figure 2). In two patients with simultaneous HG and hippocampus contacts, we additionally observed an increase in phase locking between the two regions at the onset of the retention period and the offset of the retrieval period. Clear single unit modulation was evident at various phases of the task in HG and hippocampus. In hippocampus, this modulation most commonly manifested as suppression.

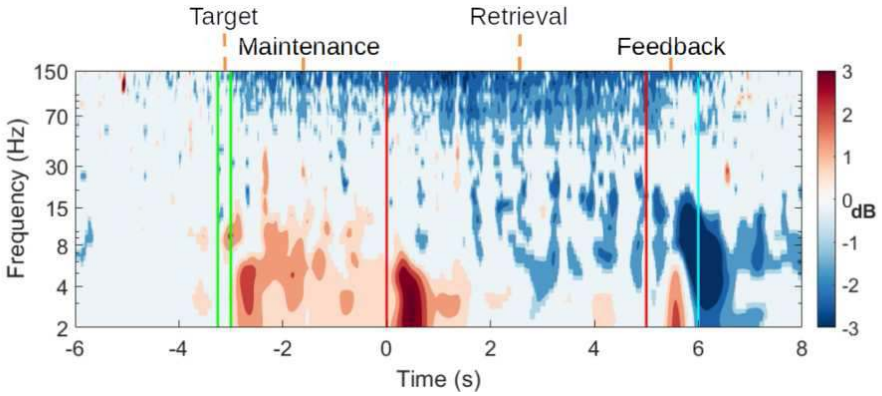

Conclusions: Overall, these data highlight neural correlates of precision of AWM and implicate the hippocampus in maintenance, retrieval and response monitoring of non-verbal AWM. The combined LFP and single unit data enable development of a model of AWM involving the hippocampus communicating to auditory cortex at various key phases.

References

1. Kumar, S.K. (2021), Oscillatory correlates of auditory working memory examined with human electrocorticography. Neuropsychologia, 150, 107691.

Poster No 1128

A brain multilayer approach to predicting cognitive decline in healthy aging

Barbara Avelar Pereira[1], Lars Bäckman[1]

[1]Karolinska Institutet, Stockholm, Stockholm

Introduction: Aging is characterized by decline in cognition. Still, individuals do not age in the same way[1]. There are large inter-individual differences in onset and rate of cognitive decline. Longitudinal research typically focuses on pathological aging, such as in Alzheimer's disease (AD). Little emphasis is given to the cognitive heterogeneity that exists in healthy older individuals or to the fact that most processes linked to normal aging, such as atrophy or inflammation, are also present in pathological aging[2]. This suggests that understanding age-related brain pathology and cognitive deficits first requires understanding brain and cognitive decline in healthy aging. Neuroimaging techniques have, individually or in conjunction with others, been shown to predict cognitive decline to different extents and at different stages of development[3]. However, most studies combining more than one modality typically report results in parallel or compare normalized findings but do not analyze data simultaneously.

Methods: We tested a multi-dimensional network framework, which aggregates data across three brain modalities into a single model capable of capturing heterogeneity in cognitive aging. For this, we used the Cognition, Brain, and Aging (COBRA) study, a large-scale cohort of 181 healthy older adults (age 64-68 at baseline; 44.8% females) followed over 10 years. There are 3 waves, separated by 5 years, and participants go through MRI (structural and functional) and PET (dopamine D2) at each wave. There is also a full cognitive battery, lifestyle, health, and genetics information. The multilayer model included three modalities (i.e., layers): (1) functional connectivity, (2) grey-matter estimates, and (3) dopamine (DA). All data underwent mean centering, regressing out covariates (e.g., age, sex, intracranial volume), and normalization. These data were used to create a subject similarity network, with nodes representing individuals and edges representing similarities between them using pairwise correlations. Finally, a multi-dimensional network framework (i.e., a multilayer network) was constructed (Fig 1). Several metrics can be derived, but the main outcome was modularity since it captures strength of network partition, which is derived using an iterative generalized Louvain community detection algorithm optimized for multilayer frameworks based on the work by Mucha et al. 2010.

Results: We postulated that, by detecting common as well as complementary signals across modalities and minimizing the effect of different scales and noise, the multilayer network would provide insights into the development and progression of cognitive decline. We have previously applied this methodology to 490 individuals at risk for AD and shown that the model can distinguish cognitively normal (CN) from AD participants (Fig 2A). The method is data driven and blind to the label of each participant (i.e., CN or AD), but these labels are still created with information included in the model[5]. As such, it remained unclear how well the network performs on a healthy sample with a comprehensive brain imaging and cognitive battery not tailored to detect a specific kind of dementia. Our framework identified groups with distinct cognitive profiles (Fig 2B). The groups differed in working memory (t(150.2)=-2.3, p=0.011) and the group with better scores also had higher white-matter integrity (t(165)=-2.8, p=0.003). There were no differences in episodic memory (p=0.445), but the group with better working memory performance and higher fractional anisotropy also had marginally better processing speed (p=0.09).

Conclusions: A full understanding of cognitive aging warrants the inclusion of interactions within and between modalities. Multimodal biomarkers seem to be good predictors of cognition in healthy aging and correlate with other estimates of brain integrity. Gray matter, functional connectivity, and DA can provide unique insights when investigating differences in healthy populations.

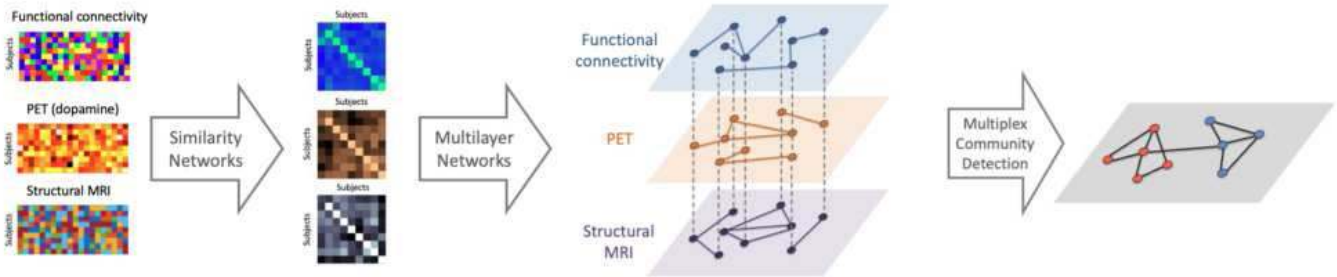

Figure 1. Multilayer framework. The 1st column displays all modalities included in the multilayer network (subjects x features, e.g., functional connectivity within and between brain regions), while the 2nd shows the corresponding similarity networks. In the 3rd column the multilayer network is displayed, with diamonds representing layers and solid and dotted lines representing intralayer and interlayer interactions, respectively. Nodes are connected across and within layers. The last column exemplifies multilayer community detection, with two communities identified.

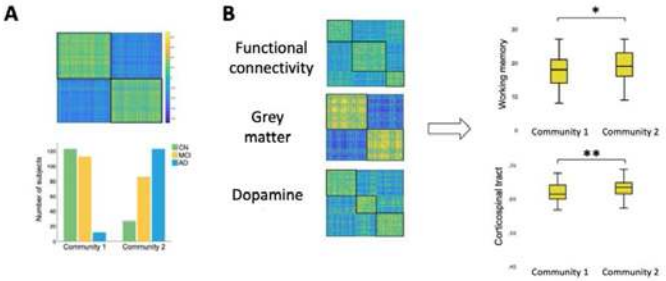

Figure 2. (a) Multilayer communities and distribution for each diagnosis. Community 1 is mostly made up of CN and community 2 of AD participants. The matrix represents the similarity between subjects across features using pairwise correlations. **(b)** Individual layers for functional connectivity, gray matter, and DA used to compute the multilayer analysis. Boxplots show working memory and white matter differences in the resulting communities.

References
1. Cabeza, R. et al. (2018). 'Maintenance, reserve and compensation: the cognitive neuroscience of healthy ageing'. Nature Reviews Neuroscience, 19(11), 701-710.
2. Jagust, W. (2013). 'Vulnerable neural systems and the borderland of brain aging and neurodegeneration'. Neuron, 77(2), 219-234.
3. Nyberg, L. et al. (2020). 'Biological and environmental predictors of heterogeneity in neurocognitive ageing: Evidence from Betula and other longitudinal studies'. Ageing research reviews, 64, p.101184.
4. Mucha, P. J. et al. (2010). 'Community structure in time-dependent, multiscale, and multiplex networks'. Science, 328(5980), 876-878.
5. Avelar-Pereira, B., et al. (2022). Decoding the heterogeneity of Alzheimer's disease diagnosis and progression using multilayer networks. Molecular Psychiatry, 1-10.

Poster No 1129

Association Between Body Mass Index and Brain Aging in Adults: A 16-Year Population-Based Cohort

Han Lv[1]

[1]Beijing Friendship Hospital, Capital Medical University, Beijing, Beijing

Introduction: High body mass index (BMI), a modifiable factor associated with poor cardiovascular health, is linked to brain health, but the causal relationship between BMI and brain health remains unclear. This study aimed to demonstrate the effect of cumulative BMI on neuroimaging features in adults of different ages and verify the causal relationship.

Methods: This study was based on the KaiLuan Study, a multicenter, long-term follow-up, community-based longitudinal cohort study of the adult population that began in 2006. The study included participants who visited the hospital at least 3 times and underwent brain MRI examination, with no evidence of dementia or mental disorders. Exclusion criteria were incomplete or poor-quality neuroimaging data and diagnosed cancer. We modeled the trajectories of BMI over 16 years to evaluate cumulative exposure. Multimodality neuroimaging data were collected using 3.0-T MRI, starting in 2020, for volumetric measurements of the brain structure, white matter hyperintensity (WMH), and skeletonized white matter tract at the voxel level. We performed two-sample Mendelian randomization analysis using genetic data from 681,275 individuals to analyze the causal relationship between BMI and neuroimaging features.

Results: In the population-based longitudinal study, clinical and neuroimaging data were obtained from 1,074 adults (aged 25–83 years). High BMI was associated with a wide range of negative brain health effects. For adults aged under 45 years, the differences in cerebral parenchyma volume between those with BMI > 26.2 kg/m2 and those with normal BMI corresponded to 12.0 years (95% confidence interval [CI], 3.0 to 20.0) of brain aging. The volumetric results corresponded to -17.9 ml (95% CI, -29.8 to -4.5). Differences in WMH were statistically significant for participants aged over 60 years, with a 6.0-ml (95% CI, 1.5 to 10.5) larger volume. Genetic analysis of 681,275 individuals indicated causal relationships among high BMI, smaller volume of the cerebral parenchyma and gray matter, and higher fractional anisotropy in projection fibers.

Conclusions: High BMI is causally associated with smaller brain volume and abnormal microstructural integrity in projection fibers, especially in young adults. These findings provide a basis for future brain health promotion and disease prevention strategies.

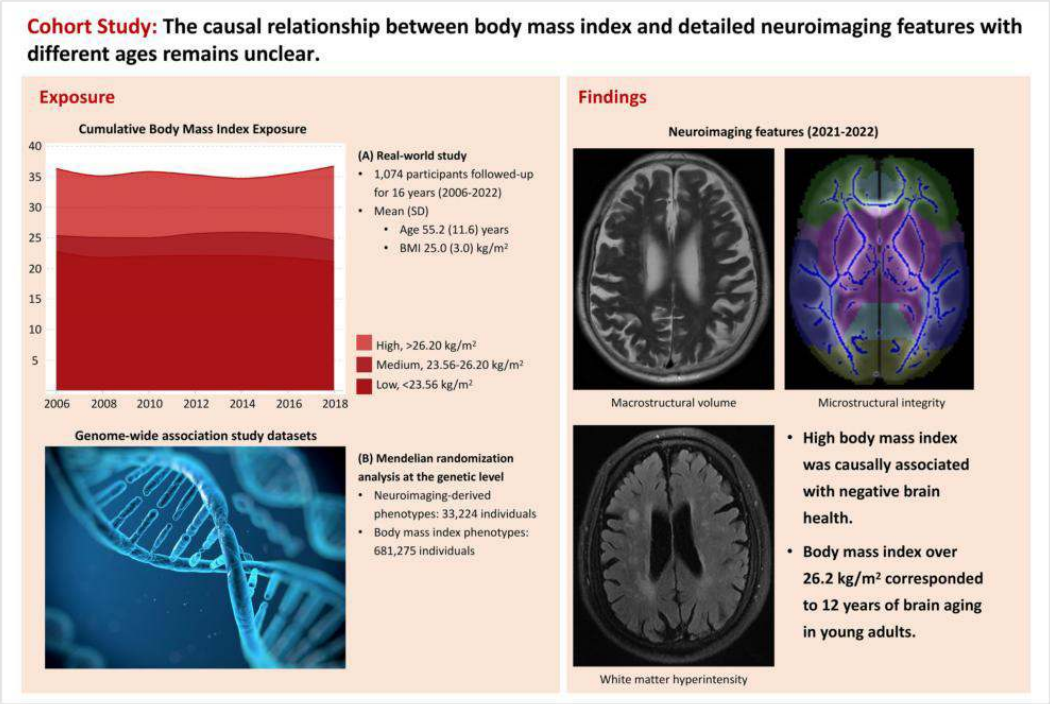

References

1. Smith, S.M. (2021), 'An expanded set of genome-wide association studies of brain imaging phenotypes in UK Biobank', Nature Neuroscience, vol. 24, no.5, pp. 737-745
2. Verbanck, M. (2018), 'Detection of widespread horizontal pleiotropy in causal relationships inferred from Mendelian randomization between complex traits and diseases'. Nature Genetics, vol. 50, no.5. pp. 693-698
3. Han, Y.P. (2021). 'Relationship between obesity and structural brain abnormality: Accumulated evidence from observational studies'. Ageing Research Reviews, vol. 71. pp. 101445

Poster No 1130

Dementia Risk Scores are significantly associated with GABA+, but not Glx, or Impulse Control

Jacob Levenstein[1], Ciara Treacy[1], Sophie Andrews[1]

[1]Thompson Institute, University of the Sunshine Coast, Birtinya, QLD

Introduction: Dementia is a neurodegenerative disease with a terminal trajectory, characterized by a complex symptomatology, including impaired memory, behavioral changes, and progressive functional decline. A Dementia risk score (DRS) quantifies an individual's risk of developing dementia, based on protective and detrimental risk-factors. Further, DRSs can be utilized to examine the neurophysiological pathogenesis of dementia risk. Recent review articles have highlighted the potential role of glutamatergic and GABAergic systems underpinning dementia etiology[1,2]. Here, we investigate whether neurochemical concentrations are associated with DRSs in an aging population without a dementia diagnosis. We aim to measure neurochemical concentrations in relation to modifiable risk factors, which have been shown to account for ~40% of dementias world-wide[3]. We hypothesize that individuals with greater DRSs will have lower GABA+ and Glx (after controlling for age and education). A secondary question explores whether behavioral measures of response inhibition relate to dementia risk and or neurochemicals. We hypothesize that individuals with worse inhibitory control will have greater DRSs, greater Glx and lower GABA+.

Methods: This study was approved by UniSC's Human Research Ethics Committee (S211620) and all participants provided informed consent. To date, 78 healthy older adults aged 50-85 completed this study. After reviewing quality metrics and model fits of the MRS data, 62 participants were included in the final cohort (31f, 67.7M-age,+/-10.01). DRSs were computed using the CogDrisk assessment[4], based on 17 modifiable and non-modifiable risk factors. All participants completed an MRI brain scan at the Thompson Institute, via a 3T Skyra (Siemens, Erlangen Germany). In brief, a T1-weighted structural scan (MPRAGE) was acquired and used for placement of the MRS volume of interest (VOI). Two single-voxel MR spectroscopy (MRS) scans were acquired using a Hadamard Encoding and Reconstruction of MEGA-Edited Spectroscopy sequence (HERMES,[5]; VOI=3cm^3, TR=2000ms, TE=80ms, flip angle=90°, averages=320, TA=10:48). MRS was acquired in the left sensorimotor cortex

(M1) and left prefrontal cortex. MRS data was analyzed using OSPREY's standard processing and fitting pipeline (v.2.4.0,[6]). Only the M1 GABA+ and Glx results are presented here, with each expressed as a ratio of creatine and phosphocreatine (tCr). A suite of behavioral tasks were collected to probe inhibitory control, attention, and cognition. Presented here are the error rate results from the Go-NoGo task administered using PsyToolKit[7] and analyzed with in-house scripts. Hierarchical linear regression was performed using SPSS (v.29.0,[8]). For all models, age and education were entered in step 1, with step 2 containing the regressor of interest.

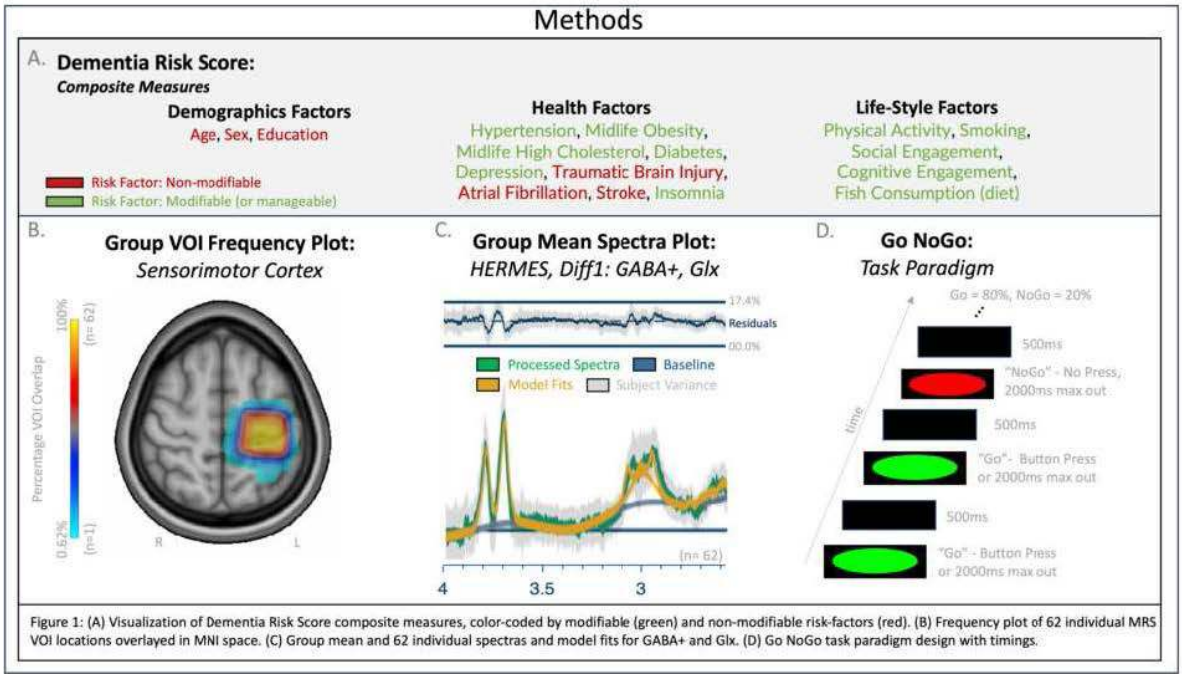

Figure 1: (A) Visualization of Dementia Risk Score composite measures, color-coded by modifiable (green) and non-modifiable risk-factors (red). (B) Frequency plot of 62 individual MRS VOI locations overlayed in MNI space. (C) Group mean and 62 individual spectras and model fits for GABA+ and Glx. (D) Go NoGo task paradigm design with timings.

Results: Hierarchical linear regression revealed that dementia risk scores were significantly associated with age, education and M1 GABA+ ($F(3,58)=20.41, p<0.001, R^2=0.514$). After controlling for age and education, GABA+ remained a significant predictor of dementia risk ($ß=-0.258, t=-2.80, p=0.007, R^2=0.119$). Age nor education were significantly correlated with GABA+ concentrations (ps. ≥ 0.31). For both Glx and Error Rate, neither were significantly associated with dementia risk, with or without controlling for age and education (ps. ≥ 0.49). Finally, Glx, but not GABA+, was significantly associated with Error Rate from the Go NoGo task ($β=-0.349, t=-2.76, p=0.008, R^2=0.118$).

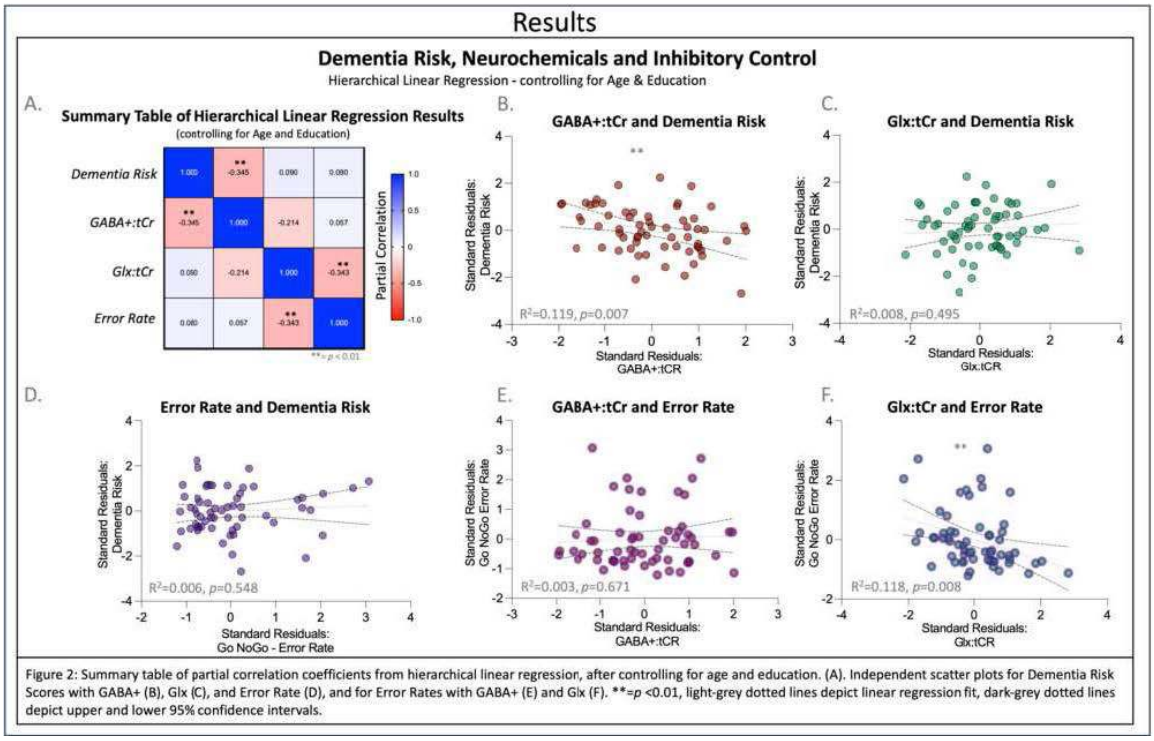

Figure 2: Summary table of partial correlation coefficients from hierarchical linear regressior, after controlling for age and education. (A). Independent scatter plots for Dementia Risk Scores with GABA+ (B), Glx (C), and Error Rate (D), and for Error Rates with GABA+ (E) and Glx (F). **=p <0.01, light-grey dotted lines depict linear regression fit, dark-grey dotted lines depict upper and lower 95% confidence intervals.

Conclusions: These results demonstrate that M1 GABA+ concentrations were significantly associated with dementia risk scores. No relationship was identified between Glx and dementia risk, suggesting that the GABAergic system at M1 may provide unique insight into the pathophysiology of modifiable dementia risk in healthy aging. To determine the mechanism(s) underpinning this relationship, further analysis of MRS VOIs, metabolites, and an evaluation of unique measures of modifiable risk factors are required.

References

1. Benussi, A., Alberici, A., Buratti, E., Ghidoni, R., Gardoni, F., Di Luca, M., ... & Borroni, B. (2019). Toward a glutamate hypothesis of frontotemporal dementia. Frontiers in neuroscience, 13, 304.
2. Calvo-Flores Guzmán, B., Vinnakota, C., Govindpani, K., Waldvogel, H. J., Faull, R. L., & Kwakowsky, A. (2018). The GABAergic system as a therapeutic target for Alzheimer's disease. Journal of neurochemistry, 146(6), 649-669.
3. Livingston, G., Huntley, J., Sommerlad, A., Ames, D., Ballard, C., Banerjee, S., ... & Mukadam, N. (2020). Dementia prevention, intervention, and care: 2020 report of the Lancet Commission. The Lancet, 396(10248), 413-446.
4. Anstey, K. J., Kootar, S., Huque, M. H., Eramudugolla, R., & Peters, R. (2022). Development of the CogDrisk tool to assess risk factors for dementia. Alzheimer's & Dementia: Diagnosis, Assessment & Disease Monitoring, 14(1), e12336
5. Saleh, M. G., Oeltzschner, G., Chan, K. L., Puts, N. A., Mikkelsen, M., Schär, M., ... & Edden, R. A. (2016). Simultaneous edited MRS of GABA and glutathione. Neuroimage, 142, 576-582.
6. Oeltzschner, G., Zöllner, H. J., Hui, S. C., Mikkelsen, M., Saleh, M. G., Tapper, S., & Edden, R. A. (2020). Osprey: Open-source processing, reconstruction & estimation of magnetic resonance spectroscopy data. Journal of neuroscience methods, 343, 108827.
7. Stoet, G. (2017). PsyToolkit: A novel web-based method for running online questionnaires and reaction-time experiments. Teaching of Psychology, 44(1), 24-31.
8. IBM Corp. Released 2022. IBM SPSS Statistics for Windows, Version 29.0. Armonk, NY: IBM Corp

Poster No 1131

Does functional system segregation mediate the effects of lifestyle on cognition in older adults?

Petar Raykov[1], Ethan Knights[1], Richard Henson[1]

[1]MRC Cognition and Brain Sciences Unit, Cambridge, United Kingdom

Introduction: Healthy aging is typically accompanied by cognitive decline (Nyberg et al., 2003). Previous work has shown that engaging in multiple, non-work activities during midlife can have a protective effect on cognition several decades later, rendering it less dependent on brain structural health; the definition of "cognitive reserve" (D. Chan et al., 2018; Gow et al., 2017). Other work has shown that increasing age is associated with reduced segregation of large-scale brain functional networks (M. Chan et al., 2021; Wig, 2017). Here we tested the hypothesis that functional segregation mediates this effect of middle-aged lifestyle on late-life cognition.

Methods: We used fMRI data acquired during three different brain states (tasks) in the CamCAN dataset (www.cam-can.org), together with cognitive data on fluid intelligence and episodic memory and retrospective lifestyle data from the Lifetime of Experiences Questionnaire (LEQ). We computed functional system segregation (SyS) as the difference between within network connectivity compared to between network connectivity. We ran regression models to examine whether SyS measures predict cognition after adjusting for linear and non-linear age and sex effects. We additionally ran mediation models examining how previous midlife activities (during ages of 30-64 years) affected SyS and cognition in late-life (65+ years old).

Results: In all three tasks, we replicated the negative association between adult age and functional segregation, and showed that functional segregation related to fluid intelligence even after adjusting for the (nonlinear) age effects. However, we found no evidence that functional segregation in late-life mediated the relationship between non-specific (non-occupation) midlife activities from the LEQ and either measure of cognition in late-life. In exploratory analyses, we also failed to find evidence that functional segregation in late-life related to youth-specific LEQ activities (i.e., education), or that functional segregation in mid-life related to current non-specific LEQ activities. These results were largely robust to use of different brain parcellations and pre-processing strategies. We tested how different pre-processing strategies affect measures of functional system segregation and its relation to fluid intelligence.

Conclusions: Our results confirm that measures of functional system segregation may be indicative of cognition. We did not find evidence that functional segregation mediated the effects non-specific midlife activities have on late life cognition. Thus, the brain correlates of cognitive reserve arising from mid-life activities remain to be discovered.

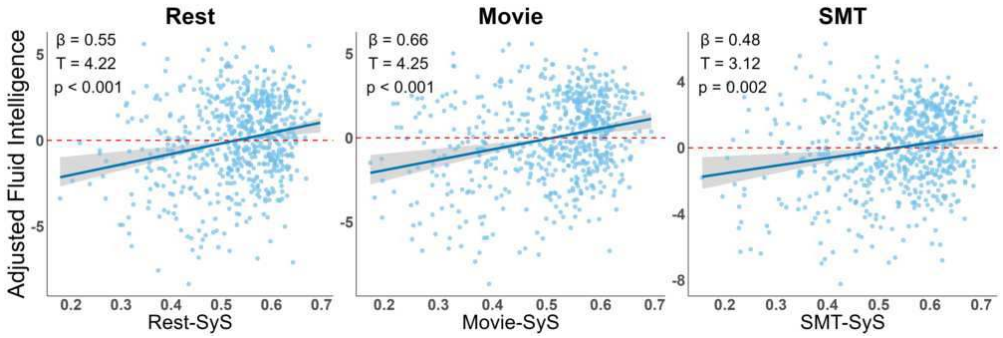

Predicting Fluid Intelligence from SyS (N=627). Fluid intelligence was positively related to SyS in each of the three brain states, after adjusting for second-order effects of age, and sex.

References

1. Chan, D., Shafto, M., Kievit, R., Matthews, F., Spink, M., Valenzuela, M., & Henson, R. N. (2018). Lifestyle activities in mid-life contribute to cognitive reserve in late-life, independent of education, occupation, and late-life activities. Neurobiology of Aging, 70, 180–183. https://doi.org/https://doi.org/10.1016/j.neurobiolaging.2018.06.012
2. Chan, M. Y., Han, L., Carreno, C. A., Zhang, Z., Rodriguez, R. M., LaRose, M., Hassenstab, J., & Wig, G. S. (2021). Long-term prognosis and educational determinants of brain network decline in older adult individuals. Nature Aging, 1(11), 1053–1067
3. Gow, A. J., Pattie, A., & Deary, I. J. (2017). Lifecourse Activity Participation From Early, Mid, and Later Adulthood as Determinants of Cognitive Aging: The Lothian Birth Cohort 1921. The Journals of Gerontology: Series B, 72(1), 25–37. https://doi.org/10.1093/geronb/gbw124
4. Nyberg, L., Maitland, S. B., Rönnlund, M., Bäckman, L., Dixon, R. A., Wahlin, Å., & Nilsson, L.-G. (2003). Selective adult age differences in an age-invariant multifactor model of declarative memory. Psychology and Aging, 18(1), 149.
5. Wig, G. S. (2017). Segregated systems of human brain networks. Trends in Cognitive Sciences, 21(12), 981–996.

Poster No 1132

Age-related differences in control energy of brain state transitions

Vibin Parakkattu[1], Lorenzo Lorenzo-Luaces[1], Youngheun Jo[1], Joshua Faskowitz[1], Alina Podschun[2], Sebastian Markett[2], Richard Betzel[1]

[1]Indiana University, Bloomington, IN, [2]Humboldt-Universität zu Berlin, Berlin, Berlin, Germany

Introduction: The brain's physical wiring – the connectome – shapes ongoing patterns of activity, tracing out a trajectory over time through a high-dimensional space (Parkes et al., 2023). Recent work has leveraged network control theory to understand how control inputs can be delivered to the brain to alter its dynamic trajectory to traverse a desired set of brain states (Cornblath et al., 2020). Control theory provides a useful measure for quantifying the effort needed to move from one brain state to another – the so-called "control energy" (Pasqualetti et al., 2014). Here, we study a lifespan dataset to understand how control energy varies across the human lifespan.

Methods: We studied the Nathan Kline Institute, Rockland Sample dataset (https://fcon_1000.projects.nitrc.org/indi/enhanced/; Nooner et al., 2012). We focused on N = 458 participants (ages 7-85 years) with high-quality and low-motion functional and diffusion MRI data. For each participant, we reconstructed a subject-specific connectome (Tournier et al., 2019) and processed the resting-state fMRI using fMRIprep (Esteban et al., 2019). To estimate brain states, we identified local peaks in the amplitude of brain-wide activity (root mean square) and extracted whole-brain activation patterns during those instants. We repeated this procedure for all participants. We then aggregated across participants and clustered them using the k-means algorithm (correlation distance and number of clusters, k = 6). For each subject, each frame (from trough to trough on either side of a given peak) was then labelled as belonging to 1 of 6 brain states. Network control theory enables us to estimate the "effort" associated with state transitions. With this framework, we then calculated, using subjects' own connectomes, the energies necessary to transition between every pair of states. We calculated the correlation of these energies with age after regressing out biological sex, intracranial volume, number of usable (low-motion) frames, as well as residual motion.

Results: We found that the k=6 clusters corresponded to three pairs; each pair consisted of an activation pattern and its near-perfect anti-correlate (Fig. 1a & b). Clusters 1 and 2 corresponded to activation/deactivation of the visual and dorsal attention networks; clusters 3 and 4 correspond to activation/deactivation of default mode with salience/ventral attention networks; clusters 5 and 6 correspond to activation/deactivation of somatomotor and visual networks with the control network (Fig. 1c). We found that, on average, control energy was greatest when transitioning between paired patterns (Fig. 1d) and, more generally, was anticorrelated with the spatial similarity of activation patterns (r = -0.93; Fig. 1e). Further, we found

heterogeneity across control sites – regions/nodes where control signal was “injected” – in terms of their regional control energies. When considering all possible transitions, we found evidence of three broad clusters, each corresponding to a different brain-wide pattern of regional control energy. These patterns were closely aligned with target states and, again, were grouped by pairs. Finally, we showed that both regional and whole-brain control energies were correlated with age (Fig 2a). In particular, control energy associated with transitioning from states 3 and 4 into 2 and 1, respectively, decreased significantly with age after regressing out covariates (r = -0.24, p < 10^-8; Fig. 2b & c). Relatedly, we found evidence of distinct regional differences in control energy with age. Broadly, these changes implicated sensorimotor systems-e.g. visual, somatomotor, and dorsal attention networks (Fig 2d & e).

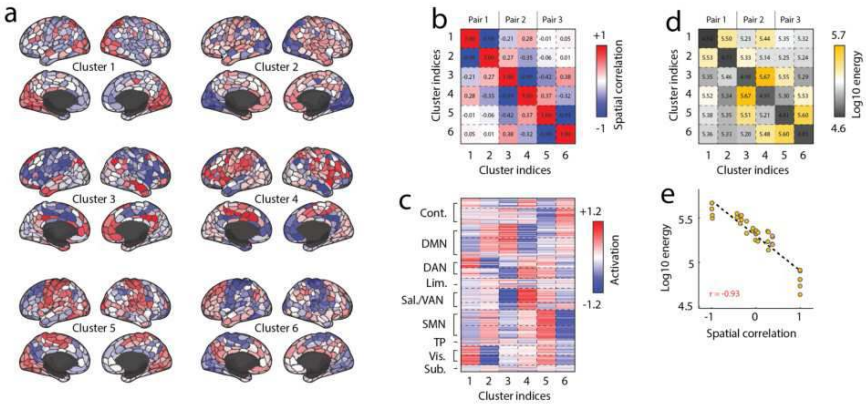

Figure 1: (a) k-means clustering algorithm produced 6 clusters, 3 pairs of near-perfect anti-correlates. (b) Spatial correlation grid for every cluster pair, indicating the three anti-correlated pairs: clusters 1 and 2, clusters 3 and 4, and clusters 5 and 6. (c) Clusters 1 and 2 correspond to activation/deactivation of the visual and dorsal attention networks. Clusters 3 and 4 correspond to activation/deactivation of the default mode with salience/ventral attention networks. Clusters 5 and 6 correspond to activation/deactivation of somatomotor and visual networks with the control network. (d) Grid indicating log of the control energy required to transition between every cluster pair, indicating highest values for energy transitions within anti-correlated cluster pairs. (e) The greater the spatial correlation between the two clusters, the lower the log of the control energy required to transition between those two clusters (r = -0.93).

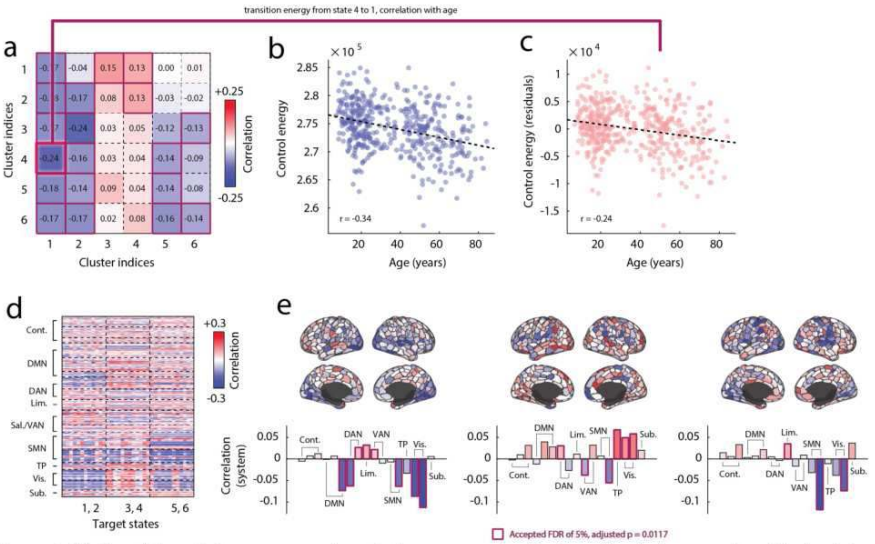

Figure 2: (a) Correlations between age and control energy required to transition between pairs of brain states. FDR-corrected statistically significant correlations highlighted with maroon border. (b) Representative correlation between age and control energy required to transition from Cluster 4 to Cluster 1. (c) Representative significant correlation between age and control energy required to transition from Cluster 4 to Cluster 1, adjusted for the effects of biological sex, intracranial volume, number of usable (low-motion) frames, as well as residual motion, after FDR correction. (d) Correlation between age and the control energy required to transition to the three paired clusters of target states (organized by functional network). (e) As age increased, transitions to Clusters 1 and 2 exhibited statistically significant decreases in activity in the default mode, dorsal attention, somatomotor, and visual networks as well as statistically significant increases in activity in the dorsal attention, limbic, and salience/ventral attention networks. As age increased, transitions to Clusters 2 and 3 exhibited statistically significant decreases in activity in the salience/ventral attention and somatomotor networks as well as statistically significant increases in activity in the dorsal attention, temporoparietal, and visual networks. As age increased, transitions to Clusters 5 and 6 exhibited statistically significant decreases in activity in the somatomotor and visual networks as well as a statistically significant increase in activity in the limbic network.

Conclusions: In conclusion, our work shows that transitions between empirically derived brain states vary with age. These findings open the possibility that observed age-related differences in cognition/behavior may be owed to differences in successfully navigating brain state transitions.

References

1. Cornblath, E. J., Ashourvan, A., Kim, J. Z., Betzel, R. F., Ciric, R., Adebimpe, A., Baum, G. L., He, X., Ruparel, K., Moore, T. M., Gur, R. C., Gur, R. E., Shinohara, R. T., Roalf, D. R., Satterthwaite, T. D., & Bassett, D. S. (2020). Temporal sequences of brain activity at rest are constrained by white matter structure and modulated by cognitive demands. Communications Biology, 3(1), 261. https://doi.org/10.1038/s42003-020-0961-x
2. Esteban, O., Markiewicz, C. J., Blair, R. W., Moodie, C. A., Isik, A. I., Erramuzpe, A., Kent, J. D., Goncalves, M., DuPre, E., Snyder, M., Oya, H., Ghosh, S. S., Wright, J., Durnez, J., Poldrack, R. A., & Gorgolewski, K. J. (2019). fMRIPrep: a robust preprocessing pipeline for functional MRI. Nature Methods, 16(1), 111–116. https://doi.org/10.1038/s41592-018-0235-4
3. Nooner, K. B., Colcombe, S. J., Tobe, R. H., Mennes, M., Benedict, M. M., Moreno, A. L., Panek, L. J., Brown, S., Zavitz, S. T., Li, Q., Sikka, S., Gutman, D., Bangaru, S., Schlachter, R. T., Kamiel, S. M., Anwar, A. R., Hinz, C. M., Kaplan, M. S., Rachlin, A. B., ... Milham, M. P. (2012). The NKI-Rockland Sample: A Model for Accelerating the Pace of Discovery Science in Psychiatry. Frontiers in Neuroscience, 6. https://doi.org/10.3389/fnins.2012.00152
4. Parkes, L., Kim, J. Z., Stiso, J., Brynildsen, J. K., Cieslak, M., Covitz, S., Gur, R. E., Gur, R. C., Pasqualetti, F., Shinohara, R. T., Zhou, D., Satterthwaite, T. D., & Bassett, D. S. (2023). Using network control theory to study the dynamics of the structural connectome. BioRxiv, 2023.08.23.554519. https://doi.org/10.1101/2023.08.23.554519
5. Pasqualetti, F., Zampieri, S., & Bullo, F. (2014). Controllability metrics, limitations and algorithms for complex networks. IEEE Transactions on Control of Network Systems, 1(1), 40–52.
6. Tournier, J.-D., Smith, R., Raffelt, D., Tabbara, R., Dhollander, T., Pietsch, M., Christiaens, D., Jeurissen, B., Yeh, C.-H., & Connelly, A. (2019). MRtrix3: A fast, flexible and open software framework for medical image processing and visualisation. NeuroImage, 202, 116137. https://doi.org/10.1016/j.neuroimage.2019.116137

Poster No 1133

Multimodal brain age prediction using 5-HT2A receptor binding and gray matter volume

Ruben Dörfel[1,2], Joan Arenas-Gomez[2], Claus Svarer[2], Gitte Knudsen[2,3], Jonas Svensson[1,2], Pontus Plavén-Sigray[1,2]

[1]Centre for Psychiatry Research, Department of Clinical Neuroscience, Karolinska Institutet, Stockholm, Sweden, [2]Neurobiology Research Unit, Copenhagen University Hospitalet Rigshospitalet, Copenhagen, Denmark, [3]Department of Clinical Medicine, University of Copenhagen, Copenhagen, Denmark

Introduction: Developing biomarkers that capture age-related biological changes in the human brain is crucial for understanding the causal role of biological aging in the genesis of neurodegenerative disorders (Mattson and Arumugam 2018). Brain serotonin 2A (5-HT2A) receptor binding, measured using positron emission tomography (PET), has been shown to decline with age and has been related to various degenerative disorders (Karrer et al. 2019; Hasselbalch et al. 2008). Similarly, gray matter (GM) volume in the brain, measured using T1 weighted magnetic resonance imaging (MRI), has been shown to decrease during adulthood (Bethlehem et al. 2022), and neuronal atrophy is a hallmark of e.g., dementia. In this study, we investigated the decline in 5-HT2A receptor binding using the brain age paradigm (Franke et al. 2010) to evaluate its usefulness as a biomarker for biological aging. Specifically, we aimed to 1) predict brain age using PET data, i.e., 5-HT2A receptor binding outcomes; 2) compare to predictions based on MRI data, i.e., gray matter volume; and 3) investigate whether a multimodal approach combining PET and MRI derived data yields improved predictions over unimodal approaches.

Methods: We investigated 209 healthy subjects between 18 and 82 years (mean=36.6, std=16.8). The data was derived from the CIMBI database (Knudsen et al. 2016). All subjects had imaging of the 5-HT2A receptor using PET and structural imaging of the brain using MRI. Binding potentials and GM volumes were quantified in 14 cortical and subcortical regions with 5-HT2A receptors (Varnäs, Halldin, and Hall 2004). Various machine learning algorithms were implemented to predict age based on imaging-derived feature sets: only PET, only MRI, and PET + MRI (Figure 1). We selected commonly used algorithms for brain age prediction (Baecker et al. 2021). Multimodal models using PET and MRI data were implemented using a stacking approach. A dummy regressor and a pre-trained structural MRI-based brain age prediction software (Leonardsen et al. 2022) were also implemented as a reference. All models were trained and evaluated using a 20-times repeated 5-fold CV setup. We reported the average mean absolute error (MAE) and the average correlation between predicted and chronological age over all hold-out folds.

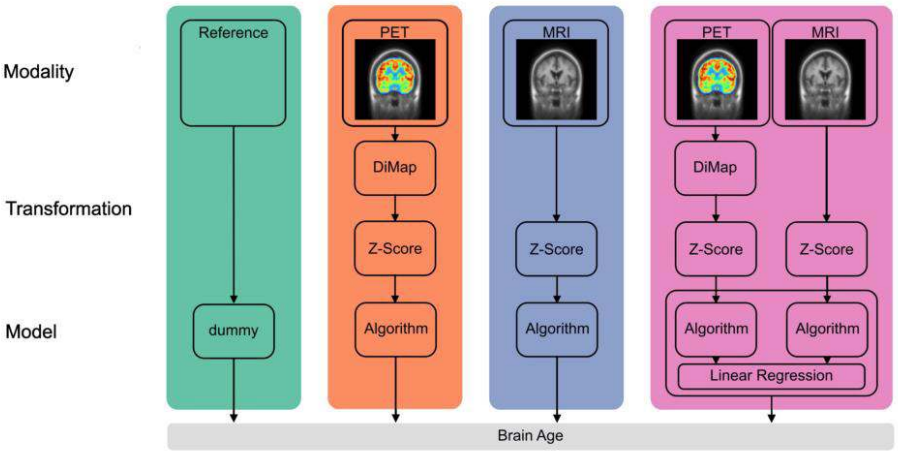

Figure 1: Overview of the various prediction pipelines. Reference: pipeline to set the predictions into the context of a pre-trained sMRI-based prediction model (pyment) and a dummy regressor always predicting the mean chronological age of subjects seen during training. **PET**: brain age predictions based on 5-HT2A receptor binding. Binding potentials derived from [11C]Cimbi-36 were transformed to [18F]Altanserin-like units using the distribution mapping (DiMap). Subsequently, BPs are z-scored. **MRI**: brain age predictions based on gray matter volumes. Volumes of cortical and subcortical regions were z-scored. **PET+MRI**: Multi-modal brain age predictions. The applied transformations for PET and MRI data were the same as for the unimodal pipelines. Brain age was predicted using a stacking ensemble method.

Results: Overall, all models using PET, MRI, and PET+MRI-derived features performed better than the dummy regressor and worse than the state-of-the-art software pyment. The results for all trained models were visualized in Figure 2. Following, we reported the results for the best model in each feature set, which was Bayesian Ridge Regression (Bridge) for PET and the Gaussian process regressor using an RBF kernel (rbfGPR) for MRI and PET+MRI. We found that cerebral 5-HT2A receptor binding predicted chronological age accurately (average MAE=6.63 years, r=0.87) and outperformed gray matter volume-based predictions (average MAE=7.76 years, r=0.79). The difference between PET and MRI-based predictions was statistically significant (p=0.04). We further found that the accuracy increased after combining MRI- and PET-derived regional measures (average MAE=5.93 years, r=0.88). However, the difference to the PET-based model was not statistically significant (p=0.14).

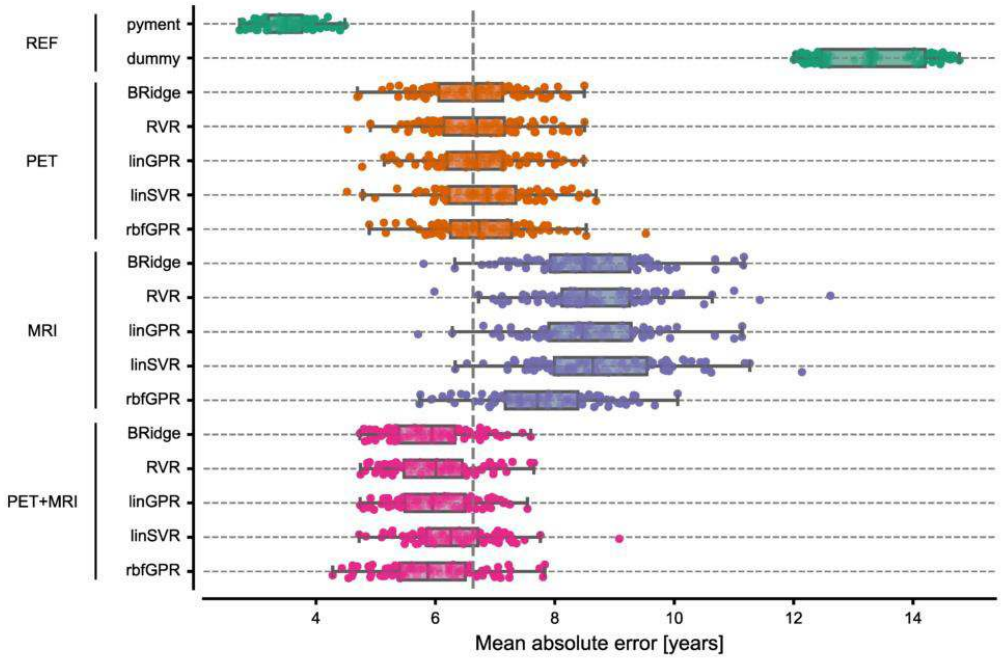

Figure 2: MAE for all the trained models. Each dot represents the mean MAE for one of the 100 CV iterations. The vertical dashed line marks the generalization error of the best PET model (BRidge). **Abbreviations:** REF - reference; BRidge - Bayesian Ridge Regressor; RVR - Reverence Vector Regression; linGPR - linear Gaussian Process Regression; linSVR - linear Support Vector Regression; rbfGPR - GPR with radial basis function kernel

Conclusions: We showed that 5-HT2A receptor binding could be used to predict chronological age accurately. Those age predictions were more accurate than predictions based solely on volumetric MRI data. Combining PET and MRI data into one model increased the accuracy, suggesting that both contribute unique information when predicting age. This indicated that

both measures were affected by distinct aging-related biological mechanisms. Therefore, 5-HT2A receptor binding might be suitable as a putative biomarker for aging-related changes in the human brain. However, further studies assessing if 5-HT2A-based age predictions are predictive of poor health outcomes are necessary to establish its use as a biomarker.

References

1. Baecker, L. et al. (2021) 'Brain age prediction: A comparison between machine learning models using region- and voxel-based morphometric data', Human Brain Mapping, 42(8), pp. 2332–2346. Available at: https://doi.org/10.1002/hbm.25368.
2. Bethlehem, R.A.I. et al. (2022) 'Brain charts for the human lifespan', Nature. Available at: https://doi.org/10.1038/s41586-022-04554-y.
3. Franke, K. et al. (2010) 'Estimating the age of healthy subjects from T1-weighted MRI scans using kernel methods: Exploring the influence of various parameters', NeuroImage, 50(3), pp. 883–892. Available at: https://doi.org/10.1016/j.neuroimage.2010.01.005.
4. Hasselbalch, S.G. et al. (2008) 'Reduced 5-HT2A receptor binding in patients with mild cognitive impairment', Neurobiology of Aging, 29(12), pp. 1830–1838. Available at: https://doi.org/10.1016/j.neurobiolaging.2007.04.011.
5. Karrer, T.M. et al. (2019) 'Reduced serotonin receptors and transporters in normal aging adults: a meta-analysis of PET and SPECT imaging studies', Neurobiology of Aging, 80, pp. 1–10. Available at: https://doi.org/10.1016/j.neurobiolaging.2019.03.021.
6. Knudsen, G.M. et al. (2016) 'The Center for Integrated Molecular Brain Imaging (Cimbi) database', NeuroImage, 124, pp. 1213–1219. Available at: https://doi.org/10.1016/j.neuroimage.2015.04.025.
7. Leonardsen, E.H. et al. (2022) 'Deep neural networks learn general and clinically relevant representations of the ageing brain', NeuroImage, 256(December 2021), p. 119210. Available at: https://doi.org/10.1016/j.neuroimage.2022.119210.
8. Mattson, M.P. and Arumugam, T.V. (2018) 'Hallmarks of Brain Aging: Adaptive and Pathological Modification by Metabolic States', Cell Metabolism, 27(6), pp. 1176–1199. Available at: https://doi.org/10.1016/j.cmet.2018.05.011.
9. Properzi, M.J. et al. (2019) 'Nonlinear Distributional Mapping (NoDiM) for harmonization across amyloid-PET radiotracers', NeuroImage, 186, pp. 446–454. Available at: https://doi.org/10.1016/j.neuroimage.2018.11.019.
10. Varnäs, K., Halldin, C. and Hall, H. (2004) 'Autoradiographic distribution of serotonin transporters and receptor subtypes in human brain', Human Brain Mapping, 22(3), pp. 246–260. Available at: https://doi.org/10.1002/hbm.20035.

Poster No 1134

Altered neuro-substrates preceding accelerated cognitive and mobility aging in older people

Pei-Lin Lee[1], Kun-Hsien Chou[2,3], Chih-Kuang Liang[4,5,1], Chih-Ping Chung[1,6], Wei-Ju Lee[1,7], Li-Ning Peng[1,8], Liang-Kung Chen[1,8,9], Ching-Po Lin[2,3,10]

[1]Center for Healthy Longevity and Aging Sciences, National Yang Ming Chiao Tung University, Taipei, Taiwan, [2]Institute of Neuroscience, National Yang Ming Chiao Tung University, Taipei, Taiwan, [3]Brain Research Center, National Yang Ming Chiao Tung University, Taipei, Taiwan, [4]Center for Geriatrics and Gerontology, Kaohsiung Veterans General Hospital, Kaohsiung, Taiwan, [5]Division of Neurology, Department of Internal Medicine, Kaohsiung Veterans General Hospital, Kaohsiung, Taiwan, [6]Department of Neurology, Neurological Institute, Taipei Veterans General Hospital, Taipei, Taiwan, [7]Department of Family Medicine, Taipei Veterans General Hospital Yuanshan Branch, Yi-Lan, Taiwan, [8]Center for Geriatric and Gerontology, Taipei Veterans General Hospital, Taipei, Taiwan, [9]Taipei Municipal Gan-Dau Hospital (managed by Taipei Veterans General Hospital), Taipei, Taiwan, [10]Department of Education and Research, Taipei City Hospital, Taipei, Taiwan

Introduction: Concurrent cognitive and mobility impairments, a condition known as physio-cognitive decline syndrome (PCDS), brings higher risks of dementia and mortality in older people[1]. Previous cross-sectional studies have identified specific clinical and neuroanatomic features linked to PCDS, indicating its potential as distinct preclinical dementia syndrome. However, the temporal relationship between neuroanatomic abnormalities and the development of PCDS has not yet been investigated. Understanding the neuroanatomical alterations preceding this syndrome is crucial for understanding the early pathophysiology of PCDS. This longitudinal study aimed to examine grey-matter volumes (GMV) and the corresponding structural covariance network (SCN) abnormalities in robust individuals to predict the conversion to PCDS.

Methods: Participants were sourced from the I-Lan Aging Longitudinal Study[2], comprising robust individuals with no initial signs of PCDS. Participants were categorized into PCDS-converter and non-PCDS converter groups based on their status in the follow-up clinical assessment. The image analytical pipeline was shown in Fig 1A. Baseline T1w images were preprocessed with the VBM pipeline under CAT12[3]. Voxel-wise ANCOVA model, accounting for age, sex, education, smoking status, and total intracranial volume, was applied to identify the regional GMV alterations. These regions served as seeds in subsequent seed-to-voxel SCN analysis to establish corresponding morphometric networks. Significant SCN changes between groups were identified using a linear regression model with a group by mean seed volume interaction term. Furthermore, individual inter-regional SC integrity was calculated using a jackknife bias estimation procedure[4] for further correlation analysis. Regional GMV and individual SCN integrity that showed abnormalities in the PCDS converter group were further analyzed for their associations with physical and cognitive performance at follow-up, using the partial Spearman correlation analysis with the same nuisance variables.

Results: The study included 343 robust individuals (60.2±6.9 years old, 49.6% men). After an average follow-up period of 5.6 years, 227 remained non-PCDS, while 116 converted to PCDS. Notable GMV reduction were identified in the cerebellum and right caudate among PCDS converters (see Fig 1B). Significant differences in SCNs between study groups for cerebellum-based (to right frontal-pole and left middle-frontal-gyrus) and caudate-based SCNs (to right caudate-putamen, right planum-temporale, left precentral-gyrus, right postcentral-gyrus, and left parietal-operculum) were observed (see Fig 1C). Furthermore, correlation analysis revealed the cerebellum's regional GMV and the integrity of the caudate-based SCNs at baseline might be linked to certain physical examination and cognitive performance at follow-up (with uncorrected $p<0.05$, see Fig 2).

Conclusions: The study uncovered early regional GMV and morphological network changes preceding PCDS in community-dwelling older individuals. PCDS converters exhibited baseline GMV reductions in cerebellum and increases right caudate volumes compared to non-converters. Seed-to-voxel SCN analysis identified distinct covariances in two cerebellum-based (to right frontal-pole and left middle-frontal-gyrus) and caudate-based SCNs (to right caudate-putamen, right planum-temporale, left precentral-gyrus, right postcentral-gyrus, and left parietal-operculum) between groups. These identified regional GMV and SCNs' integrity at baseline were also linked to physical mobility and cognitive performances over time. These findings offer an understanding of the neuroanatomical foundation of rapid declines in both physical mobility and cognitive functions, potentially guiding targeted prevention of subsequent dementia in those older people with dual cognitive and mobility impairments.

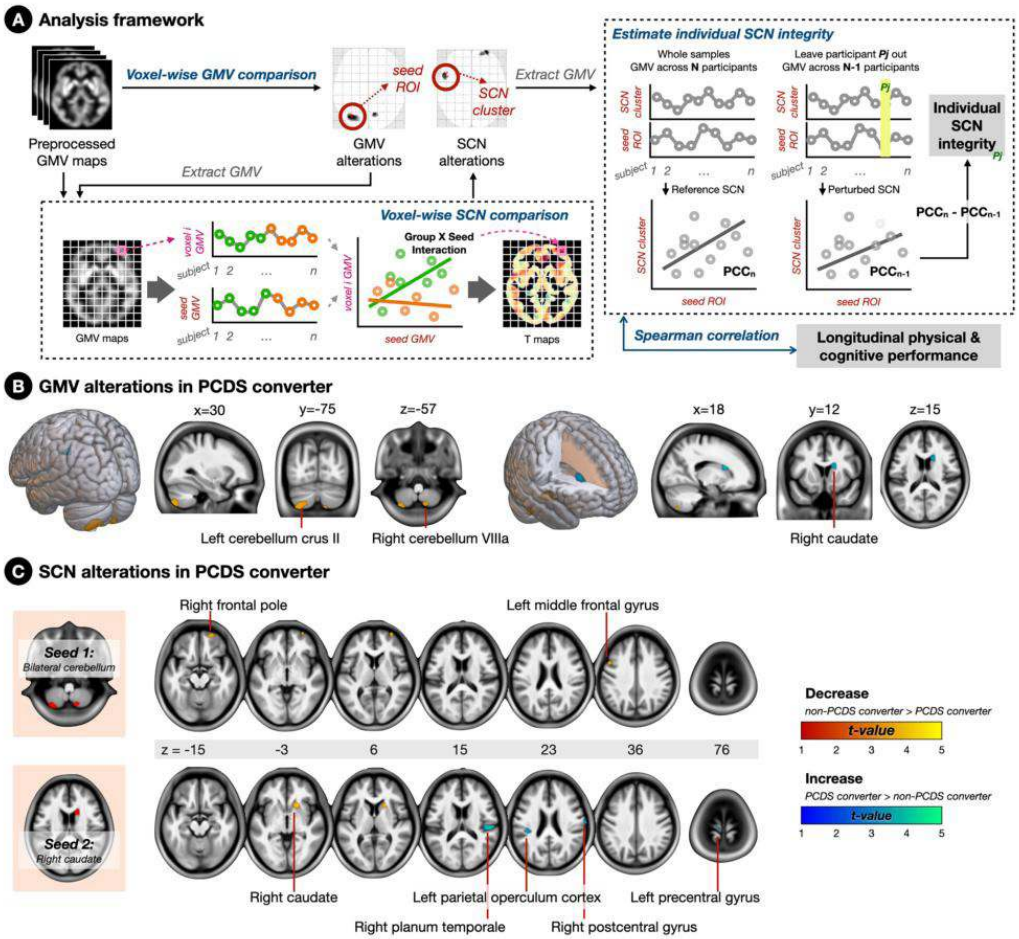

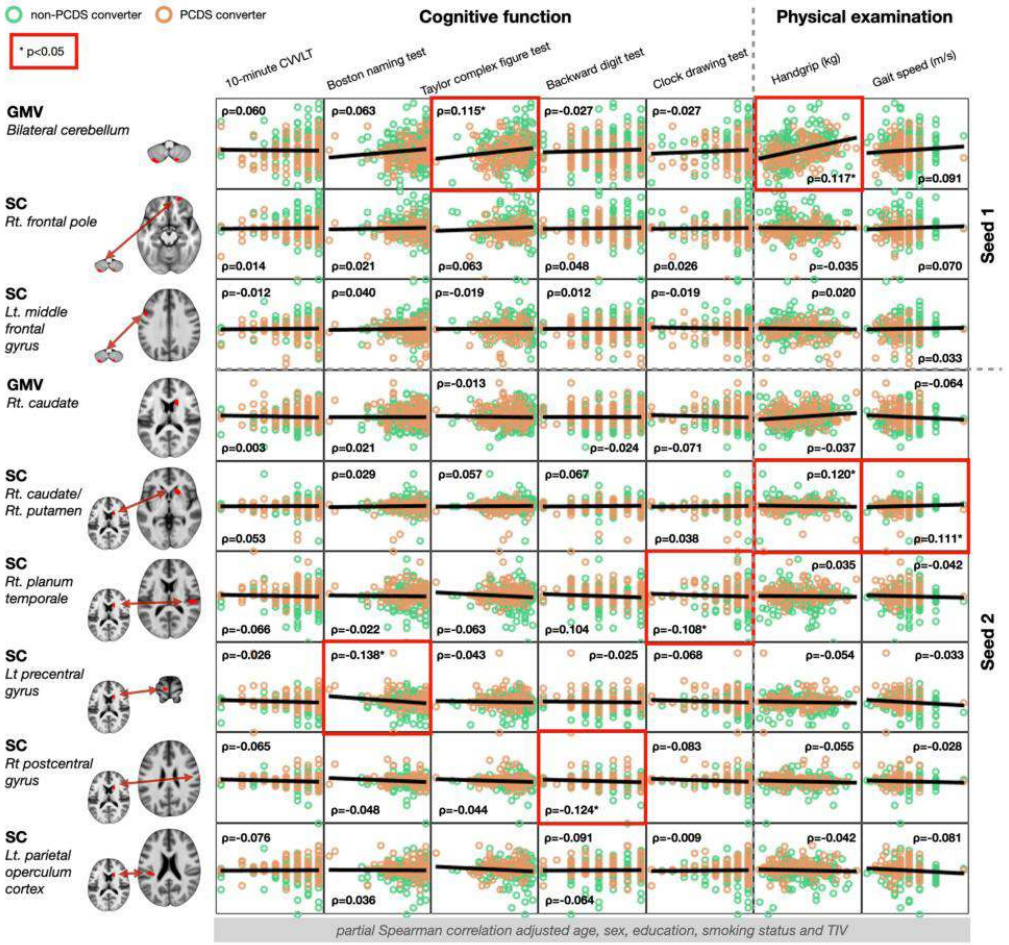

References

1. Chung, C-P., et al. "Physio-cognitive decline syndrome as the phenotype and treatment target of unhealthy aging." The journal of nutrition, health & aging (2021): 1-11.
2. Lee, Wei-Ju, et al. "Comparisons of sarcopenia defined by IWGS and EWGSOP criteria among older people: results from the I-Lan longitudinal aging study." Journal of the American medical directors association 14.7 (2013): 528-e1.
3. Gaser, Christian, et al. "CAT–A computational anatomy toolbox for the analysis of structural MRI data." biorxiv (2022): 2022-06.
4. Yang, Crystal C., et al. "Sex differences in cognition and structural covariance-based morphometric connectivity: evidence from 28,000+ UK Biobank participants." Cerebral Cortex 33.19 (2023): 10341-10354.

Poster No 1135

Atrophy Progression in People With a Family History of Alzheimer's disease is Shaped by Connectivity

Christina Tremblay[1,2], Shady Rahayel[2], Alexandre Pastor-Bernier[1], Frédéric St-Onge[3], Andrew Vo[1], François Rheault[4], Véronique Daneault[2], Filip Morys[1], Natasha Rajah[3], Sylvia Villeneuve[3], Alain Dagher[1], PREVENT-AD Research Group[3]

[1]Montreal Neurological Institute and Hospital, McGill University, Montreal, Canada, [2]Centre for Advanced Research in Sleep Medicine, Hôpital du Sacré-Cœur de Montréal, Montreal, Canada, [3]Brain Imaging Centre, Douglas Institute Research Centre, Montreal, Canada, [4]Université de Sherbrooke, Sherbrooke, Canada

Introduction: Alzheimer's disease (AD) includes a long period of presymptomatic brain changes. Different risk factors are associated with AD development, including having a family history of AD (FHAD). The Braak model suggests that tau pathology in synergy with beta-amyloid (Aβ) spreads along structural connections in AD eventually leading to atrophy (Braak & Braak, 1991). However, the pattern of atrophy progression in people with a FHAD in addition to the influence of brain structural connectivity on proteins propagation and atrophy progression remain unclear. Here we used structural MRI from three databases (ADNI (Jack et al, 2008), PREVENT-AD (Breitner et al, 2016) and Montreal Adult Lifespan Study (Elshiekh et al., 2020)) to map the atrophy progression in FHAD and AD, and build group-specific connectomes.

Methods: Longitudinal data up to 4 years enabled us to perform atrophy progression analysis in FHAD and AD compared to controls. Tau and Aβ protein distribution were quantified using [18F]AV-1451 and [18F]NAV4694 positron emission tomography processed with a standard pipeline (github.com/villeneuvelab/vlpp). Group-specific structural connectivity matrices were created using Tractoflow-ABS (Theaud et al, 2020) and Connectoflow pipelines (Rheault et al, 2021). A structural connectivity matrix from healthy adults (undamaged) was also used (Misic et al, 2015). We first derived atrophy progression maps using deformation-based morphometry (ANTs longitudinal pipeline) from three groups with similar age, education and male/female proportion at baseline (controls: N=116, FHAD: N=153, AD: N=156). The atrophy progression (group-by-age interaction) was compared between the three groups with linear mixed models (FDR corrected) controlling for sex, education, body mass index, APOe4 genotype and APOe4 interaction with age. The Cammoun atlas (448 cortical regions) was used for brain parcellation and to build the group-specific connectivity matrices (Cammoun et al., 2012). The ComBat method was applied to harmonize the multi-center imaging data (Johnson et al, 2007). For the structural connectivity analysis, Pearson's correlations with the structurally connected neighborhood regions were computed and tested against spatial null models using BrainSMASH (Burt et al., 2020).

Results: We found similar patterns of atrophy progression in FHAD and AD, notably in the cingulate cortex, temporal, and parietal lobes (Fig.1). The extent was more widespread and severe in AD. Several regions also showed less atrophy progression (-ß) in AD (mostly in the temporal and frontal lobe), suggesting a ceiling effect. Analyses of structural connectivity indicated that the atrophy pattern and its progression were associated with existing structural connectivity in FHAD (atrophy progression: r=0.31, p-valuespin=0.03; atrophy at BI: r=0.26, p-valuespin=0.04) (Fig.2A). In AD, only the atrophy at baseline was significantly correlated with that of structurally connected neighbors (atrophy progression: r=0.11, p-valuespin=0.26; atrophy at BI: r=0.50, p-valuespin=0.001). Tau and Aβ protein concentration were also higher in structurally connected regions in FHAD and AD. However, when using an undamaged connectome from healthy adults (Fig.2B bottom row), an association was found with the atrophy progression in the structurally connected regions in both FHAD and AD. These results suggests that atrophy in AD continues to propagate along pre-existing connections despite current damage while, in FHAD, structural connectivity is not significantly impaired.

Conclusions: Supporting the Braak model, in FHAD and AD, our findings showed that structural connectivity influenced the baseline distribution of tau, Aβ and atrophy. These findings also underscore the critical role of structural connectivity in the distribution of pathological markers and atrophy progression in both FHAD and AD.

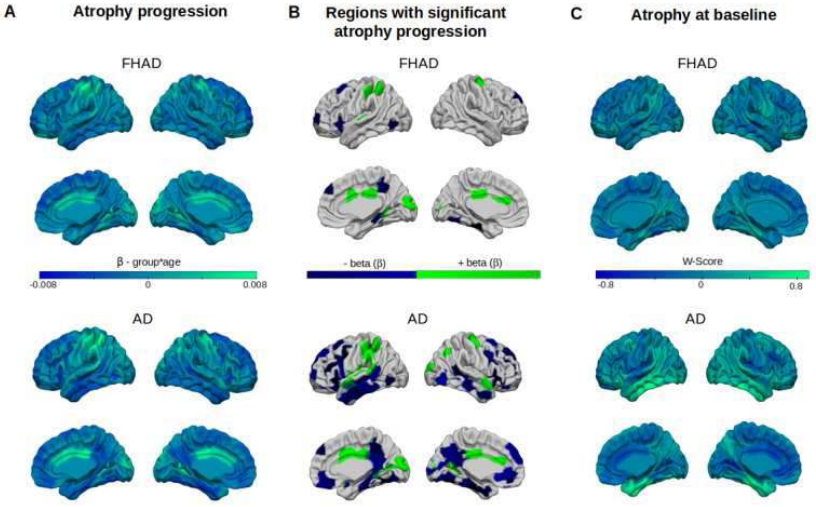

Figure 1. Atrophy progression in individuals with a family history of Alzheimer's disease (FHAD) and patients with Alzheimer's disease (AD). (**A**) Positive and negative β associated with higher (green) and lower (blue) atrophy progression in FHAD and AD, compared with the expected-age effect in healthy controls (HC). (**B**) Cortical regions showing significant atrophy progression (negative beta: blue, positive beta: green) in FHAD and AD compared with HC after FDR corrections. (**C**) Atrophy at baseline (W-scores with age and sex effects in aging regressed out) in FHAD and AD. Regions with more atrophy at baseline overlap with regions with less atrophy progression, reflecting the ceiling effect.

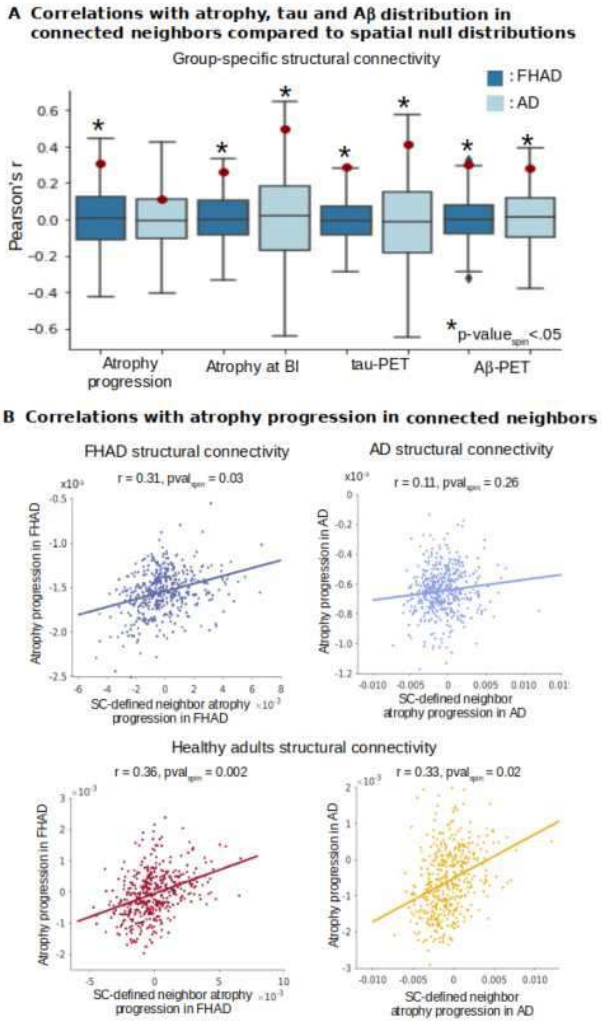

Figure 2. Relationships with structural connectivity in participants with a family history of Alzheimer's disease (FHAD) and patients with Alzheimer's disease (AD). **(A)** Pearson's correlations between cortical atrophy progression, atrophy at baseline, tau, and Aβ distribution, and those in the structurally connected regions using group-specific structural connectivity (SC) matrices. All results were compared to their spatial null distributions. **(B)** The atrophy progression in FHAD was influenced by SC independently of the connectivity matrix used (FHAD-specific (upper row) or from healthy adults (bottom row)). However, in AD, the atrophy did not propagate following the current AD SC (upper row) but seems to follow the pre-existing one (bottom row).

References

1. Braak, H., & Braak, E. (1991), 'Neuropathological stageing of Alzheimer-related changes', Acta Neuropathologica, vol. 82, no. 4, pp. 239–259. doi:10.1007/BF00308809
2. Breitner, J. et al. (2016), 'Rationale and Structure for a New Center for Studies on Prevention of Alzheimer'S Disease (Stop-Ad)', The Journal of Prevention of Alzheimer's Disease, vol. 3, no. 4, pp. 1–7. doi:10.14283/jpad.2016.121
3. Burt, J.B. et al. (2020), 'Generative modeling of brain maps with spatial autocorrelation', NeuroImage, vol. 220, pp. 117038. doi:10.1016/j.neuroimage.2020.117038
4. Cammoun, L. et al. (2012), 'Mapping the human connectome at multiple scales with diffusion spectrum MRI', Journal of neuroscience methods, vol. 203, no. 2, pp. 386-397. doi:10.1016/j.jneumeth.2011.09.031
5. Elshiekh, A. et al. (2020). 'The association between cognitive reserve and performance-related brain activity during episodic encoding and retrieval across the adult lifespan', Cortex, vol. 129, pp. 296–313. doi:10.1016/j.cortex.2020.05.003
6. Jack, C.R. et al. (2008). 'The Alzheimer's Disease Neuroimaging Initiative (ADNI): MRI methods', Journal of Magnetic Resonance Imaging, vol. 27, no. 4, pp. 685–691. doi:10.1002/jmri.21049
7. Johnson, W.E. et al. (2007). 'Adjusting batch effects in microarray expression data using empirical Bayes methods', Biostatistics, vol. 8, no. 1, pp. 118–127. doi:10.1093/biostatistics/kxj037
8. Mišić, B. et al. (2015). 'Cooperative and Competitive Spreading Dynamics on the Human Connectome', Neuron, vol. 86, no. 6, pp. 1518–1529. doi:10.1016/j.neuron.2015.05.035
9. Rheault, F. et al. (2021). 'Connectoflow: A cutting-edge Nextflow pipeline for structural connectomics', In International Society of Magnetic Resonance in Medicine (ISMRM), May 15.
10. Theaud, G. et al. (2020). 'TractoFlow: A robust, efficient and reproducible diffusion MRI pipeline leveraging Nextflow & Singularity', NeuroImage, vol. 218, p. 116889. doi:10.1016/j.neuroimage.2020.116889

Poster No 1136

Diminished Social Value Integration in Older Adults

Chris M. Stolle[1], Rongjun Yu[2], Yi Huang[1]

[1]Lingnan University, Hong Kong, China, [2]Hong Kong Baptist University, Hong Kong, China

Introduction: Older adults often make vital economic decisions, like managing retirement savings, under social influence. While research shows that social influence can alter decision-making, the impact of ageing on this process is understudied. Economic decision-making involves a mix of objective information and subjective utility (Rangel et al., 2008), with social influences integrated as 'other conferred utility' (OCU) (Chung et al., 2015). An experiment by Chung et al. showed that the OCU is encoded in the ventromedial prefrontal cortex (vmPFC). Changes in the prefrontal cortex may lead to cognitive decline (Dempster, 1992). Thus, older adults might struggle to incorporate OCU into their value estimation. They may use simpler strategies, meaning that while the OCU model may predict their behaviour, there may be no encoding in the vmPFC. We propose a "stubborn" model that assumes participants have hard-wired preference scores. This model involves a preference score for choosing risky options alone or under neutral influence (p1), and an adaptation parameter (p2) that adjusts the score based on the social influence. We hypothesise that this simpler model could predict older adults' behavior as well as the OCU model.

Methods: We conducted an fMRI study with twenty older and twenty-two young adults. Participants who always chose the same option (two older and one younger) were excluded. The experimental task was adapted from a previous experiment (Chung et al., 2015). The experiment is depicted in Figure 1. Participants had to choose between a risky and a safe gamble that would determine how much participants win: In the safe gamble, the higher and lower amounts were close together. In the risky gamble, the higher amount to win was much higher than in the safe gamble, but the lower amount was also much lower. We simulated social influence by showing participants the choice of two other (simulated) players so that there were four conditions: 1) Safe: both chose safe; 2) risky: both chose risky; 3) indifferent: one chose safe, and one chose risky; 4) non-social: We did not display any others choice.

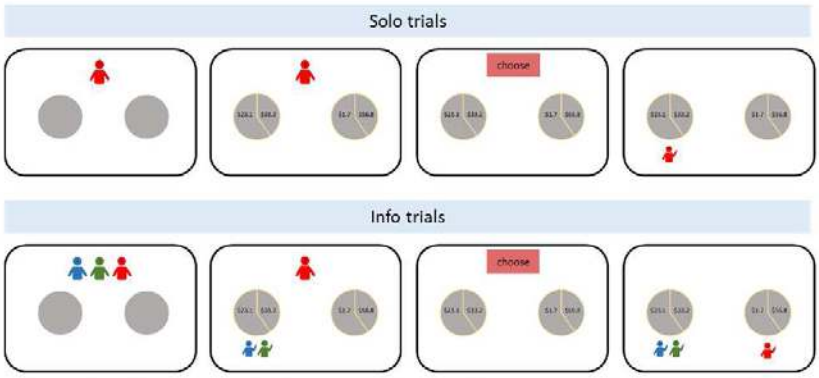

Figure1: Experimental task with solo trials (first row) and trials under social influence (second row).

Results: First, we tested whether participants understood the task or made their choice randomly. Therefore, we compared the performance of the previously described OCU model with a random choice model, in which the probability of choosing risky or safe is always .5. The OCU model outperformed the random choice model for both younger ($\chi2(3) = 35.88$, $p < 0.001$; pseudo-$R^2 = .55$) and older ($\chi2(3) = 9.89$, $p < 0.001$; pseudo-$R^2 = .18$) adults. Thus, both age groups understood the task and behaved non-randomly. We compared the OCU model to the stubborn model. For young adults, the OCU model performed significantly better than the stubborn model ($\chi2(1) = 21.92$, $p < 0.001$; pseudo-$R^2 = .16$). For older adults, the OCU model performed worse than the stubborn model (pseudo-$R^2 = .37$). The neural results (see Figure 2) showed significant activation for young adults in trials where they were faced with social influence in the vmPFC [peak voxel at x = -5, y = 42, z = -16; peak Z = 3.52; cluster size kE = 13; small volume correction (svc) at p(FEW) = 0.02]. This increased activation was absent in solo trials. For older adults, no such activation were found.

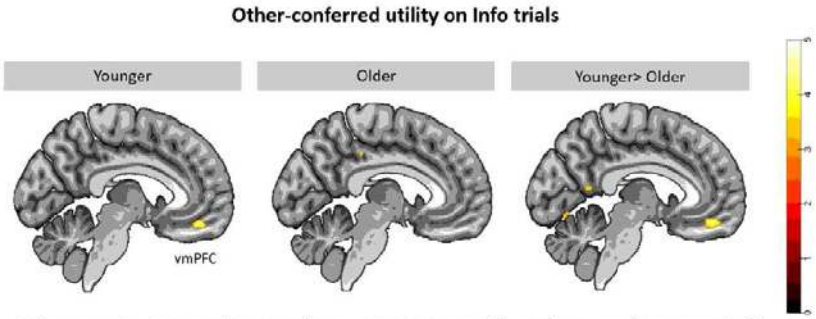

Figure 2: Neural results. VmPFC activation under social influence in young adults but not in older adults.

Conclusions: Our results showed that older adults do not incorporate other conferred utility. Instead, they use simplified compensatory strategies in which they stubbornly make risky choices at a rate that depends on the type of influence (none/indifferent, risky, safe). Correspondingly, unlike young adults, no processing of others conferred utility appears to occur in the vmPFC for older adults.

References

1. Chung, D. (2015), 'Social signals of safety and risk confer utility and have asymmetric effects on observers' choices', Nature Neuroscience, no. 18, pp. 912-916
2. Dempster, F. N. (1992), 'The rise and fall of the inhibitory mechanism: Toward a unified theory of cognitive development and aging', Developmental review, no. 12, pp. 45-75
3. Rangel, A. (2008), 'A framework for studying the neurobiology of value-based decision making', Nature Reviews: Neuroscience, no. 9(7), pp. 545-556

Poster No 1137

A layer-specific model of cortical sensory aging

Peng Liu[1], Juliane Doehler[2], Julia Henschke[2], Alicia Northall[3], Angela Serian[4], D. Samuel Schwarzkopf[5], Oliver Speck[6], Janelle Pakan[2], Esther Kühn[7]

[1]Hertie Institute for Clinical Brain Research (HIH)), Tübingen, Germany, [2]Institute for Cognitive Neurology and Dementia Research (IKND), Magdeburg, Germany, [3]Nuffield Department of Clinical Neurosciences, Oxford, United Kingdom, [4]Institute of Cognitive and Clinical Neuroscience (IKND), Heidelberg, Germany, [5]University of Auckland, Auckland, Auckland, [6]German Center for Neurodegenerative Diseases (DZNE), Magdeburg, Germany, [7]Hertie Institute for Clinical Brain Research (HIH), Tübingen, Baden-Württemberg

Introduction: Sensory processing is organized in a layered architecture with segregated input, output and modulatory circuits. This layered architecture of sensory systems is a convergent feature in animal evolution (Stacho et al., 2020). A comprehensive understanding of (dys)functional sensory systems requires a detailed understanding of alterations in the layer-specific architecture and the associated phenotypes. This is so far lacking, not only for sensory systems but for cortical dysfunction in general. Sensory dysfunction comes with different cortical phenotypes, including increases in receptive field (RF) sizes (Liu et al., 2021), functional overactivation, decreases in lateral inhibition (Pleger et al., 2016) and structural alterations such as cortical thinning (Calì et al., 2018). However, it is unclear how changes in the layer architecture may contribute to the alterations characterizing sensory cortices with reduced functionality.

Methods: Here, we employed a unique approach to target this question by combining layer-specific structural and layer-specific functional 7T-MRI of primary somatosensory cortex (SI) with behavioral assessments from two cohorts of healthy younger and older adults. Cortical aging serves as a suitable model system to investigate the layer-specific architecture of sensory dysfunction as structural and functional reorganization is observed at different levels of the processing hierarchy, and affects behavior (Popescu et al., 2021). To better understand the mechanistic underpinnings of the observed changes, we used in vivo 2-photon calcium imaging (2PCI) in younger and older mice to investigate neuronal response differences at different cortical depths (Chen et al., 2013). We also used post mortem histological examination on mice as it provides deeper insights into layer-specific structural changes.

Results: Our study presents four major results that we used to develop a novel layer model of sensory aging (see Fig. 1): (1) Increased sensory input channel: In older adults, in spite of overall cortical thinning, the middle layer (i.e., input layer IV, identified using a previously published approach, Doehler et al. 2023) presents with increased thickness, higher myelin

content, and a more pronounced antagonistic center-surround relationship between signals and cortical depth. An adult with congenital arm loss shows, on the other hand, a shrinkage specifically of layer IV of SI. This speaks towards a plasticity-mediated mechanism of layer IV thickness modulation in humans. (2) Cortical thinning driven by deep layer thinning: Reduced cortical thickness in older compared with younger adults is not homogenous across layers but driven by deep layer thinning. (3) Preserved low-myelin hand-face border in layer IV: Low-myelin borders in input layer IV are preserved older compared to younger adults as well as in an individual with congenital arm loss. (4) Altered modulation channel: Older adults show less thickness but more myelin in deep layers, which is mirrored by overall cell loss and increased PV+ cell density in older mice. This is accompanied by no alterations or even an increase in inhibitory interactions in older adults and mice, making PV-cell driven inhibition a likely underlying mechanism.

Conclusions: Taken together, the novel layer model of aging provides key and novel information on SI organization and aging sensory circuits that may explain cortical dysfunction in health and disease, which is of particular importance for developing intervention to preserve sensory functions in aging and neurodegeneration in the future. This work also provides impactful relevance for understanding the neuronal mechanisms that underlie topographic organization and plasticity in general by transferring mechanistic insights from animal to human research. Given the layer-specific profile was different from primary motor cortex, our data also motivate the detailed assessment of layer-specific circuits in different cortical areas.

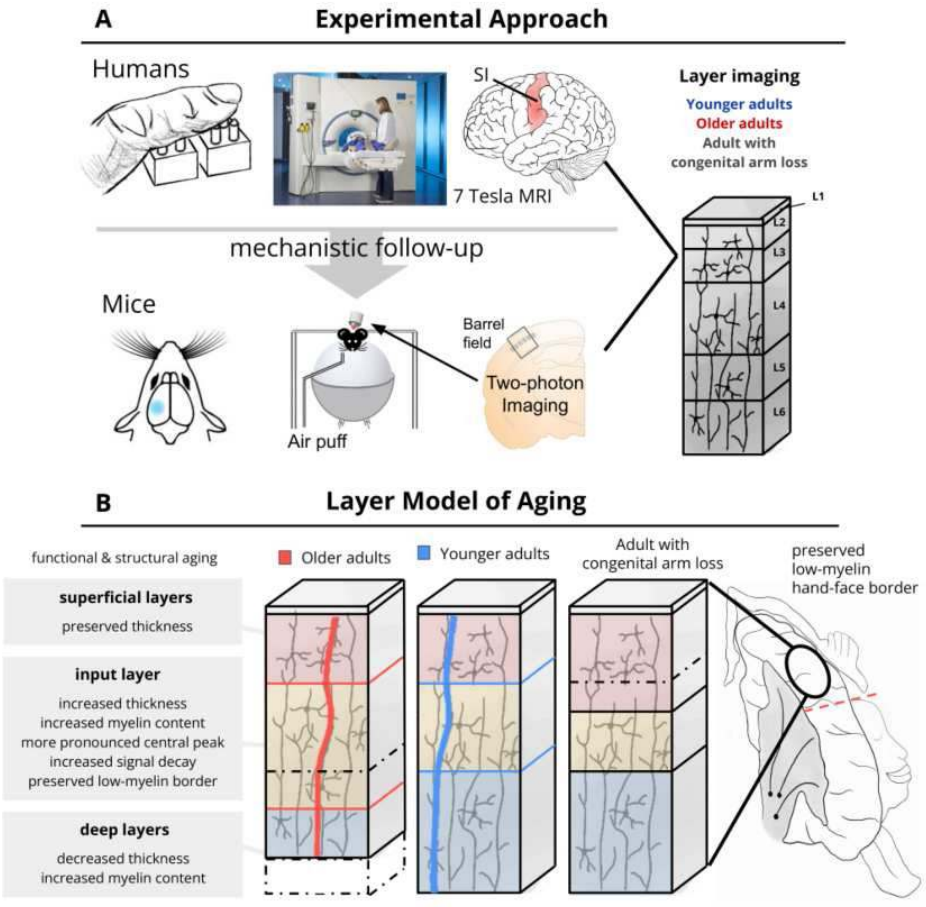

Figure 1. Experimental Approach and Layer Model of Sensory Aging. (A) 7 Tesla Magnetic Resonance Imaging (7T-MRI) was used to investigate the layer-specific structural and functional architecture of primary somatosensory cortex (SI) in younger and older adults.Participants underwent several passive tactile stimulation paradigms in the scanner. Phase-encoded data were used for Fourier-based and population receptive field (pRF) analysis. Two-photon calcium imaging (2PCI) was used to record the signal response of excitatory neurons expressing a genetically encoded calcium indicator (GCaMP6) during airpuff whisker stimulation. **(B)** The layer model of sensory aging suggests that cortical aging, as one example of cortical dysfunction, has a unique layer-specific profile. Critical characteristics are a widened input channel with aging (but a reduced input channel with sensory deprivation), a layer-specific profile of cortical thinning driven by deeper layer degeneration, and altered modulatory influences from deep layers on functional representations.

References

1. Calì, C., Wawrzyniak, M., Becker, C., Maco, B., Cantoni, M., Jorstad, A., Nigro, B., Grillo, F., Paola, V. D., Fua, P., & Knott, G. W. (2018). The effects of aging on neuropil structure in mouse somatosensory cortex—A 3D electron microscopy analysis of layer 1. PLOS ONE, 13(7), e0198131. https://doi.org/10.1371/journal.pone.0198131
2. Chen, T.-W., Wardill, T. J., Sun, Y., Pulver, S. R., Renninger, S. L., Baohan, A., Schreiter, E. R., Kerr, R. A., Orger, M. B., Jayaraman, V., Looger, L. L., Svoboda, K., & Kim, D. S. (2013). Ultrasensitive fluorescent proteins for imaging neuronal activity. Nature, 499(7458), 295–300. https://doi.org/10.1038/nature12354

3. Doehler, J., Northall, A., Liu, P., Fracasso, A., Chrysidou, A., Speck, O., Lohmann, G., Wolbers, T., & Kuehn, E. (2023). The 3D Structural Architecture of the Human Hand Area is Non-Topographic. The Journal of Neuroscience, JN-RM-1692-22. https://doi.org/10.1523/JNEUROSCI.1692-22.2023
4. Liu, P., Chrysidou, A., Doehler, J., Hebart, M. N., Wolbers, T., & Kuehn, E. (2021). The organizational principles of de-differentiated topographic maps in somatosensory cortex. eLife, 10, e60090. https://doi.org/10.7554/eLife.60090
5. Pleger, B., Wilimzig, C., Nicolas, V., Kalisch, T., Ragert, P., Tegenthoff, M., & Dinse, H. R. (2016). A complementary role of intracortical inhibition in age-related tactile degradation and its remodelling in humans. Scientific Reports, 6(1), Article 1. https://doi.org/10.1038/srep27388
6. Popescu, I. R., Le, K. Q., Ducote, A. L., Li, J. E., Leland, A. E., & Mostany, R. (2021). Increased intrinsic excitability and decreased synaptic inhibition in aged somatosensory cortex pyramidal neurons. Neurobiology of Aging, 98, 88–98. https://doi.org/10.1016/j.neurobiolaging.2020.10.007
7. Stacho, M., Herold, C., Rook, N., Wagner, H., Axer, M., Amunts, K., & Güntürkün, O. (2020). A cortex-like canonical circuit in the avian forebrain. Science, 369(6511), eabc5534. https://doi.org/10.1126/science.abc5534

Poster No 1138

Brain Aging Differences across 10 Brain Disorders by Brain Age Prediction

Chuang Liang[1], Godfrey Pearlson[2], Juan R. Bustillo[3], Peter Kochunov[4], Jessica A. Turner[5], Wei Shao[1], Rongtao Jiang[6], Jing Sui[7], Daoqiang Zhang[1], Zening Fu[5], Shile Qi[1], Vince Calhoun[5]

[1]Nanjing University of Aeronautics and Astronautics, Nanjing, China, [2]Yale School of Medicine, New Haven, CT, [3]University of New Mexico, Albuquerque, NM, [4]University of Maryland School of Medicine, Baltimore, MD, [5]Georgia State University, Atlanta, GA, [6]Yale University, New Haven, CT, [7]Beijing Normal University, Beijing, China

Introduction: Brain age can be used as a brain health index to quantify individuals' deviation from a normative brain aging trajectory[1-3]. The difference between neuroimaging-predicted brain age and the chronological age, predicted age difference (PAD), is a potential biomarker that reflects individual differences in brain developmental trajectories[4,5]. Risk factors for different brain disorders may converge on neurological aspects associated with accelerated brain aging processes[6,7]. However, most existing studies have been conducted on a limited sample-size that focused on a specific disorder without identifying interpretable neuroimaging features contributing to PAD prediction. Further understanding of brain aging trajectories and their spatial patterns among various brain disorders is important to disentangle disorder common and unique pathophysiological processes.

Methods: A total of 2752 independent patients, including attention-deficit/hyperactivity disorders (ADHD, n=344), autism spectrum disorder (ASD, n=484), schizophrenia (SZ, n=152), bipolar (BP, n=143), major depressive disorder (MDD, n=258), drinking (DRK, n=155), smoking (SMK, n=144), drinking and smoking (D&S, n=54), Alzheimer's disease (AD, n=361), mild cognitive impairment (MCI, n=657) and 2752 age-gender-quantity matched healthy controls (HCs) were collected as testing sets. Age-range matched HCs (n=53149) for each patient group were selected from 4 consortiums (including ABCD, HCP, GSP and UKB) as the corresponding training sets. Averaged gray matter volume (GMV) for each region of interest (ROI) based on Schaefer (1000 ROIs) and subcortex (16 ROIs) brain atlas[8] were used as features (Fig. 1a) in brain age prediction. Extreme gradient boosting (XGBoost) was trained on the selected age-range matched HCs, which was applied to the corresponding patient group to generate the individual brain age predictions. The accuracy of the XGBoost model[6] on training set was estimated by 10-fold cross-validation (Fig. 1b). The PAD differences (covariates: age, age2, sex and site were regressed) between HC and each patient group were conducted (Fig. 1c). Shapley additive explanations (SHAP)[9] was used to identify the interpretable brain features for PAD prediction in different diagnostic groups (Fig. 1d).

Results: (a) The high degree of correlations between chronological age and the predicted brain age in both training (r=0.67~0.94) and independent testing sets (r=0.73~0.91) confirmed the excellent prediction performance (Fig. 2a). (b) The PAD was higher in all the diagnostic groups than HCs, in which strong difference effects of PAD were observed in AD and D&S (d=0.84~0.97), moderate effects in SMK, DRK, SZ, BP and MCI (d=0.45~0.72), small effects in MDD (d=0.28), and negligible effects in ASD and ADHD (d=0.02~0.06, Fig. 2b). (3) The brain aging biomarkers that contribute the most in the PAD prediction for each diagnostic groups were: medial prefrontal cortex (mPFC)-lentiform nucleus (LN)-thalamus-amygdala in psychiatric disorders (SZ, BP and MDD), mPFC-postcentral cortex (PC)-thalamus in addiction disorders (DRK, SMK and D&S) and mPFC-superior temporal cortex-striatum-hippocampus in neurodegenerative (AD and MCI) disorders (Fig. 2c).

Conclusions: This is the first attempt to estimate brain age and its biological interpretation across 10 brain disorders in large scale cohorts. Results suggest that different brain disorders showed different brain aging, the highest aging in dementia, followed by addiction and psychiatry, (AD>D&S>SMK> DRK>SZ>BP>MCI>MDD). PAD differences were not observed in ASD and ADHD. Furthermore, the PAD in each patient group was driven by a unique spatial brain pattern, but also with some shared regions within the psychiatry (mPFC), addiction (mPFC and PC) and dementia (striatum). In summary, the observed

different brain aging, each with unique interpretable patterns, may serve as neuroimaging biomarkers for understanding the aging neural mechanisms of various brain disorders.

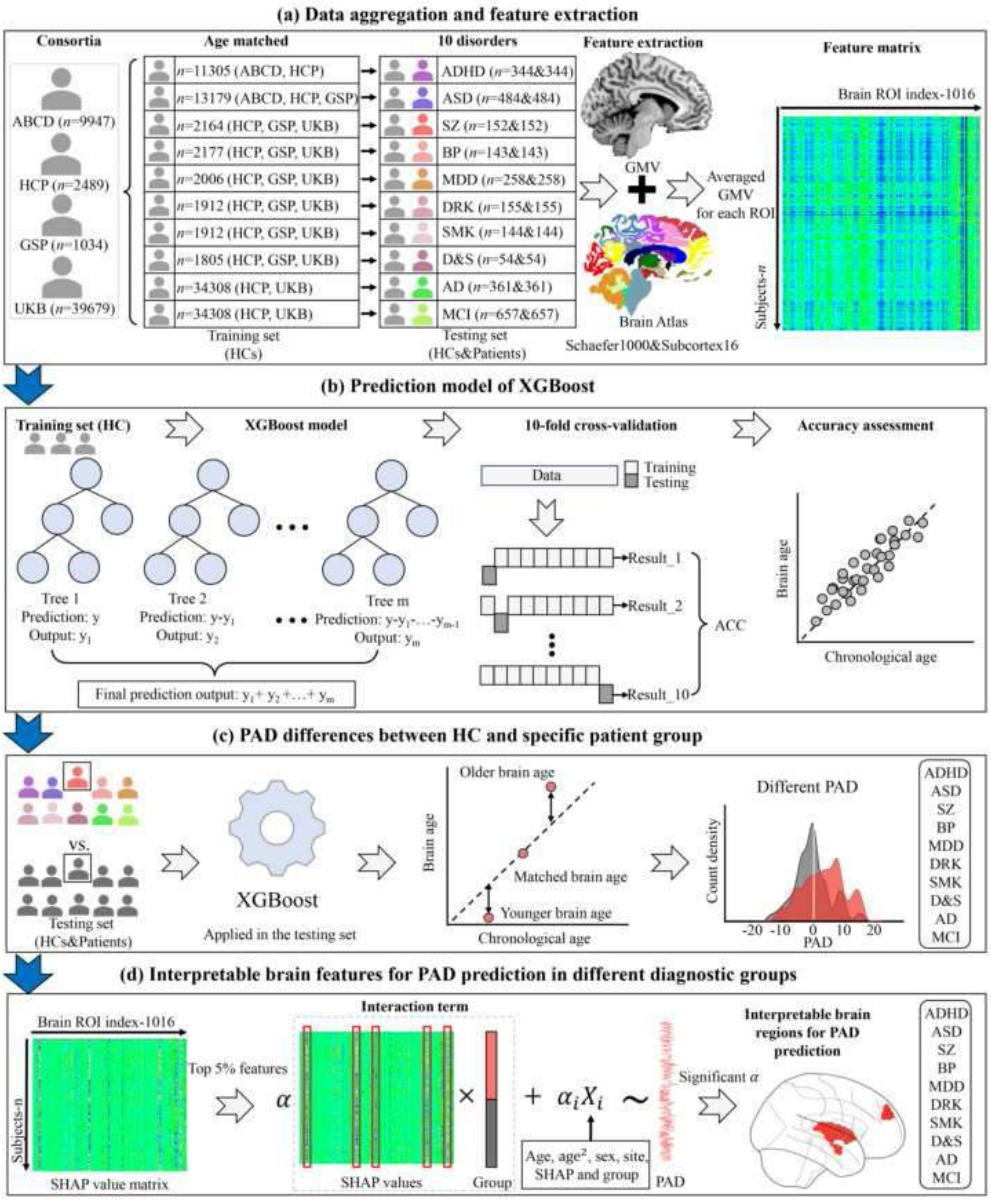

(a) The averaged GMV from each ROI were extracted based on Schaefer (1000 ROIs) and subcortex (16 ROIs) atlases as the input features. (b) The performance of the XGBoost model was verified on training set by 10-fold cross-validation. (c) XGBoost model was applied to the testing set to generate individual brain age predictions and the PAD differences between HC and specific patient group was compared. (d) Incorporating interaction terms (SHAP × group) in multiple linear regression models to identify the interpretable brain features for PAD prediction in different diagnostic groups. The age-corrected PAD was the dependent variable, while age, age², sex, site, group, SHAP value (top 5% average absolute value), and SHAP × group were the independent variables.

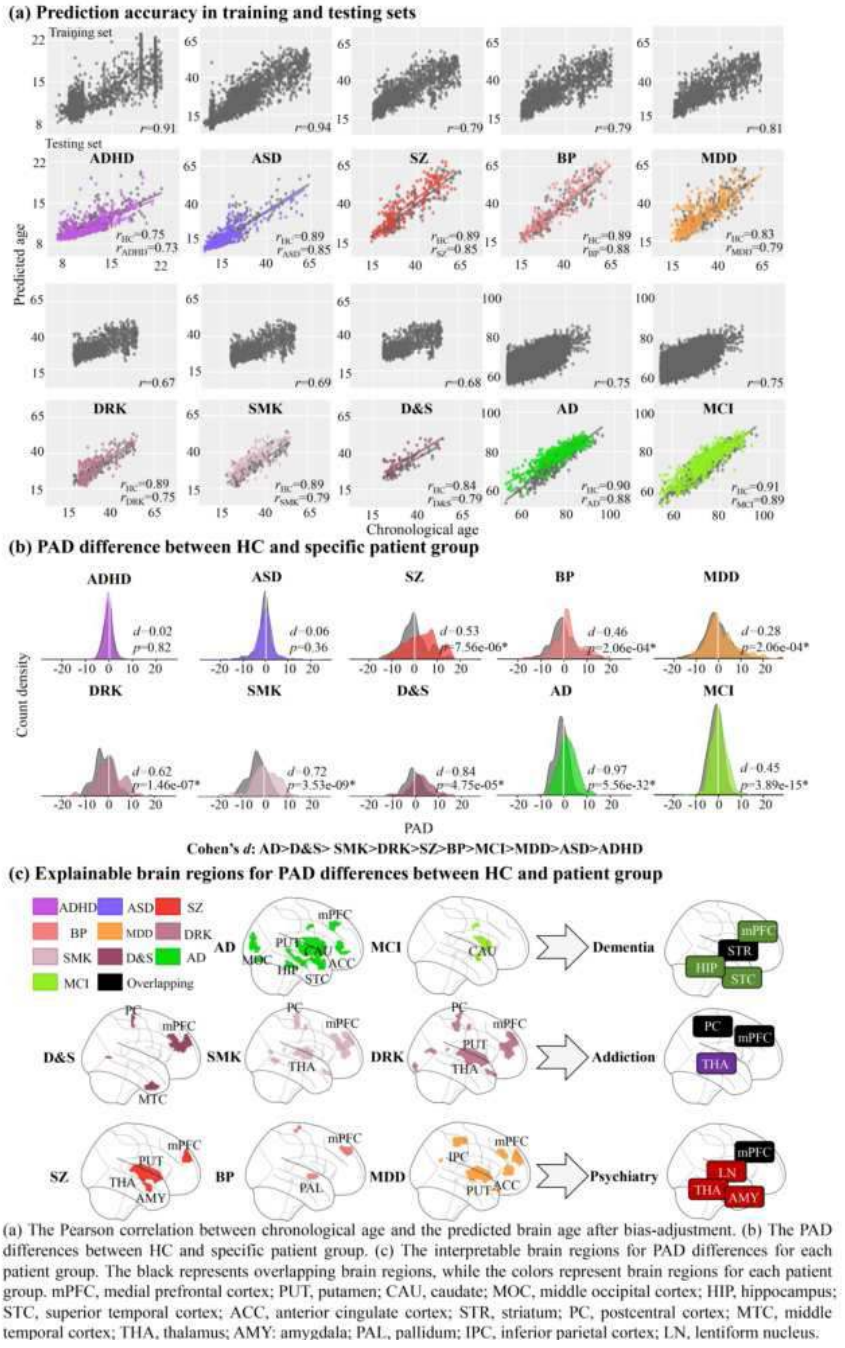

(a) The Pearson correlation between chronological age and the predicted brain age after bias-adjustment. (b) The PAD differences between HC and specific patient group. (c) The interpretable brain regions for PAD differences for each patient group. The black represents overlapping brain regions, while the colors represent brain regions for each patient group. mPFC, medial prefrontal cortex; PUT, putamen; CAU, caudate; MOC, middle occipital cortex; HIP, hippocampus; STC, superior temporal cortex; ACC, anterior cingulate cortex; STR, striatum; PC, postcentral cortex; MTC, middle temporal cortex; THA, thalamus; AMY: amygdala; PAL, pallidum; IPC, inferior parietal cortex; LN, lentiform nucleus.

References

1. Li, Y., et al., Brain connectivity based graph convolutional networks and its application to infant age prediction. IEEE Transactions on Medical Imaging, 2022. 41(10): p. 2764-2776.
2. Cole, J.H., et al., Brain age predicts mortality. Molecular psychiatry, 2018. 23(5): p. 1385-1392.
3. Bethlehem, R.A., et al., Brain charts for the human lifespan. Nature, 2022. 604(7906): p. 525-533.
4. Cole, J.H., et al., Predicting brain age with deep learning from raw imaging data results in a reliable and heritable biomarker. NeuroImage, 2017. 163: p. 115-124.
5. Cole, J.H. and K. Franke, Predicting age using neuroimaging: innovative brain ageing biomarkers. Trends in neurosciences, 2017. 40(12): p. 681-690.
6. Kaufmann, T., et al., Common brain disorders are associated with heritable patterns of apparent aging of the brain. Nature neuroscience, 2019. 22(10): p. 1617-1623.
7. Wang, J., et al., Gray matter age prediction as a biomarker for risk of dementia. Proceedings of the National Academy of Sciences, 2019. 116(42): p. 21213-21218.
8. Lawrence, R.M., et al., Standardizing human brain parcellations. Scientific data, 2021. 8(1): p. 78.
9. Ballester, P.L., et al., Gray matter volume drives the brain age gap in schizophrenia: a SHAP study. Schizophrenia, 2023. 9(1): p. 3.

Poster No 1139

Interplay of Dietary Amino Acids, Metabolic Syndrome, and ApoE ε4 on Brain Integrity at Midlife

Cherry Youn[1], Barbara Strasser[2], Dietmar Fuchs[3], Drew Gourley[4], Marie Caillaud[1], Yanrong Li[1], Isabelle Gallagher[1], Hirofumi Tanaka[4], Andreana Haley[1]

[1]Department of Psychology, University of Texas at Austin, Austin, TX, [2]Sigmund Freud University Vienna, Vienna, Vienna, [3]Institute of Biological Chemistry, Biocentre, Innsbruck, Innsbruck, [4]Department of Kinesiology and Health Education, University of Texas at Austin, Austin, TX

Introduction: Understanding the nuanced interactions between dietary components and genetic factors is critical in deciphering the mechanisms of neural aging. Tryptophan (TRP) and phenylalanine (PHE) are direct precursors of kynurenine (KYN) and tyrosine (TYR), respectively, and are large neutral amino acids (LNAA) that have been implicated in the pathogenesis of neurodegenerative diseases[1]. Their role in neurotransmitter synthesis suggests a complex interplay with cognitive function. Moreover, metabolic syndrome (MetS) has been recognized as a catalysis for accelerated cognitive decline, potentially exacerbating the aging process. This relationship may be even more pronounced in the presence of the apolipoprotein E ε4 (ApoE4) allele, a well-established genetic risk factor for Alzheimer's disease[2,3]. Despite the significant strides in identifying the deleterious effects of these variables on cognitive performance, the research remains fragmented, especially regarding the effects of LNAA on brain health across different life stages, vascular risk, and genetic backgrounds. Hence, our study aims to bridge this gap by exploring the intersection of LNAA levels, MetS, brain integrity, and the presence of the ApoE4 allele at midlife.

Methods: 65 adults aged 40-61 underwent a health assessment. All concentrations of LNAA were determined by high-performance liquid chromatography. The number of MetS components was calculated according to the unified criteria[4]. MRI was conducted on a Siemens 3T Skyra with a 32-channel head coil. Fluid-attenuated inversion recovery images and high-resolution structural images were acquired to determine white matter hyperintensity (WMH) volume, which was quantified using the Lesion Segmentation Tool in SPM8. ApoE genotyping was conducted using polymerase chain reaction amplification and Sanger sequencing[5]. Participants grouped into two: individuals carrying 1 or 2 copies of the ApoE ε4 allele (ApoE ε4 positive) or those not carrying any copy (ApoE ε4 negative). Multivariate linear regression analyses were performed using R to test the joint effect of LNAA, MetS, and ApoE4 on white matter integrity in middle-aged adults. Sex, age, and years of education were included as covariates.

Results: Multivariate linear regression analyses for assessing 3-way interaction effects indicated that the ApoE ε4 allele was a significant factor in WMH volume. Interestingly, MetS was not a significant predictor of WMH volume in participants without the ApoE ε4 allele. This suggests that MetS alone does not markedly affect neural integrity in the absence of genetic susceptibility. Furthermore, LNAA levels did not moderate the non-significant relationship between MetS and WMH volume in these individuals. However, among ApoE ε4 carriers, LNAA levels played a moderating role, over and above relevant covariates. Specifically, low LNAA levels were associated with low WMH volume in the context of MetS ($p < 0.01$). Moreover, higher LNAA appeared to accelerate the negative neural impact of MetS in these genetically at-risk individuals, revealing a nutrient-genetic interaction that may be pivotal for targeted dietary interventions.

Conclusions: This study elucidates the complex interplay of genetic predisposition, metabolic factors, and dietary amino acids on neural health. We discovered that MetS alone did not impact white matter integrity, nor did LNAA levels, in individuals without the ApoE ε4 allele. However, for ApoE ε4 carriers, LNAA levels substantially moderated WMH volume, particularly in the presence of MetS. Low LNAA levels correlated with low WMH, whereas higher levels attenuated MetS-related brain impairment. These insights underscore the potential of LNAA management as a strategic approach to mitigate the risks associated with MetS, especially in individuals genetically susceptible to neurodegeneration. Future dietary recommendations could be personalized to optimize cerebrovascular health in midlife, considering one's metabolic and genetic profiles.

References

1. Baran, H., Jellinger, K. & Deecke, L. (1999), Kynurenine metabolism in Alzheimer's disease. J Neural Transm 106, 165–181 (1999)
2. Lai, C.-L., Liou, L.-M., Liu, C.-K., Yang, Y.-H. & Lin, R.-T. (2014), Effects of metabolic syndrome, apolipoprotein E, and CYP46 on cognition among Taiwanese Chinese. Kaohsiung J Med Sci 30, 343–349
3. Feng, L. et al. (2013), Metabolic syndrome and amnestic mild cognitive impairment: Singapore Longitudinal Ageing Study-2 findings. Journal of Alzheimer's Disease 34, 649–657
4. Alberti, K. G. M. M. et al. (2009), Harmonizing the metabolic syndrome: a joint interim statement of the International Diabetes Federation Task Force on Epidemiology and Prevention; National Heart, Lung, and Blood Institute; American Heart Association; World Heart Federation; International Atherosclerosis Society; and International Association for the Study of Obesity. Circulation 120, 1640–1645
5. Sanger, F., Nicklen, S. & Coulson, A. R. (1977), DNA sequencing with chain-terminating inhibitors. Proceedings of the National Academy of Sciences 74, 5463–5467

Poster No 1140

Sensitivity of BOLD functional MRI low frequency fluctuations to age-related brain changes

Jessica Korte[1], Wilsaan Joiner[1], Audrey Fan[1]

[1]*University of California, Davis, Davis, CA*

Introduction: As the global population ages, it is vital to understand healthy aging in the brain. However, within functional MRI (fMRI) analysis, there is no established metric of healthy aging. Here, we quantify reproducibility and directly compare Amplitude of Low Frequency Fluctuations (ALFF) and fractional-ALFF (fALFF) in the cerebellum, a crucial structure for learning, motor control, and coordination, on a cohort selected from Human Connectome Project (HCP) datasets[1]. ALFF and fALFF characterize the intensity of local, spontaneous BOLD fMRI fluctuations between 0.01 and 0.08 Hz, a frequency range reflective of neuronal activity[2]. Moreover, ALFF frequency sub-bands, specifically slow-3 frequencies (slow-3f) [0.073-0.198 Hz] have demonstrated similar spectral patterns to neuronal firing[3]. Slow-3f appear stronger in cerebellar areas[5], making this sub-frequency an ideal candidate to study age-related functional changes within the cerebellum.

Methods: Data from 12 young subjects (YS; 22-35 years; 6 male) and 12 senior subjects (SS; 65-79 years; 6 male) were accessed via the HCP Young Adult S1200 and Aging datasets, respectively. Subjects successfully completed both resting-state (rs) scans without reported quality issues. MRI scans included 2 initial rs-scans and 2 follow-up rs scans. For YS, the fMRI parameters included the following: TR: 702ms, spatial resolution: 2mm isotropic, duration: 14.4 minutes, multi-band factor: 8. For SS, the parameters were: TR: 800ms, spatial resolution: 2mm isotropic, duration: 14 minutes, multi-band factor: 8. CONN was used for preprocessing of the T1 and rs-fMRI images, and included functional realignment, slice-timing correction, normalization to MNI space and resampling of the T1 image to rs-fMRI resolution. The first 5 timepoints were discarded to account for relaxation effects. Denoising included linear regression of movement, CSF, and white matter[4]. The denoised signal was then Fourier transformed, filtered to standard (f)ALFF frequencies, and later to [0.073 0.198] Hz for slow-3f (f)ALFF. ALFF is a voxel-wise measurement, calculated by summing the amplitude across the frequency-filtered spectrum, then taking the square root of this metric. fALFF is calculated similarly but is divided by the sum of amplitudes across the full, non-filtered spectrum. Both metrics were normalized to whole-brain (f)ALFF to enable comparison across participants. All statistical analysis included cluster and multiple comparison correction and was conducted in SPM12.

Results: Reproducibility analysis via paired t-tests showed high stability for (f)ALFF across rs-scans in both groups. YS demonstrated higher ALFF than fALFF in subcortical and ventricular regions, as has been shown previously[5]. SS did not demonstrate any ALFF-fALFF differences. As a result, ALFF was selected as the metric for comparison given previous demonstration of repeatability and sensitivity[5]. Slow-3f ALFF demonstrated high values (p-uncorrected<0.001, p-FWE corrected<0.05, cluster size>20) within ventricle and white matter regions relative to average whole-brain slow-3f ALFF for both groups (Fig.1), indicating sensitivity to physiological effects. Comparison between YS and SS maps of slow-3f ALFF yielded differences between senior and younger participants (p-uncorrected<0.001, p-FWE corrected<0.05, cluster size>20), as illustrated in Fig. 2.

Figure 1

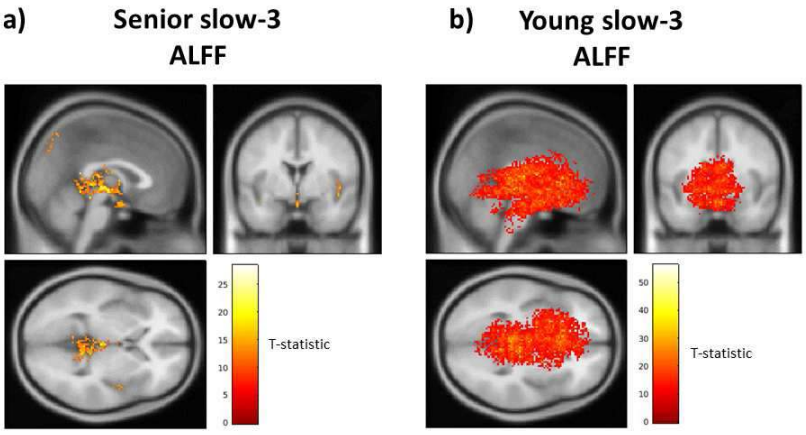

A) Areas where slow-3f ALFF was higher than average whole-brain slow-3f ALFF values for SS (p<0.001, p-FWE<0.05, cluster > 20). High values were confined to CSF areas and one posterior area.
B) Areas where slow-3f ALFF was higher than average whole-brain slow-3f ALFF values for YS (p<0.001, p-FWE<0.05, cluster > 20). YS demonstrated high values in ventricles, CSF, and throughout subcortical white matter.

Figure 2

a) Senior > Young

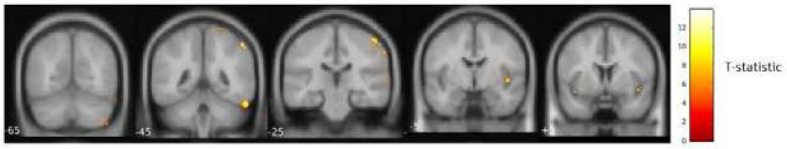

Areas of higher slow-3f ALFF in SS compared to YS. Areas included the right cerebellum exterior, right inferior temporal gyrus, right pre/post-central gyrus, and auditory canals.

b) Senior < Young

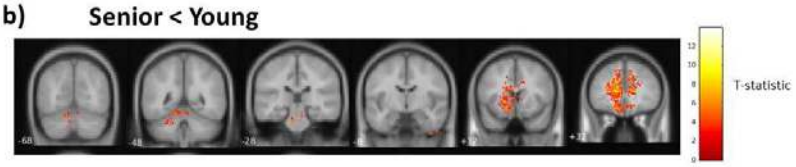

Areas of lower slow-3f ALFF in SS compared to YS. Areas included right vermal lobules I-IV, left exterior cerebellum, brain stem, frontal lobe gray and white matter

Conclusions: This preliminary study suggests that ALFF may be a more sensitive metric than fALFF in detecting healthy aging changes. Decreased vascular reactivity and pulsatile CSF movement with age may result in smaller slow-3f ALFF in ventricles and vascular areas. Slow-3f ALFF varies with age within the cerebellum, sensorimotor areas, and frontal regions. Future work will incorporate more participants into this study, apply the SUIT atlas, and will investigate the sensitivity of other sub-frequency bands changes to aging.

References

1. D. C. Van Essen et al., "The Human Connectome Project: a data acquisition perspective," Neuroimage, vol. 62, no. 4, pp. 2222–2231, Oct. 2012, doi: 10.1016/j.neuroimage.2012.02.018.
2. J. Zhang et al., "The neural correlates of amplitude of low-frequency fluctuation: a multimodal resting-state MEG and fMRI–EEG study," Cerebral Cortex, vol. 33, no. 4, pp. 1119–1129, Feb. 2023, doi: 10.1093/cercor/bhac124.
3. M. Woletz et al., "Beware detrending: Optimal preprocessing pipeline for low-frequency fluctuation analysis," Human Brain Mapping, vol. 40, no. 5, pp. 1571–1582, 2019, doi: 10.1002/hbm.24468.
4. X.-N. Zuo et al., "The oscillating brain: Complex and reliable," NeuroImage, vol. 49, no. 2, pp. 1432–1445, Jan. 2010, doi: 10.1016/j.neuroimage.2009.09.037.
5. Z. Yu-Feng et al., "Altered baseline brain activity in children with ADHD revealed by resting-state functional MRI," Brain and Development, vol. 29, no. 2, pp. 83–91, Mar. 2007, doi: 10.1016/j.braindev.2006.07.002.

Poster No 1141

Impact of Genetics on the Aging of Functional Connectivity with BrainAGE using the UK Biobank

Karen Ardila[1,2,3,4], Aashka Mohite[1,2,3,4], Emily Munro[1,2,3,4,5], Abdoljalil Addeh[1,2,3,4], Charlotte Curtis[2,6], Quan Long[4,7], M. Ethan MacDonald[1,2,3,4]

[1]Department of Biomedical Engineering, University of Calgary, Calgary, Alberta, Canada, [2]Department of Electrical Engineering & Software Engineering, University of Calgary, Calgary, Alberta, Canada, [3]Department of Radiology, University of Calgary, Calgary, Alberta, Canada, [4]Hotchkiss Brain Institute, University of Calgary, Calgary, Alberta, Canada, [5]Department of Chemical Engineering, University of Calgary, Calgary, Alberta, Canada, [6]Department of Mathematics & Computing, Mount Royal University, Calgary, Alberta, Canada, [7]Department of Biochemistry & Molecular Biology, University of Calgary, Calgary, Alberta, Canada

Introduction: Brain aging leads to altered connectivity in rfMRI studies and is influenced by genetic factors, yet the full impact of genetics remains unclear (Pang et al., 2019). Recent advances in neuroimaging and machine learning have resulted in models that predict brain aging by calculating the Brain Age Gap Estimate (BrainAGE), a useful biomarker for neurological diseases (Sanford et al., 2022), from the difference between the model's predicted age and the chronological age (Foo et al., 2020; Wilms et al., 2020; Gonneaud et al., 2021; Ardila et al., 2023). BrainAGE models suggest that brain systems vulnerable to aging overlap with those susceptible to neurodegeneration but are limited in cohort sizes and approach (Zhao et al., 2019; Brouwer et al., 2022). This research aims to investigate the genetic underpinnings of functional connectivity changes during brain aging using machine learning, neuroimaging, and genetic data from the UK Biobank.

Methods: This cross-sectional study utilized genetic and rfMRI partial correlation matrices (upper diagonal) data from 37,449 subjects (aged 44-82, mean 64 years, 52.2% female) from the UK Biobank. BrainAGE was computed by inputting measurements from each correlation matrix (Fig. 1) to a machine learning based age prediction model with bias correction (Beheshti et al., 2019). A Genome-wide association study (GWAS) was conducted using the BrainAGE as a phenotype input. The GWAS was implemented with PLINKv1.9 (Chang et al., 2015), with rigorous data quality control including filtering based on missingness, sex discrepancy, minor allele frequency, Hardy-Weinberg equilibrium, and familial relatedness (Marees et al., 2018). Associations with a p-value less than 1e-04 were considered significant genetic variants to accelerated aging of functional connectivity.

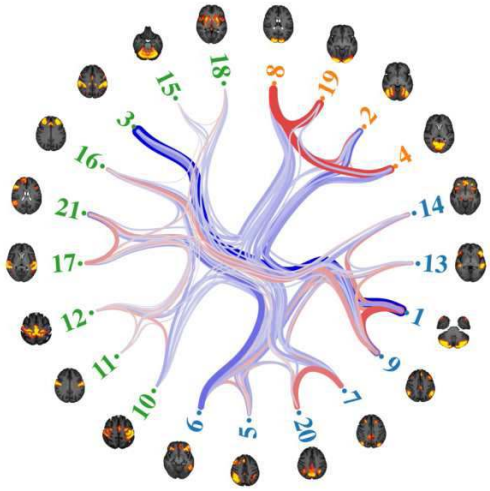

Fig. 1. Connections between brain regions from rfMRI, where the node numbers refer to the set non-artefactual group-ICA components, the color edges and scale edge width corresponds to the partial correlation values (-3.87 to 3.87).

Results: The BrainAGE model performance presented an R-squared score of 0.86 and a mean absolute error of 2.18. The GWAS identified 78 candidate single-nucleotide polymorphisms (SNPs), 10 independent significant SNPs, and 7 lead SNPs. The phenogram of the GWAS results related to accelerated brain aging shows the corresponding effect of each independent significant SNP across the human genome (Fig. 2). The genes found were TOMM40, previously related to Alzheimer's disease, body mass index, cardiovascular disease risk factors, age-related macular degeneration, longevity, and cerebrospinal fluid t-tau levels (GWAS Catalog, 2023a); APOE, with Alzheimer's disease biomarker, cholesterol levels, hippocampal volume, cerebrospinal fluid t-tau levels, parental longevity, and C-reactive protein levels (GWAS Catalog, 2023b); APOC1, with Alzheimer's disease biomarker, cholesterol levels, longevity, cerebrospinal fluid amyloid beta 42 levels, and C-reactive protein levels (GWAS Catalog, 2023c); and finally, SRXN1 with body mass index, height, autism spectrum disorder, attention deficit-hyperactivity disorder, bipolar disorder, major depressive disorder, and schizophrenia (GWAS Catalog, 2023d).

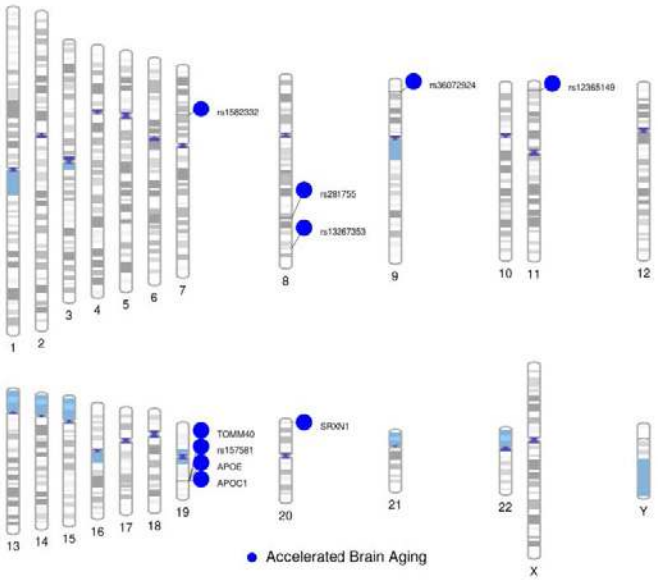

Fig. 2. Phenogram of GWAS significant SNPs and genes associated with brain alterations in connectivity, illustrating their corresponding loci in the human genome across each chromosome (http://visualization.ritchielab.org/).

Conclusions: This study investigated the genetic predisposition of specific SNPs and genes in relation to rfMRI brain correlation matrix changes and accelerated brain aging. The main contributions are the associations with genes predominantly related with longevity, Alzheimer's disease, cerebrospinal fluid t-tau levels and amyloid beta, C-reactive protein levels, and mental traits. Suggestions for future research to enhance the BrainAGE prediction model include the potential the inclusion of additional or different imaging modalities for more precise or varied detection of SNPs. The study identified several gene associations with brain aging, contributing to the knowledge of the genetic underpinnings of brain aging related to connectivity, and paving the way for potential precision medicine targets.

References

1. Ardila, K. et al. (2023) 'Using Machine Learning to Study the Effects of Genetic Predisposition on Brain Aging in the UK Biobank', Proceedings - International Symposium on Biomedical Imaging, 2023-April.
2. Beheshti, I. et al. (2019) 'Bias-adjustment in neuroimaging-based brain age frameworks: A robust scheme', NeuroImage: Clinical, 24, p. 102063.
3. Brouwer, R.M. et al. (2022) 'Genetic variants associated with longitudinal changes in brain structure across the lifespan', Nature Neuroscience, 25(4), pp. 421–432.
4. Chang, C.C. et al. (2015) 'Second-generation PLINK: Rising to the challenge of larger and richer datasets', GigaScience, 4(1), p. 7.
5. Foo, H. et al. (2020) 'Genetic influence on ageing-related changes in resting-state brain functional networks in healthy adults: A systematic review', Neuroscience & Biobehavioral Reviews, 113, pp. 98–110.
6. Gonneaud, J. et al. (2021) 'Accelerated functional brain aging in pre-clinical familial Alzheimer's disease', Nature Communications 2021 12:1, 12(1), pp. 1–17.
7. GWAS Catalog (2023a) Gene TOMM40.
8. GWAS Catalog (2023b) Gene APOE.
9. GWAS Catalog (2023c) Gene APOC1.
10. GWAS Catalog (2023d) Gene SRXN1.
11. Marees, A.T. et al. (2018) 'A tutorial on conducting genome-wide association studies: Quality control and statistical analysis'.
12. Pang, S.Y.Y. et al. (2019) 'The interplay of aging, genetics and environmental factors in the pathogenesis of Parkinson's disease', Translational Neurodegeneration 2019 8:1, 8(1), pp. 1–11.
13. Sanford, N. et al. (2022) 'Sex differences in predictors and regional patterns of brain age gap estimates', Human Brain Mapping, 43(15), pp. 4689–4698.
14. Wilms, M. et al. (2020) 'Bidirectional Modeling and Analysis of Brain Aging with Normalizing Flows', Lecture Notes in Computer Science (including subseries Lecture Notes in Artificial Intelligence and Lecture Notes in Bioinformatics), 12449 LNCS, pp. 23–33.
15. Zhao, B. et al. (2019) 'Genome-wide association analysis of 19,629 individuals identifies variants influencing regional brain volumes and refines their genetic co-architecture with cognitive and mental health traits', Nature Genetics, 51(11), pp. 1637–1644.

Poster No 1142

Significant but limited influence of cerebrovascular reactivity on age and sex in task & rest fMRI

Donna Chen[1], Xin Di[1], Xin Yu[2], Bharat Biswal[1]

[1]New Jersey Institute of Technology, Newark, NJ, [2]Harvard Medical School, Charlestown, MA

Introduction: Functional magnetic resonance imaging (fMRI) measures the blood-oxygen-level dependent (BOLD) signals, which provide an indirect measure of neural activity mediated by neurovascular responses. Cerebrovascular reactivity (CVR) affects both task-induced and resting-state BOLD activity and may confound inter-individual effects observed in BOLD-based measures, such as those related to aging and biological sex[1,2]. To disentangle these, we examined a large open-access fMRI dataset containing a breath-holding (BH) task, checkerboard task, and resting-state scans.

Methods: MRI data were collected from the Enhanced Nathan Kline Institute – Rockland Sample[3]. Participants were selected based on those without any psychiatric or neurological disorders and had undergone a baseline MRI session (8 to 85 years, mean age: 43.6 years, standard deviation: 21.5 years, 334 F, 174 M). The BH task, checkerboard task, and resting-state scans were used, and we applied voxel-wise general linear models (GLM) to estimate task activations or to remove confounding signals in the resting-state scans. For the resting-state scans, the amplitude of low-frequency fluctuations (ALFF) and regional homogeneity (ReHo) were calculated. To examine whether BH activity explains individual differences in task and resting-state activations, we calculated voxel-wise correlations between BH CVR maps and the other three maps, i.e., checkerboard activations, ALFF, and ReHo. To examine age and sex effects on each of the brain activation maps, we performed group-level voxel-wise GLM, which included age, age2, and sex regressors. After observing age or sex effects on brain activations in the checkerboard or resting-state conditions, we investigated whether the same brain regions showed correlations with CVR. We identified the regions of interest by overlapping the previously mentioned maps and extracted the mean values of both BOLD activity and CVR. To adjust the BOLD activity using CVR, two methods were used. First, we introduced CVR as a covariance in the age/sex effects model to assess how its inclusion affected the observed changes. Second, we initially regressed out CVR from the BOLD activity measurement, and then employed the same model to investigate the effects of age and sex. This allowed us to evaluate the impact of the adjustments.

Results: The ALFF activation map appeared to be similar to the BH CVR map, where the strongest values were in the lateral and medial prefrontal cortex, and subcortical regions. In contrast, the mean ReHo map had stronger values in the parietal and occipital regions (Figure 1). We observed age-effects of BH CVR, particularly in regions with large vessels (e.g., near the top of the midline region and near the insula). Sex effects were present across large brain regions compared with age effects, mainly located in the frontal white matter regions, but extended to the nearby gray matter regions in the prefrontal cortex. For the checkerboard task, significant age effects were observed in the posterior part of the thalamus and right sensorimotor regions, and no sex effects were observed. The regions with significant age effects did not overlap with the regions showing correlations with CVR (Figure 2). For resting-state ALFF, sex effects appeared to overlap with regions correlated with CVR, which is in contrast to the age effects. For the resting-state ReHo maps, we found age effects covering almost the entire cortex and subcortical regions (Figure 2).

Conclusions: Using a large-sample fMRI dataset, we showed that individual differences in CVR as measured by a BH task were correlated with BOLD activity during a simple checkerboard task and in resting-state, although the effect sizes were limited. The observed age and sex effects on task and resting-state brain activity were stronger than those explained by breath-holding activity. Adjusting for breath-holding activity had limited effects on the estimated age and sex effects.

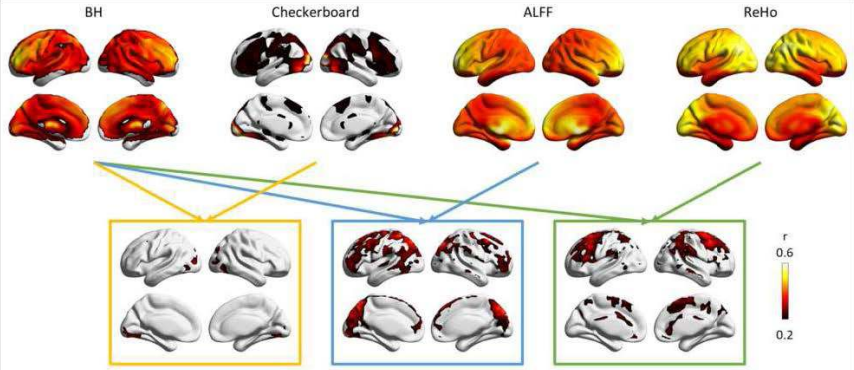

Figure 1 Top row, group averaged activation maps for the breath-holding (BH) task, checkerboard task, and resting-state task (represented as low-frequency-fluctuations (ALFF) and regional homogeneity (ReHo)). Bottom row, voxel-wise correlations between BH cerebrovascular reactivity, and checkerboard activations and resting-state parameters.

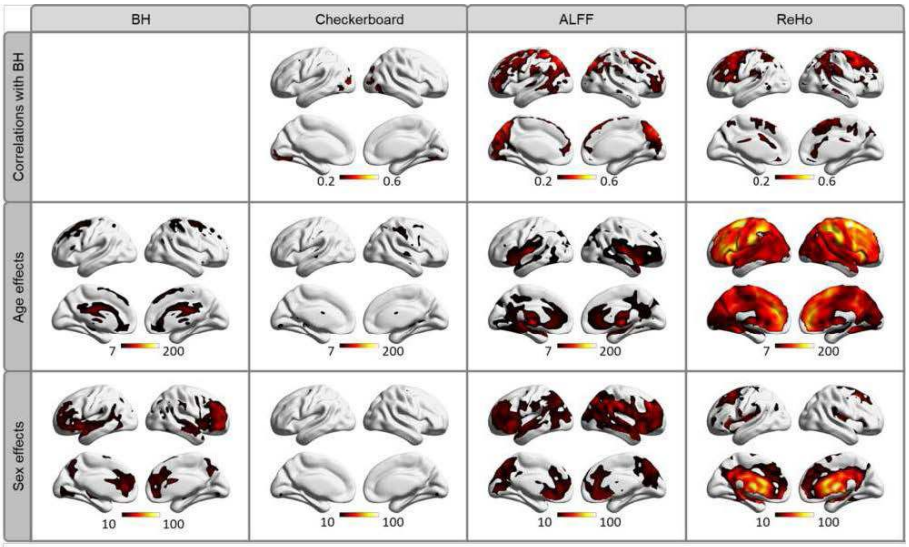

Figure 2. Top row, voxel-wise correlations of breath-holding (BH) cerebrovascular reactivity with checkerboard activation, amplitude of low-frequency fluctuations (ALFF), and regional homogeneity (ReHo). Middle row, age effects (F contrast of linear and quadratic effects) for the four maps. Bottom row, sex effects of the four maps.

References

1. Kastrup, A., Dichgans, J., Niemeier, M., & Schabet, M. (1998), 'Changes of cerebrovascular CO2 reactivity during normal aging. Stroke, 29, 1311-1314.
2. Thomason, M.E., Burrows, B.E., Gabrieli, J.D.E., & Glover, G.H. (2005), 'Breath holding reveals differences in fMRI BOLD signal in children and adults. NeuroImage, 25, 824-837.
3. Nooner, K., et al. (2012), 'The NKI-Rockland sample: a model for accelerating the pace of
4. discovery science in psychiatry. Frontiers in Neuroscience, 6.

Poster No 1143

Influences of brain iron and glutamate on changes in brain activity during working memory in aging

Jonatan Gustavsson[1], Farshad Falahati[2], Rouslan Sitnikov[3], Amirhossein Manzouri[4], Goran Papenberg[1], Alireza Salami[5], Jonas Persson[6], Grégoria Kalpouzos[7]

[1]Aging Research Center, Karolinska Institutet, Stockholm, Stockholm, [2]Aging Research Center, Karolinska Institutet, Stockholm, Sweden, [3]MRI Research Center, Karolinska University Hospital, Stockholm, Stockholm, [4]Department of Psychology, Stockholm University, Stockholm, Stockholm, [5]Karolinska Institutet & Umeå University, Stockholm, Stockholm, [6]Karolinska Institutet, Stockholm, Sweden, [7]Karolinska Institutet, Stockholm, Stockholm

Introduction: Iron is vital for several neurobiological mechanisms, such as neurotransmitters' synthesis. However, brain iron overload, associated with age-related iron dyshomeostasis, is detrimental as it leads to oxidative stress and neuroinflammation[1]. This likely contributes to alterations in neural-activity (as measured with blood oxygen level-dependent magnetic resonance imaging (BOLD MRI)) and cognitive deficits, including working memory[2,3]. Astrocytes are responsible for transporting glutamate, a neurotransmitter with antioxidant properties protecting the brain tissue from inflammatory insults[4]. They are also vulnerable to heavy metal toxicity, which can lead to BOLD alteration since astrocytes are involved in neurovascular coupling[5,6]. A healthy glutaminergic system may attenuate iron-mediated damage such as BOLD deficits. However, cross-sectional and longitudinal studies on the iron-glutamate relationship are lacking, with only one study linking more blood iron to less glutamate[7].

Methods: Using data from the 3-year longitudinal IronAge project (baseline n = 208; 20–79 years, follow-up n = 135), we aimed to investigate (1) the relationship between brain iron and glutamate as a function of age, (2) if brain iron content is linked to longitudinal changes of brain activity in normal aging, and (3) whether glutamate mediates the relationship between brain iron and brain activity. Participants underwent MRI (3.0T GE scanner) to assess brain iron, glutamate, and brain activity during an N-back working-memory task. Iron content was assessed using quantitative susceptibility mapping and glutamate concentration was measured using 1H MR spectroscopy in striatum and dorsolateral prefrontal cortex (DLPFC). Functional MRI data were processed with fmriprep and analyzed in SPM12 software. Working memory performance was calculated as d' (d-prime).

Results: Firstly, whereas there were no significant associations between iron and glutamate in the whole sample (striatum: r = -0.04, p = 0.7; DLPFC: r = 0.006, p = 0.9), we found differential relationships in DLPFC when stratifying by age group (Figure 1): In younger adults (20-39 years old), higher iron was related to higher glutamate at trend level, but in older adults (60-79) higher iron was associated with lower glutamate (younger: r = 0.34, p = 0.06; middle-aged: r = 0.014, p = 0.4; older: r = -0.33, p = 0.03). Secondly, difference of activation during 2- and 3-back (contrasted with 1-back) between the 2 timepoints showed decreased activation in right DLPFC (p < 0.001) over time at a group level (Figure 2). A multiple regression model revealed no association between activation and baseline iron in DLPFC (β = -0.097, p = 0.3). However, stratifying by age groups showed that decreased activation was associated with more baseline iron in DLPFC among younger adults only (younger: β = -0.48, p = 0.01; middle-aged: β = 0.16, p = 0.3; older: β = 0.06, p = 0.7). Further, there were no associations with glutamate at baseline (ps > 0.3). Thirdly, glutamate did not improve the fit of the model (R2 change = 0.01), nor did it attenuate the association between iron and activation. Finally, neither baseline iron nor glutamate were related to working memory performance in the whole group (ps > 0.3) nor within age groups (ps > 0.2).

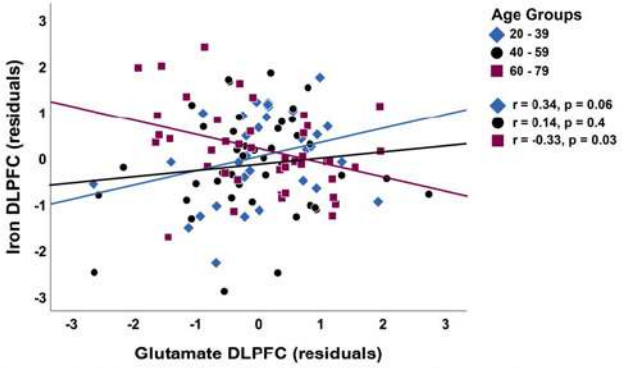

Figure 1: The relationship between brain iron and glutamate in DLPFC as a function of age (values residualised for age and DPFC volume).

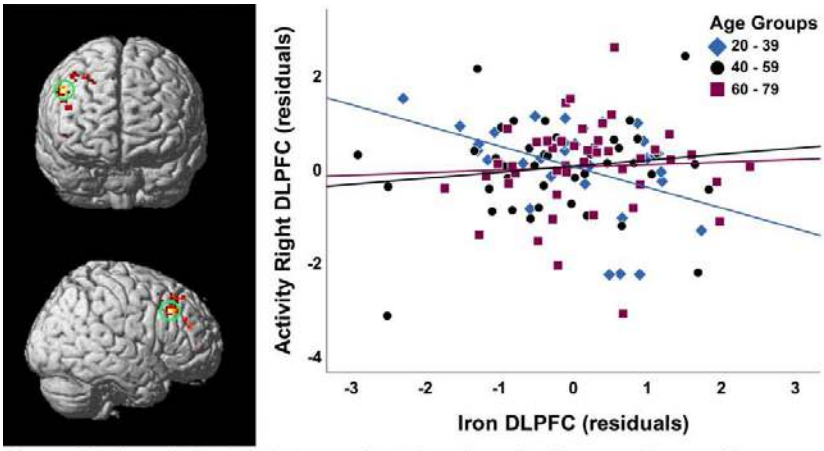

Figure 2: The relationship between frontal underactivation over time and iron. **Left:** Clusters with underactivation in right DLPFC (first eigenvariate of the cluster circled in green extracted in SPM). **Right:** The association between activation and iron in right DLPFC (values residualised for age and DPFC volume).

Conclusions: These findings indicate an association between iron and glutamate in the human brain that is modulated by age. The opposite patterns observed between younger and older adults may reflect the progress of astrocytic dysfunction; in young age iron is still in homeostasis, whereas in old age iron dyshomeostasis disrupts the glutaminergic system. Further, our results indicate that glutamate does not play a role in the relationship between iron content and decreased DLPFC activation during working memory performance.

References

1. Ward, R. J., Zucca, F. A., Duyn, J. H., Crichton, R. R., & Zecca, L. (2014). The role of iron in brain ageing and neurodegenerative disorders. The Lancet Neurology, 13(10), 1045–1060. https://doi.org/10.1016/S1474-4422(14)70117-6
2. Kalpouzos, G., Garzón, B., Sitnikov, R., Heiland, C., Salami, A., Persson, J., & Bäckman, L. (2017). Higher Striatal Iron Concentration is Linked to Frontostriatal Underactivation and Poorer Memory in Normal Aging. Cerebral Cortex, 27(6), 3427–3436. https://doi.org/10.1093/cercor/bhx045
3. Daugherty, A. M., Haacke, E. M., & Raz, N. (2015). Striatal iron content predicts its shrinkage and changes in verbal working memory after two years in healthy adults. Journal of Neuroscience, 35(17), 6731–6743. https://doi.org/10.1523/JNEUROSCI.4717-14.2015
4. Li, B., Xia, M., Zorec, R., Parpura, V., & Verkhratsky, A. (2021). Astrocytes in heavy metal neurotoxicity and neurodegeneration. Brain Research, 1752(77), 147234. https://doi.org/10.1016/j.brainres.2020.147234
5. Dringen, R., Bishop, G. M., Koeppe, M., Dang, T. N., & Robinson, S. R. (2007). The Pivotal Role of Astrocytes in the Metabolism of Iron in the Brain. Neurochemical Research, 32(11), 1884–1890. https://doi.org/10.1007/s11064-007-9375-0
6. Koehler, R. C., Roman, R. J., & Harder, D. R. (2009). Astrocytes and the regulation of cerebral blood flow. Trends in Neurosciences, 32(3), 160–169. https://doi.org/10.1016/j.tins.2008.11.005
7. Burger, A, Kotze, MJ, Stein, DJ, Janse van Rensburg, S, Howells, FM. The relationship between measurement of in vivo brain glutamate and markers of iron metabolism: A proton magnetic resonance spectroscopy study in healthy adults. Eur J Neurosci. 2020; 51: 984–990. https://doi.org/10.1111/ejn.14583

Poster No 1144

Predicting Brain Aging (Brain Age Gap) from Biomedical and Lifestyle Variables

Mostafa Mahdipour[1,2], Somayeh Maleki Balajoo[1,2], Federico Raimondo[1,2], Eliana Nicolaisen-Sobesky[1,2], Shammi More[1,2], Felix Hoffstaedter[1,2], Masoud Tahmasian[1,2,3], Simon Eickhoff[1,2], Sarah Genon[1,2]

[1]Institute of Systems Neuroscience, Heinrich Heine University Düsseldorf, Düsseldorf, Germany, [2]Institute of Neuroscience and Medicine (INM-7: Brain and Behaviour), Research Centre Jülich, Jülich, Germany, [3]Department of Nuclear Medicine, Faculty of Medicine and University Hospital Cologne, University of Cologne, Cologne, Germany

Introduction: The Brain Age Gap (BAG) can be considered as an indicator of the brain health[1,2]. BAG is defined as the difference between an individual's chronological age and the age predicted by a machine learning (ML) algorithm based on individual brain features. While some studies demonstrated univariate associations between the BAG and several lifestyle and biomedical variables[2,3], a substantial gap persists in understanding the multivariate association between these factors and BAG. Here, we addressed this question by using a wide range of biomedical, lifestyle, and sociodemographic variables conjointly to predict the BAG in a large population of the UK Biobank.

Methods: We built a ML model to predict an individual's brain age using brain structural features (cortical and subcortical parcellated grey matter volume) in a subset of specifically healthy participants in the UK Biobank (n=5,025, age range 46-

82 years, 2,579 females). In particular, we applied ridge regression implemented in the Julearn package[4]. Subsequently, the optimized predictive brain model was applied to predict brain age in the remaining UK Biobank participants (n =34,365, age range 44-82 years, 18,128 females) (Fig 1A). The BAG was then computed following the adjustment of predicted brain ages for proportional bias based on regression parameters from the training set[5]. For predicting an individual's BAG, we selected 157 variables covering biomedical (e.g., cardiovascular, respiratory, and body metabolism), lifestyle (e.g. smoking and diet) and sociodemographic (e.g.: socioeconomical status, family and social life) variables in a subset of 7,736 participants not included in the healthy subset used to build the age prediction model (age range 44-81 years, 4,272 females). In order to train the model, we used a random forest algorithm as implemented in Julearn[4] with a nested cross-validation approach including 10 inner and outer folds. Notably, we controlled for possible confounds (age, age2, sex, height, and volumetric scaling from the T1 image to standard space).

Results: We achieved a high level of accuracy in predicting chronological age using brain structural features. The average cross-validation Mean Absolute Error (MAE) of 3.75 years closely mirrored the MAE of the best model applied to the population data, which was 3.93 years and the correlation between chronological and predicted age was strong (r = 0.75 for the prediction model and 0.76 for the population data, Fig 1B). Using bias correction on the population's predicted brain age led to a relatively unbiased BAG with regards to age (Fig 1C). We then found that individual BAG could be robustly predicted to some extent by phenotypical variables with an average (across test folds) correlation between the predicted BAG and calculated BAG of 0.239±0.02, MAE of 4.54±0.10 years, and a Root Mean Square Error of 5.72±0.12 years. Examining mean features importance (Fig 2) further reveals that most features are relevant for the prediction. Nevertheless, biomedical factors, closely followed by lifestyle factors, appear to play a relatively more important role than sociodemographic variables.

Conclusions: We successfully developed a brain age prediction model in a healthy sample that enables to compute brain age gap as a sensitive estimator of individual brain structural health in an aging population. Although the relationships between any individual factor and brain structural health can be seen as negligible based on previously reported effect sizes[6], here we showed that considering a range of variables jointly enables a decent prediction of BAG. Although no set of variables appear to play a crucial role here, biomedical factors related to body metabolism and cardiovascular systems, as well lifestyle factors directly influencing these later (such as smoking and alcohol consumption) appear relatively important for structural brain health.

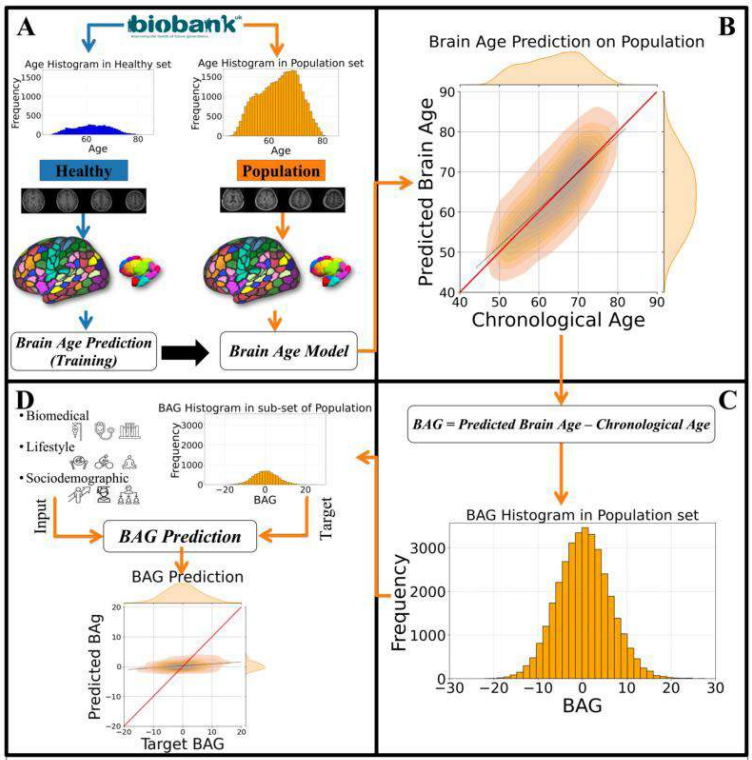

Fig 1. (A) Brain Age Prediction: After dividing the whole UK Biobank cohort into healthy and target population sub-sets, the healthy sub-set was used to design the Brain Age prediction model. In this model, Gray Matter Volumes (GMVs) of different cortical and subcortical brain parcels were used as feature inputs and chronological ages as target. Then GVMs of the population sub-set were used to predict the population's brain ages. **(B) Predicted Brain Age Vs Chronological/True Age** after bias correction; the red line is the identity line and the black dotted line is the best-fitted line based on joint scatter distribution of predicted and true ages. **(C) BAG Calculation:** By subtracting chronological/true ages from bias-corrected predicted ages Brain Age Gap (BAG) can be calculated; As shown here, some participants have positive BAG which means their brain is older than their true age while some have negative BAG. **(D) BAG Prediction:** A wide range of variables mainly in biomedical, lifestyle, and sociodemographic categories were used conjointly to predict the BAG in 7735 UK Biobank participants.

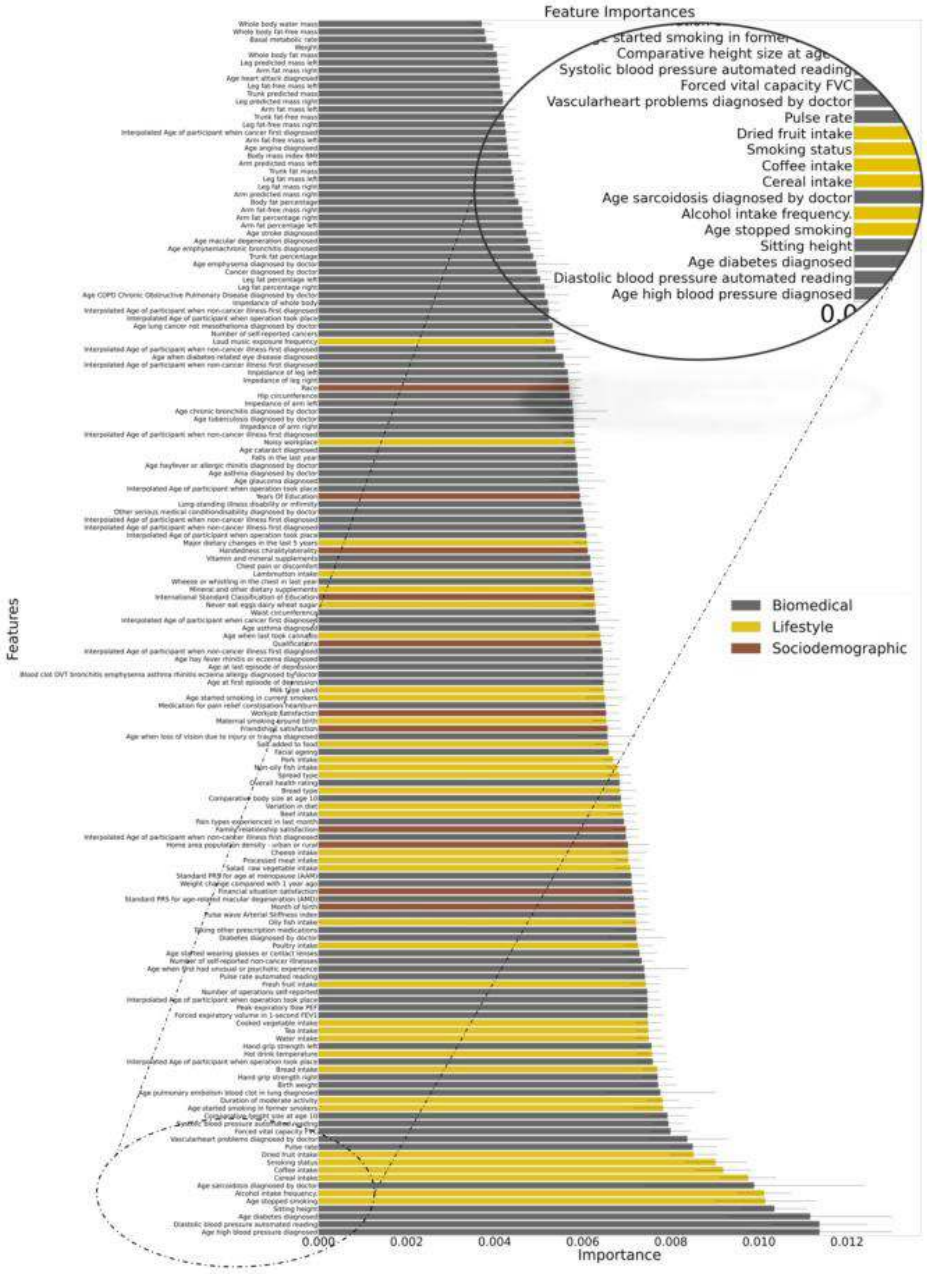

Fig 2. Mean features' importance across the outer folds for the BAG prediction: The use of random forest ML model allows us to examine the importance of features in predicting BAG based on the reduction of impurity criterion. Error bars represents standard deviation across folds.

References

1. Cole, J. H. (2020). "Multimodality neuroimaging brain-age in UK biobank: relationship to biomedical, lifestyle, and cognitive factors." Neurobiology of aging 92: 34-42.
2. Hamdan, S., et al. (2023). "Julearn: an easy-to-use library for leakage-free evaluation and inspection of ML models." arXiv preprint arXiv:2310.12568.
3. Miller, K. L., et al. (2016). "Multimodal population brain imaging in the UK Biobank prospective epidemiological study." Nature neuroscience 19(11): 1523-1536.
4. More, S., et al. (2023). "Brain-age prediction: A systematic comparison of machine learning workflows." NeuroImage 270: 119947.
5. Smith, S. M., et al. (2019). "Estimation of brain age delta from brain imaging." NeuroImage 200: 528-539.
6. Tian, Y. E., et al. (2023). "Heterogeneous aging across multiple organ systems and prediction of chronic disease and mortality." Nature Medicine 29(5): 1221-1231.

Poster No 1145

Short-range white matter tracts modulate global parameters for neurocompensation in aging

Priyanka Chakraborty[1], Suman Saha[1], Arpan Banerjee[2], Dr Dipanjan Roy[3]

[1]National Brain Research Center, Gurgaon, Haryana, [2]National Brain Research Centre, Gurgaon, Haryana, [3]School of AIDE, Center for Brain Research and Applications, IIT Jodhpur, Jodhpur, Rajasthan

Introduction: An overarching question in aging neuroscience is how the brain compensates for age-related white matter deterioration and sustains its normative pattern in neuronal dynamics across lifespan. Neuroplasticity, a recognized neurocompensatory mechanism, involves synaptic modifications and modulation of biological parameters (Park & Reuter-Lorenz 2009) in face of age related structural changes. Increased global coupling strength compensates for structural loss during healthy aging, and enhanced inter-areal coupling preserves neural synchrony (Pathak et al. 2022). Nonetheless, short-range (SR) white matter tracts allow fast and efficient local communication across the brain (Mišić & Betzel 2015), whereas, long-range (LR) tracts are crucial for integrating information among distant areas (Sporns & Zwi 2004). However, how the brain's sub-graphs comprises of SR and LR tracts contribute to this neurocompensatory mechanism keeping functional integrity intact in healthy aging process is not completely understood. We aim to investigate how two sub-communities comprising SR and LR tracts modulate biophysical parameters to compensate for age related decline and specifically explore their roles in calibrating global interaction strength and conduction delay in age-related neurocompensation. We categorize white matter fibers into SR and LR connections based on their physical length distributions and employ metastability and an anatomically constrained whole-brain network model to assess how these sub-graphs influence the model parameters using structural connectivity data from individuals.

Methods: The study includes 82 healthy subjects (43 F and 39 M) from CamCAN, which are separated into two groups: 41 young (18-33 years, mean = 25±4 years, 22 F), and 41 old subjects (60-86 years, mean = 74±6.8 years, 21 F). We used Desikan-Killany parcellation of 68 cortical regions. We defined SR and LR connections based on the fiber lengths using two thresholds selected from first quartile (70 mm for SR) and third quartile (140 mm for LR) of the average tract length distribution. The maximum fiber length is set to 250mm. We utilized the Kuramoto model (Kuramoto 1984) to capture metastability in a network, where the input to the model is SC of individual subjects. For each pair of the two parameters (κ, τ), we measure the metastability M(κ, τ) and generated a metastability map on two-parameter plane. Next, we estimate the optimal parameters utilizing the condition, [κ, τ]opt= argmax[(M(κ, τ)). The optimal parameters are estimated at the level of individuals. Next, we compared the estimated parameters between young and old groups using independent t-test.

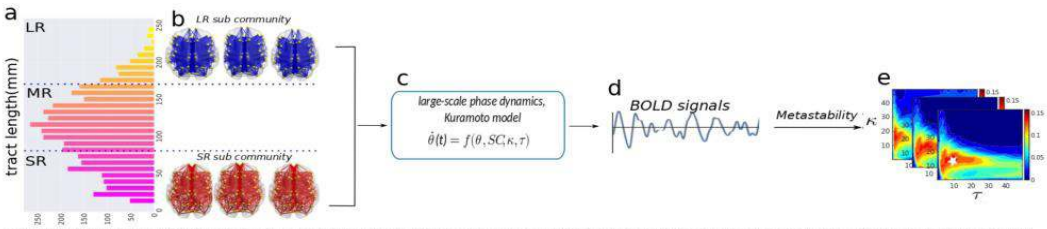

a) The graph shows the average distribution of tract length among young subjects of CamCAN dataset, where the blue vertical lines represent the lower (70mm) and upper (140mm) thresholds. The lengths are categorized into short-range (SR), middle-range (MR), and long-range (LR) based on the thresholds. (b) SR and LR sub community of each subjects. (c) Each sub community fetch to a large scale phase dynamics model, Kuramoto model. d) BOLD signals generated for each ROIs. e) Global metastability map for parameters k and τ has been calculated. White star show the region of maximaum metastability and the corresponding k and τ has been choosen as optimal parameters.

Results: The empirical structural analysis shows a significant reduction in fiber lengths and white matter counts or strengths in old subjects compared to younger participants. We also observed an age-related alteration in empirical functional network properties, whereas the empirical metastability remains constant between the two age groups. Overall, the results indicate a re-organisation in functional network and preservation in whole-brain dynamical repertoire. The simulated results reveal a significant increase in coupling strength in older adults compared to the young. We observed no significant difference between the optimal coupling strength of older adults and the short-range (SR) sub-community. Hence, the SR sub-community enhanced its coupling strength to maintain the desired set point while preserving functional integrity in the face of lost LR connections.

Conclusions: SR compensate for long-range fiber loss by modulating global coupling, effectively rescaling altered local interaction strengths (SC). Our study is useful for understanding the mechanisms underlying the brain's function in neural disorders, including Alzheimer's and Parkinson's.

References

1. Kuramoto, Y. 1984. Chemical Oscillations, Waves, and Turbulence.
2. Mišić, Bratislav, & Betzel, Richard F et al. 2015. Cooperative and competitive spreading dynamics on the human connectome. Neuron, 86(6), 1518–1529.

3. Park, Denise C, & Reuter-Lorenz, Patricia. 2009. The adaptive brain: aging and neurocognitive scaffolding. Annual review of psychology, 60, 173–196.
4. Pathak, Anagh, Sharma, Vivek, Roy, Dipanjan, & Banerjee, Arpan. 2022. Biophysical mechanism underlying compensatory preservation of neural synchrony over the adult lifespan. Communications Biology, 5(1), 567.
5. Sporns, Olaf, & Zwi, Jonathan D. 2004. The small world of the cerebral cortex. Neuroinformatics, 2, 145–162.

Poster No 1146

Lifespan music experience changes transition rates of microstate D related to executive function

Yan Li[1], Pengyu Zou[1], Liangfeng Feng[1], Jing Lu[1], Sijia Guo[1]

[1]School of Life Science and Technology, University of Electronic Science and Technology of China, Chengdu, China

Introduction: Lifespan music experience benefits older adults, which was proved by many behavioral studies, such as old musicians having higher scores on a test of executive function[1] and enhanced auditory attention in musicians[2]. The potential mechanism is still unclear but is suggested to be related to cognitive network changes, such as frontal-parietal areas[3]. The electroencephalogram (EEG) microstates can reveal the changes in the cognitive function network, and microstate D is related to attention and executive function[4,5], which have been shown to decline during aging[6,7]. Microstate analysis is, therefore, helpful in understanding how music intervention can alleviate cognitive aging. This work recruited old musicians, old non-musicians, and young non-musicians to explore the relationship between microstate D and other microstates in music intervention in cognitive aging.

Methods: Sixteen old musicians (OM) were recruited from Sichuan Conservatory of Music and nineteen age-matched old non-musicians (ONM) were recruited from communities. Twenty-five young non-musicians (YNM) were recruited from universities. Five minutes of resting EEG recordings were collected using a 64-electrode channel EEG acquisition device. These electrodes were positioned to the extended 10-20 system, and the data were recorded at a sampling rate of 1000Hz. EEG recordings were preprocessed by the EEGLAB toolbox in MATLAB and then analyzed by the EEGLAB plugin for microstates. The original instantaneous maps were clustered into four microstate classes (same as previous studies, namely, microstate A, B, C and D). Finally, the transition rates between microstates were calculated and statistically analyzed. In addition, we also collected the behavioral data of the N-back task (the accuracy and reaction time of 0, 1, 2-back).

Results: For the transition rates between microstates D and A, B, and C, all the interactions of age × music training trended significantly. For the transition rate from microstate D to A, ONM was lower than OM ($p<0.01$, $t=-4.45$) and YNM ($p<0.01$, $t=-3.51$) (Figure. 1a). For the transition rate from microstate D to B, ONM was higher than OM ($p<0.05$, $t=3.16$) and YNM ($p<0.01$, $t=9.23$), and OM was higher than YNM ($p<0.01$, $t=5.14$) (Figure. 1b). For the transition rate from microstate D to C, ONM was lower than OM ($p<0.01$, $t=-4.76$) and YNM ($p<0.01$, $t=-4.17$), and YNM was lower than OM ($p<0.05$, $t=-2.56$) (Figure.1c). P-values in the results were given after False Discovery Rate (FDR) correction. The differences of transition rates from microstates A, B, and C to microstate D between groups are similarly above results. Future more, we found that transition rate of microstate D to A in the elderly was positively correlated with the accuracy of 2-back ($p=0.024$, $r=0.3863$) (Figure.2a) and negatively correlated with the reaction time of 2-back ($p=0.0268$, $r=-0.3796$) (Figure.2b).

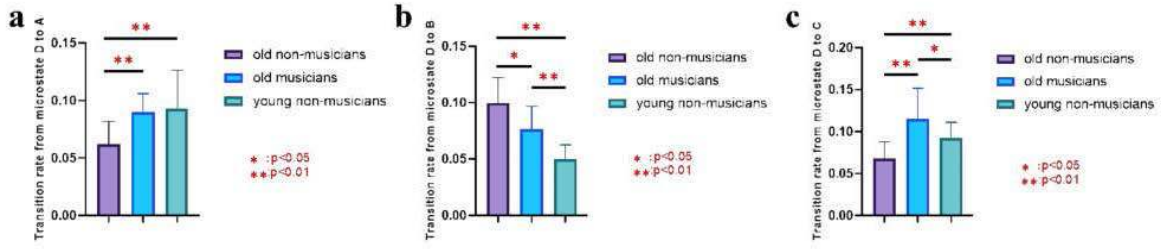

Figure. 1: The transition rates from microstate D to microstates A, B and C (FDR-corrected).

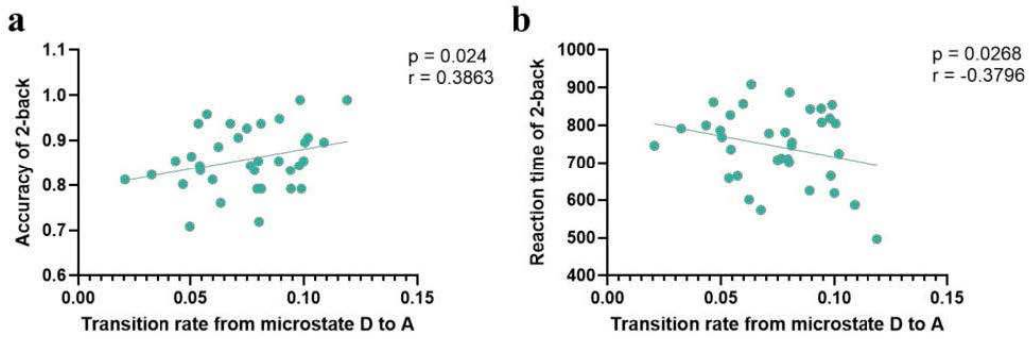

Figure. 2: The correlations between transition rate from microstate D to A and accuracy, reaction time of 2-back in the elderly.

Conclusions: As reported by existing studies, the transitions between microstates are not random[8]. Some studies have found that the possibility of such transitions between microstates is related to functional networks and exhibits a tendency in patients[9]. Similar to the above studies, we found that the changes of transition rates between microstate D and other microstates reflect cognitive aging of the elderly, specifically manifested as an increase between microstate D and C as well as a decrease between microstate D and A, B. Lifespan music experience has slowed down these changing trends and contributes to the better working memory performance. Moreover, music experience makes the auditory network more robust and enables the functional separation of auditory and frontal network to be maintained during aging, which is reflected by the correlation between transition rate and accuracy, reaction time of 2-back task. In a nutshell, these results provide more information for understanding the mechanism of music intervention in cognitive aging.

References

1. Strong, J.V. and A. Midden (2020), 'Cognitive differences between older adult instrumental musicians: Benefits of continuing to play', Psychology of Music, vol. 48, no. 1, pp. 67-83.
2. Strait, D.L., et al. (2010), 'Musical experience shapes top-down auditory mechanisms: Evidence from masking and auditory attention performance', Hearing Research, vol. 261, no. 1, pp. 22-29.
3. Zhang, L., et al. (2023), 'Successful aging of musicians: Preservation of sensorimotor regions aids audiovisual speech-in-noise perception', Science Advances, vol. 9, no. 17.
4. Seitzman, B.A., et al. (2017), 'Cognitive manipulation of brain electric microstates', Neuroimage, vol. 146, pp. 533-543.
5. Hu, N., et al. (2021), 'The modulation of salience and central executive networks by acute stress in healthy males: An EEG microstates study', International Journal of Psychophysiology, vol. 169, pp. 63-70.
6. Verhaeghen, P. and J. Cerella (2002), 'Aging, executive control, and attention: a review of meta-analyses', Neuroscience and Biobehavioral Reviews, vol. 26, no. 7, pp. 849-857.
7. Sweeney, J.A., et al. (2001), 'Inhibitory control of attention declines more than working memory during normal aging', Neurobiology of Aging, vol. 22, no. 1, pp. 39-47.
8. Khanna, A., et al. (2015), 'Microstates in resting-state EEG: current status and future directions', Neurosci Biobehav Rev, vol. 49, pp. 105-113.
9. Toplutaş, E., F. Aydın, and L.J.B.T. Hanoğlu (2023), 'EEG Microstate Analysis in Patients with Disorders of Consciousness and Its Clinical Significance', pp. 1-11.

Poster No 1147

Shared brain network response change with naturalistic social content and support recall in adults

Eric Kwun Kei Ng[1], Wan Lin Yue[1], Janice Jue Xin Koi[1], Joey Ju Yu Wong[1], Xiaoqian Li[2], W. Quin Yow[2], Juan Helen Zhou[1]

[1]National University of Singapore, Singapore, Singapore, [2]Singapore University of Technology and Design, Singapore, Singapore

Introduction: Theory of mind (ToM), a key social cognitive ability, may decline and adversely influence older adults[1,2]. Naturalistic paradigms show promise to study social cognition with better ecological validity and sensitivity to age-related differences[3], but few studies have adapted it to study ToM at older age. We examined inter-subject correlation (ISC)[5], a measure of between-subject brain response synchrony to a common stimulus and shown to be sensitive to differences in mental states[6], when participants watched a socio-affective movie. We expected 1) ISC to be higher during moments with higher ToM requirement, lower in older adults, with possible interaction such that age groups differed more during higher ToM requirement; 2) effects to be stronger in default mode network; 3) higher ISC to be associated with better recall.

Methods: 44 young (27 F, mean 22 yrs) and 46 older adults (34 F, mean 63.3 yrs) were scanned when watching a short movie about a family in local Singaporean context[11]. They then completed a recall task comprising 9 factual and 18 ToM multiple-

choice questions from 9 major scenes. FMRI data (3T Siemens Prisma(-Fit); TR 720ms, 2.5mm isotropic) were preprocessed with an in-house pipeline. Time series extracted from 430 regional[4] were split into ToM (N=56) and non-ToM (N=74) segments based on timestamps manually demarcated by 3 researchers and hemodynamic response delay (6s), followed by concatenation into a ToM (402 TRs, 5mins) and non-ToM (488 TRs, 6mins) time series per participant. Regional ISC[5] was computed separately for each age group and ToM event type by correlating the time series of each participant with the mean time series averaged across all other participants in the group (Fisher's Z, Pearson). Regions were then averaged as per functional network assignment, yielding 2 event type x (9 cortical + 3 subcortical) network-level ISC measures per participant. Network ISCs were subject to linear mixed models, with age group, ToM event type, and their interaction as variables of interest, and gender, scanner, and mean relative motion as covariates. Multiple comparisons in network analyses and post-hoc analyses were Bonferroni-adjusted. For networks showing statistically significant age-group ISC effects, partial Spearman's correlations were computed between ISC and recall scores within each age group and event type, controlling for age, gender, scanner, education, and mean relative motion.

Results: ISC was higher during ToM than non-ToM moments in most networks (ps<.004). Contrary to past findings[10], older adults tended to have higher ISC in cortical networks than young adults (ps=.025-.07 uncorrected). Age Group x Event Type interactions (Fig 1) were observed in default mode network (DMN) and salience-ventral-attention network (SN-VAN). ISC for ToM events was higher than non-ToM events in young adults (p<.001 and .008, respectively), but they were comparable in older adults. Non-ToM ISC was also higher in older than young adults (p=.052 and <.001, respectively). Higher ISC in these networks was associated with better recall for ToM moments in both groups (ps<.001; Fig 2).

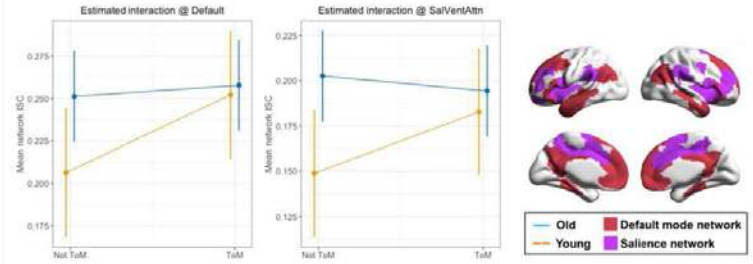

Fig 1. Synchronization of brain network activity during movie-watching shows interaction effect between age group and Theory of Mind, such that young adults showed larger ISC differences between ToM and non-ToM segments compared to older adults. Inter-subject correlations (ISC) showed Age group x Theory of Mind (ToM) interactions in the default mode network (DMN) and salience-ventral attention network (SalVentAttn) (controlled for gender, scanner and motion). Compared to young adults, older adults maintained similar level of synchrony with their peers regardless of ToM engagement; older adults also showed higher synchrony during non-ToM segments. Error bars represented 95% confidence intervals.

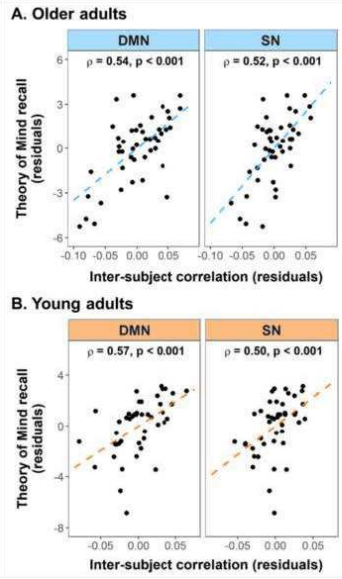

Fig 2. Higher within-group synchronization of DMN and SN-VAN activity in response to social moments was associated with better theory of mind recall in young and older adults. Inter-subject correlations (ISC) from Theory of Mind (ToM) moments in the movie showed significant positive association with ToM recall in the default mode network (DMN) and, salience-ventral attention network (SN) in both older adults (A) and young adults (B). Associations were calculated using partial Spearman's correlations after controlling for age, gender, scanner and motion (and education for older adults). Linear fits are included as visual reference.

Conclusions: Our results echoed past findings of higher neural synchrony when processing others' mental states[6]; higher ISC in older adults may be due to stimulus choice but requires further examination. Interestingly, ISC enhancement was less among older adults than young adults in the DMN (internal state representations and narrative comprehension) and SN-VAN (selective attention and regulating DMN activity). Their inclusion suggested that older adults may become less selective to the need of (or lack thereof) processing social elements, due to lower social cognitive ability or altered socioemotional preferences[7]. Positive ISC-recall association supported the hypothesis of an 'optimal way' of information processing among age-matched peers[8], with deviations reflecting idiosyncrasy in perspective taking and situational interpretation[9].

References

1. Kelly ME, Duff H, Kelly S, McHugh Power, JE, Brennan S, Lawlor BA, Loughrey DG (2017). The impact of social activities, social networks, social support and social relationships on the cognitive functioning of healthy older adults: a systematic review. Syst Rev 6(1):259.
2. Fernandes C, Barbosa F, Martins IP, Marques-Teixeira J (2021). Aging and social cognition: A comprehensive review of the literature. Psychology & Neuroscience 14(1):1.
3. Grainger SA, Rakunathan V, Adams AG, Canty AL, Henry JD (2021). An assessment of age differences in theory of mind using the virtual assessment of mentalizeng ability. Aging, Neuropsychology, and Cognition 28(1): 97-107.
4. Schaefer A, Kong R, Gordon EM, Laumann TO, Zuo XN, Holmes AJ . . . Yeo BTT (2018). Local-Global Parcellation of the Human Cerebral Cortex from Intrinsic Functional Connectivity MRI. Cereb Cortex 28(9): 3095-3114.
5. Nastase SA, Gazzola V, Hasson U, Keysers C (2019). Measuring shared responses across subjects using intersubject correlation. Soc Cogn Affect Neurosci. 14(6): 667-685.
6. Nummenmaa L, Glerean E, Viinikainen M, Jaaskelainen IP, Hari R, & Sams M (2012). Emotions promote social interaction by synchronizing brain activity across individuals. Proc Natl Acad Sci U S A 109(24): 9599-9604.
7. Carstensen LL, Isaacowitz DM, Charles ST (1999): Taking time seriously. A theory of socioemotional selectivity. Am Psychol. 54(3): 165-81.
8. Hasson U, Furman O, Clark D, Dudai Y, Davachi L (2008). Enhanced intersubject correlations during movie viewing correlate with successful episodic encoding. Neuron, 57(3): 452-462.
9. Matz SC, Hyon R, Baek EC, Parkinson C, Cerf M (2022). Personality similarity predicts synchronous neural responses in fMRI and EEG data. Sci Rep 12(1):14325.
10. Campbell KL, Shafto MA, Wright P, Tsvetanov KA, Geerligs L, Cusack R, . . . Tyler LK (2015). Idiosyncratic responding during movie-watching predicted by age differences in attentional control. Neurobiol Aging 36(11): 3045-3055.
11. Chen A (2011) The Reunion Dinner. https://asianfilmarchive.org/catalogue/the-reunion-dinner/

Poster No 1148

The negative relationship between brain-age gap and resilience in older people

Yue Gu[1], Tatia Lee[2]

[1]The University of Hong Kong, Hong Kong, [2]the University of Hong Kong, Hong Kong

Introduction: Ageing is a complex biological process (López-Otín et al., 2013). This deviation between the predicted-brain age and chronological age, referred to as the 'brain-age gap'(Franke, Ziegler, et al., 2010). There are association between individual brain-age gap and adverse outcomes such as mortality (Cole et al., 2018), neurodegenerative disorders (Franke et al. 2010; Gaser et al. 2013; Gonneaud et al. 2021). Employing brain-age gap assessments in elderly could enrich our comprehension of resilience to structural and functional insults that accumulate with advancing age, and the repercussions of diseases on the aging brain. For ageing, resilience is particularly important. Because ageing may face a variety of challenges, such as chronic illness and disability (Madsen et al., 2019; Rentz et al., 2017). We aimed to develop a deep learning-based brain age prediction model using multimodal imaging data, including resting-state fMRI, MRI and DTI scans from 124 participants aged 53-76 years old.

Methods: Demographic variables were assessed at the time of the scan. The data were obtained from a cohort of 124 right-handed older adults who underwent a comprehensive neuropsychological assessment. The final sample consisted of 93 participants, with a mean age of 61.06 years (SD = 4.90 years, range = 53-76 years), including 33 females. This study received approval from the institutional review board of the Affiliated Rehabilitation Hospital, Fujian University of Traditional Chinese Medicine, and all participants provided written informed consent. All participants underwent scanning on a 3T Scanner. The Brainnetome Atlas, which contains 246 subregions of the bilateral hemispheres, was selected for this study due to its multimodal characterization of the human brain. The brain age prediction model employed in this study integrates a multimodal set of neuroimaging features to estimate an individual's brain age. To comprehend the intricate interplay between the brain-age gap and network metrics, as well as cognitive and emotional assessments, supplementary partial correlation analyses were conducted.

Results: The model exhibited strong predictive performance, with a MSE of 19.218, indicating the model's ability to minimize prediction errors. The R^2 value of 0.968 signifies the high proportion of variance in the data that could be explained by the model, underscoring its robust predictive capacity. The selection of 159 features with the highest contribution to the prediction

model, specifically in SC. Using the partial correlation, our analysis revealed a significant negative correlation between resilience and the brain-age gap.

Conclusions: In summary, this study highlights the brain-age gap as a potential biomarker for aging, underscores the role of resilience as a protective factor.

References

1. Zhai, J., & Li, K. (2019). Predicting Brain Age Based on Spatial and Temporal Features of Human Brain Functional Networks. Frontiers in Human Neuroscience, 13, 62. https://doi.org/10.3389/fnhum.2019.00062
2. Zhang, J., Cheng, W., Liu, Z., Zhang, K., Lei, X., Yao, Y., Becker, B., Liu, Y., Kendrick, K. M., Lu, G., & Feng, J. (2016). Neural, electrophysiological and anatomical basis of brain- network variability and its characteristic changes in mental disorders. Brain, 139, 2307–2321. https://doi.org/10.1093/awwxxx
3. Wang, L., Su, L., Shen, H., & Hu, D. (2012). Decoding Lifespan Changes of the Human Brain Using Resting-State Functional Connectivity MRI. PLoS ONE, 7(8). https://doi.org/10.1371/journal.pone.0044530
4. Troy, A. S., Willroth, E. C., Shallcross, A. J., Giuliani, N. R., Gross, J. J., & Mauss, I. B. (2023). Psychological Resilience: An Affect-Regulation Framework. Annual Review of Psychology, 74(1), 547–576. https://doi.org/10.1146/annurev-psych-020122-041854
5. Rentz, D. M., Mormino, E. C., Papp, K. V., Betensky, R. A., Sperling, R. A., & Johnson, K. A. (2017). Cognitive resilience in clinical and preclinical Alzheimer's disease: The Association of Amyloid and Tau Burden on cognitive performance. Brain Imaging and Behavior, 11(2), 383–390. https://doi.org/10/gsgvdp
6. Ludwig, F. C., & Smoke, M. E. (1980). The measurement of biological age. Experimental Aging Research, 6(6), 497–522. https://doi.org/10.1080/03610738008258384
7. Lund, M. J., Alnæs, D., de Lange, A.-M. G., Andreassen, O. A., Westlye, L. T., & Kaufmann, T. (2022). Brain age prediction using fMRI network coupling in youths and associations with psychiatric symptoms. NeuroImage: Clinical, 33, 102921. https://doi.org/10.1016/j.nicl.2021.102921
8. Madsen, W., Ambrens, M., & Ohl, M. (2019). Enhancing Resilience in Community-Dwelling Older Adults: A Rapid Review of the Evidence and Implications for Public Health Practitioners. Frontiers in Public Health, 7. https://www.frontiersin.org/articles/10.3389/fpubh.2019.00014
9. Gu, Y., Li, L., Zhang, Y., Ma, J., Yang, C., Xiao, Y., Shu, N., Can, C., Lin, Y., & Dai, Z. (2022). The overlapping modular organization of human brain functional networks across the adult lifespan. NeuroImage, 253, 119125. https://doi.org/10.1016/j.neuroimage.2022.119125
10. Gu, Y., Lin, Y., Huang, L., Ma, J., Zhang, J., Xiao, Y., & Dai, Z. (2020). Abnormal dynamic functional connectivity in Alzheimer's disease. CNS Neuroscience and Therapeutics, 26(9), 962–971.

Poster No 1149

Assessment of gray matter features in reflecting advanced brain age in PCDS: A cross-national study

Chen-Yuan Kuo[1,2], Li-Ning Peng[3,4], Chih-Ping Chung[1,3], Pei-Lin Lee[3], Liang-Kung Chen[3,5], Ching-Po Lin[2,3,6], Kun-Hsien Chou[2,7]

[1]Department of Neurology, Neurological Institute, Taipei Veterans General Hospital, Taipei, Taiwan, [2]Institute of Neuroscience, National Yang Ming Chiao Tung University, Taipei, Taiwan, [3]Center for Healthy Longevity and Aging Sciences, National Yang Ming Chiao Tung University, Taipei, Taiwan, [4]Center for Geriatric and Gerontology, Taipei Veterans General Hospital, Taipei, Taiwan, [5]Taipei Municipal Gan-Dau Hospital (managed by Taipei Veterans General Hospital), Taipei, Taiwan, [6]Department of Education and Research, Taipei City Hospital, Taipei, Taiwan, [7]Brain research center, National Yang Ming Chiao Tung University, Taipei, Taiwan

Introduction: Neuroimaging-derived brain biological age serves as a widely accepted health indicator, reflecting the potential advancement or delay in brain aging compared to chronological age. Various gray matter (GM) features have been utilized for this purpose. However, the comparative sensitivity and feasibility of GM feature-derived brain age models in reflecting advanced brain aging within neurodegenerative disorders using multi-center, cross-national cohort datasets remain understudied. Physio-cognitive decline syndrome (PCDS), characterized by concurrent mobility and cognitive impairment without dementia, represents a preclinical phenotype of dementia syndrome in older individuals[1]. Our recent single-cohort study uncovered an advanced brain age in PCDS using a brain age model based on GM volume (GMV)[2]. This current study focuses on utilizing PCDS as the disease group to assess the feasibility of two GM feature-based brain age models, specifically GMV and GM density (GMD), across multi-center, cross-national studies.

Methods: Participants of clinical datasets Two cohort datasets, I-Lan Longitudinal Aging Study (ILAS) from Taiwan (N=1193, 566M/627F) and the National Institute for Longevity Sciences, Longitudinal Study of Aging (NILS-LSA) study from Japan (N=2302, 1173M/1129F), were used in this study. Using consensus criteria, participants aged 65 and above were categorized as robust or PCDS based on sex-stratified MMSE scores, grip strength, and walking speed in the bottom or top 20%. The study comprised 163 robust (age = 71.36±5.08 years, 103M/60F) and 103 PCDS (age = 74.68±6.19 years, 48M/55F) participants from ILAS, along with 137 robust (age = 70.57±4.08 years, 61M/76F) and 74 PCDS (age = 78.28±4.99 years, 43M/31F) participants from the NILS-LSA study. Brain age model construction and evaluation We gathered 1482 healthy individuals (age range: 18-92; 681M/801F) from five sites in Taiwan, training brain age prediction models with their T1-weighted MRI scans. Following

our previous brain age model construction pipeline[3], we constructed two SVR-RBF models based on gray matter GMV and GMD respectively. Model performance was assessed using minimum mean absolute error (MAE) and maximum coefficient of determination (R2) between chronological and predicted age. The optimized brain age estimators were applied to ILAS and NILS-LSA datasets for individual predicted brain age and brain age gap (BAG) calculation, representing the difference between chronological age and predicted brain age. Statistical analysis Two ANCOVA models, incorporating age, age^2, sex, education years, and total intracranial volume as confounders, compared the BAG between robust and PCDS groups in each dataset. A significance level of <0.05 was considered statistically significant.

Results: Constructing two brain age estimators based on GM features, our findings revealed superior prediction performance from the GMD brain age estimator (MAE=5.33; R2=0.81) compared to the GMV brain age estimator (MAE=6.46; R2=0.73) within the training dataset (Figure 1). Moreover, the utilization of both the optimized GMV and GMD brain age estimators consistently demonstrated advanced brain age within the PCDS group across two distinct cohort datasets (ILAS: GMV, p=0.011, η2=0.025; GMD, p=0.01, η2=0.025; NILS-LSA: GMV, p=0.027, η2=0.024; GMD, p=0.029, η2=0.023) (Figure 2).

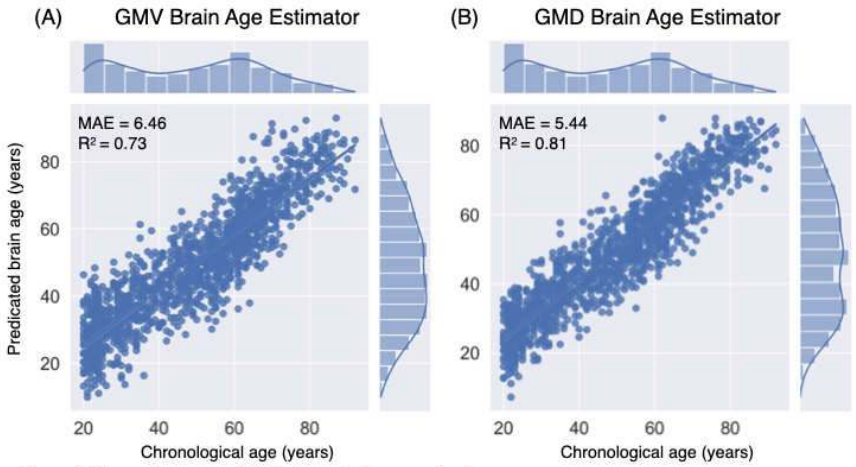

Figure 1. The performance of GM features brain age estimator.
Scatterplots illustrate the relationship between chronological age (x-axis) and predicted brain age (y-axis) within the training dataset. (A) Predicted brain ages were derived used GMV features as input data for the SVR method. (B) Predicted brain ages were derived used GMD features as input data for the SVR method. Abbreviation: GMV, gray matter volume; GMD, gray matter density; MAE, mean absolute error; R², the maximum coefficient of determination; SVR, support vector regression.

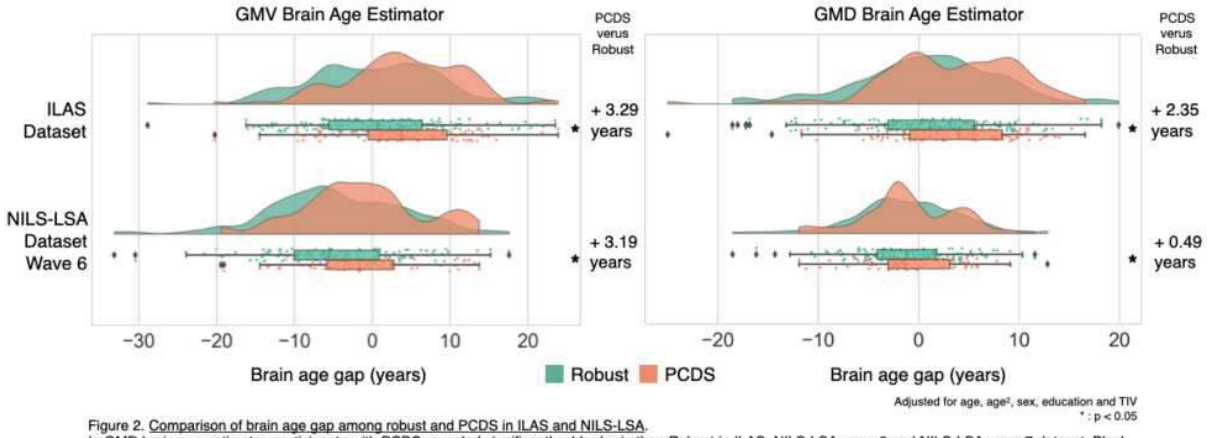

Figure 2. Comparison of brain age gap among robust and PCDS in ILAS and NILS-LSA.
In GMD brain age estimator, participants with PCDS revealed significantly older brain than Robust in ILAS, NILS-LSA wave 6 and NILS-LSA wave 7 dataset. Black star indicated significant differences. Abbreviation: ILAS, I-Lan Longitudinal Aging Study; NILS-LSA, National Institute for Longevity Sciences, Longitudinal Study of Aging; PCDS, physio-cognitive decline syndrome.

Conclusions: In summary, our study reveals the intricate relationship between diverse GM features and the effectiveness of brain age estimators. While the GMD brain age estimator shows superior predictive performance during training, both GMD and GMV estimators indicate advanced brain age within the PCDS group during subsequent case-control comparisons. This underscores the potential of neuroimaging-derived brain age as a reliable indicator of advanced brain aging, particularly within the context of PCDS. These findings provide insights for similar multicenter, multinational cohort studies exploring brain health status across diseases.

References
1. Liu LK, (2020), 'Cerebellar-limbic neurocircuit is the novel biosignature of physio- cognitive decline syndrome', Aging, vol. 12, no. 24, pp. 25319-25336.
2. Kuo CY, (2023), 'Advanced brain age in community-dwelling population with combined physical and cognitive impairments', Neurobiology of Aging, pp. 114-123.
3. Lee PL, (2022), 'Regional rather than global brain age mediates cognitive function in cerebral small vessel disease', Brain Commum., pp. 1-14.

Poster No 1150

Which white matter measures best predict processing speed and intelligence in healthy aging?

Petar Raykov[1], Rafael Henriques[2], Kamen Tsvetanov[3], Cam-CAN[3], Marta Correia[1], Richard Henson[4]

[1]MRC Cognition and Brain Sciences Unit, Cambridge, United Kingdom, [2]Champalimaud Research, Lisbon, Portugal, [3]University of Cambridge, Cambridge, Cambridgeshire, [4]MRC Cognition and Brain Sciences Unit, Great Shelford, Cambridgeshire

Introduction: Healthy aging is accompanied by decline in cognitive functions such as processing speed (PS) and fluid intelligence (gF). White matter (WM) integrity is important for both of these functions, and declines with age. However, it remains unclear which WM measures are most closely related to variation in cognitive performance. Furthermore, it's unclear whether information from different imaging modalities (e.g., T1/T2) adds complimentary information beyond the multitude of metrics derived from diffusion magnetic resonance imaging (dMRI). Here we use adult life-span data from the Cam-CAN cohort to extract commonalities across 8 different WM measures using factor analysis, and examine how many latent factors are needed. Furthermore, we compare the factors scores, as well as the original WM metrics, in their ability to predict PS and gF, after accounting for effects of age and sex.

Methods: We used multimodal neuroimaging data from 651 adults from the Cam-CAN cohort, aged between 18-88 years (www.cam-can.org). We took six dMRI metrics from a previous analysis of dMRI data across 27 WM ROIs (Henriques et al, 2023): 1) Fractional Anisotropy (FA); 2) Mean Signal Diffusion (MSD); 3) Mean Signal Kurtosis (MSK); 4) Neurite Density Index (NDI); 5) Orientation Dispersion Index (ODI); 6) Free water volume fraction (Fiso). We then added two further WM metrics: 7) the ratio of two magnetisation-weighted images (MTR) and 8) the T1/T2 ratio from T1- and T2-weighted images. PS was calculated from a factor analysis across the mean and standard deviation of reaction times on a simple and a choice reaction task; gF was calculated from a factor analysis on four Cattell subtests. We performed factor analysis on the 8 WM measures, concatenating across participants and ROIs. We then performed regression analyses to examine how much of the variance in participants' PS or gF was explained by each of the individual factor scores, or by each of the individual WM measures (averaged over all ROIs), after accounting for sex, linear and quadratic age, and their interactions. Additionally, we included a regressor to account for motion artefacts in the dMRI measures (see Henriques et al., 2023). Finally, we also regressed PS and gF on a whole-brain measure of 9) Peak Width of Skeletonized Mean Diffusivity (PSMD).

Results: We found that 3 factors captured 83% of the variance in the 8 WM measures. Given that Henriques et al. (2023) found that 3 factors also captured the majority of the variance in the 6 dMRI measures, this suggests that the addition of MTR and T1/T2-ratio measures did not add complimentary information about WM integrity. The three factors seemed to reflect 1) tissue microscopic properties; 2) free-water contamination, and 3) fibre complexity (e.g., crossing or dispersing, fanning fibres), and explained respectively 43%, 23%, 16% of the variance in data (see Fig. 1). Regression analyses showed that, of the three factors, Factor 1 explained the most variation in gF and in PS. Including all 3 factors scores in the same analysis showed that only Factor 1 explained unique variance in cognition. In terms of single metrics, MSD explained most variation in PS, but not so much variation in gF. The best individual predictor of both gF and PS was MSKI, which performed better than Factor 1 (see Table 1). The global PSMD metric showed the strongest association with age.

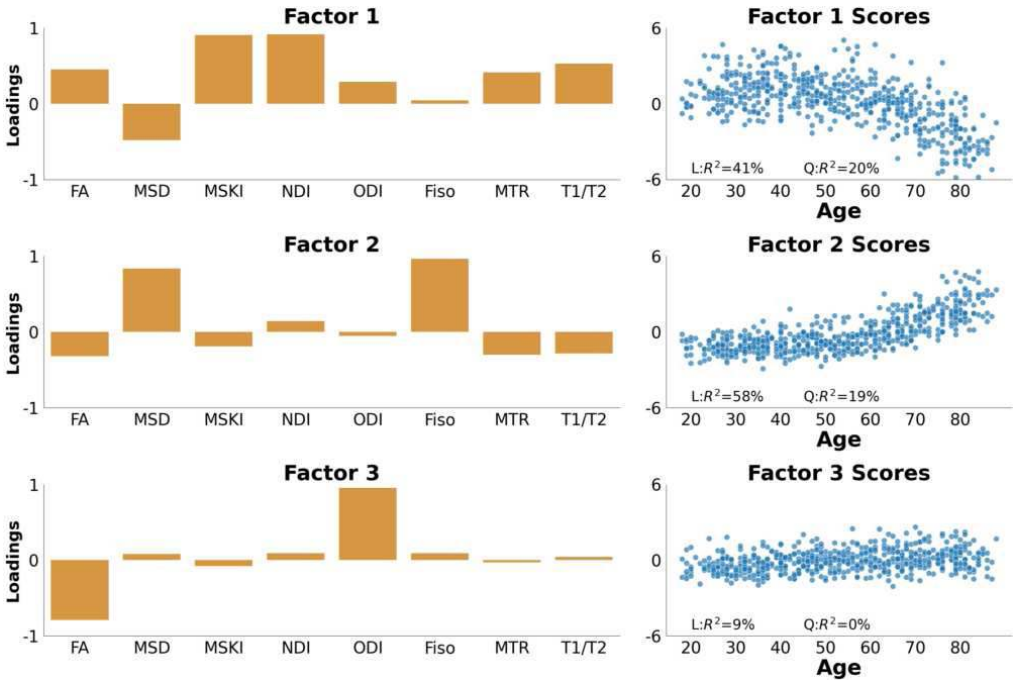

Table 1 *Effect size for different measures of WM.* Fluid Intelligence and Processing Speed columns show partial eta squared η^2 values from independent multiple regressions showing strength of relationship between different WM measures and cognition. Age column shows both combined partial eta squared for both linear and quadratic age effects on different WM measures. Regressions were fitted independently so do not take into account co-variation across WM variables.

Fluid Intelligence (gF)	Processing Speed (PS)	Age	Variable
0.014105	0.029344	0.429133	MSKI
0.012614	0.023455	0.484748	Factor 1
0.010269	0.021266	0.292598	ODI
0.007169	0.000762	0.4267	MTR
0.00687	0.023737	**0.632833**	PSMD
0.006342	0.026457	0.320238	FA
0.003713	**0.035144**	0.617694	MSD
0.002282	0.006507	0.087395	Factor 3
0.000501	0.005365	0.391751	Fiso
0.000159	0.015943	0.60838	Factor 2
5.43E-05	4.80E-06	0.120467	NDI
1.89E-05	0.001689	0.543885	T1T2

Conclusions: Our factor analysis suggest that MTR and T1/T2 measures do not add complimentary information about WM track integrity (in healthy adults) over the information already present in other dMRI metrics. Factor 1 from this analysis, reflecting age-related microscopic alterations, explained appreciable and unique variance in processing speed and fluid intelligence, after adjusting for age and sex. However, if one had to choose one MR sequence and measure, then MSKI estimated from a (multi-shell) dMRI sequence showed comparable associations across both processing speed and fluid intelligence.

References

1. Henriques, R.N., Henson, R.N., Cam-CAN & Correia, M.M. (2023) Unique information from common diffusion MRI models about white-matter differences across the human adult lifespan. Imaging Neuroscience. https://doi.org/10.1162/imag_a_00051

Poster No 1151

Impact of Defacing Procedures on Brain Age Gap Estimation

Vivien Ivan[1], Marius Vach[1], Daniel Weiß[1], Luisa Wolf[1], Shammi More[2], Kaustubh Patil[3], Dennis Hedderich[4], Nora Bittner[5], Julian Caspers[1], Christian Rubbert[1]

[1]Department of Diagnostic and Interventional Radiology, Medical Faculty and University Hospital, Duesseldorf, Germany, [2]Juelich Research Center, Juelich, Germany, [3]Institute of Neuroscience and Medicine (INM-7: Brain and Behaviour), Research Centre Jülich, Jülich, NRW, Germany, [4]Technical University of Munich, Munich, Bavaria, Germany, [5]Institute for Anatomy I, Medical Faculty, Heinrich-Heine University, Duesseldorf, Germany

Introduction: Brain Age Gap Estimation (BrainAGE) is increasingly explored as an imaging biomarker for a variety of conditions, such as neurodegenerative diseases [Gaser 2013], or in the research of atypical aging, e.g., due to lifestyle risk factors [Bittner 2021]. BrainAGE is usually derived from applying machine-learning approaches to features derived from structural magnetic resonance images of the brain [Franke 2019; More 2023]. Removal of facial features from MRI scans is increasingly deemed mandatory from a data privacy perspective [Schwarz 2019]. However, defacing procedures may cause data integrity issues, e.g. affect regional brain volume measurements [Rubbert 2022], which could also compromise the quality of BrainAGE. Thus, this study aims to systematically assess the impact of defacing on BrainAGE.

Methods: A total of 364 Alzheimer's disease (AD) patients and 717 cognitively normal (CN) participants were included from the Alzheimer's Disease Neuroimaging Initiative (ADNI). For those, unaccelerated (AD n=290 (46.2% female, 75.13±7.79 years, 55-90 years), CN n=386 (49.5% female, 74.66±5.87 years, 56-89 years)), and accelerated 3D T1 imaging (AD n=203 (40.9% female, 74.76±8.02 years, 55-90 years), CN n=500 (61% female, 71.34±6.44 years, 55-90 years)) was available. BrainAGE was derived using the best-performing model from [More 2023], trained on 2,953 non-ADNI healthy controls (18-88 years) from four large population-based studies. In essence, gray matter features were derived from standardized CAT12 for SPM12 preprocessing, smoothing with a 4 mm full-width-half-maximum kernel, resampling to 4 mm spatial resolution, and finally by principal component analysis for dimensionality reduction. Finally, Gaussian process regression was used to predict age, and BrainAGE was calculated by subtracting the chronological age from the predicted age. BrainAGE was derived for each AD and CN before and after defacing using afni_refacer, fsl_deface, mri_deface, mri_reface, PyDeface, and spm_deface. Furthermore, for AD n=74 (52.7% female, 75.51±8.19 years, 56-90 years) and CN n=84 (56% female, 75.93±4.97 years, 60-87 years) within-session unaccelerated repeat imaging was available, and BrainAGE differences between the two scans within the same session were calculated without any defacing to serve as a benchmark. The difference in BrainAGE after defacing (BrainAGEdefaced – BrainAGEfullface), as well as the mean absolute error (MAE) and mean squared error (MSE) of BrainAGE with and without defacing were calculated separately for unaccelerated and accelerated imaging. Additionally, BrainAGE outliers due to defacing were identified using BrainAGE differences above the 75th or below the 25th percentile of the benchmark and Grubbs's test.

Results: MAE and MSE for BrainAGE difference between the initial and repeat scan in the benchmark, both without defacing, were 1.15 and 2.25 for CN (BrainAGE difference -0.15±1.5), and 1.43 and 3.29 for AD (BrainAGE difference of 0.15±1.82). Preprocessing with CAT12 for SPM12 or defacing failed in 1 afni_refacer and 275 mri_deface cases. PyDeface performed best with an overall MAE of 0.33 and MSE of 0.27 (mean BrainAGE difference of 0.08±0.52, range -1.93-6.19, inter-quartile range -0.17–0.26 (see table in Figure 1) and the lowest number of outliers according to the benchmark (99, see table in Figure 1 and Figure 2). The overall MAE for fsl_deface and spm_deface was 0.35, for mri_reface 0.41, for mri_deface 0.63, and for afni_refacer 1.04. The Grubbs's test identified 23 outliers after PyDeface, with spm_deface and mri_reface leading to a lower number of outliers (20 and 11, respectively, see table in Figure 1).

	Research group	Unaccelerated Imaging						
		Failed processing	MAE	MSE	BrainAGE difference *		Outliers	
					Mean ± SD	Range (IQR)	Grubbs's test	Benchmark *
Within-session repeat imaging without defacing	CN	0/84	1.15	2.25	-0.15±1.50	-5.18–2.85 (-0.97–0.61)	1	n/a
	AD	0/74	1.43	3.29	0.15±1.82	-6.02–4.48 (-0.86–1.38)	1	n/a
afni_refacer	CN	1/414	1.16	9.87	-0.17±3.14	-40.73–14.93 (-0.58–0.71)	12	183
	AD	0/299	1.51	11.25	-0.55±3.32	-27.38–5.62 (-0.74–0.73)	21	97
fsl_deface	CN	0/414	0.31	0.2	0.02±0.45	-1.82–2.32 (-0.19–0.24)	10	33
	AD	0/299	0.4	0.39	0.06±0.62	-3.02–3.87 (-0.21–0.28)	13	21
mri_deface	CN	84/414	0.6	2.1	0.18±1.44	-8.32–13.62 (-0.23–0.32)	14	63
	AD	57/299	0.73	3.14	0.31±1.75	-3.83–13.77 (-0.24–0.41)	16	30
mri_reface	CN	0/414	0.41	0.32	0.14±0.55	-1.32–3.01 (-0.20–0.42)	2	78
	AD	0/299	0.46	0.38	0.13±0.60	-2.03–2.40 (-0.20–0.48)	2	20
PyDeface	CN	0/414	0.32	0.23	0.09±0.48	-1.62–3.18 (-0.16–0.24)	5	45
	AD	0/299	0.38	0.34	0.13±0.57	-1.93–4.37 (-0.16–0.35)	6	12
spm_deface	CN	0/414	0.32	0.19	0.07±0.43	-1.47–2.59 (-0.17–0.31)	3	35
	AD	0/299	0.35	0.32	0.16±0.54	-1.15–4.78 (-0.13–0.35)	6	13
		Accelerated Imaging						
		Failed processing	MAE	MSE	BrainAGE difference *		Outliers	
					Mean ± SD	Range (IQR)	Grubbs's test	Benchmark *
afni_refacer	CN	0/500	0.73	0.88	0.09±0.94	-3.23–3.84 (-0.57–0.69)	1	197
	AD	0/203	0.87	1.43	0.21±1.18	-4.75–3.55 (-0.32–0.92)	3	53
fsl_deface	CN	0/500	0.3	0.17	0.00±0.41	-1.72–1.54 (-0.22–0.20)	2	44
	AD	0/203	0.47	0.53	0.08±0.72	-3.44–3.22 (-0.22–0.31)	4	16
mri_deface	CN	91/500	0.58	1.52	0.19±1.22	-2.64–9.98 (-0.25–0.32)	20	83
	AD	43/203	0.7	3.55	0.36±1.86	-3.71–19.53 (-0.12–0.42)	11	19
mri_reface	CN	0/500	0.36	0.24	-0.03±0.49	-1.65–2.12 (-0.31–0.23)	2	54
	AD	0/203	0.45	0.4	0.08±0.63	-2.50–2.38 (-0.23–0.40)	5	14
PyDeface	CN	0/500	0.31	0.28	0.03±0.53	-1.64–6.19 (-0.18–0.19)	0	42
	AD	0/203	0.37	0.25	0.11±0.49	-1.24–1.62 (-0.15–0.33)	0	0
spm_deface	CN	0/500	0.39	2.16	-0.01±1.47	-30.64–5.95 (-0.21–0.27)	10	48
	AD	0/203	0.35	0.22	0.14±0.45	-2.13–1.41 (-0.11–0.37)	1	4

* BrainAGE difference = BrainAGE after defacing - BrainAGE without defacing; * Benchmark = Number of BrainAGE differences above the 75th or below the 25th percentile of the respective BrainAGE difference of the within-session repeat imaging without defacing

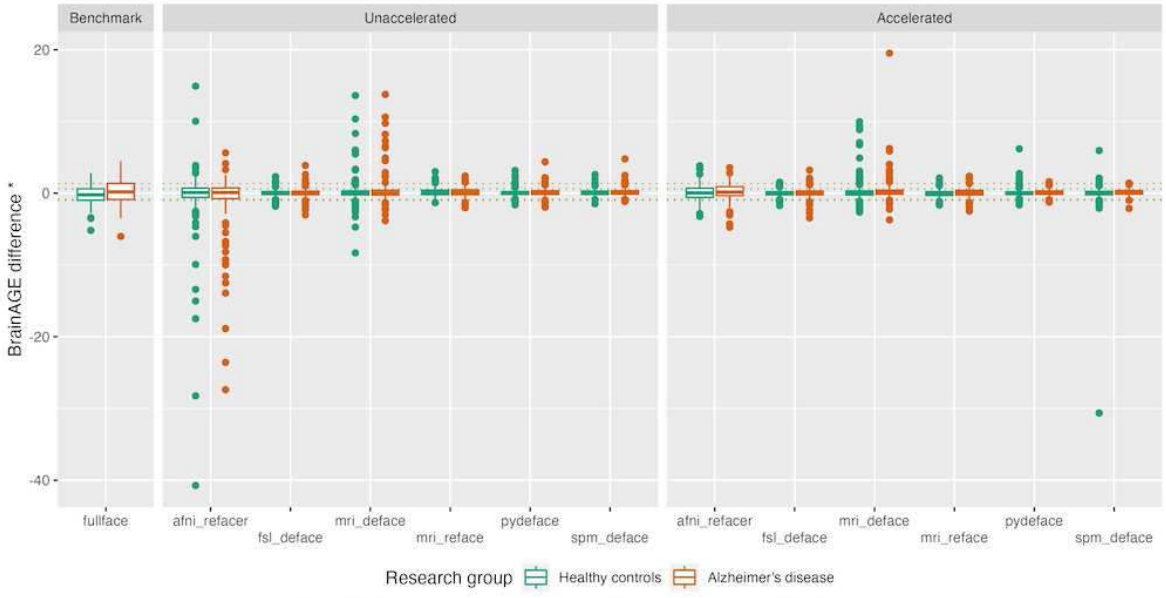

* BrainAGE difference in the benchmark = BrainAGE repeat image - BrainAGE initial image
BrainAGE difference in the (Un)Accelerated = BrainAGE after defacing - BrainAGE without defacing

Conclusions: Brain Age Gap Estimation (BrainAGE) may be affected by defacing, however, in most approaches this influence is lesser than the variability observed in BrainAGE in repeat non-defaced imaging within the same session. Overall, PyDeface had negligible impact on BrainAGE, both in AD patients and healthy controls.

References

1. Bittner N, Jockwitz C, Franke K, Gaser C, Moebus S, Bayen UJ, Amunts K, Caspers S (2021): When your brain looks older than expected: combined lifestyle risk and BrainAGE. Brain Struct Funct 226:621–645.
2. Franke K, Gaser C (2019): Ten Years of BrainAGE as a Neuroimaging Biomarker of Brain Aging: What Insights Have We Gained? Front Neurol 10:789.
3. Gaser C, Franke K, Klöppel S, Koutsouleris N, Sauer H, Initiative ADN (2013): BrainAGE in Mild Cognitive Impaired Patients: Predicting the Conversion to Alzheimer's Disease. PLoS ONE 8:e67346.
4. More S, Antonopoulos G, Hoffstaedter F, Caspers J, Eickhoff SB, Patil KR, Initiative ADN (2023): Brain-age prediction: A systematic comparison of machine learning workflows. NeuroImage 270:119947.
5. Rubbert C, Wolf L, Turowski B, Hedderich DM, Gaser C, Dahnke R, Caspers J, Initiative ADN (2022): Impact of defacing on automated brain atrophy estimation. Insights Imaging 13:54.
6. Schwarz CG, Kremers WK, Therneau TM, Sharp RR, Gunter JL, Vemuri P, Arani A, Spychalla AJ, Kantarci K, Knopman DS, Petersen RC, Jr. CRJ (2019): Identification of Anonymous MRI Research Participants with Face-Recognition Software. N Engl J Med 381:1684–1686.

Poster No 1152

Cross sectional sex differences in cortical atrophy across an indigenous Bolivian population

Nikhil Chaudhari[1], Phoebe Imms[1], Nahian Chowdhury[1], Margaret Gatz[1], Benjamin Trumble[2], Wendy Mack[1], Meng Law[3], Linda Sutherland[4], James Sutherland[4], Christopher Rowan[5], Samuel Wann[6], Adel Allam[7], Randall Thompson[8], David Michalik[9], Michael Miyamoto[10], Guido Lombardi[11], Daniel Cummings[12], Edmond Seabright[6], Sarah Alami[6], Angela Garcia[2], Daniel Rodriguez[13], Raul Quispe Gutierrez[14], Paul Hooper[15], Kenneth Buetow[2], Jonathan Stieglitz[16], Michael Gurven[15], Gregory Thomas[4], Hillard Kaplan[12], Caleb Finch[1], Andrei Irimia[1]

[1]University of Southern California, Los Angeles, CA, [2]Arizona State University, Tempe, AZ, [3]Monash University, Melbourne, Victoria, [4]MemorialCare Health Systems, Fountain Valley, CA, [5]Renown Institute for Heart and Vascular Health, Reno, NV, [6]University of New Mexico, Albuquerque, NM, [7]Al-Azhar University, Cairo, Al Mikhaym Al Daem, [8]University of Missouri, Kansas City, MO, [9]MemorialCare Miller Children's & Women's Hospital, Long Beach, CA, [10]Providence Health, Mission Viejo, CA, [11]Universidad Peruana Cayetano Heredia, Lima, Peru, [12]Chapman University, Orange, CA, [13]San Simon University, Cochabamba, Cochabamba, [14]Tsimane Health and Life History Project, San Borja, Beni, [15]University of California, Santa Barbara, CA, [16]Institute for Advanced Study in Toulouse, Toulouse, Toulouse

Introduction: The cross-sectional relationship of brain volume with age is a surrogate measure of brain atrophy, a proxy for brain health. Comparing atrophy trajectories across industrialized and non-industrialized populations can provide insights into lifestyle correlates of brain health. The Tsimane, a native Bolivian population, have lifestyles similar to those of our pre-modern ancestors (Gurven, Stieglitz et al. 2017). In contrast to the average person in developed countries, the Tsimane have higher levels of physical activity (Kraft, Stieglitz et al. 2018) and a diet richer in fiber. This unique combination of lifestyle factors renders the Tsimane uniquely attractive for studying brain atrophy. We compared Tsimane atrophy rates to those of a UK Biobank (UKBB) sample.

Methods: 746 Tsimane (346 males) aged 40-94 were scanned using computed tomography (CT). The regional brain volumes of 148 cortical brain structures were calculated using an automatic head CT tissue segmentation algorithm. These same regional volumes were computed from T1-weighted magnetic resonance imaging for 19,973 UKBB participants (same age range) using Freesurfer. Regional brain volumes were normalized by total intracranial volume to account for variation in head sizes. Linear regression coefficients describing the associations between age and Tsimane regional brain volumes (βT) were compared with those of UKBB participants (βUK). For each brain structure, Welch's two-tailed t-test for independent samples with unequal variances tested the null hypotheses H(0):βT= βUK at α = 0.05.

Results: Notably, in Tsimane males, a small but significant cross-sectional positive trend of brain volume with age was observed in occipital and parietal structures (red structures in Fig. 1A-B). Over the entire cortex, Tsimane males exhibit slower rates of volume decrease than UKBB males in frontotemporal structures (blue structures in Fig. 1E). Conversely, Tsimane females exhibit faster rates of regional brain volume decrease with age than UKBB females (red structures in Fig. 1F). In structures supporting visuospatial skills, the Tsimane exhibit age-related regional brain hypertrophy. This has not been observed in any other human population and may reflect Tsimane's high dependence on visuospatial navigation in dense Amazonian forests, a terrain with few visuospatial aids. Sex differences may involve differences in hormones, lifestyle, or health trajectories (Cowell, Turetsky et al. 1994, Blatter, Bigler et al. 1995, Coffey, Lucke et al. 1998, Trumble, Stieglitz et al.

2015). Tsimane females exhibit higher obesity rates than males (Bethancourt, Leonard et al. 2019), which may be a byproduct of lifestyle differences. Tsimane females spend more time caring for children (breastfeeding, grooming), preparing food, and engaging in light physical activity. Males, especially those under 60, engage in more moderate-to-vigorous physical activity outside the home. Figure 1. Regression coefficients for the association between cortical structures and age in Tsimane males (A), Tsimane females (B), and British males (C) and females (D) in the UK Biobank. Brighter color indicates a larger magnitude of the regression coefficient for the corresponding structures. (E, F): Structures whose regression coefficients differ significantly from the UKBB in Tsimane. Blue indicates faster volume decrease in the UKBB compared to the Tsimane. Red indicates faster volume decrease in the Tsimane compared to the UKBB.

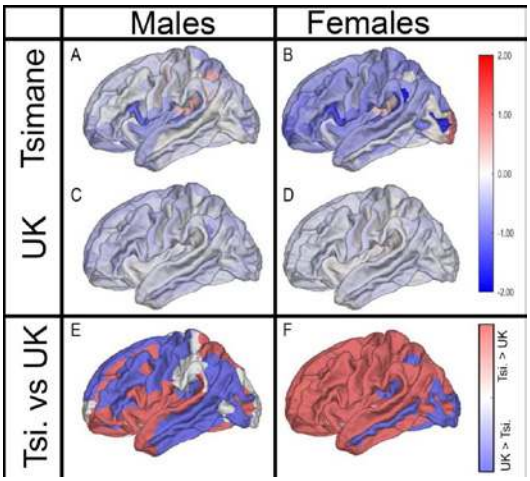

Conclusions: Living without modernization may protect men's brain health but not women's. Alternatively, unknown factors associated with industrialization may attenuate women's rate of regional volume decrease with age. Future research should clarify the relationships between regional volume trends with age, physical activity, diet, neurodegenerative disease risk, and cognitive functioning.

References

1. Bethancourt, H. J., W. R. Leonard, S. Tanner, A. F. Schultz and A. Y. Rosinger (2019). "Longitudinal changes in measures of body fat and diet among adult Tsimane'forager-horticulturalists of Bolivia, 2002-2010." Obesity 27(8): 1347-1359.
2. Blatter, D. D., E. D. Bigler, S. D. Gale, S. C. Johnson, C. V. Anderson, B. M. Burnett, N. Parker, S. Kurth and S. D. Horn (1995). "Quantitative volumetric analysis of brain MR: normative database spanning 5 decades of life." American journal of Neuroradiology 16(2): 241-251.
3. Coffey, C. E., J. F. Lucke, J. A. Saxton, G. Ratcliff, L. J. Unitas, B. Billig and R. N. Bryan (1998). "Sex differences in brain aging: a quantitative magnetic resonance imaging study." Archives of neurology 55(2): 169-179.
4. Cowell, P. E., B. I. Turetsky, R. C. Gur, R. I. Grossman, D. Shtasel and R. Gur (1994). "Sex differences in aging of the human frontal and temporal lobes." Journal of Neuroscience 14(8): 4748-4755.
5. Gurven, M., J. Stieglitz, B. Trumble, A. D. Blackwell, B. Beheim, H. Davis, P. Hooper and H. Kaplan (2017). "The Tsimane health and life history project: integrating anthropology and biomedicine." Evolutionary Anthropology: Issues, News, and Reviews 26(2): 54-73.
6. Kraft, T. S., J. Stieglitz, B. C. Trumble, M. Martin, H. Kaplan and M. Gurven (2018). "Nutrition transition in 2 lowland Bolivian subsistence populations." The American journal of clinical nutrition 108(6): 1183-1195.
7. Trumble, B. C., J. Stieglitz, M. E. Thompson, E. Fuerstenberg, H. Kaplan and M. Gurven (2015). "Testosterone and male cognitive performance in T simane forager-horticulturalists." American Journal of Human Biology 27(4): 582-586.

Poster No 1153

Senescence affects local and global prediction errors at different rates

Yi-Fang Hsu[1], Chia-An Tu[1], Jarmo Hämäläinen[2]

[1]National Taiwan Normal University, Taipei, Taiwan, [2]University of Jyväskylä, Jyväskylä, Finland

Introduction: Predictive coding is postulated to be a fundamental principle of brain functioning. Previous research suggested that senescence is accompanied by an increased weighting of prediction (Moran et al., 2014; Wolpe et al., 2016; Chan et al., 2021) and a hierarchy-selective attenuation of prediction error (PE) (Hsu et al., 2021, 2023). However, it is less clear when it starts and how it develops across lifespan.

Methods: To delineate the developmental trajectory of predictive processing, we recorded EEG from a cohort of 406 healthy participants between 15-82 years of age using an auditory local-global paradigm, which orthogonally manipulated first-order and second-order regularities to elicit local and global PE (Bekinschtein et al., 2009). Cortical responses signalling PE were

identified with a temporal principal component analysis (PCA). Participants also underwent a neuropsychological test battery where their working memory was measured with subtests in Wechsler Adult Intelligence Scale IV.

Results: Significant age-related decline can be seen on local PE (MMN and P3a), global PE (FN and P3b), as well as working memory measures. PE declines at a slower rate locally (0.010-0.017 units/yo) and a faster rate globally (0.013-0.022 units/yo). Concerning the most significant change point, for local PE it happens earlier (37-43 yo) while for global PE it happens later (44-48 yo). Both happen after working memory decline (which declines at a rate of 0.071 units/yo with the most significant change point at 32 yo) and well before retirement age. Interestingly, only 12-13% of the variability in global PE can be explained by local PE. Age effect on global PE remains significant when local PE serve as mediators. Lastly, while local P3a correlates with working memory before age is partialled out, global P3b correlates with working memory both before and after age is partialled out. Further examination of the correlation across age shows that the association only starts to emerge from ca. 34 yo onwards.

Conclusions: Senescence affects local and global PE at different rates. While the aging brain shows a hierarchy-selective attenuation of PE, the attenuated local PE only contributes partially to the attenuated global PE. The attenuated global PE does not only reflect the process of aging but might serve as a marker for cognitive impairment.

References

1. Bekinschtein TA, Dehaene S, Rohaut B, Tadel F, Cohen L, Naccache L (2009) Neural signature of the conscious processing of auditory regularities. Proc Natl Acad Sci USA 106:1672-1677.
2. Chan JS, Wibral M, Stawowsky C, Brandl M, Helbling S, Naumer MJ, Kaiser J, Wollstadt P (2021) Predictive coding over the lifespan: increased reliance on perceptual priors in older adults- a magnetoencephalography and dynamic causal modeling study. Front Aging Neurosci 13:631599.
3. Hsu YF, Waszak F, Strömmer J, Hämäläinen JA (2021) Human brain ages with hierarchy-selective attenuation of prediction errors. Cereb Cortex 31:2156-2168.
4. Hsu YF, Tu CA, Bekinschtein TA, Hämäläinen JA. (2023) Longitudinal evidence for attenuated local-global deviance detection as a precursor of working memory decline. eNeuro 10(8):ENEURO.0156-23.2023.
5. Moran RJ, Symmonds M, Dolan RJ, Friston KJ (2014) The brain ages optimally to model its environment: evidence from sensory learning over the adult lifespan. PLoS Comput Biol 10:e1003422.
6. Wolpe N, Ingram JN, Tsvetanov KA, Geerligs L, Kievit RA, Henson RN, Wolpert DM; Cam-CAN; Rowe JB (2016) Ageing increases reliance on sensorimotor prediction through structural and functional differences in frontostriatal circuits. Nat Commun 7:13034.

Poster No 1154

Predictive Modeling of Brain Age for Evaluating Cognitive Brain Aging in Hearing Loss

Yen-Jung Pan[1], Chen-Yuan Kuo[1,2], Huei-Yu Tsai[1], Liang-Kung Chen[3,4], Ching-Po Lin[1,4,5]

[1]Institute of Neuroscience, National Yang Ming Chiao Tung University, Taipei, Taiwan, [2]Department of Neurology, Neurological Institute, Taipei Veterans General Hospital, Taipei, Taiwan, [3]Taipei Municipal Gan-Dau Hospital (managed by Taipei Veterans General Hospital), Taipei, Taiwan, [4]Center for Healthy Longevity and Aging Sciences, National Yang Ming Chiao Tung University, Taipei, Taiwan, [5]Department of Education and Research, Taipei City Hospital, Taipei, Taiwan

Introduction: The occurrence of hearing loss in midlife may play a pivotal role in contributing to dementia[1]. Prior research shows that prolonged auditory deprivation not only accelerates whole-brain atrophy and impairs executive function, but also leads to alterations in both auditory and visual connectivity, potentially affecting visual processing abilities[2,3,4]. These findings suggest potential advanced brain aging in hearing loss. However, it remains uncertain whether this phenomenon impacts the whole brain or only accelerates aging in specific cognitions. Recently, the brain age prediction framework, utilizing extensive neuroimaging data and machine learning techniques, has been employed to capture and elucidate the process of brain aging[5]. Hence, our aims were to construct brain age frameworks encompassing both the whole brain and specific cognition, and to explore whether individuals with hearing loss undergo advanced brain aging.

Methods: T1-weighted MRI data from 1482 healthy participants (age range: 18-92 years; 681 males, 801 females) were obtained from 5 site for training dataset to construct the brain age estimators. The study comprised normal-hearing (NH) group (n=51, 22M/29F) and group with hearing loss (HL) (n=67, 46M/21F) from the I-Lan Longitudinal Aging Study (ILAS). All participants underwent two follow-up examinations, on average 2.28 years apart. T1-weighted image preprocessing followed a previously described procedure and individual gray matter volume (GMV) and gray matter density (GMD) maps were estimated[5]. The hearing-related cognitive masks, encompassing memory, hearing, executive, and vision, were defined through a meta-analysis utilizing a machine learning framework[6]. Subsequently, we utilized the structural covariance network framework with both the whole-brain and the hearing-related gray matter mask to independently extract 600 features of the GM signature (300 GMV and 300 GMD) for the brain age model construction. RBF-SVR algorithm was employed for constructing a brain age estimator

with a nested 5-fold cross-validation scheme on the training dataset. Model performance was assessed using the mean absolute error (MAE) and (R^2) between chronological and predicted age. Each optimized brain age estimator was then applied to the HL and NH groups to estimate individual predicted brain age and calculate the brain age gap (BAG), representing the difference between chronological age and predicted brain age. To control for confounding effects, analysis of covariance (ANCOVA) was employed to compare global and hearing-related BAGs between NH and HL groups, with age, age^2, sex, years of education, and total intracranial volume (TIV) included as nuisance variables. Significance was set at $p < 0.05$.

Results: The constructed global brain age estimator and hearing-related cognitive brain age estimators demonstrated satisfactory performance in the training dataset (global: MAE = 4.27 years, R^2 = 0.92; executive: MAE = 5.66 years, R^2 = 0.86; hearing: MAE = 6.81 years, R^2 = 0.79; memory: MAE = 6.50 years, R^2 = 0.82; vision: MAE = 6.41 years, R^2 = 0.82; Figure.1). Using the global brain age estimator, the HL group exhibited a significantly smaller BAG compared with the NH group in Wave 1 ($p = 0.034$) but not in Wave 2. In both Wave 1 and Wave 2, the HL group showed larger BAGs than the NH group in memory, hearing, and executive function, and a smaller BAG in vision, with no statistical differences (Table.1).

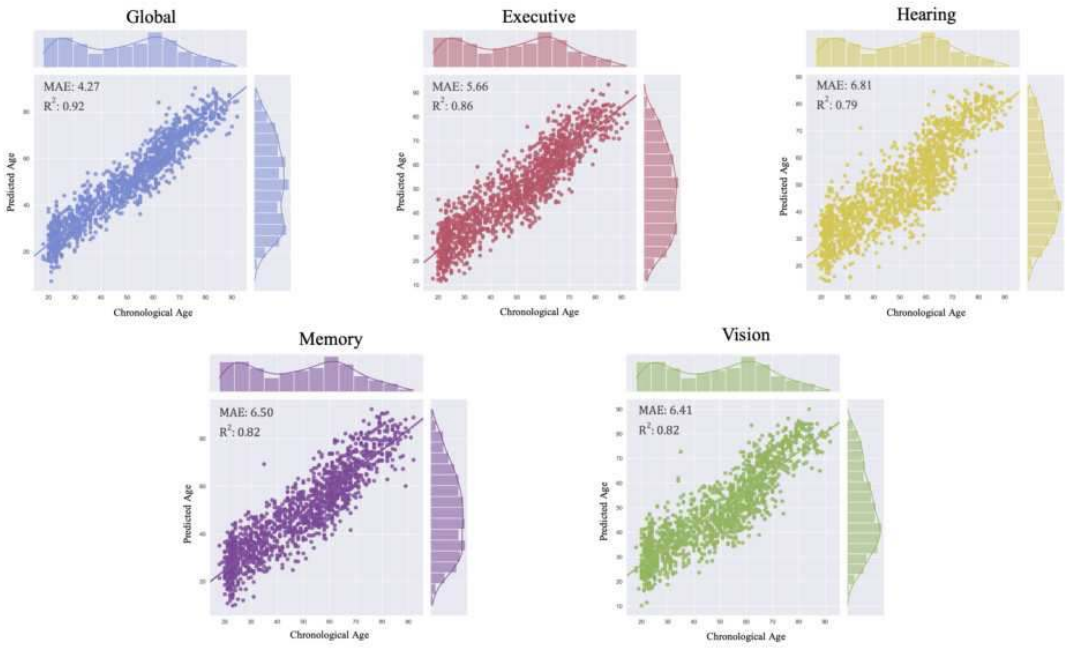

Figure.1 Prediction performances in global and hearing-related brain age estimator. MAE, mean absolute error; R^2, coefficient of determination.

Table.1 Comparison of brain age gap between normal-hearing and hearing loss

	Wave 1 BAGs				Wave 2 BAGs			
	NH	HL	Difference (HL−NH)	P value	NH	HL	Difference (HL−NH)	P value
Global	1.05±5.41	−0.17±6.60	−1.22	0.034*	2.78±6.37	1.71±5.53	−1.07	0.278
Executive	−0.26±7.70	1.21±7.04	1.47	0.966	1.57±7.09	1.98±6.82	0.41	0.925
Hearing	−2.51±10.97	0.24±10.37	2.74	0.963	−0.02±9.47	1.44±8.99	1.46	0.944
Memory	0.20±7.43	1.68±7.69.	1.47	0.546	1.84±7.39	2.71±7.68	0.87	0.400
Vision	−0.22±8.71	−1.59±9.66.	−1.37	0.059	1.57±9.01	−0.05±8.78	−1.62	0.056

*BAGs, brain age gap; NH, normal-hearing group; HL, group with hearing loss; *p<0.05.*

Conclusions: In summary, we presented a framework for hearing-related brain age estimators to explore different cognitive brain aging in hearing loss individuals. Although our study did not yield statistically significant evidence of a noteworthy increase in the BAG within each cognitive brain age estimator for the hearing loss group, we observed an increasing trend in the BAGs for hearing, memory, and executive function. Cognitive brain age estimator showed promise in elucidating the mechanisms of brain aging associated with hearing loss.

References

1. Livingston, G., et al. (2020), Dementia prevention, intervention, and care: 2020 report of the Lancet Commission. The Lancet, vol. 396, no. 10248, pp.413-446.

2. Lin, F. R., Ferrucci, L., An, Y., Goh, J. O., Doshi, J., Metter, E. J., Davatzikos, C., Kraut, M. A. & Resnick, S. M. (2014), Association of hearing impairment with brain volume changes in older adults. Neuroimage, vol. 90, pp.84-92.
3. Rosemann, S., & Thiel, C. M. (2021), No association between age-related hearing loss and brain age derived from structural neuroimaging data. Neuroimage: Reports, vol. 1(2), no. 100020.
4. Scott, G. D., Karns, C. M., Dow, M. W., Stevens, C., & Neville, H. J. (2014), Enhanced peripheral visual processing in congenitally deaf humans is supported by multiple brain regions, including primary auditory cortex. Frontiers in human neuroscience, vol. 8, no. 177.
5. Kuo, C.-Y., et al. (2021), Improving Individual Brain Age Prediction Using an Ensemble Deep Learning Framework. Front Psychiatry, vol. 12, pp. 1-11.
6. Beam, E., et al. (2021), A data-driven framework for mapping domains of human neurobiology. Nature neuroscience, vol. 24, no. 12, pp. 1733-1744.

Poster No 1155

Parcel-wise stacking ensemble provides improved age prediction and brain-aging insights

Georgios Antonopoulos[1,2], Shammi More[1,2], Federico Raimondo[1,2], Simon Eickhoff[1,2], Kaustubh Patil[1,2]

[1]Institute of Neuroscience and Medicine (INM-7: Brain and Behaviour), Research Centre Jülich, Juelich, Germany, [2]Institute for Systems Neuroscience, Medical Faculty, Heinrich-Heine University Düsseldorf, Düsseldorf, Germany

Introduction: Predicting chronological age using structural magnetic resonance imaging (MRI) has shown great potential for studying aging in health and disease. A model trained on MRI scans from healthy individuals can provide biological insights into healthy brain aging and it can also potentially assist in detection of abnormal aging in psychiatric, and neurodegenerative disorders[1,2]. Such a model may lead to novel monitoring and treatment options. However, both accuracy and explainability of age prediction models need to be improved before they can be applied in the real-world. To this end, we propose parcel-wise stacking ensemble models (SEM)[3]. In SEM the voxels in each region are not weighted equally, as in the standard approaches. Regional models evaluate the contribution of each voxel in the process making this way, better use of voxels' information. Moreover, combining predictions in sequential models leads to reduced overall bias and variance, of the final prediction.

Methods: We used T1w MRI scans of healthy subjects from 4 open datasets (IXI, eNKI, CamCAN and 1000Gehirne. N>500 each, total N=3103, age range 18-90 years). Voxel based morphometry using CAT12.8[4] was employed to estimate gray matter volume (GMV) for each subject. Performance was estimated in terms of mean absolute error (MAE) assessed in leave-one-dataset-out (LODO) set up. Proposed SEM consists of two levels, denoted as L0 and L1 (Figure 1). GLMnet[5] was used for both L0 and L1 models. The L0 uses an 873-parcel atlas and trains a model for each parcel using corresponding voxels-wise GMV. The features for the L1 model are obtained as out-of-sample (OOS) predictions from a 3-fold cross-validation scheme on L0 models. Two types of L0 models were obtained; either by pooling data from different sites (L0p) or by making predictions for each training site separately (L0s). Similarly, in L1 models were obtained by either pooling L0 predictions (L1p) or by training the L1 model for each site separately and averaging the per-site predictions (L1s). Additionally, to examine the case where enough data is available at an application site, we estimate L0 OOS predictions from that site (L0oos). These are then used to obtain predictions using the L1 models. As a baseline we also trained models using the average GMV in each parcel -by averaging predictions of the site-specific models or training models on pooled data across sites-, while ensuring use of consistent training samples across the set ups.

Results: The highest test performances were observed for the L0oos setups where L0 predictions came from the test site. The best predictions were for the L0oos-L1p (average MAE=4.8), closely followed by the L0oos-L1s (MAE=4.9). Setups using pooled L0 predictions to train L1, independently of how L0 was trained, L0p-L1p and L0s-L1p, had both MAE=5.1. Models using mean parcel-wise GMV had MAE=5.7 when the model was trained using the train sets together with the 2 folds of the test set. Performance was worse for the other two mean parcel-wise GMV models trained in three datasets, with the L1p setup up being slightly better compared to L1s (MAE=6.2 and MAE=6.7 respectively). L0 models provided robust interpretation of regional aging effects, i.e. the Pearson correlation of real age with OOS predicted-age was higher than with GMV (averaged across all datasets used for training, Figure 2). While there is a considerable overlap in the identified regions between the two methodologies, SEM distinctly emphasizes certain areas, notably the subcortex and cerebellum.

Conclusions: SEM provides improved age prediction performance compared to using parcel-wise average of GMV as well as novel biological insights regarding healthy aging. Further improvements in the SEM design could be achieved by selecting suitable learning algorithms with appropriate hyperparameter tuning for L0 and L1 models.

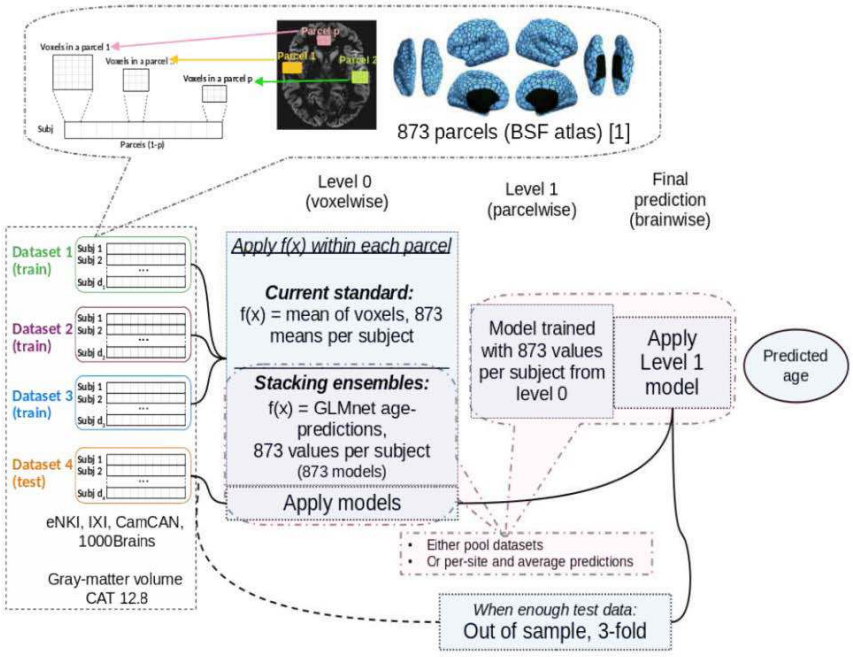

Figure 1: All voxels in a parcel, for all subjects of the train sets, are used in a 3-fold scheme to predict subjects' age using a machine learning model (here GLMnet), leading to 873 predictions per subject. Additionally, 873 models are created by fitting voxels for each parcel using pooled subjects of the train-datasets. The voxelwise age predictions of each subject are then pooled and used to fit the level 1 model (here GLMnet). The prediction of new/test data are as follows: the models fitted in level 0 are used to predict subjects' age in each parcel. These predictions serve the purpose of input features for level1 which provides the final prediction.

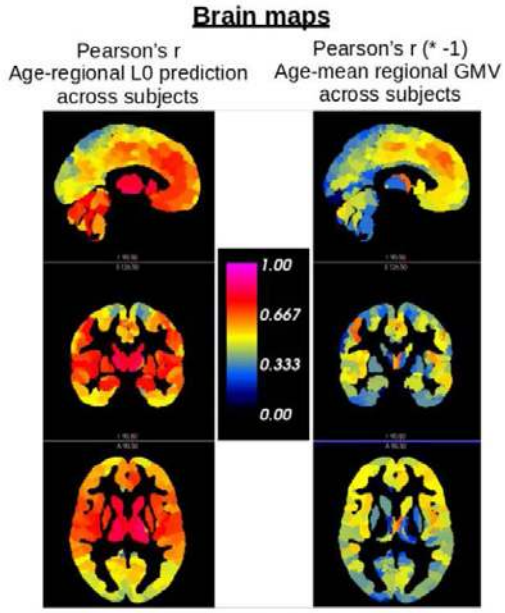

Figure 2: Biological insights produced by correlating real age to voxelwise predictions of each brain region (left) and regional mean GMV (right). For facilitating visualization of the regional-GMV to-age correlation values (right side), the values were multiplied by -1 to take into account that GMV usually decreases with age. Regions in the frontal lobe are highlighted by both methods. In SEM subcortical, lateral and cerebellum regions were prominently correlated to age.

References

1. Cole, J.H. (2018). Brain age predicts mortality. Molecular psychiatry, 23(5), pp.1385-1392.
2. Friedman, J. H. (2010) "Regularization Paths for Generalized Linear Models via Coordinate Descent", Journal of Statistical Software, 33(1), pp. 1–22. doi: 10.18637/jss.v033.i01.
3. Gaser, C. (2022). CAT–A computational anatomy toolbox for the analysis of structural MRI data. biorxiv, pp.2022-06.
4. More, S. (2023). Brain-age prediction: A systematic comparison of machine learning workflows. NeuroImage, 270, p.119947.
5. Wolpert, D.H. (1992). Stacked generalization. Neural networks, 5(2), pp.241-259.

Poster No 1156

Causal Relationship between Multiparameter Brain MRI Phenotypes and Age: Evidence from Mendelian Ran

Xinghao Wang[1], Han Lv[2], Zhenchang Wang[2]

[1]Beijing Friendship Hospital, Capital Medical University, Beijing, Beijing, [2]Beijing Friendship Hospital, Capital Medical University, Beijing, Beijing

Introduction: To explore the causal relationship between age and brain health related multiparameter imaging features using two-sample Mendelian randomization (MR).

Methods: Age was determined as chronological age of the subject. Cortical volume, white matter micro-integrity, white matter hyperintensity volume, and cerebral microbleeds of each brain region were included as phenotypes for brain health. Age and imaging of brain health related genetic data were analyzed to determine the causal relationship using inverse-variance weighted model (IVW), validated by heterogeneity and horizontal pleiotropy variables.

Results: Age is causally related to increased volumes of white matter hyperintensities (IVW, β= 0.151). For white matter micro-integrity, fibers of the inferior cerebellar peduncle (AD β= -0.128, OD β= 0.173), cerebral peduncle (AD β= -0.136), superior fronto-occipital fasciculus (ISOVF β= 0.163) and fibers within the limbic system were causally deteriorated. We also detected decreased cortical thickness of multiple frontal and temporal regions (IVW, $p<0.05$). Microbleeds were not related with aging (IVW, $p>0.05$).

Conclusions: Aging is a threaten of brain health, leading to cortical atrophy mainly in the frontal lobes, as well as the white matter degeneration especially abnormal hyperintensity and deteriorated white matter integrity around the hippocampus.

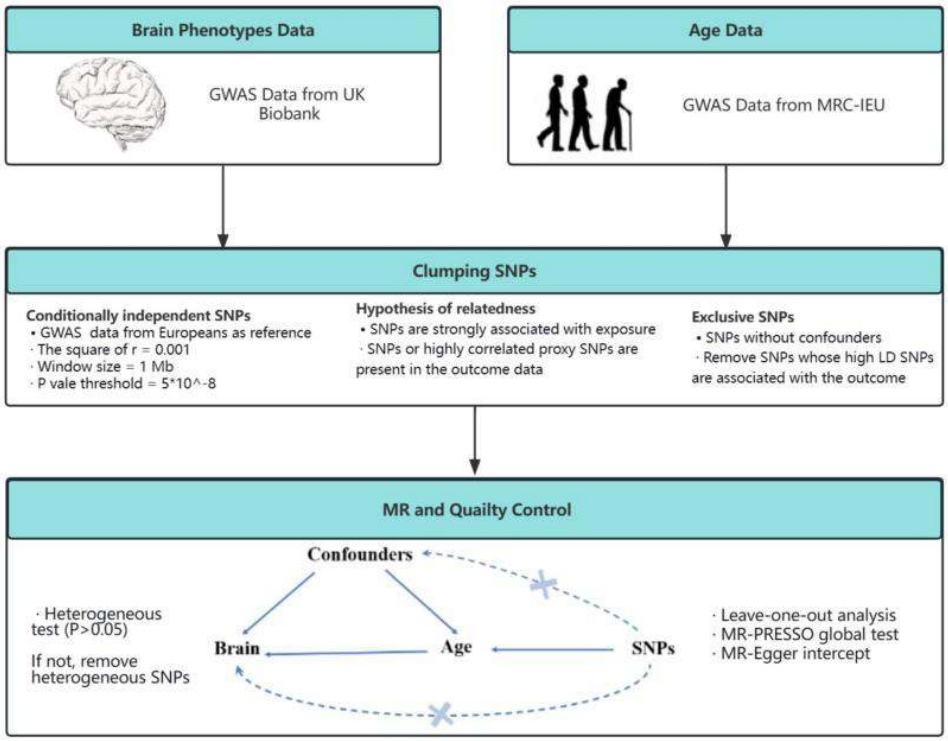

References

1. Tong T, Gao Q, Guerrero R, et al. A Novel Grading Biomarker for the Prediction of Conversion From Mild Cognitive Impairment to Alzheimer's Disease. IEEE Trans Biomed Eng. 2017;64(1):155-165. doi:10.1109/TBME.2016.2549363
2. Vinke EJ, de Groot M, Venkatraghavan V, et al. Trajectories of imaging markers in brain aging: the Rotterdam Study. Neurobiol Aging. 2018;71:32-40. doi:10.1016/j.neurobiolaging.2018.07.001
3. Bethlehem RAI, Seidlitz J, White SR, et al. Brain charts for the human lifespan [published correction appears in Nature. 2022 Oct;610(7931):E6]. Nature. 2022;604(7906):525-533. doi:10.1038/s41586-022-04554-y
4. Davies NM, Holmes MV, Davey Smith G. Reading Mendelian randomisation studies: a guide, glossary, and checklist for clinicians. BMJ. 2018;362:k601. Published 2018 Jul 12. doi:10.1136/bmj.k601
5. Skrivankova VW, Richmond RC, Woolf BAR, et al. Strengthening the Reporting of Observational Studies in Epidemiology Using Mendelian Randomization: The STROBE-MR Statement. JAMA. 2021;326(16):1614-1621. doi:10.1001/jama.2021.18236

Poster No 1157

The brain age of hippocampus-centred regions and associations with APOE genotype

Chao Dong[1], Yuangang Pan[2], Anbupalam Thalamuthu[1], Jiyang Jiang[1], Karen Mather[1], Perminder Sachdev[1], Wei Wen[1]

*[1]Centre for Healthy Brain Ageing (CHeBA), University of New South Wales, Sydney, New South Wales, [2]Centre for Frontier AI Research (CFAR), A*STAR, Singapore*

Introduction: Brain age, a promising biomarker in neuroimaging, has been widely investigated by using the whole brain image. Deep learning, specifically convolutional neural networks (CNN), has been widely used in the field of brain age prediction. A recent study which used the hippocampal-centred regions to predict brain age found that brain age gap might be a biomarker to help AD and mild cognitive impairment (MCI) diagnosis (Poloni and Ferrari 2022). Deep learning models have identified the temporal lobes and hippocampus as high-risk regions for AD classification (Qiu, Joshi et al. 2020, Wang, Honnorat et al. 2023), or related dementia (Martin, Townend et al. 2023). Grey matter density around hippocampus and amygdala has been identified as a key factor influencing age predictions (Wang, Knol et al. 2019). However, associations between the age of hippocampus-related regions, Apolipoprotein E (APOE) genotypes, and other lifestyle patterns are unknown.

Methods: Left and right hippocampus-centred regions of interest (hippocampus ROI) age prediction models were developed based on three-dimensional convolutional neural network (3D-CNN) in UK Biobank, with 31370 healthy participants in five-fold cross-validation. The unhealthy participants were excluded from the model training set to maximize sensitivity. All the 31370 healthy participants with one time point image were randomly split into five equally sized folds, with 60% for training, 20% for validation, and 20% for test set. Model performance in the training set was assessed using 5-fold cross validation. The hippocampus ROI age (HA) gap was calculated as predicted age minus chronological age. Furthermore, the longitudinal change rate of HA gap was estimated based on another 3893 participants who have two-time points imaging data. We estimated the associations between hippocampus volume, volume change rate, and APOE genotype. Similarly, we also examined the associations between HA gap, cognition, and APOE genotype, as well as the associations between longitudinal HA age change rate and APOE genotype. In addition, a Cox proportional hazards model was used to perform survival analyses (positive HA gap was used as the outcome in the model).

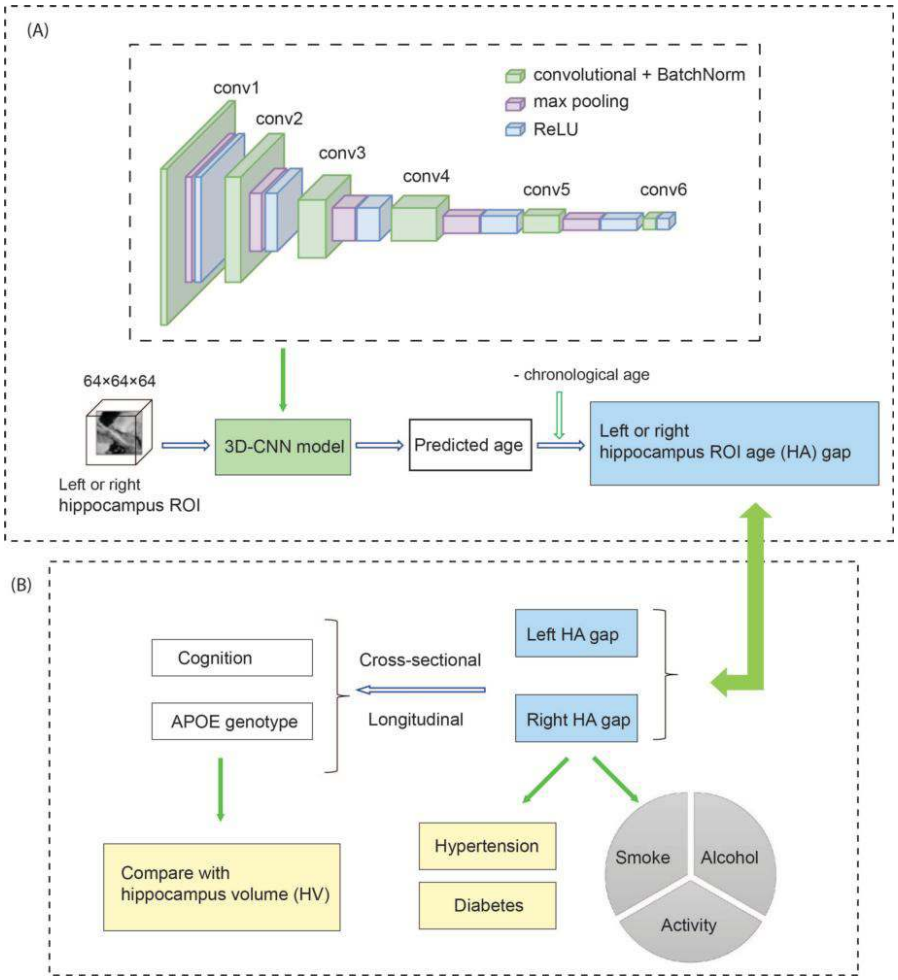

Results: Our model achieved a competitive state-of-the-art metric (MAE: 2.52 – 2.84 years in left HA model; 2.47 – 2.72 years in right HA model). In cross-sectional analysis, we found that HA gap in APOE ε4/ε4 carriers was significantly greater than that in APOE ε4 non-carriers: ε2/ε2, ε2/ε3, ε3/ε3 (left: β = 0.1663, 95% confidence interval [CI] = [0.0849, 0.2478], p = 6.30e-05; right: β = 0.1924, CI = [0.1106, 0.2742], p = 4.03e-06). Additionally, greater HA gap was correlated with worse cognitive performance. In longitudinal analysis, APOE ε4/ε4 carriers showed higher annual change rate in left HA gap compared with APOE ε2/ε2 carriers (β = 0.5805, CI = [0.0737, 1.0873], p = 0.0248), but this effect was not found in right HA gap or hippocampus volume. In survival analyses, hazard ratios (HR) with 95 % CI for sex was 1.2694 (CI = [1.1595, 1.3898], p =2.42e-07), for hypertension (HR= 1.4132, CI = [1.2711, 1.5713], p =1.61e-10), for diabetes (HR= 1.5893, CI = [1.3060, 1.9340], p =3.73e-06).

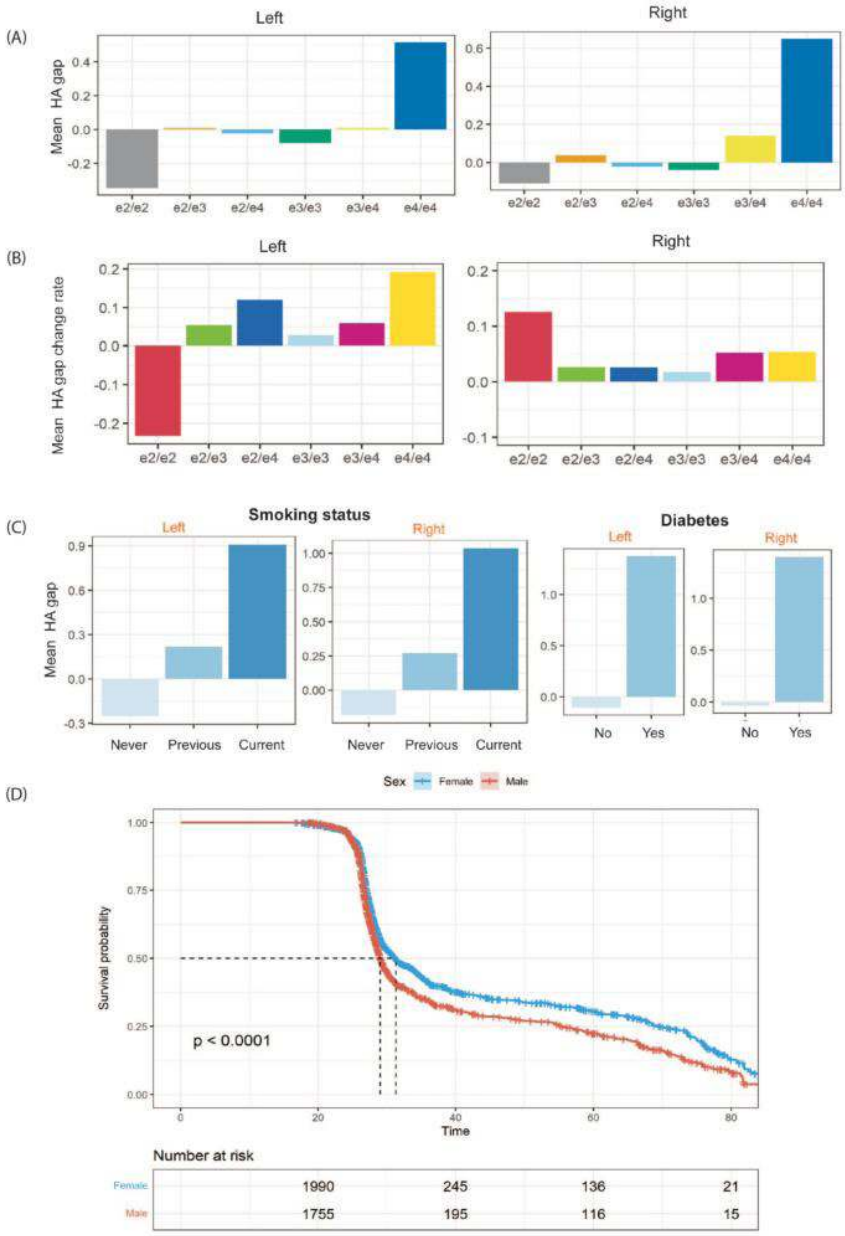

Conclusions: Our work revealed that the age gap in hippocampus ROI was associated with cognition and APOE genotypes, and demonstrated that the APOE ε4 carriers, especially homozygotes, tend to have greater HA gap and "accelerated hippocampus ROI ageing". The left HA gap could be identified as a potential biomarker linked to APOE genotype and a health indicator.

References

1. Martin, S. A., F. J. Townend, F. Barkhof and J. H. Cole (2023). "Interpretable machine learning for dementia: A systematic review." Alzheimer's & Dementia 19(5): 2135-2149.
2. Poloni, K. M. and R. J. Ferrari (2022). "A deep ensemble hippocampal CNN model for brain age estimation applied to Alzheimer's diagnosis." Expert Systems with Applications 195: 116622.

3. Qiu, S., P. S. Joshi, M. I. Miller, C. Xue, X. Zhou, C. Karjadi, G. H. Chang, A. S. Joshi, B. Dwyer, S. Zhu, M. Kaku, Y. Zhou, Y. J. Alderazi, A. Swaminathan, S. Kedar, M.-H. Saint-Hilaire, S. H. Auerbach, J. Yuan, E. A. Sartor, R. Au and V. B. Kolachalama (2020). "Development and validation of an interpretable deep learning framework for Alzheimer's disease classification." Brain 143(6): 1920-1933.
4. Wang, D., N. Honnorat, P. T. Fox, K. Ritter, S. B. Eickhoff, S. Seshadri and M. Habes (2023). "Deep neural network heatmaps capture Alzheimer's disease patterns reported in a large meta-analysis of neuroimaging studies." NeuroImage 269: 119929.
5. Wang, J., M. J. Knol, A. Tiulpin, F. Dubost, M. de Bruijne, M. W. Vernooij, H. H. H. Adams, M. A. Ikram, W. J. Niessen and G. V. Roshchupkin (2019). "Gray Matter Age Prediction as a Biomarker for Risk of Dementia." Proceedings of the National Academy of Sciences 116(42): 21213-21218.

Poster No 1158

Elevated brain iron is associated with higher R2 and more WMH in older adults

Md Tahmid Yasar[1], Ashley Bush[2], Scott Ayton[2], Puja Agarwal[3], Sonal Agrawal[3], David Bennett[3], Julie Schneider[3], Konstantinos Arfanakis[1,3]

[1]Illinois Institute of Technology, Chicago, IL, [2]The University of Melbourne, Parkville, Victoria, [3]Rush University Medical Center, Chicago, IL

Introduction: Iron is an essential micronutrient for brain health. Iron accumulates in the brain throughout lifetime and the variation in iron levels among individuals increases beyond the age of sixty[1]. Elevated iron is a source of free radicals that cause oxidative stress which has been linked to neurodegenerative and cerebrovascular pathologies as well as cognitive impairment among older adults[2]. Iron has a higher magnetic susceptibility than brain tissue and therefore magnetic resonance imaging (MRI) is sensitive to iron levels. To date, the association of iron measurements with various MRI characteristics has not been systematically investigated in older adults[3-5]. Therefore, the aim of this study was to quantify brain iron levels in a large number of community-based older adults and investigate the association of iron levels with transverse relaxation rate, R2, and white matter hyperintensities (WMH), independent of the effects of other metals and age-related neuropathologies[6-8].

Methods: Cerebral hemispheres from 437 community-based older adults participating in the Rush Memory and Aging Project[9] (Table 1) were involved in this work. All hemispheres were imaged ex-vivo at room temperature, at approximately 30 days postmortem using 3T clinical MRI scanners[6]. R2 maps were generated from multi-echo spin-echo data and then registered to an ex-vivo brain hemisphere template using ANTS[7]. WMH were segmented based on T2-weighted images[8]. WMH volume was normalized by the total hemisphere volume and then log-transformed to account for skewness. Following ex-vivo MRI, all hemispheres underwent detailed neuropathologic assessment. The assessed pathologies included Aβ plaques, neurofibrillary tangles, limbic-predominant age-related TDP-43 encephalopathy neuropathological change (LATE-NC), hippocampal sclerosis (HS), Lewy bodies, cerebral amyloid angiopathy (CAA), gross infarcts, microscopic infarcts, atherosclerosis, and arteriolosclerosis (Table 1). Inductively coupled plasma mass spectrometry was used on all participants to measure iron levels in four brain regions: mid-frontal, anterior cingulate, inferior temporal cortices, and cerebellum[10]. The log-transformed iron concentrations in the four regions were averaged to generate a global score. Other metals that were assessed included: boron, titanium, manganese, copper, zinc, selenium, rubidium, molybdenum, and mercury (Table 1). Linear regression models were used to test the voxel-wise association of R2 with iron levels, as well as the association of the total and lobar WMH burden with iron levels. All models were controlled for all other metals and neuropathologies listed above, demographics (age at death, sex, years of education), the presence of the APOE ε4 allele, postmortem interval to fixation and to imaging, and scanner. Statistical analysis was performed using PALM (FMRIB, Oxford, UK) with tail-accelerated 5,000 permutations. Statistical significance was set at $p<0.05$ after family wise error rate correction.

Characteristics	
N	437
Age at death, years (SD)	91.2 (6.0)
Male, n (%)	109 (25)
Education, years (SD)	14.5 (2.9)
Antemortem clinical diagnosis, n (%)	
- Mild cognitive impairment	101 (23)
- Dementia	194 (44)
Right hemisphere in imaging, n (%)	199 (46)
Right hemisphere in trace metal detection, n (%)	238 (54)
Iron level, mean (SD)	1.55 (0.09)
Boron level, mean (SD)	-1.19 (0.27)
Titanium level, mean (SD)	-1.00 (0.13)
Manganese level, mean (SD)	-0.57 (0.06)
Copper level, mean (SD)	0.55 (0.11)
Zinc level, mean (SD)	1.12 (0.05)
Selenium level, mean (SD)	-0.45(0.10)
Rubidium level, mean (SD)	0.23 (0.12)
Molybdenum level, mean (SD)	-1.58 (0.09)
Mercury level, mean (SD)	-2.13 (0.54)
At least one copy of the APOE-ε4 allele, n (%)	108 (25)
Postmortem interval to fixation, hours (SD)	8.6 (5.6)
Postmortem interval to imaging, days (SD)	37.8 (14.7)
MRI Scanners, n (%)	
- Siemens Trio	46 (11)
- Siemens Verio	187 (43)
- General Electric Signa	45 (10)
- Philips Achieva	159 (36)

Characteristics	
N	437
AD pathology, NIA-AA criteria, n (%)	
- low	78 (18)
- intermediate	196 (45)
- high	114 (26)
Cerebral amyloid angiopathy, n (%)	
- mild	198 (45)
- moderate	109 (25)
- severe	50 (11)
Summarized amyloid burden score, mean (SD)	1.9 (1.2)
Summarized tangle burden score, mean (SD)	1.9 (1.4)
Gross infarcts, n (%)	193 (44)
Microscopic infarcts, n (%)	162 (37)
Hippocampal sclerosis, n (%)	54 (12)
Lewy bodies, n (%)	136 (31)
Atherosclerosis, n (%)	
- mild	226 (52)
- moderate	84 (19)
- severe	31 (7)
Arteriolosclerosis, n (%)	
- mild	154 (35)
- moderate	111 (25)
- severe	26 (6)
TDP-43 pathology, n (%)	
- only amygdala	80 (18)
- amygdala and hippocampus	48 (11)
- amygdala, hippocampus, and neocortex	125 (29)

Results: The voxel-wise analysis revealed a spatial pattern of higher R2 values for higher iron levels, particularly in gray matter (Fig. 1a). The pattern included basal ganglia structures such as the globus pallidus and putamen, as well as cortical regions such as the precentral, postcentral and cuneus cortex (Fig. 1a). Higher lobar and total WMH burden were also associated with higher iron levels (Fig. 1b). No negative associations were observed.

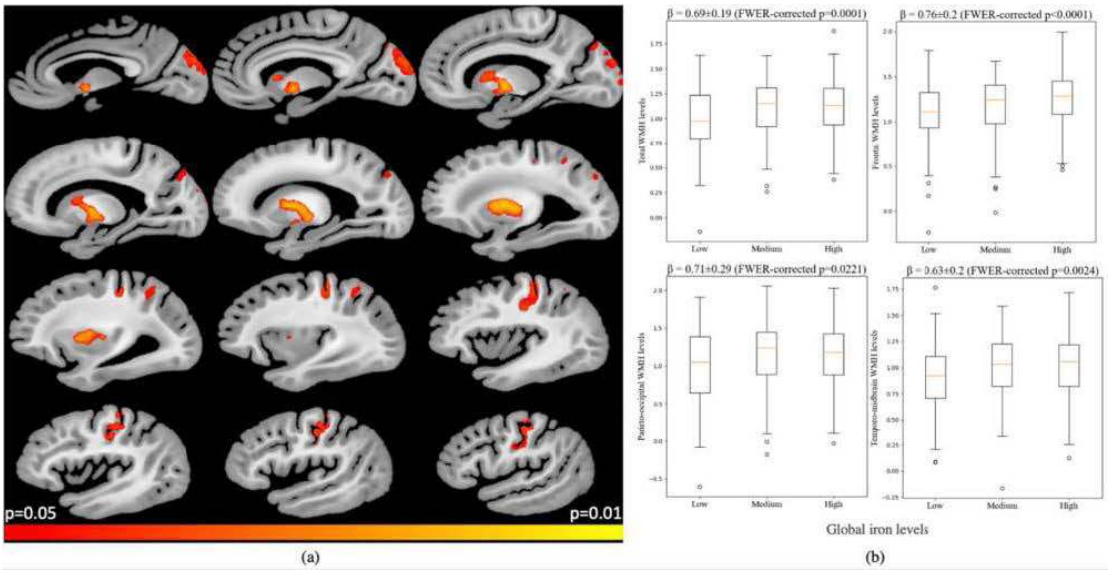

Conclusions: This investigation combined ex-vivo MRI, neuropathology and mass spectrometry in a large number of community-based older adults and showed that higher iron levels are associated with higher R2 in gray matter and higher WMH burden. These associations were independent of the effects of other metal, neuropathologies, demographic and genomic risk factors, suggesting the presence of additional mechanisms of iron accumulation.

References
1. Hallgren, B., 'The effect of age on the non-haemin iron in the human brain', J Neurochem. 1958;3(1):41-51.
2. Ayton, S., 'Brain iron is associated with accelerated cognitive decline in people with Alzheimer pathology', Mol Psychiatry. 2020;25(11):2932-2941.
3. House, M.J., 'Correlation of proton transverse relaxation rates (R2) with iron concentrations in postmortem brain tissue from alzheimer's disease patients', Magn Reson Med. 2007;57(1):172-180.
4. Langkammer, C., 'Quantitative MR imaging of brain iron: a postmortem validation study' [published correction appears in Radiology. 2011 Mar;258(3):962], Radiology. 2010;257(2):455-462.
5. Yan, S., 'Brain iron deposition in white matter hyperintensities: a 3-T MRI study', Age (Dordr). 2013;35(5):1927-1936.
6. Dawe, R.J., 'Ex vivo T2 relaxation: Associations with age-related neuropathology and cognition' Neurobiol Aging. 2014;35:1549–1561.
7. Yu, L., 'Ex vivo MRI transverse relaxation in community based older persons with and without Alzheimer's dementia', Behav Brain Res. 2017;322:233–240.
8. Arfanakis, K., 'Neuropathologic Correlates of White Matter Hyperintensities in a Community-Based Cohort of Older Adults', J Alzheimers Dis. 2020;73(1):333-345.
9. Bennett, D.A., 'Religious Orders Study and Rush Memory and Aging Project', J Alzheimer's Dis. 2018;64:S161–S189.
10. Ayton, S., 'Regional brain iron associated with deterioration in Alzheimer's disease: A large cohort study and theoretical significance', Alzheimers Dement. 2021;17(7):1244-1256.

Poster No 1159

Identity Preserving Diffusion Model for Brain Aging Modeling

Gexin Huang[1], Mengwei Ren[2], Guido Gerig[2], Xiaoxiao Li[1]

[1]The University of British Columbia, Vancouver, BC, [2]New York University, Brooklyn, NY

Introduction: Brain aging is a natural process that affects brain structure and function, leading to cognitive decline and increased risk of neurodegenerative diseases. Aging brain image generation is crucial for understanding aging, diagnosing disorders, predicting risk, and planning treatments. Deep-learning-based image-to-image generation methods could effectively study structural changes associated with aging. Keeping identity consistent in this process is crucial for understanding the underlying mechanisms and enabling personalized brain aging modeling. However, preserving identity consistency in longitudinal brain images has not been adequately addressed by previous works[1,2,3]. Thus, we propose a novel Longitudinal Transformation Diffusion model with an identity consistency module (LT-Diff) that achieves accurate brain age transformations while preserving identity using the OASIS Brain Dataset.

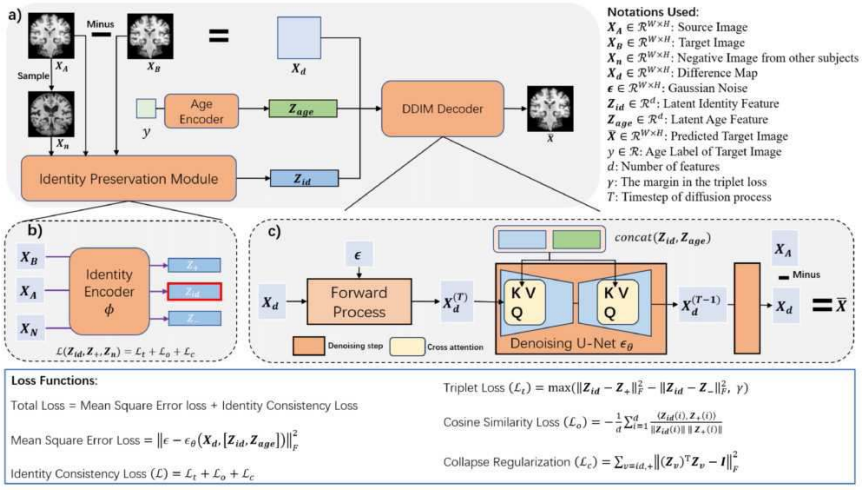

Fig. 1. Proposed pipeline of LT-Diff. (a) Difference map X_d is computed as the difference between the source image and the target image. Then, the latent age feature Z_{age} is obtained by encoding the age label of the target image from the age encoder while the latent identity feature Z_{id} is obtained from the identity preservation module. (b) Identity preservation module utilizes the identity encoder ϕ to decouple identity features from images, enhancing the similarity among features from the same subject while promoting greater dissimilarity between features from other subjects. (c) Z_{age} and Z_{id} are concatenated as the conditioning input into the DDIM decoder via the cross-attention mechanism, manipulating X_d to reconstruct the target image.

Methods: Aging brain generation is achieved via an image-2-image model that generates the target image based on the source image and the target age. We utilized the OASIS-3 brain dataset[4], consisting of longitudinal MRI imaging data collected over 15 years from ongoing studies. It includes data from 1098 individuals, 493 of whom were at various stages of cognitive decline ranging in age from 42 to 95 years. The model takes the middle slice of each 3D MRI volume as its input. The dataset covers an age range from 40 to 100, divided into four groups: 40-55, 56-70, 71-85, and 86-100. Each MRI image is labeled with

the corresponding age group. The stratified sampling strategy[5] is used for train-validation-test data split. Model Architecture: The LT-Diff model (Fig. 1a) consists of three components: the Identity Preservation Module (Fig. 1b), the Age Encoder, and the DDIM Decoder (Fig. 1c) based on the DDIM backbone[4]. Inspired by the Diffusion Autoencoder[6], the Identity Preservation Module decouples identity information using a ResNet-18 encoder, preserving identity consistency. The age encoder utilizes a four-layer MLP to generate a shared latent age feature. The DDIM decoder reconstructs the difference map between the target and source image, conditioned on concatenated identity and age features. The predicted target image is synthesized by fusing the difference map with the source image. Objective functions and Optimization: Two objectives are used for training (Fig. 1): Mean Square Error loss for difference map reconstruction and Identity Consistency Loss for preserving subject identity. The Identity Consistency Loss combines triplet loss, cosine similarity, and collapse regularization terms. The triplet loss maximizes inter-identity distance while minimizing intra-identity distance. The cosine similarity term promotes similarity within the same identity, and the collapse regularization term prevents identical features and avoids local minima during optimization[9].

Performance Comparison

a)

Methods	Metric(↓) \ Age	40-55	56-70	71-85	86-100	Average
LifeSpan GAN[9]	FID	51.71 ± 10.8	37.13 ± 4.1	42.58 ± 4.8	55.0 ± 8.6	46.61
	KID	$55.49e^{-3} \pm 7e^{-4}$	$21.5e^{-3} \pm 3e^{-4}$	$25.50e^{-3} \pm 3e^{-4}$	$56.29e^{-3} \pm 7e^{-4}$	$39.69e^{-3}$
LT-Diff	FID	$\mathbf{23.91 \pm 1e^{-1}}$	$\mathbf{23.33 \pm 1e^{-1}}$	$\mathbf{23.51 \pm 1e^{-1}}$	$\mathbf{23.59 \pm 1e^{-1}}$	**23.59**
	KID	$\mathbf{11.74e^{-4} \pm 1e^{-6}}$	$\mathbf{11.22e^{-4} \pm 1e^{-6}}$	$\mathbf{11.69e^{-4} \pm 1e^{-6}}$	$\mathbf{11.73e^{-4} \pm 1e^{-6}}$	$\mathbf{11.59e^{-4}}$

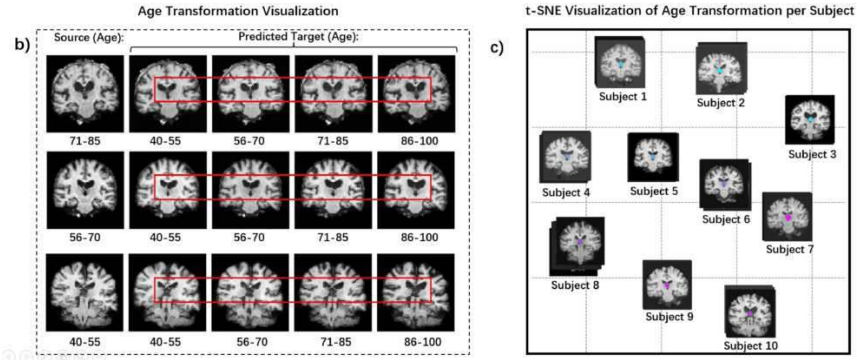

Fig. 2. (a) Performance comparison of LT-Diff with the SOTA method. Reported performances are in the (mean +/- std deviation) format with the mean being the average of 3 random runs on the test set. (b). Predicted images with varying target ages from a given source image. The ventricles within the red boxes grow larger as brain aging aggravates. (c) t-SNE visualization on identity features encoded from generated brain aging images across different subjects. Each subject generates images for four age groups and utilizes the identity encoder to obtain the identity features. The t-SNE map demonstrates that identity features of images from the same subject cluster together and are distinctly separated from features belonging to other subjects, illustrating the accurate reconstruction and preservation of identity consistency in LT-Diff.

Results: LT-Diff outperforms the state-of-the-art method (lifespan GAN)[9] with a better FID score of 23.59 and KID score of 11.59e-4 (Fig. 2a). The brain age transformation (Fig. 2b) shows ventricles growing larger with increasing brain aging while maintaining subtle geometric variations for each subject, consistent with the transformation of brain aging in prior studies [10,11]. The t-SNE visualization (Fig. 2c) confirms LT-Diff's accurate reconstruction of brain images while preserving identity consistency.

Conclusions: We propose LT-Diff, a method that preserves identity consistency in longitudinal brain imaging by leveraging decoupled identity features. By incorporating these features and age information as a condition for the diffusion decoder, LT-Diff successfully generates brain images with the desired target age. Experimental results on the Oasis-3 dataset show that LT-Diff outperforms the SOTA architecture in brain aging generation performance w.r.t aging modeling and identity preservation.

References

1. Choi, Y., Uh, Y., Yoo, J., & Ha, J. W. (2020). Stargan v2: Diverse image synthesis for multiple domains. In Proceedings of the IEEE/CVF conference on computer vision and pattern recognition (pp. 8188-8197).
2. Kanizo, Y., Hay, D., & Keslassy, I. (2013, April). Palette: Distributing tables in software-defined networks. In 2013 Proceedings IEEE INFOCOM (pp. 545-549). IEEE.
3. Sasaki, H., Willcocks, C. G., & Breckon, T. P. (2021). Unit-ddpm: Unpaired image translation with denoising diffusion probabilistic models. arXiv preprint arXiv:2104.05358.
4. LaMontagne, P. J., Benzinger, T. L., Morris, J. C., Keefe, S., Hornbeck, R., Xiong, C., ... & Marcus, D. (2019). OASIS-3: longitudinal neuroimaging, clinical, and cognitive dataset for normal aging and Alzheimer's disease. MedRxiv, 2019-12.
5. Tong, C. (2006). Refinement strategies for stratified sampling methods. Reliability Engineering & System Safety, 91(10-11), 1257-1265.
6. Preechakul, K., Chatthee, N., Wizadwongsa, S., & Suwajanakorn, S. (2022). Diffusion autoencoders: Toward a meaningful and decodable representation. In Proceedings of the IEEE/CVF Conference on Computer Vision and Pattern Recognition (pp. 10619-10629).
7. Dey, N., Ren, M., Dalca, A. V., & Gerig, G. (2021). Generative adversarial registration for improved conditional deformable templates. In Proceedings of the IEEE/CVF international conference on computer vision (pp. 3929-3941).
8. Song, J., Meng, C., & Ermon, S. (2020). Denoising diffusion implicit models. arXiv preprint arXiv:2010.02502.

9. Or-El, R., Sengupta, S., Fried, O., Shechtman, E., & Kemelmacher-Shlizerman, I. (2020). Lifespan age transformation synthesis. In Computer Vision–ECCV 2020: 16th European Conference, Glasgow, UK, August 23–28, 2020, Proceedings, Part VI 16 (pp. 739-755). Springer International Publishing.
10. Peng, L., Wang, N., Xu, J., Zhu, X., & Li, X. (2022). GATE: graph CCA for temporal SElf-supervised learning for label-efficient fMRI analysis. IEEE Transactions on Medical Imaging, 42(2), 391-402.
11. Blinkouskaya, Y., Caçoilo, A., Gollamudi, T., Jalalian, S., & Weickenmeier, J. (2021). Brain aging mechanisms with mechanical manifestations. Mechanisms of Aging and Development, 200, 111575. doi:10.1016/j.mad.2021.111575
12. Blinkouskaya, Y., & Weickenmeier, J. (2021). Brain shape changes associated with cerebral atrophy in healthy aging and Alzheimer's disease. Frontiers in Mechanical Engineering, 7, 705653.

Poster No 1160

A comparative study on thalamic subnuclear volume between premenopausal and postmenopausal women

Gwang-Won Kim[1], Kwangsung Park[2], Yun-Hyeon Kim[3], Gwang-Woo Jeong[3]

[1]Advanced Institute of Aging Science, Chonnam National University, Gwangju, Chonnam, [2]Department of Urology, Chonnam National University Medical School, Gwangju, Chonnam, [3]Department of Radiology, Chonnam National University Medical School, Gwangju, Chonnam

Introduction: Aging is a multifaceted and complex phenomenon characterized by neuro-physiological changes that exert a variety of effects on the structure and function of the brain. One such pivotal transition in women is menopause which encompasses the loss of ovarian reproductive function. However, menopause-related thalamic subnuclear changes are poorly understood. Thus, this study was aimed to compare the brain volume changes, focusing especially on the thalamic subnuclei, between premenopausal and postmenopausal women.

Methods: Twenty-one premenopausal women (mean age = 39.8 ± 7.6 years) and 21 postmenopausal women (mean age = 55.3 ± 2.5 years) participated in this study. Magnetic resonance imaging (MRI) scans were acquired using a 3.0 Tesla Magneton Tim Trio MR Scanner (Siemens Medical Solutions, Erlangen, Germany). Serum sex hormones, including total estrogen, estradiol (E2), estriol (E3), free testosterone (free-T), follicle-stimulating hormone (FSH), and luteinizing hormone (LH) were measured. The thalamic subnuclear volumes were measured using the FreeSurfer v7.2 software. Twenty-five thalamic subnuclei (50 regions of interest) were extracted extracted from each hemisphere on T1 image. Each thalamic subnuclear volume was adjusted using the following equation: Adjusted volume = (Each thalamic subnuclear volume (mm3) / Whole brain volume (mm3)) × 1000.

Results: Compared with premenopausal women, postmenopausal women showed lower levels of total estrogen ($p < 0.001$) and E2 levels ($p < 0.001$); higher levels of FSH ($p < 0.001$) and LH ($p = 0.005$). Postmenopausal women showed significantly smaller cortical surface, especially in the left medial orbitofrontal cortex, right superior temporal cortex, and right lateral orbitofrontal cortex compared to premenopausal women ($p < 0.05$, Bonferroni-corrected). Notably, the thalamic subnuclear volume, especially in the right pulvinar anterior region, in the postmenopausal women was significantly decreased ($p < 0.05$, Bonferroni-corrected). The levels of E2 were positively correlated with the adjusted volumes of the right pulvinar anterior ($r = 0.34$, $p = 0.030$).

Conclusions: This study compared differential thalamic subnuclear volumes between premenopausal and postmenopausal women. It is suggested that diminished brain volume are potentially associated with menopause-related neuro-physiological change caused by the lower sex hormone levels. Our findings will be helpful for an understanding of the effects of menopause on the altered brain volume in postmenopausal women.

References

1. Kim, G.W. (2023), 'Early Detection of Alzheimer's Disease in Postmenopausal Women Using Thalamic Subnuclear Volumetry', Journal of Clinical Medicine, vol. 12, no. 21, pp. 6844
2. Blagosklonny, M.V. (2023), 'Are menopause, aging and prostate cancer diseases', Aging, vol. 15, no. 2, pp. 298-307
3. Yureneva, S. (2021), 'Searching for female reproductive aging and longevity biomarkers', Aging, vol. 13, no. 12, pp. 16873-16894

Poster No 1161

Exploring the link between resilience, brain pathology, and cognition in old age: sex differences

Caroline Dartora[1], Anna Marseglia[1], Johan Skoog[2], Sebastian Muehlboeck[1], Silke Kern[2], Anna Zettergren[2], Ingmar Skoog[2], Eric Westman[1]

[1]Karolinska Institutet, Stockholm, Sweden, [2]University of Gothenburg, Gothenburg, Sweden

Introduction: Exposure to dementia risk factors throughout life can lead to brain atrophy and older-appearing brains on neuroimaging. Resilience mechanisms can help sustain the brain structure (brain maintenance, BM) and/or compensate for the neuropathological damage (cognitive reserve, CR), preserving cognition. Traditional proxy-based approaches (e.g., education) face challenges in measuring these mechanisms as they cannot capture the core biological dimension. However, with deep learning is possible to develop algorithms predicting the biological age of the brain from raw brain images. This study investigated whether differences between predicted brain age and chronological age (PBA-CA) can be used as a marker of BM and/or CR following the NIH-funded Collaboratory on Reserve and Resilience framework.

Methods: The study population included 719 dementia-free septuagenarians from the Gothenburg H70-1944 MRI cohort. We applied the deep learning model-developed in-house using minimally processed T1-w MRI from ~17000 neurologically intact individuals from UK Biobank, ADNI, AIBL, and GENIC and validated via a cross-validation approach to H70 participants' MRI to predict their brain age, and computed PBA-CA. MRI markers of brain pathology included cortical thickness (overall and Alzheimer's disease-related), cerebral small vessel disease (SVD; individual markers and score), and white-matter microstructural alterations (DTI's fractional anisotropy). Global and domain-specific cognitive function was based on composite scores from ten tests. Data analysis included regression models and stratification by sex.

Results: In the brain, decreasing differences between PBA and CA (reflecting younger-appearing brains) were associated with a thicker brain (overall and AD signature areas), lower SVD score-particularly lower white matter hyperintensities volume, lacunes, large infarcts-, and higher fractional anisotropy (more integrity). Decreasing differences were also related to better cognitive performance, globally and in attention/speed, executive function, and visuospatial abilities. In stratified analysis by sex, such associations were evident in men but not in women, except fractional anisotropy [robust regressions' β-coefficients for women -4.89 (95%CI -8.87,-0.90) and men -23.7 (95%CI -32.9,-14.4)].

Conclusions: Negative differences PBA<CA are related to less atrophy, less cerebrovascular alterations, and better cognition, suggesting more preserved brain structure and cognition, thus BM. However, differences between the sexes suggest that women and men may have different pathways to resilience.

References

1. Dartora, C. et al., 2023. https://doi.org/10.1101/2022.09.06.22279594

Poster No 1162

Spatiotemporal correlation between amyloid and tau underlies cognitive changes in aging

Chanmie Kim[1], Ibai Diez[1], Elisenda Bueichekú[1], Sung Ahn[1], Victor Montal[2], Jorge Sepulcre[1]

[1]Massachusetts General Hospital, Boston, MA, [2]Universitat Autonoma de Barcelona, Barcelona, Barcelona

Introduction: It is still largely unknown how the two hallmarks of Alzheimer's disease (AD) - amyloid-beta (Aβ) plaques and tau neurofibrillary tangles - interact and propagate spatiotemporally to produce synaptic dysfunction and neuronal death at the large-scale level[1,2]. This study aimed to identify the spatiotemporal cortical patterns of Aβ-and-tau and longitudinal cognitive changes in cognitively normal older adults (CN).

Methods: A total of 91 participants, all deemed CN, from the Harvard Aging Brain Study (HABS), who completed cognitive assessment, T1 MRI, 11C Pittsburg Compound B (PiB) PET, and 18F Flortaucipir (tau) PET at both baseline and two-year FU visits, were included[3]. T1 MRIs were preprocessed by FreeSurfer recon-all procedure for spatial normalization, anatomical segmentation, reconstruction of cortical surfaces, and calculation of cortical thickness[4-6]. PiB PET and tau PET images were co-registered to corresponding T1 MRIs and then spatially normalized to MNI/ICBM space. Both PET images were scaled by a mean value in the cerebellar gray reference region to calculate the standardized uptake value ratio (SUVR)[7]. We applied partial volume correction (PVC) in both PET images by using an extended Müller-Gärtner (MG) method to estimate a true concentration of radiotracer in GM[8]. After that, we resampled the PET SUVRs into the standard cortical surface. We measured vertex-wise correlations within and across PET modalities between baseline and FU. Each PET(BASE)-to-PET(FU) correlation was measured by the partial correlation between a z-score of baseline PET SUVR in vertex b and a z-score of FU PET SUVR

in the paired vertex d across all possible pairs of vertices within a cortical surface while controlling for age, sex, and a z-score of FU PET SUVR in the vertex d that was not used for the correlation as a FU PET SUVR. Then, we calculated the weighted degree (WD) in each PET(BASE)-to-PET(FU) correlation matrix to identify which baseline cortical region displays hubness properties between baseline and FU PET images. The WD of each correlation matrix at column b was calculated as the sum of the significant correlation coefficients between baseline PET SUVR in vertex b and FU PET SUVRs in all possible paired vertices. Finally, the WDs of each correlation matrix were mapped to the cortical surface at the group level. To identify the contribution of baseline & FU PET SUVRs to cognitive changes, we measured partial correlations between the merged PET SUVRs, which were calculated by averaging between baseline PET SUVRs and FU PET SUVRs across all possible vertex pairs, and FU PACC-96 scores in each correlation combination. Then, we calculated the WDs and mapped these to the standard cortical surface to visualize the spatial patterns at the group level.

Results: We found significant patterns in uni- and multi-modal PET(BASE)-to-PET(FU) analyses, indicating positive spatiotemporal relationships between a given local pathology at baseline and distributed pathology accumulations at FU (Fig. 1). The temporal accumulations of interlinked Aβ and tau pathology display distinctive spatiotemporal correlations associated with early cognitive decline (Fig. 2). Notably, we observed that baseline Aβ deposits -Thal amyloid phase II- related to future increase of tau deposits -Braak stage I-IV-, both displaying linkage to the decline in multi-domain cognitive scores (Fig. 2A). We also found unimodal tau-to-tau and cognitive impairment associations in broad areas of Braak stages I-IV (Fig. 2B).

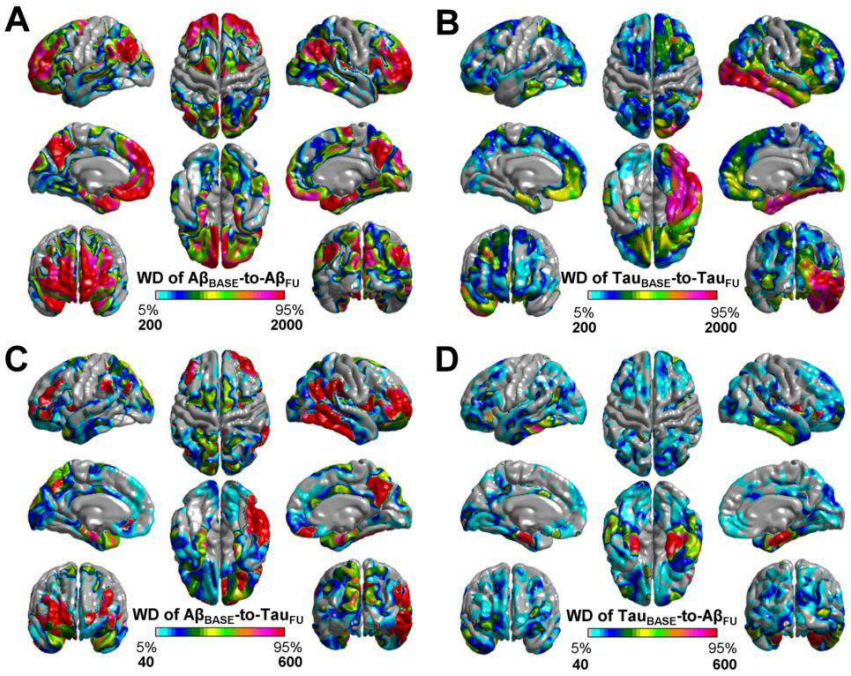

Figure 1. Surface mapped WDs of longitudinal PET correlations in CN. (A) Aβ$_{BASE}$-to-Aβ$_{FU}$, (B) Tau$_{BASE}$-to-Tau$_{FU}$, (C) Aβ$_{BASE}$-to-Tau$_{FU}$, and (D) Tau$_{BASE}$-to-Aβ$_{FU}$. Only multiple comparisons corrected significant positive correlations were included (FDR corrected q<0.05). The color bar indicates the WD value; a high score indicates that the PET SUVR of this local vertex is correlated with the other vertices.
Abbreviations: WD, weighted degree; CN, cognitively normal older adults; Aβ, 11C-Pittsburgh compound-B; tau, F18-AV-1451; SUVR, standardized uptake value ratio; and FDR, False discovery rate.

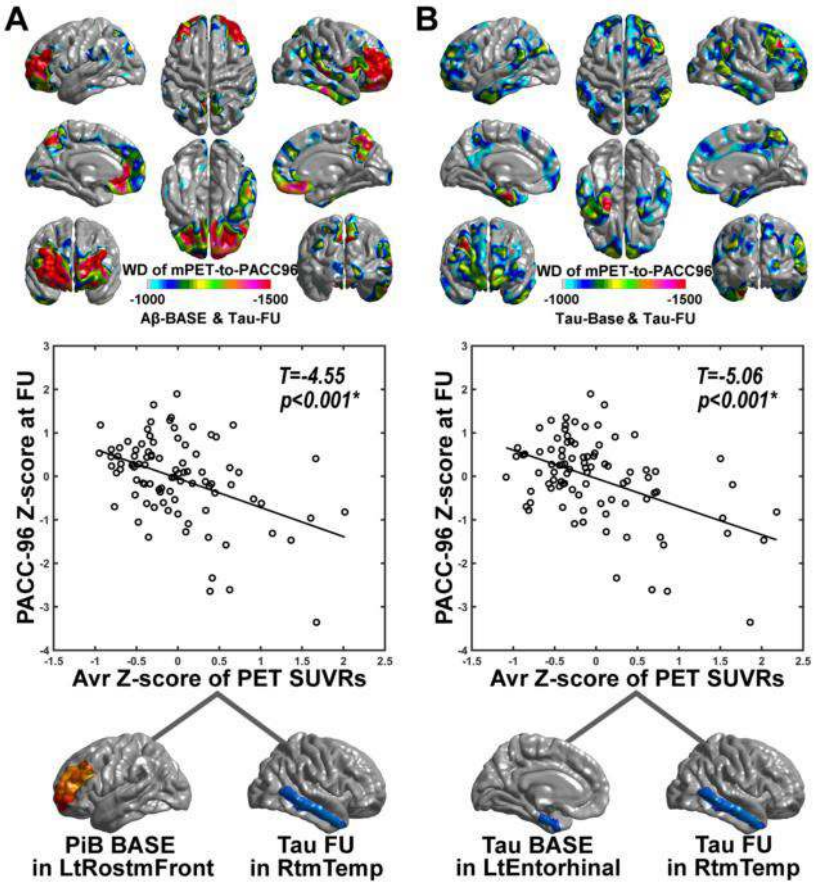

Figure 2. Surface mapped WDs of the merged PET SUVR-to-Cognition correlations and the linear regression associations between the averaged z-scores of PET SUVRs and FU PACC96 z-scores in longitudinal CN data. Only multiple comparisons corrected significant negative correlations were included (FDR corrected q<0.05). (A) Regions in which the influence of Aβ accumulation on subsequent tau accumulation, across the brain, correlate with cognitive decline include the prefrontal and precuneus. In addition, a significant negative association between the averaged PET SUVRs, which was measured by the average between the mean z-scores of PiB SUVRs of the left rostral middle frontal cortex at baseline and the mean z-scores of tau SUVRs of the right middle temporal cortex at FU, and FU PACC96 z-scores was observed in CN ($t_{(89)}$=-4.55, p<0.001). (B) the regions in which the influence of tau on subsequent tau correlate with cognitive decline include the entorhinal cortex of the left temporal lobe. A significant negative association between the averaged PET SUVRs, which was measured by the average between the mean z-scores of tau SUVRs of the left entorhinal cortex at baseline and the mean z-scores of tau SUVRs of the right middle temporal cortex at FU, and FU PACC96 z-scores was noted in CN ($t_{(89)}$=-5.06, p<0.001). The color bar indicates the WD of the merged PET SUVR-to-Cognition correlations; a low score indicates the increased averaged PET SUVR between the baseline PET's local z-score of PET SUVR and the FU PET's whole z-scores of PET SUVRs is strongly correlated with the decreased FU PACC-96 z-scores.

Abbreviations: WD, weighted degree; CN, cognitively normal older adults; Aβ, 11C-Pittsburgh compound-B; tau, F18-AV-1451; SUVR, standardized uptake value ratio; mPET, merged PET; FU, follow-up; PACC96, Preclinical Alzheimer cognitive composite; HABS, Harvard Aging Brain Study; Avr, averaged; LtRostmFront, left rostral middle frontal cortex; RtmTemp, right middle temporal cortex; LtEntorhinal, left entorhinal cortex; and FDR, False discovery rate.

Conclusions: AD-related pathology is considered to affect the human brain via disconectomic processes, and interdigitated spatial correlations of Aβ and tau seem to be upstream factors that might promote the breakdown of brain circuits and produce, in turn, cognitive decline in older adults. Our findings suggest that those spatiotemporal network relationships between Aβ and tau contribute to cognitive changes in the trajectory toward AD.

References

1. Bloom GS. Amyloid-β and tau: the trigger and bullet in Alzheimer disease pathogenesis. JAMA neurology. 2014;71:505-8.
2. Busche MA, Hyman BT. Synergy between amyloid-β and tau in Alzheimer's disease. Nature neuroscience. 2020;23:1183-93.
3. Dagley A, LaPoint M, Huijbers W, Hedden T, McLaren DG, Chatwal JP, et al. Harvard Aging Brain Study: Dataset and accessibility. Neuroimage. 2017;144:255-8.
4. Dale AM, Fischl B, Sereno MI. Cortical surface-based analysis. I. Segmentation and surface reconstruction. Neuroimage. 1999;9:179-94.
5. Fischl B, Sereno MI, Tootell RB, Dale AM. High-resolution intersubject averaging and a coordinate system for the cortical surface. Human brain mapping. 1999;8:272-84.
6. Desikan RS, Segonne F, Fischl B, Quinn BT, Dickerson BC, Blacker D, et al. An automated labeling system for subdividing the human cerebral cortex on MRI scans into gyral based regions of interest. Neuroimage. 2006;31:968-80.
7. Sepulcre J, Grothe MJ, d'Oleire Uquillas F, Ortiz-Terán L, Diez I, Yang H-S, et al. Neurogenetic contributions to amyloid beta and tau spreading in the human cortex. Nature medicine. 2018;24:1910-8.
8. Müller-Gärtner HW, Links JM, Prince JL, Bryan RN, McVeigh E, Leal JP, et al. Measurement of radiotracer concentration in brain gray matter using positron emission tomography: MRI-based correction for partial volume effects. Journal of Cerebral Blood Flow & Metabolism. 1992;12:571-83.

Poster No 1163

Brain-Age: Advancing Dementia Biomarkers in Clinical Settings

Marcella Montagnese[1,2], Serena Verdi[3], James Cole[3], Timothy Rittman[1]

[1]Department of Clinical Neurosciences, University of Cambridge, Cambridge, United Kingdom, [2]Christ's College, University of Cambridge, Cambridge, United Kingdom, [3]Centre for Medical Image Computing, Department of Computer Science, University College London, London, United Kingdom

Introduction: The escalating incidence of dementia poses a great challenge to global healthcare, with projections indicating 135 million affected individuals by 2050[1]. Neuroimaging has become an important tool in diagnosing dementia, with the potential to use imaging-derived metrics to revolutionise the field. An innovation in this domain is the 'brain-age' metric[2], a computational estimation of the brain's biological age, which is based on MRI scans and is indicative of brain atrophy. A brain that appears biologically 'older' than its chronological counterpart signals increased risk of age-related deterioration and death[3]. However, implementing these computational solutions in healthcare presents several barriers, including data-privacy and governance issues - limiting the application of such approaches to routinely collected clinical data. Computational tools for dementia are therefore often developed and tested on data that does not accurately represent real-life patients[4]. One important study to date has examined the prognostic value of brain-age within clinical cohorts[5]. Our work seeks to extend this exploration to encompass its diagnostic usefulness alongside routine cognitive tests in multiple diagnoses within memory clinics.

Methods: We used T1w MPRAGE scans from participants in the QMIN-MC cohort - recruited from memory clinics and community-based psychiatry-led clinics within the UK National Health Service (NHS) – encompassing a representative range of individuals. Patients were categorised into groups according to their diagnoses: Alzheimer's Disease (N=111, 74.1 ± 8.6 years); Mild Cognitive Impairment (N=53, 74.5 ± 7.7 years); Non-Alzheimer's Dementia (N=40, 76.1 ± 7.9 years), and Functional/Attentional Memory Symptoms (N=50, 59.5 ± 9.2 years). The brainageR tool (v2.1, https://github.com/james-cole/brainageR) was used to estimate brain age from raw T1w scans. For the initial pre-processing phase, SPM12 software was used for data segmentation and normalisation, followed by a predictive analysis. Brain-predicted age difference (brain-PAD), was determined by subtracting the individual's age at scanning from predicted brain age. See schematics in Figure 1. For multi-diagnosis classification, a Gradient Boosting approach was employed, using brain-PAD and routine cognitive scores. Multicollinearity was evaluated with Variance Inflation Factors and feature importance with Recursive Feature Elimination. Model robustness was ensured through k-fold cross-validation, with model efficacy quantified by weighted F1-scores to account for class imbalance. Comparative analyses were then done to evaluate the added diagnostic value of brain-PAD, including permutation tests for p-value calculations.

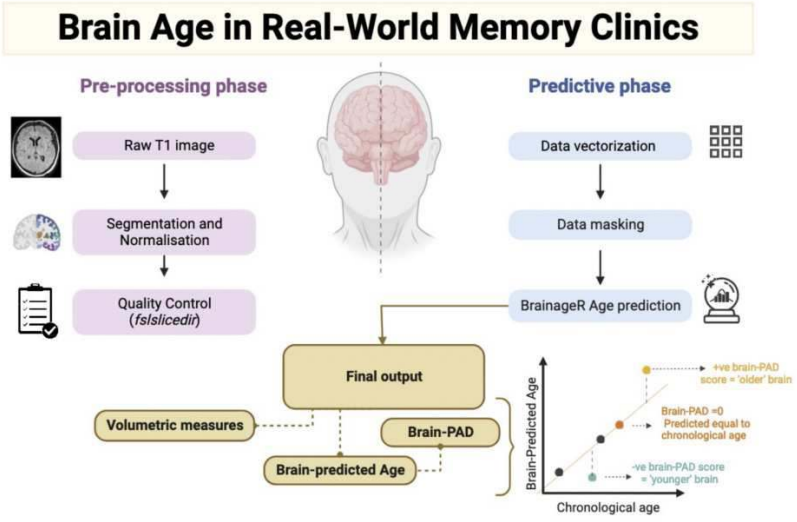

Figure 1- Schematics of the steps required for the brain-age algorithm (https://github.com/james-cole/brainageR). On the left, the flowchart of the pre-processing phase; on the right, the information about the predictive phase. Bottom section shows the final outputs and the calculation of the Brain-PAD metric.

Results: Comparative analyses between models (with vs without brain-PAD) revealed classification improvements across all diagnoses, alongside shifts in feature importance. Mean F1-score improved from 0.51 to 0.56 (p=.22). For Non-AD Dementia, precision improved from 0.23 to 0.41 (p<0.001), and F1-scores from 0.11 to 0.25. AD precision went from 0.61 to 0.63 (p<0.05),

and F1-score to 0.71. The model also showed gains for Functional/Attentional Memory Symptoms (F1-score 0.71; precision from 0.62 to 0.74, p<0.001), and MCI (F-score 0.39, precision from 0.39 to 0.41, p<0.05). The brain-PAD model was more parsimonious (3 vs 6 features), suggesting a simplification in the cognitive subdomains, with more reliance on brain-PAD. Shapley Additive exPlanations (SHAP)[6] values echoed the feature importance findings, with brain-PAD showing higher impact on model output, particularly for the correct classification of AD and Non-AD Dementia. See Figure 2.

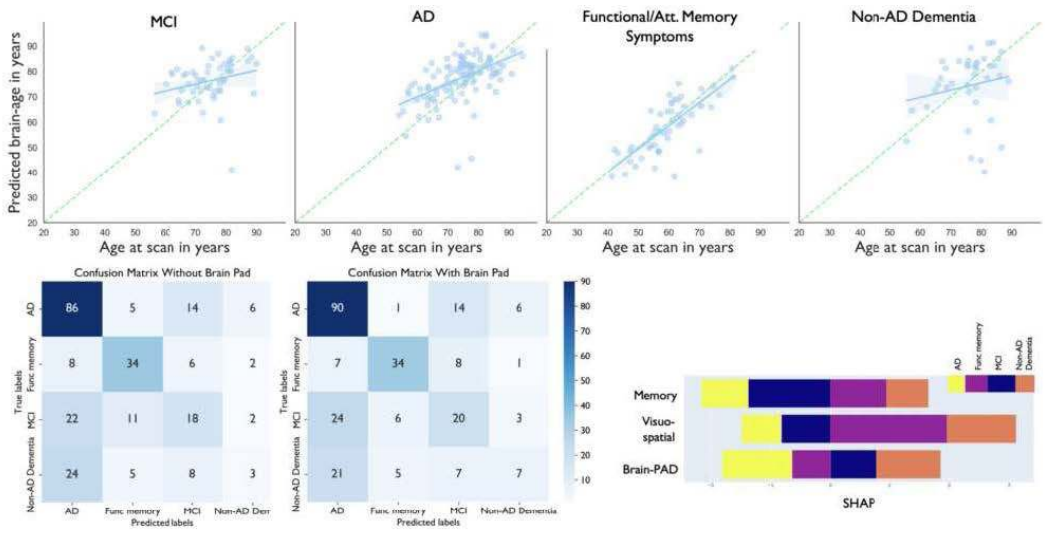

Figure 2- Multifaceted Diagnostic Model Evaluation Using Brain-PAD. Top-panel: Age at scan vs. Brain-Age Scatter Plots for each diagnosis. The identity lines, shown in green, represent the ideal scenario where the chronological age matches the brain-age estimates (y = x). In blue are the best-fit lines for each diagnostic group. **Bottom Left Panel**: Confusion matrices contrasting model performance without (left) and with (right) the inclusion of Brain-PAD**; Bottom Right Panel:** SHAP (Shapley Additive exPlanations) value summary for the cognitive subdomains and brain-PAD. The colour show the different diagnostic classes.

Conclusions: The integration of brain-PAD showed a relatively small but consistent boost in predictive performance across diagnoses. Looking at features importance showed that brain-PAD has the potential to be a crucial biomarker in the heterogeneous and multiclass diagnostic landscape of dementia even in smaller samples.

References

1. Nichols, E., Steinmetz, J. D., Vollset, S. E., Fukutaki, K., Chalek, J., Abd-Allah, F., ... & Liu, X. (2022). Estimation of the global prevalence of dementia in 2019 and forecasted prevalence in 2050: an analysis for the Global Burden of Disease Study 2019. The Lancet Public Health, 7(2), e105-e125
2. Cole, J. H., Ritchie, S. J., Bastin, M. E., Hernández, V., Muñoz Maniega, S., Royle, N., ... & Deary, I. J. (2018). Brain age predicts mortality. Molecular psychiatry, 23(5), 1385-1392.
3. Borchert, R. J., Azevedo, T., Badhwar, A., Bernal, J., Betts, M., Bruffaerts, R., ... & Rittman, T. (2023). Artificial intelligence for diagnostic and prognostic neuroimaging in dementia: A systematic review. Alzheimer's & Dementia.
4. Cole, J. H., Ritchie, S. J., Bastin, M. E., Hernández, V., Muñoz Maniega, S., Royle, N., ... & Deary, I. J. (2018). Brain age predicts mortality. Molecular psychiatry, 23(5), 1385-1392
5. Biondo, F., Jewell, A., Pritchard, M., Aarsland, D., Steves, C. J., Mueller, C., & Cole, J. H. (2022). Brain-age is associated with progression to dementia in memory clinic patients. NeuroImage: Clinical, 36, 103175.
6. Lundberg, S. M., & Lee, S. I. (2017). A unified approach to interpreting model predictions. Advances in neural information processing systems, 30.

Poster No 1164

Brain Age Gap Estimation (BrainAGE): Influence of scanner manufacturer, field strength and sequence

Vivien Lorena Ivan[1], Marius Vach[1], Daniel Weiß[1], Luisa Wolf[1], Shammi More[2,3], Kaustubh Patil[2,3], Dennis Hedderich[4,5], Nora Bittner[6], Julian Caspers[1], Christian Rubbert[1]

[1]Department of Diagnostic and Interventional Radiology, Medical Faculty and University Hospital, Düsseldorf, NRW, Germany, [2]Institute of Neuroscience and Medicine, Brain & Behaviour (INM-7), Research Centre Jülich, Jülich, NRW, Germany, [3]Institute of Systems Neuroscience, Medical Faculty, Düsseldorf, NRW, Germany, [4]Department of Neuroradiology, School of Medicine, Technical University of Munich, Munich, Bavaria, Germany, [5]TUM-NIC Neuroimaging Center, School of Medicine, Technical University of Munich, Munich, Bavaria, Germany, [6]Institute for Anatomy I, Medical Faculty, Heinrich-Heine University, Düsseldorf, NRW, Germany

Introduction: Brain Age Gap Estimation (BrainAGE) is explored as an imaging biomarker for several conditions, such as neurodegenerative diseases [Gaser 2013], or in lifestyle-choices-driven aging [Bittner 2021]. BrainAGE is usually derived from applying machine-learning approaches to features derived from structural magnetic resonance images of the brain [Franke 2019]. In cognitively normal, healthy subjects a BrainAGE of zero is expected, i.e. the predicted and the chronological age are the same, which is the underlying assumption of the current study. However, differences in BrainAGE, especially outside of the training cohorts, could arise due to different combinations of, e.g., study in- and exclusion criteria, MRI scanners, field strength or sequence parameters. Thus, this study aims to systematically assess the influence of the aforementioned.

Methods: A total of 2,414 normal participants from four population based studies were included, specifically from ADNI (n = 914, 55% female, 72.8±6.4 years, 55-90 years), HCPA (n = 725, 56% female, 60.3±15.7 years, 36-100 years), OASIS3 (n = 609, 58.9% female, 67.8±8.9 years, 42-95 years) and PPMI (n = 166, 36.7% female, 60.5±11.6 years, 30-82 years). BrainAGE was derived for each subject using the best-performing model from [More 2023], trained on 2,953 healthy controls (18-88 years, 3T scans only) from four population-based studies not used in the current study. In essence, gray matter features were derived from standardized CAT12 for SPM12 preprocessing, smoothing with a 4 mm full-width-half-maximum kernel, resampling to 4 mm spatial resolution, and finally by principal component analysis for dimensionality reduction. Finally, Gaussian process regression was used to predict age, and BrainAGE was calculated by subtracting the chronological from the predicted age. BrainAGE was then compared across the different cohorts. Furthermore, differences in BrainAGE based on scanner manufacturer, field strength, and choice of unaccelerated or accelerated T1-imaging were analyzed for each cohort, when data was available. Statistically significant differences ($p<0.05$), were analyzed using Welch two sample t-test or ANOVA, including the Tukey post-hoc test, as applicable. The mean absolute error between chronological and predicted age was calculated.

Results: Across the different cohorts, the BrainAGE for ADNI was -5.9±5.5 years (MAE 6.7), for HCPA -4.1±6.2 (MAE 5.9), for OASIS3 -4.8±5.4 (MAE 5.8), and for PPMI -3±5.8 (MAE 5.3) with a $p<0.0001$ (ANOVA) (Figure 1A). Only OASIS3/HCPA ($p=0.17$) and PPMI/HCPA ($p=0.1$) did not show significant differences. Comparing the field strength (Figure 1B), we found that scans performed at 1.5T resulted in a smaller BrainAGE (ADNI: -2.6±4.9 years, MAE 4.2; OASIS3: -2.4±4.6, MAE 4.1, PPMI: -1.6±4.8, MAE 4.2) than scans acquired at 3T (ADNI: -6.9±5.3 years, MAE 7.5; OASIS3: -4.9±5.5, MAE 5.9, PPMI: -3.5±6.1, MAE 5.8). $p<0.0001$ for ADNI, $p=0.007$ for OASIS3, and $p=0.03$ for PPMI. HCPA only acquired scans at 3T. Scans in ADNI and PPMI were acquired on scanners from different vendors (Figure 2A). In ADNI, scans acquired on GE scanners resulted in a BrainAGE of -6.3±6.2 years (MAE 7.3), on Philips of -4.9±5.1 years (MAE 6), and on Siemens of -6.1±5.3 years (MAE 6.7). $p=0.03$ (ANOVA), with statistically significant differences between Philips/GE ($p=0.008$) in the post-hoc analysis. For PPMI, the results were -0.5±7.7 years for GE scanners (MAE 6.2), -1.8±6.2 for Philips (MAE 5.1), and -4.1±4.8 for Siemens (MAE 5.1). $p=0.005$ (ANOVA), with statistically significant difference between Siemens/GE ($p=0.008$) in the post-hoc analysis. In ADNI, accelerated (-7±5.3 years, MAE 7.6) and unaccelerated (-7±5.3, MAE 7.3) imaging was available acquired at 3T ($p=0.47$, Figure 2B).

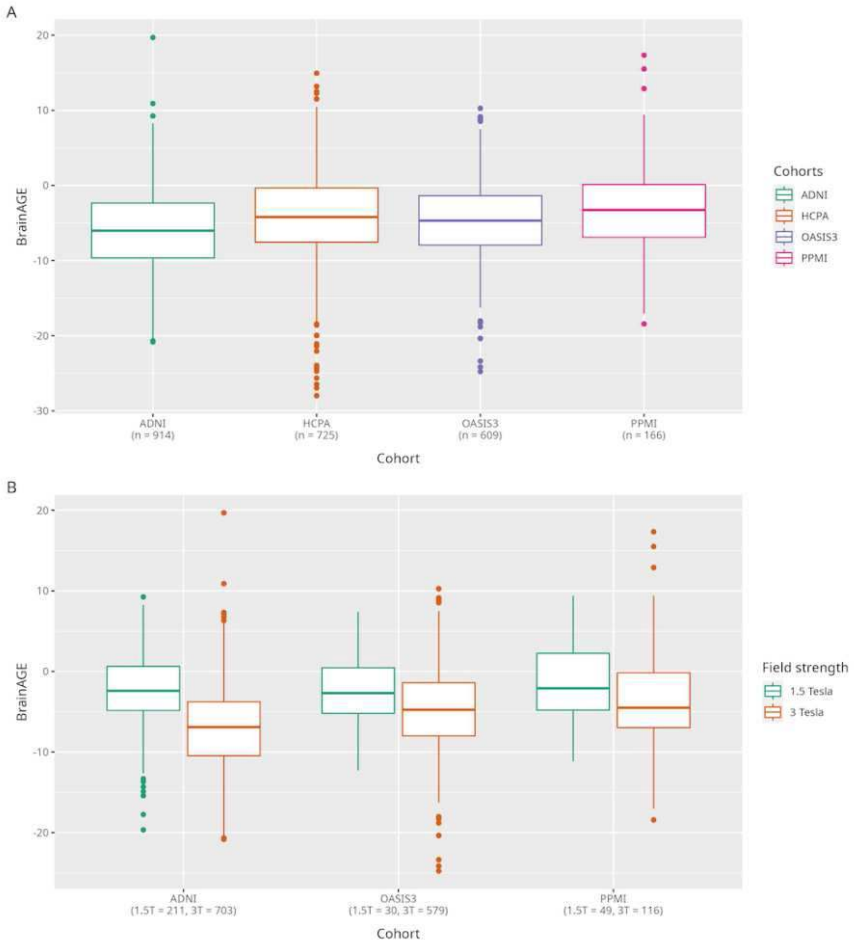

Conclusions: Researchers and clinicians should be aware that several factors, such as choice of scanner manufacturer and field strength, may influence certain Brain Age Gap Estimation (BrainAGE) and that comparisons across cohorts may not be suitable.

References

1. Bittner N, Jockwitz C, Franke K, Gaser C, Moebus S, Bayen UJ, Amunts K, Caspers S (2021): When your brain looks older than expected: combined lifestyle risk and BrainAGE. Brain Struct Funct 226:621–645.
2. Franke K, Gaser C (2019): Ten Years of BrainAGE as a Neuroimaging Biomarker of Brain Aging: What Insights Have We Gained? Front Neurol 10:789.
3. Gaser C, Franke K, Klöppel S, Koutsouleris N, Sauer H, Initiative ADN (2013): BrainAGE in Mild Cognitive Impaired Patients: Predicting the Conversion to Alzheimer's Disease. PLoS ONE 8:e67346.
4. More S, Antonopoulos G, Hoffstaedter F, Caspers J, Eickhoff SB, Patil KR, Initiative ADN (2023): Brain-age prediction: A systematic comparison of machine learning workflows. NeuroImage 270:119947.

Poster No 1165

Multivariate Association Between Cognitive Function and Brain Tissue in Healthy Older Adults

Christophe Phillips[1], Daphné Chylinski[2], Maxime Van Egroo[3], Justinas Narbutas[4], Eric Salmon[2], Pierre Maquet[2], Fabienne Collette[2], Gilles Vandewalle[5], Christine Bastin[2], Soodeh Moallemian[2]

[1]University of Liège, Liège, Belgium, [2]University of Liège, Liège, Liege, [3]Maastricht University, Maastricht, Netherlands, [4]Leibnitz research centre for working environment and human factors, Dortmund, Germany, [5]Sleep and Chronobiology Lab, GIGA-Institute, CRC-In Vivo Imaging Unit, University of Liège, Liège, Belgium

Introduction: The aging process is often accompanied by cognitive alterations, collectively known as cognitive aging, which can lead to a decline in functional capacity[1]. Normal aging is also accompanied by macro- and micro- structural changes in the brain, such as gray matter (GM) and white matter (WM) atrophy[2–4], iron accumulation, and demyelination[5–7]. Microstructural changes in the brain are interconnected; for instance, elevation in iron content is associated to demyelination, collectively

contributing to synaptic density loss and brain atrophy[8–10]. Therefore, a comprehensive examination of these concurrent brain microstructural properties with respect to cognitive aging is imperative. This exploration can reveal regions in the brain that undergo changes at an earlier stage, potentially serving as early indicators preceding the onset of cognitive issues.

Methods: This study investigates the association between cognition and various brain micro- and macro-structural properties, as assessed by multiparametric quantitative MRI maps, in healthy older adults (baseline: n=101, 31.68% male, follow-up: n=67, 32.84% male). Participants underwent cognitive assessments at baseline and after 2 years, resulting in composite scores for attention, executive function, and memory. The preclinical Alzheimer's cognitive composite (PACC5) was calculated for all participants[11]. Quantitative MRI data were obtained at baseline using a multiparametric mapping protocol. The association between cognitive composite scores and tissue properties, both at baseline and for the rate of cognitive decline over 2 years, was tested using univariate and multivariate general linear models.

Results: The univariate analyses conducted at baseline revealed several significant associations between cognition and brain structural properties. Executive function showed a positive correlation with GM volume in the cerebellum, while memory exhibited positive associations with myelin content in the cerebellum and hippocampus. GM iron levels were linked to lower memory scores in the right insula. A significant positive correlation emerged between WM myelin content and PACC5 in the left middle temporal region. Conversely, higher iron levels in the medial orbitofrontal cortex were associated with smaller PACC5 values. Results from the univariate regression analysis are presented in Table 1. As illustrated in Figure 1, the multivariate regression analyses at baseline revealed significant associations between executive function and the combination of macro- and microstructural changes in the cerebellum, as well as between memory and combined changes in the cingulate gyrus and insula (See Table 2 for detailed results). Finally, multivariate regression did not reveal any significant correlations between the different maps and the rate of decline in cognition. Moreover, it is important to note that, throughout the study duration, we did not observe a decline in cognition among the subjects.

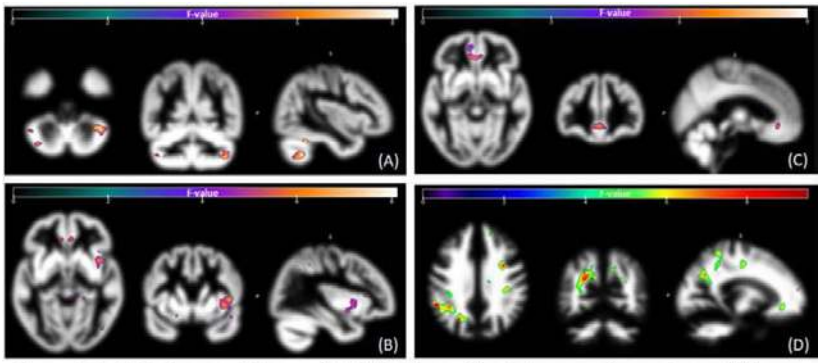

Figure 1. Statistical parametric maps (SPM) for the multivariate regression analyses within gray and white matter. The multivariate SPMs (mSPMs) show correlations between all modalities within either white matter or gray matter with respect to different cognitive composite scores (A) executive function, (B) memory, and (C) PACC5, within the gray matter; (D) memory within the white matter. The mSPMs are illustrated at p<.001 uncorrected for illustration purposes, and they are overlayed on the mean population gray matter and white matter maps in MNI space.

Table 1. Univariate regression results at the baseline, showing the correlation between different maps and cognition. Brain regions were labeled with the AAL3 atlas toolbox in SPM. Coordinates are reported in MNI space. FWER correction was applied for $p < 0.05$ at either voxel or cluster level.

peak [x y z] Coordinates	Tissue	Modality	Cluster P-value FWERcorr (voxel-level)	Cluster Size #voxels	Brain Region
Executive function (df=96)					
[35 -53 -45]	GM	GMvol	0.000(0.000)	6156	Right Cerebellum
[39 -27 -17]	WM	PD	0.020(0.003)	1170	Right Fusiform
Global memory (df=96)					
[-11 -46 -45]	GM	MTsat	0.009(0.026)	1991	Left Cerebellum
[-29 -18 -14]	GM	MTsat	0.002(0.004)	1105	Left Hippocampus
[9 -48 -23]	GM	MTsat	0.011(0.631)	1908	Right Cerebellum
[-24 -64 29]	WM	MTsat	0.000(0.009)	16565	Left Mid. Occipital
[-9 -48 -27]	WM	MTsat	0.003(0.009)	7305	Left Cerebellum
[9 -33 57]	WM	MTsat	0.000(0.054)	23922	Right Paracentral lobule
[-17 5 -18]	GM	PD	0.040(0.372)	1359	Left Olfactory bulb
[36 -26 35]	WM	PD	0.033(0.010)	1025	Right Postcentral
[29 37 19]	WM	PD	0.004(0.019)	1662	Right Mid. Frontal Gyrus
[-52 -45 40]	WM	PD	0.676 (0.023)	236	Left Inf. Parietal
[-31 -32 48]	WM	PD	0.017(0.030)	1218	Left Postcentral
[-14 55 17]	WM	PD	0.385(0.046)	390	Left. Sup. Frontal Gyrus
[46 13 0]	GM	R2*	0.005(0.214)	2276	Right Insula
PACC5 (df=96)					
[-60 -28 -12]	WM	MTsat	0.467(0.036)	652	Left Mid. Temporal Gyrus
[0 36 -9]	GM	R2*	0.138(0.032)	979	Left Pre ACC

Key: GM: gray matter, WM: white matter, ACC: anterior cingulate cortex.

Table 2. Multivariate regression results at the baseline, showing the correlation between different maps together (in GM or WM) and cognition. Brain regions were labeled with the AAL3 atlas toolbox in SPM. Coordinates are reported in MNI space. FWER correction was applied for $p < 0.05$ at voxel or cluster level.

peak [x y z] Coordinates	Tissue	Cluster P-value (voxel-level)	Cluster Size #voxels	Brain Region
Executive function				
[41 -53 -45]	GM	0.026(0.089)	1370	Right Cerebellum
Global memory				
[3 34 -12]	GM	0.015(0.057)	1557	Right ACG
[47 10 4]	GM	0.005(0.435)	1974	Right Insula
[-50 -47 31]	WM	0.001(0.005)	3402	Left Supramarginal
[30 37 19]	WM	0.074(0.016)	1253	Right Mid. Frontal
[-21 -62 29]	WM	0.003(0.036)	3011	Left Sup. Occipital
[33 3 36]	WM	0.210(0.045)	794	Right Mid. Frontal
[-49 -49 33]	WM	0.000(0.000)	1577	Left Sup. Marginal area
[32 4 37]	WM	0.002(0.000)	801	Right Mid. Frontal gyrus
PACC5				
[-2 36 -9]	GM	0.026(0.254)	1379	Left ACG

Key: ACG: anterior cingulate Gyrus

Conclusions: In summary, these findings highlight the intricate connections between cognition and brain micro- and macro-structural properties in aging, with a particular emphasis on the role of the cerebellum in cognitive aging. However, a more prolonged study is needed to further explore the association between the decline in cognition and concurrent changes in the brains.

References

1. Y. Yang, D. Wang, W. Hou, and H. Li, "Cognitive Decline Associated with Aging," in Cognitive Aging and Brain Health, Z. Zhang, Ed., in Advances in Experimental Medicine and Biology., Singapore: Springer Nature, 2023, pp. 25–46. doi: 10.1007/978-981-99-1627-6_3.
2. S. Ramanoël et al., "Gray Matter Volume and Cognitive Performance During Normal Aging. A Voxel-Based Morphometry Study," Front. Aging Neurosci., vol. 10, p. 235, Aug. 2018, doi: 10.3389/fnagi.2018.00235.
3. C. D. Good, I. S. Johnsrude, J. Ashburner, R. N. A. Henson, K. J. Friston, and R. S. J. Frackowiak, "A Voxel-Based Morphometric Study of Ageing in 465 Normal Adult Human Brains," NeuroImage, vol. 14, no. 1, pp. 21–36, Jul. 2001, doi: 10.1006/nimg.2001.0786.
4. L. Pini et al., "Brain atrophy in Alzheimer's Disease and aging," Ageing Res. Rev., vol. 30, pp. 25–48, Sep. 2016, doi: 10.1016/j.arr.2016.01.002.
5. M. F. Callaghan et al., "Widespread age-related differences in the human brain microstructure revealed by quantitative magnetic resonance imaging," Neurobiol. Aging, vol. 35, no. 8, pp. 1862–1872, Aug. 2014, doi: 10.1016/j.neurobiolaging.2014.02.008.
6. M. Taubert et al., "Converging patterns of aging-associated brain volume loss and tissue microstructure differences," Neurobiol. Aging, vol. 88, pp. 108–118, Apr. 2020, doi: 10.1016/j.neurobiolaging.2020.01.006.
7. J. Acosta-Cabronero, M. J. Betts, A. Cardenas-Blanco, S. Yang, and P. J. Nestor, "In Vivo MRI Mapping of Brain Iron Deposition across the Adult Lifespan," J. Neurosci., vol. 36, no. 2, pp. 364–374, Jan. 2016, doi: 10.1523/JNEUROSCI.1907-15.2016.
8. S. Moallemian et al., "Multimodal imaging of microstructural cerebral alterations and loss of synaptic density in Alzheimer's disease," Neurobiol. Aging, vol. 132, pp. 24–35, Dec. 2023, doi: 10.1016/j.neurobiolaging.2023.08.001.
9. T. K. Steiger, N. Weiskopf, and N. Bunzeck, "Iron Level and Myelin Content in the Ventral Striatum Predict Memory Performance in the Aging Brain," J. Neurosci., vol. 36, no. 12, pp. 3552–3558, Mar. 2016, doi: 10.1523/JNEUROSCI.3617-15.2016.
10. G. Bartzokis, "Alzheimer's disease as homeostatic responses to age-related myelin breakdown," Neurobiol. Aging, vol. 32, no. 8, pp. 1341–1371, Aug. 2011, doi: 10.1016/j.neurobiolaging.2009.08.007.
11. M. C. Donohue et al., "The Preclinical Alzheimer Cognitive Composite: Measuring Amyloid-Related Decline," JAMA Neurol., vol. 71, no. 8, p. 961, Aug. 2014, doi: 10.1001/jamaneurol.2014.803.

Poster No 1166

Aging Effects the Glutamate-enriched Functional Connectivity in Resting-state fMRI

Zihao Zheng[1,2], Ao Xie[1,2], Wei Jian[1,2], Yulin He[1,2], Haiyang Sun[1,2], Yulan Zhou[1,2], Jianfu Li[1,2], Li Dong*[1,2], Dezhong Yao[1,2]

[1]The Clinical Hospital of Chengdu Brain Science Institute, MOE Key Lab for Neuroinformation, University of Electronic Science and Technology of China, Chengdu, China, [2]School of Life Science and Technology, Center for information in medicine, University of Electronic Science and Technology of China, Chengdu, China

Introduction: In recent years, age-related changes in functional connectivity of older adults have been researched widely. According to the previous studies, obtained results are different which illustrated the functional connectivity decreased in large part of the brain (e.g. default mode network) and increased in some particular regions and areas such as sensorimotor areas (Farras-Permanyer et al., 2019). The glutamate receptor is a necessary component in the brain glutamatergic system and this receptor was proved to be associated with cognitive function and brain aging (Mecca et al., 2021). However, because the functional magnetic resonance imaging (fMRI) cannot directly provide a molecular insight into the main effect of compounds in brain aging research (Attwell and Iadecola, 2002), the potential functional network changes in older related to specific molecular systems of glutamate still unclear. Here we used a new method which utilizes the glutamate information about target distribution provide by Positron Emission Tomography (PET) to enrich the fMRI connectivity analysis in brain aging.

Methods: The resting-state fMRI (rs-fMRI) data were collected from the Cambridge Centre for Ageing and Neuroscience (Cam-CAN, http://www.cam-can.org/) (Taylor et al., 2017). All fMRI images (Older:185, younger:198) were preprocessed using SPM as implemented in the Neuroscience Information Toolbox (http://www.neuro.uestc.edu.cn/NIT.html) (Dong et al., 2018). The first 5 scans were deleted. Then the images were preprocessed by following steps: realignment, slice time correction, spatial normalization (3×3×3mm3) and smoothing (8-mm full width at half maximum kernel, FWHM). The metabotropic glutamate receptor 5 (mGluR5) (Hansen et al., 2022) was used to enrich the resting-state fMRI by applying Receptor-Enriched Analysis of Functional Connectivity by Targets (REACT) (Dipasquale et al., 2019) to estimate subject-specific functional connectivity (FC) map in each group. Next, these glutamate-enriched connectivity maps of the older and younger were compared using two sample T-test. All voxel-wise statistical analyses were performed with false discovery rate correction (P<0.05, FDR corrected). In addition, we sought to describe whether effects of aging tend to be in specific functional brain networks, conducting network enrichment analysis (a spin-based spatial permutation test) (Baller et al., 2022).

Results: The effect of aging on FCs in the glutamate enriched maps involves different cerebral cortex and deep regions. Compared with young group (P<0.05, FDR corrected), FCs significantly decreased in the precentral gyrus and middle temporal gyrus in older group. And, FCs in older group increased in the middle frontal gyrus and middle occipital gyrus, as well as in the. caudate and thalamus regions. Network enrichment analysis further revealed that age-related declines in glutamate enriched FCs were most prominent in the ventral attention network (VAN, P=0.006) and somatomotor network (SMN, P=0.04). In addition, the FCs in SMN were significantly related with fluid intelligence (r=0.18, P=0.0008), and the FC in thalamus showed negative relationship with fluid intelligence (r=-0.20, P=0.00007). The details can be found in Figure1.

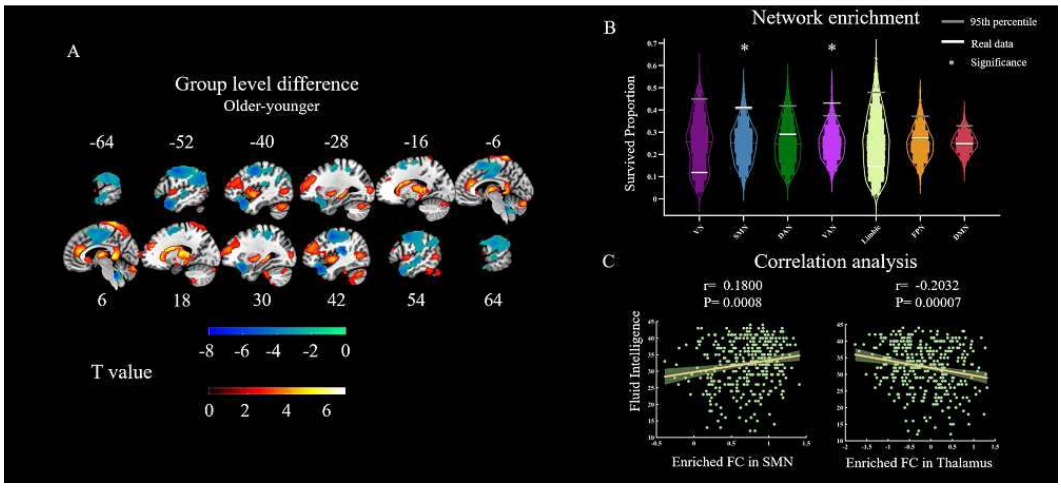

Conclusions: In conclusion, our results showed that aging related glutamate-enriched networks were mainly involved in the somatomotor network, ventral attention network and deep brain regions, and these effects perhaps were correlated with cognitive functions. The glutamate enriched FCs may provide insights into understanding brain aging in the light of the molecular mechanisms.

References
1. Attwell, D. (2002). 'The neural basis of functional brain imaging signals'. Trends Neurosci. 25, 621-5.
2. Baller, E.B. (2022). 'Developmental coupling of cerebral blood flow and fMRI fluctuations in youth'. Cell Rep. 38, 110576
3. Dipasquale, O. (2019). 'Receptor-Enriched Analysis of functional connectivity by targets (REACT): A novel, multimodal analytical approach informed by PET to study the pharmacodynamic response of the brain under MDMA'. Neuroimage. 195, 252-260.
4. Dong, L., (2018). 'Neuroscience Information Toolbox: An Open Source Toolbox for EEG-fMRI Multimodal Fusion Analysis'. Frontiers in Neuroinformatics. 12.
5. Farras-Permanyer, L. (2019). 'Age-related changes in resting-state functional connectivity in older adults'. Neural Regen Res. 14, 1544-1555.
6. Hansen, J.Y. (2022). 'Mapping neurotransmitter systems to the structural and functional organization of the human neocortex'. Nat Neurosci. 25, 1569-1581.
7. Mecca, A.P. (2021). 'Effect of age on brain metabotropic glutamate receptor subtype 5 measured with [(18)F]FPEB PET'. Neuroimage. 238, 118217.
8. Taylor, J.R. (2017). 'The Cambridge Centre for Ageing and Neuroscience (Cam-CAN) data repository: Structural and functional MRI, MEG, and cognitive data from a cross-sectional adult lifespan sample'. Neuroimage. 144, 262-269.

Poster No 1167

Network segregation mediates the association between motor imagery fMRI and walking function

Sumire Sato[1], Valay Shah[1], Grant Tays[1], David Clark[1], Daniel Ferris[1], Chris Hass[1], Todd Manini[1], Rachael Seidler[1]

[1]University of Florida, Gainesville, FL

Introduction: Functional magnetic resonance imaging (fMRI) during imagined walking in older adults has shown increased recruitment in the premotor cortex and hippocampus compared to younger adults[1,2]. These brain regions are key projection areas from the vestibular cortex, which show structural declines in aging[3]. Resting state functional connectivity is associated with task-based fMRI activity during cognitive tasks[4,5]. Investigating the role of vestibular resting state brain activity on the association between motor imagery fMRI and function may help better understand how the brain activates in response to task demands. The objective of this study was to examine the mediation effect of vestibular resting state network segregation on the relationship between imaginary walking fMRI brain activation and walking function.

Methods: 20 typical younger adults (Age: 23 ± 3.5 yrs) and 36 typical older adults (Age: 75 ± 6.4 yrs) participated in this study (Full exclusion/inclusion criteria in[6]). Self-selected walking speed was assessed with a 400m walk. Brain images were collected using a Siemens Prisma 3T scanner with a 64-channel head coil. Structural T1-weighted images were collected using a magnetization-prepared rapid gradient echo sequence. fMRI scans were collected using a multiband, interleaved echo planar imaging sequence. During the motor imagery fMRI scan, participants were shown pictures of four conditions of uneven terrains with colored disks on which they had walked previously (For details, see[7]), and were instructed to imagine themselves walking on the treadmill belts (Figure 1A). Standard preprocessing steps were followed for structural and fMRI images[8]. For task-based fMRI, spherical ROIs were created from[1] and[2] for the left and right premotor cortex and left and right hippocampus. First-level contrasts (task > rest) were used to extract mean beta values from the ROIs. For resting state connectivity analysis we identified vestibular seed regions from a meta-analysis[9]. We quantified left and right vestibular network segregation as the difference of the mean within-network connectivity and the mean between-network connectivity divided by the mean within-network connectivity[10]. Group and terrain differences in motor imagery brain activation were assessed through one-way ANCOVA (covariate = biological sex). The relationship between vestibular network segregation and motor imagery brain activation was assessed with a partial correlation. For the pairs of variables that demonstrated a significant relationship, we assessed mediation of vestibular network segregation on the association between motor imagery brain activation and walking function. Statistical significance was established with an alpha level = 0.05.

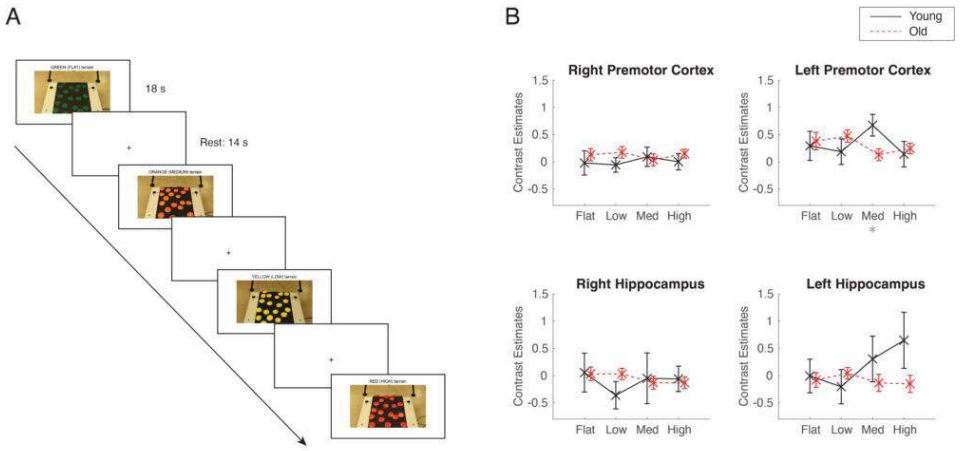

Figure 1. Motor imagery task methods (A) and results (B). A. Participants were shown four different difficulty levels of terrain for imaginary walking in the MRI scanner. The different conditions were shown pseudorandomly; conditions were presented twice within each run, for four runs. B. Means and standard error for young (in black) and older adults (In red). Main group effect was not significant, but pairwise comparisons showed higher activation in the left premotor cortex during medium terrain imaginary walking in younger adults compared to older adults. ⁎ = Post-hoc pairwise group comparison p< 0.05.

Results: We found no significant Group, Terrain, or Group x Terrain interaction effect for left and right hippocampus and left and right premotor brain activation during motor imagery (Figure 1B; all p-values > 0.05). We performed three mediation analyses based on the correlations found between motor imagery brain activity and resting state vestibular network segregation (Figure 2A), with walking speed as the dependent variable. Left vestibular network segregation mediated (1) the effect of left premotor activation during medium level terrain on walking speed and (2) right premotor activation during medium level terrain on walking speed. (3) Left premotor activation during medium level terrain showed a significant total effect on walking speed, but mediation effect of right vestibular network segregation was not significant (See Figure 2B and 2C for detailed statistical output).

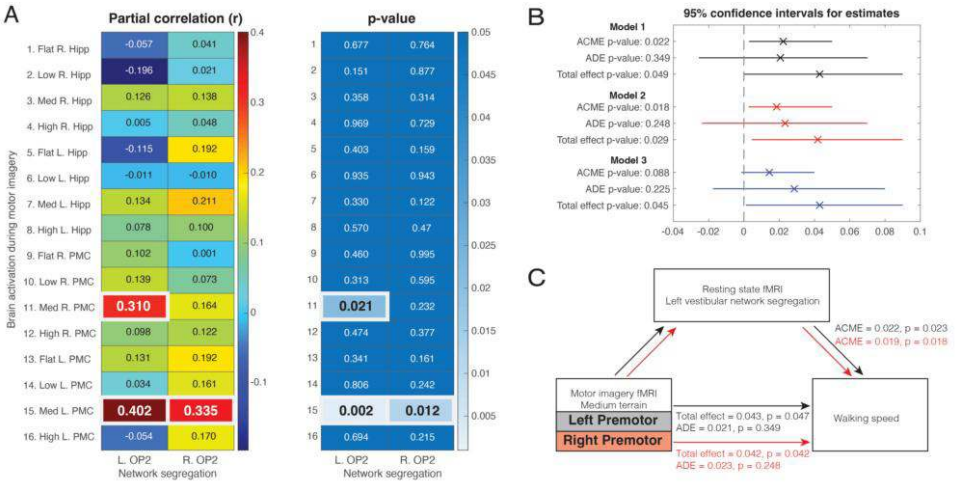

Figure 2. Partial correlation analysis between motor imagery fMRI and resting state network segregation (A) and mediation analysis results (B-C). A. Partial correlation r values (left) and p-values (right) between resting state network segregation (x-axis) and brain activation during motor imagery (y-axis). Bolded squares with white outline indicates a significant relationship. OP2 = Vestibular. Hipp = Hippocampus. PMC = Premotor cortex. B. Mediation analysis for three models dependent variable (Y) for all models was the walking speed controlled for biological sex. Model 1: Independent variable (X) = Med left premotor cortex (PMC) activation, Mediator variable (M) = left vestibular network segregation. Model 2: X = Med right PMC activation, M = left vestibular network segregation. Model 3: X = Med left PMC activation, M = right vestibular network segregation. C. Framework demonstrating significant mediations demonstrated from models 1 (in black) and 2 (in red). ADE = Average direct effect. ACME = Average causal mediated effect.

Conclusions: Left vestibular network segregation may be especially important for age differences in brain activation in the premotor cortex that is associated with walking. Identifying the role of resting state network connectivity may be a promising biomarker to assess age differences in brain activation when individuals walk with different task demands.

References

1. Allali, G., et al. (2014). The neural basis of age-related changes in motor imagery of gait: an fMRI study. J Gerontol A Biol Sci Med Sci. 69(11): p. 1389-98.

2. Gerver, C.R., et al. (2020). Shared neural recruitment across working memory and motor control tasks as a function of task difficulty and age. Aging, Neuropsychology, and Cognition. 27(6): p. 864-879.
3. Hupfeld, K.E., et al. (2022). Sensory system-specific associations between brain structure and balance. Neurobiology of Aging. 119: p. 102-116.
4. Mennes, M., et al. (2010). Inter-individual differences in resting-state functional connectivity predict task-induced BOLD activity. NeuroImage. 50(4): p. 1690-1701.
5. Zou, Q., et al. (2013). Intrinsic resting-state activity predicts working memory brain activation and behavioral performance. Human Brain Mapping. 34(12): p. 3204-3215.
6. Clark, D.J., et al. (2019). Multimodal Imaging of Brain Activity to Investigate Walking and Mobility Decline in Older Adults (Mind in Motion Study): Hypothesis, Theory, and Methods. Front Aging Neurosci. 11: p. 358.
7. Downey, R.J., et al. (2022). Uneven terrain treadmill walking in younger and older adults. PLOS ONE. 17(12): p. e0278646.
8. Cassady, K., et al. (2019). Sensorimotor network segregation declines with age and is linked to GABA and to sensorimotor performance. NeuroImage. 186: p. 234-244.
9. zu Eulenburg, P., et al. (2012) Meta-analytical definition and functional connectivity of the human vestibular cortex. NeuroImage. 60(1): p. 162-169.
10. Chan, M.Y., et al. (2014). Decreased segregation of brain systems across the healthy adult lifespan. Proceedings of the National Academy of Sciences. 111(46): p. E4997-E5006.

Poster No 1168

Mapping Intrinsic Timescales of the Elderly Brain and the Relationship with Mnemonic Discrimination

Kaichao Wu[1], Leonardo Gollo[1]

[1]Monash University, Melbourne, Victoria

Introduction: Intrinsic timescales of brain regions indicate the duration of which neural information is likely stored in a given brain region, and may represent a fundamental property for understanding cognitive processes[1-2]. This study seeks to evaluate the alteration of intrinsic timescales in the elderly compared with young adults. Considering the neural timescale a basis of the functional hierarchy in the brain[3-4], we examine the intrinsic timescales of fMRI BOLD signals across brain networks. In addition, as a typical example of brain processing sensory inputs, the mnemonic distinguish ability (the ability to distinguish existing memories from input[5-6]) of the brain was investigated together with its association with intrinsic timescales.

Methods: Resting-state fMRI scans were obtained from the University of North Carolina samples at Greensboro[5]. The participants were 28 elderly adults (61–80 years old, mean: 69.82, SD:5.64) and 34 young (18–32 years old, mean: 22.21, SD: 3.65). Participants' mnemonic discrimination ability was measured by the lure discrimination index (LDI, the younger group: mean: 0.2630, SD: 0.1918; the elderly group: mean: 0.0992, SD: 0.1946), calculated as the difference in response probabilities if the participants give a similar response to lures and foils in the mnemonic discrimination task[5]. A spatial group ICA with a set of 100 components was performed on the preprocessed and denoised BOLD signal[7] (see Fig. 1 A). After the removal of noise-related components, the 60 top components were retained. The time courses of non-noise components were then post-processed, and a band-pass filtered was applied (0.023–0.1 Hz). The intrinsic timescale was defined as the area under the curve of the autocorrelation function (ACF) from one to the time lag in which the autocorrelation first reaches a zero value (See Fig. 1 B). Repeating this procedure for all ICA components, an intrinsic timescale map of the whole brain was computed for each participant.

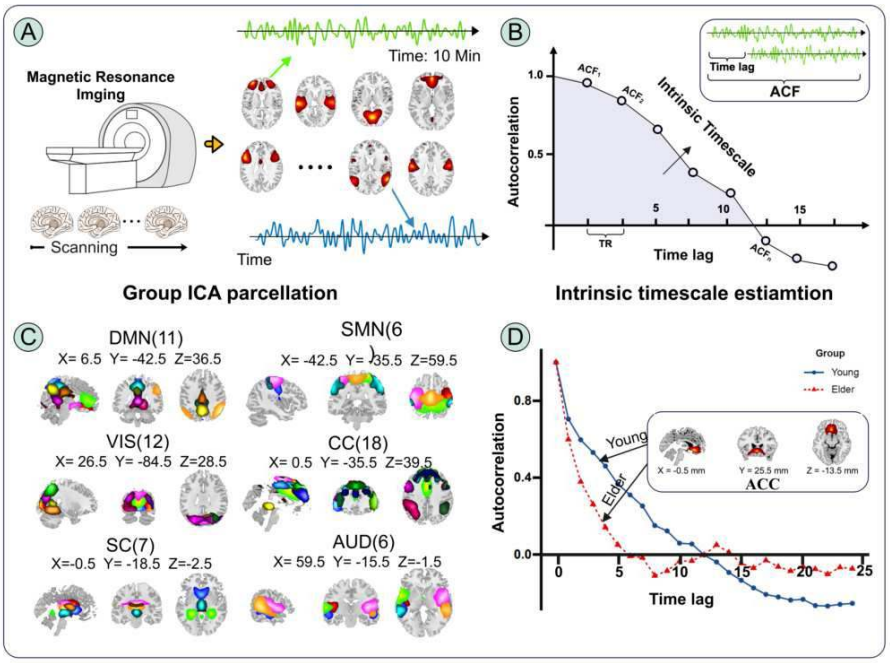

Fig 1. A. Group ICA for brain parcellation with the collected fmri and behavior data. **B**. Estimation of the intrinsic timescale per participant. **C.** The spatial map of recongized 60 conponents from the group ICA. The color pitchs indicate the exact spatial location of ICA conponents and the number in parentheses indicates the number of recongized conponents in the corresponding resting state networks. DMN: default mode network, SMN: sensormotor network, VIS: visual network, CC: cognitive control netwrok, SC: subcortical network, AUD: auditory network. **D.** The representative example of autocorrelation function curve from the Anterior cingulum cortex (ACC) of 34th young and 5th elder adult.

Results: The spatial map of the 60 recognized ICA components where they were assigned to 6 functional networks (details can be seen in Fig. 1C). As an example, Fig.1 D illustrates representative autocorrelation functions of the Anterior cingulum cortex (ACC). Figure 2 A shows that the elderly population exhibits reduced whole-brain intrinsic timescales across all functional networks compared to younger adults. For the elderly cohort, the ANOVA test shows that the intrinsic timescale is different across networks ($F = 15.76$). In particular, a post-hoc t-test shows that the subcortical network has a significantly lower intrinsic timescale than the networks in the high-order functions ($^*p < 0.001$, FDR corrected, see Fig. 2 B), demonstrating the hierarchical structure of intrinsic timescale in the elder brain. Furthermore, we found that the cuneus area in the VIS network, which is most known for its involvement in basic visual processing, has a significant correlation with the LDI ($r = 0.2532$, $p < 0.05$, FDR corrected. Fig. 2 C).

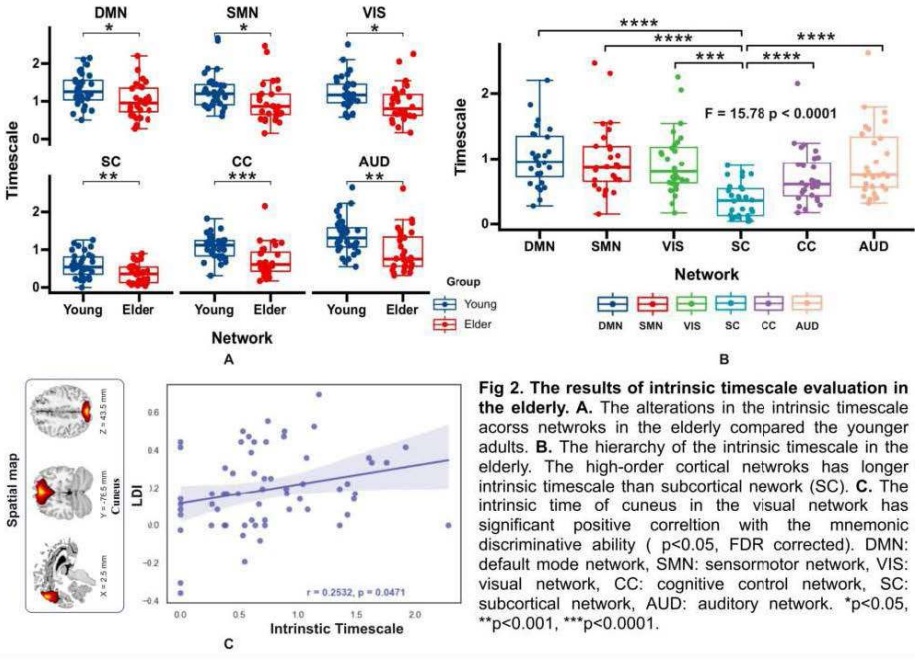

Fig 2. The results of intrinsic timescale evaluation in the elderly. A. The alterations in the intrinsic timescale acorss netwroks in the elderly compared the younger adults. **B.** The hierarchy of the intrinsic timescale in the elderly. The high-order cortical netwroks has longer intrinsic timescale than subcortical nework (SC). **C.** The intrinsic time of cuneus in the visual network has significant positive correltion with the mnemonic discriminative ability ($p<0.05$, FDR corrected). DMN: default mode network, SMN: sensormotor network, VIS: visual network, CC: cognitive control network, SC: subcortical network, AUD: auditory network. $^*p<0.05$, $^{**}p<0.001$, $^{***}p<0.0001$.

Conclusions: Our findings demonstrate that the intrinsic timescale of the elderly is significantly reduced. The reduced intrinsic timescales in the elderly brains could be associated with cognitive changes associated with aging, such as reduced Information Integration, and cognitive flexibility[8]. The elder brain exhibits a hierarchy of the intrinsic timescales with shorter intrinsic timescales at the subcortical regions than other functional networks. Finally, we found a significant association between the intrinsic timescales of the cuneus area and mnemonic discrimination ability. This finding indicates that decreased intrinsic timescale in the cuneus can be linked to challenges in the discrimination and accurate retrieval of memories in the elderly. By examining the temporal dynamics of the brain's functional networks, this study not only advances our understanding of the aging brain but also offers cues for investigating cognitive changes in the elderly.

References

1. Watanabe, T., Rees, G. and Masuda, N., 2019. Atypical intrinsic neural timescale in autism. Elife, 8, p.e42256.
2. Himberger, K.D., Chien, H.Y. and Honey, C.J., 2018. Principles of temporal processing across the cortical hierarchy. Neuroscience, 389, pp.161-174.
3. Gollo, L.L., Zalesky, A., Hutchison, R.M., Van Den Heuvel, M. and Breakspear, M., 2015. Dwelling quietly in the rich club: brain network determinants of slow cortical fluctuations. Philosophical Transactions of the Royal Society B: Biological Sciences, 370(1668), p.20140165.
4. Stephens, G.J., Honey, C.J. and Hasson, U., 2013. A place for time: the spatiotemporal structure of neural dynamics during natural audition. Journal of neurophysiology, 110(9), pp.2019-2026.
5. Wahlheim, C.N., Christensen, A.P., Reagh, Z.M. and Cassidy, B.S., 2022. Intrinsic functional connectivity in the default mode network predicts mnemonic discrimination: A connectome-based modeling approach. Hippocampus, 32(1), pp.21-37.
6. Wu, K., Jelfs, B., Mahmoud, S.S., Neville, K. and Fang, J.Q., 2023. Tracking functional network connectivity dynamics in the elderly. Frontiers in Neuroscience, 17, p.1146264.
7. Allen, E. A., Damaraju, E., Plis, S. M., Erhardt, E. B., Eichele, T., & Calhoun, V. D. (2014). Tracking whole-brain connectivity dynamics in the resting state. Cerebral Cortex, 24, 663–676.
8. Wang, M., Gamo, N.J., Yang, Y., Jin, L.E., Wang, X.J., Laubach, M., Mazer, J.A., Lee, D. and Arnsten, A.F., 2011. Neuronal basis of age-related working memory decline. Nature, 476(7359), pp.210-213.

Poster No 1169

Links between gray-matter stiffness, age and memory using Magnetic Resonance Elastography

Grégoria Kalpouzos[1], Zuzana Istvanfyova[1,2], Göran Hagman[1,2], Rebecca Ericsson[1], Ronja Löfström[1], Farshad Falahati[1], Christoffer Olsson[3], Rodrigo Moreno[3], Jonas Persson[1,4]

[1]Karolinska Institutet, Stockholm, Sweden, [2]Karolinska University Hospital, Stockholm, Sweden, [3]KTH Royal Institute of Technology, Stockholm, Sweden, [4]Örebro University, Örebro, Sweden

Introduction: Magnetic Resonance Elastography (MRE) applied to the brain has been recently developed to assess the biomechanical properties of the neural tissue such as stiffness (Yin et al 2018). Little is known about age effects on cerebral stiffness, and whether it can explain interindividual variability in cognitive performance. The few MRE studies in normal aging suggested a local reduction of cerebral stiffness and an association between hippocampal stiffness and memory (Coelho & Sousa 2022; Delgorio et al 2022). Our aims were to (1) characterize gray-matter stiffness as a function of age voxel-by-voxel, and (2) investigate age-independent associations between stiffness and visuospatial learning. Besides, we tested whether adding gray-matter volume or density (GMv, GMd) contributed to the associations between stiffness, age and cognition.

Methods: Twenty-six healthy volunteers (age range: 26-79 years old, 12 women) underwent magnetic resonance imaging and a battery of cognitive tests. MRI was performed on a 3.0T Philips Ingenia scanner, equipped for MRE with a pump connected to the scanner that sends waves through vibrations to a pillow on which the head lies, and a validated pulse sequence together with a direct inversion algorithm (Mayo Clinic, USA) that estimates the shear stiffness (i.e., resistance of a material to a shear deformation) and damping ratio (i.e., resistance of a material to oscillations). We here used the reconstructed stiffness maps whose values were expressed in pascals, and the T1-weighted images. Visuospatial learning was assessed using the Hagman test (Holleman et al 2022). The subjects were presented for 45 seconds with a 3x3 cells matrix, in which different symbols in a particular rotation and color were displayed. The instructions were to memorize the content and draw it in an empty matrix immediately after. The same test was repeated 30 minutes later to test learning. The T1-weighted images were segmented in Statistical Parametric Mapping (SPM12), and further processed using DARTEL (Ashburner 2007) to obtain spatially normalized maps of GMv (modulated images) and GMd (unmodulated images) into MNI space. The stiffness maps, coregistered to the T1s, were normalized using the flow fields from DARTEL. Images were smoothed with an 8-mm kernel. A GM mask was applied to all voxel-based analyses. To address aim 1, voxel-based regressions were performed between the stiffness maps and age at p FWE-corrected < .05. To address aim 2, voxel-based correlations were performed between the stiffness maps and performance at Hagman trial-2 at $p < .001$ (uncorrected), controlling for age and Hagman trial-1 score. Using

MarsBaR toolbox, mean stiffness was extracted from the significant MRE-clusters and applied to the GMv and GMd maps to further extract volume and density for follow-up stepwise regression analyses.

Results: With older age, lower stiffness was found in inferior frontal regions (BA 44/45, 47), premotor and somatosensory regions (BA 6, 3), lateral temporal areas (BA 21/22, 42) and insula (Fig 1A). These associations remained largely unaltered when adding GMv or GMd to the models (e.g., left frontal cluster: R2 model 1=0.792, R2 model 2 (adding GMd)=0.797, p for R2 change=.44). Controlling for age and Hagman test trial-1, better visuospatial learning was related to higher stiffness in posterior cingulate/retrosplenial area, frontal cortex, insula, striatum, and posterior hippocampus (Fig 1B). These associations remained largely significant when GMd or GMv were added to the models (e.g., for retrosplenial cluster: R2 model 1=0.560, R2 model 2=0.560, p for R2 change = .95).

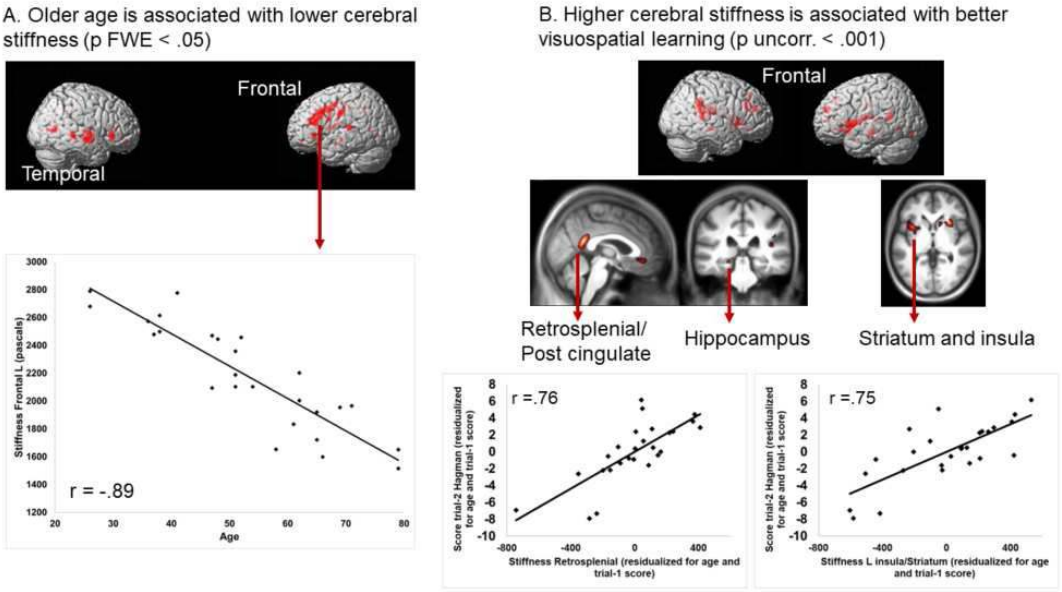

Conclusions: Reduced GM stiffness may contribute to brain aging independently of atrophy. GM stiffness may also contribute to interindividual differences in cognition, as higher stiffness in key-regions for visuospatial processing and memory was associated with better visuospatial learning independently of age.

References

1. Ashburner, J. (2007), "A fast diffeomorphic image registration algorithm", NeuroImage, vol. 38, no. 1, pp. 95-113
2. Coelho, A. (2022), "Magnetic resonance elastography of the ageing brain in normal and demented populations: A systematic review", Human Brain Mapping, vol. 43, no. 13, pp. 4207-4218
3. Delgorio, P.L. (2022), "Structure-Function Dissociations of Human Hippocampal Subfield Stiffness and Memory Performance", Journal of Neuroscience, vol. 42, no. 42, pp. 7957-7968
4. Holleman, J. (2022), "Cortisol, cognition and Alzheimer's disease biomarkers among memory clinic patients", BMJ neurololy open, vol. 4, no. 2, pp. e00034
5. Yin, Z. (2018), "Stiffness and Beyond: What MR Elastography Can Tell Us About Brain Structure and Function Under Physiologic and Pathologic Conditions", Topics in Magnetic Resonance Imaging, vol. 27, no. 5, pp. 305-318.

Poster No 1170

AgeML: a Python package for Age Modelling with Machine Learning made easy

Jorge Garcia Condado[1,2], Iñigo Tellaetxe Elorriaga[1,2], Asier Erramuzpe[1,2,3], Jesus Cortes[1,2,3]

[1]Biobizkaia Health Research Institute, Barakaldo, Spain, [2]UPV/EHU, Leioa, Spain, [3]Ikerbasque, Bilbao, Spain

Introduction: BrainAge models (Franke et al. 2010, Neuroimage) have had success in exploring the relationship between healthy and pathological ageing of the brain. Furthermore, this type of age modelling can be extended to multiple body systems and modelling of the interactions between them (Tian et al 2023, Nature Medicine). However, there is no standard for age modelling. There have been works attempting to describe proper procedures, especially for age-bias correction (de Lange and Cole 2020, Neuroimage: Clinical). In this work we developed an Open-Source software that allows anyone to do age modelling following well-established and tested methodologies for any type of clinical data. Age modelling with machine learning made easy.

Methods: AgeML is an Open-Source Python library for age modelling which can be found at https://github.com/compneurobilbao/AgeModelling. The package can currently do four types of processing: age modelling and prediction and calculation of age delta (the difference between predicted and chronological age), the association of age delta with lifestyle factors, evaluation of age delta for different clinical groups, and classification of groups based on age deltas. Age is modelled using classical machine learning algorithms to perform a supervised task of using the provided features to predict subject-wise chronological age using cross-validation. Age bias correction is also applied (de Lange and Cole 2020, Neuroimage: Clinical). The user can specify a covariate, such as gender, to train separate models and provide a file with information about clinical status to train only on controls. After the model is trained on controls it is applied to the other groups. A file is saved with the predicted ages and the age delta for possible further analysis. The three extra workflows require as input the output from the age modelling workflow. The association of the age deltas with lifestyle factors is done by running a correlation analysis between the deltas and the provided factors. Given a clinical file showing different clinical groups (healthy vs ill, disease subtypes) it computes which groups have deltas that are statistically significantly different. Finally, given two clinical groups and their age deltas, it can train a logistic regressor to classify between each group.

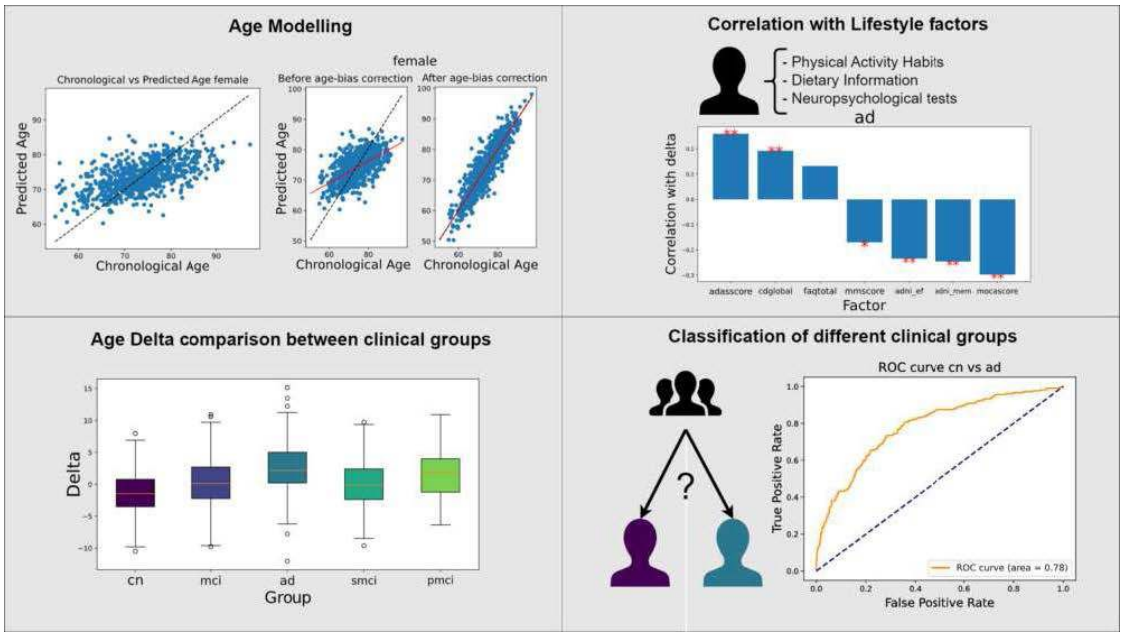

Results: To validate the workflow of this project data were obtained from the Alzheimer's Disease Neuroimaging Initiative (ADNI) database (Petersen et al 2010, Neurology). This included 629 healthy controls (CN), 635 MCI and 208 AD subjects. From the MCI subjects, there were 152 pMCI subjects, those who converted to AD within 3 years from baseline, and 152 sMCI subjects, those who remained MCI for 3 years from baseline, were chosen at random to balance the dataset. This was used to train BrainAge models, show differences in deltas between CN, MCI, AD, pMCI and sMCI, and look at the classification power of the age delta between groups as shown in previous studies (Garcia Condado and Cortes 2023, Alzheimer's & Dementia: DADM). The software package follows well-established Open Source development practices. It has a continuous integration pipeline to check for PEP8 compliance, unit testing and testing coverage. It is also open source and publicly available to encourage community-driven development, testing and transparency.

Conclusions: The objective of AgeML is to standardise procedures, lower the barrier to entry into age modelling and ensure reproducibility. The project is Open-Source to create a welcoming environment and a community to work together to improve and validate existing methodologies. We are actively seeking new developers who want to contribute to growing and expanding the package. Future steps are the implementation and easy access of foundational age models within the package.

References

1. De Lange, A.-M. G., & Cole, J. H. (2020). Commentary: Correction procedures in brain-age prediction. NeuroImage: Clinical, 26, 102229. https://doi.org/10.1016/j.nicl.2020.102229
2. Franke, K., Ziegler, G., Klöppel, S., & Gaser, C. (2010). Estimating the age of healthy subjects from T1-weighted MRI scans using kernel methods: Exploring the influence of various parameters. NeuroImage, 50(3), 883–892. https://doi.org/10.1016/j.neuroimage.2010.01.005
3. Garcia Condado, J., Cortes, J. M., & for the Alzheimer's Disease Neuroimaging Initiative. (2023). NeuropsychBrainAge: A biomarker for conversion from mild cognitive impairment to Alzheimer's disease. Alzheimer's & Dementia: Diagnosis, Assessment & Disease Monitoring, 15(4), e12493. https://doi.org/10.1002/dad2.12493
4. Tian, Y. E., Cropley, V., Maier, A. B., Lautenschlager, N. T., Breakspear, M., & Zalesky, A. (2023). Heterogeneous aging across multiple organ systems and prediction of chronic disease and mortality. Nature Medicine, 29(5), 1221–1231. https://doi.org/10.1038/s41591-023-02296-6

Poster No 1171

Biopsychosocial Correlates of Edge-community Entropy and Modularity Across the Adult Lifespan

Anita Shankar[1], Madhura Phansikar[1], Richard Betzel[2], Ruchika Prakash[1]

[1]The Ohio State University, Columbus, OH, [2]Indiana University, Bloomington, IN

Introduction: Contemporary models of cognitive aging emphasize the complex relationship between biological, environmental, and lifestyle factors as determinants of cognitive and brain health[1-3]. However, few studies have examined demographic and biopsychosocial determinants of functional brain networks across the lifespan, and none, to our knowledge, have attempted to comprehensively account for collinearity among potential predictors. In our previous work, we used an edge-centric approach to demonstrate that community entropy, a measure of nodal despecialization, increases significantly across the lifespan and negatively impacts fluid cognitive performance[4,5]. In the current study, we used elastic-net regression to identify candidate biopsychosocial features that correlate with entropy cross-sectionally and potentially mediate these age-related entropy changes.

Methods: The current study used a subset of data from the Human Connectome Project 2.0 Lifespan Release from 528 individuals between the ages of 35 and 100 years with task fMRI, physical and emotional health, and demographic data for 33 literature-informed predictors. Entropy was calculated at the level of individual nodes as described in previous work[4,5] and averaged across the whole brain. Elastic net regression was used to identify features associated with entropy from four conceptual groups: demographic factors, stress, physical health, and emotional well-being. We used a 70/30 training-test set split, using the training set to tune the model's hyperparameters and select predictors, and using the test set to determine the model's generalizability to unseen data.

Results: The final model identified 11 biopsychosocial factors, in addition to demographic factors of age, sex, and education, that predicted entropy across the lifespan. Application of the final model to the test set yielded a significant correlation between predicted and observed entropy values ($R = 0.58$, $p = 1.33e\text{-}15$; Figure 1a), which includes variance accounted for by age and variance accounted for by mediators of the relationship between age and entropy. Significant predictors above and beyond age consisted of, in order of importance: body mass index, sex, instrumental social support, average hours of sleep, visual acuity, hs-C reactive protein, perceived stress, life meaning and purpose, diastolic blood pressure, education, triglyceride levels, hemoglobin A1C, and social isolation. Removing the variance contributed by age completely, biopsychosocial factors still accounted for a significant portion of the variance in entropy ($R=0.24$, $p = 0.002$), suggesting certain factors act on entropy independent of the process of aging. We also probed how these features interact with age by running a second model that included the original features and their age-interaction terms. In the interaction model ($R = 0.59$, $p = 6.17e\text{-}16$), sex exhibited the most significant moderation effect, with males demonstrating higher entropy across all ages and greater lifespan increases in entropy than females, starting at age 54 (Figure 1b). Finally, we performed these analyses using the network property whole-brain modularity and found similar model performance ($R = 0.57$, $p = 6.26e\text{-}15$) and feature selection differed by only a single predictor (systolic blood pressure instead of diastolic blood pressure), suggesting these biopsychosocial factors reliably influence multiple measures of whole-brain network organization.

Conclusions: In the current study, we examined biopsychosocial correlates of whole-brain entropy and modularity across the adult lifespan. We present evidence that certain demographic, metabolic, cardiovascular, and psychosocial factors have system-wide influences on the function of the human brain and identify candidate age-dependent and independent predictors of network measures across the lifespan. Given previous research implicating modularity and entropy's relationship with cognition, these results may inform treatment targets for cognitive health in aging.

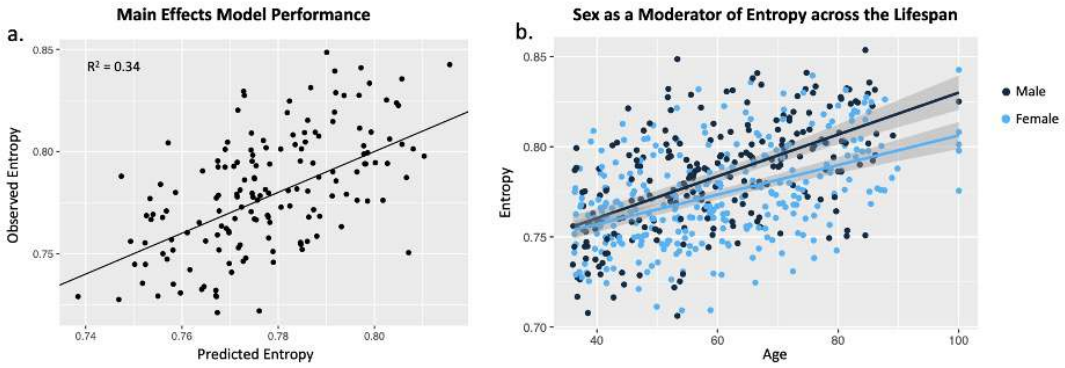

Figure 1. a) Performance of overall model prediction of the elastic net regression model applied to unseen test data assessed as the correlation between observed and predicted entropy scores. **b)** Influence of sex as a predictor of entropy and its relationship with entropy in a lifespan sample. Sex significantly predicts higher entropy (lower specialization) in males at all observed ages and this sex difference increases with increased age.

References

1. Josefsson, M., De Luna, X., Pudas, S., Nilsson, L. G., & Nyberg, L. (2012). Genetic and lifestyle predictors of 15-year longitudinal change in episodic memory. Journal of the American Geriatrics Society, 60(12), 2308–2312. https://doi.org/10.1111/jgs.12000
2. Reuter-Lorenz, P. A., & Park, D. C. (2014). How Does it STAC Up? Revisiting the Scaffolding Theory of Aging and Cognition. In Neuropsychology Review (Vol. 24, Issue 3, pp. 355–370). Springer Science and Business Media, LLC. https://doi.org/10.1007/s11065-014-9270-9
3. Alvares Pereira, G., Silva Nunes, M. V., Alzola, P., & Contador, I. (2022). Cognitive reserve and brain maintenance in aging and dementia: An integrative review. In Applied Neuropsychology:Adult (Vol. 29, Issue 6, pp. 1615–1625). Routledge. https://doi.org/10.1080/23279095.2021.1872079
4. Shankar, A., Tanner, J., Mao, T., Betzel, R., Prakash, R.S. (under review). Edge-community Entropy as a Novel Neural Correlate of Aging and Moderator of Fluid Cognition.
5. Preprint available: https://www.biorxiv.org/content/10.1101/2023.10.11.561957v1
6. Faskowitz, J., Esfahlani, F. Z., Jo, Y., Sporns, O., & Betzel, R. F. (2020). Edge-centric functional network representations of human cerebral cortex reveal overlapping system-level architecture. Nature Neuroscience, 23(12), 1644–1654. https://doi.org/10.1038/s41593-020-00719-y

Poster No 1172

An ENIGMA Consortium Genome-Wide Association Study of Brain Age

Vilte Baltramonaityte[1], Constantinos Constantinides[1], Marlene Staginnus[1], Neda Jahanshad[2], Paul Thompson[2], James Cole[3], Sarah Medland[4], Danai Dima[5], Esther Walton[1], ENIGMA consortium[6]

[1]University of Bath, Bath, United Kingdom, [2]Imaging Genetics Center, Keck School of Medicine of University of Southern California, Los Angeles, USA, [3]University College London, London, United Kingdom, [4]QIMR Berghofer Medical Research Institute, Brisbane, Australia, [5]City University London, London, United Kingdom, [6]Imaging Genetics Center, Mark and Mary Stevens Neuroimaging and Informatics Institute, Marina del Rey, CA, CA

Introduction: Deviations from a typical ageing trajectory are an important risk factor for poor health outcomes.[1] Brain-predicted age difference (PAD) – conceptualised as the difference between chronological and brain predicted age – is one such measure of deviation from healthy ageing and has been linked to over 40 traits.[2] While brain-PAD is generally thought to be heritable, specific genetic loci that influence these deviations are still largely unknown. Three recent genome-wide association studies (GWASs) on brain-PAD in UK Biobank (n up to 28,104; age range: 40 to 84) identified a small number of associated genetic variants.[3-5] This small number might be explained by the narrow age range and moderate sample size used in these studies. Larger samples covering the complete adult lifespan are needed to elucidate the genes implicated in brain-PAD, their impact on other biological systems in the brain and peripheral tissues, and the causal relationship between PAD and mental health.

Methods: Brain-PAD was derived using a ridge regression model with 77 FreeSurfer-derived structural brain imaging features of surface area, cortical thickness and subcortical volume as an input in a total of n=47,167 participants from 28 datasets within the ENIGMA consortium.[6] For a subset of these (n=34,112), we carried out a genome-wide association meta-analysis (GWAS) of brain-PAD. Additive effects of genetic variants on brain-PAD were tested, adjusting for age, age2, sex, total intracranial volume, genetic ancestry, imaging covariates (e.g. multiple scanners) and disease status (for case-control studies). We applied

linear (mixed) models using BOLT-LMM, RareMetalWorker or PLINK2. Preliminary results were meta-analysed in METAL, weighing each cohort according to sample size.

Results: A total of n=47,167 participants were included in the phenotypic analysis (age range 18-75 years; 52.8% females). Brain age was predicted with meanunweighted absolute error of 9.58 years (range 4.67-21.29). For the subset of datasets included in the GWAS, the meanunweighted absolute error was slightly larger (14.25 years; range 6.30-21.29; age-bias correctedunweighted=9.08). Fixed effect meta-analysis using METAL identified 66 genome-wide significant variants associated with brain-PAD at P = 5 x 10-8 (Figure 1). Three of these variants (on chromosomes 2, 15 and 16) were independent using r2 = 0.1 and 500 kb window size. Two out of three variants identified had been previously implicated in brain-related phenotypes. SNP-based heritability was estimated at 0.1923 (SE=0.0167).

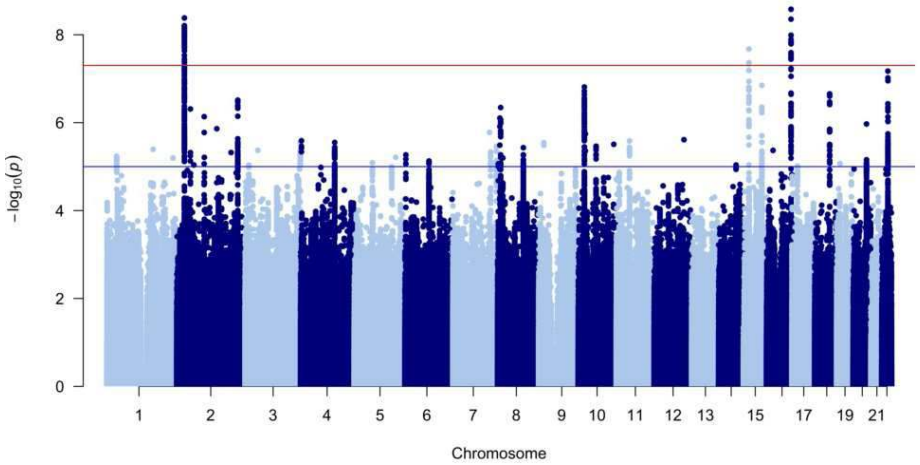

Figure 1. Manhattan plot for METAL meta-analysis of Brain-PAD. Red line: P=5x10-8, blue line: P=5x10-5. Brain-PAD=brain predicted age difference (calculated as predicted minus chronological age).

Conclusions: Our findings indicate that brain age deviations in adulthood might be moderately heritable. Genetic loci overlapped partially with previous studies using overlapping data (e.g., UK Biobank), but different brain age estimation methods, suggesting a degree of consistency across methods.[3,7] Identifying the underlying genetic loci can help to shed light on the causal risk factors involved in brain aging, aiding in the prevention and treatment of age-related poor health outcomes, such as schizophrenia, Alzheimer's disease, and other cognitive impairments.

References

1. Cole, J. H. (2018), 'Brain age predicts mortality', Molecular Psychiatry 23, 1385–1392.
2. Kolbeinsson, A. (2020), 'Accelerated MRI-predicted brain ageing and its associations with cardiometabolic and brain disorders'. Scientific Reports 10, 19940.
3. Smith, S. M. (2020), 'Brain aging comprises many modes of structural and functional change with distinct genetic and biophysical associations', eLife 9, e52677.
4. Jonsson, B. A. (2019), 'Brain age prediction using deep learning uncovers associated sequence variants', Nature Communications 10, 5409.
5. Leonardsen, E. H. (2023), 'Genetic architecture of brain age and its causal relations with brain and mental disorders', Molecular Psychiatry 28, 3111–3120.
6. Han, L. K. M. (2021), 'Brain aging in major depressive disorder: results from the ENIGMA major depressive disorder working group', Molecular Psychiatry 26, 5124–5139.
7. Kim, J. (2023), 'Investigation of genetic variants and causal biomarkers associated with brain aging', Scientific Reports 13, 1526.

Poster No 1173

Age-related changes in gray matter asymmetry: Will brains get more (a)symmetric?

Florian Kurth[1], Nicolas Cherbuin[2], Christian Gaser[3], Eileen Luders[1]

[1]University of Auckland, Auckland, New Zealand, [2]National Centre for Epidemiology and Population Health, Canberra, Australia, [3]Jena University Hospital, Jena, Germany

Introduction: Structural and functional differences between the hemispheres are known to change over time (Ocklenburg and Gunturkun, 2018; Toga et al., 2009). Some theories suggest a progressive recruitment of homotopic contralateral brain regions with increasing age, which may manifest as decreases in asymmetry (Cabeza, 2002). Other theories support the assumption

of an accelerated atrophy of one hemisphere compared to the other (Kong et al., 2018; Minkova et al., 2017; Thompson et al., 2003), which may manifest as increases in asymmetry. Here we set out to explore age-related changes in gray matter asymmetry using a longitudinal design in a large sample of 2,324 participants (1151 women / 1173 men) spanning a wide age range (47 – 80 years).

Methods: T1-weighted brain images were obtained from the UK Biobank, only including participants who were scanned at two time points and without a history of neuropsychiatric conditions, cancer, or stroke. The time between baseline and follow-up scans ranged between 1 and 7 years (mean ± SD: 2.39 ± 0.82). All brain images were preprocessed using the CAT12 toolbox (Gaser et al., 2022) applying the longitudinal workflow for age effects. The resulting tissue segments were registered to MNI space using affine transformations, flipped in the x-axis, and both original and flipped tissue segments were then warped to a symmetric Shooting Template in MNI space and modulated (Kurth et al., 2015). Subsequently, the asymmetry index was calculated as AI = (right-left)/(0.5 x [right+left]), duplicate information in the left hemisphere was discarded and the AI values within the remaining right hemisphere were smoothed using an 8 mm FWHM kernel (Kurth et al., 2015). Finally, all AI values were converted into absolute values and the absolute AI values at baseline were subtracted from the absolute AI values at follow-up. The resulting difference maps served as the dependent variable in the statistical model. Changes in asymmetry were assessed in a general linear model with sex and brain volume as covariates. Results were corrected for multiple comparisons on cluster level by controlling the family-wise error, using a cluster-forming threshold at $p \leq 0.001$ and correcting for non-stationarity (Hayasaka et al., 2004).

Results: Our study revealed brain regions where (a) asymmetry remains stable over time, (b) significantly decreases over time (Figure 1), or (c) significantly increases over time (Figure 2). More specifically, decreases in asymmetry were detected in the temporal lobe, extending into inferior parietal and occipital regions. In contrast, increases in asymmetry were evident in the frontal cortex and orbitofrontal regions as well as the insula, posterior parietal and medial frontal/parietal regions.

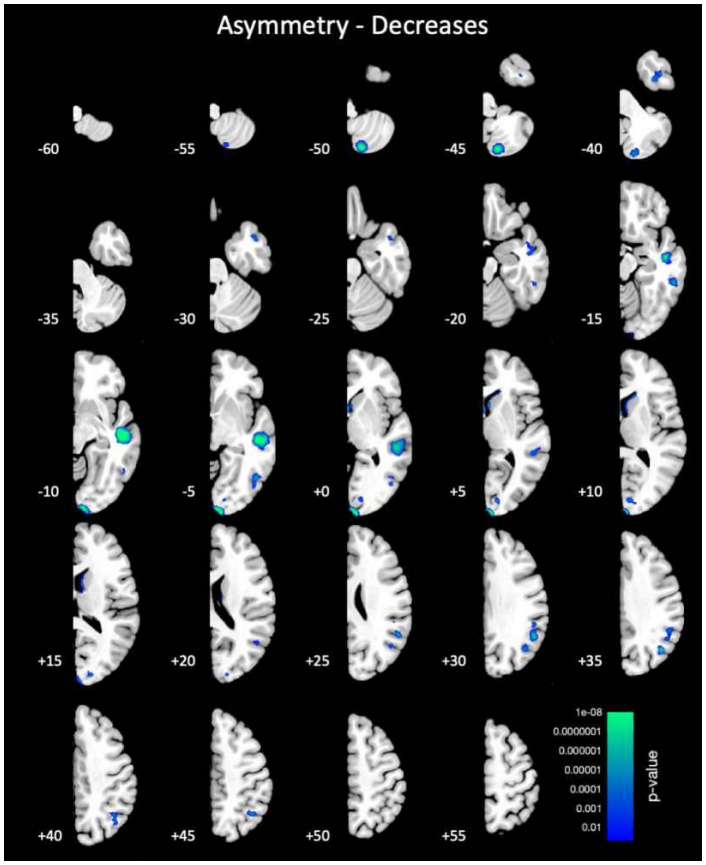

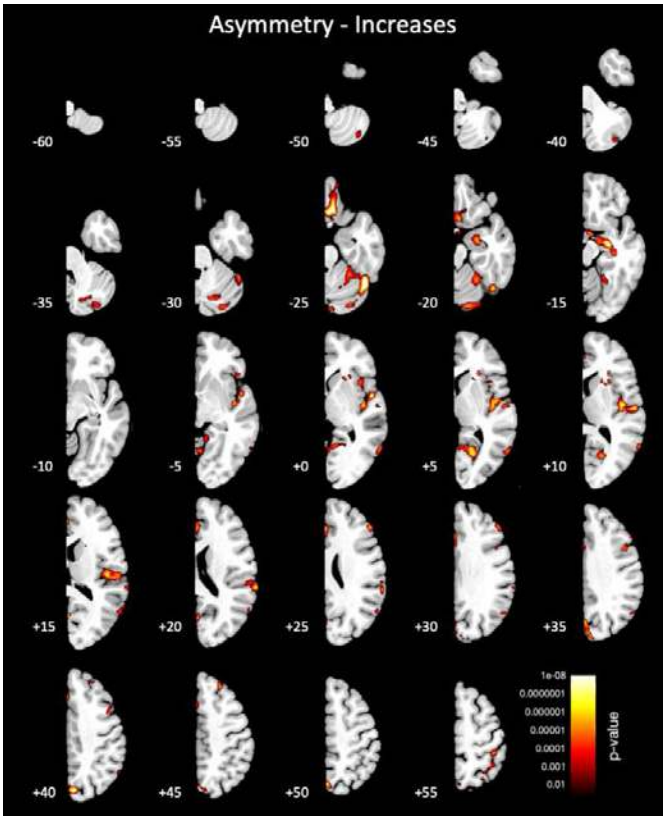

Conclusions: Our study revealed that asymmetry remains stable over time in most parts of the brain. However, there were some regions where asymmetry significantly increased or decreased. As far as this change over time is concerned, there seems to be a predominant decrease of leftward asymmetries as well as an increase of rightward asymmetries. Overall, the observed effects suggest a more pronounced gray matter loss in the left hemisphere compared to the right, supporting previous reports (Thompson et al., 2003).

References

1. Cabeza, R. (2002) Hemispheric asymmetry reduction in older adults: the HAROLD model. Psychol Aging, 17:85-100.
2. Gaser, C., Dahnke, R., Thompson, P.M., Kurth, F., Luders, E. (2022) CAT – A Computational Anatomy Toolbox for the Analysis of Structural MRI Data. bioRxiv, 2022.06.11.495736.
3. Hayasaka, S., Phan, K.L., Liberzon, I., Worsley, K.J., Nichols, T.E. (2004) Nonstationary cluster-size inference with random field and permutation methods. Neuroimage, 22:676-87.
4. Kong, X.Z., Mathias, S.R., Guadalupe, T., Group, E.L.W., Glahn, D.C., Franke, B., Crivello, F., Tzourio-Mazoyer, N., Fisher, S.E., Thompson, P.M., Francks, C. (2018) Mapping cortical brain asymmetry in 17,141 healthy individuals worldwide via the ENIGMA Consortium. Proc Natl Acad Sci U S A, 115:E5154-E5163.
5. Kurth, F., Gaser, C., Luders, E. (2015) A 12-step user guide for analyzing voxel-wise gray matter asymmetries in statistical parametric mapping (SPM). Nat Protoc, 10:293-304.
6. Minkova, L., Habich, A., Peter, J., Kaller, C.P., Eickhoff, S.B., Kloppel, S. (2017) Gray matter asymmetries in aging and neurodegeneration: A review and meta-analysis. Hum Brain Mapp, 38:5890-5904.
7. Ocklenburg, S., Gunturkun, O. (2018) Hemispheric Asymmetries Over the Lifespan. The lateralized brain: the neuroscience and evolution of hemispheric asymmetries. London: Academic Press. p 263-288.
8. Thompson, P.M., Hayashi, K.M., de Zubicaray, G., Janke, A.L., Rose, S.E., Semple, J., Herman, D., Hong, M.S., Dittmer, S.S., Doddrell, D.M., Toga, A.W. (2003) Dynamics of gray matter loss in Alzheimer's disease. J Neurosci, 23:994-1005.
9. Toga, A.W., Narr, K.L., Thompson, P.M., Luders, E. (2009) Brain Asymmetry: Evolution. In: Squire, L.R., editor. Encyclopedia of Neuroscience. Oxford: Academic Press. p 303-311.

Poster No 1174

Investigating network changes in typical aging trajectories of adulthood by cross-frequency coupling

Taha Liaqat[1], Vasily Vakorin[1], Hayyan Liaqat[1], Sam Doesburg[1], Sylvain Moreno[1]

[1]Simon Fraser University, Vancouver, British Columbia

Introduction: Typical cognitive aging trajectories can be understood as changes in neurophysiological mechanisms over the lifespan. Such mechanisms can be described with Magnetoencephalography (MEG) (Ishii et al., 2018). In turn, MEG rhythms

provide insights into the temporal hierarchy of information processing in the brain through the mechanism of cross-frequency coupling (CFC) (Buzsáki & Watson, 2012). A specific form of CFC is phase-amplitude coupling (PAC), which has been linked to cognitive performance across resting-state brain networks (Canolty & Knight., 2010). However, how PAC evolves within different networks across the lifespan is still an open question. In our study, we define trajectories of cross-frequency coupling in healthy brain aging over a wide age range and explore how they vary across resting-state networks.

Methods: We analyzed data from the Cambridge Centre for Ageing and Neuroscience (Cam-CAN) cohort study (Taylor et al., 2017). The dataset included resting-state MEG scans for 605 healthy participants aged 19 to 89. We divided all participants into five non-overlapping age groups. We reconstructed source dynamics mapped onto Schaefer's cortical atlas with 400 regions of interest (ROI) representing 17 fMRI-defined resting-state networks (Schaefer et al., 2018). For each ROI, we estimated PAC as a normalized modulation index, quantifying associations between the phase of lower frequency oscillations and the amplitude of higher frequency oscillations (Roehri et al., 2022). Specifically, we applied a complex wavelet transform to compute the phase of twenty frequencies between 1Hz and 12Hz, and the amplitude at thirty frequencies between 13Hz and 75Hz, equally spaced on a logarithmic scale. For each network, we applied a multivariate analysis, Mean-Centered Partial Least Squares (MC PLS), to explore how PAC changed across age groups (Krishnan et al., 2011). The PLS analysis decomposed our data into a set of latent variables (LV). We focused on the first LV, which explains the largest variance in the data. Each LV was associated with (i) a vector of group contrasts, representing changes in PAC strength across age groups, and (ii) a vector of z-scores, representing how the PAC for each ROI and given higher and lower frequency combination contributes to the identified group contrast. To focus on the most robust effect in each network, we computed the median of z-scores across ROIs within each network.

Results: The PLS analysis revealed statistically significant results for 14 of the 17 networks. The group contrasts, representing the ageing trajectories in PAC demonstrated either monotonic decreases or U-shaped changes in PAC strength across the lifespan, depending on the network. The median z-scores showed the most robust change in phase-amplitude coupling between the theta (6 Hz–8 Hz) and lower beta (15 Hz–18 Hz) frequency bands. To exemplify the effect, we showed the results for the Control A network (Figure 1). Here the contrast represented a trend of monotonically decreasing PAC strength across the five age groups. The largest z-scores, reflecting the most robust effects, are clustered around theta-beta cross-frequency coupling.

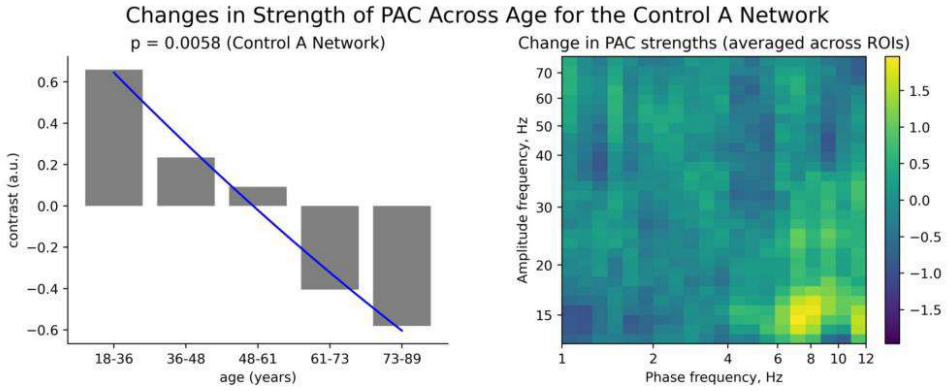

Conclusions: We identified distinct spatiotemporal patterns of age-related changes in PAC, showing their variability across resting-state networks. In turn, these patterns can be considered part of the complex neurophysiological profile in which the synchrony of distinct neural rhythms can serve as a biomarker for cognitive changes in aging in adulthood. By evaluating multiple networks under the same methodology, we have shown that the shape of the trajectories depends on the network, highlighting the variability in the aging brain at the functional level. This aligns with similar findings based on the structural parameters of the brain (Nyberg et al., 2023). Understanding relationships between this network variability and cognitive performance will further help to understand ageing trajectories in typical cognitive ageing.

References

1. Buzsáki, G. (2012), 'Brain rhythms and neural syntax: implications for efficient coding of cognitive content and neuropsychiatric disease', Dialogues in clinical neuroscience, 14(4), 345-367
2. Canolty, R. T. (2010), 'The functional role of cross-frequency coupling', Trends in cognitive sciences, 14(11), 506-515
3. Ishii, R. (2018), 'Healthy and pathological brain aging: from the perspective of oscillations, functional connectivity, and signal complexity', Neuropsychobiology, 75(4), 151-161
4. Krishnan, A. (2011), 'Partial Least Squares (PLS) methods for neuroimaging: a tutorial and review', NeuroImage, 56(2), 455-475
5. Nyberg, L. (2023), 'Individual differences in brain aging: heterogeneity in cortico-hippocampal but not caudate atrophy rates', Cerebral Cortex, 33(9), 5075-5081

6. Roehri, N. (2022), 'Phase-amplitude coupling and phase synchronization between medial temporal, frontal and posterior brain regions support episodic autobiographical memory recall', Brain Topography, 35(2), 191-206
7. Schaefer, A. (2018), 'Local-global parcellation of the human cerebral cortex from intrinsic functional connectivity MRI', Cerebral cortex, 28(9), 3095-3114
8. Taylor, J. R. (2017), 'The Cambridge Centre for Ageing and Neuroscience (Cam-CAN) data repository: Structural and functional MRI, MEG, and cognitive data from a cross-sectional adult lifespan sample', NeuroImage, vol. 144, 262-269

Poster No 1176

Neuroimaging-based brain age estimation using Artifical Intelligence(AI)-integrated prediction model

Eun Ji Yang[1], Young Hyun Lee[1], Ji Eun Park[1], Song E Kim[1], Hyang Woon Lee[1]

[1]Ewha Womans University, Seoul, Korea, Republic of

Introduction: Estimated Brain Age, derived from brain Magnetic Resonance Imaging(MRI) data, serves as a biomarker for assessing brain aging compared to chronological age. The gap between brain age and actual chronological age, known as the Brain Age Gap (BAG), is an important indicator of the acceleration or delay in the biological aging process. A brain age predicted higher than the chronological age suggests accelerated aging of the brain, potentially associated with cognitive decline and the onset of brain diseases. Alzheimer's and similar neurodegenerative diseases have been shown to exhibit older brain ages in affected individuals, with differences in the brain age gap based on sex. This study aims to predict brain age and calculate the brain age gap using an Artificial Intelligence(AI)-integrated prediction model, focusing on the differences based on sex.

Methods: This study utilizes the Human Connectome Project's HCP-YoungAdult (ages 22-35, 1,206 individuals, of which 1,113 underwent structural MR scans) and HCP-Aging (ages 36-100, 725 individuals) datasets. Our analysis involves structural MRI images obtained from the HCP's structural preprocessing pipeline and brain volume values derived from FreeSurfer files. To estimate brain age, we employed an AI-integrated prediction model using the Simple Fully Convolutional Network (SFCN) model, which is based on three-dimensional(3D) T1-weighted images. This SFCN model was pre-trained using the extensive and diverse UK Biobank dataset, enhancing its accuracy and generalizability. Additionally, advanced visualization techniques were applied to generate heatmaps, highlighting areas significant for model predictions. This approach provides better interpretation of the model's predictions and enhance the transparency of the analysis results.

Results: In this study, the aforementioned heatmaps revealed notable differences in the brain regions influencing aging in males and females. Certain brain areas were more pronounced in one sex compared to the other, suggesting the possibility of sex-specific patterns in brain aging. Furthermore, our preliminary results indicated clear differences in the brain age gap (BAG) based on sex. This finding suggests that the process of brain aging and its potential impact on neurological health may significantly differ between males and females. Such insights are crucial for understanding sex-specific aging patterns and could influence future research and clinical approaches in the field of neuroscience.

Conclusions: Our findings including AI-derived brain age predictions, associated brain age gaps and sex differences offer significant insights into understanding the progression of brain aging. These results are instrumental in suggesting practical measures for early diagnostic strategies in patients with neurological conditions, highlighting the potential of AI in contributing to advanced healthcare solutions. Supported by the National Research Foundation of Korea (NRF) (No.2020R1A2C2013216, 2019M3C1B8090803, 2019M3C1B8090802, and RS-2023-00265524), Institute of Information & Communication Technology Planning & Evaluation (IITP) grant (No. RS-2022-00155966) by the Korea government (MSIT), and BK21-plus FOUR and Artificial Intelligence Convergence Innovation Human Resources Development programs of Ewha Womans University.

References

1. Dibaji, M. (2023). 'Studying the Effects of Sex-Related Differences on Brain Age Prediction Using Brain MR Imaging', Workshop on Clinical Image-Based Procedures, Springer.
2. Peng, H. (2021). 'Accurate brain age prediction with lightweight deep neural networks', Medical Image Analysis, vol. 68, pp. 101871.
3. Sajedi, H. (2019). 'Age prediction based on brain MRI image: a survey', Journal of Medical Systems, vol. 43, pp. 1-30.
4. Sanford, N. (2022). 'Sex differences in predictors and regional patterns of brain age gap estimates', Human Brain Mapping, vol. 43, no. 15, pp. 4689-4698.
5. Yin, C. (2023). 'Anatomically interpretable deep learning of brain age captures domain-specific cognitive impairment', Proceedings of the National Academy of Sciences, vol. 120, no. 2, e2214634120.

Poster No 1177

Cortical Depth Dependent Microstructural Variations in Aging using Diffusion Tensor Imaging

Yutong Sun[1], Jordan Chad[2], J. Jean Chen[1]

[1]Medical Biophysics, University of Toronto, Toronto, Ontario, [2]Rotman Research Institute, Baycrest Health Sciences, Toronto, Ontario

Introduction: Although the utilization of diffusion-tensor imaging (DTI) in cortical gray matter (GM) is limited, previous findings have demonstrated an increased GM mean diffusivity (MD) and fractional anisotropy (FA) with aging[1,2]. However, their interpretations remain unclear. Since the cyto- and myelo-architecture vary along the cortical laminae[3], we hypothesize that age effects in DTI parameters also vary across cortical layers. In this study, using a recently published approach[6], we investigate the cortical depth dependence of DTI age effects.

Methods: 700 subjects were taken from the UK Biobank, with 100 subjects of balanced sex ratio in each quinquennial. Data were collected using a Skyra 3T scanner with 50x b=1000 and 50 2000s/mm2, voxel resolution=2mm3. We applied eddy-current and susceptibility-induced distortions using EDDY, as well as 3D gradient distortion correction. The b=1000 data was used to calculate MD. The norm of anisotropy (NA) was calculated using the orthogonal-tensor decomposition method to measure anisotropy without bias from MD[5]. For MD and NA, age effects (%change/year) were projected onto the FreeSurfer cortical surface. These were sampled between projfrac of 0.0 (representing the WM boundary) and 1.0 (representing the pial surface) at step of 0.1.

Results: We found a positive association between MD and age across the cortex, and both positive and negative age-associations in NA. Stronger MD-age effects on the pial surface (Fig. 1): This is true in most cortical regions, whereby for most regions showing a strong positive NA-age association, it was stronger on the pial surface. There was no such preference for the negative NA-age associations. Stronger MD-age effects on the WM surface (Fig. 2): MD-age effects were stronger on the WM surface for the right entorhinal, right isthmus cingulate, as well as the parahippocampal gyrus. NA-age effects displayed different depth dependencies across hemispheres. For instance, the parahippocampal and left entorhinal regions showed a negative NA-age association stronger on the WM surface, whereas the negative association in the right entorhinal region was stronger on the pial surface. Lastly, a positive NA-age association was only found in the right but not the left isthmus cingulate, being stronger on the WM surface. The few regions (e.g. left isthmus cingulate) without cortical depth dependence for MD-age associations also lacked it for NA-age associations.

Conclusions: For the dominant trend of MD-age effects being positive and stronger on the pial surface, negative NA-age associations greater on the pial surface may suggest increasing partial-volume effects with cerebrospinal fluid (CSF), resulting from cortical atrophy (Fig.1a, b). Positive NA-age associations stronger on the pial surface may suggest selective degeneration of crossing fibres in the superficial cortical layers (Fig. 1c, d). Positive NA-age associations stronger on the WM surface may indicate the co-existence of cortical atrophy and selective degeneration of crossing fibres in the base cortical layers (Fig. 1e, f). Negative NA-age associations stronger at the WM surface may be driven by a co-existence of atrophy and demyelination in the base cortical layers (Fig. 1g, h). With positive MD-age associations stronger on the WM boundary, a concurrent positive NA-age associations stronger on the WM surface (Fig. 2c, d) could suggest selective degeneration of crossing fibres in the base cortical layers. A negative NA-age association stronger at the pial surface (Fig. 2a, b) could suggest the tensor shape is becoming more isotropic but disproportionate to demyelination. Lastly, a negative NA-age association stronger on the WM boundary (Fig. 2b) could suggest demyelination potentially accompanied loss of WM packing density in the base cortical layers. Stronger MD-age effects on the WM boundary versus the pial surface likely suggests different stages of degeneration.

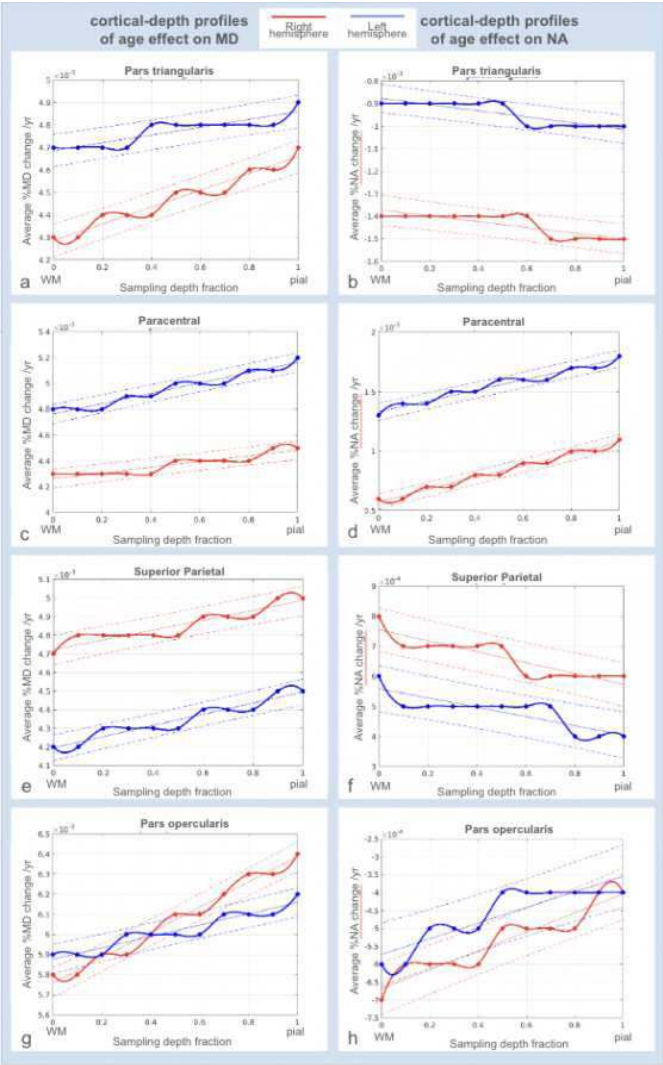

Figure 1. Cortical-depth profiles of age effects for regions with stronger MD-age effects on the pial surface. Age effects for each parameter are shown in terms of %change per year. NA is negatively associated with age on pars triangularis, with the effect being stronger on the pial surface, while for paracentral gyrus, there is a positive NA-age association that is stronger on the pial surface. There is also a positive association between NA and age in the superior parietal gyrus, but with the effect being stronger on the WM boundary. For pars opercularis, there is a negative association between age and NA, also stronger on the WM boundary.

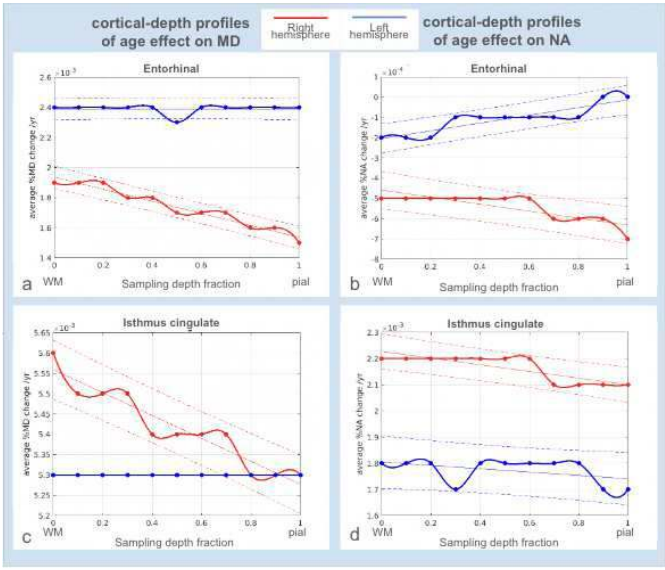

Figure 2. Cortical-depth profiles of age effects for regions stronger MD-age effects on the WM surface. Age effects for each parameter are shown in terms of % change per year. The entorhinal cortex undergoes age effect differently in the two hemispheres, with the negative NA-age association being stronger on the WM surface for the left hemisphere, and stronger on the pial surface for the right hemisphere. In the right isthmus cingulate, a positive association between NA and age is stronger on the WM surface.

References
1. Salminen, L. E., Conturo, T. E., Laidlaw, D. H., Cabeen, R. P., Akbudak, E., Lane, E. M., ... & Paul, R. H. (2016). Regional age differences in gray matter diffusivity among healthy older adults. Brain imaging and behavior, 10, 203-211.
2. Rathi, Y., Pasternak, O., Savadjiev, P., Michailovich, O., Bouix, S., Kubicki, M., ... & Shenton, M. E. (2014). Gray matter alterations in early aging: a diffusion magnetic resonance imaging study. Human brain mapping, 35(8), 3841-3856.
3. Zilles, K., Palomero-Gallagher, N., & Amunts, K. (2015). Cytoarchitecture and maps of the human cerebral cortex.
4. UK Biobank - UK Biobank. (2022) [cited 2022Nov6]. Available from: https://www.ukbiobank.ac.uk/
5. Chad, J. A., Pasternak, O., & Chen, J. J. (2021). Orthogonal moment diffusion tensor decomposition reveals age-related degeneration patterns in complex fiber architecture. Neurobiology of Aging, 101, 150-159.
6. Truong, T. K., Guidon, A., & Song, A. W. (2014). Cortical depth dependence of the diffusion anisotropy in the human cortical gray matter in vivo. PloS one, 9(3), e91424.

Poster No 1178

Exploring Age-Related Morphological Changes in Cerebral Arteries: A 7T TOF MRA Study

Zonghua Shi[1], Jiatai Li[2], Yuanzhe Huang[3], Noah Schweitzer[3], Bistra Iordanova[3], Tamer Ibrahim[3], Shaolin Yang[3], George Stetten[3], Howard Aizenstein[3], Minjie Wu[3]

[1]Washington University in St. Louis, St. Louis, MO, [2]Carnegie Mellon University, Pittsburgh, PA, [3]University of Pittsburgh, Pittsburgh, PA

Introduction: Aging-related changes in cerebrovascular health include vessel structural alterations, reduced vessel elasticity, reduced blood flow, and impaired blood-brain barrier permeability, which may contribute to neurological and neurodegenerative diseases, such as Alzheimer's Disease (AD) (Zimmerman et al., 2021). In this study, we used 7T Time-of-flight (TOF) magnetic resonance angiography (MRA) to investigate age-related differences in arterial diameter and tortuosity in the brain in cognitively normal older adults.

Methods: Our study comprised 25 older adults with normal cognition (20 females, average age of 68.3 ± 9.7 years). Whole-Brain TOF MRA images were acquired using a 7T Siemens scanner at the University of Pittsburgh, slice number=354, voxel size=0.38*0.38*0.38 mm^3, 12 mins. Manual skull-stripping was performed to remove non-brain tissues on each TOF image, and the resulting brain mask was further dilated with 2-mm sphere to preserve vessels traveling along the surface of the brain. The cerebral arterial tree was segmented using VesselMapper, an automated vessel segmentation tool recently developed in our lab (Li et al., 2023). Arterial morphology was assessed using vessel diameter and vessel tortuosity. For each subject, vessels were further categorized into three types based on vessel diameter, in which large vessels were defined as vessels with the top 33% diameter size, and small vessels as vessels with the bottom 33% diameter size. Pearson correlation analysis was performed to evaluate the association between age and vessel diameter and tortuosity.

Results: As seen in Fig. 1, there is a significant positive association between age and large vessel diameter, so that older age is associated with a larger median diameter (r=0.42, p=0.03) (Fig. 1b). In contrast, there is a significant negative association between age and small vessel diameter, so that older age is associated with a smaller median diameter (r=-0.44, p=0.03) (Fig. 1c). As seen in Fig. 2, while large vessel tortuosity is not associated with age (r=0.06, p=0.78) (Fig. 2b), small vessels demonstrate an age-related decrease in median vessel tortuosity (r=-0.53, p=0.006) (Fig. 2c).

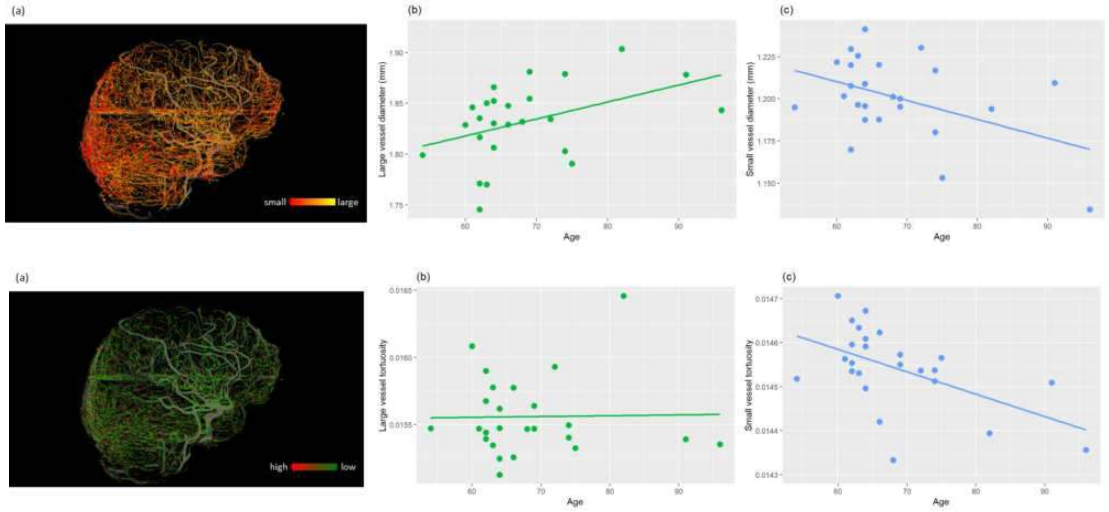

Conclusions: The observed age-related increase in large vessel diameter (Fig. 1b) aligns with the gradual diameter increase with age in central and peripheral (lower and upper limb) vessels (Mandalà & Cipolla, 2021) (Thijssen et al., 2016). Vessel diameter dilation may reflect a compensatory enlargement (Polak et al., 1996), loss of elastic fibers (Fritze et al., 2012), reduced arterial storage capacity and compromised capability to attenuate pulse propagation with aging (Zeki Al Hazzouri & Yaffe, 2014). Age-related change in large vessels is accompanied by morphologic changes in small vessels (Fig. 1b and 1c), supporting a link between large vessel damage and distal small vessel alterations in the brain. Change in diameter in small vessels is also accompanied by change in tortuosity (Fig. 1c and Fig. 2c). The challenge with the small vessels is that their conspicuity is conflated by lower blood flow velocity. Age-related decrease in tortuosity may be a reflection of lower velocity in the small tortuous vessels. Acknowledgement: This work was supported by the National Institute on Aging (R01AG067018 to Wu and RF1AG025516 to Aizenstein).

References

1. Fritze, O., Romero, B., Schleicher, M., Jacob, M. P., Oh, D. Y., Starcher, B., Schenke-Layland, K., Bujan, J., & Stock, U. A. (2012). Age-related changes in the elastic tissue of the human aorta. Journal of vascular research, 49(1), 77–86. https://doi.org/10.1159/000331278
2. Li, J., Stetten, G., Schweitzer, N., Ibrahim, T. S., Iordanova B., Aizenstein, H., Wu, M. (2023). VesselMapper - A Robust Vessel Segmentation Algorithm for 3D Images. In Annual Meeting of the Organization for Human Brain Mapping.
3. Mandalà, M., & Cipolla, M. J. (2021). Aging-Related Structural and Functional Changes in Cerebral Arteries: Caloric Restriction (CR) Intervention. Journal of vascular medicine & surgery, 9(Suppl 7), 1000002.
4. Polak, J. F., Kronmal, R. A., Tell, G. S., O'Leary, D. H., Savage, P. J., Gardin, J. M., Rutan, G. H., & Borhani, N. O. (1996). Compensatory increase in common carotid artery diameter. Relation to blood pressure and artery intima-media thickness in older adults. Cardiovascular Health Study. Stroke, 27(11), 2012–2015. https://doi.org/10.1161/01.str.27.11.2012
5. Thijssen, D. H., Carter, S. E., & Green, D. J. (2016). Arterial structure and function in vascular ageing: are you as old as your arteries?. The Journal of physiology, 594(8), 2275–2284. https://doi.org/10.1113/JP270597
6. Zeki Al Hazzouri, A., & Yaffe, K. (2014). Arterial stiffness and cognitive function in the elderly. Journal of Alzheimer's disease : JAD, 42 Suppl 4(0 4), S503–S514. https://doi.org/10.3233/JAD-141563
7. Zimmerman, B., Rypma, B., Gratton, G., & Fabiani, M. (2021). Age-related changes in cerebrovascular health and their effects on neural function and cognition: A comprehensive review. Psychophysiology, 58(7), e13796. https://doi.org/10.1111/psyp.13796

Poster No 1179

Functional alterations contribute to memory deficits in aging and AD: an fMRI and PET study

Xi Chen[1], Leah Varghese[2], Suzanne Baker[3], William Jagust[4]

[1]Stony Brook University, Stony Brook, NY, [2]Stanford University School of Medicine, Palo Alto, CA, [3]Lawrence Berkeley National Laboratory, Berkeley, CA, [4]University of California, Berkeley, Berkeley, CA

Introduction: The anterior temporal (AT) and posterior medial (PM) networks, and hippocampus in the medial temporal lobe (MTL) are functionally responsible for object/item-based, scene/context-based, and association/integrative processing for episodic memory, respectively[1]. These systems are also vulnerable to aging and Alzheimer's disease (AD)[2,3]. AD pathology of beta-amyloid (Aβ) and tau begins to emerge in cognitively normal people before clinical symptoms[4,5], and it preferentially deposits first in AT, PM, and MTL in this pre-clinical, asymptomatic stage[2]. Given the functional specificity of these regions and their particular vulnerability to AD pathology, we hypothesize that age-related and pathology-related memory deficits may be explained by functional alterations in these regions. Here, we utilized multimodal neuroimaging, including task fMRI to assess functional activation during incidental memory encoding, and PET imaging to measure Aβ and tau burden in cognitively normal older individuals. We aimed to study the neural bases of memory deficits in normal aging and early AD.

Methods: Twenty-seven young (19-34 yrs) and 51 older (60-91 yrs) participants completed a memory task[6] where the incidental encoding of object, scene, and object-in-scene pair images was scanned during fMRI and a subsequent recognition test approximately 45 minutes later was performed outside the scanner (Fig 1A). Forty-one older participants also underwent PiB and FTP PET scans to measure their Aβ and tau burden. We examined age-related (young vs. older) and AD pathology related (Aβ- vs. Aβ+, continuous tau) effects for subsequent memory performance, indexed by accuracy and d', and brain activations. The fMRI analysis was focused on the composite regions of interest (ROIs) of AT and PM (Fig 1B), as well as the hippocampus, for the pair > object + scene contrast.

Results: Behaviorally, older people had worse object and pair memory, primarily driven by an increased difficulty in distinguishing lures (Fig 1C). Older people in the pre-clinical stage of AD, evidenced by Aβ positivity and elevated temporal meta tau burden, exhibited even worse memory, with a greater difficulty in remembering the previously presented pictures, compared to those without AD pathology (Fig 1C). FMRI results show that all three ROIs had significant activations during the processing of pairs in contrast to object-alone and scene-alone materials (Fig 2A), where greater activation was predictive of better subsequent memory performance indexed by accuracy (Fig 1D). Older age was associated with reduced activation in AT

(Fig 2A), which marginally mediated the age-related differences in subsequent memory accuracy (Fig 2C). In contrast, greater tau pathology was associated with increased activation in the parahippocampal gyrus (Fig 2B), which completely mediated the tau-related differences in subsequent memory d' (Fig 2D).

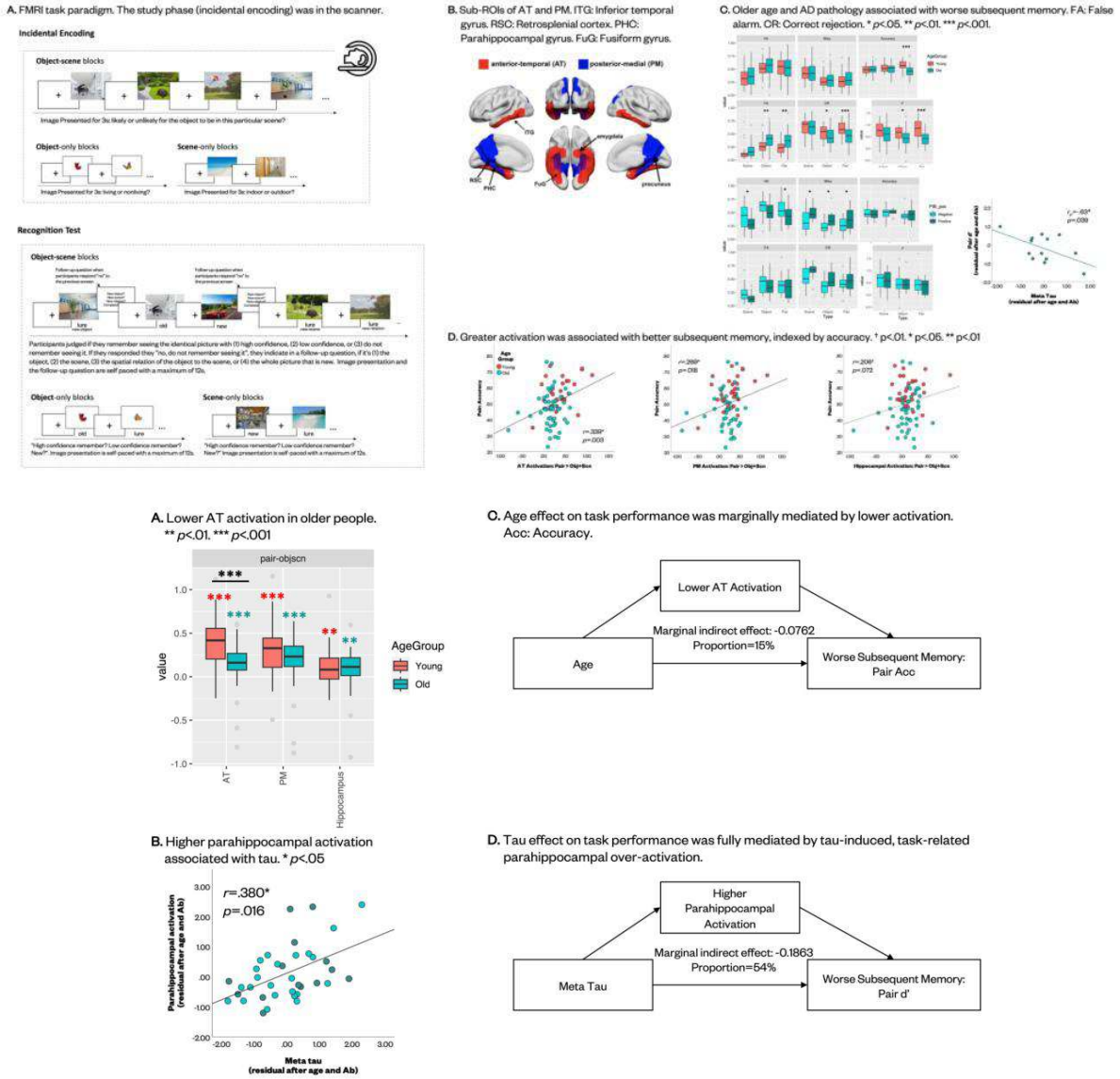

Conclusions: Older adults have worse memory, especially for complex object-in-scene pairs, primarily driven by greater false recognition of lures. AT, PM, and hippocampus are all significantly involved in processing object-in-scene pairs. The age-related functional reductions in AT regions contribute to worse task performance, especially the greater difficulty in rejecting lures. Additionally, AD pathology was associated with a further reduction in pair memory performance, most evident in failure to remember old pictures. Greater tau pathology was associated with increased activation that contributed significantly to worse subsequent memory. In conclusion, functional activation may play important roles through different mechanisms underlying memory deficits in normal aging and early AD: functional reduction in key task regions may contribute, to some extent, to worse memory task performance in aging, whereas tau-induced hyperactivation explains the disproportionately worse performance in pre-clinical AD.

References

1. Ranganath C, Ritchey M. Two cortical systems for memory-guided behaviour. Nat Rev Neurosci. 2012;13(10):713-726.
2. Braak H, Braak EVA. Staging of Alzheimer's disease-related neurofibrillary changes. Neurobiol Aging. 1995;16(3):271-278.
3. Wilson IA, Gallagher M, Eichenbaum H, Tanila H. Neurocognitive aging: prior memories hinder new hippocampal encoding. Trends Neurosci. 2006;29(12):662-670. [4] Jack Jr. CR, Bennett DA, Blennow K, et al. NIA-AA Research Framework: Toward a biological definition of Alzheimer's disease. Alzheimers Dement. 2018;14(4):535-562.
4. Sperling RA, Karlawish J, Johnson KA. Preclinical Alzheimer disease—the challenges ahead. Nat Rev Neurol. 2013;9(1):54.
5. Chen, X., Varghese, L., & Jagust, W. J. (2022). A double-edged sword: the role of prior knowledge in memory aging. Frontiers in Aging Neuroscience, 14, 874767.

Poster No 1180

Functional connectivity upregulation in post-menopause in healthy females

Ceren Tozlu[1], Parker Singleton[2], Louisa Schilling[3], Catherine Liu[4], Susan Gauthier[1], Keith Jamison[3], Amy Kuceyeski[3]

[1]Weill Cornell Medicine, NYC, NY, [2]Weill Cornell Medicine, New York, NY, [3]Weill Cornell Medicine, New York City, NY, [4]Cornell University, Ithaca, NY

Introduction: Menopause is characterized by abrupt changes in sex steroid hormones which impacts multiple organ systems, including the brain. The impact of menopause on the brain is an understudied topic; however, one of the few studies investigating brain biomarker changes during menopause found decreased white matter volume and cerebral glucose metabolism and increased cerebral blood flow during the peri-menopause compared to pre-menopause (Mosconi et al. 2021). However, it is still unclear how menopause impacts the brain's functional connectivity architecture. In a densely-sampled neuroimaging study from one healthy female, the brain's functional connectivity networks were found to be linearly associated with changes in the sex steroid hormones during the menstrual cycle (Pritschet et al, 2020). However, no study to date has investigated how menopause, which is associated with even larger changes in sex steroid hormones, impacts the brain's functional and structural connectome in the healthy female brain. Here, we compared the brain's structural and functional connectivity networks derived from advanced neuroimaging techniques between different menopause stages (i.e. pre, peri, and post-menopause) in healthy females.

Methods: Four hundred and four females (age: 60.05 ±15.74) from the Human Connectome Project-Aging (HCP-A) dataset (Van Essen et al., 2013) were used in this study. SC and FC metrics were extracted using diffusion and resting state functional MRI, respectively, via the FreeSurfer-based atlas of 86 cortical and subcortical regions. Regional SC was computed as the sum of the columns in the SC matrix, while regional FC was calculated by taking the sum of the columns in the FC matrix after removing the negative entries. Menopausal status for each individual was defined based on the STRAW criteria (Harlow et al., 2012). ANCOVA was applied to compare each region's SC and FC strength across each pair of menopause groups, with age included as a covariate. The statistics derived from the Student's t-test were visualized to show the amplitude and the direction of the difference. Group differences were considered significant when $p<0.05$ after Benjamini–Hochberg (BH) correction for multiple comparisons.

Results: There were no significant differences in the regional SC and FC between the pre vs peri-menopausal groups. However, the post-menopausal group had weaker regional SC compared to pre and peri-menopausal groups, particularly in frontal and subcortical regions. Regional FC, particularly in regions of the frontal, visual, and cerebellar networks were greater in the post-menopause compared to pre and peri-menopausal groups.

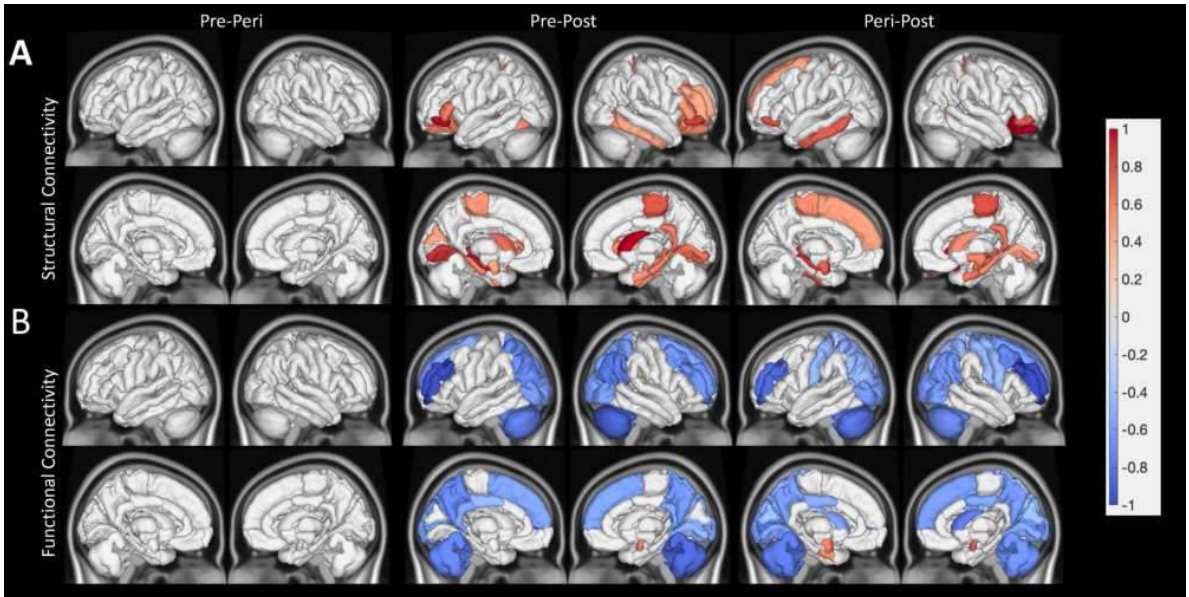

Figure 1: The statistics values extracted from the Student's t-test that was performed to compare the regional SC and FC metrics for each pair of menopause group. The statistics values were divided by the maximum of the absolute value for each comparison. The regions that (i) showed a significant difference after ANCOVA where each pair of menopause group was compared and age is included as covariate AND (ii) survived after the BH multiple comparison correction. The positive values (warm colors) represent lower SC/FC metrics in the post menopause group compared to pre and peri-menopause, while negative values (blue colors) represent higher SC/FC metrics in the post menopause group compared to pre and peri-menopause.

Conclusions: Increased regional FC in post-menopause may reveal a potential compensatory mechanism in response to decreased regional SC, as seen in other diseases associated with white matter damage (Tozlu et al., 2023). Overall, our

findings suggest that the menopausal transition impacts both the structural and functional connectome of the brain. Future studies are needed to identify how brain changes during menopause may associate with symptoms during the menopausal transition, such as hot flashes and brain fog, to provide novel and personalized treatment plans for this large portion of the population.

References

1. Pritschet L, Santander T, Taylor CM, Layher E, Yu S, Miller MB, Grafton ST, Jacobs EG. Functional reorganization of brain networks across the human menstrual cycle. Neuroimage. 2020 Oct 15;220:117091. doi: 10.1016/j.neuroimage.2020.117091. Epub 2020 Jul 2. PMID: 32621974.
2. Mosconi L, Berti V, Dyke J, Schelbaum E, Jett S, Loughlin L, Jang G, Rahman A, Hristov H, Pahlajani S, Andrews R, Matthews D, Etingin O, Ganzer C, de Leon M, Isaacson R, Brinton RD. Menopause impacts human brain structure, connectivity, energy metabolism, and amyloid-beta deposition. Sci Rep. 2021 Jun 9;11(1):10867. doi: 10.1038/s41598-021-90084-y. PMID: 34108509; PMCID: PMC8190071.
3. Van Essen DC, Smith SM, Barch DM, Behrens TE, Yacoub E, Ugurbil K; WU-Minn HCP Consortium. The WU-Minn Human Connectome Project: an overview. Neuroimage. 2013 Oct 15;80:62-79. doi: 10.1016/j.neuroimage.2013.05.041. Epub 2013 May 16. PMID: 23684880; PMCID: PMC3724347.
4. Harlow SD, Gass M, Hall JE, Lobo R, Maki P, Rebar RW, Sherman S, Sluss PM, de Villiers TJ; STRAW 10 Collaborative Group. Executive summary of the Stages of Reproductive Aging Workshop + 10: addressing the unfinished agenda of staging reproductive aging. Menopause. 2012 Apr;19(4):387-95. doi: 10.1097/gme.0b013e31824d8f40. PMID: 22343510; PMCID: PMC3340903.
5. Tozlu C, Card S, Jamison K, Gauthier SA, Kuceyeski A. Larger lesion volume in people with multiple sclerosis is associated with increased transition energies between brain states and decreased entropy of brain activity. Netw Neurosci. 2023 Jun 30;7(2):539-556. doi: 10.1162/netn_a_00292. PMID: 37397885; PMCID: PMC10312270.

Poster No 1181

Functional and microstructural measures of brain aging subgroups in cognitively unimpaired subjects

Ioanna Skampardoni[1], Junhao Wen[2], Ilya Nasrallah[1], Zhijian Yang[1], Dhivya Srinivasan[1], Guray Erus[1], Elizabeth Mamourian[1], Randa Melhem[1], Haochang Shou[1], Konstantina Nikita[3], Christos Davatzikos[1]

[1]University of Pennsylvania, Philadelphia, PA, [2]University of Southern California, LA, CA, [3]National Technical University of Athens, Athens, Attiki

Introduction: Brain aging is accompanied by several neuropathologies, often co-occurring, heterogeneously affecting brain structure and function. Unraveling the heterogeneity of complex neuroanatomical and functional changes at early asymptomatic stages may aid in revealing vulnerability or presence of neurodegeneration with potential biological and clinical implications. Here, we examine the functional connectivity (FC) and white matter (WM) integrity of three brain aging subgroups identified via a deep learning method applied to T1- and T2-weighted magnetic resonance imaging (MRI) data of a harmonized multi-cohort sample of 27,402 cognitively unimpaired individuals from the iSTAGING consortium (Habes et al. 2021).

Methods: The three subgroups were separately modeled in four decade-spanning age brackets along the 45-85 years range using the Smile-GAN method (Yang et al. 2021) built on regional volumetrics and white matter hyperintensities (WMH). We investigated internetwork connectivity based on 21 FC networks extracted using group-independent component analysis (ICA) on resting-state functional MRI (rsfMRI) data of the UK Biobank study (Miller et al. 2016). Additionally, fractional anisotropy (FA) maps derived from diffusion tensor imaging (DTI) data from the UK Biobank (Miller et al. 2016) were used to measure WM microstructural integrity. The mean FA values were extracted within 48 WM tracts using the Johns Hopkins University tract atlas. We used linear regression to associate the Smile-GAN subgroups with the 210 internetwork FC and 48 FA features, adjusting for age, sex, and subgroup labels.

Results: The three subgroups of brain volumetric measures displayed consistent patterns relative to the reference group A0 across the four age intervals: typical brain agers (A1) with mild atrophy and WMH load, and two accelerated aging subgroups, one with elevated WMH burden and vascular risk factors (VRF) enrichment but moderate atrophy (A2); and a second with diffuse severe atrophy, probably driven by lifestyle factors, and modest WMH load (A3) (Figure 1). Given the subgroup consistency across the four age intervals, functional connectivity and fractional anisotropy were examined in the entire 45-85 years age range. Internetwork connectivity analysis (N=19,143; 47% males) revealed that A3 had the most significant differences relative to the reference A0 group. We observed increased connectivity for several pairs of networks, such as the default mode - motor, somatosensory - occipital visual, and dorsal attention - occipital visual networks, and decreased connectivity for other pairs, such as the default mode - frontotemporal, subcortical - frontotemporal, and occipital visual - fronto-insular-parietal networks (Figure 2A). Our results align with the literature showing both increased (Betzel et al. 2014; Grady et al. 2016) and decreased (Onoda, Ishihara, and Yamaguchi 2012; Huang et al. 2015) internetwork connectivity, uncovering a complex functional reorganization of the brain with aging. Regarding the fractional anisotropy analysis (N=3,443; 48% males), consistent with the known associations of WMH and VRF (Power et al. 2017; Hannawi et al. 2018; Wassenaar et al.

2019) with the WM integrity, the A2 subgroup showed significant microstructural WM integrity disruption relative to A0 for 41 tracts, with the most prominent disruption observed in posterior thalamic radiation, corona radiata, superior fronto-occipital and longitudinal fasciculus, and anterior limb of the internal capsule (Figure 2B).

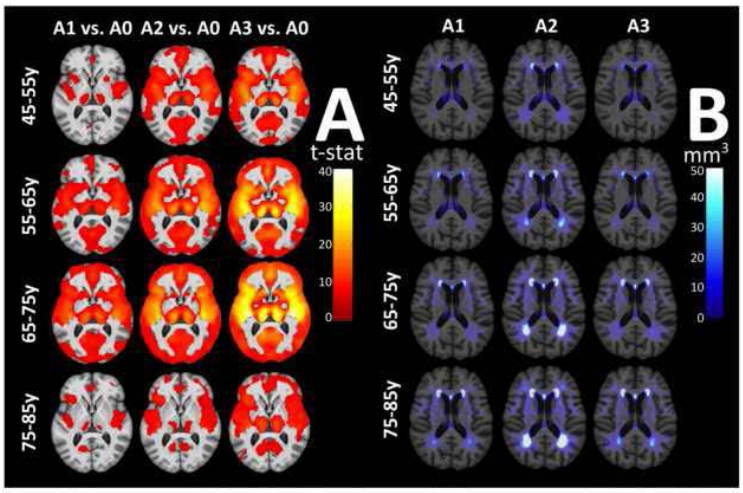

Figure 1: Neuroanatomical profile of the subgroups. A) Grey matter atrophy for the Smile-GAN subgroups (A1-3) compared to the reference A0 group. Red (white) colors correspond to regions with low (high) atrophy. B) Average white matter hyperintensity (WMH) maps for the Smile-GAN subgroups. Blue (white) colors represent regions with low (high) WMH load.

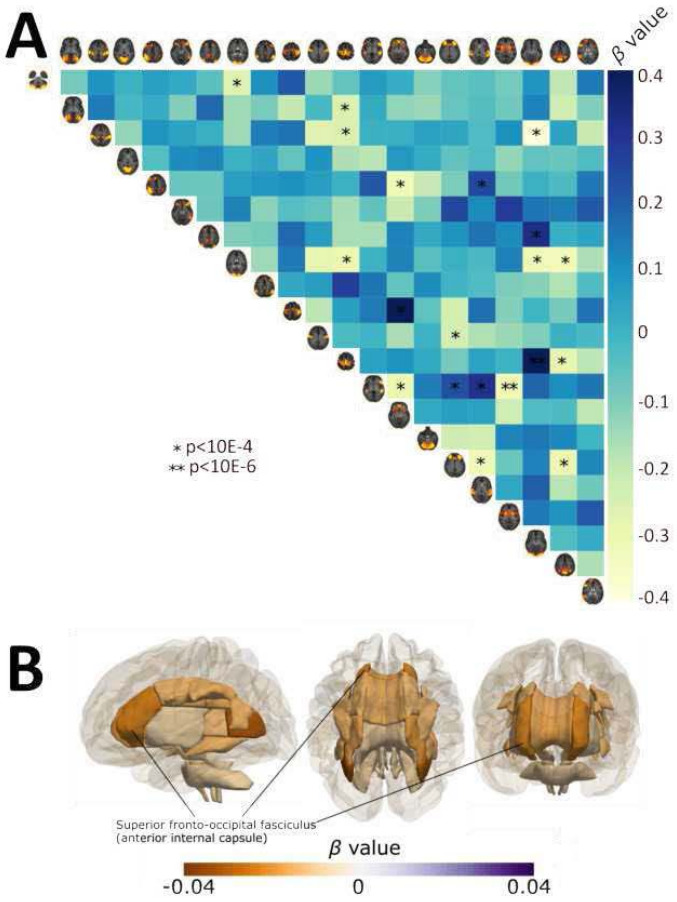

Figure 2: Functional connectivity and microstructural integrity associations of the subgroups. A) Regression coefficients for internetwork connectivity for the A3 subgroup relative to the reference group A0. Bonferroni correction for multiple comparisons adjusted the significance level at 0.05/210. B) Regression coefficients for fractional anisotropy for the A2 vs. A0 group. Bonferroni correction for multiple comparisons adjusted the significance level at 0.05/48.

Conclusions: The neuroanatomical heterogeneity of brain aging was modeled with subgroups designated by regional atrophy and WMH load in a multi-cohort cognitively unimpaired population. The subgroup characterized by elevated WMH burden and presence of VRF was associated with severely disrupted white matter integrity, while the subgroup with widespread atrophy underwent multiple changes in rsfMRI internetwork connectivity.

References

1. R. F. Betzel, L. Byrge, Y. He, J. Goñi, X.-N. Zuo, and O. Sporns, 2014. "Changes in Structural and Functional Connectivity among Resting-State Networks across the Human Lifespan." NeuroImage 102 Pt 2 (November): 345–57.
2. C. Grady, S. Sarraf, C. Saverino, and K. Campbell, 2016. "Age Differences in the Functional Interactions among the Default, Frontoparietal Control, and Dorsal Attention Networks." Neurobiology of Aging 41 (May): 159–72.
3. M. Habes et al., 2021. "The Brain Chart of Aging : Machine-Learning Analytics Reveals Links between Brain Aging, White Matter Disease, Amyloid Burden, and Cognition in the ISTAGING Consortium of 10,216 Harmonized MR Scans." Alzheimer's and Dementia: The Journal of the Alzheimer's Association 17 (1): 89–102.
4. Y. Hannawi et al., 2018. "Hypertension Is Associated with White Matter Disruption in Apparently Healthy Middle-Aged Individuals." American Journal of Neuroradiology 39 (12): 2243-2248.
5. C.-C. Huang et al., 2015. "Age-Related Changes in Resting-State Networks of a Large Sample Size of Healthy Elderly." CNS Neuroscience & Therapeutics 21 (10): 817–25.
6. K. L. Miller et al., 2016. "Multimodal Population Brain Imaging in the UK Biobank Prospective Epidemiological Study." Nature Neuroscience 19 (11): 1523–36.
7. K. Onoda, M. Ishihara, and S. Yamaguchi, 2012. "Decreased Functional Connectivity by Aging Is Associated with Cognitive Decline." Journal of Cognitive Neuroscience 24 (11): 2186–98.
8. M. C. Power et al., 2017. "Midlife and Late-Life Vascular Risk Factors and White Matter Microstructural Integrity: The Atherosclerosis Risk in Communities Neurocognitive Study." Journal of the American Heart Association 6 (5).
9. T. M. Wassenaar, K. Yaffe, Y. D. van der Werf, and C. E. Sexton, 2019. "Associations between Modifiable Risk Factors and White Matter of the Aging Brain: Insights from Diffusion Tensor Imaging Studies." Neurobiology of Aging 80: 56–70.
10. Z. Yang et al., 2021. "A Deep Learning Framework Identifies Dimensional Representations of Alzheimer's Disease from Brain Structure." Nature Communications 12 (1): 7065.

Poster No 1182

Habenula functional connectivity predicts individual sleep in healthy adults: A 5.0 T fMRI study

Lei Gao[1]

[1]Wuhan University, Wuhan, Hubei

Introduction: Sleep is an evolutionarily conserved behavior in animals and humans, which plays crucial role in strength recovery, memory consolidation, synaptic homeostasis, and waste clearance from the nervous system.(Verweij et al., 2014) Brain connectivity encoding individual sleep regulation may be rooted in small, evolutionally conservative nuclei, for example, the habenula (Hb).(Namboodiri et al., 2016) (Killgore, 2013)The habenula (Hb) is a phylogenetically brain region in a small structure with a volume of 31-36 mm3 and its accurate outlining has been a challenge on conventional functional imaging. (Aizawa et al., 2013) Despite in small size, the habenula acts as a critical neuroanatomical hub that regulates behavioral responses to pain, stress, anxiety, reward and sleep. (Boulos et al., 2017)It has been proven that intersubject variability in sleep predicts resting fMRI functional connectivity.(Li et al., 2020) Herein, we investigate the potential role of Hb in sleeprelated attention and memory loss.

Methods: 2.1 Participants The research comprised 267 healthy volunteers without DSM-V axis 1 illnesses. Sleep and water intake during the night before the MRI were self-reported. 2.2 MRI data MRI data were collected at Zhongnan Hospital of Wuhan University utilizing a 5.0 T MRI (uMR Jupiter, UIH, China) included: (1) 3D T1 (slice thickness 0.7 mm, 250 sagittal slices); (2) field map; (3) resting-state BOLD (TR = 1.6 s, multiband factor = 5, slice thickness 1.6 mm, no gap, 85 axial slices, 300 functional volumes); (4) DTI data (99 axial slices, 1.05 mm slice thickness, b values = 0, 1020, and 2025 s/mm2) in 32 directions. 2.3 Self-reported questionnaire Before the MRI scan, participants completed an online questionnaire about their sleep hours previous night, the average sleep time in the preceding three months, and their 24-hour alcohol, tea, and coffee use. Two blinded neurologists performed neurobehavioral examinations. 2.4 Habenula segmentation The Hb can be divided into lateral (LHb) and medial (MHb) parts. Using the 5T MRI and various scanning sequences, including T1-3D (0.4 mm*0.5 mm*0.5mm), T2-3D, 3D T2-FLAIR, and MTC, particularly, the MTC sequences are sensitive to neuromelanin and suitable for the outlying of the boundaries. Two senior neuroradiologists segmented the Hb from LHb and MHb. 2.5 Hb functional connectivity Hb functional connectivity was performed using the standard processing steps in the CONN toolbox (Ver 22a; https://www.nitrc.org/projects/conn). 2.6 Hb structural connectivity Hb structural connectivity was obtained using DSI Studio. 2.7 Metanalytical mapping and functional decoding of the Hb To gain a deeper understanding of the coupling network systems and functional roles associated with the identified clusters, we utilized the NeuroSynth.

Results: We have identified that the lateral and medial portions of the Hb are structurally connected to the insula and ventral prefrontal cortices. Functionally, the lateral and medial portions of the Hb are anticorrelated to the visual and salience networks. In the association analysis with individual sleep amounts, we found that average sleep amount rather than last night's sleep time predicted the anticorrelation between the visual and salience networks. Further lifespan trajectory analysis revealed that these anticorrelations are age-dependent.

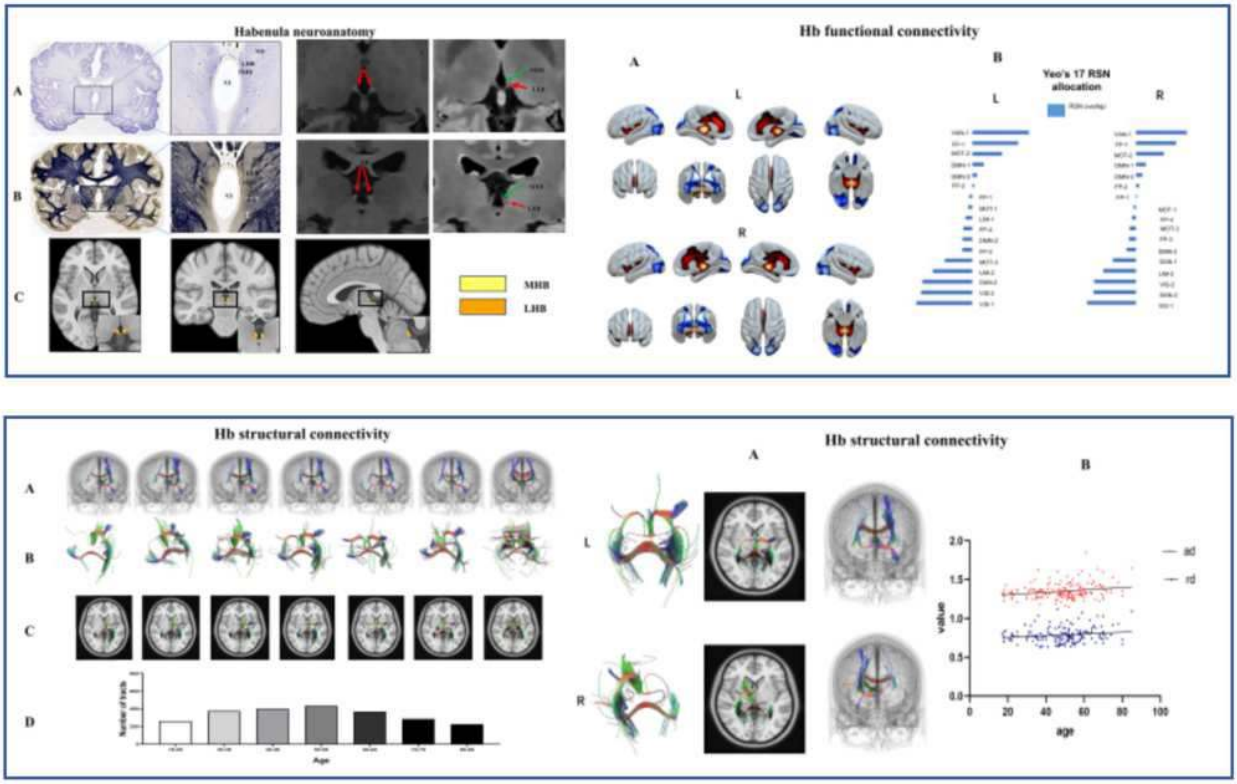

Conclusions: This high-resolution functional and structural imaging of the Hb and its association with individual sleep suggest the critical role of the Hb in the regulation of cognitive and emotional processes. Our work is the first to link the habenula to sleep in a high-resolution, large-sample population of healthy people with a lifespan trajectory. It reveals the brain underpinnings of sleep regulation and provides insight into associated sleep problems.

References

1. Aizawa, H., Cui, W., Tanaka, K., Okamoto, H., 2013. Hyperactivation of the habenula as a link between depression and sleep disturbance. Frontiers in Human Neuroscience 7, 826.
2. Boulos, L.J., Darcq, E., Kieffer, B.L., 2017. Translating the HabenulaFrom Rodents to Humans. BIOLOGICAL PSYCHIATRY 81, 296-305.
3. Killgore, W.D.S., 2013. Self-Reported Sleep Correlates with Prefrontal-Amygdala Functional Connectivity and Emotional Functioning. SLEEP 36, 1597-1608. Li, C., Fronczek Poncelet, J.,
4. Lange, D., Hennecke, E., Kroll, T., Matusch, A., Aeschbach, D., Bauer, A., Elmenhorst, E.M., Elmenhorst, D., 2020. Impact of acute sleep deprivation on dynamic functional connectivity states. HUMAN BRAIN MAPPING 41, 994-1005. Namboodiri,
5. V.M., Rodriguez-Romaguera, J., Stuber, G.D., 2016. The habenula. CURRENT BIOLOGY 26, R873-R877. Strotmann, B.,
6. Heidemann, R.M., Anwander, A., Weiss, M., Trampel, R., Villringer, A., Turner, R., 2014. High-resolution MRI and diffusionweighted imaging of the human habenula at 7 tesla. JOURNAL OF MAGNETIC RESONANCE IMAGING 39, 1018-1026.
7. Verweij, I.M., Romeijn, N., Smit, D.J., Piantoni, G., Van Someren, E.J., van der Werf, Y.D., 2014. Sleep deprivation leads to a loss of functional connectivity in frontal brain regions. BMC NEUROSCIENCE 15, 88.

Poster No 1183

Distinctive Brain Aging Patterns and Risk Factors in Middle- to Old-aged Men and Women

aram cho[1], Maithreyee Devi[2], Song E Kim[3], Hyang Woon Lee[3]

[1]Ewha womans university, Seoul, seoul, [2]EWHA Womans University Mokdong Hospital, 1071, Anyangcheon-ro, Yangcheon-gu, Seoul, [3]Ewha Womans University, Seoul, Korea, Republic of

Introduction: There have been clear evidences that the trajectory of brain aging exhibits variations based on gender. However, distinct brain regions related to aging and their sex differences have not well-documented yet. Moreover, there

are discernible differences between sexes in the clinical risk factors influencing brain atrophy and/or cognitive decline by aging have not been understood so far. This study aims to underscore the impacts of modifiable risk factors in brain atrophy and cognitive impairment in middle-to-old-aged general population, with the emphasis on sex differences between men and women.

Methods: A total of 1,227 participants between the ages of 49 to 80 were enrolled in the Korean genome and epidemiology study (KoGES), which provided the data for this population-based cohort study. The comprehensive evaluator methods including biochemical, metabolic, psychiatric assessment as well as whole night polysomnography & T1-weighted magnetic resonance imaging (MRI). Sleep habits by sleep efficiency (%) scores and Beck's Depression Inventory (BDI) for depressive symptoms. Physical activity was evaluated using metabolic equivalent of task (METs) to assess intensity. Analysis of covariance (ANCOVA) was utilized to interaction effects, with the aim of discerning potential sex differences in the process of brain aging. In addition, mediation analyses were performed after adjusting demographic and clinical factors to find out the mediating effects of each risk factor in between age-associated cognitive decline in each sex.

Results: Risk factors in cognitive decline for females are physical activity, sleep deficiency, depression, and menopausal changes. The analysis of covariance (ANCOVA) demonstrated a reduction in central cingulate cortex volume in post-menopausal compared to menopausal and pre-menopausal groups. Additionally, simple mediation model highlighted, age had direct effects on executive function tests, with indirect path via Sleep efficiency and depressive symptoms (BDI) respectively. Similarly, physical activity, as a mediator showed significant indirect effects in age related gray matter volume changes. In males, the change in cognitive function according to aging does not differ by education level, while for female, the group of under middle school and graduate showed a steep decline in cognitive function in the age of 65 or older.

Conclusions: Our findings suggest risk factors for accelerated brain aging in female. More specifically females are more vulnerable to early brain aging attributable to factors such as physical activity, sleep deprivation, menopausal transition and psychological, education level influences. These changes highlight the significance of improving lifestyle choices and identifying factors for preserve brain health in each sex.

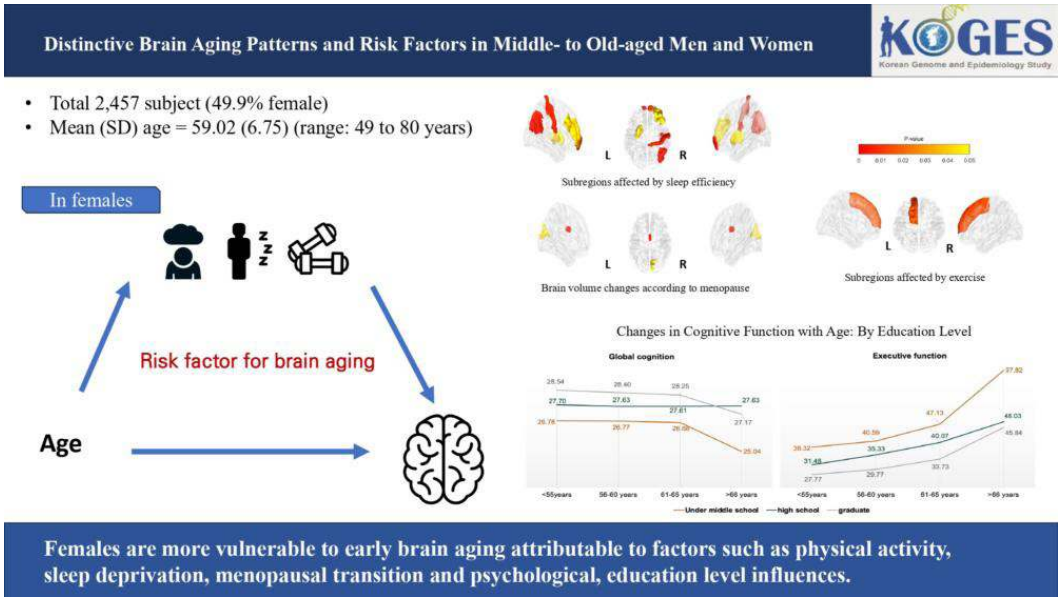

References

1. Anstey, K.J. (2021). 'Association of sex differences in dementia risk factors with sex differences in memory decline in a population-based cohort spanning 20–76 years'. Scientific Reports, vol. 11, pp. 7710
2. Armstrong N.M. (2019). 'Sex differences in brain aging and predictors of neurodegeneration in cognitively healthy older adult'. Neurobiol Aging. vol. 81, pp.146-156
3. Murphy, D.G. (1996). 'Sex differences in human brain morphometry and metabolism: an in vivo quantitative magnetic resonance imaging and positron emission tomography study on the effect of aging'. Archives of general psychiatry, Vol. 53, no. 7, pp. 585-594.

Poster No 1184

Quantifying spatially-specific impact of white matter hyperintensity on cortical atrophy in aging

Ami Tsuchida[1], Iana Astafeva[1], Victor Nozais[2], Philippe Boutinaud[2], Stéphanie Debette[1], Marc Joliot[1]

[1]Bordeaux University, Bordeaux, Gironde, [2]Fealinx, Lyon, Rhône

Introduction: Covert cerebral small vessel disease (cSVD) is common among neurologically asymptomatic older adults, and is a leading cause of stroke and dementia[1]. Among the established markers of cSVD, white matter hyperintensity (WMH) is one of the most frequently observed. Although less specific, brain atrophy is also considered as the recurring pathology in cSVD, and it has been hypothesized that it may occur as a secondary degeneration through the damaged white matter tracts[2]. However, the direct evidence for the effects of WMH on atrophy in the connected grey matter (GM) regions is lacking. Here we present a preliminary analysis from 800 UK Biobank subjects spanning the age range of 40 to 80 years, testing the regionally-specific effects of WMH on the GM volumes by deriving subject-specific disconnectome maps[3] from the WMH masks.

Methods: Two hundred UK Biobank subjects (50% female) were randomly selected from each decade of age-range from 40 to 80 years, based on the availability of both WMH lesion map and FreeSurfer-derived grey matter volumetric phenotypes computed by the UK Biobank neuroimaging pipeline[4]. Disconnectome maps were computed using the individual WMH mask as a lesion mask in QuickDisco tool in Functionnectome package[5]. The mean disconnectivity scores were extracted for each cortical region of DKT atlas (31 regions per hemisphere) using subject-specific FreeSurfer-derived parcellations (Fig. 1). For each region, we tested the impact of WMH-derived disconnectivity scores on the GM volume, in a linear model with GM volume as a dependent variable and age and disconnectivity score as main predictors, and sex and total intracranial volume as additional covariates. We also replaced the disconnectivity score with the overall WMH load to gauge whether disconnectivity derived from WMH rather than the overall load per se had stronger association with regional GM volume variations across subjects.

Results: Fig. 1 shows the age-related variations in the overall WMH volumes across the sampled population, and the examples of WMH and disconnectome maps derived from them in subjects with extensive or limited WMH. Fig. 2A shows the median disconnectivity scores across DKT atlas regions, indicating a higher disconnection in frontal region, likely as a result of WMH caps commonly found in anterior periventricular regions. The analysis of relative effects of age and WMH disconnectivity on regional GM volume revealed a wide-spread negative effect of age on cross-sectional GM volume variations (Fig. 2B). In contrast, the negative effects of WMH disconnection were limited to a few cortical regions that were somewhat right-lateralized after Bonferroni correction for the 62 regions tested (Fig. 2C). There were paradoxical positive effects on bilateral pericalcarine region, which may indicate erroneous over-segmentation of this cortical region in the proximity of posterior horn WMH. Importantly, repeating the same analysis by replacing the region-specific disconnectivity score with the global WMH load failed to show any significant impact of WMH on GM cortical volume after multiple comparison corrections.

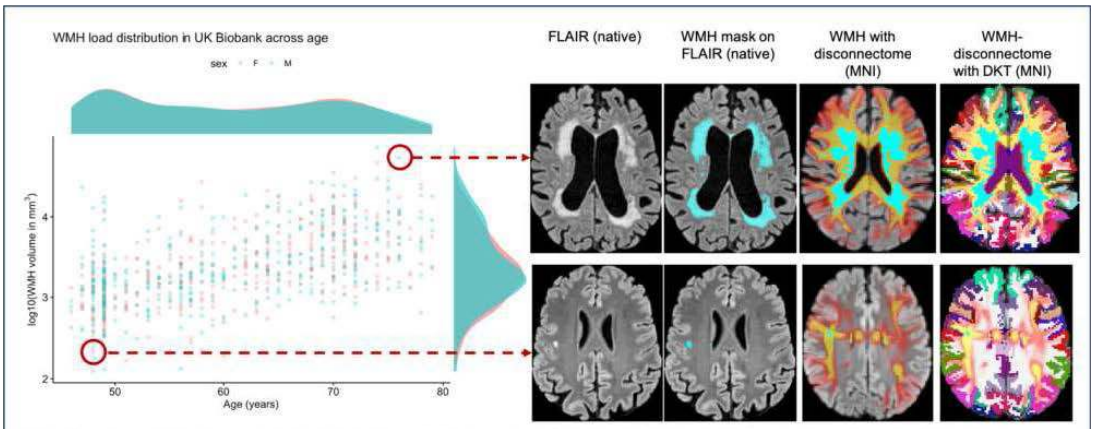

Figure 1. Age-related changes in the WMH load distributions in the 800 UK Biobank subjects and examples of WMH-derived disconnectivty scores from subjects at two extreme ends of WMH distribution.

The left panel shows the log-transformed WMH volume as a function of age in the 800 UK Biobank subjects spanning 40 to 80 years of age, together with distribution density plots (cyan for male, pink for female). The right panel shows the example FLAIR image, WMH mask, and disconnectivity map derived from the WMH mask from two subjects with either very high (top) or low (bottom) WMH load.

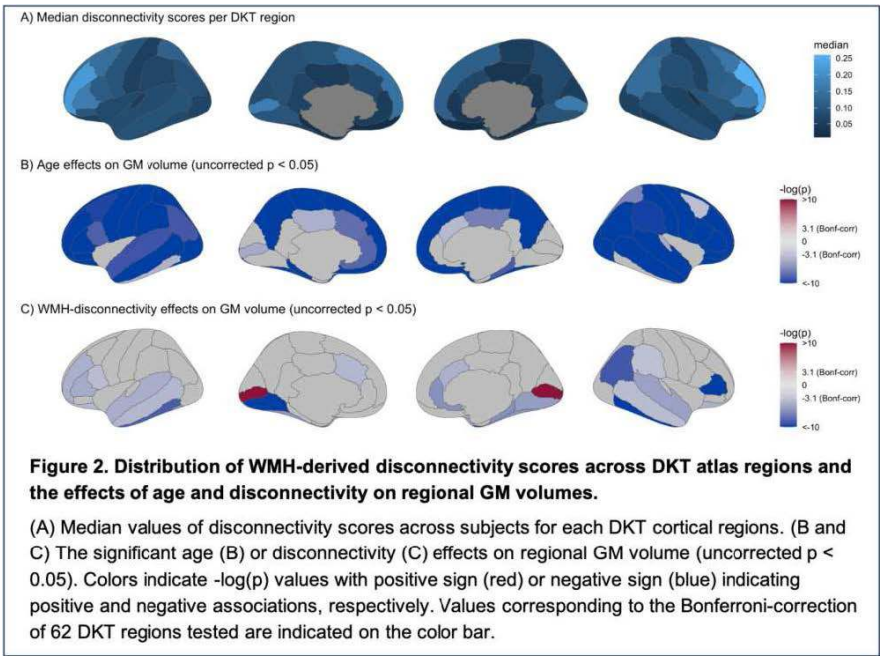

Figure 2. Distribution of WMH-derived disconnectivity scores across DKT atlas regions and the effects of age and disconnectivity on regional GM volumes.

(A) Median values of disconnectivity scores across subjects for each DKT cortical regions. (B and C) The significant age (B) or disconnectivity (C) effects on regional GM volume (uncorrected $p < 0.05$). Colors indicate -log(p) values with positive sign (red) or negative sign (blue) indicating positive and negative associations, respectively. Values corresponding to the Bonferroni-correction of 62 DKT regions tested are indicated on the color bar.

Conclusions: Our findings revealed a relatively circumscribed association of WMH-derived disconnectivity scores to the individual variability in the regional GM volumes and wide-spread age effects, suggesting that age-related GM atrophy may be largely independent of WMH-derived disconnection. Nonetheless, disconnectivity scores showed more robust associations with regional GM volumes than global WMH load. Future work is needed to clarify relative contributions of cortical atrophy and WMH disconnectivity to the age-related cognitive decline.

References

1. Debette, S. et al. (2019), 'Clinical Significance of Magnetic Resonance Imaging Markers of Vascular Brain Injury: A Systematic Review and Meta-analysis', JAMA Neurol, vol. 76, pp. 81–94
2. Duering, M. et al. (2023)., 'Neuroimaging standards for research into small vessel disease-advances since 2013', Lancet Neurol, vol. 22, pp. 602–618
3. Foulon, C. et al. (2018), 'Advanced lesion symptom mapping analyses and implementation as BCBtoolkit', Gigascience, vol. 7, pp. 1–17
4. Alfaro-Almagro, F. et al. (2018), 'Image processing and Quality Control for the first 10,000 brain imaging datasets from UK Biobank', Neuroimage, vol. 166, pp. 400–424
5. Nozais, V. et al. (2023), 'Atlasing white matter and grey matter joint contributions to resting-state networks in the human brain', Commun. Biol. vol. 6, pp. 726

Poster No 1185

Sex Differences in the Impact of Obstructive Sleep Apnea on Age-Related Brain Aging: A KoGES Study

Maithreyee Devi[1], aram cho[2], Song E Kim[3], Regina EY Kim[4], Soriul Soriul Kim[4], Seung Ku Lee[4], Hyeon Jin Kim[5], Chol Shin[4], Hyang Woon Lee[6]

[1]Computational Medicine, System Health Science & Engineering Program, Ewha Womans University, Seoul, South Korea, [2]Nursing Science, System Health Science & Engineering Program, Ewha womans university, Seoul, South Korea, [3]Departments of Neurology, College of Medicine, Ewha Womans University, Seoul, South Korea, [4]Institute for Human Genomic Study, College of Medicine, Korea University, Ansan, South Korea, [5]Department of Neurology, College of Medicine, Korea University, Ansan, South Korea, [6]Departments of Neurology,Computational Medicine, College of Medicine, Ewha Womans University, Seoul, South Korea

Introduction: The intrinsic connection of obstructive sleep apnea (OSA), a sleep-breathing disorder with accelerated cognitive aging, has been the center of interest in recent studies. Individuals with obstructive sleep apnea are found to exhibit structural and functional brain alterations. Furthermore, the pattern of brain aging differs by sex and/or gender. This study targets to investigate sex/gender-specific changes in the complex relationships between age and cognitive function, underscoring the impact of the severity of OSA on brain atrophy and cognitive impairment among middle- to elderly-aged healthy individuals.

Methods: In this population-based cohort study, data were provided by the Korean Genome and Epidemiology Study (KoGES), where approximately 2,457 individuals (50.1% men) aged between 49 and 80 years were participated. For the study purpose,

participants were categorized into four age groups: ~55 years (36.5%), 56-60 years (31.9%), 61-65 years (13.6%), and ~66 years (18.1%). The comprehensive evaluation methods include whole-night polysomnography, neuropsychological assessment, and T1-weighted magnetic resonance imaging (MRI). OSA was assessed by apnea-hypopnea index (AHI) scores. An analysis of covariance (ANCOVA) interaction effects was done to determine sex differences in the severity of OSA in various age ranges. In addition, multiple mediation analyses were performed after adjusting demographic and clinical factors to find out the mediating effects of OSA in between age-associated cognitive declines.

Results: Analysis of covariance (ANCOVA) showed a significant interaction effect between the sex* age subgroups on AHI (F:4.56, p:0.003), suggesting the association between sex and AHI scores is influenced by age. Notably, scores of AHI increase were generally higher for men in most age groups, showing a tendency for accelerated deterioration in older adulthood. Additionally, in men, multiple mediation results revealed the significance of AHI alongside total gray matter volume, particularly involving cortical areas in the parietal and cerebrum, as mediators between age and cognitive scores, including verbal fluency, mini-mental state examination (MMSE), and trail-making test, respectively. whereas there is no significance for women.

Conclusions: Our findings suggest the sex-specific effects of obstructive sleep apnea on accelerated brain aging, as demonstrated by MRI volumetry across diverse age groups. Notably, this study highlights the complex relationships among OSA severity on brain aging and how these factors are influenced by age and sex. Men are more vulnerable to the detrimental effects of OSA related to early cognitive decline, affecting a wide range of brain areas, including the cortical gray matter. These findings highlight the significance of improving lifestyle choices to maintain optimal brain health, particularly in men, who tend to have greater rates of hazardous lifestyle habits and substantial cardiovascular co-morbidity. However, further investigation is warranted to unravel the underlying factors contributing to these sex-specific differences.

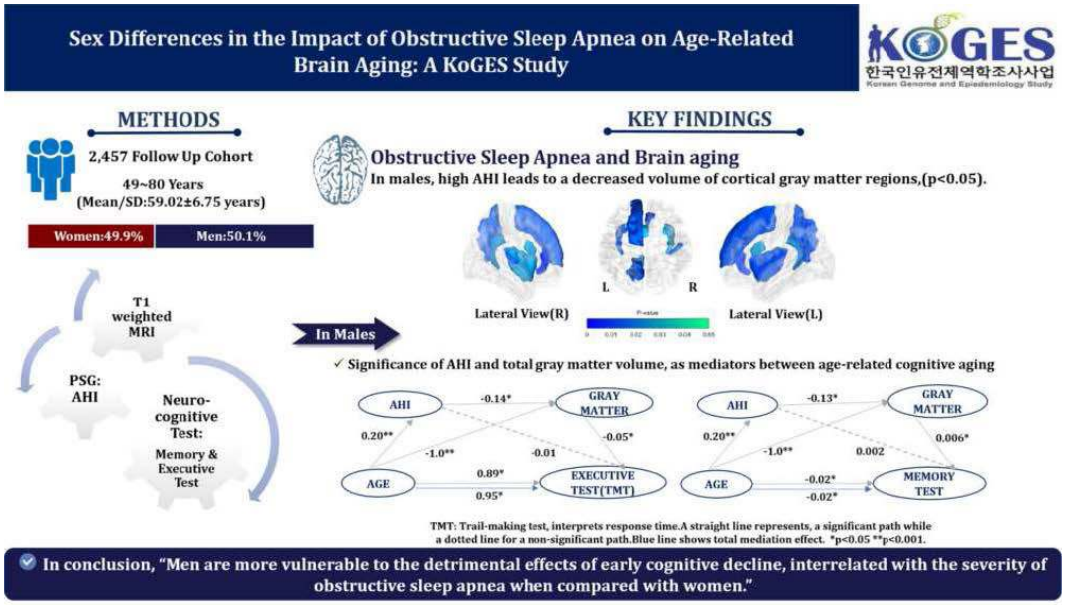

References

1. Armstrong NM, An Y, Beason-Held L, Doshi J, Erus G, Ferrucci L, Davatzikos C, Resnick SM. (2019), "Sex differences in brain aging and predictors of neurodegeneration in cognitively healthy older adults", Neurobiol Aging, vol.81, pp.146-156.
2. Gur RC, Mozley PD, Resnick SM, Gottlieb GL, Kohn M, Zimmerman R, Herman G, Atlas S, Grossman R, Berretta D. (1991), "Gender differences in age effect on brain atrophy measured by magnetic resonance imaging", Proc Natl Acad Sci, vol.88, no.7, pp.2845-9.
3. Macey PM, Henderson LA, Macey KE, Alger JR, Frysinger RC, Woo MA, Harper RK, Yan-Go FL, Harper RM. (2022), "Brain morphology associated with obstructive sleep apnea", Am J Respir Crit Care Med, vol.15, no.166(10), pp.1382-7.
4. O'Donoghue FJ, Briellmann RS, Rochford PD, Abbott DF, Pell GS, Chan CH, Tarquinio N, Jackson GD, Pierce RJ. (2005), "Cerebral structural changes in severe obstructive sleep apnea", Am J Respir Crit Care Med, vol.15, no.171(10), pp.1185-90.

Poster No 1186

Functional reorganization of the prefrontal cortex in aging

Ping Wang[1], Zi-Xuan Zhou[1], Peng Gao[2], Hai-Yan Hou[3], Jia-Xin Zhang[3], Hui-Jie Li[3], Xi-Nian Zuo[4]

[1]Beijing Normal University, Beijing, Beijing, [2]Taiyuan University of Technology, Taiyuan, Shanxi, [3]Institute of Psychology, Chinese Academy of Sciences, Beijing, Beijing, [4]Xi-Nian Zuo, Professor, Beijing Normal University, Beijing

Introduction: The posterior-to-anterior developmental trajectory of brain structure leads to posterior-to-anterior reorganization of brain function in aging (Grydeland et al., 2013), with the relative preserved prefrontal cortex compensating for decline in primary sensory cortex through increased functional activity (Davis et al., 2008). However, the prefrontal cortex itself undergoes differential subregional decline, with the rostral prefrontal cortex showing relative preservation throughout life (Bethlehem et al., 2022). We propose a posterior-to-anterior functional organization in the prefrontal cortex, with the preserved rostral prefrontal cortex compensating for decline in the dorsolateral prefrontal cortex, located in the middle and posterior regions and considered as the apex of the prefrontal cortex's functional hierarchy (Badre et al., 2018). To test this hypothesis, a gamified working memory training was conducted with older adults, targeting the dorsolateral prefrontal cortex, while the rostral prefrontal cortex is considered lack of involvement in working memory (Mansouri et al. 2017). If no functional reorganization occurs, the training would affect the dorsolateral prefrontal cortex and related brain regions, leaving the rostral prefrontal cortex unaffected. Conversely, if a posterior-to-anterior shift exists, the training would not only affect the dorsolateral prefrontal cortex but may also induce changes in the rostral prefrontal cortex.

Methods: We developed a gamified working memory intervention based on the classic n-back task and created an active control game with similar features. Seventy-six older adults were randomly assigned to either the working memory intervention group (n-back game) or the active control group (0-back control game). All participants completed 12 1-hour training sessions over 6 weeks. Structural magnetic resonance imaging (MRI) and resting-state functional MRI scans were conducted before and after the intervention. Cognitive assessments targeting working memory and other cognitive domains, such as processing speed, attention, visuospatial ability, episodic memory, and inhibition, were administered at pretest, posttest, and six months after the intervention. Changes in structure (cortical thickness, surface area and volume) and function (surface-based regional homogeneity and functional connectivity) of each subregion in prefrontal cortex, as well as changes in cognitive functions induced by the training was examined. The multivariate pattern classification analysis was conducted to test the consistency and discriminative power of changes induced by the intervention in both the structure and function of the prefrontal cortex, as well as working memory performance.

Results: The results indicated that the working memory, inhibition, visuospatial processing, and episodic memory of older adults were all significantly improved after the intervention. The MRI analyses revealed thickening of the left frontal pole (part of rostral prefrontal cortex) in the prefrontal cortex and weakened regional homogeneity and functional connectivity with the left inferior temporal gyrus. Further statistical learning analytics showed that these neurocognitive changes might be the neurobiological mechanisms underlying the working memory improvements due to the current gamified digital working memory intervention.

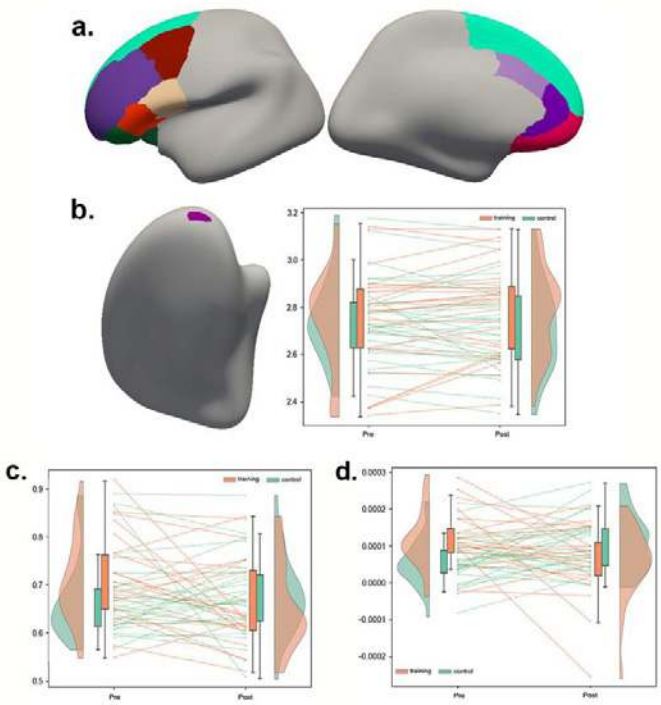

Figure 1. Parcellations of the prefrontal cortex from the Desikan-Killiany cortical atlas (a), significant cortical thickness changes in the left frontal pole (b), 2dReho changes in the left frontal pole (c), and functional connectivity changes between the left frontal pole and the left inferior temporal gyrus (d)

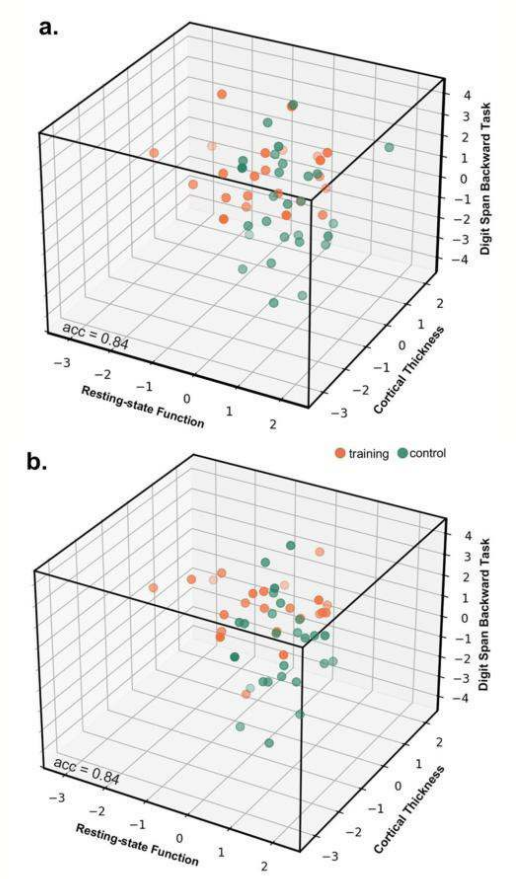

Figure 2. Multivariate pattern classification according to the post-pre structure changes and functional changes in the left frontal pole, as well as post-pre (a) or follow-up-pre (b) performance changes of working memory

Conclusions: The training-induced structural and functional changes observed in the frontal pole, rather than the typically assumed dorsolateral prefrontal cortex, suggest that the frontal pole may play a crucial role in working memory in aging. This finding implies a functional reorganization of the prefrontal cortex with increasing age. The current study provides preliminary evidence for a potential posterior-to-anterior functional shift within the prefrontal cortex, highlighting the importance of the rostral prefrontal cortex as a critical biomarker for maintaining normal cognitive function in older adults.

References

1. Badre, D. (2018). Frontal cortex and the hierarchical control of behavior. Trends in Cognitive Sciences, vol. 22, no. 2, pp. 170–188.
2. Bethlehem, R. A. I. (2022), Brain charts for the human lifespan, Nature, vol. 604, no. 7906, pp. 525–533.
3. Davis, S. W. (2008), Que PASA? The posterior-anterior shift in aging, Cerebral Cortex, vol. 18, no. 5, pp. 1201–1209.
4. Grydeland, H. (2013), Brain development and aging: overlapping and unique patterns of change, NeuroImage, vol. 68, pp. 63–74.
5. Mansouri, F. A. (2017). Managing competing goals - a key role for the frontopolar cortex. Nature Reviews Neuroscience, vol. 18, no. 11, pp. 645–657.

Poster No 1187

Brain age based signatures as a tool for differentiating neurological conditions

Rafael Navarro-González[1], James Cole[2,3], Rodrigo De Luis-García[1], Santiago Aja-Fernández[1]

[1]Laboratorio de Procesado de Imagen, UVA, Valladolid, España, [2]Centre for Medical Image Computing, UCL, London, United Kingdom, [3]Dementia Research Centre, UCL, London, United Kingdom

Introduction: Brain age, a measurment derived aplying machine learning to brain MRI images for age prediction, has demonstrated being valuable in characterizing diseases like Alzheimer's and multiple sclerosis[2-3]. However, it is a reductionist approach which simplifies all the information of an image into one number, the predicted age. Further information about different diseases could be captured if the image is transformed into a brain age signature which could be later used as the input of a classification task among different diseases. In this work, we study this approach by training a brain age model

on the output of the brain volume segmentation of a manifold of T1w MRI images from healthy adults. The selected features for the brain age task were then used for a classification task between healthy adults, chronic schizophrenic and chronic migraine patients.

Methods: A total of 2850 T1w MRI images from different free access datasets and 191 local data acquisitions have been used for the brain age task, while 65 schizophrenic patients, 74 chronic migraine patients, from our own institution and 94 healthy individuals, subset of the healthy patients selected for the study, ages between 18 to 60, were selected for the classification task (See Table 1). FastSurfer[4], a deep learning whole brain segmentation method trained on the Desikan-Killiany atlas[5], was utilized to segment the dataset acquisitions and feature extraction. A total of 624 morphological features were calculated over the segmented regions of interest (ROIs) encompassing area, volume, curvature and thickness of cortical and subcortical brain ROIs. The dataset was split into training and testing (80/20 ratio). Training involved a three-fold cross-validation with a Multilayer perceptron (MLP) regressor. In each fold, outliers (defined as 2.5 and 97.5 quantile values) were removed, data was normalized (range -1, 1) and feature selection was performed. Three feature sets (25, 50, and 100 features) were created using a two-step method: initial filtering for the top 20% of features by mutual information with age, followed by refinement with a forward feature selection algorithm using Gaussian mixture models. The same process was used for an MLP classifier. Hyperparameters for both MLPs were determined during validation, and models were retrained on the entire training cohort and tested on test data. Brain age prediction was evaluated using mean absolute error (MAE), Pearson's correlation (r), and R-squared (R^2), while classification performance was measured by Precision, Recall, Area Under the Curve (AUC), and Matthew's Correlation Coefficient (MCC). Following the same scheme, another MLP was trained in selecting features with the disease label as the target. A comparison between the brain age-based classification and this procedure was performed.

Dataset	n	Age (years, mean)	Age σ	Age range	Sex (M/F)	Scanner Bo
CoRR	894	*25.03*	*9.23*	18-60	440/454	3.0T
SALD	383	*39.19*	*14.36*	19-60	140/243	3.0T
CamCan	380	*41.32*	*11.33*	18-60	187/193	3.0T
IXI	374	*39.69*	*11.69*	19.98-59.90	178/196	1.5T and 3.0T
OASIS-1	211	*31.82*	*13.42*	18-60	89/122	1.5T
Private Dataset	191	*32.74*	*11.48*	18-60	83/108	3.0T
NeuroCog	182	*24.26*	*8.33*	18-60	78/104	3.0T
DLBS	170	*39.27*	*11.67*	20.57-59.96	60/110	3.0T
NKI	138	*35.50*	*12.07*	18-60	51/87	3.0T
AgeRisk	118	*35.94*	*12.29*	18.23-58-58	55/63	3.0T
Regression dataset	**3041**	**33.26**	**13.18**	**18-60**	**1680/1361**	**1.5T and 3.0T**
Healthy Patients	94	33.23	13.66	18-60	43/51	3.0T
Chronic Schizophrenic	65	38.27	9.94	19-56	28/37	3.0T
Chronic Migraine	74	37.84	9.70	18-60	68/6	3.0T
Classification dataset	**233**	**36.10**	**11.72**	**18-60**	**86/147**	**3.0T**

Table 1: Datasets used in this work. All datasets are available online, except for the private dataset and the chronic migraine and chronic schizophrenic group Datasets have been acquired from different scanners and vendors, with different Bo field and acquisition parameters.

Results: The models trained on 100 features were selected since they showed the best performance during validation. Validation results for the brain age task presented an MAE, r and R^2 of 5.15 years 0.85, 0.70, respectively using 100 features, while test results were 5.08 years, 0.87 and 0.73 (See figure 2C). Validation for the classification task using the 100 brain age signature showed the next results:metrics among the 0.6-0.7 level Prec = 0.70, recall = 0.67, AUC = 0.83, MCC = 0.51 (see figure 2D). While on the test group results were, Prec = 0.63, recall = 0.63, AUC = 0.78, MCC = 0.45. Furthermore, these results

are similar, although slightly inferior, to a classification task based on features selected on the disease labels (Test results 100 features: Prec = 0.64, recall = 0.66, AUC = 0.81, MCC = 0.49).

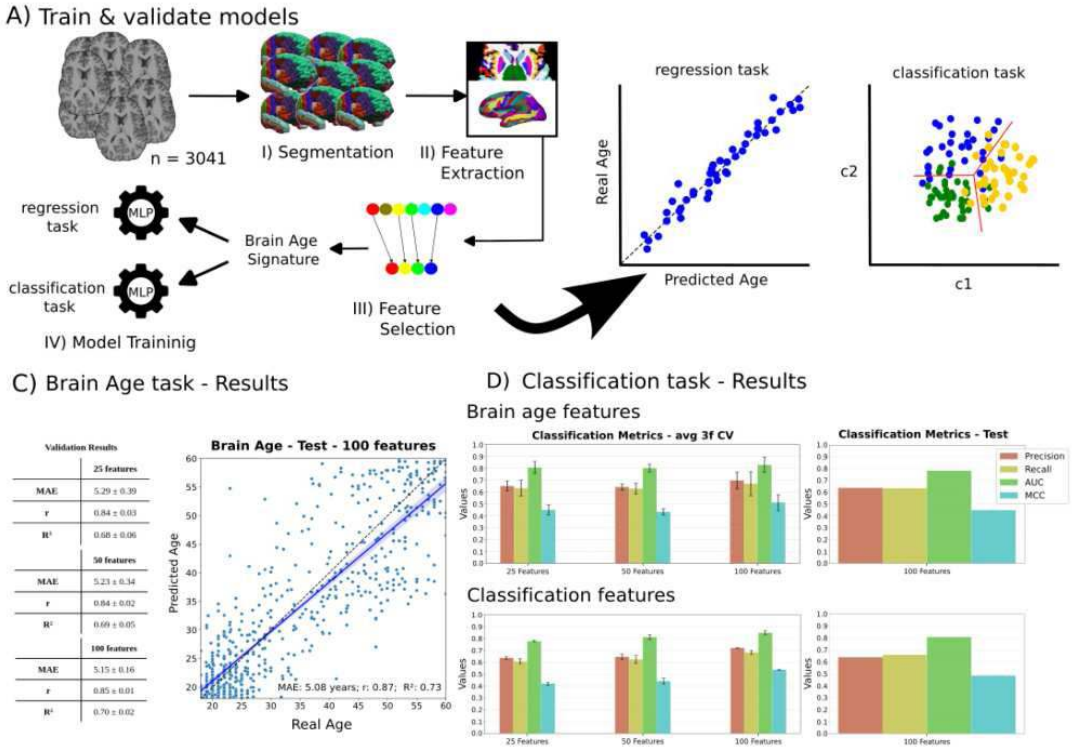

Conclusions: Features selected for brain age estimation effectively classify conditions such as schizophrenia and chronic migraine. These brain age signatures accurately predict brain age and capture disease degeneration patterns. Future work could apply these methods in broader clinical settings, enhancing understanding of neurodegenerative diseases.

References

1. Franke, K. (2010), "Estimating the age of healthy subjects from T1-weighted MRI scans using kernel methods: exploring the influence of various parameters." Neuroimage 50.3 883-892.
2. Beheshti, I. (2020) "T1-weighted MRI-driven brain age estimation in Alzheimer's disease and Parkinson's disease." Aging and disease 11.3 618
3. Cole, J. H. (2020), "Longitudinal assessment of multiple sclerosis with the brain-age paradigm." Annals of neurology 88.1 93-105.
4. Henschel, L. (2020), "Fastsurfer-a fast and accurate deep learning based neuroimaging pipeline." NeuroImage 219 117012.
5. Klein, A. (2012), "101 labeled brain images and a consistent human cortical labeling protocol." Frontiers in neuroscience 6 171.
6. Maia, F. (2022), "Effective sample size, dimensionality, and generalization in covariate shift adaptation." Neural Computing and Applications 1-13.

Acknowledgements

This work was supported by Ministerio de Ciencia e Innovación of Spain with research grants PID2021-124407NB-I00, TED2021-130758B-I00 and PRE2019-089176.

Poster No 1188

Multimodal phenotyping of successful cognitive aging

Eoin Molloy[1,2], Niklas Behrenbruch[2], Svenja Schwarck[1,2], Beate Schumann-Werner[1,2], Berta Garcia-Garcia[2,1], Niklas Vockert[2], Barbara Morgado[3], Michael Rullman[4], Patrick Mueller[1,2], Anne Hochkeppler[1], Larissa Fischer[2], Kathrin Baldauf[2], Peter Schulze[2], Andrew Stephens[5], Marianne Patt[4], Andreas Schildan[4], Hermann Esselmann[5], Jens Wiltfang[6,7,8], Henryk Barthel[4], Osama Sabri[4], Michael Kreißl[1,2], Emrah Düzel[1,2], Anne Maass[2]

[1]Otto von Guericke University Magdeburg, Magdeburg, Germany, [2]German Center for Neurodegenerative Diseases, Magdeburg, Germany, [3]University Medical Center Göttingen, Göttingen, Germany, [4]University Hospital Leipzig, Leipzig, Germany, [5]Life Molecular Imaging, Berlin, Germany, [6]Department of Psychiatry and Psychotherapy, Medical University Göttingen, Göttingen, Germany, [7]German Center for Neurodegenerative Diseases, Göttingen, Germany, [8]University of Aveiro, Aveiro, Portugal

Introduction: While some memory decline in old age is “normal”, there is a small group of “SuperAgers” that maintain mnemonic performance in older age. While many approaches have attempted to study this, exactly how these individuals maintain performance is unclear, with key questions relating to how the brains of these older adults differ in terms of tau load and brain structure. Using a multimodal approach including neuroimaging, blood, and fitness markers, we aim to test which factors are related to successful cognitive aging.

Methods: A sample of 166 cognitively normal (based on age-, sex- and education-adjusted scores on the CERAD neuropsychological battery) older adults age ≥ 60 years were included in the current analyses. Participants were on average 71 years old (SD=7.6), 43% female and highly educated (152 years). The sample is part of an ongoing study (SFB1436 - Neural Resources of Cognition). For all participants, we determined Abeta42/40 ratio from blood plasma (assay: Lumipulse G Fujirebio). T1-weighted images (0.8×0.8×0.8 mm3; N=89) were segmented with FreeSurfer, focusing on the medial temporal lobe (MTL; composite of entorhinal, parahippocampal and fusiform), anterior cingulate cortex (ACC) and whole brain thickness. We also determined temporal lobe tau burden with 60-minutes dynamic 18F-PI-2620 tau PET imaging (n=53). We calculated distribution volume ratio (DVR) images using Multilinear Reference Tissue Model2, with the inferior cerebellum as reference region. Cardiovascular fitness (aerobic capacity) and muscular capacity (hand grip strength, appendicular skeletal muscle mass, and walking performance) were measured in 95 participants. Measures of state and trait anxiety were available in 160 individuals based on self-reports (State-Trait Anxiety Inventory). To assess differences in tau pathology, brain structure, fitness or mental health measures related to “SuperAging”, we grouped individuals age ≥ 79.5 years into SuperAgers (based on delayed verbal recall performance at or above average normative values of 50-60 years) versus typical agers. In addition, we calculated a cognitive age gap (CAG) based on the difference between cognition-predicted age and chronological age. We derived cognition-predicted age with partial least square regression using 16 scores of different memory tests in a larger cohort of 187 older individuals with available cognitive data (see Figure 2A). In multiple regression models, we then assessed how CAG is related to Abeta/tau, brain structure, fitness and metal health measures covarying for chronological age, sex and education.

Results: Our sample included 37 individuals aged ≥ 79.5 years, of whom 18 were SuperAgers and 19 typical agers. SuperAgers and typical agers did not differ in age, sex, years of education, fitness measures, mental health measures (anxiety) or Abeta42/40 plasma ratio (all p-values>0.1). However, in the small subgroup with available PET data, SuperAgers (N=6) had less temporal tau burden than typical agers (N=8; t(12)=-2.9, p=0.01; Figure 1). In addition, SuperAgers trended towards higher ACC thickness (t(20)=2.0, p=0.06) with no differences in the other regions of interest (all p>0.5). In the whole sample, including participants between 60 and 89 years of age, lower CAG (i.e. younger cognitive age) related to less anxiety, higher hand grip strength, and higher cortical thickness in the MTL as well as whole cortex (all p<0.05; Figure 2B). There were no significant associations between CAG and Abeta42/40 or temporal lobe tau (p>0.1).

Conclusions: These are the first results from our ongoing study and suggest that SuperAgers have less temporal lobe tau and may have increased thickness in the ACC. These results tentatively support outcomes from previous studies. Furthermore, younger cognitive age is linked to better mental and physical health as well as higher global cortical thickness independent of education.

Figure 1. Differences in Alzheimer‘s disease pathology markers and brain thickness between SuperAgers and Typical Agers

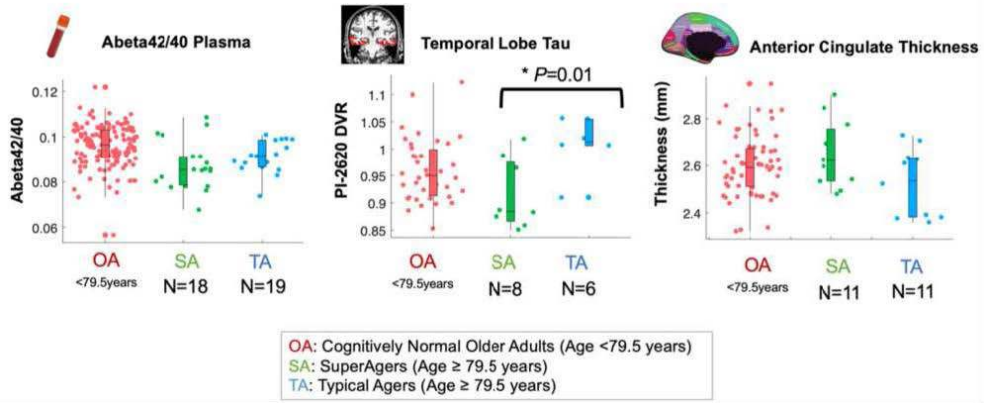

Figure 2

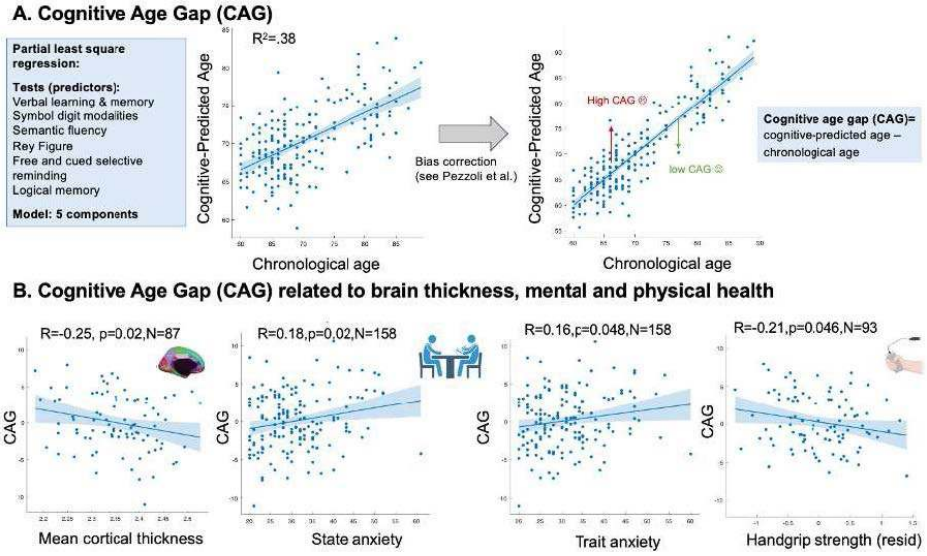

Poster No 1189

Are older adults meaner to others? Age differences in emotion-related social decision making

Hong-Zhou Xu[1], Xue-Rui Peng[1,2], Jing Yu[1,3]

[1]Faculty of Psychology, Southwest University, Chongqing, China, [2]Chair of Lifespan Developmental Neuroscience, Faculty of Psychology, Technische Universität Dresden, Dresden, Germany, [3]Key Laboratory of Mental Health, Institute of Psychology, Chinese Academy of Sciences, Beijing, China

Introduction: In social interaction, there are often differences in emotional processing between young and older adults, such us the perception of others' sadness (Löckenhoff, Costa Jr et al. 2008, Hayes, McLennan et al. 2020), which may affect emotion-related social decision making in older adults. With aging, brain functions related to social-emotional processing deteriorate in older adults (Dobrushina, Arina et al. 2020, Baez-Lugo, Deza-Araujo et al. 2023), and alterations in the function and structure of the medial prefrontal cortex are likely to influence their value representation in decision making (Samanez-Larkin and Knutson 2015). However, how these neural changes would affect emotion-related social decision making in older adults remains unresolved. Thus, a more comprehensive investigation is warranted to elucidate the nuanced connections between aging, others' emotions, and the neural bases of social decision making.

Methods: Thirty-one young adults (aged 18~24 years) and 32 older adults (aged 59~78 years) were recruited to perform a variation of the dictator game task in the fMRI scanner (Figure 1A). In this task, we used neutral and sad emotional fascial pictures to manipulate the emotional characteristics of the recipients and to investigate how others' emotions influence social decision making in young and old individuals from both behavioral and neurological perspectives. After the experiment, participants also completed a questionnaire outside of the scanner and were asked to self-report how much they had allocated. Repeated measures analysis of variance was used to analyze the behavioral data, while representational similarity analysis was used to analyze the fMRI data. Mediation analysis was also used to examine the mediating role of neural representation between age and allocation behavior. Given the significant differences in education between young and older adults, this was controlled for as a covariate in all analyses.

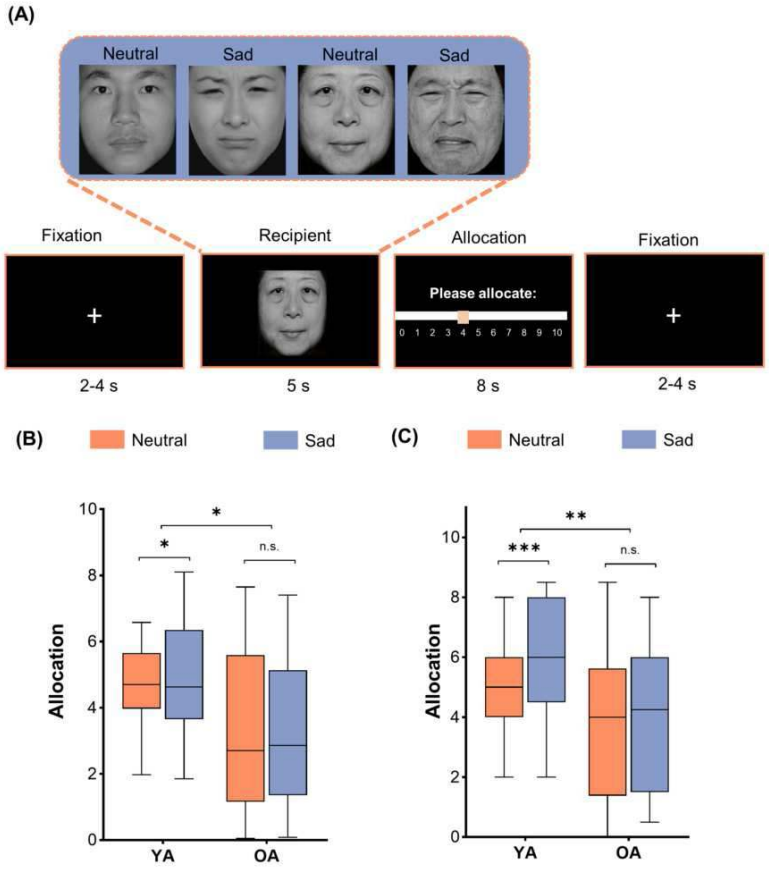

Figure 1. (A) The experimental procedure and types of recipients. (B) The behavioral results in scanner. (C) The behavioral results outside scanner.

Results: Behavioral results showed that young adults' allocation behavior was regulated by others' emotions, as young adults allocated more money to sad recipients than to neutral recipients, whereas there was no significant difference in older adults' allocation behavior (Figure 1B&1C). Neurally, the similarity scores of the neural representation in the right insula, the left dorsomedial prefrontal cortex (DMPFC), left caudate and left anterior cingulate cortex (ACC) were higher in young adults than in older adults, but the similarity scores in the right angular gyrus in older adults was higher than in young adults (Figure 2A). Besides, the neural representation between the right insula and the DMPFC played a significant mediating role between age and allocation behavior (Figure 2B).

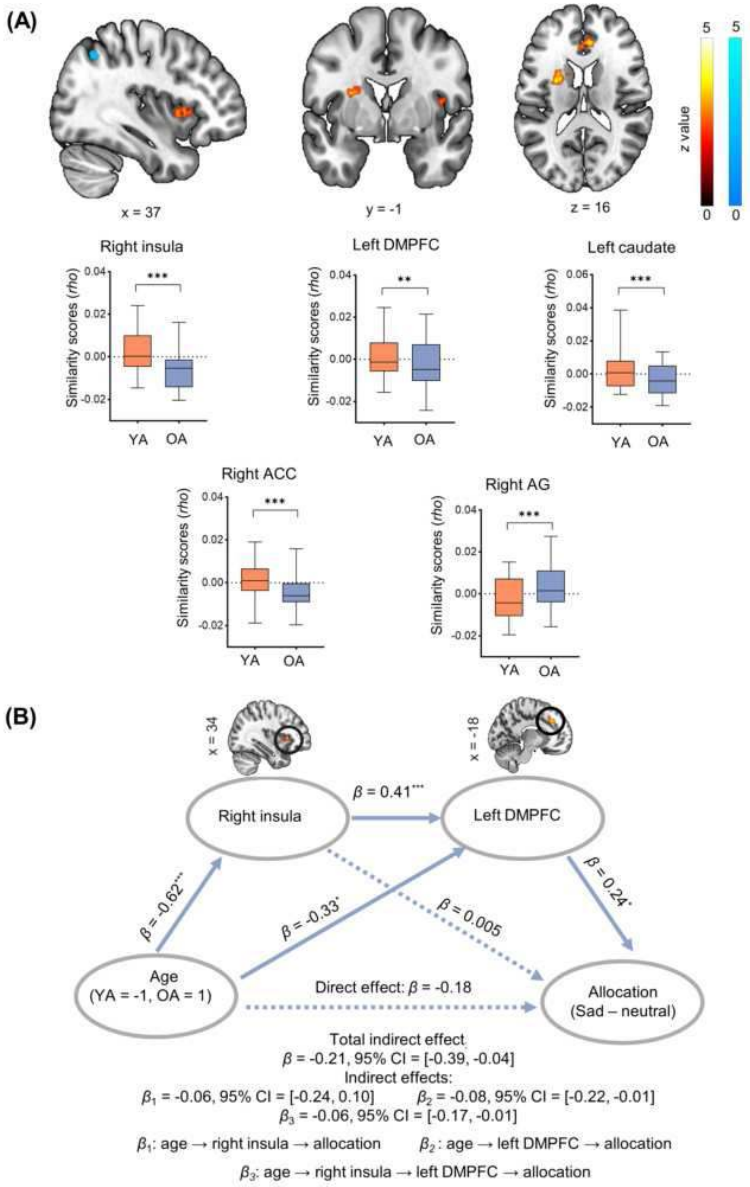

Figure 2. (A) Brain regions that differ in similarity scores between young and older adults. (B) The results of serial mediation analysis.

Conclusions: In conclusion, the present sturdy indicated that aging weakened the regulatory effect of others' emotions on social decision making from behavioral and neural perspectives. More importantly, the neural representation between the right insula and the left DMPFC played an important mediating role between age and allocation behavior. Considering that the insula and the DMPFC had important roles in processing social emotions and representing value for others, respectively (Rogers-Carter and Christianson 2019, Tomova, Saxe et al. 2020, Gangopadhyay, Chawla et al. 2021). One possible explanation is that the diminished moderating effect of others' emotions on older adults' decision making may be related to their reduced ability to process sadness and further affect their value representation for others, rather than because older adults are more miserly. Therefore, this study provided a potential neural pathway to explain age differences in emotion-related social decision making.

References

1. Baez-Lugo, S., Y. I. Deza-Araujo, C. Maradan, F. Collette, A. Lutz, N. L. Marchant, G. Chételat, P. Vuilleumier and O. Klimecki (2023). "Exposure to negative socio-emotional events induces sustained alteration of resting-state brain networks in older adults." Nature Aging 3(1): 105-120.
2. Dobrushina, O. R., G. A. Arina, L. A. Dobrynina, A. D. Suslina, P. O. Solodchik, A. V. Belopasova, M. V. Gubanova, A. N. Sergeeva, E. I. Kremneva and M. V. Krotenkova (2020). "The ability to understand emotions is associated with interoception-related insular activation and white matter integrity during aging." Psychophysiology 57(5): e13537.
3. Gangopadhyay, P., M. Chawla, O. Dal Monte and S. W. Chang (2021). "Prefrontal–amygdala circuits in social decision-making." Nature neuroscience 24(1): 5-18.

4. Hayes, G. S., S. N. McLennan, J. D. Henry, L. H. Phillips, G. Terrett, P. G. Rendell, R. M. Pelly and I. Labuschagne (2020). "Task characteristics influence facial emotion recognition age-effects: A meta-analytic review." Psychology and Aging 35(2): 295.
5. Löckenhoff, C. E., P. T. Costa Jr and R. D. Lane (2008). "Age differences in descriptions of emotional experiences in oneself and others." The Journals of Gerontology Series B: Psychological Sciences and Social Sciences 63(2): P92-P99.
6. Rogers-Carter, M. M. and J. P. Christianson (2019). "An insular view of the social decision-making network." Neuroscience & Biobehavioral Reviews 103: 119-132.
7. Samanez-Larkin, G. R. and B. Knutson (2015). "Decision making in the ageing brain: changes in affective and motivational circuits." Nature Reviews Neuroscience 16(5): 278-289.
8. Tomova, L., R. Saxe, M. Klöbl, R. Lanzenberger and C. Lamm (2020). "Acute stress alters neural patterns of value representation for others." Neuroimage 209: 116497.

Poster No 1190

Quantifying late-life alterations in brain white matter microstructural properties

Rowena Chin[1], Carrisa Cocuzza[1], Avram Holmes[2]

[1]Yale University, New Haven, CT, [2]Department of Psychiatry, Brain Health Institute, Rutgers University, Piscataway, NJ

Introduction: Understanding brain aging requires characterizing how and where brain changes vary with age. White matter (WM) is highly relevant to aging: late-life cognitive decline may partly be caused by microstructural deterioration of the brain's connective pathways through processes such as axonal demyelination that reduces information transfer efficiency across networks. Although evidence exists for cognitive dedifferentiation and in task-based fMRI work, there is a gap regarding the dedifferentiation hypothesis in whole brain neural aging, which suggests that interindividual differences in brain structure and function become increasingly related in older age. This stems from a common cause theory of neurodegeneration which posits a general system-wide breakdown of physiological function shifts overall levels of integrity across brain areas. Given these sources of variance are shared across brain regions, the resultant signature should be a stronger relationship among regionally distributed neuronal measures with age. Using a large-scale cohort study, we seek evidence for structural dedifferentiation from mid to old age, which could be an important marker of an aggregation of deleterious effects operating on distributed brain connections.

Methods: Diffusion metrics for structural white matter tracts were derived from the UK Biobank, a large-scale population-based cohort (N=29,862). We first undertook an analysis of age associations by conducting regression analyses independently across the 9 diffusion measures for 48 white matter tracts. Quantitative variables were z-transformed. The effect of age on the respective white matter diffusivity measures were estimated, covarying for height, weight, sex, age, age2, age*sex, combined gray/white matter volume, T1 inverse SNR, number of dMRI outlier slices, diastolic and systolic blood pressure, head position coordinates (X, Y, Z), and UKB imaging acquisition center. Following this, we examined de-differentiation of white matter microstructure, i.e., do white matter tracts tend to lose their individuality in older age? Cross-sectionally, we tested the de-differentiation hypothesis that microstructural properties of WM tracts across the brain become more similar at later ages across diffusivity measures.

Results: Older age was significantly associated with lower coherence of water diffusion (FA;$\beta \geq -0.436$), lower neurite density (ICVF;$\beta \geq -0.284$), lower tract complexity (OD;$\beta \geq -0.167$) and conversely, with a higher magnitude of water diffusion (MD;$\beta \leq 0.426$) and ISOVF ($\beta \leq 0.476$) across whole brain WM tracts (Figure 1). Across a range of varying diffusion measures, these results broadly indicate a decline in WM microstructure health with older age. We next present a series of six heatmaps (Figure 2) to illustrate the increasing relatedness of white matter tract microstructure across six age groups with approximately ~5 year intervals (age range: 45-75 years). Age groups created were respectively: 44.99–50.00 years (n=1091, M=49.1±1.05); 50.01–54.99 (n=4120, M=53.2 ±1.39); 55.00–60.00 (n=5174, M=58.1 ±1.41); 60.01–65.00 (n=6378, M=63.0±1.42); 65.01–70.00 (n=7182, M=68.0±1.41); 70.01–78.00 (n=6055, M=73.6±2.34). Qualitatively stronger associations among tracts with increasing age were evident for FA, MD, and NODDI measures such as ICVF, ISOVF and OD.

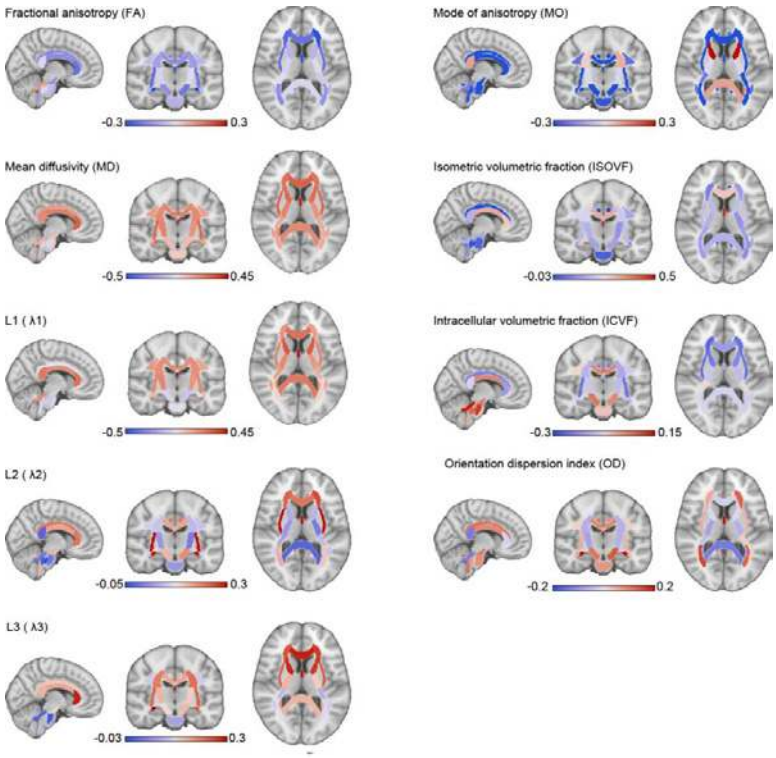

Figure 1. Spatial distribution of aging effects on 48 whole brain white matter tracts across 9 diffusion MRI measures. Positive age associations were marked in red, while negative age associations were marked in blue.

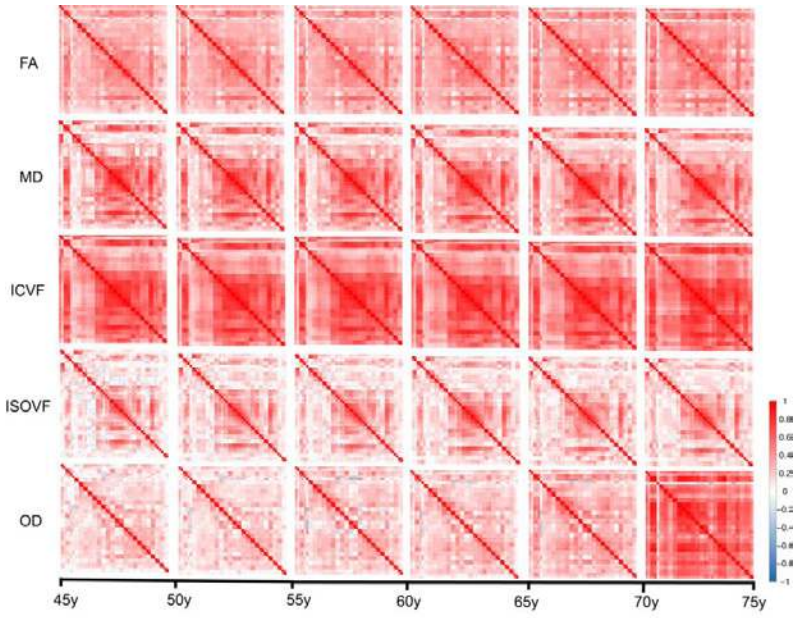

Figure 2. Illustrative whole brain heatmaps of tract de-differentiation for diffusion parameters across age groups (45-75 years; in ~5 year increments). These maps reflect 48x48 whole brain tract comparisons. Higher, positive tract inter-correlations (Spearman's rho) are indicated in darker red shades, white and blue shades denote lower and negative magnitudes respectively.

Conclusions: Consistent with prior work, spatial distribution of age associations across whole brain WM depicts significant age associations across multiple diffusivity measures. Higher covariation across WM microstructural tract phenotypes was observed with age increments, supporting age-related de-differentiation and a decrease in prominence of interindividual tract variation. Future analyses including examining whole brain functional networks could provide converging evidence for neural dedifferentiation and if these vary across networks. Probing cellular mechanisms and the role of neurotransmitter systems underlying this increasing generality may shed light on the brain basis of aging.

References

1. Chan MY (2014),' Decreased segregation of brain systems across the healthy adult lifespan'. Proc Natl Acad Sci USA 111: E4997–E5006.
2. Chong JSX (2019), 'Longitudinal changes in the cerebral cortex functional organization of healthy elderly.' J Neurosci 39: 5534–5550.

3. de Mooij, (2018), 'Age Differentiation within Gray Matter, White Matter, and between Memory and White Matter in an Adult Life Span Cohort.', The Journal of neuroscience: the official journal of the Society for Neuroscience, 38(25), 5826–5836.
4. Koen, J. D. (2019), 'Neural Dedifferentiation in the Aging Brain', Trends in cognitive sciences, 23(7), 547–559.
5. Park DC. (2004), 'Aging reduces neural specialization in ventral visual cortex', Proc. Natl. Acad. Sci, 101, 13091–13095.
6. Zuo XN (2017), 'Human connectomics across the life span', Trends Cogn Sci 21: 32–45.

Poster No 1191

Mind-body and physical training on cognitive functions of elderly with mild cognitive impairment

Sam Chi Chung Chan[1], Wayne L. S. Chan[1], Tom C. W. Tsoi[1], Michael K. C. Yeung[2], Sunny H.W. Chan[3]

[1]The Hong Kong Polytechnic University, Hong Kong, [2]The Education University of Hong Kong, Hong Kong, [3]University of the West of England, Bistrol, United Kingdom

Introduction: It has been shown that cognitive or physical training approaches could improve the cognitive functions of those with mild cognitive impairment (MCI)[1-4]. The effects of cognitive and physical trainings on cognitive, affective and physical functions of people with MCI have not been well studied. This study aimed to investigate the differential effects of the mind-body intervention (MBI) and physical exercises (PE) on cognitive, affective and physical functions of older adults with MCI in terms of neuropsychological measures and functional near-infrared spectroscopy (fNIRS).

Methods: Fifty-seven participants with MCI (mean age 68.3 (4.94)) were randomized into (1) 4-week MBI, (2) 4-week PE or (3) control group. Each participant was required to complete a series of neuropsychological and fNIRS before and after the completion of the group assigned. The neuropsychological measures were used to capture the between-group treatment effects, including Color Trails Test, Hong Kong List Learning Test, 10-meter walk test, 6-minute walk test. The participants were also engaged in emotional recognition task, N-back task, and single-task and dual-task walking while counting numbers backward. Frontal cortical activities were concurrently acquired using fNIRS.

Results: Repeated measures ANOVA showed significant group x time significance effect between the reaction time of exercise and control groups ($F_{1,41}=3.73$, $p=0.05$) with exercise group performing 2-back task faster across time. It also showed marginal group x time significance at right VLPFC activation of the mindfulness and control groups ($F_{1,24}=6.02$, $p=0.022$) with VLPFC activity reduced in the mindfulness group. Besides, Repeated measures ANOVA showed significant group x time interaction in accuracy rate of both exercise ($F_{1,38}=4.66$, $p=0.037$) and mindfulness groups ($F_{1,33}=5.73$, $p=0.022$) performing backward counting task. In terms of brain activations, repeated measures ANOVA showed significant group x time interaction at the right VLPFC in mindfulness group ($F_{1,24}=4.52$, $p=0.044$). Repeated measures ANOVA showed significant group x time interaction in accuracy rate of mindfulness groups ($F_{1,33}=5.51$, $p=0.025$) when performing dual-task with walking and backward counting. Repeated measures ANOVA showed significant group x time interaction at left OFC in the exercise group ($F_{1,24}=7.66$, $p=0.009$).

Conclusions: This would suggest that mindfulness training was showed to enhance working memory function. Both exercise and mindfulness training would enhance sustained attention, as reflected in backward counting and executive function as shown in dual task. Mindfulness training may lead to more mental effort to monitor the level of attention as shown by higher activation of the VLPFC. Exercise may enhance to more executive as shown in increased OFC activation. Long-term effect of mindfulness and physical training could be further investigated in future studies.

References

1. Marciniak, R., Sumec, R., Vyhnalek, M., Bendickova, K., Laznickova, P., Forte, G., . . . Sheardova, K. (2020), 'The Effect of Mindfulness-Based Stress Reduction (MBSR) on Depression, Cognition, and Immunity in Mild Cognitive Impairment: A Pilot Feasibility Study', Clinical Interventions in Aging, vol. 15, pp. 1365-1381.
2. Fam, J., Sun, Y., Qi, P., Lau, R. C., Feng, L., Kua, E. H., & Mahendran, R. (2020). Mindfulness practice alters brain connectivity in community-living elders with mild cognitive impairment. Psychiatry and Clinical Neurosciences, vol. 74, no.4, pp. 257-262.
3. Biazus-Sehn, L. F., Schuch, F. B., Firth, J., & Stigger, F. de S. (2020), 'Effects of physical exercise on cognitive function of older adults with mild cognitive impairment: A systematic review and meta-analysis', Archives of Gerontology and Geriatrics, vol. 89, p. 104048.
4. Song, D., Yu, D. S. F., Li, P. W. C., & Lei, Y. (2018), 'The effectiveness of physical exercise on cognitive and psychological outcomes in individuals with mild cognitive impairment: A systematic review and meta-analysis', International Journal of Nursing Studies, vol. 79, pp. 155–164.

Poster No 1192

Aging effects on task-based activity and functional networks during semantic processing and rest

Sandra Martin[1], Philipp Kuhnke[2], Curtiss Chapman[3], Gesa Hartwigsen[2]

[1]Max Planck Institute for Human Cognitive and Brain Sciences, Leipzig, Saxony, [2]Leipzig University, Leipzig, Saxony, [3]MPI CBS, Leipzig, Saxony

Introduction: Semantic knowledge is essential for everyday human cognition, such as recognizing and using objects, or speaking and comprehending language. It is usually well preserved in healthy aging (Verhaeghen, 2003). However, semantic control processes, which guide semantic access and retrieval, decline with age (Hoffman, 2018). In light of the intact semantic knowledge system in healthy older adults, these changes have been attributed to declining cognitive control functions, which contribute to successful semantic processing when ambiguities need to be resolved or irrelevant information needs to be inhibited (DeDe and Knilans, 2016). A central question is how cognitive aging modulates the contribution of cognitive control networks to semantic processing in the brain. To date, most studies focused on large-scale network interactions at rest but little is known about the differences in network organization between rest and task states and their age-related modulation. To address these questions, the current neuroimaging study explored the interaction between neural resources of domain-specific semantic processing and domain-general cognitive control in healthy young and older adults. We applied univariate task-based analyses and characterized whole-brain functional connectivity profiles during rest and semantic processing to explore the relationship between these states and their modulation through age.

Methods: 41 older adults (M: 66, SD: 3.17 years) and 43 young adults (M: 28, SD: 4.3 years) performed semantic judgment tasks (taxonomic or thematic judgments) on pairs of images (e.g. monkey and banana) during fMRI. A scrambled mirror judgment task was included as a non-semantic control task. Task-related whole-brain activation was investigated via two-level GLM analyses in SPM12. Individual time series of 400 parcels (Schaefer, 2018) were extracted for rest and task runs separately, while performing rigorous denoising. Whole-brain functional connectivity estimates were calculated across the time series using Fisher's z coefficients. Matrices of rest and semantic processing were correlated within participants and an effect of age was explored via a t-test.

Results: fMRI analyses showed activity in a left-lateralized fronto-temporo-parietal network for semantic > non-semantic tasks (Fig. 1). In both groups, activation peaks lay within networks of semantic control and domain-general cognitive control. Interaction analyses showed that young adults more strongly activated left frontal and parietal regions, and fusiform gyrus, for semantic vs. non-semantic tasks than older adults. Older adults, on the other hand, showed increased activity only in right-hemispheric frontal and parietal regions (Fig. 1 bottom). Whole-brain functional connectivity analyses revealed enhanced connectivity in young relative to older adults during rest and task states (Fig. 2A). Whole-brain connectivity matrices for rest and semantic processing were strongly interrelated within participants (Fig. 2B). However, these correlations did not show an effect of age ($t(82) = 1.08$, $p = 0.28$).

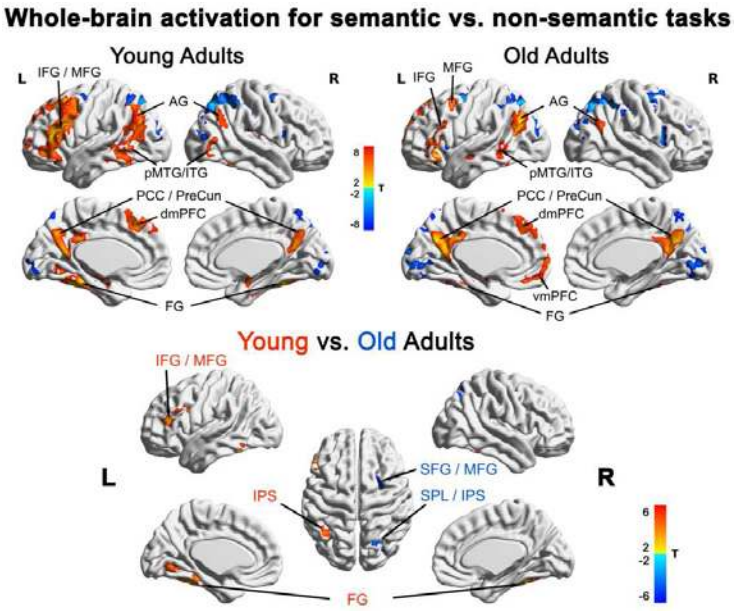

Figure 1: Whole-brain activation for semantic vs non-semantic tasks. Upper figures show contrast Semantic > Non-semantic task in each age group.

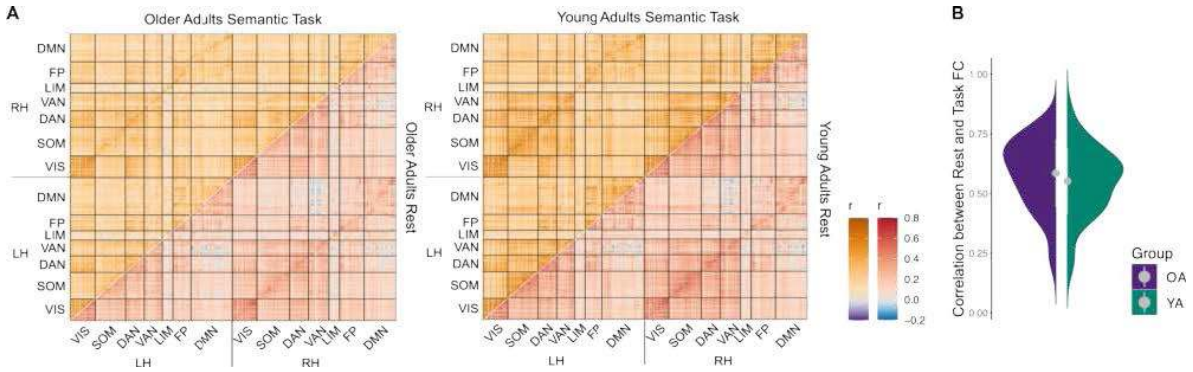

Figure 2: A) Average whole-brain correlation matrices per age group and state (semantic tasks, rest). B) Correlation between resting-state and task functional connectivity (FC) in each age group.

Conclusions: Our results demonstrate age-related changes in functional activity during semantic processing, driven by neural reorganization. While young adults showed increased activity in domain-specific semantic regions in left frontal, parietal, and inferior temporal lobes, older adults showed upregulation in right-hemispheric frontal and parietal regions, which have been associated with the frontoparietal control network. These results illustrate the increased involvement of domain-general resources in the aging brain to maintain goal-directed task processing when cognitive demands are high (Martin et al., 2022). We did not detect age differences in the synchronization of whole-brain networks during rest and task demonstrating a relatively stable functional network architecture across age groups.

References

1. Verhaeghen, P. (2003). Aging and vocabulary scores: A meta-analysis. Psychology and Aging, 18(2), 332–339. https://doi.org/10.1037/0882-7974.18.2.332
2. Hoffman, P. (2018). An individual differences approach to semantic cognition: Divergent effects of age on representation, retrieval and selection. Scientific Reports, 8(1), Article 1. https://doi.org/10.1038/s41598-018-26569-0
3. DeDe, G., & Knilans, J. (2016). Language comprehension in aging. In H. H. Wright (Ed.), Cognition, Language and Aging (pp. 107–133). John Benjamins Publishing Company. https://doi.org/10.1075/z.200.05ded
4. Schaefer, A., Kong, R., Gordon, E. M., Laumann, T. O., Zuo, X.-N., Holmes, A. J., Eickhoff, S. B., & Yeo, B. T. T. (2018). Local-Global Parcellation of the Human Cerebral Cortex from Intrinsic Functional Connectivity MRI. Cerebral Cortex (New York, N.Y.: 1991), 28(9), 3095–3114. https://doi.org/10.1093/cercor/bhx179
5. Martin, S., Saur, D., & Hartwigsen, G. (2022). Age-Dependent Contribution of Domain-General Networks to Semantic Cognition. Cerebral Cortex, 32(4), 870–890. https://doi.org/10.1093/cercor/bhab252

Poster No 1193

Brain change in healthy adults links with genetic Alzheimer's risk and lifespan memory decline

James Roe[1], Didac Vidal-Piñeiro[2], Esten Leonardsen[3], Øystein Sørensen[2], Håkon Grydeland[1], Olena Iakunchykova[1], Kristine Beate Walhovd[4], Anders Fjell[5], Yunpeng Wang[1]

[1]University of Oslo, Oslo, Norway, [2]Centre for Lifespan Changes in Brain and Cognition, Department of Psychology, University of Oslo, Oslo, Norway, [3]NORMENT; University of Oslo, Oslo, Norway, [4]Univeristy of Oslo, Oslo, Oslo, [5]Department of Psychology, Center for Lifespan Changes in Brain and Cognition, University of Oslo, Oslo, Oslo

Introduction: Across healthy adult life our brain's undergo widespread structural change. Many of these changes occur gradually and are qualitatively similar to atrophy patterns that are accelerated in Alzheimer's disease (AD)[1-2], raising the possibility accelerated brain change across healthy adult life may relate to genetic AD-risk.

Methods: We modelled subject-specific structural brain change relative to that expected given age, in dense longitudinal adult lifespan data (1430 scans from 420 individuals aged 30 to 89 years; 2-7 timepoints). Using polygenic AD scores (PRS-AD) from four GWAS[3-6], we first tested PRS-AD associations with age-relative change in early Braak stage regions – namely hippocampus, entorhinal cortex, amygdala, and medial temporal cortex. Next, following the hypothesis that brain changes in ageing and AD are largely shared, we performed machine learning classification on brain change trajectories conditional on age in longitudinal AD patient-control data, to obtain a list of AD-accelerated features and model change in these in adult lifespan data, and test PRS-AD-change associations via multivariate methods. Lastly, we tested whether high PRS-AD individuals also high on a multivariate marker of brain change exhibit more longitudinal memory decline over their healthy adult life (30-89 years).

Results: Healthy individuals losing more brain volume than expected for their age in early Braak stage regions had significantly higher genetic risk for AD, beyond the risk conferred by APOE alone. We found PRS-AD was associated with a multivariate marker of accelerated change in many AD-accelerated features in healthy adults, and that most individuals above ~50 years of age are on an accelerated change trajectory in AD-accelerated brain regions. Directly applying the AD-derived model weights to healthy adult lifespan data also enabled detection of PRS-AD-change associations in healthy adults. Finally, high PRS-AD individuals also high on a multivariate marker of change showed more adult lifespan memory decline, compared to high PRS-AD individuals with less brain change.

Conclusions: The results support a dimensional account linking gradual lifespan brain changes with AD, suggesting AD risk genes speed up the shared pattern of ageing- and AD-related neurodegeneration that starts early, occurs along a continuum, and tracks memory change in healthy adults.

References

1. Fjell, A. M., McEvoy, L., Holland, D., Dale, A. M., & Walhovd, K. B. (2013). Brain changes in older adults at very low risk for Alzheimer's disease. Journal of Neuroscience, 33(19), 8237–8242. https://doi.org/10.1523/JNEUROSCI.5506-12.2013
2. Fjell, A. M., Walhovd, K. B., Fennema-notestine, C., Mcevoy, L. K., Hagler, D. J., Holland, D., … Dale, A. M. (2009). One-Year Brain Atrophy Evident in Healthy Aging, 29(48), 15223–15231. https://doi.org/10.1523/JNEUROSCI.3252-09.2009
3. Jansen, I. E., Savage, J. E., Watanabe, K., Bryois, J., Williams, D. M., Steinberg, S., … Posthuma, D. (2019). Genome-wide meta-analysis identifies new loci and functional pathways influencing Alzheimer's disease risk. Nature Genetics, 51(3), 404–413. https://doi.org/10.1038/s41588-018-0311-9
4. Kunkle, B. W., Grenier-Boley, B., Sims, R., Bis, J. C., Damotte, V., Naj, A. C., … Pericak-Vance, M. A. (2019). Genetic meta-analysis of diagnosed Alzheimer's disease identifies new risk loci and implicates Aβ, tau, immunity and lipid processing. Nature Genetics, 51(3), 414–430. https://doi.org/10.1038/s41588-019-0358-2
5. Lambert, J. C., Ibrahim-Verbaas, C. A., Harold, D., Naj, A. C., Sims, R., Bellenguez, C., … Seshadri, S. (2013). Meta-analysis of 74,046 individuals identifies 11 new susceptibility loci for Alzheimer's disease. Nature Genetics, 45(12), 1452–1458. https://doi.org/10.1038/ng.2802
6. Wightman, D. P., Jansen, I. E., Savage, J. E., Shadrin, A. A., Bahrami, S., Holland, D., … Posthuma, D. (2021). A genome-wide association study with 1,126,563 individuals identifies new risk loci for Alzheimer's disease. Nature Genetics, 53(9), 1276–1282. https://doi.org/10.1038/s41588-021-00921-z

Poster No 1194

Age-related changes in the neural representation of naturalistic events

Selma Lugtmeijer[1], Djamari Oetringer[2], Linda Geerligs[3], Karen Campbell[4]

[1]University of Birmingham, Birmingham, West Midlands, [2]Radboud University, Nijmegen, Gelderland, [3]Donders Institute, Nijmegen, Gelderland, [4]Brock Univeristy, St. Catharines, Ontario

Introduction: How do people segment ongoing experiences into separate events? Segmentation is a crucial process that improves understanding of current events (Zacks et al., 2001) and the recall of past events (Flores et al., 2017). Naturalistic stimuli like movies provide an opportunity to study event segmentation with functional magnetic resonance imaging (fMRI). Transitions between distinct neural states may be the mechanism underlying event segmentation (Baldassano et al., 2017). Neural state boundaries are organized in a hierarchical manner across the cortex, with short states in primary sensory regions, and long states in the prefrontal cortex (Geerligs, 2022). Perceived event boundaries overlap with neural state changes across the cortical hierarchy, especially state changes that are shared between many regions. An open question is whether these neural state changes related to event segmentation are stable across the adult lifespan.

Methods: Participants from a lifespan cohort (N = 577, age 18–88; Cam-CAN; Shafto et al., 2014) viewed an 8 min movie during an fMRI scan. To identify neural state boundaries, we applied the greedy state boundary search (GSBS; Geerligs et al., 2021). Participants were sorted into 34 age groups (Geerligs et al., 2021). GSBS identifies the optimal number of state boundaries based on brain activity time courses from spherical searchlights covering the entire cortex. This metric identifies the optimal number of state boundaries within a timeseries, such that the correlations of timepoints within a state are maximized and correlations of timepoints in consecutive states are minimized. Perceived event boundaries were based on an external dataset in which participants were asked to indicate when they felt one event ended and another began (Ben-Yakov and Henson, 2018). To determine the similarity between neural state boundaries and perceived event boundaries, we computed the boundary overlap defined as the number of timepoints where neural state and perceived event boundaries overlapped. We computed Spearman correlations (FDR corrected) to relate neural state duration and boundary overlap to age.

Results: The median duration of neural states differed greatly between brain regions. In line with Geerligs et al (2022), we observed particularly short neural states in visual cortex, early auditory cortex, and somatosensory cortex. The longest states were observed in high-level regions such as the medial prefrontal gyrus and anterior portions of the lateral prefrontal cortex

(Figure 1). There was a significant effect of age on neural state duration, with longer states with increasing age. This effect was strongest in the visual cortex and medial and lateral frontal cortex (Figure 2). Brain regions throughout the cortical hierarchy, showed significant overlap between neural state boundaries and perceived event boundaries. In particular, we observed that the anterior cingulate cortex, dorsal medial prefrontal cortex, frontal gyrus, and anterior insula show strong overlap. This suggests that neural state changes in these regions are most likely to underlie the experience of an event boundary. There was no significant effect of age on the overlap between neural state boundaries and perceived boundaries.

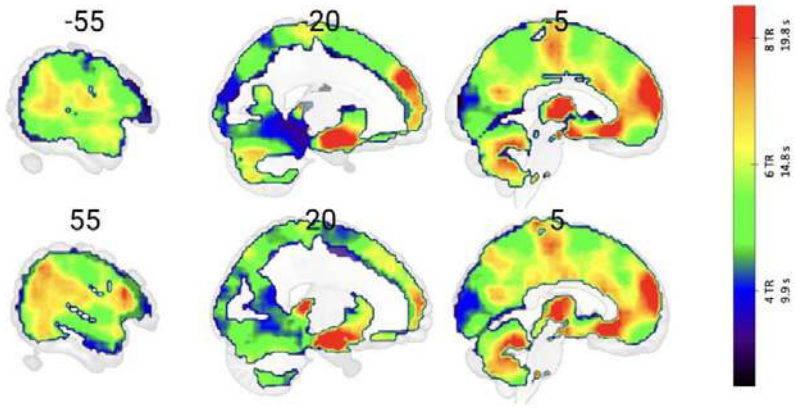

Figure 1: The cortical hierarchy of neural state durations. Median state duration varied greatly between regions.

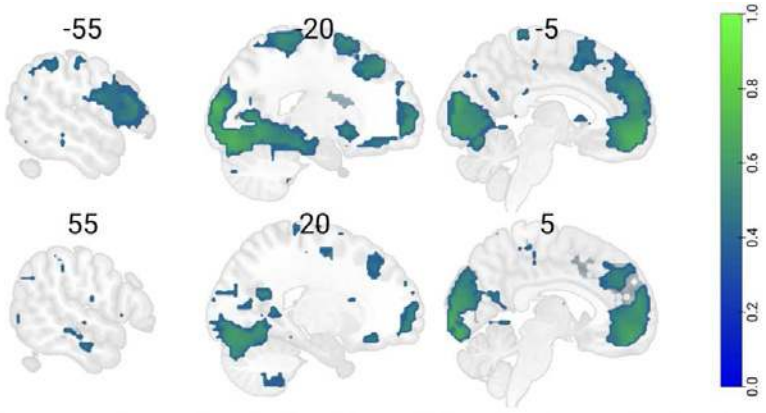

Figure 2: Effect of age on median state duration. Significant correlations after false discovery rate (FDR) correction.

Conclusions: Our results show a hierarchy of neural states during movie viewing in a large lifespan cohort. We found that neural state durations were longer in older than younger adults in many cortical areas. This suggests that neural dedifferentiation with aging is not only reflected in decreased category specificity (Koen and Rugg, 2019) but also decreased temporal differentiation. Critically, the relationship between neural states and perceived event boundaries remained similar with age, suggesting that neural state boundaries that may underlie the experience of distinct events remains stable across the adult lifespan. This is in line with findings that show that older adults identify the same event boundaries as younger adults (Reagh et al., 2020).

References

1. Baldassano, C., Chen, J., Zadbood, A., Pillow, J. W., Hasson, U., & Norman, K. A. (2017). 'Discovering event structure in continuous narrative perception and memory', Neuron, vol. 95, no. 3, pp. 709-721.
2. Ben-Yakov, A., & Henson, R. N. (2018). 'The hippocampal film editor: sensitivity and specificity to event boundaries in continuous experience', Journal of Neuroscience, vol. 38, no. 47, pp. 10057-10068.
3. Geerligs, L., van Gerven, M., & Güçlü, U. (2021). 'Detecting neural state transitions underlying event segmentation', NeuroImage, vol. 236, 118085.
4. Geerligs, L., Gözükara, D., Oetringer, D., Campbell, K. L., van Gerven, M., & Güçlü, U. (2022). 'A partially nested cortical hierarchy of neural states underlies event segmentation in the human brain', ELife, vol. 11, e77430.
5. Flores, S., Bailey, H. R., Eisenberg, M. L., & Zacks, J. M., 2017. 'Event segmentation improves event memory up to one month later', Journal of Experimental Psychology. Learning, Memory, and Cognition, vol. 43, pp. 1183–1202.
6. Koen, J. D., & Rugg, M. D. (2019). 'Neural dedifferentiation in the aging brain', Trends in cognitive sciences, vol. 23, no. 7, pp. 547-559.
7. Kurby, C. A., Asiala, L. K., & Mills, S. R. (2014). 'Aging and the segmentation of narrative film', Aging, Neuropsychology, and Cognition, vol. 21, no. 4, pp. 444-463.
8. Reagh, Z. M., Delarazan, A. I., Garber, A., & Ranganath, C. (2020). 'Aging alters neural activity at event boundaries in the hippocampus and Posterior Medial network', Nature Communications, vol. 11, no. 1, pp. 3980.
9. Zacks, J. M., Braver, T. S., Sheridan, M. A., Donaldson, D. I., Snyder, A. Z., Ollinger, J. M., Buckner, R. L., & Raichle, M. E., 2001. 'Human brain activity time-locked to perceptual event boundaries', Nature Neuroscience, vol. 4, pp. 651–655.

Poster No 1195

Predicting Brain Age from T2-FLAIR Captures White Matter Aging Associated with Cardiovascular Risks

Cong Zang[1], Elizabeth Haddad[2], Gilsoon Park[1], Sook-Lei Liew[3], Neda Jahanshad[4], Hosung Kim[5]

[1]University of Southern California, Los Angeles, CA, [2]USC, Marina Del Rey, CA, [3]University of Southern California, San Diego, CA, [4]Imaging Genetics Center, Keck School of Medicine of University of Southern California, Los Angeles, California, [5]University of Southern California, Los Angeles, CA

Introduction: In brain age prediction (BAP) studies, machine learning, especially deep learning, is commonly used to estimate 'brain age' (BA). The brain age gap (BAG) is measured as the difference between predicted brain age and chronological age (CA) and offers a quantitative measure for assessing normal versus abnormal aging. Various modalities of brain MRI data, including T1, T2-FLAIR, functional, and diffusion MRI, provide distinct features of brain structure and function that change with aging. T1 MRI is optimal for evaluating morphological changes in the gray matter (GM) and white matter (WM), while the visibility of lesions, such as white matter hyperintensities (WMH) or ischemic stroke lesions, is more pronounced on T2-FLAIR[8]. Recently, studies have employed T2-FLAIR to predict brain age trajectories from the whole WM volume[7] or WMH volumes[2]. However, they do not examine the relationship between the spatial distribution of WMH and aging. Given the distinctive association of cardiovascular diseases with WMHs in deep WM and periventricular WMHs[4], we aimed to examine brain age as predicted by the spatial distribution of WMH. We modeled medial surfaces generated at various depths from the WM-GM boundary to the ventricles and projected T2-FLAIR intensity values onto these medial surfaces. These values at different depth surfaces were then inputted into graph convolutional networks (GCN) to predict brain age. We hypothesize that the BAGs derived from T2-FLAIR signals sampled at various depth levels within WM represent WM-specific brain aging and will be associated with cardiovascular risks.

Methods: The UK BioBank dataset was used in this study (Fig. 1A). T1 images were processed through the CIVET pipeline (Fig. 1B) to construct inner cortical surfaces (namely WM surfaces)[9]. SynthSeg was used to run whole-brain segmentation[1]. We generated the Laplacian field vectors (LFV) from the WM surface to the ventricular boundary[5,6]. Vertices on the GM-WM boundary were deformed along the LFV, and medial surfaces were constructed using vertices at the given depth ratios (Fig. 1C) whose mesh topology was kept as the original GM-WM boundary (SurfStat, 2009). T2-FLAIR images were sampled onto the nearest neighboring vertices across all medial surfaces to form a feature matrix (5124 vertices x 9 surfaces, Fig. 1D). We then randomly split the dataset into i) training data (7631 subjects, age = 62.7±7.4 years, range 46-80) and test data (3370 subjects, age = 62.1±7.1 years, range = 48-77). The feature matrix was normalized to (0,1) before feeding it into the GCN. In this preliminary study, one BAG representing the whole WM was calculated. However, with this method, we could compute BAGs for different WM depth surfaces and left and right hemispheres separately. We then applied a general linear model, including risk factors, diseases and life habits as covariates. Results are Bonferroni-corrected by multiplying the original p-value with the number of comparisons (23 in total) made.

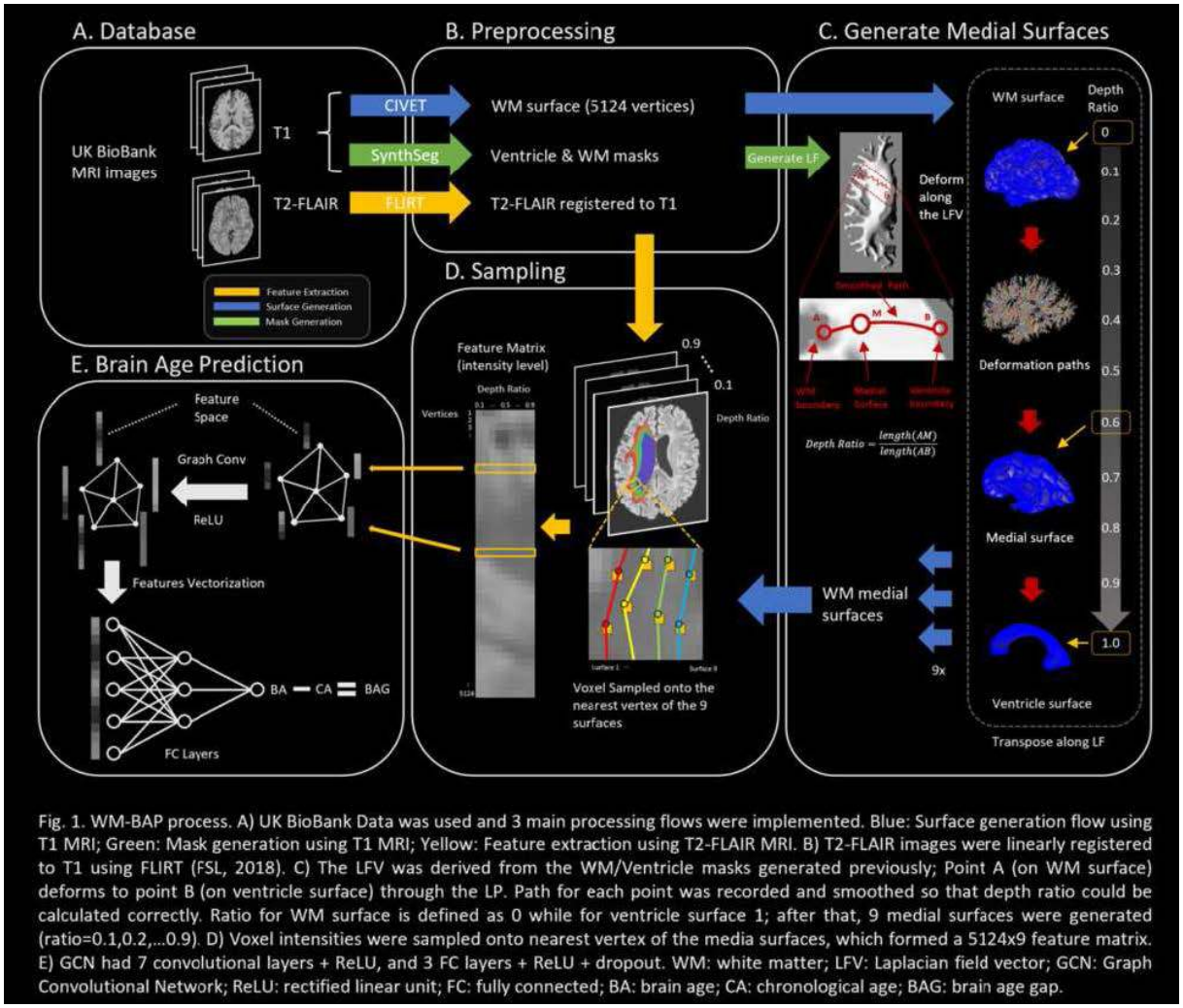

Fig. 1. WM-BAP process. A) UK BioBank Data was used and 3 main processing flows were implemented. Blue: Surface generation flow using T1 MRI; Green: Mask generation using T1 MRI; Yellow: Feature extraction using T2-FLAIR MRI. B) T2-FLAIR images were linearly registered to T1 using FLIRT (FSL, 2018). C) The LFV was derived from the WM/Ventricle masks generated previously; Point A (on WM surface) deforms to point B (on ventricle surface) through the LP. Path for each point was recorded and smoothed so that depth ratio could be calculated correctly. Ratio for WM surface is defined as 0 while for ventricle surface 1; after that, 9 medial surfaces were generated (ratio=0.1,0.2,...0.9). D) Voxel intensities were sampled onto nearest vertex of the media surfaces, which formed a 5124x9 feature matrix. E) GCN had 7 convolutional layers + ReLU, and 3 FC layers + ReLU + dropout. WM: white matter; LFV: Laplacian field vector; GCN: Graph Convolutional Network; ReLU: rectified linear unit; FC: fully connected; BA: brain age; CA: chronological age; BAG: brain age gap.

Results: Our WM-BAP model predicted brain age with a mean absolute error of 3.08 on test data. Various cardiovascular risk factors such as hypertension, high BMI, high WMH burden, high blood pressure, and high heart rate were associated with increased WM-BAG (Fig 2).

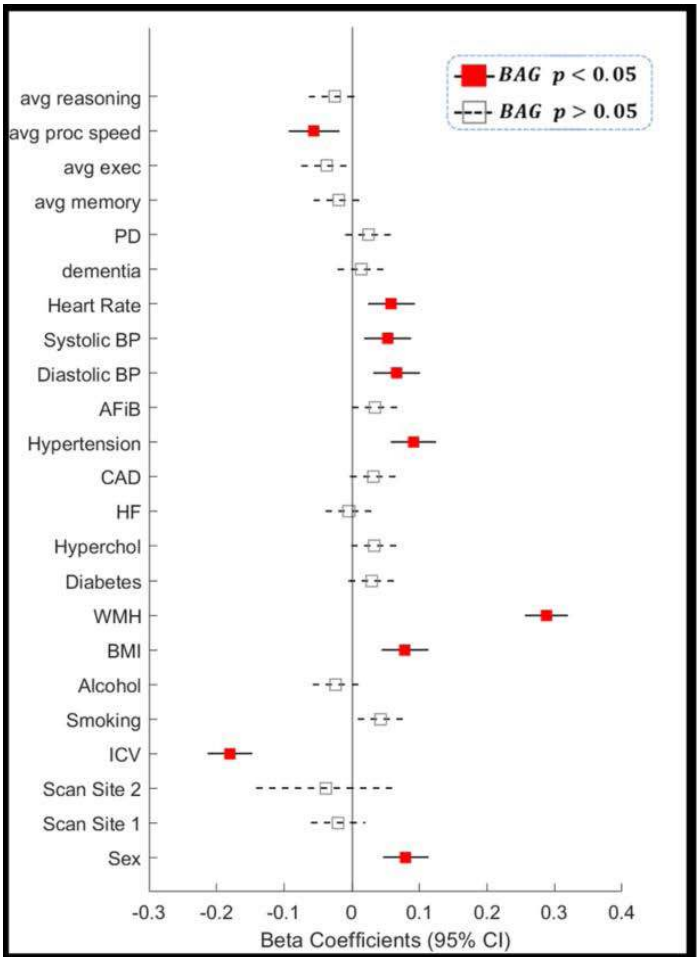

Fig. 2. GLM coefficients and p-values for *WM-BAG*. Straight lines indicate 95% CI range. p-values less than 0.05 are marked as red (Bonferroni Corrected). PD: Parkinson's Disease; HF: Heart Failure; HTN: Hypertension; CAD: Coronary Artery Disease; WMH: White matter hyperintensity volume; ICV: Intracranial volume; BMI: Body mass index.

Conclusions: Our BAP model based on T2-FLAIR signals at various WM depths captured accelerated aging associated with cardiovascular risk factors and diseases. WMH at different depths may impact brain aging differently, e.g. periventricular WMH may be associated with mild parenchymal changes, possibly due to nonischemic causes such as ependymal gliosis, demyelination, and discontinuation of the subependymal lining, while deep WM WMH may show more severe parenchymal changes, considered to be of ischemic origin[3,10]. This study establishes a foundation for WM BAP studies, which could enable future analyses of aging trajectories in specific depths of WM and their contribution to cerebrovascular diseases.

References

1. Billot B, (2023), 'SynthSeg: Segmentation of brain MRI scans of any contrast and resolution without retraining'. Medical Image Analysis, vol. 86:102789
2. de Lange AG. (2020), 'Multimodal brain-age prediction and cardiovascular risk: The Whitehall II MRI sub-study', Neuroimage, vol. 222:117292
3. Ghaznawi R, (2021), 'Association of White Matter Hyperintensity Markers on MRI and Long-term Risk of Mortality and Ischemic Stroke: The SMART-MR Study', Neurology, vol. 96(17):e2172-e2183
4. Jin, H. (2023), 'Is coronary artery calcium an independent risk factor for white matter hyperintensity?', BMC neurology, vol. 23(1), 313
5. Kim, H. (2014), 'Multivariate Hippocampal Subfield Analysis of Local MRI Intensity and Volume: Application to Temporal Lobe Epilepsy', Medical Image Computing and Computer-Assisted Intervention, Lecture Notes in Computer Science, vol. 8674.
6. Kim JS. (2005), 'Automated 3-D extraction and evaluation of the inner and outer cortical surfaces using a Laplacian map and partial volume effect classification', Neuroimage, vol. 27(1):210-21
7. Liem F. (2017), 'Predicting brain-age from multimodal imaging data captures cognitive impairment', Neuroimage, vol. 148:179-188
8. Lee, S. (2023), 'Automatic segmentation of white matter hyperintensities in T2-FLAIR with AQUA: A comparative validation study against conventional methods', Brain research bulletin, vol. 205, 110825
9. MacDonald D. (1999), 'Automated 3-D extraction of inner and outer surfaces of cerebral cortex from MRI', Neuroimage, vol. 12(3):340-56
10. Spilt A. (2006), 'Not all age-related white matter hyperintensities are the same: a magnetization transfer imaging study', American Journal of Neuroradiology, vol. 27(9):1964-8

Poster No 1196

Disentangling the Effect of Brain Size from Sex Differentiated Aging Trajectories

Aliza Brzezinski-Rittner[1,2], Mahsa Dadar[1,2], Yashar Zeighami[1,2]

[1]McGill University, Montreal, Quebec, [2]Douglas Mental Health University Health Centre, Montreal, Quebec

Introduction: The aging process leads to loss of cortical and subcortical gray and white matter volumes, and these changes are differentiated between females and males (Bethlehem et al., 2022). Although there are general aging trajectories, different biological and environmental factors lead to distinct outcomes, and sex is one of these factors. However, many volumetric sex differences found in the brain are induced by differences in brain size and disappear once adjusting for intracranial volume (Sanchis-Segura et al., 2020). In this work, we seek to disentangle the effects of sex from those derived by allometric differences in regional aging trajectories as estimated by deformation based morphometry (DBM), and volumetric data from the UK Biobank (UKBB) dataset.

Methods: Average cortical and subcortical DBM values (Zeighami et al., 2015) were extracted based on Schaeffer 1000 (Schaefer et al., 2018) and Xiao (Xiao et al., 2019)atlases, respectively. Precomputed FreeSurfer-based volumetric information was provided by the UKBB based on the DKT atlas (Desikan et al., 2006). Following visual quality control, data from 35,752 participants was included. We then created an age and total intracranial volume (TIV) matched sample of males and females (with a threshold of maximum one month of age difference at acquisition time and 0.2% difference in TIV) of 13,200 participants (referred to as matched sample), another sample of the same size matched just by age (age matched sample), and a non-matched sample of the same size (non matched sample). We modeled the sex differentiated aging trajectories for all the regions in each of the samples. We examined how the model estimates for different statistical contrasts change between these matching strategies and which coefficients were significant before and after multiple comparisons corrections for the different samples. We tested two different linear models to model aging trajectories. Model one tested the linear interaction between age and sex (ROI ~ 1 + age * sex), while the second model also included a quadratic interaction (ROI ~ 1 + (age + age2) * sex). A series of paired t-tests were used to assess the significance of the differences in model estimates for each sample.

Results: For the DBM data, overall, model one fit the regional sex differentiated aging trajectories best according to the Akaike information criterion (AIC). We found that after multiple comparisons correction, the proportion of regions in which sex showed a significant effect in their aging trajectories was smaller in the matched sample than in the others (8.1% for the non matched sample, 3.2% for the age match sample and only 0.8% for the matched sample for the interaction between sex and age) (Fig. 1). Interestingly, only one subcortical region showed a significant effect of sex in the matched sample, namely the right nucleus accumbens. Model estimates were significantly different between the samples (Fig. 2, A). For the Freesurfer volumetric data, overall, model two fit the regional sex differentiated aging trajectories best according to the AIC. Model estimates were significantly different among samples (Fig. 2, B). For both DBM and the volumetric models, the linear effect of age was negative for all samples, showing a general trend of loss of gray matter tissue. The main effect of sex was very pronounced in the non-matched sample and even in the age-matched sample, however, after matching for age and TIV, this effect diminished and in some cases it disappeared altogether. Furthermore, in the case of the volumetric data, there was a sex differentiated effect of the quadratic term for age, however, in the matched sample, this trend diminished greatly, while the main effect of the quadratic term of age became stronger (Fig. 2).

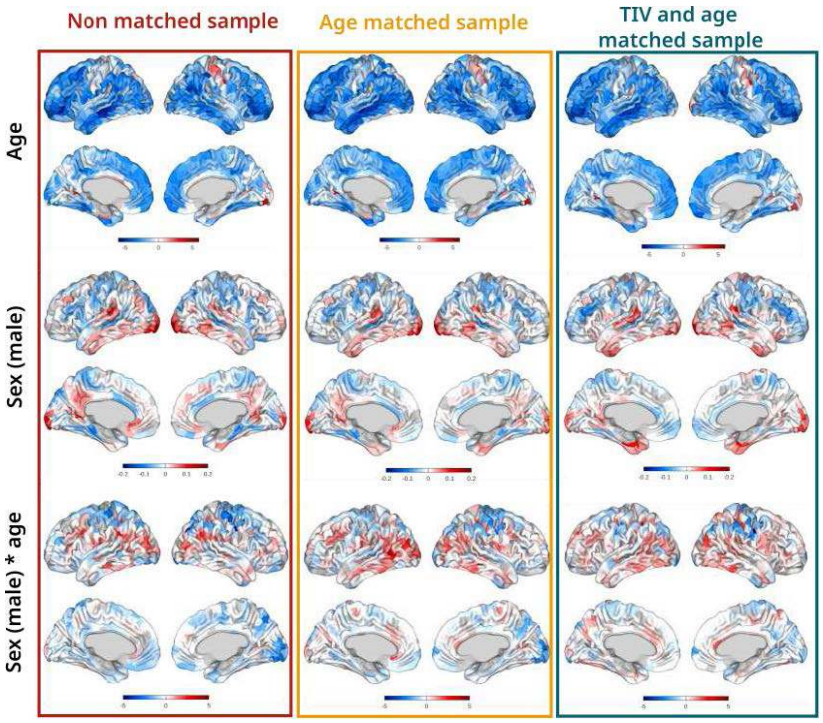

Figure 1: shows the estimates for the regional DBM aging trajectories modeled by linear interaction between age and sex projectec onto the brain surface, for each of the three samples (left column: non matched sample, middle: age matched sample. right: matched sample) and the different model terms (top row: age, middle row: sex (male), bottom row: interaction between sex (male) and age).

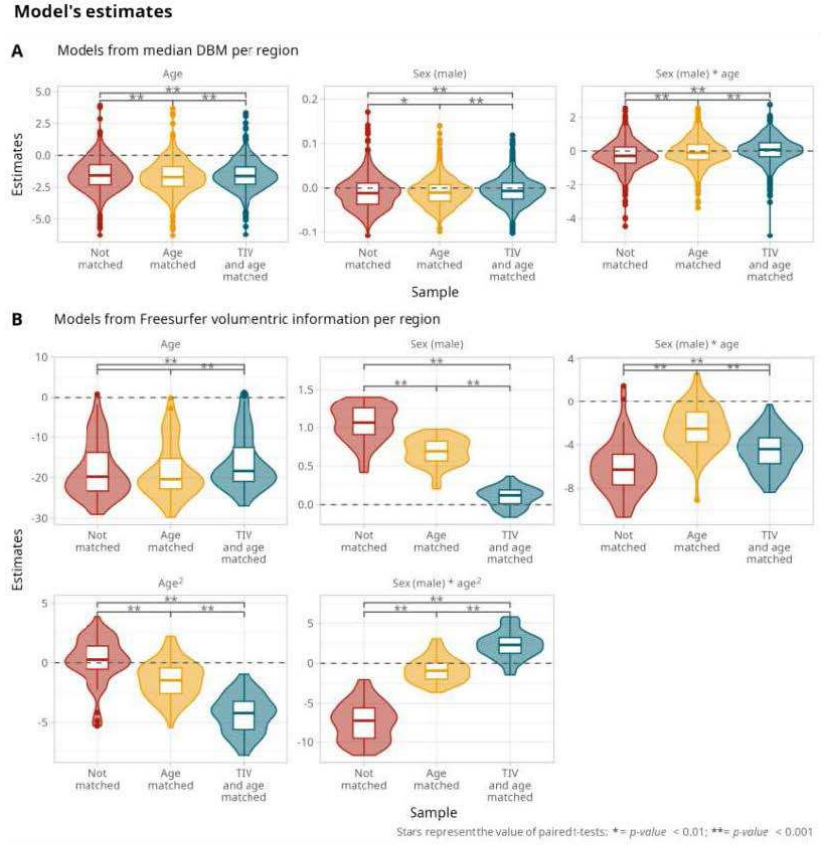

Figure 2: shows the distribution of the estimates for the regional aging trajectories modeled for each of the three samples. On red are the estimates for the non matched sample, on yellow for the age matched and on blue for the matched sample. **A.** shows the estimates for the linear interaction models used for DBM regional data. The main effect of sex, as well as the effect of age interacting with sex diminish in the matched sample in comparison to the other two. B. shows the estimates for the quadratic interaction models used for volumetric regional data. The main effect of sex diminishes in the matched sample in comparison to the other two. There is a sex differentiated effect of the quadratic term for age, however, in the matched sample, this trend diminishes greatly, while the main effect of the quadratic term of age gets stronger,

Conclusions: Our results suggest that in most cases, the regional differences that can be found between females and males in aging trajectories can be attributed to the brain size differences between the two populations.

References
1. Bethlehem, R., et. al. (2022). Brain charts for the human lifespan. Nature, 604(7906), 525–533.
2. Desikan, R. S., et. al. (2006). An automated labeling system for subdividing the human cerebral cortex on MRI scans into gyral based regions of interest. NeuroImage, 31(3), 968–980.
3. Sanchis-Segura, C., et. al. (2020). Effects of different intracranial volume correction methods on univariate sex differences in grey matter volume and multivariate sex prediction. Scientific Reports, 10(1), Article 1.
4. Schaefer, A., et. al. (2018). Local-Global Parcellation of the Human Cerebral Cortex from Intrinsic Functional Connectivity MRI. Cerebral Cortex, 28(9), 3095–3114.
5. Xiao, Y., et. al. (2019). An accurate registration of the BigBrain dataset with the MNI PD25 and ICBM152 atlases. Scientific Data, 6(1), Article 1.
6. Zeighami, Y., et. al. (2015). Network structure of brain atrophy in de novo Parkinson's disease. eLife, 4, e08440.

Poster No 1197

Relationship of fMRI-derived arousal patterns to healthy aging

Sarah Goodale[1], Shiyu Wang[1], Kate Wang[1], Catie Chang[1]

[1]*Vanderbilt University, Nashville, TN*

Introduction: In aging populations, daytime fatigue and sleepiness can be prominent and can impact everyday behavior and cognitive function[1-4]. Moreover, aging can be accompanied by disruptions of subcortical brain regions that are implicated in the regulation of arousal. Investigating the whole brain correlates of arousal may, therefore, contribute to our understanding of age-related functional changes. In this study, we leverage subject-specific arousal patterns to investigate how arousal-related hemodynamic fluctuations across the brain correlate with healthy aging.

Methods: This study used 3T fMRI data (n = 499) from the Human Connectome Project – Aging dataset[5], spanning an age range of 36-85 years. We use an established arousal "template" map[6,7], created from simultaneous EEG-fMRI data, to extract subject-specific arousal maps for each subject using a method akin to dual regression[8]. We then evaluated how arousal patterns correlate to healthy adult aging using voxel-wise regression to evaluate their relationship. We co-varied for sex, race, education, and total intracranial volume. Significant clusters were identified using a threshold-free cluster enhancement from FSL Randomize[9].

Results: Voxel-wise regression analysis demonstrated that arousal-related fMRI activity was significantly ($p < 0.01$, TCFE multiple comparisons) associated with age in regions such as the lingual gyrus, superior temporal gyrus, insula, cuneus, post-central gyrus, amygdala, thalamus, and lateral ventricles (Figure 1).

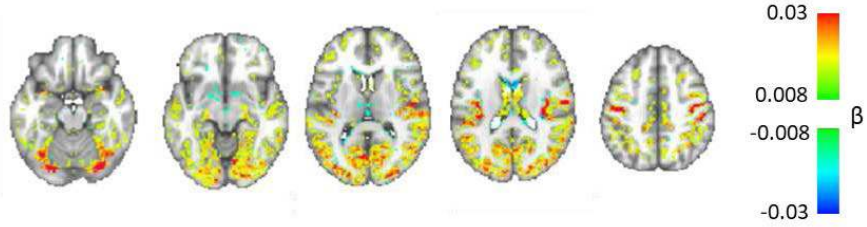

Figure 1. Relationship between whole-brain arousal patterns and aging. Map was thresholded to reveal only regions that were significant at p<0.01 corrected, using threshold-free cluster enhancement from FSL Randomise.

Conclusions: Overall, this analysis reveals significant relationships between age and fMRI arousal fluctuations, suggesting that further investigation of the functional circuits linked with arousal could contribute to our understanding of age-related changes in the brain. Future work will conduct complementary analysis of arousal-related brain signals, leverage other forms of tracking arousal such as simultaneous pupil data, and compare these findings with age-related changes in the fMRI global signal[10]. Additionally, we will explore how age-related changes in whole-brain arousal fluctuations could be implicated in cognitive decline.

References
1. Carskadon, M. A., Van den Hoed, J., & Dement, W. C. (1980). Sleep and daytime sleepiness in the elderly. Journal of geriatric psychiatry.
2. Bartolacci, C., Scarpelli, S., D'Atri, A., Gorgoni, M., Annarumma, L., Cloos, C., ... & De Gennaro, L. (2020). The influence of sleep quality, vigilance, and sleepiness on driving-related cognitive abilities: a comparison between young and older adults. Brain sciences, 10(6), 327.
3. Berardi, Raja Parasuraman, James V. Haxby, A. (2001). Overall vigilance and sustained attention decrements in healthy aging. Experimental aging research, 27(1), 19-39.

4. Staub, B., Doignon-Camus, N., Després, O., & Bonnefond, A. (2013). Sustained attention in the elderly: What do we know and what does it tell us about cognitive aging?. Ageing research reviews, 12(2), 459-468.
5. Bookheimer, S. Y., Salat, D. H., Terpstra, M., Ances, B. M., Barch, D. M., Buckner, R. L., ... & Yacoub, E. (2019). The lifespan human connectome project in aging: an overview. Neuroimage, 185, 335-348.
6. Chang, C., Leopold, D. A., Schölvinck, M. L., Mandelkow, H., Picchioni, D., Liu, X., ... & Duyn, J. H. (2016). Tracking brain arousal fluctuations with fMRI. Proceedings of the National Academy of Sciences, 113(16), 4518-4523.
7. Goodale, S. E., Ahmed, N., Zhao, C., de Zwart, J. A., Özbay, P. S., Picchioni, D., ... & Chang, C. (2021). fMRI-based detection of alertness predicts behavioral response variability. Elife, 10, e62376.
8. Beckmann, C. F., Mackay, C. E., Filippini, N., & Smith, S. M. (2009). Group comparison of resting-state FMRI data using multi-subject ICA and dual regression. Neuroimage, 47(Suppl 1), S148.
9. Winkler, A. M., Ridgway, G. R., Webster, M. A., Smith, S. M., & Nichols, T. E. (2014). Permutation inference for the general linear model. Neuroimage, 92, 381-397.
10. Nomi, J. S., Bzdok, D., Li, J., Bolt, T., Chang, C., Kornfeld, S., ... & Uddin, L. Q. (2022). Global fMRI signal topography differs systematically across the lifespan. bioRxiv, 2022-07.

Poster No 1198

Network-BrainAGE: A New Metric to Assess Network-Based Brain Aging

Shalaila Haas[1,2], Yuetong Yu[3], Hao-Qi Cui[3], Faye New[1], Ruiyang Ge[3], Sophia Frangou[3]

[1]Icahn School of Medicine at Mount Sinai, New York, NY, [2]Tri-institutional Center for Translational Research in Neuroimaging and Data Science (TReNDS), Atlanta, GA, [3]University of British Columbia, Vancouver, British Columbia

Introduction: Extensive research has established the difference between neuroimaging-predicted and actual chronological age (brainAGE), as a robust and biologically meaningful measure of brain health (Franke et al., 2019). We have previously released brainAGE models in development (Modabbernia et al., 2022) and across the lifespan (Yu et al., 2023). However, brainAGE is generally computed as a global index of age-related brain changes, disregarding information about spatial variation. In this study, we expand on our previous work to develop large-scale brainAGE models for specialized brain networks in healthy individuals across the lifespan.

Methods: The process for generating network-based brainAGE will follow our previous work (Modabbernia, 2022). The T1w structural images will be processed using standard pipelines in the Freesurfer software (version 7.1) in 9473 healthy individuals (aged 3-92 years; mean [SD] = 24.89[20.49]; N [%] female = 5126 [54.11%]) across 9 datasets: Adolescent Brain Cognitive Development (N = 3779); Pediatric Imaging, Neurocognition, and Genetics (N = 736); Brain Genomics Superstruct (N = 1570); 1000 Functional Connectomes (N = 1000); Brain Imaging Consortium (N = 203); Southwest University Adult Lifespan Dataset (N = 494); Information eXtraction from Images (N = 563); Cambridge Centre for Ageing and Neuroscience (650); and Australian Imaging Biomarkers and Lifestyle Study of Ageing datasets (N = 478). Subsequently, the Schaefer atlas was used to generate parcels (200, 400, 600, 800, 1000) of cortical thickness and cortical surface area, each assigned to one of the 7 Yeo networks (Yeo et al., 2011). Sex-specific pooled datasets were split into a training (80%) and testing (20%) subsets. Model performance was assessed by mean-absolute-error, root-mean-squared-error, and the correlation between predicted and chronological age in the test set after age-related bias adjustment.

Results: For all networks except the visual network, the mean-absolute-error reduced with increasing number of parcels (ranges across all: visual = 6.00 - 6.70; somatomotor = 5.00 - 5.67; dorsal-attention = 6.91 - 7.32; salience = 5.31 - 5.92; limbic = 5.82 - 6.65; control = 5.46 - 6.20; default = 4.89 - 5.51). For all networks, the root-mean-squared-error reduced with increasing number of parcels (ranges across all: visual = 8.03 - 9.32; somatomotor = 6.71 - 7.97; dorsal-attention = 9.22 - 9.86; salience = 7.43 - 8.41; limbic = 8.00 - 9.27; control = 7.63 - 8.68; default = 6.73 - 7.83). The correlation between predicted and chronological age was high across all networks (mean correlation across networks = 0.93) and varied by maximally 0.02 with increasing parcels. The results for the models using the 1000 parcels of the Schaefer atlas are presented in Figure 1. Correspondence between males and females for mean-absolute-error across networks was high (>0.97).

Conclusions: This study introduces novel network-specific brainAGE models indicating variability in model performance across specialized networks. These models offers potential applications in clinical samples that might demonstrate stronger associations with cognitive deficits, psychopathology, and risk factors.

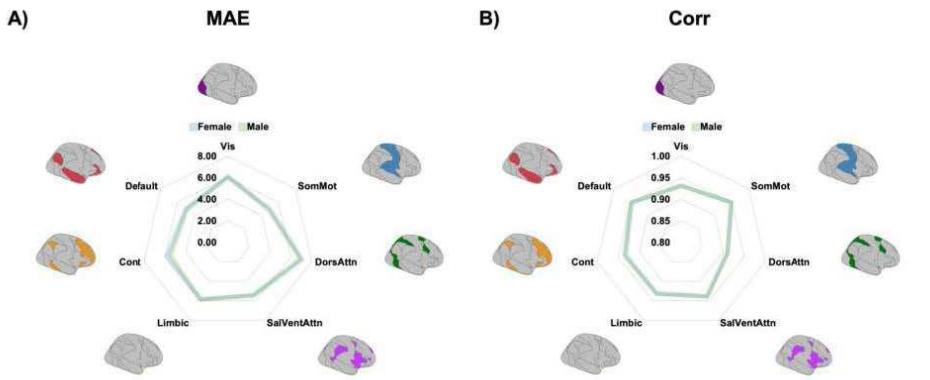

Figure 1. Sex-specific model performance of the network-based brainAGE models for each of the 7 Yeo networks based on the best performing model with 1000 parcels of the Schaefer atlas based on A) mean absolute error (MAE) and B) correlation between predicted and chronological age. Cont = control network; Default = default network; DorsAttn = dorsal attention network; Limbic = limbic network; SalVenAttn = salience/ventral attention network; SomMot = somatomotor network; Vis = visual network;

References

1. Franke, K. (2019), 'Ten Years of BrainAGE as a Neuroimaging Biomarker of Brain Aging: What Insights Have We Gained?', Frontiers in neurology, vol. 10, no. 789.
2. Modabbernia, A. (2022), 'Systematic evaluation of machine learning algorithms for neuroanatomically-based age prediction in youth', Human brain mapping, vol. 43, no.17, pp. 5126–5140.
3. Yeo, B. T. (2011), 'The organization of the human cerebral cortex estimated by intrinsic functional connectivity', Journal of neurophysiology, vol. 106, no. 3, pp. 1125–1165.
4. Yu, Y. (2023), Brain-Age Prediction: Systematic Evaluation of Site Effects, and Sample Age Range and Size. bioRxiv, 2023.11.06.565917.

Poster No 1199

Cerebrovascular Reactivity, Brain Structure, and Cognition in Aging: Heart and Brain Study

Congxiyu Wang[1,2], Raihaan Patel[1,2], Lucy Jobbins[3], Clare Mackay[1,2], Graham Reid[1], Georgina Hobden[4], Klaus P. Ebmeier[1,5], Daniel Bulte[6], Sana Suri[1,2]

[1]Department of Psychiatry, University of Oxford, Oxford, United Kingdom, [2]Oxford Centre for Human Brain Activity (OHBA), Wellcome Centre for Integrative Neuroimaging (WIN), Oxford, United Kingdom, [3]Nuffield Department of Clinical Neuroscience, University of Oxford, Oxford, United Kingdom, [4]Department of Experimental Psychology, University of Oxford, Oxford, United Kingdom, [5]Wellcome Centre for Integrative Neuroimaging (WIN), Oxford, United Kingdom, [6]Department of Engineering Science, University of Oxford, Oxford, United Kingdom

Introduction: Cerebrovascular reactivity (CVR) refers to a vasodilation response of brain blood vessels to vasoactive stimuli. Impaired CVR is related to neurodegenerative diseases including dementia (Hayes et al., 2022). However, the mechanisms underlying the relationship between CVR and age-related cognitive impairments remain unclear. As brain atrophy is a biomarker for Alzheimer's Disease and aging (Pini et al., 2016), our study aims to explore the relationships between CVR, grey matter volume, white matter hyperintensities, white matter integrity, and cognitive function in aging. Additionally, we examined the moderating effect of dementia risk, computed using an established score, on these relationships, aiming to inform the potential interventions of the modifiable dementia risk factors in midlife.

Methods: We recruited 163 participants (mean age=76.9±4.5) for the Heart and Brain Study (Suri et al., 2021). Participants underwent functional magnetic resonance imaging (MRI) to measure CVR under a 5% carbon dioxide respiratory challenge, structural MRI for grey matter volume (GMV), fluid attenuated inversion recovery for white matter hyperintensities (WMH), and diffusion tensor imaging for assessing white matter integrity (WMI). Cognition was evaluated using a battery of cognitive tests. Participants were stratified into high- or low-risk groups using the UK Biobank Dementia Risk Score (UKBDR) (Anatürk et al., 2023), which estimates midlife (mean age=52.5±4.4) dementia risk using retrospective records. Linear regression was performed to analyse associations between CVR (whole brain and lobe), and the MRI and cognitive outcomes while adjusting for age, sex, and total GMV. We also examined these associations separately for the high- and low-risk groups. Figure1 shows the details about the explanatory and outcome variables.

Variables		Information on variables
Explanatory variable		
Cerebrovascular reactivity (CVR)		Whole brain CVR, Frontal lobe CVR, Occipital lobe CVR, Parietal love CVR, Temporal love CVR
Outcome variables		
Volume of Grey Matter	Whole brain grey matter	Total Grey matter
	Subcortical region (left/right)	Nucleus accumbens, Amygdala, Caudate nucleus, Hippocampus, Pallidum, Thalamus, Putamen
	Cortical region	Default mode network: Posterior cingulate cortex & precuneus, Medial prefrontal cortex, Angular gyrus, Dorsal medial prefrontal cortex, Temporoparietal junction, Lateral temporal cortex, Anterior temporal pole, Parahippocampus, Posterior inferior parietal lobe
White matter hyperintensities (WMH)		Logarithm (log) of the normalised volume of white matter hyperintensities
White matter integrity (WMI)		Fractional Anisotropy (FA), Mean Diffusivity (MD), Radial Diffusivity (RD) of whole brain
Cognitive domains		Episodic memory, Working memory, Executive function, Fluency, Intelligence, Visuospatial memory

Results: In all participants, lower whole brain CVR significantly associated with smaller left nucleus accumbens (NAc) ($p<0.01$) and left thalamus volumes ($p<0.05$). Lobar analysis showed significant positive associations: parietal CVR with left hippocampus volume ($p<0.05$); temporal CVR with thalamus volume ($p<0.05$); frontal CVR with left thalamus and right NAc volumes ($p<0.05$); occipital CVR with right putamen ($p=0.05$). When stratifying by risk group, temporal CVR was positively related to left thalamus volume ($p<0.05$) exclusively in the high-risk group. In the low-risk group, whole brain CVR positively associated with temporoparietal junction volume ($p<0.01$). Left hippocampus volume positively associated with whole brain, frontal, parietal, and temporal CVR ($p<0.05$); frontal CVR positively related to right NAc volume ($p<0.05$). Regarding cognition, lower whole brain CVR was associated with worse fluency ($p<0.01$, primarily influenced by parietal CVR) and lower intelligence ($p<0.05$, primarily influenced by temporal CVR) only in the high-risk group. We found no associations between CVR with WMH or WMI in all participants or in either risk group.

Conclusions: This study demonstrates how global and lobar CVR relates to brain structure and cognitive functions, and how these relationships are moderated by dementia risk, contributing to a more comprehensive understanding of cognitive aging. Impaired CVR associates with smaller NAc (reward processing) and smaller thalamus (sensory perception and memory). Significant positive associations between the hippocampus (cognitive processes), temporoparietal junction (social cognition and theory of mind), and CVR were only shown in the low dementia risk group. Conversely, positive associations between fluency and intelligence were evident only in the high dementia risk group. There could potentially be a cerebrovascular-brain structure reserve for individuals with high midlife dementia risk. However, they may exhibit diminished CVR and cognitive function in later life. Future research could explore mediating relationships among midlife dementia risk, vascular health, brain structure, and cognition.

References

1. Anatürk, M., Patel, R. (2023). Development and validation of a dementia risk score in the UK Biobank and Whitehall II cohorts. BMJ Ment Health, 26(1).
2. Hayes, G. (2022). Vascular smooth muscle cell dysfunction in neurodegeneration. Frontiers in Neuroscience, 16, 1010164.
3. Pini, L. (2016). Brain atrophy in Alzheimer's disease and aging. Ageing research reviews, 30, 25-48.
4. Suri, S. (2021). Study Protocol: The Heart and Brain Study. Frontiers in Physiology, 12, 364.

Poster No 1200

Interrogating network connectivity differences in older adults using music

Sarah Faber[1], Alexander Belden[2], Psyche Loui[2], Randy McIntosh[3]

[1]Simon Fraser University, Burnaby, BC, [2]Northeastern University, Boston, MA, [3]Simon Fraser University, Vancouver, BC

Introduction: Music is an enjoyable stimulus that has been used therapeutically in a variety of health care settings. Despite many promising clinical reports, how music is able to effect change, and how it remains accessible to individuals with neurodegeneration remains unknown. In the present study, older adults listened to a selection of music excerpts both familiar and novel while fMRI was recorded before and after an eight week music listening intervention. We used hidden markov modelling (HMM, Vidaurre et al., 2016) and partial least squares (PLS; McIntosh et al., 1996) to identify patterns of network engagement and transition during music listening and how these patterns differed before and after the intervention.

Methods: We collected fMRI data from 15 cognitively healthy older adults (M = 62.67, SD = 15.35) during a music listening task. Excerpts were 20 seconds long and included self-selected familiar, well-liked songs; and excerpts selected by experimenters (popular and novel excerpts). Participants provided liking and familiarity ratings on a 4-point Likert scale following each excerpt. This protocol was completed twice: once before the intervention, and once following the intervention. We processed the fMRI data using the TVB-UKBB pipeline (Frazier-Logue et al., 2022) and completed all analyses in MatLab (Mathworks, 2019).

Results: We identified 4 brain states or functional networks. We calculated the fractional occupancy (time spent in each network) and transitional probability (the weighted, directed pairwise likelihood of transitioning between networks) for each excerpt, pre- and post-intervention. We averaged these values by stimulus category and modelled intervention effects using PLS. PLS results showed higher fractional occupancy in a bilateral temporal network pre-intervention, and higher fractional occupancy in a bilateral temporal mesolimbic network post-intervention. These networks are functionally analogous to the auditory network and auditory-reward network respectively. Transitional probability was higher for the temporal network pre-intervention, and higher for the temporal mesolimbic network post-intervention. Liking and familiarity ratings did not differ significantly between pre- and post-intervention scans.

Conclusions: Activity in a network containing regions related to auditory and reward processing was increased in a population of older adults following 8 weeks of music-based intervention. These findings indicate that music listening may be able to change dynamic network activity patterns in favour of musical reward. Increased reward stemming from increased music listening is one way music may be an effective therapeutic tool, and these findings raise many fascinating questions for future work with clinical populations.

References

1. Frazier-Logue, N., Wang, J., Wang, Z., Sodums, D., Khosla, A., Samson, A. D., ... & Shen, K. (2022). A robust modular automated neuroimaging pipeline for model inputs to TheVirtualBrain. Frontiers in Neuroinformatics, 16, 883223.
2. McIntosh, A. R., Bookstein, F. L., Haxby, J. V., & Grady, C. L. (1996). Spatial pattern analysis of functional brain images using partial least squares. Neuroimage, 3(3), 143-157.
3. Schaefer, A., Kong, R., Gordon, E. M., Laumann, T. O., Zuo, X. N., Holmes, A. J., ... & Yeo, B. T. (2018). Local-global parcellation of the human cerebral cortex from intrinsic functional connectivity MRI. Cerebral cortex, 28(9), 3095-3114.
4. Tian, Y., Margulies, D. S., Breakspear, M., & Zalesky, A. (2020). Topographic organization of the human subcortex unveiled with functional connectivity gradients. Nature neuroscience, 23(11), 1421-1432.
5. Vidaurre, D., Quinn, A. J., Baker, A. P., Dupret, D., Tejero-Cantero, A., & Woolrich, M. W. (2016). Spectrally resolved fast transient brain states in electrophysiological data. Neuroimage, 126, 81-95.
6. Vidaurre, D., Abeysuriya, R., Becker, R., Quinn, A. J., Alfaro-Almagro, F., Smith, S. M., & Woolrich, M. W. (2018). Discovering dynamic brain networks from big data in rest and task. Neuroimage, 180, 646-656.

Poster No 1201

Subclinical Vestibular Function is Associated with Surface Shape Changes in the Prefrontal Cortex

Dominic Padova[1], Andreia Faria[1], Yuri Agrawal[2], Tilak Ratnanather[1]

[1]Johns Hopkins University, Baltimore, MD, [2]University of Colorado School of Medicine, Denver, CO

Introduction: Aging-associated decline in peripheral vestibular function is linked to deficits in cognitive abilities like attention, executive function, and motor planning, highlighting the prefrontal cortex's significance. Functional neuroimaging suggests a vestibular-thalamus-prefrontal cortex pathway, with notable activations in the frontal gyri, but the exact neuroanatomical pathways remain unclear. Subclinical declines in vestibular function correlate with thalamic shape abnormalities, yet the specific involvement of prefrontal cortex subregions is not consistently demonstrated in structural neuroimaging of vestibular patients. To bridge this knowledge gap, this study investigates the relationship between subclinical vestibular function and surface shape changes in eight prefrontal cortex subfields, considering age, intracranial volume, and sex.

Methods: Data from 117 participants aged 60+ from the Baltimore Longitudinal Study of Aging, who underwent concurrent end-organ-specific vestibular tests (cVEMP for the saccule, oVEMP for the utricle, and vHIT for the horizonal canal) and T1-weighted MRI scans, were analyzed. This data was used in a previous study of a different cognitive network. MRI scans were segmented automatically using MRICloud. Surface meshes were generated using a restricted Delaunay triangulation. Population templates were created independently for each hemisphere of every region of interest and mapped to individual surfaces to measure surface shape change (tangent, normal). To streamline statistical testing, the 800 surface vertices were clustered into k patches of ≈150 mm2 based on surface geometry, reducing the number of comparisons thirtyfold. Shape variables were linearly regressed on standardized vestibular variables and covariates. Hypotheses were tested using 10,000

permutations, with a FWER rejection threshold set at the 0.05 level based on the maximum test statistic across the surface. Quality control was performed at each stage.

Results: No relationships between vestibular function and the shape of the superior frontal gyrus (SFG, SFG_PFC, SFG_pole) or the MFG_DPFC survived FWER correction at 0.05 level. A 1 standard deviation (SD) increase in saccular function was associated with ≈0.102% compression tangent to the cortical surface in Cluster 11 of the left pars opercularis (p≈0.027) and with ≈0.077% expansion normal to the cortical surface in Cluster 13 of the left middle frontal gyrus (p≈0.072). A 1 SD increase in utricular function correlated with ≈0.093% and ≈0.065% compressions tangent and normal to the cortical surface in Cluster 3 of the right pars orbitalis, respectively (p≈0.017 and p≈0.008). A 1 SD increase in horizontal semi-circular canal function correlated with ≈0.1% and ≈0.074% compression tangent and normal to the cortical surface in Cluster 4 of the left pars triangularis (p≈0.004 and p≈0.0001).

Conclusions: We found associations between reduced saccular function and significant cortical surface compression in the middle frontal gyrus and expansion in the pars opercularis, and reduced utricular and canal functions and significant surface expansion in the pars orbitalis and pars triangularis of the inferior frontal gyrus, respectively. Our significant regions agree with some of those reported in several neuroimaging studies of healthy adults and vestibular patients, clarifying previous equivocal findings. Furthermore, these findings may provide the neuroanatomical links through which vestibular end-organ function impacts higher-order cognitive abilities in the aging population.

References

1. Bigelow, R. T., & Agrawal, Y. (2015). Vestibular involvement in cognition: Visuospatial ability, attention, executive function, and memory. Journal of Vestibular Research, 25(2), 73-89.
2. Lopez C, Blanke O. (2011). 'The thalamocortical vestibular system in animals and humans', Brain research reviews, vol. 67, no. 1-2, pp. 119-146.
3. De Waele, C., Baudonnière, P., Lepecq, J., Tran Ba Huy, P., & Vidal, P. (2001). Vestibular projections in the human cortex. Experimental brain research, 141, 541-551.
4. Miyamoto, T., Fukushima, K., Takada, T., de Waele, C., & Vidal, P. P. (2007). Saccular stimulation of the human cortex: a functional magnetic resonance imaging study. Neuroscience letters, 423(1), 68-72.
5. Jacob A, Tward DJ, Resnick S, Smith PF, Lopez C, Rebello E, Wei EX, Ratnanather JT, Agrawal Y. (2020). 'Vestibular function and cortical and sub-cortical alterations in an aging population', Heliyon, vol. 6, no. 8, pp. e04728.
6. Hong, S. K., Kim, J. H., Kim, H. J., & Lee, H. J. (2014). Changes in the gray matter volume during compensation after vestibular neuritis: a longitudinal VBM study. Restorative Neurology and Neuroscience, 32(5), 663-673.
7. Hufner K, Stephan T, Hamilton D, Kalla R, Glasauer S, Strupp M, Brandt T. (2009). 'Gray-matter atrophy after chronic complete unilateral vestibular deafferentation', Annals of the New York Academy of Sciences, vol. 1164, no. 1, pp. 383-5.
8. zu Eulenburg P, Stoeter P, Dieterich M. (2010). 'Voxel-based morphometry depicts central compensation after vestibular neuritis', Annals of neurology, vol. 68, no. 2, pp. 241-9.
9. Wurthmann S, Naegel S, Steinberg BS, Theysohn N, Diener HC, Kleinschnitz C, Obermann M, Holle D. (2017). 'Cerebral gray matter changes in persistent postural perceptual dizziness', Journal of psychosomatic research, vol. 103, pp. 95-101.

Poster No 1202

The virtual ageing brain: structure-function relationship and cognitive decline in longitudinal data

Jan Fousek[1], Christiane Jockwitz[2], Nora Bittner[2], Meysam Hashemi[3], Spase Petkoski[3], Svenja Caspers[2], Viktor Jirsa[3]

[1]CEITEC, Masaryk University, Brno, Czech Republic, [2]Institute for Anatomy I, Medical Faculty, Heinrich-Heine University, Düsseldorf, Germany, [3]Institut de Neurosciences des Systèmes, Aix-Marseille University, Marseille, France

Introduction: The human brain changes during healthy aging with large individual variation in the cognitive decline (Oschwald 2020). Sources and mechanisms of this variability have been previously linked with whole-brain reorganisation, specifically in terms of the white-matter fibre tracts (structural connectivity, SC), and functional co-activations (functional connectivity, FC) of brain regions (Suárez 2020, Cabeza 2002), e.g. hemispheric asymmetry reduction. Recently, a causal framework employing whole-brain modelling where the individual SC informs a computational brain network model (Lavanga 2023) was developed on cross-sectional data of a large ageing cohort. Here, we validate the virtual ageing brain on the longitudinal data, and use it to unfold the variability of the individual cognitive decline. The prediction from the cross-sectional study was such that the subjects with stronger cognitive decline will move away from their optimal working point in terms of the network coupling, that is have a smaller slope of the change in parameter G than the subjects with well maintained cognitive performance.

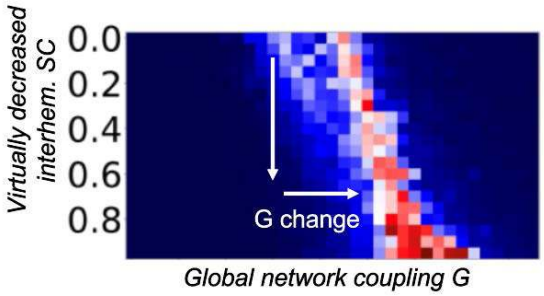

Methods: We used the SC and regional BOLD (Schaefer parcellation with 100 regions) signal of older subjects from the 1000BRAINS dataset (Caspers 2014) (full cohort: n=649, age range [51.1–85.4], nfemales=317; subjects with a follow-up: n=220, mean Δt=3.8 years). In particular, we have focused on data features with significant cross-sectional trends: from the SC we computed the average weight of the inter-hemispheric connections, from the FC we used the mean of weights of the homotopic connections, and from the FC dynamics (FCD, that is FC in a sliding window) we computed fluidity: variance of the upper triangle of the FCD (Lavanga 2023). The brain network model implemented in The Virtual Brain (Schirner 2022) was constructed from individual SC with the neural mass model (Montbrió 2015) governing the node dynamics enabling simulation of resting-state BOLD data. For each subject we employed Simulation Based Inference (SBI) to compute the posterior estimate of the global modulation from the empirical functional data (Gonçalves 2020). To assess the longitudinal change of the empirical data features and estimated parameters of the model, we computed the rate of change for the individual variables as X(t2)-X(t1) / (t2-t1).

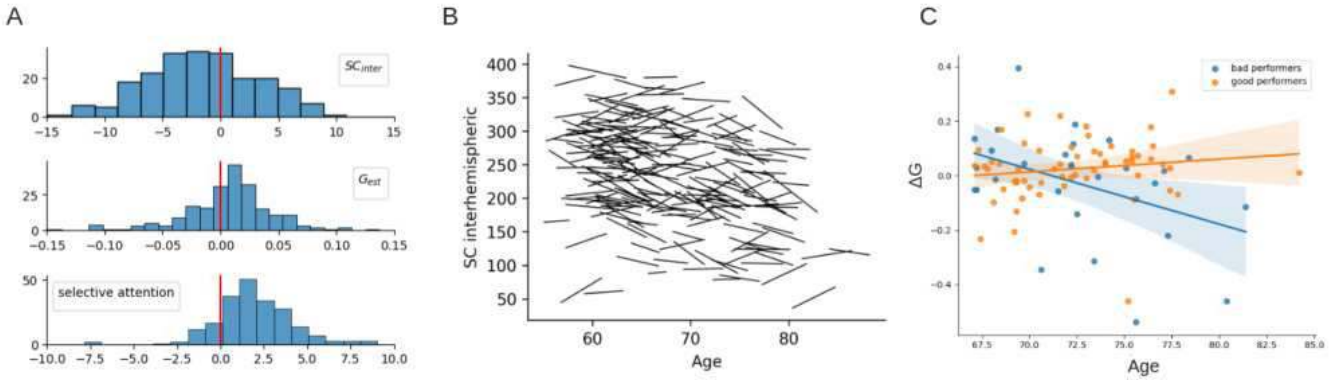

Results: The cross-sectional study relied on three pillars: structural and functional data features, individualized model parameters, and cognitive scores. Compared to the cross-sectional trends, the rates of change in the longitudinal dataset (Figure 2A,B) were preserved for the structural data (decrease of interhemispheric connections), estimated model parameters (increase of the global coupling strength), and in the cognitive scores (increased time to complete the selective attention task). Furthermore, for the older subjects (age >67) the change in estimated global coupling between the two sessions was higher for the subjects with good cognitive performance (Figure 2C).

Conclusions: Our results indicate that the deterioration of the interhemispheric SC is accompanied by increased modulation of the functional brain dynamics. The SC reorganisation might reflect a potential scaffolding of the brain during the ageing process. This effect is weaker for the cognitively well performing subjects, which suggests a process of brain maintenance. The decline in functional data features was not significant in the relatively short time span between the two visits, however it was sufficiently informative on the individual level for the estimation of the global coupling. The confrontation of this framework with the longitudinal dataset provides an important validity check as well as it opens an opportunity for further extensions by including other factors beyond 'age' and more nuanced relationships between aspects of cognitive decline and the brain changes.

References

1. Oschwald, J. (2020). Brain structure and cognitive ability in healthy aging: a review on longitudinal correlated change. Reviews in the Neurosciences, 31(1), 1–57.
2. Suárez, L. E. (2020). Linking Structure and Function in Macroscale Brain Networks. Trends in Cognitive Sciences, 24(4), 302–315.
3. Cabeza, R. (2002). Hemispheric asymmetry reduction in older adults: The HAROLD model. Psychology and Aging, 17(1), 85–100.
4. Lavanga, M. (2023). The virtual aging brain: Causal inference supports interhemispheric dedifferentiation in healthy aging. NeuroImage, 283, 120403.

5. Caspers, S. (2014). Studying variability in human brain aging in a population-based German cohort-rationale and design of 1000BRAINS. Frontiers in Aging Neuroscience, 6, 149.
6. Schirner, M. (2022). Brain simulation as a cloud service: The Virtual Brain on EBRAINS. NeuroImage, 251, 118973.
7. Montbrió, E. (2015). Macroscopic Description for Networks of Spiking Neurons. Physical Review X, 5(2), 021028.
8. Gonçalves, P. J. (2020). Training deep neural density estimators to identify mechanistic models of neural dynamics. eLife, 9.

Poster No 1203

Presbycusis impacts resting-state networks

Yingying Wang[1], Lauren Secilmis[2], Jordan Bollinger[3]

[1]Special Education and Communication Disorders, Lincoln, NE, [2]University of nebraska Lincoln, Lincoln, NE, [3]University of Nebraska-Lincoln, Lincoln, NE

Introduction: Presbycusis occurs in one in three people in the United States between the ages of 65 and 74 years[1]. Sensory degradation and/or deprivation due to hearing loss can result in significant changes in the gray and white matter of the brain[2,3]. Presbycusis presents a multifactorial and complex problem. The neural mechanism of presbycusis remains unclear and is controversial at many levels. The present study investigated the brain-behavioral relationship between the degree of hearing loss and functional connectivity using resting-state functional magnetic resonance imaging (fMRI) in 35 adults aged range from 40.0 to 74.3 years old.

Methods: Participants: A group of 35 native-English-speaking adults with self-reported normal hearing (age range: 40.0-74.3, 9 male and 26 female, 34 right-handed and one left-handed) were included in this study. We divided them into three age groups, including middle age (40.0-49 years old, N=8), young old (50 – 64 years old, N=16), and old (65 years and older, N=11). The study was approved by the Institutional Review Board at the University of Nebraska–Lincoln. Written consent forms were obtained from each participant prior to the research visit. Imaging acquisition: Brain imaging data were acquired by using a 3.0 Tesla Siemens Skyra scanner (Siemens Medical Solutions, Erlangen, Germany) with a 64-channel head coil. A high-resolution T1-weighted 3D structural image and EPI functional image were acquired. Imaging data analysis: Preprocessing of the Rs-fMRI imaging was performed with the CONN toolbox including functional realignment, outlier scrubbing, structural segmentation, normalization (MNI space normalization), and spatial smoothing. A band-pass filter (0.01 – 0.09 Hz) was applied to the time series. White matter and cerebrospinal fluid time series were regressed out. Linear detrending was performed during the denoising step. After the denoising step, the distribution of voxel-to-voxel connectivity was visualized for each step. All participants showed normally distributed data after denoising and were included in further analyses. Identifying the central auditory network: The data-driven approach uses group independent component analysis (gICA) in GIFT (version 4.0b) to decompose all preprocessed data into independent components (ICs), including dimensionality reduction, IC estimation, and back-reconstruction. Specifically, a two-step principal component analysis (PCA) was applied to reduce the data. The auditory network (AN) was then manually identified[6] to include mainly the primary auditory center (Brodmann areas 41, 42, 22) and back-reconstructed into individual time courses and spatial maps using a spatial-temporal dual-regression model. At the individual level, voxels in each subject-specific AN spatial map were used to compute the intra-network functional connectivity (FC) values, which represent the degree of synchronization between regions within AN. At last, the intra-network FC were converted into Z scores[7]. Statistical Analysis: The group differences were investigated by regression analyses. The group was defined as independent variable, while the intra-network FC values defined as dependent variables with age, PTA scores, and sex included as covariates. Results were reported at the significant level of $p < 0.05$ (cluster-wise AlphaSim threshold).

Results: The final cohort information was summarized in Figure 1. There were significant differences in the left PTA average of 4kHz and 8kHz ($p = 0.046$, Kruskal-Wallis rank sum test) and in the right PTA average of 4kHz and 8kHz ($p = 0.006$, Kruskal-Wallis rank sum test). The intra-network FC values of AN showed significant group effects in the left middle temporal gyrus within the AN.

Figure 1. Demographic characteristics

	Middle-aged	Young-old	Old	*p* Value
Sample Size	8	18	11	---
Sex (female/male)	5/3	14/2	7/4	0.26*
Age (mean ± SD)	43.2 ± 2.0	56.8 ± 4.0	70.2 ± 3.0	---
Left PTA for 4000 and 8000 Hz (mean ± SD)	15.9 ± 16.3	18.1 ± 10.6	33.9 ± 17.7	0.047†‡
Right PTA for 4000 and 8000 Hz (mean ± SD)	9.4 ± 9.8	15.9 ± 10.2	31.6 ± 16.2	0.006†‡

*Chi-square test was done using https://www.icalcu.com/stat/chisqtest.html.
†Kruskal-Wallis rank sum test was done using RStudio.
‡$p < 0.05$. PTA: pure tone average.

Conclusions: Our findings suggest that age-related hearing loss can be reflected by resting-state connectivity in AN. The causal relationship between the two needs longitudinal investigation.

References
1. NIDCD 2022
2. Zhang et al. 2020 Front Neurosci. 14:200
3. Jang et al. 2020 Medicine (Baltimore) 99(9): e19344
4. Dosenbach et al. 2017 NeuroImage Nov 1: 161: 80-93
5. Whitfield-Gabrieli et al. 2012 Brain connectivity, 2(3), 125-141.
6. Rademacher et al. 2001 NeuroImage, 13 (4): 669-683
7. Wang et al. 2014 Journal of cerebral blood flow & metabolism, 34 (4), 597-605

Poster No 1204

Distinct Structural Covariance in the Limbic Cortical Network between Women and Men along with Aging

Chang-Le Chen[1], Hecheng Jin[1], Mary Pangburn[1], Akiko Mizuno[1], Howard Aizenstein[1], Minjie Wu[1]

[1]University of Pittsburgh, Pittsburgh, PA

Introduction: The topological configuration of structural connections across the human brain is hypothesized to underlie functional organizations[1]. The patterns of morphological covariance are presumed to be vulnerable to disruption from aging, neurodegeneration, and other biological effects[2,3]. Covariance in local morphological metrics such as cortical thickness is frequently associated across disparate neuroanatomical regions between individuals, reflecting mutual trophic influences across distributed networks[4]. To elucidate age-related alterations in coordinated structural brain networks, we investigated structural covariance specifically within limbic-affiliated cortical circuits, which are critical hubs for multiple cognitive abilities[5], across an extensive age span in a population-based cohort. We postulated that altered structural covariance would be relevant to both advancing age and sex-dependent dimorphic processes.

Methods: We analyzed T1-weighted structural MRI data of 725 cognitively normal healthy adults aged from 36 to 100 years old from the Lifespan Human Connectome Project in Aging Project[6]. All T1-weighted images went through quality assurance[7], and surface-based morphometry was used to estimate cortical thickness using CAT12[7]. Regional cortical thickness within the limbic cortical network was sampled according to DK40 atlas[8] including orbitofrontal gyri, anterior, posterior, and isthmus cingulate gyri, parahippocampal gyri, entorhinal gyri, temporal pole, and insula. Since the images were acquired from four distinct scanners, thickness measures were harmonized using ComBat[9]. All subjects were stratified into female and male cohorts, and each cohort was further stratified into three age cohorts including young-middle (YM, 36-50 years, 131 females and 99 males), middle-old (MO, 51-70 years, 158 females and 118 males), and elder (EL, 71-100 years, 117 females and 102 males) cohorts considering the balanced sample size and the menopause record in the dataset. To calculate structural covariance in the limbic cortical network, we estimated partial correlation between regions of interest based on cortical thickness measures while adjusting for age, education, race handedness, and follicle-stimulating hormone levels within each cohort. To analyze structural covariance matrices, graph analysis was used to estimate global connectivity for the entire network and betweenness centrality for each node to represent general network properties[10]. Bootstrapping was used to estimate the empirical distribution of graph estimates.

Results: The general partial correlation between regions displayed a pattern of stronger connection with age in females than in males (Figure 1A). The analysis of variance further supported the observed pattern with a significant age-by-sex interaction ($p < 0.001$) and age main effect ($p < 0.001$) in terms of global connectivity while the sex main effect was not significant ($p = 0.758$) (Figure 1B). Additionally, specific regions exhibited heightened betweenness centrality in young-middle aged females that appeared to progressively decline with advancing age (Figure 2). An opposing pattern was observed in males with centrality measures increasing from young-middle to elder cohorts. However, the interaction between age and biological sex on centrality averages was only marginally significant ($p = 0.057$).

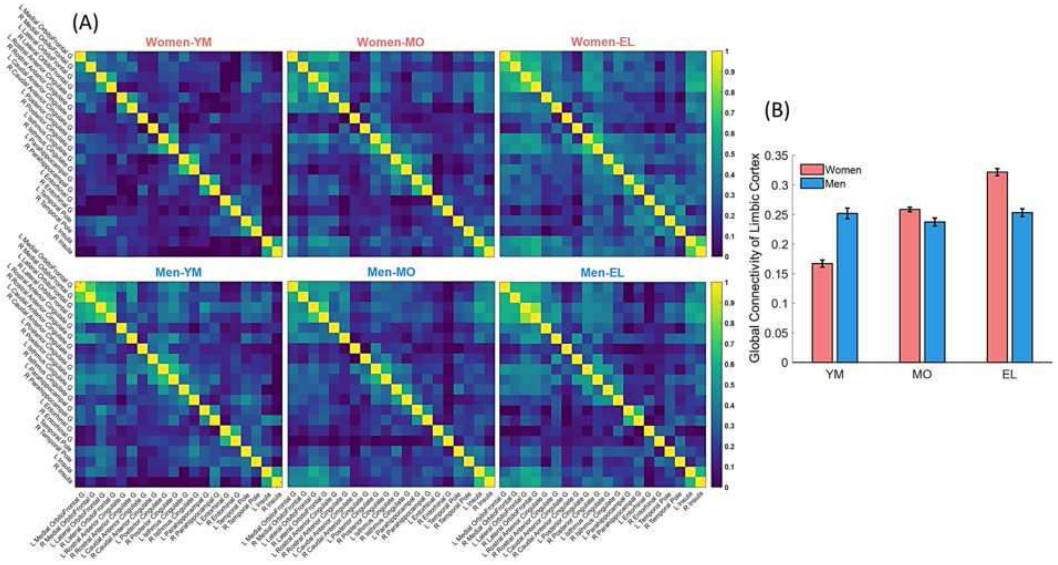

Figure 1. Structural covariance matrices of limbic cortical network in women and men across age levels including young-middle (YM), middle-old (MO), and elderly (EL) cohorts (A) and bar chart for the graph estimate, global connectivity (B).

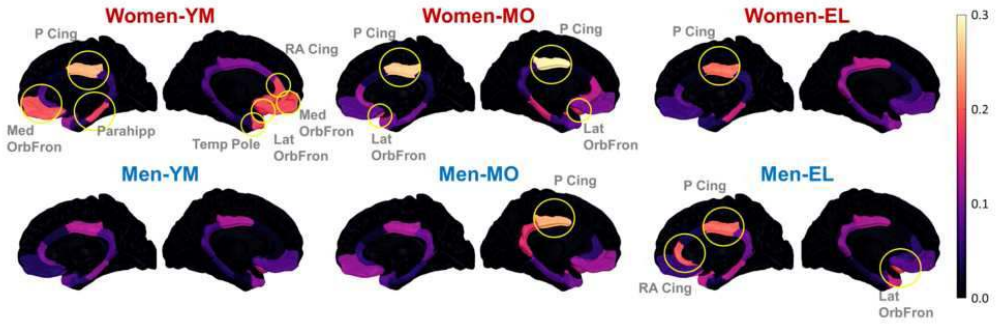

Figure 2. The mapping of betweenness centrality for each region of interest within limbic cortical network. Regions with top 10% centrality are highlighted.

Conclusions: Distinct patterns of structural covariance between females and males were observed along with aging; the overall network connectivity became stronger in women than men, implying a more aggregated limbic network in healthily aged women. This could also be a survival bias as compensating for higher prevalence of cognitive decline in women population. Also, the centralities became weaker in women cohorts, suggesting less cluster hubs exist over time and may be relevant to age-related de-differentiation. Collectively, these results suggest divergent network trajectories between women and men in the limbic network.

References

1. Smith, S., Duff, E., Groves, A., Nichols, T. E., Jbabdi, S., Westlye, L. T., ... & Douaud, G. (2019). Structural variability in the human brain reflects fine-grained functional architecture at the population level. Journal of Neuroscience, 39(31), 6136-6149.
2. Forsberg, L., Sigurdsson, S., Launer, L. J., Gudnason, V., & Ullén, F. (2019). Structural covariability hubs in old age. NeuroImage, 189, 307-315.
3. Wang, E., Jia, Y., Ya, Y., Xu, J., Mao, C., Luo, W., ... & Jiang, Z. (2021). Abnormal Topological Organization of Sulcal Depth-Based Structural Covariance Networks in Parkinson's Disease. Frontiers in Aging Neuroscience, 12, 575672.
4. Alexander-Bloch, A., Giedd, J. N., & Bullmore, E. (2013). Imaging structural co-variance between human brain regions. Nature Reviews Neuroscience, 14(5), 322-336.
5. Catani, M., Dell'Acqua, F., & De Schotten, M. T. (2013). A revised limbic system model for memory, emotion and behaviour. Neuroscience & Biobehavioral Reviews, 37(8), 1724-1737.
6. Bookheimer, S. Y., Salat, D. H., Terpstra, M., Ances, B. M., Barch, D. M., Buckner, R. L., ... & Yacoub, E. (2019). The lifespan human connectome project in aging: an overview. Neuroimage, 185, 335-348.
7. Gaser, C., Dahnke, R., Thompson, P.M., Kurth, F., Luders, E., (2022). CAT-a computational anatomy toolbox for the analysis of structural MRI data. BioRxiv, 2022.2006. 2011.495736.
8. Desikan, R. S., Ségonne, F., Fischl, B., Quinn, B. T., Dickerson, B. C., Blacker, D., ... & Killiany, R. J. (2006). An automated labeling system for subdividing the human cerebral cortex on MRI scans into gyral based regions of interest. Neuroimage, 31(3), 968-980.
9. Orlhac, F., Eertink, J. J., Cottereau, A. S., Zijlstra, J. M., Thieblemont, C., Meignan, M., ... & Buvat, I. (2022). A guide to ComBat harmonization of imaging biomarkers in multicenter studies. Journal of Nuclear Medicine, 63(2), 172-179.
10. Rubinov, M., & Sporns, O. (2010). Complex network measures of brain connectivity: uses and interpretations. Neuroimage, 52(3), 1059-1069.

Poster No 1205

Complex Regulation of Protocadherin Epigenetics on Aging-Related Brain Health

Vanessa Schmithorst[1], Daryaneh Badaly[2], Julia Wallace[3], Vince Lee[1], Cecilia Lo[4], Ashok Panigrahy[3]

[1]UPMC Children's Hospital, Pittsburgh, PA, [2]Child Mind Institute, New York, NY, [3]UPMC Children's Hospital of Pittsburgh, Pittsburgh, PA, [4]University of Pittsburgh, Pittsburgh, PA

Introduction: The clustered protocadherin (PCDH) gene clusters comprising three distinct gene families (α, β and γ) encode homotypic cell adhesion proteins regulating synaptic connectivity via specification of neuronal identity with combinatorial expression of genes in the three clusters (Yagi, 2008; Flaherty & Maniatis, 2020; Jia & Wu, 2020). Epigenetic alterations are a hallmark of aging; we investigate the impact of DNA methylation in the PCDH clusters on brain volume and neurocognitive outcomes.

Methods: We acquired subject data (N = 1936) from the Framingham Heart Study (FHS) Offspring Cohort, which was formed in 1971 to include children of participants consented into the original study. MR brain imaging outcomes were acquired using 1.0/1.5T scanners, and volumes were quantified from T2-weighted double spin-echo coronal sequences. Neuropsychological measures included: measures of language/verbal reasoning, verbal/visual memory, executive functions, and visuospatial skills. DNA methylation levels were quantified using the Infinium HumanMethylation450 BeadChip platform from Illumina. For the current study, we investigated total, PCDHA, PCDHB, and PCDHG methylation. To examine the relationship between age, methylation, brain volumes and neurocognitive outcomes, we performed the following analyses. The outcomes (dependent variables) were either brain volumes or cognitive performance. The best model for each outcome was found using the following procedure. Models were tested for each methylation value: 1) Completely excluded from the model; 2) Main effect only; 3) Main effect and interaction (with the independent variable); 4) Main effect and quadratic term; 5) Main effect, interaction, and quadratic term. As there are 5 options for each of four methylation values, a total of 5^4 = 625 linear regression models were tested. The best model was selected using the Aikake's Information Criterion (AIC).

Results: For each brain region and type (gray/white matter) except frontal gray, an increase in PCDHA methylation resulted in a retardation of age-related volume loss in both white and gray matter (Figure 1). An increase in PCDHB methylation resulted in a retardation of age-related volume loss in frontal gray matter. However, an increase in PCDHG methylation resulted in an acceleration of age-related volume loss in parietal white matter and temporal white matter. An increase in PCDHA methylation (Figure 2) also results in age-related preservation of acquired verbal skill as measured by Word Reading on the Wide Range Achievement Test (WRAT), while an increase in PCDHB methylation results in a retardation in age-related cognitive decline for the similarities test (SIM; verbal reasoning). However, an increase in PCDHG methylation results in an acceleration of age-related cognitive decline for the WRAT and the SIM tests.

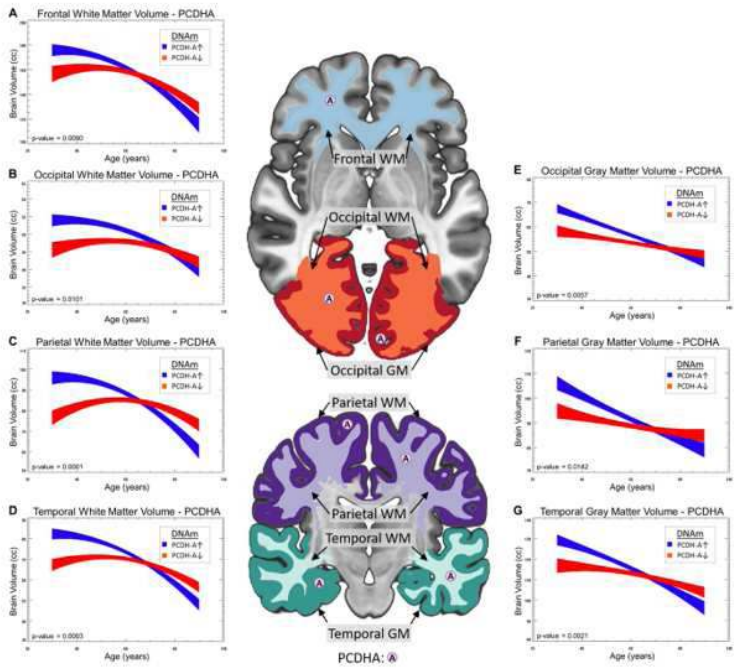

Figure 1. An increase in PCDHA methylation resulted in a retardation of age-related volume loss in both white matter and gray matter of multiple lobes.

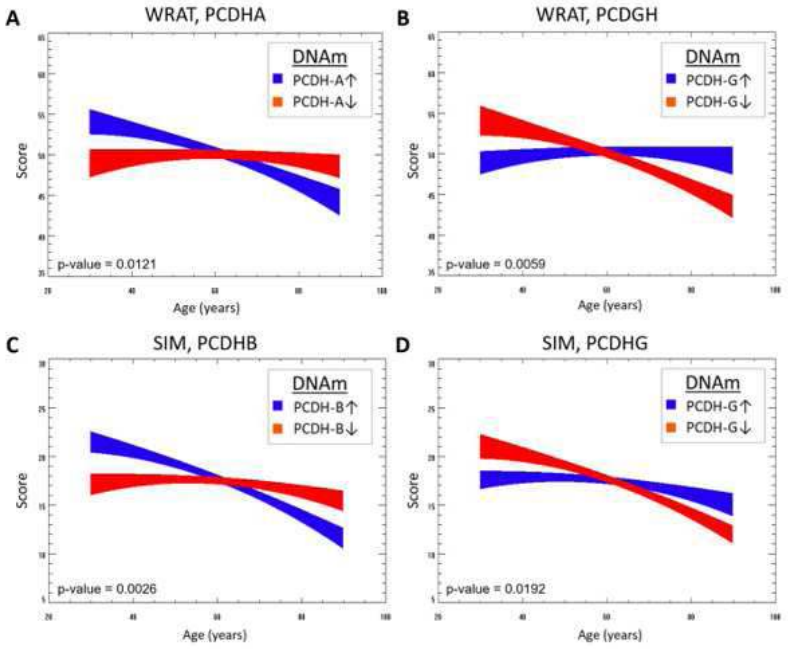

Figure 2. An increase in PCDHA/PCDHB methylation or a decrease in PCDHG methylation results in age-related retardation of cognitive loss as measured by the WRAT/SIM.

Conclusions: Our results show that normal aging processes affecting the brain and cognition are regulated by epigenetic configurations, particularly at PCDH loci. Unlike the characteristic pattern often seen for Alzheimer's, in which memory impairments are often an initial and core feature, we showed that PCDH methylation affects a set of cognitive skills unrelated to memory. We hypothesize that these results reflect optimal conditions for synaptogenesis during aging, specifically synaptic specificity, which differ from optimal conditions during neurodevelopment. Synaptogenesis during normal aging is a likely mechanism for maintaining cognitive function in the presence of synaptic loss and efficiency, as well as retarding the process of synaptic loss. Synaptogenesis likely enables aging individuals to retain more language ability in a manner similar to second language acquisition, as distinct from executive function and memory, involving a refinement process and increased specialization.

References

1. Flaherty, E. & Maniatis, T. The role of clustered protocadherins in neurodevelopment and neuropsychiatric diseases. Current Opinion in Genetics & Development 65, 144-150 (2020).
2. Jia, Z. & Wu, Q. Clustered protocadherins emerge as novel susceptibility loci for mental disorders. Frontiers in Neuroscience, 1191 (2020).
3. Yagi, T. Clustered protocadherin family. Development, growth & differentiation 50, S131-S140 (2008).

Poster No 1206

The age effect on the genetic architecture of the WM microstructure as measured by FA

Long Wei[1], Xin Xu[1], Suyu Zhong[2]

[1]Shandong Jianzhu University, Jinan, Shandong, [2]Beijing University Of Posts And Telecommunications, Beijing, Beijing

Introduction: Using diffusion MRI, a number of studies have explored white matter microstructure highly relevant to ageing[1]. It has been shown that the white matter microstructure may be influenced by genetic variants[2-3]. However, how the genetic contributions affect brain microstructural aging and particularly if existing homogeneous heritability aging pattern and distinct genetic architecture remain largely unknown. Here, we aim to identify the underlying genetic aging pattern and genetic variants of the white matter microstructure measured by fractional anisotropy (FA), which explains the mechanisms of aging changes.

Methods: We used dMRI and imputed SNP data from 22936 UKB individuals. We firstly performed the following SNP data quality controls using PLINK[4], excluding subjects with >2% missing genotypes, only including SNPs with MAF > 0.01, INFO score >0.7, and passing Hardy–Weinberg test (p value > 1 × 10−7)[5]. This resulted in 15847 individuals and 8063,552 biallelic

variants. We further used a sliding window approach of every 16 years range to examine genetic contributions vary with age (i.e., 40–55 years, 41–56 years, ...,55–70 years). Specifically, we estimated the proportion of variation explained by all autosomal SNPs with using GCTA-GREML analysis[6] to estimate the SNP-based heritability for FA of each tract. Then we assessed whether heritability estimates exhibited a homogeneous trend with age and explored heritability aging patterns. To capture the distinct, significantly SNP association, and independent lead SNPs with FA of each age range, we finally used FUMA (versionv1.4.0)[7] applying to the results from GWAS. In addition, we re-ran the above analyses with the second sliding window strategies for all subjects to further assess the genetic influence reproducibility.

Results: Fig. 1 showed FA heritability varying pattern of left and right tract with age. As shown in Fig.1, there were 12 tracts exhibiting a significant hemisphere × age interaction effect on the heritability, suggesting a significant hemisphere difference in the association between heritability and age. Specifically, there are three pattern types of these tracts. Fig.1A illustrated 7 tracts showing a significant reduced trajectory for left tract heritability as age increased. Fig. 1B illustrated 4 tracts showing a significant trajectory of first decreasing and then increasing for left tract heritability as age increased. And Fig.1C exhibited 1 tract of a significant increased trajectory for left tract heritability. Mean age of each age range was shown in Fig.1D. Based on the heritability trajectory pattern of left tract, we summarized them into 3 categories (Fig. 2). As illustrated in Fig. 2, the number of significant SNPs discovered for tracts with decreased heritability in the left hemisphere (Fig. 2A), increased heritability in the left hemisphere (Fig. 2B) and first decreasing and then increasing heritability in the left hemisphere (Fig. 2C) were exhibited. And we annotated SNPs to genes by three strategies: physical position, expression quantitative trait locus (eQTL) information, and chromatin interactions. The numbers of annotated genes were shown in Fig. 2D-E.

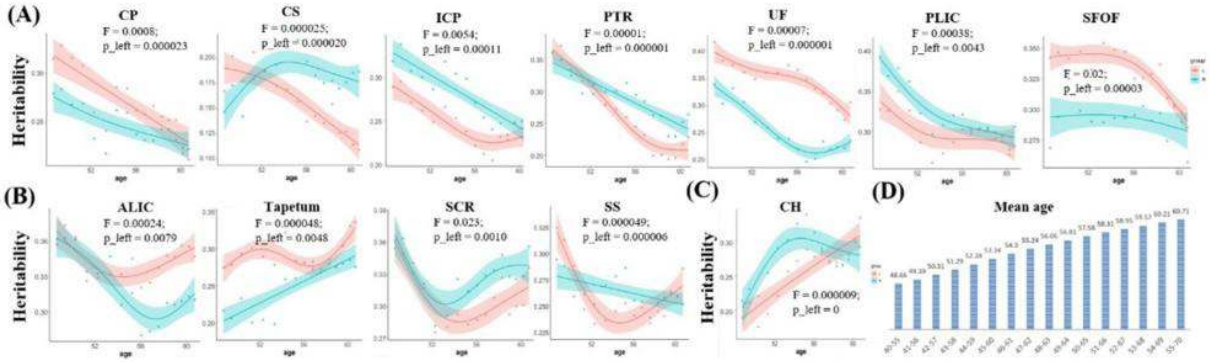

Fig. 1 The FA heritability trajectory of left and right tract with age. (A) Scatter plot of significant reduced trajectory for left tract heritability as age increased. (B) Scatter plot of significant trajectory of first decreasing and then increasing for left tract heritability as age increased. (C) Scatter plot of significant increased trajectory for left tract heritability as age increased. (D) Mean age of each age range. CP = Cerebral Peduncle; CS = Cortical Spinal; ICP = Inferior Cerebellar Peduncle; PTR = Posterior Thalamic Radiation; UF = Uncinate Fasciculus; PLIC = Posterior Limb Internal Capsule; SFOF = Superior Fronto_occipital Fasciculus; ALIC = Anterior Limb Internal Capsule; SCR = Superior Corona Radiata; SS = Sagittal Stratum; CH = Cingulum Hippocampus.

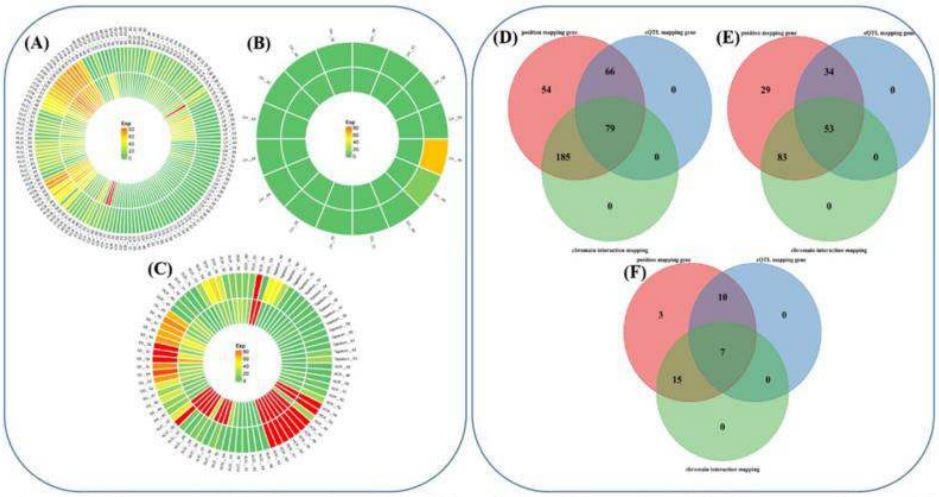

Fig. 2 Numbers of significant SNPs and annotated genes. The left panel showed the numbers of significant SNPs discovered for tracts. Outer layer: right tract; Inner layer: left tract. (A) Numbers for left tract heritability as age increased. (B) Numbers of significant increased trajectory for left tract heritability as age increased. (C) Numbers of first decreasing and then increasing for left tract heritability as age increased. The right panel showed numbers of annotated genes using three mapping strategies: physical position, expression quantitative trait locus (eQTL) information, and chromatin interactions. (D) Numbers for left tract heritability as age increased. (E) Numbers of first decreasing and then increasing for left tract heritability as age increased. (F) Numbers of significant increased trajectory for left tract heritability as age increased.

Conclusions: Our study has demonstrated that genetic contributions varied with brain microstructural aging. Particularly, three types of genetic influences were explored based that some tracts exhibited relatively consistent heritability trajectory pattern. In addition, our genetic variants analysis revealed the significant genetic effects on each type tracts as well as the gene mapping for the three patterns. Taken together, the present study explored the age effects on genetic architecture of white matter microstructure and identify some genetic age_varying patterns and variants, which may provide valuable implications for understanding observed white matter microstructure aging mechanisms.

References

1. Cox SR, et al. Ageing and brain white matter structure in 3,513 UK Biobank participants. Nat Commun. 2016, 7:13629.
2. Rutten-Jacobs LCA, et al. Genetic Study of White Matter Integrity in UK Biobank (N=8448) and the Overlap With Stroke, Depression, and Dementia. Stroke. 2018, 49(6):1340-1347.
3. Zhao B, et al. Heart-brain connections: Phenotypic and genetic insights from magnetic resonance images. Science. 2023, 380(6648):abn6598.
4. Purcell S, et al. PLINK: a tool set for whole-genome association and population-based linkage analyses. Am J Hum Genet. 2007, 81(3):559-575.
5. Makowski C, et al. Discovery of genomic loci of the human cerebral cortex using genetically informed brain atlases. Science. 2022, 375(6580):522-528.
6. Yang J, et al. GCTA: a tool for genome-wide complex trait analysis. Am J Hum Genet. 2011 Jan 7;88(1):76-82
7. Watanabe K, et al. Functional mapping and annotation of genetic associations with FUMA. Nat Commun. 2017, 8(1):1826.

Poster No 1207

Sex Differences in Age-Related Changes in Brain Network Segregation

Abhijot Sidhu[1], Kauê Duarte[1], Louis Lauzon[1], Cheryl McCreary[1], Andrea Protzner[1], Bradley Goodyear[1], Richard Frayne[1]

[1]University of Calgary, Calgary, Alberta

Introduction: The cortical regions of the human brain are organized into several functional networks that interact to facilitate higher-order cognition[1]. Resting-state functional magnetic resonance imaging (rs-fMRI) studies suggest that this interaction changes over the healthy adult lifespan, such that connectivity between networks strengthens as we age[2-3]. This redistribution is thought to be a compensatory response to age-related neurodegeneration to preserve cognitive function[2,4]. Sex differences in this aging process, however, have not been well characterized across the lifespan. Here we examine the influence of sex differences in a large cognitively healthy cohort.

Methods: rs-fMRI and 3D T1-weighted magnetic resonance (MR) data from 377 cognitively healthy adults (age range: 18.2–91.8 y; 56.1% female; MoCA ≥ 24) of the Calgary Normative Study were used for this study[5]. Follow-up data from 77 participants (21.3–80.8 y, 64.9% F, interval 2.0–3.9 y) were also included. Connectivity within and between the somatomotor (SMN), ventral attention (VAN), dorsal attention (DAN), frontoparietal (FPN), default mode (DMN), and visual (VIS) networks were computed. For each network, the average within- and between- network z-transformed connectivity (zw and zb, respectively) were used to compute the segregation index: SI=(zw– zb)/zw. A linear-mixed effects model (LME) was used to investigate the relationship between SI and age, age2, sex, and age×sex, with subject as a random effect to account for longitudinal interindividual differences. Post-hoc LME tests were used to investigate which specific pairs of networks were associated with the observed network effects. Network and pairwise LME results were adjusted using Holm-Bonferroni multiple comparison correction.

Results: Significant age effects were observed on SI for VIS ($p < 0.001$), SMN ($p < 0.001$), FPN ($p = 0.049$), VAN ($p < 0.001$), and DMN ($p < 0.001$), such that SI linearly decreased with increasing age for these networks. Significant sex effects were observed on SI for VAN ($p < 0.001$) and DMN ($p < 0.001$); females exhibited greater SI values regardless of age (Figure 1). Post-hoc pairwise analyses revealed significant age-associated increases in connectivity between FPN–VIS ($p = 0.005$), FPN–SMN ($p = 0.039$), and FPN–DAN ($p = 0.006$) network pairs. Post-hoc pairwise analyses also revealed significant sex differences in between-network connectivity for the SMN–DMN ($p = 0.038$), DAN–VAN ($p < 0.001$), DAN–FPN ($p = 0.003$), DAN–DMN ($p = 0.026$), and SVAN–FPN ($p < 0.001$) network pairs; females exhibited lower between-network connectivity for all network pairs regardless of age. No significant age2 and age×sex effects were observed.

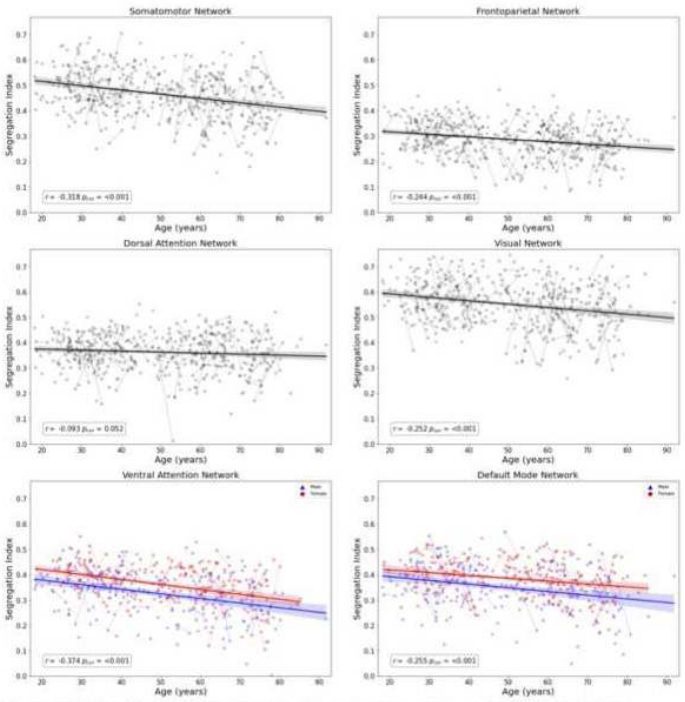

Figure 1: Segregation index significantly decrease with age for both sexes (grey) for the somatomotor, visual, ventral attention, frontoparietal, and default mode networks. Females (red) exhibit increased default mode and ventral attention network segregation relative to males (blue), independent of age. Shaded areas represent 95% confidence interval for fitted linear mixed effects model.

Conclusions: VIS, SMN, FPN, VAN, and DMN were all found to become less segregated across the healthy adult lifespan. Specifically, age-associated increases in between-network connectivity were restricted to pairs of sensory-associative and associative-associative networks. Females were observed to preserve VAN and DMN segregation relative to males, independent of age, and specifically, between associative networks. This suggests that female brains retain brain network segregation, which has been linked to healthy younger brains[1]. How sex differential brain aging patterns relate to cognitive function and how they are altered during pathological aging warrants further investigation.

References

1. Edde, M. (2020), 'Functional brain connectivity changes across the human life span: From fetal development to old age', Journal of Neuroscience Research, vol. 99, no. 1, pp. 236-262.
2. Chan, C. (2014), 'Decreased segregation of brain systems across the healthy adult lifespan', Proceedings of the National Academy of Sciences, vol. 111, no.46, pp. E4997-E5006.
3. Malagurski, B. (2020), 'Functional dedifferentiation of associative resting state networks in older adults – a longitudinal study', Neuroimage, vol. 214, pp. 116680-116691.
4. Goh, JO. (2009), 'Neuroplasticity and cognitive aging: The scaffolding theory of aging and cognition. Restorative Neurology and Neuroscience', Restorative Neurology and Neuroscience, vol. 27, no. 5, pp. 391-403.
5. McCreary, C. (2020), 'Calgary normative study: Design of a prospective longitudinal study to characterise potential quantitative MR biomarkers of neurodegeneration over the adult lifespan', BMJ Open, vol. 10, no. 8.

Poster No 1208

The Neural Substrates Underlying different subgroups across Apathy Depression Anhedonia and Fatigue

Jing Tian[1], Maiya Geddes[1]

[1]Montreal Neurological Institute, McGill University, Montreal, Canada

Introduction: Depression, apathy, anhedonia, and fatigue are common neuropsychiatric symptoms in Alzheimer's disease and have a profound impact on health-related quality of life[1]. However, because of the high correlation of these symptoms, analyzing them independently is limited[2]. Therefore, this study aims to conduct a comprehensive cross-sectional analysis of the performance differences and associated brain structural variances of these neuropsychiatric symptoms in older adults at a high risk of AD dementia.

Methods: We collected 119 at high-risk of developing AD dementia subjects from the PRe-symptomatic Evaluation of Experimental or Novel Treatments for Alzheimer's Disease (PREVENT-AD) cohort[3] with the same year of available clinical data and structural MRI data. We implemented a hierarchical clustering model on the clinical scores from four scales, identified two distinct groups. Lower scores across all items characterized subtype 1, while higher scores across all items characterized subtype 2. Specifically, the four scales include the Geriatric Depression Scale (GDS), a 15-item questionnaire assessing depressive symptoms in older adults; the Apathy Evaluation Scale (AES), an 18-item questionnaire evaluating the presence and severity of apathy; the Snaith-Hamilton Pleasure Scale (SHAPS), a 14-item questionnaire designed to assess an individual's ability to experience pleasure or enjoyment; and the Modified Fatigue Impact Scale (MFIS), a 21-item questionnaire designed to assess the impact of fatigue on various aspects of daily functioning. Subsequently, we combined cortical and subcortical gray matter volume (GMV) based on the structural MRI data of the same 119 subjects. Applied Logistic regression to match brain features with subtypes. We then applied the bootstrap technique to identify significant brain regions with a 90% confidence interval (Fig 2). Prior to classification, we controlled for age, sex, education year, APOE4 states, and eTIV (Estimated Total Intracranial Volume) through regression.

Results: In our clustering analysis, we find two groups (subtype 1 refers to the lower scores across the items; subtype 2 refers to the higher scores across the items.) shown in Fig 1A. Here, lower scores indicate higher levels of apathy, anhedonia, depression, and fatigue. Group 1 exhibits lower motivation, less pleasure, increased depression, and greater fatigue compare to group 2. Figure 1B presents the mean scores for each item in these two subtypes. Left nucleus accumbens, right pericalarine, right hippocampal, and left frontal are associated with the amotivational performances, which were shown on Figure 2. Specifically, compared to subtype 2, left accumbens, right pericalarine, and left frontal shows larger GMV in subtype 1, while right hippocampal shows smaller GMV in subtype 1.

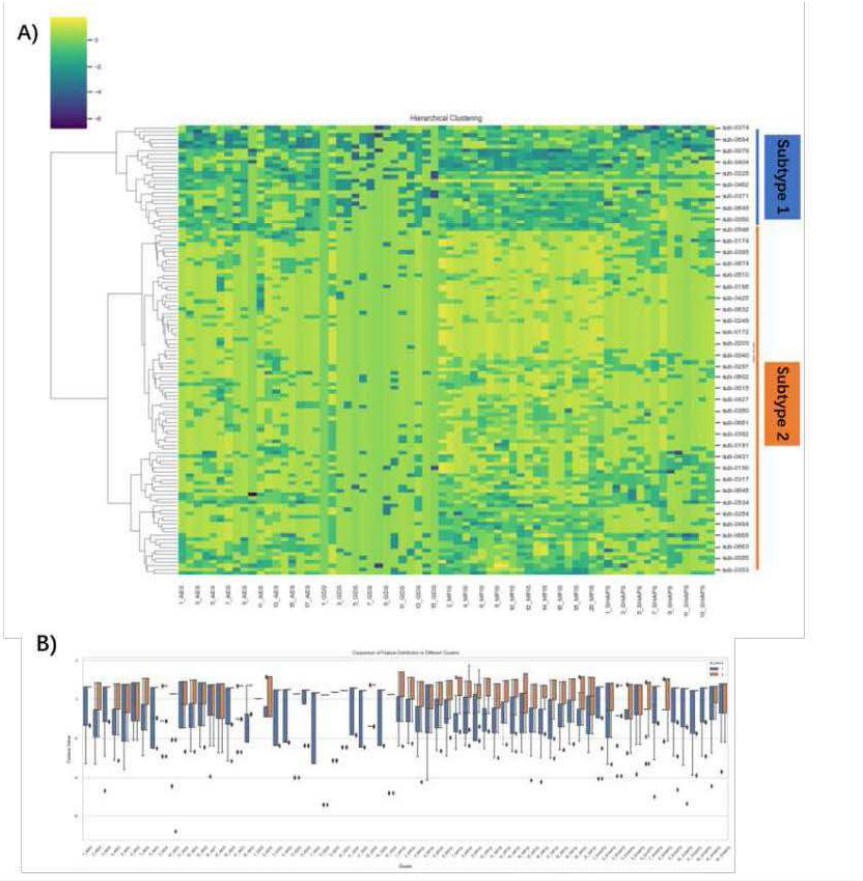

Figure 1. Subtype hierarchical clustering. **A)** 119 subjects (rows) with the same year of 68 items scores (columns) were used as input to hierarchical clustering. The color indicates the standard clinical score for each item. Euclidean distance between score vectors was used as a similarity metric between the two subjects. Ward's method was used as a linkage criterion. **B)** Clinical score distribution at each item of different subtypes (lower scores vs. higher scores) derived from hierarchical clustering. Mean scores for each item are presented to these two subtypes.

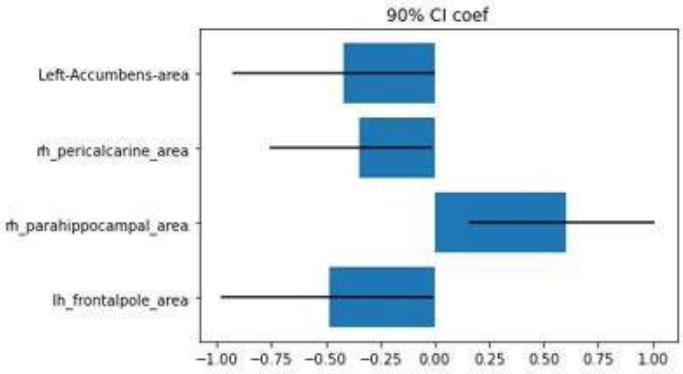

Fig 2. Distinct brain features of the two subtypes.

Conclusions: In our study, we identified significant associations between motivational factors, blood pressure levels, depression, and fatigue, and the gray matter volumes in specific brain regions. Notably, larger gray matter volumes were observed in the nucleus accumbens, a crucial component of the reward system, suggesting a potential link between reduced motivation, lower pressure, elevated depression, and fatigue. This finding aligns with research indicating that frequent Facebook use on smartphones is associated with smaller gray matter volumes in the nucleus accumbens, indicative of a heightened motivation for self-reward[3]. Additionally, individuals in this group exhibited reduced volumes in the hippocampal region, a key network hub involved in various cognitive functions, including memory, executive functions, and emotional regulation[4]. Above all, by identifying the subtype of motivational states, our study shed light on the neurobiology of different motivational states of aging people.

References

1. M. Amboni, et al., "Depression, Apathy, Anhedonia, and Fatigue in Parkinson's Disease," in Neuropsychiatric Symptoms of Movement Disorders, H. Reichmann, Ed., in Neuropsychiatric Symptoms of Neurological Disease., Cham: Springer International Publishing, 2015, pp. 1–28. doi: 10.1007/978-3-319-09537-0_1.
2. L. Daumas et al., "Associations, overlaps and dissociations between apathy and fatigue," Sci. Rep., vol. 12, no. 1, Art. no. 1, May 2022, doi: 10.1038/s41598-022-11071-5.
3. J. Tremblay-Mercier et al., "Open science datasets from PREVENT-AD, a longitudinal cohort of pre-symptomatic Alzheimer's disease," NeuroImage Clin., vol. 31, p. 102733, Jan. 2021, doi: 10.1016/j.nicl.2021.102733.
4. C. Montag et al., "Facebook usage on smartphones and gray matter volume of the nucleus accumbens," Behav. Brain Res., vol. 329, pp. 221–228, Jun. 2017, doi: 10.1016/j.bbr.2017.04.035.
5. K. Brosch et al., "Reduced hippocampal gray matter volume is a common feature of patients with major depression, bipolar disorder, and schizophrenia spectrum disorders," Mol. Psychiatry, vol. 27, no. 10, Art. no. 10, Oct. 2022, doi: 10.1038/s41380-022-01687-4.

Poster No 1209

Factors Influencing Neuroimaging-Based Advanced Brain Aging in Drug-Resistant Epilepsy

Ezequiel Gleichgerrcht[1], Kathryn Davis[2], Rebecca Roth[1], Sarah Newman-Norlund[3], Alexandra Parashos[4], Jennifer Cashwell[4], Neha Gandhi[5], Samaneh Nemati[3], Erik Kaestner[6], Carrie McDonald[7], Sigfus Kristinsson[3], Anto Bagić[8], Patricia Dugan[9], Daniel Deane[1], Julius Fridriksson[3], Ruben Kuzniecky[10], Leonardo Bonilha[3]

[1]Emory University, Atlanta, GA, [2]Perelman School of Medicine, University of Pennsylvania, PA, USA, Philadelphia, PA, [3]University of South Carolina, Columbia, SC, [4]Medical University of South Carolina, Charleston, SC, [5]Texas Institute of Neurology, Dallas, TX, [6]University of California San Diego, San Diego, CA, [7]University of California, San Diego, San Diego, CA, [8]University of Pittsburgh, Pittsburgh, PA, [9]New York University School of Medicine, New York, NY, [10]Northwell/Hosftra, Hampstead, NY

Introduction: Temporal lobe epilepsy demonstrates patterns of atrophy comparable to those seen in neurodegenerative disorders. However, the factors influencing these patterns of atrophy remain poorly understood. Here, we sought to evaluate the independent contribution of epilepsy-related variables and modifiable risk factors, as well as their interaction, on premature brain aging in epilepsy.

Methods: Brain age was estimated using a machine learning model from MRI in 515 patients with TLE and 615 neurologically healthy controls (HC). The difference between the MRI-estimated brain age and chronological age, i.e., the brain age gap (BAG) was computed for each participant. Complete risk factor data were available for 301 HC and 167 patients with TLE. Group-wise differences in BAG were determined, including voxel-wise comparisons of regional contributors to BAG specific to

each group. Propensity score matching was used to balance the datasets based on demographic and risk factor profiles, and multiple linear regression with interaction terms was used to evaluate the contributions of epilepsy and comorbidities on BAG.

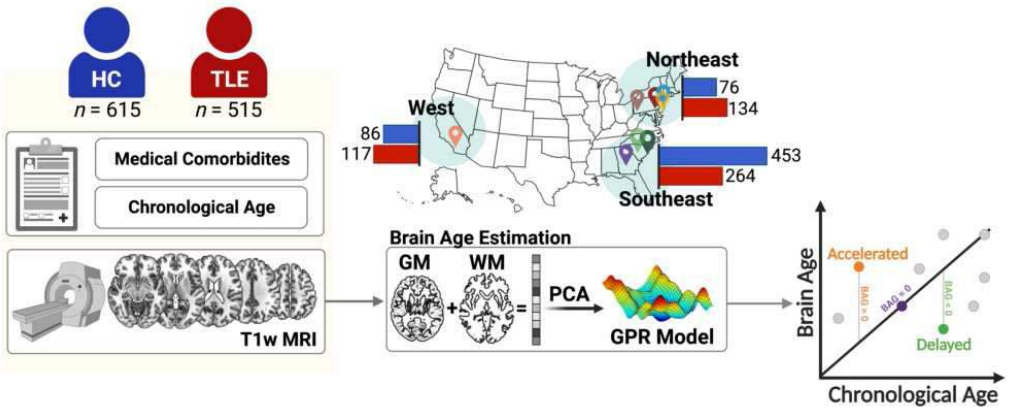

Fig. Visual overview of the study methods

Results: Compared with HC, TLE was associated with double the risk of advanced brain aging. Epilepsy was independently associated with 3.35 additional brain years. Brain regions disproportionally affected in TLE contributing to advanced BAG were medial temporal, perisylvian, and subcortical areas. An average increase of 0.97 years in BAG was observed per comorbidity, with an additional 0.83 BAG increase per comorbidity due to an interaction with epilepsy.

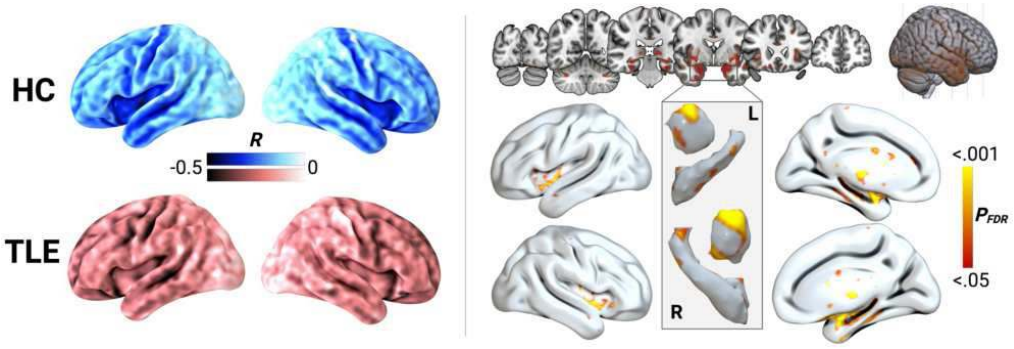

Fig. Summary of brain regions driving the patterns of brain aging seen in patients and healthy controls

Conclusions: Advanced brain aging is pervasive in TLE and is related to epilepsy-specific and modifiable risk factors. This observation has direct public health relevance since attention to modifiable risk factors is not typically at the forefront of epilepsy care, but targeted interventions could directly affect brain health in epilepsy.

References

1. Spencer S, Huh L. Outcomes of epilepsy surgery in adults and children. Lancet Neurol. 2008 Jun;7(6):525-37.
2. Helmstaedter C, Kurthen M, Lux S, Reuber M, Elger CE. Chronic epilepsy and cognition: a longitudinal study in temporal lobe epilepsy. Ann Neurol. 2003 Oct;54(4):425-32.
3. Lin JJ, Mula M, Hermann BP. Uncovering the neurobehavioural comorbidities of epilepsy over the lifespan. Lancet. 2012 Sep 29;380(9848):1180-92.
4. McDonald CR, Hagler DJ, Jr., Ahmadi ME, et al. Regional neocortical thinning in mesial temporal lobe epilepsy. Epilepsia. 2008 May;49(5):794-803.
5. Mueller SG, Laxer KD, Barakos J, Cheong I, Garcia P, Weiner MW. Widespread neocortical abnormalities in temporal lobe epilepsy with and without mesial sclerosis. Neuroimage. 2009 Jun;46(2):353-9.
6. Dabbs K, Becker T, Jones J, Rutecki P, Seidenberg M, Hermann B. Brain structure and aging in chronic temporal lobe epilepsy. Epilepsia. 2012 Jun;53(6):1033-43.
7. Lin JJ, Salamon N, Lee AD, et al. Reduced neocortical thickness and complexity mapped in mesial temporal lobe epilepsy with hippocampal sclerosis. Cereb Cortex. 2007 Sep;17(9):2007-18.
8. Bonilha L, Elm JJ, Edwards JC, et al. How common is brain atrophy in patients with medial temporal lobe epilepsy? Epilepsia. 2010 Sep;51(9):1774-9.

Poster No 1210

Neurochemical Correlates of White Matter Hyperintensities in Cognitively Normal Older Adults

Shaolin Yang[1], Minjie Wu[1], Olusola Ajilore[2], Howard Aizenstein[1], Anand Kumar[2]

[1]University of Pittsburgh, Pittsburgh, PA, [2]University of Illinois at Chicago, Chicago, IL

Introduction: White matter hyperintensities (WMH) on T2-FLAIR MR brain images is the traditional radiologic marker of cerebral small vessel disease (SVD). Pathological changes associated with WMH are heterogeneous including components of edema, gliosis, ischemia, and inflammation. However, conventional T2-FLAIR imaging is non-specific and does not differentiate these types of lesions. In this study, we evaluated the association between neurochemical measures and WMH in cognitively normal older adults. Findings from this study will provide insight into the heterogeneity of WMH.

Methods: Our study consisted of 42 cognitively normal older adults (mean age=68.8 years, age range: 60-84 years, 26 female). Brain MRI and MRS were acquired on a Philips Achieva 3T scanner, including T1w MPRAGE, T2-FLAIR, single-voxel 1H-MRS with voxels placed at bilateral frontal white matter. Specifically, the 1H-MRS spectra were acquired from the frontal white matter left (FWM-L) and right (FWM-R) (2x1x2 cm3). Spectral quantification was carried out in LCModel (Provencher et al., 1993) using unsuppressed water signal for scaling. Only the metabolite concentrations with a Cramer-Rao Lower Bound (CRLB) less than 20% were included in the data analysis. WMH volume was quantified on T2-FLAIR images using a 2D U-Net machine learning method implemented and validated by our lab (Li et al., 2023). WMH was parcellated into deep WMH, periventricular WMH, and frontal WMH. These global and regional WMH volumes were normalized by intracranial volume and log-transformed for second level analyses. Regression analyses were performed to evaluate the association between neurochemical measures in frontal white matter and normalized white matter hyperintensities, controlling for age.

Results: N-acetylaspartate (NAA) plus N-acetylaspartyl-glutamate (NAAG) in frontal WM was negatively associated with whole-brain normalized WMH (r = -0.403, p = 0.009), controlling for age (Fig. 1 top left). Myo-inositol (Ins) in the frontal WM is marginally positively associated with deep WMH (r = 0.282, p = 0.074) (Fig.1 top right) and frontal WMH (r = 0.294, p = 0.062) (data not shown). In addition, glutamate level in frontal WM is negatively associated with whole-brain WMH (r = -0.415, p = 0.016) (Fig. 1 bottom left) and periventricular WMH (r = -0.452, p = 0.008) (data not shown), controlling for age.

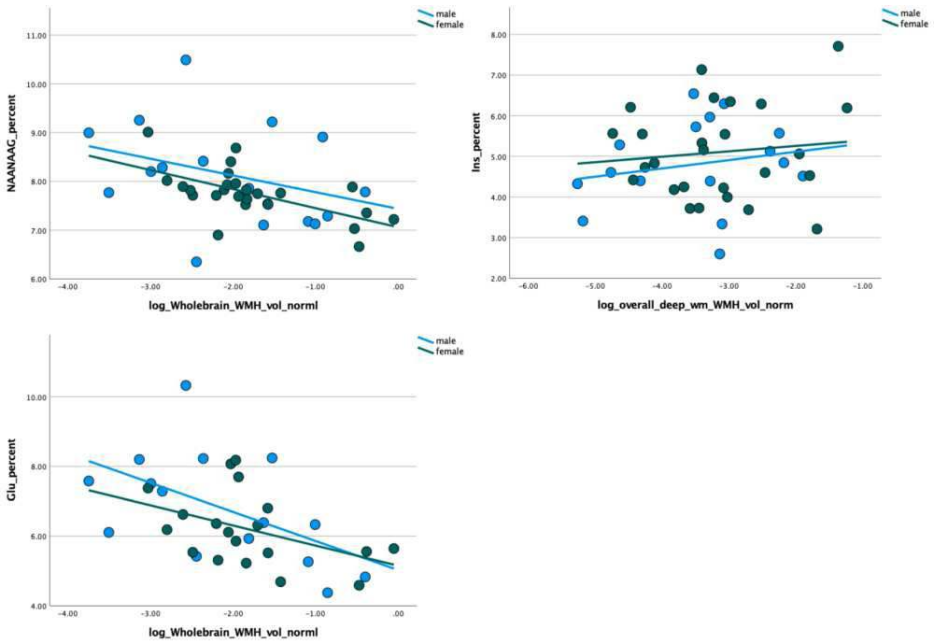

Fig. 1. Significant associations between frontal WM neurochemical measures and WMH burden, controlling for age: NAA+NAAG (top left), Ins (top right), and Glutamate (bottom left).

Conclusions: Our data reveal greater burden of WMH is associated with lower NAA level and greater Ins level. NAA is found almost exclusively in neurons. Reduced NAA + NAAG level in white matter reflects deficits in maintaining axonal-glial system (Moffett et al., 2007) and myelin synthesis (Chakraborty et al., 2001). Ins is primarily located in glial cells. Elevated Ins is believed to be a marker for gliosis and ongoing neuroinflammation (Heckova et al., 2022). Our findings provide insight into heterogeneity of WMH, suggesting SVD-related astrogliosis and axonal impairment (Llufriu et al., 2014).

References

1. Chakraborty, G., Mekala, P., Yahya, D., Wu, G. & Ledeen, R. W. (2001), "Intraneuronal N-acetylaspartate supplies acetyl groups for myelin lipid synthesis: evidence for myelin-associated aspartoacylase", J Neurochem 78, 736-745.
2. Heckova, E. et al. (2022), "Extensive Brain Pathologic Alterations Detected with 7.0-T MR Spectroscopic Imaging Associated with Disability in Multiple Sclerosis", Radiology 303, 141-150.
3. Li, J.H., Diniz, E., Forry T., Ibrahim, T.S., Aizenstein, H.J., Wu, M. (2023), "7T to 3T domain adaptation in white matter lesion segmentation on FLAIR images using deep learning", ISMRM, 03-08 June 2023, in Toronto, ON, Canada.
4. Llufriu, S. et al. (2014), "Magnetic resonance spectroscopy markers of disease progression in multiple sclerosis", JAMA Neurol 71, 840-847.
5. Moffett, J. R., Ross, B., Arun, P., Madhavarao, C. N. & Namboodiri, A. M (2007), "N-Acetylaspartate in the CNS: from neurodiagnostics to neurobiology", Prog Neurobiol 81, 89-131.
6. Provencher, S. W. (1993), "Estimation of metabolite concentrations from localized in vivo proton NMR spectra", Magn Reson. Med 30, 672-679.

Poster No 1211

G-Ratio and Conduction Velocity are Associated with Aging but Differentially with Cognitive Decline

Benjamin Newman[1], Jason Druzgal[1], John Van Horn[1]

[1]University of Virginia, Charlottesville, VA

Introduction: Recent efforts to quantify brain cellular microstructure have developed metrics of brain structure with implications for neuronal function. Termed aggregate g-ratio and aggregate conduction velocity, these metrics incorporate measures of myelin and intra-axonal volume. However it is not currently known how these metrics compare to age in an aging cohort nor how they predict cognition within this group. White matter hyperintensities (WMH) are a marked appearance of the aging brain, and should provide an ideal validation for the loss of myelin and subsequent functional disruption, estimated by these metrics.

Methods: Participants: 86 subjects were recruited for baseline neuroimaging with an age range between 58-81 (mean = 68.2 ± 5.84 S.D.) years old. There were 27 male and 58 female participants with average ages of 66.70 ± 4.97 S.D. and 68.87 ± 6.04 S.D., respectively. Image Acquisition: T1-weighted images were acquired using the ADNI3 designed MP-RAGE sequence with an isotropic voxel size 1.0×1.0×1.0mm3, TE=2980ms and TR=2300ms. Diffusion-weighted images were acquired with an isotropic voxel size of 1.7×1.7×1.7mm3, TE=70ms and TR=2900ms; 10 b=0 images and 64 gradient directions were collected at both b=1500s/mm2 and b=3000s/mm2. Behavioral and Cognitive Metrics: All subjects participated in the Trail Marking Task A & B, a measure of executive function where subjects are timed to completion of the task. B is considered more cognitively demanding as subjects must switch between letters and numbers in sequence. Image Processing: As described in more detail in previous work3 images were preprocessed with MRtrix34, FSL5, and Freesurfer6 to calculate voxel-wise aggregate g-ratio and aggregate conduction velocity with the mean b=0 images being used in lieu of T2-weighted images. WMH were automatically segmented out from the T1w images using Freesurfer. The mean value of these metrics was measured within each of the 48 regions of the JHU WM Atlas as a singular whole white matter ROI. Within subjects T-tests were used to evaluate the differences between differences within WMH and WM. Linear models tested the association between the trails tasks and cellular microstructure with controls for subject age and sex.

Results: Aggregate g-ratio was significantly reduced in WMH compared to the whole WM skeleton (T_{84}=-13.898, $p<0.001$; Fig. 1). Aggregate conduction velocity was also significantly reduced in WMH compared to the whole WM skeleton (T_{84}=-26.633, $p<0.001$; Fig. 1). However, the microstructure of the WMH was not significantly associated with age (g-ratio $F_{2,84}$=0.00086, $p=0.59$ n.s.; conduction velocity $F_{2,84}$=-0.0023, $p=0.277$ n.s.) nor performance on either Trail Marking Tasks (Trail A, g-ratio: $F_{2,84}$=0.304, $p=0.983$ n.s.; Trail A, conduction velocity: $F_{2,84}$=-6.439, $p=0.54$ n.s.; Trail B, g-ratio: $F_{2,84}$=26.35, $p=0.551$ n.s.; Trail B, conduction velocity: $F_{2,84}$=-2.513, $p=0.938$ n.s. Fig. 2). In the whole WM skeleton though Trail A & B was significantly associated with aggregate conduction velocity (Trail A: $F_{2,84}$=-41.03, $p<0.05$; Trail B: $F_{2,84}$=-176.080, $p<0.01$) but not aggregate g-ratio (Trail A: $F_{2,84}$=-34.45, $p=0.379$; Trail B: $F_{2,84}$=-30.66, $p=0.797$ n.s.). Both aggregate conduction velocity and aggregate g-ratio were observed to have a negative relationship with age in the WM skeleton ($F_{2,84}$=-0.0023, $p<0.05$; $F_{2,84}$=-0.0015, $p<0.05$, respectively).

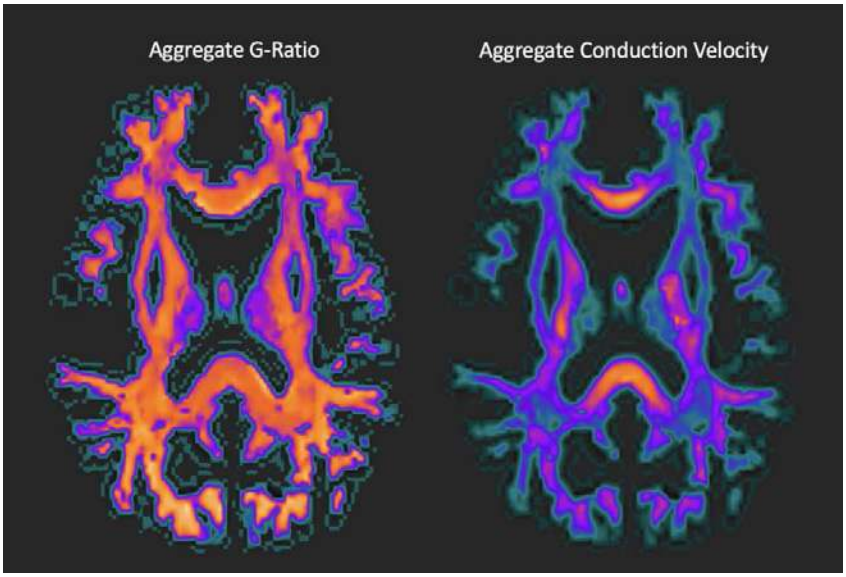

Figure 1: Visual comparison of a single subject's aggregate g-ratio and aggregate conduction velocity maps, MWH are far more visible in posterior regions as measured by aggregate conduction velocity.

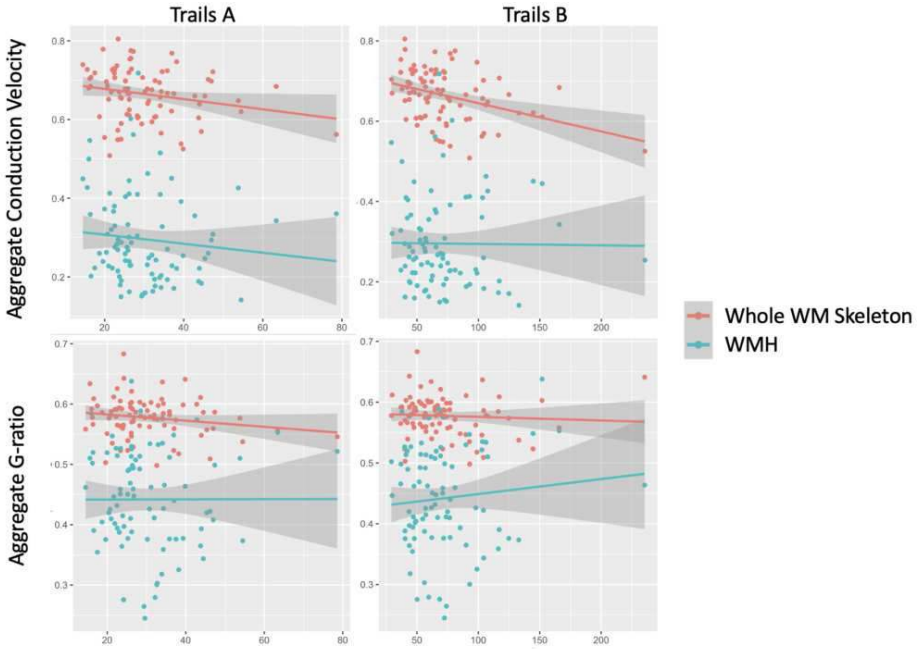

Figure 2: Chart showing variation between microstructural metrics and Trails performance in WMH and whole WM skeleton.

Conclusions: These results demonstrate that reductions in aggregate conduction velocity within the normal appearing WM skeleton, are associated with poorer cognitive performance. Aggregate g-ratio showed similar patterns of WMH damage and age-related decline, but did not have a similar relationship with cognitive performance. These results suggest that not only are aggregate conduction velocity and g-ratio measuring different microstructural features, but that the loss of larger diameter axons may drive cognitive decline in aging.

References

1. Newman BT, Jacokes Z, Venkadesh ST, et al. Conduction Velocity, G-ratio, and Extracellular Water as Microstructural Characteristics of Autism Spectrum Disorder. bioRxiv. Published online 2023:2023.07. 23.550166.
2. Tournier JD, Smith R, Raffelt D, et al. MRtrix3: A fast, flexible and open software framework for medical image processing and visualisation. NeuroImage. 2019;202:116137.
3. Jenkinson M, Beckmann CF, Behrens TE, Woolrich MW, Smith SM. Fsl. Neuroimage. 2012;62(2):782-790.
4. Fischl B. FreeSurfer. Neuroimage. 2012;62(2):774-781.

Poster No 1212

Early Life Adversity and Mental Health links clarified by Interhemispheric Functional Connectivity

Corentin Vallée[1], Xuemei Ma[1], Rebecca Pollard[1], Andrew Lawrence[1], Svenja Kretzer[1], Pei-Jung Cheng[1,2], Craig Morgan[1,3], Seeromanie Harding[1], Giovanni Montana[4], Ana Rodriguez-Mateos[5], Gunther Schumann[1], Carmine Pariante[1,6], Chiara Nosarti[1,7], Mitul Mehta[8,6], Paola Dazzan[1,6]

[1]Institute of Psychiatry, Psychology, and Neuroscience, King's College London, London, United Kingdom, [2]Department of Psychiatry, Chang Gung Memorial Hospital, Taoyuan, Taiwan, [3]SRC Centre for Society and Mental Health, King's College London, London, United Kingdom, [4]Department of Statistics, University of Warwick, Coventry, United Kingdom, [5]Faculty of Life Sciences and Medicine, King's College London, London, United Kingdom, [6]National Institute for Health Research (NIHR) Mental Health Biomedical Research Centre at South London and Maudsley NHS Foundation Trust and King's College London, London, United Kingdom, [7]School of Biomedical Engineering & Imaging Sciences, King's College London, London, United Kingdom, [8]Centre of Neuroimaging Sciences, King's College London, London, United Kingdom

Introduction: Early life adversity (ELA) refers to childhood and adolescence adverse circumstances such as physical or emotional abuse, bullying or family dysfunction. ELA exposure increases the risk of poor mental health (MH), including anxiety, depression, psychosis, and behavioral problems [Juwariah2022]. Recent resting-state fMRI studies suggest brain function may play a role in explaining the link between ELA and poor mental health [Rakesh2021,Banihashemi2022]. We have investigated here the relationship between ELA, mental health problems and resting-state interhemispheric functional connectivity (IHFC).

Methods: We recruited 230 young adolescents (11.2-14.9 years) from Southeast London schools. The presence of ELA was assessed with the Difficult and Harmful Life Event questionnaire and the England Index of Multiple Deprivation for Area-level adversity. Mental health was assessed using the Generalized Anxiety Disorder 7, the Short Mood and Feelings Questionnaire (depression), the Adolescent Psychotic-like Symptom Screener, the Strengths and Difficulties Questionnaire (well-being/ behavioral traits). Participants were considered negative for ELA if they 1) endured no more than two events of the Difficult and Harmful Life Event questionnaire, of lowest level of severity and frequency, no distress, and no injury; and 2) lived in a non-deprived area according to the Index of Multiple Deprivation. Participants were sorted in three groups: 1) ELA-positive and MH problems-negative (Group 1, n=81); 2) ELA-positive and MH problems-positive (Group 2, n=71); 3) ELA-negative and MH problems-negative (Control group, n=29). Numbers are given after questionnaire incompletion exclusion and fMRI quality control. Resting-state BOLD fMRI data were acquired on a 3T GE scanner. Images were processed with fMRIprep and denoised with CONN using fMRIprep calculated confounders. Functional connectivity was modelled by linear correlation (between pairs of contralateral voxels signal for IHFC). Group-level analyses used a general linear model with groups predicting connectivity. Voxel-level hypotheses were tested using multivariate parametric statistics with random-effects across. Inferences were performed at the level of individual clusters, based on non-parametric permutation testing (1000 iterations). Results use a combination of a cluster-forming voxel-level threshold (α_voxel=1%), and a cluster-mass threshold, corrected for false discovery rate (α_cluster=5%).

Results: Figure 1 shows differences of ROI-ROI connectivity between the control group and the other two groups exposed to ELA. We found large-scale, low effect size differences across the brain with noticeably larger effect size for homotopic structures, suggesting IHFC as a feature of interest. Figure 2 shows groups differences in interhemispheric connectivity. Compared to the control group, individuals in Group 1 showed lower IHFC in posterior brain areas (top slices). Individuals in Group 2 also showed lower IHFC in similar posterior areas when compared to the control group, but additionally showed increased IHFC in the cerebellum (middle slices). When comparing Group 1 and Group 2, both exposed to ELA but differing for MH problems, we still found an IHFC increase in cerebellum, while there were no more posterior alterations (bottom slices).

Conclusions: Our finding shows that a history of ELA is associated with distinctive alterations in interhemispheric functional connectivity depending on the co-occurence of MH problems. Alterations in IHFC connectivity may result from corpus callosum structural changes as diffusion MRI suggests corpus callosum fractional anisotropy is reduced in subjects with ELA, indicative of possible myelin atrophy or local neuroinflammation [McCarthy-Jones2018]. The cerebellum specific involvement in the co-occurrence of ELA and MH problems, may underlie symptom manifestation or be an indicator of low resilience. Its role warrants exploration in larger, longitudinal studies.

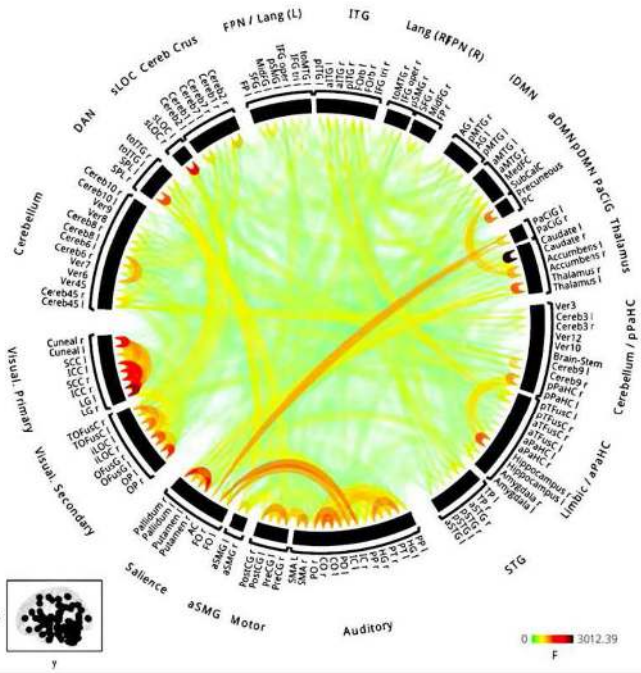

Figure 1: ROI-ROI functional connectivity – Control Group vs Group 1 and 2

Differences of ROI-ROI functional connectivity distribution between the control group (n=29) and group 1 and 2 (n=152). The ROIs used are the 132 ROIs composing the Harvard-Oxford AAL atlas (labels in the inner circle). The subcortical structures are grouped according to a priori functions labelled on the outer circle.

We found large scale, low effect size differences. The effect size of ELA looks much larger for roughly half of the homotopic location, in particular in posterior areas of the brain. Interhemispheric functional connectivity looks hence a feature of interest to investigate the association of ELA and functional connectivity

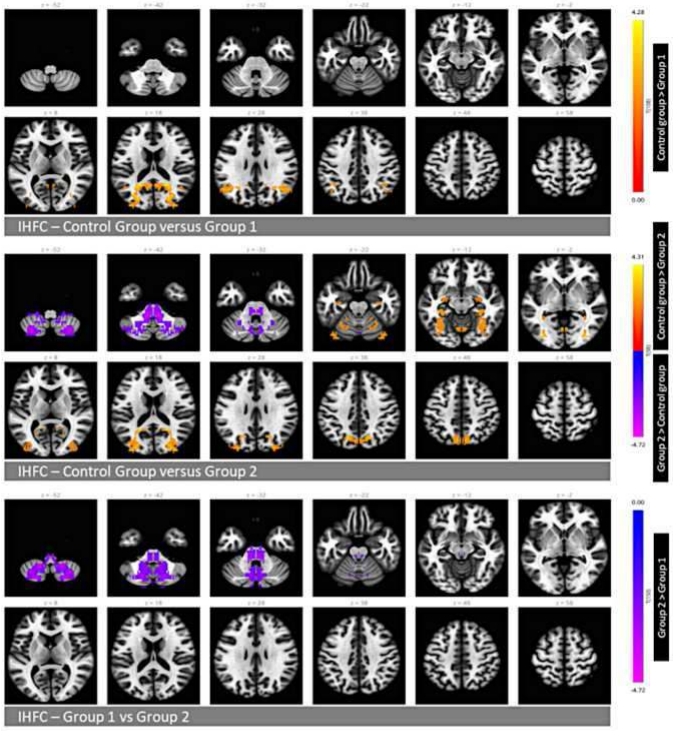

Figure 2: Differences of IHFC between Control group, Group 1 and Group 2

Differences of IHFC are shown on a MNI152 template, and the colors corresponds to the T(n) scores, where n is the degrees of freedom. Z is the axial coordinate in MNI space. The decrease of IHFC overlaps strongly around z=-8 and z=-18 between (top: Control group vs Group 1) and (middle: Control group vs Group 2). This decrease extend is however larger in lower part around z=12 for the (middle: Control group vs Group 2) comparison. The cerebellum IHFC decrease overlaps well between (middle: Control group vs Group 2) and (bottom: Group 1 vs Group 2).

IHFC map	Cluster location (MNI)	Size (Voxels)	p-value uncorrected	p-value FDR corrected
Top	±22 -54 +16	1366	0.000127	0.025703
Middle (Posterior)	±17 -70 +40	2585	0.000283	0.027140
Middle (Cerebellum)	±04 -36 -40	2378	0.000269	0.027140
Bottom	±16 -48 -48	2816	0.000165	0.032742

References
1. Juwariah, (2022). “Childhood adversities and mental health problems: A systematic review.” J Public Health Res, 11(3), 22799036221106613. https://doi.org/10.1177/22799036221106613
2. Rakesh, (2021). “Unraveling the Consequences of Childhood Maltreatment: Deviations From Typical Functional Neurodevelopment Mediate the Relationship Between Maltreatment History and Depressive Symptoms.” Biological psychiatry. Cognitive neuroscience and neuroimaging, 6(3), 329–342. https://doi.org/10.1016/j.bpsc.2020.09.016
3. Banihashemi, (2022). éChildhood Threat Is Associated With Lower Resting-State Connectivity Within a Central Visceral Network. Frontiers in psychology, 13, 805049.” https://doi.org/10.3389/fpsyg.2022.805049
4. McCarthy-Jones, (2018). “Childhood adversity associated with white matter alteration in the corpus callosum, corona radiata, and uncinate fasciculus of psychiatrically healthy adults.” Brain Imaging Behav, 12(2), 449-458. https://doi.org/10.1007/s11682-017-9703-1

Poster No 1213

Edge Participation Coefficient Unveiling the Development of Functional Connectome during Infancy

Tianyu Fang[1], Yue Wang[2], Qiuyun Fan[3], Yuanyuan Chen[4]

[1]Medical School of Tianjin University, Tianjin University, Tianjin, China, [2]Tianjin University, Tinajin, China, [3]Tianjin University, Tianjin, Tianjin, [4]Tianjin University, Tianjin, China

Introduction: Previous research has delved into the intricacies of the brain’s community structure in adults by employing methodologies that segment co-fluctuating edges into non-overlapping communities. However, our understanding of the brain’s community structure during infancy, a critical period marked by vital refinements in functional systems, remains relatively limited. In this study, we aim to bridge this gap by investigating how different functional connections within the infant brain interact and evolve as the brain undergoes development based on edge-centric functional analyses.

Methods: All participants in this study were recruited as part of the developing Human Connectome Project, approved by the UK National Research Ethics Authority. we selected 781 structural-functional scans from the third release, including scans acquired at 37–44.5 weeks postmenstrual age (PMA), at and before term-equivalent age (TEA). All scans were collected in the Evelina Newborn Imaging Centre, Evelina London Children’s Hospital, using a 3T Philips Achieva system during natural sleep without sedation. fifteen minutes of high temporal resolution rs-fMRI optimized for neonates was acquired using a multislice gradient-echo echo planar imaging sequence with multiband excitation. The rs-fMRI data were preprocessed by dHCP minimal processing pipeline and then followed with a nuisance regression, bandpass filtering and registration to template space, which was the UNC-neonate brain template and AAL atlas. Edge-centric functional connectivity (eFC) matrix was calculated between co-fluctuations of paired reginal signals. Then, edge time series were clustered into 10 communities utilizing a standard k-means algorithm with Euclidean distance. The representative edge community assignments were used as the initial centroids to cluster the edge time series of each single subject. We subsequently calculated edge participation coefficient (edge PC) of a given node within the modular eFC networks.

Results: Fig. 1 illustrated representative communities of brain connections obtained in term-born infants. Regions within sensorimotor system exhibited the greatest levels of within-system similarity. The overlapping community structure of infant cerebral cortex was displayed in Fig. 1e and f. In line with previous study on adults, regions within sensorimotor system were simultaneously involved in many communities, thereby connecting regions from multiple other systems. Fg. 2 illustrated changes in edge participant coefficient during infant brain maturation. Notably, edge PC values were significantly higher in preterm born infants compared to term born infants. When visualizing the association between edge PC and PMA at scan by node, significant negative correlation was observed with 89 regions surviving FWE correction. Further investigation at both interconnected network and connection level revealed that PC values of edges connecting the visual system with other networks and within “higher-order” networks displayed robust associations with the early brain maturation of normal neonates.

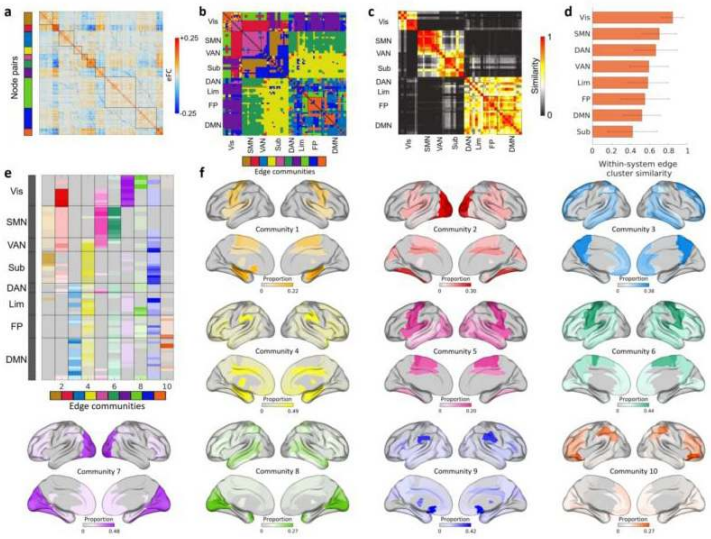

Figure 1. The overlapping community structure of cerebral cortex in term-born infant. (a) The eFC matrix reordered according to ten communities. Note that, on average, within-community eFC is greater than between-community eFC. (b) Edge communities mapped into a $[N \times N]$ matrix. The element of the edge community matrix denotes the community label of the corresponding edge. (c) The similarity of edge communities obtained by comparing the values of any two columns in (b). (d) Comparison of within-system similarity values for each of the 8 pre-defined brain systems. (e) Proportion of all edges assigned to the community that included that node as one of its endpoints. The brighter color is, the more edges were assigned to that community. (f) Topographic distribution of communities by overlaying the proportions onto a brain render.

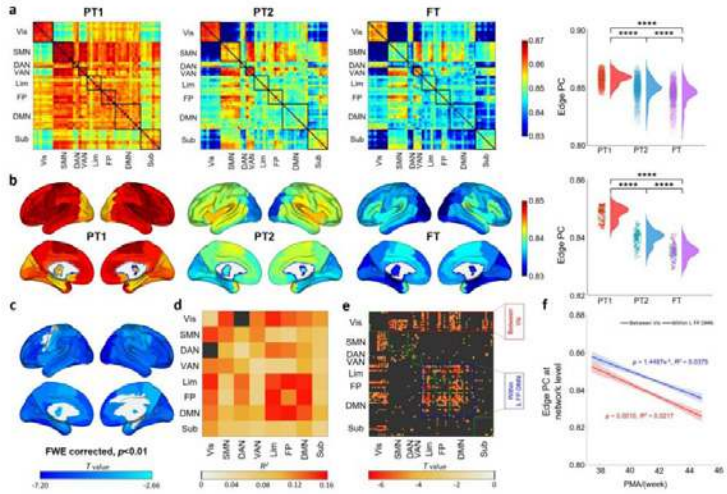

Figure 2. Changes in edge participant coefficient during infant brain maturation. (a) Group averaged edge PC values in matrix form were displayed for three groups. Violin plots on the right side illustrate the inter-group differences in terms of edge PC values (b) Topographic distribution of edge PC values averaged for each brain region (calculated as the mean of each row in the matrix shown in (a)). Violin plots show the inter-group differences in terms of edge PC values for each brain region. (c) Association between PMA at scan and edge PC by node in FT group. T-values visualized were thresholded at p<0.01 (FEW corrected for multiple comparisons). (d) Relationship between PMA at scan and edge PC at interconnected network level in FT group. The presented pattern was thresholded at p<0.01 (FDR corrected). (e) Edgewise relationship between PMA at scan and edge PC in FT group. T-values were thresholded at p<0.01 (FEW corrected for multiple comparisons). Red box highlights connections between the visual system and other systems. Blue box highlights connections within limbic, frontoparietal (FP) and default mode network (DMN). (f) Correlations between PMA at scan and edge PC at network level in FT group with 95% confidence intervals.

Conclusions: The overlapping community structure of human cerebral cortex becomes established in the early stage of development. Edge-centric approach demonstrates a high level of participant specificity, capturing unique features of individuals. Decrease in functional diversity suggests the specialization of functional systems as the infant brain matures.

References

1. Fitzgibbon, S. P. (2020), 'The developing Human Connectome Project (dHCP) automated resting-state functional processing framework for newborn infants', Neuroimage, vol. 223, p. 117303
2. Faskowitz, J. (2020). 'Edge-centric functional network representations of human cerebral cortex reveal overlapping system-level architecture', Nature neuroscience, vol. 23, no. 12, pp. 1644-1654.
3. Hughes, E. J. (2017). 'A dedicated neonatal brain imaging system', Magnetic resonance in medicine, vol. 78, no. 2, pp. 794-804.

Poster No 1214

Deciphering the Dynamic Spatiotemporal Maturation from Childhood to Adolescence

Kyoungseob Byeon[1], Shinwon Park[1], Jon Clucas[1], Kahini Mehta[2], Matthew Cieslak[2], Seok-Jun Hong[3], Hyunjin Park[3], Jonathan Smallwood[4], Theodore Satterthwaite[2], Michael Milham[1], Ting Xu[1]

[1]Child Mind Institute, New York, NY, [2]University of Pennsylvania, Philadelphia, PA, [3]Sungkyunkwan University, Suwon, South Korea, [4]Queen's University, Ontario, Canada

Introduction: Cortical maturation from childhood to adolescence plays a crucial role in neurodevelopment, shaping cognition, emotions, and behaviors. Convergent evidence suggests that neurodevelopment proceeds in a hierarchical manner, with heterogeneous structural and functional maturation patterns. However, the relationship between the established static functional patterns and the brain's intrinsic spatiotemporal dynamics remains underexplored. To address this gap, we employ Complex Principal Component Analysis (CPCA), a technique capable of reducing the complexity of high-dimensional spatiotemporal data on multiple development datasets. In this study, we aim to understand how spatiotemporal patterns develop with age, both locally and globally, focusing on three distinct propagation pathways from childhood to adolescence.

Methods: We utilized resting-state fMRI data across a developmental continuum, including Human Connectome Project Development (HCP-D, ages 8.1-21.9, n=408) and Aging (HCP-A, ages 36.0-64.9, n=399) datasets, NKI-Rockland Sample (n=839), and CCNP dataset (n=152) cohorts. The preprocessed data were parcellated followed by CPCA to extract components (i.e. spatiotemporal patterns), aligning them based on their spatial similarity with static functional gradients. Utilizing a dual-regression framework, we reconstructed individual dynamic patterns and assessed the reproducibility across cohorts, test-retest reliability across sessions, and age effects by comparing the individual patterns with the adult reference from HCP-A dataset. Additionally, we examined the age effect of amplitude for the temporal fluctuations and decoded using NeuroQuery and gene ontology enrichment analysis.

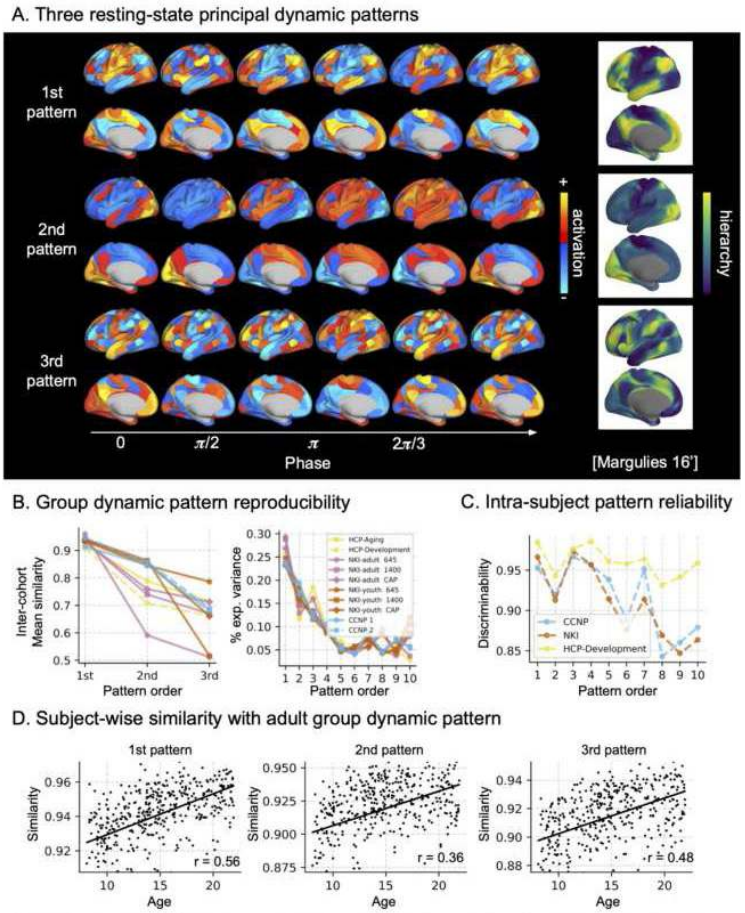

Figure 1. Reproducibility and Neurodevelopment of Resting-State Dynamic Brain Patterns.
This figure delineates the intricate nature of resting-state dynamic brain patterns, capturing their evolution across developmental and aging cohorts. A. Three phase-dependent spatiotemporal patterns identified through Complex Principal Component Analysis (CPCA) with HCP-Aging cohort. B. The reproducibility of these dynamic patterns across groups, quantified through a spatiotemporal correlation similarity index [-1, 1], which underscores the consistency of these patterns across varied datasets. This consistency is further validated by the explained variance ratio depicted across the components, emphasizing the robust nature of these patterns. C. Presents the intra-subject reliability of these dynamic patterns, emphasizing the stability within individuals over different cohorts. D. Correlation plots reveal the maturation trajectory, indicating a progressive alignment with adult-like dynamic states across the age spectrum.

Results: We identified phase-dependent spatiotemporal components and focused on the first three dynamic states (Fig. 1A). These were reproducible across cohorts and each explained over 10% of the variation in each datasets (Fig 1B). High test-retest reliability was observed for the first three patterns ($r > 0.9$), revealing individual-specific patterns can be differentiated from other participants (Fig. 1C). Compared to the adult reference, a linear increased similarity with age (r=.36-.56) was observed, indicating maturation towards adult-like dynamic states (Fig. 1D). As shown in Fig 2A, occurrence time ratio (OTR), representing the time spent in each dynamic state, exhibited a positive age effect for pattern 1 (r=.25) but a negative age effect for pattern 2 (r=-.14). A strong correlation (r=.93) was observed between OTR and the EVR, suggesting the significant contribution of time spent in each state to their altered EVR. We also calculated the proportion of bottom-up (sensory-to-association) and top-down (association-to-sensory) contributions to the first dynamic pattern. Interestingly, with increasing age, individuals spent less time in bottom-up but more time in states characterized by top-down propagation (Fig. 2B). Additionally, the amplitude of regional fluctuations for each dynamic state varied across individuals. From childhood to adolescence, amplitude increased in specific brain regions for patterns 1 and 3, while it decreased for pattern 2. (Fig. 2C), which appears to be related to cell proliferation, protein synthesis, and metal ion regulations.

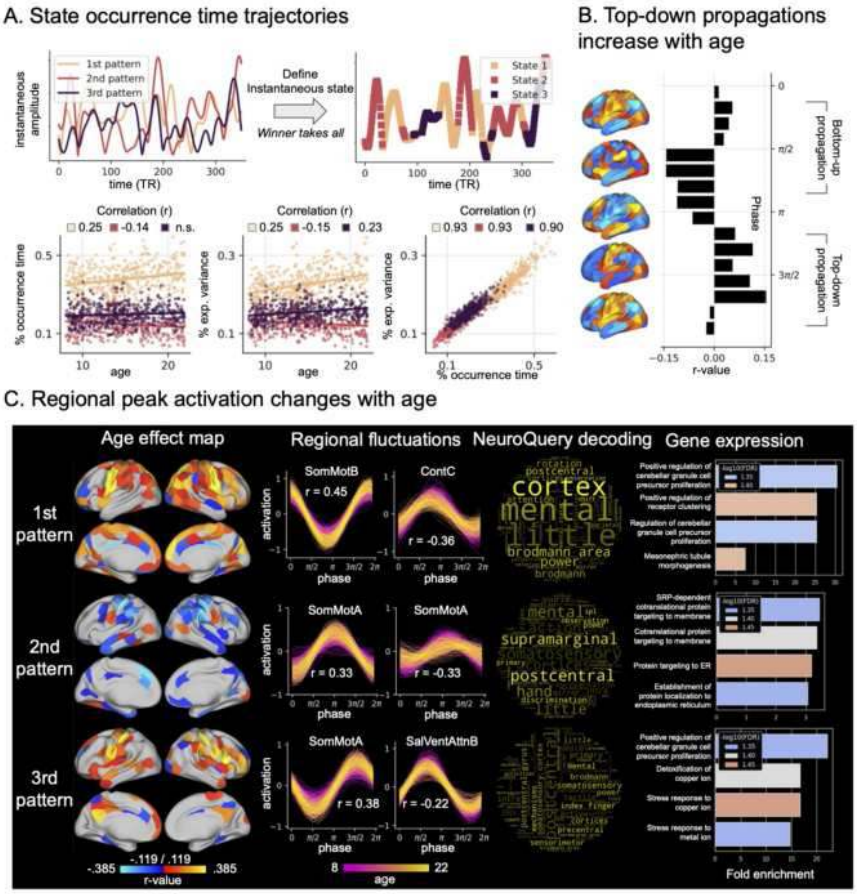

Figure 2. Age-Dependent Dynamics Associations in Brain Maturation.
This figure delves into the age-related changes within dynamic brain states and their structural underpinnings. A. Displays the relationship between age and the occurrence time ratio of dynamic states, illustrating developmental shifts in brain state occupancy. B. Shows maturation of directionality within the brain's sensory-to-association hierarchical dynamics (1st pattern). The bar graph depicting the correlation between age and proportion of time for directionality. As shown in the Fig.1, the first pattern shows both bottom-up [0 - π] and top-down propagation [π - 2π]. The significant positive correlation of top-down propagation highlights the maturation process directionality. C. Regional peak activation was calculated from regional fluctuations of each dynamic pattern. This panel presents visualization of regional peak activation changes with age, sample regional fluctuations showing highest and lowest correlation, integrating meta analysis via neuroquery and transcriptomics analysis.

Conclusions: Our study characterized reproducible and reliable spatiotemporal dynamic patterns across cohorts, establishing their developmental trajectory from childhood to adolescence. We observed the progressive maturation of dynamic brain states across development, with both sensory-centered and hierarchical propagations present in childhood. However, from childhood to adolescence, hierarchical top-down propagations become more common suggesting prior work examining cortical development using static measures of functional connectivity may instead reflect a developmental trend towards the emergence of states where brain dynamics are maintained via hierarchical propagation.

References
1. Bolt T, 'A parsimonious description of global functional brain organization in three spatiotemporal patterns', Nature neuroscience. 2022 Aug;25(8):1093-103.
2. Ge SX, 'ShinyGO: a graphical gene-set enrichment tool for animals and plants', Bioinformatics. 2020 Apr 15;36(8):2628-9.
3. Markello RD, 'Standardizing workflows in imaging transcriptomics with the abagen toolbox', elife. 2021 Nov 16;10:e72129.
4. Margulies DS, 'Situating the default-mode network along a principal gradient of macroscale cortical organization', Proceedings of the National Academy of Sciences. 2016 Nov 1;113(44):12574-9.
5. Schaefer A, 'Local-global parcellation of the human cerebral cortex from intrinsic functional connectivity MRI', Cerebral cortex. 2018 Sep 1;28(9):3095-114.
6. Sydnor VJ, 'Neuroimaging of plasticity mechanisms in the human brain: from critical periods to psychiatric conditions', Neuropsychopharmacology. 2023 Jan 1;48(1):219-20.

Poster No 1215

Early life adversity differently affects cerebellar growth in NICU survivors

Sarah Palmis[1,2,3], Camille Heguy[4,2,3], Emmanouil Rampakakis[5], Pia Wintermark[6], Charles Rohlicek[7], Christine Saint-Martin[8], Guillaume Gilbert[9], Marie Brossard-Racine[10,3,11,12]

[1]Research Institute of McGill University Health Centre, Montreal, Quebec, [2]Advances in Brain and Child Health Development Research Laboratory, Montreal, Canada, [3]Department of Neurology & Neurosurgery, Faculty of Medicine, McGill University, Montreal, Canada, [4]McGill University, Montreal, Quebec, [5]Department of Pediatrics, Montreal Children's Hospital, McGill, Montreal, Quebec, [6]Department of Pediatrics, Division of Neonatology, Montreal Children's Hospital, McGill Universit, Montreal, Quebec, [7]Montreal Children's Hospital, McGill University Health Centre, Montreal, Quebec, [8]Department of Medical Imaging, Division of Pediatric Radiology, Montreal Children's Hospital, Mcg, Montreal, Quebec, [9]MR Clinical Science, Philips Healthcare, Mississauga, Ontario, [10]Advances in Brain and Child Health Development Research Laboratory, Montreal, Quebec, [11]Department of Medical Imaging, Division of Pediatric Radiology, Montreal Children's Hospital, Montreal, Canada, [12]School of Physical and Occupational Therapy, McGill University, Montreal, Canada

Introduction: The cerebellum undergoes its most intense period of growth during the third trimester of pregnancy and the first year of life, making this brain structure vulnerable to perinatal adversities. Recent evidence supports that cerebellar development is altered in two common clinical groups that populate the neonatal intensive care units, infants born preterm (PT) or born with congenital heart disease (CHD). These infants will experience early life adversities (ELA) that are specific to their conditions. Neonates born PT are exposed to the extra-uterine environment prematurely, while neonates with complex CHD experience delayed intra-uterine development and undergo cardiac surgery during the first months of life. PT and CHD children have comparable developmental challenges and also present with hindered cerebellar development. However, no study to date has directly compared cerebellar growth between these two groups. Studies of growth trajectories have the potential to identify subtle variation patterns not detected by cross-sectional analyses and may provide new diagnostic insight. This study aims to compare the cerebellar growth trajectories during the first year of life, as assessed by quantitative MRI, between infants born PT and those with CHD.

Methods: As part of this ongoing study, 31 PT infants (<37 weeks of gestation) and 19 infants born with complex CHD who underwent open-heart surgery were enrolled. Participants completed a brain MRI under natural sleep, on a 3.0 Tesla MRI system (Achieva X-Series, Philips Healthcare) with a 32-channel head coil, at the targeted time of 3, 6 and/or 12 months. 91 high-resolution anatomical T1-weighted images (55 PT and 36 CHD) were included in our analyses. Images were first preprocessed using N4 BiasFieldCorrection algorithm. Then, using Infant Freesurfer we automatically segmented the total brain volume (TBV), the total cerebellum (TCBL), the bilateral cerebellar hemispheres (Left and Right CBL) and the vermis. Trajectories were characterized for the four cerebellar regions, using mixed-effects models for repeated measured (MMRM), and linear, quadratic, logarithmic and exponential regressions were compared using R-Squared values to determine the best fit. Comparisons of cerebellar volumes between groups at each time-point were conducted using the least squared means derived from the linear MMRM models with and without adjustment for TBV. Volume differences between the two groups were calculated using the following formula: (mean volume PT – mean volume CHD)/(mean volume CHD)x100.

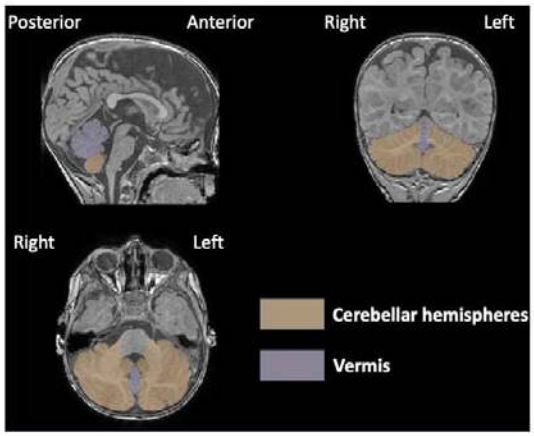

Figure 1. Example of cerebellar segmentation on a 12-months PT infant.

Results: Different growth trajectories functions were identified between the two groups. While all cerebellar regions followed a quadratic trajectory in the PT group, all cerebellar regions in the CHD group followed a logarithmic trajectory. When unadjusted for TBV, cerebellar regions were significantly smaller in CHD when compared to PT at 3 months only ($p<0.001$, volume differences TCBL:20,27%; Left CBL:20.51%; Right CBL:20.56%; Vermis:17.45%). However, volumetric differences were not significant at 6 and 12 months of age (volume difference <7%). When adjusted for TBV, no differences remained significant.

Conclusions: Our preliminary results suggest that ELA differently affects the cerebellar growth trajectories of PT and CHD infants. Smaller cerebellar volumes observed at 3 months in the CHD may be related to the different underlying mechanism of cerebellar growth disruption. Indeed, cerebellum underdevelopment is already present during the second and third trimester of pregnancy, while disruption of cerebellar growth seems to be most affected postnatally in the PT infants. Yet, the CHD group seems to catch-up at 6 months. Volumetric differences found between the two groups seem to represent a more global reduction of the TBV in CHD as compared to PT. Future studies with comparison to healthy term-born infants and with measures of outcomes are needed to confirm the clinical significance of our findings.

References

1. Leto, K., Arancillo, M., Becker, E. B., Buffo, A., Chiang, C., Ding, B., ... & Hawkes, R. (2016). Consensus paper: cerebellar development. The Cerebellum, 15, 789-828.
2. Stoodley, C. J. (2016). The cerebellum and neurodevelopmental disorders. The Cerebellum, 15, 34-37.
3. Ceschin, R., Zahner, A., Reynolds, W., Beluk, N., & Panigrahy, A. (2022). Reduced cerebellar volume in term infants with complex congenital heart disease: correlation with postnatal growth measurements. Diagnostics, 12(7), 1644.
4. Wu, Y., Stoodley, C., Brossard-Racine, M., Kapse, K., Vezina, G., Murnick, J., ... & Limperopoulos, C. (2020). Altered local cerebellar and brainstem development in preterm infants. Neuroimage, 213, 116702.
5. Dovjak, G. O., Hausmaninger, G., Zalewski, T., Schmidbauer, V., Weber, M., Worda, C., ... & Ulm, B. (2022). Brainstem and cerebellar volumes at magnetic resonance imaging are smaller in fetuses with congenital heart disease. American Journal of Obstetrics and Gynecology, 227(2), 282-e1.

Poster No 1216

Covariate Correcting Network for Isolating the Impact of Long-term SES Changes on Brain Development

Hyuna Cho[1], Yubin Han[1], Amal Isaiah[2], Won Hwa Kim[1]

[1]Pohang University of Science and Technology (POSTECH), Pohang, Korea, Republic of, [2]University of Maryland School of Medicine, Baltimore, MD

Introduction: Socioeconomic status (SES) is associated with brain development in children; however, the impact of changes in SES on longitudinal brain development is under-examined. Previous cross-sectional studies have mainly focused on single-modal macrostructural aspects of the cerebral cortex such as thickness and volume. In contrast, our study analyzed the association between the changes in SES over time and the changes in both microstructural and macrostructural properties across the whole brain. We performed two independent analyses on each brain measure by comparing two groups: one with increased household income and the other with decreased income over time. We used Covariate Correcting Network (CoCoNet)[2], an artificial neural network for correcting confounders for whole-brain analysis, to isolate the sole effect of the changes in SES on each region of interest (ROI). As a result, CoCoNet found 12 ROIs affected by the changes in SES on the

fractional anisotropy (FA). For the macrostructural analysis with cortical thickness, the model detected the left suborbital sulcus and right superior frontal sulcus, which are subsumed by the 12 ROIs from the previous analysis.

Methods: Dataset. We used the Adolescent Brain and Cognitive Development study data (v4.0)[1] with a total of 2488 children aged 9-10. Two brain measurements were provided: 1) fractional anisotropy (FA) as a microstructural property and 2) cortical thickness (CT) as a macrostructural property. Both were processed on Destrieux[4] atlas comprising 148 ROIs. Along with the imaging measures, individual annual household incomes, age, sex, scanner type, and race were examined at two timepoints with a 2-year interval. We divided the cohort into two groups based on their income changes: the income-increased (Up, N=1802) and income-decreased (Down, N=686) groups. Proposed Method. The region-wise long-term differences of brain measures (e.g., follow-up FA - baseline FA) were calculated to quantify how much the brain changed over a 2-year span, which became a dependent variable. As we aimed to investigate the true effect of longitudinal SES changes, the group information was used as a variable of interest. Age, gender, scanner, and race were chosen as the covariates to be corrected. Conventionally, these confounders are corrected via analysis of variance using the General Linear Model (GLM). Under the normality assumption, CoCoNet shares the same hypothesis space with the GLM. However, unlike GLM, CoCoNet allows a whole-brain analysis with increased sensitivity as it performs multiple F-tests across multiple ROIs simultaneously by maximizing overall F-statistics over the whole brain. Also, the model sparsely selects the key ROIs with an L1-regularizer within its loss function.

Results: The brain measures from the Up and Down groups were compared with GLM, GLM with Neural Network (GLM_NN), GLM with Lasso (GLM_Lasso), and CoCoNet. For the FA analysis (Fig 1), CoCoNet identified 12 ROIs of which p-values survived Bonferroni correction, while all baselines identified only the left lateral orbital sulcus among the 12 ROIs. CoCoNet uniquely identified key ROIs such as the right posterior transverse collateral sulcus and the right superior frontal sulcus. These ROIs are related to texture processing[7] and spatial working memory[3], which are critical in brain development. In the CT analysis (Fig 2), 2 regions were identified from CoCoNet: 1) left suborbital sulcus and 2) right superior frontal sulcus, which were also found in the FA analysis. These two ROIs are implicated in schizophrenia[5] and attention[6]. Notably, GLM and GLM_NN did not yield any ROIs, while CoCoNet sensitively identified them with small p-values.

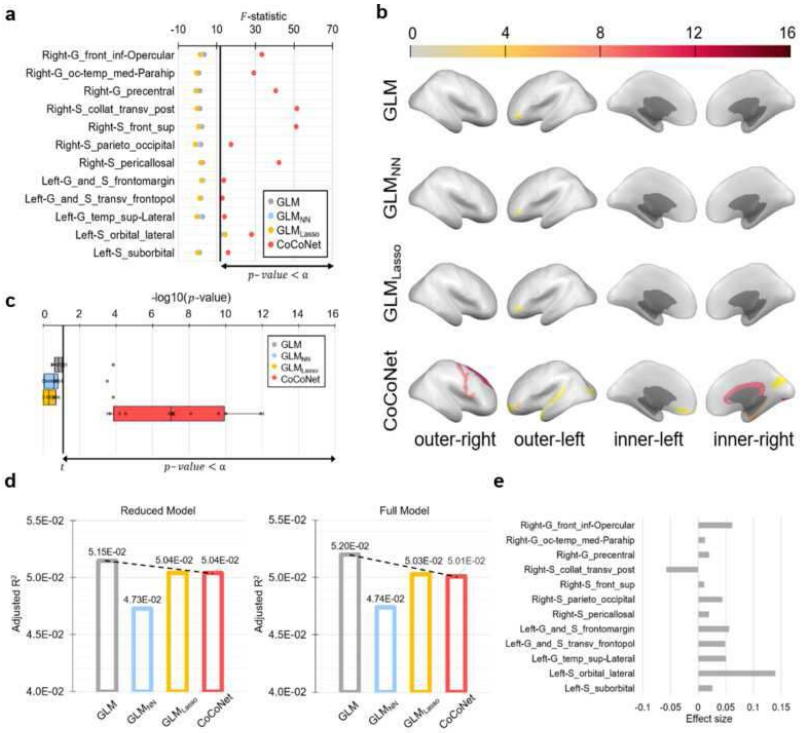

Fig. 1. Statistical analyses of identified ROIs from linear models fitted on fractional anisotropy. Multiple ANOVA F-tests were performed independently for 148 ROIs with Bonferroni correction at α=0.05. To investigate whether the identified ROIs have statistically significant group differences from income changes, the effects of nuisance variables such as age, scanner type, sex and race were marginalized via *F*-tests. **a**, Identified ROIs from CoCoNet and baseline methods that survived Bonferroni correction and their region-wise *F*-statistics from ANOVA. While baseline linear methods identified only one ROI, i.e., left lateral orbital sulcus, CoCoNet identified 11 ROIs subsuming the region with higher *F*-statistics magnitude. **b**, Visualization of -log10 scaled *p*-value maps for the identified ROIs. **c**, -log10 scaled *p*-value distributions for detected ROIs. Notably, compared to the baselines', the *p*-values of CoCoNet were distributed at much smaller ranges (i.e., higher ranges with -log10 scaling). **d**, Averaged adjusted R-squared score across 148 ROIs. **e**, ROI-wise effect sizes of longitudinal CT changes from Up vs. Down group comparison.

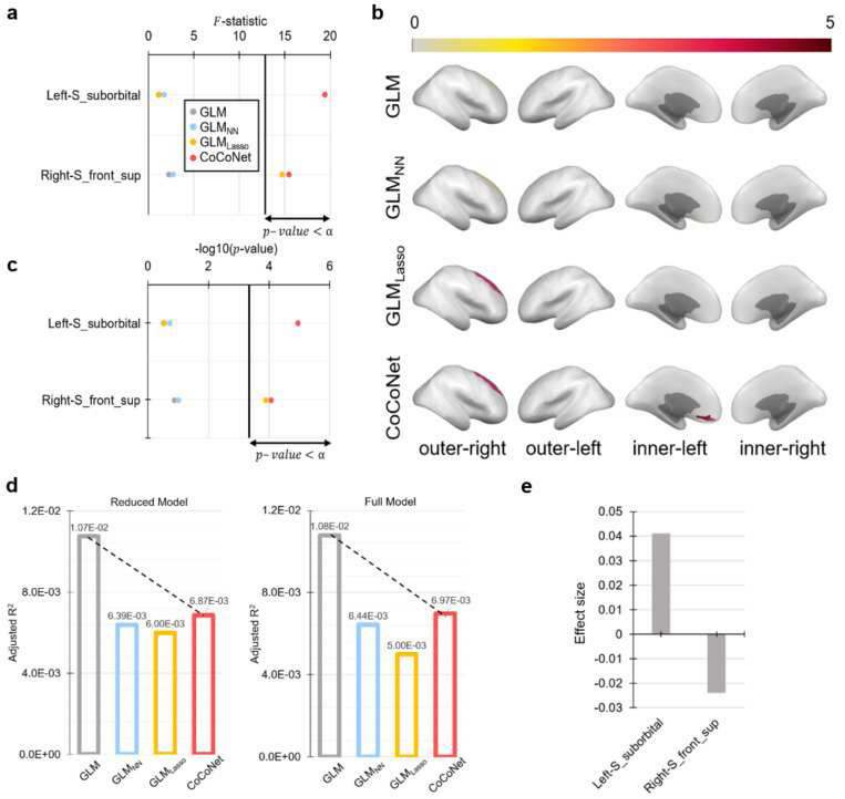

Fig. 2. Statistical analyses of identified ROIs from linear models fitted on cortical thickness. As in Fig. 2, multiple ANOVA F-tests were performed independently for 148 ROIs with Bonferroni correction at α=0.05 to observe which ROIs were affected by income changes. The effects of nuisance variables including age, scanner type, sex and race were marginalized via F-tests. **a**, Identified ROIs from CoCoNet and baseline methods that survived Bonferroni correction and their region-wise F-statistics from ANOVA. GLM and GLM_{NN} detected no ROI. However, GLM_{Lasso} and CoCoNet commonly detected right superior frontal sulcus, and CoCoNet additionally identified left suborbital sulcus. **b**, Visualization of -log10 scaled p-value maps for the identified ROIs. **c**, -log10 scaled p-values for detected ROIs. Compared to the baselines', the p-values of CoCoNet were distributed at much smaller ranges (i.e., higher ranges with -log10 scaling). **d**, Averaged adjusted R-squared score across 148 ROIs. CoCoNet showed marginal decrease compared to GLM. **e**, ROI-wise effect sizes of longitudinal CT changes from Up vs. Down group comparison.

Conclusions: We observed the true association between the long-term changes in SES and ROI-wise adolescent brain development by controlling confounders. As a result, CoCoNet sensitively found that the left suborbital sulcus and right superior frontal sulcus were affected by changes in SES. This work was supported by the National Research Foundation of Korea (NRF) grant funded by the Korea government (MSIT) (No. NRF-2022R1A2C2092336).

References

1. Casey, B. J. (2018), 'The adolescent brain cognitive development (ABCD) study: imaging acquisition across 21 sites.' Developmental cognitive neuroscience 32: 43-54.
2. Cho, H. (2021), 'Covariate Correcting Networks for Identifying Associations Between Socioeconomic Factors and Brain Outcomes in Children', International Conference on Medical Image Computing and Computer-Assisted Intervention, Springer, Cham, pp. 421-431.
3. Courtney, S. M. (1998), 'An area specialized for spatial working memory in human frontal cortex' Science 279.5355: 1347-1351.
4. Destrieux, C. (2010), 'Automatic parcellation of human cortical gyri and sulci using standard anatomical nomenclature', Neuroimage 53(1), 1–15.
5. Kim, S. (2020), 'Altered cortical thickness-based individualized structural covariance networks in patients with schizophrenia and bipolar disorder.' Journal of Clinical Medicine 9.6: 1846.
6. Nee, D. E. (2015), 'Working memory.', Brain Mapping 2: 589-595.
7. Puce, A. (1996), 'Differential sensitivity of human visual cortex to faces, letterstrings, and textures: a functional magnetic resonance imaging study.' Journal of neuroscience 16.16: 5205-5215.

Poster No 1217

Association between fALFF of white matter and postmenstrual age in newborns

Yali Huang[1], Xiaoxu Na[1], Xiawei Ou[1,2]

[1]Department of Radiology, University of Arkansas for Medical Sciences, Little Rock, AR, [2]Department of Pediatrics, University of Arkansas for Medical Sciences, Little Rock, AR

Introduction: Blood oxygenation level dependent (BOLD) contrast has been exploited for detecting neural activity in the brain using fMRI. While BOLD signals have been reliably detected in gray matter, such signals have long been ignored in white matter (Ding et al. 2018, Gore et al. 2019). The objective of the study is to investigate the relationships between fractional amplitude of low-frequency fluctuations (fALFF) in both white and gray matter and postmenstrual age in term-born infants using resting-state BOLD functional magnetic resonance imaging (BOLD-fMRI).

Methods: A total of 40 newborns (average postmenstrual age: 289 days) were analyzed. We initially performed independent component analysis (ICA) on the fMRI white and gray matter data of newborns to obtain group-level components. White matter BOLD data were decomposed into functional networks (independent components) using a group-level spatial ICA as implemented in the GIFT toolbox, and Group-ICA was performed to generate a set of group-average parcels (Calhoun et al. 2001). Subject-specific spatial maps and time courses were estimated using the GICA back-reconstruction method (Allen et al. 2014). A similar processing scheme was also applied to the gray matter BOLD signal. Here we calculated the ratio of power spectrum of three frequency bands (Frequency band: 0.001~0.027 Hz; Frequency band: 0.027~0.073 Hz; Frequency band: 0.073~0.198 Hz) to that of the frequency range (0.001~0.198 Hz), which denote the power of BOLD signal fluctuation. For each group spatial component, time course was extracted to compute fALFF at different frequency band (0.001~0.027 Hz, 0.027~0.073 Hz, 0.001~0.198 Hz) for every subject. Specifically, as the ICA decomposition order is set as 12, 12(components)*3(frequency bands)*40(subjects) fALFF values were calculated for all subjects. These 1440 (12*3*40) features represent spontaneous brain activity energy (the power of low frequency fluctuation) of the subjects, as shown in Fig. 1.

Results: To examine potential relationships between white matter fALFF and postmenstrual age of newborns, the Pearson correlation between fALFF (including 12 components, and each component comprise 3 frequency bands) and postmenstrual age was calculated. A 12*3 correlation matrix between the fALFF and postmenstrual age was obtained. To further evaluate the statistical significance of the correlation matrix, a permutation test was performed. The age labels were randomly permuted 10000 times to generate the null organization. Permutation analysis revealed that there is significant relationship between the fALFF of one component and postmenstrual age. Specifically, the fALFF of an independent component from white matter in frequency range 0.027 - 0.073 Hz is positively correlated with postmenstrual age ($r=0.35$, $p = 0.018$), while the fALFF in frequency range 0.073 - 0.198 Hz is negatively correlated with postmenstrual age ($r = -0.43$, $p = 0.007$). The spatial map of this white matter component is shown in Fig. 2A, which is located in the parietal lobe. The similar processing were conducted to the gray matter. The non-parametric permutation also demonstrated that there is one significant correlation between the fALFF of one independent component in grey matter and postmenstrual age. Specifically, it was found that there is positively correlation with postmenstrual age ($r=0.40$, $p = 0.005$) in frequency range 0.027 - 0.073 Hz, while negatively correlation with postmenstrual age ($r = -0.43$, $p = 0.004$) in frequency range 0.073 - 0.198 Hz . The spatial map of this gray matter component is shown in Fig. 2B, which is located in the parietal lobe, similar to that in Fig. 2A.

Conclusions: Our studies showed that fALFF in the parietal lobe in both white and gray matter is significantly correlated with postmenstrual age in neonates, suggesting that it may serve as an indicator of normal brain development during the perinatal age window. Further study will be needed to understand the implication of this finding.

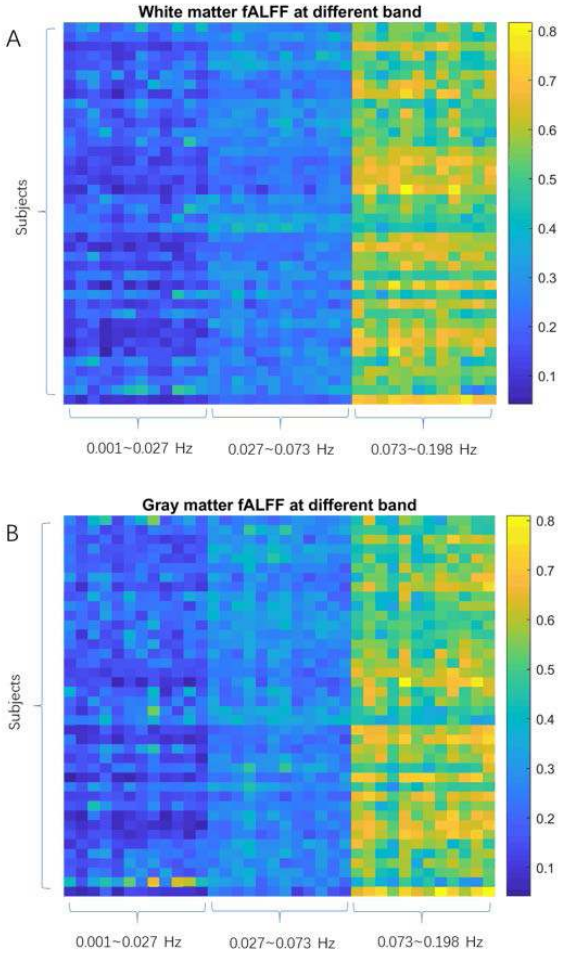

Figure 1. A) the fALFF of white matter (including 12 independent components) in different frequency bands; B) the fALFF of grey matter (including 12 independent components) in different frequency band.

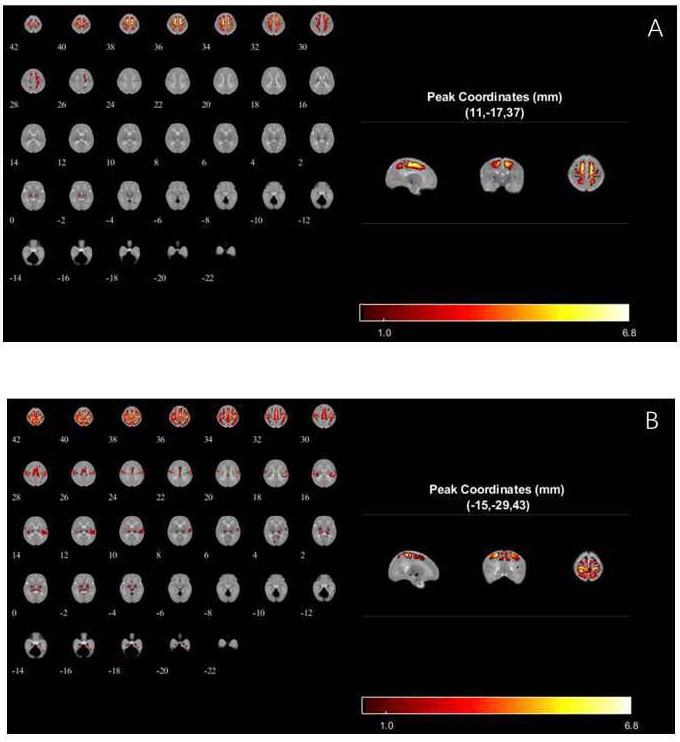

Figure 2. A) The age-related components in white matter; B) the age-related components in gray matter.

References
1. Allen, E. A., E. Damaraju, S. M. Plis, E. B. Erhardt, T. Eichele and V. D. Calhoun (2014). "Tracking whole-brain connectivity dynamics in the resting state." Cerebral cortex 24(3): 663-676.
2. Calhoun, V. D., T. Adali, G. Pearlson and J. J. Pekar (2001). "Spatial and temporal independent component analysis of functional MRI data containing a pair of task-related waveforms." Human brain mapping 13(1): 43-53.
3. Ding, Z., Y. Huang, S. K. Bailey, Y. Gao, L. E. Cutting, B. P. Rogers, A. T. Newton and J. C. Gore (2018). "Detection of synchronous brain activity in white matter tracts at rest and under functional loading." Proc Natl Acad Sci USA 115(3): 595-600.
4. Gore, J. C., M. Li, Y. Gao, T.-L. Wu, K. G. Schilling, Y. Huang, A. Mishra, A. T. Newton, B. P. Rogers and L. M. Chen (2019). "Functional MRI and resting state connectivity in white matter-a mini-review." Magn Reson Imaging 63: 1-11.

Poster No 1218

The brain's functional activation dynamics are associated with female hormone levels

Ceren Tozlu[1], Louisa Schilling[2], Parker Singleton[3], Keith Jamison[2], Amy Kuceyeski[2]

[1]Weill Cornell Medicine, NYC, NY, [2]Weill Cornell Medicine, New York City, NY, [3]Weill Cornell Medicine, New York, NY

Introduction: Sex hormones play an important role in shaping how the brain's structural and functional architecture evolve across the lifespan[1,2,3]. One of the ways to investigate the brain's structure-function relationship is to analyze how the brain's structural connectivity architecture constrains its dynamic functional activation via Network Control Theory (NCT)[4]. NCT uses the brain's structural connectivity networks to identify the minimum transition energy (TE) required for the transition between the commonly recurring brain activation states. NCT has previously been applied in disease[5] and health[6,7], for example across developing populations[8]. However, no study to date has investigated how TE is associated with female hormones, and more specifically how these relationships are impacted by menopause when striking changes in hormone levels are observed.

Methods: Four hundred and four females (age: 60.05 ± 15.74) from the Human Connectome Project-Aging (HCP-A) dataset[9] were used in this study. First, k-means was applied to the regional fMRI time series to identify commonly recurring dynamic brain states. The time series were analyzed using regional averages of 86 FreeSurfer-based regions (68 cortical and 18 subcortex/cerebellum), and the structural connectivity matrices were extracted using diffusion MRI and deterministic tractography. Second, NCT was applied to calculate the minimum energy required to transition between each pair of dynamic brain states (or to remain in the same state - i.e. persistence energy). Global TE was calculated as the average of the pairwise TEs between dynamic states and the persistence energy in each state. The regional fMRI time series were also used to calculate their entropy, which quantifies the amount of temporal regularity/unpredictability in brain activity. Global entropy is calculated as the average of regional entropy. Linear models were used to investigate the association of global TE and entropy with hormones such as estradiol, Luteinizing Hormone (LH), and Follicle-Stimulating Hormone (FSH), after controlling for age and framewise displacement (FD). The state-wise TEs were also compared between pre- (n=59), peri- (n=42), and post-menopausal (n=87) females who were between 40-60 years old using ANCOVA where age and FD were used as covariates. Group differences were considered significant when $p<0.05$ after Benjamini–Hochberg (BH) correction for multiple comparisons.

Results: Increased global TE was associated with higher levels of estradiol ($p=0.03$) and lower levels of LH ($p=0.01$), and FSH ($p=0.005$) (see Figure 1), while there was no significant association between entropy and hormone levels. Recurrent brain states included those defined by high-amplitude activity (+) or low-amplitude activity (-) in various canonical networks, including visual network (VIS+), dorsal attention (DAN-), fronto-parietal (FP+), and somato-motor (SOM+) (see Figure 2). All state-wise TEs were significantly greater in pre-menopause compared to post-menopause, while the TE between SOM+ and VIS+ networks was greater in peri-menopause compared to post-menopause.

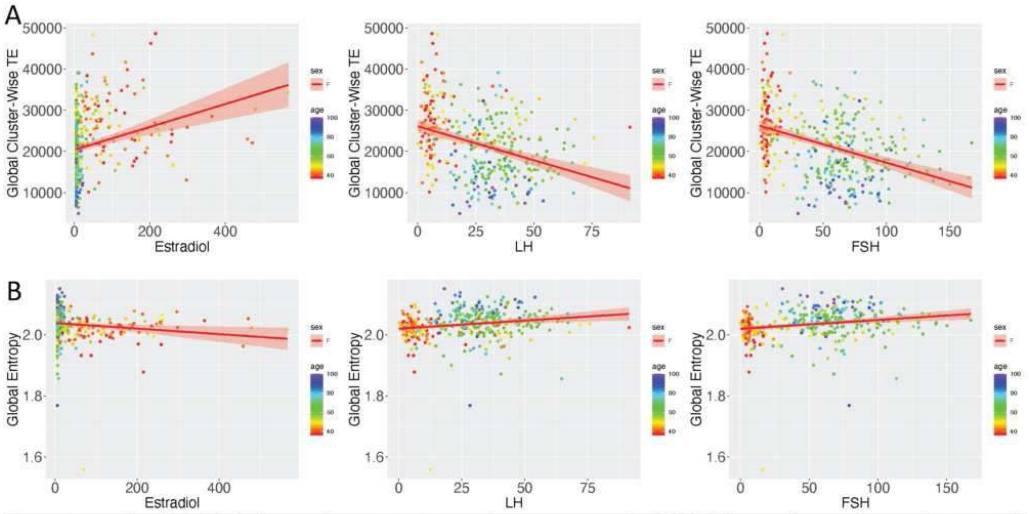

Figure 1: Scatterplot of (A) global TE (averaged over 16 transitions and persistence energy) and (B) global entropy (averaged over 86 brain regions) with hormone levels (estradiol, LH, and FSH). The dots are color-coded using the age information (i.e. red colors younger individuals and blue/purple color for older individuals)

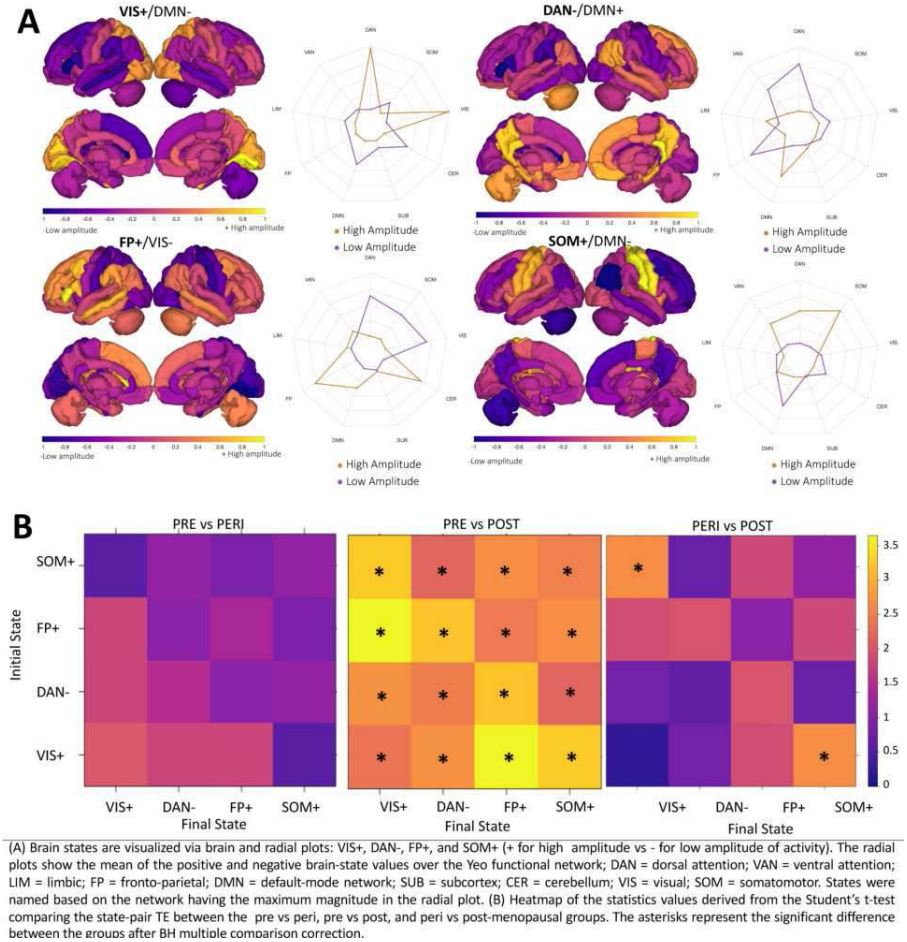

(A) Brain states are visualized via brain and radial plots: VIS+, DAN-, FP+, and SOM+ (+ for high amplitude vs - for low amplitude of activity). The radial plots show the mean of the positive and negative brain-state values over the Yeo functional network; DAN = dorsal attention; VAN = ventral attention; LIM = limbic; FP = fronto-parietal; DMN = default-mode network; SUB = subcortex; CER = cerebellum; VIS = visual; SOM = somatomotor. States were named based on the network having the maximum magnitude in the radial plot. (B) Heatmap of the statistics values derived from the Student's t-test comparing the state-pair TE between the pre vs peri, pre vs post, and peri vs post-menopausal groups. The asterisks represent the significant difference between the groups after BH multiple comparison correction.

Conclusions: Our results revealed that the known hormonal changes that occur during menopause may be accompanied with shifts in the brain's dynamic activity landscape. Being able to map how hormonal changes like puberty, pregnancy, postpartum, and menopause affect the brain is necessary for improving the healthcare of females.

References

1. Pritschet L, Santander T, Taylor CM, Layher E, Yu S, Miller MB, Grafton ST, Jacobs EG. Functional reorganization of brain networks across the human menstrual cycle. Neuroimage. 2020 Oct 15;220:117091.
2. Zamani Esfahlani F, Faskowitz J, Slack J, Mišić B, Betzel RF. Local structure-function relationships in human brain networks across the lifespan. Nat Commun. 2022 Apr 19;13(1):2053.
3. Yaqian Yang, Shaoting Tang, Xin Wang, Yi Zhen, Yi Zheng, Hongwei Zheng, Longzhao Liu, Zhiming Zheng. Brain structure-function relationships across the human lifespan based on network eigenmodes. bioRxiv 2023.03.08.531719

4. Gu S, Pasqualetti F, Cieslak M, Telesford QK, Yu AB, Kahn AE, Medaglia JD, Vettel JM, Miller MB, Grafton ST, Bassett DS. Controllability of structural brain networks. Nat Commun. 2015 Oct 1;6:8414.
5. Tozlu C, Card S, Jamison K, Gauthier SA, Kuceyeski A. Larger lesion volume in people with multiple sclerosis is associated with increased transition energies between brain states and decreased entropy of brain activity. Netw Neurosci. 2023 Jun 30;7(2):539-556.
6. Singleton SP, Timmermann C, Luppi AI, Eckernäs E, Roseman L, Carhart-Harris RL, Kuceyeski A. Time-resolved network control analysis links reduced control energy under DMT with the serotonin 2a receptor, signal diversity, and subjective experience. bioRxiv [Preprint]. 2023 May 12:2023.05.11.540409.
7. Singleton SP, Luppi AI, Carhart-Harris RL, Cruzat J, Roseman L, Nutt DJ, Deco G, Kringelbach ML, Stamatakis EA, Kuceyeski A. Receptor-informed network control theory links LSD and psilocybin to a flattening of the brain's control energy landscape. Nat Commun. 2022 Oct 3;13(1):5812.
8. Tang E, Giusti C, Baum GL, Gu S, Pollock E, Kahn AE, Roalf DR, Moore TM, Ruparel K, Gur RC, Gur RE, Satterthwaite TD, Bassett DS. Developmental increases in white matter network controllability support a growing diversity of brain dynamics. Nat Commun. 2017 Nov 1;8(1):1252
9. Van Essen DC, Smith SM, Barch DM, Behrens TE, Yacoub E, Ugurbil K; WU-Minn HCP Consortium. The WU-Minn Human Connectome Project: an overview. Neuroimage. 2013 Oct 15;80:62-79. doi: 10.1016/j.neuroimage.2013.05.041. Epub 2013 May 16. PMID: 23684880; PMCID: PMC3724347.

Poster No 1219

Differential Structural Brain Development in Adolescents with Different Apolipoprotein Eε Genotypes

Linda Chang[1], Mahsa Mayeli[1], Amal Isaiah[1], Shuo Chen[2], Thomas Ernst[1]

[1]University of Maryland School of Medicine, Baltimore, MD, [2]university of maryland, baltimore, baltimore, MD

Introduction: Apolipoprotein E epsilon (APOEε) allele has three isoforms, yielding six genotypes (ε2ε2, ε2ε3, ε2ε4, ε3ε3, ε3ε4, ε4ε4). Children with different APOEε genotypes showed differential brain maturation in a cross-sectional study (Chang 2016). Specifically, children with ε2ε4 had smallest hippocampi and young children (<10 years) with ε4ε4 had the lowest hippocampal fractional anisotropy relative to those with other APOEε genotypes. Furthermore, young children with ε2ε4 genotype performed worst on attention tasks while those with ε4ε4 had lowest scores on executive function and working memory. The ε4 allele is associated with greater risks for Alzheimer's disease (Fernández-Calle, 2022), or poorer outcomes from brain injuries (Chang, 2011; Kassam 2016). Understanding the effects of ε4 allele on brain development may provide useful early biomarkers. The current study aims to validate prior findings using the large longitudinal dataset of typically developing adolescents from the Adolescents Brain Cognitive Development (ABCD) study.

Methods: Data release 4.0 included data from 11,875 healthy children (www.abcdstudy.org). We extracted the genomics data and identified six APOEε genotypes for the associated single nucleotide polymorphisms (rs429358 and rs7412) using Plink 2.0. We included 2,476 participants with complete datasets from baseline (ages 9-10 years), 2-year and 4-year follow-up visits. We analyzed structural MRI [processed with Freesurfer v5.3+ using regions of interests (ROIs) from the Desikan-Killiany atlas (Halger, 2019)] and cognitive scores from the NIH Toolbox-Cognitive Battery (NIHTB-CB). APOEε2/ε2 were excluded due to the small sample size. We investigated APOEε genotype differences and APOEε genotype-by-Age interactions in thickness, surface area, and volume for cortical ROIs, and in subcortical ROI volumes. Longitudinal changes in these measures were assessed using a linear mixed-effects model, incorporating APOEε group, age, sex at birth, family income, study site, scanner ID, and intracranial volume (for volume measurements only) as fixed effects, and participant as random effect. The false discovery rate (FDR) was used to correct for multiple comparisons. All analyses were conducted in R 4.3.1.

Results: Participant characteristics are summarized (Figure 1). APOEε genotype effects or APOEε*Age interactions were significant in multiple ROIs for cortical thickness, surface area or volumes, and for subcortical volumes. Only six cortical measures remained significant after FDR-correction: cortical thickness of bilateral Cuneus, bilateral Pericalcarine cortices, left Lingual gyrus and left postcentral gyrus (Figure. 1). However, all subcortical gray matter volumes remained significant after FDR-correction for APOEε-main effects ($p<0.001$) or APOEε*Age interactions ($p<0.0001$), marginal effect size $R2=0.19-0.45$ (Figure 2). Specifically, relative to the other genotypes, the ε2ε4 group (red lines) had the smallest hippocampi and amygdalae, but largest pallidum, caudate and putamen bilaterally. Conversely, the ε4ε4 group (green lines) had the smallest putamen and largest amygdalae. In addition, the volumes of the corpus callosum showed group differences (Posterior: Age*APOEε-corrected-$p=0.005$, APOEε-corrected-$p<0.001$, Middle and Central: APOEε-corrected-$p<0.001$). Furthermore, global volumes of cerebral white matter, cerebellar cortex and white matter all showed APOEε and APOEε*Age effects (corrected-$p<0.001$). However, no significant effects for APOEε or APOEε*Age were found for any of the NIH-TB-CB test scores.

Figure 1. Cortical Thickness ROIs with significant *APOEε Genotype* and/or *APOEε Genotype*Age* Effects

Table 1. Participant characteristics and Numbers (#)

	Baseline	2-year Follow-Up	4-year Follow-Up
Age (years ± S.D.)	9.91 ± 0.63	11.9 ± 0.65	14.02 ± 0.68
Sex at Birth	1359 Boys / 1117 Girls		
Race (#)	White (1321); African American (330); Hispanic (496); Asian (54); Others (275)		
Family Income (#)	<$50K (648); 50K_<100K (729); >_100K (933)		
APOE ε Genotype (#)	ε2-ε3 (288); ε2-ε4 (56); ε3-ε3 (1531), ε3-ε4 (543), ε4-ε4 (58)		

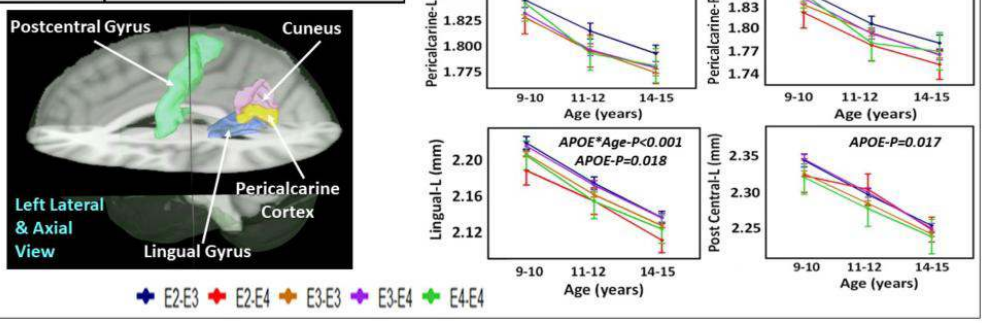

Figure 2. Subcortical ROIs with Significant *APOEε* Genotype and *APOEε Genotype*Age* Effects

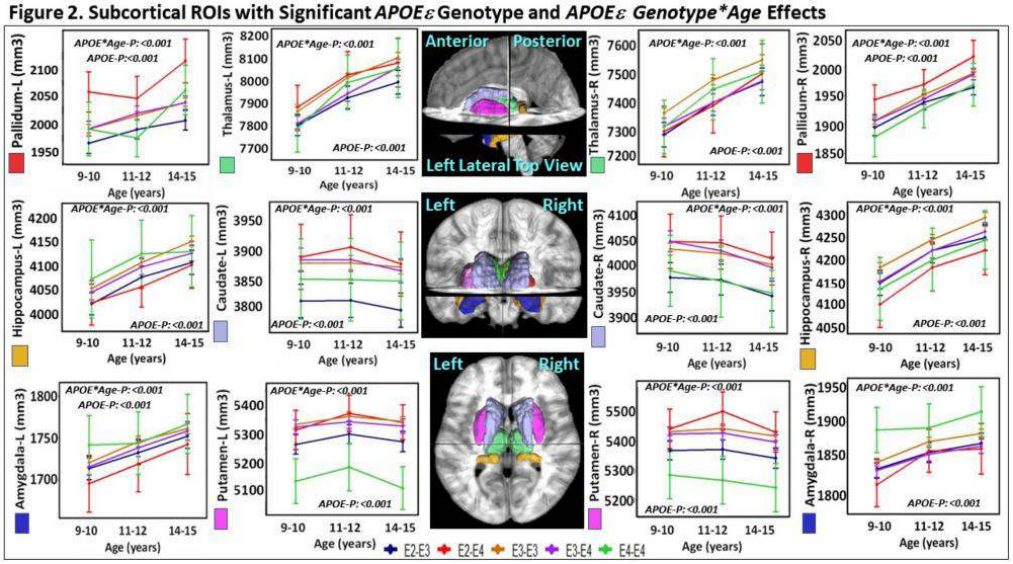

Conclusions: Adolescents with different APOEε genotypes show significant variations in the growth trajectories of their cortical thickness and subcortical gray matter volumes, especially those with ε2ε4 and ε4ε4, validating prior observations (Chang, 2016). Whether these early morphometric differences persist into adulthood, leading to greater vulnerability for brain injury or lower repair capacity at later life, requires further follow-up studies.

References

1. Chang L (2011). "Impact of apolipoprotein E ε4 and HIV on cognition and brain atrophy: antagonistic pleiotropy and premature brain aging", Neuroimage, Vol, 58, No. 4, pp. 1017-1027.
2. Chang L (2016), "Gray matter maturation and cognition in children with different APOE ε genotypes", Neurology Vol. 87, No. 6, pp. 585-594.
3. Fernández-Calle R. (2022), "APOE in the bullseye of neurodegenerative diseases: impact of the APOE genotype in Alzheimer's disease pathology and brain diseases", Molecular Neurodegeneration. Vol. 17, No. 1, pp. 62-109.
4. Hagler, D.J. Jr. (2019), "Image processing and analysis methods for the Adolescent Brain Cognitive Development Study." Neuroimage. Vol. 202, pp. 116091-116108.
5. Kassam I. (2016), "Association of the APOE-ε4 allele with outcome of traumatic brain injury in children and youth: a meta-analysis and meta-regression." Journal of Neurology Neurosurgery and Psychiatry Vol. 87, No. 4, pp. 433-440.

Poster No 1220

Development of brain state dynamics involved in working memory

Ying He[1]

[1]McGill University, Montreal, Quebec

Introduction: The human brain is an open complex system that is dynamically organized to support cognitive and behavioral flexibility, as well as rapid adaptation to ever-changing environmental or task demands. A wealth of recent neuroimaging studies in adults has demonstrated that the dynamical organization of functional brain networks is essential to support the performance of various cognitive and affective functions. Alterations in the dynamical organization of large-scale functional brain networks are linked to cognitive impairments in a variety of psychiatric and neurodevelopmental disorders. As childhood is a critical period during which the human brain function and structure undergo protracted development with prominent changes in higher-order cognitive functions such as working memory, it is thus pivotal to understand how the dynamical organization of functional brain networks contributes to children's cognitive development and the architecture of structural connectivity underlying brain dynamics.

Methods: To address above open questions, we set up a developmental functional Magnetic Resonance Imaging (fMRI) study with advanced analytic approaches and Diffusion Tensor Imaging (DTI) study in 69 children (aged 7–12-year-old) and 51 adults (aged 19–24-year-old) to investigate developmental differences in dynamical brain states of the frontal-parietal network (FPN) and default mode network (DMN) during working memory task and white matter structural connectivity. Observed fMRI data are modeled by a novel Bayesian switching dynamical systems (BSDS) approach. The BSDS model was applied to the time courses which could provide the temporal evolution of the states, the occupancy rate and mean lifetime of states, the transition probability matrix and mean and covariance of states. For each subject, we also calculated the mean fractional anisotropy (FA) values across all voxels in the tract between each two ROIs to weighted the white matter connectivity matrix. And then, the structure-function coupling was measured as Spearman rank correlation between nonzero element of structural and functional connectivity profiles.

Results: We identified five brain states with rapid transitions, characterized by dynamic configurations among FPN and DMN nodes with active and inactive engagement in different task demands. Compared with adults, children exhibited less brain states with highest activity in FPN nodes dominant to high demand, and its occupancy rate increased with age. Children preferred to attain inactive brain states with low activity in both FPN and DMN nodes. Moreover, children exhibited lower transition probability from low-to-high demand states and such transition was positively related with working memory performance. Notably, higher transition probability from low-to-high demand states was associated with stronger structural connectivity across FPN and DMN, but weaker structure-function coupling of these two networks.

Conclusions: In conclusion, our study demonstrates immature dynamical organization of the FPN and DMN nodes during WM, characterized by less occupancy rate and more transitions to inactivated state but weaker transitions among brain states dominant to high task demand condition. And effective brain dynamics is related with stronger structural connectivity but weaker structure-function coupling among FPN and DMN. Our findings extend our current understanding of how the FPN and DMN nodes are dynamically organized into a set of nuanced brain sates to support moment-to-moment information updating during WM and its links to structural connectivity.

References

1. Chen M.(2023), 'Default mode network scaffolds immature frontoparietal network in cognitive development', Cerebral Cortex, vol.33, no.9, pp. 5251-5263.
2. Taghia, J.(2018), 'Uncovering hidden brain state dynamics that regulate performance and decision-making during cognition', Nature communications, vol.9, no.1, pp. 2505.

Poster No 1221

The efficiency of dynamic brain state transitions in working memory improves in youth

Xiaoyu Xu[1,2], Zaixu Cui[2]

[1]State Key Laboratory of Cognitive Neuroscience and Learning, Beijing Normal University, Beijing, China, [2]Chinese Institute for Brain Research, Beijing, China

Introduction: Dynamic brain state transitions are required for working memory, such as moving from a low cognitive load to a working memory state (Braun et al., 2015). However, it remains unclear how the development of structural network topology supports the process of such dynamic brain state transitions. Network control theory (NCT) provided a powerful framework

for studying how structural network topology informs and constrains functional dynamics (Gu et al., 2015). NCT can be used to quantify the energetic costs, namely control energy, required to facilitate the transition between different states. Our previous work reports control energy for frontoparietal activation decreased with development (Cui et al., 2020). In the current study, we depict how the development of structural networks facilitates the dynamic transitions in working memory execution in youth under the framework of NCT.

Methods: The present study leveraged magnetic resonance imaging (MRI) data from the Lifespan Human Connectome Project Development (HCP-D) study (Somerville et al., 2018). The final sample included 590 subjects aged 8-22 with complete anatomical and diffusion MRI (dMRI) data. We preprocessed dMRI data and reconstruct the structural networks using the pipeline integrated within qsiprep (Cieslak et al., 2021). The functional activation map for the n-back task was extracted from the Human Connectome Project (Glasser et al., 2016). To depict the transition from 0-back to 2-back, we defined the initial brain states as all zero, and the target state as the contrast map between 2-back and 0-back conditions. Based on NCT, we calculated the control energy required by all brain regions during the transition (Fig.1A). To validate the facilitation of structural network topology on brain state transition, we compared the control energy of the actual networks to the null networks with the same degree and strength distribution. Next, we used general additive models to assess the developmental effects of control energy at the levels of the whole brain, systems, and nodes. Multiple comparisons were accounted for using the False Discovery Rate (Q<0.05). All the developmental effects were compared to the effects observed in the null networks. Furthermore, we described the developmental patterns among different systems leveraging the first derivative. We also correlated the age effect sizes of nodes to the sensorimotor-association axis (S-A axis) (Sydnor et al., 2021) using the Spearman method and spin test (Alexander-Bloch et al., 2018).

Results: The frontoparietal system exhibits the highest energy consumption in facilitating the transition of brain states from 0-back to 2-back (Fig.1B, C). The energetic cost of real structural networks is significantly lower than that of null networks (t=-175.14, P<2.2e-16, Fig.1D). The average energetic cost required for the whole brain declines with development (P=3.53e-09, r=-0.25, Fig2.A), and the age effect size of real networks is significantly stronger than that of null networks. As to the system level, both the average energetic costs of the frontoparietal and somatomotor systems exhibit strong developmental effects. However, the decreasing of energetic cost is consistent in the frontoparietal system from childhood to adulthood, while the cost of the somatomotor system hits a plateau in the middle of adolescence (Fig.2B, C, D). Furthermore, the age effect size (Z stats) of nodes tends to converge towards the S-A axis (r=0.28, Pspin=0.004, Fig.2E, F). This tendency reflects a hierarchical pattern of development of structural network topology.

Conclusions: Our results reveal how the development of structural network topology supports the dynamic brain state transitions in working memory. The theoretical energy consumption declined during development, which illustrates that the efficiency of dynamic brain state transitions in working memory improves from childhood to adulthood.

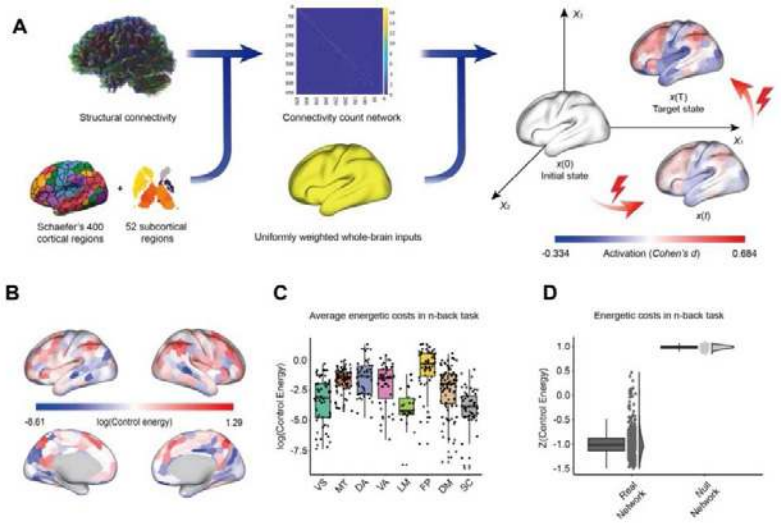

Figure 1. Schematic of methods. (A) We calculated the control energy required for the transition from the initial to the target state under the constraint of structural connectivity networks. The 452-node structural networks were estimated using diffusion and anatomical imaging. All the nodes were defined as control nodes through which energy can be input. (B) The regional control energy required to complete the transition. (C) The average energetic costs required by 7 cortical systems and a sub-cortical system. (D) The average energetic cost of real structural networks is significantly lower than that of the null networks with the same strength and degree distribution.

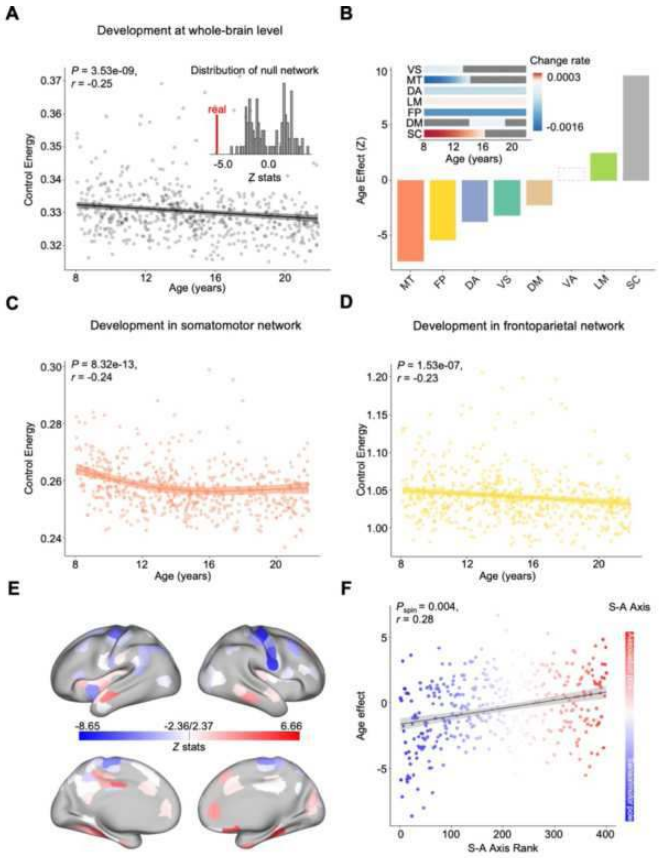

Figure 2. Energetic costs in n-back task change with age. (A) The average energetic cost of the whole brain keeps decreasing from childhood to adulthood. The age effect on cost is greater for real networks than null networks, indicating that the refinement of structural network topology facilitates the cost declination. (B) Age effect sizes and the developmental periods with significant age-related change in average energetic costs vary across 8 systems. The 95% confidence interval of the first derivative of GAM fits is used to define significant age-related changes. (C) The developmental trajectory of the average energetic cost of the somatomotor system hits a plateau at the age of around 14. (D) The average energetic cost of the frontoparietal system continuously declines in youth. (E) The age effect size of the energetic costs of nodes. (F) The age effect size of nodes tends to converge towards the S-A axis.

References

1. Alexander-Bloch. (2018). On testing for spatial correspondence between maps of human brain structure and function. Neuroimage, 178, 540-551.
2. Braun, U. (2015). Dynamic reconfiguration of frontal brain networks during executive cognition in humans. Proc Natl Acad Sci U S A, 112(37), 11678-11683.
3. Cieslak, M. (2021). QSIPrep: an integrative platform for preprocessing and reconstructing diffusion MRI data. Nat Methods, 18(7), 775-778.
4. Cui, Z. (2020). Optimization of energy state transition trajectory supports the development of executive function during youth. Elife, 9.
5. Glasser, M. F. (2016). The Human Connectome Project's neuroimaging approach. Nat Neurosci, 19(9), 1175-1187.
6. Gu, S. (2015). Controllability of structural brain networks. Nat Commun, 6, 8414.
7. Somerville, L. H. (2018). The Lifespan Human Connectome Project in Development: A large-scale study of brain connectivity development in 5-21 year olds. Neuroimage, 183, 456-468.
8. Sydnor, V. J. (2021). Neurodevelopment of the association cortices: Patterns, mechanisms, and implications for psychopathology. Neuron, 109(18), 2820-2846.

Poster No 1222

Large Data on the Small Brain: Population-wide Cerebellar Growth Models of Children and Adolescent

Carolin Gaiser[1], Rick van der Vliet[1], Augustijn de Boer[2], Opher Donchin[3], Pierre Berthet[4], Gabriel Devenyi[5], Mallar Chakravarty[6], Jörn Diedrichsen[7], Andre Marquand[2], Maarten Frens[1], Ryan Muetzel[1]

[1]Erasmus Medical Center, Rotterdam, Zuid Holland, [2]Radboud University Nijmegen, Nijmegen, Gelderland, [3]Ben-Gurion University of the Negev, Be'er Sheva, Be'er Sheva, [4]University of Oslo, Oslo, Oslo, [5]McGill University, Montreal, Quebec, [6]Brain Imaging Centre, Douglas Research Centre, Montreal, Quebec, [7]The Brain and Mind Institute, University of Western Ontario, London, Ontario

Introduction: The cerebellum is known to be engaged in a broad spectrum of functions. While its involvement in motor control is best documented, recent efforts have made clear that it is also involved in cognitive function. In the current study, we describe and provide openly available normative models of anatomical and functional subregions of the cerebellum from a large pediatric population that 1) can be used as reference models to obtain accurate normative ranges, also in smaller datasets, by benefitting from informative hyperpriors based on a large sample, and that 2) can be updated with data from new sites and extended age ranges without the necessity of sharing sensitive patient or participant data. We furthermore illustrate the usefulness and practicality of the current approach by mapping the deviations from typical cerebellar development at the level of the individual in a subpopulation of children with autistic traits (Constantino et al., 2003). These models have the potential to facilitate and maximize the use of cerebellar outcomes in neuroimaging research and as a result aid to better understand the role of the cerebellum in typical as well as atypical neurodevelopment.

Methods: Anatomical Parcellation The cerebellum was parcellated in the native space into 35 anatomical subdivisions using the MAGeT pipeline (Chakravarty et al., 2013; Park et al., 2014). Functional Parcellation As lobular boundaries of the cerebellum have shown limited correspondence with functional boundaries, we also employed the functional subregions proposed by King and colleagues (King et al., 2019). Normative Models To generate normative models for anatomical and functional subregions of the cerebellum, we made use of the PCNtoolkit python package version 0.27 (de Boer et al., 2022; Rutherford et al., 2022b) using Python 3.10.6. Using Hierarchical Bayesian Regression, we estimated normative models of the cerebellum using both the volumes from the anatomical parcellation and the morphological indicators (i.e., grey and white matter densities as well as volumes) of the functional parcellation from age, for each region of interest (ROI) separately. Sex and scanner were modeled as batch-effects.

Results: The anatomical and functional regions show similar overall growth trends. As expected in this age range traversing late-childhood into adolescence, we see increasing volumes throughout all ROIs in both parcellations. Consistent with previous findings, we observed an anterior-posterior gradient in cerebellar development likely to reflect and mirror the age-related improvements in underlying functions, with sensorimotor areas predominantly located anteriorly and cognitive areas posteriorly in the cerebellum (King et al., 2019; Klein et al., 2016; Liu et al., 2022). Anterior sensorimotor areas show smaller age-related effects compared to posterior cognitive areas, possibly reflecting protracted growth trajectories for higher-order cognitive compared to sensorimotor regions in the cerebellum.

Conclusions: We present models of cerebellar growth during childhood and adolescence, an important time period for brain development, based on a large, prospective population cohort. We find an anterior-posterior growth gradient mirroring the age-related improvements of underlying behavior and function. The anterior/sensorimotor-posterior/cognitive growth gradient follows a recently proposed functional gradient related to cognitive load as well as cerebral maturation patterns, thus providing evidence for directly related cerebello-cortical developmental trajectories. In recent years, the cerebellum has received increasing attention as a critical node in fundamental cognitive and emotional functions as well as brain development. The current openly accessible growth models will therefore be of great value for uncovering cerebellar deviations and understanding their implications in neuropathology.

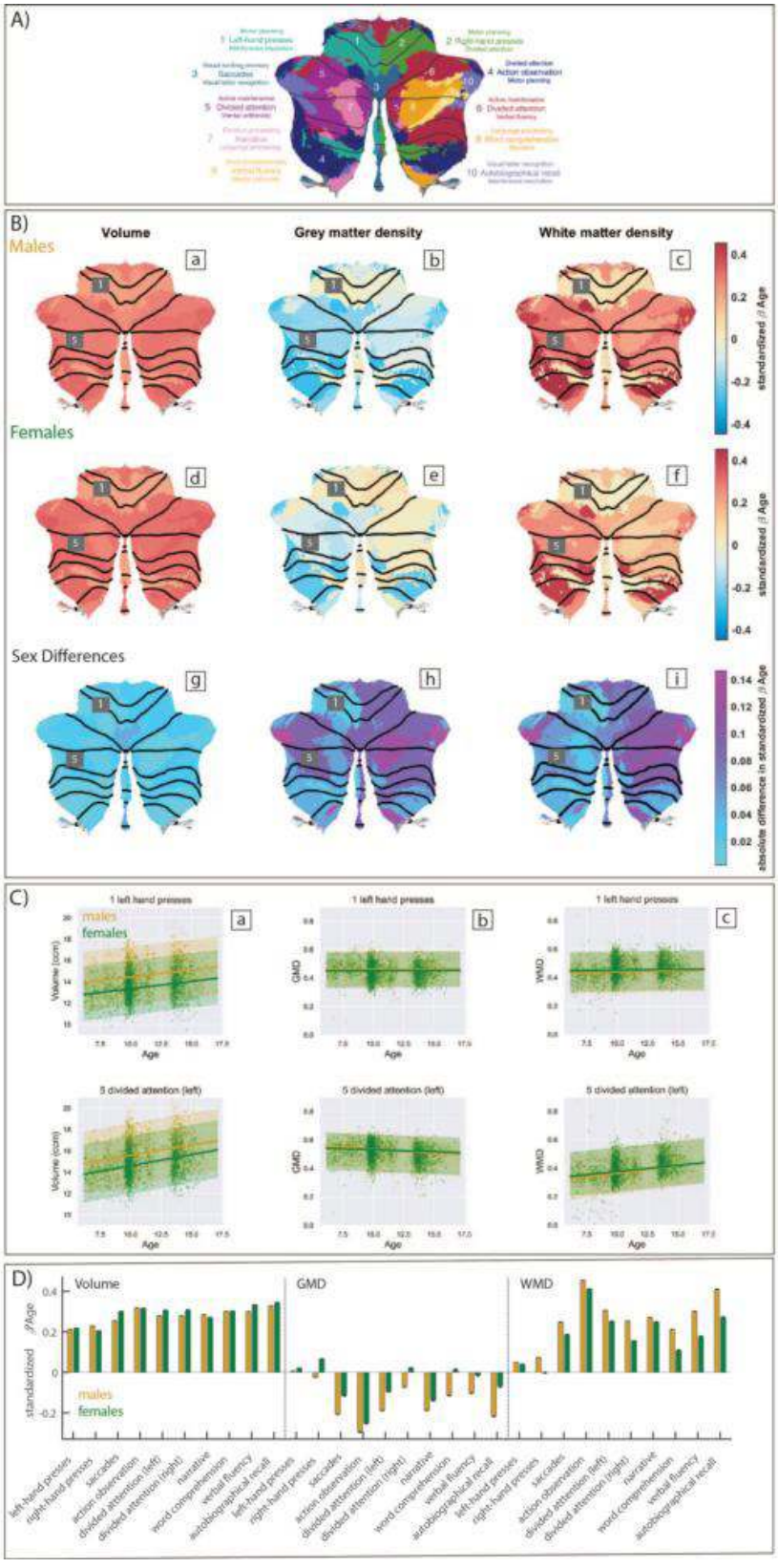
A)
B)
Volume
Grey matter density
White matter density
Males
Females
Sex Differences
standardized β Age
absolute difference in standardized β Age
C)
1 left hand presses
5 divided attention (left)
males
females
Volume (ccm)
GMD
WMD
Age
D)
Volume
GMD
WMD
β Age
standardized
left hand presses
right hand presses
saccades
action observation
divided attention (left)
divided attention (right)
narrative
word comprehension
verbal fluency
autobiographical recall

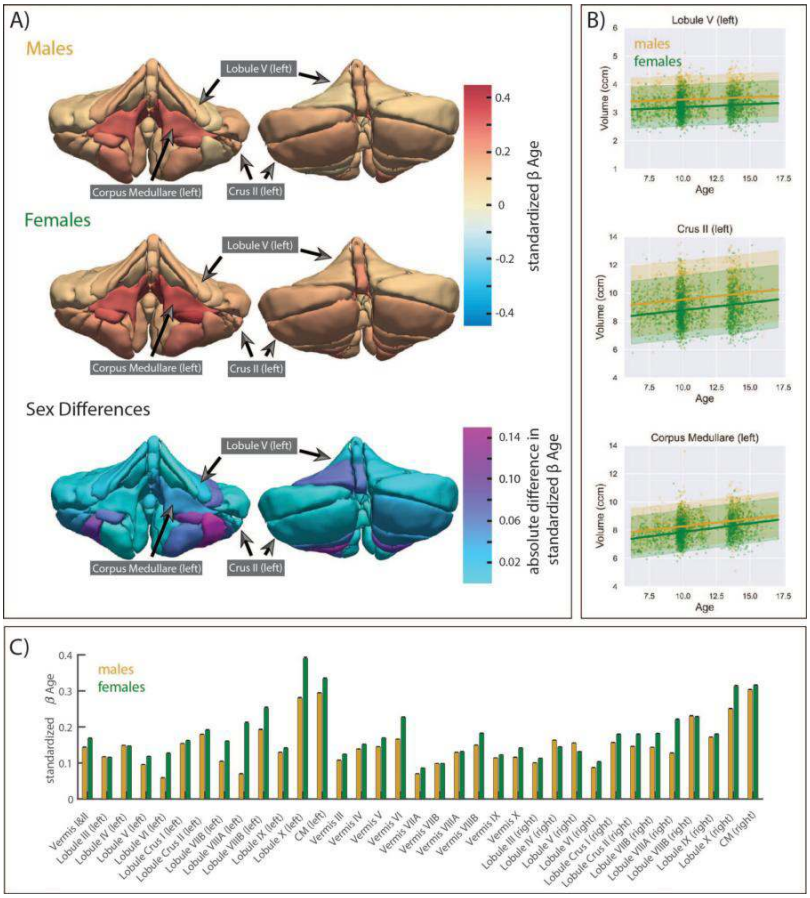

References

1. Rutherford, S., Kia, S. M., Wolfers, T., Fraza, C., Zabihi, M., Dinga, R., ... & Marquand, A. F. (2022). The normative modeling framework for computational psychiatry. Nature protocols, 17(7), 1711-1734.
2. Kia, S. M., Huijsdens, H., Rutherford, S., de Boer, A., Dinga, R., Wolfers, T., ... & Marquand, A. F. (2022). Closing the life-cycle of normative modeling using federated hierarchical Bayesian regression. Plos one, 17(12), e0278776.
3. Constantino, J. N., Davis, S. A., Todd, R. D., Schindler, M. K., Gross, M. M., Brophy, S. L., ... & Reich, W. (2003). Validation of a brief quantitative measure of autistic traits: comparison of the social responsiveness scale with the autism diagnostic interview-revised. Journal of autism and developmental disorders, 33, 427-433.
4. Kooijman, M. N., Kruithof, C. J., van Duijn, C. M., Duijts, L., Franco, O. H., van IJzendoorn, M. H., ... & Jaddoe, V. W. (2016). The Generation R Study: design and cohort update 2017. European journal of epidemiology, 31, 1243-1264.
5. Chakravarty, M. M., Steadman, P., Van Eede, M. C., Calcott, R. D., Gu, V., Shaw, P., ... & Lerch, J. P. (2013). Performing label-fusion-based segmentation using multiple automatically generated templates. Human brain mapping, 34(10), 2635-2654.
6. Park, M. T. M., Pipitone, J., Baer, L. H., Winterburn, J. L., Shah, Y., Chavez, S., ... & Chakravarty, M. M. (2014). Derivation of high-resolution MRI atlases of the human cerebellum at 3 T and segmentation using multiple automatically generated templates. Neuroimage, 95, 217-231.
7. King, M., Hernandez-Castillo, C. R., Poldrack, R. A., Ivry, R. B., & Diedrichsen, J. (2019). Functional boundaries in the human cerebellum revealed by a multi-domain task battery. Nature neuroscience, 22(8), 1371-1378.
8. Klein, A. P., Ulmer, J. L., Quinet, S. A., Mathews, V., & Mark, L. P. (2016). Nonmotor functions of the cerebellum: an introduction. American Journal of Neuroradiology, 37(6), 1005-1009.
9. Liu, X., d'Oleire Uquillas, F., Viaene, A. N., Zhen, Z., & Gomez, J. (2022). A multifaceted gradient in human cerebellum of structural and functional development. Nature neuroscience, 25(9), 1129-1133.

Poster No 1223

Intrinsic timescale evolves along a sensorimotor-association cortical axis in neurodevelopment

Golia Shafiei[1], Valerie Sydnor[2], Matthew Cieslak[3], Arielle Keller[1], Audrey Luo[1], Kahini Mehta[1], Taylor Salo[1], Dani Bassett[3], Russell Shinohara[1], Theodore Satterthwaite[3]

[1]University of Pennsylvania, Philadelphia, PA, [2]University of Pittsburgh, Pittsburgh, PA, [3]UPenn, Philadelphia, PA

Introduction: Intrinsic timescale is a commonly used measure of spontaneous neural dynamics that quantifies the time window of information processing of neuronal populations and is associated with cognition and complex behavior[1]. Intrinsic timescale displays a hierarchical cortical organization across multiple species and modalities, such that neural activity

at the sensory cortex demonstrates a shorter timescale–adapting to rapid changes in the environment–and association cortex exhibits longer timescales–sustaining neural activity for a longer time to process higher order functions. A similar organizational pattern is observed across a range of neurobiological properties that largely align to an archetypical axis spanning from sensorimotor to association cortices (S-A axis)[2]. Recent work in human neurodevelopment has demonstrated that the S-A axis also constrains developmental patterns of functional brain organization in youth[3,4]. However, less is known about age-related changes in intrinsic timescale during development and whether its cortical maturation patterns follow the same large-scale organizational principles. Here we estimate intrinsic timescale in youth and investigate its neurodevelopmental trajectories with respect to the S-A axis of brain organization.

Methods: We used functional Magnetic Resonance Imaging (fMRI) data from the Human Connectome Project: Development (HCP-D[5]; N = 610, age range 8-21 years, 327 female). Functional MRI data were preprocessed using fMRIPrep and XCP-D. The autocorrelation function (ACF) of the preprocessed time-series was used to estimate an intrinsic timescale for each region as the sum of its positive autocorrelation values, indicating the timescale at which the ACF of a given region decays[6]. A Generalized Additive Model (GAM) was first applied to assess neurodevelopmental variations in the whole-cortex average timescale across individuals, including age as the smooth variable and in-scanner motion and sex as covariates. Region-wise GAMs were then used to estimate neurodevelopmental trajectories of intrinsic timescale at each cortical region. Age effects on regional timescales were estimated as partial R2, calculated as differences in the model fit with and without including the smooth term (i.e., age). Regional neurodevelopmental trajectories were compared with an archetypical organizational map of the cortex that spans the S-A axis, obtained from the neuromaps toolbox[1,7].

Results: Applying GAM on whole-cortex data, we found that the average timescale increases during development in youth (Fig 1a). Region-wise GAM analysis demonstrated that regional neurodevelopmental trajectories of intrinsic timescale were heterogeneous across the cortex, with smaller age effects in sensorimotor cortex and larger positive age effects in association cortex (Fig. 1b). Comparing regional age effects with S-A axis rankings, we found that intrinsic timescales mature along the cortical hierarchy captured by the S-A axis (Fig. 1c; $r_s = 0.38$, $p_{spin} = 0.0024$). Further inspection of regional GAM fits confirmed that intrinsic timescale remains relatively stable in sensorimotor regions during child and adolescent development whereas timescale increases in association regions (Fig. 1d). Finally, we compared intrinsic timescale derived from task fMRI (Go/NoGo Task) with resting-state data to assess the extent to which cognitive demand influences intrinsic timescale in a neurodevelopmental cohort. Consistent with previous reports in adults, we found that the average whole-cortex intrinsic timescale significantly increases with higher task demand (Fig. 1e; paired t-test: $t = 30.95$, $p < 0.05$).

Conclusions: Intrinsic timescale increases during development, in particular in the association cortex at the top of the cortical hierarchy. Developmental effects follow a hierarchical pattern and recapitulate the S-A axis of cortical organization, revealing convergence between major axes of cortical organization and development.

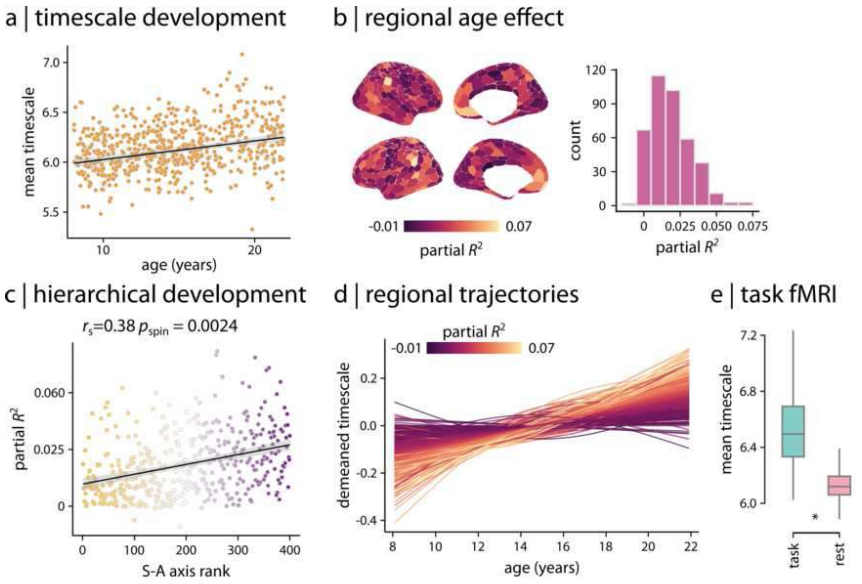

Figure 1. Neurodevelopmental trajectories of intrinsic timescale | (a) Intrinsic timescale was estimated as the sum of positive autocorrelation values for each cortical region and each individual. A whole-brain GAM was applied to model developmental changes in cortex-wide average timescale. GAM results demonstrate that average timescale increases during development in youth. (b) Region-wise GAMs were used to examine developmental changes in intrinsic timescale at the region level. Age effects quantified as partial R^2 are depicted across the cortex, displaying a heterogeneous spatial distribution. (c) Age effects on intrinsic timescale were compared to an organizational axis of the cortex that spans sensorimotor to association cortices (S-A axis), identifying a hierarchical pattern of developmental changes in intrinsic timescale along the S-A axis. Significance of the association between age effects and S-A axis rank was assessed using 10,000 spatial autocorrelation-preserving permutation tests (i.e., spin test [8]). r_s denotes Spearman's rank correlation coefficient. Linear regression line is added for visualization purposes only. (d) Regional trajectories of developmental changes in intrinsic timescale were obtained from region-wise GAM results (as shown in panel b). Each line corresponds to the model fit of each cortical region and is colored based on the brain map in panel b. The results demonstrate that intrinsic timescale in association regions increases during development in youth while it remains relatively stable in sensorimotor regions. (e) Intrinsic timescale was estimated using task fMRI data (Go/NoGo task). Whole-brain timescale maps were calculated for task and resting-state fMRI as the average timescale across individuals. Task-based timescale brain map was compared to resting-state timescale brain map, demonstrating an overall increase in intrinsic timescale with task demand (t = 30.95). Asterisk denotes significant difference in the means (two-tailed t-test).

References

1. Kiebel, S. J., Daunizeau, J., & Friston, K. J. (2008). A hierarchy of time-scales and the brain. PLoS computational biology, 4(11), e1000209.
2. Sydnor, V. J., Larsen, B., Bassett, D. S., Alexander-Bloch, A., Fair, D. A., Liston, C., ... & Satterthwaite, T. D. (2021). Neurodevelopment of the association cortices: Patterns, mechanisms, and implications for psychopathology. Neuron, 109(18), 2820-2846.
3. Sydnor, V. J., Larsen, B., Seidlitz, J., Adebimpe, A., Alexander-Bloch, A. F., Bassett, D. S., ... & Satterthwaite, T. D. (2023). Intrinsic activity development unfolds along a sensorimotor–association cortical axis in youth. Nature Neuroscience, 26(4), 638-649.
4. Luo, A., Sydnor, V. J., Pines, A., Larsen, B., Alexander-Bloch, A. F., Cieslak, M., ... & Satterthwaite, T. D. (2023). Functional Connectivity Development along the Sensorimotor-Association Axis Enhances the Cortical Hierarchy. BioRxiv, 2023-07.
5. Somerville, L. H., Bookheimer, S. Y., Buckner, R. L., Burgess, G. C., Curtiss, S. W., Dapretto, M., ... & Barch, D. M. (2018). The Lifespan Human Connectome Project in Development: A large-scale study of brain connectivity development in 5–21 year olds. Neuroimage, 183, 456-468.
6. Watanabe, T., Rees, G., & Masuda, N. (2019). Atypical intrinsic neural timescale in autism. Elife, 8, e42256.
7. Markello, R. D., Hansen, J. Y., Liu, Z. Q., Bazinet, V., Shafiei, G., Suárez, L. E., ... & Misic, B. (2022). Neuromaps: structural and functional interpretation of brain maps. Nature Methods, 19(11), 1472-1479.
8. Alexander-Bloch, A. F., Shou, H., Liu, S., Satterthwaite, T. D., Glahn, D. C., Shinohara, R. T., ... & Raznahan, A. (2018). On testing for spatial correspondence between maps of human brain structure and function. Neuroimage, 178, 540-551.

Poster No 1224

Multi-scale cortical morphometry reveals regional and scale-dependent variations across the lifespan

Karoline Leiberg[1], Bethany Little[1], Yujiang Wang[1]

[1]Newcastle University, Newcastle, United Kingdom

Introduction: Characterising the changes in cortical morphology across the lifespan is fundamental for a range of research and clinical applications. Most studies to date have found a monotonic decrease in commonly used morphometrics, such as cortical thickness and volume, across the entire brain with increasing age. Any regional variations reported are subtle changes in the rate of decrease. However, these descriptions of morphological changes have been limited to a single length scale. Here, we delineate the morphological changes associated with the healthy lifespan in multi-scale morphometrics.

Methods: Using MRI from subjects aged 6-88 years from NKI (n=833) and CamCAN (n=641), we computed several morphometrics at spatial scales ranging from 0.32 mm to 3 mm. These were obtained at both the cortical hemisphere and lobe level. We used generalised additive mixed models (GAMMs) to account for site differences before extracting age trajectories. In a proof-of-principle application, we compared brain age estimations based on a single metric (pial surface area) computed at a single scale vs. multiple scales.

Results: On the level of whole cortical hemispheres, lifespan trajectories show diverging and even opposing trends at different spatial scales, in contrast to the monotonic decreases of volume and thickness described so far. Pronounced regional differences between lobes also became apparent in scales over 0.7 mm. Using two complementary scales improved brain age estimates in RMSE by about 5 years.

Conclusions: Our study provides a comprehensive multi-scale description of lifespan effects on cortical morphology in an age range from 6-88 years. In future, this can be used as a normative model to compare individuals or cohorts, hence identifying morphological abnormalities. Our results reveal the complementary information contained in different spatial scales, demanding that morphometrics should not be considered as mere numbers, but as functions of length scale.

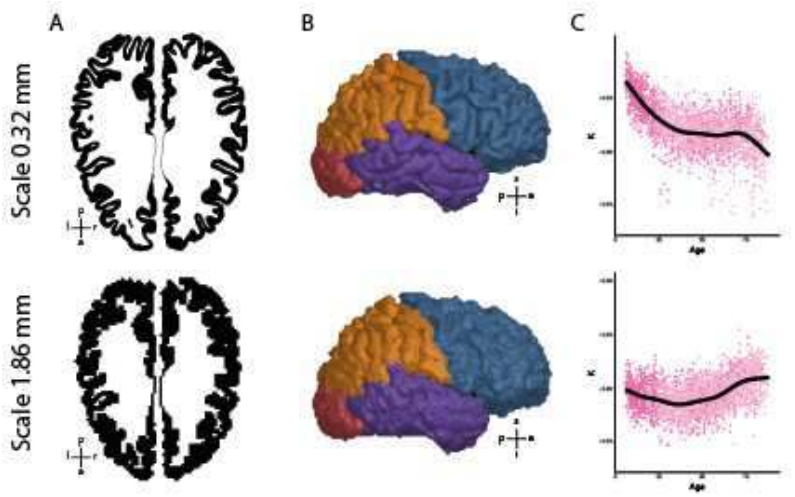

Fig. Computation of lifespan trajectories in scale-dependent morphometrics in cortical regions.

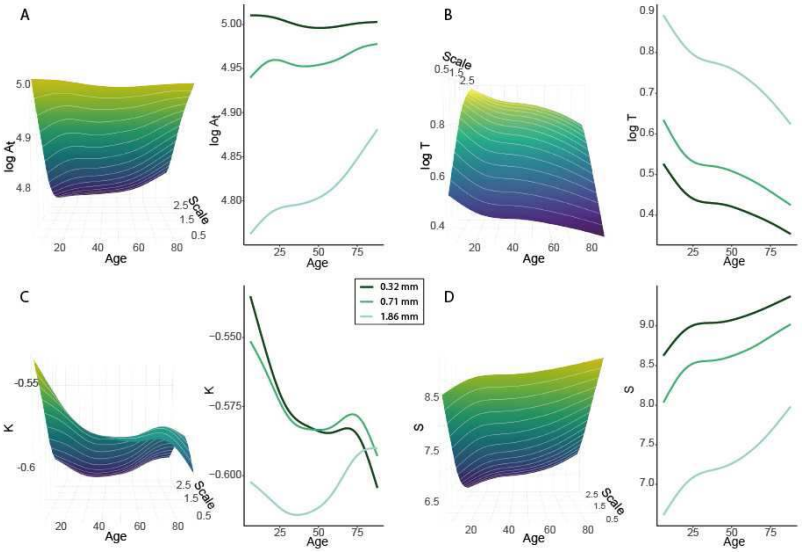

Fig. Lifespan effects on cortical hemispheres measured in scale-dependent morphometrics.

References

1. Barrick, T.R. (2010), NeuroImage, vol. 51, no. 2, pp. 565–77
2. Bethlehem, R.A.I. (2022), Nature, pp. 1–11
3. Chen, Y. (2022), eLife, pp. 1–28
4. Cole, J.H. (2020), Neurobiology of Aging, vol. 92, pp. 34–42
5. de Moraes, F.H.P. (2022), Frontiers in Neuroscience, vol. 16, pp. 1–13
6. Fjell, A.M. (2010), Reviews in the Neurosciences, vol. 21, no. 3, pp. 187–221
7. Frangou, S. (2021), Human Brain Mapping, pp. 1–21

8. Good, C.D. (2001), NeuroImage, vol. 14, no. 1 I, pp. 21–36
9. Guan, S. (2023), GeroScience, no. 0123456789
10. Gunning-Dixon, F.M. (2009), International Journal of Geriatric Psychiatry, vol. 24, no. 2, pp. 109–17
11. Kumar, S. (2021), NeurIPS, pp. 1–10
12. Le, T.T., (2018), Frontiers in Aging Neuroscience, vol. 10, p. 317
13. Leiberg, K. (2021), Medical Image Computing and Computer Assisted Intervention, vol. 12907 LNCS, pp. 691–700
14. Liang, H. (2019), Human Brain Mapping, vol. 40, no. 11, pp. 3143–52
15. Mota, B. (2015), Science, vol. 349, no. 6243, pp. 74–77
16. Nooner, K.B. (2012), Frontiers in Neuroscience, vol. 6
17. Pomponio, R. (2020), NeuroImage, vol. 208, p. 116450
18. Resnick, S.M. (2003), Journal of Neuroscience, vol. 23, no. 8, pp. 3295–301
19. Rokicki, J. (2021), Human Brain Mapping, vol. 42, no. 6, pp. 1714–26
20. Rutherford, S. (2022), eLife, vol. 11, pp. 1–15
21. Rutherford, S. (2023), eLife, vol. 12, pp. 1–24
22. Salat, D.H. (2004), Cerebral Cortex, vol. 14, no. 7, pp. 721–30
23. Schilling, K.G. (2023a), Aging Brain, vol. 3, p. 100067
24. Schilling, K.G. (2023b), Brain Structure and Function, vol. 228, no. 3–4, pp. 1019–31
25. Shafto, M.A. (2014), BMC Neurology, vol. 14, no. 1, pp. 1–25
26. Storsve, A.B. (2014), Journal of Neuroscience, vol. 34, no. 25, pp. 8488–98
27. Taylor, J.R. (2017), NeuroImage, vol. 144, pp. 262–69
28. Thambisetty, M. (2010), NeuroImage, vol. 52, no. 4, pp. 1215–23
29. Wang, Y. (2019), Communications Biology, vol. 2, no. 1, pp. 1–8
30. Wang, Y. (2021), NeuroImage, vol. 226, p. 117546
31. Wang, Y. (2022), 'Neuro-Evolutionary Evidence for a Universal Fractal Primate Brain Shape', Preprint
32. Wang, Y. (2016), Proceedings of the National Academy of Sciences of the United States of America, vol. 113, no. 45, pp. 12820–25

Poster No 1225

The development of object recognition in infancy: findings from neuroimaging and deep learning

Cliona O'Doherty[1], Áine Dineen[1], Anna Truzzi[1], Graham King[1], Keelin Harrison[1], Lorijn Zaadnoordijk[1], Enna-Louise D'Arcy[1], Jessica White[1], Tamrin Holloway[1], Chiara Caldinelli[1], Anna Kravchenko[1], Sojo Joseph[1], Eleanor Molloy[2], Adrienne Foran[3], Ailbhe Tarrant[3], Angela Byrne[2], Rhodri Cusack[1]

[1]Trinity College Dublin, Dublin, Ireland, [2]The Coombe Hospital, Dublin, Ireland, [3]The Rotunda Hospital, Dublin, Ireland

Introduction: Object recognition and categorisation are foundational skills required to build conceptual knowledge. Although categorisation is well-studied in young cohorts there is still debate surrounding its origin in the ventral visual cortex (VVC). Initial infant neuroimaging shows that category representations appear early [Kosakowski et al., 2022] but the success of deep neural networks (DNNs) as models for the ventral stream suggests that categories are formed according to a hierarchy of feature complexity. In agreement with this, behavioural studies show very young infants can form mental groups according to perceptual features [Quinn et al., 1993] with grouping by conceptual features emerging later [Younger & Cohen 1993]. However, behavioural studies are limited as they test if an infant is acting upon knowledge and cannot provide evidence for the absence of a capacity for such knowledge. Neuroscience and computational modelling can provide unique insights richly complementing behavioral measures. To date, it has not been possible to probe infant brain representations underlying categorisation at scale. With pioneering advances in awake infant fMRI [Ellis et al., 2020] we have begun to tackle these questions by collecting the largest cohort of awake, behaving infants in an fMRI study to-date and quantifying their visual representations to a broad variety of categories.

Methods: Infants (n=134) attended two scanning sessions at 2- and 9-months and were scanned in a Siemens 3T MAGNETOM Prisma. We measured brain responses to looming images: 12 categories of objects with 3 exemplars across viewpoints. The chosen categories had varying degrees of familiarity to young infants and spanned cortical organisation principles such as animacy and real-world size [Konkle & Caramazza, 2013]. Using multivariate pattern analysis, we quantified the distributed patterns of visual responses within the VVC and compared infant category organisation to adults. Representational similarity analysis with perceptual and categorical models was used to test the feature complexity in infant cortex and quantify the level of abstraction encoded across development. Infant brain activity was also compared to DNNs that were either untrained or trained to recognise 1000 categories of natural images. We measured the similarity to each layer of the DNN assuming that lower layers encode simpler features than later layers.

Results: At 2-months we observed an impressive organisation by category in ventral visual stream with significant distinctions for within versus between category representations as well as organisation by animacy and real-world size. This initial representation becomes more adult-like by 9-months and interestingly, anterior ventral regions were found to become more similar to adults earlier than posterior visual regions. Analogously, comparison to a DNN trained on an object recognition task

showed that anterior regions become closer to adults in their correlations to later layers of a DNN encoding complex features. In contrast, infants' early visual regions are more similar to an untrained network than adults as well as to earlier layers in the DNN.

Conclusions: We have demonstrated that the neural basis of categorisation is present from as early as 2-months and that anterior ventral regions become more adult-like before posterior regions. The presence of this organisation is prior to its documented functional emergence from behavioural literature and contrary to the idea that simpler features in early visual cortex develop before complex category representations. For the first time we apply multivariate analysis methods to a large, innovative infant neuroimaging dataset and successfully define similarities between the infant brain and AI models. This provides novel insight into the workings of the youngest of humans and demonstrates the promise of awake infant fMRI for the future of understanding the brain and mind in early life.

References

1. Ellis, C. T., Skalaban, L. J., Yates, T. S., Bejjanki, V. R., Córdova, N. I., & Turk-Browne, N. B. (2020). Re-imagining fMRI for awake behaving infants. Nature Communications, 11(1), 4523.
2. Konkle, T., & Caramazza, A. (2013). Tripartite organization of the ventral stream by animacy and object size. Journal of Neuroscience, 33(25), 10235-10242.
3. Kosakowski, H. L., Cohen, M. A., Takahashi, A., Keil, B., Kanwisher, N., & Saxe, R. (2022). Selective responses to faces, scenes, and bodies in the ventral visual pathway of infants. Current Biology, 32(2), 265-274.
4. Quinn, P. C., Eimas, P. D., & Rosenkrantz, S. L. (1993). Evidence for representations of perceptually similar natural categories by 3-month-old and 4-month-old infants. Perception, 22(4), 463-475.
5. Younger, B. A., & Cohen, L. B. (1986). Developmental change in infants' perception of correlations among attributes. Child development, 803-815.

Poster No 1226

Exploring Longitudinal Brain Connectivity Dynamics In Adolescent: A Multimodal MRI Analysis

Rekha Saha[1], Debbrata Kumar Saha[2], Zening Fu[3], Rogers Silva[4], Vince Calhoun[5]

[1]Georgia State University, Atlanta, GA, [2]Georgia Institute of Technology, Atlanta, GA, [3]Tri-institutional Center for Translational Research in Neuroimaging and Data Science (TReNDS) Georgi, Atlanta, GA, [4]TReNDS Center, Atlanta, GA, [5]GSU/GATech/Emory, Decatur, GA

Introduction: Functional and structural MRI play vital roles in brain development analysis. Our study explores brain development using fMRI/sMRI, merging modalities to capture nuanced brain changes during adolescence. Employing a novel symmetric multimodal fusion approach, we analyze FNC and GM data from the Adolescent Brain and Cognitive Development (ABCD) dataset, unveiling significant longitudinal change patterns. This approach reveals structured alterations in visual-sensorimotor connectivity and bilateral sensorimotor cortex. Through this analysis, we emphasize age-related multivariate brain changes, showcasing the dynamic nature of brain structure and connectivity during adolescence. This study emphasizes the dynamic nature of brain structure and connectivity during adolescence, showcasing the efficacy of our method in unraveling these changes across modalities.

Methods: In our study, we utilized subject-specific fMRI and sMRI data collected at baseline and two-years later. To capture alterations in functional network connectivity (FNC) and gray matter (GM), we computed differences between the baseline and two-year datasets, creating ΔFNC and ΔGM matrices to represent their respective changes over time. Employing the mCCA+jICA (define) method, we deconstructed these matrices, extracting co-varying change patterns: functional change patterns (FCPs) and structural change patterns (SCPs). Utilizing an elbow criterion, we estimated five components for both GM and FNC data. Following the mCCA+jICA estimation, we analyzed loading parameters and the source matrix. To identify significant longitudinal changes, we conducted one-sample t-tests on the loading parameters aF and aG for both modalities, assessing their statistical significance at a 95% confidence level with corrections for multiple comparisons.

Results: The study leverages the Neuromark template featuring 53 replicable networks grouped into 7 domains[1]. Figure 1 portrays the experimental findings, showcasing spatial maps illustrating the connections between multivariate FCPs and SCPs. These visualizations exhibit 2 FCP components (component 3 and 2) and their corresponding spatial maps of SCPs, represented with associated T-values indicating increased or decreased expression with age[2]. Notably, the upper aspects demonstrate associations of FCPs and SCPs components with increased age. Specifically, components 2 and 3 of FCPs reveal significant changes in brain functional connectivity with age, showing an increasing trend. Component 3 exhibits heightened connectivity between visual and sensorimotor domains in FNC data, complemented by decreasing changes in the bilateral sensorimotor cortex in sMRI data over two years. Additionally, FCP component 3 displays a decreasing trend

with age in functional connectivity between visual and cerebellar domains, as well as between sensorimotor and cognitive control domains.

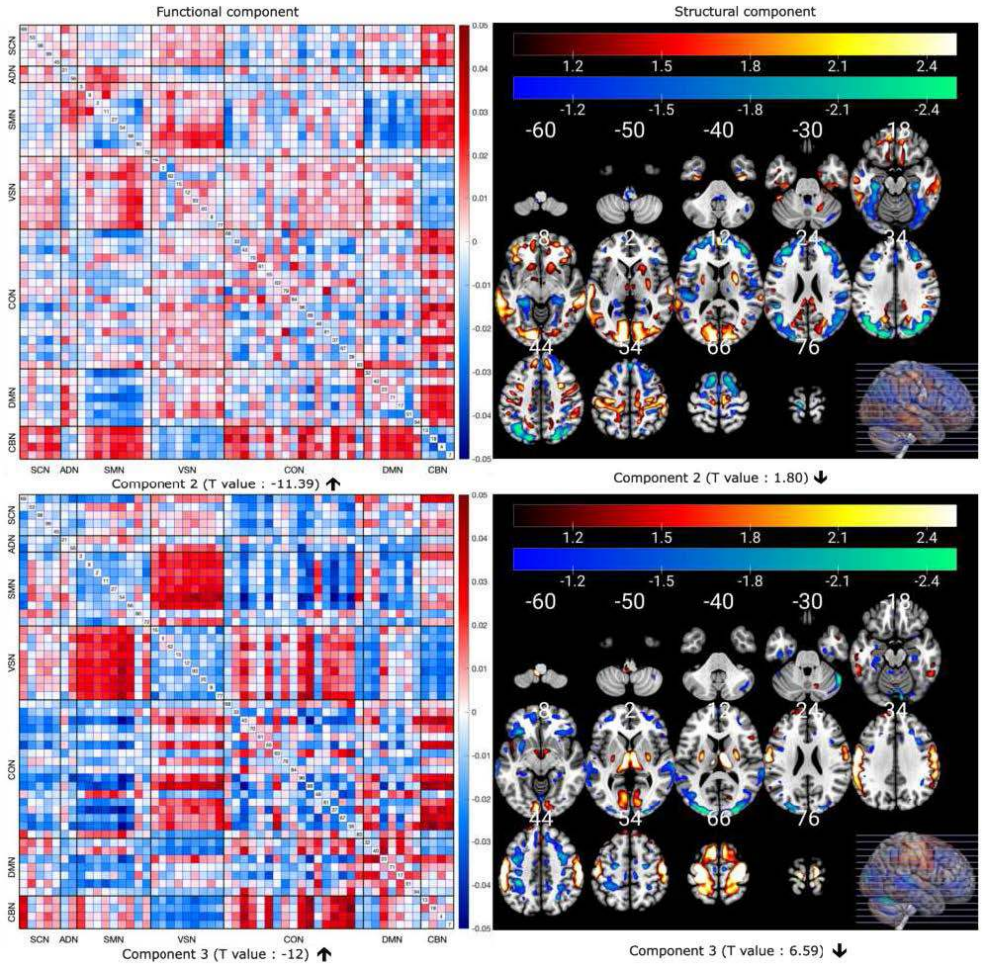

Conclusions: This study introduces an innovative method to explore links between brain functional and structural changes using FNC matrices and GM data. It investigates whole-brain structural and functional alterations over two years, revealing age-related trends and associations between these changes. Analyzing ABCD dataset data, the research identifies significant alterations in functional and structural change patterns within this period. These outcomes underscore the potential of our proposed methodology as a valuable approach for assessing holistic brain functional and structural alterations and their interplay in longitudinal investigations.

References

1. T. DeRamus, A. Iraji, Z. Fu, R. Silva, J. Stephen, T. W. Wilson, Y. P. Wang, Y. Du, J. Liu, and V. Calhoun, "Stability of functional network connectivity (fnc) values across multiple spatial normalization pipelines in spatially constrained independent component analysis," in 2021 IEEE 21st International Conference on Bioinformatics and Bioengineering (BIBE). IEEE, 2021, pp. 1–6.
2. R. Saha, D. K. Saha, M. A. Rahaman, Z. Fu, and V. D. Calhoun, "Longitudinal whole-brain functional network change patterns over a two-year period in the abcd data," in 2022 IEEE 19th International Symposium on Biomedical Imaging (ISBI). IEEE, 2022, pp. 1–4.

Poster No 1227

The rise of synergistic structure in the newborn brain

Anton Tokariev[1], Thomas Varley[2], Michael Myers[3], Martha Welch[3], Sampsa Vanhatalo[1], Olaf Sporns[2]

[1]University of Helsinki, Helsinki, Finland, [2]Indiana University, Bloomington, IN, [3]Columbia University Medical Center, New York, NY

Introduction: During the third trimester infant human brain actively self-organises into a unified complex system. Discrete local neurons wire together, their populations connect into large-scale networks, which, in turn, cooperate on a global scale. This happens at both structural and functional levels. Neural dynamics of the whole brain goes far beyond just the sum of its individual elements and this property is known as "synergy". Previously it was shown that synergy is crucial for many complex

brain functions and cognition. But the timing of emergence and early formation principles of synergistic system in the human brain is currently unknown. We hypothesized that changing patterns of synergy would be seen during early development of the infant brain, and that the emergence of a consolidated "synergistic scaffold" would be associated with the later neurocognitive performance at individual level.

Methods: In this study, we analysed high-density (124-channels) longitudinal EEG data collected from preterm infants (N = 135; born at 31 ± 2.4 weeks) and spanning over period from the third trimester to postnatal age (33–45 weeks). Each subject had 1–3 recordings done during daytime sleep (in total N = 289 recordings). The general cohort included standard care infants (SC; N = 61) and those participated in Family Nurture Intervention (FNI; N = 74) program, which was aimed to enhance mother-infant emotional connection. Artifact-free 5-min-long epochs of quiet sleep EEG were filtered into delta (1.5–4 Hz), theta (4–8 Hz), alpha (8–13 Hz), and beta (13–22 Hz) frequency bands. The filtered signals were source reconstructed into 58 cortical parcel activity using a realistic infant head model and dynamic statistical parametric mapping approach. Next, we estimated O-information (measure of higher-order structure showing the balance between redundancy and synergy) from cortical activity of each infant and correlated to their age (Spearman). Further, we computed nodal frequencies of being a part of the "synergistic scaffold" across different age groups. The developmental trajectories of O-information for each group were computed as mean values in a two-weeks-wide sliding windows and compared within each age bin using two-sample t-test. Finally, we correlated O-information levels at term equivalent age to cognitive outcomes (Bayley) at 18 months.

Results: We found that at ages corresponding to the third trimester, infant brain organization dynamically changes from redundant to synergy-dominated with O-information negatively correlating to age at all frequencies (rho < −0.42, p < 0.001; see Fig.1A for theta band). The size of the "synergistic scaffold" was also increasing with maturation (Fig.1A left). Spatially (Fig.1B), the scaffold mostly consisted of frontal nodes at preterm age (33–36 weeks), but then it expanded over visual areas before term (37–40 weeks) and further incorporated central and temporal cortices during early postnatal period (40–43 weeks). Strikingly, our analysis revealed different developmental trajectories (Fig.1C) between clinical cohorts (SC vs. FNI) with significant group differences at 35 and 38 weeks (p < 0.01). FNI infants showed a steadily decreasing trend, while SC showed bi-phasic trajectory: redundancy was slightly increasing until 38th week ("plateau" phase) followed by abrupt changes towards synergetic structure ("steep" phase). Finally, O-information values around term age were negatively correlated to later cognitive assessments (Fig.1C; rho = −0.45, p = 0.004) suggesting that brain synergy may be a biomarker of future neurodevelopment.

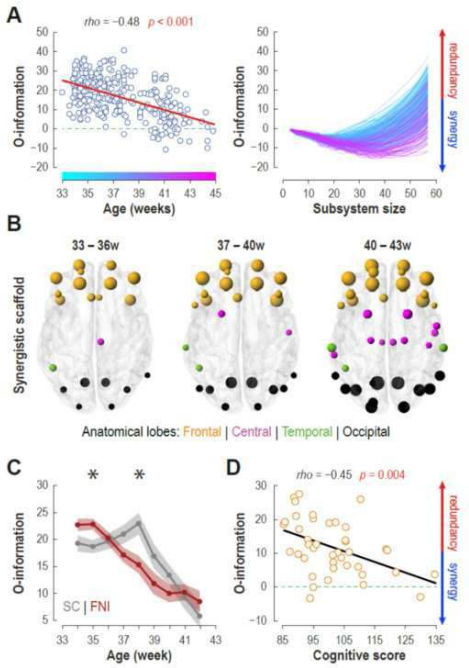

Figure 1. Emergence of synergistic structure in the infant brain at early maturation (theta band). A, O-information negatively correlates to gestational age (left), at the same time the size of the optimal synergistic subsystem (scaffold) increases (right). B, Early spatial development of the synergistic scaffold. The ball size shows consistency, or participation frequency, of each cortical region in the "synergistic scaffold" at different ages. C, Standard care (SC) and Family Nurture Intervention (FNI) groups show distinct developmental trajectories with significant differences at 35 and 38 weeks. D, O-information levels estimated around term age correlates to cognitive scores at 18 months of age.

Conclusions: Our results suggest that starting from the third trimester infant human brain rapidly develops synergetic structure and that this predicts later clinical outcomes. Moreover, support of natural mother-infant connection (environmental enrichment) modulates the developmental trajectory of these changes and associates with more gradual reorganization processes in the maturing brain.

References

1. Dale, A.M. (2000), 'Dynamic statistical parametric mapping: combining fMRI and MEG for high-resolution imaging of cortical activity', Neuron no. 26, pp. 55-67.
2. Luppi, A.I. (2022), 'A synergistic core for human brain evolution and cognition', Nature Neuroscience, 25(6), p. 771-782.
3. Rosas, F.E. (2019), 'Quantifying high-order interdependencies via multivariate extensions of the mutual information', Physical Review E, 100(3).
4. Tokariev, A. (2019a), 'Preterm birth changes networks of newborn cortical activity', Cerebral Cortex, 29(2), pp. 814-826.
5. Tokariev, A. (2019b), 'Large-scale brain modes reorganize between infant sleep states and carry prognostic information', Nature Communications, 10(1), p. 2619.
6. Varley, T.F. (2023), 'Multivariate information theory uncovers synergistic subsystems of the human cerebral cortex', Communications Biology, 6(1), p. 451.
7. Varley, T.F. (2023), 'Partial entropy decomposition reveals higher-order information structures in human brain activity', Proceedings of the National Academy of Sciences, 120(30).
8. Welch, M.G. (2012), 'Family nurture intervention (FNI): methods and treatment protocol of a randomized controlled trial in the NICU', BMC Pediatrics, 12(14).
9. Yrjölä, P. (2022), 'Facilitating early parent-infant emotional connection improves cortical networks in preterm infants', Science translational medicine, vol. 14, no. 664.

Poster No 1228

Triple Interactions Between the Environment, Brain, and Behavior in Children: An ABCD Study

Dongmei Zhi[1], Rongtao Jiang[2], Godfrey Pearlson[2], Zening Fu[3], Shile Qi[4], Weizheng Yan[5], Aichen Feng[6], Ming Xu[6], Vince Calhoun[7], Jing Sui[8]

[1]Beijing Normal University, Beijing, [2]Yale School of Medicine, New Haven, CT, [3]Tri-institutional Center for Translational Research in Neuroimaging and Data Science (TReNDS) Georgi, Atlanta, GA, [4]Nanjing University of Aeronautics and Astronautics, Nanjing, Jiang Su, [5]Emory University, Atlanta, GA, [6]Institute of Automation, Chinese Academy of Sciences, Beijing, [7]GSU/GATech/Emory, Decatur, GA, [8]Beijing Normal University, Beijing, China

Introduction: Despite the well-known fact that environmental exposures play a critical role in influencing behaviors[1], we have limited understanding of how these exposures interact with the brain and in turn shape our behaviors, especially during adolescence with rapid development of brain and behaviors[2].

Methods: In this work, we investigated the comprehensive environment-brain-behavior triple interactions among whole-brain functional network connectivity (FNC) derived from a spatially constrained single-subject ICA method[3], 41 environmental exposures (spanning perinatal, family, school, neighborhood and individual lifestyle), and 23 behaviors related to cognitive ability and mental health in 7655 children selected from the ABCD study at both baseline and longitudinally (Fig. 1)[4,5]. Linear mixed-effect models were adopted to examine the associations between 41 environmental exposures and 1378 whole-brain FNC pairs, 10 cognitive abilities, and 13 mental health measures at both baseline and longitudinally, while adjusting for multiple confounders. Furthermore, we used partial least squares regression to identify key predictive FNC signatures and environmental exposures that support individual-level prediction of behaviors at both baseline and longitudinally. Most importantly, mediation analysis was used to examine whether and to what extent the 'predictome' FNC signatures mediated the significant environment-behavior associations.

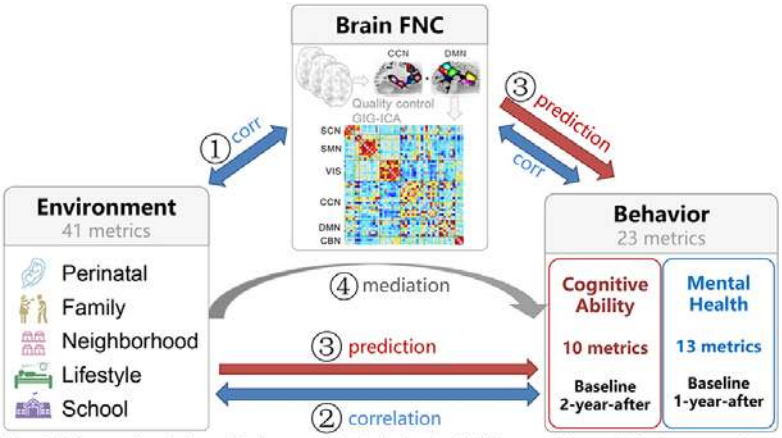

Fig. 1. Research design. Environment-brain-behavior triplet correlations 1) between environmental exposures and whole-brain functional network connectivity (FNC); and 2) between environmental exposures and multi-behaviors (baseline and 1-year, 2-year follow-up). 3) Building behavior (baseline and follow-up) prediction models using FNCs, environmental exposures, and their combinations respectively, identifying the most predictive functional network modules and environmental exposures. 4) Examining the mediating effect of the identified predictive FNCs for significant associations between environmental exposures and two types of behaviors.

Results: We found family and neighborhood exposures such as family income and area deprivation index were common critical environmental influencers on cognitive ability and mental health at both baseline and longitudinally (Fig. 2A). Healthy perinatal development was unique protective factor for evolving better cognitive ability, whereas sleep problems, family conflicts and adverse school environments specifically increase risk of mental health. As illustrated in Fig. 2B, family income and caregiver education are the top 2 ranked exposures influencing most FNCs, which manifest as similar network architectures, especially the cross-module connections. Subcortical network stands out with the highest vulnerability to environment, mainly in domains of family, perinatal and neighborhood exposures, where the thalamus was the most susceptible to environmental influences (Fig. 2C, D, E). Moreover, FNC demonstrated more predictive power for cognitive abilities than mental health, where thalamus and hippocampus play important roles in longitudinal prediction, while environmental exposures demonstrated more predictive power than FNC in both baseline and longitudinal prediction of all behaviors, especially for mental health ($r = 0.31 \sim 0.63$) (Fig. 2F). Results highlighted FNCs within subcortical (SCN) and cognitive control (CCN) networks, and between SCN-SMN as the most contributing networks to predict mental problems, and within CCN, default mode networks (DMN), and between DMN-CCN for predicting cognitive abilities (Fig. 2G). Notably, these predictions remained significant even controlling for multiple covariates, and site harmonization via ComBat (Fig. 2H). Most importantly, we successfully validated the FNC-based prediction of fluid intelligence using independent UK Biobank data ($N = 20,852$, Fig. 2I). Finally, the identified predictive FNCs can also mediate the environment-behavior associations significantly, implicating the plastic and flexible environment-brain-behavior interactive loops.

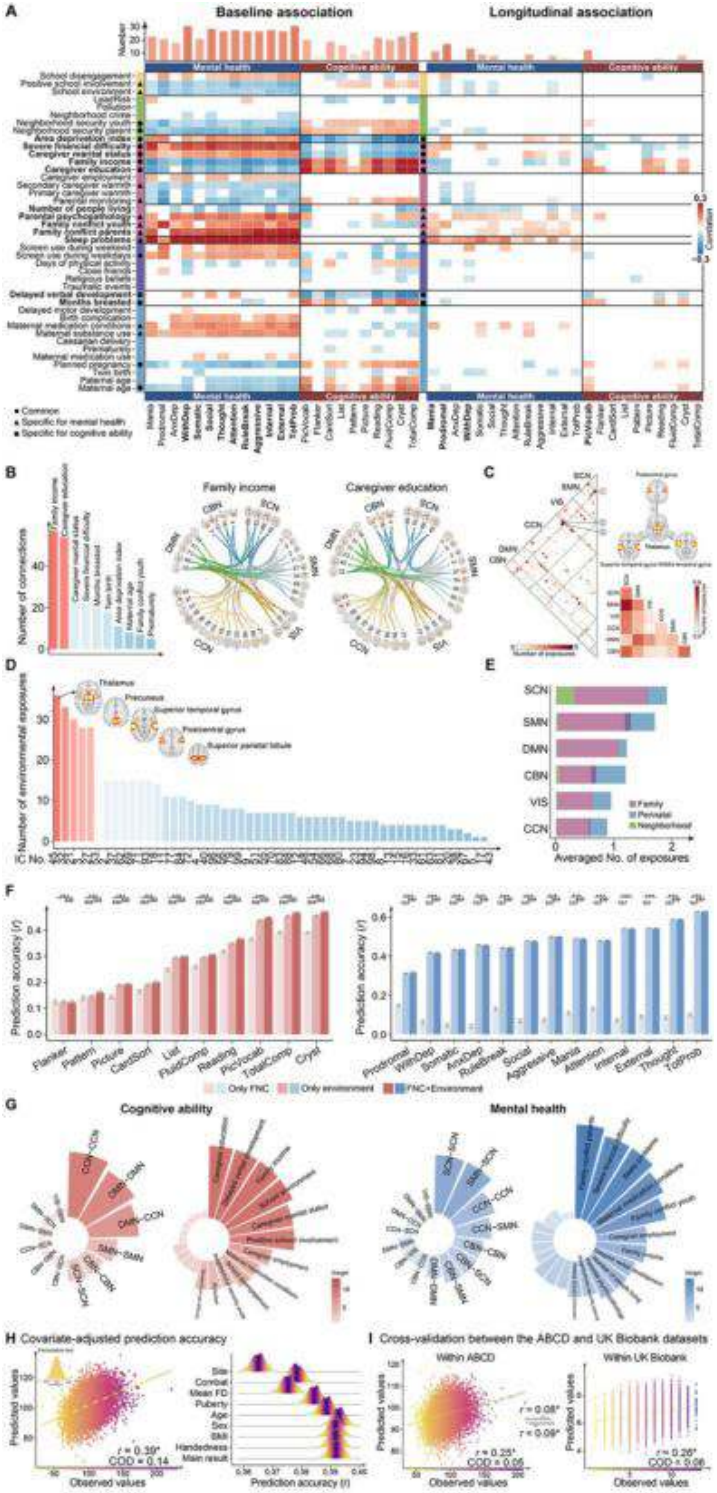

Fig. 2. **(A)** Environment-behavior association. The summarized correlation mapping between 5 domains of environmental exposures and 23 behaviors, at both baseline and longitudinally, where the triangle, square and round black dots denote the mental health-specific, cognition-specific and shared environmental exposures respectively. The bar above denotes the number of environmental exposures significantly correlated with each of the 23 behavioral items (Bonferroni corrected, $p < 0.05$). **(B)** Summary of associations between whole-brain FNC with 41 environmental exposures (FDR corrected, $p < 0.05$), and ranking of environmental factors influencing more FNC pairs, and the top two FNC patterns. **(C)** Ranking of FNC nodes associated with more exposures, and the top 5 nodes (independent component, ICs). **(D)** Mapping of the number of environmental exposures correlated with each FNC, and within each network module, where the top FNC nodes are illustrated. **(E)** Distribution of environmental exposures correlated with each FNC module. **(F)** The prediction results for behaviors. Comparison of prediction accuracy using only FNC, only environment, or their combination for 10 types of cognitive abilities and 13 types of mental measures. **(G)** The summarized top contributing FNC modules and environmental exposures for predicting cognition or mental health. **(H)** Prediction of Cognition Total Composite based on FNC only and after adjusting for covariates including site, harmonization by Combat, mean frame displacement, puberty, age, sex, BMI, and handedness, across 200 repetitions of 10-fold cross-validation. **(I)** Cross-validation between the ABCD and UK Biobank datasets for prediction of fluid intelligence using FNC. Abbreviation: SCN, subcortical network; SMN, somatomotor network; CCN, cognitive control network; DMN, default mode network; CBN, cerebellum network.

Conclusions: Collectively, this work investigated the environment-brain-behavior triple interactions in children comprehensively based on ABCD data at both baseline and longitudinally, identified CCN, DMN, and SCN as the most predictive functional networks for a wide repertoire of behaviors, and underscored the long-lasting impact of critical environmental exposures on childhood development, especially the attainable targets with family conflict, sleep quality, school and neighborhood environments to promote the healthy development of adolescents.

References

1. Rosenzweig, M.R.J.D.n., Effects of differential experience on the brain and behavior. Developmental Neuropsychology, 2003. 24(2-3): p. 523-540.
2. Dahl, R.E.J.A.o.t.n.Y.A.o.S., Adolescent brain development: a period of vulnerabilities and opportunities. Keynote address. 2004. 1021(1): p. 1-22.
3. Du, Y., et al., NeuroMark: An automated and adaptive ICA based pipeline to identify reproducible fMRI markers of brain disorders. NeuroImage: Clinical, 2020. 28: p. 102375.
4. Modabbernia, A., et al., Multivariate patterns of brain-behavior-environment associations in the adolescent brain and cognitive development study. Biological Psychiatry, 2021. 89(5): p. 510-520.
5. Casey, B., et al., The adolescent brain cognitive development (ABCD) study: imaging acquisition across 21 sites. Developmental Cognitive Neuroscience, 2018. 32: p. 43-54.

Poster No 1229

Longitudinal Changes in Regional Fiber Length Map in Early School-age Children

Yanlin Yu[1], Qing Cai[1], Chu-Chung Huang[1]

[1]*East China Normal University, Shanghai, China*

Introduction: The understanding of brain networks is of great significance for human cognition and behavior, especially in the development stage. The non-invasive neuroimaging techniques that estimate the structural connectivity in brain white matter (WM) using diffusion MRI tractography were proposed to identify the human brain's fundamental organization. However, mapping structural connectome using diffusion MRI has been challenging due to streamline quantification bias and may impede the sensitivity of change in network metrics (Yeh et al., 2021). Recent study suggested that the fiber length distribution could be a novel way to differentiate a brain region served as the functional integrator or local modules (Bajada et al., 2019). Here, we aim to generate a regional index characterized by length distribution of specific regions to investigate the developmental change during early school age. We hypothesized that longitudinal changes in regional fiber length distribution provide insight into how brain regions modulate their communication cost and may mirror the network hierarchy's developmental process.

Methods: A total of 30 typically developing children were included in this study (7.5 ± 0.3 yr, 18 females and 12 males) at the first year in primary school and received the follow-up scanning in 1 year (8.6 ± 0.3 yr). To control the effect of brain size on fiber length, the longitudinal group FOD (fiber orientation distribution) template was generated and each individual's FOD was transformed into this template for whole-brain tractography (Genc et al., 2018). The individual length connectome was reconstructed for the whole-brain tractogram based on the HCPex atlas (426 brain regions) (Huang et al., 2022). The length distribution was defined as the connected length distribution of a specific node, the median length of which was then calculated to represent the distribution characteristic. We compared the length median of brain regions in two time points using paired two-sample permutation test to identify the significant developmental changes in regional length distribution (1000 permutations, $p < 0.01$) (Figure 1). To explain the mechanism underlying developmental changes in median length, we compared the count of edges constituting the distribution across various length range at two time points. To further investigate the topological meaning of regional length map, we examined the correlation between length median and graph metrics based on the binary structural connectome (FDR corrected, $p < 0.05$).

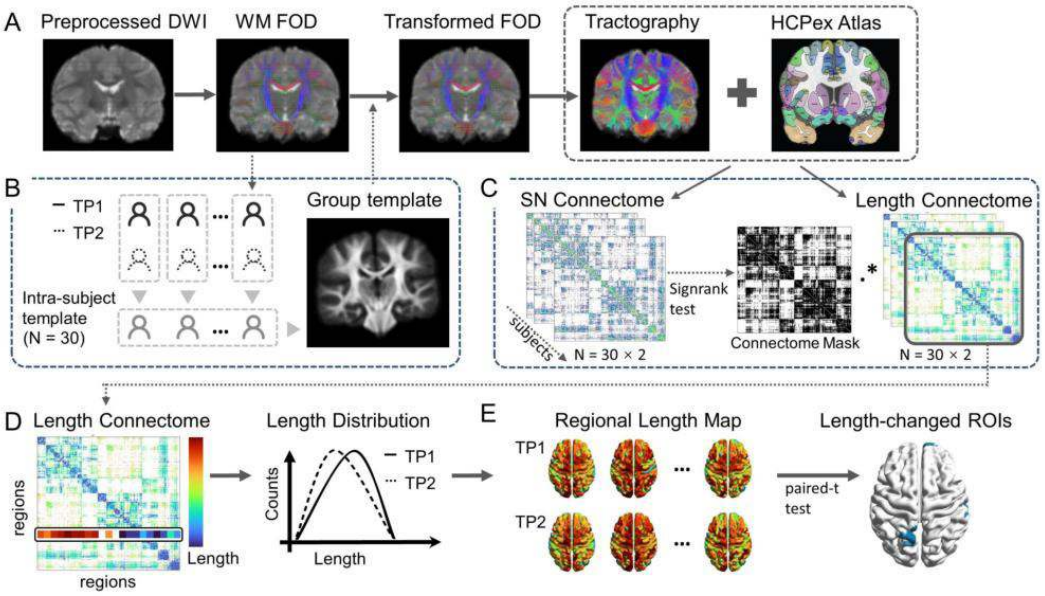

Figure 1. The framework of the longitudinal group template and length distribution reconstruction. A, The tractography-based connectome was reconstructed using the HCPex atlas. **B**, Longitudinal group FOD template generation. **C**, Connectome reconstruction. **D**, Length distribution. **E**, Comparison of regional map between timepoint 1 and timepoint 2.

Results: Most brain regions' length median decreased during development, the brain regions with significantly decreased in length median (termed length-decreased ROIs) includes L_TF, L_PHA1, L_TE1m, L_7Am, L_7PL, L_VIP, L_25, L_a24, R_PBelt and R_10d. Whereas, only R_FOP1 show a significant increase in length median (termed length-increased ROI). We observed a general pattern that there was an increase in short-range connections, accompanied by a decrease in long-range connections in length-decreased ROIs, and conversely, an increase in long-range connections in length-increased ROI. Additionally, the regional length map was positively correlated with degree and centrality but negatively correlated with the clustering coefficient and local efficiency (Figure 2).

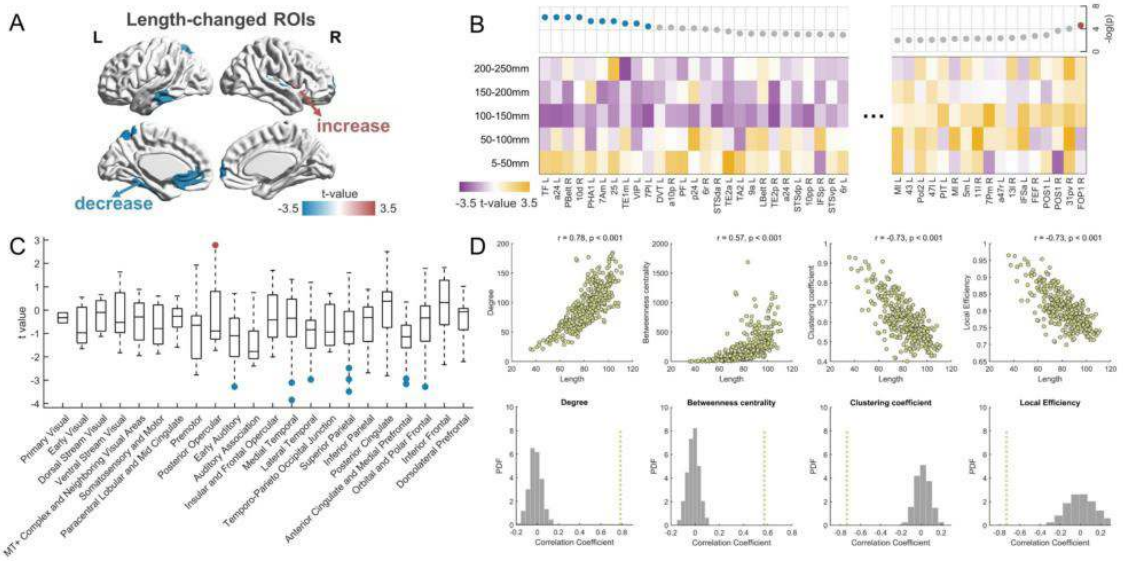

Figure 2. Developmental changes in regional length map. A, The brain regions with significant longitudinal changes (1000 permutations, $p < 0.01$). **B**, The mechanism leading to the changes in regional length distribution. **C**, The spatial pattern of altered length median of brain regions ordered by their belonging cortex based on the HCPex atlas. **D**, The association with topological characteristics of network. The upper row is the correlation between regional length map and graph metrics at baseline. The bottom row is the histograms representing the Spearman correlation coefficients across regional length map and graph metrics of null model derived from 1000 permutations.

Conclusions: This study first proposed the regional length map to investigate the developmental changes in WM during early school age. For most brain areas, the length distributions decreased with age, which could be explained by the pruning of long-range WM and the growth of short-range WM connections. Moreover, the length map positively correlated with integration and negatively correlated with segregation of structural network. Our findings suggest that, compared to streamline-based structural network metrics, the length map of brain regions may serve as a potential biomarker for assessing the development of brain topological organization at a structural level.

References
1. Bajada, C. J. (2019). Fiber length profiling: A novel approach to structural brain organization. NeuroImage, 186, 164–173. https://doi.org/10.1016/j.neuroimage.2018.10.070
2. Genc, S. (2018). Development of white matter fibre density and morphology over childhood: A longitudinal fixel-based analysis. NeuroImage, 183, 666–676. https://doi.org/10.1016/j.neuroimage.2018.08.043
3. Huang, C.-C. (2022). An extended Human Connectome Project multimodal parcellation atlas of the human cortex and subcortical areas. Brain Structure and Function, 227(3), 763–778. https://doi.org/10.1007/s00429-021-02421-6
4. Yeh, C.-H. (2021). Mapping Structural Connectivity Using Diffusion MRI: Challenges and Opportunities. Journal of Magnetic Resonance Imaging, 53(6), 1666–1682. https://doi.org/10.1002/jmri.27188

Poster No 1230

Prenatal Adversity and Inflammation at Birth Predict White Matter Integrity at Age 7 Years

Justin Yuan[1], Jessica Buthmann[1], Zhen Ming Ngoh[2], Aisleen Manahan[2], Ai Peng Tan[2], Michael Meaney[2,3,4], Ian Gotlib[1]

[1]Stanford University, Stanford, CA, [2]Singapore Institute for Clinical Sciences, Agency for Science, Technology and Research in Singapore, Singapore City, Singapore, [3]Liggins Institute, University of Auckland, Grafton, Auckland, New Zealand, [4]Douglas Hospital Research Centre, McGill University, Montreal, Quebec, Canada

Introduction: Elevated levels of inflammation are associated with difficulties in psychological functioning. Specifically, neuroimaging studies have shown that even in nonclinical populations, such as typically developing adolescents, higher concentrations of inflammatory markers are associated with problems in emotion regulation and reward processing[1], suggesting an important role of immune function in neurodevelopment. This may occur through the impact of acute inflammation on developmental processes such as cell migration, synaptogenesis, and pruning[2], associations that appear to be potentiated by the experience of adversity early in life[3]. Evidence of these relations in humans has typically come from studies of samples of adolescents or older individuals[4-7]. Here we examined whether these associations are present in early childhood. Specifically, we examined whether prenatal adversity significantly moderates the association between inflammatory status at birth and white matter maturation in the cingulum tract at age seven years.

Methods: We analyzed data from 201 mother-child dyads participating in the Growing Up in Singapore Towards Healthy Outcomes (GUSTO) study. Participants provided data relevant to three constructs: prenatal adversity, inflammatory cytokine concentration at birth, and limbic white matter maturation at age 7. Prenatal adversity was assessed by creating a composite score derived from multiple adversity factors, including maternal physical and mental health, socioeconomic status, family function, and the child's birthweight and preterm status. Inflammatory levels were assessed by measuring the concentration of the proinflammatory cytokine interleukin 6 (IL-6) from a sample of cord blood obtained at birth. Concentration values were measured using a Quanterix SIMOA HD-1 3-plex immunoassay and log-transformed. White matter maturation was assessed using data from an MRI scan conducted when the child was age 7 years (M[SD]; range=7.0[0.1]; 6.9-7.3 years). We assessed fractional anisotropy (FA) of the cingulum tract (cingulate gyrus portion), yielding an index of maturation of a brain structure underlying limbic system function. FA values were obtained from a 3T multi-shell diffusion weighted sequence, processed using FSL's probabilistic tractography pipeline (BEDPOSTX and PROBTRACKX). To analyze the data, we conducted stepwise regression, first testing for the main effects of prenatal adversity and IL-6, separately, predicting cingulum FA. To test whether adversity moderated this association, we modeled the interaction of prenatal aversity and IL-6 predicting cingulum FA at age 7 years. The interaction was probed using simple slopes analysis and the Johnson-Neyman technique. Child sex, race, and exact age at scan were included as covariates in the model.

Results: There was a significant positive main effect of prenatal adversity (β=0.16, p=0.031), but not of cord blood IL-6 (β=0.06, p=0.379), predicting year 7 cingulum FA. There was also a significant interaction between prenatal aversity and cord blood IL-6 predicting cingulum FA (β=0.16, p=0.028). Specifically, in children exposed to higher levels of prenatal adversity, elevated IL-6 was associated with higher cingulum FA (Figure 1).

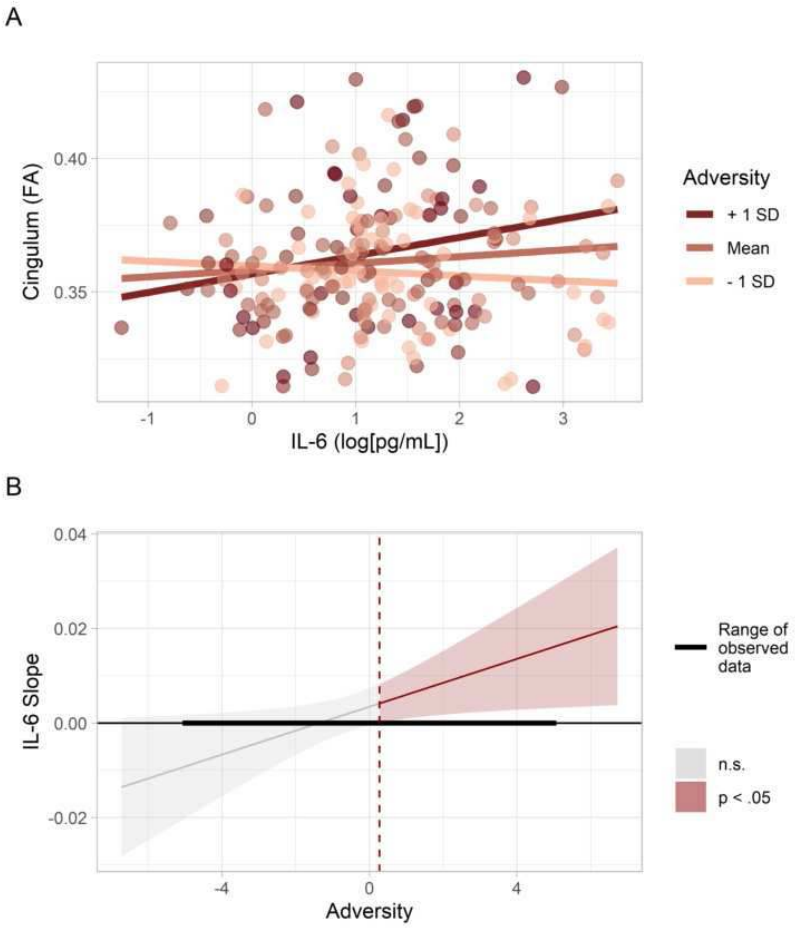

Figure 1. Interaction of prenatal adversity and inflammatory status at birth predicting cingulum tract maturation seven years later. A) Simple slopes of the adversity-IL-6 interaction. In children with greater prenatal adversity (dark red), elevated cord IL-6 concentration is associated with higher cingulum FA; points represent partial residuals of the model. B) Johnson-Neyman plot displaying the severity of adversity at which the slope of IL-6 was significant (red area). The dashed red line indicates the upper boundary of the interval (0.27), and the black bar visualizes the observed adversity scores.

Conclusions: We found in this study that exposure to prenatal adversity significantly moderated the association between inflammatory status at birth and maturation of the cingulum. These findings are consistent with past neuroimmune research, suggesting that the immune system influences neurodevelopment at a younger age than has previously been documented. Further, our results are consistent with theoretical frameworks suggesting that adversity exposure is associated with accelerated development[8] across various indices of biological aging[9]. Overall, these findings underscore the long-term effects of experiencing prenatal adversity and highlight how the immune system may shape early neurodevelopment.

References

1. Felger, J. C. Imaging the Role of Inflammation in Mood and Anxiety-related Disorders. Curr Neuropharmacol 16, 533–558 (2018).
2. Reid, B. & Danese, A. Challenges in researching the immune pathways between early life adversity and psychopathology. Development and Psychopathology 32, 1597–1624 (2020).
3. Nusslock, R. & Miller, G. E. Early-Life Adversity and Physical and Emotional Health Across the Lifespan: A Neuroimmune Network Hypothesis. Biological Psychiatry 80, 23–32 (2016).
4. Miller, G. E., White, S. F., Chen, E. & Nusslock, R. Association of Inflammatory Activity With Larger Neural Responses to Threat and Reward Among Children Living in Poverty. AJP 178, 313–320 (2021).
5. Yuan, J. P., Coury, S. M., Ho, T. C. & Gotlib, I. H. Early life stress moderates the relation between systemic inflammation and neural activation to reward in adolescents both cross-sectionally and longitudinally. Neuropsychopharmacol. 1–9 (2023) doi:10.1038/s41386-023-01708-y.
6. Kraynak, T. E., Marsland, A. L., Hanson, J. L. & Gianaros, P. J. Retrospectively reported childhood physical abuse, systemic inflammation, and resting corticolimbic connectivity in midlife adults. Brain, Behavior, and Immunity 82, 203–213 (2019).
7. Chat, I. K.-Y. et al. Residence in High-Crime Neighborhoods Moderates the Association Between Interleukin 6 and Social and Nonsocial Reward Brain Responses. Biological Psychiatry Global Open Science (2022) doi:10.1016/j.bpsgos.2022.04.006.
8. Callaghan, B. L. & Tottenham, N. The Stress Acceleration Hypothesis: effects of early-life adversity on emotion circuits and behavior. Current Opinion in Behavioral Sciences 7, 76–81 (2016).
9. Miller, J. G., Chahal, R. & Gotlib, I. H. Early Life Stress and Neurodevelopment in Adolescence: Implications for Risk and Adaptation. in Neuroscience of Social Stress (eds. Miczek, K. A. & Sinha, R.) vol. 54 313–339 (Springer International Publishing, 2022).

Poster No 1231

Known and unknown probability information separably modulate insula activity in adolescents

Natalie Melville[1,2], Flora Li[3], Sheryl Ball[1,4,5], Jungmeen Kim-Spoon[5], Pearl Chiu[1,5], Brooks Casas[1,5,4]

[1]Fralin Biomedical Research Institute at Virginia Tech Carilion, Roanoke, VA, [2]Translational Biology Medicine & Health, Virginia Tech, Roanoke, VA, [3]Economics Experimental Lab, Nanjing Audit University, Nanjing, Jiangsu, [4]Department of Economics, Virginia Tech, Blacksburg, VA, [5]Department of Psychology, Virginia Tech, Blacksburg, VA

Introduction: Adolescence is a developmental period marked by increasing independence and exploration of novel situations with uncertain outcomes. Previous research suggests that adolescents' willingness to engage in health risk behaviors (HRBs) is related to tolerance of ambiguity (Blankenstein, et al. 2016; Tymula, et al. 2012; Van Den Bos, et al. 2017), in which the probability of an outcome is unknown, while other research finds HRBs correlated to tolerance for risk (Rao, et al. 2011; Steinberg 2008), in which the probability of an outcome is known. This study aims to identify individual biases in using known and unknown probability information during decision-making in ambiguous contexts and examines their impact on neural activity.

Methods: One hundred and fifty-one adolescents, with an initial mean age of 13.5 (s.d. = 0.54), participated in yearly assessments across five waves. Participants underwent functional magnetic resonance imaging while making choices between two options with varying levels of risk and ambiguity. A behavioral model estimated two behavioral parameters associated with ambiguity: the first capturing optimism or pessimism linked to unknown likelihoods, and the second quantifying the influence of the known probability information on unknown likelihoods. Individual levels of neural activity in the mid-posterior insula (PI) and the dorsal anterior insula (dAI) were extracted during decision-making as well as the neural activity modulated by the known likelihood information. The resulting neural activity was related to ambiguity parameters using mixed effect regressions. Similarly, neural activity was predicted by visit to identify the relationship between visit and insula activation by region.

Results: Adolescents initially exhibited optimism toward the ambiguous portion of the gamble ($\beta = 0.7$, $p < 0.001$) and became more neutral as they aged ($\beta = -0.03$, $p < 0.001$). Neuroimaging revealed that more optimistic individuals exhibited diminished activity in the PI during decisions under ambiguity ($\beta = -0.24$, $p = 0.02$). Additionally, PI activity increased with age when viewing ambiguous gambles ($\beta = 0.047$, $p = 0.01$). Known outcome probabilities were found to influence preference for ambiguity ($\beta = -0.48$, $p < 0.001$). More specifically, adolescents exhibited an aversion to ambiguity when the known information indicated a high probability of receiving a large outcome. In contrast, when the probability of receiving a large outcome was low, adolescents exhibited a preference for ambiguity. This relationship between known probability information and ambiguity diminished across time ($\beta = 0.04$, $p < 0.001$). Neurally, the known probability of a high outcome was positively related to dAI during choice. This relationship was (i) diminished among adolescents showing the strongest probability-related ambiguity bias ($\beta = 0.475$, $p = 0.01$) and (ii) increased across development ($\beta = 0.076$, $p < 0.001$).

Conclusions: While prior work has focused on ambiguity tolerance independent of known probability information, this study highlights that known probability information also significantly influences choice behavior under ambiguity. Specifically, early in adolescence, known probability information strongly biases preferences for ambiguity, and this bias diminishes into late adolescence. The separable ambiguity parameters, dependent and independent of known probability information, were associated with spatially distinct activity across anterior to posterior insula, and these neural correlates changed across time consistent with the observed behavioral patterns.

References

1. Blankenstein, N. E., et al. (2016). "Dealing With Uncertainty: Testing Risk- and Ambiguity-Attitude Across Adolescence." Developmental Neuropsychology 41(1-2): 77-92.
2. Rao, U., et al. (2011). "Relationship Between Adolescent Risk Preferences on a Laboratory Task and Behavioral Measures of Risk-Taking." Journal of Adolescent Health 48(2): 151-158.
3. Steinberg, L. (2008). "A Social Neuroscience Perspective on Adolescent Risk-Taking." Dev Rev 28(1): 78-106.
4. Tymula, A., et al. (2012). "Adolescents risk-taking behavior is driven by tolerance to ambiguity." Proceedings of the National Academy of Sciences 109(42): 17135-17140.
5. van den Bos, W., et al. (2017). "Adolescents display distinctive tolerance to ambiguity and to uncertainty during risky decision making." Sci Rep 7: 40962.

Poster No 1232

Dimensions of early life adversity links to trimodal brain age in youth

Dani Beck[1], Lucy Whitmore[2], Niamh MacSweeney[1], Alexis Brieant[3], Ann-Marie de Lange[4], Lars Westlye[5], Kathryn Mills[2], Christian Tamnes[1]

[1]University of Oslo, Oslo, Norway, [2]University of Oregon, Eugene, OR, [3]University of Vermont, Vermont, VT, [4]University of Lausanne, Oslo, Norway, [5]Norwegian Centre for Mental Disorders Research (NORMENT), Oslo University Hospital, Oslo, Norway

Introduction: Exposure to early-life adversity (ELA) impacts brain development[1,2]. Research suggests a discordant relationship between ELA factors related to threat and deprivation on brain maturation. Threat factors such as physical abuse are linked with smaller brain volumes and increased functional activity, while this is not observed with deprivation[1]. With increasing evidence of different features of ELA associated with unique brain outcomes, data-driven efforts that characterise the dimensionality of ELA have been developed[3]. The ABCD Study (N=11,900, age mean=10.75) overcomes existing limitations of small samples and cross-sectional designs. Brain age prediction offers an individualised marker for assessing brain maturity. Looking at the deviation from age-expected patterns (i.e., brain age gap (BAG)) and how deviation changes over time provides an indication of whether ELA factors are associated with accelerated or delayed brain maturation. We aimed to investigate cross-sectional and longitudinal associations between ten dimensions of ELA and BAGs derived from three brain age models trained on T1, DTI, and rsfMRI data. We expected threat-related dimensions of ELA to be linked with higher BAGs, and deprivation-related dimensions to be linked with lower BAGs. We also expected links to exacerbate over time.

Methods: Age prediction was carried out using XGBoost regression[4]. Here, 50% of the ABCD Study sample (baseline and two-year follow-up; N=~9000) was used as the test set and 50% was used for model training (N=~7200) and ten-fold cross-validation (N=~1800). R2, RMSE, and MAE assessed prediction accuracy; age bias was statistically corrected. Bayesian multilevel modelling tested the associations between dimensions of ELA and T1, DTI, and rsfMRI BAG. BAG was entered as the dependent variable with each ELA dimension separately entered as the independent fixed effect along with sex, with subject ID as the random effect. Longitudinal ELA effects were assessed with interaction effects of time-point.

Results: The DTI brain age model was the most accurate (r=.66, p<.01, MAE=.71), followed by T1 (r=.59, p<.01, MAE=.79) and rs-fMRI (r=.41, p<.01, MAE=.89). We found a positive association between ELA dimension F2, representing factor loadings from measures of socioeconomic disadvantage and neighbourhood safety, and T1 BAG, indicating that this dimension was associated with older-looking brains. Further, we found a negative association between ELA dimensions F3 (secondary caregiver lack of support) and F4 (primary caregiver lack of support) and T1 BAG, indicating that dimensions related to neglect are associated with younger-looking brains. In terms of interaction effects, we found negative associations between F10 (lack of supervision) and T1 BAG, indicating that unsupervised youth diverge more from normative age patterns over time. In line with the T1 BAG findings, we found a positive association between F2 and DTI BAG. In terms of interaction effects, we found a positive association between ELA dimension F1 (caregiver psychopathology) and DTI BAG. For fMRI, we found a positive association between F2 and fMRI BAG, aligning with findings with T1 and DTI BAG. Positive associations were also found for F1 and fMRI BAG, aligning with DTI findings, and F6 (caregiver substance abuse and separation from biological parents), F8 (family aggression), and F9 (trauma exposure) and fMRI BAG. These positive associations indicate that dimensions related to threat are related to older-looking brains. A negative association was found between F4 and fMRI BAG, in line with findings from T1 BAG. In terms of interaction effects, we found a negative association between F3 and F5 (family conflict) and fMRI BAG, and a positive association between F6 and fMRI BAG.

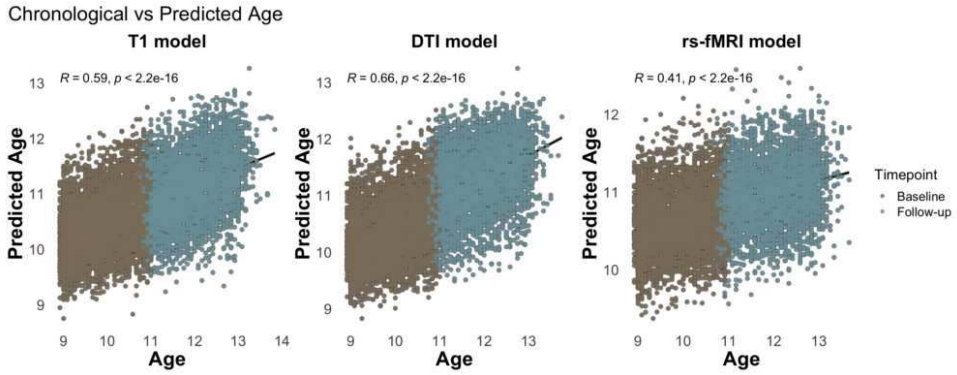

Figure 1. Trimodal brain age prediction. Performance of T1, DTI, and rsfMRI brain age models.

Early-Life Adversity Variables	Factor 1 Caregiver Psycho-pathology	Factor 2 Socio-economic disadvantage and neighbour-hood safety	Factor 3 Secondary caregiver lack of support	Factor 4 Primary caregiver lack of support	Factor 5 Youth report of family conflict	Factor 6 Caregiver substance use and separation from biological parent	Factor 7 Family anger and arguments	Factor 8 Family aggression	Factor 9 Trauma exposure	Factor 10 Lack of supervision
Caregiver ADHD symptoms (CG)	0.72									
Caregiver antisocial symptoms (CG)	0.551									
Caregiver anxiety symtpoms (CG)	0.728									
Caregiver avoidant symptoms (CG)	0.704									
Caregiver depression symptoms (CG)	0.91									
Caregiver somatic problems (CG)	0.557									
Caregiver makes feel better when worried* (Y)				0.842						
Caregiver smiles* (Y)				0.581						
Caregiver makes feel better when upset* (Y)				0.775						
Caregiver shows love* (Y)				0.65						
Caregiver easy to talk to* (Y)				0.682						
Secondary caregiver makes feel better when worried* (Y)			0.758							
Secondary caregiver smiles* (Y)			0.597							
Secondary caregiver makes feel better when upset* (Y)			0.772							
Secondary caregiver shows love* (Y)			0.793							
Secondary caregiver easy to talk to* (Y)			0.596							
Household income* (CG)		0.947								
Inability to pay for necessities (rent, food, utilities) (CG)		0.6								
Inability to pay for necessities (healthcare) (CG)		0.473								
Caregiver marital separation (CG)		0.608								
Separation from biological caregiver (CG)						0.668				
Caregiver(s) level of education* (CG)		0.736								
Family fights a lot (CG)							0.5			
Family members rarely angry* (CG)							0.822			
Family throws things when angry (CG)								0.601		
Family hardly loses temper* (CG)							0.805			
Family criticizes each other (CG)								0.517		
Family hit each other (CG)								0.798		
Family keeps the peace* (CG)							0.405			
Family tries to outdo each other (CG)								0.625		
Family does not raise voice* (CG)							0.355			
Family fights a lot (Y)					0.723					
Family members rarely angry* (Y)					0.563					
Family throws things when angry (Y)					0.635					
Family hardly loses temper* (Y)					0.663					
Family criticizes each other (Y)					0.541					
Family hit each other (Y)					0.676					
Family keeps the peace* (Y)					0.364					
Family tries to outdo each other (Y)					0.499					
Family does not raise voice* (Y)										
Father alcohol problems (CG)						0.705				
Father drug problems (CG)						0.797				
Mother alcohol and drug problems (CG)						0.747				
Car accident (CG)									0.448	
Another significant accident (CG)									0.416	
Witnessed or caught in fire (CG)									0.524	
Witnessed or caught in natural disaster (CG)									0.597	
Witnessed terrorism, war zone, or community violence (CG)									0.841	
Physically assaulted or threatened to be killed (CG)									0.772	
Witness domestic violence (CG)						0.422			0.378	
Sexual abuse (CG)									0.673	
Sudden unexpected death of loved one (CG)										
Neighborhood safety* (Y)										
Neighborhood safety* (CG)		0.382								
Caregivers know where they are*										0.48
Caregivers know who they are with*										0.605
In contact with caregivers when home alone*										
Discuss plans with caregivers*										
Eat dinner with caregivers*										
Neighborhood area deprivation index		0.522								

* indicates that the variable was reverse-scored. Y = Youth Report; CG = Caregiver Report.

Measures

- Adult self Report
- Child Report of Parent Behaviour Inventory
- Parent Demographics survey
- Family Environment Scale
- Family History Inventory
- Diagnostic Interview for Traumatic Events (KSAI
- Neighbourhood Safety/Crime Survey
- Parental Monitoring Survey
- Residential History Derived Scores

Figure 2. ELA Dimensions. Factor loadings from the ten early-life adversity dimensions. * indicates that the variable was reverse-scored. Y = Youth Report; CG = Caregiver Report.

Conclusions: Different ELA features uniquely impact brain outcomes in youth. Deprivation-related features suggest delayed maturation, while threat-related features indicate accelerated maturation.

References

1. McLaughlin, K. A., Weissman, D. & Bitrán, D. Childhood Adversity and Neural Development: A Systematic Review. SSRN Scholarly Paper at https://doi.org/10.1146/annurev-devpsych-121318-084950 (2019).
2. McLaughlin, K. A. & Sheridan, M. A. Beyond Cumulative Risk: A Dimensional Approach to Childhood Adversity. Curr. Dir. Psychol. Sci. 25, 239–245 (2016).
3. Brieant, A. et al. Characterizing the dimensional structure of early-life adversity in the Adolescent Brain Cognitive Development (ABCD) Study. Dev. Cogn. Neurosci. 61, 101256 (2023).
4. Chen, T. & Guestrin, C. XGBoost: A Scalable Tree Boosting System. in Proceedings of the 22nd ACM SIGKDD International Conference on Knowledge Discovery and Data Mining 785–794 (ACM, 2016). doi:10.1145/2939672.2939785.
5. Bürkner, P.-C. brms : An R Package for Bayesian Multilevel Models Using Stan. J. Stat. Softw. 80, (2017).

Poster No 1233

Structural measures differences between early pubertal gender-diverse and cisgender youth

Melanie Camejo Coffigny[1], Charlotte Rosario[2], Cat Bui[1], Taiga Nishida[2], Javad Ansarifar[1], Manu Kaur[1], David Hong[1]

[1]Stanford University, Stanford, CA, [2]Nueva High School, Palo Alto, CA

Introduction: Transgender youth are a vulnerable population often underrepresented in research (Gower et al., 2018). While previous studies have indicated that the hormonal fluctuations accompanying puberty contribute to neural reorganization and maturational progression in adolescents (Goddings et.al, 2019), these insights are derived from findings on cisgender youth, leaving a notable gap in our understanding of the neural implications for transgender adolescents. To address this gap, our study assessed global and regional differences in brain volume, cortical thickness and surface area among early pubertal transgender youth compared to cisgender youth.

Methods: As part of an ongoing longitudinal study at Stanford University, structural measures were examined in a cohort of 23 transgender (60.8% female) and 24 cisgender (58.3% female) participants recruited during the early stages of puberty, e.g. Tanner Stages I-III, ranging in age from 10 to 15 years at the time of enrollment. Participants were categorized into four gender groups: cisgender male (MC), cisgender female (FC), transgender female (FtM), and transgender male (MtF). The MRI sequence used was T1-weighted image: TR: 8.5 ms, TE: 3.4 ms, flip: 15 degrees, TI: 400 ms, FOV: 22 cm, slice thickness: 1.5 mm, 128 slices, 256x256 matrix, NEX 1, scan time: 4 min 34 sec. Cortical reconstruction and volumetric segmentation were performed using Freesurfer v.7.3.2., with 10mm FWHM smoothing. Global differences of total cortical volume (TCV) amongst groups were estimated using a one-way ANOVA, while differences in total surface area (TSA) and total cortical thickness (TCT) were estimated using a one-way ANCOVA whilst controlling for eTIV. Assumptions for Levene's test and normality checks were met. Regional statistical analyses were conducted using a Generalized Linear Model, cluster-corrected for multiple comparisons. Right and left hemispheres were analyzed separately.

Results: There was a significant difference in global intracranial volume ($F(3,21.4)=5.35$, $p=0.007$) between groups. Post-hoc tests found a significant difference between cisgender females and males ($p=0.015$), and cisgender females and transgender males ($p=0.014$). There were no significant differences in TSA and TCT between groups. Regional analyses of CV, SA and CT showed significant differences between groups in the superior frontal (SFG), rostral middle frontal (RMFG), and inferior temporal gyri (ITG), with most clusters found on the left hemisphere (see Table 1 for details).

Hemisphere and Measure	Groups	Cluster	Size(mm²)	X	Y	Z	CWP	Annot
L-Area	MC vs. FC	1	928.05	-16.5	41.7	37.6	0.0002	superiorfrontal
		2	380.83	-54.6	-34.9	-16.6	0.02484	inferiortemporal
	MC vs. FtM	1	562.77	-27.1	33.1	24.2	0.0034	rostralmiddlefrontal
L-Volume	MC vs. FC	1	422.66	-7.2	52.5	32.4	0.0004	superiorfrontal
	MC vs. FtM	1	317.74	-7.1	53.4	32.9	0.003	superiorfrontal
		2	176.06	-22.6	51.6	-12.2	0.04918	rostralmiddlefrontal
	MC vs. MtF	1	211.71	-7.2	52.5	32.4	0.02544	superiorfrontal
L-Thickness	FC vs. MtF	1	255.91	-40.5	27.1	13.6	0.00858	rostralmiddlefrontal
	MC vs. MtF	1	199.87	-7.4	49	33.2	0.03292	superiorfrontal
R-Thickness	FC vs. FtM	1	295.72	11.3	50.6	11.3	0.003	superiorfrontal
	FC vs. MtF	1	1197.41	7.9	51.3	17.7	0.0002	superiorfrontal
	MC vs. MtF	1	433.45	13.7	60.5	15.3	0.0002	superiorfrontal

Table 1.Significant clusters for differences in surface area, volume and cortical thickness between transgender and cisgender youth.

Conclusions: The global differences in total cranial volume between cisgender and transgender groups found in this study align with previous findings based on assigned sex at birth. Given that this group of transgender youth had not undergone gender-affirming hormone therapy, it is not surprising these findings are in alignment. However, the regional differences we found in CV, SA and CT, have not been previously reported in prior literature due to the lack of research on early pubertal transgender youth. In the future, we hope to further expand these novel contributions to the field of human brain mapping by assessing the neural development of transgender youth undergoing gender-affirming hormone therapy.

References
1. Dale, A.M.,1999. Cortical surface-based analysis. I. Segmentation and surface reconstruction. Neuroimage 9, 179-194.
2. Fischl, B., 2000. Measuring the thickness of the human cerebral cortex from magnetic resonance images. Proc Natl Acad Sci U S A 97, 11050-11055.
3. Hagler, D. J., (2006). Smoothing and cluster thresholding for cortical surface-based group analysis of fMRI data. NeuroImage, 33(4), 1093–1103.

Poster No 1234

Segregation of the Regional Radiomics Similarity Network Exhibited an Increase in Children

Lei Chu[1], Debin Zeng[1], Yirong He[2], Xiaoxi Dong[2], Qiongling Li[2], Shuyu Li[2]

[1]Beihang University, Beijing, China, [2]Beijing Normal University, Beijing, China

Introduction: Gaining a comprehensive understanding of the typical developmental trajectory of the human brain during late childhood to early adolescence is crucial for profound insights into its structure, function, and underlying mechanisms of developmental psychiatric and behavioral disorders(Blakemore, 2012; Vijayakumar et al., 2018). Using texture features of each brain region and calculating their similarities between nodes as edges to construct a network for each subject, R2SN has been well characterized with high reproducibility and significantly correlated with both genetic similarity networks and cognition in adults and been well applied to the diagnosis and staging of Alzheimer's disease(Zhao et al., 2022). Brain development exhibits increasing functional segregation to support cognition procession specialization within the framework of network neuroscience. Although coordinated variations in brain morphology have been extensively utilized to infer the macroscopic structural bases for developmental evolution of brain function, little is known about how microscopic features contribute to this process and their relationship with cognition. We hypothesized that alterations in the segregation of R2SN during development may be also associated with refinements in executive function (EF), a broad cognitive domain that encompasses multiple subdomains, including working memory, response inhibition, and set shifting, paralleling the human brain's protracted maturational time course.

Methods: Participants. The longitudinal dataset of cognitively normal children was derived from the Children School Functions and Brain Development Project in China (CBD, Beijing Cohort) with a sample comprising 494 MR scans from 309 typically developing children ages 6.2-13 years at baseline (142 females and 167 males). 44 children were scanned at three separate times, 97 children managed to visit 2 with a scan interval of approximately one year. We uesed high-resolution anatomical images acquired with three dimensional 1mm3 isotropic T1-weighted magnetization-prepared rapid gradient echo (MPRAGE) sequence. R2SN construction and statistical analysis. The anatomical MR images underwent Human Connectome Project (HCP) minimum preprocessing pipeline(Glasser et al., 2013) with several modifications for child's brain. we constructed individual regional radiomics similarity networks (R2SNs) based on similarities of radiomics features across 246 brain regions using CBD dataset. To characterize R2SNs' segregation, we measured segregation indexes at both system and local levels. We corrected for multiple comparisons across all pairs of network metrics with false discovery rate (pFDR) < 0.05. To dimensionally delineate the longitudinal changes of the topology of similarity networks, we conducted several mixed-effect models to explore the developmental trajectories of each graph theoretical measures.

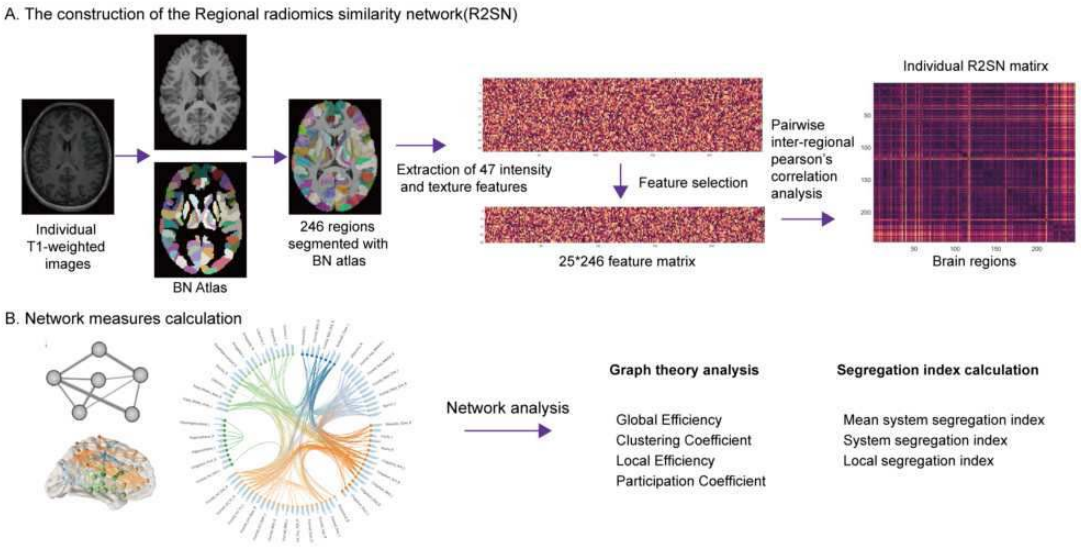

Results: Regarding fundamental properties of graph theory, we exclusively observed progressive linear increments in both the global clustering coefficient and local efficiency during the late childhood and early adolescence stages, indicating a heightened level of network segregation (Fig2A). Mixed-effect models revealed longitudinal increases in R2SNs' segregation, particularly evident in system-level segregation within subcortical regions, as well as decreasing segregation within the ventral attention network. (Fig2B-G)Furthermore, superior working memory and inhibitory control performance were associated with higher system-level segregation indexes in default and subcortical systems, along with lower local-level segregation indexes in several brain regions belonging to the visual network regardless of age(Fig2H-M).

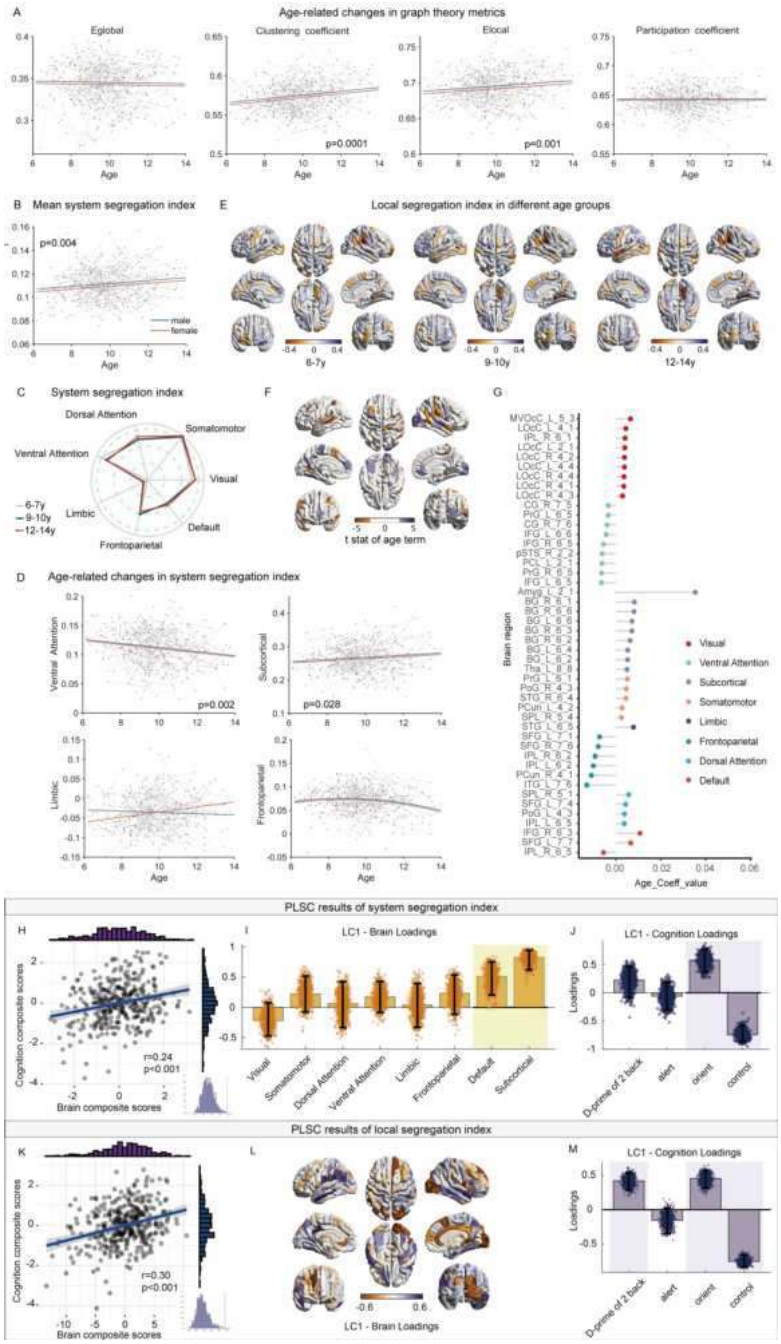

Conclusions: Our findings offer novel insights into typical brain developmental changes as indicated by the segregation index computed using R2SN approaches, which can be a valuable tool for comprehending human brain structural and cognition maturation.

References

1. Blakemore, S.J., 2012. Development of the social brain in adolescence. J R Soc Med. 105, 111-6.
2. Glasser, M.F., et al., 2013. The minimal preprocessing pipelines for the Human Connectome Project. Neuroimage. 80, 105-24.
3. Vijayakumar, N., et al., 2018. Puberty and the human brain: Insights into adolescent development. Neurosci Biobehav Rev. 92, 417-436.
4. Zhao, K., et al., 2022. Regional Radiomics Similarity Networks Reveal Distinct Subtypes and Abnormality Patterns in Mild Cognitive Impairment. Adv Sci (Weinh). 9, e2104538.

Poster No 1235

The differentiation of multiscale structural gradients from children to adolescents

Yirong He[1], Qiongling Li[1], Debin Zeng[2], Lei Chu[3], Xiaoxi Dong[1], Shuyu Li[4]

[1]Beijing Normal University, Beijing, Beijing, [2]Beihang University, Beijing, Beijing, [3]Beihang University, Beijing, Beijing, [4]Beijing Normal University, Beijing, China

Introduction: The brain development of children and adolescents is accompanied by maturation of cortical myelination and white matter network. Many studies have revealed that cortical maturation follows a pattern of spatiotemporal hierarchy(Sydnor, Larsen et al. 2021). Connectome gradient techniques representing brain topological organization in a low-dimensional space can smoothly capture the cortical macroscale hierarchy(Margulies, Ghosh et al. 2016). A recently introduced in vivo model integrated three features of structural connectivity, including diffusion MRI tractography, geodesic distance, and microstructural similarity(Paquola, Seidlitz et al. 2020). Here, we leveraged this approach to investigate structural connectome development from childhood to adolescence and related it with maturation of cortical morphology and function.

Methods: Dataset. We collected a longitudinal cohort of 276 participants (aged 6-14 years, 135 females) with 437 scans from Children School Functions and Brain Development Project in China (Beijing Cohort). We obtained structural MRI and diffusion MRI using a 3T Siemens Prisma scanner at Peking University. Compute multiscale structural connectome gradients. Base on T1w, T2w, and diffusion MRI, we computed geodesic distances, microstructural profile covariance (MPC), and tact strength between brain regions. After connecting the MPC, geodesic matrix, and structural connectivity network horizontally, we calculated the normalized angle similarity between each of the two rows(Paquola, Seidlitz et al. 2020). To compute connectome gradients, the normalized angle matrix was then fed into the diffusion map embedding algorithm, which mapped the high-dimensional multiscale structural connectome data into a low-dimensional space(Coifman, Lafon et al. 2005). We calculated several global features to measure the gradient transitions during development, including gradient range, explanation ratio, standard deviation, and dispersion. By leveraging a mixed effect linear model, we identified the developmental trajectories at both the global level and node-wise level. Meanwhile, we calculated eccentricity measure as Euclidean distance between each node and the centroid of template space. Association with development of morphometric features. We utilized 5 cortical morphometric measures to investigate the relationships between multiscale structural gradients and morphometric features. We performed principle component analysis (PCA) to summarize these 5 features and related the PC 1 to the multiscale structural gradient 1. Multiscale structure-function coupling. We conducted an analysis on the coupling between structure and function. Coupling was computed as Spearman rank correlation between connectivity profiles of structure and function.

Results: During development, the first gradient showing differentiation between transmodal and primary regions, and the second gradient separating anterior and posterior regions (Fig 1A). According to the trajectories of global measures, the first gradient increased with development and vice versa for the second gradient. Age-related changes in multiscale structural gradient 1 during development revealed the gradual maturation of the S-A axis (Fig. 1). The first principal component of morphological features was associated with the first gradient, and the age-related patterns of change were also correlated (Fig. 2A-D). The pattern of coupling between multiscale structure and functional connectivity adhered to the S-A axis, and the majority of systems exhibited an increase in coupling with development (Fig. 2E-F).

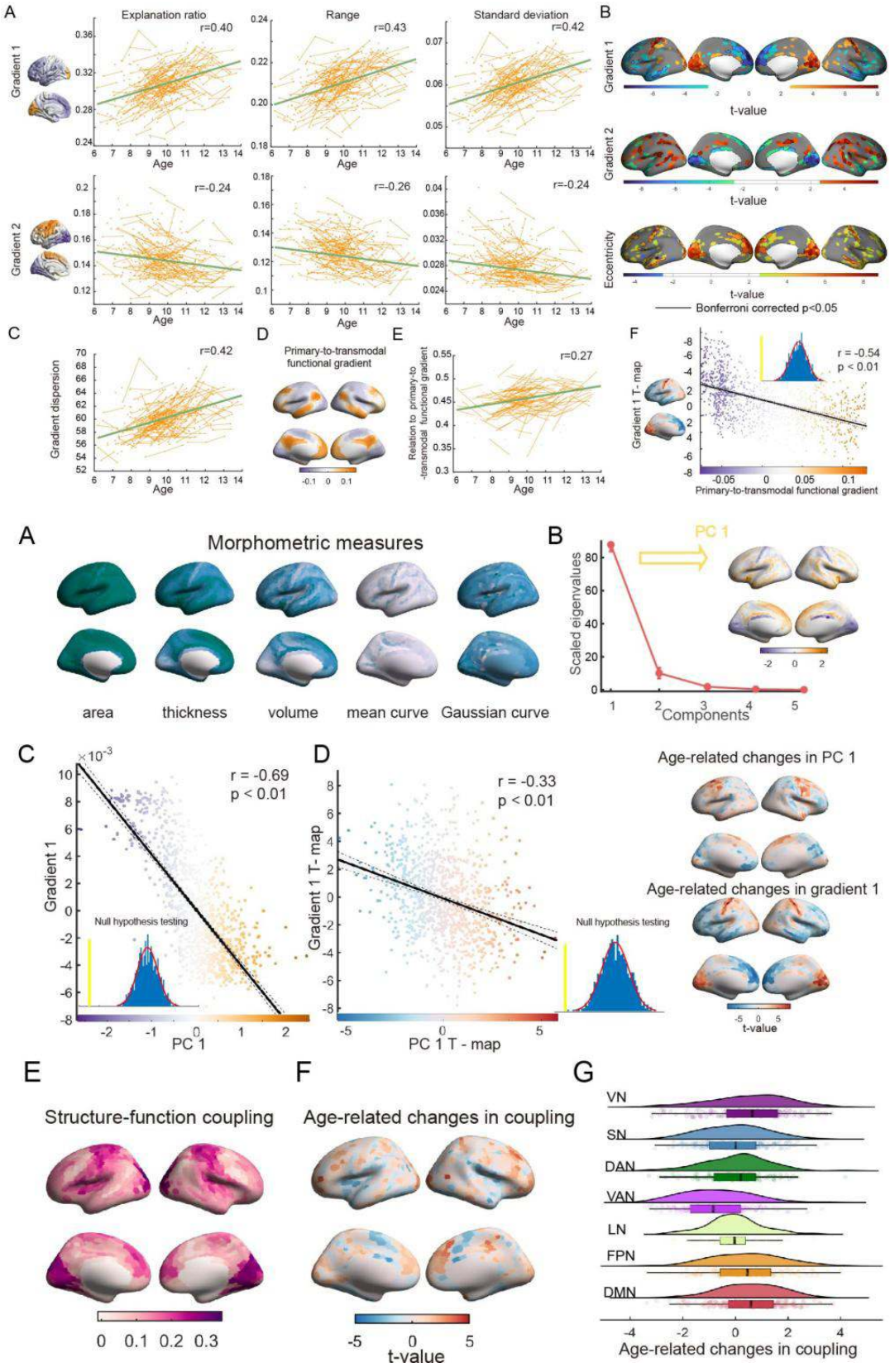

Conclusions: In conclusion, by applying connectome gradient analysis, we revealed a progressive transition of multiscale structural connectome from childhood to adolescence. Our findings suggested that the organization of structural connectome moves toward a more distributed direction with development, which correlates with maturation of cortical macrostructure and function.

References

1. Coifman, R. R., S. Lafon, A. B. Lee, M. Maggioni, B. Nadler, F. Warner and S. W. Zucker (2005). "Geometric diffusions as a tool for harmonic analysis and structure definition of data: Diffusion maps." Proceedings of the national academy of sciences 102(21): 7426-7431.
2. Margulies, D. S., S. S. Ghosh, A. Goulas, M. Falkiewicz, J. M. Huntenburg, G. Langs, G. Bezgin, S. B. Eickhoff, F. X. Castellanos, M. Petrides and others (2016). "Situating the default-mode network along a principal gradient of macroscale cortical organization." Proceedings of the National Academy of Sciences 113(44): 12574-12579.
3. Paquola, C., J. Seidlitz, O. Benkarim, J. Royer, P. Klimes, R. A. I. Bethlehem, S. Larivière, R. V. de Wael, R. Rodríguez-Cruces, J. A. Hall, B. Frauscher, J. Smallwood and B. C. Bernhardt (2020). "A multi-scale cortical wiring space links cellular architecture and functional dynamics in the human brain." PLoS Biology 18(11).
4. Sydnor, V. J., B. Larsen, D. S. Bassett, A. Alexander-Bloch, D. A. Fair, C. Liston, A. P. Mackey, M. P. Milham, A. Pines, D. R. Roalf and others (2021). "Neurodevelopment of the association cortices: Patterns, mechanisms, and implications for psychopathology." Neuron 109(18): 2820-2846.

Poster No 1236

Adolescent maturation of cortical microcircuits based on individualized biophysical network modeling

Amin Saberi[1,2,3], Kevin Wischnewski[1], Kyesam Jung[1], Leon Lotter[1], Lina Schaare[2], Juergen Dukart[1], Oleksandr Popovych[1], Simon Eickhoff[1], Sofie Valk[2]

[1]INM-7, Research Centre Jülich, Jülich, Germany, [2]Max Planck Institute for Human Cognitive and Brain Sciences, Leipzig, Germany, [3]Institute of Systems Neuroscience, Heinrich Heine University Düsseldorf, Düsseldorf, Germany

Introduction: Adolescence is a critical period of development with substantial macro- and microscale changes in the brain, including maturation of cortical microcircuits and the excitation-inhibition (E-I) balance[1,2]. However, the in vivo and non-invasive assessment of E-I is a challenge limiting the extent of current available evidence in humans[3,4]. Biophysical network modeling (BNM) is a promising approach that can bridge the functional imaging data at the macroscale to the hidden features of cortical microcircuits at the microscale[5,6]. Here, we used individualized BNM on magnetic resonance imaging data to study typical E-I maturation and its association to psychopathology throughout adolescence.

Methods: We studied adolescents from the cross-sectional Philadelphia Neurodevelopmental Cohort (PNC; N = 764, 421 female, age: 15.3±2.6 [10-19]) and the longitudinal IMAGEN dataset (N = 148, 74 female) with follow-ups from age 14 to 19. The imaging data was processed to calculate individual structural connectomes (SC), empirical functional connectomes (FC), and empirical functional connectivity dynamics (FCD) matrices. Next, we performed BNM simulation-optimization at the level of each individual (Fig. 1). We simulated the activity of 100 cortical regions of the Schaefer atlas as network nodes governed by the reduced Wong-Wang model with feedback inhibition control[7,8] and the Balloon-Windkessel model for calculation of simulated BOLD signals[9]. The model was controlled by 15 free parameters, including global coupling (G), in addition to bias and coefficient terms which determine the regional excitatory-to-excitatory (wEE) and excitatory-to-inhibitory (wEI) connection weights as a combination of six biological maps (T1w/T2w, cortical thickness, FC principal gradient, gene expression principal axis, NMDA-R and GABAA PET maps). The goodness-of-fit of the simulations to the empirical functional data of each subject was defined as the correlation of FC matrices subtracted by the absolute difference in their means and Kolmogorov-Smirnov distance of FCD matrices (Fig. 1A). Model optimization was performed using covariance matrix adaptation evolution strategy (Fig. 1B). We subsequently used the optimal simulation of each subject to calculate the mean simulated excitatory firing rates (<rE>) as regional markers of E-I balance (Fig. 1C). Following, we studied the effect of age on <rE> through adolescence. We assessed spatial correlation of age effects derived from different datasets or conditions through using spin-permutated surrogates. Last, we explored potential alterations of E-I maturation associated with psychopathology by evaluating age-by-group interaction effects on <rE> in typical and atypical developing subgroups, as defined by Global Assessment Scale ratings (PNC) or presence of DSM diagnoses (IMAGEN).

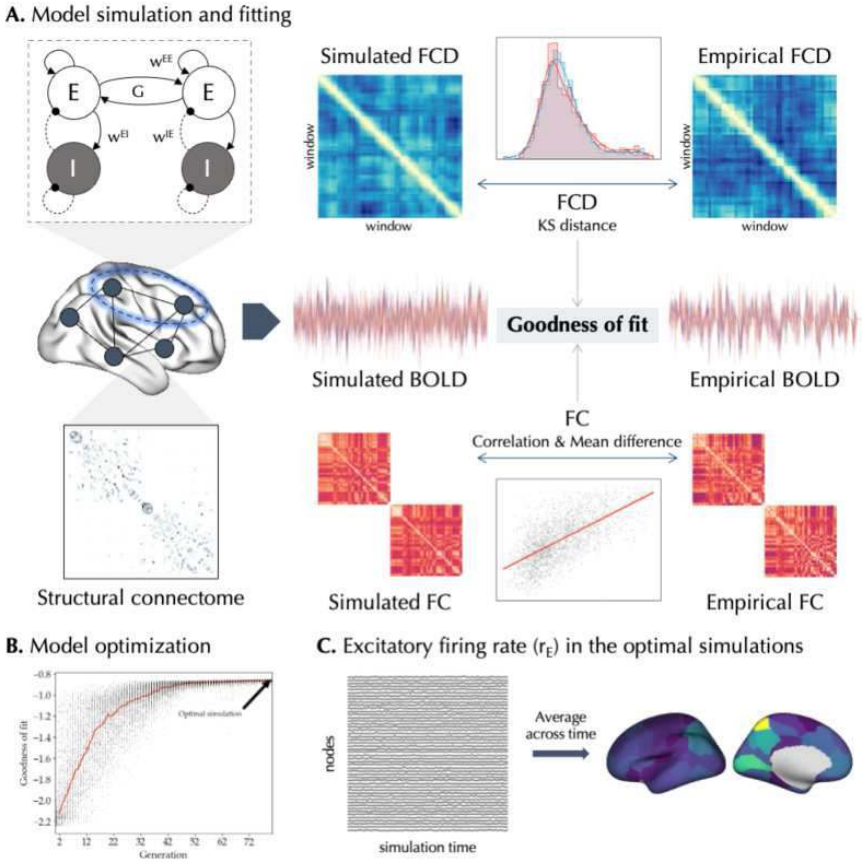

Fig. 1. Modeling framework. A. The BOLD signal is simulated based on the reduced Wong-Wang model (*left*) given a set of plausible model parameters. Goodness of fit of the simulation to empirical data is evaluated as the correlation of functional connectivity (FC) matrices subtracted by their absolute mean difference and the Kolmogorov-Smirnov distance of functional connectivity dynamics (FCD) matrices. **B.** The free model parameters are optimized using covariance matrix adaptation evolution strategy (CMAES). The variations of goodness of fit across the generations of an exemplary CMAES execution are shown. Each point is a simulation, the red line shows the median goodness of fit in each generation, and the arrow indicates the optimal simulation. **C.** From the optimal simulation of each subject we extract the mean excitatory firing rate ($\langle r_E \rangle$) across time as a marker of excitation-inhibition balance in each node.

Results: In the PNC dataset, <rE> significantly decreased with age in transmodal areas but increased in unimodal regions (Fig. 2A). This pattern was replicable across random subsamples (Fig. 2A) and was robust to age-related variations of SC, as similar age effects were observed with group-averaged SC ($r = 0.82$, $p < 0.01$). Longitudinal changes of <rE> from age 14 to 19 in IMAGEN showed a pattern largely similar to PNC ($r = 0.67$, $p < 0.01$; Fig. 2B). The age-by-group interaction effects, testing for associations between E-I maturation and psychopathology, were not significant in both datasets in any node after FDR correction (Fig. 2).

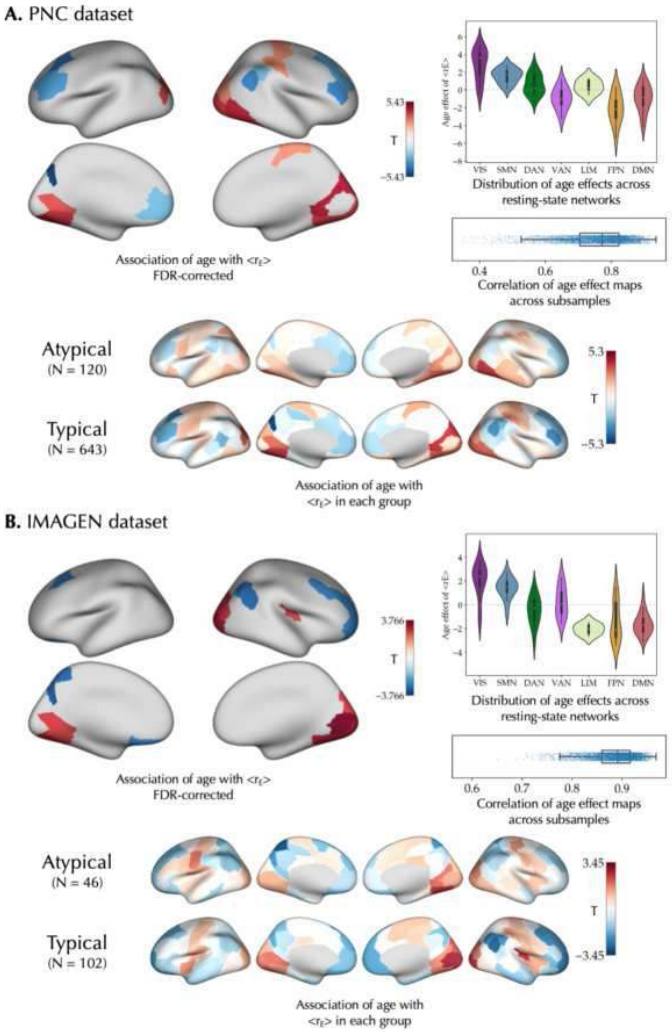

Fig. 2. The association of age with mean excitatory firing rate (<r_E>) in PNC (**A**) and IMAGEN (**B**) datasets. In each panel, the FDR-corrected age effects across all subjects (*top left*) as well as non-thresholded age effects in the atypical and typical subgroups (*bottom*) are shown. At the *top right* of each panel, the distribution of non-thresholded age effects of the whole sample across resting-state networks as well as the distribution of correlation of non-thresholded age effects between subsamples are plotted.

Conclusions: We find E-I ratio during adolescence to decrease in association cortices and increase in unimodal regions. This corroborates previous animal and human studies showing a decreased E-I ratio in association areas[3,4,10]. Individualized modeling holds promise for further interrogation of the interrelationship between microcircuit maturation and cognitive as well as clinical variation.

References

1. Sydnor VJ, Larsen B, Bassett DS, Alexander-Bloch A, Fair DA, Liston C, et al. Neurodevelopment of the association cortices: Patterns, mechanisms, and implications for psychopathology. Neuron. 2021. 15 July 2021. https://doi.org/10.1016/j.neuron.2021.06.016.
2. Caballero A, Orozco A, Tseng KY. Developmental regulation of excitatory-inhibitory synaptic balance in the prefrontal cortex during adolescence. Semin Cell Dev Biol. 2021;118:60–63.
3. Larsen B, Cui Z, Adebimpe A, Pines A, Alexander-Bloch A, Bertolero M, et al. A developmental reduction of the excitation:inhibition ratio in association cortex during adolescence. Science Advances. 2022. February 2022. https://doi.org/10.1126/sciadv.abj8750.
4. Ghisleni C, Bollmann S, Poil S-S, Brandeis D, Martin E, Michels L, et al. Subcortical Glutamate Mediates the Reduction of Short-Range Functional Connectivity with Age in a Developmental Cohort. J Neurosci. 2015;35:8433–8441.
5. Popovych OV, Manos T, Hoffstaedter F, Eickhoff SB. What Can Computational Models Contribute to Neuroimaging Data Analytics? Frontiers in Systems Neuroscience. 2019;12:68.
6. Deco G, Kringelbach ML. Great Expectations: Using Whole-Brain Computational Connectomics for Understanding Neuropsychiatric Disorders. Neuron. 2014;84:892–905.
7. Deco G, Ponce-Alvarez A, Hagmann P, Romani GL, Mantini D, Corbetta M. How local excitation-inhibition ratio impacts the whole brain dynamics. J Neurosci. 2014;34:7886–7898.
8. Demirtaş M, Burt JB, Helmer M, Ji JL, Adkinson BD, Glasser MF, et al. Hierarchical Heterogeneity across Human Cortex Shapes Large-Scale Neural Dynamics. Neuron. 2019;101:1181-1194.e13.
9. Friston KJ, Harrison L, Penny W. Dynamic causal modelling. Neuroimage. 2003;19:1273–1302.
10. Hoftman GD, Datta D, Lewis DA. Layer 3 excitatory and inhibitory circuitry in the prefrontal cortex: Developmental trajectories and alterations in schizophrenia. Biological Psychiatry. 2017;81:862.

Poster No 1237

A robust brain network for sustained attention from adolescence to adulthood

Yihe Weng[1], Johann Kruschwitz[2], Laura Rueda-Delgado[1], Kathy Ruddy[1], Rory Boyle[1], Emin Serin[3], Robert Whelan[1]

[1]Trinity College Dublin, Dublin, Dublin, [2]Department of Psychiatry and Psychotherapy CCM, Charité – Universitätsmedizin Berlin, Corporate Mem, Berlin, Germany, [3]Charité Universitätsmedizin Berlin, Berlin, Germany

Introduction: Sustained attention, crucial for daily life, refers to the ability to maintain attentional focus on relevant stimuli with repeated presentation over extended periods. This cognitive process significantly impacts academic achievement, safety, social communication, and mental health[1]. Sustained attention typically improves from mid-adolescence to adulthood[2]. Previous studies have identified predictive network predicting sustained attention[3]. However, the stability of underlying brain networks from adolescence to early adulthood remains relatively unexplored. Here, we examine the trajectory of functional brain networks predicting sustained attention from age 14 to 23.

Methods: Subjects: Functional MRI data from adolescents at ages 14 (N=717) 19 (N=1079) and 23 (N=1120) were obtained from the Stop Signal Task of the IMAGEN study[4]. Subjects responded to a Go signal, while withholding their response if the Go signal was followed unpredictably by a Stop signal. Intra-individual coefficient of variation (ICV) indexed sustained attention by quantifying trial-to-trial reaction time (RT) consistency using Go trials. The ICV was the standard deviation of GO RT divided by mean GO RT. Lower ICV reflects better sustained attention. Preprocessing: All images were pre-processed within SPM12: slice timing, head motion correction, normalization, and smoothed. Subjects were excluded if mean framewise displacement>0.5mm. CPM analysis: A generalized psychophysiological interaction analysis[5] was performed across the whole-brain using the Shen atlas to yield task-related connectivity under Go trials condition. Connectome-based predictive modelling (CPM), a machine learning method[6] was applied to predict ICV at each timepoint. This involved four key steps: 1) feature selection, 2) feature summarization, 3) model building, and 4) assessment of prediction significance. The CPM analysis was performed across timepoint, applying the model defined at one timepoint to predict ICV at subsequent timepoints (e.g., using the model defined at age 14 to predict ICV at ages 19 and 23). Finally, the generalizability of model defined at age 23 in an external dataset of the same age, STRATIFY.

Results: 2.1 Predicting ICV at each timepoint. Positive, negative, and combined networks significantly predicted ICV: at age 14 ($r = 0.25$, $r = 0.25$, and $r = 0.28$, respectively, all $P < 0.001$), 19 ($r = 0.27$, $r = 0.25$, $r = 0.28$, respectively, all $P < 0.001$) and 23 ($r = 0.38$, $r = 0.33$, and $r = 0.37$, respectively, all $P < 0.001$). 2.2 Predicting ICV across timepoints. Positive, negative, and combined networks defined at age 14 predicted ICV at ages 19 ($r = 0.16$, $r = 0.14$, and $r = 0.16$, all $P < 0.001$) and 23 ($r = 0.20$, $r = 0.12$, and $r = 0.17$, all $P < 0.001$) respectively. Likewise, positive, negative, and combined networks defined at age 19 predicted ICV at age 23 ($r = 0.30$, $r = 0.26$, and $r = 0.31$, respectively, all $P < 0.001$). 2.3 Generalization Positive, negative, and combined networks at age 23 in IMAGEN predicted ICV in STRATIFY ($r = 0.34$, $r = 0.34$, and $r = 0.35$, respectively, all $P < 0.001$).

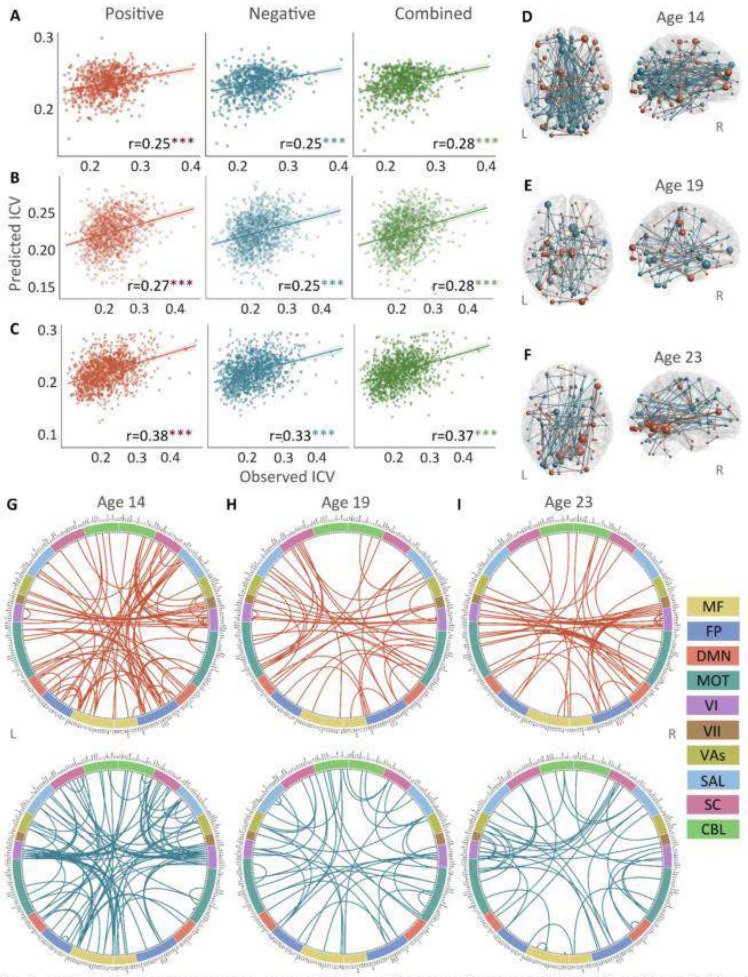

Fig. 1 The predictive performances and networks of intra-individual coefficient of variation (ICV) per timepoint derived from Go trials. Correlation between observed and predicted ICV in positive, negative, and combined networks at **(A)** age 14 **(B)** age 19 and **(C)** age 23. Predictive networks for ICV at **(D)** age 14 **(E)** age 19 and **(F)** age 23. Connectome of positive and negative networks of ICV at **(G)** age 14 **(H)** age 19 and **(I)** age 23. The edges depicted above are those selected in at least 95% of cross validation folds. Red, blue, and green spheres/lines/scatters separately represent positive, negative, and combined networks. MF, Medial frontal; FP, Frontoparietal; DMN, Default mode; MOT, Motor; VI, Visual I; VII, Visual II; VAs, Visual association; SAL, Salience; SC, Subcortical; CBL, Cerebellar. R/L, right/left hemisphere. ***, $P < 0.001$.

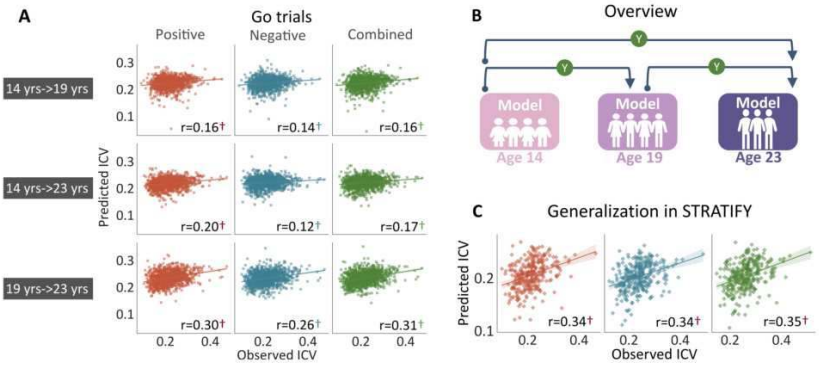

Fig. 2 Intra-individual coefficient of variation (ICV) prediction across timepoints and generalization in STRATIFY. (A) Predictive performances of ICV across timepoint. The top, middle, and bottom rows of (A) panel shows the predictive performance: using models defined at age 14 to predict age 19 (i.e., 14 yrs -> 19 yrs), using models defined at age 14 to predict age 23 (i.e., 14 yrs -> 23 yrs), and using models defined at age 19 to predict age 23 (i.e., 19 yrs ->23 yrs) respectively. **(B)** Overviews of predicting ICV across time. The green circle represents that the predictive models identified at this timepoint could be used to predict ICV at another timepoint. **(C)** Predictive performance using models defined at age 23 to predict the STRATIFY. The red, blue, and green scatter represent positive, negative, and combined networks. *, $P < 0.05$; **, $P < 0.01$; †, $P < 0.001$.

Conclusions: Sustained attention networks derived from Go trials predicted behavior at different timepoints, suggesting that individual differences in these networks were preserved throughout development. In neurodiverse youth, attention networks in individuals remain stable across months to years, as shown using connectome-based identification and longitudinal scans[7]. Here, we demonstrate that attention-network stability also holds in a large cohort of healthy participants. In addition, a predictive network defined at one timepoint predicted another timepoint, indicating that sustained attention relies on

global brain activation (i.e., network strength) rather than specific regions or networks (see also[8]). In summary, the identified predictive networks involved in sustained attention are robust from ages 14 to 23.

References

1. Di, X. and B. B. Biswal (2019). "Toward Task Connectomics: Examining Whole-Brain Task Modulated Connectivity in Different Task Domains." Cerebral Cortex 29(4): 1572-1583.
2. Esterman, M. and D. Rothlein (2019). "Models of sustained attention." Curr Opin Psychol 29: 174-180.
3. Horien, C., A. S. Greene, X. Shen, D. Fortes, E. Brennan-Wydra, C. Banarjee, R. Foster, V. Donthireddy, M. Butler, K. Powell, A. Vernetti, F. Mandino, D. O'Connor, E. M. R. Lake, J. C. McPartland, F. R. Volkmar, M. Chun, K. Chawarska, M. D. Rosenberg, D. Scheinost and R. T. Constable (2022). "A generalizable connectome-based marker of in-scan sustained attention in neurodiverse youth." Cereb Cortex.
4. Mascarell Maricic, L., H. Walter, A. Rosenthal, S. Ripke, E. B. Quinlan, T. Banaschewski, G. J. Barker, A. L. W. Bokde, U. Bromberg, C. Buchel, S. Desrivieres, H. Flor, V. Frouin, H. Garavan, B. Itterman, J. L. Martinot, M. P. Martinot, F. Nees, D. P. Orfanos, T. Paus, L. Poustka, S. Hohmann, M. N. Smolka, J. H. Frohner, R. Whelan, J. Kaminski, G. Schumann, A. Heinz and I. consortium (2020). "The IMAGEN study: a decade of imaging genetics in adolescents." Mol Psychiatry 25(11): 2648-2671.
5. Rosenberg, M. D., W. T. Hsu, D. Scheinost, R. Todd Constable and M. M. Chun (2018). "Connectome-based Models Predict Separable Components of Attention in Novel Individuals." J Cogn Neurosci 30(2): 160-173.
6. Shen, X., E. S. Finn, D. Scheinost, M. D. Rosenberg, M. M. Chun, X. Papademetris and R. T. Constable (2017). "Using connectome-based predictive modeling to predict individual behavior from brain connectivity." Nat Protoc 12(3): 506-518.
7. Thomson, P., C. B. Malpas, N. Vijayakumar, K. A. Johnson, V. Anderson, D. Efron, P. Hazell and T. J. Silk (2022). "Longitudinal maturation of resting state networks: Relevance to sustained attention and attention deficit/hyperactivity disorder." Cogn Affect Behav Neurosci 22(6): 1432-1446.
8. Zhao, W., C. E. Palmer, W. K. Thompson, B. Chaarani, H. P. Garavan, B. J. Casey, T. L. Jernigan, A. M. Dale and C. C. Fan (2021). "Individual Differences in Cognitive Performance Are Better Predicted by Global Rather Than Localized BOLD Activity Patterns Across the Cortex." Cereb Cortex 31(3): 1478-1488.

Poster No 1238

Prenatal Famine Exposure and Late-Life Functional Brain Network Connectivity: A Longitudinal Study

Amber Boots[1], Jessica Damoiseaux[2], Youjin Yung[2], Aline Marileen Wiegersma[3], Anouk Schrantee[3], Daphne Boucherie[3], Tessa Roseboom[3], Susanne de Rooij[3]

[1]Amsterdam UMC, Amsterdam, NA, [2]Wayne State University, Detroit, MI, [3]Amsterdam UMC, Amsterdam, Netherlands

Introduction: The effects of the prenatal environment on resting-state functional connectivity can be detected up into older adulthood. In the Dutch famine birth cohort study, we previously identified differences in resting-state functional connectivity of the default mode network (DMN),salience network (SN), and central executive network (CEN) at age 68 between men and women who had been exposed or unexposed to famine in early gestation. In the current study, we aimed to investigate longitudinal changes in resting-state functional connectivity of the DMN, SN and CEN in the same cohort between ages 68 and 74. Our hypothesis posited that prenatal famine exposure would be associated with more pronounced aging-related changes in functional connectivity, expressed as network desegregation with reduced within-network functional connectivity.

Methods: We performed a longitudinal follow-up resting-state functional magnetic resonance imaging study in the Dutch famine birth cohort at ages 68 (N = 115) and 74 (N = 80). Within-network functional connectivity of the DMN, SN and CEN was determined using the CONN toolbox ROI-to-ROI connectivity pipeline and was compared between individuals unexposed (born before or conceived after) or exposed to famine in early gestation using a latent change score modeling approach with full information maximum likelihood estimation (Fig. 1).

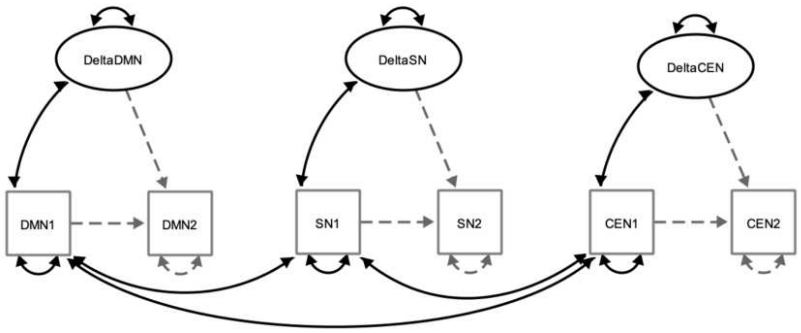

Fig. 1. Latent change score model path diagram of within-network functional connectivity. Squares represent observed variables, circles are latent variables. Grey dotted lines indicate fixed effects,

Results: No group differences were observed in baseline score (intercept) or rate of change (slope) of the DMN, SN and CEN between individuals exposed or unexposed to famine in early gestation ($\Delta\chi 2 = 1.408$, $p = 0.704$). Across both groups, there was a significant increase in DMN connectivity over time. Additional exploratory analyses revealed that the increase in DMN connectivity was mainly driven by connectivity within the posterior cingulate cortex and parietal regions of the DMN.

Conclusions: This study did not reveal more pronounced aging-related alterations in network connectivity among individuals exposed to famine in early gestation compared to unexposed individuals. This does not provide support for the hypothesis of accelerated brain aging, but may align with persistent developmental effects of prenatal undernutrition on late-life brain health. Future analyses will examine changes in between-network functional connectivity as well.

Poster No 1239

Allometric constraints on brain tissue configuration

Jakob Seidlitz[1], Margaret Gardner[1], Lena Dorfschmidt[2], Gabriel Devenyi[3], Mallar Chakravarty[4], Chet Sherwood[5], William Hopkins[6], Yaniv Assaf[7], Yossi Youvel[7], Ting Xu[8], Samuel Alldritt[8], Julian Ramirez[8], Gareth Ball[9], Jacob Vogel[10], Edward Bullmore[11], Richard Bethlehem[12], Aaron Alexander-Bloch[1]

[1]University of Pennsylvania, Philadelphia, PA, [2]The Children's Hospital of Philadelphia, Philadelphia, PA, [3]McGill University, Montreal, Quebec, [4]Brain Imaging Centre, Douglas Research Centre, Montreal, Quebec, [5]The George Washington University, Washington, DC, [6]MD Anderson Cancer Center Texas, Houston, TX, [7]Tel Aviv University, Tel Aviv, Israel, [8]Child Mind Institute, New York, NY, [9]Murdoch Children's Research Institute, Melbourne, VIC, [10]Lund University, Lund, n/a, [11]University of Cambridge, Cambridge, United Kingdom, [12]Autism Research Centre, Department of Psychiatry, University of Cambridge, Cambridge, United Kingdom

Introduction: A critical event in human evolution was the emergence of increased brain size variation relative to other species[1,2]. Total brain size can vary ~700-fold across primate species[3], as much as 2-fold in adult humans[4], and dynamically changes across the lifespan[5]. In humans, scaling of brain regions with total brain size is largely non-linear (allometric)[4], with areas of extreme allometric scaling subserving highly specialized functions, greater interindividual variability, and elevated disease vulnerability[4]. However, the comparative allometric relationships within (static) and between (evolutionary) species of brain tissue compartments remains unknown.

Methods: We assessed brain scaling across multiple structural magnetic resonance imaging datasets comprising 101,457 humans aged 115 days post conception to 100 years[5], 210 chimpanzees aged 6 years to 56 years, 87 macaques aged 85 days post conception to 23 years, and 226 mammals across 123 species (MaMI)[6]. Tissue segmentation for whole-brain gray matter volume (GMV), white matter volume (WMV), and cerebrospinal fluid (CSF) was performed using FreeSurfer (v5.3, v6.1, or infant), CIVET (v.1.1.10 or v2.1.0), or custom pipelines in the human datasets (and harmonized across studies[5]); and custom pipelines for the chimpanzee[7] and macaque[8] datasets. Brain size was indexed as total cerebrum volume (TCV) for human data or total brain volume (TBV) for the chimpanzee and macaque datasets, after observing high correlations ($r>0.98$) of TCV and TBV in the largest studies within the human dataset (ABCD, UK Biobank). To evaluate allometric tissue volume relationships with total brain size, log-log regressions were performed in R using linear mixed-effects models (multi-species) and generalized additive models for within-species tests[4]. As such, a coefficient of one represents linear scaling (isometric) and values less than (hypo-allometric) or greater than (hyper-allometric) one represent non-linear scaling.

Results: Within-species (static) allometric scaling coefficients were similar for humans (GMV=0.89, WMV=1.14, CSF=0.95), chimpanzees (GMV=0.89, WMV=1.15, CSF=0.86), and macaques (GMV=0.88, WMV=1.19, CSF=1.01). Across-species compartmental allometric scaling coefficients were similar to previously reported estimates (MaMi: GMV=0.98, WMV=1.16; Previous[9]: GMV=0.96, WMV=1.17), with notable static (relative to evolutionary) hypo-allometry of GMV. A sliding-window approach revealed highly dynamic scaling relationships for each tissue class across the human lifespan (Fig. 1A). Interestingly, despite static isometry, CSF volume shifted from being hypo-allometric in the perinatal and childhood periods to hyper-allometric for adolescence and adulthood. GMV showed a similar but opposing pattern, decreasing at a faster rate than TBV (increased hypo-allometry) in adulthood. Cortical regional analyses using age epochs defined by scaling inflection points showed that while higher-order association areas changed from hyper- to hypo-allometric scaling, primary sensory and insular areas remained consistently hypo-allometric relative to TBV (Fig. 1A). Comparing the variance of total brain size (vT) to the summed variances of the constituent tissues (vC), we observed a marked shift from a period of compensation in the first two years of life ($vT < vC$) to a period of increased coordination ($vT > vC$), peaking in mid-adolescence and declining thereafter, demonstrating the dynamics of human brain compartmentalization[10] (Fig. 1B).

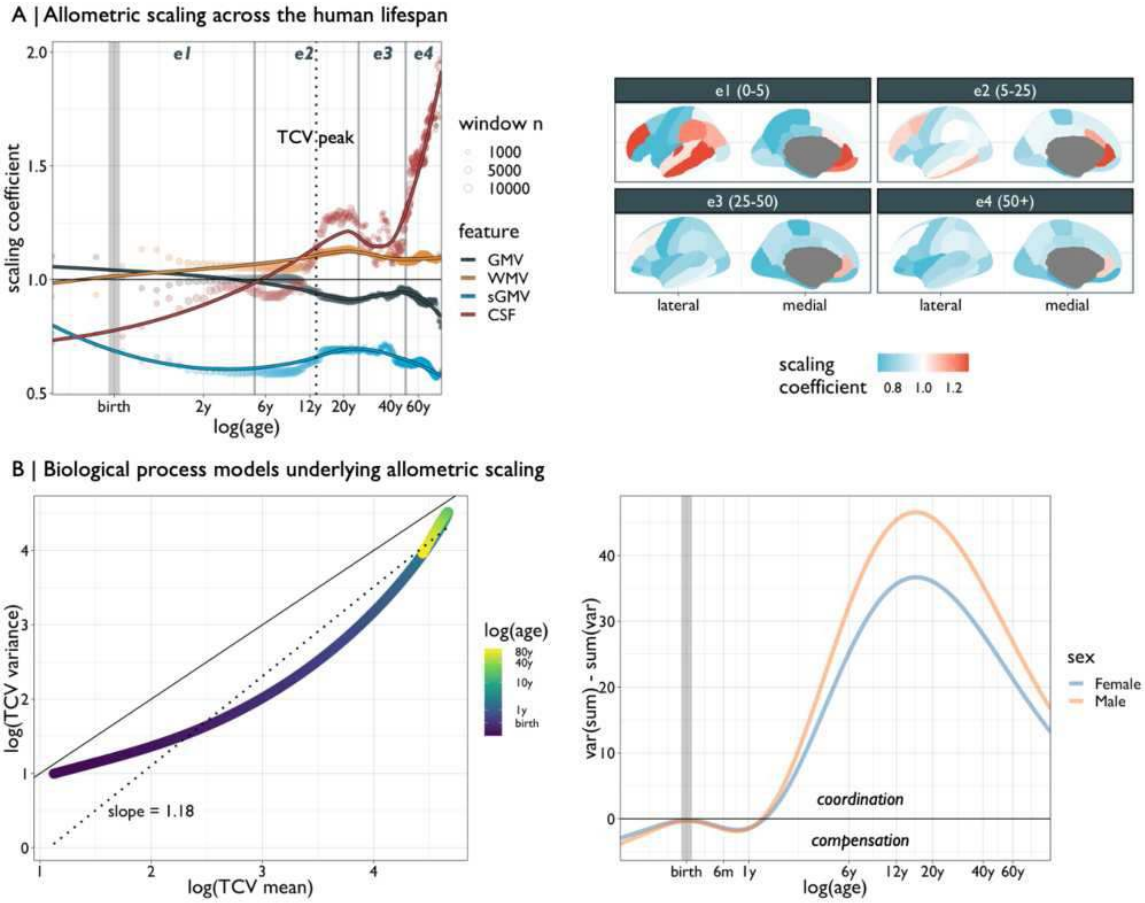

Figure 1. A | Allometric scaling of major tissue classes across the human lifespan, using sliding windows of 800 days at 100-day intervals (N=356) to accommodate age-varying differences in the number of subjects. Size of circles represents the number of subjects within a window. Color denotes tissue class. Dotted line represents the age at peak total cerebrum volume (TCV), thick gray line defines term-equivalent birth (37-41 gestational weeks) for visualization, and thin solid gray lines denote qualitatively defined epochs (e) based on changes in tissue class scaling coefficients. (Right) Brain plots showing cortical region volume scaling per lifespan epoch across 34 regions, defined by the Desikan-Killiany atlas. Region volumes were bilaterally averaged (plotted on the left hemisphere for visualization). Color denotes scaling coefficient. **B |** (Left) Comparison of mean and variance of total brain size across the human lifespan (using predicted 50th percentile lines), plotted on a log scale and colored by age (also log scaled). (Right) Difference of the variance of TCV and sum of the variances of constituent tissue classes (GMV, WMV, CSF) across age (log scaled). A cross-sectional variance of TCV (denoted var(sum)) greater than the sum of the variances of the constituent tissue classes comprising TCV (denoted sum(var)) signals a dominance of coordinating over compensatory processes[10]. GMV: gray matter volume, WMV: white matter volume, sGMV: subcortical gray matter volume, CSF: ventricular cerebrospinal fluid volume.

Conclusions: Despite marked evolutionary changes in brain size and variation, patterns of allometric scaling were similar across species. However, the flexibility of developmental scaling across the human lifespan highlighted strong hyper-allometric scaling of association cortical regions during the greatest period of brain growth in infancy and early childhood.

References

1. Gonda, A., Herczeg, G. & Merilä, J. Evolutionary ecology of intraspecific brain size variation: a review. Ecol. Evol. 3, 2751–2764 (2013).
2. Isler, K. & van Schaik, C. P. How Our Ancestors Broke through the Gray Ceiling: Comparative Evidence for Cooperative Breeding in Early Homo. Curr. Anthropol. 53, S453–S465 (2012).
3. Heuer, K. et al. Evolution of neocortical folding: A phylogenetic comparative analysis of MRI from 34 primate species. Cortex 118, (2019).
4. Reardon, P. K. et al. Normative brain size variation and brain shape diversity in humans. Science 360, (2018).
5. Bethlehem, R. A. I. et al. Brain charts for the human lifespan. Nature 604, 525–533 (2022).
6. Assaf, Y., Bouznach, A., Zomet, O., Marom, A. & Yovel, Y. Conservation of brain connectivity and wiring across the mammalian class. Nat. Neurosci. 23, 805–808 (2020).
7. Devenyi, G. A., Sherwood, C., Hopkins, W. D. & Raznahan, A. Chimpanzee High-Resolution Minimum Deformation Average and Application To Aging and Sex Differences. Organization for Human Brain Mapping.
8. Seidlitz, J. et al. A population MRI brain template and analysis tools for the macaque. Neuroimage 170, (2018).
9. Zhang, K. & Sejnowski, T. J. A universal scaling law between gray matter and white matter of cerebral cortex. Proc. Natl. Acad. Sci. U. S. A. 97, 5621–5626 (2000).
10. Mitteroecker, P. et al. Morphometric Variation at Different Spatial Scales: Coordination and Compensation in the Emergence of Organismal Form. Syst. Biol. 69, 913–926 (2020).

Poster No 1240

Normative Brain Development of Cortical Thickness in Early-School Age Children: A Longitudinal Study

Baitao Li[1], Xiao Wang[1], Qing Cai[1], Chu-Chung Huang[1]

[1]East China Normal University, Shanghai, China

Introduction: Normative modeling has emerged as an essential analytical tool in neuroimaging, providing a framework to delineating individual difference, especially in brain development (Marquand et al., 2016). However, most previous studies relied solely on cross-sectional data to model the age-related brain changes, potentially leading to an incomplete understanding of the variability present in longitudinal data (Di Biase et al., 2023). To address this limitation of cross-sectional normative modeling, our research shifts focus to the use of longitudinal data for modeling developmental changes. In this study, we integrated the gamlssNP method (Stasinopoulos et al., 2017), specifically tailored for longitudinal data analysis. Considering the considerable environmental change experienced by early-school-age children, we model a longitudinal cohort of children aged 7 to 10 years, with at least two MRI data points. This study aims to establish a less-biased normative model based on longitudinal data to depict cortical thickness development in early-school-age children.

Methods: We selected participants with at least two data time points, which yielded 529 T1-weighted (T1w) MRI images. These T1w images were processed using FreeSurfer (v7.3.2), to extract cortical thickness in various brain regions using DKT atlas of each participant. We fitted normative centile curves were fit to cortical thickness using gamlssNP(gamlss.mx) method in R version 4.3.0 (2023-04-21). For model selection and diagnostic, we employed 5-fold cross-validation to determine the optimal parameter combination of degrees of freedom (df) and the number of components (K) for gamlssNP model. The final model parameters were chosen to achieve a balance between fit (lower AIC) and generalization (lower VGD) across all brain regions.

Results: After a 5-fold cross-validation, the (df = 2, K = 2) parameter combination emerges as notably effective among all tested configurations, with an VGD percentile of 0.1461 ± 0.0255, suggesting the model robustness and consistency. Normative model analysis revealed significant age correlations in several brain regions. Among the regions, precentral, paracentral, and entorhinal, exhibited a positive correlation, whereas 14 regions, including the insula, rostral anterior cingulate, and medial orbitofrontal, showed a negative correlation with age (Fig. 1). Here we showed the most significant six regions for demonstration.

Conclusions: Our study found that the precentral, paracentral, and entorhinal cortices, increase in cortical thickness with age. This increase may imply development in motor and cognitive abilities in children. In contrast, the insula and rostral anterior cingulate show reduced thickness, suggesting neural maturation (Gilmore et al., 2018). Overall, these patterns reveal a complex developmental timeline, wherein some regions mature early, playing roles in emotional and cognitive functions. Future work should investigate the individual differences between actual and predicted cortical thickness in these regions and associate them with cognitive development, especially in early school-age children.

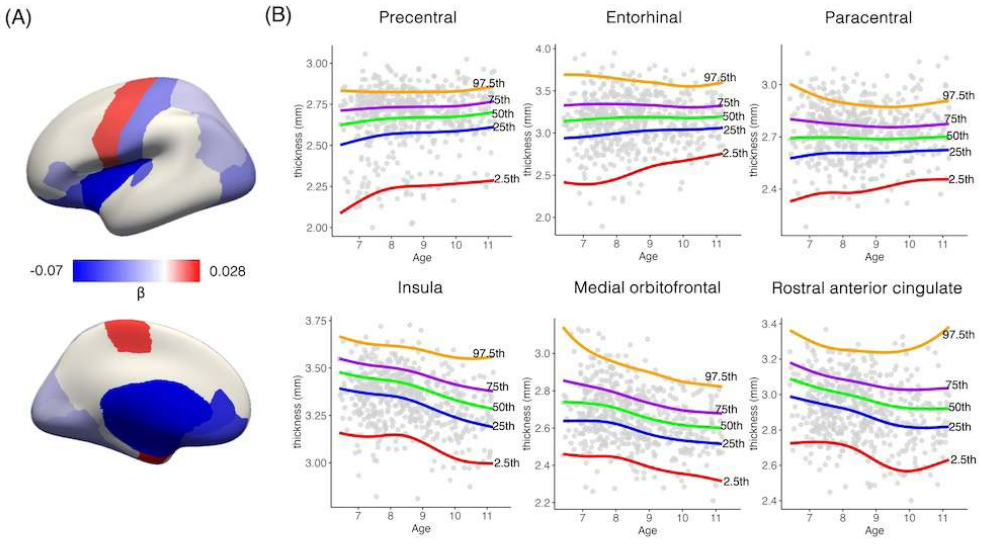

Fig1. Age-related cortical thickness change in left hemisphere. **(A)** Shows the brain regions significantly associated with age in the model, **(B)** Top row depicts the growing trend in brain regions significantly correlated with age; Bottom row illustrates the decreasing trend in brain regions significantly correlated with age. The lines in the curve graph on the right indicate the distribution of quantile lines predicted by the model.

References

1. Marquand, A. F., Rezek, I., Buitelaar, J., & Beckmann, C. F. (2016). Understanding heterogeneity in clinical cohorts using normative models: Beyond case-control studies. Biological Psychiatry, 80, 552–561.
2. Di Biase, M. A., Tian, Y. E., Bethlehem, R. A. I., Seidlitz, J., Alexander-Bloch, A. F., Yeo, B. T. T., & Zalesky, A. (2023). Mapping human brain charts cross-sectionally and longitudinally. Proceedings of the National Academy of Sciences of the United States of America, 120(20), e2216798120.
3. Stasinopoulos, M. D., Rigby, R. A., Heller, G. Z., Voudouris, V., & De Bastiani, F. (2017). Flexible Regression and Smoothing: Using GAMLSS in R. CRC Press.
4. Gilmore, J. H., Knickmeyer, R. C., & Gao, W. (2018). Imaging structural and functional brain development in early childhood. Nature Reviews Neuroscience, 19, 123-137.

Poster No 1241

Brain aging after prenatal undernutrition: longitudinal BrainAGE estimations

Amber Boots[1], Aline Marileen Wiegersma[2], Christian Gaser[3], Tessa Roseboom[2], Susanne de Rooij[2]

[1]Amsterdam UMC, Amsterdam, NA, [2]Amsterdam UMC, Amsterdam, Netherlands, [3]Jena University Hospital, Jena, Germany

Introduction: Environmental exposures during critical periods of early human development have been associated with late-life brain structure and function. It is currently unknown whether these long-term effects represent persistent developmental effects or signal ongoing processes of accelerated brain aging. In the current study, we aimed to investigate longitudinal changes in neuroanatomical brain aging between ages 68 and 74 in men and women exposed or unexposed to the Dutch famine in early gestation.

Methods: We performed a longitudinal follow-up magnetic resonance imaging study in the Dutch famine birth cohort at ages 68 (N = 118) and 74 (N = 81). Brain Age Gap Estimation (BrainAGE), a neuroimaging-based biomarker for neuroanatomical brain aging, was determined for all participants using a longitudinal machine-learning approach. Pace of aging was calculated by taking the difference between BrainAGE scores at age 68 and 74. Additionally, we associated BrainAGE scores to self-reported cognitive problems at age 74.

Results: Men and women exposed to famine in early gestation had higher BrainAGE scores at age 74, similar to the results observed at age 68 (Fig. 1). This was strongest in exposed men. Pace of aging between time points is currently being investigated. Individuals with higher BrainAGE scores had higher odds of reporting cognitive problems at age 74. This association was mostly driven by individuals exposed to famine in early gestation.

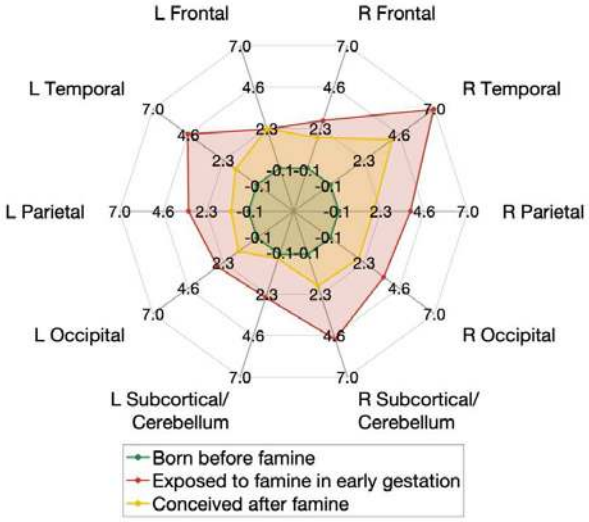

Fig. 1. Regional gray matter BrainAGE scores according to prenatal exposre to famine.

Conclusions: The higher BrainAGE scores among those exposed to famine in early gestation at both ages 68 and 74 indicate that the neuroanatomical correlates of adverse prenatal exposures can be identified consistently throughout late life. In addition, this study revealed a clear association between BrainAGE and self-reported cognitive problems, underlining the strength of BrainAGE as a biomarker of brain aging and cognitive decline.

Poster No 1242

A Novel Method to Investigate Neurodevelopment Using Ising Temperature and Graph Neural Networks

Rodrigo Carvalho[1], Walter Pinaya[2], João Sato[1]

[1]Federal University of ABC, São Bernardo do Campo, São Paulo, [2]King's College London, London, London

Introduction: One of the biggest challenges in neuroscience is comprehending brain function mechanisms on different temporal and spatial scales. In particular, the topic of neurophysiology during the resting state at the macroscopic level is of great interest, not only in contribution to neurodevelopment and psychiatry but also to emergent patterns that microscopic components cannot explain. Recent studies show that brain dynamics may be modelled by lattice models near criticality, such as the 2D Ising Model[1,2]. The Ising temperature, which is the order parameter dictating the phase transitions of the model, is being used to better understand different brain states[3,4]. This work aims to investigate neurodevelopment through a novel method to estimate the Ising Temperature of the brain from functional Magnetic Resonance Imaging (fMRI) data using functional connectivity and Graph Neural Networks (GNNs) trained with Ising Model networks.

Methods: The Attention Deficit Hyperactivity Disorder 200 (ADHD200) dataset (491 healthy subjects, 285 subjects with ADHD, 7–21 years, M=11.99, SD=3.2 years) was used. The functional connectivity graphs of the whole brain were calculated by Pearson's correlation of the 190 ROIs. The 2D Ising model was simulated using a lattice of 330x330 spins fluctuating over 200 time steps after thermal equilibrium, where each time step gives all the spins of the lattice the opportunity to change their state. Then, the lattice is averaged over blocks of 23x23 spins, in order to get a continuous time series representative of the fMRI signal. The 2D Ising Model graphs were calculated by Pearson's correlation, resulting in 190 nodes. To prepare the graphs for the GNN, the edges were selected by a 10-nearest-neighbours algorithm using the FC matrix, each node represented a ROI and the node features were the connectivity with the other ROIs[5]. To calculate the Ising Temperature for the brain networks, a GNN was trained, with 3 graph convolutional layers, a global average pooling process, and 2 linear layers. The activation function was Leaky-ReLu, the dropout technique was also used, and the loss function used was the Mean Absolute Error (MAE). The GNN was trained over 300 epochs, using 1200 simulations of the 2D Ising Model around the criticality, and evaluated in 400 simulations. Therefore, the trained GNN was used on whole brain networks to estimate the brain temperature over neurodevelopment. The methodology is shown in Fig. 1.

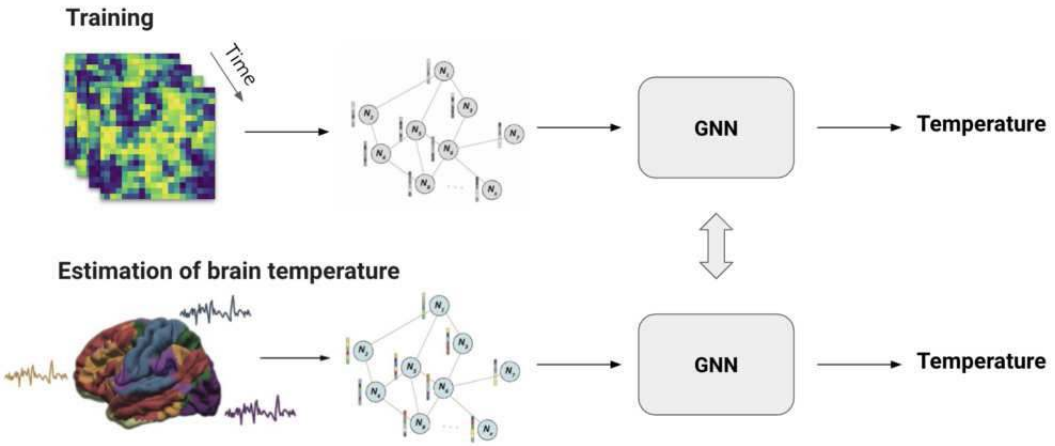

Results: The GNN performance predicting the temperature on the test set was MAE = 0.08 and r2 = 0.70. For the whole brain graphs, age and temperature for healthy subjects were negatively correlated (r = -0.32, two-sided p<0.001). Subjects with ADHD were negatively correlated (r = -0.34, two-sided p<0.001). Moreover, to evaluate the influence of head motion on the Ising Temperate estimation, a linear regression was used. The only variable significant to explain the age was temperature, and it's also negatively associated (coef = -0.92(0.08), two-sided p<0.001).

Conclusions: In this work, functional connectivity and Graph Neural Networks were used to estimate the Ising Temperature of the brain, in order to investigate neurodevelopment. The main finding indicates a statistically significant negative correlation between age and temperature, suggesting that the brain gets distant from criticality as age increases. Moreover, this novel methodology allows more works to investigate the brain network from GNNs trained on simulated dynamical models.

References

1. Chialvo, (2010), "Emergent complex neural dynamics", Nature Phys, vol. 6, pp. 744–750.
2. Fraiman, (2009), "Ising-like dynamics in large-scale functional brain networks", Phys Rev, vol. 79, pp. 061922.

3. Ruffini, (2023), "LSD-induced increase of Ising temperature and algorithmic complexity of brain dynamics", PLoS Computational Biology, vol. 19, pp. 1010811.
4. Kandeepan, (2020), "Modeling an auditory stimulated brain under altered states of consciousness using the generalized Ising model", NeuroImage, vol. 223, pp. 117367.
5. Qin, (2022), "Using graph convolutional network to characterize individuals with major depressive disorder across multiple imaging sites", EBioMedicine, vol. 78, pp. 103977.

Poster No 1243

Perinatal development of the corpus callosum in term and preterm infants

Wei Wang[1], Liyuan Yang[1], Gaolang Gong[1]

[1]State Key Laboratory of Cognitive Neuroscience and Learning & IDG/McGovern Institute for Brain Resea, Beijing, Beijing

Introduction: The corpus callosum (CC) is the largest commissural tract, supporting interhemispheric communication and hemispheric specialization of various brain functions[1]. In fetuses and newborns, the development of this particular structure has been frequently adopted as a key indicator of the entire brain development, possibly due to the easy identification and quantification of the midsagittal CC on MRI or ultrasound images[2]. Previous studies have demonstrated CC abnormalities in adults with preterm birth[3,4], but the impact of preterm birth on perinatal CC development remains unexplored. To address this, we included multimodal perinatal MRI dataset from term and preterm babies and compared their MRI-derived measures. Furthermore, we evaluated the association between perinatal CC microstructures and neurobehavioral outcomes at 18 months old.

Methods: In total, 59 preterm and 381 term infants from the developing Human Connectome Project (dHCP) were included (Preterm group: 37 males, gestational age (GA) = 23.7-36.9 wks, postmenstrual age (PMA) = 37-44.9 wks; Term group: 205 males, GA = 37-42.3 wks, PMA = 37.4-44.7 wks). The dHCP preprocessed structural and diffusion MRI dataset was used[5]. For each baby, the CC was manually delineated on the native-space midsagittal slice of aligned T2w images. The outlined midsagittal CC was then divided into five subregions according to the Hofer scheme[6]. Diffusion tensor and neurite orientation dispersion and density imaging (NODDI) were estimated. The mean fractional anisotropy (FA), diffusivity (MD), neurite density index (NDI), orientation dispersion index (ODI), and total area were calculated for each midsagittal CC subregion. For each subregional measure above, we applied the normative modeling (implemented in the PCNtoolkit[7]) with data from all term infants. For this model, PMA and sex were input as predictors, and 10-fold cross-validation was applied. For each infant (both term and preterm), an individual z-score was derived from the normative model, representing his/her deviation from the normative trajectory during perinatal period. For each infant, neurobehavioral outcomes at 18 months old were assessed by the Bayley III Scales, yielding 5 scores for the cognition, receptive language, expressive language, gross motor, and fine motor ability, respectively. For each measure, two-sample t-test was used to test group difference in the z-scores. In the two groups, partial least square correlation (PLSC) analysis was separately performed to examine the association between perinatal CC microstructural measures and Bayley III scores at 18 months old. The Bonferroni method was applied to correct for multiple comparisons, and corrected $p < 0.05$ was considered as the significance level.

Results: As shown in Fig. 1, there were significant group differences in microstructural measures in at least one CC subregion. Particularly, preterm infants showed significantly lower NDI in all subregions. In contrast, no group difference of 2D midsagittal area was found in any of the subregions. The PLSC analysis only showed a significant latent component (LC) in the preterm group ($r = -0.52$, $p = 0.006$; Fig. 2A). In term infant, applying the associated coefficients of the observed significant LC did not show a significant correlation between CC microstructural measures and neurobehavioral scores ($r = 0.04$, $p = 0.442$; Fig. 2B), suggesting the specificity of the observed LC to the preterm infants. For each CC measure and neurobehavioral score, its contribution to this significant LC (as referred to as salience) were illustrated in Fig. 2C.

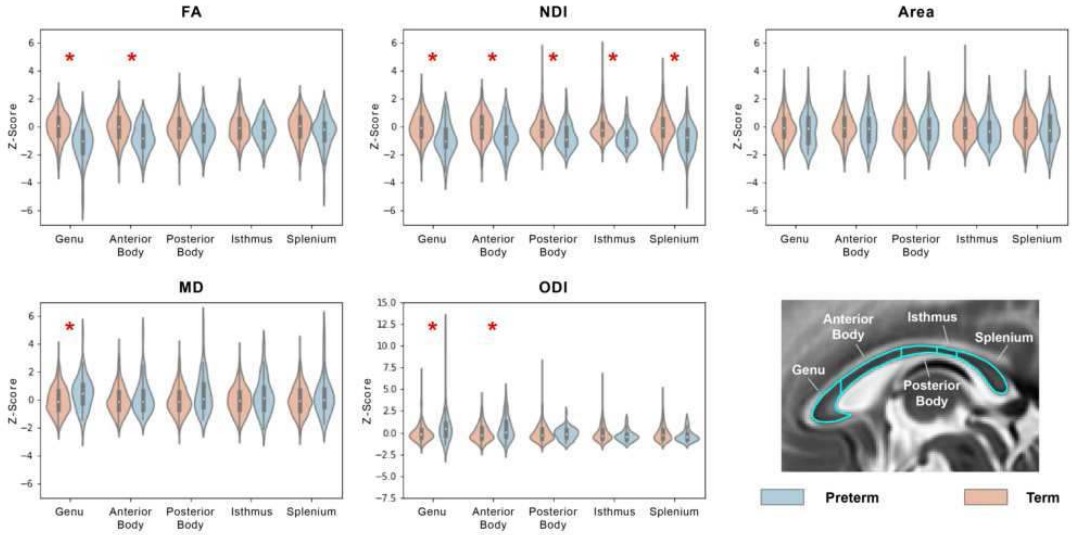

Fig. 1. Group differences in z-scores based on two-sample t-test analysis, and schematic of midsagittal CC under Hofer scheme. *corrected $p < 0.05$.

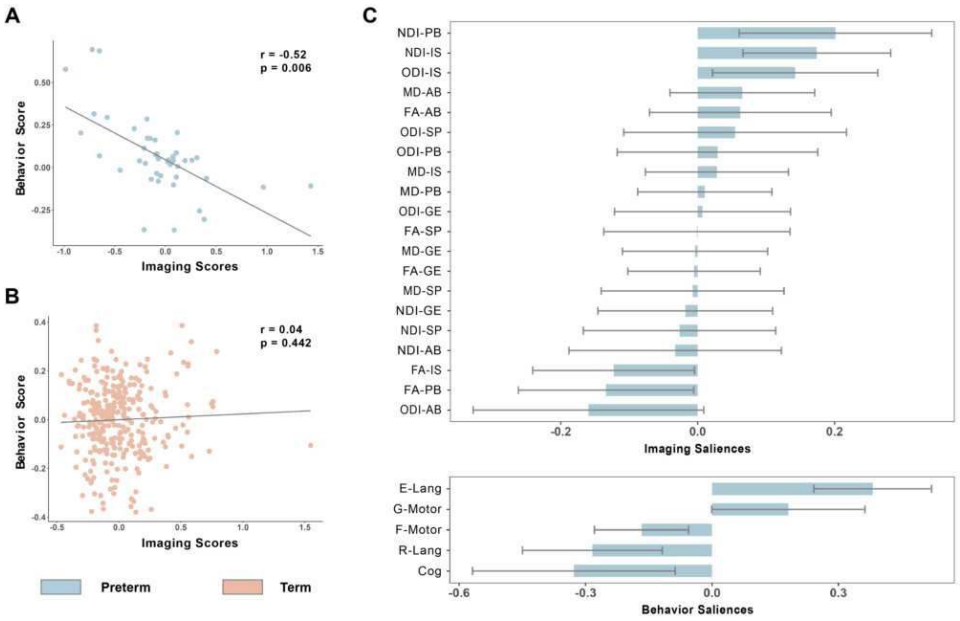

Fig. 2. Association between CC microstructural measures at TEA and Bayley III scores at 18m CA based on PLSC analysis. **A**, The correlation between imaging scores and behavior scores of significant LC in preterm infants. **B**, The imaging saliences and behavior saliences of significant LC in preterm infants. **C**, The correlation between imaging scores and behavior scores in term infants (the scores were calculated based on the significant LC coefficient of preterm infants). GE, genu; AB, anterior body; PB, posterior body; IS, isthmus; SP, splenium; Cog, cognition; R-Lang, receptive language; E-Lang, expressive language; G-Motor, gross motor; F-Motor, fine motor.

Conclusions: The present study demonstrated microstructural underdevelopment of the CC around the perinatal period in preterm infants, especially around the genu and anterior body of the CC. Moreover, the perinatal CC microstructures are multivariably associated with neurobehavioral outcomes at 18 months old, highlighting a crucial role of CC early development in behavioral capability of later life.

References

1. Fame, R. M. et al. (2011), 'Development, specification, and diversity of callosal projection neurons', Trends in Neurosciences, vol. 34, no. 1, pp. 41–50.
2. De León Reyes, N. S. et al. (2020), 'Development and plasticity of the corpus callosum', Development, vol. 147, no. 18, pp. dev189738.
3. Thompson, D. K. et al. (2011), 'Characterization of the corpus callosum in very preterm and full-term infants utilizing MRI', NeuroImage, vol. 55, no. 2, pp. 479–490.
4. Siffredi, V. et al. (2023), 'Corpus callosum structural characteristics in very preterm children and adolescents: Developmental trajectory and relationship to cognitive functioning', Developmental Cognitive Neuroscience, vol. 60, pp. 101211.
5. Edwards, A. D. et al. (2022), 'The Developing Human Connectome Project Neonatal Data Release', Frontiers in Neuroscience, vol. 16, pp. 886772.
6. Hofer, S. et al. (2006), 'Topography of the human corpus callosum revisited--comprehensive fiber tractography using diffusion tensor magnetic resonance imaging', NeuroImage, vol. 32, no. 3, pp. 989–994.
7. Rutherford, S. et al. (2022), 'The normative modeling framework for computational psychiatry', Nature Protocols, vol. 17, no. 7, pp. 1711–1734.

Poster No 1244

Mental attention: Common and distinct brain areas across development

Andrei Faber[1], Marie Arsalidou[2]

[1]HSE University, Moscow, Russian Federation, [2]York University, Toronto, Canada

Introduction: Cognitive abilities develop with age as reflected by improved performance in tasks of executive function and working memory. Working memory is a well-established concept and its neural correlates have been documented with neuroimaging (Owen et al., 2005). We consider mental attention as the maturational component of working memory (Arsalidou et al., 2010). Critically, little is known about the development of the brain correlates of mental attention through childhood and adolescence. We used a developmental construct of mental attention to investigate brain correlates related to solving tasks with multiple levels of difficulty in children, adolescents, and adults using functional magnetic resonance imaging (fMRI).

Methods: Data from children (9–12 years, n = 24), adolescents (13–16 years, n = 27), and adults (21-29 years, n = 31) were analysed. MRI acquisition was performed on a 3T Philips scanner. An anatomical T1-weighted image (TR = 2300 ms; TE = 2.62 ms; FOV = 256 × 256 × 192 mm^3; voxel size = 1×1×1 mm^3) was collected for the registration with functional images (TR = 1500 ms; TE = 35 ms; FOV = 230 × 230 × 150 mm^3; voxel size = 1.75 × 1.75 × 3.0 mm^3), which were collected while children completed the CMT (Color Matching Task). In a blocked design, participants were asked to indicate whether the relevant colors match those presented in the previous slide. Task difficulty was indexed by the number of relevant colors (n = 1-6). MRI data preprocessing and analyses were conducted using AFNI (Cox, 1996). Statistical maps were obtained for six contrasts by subtracting task-related blood oxygenation level dependent (BOLD) signal associated with each difficulty level from the signal related to control blocks with fixation cross. A linear regression was applied to whole-brain activity using general linear model (GLM) analyses. The statistical threshold was set at $p < .001$ with a cluster size threshold of 40 voxels, which is equivalent to cluster-level $q < .05$, FDR corrected.

Results: The first analytical goal was to examine mental attention activations modulated by level of difficulty separately for each age group. Conjunction analysis revealed common brain areas for each level of difficulty across three age groups. Specifically, common regions of significant activation for easy and moderate levels were the right dorsolateral prefrontal cortex (DLPFC), bilateral superior parietal lobule (SPL), right inferior parietal lobule (IPL), pre-supplementary motor area (Pre-SMA), and bilateral cerebellum lobules VII, VIII in all three age groups (Figure 1). The right intraparietal sulcus was the only common brain area across age groups for the hard levels of difficulty. However, implication and lateralization of other brain regions such as middle frontal gyrus, inferior frontal gyrus, and dorsal anterior cingulate cortex varied by both age and level of difficulty in CMT.

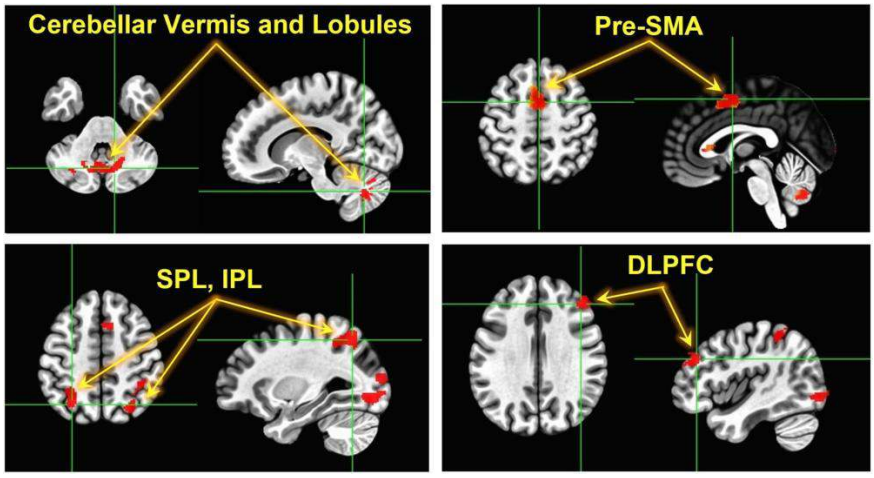

Conclusions: The study revealed that mental attention is expressed in frontoparietal regions in children, adolescents and adults, which is consistent with past research on working memory (e.g., Yaple et al., 2019 for meta-analysis). However, we observe the common brain regions becoming distinct as a function of age group, especially at hard levels of CMT, expressed by effects of hemispheric variation and spatial extent. For instance, children rely primarily on the right dorsolateral prefrontal cortex, whereas adolescents elicit activity in the prefrontal cortex bilaterally. Overall, results highlight the protracted development of the prefrontal cortex and support the notion of functional reorganization during school-age years. Findings have practical and theoretical applications for understanding of cognitive development.

References
1. Arsalidou, M. (2010), 'Misleading cues improve developmental assessment of working memory capacity: the colour matching tasks', Cognitive Development, vol. 25, pp. 262–277
2. Cox, R. (1996), 'AFNI: Software for Analysis and Visualization of Functional Magnetic Resonance Neuroimages', Computers and Biomedical Research, vol. 29, no. 3, pp. 162-173
3. Owen, A. M. (2005), 'N-Back Working Memory Paradigm: A meta-analysis of normative functional neuroimaging studies', Human Brain Mapping, vol. 25, no. 1, pp. 46–59
4. Yaple, Z. (2019), 'Meta-analyses of the n-back working memory task: fMRI evidence of age-related changes in prefrontal cortex involvement across the adult lifespan', Neuroimage, vol. 196, pp. 16-31

Poster No 1245

Developmental Mismatches in Amygdala and PFC Macrostructure and White Matter Tract Integrity

Jamie Roeske[1], Xiangyu Long[1], Meaghan Perdue[1], Madison Long[1], Bryce Geeraert[1], Mohammad Ghasoub[1], Catherine Lebel[1]

[1]*University of Calgary, Calgary, Alberta*

Introduction: Brain development varies regionally, with the volumes of subcortical regions like the amygdala plateauing before prefrontal cortex (PFC) volumes. The development of white matter tracts that terminate in the PFC has also been shown to plateau later than other major tracts. As theories like the Developmental Mismatch Hypothesis propose that differences in amygdala and PFC developmental rates drive behaviour development, studying the developmental trajectories of these regions is critical to understanding behaviour and the causes of neurodevelopmental disorders. While previous work has established that amygdala and PFC macrostructural trajectories are mismatched, findings are limited by small sample sizes (~n=30) and do not include the period of most dramatic development, birth to 5 years of age. Few studies have investigated macrostructure and tract integrity within the same sample, with amygdala-PFC connectivity particularly overlooked. Here, we used a large longitudinal dataset to characterize and compare amygdala and PFC volumes and amygdala-PFC tract integrity trajectories in children and adolescents.

Methods: 518 magnetic resonance imaging (MRI) scans from 95 typically developing participants aged 1.95-12.99 were included (48 females). T1 (FSPGR BRAVO, 0.9mm isotropic voxels, TR=8.23ms, TE=3.76ms) and diffusion-weighted (spin-echo EPI, 1.6x1.6x2.2mm voxels, TR=6750ms, TE=79ms, 5 b=0 s/mm2 volumes, 30 b=750 s/mm2 volumes) scans were acquired on a 3T GE Discovery MR750w system with a 32-channel head coil at the Alberta Children's Hospital. Advanced Normalization Tools (ANTs) and Analysis of Functional Neuroimages (AFNI) were used to perform an N4 bias correction and 1mm voxel size resampling, respectively, on raw T1 scans. Preprocessed T1 scans were segmented using Multi-atlas Cortical Reconstruction Using Implicit Surface Evolution (MaCRUISE), and amygdala and PFC (middle frontal gyrus (MFG), inferior frontal gyrus (IFG), frontal pole (FP)) volumes were extracted. Diffusion images were preprocessed in ExploreDTI, and then semiautomated deterministic tractography was performed to isolate the amygdala-PFC tract in each hemisphere. Mean fractional anisotropy (FA) and mean diffusivity (MD) were computed for each tract. Volumes and tract metrics were standardized to Z-scores across the full study cohort. Trajectories were modelled using generalized additive mixed effects models (GAMMs) from the mgcv package in RStudio. Age, age+sex, and age*sex models were tested for each metric bilaterally. All volume models contained intracranial volume as a covariate. Models with the lowest Bayesian information criterion values were selected. Metric developmental rates were calculated from the first derivative of the GAMM trendlines. Periods with significant age-related change had first derivative 95% confidence intervals that excluded zero.

Results: Significant age effects were found for all metrics (Figures 1 and 2). Bilateral amygdala volume gradually increased between ages 1.95-5.28. Left amygdala volume decreased slightly between ages 7.89-9.16. Bilateral MFG volume steadily decreased across the age span. Right IFG volume increased slightly between ages 3.23-4.22. Bilateral IFG and FP volumes steadily decreased between 5.06-12.99 years and 5.33-12.99 years, respectively. Bilateral tract FA increased rapidly at early ages and then more gradually across the age span. Bilateral tract MD decreased rapidly at early ages and plateaued by 10.44 years.

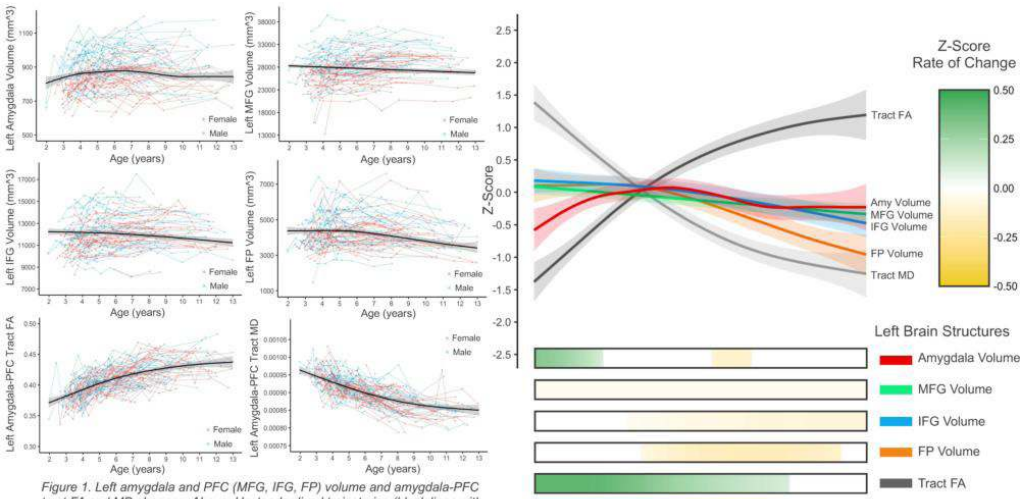

Figure 1. Left amygdala and PFC (MFG, IFG, FP) volume and amygdala-PFC tract FA and MD changes. Above: Unstandardized trajectories (black lines with shaded confidence intervals) over raw data. Raw data circles represent individual visits. Longitudinal visits are connected by straight lines. Right: Combined Z-score trajectories with confidence intervals. Bars reflect metric rates of change. Green and yellow represent significant metric increases and decreases, respectively.

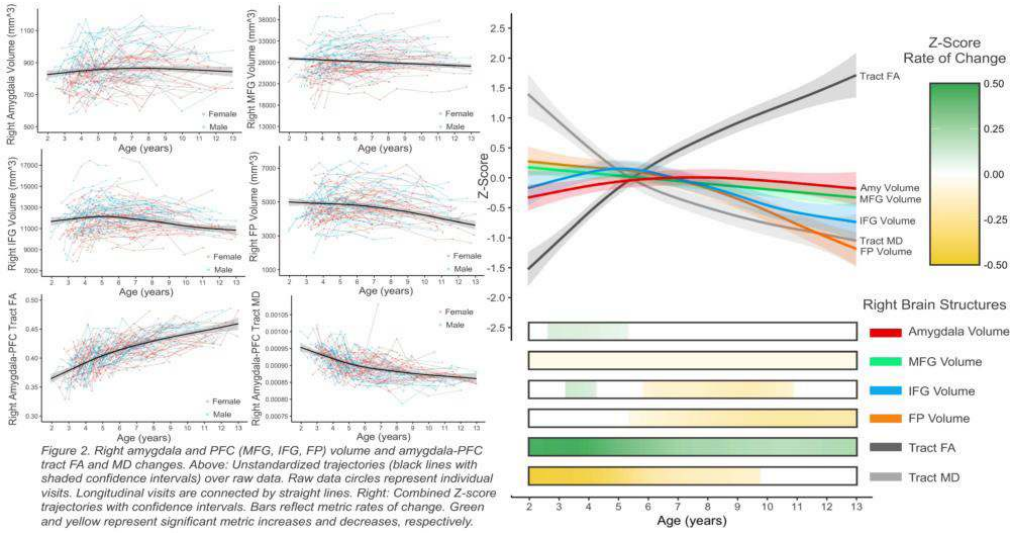

Figure 2. Right amygdala and PFC (MFG, IFG, FP) volume and amygdala-PFC tract FA and MD changes. Above: Unstandardized trajectories (black lines with shaded confidence intervals) over raw data. Raw data circles represent individual visits. Longitudinal visits are connected by straight lines. Right: Combined Z-score trajectories with confidence intervals. Bars reflect metric rates of change. Green and yellow represent significant metric increases and decreases, respectively.

Conclusions: Our findings show that amygdala, PFC, and amygdala-PFC tract trajectories are qualitatively mismatched. Amygdala development predominantly occurred in early childhood, while PFC development occurred in late childhood and early adolescence. The amygdala-PFC white matter tract changed most in early childhood and showed larger changes than amygdala and PFC volumes. Future directions include expanding the age range up to age 17 and relating mismatches to behaviour development.

References

1. Donnici, C. (2023), 'Prenatal depressive symptoms and childhood development of brain limbic and default mode network structure', Human Brain Mapping, vol. 44, no. 6, pp. 2380-2394.
2. Geeraert, B.L. (2020), 'Multimodal principal component analysis to identify major features of white matter structure and links to reading', Public Library of Science Open, vol. 15, no. 8, pp. e0233244.
3. Hay, R.E. (2020), 'Amygdala-prefrontal structural connectivity mediates the relationship between prenatal depression and behaviour in preschool boys', Journal of Neuroscience, vol. 40, no. 36, pp. 6969-6977.
4. Lebel, C. (2011), 'Longitudinal development of human brain wiring continues from childhood into adulthood', Journal of Neuroscience, vol. 31, no. 30, pp. 10937-10947.
5. Lebel, C. (2021), 'Prenatal Exposure And Child brain and mental Health (PEACH) study: protocol for a cohort study of children and youth with prenatal alcohol exposure, British Medical Journal Open, vol. 11, no. 5, pp. e051660.
6. Mills, K.L. (2014), 'The developmental mismatch in structural brain maturation during adolescence', Developmental Neuroscience, vol. 36, no. 3-4, pp. 147-160.
7. Reynolds, J.E. (2020), 'Calgary preschool magnetic resonance imaging (MRI) dataset', Data Brief, vol. 29, pp. 105224.
8. Tottenham, N. (2017), 'The developing amygdala: a student of the world and a teacher of the cortex, Current Opinion in Psychology, vol. 17, pp. 55-60.
9. Van Duijenvoorde, A.C.K. (2019), 'A three-wave longitudinal study of subcortical-cortical resting-state connectivity in adolescence: Testing age- and puberty-related changes' Human Brain Mapping, vol 40, no. 13, pp. 3769-3783.
10. Wood, S. (2017), 'Generalized additive models: An introduction with R (Second Edition)', Boca Raton: Chapman and Hall/CRC, pp. 253-496.

Poster No 1246

Impacts of Short Wavelength Light on Cortical Excitability

Roya Sharifpour[1], Fermin Aizpurua[1], Ilenia Paparella[1], Islay Campbell[1], Elise Beckers[1], Nasrin Mortazavi[1], Ekaterina Koshmanova[1], Christophe Phillips[2], Gilles Vandewalle[1]

[1]Sleep and Chronobiology Lab, GIGA-Institute, CRC-In Vivo Imaging Unit, University of Liège, Liège, Belgium, [2]University of Liège, Liège, Belgium

Introduction: Given the high levels of short wavelength blue light we are exposed to in modern life and the biological impact of light on sleep-wake regulation (Münch 2017, Gooley 2011), it is important to fully understand the impact of light on brain function, especially in adolescents, as they may be more susceptible to the biological effects of light. Cortical excitability is a basic and yet fundamental aspect of brain function and cognition that depends on sleep-wake regulation (Ly 2016). Here, we assessed whether cortical excitability of healthy adolescents and young adults was affected by blue light exposure using electroencephalogram (EEG) recordings of transcranial magnetic stimulation (TMS).

Methods: Thirty participants, 16 adolescents (16.9±1.1y, 5 Females) and 14 young adults (24.0±3.6y, 6 Females) were included in the study. Participants followed a loose sleep-wake schedule for 5 days prior to the experiment (±1h) to avoid excessive sleep restriction. On the experiment day, participants arrived at the laboratory ~8h after wakeup time and were maintained in dim-light (< 10 lux) for 1h prior to the first TMS-EEG session. The stimulation target was set to the supplementary motor area on the dominant hemisphere. TMS-evoked responses (TEP) were recorded in 2 sessions under 2 different light conditions including a control orange light (30 lux, 24 melEDI lux) and an active blue light (30 lux, 312 melEDI lux). Sessions were separated by at least a 15-minute washout period in dim light (< 10 lux). The order of the sessions was randomized. Each session included around 250 trials and TEP were recorded using a 60-channel EEG amplifier. Data preprocessing was performed using MNE python package. Continues EEG data was filtered, visually inspected, re-referenced to the average of good channels and epoched. Independent components of the epochs were computed and components representing TMS artifacts were set to zero. Artifact free epochs were split to shorter epochs (-300 to 300 ms), re-referenced to the average of good channels and baseline corrected (-100 to -1.5ms). Cortical excitability was then inferred from the amplitude and slope of the first EEG component (0–30 ms) of the mean TEP measured at the closest electrode to the stimulation. Statistical analyses consisted of Generalized Linear Mixed Models, with subject as random factor, light condition as repeated measures, and age group sex and BMI as covariates.

Results: GLMM analysis also showed yielded a illuminance by age group interaction ($p = 0.03$) (Fig1). Post hoc comparisons indicated that amplitude was higher during the blue light session compared to the orange in young adults ($p=0.007$), while in adolescents the amplitude did not change significantly ($p = 0.8$). GLMM analysis of the TEP slope did not reveal any main effects ($p > 0.05$) neither any illuminance by age group interaction ($p=0.1$). However, post hoc comparisons revealed significantly higher slope during the blue session compared to the orange in young adults ($p=0.03$), and no significant change in adolescents ($p=0.9$).

Conclusions: These preliminary findings suggest that adolescents may not be more sensitive to the biological impact of blue light on sleep-wake regulation or that they are very sensitive to it and reached saturation under the orange light. Funding: European Union (LIGHTCAP Project), FNRS, ULiège, FEDER, Fondation Léon Frédéric.

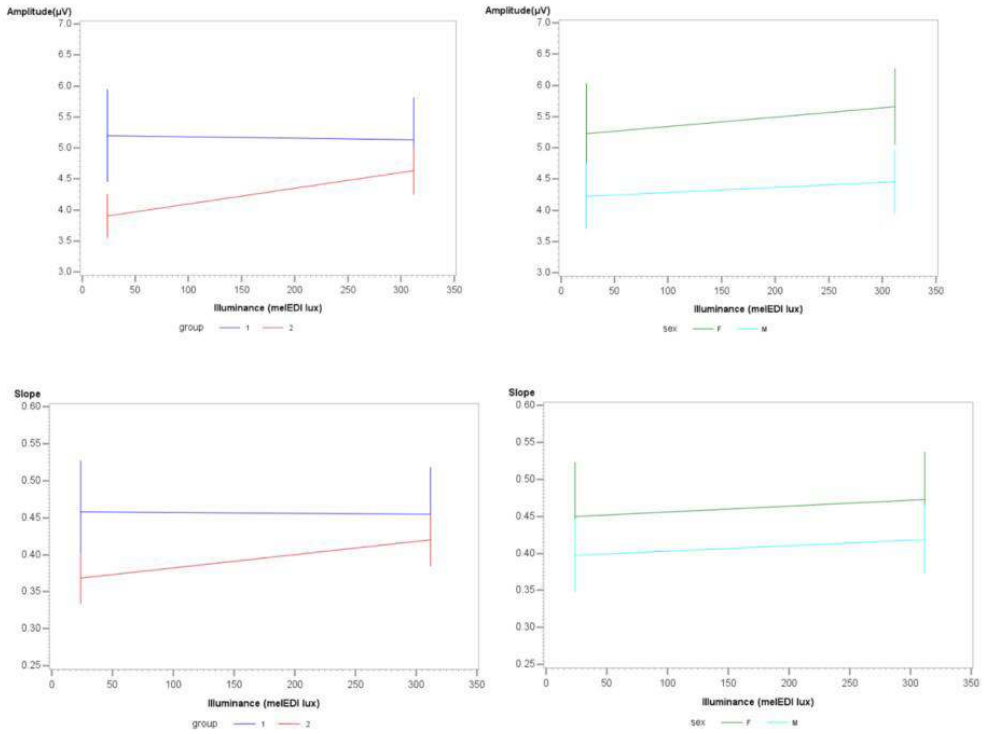

References

1. Gooley, J. J., (2011), 'Exposure to room light before bedtime suppresses melatonin onset and shortens melatonin duration in humans'. The Journal of Clinical Endocrinology & Metabolism, vol. 96, no. 3, pp. E463-E472.
2. Ly, J. Q., (2016), 'Circadian regulation of human cortical excitability'. Nature communications, vol. 7, no. 1, p.11828.
3. Münch, M., (2017), 'Blue-enriched morning light as a countermeasure to light at the wrong time: effects on cognition, sleepiness, sleep, and circadian phase'. Neuropsychobiology, vol. 74, no. 4, pp. 207-218.

Poster No 1247

Between-sex differences not greater than within-sex differences in early adolescent brain structure

Carinna Torgerson[1], Hedyeh Ahmadi[1], Megan Herting[1], Jeiran Choupan[1]

[1]*University of Southern California, Los Angeles, CA*

Introduction: Neuroimaging studies of sex differences in the pediatric human brain predominantly examine mean differences between males and females (Giedd et al., 2012; Giedd & Denker, 2015; Kaczkurkin et al., 2019; Lenroot & Giedd, 2010). Yet, during development, inter-individual variability in brain structure is high (Bottenhorn et al., 2023). Significant sex differences in variance have also been reported in children and adolescents (Bottenhorn et al., 2023; Forde et al., 2020; Wierenga et al., 2018). Unequal variance between groups violates the assumptions of many of the traditional statistical methods for evaluating sex differences - such as ANOVA and t-tests. Without investigating the amount of individual variability within sexes, we cannot say definitively whether the mean differences actually reflect distinct male and female phenotypes (e.g., sexual dimorphism) of the brain.

Methods: We aimed to characterize the relationship between sex and brain macro- and micro-structure in early adolescence using a large sample of 9-11 year-olds from the Adolescent Brain Cognitive Development (ABCD) Study (N=8,272). To do so, we examined homogeneity of variance between sexes, overlap between male and female distributions, and performed an analysis of similarities (ANOSIM) on global metrics of brain structure. For completeness, we performed all statistical tests using both uncorrected (raw) measures of brain structure and after correcting for age, pubertal development, socioeconomic status, race, ethnicity, and MRI scanner manufacturer.

Results: Although mean sex differences were significant in the mixed-effects models of total brain volume, average cortical thickness, and whole-brain mean diffusivity, there was more overlap than difference between male and female distributions for all measurements (Figure 1). Furthermore, we found significant sex differences in variance of total brain volume and mean diffusivity. ANOSIM results showed that within-sex and between-sex variance were similar for all measures.

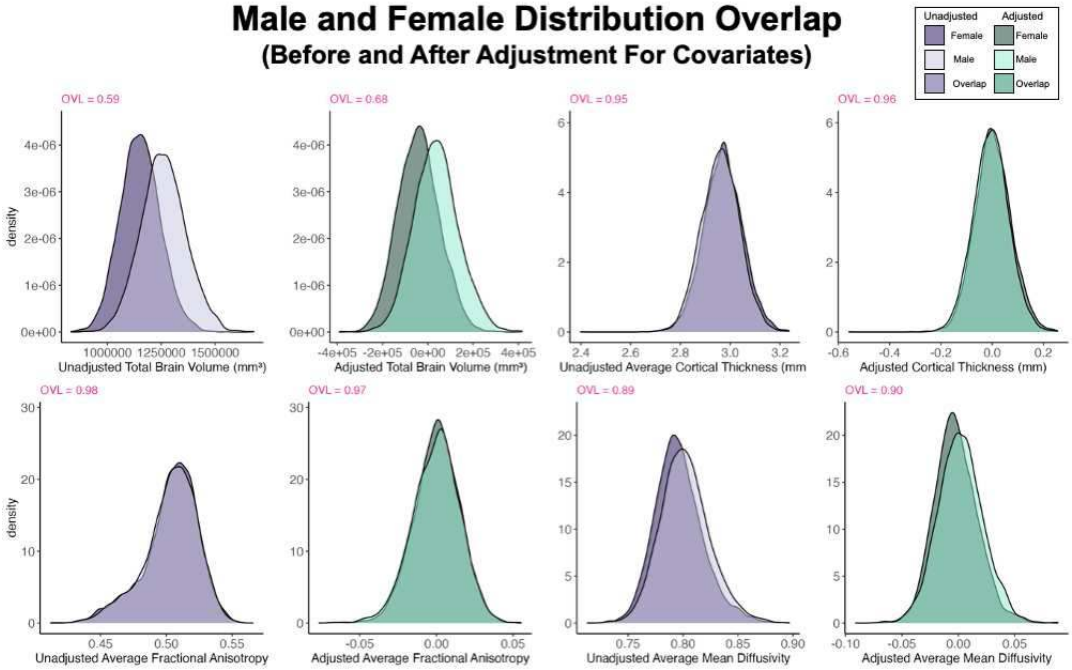

Conclusions: We found high similarity and low difference between sexes on four common measures of adolescent brain structure. In particular, the ANOSIM results suggest that two random adolescents of the same sex will differ as much as a random female and random male differ. In conjunction with our finding of significant inhomogeneity of variance between males and females, these findings suggest that reported sex differences in global measures of early adolescent brain structure are likely driven by disparities in variance, rather than distinctive sex-based phenotypes. Such results contradict previous reports of consistent, meaningful sex differences in total brain volume throughout the lifespan (Giedd et al., 1997, 2015; Lenroot et al., 2007), but support studies which have found significant variance sex differences in brain structure (Bottenhorn et al., 2023; Forde et al., 2020; Wierenga et al., 2018). The findings also serve as a reminder that aggregate differences should not be applied to inter-individual comparisons.

References

1. Bottenhorn, K. L. (2023). Profiling intra-and inter-individual differences in brain development across early adolescence. NeuroImage, 279, 120287.
2. Forde, N. J. (2020). Sex Differences in Variability of Brain Structure Across the Lifespan. Cerebral Cortex, 30(10), 5420–5430. https://doi.org/10.1093/cercor/bhaa123
3. Giedd, J. N. (1997). Sexual dimorphism of the developing human brain. Progress in Neuro-Psychopharmacology & Biological Psychiatry, 21(8), 1185–1201. https://doi.org/10.1016/s0278-5846(97)00158-9
4. Giedd, J. N. (2012). Magnetic resonance imaging of male/female differences in human adolescent brain anatomy. Biology of Sex Differences, 3(1), 1–9.
5. Giedd, J. N. (2015). The Adolescent Brain: Insights from Neuroimaging. In: Brain Crosstalk in Puberty and Adolescence (pp. 85–96). Springer International Publishing. https://doi.org/10.1007/978-3-319-09168-6_7
6. Kaczkurkin, A. N. (2019). Sex differences in the developing brain: Insights from multimodal neuroimaging. Neuropsychopharmacology, 44(1), 71–85. https://doi.org/10.1038/s41386-018-0111-z
7. Lenroot, R. K. (2007). Sexual dimorphism of brain developmental trajectories during childhood and adolescence. Neuroimage, 36(4), 1065–1073.
8. Lenroot, R. K. (2010). Sex differences in the adolescent brain. Brain and Cognition, 72(1), 46–55.
9. Wierenga, L. M. (2018). A key characteristic of sex differences in the developing brain: Greater variability in brain structure of boys than girls. Cerebral Cortex, 28(8), 2741–2751.

Poster No 1248

Neurotransmitter systems explain lifespan changes of human resting-state brain activity

Leon Lotter[1,2,3], Jan Kasper[1,2], Simon Eickhoff[1,2], Juergen Dukart[4,2]

[1]INM-7, Research Centre Jülich, Jülich, NRW, Germany, [2]Institute of Systems Neuroscience, Heinrich Heine University, Düsseldorf, NRW, Germany, [3]Max Planck School of Cognition, Leipzig, Saxony, Germany, [4]INM-7, Forschungszentrum Jülich, Jülich, NRW, Germany

Introduction: Human brain activity, as measured using resting-state functional (rsf)MRI, changes during neurodevelopment and aging (Ferreira & Busatto, 2013; Hu et al., 2014; Uddin et al., 2010). Despite solid evidence for age-related alterations, their interpretation often remains unspecific, due to a lack of non-invasive methods that provide insights into the underlying neurobiological processes. We approach this problem using a framework that was previously successfully applied to identify potential neurobiological mechanisms contributing to structural brain development (Lotter et al., 2023): We first establish regional developmental trajectories of an rsfMRI measure of brain activity – the fractional Amplitude of Low Frequency Fluctuations (fALFF) (Zou et al., 2008) – in a lifespan sample of 2444 individuals. Using these modeled trajectories, we construct "representative" fALFF change brain maps across the lifespan. We hypothesize that fALFF spatial change patterns (i.e., stronger vs. weaker change in one vs. another brain region during a given age span) reflect developmental changes in specific neurobiological systems (Dukart et al., 2021; Lotter et al., 2023). For this, we compute spatial colocalization analyzes testing the extent to which lifespan fALFF changes are explained by distributions of specific neurotransmitter systems and brain metabolism.

Methods: We employed the lifespan Human Connectome Project dataset (HCP-D: n = 642, 5–22 years; HCP-YA: n = 1093, 22–37 years, HCP-A: n = 709, 36–90 years). HCP-preprocessed MRI data was cleaned from white matter and CSF signals, parcellated into 416 cortical and subcortical regions (Huang et al., 2022), and fALFF was calculated on each region's time series (0.01–0.1 Hz). We used "normative" warped Bayesian linear regression models to model fALFF per brain region across age, accounting for effects of sex, study site, and motion (Rutherford et al., 2021). Predictions from these models were used to construct fALFF change maps across 5-year time windows from 5 to 90 years. As potential biological correlates of fALFF change patterns, we gathered and parcellated a collection of group-average PET maps (Markello et al., 2022). To account for their intercorrelation, we applied hierarchical clustering to group them according to their spatial correlation. Following this hierarchy, we used linear regression models to examine if fALFF change patterns are explained by specific PET-derived neurotransmitter and metabolism maps (outcome: fALFF change, predictor(s): PET maps in a cluster, observations: parcel-wise values, controlled for partial volume effects). Statistical significance was established using spatial null maps and FDR correction (Lotter et al., 2023; Lotter & Dukart, 2022).

Results: Developmental models explain up to 56% of variance in fALFF data and revealed a general trend towards lower brain activity with higher age in mostly transmodal cortical brain areas (examples in Fig. 1A). PET maps cluster broadly according to receptors with high density in subcortical areas (high-striatal vs. high-thalamic) and those concentrate in cortical areas (brain metabolism vs. "general": serotonergic, glutamatergic, GABAergic transmitter systems; Fig. 1B). Modeled fALFF change patterns are explained to large extents by both main clusters (multivariate R2 up to 49%; Fig. 2: top), with the strongest contribution by major cortical transmitter systems (multivariate R2 up to 42%; center) and an emphasis on glutamatergic and GABAergic receptors (univariate R2 up to 29%; bottom).

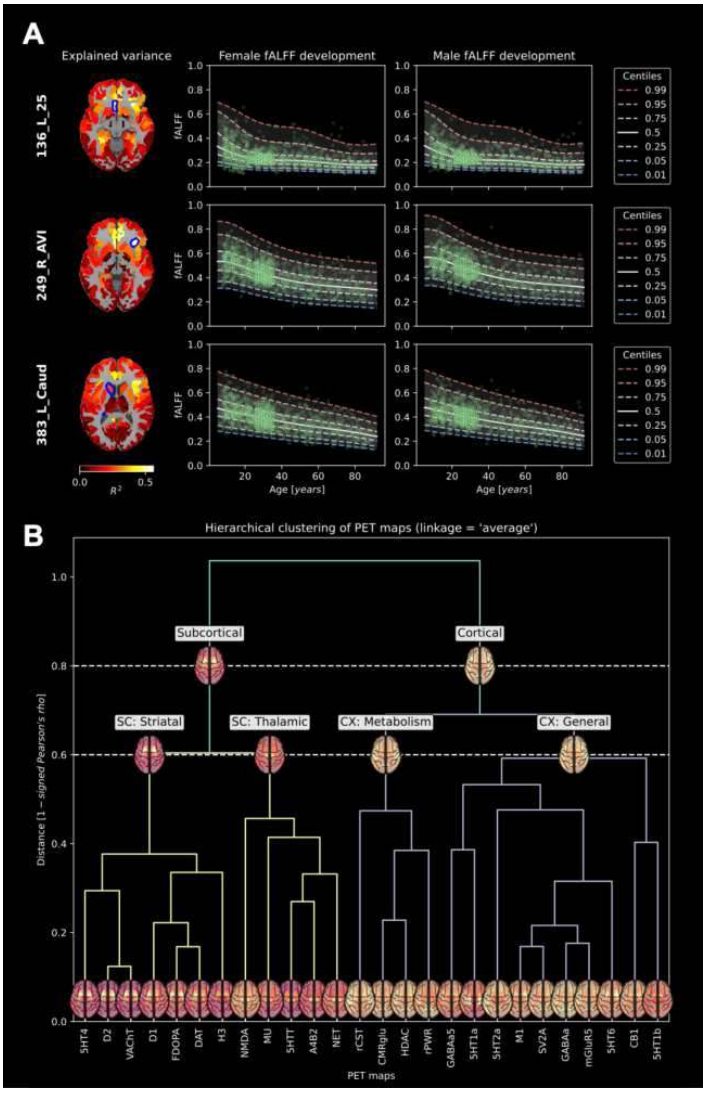
A
Explained variance
Female fALFF development
Male fALFF development
136_L_25
249_R_AVI
383_L_Caud
Centiles
0.99
0.95
0.75
0.5
0.25
0.05
0.01
fALFF
Age [years]
B
Hierarchical clustering of PET maps (linkage = 'average')
Subcortical
Cortical
SC: Striatal
SC: Thalamic
CX: Metabolism
CX: General
Distance [1 − signed Pearson's rho]
5HT4
D2
VAChT
D1
FDOPA
DAT
H3
NMDA
MU
5HTT
A4B2
NET
rCST
CMRglu
HDAC
rPWR
GABAa5
5HT1a
5HT2a
M1
SV2A
GABAa
mGluR5
5HT6
CB1
5HT1b
PET maps

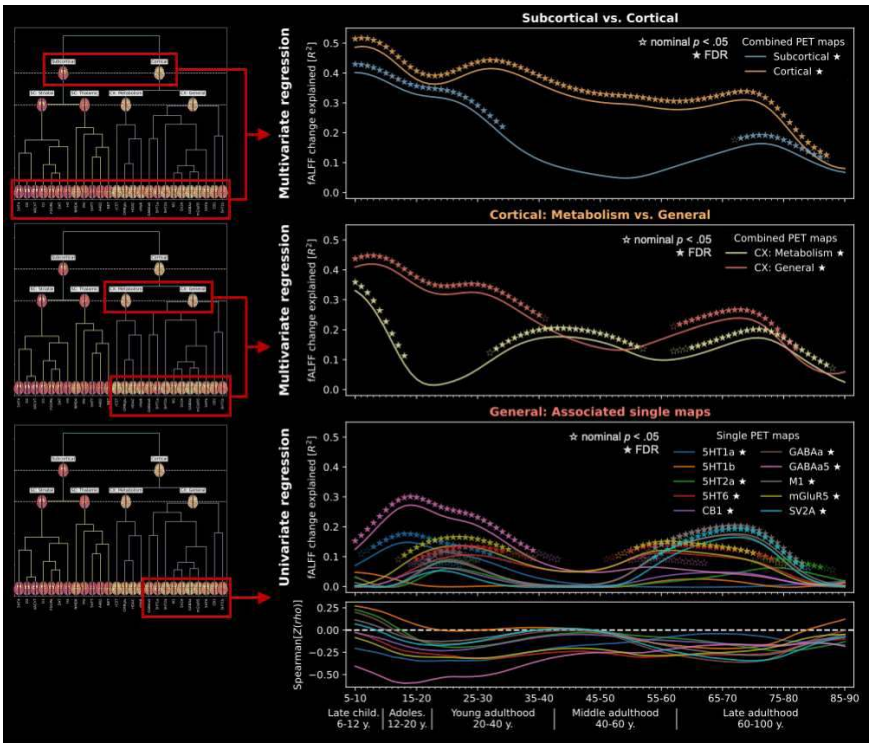
Subcortical vs. Cortical
Multivariate regression
fALFF change explained [R²]
☆ nominal p < .05
★ FDR
Combined PET maps
Subcortical ★
Cortical ★
Cortical: Metabolism vs. General
CX: Metabolism ★
CX: General ★
General: Associated single maps
Univariate regression
Single PET maps
5HT1a ★
5HT1b
5HT2a ★
5HT6 ★
CB1 ★
GABAa ★
GABAa5 ★
M1 ★
mGluR5 ★
SV2A ★
Spearman|Z(rho)|
5-10
15-20
25-30
35-40
45-50
55-60
65-70
75-80
85-90
Late child. 6-12 y.
Adoles. 12-20 y.
Young adulthood 20-40 y.
Middle adulthood 40-60 y.
Late adulthood 60-100 y.

Conclusions: Development of human brain activity measured with rsfMRI follows the distributions of specific neurotransmitter systems. Our approach not only identifies neurobiological mechanisms associated with human brain-functional development, but also constitutes the foundation for future biologically grounded biomarkers based on individual functional MRI.

References

1. Dukart, J. et al. (2021). JuSpace: A tool for spatial correlation analyses of magnetic resonance imaging data with nuclear imaging derived neurotransmitter maps. Human Brain Mapping, 42(3), 555–566. https://doi.org/10.1002/hbm.25244
2. Ferreira, L. K. & Busatto, G. F. (2013). Resting-state functional connectivity in normal brain aging. Neuroscience & Biobehavioral Reviews, 37(3), 384–400. https://doi.org/10.1016/j.neubiorev.2013.01.017
3. Hu, S. et al. (2014). Changes in cerebral morphometry and amplitude of low-frequency fluctuations of BOLD signals during healthy aging: Correlation with inhibitory control. Brain Structure & Function, 219(3), 983–994. https://doi.org/10.1007/s00429-013-0548-0
4. Huang, C.-C. et al. (2022). An extended Human Connectome Project multimodal parcellation atlas of the human cortex and subcortical areas. Brain Structure and Function, 227(3), 763–778. https://doi.org/10.1007/s00429-021-02421-6
5. Lotter, L. D. & Dukart, J. (2022). JuSpyce—A toolbox for flexible assessment of spatial associations between brain maps [Computer software]. Zenodo. https://doi.org/10.5281/zenodo.6884932
6. Lotter, L. D. et al. (2023). Human cortex development is shaped by molecular and cellular brain systems (p. 2023.05.05.539537). bioRxiv. https://doi.org/10.1101/2023.05.05.539537
7. Markello, R. D. et al. (2022). neuromaps: Structural and functional interpretation of brain maps. Nature Methods, 1–8. https://doi.org/10.1038/s41592-022-01625-w
8. Rutherford, S. et al. (2021). The Normative Modeling Framework for Computational Psychiatry (p. 2021.08.08.455583). https://doi.org/10.1101/2021.08.08.455583
9. Uddin, L. Q. et al. (2010). Typical and atypical development of functional human brain networks: Insights from resting-state fMRI. Frontiers in Systems Neuroscience, 0. https://doi.org/10.3389/fnsys.2010.00021
10. Zou, Q.-H. et al. (2008). An improved approach to detection of amplitude of low-frequency fluctuation (ALFF) for resting-state fMRI: fractional ALFF. Journal of Neuroscience Methods, 172(1), 137–141. https://doi.org/10.1016/j.jneumeth.2008.04.012

Poster No 1249

White matter integrity change across the lifespan: a systematic review and meta-analysis

Karis Colyer-Patel[1], Jalmar Teeuw[1], Vivien Maes[2], Rachel Brouwer[3], Paul Thompson[4], Hilleke Hulshoff Pol[2]

[1]University Medical Center Utrecht, UMC Brain Center, Department of Psychiatry, Utrecht, Netherlands, [2]Utrecht University, Department of Experimental Psychology, Helmholtz Institute, Utrecht, Netherlands, [3]Department of Complex Trait Genetics, Center for Neurogenomics and Cognitive Research, Amsterdam, Netherlands, [4]Imaging Genetics Center, Mark and Mary Stevens Neuroimaging and Informatics Institute, Los Angeles, USA

Introduction: Across the lifespan the brain undergoes significant changes during development and aging which coincide with the maturation of cognition and behaviour during development, and with functional decline later in life. White matter (WM) microstucture changes with development and aging (Lebel et al., 2019; Madden et al., 2012) and is associated with risk and resilience to psychiatric and neurological disorders (Meyer & Lee, 2019; Sorond & Gorelick, 2019). The extent to which and how measures of WM microstructure, including fractional anisotropy (FA), evolve over the lifespan is still not fully understood. Genetic factors influence various metrics of WM microstructure (Kochunov et al., 2015; Koenis et al., 2015) and change-rates of WM volume (Brouwer et al., 2022). However, it is less clear whether change-rates of WM microstructure across the lifespan are also influenced by genetics. The aims of this systematic review are twofold: (1) to investigate how FA changes across the lifespan based on longitudinal data, and (2) to investigate evidence of genetic influences on change rates.

Methods: We systematically reviewed longitudinal studies investigating FA changes across the lifespan. Searches were conducted in Medline, PsycInfo, and EMBASE up to 9th August 2023, with terms related to DTI/FA and longitudinal/change. Inclusion criteria included participants in the age range of 0-99 and included both healthy and patient groups with a sample size of ≥ 75. For the meta-analysis investigating annual whole-brain FA change, a cubic-spline function was applied. When estimating the trajectories of whole-brain FA values across the lifespan, a LOESS curve was used to fit the data. To review the evidence of influences of genetic variants on WM integrity change, we conducted an additional search adding the following search terms: i.e., genes, genome-wide association study, polygenic, family, twins and heritability. The search terms were broadened to include other DTI measures: i.e., mean diffusivity (MD), global and local efficiency.

Results: Our systematic search resulted in 3,017 studies, of which 125 studies measured FA across two timepoints. From these studies, 9 studies had quantified whole-brain FA change and had reported the actual annual changes. A further 9 studies which did not report the actual annual whole-brain FA change, but annual changes could be estimated were also included. Across childhood and adolescence, FA increased and started to plateau in adulthood. Between ages 25-50 there was non-significant change. Beyond 50, significant decreases emerged, which continued to the upper limit of our age range (age 65). Longitudinal studies of FA change above the age of 65 that met are inclusion criteria were sparse. Maximum annual

increase in FA was 0.02 and maximum decrease was -0.025. The additional systematic search focusing on genetic studies resulted in 828 studies, of which thirteen were identified as suitable for the systematic review, including 3 familial risk studies, 1 heritability study and 9 studies investigating specific genetic variants. Overall, findings from the familial and heritability studies provide limited evidence of genetic influences on change in WM integrity across time. In the studies of specific genetic variants, five provided evidence of an influence on changes of both FA and MD over time. These studies investigated genetic variants associated with Alzheimer's disease, schizophrenia, Huntington's disease and frontotemporal dementia.

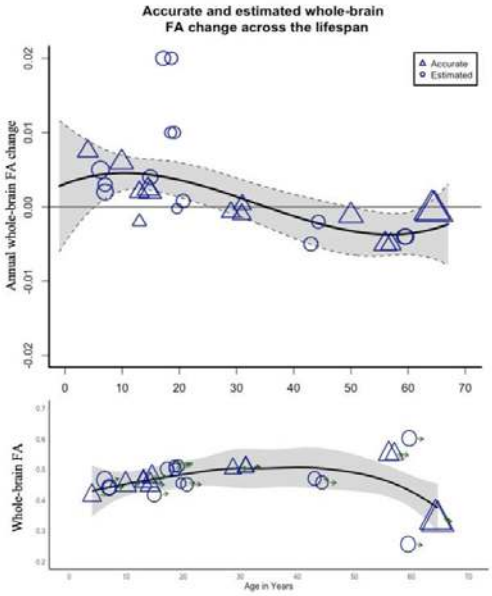

Figure 1A. Meta-analysis of whole-brain FA change across the lifespan. Annual FA change represents the FA at timepoint 2 minus FA at timepoint 1, divided by the number of years between timepoints. Each circle represents a cohort; the size of the circle represents the size of the cohort (up to 2,962 Individuals). The triangles represent studies that reported the annual whole-brain FA change, and the circles represent studies that did not report the actual annual whole-brain FA change, and so annual changes were estimated based on the information available. These studies included both healthy controls and patient groups. A cubic-spline function was used to fit the data, shown here with the 95% confidence intervals. **B.** The estimated trajectories of whole-brain FA values across the lifespan. A LOESS curve was fit to the data with a smoothing window of 0.8, represented with the 95% confidence intervals.

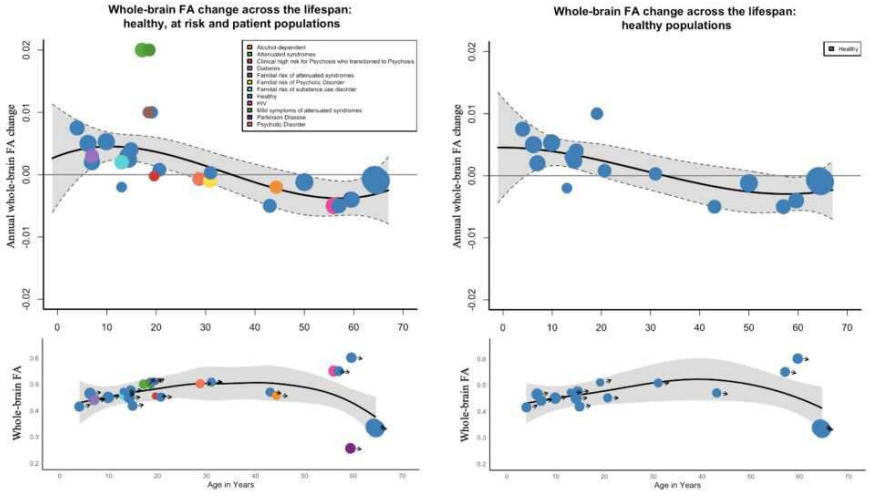

Figures 2 & 3. Meta-analysis of whole-brain FA change across the lifespan. Annual FA change represents the FA at timepoint 2 minus FA at timepoint 1, divided by the number of years between timepoints. Each circle represents a cohort; the size of the circle represents the size of the cohort (up to 2,962 individuals). **2A.** The blue circles represent studies that included a sample of healthy individuals. The rest of the coloured circles represent different patient or high-risk groups. A cubic-spline function was used to fit the data, shown here with the 95% confidence intervals. **2B.** The estimated trajectories of whole-brain FA values across the lifespan. A LOESS curve was fit to the data with a smoothing window of 0.8, represented with the 95% confidence intervals. **3A.** The blue circles represent studies that included a sample of healthy individuals. A cubic-spline function was used to fit the data, shown here with the 95% confidence intervals. **3B**. The estimated trajectories of whole-brain FA values across the lifespan. A LOESS curve was fit to the data with a smoothing window of 0.8, represented with the 95% confidence intervals

Conclusions: There are significant changes in FA across the lifespan, with average increases up to age 25, non-significant change between 25-50 years, and beyond age 50 decreases up to (at least) age 65. While WM microstructure is substantially heritable, in the sparse studies investigating heritability of change in WM integrity so far, most evidence suggests there is

no significant influence of genes. GWAS in larger samples may be required to identify robust effects of specific common genetic variants.

References
1. Brouwer, R. (2022). Genetic variants associated with longitudinal changes in brain structure across the lifespan. Nature Neuroscience, 25(4), 421-432.
2. Kochunov, P. (2015). Heritability of fractional anisotropy in human white matter: a comparison of Human Connectome Project and ENIGMA-DTI data. NeuroImage, 111, 300-311.
3. Koenis, M. M. (2015). Development of the brain's structural network efficiency in early adolescence: a longitudinal DTI twin study. Human Brain Mapping, 36(12), 4938-4953.
4. Lebel, C. (2019). A review of diffusion MRI of typical white matter development from early childhood to young adulthood. NMR in Biomedicine, 32(4), e3778.
5. Madden, D. J. (2012). Diffusion tensor imaging of cerebral white matter integrity in cognitive aging. Biochim Biophys Acta, 1822(3), 386-400.
6. Meyer, H. C. (2019). Translating developmental neuroscience to understand risk for psychiatric disorders. American Journal of Psychiatry, 176(3), 179-185.
7. Sorond, F. A. (2019). Brain white matter: a substrate for resilience and a substance for subcortical small vessel disease. Brain sciences, 9(8), 193.

Poster No 1250

Functional and Anatomical Growth Charts of the Cerebellum from Infancy to Young Adulthood

Aikaterina Manoli[1,2,3,4], Neville Magielse[5,6,1], Felix Hoffstaedter[7,6], Nilsu Saglam[1], Lorenz Ahle[1], Ceyda Yalcin[1], Hidir Arslan[1], Charlotte Grosse Wiesmann[1], Jörn Diedrichsen[8,9,10], Sofie Valk[1,3,6]

[1]Max Planck Institute for Human Cognitive and Brain Sciences, Leipzig, Germany, [2]International Max Planck Research School on Cognitive Neuroimaging, Leipzig, Germany, [3]Institute of Neuroscience and Medicine, Brain & Behavior (INM-7), Research Centre Jülich, Jülich, Germany, [4]Faculty of Medicine, Leipzig University, Leipzig, Germany, [5]INM-7, Research Center Jülich, Jülich, NRW, [6]Institute of Systems Neuroscience, Medical Faculty, Heinrich Heine University Düsseldorf, Düsseldorf, Germany, [7]Institute of Neuroscience and Medicine (INM-7: Brain and Behaviour), Research Centre Jülich, Jülich, NRW, [8]The Brain and Mind Institute, University of Western Ontario, London, Ontario, Canada, [9]Department of Statistical and Actuarial Sciences, University of Western Ontario, London, Ontario, Canada, [10]Department of Computer Science, University of Western Ontario, London, Ontario, Canada

Introduction: Apart from its role in motor processing, the cerebellum is involved in a wide range of cognitive functions, extending its relevance for clinical conditions. Accumulating evidence from paediatric populations suggests that early-life cerebellar abnormalities are linked to neurocognitive deficits in autism and schizophrenia (Olson et al., 2023). Despite these periods being closely linked to the development of neuropsychiatric disorders, a normative framework of cerebellar development is currently lacking. Here, we constructed normative models of cerebellar volumetric growth from infancy to adulthood, by focusing on both anatomical and functional cerebellar parcellations.

Methods: We leveraged open structural (T1-weighted) MRI data from the Baby Connectome Project (BCP; Howell et al., 2019) and the Lifespan Human Connectome Project in Development (HCP-D; Somerville et al., 2018) (Ntotal=993; age range: 0.5-22 years). Infant scans (< 2 years) were preprocessed with iBEAT (Dai et al., 2013), a toolbox optimized for infant brain processing and extraction. Child and adolescent scans (> 2 years) were processed with the standard HCP minimal preprocessing pipelines (Glasser et al., 2013). We obtained native-space anatomical volumes using ACAPULCO (Han et al., 2020), a convolutional neural network-based algorithm that segments the cerebellum into 28 lobules. For functional models, we used an atlas of 10 cerebellar regions spanning cognitive, affective and motor domains (King et al., 2019). We extracted functional parcel volumes by resampling the MNI-space atlas to each subject's native space with trilinear interpolation. Manual correction of anatomical and functional parcel masks was employed to account for over- or under-inclusion of cerebellar boundaries. We constructed anatomical and functional growth models using hierarchical Bayesian regression (HBR), which allowed us to control for sex and scanner site variability by specifying them as batch effects (Gaiser et al., 2023). We generated linear and 3rd-order b-spline models of cerebellar growth across age for each parcel, after splitting the dataset into a training (80%) and test set (20%). Inference was performed with Markov chain Monte Carlo methods (4 chains with 2000 samples). Finally, linear and b-spline model performance was compared via leave-one-out cross-validation.

Results: We found divergent effects of age on cerebellar volumes within anatomical (Fig. 1A) and functional parcels (Fig. 1B). Anterior anatomical parcels (lobules I–VI) demonstrated larger age-related effects (i.e., steeper growth trajectories) compared to posterior parcels (lobules VII–IX). Contrarily, all functional parcels demonstrated consistent volumetric increases across

age. Lastly, models stratified by sex revealed steeper growth trajectories for males compared to females, with females also demonstrating patterns of slight volumetric decrease across development in anatomical parcels.

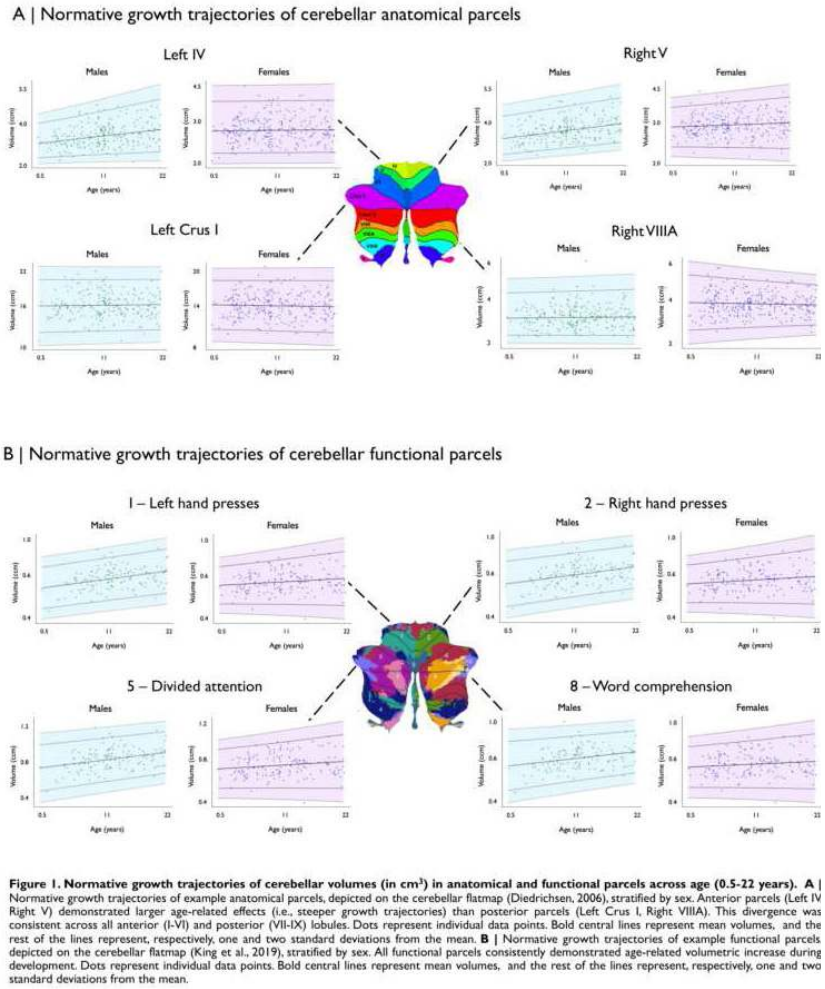

Figure 1. Normative growth trajectories of cerebellar volumes (in cm³) in anatomical and functional parcels across age (0.5-22 years). A | Normative growth trajectories of example anatomical parcels, depicted on the cerebellar flatmap (Diedrichsen, 2006), stratified by sex. Anterior parcels (Left IV Right V) demonstrated larger age-related effects (i.e., steeper growth trajectories) than posterior parcels (Left Crus I, Right VIIIA). This divergence was consistent across all anterior (I-VI) and posterior (VII-IX) lobules. Dots represent individual data points. Bold central lines represent mean volumes, and the rest of the lines represent, respectively, one and two standard deviations from the mean. **B |** Normative growth trajectories of example functional parcels depicted on the cerebellar flatmap (King et al., 2019), stratified by sex. All functional parcels consistently demonstrated age-related volumetric increase during development. Dots represent individual data points. Bold central lines represent mean volumes, and the rest of the lines represent, respectively, one and two standard deviations from the mean.

Conclusions: We found differences in normative trajectories between anatomical and functional cerebellar parcellations. Functional regions, involved in distinct cognitive processes, demonstrated consistent volumetric growth, which could reflect improvement in cognitive tasks across age. By contrast, anatomical regions showed a posterior-anterior gradient, in which anterior volumes increased more steeply than posterior volumes. This can be interpreted in light of the lack of convergence between functional and anatomical boundaries in the cerebellum (King et al., 2019). Anterior anatomical regions, uniformly involved in motor functions, demonstrate consistent growth across development. Conversely, the size of posterior anatomical regions encompasses a mosaic of functional subregions, which span several anatomical boundaries. This highlights a greater relevance of functional maps of the cerebellum for early-life diagnosis of neurodevelopmental disorders, based on deviations from normative trajectories related to specific cognitive functions.

References

1. Dai, Y. (2012). 'iBEAT: A Toolbox for Infant Brain Magnetic Resonance Image Processing', Neuroinformatics, vol. 11, no. 2, pp. 211–225.
2. Diedrichsen, J. (2009). 'A Probabilistic MR Atlas of the Human Cerebellum', NeuroImage, vol. 46, no. 1, pp. 39–46.
3. Gaiser, C. (2023). 'Large Data on the Small Brain: Population-Wide Cerebellar Growth Models of Children and Adolescents', bioRxiv (Cold Spring Harbor Laboratory).
4. Glasser, M. F. (2013). 'The Minimal Preprocessing Pipelines for the Human Connectome Project', NeuroImage, vol. 80, pp. 105–124.
5. Han, S. (2020). 'Automatic Cerebellum Anatomical Parcellation Using U-Net with Locally Constrained Optimization', NeuroImage, vol. 218, pp. 116819.
6. Howell, B. (2019). 'The UNC/UMN Baby Connectome Project (BCP): An Overview of the Study Design and Protocol Development', NeuroImage, vol. 185, pp. 891–905.
7. King, M. (2019). 'Functional Boundaries in the Human Cerebellum Revealed by a Multi-Domain Task Battery', Nature Neuroscience, vol. 22, no 8, pp. 1371–1378.
8. Olson, I. R. (2023). 'Little Brain, Little Minds: The Big Role of the Cerebellum in Social Development', Developmental Cognitive Neuroscience, vol. 60, pp. 101238.
9. Somerville, L. H. (2018). 'The Lifespan Human Connectome Project in Development: A Large-Scale Study of Brain Connectivity Development in 5–21 Year Olds', NeuroImage, vol. 183, pp. 456–468.

Poster No 1251

Neurodynamic complexity links with early brain development: a resting-state fMRI study on infants

Wenchao Zhou[1], Ziwei Zhang[1], Teng Liang[1], Qiongyu Yan[1], Guobin Ding[1], Shiyu Xia[1], Cunyi Li[1], Ziqian Zhang[1], Chun Meng[1]

[1]*University of Electronic Science and Technology of China, Chengdu, China*

Introduction: The neonatal maturation of neural activity holds pivotal significance for functional manifestation and long-term development in human brain (Tang et al., 2020), which can be assessed by hierarchical cortical dynamics, i.e. intrinsic timescale (Raut, Snyder and Raichle, 2020). Meanwhile the Hurst exponent delineates fractal-based self-similarity and long-range dependence in the BOLD signals, providing another perspective about neurodynamic complexity (Guan et al., 2023). To better understand neurodevelopment differentiation, it is important to elaborate on early-life cortical dynamic properties.

Methods: This study examined fMRI data from 120 neonates (postmenstrual age approximately 40 weeks, gestational age (GA) ranging from 25 to 41 weeks). Timescale and fractal metrics were computed for preprocessed and averaged time series using Yeo-400 atlas (Schaefer et al., 2018). The complexity metrics dependent on GA were modeled using linear and quadratic models in Matlab, separately for unimodal and transmodal area. Further, averaged complexity metric across whole brain was correlated between timescale and Hurst exponent across subjects. The spatial correspondence was computed by Spearman correlation between timescale and Hurst exponent across whole brain at the individual level, and then fitted into a linear and quadratic model against GA. The spin test was used to detect significant spatial correspondence.

Results: We found longer timescale and higher Hurst exponent within unimodal compared to transmodal area in neonates, which is contrary pattern compared to young adults (Dong et al., 2018; Ito, Hearne and Cole, 2020), and may be attributed to varying developmental milestones for different brain regions (Bethlehem et al., 2022). Preterm birth demonstrated nonlinear effect on neurodynamic complexity for neonatal brain developing into 40 weeks. Importantly, 29th week seemed to be critical for timescale development (Heikkilä et al., 2023), and Hurst exponent increased linearly with higher GA (<38 weeks), suggesting that preterm birth is associated with more chaotic brain dynamics (Campbell and Weber, 2022). Moreover, our results also confirm that intrinsic timescale and Hurst exponent represent different facets of temporal complexity in early brain development.

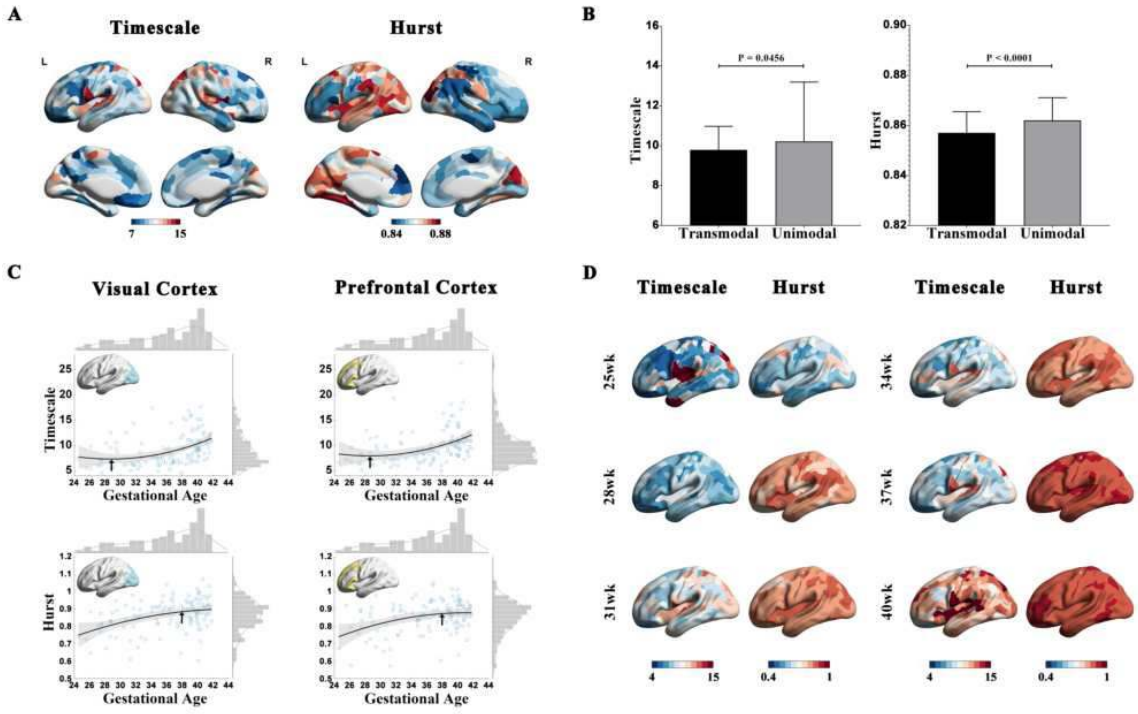

Figure 1. Results of neurodynamic complexity analyses. A) across-subject averaged maps for timescale and Hurst exponent. B) significant differences of timescale and Hurst exponent between unimodal and transmodal area. Unimodal area showed longer timescale and higher Hurst exponent than transmodal area in neonates, which is contrary pattern compared to young adults. C) Results of linear and quadratic regression analysis. D) average brain patterns affected by GA (from 25 to 41 week) for timescale and Hurst exponent. Our results suggest that, after the first 40 weeks of brain maturation, unimodal and transmodal systems develop pronounced long-range dependence (Hurst > 0.5), and similar extent of self-similarity and processing speed. The higher GA is, the higher Hurst and timescale are. Notably, GA>38 seemed to minimally affect Hurst, while GA<29 had strong constraint on timescale. For GA>29, brain's timescale increased rapidly.

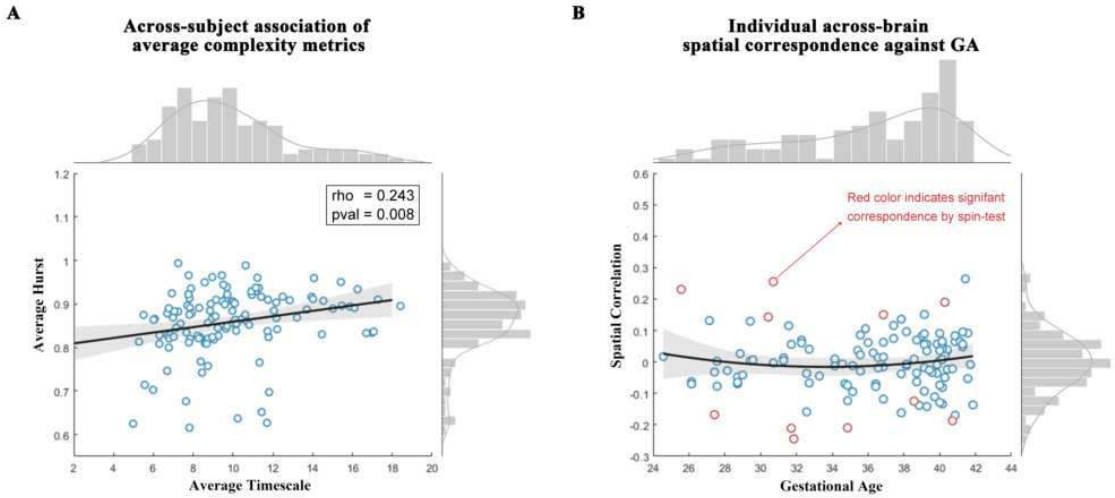

Figure 2. Correspondence between timescale and Hurst exponent across subjects and across whole brain. A) average complexity metrics over whole brain showed significant positive correlation across subjects, meaning infants who have slower timescale also have higher long-range dependence. B) Linear and quadratic model demonstrated that, first the individual spatial correspondence across whole brain between two complexity metrics remained low around zero across all subjects, and second was unlikely to be affected by preterm birth. Results confirmed our hypothesis that intrinsic timescale and Hurst exponent represent different facets of temporal complexity of functional brain activity, although they are significantly correlated with each other across subjects.

Conclusions: Hierarchical cortical dynamics was found to be structured, but contrary to young adults, suggesting they may develop with maturation. Neurodynamic complexity follows nonlinear principle during neonatal development. Very preterm birth earlier than 29 weeks may increase the risk of early brain development.

References

1. Bethlehem, R.A.I. et al. (2022) 'Brain charts for the human lifespan', Nature, 604(7906), pp. 525–533. Available at: https://doi.org/10.1038/s41586-022-04554-y.
2. Campbell, O.L. and Weber, A.M. (2022) 'Monofractal analysis of functional magnetic resonance imaging: An introductory review', Human Brain Mapping, 43(8), pp. 2693–2706. Available at: https://doi.org/10.1002/hbm.25801.
3. Dong, J. et al. (2018) 'Hurst Exponent Analysis of Resting-State fMRI Signal Complexity across the Adult Lifespan', Frontiers in Neuroscience, 12, p. 34. Available at: https://doi.org/10.3389/fnins.2018.00034.
4. Guan, S. et al. (2023) 'Multifractal long-range dependence pattern of functional magnetic resonance imaging in the human brain at rest', Cerebral Cortex, p. bhad393. Available at: https://doi.org/10.1093/cercor/bhad393.
5. Heikkilä, K. et al. (2023) 'Preterm birth and the risk of multimorbidity in adolescence: a multiregister-based cohort study', The Lancet Public Health, 8(9), pp. e680–e690. Available at: https://doi.org/10.1016/S2468-2667(23)00145-7.
6. Ito, T., Hearne, L.J. and Cole, M.W. (2020) 'A cortical hierarchy of localized and distributed processes revealed via dissociation of task activations, connectivity changes, and intrinsic timescales', NeuroImage, 221, p. 117141. Available at: https://doi.org/10.1016/j.neuroimage.2020.117141.
7. Raut, R.V., Snyder, A.Z. and Raichle, M.E. (2020) 'Hierarchical dynamics as a macroscopic organizing principle of the human brain', Proceedings of the National Academy of Sciences, 117(34), pp. 20890–20897. Available at: https://doi.org/10.1073/pnas.2003383117.
8. Schaefer, A. et al. (2018) 'Local-Global Parcellation of the Human Cerebral Cortex from Intrinsic Functional Connectivity MRI', Cerebral Cortex, 28(9), pp. 3095–3114. Available at: https://doi.org/10.1093/cercor/bhx179.
9. Tang, A. et al. (2020) 'Infant behavioral inhibition predicts personality and social outcomes three decades later', Proceedings of the National Academy of Sciences, 117(18), pp. 9800–9807. Available at: https://doi.org/10.1073/pnas.1917376117.

Poster No 1252

Development of cortical and subcortical asymmetry from mid gestation to old age

Lena Dorfschmidt[1], Simon White[2], Jenna Schabdach[3], Zhiqiang Sha[1], Margaret Gardner[4], Shreya Gudapati[11], Dabriel Zimmerman[1], Logan Williams[5], Vanessa Kyriakopoulou[5], Emma Robinson[5], A. Edwards[5], Lifespan Brain Chart Consortium[1], Edward Bullmore[2], Russell Shinohara[4], Richard Bethlehem[6], Jakob Seidlitz[4], Aaron Alexander-Bloch[4]

[1]University of Philadelphia, Philadelphia, PA, [2]University of Cambridge, Cambridge, UK, [3]Children's Hospital of Philadelphia, Philadelphia, PA, [4]University of Pennsylvania, Philadelphia, PA, [5]King's College London, London, UK, [6]Autism Research Centre, Department of Psychiatry, University of Cambridge, Cambridge, UK

Introduction: Asymmetry is a key organizing principle of the brain, and has previously been shown to support healthy cognition[1], with alterations in asymmetry observed across neuropsychiatric disorders[2,3]. While asymmetry emerges during fetal development[4], its lifelong dynamics and variability remain unknown[4]. The recent development of normative reference charts for the human brain have enabled individuals to be benchmarked against population-level norms across the lifespan[5]. This

study significantly extends this previous work by including regional (left/right) cortical and subcortical brain areas from over 100,000 participants, and comprehensively mapping left-right asymmetry trajectories across the human lifespan and between clinical cohorts.

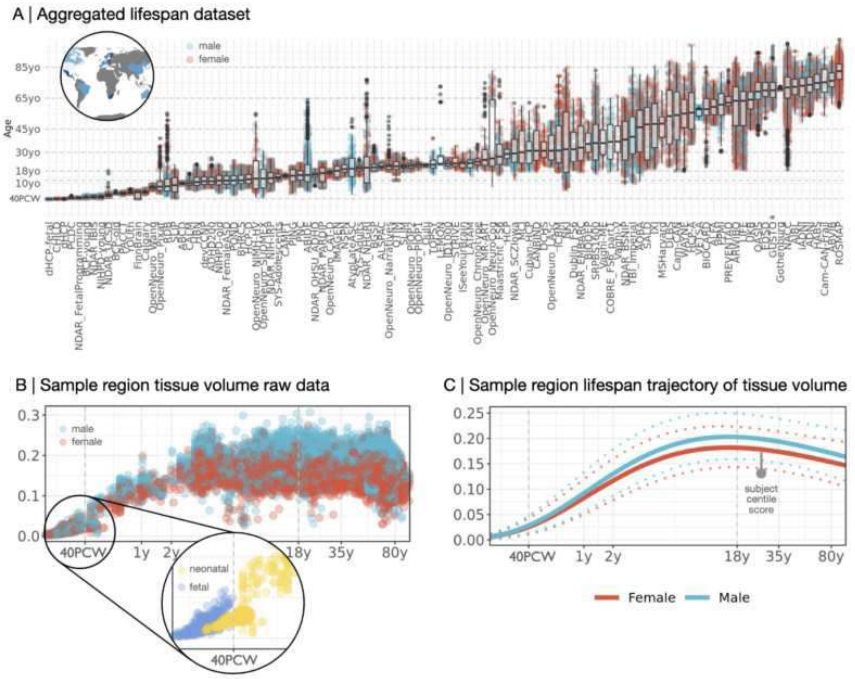

Fig. 1: (A) We collected T1- and T2-weighted MRI data from 103 primary studies from 25 countries to form an aggregated dataset of 129,963 scans from 103,013 subjects, that collectively spanned the age range from mid-gestation to 102 postnatal years. The box-plots show the age distribution for each study, with individual points colored by sex. Term birth is indicated at 40 PCW. The world map depicts the origin of the studies, with darker colors indicating an increased number of subjects from a given county. (B) Sample regions showing the raw gray matter volume of the right amygdala plotted for each cross-sectional scan as a function of age (log-scaled). Colors indicate sex. We further highlight the fact that we included overlapping samples of fetal scans and preterm born neonatal scans to cover the early life period. (C) We estimated normative trajectories of tissue development using GAMLSS, stratified by sex, with site- and study-specific batch effects, resulted in sex-specific lifespan trajectories of development of the median of each phenotype. We show the non-linear trajectory of the sample region's median gray matter volume (with 2.5 and 97.5% centiles denoted as dotted lines) as a function of age (log-scaled).

Methods: We aggregated a dataset of 103 primary studies from 25 countries (Fig. 1A), comprising 129,963 scans from 103,013 subjects spanning 21 post conception weeks (PCW) to 102 years of age (Fig. 1B). We mapped lifespan trajectories of regional subcortical gray matter volume (GM), surface area (SA), cortical thickness (CT) and ventricular volume for 68 cortical regions of the Desikan-Killiany and 12 subcortical regions defined by FreeSurfer[6]. We fit generalized additive models for location, scale and shape (GAMLSS)[7] to estimate the nonlinear effects of age, stratified by sex, on all phenotypes, while accounting for study effects using random effects (Fig. 1C). Key developmental milestones were defined by deriving the peak and peak rate-of-change of the trajectories. Next, we derived an index of regional brain asymmetry in each phenotype as (L-R)/(L+R), where L and R are the respective values of the regional phenotype in the left and right hemisphere. Accordingly, an asymmetry score of > 0 indicates a left-dominant region, whereas a score < 0 indicates right-dominance. We then used similar GAMLSS methods for modeling lifespan trajectories of regional brain asymmetry, deriving (per)centile scores for each phenotype for each individual. Group effects across multiple brain disorders with more than 1000 subjects each were estimated using the (signed) Cohen's d of the pairwise difference versus controls. Lastly, we derived a map of hemispheric asymmetry in case-control differences for each disorder and phenotype as the difference between left and right case-control differences. We then computed the first principal component of the (disorder*phenotypes) x regions map as a measure of cross-disorder effects on brain asymmetry.

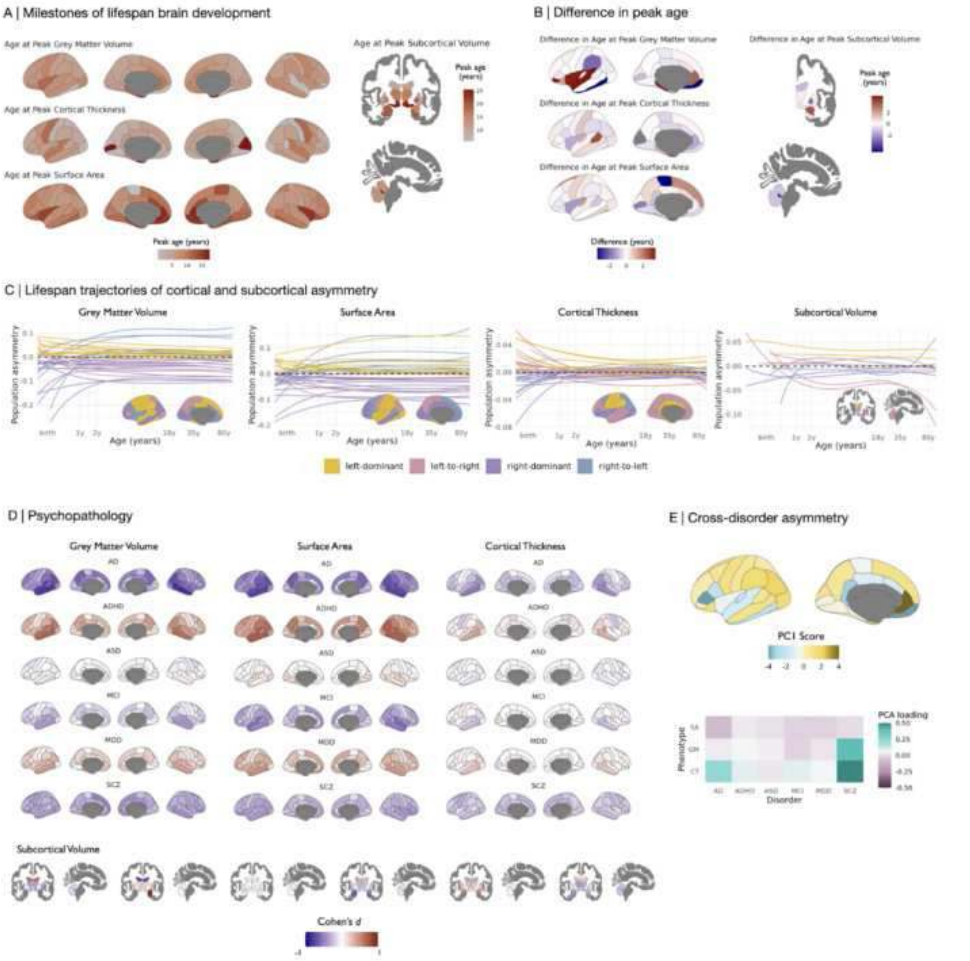

Fig. 2: (A) We derived milestones of lifespan brain development. Here we show the age at peak regional GM, CT, SA, and subcortical volume. (B) We estimated the hemispheric difference (left-right) in age at peak regional GM, CT, SA, and subcortical volume. There were left-right age differences in hemispheric peaks of up to 3 years across phenotypes, indicating hemispheric asymmetries across the cortex and subcortex. (C) We next estimated lifespan trajectories of regional asymmetry. (D) We estimated subject-specific centile scores, i.e. deviations from the norm, in healthy controls and multiple patient groups: Alzheimer's (AD, *N=2861*), mild cognitive impairment (MCI, *N=1477*), major depression (MDD, *N=5330*), schizophrenia (SCZ, *N=1054*), autism spectrum disorder (ASD, *N=2190*), attention deficit hyperactivity disorder (ADHD, *N=937*). A Cohen's $d < 0$ indicates decreased phenotypic values in patients compared to controls. (E) Next, we estimated hemispheric difference maps in case-control effects for each phenotype and disorder. We then derived a cross-disorder asymmetry map, as the first principal component of all hemispheric difference maps (i.e. across disorders and phenotypes). This component thus summarizes variation in asymmetry across disorders. The bottom plot shows the PCA loadings onto the component. A negative loading indicates that positive PC1 scores are associated with greater case-control differences in the right compared to the left hemisphere, for instance, regions colored yellow in the anatomical plot have greater SA case-control differences in the right hemisphere compared to the left hemisphere across disorders.

Results: We found that L/R regional tissue trajectories largely peaked in (early) childhood and adolescence (Fig. 2A), with left-right age differences in hemispheric peaks of up to 3 years across phenotypes (Fig. 2B), in line with previous bilaterally-combined results[7]. Brain asymmetry trajectories across phenotypes and regions showed the greatest dynamics in the first two years of life, generally stabilizing thereafter (Fig. 2C). Overall, asymmetry was greater in GM and SA compared to CT. We found widespread case-control differences in centile scores across phenotypes and disorders, with the largest decreases in GM, SA and CT in AD and MCI, followed by SCZ. Lastly, we estimated a map of cross-disorder asymmetry effects (Fig. 2E). We found that for SA and GM, most disorders negatively loaded onto this component, indicating that the majority of cortical regions were associated with greater case-control differences in the right compared to the left hemisphere (Fig. 2E).

Conclusions: Our findings highlight changes in brain asymmetry over the course of the lifespan and underscore the potential clinical relevance of assessing brain asymmetry in the context of brain disorders across development and aging. The identification of specific deviations and their cross-disorder implications provides a foundation for future research and clinical applications in the realm of brain development and mental health.

References

1. Brancucci, A., Lucci, G., Mazzatenta, A., & Tommasi, L. (2009). Asymmetries of the human social brain in the visual, auditory and chemical modalities. Philosophical Transactions of the Royal Society B: Biological Sciences, 364(1519), 895-914.
2. Okada, N., Fukunaga, M., Yamashita, F., Koshiyama, D., Yamamori, H., Ohi, K., ... & Hashimoto, R. (2016). Abnormal asymmetries in subcortical brain volume in schizophrenia. Molecular psychiatry, 21(10), 1460-1466.
3. Postema, M. C., Van Rooij, D., Anagnostou, E., Arango, C., Auzias, G., Behrmann, M., ... & Francks, C. (2019). Altered structural brain asymmetry in autism spectrum disorder in a study of 54 datasets. Nature communications, 10(1), 4958.
4. Francks, C. (2015). Exploring human brain lateralization with molecular genetics and genomics. Annals of the New York Academy of Sciences, 1359(1), 1-13.
5. Roe, J. M., Vidal-Pineiro, D., Amlien, I. K., Pan, M., Sneve, M. H., de Schotten, M. T., ... & Westerhausen, R. (2023). Tracing the development and lifespan change of population-level structural asymmetry in the cerebral cortex. Elife, 12, e84685.
6. Bethlehem, R. A., Seidlitz, J., White, S. R., Vogel, J. W., Anderson, K. M., Adamson, C., ... & Bullmore, E.T., Alexander-Bloch, A. (2022). Brain charts for the human lifespan. Nature, 604(7906), 525-533.
7. Fischl, B., Salat, D. H., Busa, E., Albert, M., Dieterich, M., Haselgrove, C., ... & Dale, A. M. (2002). Whole brain segmentation: automated labeling of neuroanatomical structures in the human brain. Neuron, 33(3), 341-355.
8. Stasinopoulos, D. M., & Rigby, R. A. (2008). Generalized additive models for location scale and shape (GAMLSS) in R. Journal of Statistical Software, 23, 1-46.

Poster No 1253

T2 MRI visible perivascular spaces preterm and term born neonates

Lena Meinhold[1], Antonio Gennari[1], Giancarlo Natalucci[2], Beatrice Latal[3], Brigitte Koller[4], Jean-Claude Fauchere[4], Cornelia Hagmann[5], Ruth Tuura[1]

[1]Centre for MR Research, University Children`s Hospital Zurich, Zurich, Switzerland, [2]FLRF Center for Neurodevelopment, Growth and Nutrition of the Newborn Zurich, Zurich, Switzerland, [3]Child Development Centre, University Children's Hospital Zurich, Zurich, Switzerland, [4]Department of Neonatology, University Hospital Zurich, Zurich, Switzerland, [5]University Children`s Hospital Zurich, Zurich, Switzerland

Introduction: Target audience: Researchers and clinicians interested in the clinical implications and developmental correlates of enlarged perivascular spaces in preterm and term born neonates. Background: Human perivascular spaces (PVS) are recognized as important immunological sites and form part of the brain`s neurofluid clearance system (Iliff et al., 2012). PVS are known to become enlarged with aging and may be associated with several CNS disorders (Wardlaw et al., 2020), however very little is known about PVS in the neonatal brain and PVS alterations in preterm birth (Kim et al., 2023). The purpose of this study was to investigate PVS in preterm and term born neonates and explore potential associations of PVS with preterm birth, maturation and developmental outcome.

Methods: In this retrospective study, we evaluated a cohort of 86 preterm born neonates and 21 term born neonates. T2-weighted fast spin echo (FSE) MRI data were acquired at term equivalent age with a 3T GE HD.xt scanner, using an 8-channel head coil, with TE/TR= 109/5700 ms, FOV=25.6 cm, acquisition matrix=256x256, reconstruction matrix=512x512, slice thickness = 2 mm. T2-weighted images were visually inspected and PVS counts were estimated manually in the basal ganglia (BG) and centrum semiovale (CSO), using a validated scoring system (Wardlaw et al,. 2013). Developmental outcome in the preterm group was evaluated with the mental development index (MDI) and psychomotor developmental index (PDI) of the Bayley scales of infant development II. Developmental outcome in the control group was evaluated with the cognitive, language and motor composite scores of the Bayley scales of infant development III. Groupwise differences in PVS counts and associations with postmenstrual age, preterm birth and developmental outcomes were evaluated with Mann-Whitney tests, Kendall`s correlation coefficients and regression analyses, respectively. All statistical analyses were performed with RStudio, R version 4.1.2.

Results: PVS counts in the basal ganglia did not differ between groups, whereas PVS counts in the CSO were significantly higher in preterm born neonates (mean = 1.42, sd = 2.24), compared to control subjects (mean = 0.43, sd = 1.12, $p < 0.01$). CSO PVS were positively associated with postmenstrual age both before and after controlling for gestational age $b = 0.27$, $p < 0.01$, CI [0.08, 0.47] and $b = 0.39$, $p < 0.01$, CI [0.19, 0.6], respectively. The effect of gestational age on CSO PVS was significant with $b = -0.13$, $p < 0.01$, CI [-0.23, -0.04]. We found no evidence for an association of PVS with developmental outcome. Discussion: To our knowledge, only one other study investigated perivascular spaces in preterm born neonates, demonstrating a lower basal ganglia PVS fraction with increasing maturation (postmenstrual age) (Kim et al., 2023). Interestingly, in our cohort, we identified significantly more white matter PVS in preterm born neonates which increased with maturation, and more PVS were seen in those with lower gestational age, suggesting two separate underlying processes: A) PVS evolve naturally with maturation and B) PVS may be associated with preterm birth. Premature births are often accompanied by neonatal cerebral white matter injury, inflammation and glial activation (Back, 2017) and PVS swelling may be part of the brain`s protective

response to white matter injury but may also influence the development of the neuroimmune and neurofluid clearance system in neonates.

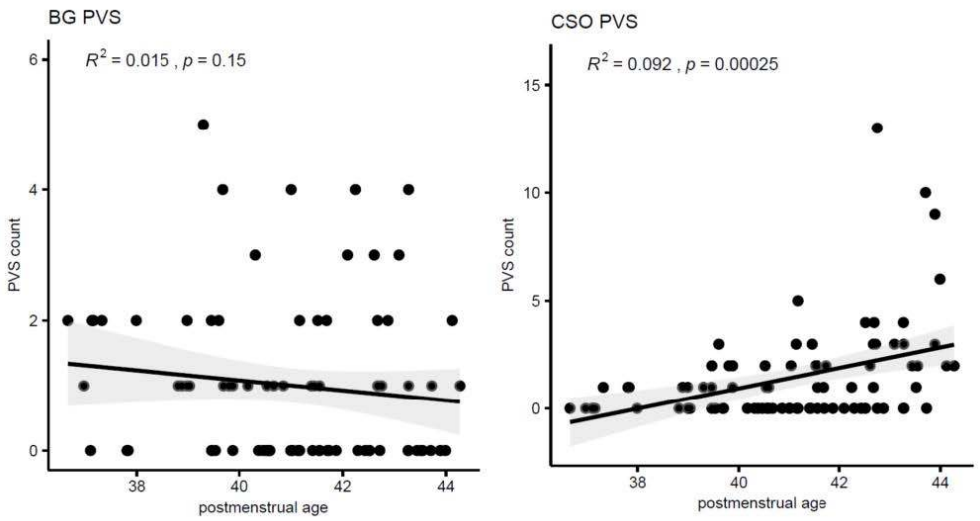

Fig. Association of centrum semiovale PVS with postmenstrual age at MRI in preterm and term born neonates.

Conclusions: These results demonstrate an increase of CSO PVS with maturation in both preterms and healthy controls, as well as an association of CSO PVS with preterm birth. Longitudinal studies may shed further light on the role of preterm birth in the brain`s neurofluid clearance system during development.

References

1. Back, S.A. (2017). White matter injury in the preterm infant: pathology and mechanisms. Acta neuropathologica, 134(3), 331-349. ;
2. Iliff, J.J. et al.,(2012). A Paravascular Pathway Facilitates CSF Flow Through the Brain Parenchyma and the Clearance of Interstitial Solutes, Including Amyloid β. Science Translational Medicine, 4(147), 147ra111-147ra111. ;
3. Kim, J. Y., et al (2023). MRI-visible perivascular spaces in the neonatal brain. Radiology, 307(2), e221314. ;
4. Wardlaw, J.M. et al.,(2013). Neuroimaging standards for research into small vessel disease and its contribution to ageing and neurodegeneration. The Lancet Neurology, 12(8), 822-838. ;
5. Wardlaw, J.M., et al., (2020). Perivascular spaces in the brain: anatomy, physiology and pathology. Nature Reviews Neurology, 16(3), 137-153.

Poster No 1254

Sex- and Obesity-related Differences in Amygdala Subnuclei Apportionment Exist during Preadolescence

L. Nate Overholtzer[1], J. Max Landa[1], Jade Li[1], Jessica Morrel[2], Hedyeh Ahmadi[1], Megan Herting[1]

[1]University of Southern California, Los Angeles, CA, [2]University of Southern California, Los Angles, CA

Introduction: The amygdala is a subcortical limbic system structure critical for emotional processing, sensory perception, decision-making, and appetitive behaviors (Baxter and Murray, 2002; Izadi and Radahmadi, 2022). Neuroanatomical and imaging techniques demonstrate the amygdala can be cytoarchitecturally, genetically, and functionally divided into distinct subnuclei (Ou et al. 2023). Using the novel CIT168 atlas, 9 subnuclei can be assessed in vivo: lateral (LA), dorsal and intermediate basolateral (BLDI), basomedial nucleus (BM), central (CEN), cortical and medial (CMN), basolateral ventral and paralaminar subdivision (BLVPL), amygdala transition areas (ATA), amygdalostriatal transition area (ASTA), anterior amygdala area (AAA), and other non-classified amygdala areas (OTHER) (Pauli, et al., 2018; Tyszka and Pauli, 2016). Prior research in a group of about 400 adolescents spanning ages 10-17 years old indicated sex-related differences but no effects of obesity in amygdala subnuclei apportionment (Campbell et al. 2021). The current study aims to characterize the relationship between (1) obesity and (2) sex differences with proportional amygdala subnuclei volumes in a large, diverse sample of preadolescents.

Methods: We utilized cross-sectional Siemens Prisma MRI data from 4,155 participants aged 9-10 (Males: 55.4%, Females: 44.6%) from 12 sites of the Adolescent Brain Cognitive Development (ABCD®) Study. B-spline bivariate symmetric normalization (SyN) diffeomorphic registration algorithm from ANTs version 2.2.0 was adapted for image registration of T1w and T2w participant images to the high-resolution CIT168 probabilistic atlas (Figure 1). We measured the probabilistic volumes of 9 subnuclei and calculated the relative volume fraction (RVF) for each subnuclei as the proportion of subnuclei volume

relative to the total hemispheric amygdala volume. We excluded participants with an intra-amygdala contrast to noise-ratio (CNR) less than 1.0 in either hemisphere (Campbell, et. al, 2021). Multilevel modeling was employed to examine the effect of (1) BMIz and (2) sex on subnuclei RVFs while adjusting for covariates (i.e., pubertal status, handedness, race/ethnicity, household income, parental education) and study site. Standardized beta coefficients and confidence intervals are reported; P-values were FDR corrected and p-FDRs < 0.05 were considered statistically significant.

Figure 1. Probablistic amygdala subnuclei segmentation in a representative subject with the CIT168 Atlas. Structural T1w and probablistic estimates of 9 subnuclei shown in the coronal plane and thresholded at 0.5 for visualization purposes. Amygdalostriatal transition area not depicted in image.

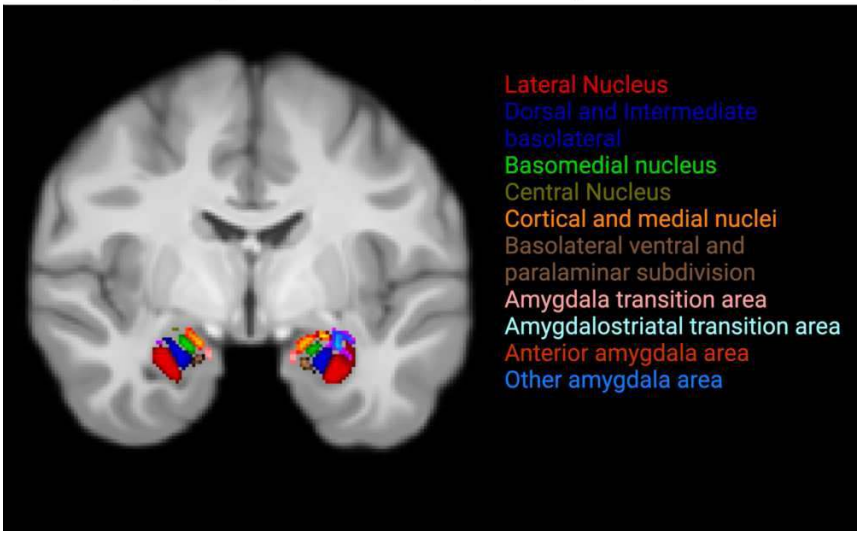

Results: For BMIz, we observed a significant association between obesity and RVFs, including a smaller LA as well as larger BM, CMN, and ATA (all p-FDRs ≤ 0.05, Figure 2a). Also, we saw an association obesity with smaller BLDI RVF in the right amygdala (p-FDRs = 0.03), which trended towards significance in the left amygdala (p-FDR = 0.06, Figure 2a). In both hemispheres, we saw significant sex differences, with smaller RVFs of the BLVPL and ATA, but larger RVFs of the CEN and CMN, in female as compared to male preadolescents (all p-FDR < 0.05, Figure 2b). Sex differences were also noted in some additional left hemisphere subnuclei, with smaller RVFs of LA and OTHER, but larger RVFs of ASTA and BM, in females (all p-FDR < 0.05, Figure 2b).

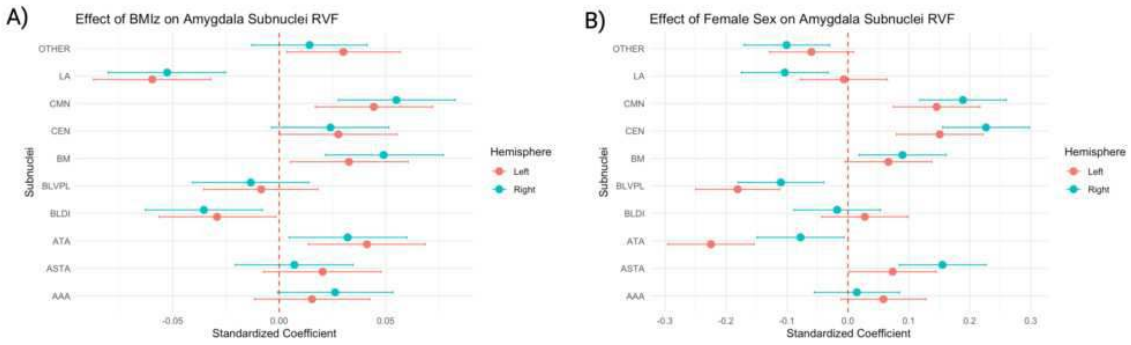

Figure 2. Results from multilevel regression models. Standardized beta coefficients and confidence intervals for effects of (A) BMIz and (B) Sex (female vs. male) on subnuclei RVFs.

Conclusions: In a large, diverse sample of preadolescents, we were able to identify distinct associations between obesity and sex in amygdala subnuclei apportionment. This research expands upon prior work (Campbell et al., 2021) in identifying sex differences in additional subnuclei and expands upon obesity-related differences in amygdala subnuclei previously found in a small sample of youth 8-22 years of age (Kim et al., 2020). Given that several subnuclei have been implicated in reward learning and homeostatic regulation of eating behavior, additional research could contextualize how these findings influence self-regulation during preadolescence.

References

1. Baxter, M. G., & Murray, E. A. (2002). The amygdala and reward. Nature Reviews Neuroscience, 3(7), 563-573.
2. Campbell, C. E., Mezher, A. F., Eckel, S. P., Tyszka, J. M., Pauli, W. M., Nagel, B. J., & Herting, M. M. (2021). Restructuring of amygdala subregion apportion across adolescence. Developmental Cognitive Neuroscience, 48, 100883.

3. Izadi, M. S., & Radahmadi, M. (2022). Overview of the central amygdala role in feeding behaviour. British Journal of Nutrition, 127(6), 953-960.
4. Kim, M. S., Luo, S., Azad, A., Campbell, C. E., Felix, K., Cabeen, R. P., ... & Herting, M. M. (2020). Prefrontal cortex and amygdala subregion morphology are associated with obesity and dietary self-control in children and adolescents. Frontiers in Human Neuroscience, 14, 563415.
5. Ou, Y. N., Wu, B. S., Ge, Y. J., Zhang, Y., Jiang, Y. C., Kuo, K., ... & Yu, J. T. (2023). The genetic architecture of human amygdala volumes and their overlap with common brain disorders. Translational Psychiatry, 13(1), 90.
6. Pauli, W. M., Nili, A. N., & Tyszka, J. M. (2018). A high-resolution probabilistic in vivo atlas of human subcortical brain nuclei. Scientific Data, 5(1), 1-13.
7. Tyszka, J. M., & Pauli, W. M. (2016). In vivo delineation of subdivisions of the human amygdaloid complex in a high-resolution group template. Human Brain Mapping, 37(11), 3979-3998.

Poster No 1255

Development of functional connectivity gradients in multiple frequency bands

Zhu-Qing Gong[1], Xi-Nian Zuo[1]

[1]Beijing Normal University, Beijing, China

Introduction: A wide frequency range of brain oscillations can be recorded by various techniques. In the near century, a large number of electrophysiological studies have gradually accumulated evidence that oscillations in different frequencies are associated with different functions. In summary, high-frequency oscillations have more local connections and participate in bottom-up processes, while low-frequency oscillations have more long-distance connections and dominate in top-down processes (Buzsaki et al., 2004). In the past decade, an increasing number of functional magnetic resonance imaging (fMRI) studies have investigated the whole frequency range of blood oxygen level-dependent (BOLD) oscillations using multiband frequency analysis and found that BOLD oscillations have similar functional organization hierarchies in that different frequency bands dominate different functions (Zuo et al., 2010; Thompson et al., 2015; Gong et al., 2023). However, the multiband functional organization during development has not been revealed. In this study, we aimed to investigate the developmental patterns of functional organization in multiple frequency bands in school-aged children. Our hypothesis is that since the functions are different among frequency bands, the developmental processes would also differentiate among frequencies.

Methods: Resting-state fMRI data from 381 school-aged children from the Chinese Color Nest Project, an accelerated longitudinal dataset, were chosen for this research (Fan et al., 2023). The data were divided into different age groups from 6 to 18 years old, one for each year of age. After preprocessing, BOLD oscillations were decomposed into three frequency bands: slow-3 (0.082-0.200 Hz), slow-4 (0.031-0.082 Hz) and slow-5 (0.013-0.031 Hz). Then, we performed functional connectivity gradient analysis for each age group in all frequency bands. For each frequency band, spatial correlation of gradient distribution between every two age groups was conducted to quantify the phases and continuity of the developmental changes in gradient distribution patterns.

Results: We mainly considered the first two gradients in this study since they account for the most variation. In each frequency band, the development of the two gradients throughout the school age can be divided into three stages (Fig. 1). In stage 1, the first gradient exhibited functional segmentation among primary sensory and motor regions; the second gradient exhibited functional integration from primary regions to associative regions. Stage 2 shows mixed transition modes for both gradients. In stage 3, the distribution pattern of the first and second gradients is reversed. Fig. 2 shows the developmental stages of the first and second gradients across different frequency bands. Overall, the first gradient maturated earlier than the second gradient, indicating that during the development of brain functional reorganization, functional segmentation is continuously optimized even after functional integration matures. The three frequency bands showed divergent developmental rates, as expected. For the first gradient, slow-3 matured the earliest, followed by slow-5 and then slow-4. For the second gradient, slow-5 matured the earliest, followed by slow-3 and finally slow-4. A recent study reported that slow-3, slow-4 and slow-5 are associated with sensory integration and language-related functions, executive functions, and self-related functions, respectively, offering an explanation for the current results that brain oscillations support these different functions having unique development courses (Gong et al., 2023).

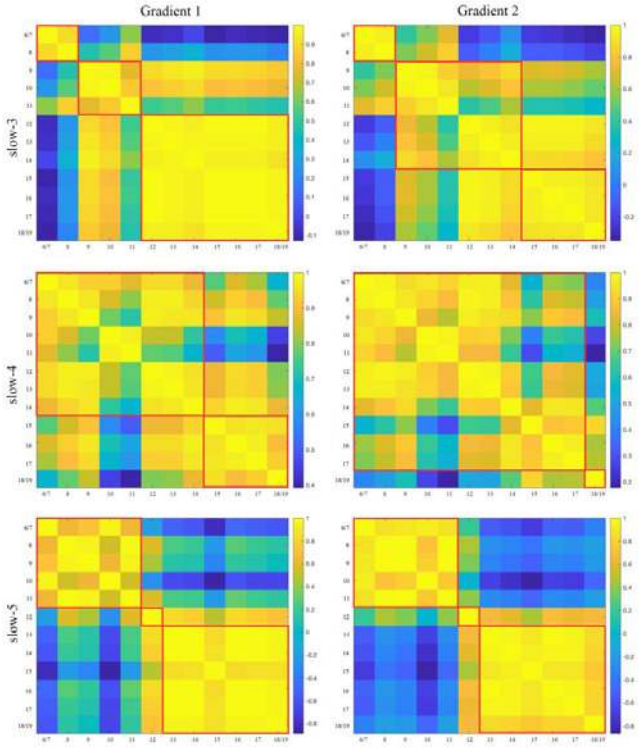

Fig. 1 The spatial correlation of gradient patterns in every two age groups.

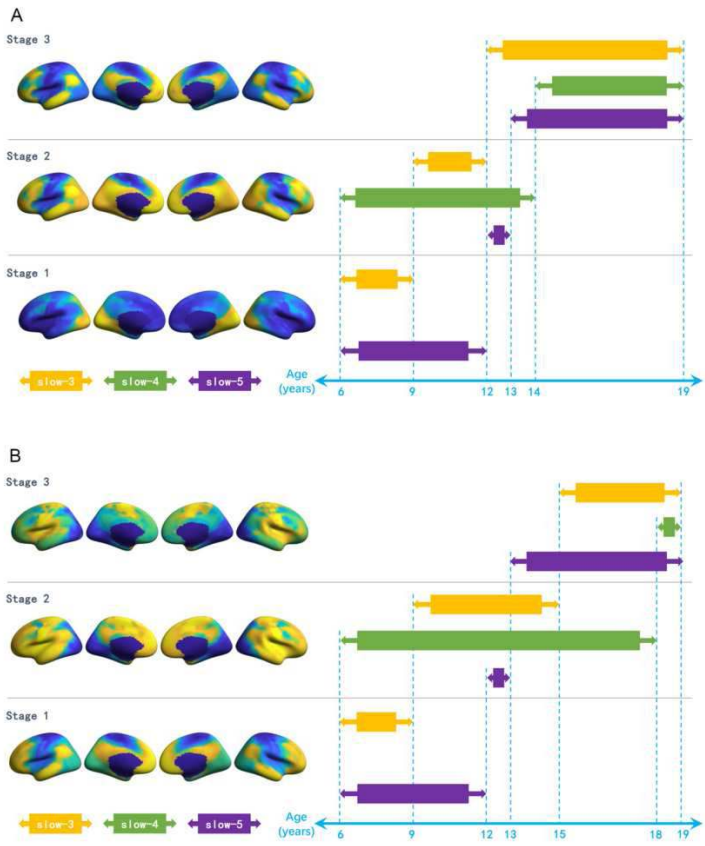

Fig. 2 The developmental stages of the first (A) and second (B) gradients across different frequency bands.

Conclusions: Our study characterized the developmental patterns of BOLD oscillations in different frequency bands. The results revealed that the development of brain function is both phased and continuous. The divergent developmental courses for different frequency bands provide evidence for the frequency specificity of brain function.

References
1. Buzsaki, G. and A. Draguhn (2004). "Neuronal oscillations in cortical networks." Science 304(5679): 1926-1929.
2. Fan, X.-R., et al. (2023). "A longitudinal resource for population neuroscience of school-age children and adolescents in China." Scientific Data 10(1).
3. Gong, Z.-Q. and X.-N. Zuo (2023). "Connectivity gradients in spontaneous brain activity at multiple frequency bands." Cerebral Cortex 33(17): 9718-9728.
4. Thompson, W. H. and P. Fransson (2015). "The frequency dimension of fMRI dynamic connectivity: Network connectivity, functional hubs and integration in the resting brain." Neuroimage 121: 227-242.
5. Zuo, X. N., et al. (2010). "The oscillating brain: Complex and reliable." Neuroimage 49(2): 1432-1445.

Poster No 1256

Distinctive Effects of Depression and Anxiety on Children's Cognition and Emotional Bias

Jisu Chung[1], Sang Ah Lee[1]

[1]Seoul National University, Gwanak-gu, Seoul

Introduction: Emotional wellness, such as depression and anxiety, has an impact on cognitive processes such as emotional bias, attention, and inhibitory control. However, while there is a high level of comorbidity in depression and anxiety[1], their cognitive effects may be dissociable[2]. The present study aimed to extend such infestation to the cognitive effects of anxiety and depression symptoms in childhood. To address the challenge of conducting tests involving many trials on children, we used modified versions of the emotional flanker task, emotional stroop task, and an emotion-color conjunction task using animated faces.

Methods: 45 children aged between 5 to 9 were recruited for participation at the children's museum. 33 (mean age = 7.44, female 18) successfully completed the task and surveys. Three different emotional attentional tasks were employed to examine cognitive abilities and behavioral characteristics of children: an emotional flanker task, an emotional stroop task, and an emotional feature conjunction task. In the emotional conjunction task, participants had to select the target defined with a conjunction of color and facial expression. All three tasks used animated cat faces and a children-friendly interface to draw and sustain children's attention. Self-report questionnaires, including a depression scale (CES-DC)[5], anxiety scale (STAI-CH[4], and ADHD scale (K-ARS)[3], were collected to assess children's emotional health and parent-reported ADHD symptoms. All experiments were conducted in a room within a children's museum.

Results: Depression and trait anxiety scores were highly correlated ($r = 0.461$, $p = 0.002$). However, ADHD surveys (K-ARS) showed a correlation with depression scores ($r = 0.403$, $p = 0.008$) but not with anxiety scores ($r= 0.143$, $p=0.368$). These results suggest that depression and anxiety may have different effects on cognition. In the emotional flanker task, overall reaction time showed a correlation with depression scores ($r = 0.397$, $p = 0.024$, STAI-CH as covariate), but not with anxiety scores ($r = -0.188$, $p = 0.302$, CES-DC as covariate). Interestingly, this correlation was driven by the congruent emotion conditions (all positive or negative faces) (positive; $r = 0.357$, $p = 0.045$, negative; $r = 0.576$, $p = 0.001$, STAI-CH as covariate), showing that a highly emotional stimulus took more time to process in children with depressive symptoms. In contrast, the emotional Stroop task showed slower response times with higher anxiety ($r = 0.345$, $p = 0.053$, CES-DC as covariate), particularly in the negative condition ($r = 0.373$, $p = 0.036$, CES-DC as covariate). The emotional conjunction task also showed a correlation between response time and anxiety ($r = 0.39$, $p = 0.044$), but not with depression ($r = 0.139$, $p = 0.49$), particularly when the target was a negative face($r = 0.44$, $p = 0.02$). These results suggest that children with high trait anxiety may have maladaptive emotion regulation, especially with negative emotional stimuli.

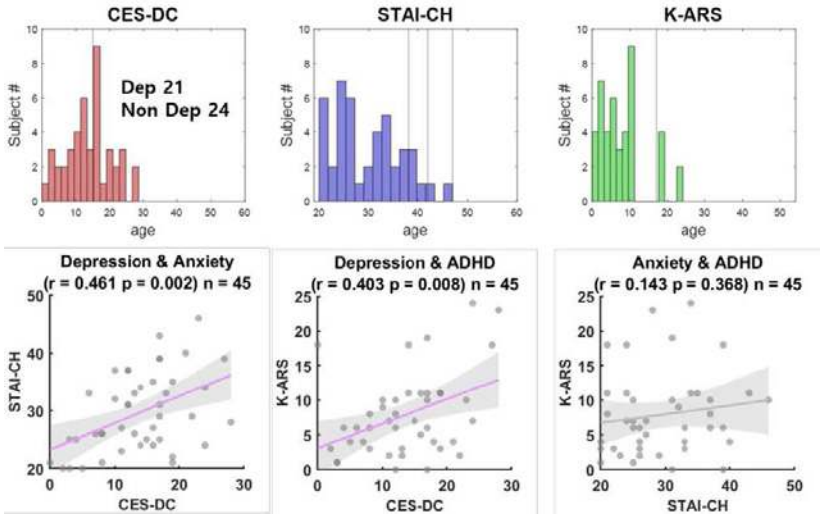

Fig. Affective health surveys and relationship

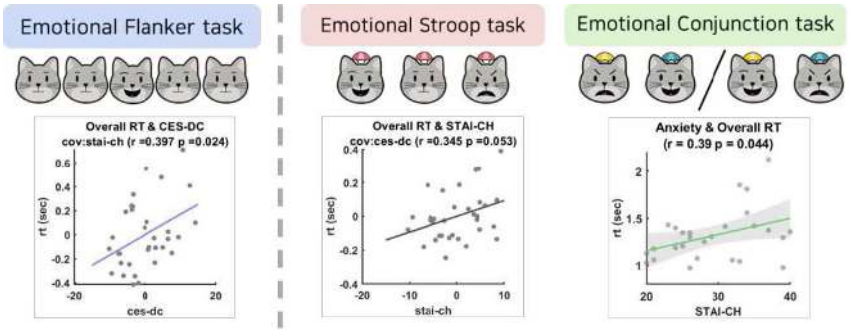

Fig. Relationship between emotional attentive task and affective health survey

Conclusions: Our findings suggest that children's depression and trait anxiety show distinct effects in emotion-related cognitive tasks. We speculate that delayed executive function and conflict resolution are related to depressive symptoms, while decrease in inhibitory function, particularly with respect to negative emotional processing, is associated with children's anxiety. Such tasks can be useful for younger children who may not be able to recognize nor explain their cognitive symptoms.

References

1. Belzer, Kenneth PhD; Schneier, Franklin R. MD. Comorbidity of Anxiety and Depressive Disorders: Issues in Conceptualization, Assessment, and Treatment. Journal of Psychiatric Practice 10(5):p 296-306, September 2004.
2. MacLeod, C., & Hagan, R. (1992). Individual differences in the selective processing of threatening information, and emotional responses to a stressful life event. Behaviour Research and Therapy, 30, 151 – 161.
3. McGoey, K. E., DuPaul, G. J., Haley, E., & Shelton, T. L. (2007). Parent and teacher ratings of attention-deficit/hyperactivity disorder in preschool: The ADHD rating scale-IV preschool version. Journal of Psychopathology and Behavioral Assessment, 29(4), 269–276.
4. Spielberger, C. D., Edwards, C. D., Montouri, J., & Lushene, R. (1973). State-Trait Anxiety Inventory for Children (STAI-CH) [Database record]. APA PsycTests.
5. Weissman, M. M., Orvaschel, H., & Padian, N. (1980). Children's Symptom and Social Functioning Self-Report Scales Comparison of Mothers' and Children's Reports. The Journal of nervous and mental disease, 168(12), 736-740.

Poster No 1257

A Normative Model of Brain Microstructure based on Diffusion MRI in 52,719 Participants

Julio Villalón Reina[1], Alyssa Zhu[2], Talia Nir[3], Neda Jahanshad[4], Paul Thompson[5], Elnaz Nourollahimoghadam[2], Sebastian Benavidez[1], Clara Moreau[1], Tamoghna Chattopadhyay[1], Sophia Thomopoulos[6], Leila Nabulsi[1], Yixue Feng[7], Emily Laltoo[8]

[1]University of Southern California, Los Angeles, CA, [2]USC, Marina Del Rey, CA, [3]University of Southern California Keck School of Medicine, Marina del Rey, CA, [4]Imaging Genetics Center, Keck School of Medicine of University of Southern California, Los Angeles, California, [5]Imaging Genetics Center, Keck School of Medicine of University of Southern California, Los Angeles, CA, [6]USC, Marina del Rey, CA, [7]University of Southern California, Marina Del Rey, CA, [8]University of Southern California, Mark and Mary Stevens Neuroimaging and Informatics Institute, Los Angeles, CA

Introduction: Normative models (NM) estimate the centiles of variation of a brain measure as a function of specific explanatory covariates. Assembling a large, representative reference dataset to train the NM requires the pooling of multi-site data, to increase the size of the training sample and improve the reproducibility and generalizability of findings. Even so, acquisition protocols influence diffusion tensor imaging (DTI) metrics, making it important to model protocol and site effects. To create a generalizable NM of brain DTI metrics across the lifespan, we trained a large scale NM on data from 52,719 subjects, using state-of-the-art tools to model and adjust for site-dependent effects, and to detect individual deviations from the norm.

Methods: We analyzed DTI data from: ABCD, AOMIC, CAMCAN, CHBMP, CHCP, HBN, HCP-A, HCP-D, HCP-YA, PedsDTI, PING, PNC, QTAB, QTIM, SLIM, UKBB, ADNI3, OASIS3 and PPMI. Fig.1 summarizes demographic information for the cohorts. We preprocessed all cohorts' data with the ENIGMA-DTI protocol. Mean fractional anisotropy (FA) and mean diffusivity (MD) were extracted for 21 bilateral ROIs from the JHU-WM atlas and the skeletonized Average-WM. Hierarchical Bayesian Regression (HBR) was run to estimate the age trajectory and centile curves of DTI metrics across the lifespan (3-92 years), for FA and MD. We used age and sex as covariates, with each metric per ROI as the dependent variable and the dMRI protocol as the batch effect (35 protocols). Most sites were acquired at 3T, four sites at 1.5T and one site at 4T; b-values=1000 to 1500s-mm2; gradient directions=12 to 92. We modeled the effect of age with a cubic b-spline basis. Using the model trained on healthy controls' data, we characterized the main effect and age-dependent effects of Alzheimer's disease (AD) and mild cognitive ilmpairment (MCI) on these brain metrics. For testing, we included 81 patients with AD (mean age: 77y±8.4, 46M/35F) and 225 MCI participants (mean age: 75.1y±8.1, 127M/98F). Training and testing data sets were created with an 80% to 20% sample split. Z-scores were calculated for the 20% test control subjects. Likewise, Z-scores for the AD and MCI subjects were also calculated. Probabilities of abnormality (p-values) were derived from all Z-scores. ROI-wise areas under the ROC curves (AUCs) were calculated to determine the classification accuracy of the computed deviations, for AD and MCI. We controlled the false discovery rate (FDR) for each DTI metric separately across ROIs to identify those with significant group differences. For the significant ROIs, we calculated the average of extreme deviations (Z>|2|) for each disease. To achieve stability, we repeated the same procedure 10 times. We report the deviations for the ROIs that passed the FDR correction in 9 out of 10 times.

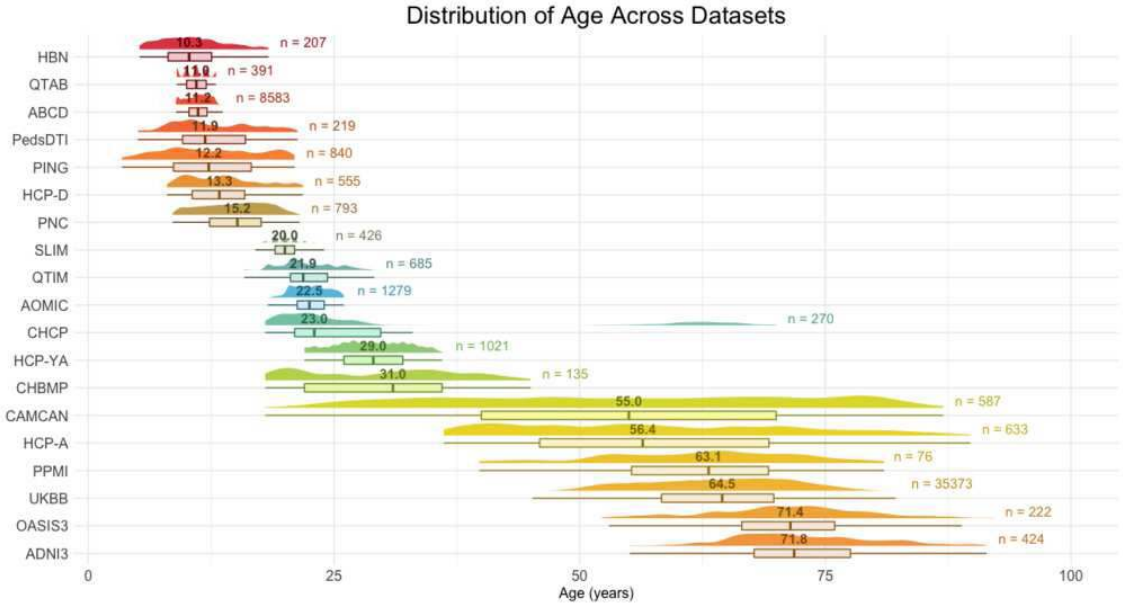

Results: Normative modeling with HBR (NM-HBR) was able to create lifespan trajectories for the DTI metrics by pooling large-scale multi-site DTI data. The average FA across all WM reached a peak at 29 years; average MD reached a minimum at 42 years (Fig.2). With NM-HBR, we were able to create site-specific NMs, allowing the intercept and the reference values for DTI metrics to vary across protocols (Fig.2C). NM-HBR quantified extreme deviations in the WM for AD and MCI with high anatomical precision. For AD classification, the cingulum of the hippocampus (CGH) attained an AUC=0.68 for FA and AUC=0.71 for MD. In MCI, MD measures in the BCC attained best classification accuracy (AUC=0.58). We found extreme deviations (Z>|2|) in both directions for AD and MCI. Fig. 2D shows the AUCs of the Z-scores across all JHU-WM ROIs for AD in the CGH and GCC.

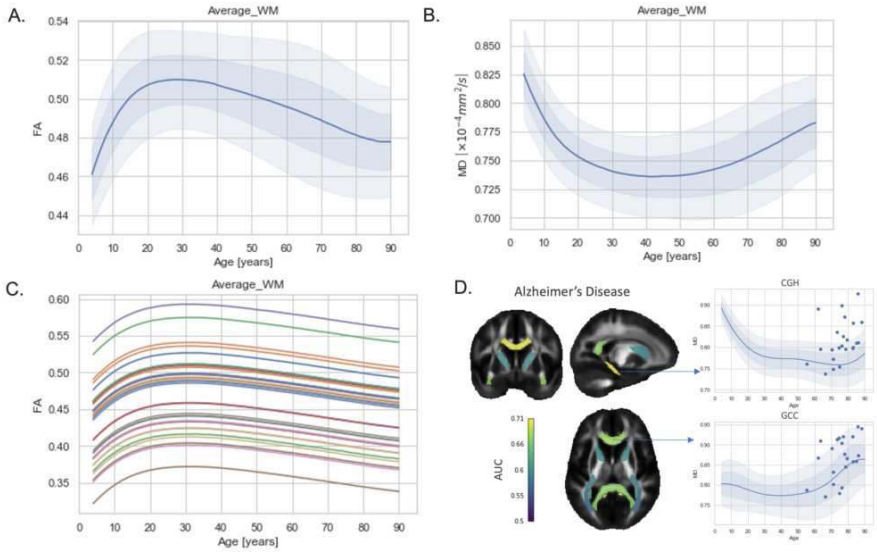

Conclusions: These NM will be available to the neuroimaging community with DTI data in the ENIGMA-DTI template space and may be applied to multi-site samples of patients with neurologic and psychiatric diseases to detect deviations from age- and sex-specific norms and at different stages of brain disease.

References

1. B. J. Casey et al. (2018), Developmental Cognitive Neuroscience, vol. 32, pp. 43-54, 2018.
2. J. Ge et al. (2023), Nature Neuroscience, vol. 26, no. 1, pp. 163-172.
3. B. A. Landman et al. (2007), NeuroImage, vol. 36, no. 4, pp. 1123-1138.
4. M. P. Harms et al. (2018), Neuroimage, vol. 183, pp. 972-984.
5. N. Jahanshad et al. (2013), NeuroImage, vol. 81, pp. 455-469.
6. T. L. Jernigan et al. (2016), NeuroImage, vol. 124, pp. 1149-1154.
7. S. M. Kia et al. (2022), PLOS ONE, vol. 17, no. 12, p. e0278776.
8. W. Liu et al. (2017), Sci Data, vol. 4, p. 170017.
9. K. L. Miller et al. (2016), Nature Neuroscience, vol. 19, no. 11, pp. 1523-1536.
10. J. L. Pamela et al. (2011), medRxiv, p. 2019.12.13.19014902, 2019.
11. K. Marek et al. (2011), Progress in Neurobiology, vol. 95, no. 4, pp. 629-635.
12. G. Ruiyang et al. (2023), bioRxiv, p. 2023.01.30.523509.
13. S. Rutherford et al. (2022), Nature Protocols, vol. 17, no. 7, pp. 1711-1734.
14. L. Snoek et al. (2021), Scientific Data, vol. 8, no. 1, p. 85.
15. L. T. Strike et al. (2023), Scientific Data, vol. 10, no. 1, p. 195.
16. J. R. Taylor et al. (2017), NeuroImage, vol. 144, pp. 262-269.
17. P. A. Valdes-Sosa et al. (2021), Scientific Data, vol. 8, no. 1, p. 45.
18. D. C. Van Essen et al. (2012), NeuroImage, vol. 62, no. 4, pp. 2222-2231.
19. L. Walker et al. (2016), Neuroimage, vol. 124, no. Pt B, pp. 1125-1130.
20. A. Zavaliangos-Petropulu et al. (2019), Frontiers in Neuroinformatics, Original Research vol. 13.
21. G. I. de Zubicaray et al. (2008), Brain Imaging and Behavior, vol. 2, no. 4, pp. 258-263.

Poster No 1258

Prenatal Familial Income Volatility and Infant Subcortical Brain Volumes

Genevieve Patterson[1], Alexander Dufford[2], Sun Hyung Kim[3], Martin Styner[4], Pilyoung Kim[1]

[1]University of Denver, Denver, CO, [2]Oregon Health & Science University, Portland, OR, [3]The University of North Carolina at Chapel Hill, Chapel Hill, NC, [4]Department of Psychiatry, University of North Carolina at Chapel Hill, Chapel Hill, NC

Introduction: Unpredictable environments can be a source of stress influencing the developing brain, including during the prenatal period. Subcortical regions including the amygdala and hippocampus have been previously shown to be especially sensitive to stress exposure, in part due to the high number of glucocorticoid receptors present in these regions (Badihian et al., 2020). Emerging evidence suggests that socioeconomic status (SES) is associated with child brain development including in infancy (Betancourt et al. 2016; Ramphal et al., 2020; Gao et al., 2015). Prior studies have consistently reported associations between lower SES and smaller hippocampal volumes with more mixed results for amygdala volume (Rakesh & Whittle, 2021). Household chaos and unpredictability have also been associated with child development at a behavioral (Evans et al. 2005; Davis et al., 2019), physiological (Tarullo et al., 2020; Noroña-Zhou et al. 2020), and neural (Granger et al., 2021) level. Income

volatility, specifically income losses, has been associated with both externalizing and internalizing symptoms throughout development (Miller et al. 2021). However, little is known about the role of income instability and infant brain development. Here we examine the association between familial income instability and subcortical brain volumes in early infancy.

Methods: The current study includes 63 infants from a prospective longitudinal study of pregnant individuals and their infants from diverse socioeconomic backgrounds (31.7% low income, prenatal income to needs ratio <=2)). Arc Percent Change (APC) in household earned income was calculated for each month compared to the previous month for the time period covering conception to the month of the child's birth. An income shock was defined as APC > 25% for a given month, with decreases defined as a negative shock. The number of negative income shocks were summed across the prenatal time period. Infants completed an MRI after birth during natural sleep (Mean Age = 34.9 days, SD = 19.9 days; 52.4% female). Infant amygdala and hippocampus as well as tissue segmentation were individually segmented using a multimodality, multi-template-based automatic method combining T1- and T2-weighted MR images via the MultiSegPipeline v2.2.1 tool (Cherel et al., 2015), which employs deformable registration and label fusion from the ANTs toolset (Tustison et al., 2021). Bivariate correlations were conducted to test the following as potential covariates: total intercranial volume (ICV), postconceptional age at scan (sum of gestational age at birth and age at scan), sex at birth, birthweight, average prenatal income to needs ratio, and NICU stay. Covariates significantly associated with hippocampus and amygdala volumes were included in further multiple regression analysis predicting infant right and left hippocampus and amygdala volume from the total number of negative income shocks.

Results: The number of negative income shocks was significantly associated with smaller right hippocampal volume (β = -33.60, p = .01) covarying for ICV and birthweight. The number of negative income shocks was significantly associated with smaller right amygdala volume (β = -11.55, p = .008) covarying for ICV and postconceptional age at scan.

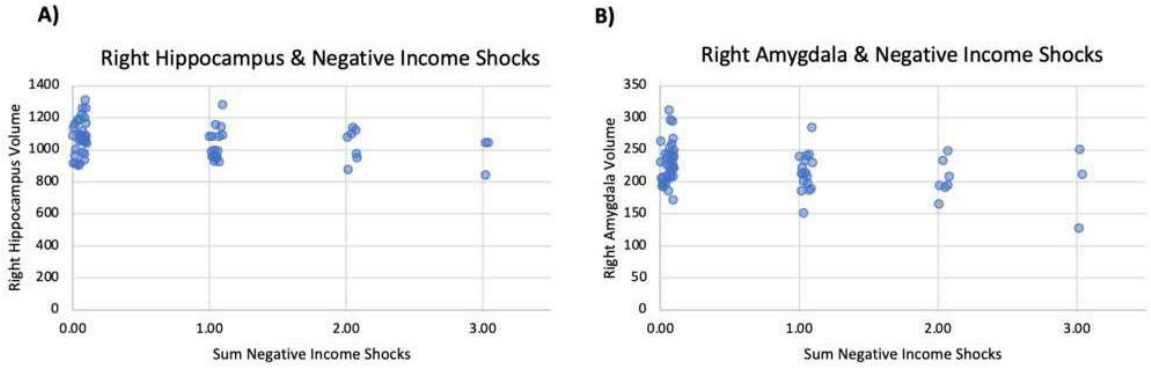

Figure 1: A) Scatter plot for sum of negative income shocks and infant right hippocampus volume B) Scatter plot for sum of negative income shocks and infant right amygdala volume

Conclusions: We found evidence that familial income volatility during the perinatal period is associated with infant brain structure after birth. These early differences in brain structure may potentially influence infant's developmental trajectories with implications for later brain structure, function, and associated behavior. These findings provide support for the development of public programs that prioritize consistency, especially for families and during sensitive periods like pregnancy.

References

1. Badihian, N. (2020). Transcriptional and epigenetic changes of brain derived neurotrophic factor following prenatal stress: A systematic review of animal studies. Neuroscience & Biobehavioral Reviews, 117, 211-231.
2. Betancourt, L. M. (2016). Effect of socioeconomic status (SES) disparity on neural development in female African-American infants at age 1 month. Developmental Science, 19(6), 947-956.
3. Cherel, M. (2015). Automatic tissue segmentation of neonate brain MR Images with subject-specific atlases. SPIE Medical Imaging, 941311-941311–11.
4. Davis, E. P. (2019). Across continents and demographics, unpredictable maternal signals are associated with children's cognitive function. EBioMedicine, 46, 256–263.
5. Evans, G. W. (2005). The Role of Chaos in Poverty and Children's Socioemotional Adjustment. Psychological Science, 16(7), 560–565.
6. Gao, W. (2015). Functional Network Development During the First Year: Relative Sequence and Socioeconomic Correlations. Cerebral Cortex 25(9), 2919-2928.
7. Granger, S.J. (2021). Aberrant Maturation of the Uncinate Fasciculus Follows Exposure to Unpredictable Patterns of Maternal Signals. Journal of Neuroscience, 41(6), 1242-1250.
8. Miller, P. (2021). Income dynamics and behavior problems in early childhood, middle childhood, and the transition to adolescence. Journal of Applied Developmental Psychology, 77, 101345.
9. Noroña-Zhou, A. N. (2020). Unpredictable maternal behavior is associated with a blunted infant cortisol response. Developmental Psychobiology, 62(6), 882–888.
10. Rakesh, D. (2021). Socioeconomic status and the developing brain–A systematic review of neuroimaging findings in youth. Neuroscience & Biobehavioral Reviews, 13

11. Ramphal, B. (2020). Brain connectivity and socioeconomic status at birth and externalizing symptoms at age 2 years. Developmental Cognitive Neuroscience, 45, 100811.
12. Tarullo, A. R., (2020). Cortisol and socioeconomic status in early childhood: A multidimensional assessment. Development and Psychopathology, 32(5), 1876–1887.
13. Tustison, N. J. (2021). The ANTsX ecosystem for quantitative biological and medical imaging. Scientific Reports, 11(1), 9068.

Poster No 1259

Brain Charts for the Rhesus Macaque

Samuel Alldritt[1], Julian Ramirez[1], Jakob Seidlitz[2], Richard Bethlehem[3], Karl-Heinz Nenning[4], David Amaral[5], Damien Fair[6], Andrew Fox[7], Alexandre Franco[4], Jeff Bennett[8], Ned Kalin[9,10], Brian Russ[4], Lena Dorfschmidt[11], Aaron Alexander-Bloch[2], Daniel Margulies[12], Jonathan Smallwood[13], Charles Schroeder[14], Becker Guillaume[15], Mar Sanchez[16], Lucie Chalet[17], Daniel Gale[13], Zsofie Kovacs-Balint[18], Jason Gallivan[19], Joseph Nashed[20], Clement Garin[21], John Erdman[22], Matthew Kuchan[23], Martha Neuringer[24], Viola Neudecker[25], Oscar Miranda Dominguez[26], Ansgar Brambrink[25], Christopher Kroenke[24], Christopher Petkov[27], Jiaojing Wang[28], Chris Klink[29], Adam Messinger[30], PRIME-DE Consortium[1], Michael Milham[1], Ting Xu[1]

[1]Child Mind Institute, New York, NY, [2]University of Pennsylvania, Philadelphia, PA, [3]Autism Research Centre, Department of Psychiatry, University of Cambridge, Cambridge, United Kingdom, [4]Nathan Kline Institute, Orangeburg, NY, [5]University of California Davis MIND Institute, Sacramento, CA, [6]Masonic Institute for the Developing Brain, University of Minnesota Medical School, Minneapolis, MN, [7]University of California Davis, Davis, CA, [8]California National Primate Research Center, Davis, CA, [9]University of Wisconsin Madison, Madison, WI, [10]Department of Psychiatry, University of Wisconsin School of Medicine and Public Health, Madison, WI, [11]The Children's Hospital of Philadelphia, Philadelphia, PA, [12]Université Paris Cité, CNRS, Integrative Neuroscience and Cognition Center, Paris, France, [13]Department of Psychology, Queen's University, Ontario, Canada, [14]Nathan S. kline Institute for Psychiatric Research, Orangeburg, NY, [15]Université de Lyon, Lyon, France, [16]Emory National Primate Research Center, Atlanta, GA, [17]Claude Bernard University Lyon 1, Villeurbanne, France, [18]Emory University, Budapest, Hungary, [19]Department of Psychology, Queens University, Ontario, Canada, [20]Centre for Neuroscience Studies, Queen's University, Ontario, Canada, [21]Department of Biomedical Engineering, Vanderbilt University, Nashville, TN, [22]Beckman Institute for Advanced Science and Technology, Champaign, IL, [23]Abbott Laboratories, Columbus, OH, [24]Oregon National Primate Research Center, Portland, OR, [25]Columbia University, New York, NY, [26]University of Minnesota, Minneapolis, MN, [27]Newcastle University, Newcastle, United Kingdom, [28]Kunming University of Science and Technology, Kunming, China, [29]Netherlands Institute for Neuroscience Royal Netherlands Academy of Arts and Sciences, Meibergdreef, Netherlands, [30]National Institute of Health, Baltimore, MD

Introduction: The rhesus macaque is one of the most widely used non-human primate (NHP) models for the human brain, due to resemblance in brain structure, function, and social behaviours. Notably, comparative developmental models of human and macaque provides opportunities to investigate neural plasticity, developmental trajectories, and pathological processes. Recently, analysis of multisite MRI datasets have successfully characterized human brain development across the lifespan[1]. However, due to multifaceted challenges in NHP studies, we lack comparative brain growth charts for macaques. This study aimed to establish reference standards for macaque brain development that facilitates the comparison of development phases across humans and macaques.

Methods: We studied a collaborative multisite collection of MRI data including the PRIMatE Data Exchange (PRIME-DE) consortium. Structural images were preprocessed through the 'nhp-abcd-bids-pipeline'[2-4], with customized templates for early developmental data (age < 0.3 yr), followed by visual inspections for quality assessment. Prenatal data was manually segmented[5]. A total of 1,522 scans (1024 macaques, 554 F, age: -.23 - 30.64 yr) across 23 sites were included in the analysis. We estimated global and regional volume, cortical thickness, and surface area and applied a GAMLSS, fitting nonlinear growth curves stratified by sex and site as a random effect. We identified the macaque developmental milestones (i.e. growth rates and peak age of trajectories) and transformed them to human surfaces for comparing the developmental phases between humans and macaques.

Results: Overall, macaque trajectories demonstrate similar patterns in total volume of gray matter (GMV), white matter, and subcortical GM compared to humans. However, unlike humans, where GMV peaks in childhood (~6 yr), macaque GMV peaked earlier during infancy (~8 mon), followed by a plateau and gradual decline. Ventricular volume sharply decreases before birth, with a steady postnatal increase, followed by a slight increase towards the end of the lifespan. At the GMV peak age (Fig 1C), the growth rate in volume, area, and cortical thickness shows regional variations[6]. Except for the frontal pole, volumes in the lateral and medial frontal, middle temporal, and parahippocampal regions continue to increase, while the visual and parietal lobes show a reduction. Cortical thickness mirrors a similar pattern to volume, while surface area displays

continued expansion in most brain regions, except for the visual cortex. Figure 2 illustrates regional peak ages for volume, area, and thickness. Notably, volume and area share a similar peak age scale across regions, with a late peak age observed in the precentral gyrus and anterior cingular cortex (ACC). In contrast, thickness exhibits an earlier overall peak age. Upon comparing the human peak age with that of macaque transformed on the human surface (Fig 2C-D), a development delay was detected in the insular and ACC across all measures (Fig 2F), highlighting functional relationships including social cognition, autobiographical memory, and affective processing.

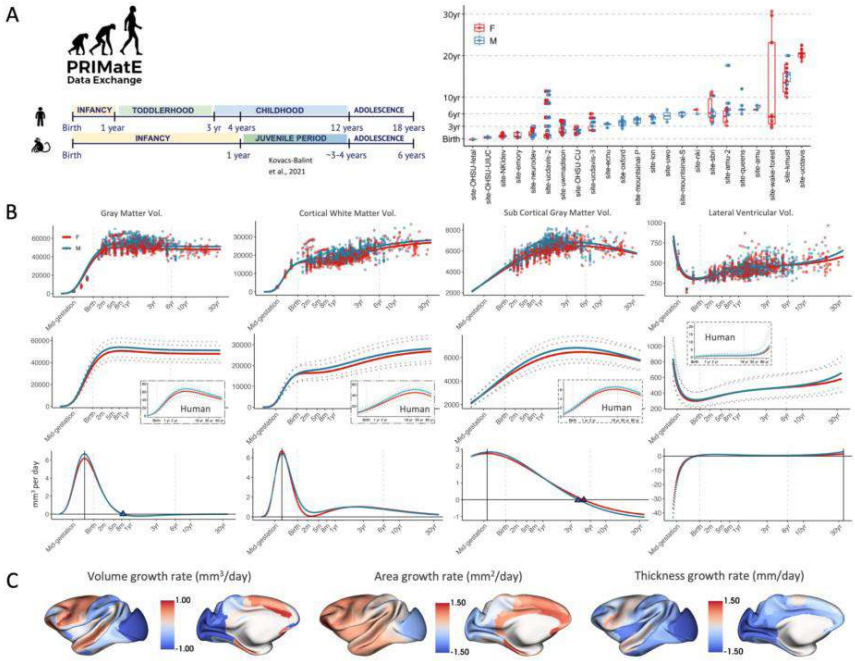

Figure 1. Brain charts for rhesus macaque. A) Human and macaque approximate lifecycle stages and demographic information of MRI data. B) Brain volume trajectories and growth rates (per day) over the lifespan shown over a log scale, with comparable human charts from Bethlehem & Seidlitz et al., (2022). C) Growth rates of volume (mm^3/day), surface area (mm^2/day), and cortical thickness (mm/day) at total gray volume peak age (8 months).

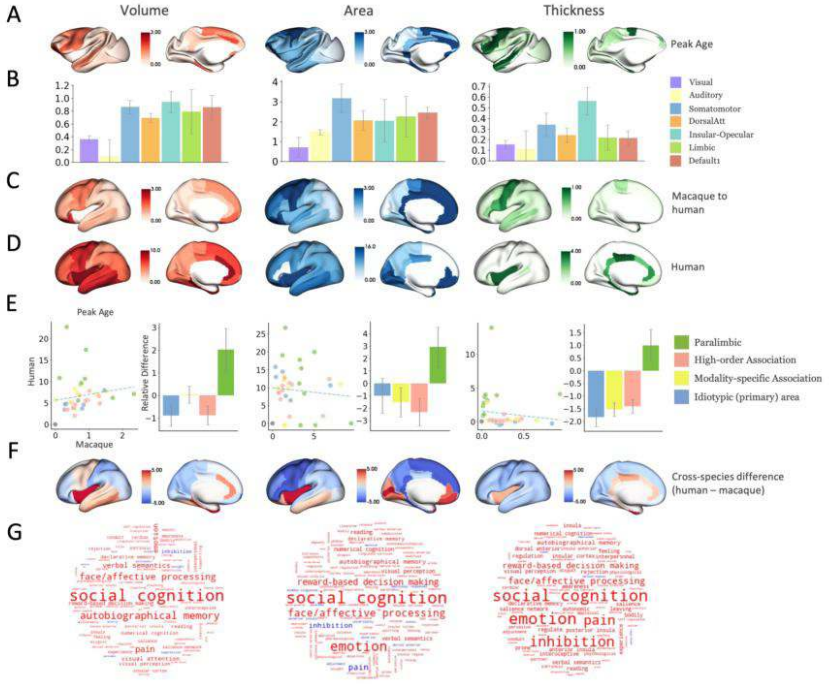

Figure 2. Peak ages for volume, surface area, and cortical thickness. A) Macaque regional peak ages in years. B) Macaque peak ages at the network level. C) Macaque peak ages aligned to the human surface in the Deskian-Killiany parcellation. D) Human peak age in years in the Deskian-Killiany parcellation. E) Scatterplots represent the comparison of peak age between humans (y-axis) and macaque(x-axis), colored by the cytoarchitectonic classes. Bar plots show relative differences (human - macaque) in age peak normalized by the GMV peak age). F) Difference in peak age between humans and macaques normalized by the GMV peak age within species. G) A Neuroquery meta-analysis of the difference maps, colored matches with difference map in Fig 2F.

Conclusions: This study established normative brain development trajectories for macaque. Compared to human, macaque brain grows faster and plateaus earlier, particularly in regions with functional associations with social cognition, autobiographical memory, and affective processing. Our findings suggest neotenic changes in human brain development with prolonged periods of postnatal brain growth during childhood, which may facilitate cellular maturation, myelination, synaptic wiring, and pruning. Functionally these changes are important for the development of complex cognitive and social behaviours that are core features of human cognition. The normative brain charts offer a window into the brain development of nonhuman primates that provides a baseline from which we can gain an understanding of how human brain development shapes how we think and feel.

References

1. Bethlehem RAI, Seidlitz J, White SR, Vogel JW, Anderson KM, Adamson C, et al. Brain charts for the human lifespan. Nature. 2022;604: 525–533.
2. Autio JA, Glasser MF, Ose T, Donahue CJ, Bastiani M, Ohno M, et al. Towards HCP-Style macaque connectomes: 24-Channel 3T multi-array coil, MRI sequences and preprocessing. Neuroimage. 2020;215: 116800.
3. Donahue CJ, Sotiropoulos SN, Jbabdi S, Hernandez-Fernandez M, Behrens TE, Dyrby TB, et al. Using Diffusion Tractography to Predict Cortical Connection Strength and Distance: A Quantitative Comparison with Tracers in the Monkey. J Neurosci. 2016;36: 6758–6770.
4. Glasser MF, Sotiropoulos SN, Wilson JA, Coalson TS, Fischl B, Andersson JL, et al. The minimal preprocessing pipelines for the Human Connectome Project. Neuroimage. 2013;80: 105–124.
5. Ryali S, Chen T, Supekar K, Menon V. A parcellation scheme based on von Mises-Fisher distributions and Markov random fields for segmenting brain regions using resting-state fMRI. Neuroimage. 2013;65: 83–96.
6. Bezgin, Gleb, Vasily A. Vakorin, A. John van Opstal, Anthony R. McIntosh, and Rembrandt Bakker. 2012. “Hundreds of Brain Maps in One Atlas: Registering Coordinate-Independent Primate Neuro-Anatomical Data to a Standard Brain.” NeuroImage 62 (1): 67–76.
7. Mesulam, M.-M. (Ed.). (2000). Principles of behavioral and cognitive neurology (2nd ed.). Oxford University Press.

Poster No 1260

Associations Between Prenatal Stress, Maternal Anxiety, and Infant Functional Connectivity

Jenna Chin[1], Haitao Chen[2], Wei Gao[3], Pilyoung Kim[1]

[1]University of Denver, Denver, CO, [2]Cedars-Sinai Medical Center, Los Angeles, CA, [3]Biomedical Imaging Research Institute (BIRI), Cedars-Sinai Medical Center, Los Angeles, CA

Introduction: There is emerging evidence demonstrating associations between prenatal stress and infant brain outcomes. However, studies examining the specific role of prenatal life events in shaping infant functional connectivity (FC) remain limited. It is also unclear how prenatal psychological distress may interact with stressful event exposure. Here we use resting-state fMRI (rs-fMRI) to examine the effects of stressful event exposure and gestational parent anxiety symptoms on amygdala (amyg)–anterior cingulate cortex (ACC) FC, a neural circuit with known stress-related alterations.

Methods: Participants were 56 gestational parent–infant dyads. Gestational parents (M age=29.86, SD=5.51 years) were recruited for a longitudinal study of pregnancy. Prenatal stress was measured at three prenatal time points using a Life Events Interview (Lobel et al., 1992). Participants rated the severity of endorsed events from neither negative nor undesirable (1) to extremely negative or undesirable (5). Severity scores were summed to compute severity-weighted life event totals. To assess prenatal anxiety symptoms, gestational parents completed the State-Trait Anxiety Inventory at three prenatal time points (Spielberger, 1989). Scores across the three prenatal time points were averaged to create a composite prenatal anxiety score. Infants completed a rs-fMRI scan (M=32.31, SD=16.14 days). Amyg to ACC FC values were computed based on the infant 2-year AAL atlas (Shi et al., 2011). The average fMRI time series for each ROI were calculated by averaging the time series across all voxels within the region. Pair-wise correlations were calculated and values were Fisher-Z transformed. First, associations between each ROI to ROI FC (i.e., left amyg–left ACC, left amyg–right ACC, right amyg–left ACC, right amyg–right ACC) and prenatal stress were tested using four separate regressions. All analyses controlled for infant postnatal age and sex. We then tested whether gestational parent prenatal anxiety symptoms mediated significant associations between prenatal stress and infant rs-FC.

Results: Higher prenatal stress, operationalized as severity-weighted stressful life event totals, was associated with decreased left amyg–left ACC FC values (B= -.294, SE = .002, p =.030; Fig. 1a) and decreased right amyg–left ACC FC values (B= -.312, SE = .002, p =.021; Fig. 1b). Prenatal stress was not significantly associated with left amyg–right ACC FC or right amyg–right ACC FC. The effect of prenatal stressful events on infant left amyg–left ACC was fully mediated by prenatal anxiety symptoms, such that the indirect effect of prenatal stressful events on left amyg–left ACC FC was significant (b = -.003, [-.0053, -.0003]; Fig. 2a). The remaining direct effect of prenatal stressful events on left amyg–left ACC was not significant. We did not find evidence that the effect of prenatal stress on infant right amyg–left ACC was mediated by prenatal anxiety symptoms (Fig. 2b).

Figure 1

Associated between prenatal severity-weighted stressful life events and left amygdala–left ACC (A) and right amygdala–left ACC (B).

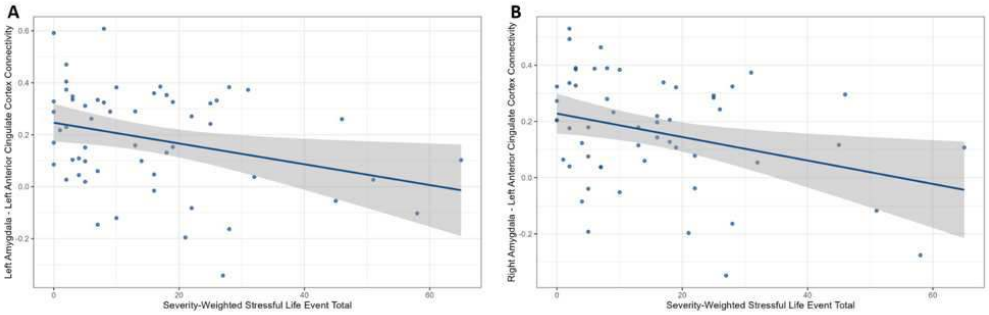

Figure 2

Path model of mediation analysis of severity-weighted stressful life events predicting left amygdala–left ACC (A) and right amygdala–left ACC (B). Note: analyses included infant postnatal age at scan and sex assigned at birth as control variables, but not pictured here.

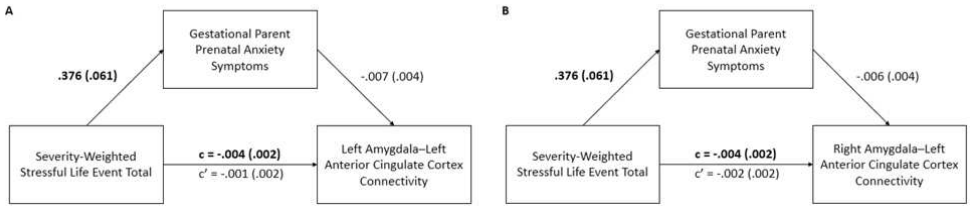

Conclusions: We found evidence that prenatal stress characterized as severity-weighted stressful life events is associated with infant functional connectivity. We also found evidence that gestational parent prenatal anxiety symptoms may mediate this relationship. Our findings contribute to the growing literature on prenatal stress exposure and the functional connectivity of emotional circuits in infants and highlight the prenatal period as target for interventions that improve infant and family well-being.

References

1. Lobel, M. (1992). Prenatal maternal stress and prematurity: a prospective study of socioeconomically disadvantaged women. Health psychology, 11(1), 32.
2. Spielberger, C.D. (1989) State-Trait Anxiety Inventory: Bibliography. 2nd Edition, Consulting Psychologists Press, Palo Alto.

Poster No 1261

Functional Connectivity in Adolescents with Congenital Heart Disease or Neonatal Encephalopathy

Megan Martin[1], Lauren Harasymiw[1], Shabnam Peyvandi[1], Elizabeth George[1], Patrick McQuillen[1], Duan Xu[1]

[1]University of California, San Francisco, San Francisco, CA

Introduction: Although congenital heart disease (CHD) and hypoxic ischemic encephalopathy (HIE) are different pathological conditions, CHD restricts oxygen delivery to the neonatal brain and HIE results from restricted oxygen delivery to the neonatal brain. Both are associated with high incidence of neonatal brain injury and altered brain development. Prior studies have shown differences between these groups in brain size and microstructural development as well as associations between graph theory metrics and intellectual performance derived from functionally connected neural networks using resting state functional MR images (rsfMRI). A negative association between average pathlength and intellectual performance and a positive relationship between global efficiency and intellectual performance have been observed. In this study, we compare graph theory metrics of functionally connected neural networks of adolescents who were born with CHD or HIE to examine similarities and differences.

Methods: We evaluated rsfMRI in adolescents with CHD (n=23) between the ages of 8 and 19 years old and HIE (n=20) between the ages of 10 and 15 years old. These adolescents were enrolled in respective longitudinal cohort studies as neonates. An fMRI sequence with 3mm resolution, a repetition time of 2 seconds and 200 passes was acquired continuously

on a 3T GE MR750 scanner (GE Healthcare, Waukesha, WI, USA) while the subjects were at rest. Additionally, subjects underwent detailed neuropsychological testing. The CONN toolbox (version 22a) was used to preprocess and denoise the rsfMRI data, co-register with the T1 weighted anatomical image and MNI adult brain atlas, and compute functional brain connectomes, adjacency matrices, and graph theory metrics. The graph theory metrics included in this analysis were global and local efficiency, betweenness, closeness centrality, eigenvector centrality, eccentricity, cost, average pathlength, clustering coefficient, and degree. An ANCOVA test was used to assess age as a covariant of neural network graph theory metrics and evaluate groupwise significant differences between CHD and HIE. Groupwise mean and standard deviation were computed when a significant difference was present in a network graph theory metric.

Results: With age evaluated as a covariant, significant differences by diagnosis were identified in two or more graph theory metrics of the sensory motor, visual, salience, dorsal attention, language, and cerebellar networks. No significant differences by diagnosis were identified in the default mode or frontoparietal networks. When significantly different, mean average pathlength was lower in the CHD cohort than in the HIE cohort, except in the cerebellar posterior network, where it was lower in the HIE cohort (Figure 1). Conversely, when significantly different, global efficiency was generally higher in the CHD cohort than in the HIE cohort, except in the dorsal attention frontal eye field and the cerebellar posterior networks where this metric was higher in the HIE cohort (Figure 1).

			Graph Theory Metric									
			Global Efficiency	Local Efficiency	Betweenness	Closeness Centrality	Eigenvector Centrality	Cost	Average pathlength	Degree	Eccentricity	Clustering Coefficient
Neural Network	Sensory Motor Lateral L	HIE	0.513 ± 0.068	–	–	0.442 ± 0.056	1.072 ± 1.059	0.169 ± 0.086	2.302 ± 0.328	27.60 ± 14.07	–	–
		CHD	0.562 ± 0.047	–	–	0.483 ± 0.040	2.027 ± 0.747	0.238 ± 0.068	2.083 ± 0.191	38.78 ± 11.12	–	–
	Sensory Motor Superior	HIE	–	–	–	0.409 ± 0.055	–	–	2.492 ± 0.375	–	–	–
		CHD	–	–	–	0.435 ± 0.037	–	–	2.315 ± 0.199	–	–	–
	Visual Occipital	HIE	–	–	–	–	–	–	–	–	3.85 ± 0.75	0.544 ± 0.085
		CHD	–	–	–	–	–	–	–	–	4.39 ± 0.72	0.617 ± 0.158
	Salience ACC	HIE	0.497 ± 0.071	–	–	0.433 ± 0.063	0.921 ± 0.856	0.146 ± 0.067	–	23.75 ± 10.97	–	–
		CHD	0.554 ± 0.047	–	–	0.484 ± 0.034	1.737 ± 0.806	0.212 ± 0.064	–	34.61 ± 10.49	–	–
	Salience AInsula L	HIE	0.529 ± 0.038	–	–	0.454 ± 0.036	1.185 ± 1.008	0.183 ± 0.049	2.216 ± 0.208	29.85 ± 8.02	–	–
		CHD	0.562 ± 0.038	–	–	0.483 ± 0.028	2.064 ± 0.706	0.234 ± 0.057	2.075 ± 0.119	38.09± 9.29	–	–
	Salience AInsula R	HIE	–	–	–	0.448 ± 0.048	1.207 ± 1.034	–	2.264 ± 0.292	–	–	–
		CHD	–	–	–	0.486 ± 0.029	2.048 ± 0.740	–	2.065 ± 0.126	–	–	–
	Salience SMG R	HIE	0.497 ± 0.044	–	–	0.429 ± 0.043	0.737 ± 0.739	0.148 ± 0.044	2.359 ± 0.295	24.15 ± 7.20	–	–
		CHD	0.542 ± 0.033	–	–	0.477 ± 0.025	1.561 ± 0.550	0.188± 0.047	2.100 ± 0.110	30.57± 7.64	–	–
	Dorsal Attention FEF R	HIE	0.472 ± 0.042	–	0.00602 ± 0.00476	–	–	–	–	–	4.15 ± 0.67	–
		CHD	0.428 ± 0.049	–	0.00237 ± 0.00511	–	–	–	–	–	4.57 ± 0.59	–
	Dorsal Attentions IPS L	HIE	0.487 ± 0.051	–	–	0.419 ± 0.046	–	–	2.416 ± 0.287	–	–	0.590 ± 0.103
		CHD	0.520 ± 0.041	–	–	0.460 ± 0.031	–	–	2.184 ± 0.155	–	–	0.521 ± 0.099
	Dorsal Attentions IPS R	HIE	–	0.797 ± 0.051	–	0.422 ± 0.050	–	–	2.406 ± 0.349	–	–	0.600 ± 0.094
		CHD	–	0.754 ± 0.058	–	0.459 ±0.024	–	–	2.183 ± 0.119	–	–	0.525 ± 0.104
	Language IFG L	HIE	–	0.742 ± 0.087	–	–	–	–	–	–	–	0.515 ± 0.123
		CHD	–	0.791 ± 0.069	–	–	–	–	–	–	–	0.592 ± 0.129
	Language pSTG R	HIE	0.532 ± 0.051	–	–	0.458 ± 0.046	–	0.187 ± 0.066	2.211 ± 0.280	30.45 +10.80	3.75 ± 0.97	–
		CHD	0.572 ± 0.026	–	–	0.497 ± 0.018	–	0.238 ± 0.0593	2.013 ± 0.074	38.78 ± 9.68	4.22 ± 0.60	–
	Cerebellar Anterior	HIE	–	0.716 ± 0.077	0.014 ± 0.010	–	1.277 ±1.084	–	–	–	–	0.474 ± 0.112
		CHD	–	0.630 ± 0.079	0.021 ± 0.012	–	0.585 ± 0.582	–	–	–	–	0.361 ± 0.077
	Cerebellar Posterior	HIE	0.504 ± 0.069	0.720 ± 0.096	–	0.438 ± 0.061	1.059 ± 0.962	0.153 ± 0.076	2.331 ± 0.376	25.00 ± 12.33	–	0.488 ± 0.101
		CHD	0.453 ± 0.072	0.757 ± 0.103	–	0.407 ± 0.059	0.409 ± 0.513	0.103 ± 0.057	2.511 ± 0.382	16.83 ± 9.27	–	0.547 ± 0.165

Figure 1. Significantly different graph theory metrics of brain networks by diagnosis. Values reported as means ± standard deviation.

Conclusions: Our study suggests differences in functional connectivity of neural networks between adolescents with CHD as compared to those with HIE. Further work is needed to determine the association of these differences with detailed cognitive or functional outcomes available for these cohorts.

References

1. Kebaya, L.M.N. (2023) 'Subcortical brain volumes in neonatal hypoxic–ischemic encephalopathy', Pediatric Research, vol. 94, pp. 1797-1803.
2. McQuillen, P.S. (2011), 'Effects of congenital heart disease on brain development', Progress in Pediatric Cardiology, vol. 29, no. 2, pp. 79-85.
3. Nieto-Castanon, A. & Whitfield-Gabrieli, S. (2022). 'CONN functional connectivity toolbox: RRID SCR_009550, release 22'.
4. Parmentier, C.E.J. (2022) 'Magnetic Resonance Imaging in (Near-)Term Infants with Hypoxic-Ischemic Encephalopathy', Diagnostics, vol. 12, no. 3, pp. 645.
5. Van den Heuvel, M.P. (2009) 'Efficiency of functional brain networks and intellectual performance', Journal of Neuroscience, vol. 29, no. 23, pp. 7619-24.
6. Whitfield-Gabrieli, S. & Nieto-Castanon, A. (2012). 'Conn: A functional connectivity toolbox for correlated and anticorrelated brain networks', Brain connectivity, vol. 2, no. 3, pp. 125-141.

Poster No 1262

Lessons learned from longitudinal MRI study of infant and toddler brain development

Leslie Gaines[1], Bosi Chen[1], Alexis McKay[1], Seyeon Yim[1], Cassandra Hendrix[2], Natalie Brito[3], Moriah Thomason[4]

[1]Department of Child and Adolescent Psychiatry, New York University Langone, New York, NY, [2]NYU Langone, New York, NY, [3]New York University, New York, NY, [4]NYU Langone Medical Center, New York, NY

Introduction: Infant and toddler MRI provides a unique opportunity to study rapid changes in both brain anatomy and functional organization in the first years of life[1,2]. However, scanning infants and toddlers presents multiple practical challenges that often result in limited sample sizes and variable data quality[3]. In particular, longitudinal MRI studies across infancy and toddlerhood require careful considerations for MRI acquisition strategies during different developmental stages. In an effort to promote communication with other infant toddler imaging labs, we are reporting our scanning protocols, success rates across scan sequences, and motion characterization in our longitudinal infant MRI study as well as planned modifications to our protocol in preparation for scanning toddlers at 4 years of age.

Methods: Participants included infants of women enrolled in the COVID-19 and Perinatal Experiences Study, conducted at NYU Langone Health. 88 infants (47 males) were scanned within the first 5 months after birth (ages 1-5 months; neonatal visit) and 64 infants (36 males) were scanned at around 12 months of age (ages 9-17 months; 1-year-old visit) during natural sleep. All infants were scanned during daytime napping for the neonatal MRI visit but the majority (63%) of infants were scanned during nocturnal sleep for the 1-year-old MRI visit. The MRI acquisition sequence includes T1-weighted and T2-weighted anatomical scans, fMRI, diffusion tensor imaging (DTI), and relaxometry imaging on a 3T Siemens Prisma MRI using a 32-channel head coil. We defined a scan being successful if at least one type of usable data is available. Head motion indexed by framewise displacement (FD) was extracted for each fMRI scan.

Results: The success rate for neonatal MRI scans (84%) is significantly higher than the success rate for 1-year-old MRI scans (56%; $X2$ (1, $N = 88$) = 13.03, $p < .001$). Anatomical T1 were acquired in 83% of the neonatal and 56% of 1-year-old scans. FMRI data were acquired in 74% of the neonatal scans and in 52% of the 1-year-old scans. Full or partial DTI were acquired in 32% of the neonatal scans and in 34% of the 1-year-old scans. While the acquired fMRI data length is comparable between the two timepoints ($t(63) = .13$, $p = .45$), head motion is significantly higher during the neonatal scans ($t(78.19) = 2.38$, $p = .02$). For the 1-year-old MRI visit, the success rate during nocturnal sleep (66%) is significantly higher than during daytime napping (33%; $X2$ (1, $N = 64$) = 6.67, $p = .01$).

Conclusions: Consistent with reports by other infant MRI research groups[4], sleep MRI success rates are higher among younger infants than older infants. Increased awareness of surroundings at 1 year old may hinder children's ability to fall asleep in unfamiliar environments. Neonates display greater head motion than older infants during MRI, likely related to developmental differences in sleep patterns. For older infants, we attribute greater success rates during nocturnal sleep compared to daytime napping to the higher likelihood of achieving deeper and longer sleep periods at night. Our group is currently preparing for the third longitudinal MRI visit to scan children at age 4 years during nocturnal sleep. These combined findings have informed the development of preparation and scanning protocols for toddlers. A comprehensive preparation protocol, including an age-appropriate social story, a narrated video of the MRI visit, and a 7-day at-home habituation process, is under development and will be included as part of this presentation.

References

1. Gilmore, J. H., Shi, F., Woolson, S. L., Knickmeyer, R. C., Short, S. J., Lin, W., . . . Shen, D. (2012). Longitudinal development of cortical and subcortical gray matter from birth to 2 years. Cereb Cortex, 22(11), 2478-2485. doi:10.1093/cercor/bhr327
2. Gao, W., Alcauter, S., Elton, A., Hernandez-Castillo, C. R., Smith, J. K., Ramirez, J., & Lin, W. (2015). Functional Network Development During the First Year: Relative Sequence and Socioeconomic Correlations. Cereb Cortex, 25(9), 2919-2928. doi:10.1093/cercor/bhu088
3. Turesky, T. K., Vanderauwera, J., & Gaab, N. (2021). Imaging the rapidly developing brain: Current challenges for MRI studies in the first five years of life. Developmental Cognitive Neuroscience, 47, 100893. https://doi.org/10.1016/j.dcn.2020.100893
4. Hendrix, C. L., & Thomason, M. E. (2022). A survey of protocols from 54 infant and toddler neuroimaging research labs. Developmental Cognitive Neuroscience, 54, 101060. https://doi.org/10.1016/j.dcn.2022.101060.

Poster No 1263

Developmental Sex Differences in White Matter using Advanced and Conventional dMRI Models

Sebastian Benavidez[1], Katherine Lawrence[1], Gaon Kim[1], Zvart Abaryan[2], Emily Laltoo[1], James McCracken[3], Paul Thompson[1]

[1]Imaging Genetics Center, Mark and Mary Stevens Neuroimaging & Informatics Institute, USC, Marina del Rey, CA, [2]Children's Hospital of Los Angeles, Los Angeles, CA, [3]Department of Psychiatry, University of California San Francisco, San Francisco, CA

Introduction: Childhood and adolescence are periods of substantial white matter (WM) maturation. WM abnormalities have also been implicated in adolescent-onset psychiatric disorders. Understanding sex differences in the typically developing brain may offer insight into sex-specific variation in these brain-based disorders (Boyd et al., 2015). Although prior research has extensively characterized WM sex differences in adults (Salminen et al., 2022), WM sex differences during development are less well understood. Here we aimed to characterize sex differences in WM microstructure during typical development – from early childhood through emerging adulthood – using diffusion-weighted MRI (dMRI) data modeled with conventional diffusion tensor imaging (DTI) (Basser et al., 1994) and the advanced tensor distribution function (TDF) (Leow et al., 2009).

Methods: We analyzed dMRI data sourced from the Healthy Brain Network (Alexander et al., 2017), from 239 typically developing participants aged 5-22 years (46.0% female). Participants were included in our sample if they received a full clinical evaluation and were not given a clinical diagnosis. dMRI scans were acquired across four scanners: three 3T scanners (1.8 mm isotropic voxel size, 72 slices), and one 1.5T scanner (2.0 mm isotropic voxel size, 72 slices). All dMRI scans had one b = 0 s/mm2 volume and 64 directions at b = 1000 s/mm2. All dMRI scans were preprocessed using the ENIGMA-DTI protocol (Jahanshad et al., 2013). Measures of fractional anisotropy (FADTI), mean diffusivity (MD), axial diffusivity (AD), and radial diffusivity (RD) were generated using DTI. The TDF model was used to generate FATDF, which is similar to FADTI but more accurately describes voxels with crossing fibers. These measures were then skeletonized using tract-based spatial statistics. Using the JHU WM brain atlas (Mori et al., 2008), the average value along the WM skeleton was extracted for each metric in 25 regions of interest (ROI). We harmonized the ROI data using ComBat within each metric (Radua et al., 2020; Fortin et al., 2018). A fixed-effects linear regression was used to assess WM sex differences, adjusting for age, age-squared, the interaction between sex and age, and the interaction between sex and age-squared. The false discovery rate (Benjamini & Hochberg, 1995) was used to correct for multiple comparisons across the 25 ROIs, and significance was determined by a corrected p-value of 0.05.

Results: The effect of sex was regionally consistent, as boys generally exhibited lower FADTI and FATDF and higher MD, AD, and RD than girls. For the DTI metrics, boys displayed significantly lower FADTI in the sagittal stratum (SS); higher MD across the whole brain, in the corona radiata (CR), posterior corona radiata (PCR), anterior corona radiata (ACR), external capsule (EC), uncinate fasciculus (UNC), posterior thalamic radiation (PTR), superior longitudinal fasciculus (SLF), and SS; higher AD in the PCR, SLF, and SS; and higher RD in the SS compared to girls. For FATDF, boys exhibited significantly lower values than girls in the CR, superior corona radiata (SCR), PCR, EC, fornix/stria terminalis (FXST), PTR, retrolenticular limb of the internal capsule (RLIC), SLF, SS, and tapetum (TAP). The TDF model was more sensitive to sex differences than DTI, detecting more significant ROIs than the DTI model (Fig. 1).

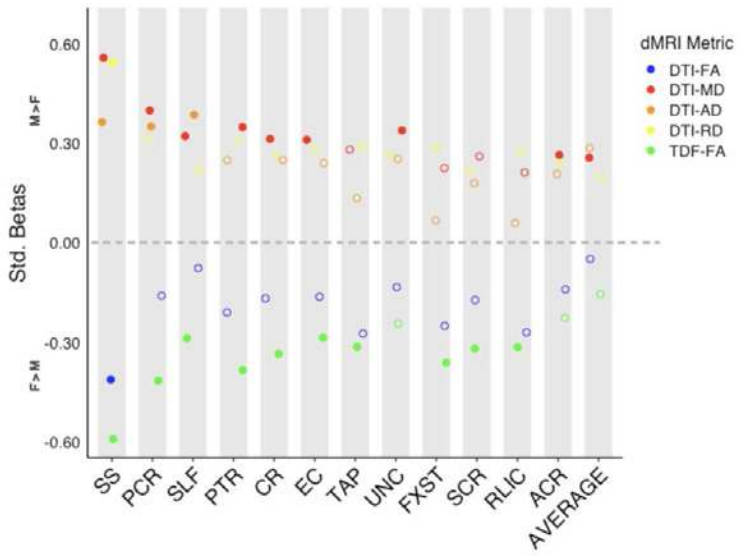

Fig. 1 Effect sizes for the main effect of sex. We show ROIs that exhibited significance for at least one dMRI metric: solid circles represent significant effects, and hollow circles represent non-significant effects. Positive values represent metrics that were greater in boys compared to girls, and negative values represent metrics that are greater in girls compared to boys.

Conclusions: We found widespread sex differences in WM microstructure during typical development. The observed sex differences across WM regions suggest greater FA and lower diffusivity for females compared to males, which may have implications for understanding sex-specific vulnerabilities in psychiatric disorders. As a whole, these findings highlight the need to consider sex in neurodevelopmental research and underscore the value of the advanced TDF model.

References

1. Alexander, L.M. (2017), 'An open resource for transdiagnostic research in pediatric mental health and learning disorders', Sci Data, vol. 4, no. 1, Art. no. 1
2. Basser, P.J. (1994), 'MR diffusion tensor spectroscopy and imaging', Biophys J, vol. 66, no. 1, pp. 259–267
3. Benjamini, Y. (1995), 'Controlling the False Discovery Rate: A Practical and Powerful Approach to Multiple Testing', Journal of the Royal Statistical Society: Series B (Methodological), vol. 57, no. 1, pp. 289–300
4. Boyd, A. (2015), 'Gender differences in mental disorders and suicidality in Europe: Results from a large cross-sectional population-based study', Journal of Affective Disorders, vol. 173, pp. 245–254
5. Fortin, J.P. (2018), 'Harmonization of cortical thickness measurements across scanners and sites', NeuroImage, vol. 167, pp. 104–120
6. Jahanshad, N. (2013), 'Multi-site genetic analysis of diffusion images and voxelwise heritability analysis: A pilot project of the ENIGMA–DTI working group', NeuroImage, vol. 81, pp. 455–469
7. Leow, A.D. (2009), 'The tensor distribution function', Magnetic Resonance in Medicine, vol. 61, no. 1, pp. 205–214
8. Mori, S. (2008), 'Stereotaxic white matter atlas based on diffusion tensor imaging in an ICBM template', NeuroImage, vol. 40, no. 2, pp. 570–582
9. Radua, J. (2020), 'Increased power by harmonizing structural MRI site differences with the ComBat batch adjustment method in ENIGMA', NeuroImage, vol. 218, p. 116956
10. Salminen, L.E. (2022), 'Sex is a defining feature of neuroimaging phenotypes in major brain disorders', Human Brain Mapping, vol. 43, no. 1, pp. 500–542

Poster No 1264

Cerebello-cortical Connectivity During Early Brain Development

Wenjiao Lyu[1], Kimhan Thung[1], Li Wang[1], Weili Lin[1], Sahar Ahmad[1], Pew-Thian Yap[1]

[1]*University of North Carolina at Chapel Hill, Chapel Hill, NC*

Introduction: The cerebello-cortical system stands out as one of the most crucial networks in the human brain. In comparison to other primates, the expansion of key regions within the human cerebello-cortical system has undergone the highest evolutionary rate, suggesting a pivotal role of the cerebellum in the cognitive evolution of humans[1]. The cerebellum undergoes rapid growth in the late stages of gestation and continues to develop after birth, establishing long-range connections with the brain through the formation of white matter fibers[2]. However, during the early childhood period, when the cerebellum undergoes continuous development, a clear picture of the evolution of cerebello-cortical connectivity remains elusive. Abnormal connections between the cerebellum and the cerebral cortex have been found to be associated with disorders such as autism spectrum disorder and hyperactivity disorder, which tend to manifest in childhood and are associated with cognitive

and motor abnormalities[3]. It is therefore crucial to investigate the fundamental patterns of cerebello-cortical connectivity during early childhood. Here, we map the typical developmental patterns of cerebello-cortical connectivity in early children.

Methods: Over 1000 BCP scans from 285 healthy participants (M/F:137/148), aged between birth and 5 years were collected in this study[4]. The rs-fMRI data were processed using the following steps[5]: head motion correction, EPI distortion correction, brain extraction, registration to structural MRI, high-pass filtering, ICA-AROMA denoising, and co-registration to MNI space. Then 2 stages of group independent component analysis (GICA) were used to generate the independent components. Based on the anatomical location of the individual components, 26 components were selected from 35 components and further grouped as 9 cortical functional networks (FNs). Dual regression was used to obtain individual FNs[6]. For each individual non-overlapping FN, a representative eigen time series was computed. For each cerebellar voxel, partial correlations were computed with respect to all the FN eigen time series. Finally, the correlations were converted to z-scores using Fisher r-to-z transform. SUIT and R were used for visualization.

Results: We identified 26 components and categorized them into nine brain functional networks, namely the Sensorimotor Network (SMN), Default Mode Network (DMN), Salience Network (SN), Executive Control Network (ECN), Visual Network (VIS), Auditory Network (AUD), Dorsal Attention Network (DAN), Ventral Attention Network (VAN), and Limbic Network. Cerebello-cortical functional connectivity maps across months were derived through partial correlation analyses involving all the specified components. Generally, the connectivity between the SMN and the cerebellum surpasses that of other cortical brain networks. Particularly, connectivity is more pronounced in Lobule I-IV, Lobule V, and Lobule VIII. Robust connectivity has been identified between the visual network and Lobule VI. Connectivity between higher-order functional networks and the cerebellum is typically weaker in early childhood. Around age one, children display cerebello-cortical connectivity patterns similar to those seen in adults (Figure 1). During childhood, the overall strength of cerebello-cortical connectivity exhibits an ascending trend. Connection between the cerebellum and different brain functional networks develops asynchronously and heterogeneously. Certain brain networks demonstrate gender differences in connectivity with the cerebellum (Figure 2).

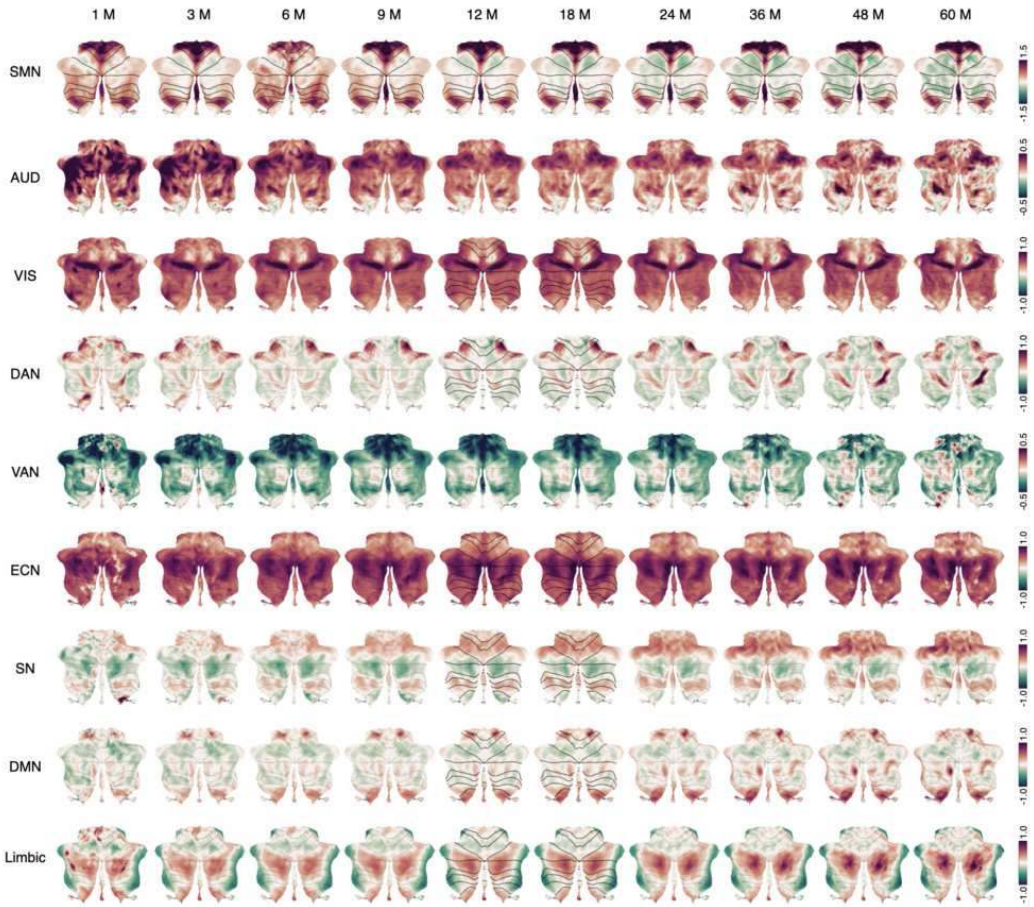

Figure 1. Cerebello-cortical connectivity during early brain development.

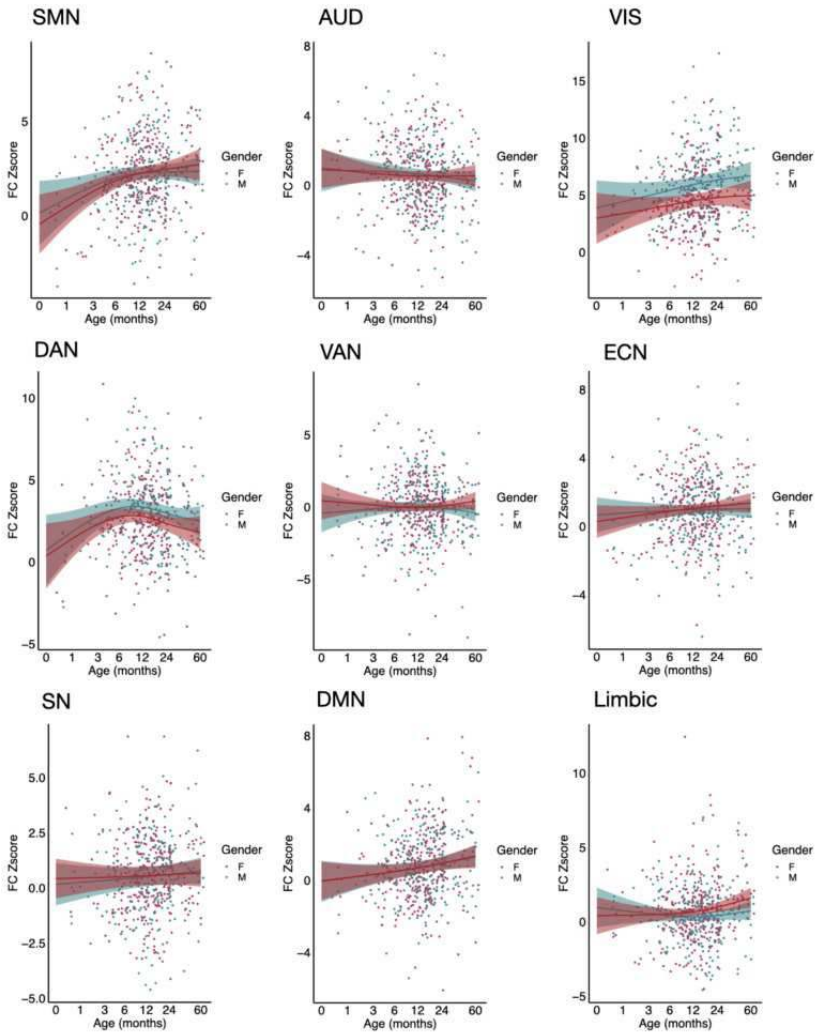

Figure 2. Developmental trajectories of cerebello-cortical functional connectivity.

Conclusions: We mapped the cerebello-cortical functional connections from 0 to 5 years of age, capturing the asynchronous and heterogenous patterns of development during this early phase of brain development.

References

1. Barton et al. (2014), "Rapid evolution of the cerebellum in humans and other great apes," Current Biology, 24(20), 2440-2444.
2. Volpe (2009), "Cerebellum of the premature infant: rapidly developing, vulnerable, clinically important," Journal of Child Neurology, 24(9), 1085-1104.
3. ten Donkelaar et al. (2003), "Development and developmental disorders of the human cerebellum," Journal of Neurology, 250, 1025–1036.
4. Howell et al. (2019), "The UNC/UMN Baby Connectome Project (BCP): An overview of the study design and protocol development," NeuroImage, 185, 891-905.
5. Thung et al. (2022), "Analysis of ICA-AROMA motion denoising on fMRI data in infant cohort," OHBM.
6. Beckmann et al. (2009), "Group Comparison of Resting-State FMRI Data Using Multi-Subject ICA and Dual Regression," NeuroImage, 47(Suppl 1), S148.

Poster No 1265

Distinct spatial dimensions of changes in cortical structure during early adolescence

Mari Shishikura[1], Alain Dagher[2]

[1]McGill University, Montreal, QC, [2]Montreal Neurological Institute and Hospital, McGill University, Montreal, QC

Introduction: Adolescence is a critical period when the brain undergoes structural and functional maturation. Previous studies have shown that mean cortical thickness peaks at 1-2 years of life and decreases thereafter, whereas total cortical surface area

continues to expand during childhood until it peaks in late childhood/adolescence[1,2]. However, less is known about region-specific trajectories of these cortical structures during the maturation process. Moreover, we have yet to elucidate if different regions are coordinated in the way they mature. In this study, we aimed to depict the region-specific developmental trajectory in the cortex during early adolescence. We further identified clusters of regions that had a common structural change pattern. Finally, we investigated whether these common change factors were associated with changes in impulsivity scores over the same period.

Methods: We used T1-weighted magnetic resonance images from Adolescent Brain Cognitive Development study[3], an ongoing longitudinal study where subjects were recruited at age 9-10 and are scanned every two years (baseline, 2-year-, and 4-year-follow-up data are currently available). We included subjects who were scanned at least twice, totaling 7904 subjects. Images were pre-processed and the cortex was segmented into 68 regions (DK atlas) by the ABCD working group. Site differences were corrected using Longitudinal ComBat[4]. For each region, we fitted a separate latent growth curve model[5] to obtain baseline measures (intercept) and annual change (slope) of cortical surface area and thickness. Estimate of change is reported as % change per annum. We then simultaneously estimated growth curves of all regions in the left hemisphere and obtained a latent correlation matrix, which represents how correlated slopes are among regions. Exploratory factor analysis (EFA) was conducted on the matrix to identify latent factors, which capture spatially distinct dimensions of cortical structural change. As a confirmatory factor analysis (CFA), we modeled growth curves simultaneously in the right hemisphere with the identified latent factors. Model fit was assessed based on Comparative Fit Index (CFI) and Standardized Root Mean Squared Residual (SRMR), with CFI>0.9 and SRMR<0.08 as a good fit. Finally, we assessed the Pearson correlation between the latent change factors and the change in UPPSP impulsivity scores[6].

Results: Latent growth curve modeling revealed that while all regions undergo cortical thinning from age 10 to 14 (maximum in cuneus, 1.13%, minimum in entorhinal cortex, 0.13%), surface area show mixed direction of change. Specifically, regions in frontal lobe had surface area expansion (maximum in anterior cingulate, 0.54%), whereas regions in parietal and occipital lobe showed decrease in surface area (maximum in precuneus, 0.6%) (Fig 1). Although EFA suggested a two-factor solution for cortical thickness changes, CFA showed a moderate fit (CFI=0.81, SRMR=0.08). For cortical surface area, four-factor model had a good fit (CFI=0.94, SRMR=0.02). The loadings of the four factors are shown in Fig2. Factor 3, which had high loadings on frontal cortex, showed significant association with UPPSP lack of planning (r = -0.059, p=0.006).

Conclusions: We showed that cortical regions can be grouped together in regard to the trajectory of development during early adolescence. These underlying spatial patterns may be crucial in assessing brain-behavior associations during development.

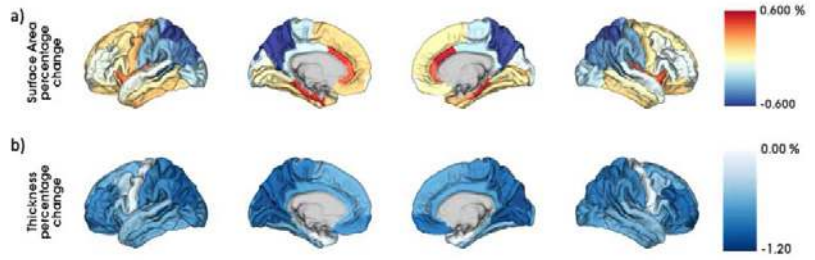

Fig 1. Results of latent growth curve modeling for each region. Values represent annual % change.

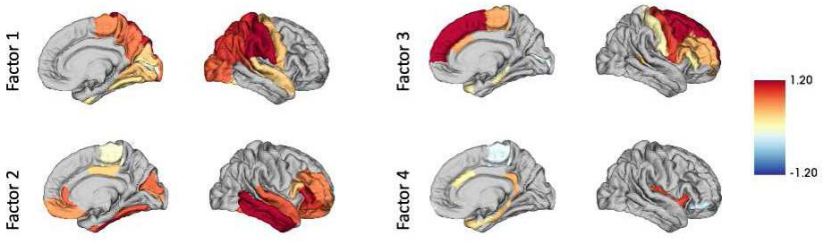

Fig 2. Standardized factor loadings of regional surface area on each cortical change factors identified in the confirmatory factor analysis.

References

1. Bethlehem, R. a. I. et al. (2022), 'Brain charts for the human lifespan.' Nature 604, 525–533.
2. Gilmore, J. H., Knickmeyer, R. C. & Gao (2018), W. 'Imaging structural and functional brain development in early childhood.' Nat Rev Neurosci 19, 123–137.

3. Karcher, N. R. & Barch, D. M. (2021), 'The ABCD study: understanding the development of risk for mental and physical health outcomes.' Neuropsychopharmacol. 46, 131–142.
4. Beer, J. C. et al. (2020), 'Longitudinal ComBat: A method for harmonizing longitudinal multi-scanner imaging data.' NeuroImage 220, 117129 (2020).
5. Burant, C. J. (2016), 'Latent Growth Curve Models: Tracking Changes Over Time.' Int J Aging Hum Dev 82, 336–350.
6. Lynam, D. R., Smith, G. T., Whiteside, S. P. & Cyders, M. A. (2006), 'The UPPS-P: Assessing Five Personality Pathways to Impulsive Behavior (Technical Report).'

Poster No 1266

The leading influence of life stressful events on the dynamic reconfiguration of brain networks

Xinnan Wang[1], Ying He[2]

[1]Beijing Normal University, Chengdu, Sichuan, [2]Beijing Normal University, Beijing, Beijing

Introduction: The occurrence of stressful events in life will increase the risk of emotional and behavioral problems. Some studies have found that among adolescents, Previously experienced stressful life events can accurately predict the emergence of problem behaviors one year later (Kim et al. 2003) and have also been shown to affect behavioral, emotional, social, physical, and cognitive development. Many previous studies have focused on the influence of the occurrence of previous life stressful events on subsequent brain structural features, the occurrence of stressful events, represented by neglect or deprivation (financial or parental care), has also been shown to be associated with changes in activation and functional connectivity of the frontoparietal network and the default network (Chahal et al. 2022).

Methods: Participants: A total of 2774 twins have finished the questionaires through two time poins. A total of 108 pairs of twins completed MRI scans at the third timepoints.. Questionnaire: SLE were measured for all participants for stressful life events. CBCL were adopted to measure the externalized behavioral factors and attention deficits of the subjects. fMRI Data: A total of 73 pairs (146 subjects) were used for brain image data analysis. A template containing 1024 uniformly sized gray matter regions was selected, the average time series of each voxel in each region was extracted, and then the dynamic functional connection matrix was calculated using the sliding time window method. The iterative and ordered Louvain algorithm is used by Matlab2016 to modularise the functional connections for each time window.

Results: There are significant differences in visual network, somatic motor network, dorsal attention network, default network, and subcortical network (visual network: t (140) = 3.123, pcorrected = 0.0174; Physical motor network: t (140) = 2.657, pcorrected = 0.0176 ; Dorsal attention network: t (140) = 2.739,pcorrected = 0.0176; Default network: t (140) = 2.303, pcorrected = 0.0364; Subcortical network: t (140) = 2.731,pcorrected = 0.0176). The ventral attention network, limbic system and frontoparietal network also showed a trend of more dynamic activities in the low life stress group. In terms of module variation rate, the low life stress group also showed a trend of more dynamic activities, and the visual network, the somatic motor network and the dorsal attention network showed marginal significance (visual network: pcorrected = 0.0529; Physical motor network: pcorrected = 0.0529; Dorsal attention network: pcorrected = 0.0529). The occurrence of prior disciplinary behavior significantly predicted the MV rate of the brain frontoparietal network and the default network (FPN: t = -2.226, p = 0.0285; DMN: t= -2.160, p = 0.0335), and in the NSR, DMN showed a significant edge (t= -1.793, p = 0.076), and PFN only showed a trend, but not significant (t= -1.130, p = 0.261). Also, the results show that the reduced NSR of the subcortical network is associated with an increased problem of aggressive behavior (t = -2.762, pcorrected=0.0260), problem of external behavior (t = -2.608, pcorrected=0.0260), and the overall score of behavior problems (t = -2.36, pcorrected=0.0328). On the basis of NSR, the increase of externalized behavior problems is also correlated with less MSR (attack behavior: t = -2.010, p = 0.0473; Externalized behavior problems: t = -2.260, p = 0.0263), while the total score of behavior problems showed a negative correlation trend(t = -1.835, p = 0.0699).

Conclusions: We found that the dynamic recombination activity of brain regions, such as the frontoparietal network and the default network, is mainly influenced by environmental factors, and stressful life events may be an important factor. These findings contribute to a better understanding of the factors behind the organizational patterns and changes of brain functional networks and provide a basis for prevention and intervention of abnormal development in children and adolescents.

References

1. Kim et al., 2003. "Reciprocal Influences between Stressful Life Events and Adolescent Internalizing and Externalizing Problems." Child Development 74(1):127–43. doi: 10.1111/1467-8624.00525.
2. Chahal et al.,(2022). "An Exploration of Dimensions of Early Adversity and the Development of Functional Brain Network Connectivity during Adolescence: Implications for Trajectories of Internalizing Symptoms." Development and Psychopathology 34(2):557–71. doi: 10.1017/S0954579421001814.

3. Papagni et al., 2011. "Effects of Stressful Life Events on Human Brain Structure: A Longitudinal Voxel-Based Morphometry Study." Stress 14(2):227–32. doi: 10.3109/10253890.2010.522279.

Poster No 1267

Brain-Age Prediction: Systematic Evaluation of Site Effects, and Sample Age Range and Size

Yuetong Yu[1], Hao-Qi Cui[1], Shalaila Haas[2], Faye New[2], Nicole Sanford[1], Kevin Yu[1], Denghuang Zhan[1], Guoyuan Yang[3], Jia-hong Gao[4], Dongtao Wei[5], Jiang Qiu[5], Boris Bernhardt[6], Paul Thompson[7], Sophia Frangou[1], Ruiyang Ge[1], ENIGMA consortium[8]

[1]University of British Columbia, Vancouver, British Columbia, [2]Icahn School of Medicine at Mount Sinai, New York, NY, [3]Beijing Institute of Technology, Beijing, China, [4]Peking University, Beijing, Beijing, [5]Southwest University, Chongqing, Chongqing, [6]Montreal Neurological Institute and Hospital, Montreal, Quebec, [7]USC, Marina Del Rey, CA, [8]Imaging Genetics Center, Mark and Mary Stevens Neuroimaging and Informatics Institute, Marina del Rey, CA, CA

Introduction: Structural neuroimaging data have been utilized to estimate the biological age of the brain (brain-age). This metric has shown associations with other biologically and behaviorally significant indicators of brain development and aging. The continuous interest in brain age research underscores the necessity for robust, publicly accessible pre-trained brain age models, constructed using extensive data from healthy individuals. In response to this demand, we previously introduced a developmental brain age model (5-22 years). In this work, we expand upon our prior efforts to create, empirically validate, and share a pre-trained brain age model that spans across a broader spectrum of the human lifespan.

Methods: We examined the impact of site harmonization, age range, and sample size on brain age prediction using a discovery sample comprising 35,683 healthy individuals (53.59% female, age range 5-90 years), a replication sample (N=2101, 55.35% female, age range 8-80 years), and a longitudinal consistency sample (N=377, 49.87% female, age range: 9-25 years). Morphometric features were extracted from FreeSurfer processing, and included Desikan-Killiany atlas measures of cortical thickness (n=68), cortical surface area (n=68), and regional subcortical volumes (n=14) based on the Aseg atlas. Following our previous work[1], support vector regression with radial basis function kernel was adopted to train the sex-specific brain-age models. The primary performance measures for all models were the mean absolute error (MAE), and the correlation coefficient (CORR) between brain-age and chronological age. The procedures used to generate optimized sex-specific models are illustrated in Figure 1. For all models, hyper-parameter tuning was performed in the discovery sample using a grid search approach in a 10-fold cross-validation scheme across five repetitions. We evaluated 3 site handling strategies in each of 5 scenarios after partitioning the discovery sample into different age bins as follows: (i) a single bin with the full sample age range (5-90 years); (ii) nine bins each covering sequential 10-year intervals; (iii) four bins each covering sequential 20-year intervals; (iv) three bins each covering sequential 30-year intervals; (v) two age bins each covering sequential 40-year intervals. The following 3 site handling strategies were applied to each bin: (i) data residualization with respect to the scanning site using Combat-GAM[2]; (ii) data residualization with respect to the scanning site using a generalized linear model[3], and (iii) no site harmonization. The approach and age partition with the best-performing MAE and CORR values were considered for further evaluation. To estimate the minimum sample size required for a stable model, the discovery sample was randomly partitioned into 30 sex-specific subsets, ranging from 200 to 6,000 participants in increments of 200, without replacement. The model with the lowest replication MAE and highest replication CORR in the replication sample and in the longitudinal consistency sample was chosen as the preferred model.

Results: (1) The accuracy of age prediction from morphometry data was higher when no site harmonization was applied (Fig 1A); (2) dividing the sample into two age-bins (5-40 and 40-90 years) provided a better balance between model accuracy and explained age variance than any other alternatives (Fig1A, Fig2A), as well as achieved optimal consistency on the longitudinal data (Fig2B); (3) model accuracy for brain-age prediction plateaued at a sample size exceeding 1,600 participants (Fig1B). These findings have been incorporated into an open platform for individualized neuroimaging metrics[4].

Conclusions: In this work, we present empirically validated models for brain-age that can accommodate studies using data across most of the lifespan. We outline the methodological choices that have led to these models and their performance within and across samples as well as longitudinally.

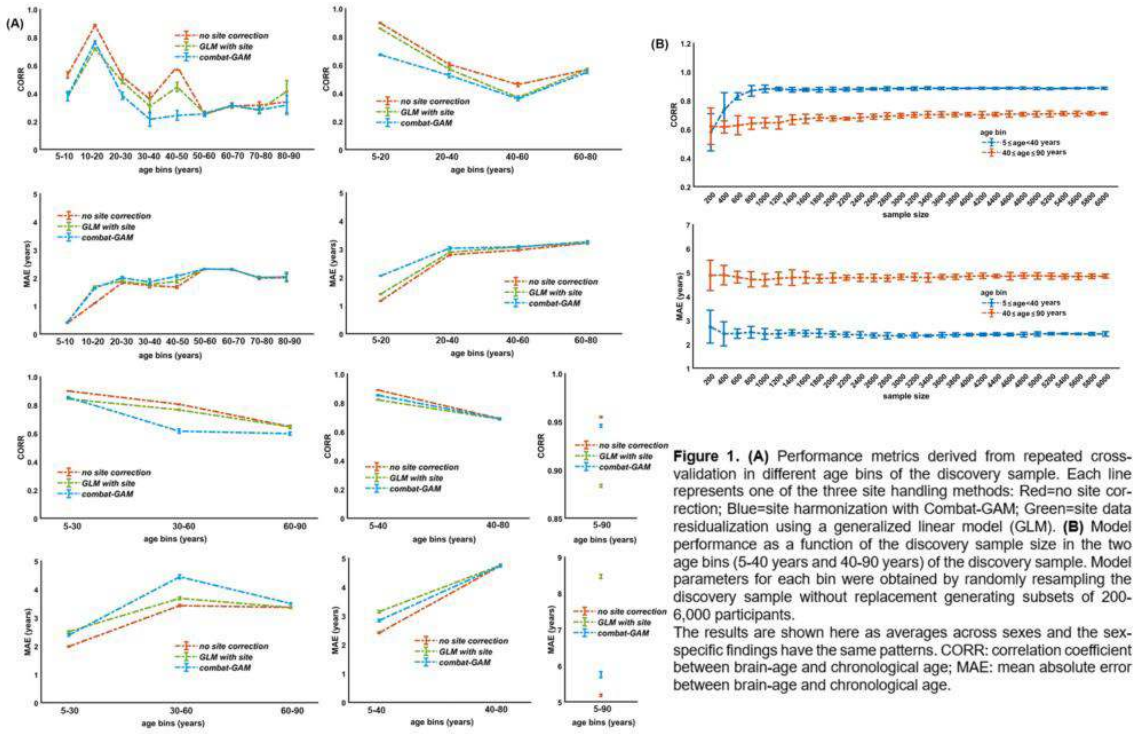

Figure 1. (A) Performance metrics derived from repeated cross-validation in different age bins of the discovery sample. Each line represents one of the three site handling methods: Red=no site correction; Blue=site harmonization with Combat-GAM; Green=site data residualization using a generalized linear model (GLM). **(B)** Model performance as a function of the discovery sample size in the two age bins (5-40 years and 40-90 years) of the discovery sample. Model parameters for each bin were obtained by randomly resampling the discovery sample without replacement generating subsets of 200-6,000 participants.
The results are shown here as averages across sexes and the sex-specific findings have the same patterns. CORR: correlation coefficient between brain-age and chronological age; MAE: mean absolute error between brain-age and chronological age.

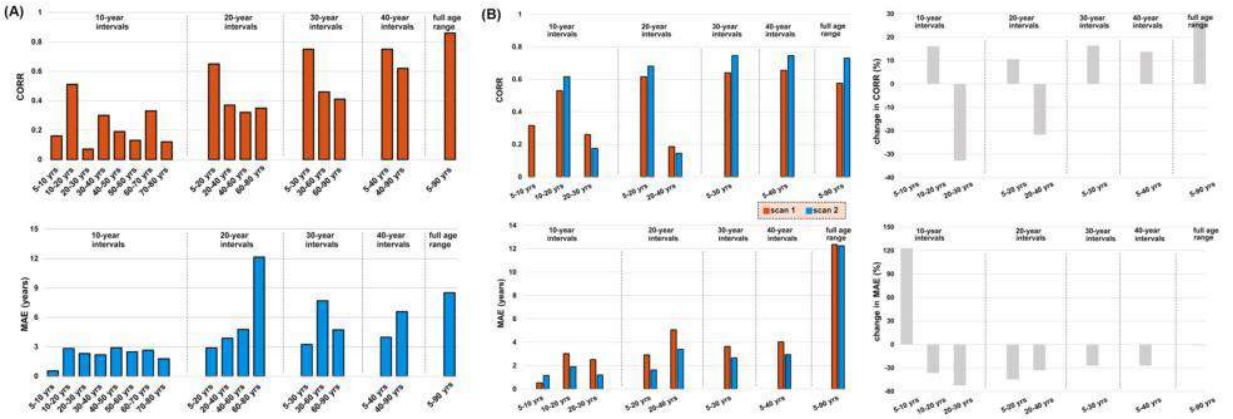

Figure 2. **(A)** Performance metrics derived from the application of the models pre-trained on different age bins of the discovery sample to the corresponding age bins of the replication sample. **(B)** Model performance in longitudinal data. The left panel presents the CORR and MAE values for the first and second MRI scans, while the right panel exhibits the percentage changes (%) in CORR and MAE for the second scan compared to the first scan. The results were generated by employing models that had been trained on discovery samples from each age range division and then applied to the longitudinal consistency sample.
The results are shown here as averages across sexes and the sex-specific findings have the same patterns. CORR: correlation coefficient between brain-age and chronological age; MAE: mean absolute error between brain age and chronological age.

References

1. Modabbernia, A., et al., Systematic evaluation of machine learning algorithms for neuroanatomically-based age prediction in youth. Human Brain Mapping, 2022. 43(17): p. 5126-5140.
2. Pomponio, R., et al., Harmonization of large MRI datasets for the analysis of brain imaging patterns throughout the lifespan. NeuroImage, 2020. 208: p. 116450.
3. de Lange, A.M.G., et al., Mind the gap: Performance metric evaluation in brain-age prediction. Human Brain Mapping, 2022. 43(10): p. 3113-3129.
4. https://centilebrain.org/#/brainAge2

Poster No 1268

Normative modeling of thalamic nuclear volumes

Manojkumar Saranathan[1], Taylor Young[1]

[1]*University of Massachusetts Chan Medical School, Worcester, MA*

Introduction: The thalamus and its constituent nuclei are implicated in several neurological and neuropsychiatric disorders, but the roles of specific nuclei are still being elucidated as thalamic nuclei segmentation methods have been suboptimal, until

recently. Thalamus optimized multi-atlas segmentation (THOMAS) is a recently developed state-of-the-art method[1] that utilizes the improved contrast of white-matter nulled (WMn) MRI to generate accurate nuclei parcellations. It has been validated against manual segmentation guided by the Morel atlas. Recently, THOMAS has been adapted for standard 3T T1 MRI[2] by synthesizing WMn-MRI data from standard T1 MRI prior to segmentation. Normative modeling[3,4] is an emerging framework that has proven sensitive in detecting subtle heterogeneity often present in mental disorders, missed by conventional case-control analyses. Using the modified THOMAS method, we analyzed thousands of T1 MRI datasets from publicly available databases and created what we believe to be the first normative model of thalamic nuclear volumes across the lifespan. We then used this normative model to examine data from patients with dementia (early and late mild cognitive impairment, Alzheimer's disease), ADHD, bipolar disorder, affective and non-affective psychosis, and schizophrenia.

Methods: Volumes of the whole thalamus and 12 nuclei were generated for each side using THOMAS in control subjects (n=2374, 1279 female 1095 male) and disease cohorts (n=694, 301 female 393 male). Site effects were harmonized using COMBAT-GAM and volumes were adjusted by total intracranial volume (FreeSurfer eTIV output). Multiple modeling approaches have been presented for normative modeling. To determine the optimal model for thalamic nuclear volumes, three models- Ordinary least squares regression (OLS), multiple fractional polynomial models (MFP), and generalized additive models of location shape and scale (GAMLSS)- were evaluated with 5-fold cross validation on a subset of 200 subjects. Using maximum absolute error and mean squared error as metrics, MFP models performed the best and were computationally efficient (in concordance with[4]) and was used for creating NMs on the whole dataset. For each nucleus and hemisphere, an MFP-based NM was trained on control subjects in sex-stratified datasets with age as a covariate, resulting in 13*2*2=52 models. These models were then applied to patient data from the disease cohorts. For each control subject and patient, z-scores were calculated from model residuals. Infranormal (z<=-2) and supranormal (z>=2) deviations were tabulated. Multi group comparisons were performed using the Kruskal-Wallis rank sum test and z-score distributions were compared using the z-test.

Results: Figure 1 shows a normative model for left mediodorsal nucleus as a function of age with the different quantiles. Ridge plots of z-score distributions showed shifts in specific nuclei associated with the conditions. For example, significant (Bonferroni p<0.05) shifts in z-score distributions showed a gradual progression from predominantly left anteroventral, mediodorsal, and pulvinar in early MCI to nearly all nuclei bilaterally in AD. Figure 2 summarizes extreme infranormal z-score deviations (<2) as a function of disease diagnosis. Note the progression from EMCI to AD as well as significant deviations in non-affective psychosis and schizophrenia. Supranormal z-score deviations (>2) were all non-significant.

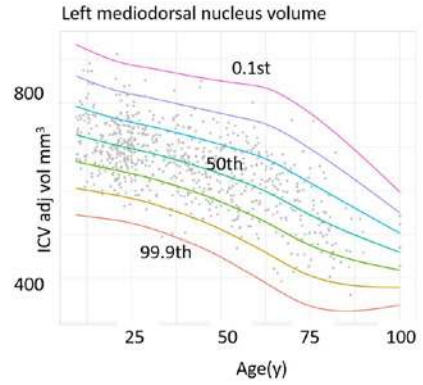

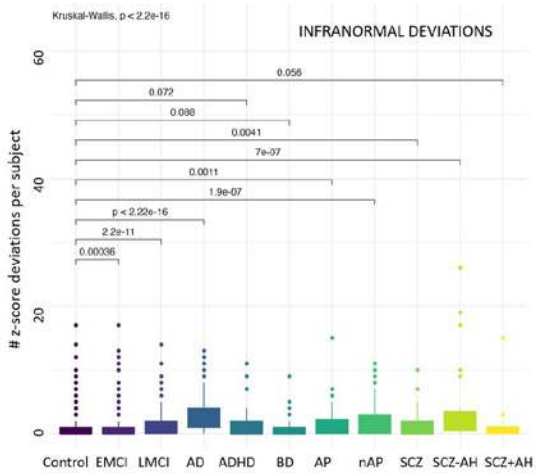

Conclusions: We have created the first normative models of thalamic nuclear volumes from large cohorts of publicly available MRI data. Preliminary analyses on neurodegenerative and neuropsychiatric disease cohorts show the utility of NM in the elucidating heterogeneity (e.g. in schizophrenia) that is missed by traditional case-control (average volume) studies. Future work will fine tune these models to detect hitherto undetected changes in thalamic nuclear volumes in earlier disease stages to help in drug discovery and mechanistic modeling.

References

1. Su, J. H., Thomas, F. T., Kasoff, W. S., Tourdias, T., Choi, E. Y., Rutt, B. K., & Saranathan, M. (2019). Thalamus Optimized Multi Atlas Segmentation (THOMAS): fast, fully automated segmentation of thalamic nuclei from structural MRI. NeuroImage, 194, 272–282. https://doi.org/10.1016/j.neuroimage.2019.03.021
2. Vidal et al. (2023). Robust thalamic nuclei segmentation from T1-weighted MRI. arXiv:2304.07167 doi: https://doi.org/10.48550/arXiv.2304.07167
3. Rutherford S, Kia SM, Wolfers T, Fraza C, Zabihi M, Dinga R, Berthet P, Worker A, Verdi S, Ruhe HG, Beckmann CF, Marquand AF (2022). The normative modeling framework for computational psychiatry. Nat Protoc. (7):1711-1734. doi: 10.1038/s41596-022-00696-5.
4. Ge et al. (2023). Normative Modeling of Brain Morphometry Across the Lifespan using CentileBrain: Algorithm Benchmarking and Model Optimization. bioRxiv 2023.01.30.523509; doi: https://doi.org/10.1101/2023.01.30.523509

Poster No 1269

Functional connectome through the human life span

Lianglong Sun[1], Tengda Zhao[1], Xinyuan Liang[1], Mingrui Xia[1], Qiongling Li[1], Xuhong Liao[2], Gaolang Gong[1], Qian Wang[1], Chenxuan Pang[1], Qian Yu[1], Yong He[1]

[1]State Key Laboratory of Cognitive Neuroscience and Learning, Beijing Normal University, Beijing, China, [2]School of Systems Science, Beijing Normal University, Beijing, China

Introduction: The emergence, development, and aging of the intrinsic connectome architecture enables the dynamic reorganization of functional specialization and integration throughout the lifespan, contributing to continuous changes in human cognition and behavior (Zuo et al., 2017). Understanding the spatiotemporal growth process of the typical functional connectome is critical for elucidating network-level developmental principles in healthy individuals and for pinpointing periods of heightened vulnerability or potential. The growth chart framework provides an invaluable tool for charting normative reference curves in the human brain (Bethlehem et al., 2022; Rutherford et al., 2022). However, the normative growth trajectory of the functional brain connectome across the human lifespan remains unknown.

Methods: We employed a comprehensive data quality control framework that combined automated assessment tools and expert manual review to assess both structural and functional images across all 45,525 scans. The final sample included 33,809 scans (N = 32,328) with high-quality images from 119 sites (Fig. 1a). Using the standardized and highly uniform processing pipeline, we obtained the surface-based preprocessed BOLD signals in fsaverage4 space for each individual. We then constructed a vertex-wise functional connectome matrix by calculating the Pearson correlation coefficient between the time courses of each vertex. We examined the individual connectome at the whole-brain, system, and regional levels, harmonizing all measures across sites. Guided by the WHO recommendation (Borghi et al., 2006), we used GAMLSS to elucidate the age-related nonlinear trajectories for healthy populations, with sex and in-scanner head motion as fixed effects. To assess the rate of change and inflection points, we calculated first derivatives of the trajectories. By proposing a Gaussian-weighted iterative age-specific group atlas generation approach, we established a set of continuous growth atlases with accurate system correspondences across the life course.

Results: The lifespan curve of global mean functional connectivity (Fig. 1c) showed a nonlinear increase from 32 postmenstrual weeks onward, peaking at 40.0 years (95% CI 39.4-40.5), followed by a nonlinear decline. The peak of the increased rate of growth occurred at 17.8 years (95% CI 14.8-20.0), while the maximum rate of decline was observed at 57.4 years (95% CI 55.8-59.9). Global variance in whole-brain functional connectivity (Fig. 1d) also showed a nonlinear growth pattern, peaking in adulthood at 34.7 years (95% CI 32.4-37.2), with maximum rates of increase and decline occurring at 32 postmenstrual weeks and 59.0 years (95% CI 57.4-62.9), respectively. Consistent with the developmental pattern of the age-specific atlas (Fig. 2a, 2b), the normative growth trajectories showed that the similarity of the individualized atlas to the reference increased from 32 postmenstrual weeks, peaked at 31.7 years (95% CI 30.7-32.6), remained stable until 54.1 years (95% CI 53.7-54.6), and then continuously declined at an accelerated rate until 80 years of age (Fig. 2c). Whole-brain system segregation across all systems peaked at 24.7 years (95% CI 23.0-26.0) and showed a more pronounced accelerated decline around the sixth decade of life (Fig. 2d). Different networks manifested heterochronous growth patterns (Fig. 2e). Lifespan growth of functional connectivity at the regional level reveals a spatial gradient pattern (Fig. 2f, 2g).

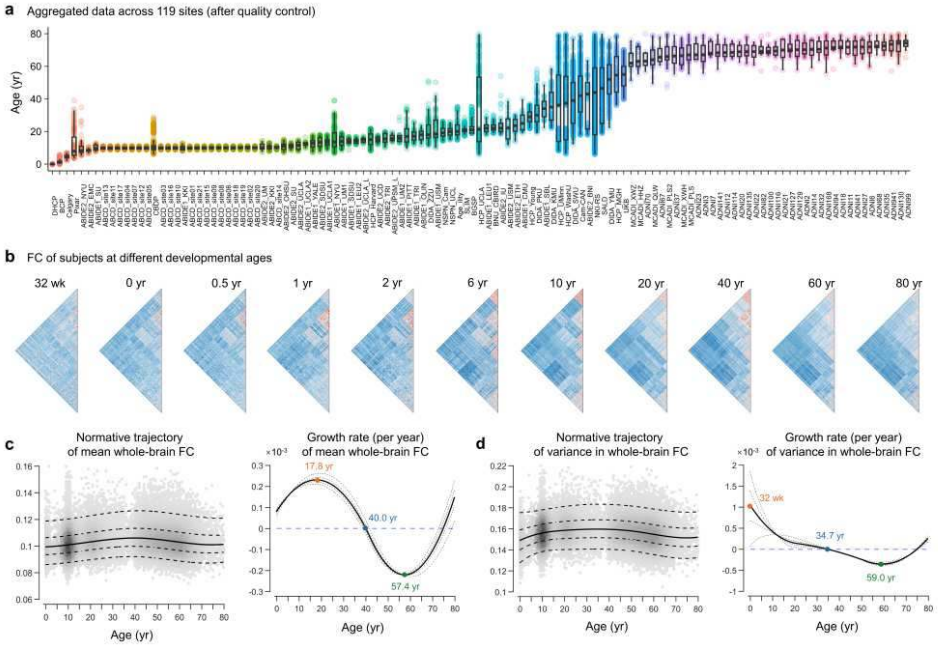

Fig. 1 | Data samples, functional connectome and global growth of the connectome over the lifespan. a, Quality-controlled MRI data from 119 scanning sites. Box plots show the age distribution of individuals for each site of data acquisition. **b**, The functional connectivity (FC) matrices of representative subjects at different developmental ages. **c**, Normative trajectory (left panel) and growth rate (right panel) of whole-brain mean FC as estimated by GAMLSS. The median (50% centile) is represented by a solid line, while the 5%, 25%, 75%, and 95% centiles are indicated by dotted lines. The growth velocity is characterized by the first derivative of the trajectory. Critical milestones in the lifespan developmental trajectory include a stabilization of the growth rate at 40.0 years (95% bootstrap confidence interval (CI) 39.4-40.5), a maximum increase at 17.8 years (95% bootstrap CI 14.8-20.0), and a maximum decline at 57.4 years (95% bootstrap CI 55.8-59.9). **d**, Normative trajectory and growth rate of variance in whole-brain FC, with a peak age at 34.7 years (95% bootstrap CI 32.4-37.2), a maximum increase occurring at 32 postmenstrual weeks, and a maximum decline occurring at 59.0 years (95% bootstrap CI 57.4-62.9). wk, week; mon, month; yr, year.

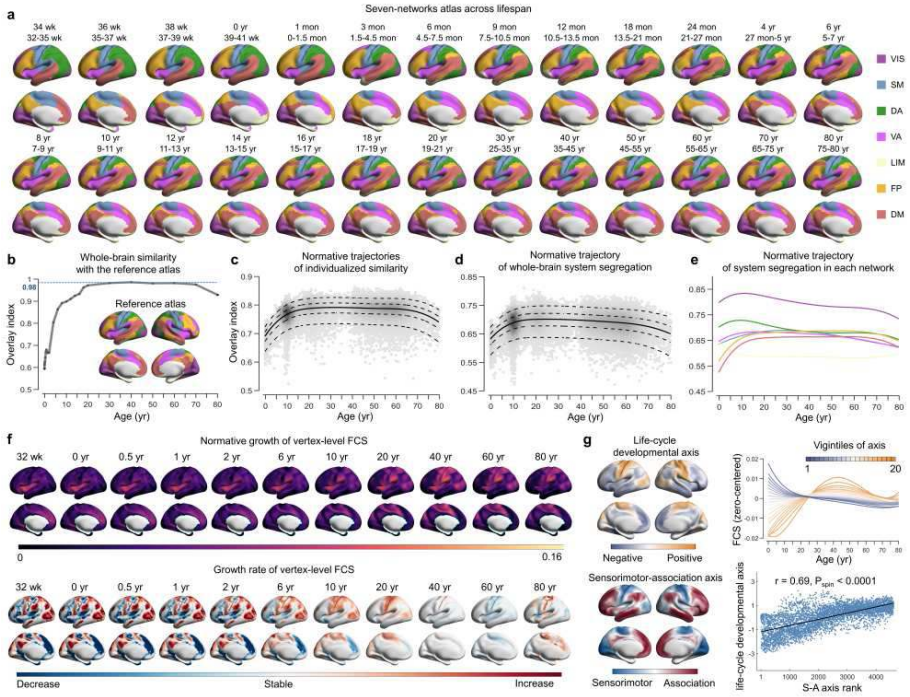

Fig. 2 | System-level and region-level growth of the connectome throughout the lifespan. a, Employing the Gaussian-weighted iterative group atlas generation approach, the first life-cycle set of functional seven-network atlases from 32 postmenstrual weeks to 80 years was established. **b**, Whole-brain similarity of each age-specific atlas with the reference atlas. **c**, Normative trajectory of individualized atlas similarity with the reference atlas. The similarity increased from 32 postmenstrual weeks, peaking at 31.7 years (95% bootstrap CI 30.7-32.6), and undergoing a continually accelerated decline starting at approximately 54.1 years (95% bootstrap CI 53.7-54.6) until 80 years of age. **d**, Normative trajectory of whole-brain system segregation. The developmental peak occurred at 24.7 years (95% bootstrap confidence interval 23.0-26.0). **e**, Normative trajectory of system segregation for each network. **f**, The fitted 50% centiles (top panel) and their growth rates (bottom panel) for all vertices at several key age points. **g**, The life-course developmental axis of brain functional connectivity, represented by the first principal component from a PCA on vertex-level FCS trajectories. Based on the lifespan principal axis, all vertices across the brain were equally divided into 20 bins. The zero-centered trajectories of all vertices within each bin were averaged. The first vigintile (depicted in darkest yellow) represents one pole of the axis, while the twentieth vigintile represents the opposite pole (depicted in darkest blue). The patterns of developmental trajectories vary continuously along the axis, with the greatest differences observed between the two poles. The sensorimotor-association (S-A) axis, as formulated by Sydnor et al. (2021), represents a cortical continuum that transitions from primary regions to transmodal areas. A strong correlation was observed between the life-course principal developmental axis and the S-A axis (linear association shown with a 95% confidence interval). VIS, visual; SM, somatomotor; DA, dorsal attention; VA, ventral attention; LIM, limbic; FP, frontoparietal; DM, default mode. wk, week; mon, month; yr, year.

Conclusions: Through systematic analysis at the whole-brain, system, and regional levels, we charted the multiscale, nonlinear trajectories of functional connectome and revealed previously unidentified key growth milestones. We created the lifespan age-specific atlases, serving as a foundational resource for future research on brain network development and aging.

References
1. Zuo X N et al. (2017), 'Human connectomics across the life span'. Trends in Cognitive Sciences, vol. 21, no. 1, pp. 32-45.
2. Bethlehem R A I et al. (2022), 'Brain charts for the human lifespan'. Nature, vol. 604, no. 7906, pp. 525-533.
3. Rutherford S et al. (2022), 'Charting brain growth and aging at high spatial precision'. Elife, vol. 11, no. e72904, pp.
4. Borghi E et al. (2006), 'Construction of the World Health Organization child growth standards: selection of methods for attained growth curves'. Statistics in Medicine, vol. 25, no. 2, pp. 247-265.
5. Sydnor V J et al. (2021), 'Neurodevelopment of the association cortices: Patterns, mechanisms, and implications for psychopathology'. Neuron, vol. 109, no. 18, pp. 2820-2846.

Poster No 1270

An Optimised Surface Projection Pipeline for Enhanced Analysis of Fetal Brain Connectivity

Pablo Prieto Roca[1], Logan Williams[1,2], Sean Fitzgibbon[3], Vanessa Kyriakopoulou[2], Alice Davidson[2], Alena Uus[1,2], Antonis Makropoulos[1], Andreas Schuh[4], Lucilio Cordero-Grande[5], Emer Hughes[2], Anthony Price[2], Eugene Duff[6,3], Tomoki Arichi[2,7,8], A. Edwards[2,7,9], Daniel Rueckert[10,4], Stephen Smith[3], Joseph Hajnal[2], Emma Robinson[1,2], Vyacheslav Karolis[2]

[1]Biomedical Engineering Department, King's College London, London, United Kingdom, [2]Centre for the Developing Brain, King's College London, London, United Kingdom, [3]Wellcome Centre for Integrative Neuroimaging, FMRIB, University of Oxford, Oxford, Oxfordshire, United Kingdom, [4]Department of Computing, Imperial College London, London, United Kingdom, [5]Universidad Politécnica de Madrid & CIBER-BBN, Madrid, Spain, [6]UK Dementia Research Institute, Department of Brain Sciences, Imperial College London, London, United Kingdom, [7]MRC Centre for Neurodevelopmental Disorders, King's College London, London, United Kingdom, [8]Paediatric Neurosciences, Evelina London Children's Hospital, Guy's and St Thomas' NHS Foundation Trust, London, United Kingdom, [9]Neonatal Intensive Care Unit, Evelina London Children's Hospital, London, United Kingdom, [10]Klinikum rechts der Isar, Technical University of Munich, Munich, Bavaria, Germany

Introduction: The human fetal period is a key time for the formation of the functional brain connectome[1,2]. Detailed exploration of this process is now possible with the availability of the open-access dataset from the Developing Human Connectome Project (dHCP) and advancements in fMRI in-utero methodology[3]. However, studying this is particularly challenging, partly due to the rapidly changing shape of the fetal brain, which complicates the alignment of cortical areas across subjects and different ages. In this context, surface-based methods markedly improve the accuracy of co-localizing cortical areas compared to volume-based methods[4]. Here we describe an optimized pipeline for projecting fetal volumetric functional data onto surfaces, enabling robust population-level inference.

Methods: Resting-state in-utero dHCP fMRI data from 164 healthy developing fetuses (87 males and 77 females, age range of 24.5-38.5 gestational weeks) were acquired using a 3T Philips Achieva system, and underwent dynamic geometric and slice-to-volume motion corrections, and temporal denoising[1]. A recently developed spatiotemporal surface fetal brain atlas[5], which encompasses individual templates for each gestational week, ranging from 21 to 36 weeks, was used as a template space. Our projection pipeline, illustrated in Figure 1, represents a modified version of the HCP pipeline for volume-to-surface mapping and incorporates tools from the Connectome Workbench software and FSL[6,7]. The process involves 5 steps: (1) the structural surface is mapped into native functional space; (2) individual functional data features are then mapped onto the surface through a ribbon-constrained volume-to-surface mapping process; (3) Surface matching between the individual surface and the 36th week of the spatio-temporal fetal surface template[5] was then calculated using Multimodal Surface Matching (MSM)[8] in two stages. First, (3.1) individual surfaces were mapped to the "nearest" template (from the closest gestational age); then (3.2) template-to-template registration was performed between consecutive weekly templates (e.g. from 25 to 26 weeks, and 26 to 27 weeks etc); finally (3), these mappings were concatenated together in order to map all individuals to the 36 week template in which the group-level analysis was done, the latter serves two primary purposes: 1) It allows a gradual transition between spaces, through expected cortical development patterns. This aspect is particularly emphasised by the kernel-weighted averaging across subjects utilised for the template construction[5]; 2) It enables the transition from any specific week's template to a desired group-level template in a single interpolation step, simplifying the workflow and enhancing efficiency. To demonstrate the utility of our pipeline, we performed a group-level ICA with 25-dimensional factorization using FSL MELODIC[10].

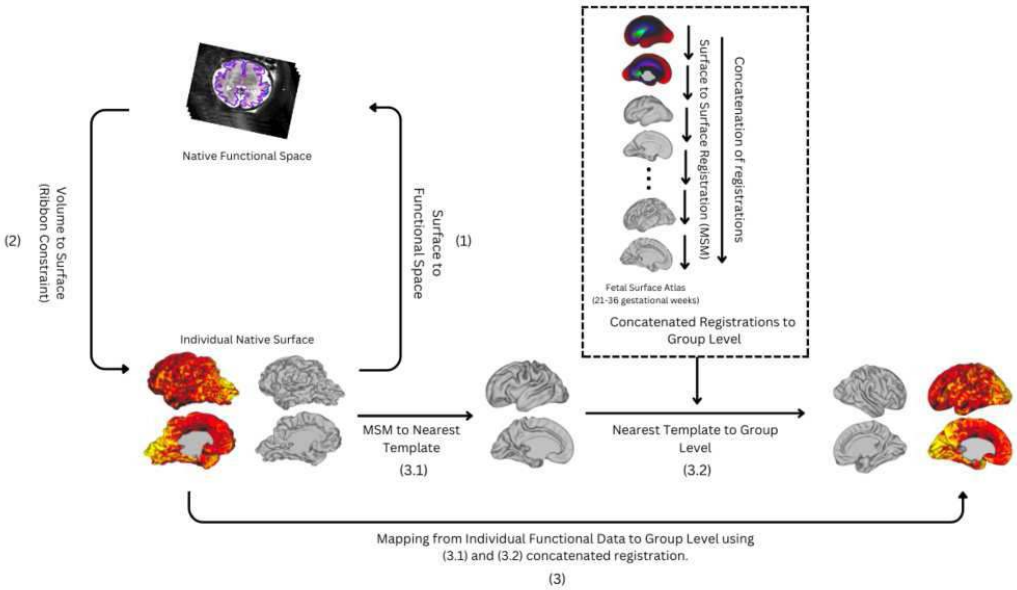

Figure 1: Schematic of a five-step pipeline for analysing brain development. (1) Aligns the structural surface with functional brain data. (2) Maps functional data onto the surface. (3.1) Matches surfaces with the nearest gestational age template, focusing on sulcal depth. (3.2) Registers surfaces between consecutive weekly templates from 25 to 38 weeks of gestation, emphasizing sulcal depth. (3) Concatenates these registrations for direct mapping to the target gestational week for group analysis

Results: Figure 2 presents the outcomes of the Group-ICA with our pipeline, the first-ever performed on the fetal cortical surface. ICA components were excluded if upon visual inspection they were likely to be related to noise which was non-neural in origin. Although derived single components lack distributed network properties, several pairs of maps showed a distinctive interhemispheric symmetry, suggesting a coordinated emergence of activity across hemispheres.

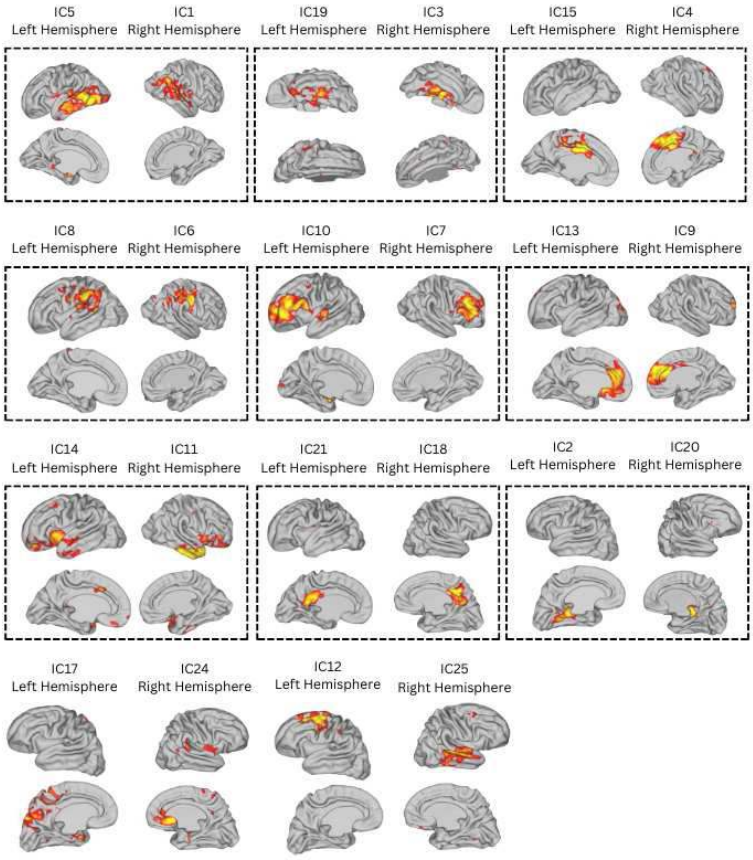

Figure 2: The boxed areas highlight ICA components exhibiting significant interhemispheric symmetry. Other components also show significant activity, none display symmetry similar to the highlighted ICA components.

Conclusions: Our study's projection pipeline contributes to the field of fetal brain imaging by the mapping of volumetric functional data onto the cortical surface for subsequent application of a surface-based registration to template framework. This method has the potential of improving the analysis of in utero brain activity, offering insights into functional connectivity during the critically important fetal period. Such insights could be valuable for prenatal health and developmental neuroscience research, although further studies are required to fully understand their implications.

References

1. Karolis, V. R. et al. (2023). Maturational networks of fetal brain activity. Nature. doi: 10.1101/2022.06.14.495883v2. Available at: https://www.biorxiv.org/content/10.1101/2022.06.14.495883v2.
2. Moriah E. Thomason et al. "Cross-hemispheric functional connectivity in the human fetal brain". In: Science Translational Medicine 5.173 (Feb. 2013). issn: 19466234. doi: 10.1126/scitranslmed.300497
3. The Developing Human Connectome Project (dHCP). (2021). Approaches to the in-utero fMRI denoising in the Developing Human Connectome Project (dHCP). In: Organisation for Human Brain Mapping Annual Meeting, Vol. 2112.
4. Coalson, T. S., Van Essen, D. C., & Glasser, M. F. (2018). The impact of traditional neuroimaging methods on the spatial localization of cortical areas. Proceedings of the National Academy of Sciences of the United States of America, 115(27), E6356–E6365. doi: 10.1073/pnas.1801582115. ISSN: 10916490.
5. Karolis, V. et al. (2023). Developing Human Connectome Project spatio-temporal surface atlas of the fetal brain. doi: 10.12751/g-node.qj5hs7.
6. Human Connectome Project. (2021). Connectome Workbench. Available at: https://www.humanconnectome.org/software/workbench-command.
7. Jenkinson, M. et al. (2012). FSL. NeuroImage, 62(2), 782–790. doi: 10.1016/j.neuroimage.2011.09.015. ISSN: 10538119. Available at: https://linkinghub.elsevier.com/retrieve/pii/S1053811911010603.
8. Robinson, E. C. et al. (2018). Multimodal surface matching with higher-order smoothness constraints. NeuroImage, 167, 453–465. doi: 10.1016/j.neuroimage.2017.10.037. ISSN: 10959572.
9. Logan Z.J. Williams et al. "Structural and functional asymmetry of the neonatal cerebral cortex". In: Nature Human Behaviour 7.6 (June 2023), pp. 942–955. issn: 23973374. doi: 10.1038/s41562-023-01542-8.
10. Beckmann, C. F., & Smith, S. M. (2004). Probabilistic Independent Component Analysis for Functional Magnetic Resonance Imaging. IEEE Transactions on Medical Imaging, 23(2), 137–152. doi: 10.1109/TMI.2003.822821. ISSN: 02780062.

Poster No 1271

Functional Connectivity Changes of the Paternal Brain: A Longitudinal Study

Negin Daneshnia[1], Natalia Chechko[1], Susanne Nehls[1]

[1]RWTH University Hospital Aachen, Aachen, Germany

Introduction: During the last two decades a global shift in fatherhood has been observed, including factors such as paid paternal leave and increased involvement in child-care (McGill, 2014). Along with that, a growing scientific interest in the neurobiological underpinnings of fatherhood can be noted. While our preliminary findings hint at paternal brain neuroplasticity, with dynamic structural changes during the first 12 weeks postpartum, others hint at paternal-specific networks involved in aspects such as infant cry perception (Witteman et al., 2019). Nonetheless, findings are sparse and inconsistent. Based on that, the present longitudinal study investigated functional connectivity in the paternal brain during a 6-month postpartum period.

Methods: We examined paternal (N=23) brain function within the first week of childbirth, as well as after 3, 6, 9, 12 and 24 weeks postpartum. The subjects (mean age = 32.46, SD= 7.85) were healthy and the biological fathers of healthy infants who had been born at the University Hospital Aachen. Resting state fMRI images were obtained during every of the six sessions and data was analyzed using the CONN toolbox (Nieto-Castanon, 2020). Seed-based connectivity (SBC) and whole-brain ROI-to-ROI analysis were conducted to examine functional connectivity (FC) changes over the period of 24 weeks postpartum. For the SBC analysis, connectivity strength (z) across a-priori-defined regions of the default mode network (DMN) (the MPFC, the PCC, the left and right lateral parietal cortices) was calculated. Statistical thresholds were set for both analyses, with cluster threshold $p < .05$ (FDR corrected); voxel threshold $p < .001$ (p-uncorrected), and connection threshold $p < .05$ (p- uncorrected); cluster threshold $p < .05$ (p-uncorrected) for the SBC and ROI-to-ROI analysis respectively.

Results: SBC analysis displayed significant connectivity patterns between the DMN to other brain areas throughout the postpartum period. More specifically, enhanced connectivity was observed as soon as 3 weeks postpartum, persisting through week 6. These associations encompassed regions in the bilateral cerebellum and frontal lobules, as well as the right thalamus and the middle and superior temporal gyri. Notably, connectivity changes appeared to fade in weeks 9 and 12 postpartum, with FC observed only in the left postcentral gyrus. In contrast, at 24 weeks postpartum, connectivity associations were revealed in bilateral temporal areas, particularly in Heschl's and temporal gyri, as well as in the left cerebellum, the angular gyrus, the insula and right thalamus. Additional whole-brain ROI-to-ROI analysis was conducted, comparing 1 week to 24 weeks postpartum, to identify possible connections outside the DMN. The cluster of FCs included, inter alia, parts of the

mesolimbic pathway (e.g. the right accumbens, left amygdala), the central executive network (CEN) (e.g. the left middle frontal gyrus) and the salience network (SN) (e.g. the bilateral rostral prefrontal cortex).

Conclusions: The observed results hint at significant functional connectivity in men shortly after childbirth and up to 24 weeks postpartum, supporting the notion of a paternal brain that appears to adapt to the demands of fatherhood. That is particularly emphasized by the rapid onset of connectivity associations observed as early as 3 weeks postpartum, including regions that have previously been reported as emerging paternal brain areas (Feldman et al., 2019). More precisely, we found support for connectivity changes in mentalizing networks (e.g. angular gyrus), emotion regulation networks (e.g., frontal gyri, insula) and the subcortical parenting network (e.g., putamen, pallidum, thalamus, amygdala). When considering the emerging connectivity between the core networks CEN, SN and DMN, the postpartum paternal brain appears to modify critical networks that may facilitate the transition to parenthood.

References

1. Feldman R., Braun K., Champagne F.A. (2019) The neural mechanisms and consequences of paternal caregiving. Nat. Rev. Neurosci.;20:205–224. doi: 10.1038/s41583-019-0124-6.
2. McGill B.S. (2014) Navigating New Norms of Involved Fatherhood. J. Fam. Issues; 35:1089–1106. doi: 10.1177/0192513X14522247.
3. Nieto-Castanon, A. (2020). FMRI minimal preprocessing pipeline. In Handbook of functional connectivity Magnetic Resonance Imaging methods in CONN (pp. 3-16). Hilbert Press.
4. Witteman J., Van IJzendoorn M.H., Rilling J.K., Bos P.A., Schiller N.O., Bakermans-Kranenburg M.J. (2019) Towards a neural model of infant cry perception. Neurosci. Biobehav. Rev.;99:23–32. doi: 10.1016/j.neubiorev.2019.01.026.

Poster No 1272

Variations of the Corpus Callosum in Congenital Adrenal Hyperplasia (CAH)

Eileen Luders[1], Debra Spencer[2], Caitlin Dale[1], Melissa Hines[2], Florian Kurth[1]

[1]University of Auckland, Auckland, New Zealand, [2]University of Cambridge, Cambridge, United Kingdom

Introduction: Congenital adrenal hyperplasia (CAH) is a genetic variant that causes high levels of androgens during gestation in females, whereas levels in males are largely normal. Only little is known about the brain in CAH, and no study has specifically focused on the corpus callosum.

Methods: Here we compared callosal area measures between 53 individuals with CAH and 53 control participants, who were pair-wise matched with respect to sex (33 women/20 men) and age (mean±SD: 30.2±7.8 years). The corpus callosum was manually outlined on T1-weighted brain images, obtained on a 3 Tesla scanner, and divided into seven sections according to the Witelson scheme (i.e., rostrum, genu, rostral body, anterior midbody, posterior midbody, isthmus, and splenium). The midsagittal callosal areas were compared using a two-way ANOVA, while co-varying for age and total brain volume.

Results: Neither the main effect of biological sex (women vs. men) nor the group-by-sex interaction was significant. In contrast, there was a significant main effect of group (CAH vs. controls) for some callosal areas. More specifically, women/men with CAH had significantly smaller callosal areas than control women/men within the isthmus ($p=0.0024$) and splenium ($p=0.0048$), both effects surviving Bonferroni corrections for multiple comparisons. In addition, there was a trend for a smaller posterior midbody in women/men with CAH compared to control women/men ($p=0.0586$).

Conclusions: Given the lack of significant group-by-sex interactions (CAH-related effects were present in both sexes) it is likely that callosal abnormalities do not manifest as effects of prenatal androgens (otherwise effects would be restricted to women). Instead, they may reflect aspects of the disease and/or effects of treatment as both women and men with CAH receive supplements of glucocorticoids. The latter seems especially noteworthy because glucocorticoids are applied in a wide range of medical conditions, and possible adverse effects on the human brain may not be restricted to CAH.

Poster No 1273

Protective Role of Parenthood on Age-Related Brain Function

Edwina Orchard[1], Sidhant Chopra[1], Leon Ooi[2], Pansheng Chen[3], Lijun An[2], Sharna Jamadar[4], B. T. Thomas Yeo[2], Helena Rutherford[1], Avram Holmes[5]

[1]Yale University, New Haven, CT, [2]National University of Singapore, Singapore, Singapore, [3]National University of Singapore, Queenstown, Queenstown, [4]Monash University, Melbourne, NA, [5]Department of Psychiatry, Brain Health Institute, Rutgers University, Piscataway, NJ

Introduction: Parenthood is a largely ubiquitous experience, yet little is known about how the extreme environmental and biological changes of parenting impact humans across their lifespan. Emerging research in humans and non-human animals suggests parenting may confer long-term benefits to cognition and brain structure, however the effect on brain function remains unknown.

Methods: Here, we investigate the effect of number of children parented (parity), and age on brain function using a large population-based adult sample of females (N=19,964) and males (N=17,607) from the UK Biobank. For each participant, we mapped brain-wide inter-regional functional connectivity between 419 brain regions. To characterize the effect of parity and age on brain function, we examined the Spearman correlation with functional connectivity at each edge, using the Network Based Statistic (NBS) for inference at the level of connected-components of edges showing a common effect.

Results: In both sexes, we observed widespread increases in functional connectivity associated with increased parity (pFWE<.001; Fig1A-B), largely concentrated within the somato/motor network, and between the default network and the rest of the brain. While these effects could indicate neural changes resulting from the early stages of parenthood that stabilize and endure throughout the lifespan, it also could indicate networks and regions that are impacted at later stages. As we show an association between number of children parented (parity) and brain function, this suggests a cumulative impact of parenthood on brain function, such that having additional children continues to alter brain function in a dose-dependent manner. We find widespread functional connectivity decreases associated with age (pFWE<.001; Fig1D-E), largely within the somato/motor networks, and increases between subcortical and association networks and the rest of the brain. This pattern of dysconnectivity has been described in studies characterizing normative ageing trajectories, where the dysconnectivity of the somatomotor network is among the first age-related functional brain changes, consistent with our mid-life sample. Both the effect of parity (r=.67; p<.001; Fig1C) and age (r=.90;p<0.001; Fig1F) on functional connectivity were consistent between females and males. Critically, we find that the effects of parity on functional connectivity were negatively correlated with the effects of age on functional connectivity for females (r=-.41; p<.001; Fig1G), and males (r=-.56; p<.001; Fig1H), suggesting that an increasing number of children is associated with patterns of brain function that are in the opposite direction to age-related brain changes in both sexes.

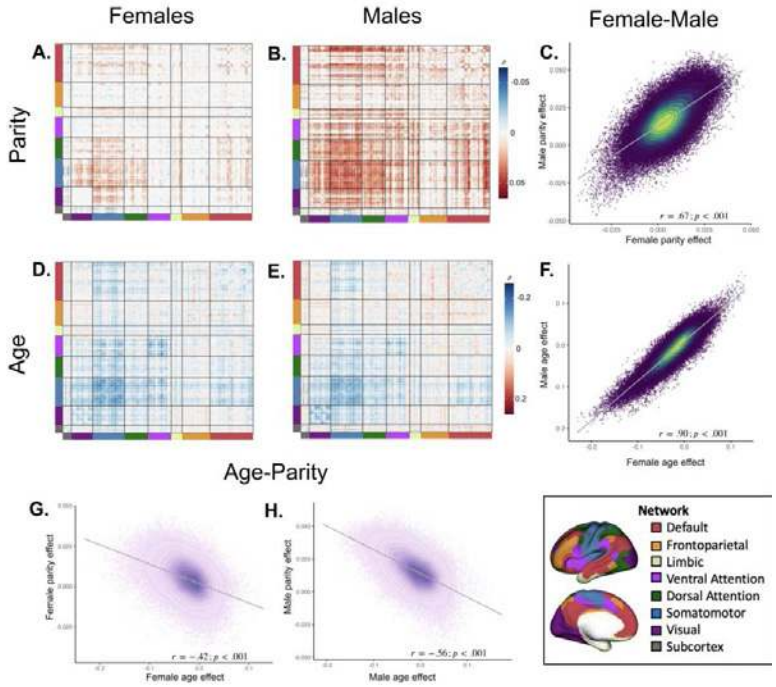

Conclusions: Overall, our results align with prior work in humans and animals to suggest that parity may be protective against age-related brain changes, with the biological and environmental changes accompanying parenthood conferring benefits to brain health across the lifespan. As these relationships exist consistently for both males and females, they implicate the parental environment. This could include direct parenting mechanisms which alter the brain via behavioral actions of caregiving. If so, this could imply that these effects may also exist for other types of caregiving experience, with a potential impact for non-gestational parents of all genders, as well as for any other person with a strong relationship with or responsibility for children, including grandparents, and childcare workers.

References

1. Orchard, Chopra et al., 2024, in Preparation

Poster No 1274

Human brain normative modeling by brain eigenmodes

Sina Mansour L.[1], B. T. Thomas Yeo[2], Maria Di Biase[3], Andrew Zalesky[4]

[1]National University of Singapore, Singapore, NA, [2]National University of Singapore, Singapore, Singapore, [3]The University of Melbourne, Parkville, Victoria, [4]The University of Melbourne, Melbourne, Victoria

Introduction: Normative models (NMs) construct reference charts for population-wide distributions of a biological phenotype[1]. Analogous to growth charts in medicine, assessing a child's height relative to their age and sex, normative brain charting is a framework for modeling variations in structural brain phenotypes, such as cortical thickness. Previous research has demonstrated NM's efficacy in accurately capturing the heterogeneity of normative deviations in brain structure[2]. Normative charting of brain MRI data holds the potential to yield insightful spatial estimates of variations in cortical phenotypes[3]. Nevertheless, methodological limitations have thus far impeded the development of NMs with high spatial precision. Recent advances have increased the spatial resolution of NMs to predefined brain atlases[4]. Despite these notable efforts, existing approaches fall short of achieving spatially detailed norms comparable to the original resolution of MRI data. The establishment of a normative framework to detect subtle spatial nuances remains an unfulfilled aspiration for precision psychiatry.

Methods: To establish and evaluate our normative reference models, we combined data from three distinct Human Connectome Project (HCP) cohorts to cover the human lifespan (HCP Development[5], Young Adult[6], and Aging[7]), comprising 2,473 individuals (54.7% female) aged 5 to 100. Cortical thickness was extracted for each scan using HCP's minimal preprocessing pipeline[8]. Computing high-resolution NMs is challenging due to the high dimensionality of the feature space. Appropriate low-dimensional encoding of cortical phenotypes could hence enable the development of computationally tractable high-resolution normative references. To this end, we utilized brain eigenmodes[9] as basis functions for information reconstruction (Fig. 1a,b). We constructed a sparse, high-resolution connectome and used graph signal processing techniques to generate connectome eigenmodes via singular value decomposition of a random-walk Laplacian shift operator. These eigenmodes were utilized as a basis for normative reconstruction by graph signal filtering[10]. Specifically, 2,000 brain eigenmodes encoded the high-resolution thickness information in the graph frequency domain. Thickness loading on each eigenmode formed a distinct spectral phenotype of the cohort. Distinct hierarchical Bayesian regression NMs were trained to model spectral phenotypes as a function of age and sex while accounting for scanner/site effects. This facilitated the generalization of pre-trained reference NMs to unseen spatial normative queries (Fig. 1c,d).

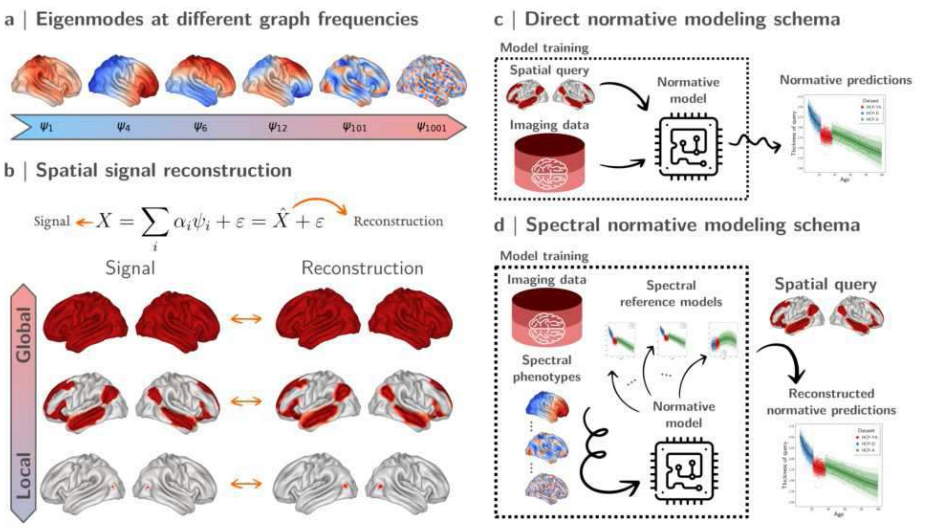

Figure 1. Illustration of the spectral normative modeling framework. (a) Spectral brain connectivity eigenmodes, derived via singular vector decomposition of the graph Laplacian, form an orthogonal basis set for information reconstruction. (b) Utilizing graph Fourier transformation of graph frequency domain signal encoding, we are able to reconstruct signals with varying spatial characteristics (global to local). Using this framework, conventional direct normative modeling designs can be extended to reconstructive spectral normative models. (c) Direct normative models use a fixed spatial query during training, requiring access to preprocessed imaging data. (d) Conversely, the spectral counterpart trains a comprehensive set of normative models for various brain eigenmodes. These pre-trained models are stored for subsequent evaluation of normative ranges for arbitrary spatial queries. This innovative approach eradicates the necessity for retraining the model when encountering new queries, thus removing the requirement for processing imaging data to gain novel normative insights.

Results: After training spectral NMs, we conducted a comprehensive evaluation of their ability to infer norms in comparison to a direct model. Posterior predictive distributions of spectral NMs were used to reconstruct normative ranges for alternative families of spatial queries. Notably, global spatial queries (e.g., mean thickness), regional spatial queries (e.g., thickness of a functional network), and high-resolution queries focused on specific cortical vertices were tested to evaluate goodness of fit (Fig. 4). Our findings indicate that spectral NMs are capable of generating effective normative ranges at various spatial resolutions.

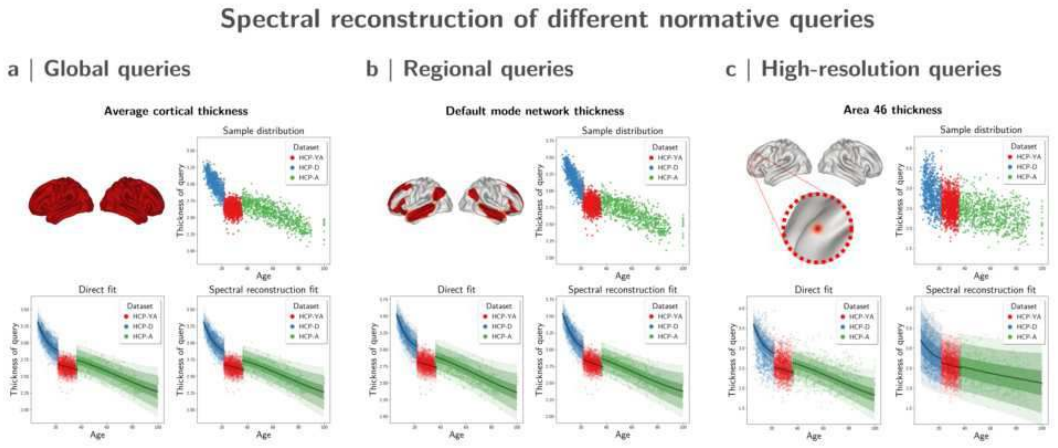

Figure 2. Comparison of spectral normative ranges with direct fits for diverse spatial query types. Normative modeling performance assessed across three distinct spatial query families: (a) global, (b) regional, and (c) high-resolution queries. Each panel showcases the spatial query (top left) alongside a scatter plot depicting the population-wide distribution of respective thickness queries against age (top right). Normative estimations from both direct modeling and spectral normative reconstructions are displayed in the bottom left and right corners, respectively. Scatter plot colors distinguish between three HCP datasets (D: Development, YA: Young Adult, A: Aging).

Conclusions: We present a novel approach to extract versatile normative ranges from a set of pre-trained NMs constructed from brain eigenmodes. Our findings underscore the effectiveness of spectral NMs in generating accurate normative ranges. This obviates the necessity for the computationally intensive task of fitting new reference models for distinct spatial queries. This can inform clinical studies investigating normative trajectories of healthy brain development and aging, all without the need for direct access to or extensive processing of large imaging datasets.

References

1. Marquand, A. F., Rezek, I., Buitelaar, J., & Beckmann, C. F. (2016). Understanding heterogeneity in clinical cohorts using normative models: beyond case-control studies. Biological psychiatry, 80(7), 552-561.
2. Marquand, A. F., Kia, S. M., Zabihi, M., Wolfers, T., Buitelaar, J. K., & Beckmann, C. F. (2019). Conceptualizing mental disorders as deviations from normative functioning. Molecular psychiatry, 24(10), 1415-1424.
3. Bethlehem, R. A., Seidlitz, J., White, S. R., Vogel, J. W., Anderson, K. M., Adamson, C., ... & Schaare, H. L. (2022). Brain charts for the human lifespan. Nature, 604(7906), 525-533.
4. Rutherford, S., Fraza, C., Dinga, R., Kia, S. M., Wolfers, T., Zabihi, M., ... & Marquand, A. F. (2022). Charting brain growth and aging at high spatial precision. elife, 11, e72904.
5. Somerville, L. H., Bookheimer, S. Y., Buckner, R. L., Burgess, G. C., Curtiss, S. W., Dapretto, M., ... & Barch, D. M. (2018). The Lifespan Human Connectome Project in Development: A large-scale study of brain connectivity development in 5–21 year olds. Neuroimage, 183, 456-468.
6. Van Essen, D. C., Smith, S. M., Barch, D. M., Behrens, T. E., Yacoub, E., Ugurbil, K., & Wu-Minn HCP Consortium. (2013). The WU-Minn human connectome project: an overview. Neuroimage, 80, 62-79.
7. Harms, M. P., Somerville, L. H., Ances, B. M., Andersson, J., Barch, D. M., Bastiani, M., ... & Yacoub, E. (2018). Extending the Human Connectome Project across ages: Imaging protocols for the Lifespan Development and Aging projects. Neuroimage, 183, 972-984.
8. Glasser, M. F., Sotiropoulos, S. N., Wilson, J. A., Coalson, T. S., Fischl, B., Andersson, J. L., ... & Wu-Minn HCP Consortium. (2013). The minimal preprocessing pipelines for the Human Connectome Project. Neuroimage, 80, 105-124.
9. Robinson, P. A., Zhao, X., Aquino, K. M., Griffiths, J. D., Sarkar, S., & Mehta-Pandejee, G. (2016). Eigenmodes of brain activity: Neural field theory predictions and comparison with experiment. NeuroImage, 142, 79-98.
10. Huang, W., Bolton, T. A., Medaglia, J. D., Bassett, D. S., Ribeiro, A., & Van De Ville, D. (2018). A graph signal processing perspective on functional brain imaging. Proceedings of the IEEE, 106(5), 868-885.

Poster No 1275

Unraveling lifespan signatures: Time-series phenotyping and age prediction using MEG

Christina Stier[1,2], Elio Balestrieri[1,2], Jana Fehring[1,2], Andreas Wollbrink[1], Niels Focke[3], Joachim Gross[1,2]

[1]Institute for Biomagnetism and Biosignal Analysis, University of Muenster, Muenster, Germany, [2]Otto Creutzfeldt Center for Cognitive and Behavioral Neuroscience, University of Muenster, Muenster, Germany, [3]Clinic of Neurology, University Medical Center, Goettingen, Goettingen, Germany

Introduction: Understanding the developing and aging brain is critical for predicting and assessing individual health risks. While the effects of age on the structural architecture of the brain have been studied previously for a wide age range (Bethlehem et al., 2022), similar efforts for neurophysiological dynamics have been sparse. In particular, it remains unclear which functional metrics predict individual age and can be used to estimate deviations from the normative lifespan.

Methods: We extensively characterized 5 min of MEG resting-state signals derived from the Cambridge Center for Ageing and Neuroscience (CamCAN, Taylor et al., 2017) using 5988 features and whole-brain anatomical parcellation. We extracted features from the highly comparative time-series analysis toolbox (hctsa, Fulcher et al., 2017) and conventional features encompassing frequency-specific power, amplitude- and phase-based connectivity, the 1/f exponent (slope), and alpha peak frequency (instantaneous alpha peak frequency, center of gravity). Each feature was used to predict the individual age of participants (n = 350, 18-88 years) using partial least squares regression (PLS, 5 components) and 10-fold cross-validation (15 repetitions). The model performance was evaluated with the correlation between the true and predicted age (Pearson's r) and the mean absolute error (MAE), and potential confounding bias by sex and estimated intracranial volume (eTIV) tested (Spisak, 2022). To elaborate on the regional information of well-performing features, we applied k-means clustering on transformed PLS regression weights (Haufe et al., 2014).

Results: Conventional features showed a prediction accuracy between r = 0.17 (MAE = 17.1) and r = 0.65 (MAE = 11.99), with the lowest performances of amplitude- and phase-coupling measures and best performances of measures depicting alpha peak frequencies (Figure 1). 107 features extracted from the hctsa toolbox outperformed conventional ones (r > 0.7), with the highest accuracies for the autocorrelation function at a time delay of 36 ms (lag 11; r = 0.75, MAE = 10.38, Figure 2). The prediction analyses for each feature were not confounded by sex or eTIV (pFDR > 0.05). Clustering of the PLS weights for high-performing features (r > 0.73) showed that signal changes in the visual cortex, frontal-parietal areas, and central-temporal areas were most indicative of age.

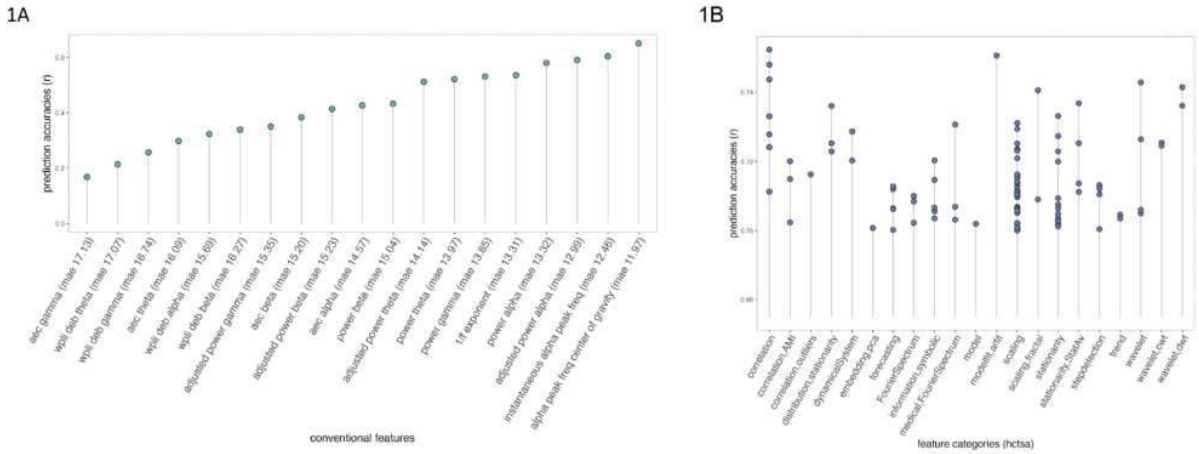

Figure 1
A) Green dots indicate the prediction accuracies of commonly studied metrics quantified by the correlation (r) between true and predicted age. Adjusted power refers to aperiodic-adjusted power as computed using spectral parametrization methods.
B) Blue dots indicate the predictive performance of hctsa features with higher accuracies (r > 0.7) than conventional features shown in 1A). The labels show operational categories to which the investigated features belong.

Abbreviations: aec = amplitude coupling, mae = mean absolute error, wpli deb = debiased weighted phase-lag index

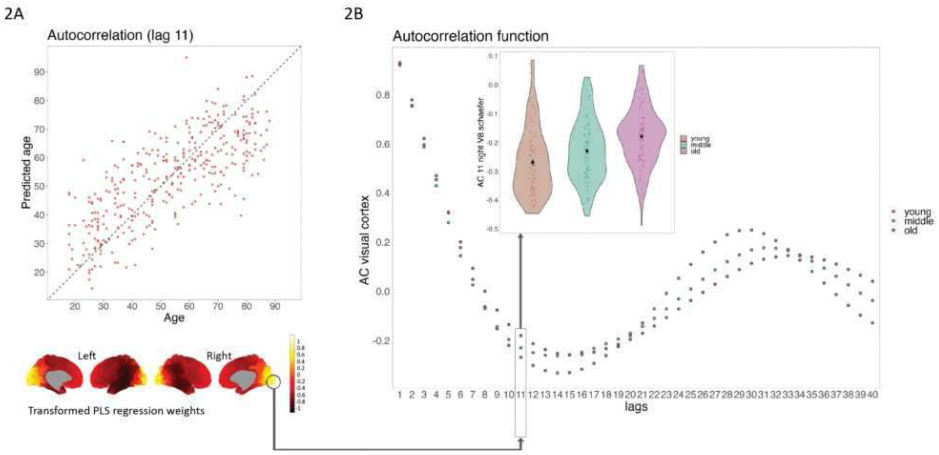

Figure 2
A) Shown is a scatterplot for the most predictive feature investigated (Autocorrelation at lag 10) and the transformed beta weights (Haufe et al., 2014) of the partial least squares regression analysis (PLS).
B) The plot shows the autocorrelation function for different time-delays at Schaefer atlas parcel V8 (visual cortex, right hemisphere) and averaged for three age groups (young: 18-38 years (n=100); middle: 39-68 years (n=150), old: 69-88 years (n = 100)).

Conclusions: We provide an overview of the predictive value of neurophysiological metrics commonly studied to describe the healthy or diseased brain and a comprehensive set of time-series features in the context of development and aging. The profiling of regional MEG signals revealed lifespan patterns that can be captured by simple linear time-series measures, which were more accurate than the conventional spectral features. While further investigations on the relationship between informative features are needed to shed light on aging mechanisms, they all point to profound functional alterations in the visual, central-temporal, and frontal-parietal brain regions during adulthood.

References

1. Bethlehem, R. A., Seidlitz, J., et al. (2022), Brain charts for the human lifespan. Nature, 604(7906), 525-533;
2. Fulcher, B. D. et al. (2017), hctsa: A computational framework for automated time-series phenotyping using massive feature extraction. Cell Systems, 5(5), 527-531;
3. Haufe, S., et al. (2014), On the interpretation of weight vectors of linear models in multivariate neuroimaging. Neuroimage, 87, 96-110.
4. Spisak, T. (2022), Statistical quantification of confounding bias in machine learning models. GigaScience, 11, giac082;
5. Taylor, J. R., et al. (2017), The Cambridge Centre for Ageing and Neuroscience (Cam-CAN) data repository: Structural and functional MRI, MEG, and cognitive data from a cross-sectional adult lifespan sample. Neuroimage, 144, 262-269

Poster No 1276

White matter brain charts: modelling diffusion imaging data across the lifespan

Ramona Cirstian[1], Natalie Forde[2], Christian Beckmann[3], Andre Marquand[4]

[1]Donders Institute for Brain, Cognition and Behaviour, Nijmegen, Gelderland, [2]Donders Institute for Brain, Cognition, and Behavior, Radboud University Nijmegen, Nijmegen, NL, Nijmegeb, Netherlands, [3]Radboud University Medical Centre, Donders Institute for Brain, Cognition and Behaviour, Nijmegen, Gelderland, [4]Radboud University Nijmegen, Nijmegen, Gelderland

Introduction: Diffusion MRI (dMRI) is a neuroimaging modality used to evaluate brain structure at a microscopic level and can be exploited to map the direction of the white matter fibers in the brain. In this study, we curated a reference cohort comprising high-quality multi-shell diffusion neuroimaging data from 10 sites across 5 different studies (N=25104; ages 2–100) and using normative modeling, we delineated lifespan trajectories of fractional anisotropy and mean diffusivity for 50 white matter tracts based on the JHU white matter tract atlas. Normative modelling is an innovative method used to model biological and behavioral variation across a study population and can be used to make statistical inferences at an individual level[1]. This is achieved by mapping a response variable (e.g., neuroimaging derived phenotypes) to a covariate (e.g., age) in a similar way growth charts are used in pediatric medicine to map the height or weight of children to their age. Establishing reference models to capture population variations and examining individual deviations is important for comprehending inter-individual variability and its connection to the onset and advancement of medical conditions[2].

Methods: We compiled data from four large open-source datasets for this analysis: UK Biobank (N = 22654, age 46-82), HCP Young Adult (N = 1065, age 22-37), HCP Development (N = 454, age 8-21), HCP Aging (N = 239, 35-100) and Developing HCP (age 2-3). The data were pre-processed using the HCP pipeline with the exception of the UK Biobank which was obtained

already pre-processed[3]. The data were later processed using DTIfit and TBSS to obtain the FA and MD means for each tract using the JHU atlas. A normative model was trained with the training set (n=16736) to estimate the normal range of each IDPs value according to age. To account for the possible non-linear effects and non-Gaussian distributions within the dataset, we used a warped Bayesian linear regression (BLR) model[4]. We used fixed effects to model the effect of site as demonstrated in our previous publications[5]. Next, the test set was used to estimate each subjects' deviation from the normal range of each IDP by computing the individual z-score (equation 2). The fit statistics of the model were computed including explained variance, skew, and kurtosis. The deviation for each subject was visualized by plotting the individual z-scores across the mean and centiles of variation predicted by the model.

Results: The initial concatenation of the five datasets showed severe site effects caused by discrepancies between scanner parameters, resulting in data scaling. These effects are visualized in Figure 1 and 2 on the left side of each panel. Figure 1A displays the scatterplot of average FA values within the body of the corpus callosum obtained from the skeletonized data. Each dataset is color-coded to emphasize the discrepancy in data distribution and scaling. The same principle applies to Figure 1C, which represents the average FA values within the uncinate fasciculus right (on the skeleton). In contrast, on the right-hand side in Figure 1C and 1D, the datapoints represent the z-scores obtained from applying the BLR normative modeling, which predicts the centiles of variation across the entire lifespan. This approach accounts for the non-Gaussianity of the dataset while adjusting and rescaling the datapoints to correct for site effects. The same principles are applied to Figure 2, where the MD values for the same two tracts are represented.

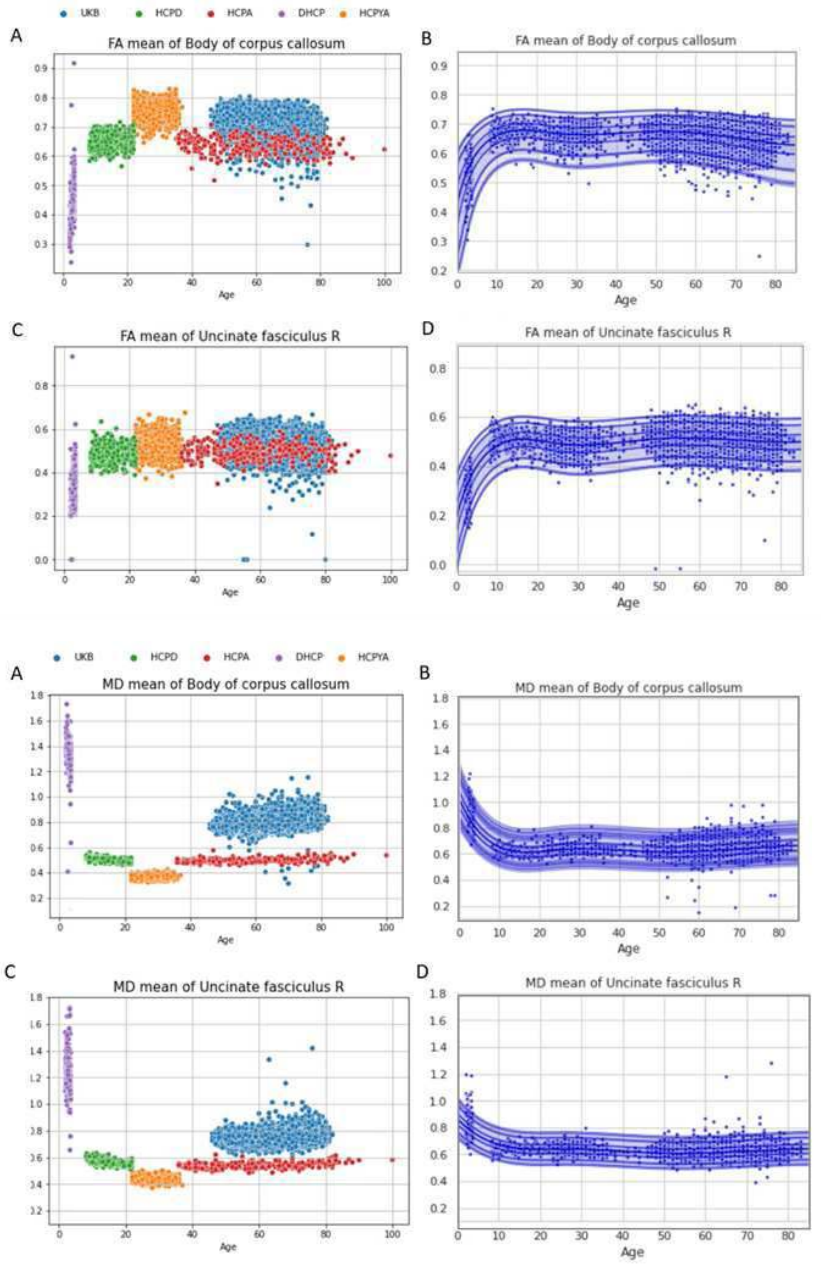

Conclusions: In this study, we developed normative brain charts for fractional anisotropy (FA) and mean diffusivity (MD) using a diverse lifespan dataset. Our models, adaptable to non-Gaussian distributions, accommodate new sites and prioritize individual variations, moving beyond group-level inferences for personalized insights.

References

1. Marquand AF, Rezek I, Buitelaar J, Beckmann CF. Understanding heterogeneity in clinical cohortsusing normative models: beyond case-control studies. Biological psychiatry. 2016 Oct1;80(7):552-61.
2. Rutherford, S., Fraza, C., Dinga, R., Kia, S.M., Wolfers, T., Zabihi, M., Berthet, P., Worker, A.,Verdi, S., Andrews, D. and Han, L.K., 2022. Charting brain growth and aging at high spatialprecision. elife, 11, p.e72904.
3. Alfaro-Almagro, F., Jenkinson, M., Bangerter, N.K., Andersson, J.L., Griffanti, L., Douaud, G.,Sotiropoulos, S.N., Jbabdi, S., Hernandez-Fernandez, M., Vallee, E. and Vidaurre, D., 2018. Imageprocessing and Quality Control for the first 10,000 brain imaging datasets from UK Biobank.Neuroimage, 166, pp.400-424.
4. Fraza, C.J., Dinga, R., Beckmann, C.F. and Marquand, A.F., 2021. Warped Bayesian linearregression for normative modelling of big data. Neuroimage, 245, p.118715.ckveq
5. Rutherford, S., Kia, S.M., Wolfers, T., Fraza, C., Zabihi, M., Dinga, R., Berthet, P., Worker, A.,Verdi, S., Ruhe, H.G. and Beckmann, C.F., 2022. The normative modeling framework forcomputational psychiatry. Nature protocols, 17(7), pp.1711-1734.

Poster No 1277

Neural correlates of device-based sleep characteristics in adolescents

Qing Ma[1], Wei Cheng[1]

[1]Fudan University, Shanghai

Introduction: Adolescence is marked by significant transformations in sleep patterns, including shortened sleep duration, delayed sleep time and shifted circadian rhythm[2]. These predictable changes often coincide with ongoing development of key cognitive and regulatory neural systems that is essential for cognitive development preparing for adult life[1,3]. Therefore, investigating the relevance between sleep characteristics and the underlying brain development that facilitates cognitive development becomes particularly significant.

Methods: 3300 adolescents aged11-12 years old (the 2-year follow-up data) from Adolescent Brain Cognitive Development (ABCD 5.0) study, integrating extensive device-based sleep characteristics and multimodal imaging data. The replication sample consisted of 1,271 adolescents aged 13-14 years old (the 4-year follow-up data). Sleep characteristics were objectively collected through wristband records using Fitbit. An average of 18 sleep indicators were collected daily over the three-weeks period. For brain imaging, we collected 85 regional volumes, including 68 cortical and 17 subcortical areas, respectively. Resting state functional connectivity among 12 networks and subcortical regions were also involved. Specific functional networks are auditory, cingulo-opercular, cingulo-parietal, default-mode, dorsal-attention, fronto-parietal, retrosplenial-temporal, salience, sensorimotor-hand, sensorimotor-mouth, ventral-attention, and visual networks. Cognitive performance was measured using NIH Toolbox. Here, we first applied sparse canonical correlation (sCCA) analysis to obtain the relationship between dimensional sleep and brain structure and function. Subsequently, significant canonical variates derived from brain imaging data were used to cluster adolescents into distinct biotypes. Then, we used one-way analysis of covariance (ANCOVA) to identify sleep characteristics, cognitive performance, academic attainment, and brain imaging measures that differed between relatively homogeneous biotypes.

Results: 1. Two sleep-brain dimensions. We revealed two sleep-brain dimensions: one characterized by later being asleep and shorter duration, linked to decreased subcortical-cortical network functional connectivities; the other showed higher heart rate and shorter light sleep duration, associated with lower brain volumes and decreased functional connectivities. 2. Three adolescent biotypes based on dimension of brain measures. Hierarchical clustering based on brain dimension associated with sleep characteristics revealed three biotypes of adolescents, marked by unique sleep profiles: biotype 1 exhibited delayed and shorter sleep, coupled with higher heart rate during sleep; biotype 3 with earlier and longer sleep, accompanied by lower heart rate; and biotype 2 with intermediate pattern. 3. Biotype-specific cognitive performance, academic attainment, and brain measures. Results showed that the three biotypes differed significantly in the cognitive performances (FDR correction at $P < 0.05$), including crystalized intelligence ($F = 22.21$, $P < 0.001$), picture vocabulary ($F = 20.04$, $P < 0.001$), and oral reading recognition ($F = 13.35$, $P < 0.001$. 4. Longitudinal analyses revealed that all three biotypes exhibited progressive improvements in cognitive ability, specifically in crystallized intelligence, picture vocabulary, and oral reading recognition, over the four-year span.

Conclusions: Collectively, our novel findings delineate a linkage between objective sleep characteristics and developing brain in adolescents, underscoring their significance in cognitive development and academic attainment, which could serve

as references for individuals with sleep difficulties and offer insights for optimizing sleep routines to enhance better cognitive development and school achievement.

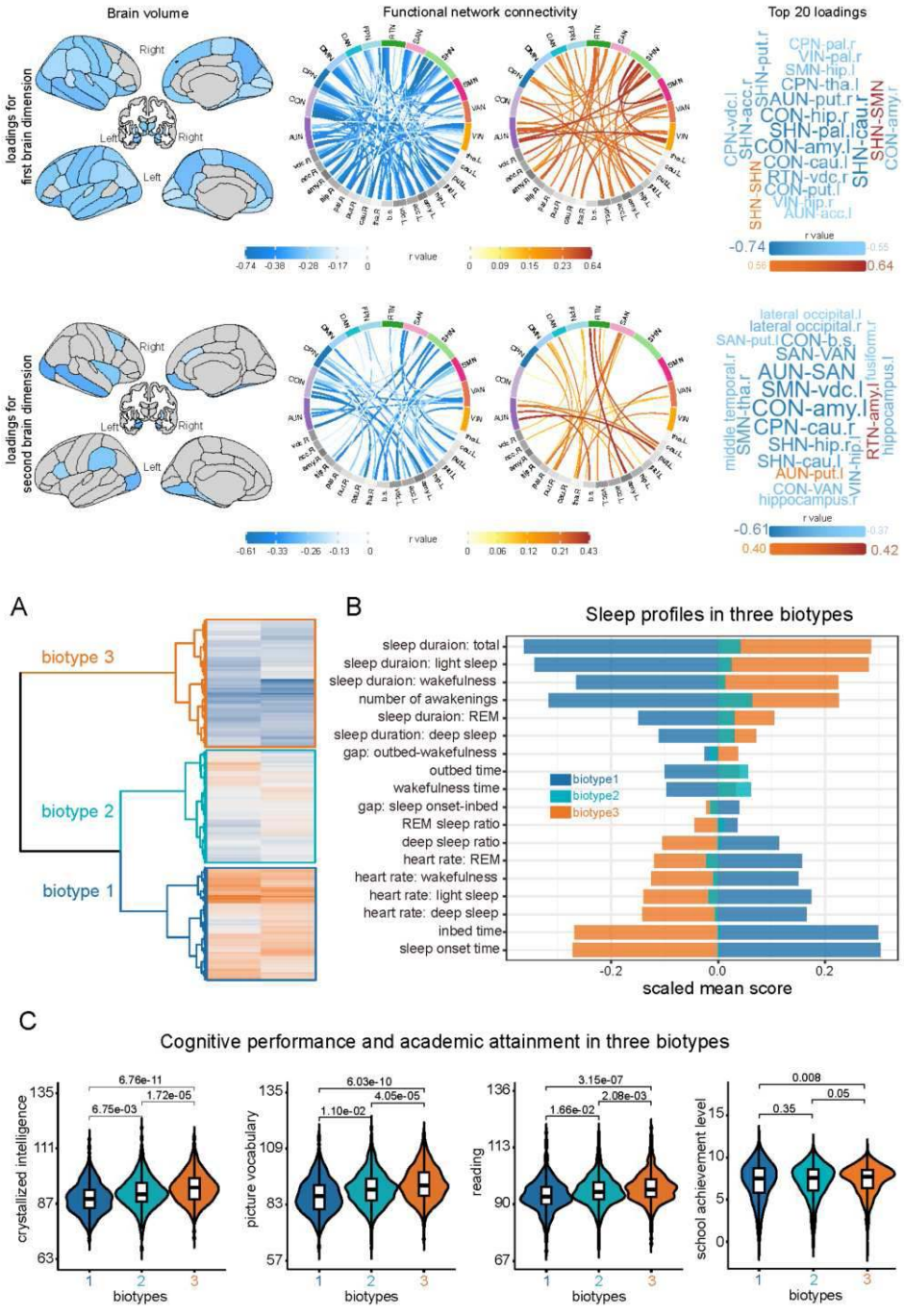

References

1. Leong, R. L. F. & Chee, M. W. L. Understanding the Need for Sleep to Improve Cognition. Annual Review of Psychology 74, 27-57, doi:10.1146/annurev-psych-032620-034127 (2023).
2. Galván, A. The Need for Sleep in the Adolescent Brain. Trends Cogn Sci 24, 79-89, doi:10.1016/j.tics.2019.11.002 (2020).
3. Anastasiades, P. G., de Vivo, L., Bellesi, M. & Jones, M. W. Adolescent sleep and the foundations of prefrontal cortical development and dysfunction. Prog Neurobiol 218, 102338, doi:10.1016/j.pneurobio.2022.102338 (2022).

Poster No 1278

Elevated ALFF in Early Developing Brain Systems from Birth to Three Years

Ashley Nielsen[1], Alyssa Labonte[2], Max Herzberg[1], Deanna Barch[3], Joan Luby[2], Cynthia Rogers[2], Chad Sylvester[2], Christopher Smyser[2]

[1]Washington University in St. Louis, Saint Louis, MO, [2]Washington University in St. Louis, St. Louis, MO, [3]Washington University, Saint Louis, MO

Introduction: The blood oxygen level dependent (BOLD) signal measured with functional magnetic resonance imaging (fMRI) indirectly reflects the synaptic activity of neural populations. Early in development, the maturation of inhibitory interneurons refines the synaptic activity of neural populations, shifting from synchronous, high amplitude activity to sparse, suppressed activity and marks the closing of sensitive periods. Thus, the amplitude of the low-frequency fluctuations (ALFF) in the BOLD signal has been proposed as a putative indicator of cortical maturity and neuroplasticity, illuminating changes in the balance of excitation and inhibition. Developmental patterns of ALFF during childhood and adolescence differ across the brain (Sydnor et al. 2023). In sensorimotor areas that develop early, ALFF decreases in childhood, while, in association areas that develop late, ALFF increases across adolescence and then decreases into adulthood. How ALFF emerges beginning at birth when neuroplasticity and developmental change are greatest has yet to be characterized. Here, we aimed to chart the developmental trajectory of ALFF during the first three years of life to potentially uncover how developmental neuroplasticity differs across the brain in humans.

Methods: fMRI was acquired during natural sleep at birth (n=261), age 2 years (n=98), and age 3 years (n=80) as part of the Early Life Adversity and Biological Embedding Study. Functional data were mapped to individual surfaces. ALFF, the amplitude of low-frequency (0.01-0.08 Hz) fluctuations, was derived using the Fast Fourier transform for each vertex in the cortical surface and each voxel in the subcortex and cerebellum. Longitudinal change in ALFF from birth to age 2 years (n=75) and from age 2 years to age 3 years (n=39) was determined. We also examined how sub-millimeter head motion in the scanner impacts estimates of ALFF to avoid inflating or obfuscating true developmental change. Head motion was quantified as mean frame-wise displacement (meanFD) and de-noising strategies were applied to evaluate the relationship between head motion and ALFF.

Results: Across all three timepoints (Figure 1 A-C), ALFF was highest in sensorimotor areas (somatosensory, visual, auditory) and the subcortex (thalamus, amygdala, hippocampus). The change in ALFF between birth and age 2 years was four times greater than between age 2 years and 3 years. ALFF increased the most in somatosensory and visual areas as well as parts of the thalamus and putamen (Figure 1 D-E). ALFF remained low in the majority of frontal cortex from birth to age 3 years. ALFF varied with head motion (meanFD) such that greater head motion was associated with greater ALFF, but the effect was reduced by applying de-noising strategies.

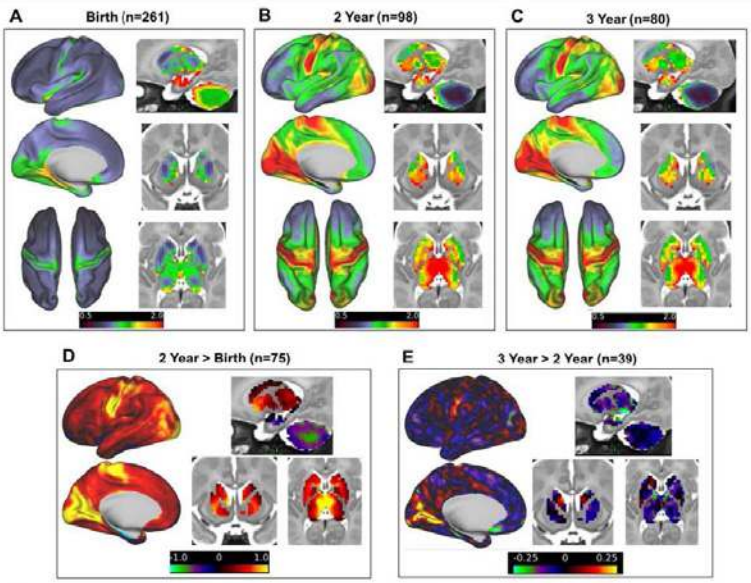

Figure 1. *The Amplitude of Low Frequency Fluctuations (ALFF) in the BOLD signal across the first three years of life.* **A.** ALFF measured at birth (within the first 6 weeks of life) averaged across subjects is depicted. **B.** ALFF measured at age 2 years (between 2-2.5 years) averaged across subjects is depicted. **C.** ALFF measured at age 3 years (between 3-3.75 years) averaged across subjects is depicted. **D.** For the 75 subjects with ALFF at birth and age 2, the longitudinal difference in ALFF (2 years – birth) were averaged across subjects. **E.** For the 39 subjects with ALFF at age 2 and age 3, the longitudinal difference in ALFF (3 years – 2 years) were averaged across subjects.

Conclusions: ALFF has been proposed as a marker of neuroplasticity and maturation. These findings demonstrate that, during the first three years of life, ALFF is highest in brain regions known to undergo the earliest maturation. The greatest change in ALFF occurred between birth and age 2 years, potentially indicating the opening of sensitive periods and/or the rapid developmental change occurring during this period. Later developing brain areas, like frontal cortex, did not exhibit increases in ALFF, consistent with the notion that the greatest developmental change in the balance of excitation and inhibition has not yet occurred for this region. During this developmental window decreases in ALFF were not observed (except for the cerebellum), potentially indicating that early developing sensorimotor systems are still sensitive to environmental exposures and have not yet completed maturation. Charting how ALFF varies across the brain during early development as a potential guide to when plasticity is greatest could greatly facilitate efforts to promote healthier brain development and prevent adverse exposures during sensitive developmental windows.

References

1. Sydnor, V.J., et al. (2023), 'Intrinsic activity development unfolds along a sensorimotor-association cortical axis in youth', Nature Neuroscience vol 26, no. 4, pp. 638-649

Poster No 1279

Development of Infant Brain Structure-function Coupling Indicates Spatiotemporal Disassociation

Rui Zhou[1], Lingbin Bian[1], Jiawei Huang[1], Feihong Liu[2,1], Yajuan Zhang[1], Tianli Tao[1], Mianxin Liu[1], Zhuoyang Gu[1], Xinyi Cai[1], Lianghu Guo[1], Feiyu Quan[1], Yan Liang[1], Dinggang Shen[1,3,4], Han Zhang[1,4]

[1]School of Biomedical Engineering, ShanghaiTech University, Shanghai, China, [2]School of Information Science and Technology, Northwest University, Xi'an, China, [3]Department of Research and Development, United Imaging Intelligence Co., Ltd., Shanghai, China, [4]Shanghai Clinical Research and Trial Center, Shanghai, China

Introduction: The infant brain rapidly matures after birth with distinct brain regions interconnecting for unique functions at different developmental stages, underpinning different behavioral milestones (Tierney 2009). A critical knowledge gap is how the interweaved relation between brain structure and function evolves during early development and whether such relation can predict later outcomes. Most previous studies focused on the youths or adults, holding divergent views on how such a relationship is built in infancy (Suárez 2020). We systematically studied infant brain structure-function coupling, including its spatial and longitudinal patterns, hemispheric lateralization, and the association with developmental scores such as fine motor skills. Our findings provide insights into how the infant brain's wiring influences brain functioning and behavior.

Methods: We utilized resting-state fMRI and diffusion MRI data from the Baby Connectome Project (Howell 2019), comprising 318 scans with 180 subjects within the 0-36 month age range. Our data preprocessing involved motion correction, distortion correction, functional-anatomical registration, one-time resampling, and a deep learning-based denoising for fMRI, as well as denoising, distortion/eddy-current correction, ODF fitting, and probabilistic fiber tracking for diffusion MRI. We used Schaefer's (Schaefer 2018) and Yeo's (Yeo 2011) atlases to parcellate the brain into 400 ROIs and 7 subnetworks for connectivity analysis. Structure-function coupling was determined through Spearman correlations of both nodal and global connectivity profiles, generating ROI-level and brain-level measures. Hemispheric asymmetry in structure-function coupling was assessed. Longitudinal changes in the coupling were depicted using a linear mixed-effect model. The relationship between the coupling and the developmental outcomes measured by the Mullen Scale was examined(Mullen 1995).

Results: Fig. 1A shows the spatial distribution of ROI-wise structure-function coupling in the brain averaged across 0-36 months of age. The primary areas exhibit higher coupling, indicating efficient sensory information processing due to their maturing priorities. Conversely, lower coupling at the high-order cortices suggests immature high-level cognitive functions during early infancy(Molloy 2022). Fig. 1B depicts a logarithmic longitudinal changing pattern of the global structure-function coupling, with a faster change after birth which is slowing down later. Fig. 1C displays the logarithmic slopes of ROI-wise structure-function coupling changes. The primary areas again show steeper decreases compared to the high-order areas. Only bilateral inferior prefrontal cortices and the temporal pole exhibit slightly increasing yet statistically insignificant coupling. This may indicate that the primary cortices develop faster with quicker indirect connection being formatted while functioning of the high-order cortices was still largely defined by their prototypic hard wiring(Dehaene-Lambertz 2015). Fig. 2A reveals hemisphere disparities in the subnetwork-level structure-function coupling trajectories. The ventral attention network consistently exhibits a higher rightward coupling toward the right hemisphere, while the default mode network (DMN) shows a consistent leftward lateralization (Fig. 2B), suggesting their functional specialization(Baum 2020). We found significant associations between the coupling of the right DMN/left frontoparietal control network (FPC) and fine motor skills (Fig. 2C&D), indicating that the structure-function coupling can predict developmental outcomes.

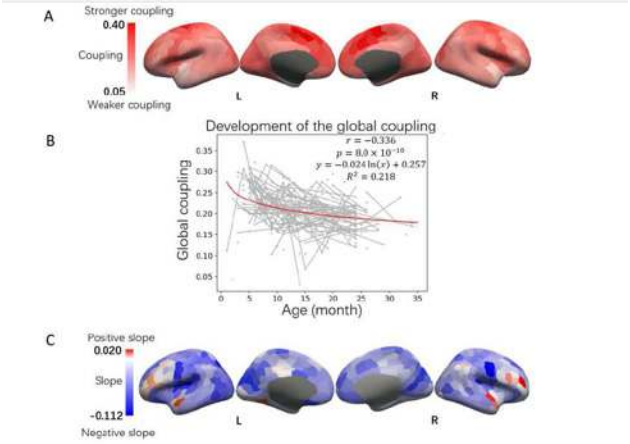

Fig. 1 (A) The spatial distribution of the structure-function coupling averaged across all subjects and ages. (B) The developmental trajectory of the global structure-function coupling fitted with a logarithmic linear mixed-effect model with covariates of gender, mean frame-wise displacement, and scanning sites. (C) The logarithmic slope of structure-function coupling changes in early development for each ROI.

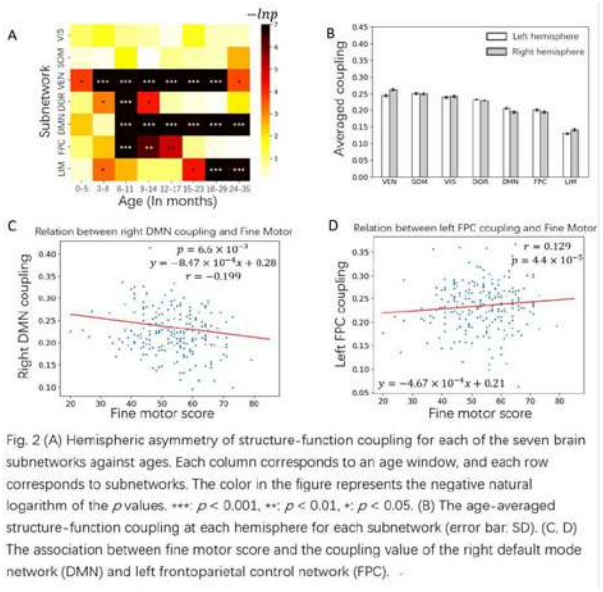

Fig. 2 (A) Hemispheric asymmetry of structure-function coupling for each of the seven brain subnetworks against ages. Each column corresponds to an age window, and each row corresponds to subnetworks. The color in the figure represents the negative natural logarithm of the p values. ***: $p < 0.001$, **: $p < 0.01$, *: $p < 0.05$. (B) The age-averaged structure-function coupling at each hemisphere for each subnetwork (error bar: SD). (C, D) The association between fine motor score and the coupling value of the right default mode network (DMN) and left frontoparietal control network (FPC).

Conclusions: We present infant brain structure-function coupling and their developmental trajectories for the first time, describing how the white matter structure is related with neuron activity in different regions and indicating rapidly developing functional specialization in early infancy and their neurodevelopmental significance.

References

1. Baum, G. L. (2020). "Development of structure–function coupling in human brain networks during youth." Proceedings of the National Academy of Sciences 117(1): 771-778.
2. Dehaene-Lambertz, G. (2015). "The infancy of the human brain." Neuron 88(1): 93-109.
3. Howell, B. R. (2019). "The UNC/UMN Baby Connectome Project (BCP): An overview of the study design and protocol development." NeuroImage 185: 891-905.
4. Molloy, M. F. (2022). "Individual variability in functional organization of the neonatal brain." NeuroImage 253: 119101.
5. Mullen, E. M. (1995). Mullen scales of early learning, AGS Circle Pines, MN.
6. Schaefer, A. (2018). "Local-global parcellation of the human cerebral cortex from intrinsic functional connectivity MRI." Cerebral cortex 28(9): 3095-3114.
7. Suárez, L. E. (2020). "Linking structure and function in macroscale brain networks." Trends in cognitive sciences 24(4): 302-315.
8. Tierney, A. L. (2009). "Brain development and the role of experience in the early years." Zero to three 30(2): 9.
9. Yeo, B. T. (2011). "The organization of the human cerebral cortex estimated by intrinsic functional connectivity." Journal of neurophysiology.

Acknowledgements

This work utilizes data acquired with support by an NIH grant (1U01MH110274) and the efforts of the UNC/UMN Baby Connectome Project (BCP) Consortium. This work is partially supported by The National Key Technology R&D Program (No. 2022ZD0209000), Shanghai Pilot Program for Basic Research - Chinese Academy of Science, Shanghai Branch (No. JCYJ-SHFY-2022-014), Open Research Fund Program of National Innovation Center for Advanced Medical Devices (No. NMED2021ZD-01-001), Shenzhen Science and Technology Program (No. KCXFZ20211020163408012), and Shanghai Pujiang Program (No.21PJ1421400).

Poster No 1280

Using Infant fMRI to Study the Developing Social Brain in the First Year of Life

Sohye Kim[1], Hannah Spear[1], Satrajit Ghosh[2,3], Rahul Brito[2,3], Tiffany Moore Simas[1], Nancy Byatt[1], Stephen Nicholas[1,4], Lawrence Rhein[1], Sarabeth Broder-Fingert[1], David Kennedy[1], Jean Frazier[1]

[1]University of Massachusetts Chan Medical School, Worcester, MA, [2]Massachusetts Institute of Technology, Cambridge, MA, [3]Harvard University, Cambridge, MA, [4]William James College, Newton, MA

Introduction: The fundamental architecture of the social brain is developed in infancy, and early deficits in social development are difficult to compensate for later in life (Ma, 2015). However, current techniques limit our ability to assess early differences and deficits in the infant's social brain. This has limited our fundamental knowledge of the developing social brain in human infants and has delayed the development of new diagnostics and therapeutics targeting these crucial earliest years. The goal of the present study was to demonstrate the feasibility of using a novel fMRI paradigm to measure infants' developing social responsiveness to the first social partner–the mother–at 6 months of age.

Methods: Our novel fMRI paradigm uses an established MRI protocol to scan infants during natural sleep and relies on the infant's fully developed auditory responsiveness present by 6 months and well preserved under sleep (Blasi, 2011; Wild, 2017). Twenty-four (15 males) typically developing 6-month-old infants underwent scanning during natural sleep, listening to maternal voice, unfamiliar female voice, and speech-shaped noise. Unfamiliar voices were distinct from maternal voice on 512 features extracted by the Pyannote machine learning model (Bredin, 2020; Coria, 2020). Speech-shaped noise consisted of white noise edited to match maternal voice on frequency and loudness. FMRI data was processed using FEAT (FMRI Expert Analysis Tool) version 6.00, part of FSL. A total of 54 runs from 18 infants (11 males) passed quality assurance, showing distinct auditory activation and no excessive movement, and were included in the analysis. Voxel-wise whole-brain analyses examined the infant's fMRI response to: (a) human (maternal and unfamiliar) voice compared to speech-shaped noise, and (b) maternal voice compared to unfamiliar voice, adjusting for infant sex, infant age (in weeks), and maternal age. Z-statistic images were thresholded using clusters determined by $Z > 3.1$ and a corrected cluster threshold of $p = .05$. Correlational analysis examined Pearson's r between the infant's fMRI responses to the maternal > unfamiliar voice contrast and concurrent behavioral measures of maternal anxiety (State-Trait Anxiety Inventory; Spielberger, 1989), maternal stress (Perceived Stress Scale; Cohen, 1983), maternal depression (Edinburgh Postnatal Depression Scale; Cox, 1987), and infant negative emotionality (Infant Behavior Questionnaire-Revised, Very Short Form; Putnam, 2014).

Results: Compared to speech-shaped noise, human voice elicited increased activations in multiple cortical regions of the infant's social brain (Figure 1A), including the superior temporal gyrus, temporoparietal junction, and medial prefrontal cortex. Compared to unfamiliar voice, maternal voice elicited increased activations in all aforementioned cortical regions, and additionally in key dopamine- and oxytocin-rich subcortical regions (Figure 1B), including the striatum, amygdala, and ventral diencephalon (encompassing the hypothalamus, ventral tegmental area, and substantia nigra). Compared to maternal voice, unfamiliar voice did not elicit any additional activations. Maternal anxiety, stress, depression, and infant negative emotionality negatively correlated with the infant's preferential brain responses to maternal voice in key social brain regions (Figure 2).

Conclusions: Six-month-old infants show preferential brain responses to human voice and voice of their first social partner. Our findings provide support for the feasibility of using fMRI to measure the developing brain's responsiveness to social cues. Our findings also provide preliminary evidence that the infant's preferential response to social cues is negatively associated with maternal anxiety, stress, and depression, and infant negative emotionality. When extended to at-risk infants, this work has the potential to yield breakthroughs in identifying novel neural markers that can detect early differences and deficits in an infant's developing social brain.

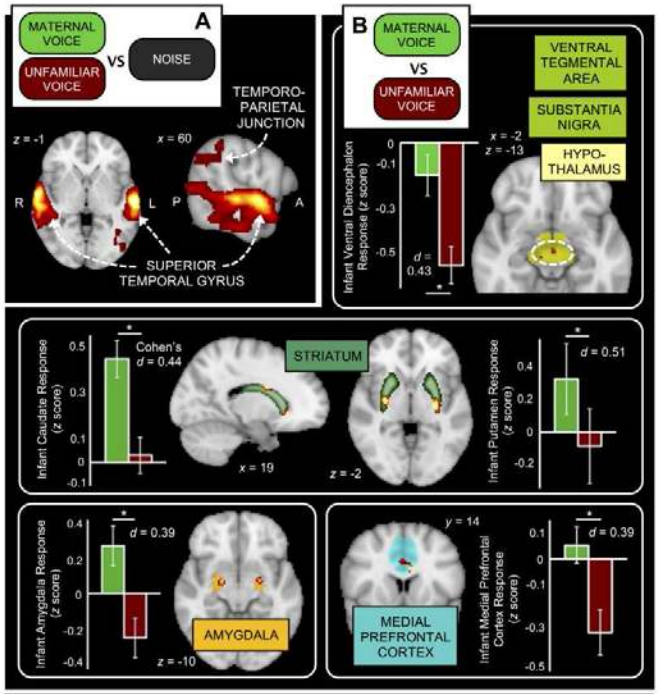

Figure 1. **fMRI can be used to measure early differences and deficits in the developing social brain.** (A) **Infants show preferential brain response to human voice**: Human voice (Maternal voice + Unfamiliar voice) > Speech-shaped noise contrast (at corrected $p < .05$). (B) **Infants show preferential brain response to maternal voice**: Maternal voice > Unfamiliar voice contrast (at corrected $p < .05$). *Note*. *$p < .01$ for bar graphs.

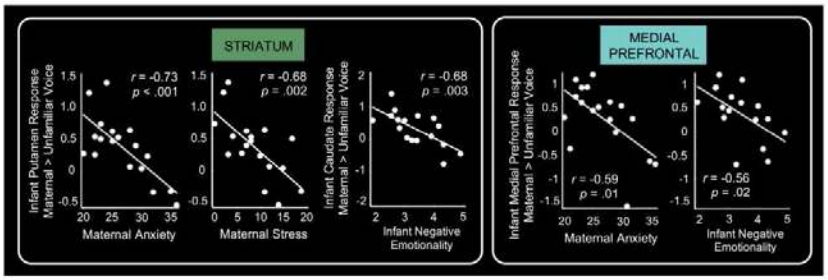

Figure 2. Maternal anxiety, stress, and infant negative emotionality negatively correlates with the infant's preferential brain responses to maternal voice.

Note. Maternal Anxiety: State-Trait Anxiety Inventory; Maternal Stress: Perceived Stress Scale; Infant Negative Emotionality: Infant Behavior Questionnaire-Revised.

References

1. Blasi, A. (2011), 'Early specialization for voice and emotion processing in the infant brain', Current Biology, vol. 21, no. 14, pp. 1220-1224.
2. Bredin, H. (2020), 'Pyannote.audio: Neural building blocks for speaker diarization', ICASSP 2020 – IEEE International Conference on Acoustics, Speech, and Signal Processing, Barcelona, Spain, pp. 7124-7128.
3. Cohen S. (1983), 'A global measure of perceived stress', Journal of Health and Social Behavior, vol. 24, no. 4, pp. 386-396.
4. Coria J.M. (2020), 'A comparison of metric learning loss functions for end-to-end speaker verification', In: Espinosa-Anke, L., Martin-Vide, C., & Spasic, I., eds. Statistical Language and Speech Processing, 2020. Cardiff, UK, Springer. pp. 137-148.
5. Cox, J.L. (1987), 'Detection of postnatal depression. Development of the 10-item Edinburgh Postnatal Depression Scale', British Journal of Psychiatry, vol. 150, no. 6, pp. 782-786.
6. Ma, S. (2015), 'Early childhood health promotion and its life course health consequences', In: Reynolds, A.J., Rolnick, A.J., & Temple, J.A., eds. Health and Education in Early Childhood: Predictors, Interventions, and Policies. Cambridge, UK: Cambridge University Press.
7. Putnam, S.P. (2014), 'Development and assessment of short and very short forms of the infant behavior questionnaire-revised', Journal of Personality Assessment, vol. 96, no. 4, pp. 445-458.
8. Spielberger, C.D. (1989), State-Trait Anxiety Inventory: a comprehensive bibliography. Palo Alto, CA: Consulting Psychologists Press.
9. Wild, C.J. (2017), 'Adult-like processing of naturalistic sounds in auditory cortex by 3- and 9-month old infants', Neuroimage, vol. 157, no. 15, pp. 623-634.

Poster No 1281

Hierarchical Development of White Matter Tracts in Youth

Audrey Luo[1,2], Valerie Sydnor[3], Joelle Bagautdinova[1], Aaron Alexander-Bloch[1], Bart Larsen[4], Fang-Cheng Yeh[5], Fengling Hu[1], Marc Jaskir[6], Arielle Keller[1], David Roalf[7], Golia Shafiei[1], Russell Shinohara[1], Matthew Cieslak[8], Theodore Satterthwaite[8]

[1]University of Pennsylvania, Philadelphia, PA, [2]Penn Lifespan Informatics and Neuroimaging Center (PennLINC), Perelman School of Medicine, University of Pennsylvania, Philadelphia, PA, [3]Department of Psychiatry, University of Pittsburgh, Pittsburgh, PA, [4]University of Minnesota, Minneapolis, MN, [5]Department of Bioengineering, University of Pittsburgh, Pittsburgh, PA, [6]Center for Neuroengineering and Therapeutics, University of Pennsylvania, Philadelphia, PA, [7]Department of Psychiatry, Perelman School of Medicine, University of Pennsylvania, Philadelphia, PA, [8]UPenn, Philadelphia, PA

Introduction: Previous work has shown regional variation in the pattern and timing of white matter (WM) development, but the relationship between WM development and hierarchical brain organization remains sparsely investigated. Recent studies have shown that spatiotemporal developmental patterns of functional connectivity align with the sensorimotor-association (S-A) axis[1,2]. Studying WM development in the context of cortical organization can provide insight into how structural connectivity develops to support cortical activity. We hypothesized that the pattern and timing of developmental changes in WM tracts occur hierarchically along the S-A axis of cortical development.

Methods: We used diffusion MRI data in youth ages 8-22 from the Human Connectome Project: Development (N=569). All images were preprocessed using QSIPrep 0.16.1[3]. Next, 50 white matter tracts were mapped using automated fiber tracking from DSI studio[4] as part of a QSIPrep reconstruction workflow. We used mean fractional anisotropy (FA) along each tract to characterize WM. Site effects were harmonized using CovBat, in which age was modeled as a smooth term via a generalized additive model (GAM)[5,6]. To model both linear and non-linear associations between FA and age, we used GAMs with penalized splines while covarying for sex and in-scanner motion. The age of maturation was defined as the earliest age at which the first derivative of the smooth was not significant. To define S-A ranks for each tract, we used a population-based WM tract-to-cortical region connectome mapping[7] based on HCP-MMP atlas regions[8], which identified the population probability that a given tract was connected to each HCP-MMP atlas region. Tract-to-region connections present in at least 5% of the population were retained. We parcellated the S-A axis using the HCP-MMP atlas, yielding regional S-A ranks. Next, a weighted mean S-A rank was computed for each tract by weighing the average S-A ranks of the regions that a tract connected to by the population probability of each tract-to-region connection. We used Spearman's rank correlations to characterize the spatial association between developmental effects and S-A axis ranks. Spin-based spatial permutation tests were used for significance testing[9].

Results: We visualized each tracts' weighted mean S-A rank and the cortical regions each tract connected to using Yeh's tract-to-region probabilities (Fig. 1). Weighted mean S-A rank tended to correspond to associated tract functions described in literature; for example, the optic radiation ranked lowest whereas arcuate fasciculus ranked high on the S-A axis (Fig. 1A-B). Mid-ranking tracts tended to connect diverse cortical regions spanning across the S-A axis (Fig. 1D). A tract's rank was significantly associated with its age of maturation (Fig. 2A, $r = 0.41$, $p_{spin}<0.001$). Sensorimotor tracts tended to mature earlier, including corticospinal tracts and the optic radiations. In contrast, higher order tracts (i.e., those with higher S-A ranks) tended to mature later, such as the frontal aslant tracts and anterior thalamic radiations. The uncinate fasciculus uniquely matured earlier among higher order tracts. Fitted smooths based on model-predicted data were computed in all tracts (Fig. 2B-E). The FA of lowest-order tracts (rank less than 100) tended to have flatter trajectories of developmental change (Fig. 2B and C). In contrast, FA in many higher order tracts (rank greater than 200) continued to increase throughout adolescence (Fig. 2E), though several tracts displayed earlier flattening, including the uncinate fasciculus.

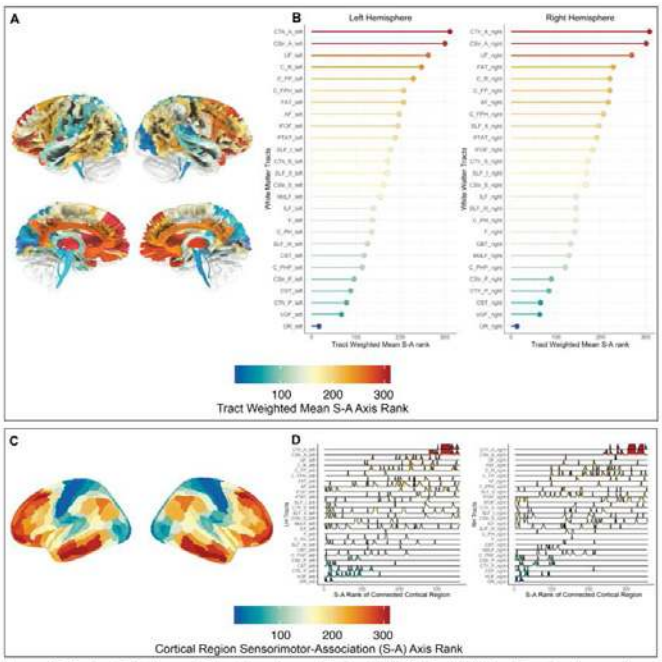

Figure 1. Tract weighted mean S-A axis ranks are displayed. **(A-B)** Each WM tract is colored according to its weighted mean S-A rank. **(C)** The cortical S-A axis is displayed using the HCP-MMP atlas. **(D)** Ridgeline plots display white matter tracts in the left and right hemispheres plotted against the S-A axis ranks of the cortical regions the tracts connect to. The tract-to-region population probabilities are represented by the height values. Tracts are colored by weighted mean S-A rank. Mid-ranking tracts (yellow, orange) tend to display connections to cortical regions with varying positions on the S-A axis.

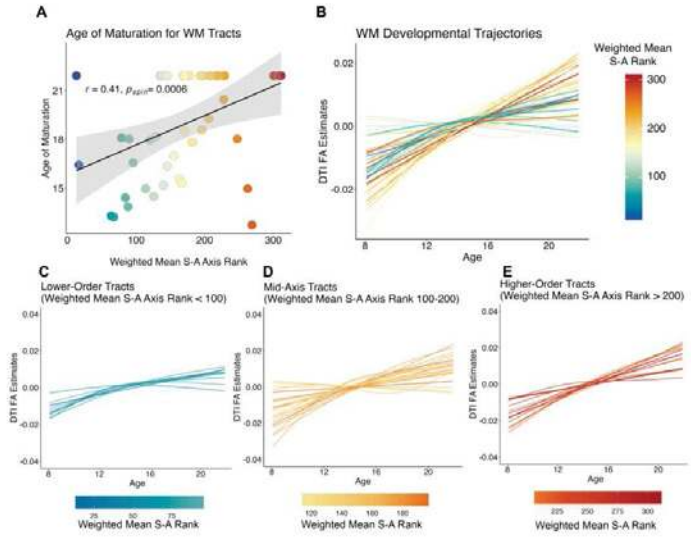

Figure 2. Timing of white matter maturation varies depending on a given tract's weighted mean sensorimotor-association (S-A) axis rank. **(A)** The age of maturation, defined as the maximum age where the first derivative of the age smooth is significant based on a simultaneous credible interval, for each white matter tract is plotted against a given tract's weighted mean S-A rank. **(B)** Using generalized additive models, age-related change in fractional anisotropy (FA) is modeled for every tract across childhood and adolescence. Each line represents the predicted FA for each tract at each age. DTI FA estimates are zero-centered. **(C-D)** Plots display the developmental pattern of tracts grouped by S-A rank. Colors indicate weighted mean S-A rank of a given tract. The S-A axis was parcellated with the HCP-MMP atlas to compute weighted mean S-A ranks using the population-based tract-to-region connectome.

Conclusions: We found WM maturation occurs hierarchically along a major axis of cortical organization. Characterizing patterns of healthy WM development is important for understanding how deviations from normative hierarchical development may confer risk for diverse psychopathology. Replication of these results in additional datasets is necessary to establish generalizability.

References

1. Sydnor, V. J., et al. (2021), Neurodevelopment of the association cortices: Patterns,
2. mechanisms, and implications for psychopathology. Neuron, 109(18), 2820–2846.
3. Luo, A., et al. (2023), Functional Connectivity Development along the Sensorimotor-Association Axis Enhances the Cortical Hierarchy. bioRxiv.

4. Cieslak, M., et al. (2021), QSIPrep: An integrative platform for preprocessing and reconstructing diffusion MRI data. Nature Methods, 18(7), Article 7.
5. Yeh, F.-C., et al. (2018), Population-averaged atlas of the macroscale human structural
6. connectome and its network topology. NeuroImage, 178, 57–68.
7. Chen, A. A., et al. (2022), Mitigating site effects in covariance for machine learning in neuroimaging data. Human Brain Mapping, 43(4), 1179–1195.
8. Pomponio, R., et al. (2020), Harmonization of large MRI datasets for the analysis of brain imaging patterns throughout the lifespan. NeuroImage, 208, 116450.
9. Yeh, F.-C. (2022), Population-based tract-to-region connectome of the human brain and its hierarchical topology. Nature Communications, 13(1), Article 1.
10. Glasser, M. F., et al. (2016), A multi-modal parcellation of human cerebral cortex. Nature, 536(7615), 171–178.
11. Alexander-Bloch, A. F., et al. (2018), On testing for spatial correspondence between maps of human brain structure and function. NeuroImage, 178, 540–551.

Poster No 1282

Unveiling Co-Development of Cortical Surface Area and Thickness Asymmetry in Young Brain

Xinran Wu[1], Xiangzhen Kong[2], Lena Palaniyappan[3], Gunter Schumann[4], Jianfeng Feng[5], Jie Zhang[6]

[1]Institute of Science and Technology for Brain-inspired Intelligence, Fudan University, Shanghai, Shanghai, [2]Department of Psychology and Behavioral Sciences, Zhejiang University, Zhejiang, China, Hangzhou, Zhejiang, [3]Orygen, The National Centre of Excellence in Youth Mental Health, Parkville, VIC, Australia, Parkville, Victoria, [4]Centre for Population Neuroscience and Stratified Medicine (PONS), Fudan University and Charite, Shanghai, Shanghai, [5]Institute of Science and Technology for Brain inspired Intelligence, Shanghai, Shanghai, [6]Institute of Science and Technology for Brain-inspired Intelligence (ISTBI), Shanghai, Shanghai

Introduction: Hemispheric asymmetry is a fundamental aspect of human brain organization (Duboc et al., 2015), yet its developmental processes remain poorly understood. Unique asymmetrical patterns have been identified in cortical surface area (CSA) and cortical thickness (CT) (Kong et al., 2018), and undergoing various developmental changes with age (Roe et al., 2023). Abnormal alterations in asymmetry have been linked to certain neurodevelopmental disorders in adolescents, such as autism (Postema et al., 2019), underscoring the significance of comprehending the asymmetric development of the brain for overall brain health. However, the current study exclusively delineated the trajectories of asymmetry development for different features, and the correlation between the asymmetry development of distinct modalities remains incompletely understood.

Methods: This study investigates brain structural asymmetry development, genetic factors, and cognitive/psychiatric associations in youths. We used MRI data from two longitudinal datasets: Adolescent Brain Cognitive Development (ABCD) study (N>11,000, 2 time points: 10 and 12 years) and IMAGEN study (N>2,000, 3 time points: 14, 19, 22 years). Asymmetry indices (AI) from CT, CSA, and subcortical volume were assessed with linear mixed models (LMM) for age-related effects. Cognitive processes associated with CSA and CT asymmetry developmental pattern were determined through a Neurosynth-based meta-analysis. Besides, the associations between AI and cognitive / psychiatric phenotype were investigated using LMM. Finally, genetic association analysis (GWAS), gene enrichment analysis, and temporal expression analysis using BrainSpan dataset were performed on ABCD genetic sequencing data to investigate genetic factors influencing CSA and CT asymmetry and its changing rates (ΔAI) from ages 10 to 12.

Results: Despite baseline CT and CSA AI pattern differences with each other (Fig 1A), CT and CSA asymmetry showed similar developmental trajectories: Frontal and temporal regions exhibited increasing left-lateralization with age (Fig 1B, C), which associated with language and emotion functions (by Neurosynth, Fig 1D, E). Age-related changes in CSA and CT within these regions indicated that asymmetry development was driven by more rapid CSA and CT reduction in the right frontotemporal regions during adolescence than their left homotopic regions. Phenotype association analysis suggested prolonged CT asymmetry development in the superior frontal cortex (less leftward than peers) related to better cognitive function (Fig 2A). Genetic analysis revealed more genes linked to ΔAI than AI, and enrichment analysis revealed the genes influencing both CSA and CT ΔAI primarily associated with neural and synapse development (Fig 2B, C, D); besides, these genes had increased expression upon adolescence (especially in frontal lobe) (Fig2 E).

Conclusions: In summary, this study showed that despite CSA and CT were influenced by distinct developmental and genetic mechanism, a similar co-developmental trajectory still exists between asymmetry of the two different morphological features, primarily in frontotemporal regions. This shared trajectory may result from common biological pathways in adolescent brain like synaptic pruning and dendritic changes affecting both CSA and CT. Leftward development in these regions may underlie advanced cognitive abilities, including language. Prolonged cortical thickness asymmetry growth in superior frontal gyrus correlated with higher cognitive abilities, which might suggest more neural plastic and less inflammation (Tooley, Bassett, &

Mackey, 2021) that can preserve neurons and synapses, and finally enhanced brain function. These findings hold important implications for understanding normal and abnormal brain development.

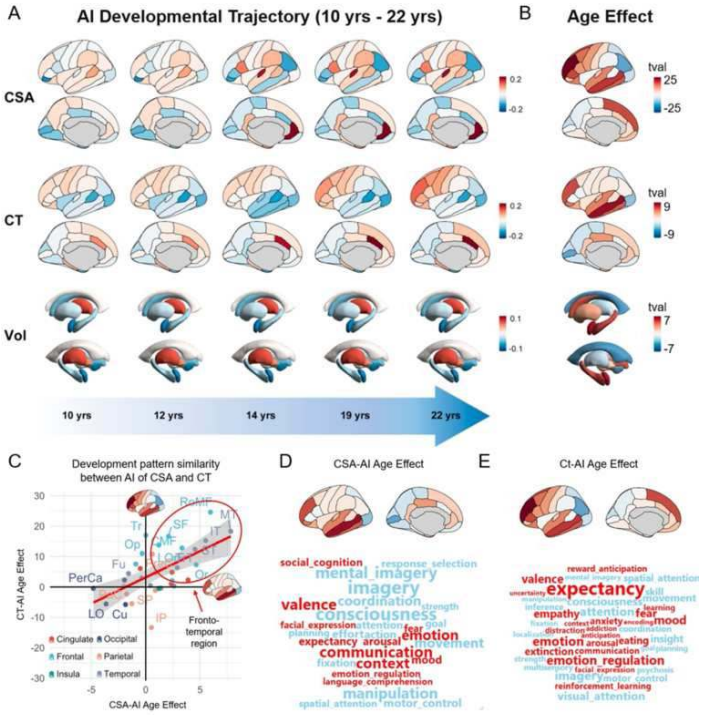

Figure 1. Developmental trajectories of cortical thickness and surface area. (A) Average asymmetry patterns across five age groups.(B) The age effects obtained from the linear mixed-effects models (t values with age as linear predictor).(C) Spatial similarity of t-value maps for CSA-AI and CT-AI. The horizontal axis represents the age-effect of AI for CSA, while the vertical axis represents age-effect of AI for CT. CSA-AI and CT-AI t-maps are correlated spatially with each other, with the most prominent cross-modal co-varying regions primarily located in the frontotemporal regions (circled in red). (D-E) Meta-analysis results. Spatial similarity was computed between the age effect maps for CSA-AI and CT-AI and 217 meta-analytic spatial maps corresponding to different cognitive terms from Neurosynth. Positively correlated terms are presented in red, and negatively correlated terms in blue in the word cloud. The size of the words in the word cloud corresponds to the significance of spatial correlation (-log10(p)). Only terms with a significant correlation ($p < 0.05/217$, Bonferroni correction) are presented.

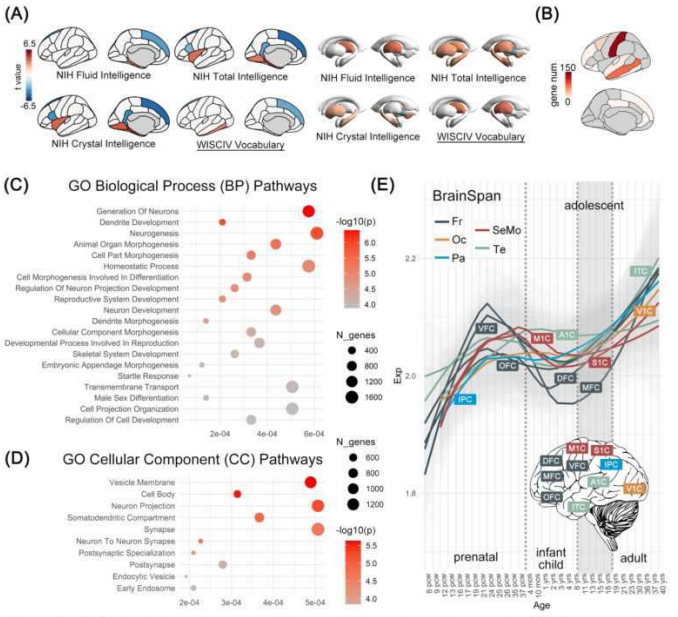

Figure 2. Behavioral phenotype association analysis and genetic analysis. (A) The asymmetry of cortical thickness and subcortical volume and its association with cognitive abilities. The figure displayed the t-values of regressive coefficients for each phenotype (FDR $q < 0.05$). Cognition phenotypes were estimated separately due to differences in the scales used in ABCD and IMAGEN. Items with titles underlined are from the IMAGEN cohort. NIH: NIH Cognitive Battery. WISC-IV: Wechsler Intelligence Scale for Children–Fourth Edition. (B) Genetic correlations of longitudinal change rates (ΔAI) from ages 10 to 12. Here we present ΔAI within regions becoming more left-lateralized with age (L-ΔAI genes) because only this subset of regions showed significant enrichment results. Color indicates the number of significant genes. (C-D) Genetic enrichment results for L-ΔAI genes, localized to Gene Ontology (GO) pathways. (C) Biological process (BP) pathways. The x-axis represents the overlap rate of gene sets corresponding to the GO term, bubble size indicates the number of overlapping genes, and color intensity indicates significance (-log10(p)). (D) Cellular component (CC) pathways. (E) Gene expression of L-ΔAI genes across cortical regions exhibits a resurgence during adolescence. PCW, post-conceptional weeks. Mos, Months. Brain region abbreviations are listed in supplemental materials: Fr, Frontal lobe; Pa, Parietal lobe; Te, Temporal lobe; SeMo, Sensory-Motor cortex; Oc, Occipital lobe.

References
1. Duboc, V., Dufourcq, P., Blader, P., & Roussigné, M. (2015). 'Asymmetry of the Brain: Development and Implications'. Annual Review of Genetics, vol 49(1), pp. 647-672.
2. Kong, X.-Z., Mathias, S. R., Guadalupe, T., Glahn, D. C., Franke, B., Crivello, F., . . . Francks, C. (2018). 'Mapping cortical brain asymmetry in 17,141 healthy individuals worldwide via the ENIGMA Consortium'. Proceedings of the National Academy of Sciences, 115(22), E5154-E5163.
3. Postema, M. C., van Rooij, D., Anagnostou, E., Arango, C., Auzias, G., Behrmann, M., . . . Francks, C. (2019). 'Altered structural brain asymmetry in autism spectrum disorder in a study of 54 datasets'. Nat Commun, 10(1), 4958.
4. Roe, J. M., Vidal-Pineiro, D., Amlien, I. K., Pan, M., Sneve, M. H., Thiebaut de Schotten, M., . . . Westerhausen, R. (2023). 'Tracing the development and lifespan change of population-level structural asymmetry in the cerebral cortex'. Elife, 12, e84685. doi:10.7554/eLife.84685
5. Tooley, U. A., Bassett, D. S., & Mackey, A. P. (2021). 'Environmental influences on the pace of brain development'. Nature Reviews Neuroscience, 22(6), 372-384.

Poster No 1283

Chinese Baby Connectome Project (CBCP): Advanced and Comprehensive Infant Cohort Protocols

Lixuan Zhu[1], Qing Yang[1], Feiyu Quan[1], Yan Liang[1], Qiong He[1], Ying Lin[2], Jian Sun[1], Ruili Ma[1], Jiayang Guo[1], Weijia Zhang[1], Zhixin Wang[1], Yajuan Zhang[1], Tianli Tao[1], Xinyi Cai[1], Lin Zhang[2], Mingwen Yang[2], Zuozhen Lan[2], Chaowei Zhang[3], Dan Cai[4], Na Hu[4], Xianghui Huang[5], Wei Wei[6], Xuechen Ding[4], Xinpei Xu[6], Mingming Zhang[4], Xiaoqian Yan[7], Chenbo Wang[8], Weijun Zhang[9], Jiayu Zhu[9], Jian Cheng[10], Kunyu Xu[11], Geng Chen[12], Qian Wang[1], Feng Shi[13], Anqi Qiu[14], Chunfeng Lian[15], Jungang Liu[2], Dan Li[4], Guoqiang Cheng[16], Han Zhang[1,17], Dinggang Shen[1,13,17]

[1]School of Biomedical Engineering, ShanghaiTech University, Shanghai, China, [2]Department of Radiology, Xiamen Children's Hospital, Children's Hospital, Fujian, China, [3]Fujian Key Laboratory of Neonatal Diseases, Children's Hospital of Fudan University (Xiamen Branch), Fujian, China, [4]School of Psychology, Shanghai Normal University, Shanghai, China, [5]Fujian Key Laboratory of Neonatal Diseases, Children's Hospital of Fudan University (Xiamen Branch), Xiamen, Fujian, [6]Shanghai Institute of Early Childhood Education, Shanghai Normal University, Shanghai, China, [7]Institute of Science and Technology for Brain-Inspired Intelligence, Fudan University, Shanghai, China, [8]School of Psychology and Cognitive Science, East China Normal University, Shanghai, China, [9]Shanghai United Imaging Healthcare Co., Ltd., Shanghai, China, [10]School of Computer Science and Engineering, Beihang University, Beijing, China, [11]Institute of Modern Languages and Linguistics, Fudan University, Shanghai, China, [12]School of Computer Science and Engineering, Northwestern Polytechnical University, Xi'an, China, [13]Shanghai United Imaging Intelligence Co., Ltd., Shanghai, China, [14]Department of Biomedical Engineering, National University of Singapore, Singapore, [15]School of Mathematics and Statistics, Xi'an Jiaotong University, Xi'an, China, [16]Department of Neonatology, Children's Hospital of Fudan University, Fujian, China, [17]Shanghai Clinical Research and Trail Center, Shanghai, China

Introduction: Studies based on the developing Human Connectome Project (dHCP) (Edwards et al., 2022) and the UNC/UMN Baby Connectome Project (BCP) (Howell et al., 2019) have significantly advanced our understanding of the early development of brain. Our research extends cutting-edge magnetic resonance imaging (MRI) acquisition techniques, including AI-driven approaches, to investigate infant brain development. In the Chinese Baby Connectome Project (CBCP), we integrate infant-tailored, accelerated imaging with comprehensive non-imaging data collection, aiming to build the first longitudinal atlas in China (Fig. 1b). Aligned with children aged 0-6 years, the CBCP protocol covers imaging, physiological, genetic, environmental, and behavioral data, providing a holistic perspective on brain development.

Methods: Cohort Design: CBCP aims to gather full-spectrum data from over 1000 healthy infants aged 0-6 in 12 sub-cohorts, utilizing an accelerated longitudinal design. Rigorous criteria ensure enrollment of term-birth children without adverse prenatal conditions. Preparations: Lab layout (Fig. 1a) and experimental procedure (Fig. 1c) are detailed. Pre-MRI preparation includes 25-min mock scanner training with motion monitoring, sleeping with noise training, and sleep deprivation to increase success rate. MRI scan: we encourage children of age 0-3 undergo MRI scans during natural sleep and those of age 3-6 take awake scans while watching cartoons (black screen for resting-state fMRI (rfMRI)), but allow overlapped age period between sleep and awake scans. All sites use 3.0T MRI scanners of the same model (uMR 890, United Imaging) with a 64-channel head coil. Informed by pilot studies, CBCP MRI protocol (Table 1) encompass T1w and T2w structural MRI (sMRI), rfMRI, diffusion MRI (dMRI), and multiplex imaging (MTP) (Ye et al., 2022). For sMRI, we utilize AI-assisted compressed sensing (ACS) (Liu et al., 2023) to ensure fast acquisition of 3D sMRI (0.8mm isotropic), saving 37.8% time compared to BCP. To further "freeze" head motion and increase success rate for certain infants who prone to move, 1-min ultra-fast 3D sMRI scans are implemented. Compared to BCP with 2mm isotropic rfMRI, CBCP collects rfMRI with higher spatial resolution (1.8mm isotropic) at a 800ms TR. dMRI with complete incremental acquisitions of 3-shell scheme at both AP and PA phase encoding directions. MTP

incorporates dual repetition time, dual flip angle, multi-echo, and optional flow modulation features, which provides 16 qualitative and 9 quantitative images (Fig. 1b). Quality control (QC): a pilot study with traveling subjects ensured data quality across centers. Phantom scans before the experiment assure scanner stability. All the MRI data will be immediately uploaded to a data-management platform for QC. An automated infant MRI preprocessing pipeline, using deep learning, guarantees reliable retrieval of subjects' attributes. Non-imaging data: includes EEG/ERP for infants (0-6) during various tasks and resting state. Behavioral observations, audio/video recordings, social assessments, IQ, and Griffiths developmental evaluations are conducted following a comprehensive digitized questionnaire on environmental, perinatal, and family factors. Genetic data will be collected for deep sequencing.

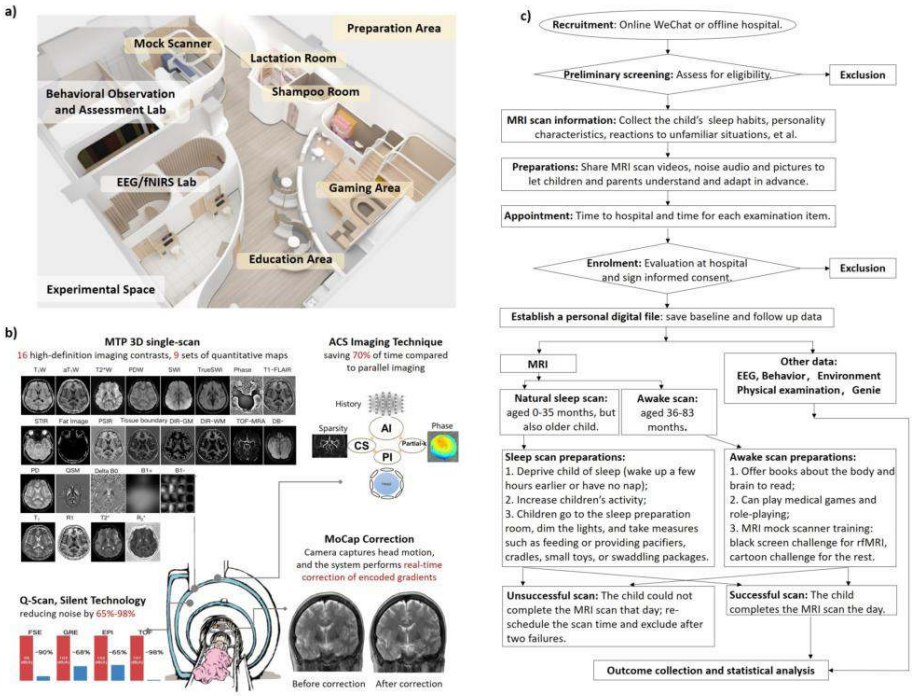

Figure 1 a) Integrated child-friendly experimental preparation and data collection laboratory layout. b) Specialized new technologies used in the construction of CBCP corhorts: MTP, ACS, Q-Scan, and MoCap Correction. c) The flowchart of the CBCP data collection process, primarily focusing on the MRI section. It covers the recruitment of participants, participant screening for inclusion, preliminary practice and preparation for data collection, scheduling appointments, obtaining informed consent through signature, establishing individual data profiles, and detailing the process of MRI data collection. This includes distinctions between scans conducted during natural sleep and those during wakefulness. The flowchart also addresses response measures and plans for handling various scenarios.

Table 1 CBCP MR imaging protocol

Sequences	Matrix	FoV (mm)	Resolution (mm)	TE (msec)	TR (msec)	Slices/ Orientation	Time (min:sec)	Acceleration
gre_scout	255×255	260×260	1.02×1.02×8	4.02	8.4	1/Sag	00:07	
gre_scout_ref	255×255	260×260	1.02×1.02×8	4.02	8.4	1/Sag	00:07	
Fast T1-weighted	320×300	256×240	0.8×0.8×0.8	2	6.2	208/Sag	01:03	ACS 8, ×12 .6
Fast T2-weighted	320×300	256×240	0.8×0.8×0.8	540	3000	208/Sag	01:00	ACS 10, ×19.9
T1-weighted	320×300	256×240	0.8×0.8×0.8	2.3	6.5	208/Sag	03:46	ACS 2, ×3.2
T2-weighted	320×300	256×240	0.8×0.8×0.8	452	3000	208/Sag	04:09	ACS 2, ×3.8
Field Map	116×116	209×209	1.8×1.8×1.8	81.1	8750	72/Axial	00:45	-
rfMRI PA	116×116	209×209	1.8×1.8×1.8	37	800	72/Axial	06:31	Multi-Band=8
dMRI AP, b0	140×140	210×210	1.5×1.5×1.5	77.1	3017	92/Axial	00:44	Multi-Band=4
dMRI PA, b = 500, 1000, 3000	140×140	210×210	1.5×1.5×1.5	77.1	3017	92/Axial	04:12	Multi-Band=4, 3 shells, 72 directions
dMRI AP, b = 500, 1000, 3000	140×140	210×210	1.5×1.5×1.5	77.1	3017	92/Axial	04:12	
MTP	192×192	230×190	0.8×0.8×1.6	3.91	48.1	90/Axial	6:58	ACS 4.4, ×5.91
Contingent on the baby continuing to sleep or cooperating								
rfMRI AP	116×116	209×209	1.8×1.8×1.8	37	800	72/Axial	06:31	Multi-Band=8
dMRI PA, b = 1500, 2000, 2500	140×140	210×210	1.5×1.5×1.5	77.1	3017	92/Axial	04:32	Multi-Band=4, 3 shells, 72 directions
dMRI AP, b = 1500, 2000, 2500	140×140	210×210	1.5×1.5×1.5	77.1	3017	92/Axial	04:32	

Results: As of 10/23, we've collected MRI data from 298 infants with a 78% success rate (sMRI, fMRI, and dMRI complete acquisition). CBCP QC standards show pass rates: T1w, 94.4%; T2w, 85.7%; rfMRI, 69.4%; dMRI, 87.1%. Applying the same criteria to BCP data yields: T1w, 95.8%; T2w, 93.2%; rfMRI, 56%; dMRI, 72.1%.

Conclusions: We report our protocol for this ongoing CBCP project aiming to build China's largest, high-quality, longitudinal infant brain-behavior dataset. CBCP embraces advanced imaging techniques for a comprehensive longitudinal cohort, offering a unified and standardized protocol from acquisition to analysis for both imaging and non-imaging data in depicting healthy brain developmental trajectories.

References

1. Edwards, A.D. et al. (2022) 'The Developing Human Connectome Project Neonatal Data Release', Frontiers in Neuroscience, 16. Available at: https://doi.org/10.3389/fnins.2022.886772.
2. Van Essen, D.C. et al. (2013) 'The WU-Minn Human Connectome Project: An overview', NeuroImage, 80, pp. 62–79. Available at: https://doi.org/10.1016/j.neuroimage.2013.05.041.
3. Howell, B.R. et al. (2019) 'The UNC/UMN Baby Connectome Project (BCP): An overview of the study design and protocol development', NeuroImage, 185, pp. 891–905. Available at: https://doi.org/10.1016/j.neuroimage.2018.03.049.
4. Liu, K. et al. (2023) 'The clinical feasibility of artificial intelligence-assisted compressed sensing single-shot fluid-attenuated inversion recovery (ACS-SS-FLAIR) for evaluation of uncooperative patients with brain diseases: comparison with the conventional T2-FLAIR with parallel imaging', Acta Radiologica, 64(5), pp. 1943–1949. Available at: https://doi.org/10.1177/02841851221139125.
5. Ye, Y. et al. (2022) 'MULTI-parametric MR imaging with fLEXible design (MULTIPLEX)', Magnetic Resonance in Medicine, 87(2), pp. 658–673. Available at: https://doi.org/10.1002/mrm.28999.
6. Acknowledgement
7. This work is partially supported by the STI 2030—Major Projects (2022ZD0209000 and 2021ZD0200516), Shanghai Pilot Program for Basic Research—Chinese Academy of Science, Shanghai Branch (JCYJ-SHFY-2022-014), and Shenzhen Science and Technology Program (No. KCXFZ20211020163408012).

Poster No 1284

7T BOLD fMRI characterisation of depth dependent hemodynamics in developing human cortex

Jucha Willers Moore[1], Elisabeth Pickles[1], Philippa Bridgen[2], Pierluigi Di Cio[2], Alena Uus[1], Ines Tomazinho[1], Beya Bonse[1], Maria Deprez[1], Sharon Giles[2], A. Edwards[1], Joseph Hajnal[1], Shaihan Malik[1], Tomoki Arichi[1], Jonathan Polimeni[3]

[1]King's College London, London, United Kingdom, [2]London Collaborative Ultra high field System (LoCUS), London, United Kingdom, [3]Athinoula A. Martinos Center for Biomedical Imaging, Massachusetts General Hospital, Charlestown, MA

Introduction: Neuronal activity, neurovascular coupling and vascular dynamics undergo rapid maturation in the perinatal period[1-3]. The amplitude and temporal features of the neonatal hemodynamic response to neuronal activity therefore differs markedly from that typically seen in adults[4]. It is thus unclear if cerebral cortical depth-dependent hemodynamic responses features related to differences in hemodynamics across different levels of the intracortical vascular hierarchy[5] can be generalised to the developing newborn brain[1,2]. To address this, we developed a platform for high-resolution 7T fMRI studies in newborn infants and performed a cortical-depth analysis of task-driven BOLD responses in primary motor cortex (M1).

Methods: NHS research ethics committee approval and written parental consent was provided for data collection. Data were acquired from 10 healthy infants at term equivalent age (median: 39.7 weeks postmenstrual age at scan (range: 37.4–42.9), 5 female) during natural sleep using a Siemens 7T system (MAGNETOM Terra, Siemens Healthineers, Erlangen, DE) and a 1TX-32RX Nova Medical head coil (Wilmington, MA, USA) with locally imposed safety restrictions[6]. A GRE-EPI sequence was used to acquired BOLD fMRI data over 6 m 51 s with parameters: resolution=0.8 mm isotropic (full Fourier), TR/TE=2660/48 ms, 25 slices, 1.06 ms nominal echo spacing, and R=2 acceleration with Dual-Polarity GRAPPA reconstruction[7]. Sensorimotor stimulation (on/off blocks of 26.6 s) was elicited with a custom robotic device[8] (Fig. 1A). After pre-processing using tools implemented in FSL, ROIs spanning the full cortical thickness were manually defined within significant clusters of activation (Z>2) in M1; data were up-sampled; 3 equi-volume layers were defined using LAYNII[9]; and layer-specific BOLD timeseries were extracted, from which normalized trial responses of percent signal change were calculated and then averaged across infants (Fig. 1B-D).

Results: fMRI data were successfully acquired in 7/10 infants with significant activation identified in the contralateral hand area of M1 in response to sensorimotor stimulation (Fig. 1B). Trial-averaged responses showed a rise in BOLD signal around 8 s after stimulus onset in the superficial cortical depths (Fig. 1E, F) with a median positive peak of 5.54 % BOLD signal change (Fig. 2B). Conversely, at deeper cortical depths, a subtle initial dip was seen followed by a trend for a delayed rise in BOLD signal and a significantly lower median peak amplitude of 3.08 % signal change (p=0.004) and 1.79 % signal change (p=0.002) in the middle and deep cortical depths respectively (Fig. 2A, B). A trend emerged for a more pronounced post-stimulus undershoot in the BOLD response at superficial cortical depths, but it did not reach significance.

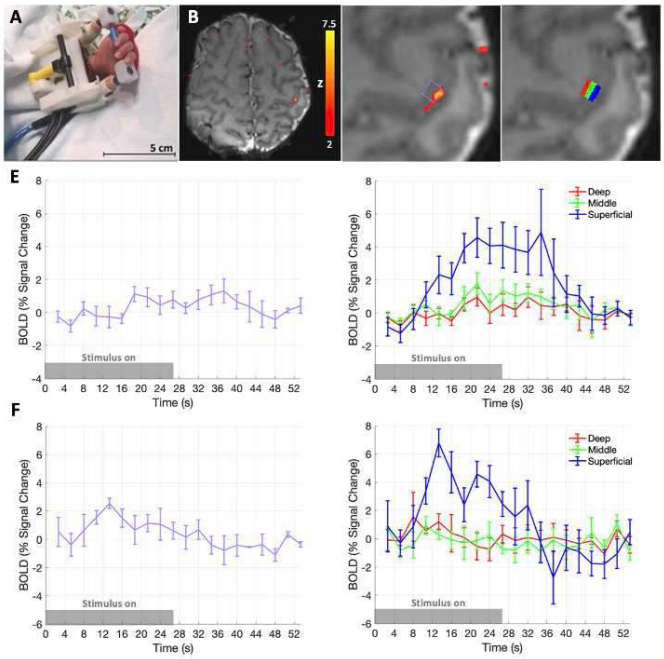

Figure 1. BOLD signal shows a cortical depth specific response profile in the neonatal motor cortex. (A) Robotic wrist sensorimotor stimulation device. (B) Exemplar activation in left M1 following wrist sensorimotor stimulation (Z>2), (C) activation region of interest (ROI; purple) and (D) three cortical depth/layer definitions overlaid onto the mean EPI image in one infant. Cortex is 1.5–2 mm in thickness. (E) Hemodynamic response across whole ROI (left) and in each ROI layer (right) as group mean (+/– SEM, N=7 infants) and (F) exemplar mean (+/– SEM, N=7 trials) in one infant.

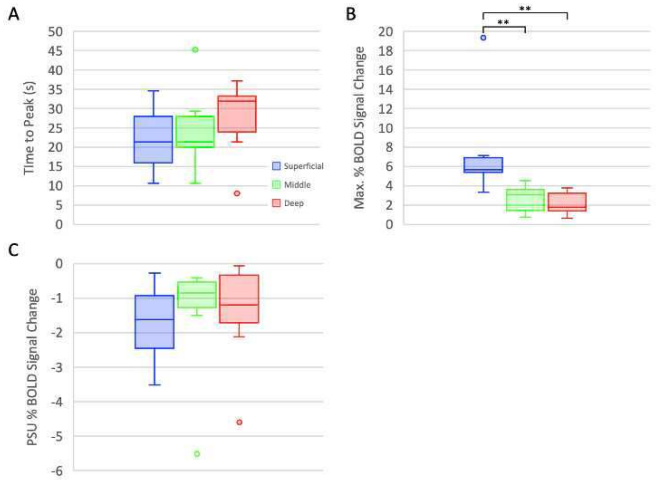

Figure 2. Parameters of BOLD signal change across cortical depths in individual subjects in response to a sensorimotor stimulus to the wrist. (A) No significant difference seen in time to peak across deep, middle, and superficial cortical depths. (B) Greater peak % BOLD signal change seen in the superficial depth compared with middle (p=0.004) and deep (p=0.002) cortical depths. (C) No significant difference seen in the minimum % BOLD signal change of the post-stimulus undershoot (PSU) change. Boxplots represent the median, 25th and 75th centiles; N=7 infants, circle points are outliers, Mann-Whitney-Wilcoxon test, p<0.01**).

Conclusions: We present the first evidence of differing hemodynamic responses across cortical depths in the neonatal brain, which differ markedly than those typically seen in adults. This may reflect differences in the vasculature, such as the endothelium of the diving arterioles which dilate first in the deeper cortical depths in adults, propagating vasodilation upstream to the pial surface[5]. As the arteriolar endothelium develops postnatally, propagation likely differs in neonates[1] resulting in a delayed BOLD response in the deeper cortical layers. The increased functional contrast-to-noise ratio at 7T[10] provides a unique opportunity for detailed in vivo studies of neurovascular coupling and hemodynamics during the critically important perinatal period. This offers new insight into the early development of cortical hemodynamics and a means to explore generalisability of our mechanistic understanding of adult cortical hemodynamics. Future work can investigate how hemodynamics evolve during early development, whether the sleeping state during our task affects hemodynamics, and whether alterations are seen in pathology.

References
1. Allievi, A. G. (2013), 'An fMRI Compatible Wrist Robotic Interface to Study Brain Development in Neonates', Annals of Biomedical Engineering, 41(6), 1181–1192.
2. Arichi, T. (2012), 'Development of BOLD signal hemodynamic responses in the human brain', Neuroimage, 63(2), 663–673.
3. Harris, J. J. (2011), 'The physiology of developmental changes in BOLD functional imaging signals', Developmental Cognitive Neuroscience, 1(3), 199–216.
4. Hoge, W. S. (2016), 'Dual-Polarity GRAPPA for simultaneous reconstruction and ghost correction of EPI data', Magnetic Resonance in Medicine, 76(1), 32–44.
5. Huber, L (2021), 'LayNii: A software suite for layer-fMRI', NeuroImage, 237, 118091.
6. Kozberg, M. (2016), 'Neurovascular coupling and energy metabolism in the developing brain', Progress in Brain Research, 225, 213–242.
7. Malik, S. J. (2021), 'Specific absorption rate and temperature in neonate models resulting from exposure to a 7T head coil', Magnetic Resonance in Medicine, 86(3), 1299–1313.
8. Norman, M. G. (1986), 'The Growth and Development of Microvasculature in Human Cerebral Cortex', Journal of Neuropathology & Experimental Neurology, 45(3), 222–232.
9. Siero, J. C. W. (2013), 'BOLD Specificity and Dynamics Evaluated in Humans at 7 T: Comparing Gradient-Echo and Spin-Echo Hemodynamic Responses', PLoS ONE, 8(1), e54560.
10. Viessmann, O. (2021), 'High-resolution fMRI at 7 Tesla: Challenges, promises and recent developments for individual-focused fMRI studies', Current Opinion in Behavioral Sciences, 40, 96–104.

Poster No 1285

Prenatal environment is associated with the pace of network development over the first 3 years

Ursula Tooley[1], Aidan Latham[2], Jeanette Kenley[2], Dimitrios Alexopoulos[2], Tara Smyser[2], Barbara Warner[2], Joshua Shimony[2], Jeffrey Neil[2], Joan Luby[2], Deanna Barch[3], Cynthia Rogers[2], Christopher Smyser[2]

[1]Washington University in Saint Louis, Saint Louis, MO, [2]Washington University in St. Louis, St. Louis, MO, [3]Washington University, Saint Louis, MO

Introduction: Environmental influences on brain structure and function during development have been well-characterized, and the pace of early brain development has been associated with important risk factors and behavioral outcomes (Shaw et al. 2010; Farah 2017). As children mature, intrinsic cortical networks become more segregated, with sets of brain regions displaying more densely interconnected patterns of connectivity and large-scale systems becoming increasingly distinct (Grayson & Fair 2017). Some theoretical models posit that environmental influences on brain development might arise by way of effects on the pace of brain development, such that brain development proceeds faster in neonates and toddlers from lower-SES backgrounds (Tooley et al. 2021).

Methods: In a set of pre-registered analyses (AsPredicted #128836), we explicitly test whether early SES is associated with differences in the pace of intrinsic cortical network segregation during the first three years of life. We capitalize on a unique cohort of neonates and toddlers (n=261, M=41.3 weeks at first scan) with longitudinal fMRI neuroimaging data and extensively characterized early environments (Stout et al. 2022), using generalized additive mixed models (Wood 2004) to examine moderating effects of prenatal SES (Luby et al. 2023) on development of cortical network segregation, controlling for sex at birth, amount of uncensored data included, in-scanner motion, and average network connectivity. We take a hierarchical approach, first examining measures of cortical network segregation (Figure 1a-c) at whole brain resolution, then analyzing at the level of functional brain systems, and finally in individual brain regions. Finally, we examine whether differences in measures of cortical network segregation at age two years are associated with language and cognitive abilities (Bayley Scales of Development-III).

Results: Cortical network segregation increases with age during the first three years of life (Figure 1d-f), and prenatal SES significantly moderates trajectories of cortical network segregation across scales (Figure 1g-i). Neonates and toddlers from lower-SES backgrounds show a steeper increase in cortical network segregation with age, consistent with accelerated network development. We find that associations between SES and cortical network segregation are present primarily at the local scale. Effects of prenatal SES are strongest in the somatomotor and dorsal attention systems (Figure 2a-b) and conform to a sensorimotor-association hierarchy of cortical organization (Figure 2c). Importantly, SES-associated differences in cortical network segregation are associated with language abilities at age two years, such that lower segregation is associated with improved language abilities, even when controlling for prenatal SES (Figure 2d-f).

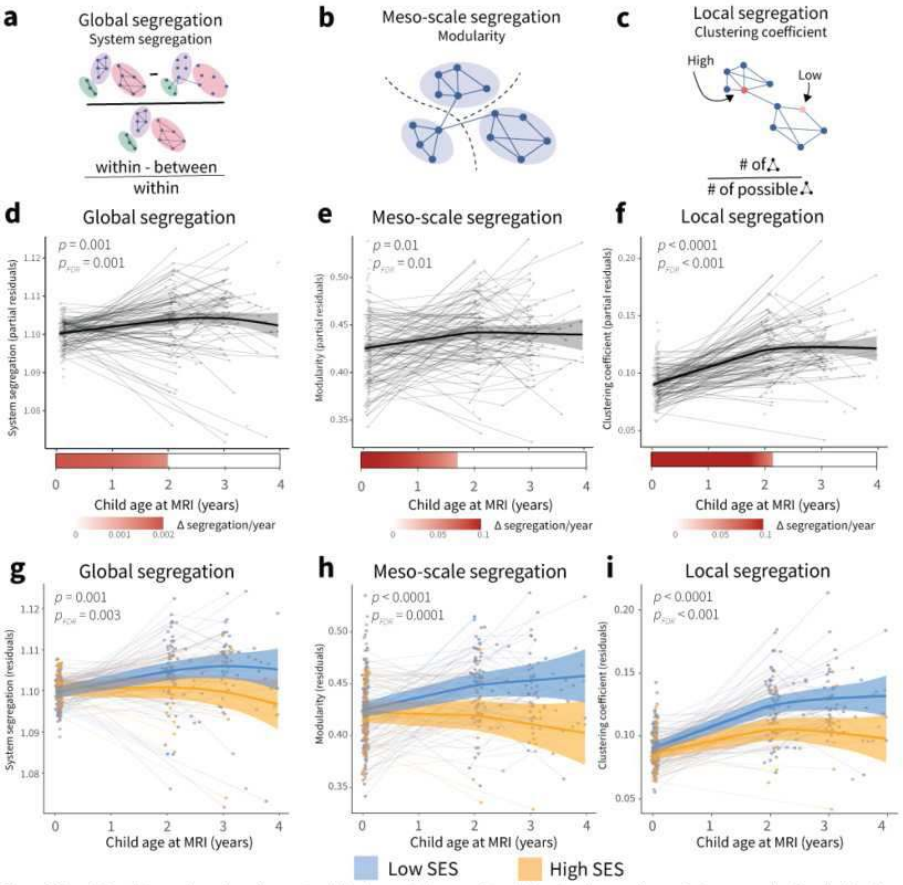

Figure 1. Associations between the early environment and developmental increases in cortical network segregation. **a,** System segregation is a whole-brain measure of functional network segregation that quantifies the difference between mean within-system connectivity and mean between-system connectivity as a proportion of mean within-system connectivity. **b,** Modularity is a measure of network segregation that estimates the extent to which the nodes of a network, or in this case brain regions, can be subdivided into modules characterized by strong, dense intramodular connectivity and weak, sparse intermodular connectivity. **c,** The clustering coefficient is a measure of local segregation that quantifies the amount of connectivity between a node and its immediate neighbors. **d,** Global segregation increases significantly with age (F_{segage} = 6.26, p = 0.001, p_{FDR} = 0.001). **e,** Meso-scale segregation increases significantly with age (F_{segage} = 3.93, p = 0.01, p_{FDR} = 0.01). **f,** Local segregation increases significantly with age (F_{segage} = 43.23, p < 0.0001, p_{FDR} < 0.0001). **g,** Prenatal SES moderates trajectories of global cortical network segregation ($F_{segageSES}$ = 6.38, p = 0.001, p_{FDR} = 0.003). **h,** Prenatal SES moderates trajectories of meso-scale cortical network segregation ($F_{segageSES}$ = 9.86, p < 0.0001, p_{FDR} = 0.0001). **i,** Prenatal SES moderates trajectories of local cortical network segregation ($F_{segageSES}$ = 13.40, p < 0.0001, p_{FDR} < 0.0001). Bars below the x-axis in **d-f** depict the derivative of the fitted smooth function of age. The filled portion of the bar indicates periods where the magnitude of the derivative of the fitted curve is significant, with the saturation of the fill representing the value of the derivative. SES was modeled continuously, here we show model trajectories from lowest (blue) and highest (orange) deciles of SES. Individual points represent individual scans, with lines indicating scans from the same participant. Panels **a-c** reprinted with permission from [3].

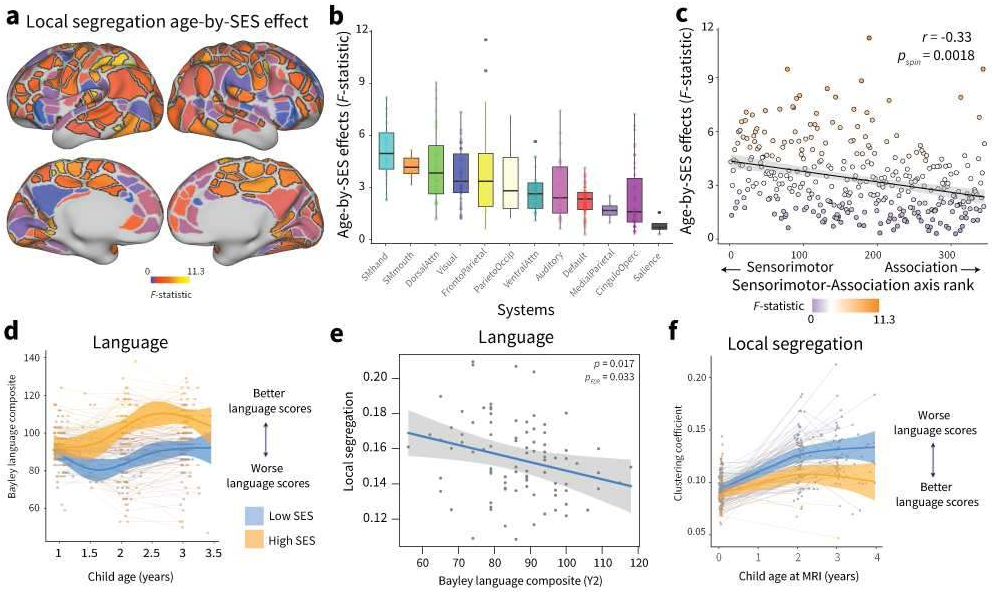

Figure 2. Environmental effects on developmental increases in local segregation are enriched in somatomotor systems and associated with language abilities. **a,** The heterogenous patterning of the magnitude of age-by-SES effects (*F*-statistic) on local segregation is shown on the cortical surface. Regions that show significant age-by-SES effects passing FDR correction at p_{FDR} < 0.05 are outlined in black. **b,** SES effects on developmental increases in local segregation are enriched in somatomotor systems. Boxplots show median and interquartile range of the magnitude of age-by-SES effects; each point is an individual parcel. **c,** The magnitude of age-by-SES effects is related to a canonical sensorimotor-to-association axis of cortical organization. Each point is an individual parcel, the color of the points represents the magnitude of age-by-SES effects. A Spearman's correlation between these two measures assessed by a conservative spin-based rotation test was significant (r = -0.33, p_{spin} = 0.0018). **d,** Effects of prenatal SES on trajectories of age-standardized Bayley language composite scores ($F_{segageSES}$ = 7.54, p < 0.0001, p_{FDR} < 0.0001). **e,** Local segregation at two years of age was negatively associated with language abilities at two years (β = -0.23, p = 0.017, p_{FDR} = 0.033), even after controlling for prenatal SES (β = -0.25, p = 0.017) . **f,** The directionality of this association is such that higher levels of local segregation, found in toddlers from lower-SES backgrounds, are associated with worse performance on measures of language ability.

Conclusions: We find that the development of cortical brain networks during the first three years of life is strongly associated with features of the early environment, suggesting these influences may play a key role in shaping this trajectory. Being born into a more advantaged (higher SES) environment is associated with a more protracted trajectory of cortical functional network development in early childhood; more protracted cortical network development might reflect prolonged periods of plasticity or alterations in synaptic proliferation and pruning (Tanti et al. 2013; Manzano Nieves et al. 2020). Importantly, environmental influences on development of cortical network segregation might underlie SES-associated differences in language abilities observed later in development. Our results suggest that infancy and toddlerhood may be an important period for promoting healthy brain development, emphasizing the first years of life as a target for policies supporting optimal child development.

References

1. #128836 | AsPredicted. (2023). Retrieved November 23, 2023, from https://aspredicted.org/eb5pd.pdf
2. Farah, M. J. (2017). The neuroscience of socioeconomic status: Correlates, causes, and consequences. Neuron, 96(1), 56–71. https://doi.org/10.1016/j.neuron.2017.08.034
3. Grayson, D. S. (2017). Development of large-scale functional networks from birth to adulthood: A guide to the neuroimaging literature. NeuroImage, 160, 15–31. https://doi.org/10.1016/j.neuroimage.2017.01.079
4. Luby, J. L. (2023). Social disadvantage during pregnancy: Effects on gestational age and birthweight. Journal of Perinatology, 43(4), Article 4. https://doi.org/10.1038/s41372-023-01643-2
5. Manzano Nieves, G. (2020). Early life adversity decreases pre-adolescent fear expression by accelerating amygdala PV cell development. eLife, 9, e55263. https://doi.org/10.7554/eLife.55263
6. Shaw, P. (2010). Childhood psychiatric disorders as anomalies in neurodevelopmental trajectories. Human Brain Mapping, 31(6), 917–925. https://doi.org/10.1002/hbm.21028
7. Stout, M. J. (2022). A multidisciplinary Prematurity Research Cohort Study. PLOS ONE, 17(8), e0272155. https://doi.org/10.1371/journal.pone.0272155
8. Tanti, A. (2013). Region-dependent and stage-specific effects of stress, environmental enrichment, and antidepressant treatment on hippocampal neurogenesis. Hippocampus, 23(9), 797–811. https://doi.org/10.1002/hipo.22134
9. Tooley, U. A. (2021). Environmental influences on the pace of brain development. Nature Reviews Neuroscience, 22(6), 372–384. https://doi.org/10.1038/s41583-021-00457-5
10. Tooley, U. A. (2022). The age of reason: Functional brain betwork development during childhood. Journal of Neuroscience, 42(44), 8237–8251. https://doi.org/10.1523/JNEUROSCI.0511-22.2022
11. Wood, S. N. (2004). Stable and efficient multiple smoothing parameter estimation for generalized additive models. Journal of the American Statistical Association, 99(467), 673–686. https://doi.org/10.1198/016214504000000980

Poster No 1286

High field multi-echo fMRI in infants

Julia Moser[1,2], Kimberly Weldon[1], Sooyeon Sung[1,2], Alireza Sadeghi-Tarakameh[3], Thomas Madison[1], Hannah Pham[1,4], Jacob Lundquist[1], Edward Auerbach[3], Gregor Adriany[3], Yigitcan Eryaman[3], Steve Nelson[1,5], Jed Elison[1,2,5], Damien Fair[1,2,5], Essa Yacoub[3]

[1]Masonic Institute for the Developing Brain, University of Minnesota, Minneapolis, MN, [2]Institute of Child Development, University of Minnesota, Minneapolis, MN, [3]Center for Magnetic Resonance Research, University of Minnesota, Minneapolis, MN, [4]Department of Neuroscience, University of Minnesota, Minneapolis, MN, [5]Department of Pediatrics, University of Minnesota, Minneapolis, MN

Introduction: Important insight into brain structure and function during early development can be gained from fMRI in infants. However, a number of methodological challenges arise when working with this age group that go beyond practical considerations. Lacking commercially available head coils optimized for developmental populations, the use of head coils designed for adults results in sub-optimal signal-to-noise ratios and increases in partial voluming because of the smaller brain sizes relative to the standard voxel sizes[1]. Higher spatial resolutions can be achieved by moving to higher field strengths (i.e. > 3T). However, despite the availability of FDA approved 7T MRI scanners, they are rarely used in infants because it requires additional safety considerations[2]. Further, the most popular 7T system, the Siemens Magnetom Terra, is currently not FDA-approved for subjects as light as infants (<30kg). Independent of field strength, finding optimal acquisition protocols, which consider the tissue properties of the developing brain, is an additional challenge. We recently showed that multi-echo (ME) fMRI at 3T could be a promising tool to account for this in a developmental population[3]. Up to now, the application of ME fMRI sequences have not been tested in infants at 7T. We show initial results from a high resolution 7T ME-fMRI acquisition and compare them to an adult as a reference.

Methods: The example infant presented here was a healthy full-term infant, seven weeks old from whom we acquired 3T and 7T data within a four day period. To make 7T acquisition possible, we developed an in-house system to assess the safe operating power limits for a newborn infant. Functional data at 3T was acquired using a four-echo sequence (14ms, 39ms,

64ms, 88ms, TR = 1.761s, 2mm res). Functional data at 7T was acquired using a three-echo sequence (14ms, 35ms, 57ms, TR = 1.768s, 1.6mm res). T2w and T1w anatomical references were acquired at 3T. All data acquisitions were performed during natural sleep. We preprocessed data using NORDIC[4] for thermal denoising, BIBSnet[5] for creating segmentations of the anatomical data, Nibabies[6] with its multi-echo preprocessing workflow and XCP-D[7] for functional connectivity processing. Functional connectivity matrices were calculated using low motion data (framewise displacement < 0.3mm) only.

Results: All ME data acquired at 3T and 7T showed high functional tissue contrast, indicating that despite halving the voxel volume at 7T, sensitivity was still not limited (Figure 1). As expected, T2* relaxation times for the same infant across both field strengths were shorter in 7T compared to 3T, to a similar extent than in the adult (Figure 2A). At both field strengths, T2* across the cortex revealed a similar variance and showed similar areas with shorter T2*s due to susceptibility artifacts, highlighting the benefits of ME imaging. Functional connectivity matrices showed similar correlation patterns between brain regions for data acquired at 3T and 7T. However, the absolute magnitude of functional connections was higher in data acquired at 7T (Figure 2B).

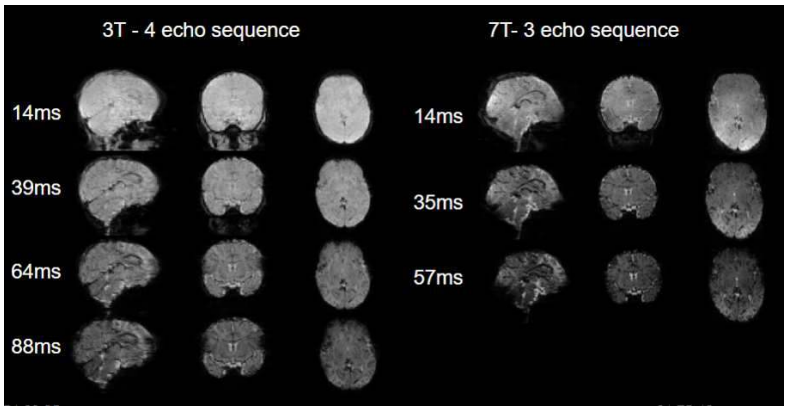

Figure 1: Multi-echo fMRI data of same infant acquired at 3T and 7T.

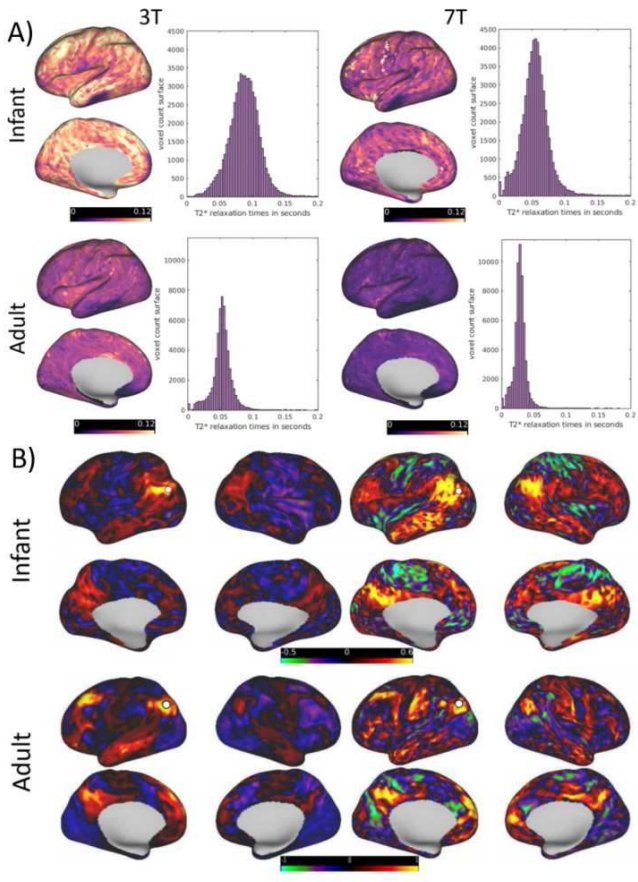

Figure 2: A) T2* relaxation times. Histograms show distribution across the surface. B) Example functional connectivity seedmap showing increase in magnitude of functional connections.

Conclusions: Our initial results show that ME fMRI in infants at 7T is not only feasible but feasible with much higher resolutions, resulting in data with high specificity and sensitivity. Investigation of T2* relaxation times points towards similar advantages of ME fMRI in infants in 7T as previously shown in 3T[3]. The observed increase in functional connectivity strength is consistent with the adult literature[8] and our example adult subject. Given careful safety considerations and suitable acquisition protocols, 7T imaging could be established as a promising tool for developmental neuroimaging as the smaller voxel size achievable at 7T is more suitable for the size of an infant brain. Moving forward, further benefits for functional connectivity research that go beyond the absolute strength of connections can be explored as well as even smaller voxel sizes.

References

1. Dubois, J., Alison, M., Counsell, S. J., Hertz-Pannier, L., Hüppi, P. S., & Benders, M. J. N. L. (2021). MRI of the Neonatal Brain: A Review of Methodological Challenges and Neuroscientific Advances. Journal of Magnetic Resonance Imaging: JMRI, 53(5), 1318–1343.
2. Malik, S. J., Hand, J. W., Carmichael, D. W., & Hajnal, J. V. (2022). Evaluation of specific absorption rate and heating in children exposed to a 7T MRI head coil. Magnetic Resonance in Medicine: Official Journal of the Society of Magnetic Resonance in Medicine / Society of Magnetic Resonance in Medicine, 88(3), 1434–1449.
3. Moser, J., Koirala, S., Madison, T., Labonte, A. K., Carrasco, C. M., Feczko, ..., Sylvester, C. M., & Fair, D. A. (2023). Multi-echo Acquisition and Thermal Denoising Advances Infant Precision Functional Imaging. In bioRxiv (p. 2023.10.27.564416). https://doi.org/10.1101/2023.10.27.564416
4. Vizioli, L., Moeller, S., Dowdle, L., Akçakaya, M., De Martino, F., Yacoub, E., & Uğurbil, K. (2021). Lowering the thermal noise barrier in functional brain mapping with magnetic resonance imaging. Nature Communications, 12(1), 5181.
5. Hendrickson, T. J., Reiners, P., Moore, L. A., Perrone, A. J., Alexopoulos, D., Lee, E. G., ..., & Feczko, E. (2023). BIBSNet: A Deep Learning Baby Image Brain Segmentation Network for MRI Scans. In bioRxiv (p. 2023.03.22.533696). https://doi.org/10.1101/2023.03.22.533696
6. Goncalves, M., Markiewicz, C. J., Esteban, O., Feczko, E., Poldrack, R. A., & Fair, D. A. (2023). NiBabies: a robust preprocessing pipeline for infant functional MRI. https://doi.org/10.5281/zenodo.7562647
7. Mehta, K., Salo, T., Madison, T., Adebimpe, A., Bassett, D. S., Bertolero, M.,...., & Satterthwaite, T. D. (2023). XCP-D: A Robust Pipeline for the post-processing of fMRI data. In bioRxiv (p. 2023.11.20.567926). https://doi.org/10.1101/2023.11.20.567926
8. Vu, A. T., Jamison, K., Glasser, M. F., Smith, S. M., Coalson, T., Moeller, S., Auerbach, E. J., Uğurbil, K., & Yacoub, E. (2017). Tradeoffs in pushing the spatial resolution of fMRI for the 7T Human Connectome Project. NeuroImage, 154, 23–32.

Poster No 1287

Identifying a common cause of macrocephaly using brain growth charts

Ayan Mandal[1], Barbara Chaiyachati[2], Jenna Schabdach[2], Margaret Gardner[1], Susan Sotardi[2], Maria Henry[2], Joanne Wood[2], Aaron Alexander-Bloch[1], Jakob Seidlitz[1]

[1]University of Pennsylvania, Philadelphia, PA, [2]Children's Hospital of Philadelphia, Philadelphia, PA

Introduction: Macrocephaly, defined as a head circumference measurement of greater than two standard deviations from the mean on typical growth charts, is among the most common clinical indications for an MRI scan in young children. The differential diagnosis for macrocephaly is broad, constituting potentially serious etiologies such as non-accidental head trauma or neurogenetic disorders as well as benign causes. A common cause of macrocephaly is benign enlargement of the subarachnoid space (termed "BESS"), a condition marked by elevated thickness of extra-axial CSF (eaCSF) which typically self-resolves after 1-2 years of age.[1] The diagnosis of BESS is complicated by the dynamic nature of eaCSF in early infancy as well as a lack of supporting quantitative diagnostic criteria for this condition. Growth charts of eaCSF could be a tremendous aid to clinicians seeking to differentiate BESS from other more clinically concerning causes of macrocephaly.[2]

Methods: We accessed 457 clinically-acquired T1w MRI scans from pediatric patients (ages 0 -22) at the Children's Hospital of Philadelphia (CHOP) to form a cohort of clinical controls, termed Scans with Limited Imaging Pathology (SLIP), described previously.[3] In parallel, nine T1w MRI scans from subjects with a diagnosis of BESS from a board-certified radiologist were also accessed. SynthSeg, a segmentation algorithm based on convolutional neural networks, was used to segment each T1w scan into various tissue types, including eaCSF.[4] To isolate the components of eaCSF relevant to BESS, we isolated the eaCSF superior to the anterior commissure for each patient, consistent with prior studies.[5] Extra-axial CSF thickness was measured using the function "measure_bb_thick" in AFNI and then averaged to produce a mean thickness for each subject (Figure 1).[6] Growth charts of eaCSF thickness were modeled in R using generalized additive models for location, scale, and shape (GAMLSS) within the total cohort.[7]

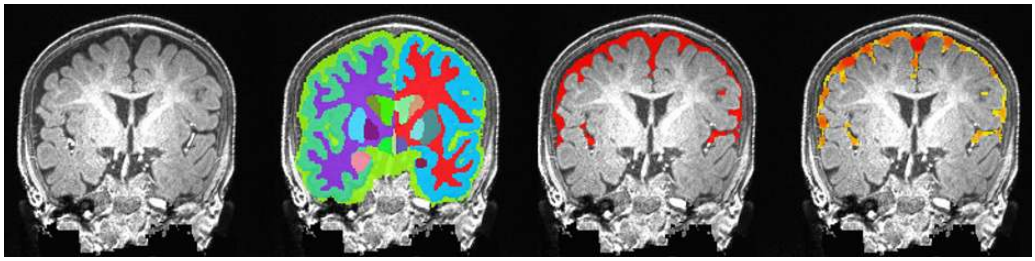

Figure 1: Coronal T1 MRI with sequential method processing. From left to right: Raw, Total segmented, Supratentorial eaCSF restricted segmentation mask, Voxel-thickness estimation.

Results: In the SLIP cohort, eaCSF thickness varied nonlinearly with age, increasing from birth to six months, then gradually declining until around eight years, when it rises again and trends upwards throughout adolescence (Figure 2). Based on these normative trajectories of eaCSF thickness, seven of the nine patients with a clinical diagnosis of BESS were above the 97.5% percentile for their age.

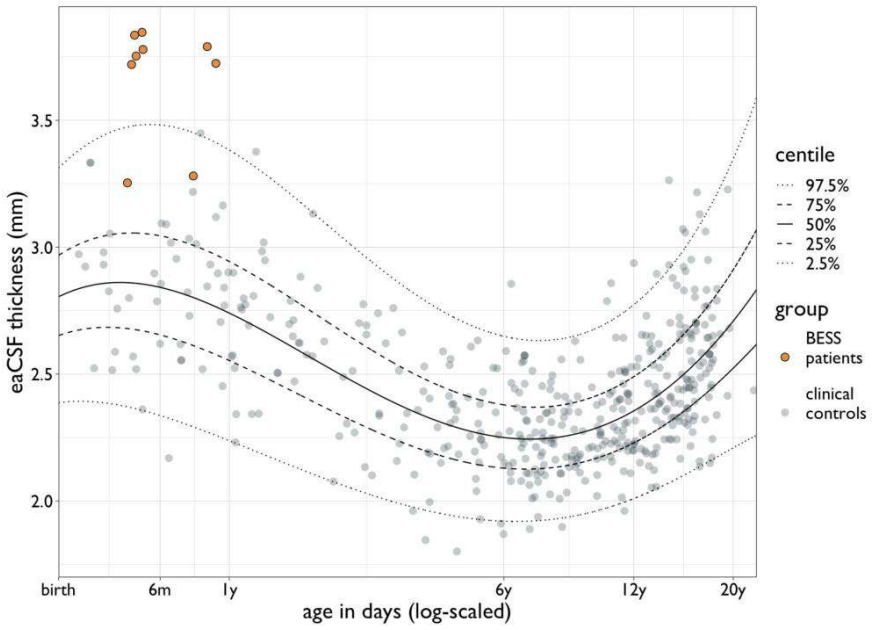

Figure 2: Extra-axial CSF Thickness in Childhood and Adolescence. Thickness reflects voxel-based average of supratentorial eaCSF mask from clinically acquired images in normal (gray) and BESS (orange)

Conclusions: We demonstrate that the thickness of the subarachnoid space changes in a dynamic but relatively predictable pattern throughout childhood and adolescence. The dynamic nature of these changes complicates the diagnosis of BESS, a common cause of macrocephaly. We show that patients with BESS can be reliably differentiated from clinical controls using computational measurements of eaCSF thickness paired with normative modeling. Our findings demonstrate the feasibility of updating diagnostic guidelines and aiding clinical decision-making for BESS and likely other macrocephalic conditions using brain growth charts.

References

1. Tucker, J., Choudhary, A. K. & Piatt, J. Macrocephaly in infancy: benign enlargement of the subarachnoid spaces and subdural collections. J. Neurosurg. Pediatr. 18, 16–20 (2016).
2. Bethlehem, R. A. I. et al. Brain charts for the human lifespan. Nature 604, 525–533 (2022).
3. Schabdach, J. M. et al. Brain Growth Charts for Quantitative Analysis of Pediatric Clinical Brain MRI Scans with Limited Imaging Pathology. Radiology 309, e230096 (2023).
4. Billot, B. et al. Robust machine learning segmentation for large-scale analysis of heterogeneous clinical brain MRI datasets. Proc. Natl. Acad. Sci. U. S. A. 120, e2216399120 (2023).
5. Shen, M. D. et al. Extra-axial cerebrospinal fluid in high-risk and normal-risk children with autism aged 2-4 years: a case-control study. Lancet Psychiatry 5, 895–904 (2018).
6. Glen D, Taylor PA, Seidlitz J, et al. Through Thick and Thin: Measuring Thickness in MRI with AFNI. presented at: 24th Annual Meeting of the Organization for Human Brain Mapping; 2018; Singapore. https://afni.nimh.nih.gov/pub/dist/HBM2018/OHBM_2018_Thickness.pdf
7. Rigby RA, Stasinopoulos MD, Heller GZ, De Bastiani F. Distributions for modeling location, scale, and shape: Using GAMLSS in R. CRC press (2019)

Poster No 1288

Is corpus callosum biometry at school age related to preterm birth in children with cerebral palsy?

Monica Crotti[1,2,3], Manuel Lubián-Gutiérrez[4,5], Nofar Ben Itzhak[1,2], Lisa Mailleux[2,6], Lize Kleeren[2,3,6], Lisa Decraene[2,6,7], Els Ortibus[1,2,8]

[1]KU Leuven, Department of Development and Regeneration, B-3000 Leuven, Belgium, [2]KU Leuven, Child and Youth Institute, B-3000 Leuven, Belgium, [3]KU Leuven, Leuven Brain Institute, B-3000 Leuven, Belgium, [4]Puerta del Mar University, Biomedical Research and Innovation Institute of Cádiz (INiBICA), Cádiz, Spain, [5]Puerta del Mar University Hospital, Department of Paediatrics, Division of Neonatology, Cádiz, Spain, [6]KU Leuven, Department of Rehabilitation Sciences, Research group for Neurorehabilitation, B-3000 Leuven, Belgium, [7]Hasselt University, Rehabilitation Research Centre, B-3590 Diepenbeek, Belgium, [8]University Hospitals Leuven, Cerebral Palsy Reference Center, B-3000 Leuven, Belgium

Introduction: Cerebral palsy (CP) is a motor developmental disorder caused by damage to the developing fetal or infant brain (Rosenbaum et al., 2007). Previous findings showed a reduction in the length of the corpus callosum (CC) in infants with CP compared to those with neurotypical development (Panigrahy et al., 2005). Half of the children diagnosed with CP are born preterm (PT; gestational age≤36 weeks) (Van Naarden Braun et al., 2016), a condition associated with a reduction in CC total length compared to birth at term (Caldú et al., 2006). Nevertheless, there is a lack of research specifically investigating the relation between PT birth and CC biometry assessed at school-age in children with unilateral CP (uCP). Here, we aim to investigate if CC total length and the thickness of its subdivision (i.e., genu, body, isthmus, and splenium) differ between children with uCP born PT and at term (T).

Methods: T1-weighted images were acquired (TE/TR/TI 4.2/9.1/760.3 ms, voxel size 0.9×0.9×0.9 mm^3, matrix 284x269x200) using a 3.0-T scanner (Hercules, Philips Medical Systems) in 38 children with uCP (age=11y6m±2y9m, 21 males). CC biometry (total CC length; thickness of genu, body, isthmus, splenium; Figure 1) was measured manually using the midline sagittal T1 scan and classified as above or below the median according to age normative values of Garel et al. (2011). Children were divided according to gestational age (GA) in PT (N=18; median GA=32.50, IQR [30.75-36]) and T (N=20; median GA=40, IQR [39-40]). Differences in CC biometry between children born PT and at T were investigated with one-way ANCOVA with birth weight and age at MRI as covariates. Statistics were performed using IBM SPSS Statistics (Version 28.0.1).

Figure 1. Biometric parameters measured on the midsagittal T1 MRI scan on a storage system of the clinical workstation of the University Hospitals of Leuven (Belgium), according to Garel et al. (2011). (A) Example of measurement of the total length of the CC as the distance between the anterior aspect of the genu and the posterior aspect of the splenium. (B) Measurement of the thickness of the CC at the level of the genu (a), body (b), isthmus (c), and splenium (d).

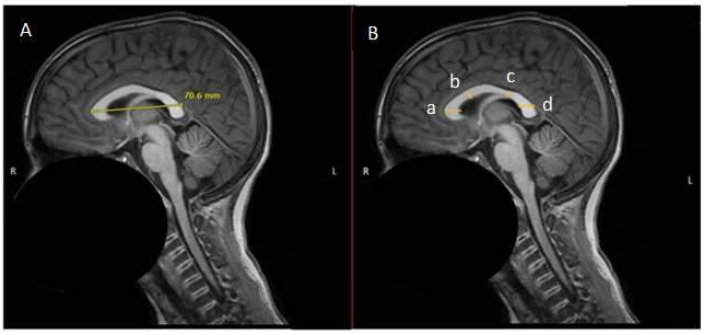

Results: Biometry below the normative range (Table 1) was found in 66% (n=25) of children with uCP for the CC total length (n(PT)=10; n(T)=15); in 34% for the genu (n(PT)=7; n(T)=6); in 76% for the body (n(PT)=12; n(T)=17); in 85% for the isthmus (n(PT)=15; n(T)=17); and in 74% of the splenium (n(PT)=14; n(T)=14). No significant difference was found in CC biometry between children with uCP born PT and born at term (p>0.05).

Table 1. Corpus callosum biometry in children with unilateral cerebral palsy born preterm and at term

CC biometry	Children with uCP born preterm (*N*=18)		Children with uCP born at term (*N*=20)	
	median (IQR)	*n*(%) of children below the median	median (IQR)	*n*(%) of children below the median
Total length	66.95 (49.80-72.50)	10 (56)	65.40 (55.30-73.10)	15 (75)
Genu	11.00 (5.60-14.20)	7 (39)	11.10 (7.50-14.70)	6 (30)
Body	4.85 (2.90-7.20)	12 (67)	4.60 (3.10-6.80)	17 (85)
Isthmus	2.80 (1.20-5.20)	15 (83)	2.85 (1.20-5.20)	17 (85)
Splenium	9.35 (4.60-13.50)	14 (78)	10.00 (6.40-13.90)	14 (70)

CC: corpus callosum; uCP: unilateral cerebral palsy; N: number of children out of the total sample of 38 children with uCP; n: number of children out of the sample of children born preterm (18) and at term (20); %: percentage of children.

Conclusions: Our results suggest that preterm birth does not influence CC biometry assessed at school-age in children with uCP. Plasticity processes occurring through infancy might compensate for differences between children born at term and PT. Nevertheless, a high number of children with uCP still present with reduced CC biometry when assessed at school-age, in particular in the mid-posterior part. Further research is warranted to unravel if CC biometry in earlier stages could potentially help to predict CP diagnosis in both children born at term and PT.

References

1. Caldú, X., Narberhaus, A., Junqué, C., Giménez, M., Vendrell, P., Bargalló, N., Segarra, D., & Botet, F. (2006). Corpus Callosum Size and Neuropsychologic Impairment in Adolescents who Were Born Preterm. Http://Dx.Doi.Org/10.1177/08830738060210050801, 21(5), 406–410. https://doi.org/10.1177/08830738060210050801
2. Garel, C., Cont, I., Alberti, C., Josserand, E., Moutard, M. L., & Ducou Le Pointe, H. (2011). Biometry of the corpus callosum in children: MR imaging reference data. American Journal of Neuroradiology, 32(8), 1436–1443. https://doi.org/10.3174/ajnr.A2542
3. Panigrahy, A., Barnes, P. D., Robertson, R. L., Sleeper, L. A., & Sayre, J. W. (2005). Quantitative analysis of the corpus callosum in children with cerebral palsy and developmental delay: Correlation with cerebral white matter volume. Pediatric Radiology, 35(12), 1199–1207. https://doi.org/10.1007/s00247-005-1577-5
4. Rosenbaum, P., Paneth, N., Leviton, A., Goldstein, M., & Bax, M. (2007). A report: The definition and classification of cerebral palsy April 2006. Developmental Medicine and Child Neurology, 49(SUPPL. 2), 8–14. https://doi.org/10.1111/j.1469-8749.2007.tb12610.x
5. Van Naarden Braun, K., Doernberg, N., Schieve, L., Christensen, D., Goodman, A., Yeargin-Allsopp, M., & Naarden Braun, V. (2016). Birth Prevalence of Cerebral Palsy: A Population-Based Study. PEDIATRICS, 137(1). https://doi.org/10.1542/peds.2015-2872

Poster No 1289

Identifying spatiotemporal changes in cortical neurodevelopment using post-mortem and in vivo data

Thanos Tsigaras[1], Juergen Dukart[1], Simon Eickhoff[1], Casey Paquola[1]

[1]INM-7, Forschungszentrum Jülich, Jülich, North Rhine Westphalia

Introduction: Despite numerous attempts to model human cortical neurodevelopment, we lack details on spatiotemporal changes occurring within the cortex. Here, we leverage the complementarity of post-mortem and in vivo approaches to track cortical microstructure throughout early development.

Methods: We assessed age-related changes in cortical cytoarchitecture using photomicrographs of cresyl-stained post-mortem human brain tissue (254 cortical patches from 29 Von Economo areas; 0, 1, 3, 15, 24 and 48 months; 6-7 brains per age)[1-6]. We identified the contours of individual cells using a tailored segmentation algorithm[7] and used a sliding-window approach to extract the number of cells per window and the percentage of area covered by cells in each window (Fig. 1A). Measurements were averaged across matching depths (Fig. 1B). To examine temporal changes of the cytoarchitectural features, we calculated the product-moment correlation coefficients (r) between age and cytoarchitecture for each area and depth. We characterised cortical microstructure in vivo using T1w/T2w images from the developing Human Connectome Project (dHCP, n=328, 37-44 weeks post-menstrual age)[8]. We sampled T1w/T2w intensities at 14 intracortical depths[9], producing microstructure profiles at each vertex (Fig. 2A). Given these profiles are inherently smoother than the histological profiles, we synopsised their shape using central moments (CMs; mean, centre of gravity, standard deviation). We assessed the influence of age on microstructure via area-specific product-moment correlations with the CMs. To test whether the CMs can be explained by depth-specific cytoarchitecture changes, we linearly modelled their relationships. Post hoc univariate tests were performed to better interpret how depth-specific changes in cytoarchitecture contribute to in vivo changes in microstructure.

Results: Number of cells per window decreases with age at all cortical depths in most brain areas, though the magnitude of the effect varied (Fig. 1C). In contrast, the area covered by cells increased or decreased with age depending on cortical depth. Age-related increases were prominent deeper in the cortex, whereas decreases were widespread in superficial cortex. This depth-wise shift was most prominent in association cortex, including prefrontal cortex and temporo-parietal areas that neighbour the occipital lobe. We observed significant global increases in mean intensity of MRI-derived profiles, but region-specific changes in the balance of microstructure across cortical depths (Fig. 2B). Specifically, the centre of gravity increased in areas on the inferior surface of the cortex, suggestive of microstructural increases deeper in the cortex. In contrast, the standard deviation of the profiles decreased with age in the frontal and temporal lobes, signifying increasingly balanced microstructural density across cortical depths. Multivariate regressions showed more than 60% of variance in CM changes could be explained by depth-specific changes in cytoarchitecture. Effects were more prominent in mid-cortical depths, pointing towards a depth-specific correlation between cytoarchitecture and MRI-derived microstructure.

Conclusions: Our study provides novel insights into the cellular basis of intracortical development. We found evidence for selective decreases in cellular density, as well as increases in cell size. Furthermore, by demonstrating the statistical

relationship between histology- and MRI-derived changes, our work provides the foundation for further investigations into the multi-scale nature of cortical development, involving microstructure, morphology and connectivity.

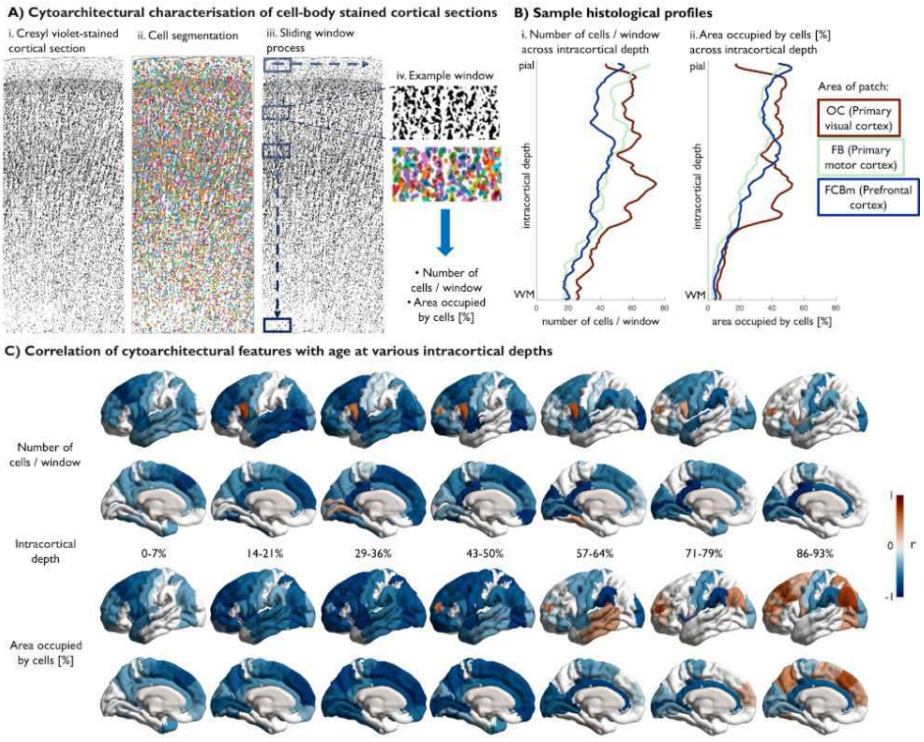

Figure 1: A) Sample cortical patch of a Cresyl-stained brain slice (*left*). A cell-segmentation algorithm was applied (*middle*) and using a sliding-window approach, we extracted the number of cells and the area occupied by cells across cortical depths (right). To account for the different cortical thicknesses and improve comparability to the *in vivo* dataset, all profiles were resampled, averaged across duplicate areas, and clustered into 14 depths. **B)** Sample histological profiles of cell number per window and area occupied by cells across cortical depths between the pial and white matter (WM). Each line corresponds to the profile of a different Von Economo's cortical area, OC (*red*), FB (*green*) and FCBm (*blue*). **C)** Statistically significant product-moment correlation coefficients (r) of age with number of cells and area occupied by cells at different cortical depths. White regions correspond to areas where no cortical patches were available or to areas with non-significant correlation coefficients. Histological patches were originally labelled using the terminology of Von Economo and Koskinas. We thus used these labels to accurately project the correlation coefficients onto *fsaverage* using the Von Economo parcellation[10].

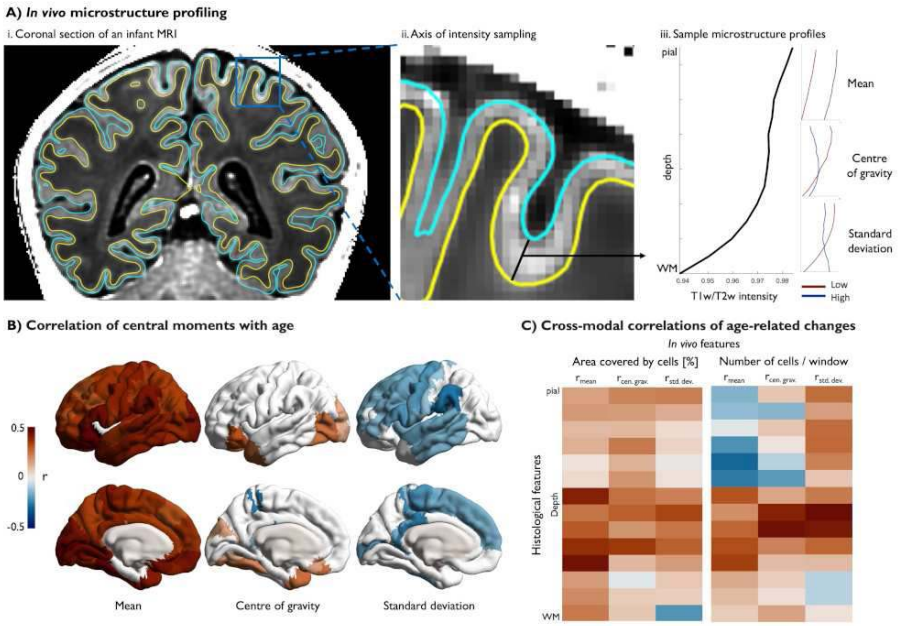

Figure 2: A) *In vivo* microstructure profiles were extracted from T1w/T2w images of infant brains. Subsequently, the shape of each microstructure profile was characterised by three central moments (mean, centre of gravity and standard deviation). On the right side of the main sample profile, three graphs show sample profiles with a high and a low value of each corresponding central moment. **B)** Product-moment correlation coefficients (r) of gestational age with each central moment. White regions correspond to areas with non-significant correlation coefficients ($p_{FDR} > 0.05$). **C)** Interaction of the age-related changes in central moments and the age-related, depth-specific changes in histological features. The correlation matrix shows the product-moment correlation coefficients between each pair of variables. For this analysis, only post-mortem samples with an age overlap to the *in vivo* dataset were used.

References

1. Conel J. L. (1939). The postnatal development of the human cerebral cortex. The cortex of the newborn: Vol. I. Harvard University Press.
2. Conel J. L. (1942). The postnatal development of the human cerebral cortex. The cortex of the one-month infant: Vol. II. Harvard University Press.
3. Conel J. L. (1947). The postnatal development of the human cerebral cortex. The cortex of the three-month infant: Vol. III. Harvard University Press.
4. Conel J. L. (1955). The postnatal development of the human cerebral cortex. The cortex of the fifteen-month infant: Vol. V. Harvard University Press.
5. Conel J. L. (1959). The postnatal development of the human cerebral cortex. The cortex of the twenty-four-month infant: Vol. VI. Harvard University Press.
6. Conel J. L. (1963). The postnatal development of the human cerebral cortex. The cortex of the four-year child: Vol. VII. Harvard University Press.
7. Upschulte, E., Harmeling, S., Amunts, K., & Dickscheid, T. (2022). Contour proposal networks for biomedical instance segmentation. Medical Image Analysis, 77, 102371. https://doi.org/10.1016/j.media.2022.102371
8. Makropoulos, A., Robinson, E. C., Schuh, A., Wright, R., Fitzgibbon, S., Bozek, J., Counsell, S. J., Steinweg, J., Vecchiato, K., Passerat-Palmbach, J., Lenz, G., Mortari, F., Tenev, T., Duff, E. P., Bastiani, M., Cordero-Grande, L., Hughes, E., Tusor, N., Tournier, J.-D., ... Rueckert, D. (2018). The developing human connectome project: A minimal processing pipeline for neonatal cortical surface reconstruction. NeuroImage, 173, 88–112. https://doi.org/10.1016/j.neuroimage.2018.01.054
9. Paquola, C., Vos De Wael, R., Wagstyl, K., Bethlehem, R. A. I., Hong, S.-J., Seidlitz, J., Bullmore, E. T., Evans, A. C., Misic, B., Margulies, D. S., Smallwood, J., & Bernhardt, B. C. (2019). Microstructural and functional gradients are increasingly dissociated in transmodal cortices. PLOS Biology, 17(5), e3000284. https://doi.org/10.1371/journal.pbio.3000284
10. Scholtens, L. H., de Reus, M. A., & van den Heuvel, M. P. (2015). Linking contemporary high resolution magnetic resonance imaging to the von economo legacy: A study on the comparison of MRI cortical thickness and histological measurements of cortical structure. Human Brain Mapping, 36(8), 3038–3046. https://doi.org/10.1002/hbm.22826

Poster No 1290

Structural Development of Early Emerging Sulcal Folds During the First Year of Human Life

Sarah Tung[1], Xiaoqian Yan[2], Bella Fascendini[3], Christina Tyagi[1], Charleny Martinez Reyes[1], Keithan Ducre[1], Karla Perez[1], Ahmad Allen[1], Juliet Horenziak[1], Hua Wu[4], Vaidehi Natu[1], Kalanit Grill-Spector[1,5]

[1]Psychology Department, Stanford University, Stanford, USA, [2]Institute of Science and Technology for Brain-Inspired Intelligence, Fudan University, Shanghai, China, [3]Department of Psychology, Princeton University, Princeton, USA, [4]Center for Cognitive and Neurobiological Imaging, Stanford, USA, [5]Wu Tsai Neurosciences Institute, Stanford University, Stanford, USA

Introduction: Cortical folding varies widely among mammals and is particularly pronounced in human brains[1]. Sulcal deepening begins in utero and continues in the first two years of life[2]. It has been hypothesized that sulci deepen to accommodate for cortical expansion. However, how early emerging sulcal folds deepen during infancy remains largely unknown. Here, we examined how early emerging sulcal folds deepen in the first year of human life and whether sulcal deepening is associated with changes in (1) macrostructural features such as curvature, surface area, and cortical thickness, and (2) microstructural tissue properties in gray and adjacent white matter such as increases in tissue microstructure associated with myelination[3,4].

Methods: We used MRI to measure T1- and T2-weighted anatomicals and quantitative MRI to measure relaxation rate (R1) in 43 infants over 87 session (27 infants are longitudinal) in newborns (n=27, 10 females, M= 29.1 days, SD=9.9 days), 3-month-olds (n=27, 14 females, M=105.8 days, SD=18.6 days), 6-month-olds (n= 22, 10 females, M=189.3 days, SD=15.8 days), and 1-year-olds (n=11, 4 females, M=385.1 days, SD=16.9 days). Higher R1 indicates higher tissue density and a more developed cortex. To test sulcal development, we analyzed 12 sulcal folds that emerge in utero between 16 - 31 gestational weeks[5], distributed across the cortical surface (Fig 1A). We used the adult average FreeSurfer brain and cortex-based alignment to identify each sulcal fold in every individual infant's brain and age (Fig 1B). We validated the reliability of automated sulcal fold identification by comparing the accuracy of automated versus hand-drawn sulci using dice coefficients. We found no significant age-related effect of dice coefficient (3-way ANOVA, with factors: age, hemisphere, and sulcus, no main effect of age: F=0.20, p=0.90, sulcus: F=0.73, p=0.70, or hemisphere: F=1.04, p=0.31). Then, in each individual sulcus, we measured the average sulcal depth, surface area, thickness, curvature, and R1. Using linear mixed models (LMMs), we quantified the development of sulci as a function of age and tested if sulcal deepening is significantly related to macro- and microstructural properties.

Results: Our study revealed five main findings: First, all sulcal folds significantly deepen in the first year of life, except for the calcarine sulcus, which remains unchanged (Fig 1C). Second, early emerging sulci are deeper at birth than later emerging sulci, but deepen more slowly after birth (Fig 1I,O). Third, surface area and cortical thickness increase with age (Fig 1D,E), but all sulci become less concave (Fig 1F). Fourth, R1 linearly increases in both gray and white matter in all sulci, with R1 being larger at birth in gray matter than in white matter (Fig 1G,H). However, this pattern reverses after birth, whereby the rate of R1 development in white matter is higher than that in gray matter (Fig 1M,N). Together, these data suggest heterogenous

development of macro- and microstructural properties in these sulci. LMMs relating sulcal depth with macro- and microstructural properties revealed that a linear combination of surface area, curvature, thickness, and R1 best predict sulcal depth across the first year of life (R2=0.78; AIC= 2150). This combined model demonstrated a significant positive relationship between sulcal depth and R1 (β=2.08; p=0.0005), thickness (β=0.248, p=0.005), surface area (β=0.0008, p<0.0001), and a negative relationship with curvature (β=-6.09, p=6.46x10-6).

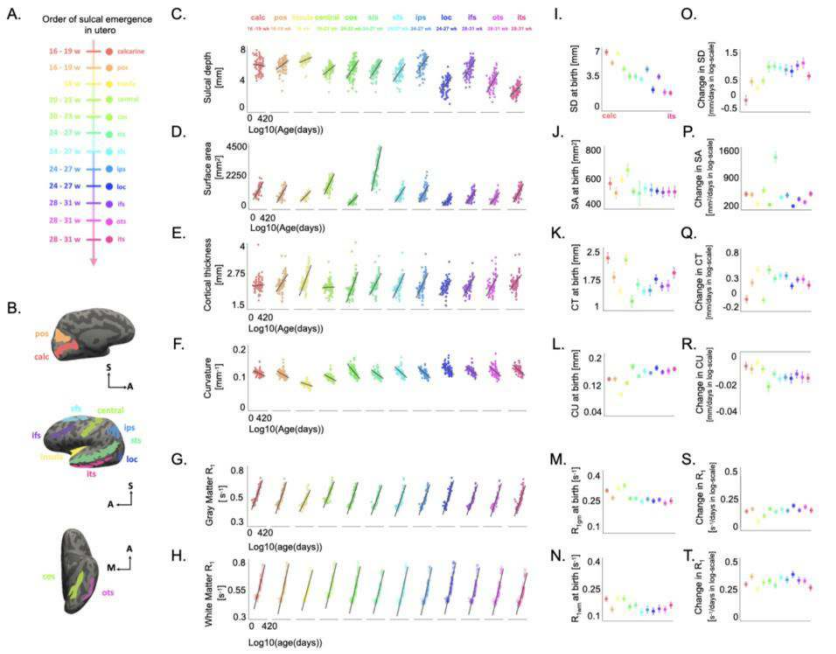

Figure 1. Development of macro- and microstructural properties in early emerging sulcal folds is heterogenous in the first year of life. (A) Timeline of when the 12 sulcal folds emerge *in utero* [5]. (B) Left hemisphere sulcal folds displayed on an inflated cortical surface of an example 1-year-old infant. (C-H) Individual macro- and microstructural properties as a function of infant age in the 12 sulcal folds. *Each dot*: mean macro- or microstructural value per sulcal fold per infant session. *Line:* Linear mixed model line fit. (I-N) Estimates of macro- and microstructural properties at birth (LMM intercept). (O-T) Rate of macro- and microstructural development (LMM slope). *Error bars:* standard error on estimates of intercepts and slopes. Data shown are from the left hemisphere.

Conclusions: Our results indicate that there are differential developments in macro- and microstructural properties of early emerging sulcal folds of the human brain. Mechanistically, we propose that cortical expansion, characterized by changes in surface area, thickness, and curvature, and microstructural tissue growth contribute to sulcal deepening during the first year of human life.

References

1. Zilles, K. et al. (2013), 'Development of cortical folding during evolution and ontogeny', Trends in Neurosciences, 36, 275-284.
2. Meng, Y. et al. (2014), 'Spatial distribution and longitudinal development of deep cortical sulcal landmarks in infants', NeuroImage, 100, 206–218.
3. Van Essen, D. (1997), 'A tension-based theory of morphogenesis and compact wiring in the central nervous system', Nature, 385, 313–318.
4. Van Essen, D. (2020), 'A 2020 view of tension-based cortical morphogenesis', Proceedings of the National Academy of Sciences of the United States of America, 117(52), 32868–32879.
5. Chi, J. G. et al. (1977), 'Gyral development of the human brain,' Annals of neurology, 1(1), 86–93.

Poster No 1291

Structural neural basis underlying externalization-internalization transition during adolescence

Deying Li[1], Haiyan Wang[1], Yufan Wang[1], Congying Chu[1], Lingzhong Fan[1]

[1]Institute of Automation,Chinese Academy of Sciences, Beijing, China

Introduction: Adolescence, marked by swift neurodevelopment and cognitive-behavioral transformations impacting cognition, personality, and mental health, witnesses problematic behaviors categorized as internalizing or externalizing (Fuhrmann, Knoll et al. 2015, Achenbach, Ivanova et al. 2016), which is correlated with various adverse developmental outcomes. Neuroimaging objectively quantifies developmental changes. Specifically, the geometry of the cerebral cortex and neural connectivity

are acknowledged to mutually influence and undergo adaptations during developmental processes(Vasung, Lepage et al. 2016, Wu, Palaniyappan et al. 2023). Comprehending the dynamics of cortical geometry and connectivity changes can yield insights into the emergence of cognitive functions and behaviors(Giedd, Blumenthal et al. 1999). A significant challenge lies in the lack of well-established methodologies for seamlessly integrating cerebral cortex geometry and neural connectivity to comprehensively understand the interplay between brain structure and externalizing/internalizing behaviors in adolescence. This understanding is crucial for determining the optimal timing and nature of interventions. In this study, we propose a novel structural indicator that combines both gray matter and white matter measurements to assess the internalizing and externalizing transition processes during adolescence.

Methods: IMAGEN, a large-scale longitudinal neuroimaging cohort study, spanned ages 14, 19, and 22, involving 647 unrelated subjects. T1-weighted images and DWI data underwent preprocessing (Li, Wang et al. 2023), with subsequent probabilistic tractography mapping the whole-brain anatomical connectivity pattern. We reconstructed 72 tracts identified by TractSeg (Wasserthal, Neher et al. 2018). The fiber connection fingerprint results from projecting each fiber onto the white surface, computed using the LaPy Python library (Pang, Aquino et al. 2023). Geometric modes of the white surface mesh were computed for each age and utilized to reconstruct the fiber connection fingerprint. Reconstruction coefficients were then extracted, forming the novel Fiber Decomposition Index (FDI). Behavioral symptoms in IMAGEN participants were assessed using screening questions from DAWBA and SDQ, covering externalizing and internalizing symptoms(Xie, Xiang et al. 2023). PLSCanonical(PLSC) analysis of FDI with internalizing and externalizing behavioral symptoms was conducted. To avoid overfitting, we implemented a train/test design, assigning 90% to the training set and 10% to the test set. This study specifically focuses on the first principal component, possessing the largest explainable variance.

Results: We examined the explanatory power of geometric eigenmodes for diverse aspects of the white matter fiber connection fingerprint, derived from the white surface mesh at three time points. 200 modes were selected for the study. This decomposition was used to assess the accuracy of geometric eigenmodes in capturing the fiber connection fingerprint in 647 individuals from the IMAGEN dataset. Reconstruction accuracy, measured by vertex-wise Pearson correlation between empirical and reconstructed maps, exceeding a correlation coefficient (r) of 0.80 with 200 modes. The PLSC analysis is conducted on the same participant cohort at both 14y and 19y. A noteworthy relationship is identified between externalizing symptoms with FDI at 14y and internalizing symptoms in 19y.

Conclusions: The geometric foundation of the cerebral cortex aligns well with fiber projection across the cortex. The fitting coefficients exhibit statistically significant associations with both internalizing and externalizing behaviors at ages 14 and 19. Our findings indicate that, at 14y, FDI is significantly linked to externalizing behaviors. Conversely, at 19y, it shows significant associations with internalizing behaviors. This unveils a developmental pattern wherein adolescents transition from externalizing to internalizing behavioral problems.

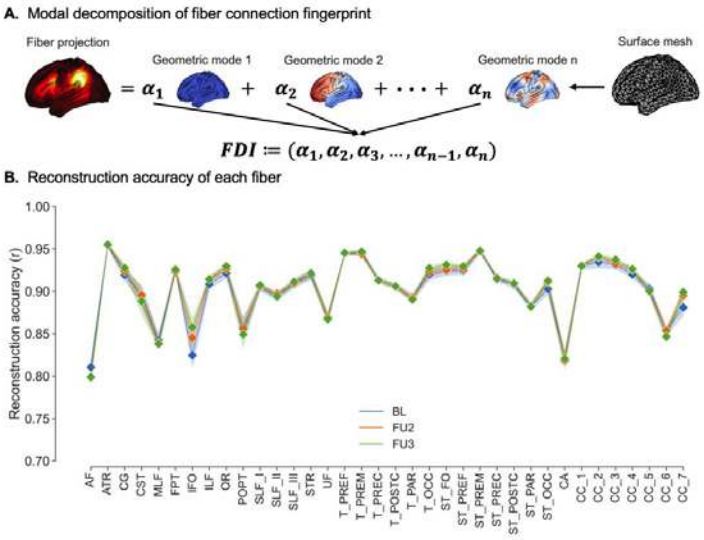

Fig.1 | Reconstruction of fiber connection fingerprint with geometric eigenmodes. A) Geometric eigenmodes are derived from the cortical surface mesh in each age. The connection pattern of 36 fibers can be decomposed as a weighted sum of geometry modes with varying wavelengths. The Fiber Decomposition Index (FDI) is defined by the modulus of top 200 modes. **B)** Reconstruction accuracy of fiber connection fingerprint in each age.

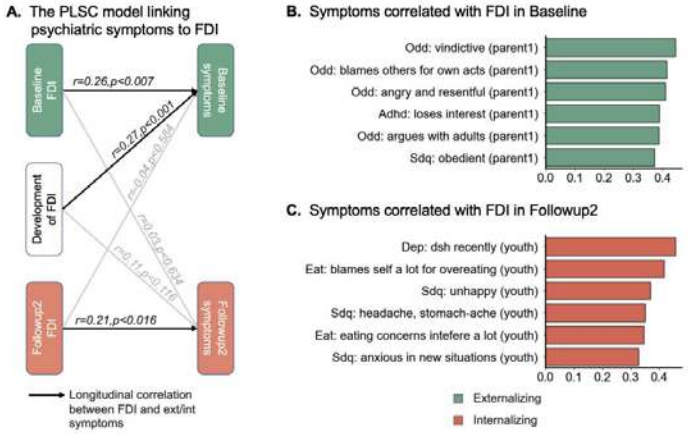

Fig2 | A) The longitudinal analysis of FDI and psychiatric symptoms. FDI correlated behavioral symptoms at age 14 (*r=0.26, p<0.007*) but not at age 19 (*r=0.03, p<0.634*). FDI correlated behavioral symptoms at age 19 (*r=0.21, p<0.016*) but not at age 14 (*r=-0.04, p<0.584*). The changed between FDI in age 14 and age 19 correlated behavioral symptoms at age 14 (*r=0.27, p<0.001*) but not age 19 (*r=0.11, p<0.116*). **B)** The PLSC model linking externalizing symptoms with the FDI in Baseline. **C)** The PLSC model linking internalizing symptoms with FDI in Followup2.

References

1. Achenbach, T. M., M. Y. Ivanova, L. A. Rescorla, L. V. Turner and R. R. Althoff (2016). "Internalizing/Externalizing Problems: Review and Recommendations for Clinical and Research Applications." J Am Acad Child Adolesc Psychiatry 55(8): 647-656.
2. Fuhrmann, D., L. J. Knoll and S. J. Blakemore (2015). "Adolescence as a Sensitive Period of Brain Development." Trends Cogn Sci 19(10): 558-566.
3. Giedd, J. N., J. Blumenthal, N. O. Jeffries, F. X. Castellanos, H. Liu, A. Zijdenbos, T. Paus, A. C. Evans and J. L. Rapoport (1999). "Brain development during childhood and adolescence: a longitudinal MRI study." Nat Neurosci 2(10): 861-863.
4. Li, D., Y. Wang, L. Ma, W. Shi, Y. Lu, H. Wang, X. Cheng, Y. Wang, C. Gao, L. Cheng, C. Erichsen, Y. Zhang, Z. Yang, S. Eickhoff, C.-h. Chen, C. Chu and L. Fan (2023).
5. Pang, J. C., K. M. Aquino, M. Oldehinkel, P. A. Robinson, B. D. Fulcher, M. Breakspear and A. Fornito (2023). "Geometric constraints on human brain function." Nature 618(7965): 566-574.
6. Vasung, L., C. Lepage, M. Rados, M. Pletikos, J. S. Goldman, J. Richiardi, M. Raguz, E. Fischi-Gomez, S. Karama, P. S. Huppi, A. C. Evans and I. Kostovic (2016). "Quantitative and Qualitative Analysis of Transient Fetal Compartments during Prenatal Human Brain Development." Front Neuroanat 10: 11.
7. Wasserthal, J., P. Neher and K. H. Maier-Hein (2018). "TractSeg - Fast and accurate white matter tract segmentation." Neuroimage 183: 239-253.
8. Wu, X., L. Palaniyappan, G. Yu, K. Zhang, J. Seidlitz, Z. Liu, X. Kong, G. Schumann, J. Feng, B. J. Sahakian, T. W. Robbins, E. Bullmore and J. Zhang (2023). "Morphometric dis-similarity between cortical and subcortical areas underlies cognitive function and psychiatric symptomatology: a preadolescence study from ABCD." Mol Psychiatry 28(3): 1146-1158.
9. Xie, C., S. Xiang, C. Shen, X. Peng, J. Kang, Y. Li, W. Cheng, S. He, M. Bobou, M. J. Broulidakis, B. M. van Noort, Z. Zhang, L. Robinson, N. Vaidya, J. Winterer, Y. Zhang, S. King, T. Banaschewski, G. J. Barker, A. L. W. Bokde, U. Bromberg, C. Buchel, H. Flor, A. Grigis, H. Garavan, P. Gowland, A. Heinz, B. Ittermann, H. Lemaitre, J. L. Martinot, M. P. Martinot, F. Nees, D. P. Orfanos, T. Paus, L. Poustka, J. H. Frohner, U. Schmidt, J. Sinclair, M. N. Smolka, A. Stringaris, H. Walter, R. Whelan, S. Desrivieres, B. J. Sahakian, T. W. Robbins, G. Schumann, T. Jia, J. Feng, I. Consortium, S. E. Consortium and Z. I. B. Consortium (2023). "A shared neural basis underlying psychiatric comorbidity." Nat

Poster No 1292

Maturation of cortical connectivity in the core functional systems – infancy through childhood

Jiaxin Tu[1], Aidan Latham[1], Jeanette Kenley[1], M. Camacho[1], Omid Kardan[2], Eric Feczko[3], Sydney Kaplan[1], Trevor Day[3], Chad Sylvester[1], Oscar Miranda Dominguez[3], Lucille Moore[3], Damien Fair[3], Christopher Smyser[1], Jed Elison[3], Timothy Laumann[4], Evan Gordon[4], Adam Eggebrecht[5], Muriah Wheelock[1]

[1]Washington University in St. Louis, St. Louis, MO, [2]University of Michigan, Ann Arbor, MI, [3]University of Minnesota, Minneapolis, MN, [4]Washington University, St. Louis, MO, [5]Washington University School of Medicine, St. Louis, MO

Introduction: Resting-state functional correlations (FC) of BOLD time-series detects brain regions that activate together at rest, revealing functional systems with distinguishable functionalities(Seitzman et al., 2019; Wig, 2017). Prior evidence suggested that the degree to which these systems are segregated – showing strong within-system FC relative to between-system FC – increases with brain development(Cao et al., 2017; Grayson & Fair, 2017; Tooley et al., 2022a), but the results

were inconclusive and sometimes conflicting. Furthermore, FC within the same system are typically closer in space than those between systems(Zhi et al., 2022), yet the most significant developmental changes in connectivity are observed over longer distances(Liu et al., 2022), further complicating the interpretations.

Methods: We analyzed group-average vertex-wise FC resting-state fMRI data from three developmental windows: babies (0-3 years)(Howell et al. 2019; Kaplan et al. 2022), children (6-15 years)(Alexander et al. 2017), and young adults (19-32 years)(Power et al. 2014), assessing the six core functional systems widely recognized for their distinct roles(Wig 2017; Uddin, Yeo, and Spreng 2019). Unlike traditional single-seed-based methods, we evaluated the average connectivity of all brain vertices within a system (Fig. 1A, 1B). We quantified the maturity of this system-average FC map using its eta-squared (η^2) coefficient(Cohen et al. 2008) to that in the young adult. We additionally calculated the within and outside system FC for geodesic distance in fsLR standard mesh up to 150 mm in 10 mm bins to examine system segregation as a function of distance.

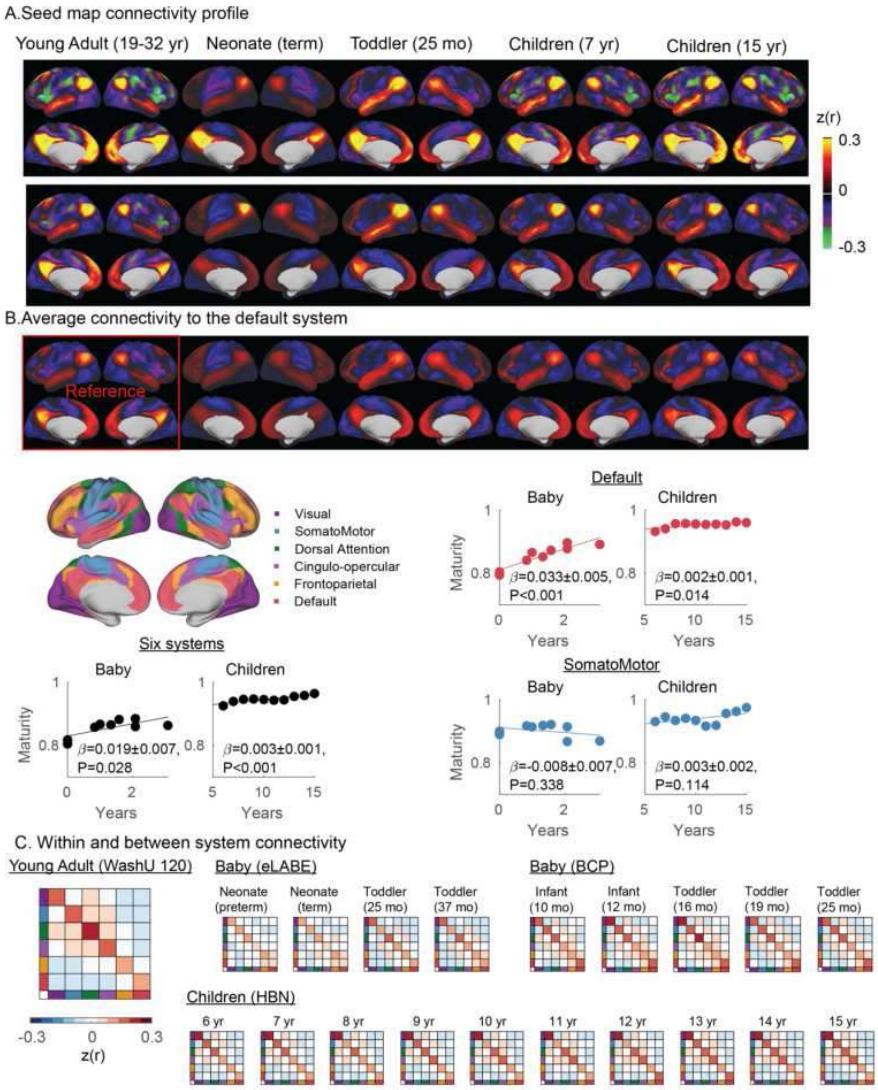

Figure 1. System-average connectivity across development.

Results: Our analysis revealed that system-average FC in full-term neonates closely resembles that in adults (η^2 = 0.82), with this similarity increasing throughout development in babies (0-3 year, growth rate of η^2 =0.019/year, P = 0.028) and children (6-15 year, growth rate of η^2 =0.003/year, P <0.001) (Fig. 1B). An age-group interaction showed a significant difference in growth rate (β = 0.016, P = 0.007). The maturity of connectivity in full-term neonates also varied across system (MI = 0.81±0.07 across six systems). There was a significance increase in maturity of connectivity in the default system for babies and children but not in the somatomotor system (Fig. 1B). We also obtain a matrix of within and between system FC by summing these average FC map within predefined system topography(Yeo et al., 2011) (Fig. 1C). We noted that while within-system FC generally increased from infancy to adulthood, between-system FC changes were more nuanced: the FC between default and frontoparietal systems decreased, but the FC between visual, somatomotor, dorsal attention and cingulo-opercular systems increased across development. Furthermore, we found that FC was higher within than outside systems across all distance bins (Fig.

2A) and systems (Fig. 2B) in young adults. System-specific long-range connectivity was also present in neonates, suggesting that it was established before birth, rather than developing throughout the first year of life (Fig. 2C). During development from neonate to adult, the within-system FC at >50 mm increased, and the within- and between-system FC at <50 mm decreased, leading to an overall increase in the difference between within-and between-system FC (Fig. 2C). These dynamics can be observed in all systems, with varying degrees of short-distance and long-distance system segregation across stages of development (Fig. 2D).

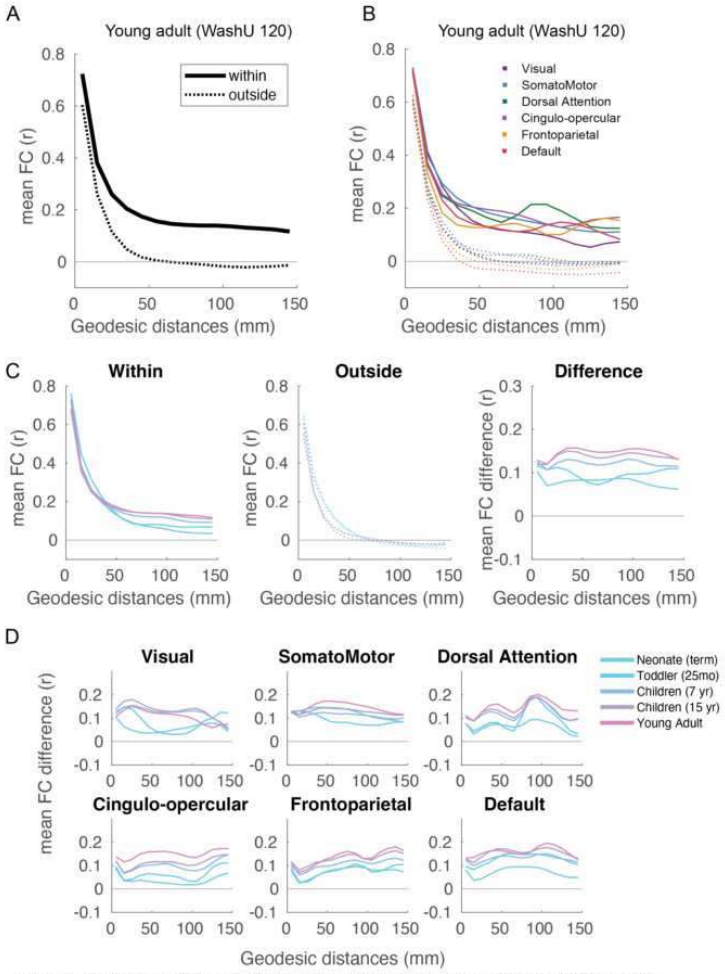

Figure 2. *Difference in within and outside system FC for each 10mm spatial bins.* A) Mean within and outside system FC. B) Mean within and outside system FC for the six functional systems in Fig.1. C) Mean within and outside system FC and their difference across different stages of development. D) Mean within and outside system FC difference across development for the six functional systems.

Conclusions: Our findings affirm that from birth, within-system connectivity is stronger than between-system connectivity for the core functional networks, and this disparity expands throughout development.

References

1. Alexander, L. M., Escalera, J., Ai, L., Andreotti, C., Febre, K., Mangone, A., Vega-Potler, N., Langer, N., Alexander, A., Kovacs, M., Litke, S., O'Hagan, B., Andersen, J., Bronstein, B., Bui, A., Bushey, M., Butler, H., Castagna, V., Camacho, N., … Milham, M. P. (2017). An open resource for transdiagnostic research in pediatric mental health and learning disorders. Scientific Data, 4(1), Article 1.
2. Baum, G. L., Ciric, R., Roalf, D. R., Betzel, R. F., Moore, T. M., Shinohara, R. T., Kahn, A. E., Vandekar, S. N., Rupert, P. E., Quarmley, M., Cook, P. A., Elliott, M. A., Ruparel, K., Gur, R. E., Gur, R. C., Bassett, D. S., & Satterthwaite, T. D. (2017). Modular Segregation of Structural Brain Networks Supports the Development of Executive Function in Youth. Current Biology, 27(11), 1561-1572.e8.
3. Cao, M., He, Y., Dai, Z., Liao, X., Jeon, T., Ouyang, M., Chalak, L., Bi, Y., Rollins, N., Dong, Q., & Huang, H. (2017). Early Development of Functional Network Segregation Revealed by Connectomic Analysis of the Preterm Human Brain. Cerebral Cortex, 27(3), 1949–1963.
4. Chan, M. Y., Park, D. C., Savalia, N. K., Petersen, S. E., & Wig, G. S. (2014). Decreased segregation of brain systems across the healthy adult lifespan. Proceedings of the National Academy of Sciences, 111(46), E4997–E5006. https://doi.org/10.1073/pnas.1415122111
5. Cohen, A. L., Fair, D. A., Dosenbach, N. U. F., Miezin, F. M., Dierker, D., Van Essen, D. C., Schlaggar, B. L., & Petersen, S. E. (2008). Defining functional areas in individual human brains using resting functional connectivity MRI. NeuroImage, 41(1), 45–57.
6. Cui, Z., Li, H., Xia, C. H., Larsen, B., Adebimpe, A., Baum, G. L., Cieslak, M., Gur, R. E., Gur, R. C., Moore, T. M., Oathes, D. J., Alexander-Bloch, A. F., Raznahan, A., Roalf, D. R., Shinohara, R. T., Wolf, D. H., Davatzikos, C., Bassett, D. S., Fair, D. A., … Satterthwaite, T. D. (2020). Individual Variation in Functional Topography of Association Networks in Youth. Neuron, 106(2), 340-353.e8.
7. Gao, W., Alcauter, S., Elton, A., Hernandez-Castillo, C. R., Smith, J. K., Ramirez, J., & Lin, W. (2015). Functional Network Development During the First Year: Relative Sequence and Socioeconomic Correlations. Cerebral Cortex (New York, N.Y.: 1991), 25(9), 2919–2928.

Poster No 1293

The associations between microglia function, prenatal environment and white matter development

Shi Yu Chan[1], Eamon Fitzgerald[2], Zhen Ming Ngoh[3], Janice Lee[1], Jasmine Chuah[1], Marielle Fortier[4], Juan Helen Zhou[5], Patricia Silveira[2], Michael Meaney[3], Ai Peng Tan[6]

[1]Singapore Institute for Clinical Sciences, Singapore, Singapore, [2]McGill University, Montreal, Quebec, [3]Singapore Institute for Clinical Sciences, Agency for Science, Technology and Research in Singapore, Singapore City, Singapore, [4]KK Women's and Children's Hospital, Singapore, Singapore, [5]National University of Singapore, Singapore, Singapore, [6]National University Hospital, Singapore, Others

Introduction: The biological embedding of early life experiences on neurodevelopment is postulated to be mediated through the immune system (Berens, Jensen et al. 2017). As the brain's resident immune cell, microglia play a role in environmental surveillance and respond to both adverse and enriched environments (Cathomas, Holt et al. 2022). Microglia have also been shown to regulate neurodevelopment, including synaptic plasticity (Cathomas, Holt et al. 2022). White matter development, indexed by changes in fractional anisotropy (FA), affect a variety of psychopathological outcomes (Stephens, Langworthy et al. 2020), and is shaped by early life environment and genetic factors (Lebel and Deoni 2018). Thus, individual variation in microglia function may interact with early life experiences to influence white matter development. In this study, we examined the associations between microglia function, early life environment and white matter FA slopes. We also explored the sex-dependency of these associations.

Methods: Diffusion imaging data and T1-weighted images were collected from the Growing Up in Singapore Towards Healthy Outcomes (GUSTO) cohort (Soh, Tint et al. 2014) over three time-points (age 4.5, 6.0, 7.5 years) from early to mid-childhood. 351 participants had diffusion imaging data collected at more than one time-point and were included in the current study. Diffusion datasets were processed in FMRIB's Software Library (FSL v6.0.4) (Smith, Jenkinson et al. 2004) to calculate parametric maps of FA. T1-weighted images were processed with the FreeSurfer v6.0 recon-all pipeline (Fischl 2012) to obtain bilateral cerebral white matter masks. We applied the bilateral white matter mask to the FA maps to extract mean white matter FA. Individual variation in microglia function was indexed by an expression-based microglia polygenic score (ePGS). Two cumulative prenatal environment scores (adverse and advantageous) were derived from demographic and maternal health measures during pregnancy (Silveira, Pokhvisneva et al. 2017). Linear mixed effects models were used to estimate white matter FA slopes over childhood for each participant. Spearman's correlation and linear regression models were used to examine the associations between microglia ePGS, white matter FA slopes, sex and prenatal environment.

Results: We observed a significant association between individual estimates of white matter FA slopes and microglia ePGS scores (Spearman's rho = 0.144, p = 0.008). This association was modulated by sex (Microglia ePGS:sex interaction: p = 0.026), where a significant positive correlation was only observed for females (Spearman's rho = 0.243, p = 0.0013). Similarly, a significant interaction between microglia ePGS and an advantageous prenatal environment on white matter FA slopes was observed for females (estimate = -0.221, Std Error = 0.084, t-value = -2.63, p = 0.01), but not for males (p = 0.745). In addition, we did not observe a significant interaction between microglia ePGS and an adverse prenatal environment on white matter FA slopes for both males and females (all p > 0.3).

Conclusions: We show that a significant association between an advantageous prenatal environment and white matter development was only observed in females with high microglia ePGS. Our findings suggest that variations in microglia function may explain the heterogeneity in individual susceptibility to early life environment on white matter development.

References

1. Berens, A. E. (2017). "Biological embedding of childhood adversity: from physiological mechanisms to clinical implications." BMC Medicine 15(1): 135.
2. Cathomas, F. (2022). "Beyond the neuron: Role of non-neuronal cells in stress disorders." Neuron 110(7): 1116-1138.
3. Fischl, B. (2012). "FreeSurfer." Neuroimage 62(2): 774-781.
4. Lebel, C. (2018). "The development of brain white matter microstructure." Neuroimage 182: 207-218.
5. Silveira, P. P. (2017). "Cumulative prenatal exposure to adversity reveals associations with a broad range of neurodevelopmental outcomes that are moderated by a novel, biologically informed polygenetic score based on the serotonin transporter solute carrier family C6, member 4 (SLC6A4) gene expression." Development and Psychopathology 29(5): 1601-1617.
6. Smith, S. M. (2004). "Advances in functional and structural MR image analysis and implementation as FSL." Neuroimage 23 Suppl 1: S208-219.
7. Soh, S. E. (2014). "Cohort profile: Growing Up in Singapore Towards healthy Outcomes (GUSTO) birth cohort study." International Journal of Epidemiology 43(5): 1401-1409.
8. Stephens, R. L. (2020). "White Matter Development from Birth to 6 Years of Age: A Longitudinal Study." Cerebral Cortex 30(12): 6152-6168.

Poster No 1294

The Development of Brain Morphometric Similarity Network in School-aged Children

Xiao Wang[1], Chu-Chung Huang[1], Qing Cai[1]

[1]*East China Normal University, Shanghai, China*

Introduction: The development of brain networks in early school-age children plays a pivotal role in the maturation of complex cognitive and behavioral functions (Dong et al., 2021; Shaffer & Kipp, 2013). Evidence suggests that brain structural maturation involves a process of interconnected networking, in which multiple brain regions undergo synchronized morphometric changes in a coordinated manner (Wu et al., 2023). Therefore, exploring the cortical similarity networks is likely to provide a comprehensive understanding of brain maturation trajectories. However, the developmental pattern of the brain morphometric similarity networks in school-age children has yet to be fully revealed and validated through longitudinal data.

Methods: Utilizing the T1-weighted longitudinal imaging data (N = 639, 1-5 time points, aged 6-11) from East China Normal University, we investigated the developmental trajectories of the cortical similarity networks using linear mixed effects model (Figure 1). The Morphometric INverse Divergence (MIND) approach was employed to estimate the within-subject similarity between cortical areas based on the divergence between their multivariate distributions of multiple morphometric features (Sebenius et al., 2023). To investigate the topographical properties of MIND networks systematically, we detected the modular structure using a community detection approach. Additionally, we associated the MIND similarity with both the Raven IQ and the working memory ability.

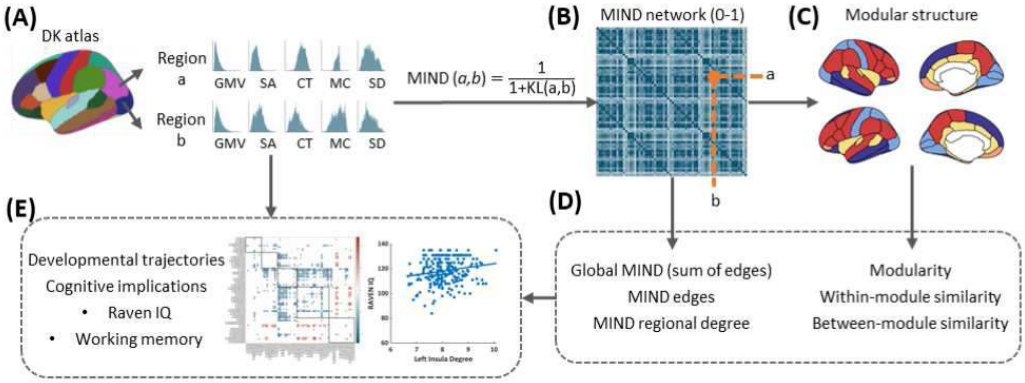

Figure 1. Flowchart of data analytical pipeline in this study. (A) The T1-weighted images of each scan were preprocessed using FreeSurfer to extract five cortical surface-based, vertex-wise morphometric maps, including gray matter volume, surface area, cortical thickness, mean curvature and sulcal depth. For each pair of regions, the interregional morphometric similarity was estimated using the Kullback–Leibler divergence approach to construct the Morphometric INverse Divergence (MIND) Network (B) for each scan data. (C) Community detection was performed for the each MIND network and the group mean matrix to identify the modular structure systematically. (D) The global MIND (sum of similarity in network), MIND edges and the regional degree (sum of similarity between this region and the rest of regions, e.g. sum of each row or column of the matrix) were computed to quantify the MIND network for each scan data. And, the modularity, within- and between-module similarity were calculated to characterize the topological modular structure for each scan data. (E) The developmental trajectories and the cognitive association of each single morphometric feature, the MIND network and the modular structural properties were examined. Abbreviation: GMV, Gray matter volume; SA, Surface area; CT, Cortical thickness; MC, Mean curvature; SD, Sulcal depth; MIND, Morphometric INverse Divergence.

Results: The prominent developmental pattern observed in multiple morphometric features during the school-age period was the expansion of surface area and the thinning of cortical thickness, together with the increased gray matter volume in the higher-level transmodal areas and the decreased volume in the primary areas (Figure 2A). The modularity of MIND networks shown increased with age (Figure 2D). Five modules including Frontal-Temporal Area 1 and 2, Sensory-Motor Area, Insula-Limbic Area, and Orbital-Frontal Area were identified (Figure 2B). The morphometric similarities within and between the modular structure decline with age, except for the similarity between the Insula-Limbic Area and Frontal-Temporal Area (Figure 2C). The morphometric similarity of MIND network was decreased with age, while the regional degrees of bilateral insula and anterior cingulate cortex increased (Figure 2E-G). No significant association between cognitive scores (Raven IQ and working memory ability) and the morphometric features or the MIND network was found.

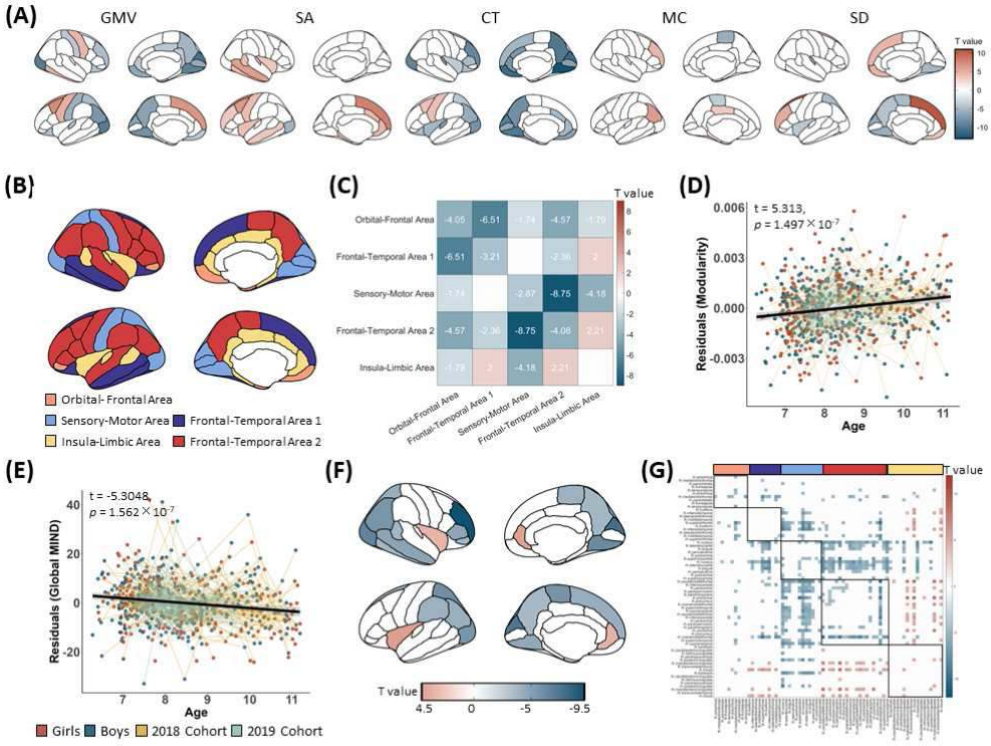

Figure 2. The developmental trajectories of the morphometric features and MIND network. (A) The developmental trajectories of gray matter volume, surface area, cortical thickness, mean curvature and sulcal depth. (B) The modular structure of MIND network. (C) The age effects of within- and between-module similarity. (D) The association between age and modularity, control the effects of gender, site, cohort and total gray matter volume. (E) The association between age and global MIND (sum of similarity in network), control the effects of gender, site, cohort and total gray matter volume. (F) The age effects of regional degree of MIND network. (G) The age effects of MIND edges. Warm color, positive age effects; cool color, negative age effects. Red dots, girls; blue dots, boys; yellow lines, 2018 cohort; green lines, 2019 cohort. Abbreviation: GMV, Gray matter volume; SA, Surface area; CT, Cortical thickness; MC, Mean curvature; SD, Sulcal depth; MIND, Morphometric INverse Divergence.

Conclusions: In summary, we longitudinally investigated the developmental trajectories of brain morphometric similarity network in school-aged children using T1w images. We observed that the MIND networks displayed a modular architecture, where most modules exhibited a decreased in similarity with age increased. Notably, higher-level transmodal areas, such as the bilateral insula and anterior cingulate cortex, demonstrated an opposite trend. These findings highlight the pattern of the brain segregation in fronto-temporal areas and increased inter-modular integration in insula-limbic areas. This study suggested that the cortical morphometric similarity can serve as a maturational marker during the school-age stage and provided insights into typical brain development.

References

1. Dong, H. M., Margulies, D. S., Zuo, X. N., & Holmes, A. J. (2021). Shifting gradients of macroscale cortical organization mark the transition from childhood to adolescence. Proc Natl Acad Sci U S A, 118(28). https://doi.org/10.1073/pnas.2024448118
2. Sebenius, I., Seidlitz, J., Warrier, V., Bethlehem, R. A. I., Alexander-Bloch, A., Mallard, T. T., Garcia, R. R., Bullmore, E. T., & Morgan, S. E. (2023). Robust estimation of cortical similarity networks from brain MRI. Nature Neuroscience, 26(8), 1461-1471. https://doi.org/10.1038/s41593-023-01376-7
3. Shaffer, D. R., & Kipp, K. (2013). Developmental psychology: Childhood and adolescence. Cengage Learning.
4. Wu, X., Palaniyappan, L., Yu, G., Zhang, K., Seidlitz, J., Liu, Z., Kong, X., Schumann, G., Feng, J., Sahakian, B. J., Robbins, T. W., Bullmore, E., & Zhang, J. (2023). Morphometric dis-similarity between cortical and subcortical areas underlies cognitive function and psychiatric symptomatology: a preadolescence study from ABCD. Mol Psychiatry, 28(3), 1146-1158. https://doi.org/10.1038/s41380-022-01896-x

Poster No 1295

Unveiling Fetal Cortical Folding: Neuroimaging and Genetic Insights

Xinyi Xu[1], Ruike Chen[1], Tianshu Zheng[1], Zhiyong Zhao[1], Mingyang Li[1], Dan Wu[1]

[1]College of Biomedical Engineering & Instrument Science, Zhejiang University, Hangzhou, Zhejiang

Introduction: The human fetal cerebral cortex undergoes genetically orchestrated gyrification (cortical folding) during the prenatal period. Recent fetal brain MRI advancements allow spatiotemporal quantification of macro- and microstructures

during cortical folding (Figure 1a). Researchers aim to understand the relationship between morphological changes and underlying microstructural alterations associated with cortical folding (Garcia et al., 2021). Transcriptomic technologies revealed regional gene expression patterns during prenatal development (Miller et al., 2014, Li et al., 2018). Pioneering studies by (Huang et al., 2013) and (Vasung et al., 2021) correlated MRI measurements with relevant genes using ex-vivo and in-vivo fetal brains but fell short in describing cortical folding. Therefore, we aim to comprehensively characterize spatiotemporal macro- and microstructural development of the fetal cerebral cortex by integrating in-utero fetal structural MRI, diffusion MRI, and gene expression.

Methods: Fetal brain MRI data: We used fetal brain T2 atlas (Xinyi et al., 2022) and diffusion MRI atlas data (Chen et al., 2022) from 23-38w gestational age (GA), served as standard average representations of a healthy fetal population. Macro- and microstructural characterization of cortical folding was conducted weekly (Figure 1a). Curvature, indicating the degree of cortical folding, was computed as the morphological representation. The Diffusion Basis Spectrum Imaging (DBSI) model (Wang et al., 2011) estimated the fiber, restricted, hindered, and water components of brain tissue using the DBSI toolbox (Spees et al., 2018). Bulk tissue gene expression data: Cortical gene expression data, quantified as Reads Per Kilobase Million (RPKM), were obtained from PsychEncode project (Li et al., 2018). Postmortem human brains underwent regional dissection encompassing 11 neocortical regions (Figure 1b). For this study, we selectively incorporated RPKM data from 4 prenatal specimens (two at 21 pcw, one at 35 pcw, and another at 37 pcw) to match GAs of fetal brain MRI atlases (Figure 1c). Structural equation modeling (SEM): To examine directional influence between early macrostructural cortical folding changes and late microstructural alterations, we conducted SEM in R (lavaan package). This analysis focused on curvature and four DBSI metrics at early (23w) and late (35w-38w) stages (Figure 1d). FDR correction was applied within each DBSI metric. Correlation of Gene experession and Macro-/Micro-structural Measures: We compared regional variation in cortical MRI measures (curvature and DBSI metrics) with prenatal gene expression in correspondent cortical regions (Figure 1b). Pearson correlation between MRI measures and log of RPKM for selected 5438 marker genes (similar selection process to (Ball et al., 2020)) was performed. Enrichment analysis of significant associated genes was conducted using WebGestalt (https://www.webgestalt.org/#).

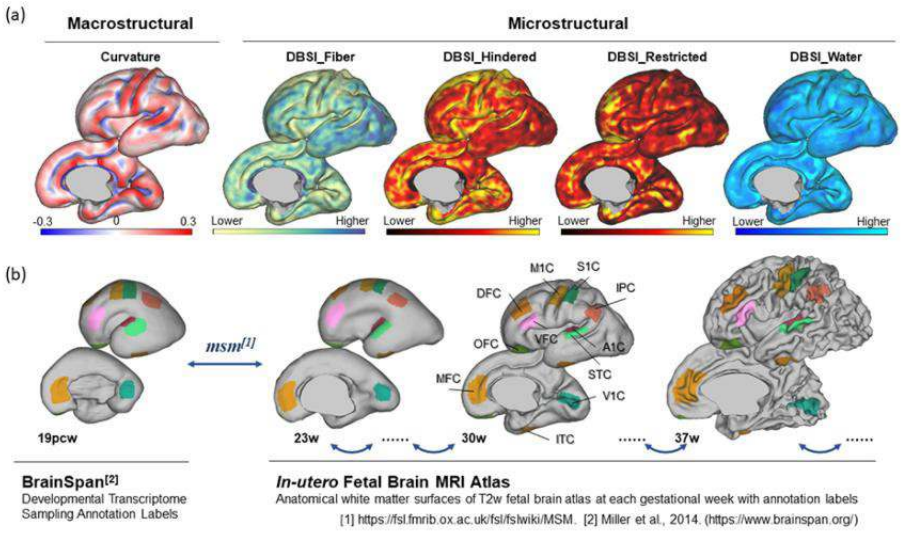

(c) Included gene expression data from PsychEncode

Braincode	Age	Hemisphere	sex	Ethnicity
HSB107	21pcw	L	F	European
HSB92	21pcw	R	M	African
HSB155	35pcw	R	F	European
HSB194	37pcw	L	M	European

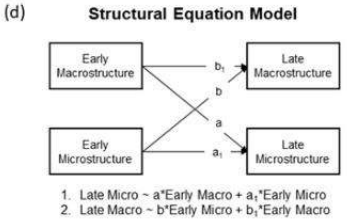

Figure 1. (a) Cortical macro- and microstructural neuroimaging metrics at 30w gestational age: curvature from structural MRI and four DBSI metrics from diffusion MRI. (b) 11 cortical labels for spatially comparing transcriptomic and neuroimaging data, transferred onto fetal brain atlas surfaces by *msm*, a surface registration method, and manual refinement. (c) Specimen/sample details for included PsychEncode gene expression data. (d) Structural equation model depicting macro- and microstructure relationships at different developmental stages. Abbreviations: DFC, dorsolateral prefrontal cortex (PFC); VFC, ventrolateral PFC; MFC, medial PFC; OFC, orbital PFC; M1C, motor cortex; S1C, somatosensory cortex; IPC, posterior inferior parietal cortex; A1C, primary auditory cortex; STC, posterior superior temporal cortex; ITC, inferior temporal cortex; V1C, primary visual (occipital) cortex.

Results: Early changes (23w) in curvature were significantly associated with changes in DBSI fiber and hindered fractions at later stages (35w-38w) (Figure 2a-c). Based on these SEM results, we further analyzed the correlations of curvature at 23w and two DBSI metrics at 37w-38w with gene expression data. Of 5438 genes, 87 correlated significantly with curvature, 79 with DBSI fiber fraction, and 30 with DBSI hindered fraction after FDR correction ($p<0.05$) (Figure 2d). Significant enrichment of the genes that were significantly associated with curvature identified neurodevelopmental terms, including neurogenesis and neuron differentiation (Figure 2e). Genes significantly correlated with DBSI fiber and hindered fractions were both enriched for cell adhesion, biological adhesion, and extracellular matrix organization.

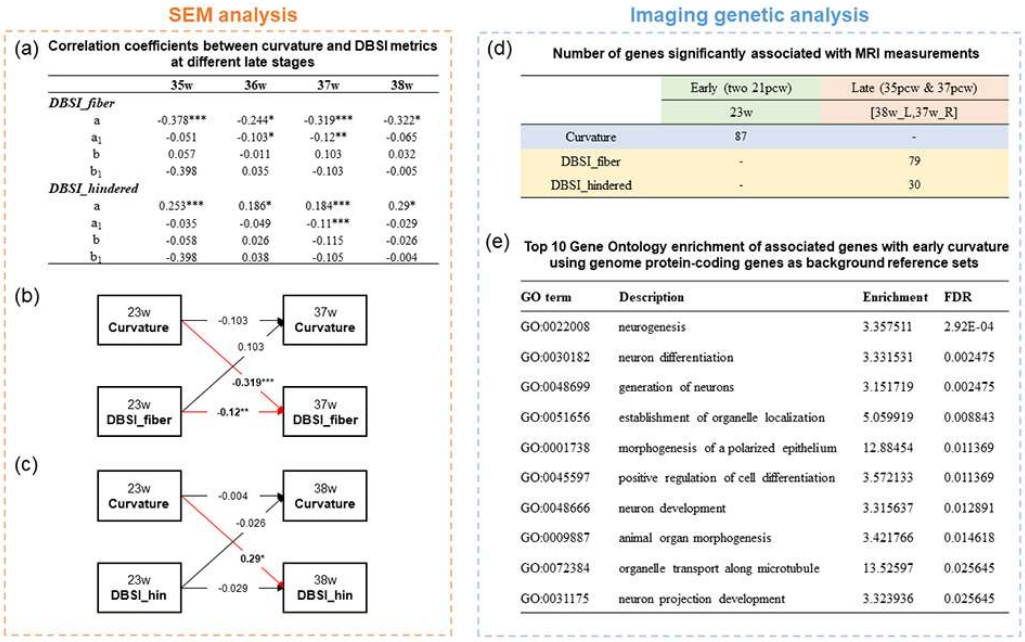

Figure 2. Results of SEM analysis (a-c) and Imaging genetic analysis (d-e). (a) Correlation coefficients estimation between curvature and two DBSI metrics at 35w-38w. Representative path graphs illustrating results of Curvature and DBSI fiber fraction at early 23w and late 37w (b), curvature and DBSI hindered fraction at early 23w and late 38w (c). (d) Number of genes significantly associated with neuroimaging macro- and microstructural metrics at two stages. (e) Gene Ontology enrichment of genes associated with early curvature using genome protein-coding genes as background reference sets. * corrected p-value <0.05, ** <0.01, *** <0.001.

Conclusions: Our study combines advanced imaging modalities and genetic analysis to probe fetal cortex development dynamics, enhancing our understanding of macro- and microstructural interplay in neurodevelopment.

References

1. Ball G, et al. (2020), 'Cortical morphology at birth reflects spatiotemporal patterns of gene expression in the fetal human brain', PLoS Biology, vol. 18, no. 11, pp. e3000976-e3000976.
2. Chen R, et al. (2022), 'Deciphering the developmental order and microstructural patterns of early white matter pathways in a diffusion MRI based fetal brain atlas', Neuroimage, vol. 264, no. pp. 119700.
3. Garcia K E, et al. (2021), 'A model of tension-induced fiber growth predicts white matter organization during brain folding', Nature Communications, vol. 12, no. 1, pp. 6681.
4. Huang H, et al. (2013), 'Coupling Diffusion Imaging with Histological and Gene Expression Analysis to Examine the Dynamics of Cortical Areas across the Fetal Period of Human Brain Development', Cerebral Cortex, vol. 23, no. 11, pp. 2620-2631.
5. Li M, et al. (2018), 'Integrative functional genomic analysis of human brain development and neuropsychiatric risks', Science (New York, N.Y.), vol. 362, no. 6420, pp. eaat7615.
6. Miller J A, et al. (2014), 'Transcriptional landscape of the prenatal human brain', Nature, vol. 508, no. 7495, pp. 199-206.
7. Spees W M, et al. (2018), 'MRI-based assessment of function and dysfunction in myelinated axons', Proceedings of the National Academy of Sciences, vol. 115, no. 43, pp. E10225-E10234.
8. Vasung L, et al. (2021), 'Association between Quantitative MR Markers of Cortical Evolving Organization and Gene Expression during Human Prenatal Brain Development', Cerebral Cortex, vol. 31, no. 8, pp. 3610-3621.
9. Wang Y, et al. (2011), 'Quantification of increased cellularity during inflammatory demyelination', Brain, vol. 134, no. Pt 12, pp. 3590-3601.
10. Xinyi X, et al. (2022), 'Spatiotemporal Atlas of the Fetal Brain Depicts Cortical Developmental Gradient', The Journal of Neuroscience, vol. 42, no. 50, pp. 9435.

Poster No 1296

Dual long-axis reorganization of hippocampus in youth

Debin Zeng[1], Qiongling Li[2], Deyu Li[1], Yirong He[2], Xiaoxi Dong[2], Shaoxian Li[2], Shenghan Bi[2], Yong He[2], Xi-Nian Zuo[2], Shuyu Li[2]

[1]Beihang University, Beijing, China, [2]Beijing Normal University, Beijing, China

Introduction: The reorganization of human hippocampus, especially its interaction with cortex, remains largely undefined in youth. The organization of a single hippocampal long-axis has been predominantly characterized as monotonic(Genon et al. 2021; Strange et al. 2014), despite recent indications of nonmonotonic features in neuron density(Gandolfi et al. 2023) and geometric eigenmodes(Pang et al. 2023). While the human cortical hierarchy has been well recognized for significant developmental and evolutionary advantages(Dong et al. 2021; Tong et al. 2022), hippocampus has been typically considered an evolutionarily conserved brain structure(Strange et al. 2014; Pandya et al. 2015), and overlooked regarding its integrative role of cortical hierarchical processing during development.

Methods: Our study utilized data from the Human Connectome Project Development (HCP-D) with 652 participants (5-21 years) and the Children School Functions and Brain Development Project (CBD, Beijing Cohort) with 300 children (6-13 years). We used the HippUnfold tool(DeKraker et al. 2022) to segment the hippocampus and generate mid-thickness surfaces. Hippocampal-cortical connectomes were created by correlating rs-fMRI time series between hippocampal vertices and cortical regions (defined by the Glasser atlas(Glasser et al. 2016)). A diffusion embedding method yielded the hippocampal functional gradient (Fig. 1a), and cortical projections were computed by taking the dot product between the gradient and the hippocampal functional connectivity for each cortical region. Geometric eigenmodes for each hippocampus were obtained through Laplace–Beltrami operator-based analysis. All developmental effects were studied using generalized additive models. Lastly, transcriptomic association and developmental enrichment analyses were conducted to explore the neurobiological basis of dual long-axis functional gradient development.

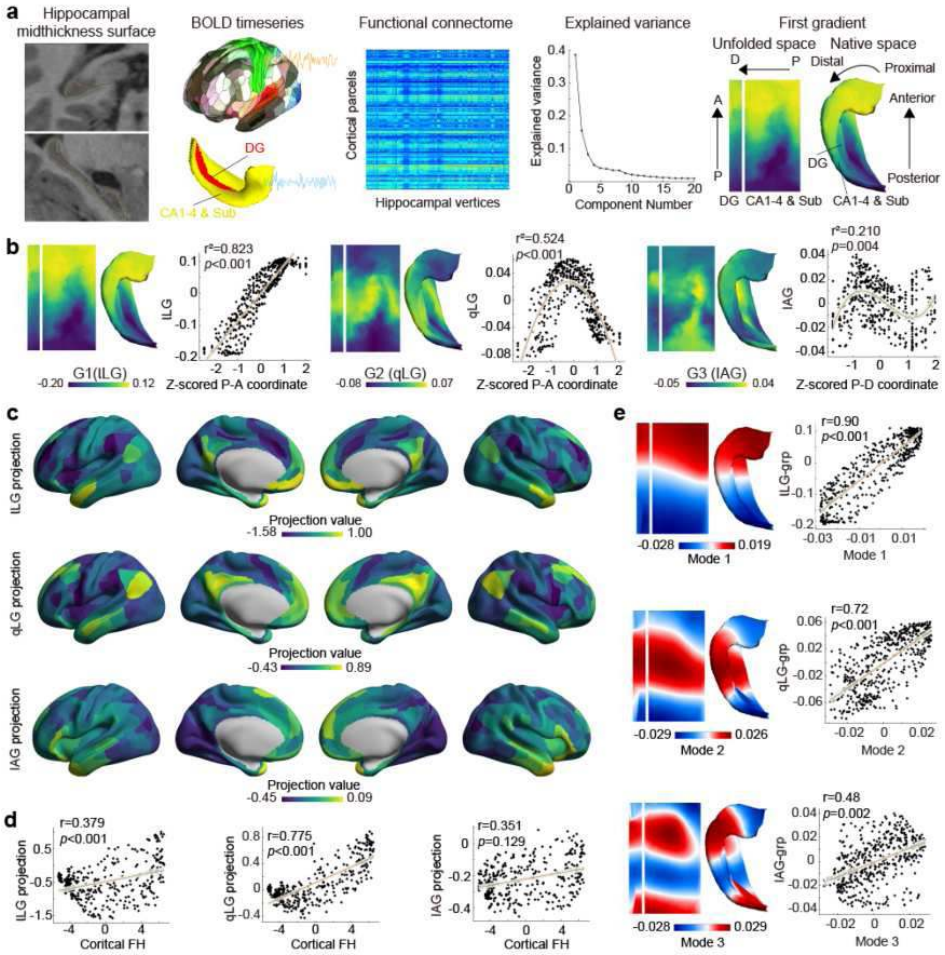

Fig. 1 | Topographic characterization, cortical projection, and geometric constraints of major hippocampal gradients in youth. a, Methodological overview for identifying hippocampal gradients. **b**, Topographic characterization of the first three hippocampal gradients at the overall group level and relationships between hippocampal gradients and anatomical positions. **c**, Group-averaged cortical projection of the left hippocampal gradients. **d**, Correlation between the projection pattern of specific gradients in the left hippocampus and cortical functional hierarchy (FH). **e**, Group-averaged first three geometric eigenmodes and relationship between these eigenmodes and hippocampal gradients.

Results: Here, we corroborated the presence and significance of a dual long-axis representation of the hippocampal connectome and geometry including both linear and quadratic gradients along its long-axis in youth (Fig. 1b and e). This finding was robust across two independent large-scale developmental cohorts. Projecting the connectome gradients onto the cortex, we clarified how distinct cortical hierarchies allocate functional connectivity differently along the long-axis, thus coding the hippocampus's intricate and multifaceted role in cortical hierarchical processing (Fig. 1c and d). These discoveries challenge classical views that propose a monotonic gradient of structural and functional differentiation along the hippocampal long-axis, and question the traditional notion of the hippocampus as being evolutionarily conserved in terms of its organization. We observed substantial developmental reorganization of dual long-axis gradients in supporting the maturation of the cortical hierarchy in youth (Fig. 2b). The reorganization further unfolds that the human hippocampus continues to loosen its geometric gradient constraints on functional gradients to support the executive function performance (Fig. 2c and d). Notably, we revealed that neurodevelopmental variability in the functional gradient profiles mirrors a gradient associated with a plasticity-limiting factor (myelin content, estimated by T1w/T2w ratio) (Fig. 2a). At micro-level, we found that neural growth, stress hormone regulation, and neuroactive signaling are involved in this geometry-function-cognition alignment, facilitating such reorganization of the dual hippocampal long-axis gradients in youth (Fig. 2e).

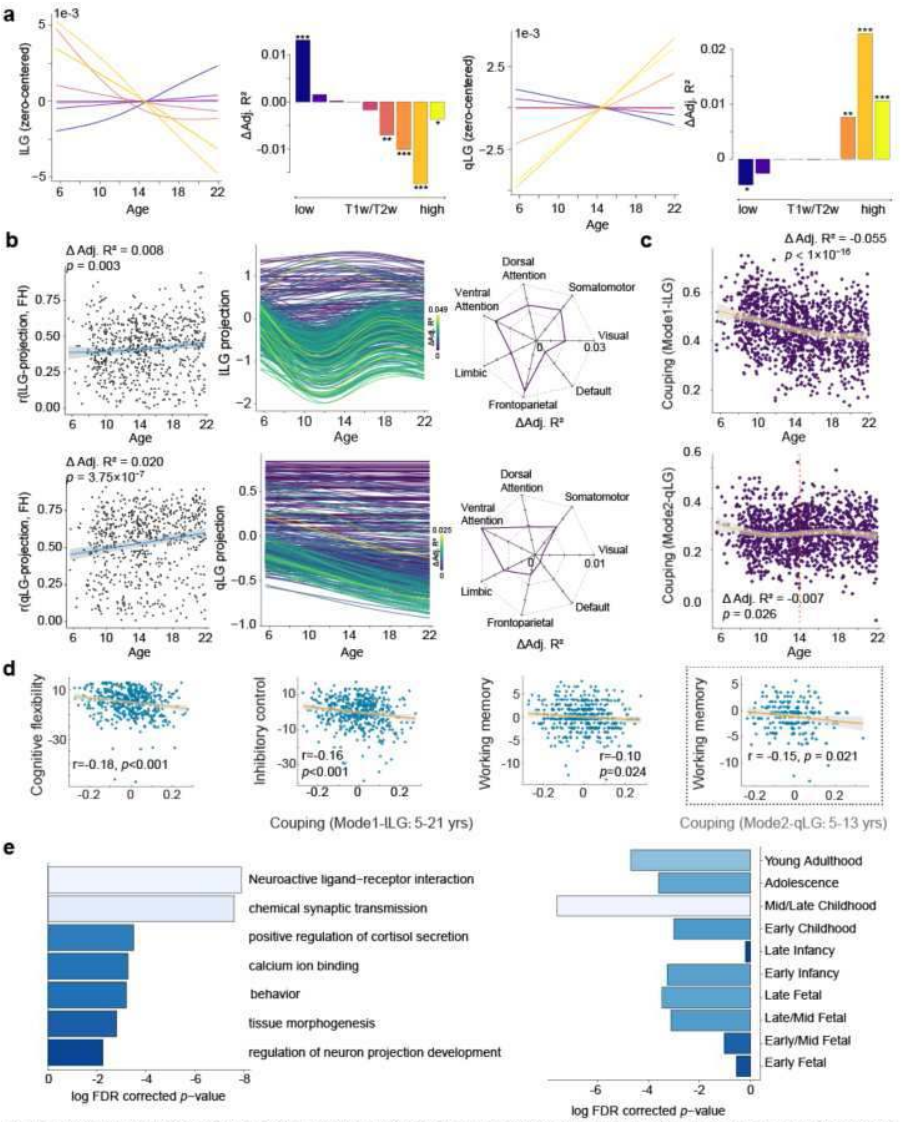

Fig. 2 | Understanding hippocampal-cortical reorganizational principles across structural, functional, and molecular dimensions as well as its maturation. a, Development of dual long-axis dimensions of hippocampal gradient parallels myelin maturation. **b**, Cortical projection of the hippocampal gradient links to the maturation of the cortical hierarchy in youth (left) and the cortical region-specific trajectories indicated that the frontoparietal and ventral attention systems plays a critical role in this process (middle and right). **c**, Developmental trajectories of geometric-functional coupling of dual long-axis gradients. **d**, Relationship between the geometric-functional coupling and executive function performance. **e**, The enriched biological pathways and gene ontology terms linked to important gene set for lLG (left) and developmental enrichment analysis for this gene set (right).

Conclusions: Our findings enrich the understanding of hippocampal-cortical reorganizational principles across structural, functional, and molecular dimensions as well as its maturation, and define the plasticity distribution within the human hippocampus at systems level, holding potentials to enhance and translate neurodevelopment and neuropsychiatric healthcare.

References
1. DeKraker, Jordan, Roy A. M. Haast, Mohamed D. Yousif, Bradley Karat, Jonathan C. Lau, Stefan Köhler, and Ali R. Khan. 2022. 'Automated hippocampal unfolding for morphometry and subfield segmentation with HippUnfold', eLife, 11: e77945.
2. Dong, Hao-Ming, Daniel S. Margulies, Xi-Nian Zuo, and Avram J. Holmes. 2021. 'Shifting gradients of macroscale cortical organization mark the transition from childhood to adolescence', Proceedings of the National Academy of Sciences, 118: e2024448118.
3. Gandolfi, Daniela, Jonathan Mapelli, Sergio M. G. Solinas, Paul Triebkorn, Egidio D'Angelo, Viktor Jirsa, and Michele Migliore. 2023. 'Full-scale scaffold model of the human hippocampus CA1 area', Nature Computational Science, 3: 264-76.
4. Genon, Sarah, Boris C. Bernhardt, Renaud La Joie, Katrin Amunts, and Simon B. Eickhoff. 2021. 'The many dimensions of human hippocampal organization and (dys)function', Trends in Neurosciences, 44: 977-89.
5. Glasser, Matthew F, Timothy S Coalson, Emma C Robinson, Carl D Hacker, John Harwell, Essa Yacoub, Kamil Ugurbil, Jesper Andersson, Christian F Beckmann, and Mark Jenkinson. 2016. 'A multi-modal parcellation of human cerebral cortex', Nature, 536: 171-78.
6. Pandya, Deepak, Benjamin Seltzer, Michael Petrides, and Patsy Benny Cipolloni. 2015. Cerebral Cortex: Architecture, Connections, and the Dual Origin Concept (Oxford University Press).
7. Pang, James C., Kevin M. Aquino, Marianne Oldehinkel, Peter A. Robinson, Ben D. Fulcher, Michael Breakspear, and Alex Fornito. 2023. 'Geometric constraints on human brain function', Nature, 618: 566-74.
8. Strange, Bryan A, Menno P Witter, Ed S Lein, and Edvard I Moser. 2014. 'Functional organization of the hippocampal longitudinal axis', Nature Reviews Neuroscience, 15: 655-69.
9. Tong, Chuanjun, Cirong Liu, Kaiwei Zhang, Binshi Bo, Ying Xia, Hao Yang, Yanqiu Feng, and Zhifeng Liang. 2022. 'Multimodal analysis demonstrating the shaping of functional gradients in the marmoset brain', Nature Communications, 13: 6584.

Poster No 1297

Microstructural Features Linking White Matter and Mathematics in Childhood and Adolescence

Bryce Geeraert[1], Kiara Kunimoto[1], Marc Lebel[1], Catherine Lebel[1]

[1]University of Calgary, Calgary, Alberta

Introduction: Mathematics is a complex skill requiring the coordination of distributed gray matter brain regions connected by white matter tracts[1]. Diffusion imaging (dMRI) studies have revealed a network of white matter tracts that facilitate math processing[2], but it remains unclear how the microstructural features of these tracts support math. Additional modalities can provide higher specificity to white matter microstructure. The neurite density index (NDI) and orientation dispersion index (ODI) probe axon packing and coherence, myelin volume fraction (VFm) is sensitive to myelin content, while the g-ratio reports axon diameter to myelin thickness, which relates to communication efficiency in white matter[3-5]. We combined dMRI with these more specific metrics to evaluate links between white matter microstructural development and math in a longitudinal cohort of adolescents.

Methods: 33 healthy children (16M/17F, 12.7 ± 2.4 years) were scanned on a GE 3T Discovery MR750w scanner, and again after two years (66 datasets total). DTI/NODDI: spin echo EPI, TR/TE = 12s/88ms, 2.2mm isotropic resolution, b=900 & 2000 s/mm2, 30 directions and 5 b0 per shell. McDESPOT: multi-α SPGR, 18° max α, 1.72x0.86x1.7mm res.; IR-SPGR, 2.29x0.86x3.4mm res., 5° α; two bSSFP images with phase of 0° and 180°, 1.72x0.86x1.7 mm resolution, max α 60°, TR/TE = min+0.1ms/min for all. Participants completed WIAT-III CDN subtests for Mathematics and Math Fluency composite scores at both time points[6]. Following preprocessing, four math-related tracts-the left superior longitudinal (SLF) and inferior longitudinal fasciculi (ILF), corticospinal tract (CST), and the splenium-were segmented in ExploreDTI. Fractional anisotropy (FA), mean diffusivity (MD), NDI, ODI, VFm, and g-ratio maps were produced. Partial correlations between time 1 and annual change in white matter metrics and math scores, controlling for age and gender, were computed per tract. Multiple comparisons were corrected via the false discovery rate (FDR) method[7].

Results: ODI of the SLF and CST correlated to Mathematics in cross-sectional analysis of time 1 data. Longitudinally, annual change in Mathematics correlated with change of NDI in the SLF, MD in the CST, and VFm in the splenium. Math Fluency correlated with VFm in the ILF and splenium, and with g-ratio in the ILF and CST. No significant correlations were observed between FA and math scores in any investigated region (Table 1, Figure 1). Correlations did not survive FDR correction. Follow-up analyses of math subtests suggested white matter microstructure was most closely related to rapid information processing, although some links to higher-order mathematical skills were observed.

Table 1. Partial correlations between cross-sectional and annual change in imaging metrics and mathematics scores from the WIAT-III CDN, controlling for age at time 1 and parent-reported gender. C.S.: cross-sectional, Long.: longitudinal.

Region	Data	Imaging Metric	Math Metric	Correlation	p-value	Sample	Power
SLF	C.S.	ODI	Mathematics	r = -0.418	p = 0.038	n = 27	0.752
CST	C.S.	ODI	Mathematics	r = -0.464	p = 0.017	n = 27	0.842
SLF	Long.	NDI	Mathematics	r = 0.411	p = 0.041	n = 27	0.664
ILF	Long.	VF_m	Fluency	ρ = - 0.539	p = 0.047	n = 16	0.694
	Long.	g-ratio	Fluency	r = 0.641	p = 0.013	n = 16	0.895
CST	Long.	MD	Mathematics	ρ = - 0.407	p = 0.039	n = 28	0.622
	Long.	g-ratio	Fluency	r = 0.550	p = 0.042	n = 16	0.719
Splenium	Long.	VF_m	Mathematics	ρ = - 0.635	p = 0.020	n = 15	0.863
	Long.	VF_m	Fluency	ρ = - 0.646	p = 0.017	n = 15	0.882

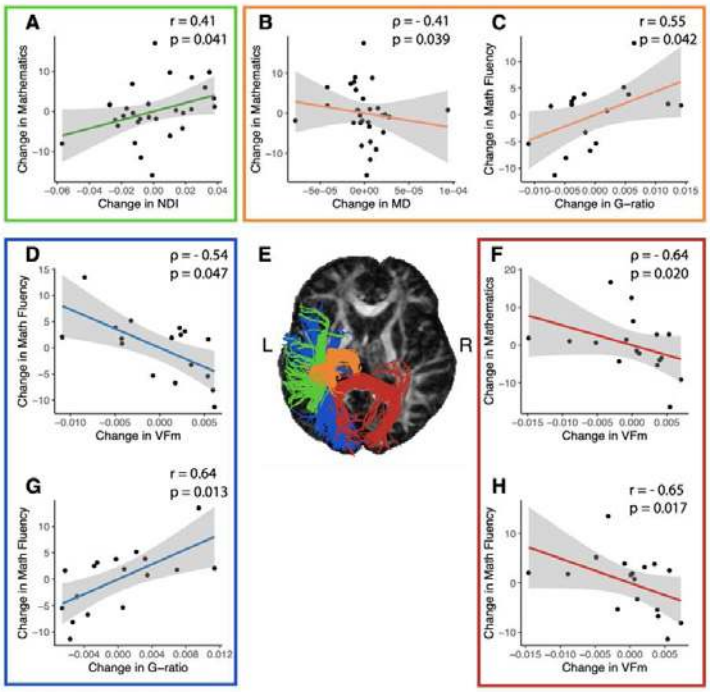

Figure 1. Partial correlations between annual change in white matter microstructure (x axes) and Mathematics or Math Fluency composite scores (y axes), controlling for age and parent-reported gender. Correlation fit lines are colored by their corresponding region.

Conclusions: We applied measures specific to white matter microstructure in a longitudinal cohort to show that links between DTI metrics and math skill are primarily driven by changes in axonal packing and myelin. Our findings suggest axonal packing in the math network supports sophisticated processing and problem solving, while myelin predominantly supports rapid information processing. Correlations were moderate to high magnitude and achieved high power, despite not surviving FDR correction. This, combined with the near absence of correlations between DTI metrics and math, highlights the strength of microstructurally-sensitive metrics to detect subtle relationships that may be missed by traditional methods. While most relationships were such that indications of more mature white matter were positively correlated to math, decreases in myelin content were linked to improvements in mathematics in adolescence. This suggests adolescence is a period of refinement to the already established structural network underlying mathematical processing. These findings shed light on the role of white matter tracts in complex cognitive tasks such as mathematical processing, and may be applied to better understand the biological underpinnings of learning disabilities.

References

1. Arsalidou, M. & Taylor, M. J. Is 2+2=4? Meta-analyses of brain areas needed for numbers and calculations. NeuroImage 54, 2382–2393 (2011).
2. Matejko, A. A. & Ansari, D. Drawing connections between white matter and numerical and mathematical cognition: A literature review. Neurosci. Biobehav. Rev. 48, 35–52 (2015).
3. Zhang, H., Schneider, T., Wheeler-Kingshott, C. A. & Alexander, D. C. NODDI: Practical in vivo neurite orientation dispersion and density imaging of the human brain. NeuroImage 61, 1000–1016 (2012).
4. Varma, G., Duhamel, G., de Bazelaire, C. & Alsop, D. C. Magnetization transfer from inhomogeneously broadened lines: A potential marker for myelin: Magnetization Transfer from Inhomogeneously Broadened Lines. Magn. Reson. Med. 73, 614–622 (2015).
5. Stikov, N. et al. In vivo histology of the myelin g-ratio with magnetic resonance imaging. NeuroImage 118, 397–405 (2015).
6. Wechsler D. Wechsler Individual Achievement Test -- Third Edition: Canadian (WIAT-III CDN). (Pearson Canada Assessment Inc, 2010).
7. Benjamini, Y. & Hochberg, Y. Controlling the False Discovery Rate: A Practical and Powerful Approach to Multiple Testing. J. R. Stat. Soc. Ser. B Methodol. 57, 289–300 (1995).

Poster No 1298

Regional cortical thickness growth pattern during early fetal stage

Hyukjin Yun[1], Sungmin You[1], Seungyoon Jeong[1], Pablo Jáquez Vergara[1], Sian Wilson[2], Ellen Grant[1], Kiho Im[1]

[1]Boston Children's Hospital, Boston, MA, [2]King's College London, London, England

Introduction: Fetal brain magnetic resonance imaging (MRI) has been employed to visualize fetal brain growth during pregnancy. The cortical plate (CP) is one of distinguishable tissues in fetal brain MRI which is a transient tissue formed as a result of the migration of neuronal precursors from the germinal matrix and ganglionic eminence, giving rise to the developing cerebral cortex[1]. In an ex vivo fetal MRI study, the CP thickness showed a small change (< 1 mm) between 15 and 40 weeks of gestational age (GA), however, it varied significantly across cortical regions[2]. The regionally different growth of the CP thickness may be related to rapid growth and regional expansion of functional areas under genetic controls[3,4]. Investigating regionally different growth pattern of the CP thickness in living fetuses may provide more regional information of functional development in human brain development. In this study, we measured the CP thickness using multi-site fetal brain MRI data and quantify regionally growth rates of the CP thickness.

Methods: The study was approved by the local Institutional Review Board at Boston Children's Hospital (BCH) and by the Ethics Committee of Hospital Clínic Barcelona, Spain (HCB/2020/0267). A total of 28 typically developing (TD) fetuses (GA: 27.6 ± 3.5 [mean ± standard deviation]) were included in this study (twenty from BCH and eight from developing Human Connectome Project (dHCP, https://www.developingconnectome.org/project/)). Multiplanar MRI stacks of thick 2D slices from BCH and dHCP data were acquired using T2-weighted Half-Fourier Acquisition Single-Shot Turbo Spin-Echo and Single-shot fast spin-echo sequences, respectively. After motion correction of MRI stacks[5,6], we performed CP segmentation[7] and extracted the inner CP surface using Marching cube algorithm[8]. The outer CP surfaces was expanded from the inner surface using a topology-preserving deformation technique[9,10]. Based on vertex-wise correspondence between the inner and outer surfaces we estimated cortical thickness by distance between the corresponding vertices[11]. For inter-subject vertex correspondence, we aligned the surfaces to 29 GW template surface[12]. On the template surface, we manually 21 parcellated cortical regions (Figure 1A) based on the Freesurfer Desikan atlas[13]. Then the regional linear growth rates were calculated by fitting a line to the average thickness and GA.

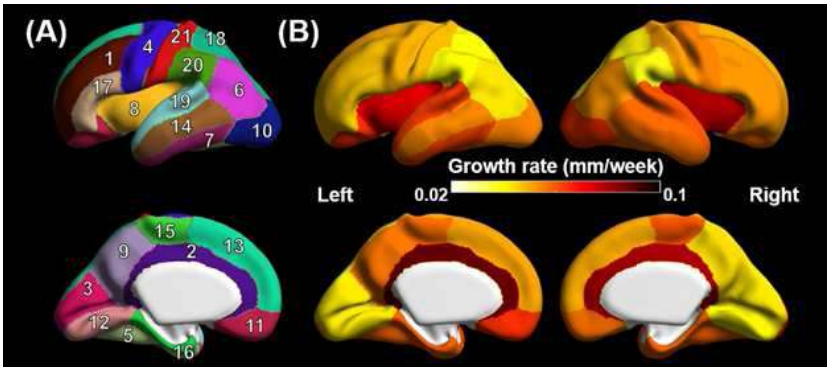

Figure 1. Cortical regions defined in a template brain (A) and regional growth rates of cortical plate thickness (B). Anatomical lables: 1. middle frontal, 2. cingulate cortex, 3. cuneus, 4. precentral, 5. fusiform, 6. inferior parietal, 7. inferior temporal, 8. insula, 9. precuneus, 10. lateral occipital, 11. orbital frontal, 12. lingual, 13. superior frontal, 14. middle temporal, 15. paracentral, 16. parahippocampal, 17. inferior frontal, 18. superior parietal, 19. superior temporal, 20. supramarginal, 21. postcentral.

Results: All the regions showed small growth rates (< 0.1mm/week) but the rates were regionally diverse (Table 1). Among the regions, bilateral cingulate cortex and insular showed high growth rate (> 0.7 mm/week) (Figure 1B). Superior and inferior temporal cortices also showed relatively high growth rate (> 0.6mm/week). In contrast, the regions belonging to parietal and occipital lobes showed relatively low growth rate (< 0.45mm/week).

Table 1. Regional growth rates of cortical plate thickness and R-squared values.

Region	Left		Right	
	Growth rate (mm/week)	R-squared	Growth rate (mm/week)	R-squared
Middle frontal	0.0473	0.5285	0.0521	0.6493
Cingulate cortex	0.0880	0.8136	0.0801	0.8121
Cuneus	0.0424	0.4158	0.0426	0.4376
Precentral	0.0494	0.5337	0.0546	0.6191
Fusiform	0.0578	0.5846	0.0580	0.4861
Inferior parietal	0.0429	0.4447	0.0523	0.5225
Inferior temporal	0.0619	0.6917	0.0564	0.5615
Insula	0.0737	0.6475	0.0795	0.6946
Precuneus	0.0561	0.5315	0.0439	0.4668
Lateral occipital	0.0542	0.5652	0.0642	0.6548
Orbital frontal	0.0644	0.7630	0.0566	0.7452
Lingual	0.0424	0.3714	0.0409	0.3783
Superior frontal	0.0503	0.5554	0.0496	0.5945
Middle temporal	0.0539	0.6495	0.0572	0.6887
Paracentral	0.0569	0.5404	0.0599	0.6754
Parahippocampal	0.0585	0.5668	0.0579	0.5964
Inferior frontal	0.0462	0.6017	0.0521	0.6523
Superior parietal	0.0394	0.2873	0.0418	0.3206
Superior temporal	0.0630	0.7337	0.0597	0.7292
Supramarginal	0.0401	0.4660	0.0387	0.3860
Postcentral	0.0478	0.4871	0.0511	0.4970

Conclusions: This study presented regional growth rates of the CP thickness in the TD fetuses. We observed high thickness growth rates in the central region compared to the peripheral regions. The age-related growth patterns of the CP thickness are similar to gyrification. In our previous studies, we found that early cortical folding emerged in the central regions and proceeded in the temporo-parieto-occipital lobes, and then the frontal lobe[12,14]. This regional pattern of growth rates may reflect the phylogenic and functional localization of the cerebral cortex. The phylogenetically older allocortex cortical regions such as the anterior insular cortex mature earlier than the newer cortical regions[15,16]. Therefore, the diverse growth rates of CP thickness during early fetal life may agree with regionally relevant indices in functional development in the human brain. The findings in this study may be used in the future investigations to reveal the relationship between CP thickness and functional development with a large sample of fetal brain MRI in wide GA range.

References

1. I. Kostović (2007), Transient patterns of cortical lamination during prenatal life: Do they have implications for treatment?, Neuroscience & Biobehavioral Reviews. 31 1157–1168.
2. L. Vasung (2016), Quantitative and Qualitative Analysis of Transient Fetal Compartments during Prenatal Human Brain Development, Frontiers in Neuroanatomy. 10 11.
3. L. Ronan (2015), From genes to folds: a review of cortical gyrification theory, Brain Structure and Function. 220 2475–2483.
4. W. Welker (1990), Why Does Cerebral Cortex Fissure and Fold?, in: Cerebral Cortex, Springer, Boston, MA, : pp. 3–136.
5. M. Kuklisova-Murgasova (2012), Reconstruction of fetal brain MRI with intensity matching and complete outlier removal, Med Image Anal.
6. A. Makropoulos (2018), The developing human connectome project: A minimal processing pipeline for neonatal cortical surface reconstruction, NeuroImage. 173 88–112.
7. J. Hong (2020), Fetal Cortical Plate Segmentation Using Fully Convolutional Networks With Multiple Plane Aggregation, Frontiers in Neuroscience. 14.
8. C. Lepage (2017), Human MR evaluation of cortical thickness using CIVET v2. 1, Organization for Human Brain Mapping.
9. J.S. Kim (2005), Automated 3-D extraction and evaluation of the inner and outer cortical surfaces using a Laplacian map and partial volume effect classification, NeuroImage. 27 210–221.
10. M. Liu (2021), Robust Cortical Thickness Morphometry of Neonatal Brain and Systematic Evaluation Using Multi-Site MRI Datasets, Frontiers in Neuroscience. 15.
11. S. Robbins (2004), Tuning and comparing spatial normalization methods, Med Image Anal. 8 311–323.
12. H.J. Yun (2020), Temporal Patterns of Emergence and Spatial Distribution of Sulcal Pits During Fetal Life, Cereb Cortex. 30 4257–4268.
13. R.S. Desikan (2006), An automated labeling system for subdividing the human cerebral cortex on MRI scans into gyral based regions of interest, NeuroImage. 31 968–980.
14. H.J. Yun (2022), Quantification of sulcal emergence timing and its variability in early fetal life: Hemispheric asymmetry and sex difference, NeuroImage. 263 119629.
15. N. Gogtay (2004), Dynamic mapping of human cortical development during childhood through early adulthood, Proceedings of the National Academy of Sciences. 101 8174–8179.
16. J.L.R. Rubenstein (1999), Genetic Control of Cortical Development, Cereb Cortex. 9 521–523.

Poster No 1299

Preschool-age sensorimotor network segregation supports motor and cognitive maturation in childhood

Xing Qian[1], Marcus Qin Wen Ong[1], Jia Ming Lau[1], Shayne Siok Peng Yeo[2], Zhen Ming Ngoh[2], Ai Peng Tan[3], Peter D. Gluckman[4], Evelyn Chung Ning Law[2], Juan Helen Zhou[1]

[1]National University of Singapore, Singapore, Singapore, [2]Singapore Institute for Clinical Sciences, Agency for Science, Technology and Research in Singapore, Singapore, Singapore, [3]National University Hospital, Singapore, Singapore, [4]Liggins Institute, University of Auckland, Auckland, New Zealand

Introduction: The human brain undergoes early maturation of primary sensorimotor regions and more protracted development of high-order association regions, generally paralleling motor and cognitive milestones[1]. Research finds that preadolescent children with more physical activity (PA) show more efficient patterns of brain activity and superior cognitive performance[2], supporting Piaget's postulation that sensorimotor system provides necessary foundations upon which higher-order cognition is built[3]. In childhood, brain functional networks became increasingly segregated with increased age, which was suggested to support vast improvements in executive function (EF)[4]. However, little is known on the longitudinal changes of functional segregation and their associations with EF and PA, particularly in preschool children. We aimed to study this gap in children from 4.5 to 10.5 years old (YO) using longitudinal GUSTO dataset[5]. We expected differential system-specific trajectories of the network segregation and hypothesized that earlier sensorimotor network segregation would play a dominant role in the behavioral prediction.

Methods: We studied 574 children who had at least one timepoint brain images of good quality, including 157, 211, 400 and 380 children at the visits of 4.5, 6, 7.5 and 10.5 YO respectively. The average daily time of moderate to vigorous physical activities (MVPA) was measured at 5.5, 8 and 10 YO[6]. To assess EF, the BRIEF[7] were administered at 4.5, 7 and 8.5 YO, and the D-KEFS[8] was administered at 10.5 YO. To calculate functional connectivity (FC), region-of-interest (ROI) time series were extracted from resting state fMRI data using a 144-ROI parcellation[9]. We performed a 2-stage consensus community detection on FC matrices to derive the individual- and group-level network community structures[10]. To characterize the network segregation of each child at each visit, we calculated the modularity, and the global and system/module level system segregation (SS) and participation coefficient (PC)[11]. We examined the longitudinal changes of these measures using linear mixed effect model and the associations with EF, MVPA and future brain measures.

Results: We observed the sensorimotor modules (i.e., visual and somatomotor) were already detected at younger ages (i.e., 4.5 and 6 YO), while the higher-order cognitive modules (i.e., salience/ventral attention [S/VA] and control) were formed at older ages (i.e., 7.5 and 10.5 YO) (Fig 1A). Whole-brain functional network segregation was increased longitudinally represented by higher modularity/SS and lower PC (Fig 1B). When navigating at different system types, the SS of both sensorimotor and association systems was increased, indicating increased functional system differentiation across the sensorimotor-association axis (Fig 1C). At the module level, all the cortical modules showed declined PC over time. The default mode (DM) module showed increased SS over time, while the visual/dorsal attention A (VS+DAA) module showed decreased SS (Fig 1D), indicating more integration with other modules over time. Moreover, girls showed higher functional segregation, i.e., lower PC in the DM, control, S/VA-B and SC modules and higher SS in association system than boys. More segregation of sensorimotor systems at earlier ages dominantly predicted better EF and longer MVPA (both cross-sectionally and future) (Fig 2, A&B). In contrast, as the children grew up, this role was predominantly replaced by the association systems (Fig 2, C&D). Moreover, preschool children with more segregation in the sensorimotor system at early ages (i.e., 4.5 to 6 YO) had more segregation in the association system in middle or late childhood (i.e., 7.5 to 10.5 YO) (Fig 2, E&F).

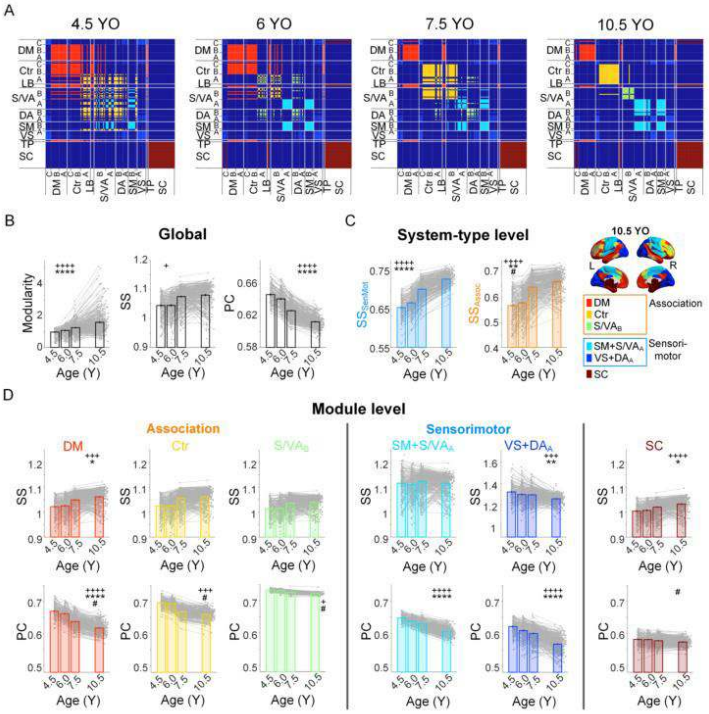

Figure 1. Changes of brain modular structure and segregation during development. A. Sensorimotor modules segregated earlier than association modules during development. The edges connecting nodes in the same community are highlighted using the same color. The sensorimotor communities, i.e., visual (blue) and somatomotor (cyan), and the subcortical community could already be detected at younger ages (i.e., 4.5 YO and 6 YO), while the higher-order cognitive communities (i.e., the salience and control) were formed at older ages (i.e., 7.5 YO and 10.5 YO). **B.** Whole-brain functional network segregation measured by modularity, system segregation (SS) and participation coefficient (PC) increased longitudinally. **C.** The segregation of both sensorimotor and association systems was increased longitudinally and cross-sectionally. **D.** At module level, all the modules except for subcortical module showed declined mean PC over time. The DM and subcortical modules showed increased SS over time while the VS+DAA module showed decreased SS over time. Girls showed significantly lower PC in DM, Ctr, S/VAB and Sc modules and higher SS of association system than boys during the development. The bar charts with error bars represent the mean and standard error values. The sign '+' represents a significant time effect. The sign '*' represents a significant age effect. The sign '#' represents a significant gender effect. Four signs represent $p < 0.0001$, three signs represent $p < 0.001$, two signs represent $p < 0.005$, and one sign represents $p < 0.05$. For module and system type level p-values, we performed FDR correction for multiple comparison correction. Abbreviations: SM = Somatomotor; S/VA = Salience/Ventral Attention; Vs = Visual; DA = Dorsal Attention; Ctr = Control; DM = Default Mode; Sc = Subcortical; SS = system segregation; PC = participation coefficient.

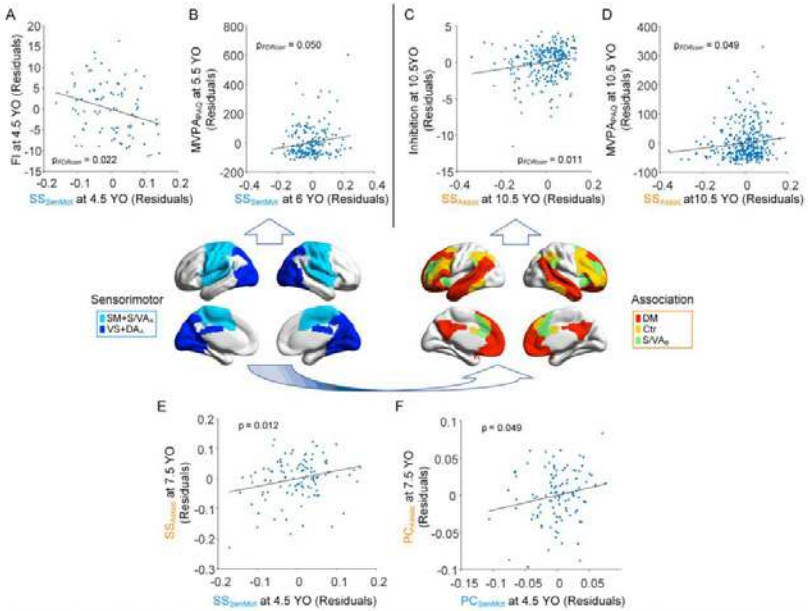

Figure 2. Differential behavior associations of the sensorimotor and association system segregation from preschool to late childhood. A & B. Sensorimotor in preschool age. Higher system segregation (SS) of sensorimotor system was associated with lower risk of flexibility dysfunction at 4.5 YO (A). Higher SS of sensorimotor system at 6 YO was associated with longer time spent on MVPA at 5.5 YO (B). **C & D. Association in late childhood.** Higher SS of association system was associated with better inhibition and longer time spent on MVPA and at 10.5 YO. **E & F.** Higher SS and lower participation coefficient (PC) of sensorimotor system at 4.5 YO predicted higher SS and lower PC of association system at 7.5 YO, respectively. Abbreviations: MVPA= moderate to vigorous physical activities. FI = Flexibility Index. SS = system segregation. PC = participation coefficient.

Conclusions: Our study provides novel evidence characterizing the differential longitudinal maturation of brain sensorimotor and association network segregation, which underscore the important role of sensorimotor system to future motor and cognitive development across the childhood.

References
1. Gogtay N, et al. Dynamic mapping of human cortical development during childhood through early adulthood. Proceedings of the National Academy of Sciences 101, 8174-8179 (2004).
2. Erickson KI, Hillman CH, Kramer AF. Physical activity, brain, and cognition. Current opinion in behavioral sciences 4, 27-32 (2015).
3. Piaget J. The construction of reality in the child. Routledge (2013).
4. Baum GL, et al. Modular segregation of structural brain networks supports the development of executive function in youth. Current Biology 27, 1561-1572. e1568 (2017).
5. Nguyen TT, et al. Variations in Cortical Functional Gradients Relate to Dimensions of Psychopathology in Preschool Children. Journal of the American Academy of Child & Adolescent Psychiatry, (2023).
6. Dwyer GM, Hardy LL, Peat JK, Baur LA. The validity and reliability of a home environment preschool-age physical activity questionnaire (Pre-PAQ). International Journal of Behavioral Nutrition and Physical Activity 8, 1-13 (2011).
7. Gioia GA, Andrwes K, Isquith PK. Behavior rating inventory of executive function-preschool version (BRIEF-P). Psychological Assessment Resources Odessa, FL (1996).
8. Lippa SM, Davis RN. Inhibition/switching is not necessarily harder than inhibition: An analysis of the D-KEFS color-word interference test. Archives of Clinical Neuropsychology 25, 146-152 (2010).
9. Yeo BT, et al. The organization of the human cerebral cortex estimated by intrinsic functional connectivity. Journal of neurophysiology, (2011).
10. Braun U, et al. Dynamic reconfiguration of frontal brain networks during executive cognition in humans. Proceedings of the National Academy of Sciences 112, 11678-11683 (2015).
11. Chan MY, Park DC, Savalia NK, Petersen SE, Wig GS. Decreased segregation of brain systems across the healthy adult lifespan. Proceedings of the National Academy of Sciences 111, E4997-E5006 (2014).

Poster No 1300

Ultra-high field quantitative susceptibility mapping of the neonatal brain

Chiara Casella[1,2], Katy Vecchiato[1,2], Ayse Sila Dokumaci[3], Philippa Bridgen[4,5], Beya Bonse[1,5], Pierluigi Di Cio[4,5], Joseph Hajnal[1,3,4], Sharon Giles[3,4], Jucha Willers Moore[1,6], Jan Sedlacik[4,7,8], Wilkinson Thomas[3], Raphael Tomi-Tricot[3,9], David Carmichael[3], Jonathan O'Muircheartaigh[1,2,6], Tomoki Arichi[1,5,6], Shaihan Malik[1,3,4]

[1]Centre for the Developing Brain, King's College London, London, United Kingdom, [2]Institute of Psychiatry, Psychology and Neuroscience, King's College London, London, United Kingdom, [3]Biomedical Engineering Department, King's College London, London, United Kingdom, [4]London Collaborative Ultra high field System (LoCUS), London, United Kingdom, [5]Guys and St Thomas' NHS Foundation Trust, London, United Kingdom, [6]MRC Centre for Neurodevelopmental Disorders, London, United Kingdom, [7]Mansfield Centre for Innovation, Imaging Sciences, Institute of Clinical Sciences, Imperial College, London, United Kingdom, [8]Robert Steiner MR Unit, MRC Laboratory of Medical Sciences, Hammersmith Hospital, London, United Kingdom, [9]MR Research Collaborations, Siemens Healthcare Limited, London, United Kingdom

Introduction: Iron is essential for healthy brain development[1], but its non-invasive quantification in early life is extremely challenging. 7T MRI provides enhanced SNR, resolution, and susceptibility effects, which can greatly enhance the ability to image brain iron. Specifically, 7T quantitative susceptibility mapping (QSM)[2] affords uniquely high sensitivity for detecting subtle variations in brain iron deposition, but has never been used to study the newborn brain. Here, we explore the feasibility and sensitivity of 7T QSM for assessing brain iron in the first weeks after birth.

Methods: Subjects and data acquisition: 5 neonates (median age: 39.7 weeks postmenstrual age (PMA), range: 37-41.28) were imaged in natural sleep at 7T (MAGNETOM Terra, Siemens Healthineers) with 2D T2w acquisitions for anatomical information (axial, sagittal, coronal: 0.6x0.6x1.2mm resolution, TR=8640ms, TE=156ms, flip angle=120°) and a 3D T2*w GRE sequence for QSM (0.7mm isotropic, TR=32.2ms, flip angle= 15°, 6 TEs, TE1=2.92ms, echo spacing=5.19ms). For comparison, 11 children (mean age: 11.9 years, range: 8-14) were imaged on the same scanner with 3D MP2RAGE 3 (0.65mm isotropic, TE/TR=3.15/4000ms,TIs=650/2280ms), 3D FLAIR (0.8mm isotropic, TE/TR=240/9000ms,TI=2600ms), and 3D T2*w GRE sequences (0.7mm isotropic, TR=29ms, flip angle=15.5°, 6 TEs, TE1=2.68ms, echo spacing=4.69ms). QSM reconstruction: Combination of complex data and QSM computation were carried out using the approaches outlined in[4]. Image registration and tissues segmentation: Neonates: T2w images were non-linearly registered to a 37 week PMA template[5] . Magnitude images were rigidly co-registered to the corresponding T2w volume. QSM normalization to the template was achieved through composition of the above transformations. Tissue segmentations and surfaces were generated in template space using the developing Human Connectome Project (HCP) pipeline[6]. Children: Magnitude images were rigidly co-registered to the corresponding MP2RAGE volume, and QSM normalization was achieved through the composition of the above transformations. FLAIR and T1w images were analyzed with the HCP pipeline[7] to perform tissue segmentation and surface reconstruction in native space. Analysis: Susceptibility (χ) was examined in caudate, lentiform nucleus, corpus callosum (CC) and lateral ventricles. Additionally, χ was sampled along the grey/white matter (GM/WM) boundary.

Results: The susceptibility contrast between GM and WM in neonates is low. χ in GM nuclei is negative in neonates and positive in children, where clearer structural boundaries are observed, reflecting greater iron deposition. χ is negative in the CC of neonates, underscoring a significant effect of diamagnetic myelin on WM susceptibility even in the initial weeks after birth. In children, χ in the CC is more negative, reflecting increased myelination. χ in ventricles is higher in the neonatal brain. This finding is consistent with previous 3T evidence[8] and is possibly due to the higher content of iron-containing neutrophils in the newborn brain[9]. Positive χ values are observed in posterior auditory and visual cortical areas in neonates, while in children positive χ values are more widespread, consistent with a high iron layer in the deeper cortex corresponding to underlying myeloarchitecture[10], and with a posterior to anterior pattern of myelination in neurodevelopment.

Conclusions: We demonstrate the feasibility of QSM of the neonatal brain at 7T and show that it can detect regional variations in tissue composition through different stages of brain development. These findings implicate the huge potential of this approach for providing novel insights into neurodevelopment and for improving understanding of iron-related tissue damage in the initial months after birth, as well as its association with prognosis.

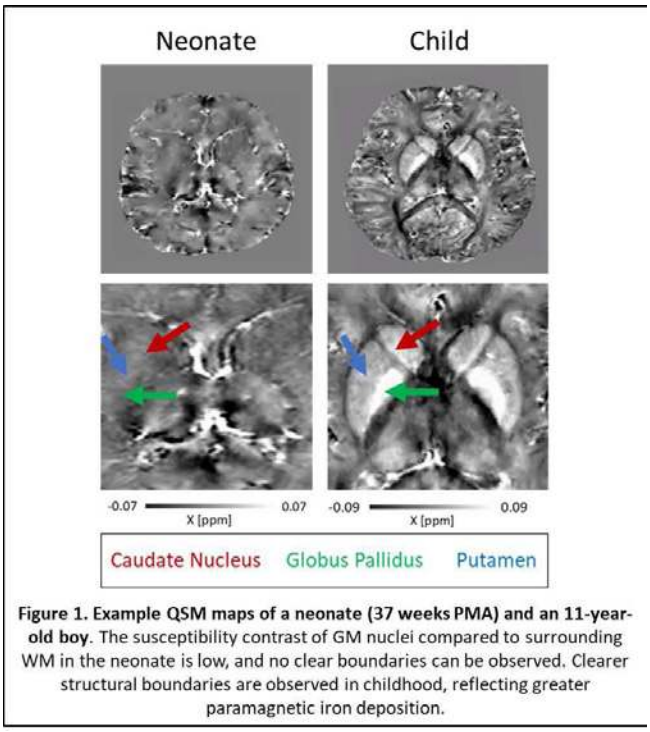

Figure 1. Example QSM maps of a neonate (37 weeks PMA) and an 11-year-old boy. The susceptibility contrast of GM nuclei compared to surrounding WM in the neonate is low, and no clear boundaries can be observed. Clearer structural boundaries are observed in childhood, reflecting greater paramagnetic iron deposition.

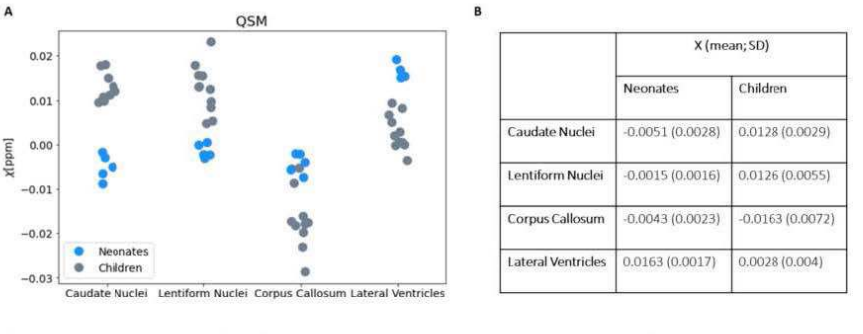

Figure 2. Exploration of susceptibility values in neonates and children. Mean and standard deviation values across Caudate Nuclei, Lentiform Nuclei, Corpus Callosum and Lateral Ventricles are plotted in (A) and listed in (B). In (C) the distribution of mean χ values across the GM/WM boundary are displayed for neonates and children.

References
1. Lozoff, B. Iron deficiency and child development. Food and nutrition bulletin 28, S560–S571 (2007).
2. Liu, C. et al. Quantitative Susceptibility Mapping: Contrast Mechanisms and Clinical Applications. Tomography 1, 3–17 (2015).
3. Dokumacı, A. S. et al. Simultaneous Optimization of MP2RAGE T1-weighted (UNI) and FLuid And White matter Suppression (FLAWS) brain images at 7T using Extended Phase Graph (EPG) Simulations. Magnetic Resonance in Medicine 89, 937–950 (2023).
4. Chari, A. et al. Epileptogenic Tubers Are Associated with Increased Kurtosis of Susceptibility Values: A Combined Quantitative Susceptibility Mapping and Stereoelectroencephalography Pilot Study. American Journal of Neuroradiology 44, 974–982 (2023).
5. Makropoulos, A. et al. Regional growth and atlasing of the developing human brain. Neuroimage 125, 456–478 (2016).
6. Makropoulos, A. et al. The developing human connectome project: A minimal processing pipeline for neonatal cortical surface reconstruction. NeuroImage 173, 88–112 (2018).
7. Glasser, M. F. et al. The minimal preprocessing pipelines for the Human Connectome Project. Neuroimage 80, 105–124 (2013).
8. Zhang, Y. et al. Neonate and Infant brain development from birth to 2 years assessed using MRI-based quantitative susceptibility mapping. Neuroimage 185, 349–360 (2019).
9. Zimmermann, P. & Curtis, N. Normal values for cerebrospinal fluid in neonates: a systematic review. Neonatology 118, 629–638 (2021).
10. Lorio, S. et al. Quantitative MRI susceptibility mapping reveals cortical signatures of changes in iron, calcium and zinc in malformations of cortical development in children with drug-resistant epilepsy. NeuroImage 238, 118102 (2021).

Poster No 1301

Cortical Thickness and Myelination in Preterm and Full-term Infant Brains

Fumitaka Homae[1], Daisuke Tsuzuki[2]

[1]Tokyo Metropolitan University, Tokyo, [2]Kochi University, Kochi

Introduction: The cerebral cortex exhibits a thicker profile at convex regions, such as the crown near the vertices of cortical gyri, compared to concave regions at the fundi of cortical sulci. This tendency has been observed in adults through structural magnetic resonance imaging (MRI) measurements (Fischl & Dale, 2000), neonates, and infants (Holland et al., 2020). The difference between convex and concave regions is also evident in their degree of myelination, as measured by quantitative relaxation rate mapping (Sereno et al., 2013) and in the ratio of T1-weighted (T1w) and T2-weighted (T2w) MRI images (Shafee et al., 2015). Since not all sulci and gyri are fully matured at term, we anticipate that cortical thickness and the degree of myelination will vary based on the morphological changes of the cortical surface during early infancy.

Methods: In this study, we parameterized the local shape of the cortical surface and examined the profiles of cortical thickness in convex and concave regions relative to gestational age. We analyzed infant MRI data from the second release of the Developing Human Connectome Project (Hughes et al., 2017). The dataset included brain images of preterm and full-term infants (N = 401; range of the scans: 37.0–44.7 gestational weeks). Each infant was classified into eight groups based on the scan week, ranging from 37 to 44 weeks. The database provided cortical mesh data reconstructed from structural MRIs. Cortical thickness was defined as the distance between pial and white-matter surfaces (Bozek et al., 2018; Makropoulos et al., 2018). The values of T1w/T2w at each vertex of the surface mesh were also utilized in the analysis. We calculated the principal curvatures at each vertex and determined vertex-wise shape indexes (Koenderink & Van Doorn, 1992). Based on the shape index, vertices were categorized into one of seven morphological definitions: spherical cup, rut, saddle rut, saddle, saddle ridge, ridge, and dome (Vezzetti & Marcolin, 2012). The spherical cup and dome categories predominantly appeared in the sulcal fundi and gyrus crowns, respectively. For each infant, we obtained the mean values of cortical thickness and T1w/T2w across vertices within each morphological category.

Results: The cortical thickness and T1w/T2w values increased with gestational weeks. At 44 weeks, the cortical thickness increased gradually from the spherical cup regions (lowest) to the dome regions (highest thickness). However, in full-term infants younger than 39 gestational weeks at MRI scanning, the cortical thickness in the dome regions was lower than in the ridge and saddle ridge regions. Furthermore, at around 40 weeks, preterm infants had a thicker cortex than full-term infants. Conversely, the T1w/T2w values showed the opposite trend; the values were higher in full-term infants than in preterm infants. In both infant groups, the spherical cup regions exhibited the lowest T1w/T2w values.

Conclusions: These results suggest that the cortical thickness changes with the formation of cortical sulci and gyri and that its distribution depends on the gestational age at birth. Furthermore, the differences between the infant groups suggest that the cerebral cortex in preterm infants at approximately 40 gestational weeks contained relatively large amounts of astrocytes and extracellular matrix.

References
1. Bozek, J. (2018). Construction of a neonatal cortical surface atlas using Multimodal Surface Matching in the Developing Human Connectome Project. Neuroimage, 179, 11-29.
2. Fischl, B. (2000). Measuring the thickness of the human cerebral cortex from magnetic resonance images. Proc Natl Acad Sci U S A, 97(20), 11050-11055.

3. Holland, M. A. (2020). Folding drives cortical thickness variations. Eur Phys J Spec Top, 229(17-18), 2757-2778.
4. Hughes, E. J. (2017). A dedicated neonatal brain imaging system. Magn Reson Med, 78(2), 794-804.
5. Koenderink, J. J. (1992). Surface shape and curvature scales. Image and vision computing, 10(8), 557-564.
6. Makropoulos, A. (2018). The developing human connectome project: A minimal processing pipeline for neonatal cortical surface reconstruction. Neuroimage, 173, 88-112.
7. Sereno, M. I. (2013). Mapping the human cortical surface by combining quantitative T(1) with retinotopy. Cereb Cortex, 23(9), 2261-2268.
8. Shafee, R. (2015). Gray matter myelination of 1555 human brains using partial volume corrected MRI images. Neuroimage, 105, 473-485.
9. Vezzetti, E. (2012). Geometry-based 3D face morphology analysis: soft-tissue landmark formalization. Multimedia Tools and Applications, 68(3), 895-929.

Poster No 1302

Resting-state neural activity and brain structure associations in infants and children

James Edgar[1], Heather Green[1], Kylie Mol[1], Marybeth McNamee[1], Mina Kim[1], Yuhan Chen[1]

[1]*Children's Hospital of Philadelphia, Philadelphia, PA*

Introduction: Many electrophysiology studies have reported on resting-state (RS) neural activity in humans. This research often focuses on RS alpha-band activity (8-12 Hz in adults), with RS alpha activity commonly interpreted as reflecting the brain's readiness to process information (Klimesch et al., 2007), predicting task performance and processing speed (Klimesch, 1999), and being integral to local- and long-range functional connectivity (Osipova et al., 2008). Infant RS studies seek to understand the maturation of RS neural processes, with the first two years of life a period of rapid neural development. This line of research is constrained by difficulty obtaining prototypical high signal-to-noise ratio (SNR) eyes-closed RS electrophysiology measures in infants and toddlers, with almost all infant studies obtaining RS measures while infants view visual stimuli, and with an eyes-open condition not generating a robust infant 'alpha' response (here referred to as the 'dominant oscillation' response; (Edgar et al., 2023)). In the present study, a RS task optimized for infants was used to examine the maturation of RS activity from 0 to 28 months, with associations between RS neural activity and brain structure also examined.

Methods: Whole-head magnetoencephalography (MEG) data were obtained while infants underwent an eyes-open dark room (DR) RS task (Edgar et al., 2023). The infants rested with eyes open in total darkness for 30s, then viewed the Inscape video for 20 s (Vanderwal et al., 2015), alternating 6 times. 300s of DR data were collected to obtain 180s of video off and 120s of video on data. Following the MEG exam, MRI data were collected on a Siemens Prisma 3T: a T1-weighted magnetization-prepared rapid gradient-echo image, a T2-weighted image, and a diffusion-weighted spin-echo single-shot EPI sequence with opposed phase encoding direction pairs. RS DR activity was examined in brain space using distributed source modeling, with analyses examining periodic and aperiodic activity RS measures (Ostlund et al., 2022) in a parietal-occipital ROI. Parietal-occipital gray matter (cortical thickness) and local diffusion measures (e.g., fractional anisotropy) were obtained to assess associations between RS neural activity and brain structure.

Results: MEG data were obtained from 26 infants (0 to 18 months). As shown in Figure 1a, comparison of the total darkness (black line) and the video-on (red line) power spectrum shows that the infant dominant oscillation was easily identified in the infants/toddlers in the total darkness condition but not the video-on condition (x axis shows frequency and y axis RS power). Figure 1b shows the expected age-related increase in the infant dominant oscillation frequency in the total darkness condition. MEG, T1, and DTI data were obtained from 23 infants. As shown in Figure 2, more mature parietal-occipital gray matter (in infants, less gray-matter cortical thickness) as well as more mature parietal-occipital white matter (in infants, higher fractional anisotropy and lower mean diffusivity) predicted a more mature RS dominant oscillation frequency (higher frequency) as well as more mature aperiodic offset and exponent values (in infants, these values decreasing as a function of age).

Figure 1a

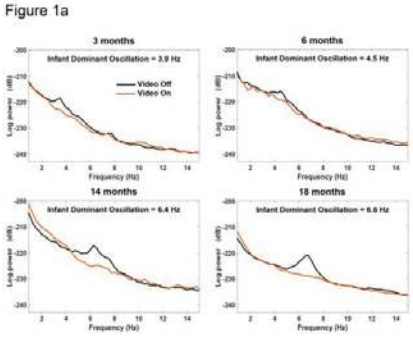

Figure 1b

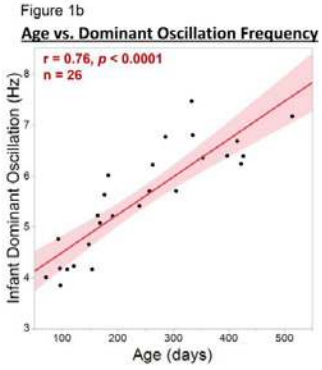

Figure 2

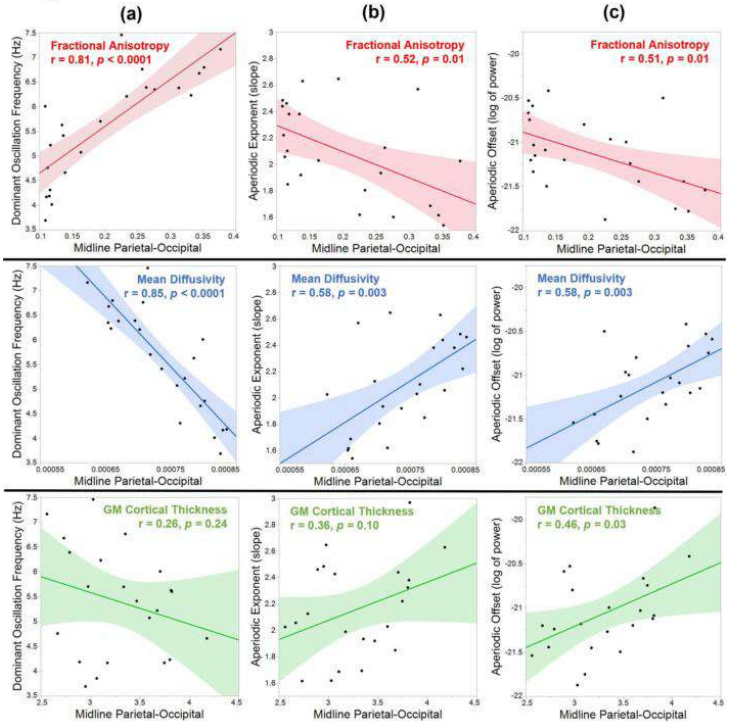

Figure 2 legend: Associations with RS activity are shown for parietal-occipital midline white-matter fractional anisotropy in the top row (red), white-matter radial diffusivity in the middle row (blue), and parietal-occipital gray matter in the bottom row (green). Associations with source-localized RS activity are shown for the periodic dominant oscillation frequency (column a), the aperiodic offset (column b), and the aperiodic exponent (column c). Associations in the opposite direction for fractional anisotropy and mean diffusivity are expected, with infants' fractional anisotropy values increasing and mean diffusivity values decreasing as a function of age. Associations are strong, with regression analyses showing that, combined, these brain structure measures account for 30 to 60% of the variance in the RS measures.

Conclusions: The eyes-open DR task provides RS measures with a high-SNR dominant oscillation response in awake infants, with a periodic dominant oscillation (3 to 8 Hz) observed in all infants (and thus indicating the presence of a 'dominant oscillation' in even young infants), and with a higher frequency dominant oscillation observed in older than younger infants. Present findings build on and extend the few older child and adult studies examining RS neural activity and brain structure association (Edgar et al., 2015; Green et al., 2021; Valdes-Hernandez et al., 2010), with the maturation of parietal-occipital gray and white matter associated with the maturation of periodic as well as aperiodic RS neural activity.

References

1. Edgar, J.C. (2023). A comparison of resting-state eyes-closed and dark-room alpha-band activity in children. Psychophysiology, e14285. doi:10.1111/psyp.14285
2. Edgar, J. C. (2015). Resting-state alpha in autism spectrum disorder and alpha associations with thalamic volume. Journal of Autism and Developmental Disorders, 45(3), 795-804. doi:10.1007/s10803-014-2236-1
3. Green, H. L., (2021). Peak Alpha Frequency and Thalamic Structure in Children with Typical Development and Autism Spectrum Disorder. Journal of Autism and Developmental Disorders, doi:10.1007/s10803-021-04926-9
4. Klimesch, W. (1999). EEG alpha and theta oscillations reflect cognitive and memory performance: a review and analysis. Brain Research Reviews, 29(2-3), 169-195.
5. Klimesch, W. (2007). EEG alpha oscillations: the inhibition-timing hypothesis. Brain Research Reviews, 53(1), 63-88. doi:10.1016/j.brainresrev.2006.06.003
6. Osipova, D., (2008). Gamma power is phase-locked to posterior alpha activity. PLoS One, 3(12), e3990. doi:10.1371/journal.pone.0003990
7. Ostlund, B. (2022). Spectral parameterization for studying neurodevelopment: How and why. Developmental Cognitive Neuroscience, 54, 101073. doi:10.1016/j.dcn.2022.101073
8. Valdes-Hernandez, P. A. (2010). White matter architecture rather than cortical surface area correlates with the EEG alpha rhythm. Neuroimage, 49(3), 2328-2339. doi:10.1016/j.neuroimage.2009.10.030
9. Vanderwal, T. (2015). Inscapes: A movie paradigm to improve compliance in functional magnetic resonance imaging. Neuroimage, 122, 222-232. doi:10.1016/j.neuroimage.2015.07.069

Poster No 1303

Impacts of perinatal factors on white matter outcome at 8 to 10 years by diffusion tensor imaging

Injoong Kim[1,2], Omar Azrak[2], Mark Foster[2], Emil Cornea[2], Sang Kyoon Park[2], Martin Styner[2], John Gilmore[2]

[1]Department of Radiology, Veterans Health Service Medical Center, Seoul, Republic of Korea, [2]Department of Psychiatry, University of North Carolina Chapel Hill, Chapel Hill, NC, United States

Introduction: Postnatal brain development is a complex process that is under active investigation. Diffusion tensor imaging (DTI) can reveal altered white matter microstructure by using the orientation and integrity of white matter tracts. Here, we aimed to investigate how common neonatal indicators of health (birthweight [BW], gestational age [GA], head circumference at birth [HC]) and brain development are related to DTI-based measurement of white matter microstructure in 8 to 10 years old near-term-born children. Recent study (Nivins et al, 2023) showed how these indicators predict brain volume and white matter microstructure in the same age group, with only BW showing predictive power for white matter microstructure via a traditional tract-based spatial statistics (TBSS) analysis. Building on these results, the goal of the current study was to replicate their findings in a separate sample via an alternative, more sensitive DTI analysis framework.

Methods: From the University of North Carolina's Early Brain Development Study (EBDS) database, we selected participants with MRI scans collected within 8 to 10 years of age on a 3T Siemens Tim Trio (b=0[13], 300[8], 700 [32], 2000 [64 unique gradients]; 2x2x2mm resolution) and perinatal clinical information. Ninety-two children born at≥30 weeks' gestation age were included (male, 42 [45%]; median age, 10 [range 8-10.9 years]). A study-specific quality control protocol was applied to all raw DTI data using the dmriprep (Dubos et al, 2023) module in the DMRIPlayground toolkit (https://github.com/NIRALUser/DTIPlayground). A study-specific DTI atlas was created via the dmriatlas module in DMRIPlayground. Fifty-three major white matter tracts were determined in that DTI atlas space via propagation and automated tracking (Ngattai Lam et al, 2018) of the EBDS pediatric DTI atlas (Short et al, 2022). Diffusion tensor metrics (fractional anisotropy [FA], axial diffusivity [AD], radial diffusivity [RD]) were extracted at evenly spaced points (arc lengths) along each fiber tract. Statistical analysis was performed via FADTTS (Zhu et al, 2011), covarying for gender, yielding tract-wise global as well as local p-value maps. For each tract, a multivariate analysis was first performed combining all three DTI metrics, followed by a posthoc analysis for each FA, RD and AD separately.

Results: Among the three factors (BW, GA, HC), BW showed the most widespread significant associations ($p<0.05$) with white matter diffusion metrics globally (28 out of 53 white matter tracts) and locally (see Figure 1). GA (15 out of 53) and HC (16 out of 53) also showed significant associations though with a lower number of tracts affected. Gender was also highly associated with the diffusion metrics globally in most white matter tracts. In the posthoc analysis, we found surprisingly far more correlations for all three perinatal factors with AD and RD than with FA. AD and RD associations with BW, GA and HC were found in 18, 8, 9 and 17, 8, 9 out of 53 white matter tracts, respectively. For FA, 5, 4, 3 out of 53 white matter tracts showed significant associations.

Figure 1. Fiber tract-based analysis results showing significant correlation ($p<0.05$) with Birthweight (a), Gestational age (b), and Head circumference at birth (c) for all major 53 tracts. Red to blue indicates the level of the p values (red = non-significant).

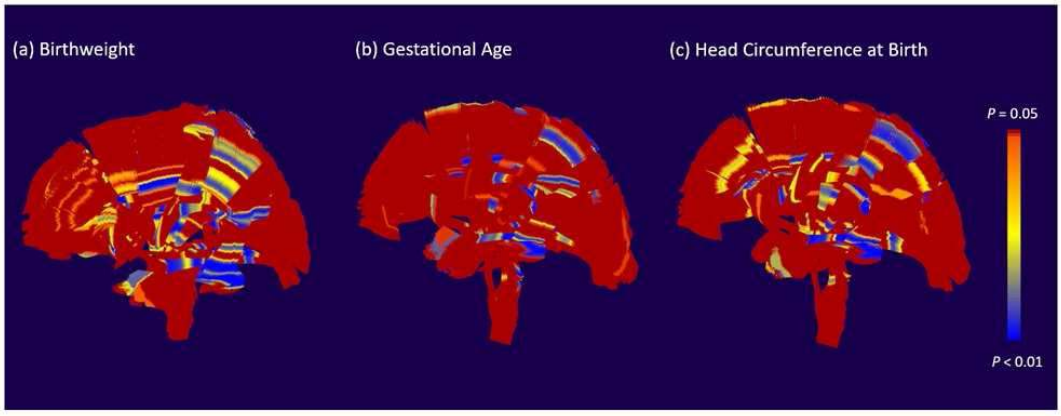

Conclusions: In comparison with previous study (Nivins et al, 2023), we show that neonatal measures of birthweight, gestational age, and head circumference at birth are all significantly predictive of white matter microstructure at age 8-10 years across many fiber tracts, with a focus on central white matter locations. These findings might hold the potential to offer substantial insights into the intricate relationship between perinatal factors and the development of the brain's white matter

during childhood. Please note that the presented analysis is based on a mid-size sample (n=92) scanned on a single 3T scanner. We are currently in the process to extend this study to include all EBDS subjects scanned at the ages of 8-10 years, increasing the sample size to over 300 subjects acquired on 3 different 3T Siemens scanners.

References

1. Dubos, J. (2023). "Dmriprep: open-source diffusion MRI quality control framework with graphical user interface." Proceedings of SPIE- the International Society for Optical Engineering 2023 Feb; 12464: 124643A.
2. Ngattai Lam, P. (2018). "TRAFIC: fiber tract classification using deep learning." Proceedings of SPIE- the International Society for Optical Engineering 2018 Feb; 10574: 1057412.
3. Nivins, S. (2023). "Size at birth predicts later brain volumes." Scientific Reports 2023; 13: 12446.
4. Short, S. J. (2022). "Diffusion Tensor Based White Matter Tract Atlases for Pediatric Populations." Frontiers in Neuroscience 2022; 16: 806268.
5. Zhu, H. (2011). "FADTTS: functional analysis of diffusion tensor tract statistics." Neuroimage 2011 Jun 1; 56(3): 1412–1425.

Poster No 1304

Subtle differences in attentional networks when contrasting very preterm with term-born infants

Florian Fischmeister[1], Nadine Pointner[1], Sophie Weinmüller[1], Alfredo Spagna[2], Galatee Reme[1], Vito Giordano[1], Karin Pichler[1], Gregor Kasprian[1], Kathrin Kollndorfer[1]

[1]Medical University of Vienna, Vienna, Austria, [2]Columbia University, New York, NY

Introduction: Children who are born very preterm (before 33 weeks of gestation) are up to 4 times more likely to be diagnosed with attention deficits compared to their term-born peers. Attention is an essential neuropsychological component that is crucial for effective cognitive functioning. According to the neurocognitive model developed by Posner and Petersen in 1990, attention comprises three distinct neural networks: alerting, orienting, and executive control. These networks develop during infancy and are related to differences in an individual's self-regulation. The efficiency of these attentional networks can be assessed using the Attentional Networks Test (ANT; Fan et al., 2002). In this study, we present initial data that examines these networks and evaluates their efficiency for both term-born and very preterm-born children.

Methods: Nineteen healthy children aged between 5 and 6 years old, consisting of 7 very preterm and 12 term-born controls, underwent a comprehensive assessment, which included clinical, behavioral, and socio-demographic evaluations. The assessment also featured a child-friendly version of the Attentional Network Test for Interaction (ANTI) called ANTI-Birds (Casagrande et al., 2021). The ANTI-Birds task was presented twice, once during the assessment and once while functional magnetic resonance images were acquired using a 3T Prisma MRI (Siemens, Erlangen, Deutschland). Task-based data were analyzed using fMRIPrep (Esteban et al., 2019) with age-specific templates created by Fonov et al. (2011). The first and second levels were modeled with fixed-effects models using FitLinS (Markiewicz et al., 2022).

Results: On a behavioral level, preterm and term-born children performed equally well, with only marginal differences in the Kaufmann Assessment Battery for Children (K-ABC). The results of the fMRI study indicate that all three attention networks can be found consistently across both groups. The alerting network, which represents a change in internal state, involves frontal and parietal regions, particularly of the right hemisphere. Activation associated with the orienting network, which is involved in the selection of information, was found within the frontal eye fields, interior parietal lobe, midbrain, and thalamic regions. The executive control network, representing more complex mental operations like monitoring conflicting information, can be aligned with activated regions along midline frontal areas such as the anterior cingulate cortex, lateral prefrontal cortex, and basal ganglia. Contrary to the behavioral data, a marked difference in a specific network within preterm-born children was observed. While the executive control network revealed increased activation in prefrontal regions, indicating a higher demand for cognitive resources within preterms, the alerting network showed the opposite pattern. Here, a global increase in activation across the whole network was observed.

Conclusions: There is ample evidence that the three aspects of attention - alerting, orienting, and executive control - are anatomically separable in adolescents and adults. However, it is discussed if this is also the case in the developing brain. This study is one of the first to investigate whether these three aspects of attention are independent and linked to separate brain regions in children, both term and preterm. Variations observed across the two groups may indicate differences in processing style and/or developmental levels within the subcomponents of the attention network.

References

1. Casagrande, M., Marotta, A., Martella, D., Volpari, E., Agostini, F., Favieri, F., Forte, G., Rea, M., Ferri, R., Giordano, V., Doricchi, F., & Giovannoli, J. (2021). Assessing the three attentional networks in children from three to six years: A child-friendly version of the Attentional Network Test for Interaction. Behavior Research Methods.

2. Fan, J., McCandliss, B. D., Sommer, T., Raz, A., & Posner, M. I. (2002). Testing the efficiency and independence of attentional networks. Journal of Cognitive Neuroscience, 14(3), 340–347.
3. Fonov V, Evans AC, Botteron K, Almli CR, McKinstry RC, Collins DL, et al. Unbiased average age-appropriate atlases for pediatric studies. Neuroimage. 2011;54(1):313–27.
4. Markiewicz, Christopher J., De La Vega, Alejandro, Wagner, Adina, Halchenko, Yaroslav O., Finc, Karolina, Ciric, Rastko, Goncalves, Mathias, Nielson, Dylan M., Kent, James D., Lee, John A., Bansal, Shashank, Poldrack, Russell A., & Gorgolewski, Krzysztof J. (2022). poldracklab/fitlins: 0.11.0 (0.11.0). Zenodo.
5. Posner, M. I., & Petersen, S. E. (1990). The attention system of the human brain. Annual Review of Neuroscience, 13(1), 25–42.

Poster No 1305

Mapping infant brain functional regionalization with multiview functional cortical parcellation

Tianli Tao[1], Jiawei Huang[1], Xinyi Cai[1], Feihong Liu[1], Rui Zhou[1], Zhuoyang Gu[1], Lianghu Guo[1], Lixuan Zhu[1], Feng Shi[2], Han Zhang[1]

[1]School of Biomedical Engineering, ShanghaiTech University, China, Shanghai, China, [2]Shanghai United Imaging Intelligence Co., Ltd, Shanghai, China, Shanghai, China

Introduction: The human brain demonstrates higher spatial and functional heterogeneity during the first two postnatal years than any other period of life (Johnson, 2000). Understanding the changes in brain function and structure has profound implications for comprehending early brain development. While existing research has provided substantial insights into the development of brain structure, our understanding of the development of cortical functions remains limited. Using advanced infant cortical functional parcellation, we investigate the relationship between functional regionalization and cognitive development. This work aims to address two questions: First, what is the functional hierarchy of brain functional regionalization? Second, what is the relationship between longitudinal functional regionalization and cognitive development?

Methods: A total of 467 scans collected from the Baby Connectome Project (BCP) (Howell, et al., 2019) were included in the current study. These scans comprised paired T1-weighted (T1w) MRI and resting-state fMRI data from 221 infants aged between 2 weeks and 24 months. Infant-based preprocessing procedures were applied to the T1w MRI and resting-state fMRI data. (Li, et al., 2013) We utilized our previously developed multiview functional parcellation with 9 brain subnetworks (Tao, et al., 2023) as the infant brain functional atlas. Consistent with the methodology outlined in the prior study, we calculated the multiview fMRI fingerprint and projected the data onto the individual cortical surface using Freesurfer (Fischl, 2012). Each subject's sphere has been registered to the fsaverage standard sphere, ensuring that corresponding vertices for each individual are aligned at the same location. First, we employed a dendrogram analysis to explore the hierarchical relationships among the 9 subnetworks. Specifically, we utilized the multiview fMRI fingerprint to calculate the pairwise correlations among 9 subnetworks for each scan. Based on these correlations, we constructed a dendrogram to depict the hierarchical organization among the regions. Then, we utilized a linear mixed model to model the correlations between these subnetworks and five standardized Mullen scores (Mullen, 1995), namely Gross Motor (GM), Fine Motor (FM), Visual Reception (VR), Receptive Language (RL), and Expressive Language (EL).

Results: Upon dendrogram analysis, we observed that the 9 subnetworks of the brain could be primarily categorized into three different clusters of functional development: 1) subnetwork 3 (Visual); 2) subnetworks 1, 7, 8 (Dorsal attention, Default mode, Parietal); and 3) subnetworks 2, 4, 5, 6, 9 (Limbic, Somatomotor, Superior temporal Frontal, Inferior temporal) (Fig. 1). This hierarchical organization suggests a prioritization in the functional development of different subnetworks, with a higher priority in the development of visual areas. This implies a more urgent need for visual capabilities during development in infancy. As shown in Fig. 2, we found a significantly negative correlation between the subnetworks 1, 5, 7, 8 and receptive language scores, as well as between subnetworks 3, 9 and visual reception scores. No significant correlation was observed between any other Mullen scores and other subnetworks. Such results suggest that lower regional homogeneity, or higher functional diversity, maybe associated with enhanced information acquisition abilities (such as receptive language and vision) in infants. This finding may reflect the notion that functional differentiation within these specific brain subnetworks contributes to heightened perceptual and language capabilities.

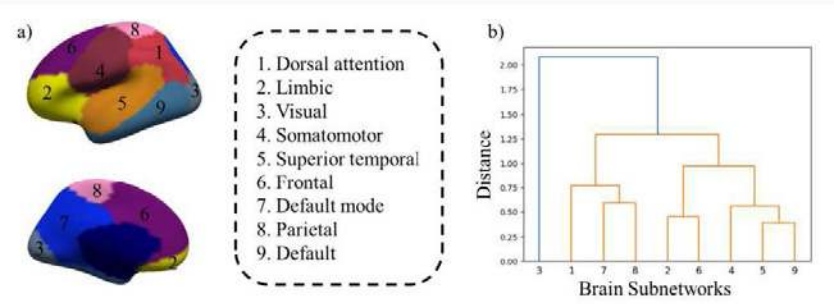

Fig. 1. a) The functional parcellation with 9 subnetworks based on the multiview fMRI fingerprint. b) The dendrogram among the brain subnetworks from BCP.

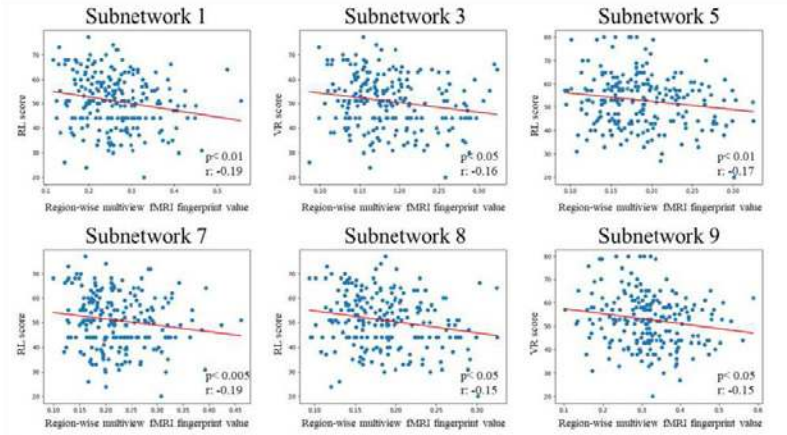

Fig. 2. Negative correlation patterns observed between the region-wise multiview fMRI fingerprint value of subnetworks 1, 5, 7, 8 and receptive language (RL) score, as well as between the region-wise multiview fMRI fingerprint value of subnetworks 3, 9 and visual reception (VR) scores.

Conclusions: Our study reveals a hierarchical organization in the brain functional development and its significant association with receptive language and vision abilities during early development. This suggests that the heterogeneity in functional development may contribute to elevated cognitive levels in infants.

References

1. Johnson, Mark H. (2000), "Functional brain development in infants: Elements of an interactive specialization framework." Child development 71.1: 75-81.
2. Li, Gang, et al. (2013), "Mapping region-specific longitudinal cortical surface expansion from birth to 2 years of age." Cerebral cortex 23.11: 2724-2733.
3. Howell, Brittany R., et al. (2019), "The UNC/UMN Baby Connectome Project (BCP): An overview of the study design and protocol development." NeuroImage 185: 891-905.
4. Tao, Tianli, et al. (2023), "Regionalized Infant Brain Cortical Development Based on Multi-view, High-Level fMRI Fingerprint." International Workshop on Machine Learning in Medical Imaging. Cham: Springer Nature Switzerland.
5. Fischl, Bruce. (2012), "FreeSurfer." Neuroimage 62.2: 774-781.
6. Mullen, Eileen M. (1995), Mullen scales of early learning. Circle Pines, MN: AGS.
7. This work is partially supported by the STI 2030—Major Projects (2022ZD0209000 and 2021ZD0200516), Shanghai Pilot Program for Basic Research—Chinese Academy of Science, Shanghai Branch (JCYJ-SHFY-2022-014), and Shenzhen Science and Technology Program (No. KCXFZ20211020163408012).

Poster No 1306

Developmental Shifts in Neurobehavioral Substrates of Attentional Networks:A Longitudinal fMRI Study

Siya Peng[1], Rui Ding[1], Yuyao Zhao[1], Lei Hao[1], Shaozheng Qin[1]

[1]Beijing Normal University, Beijing, Beijing

Introduction: Human brain undergoes a prolonged maturation process to support nuanced cognitive functions, wherein developmental shifts may occur, giving rise to sensitive periods of development. However, hindered by small sample sizes,

cross-sectional designs, and limited age range distribution, the impact of age maturation on the neurobehavioral substrates of attention networks, and dynamic shifts in these substrates during development, still remain elusive. Utilizing longitudinal data to capture developmental changes in attention can contribute to early clinical detection.

Methods: This study is part of the Beijing Cohort of the Children School Functions and Brain Development Project. A total of 846 scans were completed, spanning over ages 6 to 16, at an interval of one year for three years, with 400, 281, and 165 scans per year. An additional fMRI dataset from 84 healthy young adults (final sample of 73) was used for comparative purposes. Based on the neural specialization perspective, we investigated changes in brain systems involved in three attentional components (i.e., alerting, orienting, and executive attention). The child-friendly version of the Attention Network Test (ANT) developed by Fan et al., (2002) was used. This version includes four cue-prompt conditions and two target-response flanker tasks to measure alerting, orienting, and executive attention processes. In order to investigate the developmental trajectories of behavioral indices for three attentional processes with age, we analyzed behavioral performance in the ANT by calculating the average reaction times (RTs) for different cue and target conditions, and fitted the developmental trajectories using linear mixed-effects (LME) models. In terms of neural activity, we used voxel-based linear mixed-effects models to analyze the interaction between age and behavior during attention using the 3dLMEr in AFNI. We also extracted regions of interest (ROIs) and studied the activation patterns of these regions. Finally, we performed a generalized psychophysiological interaction (gPPI) analysis to explore the functional connectivity patterns that support differences in attentional behaviors.

Results: Behaviorally, the three attention processes-alerting, orienting, and executive control-follow distinct age-related developmental paths, ultimately converging towards adult proficiency, indicative of attentional maturation. The alerting network's efficiency demonstrates an inverted U-shaped trajectory, while the orienting network's efficiency marginally declines, and the executive control network's efficiency consistently enhances with age. Neurally, there is a shifting point from 9 to 10 in age by performance interactions. Specifically, in alerting and orienting networks, an interaction between age and behavioral performance was observed in the activation of the frontal eye fields (FEF) and supplementary motor area (SMA). Younger children show better performance with higher activation, a trend that reverses in older children. Furthermore, children with poorer attention performance relied on functional connectivity between the SMA and other brain regions like the thalamus and precuneus to maintain attention efficiency, a dependency that diminishes with age. Similarly, stronger activation of the right rostrolateral prefrontal cortex (RLPFC) and temporoparietal junction (TPJ), along with higher levels of ventral striatum-dorsomedial prefrontal cortex (VS-dmPFC) functional connectivity, support the development of children with poorer executive attention performance.

Conclusions: Overall, brain regions that facilitate the transition of higher cognitive functions and their co-activation patterns with other cortical/subcortical regions play a central role throughout development. And children with lower executive attention performance demonstrate an increased reliance on the functional connectivity of prefrontal-striatal pathway, indicating impairments related to goal-directed processes.

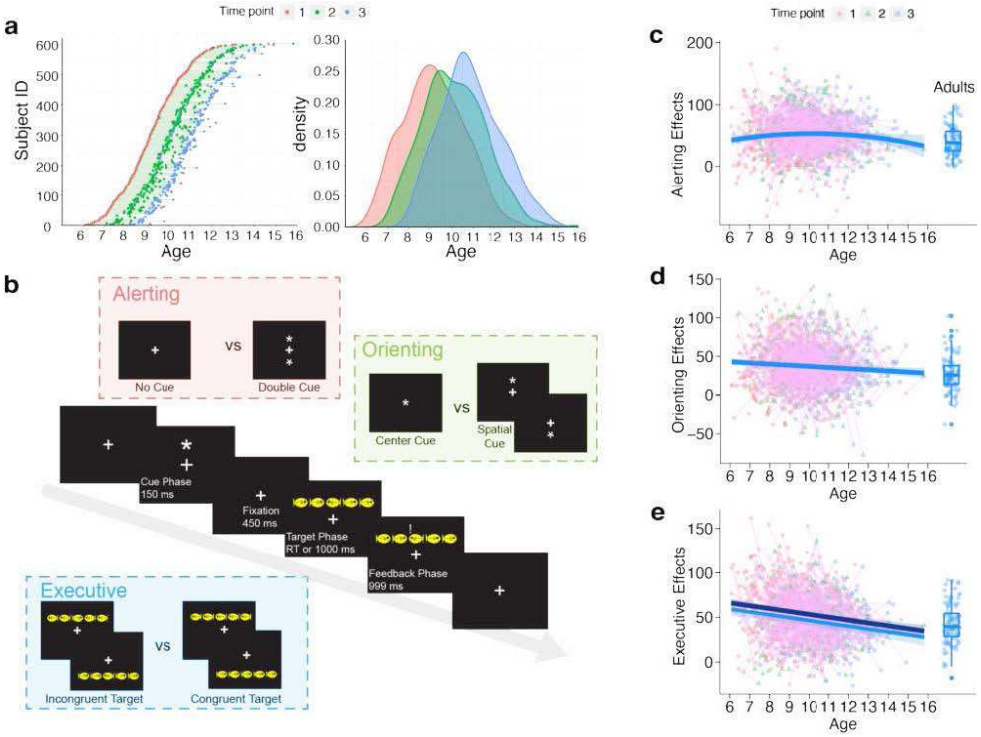

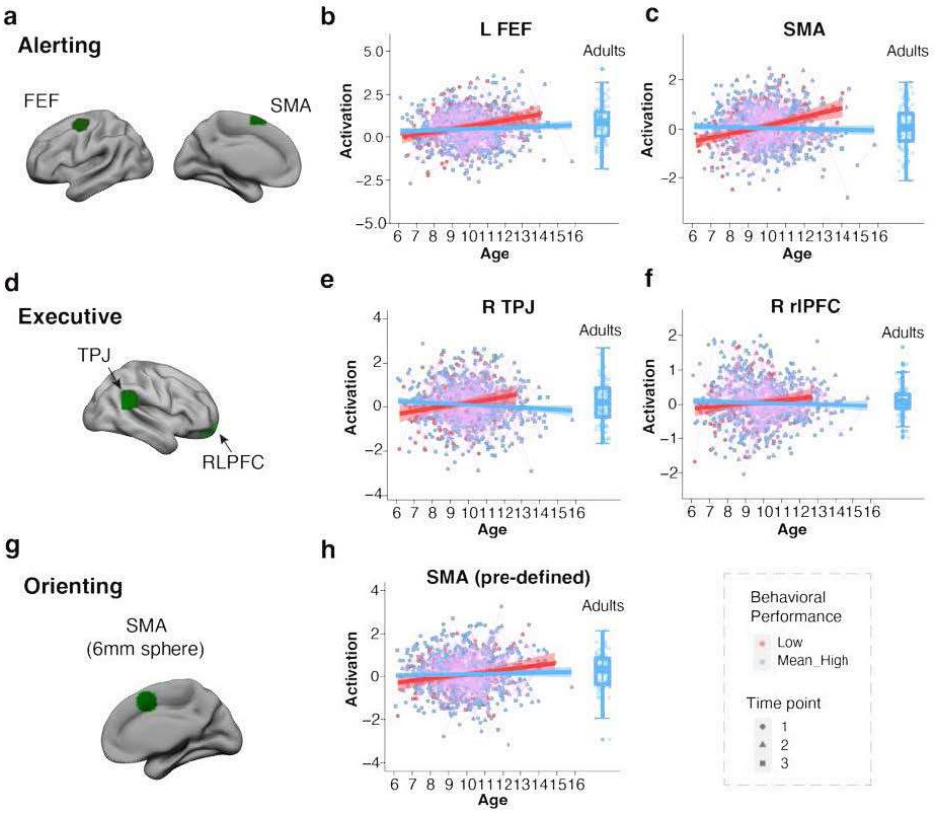

References

1. Chen, G. (2013). Linear mixed-effects modeling approach to FMRI group analysis. NeuroImage, vol. 73, pp. 176–190.
2. Fan, J. (2002). Testing the Efficiency and Independence of Attentional Networks. Journal of Cognitive Neuroscience, vol. 14, no. 3, pp. 340–347.
3. Petersen, S.E., & Posner, M.I. (2012). The Attention System of the Human Brain: 20 Years After. Annual review of neuroscience, vol. 35, pp. 73–89.
4. Raz, A., & Buhle, J. (2006). Typologies of attentional networks. Nature Reviews Neuroscience, vol. 7, no. 5, pp. 367–379.

Poster No 1307

Divergent Developmental Trajectories of Primary and Secondary Brain Sulci in Late Childhood

Yijin Shan[1], Yirong He[2], Debin Zeng[3], Xiaoxi Dong[2], Lei Chu[4], Shuyu Li[5]

[1]Beihang University, Beijing, Beijing, [2]Beijing Normal University, Beijing, Beijing, [3]Beihang university, Beijing, Beijing, [4]Beihang University, Beijing, Beijing, [5]Beijing Normal University, Beijing, China

Introduction: The primary sulcus can be identified after 25th GW, followed by the emergence of the secondary sulcus at the 32nd GW and the tertiary sulcus at the 36th GW (Chi, Dooling, and Gilles 1977). As cortical morphology continues to change during late childhood, there have been relatively few studies of developmental changes in specific sulcal morphology. What are the differences between the developmental patterns of the primary and secondary sulci in late childhood, and are such differences associated with cognition. To explore these questions, we used a widely used sulcus recognition toolbox to investigate the developmental changes of different primary and secondary sulci separately in children aged 6-14 years.

Methods: Subjects The dataset consisted of 312 typically developing children aged 6.1-13.9 years (F/M = 145/167) from the Children School Functions and Brain Development project (CBD, Beijing Cohort). Specifically, 47 children had 3 scans available, 97 children had 2 scans and 168 children had 1 for a total of 490 MRI scans. MRI acquisition The MRI data was acquired utilizing a 3T SIEMENS Prisma scanner(Fan et al. 2021). For every subject, T1-weighted structural images were acquired with the following parameters: TR = 2530 ms, TE = 2.98 ms, inversion time = 1100 ms, FA = 7°, FOV = 256 × 224 mm2, matrix size = 256 × 224, slice thickness = 1 mm, and scan time = 5 min and 58 s. Image analyses All T1w images were processed using FreeSurfer (v5.1), and the outputs were directly imported into the Morphologist toolbox in BrainVISA for sulcus classification and labeling according to predefined anatomical nomenclature (Borne et al. 2020). After filtering out the sulci with extraction success rate less than 75%, we retained the cortical thickness, sulcus width, surface area, maximum

depth, mean depth, and sulcus length in standardized talairach space of a total of 91 sulci in the left and right hemisphere (Fig. 1). Statistics The extracted morphological features were analyzed using a mixed-effects model (MEM), where effects affecting the dependent variable were categorized as either “fixed effects”, such as the effects of age and sex, or “random effects”, such as measurements of the same individual at different time points. After model fitting, the fitted models were selected by Bayesian Information Criterion (BIC). Cognitive Data Acquisition and Analysis Participants’ cognitive performance was assessed using the classic numerical N-back Working Memory Task (WM) and a child-friendly version of the Attention Network Task (ANT) (Hao et al. 2021). To assess the interaction between cognitive scores and sulcus morphology a partial least squares correlation analysis (PLSC) was performed(Krishnan et al. 2011).

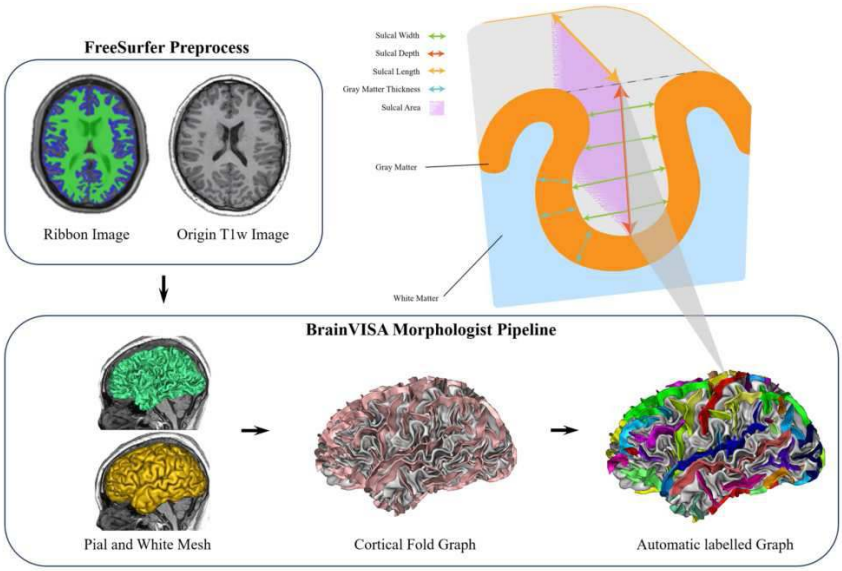

Fig. 1 Flowchart of data processing

Results: Similar to previous studies in late childhood, both primary and secondary sulci showed significant decreases in surface area, mean depth, and cortical thickness, with the primary sulcus showing the most significant changes (Fig. 2). Notably, sulcus width was significantly increased in the secondary sulcus but not in the primary. By plotting the t-values of the significant changes in each sulcus on a colormap at the sulcus level, it can be more intuitively found that the changes in sulcus morphology of the motor-sensory cortex are more obvious. The PLSC results showed that although the morphology of both primary and secondary sulci interacted significantly with cognition, they were associated with different kinds of cognitive abilities.

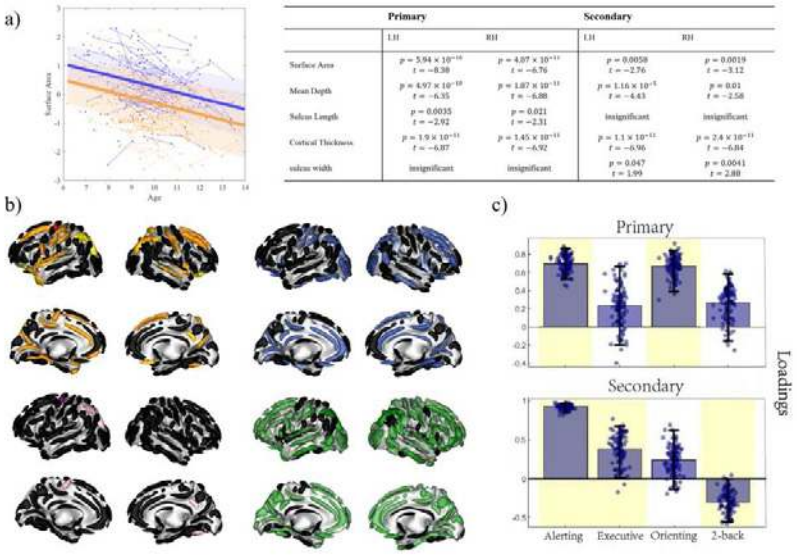

Fig. 2 a) demonstrates the effect of the MEM fit and the changes in each feature of the primary and secondary sulci, b) shows the color shades representing the magnitude of the changes in this sulcus (Yellow: surface area, Blue: mean depth, Rose: sulcus length, Green: sulcus width) c) demonstrates the interactions of the four cognitive metrics with the primary and secondary sulci, with the yellow background representing significance.

Conclusions: The present work uses a extensive sample size to longitudinally and systematically investigate the trajectory of developmental changes across primary and secondary brain sulci in late childhood, suggesting that developmental changes in brain morphology during this period may be associated with different cognitive functions.

References

1. Borne, Léonie, Denis Rivière, Martial Mancip, and Jean-François Mangin. 2020. 'Automatic Labeling of Cortical Sulci Using Patch- or CNN-Based Segmentation Techniques Combined with Bottom-up Geometric Constraints'. Medical Image Analysis 62 (May): 101651.
2. Chi, J. G., E. C. Dooling, and F. H. Gilles. 1977. 'Gyral Development of the Human Brain'. Annals of Neurology 1 (1): 86–93.
3. Fan, Fengmei, Xuhong Liao, Tianyuan Lei, Tengda Zhao, Mingrui Xia, Weiwei Men, Yanpei Wang, et al. 2021. 'Development of the Default-Mode Network during Childhood and Adolescence: A Longitudinal Resting-State fMRI Study'. NeuroImage 226 (February): 117581. https://doi.org/10.1016/j.neuroimage.2020.117581.
4. Hao, Lei, Lei Li, Menglu Chen, Jiahua Xu, Min Jiang, Yanpei Wang, Linhua Jiang, et al. 2021. 'Mapping Domain- and Age-Specific Functional Brain Activity for Children's Cognitive and Affective Development'. Neuroscience Bulletin 37 (6): 763–76.
5. Krishnan, Anjali, Lynne J. Williams, Anthony Randal McIntosh, and Hervé Abdi. 2011. 'Partial Least Squares (PLS) Methods for Neuroimaging: A Tutorial and Review'. NeuroImage 56 (2): 455–75.

Poster No 1308

Aperiodic and Hurst EEG exponents across early human brain development: a systematic review

Ryan Stanyard[1], David Mason[1], Claire Ellis[1], Hannah Dickson[1], Roxanna Short[1], Dafnis Batalle[1], Tomoki Arichi[1]

[1]King's College London, London, United Kingdom

Introduction: Electrophysiological recordings of human brain activity are characterised by a negative power law relationship between frequency (Hz) and spectral power (μV^2). Frequency-power slope exponents (termed β or χ) have been proposed to be of physiological relevance as proxies of neural activity excitation:inhibition (E:I) balance. As alterations in E:I balance may contribute to the pathophysiology underlying neurodevelopmental conditions (e.g. autism), understanding how exponents (1/f^β) evolve across childhood may have key implications for their early assessment and intervention. Common 1/f frequency-based measures include power law exponents (PLE), and aperiodic components (AE) which account for the influence of oscillations on the slope. We explore evidence surrounding the maturation of these exponents as well as their analogue in the temporal domain, the resting Hurst exponent (HE). To synergise the 1/f literature, we convert HE into AE, where AE=2*HE-1. This systematic review aims to characterise how and when 1/f measures change in early typical human development, thereby offering a more nuanced perspective of sensitive periods of neurodevelopment.

Methods: The systematic review was completed according to the PRISMA guidelines and pre-registered with PROSPERO (CRD42023363294). Relevant literature referred to the development/maturation of the 1/f^β signal including the maturation of AE, PLE or HE across the early human lifespan (from birth to young adulthood) as measured using EEG recorded during eyes open or closed rest (EOR, ECR) from typically developing individuals. Searches were performed across Ovid-Embase, Ovid-PsycInfo, Ovid-Medline, Scopus and Web of Science (with appropriate MESH headings and adjacency terms where possible), during March 2023. Risk of bias was assessed using the Quality Assessment for Diverse Studies tool; rater scores (91.07% agreement) were compared to ensure differences of <2 points (0.01%, 6/504 cases), with differing cases discussed, agreed and calibrated. As few studies reported age correlations or effect sizes (N=8) and raw AE effect size interpretation is ambiguous, with no comparison state uniform to all studies, a meta-analysis was not performed. Rather, we qualitatively synthesised findings from infancy-young adulthood across global and regional scales for each method and condition (ECR/EOR).

Results: Forty-two studies were identified containing one or more available 1/f measures (N=3478 participants). Risk of bias analysis showed the performance of included studies was generally strong across all items with scores >2 (scale 0-3). Studies were generally poorer at providing recruitment data, discussing study strengths and limitations and providing clearly defined research aims/hypotheses. Article synthesis revealed that HE consistently exceeded 0.50 throughout early development. Overall, age-related trends were complex (largely owing to large within- and between-study variance), with a rapid decrease in AE during infancy and heterogenous changes thereafter, consistent across methods of calculating AE. AE values in ECR consistently exceeded those in EOR. Regionally, AE maxima shifted topologically during development, from posterior to frontocentral.

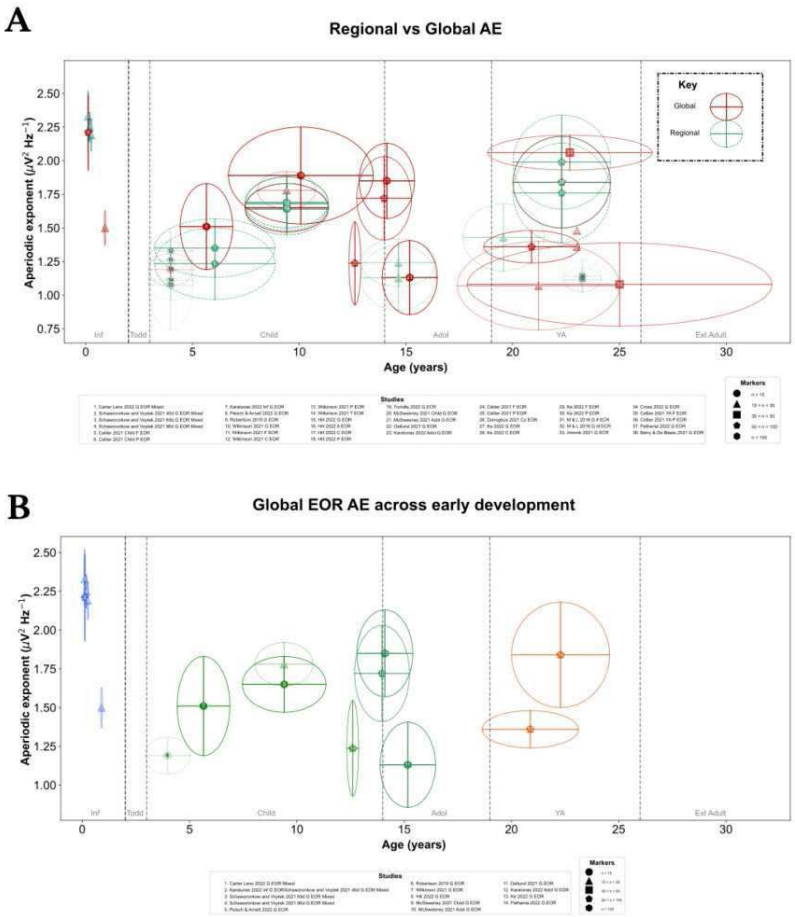

Fig. Consistency of the (a) global aperiodic exponent across global (solid lines) and regional (dotted lines) scales and (b) the global trend of eyes-open rest AE. Colour alpha: sample size, whiskers: SD.

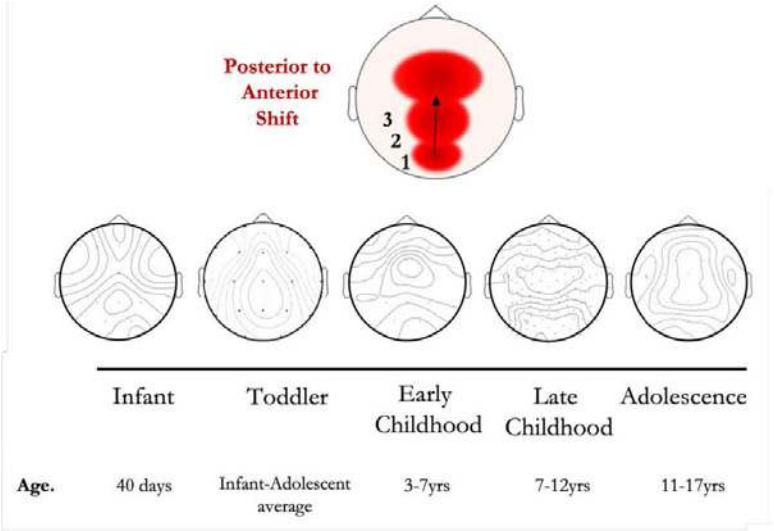

Fig. Illustrative regional maturation of the aperiodic exponent with age. Due to limited access to study data in each lifespan stage, topoplots have been generated from available eyes-open data.

Conclusions: Age-related AE changes in early development are complex, with significant gaps in the published literature preventing clear identification of directions of change and reliable AE ranges, particularly in infancy and toddlerhood. We identify consistent AE across methods, scales and in terms of AE being greater in ECR than EOR, as well as developmental changes in AE maxima. Topological shifts in AE maxima throughout development may potentially reflect known spatial changes in brain network hub maturation. Furthermore, characterising typical AE development provides a point of reference for exploring atypical development in neurodevelopmental conditions, and could act as a potential non-invasive biomarker.

References
1. Arnett, A.B. et al. (2022) 'Absence of dynamic neural oscillatory response to environmental conditions marks childhood attention deficit hyperactivity disorder', Journal of Child Psychology and Psychiatry, 63(12), pp. 1615–1621.
2. Barry, R.J. and De Blasio, F.M. (2021) 'Characterizing pink and white noise in the human electroencephalogram', Journal of Neural Engineering, 18(3).
3. Bornas, X. et al. (2013) 'Long-Range Temporal Correlations in Resting EEG', Journal of Psychophysiology, 27(2), pp. 60–66.
4. Bruining, H. et al. (2020) 'Measurement of excitation-inhibition ratio in autism spectrum disorder using critical brain dynamics', Scientific Reports, 10, p. 9195.
5. Carter Leno, V. et al. (2022) 'Infant excitation/inhibition balance interacts with executive attention to predict autistic traits in childhood', Molecular Autism, 13(1), pp. 1–13.
6. Cellier, D. et al. (2021) 'The development of theta and alpha neural oscillations from ages 3 to 24 years', Developmental Cognitive Neuroscience, 50, p. 100969.
7. Donoghue, T. et al. (2020) 'Parameterizing neural power spectra into periodic and aperiodic components', Nature Neuroscience, 23(12), pp. 1655–1665.
8. Fransson, P. et al. (2013) 'Early Development of Spatial Patterns of Power-Law Frequency Scaling in fMRI Resting-State and EEG Data in the Newborn Brain', Cerebral Cortex, 23(3), pp. 638–646.
9. Hill, A.T. et al. (2022) 'Periodic and aperiodic neural activity displays age-dependent changes across early-to-middle childhood', Developmental Cognitive Neuroscience, 54.
10. Houtman, S.J. et al. (2021) 'STXBP1 Syndrome Is Characterized by Inhibition-Dominated Dynamics of Resting-State EEG', Frontiers in Physiology, 12.
11. Immink, M.A. et al. (2021) 'Resting-state aperiodic neural dynamics predict individual differences in visuomotor performance and learning', Human Movement Science, 78, p. 102829.
12. Irrmischer, M. et al. (2018) 'Strong long-range temporal correlations of beta/gamma oscillations are associated with poor sustained visual attention performance', The European Journal of Neuroscience, 48(8), pp. 2674–2683.
13. Karalunas, S.L. et al. (2022) 'Electroencephalogram aperiodic power spectral slope can be reliably measured and predicts ADHD risk in early development', Developmental Psychobiology, 64(3), p. e22228.
14. Ke, L. et al. (2022) 'Short-term PM2.5 exposure and cognitive function: Association and neurophysiological mechanisms', Environment International, 170, pp. 107593.

Poster No 1309

Tracing Motor Preparation and Activation in the Developing Brain

Julia Schmidgen[1], Stephan Bender[1], Kerstin Konrad[2]

[1]University Hospital Cologne, Cologne, Germany, [2]University Hospital Aachen; Forschungszentrum Jülich, Aachen; Jülich, Germany

Introduction: The motor system shows a prolonged development throughout childhood and adolescence. The analysis of the contingent negative variation (CNV) provides valuable insights into various cognitive and motor processes, underlying cortical sources, and their development across the lifespan. The negative CNV potential is generated between a warning stimulus and a behaviorally relevant imperative stimulus that requires a fast button press. It allows to temporally disentangle response selection and early response preparation processes (early CNV) from the pre-activation of motor networks (late CNV). Currently, it remains unclear which cortical sources contribute to response selection and early response preparation in young children. This study explores cortical sources of motor network preactivation and developmental disparities in individuals aged 5 to 16 years.

Methods: We recorded EEG activity of a sample of 46 healthy right-handed children and adolescents, aged 5 to 16 years, using a 64-electrode high density sensor array. Subjects performed a CNV task with a directional warning cue, indicating the response side of the button press. To assess age related developmental differences of cortical activation, analyses of slow cortical potentials, cortical source analysis and event-related desynchronization within the alpha band were applied.

Results: Children showed increased reaction times and performed significantly more errors compared to adolescent subjects. The orienting response (early CNV) of young children (5- to 8-year-olds) was dominated by sensory post-processing of the directional warning stimulus reflected as pronounced cortical activity over posterior areas and showed only small mid-frontocentral activity, allocated by source analysis to the supplementary motor area (SMA). With increasing age, SMA activity became more prevalent and was recruited with a reduced latency. Significant contralateral alpha band desynchronization was found to be present in all age groups. Alpha rhythm during motor pre-activation (late CNV) showed decreasing event-related synchronization over ipsilateral and increasing event-related desynchronization over contralateral central areas with age. In contrast to studies investigating adult subjects, our adolescent sample (13- to 16-year-olds) showed no contralateral cortical activity during motor pre-activation yet.

Conclusions: The investigated data indicate a prolonged development of motor control up into adulthood. Behavioral results indicated less-efficient action pre-processing and a lack of inhibitory control. Besides increasing efficiency in action control,

activation of mid-frontocentral areas related to the supplementary motor area becomes more prevalent during processes of motor preparation and response evaluation with increasing age. The results supported the hypothesis of a developmental shift from a reactive to a proactive control and an immaturity of supplementary-, pre- and primary motor areas until late adolescence or early adulthood.

References
1. Schmidgen, J. (2023), 'Tracing Motor Preparation and Activation in the Developing Brain'

Poster No 1310

Alteration in macro- and micro-structures of the adolescent hippocampus after the COVID-19 pandemic

Lin Cai[1], Norihide Maikusa[1], Yinghan Zhu[1], Atsushi Nishida[2], Shuntaro Ando[1], Naohiro Okada[3], Kiyoto Kasai[1], Yuko Nakamura[1], Shinsuke Koike[1]

[1]The University of Tokyo, Tokyo, Japan, [2]Tokyo Metropolitan Institute of Medical Science, Tokyo, Japan, [3]University of Tokyo Institutes for Advanced Study, Tokyo, Japan

Introduction: Although a SARS-CoV-2 infection has been revealed to result in changes in human brain structure[1], the impact of the COVID-19 pandemic on the brain among uninfected individuals is still underexplored. Since adolescence is a sensitive period for the development of mental illnesses caused by stressful life events[2], it is important to understand the effect of stressful experiences on the adolescent brain, particularly the hippocampus. Thus, the COVID-19 pandemic, as one of extremely stressful life events, enabled us to examine the impact of stress on the adolescent hippocampus.

Methods: We analyzed 1,149 longitudinal brain structural scans from 479 participants (mean ± SD =14.5 ± 2.2 years; 214 girls) who were from a longitudinal population-neuroscience Tokyo TEEN Cohort study[3]. At the end of wave 3, due to the first state of emergency (SoE), data collection was suspended between the end of March 2020 and July 30, 2020. For the four waves of data collection, three acquisition procedures were performed. Only T1-weighted images were acquired for Procedure 1 and 2, while T1-weighted, T2-weighted, and diffusion images were acquired for Procedure 3. The HCP pipeline was utilized for image preprocessing[4]. Then, bilateral hippocampal volumes were extracted from the FreeSurfer's aseg.stats file. For Procedure 3, 12 hippocampal subfield volumes were obtained using the hippocampal subfield segmentation algorithm in FreeSurfer v6.0.0[5]. After raw diffusion scans were preprocessed, the microstructural metrics were estimated using the diffusion kurtosis imaging (DKI) model[6]. The DKI model could produce 7 microstructural indices, namely fractional anisotropy (FA), mean diffusivity, axial diffusivity, radial diffusivity, mean kurtosis, axial kurtosis, and radial kurtosis. For each scan, volumetric estimates for the bilateral hippocampi and hippocampal subfields, and the 7 microstructural indices for the bilateral hippocampi were averaged across hemispheres as indices in the following statistical analysis. To examine whether the hippocampus during the COVID-19 pandemic differed from that collected in other dates, we set a one-year time interval from 2020/07/29 to 2021/07/29 after the first SoE (2020/04/07 ~ 2020/05/25). Relative to July 29, 2020, the date of MRI scans during this one-year interval was converted into relative values using the log transformations denoted as RV.log. Subsequently, RV.log entered the generalized additive mixed models (GAMMs) or generalized linear mixed models (GLMMs) to examine how the SoE impacted the hippocampal structures. We included age as a smooth term, sex, SES, IQ, and ICV as linear terms, as well as a tensor interaction term between age and sex in the GAMMs. Additionally, the participant ID was introduced as the random intercept. For hippocampal subfield volumes and DKI indices, we used GLMMs to examine the relationships between subfield volumes and SoE. False discovery rate correction was used to account for multiple comparisons.

Results: The GAMM showed that there was a significant main effect of SoE on the mean hippocampal volume (β = 102.19, 95% CI [0.61, 203.77], p = 0.049). The GLMMs showed main effects of SoE on mean volumes in the granule cell and molecular layer of the dentate gyrus (β = 18.19, 95% CI [2.97, 33.41], uncorrected p = 0.02), CA4 (β = 12.75, 95% CI [0.38, 25.12], uncorrected p = 0.04), and hippocampus-amygdala transition area (β = 5.67, 95% CI [1.18, 10.17], uncorrected p = 0.01). A main effect of SoE on the FA values in the mean hippocampus was found (β = 0.03,95% CI [1.93e-03, 0.06], uncorrected p = 0.04).

Conclusions: Our findings revealed that the COVID-19 pandemic resulted in a transient increase in adolescent hippocampal volumes. Similar but less robust findings were observed for hippocampal subfields and microstructure. These findings provide new insight that a major life event might alter the adolescent hippocampal development.

References
1. Douaud, G.(2022), 'SARS-CoV-2 is associated with changes in brain structure in UK Biobank', Nature 604, 697-707
2. Fuhrmann, D. (2015), 'Adolescence as a sensitive period of brain development', Trends Cogn Sci 19, 558-566

3. Okada, N. (2019), 'Population-neuroscience study of the Tokyo TEEN Cohort (pn-TTC): Cohort longitudinal study to explore the neurobiological substrates of adolescent psychological and behavioral development', Psychiatry and Clinical Neurosciences 73, 231-242
4. Glasser, M. F. (2013), 'The minimal preprocessing pipelines for the Human Connectome Project', Neuroimage 80, 105-124
5. Iglesias, J. E. (2015), 'A computational atlas of the hippocampal formation using ex vivo, ultra-high resolution MRI: application to adaptive segmentation of in vivo MRI', Neuroimage 115, 117-137
6. Jensen, J. H. (2005), 'Diffusional kurtosis imaging: the quantification of non-gaussian water diffusion by means of magnetic resonance imaging', Magnetic Resonance in Medicine: An Official Journal of the International Society for Magnetic Resonance in Medicine 53, 1432-1440

Poster No 1311

How nutrition contributes to myelination and structural connectivity in school age

Diandra Brkic[1], Fabio Mainardi[2], Jonas Hauser[3], Sean Deoni[4]

[1]Nestlé Institute of Health Sciences, Lausanne, Vaud, [2]Nestlé Institute of Health Sciences, Lausanne, Switzerland, [3]Brain Health Department, Nestlé Institute of Health Sciences, Lausanne, Switzerland, [4]Department of Pediatrics, Warren Alpert Medical School at Brown University, Providence, RI

Introduction: School-age period, typically from 2 to 15 years old, is a critical phase in child development that significantly impacts cognition, learning, behaviour, and social-emotional development. This age is characterized by heightened sensitivity, making it a crucial time for shaping and nurturing a child's overall growth and well-being. From a brain development perspective, it is also a pivotal period characterized by significant reorganization. For instance, there is a remarkable restructuring of synaptic plasticity, and notable changes in the structural and functional networks, associated with learning (Dean et al., 2015). Although numerous studies have investigated the impact of the environment, socioeconomic status (SES), and genes on neurodevelopment, there is a huge knowledge gap regarding the specific influence of nutrition on cortical changes, particularly in this age range (Saavedra & Prentice, 2023). In this study, we have assessed how nutrition shapes brain myelination and white matter network organisation, and how this affects cognition and learning skills in a large cohort of school-age children (Brown University RESONANCE cohort).

Methods: A large sample (N=282) of school-age children (mean age 7.5 y.o.), from the Brown University RESONANCE cohort, was included in this study. All participants had morphological and structural brain measures (Water fraction myelination and fractional anisotropy, FA), full cognitive (WPPSI, WASI) and learning (AAB) assessments, and dietary intake (ASA-24h recall questionnaire) completed. Specifically we investigated how dietary intake affects both myelination and structural connectivity, linked to learning and cognitive skills. In order to capture this relationship in a data driven fashion, we performed a series of mediation models (Rijnhart et al., 2021). This allowed us to assess the indirect effects and shed light on the underlying pathways between important nutrients for, cognition and learning, mediated by brain structure and morphology, while controlling for age and parental education.

Results: Four different mediation analyses were performed to explore the causal relationship between 64 nutrients and 35 food groups and cognitive and learning performance, with myelination and FA, as mediating factors. Mediation models identified the most significant nutrients contributing to cognitive and learning skills outcomes, via myelination and structural connectivity. Specifically, the models were: a) nutrition, myelination, cognition; b) nutrition, myelination, learning (reading); c) nutrition, FA (DTI), cognition; d) nutrition, FA (DTI), learning. Each of the models provided a set of most important essential nutrients (e.g. iron, vit B) affecting both learning and cognition, in different related brain networks and ROIs. Importantly we found consistency across all models, defining how dietary intake affects both learning and cognition, via correlated brain measures

Conclusions: To the best of our knowledge this is the first study offering a deeper understanding of the intricate interplay between nutrition, brain development and structural changes, and cognitive and learning outcomes. Our results provide a unique perspective on which nutrients may support learning and cognition in school age children. In addition, it assesses how this relationship is mediated by myelination rate and structural efficiency in learning-related brain areas. In short, this study emphasizes the significance of considering the impact of nutrition on child development. It highlights the need to incorporate nutrition as a crucial factor when studying key determinants influencing brain development, learning, and cognitive abilities in school age. By recognizing the role of nutrition in shaping these domains, we can better understand the multifaceted factors that contribute to optimal brain development and promote effective strategies for fostering learning and cognition in children.

References

1. Dean, D. C., O'Muircheartaigh, J., Dirks, H., Waskiewicz, N., Walker, L., Doernberg, E., Piryatinsky, I., & Deoni, S. C. L. (2015). Characterizing longitudinal white matter development during early childhood. Brain Structure and Function, 220(4), 1921–1933. doi: 10.1007/s00429-014-0763-3
2. Rijnhart, J. J. M., Lamp, S. J., Valente, M. J., MacKinnon, D. P., Twisk, J. W. R., & Heymans, M. W. (2021). Mediation analysis methods used in observational research: A scoping review and recommendations. BMC Medical Research Methodology, 21(1), 226. doi: 10.1186/s12874-021-01426-3
3. Saavedra, J. M., & Prentice, A. M. (2023). Nutrition in school-age children: A rationale for revisiting priorities. Nutrition Reviews, 81(7), 823–843. doi: 10.1093/nutrit/nuac089

Poster No 1312

Systematic shift of cortical thickness distribution within newborns between two dHCP releases

Daisuke Tsuzuki[1], Fumitaka Homae[2]

[1]Kochi University, Kochi, Japan, [2]Tokyo Metropolitan University, Tokyo, Japan

Introduction: The Developing Human Connectome Project (dHCP) is a study to map the growth of the baby's brain and has made major scientific progress by creating a 4-dimensional connectome for early human life (Hughes et al. 2017). In 2019, they began providing 558 neonatal scans, including structural imaging, structural connectivity and functional connectivity data as the second release of data. In 2021, the third dHCP data release was announced, and scans from 783 infants, of whom 583 were healthy infants born at term, are currently available (Edwards et al. 2022). Many studies have been conducted, and a large number of studies have been published using dHCP data. In contrast, we observed significant and systematic differences in the cortical thickness calculated on identical individual structural MRIs between the second and third releases of the dHCP. However, these differences have not been fully estimated or reported.

Methods: We used two structural datasets, "dHCP second data release" (https://www.developingconnectome.org/data-release/second-data-release/) and "dHCP third data release" (https://www.developingconnectome.org/data-release/third-data-release/) to investigate the characteristics of cortical thickness in newborns. More precisely, we chose the 556 neonatal scans (222 girls and 281 boys, including multiple sessions; 40.0 ± 3.0 post-menstrual age in weeks) contained in both the second and third data releases of dHCP and analyzed their cortical thickness (Makropoulos et al. 2018). A two-sample Kolmogorov-Smirnov test was performed to test for differences between the two distributions of cortical thickness for each newborn. The same test was then applied to the mean curvature of the white matter surface to compare the tendencies.

Results: In this study, we examined the differences in the cortical thickness distributions calculated on identical individual structural MRIs between dHCP releases 2 and 3. The extracted pial surfaces included in dHCP release 3 show a relatively large and expanded gyrus compared to those of release 2 (Fig. 1). The results of the statistical test suggest that the cortical thickness of dHCP release 3 increased systematically (Fig. 2) via the dHCP structural pipeline process (Makropoulos et al. 2018). In contrast, differences in the mean curvature of the white matter surface calculated for both dHCP releases were rarely shown (Fig. 2). In the cortical thickness analysis, the distributions of dHCP release 2 and release 3 differed significantly for every 556 measurements (all p-values <0.0001, Bonferroni adjusted, by two-tailed, two-sample Kolmogorov-Smirnov test). The distributions of cortical thickness for dHCP release 3 were fully shifted to the larger side compared with those for release 2. In the mean curvature of the white matter surface analysis, the distributions between dHCP release 2 and release 3 showed partly significant differences (12 of 556 p-values <0.0001, Bonferroni adjusted, by two-tailed, two-sample Kolmogorov-Smirnov test).

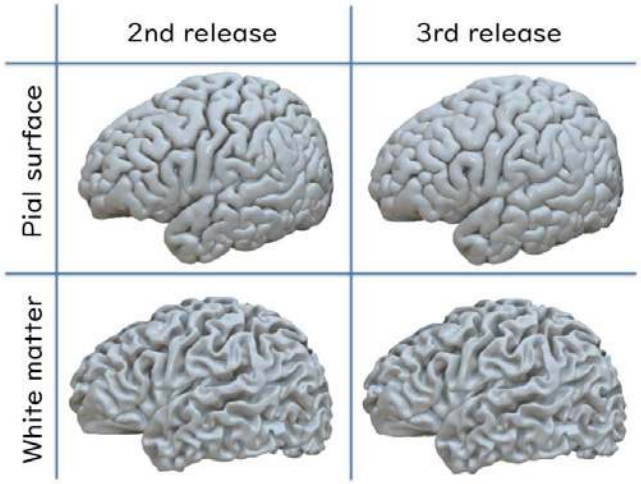

Fig. 1 The appearances of pial surface and white matter surface for identical newborn from two dHCP releases (sample: CC00502XX07)

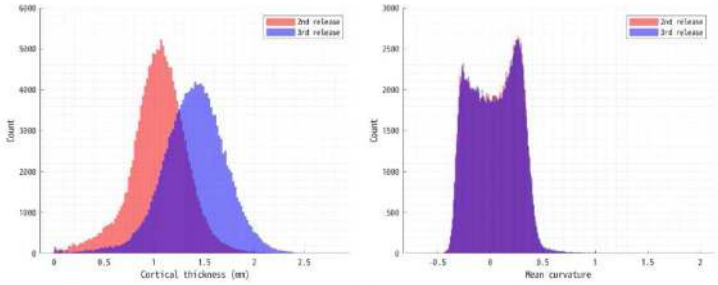

Fig. 2 Comparing distributions of cortical thickness and mean curvature between two dHCP releases (sample: CC00502XX07)

Conclusions: This result implies that the shapes of the white matter surfaces extracted from the structural MRIs of the two dHCP releases do not differ morphologically, as shown by the cortical thickness. Further work is needed to clarify which part of the dHCP structural pipeline affects the differences in cortical thickness between the two dHCP releases.

References

1. Hughes, E. J., Winchman, T., Padormo, F., Teixeira, R., Wurie, J., Sharma, M., ... & Hajnal, J. V. (2017). A dedicated neonatal brain imaging system. Magnetic resonance in medicine, 78(2), 794-804.
2. Edwards, A. D., Rueckert, D., Smith, S. M., Abo Seada, S., Alansary, A., Almalbis, J., ... & Hajnal, J. V. (2022). The developing human connectome project neonatal data release. Frontiers in neuroscience, 16, 886772.
3. Makropoulos, A., Robinson, E. C., Schuh, A., Wright, R., Fitzgibbon, S., Bozek, J., ... & Rueckert, D. (2018). The developing human connectome project: A minimal processing pipeline for neonatal cortical surface reconstruction. Neuroimage, 173, 88-112.

Poster No 1313

The relationship between GABA levels and spectral oscillatory dynamics in the neonatal brain

Alice Thomson[1], Juliette Champaud[2], Jucha Willers Moore[1], Ines Tomazinho[1], Beya Bonse[1], Kathleen Colford[1], Parvaneh Adibpour[1], Lorenzo Fabrizi[2], Nicolaas Puts[1], Tomoki Arichi[1]

[1]King's College London, London, UK, [2]University College London, London, UK

Introduction: In the adult brain, GABA levels positively correlate with the power of beta and gamma band oscillations in multiple brain regions including the visual cortex[1-4]. This is driven by GABAergic interneuron activity within cortical circuits which in turn shapes neural synchrony[1-4]. During early brain development this relationship may differ because of changes in GABA function[5]. Here, we probe the relationship between magnetic resonance spectroscopy (MRS) measures of brain GABA levels and resting state electroencephalography (EEG) power spectral densities in the occipital lobe of healthy term neonates. We hypothesise that the relationship between GABA levels and neuronal oscillations is not present in the developing brain.

Methods: Data were acquired from 8 term neonates. Three datasets were excluded following post-acquisition data quality checks. Data is thus reported from 5 neonates with a median age of 39.7 (range: 37.28 - 43.29) weeks postmenstrual age and 3 (range: 1-27) post-natal days at scan, 2 females. All infants were healthy at the time of scanning and had normal brain appearances. Both and EEG and MRS recordings were performed during natural sleep. Studies were performed with NHS ethics committee approval and written parental consent. A Philips Achieva 3T at St. Thomas' Hospital London (32-channel neonatal head coil[6] was used to acquire MRS data from a 27ml voxel placed over the occipital lobe (OCC), centered on the midline (Figure 1). MRS was performed using GABA editing MEGA-PRESS[7]; 320 transients, 2048 data points, TE/TR:68/2000ms, VAPOR water suppression. MRS data were processed in Osprey. T2-weighted anatomical images were segmented using the developing Human Connectome Project pipeline[8] for alpha tissue correction of GABA concentrations[9]. Concentrations are reported in institutional units (i.u) and reported as GABA+ (GABA plus macromolecule contribution). Resting-state EEG data were acquired same day prior to the MRI for 10-15 mins using a 32- or 25-channel cap (EasyCap GMbH) and a BrainProducts EEG system. Pre-processing steps were performed in MATLAB (2021a) and EEGLAB[10]. Raw data were filtered with a notch (48-52 Hz) and second-order bidirectional Butterworth bandpass (0.1 and 70Hz). Data were then epoched into 60-150s sections and denoised using ICA (0-5 components rejected; Figure 1C). Power spectral densities estimated with the Welch's method for each channel/subject and averaged across O1, O2, Oz, POz channels spanning the occipital area (Figure 1D). Spearman's rho correlation coefficients were first calculated between GABA+ and frequency power in 1Hz-intervals from 0-70Hz before averaging across frequency bands (1-4Hz for delta, 4 –8Hz for theta, 8-12Hz for alpha, 13-30Hz for beta and 30-40Hz for gamma).

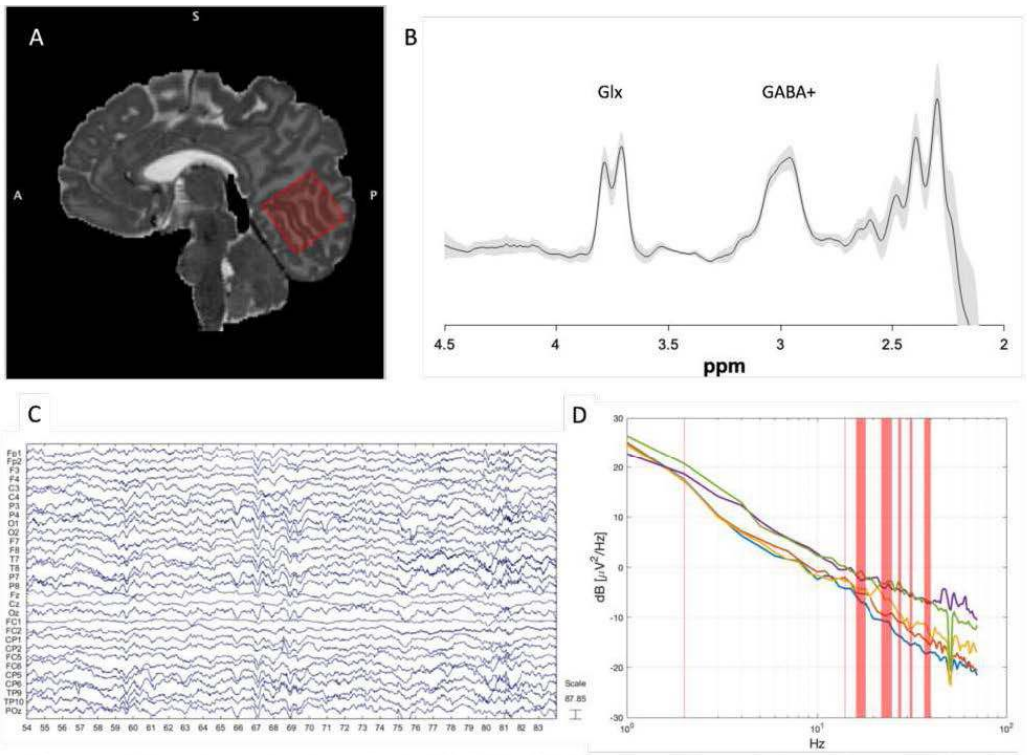

Figure 1. (A) A voxel was placed over the Occipital lobe (27ml; N = 6; red) for acquisition of in vivo MRS spectra. (B) MEGA-PRESS was used to resolve GABA+, a group averaged MRS difference spectrum is shown with +1/-1 standard deviation in grey. (C) Thirty-second EEG recording from example subject with 32-channel BrainProducts BrainCap. (D) Each individual's Power Spectral Density averaged across O1, O2, Oz, POz with highlighted in red frequency samples significantly correlating with GABA concentration.

Results: Occipital GABA+ levels was positively correlated with beta (rho = 0.90, $p < 0.05$) and gamma power (rho = 0.90, $p < 0.05$; Figure 2). There was no significant relationship between GABA+ levels and other frequency bands; delta (1-4Hz): rho = 0.10, p = 0.87, theta (4-8Hz): rho = 0.60, p = 0.28, alpha (8 – 12Hz): rho = 0.6, p = 0.228.

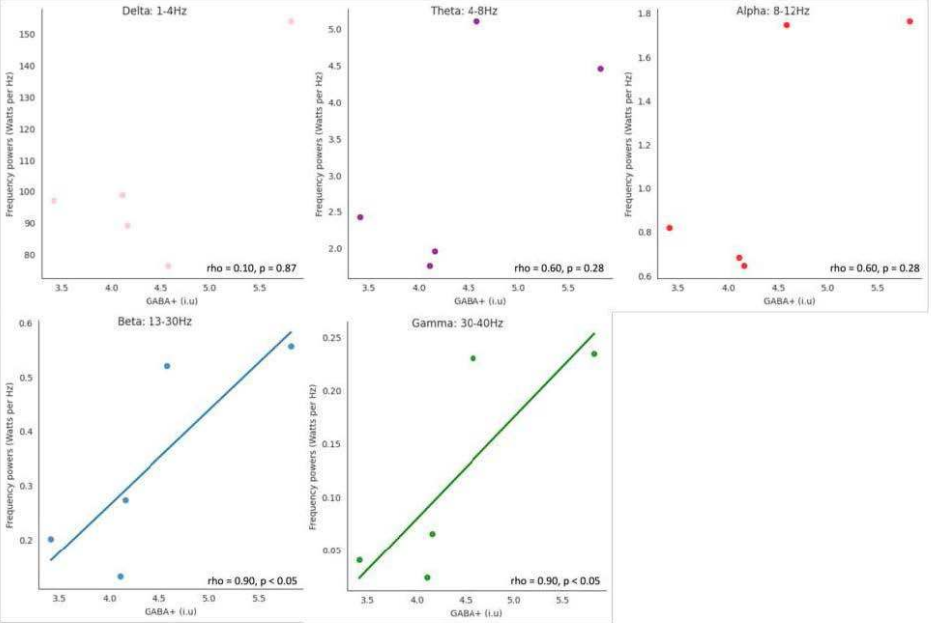

Figure 2. Correlations between occipital GABA+ levels (as measured by MRS) and delta (1 – 4 Hz), theta (4 – 8Hz), alpha (8 – 12Hz), beta (13 – 30Hz) and gamma (30 – 40Hz) EEG power (Watts per Hz). Spearman rho correlation coefficients are shown with significance indicated, trend lines are for visual reference only.

Conclusions: Our findings show a positive correlation between GABA+ levels and EEG beta and gamma frequency powers in the neonatal brain. This suggests that GABAergic activity may have a similar role in influencing neuronal oscillations in the early post-natal period, as has been observed in the adult brain[1-4]. This can provide new insight into the development of the relationship between neurochemistry and synchronous neuronal activity in the human brain, which can be further complemented by exploring relationships with emerging patterns of functional connectivity.

References

1. Brunel, N., & Wang, X. J. (2003), 'What determines the frequency of fast network oscillations with irregular neural discharges? I. Synaptic dynamics and excitation-inhibition balance', Journal of neurophysiology, vol. 90(1), pp. 415–430.
2. Baumgarten, T. J., Oeltzschner, G., Hoogenboom, N., Wittsack, H. J., Schnitzler, A., and Lange, J. (2016), 'Beta peak frequencies at rest correlate with endogenous GABA+/Cr concentrations in sensorimotor cortex areas', PLoS One, vol.11:e0156829.
3. Gaetz, W., Edgar, J. C., Wang, D. J., and Roberts, T. P. (2011), 'Relating MEG measured motor cortical oscillations to resting gamma-aminobutyric acid (GABA) concentration', Neuroimage, vol.55, pp. 616–621.
4. Kujala, J., Jung, J., Bouvard, S., Lecaignard, F., et al. (2015), 'Gamma oscillations in V1 are correlated with GABA(A) receptor density: A multi-modal MEG and Flumazenil-PET study', Scientific reports, vol.5, pp. 16347.
5. Rivera, C., Voipio, J., Payne, J. A., Ruusuvuori, E., et al. (1999), 'The K+/Cl- co-transporter KCC2 renders GABA hyperpolarizing during neuronal maturation', Nature, vol.397(6716), pp. 251–255.
6. Hughes, E. J., Winchman, T., Padormo, F., Teixeira, R., et al. (2017), 'A dedicated neonatal brain imaging system', Magnetic resonance in medicine, vol. 78(2), pp. 794–804.
7. Mescher, M., Merkle, H., Kirsch, J., Garwood, M., & Gruetter, R. (1998), 'Simultaneous in vivo spectral editing and water suppression', NMR in biomedicine, vol. 11(6), pp. 266–272.
8. Makropoulos, A., Robinson, E. C., Schuh, A., Wright, R., Fitzgibbon, S., Bozek, J., et al (2018), 'The developing human connectome project: A minimal processing pipeline for neonatal cortical surface reconstruction', NeuroImage, vol. 173, pp. 88–112.
9. Harris, A. D., Puts, N. A., & Edden, R. A. (2015), 'Tissue correction for GABA-edited MRS: Considerations of voxel composition, tissue segmentation, and tissue relaxations', Journal of magnetic resonance imaging: JMRI, vol. 42(5), pp. 1431
10. Delorme, A., & Makeig, S. (2004), 'EEGLAB: an open source toolbox for analysis of single-trial EEG dynamics including independent component analysis', Journal of Neuroscience Methods, vol. 134(1), pp. 9–21.

Poster No 1314

Early-life Human Milk Oligosaccharides and their effect on cortical thickness at 6 years of age

Jonatan Ottino-Gonzalez[1], Shana Adise[1], Christopher Machle[1], Lars Bode[2], Ravi Bansal[3], Bradley Peterson[3], Michael Goran[1]

[1]CHLA, Los Angeles, CA, [2]University of California San Diego, La Jolla, CA, [3]Children's Hospital Los Angeles, Los Angeles, CA

Introduction: Neurodevelopment starts in conception and extends into adulthood yet most of its critical processes take place during gestation and the first postnatal years[1]. The optimal growth of brain structures work as foundation for cognitive activity and both relate to better psychosocial adjustment later in life[2]. Breastfeeding overlaps with a period of rapid brain

growth during the first year of life[3] and it thus constitutes an important factor to consider in neurodevelopment. Despite evidence showing that breastfeeding is positively related to grey and white matter volumes[4,5], very few studies have studied what compounds in human milk are involved. Human milk oligosaccharides (HMOs) are non-digestible sugars involved in neurodevelopmental processes such as myelination, neuronal outgrowth and migration, or microglia maturation[6,7]. In previous work, we showed that exposure to 2'fucosylactose (2`FL), 3-fucosylactose (3FL) and 3'-sialylactose (3'SL) was associated with variations in brain microstructure in newborns[8]. For this study, we examine the extent to which the accumulated exposure to 2`FL, 3FL and 3'SL during the first 6 months of life is related to variations in brain cortical thickness at 6 years of age.

Methods: Forty mother-infant dyads from the Mother's Milk and El Sendero cohorts with data available at 1-month, 6-month and 72-month were included in the study. Inclusion criteria was being a first-time mother of a singleton healthy pregnancy, active breastfeeding, and enrollment by 1-month postpartum. Exclusion criteria involved medical disease or use of medication, tobacco or drug use, pre-term/low-birth weight, and or/fetal malformations. Family history and physical examinations were taken at the 1-month visit. Human milk sample was collected during the 1 and 6-month visits. Mothers were told to fast and refrain from feeding or pumping milk for 1.5h before collection. HMOs were isolated with high-throughput solid-phase extraction, fluorescently labeled, and measured with High-Performance Liquid Chromatography. HMO concentrations are expressed in nanomoles per milliliter (nmol/ml) and aggregated from 1 and 6-month visits. Scores were checked for skewness and box-cox transformed as needed. At the 72-month visit, child MRI data was collected with a 3 Tesla Phillips Achieva. T1-weighted scans were processed in FreeSurfer (v.7.3.2) and the thicknesses of 68 Desikan-labeled cortical regions were bilaterally averaged and regressed against age, sex and the total euler number for further adjustment. The main analysis involved multiple linear regression models with each region as the dependent variable. Separate models were run for each HMO. Mother's age at delivery, delivery type (i.e., C-section or Vaginal) and average human milk proportion from 1 to 6-months (0 to 1, values closer to 0 indicate mostly formula-fed) were used as nuisance covariates. All reported p-values are uncorrected. The study was performed with the approval of the IRB of the Children's Hospital of Los Angeles (CHLA-18-00576) and the participants' written consent.

Results: No significant associations were found with regard to 2`FL exposure. The exposure to 3FL was positively related to the frontal pole (b = 0.48 [0.17, 0.80], p = 0.004) and paracentral (b = 0.46 [0.14, 0.78], p = 0.006) thickness. The exposure to 3'SL was positively associated with the thickness in the rostral middle frontal (b = 0.35, [0.27, 0.67], p = 0.034).

Conclusions: In previous work, we showed that the exposure to 2`FL, 3FL and 3'SL was related to brain microstructure in newborns. In the current work, we showed that the exposure to 3FL and 3'SL may have positive long-lasting effects on grey matter structure at 6 years of age. Future work will be able to help to determine causalities and the underlying mechanisms (i.e., increases in neuronal and/or dendritic density, underlying white matter changes, etc.).

References

1. Budday S, Steinmann P, Kuhl E. Physical biology of human brain development. Front Cell Neurosci. 2015;9. doi:10.3389/fncel.2015.00257
2. Jokela M. Why is cognitive ability associated with psychological distress and wellbeing? Exploring psychological, biological, and social mechanisms. Pers Individ Dif. 2022;192:111592. doi:10.1016/J.PAID.2022.111592
3. Knickmeyer RC, Gouttard S, Kang C, et al. A Structural MRI Study of Human Brain Development from Birth to 2 Years. Journal of Neuroscience. 2008;28(47):12176-12182. doi:10.1523/JNEUROSCI.3479-08.2008
4. Kafouri S, Kramer M, Leonard G, et al. Breastfeeding and brain structure in adolescence. Int J Epidemiol. 2013;42(1):150-159. doi:10.1093/ije/dys172
5. Deoni SCL, Dean DC, Piryatinsky I, et al. Breastfeeding and early white matter development: A cross-sectional study. Neuroimage. 2013;82:77-86. doi:10.1016/j.neuroimage.2013.05.090
6. Silva YP, Bernardi A, Frozza RL. The Role of Short-Chain Fatty Acids From Gut Microbiota in Gut-Brain Communication. Front Endocrinol (Lausanne). 2020;11:25. doi:10.3389/FENDO.2020.00025/BIBTEX
7. Schnaar RL, Gerardy-Schahn R, Hildebrandt H. Sialic acids in the brain: gangliosides and polysialic acid in nervous system development, stability, disease, and regeneration. Physiol Rev. 2014;94(2):461-518. doi:10.1152/PHYSREV.00033.2013
8. Berger PK, Bansal R, Sawardekar S, et al. Associations of Human Milk Oligosaccharides with Infant Brain Tissue Organization and Regional Blood Flow at 1 Month of Age. Nutrients. 2022;14(18):3820. doi:10.3390/nu14183820

Poster No 1315

Untangling microstructural development: insights from soma, neurite, and myelin imaging on macaques

Ting Gong[1], Evan Dann[1], Chiara Maffei[1], Hong-Hsi Lee[1], Hansol Lee[1], Jocelyne Bachevalierb[2], Susie Huang[1], Suzanne Haber[3,4], Anastasia Yendiki[1]

[1]Athinoula A. Martinos Center for Biomedical Imaging, Massachusetts General Hospital, Boston, MA, [2]Emory National Primate Research Center, Emory University, Atlanta, GA, [3]Department of Pharmacology and Physiology, University of Rochester, Rochester, NY, [4]McLean Hospital, Belmont, MA

Introduction: Early brain development involves dynamic biological processes, such as synaptogenesis and myelination, that shape cellular organization and are essential for normal brain function. Current methods used in developmental studies lack specificity to cellular microstructure. Thus, their findings are hard to interpret, especially in the gray matter (GM). In this study, we use advanced biophysical models to measure changes of cell soma density, neurite density and myelin concentration in developmental brains. Our goal is to validate biomarkers of major biological processes that are relevant to studies of healthy and disordered brain development.

Methods: Five fixed macaque brains, three developmental (3-week, 3-month, and 1-year old) and two adult, were scanned in a small-bore 4.7 T Bruker BioSpin MRI system. Quantification of cell soma and neurites. Soma and neurite density imaging (SANDI)[1] models diffusion weighted (DW) signals in a voxel from within the soma (cell bodies of neurons and neuroglia), the neurite (dendritic processes and axons) and the extra-cellular water. This provides histology-correlated estimates of apparent soma density, soma size and neurite density[2]. For SANDI analysis, DW images were collected using a two-shot, 3D echo-planar imaging sequence at 0.5 mm isotropic resolution; DW gradient directions were uniformly sampled over the hemisphere for each of 8 shells: 12 directions for b=1, 2.5, 5, 7.5 and 32 directions for b=11.1, 18.1, 25, 43 ms/µm2. The diffusion gradient pulse duration and separation was 11 and 15 ms. We also use a subset of the DWI datasets to estimate FA and MD from conventional DTI[3] and neurite density index (NDI) and orientation dispersion index (ODI) from NODDI model[4], which has been widely studied in mainly white matter (WM) development[5–7]. Quantification of myelin and R2. Commonly used myelin measures include T1w/T2w ratio[8], R1[9,10], R2 and more specific myelin water fraction (MWF)[11]. For our ex vivo data, we collected multi-slice multi-echo images for quantitative R2 mapping and MWF estimation (20 spin echo images with echo times from 8-160 ms and an equal echo spacing of 8 ms; TR = 3000 ms). The data were fitted for voxel-wise R2 values as well as a spectrum of T2 to extract the MWF.

Results: Figure 1 illustrates that SANDI can provide more specific interpretation of DW signal changes in GM during development. Compared to adult brains, the developmental brains generally show higher soma density, lower neurite density and smaller soma size. This agrees with histological evidence of similar or even higher number of neurons in infants than adults[12], but much less complex neuronal projections in the former. A smaller average soma size could reflect microglia proliferation in developmental brains as glia have smaller soma than neurons. Compared to SANDI findings in the same GM ROIs, DTI shows somewhat lower MD in developmental brains than adult but no clear trend in FA. Furthermore NODDI-derived NDI could not differentiate developmental stages, and ODI showed similar information to FA. Descriptions of developmental trends and major processes are provided in Fig1A. In measuring myelination, MWF estimation is sensitive to SNR, thus less robust in GM of developmental brains due to low concentration. R2 is used as a measure of myelination in some developmental studies because myelin has higher R2 than other tissue components. We show in Figure 2 that R2 is confounded by soma density when there is little myelination, due to higher R2 in soma than neurites and extra-cellular space[13]. This suggests that, while R2 (and other relaxation-based measures[14]) can measure maturation, it cannot be interpreted specifically as a myelin measure in the developing brain.

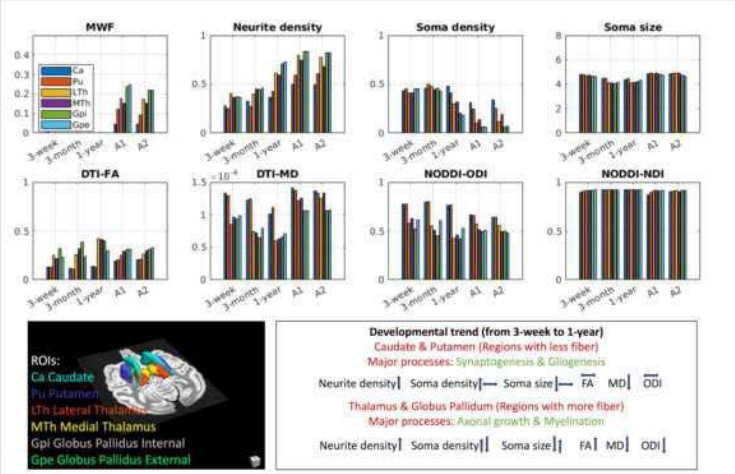

(A) Subcortical GM development measured by different microstructure parameters

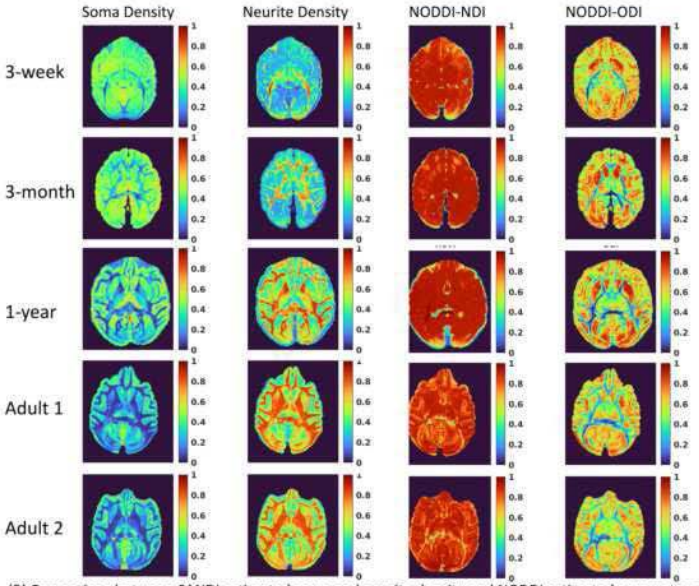

(B) Comparison between SANDI estimated soma and neurite density and NODDI estimated parameters

Figure 1. Mean microstructure measures showing different developmental trends in GM ROIs with different tissue properties. In caudate and putamen, the increased neurite density and decreased MD and soma size could reflect synaptogenesis and membrane proliferation associated with gliogenesis. In regions with higher fiber content, the increased neurite density and FA likely reflect axonal growth and myelination; changes in soma size could be related to changes of oligodendrocytes for myelin production. As in a previous study [15], the T2 spectrum failed to show a peak for myelin water in most regions of the developmental brains (thus MWF not shown) likely due to very low SNR of myelin signal.

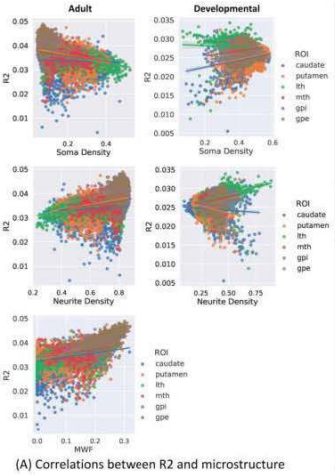

(A) Correlations between R2 and microstructure

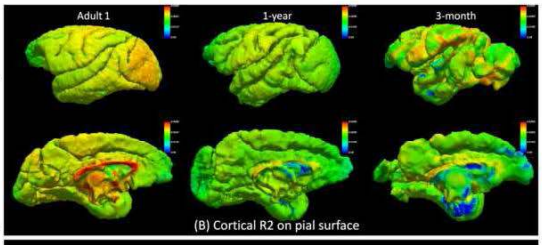

(B) Cortical R2 on pial surface

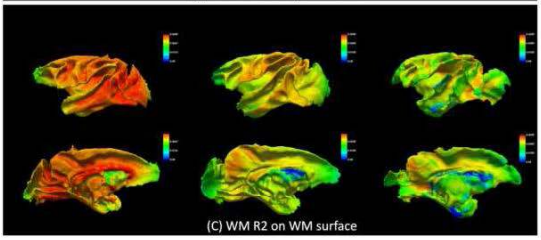

(C) WM R2 on WM surface

Figure 2. R2 as measure of maturation. (A) Voxel-wise R2 contains contributions from all tissue compartments, including myelin, soma, and neurites. In adult brain, because of higher myelination, R2 is positively correlated with MWF and negatively correlated with soma density; this is because higher myelination introduces higher neurite density (positive correlation not shown), thus lower soma density. In developing brain, R2 is positively correlated with soma density due to low myelination. This suggests that R2 in the cortex reflects both myelin and soma (B; middle cortical layer) while it reflects mostly myelin in the adult WM (C; 0.5 mm below WM surface).

Conclusions: We show the promise of combining SANDI and myelin imaging to disentangle biological processes in brain development. Future work will include histological staining to validate MRI findings.

References

1. Palombo, M. et al. SANDI: A compartment-based model for non-invasive apparent soma and neurite imaging by diffusion MRI. Neuroimage 215, (2020).
2. Ianuş, A. et al. Soma and Neurite Density MRI (SANDI) of the in-vivo mouse brain and comparison with the Allen Brain Atlas. Neuroimage 254, (2022).
3. Basser, P. J. et al. MR diffusion tensor spectroscopy and imaging. Biophys J 66, 259–267 (1994).
4. Zhang, H. et al. NODDI: Practical in vivo neurite orientation dispersion and density imaging of the human brain. Neuroimage 61, 1000–1016 (2012).
5. Qiu, A. et al. Diffusion Tensor Imaging for Understanding Brain Development in Early Life. (2015) doi:10.1146/annurev-psych-010814-015340.
6. Ouyang, M. et al. Delineation of early brain development from fetuses to infants with diffusion MRI and beyond. (2018) doi:10.1016/j.neuroimage.2018.04.017.
7. Dipiero, M. et al. Applications of advanced diffusion MRI in early brain development: a comprehensive review. 228, 367–392 (2023).
8. Glasser, M. F. et al. Mapping Human Cortical Areas In Vivo Based on Myelin Content as Revealed by T1- and T2-Weighted MRI. Journal of Neuroscience 31, 11597–11616 (2011).
9. Lutti, A. et al. Using high-resolution quantitative mapping of R1 as an index of cortical myelination. Neuroimage 93 Pt 2, 176–188 (2014).
10. Grotheer, M. et al. White matter myelination during early infancy is linked to spatial gradients and myelin content at birth. Nature Communications 2022 13:1 13, 1–12 (2022).
11. Mackay, A. L. et al. Magnetic Resonance of Myelin Water: An in vivo Marker for Myelin. Brain Plasticity 2, 71–91 (2016).
12. O'Kusky, J. et al. Postnatal changes in the number of neurons and synapses in the visual cortex (area 17) of the macaque monkey: A stereological analysis in normal and monocularly deprived animals. Journal of Comparative Neurology 210, 291–306 (1982).
13. Gong, T. et al. Multi-TE SANDI: Quantifying compartmental T2 relaxation times in the grey matter. (2023).
14. Sandrone, S. et al. Mapping myelin in white matter with T1-weighted/T2-weighted maps: discrepancy with histology and other myelin MRI measures. Brain Struct Funct 228, 525–535 (2023).
15. Bartels, L. M. et al. Orientation dependence of R2 relaxation in the newborn brain. Neuroimage 264, 119702 (2022).

Poster No 1316

Automated fetal ICV annotation in 3D-ultrasound: sex-specific brain development and outcome at age 3

Sonja de Zwarte[1], Jalmar Teeuw[2], Mireille Bekker[3], Ruud van Sloun[4], Hilleke Hulshoff Pol[2]

[1]Department of Psychiatry, UMC Brain Center, University Medical Center Utrecht, Utrecht, Netherlands, [2]Department of Experimental Psychology, Helmholtz Institute, Utrecht University, Utrecht, Netherlands, [3]Department of Obstetrics, University Medical Center Utrecht, Utrecht, Netherlands, [4]Lab of Biomedical Diagnostics, Department of Electrical Engineering, Eindhoven, Netherlands

Introduction: The human brain undergoes major developmental changes during pregnancy. Three-dimensional (3D) ultrasound images provide the opportunity to investigate prenatal brain development in detail on a large scale. Prenatal brain development can be linked to mental and other health outcomes later in life (Clifford et al., 2016; Davies et al., 2020; Gao et al., 2019; Hulshoff Pol et al., 2000); however, it remains largely unknown to what extent typical brain development can be linked to behavioral outcome early in life.

Methods: We developed a convolutional neural network model for automated segmentation of fetal intracranial volume (ICV) from 3D ultrasound. In addition, we developed an automated quality control procedure to deal with many within-subject images. We applied the trained model in a large longitudinal population sample from the YOUth Baby and Child cohort (www.uu.nl/youthcohort) measured at 20- and 30-week of gestational age to investigate biological sex differences in fetal ICV (N=2,235 individuals with 43,492 ultrasounds) (de Zwarte et al., 2022). To link prenatal brain development to postnatal outcome, behavioral and emotional problems were assessed at age 3 using the Child Behavior Check List (CBCL; 1.5–5 years). In total, N=630 children were included (296 boys, 334 girls) with at least one good-quality ultrasound and completed CBCL.

Results: Our trained model estimated ICV and ICV growth in 7,672 ultrasounds of 1,762 participants that passed the automatic quality control procedure. This was 18% of the available ultrasound scans and 72% of the participants. Most unsuccessful predictions were due to non-brain ultrasound, low-quality ultrasound (e.g., due to motion of fetus or high maternal BMI), or incomplete coverage of the entire fetal brain. Boys had significantly larger ICV at 20- (B=2.86; p=5.7e-14) and 30-weeks (B=12.35; p=8.2e-27) of pregnancy, and more pronounced ICV growth than girls (0.12ml/day; p=1.8e-5) (Figure 1). Lower ICV20weeks was associated with higher scores on anxious/depressed, somatic complaints, internalizing-, other-, total-, stress- and attention deficit hyperactivity-problems scales (standardized beta coefficients=[-0.091;-0.123], p<0.05). There was significant interaction effect between sex and ICV20weeks in the anxious/depressed scale; with no relationship between

ICV and behavior in boys and a negative relationship in girls (respectively standardized beta coefficients -0.001 and -0.237; picvXsex<0.05). There were also significant interaction effects between sex and ICVgrowth (ml/day) in the anxious/depressed, somatic complaints and internalizing behavior scales (picvXsex<0.05). In boys, less ICV growth per day was associated with more problems (standardized beta coefficients=[-0.083;-0.108]) and in girls more ICV growth per day was associated with more problems (standardized beta coefficients=[0.116;0.133]). See Figure 2 for an example of these interaction effects in the anxious/depressed syndrome scale.

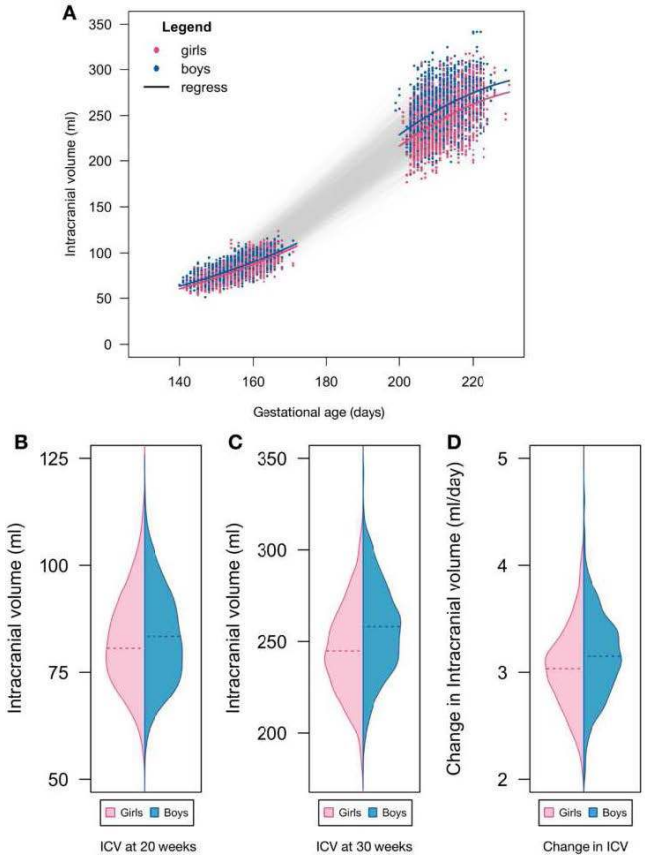

Figure 1. Growth curve and sex effects for fetal intracranial volume (ICV) in boys and girls.

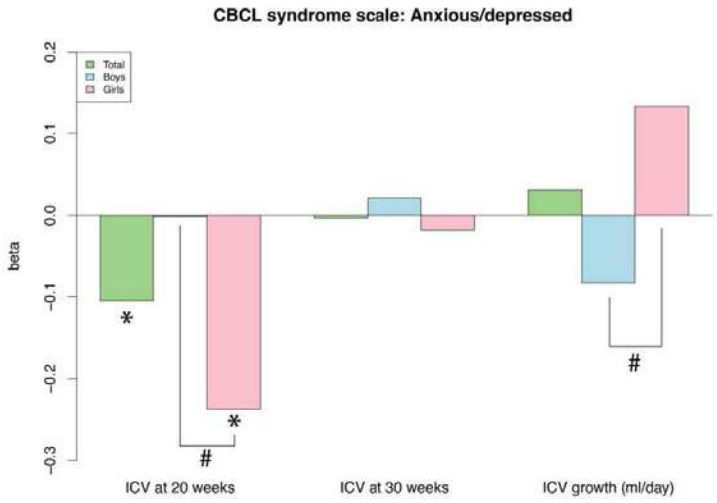

Figure 2. Relationship prenatal intracranial volume (ICV) and Child Behavior Check List (CBCL) anxious/depressed syndrome scale and age 3.

Conclusions: We report sex-specific prenatal brain development, which might have different implications for behavior in children at age 3. In particular, brain structure and growth in mid-gestation seemed linked to behavioral outcome, rather than ICV in the third trimester. These findings are potentially in line with findings in the Born in Bradford cohort, where positive associations between fetal size and growth in early and mid-gestation and academic attainment in childhood rather than in the third trimester (Norris et al., 2018). However, more longitudinal research is needed. Automated artificial intelligence approaches provide an opportunity to investigate fetal brain development on a much larger scale and to answer fundamental questions related to prenatal brain development (Namburete et al., 2023).

References

1. Clifford, A., Lang, L., Chen, R., Anstey, K.J., Seaton, A. (2016), 'Exposure to air pollution and cognitive functioning across the life course - A systematic literature review' Environ Res, vol. 147, pp. 383-398.
2. Davies, C., Segre, G., Estradé, A., Radua, J., De Micheli, A., Provenzani, U., et al. (2020). 'Prenatal and perinatal risk and protective factors for psychosis: a systematic review and meta-analysis' Lancet Psychiatry, vol. 7, no. 5, pp. 399-410.
3. De Zwarte, S.M.C., Teeuw, J., He, J., Bekker, M.N., van Sloun, R.J.G., Hulshoff Pol, H.E. (2022), 'Automated segmentation of fetal intracranial volume in 3D ultrasound using deep learning: identifying sex differences in prenatal brain development' BioRxiv, https://doi.org/10.1101/2022.12.19.521094
4. Gao, W., Grewen, K., Knickmeyer, R.C., Qiu, A., Salzwedel, A., Lin, W., Gilmore, J.H. (2019), 'A review on neuroimaging studies of genetic and environmental influences on early brain development' NeuroImage, vol. 185, pp. 802-812.
5. Hulshoff Pol, H.E., Hoek, H.W., Susser, E., Brown, A.S., Dingemans, A., Schnack, H.G., et al. (2000), 'Prenatal exposure to famine and brain morphology in schizophrenia' Am J Psychiatry, vol. 157, no. 7, pp. 1170-1172.
6. Namburete, A.I.L., Papież, B.W., Fernandes, M., Wyburd, M.K., Hesse, L.S., Moser F.A., et al. (2023), 'Normative spatiotemporal fetal brain maturation with satisfactory development at 2 years', Nature, vol. 623, no. 7985, pp. 106-114.
7. Norris, T., Johnson, W., Petherick, E., Cameron, N., Oddie, S., Johnson, S., et al. (2018), 'Investigating the relationship between fetal growth and academic attainment: secondary analysis of the Born in Bradford (BiB) cohort' Int J Epidemiol, vol. 47, no. 5, pp. 1475-1484.

Poster No 1317

A simultaneous EEG-fMRI protocol for exploring the development of hierarchical sensory processing

Parvaneh Adibpour[1], Vyacheslav Karolis[1], Ines Tomazinho[2], Beya Bonse[2], Kamilah St Clair[2], Wendy Norman[2], Kathleen Colford[2], Massimo Marenzana[2], Fraser Aitken[3], Claire Kabdebon[4], Jonathan O'Muircheartaigh[5], Tomoki Arichi[1,6,7]

[1]Centre for the Developing Brain, Department of Perinatal Imaging and Health, King's College London, London, United Kingdom, [2]Guys and St Thomas' NHS Foundation Trust, London, United Kingdom, [3]School of Biomedical Engineering and Imaging Sciences, King's College London, London, United Kingdom, [4]Laboratoire de Sciences Cognitives et Psycholinguistique, Département d'études cognitives, ENS, CNRS, Paris, France, [5]Department of Forensic and Neurodevelopmental Sciences, King's College London, London, United Kingdom, [6]Department of Bioengineering, Imperial College London, London, United Kingdom, [7]Evelina London Children's Hospital, Guy's and St Thomas' NHS Foundation Trust, London, United Kingdom

Introduction: According to the predictive coding framework, sensory information is processed along a hierarchy, where higher-level processing areas generate predictions that are compared against incoming sensory evidence, and when not matched (i.e., deviance), a prediction error is generated, and the brain revises its model of the world[1]. Little is known about how the neural substrates of predictive processing emerge in the developing brain, which is of particular relevance for neurodevelopmental conditions such as Autism Spectrum Condition where atypical sensory network profiles[2] and predictive abilities[3] are reported. We aimed to establish a protocol for investigating the hierarchy of auditory predictive processing across development that can disentangle the different components of predictive processing in time and space by combining EEG and fMRI.

Methods: The paradigm consists of blocks of sounds with 6 repetitions of a sequence composed of four speech syllables. Blocks consisted of either repetition of the same sound sequence (standard blocks) or occasional violation of regularities with sequences involving a deviant or a missing sound (deviant or omission blocks-Figure.1). To test the paradigm, simultaneous EEG-fMRI data were acquired from 8 adults and a pilot dataset of 4 neonates (birth age =39.8 [37.6-40.9] gestational weeks, scan age = 41.3 [40-44.1] weeks). BOLD fMRI data were acquired on a Philips Achieva 3T MRI scanner with a 32-channel head coil, using an echo-planar imaging sequence with TR (infant 2001/adult 2500) ms, resolution (infant 2.08x2.08x2.9; adult 3.5x3.5x4.5 mm3). Preprocessing and GLM analysis were performed in FSL[4] to define subject-level activation maps. For adult group analysis, z-statistical maps from each subject were aligned to the subject's T1-weighted image and warped to the MNI152 space using ANTs[6], and group average effects were identified using nonparametric permutation testing. EEG data was acquired using a 32-channel MR-compatible Brain Products system. MR gradient and pulse artefacts were removed from recorded data using Analyzer II software. Recordings were filtered (0.5-30 Hz), cleaned for motion artifacts using

APICE preprocessing pipeline[6], interpolated for noisy channels, re-referenced with respect to average-reference, and then segmented into epochs relative to the onset of the last sound in the sequence. Auditory evoked responses were obtained by averaging the trials corresponding to each experimental condition. Average activity over fronto-central channels were compared between conditions using a paired t-test.

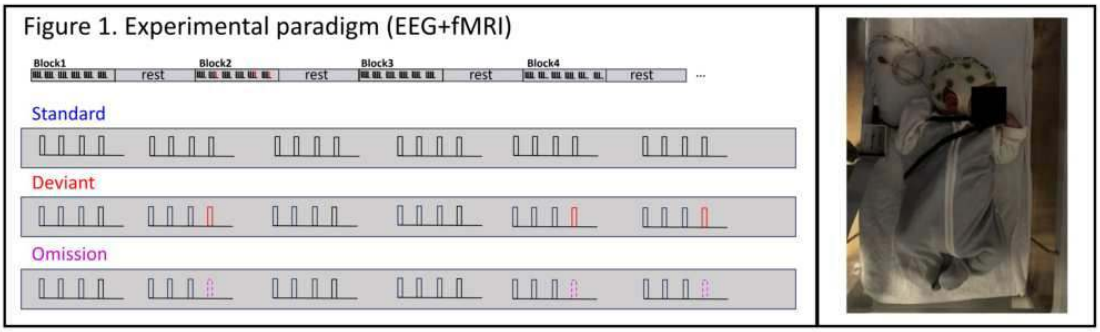

Figure 1. Left: Experimental paradigm showing the stimulation blocks interleaved with resting periods. Each row illustrates one experimental block. Right: a neonate wearing an EEG cap before entering the MRI machine.

Results: Preliminary analyses indicated EEG auditory evoked responses to the sequence of 4 sounds with a decrease in amplitude from the 1st to the 3rd sound consistent with habituation (Figure 2.a). For the last (4th) sound, a mismatch response to deviance (deviant/omission vs standard) was elicited in both adults and neonates (Figure 2.b). Mismatch responses had a frontocentral scalp distribution, with a negative polarity in adults and a positive polarity in neonates; and were slower in neonates. FMRI analyses identified significant clusters of functional activity in response to sound blocks within the primary auditory cortices, planum temporal as well as superior temporal and frontal gyri (Figure 2.c).

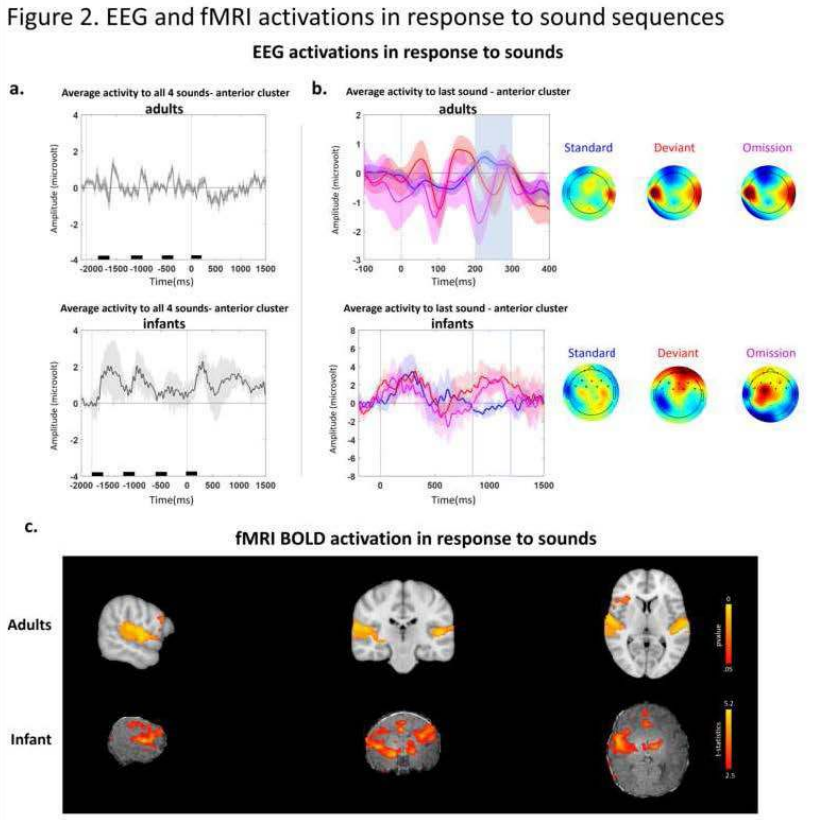

Figure 2. EEG: a) Average activity over the anterior cluster in response to the sequence of 4 sounds in adults (top, n = 8) and neonates (bottom, n = 4), showing a decrease in amplitude from the 1st to the 3rd sound following habituation. b) Average activity over the anterior cluster in response to the last sound in adults (top) and neonates (bottom) illustrate the mismatch response in the highlighted time-window. c) fMRI activations in response to sound blocks in adults (top, n=8, group-level analysis) and one example neonate (bottom, subject-level analysis) covering the primary auditory cortices, planum temporale, and superior temporal and frontal gyri.

Conclusions: We have established an experimental procedure for simultaneous EEG-fMRI studies to explore the neural correlates of detecting violations of regularity during sound sequence processing. In-scanner EEG mismatch responses were consistent with previous reports[7], confirming that although less mature in their responses than adults, neonates are sensitive to the statistics of auditory sequences. This will enable detailed investigation of the link between EEG and fMRI activations such as the spatial correlates of individual components of the EEG responses involved in predictive processing.

References

1. Clark, A. (2013). Whatever next? Predictive brains, situated agents, and the future of cognitive science. Behavioral and brain sciences, 36(3), 181-204.
2. Guiraud, J. A., Kushnerenko, E., Tomalski, P., Davies, K., Ribeiro, H., Johnson, M. H., & BASIS team. (2011). Differential habituation to repeated sounds in infants at high risk for autism. Neuroreport, 22(16), 845-849.
3. Sinha, P., Kjelgaard, M. M., Gandhi, T. K., Tsourides, K., Cardinaux, A. L., Pantazis, D., ... & Held, R. M. (2014). Autism as a disorder of prediction. Proceedings of the national academy of sciences
4. Woolrich, M. W., Ripley, B. D., Brady, M., & Smith, S. M. (2001). Temporal Autocorrelation in Univariate Linear Modeling of FMRI Data. NeuroImage, 14(6), 1370–1386 www.fmrib.ox.ac.uk/fsl
5. Avants, B. B., Tustison, N., & Song, G. (2009). Advanced normalization tools (ANTS). Insight j, 2(365), 1-35.
6. Fló, A., Gennari, G., Benjamin, L., & Dehaene-Lambertz, G. (2022). Automated Pipeline for Infants Continuous EEG (APICE): A flexible pipeline for developmental cognitive studies. Developmental Cognitive Neuroscience, 54, 101077.
7. Dehaene-Lambertz, G., & Gliga, T. (2004). Common neural basis for phoneme processing in infants and adults. Journal of cognitive neuroscience, 16(8), 1375-1387.

Poster No 1318

Estimation of iron levels via T2* mapping increases with age in the fetal brain

Mark Duffy[1], Amyn Majbri[2], Ellyn Kennelly[3], Tanya Bhatia[2], Lanxin Ji[1], Moriah Thomason[4]

[1]NYU Langone Health, New York, NY, [2]New York University Medical Center, New York, NY, [3]Wayne State University, Detroit, MI, [4]NYU Langone Medical Center, New York, NY

Introduction: Iron is highly expressed in the brain, playing an essential role in neurodevelopmental processes including DNA and neurotransmitter synthesis, myelination and mitochondrial function[1]. Studies in children and adults have shown iron deficiency to have a significant effect on neurological mechanisms[2,3]. Recent studies have shown brain iron in subcortical regions, such as the thalamus, caudate, putamen and striatum, to be linked with cognitive function[4,5]. T2* mapping is an established method for attaining an indirect measure of brain iron levels[6,7]. Approximation of infant brain iron levels using T2* mapping has shown iron to increase across the entire brain directly after birth[8]. However, the study of brain iron levels in the fetus and their implications is an area relatively unexplored. This study aims to assess the relationship between fetal brain iron levels in subcortical regions and age via a T2*-based measure.

Methods: Multi-echo (ME) fMRIs for 41 fetuses gestational aged 30.69 ± 4.26 weeks were attained from the Perinatal Imaging of Neural Connectivity (PINC) project. Imaging data was obtained on a Siemens Magnetom Verio syngo MRI system with a 550g abdominal 4-channel Siemens Flex Coil. Two sets of ME-fMRI data were attained via 12-min ME-fMRI (360 volumes), with the following scanning parameters: dataset a) TR = 2000ms; TE = 18, 31.07, 44.14ms (3 echoes); flip angle: 83 degrees; voxel size: 3.5 x 3.5 x 3.5 mm3; N=10 runs, dataset b) TR = 2000ms; TE = 18, 34, 50ms (3 echoes); flip-angle: 83 degrees; voxel-size: 3.487 x 3.487 x 3.5 mm3, N=130 runs. Pre-processing of fMRI data was performed using SPM and FSL software. A measure for motion, DVARS, was estimated for each volume. Ten consecutive volumes with the lowest DVARS were identified and averaged for T2* estimation[9,10]. T2* maps were generated through the fitting of a logarithmic curve across echoes for each voxel. Voxels of T2* value outside the accepted range (0-200ms) were replaced by zero in FSL. T2* maps were then normalized to a 32-week template, by applying the transformation matrix estimated from the fMRI data using SPM. The reciprocal of T2*, R2*, was then estimated in 12 bilateral sub-cortical regions of interest (ROIs); anterior and posterior thalamus, putamen and caudate. The ROIs are defined by a data-driven parcellation approach. Mean values of the non-zero voxels within ROIs were calculated in FSL. Pearson's correlation analysis was performed via Python and SciPy/Pandas libraries to assess the relationship between T2* voxel values for ROIs and fetal age (weeks).

Results: Significant positive correlations were observed between mean voxel values in specific ROIs and increase in age. The left thalamic regions, caudate and putamen increased significantly with age (caudate: R=0.3965 p=0.0084; putamen: R=0.5886 p=0.00005; anterior thalamus: R=0.4485 p=0.0033; posterior thalamus: R=0.4063 p=0.0084). Similar trends were also seen in the right anterior thalamus and right putamen (thalamus: R=0.1431; putamen: R=0.1511).

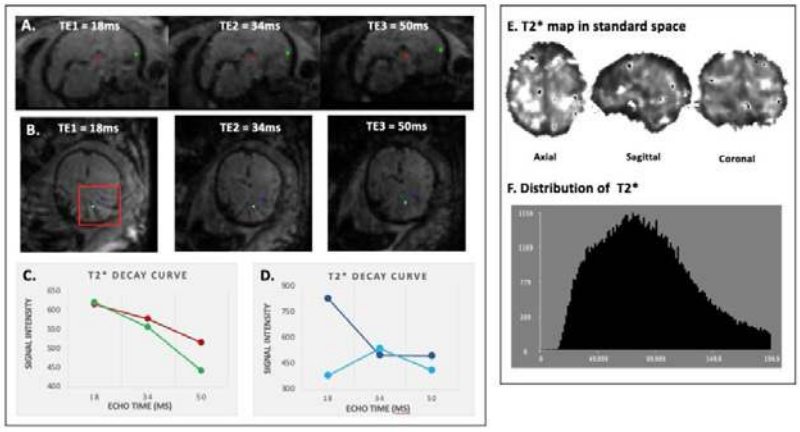

Fig.1. T2* decay curve across 3 echo times (TEs) (A-D). Example T2* map and distribution (E-F). (A+C) T2* decay curves for specific voxels (red and green) across echo 1 (18ms), echo 2 (34ms) and echo 3 (50ms) represent the decay in T2* signal over time. (B) Unsuccessful T2* curve fitting in specific voxels (light blue and navy) due to artefact present in volume disrupting signal, (D) resulting in T2 curve-fitting failure. (E) T2 generated from averaging 10 volumes with lowest DVARS per session and producing a map by fitting of a log curve across all 3 echoes for each voxel. (F) The distribution of voxel signal intensity across full volume of a T2* map.

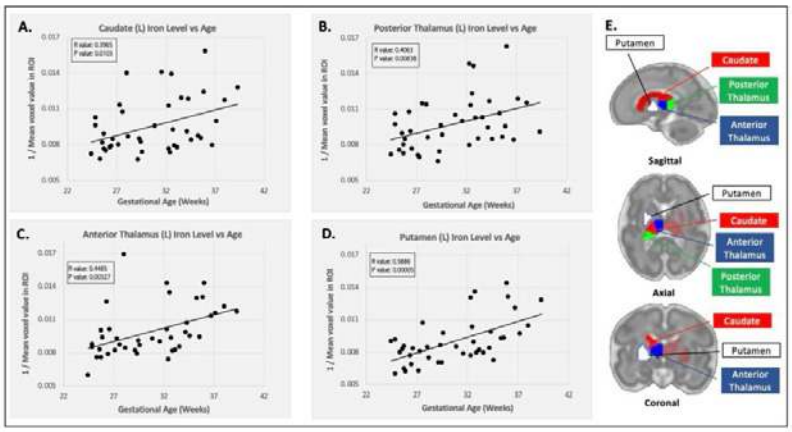

Fig.2. Iron levels increase with age (A-E). (A) Significant positive correlation between mean R2* voxel values across subjects and age in the left caudate (R=0.3965 p=0.0103). (B) Significant positive correlation between mean R2* voxel values across subjects and age in the left posterior thalamus (R=0.4063 p=0.0084). (C) Significant positive correlation between mean R2* voxel values across subjects and age in the left anterior thalamus (R=0.4485 p=0.0033). (D) Significant positive correlation between mean R2* voxel values across subjects and age in the left putamen (R=0.5886 p=0.00005). (E) Bilateral ROIs as defined by 32-week fetal template. 12 ROIs in total, 6 in each hemisphere; putamen (white), posterior (green) and anterior (navy) thalamus, caudate regions (x3) (red), right hemisphere regions (pink).

Conclusions: This study is the first to demonstrate the simulation of iron in brain development before birth. Our results indicate that fetal brain iron levels increase with age in subcortical regions that are high in iron concentration and key in cognitive processes. Although significance was not determined in all ROIs, positive trends across almost all regions support positive correlation. T2* mapping from multi-echo fMRI data represents a valid method for iron estimation in fetal brains. Future studies with larger datasets are required to further establish the relationship between iron and fetal brain development. To expand analysis, iron may be estimated across the whole brain over longer age ranges, and be linked with behavioral development after birth.

References

1. Reinert A, Morawski M, Seeger J, Arendt T, Reinert T. Iron concentrations in neurons and glial cells with estimates on ferritin concentrations. BMC Neurosci. 2019;20(1):25. Epub 20190529. doi: 10.1186/s12868-019-0507-7. PubMed PMID: 31142282; PMCID: PMC6542065.
2. Beard JL, Connor JR. Iron status and neural functioning. Annu Rev Nutr. 2003;23:41-58. Epub 20030410. doi: 10.1146/annurev.nutr.23.020102.075739. PubMed PMID: 12704220.
3. Nnah IC, Wessling-Resnick M. Brain Iron Homeostasis: A Focus on Microglial Iron. Pharmaceuticals (Basel). 2018;11(4). Epub 20181123. doi: 10.3390/ph11040129. PubMed PMID: 30477086; PMCID: PMC6316365.
4. Larsen B, Bourque J, Moore TM, Adebimpe A, Calkins ME, Elliott MA, Gur RC, Gur RE, Moberg PJ, Roalf DR, Ruparel K, Turetsky BI, Vandekar SN, Wolf DH, Shinohara RT, Satterthwaite TD. Longitudinal Development of Brain Iron Is Linked to Cognition in Youth. J Neurosci. 2020;40(9):1810-8. Epub 20200127. doi: 10.1523/jneurosci.2434-19.2020. PubMed PMID: 31988059; PMCID: PMC7046454.

5. Hect JL, Daugherty AM, Hermez KM, Thomason ME. Developmental variation in regional brain iron and its relation to cognitive functions in childhood. Dev Cogn Neurosci. 2018;34:18-26. Epub 20180522. doi: 10.1016/j.dcn.2018.05.004. PubMed PMID: 29894887; PMCID: PMC6250585.
6. Aquino D, Bizzi A, Grisoli M, Garavaglia B, Bruzzone MG, Nardocci N, Savoiardo M, Chiapparini L. Age-related iron deposition in the basal ganglia: quantitative analysis in healthy subjects. Radiology. 2009;252(1):165-72. doi: 10.1148/radiol.2522081399. PubMed PMID: 19561255.
7. Péran P, Cherubini A, Luccichenti G, Hagberg G, Démonet JF, Rascol O, Celsis P, Caltagirone C, Spalletta G, Sabatini U. Volume and iron content in basal ganglia and thalamus. Hum Brain Mapp. 2009;30(8):2667-75. doi: 10.1002/hbm.20698. PubMed PMID: 19172651; PMCID: PMC6871035.
8. Ji L, Yoon YB, Hendrix CL, Kennelly EC, Majbri A, Bhatia T, Taylor A, Thomason ME. Developmental coupling of brain iron and intrinsic activity in infants during the first 150 days. Developmental Cognitive Neuroscience. 2023;64:101326.
9. Jenkinson M, Beckmann CF, Behrens TE, Woolrich MW, Smith SM. FSL. Neuroimage. 2012;62(2):782-90. Epub 20110916. doi: 10.1016/j.neuroimage.2011.09.015. PubMed PMID: 21979382.
10. Kundu P, Brenowitz ND, Voon V, Worbe Y, Vértes PE, Inati SJ, Saad ZS, Bandettini PA, Bullmore ET. Integrated strategy for improving functional connectivity mapping using multiecho fMRI. Proc Natl Acad Sci U S A. 2013;

Poster No 1319

The dlPFC mediates the association between psychological control and externalizing behavior in youth

Jalmar Teeuw[1], Sahasra Vijayanand[2], Hilleke Hulshoff Pol[2]

[1]Department of Psychiatry, University Medical Center Utrecht, Utrecht, Netherlands, [2]Department of Experimental Psychology, Helmholtz Institute, Utrecht University, Utrecht, Netherlands

Introduction: Harsh and abusive parenting can have detrimental effects on a child's wellbeing and mental health (Mehta et al., 2023), and can have long-lasting effects on brain development (Teicher et al., 2016). The reciprocal relationship between parenting and externalizing behavior in children is well-established (Pinquart, 2017). Brain structures have been implicated in externalizing behaviors (Teeuw et al., 2022). Recent reports indicate that normal variations of parenting can also impact brain development (Cortes Hidalgo, et al., 2022). This raises the question if brain structures mediate the relationship between parenting and externalizing behavior.

Methods: We analyzed data from the longitudinal YOUth Child & Adolescent cohort at 'Around 9 years' (N=1,303) and 'Around 12 years' (N=385) (Onland-Moret et al., 2020). Externalizing behavior was assessed by the Child Behavior Checklist. Dimensions of parenting behavior were extracted from the Child's Report of Parent Behavior Inventory and the Parental Control questionnaire. Gray matter volumes were extracted from MRI scans using FreeSurfer (Fischl, 2012) (Figure 1). Partial correlation analysis was used to confirm associations of brain structures with parenting and externalizing behaviors, controlling for sex and age. The mediating role of brain structures on the relationship between parenting and externalizing behavior was investigated with the PROCESS Macro (Hayes, 2017). In a post-hoc analysis, results were controlled for the household environment.

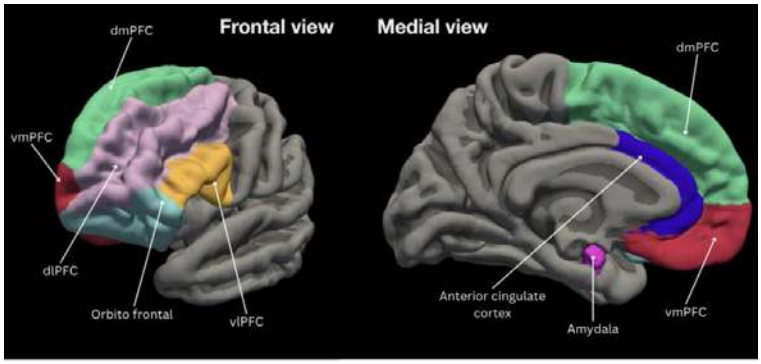

Figure 1. Overview of brain regions used in the analysis: ventral-medial prefrontal cortex (vmPFC), dorsal-medial PFC (dmPFC), dorsolateral PFC (dlPFC), ventral-lateral PFC (vlPFC), orbitofrontal cortex (OFC), anterior cingulate cortex (ACC), amygdala (AMY), and total brain volume (TBV).

Results: The factor analysis of the parenting questionnaires revealed two dimensions: (1) psychological control (accounting for 19% of the total variance) and (2) parental strictness (12% of total variance). Higher psychological control (ρ_9y=+0.16, p=2.03E−06; ρ_12y=+0.34, p=6.20E−05) and less strict parenting (ρ_9y=−0.08, p=1.28E−02) was associated with higher

levels of externalizing behavior (Figure 2A). In addition, higher psychological control at 9 years was predictive of externalizing behavior at 12 years (ρ_9y->12y=+0.21, p=4.28E−04). These effects remained significant after controlling for the household environment (p<0.034). Higher psychological control at age 9 years was associated with lower gray matter volume of the AMY, dlPFC, OFC, and TBV (range ρ_9y=[−0.11,−0.08], p_min=1.84E−03; Figure 2B). Higher levels of externalizing behavior was also negatively associated with lower gray matter volume of AMY, dmPFC, dlPFC, and TBV at age 9 years (range ρ_9y=[−0.10,−0.07], p_min=3.17E−03), and for vmPFC (ρ_12y=−0.31, p=7.37E−03) and ACC (ρ_12y=−0.27, p=2.50E−02) at age 12 years. Moreover, except for the AMY and the vmPFC, lower gray matter volume of brain structures at age 9 years was predictive of externalizing behavior at 12 years (range ρ_9y->12y=[−0.17,−0.11], p_min=1.89E−03), but not reversed. Only the associations for the AMY, dlPFC, and OFC at age 9 years remained significantly associated with psychological control and externalizing behavior at ages 9 and 12 years after controlling for the household environment. Based on these findings, the dlPFC, OFC and TBV were selected as prime candidates for the main mediation analysis. There was significant mediation of the association between psychological control of parents at age 9 years and externalizing behavior of children at age 12 years by the dlPFC (indirect effect: +0.035, 95%CI [+0.007; +0.072]; 14.7% of total effect), but was not significant for OFC (indirect effect: +0.013, 95%CI [−0.006; +0.037], 6.1% of total effect) or TBV (indirect effect: +0.007, 95%CI [−0.006; +0.028], 3.0% of total effect) (Figure 2C).

Conclusions: Psychological control of parents and externalizing behavior of children are associated with gray matter volumes, and the relationship between the two is mediated by the dlPFC. These findings suggest that normal variation in parenting can influence brain development of children with implications for their behavior, such as externalizing behavior, in adolescence.

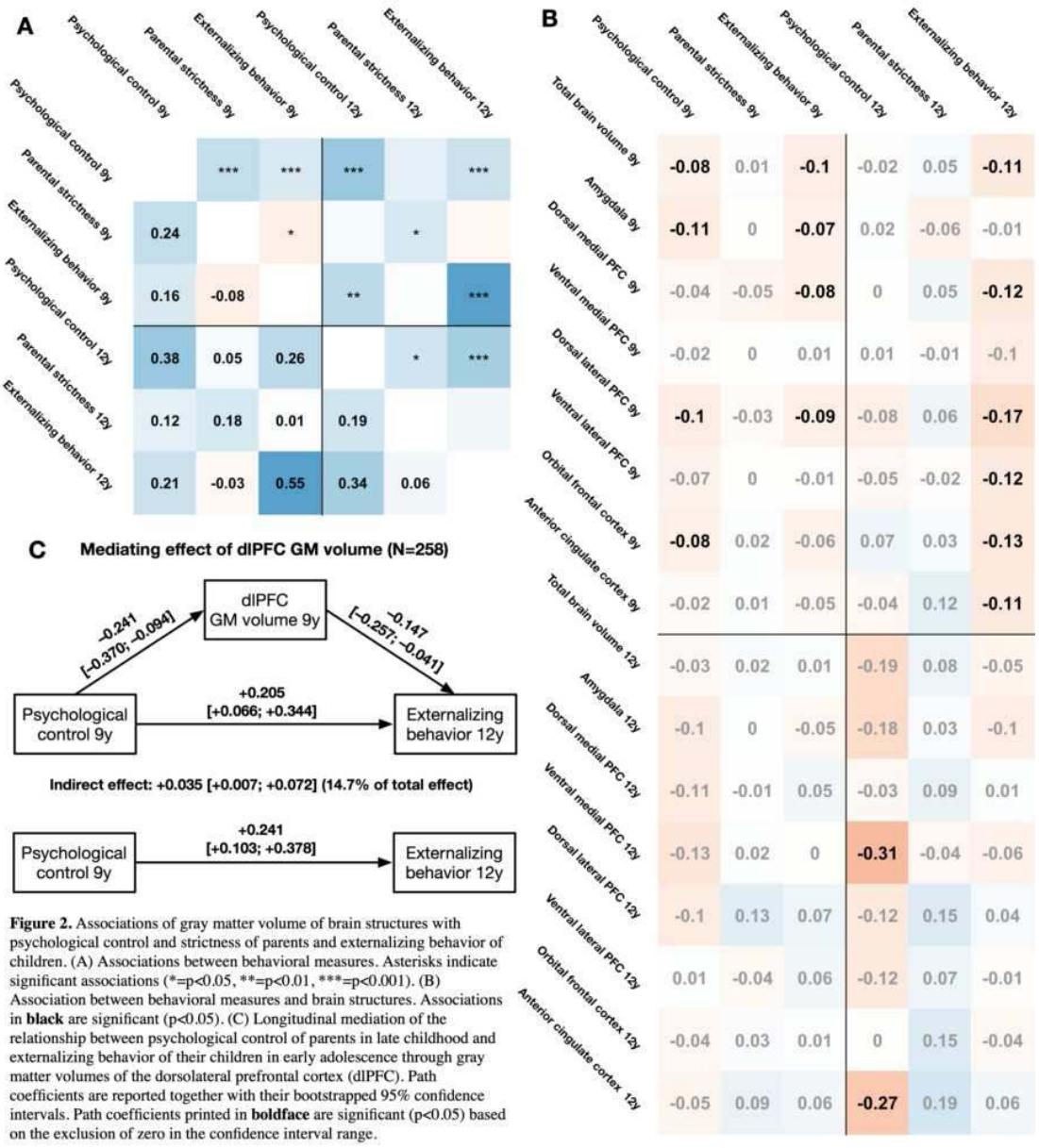

Figure 2. Associations of gray matter volume of brain structures with psychological control and strictness of parents and externalizing behavior of children. (A) Associations between behavioral measures. Asterisks indicate significant associations (*=p<0.05, **=p<0.01, ***=p<0.001). (B) Association between behavioral measures and brain structures. Associations in **black** are significant (p<0.05). (C) Longitudinal mediation of the relationship between psychological control of parents in late childhood and externalizing behavior of their children in early adolescence through gray matter volumes of the dorsolateral prefrontal cortex (dlPFC). Path coefficients are reported together with their bootstrapped 95% confidence intervals. Path coefficients printed in **boldface** are significant (p<0.05) based on the exclusion of zero in the confidence interval range.

References

1. Cortes Hidalgo, A.P., Thijssen, S., Delaney, S.W., Vernooij, M.W., Jansen, P.W., Bakermans-Kranenburg, M.J., van IJzendoorn, M.H., White, T., Tiemeier, H. (2022). 'Harsh Parenting and Child Brain Morphology: A Population-Based Study'. Child Maltreat. vol. 27, pp. 163–173
2. Fischl, B. (2012). 'FreeSurfer'. Neuroimage vol. 62, pp. 774–781
3. Hayes, A.F. (2017). 'Introduction to Mediation, Moderation, and Conditional Process Analysis: A Regression-Based Approach'. Guilford Press, New York
4. Mehta, D., Kelly, A.B., Laurens, K.R., Haslam, D., Williams, K.E., Walsh, K., Baker, P.R.A., Carter,
5. H.E., Khawaja, N.G., Zelenko, O., Mathews, B. (2023). 'Child Maltreatment and Long-Term Physical and Mental Health Outcomes: An Exploration of Biopsychosocial Determinants and Implications for Prevention'. Child Psychiatry Hum. Dev. vol. 54, pp. 421–435
6. Onland-Moret, N.C., Buizer-Voskamp, J.E., Albers, M.E.W.A., Brouwer, R.M., Buimer, E.E.L., Hessels, R.S., de Heus, R., Huijding, J., Junge, C.M.M., Mandl, R.C.W., Pas, P., Vink, M., van der Wal, J.J.M., Hulshoff Pol, H.E., Kemner, C. (2020). 'The YOUth study: Rationale, design, and study procedures'. Dev. Cogn. Neurosci. vol. 46, 100868
7. Pinquart, M. (2017). 'Associations of parenting dimensions and styles with externalizing problems of children and adolescents: An updated meta-analysis'. Dev. Psychol. vol. 53, pp. 873–932
8. Teeuw, J., Klein, M., Mota, N.R., Brouwer, R.M., van 't Ent, D., Al-Hassaan, Z., Franke, B., Boomsma, D.I., Hulshoff Pol, H.E. (2022). 'Multivariate Genetic Structure of Externalizing Behavior and Structural Brain Development in a Longitudinal Adolescent Twin Sample'. Int. J. Mol. Sci. vol. 23, 3176
9. Teicher, M.H., Samson, J.A., Anderson, C.M., Ohashi, K. (2016). 'The effects of childhood maltreatment on brain structure, function and connectivity'. Nat. Rev. Neurosci. vol. 17, pp. 652–666

Poster No 1320

CentileBrain Normative Models of Brain Morphometry Can Generalize to Diverse Ethnoracial Groups

Ruiyang Ge[1], Yuetong Yu[1], Guoyuan Yang[2], Jia-hong Gao[3], Ryota Hashimoto[4], Masaki Fukunaga[5], Junya Matsumoto[4], Kiyotaka Nemoto[6], Neda Jahanshad[7], Paul Thompson[8], Sophia Frangou[1]

[1]University of British Columbia, Vancouver, British Columbia, [2]Beijing University of Technology, Beijing, China, [3]Peking University, Beijing, Beijing, [4]National Center of Neurology and Psychiatry, Kodaira, Japan, [5]National Institute for Physiological Sciences, Okazaki, Aichi, [6]Department of Psychiatry, University of Tsukuba, Ibaraki, Japan, [7]Imaging Genetics Center, Keck School of Medicine of University of Southern California, Los Angeles, California, [8]Imaging Genetics Center, Keck School of Medicine of University of Southern California, Los Angeles, CA

Introduction: Application of the normative modeling to brain morphometry data has the potential to inform about the significance of normative deviation in brain morphometry for health and disease[1,2]. However, the majority of data collected are from individuals of European ancestry or those who may self-identify as non-Hispanic Whites[3], and the generalization of the fit of established brain morphological norms to a broad range of ethnoracial groups remains largely unexamined.

Methods: We have developed robust age- and sex-specific CentileBrain normative models (https://centilebrain.org/)[4] of regional measures of cortical thickness, cortical surface area, and subcortical volumes using structural brain scans from a pooled sample of 37,407 healthy individuals (53.33% female; aged 3 to 90 years) with diverse but mostly European background. In the present report, model parameters computed in the model development sample were tested for their generalizability to independent samples, each comprising healthy individuals either self-identifying as Black (n=284), South Asian (n=376), East Asian Chinese (n=1,136), and East Asian Japanese (n=970) or using genetic data to label ancestry as African (n=104), Admixed American (n=57), East Asian (n=415), and European (n=428). Mean-absolute-error (MAE) and root-mean-square-error (RMSE) served as the main measure of model performance.

Results: Regardless of the definition of the ethnoracial groupings, the correlation coefficient between the MAE and RMSE values of regional morphometric measures obtained from the model development sample and the MAE and RMSE values of the corresponding morphometric measures obtained in each ethnoracial sample were all greater than 0.96 for all ethnoracial groups (Figure 1 and Figure 2).

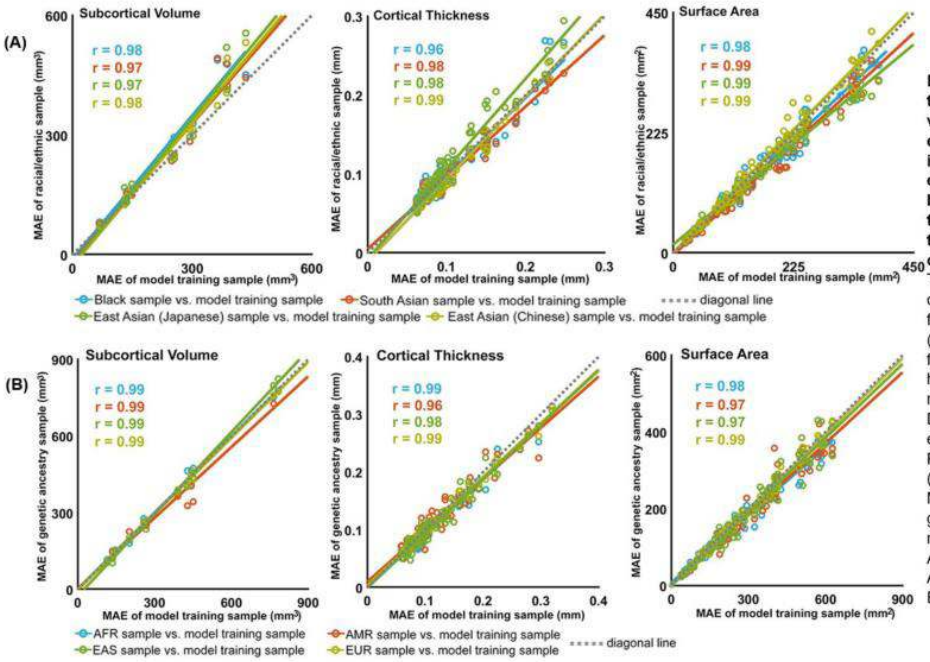

Figure 1. Scatterplots illustrate the mean-absolute-error (MAE) values derived from (A) ethnoracial groups self-identified by participants, (B) ethnoracial groups determined by genetic ancestry, alongside the corresponding values from the model optimization/training sample. The observed pattern remained consistent across both sexes and for the root-mean-square-error (RMSE) metric The results for female participants are shown here. Each circle denotes a regional morphometric measure. Different colors indicate different ethnoracial groups. The Pearson's correlation coefficient (r) was computed between the MAE values of each ethnoracial group with those obtained in the model optimization samples. AFR=African; AMR=Admixed American; EAS=East Asian; EUR=European.

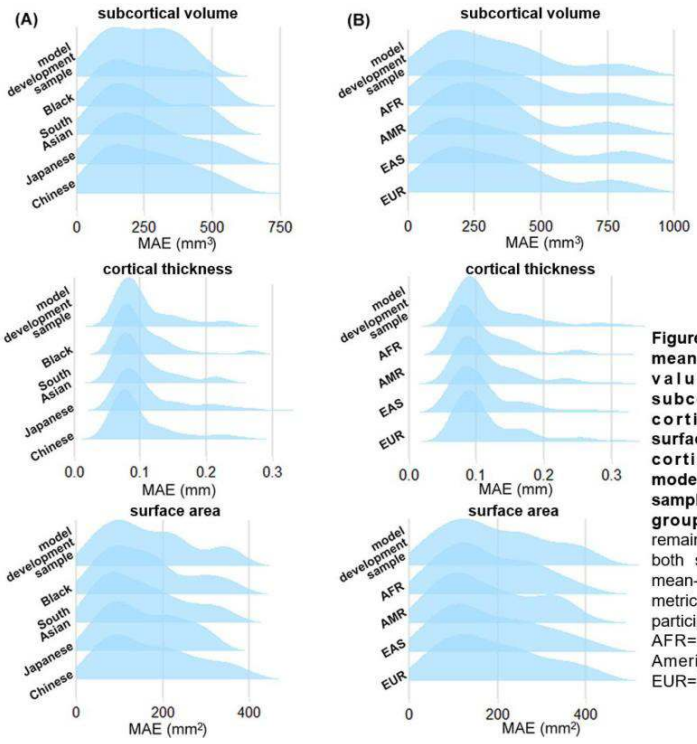

Figure 2. Distributions of the mean-absolute-error (MAE) values across the 14 subcortical volumes and cortical thickness and surface area across the 68 cortical regions for the model development/training sample and each ethnoracial group. The observed pattern remained consistent across both sexes and for the root-mean-square-error (RMSE) metric The results for female participants are shown here. AFR=African; AMR=Admixed American; EAS=East Asian; EUR=European.

Conclusions: This study provides evidence that our pre-trained CentileBrain normative models for brain morphometric measures can be applied to samples of diverse ethnoracial backgrounds across the human lifespan.

References

1. Marquand, A., et al. (2016). Understanding Heterogeneity in Clinical Cohorts Using Normative Models: Beyond Case-Control Studies. Biological Psychiatry, 80, 552-561.
2. Haas, S., et al. (2023). Normative modeling of brain morphometry in Clinical High-Risk for Psychosis. JAMA Psychiatry, in press.
3. Palk, A., et al. (2020). Ethical issues in global neuroimaging genetics collaborations. NeuroImage, 221, 117208.
4. Ge, R., et al. (2023). Normative modeling of brain morphometry across the lifespan using CentileBrain: Algorithm benchmarking and model optimization. Lancet Digital Health (accepted).

Poster No 1321

The overgrowth of structure-function coupling level in premature brain during infancy

Rong Wang[1], Jing Yu[1], Tianyu Fang[1], Yue Zhang[1], Qiuyun Fan[1], Yuanyuan Chen[1]

[1]Academy of Medical Engineering and Translational Medicine, Medical School of Tianjin University, Tianjin, China

Introduction: There are plenty of literatures about the two parallel development of infant brain during infancy, brain structure and brain function, but not about their coupling together with development, which also have been indicated to be very coupled in adult brain. In this study, we explore the concurrent development of brain structure and function in infants, a process known to be closely interlinked in adults. We are aimed to explore how the brain structure function couple during infancy, develop with age and alter with prematurity.

Methods: All data were acquired from the Developing Human Connectome Project(Hughes, Winchman et al. 2017). This study included 436 full-term infants (202 females; mean gestational age at birth: 39.9±1.27 weeks; mean PMA at scan:41.14±1.71 weeks) and 174 preterm infants (78 females, mean gestational age at birth: 32.24±3.44 weeks), out of which 63 preterm infants underwent two scans (PMA of 1th scan at birth: 34.49±1.77 weeks; PMA at 2th scan at term-equivalent age: 40.96±2.10 weeks). Cognitive assessments were collected at approximately 18 months of age using the Bayley Scale of Infant Development third edition (BSID-III). Image preprocessing was done including distortion correction, motion correction, scrubbing, interpolation, filtering, nuisance regression of spectrally matched motion parameters plus signals within CSF, white-matter, and grey-matter tissues. The UNC neonatal brain template as well as the AAL-aligned brain parcellation with 90 nodes were used to define the final space, and to construct the structural and functional connectome. Functional connectivity matrixes were calculated based on Fisher-Z transformed correlation. Structural connectivity matrixes were obtained from the fiber bundle density between two regions. The structural and functional connectivity coupling index was calculated for each brain regions individually, based on a multilinear regression model. The regression model incorporated multiple cortical connectivity including Euclidean distance, shortest path length and communicability, which were obtained from the sparse structural connectivity matrix and used to predict functional connectivity for the connectivity profile at each region. And the R-square value of the regression model was considered as the coupling index between regional structure and function.

Results: The brain structure-function coupling at the whole brin level showed significant group difference between the preterm at birth, the preterm at TEA and the full-term group (see Figure 1a). The preterm group showed a lower coupling level at birth and followed with a great growth at TEA, which was even higher than the coupling level of full-term group and consistent across all sub systems (Figure 1b). However, the spatial pattern of coupling index for two groups showed quite similar, with higher level for unimodal cortex and lower level for transmodal cortex. The developmental dynamics with PMA showed a rapid increase for both whole brain and reginal coupling index in full-term group but not in preterm at TEA group (Figure 2a and 2b). Highlighted regions were located within unimodal networks (Figure 2c). Finally, the coupling index for both groups showed significant association with cognitive outcomes at 19 months age, controlling covariables like gestational age at birth, PMA at scan, gender and motion parameters (Figure 2 d and e). Noteworthy, negative association for preterm and positive association for full-term between coupling index and cognitive score were identified.

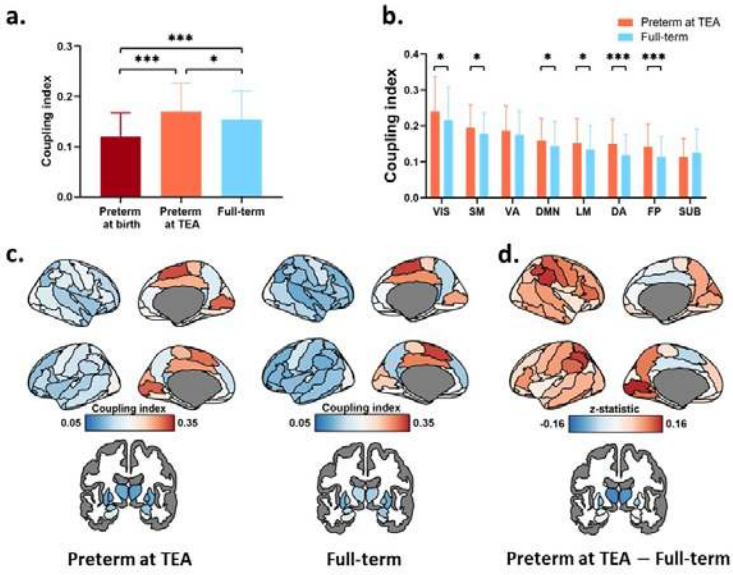

Fig.1 The differences and spatial distribution of SC-FC couping index in preterm and full-term infants. a) The group differences in whole-brain coupling index; **b)** The group differences in structural-functional connectivity coupling index between preterm at TEA and full-term at the level of networks (visual (VIS), sensorimotor (SM), ventral attention (VA), Default mode (DMN), limbic system (LM), dorsal attention (DA), frontoparietal control (FP), and subcortical (SUB) network); **c)** The spatial distribution of coupling index in preterm at TEA and full-term at the level of regions; **d)** The group differences in regional coupling index (z stats value from Two-Independent-Sample Mean z-Test). *: p<0.05, **:p<0.01, ***: p<0.001.

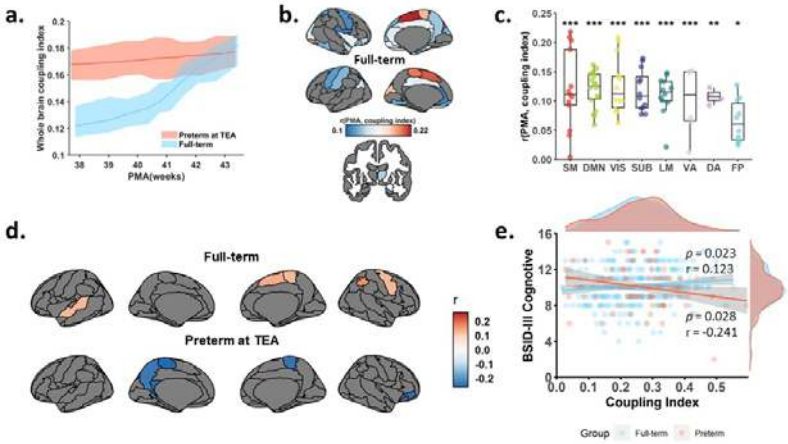

Fig 2. Coupling index development during the perinatal period and the correlation of coupling index with cognitive performance at 19 months age. a) The development trend of gradually increasing whole-brain coupling index in preterm at TEA and full-term. Infants in each group were divided into 10 bins based on PMA, and the average PMA and average whole-brain coupling index were calculated for each bin. Smooth processing was applied to the original folded line. The shaded envelope denotes the standard error for each bin; **b)** The r-values from Pearson's correlation with PMA and coupling index in full-term group. The grey area indicates no statistical significance. **c)** Correlation between PMA and coupling index grouped by brain network (asterisks indicate statistical significance). Each point represents a brain region. The x-ticks are arranged in descending order based on the network's r-values, with the larger values closer to the y-axis. *: p<0.05, **:p<0.01, ***: p<0.001; **d)** The r-values from Pearson's correlation with regional coupling index and cognitive scores. The grey area indicates no statistical significance. **e)** Correlation between coupling index and cognitive scores for the region of right paracentral lobule. Each point represents an individual. The shaded envelope denotes the 95% confidence interval.

Conclusions: The immaturity of brain is very sensitive and vulnerable to the explosive environment inputs. The preterm infant brain possesses low level of structure-function coupling at birth and goes through an overgrowth to the term equivalent age. This overgrowth of brain structure-function coupling for preterm infants was verified to be negative correlated with the 19-month-old cognition outcome.

References

1. Esfahlani, F. Z., J. Faskowitz, J. Slack, et al. (2022). "Local structure-function relationships in human brain networks across the lifespan." Nature Communications vol. 13(1).
2. Hughes, E. J., T. Winchman, F. Padormo, et al. (2017). "A dedicated neonatal brain imaging system." Magnetic Resonance in Medicine vol. 78(2): 794-804.
3. Liu, Z. Q., B. Vázquez-Rodríguez, R. N. Spreng, et al. (2022). "Time-resolved structure-function coupling in brain networks." Communications Biology vol. 5(1).

Poster No 1322

Neural development of language and speech in infants and toddlers

Kelly Hiersche[1], Zeynep Saygin[1]

[1]*The Ohio State University, Columbus, OH*

Introduction: Children acquire language without formal instruction. The "language-ready" brain hypothesis suggests infant brains are prewired for language acquisition due to the asymmetries in anatomical regions associated with language processing (Boeckx, 2014; Dehaene-Lambertz, 2006). Testing this hypothesis requires using both structural and functional MRI in the same infant, ideally using similar rigor as neuroimaging in adults; however, because children are notoriously difficult to scan with task fMRI during these early years of language acquisition, this hypothesis has not yet been explored. How early in human development can we observe selectivity within the language network to linguistically meaningful stimuli vs. human-produced speech sounds that are not linguistically meaningful? Are the early structural asymmetries actually precursors to this neural tuning for language or speech? In this study, we leverage novel neuroimaging and analysis methods to examine the response of the infant brain (ages 2-35 months) in native space to language and speech and their association with structural asymmetries both in anatomical regions (sROIs) and subject-specific functional regions (fROIs).

Methods: All infants completed at least one high-resolution T1-weighted MPRAGE scan (TR=2300ms, TE=2.9ms, voxel size=1.00 isotropic). We repeated structural scans until data quality was high enough for subsequent processing based on visual inspection during data acquisition. Structural data was processed using FreeSurfer's infant_recon_all (Zollei, 2020), visually checked for correctness. The outputs were used to examine height/depth of brain folds and curvature. Additionally, each infant completed at least two runs of a language localizer task (all TR=1000ms, TE=28ms, vox size=2x2x3mm) where they listened to audio recordings of male and female experimenters reading a children's book, with 3 conditions commonly used in language fMRI studies in adults: sentences (Sn), reverse sentences (Rv, Sn played in reverse; controls length, prosody and tone, but speech is meaningless), and a texturized sound condition (Tx, auditorily degraded Sn, unrecognizable as speech, low-level auditory control). All functional data was preprocessed with a similar protocol and exclusion criteria as prior fMRI work in infants (Deen 2017, Kosakowski, 2022). Functional to anatomical registration was completed using FSL's linear registration tool, FLIRT (Jenkinson 2001 & 2002) (affine, 12 dof; best registration method across all infants), and all registrations were visually examined for accuracy. Resulting GLM contrast were applied to an individualized-subject approach, mirroring rigor applied to adult neuroimaging, for creating fROIs (top 5% most responsive voxels in search spaces (Fedorenko, 2010); language Sn>Rv; speech SnRv>Tx). Anatomical parcellations in native space generated sROIs.

Results: We found no evidence of language (Sn-Rv) or speech (SnRv-Tx) selectivity in the sROIs (except RH orbital inferior frontal), perhaps due to functional heterogeneity within anatomical regions. Additionally, we do not see clear anatomical asymmetries. However, when using fROIs we found evidence of speech selectivity in RH superior temporal and LH inferior frontal fROIs, and quite surprisingly some initial sensitivity to linguistic stimuli as compared to reverse speech in the LH inferior frontal fROI (Fig. 1B). Interestingly, we also see greater LH inferior frontal fROI sulcal depth than RH (Fig. 1C).

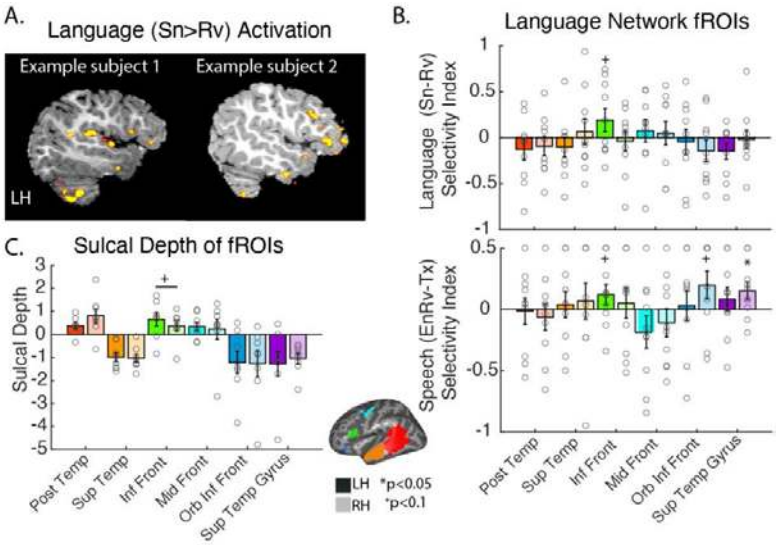

Figure 1: A. Sn>Rv activation in two example subjects. B. Mean selectivity to language (top) and speech (bottom) in 6 bilateral individually-defined fROIs, with standard error bars and individual subject data points. One-tailed t-tests of selectivity compared to zero used to assess significance. Inset shows language parcel search spaces used for fROIs on fsaverage inflated left hemisphere. C. Mean sulcal depth for fROIs. Two-tailed, paired samples t-tests used to assess differences between left and right fROIs.

Conclusions: These results highlight the importance of individually-defining fROIs even in infants, and show novel evidence in support of the early emergence (and developmental timecourse) of language selectivity and laterality in frontal cortex. We also identify a possible anatomical substrate for the development of this uniquely human skill. Future investigations will explore longitudinal development of this structure-function relationship, connectivity asymmetries, and extended language network (e.g. cerebellum, Fig.1A).

References

1. Boeckx, C. (2014). The shape of the human language-ready brain. Frontiers in psychology, 5, 282.
2. Deen, B. (2017). Organization of high-level visual cortex in human infants. Nature communications, 8(1), 13995.
3. Dehaene-Lambertz, G. (2006). Nature and nurture in language acquisition: anatomical and functional brain-imaging studies in infants. Trends in neurosciences, 29(7), 367-373.
4. Fedorenko, E. (2010). New method for fMRI investigations of language: defining ROIs functionally in individual subjects. Journal of neurophysiology, 104(2), 1177-1194.
5. Kosakowski, H. L. (2022). Selective responses to faces, scenes, and bodies in the ventral visual pathway of infants. Current Biology, 32(2), 265-274.
6. M. Jenkinson. (2001). A global optimisation method for robust affine registration of brain images. Medical Image Analysis, 5(2):143-156
7. M. Jenkinson. (2002). Improved optimisation for the robust and accurate linear registration and motion correction of brain images. NeuroImage, 17(2):825-841.
8. Zöllei, L. (2020). Infant FreeSurfer: An automated segmentation and surface extraction pipeline for T1-weighted neuroimaging data of infants 0–2 years. Neuroimage, 218, 116946.

Poster No 1323

Higher criticism statistics for fMRI: a secondary analysis of NARPS team results

Benedikt Sundermann[1,2], Anke McLeod[3], Christian Mathys[3,2]

[1]Evangelisches Krankenhaus Oldenburg, Medical Campus University of Oldenburg, Oldenburg, Lower Saxony, [2]Research Center Neurosensory Science, University of Oldenburg, Oldenburg, Germany, [3]Evangelisches Krankenhaus Oldenburg, Medical Campus University of Oldenburg, Oldenburg, Germany

Introduction: The Neuroimaging Analysis Replication and Prediction Study (NARPS) (Botvinik-Nezer et al. 2020) highlighted the heterogeneity of results obtained by different teams analyzing the same task-fMRI dataset (Botvinik-Nezer et al. 2019) and thus potential problems associated with analytical variability. Most NARPS-teams used mass-univariate testing, combined with cluster-based thresholding for multiple comparison (MC) correction. This raises the question, to what extent the variability of conclusions by different NARPS-teams was triggered by the limited capability of identifying consistent effects within areas of interest using mass-univariate approaches across the different original analyses. In this secondary analysis of NARPS data we used an alternative statistical approach, higher criticism (HC) to search for at least rare or weak effects in intermediate team results (unthresholded result maps). HC is a statistical approach for testing a global hypothesis that such effects are present within a large number of primary statistical tests by quantifying an excess of low p-values (Donoho and Jin 2015). HC has been introduced to assess subthreshold effects in fMRI avoiding limitations of conventional mass-univariate testing (Gerlach et al. 2021, Sundermann et al. 2023). Purpose of this analysis was: to assess whether HC-based global hypothesis testing for rare/weak effects based on result maps from different teams reduces the variability of results.

Methods: Analysis of publicly available intermediate results (unthresholded result maps; aggregate data, not individual subjects) from 64 teams in NARPS. Calculation of z-value maps with original published NARPS code and conversion to p-value maps representing equivalents of two-sided tests as a prerequisite for the rationale of p-value histogram interpretation underlying HC (different from original one-sided NARPS hypothesis tests). Extraction of p-values of all covered voxels from the regions of interests (ventro-medial prefrontal cortex, ventral striatum, and amygdala) from the NARPS common thresholding analysis. Visualization of p-value histograms and global hypothesis tests using the classical HC statistic. Comparison of HC-based global hypothesis test results and original team decisions for the 9 ROI/hypothesis-combinations.

Results: Most p-value histograms exhibited typical distributions as a prerequisite for an HC-based analysis. The global null hypothesis was rejected more frequently in HC-based analyses (82.1 % of tests) compared with rejected null hypotheses in the original NARPS team results (26.9 %), see Figure. For 5 out of 9 hypotheses with ambiguous results (null hypothesis rejected in 29.1 %) in the original analysis, HC rejected the global null hypothesis in a majority of teams (87.8 %). For 3 out of 9 hypotheses (amygdala) with originally negative results (null hypothesis rejected in 4.1 %), HC-based results were ambiguous (null hypothesis rejected in 68.2 % of tests). Secondary analyses revealed a small association of smoothness estimates from team maps with the HC decisions.

Conclusions: HC-based analyses revealed at least rare or weak effects within ROIs despite negative or ambiguous findings in conventional mass-univariate analyses of task-based fMRI data of mixed gambles reported in NARPS. It thus reduced variability of conclusions in a subset of NARPS hypotheses. HC-based findings also include effects in the amygdala, discussed as a negative result in the original fMRI study (Tom et al. 2007). Thus, HC-based analyses appear to have a higher probability of positive results than conventional thresholding of mass-univariate tests. They could not solve the problem with heterogeneous results across NARPS teams in general. HC rather shifted ambiguity towards hypotheses with negative results in the original analyses. While there is small effect of spatial map smoothness, smoothness does not appear to be the main driver of differences of HC-based results.

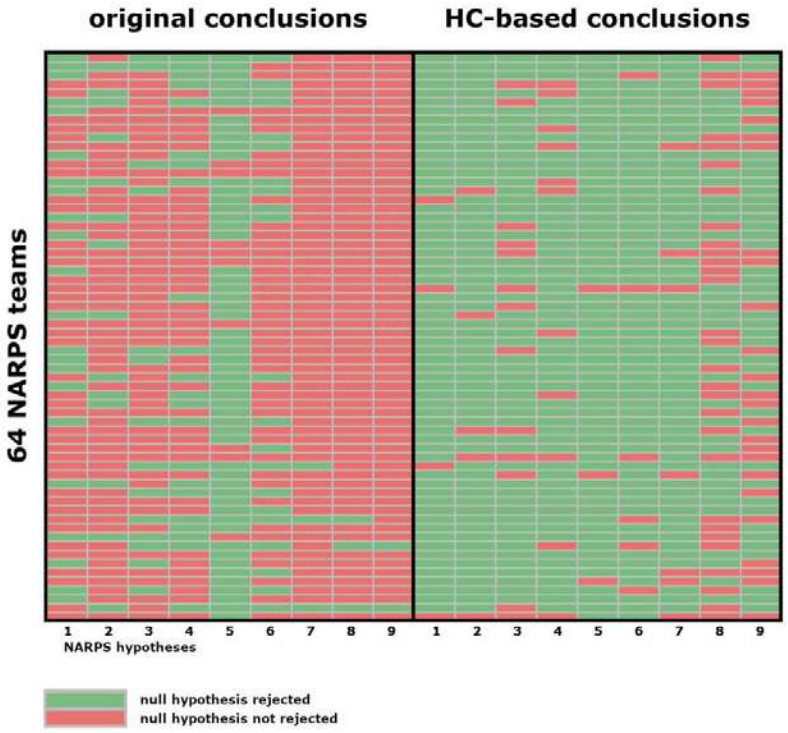

Figure - Comparison of original conclusions by 64 teams in NARPS vs. conclusions based on HC global hypothesis testing

References

1. Botvinik-Nezer, R., Holzmeister, F., Camerer, C. F., Dreber, A., Huber, J., Johannesson, M., et al. (2020). 'Variability in the analysis of a single neuroimaging dataset by many teams.' Nature, vol. 582, no. 7810, pp. 84-88.
2. Botvinik-Nezer, R., Iwanir, R., Holzmeister, F., Huber, J., Johannesson, M., Kirchler, M., Dreber, A., Camerer, C.F., Poldrack, R.A. and Schonberg, T., (2019). 'fMRI data of mixed gambles from the Neuroimaging Analysis Replication and Prediction Study.' Sci Data, vol. 6, no. 1, pp. 106.
3. Donoho, D. and Jin, J. (2015). 'Higher Criticism for Large-Scale Inference, Especially for Rare and Weak Effects.' Statistical Science, vol. 30, no. 1, pp. 1-25.
4. Gerlach, A. R., Karim, H. T., Kazan, J., Aizenstein, H. J., Krafty, R. T. and Andreescu, C. (2021). 'Networks of worry-towards a connectivity-based signature of late-life worry using higher criticism.' Transl Psychiatry, vol. 11, no. 1, pp. 550.
5. Sundermann, B., Pfleiderer, B., McLeod, A. and Mathys, C. (2023). 'Seeing more than the tip of the iceberg: Approaches to subthreshold effects in functional magnetic resonance imaging of the brain.' PsyArXiv Preprints. https://doi.org/10.31234/osf.io/fyhst
6. Tom, S. M., Fox, C.R., Trepel, C. and Poldrack, R.A. (2007). 'The neural basis of loss aversion in decision-making under risk.' Science, vol. 315, no. 5811, pp. 515-518.

Poster No 1324

An Electrophysiology-Silent fMRI Study to Inform the Neurofunctional Basis of Startle Habituation

Laura Naysmith[1], Owen O'Daly[1], Ana Beatriz Solana[2], Florian Wiesinger[2], Simon Hill[1], Steven Williams[1], Veena Kumari[3]

[1]King's College London, London, England, [2]GE Healthcare, Munich, Germany, [3]Brunel University, London, England

Introduction: The acoustic startle reflex provides an important model system for exploring information processing mechanisms and stem from acoustic-focused rodent models, translating to human neuroimaging findings. The startle reflex is subject to modulation, such as habituation which leads to attenuation of the reflex response, and is thought to reflect

attentional filtering of redundant information (Thompson & Spencer, 1966). Indeed, startle habituation impairments have been observed in disorders such as Parkinson's disease, schizophrenia, post-traumatic stress disorder, and Huntington's disease (review, McDiarmid, Bernandos & Rankin, 2017). To better understand information processing in healthy populations and, subsequently, dysfunction in clinical populations, the current study aimed to explore the neurofunctional basis of startle habituation, which remains poorly understood. In a mixed-sex, healthy young adult sample, the study combined simultaneous electromyography (EMG) to measure the startle reflex as an eyeblink, and fMRI to provide a closer coupling of stimulus, behaviour, and BOLD MR signal and hence, greater inference of the association of regional brain activation with startle behaviour and startle stimulus processing. Secondly, we present a major advancement in this work with the application of a silent fMRI sequence, Looping Star (Wiesinger, Menini, & Solana, 2019), which allowed for the continuous presentation of acoustic stimuli by minimising gradient-related acoustic noise. Neural circuitry underpinning startle habituation was hypothesised in the brainstem (Kuhn et al., 2020) and thalamus (McDowell et al., 2006) and when EMG-assessed measures of startle habituation were modelled as a covariate at the group-level fMRI analysis, neural activity was expected to decrease with more startle habituation.

Methods: Forty-two participants (M= 23.71 years) were presented with a passive auditory startle paradigm in the 3T MRI scanner, which consisted of loud auditory clicks to elicit startle. EMG measures of startle were acquired in real-time using AcqKnowledge (BIOPAC Systems Inc.) and required online band-pass filtering and offline filtering, of which an innovative pipeline was developed to suit the frequency spectrum of Looping Star. We used a silent functional MRI multi-echo sequence called Looping Star (TE1/ TE2/ TE3/ TR= 0ms/ 17.9ms/ 35.8ms/ 2.62s). Imaging data were pre-processed and analysed in SPM12. An optimal combination of the gradient echoes (TE= 17.9ms and 35.8ms) was used (Fig 1). At the group-level, a linear regression was conducted. EMG data, analysed in SPSS Statistics, calculated startle habituation as a regression slope per participant and these regression slope values were included as a covariate of interest at group-level. We conducted a regions of interest (ROI) approach (thalamus, McDowell et al., 2006; brainstem, Kuhn et al., 2020). We also tentatively conducted a whole brain analysis, as Hermann et al. (2020) highlighted the Default Mode Network (DMN) during startle habituation.

Results: BOLD fMRI activity in the thalamus, brainstem, and a cluster surmising the right putamen and extending to the right insula was observed (Fig 2). BOLD response in these regions correlated significantly positive with startle habituation slope values, thus indicating a decrease in BOLD MR response with more startle habituation (negative startle habituation slope value).

Conclusions: Simultaneous EMG data enriched fMRI findings of the neural basis of startle habituation by identifying a positive relationship between acoustic startle habituation and sub/cortical regions. The direction of relationship between fMRI BOLD and startle habituation can be used to further examine how the acoustic primary startle circuit is mediated, such as through reticular activating system (McDowell et al., 2006) or cortical networks such as the DMN (Hermann et al., 2020) and encourage further fMRI investigations in clinical populations which show aberrations in startle habituation.

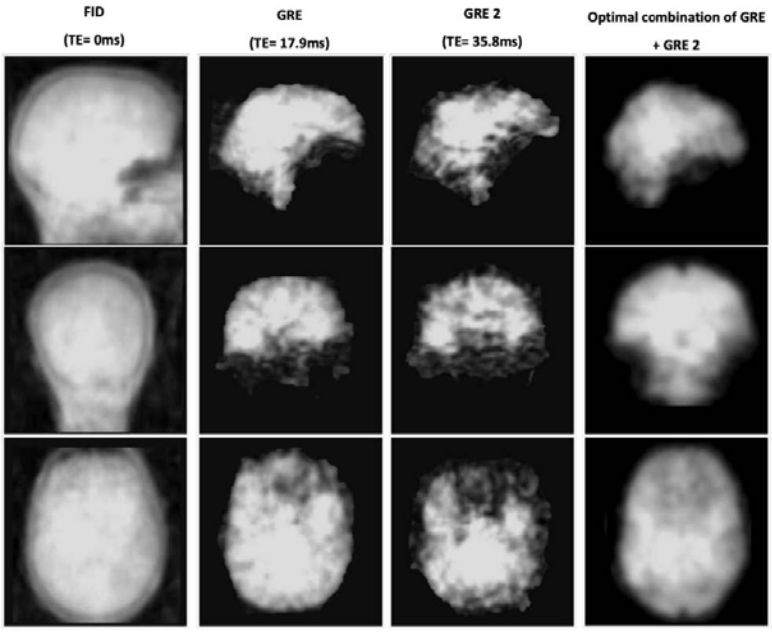

Fig. Sagittal, coronal, and axial slices of free induction decay (FID), gradient echoes (GRE) (1 and 2), and optimal combination of gradient echoes of one participant.

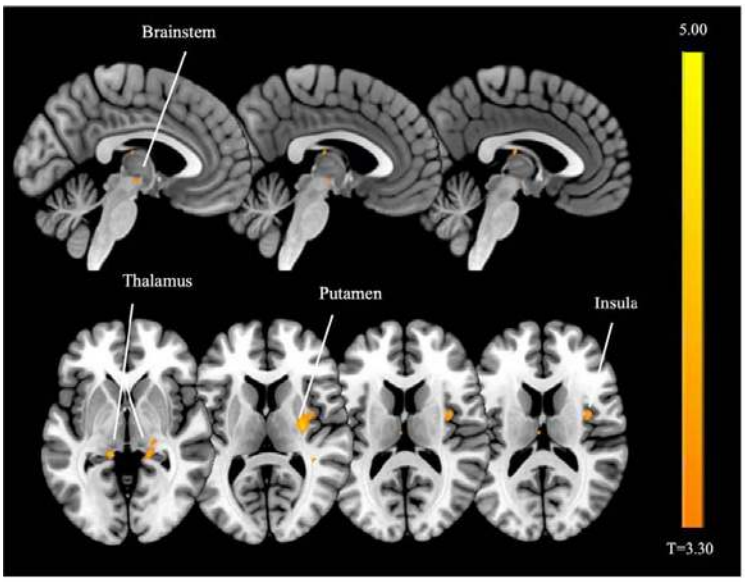

Fig. ROI BOLD activity (bilateral thalamus and brainstem) and a BOLD activity in a cluster surmising right putamen to ig. right insula showed a decrease in MR response with more startle habituation.

References

1. Hermann, B., Salah, A. B., Perlbarg, V., Valente, M., Pyatigorskaya, N., Habert, M. O., Raimondo, F., Stender, J., Galanaud, D., Kas, A., Puybasset, L., Perez, P., Sitt, J. D., Rohaut, B., & Naccache, L. (2020). Habituation of auditory startle reflex is a new sign of minimally conscious state. Brain, 143(7), 2154-2172.
2. Kuhn, M., Wendt, J., Sjouwerman, R., Buchel, C., Hamm, A., & Lonsdorf, T. B. (2020). The Neurofunctional Basis of Affective Startle Modulation in Humans: Evidence From Combined Facial Electromyography and Functional Magnetic Resonance Imaging. Biol Psychiatry, 87(6), 548-558.
3. McDiarmid, T. A., Bernardos, A. C., & Rankin, C. H. (2017). Habituation is altered in neuropsychiatric disorders—A comprehensive review with recommendations for experimental design and analysis. Neuroscience & Biobehavioral Reviews, 80, 286-305. https://doi.org/10.1016/j.neubiorev.2017.05.028
4. McDowell, J. E., Brown, G. G., Lazar, N., Camchong, J., Sharp, R., Krebs-Thomson, K., Eyler, L. T., Braff, D. L., & Geyer, M. A. (2006). The neural correlates of habituation of response to startling tactile stimuli presented in a functional magnetic resonance imaging environment. Psychiatry Res, 148(1), 1-10.
5. Thompson, R. F., & Spencer, W. A. (1966). Habituation: a model phenomenon for the study of neuronal substrates of behavior. Psychological review, 73(1), 16.
6. Wiesinger, F., Menini, A., & Solana, A. B. (2019). Looping Star. Magn Reson Med, 81(1), 57-68.

Poster No 1325

BayesfMRI: User-friendly spatial Bayesian modeling for task fMRI

Damon Pham[1], David Bolin[2], Martin Lindquist[3], Thomas Nichols[4], Amanda Mejia[1]

[1]Indiana University, Bloomington, IN, [2]King Abdullah University of Science and Technology, Thuwal, Saudi Arabia, [3]Johns Hopkins University, Baltimore, MD, [4]University of Oxford, Oxford, United Kingdom

Introduction: Spatial Bayesian models are a powerful way to account for spatial dependencies in fMRI analysis[3]. While massive univariate modeling treats each voxel or vertex as a separate entity, spatial Bayesian models place a multivariate prior distribution on the underlying maps of activation, which encodes the spatial dependence and implicitly smoothes the activation estimates. This avoids ad-hoc data smoothing, which induces spatially dependent noise and can lead to false positive clusters[2]. In addition, spatial Bayesian models can use the joint posterior distribution across brain locations to identify areas of activation. This dramatically increases power to detect activations and facilitates the use of meaningful minimum effect sizes, even in individual-level analysis[5]. The open-source BayesfMRI R package provides a user-friendly interface for spatial Bayesian models for task fMRI analysis. Importantly, the spatial Bayesian models implemented in BayesfMRI are surface-based and subcortical parcel-constrained. These grayordinates-based models leverage spatial dependencies in a neurobiologically appropriate way and avoid the mixing of signals known to occur with whole-brain volumetric smoothing or spatial modeling[1].

Methods: Fig. 1 illustrates the main functions of the BayesfMRI package. The BayesGLM function fits a spatial Bayesian model for subject-level task fMRI analysis. Wrapper functions provide direct compatibility with CIFTI, GIFTI and NIFTI-format data. The id_activations function identifies areas of significant activation above a specified minimum effect size, using the joint posterior distribution across locations. This substantially increases power to detect activations while controlling the family-wise error rate (FWER). Second-level analysis relies on the BayesGLM2 function, which uses group-average spatial Bayesian modeling[5]. Alternatively, the function act_prevalence produces group prevalence maps based on the subject-level activation maps. The plot function can be used to produce user-friendly visualizations of all results. BayesfMRI also includes fast prewhitening using spatially variable high-order AR modeling to effectively mitigate autocorrelation[4]. Planned future functionality includes Bayesian estimation and inference of hemodynamic response function (HRF) shape (e.g. height, width, onset) and data-driven individualized HRF estimation.

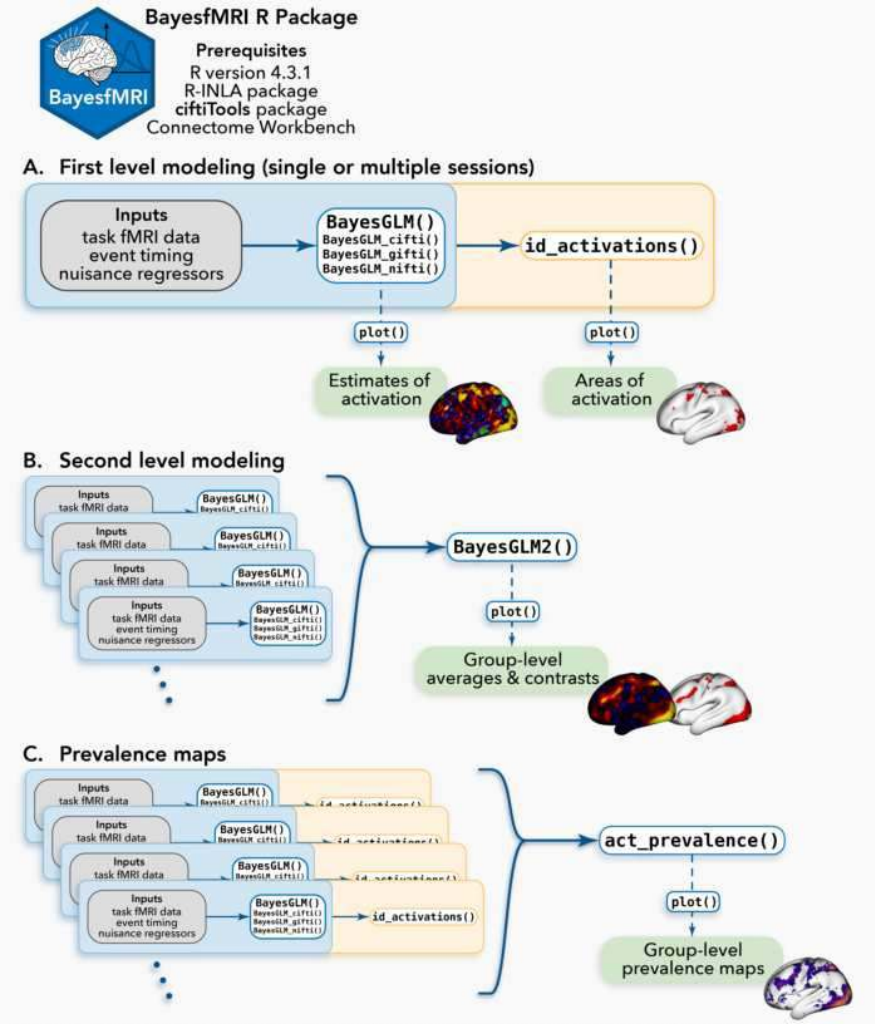

Figure 1. Schematic of BayesfMRI functions. (A) `BayesGLM` fits a spatial Bayesian model for subject-level task fMRI analysis. It includes prewhitening, nuisance regression, and inclusion of HRF derivatives. Wrapper functions provide direct compatibility with CIFTI, GIFTI and NIFTI-format data. `id_activations` identifies areas of significant activation above a specified minimum effect size, based on the joint posterior distribution across locations (see Technical Notes). This substantially increases power to detect activations while controlling the family-wise error rate (FWER). **(B)** `BayesGLM2` produces group-average estimates using spatial Bayesian modeling, and identifies areas of activation based on the joint posterior distribution of the group averages, as described in [3]. **(C)** `act_prevalence` produces group prevalence maps based on the subject-level activation maps from (A). The ability to produce robust prevalence maps is due to the relatively high power of spatial Bayesian modeling for first-level analysis. *Technical Notes: Activations defined as locations with activation amplitude significantly greater than a specified local signal change. Significance based on the joint posterior distribution across all locations. A significance level of 0.05 means that with posterior probability 0.95, all locations are "activated", i.e. the posterior probability of a single false positive, aka FWER, is 0.05.*

Results: Fig. 2 provides a demo of BayesfMRI, with pseudo-code and sample results based on an analysis of the HCP working memory task (n=20). First- and second-level spatial Bayesian models are illustrated. Example visualizations based on the real data are shown on the right. These show smooth estimates and robust areas of activation at both the individual and group level. As an alternative to group averages, group prevalence maps show the proportion of subjects exhibiting activation at each location. This shows similar patterns as the group-average activations but provide greater nuance and extent. These robust prevalence maps are possible due to high power at the first level provided by spatial Bayesian modeling.

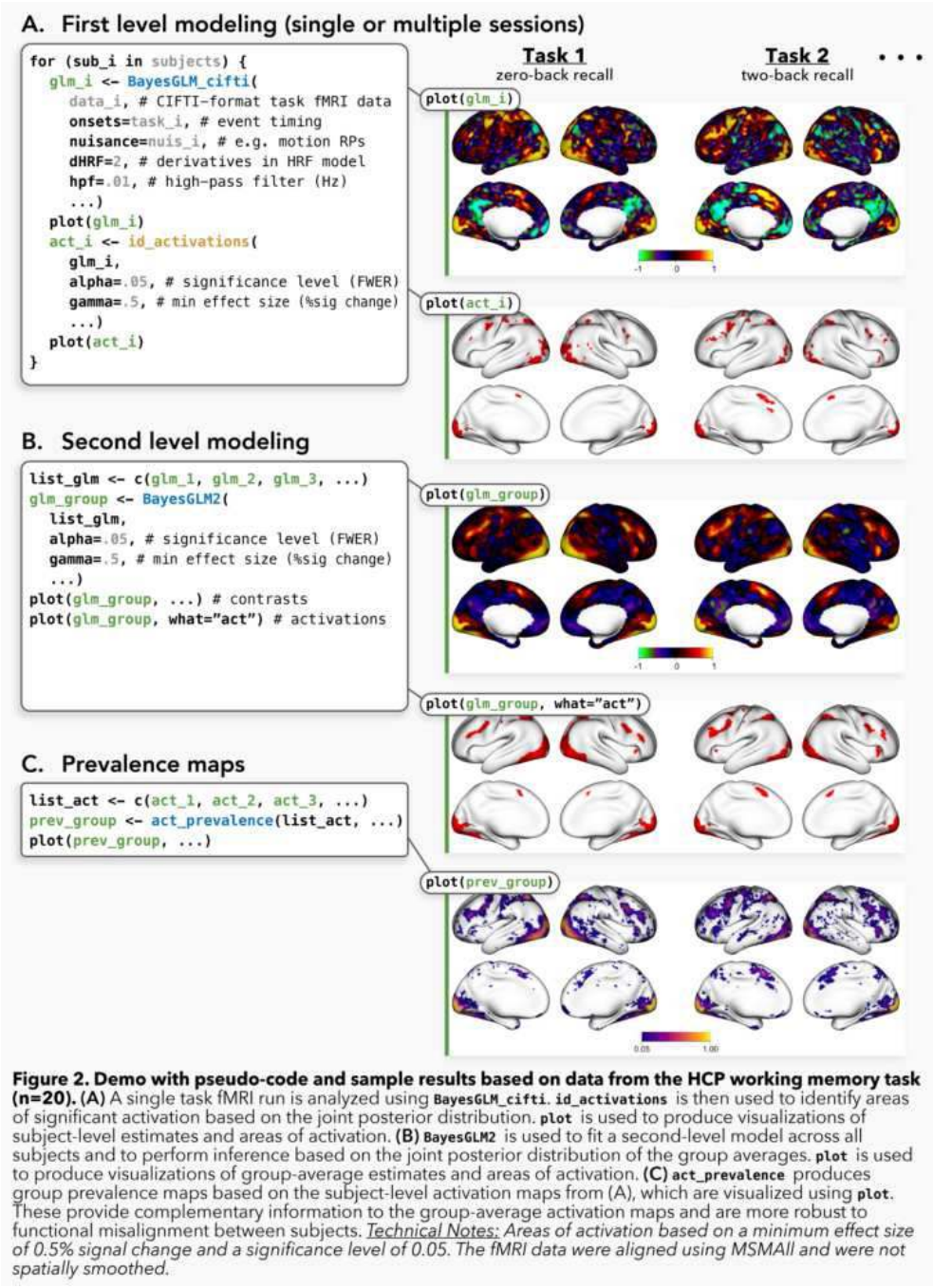

Figure 2. Demo with pseudo-code and sample results based on data from the HCP working memory task (n=20). **(A)** A single task fMRI run is analyzed using `BayesGLM_cifti`. `id_activations` is then used to identify areas of significant activation based on the joint posterior distribution. `plot` is used to produce visualizations of subject-level estimates and areas of activation. **(B)** `BayesGLM2` is used to fit a second-level model across all subjects and to perform inference based on the joint posterior distribution of the group averages. `plot` is used to produce visualizations of group-average estimates and areas of activation. **(C)** `act_prevalence` produces group prevalence maps based on the subject-level activation maps from (A), which are visualized using `plot`. These provide complementary information to the group-average activation maps and are more robust to functional misalignment between subjects. *Technical Notes: Areas of activation based on a minimum effect size of 0.5% signal change and a significance level of 0.05. The fMRI data were aligned using MSMAll and were not spatially smoothed.*

Conclusions: BayesfMRI is a user-friendly, open-source R package that facilitates spatial Bayesian modeling for task fMRI analysis. The spatial models are based on grayordinates data to leverage spatial dependencies along the cortical surface and within subcortical structures, which avoids blurring anatomically distinct areas. BayesfMRI implements single- and multi-session/longitudinal subject-level analysis, second-level group analysis, prewhitening, and powerful joint posterior inference to identify areas of activation above a specified minimum effect size. Convenient visualizations are also provided. BayesfMRI is available through both CRAN and GitHub.

References

1. Brodoehl, S., Gaser, C., Dahnke, R., Witte, O. W., & Klingner, C. M. (2020). Surface-based analysis increases the specificity of cortical activation patterns and connectivity results. Scientific reports, 10(1), 5737.
2. Lindquist, M. A., & Mejia, A. (2015). Zen and the art of multiple comparisons. Psychosomatic medicine, 77(2), 114.
3. Mejia, A. F., Yue, Y. R., Bolin, D., Lindgren, F., & Lindquist, M. A. (2020). A Bayesian general linear modeling approach to cortical surface fMRI data analysis. Journal of the American Statistical Association.
4. Parlak, F., Pham, D. D., Spencer, D. A., Welsh, R. C., & Mejia, A. F. (2023). Sources of residual autocorrelation in multiband task fMRI and strategies for effective mitigation. Frontiers in Neuroscience, 16, 1051424.
5. Spencer, D., Yue, Y. R., Bolin, D., Ryan, S., & Mejia, A. F. (2022). Spatial Bayesian GLM on the cortical surface produces reliable task activations in individuals and groups. NeuroImage, 249, 118908.

Poster No 1326

Assessing motion-associated tSNR of brainstem and spinal cord fMRI in a post-stroke cohort

Neha Reddy[1], Kimberly Hemmerling[1], Julius Dewald[1], Molly Bright[1]

[1]*Northwestern University, Chicago, IL*

Introduction: Motor-task fMRI is a critical modality to study neural changes after a stroke. Although current work has focused on cortical activity patterns in post-stroke cohorts, brainstem and spinal cord fMRI will be equally important to understanding overall adaptation within the central nervous system[7]. However, one challenge of motor-task fMRI in a cohort with stroke is that participants exhibit higher head motion[10], which can decrease data quality. This problem is compounded in the brainstem and spinal cord, which already have lower data quality. Therefore, we aimed to (1) anticipate the degree of head motion in post-stroke participants before an MRI scan, and (2) assess how head motion affects fMRI data quality in the brain, brainstem, and spinal cord.

Methods: Data collection: 6 individuals (62±7y, 6M) with chronic hemiparetic stroke and a paretic upper limb underwent 3 study sessions: 1 outside the scanner and 2 MRI scans in a Siemens 3T Prisma with a 64-channel head/neck coil. Participants performed a hand-grasp task at 40% maximum force: 10-s 'squeeze', 15-s 'relax', 11 trials/hand. During the first visit, participants lay on an exam table in an out-of-use head coil to simulate the MRI environment, while grip force and head motion data were collected (Fig1). During MRI sessions, participants performed the hand-grasp task during a cortical-brainstem GRE EPI scan (TR=2.2s, TEs=13.4/39.5/65.6ms, FA=90°, MB factor=2, voxel size=1.731x1.731x4.0mm^3) and a spinal cord (~C4-C7) GRE EPI scan with ZOOMit selective excitation (TR=2.13s, TE=30ms, FA=90°, voxel size=1x1x3mm^3). Axial slices were aligned perpendicular to the base of the 4th ventricle or longitudinal cord axis, respectively. Structural scans were also acquired. Lab session analysis: Motion data were downsampled to 0.5Hz to approximate the fMRI TR, and Framewise Displacement (FD) was calculated as the sum of the difference in head motion between samples[8]. Cortical-brainstem fMRI analysis[1,5]: The first 10 fMRI volumes were removed to allow for steady-state magnetization, then scans were distortion-corrected. Head-motion realignment parameters were computed for the first echo with respect to the Single Band reference image, then applied to all echoes. An optimally combined image was calculated[4]. The hand-grasp task and motion parameters were modeled out before mean tSNR was calculated in two ROIs transformed to functional space: gray matter segmented from the T1-w scan, thresholded at 75%; and brainstem, using the Harvard-Oxford subcortical structural atlas brainstem[3] thresholded at 50%. FD was calculated using parameters from volume realignment. Spinal cord fMRI analysis[1,2,5]: 2D slicewise motion correction was performed and FD calculated using X and Y motion parameters. The spinal cord was manually segmented. Mean cord tSNR was calculated after task and motion regressors were modeled out.

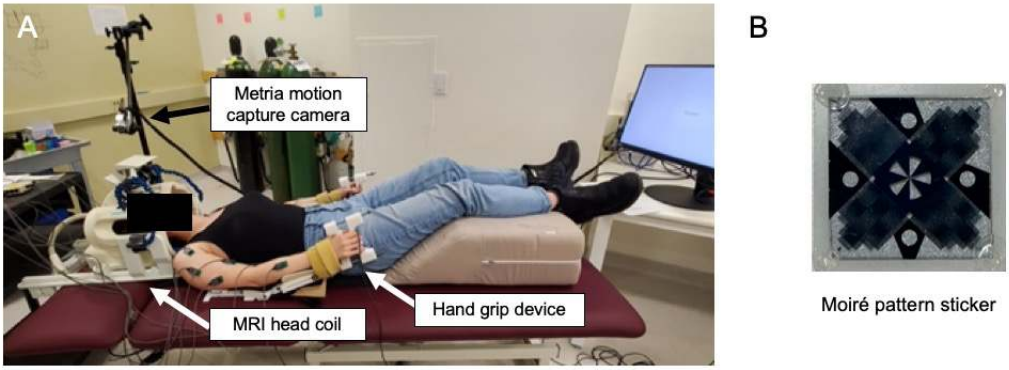

Figure 1. Experimental setup in lab environment. (A) Participant positioned with their head in an out of use MRI head coil and arms placed in the hand grip device. Grip force was sampled via two load cells (Interface) in a custom device. Head-motion data (6-DOF) were sampled at 66 Hz, using a camera to track a moiré-patterned marker on the subject's forehead (Metria Innovation Inc). The Metria motion capture camera is positioned above the participant's head, directed at a moiré pattern sticker on their forehead. Medical tape was placed across the forehead during the lab and MRI sessions to reduce head motion. **(B)** The moiré pattern sticker that is placed on participant foreheads.

Results: Head motion in the lab was significantly correlated with both head and spinal cord motion (FD) during fMRI (Fig2A). Head and spinal cord motion was significantly negatively correlated with mean tSNR in cortical, brainstem, and spinal cord ROIs (Fig2D).

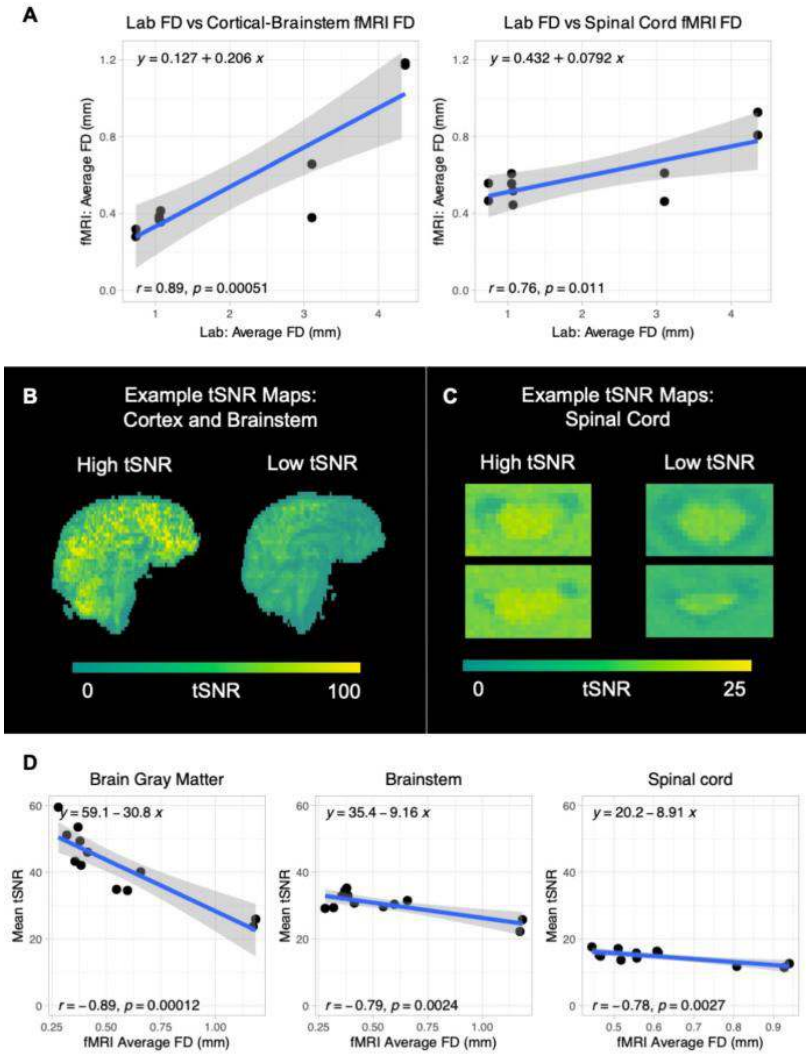

Figure 2. (A) Average FD during a hand-grasping task in the lab environment vs. the average (left) cortical-brainstem and (right) spinal cord FD during a similar task. **(B)** Example of high and low tSNR in the cortex and brainstem and **(C)** in the spinal cord. **(D)** Average FD vs. mean tSNR in the brain gray matter, brainstem, and spinal cord.

Conclusions: In cohorts with increased movement during motor-task fMRI, motion can be evaluated in a mock-MRI environment before scanning. However, while the lab session is designed to simulate the MRI session, minor differences in setup still exist, causing variability in the lab vs. MRI motion relationship. Even after motion correction and denoising, spinal cord tSNR was lower in this stroke cohort compared to a similar spinal cord dataset in younger controls[6], indicating the importance of other physiological denoising techniques for brainstem and spinal cord fMRI. We anticipate that multi-echo independent component analysis for cortical-brainstem scans will improve tSNR[9]. Overall, our findings demonstrate that a motion-capture lab session can help anticipate and plan for potential decreases in tSNR throughout the CNS in a clinical population.

References

1. Cox R. W. (1996). AFNI: software for analysis and visualization of functional magnetic resonance neuroimages. Computers and biomedical research, an international journal, 29(3), 162–173. https://doi.org/10.1006/cbmr.1996.0014
2. Deshpande, R. (2022). Neptune: A toolbox for spinal cord functional MRI data processing and quality assurance [Abstract]. International Society for Magnetic Resonance in Medicine.
3. Desikan, R. S. (2006). An automated labeling system for subdividing the human cerebral cortex on MRI scans into gyral based regions of interest. NeuroImage, 31(3), 968–980. https://doi.org/10.1016/j.neuroimage.2006.01.021
4. Dupre, E. (2021). TE-dependent analysis of multi-echo fMRI with tedana. The Journal of Open Source Software, 6(59), 1–5. https://doi.org/10.21105/joss.03103
5. Jenkinson, M. (2012). FSL. NeuroImage, 62, 782–790. https://doi.org/10.1016/j.neuroimage.2011.09.015
6. Hemmerling, K. J. (2023). Spatial distribution of hand-grasp motor task activity in spinal cord functional magnetic resonance imaging. Human Brain Mapping, 44(17), 5567–5581. https://doi.org/10.1002/hbm.26458
7. Li, S. (2019). A unifying pathophysiological account for post-stroke spasticity and disordered motor control. In Frontiers in Neurology (Vol. 10, Issue MAY). https://doi.org/10.3389/fneur.2019.00468

8. Power, J. D. (2012). Spurious but systematic correlations in functional connectivity MRI networks arise from subject motion. NeuroImage, 59(3), 2142–2154. https://doi.org/10.1016/j.neuroimage.2011.10.018
9. Reddy, N. A. (2023). Multi-echo ICA denoising increases tSNR in combined cortical and brainstem task-fMRI [Abstract]. Organization for Human Brain Mapping Annual Meeting.
10. Seto, E. (2001). Quantifying head motion associated with motor tasks used in fMRI. NeuroImage, 14(2), 284–297. https://doi.org/10.1006/nimg.2001.0829

Poster No 1327

Effects of NORDIC denoising on population receptive field maps

David Linhardt[1], Garikoitz Lerma-Usabiaga[2], Michael Woletz[1], Christian Windischberger[1]

[1]High Field MR Center, Medical University of Vienna, Austria, [2]Basque Center On Cognition, Brain and Language, BCBL, San Sebastian, Spain

Introduction: In fMRI studies it is a common goal to achieve higher spatial resolution. However, measuring smaller voxels reduces the signal-to-noise ratio (SNR). NORDIC[1,2] is a noise reduction method aiming to tackle this issue. Based on a patchwise principal component analysis (PCA), NORDIC identifies and removes components that are similar to thermal noise. This SNR increase goes hand in hand with an increase in image smoothness, however it was found that the increase is less than with other denoising methods[3]. In the special fMRI application of population receptive field (pRF) mapping, Gaussian smoothing of the image is directly corresponding to an increase in pRF size parameter estimation[4]. Within this work, we investigated the effects of NORDIC denoising on the resulting pRF parameter estimations.

Methods: We acquired fMRI data in three participants (two female, age: 20.3∓0.9) on a SIEMENS PrismaFit 3T scanner using the lower part of a 64-channel head coil. Subjects were scanned for one 5-minute functional run (TE/TR=1000/38ms, 1.5mm isotropic) while being presented a bar aperture (width=1.2°) moving through the visual field in eight different directions, revealing reversing checkerboards. The stimulated field of view was 9° radius. NORDIC denoising was applied on the NIFTI files after standard scanner reconstruction (NIFIT_NORDIC, github.com/SteenMoeller/NORDIC_Raw). Both the original and noise-reduced versions were minimally preprocessed using fMRIPrep v23.0.1 (fmriprep.org). The pRF mapping analysis was conducted on both conditions using the containerized solution prfprepare v1.3.5 (github.com/dlinhardt/prfprepare) and prfanalyze-vista v2.2.2_3.1.1 (github.com/vistalab/PRFmodel). Only voxels in V1-3 (Benson atlas[5]) and above the 20% variance explained threshold were used for the comparison. Assessment of NORDIC effects were performed in a voxel-by-voxel comparison.

Results: The pRF position eccentricity and polar angle estimations did not show any systematic differences between the two conditions (Fig 1A and B), but including NORDIC in the preprocessing pipeline substantially increased the pRF size (Fig 1C). As expected for a noise-reduction method, NORDIC-processed results show higher variance-explained values (Fig 1D). To quantify the differences, we calculated Cohen's d effect sizes[6] for the different comparisons. These effect sizes confirm the quantitative results and yield no effects for the pRF center position (eccentricity 0.06; polar angle 0.01), a small effect in the pRF size (0.33) and a large effect for the variance explained (1.66). Further quantification was conducted to assess the magnitude of pRF size increase. For that, we computed the ratio of pRF sizes estimation with and without NORDIC correction. As illustrated in Figure 2, a histogram of this ratio reveals a predilection for values greater than 1, substantiating an amplification in pRF size. The median of this distribution is positioned at 1.22, signifying a 22% increase in pRF size attributable to the removal of noise using NORDIC.

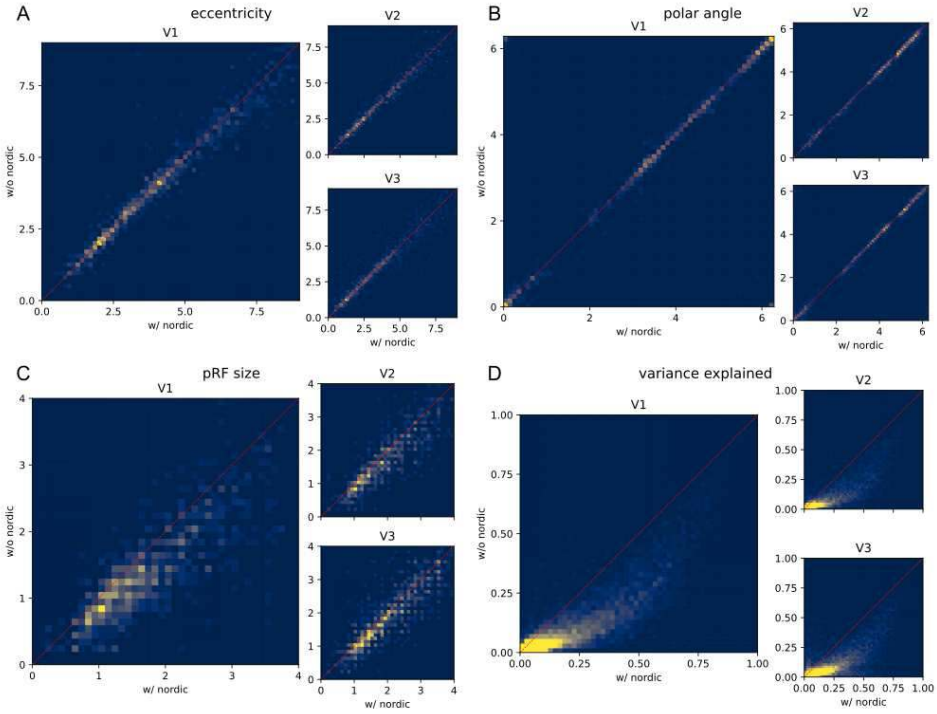

Figure 1: pRF parameter comparison
2D histograms showing direct voxel-to-voxel comparisons of the resulting pRF parameter between the two conditions with and without prior NORDIC denoising. Values around the identity line (red line) represent similar results of the two conditions. The pRF center position is not effectively changed by the denoising (A & B) while the pRF size (C) as well as the variance explained (D) shows a bias towards higher values for the denoised condition.

Conclusions: The application of NORDIC denoising in pRF mapping, results in a median 22% increase in pRF size estimations. These increases in pRF size estimation can not directly be linked to overall image smoothness (AFNI 3dFWHMx). Instead, we argue it arises from the integration of information from adjacent voxels with differing pRF characteristics, leading to peak broadening. This phenomenon is based on the inherent retinotopic organization of neighboring voxels. Previous studies have demonstrated that standard Gaussian spatial smoothing impacts pRF size[4], showing the described effect. Even though image smoothness is hardly increased using NORDIC[3], the effect of neighboring voxel integration most probably leads to the measured pRF size increases. Therefore, the use of NORDIC in preprocessing, despite its benefits in noise reduction, requires cautious interpretation due to its influence on pRF size estimations.

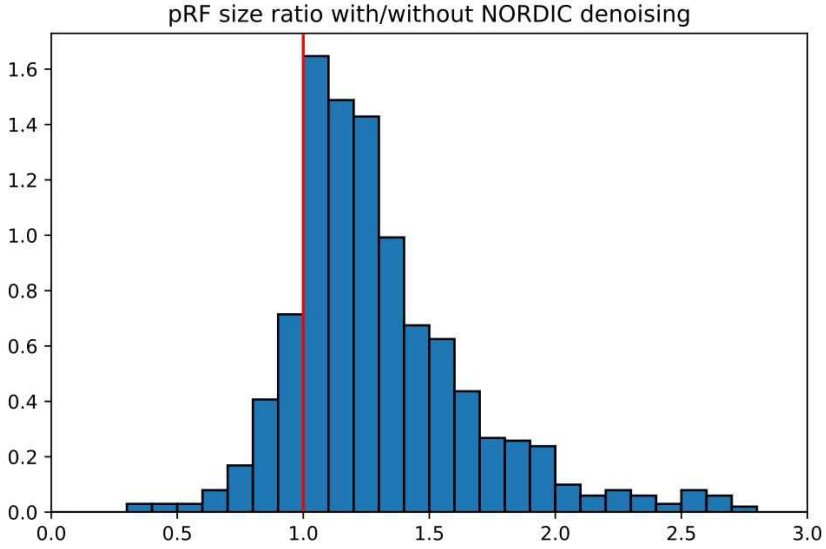

Figure 2: Histogram showing the ratio of pRF sizes from analyses with and without prior NORDIC denoising. Values around 1 (red line) correspond to equal sizes. Mean of this distribution is 1.37, indicating an average 37% increase of pRF size.

References
1. Moeller, S., Pisharady, P.K., Ramanna, S., Lenglet, C., Wu, X., Dowdle, L., Yacoub, E., Uğurbil, K., Akçakaya, M.: NOise reduction with DIstribution Corrected (NORDIC) PCA in dMRI with complex-valued parameter-free locally low-rank processing. NeuroImage. 226, 117539 (2021). https://doi.org/10.1016/j.neuroimage.2020.117539
2. Vizioli, L., Moeller, S., Dowdle, L., Akçakaya, M., De Martino, F., Yacoub, E., Uğurbil, K.: Lowering the thermal noise barrier in functional brain mapping with magnetic resonance imaging. Nat. Commun. 12, 5181 (2021). https://doi.org/10.1038/s41467-021-25431-8
3. Dowdle, L.T., Vizioli, L., Moeller, S., Akçakaya, M., Olman, C., Ghose, G., Yacoub, E., Uğurbil, K.: Evaluating increases in sensitivity from NORDIC for diverse fMRI acquisition strategies. NeuroImage. 270, 119949 (2023). https://doi.org/10.1016/j.neuroimage.2023.119949
4. Windischberger, C., Linhardt, D., Angerer, Pawloff, M., Ritter, M., Schmidt-Erfurth, U.: (ISMRM 2022) Population-receptive field size estimates are biased by acquisition and preprocessing parameters: a 7T fMRI study, https://archive.ismrm.org/2022/2198.html
5. Benson, N.C., Butt, O.H., Brainard, D.H., Aguirre, G.K.: Correction of distortion in flattened representations of the cortical surface allows prediction of V1-V3 functional organization from anatomy. PLoS Comput. Biol. 10, e1003538–e1003538 (2014). https://doi.org/10.1221/journal.pcbi.1003538
6. Cohen, J.: Statistical Power Analysis for the Behavioral Sciences. Routledge (1988)

Poster No 1328

Corticospinal pain processing and modulation in fibromyalgia: a combined brain-cord fMRI study

Dario Pfyffer[1], Merve Kaptan[1], Christine Law[1], Kenneth Weber[1], Valeria Oliva[1], Sandrine Bédard[1], Tara Maronesy[1], Gary Glover[1], Sean Mackey[1]

[1]Stanford University, Palo Alto, CA

Introduction: Chronic widespread pain represents the cardinal symptom of fibromyalgia (FM)[1]. While physical therapy was found to relieve pain[2], its modulatory mechanisms in the central nervous system remain understudied. Brain and more recently spinal cord (SC) functional magnetic resonance imaging (fMRI) have advanced knowledge of neural correlates of pain processing[3,4]. Regions showing increased pain-related activity in FM include the thalamus, insula, somatosensory cortices, and SC dorsal horn[5]. Moreover, dysfunctions in cerebral pain-modulatory systems were reported[6], but their link to the SC is missing. We currently lack understanding of the intricate interplay between spinal and supraspinal networks during pain perception as brain and SC fMRI are conventionally performed separately. Here, we characterize corticospinal mechanisms of aberrant nociceptive processing in FM, by means of combined brain-SC fMRI, and explore descending pain-modulatory effects related to physical activity.

Methods: This preliminary study includes 6 female FM patients (age range: 22-62) and 4 female healthy volunteers (HV, age range: 33-62 years). The imaging protocol consisted of the combined brain-SC sequence7 (EPI pulse sequence, dynamic per slice shimming; 3T GE SIGNA 750 scanner; 16-channel neurovascular array coil; TR=2.5s, TE=30ms, GRAPPA=2), 30 brain slices (3.4x3.4x5.0mm3) and 13 cervical SC slices (1.25x1.25x5.0mm3) centered at C5 vertebral level, axial (FOV=22cm, matrix size=128x128, ΔTE=1ms) and sagittal (FOV=30cm, matrix size=256x64, ΔTE=1ms) field maps for shimming, and anatomical scans (brain: T1w 3DFSPGR (1.0x1.0x1.0mm3); SC: T2w reduced-FOV 3D turbo spin-echo (0.7x0.5x0.5mm3)). The experimental design included four conditions (8x each, 13s) in randomized order: stimulation ON/OFF paired with motor task ON/OFF. Thermal stimuli were applied at the right volar forearm (C6 dermatome) at individual temperatures producing a 6 on the Numeric Rating Scale (0-10), using an ATS thermode (Medoc, 3x3cm2 surface). The motor task consisted of repetitive isometric right-hand gripping with visual feedback (60% of maximal voluntary contraction) using a Dynamometer (BIOPAC). Blocks were followed by 5s pain rating and 6s rest periods. SC and brain images were processed (slice-time correction, motion correction, spatial normalization, smoothing) using FSL and Spinal Cord Toolbox. Preprocessing included RETROICOR8 correction and cerebrospinal fluid regression to account for the physiological noise. Activation maps (fixed effects) were cluster-corrected ($z>2.3$) for the brain and uncorrected for the SC, with a threshold of $p=0.05$.

Results: While average pain ratings decreased by 0.6 points for stimulations during motor task vs. stimulations at rest for HV, they only dropped by 0.2 points for FM. Upon stimulation during motor task, greater activity was found within regions implicated in sensory pain aspects (S1, ACC, insula) in FM compared to HV (Fig. 1, red). Enhanced activity was demonstrated in regions implicated in pain regulation (PFC, PAG, pgACC, PCC, motor cortices) in HV compared to FM (Fig. 1, green). SC dorsal horns exhibited higher and more widespread activity at the level corresponding to the site of stimulation (C6) in FM (red) than HV (green) during the motor task (Fig. 2A). This is supported by the greater activity observed in the same region when contrasting FM > HV (Fig. 2B, red).

Conclusions: Our findings expand previous work detecting elevated activity in pain-related brain regions upon noxious thermal stimulation by showing the same pattern in the SC. Crucially, executing a motor task during stimulation reduced pain ratings and engaged brain regions implicated in descending pain modulation in HV[9]. FM, in contrast, exhibited greater activity

in brain regions processing sensory pain and SC dorsal horns. Using combined brain-SC fMRI, we identified neural correlates of aberrant pain modulation in FM which can advance development of objective biomarkers of chronic pain.

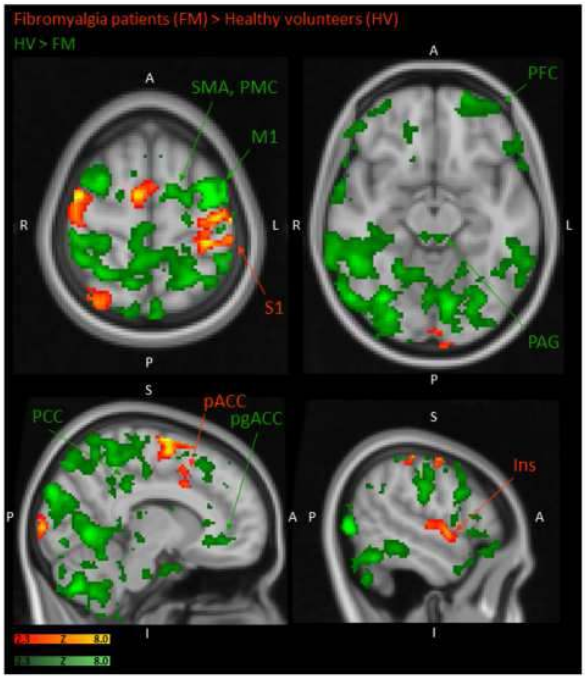

Figure 1: Brain regions showing higher activity upon noxious thermal stimulation during the motor task in FM than HV include S1, ACC, and Ins (highlighted in red). SMA, PMC, M1, PFC, PAG, PCC, and pgACC, all of which are involved in pain regulation, exhibit greater activity in HV than FM (highlighted in green). Fixed effects, Z>2.3. S1, primary somatosensory cortex; pACC, posterior anterior cingulate cortex; Ins, insula; SMA, supplementary motor area; PMC, premotor cortex; M1, primary motor cortex; PFC, prefrontal cortex; PAG, periaqueductal gray; PCC, posterior cingulate cortex; pgACC, pregenual anterior cingulate cortex.

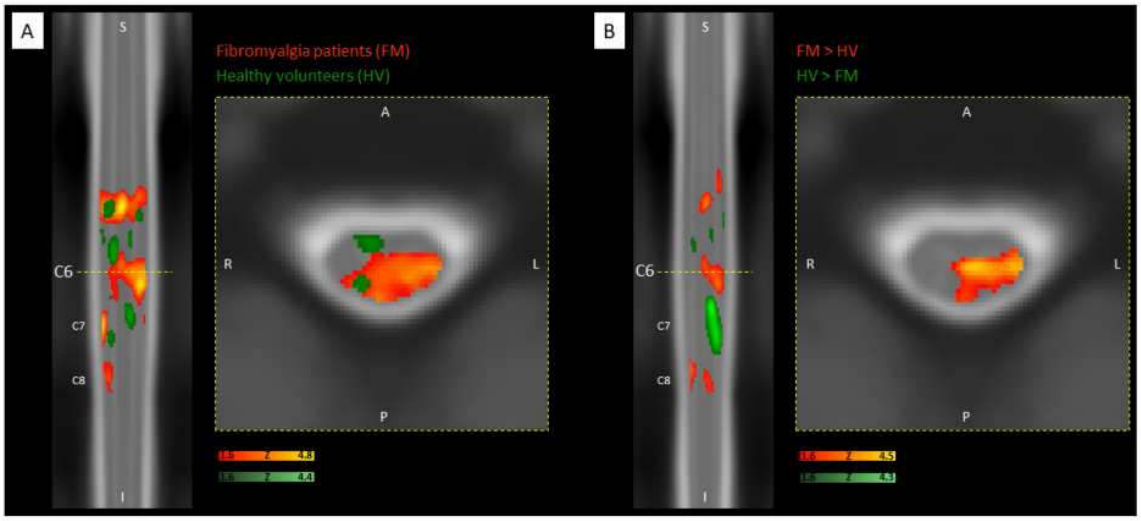

Figure 2: (A) Noxious thermal stimulation during the motor task elicited activity predominantly within spinal cord dorsal horns at the cervical level corresponding to site of stimulation (C6) in HV (highlighted in green) and FM (highlighted in red), the latter showing more widespread activity. (B) Contrasting both groups demonstrates the greater activity observed in FM than HV (highlighted in red). Spinal cord activity induced by the motor task can be seen more inferior at levels corresponding to activated muscles during hand grip (C7/C8). Fixed effects, Z>1.6 (uncorrected).

References

1. Bosma RL. (2016) FMRI of spinal and supra-spinal correlates of temporal pain summation in fibromyalgia patients. Human Brain Mapping. 37(4):1349-60.
2. Glover GH. (2000) Image-based method for retrospective correction of physiological motion effects in fMRI: RETROICOR. Magnetic Resonance in Medicine. 44(1), 162–167.
3. Islam H. (2019) Dynamic per slice shimming for simultaneous brain and spinal cord fMRI. Magnetic Resonance in Medicine. 81(2):825-838.
4. Martucci KT. (2016) Imaging Pain. Anesthesiology Clinics. 34(2):255-269.
5. Mosch B. (2023) Neural correlates of control over pain in fibromyalgia patients. Neuroimage Clinical. 37:103355.
6. Neumann L. (2003) Epidemiology of fibromyalgia. Current Pain and Headache Reports. 7(5):362-368.
7. Offenbacher M. (2000) Physical therapy in the treatment of fibromyalgia. Scandinavian Journal of Rheumatology Suppl. 113:78-85.
8. Reddan MC. (2018) Modeling Pain Using fMRI: From Regions to Biomarkers. Neuroscience Bulletin. 34(1):208-215.
9. Weber KA. (2018) Thermal Stimulation Alters Cervical Spinal Cord Functional Connectivity in Humans. Neuroscience. 369:40-50.

Poster No 1329

The Impact of TMS Intensity and Location on Neural Activation: An iTBS-fMRI Study

Kai-Yen Chang[1], Martin Tik[2], Yuki Mizutani-Tiebel[1], Lucia Bulubas[1], Frank Padberg[1], Daniel Keeser[1]

[1]Department of Psychiatry and Psychotherapy, University Hospital LMU, Munich, Germany, [2]Center for Medical Physics and Biomedical Engineering, Medical University of Vienna, Vienna, Austria

Introduction: The determination of intermittent theta burst stimulation (iTBS) intensity relies on motor threshold (MT) measured in the primary motor cortex (M1). Despite the common practice of using 80% to 120% of M1 resting MT for prefrontal cortex stimulation, the transferability and adequacy of this approach remain unclear. Utilizing concurrent TMS-fMRI, we investigate the impact of subthreshold intensities (80% rMT) and low stimulation intensity (40% rMT) on the left DLPFC. We also include 80% rMT over the left M1 as a reference. By comparing these conditions within the same subjects, we seek to understand how varying TMS intensities influence neural activation in the prefrontal region and whether left M1 intensity induces similar patterns in the left DLPFC. This exploration is crucial for establishing the appropriate stimulation intensity for clinical treatment, shedding light on the differentiated relationship between stimulation intensity and neuronal activation in the prefrontal brain region.

Methods: All participants signed informed consent approved by the local LMU ethical committee. 18 healthy participants (10 males, mean age = 26.4, SD = 3.1) were included. We randomized three conditions for each participant: 80% or 40% rMT intensity over the left DLPFC (-38, 44, 26)[1] and 80% rMT over the left M1. In these sessions, we acquired a structural and interleaved iTBS-fMRI sequence. Apart from the standard MRI data preprocessing[2], we used independent component analysis (ICA) to remove general noise such as ventricular and motion artifacts in addition to potential coil artifacts in the fMRI data as suggested in[3]. To establish a correlation between simulated electric field (E-field) and fMRI BOLD activation in each subject under the conditions of 80% rMT in the DLPFC and M1, we adopted predefined targets for the left DLPFC and M1 (-37, -21, 58)[4], and calculated the mean E-field magnitude on SimNIBS 4.0 and the mean beta value from fMRI data within a 10mm radius of region of interest.

Results: At 80% rMT over left DLPFC, significantly increased BOLD was observed under the stimulated location, M1, anterior cingulate gyrus (ACC), anterior insula, and bilateral auditory cortices. It is noteworthy that the activation of the bilateral ACC and anterior insula represents a classic marker for the so-called salience network. While lower iTBS intensity resulted only in the presence of BOLD activity on the contralteral right DLPFC, bilateral auditory cortices and ACC. In M1 condition, activations were observed in the bilateral primary motor cortices, right DLPFC, auditory cortex, and primary somatosensory cortex. In the subcortical regions, the BOLD activations were found in putamen region and left caudate region. The correlation analysis examined E-field magnitude and fMRI beta values in two conditions: DLPFC 80% rMT and M1 80% rMT. A weak positive correlation (r = 0.31) was found in the DLPFC condition, while the M1 condition showed a strong positive correlation (r = 0.65).

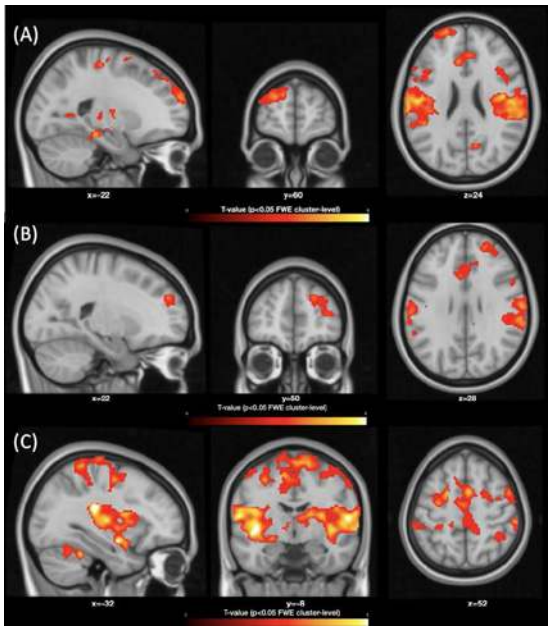

Figure 1. (A) Immediate BOLD during 80% rMT left DLPFC. (B) Immediate BOLD during 40% rMT left DLPFC. (C) Immediate BOLD during 80% rMT left M1.

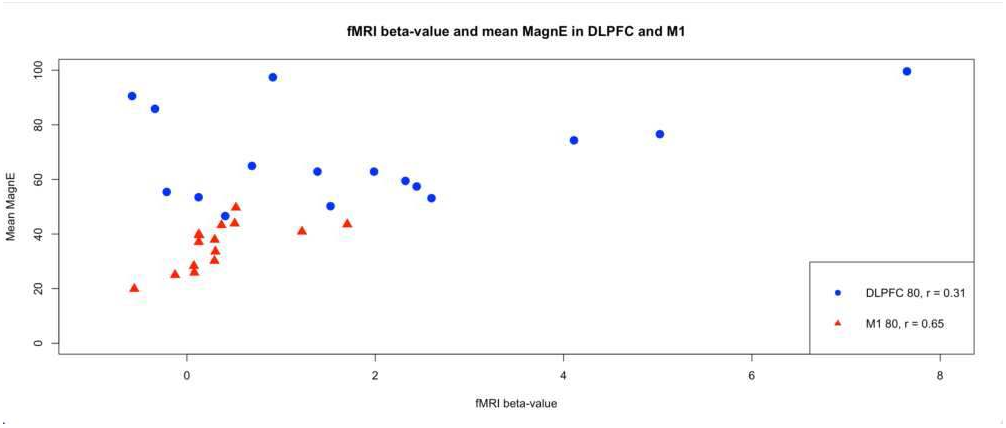

Figure 2. Correlation analysis of E-Field magnitude and fMRI beta values in DLPFC and M1 80% rMT conditions.

Conclusions: The results of our study revealed that focal BOLD activations were found under stimulated region in the left DLPFC after ICA denoising was applied. This observation suggests that artifacts from the TMS coil or TMS-MRI hardware coupling were removed. Moreover, it revealed activation in the salience network, containing the anterior insula and anterior cingulate gyrus, aligning with Hawco et al.'s findings[5]. Conversely, the 40% rMT DLPFC condition did not exhibit this specific pattern; only the right DLPFC showed activity, potentially indicating interhemispheric compensation. The correlation analysis suggests that higher E-field magnitudes in the cortex generally correlate with higher BOLD signals in fMRI. Due to the higher complexity of the DLPFC, the prediction of simulation results becomes more difficult, highlighting the challenge in predicting outcomes under the same TMS intensity for DLPFC and M1.

References

1. Blumberger DM, Vila-Rodriguez F, Thorpe KE, Feffer K, Noda Y, Giacobbe P, et al. Effectiveness of theta burst versus high-frequency repetitive transcranial magnetic stimulation in patients with depression (THREE-D): a randomised non-inferiority trial. The Lancet. 2018 Apr;391(10131):1683–92.
2. Tik M, Woletz M, Schuler AL, Vasileiadi M, Cash RFH, Zalesky A, et al. Acute TMS/fMRI response explains offline TMS network effects – An interleaved TMS-fMRI study. NeuroImage. 2023 Feb;267:119833.
3. Riddle J, Scimeca JM, Pagnotta MF, Inglis B, Sheltraw D, Muse-Fisher C, et al. A guide for concurrent TMS-fMRI to investigate functional brain networks. Front Hum Neurosci. 2022 Dec 15;16:1050605.
4. Mayka MA, Corcos DM, Leurgans SE, Vaillancourt DE. Three-dimensional locations and boundaries of motor and premotor cortices as defined by functional brain imaging: A meta-analysis. NeuroImage. 2006 Jul;31(4):1453–74.
5. Hawco C, Voineskos AN, Steeves JKE, Dickie EW, Viviano JD, Downar J, et al. Spread of activity following TMS is related to intrinsic resting connectivity to the salience network: A concurrent TMS-fMRI study. Cortex. 2018 Nov;108:160–72.

Poster No 1330

Reducing individual differences in task fMRI with OGRE preprocessing for FSL

Mark McAvoy[1], Lei Liu[1], Ruiwen Zhou[1], Mark McAvoy[1]

[1]*Washington University School of Medicine, St. Louis, MO*

Introduction: Volumetric preprocessing methods continue to enjoy great popularity in the analysis of functional MRI (fMRI) data. Among these methods, the software packages FSL (Jenkinson et al., 2012) and FreeSurfer (Fischl et al., 2004) are omnipresent throughout the field. However, it remains unknown what advantages an integrated FSL+FreeSurfer preprocessing approach might provide over FSL alone. Here we developed the One-step General Registration and Extraction (OGRE) pipeline to combine FreeSurfer and FSL tools for brain extraction and registration of fMRI data for FSL volumetric analysis.

Methods: OGRE preprocessing included coarse registration with FSL tools followed by fine registration with FreeSurfer (Glasser et al., 2013), then formatted for integration with FSL. OGRE preprocessing was compared to traditional FSL preprocessing with a dataset of adult volunteers (N=26) performing a precision drawing task with a MRI-compatible tablet during fMRI scanning. The task followed a blocked design with 15.2s draw/rest, TR = 662 ms, 6×5.4min runs alternating between runs with right hand (RH) drawing and left hand (LH) drawing. Data were preprocessed with FSL or OGRE, and then analyzed with the FSL FEAT general linear model which included explanatory variables for Task (i.e. drawing) and its temporal derivative, each formed by convolving the hemodynamic response with a double-gamma function. Additional variables addressed volumes with excess head motion (framewise displacement > 75th percentile + 1.5* interquartile range). The contrast, Task > rest, was averaged across runs for each participant, and then an across-participants mixed effects

analysis was performed to identify a whole-brain voxel-wise effect of Method (OGRE vs. FSL-only) with cluster threshold Z > 3.1 ($p < 0.05$ corrected). In addition, participant-level data were quantified via a region of interest (ROI) analysis. 42 ROIs were defined from: primary motor representations of hand, lip and foot (Smith & Frey, 2011); the Yeo-7 atlas (Yeo et al., 2011); and the whole brain. For direct statistical comparison of mean signal magnitude and inter-individual standard deviation, these ROIs were entered into a 2 (Method: OGRE vs. FSL-only) * 10 (Area) * 2 (Hemisphere: left, right) * 2 (Condition: LH-draw, RH-draw) repeated measures ANOVA with participants as the random factor.

Results: OGRE preprocessing, compared to traditional FSL preprocessing, led to consistently lower inter-individual variability of task-related BOLD activation (Task > Rest) with a decrease of 44 ± 12%, as shown in Figure 1. This decrease in inter-individual variability was found in all 42 ROIs, and statistically significant ($p < 0.001$) in 37/42 ROIs (88%). Signal magnitude did not differ systematically between OGRE and FSL: magnitude increased numerically in 28/42 ROIs (67%), and this difference was significant in only 6/42 ROIs (14%). Nevertheless, in a whole-brain analysis, OGRE showed significantly more activation than FSL preprocessing in 5-7 clusters including sensorimotor areas contralateral to movement, while no areas showed more activation for FSL preprocessing than OGRE preprocessing.

Conclusions: The integration of FreeSurfer tools via OGRE preprocessing can improve fMRI data analysis in the context of FSL's volumetric approach. Specifically, OGRE preprocessing led to decreased inter-individual variability, which in turn led to increased detection of task-relevant BOLD activity (sensorimotor areas contralateral to movement). The OGRE pipeline provides a turnkey method to integrate FreeSurfer-based brain extraction and registration with FSL analysis of task fMRI data.

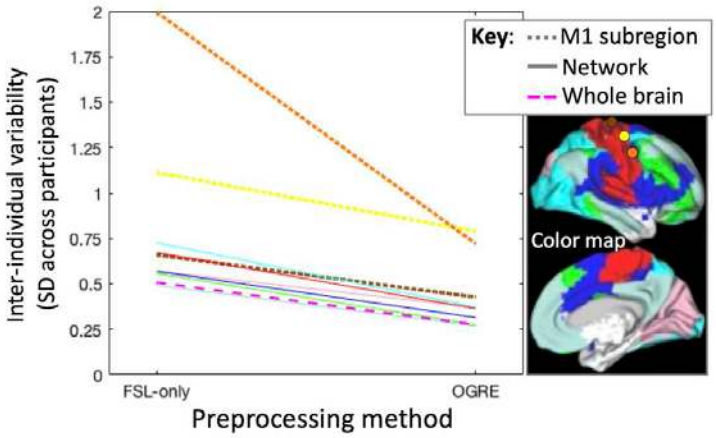

Figure 1. OGRE preprocessing leads to lower inter-individual variability in BOLD signal (Task > Rest) across the brain. Representative data shown here: right hemisphere ROIs during left hand drawing. Locations of M1 subregions (circles in color map) are approximate.

References

1. Jenkinson M, Beckmann CF, Behrens TE, Woolrich MW, Smith SM. FSL. Neuroimage. 2012;62(2):782-90.
2. Fischl B, Salat DH, van der Kouwe AJ, Makris N, Segonne F, Quinn BT, Dale AM. Sequence-independent segmentation of magnetic resonance images. Neuroimage. 2004;23 Suppl 1:S69-84. doi: 10.1016/j.neuroimage.2004.07.016. PubMed PMID: 15501102.
3. Glasser MF, Sotiropoulos SN, Wilson JA, Coalson TS, Fischl B, Andersson JL, et al. The minimal preprocessing pipelines for the Human Connectome Project. Neuroimage. 2013;80:105-24. Epub 20130511. doi: 10.1016/j.neuroimage.2013.04.127. PubMed PMID: 23668970; PubMed Central PMCID: PMCPMC3720813.
4. Smith JC, Frey SH. Use of independent component analysis to define regions of interest for fMRI studies. International Society for Magnetic Resonance in Medicine (ISMRM); Feb 09; Montreal, Canada2011.
5. Yeo BT, Krienen FM, Sepulcre J, Sabuncu MR, Lashkari D, Hollinshead M, et al. The organization of the human cerebral cortex estimated by intrinsic functional connectivity. J Neurophysiol. 2011;106(3):1125-65. Epub 20110608. doi: 10.1152/jn.00338.2011. PubMed PMID: 21653723; PubMed Central PMCID: PMCPMC3174820.

Poster No 1331

Meditation attenuates activity of a trans-diagnostic brain network: 3T and 7T fMRI evidence

Saampras Ganesan[1], Bradford Moffat[2], Nicholas Van Dam[3], Valentina Lorenzetti[4], Andrew Zalesky[1,5]

[1]Department of Biomedical Engineering, The University of Melbourne, Melbourne, Victoria, [2]Melbourne Brain Centre Imaging Unit, The University of Melbourne, Melbourne, Victoria, [3]Melbourne School of Psychological Sciences, The University of Melbourne, Melbourne, Victoria, [4]Faculty of Health, Australian Catholic University, Melbourne, Victoria, [5]Department of Psychiatry, The University of Melbourne, Melbourne, Victoria, Australia

Introduction: Burgeoning fMRI research in meditation alongside advancements in ultra-high field fMRI and real-time neuroimaging uniquely enable multi-faceted investigations into the neurobiology of meditation. Meditation encompasses mind-body attentional training[7], that can alleviate core psychopathological symptoms, such as dysfunctional self-referential thinking and mood[1,5,6], prevalent across multiple internalizing psychiatric disorders including depression, anxiety, schizophrenia, etc. Elucidating the most robust neurobiological underpinnings of meditation can help objectively inform and develop the therapeutic value of meditation in treating prevalent psychiatric disorders[6].

Methods: Here, we present and distil fMRI-measured brain activations reported across 3 independent studies of task-fMRI meditation research (Figure 1), comprising N=210 healthy individuals that either: i) meditated by paying attention to breathing sensations (meditation condition) or; ii) engaged in a non-meditative control condition (e.g., let their minds wander freely) inside the MRI scanner. The first study (N=174) involves whole-brain random-effects activation likelihood estimation (ALE) meta-analysis of significant brain activation coordinates reported in PRISMA-eligible 3T meditation task-fMRI studies[3]. The second study (N=10) involves group-level whole-brain general linear modelling (GLM) inferences from first-of-a-kind ultra-high field 7T meditation task-fMRI following stringent artefact modelling[4]. The final study (N=26) involves group-level inferences from a real-time 7T fMRI neurofeedback paradigm (2-day fMRI sessions) that aimed to train participant self-regulation of BOLD activation within a target brain region via meditation.

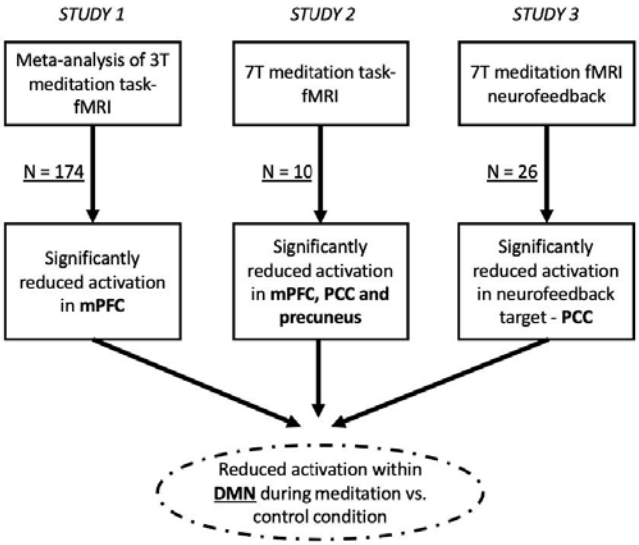

Figure 1: Schematic representing the 3 independent fMRI studies, their notable findings, and the overarching outcome emerging across the studies. mPFC – medial prefrontal cortex, PCC – posterior cingulate cortex, DMN – Default-mode network

Results: Key nodes of the default-mode network (DMN) were implicated commonly across all 3 independent studies, demonstrating significantly reduced activation during meditation compared to control condition (Figure 2). Specifically, the coordinate-based meta-analysis revealed significantly reduced activation (FWE-corrected $p<0.05$, 1000 permutations) during meditation vs. control condition in the medial prefrontal cortex (mPFC). Group-level GLM of the 7T meditation task-fMRI, adjusted for head-motion, physiological (RETROICOR) and arousal (self-report) variables, found significantly reduced activation (FWE-corrected $p<0.05$, $z>3.1$, 1024 permutations) during meditation vs. rest in precuneus, posterior cingulate cortex (PCC) and mPFC. Finally, mean BOLD percent-signal change within PCC (neurofeedback target region) estimated in real-time during neurofeedback self-regulation, after real-time adjustment for physiological confounds, was found to be significantly negative ($T(25) = -4.0$, $p = 0.0005$) at the group-level for meditation vs. rest.

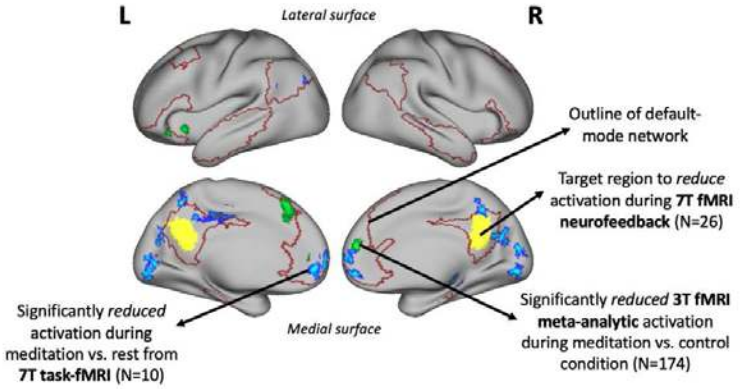

Figure 2: Areas of significantly reduced activation during meditation vs. control condition displayed on the cortical brain surface along with the boundaries (maroon) of the default-mode network. The different colors of activation clusters represent findings from different studies, i.e., meta-analysis (green), 7T task-fMRI (blue) and neurofeedback (yellow).

Conclusions: The distillation of multifaceted brain activation findings from 3T task-fMRI meta-analysis, 7T task-fMRI and 7T fMRI neurofeedback conclusively demonstrates that meditation attenuates activation within the DMN, a brain network predominantly associated with self-referential processing. Notably, given the trans-diagnostic implication of dysfunctional self-referential processing and DMN in psychiatric conditions[2], our findings highlight the potential utility of meditation-based therapeutics in alleviating excessive and aberrant self-referential processing characteristic of several internalizing psychiatric disorders. This work also highlights the value of synthesising multifaceted findings across 3T and 7T MRI to illuminate putative neurobiological mechanisms underlying complex subjective states of awareness (i.e., meditation).

References

1. Creswell, J.D., Mindfulness Interventions. Annual Review of Psychology, 2017. 68(1): p. 491-516.
2. Doucet, G.E., et al., Transdiagnostic and disease-specific abnormalities in the default-mode network hubs in psychiatric disorders: A meta-analysis of resting-state functional imaging studies. European Psychiatry, 2020. 63(1): p. e57.
3. Ganesan, S., et al., Focused attention meditation in healthy adults: A systematic review and meta-analysis of cross-sectional functional MRI studies. Neuroscience & Biobehavioral Reviews, 2022. 141: p. 104846.
4. Ganesan, S., et al., Meditation attenuates default-mode activity: A pilot study using ultra-high field 7 Tesla MRI. Brain Research Bulletin, 2023. 203: p. 110766.
5. Hölzel, B.K., et al., How Does Mindfulness Meditation Work? Proposing Mechanisms of Action From a Conceptual and Neural Perspective. Perspectives on Psychological Science, 2011. 6(6): p. 537-559.
6. Lin, Y., C.P. Callahan, and J.S. Moser, A mind full of self: Self-referential processing as a mechanism underlying the therapeutic effects of mindfulness training on internalizing disorders. Neuroscience & Biobehavioral Reviews, 2018. 92: p. 172-186.
7. Lutz, A., et al., Attention regulation and monitoring in meditation. Trends in cognitive sciences, 2008. 12(4): p. 163-169.

Poster No 1332

Bounded contribution of human early visual cortex to topographic bias in spatial extent perception

Juhyoung Ryu[1], Sang-Hun Lee[1]

[1]*Seoul National University, Seoul, South Korea*

Introduction: Accurate perception of object's spatial extent, an enclosed region they occupy in space, is crucial for successful interaction with the environment. The topographic representation of space in the early visual cortex (EVC) has been favored as a neural correlate of spatial extent perception. However, it remains mostly unexplored whether and how the topographic anisotropies in EVC relate to those in perceived spatial extent. In this study, we examined the topographic representations of the EVC and individuals' perception, focusing on the influence of orientation (co-axiality) and radial position (radiality) of stimuli: radial when elongated along the radial axis on which the RF is positioned in retinotopic space, and co-axial when elongated along the axis aligned to the stimulus orientation in visual space. We conducted fMRI and psychophysics experiments to examine the dominant factor in topographic bias of the pRF and perceived anisotropy and the relationships of anisotropies between the pRF and perception at the individual level. The results revealed a mismatch in bias, with EVC showing a radial bias and perception showing a co-axial bias. Despite of this mismatch, inter-individual variabilities in EVC's anisotropy were correlated with that in perception. The results suggest the involvement of additional mechanisms beyond EVC in transforming information to match perceived spatial extent.

Methods: we estimated the pRFs of individual voxels in EVC using visual stimuli with two types of gratings with different orientations in the retinotopic polar space: radially and tangentially oriented gratings (Fig. 1c, 2a-1). Due to the correlation between preferred orientations and polar-angle positions of neurons (Fig. 1a,b), how the two anisotropy factors affect the pRF anisotropy is inconclusive. To overcome this, we used radially and tangentially oriented gratings, decorrelating orientation and polar-angle position. By inspecting elongation axes in tangential orientation condition, the study distinguishes whether co-axiality or radiality dominates. Furthermore, comparing degrees of elongation between stimulus orientations reveals the modulatory influence of the non-governing factor (Fig. 1e,f).

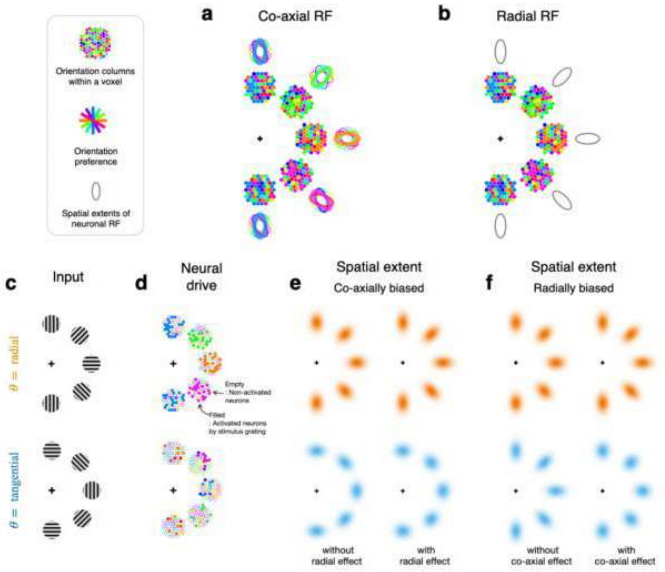

Figure 1. The rationale for pRF estimation using radially and tangentially oriented gratings to evaluate the respective influences of topographic factors on the spatial representation of EVC. **a,b)** Schematic illustrations of two hypothetical factors, radiality (**a**) and co-axiality (**b**), that govern the anisotropy of individual RFs of orientation-tuned neurons in the presence of a strong correlation between their orientation preference and polar-angle position. The fixation location is marked by crosshairs. Each cluster of colored dots represents orientation columns that are aggregated within a voxel representing a specific retinotopic position. The colors represent orientation preference, and their distributional biases reflect the strong correlation between columns' preferred orientation and polar-angle position. The ellipsoids surrounding the dot clusters represent the topographical anisotropy of neurons' RFs. If co-axiality governs, the RFs are elongated along their preferred orientation (**a**). If radiality governs, the RFs are elongated along the radial axis (**b**). **c)** Visual inputs with radially (top) and tangentially (bottom) oriented gratings. **d)** The neural drives by the gratings shown in **c**. **e,f)** Illustrations of how the same neural drives shown in **d** induce different neural spatial extents depending on how strongly radiality and co-axiality govern the RF anisotropy. If only co-axiality influences the anisotropy, the neural spatial extent will be co-axially elongated, while the degree of co-axial elongation will not differ between the two orientation conditions (**e**, left). If co-axiality has a stronger influence on anisotropy than radiality, the neural spatial extent will be elongated in the co-axial direction, with a relatively high degree of elongation in the radial orientation condition (**e**, right). If only radiality influences the anisotropy, the neural spatial extent will be radially elongated, while the degree of radial elongation will not differ between the two orientation conditions (**f**, left). If radiality has a stronger influence on anisotropy than co-axiality, the neural spatial extent will be elongated in the radial direction, with a relatively high degree of elongation in the radial orientation condition (**f**, right).

Results: We quantified the degree of radial elongation with the radial bias index, RI_pRF, derived from the subtractive contrast between the radial and tangential spatial extents of the pRFs. We found that radiality is the dominant factor governing the pRF anisotropy, with pRFs extending farther along the radial axis than the tangential axis, regardless of the stimulus orientation conditions (Fig. 2b). RI_pRF tended to be smaller in the tangential orientation condition than in the radial orientation condition for all three areas of EVC, indicating that the pRF spatial extent is radially biased, with a weak modulation by co-axiality, albeit statistically insignificant. Next, we acquired psychophysical data and estimated radial bias index of the perceived anisotropy, RI_perc, from the observers whose pRF anisotropy was estimated. The perceptual anisotropy is co-axially biased with radial modulation (Fig. 2c). Despite of the mismatch in anisotropy between EVC and perception, there were the substantial inter-individual correlations in the influence of radiality and co-axiality on both the pRF and perceptual anisotropies (Fig. 2c,e).

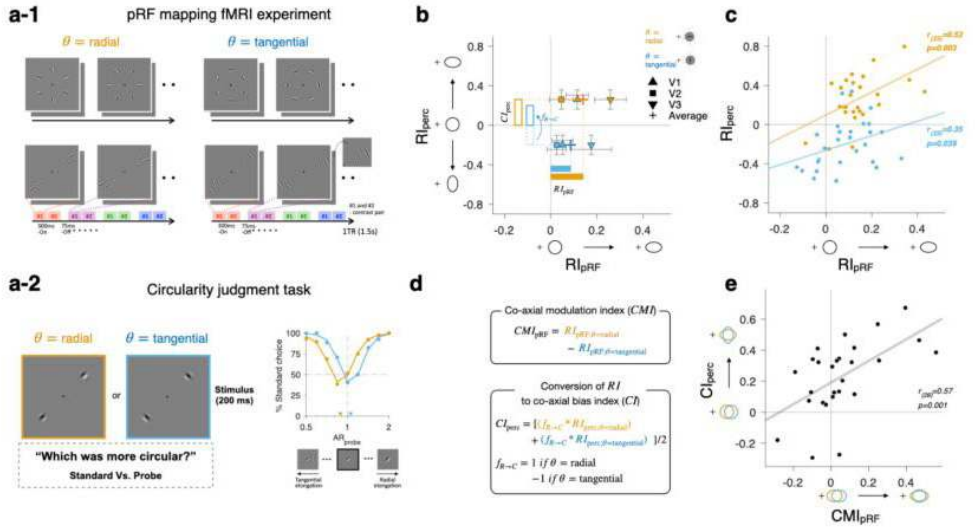

Figure 2. FMRI and psychophysical experimental design (**a**), a mismatch in bias and co-variations in the inter-individual difference between the pRF anisotropy and the perceptual anisotropy (**b-e**). **a-1)** Spatial arrangements and temporal sequence of pRF mapping stimuli. **a-2)** Circularity judgment task and example psychometric curves. Left, Example pairs of Gabor stimuli under the radial and tangential orientation conditions. Right, Example psychometric curves from a representative observer. The fraction of trials in which the standard stimulus was chosen is plotted as a function of the *AR* of the probe (AR_{probe}) in a given trial. By inverting these values of AR_{probe} at the minima of the psychometric curves, the perceived aspect ratio (AR_{perc}) was estimated. Dots, observed data; Solid lines, fitted psychometric functions; downward triangle, $1/AR_{perc}$; Inset images on the x-axis, the probe Gabors at three *AR* values (0.5, 1, 2). **b)** Across-individual averages of the radial bias indices of the pRF (RI_{pRF}) and perceptual (RI_{perc}) anisotropies in the radial and tangential orientation conditions. The x-axis values of the symbols are the across-individual averages of RI_{pRF} for V1, V2, and V3. As for the y-axis values, the one and same across-individual average of RI_{perc} is repeatedly used for the symbols in each stimulus orientation condition. Symbols and error bars, mean and 95% CI; Upward triangle, square, downward triangle and crosshair symbols represent V1, V2, V3, and the average of V1-3. **c)** Across-individual co-variations between the influences of radiality on the pRF and perceptual anisotropies, shown separately for the radial (orange) and tangential (blue) orientation conditions. *r* and *p*, Pearson's r and one-tail p-value; solid lines, linear regression fits. **d)** Definition of the co-axial modulation index of pRF anisotropy (CMI_{pRF}) and the mean co-axial bias index of perceptual anisotropy ($\overline{CI}_{perc}$). **d)** Across-individual co-variations between the influences of co-axiality on the pRF and perceptual anisotropies. **a-d)** Orange and blue colors, the radial and tangential orientation conditions. **b,c,e)** Schematically depicted ellipsoids are used as guides on the x and y axes to visually illustrate the topographic anisotropies corresponding to the RI_{pRF} and RI_{perc} values (**b,c**) or the CMI_{pRF} and the $\overline{CI}_{perc}$ values (**e**).

Conclusions: Our study highlights a mismatch in bias between the pRF of EVC and perceived anisotropies, with inter-individual correlation between them, suggesting a limited role for EVC in spatial extent perception. The findings implicate that spatial extent perception builds on EVC's spatial representation but requires an additional mechanism to transform its topographic bias.

References

1. Lee, S. H., & Ryu, J. (2023). A mismatch between human early visual cortex and perception in spatial extent representation: Radial bias shapes cortical representation while co-axial bias shapes perception. bioRxiv, 2023-02.

Poster No 1333

Stable degenerate brain systems that underlie visual short-term memory across the adult lifespan

Michelle Jansen[1], Alireza Salami[2], Fernando Martínez[1], Daniel Mitchell[3], . Cam-CAN[3], Linda Geerligs[1]

[1]Donders Institute, Radboud University, Nijmegen, Gelderland, [2]Karolinska Institutet & Umeå University, Stockholm, Stockholm, [3]MRC Cognition and Brain Sciences Unit, University of Cambridge, Cambridge, Cambridgeshire

Introduction: Cognitive task performance may be supported through multiple neural pathways, a concept referred to as "brain degeneracy"[1]. We used a novel approach to consider brain degeneracy during a visual short-term memory (VSTM) task across the adult lifespan. Here, we identified groups of participants whose VSTM performance was characterized by different brain activation patterns and investigated whether these groups differed in age, task performance, grey matter (GM), and white matter (WM) integrity.

Methods: We analyzed data of 113 participants from the Cam-CAN cohort (47.8% female, mean age 52.66, SD = 17.99)[2]. Participants engaged in a VSTM fMRI paradigm[3]. Our effect of interest was the activation difference between the highest and the lowest memory load during the maintenance period. To identify modules of brain regions that responded similarly to VSTM load across different participants, we applied consensus partitioning based on the Louvain modularity algorithm[4,5].

We chose the partition with the highest resemblance to earlier detected age-representative networks[6]. To find groups of participants who showed differential recruitment patterns of the resulting brain modules, latent profile analysis was applied using the residual activity in each brain module and overall network responsivity. Group differences in age, task performance, GM volumes, and mean kurtosis were examined using Welch's ANOVA and pairwise t-tests, corrected for age, total GM, and total intracranial volume (ICV) where appropriate. Within group associations between brain activity and task performance were investigated with Pearson correlations, controlling for age and mean responsivity across all ROIs.

Results: We identified seven distinct brain modules that resembled earlier identified functional networks. A model with 4 latent groups resulted in the most optimal fit (n=35, n=24, n=42, n=12 in groups 1-4). Group differences were most evident for the frontal control module (FCM), visual module (VM), and default mode module (DMM; Fig 1). Group 4 tended to be younger (group 1, $p<0.01$; group 2, $p=0.03$; group 3, $p=0.06$). Significant group differences were observed in mean kurtosis for the left uncinate fasciculus and the left inferior longitudinal fasciculus, after correcting for ICV (all $p<0.001$). Group 2, the subgroup with low FCM and high VM recruitment, showed reduced WM integrity in these tracts. We observed negative associations between FCM activation and memory precision in group 1 and 2 ($r=-0.46$, $p=0.006$; $r=-0.41$, $p=0.055$). Notably, these groups also showed lower levels of FCM recruitment during the task. Further, we noted a negative association between activity in the DMN and the number of items in memory in group 1 ($r=-0.35$, $p=0.045$), suggesting that the reduced DMN suppression in this group was negatively affecting performance.

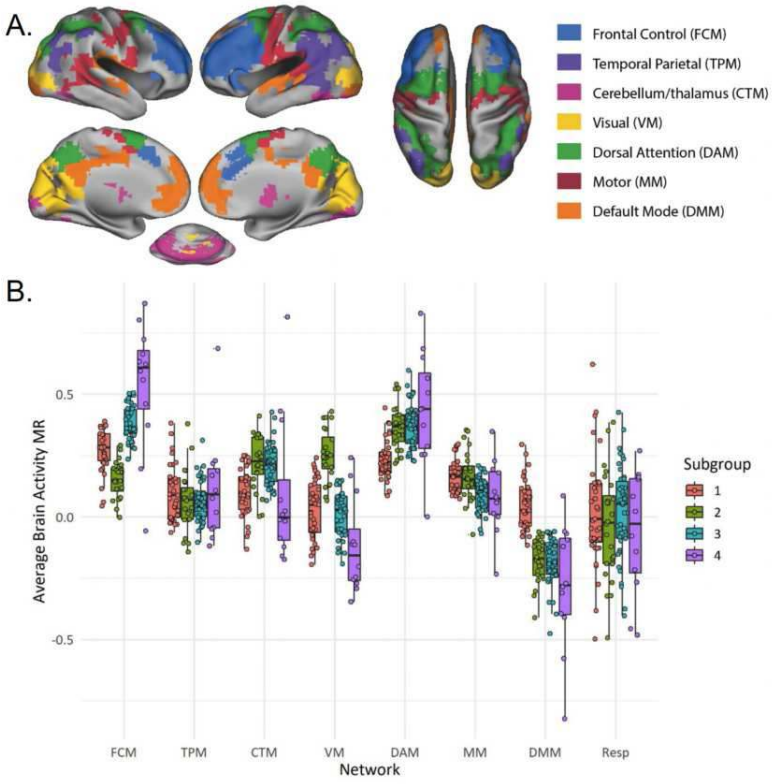

A) Illustration of the seven brain modules that demonstrated different load-dependent activation during the VSTM; B) For each of the four identified groups, this figure displays the average residual brain activity for each of the seven brain modules and overall responsivity across all ROIs (Resp). Group differences were most prominent for the FCM, VM, and DMM.

Conclusions: We identified groups of participants that were characterized by different brain activation patterns. These groups did not differ in task performance, but were characterized by differential associations between brain activity and performance, particularly in the FCM. We also observed age-independent differences in WM integrity between groups, particularly in the uncinate fasciculus. This suggests that differences in brain activity during task performance might have been shaped by individual differences in brain structure. Individuals can use different cognitive strategies to complete the VSTM task (e.g., verbalizing the memory representation or visualizing the items)[7]. Notably, the uncinate fasciculus has been implicated in semantic language processing, associative learning, and working memory. We could speculate that group 2 relied more on maintaining visual representations by recruiting the VM due to the reduced integrity in the left uncinate fasciculus. Altogether, our novel analysis approach may help to further understand how multiple neural pathways could underlie cognitive performance.

References

1. Edelman, G. M., & Gally, J. A. (2001), 'Degeneracy and complexity in biological systems. Proceedings of the National Academy of Sciences', vol. 98, no. 24, pp. 13763-13768.
2. Shafto, M. A., Tyler, L. K., Dixon, M., Taylor, J. R., Rowe, J. B., Cusack, R., ... & Cam-CAN. (2014), 'The Cambridge Centre for Ageing and Neuroscience (Cam-CAN) study protocol: a cross-sectional, lifespan, multidisciplinary examination of healthy cognitive ageing', BMC neurology, vol. 14, pp. 1-25.
3. Emrich, S. M., Riggall, A. C., LaRocque, J. J., & Postle, B. R. (2013), 'Distributed patterns of activity in sensory cortex reflect the precision of multiple items maintained in visual short-term memory', Journal of Neuroscience, vol. 33, no. 15, pp. 6516-6523
4. Bassett, D. S., Porter, M. A., Wymbs, N. F., Grafton, S. T., Carlson, J. M., & Mucha, P. J. (2013), 'Robust detection of dynamic community structure in networks', Chaos: An Interdisciplinary Journal of Nonlinear Science, vol. 23, no. 1.
5. Rubinov, M., & Sporns, O. (2010), 'Complex network measures of brain connectivity: uses and interpretations', NeuroImage, vol. 52, no. 3, pp. 1059–1069.
6. Geerligs, L., Rubinov, M., & Henson, R. N. (2015), 'State and trait components of functional connectivity: individual differences vary with mental state', Journal of Neuroscience, vol. 35, no. 41, pp. 13949-13961.
7. Pearson, J., & Keogh, R. (2019), 'Redefining visual working memory: A cognitive-strategy, brain-region approach', Current Directions in Psychological Science, vol. 28, nr. 3, pp. 266-273.

Poster No 1334

Dissection of tectal feedback connections in the rat visual system using MRI

Rita Gil[1], Mafalda Valente[1], Noam Shemesh[1]

[1]Champalimaud Research, Champalimaud Foundation, Lisbon, Lisbon

Introduction: Previous work from the lab has shown positive to negative BOLD transitions in the rat superior colliculus (SC) when moving from low to high frequency visual stimulation[1]. Such modulations have been associated with high visual frequency stimulation-induced neuronal suppression and the entrance in the continuity illusion regime: individual light flashes discriminated in the low frequency static vision mode become fused in the high frequency dynamic vision mode and animals report seeing an illusory continuous light. Since retinal evoked potentials can still track individual light flashes at very high frequencies[2,3], SC's response modulation could result from feedback arriving to the region, namely from the primary visual cortex (V1) - corticotectal connections[4,5]- and between SCs –tectotectal connections[5-7]. In this work we investigate the effect of such feedback connections on the SC response modulations using fMRI.

Methods: Study in Long-Evans rats under medetomidine sedation in accordance with European Directive 2010/63. Stimulation: Binocular/monocular stimulation at 1Hz and 25Hz (flash duration=10 ms) was performed with an optic fibre connected to a blue LED (λ = 470nm). Ibotenic Acid Lesions: Injections of 1% ibotenic solution diluted in a 0.1M NaOH solution were performed along the left SC and/or both V1s. Animals were imaged one week after surgery to avoid inflammation. fMRI: Spin-echo echo planar imaging (SE-EPI) sequence in a 9.4T scanner: TR/TE=1500/40ms; resolution=268x268μm^2, slice=1.5mm. Pre-processing: Outlier, motion and slice-timing correction, isotropic smoothing. Runs were detrended with a polynomial fit to rest periods.

Results: The visual pathway is shown in Fig.1A. BOLD t-maps for the controls (Fig.1B) and V1 lesion group (Fig.1C), with reduced cortical feedback, show SC response modulation as a function of frequency: monocular stimulation at high frequency reveals positive/negative responses in the ipsilateral/contralateral SC (iSC/cSC), respectively. V1 lesioning reduces response amplitudes in both stimulation frequencies and modalities suggesting a general cortical gain effect (Fig.1D). To investigate the tectotectal connections, monocular stimulation (Fig.2A) is used, along with iSC and/or V1 lesions (Fig.2B). While for the 1Hz regime iSC lesions have little effect on the cSC responses, for the 25Hz regime the cSC responses are driven towards stronger negative values (Fig.2C). High frequency regimes lead to iSC positive responses that appear to counterbalance the negative cSC responses. Once such positive responses are abolished (through iSC lesions) the cSC responses are amplified. In Fig.2D we propose a mechanism for the tectotectal interactions in the different frequency stimulation regimes.

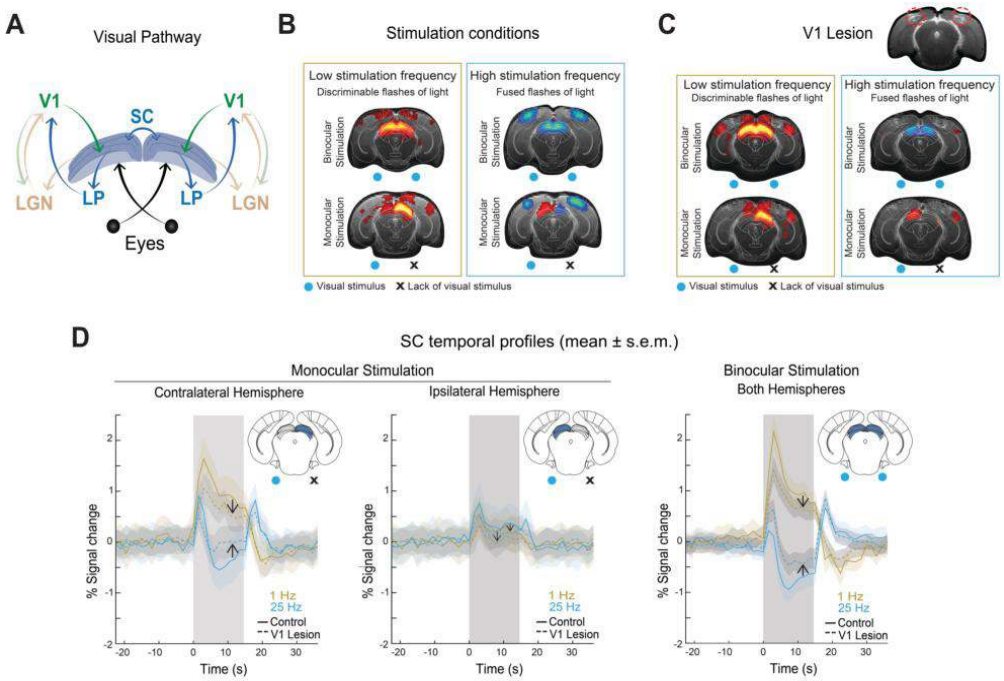

Figure 1: Corticotectal Feedback Connections
(A) Visual pathway schematic; BOLD t-maps for the control group **(B)** and bilateral V1 lesion group **(C)**; **(D)** SC BOLD temporal profiles for the monocular and binocular stimulation regimes. After V1 was bilaterally lesioned, therefore reducing corticotectal feedback, a reduction of response amplitude is observed for all conditions. This suggest a general cortical gain effect from corticotectal feedback on SC BOLD responses.

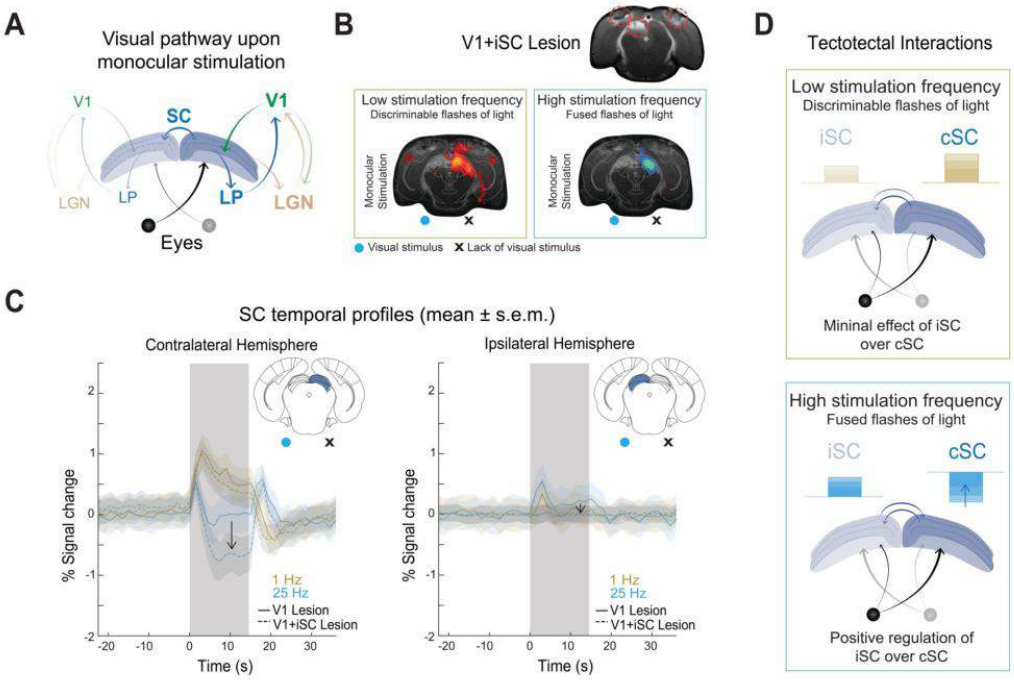

Figure 2: Tectotectal Feedback Connections (A) Visual pathway schematic upon monocular stimulation; **(B)** BOLD t-maps for the iSC+V1 lesion group; **(C)** SC BOLD temporal profiles for the iSC+V1 and V1 lesion groups. For the 1 Hz regime, lesioning iSC has little effect on the cSC responses. For the 25 Hz regime, once the iSC positive responses are abolished through lesioning, the cSC responses are amplified towards negative values; **(D)** Proposed tectotectal interactions for the two frequency regimes: iSC exerts a positive regulation of negative contralateral BOLD responses at high frequency regimes.

Conclusions: While cortical feedback serves as general gain control of the SC responses, the interaction between the SCs appears to depend on the operating vision mode. During the static vision mode, tectotectal feedback does not play a big role; however, at high frequency stimulation regime (when animals enter the dynamic vision mode) tectotectal feedback appears to exert a push-pull effect where the iSC counterbalances the neuronal suppression in the visually stimulated SC (cSC). Future studies are needed to better understand the behavioural relevance of these measured opposite responses in SCs at high frequency regimes.

References
1. Gil, Rita, Mafalda Valente, and Noam Shemesh. "Activation/suppression balances in rat Superior Colliculus encode the visual continuity illusion." bioRxiv 2022-11 (2022)
2. Yang, S. et al. (2012), 'The electroretinogram of mongolian gerbil (Meriones unguiculatus): Comparison to mouse.' Neuroscience Letters 589, 7–12.
3. Lisney, T. J., et al. (2012), 'Using electroretinograms to assess flicker fusion frequency in domestic hens Gallus gallus domesticus.' Vision Research 62, 125–133.
4. Zhao, Xinyu, et al. (2014), "Visual cortex modulates the magnitude but not the selectivity of looming-evoked responses in the superior colliculus of awake mice.", Neuron 84.1, 202-213.
5. Goodale, M. A., (1973), 'Cortico-tectal and intertectal modulation of visual responses in the rat's superior colliculus.', Experimental Brain Research 17.1, 75-86.
6. Bereshpolova, Yulia, et al. (2006), 'The impact of a corticotectal impulse on the awake superior colliculus.', Journal of Neuroscience 26.8, 2250-2259.
7. Olivier, Etienne, et al. (2000) 'Evidence for glutamatergic tectotectal neurons in the cat superior colliculus: a comparison with GABAergic tectotectal neurons.', European Journal of Neuroscience 12.7, 2354-2366.

Poster No 1335

Nonlinear kernel-based fMRI activation detection

Chendi Han[1], Zhengshi Yang[1], Xiaowei Zhuang[1], Dietmar Cordes[1]

[1]Cleveland Clinic Lou Ruvo Center for Brain Health, Las Vegas, NV

Introduction: Kernel Canonical Correlation Analysis (KCCA) is an efficient way to detect brain activation globally with less computational complexity. However, the current KCCA is limited to the linear kernel, and the performance for other more general types of kernels is not completely understood due to a lack of inverse mapping i.e. Back Construction (BC) methods. This study aims to expand the current KCCA method to arbitrary nonlinear kernels. The general linear model (GLM) is commonly used in task fMRI data analysis. Several related methods such as an isotropic GLM with Gaussian Smoothing (GS)[1], Canonical Correlation Analysis (CCA) and Linear KCCA[2-5] have been used to obtain activation maps. Beyond linear methods, nonlinear kernel-based methods, such as the Support Vector Machine (SVM), are very powerful in data classification and prediction[6], but there is no method available to define an inverse mapping from the feature space to the original space for obtaining an activation map. In this study, we proposed a general type of BC technique which allows us to get the activation pattern for any type of linear or nonlinear kernel mapping. The new method was applied to real fMRI data for activation analysis.

Methods: Structural and functional MRI data were obtained from the Human Connectome Project (HCP) database[7], which contains 3T MRI imaging data from 87 males aged 26-30 old. We focus on the working memory task fMRI study. fMRI data were acquired with 405 timeframes with multiband factor 8, TR/TE=720/33.1ms; FA=52 degrees; 72 slices; spatial resolution=2mm^3 with size=104 × 90. The data were minimally preprocessed (realignment, slice-timing correction, normalization to MNI, linear detrending). No spatial smoothing was performed. The task itself represents an event-related task design consisting of targets, non-targets, and lures contrasts. Figure 1 shows a flow chart of our data analysis. fMRI signal Y is transformed to feature space Y ~ by Y ~=YA∈R^(t×p), A∈R^(q×p) where A is the spatial transformation matrix, then map to the kernel space K_Y by an arbitrary kernel function. For the design matrix X, we define the contrast vector c=[1,-1,0] and map X to X_eff[8]. Then, map the X_eff to kernel space by K_X=X_eff X'_eff. Using KCCA, the solution vectors v_X and v_Y are found to maximize the canonical correlation corr(K_X v_X,K_Y v_Y) in the feature space with penalty term γ to avoid overfitting[9]. To transform back to the ordinary space, we propose a BC method by r=|∑_t(∂ [(K_Y v_Y)]_t)/(∂ Y_t)|∈R^q where the (voxel-specific) correlation vector r measures the importance of each voxel's contributing to the signal in kernel space.

Results: In Figure 2 (a1)-(e1), we show the activation pattern for one selected subject, with the color indicating the top 10% of voxels with high r value. In Figure 2 (a2)-(e2), we plot the same results using Gray Matter (GM) as a background. The GM is computed using spm package with segmentation probability p>0.5. The Hyperbolic tangent kernel avoids most activations arising outside the GM. To further characterize the overlapping, we treat the GM as the ground truth, using different thresholds to compute the true positive (activation appears on the GM) and false positive (activation not on the GM), with the ROC curve as shown in Figure 2 (f). Then using the 5mm GS as the reference, we define the subject-specific parameter α=(AUC)_Kernel/(AUC)_GS as a ratio measuring how many increasements compared with the GS. The distribution of α among all subjects are shown in Figure 2 (a3)-(e3), with the mean and average shown in Figure 2 (g). On average the Hyperbolic tangent kernel has highest α value among all other kernels.

Conclusions: The key findings of this study are: 1) BC is an efficient method to compute activation maps for general types of kernel representations. 2) Hyperbolic tangent kernel can get activation in an optimum location compared with other kernels.

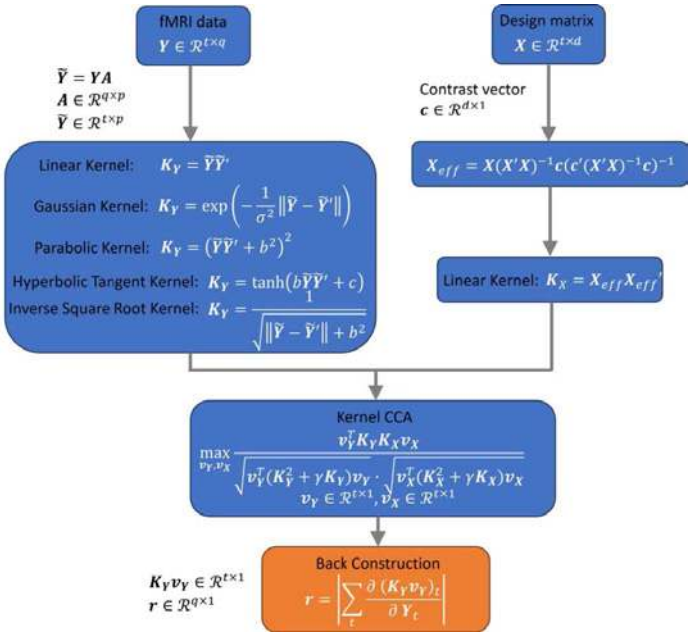

Figure 1: A schematic diagram of regularized kernel canonical correlation analysis for task fMRI activation analysis.

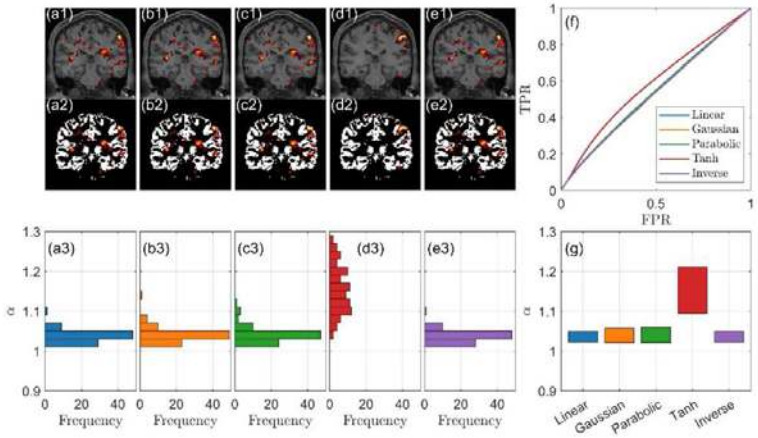

Figure 2: (a1)-(e1), activation pattern obtained from Linear kernel, Gaussian kernel, Parabolic kernel, Hyperbolic tangent kernel and Inverse square root kernel respectively. The color indicates the top 10% of voxels with high r value. The background is the T1 image at the corresponding location. (a2)-(e2) The same activation pattern but using the gray matter as background. The activation pattern obtained from the Hyperbolic tangent kernel has maximum overlapping on the gray matter. (f) ROC curves computed from five different kernels which are used to characterize the overlapping between the activation and the gray matter. (a3)-(e3) histogram for α computed from Linear kernel, Gaussian kernel, Parabolic kernel, Hyperbolic tangent kernel and Inverse square root kernel respectively. (g) Mean and variance for α based on 87 subjects.

References

1. Friman, O., et al. (2003), Adaptive analysis of fMRI data. Neuroimage, vol. 19, pp. 837-845.
2. Friman, O., et al. (2001), Detection of neural activity in functional MRI using canonical correlation analysis. Magnetic Resonance in Medicine: An Official Journal of the International Society for Magnetic Resonance in Medicine, vol. 45, pp. 323-330.
3. Cordes, D., et al. (2012), Optimizing the performance of local canonical correlation analysis in fMRI using spatial constraints. Human brain mapping, vol. 33, pp. 2611-2626.
4. Yang, Z., et al. (2018), 3D spatially-adaptive canonical correlation analysis: Local and global methods. Neuroimage, vol. 169, pp. 240-255.
5. Boser, B. E, I., et al. (1992), A training algorithm for optimal margin classifiers. Proceedings of the fifth annual workshop on Computational learning theory, pp. 144-152.
6. Barch, D.M., et al. (2013), Function in the human connectome: task-fMRI and individual differences in behavior. Neuroimage, vol. 80, pp. 169-189.
7. Cordes, D., et al. (2012), Optimizing the performance of local canonical correlation analysis in fMRI using spatial constraints. Human brain mapping, vol. 33, pp. 2611-2626.
8. Hardoon, D.R., et al. (2004), Canonical correlation analysis: An overview with application to learning methods. Neural computation 2004. vol. 16, pp. 2639-2664.

Acknowledgements

This study was funded by NIH-RF1AG071566.

Poster No 1336

Tedana: multi-echo fMRI noise removal software and resources

Daniel Handwerker[1], Peter Bandettini[1], Logan Dowdle[2], Elizabeth DuPre[3], Javier Gonzalez-Castillo[1], Christopher Markiewicz[3], Stefano Moia[4], Peter Molfese[1], Neha Reddy[5], Taylor Salo[6], Joshua Teves[1], Eneko Uruñuela[7]

[1]National Institute of Mental Health, Bethesda, MD, [2]Center for Magnetic Resonance Research, Minneapolis, MN, [3]Stanford University, Stanford, CA, [4]Maastricht University, Maastricht, Netherlands, [5]Northwestern University, Chicago, IL, [6]University of Pennsylvania, Philadelphia, PA, [7]Basque Center on Cognition, Brain and Language, Gipuzkoa, Spain

Introduction: Multi-echo fMRI involves the collection of data at multiple echo times for each excitation pulse. Three or more volumes of fMRI data can be collected at every time point with minimal acquisition cost. These additional data can be used to reduce acquisition noise and better estimate and remove signals that are not blood oxygen level dependent [Kundu 2012, Posse 1999]. Tedana [DuPre, Salo 2021] is an open source software that provides ways to apply multi-echo noise removal methods. Tedana also includes educational resources to help researchers better understand and use multi-echo fMRI data, whether or not they use tedana's software.

Methods: Tedana uses modern software techniques combined with an accessible community of developers and users to continue to improve the software (github.com/ME-ICA/tedana) and resources (tedana.readthedocs.io). Tedana is integrated into the AFNI [Cox 1996] and fMRIPrep [Esteban et al 2018] preprocessing pipelines. We also monitor and respond to questions at neurostars.org using the "multi-echo" and "tedana" tags to better support our software and have built a welcoming community of multi-echo fMRI users.

Results: A major software update over the past year was modularization of the ICA classification "decision tree." The central multi-echo fMRI denoising method in tedana applies ICA to the data and then selects which components should be classified as noise and removed [Kundu 2012]. In the modularized code, each step in the decision tree can be defined in a text file, and all classifications that change in each step are fully tracked. With this new system, it is now possible to alter the decision process to address study-specific needs. The new process and how to design a new decision tree are fully documented to make new innovations within tedana accessible to more researchers. We have additionally improved our methods for tracking and automatically enforcing code style consistency and removed unnecessary dependencies that limited the integration of tedana with other software packages. In responding to user questions, we have also identified and fixed several issues with the code or documentation.

Conclusions: The changes during the past year make it easier for new contributors to join and will support planned improvements to denoising methods. A key planned improvement is to allow external information, such as motion regressors, into the decision process so that multi-echo methods can be combined with other ICA-based denoising methods, like AROMA [Pruim et al 2015].

References

1. Cox R. W. (1996). AFNI: software for analysis and visualization of functional magnetic resonance neuroimages. Computers and biomedical research, an international journal, 29(3), 162–173. https://doi.org/10.1006/cbmr.1996.0014
2. DuPre, Salo et al., (2021). "TE-dependent analysis of multi-echo fMRI with tedana." Journal of Open Source Software, 6(66), 3669 https://doi.org/10.21105/joss.03669
3. Esteban, O., Markiewicz, C.J., Blair, R.W. et al. fMRIPrep: a robust preprocessing pipeline for functional MRI. Nat Methods 16, 111–116 (2019). https://doi.org/10.1038/s41592-018-0235-4
4. Kundu, Inati, Evans, Luh, Bandettini (2012). Differentiating BOLD and non-BOLD signals in fMRI time series using multi-echo EPI. NeuroImage, 60(3), 1759-1770. https://doi.org/10.1016/j.neuroimage.2011.12.028.
5. Posse, S., Wiese, S., Gembris, D., Mathiak, K., Kessler, C., Grosse-Ruyken, M.-L., Elghahwagi, B., Richards, T., Dager, S.R. and Kiselev, V.G. (1999), Enhancement of BOLD-contrast sensitivity by single-shot multi-echo functional MR imaging. Magn. Reson. Med., 42: 87-97. https://doi.org/10.1002/(sici)1522-2594(199907)42:1%3C87::aid-mrm13%3E3.0.co;2-o
6. Pruim, R. H. R., Mennes, M., van Rooij, D., Llera, A., Buitelaar, J. K., & Beckmann, C. F. (2015). ICA-AROMA: A robust ICA-based strategy for removing motion artifacts from fMRI data. NeuroImage, 112, 267–277. https://doi.org/10.1016/j.neuroimage.2015.02.064

Poster No 1337

Combined Transcranial Magnetic Stimulation with Spinal Cord fMRI to Probe Spinal Motor Circuitry

Ekansh Sareen[1,2], Nawal Kinany[1,2], Estelle Raffin[1], Rebecca Jones[1], Loan Mattera[3], Roberto Martuzzi[3], Friedhelm Hummel[1], Dimitri Van De Ville[1,2]

[1]École Polytechnique Fédérale de Lausanne, Lausanne, Switzerland, [2]Department of Radiology and Medical Informatics, University of Geneva, Geneva, Switzerland, [3]Fondation Campus Biotech Geneva, Geneva

Introduction: The spinal cord, a pivotal neurological center within the central nervous system, houses intricate neural pathways facilitating and modulating sensorimotor activity for diverse human functions. Despite its significance, the exploration of its functional intricacies, particularly the independent characterization of underlying motor mechanisms, remains an evolving area of research. To tackle this challenge, our ongoing investigation employs a multimodal approach that combines transcranial magnetic stimulation (TMS) for targeted motor cortex stimulation with functional magnetic resonance imaging (fMRI) of subsequent spinal cord activity. This holds the potential for a systematic and comprehensive delineation of the motor aspect of spinal circuitry.

Methods: Ten healthy volunteers were included in this study. The experiments were performed on a Siemens 3T Prisma scanner using a concurrent TMS-fMRI acquisition protocol, previously used in[1]. Single-pulse TMS was applied over the right primary motor cortex, targeted over first dorsal interosseous (FDI) and abductor digiti minimi (ADM) muscle groups on the left hand, using the MagPro XP stimulator system. EMG electrodes were placed over the targeted muscle groups to record motor evoked potential (MEP) responses to the applied TMS. The study included two sessions of acquisitions (S1 and S2), with identical protocols separated by a week (Fig. 1A). The TMS pulse was applied with three varying intensities of pre-estimated subject-specific resting motor threshold (rMT), i.e., sub-threshold (0.8% rMT), threshold, (rMT), and supra-threshold (1.2% rMT). The functional images of the spinal cord were acquired using a gradient-echo EPI sequence with inner field-of-view (TR = 2500 ms, TE = 34 ms, resolution = 1x1x3 mm3), spanning over C2 to C8 spinal levels. The acquired data were preprocessed using the pipeline introduced in[2] as implemented in the Spinal Cord Toolbox[3]. Preprocessed images were then analyzed using the GLM to extract spinal activation maps. We used an event-based design matrix with two explanatory variables: non-modulated (NM) and modulated (M, orthogonal to NM, derived from recorded MEP responses) (Fig. 1B). Average group-level activation maps were computed using fixed effects analysis (n=9 for S1, n=10 for S2).

Results: Fig. 1C illustrates the average peak-to-peak MEP amplitude across subjects for three intensity modulation conditions. Fig. 1D illustrates the average group activation maps for S1 and S2 for NM and M regressors. In S1, activation maps for the NM condition present localized activity at C5 within descending white matter tracts and right ventral horns. For the M condition, a left-dominant bilateral activity was observed in the ventral horns at C7. In S2, NM condition activity localizes primarily at C7-C8 within descending white matter tracts, with additional activity observed in the right intermediate zone of ventral horn. For the M condition, no significant activity was found. Applied TMS (NM regressor) in both sessions predominantly induces activity in descending white matter tracts carrying motor information from the cortex. Conversely, TMS intensity modulation (M regressor) in S1 induces stimulation-side dominated bilateral activity in the ventral gray matter horns, housing motor neurons. We only observed the modulation effect in S1, which is coherent with our observation from the recorded MEP responses (Fig 1C).

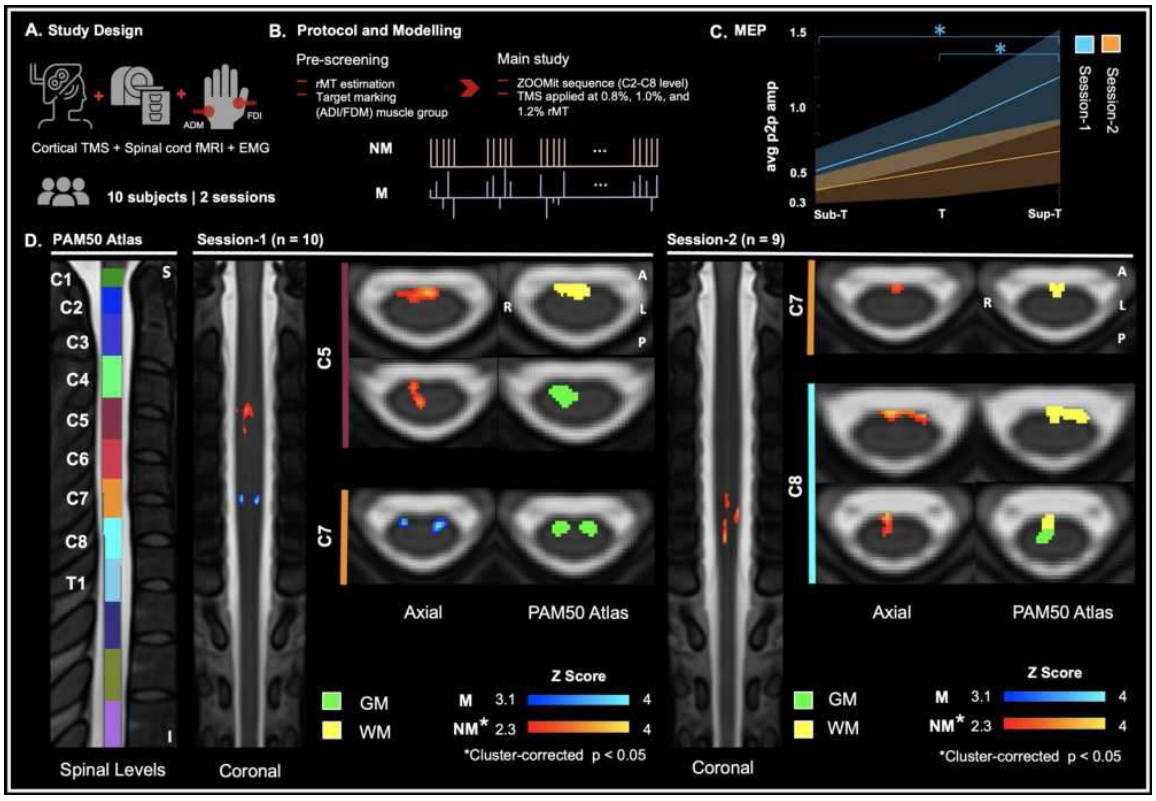

Conclusions: This investigation demonstrates the viability of our proposed multimodal setup for simultaneous stimulation and imaging of corticospinal circuits, specifically the spinal motor circuitry. Our findings underscore the involvement of spinal motor neurons in response to modulating TMS intensity. Nevertheless, notable inter-subject and inter-session variability necessitates further exploration with an expanded subject pool.

References

1. Raffin, E., Salamanca-Giron, R. F., Huxlin, K. R., Reynaud, O., Mattera, L., Martuzzi, R., & Hummel, F. C. (2022). Concurrent TMS-fMRI to determine adaptive brain changes to virtual lesions interfering with visual processing. bioRxiv 2022.03.03.482512.
2. Kinany, N., Pirondini, E., Martuzzi, R., Mattera, L., Micera, S., & Van de Ville, D. (2019). Functional imaging of rostrocaudal spinal activity during upper limb motor tasks. Neuroimage, 200, 590-600.
3. De Leener, B., Lévy, S., Dupont, S. M., Fonov, V. S., Stikov, N., Collins, D. L., & Cohen-Adad, J. (2017). SCT: Spinal Cord Toolbox, an open-source software for processing spinal cord MRI data. Neuroimage, 145, 24-43.

Poster No 1338

Effects of Caffeine Intake as a Sympathetic Stimulant on Brain Dynamics during Cognitive Tasks

Cem Karakuzu[1], Kübra Eren[1], Elif Can[1], Belal Tavashi[1], Kadir Yildirim[1], Lina Alqam[1], Alp Dincer[2], Pinar S Ozbay[1]

[1]Bogazici University, Istanbul, Turkey, [2]Acibadem University, Istanbul, Turkey

Introduction: This study explores the impact of caffeine, a sympathetic stimulant, on cognitive brain dynamics, leveraging the power of functional magnetic resonance imaging (fMRI) and independent component analysis (ICA), which is a data-driven clustering method to construct statistically independent spatial maps of fMRI data. This integrative approach promises a more nuanced perspective on the effects of caffeine on cognitive functions.

Methods: Data were obtained at 3T with GRE-EPI (FA = 90, TR = 3 s, TE = 36 ms, in-place resolution = 2.5 mm, number of TRs = 135). The participant was asked to find the unknown while seeing the equation (see Figure 1A). Preprocessing of fMRI data followed the suggested 'afni_proc' pipeline, including removal of signal drifts, slice-timing correction, realignment of consecutive volumes, registration to MNI template, smoothing (3 mm FWHM), and regression of motion parameters while removing outliers (threshold = 0.2) (Taylor et al., 2018; Cox 1996). PPG and respiratory signals were collected with a pulse oximeter attached to the fingertip and respiratory bellows, respectively. We used RETROICOR to reduce the effects of their cycles in the fMRI. There were four participants who attended the experiment. Repeated scans were performed following immediate intake of caffeine pills, first scan 10 minutes and second scan 30 minutes following intake. The subjects were not informed if the pill was caffeine or placebo. Firstly, ICA performed for all subjects by FSL's MELODIC (Jenkinson et al., 2012). Thus, task-related components and RVT related components were determined by examining the association between components' time-courses and experimental design. RVT related components were identified by cross-correlation analysis between the time-course and RVT in MATLAB (MathWorks, 2023). Secondly, those components were investigated to describe how spatial maps changed when RETROICOR was not performed. Finally, we applied group-ICA on three participants' first sessions and second sessions.

Results: Controlling physiological signals with RETROICOR might make the components take the early places if the physiological signals are controlled. The relationship between RVT and time-course was explored. Cross-correlations between the RVT and the signal in sessions gave contrary results. Moreover, in session 2 of the participant 2, the task-related component 1 has also the highest cross-correlation with RVT. Group-ICA: component 16 shows distinct patterns of the effect of increased activity of cerebral arteries, unlike the other group (see figure 2A). Also, explained variance of insula activation is higher in the 30-minutes after group and the spatial map is more particular for the insula regions. Besides, task related IPS region is visible earliest in the component 6 in the 10-minutes after group. On the other hand, it can be seen at the component 2 in the 30-minutes after group. Finally, Component 18 in caffeine has a particular map covering thalamus (see figure 2B).

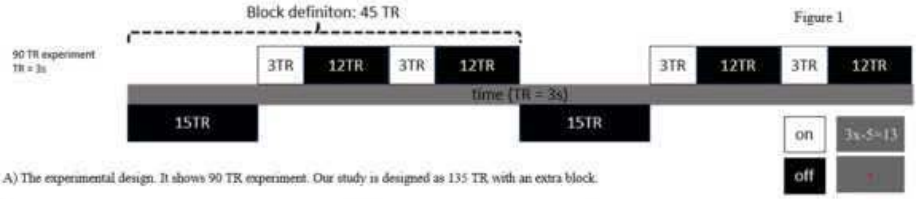

Figure 1

A) The experimental design. It shows 90 TR experiment. Our study is designed as 135 TR with an extra block.

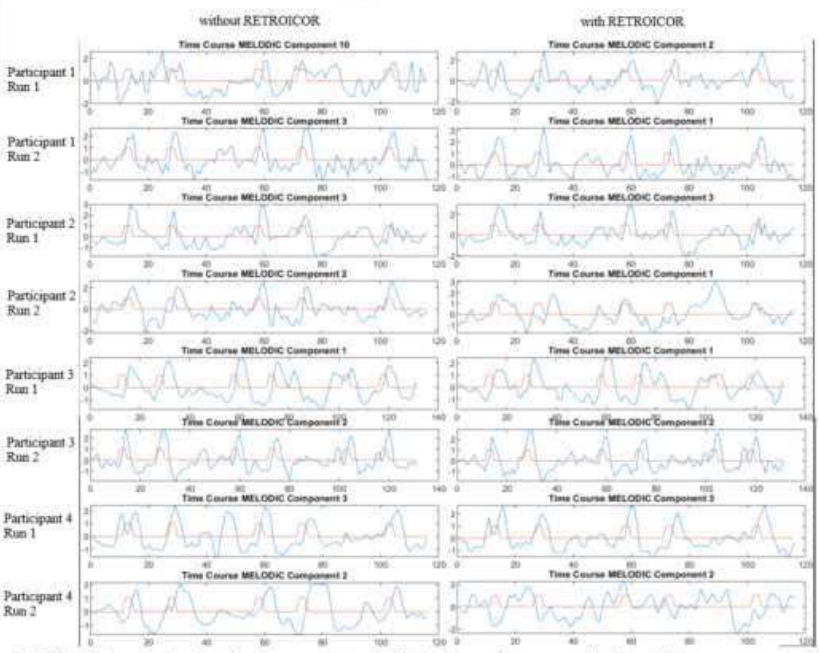

B) fMRI signal time-course from the task-related components trough all TRs. The orange line represents the task's on/off times.

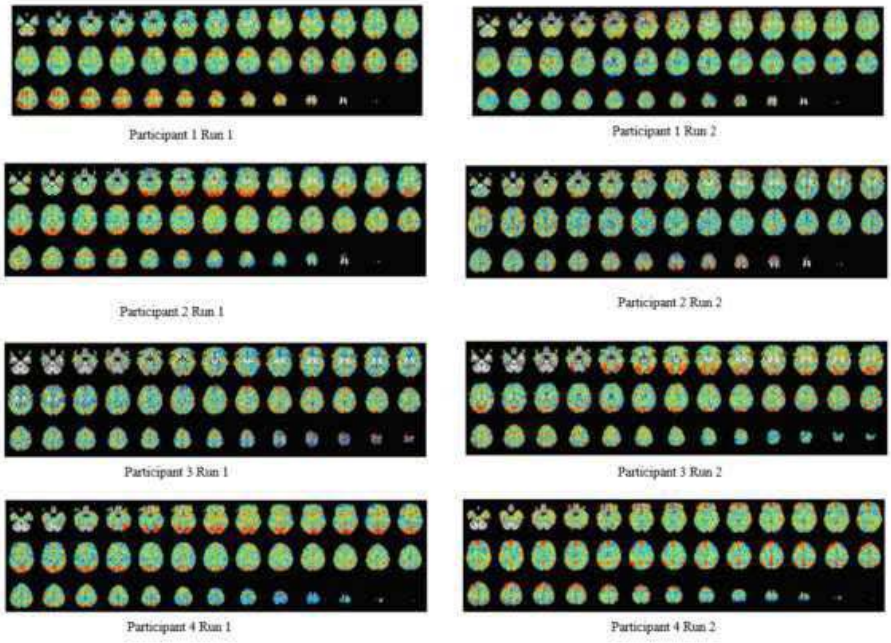

C) The spatial maps of task-related components for each session which was applied RETROICOR

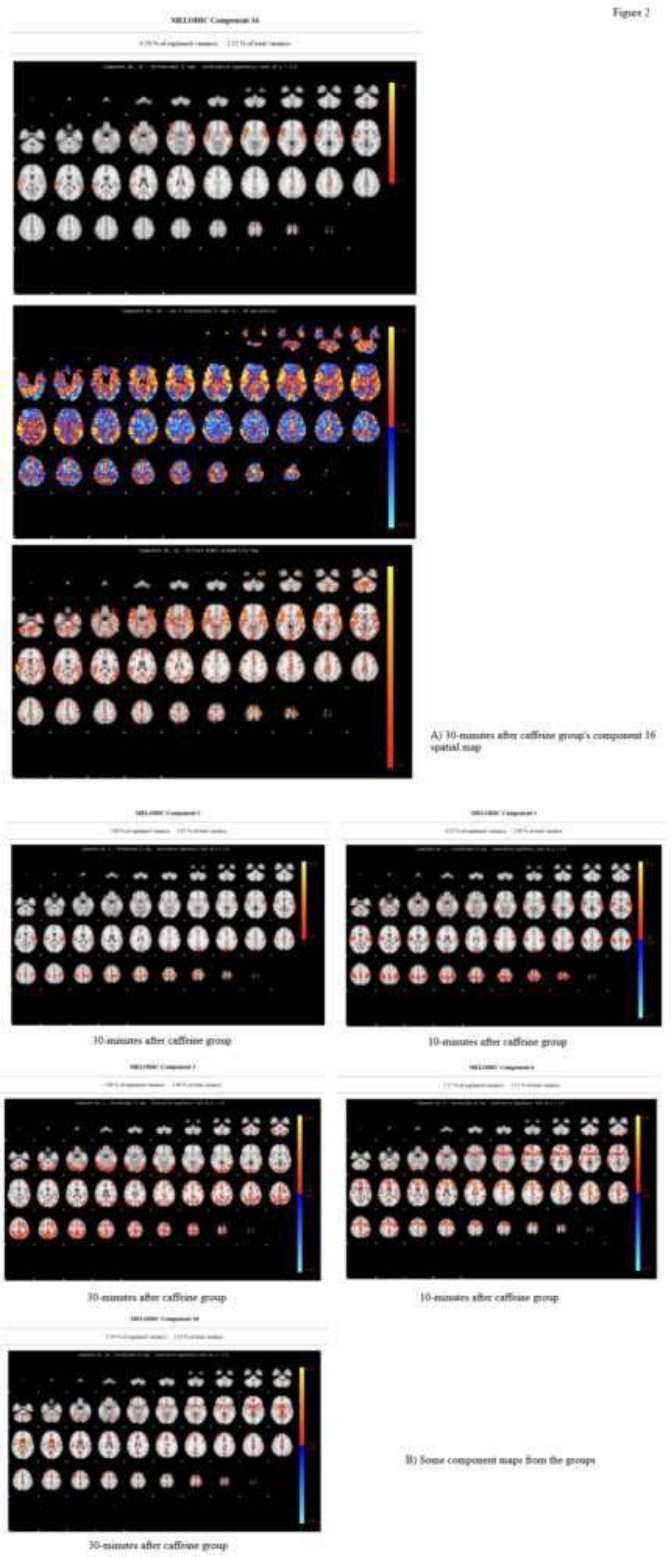

Conclusions: Controlling physiological signals is highly substantial because single subject ICAs shows that provided networks and explained variances could be changed by physiological signals. Also, RVT could be correlated with the task-related networks, which means that cardiac and respiratory activity could interfere with fMRI signals of the brain. When considering the how cerebral arteries affect the fMRI signals, the importance of this cross-correlation must be considered. Because it is also the most task-related component, the effect of caffeine trough the sympathetic activity increase and its chemical effects on the direct neuronal level requires research to distinguish impact pathways.

References
1. Cox RW (1996). AFNI: software for analysis and visualization of functional magnetic resonance neuroimages. Comput Biomed Res 29(3):162-173.
2. Jenkinson, M., Beckmann, C. F., Behrens, T. E., Woolrich, M. W., & Smith, S. M. (2012). FSL. NeuroImage, 62(2), 782–790.
3. Taylor PA, Chen G, Glen DR, Rajendra JK, Reynolds RC, Cox RW (2018). FMRI processing with AFNI: Some comments and corrections on 'Exploring the Impact of Analysis Software on Task fMRI Results'.
4. The MathWorks Inc. (2023). MATLAB version: 9.14.0 (R2023a), Natick, Massachusetts: The MathWorks Inc. https://www.mathworks.com

Poster No 1339

Autonomic Regression in fMRI: Insights from Respiration, Pupil Size and PPG Amplitude

Belal Tavashi[1], Kübra Eren[1], Kadir Yildirim[1], Elif Can[1], Cem Karakuzu[1], Lina Alqam[1], Alp Dincer[2], Pinar S Ozbay[1]

[1]Bogazici University, Istanbul, Turkey, [2]Acibadem University, Istanbul, Turkey

Introduction: To understand the impact of autonomic correction on spatiotemporal patterns in the fMRI-systemic signals relationship, we used PPG amplitude and pupil size. Stress-induced hormonal responses, affecting alertness and pulse rate, prompted our examination of removing autonomic and behavioral effects from fMRI data. We hypothesized that eliminating these components, due to their strong co-variation with fMRI data, would influence outcomes. This research aims to assess the contribution of autonomic processes to spatiotemporal correlations and active brain regions during a cognitive task.

Methods: FMRI data were obtained at 3 T with GRE-EPI (FA = 90, TR = 3 s, TE = 36 ms, in-place resolution = 2.5 mm, number of TRs = 135). The cognitive task involved solving arithmetic equations with one unknown, displayed against a grey background with a fixation dot in a block design (6 blocks, each: 45s OFF, 9s ON, and 36s OFF). Preprocessing of fMRI data followed the suggested 'afni_proc' pipeline (AFNI[1]), including removal of signal drifts, slice-timing correction, realignment of consecutive volumes, registration to MNI template, smoothing (3 mm fwhm), and regression of motion parameters while removing outliers (threshold = 0.2). PPG and respiratory signals were collected with a pulse oximeter attached to the fingertip and respiratory bellows, respectively. PPG amplitude (PPG-AMP), as an index of peripheral vascular volume[2], and respiratory volumes per time (RVT)[3] were calculated. An MRI-compatible camera was used to track a subject's eye movement. Pupil diameters were recorded automatically as a secondary measure of sympathetic activity. So far we acquired 4 subjects data, and performed the following analysis: We averaged event-locked physiological signals (based on cardiac, respiratory and pupil size variations) and fMRI responses within grey matter, task (e.g., Visual, IPS) and non-task (e.g., DMN, Insula) related regions. We performed voxel-wise correlations of PPG-AMP and pupil diameter with fMRI across subjects. Each preprocessed fMRI data set were subjected to General Linear Modelling (GLM). This part includes all timing information regarding mental task according to the experiment. The modeling step was combined with regression of motion parameters and their derivatives (3dDeconvolve) in 'afni_proc'. To incorporate further regressors of no interest, as described below, we included each time-series. Various methods developed to reduce the effects of cardiac and respiratory cycles in the fMRI data[4]. Among them, we used one of the most common approaches: RETROICOR[5], and included in the GLM as nuisance regressors, as implemented in AFNI's "RetroTS.m". To evaluate the contribution of better captured autonomic processes, we performed a regression analysis employing RETROICOR + RVT, PPG-AMP, and pupil diameter time-series (and combinations), adding time-shifted versions. To our knowledge, this will be the first study incorporating PPG-AMP or pupil diameter as regressors in such detail during wake conditions in humans.

Results: The study found task-related increases in fMRI signal, particularly in areas like IPS and visual regions, peaking at 6-9 seconds. Pupil size increased with a 6-second lag, peaking around 12 seconds, showing a time-dependent relationship with the fMRI signal. Negative correlations between pupil and fMRI in negative lags were attributed to sympathetic activity. Cross-correlation maps illustrated sympathetic-driven patterns around ventricular regions for negative lags and task-driven patterns around IPS and visual regions for positive lags. Removing time-shifted autonomic regressors reduced activity, especially in DMN and insular regions, as well as negative activations in ventricular regions.

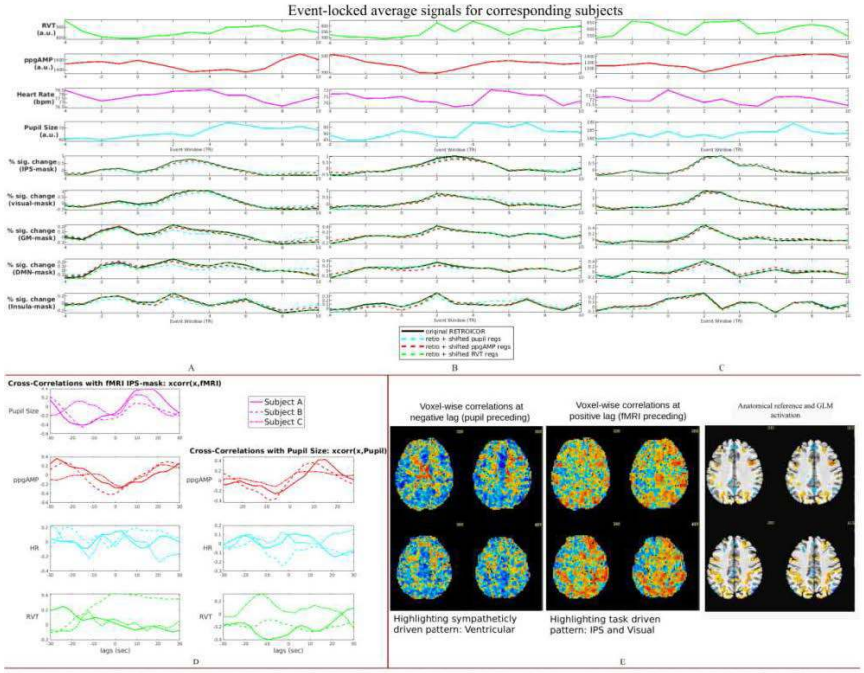

Figure 1: (A, B, C) Event-locked average signal changes of autonomic regressors and fMRI data across six task events for subjects A, B, and C, respectively. (D) Cross-correlation plots of IPS-masked fMRI signal and autonomic regressors (left), pupil size and other autonomic regressors (right). (E) Subject level voxel wise correlations of pupil size and fMRI (RETROICOR version) at the -3TR lag (left) and at the +3TR lag (middle) and GLM activation map (RETROICOR version) exhibiting the task-related region IPS (right).

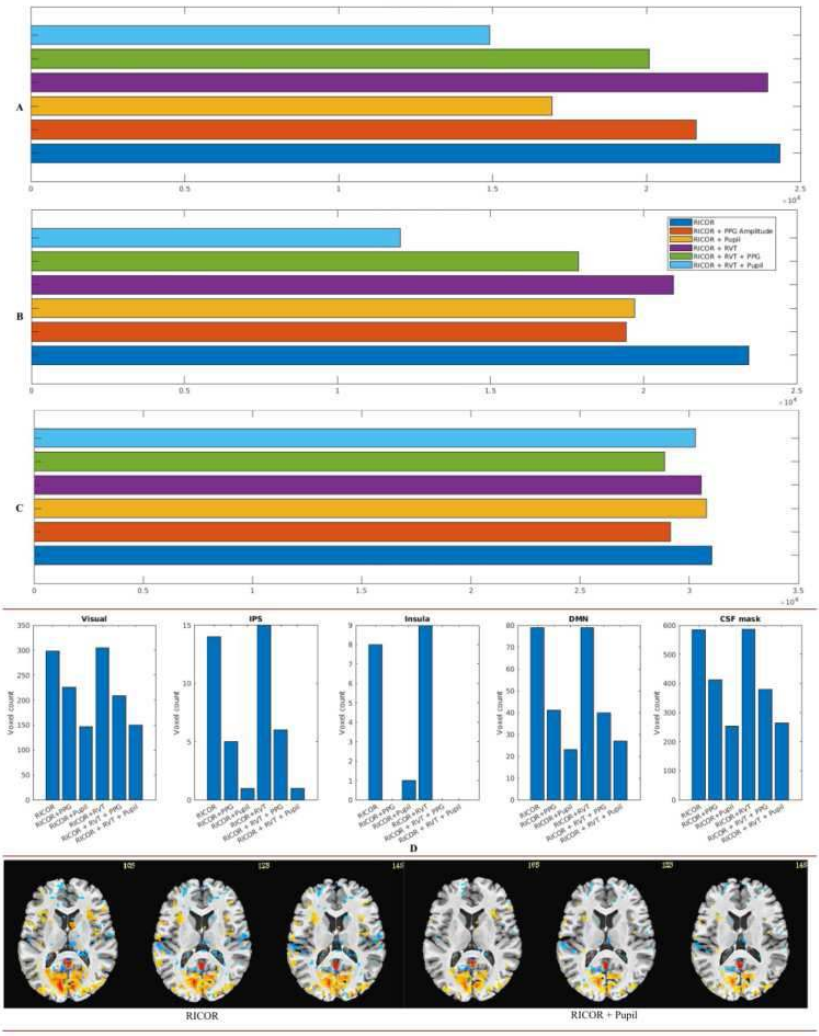

Figure 2: (A, B, and C) total voxel count for subjects A, B, and C, respectively. (D) voxel counts in specific regions of the brain in subject A ($p < 0.05$). (E) GLM activation maps for subject A ($p < 0.05$).

Conclusions: Our results showed that contributions of the sympathetic activity to fMRI signal which could not be revealed with RVT, can be explained with other autonomic signals like PPG-AMP and pupil size, which could be complementary to each other.

References
1. Cox RW. AFNI: software for analysis and visualization of functional magnetic resonance neuroimages. Computers and biomedical research, an international journal. 1996;29(3):162-73.2.
2. Özbay PS, Chang C, Picchioni D, Mandelkow H, Moehlman TM, Chappel-Farley MG, et al. Contribution of systemic vascular e!ects to fMRI activity in white matter. Neuroimage. 2018;176:541-9.3.
3. Birn RM, Diamond JB, Smith MA, Bandettini PA. Separating respiratory-variation-related fluctuations from neuronal-activity-related fluctuations in fMRI. Neuroimage. 2006;31(4):1536-48.4.
4. Caballero-Gaudes C, Reynolds RC. Methods for cleaning the BOLD fMRI signal. Neuroimage. 2017;154:128-49.5.
5. Glover GH, Li TQ, Ress D. Image-based method for retrospective correction of physiological motion e!ects in fMRI: RETROICOR. Magn Reson Med. 2000;44(1):162-7.

Poster No 1340

Higher body weight-dependent neural activation during reward processing

Maike Richter[1], Janik Goltermann[2], Lavinia Steinmann[1], Anna Kraus[2], Susanne Meinert[2], Jonathan Repple[3], Udo Dannlowski[2], Nils Opel[1]

[1]Department of Psychiatry and Psychotherapy, Jena University Hospital, Jena, Germany, [2]Institute for Translational Psychiatry, University of Münster, Münster, Germany, [3]Department of Psychiatry, Psychosomatic Medicine, and Psychotherapy, Goethe University Frankfurt, Frankfurt am Main, Germany

Introduction: Obesity is associated with alterations in brain structure and function, particularly in areas related to reward processing (García-García et. al, 2014; Opel et. al, 2015). Although brain structural investigations have demonstrated a continuous association between higher body weight and reduced gray matter in well-powered samples (Opel et. al, 2017; Shaw et. al, 2018), functional neuroimaging studies have typically only contrasted individuals from the normal weight and obese body mass index (BMI) ranges with modest sample sizes (García-García et. al, 2014; Han et. al, 2021). It remains unclear, whether the commonly found hyperresponsiveness of the reward circuit can (a) be replicated in well-powered studies and (b) be found as a function of higher body weight even below the threshold of clinical obesity.

Methods: 383 adults across the weight spectrum underwent functional magnetic resonance imaging during a common card-guessing paradigm simulating monetary reward. Multiple regression was used to investigate the association of BMI and neural activation in the reward circuit. In addition, a one-way ANOVA model comparing three weight groups (normal weight, overweight, obese) was calculated.

Results: Higher BMI was associated with higher reward response in the right (x=36, y=18, z = -14; t(379)=4.66; k=9; pFWE = 0.007) and left (x = -28, y=18, z = -4; t(379)=4.30; k=3; pFWE = 0.029) insula. This association could no longer be found when participants with obesity were excluded from the analysis. The ANOVA revealed higher activation in the right (x=34, y=18, z = -14; t(378)=4.78; k=10; pFWE = 0.005) and left (x = -28, y=20, z = -4; t(378)=4.29; k=6; pFWE = 0.033) insula in obese vs. lean individuals, but no difference between lean and overweight participants.

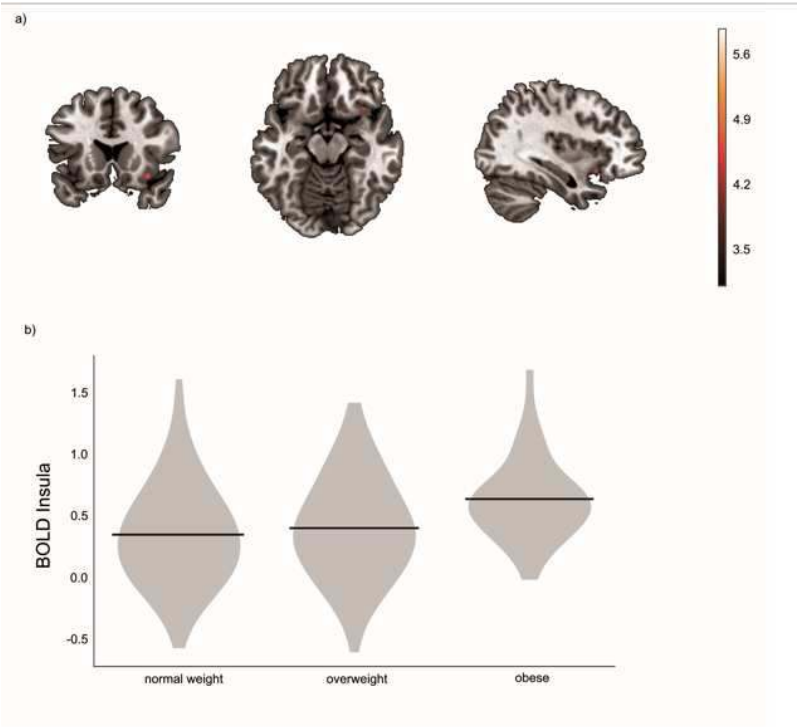

(a) Positive effect of BMI on neural responsiveness to reward in the insula. Results from the region-of-interest-analysis of the one-way ANOVA for the obesity > normal weight contrast are shown at MNI coordinates x = 36, y = 18, z = -14. Family-wise error corrected results at a voxel threshold of p < .05 are presented. Color bar: t-value.
(b) Violin plot depicting the density and group means of extracted insula BOLD values (3 mm around the peak voxel) for each weight group from the ANOVA model

Conclusions: The overactivation of reward-related brain areas in obesity is a consistent finding that can be replicated in large samples. In contrast to brain structural aberrations associated with higher body weight, the neurofunctional underpinnings of reward processing in the insula appear to be more pronounced in the higher body weight range.

References

1. García-García, I. (2014). Reward processing in obesity, substance addiction and non-substance addiction. Obesity Reviews, 15(11), 853–869.
2. Han, P. (2021). Increased brain reward responsivity to Food-Related odors in obesity. Obesity (Silver Spring, Md.), 29(7), 1138–1145.
3. Opel, N. (2015). Enhanced neural responsiveness to reward associated with obesity in the absence of food-related stimuli. Human Brain Mapping, 36(6), 2330–2337.
4. Opel, N. (2017). Prefrontal gray matter volume mediates genetic risks for obesity. Molecular Psychiatry, 22(5), 703–710.
5. Shaw, M. E. (2018). Body mass index is associated with cortical thinning with different patterns in mid- and late-life. International Journal of Obesity, 42(3), 455–461.

Poster No 1341

Brain responses to vehicles predict individual interest and forecast changes in aggregate demand

Dylan Christiano[1,2], Cynthia Wu[1], Tara Srirangarajan[1], Shabnam Hakimi[3], Matthew Klenk[3], Charlene Wu[3], Brian Knutson[1]

[1]Stanford University, Stanford, CA, [2]University of Michigan, Ann Arbor, MI, [3]Toyota Research Institute, Palo Alto, CA

Introduction: Demand for vehicles using alternative fuel sources is increasing, leading to the introduction of new vehicle models and types. Little is known, however, about market demand for these new vehicles. We sought to examine whether brain activity could predict individuals' desire to purchase and learn more about vehicles (Erk et al., 2002), as well as forecast changes in demand for vehicles out-of-sample in the US market (Knutson & Genevsky, 2018). Drawing from the AIM (Affect, Integration, Motivation) framework, we hypothesized that activity in the Nucleus Accumbens (NAcc), associated with dopaminergic signaling and positive arousal to stimuli, should predict choice (Samanez-Larkin & Knutson, 2015) and might forecast changes in demand for new vehicles.

Methods: 13 subjects who reported being interested in purchasing a vehicle in the next two years participated in a vehicle rating task as their brain activity was monitored using Functional Magnetic Resonance Imaging (FMRI). Participants viewed 48 trials per task, each lasting an average of 16 seconds. A mixed set of 12 Electric Vehicles (EV) and 12 Internal Combustion Engine (ICE) vehicles from various brands. Each vehicle appeared twice, in black or white colors, at a ¾ angle, and in a pseudorandom order. During each vehicle rating task trial, subjects initially saw a centrally presented image of the vehicle and its' model name (2 sec), followed by its fuel source (2 sec), followed by rating prompts querying interest in learning more and desire to purchase the vehicle (4 sec each). To assess changes in aggregate United States market demand, we collected publicly available data indicating units of each model sold for each quarter of 2022 (from goodcarbadcar.net). We then calculated the average and slope of units sold over quarters of 2022 to estimate average demand and change in demand. For individual prediction analyses, activity was averaged prior to choice and extracted from predicted Volumes Of Interest (VOIs) in the NAcc, Medial PreFrontal Cortex (MPFC), and Anterior Insula (AIns) and regressed against rated desire to know more and to purchse on each trial (Samanez-Larkin and Knutson, 2015). For aggregate market forecasts, activity in these VOIs was averaged by model and regressed against the slope of sales for 2022.

Results: Within individuals, both VOI and whole brain analyses revealed that subjects' initial NAcc response to vehicles predicted rated desire to know more about and purchase those vehicles. A main effect of fuel type indicated that subjects preferred electric to gas vehicles (beta=15.21±0.07, $p < 0.001$) and NAcc activity also predicted vehicle preference (beta=2.63±0.11, $p < 0.01$). At the aggregate level, average NAcc response to vehicles also forecast the slope in market demand for units sold ($p<.006$), but not the average of units sold during 2022. In combination with NAcc activity, averaged behavior (i.e., desire to know and purchase ratings), however, did not forecast the slope or average units sold.

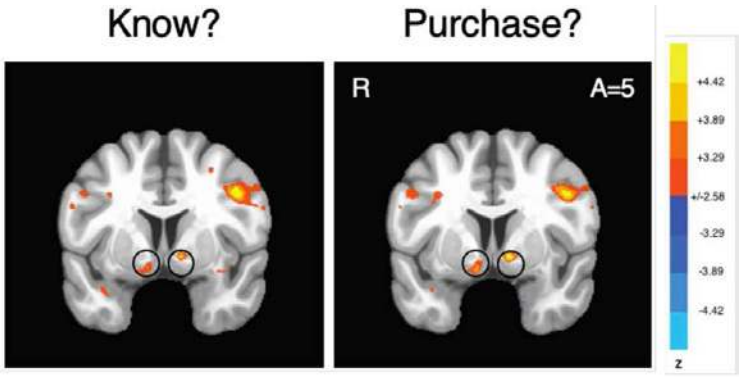

Fig. Whole brain maps confirm that NAcc activity predicts individual desire to know more and to purchase different vehicle models.

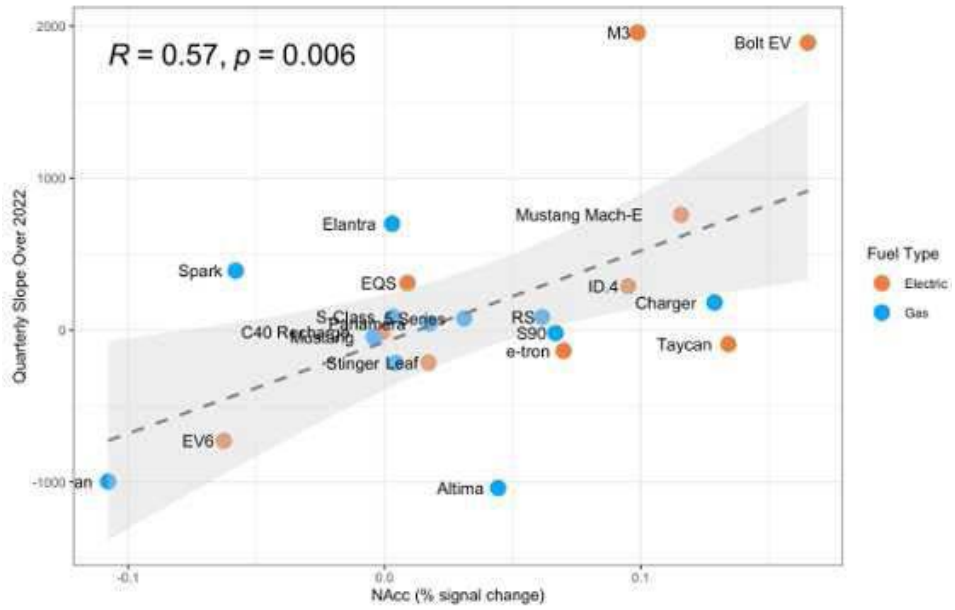

Pairwise plot indicating that NAcc response to vehicles forecasts aggregate change in U.S. demand for different models over 2022.

Conclusions: Brain responses to vehicles, specifically early responses in the NAcc, predict individuals' desire learn more about and to purchase them. Further, average group NAcc activity forecast changes in demand for cars, beyond behavioral forecasts. These findings suggest that brain activity might add value to conventional measures for forecasting market demand for new vehicles.

References

1. Erk, S., Spitzer, M., Wunderlich, A. P., Galley, L., & Walter, H. (2002). Cultural objects modulate reward circuitry. Neuroreport, 13(18), 2499-2503.
2. Knutson, B., & Genevsky, A. (2018). Neuroforecasting aggregate choice. Current Directions in Psychological Science, 27(2), 110-115.
3. Samanez-Larkin, G. R., & Knutson, B. (2015). Decision making in the ageing brain: changes in affective and motivational circuits. Nature Reviews Neuroscience, 16(5), 278-289.

Poster No 1342

Precision functional mapping of therapeutic response in task-specific focal dystonia

Vi Nguyen[1], Ashley Meyer[2], Jessica Hudson[3], Scott Norris[3], Evan Gordon[4]

[1]Washington University in St Louis, St Louis, MO, [2]Washington University in St. Louis, St. Louis, MO, [3]Washington University in St Louis School of Medicine, St Louis, MO, [4]Washington University, St. Louis, MO

Introduction: Adductor laryngeal dystonia (ADLD) is a task-specific focal dystonia that involves excessive laryngeal muscle contraction during speech. Focal dystonia like ADLD is associated with dysfunction of the basal ganglia, primary motor cortex (M1), thalamus, and cerebellum[1,4,6]. ADLD-related vocal disability improves with recurring, invasive application of botox into laryngeal muscles. A deeper understanding of central neural mechanisms related to this transient therapeutic response may improve understanding of pathophysiological mechanisms and therapeutic potential (i.e. advance engagement targets for central acting neuromodulation approaches). Prior work suggested alterations in resting-state functional magnetic resonance imaging (rs-fMRI) functional connectivity (FC) in dystonia patients after successful botox therapy[5]. However, this work collected low amounts of per-patient data, and thus could not detect individual-specific therapeutic alterations. Here, we employed precision functional mapping (PFM), which collects large quantities of per-patient data to precisely characterize individual-specific brain networks without averaging across patients[2,3]. We aimed to determine the vocalization-related functional motor network in ADLD subjects and assess how this vocalization network FC was altered in each individual patient by applying therapeutic botox injections.

Methods: We conducted a treatment response of PFM in 4 ADLD patients. In each patient, both before and after successful injections, we collected up to 5 scanning sessions totaling 125 minutes of rs-fMRI and 40 minutes of task fMRI collected while performing vocalization impairment-specific motor task. FMRI images were corrected for motion, slice-time, distortion, and registered to an MNI template. We applied nuisance regression, band-pass filtering, and motion censoring[7] to rs-MRI data. All fMRI data were sampled to the cortical surface and subcortical structures and smoothed at 4mm FWHM. To identify individual-specific vocalization-related brain regions, we fit each patient's task fMRI data to a general linear model and entered vocalization beta weights into a one-sample t-test across sessions. To determine whether vocalization-related fMRI activity differed after injection in each patient, a paired t-test compared vocalization-related beta weights between pre and post-injection timepoints. Finally, in each subject, vocalization-related regions of interest were delineated within M1 as cortical seeds for FC. FC was calculated as correlations between the ROI signal time course and every time course in the brain. A paired t-test between the pre- and post-injection timepoints determined whether FC differed after injection in each patient.

Results: Vocalization-related brain regions were identified in every subject and consisted of a dual representation in M1. Within each subject, vocalization-related activation within subcortical structures was reduced post- compared to pre-injection, most consistently in the posterior putamen and motor cerebellum, and less in the thalamus. Similarly, resting-state FC seeded from vocalization-related M1 regions was consistently reduced in motor cerebellum and posterior putamen and less in thalamus in post- compared to pre-injection.

Conclusions: Application of PFM in task-specific dystonia pinpoints a more precise patient-specific cortical and subcortical mapping of the functional motor. Further, it identifies patient-specific alterations in this network's function and connectivity resulting from therapeutic botulinum toxin injection. The identified locations of these alterations suggest potential target engagement sites for future therapeutic trials. These alterations were partially consistent across subjects, but also exhibited some degree of individual specificity, highlighting the potential for patient-specific PFM when considering pathophysiological mechanisms and advancing therapeutic potential in dystonia.

References

1. Battistella, Giovanni, Pichet Termsarasab, Ritesh A. Ramdhani, Stefan Fuertinger, and Kristina Simonyan. 2017. "Isolated Focal Dystonia as a Disorder of Large-Scale Functional Networks." Cerebral Cortex (New York, N.Y.: 1991) 27 (2): 1203–15. https://doi.org/10.1093/cercor/bhv313.
2. Gordon, Evan M., Timothy O. Laumann, Adrian W. Gilmore, Dillan J. Newbold, Deanna J. Greene, Jeffrey J. Berg, Mario Ortega, et al. 2017. "Precision Functional Mapping of Individual Human Brains." Neuron 95 (4): 791-807.e7. https://doi.org/10.1016/j.neuron.2017.07.011.
3. Gordon, Evan M., Timothy O. Laumann, Scott Marek, Dillan J. Newbold, Jacqueline M. Hampton, Nicole A. Seider, David F. Montez, et al. 2021. "Human Fronto-Striatal Connectivity Is Organized into Discrete Functional Subnetworks." bioRxiv. https://doi.org/10.1101/2021.04.12.439415.
4. Hanekamp, Sandra, and Kristina Simonyan. 2020. "The Large-scale Structural Connectome of Task-specific Focal Dystonia." Human Brain Mapping 41 (12): 3253–65. https://doi.org/10.1002/hbm.25012.
5. Nevrlý, Martin, Petr Hluštík, Pavel Hok, Pavel Otruba, Zbyněk Tüdös, and Petr Kaňovský. n.d. "Changes in Sensorimotor Network Activation after Botulinum Toxin Type A Injections in Patients with Cervical Dystonia: A Functional MRI Study | Experimental Brain Research." Accessed November 9, 2023. https://link.springer.com/article/10.1007/s00221-018-5322-3.
6. Norris, Scott A., Aimee E. Morris, Meghan C. Campbell, Morvarid Karimi, Babatunde Adeyemo, Randal C. Paniello, Abraham Z. Snyder, Steven E. Petersen, Jonathan W. Mink, and Joel S. Perlmutter. 2020. "Regional, Not Global, Functional Connectivity Contributes to Isolated Focal Dystonia." Neurology 95 (16): e2246–58. https://doi.org/10.1212/WNL.0000000000010791.
7. Power, Jonathan D., Anish Mitra, Timothy O. Laumann, Abraham Z. Snyder, Bradley L. Schlaggar, and Steven E. Petersen. 2014. "Methods to Detect, Characterize, and Remove Motion Artifact in Resting State fMRI." NeuroImage 84 (January): 320–41. https://doi.org/10.1016/j.neuroimage.2013.08.048.

Poster No 1343

Sensory Hypersensitivity and Symptoms Correlates in Juvenile Fibromyalgia: A Multisensory fMRI Study

Laura Martín Herrero[1], Maria Suñol[1], Lucia Blanc[1], Tracy Ting[2], Jon Dudley[2], Saül Pascual-Diaz[1], Susmita Kashikar-Zuck[2], Robert Coghill[2], Marina López-Solà[1]

[1]University of Barcelona, Barcelona, Barcelona, [2]Cincinnati Children's Hospital Medical Center, Cincinnati, OH

Introduction: Juvenile Fibromyalgia (JFM) is a chronic pain condition characterized by persistent widespread musculoskeletal pain, fatigue, and sleep disturbances which predominantly affects adolescent girls (Yunus and Masi, 1985, kashikar-zuck, et al., 2016). JFM patients often report heightened unpleasantness to non-painful sensory stimuli (Ting et al. 2016, Bennett et al. 2014). In the same line, studies in adults with fibromyalgia (FM) (López-Solà et al., 2014; 2017; Wilbarger and Cook, 2011; Wang and Frey-Law, 2022) have shown that patients show greater unpleasantness to these stimuli. Furthermore, when compared to healthy peers, FM patients showed reduced responses in primary sensory cortices during multisensory stimulation, which correlated with multisensory hypersensitivities in daily life and FM symptoms. Conversely, they showed hyperactivation of the right insula and the right anterior lingual gyrus. The understanding of multisensory sensitivities may help improve our knowledge of the pathophysiological components of fibromyalgia and guide treatment selection on an individualized basis (Wang and Frey-Law, 2022). Here, we investigate whether patients with JFM exhibit reduced tolerance during a multisensory fMRI task and study the relationship between brain activity and core JFM symptoms and multisensory hypersensitivity in daily life.

Methods: Forty-six adolescent girls (16.56 ± 1.01 years) diagnosed with JFM and forty-four healthy girls (16.09 ± 1.06 years) completed validated self-reported measures of multisensory hypersensitivity in daily life and core JFM symptoms. They also underwent a multisensory task inside the fMRI scanner that involved four trials of alternating 30 seconds of simultaneous multisensory stimulation (visual, auditory, and tactile-motor finger opposition task) and rest periods ranging from 20-30 seconds. The functional images were preprocess using CONN Toolbox running on MATLAB. At the subject level, we used a conventional general lineal model approach (GLM) implemented in SPM12 software to identify voxels that show significant changes in activity during the multisensory blocks compared to the baseline condition. The results from the first level analysis for all participants were used in a two-sample t-test model to assess the differences between groups in brain functional activity. We also performed regression model analysis in JFM patients group using the scores of the self-reported measures to assess the association between brain functional activity and these measures.

Results: Compared to healthy participants, JFM patients reported higher levels of unpleasantness during the multisensory task, which positively correlated with sensory hypersensitivities in daily life and core JFM symptoms in patients. Nevertheless, there were no significant differences between groups in brain functional activity ($pFWE<0.05$ at cluster level and $p<0.001$ at voxel level). Among the JFM group, patients with greater hypersensitivities in daily life and JFM core symptoms (widespread pain index, functional disability, symptom severity and PROMIS fatigue) showed increased activation of sensory-motor, prefrontal and temporal cortex areas ($pFWE<0.05$ at cluster level and $p<0.001$ at voxel level).

Conclusions: The findings in JFM patients parallel the symptom findings observed in adult patients with FM. Moreover, JFM patients reporting greater sensory hypersensitivities showed extensive hyperactivation of cortical prefrontal, sensory-motor and visual regions. The findings suggest that juvenile patients with fibromyalgia reporting less tolerance to non-painful sensory stimuli and exacerbated core clinical symptoms show amplified cortical responses in sensory integration and response-related brain regions during a multisensory task. These findings are partly different from what was observed in adult FM patients. Future studies should directly compare adult and juvenile patients to further elucidate these neurophysiological changes across the lifespan.

References

1. Bennett, R. M. (2014), 'Criteria for the diagnosis of fibromyalgia: validation of the modified 2010 preliminary American College of Rheumatology criteria and the development of alternative criteria', Arthritis care & research, 66(9), 1364-1373.
2. Kashikar-Zuck, S. (2016), 'Juvenile fibromyalgia: different from the adult chronic pain syndrome?', Current rheumatology reports, 18(4), 19.
3. López-Solà, M. (2014), 'Altered functional magnetic resonance imaging responses to nonpainful sensory stimulation in fibromyalgia patients', Arthritis & rheumatology, 66(11), 3200-3209.
4. López-Solà, M. (2017), 'Towards a neurophysiological signature for fibromyalgia', Pain, 158(1), 34.
5. Ting, T. V. (2016), '2010 American College of Rheumatology adult fibromyalgia criteria for use in an adolescent female population with juvenile fibromyalgia', The Journal of pediatrics, 169, 181-187.
6. Wang, D. (2022), 'Multisensory sensitivity differentiates between multiple chronic pain conditions and pain-free individuals', Pain, 10-1097.
7. Wilbarger, J. L. (2011), 'Multisensory hypersensitivity in women with fibromyalgia: implications for well being and intervention', Archives of physical medicine and rehabilitation, 92(4), 653-656.
8. Yunus, M. B. (1985), 'Juvenile primary fibromyalgia syndrome. A clinical study of thirty-three patients and matched normal controls', Arthritis & Rheumatology 28, 138–145

Poster No 1344

Functional and structural characterization of Human hypothalamic nuclei in eating disorders

Coleen Roger[1,2,3], Adèle Lasbleiz[4,1], Maxime Guye[1,2], Anezka Kovarova[5,1], Hugo Dary[2,1], Yu Fu[6], Patrick Cozzone[2], Anne Dutour[4], Bénédicte Gaborit[4], Jean-Philippe Ranjeva[1,2]

[1]CEMEREM, Marseille, France, [2]CNRS, Marseille, France, [3]IMCB, Astar, Singapore, Singapore, [4]AP-HM, Marseille, France, [5]Masaryk University, Brno, Czech Republic, [6]Astar, Singapore, singapore

Introduction: Energy expenditure appears as a continuous process, while energy refilling through food intake is by nature discontinuous. To keep the body fat mass stable, a system in which the hypothalamus (HT) is one of the key structures provides efficient balance between energy expenditure and energy intake. However, non-invasive exploration of such a small structure in the context of food intake networks remains challenging in humans.

Methods: We used ultra-high field (7T) MRI to study morphometry and activation pattern of hypothalamic nuclei associated to food-cue paradigm in eating disorders and healthy controls. The activation task performed after a 15h fasting period consisted in showing high-calorie and low-calorie content food as well non-food images from a standardized database[1], and images related to food contexts, to 13 HC (18,5<BMI <25 kg/m2), as well as 8 diagnosed Obese and 7 diagnosed Anorexic patients (all female, 26+4 years). After the experiment, each participants were asked to rate (score=$^{0\text{-}3}$) how appealing the food images they just saw were (palatability score).

The Neudorfer Atlas[2] registered to the average spatially normalized T1 volumes from all subjects (AntsRegistration SyN) (Fig 1A), was used to locate activation clusters as well as evaluate the modulation of morphometry/microstructure of HT nuclei in Anorexic patients or Obese patients and its potential association with BMI.

Results: Structurally, no significant difference between groups were observed in the global HT volumes (normalized by whole brain volume (WBV)), with only a trend increase of HT volumes in the Obese group ($p=0.15$) (Fig 1B). Obese patients relative to Controls, showed significant volume increases in the right and the left fornix (Fig 1B), as well as increase in T1 values in the right and the left Arcuate Nuclei (Fig 1C), ($p<0.05$, Kruskall-Wallis tests, corrected for multiple comparisons). Anorexic patients relative to Controls, showed increased T1 values in the left Paraventricular nucleus ($p<0.05$, corrected for MC) (Fig 1C). BMI scores of the whole cohort were associated to the volume of the Left Lateral HT Area (rho=0.502, $p=0.007$) (Fig 1D). The Food-NonFood contrast (modulated by palatability score) showed significant activation in Controls within the Right Arcuate Nucleus, the Right Ventromedial Nucleus and the Left Paraventricular nucleus (Fig 2A). Relative to Controls, Anorexic patients showed less activation within the left Paraventricular nucleus (Fig 2A). The Context-NonFood contrast (modulated by palatability score) showed in Controls, activation of the left Paraventricular nucleus (Fig 2B). Relative to Controls, Anorexic patients showed higher activation in the right Lateral HT Area, the Right Paraventricular nucleus, the right Periventricular nucleus and bilateral

Posterior HT nucleus (Fig 2B) while Obese patients showed higher activation in the right Paraventricular nucleus, right medial preoptic nucleus, and the right posterior HT nucleus (Fig 2B).

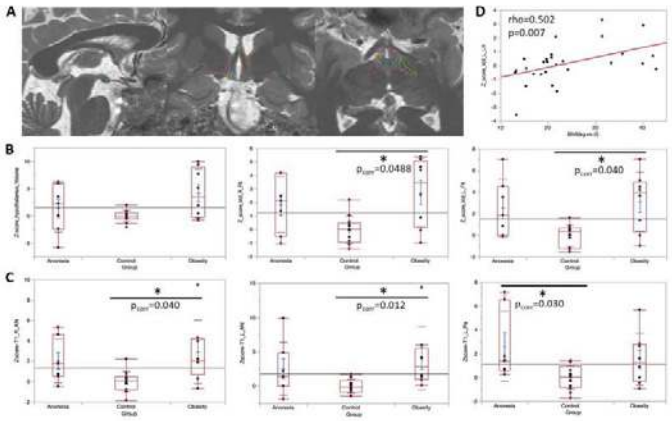

Figure 1: Morphometric and microstructural changes of HT nuclei in eating disorders

A) Coregistered Neurodorfer atlas into an individual qT1 map. B) Between group differences of volumes of the whole hypothalamus and bilateral fornix. C) Between group differences of T1 values of bilateral arcuate nuclei and PVN. D) Correlation between Left LHA volume and BMI.

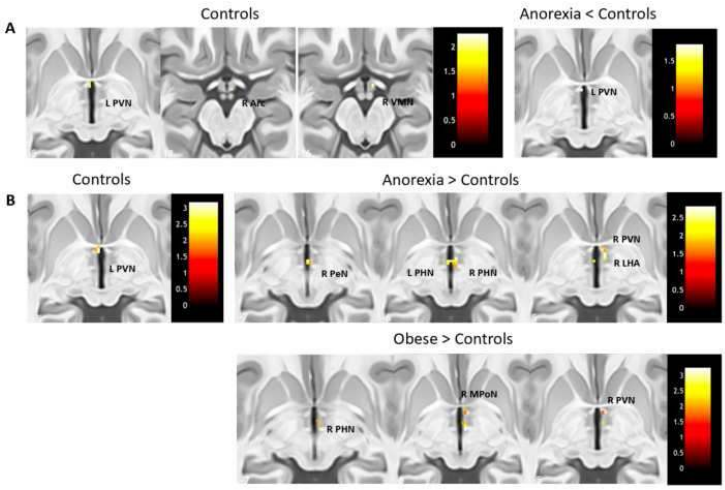

Figure 2: Hypothalamic activation induced by contrast modulated by palatability scores

A) Hypothalamic activation observed in response to Food-NonFood in Controls (left) and decreased activation observed in Anorexia relative to Controls (right). B) Hypothalamic activation observed in response to Context-NonFood in Controls (left), increased activation observed in Anorexia relative to Controls (up) and increased activation observed in Obese relative to Controls (down).

Conclusions: In a cohort of 28 subjects carefully selected according to age, sex, and condition (15h fasting), high resolution quantitative T1 MRI at 7T was sensitive enough to show morpho-structural changes of specific HT nuclei in Obesity and Anorexia in line with results obtained in large cohorts (>1000 participants) explored at 3T[3]. The significant increase in T1 in bilateral arcuate nuclei in the Obese group may reflect HT inflammation of this region[4]. During food cue stimuli, altered activation of HT nuclei involved in food networks were observed in Anorexic and Obese groups. Finally, higher activation of the right Lateral HT Area in the Anorexic group during the context condition may reflect abnormal processing of response to contextual feeding conditioning[5]. The combined study of the functional and morpho-structural characteristics of HT nuclei will allow for a better understanding and monitoring of eating disorders.

References

1. Charbonnier, L., van Meer, F., van der Laan, L.N., Viergever, M.A., & Smeets, P.A.M. (2016) Standardized food images: A photographing protocol and image database. Appetite, 96, 166–173
2. Neudorfer, C., Germann, J., Elias, G.J.B., Gramer, R., Boutet, A., & Lozano, A.M. (2020) A high-resolution in vivo magnetic resonance imaging atlas of the human hypothalamic region. Sci Data, 7, 305.
3. Brown, S.S.G., Westwater, M.L., Seidlitz, J., Ziauddeen, H., & Fletcher, P.C. (2023) Hypothalamic volume is associated with body mass index. NeuroImage Clin., 39, 103478.
4. Thaler, J.P., Yi, C.-X., Schur, E.A., Guyenet, S.J., Hwang, B.H., Dietrich, M.O., Zhao, X., Sarruf, D.A., Izgur, V., Maravilla, K.R., Nguyen, H.T., Fischer, J.D., Matsen, M.E., Wisse, B.E., Morton, G.J., Horvath, T.L., Baskin, D.G., Tschöp, M.H., & Schwartz, M.W. (2012) Obesity is associated with hypothalamic injury in rodents and humans. J. Clin. Invest., 122, 153–162.
5. Mohammad, H., Senol, E., Graf, M., Lee, C.-Y., Li, Q., Liu, Q., Yeo, X.Y., Wang, M., Laskaratos, A., Xu, F., Luo, S.X., Jung, S., Augustine, G.J., & Fu, Y. (2021) A neural circuit for excessive feeding driven by environmental context in mice. Nat. Neurosci., 24, 1132–1141.

Poster No 1345

Quantitative Analysis of Longitudinal Memory fMRI in Temporal Lobe Epilepsy Using ICN_Atlas

Azka Sohail[1], Marine Fleury[1], Meneka Sidhu[1], Lajos Kozák[2], Louis Lemieux[1]

[1]UCL Queen Square Institute of Neurology, London, United Kingdom, [2]Department of Neuroradiology, Medical Imaging Centre, Semmelweis University, Budapest, Hungary

Introduction: The impact of surgery on memory function in severe epilepsy patients and its prediction have been investigated using functional magnetic resonance imaging (fMRI). Notably, strong associations between fMRI lateralisation and postoperative verbal memory decline were observed (Sidhu et al., 2015). In a related study, Sidhu et al. (2016) assessed surgical success by examining pre- and postoperative memory reorganisation following anterior temporal resection. Traditionally, these investigations frame findings based on anatomical localisation, describing activated regions and selecting seed regions for functional connectivity analyses. Recent research has highlighted how Intrinsic Connectivity Networks (ICNs) capture fundamental aspects of the brain's functional connectivity, offering a universal framework for fMRI interpretation and quantification of activation patterns as a basis of fMRI map regional quantification. We have implemented this approach in the form of the ICN_Atlas (Kozák et al. (2017)) to quantify the degree of engagement of ICNs in fMRI maps (figure 1).

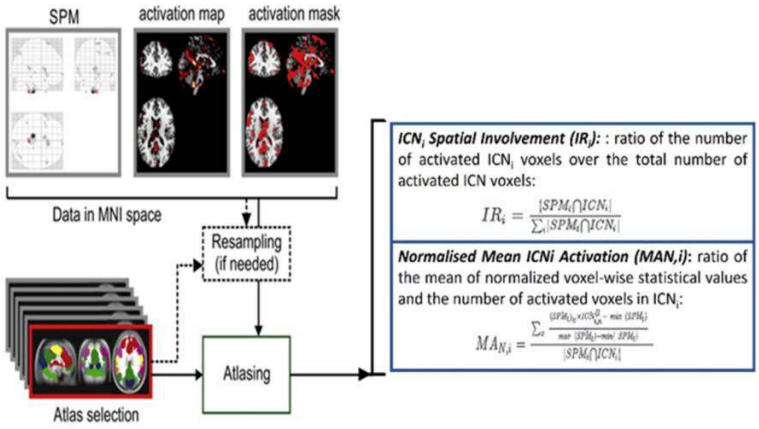

Figure 1. Schematic diagram of the ICN_Atlas atlasing process. *The input consists of an fMRI activation map of interest (in MNI space). Users can select an ICN base atlas of their choice (e.g., BRAINMAP20). The output consists of ICN engagement metric values.*

Methods: In this study, we aimed to quantify changes in memory encoding activation patterns pre and post-surgery using ICN_Atlas, introducing an objective approach to supplement previous investigations. 41 patients with temporal lobe epilepsy (20 left TLE, 21 right TLE) were scanned pre-operatively and post-operatively at 4 months. 20 healthy controls underwent the same fMRI protocol. ICN engagement was quantified using two metrics: Spatial Involvement (IRi) and Normalised Mean Activation (MAN,i) for 20 ICNs (Laird et al., 2011). We assessed the ICN-wise engagement changes using repeated measures ANOVA.

Results: A representative pattern of change is illustrated in Figure 2. In the healthy controls, the following patterns were observed for both tasks: no significant change in IRi and with an initial modest increase in MAN,i followed by a decline at 10 years. In the patient groups, the most prominent changes following surgery were observed in the motor/visual-spatial and visual ICNs. Notably, at 3 months' post-surgery, motor ICNs exhibited increased spatial engagement while visual ICNs showed little to no change in both patient sub-groups. At 10 years post-surgery, spatial engagement of the motor ICNs declined markedly, contrasting with a substantial increase in visual ICNs. The patterns for MAN,i show a pronounced change in ICN engagement, particularly for word encoding, in contrast to IRi. This indicates there are substantial changes in activation strength across different rescans. Overall, the engagement changes were more significant in the patients than in the healthy controls and greater in LTLE compared to RTLE.

Conclusions: The observed variations in ICN engagement are in line with expectations for memory encoding tasks, signifying the reorganisation of memory encoding networks. Utilising ICN_Atlas, we were able to quantify longitudinal fMRI data objectively in a whole-brain, regionally specific and functionally meaningful manner. The quantitative perspective offered here complements the anatomical focus of previous investigations (Sidhu et al., 2013, 2015, 2016) and, therefore, could lead to a better, more complete understanding of the impact of surgery and, potentially, improved prediction of functional sequela. This work is supported by the UCLH BRC and MRC grant ID MR/X031039/1 who also support MKS.

References

1. Kozák, L. R., Van Graan, L. A., Chaudhary, U. J., Szabó, Á. G., & Lemieux, L. (2018). Optimising Pre-Surgical fMRI Language Mapping Using Knowledge Derived from Intrinsic Connectivity Brain Networks for Personalised Therapy Planning. (Unpublished).
2. Kozák, L. R., Van Graan, L. A., Chaudhary, U. J., Szabó, Á. G., & Lemieux, L. (2017). ICN_Atlas: Automated Description and Quantification of Functional MRI Activation Patterns in The Framework of Intrinsic Connectivity Networks. NeuroImage, 163, 319-341.
3. Laird AR, Fox PM, Eickhoff SB, Turner JA, Ray KL, McKay DR, Glahn DC, Beckmann CF, Smith SM, Fox PT. (2011) Behavioral interpretations of intrinsic connectivity networks. J Cognitive Neuroscience. 23(12), 4022-37.
4. Laird, A. R., Eickhoff, S. B., Li, K., Robin, D. A., Glahn, D. C., & Fox, P. T. (2009). Investigating The Functional Heterogeneity of The Default Mode Network Using CoordinateBased Meta-Analytic Modelling. Journal Of Neuroscience, 29(46), 14496-14505
5. Sidhu MK, Duncan JS, Sander JW. (2018) Neuroimaging in epilepsy. Current Opinion in Neurology. 31(4):371-378.
6. Sidhu MK, Stretton J, Winston GP, Bonelli S, Centeno M, Vollmar C, Symms M, Thompson PJ, Koepp MJ, Duncan JS. (2013) A functional magnetic resonance imaging study mapping the episodic memory encoding network in temporal lobe epilepsy. Brain. 136 (6), 1868-88.
7. Sidhu MK, Stretton J, Winston GP, McEvoy AW, Symms M, Thompson PJ, Koepp MJ, Duncan JS. (2016) Memory network plasticity after temporal lobe resection: a longitudinal functional imaging study. Brain. 139(Pt 2):415-30.
8. Sidhu MK, Stretton J, Winston GP, Symms M, Thompson PJ, Koepp MJ, Duncan JS.(2015) Memory fMRI predicts verbal memory decline after anterior temporal lobe resection. Neurology. 84(15), 1512-9.83
9. Sidhu MK, Stretton J, Winston GP, Symms M, Thompson PJ, Koepp MJ, Duncan JS. (2015) Memory fMRI Predicts Verbal Memory Decline After Anterior Temporal Lobe Resection. Neurology. 84,1512–1519
10. Sidhu MK, Stretton J, Winston GP, Symms M, Thompson PJ, Koepp MJ, Duncan JS. (2015) Factors affecting reorganisation of memory encoding networks in temporal lobe epilepsy. Epilepsy Res. 110,1-9

Poster No 1346

Predicting lateralization of human language processing with non-language functional activity

Haokun Li[1], Gaolang Gong[2]

[1]State Key Laboratory of Cognitive Neuroscience and Learning & IDG/McGovern Institute for Brain Resea, Beijing, China, [2]State Key Laboratory of Cognitive Neuroscience and Learning & IDG/McGovern Institute for Brain Resea, Beijing, Beijing

Introduction: While leftward lateralization of human language processing has been well documented at the population level, determining the direction and degree of language lateralization at the individual level is still a challenge. Previous empirical studies on language lateralization largely confined to functional activity of specific component of language processing per se[1]. To date, it remains unclear how the functional lateralization of other non-language functions relates to language lateralization. In this study, we applied machine learning approaches to explore whether and how the language lateralization could be individually predicted by functional lateralization of a set of non-language functions, using fMRI data from over 1000 healthy adults.

Methods: A total of 1005 subjects (female/male: 534/471; age: 28.72±3.7 years) from the 'HCP1200' dataset were included in our analysis. All the subjects completed functional MRI scanning for language, emotion, gambling, relational, social, and working memory tasks[2]. The structural and functional images was pre-processed using the HCP pipelines[2,3]. A group-average activation map of the main contrast of language task (i.e., 'story VS. baseline') was used to locate the ROIs (Fig. 1A). The mean of positive Cohen's d values across the vertices of the entire cortex was calculated as the threshold, and the core language areas were then identified as the HCP-MMP parcels above the threshold (Fig. 1B)[45]. For each individual, the laterality effect of language was defined as (left-right) of the mean Z values across the vertices within all core language areas in each hemisphere. For the main contrasts (i.e., 'explanatory variable of interest VS. baseline') of the other 5 non-language tasks, the functional asymmetry values were calculated as above for each pair of HCP-MMP parcel (180 in total). Therefore, each individual ended up with an asymmetry feature vector of non-language tasks with a length of 180*5. A ridge regression with a nested 5-fold cross-validation approach (5F-CV) was then applied to predict the language laterality effect with the asymmetry feature vector of non-language tasks[6] (Fig. 1C). A nonparametric permutation method was used to assess the significance of the Pearson correlation coefficient, mean absolute error (MAE), and feature weight.

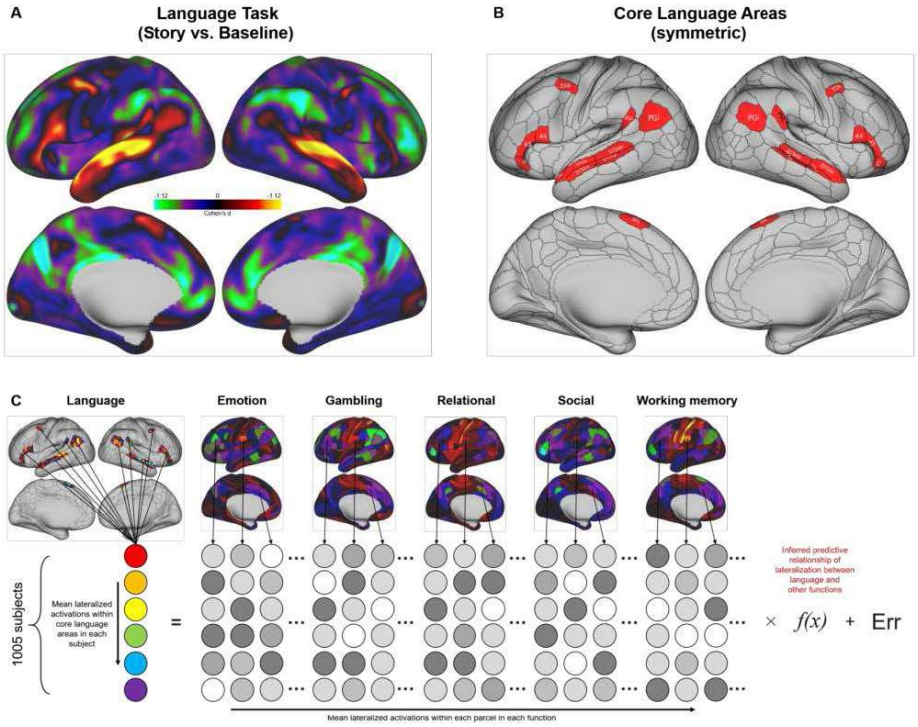

Fig. 1. (A) Group-average activation maps for the contrasts of "story versus baseline" in the language task. (B) The ROIs selected from core language areas. (C) Linear regression model. Each colored circle in the left column represents the lateralized activation (the mean z values of LH language ROIs - the mean z values of RH language ROIs) of each subject. Each row of grayscale circles represents the series connected by lateralized activation of each of 180 parcels in the hcp-mmp atlas in each function. f(x), the resulting model (predictive relationship between language and other functions). Err, model residual error. (This figure is a simple schematic representation of the model without detailed depiction of nested 5-fold cross-validation)

Results: As shown in Fig. 2A, the whole-brain functional lateralization of non-language functions could significantly predict language lateralization at the individual level (mean prediction accuracies r=0.543, p<0.0005, MAE=0.556, p<0.0005). In Fig. 2B, the absolute value of the weight represents the importance of corresponding feature in the prediction model, and the positive or negative feature value indicates whether the asymmetry feature changes in a similar way with language lateralization or the opposite. The significant or highly contributing non-language asymmetry features are always located within the core language areas across all non-language functions (the same trend for uncorrected gambling). Notably, the selected contrasts of these non-language tasks did not involve language processing, and therefore did not showed significant activation in these identified core language areas. Intriguingly, the significant asymmetry features are largely positive for the relational and working memory tasks, but negative for the other three non-language functions.

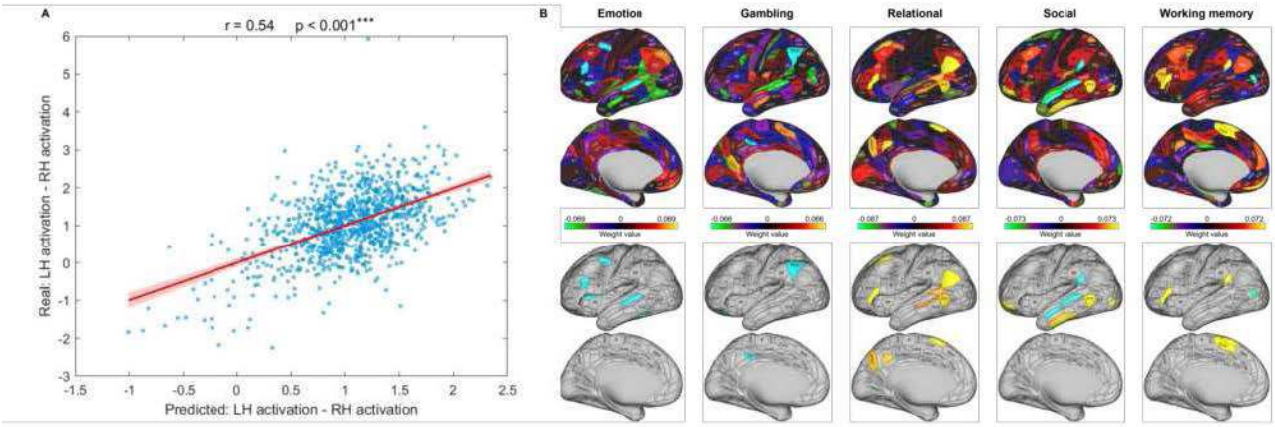

Fig. 2. (A) The scatterplot and the fitted line demonstrate the LH-RH activations of all subjects and the cross-subject correlations between predicted and real LH-RH activations. Positive values indicate stronger activation in the LH, and negative values indicate stronger activation in the RH. ***p < 0.0005. (B) The unthresholded (above) and the thresholded (below) weight maps for the five other functions. (In the permutation, one-tailed p=0.01 in the null distribution of weight corresponds to ±0.066 as the threshold)

Conclusions: The present study demonstrated that the language lateralization could be individually predicted by multivariate machine learning approach together with non-language functional lateralization features. This suggested a complex relationship of functional lateralization between language and non-language functions through core language areas.

References
1. Vingerhoets, G. (2019), "Phenotypes in hemispheric functional segregation? Perspectives and challenges", Physics of Life Reviews, vol. 30, pp. 1–18
2. Barch, D. M. et al. (2013), "Function in the human connectome: Task-fMRI and individual differences in behavior", NeuroImage, vol. 80, pp. 169–189
3. Glasser, M. F. et al. (2013), "The minimal preprocessing pipelines for the Human Connectome Project", NeuroImage, vol. 80, pp. 105–124
4. Glasser, M. F. et al. (2016), "A multi-modal parcellation of human cerebral cortex", Nature, vol. 536, no. 7615, pp. 171–178
5. Rajimehr, R. et al. (2022), "Complementary hemispheric lateralization of language and social processing in the human brain", Cell Reports, vol. 41, no. 6, pp. 111617
6. Cui, Z. et al. (2018), "The effect of machine learning regression algorithms and sample size on individualized behavioral prediction with functional connectivity features", NeuroImage, vol. 178, pp. 622–637

Poster No 1347

Cerebellar meta-analytic maps: describing bias to construct domain-specific functional topographies

Neville Magielse[1,2,3], Amin Saberi[1], Aikaterina Manoli[2], Simon Eickhoff[1], Sofie Valk[2]

[1]INM-7, Research Center Jülich, Jülich, Germany, [2]Max Planck Institute for Human Cognitive and Brain Sciences, Leipzig, Germany, [3]Institute of Systems Neuroscience, Heinrich Heine University Düsseldorf, Düsseldorf, Germany

Introduction: The cerebellum, apart from its canonical motor functions, plays important roles in most human behaviors, including language, theory of mind, working memory, and executive functioning (King et al. 2019). Cerebellar activations associated with these diverse behavioral domains have been reported in the literature (Kruithof, Klaus, and Schutter 2023; Van Overwalle, D'aes, and Mariën 2015; Stoodley 2012; Stoodley and Schmahmann 2009). However, a full cerebellar functional topography based on the accumulation of neuroimaging studies is still missing. Here, we aimed to construct such meta-analytic maps of cerebellar activity in a cross-domain manner, leveraging the BrainMap database. Together, we show both promise and challenge in consolidating cerebellar functional imaging data into cross-domain meta-analytic maps.

Methods: We used the BrainMap annotated database of the neuroimaging literature to identify task-based functional imaging experiments on healthy subjects that reported cerebellar activations (Laird et al. 2009; Fox et al. 2005). We categorized the experiments based on the five main behavioral domains (BDs) in the BrainMap including action, cognition, emotion, interoception, and perception. In each domain we performed activation likelihood estimation (ALE) to investigate convergence of findings within the cerebellar mask (Eickhoff et al. 2012). Additionally, we performed a domain-general ALE to assess whether there is spatial bias in the reported findings within the cerebellum. In this analysis we included 100 randomly selected experiments from each BD to ensure even participation of the domains. Subsequently, we reported the ALE maps and evaluated their spatial cross-correlation. Last, we studied the co-alignment of the ALE maps with an openly available atlas of cerebellar activations associated with the multi-domain task battery (King et al. 2019).

Results: We found a total of 1679 experiments reporting cerebellar task-associated activations. The ALE maps of the cognition, emotion and perception BDs were highly similar, while the ALE map of action was most similar to perception, and the ALE map of interoception showed the least similarity to the other domains (Fig. 1A, B). There was a domain-general convergence of cerebellar activations in primarily the antero-superior cerebellum, potentially indicating a spatial bias in the reported findings. Accordingly, we found that the distribution of findings across axial slices was unequal across the cerebellar volume (Fig. 1C). Zooming in, we observed positive correlations between the maps of 2-back and math tasks with the cognitive BD ALE, and finger sequence task with the action BD ALE map, while the correlation of resting-state and movie watching tasks with the BD ALE maps were generally negative (Fig. 2).

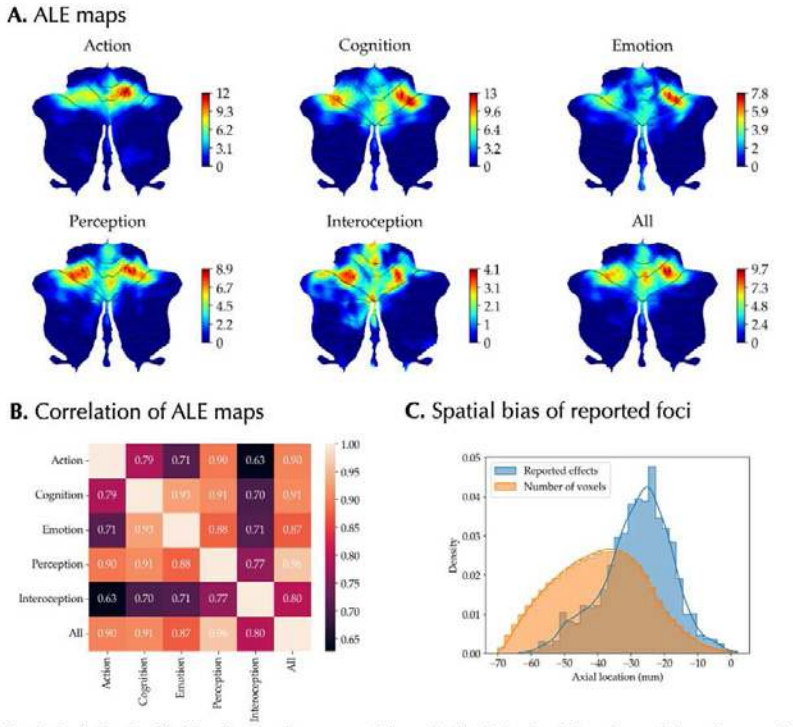

Fig. 1. A. Activation likelihood estimation maps of the main five behavioral domains and domain-general activations (all). **B.** Spatial correlation of the ALE maps. Heatmap values represent correlation coefficients. **C.** The distribution of reported foci across domains (blue) in comparison to the expected distribution based on the number of voxels (orange) across the Z-axis, i.e., axial location within the MNI template.

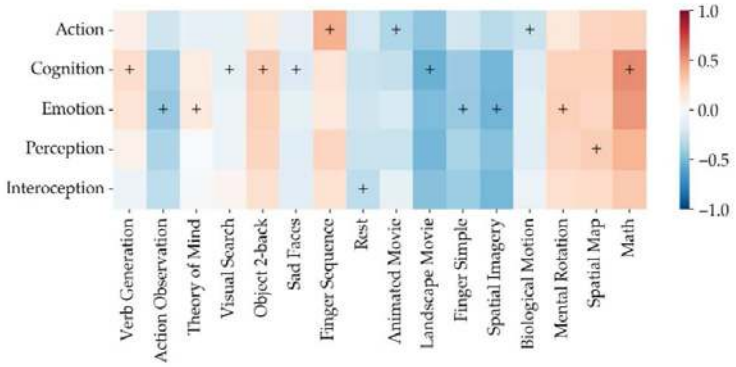

Fig. 2. The correlation of ALE maps (y-axis) with individual task-activation maps of the multi-domain task battery (x-axis). Plus signs indicate the highest absolute value of correlation coefficients in each column.

Conclusions: Together, our study shows a meta-analytic mapping of task activations in the cerebellum which extends previous studies done at the level of individuals (King et al. 2019). We observed a bias of reported findings in the anterior-superior cerebellum. Common challenges of cerebellar neuroimaging, including BOLD-bleeding of visual cortical signal, heterogeneous signal-to-noise, and primarily a severe sampling bias, should be addressed in future neuroimaging and meta-analytic studies.

References

1. Eickhoff, Simon B., Danilo Bzdok, Angela R. Laird, Florian Kurth, and Peter T. Fox. 2012. 'Activation Likelihood Estimation Meta-Analysis Revisited.' NeuroImage 59 (3): 2349–61. https://doi.org/10.1016/j.neuroimage.2011.09.017.
2. Fox, Peter T., Angela R. Laird, Sarabeth P. Fox, P. Mickle Fox, Angela M. Uecker, Michelle Crank, Sandra F. Koenig, and Jack L. Lancaster. 2005. 'BrainMap Taxonomy of Experimental Design: Description and Evaluation'. Human Brain Mapping 25 (1): 185–98. https://doi.org/10.1002/hbm.20141.
3. King, Maedbh, Carlos R. Hernandez-Castillo, Russell A. Poldrack, Richard B. Ivry, and Jörn Diedrichsen. 2019. 'Functional Boundaries in the Human Cerebellum Revealed by a Multi-Domain Task Battery'. Nature Neuroscience 22 (8): 1371–78. https://doi.org/10.1038/s41593-019-0436-x.
4. Kruithof, Eline S., Jana Klaus, and Dennis J. L. G. Schutter. 2023. 'The Human Cerebellum in Reward Anticipation and Outcome Processing: An Activation Likelihood Estimation Meta-Analysis'. Neuroscience & Biobehavioral Reviews 149 (June): 105171. https://doi.org/10.1016/j.neubiorev.2023.105171.

5. Laird, Angela R., Simon B. Eickhoff, Florian Kurth, Peter M. Fox, Angela M. Uecker, Jessica A. Turner, Jennifer L. Robinson, Jack L. Lancaster, and Peter T. Fox. 2009. 'ALE Meta-Analysis Workflows Via the Brainmap Database: Progress Towards A Probabilistic Functional Brain Atlas.' Frontiers in Neuroinformatics 3: 23. https://doi.org/10.3389/neuro.11.023.2009.
6. Stoodley, Catherine J. 2012. 'The Cerebellum and Cognition: Evidence from Functional Imaging Studies'. The Cerebellum 11 (2): 352–65. https://doi.org/10.1007/s12311-011-0260-7.
7. Stoodley, Catherine J., and Jeremy D. Schmahmann. 2009. 'Functional Topography in the Human Cerebellum: A Meta-Analysis of Neuroimaging Studies'. NeuroImage 44 (2): 489–501. https://doi.org/10.1016/j.neuroimage.2008.08.039.
8. Van Overwalle, Frank, Tine D'aes, and Peter Mariën. 2015. 'Social Cognition and the Cerebellum: A Meta-Analytic Connectivity Analysis'. Human Brain Mapping 36 (12): 5137–54. https://doi.org/10.1002/hbm.23002.

Poster No 1348

Ultrafast fMRI Reveals Laminar Specificity of Hemodynamic Profiles in Primary Somatosensory Cortex

Xiangnan Tian[1], Nadia Bouraoud[2], Stephen Dodd[2], Alan Koretsky[2], Zhiwei Ma[1]

[1]ShanghaiTech University, Shanghai, China, [2]National Institutes of Health, Bethesda, MD, USA

Introduction: Recent advancements in ultra-high-field MRI have significantly improved fMRI, enabling detailed studies of individual cortical layers. This has provided insights into the timing of brain activity. Different layers of the cortex have unique connections and interactions between neurons and blood vessels. This complex relationship reflects how neuronal activity is linked to the BOLD signal, with each layer having its specific temporal profile. The fMRI activation initiates in mid-cortical layers and subsequently extends to other layers[1,2]. Despite the strides in studying laminar-specific fMRI onset, other laminar temporal features of hemodynamic profiles, such as fMRI signal offset, are yet to be understood. Here we utilized ultrafast fMRI to capture the temporal variations of the BOLD signal across different cortical depths in rat primary somatosensory cortex to reveal laminar-specific hemodynamic profiles.

Methods: Four alpha-chloralose anesthetized Sprague-Dawley rats were imaged using an 11.7 T MRI scanner to examine fMRI responses to forepaw stimulation. For each rat, a BOLD fMRI run with a TR of 1500 ms (voxel size = 0.17 mm×0.17 mm×0.4 mm, slice number = 14) was acquired to localize S1FP based on its activation map. This guided subsequent fMRI runs with a TR of 200 ms (voxel size = 0.17 mm×0.17 mm×1.2 mm, slice number = 1) positioned on the slice in the center of the S1FP. Each of these fMRI runs included 60 blocks and the stimulation was on for 2 s within each block. In the preprocessing, NORDIC denoising was applied[3]. The MATLAB function 'imregister' was used for motion correction. The cortical depth of each voxel in the S1FP was derived using Laplace's equation[4-7]. The voxels were grouped into 10 geometric layers based on their cortical depths. A high-pass filtering of 0.0179 Hz was performed. Outlier blocks were excluded using autoencoders. The BOLD percent change data of the remaining blocks were averaged and then fitted using the double gamma function. The response height, full-width-at-half-maximum (FWHM), time-to-peak, and time constant of the BOLD signal of each geometric layer were derived based on the fitted curve. Here, the time constant was the time difference between the stimulation on time and the time when the fitted curve reached 1/e of the maximum of the curve on the decay phase. In addition, instead of using the fitted curve, the BOLD onset time was calculated using the time difference between the stimulation on time and the time when the BOLD signal was firstly two standard deviations above the baseline.

Results: Fig. 1a shows a representative result of a task fMRI activation map in S1FP and its corresponding layerification. It also shows BOLD percent change maps per geometric layers of an individual block and the average of 922 blocks after outlier exclusion. The BOLD percent change curves per geometric layers are shown in Fig. 1b. The hemodynamic profiles are shown in Fig. 2. We observed distinct laminar BOLD responses to rat forepaw stimulation. The response height decreased from superficial to deep layers (Fig. 2b). The third geometric layer of S1FP exhibited the shortest FWHM, time-to-peak, onset, and time constant (Fig. 2c-f).

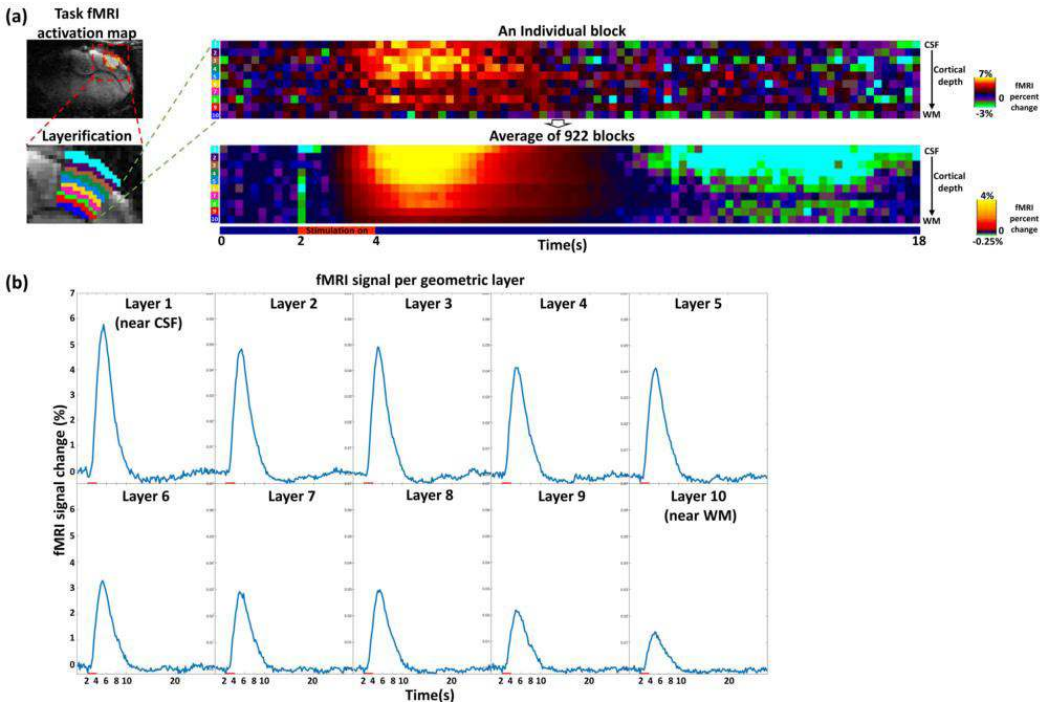

Figure 1. (a) BOLD percent change maps. (b) BOLD percent change curves per geometric layers.

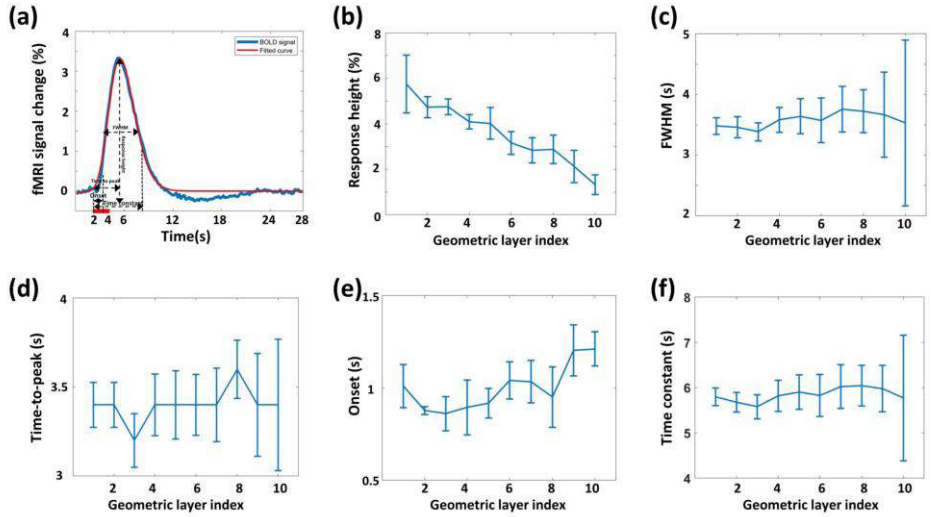

Figure 2. (a) BOLD signal change of S1FP. (b) Response height. (c) FWHM. (d) Time-to-peak. (e) Onset. (f) Time constant of BOLD decay phase.

Conclusions: This study has revealed a laminar-specific timing in the BOLD response to sensory stimuli. Consistent with previous findings[1,2], the middle layers had the shortest onset time. The cortex at its 30% depth also showed the shortest time constant of the BOLD decay phase. Ultrafast fMRI with laminar spatial resolution enhances our grasp of the neurovascular dynamics across cortical depths, offering important implications for interpreting fMRI data.

References

1. Silva, A.C. (2002), 'Laminar specificity of functional MRI onset times during somatosensory stimulation in rat', Proceedings of the National Academy of Sciences 99:15182-15187
2. Yu, X. (2014), 'Deciphering laminar-specific neural inputs with line-scanning fMRI', Nature Methods 11:55-58
3. Vizioli, L. (2021), 'Lowering the thermal noise barrier in functional brain mapping with magnetic resonance imaging', Nature communications 12:5181
4. Huber, L. (2017), 'High-Resolution CBV-fMRI Allows Mapping of Laminar Activity and Connectivity of Cortical Input and Output in Human M1', Neuron 96:1253-1263
5. Wang, Q. (2020), 'The Allen Mouse Brain Common Coordinate Framework: A 3D Reference Atlas', Cell 181:936-953
6. Jones, S.E. (2000), 'Three-dimensional mapping of cortical thickness using Laplace's equation', Human brain mapping 11:12-32
7. Haidar, H. (2005), 'New numerical solution of the Laplace equation for tissue thickness measurement in three-dimensional MRI', Journal of Mathematical Modelling and Algorithms 45:83-97

Poster No 1349

GPU-Empowered Mapping of Population Receptive Fields (GEM-pRF)

Siddharth Mittal[1], Michael Woletz[1], David Linhardt[2], Christian Windischberger[3]

[1]Medical University of Vienna, Vienna, Vienna, [2]Medical University of Vienna, Wien, Vienna, [3]Medical University of Vienna, Vienna, Austria

Introduction: Population receptive field (pRF) mapping allows for determining the retinotopic organisation in the visual cortex (Dumoulin & Wandell, 2008). It involves modelling pRFs as 2D Gaussian functions in the visual field and fitting them to time series data of the neuronal responses. While highly accurate, this process is computationally demanding due to iterative refinement. To address this, we propose a novel pRF implementation called GPU-Empowered Mapping of pRF (GEM-pRF). It uses a reformulated mathematical notation based on the originally proposed technique by Dumoulin & Wandell (2008) for faster and accurate pRF parameter estimation. Here we show that our new approach harnesses high-performance computing advantages to speed up acquisition by over 15 times.

Methods: GEM-pRF is a two-stage procedure. During the first stage, a grid search is performed to compute the coarse pRF parameters estimation. The estimated pRF parameters for a given pRF are its position and size (i.e., μx, μy, and σ). Our derived mathematical notation simplifies this step in order to use GPU-based matrix multiplication for major speed gains. In the second stage, refining the coarsely estimated pRF parameters involves a quadratic approximation of the error function in the neighbourhood of the coarse result. We use partial derivatives of the error term to find minima, thereby enabling estimation of the best pRF fitting parameters. Goodness-of-fit is based on residual sum of squares (RSS). Our novel approach was evaluated on a laptop with an NVIDIA RTX 3050Ti GPU and a university server's GPU cluster using NVIDIA Tesla V100. We assessed the accuracy of this method with both simulated and empirical data.

Results: Our GEM-pRF implementation shows notable speed enhancement without compromising accuracy. To validate our results on simulated data, we utilised a validation framework (Lerma-Usabiaga et al., 2020) for pRF mapping methods. Within this framework, we generated low- and high-noise datasets comprising 5000 voxels each. Datasets were generated for two scenarios, first for a smaller pRF located at visual field centre (i.e. μx=0, μy=0, σ=1), and second for off-centred bigger pRF (i.e. μx=3, μy=-2, σ=1.8). We compared our pRF parameter estimations with different fMRI analysis toolboxes (mrVista, SamSrf, and f-pRF ((Bhat et al., 2021) from CNI_toolbox). In Figure 1, our new implementation pRF parameter estimation (position & size) showed very good pRF parameter estimation results compared to other pRF implementations in both low- and high SNR scenarios. For evaluation on empirical data, we scanned a healthy male using a 64-channel head coil on a 3T Siemens PrismaFit scanner. The full coil was used for anatomical measurements (MP2RAGE, 1mm iso), while functional measurements (CMRR EPI, TR/TE=1000/38ms, 1.5mm iso, MB=3) used the coil's lower part only. Our pRF parameter estimates were compared to those computed by the standard mrVista implementation, a specialised software package for pRF fMRI data analysis. The comparison of results is presented in Figure 2, which shows the estimated pRF positions (μx, μy) and their sizes (σ). Figure 2(d) shows the comparison of Variance Explained (R2) values for the modelled signals. The overall comparison reveals high correspondence between our novel approach and the standard mrVista implementation. Our implementation, however, requires considerably less computation time: while mrVista and similar implementations require about 10 minutes, our implementation completes pRF parameter estimation in approx. 30-40 seconds for datasets containing up to 10,000 voxels.

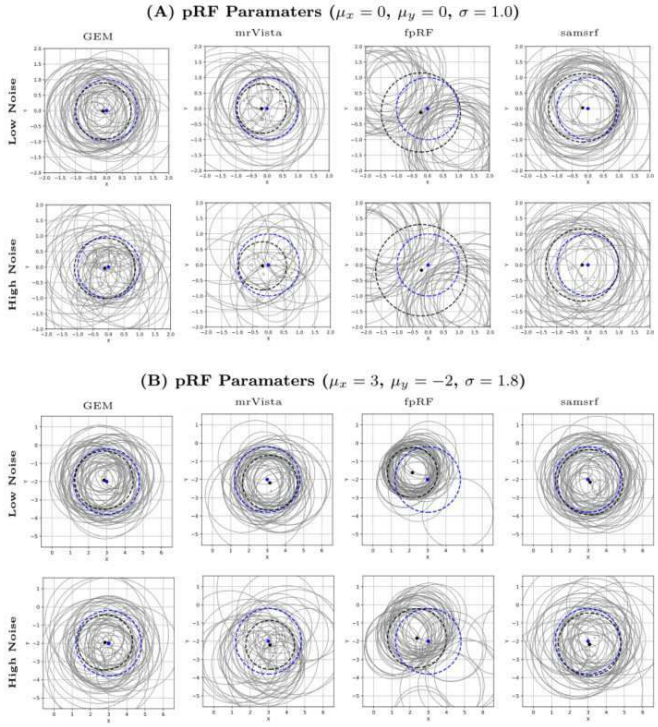

Figure 1: Comparison of pRF mapping methods on simulated data with low & high noise. Blue dot and dashed circle indicate the groundtruth pRF center and its radius, while the black dot and dashed circles represent the averaged estimated pRF center and its radius. Gray circles depict estimated circular pRFs. **(A)**: Groundtruth pRF centered at ($\mu_x = 0$, $\mu_y = 0$) deg, size $\sigma = 1.0$ with low & high noise. **(B)**: Groundtruth pRF centered at ($\mu_x = -3$, $\mu_y = 3$) deg, size $\sigma = 1.8$ with high noise.

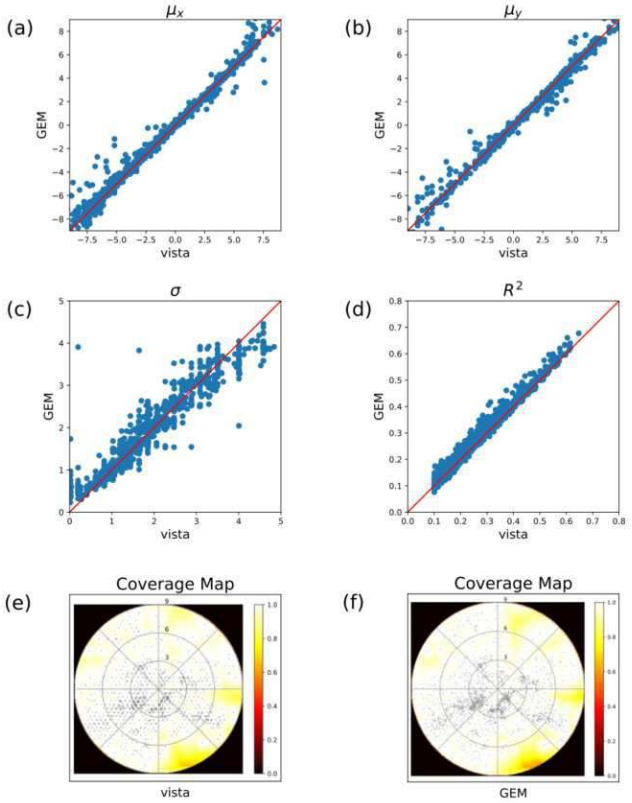

Figure 2: Evaluation of pRF estimations computed using GEM-pRF and mrVista on empirical data acquired from a 3T scanner. **(a)-(c)** Comparison of the center-X (μ_x), center-Y (μ_y), and the size of the estimated pRFs. **(d)** Comparison of mrVista vs. GEM-pRF variance explained (R^2). **(e)-(f)** Coverage maps obtained by mrVista and GEM-pRF respectively.

Conclusions: Our proposed GPU-empowered mapping of pRF (GEM-pRF) approach maintains the high-accuracy of the pRF parameters estimation results as compared to the existing popular techniques, while reducing the computational time by more than an order of magnitude.

References
1. Dumoulin, S. O., & Wandell, B. A. (2008). Population receptive field estimates in human visual cortex. NeuroImage, 39(2), 647–660. https://doi.org/10.1016/j.neuroimage.2007.09.034
2. Lerma-Usabiaga, G., Benson, N., Winawer, J., & Wandell, B. A. (2020). A validation framework for neuroimaging software: The case of population receptive fields. PLoS Computational Biology, 16(6). https://doi.org/10.1371/journal.pcbi.1007924
3. Bhat, S., Lührs, M., Goebel, R., & Senden, M. (2021). Extremely fast pRF mapping for real-time applications. NeuroImage, 245. https://doi.org/10.1016/j.neuroimage.2021.118671

Poster No 1350

Stimulus smoothness influences pRF parameters

David Linhardt[1], Johanna Bogner[1], Michael Woletz[1], D. Samuel Schwarzkopf[2], Christian Windischberger[1]

[1]High Field MR Center, Medical University of Vienna, Austria, [2]University of Auckland, New Zealand

Introduction: Population receptive field (pRF) modeling with functional MRI (fMRI) is the gold-standard method for revealing how a subject's visual field maps onto the visual cortex. Subjects maintain focus on a central point while a bar aperture moves across their visual field. Traditionally, this bar jumps to a new position with each fMRI volume captured, tying the model's temporal resolution to the scan's repetition time (TR). This method, however, also impacts spatial resolution, as it fails to distinguish small pRFs within the range of a single bar jump. Further, the jump width of the stimulus also imposes a constraint on the pRF size that cannot be effectively analyzed when too small. To assess the impact of the stimulus smoothness on pRF mapping, here we tested stimuli varying in their movement patterns, from classical jumps to smooth transitions, and explicitly incorporated stimulus temporal resolution in the pRF model.

Methods: We designed 3 stimulus conditions based on a classical pRF mapping paradigm. A bar (width=1.6°) moved through the field of view in eight different directions, revealing a reversing checkerboard pattern. Subjects were instructed to fixate on the central dot. The stimulus reached a total diameter of 12° visual angle: Standard: the bar jumped once per TR for ⅓ of the bar width Small jumps: the bar jumped twice per TR smooth: the bar jumped 8 times per TR, resulting in smooth movement A total of 6 healthy subjects (5 female, age: 24.5±2.6) were measured on a 7T SIEMENS MAGNETOM scanner. For every stimulus condition, we acquired two functional runs (TE/TR=25.6/1000ms, 1.2mm isotropic) in one session, resulting in 6 runs per subject. Together with an additional structural T1-weighted image (0.75mm isotropic) the data were minimally pre-processed using containerized solution fMRIPrep v23.1.4 (fmriprep.org). For the pRF mapping, the analysis tool SamSrf v9.7 (github.com/samsrf/samsrf)[1] was used, which allows for the creation of the pRF model at a higher temporal resolution. Using this option, the analysis created models in the native temporal resolution of the stimulus. These high resolution models were then subsampled to the timings of the acquired data (at every TR). This procedure was used to estimate the pRF position (eccentricity, polar angle) and size (sigma). Only data in V1 and exceeding a variance explained threshold of 10% were included in the analysis. Coverage plots were created as the maximum surface of all pRFs using prfresult v0.1.1 (github.com/dlinhardt/prfresult). Reproducibility was assessed using Spearman's correlation, between the two runs of each condition. For every pRF parameter, the correlation was calculated for every subject independently and then averaged across subjects.

Results: Differences in coverage plots are shown for two subjects in Figure 1. The columns represent results obtained from the standard, small jump and smooth stimulus respectively. The standard analysis revealed pronounced clustering artifacts in both subjects, with the clustered pRFs exhibiting sizes notably smaller than typical. While diminished, these artifacts persisted in the small jump stimulus. For both conditions, the distance between clusters roughly corresponds to the jump width of the bar. Only results for the smoothly moving bar in the third column are free of these artifacts. Comparative analysis of reproducibility across standard, small jump, and smooth stimuli yields negligible differences, with values for standard (eccentricity: 0.91; polar angle: 0.97; sigma: 0.26), small jump (0.92; 0.98; 0.27), and smooth (0.91; 0.96; 0.29) stimulation. Variance explained averages across subjects show a marginal increase for small (26%) and smooth (25%) compared to standard (24%) stimulation.

Conclusions: Though we could not find an improved performance of the smooth stimuli in terms of reproducibility or goodness of fit, artifacts driven by tiny pRFs were heavily reduced and we found an overall more uniform coverage using a smoother stimulus design.

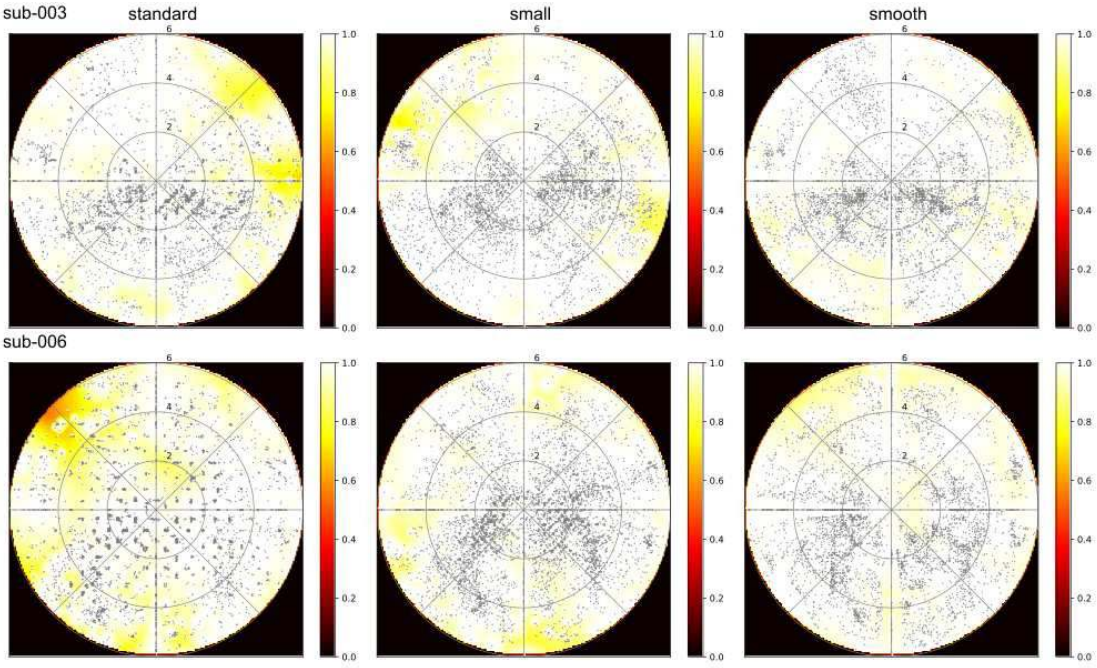

Figure 1: Coverage maps of two exemplary subjects.
The left column shows results obtained using the standard jumping bar. The following two columns show results from small jumping and smooth stimuluation. It can be seen that the standard results yield lots of clusters in the coverage map that become less distinct in the second column and completely disappear for the smooth stimulus paradigm. Every gray dot represents a single voxel's result while their underlying colour codes for the maximum surface of all pRFs.

References
1. Schwarzkopf, D.S.: SamSrf 9.8 - Matlab toolbox for pRF analysis. (2018). https://doi.org/10.17605/OSF.IO/2RGSM

Poster No 1351

Neural Correlates of Embodiment using Virtual Reality Mental Illness Avatar Body Experience

Kelssy Hitomi dos Santos Kawata[1], Wey Lem[1], Koki Ono[1], Hiroshi Oyama[1]

[1]The University of Tokyo, Bunkyo-Ku, Tokyo

Introduction: We previously demonstrated via visual-motor action synchronization that the sense of embodiment (SoE) experience into an avatar with mental illness using immersive virtual reality (IVR) increased knowledge acquisition and decreased stigma towards the mental illness person[1]. In order to maximize this effect, there is a need to verify the neural correlates of individual differences of SoE. Here, we investigated the effect of SoE through visual-motor action synchronization using embodiment into an avatar with mental illness via IVR in regard to the neural correlates of the individual difference of SoE.

Methods: We analysed data from 32 right-handed native Japanese (14 female; M = 24.00, SD = 6.10 years), and they were randomized into either the IVR-control or control-IVR sequence groups. The IVR group experienced the embodiment of an avatar with mental illness in IVR via a head-mounted display (HMD), in which they assumed the role of a company employee with mild symptoms of depression and experienced stigma. The embodiment experience was performed via visual-motor action synchronization with the hand-tracking feature, allowing for three types of interactions; grabbing a paper, holding a computer mouse, and pressing the snooze button on the alarm clock. On the other hand, the control group watched a video with the same content as the IVR group but without visual-motor action synchronization. In both groups, after each experience, participants were evaluated in terms of the SoE. During the functional magnetic resonance imaging (fMRI) scanning that occurred before and after these experiences, all participants were asked to listen to the main auditory content of the embodiment experience while wearing a sleeping mask to minimize the visual effects generated by removing the HMD. For the behavioural data, a paired t-test was conducted for the SoE scores between the IVR and control groups. In addition, the effect of individual differences of embodiment on brain activity was examined using a 2nd-level between participant regression analysis, respectively for the IVR and control groups. The voxel-wise statistics used an uncorrected p-value of <0.001 for the cluster-forming threshold and at a threshold of family-wise error (FWE)-corrected p-value of <0.05 for cluster

extent. The protocol received approval from the Research Ethics Committee of the Faculty of Medicine and Graduate School of Medicine of the University of Tokyo (2019099NI).

Results: The SoE score in the IVR group was significantly higher than those in the control group. The SoE score related to the IVR group was negatively associated with the neural response of mental illness embodied experience in the right inferior frontal gyrus, right anterior insula and left angular gyrus. These brain regions contain mirror neurons which engage in understanding visual-motor actions and emotion in various fMRI studies beyond embodiment[2-5].

Conclusions: Thus, our findings suggest that mirror neurons contributes to the mechanisms of embodiment simulation using IVR and has important implications for the development of a more objective method of SoE assessment, based on physiological data.

References

1. Lem WG, dos Santos Kawata KH, Oyama H: The Impact of Virtual Reality-Based Anti-Stigma Intervention on Mental Illness Knowledge and Associated Neural Activity. In: Proceedings of Annual Conference of Japan Society for Medical Virtual Reality 第 22 回 日本 VR 医学会学術大会: 2023: Japanese Society for Medical Virtual Reality; 2023: 25-26.
2. Yang C-J, Yu H-Y, Hong T-Y, Shih C-H, Yeh T-C, Chen L-F, Hsieh J-C: Trait Representation of Embodied Cognition in Dancers Pivoting on the Extended Mirror Neuron System: A Resting-State fMRI Study. Front Hum Neurosci 2023, 17:1173993.
3. Shimada S: Multisensory and Sensorimotor Integration in the Embodied Self: Relationship between Self-Body Recognition and the Mirror Neuron System. Sensors 2022, 22(13):5059.
4. Ku J, Lee H, Kim J-J, Kim IY, Kim SI: Brain mechanism involved in the real motion interaction with a virtual avatar. Biomedical Engineering Letters 2012, 2:164-172.
5. Horoufchin H, Bzdok D, Buccino G, Borghi AM, Binkofski F: Action and object words are differentially anchored in the sensory motor system-A perspective on cognitive embodiment. Sci Rep-Uk 2018, 8(1):6583.

Poster No 1352

Movie-specific temporal dynamics analysis in functional connectivity using the COBE method

Priyanka Mittal[1], Anil Sao[2], Bharat Biswal[3]

[1]Indian Institute of Technology, Mandi, Himachal Pradesh, [2]Indian Institute of Technology, Bhilai, Chattisgarh, [3]New Jersey Institute of Technology, Newark, NJ

Introduction: Temporal dynamics of brain states, measured using fMRI, could be associated with a sequence of well-defined functional states and can be derived using dynamic functional connectivity (FC). It has been reported that in fMRI scans made during movie watching, the transitions of functional states are temporally aligned to specific features of the movie (Meer et al., 2020). Leveraging the Hidden Markov Model (HMM), such dynamics of whole-brain networks can be modeled as hidden states, where each state can be described by the mean activation vector (Hunyadi et al., 2019; Vidaurre et. al., 2016, 2018a). Most frequently observed states for a window of time may be different across the subjects due to individual-level variations despite they have undergone the same movie stimuli during the scan. In this study, we attempted to suppress the subject level variations present in the dynamic FC observed during movie-watching fMRI data through the Common orthogonal basis extraction (COBE) algorithm. This leads to enhanced consistency in the state's temporal dynamics across the subjects that have undergone the same movie stimuli.

Methods: We have analyzed movie fMRI data from the publicly available dataset called the "HCP S1200 release." This included data from 184 individuals who underwent fMRI scanning while watching movies on a 7 Tesla scanner at the University of Minnesota (https://db.humanconnectome.org). The stimuli for MOVIE1_CC1 and MOVIE3_CC2 consisted of four short clip compilations consisting of independent Creative Commons videos. MOVIE2_HO1 and MOVIE4_HO2, on the other hand, consisted of scenes from Hollywood movies. In this study, dynamic FC matrices are computed using 160 regions of interest (ROIs) from the Dosenbach atlas using point-by-point multiplication of z-scored ROIs. To estimate the HMM states from the group of dynamic FC matrices related to four different movie stimuli, we have used the HMM-MAR toolbox (Vidaurre et. al., 2016). Further, we applied the Common Orthogonal Basis Extraction (COBE) method (Zhou et al., 2016) to extract common FC patterns across subjects for a movie. Thus movie-specific information present in dynamic FCs is extracted as the common subspace and subject level variations are separated from the FC. For the analysis of movie-specific temporal dynamics present in the dynamic FC, HMM states are extracted from the common subspace of FC across subjects.

Results: Figure 1 shows the workflow pipeline where HMM states are estimated using group analysis of all four movie stimuli-related dynamic FC matrices. HMM states were also computed in this study after the COBE application on the dynamic FC matrices of each movie stimuli separately. Using the COBE algorithm, the common information present in the dynamic FC which is movie-related (as movie stimuli are common across the subjects for a particular stimuli) is retained after removing the individual components of the COBE decomposition of FC matrices. Using the HMM model, the state path followed by each

of the subjects across time can be observed. Figure 2 shows the most frequent states for both cases (with and without using COBE) when a nonoverlapping time window of 10-time points is considered for all the subjects. It is evident from Figure 2 (b) that after COBE application, the state path of most frequent states across the subset of subjects is more consistent than the previous case Figure 2 (a). For all four movies, after the COBE application, fewer states are frequent and comparatively consistent across the subjects.

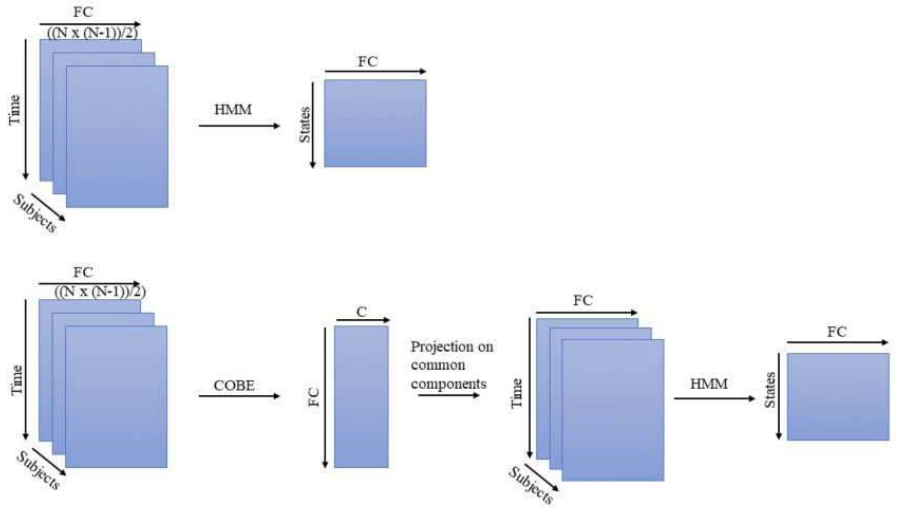

Figure 1: Workflow pipeline for extracting HMM states directly from dynamic FC matrices and after performing COBE on dynamic FC matrices while retaining their common information.

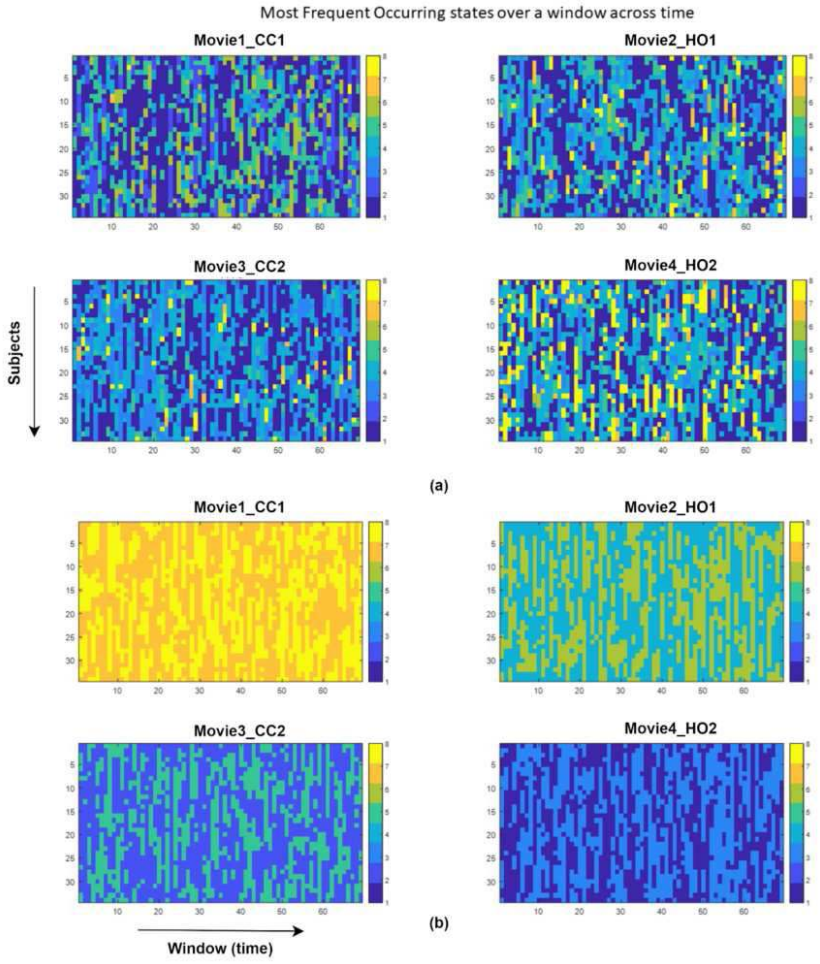

Figure 2: Most frequent States over the time windows across subjects, (no. of states =8) extracted: (a) directly from dynamic FC matrices (b) after applying COBE with no. of components = 30

Conclusions: In this study, using the COBE algorithm, we have attempted to separate the individual-level variation present in FC matrices and one can observe its effect in the form of consistent state transition across the subjects over the time window. The HMM method is used in this work to model the fMRI data as transitions of some hidden states which will be aligned to the specific features of their movie stimuli.

References

1. Hunyadi, B. et al. (2019), A dynamic system of brain networks revealed by fast transient EEG fluctuations and their fMRI correlates. NeuroImage, 185, pp. 72–82.
2. Meer, J.N.V.D. et al. (2020), Movie viewing elicits rich and reliable brain state dynamics. Nature communications, 11(1), p. 5004.
3. Vidaurre, D. et al. (2016), Spectrally resolved fast transient brain states in electrophysiological data. NeuroImage, 126, pp. 81–95.
4. Vidaurre, D. et al. (2018b), Spontaneous cortical activity transiently organizes into frequency specific phase-coupling networks. Nature Communications, 9(1), p. 2987.
5. Zhou, G. et al. (2015), Group component analysis for multiblock data: Common and individual feature extraction. IEEE transactions on neural networks and learning systems, 27(11), pp. 2426-2439.

Poster No 1353

Surprising the brain: neuroscientific inquiry into surrealistic art

Yingying Huang[1], Cristina Denk-Florea[1], Gujing Li[1], Christina Konstantinou[2], Stephen Forcer[2], Frank Pollick[1]

[1]School of Psychology and Neuroscience, University of Glasgow, Glasgow, United Kingdom, [2]School of Modern Languages and Cultures, University of Glasgow, Glasgow, United Kingdom

Introduction: How does the brain process surreal artworks that depict objects or scenes that do not exist in reality? Surrealism, an artistic and literary movement that emerged in the early 20th century, aimed to reveal hidden parts of the mind that challenge conventional notions of reality. While surrealism is often claimed to have psychological significance, it has not been extensively studied from a neuroscientific perspective. Our study seeks to contribute to the dialogue between art and neuroscience by investigating the potential neural mechanisms underlying the perception of surrealistic art, specifically in relation to surprise, error prediction, and neural representation.

Methods: We used 3T functional Magnetic Resonance Imaging (fMRI) technique to examine the brain response to images of surrealistic objects and paintings, in comparison to images of naturalistic objects and paintings. To control for confounding factors, such as valence, arousal, familiarity, and luminance, a behavioural pre-test was included to select a set of images consisting of 64 surreal objects, 64 surreal paintings, 64 natural objects, and 64 natural paintings for fMRI experimental procedure. The experiment used a 2x2 factor design (condition: surreal and natural, category: object and painting). We conducted four functional experiment runs, one anatomy, and one retinotopic mapping run. In each experimental run, participants were required to view each image for 4s and press the button when the black fixation cross changed to red, which was used to monitor participants' attention. Each block (16s) consisted of four images from the same category and was followed by an 8s baseline. All image stimuli were presented only once. A total of 27 healthy participants attended the fMRI experiment. We used BrainVoayger 22.4 to do the fMRI data analysis with a F-test to indicate interaction and main factor effects. We then used Matlab to perform a whole brain searchlight decoding analysis and a multivoxel pattern analysis (MVPA) with linear support vector machine (SVM) classifier.

Results: 1) F-test results. Using cluster thresholding ($p<0.05$) with a cluster determining threshold of $p<0.001$, we revealed a significant interaction effect in multiple brain regions, including the superior and inferior frontal gyrus in both hemispheres, as well as cuneus, precuneus, and cingulate gyrus in the right hemisphere. This suggests that surrealistic images may engage unique neural mechanisms compared to naturalistic images, possibly related to the surprising and unexpected elements often present in surrealistic art. Additionally, the main effect of condition (surreal vs natural) involved the amygdala, as well as visual cortex and frontal cortex in both hemispheres. The main effect of category (object vs painting) was found to be significant mainly in the visual cortex and frontal cortex in both hemispheres. 2) Whole-brain searchlight MVPA decoding results showed that decoding accuracy in the visual cortex was significant ($p<0.01$ after the false discovery rate (FDR) $q<0.05$ correction). 3) We further conducted MVPA decoding specifically for the brain activity patterns in the early visual cortex (EVC). The results demonstrated that voxel activity patterns between surrealism and naturalism conditions were different in the EVC and that the patterns between object and painting category were also notably distinct. This implies that the early visual cortex is sensitive to these distinctions between surreal and natural art.

Conclusions: These findings provide preliminary evidence for the neuroscientific relevance of surrealism and contribute to our understanding of how the brain processes artistic stimuli, emphasising distinct neural signatures associated with surrealism and naturalism.

References
1. Silveira, S., Graupmann, V., Frey, D., Blautzik, J., Meindl, T., Reiser, M., Chen, C., Wang, Y., Bao, Y., Pöppel, E., & Gutyrchik, E. (2012). Matching Reality in the Arts: Self-Referential Neural Processing of Naturalistic Compared to Surrealistic Images. Perception, 41(5), 569-576. https://doi.org/10.1068/p7191
2. Carr, A. N., & Zanetti, L. A. (2000). The Emergence of a Surrealist Movement and its Vital `Estrangement-Effect' in Organization Studies. Human Relations, 53(7), 891-921. https://doi.org/10.1177/0018726700537001
3. Frank, D., Kafkas, A., & Montaldi, D. (2022). Experiencing surprise: The temporal dynamics of its impact on memory. Journal of Neuroscience, 42(33), 6435-6444.

Poster No 1354

Common and distinct neural mechanisms of aversive and appetitive pain-related learning

Jialin Li[1,2], Katharina Schmidt[2], Lea Busch[2], Tamás Spisák[2], Katja Wiech[3,2], Ulrike Bingel[2]

[1]Max Planck School of Cognition, Leipzig, Germany, [2]University Medicine Essen, Essen, Germany, [3]Wellcome Centre for Integrative Neuroimaging, Oxford, United Kingdom

Introduction: Learning from signals of upcoming aversive and appetitive events is crucial for humans. Several studies have investigated the mechanisms underlying these two types of learning (Martin-Soelch et al., 2007; Fullana et al., 2016; Klein et al., 2022; van der Schaaf et al., 2022), but mostly using different sensory modalities and paradigms (e.g., pain vs. monetary reward), which limits interpretations (Klein et al., 2022). A recent study (van der Schaaf et al., 2022) addressed this issue by comparing aversive and appetitive learning within the same sensory modality (tonic heat pain increase vs. decrease) and found marked behavioural differences including stronger aversive than appetitive acquisition but no differences in extinction. However, little is known about the neural underpinnings of such findings. This study aims to elucidate common and distinct neural mechanisms of aversive and appetitive pain-related learning in healthy individuals.

Methods: N = 62 healthy individuals participated in an fMRI paradigm in which moderate continuous pain was elicited by a novel capsaicin-induced tonic heat pain model (van der Schaaf et al., 2022). Individually calibrated phasic heat pain (unconditioned stimulus, US) was experimentally induced and paired with predictive cues (conditioned stimulus, CS). Following habituation, three geometrical cues (CSincrease, CSdecrease, CSmedium) signaled pain exacerbation (USincrease), pain decrease (USdecrease) and no change in temperature (USmedium) respectively in the acquisition phase. In the subsequent extinction phase, all cues were followed by the USmedium (Fig. 1). Neuroimaging data were preprocessed using the fMRIprep pipeline. Univariate general linear model analyses were performed separately for each phase using SPM12. First-level regressors included all CS and US events during acquisition and CS events during extinction, as well as nuisance variables (ratings, head movement). To identify brain regions that show increasing engagement with learning over time, we applied time modulation to CS regressors (Forkmann et al., 2023), and individual-wise contrasts modeling time x condition interactions (e.g., aversive: CSincrease x time > CSmedium x time) were entered into group-level one-sample t-tests. Results were followed up by functional connectivity analyses (gPPI; McLaren et al., 2012) for key regions identified. Results were thresholded at $p < .05$ family-wise error (FWE) corrected at peak level with small volume correction (SVC) for brain regions included in our a priori hypotheses (SFB1280 A11 project).

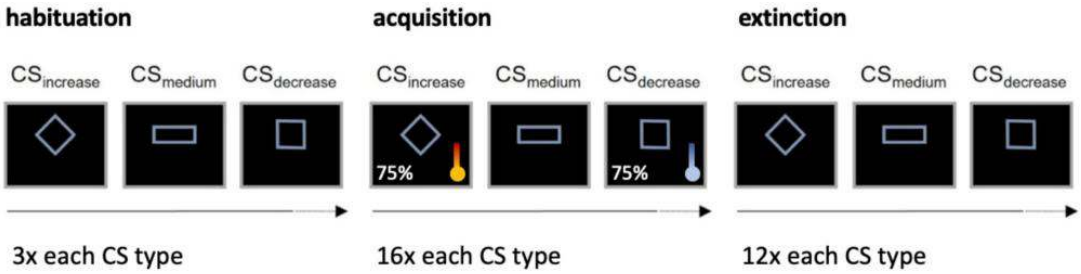

Results: The time x condition interaction indicated that compared to appetitive events, the acquisition of aversive events was associated with a stronger increase in medial thalamus activity (Fig. 2a). Conjunction analysis revealed that both types of learning were accompanied by increasing responses in the superior frontal gyrus and medial occipital cortex (Fig. 2b). Functional connectivity analysis using the occipital cortex as the seed region showed positive coupling with the frontal operculum during both types of learning (Fig. 2c), suggesting a similar connectivity pattern regardless of valence during acquisition. In the extinction phase, we found a greater decrease in activity in the lateral occipital cortex for the aversive than the appetitive condition, whereas the parahippocampal gyrus showed a stronger decrease in the appetitive condition (Fig.

2d). Both conditions showed a decrease in response over the course of the extinction phase in the vmPFC (Fig. 2e), which was negatively correlated with the activity in the periaqueductal gray (Fig. 2f).

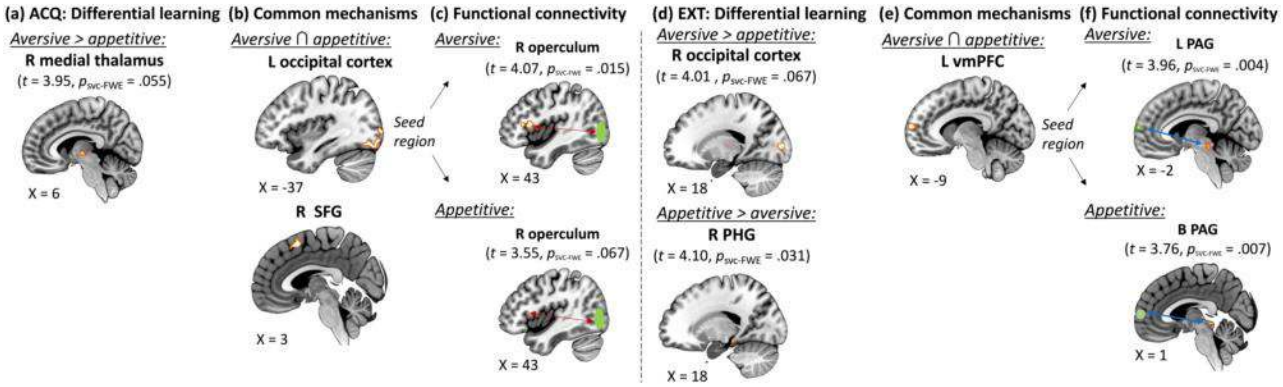

Conclusions: Our results show that in healthy individuals, aversive and appetitive learning (within the same sensory modality) involve a common set of brain regions but can also be distinguished in areas such as the medial thalamus during acquisition and the occipital cortex, parahippocampal gyrus and vmPFC during extinction.

References

1. van der Schaaf, M.E., Schmidt, K., Kaur, J., Gamer, M., Wiech, K., Forkmann, K. and Bingel, U. (2022), Acquisition learning is stronger for aversive than appetitive events. Communications Biology, vol. 5, no. 1, pp. 1-10.
2. Fullana, M.A., Harrison, B.J., Soriano-Mas, C., Vervliet, B., Cardoner, N., Àvila-Parcet, A. and Radua, J. (2016), Neural signatures of human fear conditioning: an updated and extended meta-analysis of fMRI studies. Molecular Psychiatry, vol. 21, no. 4, pp. 500-508.
3. Klein, S., Kruse, O., León, I.T., Van Oudenhove, L., van't Hof, S.R., Klucken, T., Wager, T.D. and Stark, R. (2022), Cross-paradigm integration shows a common neural basis for aversive and appetitive conditioning. NeuroImage, vol. 263, pp. 119594.
4. Martin-Soelch, C., Linthicum, J. and Ernst, M. (2007), Appetitive conditioning: neural bases and implications for psychopathology. Neuroscience & Biobehavioral Reviews, vol. 31, no. 3, pp. 426-440.
5. Forkmann, K., Wiech, K., Schmidt, K., Schmid-Köhler, J. and Bingel, U. (2023), Neural underpinnings of preferential pain learning and the modulatory role of fear. Cerebral Cortex, vol. 33, no. 16, pp. 9664-9676.
6. McLaren, D.G., Ries, M.L., Xu, G., Johnson, S.C. (2012), A generalized form of context dependent psychophysiological interactions (gPPI): a comparison to standard approaches. Neuroimage, vol. 61, no. 4, pp. 1277-1286.

Poster No 1355

Activation analysis of T2* time-series from multi-echo fMRI data

Anezka Kovarova[1,2], Michal Mikl[2]

[1]Masaryk University, Faculty of Medicine, Brno, Czech Republic, [2]CEITEC Masaryk University, Brno, Czech Republic

Introduction: The multi-echo fMRI acquisition provides enhanced sensitivity to the Blood Oxygenation Level Dependent (BOLD) signal by capturing multiple echoes within a single imaging sequence. Moreover, this advanced approach introduces the possibility of incorporating T2* mapping principles into every time point of the imaging data. This abstract explores the pilot study of the multi-echo multi-band (ME MB) fMRI approach coupled with the principles of T2* mapping, as a synergistic strategy for advancing the field of fast functional imaging. This combination may have the potential to enhance the robustness and stability of processed ME MB fMRI data.

Methods: Data was collected from 49 healthy volunteers aged 20-38 without any neurological, psychiatric, or mental disorder. The study protocol was approved by the Masaryk University Ethics Committee. The measurements were performed on the Siemens Prisma 3T MR whole-body scanner with 64-channel head-neck coil. The acquisition consisted of high-resolution anatomical images (MPRAGE, voxel size 1 x 1 x 1 mm, FOV 224 x 224x 240 mm) and then 7 different BOLD runs with block design combining visual stimulation and motor activity (pressing buttons). The acquisition time of each run was 6 minutes, echo times (TE) were 17, 35 and 52 ms, voxel size was 3 x 3 x 3 mm. Repetition times (TR), number of scans and flip angles (FA) were different for every run as follows: 1) 3.05 s / 120 / 80°; 2) 3.05 / 120 / 45°; 3) 0.8 s / 450 / 45°; 4) 0.8 s / 450 / 20°; 5)0.6 s / 600 / 45°; 6) 0.6 s / 600 / 20°; 7) 0.4 s / 900 / 20°. Acquired data was processed in as composite ME model data the optimal combinations weighted by the contrast-to-noise ratio in the standard way in SPM12. The second model was calculated as T2* estimation of the same data. The results of activation were verified by using GLM models on single-subject and group levels. We mainly focused on activation level and power of statistics, so we evaluated the differences between multi-echo and T2* models by assessing the number of active voxels, variance of residuals, percent signal change (PSC) and the power of t-statistics. We explored both global and local metrics which were chosen according to the level of activation.

Results: The comparison of ME MB data and T2* data was done using several metrics. For the global level of activation, we computed the number of active voxels, where the T2* model provided similar values as ME model and in runs 3 and 5 the T2* yielded even higher values than ME and these differences were statistically significant (shown in fig. 1). The variance of residuals was slightly worse in T2* model. We also evaluated data in chosen ROIs based on activation and then picked top 50 voxels from each ROI. When comparing the t-values, the T2* model outperformed ME model in some ROIs as shown in fig. 2 (Left precentral gyrus), especially in runs 3,4,5,6 where the difference was statistically significant. However, in some other ROIs the T2* model provided slightly worse results than ME model. Both models provided similar values of PSC in most ROIs, like in the ROI shown in fig. 2, where the T2* model performed significantly better in runs 5, 6 and 7.

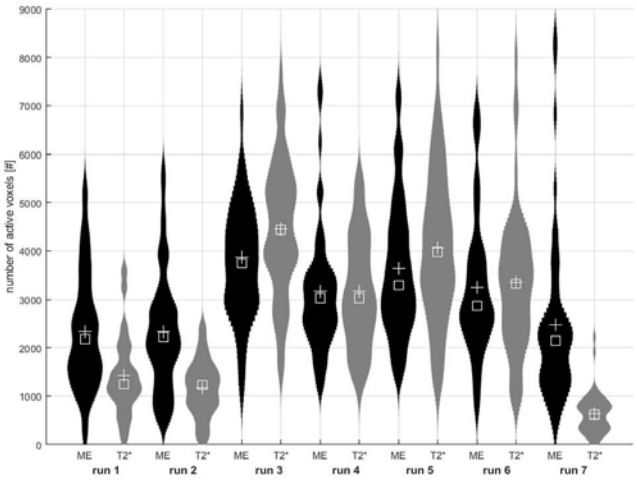

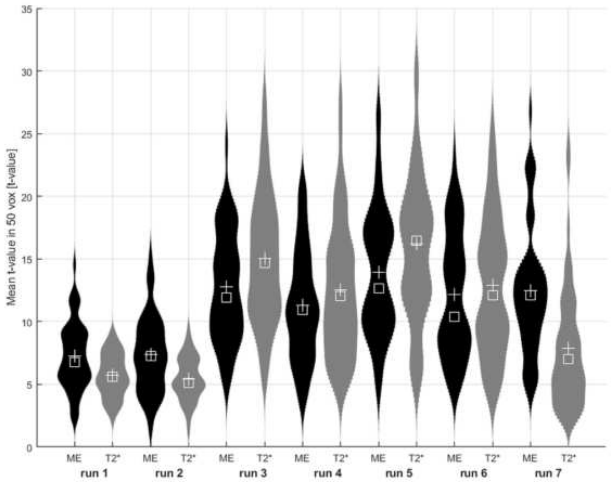

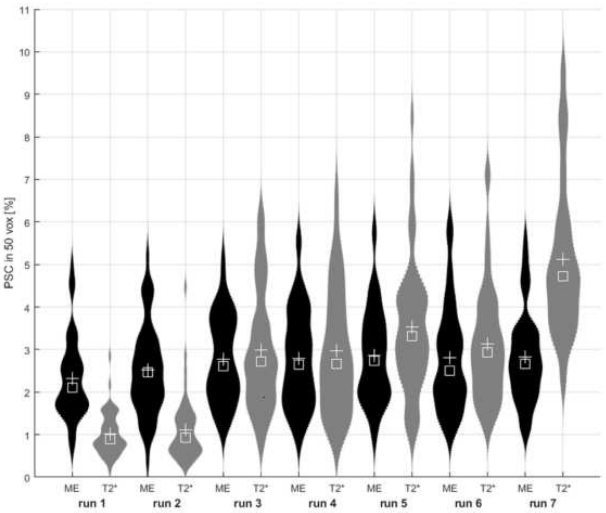

Conclusions: The pilot comparison study of ME MB data and T2* mapping showed promising results in terms of acquiring the same or even higher level of data quality in observed metrics. We hope that T2* as a quantitative parameter could contribute to the robustness and stability of the fast fMRI data processing. Although some ROIs gave slightly worse results of T2* than ME model, the overall activation in our data appears to be comparable. We are also planning to verify our theory and results on event-related data or other types of fMRI task data.

References

1. Kundu et al. (2017), 'Multi-echo fMRI: A review of applications in fMRI denoising and analysis of BOLD signals', NeuroImage, vol. 154, pp. 59-80
2. Kovářová, A. (2021), 'Contribution of the multi-echo approach inaccelerated functional magnetic resonance imaging multiband acquisition', Human Brain Mapping, vol. 43, issue 3, pp. 955-973

Poster No 1356

Adaptation to Numerosity Changes Monotonic Responses to Image Contrast in Early Visual Cortex

Liangyou Zhang[1], Evi Hendrikx[1], Yizhen Wang[2], Surya Gayet[1], Serge Dumoulin[3], Ben Harvey[1]

[1]Utrecht University, Utrecht, The Netherlands, [2]South China Normal University, Guangzhou, China, [3]Spinoza Centre for Neuroimaging, Amsterdam, The Netherlands

Introduction: Humans and many animals effortlessly perceive numerosity, the number of visual objects in an image. Numerosity perception is affected by adaptation (Burr & Ross, 2008): after viewing a particular adapter numerosity frequently or for a long time, other numerosities appear more different from this adapter than they are. Recent studies show two broad classes of neural responses to numerosity. First, parietal and frontal numerosity-tuned responses (Harvey et al., 2013; Nieder et al., 2002) show activation peaks at a specific (preferred) numerosity. We have recently shown that this preferred numerosity is affected by numerosity adaptation (Tsouli et al., 2021). Second, monotonic responses in the early visual cortex (DeWind et al., 2019; Park et al., 2015) increase in amplitude as numerosity increases. These monotonic responses are found in neural populations at the retinotopic location of the stimulus in early visual field maps (Paul et al., 2022). Furthermore, they follow spatial frequency domain image contrast more closely than they follow numerosity, though close relationships between contrast and numerosity may underlie numerosity's straightforward perception. Here we ask whether effects of numerosity adaptation on perception and numerosity-tuned responses originate in early visual contrast representations.

Methods: We used ultra-high field 7T fMRI to record responses to numerosity in early visual field maps V1-V3, hV4, LO1-2 and V3A/B. Participants viewed dot groups of gradually changing numerosity to map numerosity preferences. We repeated this under three different conditions. The low numerosity adaptation condition alternated this changing numerosity display with displays containing one item. The high numerosity adaptation condition alternated the changing numerosity with twenty items. In the control condition, every display contained the changing numerosity. In each condition, we used a general linear model (GLM) to capture the responses to the changing numerosity, where each voxel's response is predicted by the spatial frequency domain contrast energy (i.e. Fourier power) of each display. This determines the amplitude of the monotonic response to increases in Fourier power as the slope (beta) of the relationship between the display's Fourier power and each voxel's response. We used visual field mapping to determine which visual field map each voxel lay in and its preferred visual field position (Figure 1a-c). For each visual field map, we selected voxels responding within the numerosity stimulus area and showing a monotonically increasing response to Fourier power in the control condition. We tested whether the mean response slope differed between low and high numerosity adaptation conditions. We then compared, across visual field maps, the proportion by which the response slope decreased between the low and high adaptation conditions.

Results: The monotonic response's amplitude (slope or beta in the GLM) reduced during adaptation to high numerosities, compared to adaptation to low numerosities, in all visual field maps (Figure 1d). This is consistent with perceptual effects where high numerosity adaptation decreases perceived numerosity. Furthermore, the proportion by which response amplitude decreased from the low to high numerosity adaptation conditions became progressively greater from earlier visual field maps (~30% decrease in V1) to later visual field maps (~70% decrease in V3A/B and LO2) (Figure 1e).

Conclusions: These results imply that adaptation effects on numerosity-tuned neural populations' preferred numerosities, and on numerosity perception, may result from effects beginning in early visual contrast representations. These effects begin by V1 and increase through the visual processing hierarchy. Therefore, numerosity adaptation in part reflects early-stage adaptation to image contrast. However, the progressive increase in this effect suggests that adaptation may have further effects at later stages of numerosity processing.

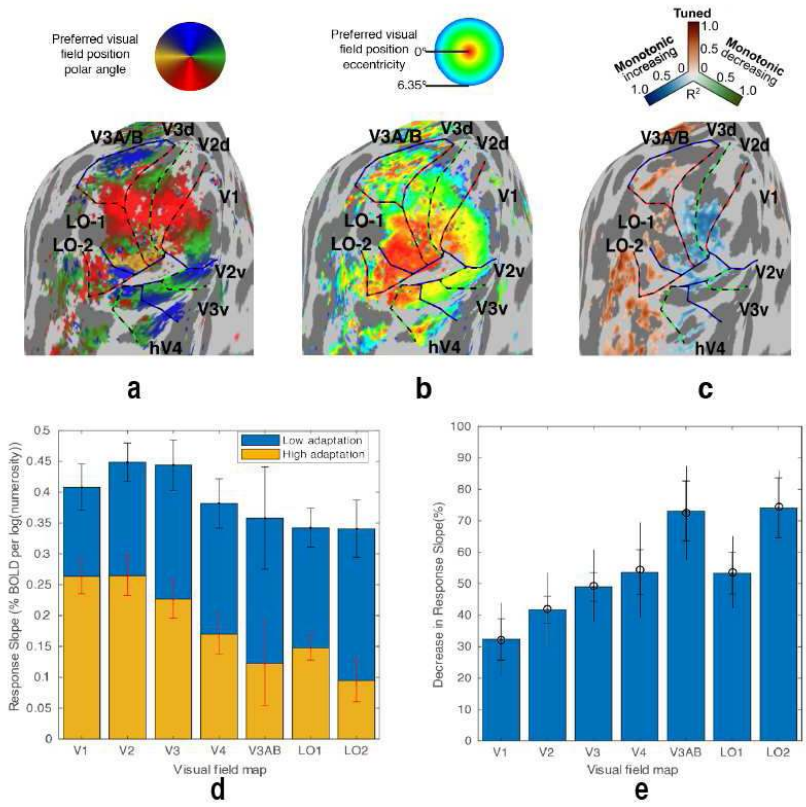

References

1. DeWind, N. K., Park, J., Woldorff, M. G., & Brannon, E. M. (2019). Numerical encoding in early visual cortex. Cortex, 114, 76–89.
2. Harvey, B. M., Klein, B. P., Petridou, N., & Dumoulin, S. O. (2013). Topographic Representation of Numerosity in the Human Parietal Cortex. Science, 341(6150), 1123–1126.
3. Nieder, A., Freedman, D. J., & Miller, E. K. (2002). Representation of the Quantity of Visual Items in the Primate Prefrontal Cortex. Science, 297(5587), 1708–1711.
4. Park, J., DeWind, N. K., Woldorff, M. G., & Brannon, E. M. (2015). Rapid and Direct Encoding of Numerosity in the Visual Stream. Cerebral Cortex, bhv017.
5. Paul, J. M., van Ackooij, M., ten Cate, T. C., & Harvey, B. M. (2022). Numerosity tuning in human association cortices and local image contrast representations in early visual cortex. Nature Communications, 13(1), 1340.
6. Tsouli, A., Cai, Y., van Ackooij, M., Hofstetter, S., Harvey, B. M., te Pas, S. F., van der Smagt, M. J., & Dumoulin, S. O. (2021). Adaptation to visual numerosity changes neural numerosity selectivity. NeuroImage, 229, 117794.

Poster No 1357

Framework for parametric fMRI fitting

Michael Woletz[1], David Linhardt[2], Siddharth Mittal[1], Christian Windischberger[3]

[1]Medical University of Vienna, Vienna, Vienna, [2]Medical University of Vienna, Wien, Vienna, [3]Medical University of Vienna, Vienna, Austria

Introduction: Most task-based fMRI analysis designs make use of a general linear model (GLM) (Friston, 1995), where a regression matrix is constructed based on the task design and the research question and fitted, along with additional nuisance regressors to the data in a least-squares way. Other, specialized methods, such as population receptive field mapping (PRF), employ models where the regression matrix is not only depending on the task, but also additional parameters, which are in turn estimated from the data using optimization methods. In this work we present a simple framework, allowing the fast comparison of different parameters during the optimization process, as well as the computation of derivatives.

Methods: A mathematical framework was developed, by making use of algebraic properties of the regressors, which simplifies the fitting process. Instead of performing least squares fitting, the fitting problem can be reduced to a matrix multiplication by enforcing orthonormality constraints, without changing the overall fit. That is, the static regressors are made orthonormal using a QR decomposition and the model regressor by subtraction of the static regressor fits (see Figure 1 for details). The constructed matrix consists of time courses, corresponding to different sets of parameters, which can be used

for a coarse fitting routine on all measured voxels at once. Once approximate parameters are found, the framework allows for the computation of derivatives with respect to the estimated parameters, which enables the use of efficient derivative based methods for the estimation of all parameters in all measured voxels. The proposed framework was tested on simulated data, simulating a PRF acquisition. Noisy time-courses were generated, representing a moving bar stimulus for a Gaussian PRF at a given position and size. Time courses were generated using the equations in Figure 1, as well as the derivative for the optimization function and used to compare the simulated ground truth results with the result from the parametric fitting framework.

$$\mathbf{X} = [\mathbf{s}(\boldsymbol{\theta}) \quad \mathbf{R}] \tag{1}$$

$$\mathbf{s}^*(\boldsymbol{\theta}) = [\mathbf{I} - \mathbf{R}\mathbf{R}^T]\,\mathbf{s}(\boldsymbol{\theta}) \tag{2}$$

$$\mathbf{s}'(\boldsymbol{\theta}) = \frac{\mathbf{s}^*(\boldsymbol{\theta})}{\sqrt{\mathbf{s}^*(\boldsymbol{\theta})^T\mathbf{s}^*(\boldsymbol{\theta})}} \tag{3}$$

$$\mathbf{X}' = [\mathbf{s}'(\boldsymbol{\theta}) \quad \mathbf{R}] \tag{4}$$

$$\hat{\mathbf{e}} = \left[\mathbf{I} - \mathbf{X}'\left(\mathbf{X}'^T\mathbf{X}'\right)^{-1}\mathbf{X}'^T\right]\mathbf{y} \tag{5}$$

$$\hat{\mathbf{e}}^T\hat{\mathbf{e}} = \mathbf{y}^T\mathbf{y} - (\mathbf{y}^T\mathbf{s}'(\boldsymbol{\theta}))^2 - \mathbf{y}^T\mathbf{R}\mathbf{R}^T\mathbf{y} \tag{6}$$

Figure 1. Modifications to the general linear model (GLM) design matrix in this work. Please note that the residual sums of squares (6) only a scalar product of the data **y** and the model signal **s** depend on the parameters **θ**, reducing the optimisation to a matrix product and allowing the computation of partial derivatives.

Results: The calculated error function and its partial derivatives as a function of the location parameters for a simulated PRF experiment can be seen in Figure 2. Our framework is very efficient, allowing the computation of both the error function and the gradient as simple matrix multiplications, enabling a fast evaluation of both for many voxel time-courses at once, without reducing the fitting accuracy.

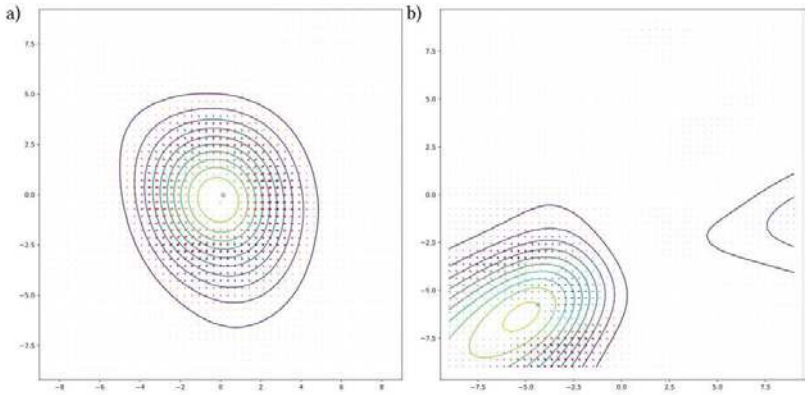

Figure 2. Examples from population receptive field (PRF) mapping. The PRF was modelled as a Gaussian function with parameters μ_x, μ_y and σ. Isolines for the residual sums of squares error are plotted along with the partial derivatives with respect to μ_x, μ_y (arrows) and σ (arrow color) as a function of μ_x and μ_y for a PRF a) near the center and b) off the center. It can be seen, that the computed gradients correspond well to the error function and that the error function has a maximum close to the ground truth value (blue cross).

Conclusions: By reformulatiing the GLM model, we have presented a framework, which allows fitting of parameters in an fMRI experiment. The new framework allows for faster fitting routines and gradient based fitting routines, not only on CPUs, but GPUs, enabling not only faster results, but also more complicated models.

References

1. Friston, K.J., (1995), 'Analysis of fMRI time-series revisited', NeuroImage. vol. 2, no. 1, pp. 45-53

Poster No 1358

BOLD fMRI effects of concurrent tDCS at the pre-SMA on inhibition in OCD patients

Daniela Rodriguez Manrique[1], Kathrin Koch[2]

[1]Technical University Munich, Munich, Bavaria, [2]Neuroradiology, Klinikum rechts der Isar der Technischen Universität München, Munich, Bavaria

Introduction: OCD Patients have difficulty inhibiting obsessive thoughts and reoccurring compulsive behaviors, two core symptoms underlying the disorder. Hence, studies have investigated brain areas and networks involved in response inhibition

in OCD patients. They find the inferior frontal gyrus and the pre-supplementary motor area (pre-SMA) as key regions involved in inhibition[5,6,9]. Previously, the pre-SMA has been chose as a target in inhibition performance tDCS studies. Post stimulation OCD studies showed modulated pre-SMA-vmPFC connectivity[7]. tDCS is an attractive method due to its cheap and mobile nature, however its underlying mechanisms are poorly understood and rarely studied in combination with imaging. Studies rarely detail the conditions between stimulation and task results. Performing concurrent fMRI-tDCS allows increased insight into the immediate and postponed blood oxygen dependent (BOLD) changes in brain regions and networks and their second-hand effects[1]. Thus, allowing studies to better investigate the neuronal basis for behavioural and symptomatic changes in patients. This study aimed to test whether tDCS at the pre-SMA could improve inhibition performance and related brain connectivity.

Methods: 54 OCD patients recruited from four clinics in and around Munich, a double-blinded crossover study, the patients received 20 minutes of tDCS during one appointment and a 30 second sham during another. Patients were stimulated in the scanner during which they performed the stop-signal task and the Stroop task (each 10min). Electrodes were placed on the FC1 and FC2 10-20 EEG positions. 46 Patients with OCD were included in the analysis upon excluding participants with outlying task performance. The imaging data recorded during the Stroop task were analysed using McIntosh's event-related approach with partial least squares[2]. This multivariate analysis technique identifies whole-brain patterns of covariance related to conditions of an experiment. Each brain voxel has a weight, referred to as salience, which specifies how strongly the voxel contributes to the covariance explained by that latent variable (LV). In the non-rotated mean-centred event-related PLS, the analysis looks for LVs which explain the maximum percentage of variance between the contrast and the BOLD signal. The LVs were determined with a permutation test using 2000 permutations, each event had a temporal window size of 14 time-points post-stimulus onset, called Lags. To answer our hypothesis on the effect of tDCS on the inhibition (incongruent) condition, we contrasted between task conditions and timepoints. Furthermore, the reliability of each voxel's contribution to a particular LV was tested by submitting all saliences to a bootstrap estimation of the standard errors (SEs), using 2,000 bootstraps. The bootstrap ratio (BSR) is calculated by dividing salience with standard error. Peak voxels with a salience/SE ratio ≥3.0 or ≤-3 for negative correlations ($p < .001$) were deemed as reliable[3].

Results: No significant differences in stroop ansd stop-signal task performance between the stimulation and sham timepoints were found. Figure 1 displays the brain scores for each condition and over time. All three timepoints included in Fig 2. Had their most significant cluster in the supramarginal gyrus. The stimulation condition did show an increase connectivity in the expected inferior frontal gyrus (Fig. 2)[6,9].

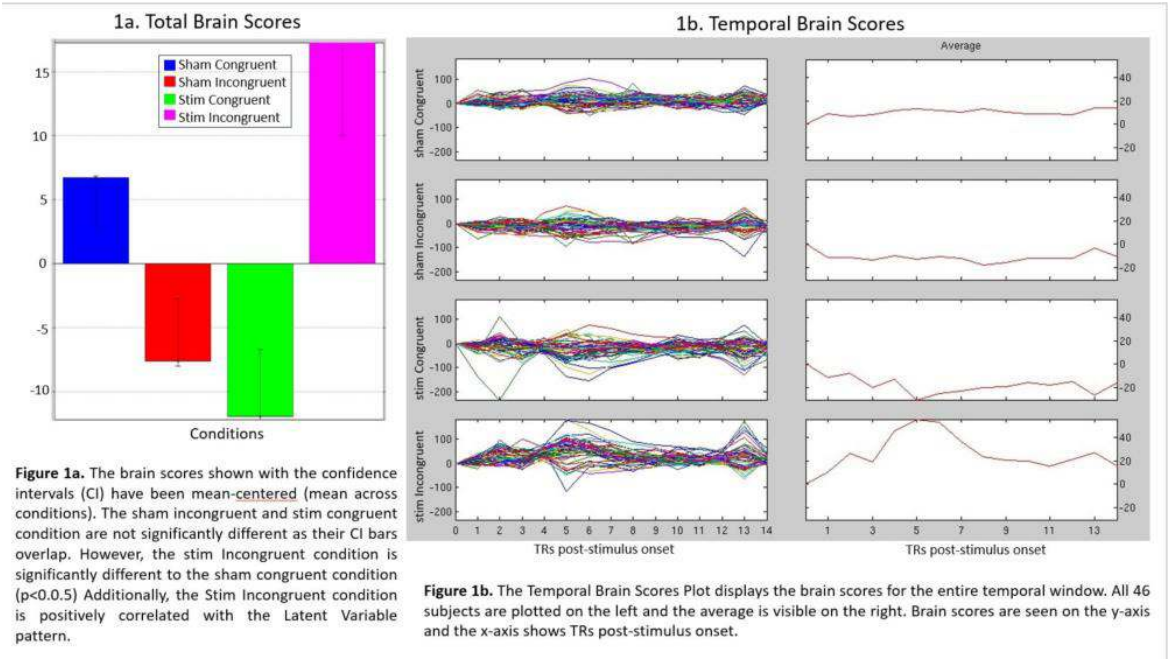

Figure 1a. The brain scores shown with the confidence intervals (CI) have been mean-centered (mean across conditions). The sham incongruent and stim congruent condition are not significantly different as their CI bars overlap. However, the stim Incongruent condition is significantly different to the sham congruent condition ($p<0.0.5$) Additionally, the Stim Incongruent condition is positively correlated with the Latent Variable pattern.

Figure 1b. The Temporal Brain Scores Plot displays the brain scores for the entire temporal window. All 46 subjects are plotted on the left and the average is visible on the right. Brain scores are seen on the y-axis and the x-axis shows TRs post-stimulus onset.

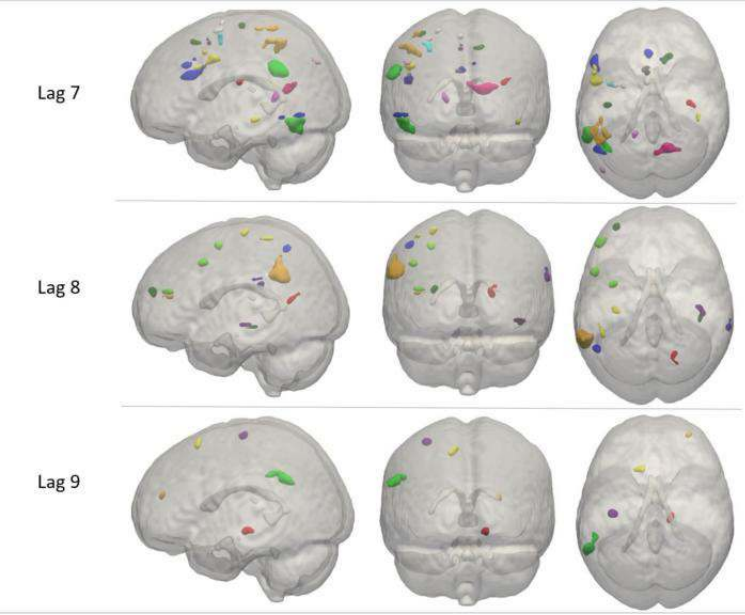

Figure 2. Shows the clusters where peak voxels have a salience/standard error ration ≥3 or ≤-3 ($p<0.001$) for the latent variable (LV) describing 100% of all the variance for our desired contrast comparing conditions and timepoints. The LV had a significance of $p<0.036$. 2000 permutations and bootstraps were used in this calculation. Lag represents the TRs post stimulus onset (this sequence had a TR of 1s).

Lag 7: cl.1 in light green, cl.2 in blue, cl.3 in yellow, cl. 4 in orange, cl.5 in purple, cl.6 dark green, cl.7 in turquoise, cl.8 in white, cl.9 in dark grey.
Negative correlation: cl.10 in red, cl.11 in magenta, cl.12 in hot pink and cl.13 in light pink.

Lag 8: cl.1 in orange, cl.2 in light green, cl.3 in dark green, cl.4 purple, cl.5 in blue, cl.6 in yellow and cl.7 in red (negative correlation)

Lag 9: cl.1 in light green, cl.2 in purple, cl.3 in yellow, cl.4 in orange and cl.5 in red (negative correlation).

Figure created following Mandan (4).

Conclusions: Correlations with behavioural performance scores including accuracy and response time will be included in further analysis. Additionally, the question whether timepoint sequence influences brain patterns remains to be answered. Finally, a separate analysis will be conducted where the effect of electric field magnitude patterns calculated for each participant using a method developed last year will be considered[8].

References

1. Ekhtiari, H. (2022) 'A checklist for assessing the methodological quality of concurrent tES-fMRI studies: a consensus study and statement', Nature Protocols, ISSN: 1754-2189.
2. McIntosh, A. R. (2004) 'Spatiotemporal analysis of event-related fMRI data using partial least squares', NeuroImage, vol. 23, 764-775.
3. Sampson, P. D. (1989). 'Neurobehavioral effects of prenatal alcohol: Part II. Partial Least Squares Analysis.', Neurotoxicology and Teratology, vol. 11, 477–491.
4. Madan, C. R. (2015) 'Creating 3D visualisations of MRI data: A brief guide [version 1; peer review:3 approved]', F1000Research, 4:466.
5. Cai, W. (2012) 'The role of the right pre-supplementary motor area in stopping action: two studies with event-related transcranial magnetic stimulation.', J Neurophysiology, vol. 108, 380-389.
6. De Wit, S. J. (2012) 'Presupplementary Motor Area Hyperactivity During Response Inhibition: A Candidate Endophenotype of Obsessive-Compulsive Disorder', Am J Psychiatry, vol. 169, 1100-1108.
7. Yu, J. (2015) 'Brain Stimulation Improves Cognitive Control by Modulating Medial-Frontal Activity and preSMA-vmPFC Functional Connectivity', Human Brain Mapping, vol. 36, 4004-4015.
8. Rodriguez-Manrique, D. (2022) 'Electrode localisation for electrical field modelling in transcranial direct current stimulation (tDCS) studies using magnetic resonance imaging (MRI).', OHBM Abstract
9. Chambers, C. D. (2006) 'Insights into the neural basis of response inhibition from cognitive and clinical neuroscience', Neuroscience & Biobehavioural Reviews, vol. 33, 631-646.

Poster No 1359

Neurological Representations of Galvanic Skin Response Under 7T fMRI. A Pilot Study

Zachary Cohen[1], Mirja Steinbrenner[2], Rishi Sharma[1], Rory Piper[1], Neo Baker[1], Mark Richardson[3], David Carmichael[1]

[1]King's College London, London, United Kingdom, [2]Department of Neurology, Charité, Berlin, Germany, [3]Department of Basic and Clinical Neuroscience, London, United Kingdom

Introduction: Galvanic skin response (GSR) represents sympathetic arousal[1]. In an inverse relationship the increase of GSR leads to a decrease in cortical excitability[2]. Furthermore, changes in GSR can lead to regionally increased activity in premotor and supplementary motor cortices[3,4]. The modulation of GSR has been explored as a potential therapy for epilepsy[5–8]. However, an incomplete understanding of the acute effects of GSR limits its potential application. This study utilised the increased spatial resolution and sensitivity of 7T MRI to investigate the neurological representations of GSR signal during functional magnetic resonance imaging (fMRI).

Methods: Seven healthy controls attended St Thomas' Hospital (London, UK) for two study sessions. In the first session, they received GSR modulation training. Electrodes were placed on their fingers and connected to a BrainAmp ExG amplifier. The GSR signal was recorded (BrainVision) and downsampled to 10Hz. Increases in GSR were represented in a game

where a bird's height increased. Participants played this game for 1.5 hours with breaks. In the second session, participants underwent scans using a 7T MRI (Terra Siemens Healthineers), acquiring 0.65mm isotropic structural MP2RAGE images[9] and 220 echo-planar images (1.1mm isotropic, TR=2600ms, TE=24ms) per run. They underwent two fMRI runs of 9 minutes, alternating between rest and attempting to increase GSR in 1 minute blocks. Additionally they tapped their right index finger to their thumb at 1hz in randomised minute blocks. Instructions were given via lights on a screen. Data was processed in Statistical Parametric Mapping (SPM), including realignment, normalisation, and smoothing (12mm kernel). The Functional Image Artifact Correction Heuristic (FIACH) tool for R[10] was used to provide a noise model from signal time courses in brain regions with high noise levels. GSR data was recorded on MR conditional Brain Products equipment. The GSR signal was convolved with a standard hemodynamic response function in SPM. A General Linear Model analysed three conditions: attempted GSR increase, finger tapping, and actual GSR-signal. T-contrasts were generated at the first level; a second level analysis determined the group effect. Resultant maps were superimposed onto normalized individual echo planar images and a standard Montreal Neurological Institute (MNI) template brain for group analysis, comparing individual and group neural activity in response to the experimental conditions.

Results: For the condition of GSR modulative increase, we found association of increased activation in attention-network related areas of the brain – specifically left frontal ($p<0.001$ unc). At the group level these findings were not significant in our number of participants ($p<0.001$ unc). Expected increases in activity of the left motor area were seen in all individuals and at the group level ($p<0.001$ unc). During periods of increasing GSR signal we observed increased bilateral frontal pole activation at a group level ($T = 5.2$ $p<0.001$ unc) (Fig1).

Conclusions: GSR modulation shows promise as a therapy for neurological and neuropsychiatric disorders, potentially reducing cortical excitability and influencing sensorimotor activity. This study aims to explore the acute effects of GSR modulation using a novel paradigm in conjunction with 7T MRI fMRI. Despite the small numbers, a prefrontal increase in activity with increasing GSR is consistent with previous literature suggesting altered frontal pole activity[5] This research establishes the feasibility for both additional healthy controls and participants with GGE to be scanned under this paradigm, interrogating if a GSR modulative increase causes reduced sensorimotor connectivity that may be associated with a reduction in seizures.

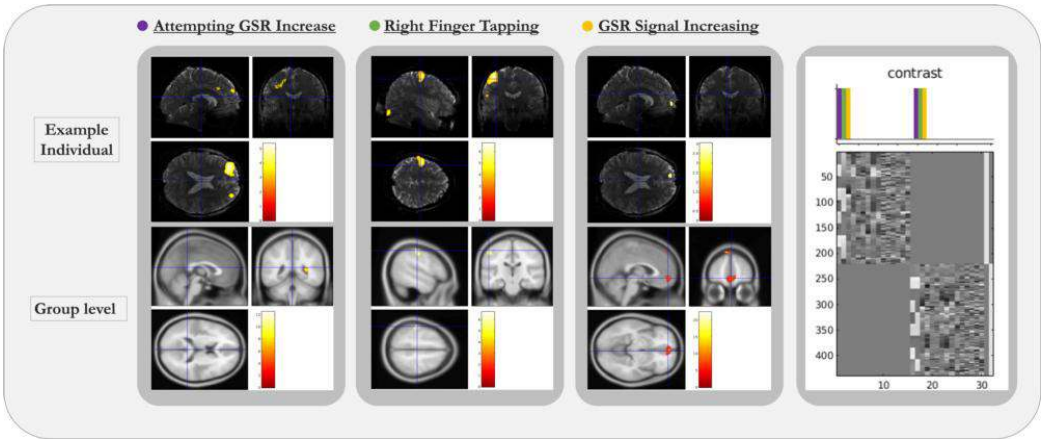

Fig. Brain activations for each task condition

References

1. Y. Nagai, C. I. Jones, and A. Sen, "Galvanic Skin Response (GSR)/Electrodermal/Skin Conductance Biofeedback on Epilepsy: A Systematic Review and Meta-Analysis," Frontiers in Neurology, vol. 10. 2019. doi: 10.3389/fneur.2019.00377.
2. Y. Nagai, L. H. Goldstein, H. D. Critchley, and P. B. C. Fenwick, "Influence of sympathetic autonomic arousal on cortical arousal: Implications for a therapeutic behavioural intervention in epilepsy," Epilepsy Res, vol. 58, no. 2–3, 2004, doi: 10.1016/j.eplepsyres.2004.02.004.
3. H. D. Critchley, R. Elliott, C. J. Mathias, and R. J. Dolan, "Neural activity relating to generation and representation of galvanic skin conductance responses: A functional magnetic resonance imaging study," Journal of Neuroscience, vol. 20, no. 8, 2000, doi: 10.1523/jneurosci.20-08-03033.2000.
4. H. D. Critchley, R. N. Melmed, E. Featherstone, C. J. Mathias, and R. J. Dolan, "Brain activity during biofeedback relaxation a functional neuroimaging investigation," Brain, vol. 124, no. 5, 2001, doi: 10.1093/brain/124.5.1003.
5. Y. Nagai et al., "Epileptic Seizures are Reduced by Autonomic Biofeedback Therapy Through Enhancement of Fronto-limbic Connectivity: A Controlled Trial and Neuroimaging Study," EBioMedicine, vol. 27, p. 112, Jan. 2018, doi: 10.1016/J.EBIOM.2017.12.012.
6. I. Kotwas, A. McGonigal, S. Khalfa, M. Bastien-Toniazzo, F. Bartolomei, and J. A. Micoulaud-Franchi, "A case-control study of skin conductance biofeedback on seizure frequency and emotion regulation in drug-resistant temporal lobe epilepsy," International Journal of Psychophysiology, vol. 123, 2018, doi: 10.1016/j.ijpsycho.2017.10.005.
7. J. A. Micoulaud-Franchi et al., "Skin conductance biofeedback training in adults with drug-resistant temporal lobe epilepsy and stress-triggered seizures: A proof-of-concept study," Epilepsy and Behavior, vol. 41, 2014, doi: 10.1016/j.yebeh.2014.10.017.

8. Y. Nagai, L. H. Goldstein, P. B. C. Fenwick, and M. R. Trimble, “Clinical efficacy of galvanic skin response biofeedback training in reducing seizures in adult epilepsy: a preliminary randomized controlled study,” 2004, doi: 10.1016/j.yebeh.2003.12.003.
9. A. S. Dokumacı et al., “Simultaneous Optimization of MP2RAGE T1-weighted (UNI) and FLuid And White matter Suppression (FLAWS) brain images at 7T using Extended Phase Graph (EPG) Simulations,” Magn Reson Med, vol. 89, no. 3, 2023, doi: 10.1002/mrm.29479.
10. T. M. Tierney et al., “FIACH: A biophysical model for automatic

Poster No 1360

Spatial Frequency Maps in Human Visual Cortex: A Replication and Extension

Jiyeong Ha[1], William Broderick[2], Kendrick Kay[3], Jonathan Winawer[4]

[1]Department of Psychology, New York University, New York, NY, [2]Center for Computational Neuroscience, Flatiron Institute, New York, NY, [3]Center for Magnetic Resonance Research, Department of Radiology, University of Minnesota, Minneapolis, MN, [4]Department of Psychology, Center for Neural Science, New York University, New York, NY

Introduction: Neurons in primary visual cortex (V1) of non-human primates are tuned to different spatial scales, often quantified in terms of spatial frequency. This tuning is known to vary systematically, such that preferred spatial frequency decreases with eccentricity. fMRI studies in human have shown that spatial frequency tuning can be measured at the millimeter scale, showing the expected decline in preferred frequency with eccentricity. However, there is still wide variability in estimates of peak spatial frequency tuning across studies, with measures at a given eccentricity differing by up to four-fold, except for the two recent studies by Aghajari, Vinke, & Ling (2020) and Broderick, Simoncelli, & Winawer, (2022), which show good agreement. To better understand the discrepancies, it is crucial to investigate the reproducibility of spatial frequency maps obtained in previous studies using identical stimulus classes and analysis techniques. In this study, we aimed to replicate Broderick et al.’s results using an independent dataset. Furthermore, we extended the analyses of Broderick et al, which was limited to V1, to extrastriate maps (V2 and V3).

Methods: We applied the parameterized approach of Broderick et al. (2022) to model spatial frequency preferences, which fits all the voxels in an entire visual area simultaneously with a relatively small number of parameters. This enables compact characterization of spatial frequency tuning across all of V1 as a function of 4 attributes: stimulus spatial frequency, voxel eccentricity, stimulus orientation (absolute orientation), and stimulus orientation relative to voxel polar angle preference (relative orientation). For this replication and extension, we used an unreleased extension of the Natural Scenes Dataset (NSD) (Allen et al., 2020) in which fMRI responses to a set of log-polar grating stimuli similar to those used by Broderick et al. were measured in the NSD subjects. To assess the reproducibility of spatial frequency maps, we compared the final parameters estimated from NSD and the original study.

Results: Despite many experimental differences between Broderick et al and NSD, including field strength (3T vs 7T), number of stimulus presentations per observer (96 vs 32), and stimulus field of view (12° vs 4.2° maximal eccentricity), NSD dataset also showed good responses to scaled gratings (Fig. 1). Specifically, the data are well captured by log Gaussian tuning function and preferred spatial frequency exhibited a noticeable decrease with eccentricity. Notably, there was good agreement in most model parameters, capturing the dependency of preferred spatial frequency on voxel eccentricity. Moreover, the effect of absolute stimulus orientation on spatial frequency maps was similar: a higher spatial period for vertical and oblique orientations compared to horizontal and cardinal orientations in both studies. Lastly, we also found systematic changes with visual hierarchy. From V1 to V3, there was an increasingly large bandwidth in the voxel spatial frequency tuning functions.

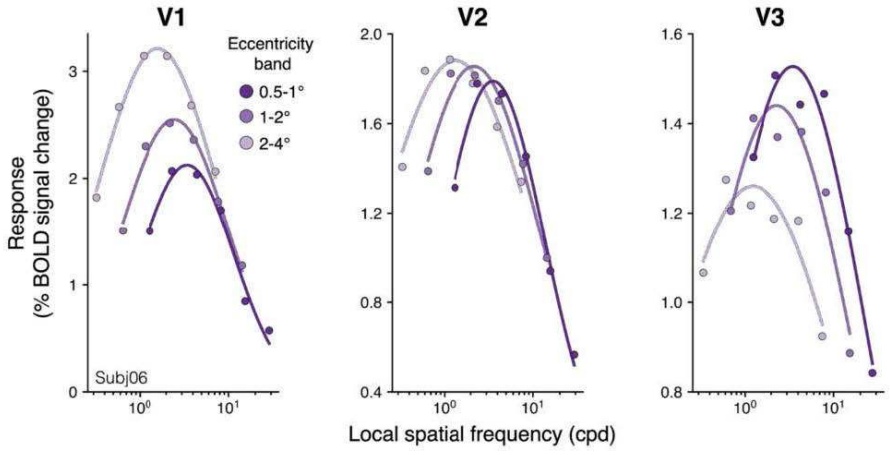

Conclusions: Using an independent dataset and the same parametric modeling approach, our results showed good agreement on spatial frequency preference maps in V1 with the two most recent studies (Fig. 2), and some systematic changes in spatial frequency representation between V1 and extrastriate areas. Together, our findings show robust reproducibility of visual fMRI experiments, and bring us closer to a systematic characterization of spatial encoding in the human visual system.

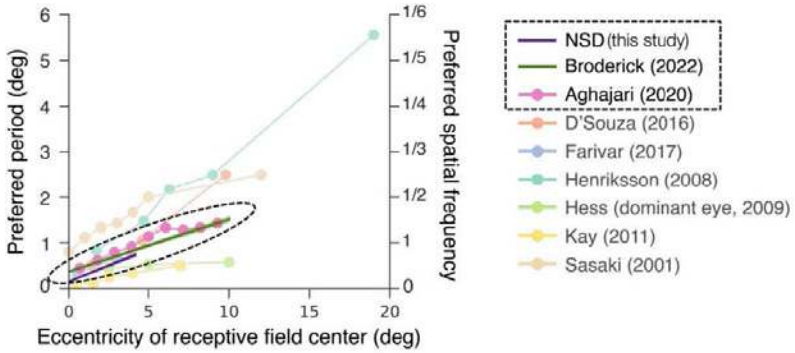

References

1. Aghajari, S., Vinke, L. N., & Ling, S. (2020). Population spatial frequency tuning in human early visual cortex. Journal of neurophysiology, 123(2), 773-785.
2. Allen, E. J., St-Yves, G., ... & Kay, K. (2022). A massive 7T fMRI dataset to bridge cognitive neuroscience and artificial intelligence. Nature neuroscience, 25(1), 116-126.
3. Broderick, W. F., Simoncelli, E. P., & Winawer, J. (2022). Mapping spatial frequency preferences across human primary visual cortex. Journal of vision, 22(4):3

Poster No 1361

Effects of phase-encoding on BOLD data with a positive control task

Céline Provins[1], Alexandre Cionca[1], Elodie Savary[1], Patric Hagmann[1], Oscar Esteban[1]

[1]Lausanne University Hospital and University of Lausanne, Lausanne, Switzerland

Introduction: Quality assessment and quality control (QA/QC) checkpoints layered throughout the dataflow are essential to ensure the reliability of neuroimaging analyses (Niso et al. 2022). In the case of functional MRI, best practices recommend collecting a 'positive control' task with which the different layers of QA/QC can be validated. These are short and simple tasks designed to elicit robust and precisely located brain activation patterns, permitting the diagnosis of potential issues in the workflow. Here, we examine how the phase-encoding direction (PE) choice in echo-planar imaging (EPI) blood-oxygen-level-dependent (BOLD) fMRI influences the resulting activation maps using a positive control task that includes visual and motor paradigms.

Methods: Data. 36 fMRI images were extracted from a dense sampling dataset, called the Human Connectome Phantom (HCPh), acquired as part of a registered report (Provins et al. 2023). A single male subject underwent repeated scans over four weeks. fMRI was acquired in a 3T Siemens Magnetom PrismaFit using a multi-echo EPI BOLD sequence varying PE across sessions in the four possible directions: anterior-posterior (AP), PA, left-right (LR), and RL. The echo times were TE=(12.60/33.04/53.48/73.92)ms. The other parameters, unchanged across sessions, were: 99 volumes with TR=1.6s, FA=64°, 2.2×2.2×2.2[mm3] resolution, distance factor 0%, 60 slices, 96×96 matrix, FOV=211mm, GRAPPA factor 2, SMS factor 4. Task. Our quality control task (QCT), implemented with PsychoPy (Peirce et al. 2019), was adapted from the 'eye-movement' variant of the tasks proposed by (Harvey et al. 2018). It consists of four paradigms: a central fixation dot (blank), gaze movement, visual grating patterns, and a finger-tapping (left/right) block. The presentation order and realization of these paradigms (e.g. the coordinates in the gaze movement and the hand in fingertapping) were randomized. Preprocessing. Data were preprocessed with fMRIPrep (Esteban et al. 2019) and further denoised by regressing out the 6 motion parameters, the WM and CSF mean signal, censoring frames with a framewise displacement above 0.4mm and smoothed to an estimated 4mm Gaussian kernel. No susceptibility distortion correction was applied to preserve the impact of different PE directions. Four QCT fMRI scans were excluded, three due to failed fMRIPrep runs and one for incorrectly defined events. Task activation analysis. We used an event-based first-level model to estimate which voxels are significantly active during the tasks. Second-level models were then constructed using PE as confounds. The models were implemented with nilearn ("Nilearn" 2023). Data & code availability. The HCPh dataset and the fMRIPrep derivatives will be publicly released with the Stage 2 culmination of the corresponding registered report. The task implementation is openly available at https://github.com/TheAxonLab/HCPh-

fMRI-tasks. Our analysis is openly available as an educational notebook at https://www.axonlab.org/hcph-sops/analysis/qct-activation/.

Results: Our QCT produces precisely-located brain activations. Confirming that the responses align with the expected activations is an integral component of the quality control protocol for our HCPh project (Figure 1). Different PE caused activation disparities beyond susceptibility distortion-prone areas. We constrasted several pairs of PE and report the most relevant one in Figure 2. The latter highlights significant differences in fingertapping-induced activation within a segment of the primary motor cortex, a region that is usually not considered impacted by susceptibility distortion.

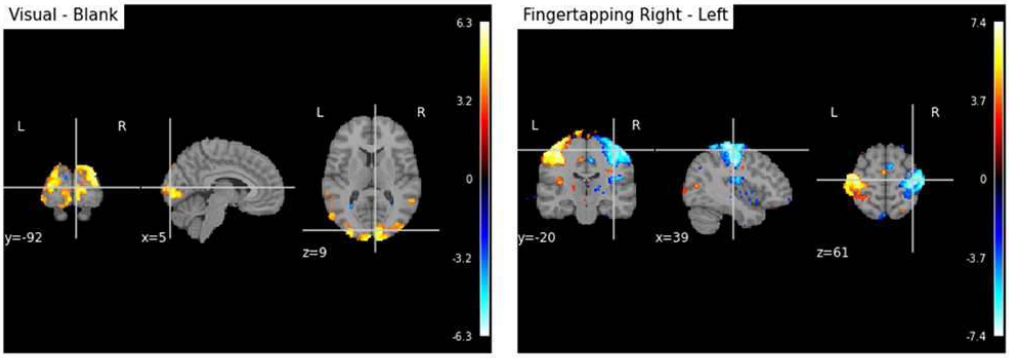

Figure 1. Brain activations elicited by our QCT are precisely-located and correspond to the expected responses. The visual grating patterns clearly activate the visual cortex in the occipital lobe. The fact that fingertapping activates the contralateral primary motor cortex is evident. These task activation maps are obtained using a second-level GLM with all the PE directions contrasting the tasks as indicated in the legend. The statistical maps were controlled for false discovery rate with alpha=0.05.

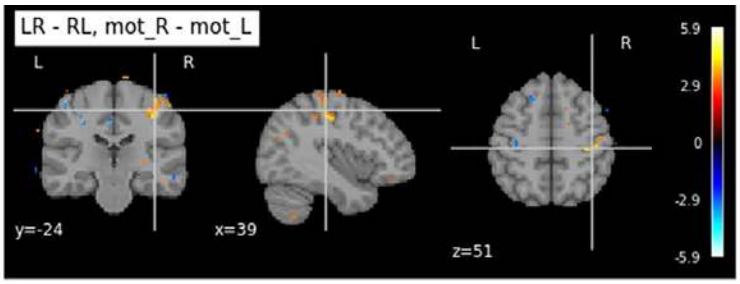

Figure 2. The change of PE direction induced significant differences in brain activations. The cortex segment with distinct fingertapping activation is distant from ear cavities and sinuses. Typically considered unaffected by susceptibility distortion, this region unexpectedly shows a significant impact of the PE direction. This statistical map corresponds to a second-level GLM contrasting LR and RL PE directions on the second level and right versus left-hand fingertapping on the first level. The statistical maps were controlled for false discovery rate with alpha=0.5.

Conclusions: Quality control tasks, acquired in just a few minutes, can easily be integrated into any acquisition protocol, serving as a potent tool to assess the integrity of analysis workflows. We showcased its potential by examining how PE affects task activation maps. Next steps include inspecting maps in subject space and further interpreting the differences among PE directions.

References

1. Esteban, Oscar, Christopher J. Markiewicz, Ross W. Blair, Craig A. Moodie, A. Ilkay Isik, Asier Erramuzpe, James D. Kent, et al. 2019. "fMRIPrep: A Robust Preprocessing Pipeline for Functional MRI." Nature Methods 16 (1): 111–16. https://doi.org/10.1038/s41592-018-0235-4.
2. Harvey, Jessica-Lily, Lysia Demetriou, John McGonigle, and Matthew B. Wall. 2018. "A Short, Robust Brain Activation Control Task Optimised for Pharmacological fMRI Studies." PeerJ 6 (September): e5540. https://doi.org/10.7717/peerj.5540.
3. "Nilearn." 2023. https://doi.org/10.5281/zenodo.8397157.
4. Niso, Guiomar, Rotem Botvinik-Nezer, Stefan Appelhoff, Alejandro De La Vega, Oscar Esteban, Joset A. Etzel, Karolina Finc, et al. 2022. "Open and Reproducible Neuroimaging: From Study Inception to Publication." NeuroImage 263 (November): 119623. https://doi.org/10.1016/j.neuroimage.2022.119623.
5. Peirce, Jonathan, Jeremy R. Gray, Sol Simpson, Michael MacAskill, Richard Höchenberger, Hiroyuki Sogo, Erik Kastman, and Jonas Kristoffer Lindeløv. 2019. "PsychoPy2: Experiments in Behavior Made Easy." Behavior Research Methods 51 (1): 195–203. https://doi.org/10.3758/s13428-018-01193-y.
6. Provins, Céline, Yasser Alemán-Gómez, Eleonora Fornari, Benedetta Franceschiello, Hélène Lajous, William H. Thompson, Ileana Jelescu, Patric Hagmann, and Oscar Esteban. 2023. "Reliability Characterization of MRI Measurements for Analyses of Brain Networks on a Human Phantom." Nat. Methods (Stage 1 accepted-in-principle) https://doi.org/10.17605/OSF.IO/VAMQ6.

Poster No 1362

Functional localization of SMA through fMRI and OPM-MEG

Jeff Soldate[1], Lester Sands[1], Michelle Hampson[2], Pendleton Montague[1], Stephen LaConte[1]

[1]Virginia Tech, Roanoke, VA, [2]Yale University School of Medicine, New Haven, CT

Introduction: Neurofeedback tracking supplementary motor area (SMA) is a promising intervention for Tourette Syndrome, reducing symptom severity[1]. Localization of tic neural correlates to the functionally heterogeneous SMA is an important step in personalizing neurofeedback. Ideally tic production during neuroimaging could be used to set the target of interest, but sensitivity to motion in MRI makes this strategy difficult. OPM-MEG, offering similar spatial resolution to MRI at higher temporal resolution and with motion resistant, wearable sensor arrays, is an ideal imaging modality for such localization. As a nascent technology, it remain to be seen how similar functional localization results are between fMRI and OPM-MEG. This work examines localization of SMA in both modalities in four healthy participants, using a bi-manual tapping task.

Methods: Participants performed synchronized and poly-rhythmic bi-manual tapping. This task has been shown to differentially activate SMA between the two task conditions (synchronized and poly-rhythmic tapping)[2]. Tapping was visually paced by matching rotation speed of two wedges in either side of a central point (adapted from[3]). Synchronized trials demanded 2 Hz tapping from both hands while poly-rhythmic trials demanded 3 Hz tapping from the right hand and 2 Hz tapping from the left. In fMRI, we used 16, 30 second blocks divided evenly between both conditions. In MEG, we used 80, 8 second long trials divided evenly between conditions. MRI images were obtained at 3T using a single band EPI sequence (TR=2000ms, TE=30ms). MEG recordings were taken using a 22 channel array of 11 dual axis, zero field magnetometers at 1200 Hz[4] in a custom built magnetically shielded room[5]. Recordings were filtered for gamma band neural oscillation (14-30Hz), corrected for the influence of homogeneous fields, and source localized using a linearly constrained minimum variance beamformer implemented in MNE[6].

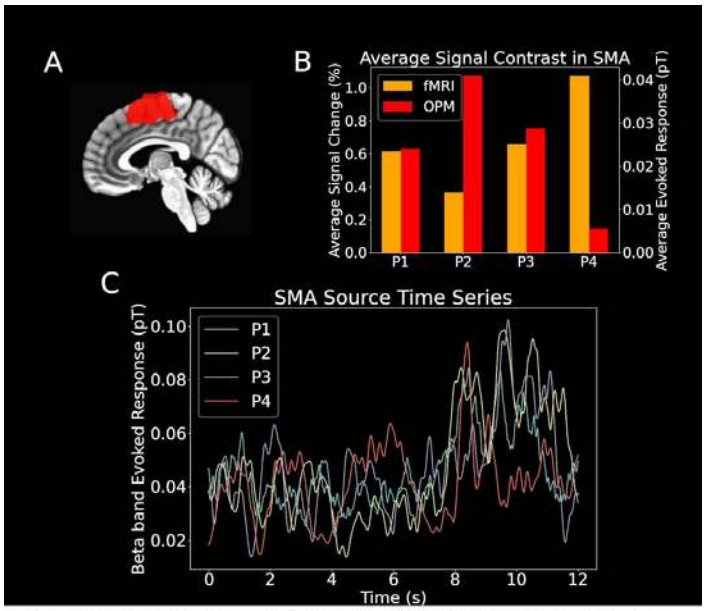

Figure 1: Part A shows SMA as defined by the Eichoff-Zilles macro labels atlas. Part B shows the average signal difference between poly-rhythmic tapping and synchroized tapping in selected voxels overlapping SMA. Part C shows sample time series for magnetic sources in SMA.

Results: Both tasks elicited difference in signal between poly-rhythmic and even tapping over SMA, as defined by the Eichoff-Zilles macro labels atlas[6]. Virtual electrodes from these clusters show a characteristic decrease in beta power during finger tapping and a rebound after cessation. Both methods showed significant clusters of active voxels overlapping with SMA, though the size and location of each cluster differed between neuroimaging method. Average deviation between active clusters (based on thresholds of $q \leq 0.0001$ and $z \geq 2.5$) was 23±9mm with the majority of disagreement in the Y (A-P) dimension. Both tasks saw increased activity during poly-rhythmic tapping over even tapping.

Conclusions: We were able to show localization of SMA within participant with a contrasting tapping task in both fMRI and OPM-MEG. OPM-MEG source localization remains a difficult problem, leading to varied and spatially dispersed regions of activity. This should decrease as the number of channels and density of sensor arrays increases. Overall, these results indicate OPM is able to identify spatial signal changes related to differing levels of SMA engagement in bi-manual finger tapping.

References

1. Sukhodolsky DG, Walsh C, Koller WN, Eilbott J, Rance M, Fulbright RK, Zhao Z, Bloch MH, King R, Leckman JF, Scheinost D, Pittman B, Hampson M. (2020), 'Randomized, Sham-Controlled Trial of Real-Time Functional Magnetic Resonance Imaging Neurofeedback for Tics in Adolescents With Tourette Syndrome', Society of Biological Psychiatry, 15;87(12):1063-1070
2. Ullén F, Forssberg H, Ehrsson HH. (2003), 'Neural networks for the coordination of the hands in time'. Journal of Neurophysiology. 89(2):1126-35
3. Klaiman E, Karniel A, (2006), 'Bimanual adaptation: internal representations of bimanual rhythmic movements', Experimental Brain Research, 171:204-14
4. Shah VK, Wakai RT, (2013), 'A compact, high performance atomic magnetometer for biomedical applications'. Physics in Medicine and Biology. 21;58(22):8153-61
5. Holmes, N., Rea, M., Chalmers, J. et al. (2022), 'A lightweight magnetically shielded room with active shielding'. Scientific Reports. 2022 12(13561)
6. Gramfort A, Luessi M, Larson E, Engemann DA, Strohmeier D, Brodbeck C, Goj R, Jas M, Brooks T, Parkkonen L, Hämäläinen M. (2013). 'MEG and EEG data analysis with MNE-Python'. Frontiers in Neuroscience 26;7:267
7. Eickhoff SB, Stephan KE, Mohlberg H, Grefkes C, Fink GR, Amunts K, Zilles K. (2005). 'A new SPM toolbox for combining probabilistic cytoarchitectonic maps and functional imaging data'. Neuroimage. 1;25(4):1325-35

Poster No 1363

Predicting Variance in Behaviour and Cognition from Task-Based fMRI-Derived Brain Networks

Maiya Rasheed[1], Zhangyu Yang[1], Kyle Mackenzie[1], Abhijit Chinchani[2], Luca Besso[3], Todd Woodward[1]

[1]University of British Columbia, Vancouver, British Columbia, [2]The University of British Columbia (UBC), Vancouver, British Columbia (BC), [3]The University of Manchester, Manchester, United Kingdom

Introduction: The field of neuroscience has been moving towards understanding behaviour and cognition by examining underlying brain activity. Beyond deepening the understanding of individual differences in these constructs, examining what brain activity relates to cognitive or behaviour traits unlocks important translational applications such as personalized neuromodulation. One way to examine brain activity is using fMRI measurements during task paradigms, where networks underlying the cognitive operations required to complete a task may be extracted (Percival et al., 2020). Task-based fMRI can provide precise brain activity parameters that describe hemodynamic activity in different networks over different phases of the task. Importantly, a supervised multivariate approach called iterative constrained principal component analysis (CPCA) may be used to derive fine relationships between brain activity and behaviour. Iterative CPCA provides benefits over traditional analyses. Rather than reducing many variables into a single summary score and restricting the analysis to only variance in one variable, CPCA includes all individual items for both sets of variables (Chinchani et al., 2021). In this study, we aimed to evaluate the relationship between brain activity in four task-based networks extracted from a social task from the human connectome project and measures of behaviour/cognition.

Methods: 1000 participants were included in this analysis. During the experiment, participants were presented with a short video (20 s) of objects either moving randomly or interacting socially, and had to respond with one of three options: 1) objects had a social interaction, 2) objects had no social interaction, or 3) unsure (Van Essen et al., 2013). fMRI-CPCA (Percival et al., 2020) was used to extract brain networks from fMRI variance related to task timing. Four components were found and classified as the auditory attention for response network, sustained attention network, re-evaluation network, and traditional default mode network. Features of each network's estimated hemodynamic response were extracted to describe brain activity (Figure 1). This project collected behavioural data such as demographics, emotions, personality, cognition, and task performance. The predictor variables were made up of the brain network parameters, while criterion variables were made up of behavioural data. First, variance in the criterions was constrained to what is explained by the predictors.(Hunter & Takane, 2011). Next, components were extracted to summarize overlap between the two sets of variables. Finally, rigorous split-half reliability and permutation testing were performed to determine specific, reliable relationships between items.

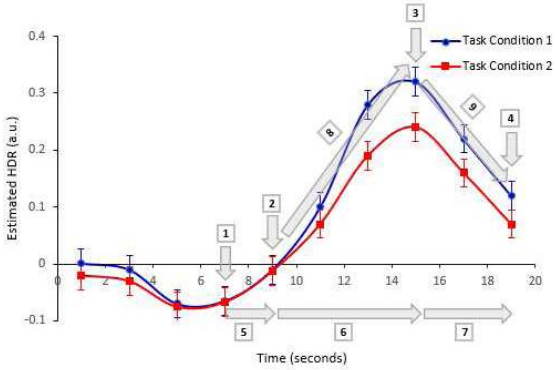

Figure 1. Sample hemodynamic response curve for one network with arrows pointing out the features quantified for the iterative CPCA analysis. 1) Subzero peak. 2) Start. 3) Peak. 4) End. 5) Decrease to suppress. 6) Start to peak. 7) Peak to end. 8) Beta weight start to peak. 9) Beta weight peak to end.

Results: Activity at the end of the trial in the sustained attention network, when participants watched videos denoting social interaction, was related to perceptions of social support (predictor loading=0.57, predictor loading reliability proportion=0.82, p=0.020). Specifically, perceptions of emotional (0.20) and instrumental support (0.15) were positively associated with this network activity, while perceptions of rejection (-0.19), loneliness (-0.13), and hostility (-0.18) were negatively associated with this network activity.

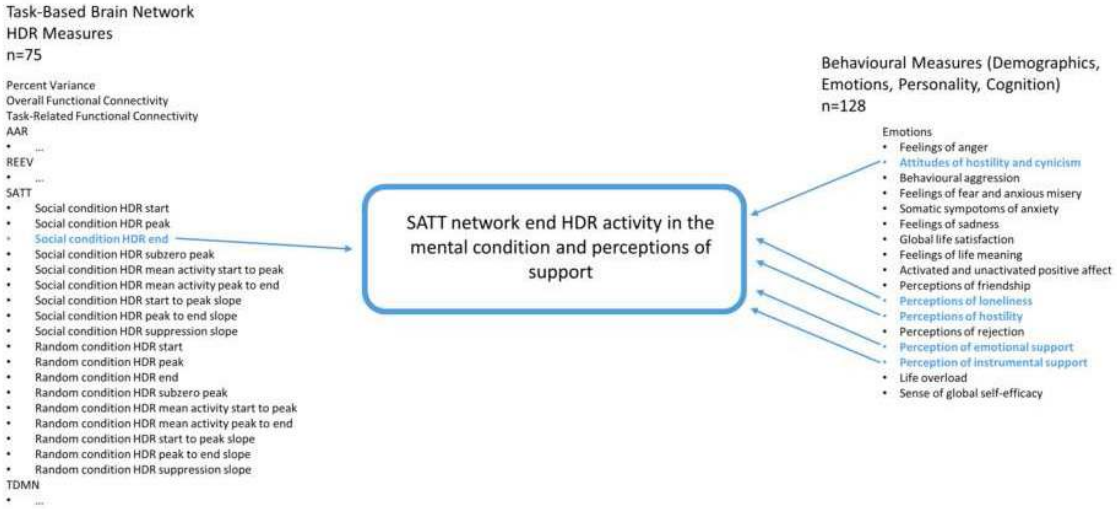

Figure 2. Diagram of the relationship between brain network hemodynamic response (HDR) parameters and behavioural data explored by iterative CPCA. Brain networks include the auditory attention for response network (AAR), re-evaluation network (REEV), sustained attention network (SATT), and traditional default mode network (TDMN).

Conclusions: In this study, we aimed to delineate fine relationships between two sets of variables describing brain activity and behaviour, specifically examining relationships between network variables extracted in a social cognition task and emotions. The association with end-trial activity in the sustained attention network in the social condition suggests that people who exhibit more hostile traits stop attending to social stimuli faster than people who have higher perceived social support. These findings shed light on the detailed interplay between brain activity and behavior, in particular, emphasizing the relevance of Theory of Mind in deciphering how individuals with varying social traits engage with and process social stimuli.

References

1. Percival, C. M. (2020). 'Set of task-based functional brain networks derived from averaging results of multiple fmri-cpca studies: CNoS-Lab/Woodward_Atlas'. Zenodo.
2. Chinchani, A. M. (2021). 'Item-specific overlap between hallucinatory experiences and cognition in the general population: A three-step multivariate analysis of international multi-site data'. Cortex, vol. 145, pp. 131-144. https://doi.org/10.1016/j.cortex.2021.08.014
3. Van Essen, D.C. (2013). 'The WU-Minn Human Connectome Project: An overview'. NeuroImage vol. 80, pp. 62-79.
4. Takane, Y., & Hunter, M. A. (2011). 'A new family of constrained principal component analysis (CPCA)'. Linear Algebra and its Applications, vol. 434, no. 12, pp. 2539-2555. https://doi.org/10.1016/j.laa.2011.01.002

Poster No 1364

The Hypothesis Race Model for evaluation of research findings

Robert Kelly[1], Matthew Hoptman[2]

[1]Weill Cornell Medicine, White Plains, NY, [2]Clinical Research Division, Nathan S. Kline Institute for Psychiatric Research, Orangeburg, NY

Introduction: Empirical results from individual research experiments are commonly evaluated with Null Hypothesis Significance Testing (NHST). The "replication crisis" refers to concerns that statistically significant findings derived from NHST often are not replicable. Benjamin et al. (2018) suggested that we "improve reproducibility" for "claims of new discoveries" by reducing the conventional α-level from 0.05 to 0.005, while increasing sample sizes to maintain study power. However, doing so can increase the total cost of "confirming" hypotheses over multiple studies. We demonstrate this problem using a Bayesian model called the Hypothesis Race Model (HRM, Fig. 1) for the case where many hypotheses are tested simultaneously, each with a small initial probability of being true. For this "Horse Race" scenario, cost-efficiency improves by reducing sample sizes and focusing testing on hypotheses that best progress toward "confirmation."

Methods: From Bayes' theorem R1 = BF1*R0, where R0 is the prior odds that our hypothesis is true (Ht; Hf if false), and R1 is the posterior odds that our hypothesis is true after obtaining the results, T1, of an experiment; and BF1 = P(T1 | Ht)/P(T1 | Hf). For the binary outcomes of statistically significant (+) or not (-), BF1+ = (1-β)/α, where 1-β is the power of the study and α, the α-level for statistical significance; and BF1- = β/(1-α). In the nonbinary approach, T1 is a measured continuous test statistic and P(T1 | Ht) and P(T1 | Hf) are the probability densities for obtaining T1 given Ht or Hf, respectively. Our illustrative "experiment": measuring tumor-cell reduction after exposure to a chemical in a petri dish, testing 10,000 chemicals, each with a 1/1000 chance of being a "winner," until we find 5 winners. Our 10,000 hypotheses were simulated with a database of candidate chemicals having effect sizes of Cohen's d=0, except for 10 cases with d = 0.2, 0.4 or 0.8 (the winners). We assessed statistical significance with one-tailed paired t-tests comparing to 0 the mean difference in number of cells in the petri dishes before and after exposure, with df=N-1, where N was the number of petri dishes in each sample. We recorded the total number of petri dishes required, over multiple trials with sample sizes of 5, 10, 20, 40, 80 or 160. A Monte Carlo simulation found the winners by repeatedly picking and testing a hypothesis with the highest R-value, confirming it as a winner when R > 100. A computer program generated the test statistic Tj (for the jth trial) that corresponded to a randomly selected point on the cumulative t-distribution with df=N-1, centered on d for the tested hypothesis. We conservatively estimated BFj for the binary HRM from the estimate d=de=0.2, calculating a fixed value of α for each N, such that the average distance traversed toward confirmation would be optimized (work not shown). The estimated value of β followed from the t-distribution corresponding to de=0.2. The nonbinary HRM followed the same pattern, except that α did not need to be specified. For each sample size, 500 iterations were performed, for the binary and non-binary applications. Mean values for total number of petri dishes needed were compared using two-tailed, unpaired t-tests, considering $p < 0.001$, uncorrected, statistically significant. Each of these 6 values were compared pairwise within each group (binary or nonbinary) and across groups for a total of 36 comparisons.

Results: Smaller trial sizes (N = 5, 10 or 20) were significantly more cost-effective in terms of total number of petri dishes needed than larger trial sizes (N = 40, 80 or 160) for both the binary and nonbinary HRM (Fig. 2). The percentage of incorrectly identified winners per iteration ranged from 0.04% to 0.68% for the 12 cases.

Conclusions: A Bayesian perspective that considers results from multiple trials can help to estimate and reduce costs of evaluating hypotheses through empirical testing.

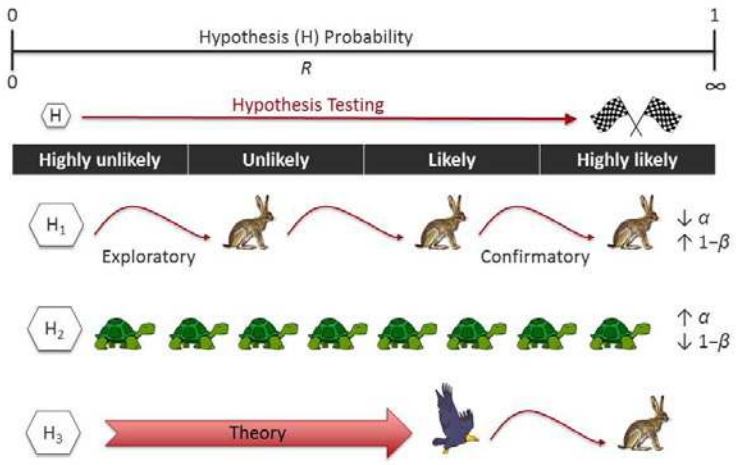

Fig. 1. The Hypothesis Race Model: A research hypothesis is "confirmed" when the combined weight of evidence from experimental trials moves the probability (or odds, *R*-value) that the hypothesis is true across the "finish line." Shown for hypotheses H_1-H_3 are the influences of alpha level (α), power ($1-\beta$) and the possible role of theory in making progress toward confirmation.

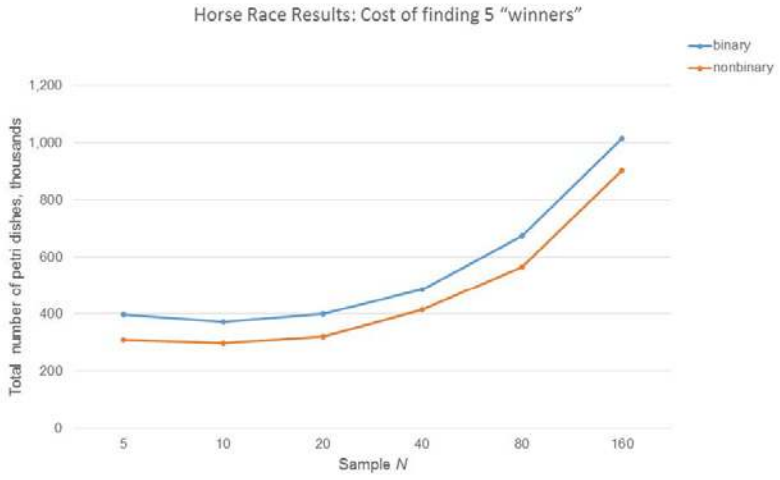

Fig. 2. "Horse Race" results, for the binary and nonbinary Hypothesis Race Models, showing the average total number of petri dishes needed to repeatedly test, with fixed sample size *N*, to find 5 chemicals that can reduce tumor cells ("winners"), from a field of 10,000 hypothesized viable chemotherapies, each with a 1/1000 chance of being a winner. This total cost was significantly lower for trials having only 5-20 petri dishes compared with larger trial sample sizes.

References

1. Aarts, A. A. et al (2015), 'Estimating the reproducibility of psychological science', Science, vol. 349, 6251.
2. Benjamin, D. J. et al (2018), 'Redefine statistical significance', Nature Human Behaviour, vol. 2, no. 1, pp. 6–10.
3. Ioannidis, J. P. A. (2005), 'Why Most Published Research Findings Are False', PLoS Medicine, vol. 2, no. 8, e124.
4. Kelly, R. E. & Hoptman, M. J. (2022), 'Replicability in Brain Imaging', Brain Sciences, vol. 12, no. 3, 397.
5. Wagenmakers, E. J. (2007), 'A practical solution to the pervasive problems of p values', Psychon Bull Rev, vol. 14, no. 5, pp. 779-804.

Poster No 1365

Scalable Gaussian Process Neural Network with application to Neuroimaging Data

Kan Keeratimahat[1], Thomas Nichols[2], Jian Kang[3]

[1]University of Oxford, Oxford, Oxfordshire, [2]University of Oxford, Oxford, United Kingdom, [3]University of Michigan, Ann Arbor, MI

Introduction: Scalar-on-image regression, modelling a univariate outcome per subject given image data, is a core machine learning task in neuroimaging but remains a challenge due to the high-dimensional, heterogeneous nature of the brain image data. While such prediction tasks must combine information from across the brain, conventional approaches neglect the complex spatial dependence and potential for nonlinear association. However, spatial Bayesian models do not necessarily

scale to biobank-sized datasets needed to detect subtle associations. Here we introduce a fast Bayesian model designed to address these issues.

Methods: We propose a Bayesian Gaussian Process-induced Neural Network (GPNN) that captures nonlinear associations while using spatial smoothness constraints[1] to establish a biologically plausible network structure. Specifically, we employ scalable approximate GPs with a modified squared exponential kernel, affording control over smoothness, concentration, and anchor points of each GP, allowing long-range, inter-regional dependencies in the association. While Bayesian approaches can be computationally intensive, our approach leverages low-rank basis functions and stochastic learning to handle large imaging datasets. Additionally, we employ Bayesian conjugate updates, eliminating the need for costly parameter grid searches while allowing the parameter distributions to adapt to the data. We propose three major architectures, each comprising a 1-layer fully-connected spatially-informed neural network: GPNN-GP-GP [Figure 1], GPNN-Linear-GP, and GPNN-GP-Linear. For instance, GPNN-Linear-GP denotes a GPNN with a linear connection in the input layer and a GP connection in the hidden layer. Additionally, we implement a scalable approximate posterior sampling method, Stochastic Gradient Langevin Dynamics[2] on the trained neural network to obtain the full posterior distribution for our parameters and their corresponding posterior predictive distributions. This equips our model with the capability to quantify the uncertainty of individual predictions, a desirable yet uncommon feature in regular machine learning techniques. We apply our method to predict Brain Age using T1-weighted structural images from the extensive UK Biobank dataset (where p >> 100,000 and n = 4,000). In this study, a brain atlas consisting of 12 grey-matter regions is employed as the spatial prior information.

Figure 1

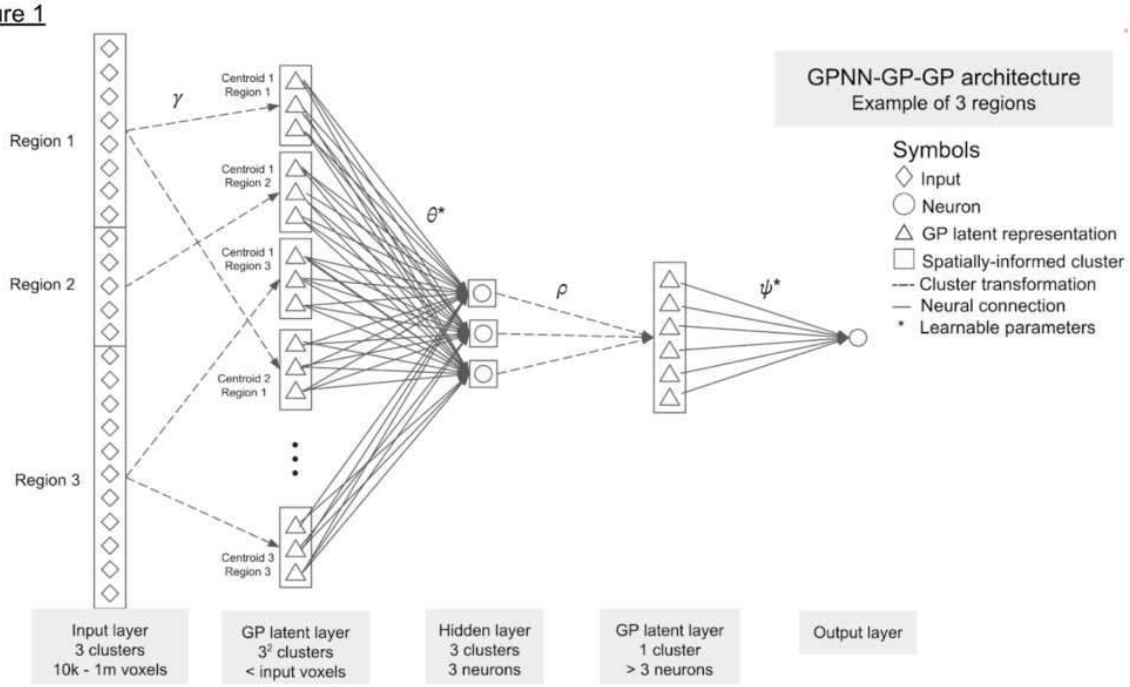

Figure 1: Visualisation of the proposed GPNN-GP-GP architecture. The example diagram illustrates a GPNN-GPGP architecture with 3 regions of interest.

Results: All the GPNN models have superior predictive accuracy relative to the GP Regression model, and in particular, the GPNN-Linear-GP outperforms Ridge and LASSO models as well [Figure 2a]. Additionally, the saliency obtained from GPNN reveals an interpretive model representation based on the incorporated spatial prior, distinguishing it from traditional methods. Specifically, the GPNN saliency maps are smooth, unlike Ridge or LASSO which lack such spatial structure [Figure 2b]. Furthermore, the adaptation of SGLD provides posterior predictive intervals, shown to be accurate relative to Metropolis-Hasting [Figure 2a].

Figure 2a

Model \ Metric	Optimisation: RMSE (train, test)	Optimisation: R-squared (train, test)	Optimisation: Total variables (non-zero)	Inference: $ECR_{95\%}$ (train, test)	Inference: Avg $PPI_{95\%}$ width (train, test) years	Inference: Run time
LASSO	3.34, 4.92	81.2%, 59.4%	628	*N/A*	*N/A*	*N/A*
Ridge	0.90, 4.59	98.6%, 64.6%	156,812	*N/A*	*N/A*	*N/A*
GPR	4.27, 5.47	69.2%, 49.9%	12,341	100%, 98.5%	4.9, 43.9	5 m
GPNN-GP-GP	2.92, 5.20	85.6%, 54.5%	21,548	-	-	-
GPNN-GP-Linear	3.39, 5.03	80.6%, 57.4%	21,277	-	-	-
GPNN-Linear-GP	0.00, 4.58	100%, 64.7%	157,096	99.0%, 94.8%	22.5, 24.7	15 h
MALA (MH)	*N/A*	*N/A*	*N/A*	97.5%, 95.7%	27.7, 27.9	26 h

Table 1: Optimisation and Inference performance of the tested models. *N/A* indicates that the model is not applicable to the specific assessment.
- $ECR_{95\%}$ is the Emipircal Coverage Rate constructed upon 95% Gaussian threshold.
- $PPI_{95\%}$ is the 95% Posterior Predictive Interval around the posterior mean of the predictions

Figure 2b

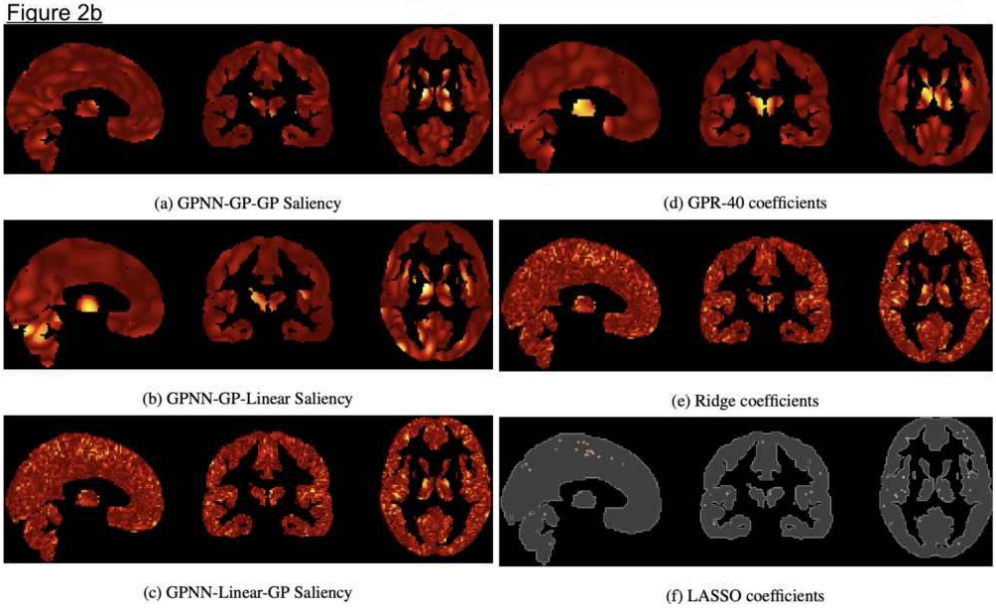

Figure 2a: Real data optimisation performances and posterior inference performances (median). Figure 2b: Absolute values of saliency (GPNN) and magnitude of fitted coefficients (regressions).

Conclusions: The proposed GPNN models demonstrate superior performance compared to traditional models, showcasing their potential for accurate and interpretable predictions. Notably, we found the GPNN-Linear-GP model to be the top-performing model. A limitation of our work is the long computation to train our network; however, in this initial work all computations were performed on a CPU, and substantial optimisations will be possible with a GPU implementation. In future work, we plan to extend the GPNN framework to incorporate multiple modalities of imaging data, as well as non-imaging data.

References

1. Kang, J. (2018). Scalar-on-image regression via the soft-thresholded gaussian process. Biometrika, 105(1):165–184.
2. Welling, M. (2011). Bayesian learning via stochastic gradient langevin dynamics. In Proceedings of the 28th international conference on machine learning (ICML-11), pages 681–688. Citeseer

Poster No 1366

Efficient Compression and Interpretation of Multimodal Data: Scalable Bayesian Factor Analysis

George Hutchings[1], Thomas Nichols[1], Chris Holmes[1], Habib Ganjgahi[1]

[1]*University of Oxford, Oxford, United Kingdom*

Introduction: There is growing interest in large-scale epidemiological studies, with both many individuals and many variables, and dimensionality reduction is an important tool for summarising the structure in these datasets. For example, the UK Biobank and NO.MS (Novartis-Oxford multiple sclerosis dataset, a longitudinal study involving 8000 individuals) include a diverse assortment of variables: from binary variables to brain images. This data, which is both high dimensional and includes discrete variables, provides challenges for existing methods like ICA and PCA, which are optimal for continuous (and even Gaussian) variables. Additionally, they only have heuristics for choosing the number of latent features. We propose an efficient data compression method, a Bayesian factor analysis which can handle high dimensional data, as well as dealing with mixed modality data and inferring the number of latent variables in a principled manner.

Methods: Our method utilizes a Bayesian model optimized through the variational EM algorithm (Fig 1). A sparsity-inducing spike & slab prior on the loading matrix promotes interpretable latent variables. Each element of the loading matrix follows a zero-mean normal distribution, with differing variances. Non-zero elements are assigned to the slab (with probability 1-w), have a large variance, while zero elements are assigned to the low variance spike (with probability w). Sparsity is induced through an Indian buffet process (IBP) prior on w, which also can shrink any unimportant latent variables to 0, inferring the number of latent features. To ensure scalability, our method utilizes a variational EM approach as opposed to more traditional MCMC which is prohibitive in high dimensions and can suffer from the label switching problem, a common issue arising from model unidentifiability. The approach maintains dependencies between variables, with only the factor scores and the continuous analogue of the discrete variables assumed to factorise. Other latent variables in the model are treated without factorisation, preserving their dependencies, this is unlike a purely mean-field approximation. For handling discrete variables, we incorporate a semiparametric Gaussian copula, providing a principled approach to address discrete data within the model.

Notation

$y_1,...,y_N$ observations of D variables

$Y_d = [[y_1]_d, ..., [y_N]_d]^\top,\ d \in \{1, ..., D\}$

C = Index set of all continuous dimensions $\subseteq \{1, ..., D\}$

$\Lambda \in \mathbb{R}^{D \times K}$ Loading matrix, with K latent factors

$Z_d \in \mathbb{R}^N$ Continuous analogue of Y_d

$\eta_n \in \mathbb{R}^N$

Hierarchical model

$Y_d = p(z_d \in D(Y_d))$ Copula (Murray-2013)

$Z_d = \mathcal{N}(Z_d|\eta\Lambda_d, \Psi_d I)$ For $d \notin C$

$Y_d = \mathcal{N}(Y_d|\eta\Lambda_d, \Psi_d I)$ For $d \in C$

$\Psi_d = I\mathcal{G}a(\Psi_d|10^{-6}, 10^{-6})$ Uninformative prior

$\eta_n = \mathcal{N}(\eta_n|0, I)$

$\Lambda_{dk} = \mathcal{N}(\eta_n|0, \tau^{-1}(1 - w_{dk})v_0 + w_{dk}v_1))$ Spike and slab variance

$\tau = \mathcal{G}a(\tau|10^{-6}, 10^{-6})$ Uninformative prior

$$w_{dk} = Ber\left(w_{dk}\middle|\prod_{i=1}^{k} u_i\right)$$

$u_k = U(u_k|0, 1)$

Figure 1

Results: The efficacy of our model is assessed with simulation studies and real data, with the noteworthy ones outlined below: Sim i) Data is simulated from loading matrix shown in fig 2a, of note is that the data is of higher dimensionality than the number of samples. The recovered loading matrix is in fig 2b. Sim ii) Binary data is simulated from loading matrix shown in fig 2c (binarized by thresholding the continuous data at 0), one should note that two latent dimensions share multiple covariates making this a challenging simulation. The recovered loading matrix is in fig 2d. One can see that in both cases the true loading matrix is recovered (the loading matrix is unidentifiable to permutation of columns) and in sim i the number of latent variables (non-zero columns) is shrunk to the true number. Additionally, we apply our method to the NO.MS clinical dataset which includes binary, count and continuous covariates, we obtain the structure of the loading matrix seen in fig 2e and 2f.

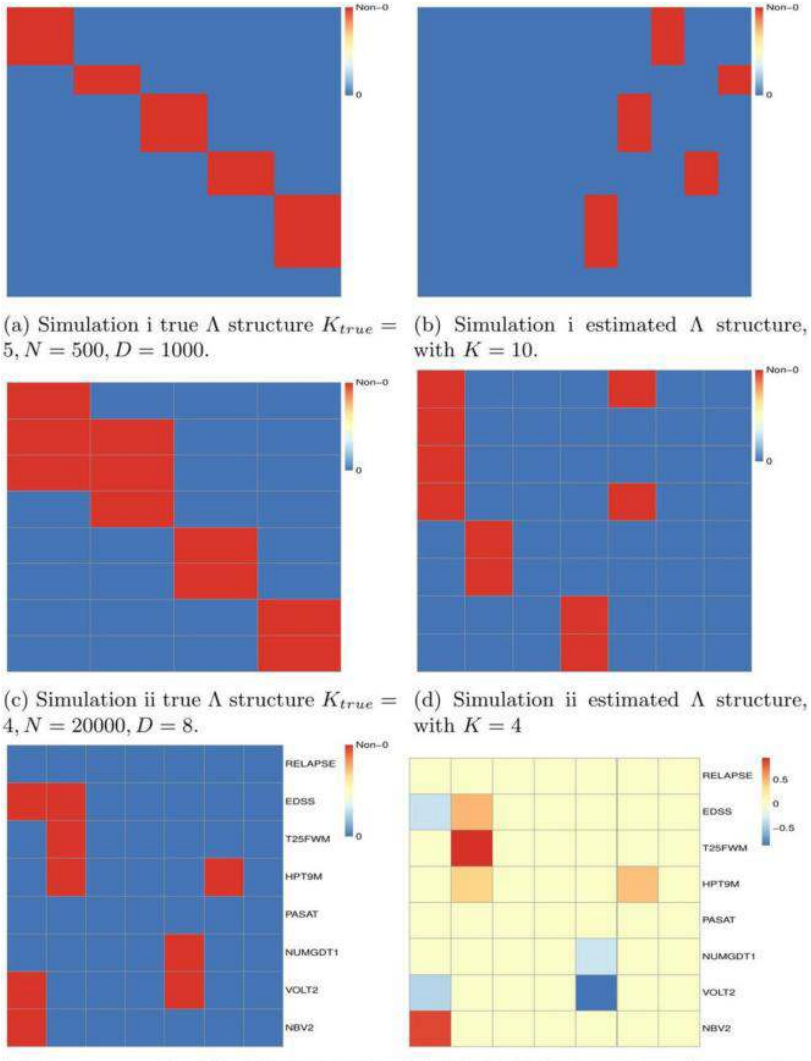

(a) Simulation i true Λ structure $K_{true} = 5, N = 500, D = 1000$.

(b) Simulation i estimated Λ structure, with $K = 10$.

(c) Simulation ii true Λ structure $K_{true} = 4, N = 20000, D = 8$.

(d) Simulation ii estimated Λ structure, with $K = 4$

(e) Λ structure for NO.MS clinical data $(D = 8, N \approx 6000)$.

(f) Λ for NO.MS clinical data $(D = 8, N \approx 6000)$.

The real data variables are respectively: Relapse (Y/N) (binary), EDSS (ordinal), Timed 25-foot walk (continous), Hand coordination (9HPT) (continuous), Cognition (PASAT) (count), Number of Gd+ T1 lesions (count), T2 lesion volume (continuous), Normalized brain volume (continuous).

Figure 2

Conclusions: We propose a scalable factor analysis method designed to handle the complexities of large-scale epidemiological studies, and imaging data. The method efficiently compresses high-dimensional, mixed modality data, using an approach inspired by probabilistic PCA. The method is then evaluated in several simulation studies and on real data.

References

1. Murray, J. S., Dunson, D. B., Carin, L., & Lucas, J. E. (2013). Bayesian Gaussian copula factor models for mixed data. Journal of the American Statistical Association, 108(502), 656-665.
2. Ročková, V., & George, E. I. (2018). The spike-and-slab lasso. Journal of the American Statistical Association, 113(521), 431-444.
3. Ročková, V., & George, E. I. (2016). Fast Bayesian factor analysis via automatic rotations to sparsity. Journal of the American Statistical Association, 111(516), 1608-1622.

Poster No 1367

Structural-Spectral Dynamic Causal Modelling for Resting-State fMRI

Matthew Greaves[1], Leonardo Novelli[2], Adeel Razi[3]

[1]Monash University, Melbourne, Victoria, [2]Monash University, Clayton, Victoria, [3]Monash University, Melbourne, Australia

Introduction: We introduce a new dynamic causal model (DCM) for resting-state functional MRI (fMRI) that utilises structural connectivity to characterise power spectra of endogenous neuronal fluctuations. Research indicates a relationship between

a brain region's structural connections (i.e., its degree) and the power spectrum of its neuronal activity, typically exhibiting a power-law (scale-free) distribution (Baria et al., 2013; Fallon et al., 2020; Lee & Xue, 2017). Regions with a higher degree exhibit higher power at lower frequencies (i.e., predominant slower fluctuations), which may be due to the role hubs play in coordinating widespread activity across the brain (He, 2014; He et al., 2010). Noting this relationship, we introduce a biologically plausible generative model in which the structural connectivity degree of each brain region characterises the power spectrum of its (random) neuronal fluctuations.

Methods: Spectral DCM models neuronal (state) noise with generic 1/f spectra, which characterises fluctuations in systems that are at a nonequilibrium steady state (Friston et al., 2014). Spectral DCM parameterises neuronal fluctuations using a power-law form for their power spectra. Under this model, amplitude and exponent parameters control the shape of these power spectra. In the proposed generative model, we provide a new forward model for spectral DCM that utilises the structural connectome. In this model, the degree of each brain region's (normalised) structural connectivity is assumed to have a linear mapping with the exponent parameter of the power spectra. To provide face validation of the proposed structural-spectral DCM, we performed both in silico and empirical illustrations involving a cortico-subcortical effective connectivity network. Thus, we evaluated the performance of the structural-spectral DCM in capturing ground-truth effective connectivity and in describing effective connectivity in a network with substantial interregional differences in terms of the power of low frequency fluctuations (Fallon et al., 2020; He et al., 2010).

Results: The in silico analyses showed that new structural-spectral DCM was superior in capturing the power spectra of intrinsic neural fluctuations, as compared to the conventional spectral DCM. The model successfully identified hub regions and their associated lower frequency fluctuations, agreeing with the existing evidence about brain network dynamics (e.g., Baria et al., 2013; Fallon et al., 2020). Likewise, this approach was more accurate than spectral DCM in recovering ground-truth effective connectivity. The empirical illustration demonstrated higher model-evidence for the new DCM relative to the spectral DCM.

Conclusions: The structural-spectral DCM introduced here represents an important advance in characterising endogenous neuronal activity by furnishing a biologically-plausible generative model of their (structurally-informed) power spectra. Although previous research has integrated structural connectivity into DCM via the introduction of empirical priors (e.g., Sokolov et al., 2019, 2020; Stephan et al., 2009), the proposed DCM gracefully fused structural connectivity into the generative model. The mechanistic understanding of how structure shapes the intrinsic functional dynamics afforded by this new DCM will have broad implications for probing pathophysiology of various brain disorders in which power spectra of neural activity is altered (e.g., Trakoshis et al., 2020).

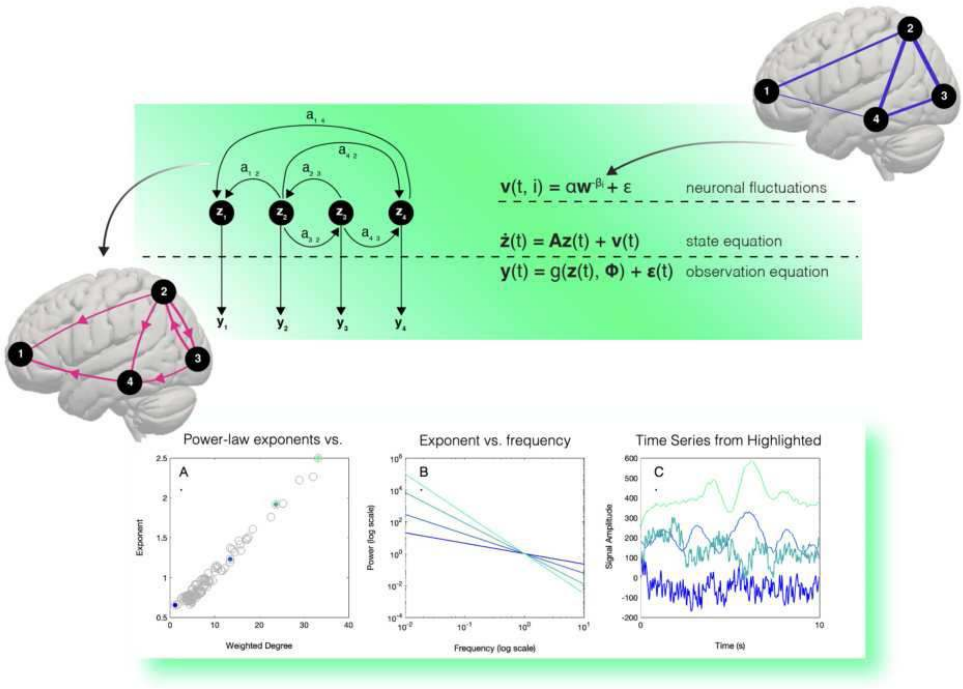

Illustration of the structural-spectral dynamic causal modelling approach. The top panel displays the generative model comprising the state and observation equations. The neuronal fluctuations are modelled as a power-law function of (angular) frequency (w) with a fixed amplitude (α) and a region-specific power-law exponent (βᵢ) as a free parameter which is modelled as a function of the degree of structural connections. On the right, a purple, undirected graph highlights the structural connectivity between four regions in a toy network. On the left, a pink, directed graph highlights the inferred effective connectivity for this network. Among the lowermost panels, panel A depicts the linear relationship between power-law exponents and the weighted degree of a synthetic connectome. Panel B represents the relationship between the exponents of power spectra and frequency, showing how the power spectra of intrinsic fluctuations is influenced by this power-law exponent. Panel C shows representative synthetic time series from the highlighted brain regions corresponding to different parametrisations of intrinsic fluctuations.

References
1. Baria, A. T. (2013). Linking human brain local activity fluctuations to structural and functional network architectures. NeuroImage, 73, 144–155. https://doi.org/10.1016/j.neuroimage.2013.01.072
2. Fallon, J. (2020). Timescales of spontaneous fMRI fluctuations relate to structural connectivity in the brain. Network Neuroscience, 4(3), 788–806. https://doi.org/10.1162/netn_a_00151
3. Friston, K. J. (2014). A DCM for resting state fMRI. NeuroImage, 94, 396–407. https://doi.org/10.1016/j.neuroimage.2013.12.009
4. He, B. J. (2014). Scale-free brain activity: Past, present, and future. Trends in Cognitive Sciences, 18(9), 480–487. https://doi.org/10.1016/j.tics.2014.04.003
5. He, B. J. (2010). The Temporal Structures and Functional Significance of Scale-free Brain Activity. Neuron, 66(3), 353–369. https://doi.org/10.1016/j.neuron.2010.04.020
6. Lee, T.-W. (2017). Linking graph features of anatomical architecture to regional brain activity: A multi-modal MRI study. Neuroscience Letters, 651, 123–127. https://doi.org/10.1016/j.neulet.2017.05.005
7. Sokolov, A. A. (2019). Linking structural and effective brain connectivity: Structurally informed Parametric Empirical Bayes (si-PEB). Brain Structure and Function, 224(1), 205–217. https://doi.org/10.1007/s00429-018-1760-8
8. Sokolov, A. A. (2020). Asymmetric high-order anatomical brain connectivity sculpts effective connectivity. Network Neuroscience, 4(3), 871–890. https://doi.org/10.1162/netn_a_00150
9. Stephan, K. E. (2009). Tractography-based priors for dynamic causal models. NeuroImage, 47(4), 1628–1638. https://doi.org/10.1016/j.neuroimage.2009.05.096
10. Trakoshis, S. (2020). Intrinsic excitation-inhibition imbalance affects medial prefrontal cortex differently in autistic men versus women. eLife, 9, e55684. https://doi.org/10.7554/eLife.55684

Poster No 1368

Validation of a dynamic causal model of NMDA receptors: sensitivity and parameter recovery analysis

Nikola Jajcay[1], Jakob Heinzle[2], Jiří Horáček[3], Klaas Stephan[2]

[1]National Institute of Mental Health, Klecany, Czech Republic, [2]Translational Neuromodeling Unit (TNU), University of Zurich & ETH Zurich, Zurich, Zurich, [3]National Institute of Mental Health, Klecany, Česká republika

Introduction: The NMDA receptor is essential for controlling synaptic plasticity and mediating learning and memory functions. Furthermore, its hypofunction may be one of the pathophysiological mechanisms of schizophrenia. To study dysfunctions in NMDA signalling, one can employ dynamic causal models (DCMs) that utilize mathematical models of neural ensembles to predict fluctuations in synaptic currents and their influence on postsynaptic potentials. DCMs allow us to infer the most likely parameters that generated brain activity. Before using such models to profile NMDA receptor (dys)function in actual data, we conducted a full model validation, including sensitivity and parameter recovery analyses, to explore the validity, identifiability, and robustness of various neurobiological model definitions and parameters.

Methods: DCMs are generative models representing the joint probability of data and model parameters. It is possible to "invert" the model and infer the posterior distribution of the parameters given the measured data. DCMs for EEG data consist of three modelling layers: the first layer models the average population membrane potential, the second layer models populations grouped into a single source, and the final layer represents a collection of sources. This work focuses on the first two layers and explores neural and noise sensitivity and parameter recoverability. We utilise the variance-based method for the parameter sensitivity analyses by computing Sobol indices, whereas for parameter recovery analysis, we sample model parameters from the prior and run the variational inference to check and compare posterior estimates. Here, we investigate a conductance-based DCM with two sources consisting of a canonical microcircuit. Finally, we formulate the problem in a Fourier domain by transforming the simulated data into cross-spectral densities (CSD) as a preparatory step for using the validated model on resting-state data.

Results: We first explored the effect of neuronal, noise and connectivity parameters on the simulated CSD using one-at-a-time prior sampling, where we estimated the CSD variance and then estimated Sobol indices using a generalised chaos polynomial estimator. Most parameters affect only the amplitude of the CSD but cannot shift the frequency peaks. The notable differences are the firing rate variance, GABA time scale, and some within-source excitatory connections. The parameters with the strongest influence on the CSD are background input, GABA synaptic time scale, magnesium block sensitivity, noise amplitude, and noise colour. The Sobol sensitivity analysis in the first order showed that the effect of these parameters varies by frequency and that the most substantial effect in the low frequencies (theta and below) is due to the background input and noise parameters. In contrast, the higher frequencies (alpha and low beta) are governed by the magnesium block parameters, thus directly relating to the NMDA signalling. Finally, the parameter recovery analysis suggests relatively high recoverability of neural parameters (such as background input and synaptic time scales). At the same time, the model struggled to recover noise parameters (correlation between sampled value from the prior and MAP posterior estimate around 0.2 for noise magnitude and 0.5 for noise colour).

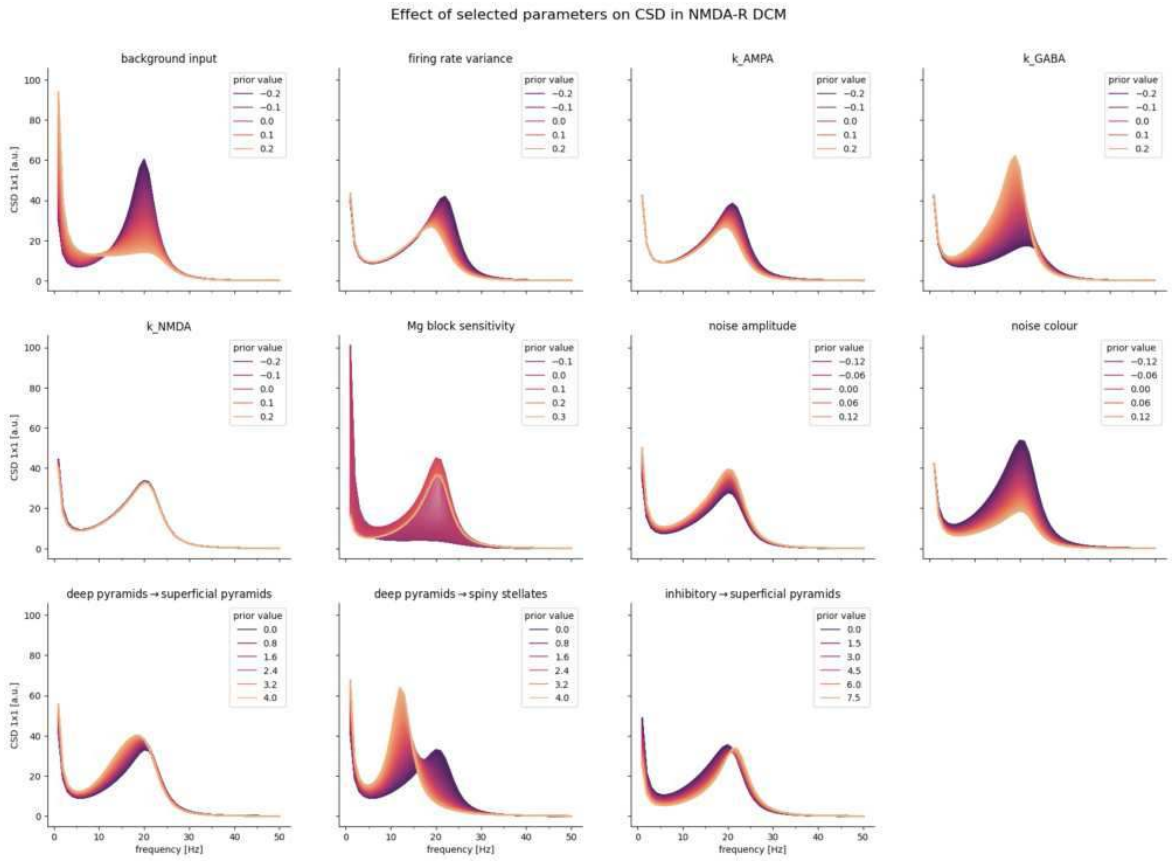

Fig. Exploration of effects of selected parameters on the CSD in NMDA-R DCM model. The values for each parameter were sampled from their default prior with twice the variance.

Conclusions: We have started a methodological sensitivity, parameter recovery, and robustness analysis of the conductance-based DCM. In the next step, we plan to examine parameter interactions more closely via n-order Sobol indices, although our preliminary results suggest that most parameters are orthogonal and second-order Sobol indices are generally relatively low. Finally, we plan to finish our model validation with prior and posterior predictive checks to compare with data of the animal pharmacological model of the NMDA antagonist, ketamine. This model validation is essential to arrive at a robust NMDA-R DCM model able to profile NMDA receptor (dys)functions.

References

1. Pereira, I., et al. (2021). Conductance-based dynamic causal modeling: A mathematical review of its application to cross-power spectral densities. NeuroImage, 245, 118662.
2. Symmonds, M., et al. (2018). Ion channels in EEG: isolating channel dysfunction in NMDA receptor antibody encephalitis. Brain, 141(6), 1691-1702.

Acknowledgements
This project has received funding from the European Union's Horizon Europe research and innovation programme under the Horizon WIDERA Talents grant agreement number 101090306.

Poster No 1369

Probabilistic Staging in Alzheimer's Disease with Deep Kernel Learning

Vasiliki Tassopoulou[1]

[1]*University of Pennsylvania, Philadelphia, PA*

Introduction: Machine learning (ML) can significantly enhance the process of subject stratification and selection in clinical trials, offering a more sophisticated and data-driven approach to these critical aspects of clinical research. In this work, we propose to learn a continuous temporal function of progression that describes the transition of subjects from several diagnosis stages. In Alzheimer's Disease (AD), we usually have clinical stages of Cognitive Normal (CN), Mild Cognitive Impairment (MCI) and finally AD. In this study, we use a deep kernel learning framework with temporal single-task Gaussian Processes to

learn the temporal function that describes the evolution of the clinical status. Our approach tailors the deep architecture to handle multimodal data including imaging, genomics and clinical information to learn a common embedding as the input to the Gaussian Process (GP) kernel.

Methods: Subjects scanned using the same scanner with more than four longitudinal MRI acquisitions from the Alzheimer's Disease Neuroimaging Initiative (ADNI) and Baltimore Longitudinal Study of Aging (BLSA) study cohorts were used for method development. T1 structural MRIs were preprocessed and segmented into 145 gray (GM) and white matter (WM) regions of interest (ROIs) using previously described methods[1]. Models were trained using 145 ROI volumes at baseline along with clinical covariates such as the Age at baseline, the Sex, the APOE4 Allele, cognitive status (CN, MCI or AD), and the number of years of education as features. The output of the model is the temporal function of the cognitive status. The learned temporal function is a function of the baseline acquisition of the subject, which means that on inference time, we need only the first scan of the subject so as to get the temporal function of the clinical status. Through the predictive posterior distribution we can obtain an estimate of the staging curve along with the uncertainty bands. Models were trained using 5-fold cross validation is applied in subject level, which indicates a leave-subjects-out validation scheme.

Results: In the first figure, we visualise the staging curve that is our model's output, along with the staging's uncertainty intervals. The red dashed lines are the critical points that indicate the progression from one stage to another. The 1 corresponds to the CN status, the 0 to the MCI and the -1 to AD. The critical threshold of 0.5 determines the progression from CN to AD, whereas the critical threshold -1 determine the progression from MCI to AD. In the first plot, we observe 6 test samples. The staging curve has been produced using only the baseline acquisition as input. In the plot, we visualize three stable subjects, one CN, one MCI and one AD, along with three converters to AD. In the stable subjects, we observe how the predicted staging curve remains stable. In the CN subject, the staging curve is above 1, on the MCI is between -0.5 and 0.5 and on the stable AD subject the test subjects that progress to AD. This plot showcases the potential of the model to predict staging curves. In the second plot, we calculate the correlation of the clinical biomarker with an imaging one,the SPARE-AD score[2], stratified based on the progression status. The CN stable have the smaller correlation with the SPARE-AD score, since the staging curve is stable and the SPARE-AD are noisy and we observse some variation. In the following progression status, the correlation increases and that indicates a positive relationship with the SPARE-AD score.

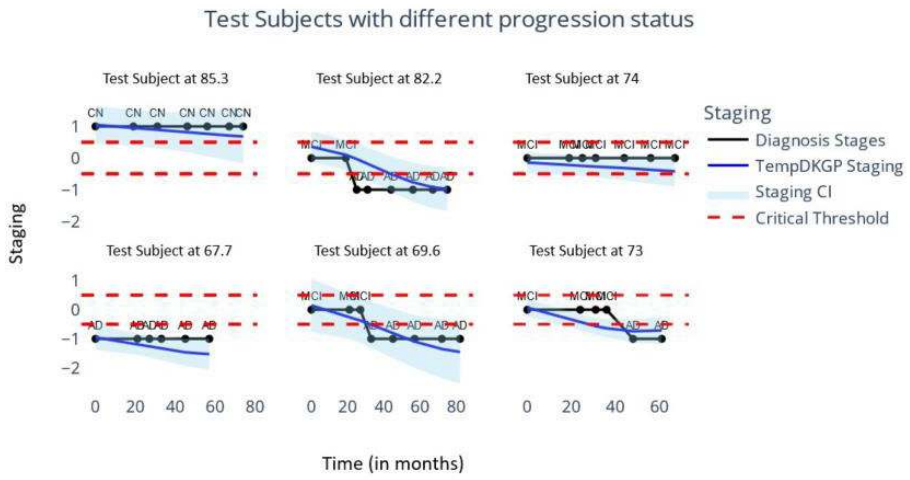

Conclusions: The two attached plots, showcase the potential of the Temporal Deep Kernel GP model to be used as a staging model for test subjects with only baseline acquisitions. Further validation, such as the correlation of the Staging Curve with other clinical variables, such as cognitive scores, is needed in order to prove further the validity of the produced staging curves. The work for further validating this model is part of our current and ongoing work.

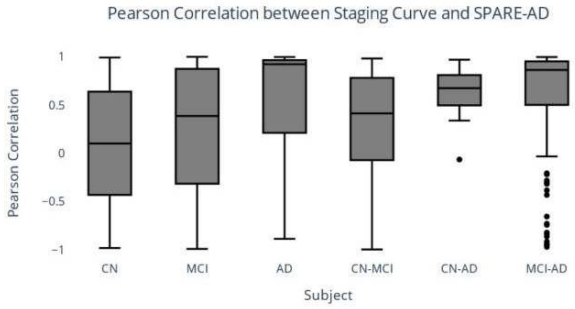

References
1. Sled, J. G., Zijdenbos, A. P., & Evans, A. C. (1998). A nonparametric method for automatic correction of intensity nonuniformity in MRI data. IEEE transactions on medical imaging, 17(1), 87–97. https://doi.org/10.1109/42.668698
2. Davatzikos, C., Xu, F., An, Y., Fan, Y., & Resnick, S. M. (2009). Longitudinal progression of Alzheimer's-like patterns of atrophy in normal older adults: the SPARE-AD index. Brain : a journal of neurology, 132(Pt 8), 2026–2035. https://doi.org/10.1093/brain/awp091

Poster No 1370

Structure in ongoing experience: extending Bayesian changepoint analysis for event segmentation

Elizabeth DuPre[1], Scott Linderman[1], Russell Poldrack[2]

[1]Stanford University, Stanford, CA, [2]Stanford University, Palo Alto, CA

Introduction: Unconstrained or "naturalistic" stimuli have become increasingly popular in computational cognitive neuroscience, demanding new methods to analyze minimally annotated data. Event segmentation-in which task or stimulus changes are inferred directly from neural data-is an important tool in this space. Commonly, segmentations are labeled using left-right Hidden Markov Models (lrHMM), as in Baldassano et al. (2017). Importantly, lrHMMs have been shown to successfully segment functional magnetic resonance imaging (fMRI) data into events that agree with human annotations, such as individual scenes in a film. Researchers can then examine how these segmentation boundaries differ across brain regions and experimental contexts. However, these models are trained on averaged subject-level fMRI data, obscuring inter-individual variability in the location of event boundaries. They also produce a single segmentation, limiting insight into the model's relative confidence in event boundaries.

Methods: Here, we jointly identify individual as well as consensus group-level event segmentations by extending existing work on Bayesian changepoint analysis (Fearnhead, 2006) to a hierarchical framework. That is, we jointly estimate changepoints for each individual subject, constrained by hierarchically-estimated group changepoints. This framework also enables us to make additional improvements on existing lrHMMs, such as identifying the model's relative confidence in a given segmentation versus other segmentations with differing numbers of changepoints. We are additionally able to allow individual voxels to exhibit unique variances, better matching the underlying fMRI signal. We showcase this model in the Sherlock dataset shared during the OHBM Naturalistic Data educational course (Chang et al., 2020) and previously collected by Chen and colleagues (Chen et al., 2017).

Results: Hierarchical Bayesian changepoint analysis reveals variability in event segmentations that is commonly missed in lrHMM analyses. In Figure 1, we show this variability at the group level, highlighting the relative confidence of the model for a range of changepoints (i.e., segmented events). We note that these segmentations still capture meaningful structure in the data, as shown in Figure 2 for an example segmentation. Our results also allow us to identify segmentation time courses for each individual in the training dataset, which has not been possible to date.

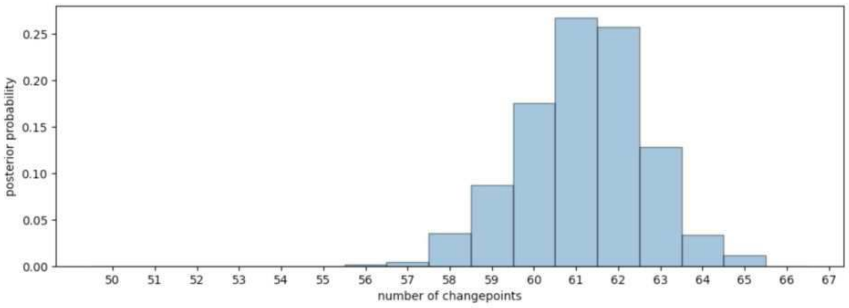

Figure 1. The posterior probability for the number of changepoints identified at the group-level analysis of eight subjects watching an episode of the series Sherlock. Each changepoint is a single boundary in the event segmentation. Here, 61 changepoints is identified as the most probable segmentation; however, other nearby values also show high-confidence.

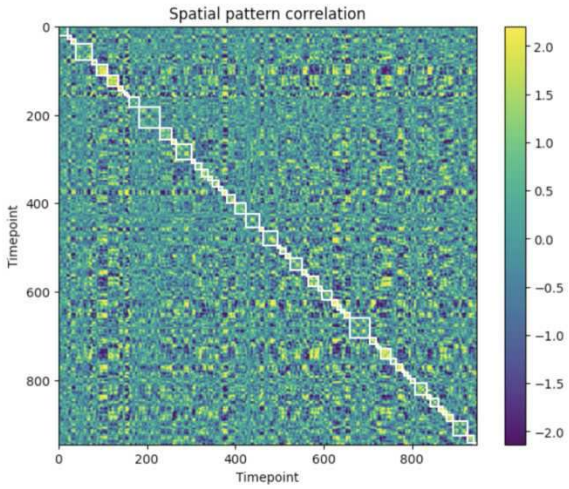

Figure 2. An example group-level event segmentation (depicted in white), overlaid on subject-averaged spatial pattern correlations over time. The segmentation matches visible structure in the data.

Conclusions: We expect this hierarchical Bayesian changepoint analysis implementation will be broadly useful in naturalistic neuroimaging, as well as in neural data recordings that show significant inter-session or inter-individual variability with limited annotations. This work will also be increasingly important in mapping individual differences in event segmentation and their changes in health and disease (Jafarpour et al., 2022).

References

1. Baldassano, C., (2017). Discovering Event Structure in Continuous Narrative Perception and Memory. Neuron, 95(3), 709–721.e5.
2. Chang, L., (2020). naturalistic-data-analysis/naturalistic_data_analysis: Version 1.0. https://doi.org/10.5281/zenodo.3937849
3. Chen, J., (2017). Shared memories reveal shared structure in neural activity across individuals. Nature Neuroscience, 20(1), 115–125.
4. Fearnhead, P. (2006). Exact and efficient Bayesian inference for multiple changepoint problems. Statistics and Computing, 16(2), 203–213.
5. Jafarpour, A., (2022). Event segmentation reveals working memory forgetting rate. iScience, 25(3), 103902.

Poster No 1371

Behavioural and brain activation differences in Hierarchical Bayesian Inference across Age

Vae Zhang[1], Wilson Lim[1], SH Annabel Chen[2]

[1]School of Social Sciences, Psychology, Nanyang Technological University Singapore, Singapore, Singapore, [2]School of Social Sciences, Psychology, Nanyang Technological University Singapore, Singapore

Introduction: Hierarchical causal relations underlie state changes in dynamic environments[1]. These relations could be encoded in the brain hierarchically[2,3] and optimal inference occurs via Bayesian estimation of the context of incoming sensory evidence[4]. The neural correlates of Hierarchical Bayesian Inference (HBI) and their changes across age are not well elucidated. Thus, we examined the neural encoding of HBI across age groups in a probabilistic task during an EEG recording (fig.1).

Methods: 30 older (age 55-72) and 30 younger adults (age21-34) were included in the analysis. Subject-wise HBI parameters were computed for each trial using the Hierarchical Gaussian Filter[4]. 64-channel EEG activity was preprocessed before computing each frequency band's relative power across epochs for all trials of each subject from different ROIs for the pre- and post-stimulus period (fig.1B). Correlations between HBI parameters and relative power were examined across trial types and age groups using linear models in R. All pairwise post-hoc comparisons were false discovery rate corrected.

Results: Older adults had lower sensory surprise ($p=0.002$), higher variances in their estimation of contextual rules($p<0.001$), and higher estimated variance in the mean rate of contextual changes ($p=0.015$) as compared to young adults. Before stimulus onset, a significant interaction between age group and trial type in the occipital region was found in the linear correlations between beta band power and sensory surprise. Opposite trends between younger and adults for these high-surprise trial correlations were significantly different (post-hoc $p = 0.031$). The linear correlation between beta power and estimated variance in sensory predictions was higher in high-surprise trials than in low-surprise trials in the parietal region ($p=0.021$). In the post-stimulus period, linear correlations between alpha band power and estimated variance in contextual

rules were significantly higher in low surprise trials as compared to high surprise trials in the parietal region (p=0.007). There was a significant interaction effect between age and trial type for the linear correlation between alpha power and subjects' estimates of the mean rate of change of context in the prestimulus period. The linear correlation between the two variables was significantly higher in younger adults for the high surprise trials compared to old adults in the central regions of the brain (post-hoc p=0.0025).

Conclusions: Hierarchical Bayesian modelling revealed that older adults may experience lower than necessary levels of sensory prediction errors which resulted in comparatively higher variances in the estimation of contextual contingencies and thus higher variance in the estimation of context volatility, as compared to younger adults. Specific neural hierarchies that might be responsible for encoding HBI were found, and changes in these hierarchies may have resulted in different uncertainty estimates across ages. Posterior beta power in the prestimulus period increased with prediction error and estimated variance in predictions which is consistent with its proposed role in signalling predictive expectancies[5,6]. This relationship was inverted in older adults which may explain why older adults experience lower sensory surprise. Alpha power is proposed to correlate both negatively and positively with stimulus uncertainty[7,8]. These differences may be resolved by looking at uncertainty from a hierarchical perspective. We found that the correlations between poststimulus parietal alpha power correlated negatively with estimated precision and update of contextual rules in high surprise trials, while central prestimulus alpha power correlated positively with context volatility which is a higher level of uncertainty. This was inverted for older adults in high surprise trials which could suggest poorer inhibition control in the central region.

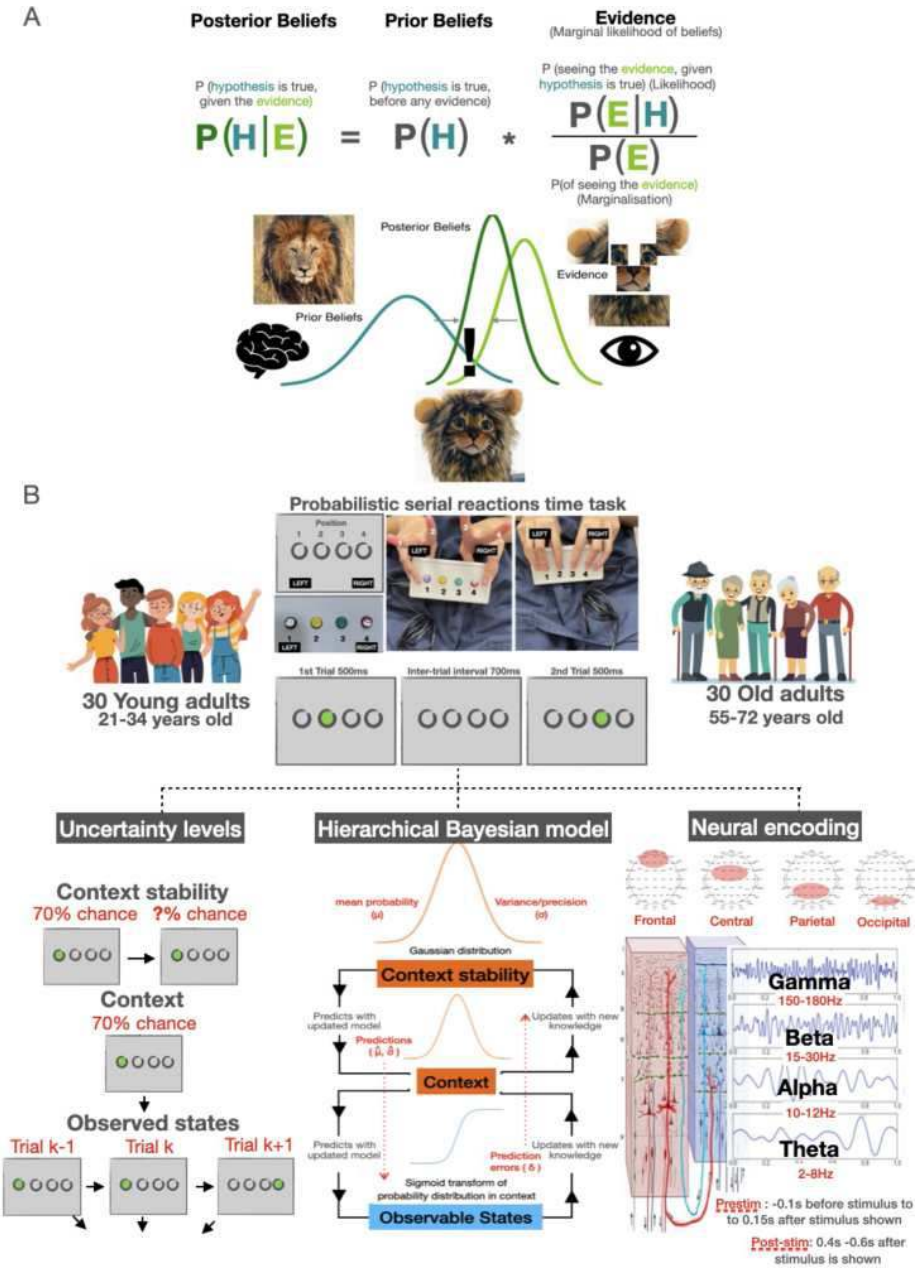

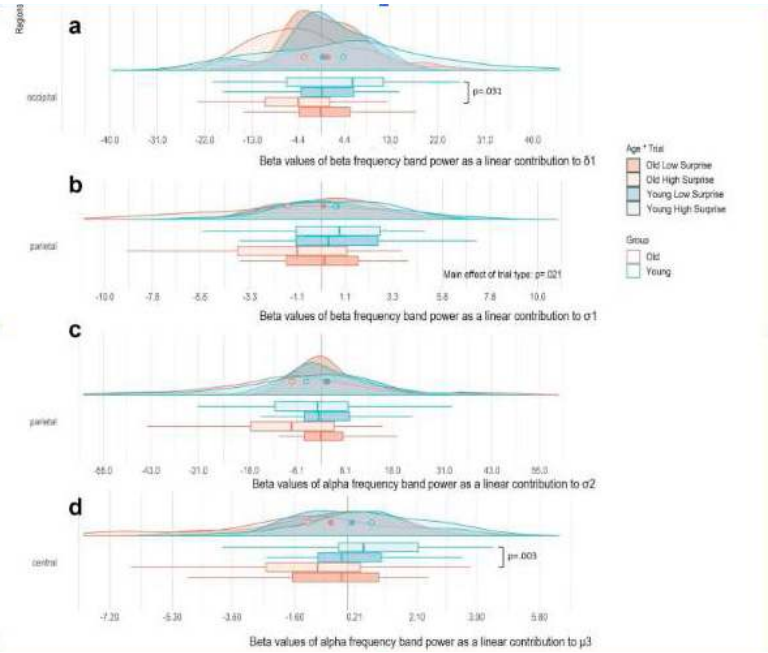

References

1. Marshall, L., Mathys, C., Ruge, D., De Berker, A. O., Dayan, P., Stephan, K. E., & Bestmann, S. (2016). Pharmacological fingerprints of contextual uncertainty. PLoS Biology, 14(11), e1002575.
2. Friston, K. (2008). Hierarchical models in the brain. PLoS computational biology, 4(11), e1000211.
3. Chao, Z. C., Huang, Y. T., & Wu, C. T. (2022). A quantitative model reveals a frequency ordering of prediction and prediction-error signals in the human brain. Communications Biology, 5(1), 1076.
4. Mathys, C., Daunizeau, J., Friston, K. J., & Stephan, K. E. (2011). A Bayesian foundation for individual learning under uncertainty. Frontiers in human neuroscience, 5
5. Fujioka, T., Trainor, L. J., Large, E. W., & Ross, B. (2009). Beta and gamma rhythms in human auditory cortex during musical beat processing. Annals of the New York Academy of Sciences, 1169(1), 89-92.
6. Arnal, L. H., & Giraud, A. L. (2012). Cortical oscillations and sensory predictions. Trends in cognitive sciences, 16(7), 390-398.
7. Darriba, Á., & Waszak, F. (2018). Predictions through evidence accumulation over time. Scientific Reports, 8(1), 494.
8. Kosciessa, J. Q., Lindenberger, U., & Garrett, D. D. (2021). Thalamocortical excitability modulation guides human perception under uncertainty. Nature Communications, 12(1), 2430.
9. Klimesch, W., Sauseng, P., & Hanslmayr, S. (2007). EEG alpha oscillations: the inhibition–timing hypothesis. Brain research reviews, 53(1), 63-88.

Poster No 1372

Influence of In-domain Pre-training on 3D Vision Transformer in Structural Neuroimaging Data

JiHoon Kim[1], Roshan Rane[2,3,4], Kerstin Ritter[2,3]

[1]Freie Universität Berlin, Department of Education and Psychology, Berlin, Germany, [2]Charité – Universitätsmedizin Berlin, Department of Psychiatry and Psychotherapy, Berlin, Germany, [3]Bernstein Center for Computational Neuroscience, Berlin, Germany, [4]Einstein Center for Neurosciences Berlin, Berlin, Germany

Introduction: Vision Transformer (ViT) is gaining attention for predictive modeling of associations between brain structure and phenotype in neuroimaging[1]. Adapting ViT to neuroimaging is challenging due to its data-hungry nature. This nature may bring a risk of overfitting, and poor generalization with limited data[2,3]. Transfer learning is crucial to overcome these challenges[4]. Two in-domain pre-trained models: one for sex classification and the other for age estimation, show promise in neuroimaging[5,6]. However, a systematic comparison of the impact of different kinds of pre-training on different phenotypes in diverse sample sizes is lacking. Therefore, we pre-train two in-domain pre-trained models and conduct a systematic comparison of the models in predicting different phenotypes across different sample sizes.

Methods: We use T1-weighted brain images from the UK Biobank dataset (N=36,598), subjected to minimal processing: skull stripping, bias correction, and Montreal Neurological Institute (MNI) template registration. Images are downsampled to 96x96x96 voxels. We utilize randomly initialized Vision Transformer (ViT) and 'DenseNet-121' Convolution Neural Network (CNN) models, referred to as Vanilla ViT and Vanilla CNN. We conduct two-stage experiments consisting of pre-training and fine-tuning stage (Figure 1). In the pre-training stage, we pre-train ViT models for sex classification (ViT w.SEX) and age

estimation (ViT w.AGE). In the fine-tuning stage, we perform three binary classification tasks: biological sex, chronological age group (68 – 82 vs. 44 – 61), and high vs. low alcohol use. Four models: ViT w.SEX, ViT w.AGE, Vanilla ViT, and Vanilla CNN are trained per task across sample sizes from 200 to 7,000. We evaluate model performance on a holdout set (N=3,055) using balanced accuracy (BACC). Lastly, we apply Chefer's feature visualization method to obtain ViT classification relevance feature values and overlay normalized mean values of true positive samples onto the MNI templates[7].

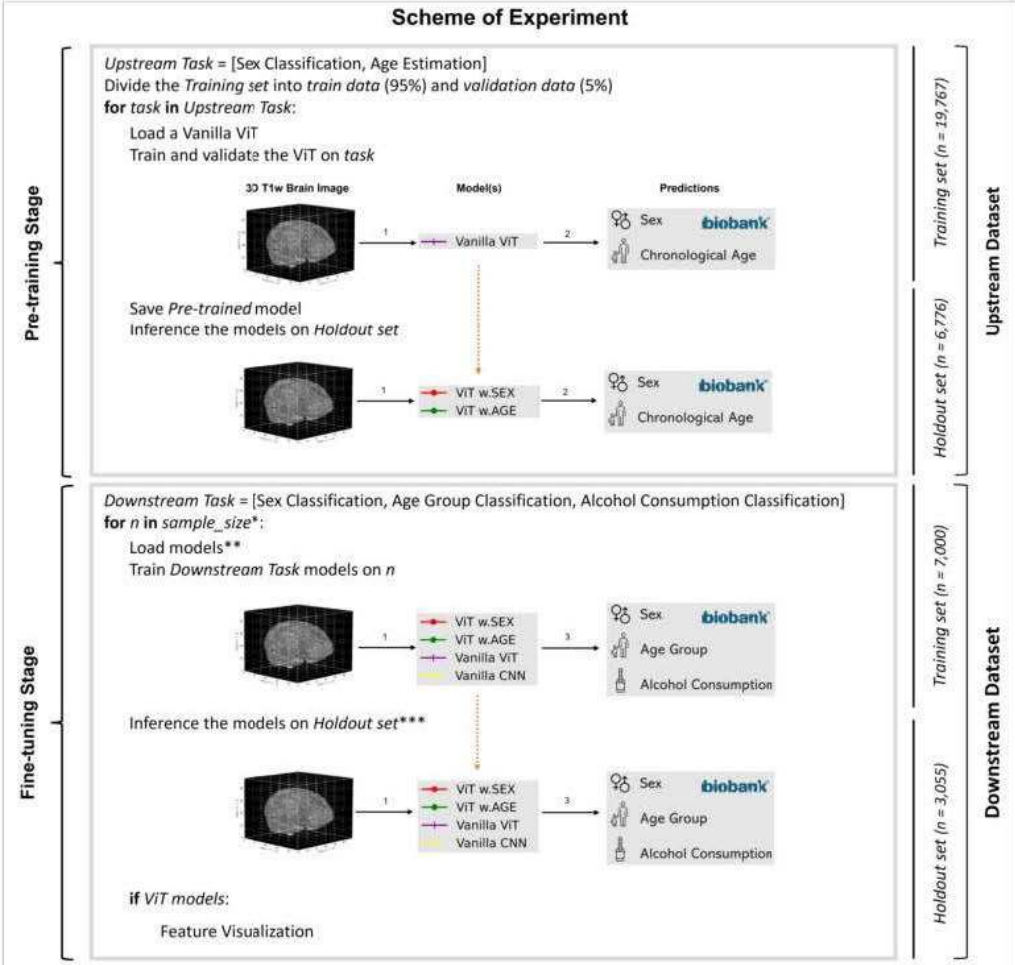

Figure 1: Scheme of Experiments. The diagram shows the *dataset* and *task* in the two stages.
dataset: subjects were categorized into four groups by two criteria: availability of alcohol consumption label and source of imaging. Subjects lacking labels are assigned to the upstream dataset for pretraining, and subjects with explicit labels are allocated to downstream datasets for finetuning. In each dataset, the holdout set had data only from Newcastle for testing, while the training set had data from Cheadle and Reading for model training.
task: model training uses batch size 20, binary cross entropy for classification, mean squared error for regression, and Adam optimizer with a learning rate of 3e-05, and execute pre-training for 20 epochs, followed by fine-tuning for 40 epochs. The model with the minimum loss is selected.
* 200, 500, 1,000, 2,000, 4,000, and 7,000. ** ViT w.SEX, ViT w.AGE, Vanilla ViT, and Vanilla CNN. *** For age group, the number of the Holdout set is 2,292.
T1w: T1-weighted, ViT w.SEX : ViT pretrained on sex classification, ViT w.AGE : ViT pretrained on age estimation, Vanilla ViT: Randomly initialized ViT, and Vanilla CNN: Randomly initialized Convolution Neural Network.

Results: After pre-training, ViT w.SEX achieved BACCs of 98.89% and 98.84%, and ViT w.AGE showed mean absolute errors of 2.94 and 2.88 in validation and holdout sets, respectively. Figure 2 (a) shows the model performance of three prediction tasks on the holdout set after fine-tuning. ViT w.SEX and ViT w.AGE outperformed other models in Sex and age group predictions, respectively. In alcohol consumption prediction, ViT w.SEX performed better than Vanilla ViT in small sample sizes (200 to 1,000). Also, ViT w.SEX reaches its best BACC of 61.53% in training size 7,000. We observed different feature importance patterns for each model. Within each model, patterns are consistent across varying training sizes. Figure 2 (b) shows the feature visualization of the high alcohol use in training size 7,000. Notably, Vanilla ViT and ViT w.SEX have common features but also ViT w.SEX highlighted brain stem, right cerebellum, left corpus callosum, and left midcingulate cortex regions, setting it apart from Vanilla ViT.

(a) Model Performance on Three Prediction Tasks

Prediction (Holdout Set N)	Model / Training Size	Balanced Accuracy of Different Training Sizes, along with their corresponding 95% Confidence Intervals					
		200	500	1,000	2,000	4,000	7,000
Sex (3,055)	ViT w.SEX	**0.9785 ± 0.0051**	**0.9855 ± 0.0042**	**0.9821 ± 0.0047**	**0.9873 ± 0.0040**	**0.9863 ± 0.0041**	**0.9885 ± 0.0038**
	ViT w.AGE	0.6569 ± 0.0168	0.7511 ± 0.0151	0.8872 ± 0.0112	0.9145 ± 0.0099	0.9479 ± 0.0079	0.9691 ± 0.0061
	Vanilla ViT	0.7850 ± 0.0146	0.8451 ± 0.0128	0.9027 ± 0.0105	0.9164 ± 0.0098	0.9590 ± 0.0070	0.9714 ± 0.0059
	Vanilla CNN	0.8657 ± 0.0121	0.9112 ± 0.0101	0.9501 ± 0.0077	0.9654 ± 0.0065	0.9739 ± 0.0057	0.9711 ± 0.0059
Age Group (2,292)	ViT w.SEX	0.7684 ± 0.0173	0.8012 ± 0.0163	0.8599 ± 0.0142	0.8912 ± 0.0127	0.9133 ± 0.0115	0.9163 ± 0.0113
	ViT w.AGE	**0.8719 ± 0.0137**	**0.8984 ± 0.0124**	**0.8985 ± 0.0124**	**0.9180 ± 0.0112**	**0.9336 ± 0.0102**	**0.9388 ± 0.0098**
	Vanilla ViT	0.8084 ± 0.0161	0.8477 ± 0.0147	0.8826 ± 0.0132	0.9041 ± 0.0121	0.9253 ± 0.0108	0.9270 ± 0.0107
	Vanilla CNN	0.7839 ± 0.0168	0.8416 ± 0.0149	0.8776 ± 0.0134	0.9019 ± 0.0122	0.9180 ± 0.0112	0.9250 ± 0.0108
Alcohol Consumption (3,055)	ViT w.SEX	**0.5924 ± 0.0174**	0.5759 ± 0.0175	0.5890 ± 0.0174	0.5835 ± 0.0175	0.5870 ± 0.0175	**0.6153 ± 0.0173**
	ViT w.AGE	0.5533 ± 0.0176	0.5468 ± 0.0177	0.5508 ± 0.0176	0.5646 ± 0.0176	0.5700 ± 0.0176	0.5869 ± 0.0175
	Vanilla ViT	0.5470 ± 0.0177	0.5398 ± 0.0177	0.5677 ± 0.0176	**0.5927 ± 0.0174**	0.6032 ± 0.0173	0.6062 ± 0.0173
	Vanilla CNN	0.5818 ± 0.0175	**0.5888 ± 0.0174**	**0.5956 ± 0.0174**	0.5905 ± 0.0174	**0.6112 ± 0.0173**	0.6091 ± 0.0173

(b) Feature Visualization on High Alcohol Use

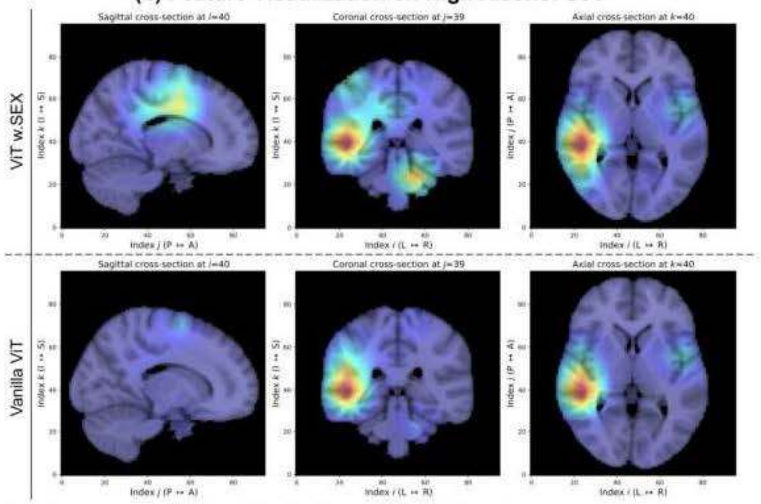

Figure 2: Model performance and feature visualization on the holdout set.
(a) Model performance - results of three prediction tasks. Larger sample sizes enhance balanced accuracy and tighten confidence intervals in sex and age group predictions, affirming increased precision for true population estimates. In contrast, smaller changes in the confidence interval occur with alcohol consumption as the sample size increases. Vanilla CNN exhibits superior performance over Vanilla ViT for sex and alcohol consumption predictions in small sample sizes. In contrast, Vanilla ViT showed a competitive model performance against Vanilla CNN in age group prediction. All values are reported as balanced accuracy with corresponding 95% confidence intervals.
(b) Feature visualization - high alcohol use interpreted from ViT w.SEX and Vanilla ViT in training size 7,000. There are common features strongly highlighted in the left superior temporal gyrus region and less highlighted in the right pre-central gyrus for both models. All visualizations are displayed with one sagittal, coronal, and axial cross-section of the images. Images are oriented in RAS+ orientation.
ViT w.SEX: ViT pretrained on sex classification, ViT w.AGE: ViT pretrained on age estimation, Vanilla ViT: Randomly initialized ViT, Vanilla CNN: Randomly initialized Convolution Neural Network, MNI: Montreal Neurological Institute, L: Left, R: Right, P: Posterior, A: Anterior, I: Inferior, and S: Superior.

Conclusions: We show that phenotype prediction strongly depends on the pre-training. The results of sex and age group prediction showed the importance of aligning pre-training tasks with target phenotypes. ViT w.SEX showed competitive results in alcohol consumption prediction, especially in smaller datasets. It may indicate that the prediction is confounded by sex. We provide feature visualizations of high alcohol use. The literature consistently reported associations between alcohol intake and alterations in grey matter volume of widespread areas such as the cerebellum, frontal, and temporal lobes, as well as various subcortical structures[8,9,10]. Our findings echo these observations. ViT w.SEX may outperform Vanilla ViT based on the distinct highlighted features. We demonstrate that the effectiveness of in-domain pre-training can vary based on factors such as the size of the fine-tuning dataset, and the relationship between the pre-training and target phenotypes.

References

1. Zhao Z (2023), 'Conventional machine learning and deep learning in Alzheimer's disease diagnosis using neuroimaging: A review', Frontier Computational Neuroscience 17:1038636
2. Dosovitskiy A (2021), 'An Image is Worth 16x16 Words: Transformers for Image Recognition at Scale', Available at: http://arxiv.org/abs/2010.11929
3. Li J (2022), 'Transforming medical imaging with Transformers? A comparative review of key properties, current progresses, and future perspectives', Available at: http://arxiv.org/abs/2206.01136
4. Gani H (2022), 'How to Train Vision Transformer on Small-scale Datasets?', Available at: http://arxiv.org/abs/2210.07240

5. Cole JH (2017), 'Predicting brain age with deep learning from raw imaging data results in a reliable and heritable biomarker', Neuroimage 163:115–124
6. Lu B (2022), 'A practical Alzheimer's disease classifier via brain imaging-based deep learning on 85,721 samples', Journal of Big Data 9:101
7. Chefer H (2020), 'Transformer Interpretability Beyond Attention Visualization', Available at: http://arxiv.org/abs/2012.09838
8. Guggenmos M (2017), 'Quantitative neurobiological evidence for accelerated brain aging in alcohol dependence', Translational Psychiatry 7:1–7
9. Nutt D (2021), 'Alcohol and the Brain', Nutrients 13:3938
10. Topiwala A (2022), 'Alcohol consumption and MRI markers of brain structure and function: Cohort study of 25,378 UK Biobank participants', Neuroimage Clinical 35:103066

Poster No 1373

Probabilistic prediction of cognitive impairment in continuous time for confidence quantification

Bruno Hebling Vieira[1], Dorothea Floris[2], Camille Elleaume[3], Franziskus Liem[4], Gaël Varoquaux[5], Nicolas Langer[1]

[1]University of Zurich, Zurich, Switzerland, [2]Methods of Plasticity Research, Department of Psychology, University of Zürich, Zürich, Switzerland, [3]University of Zurich, Zurich, Zurich, [4]ETHZ, Zurich, Switzerland, [5]SODA, Inria, Paris, France

Introduction: Machine learning models have been employed to great success in the prediction of cognitive impairment from demographic and familial risk-factors and imaging derived phenotypes (IDPs). Using MRI-based markers of brain atrophy, it is possible to obtain accurate continuous time classification of MCI and dementia patients[1], as well as predict subjects' trajectories in different staging and screening instruments[2-3]. To date most models have been trained to give point-predictions in fixed time windows, despite the added benefits of probabilistic prediction and continuous time trajectories, such as the assessment of confidence. This provides adjustable decision thresholds with guarantees for future translation of such models into actionable insights. In this work, we implement continuous time probabilistic prediction of cognitive impairment from brain regional morphometry and covariates.

Methods: We employed T1w MRI data from ADNI (1, 2, GO, 3) for training and validation, while external testing was performed on images from OASIS[4-5] (3, 4). FreeSurfer 7.3.2 morphometry estimates were used as IDPs (see Figure 1.A). We predicted Clinical Dementia Rating (CDR) Sum of Box Scores (SOB)[6] scores from 4 sets of inputs: (1) IDPs (fs2cdr), (2) other CDR session (cdr2cdr), (3) both an IDP session and a different CDR session (fscdr2cdr), (4) covariates only (cov2cdr). Modeling was performed with gradient boosted decision trees from LightGBM (4.0.0), well suited for unstructured tabular data[7] in Python (3.10.2), predicting the level of six CDR Box Scores. Covariates were included in all models, including patients' current age, sex, APOE2 and APOE4 allele counts, educational attainment, MRI scanner field strength, and the time difference(s) between the input and output time (see Figure 1.A-B). We compared probabilistic expectations to a regression model that predicts the CDR-SOB directly in the same settings as before, to identify potential performance degradation in the probabilistic model. We evaluated the calibration of predicting impairment in the future, i.e., p(CDR-SOB>0), to assess if the model is over- or under-confident in identifying abnormal cognition. Biological validity was assessed by the feature importance for the prediction of each CDR Box Score (see Figure 2).

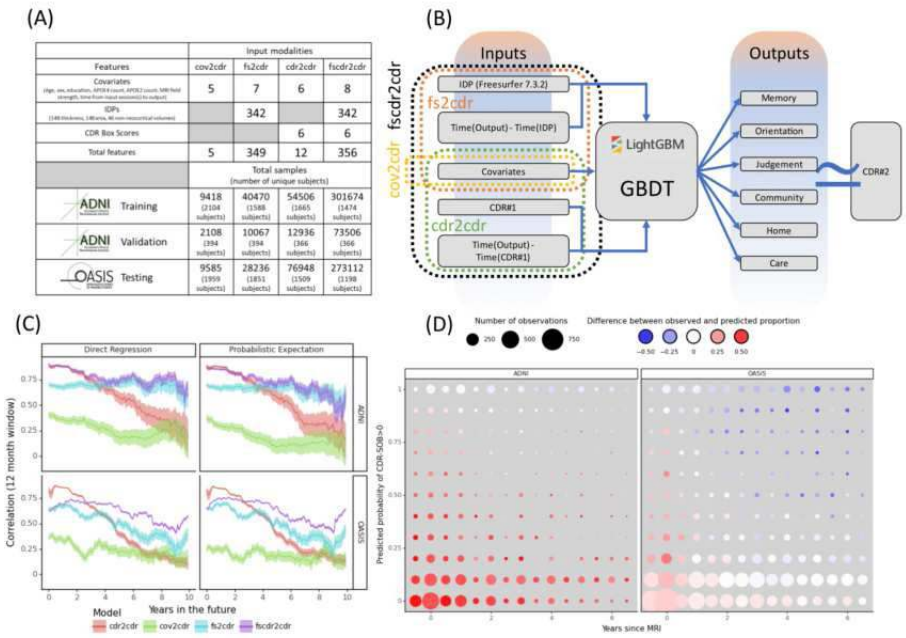

(A) shows the number of features per learning setting. IDPs include cortical morphometry estimates obtained from the Destrieux gyral-sulcal atlas and volumetry from other brain regions; (B) flowchart showing inputs, per modality, and outputs, i.e., probability for each level of each CDR Box Score, which are combined into the probability of CDR-SOB levels by the Convolution Theorem; (C) compares a direct regression model predicting CDR-SOB (left) to expectations obtained from our probabilistic model (right), in both the validation (ADNI, top) and external testing (OASIS, bottom) datasets. IDPs lead to better performance in longer time windows. Also, the probabilistic model maintains the level of performance of the direct regression model; (D) calibration plot relating the predicted probability CDR-SOB>0 to the observed proportion of samples with any impairment. A perfectly calibrated model would demonstrate the same proportion of positive cases for each probability bin. Red areas signify that the observed proportion of CDR-SOB>0 cases is higher than the predicted probability, denoting underconfidence, while blue highlight areas where the observed proportion is smaller than the predicted probability, which denotes overconfidence.

Results: Probabilistic models maintain good performance for point-predictions, on the same level as direct regression models. In short time-windows, up to 5 years in the future, present CDR provides the best predictions of future CDR according to the observed Pearson correlation between true and predicted CDR-SOB. Approximately 5 years in the future onwards, the IDP-derived model (fs2cdr) surpasses the CDR-only model (cdr2cdr). Including both CDR and IDPs (fscdr2cdr) is optimal at all time scales (see Figure 1.C). We detected underestimation (in red), and overestimation (in blue) of the probability of impairment (see Figure 1.D). This information can be used to recalibrate the underlying model in future work. The performance of point-predictions from probabilistic models can be explained by biological heterogeneity underlying different CDR Box Score domains[8]. Figure 2.A-B show feature importance for each CDR Box Score. Overall, highlighted regions resemble atrophy patterns observed in Alzheimer's. The left hippocampal volume is highly correlated with verbal episodic memory, while the right hippocampus volume correlates with spatial memory in older subjects[9]. High spatial similarity between importance scores can be explained by the positive correlation between Box Scores, shown in Figure 2.C.

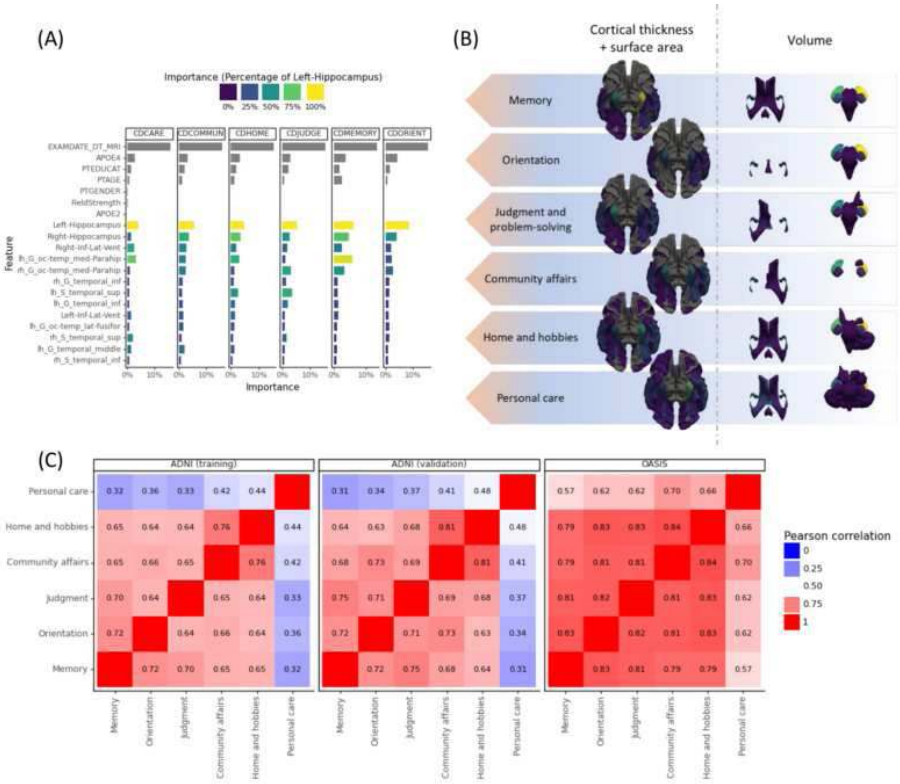

Feature importances for each CDR Box-Scores. Feature importances are defined as the gain with the inclusion of a given variable in a split in the tree ensemble, normalized by frequency of splits using said variable, in the training data. (A) shows percentage feature importance, i.e., feature importance of a feature divided by the sum of feature importances per target. (B) shows feature importances for IDPs (cortical regional average thickness plus surface area added together, and volume from hippocampi, ventricles and non-cortical regions) as a percentage of the Left-Hippocampus importance, the highest among IDPs. Regions with relative importance less than 10% of the Left-Hippocampus are not shown. (C) The correlation matrix between CDR Box Scores, which might explain the high spatial similarity between importance maps, is shown, demonstrating a high positive correlation for all Box Scores with the exception of "Personal care", which might be explained by its coarser scale. Correlations in OASIS are inflated compared to ADNI, due to the higher proportion of cognitively unimpaired participants.

Conclusions: IDPs provide optimal performance to predict cognitive impairment in longer time scales. Probabilistic predictions maintain accuracy of point-predictions with the benefit of confidence quantification. This work represents a significant step towards improving the translation of machine learning models into actionable insights, to enhance research on clinical trials and personalized medicine.

References

1. Karaman, B. K. (2022), 'Machine learning based multi-modal prediction of future decline toward Alzheimer's disease: An empirical study'. PLOS ONE 17.
2. Vieira, B. H. (2022), 'Predicting future cognitive decline from non-brain and multimodal brain imaging data in healthy and pathological aging'. Neurobiology of Aging 118, 55–65.
3. Bhagwat, N. (2018), 'Modeling and prediction of clinical symptom trajectories in Alzheimer's disease using longitudinal data'. PLoS Computational Biology 14.
4. Koenig, L. N. (2020), 'Select Atrophied Regions in Alzheimer disease (SARA): An improved volumetric model for identifying Alzheimer disease dementia'. NeuroImage Clinical, 26.
5. LaMontagne, P. J. (2019), 'OASIS-3: Longitudinal Neuroimaging, Clinical, and Cognitive Dataset for Normal Aging and Alzheimer Disease'. medRxiv Preprint
6. Cedarbaum, J. M. (2013), 'Rationale for use of the Clinical Dementia Rating Sum of Boxes as a primary outcome measure for Alzheimer's disease clinical trials'. Alzheimer's Dementia. 9, S45–S55.
7. Grinsztajn, L. (2023), 'Why do tree-based models still outperform deep learning on typical tabular data?', Neurips.
8. Lowe, D. A. (2012), 'Greater Precision when Measuring Dementia Severity: Establishing Item Parameters for the Clinical Dementia Rating Scale'. Dementia and Geriatric Cognitive Disorders, 34, 128–134.
9. Ezzati, A. (2016), 'Differential association of left and right hippocampal volumes with verbal episodic and spatial memory in older adults'. Neuropsychologia 93, 380–385.

Poster No 1374

Functional gradient boosting predicts trajectories of cognitive impairment from brain morphometry

Bruno Hebling Vieira[1], Camille Elleaume[2], Nicolas Langer[1]

[1]University of Zurich, Zurich, Switzerland, [2]University of Zurich, Zurich, Zurich

Introduction: The literature has shown that quantifiable MRI-markers of brain atrophy are highly predictive for future classification between cognitively normal (CN) individuals and Alzheimer's disease dementia (AD)[1] patients. This holds significant promise for prognostic applications, particularly in the recruitment phase of clinical trials targeting pre-clinical and subclinical stages of dementia[2]. However, cognitive impairment occurs along a continuum, not as discrete diagnostic categories. Our previous work has shown that structural MRI adds information to a model predicting the yearly rate of change in CDR-SOB and MMSE[3]. While approximating the trajectory of cognitive impairment as a linear decline is valid for small intervals, it breaks down at long intervals, since the actual evolution follows a non-linear trajectory[4]. Due to the sparsity of longitudinal data, accurately estimating non-linear trajectories for individual participants becomes a challenging task. To test the effectiveness of different trajectory classes in the prediction of future cognitive impairment we present a method that can accommodate (non-)linear trajectories independent of the number of samples per participant in a cohort. Our approach involves estimating a versatile class of 'functions' aimed at best approximating the trajectories of participants' scores from features such as brain imaging features and risk factors. We employed a large-scale dataset (ADNI) to train three distinct models for predicting CDR-SOB trajectories using regional brain morphometry. We compared the performance of a linear functional, an inverse cloglog functional, and a direct regression that incorporates time as a feature.

Methods: Features for modelling CDR-SOB trajectories were risk factors (i.e., age, sex, educational attainment, APOE2 and APOE4 allele counts), confounders (i.e., MRI magnetic field strength), covariates (i.e., the time between the input and output sessions in the direct regression model) and imaging derived phenotypes (IDPs). IDPs were obtained from Freesurfer, including cortical thickness and surface area from 148 regions in the Destrieux atlas, and volume from 46 non-neocortical regions. Data from ADNI (1, 2, GO, 3) were used for training and validation. We split ADNI into a training set comprising data of 80% of the subjects and a validation set containing the remaining 20% subjects. External validation relied on the independent dataset OASIS (3,4)[5-6] (see Figures 1.A-B). We estimated a linear trajectory model, outputting two parameters only, and two non-linear trajectory models, including an inverse cloglog functional with a Beta likelihood, and a direct non-parametrized regression functional (see Figure 1.C-E).

Results: A ll three models display a similar level of performance in ADNI and generalize to OASIS (see Figure 2.A-B,D). The models are overtly conservative, however, and tend towards flat predictions and underestimation of CDR-SOB in the case of AD due to regression-to-the-mean, which is visible in Figure 2.C. The MAE increases in longer time windows, with the best models reaching approximately 3 for AD patients, and 1 for CN individuals (see Figure 2.D). Explicit parametrization of predictions can be used to estimate rates of decline, age of onset and phase transition, and integrate prior knowledge, e.g., the inverse cloglog function is bounded between 0 and 18, as is the CDR-SOB. Direct regression can also incorporate monotonicity constraints in features, but in our experiments, it did not result in better models. Future research will investigate other parametrizations as well as other likelihood functions.

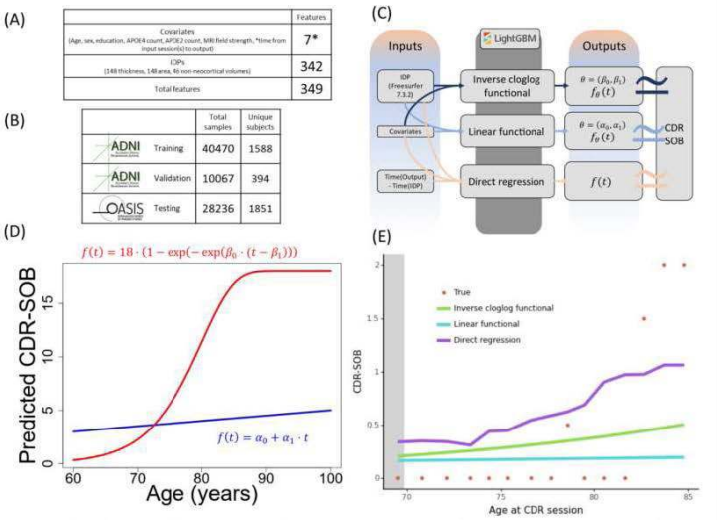

Overview of the study procedure. (A) Input features, including covariates and FreeSurfer IDPs. The time between sessions only affects the direct regression model, and not the parametrized functional models. (B) Total number of data available for training, validation and testing. (C) Different functional models were trained on ADNI data to predict CDR-SOB trajectories from brain regional morphometry estimates and covariates, including an inverse cloglog functional, a linear functional and a direct regression taking the time between the imaging session and the CDR session as an additional input. (D) The model is optimized to provide a good approximation of all CDR-SOB values available for the given subject at once. In the case of the linear trajectory, only two outputs are necessary to fully specify the functional, (α_0, α_1), assuming a Gaussian likelihood with constant variance. In the case of the inverse cloglog trajectory, the mean function is given by (β_0, β_1) and a Binomial likelihood is assumed. The direct regression model results in a non-parametric functional solution per input. (E) Example of real predictions and true CDR-SOB trajectories are shown from a 70 years old subject in OASIS. The gray area represents the past, in relation to the MRI session.

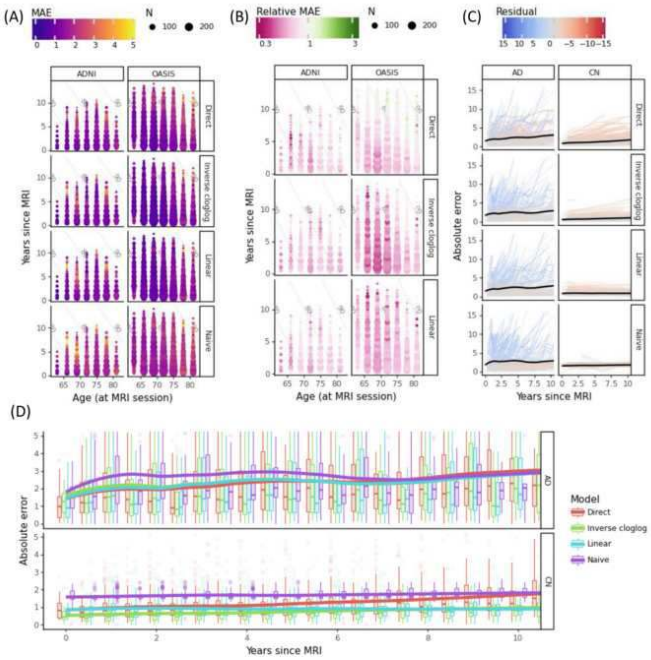

MAE (A) and relative MAE (B) according to both the age at the MRI session and the time to the target CDR session (diagonal lines show the age at the CDR session), across all data points. Relative MAE is computed as a percentage from the naïve baseline model, which consists of the expected CDR-SOB for a given age in ADNI data. All models demonstrate performance better than the baseline model. (C) Residuals for the three models in the earliest image available of cognitively normal (CN, n=477) participants and confirmed primary Alzheimer's disease dementia (AD, n=391) patients in OASIS, as a function of the time since the MRI session. Red denotes overestimation of the expected CDR-SOB and blue denotes underestimation. MAE is estimated as a function of time according to a locally estimated regression (LOESS). (D) The MAE curves from (C) are shown, superimposed on boxplots of absolute errors computed every 6 months into the future, with the y-axis limited to 5 to ease visualization. The linear and the inverse cloglog functionals provide consistently better predictions than the baseline for both AD and CN participants in several time windows.

Conclusions: Our approach enables the prediction of (non-)linear trajectories of cognitive impairment, independent of the number of data points per subject. Non-linear trajectory models did not outperform the linear functional model in the prediction of CDR-SOB in the future from IDPs.

References

1. Karaman, B. K. (2022), "Machine learning based multi-modal prediction of future decline toward Alzheimer's disease: An empirical study". PLOS ONE 17.
2. Tam, A. (2022), "Prediction of Cognitive Decline for Enrichment of Alzheimer's Disease Clinical Trials". The Journal of Prevention of Alzheimer's Disease, 9, 400–409.
3. Vieira, B. H. (2022), "Predicting future cognitive decline from non-brain and multimodal brain imaging data in healthy and pathological aging". Neurobiology of Aging,118, 55–65.
4. Delor, I. (2013), "Modeling Alzheimer's Disease Progression Using Disease Onset Time and Disease Trajectory Concepts Applied to CDR-SOB Scores From ADNI". CPT: Pharmacometrics & Systems Pharmacology, 2, 78.
5. Koenig, L. N. (2020), "Select Atrophied Regions in Alzheimer disease (SARA): An improved volumetric model for identifying Alzheimer disease dementia". NeuroImage: Clinical, 26, 102248.
6. LaMontagne, P. J., (2019). "OASIS-3: Longitudinal Neuroimaging, Clinical, and Cognitive Dataset for Normal Aging and Alzheimer Disease". medRxiv preprint.

Poster No 1375

Meta-matching to translate phenotypic predictive models from big to small data on structural MRI

Naren Wulan[1,2,3], Lijun An[1,2,3], Chen Zhang[1,2,3], Ru Kong[1,2,3], Pansheng Chen[1,2,3], Danilo Bzdok[4,5], Simon Eickhoff[6,7], Avram Holmes[8], B. T. Thomas Yeo[1,2,3,9,10]

[1]Centre for Sleep & Cognition & Centre for Translational Magnetic Resonance Research, NUS, Singapore, Singapore, [2]Department of Electrical and Computer Engineering, National University of Singapore, Singapore, Singapore, [3]N.1 Institute for Health & Institute for Digital Medicine, National University of Singapore, Singapore, Singapore, [4]McConnell Brain Imaging Centre (BIC), Montreal Neurol, McGill Universityogical Institute (MNI), Montreal, QC, Canada, [5]Mila – Quebec Artificial Intelligence Institute, Montreal, QC, Canada, [6]Institute for Systems Neuroscience, Medical Faculty, Heinrich-Heine University Düsseldorf, Düsseldorf, Germany, [7]Institute of Neuroscience and Medicine, Brain & Behavior (INM-7), Research Center Jülich, Jülich, Germany, [8]Department of Psychiatry, Brain Health Institute, Rutgers University, Piscataway, NJ, [9]Integrative Sciences and Engineering Programme (ISEP), National University of Singapore, Singapore, Singapore, [10]Martinos Center for Biomedical Imaging, Massachusetts General Hospital, Charlestown, MA, United States

Introduction: A central goal in neuroscience is understanding how brain imaging is associated with behavior. Structural MRI has been used to make individualized predictions in a variety of neurological and psychiatric disorders (Arbabshirani et al., 2017; Bhagwat et al., 2019; Cohen et al., 2021) due to its good contrasts. However, the prediction performance is strongly limited by a small sample size for many current MRI studies (Kharabian Masouleh et al., 2019; Poldrack et al., 2020; He et al., 2020). By transferring knowledge from large-scale source datasets (e.g. UK Biobank) to small target datasets, meta-matching has greatly improved prediction performance in functional MRI (He et al., 2022). Here, we tailored meta-matching approaches to predict new phenotypes in small boutique datasets with structural MRI.

Methods: Our study departed from the UK Biobank (N=36,461, 67 phenotypes; Alfaro-Almagro et al., 2018), HCP-YA (N=1017, 35 phenotypes; Van Essen et al., 2013), and HCP-Aging (N=656, 45 phenotypes; Bookheimer et al., 2019). We transferred models pretrained from meta-training set to meta-test sets. For within UK Biobank analysis, we randomly split UK Biobank dataset into meta-training set (N=26573, 33 phenotypes) and meta-test set (N=9888, 34 phenotypes). There is no overlap between participants or phenotypes across meta-training and meta-test sets. On meta-test set, K participants (K-shot, where K had a value of 10, 20, 50, 100, and 200) were randomly selected to mimic traditional small sample size studies, while the remaining participants in the meta-test set served for evaluation. Each random K-shot split was repeated 100 times to ensure stability. For cross-dataset analysis, the UK Biobank served as a meta-training set, while HCP-YA and HCP-Aging served as meta-test sets separately. We adopted meta-matching by pretraining a 3D CNN model (Peng et al., 2021) on the meta-training set structural brain imaging to improve phenotypic prediction performance on meta-test sets (Figure 1). For baseline approaches, we considered the elastic net and direct transfer learning algorithm (Figure 1). The input of elastic net was morphometric measures (volumes and thickness from cortical and/or subcortical ROIs by FreeSurfer); the input of deep learning approaches is T1 images affine transformed to MNI152 standard space.

Results: Figure 2 (A) shows the prediction accuracy (Pearson's correlation) across all test phenotypes on the UK Biobank meta-test set. The boxplots represent 100 repetitions for K-shot. We can observe that meta-matching-based approaches (meta-matching finetune and meta-matching stacking) can significantly outperform the Elastic net baseline and direct transfer

learning methods (for every K number). The previous experiment results (Figure 2 (A)) suggested that meta-matching-based methods can perform well when transferring within the same dataset (e.g. UK Biobank). To demonstrate the generalization ability of meta-matching-based methods. approaches are also applied to the meta-test set in the HCP-YA dataset Figure 2 (B), and the HCP-Aging dataset Figure 2 (C) respectively. Figure 2 (B) and Figure 2 (C) show that the meta-matching-based methods can significantly outperform baseline methods in most cases when transferring from the meta-training dataset (UK Biobank) to the meta-test dataset (HCP-YA or HCP-Aging).

Conclusions: We adopted meta-matching from functional to structural imaging and achieved superior performance over elastic net and direct transfer learning on small datasets including HCP-YA and HCP-Aging. Our results showed the great potential of meta-matching framework in structural MRI-based behavior predictions.

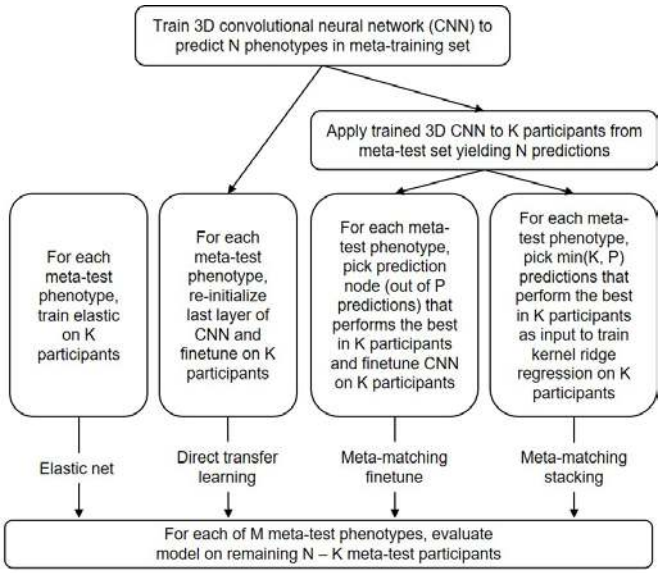

Figure 1. Overview of different approaches. We considered two baselines: elastic net and transfer learning. We proposed two meta-matching variants: meta-matching finetune and meta-matching stacking.

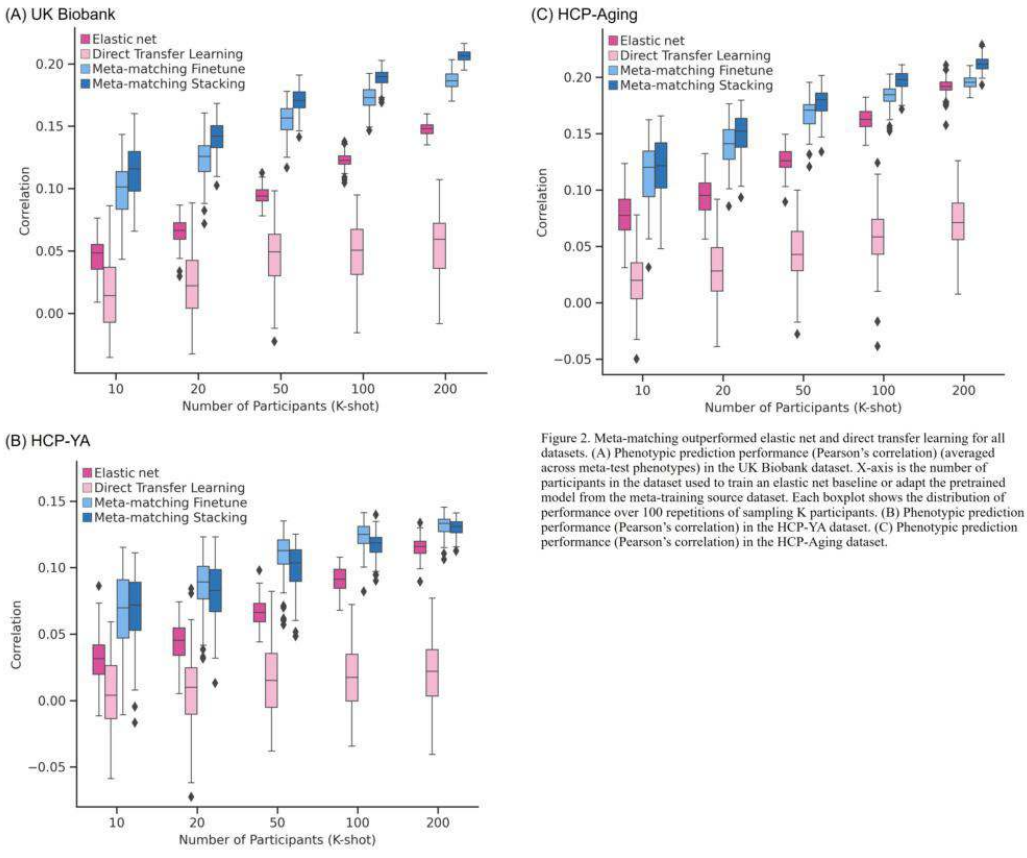

Figure 2. Meta-matching outperformed elastic net and direct transfer learning for all datasets. (A) Phenotypic prediction performance (Pearson's correlation) (averaged across meta-test phenotypes) in the UK Biobank dataset. X-axis is the number of participants in the dataset used to train an elastic net baseline or adapt the pretrained model from the meta-training source dataset. Each boxplot shows the distribution of performance over 100 repetitions of sampling K participants. (B) Phenotypic prediction performance (Pearson's correlation) in the HCP-YA dataset. (C) Phenotypic prediction performance (Pearson's correlation) in the HCP-Aging dataset.

References

1. Arbabshirani, M. R., Plis, S., Sui, J., & Calhoun, V. D. (2017). Single participant prediction of brain disorders in neuroimaging: Promises and pitfalls. NeuroImage, 145, 137-165.
2. Bhagwat, N., Pipitone, J., Voineskos, A. N., Chakravarty, M. M., & Initiative, A. s. D. N. (2019). An artificial neural network model for clinical score prediction in Alzheimer disease using structural neuroimaging measures. Journal of Psychiatry and Neuroscience, 44(4), 246-260.
3. Cohen, S. E., Zantvoord, J. B., Wezenberg, B. N., Bockting, C. L., & van Wingen, G. A. (2021). Magnetic resonance imaging for individual prediction of treatment response in major depressive disorder: a systematic review and meta-analysis. Translational psychiatry, 11(1), 168.
4. Kharabian Masouleh, S., Eickhoff, S. B., Hoffstaedter, F., Genon, S., & Initiative, A. s. D. N. (2019). Empirical examination of the replicability of associations between brain structure and psychological variables. elife, 8, e43464.
5. Poldrack, R. A., Huckins, G., & Varoquaux, G. (2020). Establishment of best practices for evidence for prediction: a review. JAMA psychiatry, 77(5), 534-540.
6. He, T., Kong, R., Holmes, A. J., Nguyen, M., Sabuncu, M. R., Eickhoff, S. B., . . . Yeo, B. T. (2020). Deep neural networks and kernel regression achieve comparable accuracies for functional connectivity prediction of behavior and demographics. NeuroImage, 206, 116276.
7. He, T., An, L., Chen, P., Chen, J., Feng, J., Bzdok, D., . . . Yeo, B. T. (2022). Meta-matching as a simple framework to translate phenotypic predictive models from big to small data. Nature neuroscience, 25(6), 795-804.
8. Alfaro-Almagro, F., Jenkinson, M., Bangerter, N. K., Andersson, J. L., Griffanti, L., Douaud, G., . . . Vallee, E. (2018). Image processing and Quality Control for the first 10,000 brain imaging datasets from UK Biobank. NeuroImage, 166, 400-424.
9. Van Essen, D. C., Smith, S. M., Barch, D. M., Behrens, T. E., Yacoub, E., Ugurbil, K., & Consortium, W.-M. H. (2013). The WU-Minn human connectome project: an overview. NeuroImage, 80, 62-79.
10. Bookheimer, S. Y., Salat, D. H., Terpstra, M., Ances, B. M., Barch, D. M., Buckner, R. L., . . . Elam, J. S. (2019). The lifespan human connectome project in aging: an overview. NeuroImage, 185, 335-348.
11. Peng, H., Gong, W., Beckmann, C. F., Vedaldi, A., & Smith, S. M. (2021). Accurate brain age prediction with lightweight deep neural networks. Medical Image Analysis, 68, 101871.

Poster No 1376

Brain-based predictions of cardiovascular risk factors in midlife populations at risk of dementia

Bolin Cao[1,2], Qing Qi[1,2], Feng Deng[1,2], Maria-Eleni Dounavi[3], Graciela Muniz-Terrera[4,5], Paresh Malhotra[6,7], Ivan Koychev[8], John O'Brien[3], Craig Ritchie[4,9], Brian Lawlor[1,2], Lorina Naci[1,2]

[1]Trinity College Institute of Neuroscience, School of Psychology, Trinity College Dublin, Dublin, Ireland, [2]Global Brain Health Institute, Trinity College Dublin, Dublin, Ireland, [3]Department of Psychiatry, School of Clinical Medicine, University of Cambridge, Cambridge, UK, [4]Edinburgh Dementia Prevention, University of Edinburgh, Edinburgh, UK, [5]Department of Social Medicine, Ohio University, Ohio, USA, [6]Department of Brain Science, Imperial College London, London, UK, [7]UK Dementia Research Institute Care Research and Technology Centre, Imperial College London and the University of Surrey, London, UK, [8]Department of Psychiatry, Oxford University, Oxford, UK, [9]Scottish Brain Sciences, Edinburgh, UK

Introduction: Dementia, particularly Alzheimer's disease (AD), is a growing public health challenge. The progression of AD underscores the critical importance of midlife as a period for preventive intervention[1-3]. As dementia is a heterogeneous neurodegenerative condition, single risk factors are inadequate for accurately identifying people who are most likely to develop dementia[4]. Instead, multifactorial risk scores, like the cardiovascular risk factors, aging, and dementia (CAIDE) risk score[5], encompassing cardiovascular (blood pressure, cholesterol, body mass index, and physical inactivity) and non-modifiable risk factors (age, sex, and APOE ε4 genotype), are crucial for dementia risk estimate. However, the underlying functional brain architecture correlating with these risk factors is poorly understood. This study seeks to bridge this gap through network-based statistic (NBS)-Predict[6], a novel predictive model aiming to identify neuroimaging biomarkers for dementia-related risks in midlife, thus aiding in personalized prevention and intervention strategies.

Methods: Resting-state fMRI imaging, CAIDE, cardiovascular and non-modifiable risk factors, and a lifetime of experiences questionnaire (LEQ) data were collected in 585 (207/378 female/male) healthy participants aged 40-59 years (mean = 50.9) enrolled in the PREVENT-Dementia study[7-9] who had useable MR data. Following standard preprocessing procedures, the Dosenbach atlas[10] was utilized to extract mean time series and construct functional connectivity (FC) matrices for each participant. We applied the NBS-Predict model to predict the CAIDE, cardiovascular, and non-modifiable risk factors scores based on the whole-brain FC (Figure 1). Specifically, our analysis employed a linear support vector machine characterized by 10-fold cross-validation (repeated 10 times), with feature selection at $p<0.05$ and 1000 permutations for statistical significance. Additionally, a hierarchical regression model was used to assess the impact of midlife LEQ score on the FC linked with cardiovascular risk factors. The LEQ specific and non-specific score, age, sex, years of education, and mean framewise displacement (FD) were set independent variables.

Results: NBS-Predict models significantly predicted the CAIDE ($r=0.214$, $p<0.001$), the cardiovascular ($r=0.201$, $p<0.001$), and the non-modifiable ($r=0.237$, $p<0.001$) risk factors scores. We observed similar FC patterns related to the CAIDE and cardiovascular risk factor score, with connections between the somatomotor and cingulo-opercular networks and within the

somatomotor network, as shown in Figure 2a. By contrast, the FC patterns for the non-modifiable risk score were different from those observed for CAIDE. Furthermore, we found that the non-specific score (physically, socially and intellectually stimulating mid-life activities) was positively associated with the FC of regions impacted by cardiovascular risk factors (β=0.001, p=0.017).

Conclusions: We found considerable overlap in FC patterns associated with CAIDE and cardiovascular risk factors in midlife, which were very different from those associated with non-modifiable risk. This suggests different neurobiological pathways for cardiovascular-based modifiable and other non-modifiable risk factors contributing to dementia risk in midlife. These results bolster the case for personalized approaches to dementia prevention decades before the onset of clinical symptoms. The research highlights the beneficial impact of an active and engaged lifestyle on brain health.

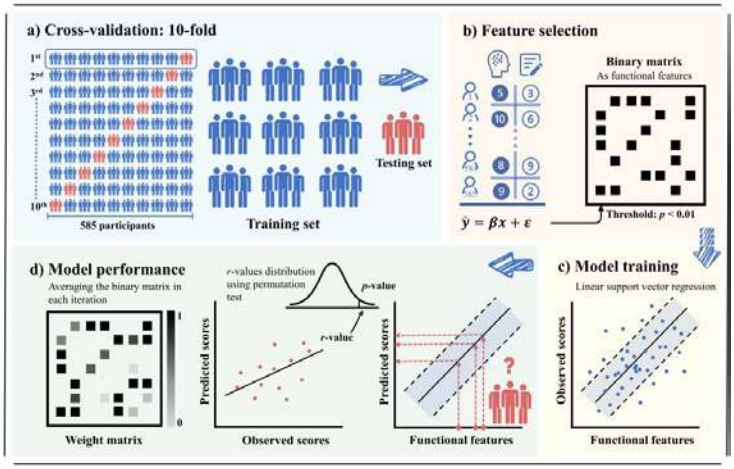

Figure 1. Schematic of the NBS-Predict. a) Cross-validation: Employed 10-fold cross-validation, randomly dividing participants into ten groups for model evaluation, with each group being used once as a test set. b) Feature selection: Extracted time series from Dosenbcah altas, forming connectivity matrices, and retained connections with significant correlations to risk scores after linear modeling, represented by a binary matrix. c) Model training: Employed linear support vector regression to model the observed scores against functional features. d) Model performance: Assessed by feeding test set features into the model and calculating Pearson's correlation between predicted and observed scores, repeating the validation ten times for reliability, and using permutation testing for significance, also averaging weight matrices to interpret the contributions of specific connections.

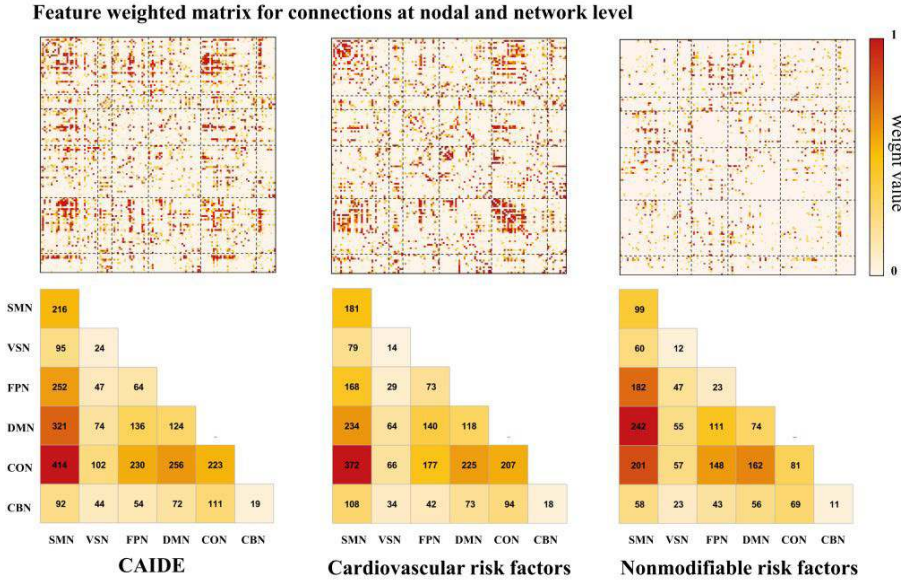

Figure 2. Feature weighted matrix for connections. Nodal and network-level feature weighted matrices. These matrices show the weighted values of connections, reflecting their importance in predicting risk factor scores. A higher weight suggests greater importance in the prediction model. For enhanced visualization and interpretation, we quantified the number of these connections at the network level. Abbreviation: DMN, default mode network; FPN, frontoparietal network; CON, cingulo-opercular network; SMN, sensorimotor network; VSN, visual network; CBN, cerebellum network.

References
1. Livingston, G., et al., Dementia prevention, intervention, and care. Lancet, 2017. 390(10113): p. 2673-2734.
2. Ritchie, K., et al., Designing prevention programmes to reduce incidence of dementia: prospective cohort study of modifiable risk factors. BMJ, 2010. 341: p. c3885.
3. Barnes, D.E. and K. Yaffe, The projected effect of risk factor reduction on Alzheimer's disease prevalence. Lancet Neurol, 2011. 10(9): p. 819-28.
4. Stephen, R., et al., Change in CAIDE Dementia Risk Score and Neuroimaging Biomarkers During a 2-Year Multidomain Lifestyle Randomized Controlled Trial: Results of a Post-Hoc Subgroup Analysis. Journals of Gerontology Series a-Biological Sciences and Medical Sciences, 2021. 76(8): p. 1407-1414.
5. Kivipelto, M., et al., Risk score for the prediction of dementia risk in 20 years among middle aged people: a longitudinal, population-based study. Lancet Neurology, 2006. 5(9): p. 735-741.
6. Serin, E., et al., NBS-Predict: A prediction-based extension of the network-based statistic. Neuroimage, 2021. 244.
7. Ritchie, C.W., K. Wells, and K. Ritchie, The PREVENT research programme - A novel research programme to identify and manage midlife risk for dementia: the conceptual framework. International Review of Psychiatry, 2013. 25(6): p. 748-754.
8. Ritchie, C.W., et al., The PREVENT Dementia programme: Baseline demographic, lifestyle, imaging and cognitive data from a midlife cohort study investigating risk factors for dementia. 2023: p. 2023.07.14.23292648.
9. Ritchie, C.W. and K. Ritchie, The PREVENT study: a prospective cohort study to identify mid-life biomarkers of late-onset Alzheimer's disease. Bmj Open, 2012. 2(6).
10. Dosenbach, N.U., et al., Prediction of individual brain maturity using fMRI. Science, 2010. 329(5997): p. 1358-61.

Poster No 1377

Brain Connectome Analysis for Alzheimer's Disease using Hodge Laplacian-based Edge Convolution

Joonhyuk Park[1], Yechan Hwang[1], Moo K Chung[2], Minjeong Kim[3], Guorong Wu[4], Won Hwa Kim[1]

[1]Pohang University of Science and Technology (POSTECH), Pohang, Korea, Republic of, [2]University of Wisconsin, Madison, WI, [3]University of North Carolina at Greensboro, Greensboro, NC, [4]University of North Carolina at Chapel Hill, Chapel Hill, NC

Introduction: Advancement of graph theory has facilitated the study of the human brain as a graph, depicting anatomical regions of interest (ROIs) as nodes and white matter connectomes as edges[2]. Recent brain network analysis employs graph neural networks (GNNs) that utilize graph convolution on node signals, where the analysis is performed on the node measures and the actual connectomic features play an indirect role as a neighborhood selector. Thus, we propose to utilize Hodge-GNN that can capture the edge-wise relationship and allow the spatial graph convolution to directly employ the higher-order connectivity (i.e., connectivity between edges) of a graph as a simplicial complex via Hodge Laplacian. Our method was validated on Alzheimer's Disease Neuroimaging Initiative (ADNI) dataset and depicted Alzheimer's Disease (AD) associated brain connectivities, which aligned with existing literatures. This research was supported by IITP-2019-0-01906 (AI Graduate Program at POSTECH), the Korea Health Industry Development Institute (KHIDI) HU22C0168 and HU22C0171, and National Research Foundation (NRF) NRF-2022R1A2C2092336.

Methods: Dataset. The dataset consists of structural brain connectivity data obtained from Diffusion Tensor Images (DTI) within ADNI using tractography. Each sample is given as a weighted graph with 160 nodes (148 cortical and 12 subcortical ROIs) from Destrieux atlas[1] and the weights denote the number of white matter fiber tracts connecting different ROIs. The dataset is composed of 1824 subjects within Control (CN, N=844), Early and Late Mild Cognitive Impairment (EMCI, N=490 and LMCI, N=250), and AD (N=240) groups. Preliminaries. A simplicial complex comprises simplices, representing objects in varying dimensions within topological space, such as nodes (0-simplex), edges (1-simplex), triangles (2-simplex), and higher-dimensional counterparts. The mapping of simplices in the p-th dimension to their (p-1)-th dimensional boundaries is facilitated by a boundary matrix, a matrix form of the boundary operator. This boundary matrix plays an important role in defining the Hodge Laplacian, enhancing the representation of higher-order graph structures. Method. The proposed method is composed of two components: 1) graph transformation of adjacency matrix to Hodge 1-Laplacian, and 2) edge-wise graph convolution using the Hodge 1-Laplacian (Fig. 1a). The Hodge 1-Laplacian is defined through the 1-simplex boundary matrix (i.e., the incidence matrix), capturing topological features associated with 1-simplices not initially discernible in the original graph form. Consequently, utilizing Hodge 1-Laplacian for spatial graph convolution not only provides the connectivity over edges, but also assigns different weights on adjacent edges based on the graph topology (Fig. 1b). 4-way graph classification on Control, EMCI, LMCI and AD was conducted via 5-fold cross validation. The performance was measured using average accuracy, Macro-(precision, recall, and F1-score), and compared with various baseline methods.

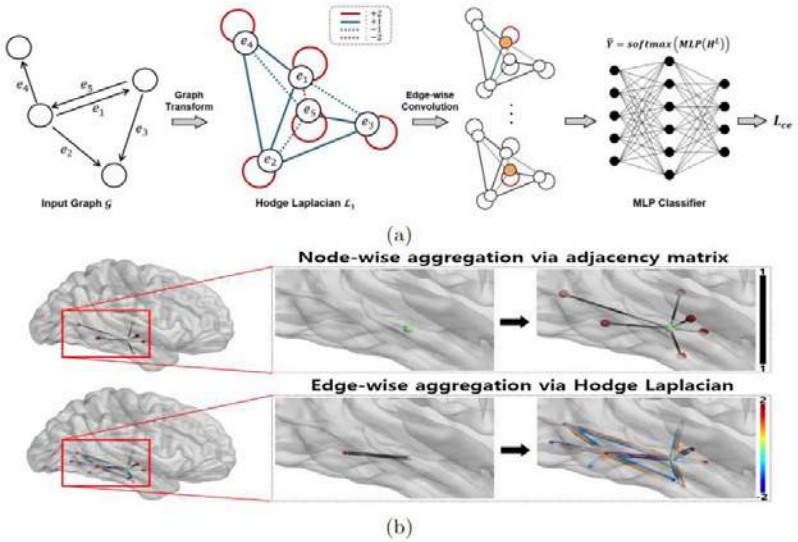

Fig. 1: **(a)** The overall process of the proposed method: 1) deriving Hodge 1-Laplacian $\mathcal{L}_1$ from input graph $\mathcal{G}$. 2) edge-wise graph convolution using $\mathcal{L}_1$. 3) Each edge (orange node) aggregates the information of neighboring edges in different weights given by $\mathcal{L}_1$. 4) MLP takes edge-convolved features as an input and is updated by the loss. **(b)** An illustration of direct neighborhood from graph Laplacian $\mathcal{L}_0$ (top) and a Hodge 1-Laplacian $\mathcal{L}_1$ (bottom). $\mathcal{L}_1$ allows edge-wise aggregation by weighted sum of neighboring edges via shared nodes with directional weights (denoted by the edge color). Node colors: base node (green), 1-hop (red), and 2-hop neighbors (blue).

Results: Experimental Results. Our method outperformed conventional graph classification methods[4], spatial and spectral GNNs[5,6], and edge convolution method[9] in all evaluation measures (Fig. 2A). Also, the significant edges depicted from the AD analysis exhibited consistency with prior works of AD, highlighting connectomes within subcortical regions, temporal lobe, and frontal lobe (Fig. 2B,C)[3]. Interestingly, some of the depicted edges showed symmetry found in both hemispheres, such as pallidum-putamen and amygdala-hippocampus connectomes, which are known to play crucial roles in the development of AD[7,8].

A

	Methods	Accuracy	Precision	Recall	F1-score
Conventional	SVM	58.31 ± 1.40	70.67 ± 3.44	44.49 ± 1.57	46.94 ± 2.36
	SLP	71.42 ± 3.42	68.91 ± 4.46	70.27 ± 3.39	69.16 ± 3.99
	MLP	72.41 ± 1.14	73.66 ± 1.29	67.47 ± 2.59	69.45 ± 1.22
	GCN ($\mathcal{G}$) [4]	70.16 ± 1.82	67.67 ± 2.46	66.82 ± 1.30	67.00 ± 1.88
	GCN ($\mathcal{G}_L$)	80.85 ± 3.10	81.21 ± 3.34	77.55 ± 2.93	79.09 ± 3.10
Spatial domain	1-2-GNN [6]	73.58 ± 1.12	71.44 ± 0.87	71.31 ± 1.41	71.15 ± 0.43
	1-2-3-GNN [6]	73.81 ± 1.91	72.39 ± 1.82	71.04 ± 2.64	71.25 ± 1.51
Spectral domain	MENET [5]	80.47 ± 1.82	79.30 ± 0.69	77.09 ± 1.59	77.92 ± 1.12
Edge Convolution	DGCNN [9]	72.61 ± 2.01	69.69 ± 2.29	69.11 ± 1.51	69.11 ± 1.90
Ours	Hodge-GNN	**83.60±1.93**	**84.75±2.19**	**80.10±1.87**	**82.03±1.93**

B

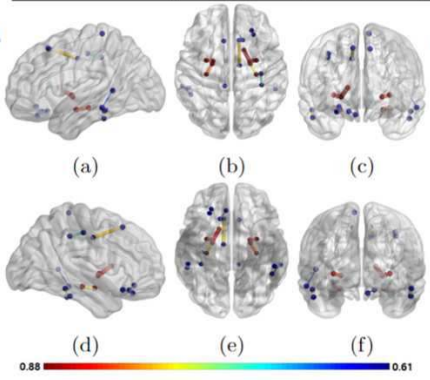

C

$\mathcal{H}$	ROI	ROI
0.88	Right-Pallidum	Right-Putamen
0.87	Left-Pallidum	Left-Putamen
0.83	Right-S_central	Right-S_postcentral
0.82	Left-G_subcallosal	Right-G_subcallosal
0.80	Left-S_temporal_inf	Left-G_temporal_inf
0.78	Right-Amygdala	Right-Hippocampus
0.78	Left-Amygdala	Left-Hippocampus
0.77	R-S_orbital_med-olfact	Right-G_rectus
0.73	Right-Pallidum	R-Thalamus-Proper
0.67	Right-S_temporal_inf	Right-G_temporal_inf
0.66	Left-G_S_paracentral	Left-G_front_sup
0.66	R-G_S_cingul-Mid-Post	Right-G_front_sup
0.62	Left-S_temporal_sup	L-G_temporal_middle

Fig. 2: **A**: Quantitative Comparison of Hodge-GNN with various Baselines. $\mathcal{G}_L$ denotes the line graph of the input graph $\mathcal{G}$. **B**: Significant edges depicted from the AD analysis; (a),(d) outer view of left/right hemisphere, (b),(e) top/bottom, (c),(f) front/rear view. Blue node: cortical, Red node: subcortical region, Edge color/thickness denote importance $\mathcal{H}$ obtained from the gradient-based class activation map. **C**: ROIs of the depicted connectomes. Among the 17 depicted ROIs, 5 ROIs (pallidum, amygdala, putamen, hippocampus, and thalamus) were from subcortical regions, denoting the critical role of subcortical areas in the stages of AD [8].

Conclusions: We proposed a novel graph edge-learning framework, Hodge-GNN, to extract edge-wise relationships within the spatial domain of graphs via Hodge 1-Laplacian. Hodge-GNN conducts graph convolution on edges directly, enabling an accurate classification of AD stages. The validation experiment proved effectiveness even in scenarios lacking node-wise measurements, a common reliance in most GNN methods, accompanied by interpretability that delineates specific connectomes and ROIs for effective AD analysis.

References

1. Destrieux, C., et al. (2010), 'Automatic parcellation of human cortical gyri and sulci using standard anatomical nomenclature', Neuroimage 53(1), 1–15
2. Farahani, F.V., et al. (2019), 'Application of graph theory for identifying connectivity patterns in human brain networks: a systematic review', Frontiers in Neuroscience, vol. 13, 585
3. Filippi, M., et al. (2020), 'Changes in functional and structural brain connectome along the Alzheimer's disease continuum', Molecular psychiatry, 25(1), 230–239
4. Kipf, T.N., et al. (2017), 'Semi-supervised classification with graph convolutional networks', International Conference on Learning Representations
5. Ma, X., et al. (2021), 'Learning multi-resolution graph edge embedding for discovering brain network dysfunction in neurological disorders', Information Processing in Medical Imaging: 27th International Conference, IPMI 2021, Virtual Event, June 28–June 30, 2021, Proceedings, pp. 253–266
6. Morris, C., et al. (2019), 'Weisfeiler and leman go neural: Higher-order graph neural networks', Proceedings of the AAAI conference on artificial intelligence, vol. 33, no. 1, pp.4602–4609
7. Tentolouris-Piperas, V., et al. (2017), 'Brain imaging evidence of early involvement of subcortical regions in familial and sporadic Alzheimer's disease', Brain research, 1655, 23–32
8. Vogt, L.K., et al. (1990), 'Pathological alterations in the amygdala in Alzheimer's disease', Neuroscience 37(2), 377–385
9. Wang, Y., et al. (2019), 'Dynamic graph CNN for learning on point clouds', ACM Transactions on Graphics (tog), 38(5), 1–12

Poster No 1378

Decoding naturalistic auditory and visual information using high-density diffuse optical tomography

Morgan Fogarty[1], Kalyan Tripathy[2], Zachary Markow[1], Jason Trobaugh[1], Joseph Culver[2]

[1]Washington University in St. Louis, St. Louis, MO, [2]Washington University School of Medicine, St. Louis, MO

Introduction: Decoding of naturalistic information from functional neuroimaging data has important neuroscience and clinical implications. Prior studies using functional magnetic resonance imaging (fMRI) have reconstructed visual (Nishimoto et al., 2011) and language (Tang et al., 2023) from neural responses. However, the physical constraints of fMRI make some natural studies and widespread application impractical. High density diffuse optical tomography (HD-DOT) is an optical imaging modality that uses many overlapping light measurements to reconstruct images similar to fMRI (Eggebrecht et al., 2014). HD-DOT has a quiet, open scanning environment, and in some cases portability, allowing for a range of decoding studies. Here, we evaluate the performance of decoding audiovisual movie clip identity through a template-matching with HD-DOT data. This work establishes the feasibility of decoding complex auditory and visual stimulus information from optical neuroimaging data.

Methods: Our HD-DOT system has 128 sources and 125 detectors distributed across posterior, lateral, and dorsal surfaces of the head with a grid spacing of 11mm. Highly sampled adults (n=3, 20-31 years old) watched a library of 20, 5-minute animated audiovisual movie clips twice each over 5 imaging sessions. A spatiotemporal template-matching approach was selected to decode the clip identity based on the HD-DOT data (Tripathy et al., 2021). Data from each session was divided into a template run and test run with one viewing of each movie clip in each half. The voxel-wise Pearson correlation coefficients were computed between the test data and the template data for each clip and averaged across the voxels to determine the mean template correlation. Decoded clip identity was assigned based on the maximum correlation between the templates and test run. Confusion matrices were generated by tracking the number of times that each test clip was decoded as each of the possible options across all imaging sessions was included in the analysis. Mean decoding accuracy was reported as the total percentage of trials across all sessions that were decoded correctly. To assess factors that impact decoding performance, the number of templates and clip duration was varied, and decoding accuracy reevaluated for each parameter.

Results: Participants viewed four movie clips twice in each imaging session. Cortical responses between independent viewings of every possible pairing of clips reveals strong correlations between runs in which the participant was presented the same movie clip (Fig 1A). Averaging inter-run correlation maps across all possible pairings of matched and mismatched movies illustrates that movies evoke reproducible, clip-specific patterns of brain activity (Fig 1B). The clip identity was decoded through template matching (Fig 1C) and aggregated across sessions and subjects (Fig 1D). The bright main diagonal of the confusion matrix illustrates that the decoded clip usually matched the clip that was presented with an accuracy of 92.3±4.4%. Decoding improved with increased clip duration but was already significantly above chance with as little as 15 seconds of data (Fig 2A). Using a fixed clip duration of 45 seconds, the number of decoding choices was varied between 4 and 16. Decoding

accuracy decreased with an increasing number of templates but remained well above chance (Fig 2B). Varying both clip duration and the number of templates across all sessions (Fig 2C-E) resulted in accuracies greater than chance for decoding 8 clip segments (90 second clip, accuracy = 76.0±5.0%, chance = 12.5%), 16 clip segments (45 seconds clip, accuracy = 53.4±6.3%, chance = 6.25%), and 64 clip segments (15 second clip, accuracy = 23.3±4.2%, chance = 3.13%).

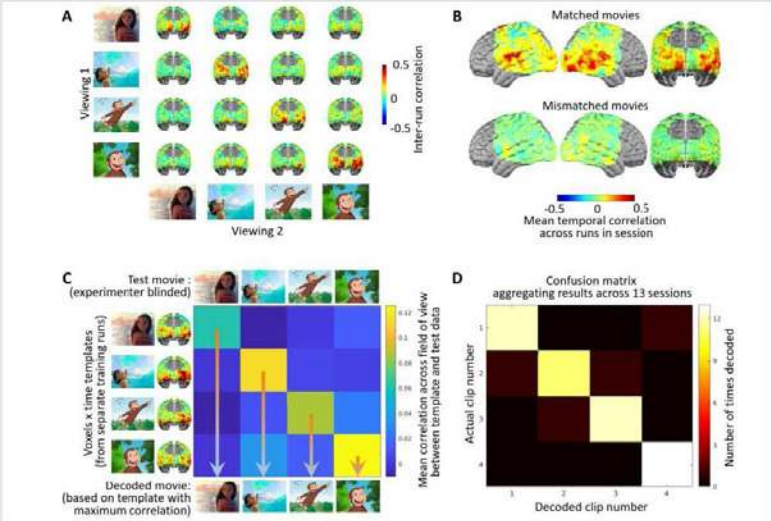

Figure 1: Voxel-wise Pearson correlation coefficients were computed across the field of view between each clip during a single imaging session (A). Higher correlations between matched clips indicates that movie evoke unique, reproducible patterns of brain activity. Across all subjects and sessions the matched and mismatched responses were averaged (B). A template decoding approach based on these correlation values was applied to determine the clip identity based on the neural responses (C). Responses across each session and subject were aggregated in a confusion matrix (D) indicating a decoding accuracy of 92.3±4.4%.

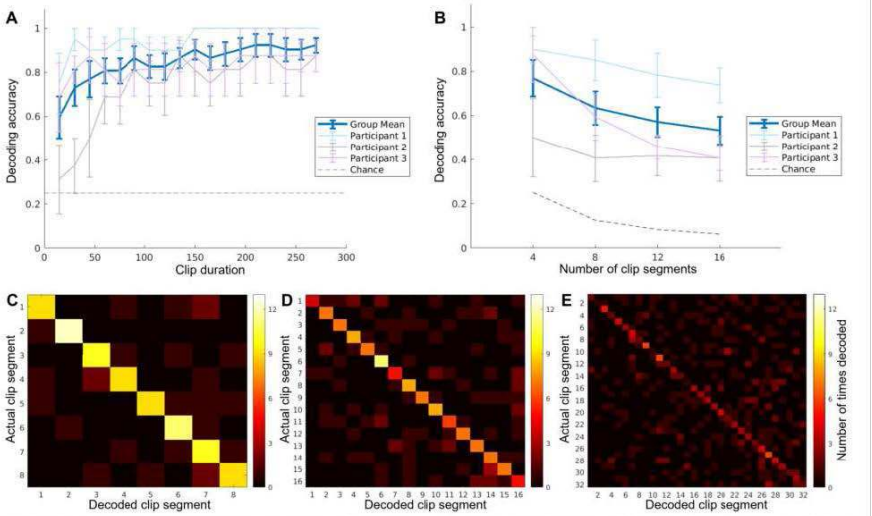

Figure 2: Decoding accuracy decreased with shorter clip lengths (A) as the clip duration was varied from 15 to 300 seconds. Similarly, the number of template options was increased from 4 to 16 templates (B) with the decoding accuracy decreasing but remaining above chance with the additional templates. Clip duration and number of templates was scaled simultaneously (C-E) resulting in accuracies greater than chance for decoding 8 clip segments (90 second clip, accuracy = 76.0±5.0%, chance = 12.5%), 16 clip segments (45 seconds clip, accuracy = 53.4±6.3%, chance = 6.25%), and 64 clip segments (15 second clip, accuracy = 23.3±4.2%, chance = 3.13%).

Conclusions: This work illustrates that complex, naturalistic information can be decoded from HD-DOT data. These results encourage further studies applying more intricate decoding algorithms to HD-DOT data, for instance to reconstruct novel scenes from optical neuroimaging data.

References

1. Eggebrecht, A. T., Ferradal, S. L., Robichaux-Viehoever, A., Hassanpour, M. S., Dehghani, H., Snyder, A. Z., Hershey, T., & Culver, J. P. (2014). Mapping distributed brain function and networks with diffuse optical tomography. Nature Photonics, 8(6), 448-454. https://doi.org/10.1038/nphoton.2014.107
2. Nishimoto, S., Vu, A. T., Naselaris, T., Benjamini, Y., Yu, B., & Gallant, J. L. (2011). Reconstructing visual experiences from brain activity evoked by natural movies. Current Biology, 21(19), 1641-1646. https://doi.org/10.1016/j.cub.2011.08.031
3. Tang, J., LeBel, A., Jain, S., & Huth, A. G. (2023). Semantic reconstruction of continuous language from non-invasive brain recordings. Nature Neuroscience. https://doi.org/10.1038/s41593-023-01304-9
4. Tripathy, K., Markow, Z. E., Fishell, A. K., Sherafati, A., Burns-Yocum, T. M., Schroeder, M. L., Svoboda, A. M., Eggebrecht, A. T., Anastasio, M. A., Schlaggar, B. L., & Culver, J. P. (2021). Decoding visual information from high-density diffuse optical tomography neuroimaging data. NeuroImage, 226. https://doi.org/10.1016/j.neuroimage.2020.117516

Poster No 1379

The magnitude of prediction error for behavior relates to sociodemographic and scan factors

Jingwei Li[1,2], Jianxiao Wu[1,2], Simon Eickhoff[2,1], B. T. Thomas Yeo[3,4], Sarah Genon[1,2]

[1]Institute of Neuroscience and Medicine (INM-7: Brain and Behaviour), Research Centre Jülich, Jülich, Germany, [2]Institute of Systems Neuroscience, Heinrich Heine University Düsseldorf, Düsseldorf, Germany, [3]CSC, TMR, ECE, WisDM, ISEP, National University of Singapore, Singapore, Singapore, [4]Martinos Center for Biomedical Imaging, Massachusetts General Hospital, Charlestown, MA

Introduction: MRI-based prediction of behavioral phenotypes is a promising approach for individualized diagnosis and treatment of mental health. However, this field lacks generalizability: some (groups of) individuals are generally misclassified or show relatively large prediction errors[1-3]. Although it has been suggested that misclassified people tended to deviate from the stereotypical patterns observed in correctly classified participants, the range of sociodemographic and neuroimaging-specific factors relating to prediction errors is unknown. In this study, we investigated the associations between the prediction error magnitude of multiple behavioral domains and a broad range of variables in developmental and young adult cohorts.

Methods: We focused on three scan-related and five sociodemographic variables of interest in three open datasets: the Adolescent Brain Cognitive Development cohort (ABCD[4]; N = 5351; 9-11y; 36 behavioral measures), the Human Connectome Project -Young Adults (HCP-YA[5]; N = 948; 22-37y; 51 behavioral measures), and the Human Connectome Project – Development (HCP-D[6]; N = 455; 8-22y; 22 behavioral measures). The preprocessing of resting-state fMRI followed our previous work (ABCD & HCP-YA:[1]; HCP-D:[7]), resulting in functional connectivity (FC) matrices across 400 cortical areas[8] and 19[9] (for ABCD & HCP-YA) / 54[10] (for HCP-D) subcortical areas. Similarly, kernel ridge regression (for ABCD & HCP-YA) and support vector regression (for HCP-D) were used to predict the behavioral measures from FC. Age, gender, education (parental education for ABCD), intracranial volume, and head movement (and family income for HCP-YA) were regressed from behavioral scores and FC. For simplicity, behavioral measures were clustered within each dataset based on their similarities in prediction errors (Fig. 1A). Prediction errors were averaged within each behavioral cluster. The associations between the averaged prediction errors and each continuous covariate were examined by Pearson's correlation. The associations of categorical covariates with prediction errors were quantified by a two-sample t-test (gender) and one-way ANOVA (other covariates). To control the effect of dataset size, we randomly subsampled 100 times in ABCD and HCP-YA to match HCP-D.

Results: In scan-related factors, head movement was widely correlated with multiple behavioral domains across datasets (Fig. 1B). In developing cohorts (ABCD, HCP-D), head size, captured by intracranial volume, was significantly negatively correlated with prediction errors of Child Behavior Checklist (CBCL), prodromal psychosis, and emotion recognition. In sociodemographic factors, consistent with our previous work[1], ethnicity was strongly associated with prediction errors for most of the behavioral domains in ABCD and HCP-YA. In addition, (parental) education and family income were even more broadly associated with prediction errors of almost all behavioral domains across all datasets. Age was correlated with prediction errors in both developing cohorts. The associations observed in the full samples still hold in subsamples. Examples of the observed associations are illustrated in Fig. 2.

Conclusions: FC-based behavioral prediction errors were broadly associated with many scan-related and sociodemographic factors in young populations. More associations were observed for the behavioral domains that were more difficult to predict, such as CBCL and prodromal psychosis in ABCD and emotion recognition in the two HCP datasets. It suggests that the predictive models might learn more information from non-neurobiological factors to predict such behavioral measures. More associations were observed in ABCD compared to the other two datasets, possibly related to the higher diversity of this dataset. In sum, this study importantly contributes to a better understanding of the insufficient prediction power and low generalizability in the field.

(A) Group of behavioral measures clustered by similarity in prediction error

ABCD (correlation between prediction errors > 0.4)					HCP-YA (correlation between prediction errors > 0.3)			HCP-D (correlation between prediction errors > 0.3)	
Verbal Memory	Cognition	Mental Rotation	CBCL (Child Behavior Checklist)	Prodromal Psychosis	Social Cognition	Positive/Negative Feelings	Emotion Recognition	Cognition	Emotion Recognition
Short delay recall	Reading (pronunciation)	Visuospatial accuracy	Anxious/Depressed	Total prodromal psychosis symptoms	Social Cognition - Random	Neuroticism (NEO)	Emot. Recog. - Total	Fluid Cognition	Emot. Recog. - Total
Long delay recall	Crystallized cognition	Visuospatial efficiency	Withdrawn/Depressed	Prodromal psychosis severity	Social Cognition - Interaction	Anger - Hostility	Emot. Recog. - Angry	Crystallized Cognition	Emot. Recog. - Fear
	Picture vocabulary		Social problems			Sadness	Emot. Recog. - Fear	Total Cognition	Emot. Recog. - Sad
	Overall cognition		Thought problems			Loneliness	Emot.Recog. - Neutral	Cognitive Flexibility (DCCS)	
	Fluid cognition		Aggressive behavior			Perceived Stress	Emot. Recog. - Sad	Inhibition (Flanker task)	
	Processing speed		Attention problems			Anger - Affect		Working Memory	
			Rule-breaking behavior			Fear - Affect		Oral Reading Recognition	
			Mania			Friendship		Processing Speed	
						Perceived Rejection		Picture Vocabulary	
						Emotional Support			
						Perceived Hostility			

Row 1: datasets. Row 2: names of behavioral groups. Row 3 – last row: behavioral measures in each group.

(B) Association with behavioral prediction errors in full samples

FDR correction across behavioral groups per dataset per covariate.

		Euler characteristic	Head size	Head motion	Age	Sex/Gender *Two-sample t-test (M-F)*	Ethnicity/race *One-way ANOVA*	(Parental) Education *One-way ANOVA*	Family Income
ABCD	Verbal Memory	R = -0.007 P = 0.595	R = -0.029 P = 0.0402	R = 0.022 P = 0.106	R = -0.035 P = 0.0128	P = 0.879 Effect size = 2.16e-3	P = 0.609 Effect size = 5.24e-4	P = 0.0130 Effect size = 4.05e-3	One-way ANOVA P = 0.0179 Effect size = 4.32e-3
	Cognition	R = -0.038 P = 7.06e-3	R = 0.003 P = 0.838	R = 0.032 P = 0.0237	R = 0.035 P = 0.0123	P = 9.52e-4 Effect size = 3.03e-2	P = 2.39e-5 Effect size = 5.17e-3	P = 1.35e-3 Effect size = 5.27e-3	One-way ANOVA P = 3.22e-3 Effect size = 5.33e-3
	Mental Rotation	R = 0.014 p = 0.310	R = 0.018 P = 0.190	R = -0.012 P = 0.399	R = 0.094 P = 1.66e-11	P = 5.26e-3 Effect size = 3.97e-2	P = 0.0147 Effect size = 2.41e-3	P = 0.535 Effect size = 1.56e-3	One-way ANOVA P = 0.0516 Effect size = 3.68e-3
	CBCL	R = -0.019 P = 0.174	R = -0.062 P = 8.70e-6	R = 0.063 P = 5.44e-6	R = -0.012 P = 0.402	P = 1.08e-15 Effect size = 0.110	P = 1.26e-14 Effect size = 1.33e-2	P = 3.71e-39 Effect size = 3.91e-2	One-way ANOVA P = 1.35e-55 Effect size = 5.63e-2
	Prodromal Psychosis	R = -0.019 P = 0.544	R = -0.092 P = 3.70e-11	R = 0.058 P = 2.92e-5	R = -0.068 P = 1.10e-6	P = 0.553 Effect size = 1.15e-2	P = 3.50e-18 Effect size = 1.69e-2	P = 7.06e-20 Effect size = 2.14e-2	One-way ANOVA P = 1.12e-18 Effect size = 2.16e-2
HCP-YA	Social Cognition	R = 0.028 P = 0.397	R = -0.065 P = 0.0440	R = 0.092 P = 4.59e-3	R = 0.022 P = 0.505	P = 0.651 Effect size = -1.85e-2	P = 2.61e-5 Effect size = 3.00e-2	P = 6.36e-5 Effect size = 3.02e-2	One-way ANOVA P = 6.70e-4 Effect size = 2.65e-2
	Positive/Negative Feelings	R = 0.025 P = 0.438	R = -0.040 P = 0.213	R = 0.095 P = 3.42e-3	R = -0.028 P = 0.396	P = 0.917 Effect size = 2.29e-3	P = 2.72e-5 Effect size = 2.99e-2	P = 2.22e-4 Effect size = 2.72e-2	One-way ANOVA P = 0.0128 Effect size = 1.87e-2
	Emotion Recognition	R = -0.002 P = 0.957	R = -0.012 P = 0.719	R = 0.124 P = 1.36e-4	R = -0.035 P = 0.284	P = 0.0657 Effect size = 4.37e-2	P = 0.481 Effect size = 4.75e-3	P = 0.278 Effect size = 7.91e-3	One-way ANOVA P = 0.0100 Effect size = 1.94e-2
HCP-D	Cognition	R = -0.026 P = 0.583	R = 0.004 P = 0.928	R = -0.011 P = 0.809	R = 0.000 P = 0.992	P = 0.788 Effect size = 9.00e-3	P = 0.0685 Effect size = 1.92e-2	P = 9.86e-5 Effect size = 6.44e-2	R = 0.009 P = 0.852
	Emotion Recognition	R = -0.128 P = 6.14e-3	R = -0.301 P = 1.64e-5	R = 0.111 P = 0.0181	R = -0.220 P = 2.24e-6	P = 0.0763 Effect size = -7.44e-2	P = 0.590 Effect size = 6.24e-3	P = 1.47e-5 Effect size = 7.36e-2	R = -0.028 P = 0.566

For ABCD and HCP-YA, the significant associations were confirmed by random subsampling.

Figure 1. (A) Detailed names of behavioral measures included in each behavioral cluster. To simplify the analyses, we grouped the behavioral measures that shared similar patterns in the prediction errors together. Later on, we only investigated the association between the averaged prediction errors for each behavioral cluster and covariates. **(B) Associations between prediction errors and covariates in the full samples.** For continuous covariates, e.g. head size (i.e. intracranial volume), both the Pearson's correlation and the corresponded p value are reported. For a binary covariate (sex/gender), two-sample t-test was used to test if significant difference in behavioral prediction error existed between the two covariate categories. For non-binary categorical covariates, e.g. education, one-way ANOVA was used to determine if significant difference in prediction error existed across covariate categories.

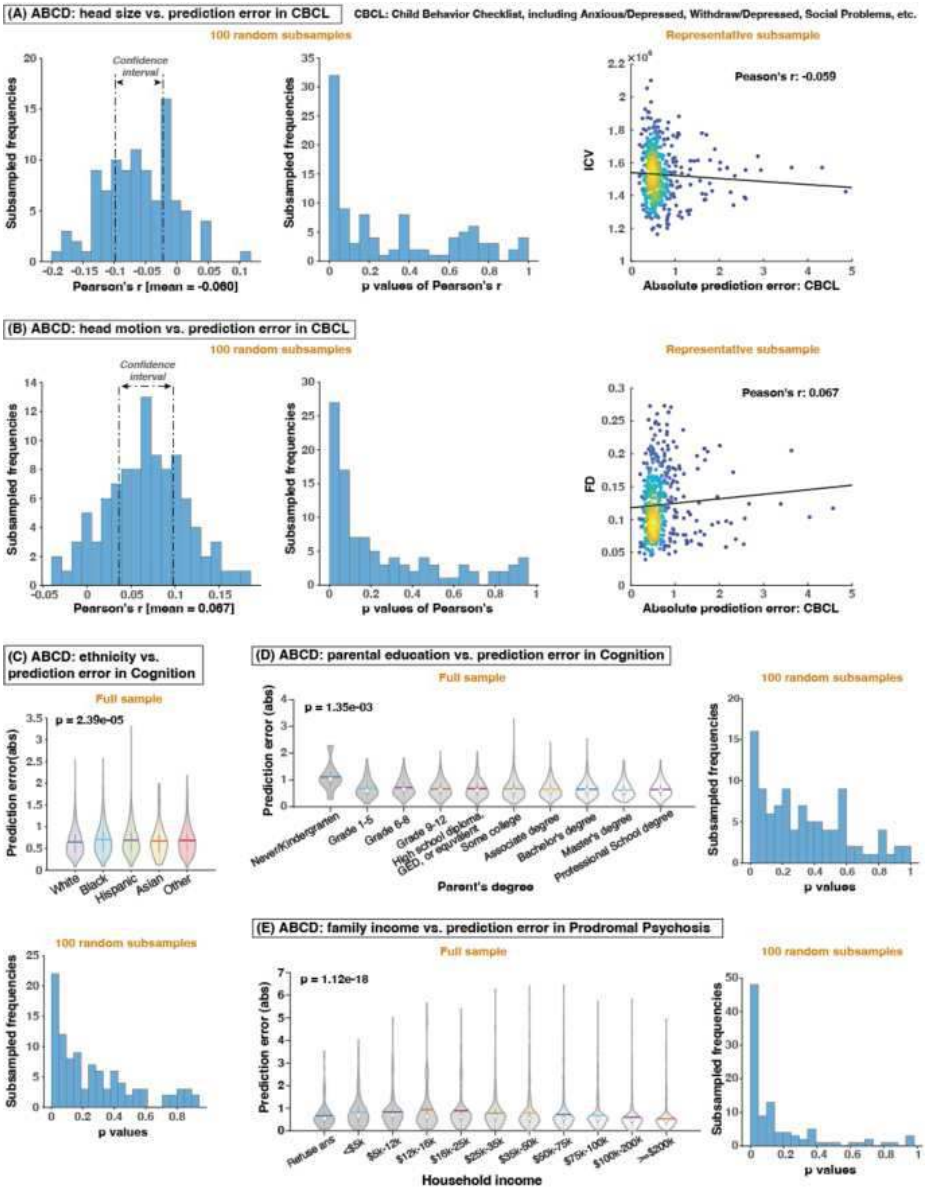

Figure 2. Examples of associations between prediction errors and scan-related / sociodemographic covariates. The discovered associations were robust, validated in 100 random subsamples. In (A-B), the left panel shows the distribution of the correlation between prediction errors and a certain continuous covariate across subsamples; the middle panel shows the distribution of the p values corresponding to the correlations in subsamples. A confidence interval of the subsampled correlations that does not overlap with 0, and the p value distributions skewed towards 0, would indicate that the observed association is stable. The right panel shows the relationship in one representative subsample as a scatter plot between prediction errors and the covariate. The correlation in this representative subsample roughly equals to the mean correlation among all subsample. In (C-E), the covariates are categorical with more than two categories. Therefore, the left/upper panel shows the prediction errors per category of the covariate in the full saprnle; the right/lower panel shows the distribution of subsampled p values of cross-category differences in prediction errors. The differences in prediction errors across covariate categories were tested by one-way ANOVA. Similarly, the p value distributions skewed towards 0 would indicate robust association.

References

1. Li, J. et al. (2022). Cross-ethnicity/race generalization failure of behavioral prediction from resting-state functional connectivity. Sci. Adv. 8, eabj1812.
2. Dhamala, E. et al. (2023). One Size Does Not Fit All: Methodological Considerations for Brain-Based Predictive Modeling in Psychiatry. Biological Psychiatry. 93(8). 717-728.
3. Greene, A.S. et al. (2022). Brain–phenotype models fail for individuals who defy sample stereotypes. Nature. 609, 109–118.
4. Casey, B.J. et al. (2018). The Adolescent Brain Cognitive Development (ABCD) study: Imaging acquisition across 21 sites. Dev. Cogn. Neurosci. 32. 43-54.
5. Van Essen, D.C. et al. (2013). The WU-Minn human connectome project: An overview. NeuroImage. 80, 62–79.
6. Somerville, L.H. et al. (2018). The Lifespan Human Connectome Project in Development: A large-scale study of brain connectivity development in 5-21 year olds. Neuroimage. 183. 456-468.
7. Wu, J. et al. (2021). A Connectivity-Based Psychometric Prediction Framework for Brain-Behavior Relationship Studies. Cereb. Cortex. 31(8). 3732-375
8. Schaefer, A. et al. (2018). Local-global parcellation of the human cerebral cortex from intrinsic functional connectivity MRI. Cereb. Cortex 28, 3095–3114.
9. Fischl, B. et al. (2002). Whole brain segmentation: Automated labeling of neuroanatomical structures in the human brain. Neuron 33, 341–355.
10. Tian, Y. et al. (2020). Topographic organization of the human subcortex unveiled with functional connectivity gradients. Nat Neurosci. 23(11):1421-1432.

Poster No 1380

The legibility of the imaged human brain

James Ruffle[1], Robert Gray[1], Samia Mohinta[1], Guilherme Pombo[1], Chaitanya Kaul[2], Harpreet Hyare[1], Geraint Rees[1], Parashkev Nachev[1]

[1]UCL Queen Square Institute of Neurology, London, London, [2]School of Computing Science, University of Glasgow, Glasgow, Glasgow

Introduction: Our knowledge of the organisation of the human brain at the population-level is yet to translate into power to predict functional differences at the individual-level, limiting clinical applications, and casting doubt on the generalisability of inferred mechanisms. It remains unknown whether the difficulty arises from the absence of individuating biological patterns within the brain, or from limited power to access them with the models and compute at our disposal.

Methods: Here we comprehensively investigate the resolvability of such patterns with data and compute at unprecedented scale. Across 23 810 unique participants from UK Biobank, we systematically evaluate the predictability of 25 individual biological characteristics, from all available combinations of structural and functional neuroimaging data. Over 4526 GPU*hours of computation, we train, optimize, and evaluate out-of-sample 700 individual predictive models, including fully-connected feed-forward neural networks of demographic, psychological, serological, chronic morbidity, and functional connectivity characteristics, and both uni- and multi-modal 3D convolutional neural network models of macro- and micro-structural brain imaging.

Results: We find a marked discrepancy between the high predictability of sex (balanced accuracy 99.7%), age (mean absolute error 2.048 years, R2 0.859), and weight (mean absolute error 2.609Kg, R2 0.625), for which we set new state-of-the-art performance, and the surprisingly low predictability of other characteristics (Figure 1). Neither structural nor functional imaging predicted an individual's psychology better than the coincidence of common chronic morbidity ($p<0.05$). Serology predicted common morbidity ($p<0.05$) and was best predicted by it ($p<0.001$), followed by structural neuroimaging ($p<0.05$) (Figure 2).

Conclusions: Our findings suggest either more informative imaging or more powerful models will be needed to decipher individual level characteristics from the human brain. We make our models and code openly available.

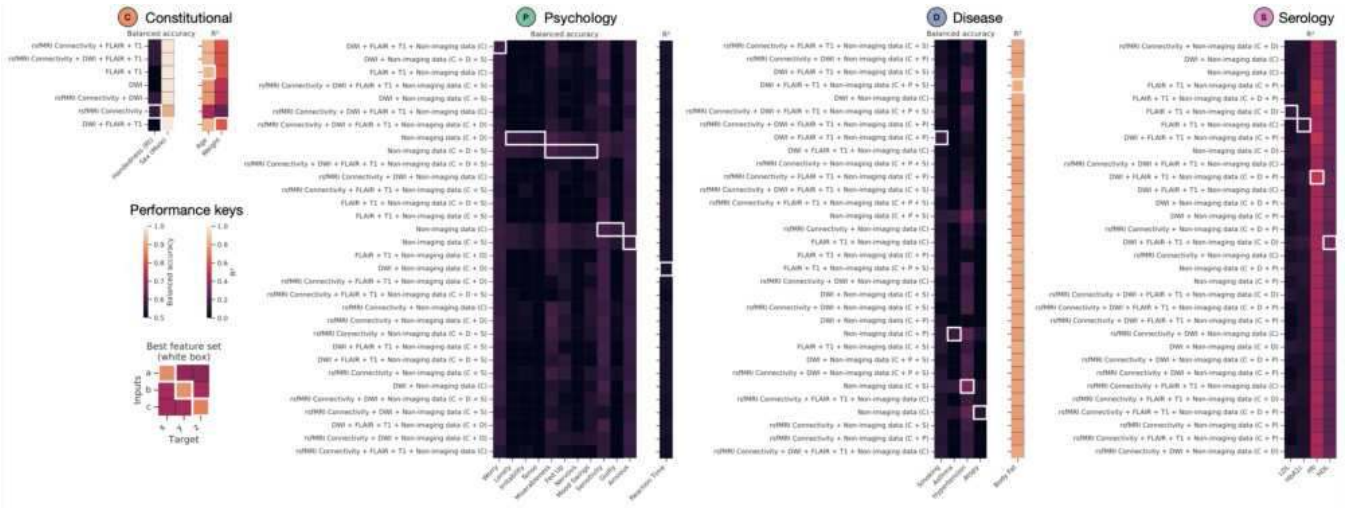

Figure 1 - Model performances. Test set performance for all models across constitutional (C) – orange, disease (D) – blue, psychology (P) – green, and serology (S) – pink feature domains. Index of performance is given as balanced accuracy for classification targets and R^2 for regression fits. The x-axis of all heatmaps depicts the model target, and y-axis depicts the range of feature inputs. White boxes demarcate the best set of inputs to achieve the greatest out-of-sample model performance.

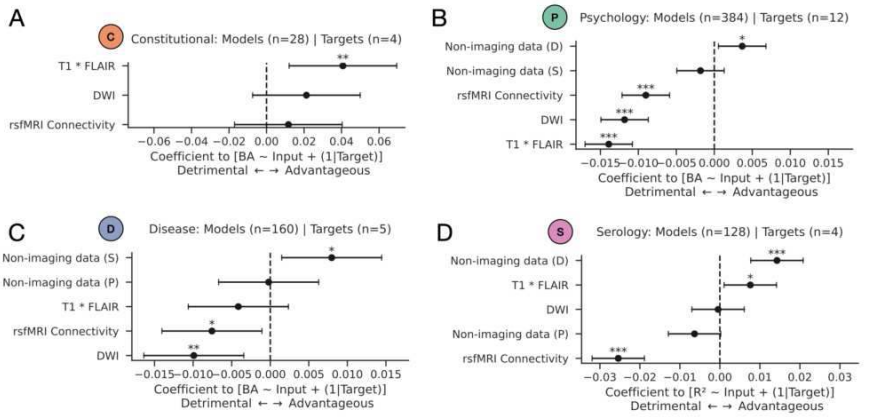

Figure 2 - Domain-specific effects. Linear mixed-effects models for predicting out of sample performance (balanced accuracy or R^2, where applicable) from structural imaging, functional imaging, and non-imaging domain feature sets. Shown are coefficient plots for models whose targets are A) constitutional, B) psychology, C) disease, and D) serology. Inputs with coefficients whose values are positive are associated with increase model performance (advantageous), whilst features with negative coefficients are associated with weaker performance (detrimental). Asterisks stipulate statistical significance as per standard convention: * denotes p<0.05; ** denotes p<0.01; *** denotes p<0.001.

References
1. MONAI: https://monai.io
2. PyTorch: https://pytorch.org
3. Nilearn: https://nilearn.github.io/stable/index.html

Poster No 1381

Automatic MRI-based Prognostic Prediction After Acute Ischemic Brain Stroke

Noam Rotenberg[1], Brian Caffo[1], Andreia Faria[1]

[1]*Johns Hopkins University, Baltimore, MD*

Introduction: Stroke is a leading cause of long-term disability. In addition to the obvious benefits to patients and families, early prognosis prediction can assist in triage, precision care, and provide benchmarks for clinical interventions. Previous studies have tried to predict mRS-90, a common measure of outcomes 90 days after stroke, using clinical and imaging features[1-3], but they encountered challenges related to their limited and homogeneous samples, and subjectivity of the lesion evaluation. We developed a comprehensive model to predict mRS-90 in patients with acute ischemic stroke, based on automatically extracted features of the acute injury. This model adds up to the "Acute stroke Detection and Segmentation" tool, ADS[1], a public and user-friendly toolbox, accessible to non-image experts clinical researchers, providing objective quantification of acute ischemic strokes in real time.

Methods: The sample includes 1154 patients with MRIs with evidence of ischemic stroke in the diffusion weighted images (DWI), and recorded mRS-90, a subset of our public dataset[4,5]. Each patient's imaging data was represented by a quantitative feature vector (QFV) that reflects the ratio of injury in brain structures[6]: basal ganglia, deep white matter (WM), internal capsule, cerebellum, insula, brainstem, thalamus, and occipital, parietal, temporal, and frontal lobes, plus injury volume and hemisphere(s) affected. A variety of machine learning models (Table 1), were trained (n = 800), tuned, and tested (n = 354). In order to make our results both interpretable and comparable with previous studies we evaluate efficiency of our models in two paradigms: 1. mRS per se: We computed: a) Flexible mRS: accuracy, where predicted mRS ±1 compared to the ground truth mRS is considered true positive; and b) 3-level mRS: accuracy, where predicted mRS and true mRS are mapped into three groups: mRS 0-2 (not affected or slightly disabled), 3-4 (moderately disabled), 5-6 (severely disabled or dead). 2. Binary statistics: predicted and true mRS are mapped into two groups: mRS-90 <=3.5 and > 3.5 (good and bad prognosis, respectively). AUROC, F1, sensitivity, and specificity were calculated. This approach makes our results comparable with those of previous studies, which commonly use a binary paradigm, and enable us to see whether the prediction efficiency differs for patients mildly or severely affected. Feature Analysis was performed with gradient boosting forest feature importance in three models, including 1) all patients; 2) patients with small strokes (below-median (5.8 mL) injury volume); and 3) patients with large strokes, which are known to exhibit more variable prognosis. Stratifying by lesion volume aims to reduce the effect of total lesion volume and to reveal the regions that mostly influences prognosis.

Results: Overall, all models had similar accuracy, both for the "per se" mRS and the binary prognostic prediction, and all had higher specificity than sensitivity (table 1). These results rival with those reported in previous studies for binary prognostic classification[1-3]. This is encouraging since the models were trained and tested in large and independent samples of real clinical data. The feature analysis (figure 1) shows that stroke volume was the most important feature in the model trained with all the patients, as expected. In small strokes, as the importance of the total injury volume diminishes, the importance of lesions in regions that are crucial for vital functions (e.g., brainstem) or in association areas (frontal lobe, WM) increases. Within the large strokes, the injury of regions within the posterior circulation (occipital and temporal lobe, thalamus, and cerebellum) lead to predict worse prognosis.

Conclusions: Our results show that prognosis can be reasonably predicted by lesion location automatically calculated from brain MRIs. This process enables lesion-functional modeling and accessible prognostic prediction for patient stratification and personalized care.

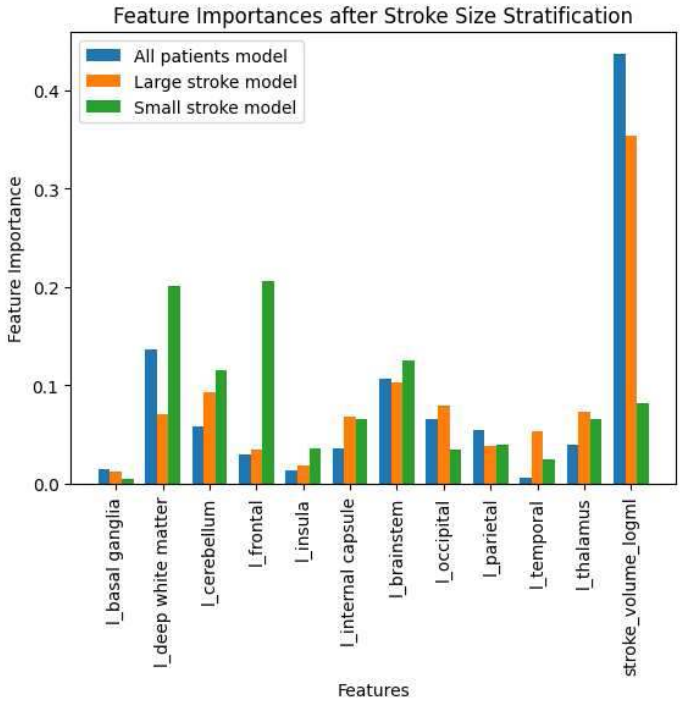

	flexible mRS	3-classes mRS	AUROC	F1 score	Sensitivity	Specificity
Gradient Boosting	0.61	0.65	0.75	0.54	0.58	0.83
Random Forest	0.61	0.64	0.74	0.54	0.49	0.89
Bayesian Ridge	0.6	0.64	0.73	0.54	0.55	0.85
Linear	0.59	0.63	0.72	0.53	0.66	0.74
Bagged Linear	0.6	0.65	0.73	0.55	0.51	0.9
Support Vector	0.68	0.63	0.72	0.54	0.53	0.87
Radius Neighbors	0.55	0.64	0.73	0.55	0.63	0.8

References

1. Gianluca, B (2020). Multimodal predictive modeling of endovascular treatment outcome for acute ischemic stroke using machine-learning. Stroke, 51(12):3541–3551
2. Helge, C (2022). Imaging-based outcome prediction in posterior circulation stroke. Journal of Neurology, 269(7):3800–3809
3. Anouk, L (2020). Prediction of functional outcome after acute ischemic stroke: comparison of the ct-dragon and a reduced features set. Frontiers in Neurology, 11:718
4. Liu, CF and Faria, AV (2023). Acute-stroke Detection Segmentation (ADS). https://www.nitrc.org/projects/ads/.
5. Liu, CF (2023). A large public dataset of annotated clinical mris of patients with acute stroke and linked metadata. Scientific Data, 10(1):458
6. Liu, CF (2023). Automatic comprehensive radiological reports for clinical acute stroke mris. Communications Medicine, 3(1):95.

Poster No 1382

Early Prediction of Long-term Cognitive Development Using Multimodal MRI in Infants Born Preterm

Nehal Parikh[1], Mekibib Altaye[2], Armin Allahverdy[2], Hailong Li[2], Beth Kline-Fath[2], Weihong Yuan[2], Abiot Yenealem Derbie[1], Lili He[2], Leanne Tamm[2]

[1]Cincinnati Children's Hospital, Cincinnati, OH, [2]Cincinnati Chiildren's Hospital, Cincinnati, OH

Introduction: Cognitive impairment remains the most common long-term adverse outcome following preterm birth. Accurate diagnosis usually takes 3 to 5 years during which time we are missing an early critical window of neuroplasticity. Detection during this window would allow for early targeted interventions to enhance therapeutic efficacy. Our goal was to improve early prediction of cognitive development by term-equivalent age (TEA) by exploiting features from brain morphometry, structural connectivity (SC), and functional connectivity (FC) derived from structural MRI, diffusion MRI (dMRI), and resting state functional MRI (rsfMRI), respectively.

Methods: We studied a multisite regional cohort of 358 very preterm (VPT) infants born at or below 32 weeks' gestational age from 5 Southwest Ohio NICUs (Cincinnati Infant Neurodevelopment Early Prediction [CINEPS] cohort). All infants were imaged at Cincinnati Children's Hospital between 39 and 44 weeks postmenstrual age on the same 3T Philips scanner and 32-channel receiver head coil with the following identical sequences: dMRI: TE: 88 msec, TR 6972 msec, FA 90°, resolution 2×2×2 mm3, 36 directions; b-value 800 s/mm2, MB factor 2; rsfMRI: TE: 45 msec, TR 893 msec, FA 90°, resolution 2.5×2.5×2.5 mm3,400 volumes, MB factor 4; Axial T2w: TE 166 msec, TR 8,300 msec, FA 90°, resolution 1×1×1 mm3. Cognitive development was assessed with the Differential Ability Scales (2nd Edition) General Conceptual Ability (GCA) score at 3 years corrected age. We used established pre- and post-processing pipelines and neonatal brain atlases from the Developing Human Connectome Project (dHCP) to generate brain volumes, cortical maturation metrics, SC and FC as previously described (Bastiani M. 2019; Kline JE, 2020; Kline JE, 2021). Missing data was handled via k-nearest neighbor imputation. We used two unsupervised approaches for feature selection/reduction from the nearly 20,000 MRI predictor variables: CONN, which generated six graph theory measures per modality for each of the 81 dHCP atlas regions of interest and non-negative matrix factorization (NMF), which decomposed these measures to 26 morphometry, 28 FC and 30 SC network components. Global efficiency from SC and FC and postmenstrual age at MRI scan were modeled separately. We selected one conventional MRI (cMRI; global brain abnormality score) and 10 known clinical predictors of cognitive development a priori (Table 1). Last, we applied support vector machine (SVM) to develop a multimodal model that included the above 86 independent variables to predict the GCA score. We created 500 bootstrap datasets to evaluate model performance and correct for over-optimism per the TRIPOD guidelines (Moons KGM, 2015). To assess model fit, we calculated optimism-corrected values for R2, root mean square error (RMSE), and difference between observed and predicted scores.

Results: The mean (SD) gestational age was 29.3 (2.5) and GCA score was 93.7 (20.0) for the 314 infants (88%) with follow-up data at or after 3 years CA (Table 1A). The 11 a priori selected clinical + cMRI predictors (Table 1) did poorly in predicting the DAS GCA score: R2 24.0%. The combined multimodal model achieved the highest accuracy with an optimism-corrected R2 value of 64.3% (95% CI: 56.3, 72.3) (Table 1B). The predicted cognitive scores of the multimodal model were closely aligned with the observed scores (Fig. 1A); Approximately two-thirds of the predicted GCA scores were within +/- 6 points (1 SD) of the observed scores (Fig. 1B).

Table 1A. Maternal and infant clinical characteristics of children born preterm with long-term cognitive outcome data.

Baseline Variables*	Preterm Infants (N=314)
Histologic chorioamnionitis (moderate-severe)	47 (15.0%)
Hypertensive disorder of pregnancy	129 (41.1%)
Multiple gestation	115 (36.6%)
Gestational age, weeks, mean (SD)	29.3 (2.5)
Female sex	152 (48.4%)
Surgical necrotizing enterocolitis / intestinal perforation	16 (5.1%)
Postnatal sepsis	33 (10.5%)
Bronchopulmonary dysplasia	
Grade 1	73 (23.3%)
Grade 2	48 (15.3%)
Grade 3	15 (4.8%)
Social risk score, median (IQR)	3 (1, 5)
Postmenstrual age at MRI scan, weeks, mean (SD)	42.8 (1.3)
Global brain abnormality score, median (IQR)#	6 (2, 8)

*These clinical and conventional MRI variables were selected *a priori* for the SVM model; all values are n (%) unless otherwise noted
#Based on Kidokoro H, et al. (2013)

Table 1B: Prediction accuracy (optimism-corrected R^2) and root mean square error (RMSE) for each of the modalities independently and in combination.

Modality	Optimism Corrected R^2 (95% CI)*	RMSE (95% CI)*
Clinical variables	0.203 (0.088, 0.290)	17.90 (16.45, 19.30)
Conventional MRI (cMRI)	0.111 (0.014, 0.176)	18.90 (17.27, 20.38)
Clinical + cMRI	0.240 (0.141, 0.338)	17.53 (15.94, 19.11)
Morphometry	0.378 (0.261, 0.484)	16.82 (13.91, 19.85)
Structural connectivity (SC)	0.517 (0.423, 0.603)	14.44 (12.67, 16.22)
Functional connectivity (FC)	0.454 (0.342, 0.571)	15.59 (12.68, 18.06)
Morphometry+SC+FC	0.596 (0.513, 0.678)	13.07 (11.54, 14.52)
Clinical+cMRI+Morphometry+SC+FC#	0.643 (0.563, 0.723)	11.94 (10.43, 13.24)

*All values are optimism-corrected after bootstrapping (Moons KGM, Ann Intern Med. 2015).
#NMF selected of 30 SC, 28 FC, and 26 morphometry components that were combined with 10 clinical and two structural MRI a priori selected variables that were added to the SVM model. GCA scores were imputed from the 5 yr. testing visits for 31 children with missing data at age 3.

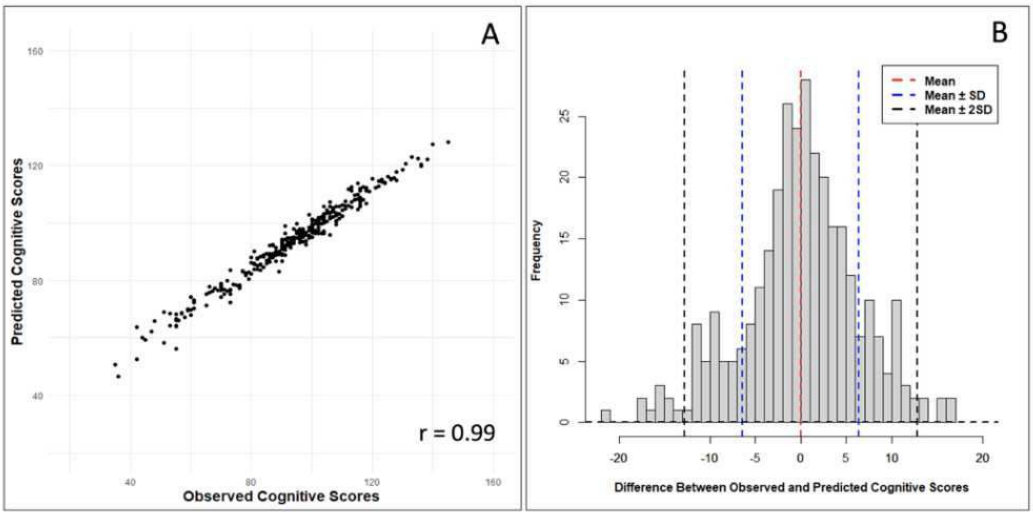

Figure 1. A) Scatter plot of observed versus predicted cognitive scores (mean scores after bootstrap and optimism correction) and B) Histogram of difference between observed and predicted scores.

Conclusions: In a regional prospective cohort of VPT infants, we used multimodal advanced neuroimaging and machine learning to enable early prediction of long-term cognitive development. Our study generated data that is considerably higher in accuracy than current prognostic models. We aim to use this internally validated model to enable targeted risk stratification for interventions that are designed to enhance cognitive development in high-risk VPT infants.

References

1. Bastiani, M. (2019). 'Automated processing pipeline for neonatal diffusion MRI in the developing Human Connectome Project. Neuroimage, vol 18, pp. 750-763.
2. Kidokoro H. (2013). 'New MR imaging assessment tool to define brain abnormalities in very preterm infants at term.' American Journal of Neuroradiology, vol. 34, no. 11, pp. 2208-2214
3. Kline JE. (2020). 'Automated brain morphometric biomarkers from MRI at term predict motor development in very preterm infants.' Neuroimage Clinical. vol 28, no. 102475.
4. Kline JE. (2021). 'Association Between Brain Structural Network Efficiency at Term-Equivalent Age and Early Development of Cerebral Palsy in Very Preterm Infants.' Neuroimage. vol 245, no.118688
5. Moons KGM (2015). 'Transparent Reporting of a multivariable prediction model for Individual Prognosis Or Diagnosis (TRIPOD): Explanation and Elaboration'. Annals of Internal Medicine, vol. 162, pp. W1-W73.

Poster No 1383

Accurate, Early Detection of Cerebral Palsy Using Multimodal MRI at Term in Infants Born Preterm

Nehal Parikh[1], Mekibib Altaye[2], Armin Allahverdy[2], Julia Kline[3], Karen Harpster[2], Hailong Li[2], Junqi Wang[2], Abiot Yenealem Derbie[4], Jean Tkach[2], Beth Kline-Fath[2], Stephanie Merhar[2], Weihong Yuan[2], Lili He[2]

[1]Cincinnati Children's Hospital, Cincinnati, OH, [2]Cincinnati Chiildren's Hospital, Cincinnati, OH, [3]National Institutes of Health, Bethesda, MD, [4]Cincinnati Children's Hospital, Cincinnati, OH

Introduction: Despite recent advances in early diagnosis of cerebral palsy (CP), accurate and timely detection remains elusive. Advances in quantitative MRI and machine learning technology appear promising to enable early, accurate prediction of CP. Our goal was to improve early CP prediction in preterm infants by exploiting advanced quantitative MRI biomarkers acquired at term-equivalent age.

Methods: We recruited a multisite regional cohort of 358 very preterm (VPT) infants born at or below 32 weeks' gestational age from 5 Southwest Ohio Neonatal Intensive Care Units (Cincinnati Infant Neurodevelopment Early Prediction Study [CINEPS]). All infants were imaged at Cincinnati Children's between 39 and 44 weeks postmenstrual age on a single 3T Philips scanner and 32-channel receiver head coil with the following identical sequences: dMRI: TE 88ms, TR 6972ms, FA 90°, resolution 2×2×2 mm3, 36 directions; b-value of 800 s/mm2; MB factor 2; rsfMRI: TE 45, TR 893ms, FA 90°, resolution 2.5×2.5×2.5 mm3; 400 volumes; MB factor 4; Axial T2w: TE 166 ms, TR 8300ms, FA 90°, resolution 1×1×1 mm3. CP was diagnosed at 2 years corrected age (CA) using the Amiel-Tison (1998) standardized neurological exam and the Gross Motor Function Classification System (GMFCS; Palisano RJ, 2000). We used established pre- and post-processing pipelines and neonatal brain atlases from the Developing Human Connectome Project (dHCP) to generate brain morphometry measures (volumes, cortical maturation), structural connectivity (SC) from diffusion MRI (dMRI), and functional connectivity (FC) from resting state functional MRI (rsfMRI) as previously described (Bastiani M, 2019; Kline JE, 2020; Kline JE, 2021). We used CONN to generate six graph theory measures per modality for each of the 81 dHCP atlas regions of interest. We used an unsupervised approach for feature selection/reduction from the nearly 20,000 MRI predictor variables. Specifically, we employed non-negative matrix factorization (NMF) to decompose these predictors into 7 network components each from morphometry, FC, and SC. We elected to include moderate-severe brain injury from conventional MRI (cMRI) and five clinically known predictors of CP a priori (Table 1). Last, we applied a support vector machine to develop a multimodal model that included the above independent variables to predict CP. We created 1,000 bootstrap datasets to evaluate model performance and correct for over-optimism per the TRIPOD guidelines (Moons KGM, 2015). To assess model fit, we calculated optimism-corrected values for sensitivity, specificity, and area under the receiver operating characteristic curve (AUC).

Results: There were no significant differences in the baseline clinical variables between the 307 VPT infants (86%) that returned for standardized CP testing at 2 years CA (shown in Table 1) and the 51 that did not (data not shown). 34 infants (11.1%) developed CP (GMFCS ≥1) of which 11 (3.6%) had moderate-severe CP (GMFCS≥2). The CP vs. non-CP groups differed in several clinical factors (Table 1). We observed moderate-severe injury on cMRI at term in 25 (8.1%) infants. The AUC was 0.657 (95% CI: .581, .730) for the clinical plus cMRI model. For the combined model that included clinical, cMRI, and quantitative MRI modalities, the AUC was 0.870 (.818, .914), sensitivity was 86.0% (73.5, 96.4), and specificity was 88.0% (79.5, 96.0) for the prediction of any CP; the corresponding values for moderate-severe CP were 0.946 (.859, .993), 93.4% (72.2, 100), and 95.8% (90.5, 99.7) (Table 2).

Table 1: Baseline characteristics of mothers and their infants born very preterm with and without cerebral palsy (CP) at 2 years corrected age.

Baseline variables*	CP (N=34)	No CP (N=273)	*P* value
Maternal characteristics			
Maternal age, years	28.71 (5.47)	29.33 (5.47)	0.53
Antenatal steroids*	29 (85.3%)	253 (92.7%)	0.17
Antenatal magnesium	28 (82.4%)	230 (84.2%)	0.78
Histologic chorioamnionitis	7/30 (23.3%)	40/245 (16.3%)	0.34
Hypertensive disorders of pregnancy	16 (47.1%)	108 (39.6%)	0.41
High-risk social status	9 (26.5%)	46 (16.8%)	0.17
Multiple gestation	8 (23.5%)	102 (37.4%)	0.11
Infant characteristics			
Gestational age, weeks, mean (SD)*	27.75 (2.66)	29.40 (2.40)	*<0.01*
Birth weight z-score, mean (SD)	0.32 (1.30)	0.05 (0.92)	0.13
Sex, female*	12 (35.3%)	138 (50.6%)	0.09
Severe IVH[δ]	8 (23.5%)	15 (5.5%)	*<0.01*
Caffeine administration	27 (79.4%)	192 (70.3%)	0.27
Sepsis	4 (11.8%)	29 (10.6%)	0.84
Necrotizing enterocolitis (stage II or higher)	4 (11.8%)	12 (4.4%)	0.09
BPD (moderate-severe)*[#]	16 (47.1%)	46 (16.8%)	*<0.01*
Retinopathy of prematurity (severe)	4 (11.8%)	15 (5.5%)	0.15
Major surgery requiring general anesthesia	5 (14.7%)	31 (11.4%)	0.57
Postmenstrual age at MRI, weeks, mean (SD)*	43.18 (1.33)	42.64 (1.33)	*0.02*
Brain injury on conventional MRI at term*[€]	12 (35.3%)	13 (4.8%)	*<0.01*

All values are n (%) unless otherwise noted.
*These six variables were selected *a priori* for the prognostic model
[δ]Severe intraventricular hemorrhage defined using Papile grades III/IV definition.
[#]Bronchopulmonary dysplasia (BPD) definition per Jenson EA, 2019 at 36 weeks postmenstrual age.
[€]Brain injury to motor regions as defined by Novak I, 2016 on structural MRI at term-equivalent age.

Table 2. Prognostic test properties for multimodal advanced MRI biomarkers and currently known clinical and conventional MRI predictors for the prediction of cerebral palsy (GMFCS≥1) and moderate-severe cerebral palsy (GMFCS≥2) at 2 years corrected age.

Modalities	Sensitivity (95% CI)	Specificity (95% CI)	PPV (95% CI)	NPV (95% CI)	AUC (95% CI)
CP (GMFCS≥1)					
Clinical predictors	57.03 (42.57,71.68)	73.09 (68.12,78.12)	20.90 (11.15,28.68)	93.19 (90.48,96.42)	0.651 (.573,.728)
Conventional MRI (cMRI)	35.38 (19.24,51.84)	95.26 (92.98,97.99)	48.66 (28.82,69.91)	92.07 (89.33,95.39)	0.653 (.571,.741)
Clinical + cMRI	60.83 (45.75,74.51)	70.50 (65.57,75.29)	19.61 (8.59,28.41)	93.69 (91.18,96.62)	0.657 (.581,.730)
Morphometry	74.17 (53.57,88.23)	89.08 (79.85,97.06)	51.41 (35.59,73.13)	96.55 (94.24,98.37)	0.816 (.739,.879)
Structural connectivity (SC)	83.32 (67.65,96.08)	88.31 (80.21,95.24)	46.79 (31.51,64.96)	97.74 (95.95,99.48)	0.858 (.800,.910)
Functional connectivity (FC)	73.65 (52.94,91.18)	85.84 (73.63,97.80)	46.00 (30.43,78.57)	96.40 (94.00,98.64)	0.797 (.723,.859)
Morphometry + SC+ FC	82.14 (69.97,93.88)	88.16 (79.49,96.70)	51.72 (36.90,73.68)	(97.57 (95.93,99.15)	0.852 (.798,.900)
Clinical + cMRI + Morphometry + SC + FC	85.96 (73.53,96.44)	87.95 (79.49,95.97)	48.78 (32.23,69.67)	98.07 (96.47,99.51)	0.870 (.818,.914)
Mod-severe CP (GMFCS≥2)					
Clinical predictors	75.24 (41.56,97.72)	75.48 (71.62,79.51)	8.25 (0,18.27)	98.91 (97.47,100)	0.754 (.591,.863)
Conventional MRI	72.52 (45.45,100)	94.30 (91.87,96.99)	32.14 (14.00,50.96)	98.91 (97.87,100)	0.834 (.698,.985)
Clinical + cMRI	75.23 (45.45,92.93)	93.56 (90.66,96.65)	28.15 (0.79,45.93)	99.04 (97.92,99.70)	0.844 (.693,.938)
Morphometry	77.33 (45.45,100)	94.78 (89.53,99.32)	40.93 (22.86,77.68)	99.12 (97.99,100)	0.861 (.722,.961)
Structural connectivity	86.65 (63.63,100)	95.77 (90.54,99.66)	50.28 (27.03,88.89)	99.50 (98.64,100)	0.912 (.810,.981)
Functional connectivity	76.15 (45.45,100)	92.44 (84.80,99.32)	33.40 (16.32,80.00)	99.06 (97.87,100)	0.844 (.694,.949)
Morphometry + SC+ FC	92.60 (72.72,100)	93.88 (89.19,98.65)	38.87 (24.44,71.43)	99.71 (98.95,100)	0.932 (.840,.981)
Clinical + cMRI + Morphometry + SC + FC	93.36 (72.72,100)	95.81 (90.54,99.66)	52.39 (28.20,90.91)	99.75 (98.99,100)	0.946 (.859,.993)

*All values except for AUC are percentages; clinical and cMRI models were performed using logistic regression

Conclusions: In a regional prospective cohort of VPT infants, we combined multimodal neuroimaging and machine learning to enable early, accurate prediction of CP that outperformed current statistical models. Our internally validated model can be immediately translated to enable targeted risk stratification for research studies following NICU discharge that are designed to prevent or reduce the severity of CP in high-risk VPT infants.

References
1. Amiel-Tison CGJ (1998). 'Neurological Development From Birth to Six Years. Baltimore, MD.' Johns Hopkins University Press.
2. Bastiani, M. (2019). 'Automated processing pipeline for neonatal diffusion MRI in the developing Human Connectome Project. Neuroimage, vol 18, pp. 750-763.
3. Kidokoro H. (2013). 'New MR imaging assessment tool to define brain abnormalities in very preterm infants at term.' American Journal of Neuroradiology, vol. 34, no. 11, pp. 2208-2214
4. Kline JE. (2020). 'Automated brain morphometric biomarkers from MRI at term predict motor development in very preterm infants.' Neuroimage Clinical. vol 28, no. 102475.
5. Kline JE. (2021). 'Association Between Brain Structural Network Efficiency at Term-Equivalent Age and Early Development of Cerebral Palsy in Very Preterm Infants.' Neuroimage. vol 245, no.118688
6. Moons KGM (2015). 'Transparent Reporting of a multivariable prediction model for Individual Prognosis Or Diagnosis (TRIPOD): Explanation and Elaboration'. Annals of Internal Medicine, vol. 162, pp. W1-W73.
7. Palisano RJ (2000). 'Validation of a model of gross motor function for children with cerebral palsy.' Physical Therapy, vol. 80, no. 10, pp. 974–985

Poster No 1384

Artificial neural network in classification of traumatic brain injury using rs-fMRI and PET imaging

Faezeh Vedaei[1], Najmeh Mashhadi[2], Mahdi Alizadeh[3], George Zabrecky[3], Daniel A. Monti[3], Nancy Wintering[3], Andrew B. Newberg[3], Feroze B. Mohamed[3]

[1]University of Pennsylvania, Philadelphia, PA, [2]University of California-Santa Cruz, Santa Cruz, CA, [3]Thomas Jefferson University, Philadelphia, PA

Introduction: Mild traumatic brain injury (mTBI) is a public health concern that may adversely affects person's quality of life, thinking, memory and behavior. Most of the complications of mTBI are brain function alterations that impact on cognitive performance and in a long-term may lead to neurodegenerative diseases.[1] Functional brain imaging including resting-state functional magnetic resonance imaging (rs-fMRI) and positron emission tomography (PET) have been used to detect brain function abnormalities in brain disorders.[2,3] While statistical group level analysis can provide spatial patterns of brain function at population level, these methods are not able to provide imaging signature of brain disorders that can be applied at single individual level. Machine learning (ML) algorithms including artificial neural network (ANN) have recently gained more popularity in medical image analysis due to their capability to learn complex representations of data.[4] We aimed to develop automatic classification model using ANN and rs-fMRI and PET imaging to distinguish between patients at chronic stage of mTBI from healthy controls (HCs).

Methods: rs-fMRI and PET were acquired from 83 patients with mTBI and 40 HCs. Voxel-wise brain maps of rs-fMRI metrics including fractional amplitude of low frequency fluctuation (fALFF), degree centrality (DC), regional homogeneity (ReHo), functional connectivity strength (FCS), and voxel-mirrored homotopic connectivity (VMHC) generated for each subject using DPARSF_V5.0 after preprocessing steps. Also, PET data was processed using PETPVE12 toolbox running on MATLAB. ANN architecture was developed using autoencoder, several hidden layers of rectified linear unit (ReLU) function and the last layer of sigmoid function. Input features were generated applying Automated Anatomical Labeling (AAL) atlas and extracting the mean values of each measurement from 116 region of interest (ROI). The classification model was developed for single modality and multimodality measurements.[5] The performance of the models was estimated via 5-fold cross validation (CV) using the receiver operator characteristic (ROC) curve analysis. Also, top 10 ROIs with the most contribution to the model prediction were extracted for each metric.[6,7]

Results: Classification performance analysis showed high scores for each single modality. However, the accuracy of classification improved using multimodality model that achieved the highest using multimodality of rs-fMRI and PET measurements (Table 1). The selected top 10 important features for all the metrics were among several main brain functional network including default mode network (DMN), sensorimotor network, visual cortex, cerebellum, and limbic system (Figure 1).

Conclusions: In the need to robust biomarkers discriminating patients with mTBI from HCs, our study for the first developed automatic classification model using deep leering (DL)-based architectures. We employed autoencoder to extract the extract hidden representations using unsupervised approach. We showed that each single modality can capture specific information from neurophysiology of mTBI providing comprehensive approach to study of brain function alteration in brain disorders including mTBI. Also, considering the complicated pathologic process of mTBI, multiple neuroimaging metrics may provide complementary information and can be investigated via multimodality classification models. Cognitive dysfunction that is accompanied with mTBI is linked with brain function alteration in specific brain areas. We have shown that brain regions located in the frontal, temporal, and parietal lobes, as well as brain regions located in the limbic system and visual cortex as well as cerebellum are among the most important features have the most contribution in model prediction.[8-10] These results

suggest that DL-based classifiers might be extended to quantitative imaging biomarker providing a new avenue for prediction of individual patients in the clinical settings.

Table 1. Classification performances of the single metrics of rs-fMRI and PET and multimodality models.

Features	AUC	Accuracy	Sensitivity	Specificity	F1-score	Precision	Recall
DC	87.95	91.67	98.75	77.14	94.21	90.31	98.75
fALFF	81.25	86.67	95.00	67.50	91.01	88.13	95.00
FCS	78.66	84.17	93.75	63.57	88.94	85.24	93.75
ReHo	75.13	80.83	91.32	58.93	86.71	84.42	91.32
VMHC	78.21	85.00	97.50	58.93	89.85	83.62	97.50
PET	72.04	79.17	92.65	51.43	85.85	80.49	92.65
rs-fMRI	92.32	94.17	97.50	87.14	95.82	94.55	97.50
rs-fMRI + PET	93.75	95.83	100	87.50	97.04	94.38	100

AUC, area under the receiver operator curve; DC, degree centrality; fALFF, fractional amplitude of low frequency fluctuation; FCS, functional connectivity strength; ReHo, regional homogeneity; VMHC, voxel mirrored homotopic connectivity; rs-fMRI, resting-state functional magnetic resonance imaging (rs-fMRI = DC + fALFF + FCS + ReHo + VMHC).

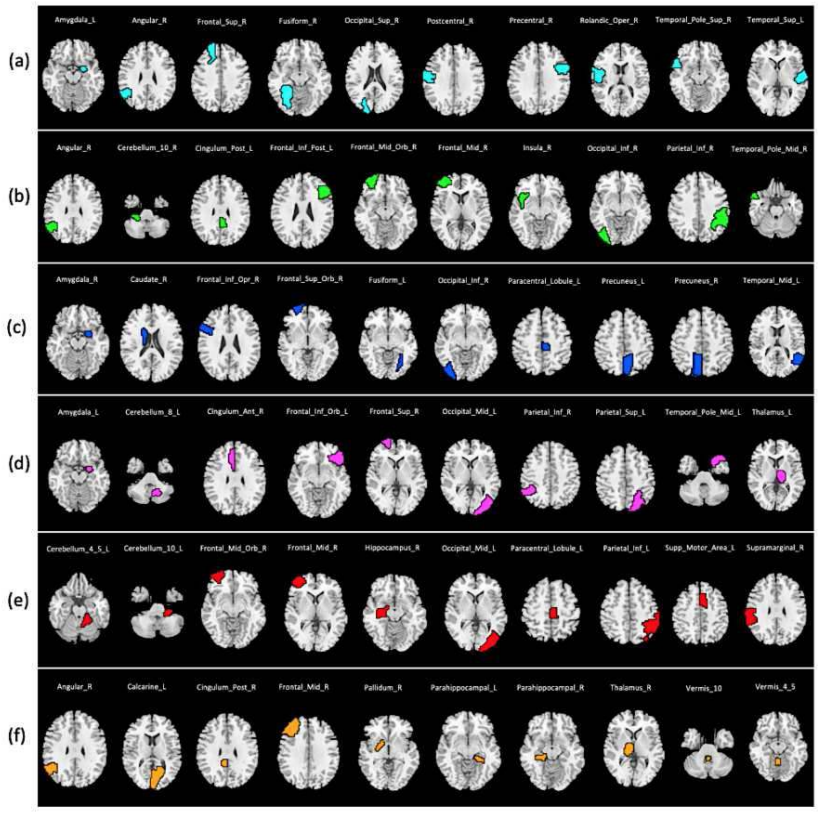

Figure 1. Top 10 ROIs defined as the most discriminative features for each single rs-fMRI metrics and PET data; (a): DC, degree centrality; (b): fALFF, fractional amplitude of low frequency fluctuation; (c): FCS, functional connectivity strength; (d): ReHo, regional homogeneity; (e): VMHC, voxel mirrored homotopic connectivity; (f): PET, positron emission tomography.

References

1. Vergara, V. M., Mayer, A. R., Damaraju, E., Kiehl, K. A. & Calhoun, V. Detection of Mild Traumatic Brain Injury by Machine Learning Classification Using Resting State Functional Network Connectivity and Fractional Anisotropy. J. Neurotrauma 34, 1045–1053 (2017).
2. Byrnes, K. R. et al. FDG-PET imaging in mild traumatic brain injury: A critical review. Front. Neuroenergetics 6, (2014).
3. Maldjian, J. A. Applications of rs-fMRI to Traumatic Brain Injury. 27, 685–696 (2018).
4. Yin, W., Li, L. & Wu, F. X. Deep learning for brain disorder diagnosis based on fMRI images. Neurocomputing 469, 332–345 (2022).
5. Zhou, T., Thung, K. H., Zhu, X. & Shen, D. Effective feature learning and fusion of multimodality data using stage-wise deep neural network for dementia diagnosis. Hum. Brain Mapp. 40, 1001–1016 (2019).

6. Hao, X. et al. Multi-modal neuroimaging feature selection with consistent metric constraint for diagnosis of Alzheimer's disease. Med. Image Anal. 60, 101625 (2020).
7. Zhang, F. et al. Multi-modal deep learning model for auxiliary diagnosis of Alzheimer's disease. Neurocomputing 361, 185–195 (2019).
8. Konstantinou, N., Pettemeridou, E., Stamatakis, E. A., Seimenis, I. & Constantinidou, F. Altered resting functional connectivity is related to cognitive outcome in males with moderate-severe traumatic brain injury. Front. Neurol. 9, (2018).
9. Schwedt, T. J., Chong, C. D., Peplinski, J., Ross, K. & Berisha, V. Persistent post-traumatic headache vs. migraine: an MRI study demonstrating differences in brain structure. J. Headache Pain 18, 1–8 (2017).
10. Stevens, M. C. et al. Multiple resting state network functional connectivity abnormalities in mild traumatic brain injury. Brain Imaging Behav. 6, 293–318 (2012).

Poster No 1385

Efficient Synthesis of 3D sMRI for Schizophrenia Classification with Generative Adversarial Networks

Alexandra Reichenbach[1], Sebastian King[1], Yasmin Hollenbenders[1]

[1]Heilbronn University, Center for Machine Learning, Heilbronn, Baden-Württemberg

Introduction: Schizophrenia (SCZ) is a heterogeneous psychiatric disease lacking reliable biomarkers (Mohammadi, Rashidi, & Amooeian, 2018) despite genetic, blood, and brain alterations being linked to it. Automated decision support for diagnosing psychiatric diseases using deep learning (DL) classifiers based on structural magnetic resonance imaging (sMRI) of the brain is currently investigated. However, these classifiers typically require large datasets for training, which are not available for SCZ patients. To overcome this obstacle, we synthesize artificial data for SCZ patients and a healthy control (HC) group using generative adversarial networks (GAN) based on 193 3D sMRI images of SCZ patients and HC from the MCIC dataset (Gollub et al., 2013). Despite rapid developments in the field of generative models, synthesis of 3D MRI brain data for psychiatric diagnosis support has not yet been demonstrated.

Methods: Four GAN architectures based on a deep convolutional GAN (DC-GAN) are adapted to address the technical challenges arising from the specific use case and evaluated for their image synthesis capabilities (Fig. 1). Spectral normalization regularization (SN-GAN) deals with the vanishing gradients problem that often occurs for small sample sizes (Miyato, Kataoka, Koyama, & Yoshida, 2018). Incorporating an encoder (α-SN-GAN) helps to alleviate mode collapse (Kwon, Han, & Kim, 2019). Both problems are also addressed by applying data augmentation during training (DiffAugment) (Zhao, Liu, Lin, Zhu, & Han, 2020). Additionally, a hierarchical approach is adapted (HA-GAN) to reduce the computational cost of the training (Sun et al., 2022) and also combined with the α-SN-GAN to join their advantages (α-HA-GAN). Subsequently, three conditioning approaches are employed for creating the two clinical groups (SZC/HC). Finally, the images are "diagnosed" using a 3D convolutional neural network (3D-CNN). Multiple training datasets consisting of different sizes and ratios of real and synthetic images are evaluated.

Results: Regularization combined with incorporating an encoder (α-SN-GAN) yields synthetic images of high fidelity and diversity shown with qualitative and quantitative evaluation (Fig. 2 left and middle). The hierarchical approaches as well as data augmentation for training produces data of lesser quality. Furthermore, we demonstrate that the α-SN-GAN conditioned with an auxiliary classifier produces synthetic images that trains the 3D-CNN equally well as the real images for the diagnostic classification task. Increasing the training dataset size with synthetic images 6-fold results in 18% improvement of classifier performance from 61% to 79% accuracy (Fig. 2 right, large dataset).

Conclusions: This work demonstrates the synthesis of high-quality 3D brain sMRI data for two clinical groups from a small dataset. A diagnostic classifier separating real sMRI data from SCZ patients and HC can be trained successfully with the synthetic data and increasing the amount of synthetic training data increases the performance of the classifier by nearly 20%. This increase suggests that the synthetic data is capable of making the algorithm more robust for classifying the real data. The systematic comparison of GAN architectures for basic training as well as for conditioning the data on the clinical group demonstrates that the architectural choices for the GAN are essential and the resulting data always needs to be evaluated carefully. This approach can be adapted to bolster other imaging modalities such as fMRI for training multimodal classifiers that have shown promise for SCZ diagnosis. Furthermore, the auxiliary α-SN-GAN has the potential to reveal underlying structural differences between the two clinical groups and might therefore also aid in the research for SCZ biomarkers.

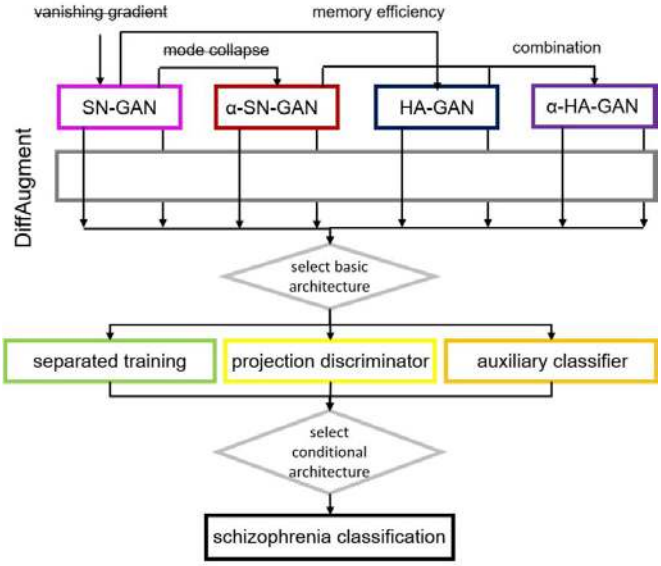

Fig. 1 Processing pipeline with architecture selection. Four basic architectures are designed to alleviate different problems during data synthesis and all four tested with and without additional augmentation during training (DiffAugment). The best basic architecture is then expanded by three approaches for generation of different classes (healthy *vs.* patients). The best conditional architecture is then used to synthesize data for training a classifier usable for decision support in schizophrenia diagnosis. Abbreviations: GAN (generative adversarial network) SN (spectral normalization regularization) HA (hierarchical approach) α (encoder)

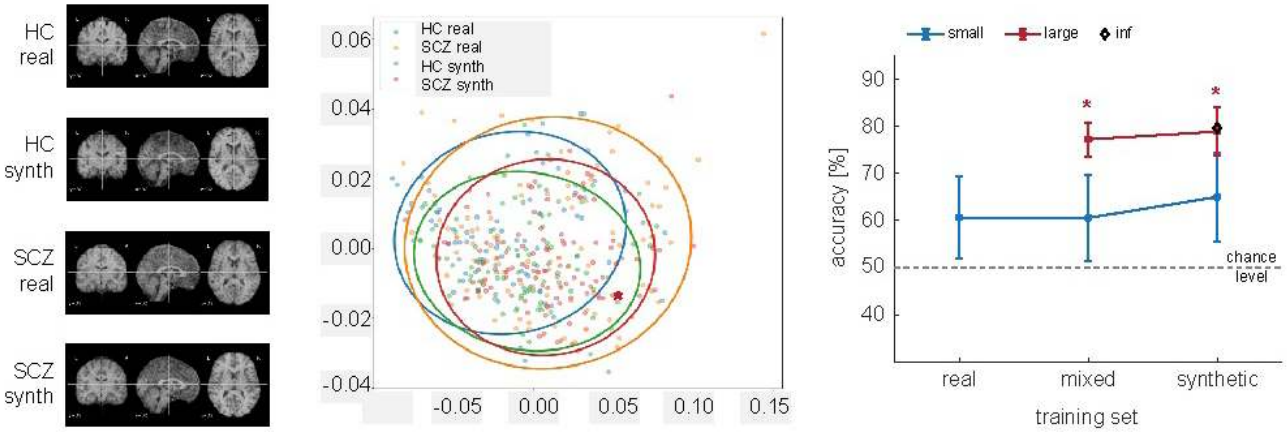

Fig. 2 Data generated with the alpha-SN-GAN and its performance. Left: Exemplary sMRI sections from real and synthetic data (qualitative comparison). Middle: Data distributions of the first two components from the PCA (qualitative comparison). Right: Performance of the diagnostic classifier. Error bars denote standard deviation. * sign. larger than real data (corrected).

References

1. Gollub, R. L. (2013). The MCIC collection: a shared repository of multi-modal, multi-site brain image data from a clinical investigation of schizophrenia. Neuroinformatics, 11, 367-388.
2. Kwon, G. (2019). Generation of 3D brain MRI using auto-encoding generative adversarial networks. Paper presented at the International Conference on Medical Image Computing and Computer-Assisted Intervention.
3. Miyato, T. (2018). Spectral normalization for generative adversarial networks. arXiv preprint arXiv:1802.05957.
4. Mohammadi, A. (2018). Brain, blood, cerebrospinal fluid, and serum biomarkers in schizophrenia. Psychiatry research, 265, 25-38.
5. Sun, L. (2022). Hierarchical amortized GAN for 3D high resolution medical image synthesis. IEEE Journal of Biomedical and Health Informatics, 26(8), 3966-3975.
6. Zhao, S. (2020). Differentiable Augmentation for Data-Efficient GAN Training.

Poster No 1386

Improved Motor Neurone Disease Prognosis Prediction with Multimodal Data Fusion

Florence Townend[1], James Chapman[1], Ayodeji Ijishakin[1], Federica Agosta[2,3], Edoardo Spinelli[2,3], Silvia Basaia[2], Yuri Falzone[3], Paride Schito[3], Massimo Filippi[2], Andrea Malaspina[4], James Cole[1]

[1]Centre for Medical Image Computing, University College London, London, UK, [2]Neuroimaging Research Unit, Division of Neuroscience, IRCCS San Raffaele Scientific Institute, Milan, Italy, [3]Neurology Unit, IRCCS San Raffaele Scientific Institute, Milan, Italy, [4]UCL Queen Square Institute of Neurology, University College London, London, UK

Introduction: Motor Neurone Disease (MND) is a multifactorial and heterogeneous neurodegenerative disease with an expected survival time of 3 to 5 years from symptom onset. During diagnosis, a multimodal set of data can be collected, including brain MRI, blood tests, and functional ratings. Accurate prognosis prediction for personalised clinical management is challenging but vital for empowering patients' and families' future planning and for clinical trial design. However, most current MND prognosis tools only use clinical measures, and the potential contribution of brain MRI to prognosis prediction has been under-explored. We aimed to explore the advantages of using multimodal data for prognosis prediction compared to using unimodal data, by modelling survival time in MND patients using baseline volumes extracted from structural MRI and clinical measures. Further, we evaluated different multimodal data fusion approaches, via the Fusilli Python package (Townend, 2023).

Methods: The study utilised two datasets, University College London Queen's Square Institute of Neurology's ALS Biomarkers Study (UK MND CSG) and Ospedale San Raffaele in Milan, Italy, containing clinical information and brain MRI. We included patients (N=110) in our analysis who had passed away and who had T1w or T2w brain MRI scans within 12 months of diagnosis. Patients were categorised into slow- and fast-progressors based on median survival time from diagnosis to death (see Table 1 for patient demographics). MRI segmentation was performed using SynthSeg, a modality-agnostic deep-learning segmentation tool (Billot, 2021), that enabled mismatched MRI modalities among patients to be included. The resulting 33 extracted volumes were z-score normalised. The clinical features were age, sex, diagnostic delay (the time between symptom onset and diagnosis), and ALSFRS-R, a functional disability rating scale. We compared 10 multimodal data fusion methods and 2 unimodal methods on their performance in classifying newly diagnosed MND patients as slow- or fast-progressing. Each method was trained with 10-fold cross validation and the training was repeated until the mean AUC (Area Under the receiver-operating characteristic Curve) stabilised over all repetitions. The AUC for each repetition was computed by aggregating validation folds from the cross-validation training and calculating the AUC of the aggregated folds. Data fusion methods were compared on their mean AUC over the stability repetitions.

Variables	MND Subjects (N=110)
Age (years)	
Mean ± SD	63.6 ± 11.7
Min-Max	28.5 - 93.6
Median (IQR)	65.1 (13.2)
Sex (%)	
Female	52 (47.3)
Male	58 (52.7)
ALSFRS-R (out of 48)	
Mean ± SD	37.5 ± 7.2
Min-Max	13.0 - 48.0
Median (IQR)	39.0 (10.0)
Survival time (months)	
Mean ± SD	29.3 ± 23.1
Min-Max	0.9 - 122.7
Median (IQR)	24.4 (28.4)

Table 1: Patient demographics in our analysis. ALSFRS-R is the revised amyotrophic lateral sclerosis functional rating scale, a functional rating scale of MND-related disability at baseline visit, with possible values ranging from 0 to 48.

Results: Figure 1 shows the performance distributions over the stability repetitions of each fusion model, arranged by mean AUC from highest to lowest. Of the ten fusion models evaluated, four outperformed the extracted volumes unimodal model (AUC=0.74), and eight outperformed the clinical features unimodal model (AUC=0.65). The highest-performing model (AUC=0.80) was the early concatenation fusion model, where extracted volumes and clinical features were concatenated before being input into a fully connected neural network. The highest AUC of 0.80 shows that there is promise in using multimodal techniques for MND prognosis prediction over standard unimodal approaches. However, to ensure robust performance on external datasets without using stability repetitions, a larger sample size is needed.

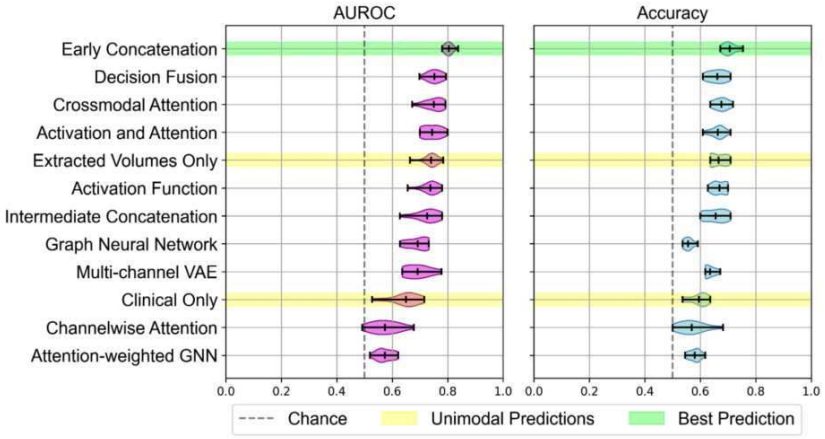

Figure 1: Performance distributions over 14 repetitions of 10-fold cross validation of ten multimodal data fusion methods and two unimodal benchmark methods. AUC (Area Under the receiver-operating characteristic Curve) and accuracy were used to measure performance. The black-dashed line represents the random chance performance.

Conclusions: Data fusion of both brain MRI and clinical features led to improved performance, showing the added value of neuroimaging features predicting MND prognosis. Crucially, the choice of data fusion method influenced predictive performance, with some performing better and some performing worse than unimodal methods. This variability in performance highlights the importance of assessing different data fusion methods and the power of the Fusilli toolbox to achieve this. Future work will explore the fusion of clinical features with voxel-wise MRI data and test generalisability in external datasets.

References

1. Townend, F.J. (2023). florencejt/fusilli (v0.0.7). Zenodo. https://doi.org/10.5281/zenodo.10137293
2. UK MND CSG, "UK MND CSG — ALS Biomarkers Study." https://www.mndcsg.org.uk/mnd-clinical-research/research-studies/als-biomarkers-study/
3. Billot, B. (2021). SynthSeg: Domain Randomisation for Segmentation of Brain Scans of any Contrast and Resolution(arXiv:2107.09559). arXiv

Poster No 1387

Enhanced inter-subject synchrony promotes phenotype prediction in naturalistic conditions

Xuan Li[1], Simon Eickhoff[1], Susanne Weis[1]

[1]Institute of Neuroscience and Medicine (INM-7), Research Centre Jülich, Jülich, North Rhine–Westphalia Land

Introduction: Recent studies have suggested that naturalistic stimuli, such as movie clips, outperform rest and conventional tasks in phenotype prediction[1,2]. Despite their promise, the impact of stimulus selection on phenotype prediction remains largely unclear. Most existing datasets of naturalistic conditions lack sufficient justifications for selecting specific stimuli, and many studies so far have used one single stimulus. Here, we investigate the impact of stimulus selection on phenotype prediction from two aspects, namely brain states (inter-subject synchrony)[3] and stimulus features. We focus on the paradigmatic case of sex classification due to the robust and well-established nature of the brain-sex relationship.

Methods: We used preprocessed fMRI data of 178 subjects while watching 13 different short movie clips provided by the Human Connectome Project. All fMRI data were truncated to 132 TRs (i.e., 2:12 min) for a direct comparison across different movie clips. For sex classification we applied our previously proposed approach[1], which allows phenotype prediction from evoked activity. Subject-specific loadings onto shared responses identified as principal components (PCs) of the fMRI time series across subjects were computed within each of 436 parcels[4]. These loadings (here we only used PC1 loadings) were used as features for classification by using a support vector machine with a radial basis function kernel[4]. Performance was quantified as average balanced accuracy over 10 repetitions of 10 cross validation folds. Family structure was controlled for and data leakage was prevented during all phases of the procedure. Group-level brain states were characterised by inter-subject synchrony, quantified as the variance explained by PC1 (the shared response) for each parcel and movie clip, with a large amount of variance indicating stronger inter-subject synchrony. A variety of movie features were extracted and analysed,

including total motion energy, visual brightness, loudness, number of TRs showing human faces, number of spoken words and semantic features.

Results: We observed large variations in both sex classification performance and inter-subject synchrony across movie clips and a significant correlation between the two (r = 0.70, p = 0.007; Fig. 1A-C). Influence of head motion was excluded (Fig. 1D-E). Better accuracy was significantly (r = 0.87, FDR corrected p<0.05; Fig. 1F) associated with higher inter-subject synchrony in the right temporal parietal junction (TPJ), a key brain area for social cognition and attention maintenance[5]. Similar findings were obtained for the 17 networks[6] (Fig. 1G). High inter-subject synchrony was associated with large variations in auditory loudness across time (RMS_std, r = 0.65, p =0.017; Fig. 2A-B) and semantic features (Fig. 2C) related to concrete objects (e.g., "living_thing", "person"), human actions and social interactions (e.g.," move","travel") and story structure (e.g., "causal_agent"). Better classification performance was associated with more spoken words (r= 0.55, p =0.049; Fig. 2D-E). Results on semantic features were highly similar between inter-subject synchrony and classification performance (Fig. 2F).

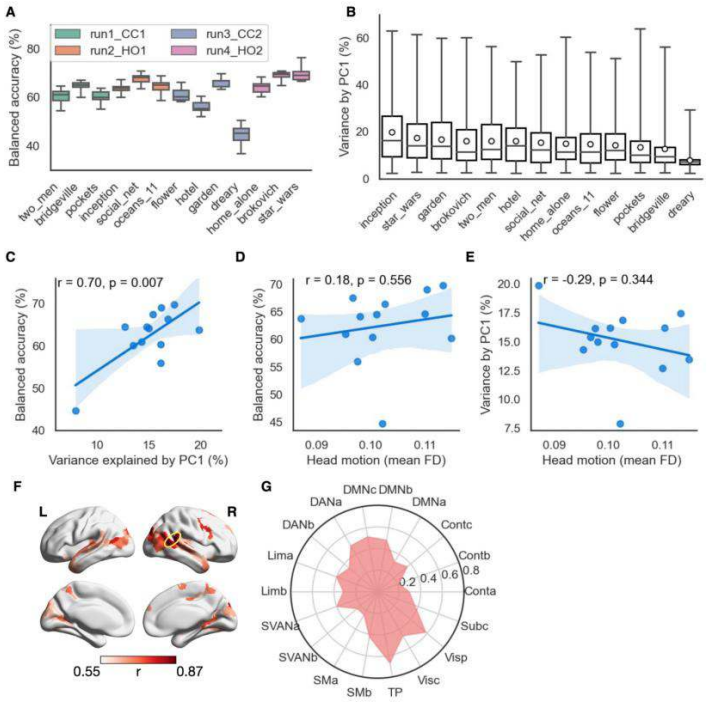

Fig. 1: Relationship between classification performance and inter-subject synchrony. **A**) Balanced accuracy for sex classification across all CV folds for each movie clip. **B**) Inter-subject synchrony (variance explained by PC1) of all parcels for each movie clip. **C**) Sex classification accuracy was significantly correlated with average inter-subject synchrony over all parcels. Each dot represents a movie clip. Both classification accuracy (**D**) and inter-subject synchrony (**E**) were not correlated with head motion (averaged over all TRs and subjects within each movie clip). **F**) Brain regions showing a significant (p<0.05) correlation between classification accuracy and inter-subject synchrony. Regions in TPJ marked by a yellow circle survived FDR correction. **G**) Correlations between classification accuracy and inter-subject synchrony for all ROIs grouped by networks.

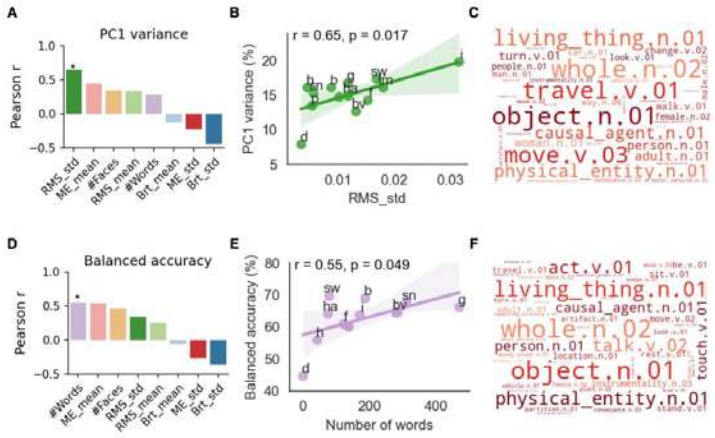

Fig. 2: Influence of features of movie stimuli. **A**) Correlation (Pearson's r) between inter-subject synchrony and each feature across movie clips. * denotes p<0.05. **B**) Variations in loudness across time (TMS_std) was significantly correlated with inter-subject synchrony. **C**) Semantic features whose occurrences were positively correlated with inter-subject synchrony. **D**) Correlation (Pearson's r) between classification accuracy and each feature across movie clips. * denotes p<0.05. **E**) Number of spoken words (#Words) was significantly correlated with classification accuracy. **F**) Semantic features whose occurrences were positively correlated with classification accuracy. Word size is proportional to the strength of the correlation in (**C**) and (**F**).

Conclusions: Contrary to intuition, we show that movie stimuli promoting similar brain states across subjects may actually enhance phenotype prediction[7]. Notably, our results here may provide very conservative lower bounds due to the very short nature of the movie stimuli. Higher inter-subject synchrony may reflect better subject engagement and higher attention levels caused by stimulus processing[8,9], suppressing noises (e.g., spontaneous thoughts) while amplifying phenotype relevant signals. Moreover, we show that stimuli with rich social content and cohesive stories may benefit phenotype prediction by promoting inter-subject synchrony[10]. These results collectively offer valuable insights for future studies in selecting an appropriate naturalistic stimulus for phenotype prediction.

References

1. Li, X. (2023), A topography-based predictive framework for naturalistic viewing fMRI. Neuroimage 120245.
2. Finn, E. S. (2021), Movie-watching outperforms rest for functional connectivity-based prediction of behavior. Neuroimage 117963.
3. Hasson, U. (2004). Intersubject synchronization of cortical activity during natural vision. Science 303, 1634– 1640.
4. Weis, S. (2020), Sex classification by resting state brain connectivity. Cerebral cortex, 30, 824-835.
5. Langner, R. (2013), Sustaining attention to simple tasks: A meta-analytic review of the neural mechanisms of vigilant attention. Psychol. Bull., 139, 870–900.
6. Yeo, B. T. T. (2011), The organization of the human cerebral cortex estimated by intrinsic functional connectivity. J. Neurophysiol.106, 1125–1165.
7. Vanderwal, T. (2017), Individual differences in functional connectivity during naturalistic viewing conditions. NeuroImage, 157, 521–530.
8. Ki, J. J. (2016), Attention Strongly Modulates Reliability of Neural Responses to Naturalistic Narrative Stimuli. J. Neurosci., 36, 3092–3101.
9. Ohad, T. (2023), Neural synchronization as a function of engagement with the narrative. NeuroImage, 276, 120215.
10. Hasson, U. (2008). Enhanced intersubject correlations during movie viewing correlate with successful episodic encoding. Neuron, 57, 452-62.

Poster No 1388

MRI meets economics: Balancing sample size and scan duration

Leon Ooi[1], Csaba Orban[1], Thomas Nichols[2], Shaoshi Zhang[1], Trevor Wei Kiat Tan[1], Ruby Kong[1], Scott Marek[3], Nico Dosenbach[3], Timothy Laumann[3], Evan Gordon[3], Juan Helen Zhou[1], Danilo Bzdok[4], Simon Eickhoff[5], Avram Holmes[6], B. T. Thomas Yeo[1]

[1]National University of Singapore, Singapore, Singapore, [2]University of Oxford, Oxford, United Kingdom, [3]Washington University, St. Louis, MO, [4]McConnell Brain Imaging Centre (BIC), Montreal Neurol, McGill Universityogical Institute (MNI), Montreal, Quebec, [5]Institute for Systems Neuroscience, Medical Faculty, Heinrich-Heine University Düsseldorf, Düsseldorf, North Rhine–Westphalia Land, [6]Rutgers University, Piscataway, NJ

Introduction: Resting-state functional connectivity (RSFC) is widely used to predict behavioral traits in individuals[1–3]. A pervasive dilemma when collecting functional MRI (fMRI) data is whether to prioritize sample size or scan duration given fixed resources. Larger sample sizes lead to better individual-level prediction accuracy and brain-behavior association reliability[4–6]. However, in parallel, other studies have emphasized the importance of longer fMRI scan duration per participant, which leads to improved data quality, reliability, and prediction performance[7]. Here, we investigate the trade-off between sample size and scan time in the context of prediction accuracy and reliability of brain-behavior relationships using RSFC.

Methods: We utilized 792 participants from the Human Connectome Project (HCP) and 2565 participants from the Adolescent Brain Cognitive Development (ABCD) study. Each participant's brain was parcellated into 419 regions of interest[8], and a FC matrix was formed by taking the correlation of BOLD signals for each pair of regions from the first T mins. The FC matrices were used to train regression models[9] for a wide set of behavioral measures[10]. A nested cross-validation procedure was used and accuracy was measured using Pearson's correlation(r) between the predicted and actual scores of participants in the test fold. The above analysis was repeated with different training set sizes, N, achieved by subsampling each training fold, while keeping the test set identical across different training set sizes to keep the results comparable across different N. The whole procedure was repeated with different values of T. T was varied from 2 mins to the maximum scan time of each dataset. To explore the reliability of univariate brain-wide association analyses, we followed a previously established split-half procedure[4]. We derived the t-statistic between each RSFC edge and behavioral measure across participants, on two non-overlapping sets of participants. Their concurrence was then computed using the intra-class correlation formula[4]. Sample size and scan duration were varied in a similar manner as before.

Results: Fig 1A shows prediction performance for a cognition factor score derived in each dataset. Accuracy increases with more training participants and scan time. Plotting prediction performance against total scan time (# training participants * scan time), reveals a logarithmic-like relationship when considering points with less than 30min of scan time (Fig 1B). Sample size and total scan time are broadly interchangeable below this point, achieving comparable prediction accuracies so long as the total scan time is similar. This relationship generalized to 19 other scores in the HCP, and 14 others in the ABCD. Fig 1C shows that total scan time explains prediction accuracy remarkably well across measures in both datasets. Reliability of brain-

behavior associations increases with more training participants and scan time as well (Fig 2A). However, plotting reliability against total scan time reveals that sample size dominates scan time much earlier, between 6 to 10 mins of scan time (Fig 2B). We similarly visualized reliability in terms of total scan time with a logarithmic function in Fig 2C to show the generalizability of this relationship across multiple behavioral measures.

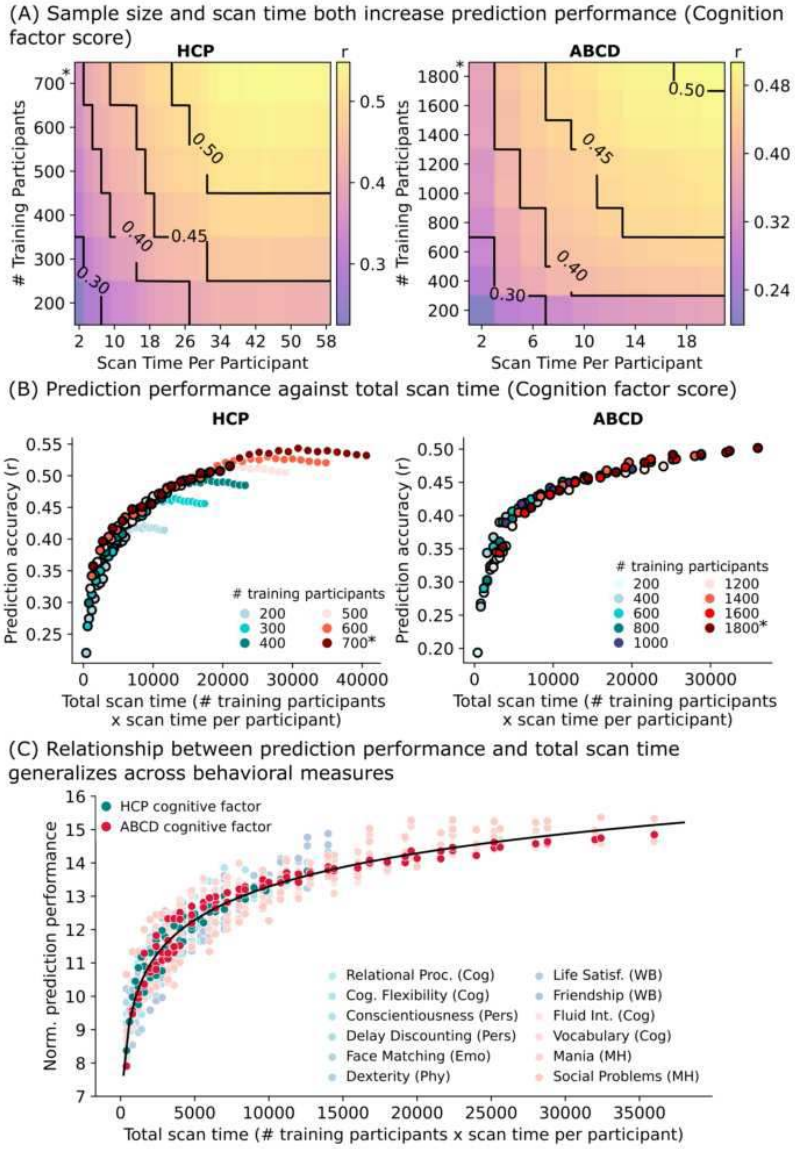

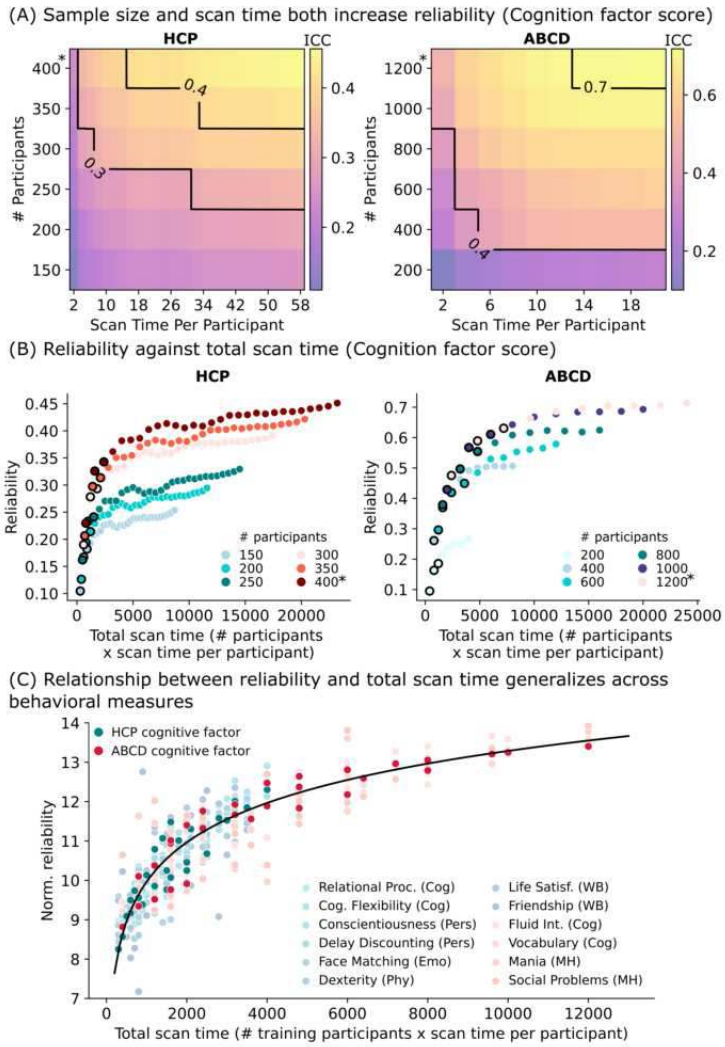

Conclusions: Total scan time explains prediction performance of behavioral measures very well, such that increasing sample size (with fixed scan time) or scan time (with fixed sample size) leads to similar accuracy. Conversely, reliability of brain-behavior association is more dependent on sample sizes rather than scan time. Notably, larger samples are important to get better sampling of intersubject variability related to features, targets and confounds. Our findings establish an empirically informed reference for calibrating scan times and sample sizes to maximize prediction and reliability of brain-behavior association.

References

1. E. S. Finn et al., “Functional connectome fingerprinting: identifying individuals using patterns of brain connectivity,” Nat. Neurosci., vol. 18, no. 11, pp. 1664–1671, Oct. 2015.
2. E. Dhamala, K. W. Jamison, A. Jaywant, S. Dennis, and A. Kuceyeski, “Distinct functional and structural connections predict crystallised and fluid cognition in healthy adults,” Hum. Brain Mapp., vol. 42, no. 10, pp. 3102–3118, Jul. 2021.
3. R. Kong et al., “Individual-specific areal-level parcellations improve functional connectivity prediction of behavior,” Cereb. Cortex, vol. 31, no. 10, pp. 4477–4500, Aug. 2021.
4. Y. Tian and A. Zalesky, “Machine learning prediction of cognition from functional connectivity: Are feature weights reliable?,” Neuroimage, vol. 245, p. 118648, Dec. 2021.
5. S. Marek et al., “Reproducible brain-wide association studies require thousands of individuals,” Nature, vol. 603, no. 7902, pp. 654–660, Mar. 2022.
6. J. Chen et al., “There is no fundamental trade-off between prediction accuracy and feature importance reliability,” bioRxiv, p. 2022.08.08.503167, 11-Aug-2022.
7. P. Feng et al., “Determining four confounding factors in individual cognitive traits prediction with functional connectivity: an exploratory study,” Cereb. Cortex, May 2022.
8. A. Schaefer et al., “Local-Global Parcellation of the Human Cerebral Cortex from Intrinsic Functional Connectivity MRI,” Cereb. Cortex, vol. 28, no. 9, pp. 3095–3114, Sep. 2018.
9. T. He et al., “Deep neural networks and kernel regression achieve comparable accuracies for functional connectivity prediction of behavior and demographics,” Neuroimage, vol. 206, p. 116276, Feb. 2020.
10. L. Q. R. Ooi et al., “Comparison of individualized behavioral predictions across anatomical, diffusion and functional connectivity MRI,” Neuroimage, vol. 263, no. 119636, p. 119636, Sep. 2022.

Poster No 1389

Subtyping Disease Progression Pattern in Dementia: BBB leakage and Cortical thinning Trajectories

Yanghee Im[1], Won-Jin Moon[2], Hong Jun Jeon[2], Hyun Woo Chung[3], Kyoung Ja Kwon[4], Min-Young Noh[5], Hee-Jin Kim[5], Seol-Heui Han[2], Yeonsil Moon[2], Hosung Kim[1]

[1]University of Southern California, Los Angeles, CA, [2]Research Institute of Medical Science, Konkuk University of Medicine, Seoul, Korea, Republic of, [3]Departments of Nuclear Medicine, Konkuk University Medical Center, Seoul, Korea, Republic of, [4]Center for Geriatric Neuroscience Research, Institute of Biomedical Science and Technology, Seoul, Korea, Republic of, [5]Department of Neurology, Hanyang University Medical Center, Hanyang University College of Medicine, Seoul, Korea, Republic of

Introduction: Dementia, a cognitive decline syndrome, often stems from neurodegenerative diseases like Alzheimer's disease. The blood-brain barrier (BBB) guards the brain against toxins but can break down, allowing harmful substances to enter and cause neuronal injury. Although BBB's impact on neuronal injury is acknowledged, our understanding of the temporal and spatial aspects remains limited. The Subtype and Stage Inference (SuStaIn), a machine-learning approach, reveals the heterogeneity and temporal complexity in diseases like Alzheimer's and Parkinson's disease. SuStaIn identifies subtypes with unique progression trajectories using cross-sectional patient data (Young et al., 2018). This study employs multimodal imaging markers, including BBB permeability and cortical thickness explaining neuronal loss, to stratify dementia into subgroups. The goal is to associate clinical symptoms with each identified subtype.

Methods: A total of 137 participants composed of 36 patients of normal cognition (NC), 52 patients of mild cognitive impairment (MCI) and 49 patients of dementia were studied. The diagnoses of MCI and dementia were based on previous criteria (Petersen et al., 1999). Patients with MCI performed normal daily living activities; nonetheless, they exhibited an objective memory impairment, implying <1.5 standard deviation from the norm in at least one memory test. Dynamic Contrast-Enhanced (DCE) using Gadobutrol (1.0 mmol/kg of body weight) and T1-weighted MRI acquisitions were conducted at the Konkuk University Medical Center using a Magnetom Skyra 3.0 Tesla unit (Siemens Medical Systems, Erlangen, Germany). The specific parameters and protocols can be found in (Moon et al., 2023). Automated brain region segmentation was conducted using the InBrain (https://www.inbrain.co.kr). The cortical thickness and BBB K-trans metrics extracted from DCE-MRI were mapped and averaged in each cortical ROI based on the Desikan Killiany atlas (Desikan et al., 2006). The SuStaIn model was applied to 12 features: two metrics, K-trans (measure of BBB-permeability) and cortical thickness (measure of neuronal loss), in six different ROIs. Each feature was z-scored transformed with respect to mean and standard deviation of NC subjects. A sequential transition of each feature from z-score of 1 to 2 and 3 represented disease progression pattern for each subtype, resulting in a series of stages. Subjects were assigned to the most probable subtype and stage by SuStaIn based on their maximum likelihood. The optimal number of subtypes was determined by the lower Cross-Validation Information Criterion (CVIC) calculated through 10-fold cross validation. Demographic comparisons between NC, MCI, and dementia groups were conducted using two-sample t-tests and chi-squared tests (Table 1). Pearson correlation analysis was performed to examine the correlation between the SuStaIn Stage and cognitive scores.

Results: The model with two subtypes was the most stable showing the lowest variation in the log likelihood (Fig. 1A). Among 137 subjects, 77 were classified as subtype 1 and 60 as subtype 2 (Fig. 1B). All patients were assigned to each subtype with high probability (>50%, Fig. 1C). Each subtype was characterized by distinct patterns of sequential increases in BBB permeability and cortical thinning (Fig. 1D and E). For subtype 1, both biomarkers become abnormal simultaneously, whereas dysfunction of BBB precedes cortical thinning for subtype 2. In subtype 1, significant correlations were found between SuStaIn stage and MMSE and CDR-SOB, but not in subtype 2 (Fig. 2).

	NC (N=36)	MCI (N=52)	Dementia (N=49)	p-value
Age	64.8±5.8	70.2±7.4	72.9±8.8	<0.001
Gender (%)	9(25.0)	21(40.4)	22(44.9)	0.160
Education, years	11.5±4.1	9.6±4.5	7.9±4.8	0.002
APOE4 carrier (%)	3(15.0)	17(40.5)	18(36.7)	0.128
HTN	16(44.4)	22(42.3)	26(54.2)	0.468
DM	3(8.3)	12(23.1)	13(27.1)	0.094
Dyslipidemia	18(50.0)	21(40.4)	11(22.9)	0.030
Depression	2(5.6)	9(17.3)	16(33.3)	0.005
MMSE	27.9±1.7	25.4±3.5	17.0±5.0	<0.001
CDR-SOB	0.4±0.8	1.3±0.8	6.1±3.4	<0.001

Table 1. Demographics of participants. NC, MCI and dementia subjects were not significantly different in gender, APOE4 carrier, HTN, DM, but in age, education, dyslipidaemia, depression, and cognitive scores.

Abbreviations: HTN, hypertension; DM, diabetes mellitus; NC, normal cognition; MCI, mild cognitive impairment; MMSE: Mini-mental State Examination; CDR-SOB: clinical dementia rating sum of boxes.

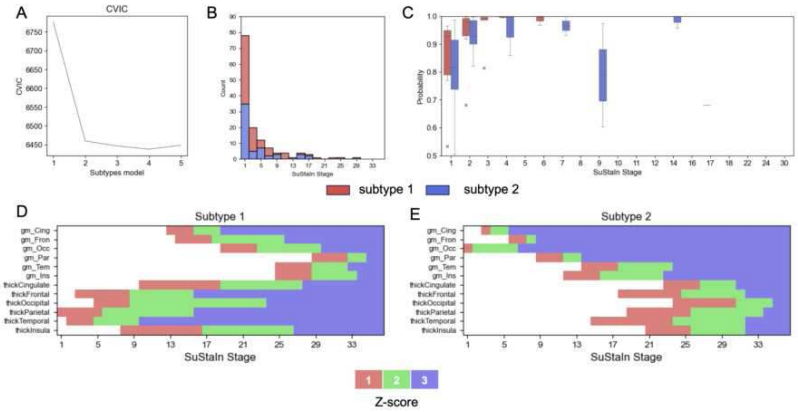

Figure 1. The patterns of neurodegenerative progression subtypes in NC, MCI and dementia groups. **A** The CVIC under different number of subtypes. Decreased CVIC indicates an improved model fit. In case of little improvement in model fit, a simpler model should be favored. Box plots display the median, upper and lower quartiles, whiskers representing 1.5 times the interquartile range, and dots representing the distribution of raw data (minima and maxima are included). While obvious improved model fit was observed from one to two subtype having a huge decrease in the CVIC value, clear improvement was not observed from further increase of number of subtypes. **B** Distribution of two dementia subtypes across SuStaIn stages likelihood subtype. **C** Boxplots of probability of maximum likelihood subtype. The lowest probability from our model was 0.503. **D** and **E** The positional variance diagrams of two dementia subtypes. y axis represents the number of events (12 variables * 3 scores). The colors and intensity of color reflects the row-wise positional density and confidence in the ordering. The location with highest score means the most probable stage/sequence of this feature.
Abbreviations: CVIC: Cross-Validation Information Criterion; SuStaIn: Subtype Stage Inference.

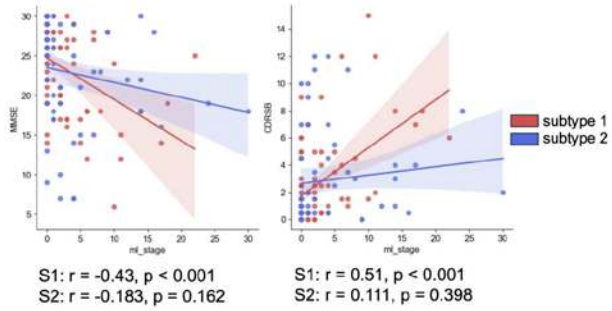

Figure 2. Correlations between SuStaIn stage and clinical symptoms in two subtypes. In subtype 1, significant correlations were found between SuStaIn stage and MMSE, and CDR-SOB, but not in subtype 2.
Abbreviations: SuStaIn: Subtype Stage Inference; MMSE: Mini-mental State Examination; CDR-SOB: clinical dementia rating sum of boxes.

Conclusions: In the present study, we revealed two different spatiotemporal trajectories of dementia using two crucial imaging biomarkers. Each subtype displayed a different relationship with clinical features. Further studies analyzing crucial factors, including various cytokines, NfL, and other biomarkers related to BBB permeability and neuronal injury, are needed.

References

1. Desikan, R. S., Ségonne, F., Fischl, B., Quinn, B. T., Dickerson, B. C., Blacker, D., Buckner, R. L., Dale, A. M., Maguire, R. P., Hyman, B. T., Albert, M. S., & Killiany, R. J. (2006), 'An automated labeling system for subdividing the human cerebral cortex on MRI scans into gyral based regions of interest', NeuroImage, 31(3), 968–980.
2. Moon, Y., Jeon, H. J., Han, S.-H., Min-Young, N., Kim, H.-J., Kwon, K. J., Moon, W.-J., & Kim, S. H. (2023), 'Blood-brain barrier breakdown is linked to tau pathology and neuronal injury in a differential manner according to amyloid deposition', Journal of Cerebral Blood Flow and Metabolism: Official Journal of the International Society of Cerebral Blood Flow and Metabolism, 43(11), 1813–1825.
3. Petersen, R. C., Smith, G. E., Waring, S. C., Ivnik, R. J., Tangalos, E. G., & Kokmen, E. (1999), 'Mild cognitive impairment: Clinical characterization and outcome', Archives of Neurology, 56(3), 303–308.
4. Young, A. L., Marinescu, R. V., Oxtoby, N. P., Bocchetta, M., Yong, K., Firth, N. C., Cash, D. M., Thomas, D. L., Dick, K. M., Cardoso, J., Van Swieten, J., Borroni, B., Galimberti, D., Masellis, M., Tartaglia, M. C., Rowe, J. B., Graff, C., Tagliavini, F., Frisoni, G. B., ... Furst, A. J. (2018), 'Uncovering the heterogeneity and temporal complexity of neurodegenerative diseases with Subtype and Stage Inference', Nature Communications, 9(1), 4273.

Poster No 1390

L2C-FNN: Longitudinal to Cross-sectional FNN for Generalizable AD-dementia Progression Prediction

Chen Zhang[1], Lijun An[1], Naren Wulan[1], Csaba Orban[1], Kim-Ngan Nguyen[1], Pansheng Chen[1], Christopher Chen[1], Juan Helen Zhou[1], B. T. Thomas Yeo[1]

[1]National University of Singapore, Singapore, Singapore

Introduction: Alzheimer's disease dementia (AD-dementia) is a neurodegenerative disorder with a prolonged prodromal phase and limited therapeutic options post-dementia onset, emphasizing the importance of early detection for timely and effective intervention (Scheltens et al., 2016). Hence, predicting longitudinal disease progression of individuals is of substantial interest (Ghazi et al., 2019; Nguyen et al., 2020). However, the absence of cross-cohort assessments in previous studies have raised concerns about clinical applicability (Wang et al., 2022) due to the cohort disparities. In this study, we introduce the Longitudinal to Cross-sectional Feedforward Neural Network (L2C-FNN), a robust model designed to mitigate cohort differences and demonstrate its superior generalizability against strong machine learning baseline models across three separate unseen cohorts.

Methods: L2C-FNN and baseline models underwent training on ADNI (N=2421; Jack et al., 2010) followed by evaluation of generalizability on external test cohorts: AIBL (N=862; Ellis et al., 2010) from Australia, MACC (N=700; Hilal et al., 2020) from Singapore, and OASIS (N=1378; LaMontagne et al., 2019) from North America. ADNI participants were randomly divided into training, validation, and test sets (ratio of 18:1:1) for model fitting, hyperparameter tuning and within-cohort evaluation. The trained models were adapted to AIBL, MACC, and OASIS for cross-cohort evaluation, with 20 repetitions to ensure result stability (Figure 1A). Care was taken to ensure non-overlapping test sets, covering the entirety of the ADNI cohort across the 20 data splits. Utilizing multimodal inputs (e.g., cognitive state measurements, cortical and/or subcortical ROI volumes) from the first 50% of timepoints of each participant, we predicted clinical diagnosis, ventricular volume, and cognitive state for the second 50% of timepoints, projecting up to 10 years into the future. All continuous variables (e.g., ROI volumes) underwent normalization through GaussRank transformation, a special form of quantile normalization (Zhao et al., 2020), with a Gaussian reference distribution. L2C-FNN (Figure 1B) is a deep feedforward neural network featuring a specialized longitudinal-to-cross-sectional format transformation, which involves computing summary statistics such as the rate of change, maximum, and minimum of each input modality from historical timeseries data. The L2C transformation offers an advantage by eliminating the reliance on error-prone recursive techniques like RNN commonly used in disease progression modeling (Fan et al., 2019). Baseline approaches included Frog, an XGBoost-based model, and MinimalRNN (Nguyen et al., 2020) an RNN-based model, which were 1st and 2nd place winners in the TADPOLE international challenge for longitudinal AD-dementia progression prediction (Marinescu et al., 2021).

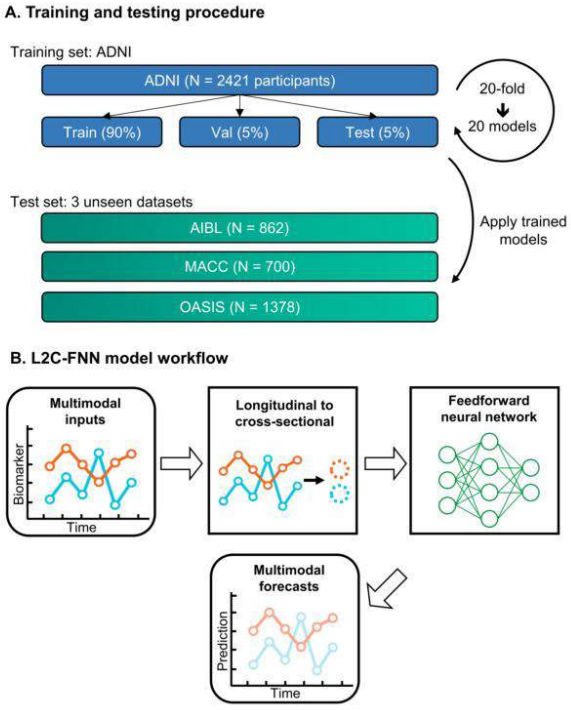

Figure 1. Training and testing procedure and L2C-FNN model structure.
(A) L2C-FNN and baseline methods are trained on ADNI and applied to three unseen test datasets to assess the generalizability. ADNI participants were randomly divided into training, validation, and test sets (ratio of 18:1:1) for hyperparameter tuning and within-cohort evaluation. The trained models were adapted to AIBL, MACC, and OASIS participants for cross-cohort evaluation, with 20 repetitions to ensure result stability.
(B) Multimodal longitudinal inputs (e.g., cognitive state measurements, cortical and/or subcortical ROI volumes, clinical diagnosis) for each participant are converted to cross-sectional format. A deep feedforward neural network takes in the transformed data and generates multimodal forecasts including clinical diagnosis, cognitive states, and brain atrophy.

Results: Figure 2A demonstrates the comparable performance of L2C-FNN with strong baseline methods (Frog and MinimalRNN) for within-cohort (ADNI) clinical diagnosis, cognitive state, and ventricular volume prediction, Notably, L2C-FNN clinical diagnosis and MMSE prediction outperformed all baselines numerically. Figure 2B shows cross-cohort evaluation in three external cohorts (AIBL, MACC, and OASIS), highlighting the superior performance of L2C-FNN over all baseline models, underscoring its robust generalizability. Particularly noteworthy is L2C-FNN's consistent achievement of significantly lower MMSE prediction errors across all test cohorts compared to the baseline methods.

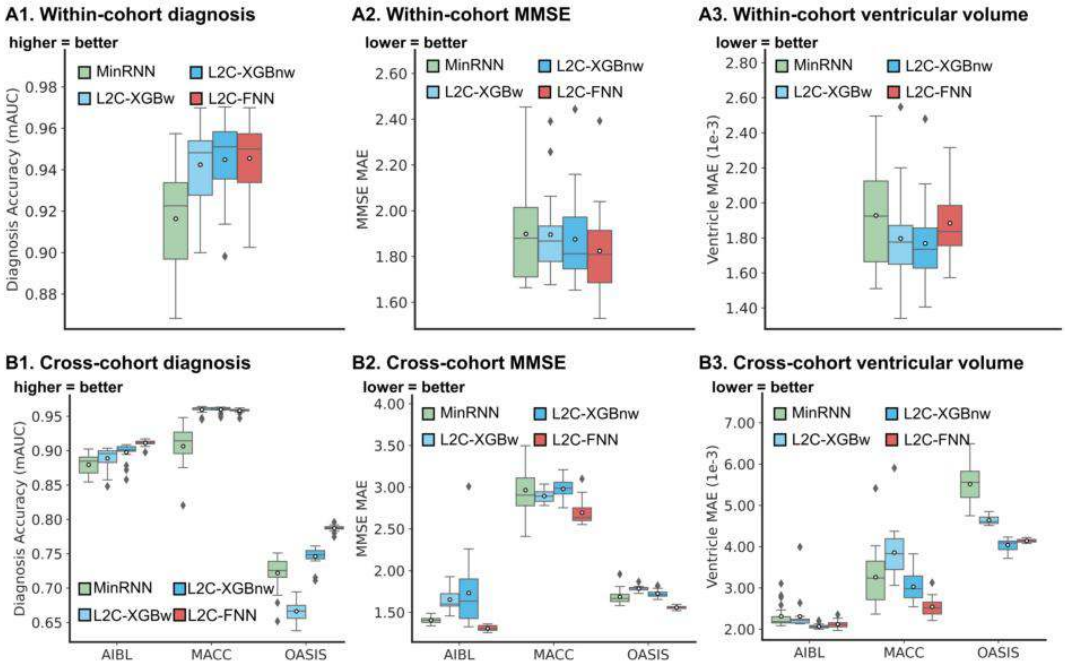

Figure 2. L2C-FNN compares favorably against strong baseline methods for within-and cross-cohort longitudinal clinical diagnosis, cognitive state (MMSE), and brain atrophy (ventricular volume) prediction. For clinical diagnosis, higher mAUC value indicate better performance. For MMSE and ventricular volume, lower MAE indicates better performance. L2C-XGBw and L2C-XGBnw are two variants of Frog. MinRNN corresponds to MinimalRNN (A) Within-cohort performance comparison. Boxplots represent variability across 20 test sets. (B) Cross-cohort comparison. Boxplots represent variability across performance of 20 trained copies of each algorithm. X-axis indicates the three unseen test cohorts.

Conclusions: Our findings demonstrate the superiority of the L2C-FNN model over baseline algorithms in longitudinal AD-dementia progression prediction when trained and tested on ADNI dataset. Crucially, this strong performance extended to previously unseen cohorts with significantly diverse populations from the training set, including AIBL, MACC, and OASIS, as confirmed by cross-cohort evaluation, emphasizing the model's superior generalizability.

References

1. Ellis, K. A. (2010), 'Addressing population aging and Alzheimer's disease through the Australian Imaging Biomarkers and Lifestyle study: Collaboration with the Alzheimer's Disease Neuroimaging Initiative', Alzheimer's & Dementia, 6(3), 291–296.
2. Fan, C. (2019), 'Assessment of deep recurrent neural network-based strategies for short-term building energy predictions', Applied Energy, 236, 700–710.
3. Hilal, S. (2020), 'Cortical cerebral microinfarcts predict cognitive decline in memory clinic patients', Journal of Cerebral Blood Flow and Metabolism: Official Journal of the International Society of Cerebral Blood Flow and Metabolism, 40(1), 44–53.
4. Jack, C. R. (2010), 'Update on the magnetic resonance imaging core of the Alzheimer's disease neuroimaging initiative', Alzheimer's & Dementia: The Journal of the Alzheimer's Association, 6(3), 212–220.
5. LaMontagne, P. J. (2019), 'OASIS-3: Longitudinal Neuroimaging, Clinical, and Cognitive Dataset for Normal Aging and Alzheimer Disease', medRxiv, 2019.12.13.19014902.
6. Marinescu, R. V. (2021), 'The Alzheimer's Disease Prediction Of Longitudinal Evolution (TADPOLE) Challenge: Results after 1 Year Follow-up' (arXiv:2002.03419). arXiv.
7. Mehdipour, Ghazi. (2019), 'Training recurrent neural networks robust to incomplete data: Application to Alzheimer's disease progression modeling', Medical Image Analysis, 53, 39–46.
8. Nguyen, M. (2020), 'Predicting Alzheimer's disease progression using deep recurrent neural networks', NeuroImage, 222, 117203.
9. Scheltens, P. (2016), 'Alzheimer's disease', The Lancet, 388(10043), 505–517.
10. Wang, C. (2022), 'A high-generalizability machine learning framework for predicting the progression of Alzheimer's disease using limited data', Npj Digital Medicine, 5(1), Article 1.
11. Zhao, Y. (2020), 'How to do quantile normalization correctly for gene expression data analyses', Scientific Reports, 10(1), Article 1

Poster No 1391

Explainable Deep Learning for Alzheimer's Disease Diagnosis and Mild-Cognitive Impairment Prognosis

Sophie Martin[1], Francesca Biondo[2], Florence Townend[3], An Zhao[1], Frederik Barkhof[4], James Cole[1]

[1]University College London, London, London, [2]UCL, London, London, [3]University College London, London, Greater London, [4]Amsterdam University Medical Centre, Amsterdam, Noord-Holland

Introduction: Deep learning provides innovative solutions for predicting Alzheimer's disease (AD) before significant cognitive decline, a key challenge of the modern era. In this work, we address two limitations of existing studies: Many studies are biased by relying only on large, curated, homogenous research datasets to train and evaluate models, limiting generalisability (Martin et al., 2023). Models are also often limited by a lack of transparency, hindering integration with existing diagnostic pipelines. Here, we leveraged a non-harmonised, multi-site dataset and the use of explainable AI methods to overcome these issues.

Methods: 3,060 3D T1-weighted MRI scans from the National Alzheimer's Coordinating Center were used to train and evaluate the models on held-out test sets. Minimal pre-processing was applied: each scan was affinely registered to the MNI152 template using EasyReg (Hoffmann et al., 2022; Iglesias et al., 2021). We used MRIqc image quality metrics and visual assessment to remove any poorly quality scans (Esteban et al., 2017). The dataset is described in Figure 1a. We implemented two state-of-the-art neural networks, a ResNet (He et al., 2015; Wightman, Touvron, et al., 2021) and Vision Transformer (ViT) (Dosovitskiy et al., 2020; Steiner et al., 2021), to classify AD dementia patients versus healthy controls (diagnosis). To overcome the challenges of training 3D ViTs on small datasets, we investigated the use of an ensemble approach, by fine-tuning 2D models pretrained on ImageNet (Wightman, Ha, et al., 2021) using single slices along three planes: axial, sagittal and coronal. A triplanar ensemble model was produced by training a multi-layer perceptron using the outputs from each single-plane model. Additionally, we explored the combination of imaging-model based probabilities with non-imaging features in a Random Forest (RF) to assess whether this improved performance. These models were benchmarked against a 3D ResNet, as well as a RF with only non-imaging features. We also evaluated each model on whether participants diagnosed with mild cognitive impairment (MCI) at baseline will progress to AD within 3 years (prognosis) to examine whether the learned features are transferable to an unseen, more challenging task. To explain the models, we applied several post-hoc explanation methods to visualise the most important features.

Results: Figure 1c shows that triplanar models provide a small improvement in the diagnostic balanced accuracy (BACC) +0.8% and +0.1% for the ViT and ResNet respectively. However, the 3D ResNet achieved a BACC 83.4%, highlighting the importance of contextual information across the brain volume. Combining the output of the imaging models with non-imaging data increased the diagnostic BACC to 95.3%, whilst balancing precision and recall better than using only non-imaging features. The advantage of including imaging data is most apparent in the absence of a bed-side screening tool for Alzheimer dementia (MMSE score). Moreover, for MCI prognosis, the multi-modal RF model with ResNet outputs showed a clear improvement in performance compared to non-imaging features alone, increasing the BACC from 65.5% to 73.1%.

A

Feature	Training sample (AD/CN)		Test sample (AD/CN)		Test sample (sMCI/pMCI)	
	n	mean±std.	n	mean±std.	n	mean±std.
Age	2754	69.5±11.0 (73.5±9.68 /68.3±11.1)	306	69.0±10.3 (72.0±8.95/68.2±10.5)	351	73.7±7.87 (72.6±7.80/74.7±7.81)
Sex (p. female)	2754	0.63 (0.51/0.66)	306	0.63 (0.56/0.65)	351	0.43 (0.44/0.42)
Education (years)	2750	15.8±2.98 (15.0±3.47/16.0±2.76)	306	15.6±3.18 (14.2±3.71/15.9±2.93)	350	15.6±3.16 (15.8±3.20/15.4±3.11)
APOE4 (p. positive)	2341	0.40 (0.63/0.33)	262	0.39 (0.55/0.35)	343	0.53 (0.50/0.55)
MMSE	1276	26.4±4.84 (20.9±5.27/28.9±1.41)	139	26.3±5.20 (19.9±5.57/28.8±1.87)	227	26.4 (27.3/25.7)

B

Model	Diagnosis (AD versus. CN)				Prognosis (sMCI versus. pMCI)			
	n (AD/CN)	BACC (%)	AUROC (%)	AUPRC (%)	n (sMCI/pMCI)	BACC (%)	AUROC (%)	AUPRC (%)
Age + Sex	306 (63/243)	50.0	50.0	20.6	351 (174/177)	50.0	50.0	50.0
Age + Sex + Education	306 (63/243)	53.7	53.7	23.8	350 (173/177)	50.8	50.8	51.0
Age + Sex + Education + APOE4	262 (56/206)	54.6	54.6	23.9	343 (170/173)	52.1	52.1	51.6
Age + Sex + Education + APOE4 + MMSE	136 (37/99)	**91.9**	**91.9**	**76.6**	220 (96/124)	**65.5**	**65.4**	**66.3**

C

Model	Diagnosis (AD versus. CN)							Prognosis (sMCI versus. pMCI)						
		Vision Transformer			ResNet				Vision Transformer			ResNet		
	n (AD/CN)	BACC (%)	AUROC (%)	AUPRC (%)	BACC (%)	AUROC (%)	AUPRC (%)	n (sMCI/pMCI)	BACC (%)	AUROC (%)	AUPRC (%)	BACC (%)	AUROC (%)	AUPRC (%)
Axial	306 (63/243)	78.6	86.8	70.2	77.2	86.5	70.0	351 (174/177)	57.5	63.7	64.3	56.6	65.2	66.1
Coronal	306 (63/243)	73.0	**90.9**	**81.1**	75.2	89.7	80.4	351 (174/177)	**59.6**	**69.8**	**68.7**	62.1	71.4	72.6
Sagittal	306 (63/243)	67.5	84.2	60.6	68.8	85.4	65.9	351 (174/177)	55.7	64.5	60.2	56.1	63.2	61.6
Triplanar-MLP	306 (63/243)	**73.8**	**90.9**	77.5	75.3	**90.1**	78.9	351 (174/177)	58.4	68.4	68.0	62.1	71.8	70.9
3D	306 (63/243)	-	-	-	**83.4**	89.5	**82.1**	351 (174/177)	-	-	-	**65.9**	**72.9**	**73.2**

D

Model	Diagnosis (AD versus. CN)							Prognosis (sMCI versus. pMCI)						
		Vision Transformer			ResNet				Vision Transformer			ResNet		
	n (AD/CN)	BACC (%)	AUROC (%)	AUPRC (%)	BACC (%)	AUROC (%)	AUPRC (%)	n (sMCI/pMCI)	BACC (%)	AUROC (%)	AUPRC (%)	BACC (%)	AUROC (%)	AUPRC (%)
Axial + Sagittal + Coronal + Age + Sex + Education + APOE4	262 (56/206)	83.4	83.4	58.7	82.8	82.8	61.1	343 (170/173)	**64.3**	**64.3**	60.3	67.5	67.5	63.7
Triplanar + Age + Sex + Education + APOE4	262 (56/206)	82.1	82.1	58.1	83.2	83.2	60.3	343 (170/173)	62.0	62.0	59.0	66.6	66.6	62.5
3D + Age + Sex + Education + APOE4	262 (56/206)	-	-	-	84.3	84.3	62.6	343 (170/173)	-	-	-	66.0	66.0	61.5
Axial + Sagittal + Coronal + Age + Sex + Education + APOE4 + MMSE	136 (37/99)	**91.1**	**91.1**	**76.5**	91.6	91.6	79.4	220 (96/124)	61.2	61.2	**63.2**	70.9	70.9	71.1
Triplanar + Age + Sex + Education + APOE4 + MMSE	136 (37/99)	88.7	88.7	71.2	91.7	91.7	82.7	220 (96/124)	59.4	59.4	62.0	**73.1**	**73.1**	**73.5**
3D + Age + Sex + Education + APOE4 + MMSE	136 (37/99)	-	-	-	**95.3**	**95.3**	**86.4**	220 (96/124)	-	-	-	71.5	71.5	70.8

Figure 1. A) Demographics of the NACC dataset. Due to missing data, we report the sample size n for each variable. Group-wise statistics are given in brackets respectively. B) Classification performance for the imaging-based deep learning models. Highest values are shown in bold. C) Classification performance for the Random Forest models based on tabular features only. Highest values are shown in bold. D) Classification performance for the multi-modal Random Forest models trained by including the probabilities associated with the imaging-based models with non-imaging features. Highest values are shown in bold.

AD = Alzheimer's disease. CN = cognitively normal. sMCI = stable mild-cognitive impairment (remained MCI for at least 3-years from baseline scan date). pMCI = progressive mild-cognitive impairment (progressed to AD after 3-4 years from baseline scan date). p. = proportion. APOE4 positive is defined as at least one copy of the APOE-e4 allele. MLP = multi-layer perceptron.

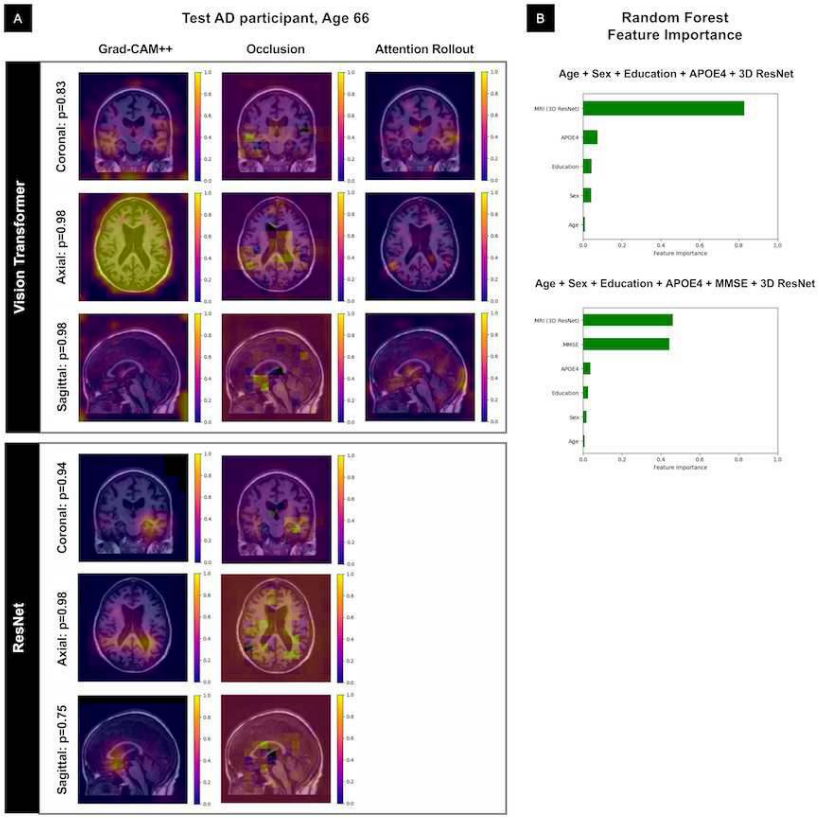

Figure 2. A) Heatmaps for three AD participants using four explanation methods and the best performing imaging-based model. B) Most important features according to the multi-modal Random Forest model with the best performance.

Conclusions: Deep learning models trained on more representative and heterogeneous datasets can still produce high diagnostic performance. A model trained only on healthy controls and AD patients was able to predict MCI conversion with a BACC of 75.3%, which is comparable with previous studies trained directly on this task. Vision Transformers achieve comparable diagnostic performance to ResNets with fewer parameters (5M and 11M respectively) but did not generalise as well to the prognosis task. Explanation methods can be used to identify salient brain regions and highlight the utility of neuroanatomical information over non-imaging features (Fig 2). Heatmaps were most consistent across methods for the ResNet model and highlighted relevant features such as ventricular atrophy.

References

1. Dosovitskiy, A. (2020). An Image is Worth 16x16 Words: Transformers for Image Recognition at Scale, arXiv.
2. Esteban, O. (2017). MRIQC: Advancing the automatic prediction of image quality in MRI from unseen sites, PLoS One, vol. 12, no. 9, e0184661.
3. He, K. (2015). Deep Residual Learning for Image Recognition, arXiv.
4. Hoffmann, M. (2022). SynthMorph: Learning Contrast-Invariant Registration Without Acquired Images, IEEE Transactions on Medical Imaging, vol. 41, no. 3, pp. 543-558.
5. Iglesias, J. E. (2021). Joint super-resolution and synthesis of 1 mm isotropic MP-RAGE volumes from clinical MRI exams with scans of different orientation, resolution and contrast. NeuroImage, vol. 237, pp. 118206-118206.
6. Martin, S. A. (2023). Interpretable machine learning for dementia: A systematic review, Alzheimer's & Dementia, vol. 19, no. 5, pp. 2135-2149.
7. Steiner, A. (2021). How to train your ViT? Data, Augmentation, and Regularization in Vision Transformers, arXiv.
8. Wightman, R. (2021). rwightman/pytorch-image-models: Minor release, Zenodo.
9. Wightman, R. (2021). ResNet strikes back: An improved training procedure in timm, arXiv.

Poster No 1392

Multi-domain and Uni-domain Fusion for domain-generalizable fMRI-based phenotypic prediction

Pansheng Chen[1], Lijun An[1], Naren Wulan[1], Chen Zhang[1], Shaoshi Zhang[1], Leon Ooi[1], Ru Kong[1], Jianxiao Wu[2], Sidhant Chopra[3], Danilo Bzdok[4], Simon Eickhoff[5], Avram Holmes[6], B. T. Thomas Yeo[1]

[1]National University of Singapore, Singapore, Singapore, [2]Institute of Neuroscience and Medicine (INM-7: Brain and Behaviour), Research Centre Jülich, Jülich, Germany, [3]Yale University, New Haven, CT, [4]McConnell Brain Imaging Centre (BIC), Montreal Neurol, McGill Universityogical Institute (MNI), Montreal, Quebec, [5]Institute for Systems Neuroscience, Medical Faculty, Heinrich-Heine University Düsseldorf, Düsseldorf, North Rhine–Westphalia Land, [6]Department of Psychiatry, Brain Health Institute, Rutgers University, Piscataway, NJ

Introduction: Resting-state functional connectivity (RSFC) is widely used to predict phenotypes in individuals[1,2]. Due to unavoidable small sample size issues[3-5], recent work has sought to translate models trained from large-sized neuroimaging datasets to predict phenotypes on small target datasets[5,6]. However, predictive models may fail to generalize to new datasets due to differences in population, data collection, and processing across datasets[7,8]. Here we proposed a method named Multi-domain and Uni-domain Fusion (MUF) to enhance model generalizability, which outperformed 4 strong baselines on 6 target datasets.

Methods: We used 419 X 419 RSFC matrices to predict phenotypes[5] from 7 datasets: UK Biobank[10,11], ABCD[12], GSP[13], HBN[14], eNKI[15], HCP-YA[16] and HCP-Aging[17]. We did a leave-one-dataset-out test on each dataset, except UK Biobank as we need the largest dataset and for training. Each dataset was iteratively used as the target dataset and all others were used as source datasets (Fig 1A). Predictive models trained from source datasets were adapted to K participants (K-shot) in the target dataset to predict target phenotypes. The adapted models were evaluated in the remaining test participants. This procedure was repeated 100 times for stability. We compared MUF against 4 baselines (Fig 1B): classical Kernel Ridge Regression (KRR), meta-matching with stacking[5], and our previous work: meta-matching with dataset stacking and multilayer meta-matching[9]. Classical KRR models were trained on K-shot to predict target phenotypes[5]. For meta-matching with stacking[5], a feedforward deep neural network (DNN) was trained on UK Biobank to predict 67 phenotypes. The base DNN was applied to K-shot and DNN predictions were used as features to train a KRR model on K-shot to predict target phenotypes (i.e. stacking). Meta-matching with dataset stacking[9] extends meta-matching with stacking by training separate KRR/DNN models for each source dataset and then performing stacking on K-shot to predict target phenotypes. To resolve the sample size imbalance across source datasets, multilayer meta-matching[9] gradually applied stacking from larger source datasets to smaller datasets to boost prediction accuracies. These predictive models then underwent another round of stacking using K-shot to predict target phenotypes. Of note, the above 4 baselines trained base models independently on each dataset. Fig 1C shows our new proposed MUF method, which combines both cross-domain and intra-domain training to learn domain-general and domain-specific information. On the basis of multilayer meta-matching, we also employed a multi-domain strategy that trains a joint

multi-task DNN using all source datasets together, enabling it to offset site differences to some extent and thus generalize better on unseen datasets. Predictions from the above joint DNN were concatenated together with predictions from the multilayer meta-matching method and then used as features of the stacking model to predict target phenotypes.

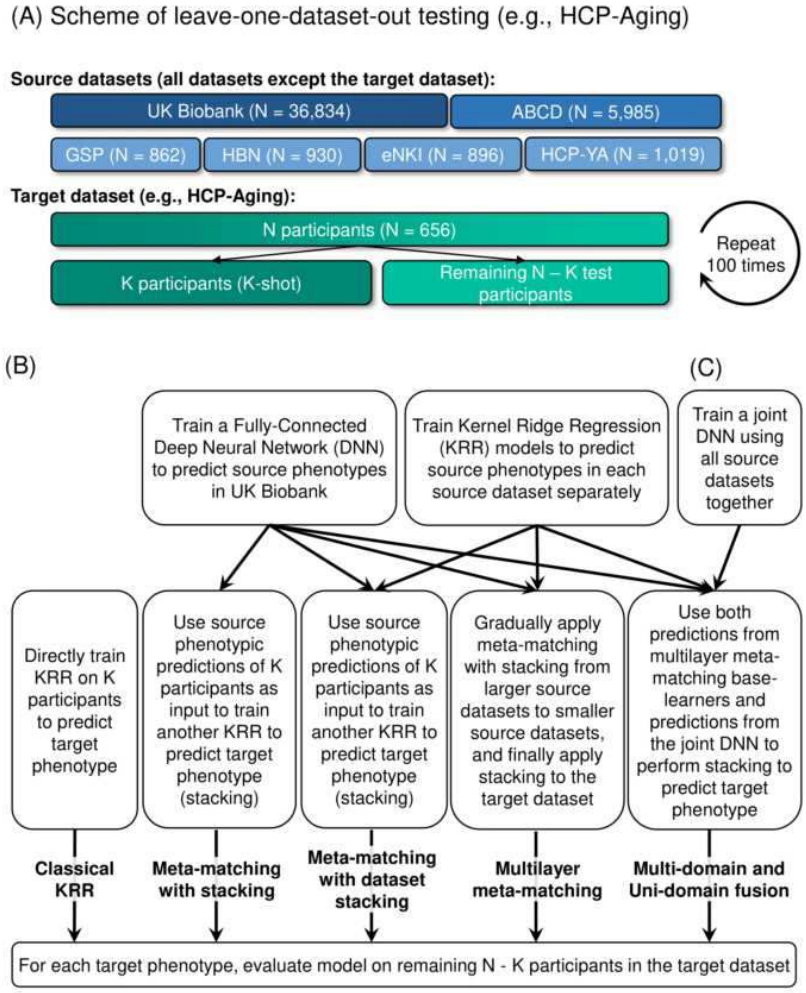

Figure 1. (A) We used 7 datasets (UK Biobank[10,11], ABCD[12], GSP[13], HBN[14], eNKI[15], HCP-YA[16] and HCP-Aging[17]) and did a leave-one-dataset-out test on each dataset (except UK Biobank). One dataset was used as the target dataset and all other datasets were used as source datasets. Predictive models from the source datasets were adapted to K participants from the target dataset to predict target phenotypes. The adapted models were evaluated in the remaining N – K participants. This procedure was repeated 100 times for stability. (B) Schematic of 4 baselines: classical KRR, meta-matching with stacking[5], meta-matching with dataset stacking and multilayer meta-matching[9]. (C) Schematic of our new proposed method: Multi-domain and Uni-domain Fusion (MUF)

Results: Fig 2 shows the prediction accuracy (Pearson's correlation) in 6 target datasets. All reported p values survived a false discovery rate of $q < 0.05$. We found that original meta-matching with stacking[5] was not better than classical KRR on some datasets (e.g., HBN), but our proposed methods improved it by incorporating more diverse source datasets. In all test datasets, MUF consistently outperformed all other baselines, indicating that MUF can better generalize from different source datasets and is more robust on new target datasets. Using Wilcoxon signed-rank test, MUF was better than meta-matching with dataset stacking[9] ($p < 0.02$ for all K) and multilayer meta-matching[9] ($p < 0.02$ for $K > 20$).

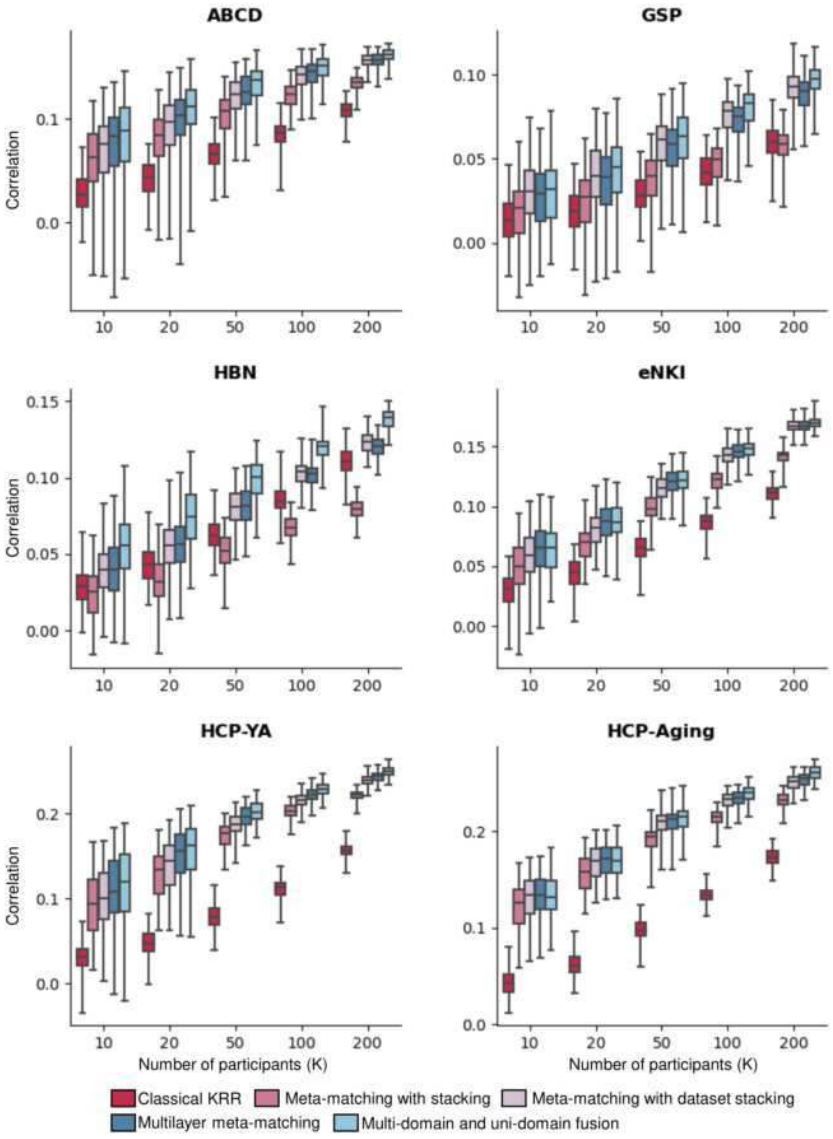

Figure 2. Prediction performance (Pearson's correlation) of 5 methods on 6 target datasets. The vertical axis is phenotypic prediction performance in terms of Pearson's correlation (averaged across all target phenotypes in the corresponding dataset). The horizontal axis is the number of K participants in the target dataset used for stacking. Boxplots represent variability across 100 repetitions of sampling K participants.

Conclusions: We propose a method using both multi-domain and uni-domain training, to translate phenotypic prediction models from multiple source datasets to small-sized target datasets. We found that our MUF performed the best on 6 test datasets.

References

1. Eickhoff, S. B. (2019). Neuroimaging-based prediction of mental traits: Road to utopia or Orwell?. PLoS biology, 17(11), e3000497
2. Varoquaux, G. (2019). Predictive models avoid excessive reductionism in cognitive neuroimaging. Current opinion in neurobiology, 55, 1-6
3. Arbabshirani, M. R. (2017). Single subject prediction of brain disorders in neuroimaging: Promises and pitfalls. Neuroimage, 145, 137-165
4. Poldrack, R. A. (2020). Establishment of best practices for evidence for prediction: a review. JAMA psychiatry, 77(5), 534-540
5. He, T. (2022). Meta-matching as a simple framework to translate phenotypic predictive models from big to small data. Nature Neuroscience, 1-10
6. Lu, B. (2022). A practical Alzheimer's disease classifier via brain imaging-based deep learning on 85,721 samples. Journal of Big Data, 9(1), 1-22
7. Kakarmath, S. (2020). Best practices for authors of healthcare-related artificial intelligence manuscripts. NPJ digital medicine, 3(1), 134
8. Abraham, A. (2017). Deriving reproducible biomarkers from multi-site resting-state data: An Autism-based example. NeuroImage, 147, 736-745
9. Sudlow, C. (2015). UK biobank: an open access resource for identifying the causes of a wide range of complex diseases of middle and old age. PLoS medicine, 12(3), e1001779
10. Chen, P. (2023). Multilayer meta-matching: translating phenotypic prediction models from multiple datasets to small data. In Prep

11. Miller, K. L. (2016). Multimodal population brain imaging in the UK Biobank prospective epidemiological study. Nature neuroscience, 19(11), 1523-1536
12. Volkow, N. D. (2018). The conception of the ABCD study: From substance use to a broad NIH collaboration. Developmental cognitive neuroscience, 32, 4-7
13. Holmes, A. J. (2015). Brain Genomics Superstruct Project initial data release with structural, functional, and behavioral measures. Scientific data, 2(1), 1-16
14. Alexander, L. M. (2017). An open resource for transdiagnostic research in pediatric mental health and learning disorders. Scientific data, 4(1), 1-26
15. Nooner, K. B., (2012). The NKI-Rockland sample: a model for accelerating the pace of discovery science in psychiatry. Frontiers in neuroscience, 6, 152
16. Van Essen, D. C. (2013). The WU-Minn human connectome project: an overview. Neuroimage, 80, 62-79
17. Harms, M. P. (2018). Extending the Human Connectome Project across ages: Imaging protocols for the Lifespan Development and Aging projects. Neuroimage, 183, 972

Poster No 1393

Accurate Detection of Mental Fatigue with LSTM Network using fNIRS

Mengshan Li[1,2], Wenchao Zhang[1,2], Jiayu Xu[1,2], Zaichen La[1,2], Huiling Zhou[1,2], Zhao Yan[1,2], Yonghuan Feng[1,2], Guanya Li[1,2], Yang Hu[1,2], Yi Zhang[1,2]

[1]Center for Brain Imaging, School of Life Science and Technology, Xidian University, Xi'an, Shaanxi 710126, China, [2]International Joint Research Center for Advanced Medical Imaging and Intelligent Diagnosis and Treatment & Xi'an Key Laboratory of Intelligent Sensing and Regulation of trans-Scale Life Information, School of Life Science and Technology, Xidian University, Xi'an, Shaanxi 710126, China

Introduction: Long-term cognitive tasks easily lead to mental fatigue, usually manifested in decreased attention, slower reaction time, and increased aversion to tasks, resulting in increased accident incidence[1]. To cope with these adverse but preventable consequences caused by mental fatigue, accurate detection of mental fatigue is required. Several ways including electroencephalography and functional Near-infrared Spectroscopy (fNIRS) have been employed, however, they used multiple channels covering the whole brain[2-4], which is less inefficient and inconvenient in applications[5]. Thus, it is necessary to identify the specific regions that are closely related to mental fatigue. In the current study, multi-channel fNIRS signals covering the frontal and parietal brain regions were measured on participants with normal and mentally fatigued states, respectively. Then, the individualized mental fatigue detection model was constructed and the contribution channels for fatigue detection were determined.

Methods: Seventeen healthy students were recruited from Xidian University to participate in the study. The Shimadzu LABNIRS device was employed to measure the fNIRS data of participants during the sustained cognitive tasks inducing mental fatigue (Figure 1A), and optrodes were arranged on the frontal-parietal brain regions according to the international 10-20 system, with a total of 46 channels (Figure 1B). Resting - state fNIRS data were measured for each participant before and after the sustained cognitive task, and their mental fatigue levels were assessed using the Karolinska Sleepiness Scale (KSS, Figure 2A). Each subject participated in the experiment twice. The two five-minute resting-state datasets before and after the sustained cognitive task were categorized into normal and mental fatigue states. A sliding window with a length of 6s and a shift of 1.5s was applied to segment the fNIRS data into 196 normal and mental fatigue samples for each participant in each experiment respectively. For each participant, a detection model based on the Long Short-Term Memory (LSTM) network was trained with the samples from the first experiment, and the samples from the second experiment were used to test the model (Model 1). The shap interpreter was employed to evaluate the weights of channels[6], and the top 20% of channels contributing most to the classification were selected as mental fatigue-related channels. Then, the detection model was retrained and tested with the selected channels (Model 2). In addition, paired t-tests were performed to test the difference in Amplitude of Low Frequency Fluctuations (ALFF) between normal and mental fatigue states for each channel, and channels with significant differences were chosen to retrain the detection models again for each participant (Model 3, Figure 1C).

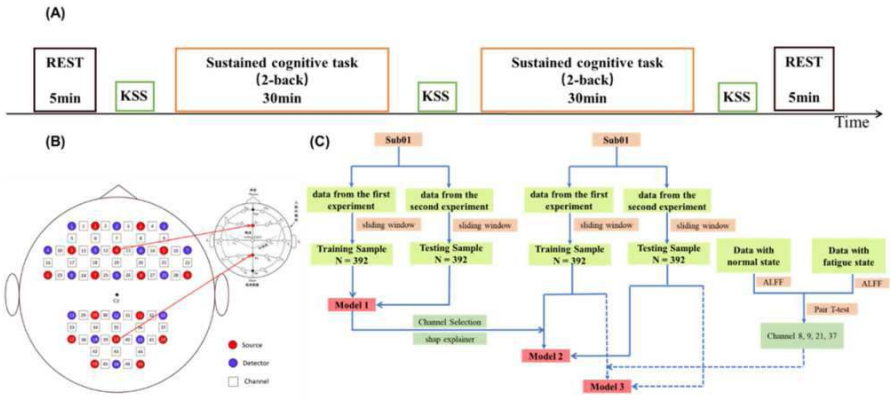

Figure 1. Experimental design. (A) The paradigm of sustained cognitive task; (B) The optrodes arrangement in frontal-parietal regions according to the international 10-20 system; (C) The flowchart of individualized detection model construction with different channels.

Results: The KSS score was significantly increased along with the sustained task progress ($P < 0.001$, Figure 2A). The average accuracy of the Model 1 was 91.93%. Channels with high contributions were located in Brodmann's area 5 (BA5) and BA7 (parietal area and somatosensory association cortex), BA6 and 9 (frontal area), and BA40 (superior temporal gyrus, Figure 2B). Model 2 used the above mental fatigue-related channels and achieved an average accuracy of 91.06%, with no significant decrease compared with Model 1. The group-level statistic method identified channels corresponding to BA8, BA9, and BA40. However, the detection model with these channels (Model 3) only yielded an accuracy of 50.64%, which was significantly lower than that of Model 1 ($P < 0.001$, Figure 2C).

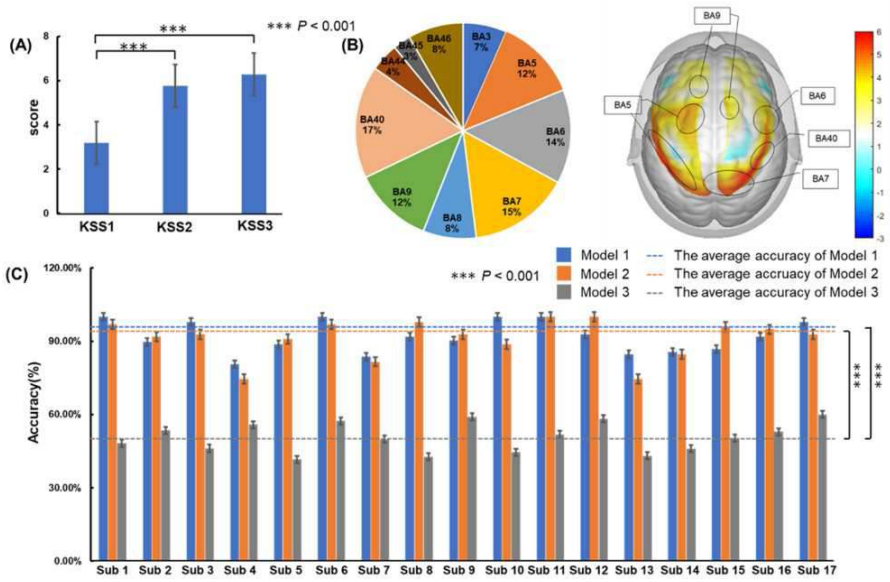

Figure 2. Mental fatigue score and performance of detection models. (A) Changes in KSS scores during the sustained cognitive task; (B) Brain regions relevant to mental fatigue; (C) Accuracy of models with three different channels.

Abbreviations: KSS, Karolinska Sleepiness Scale; BA, Brodmann's area.

Conclusions: This study identified mental fatigue-related channels within the frontal-parietal network based on individualized mental fatigue detection models, reducing the number of required optrodes without compromising detection accuracy. This study is helpful to the practical application of mental fatigue detection based on fNIRS.

References
1. Boksem MA, Meijman TF, Lorist MM. (2006). 'Mental fatigue, motivation and action monitoring', Biological psychology, vol. 72, no. 2, pp. 123-32.
2. Zhang, C., Sun, L., Cong, F., Kujala, T., Ristaniemi, T., and Parviainen, T.(2020). 'Optimal imaging of multi-channel EEG features based on a novel clustering technique for driver fatigue detection', Biomed. Signal Process and Control, vol 62, pp 1-9.
3. Peng Y, Li C, Chen Q, Zhu Y, Sun L. (2022). 'Functional Connectivity Analysis and Detection of Mental Fatigue Induced by Different Tasks Using Functional Near-Infrared Spectroscopy', Frontiers in neuroscience, vol. 15.
4. Lin, C. T., King, J. T., Chuang, C. H., Ding, W., Chuang, W. Y., Liao, L. D., & Wang, Y. K. (2020). 'Exploring the Brain Responses to Driving Fatigue Through Simultaneous EEG and fNIRS Measurements', International journal of neural systems, vol. 30, no. 2.
5. Li, R. Yang, D. Fang, F, Hong, K.-S, Reiss, A.L, Zhang, Y. (2022). 'Concurrent fNIRS and EEG for Brain Function Investigation: A Systematic, Methodology-Focused Review', Sensors (Basel, Switzerland), vol. 22, no. 15.
6. Lundberg, Scott M., and Su-In Lee.(2017). 'A unified approach to interpreting model predictions', Advances in neural information processing systems, pp. 4765-4774

Poster No 1394

Developing Replicable model for Real-World Functional Neuroimage

Jiaqi Ding[1], Tingting Dan[1], Ziquan Wei[1], Guorong Wu[1]

[1]University of North Carolina at Chapel Hill, Chapel Hill, NC

Introduction: Neuroimaging techniques have revolutionized our capacity to understand the neurobiological underpinnings of behaviorin-vivo[1]. Leveraging an unprecedented wealth of public neuroimaging data, there is a surging interest to answer novel neuroscience questions using machine learning techniques. Despite the remarkable successes in existing deep models, current state-of-the-arts[2] have not yet recognized the potential issues of experimental replicability arising from ubiquitous cognitive state changes, which might lead to spurious conclusions and impede generalizability across neuroscience studies. In this work, we first dissect the critical (but often missed) challenge of ensuring prediction replicability in spite of task-irrelevant functional fluctuations. Then, we formulate the solution as a domain adaptation where we devise a cross-attention mechanism with discrepancy loss in a Transformer backbone.

Methods: In our domain cross-attention Transformer[8], as shown in Figure 1, first, we introduce the cross-attention layer, an alternating module comprising self-attention in the source domain and cross-attention based on source and target domain. The integration of cross-attention (shown in the top right corner of Figure 1) facilitates the model's ability to relate source domain information to the target domain. Specifically, suppose the output of target domain's previous-layer constitutes the query QT, while the outputs from the source domain form the key KS and value VS, so that the model achieves enhanced information exchange and contextual representation between the two domains and minimizes the inter-domain dependencies. Then, we propose an adjusted discrepancy loss that can align the predicted probability vectors from the source and target domains, ensuring that they exhibit similar patterns in a shared feature space. We first propose a novel mathematical approach to update the correspondence between the predicted vectors of the two domains within the same batch. Then, we compute the mean discrepancy loss between the predicted probabilities in the source domain and the updated probabilities in the target domain.

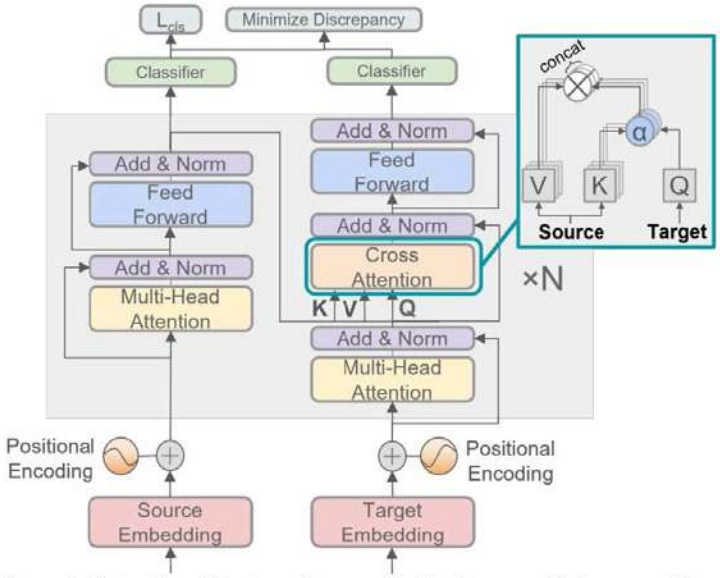

Figure 1: Network architecture of our replicable deep model for recognizing cognitive tasks from fMRI data. Our model extends the traditional transformer framework to take the intra-subject functional fluctuations into account by (1) cross-attention transformer and (2) an effective loss function for domain adaption between test and retest fMRI scans.

Results: We have evaluated the cognitive task recognition accuracy and consistency on both test and retest functional neuroimages from the Human Connectome Project. Our working memory dataset is part of the HCP-Task dataset[7], it provides valuable insights into the brain's activity during working memory tasks, including two distinct scanning sessions referred to as test data (scan 1) and retest data (scan 2). In experiments, our primary objective was to delve into the model replicability. To this end, we employed the bidirectional validation framework. Initially, we train the model on the test data and test on the retest data (i.e., test-retest experiment). This process was then reversed (i.e., retest-test experiment). By assessing the divergences in the outcome distribution patterns between these distinct scans, we aimed to unravel the model's capacity to equivalently discern the inherent features of both datasets, enabling us to make sure whether it indeed grasped the task-specific features in the disparate scans. Figure 2 (last column, whole brain) shows the task recognition accuracy (for a total of eight tasks) by different methods[3456]. It is clear that our method outperforms all the comparison methods (at a significant level $p<0.0001$) in bidirectional validation situations.

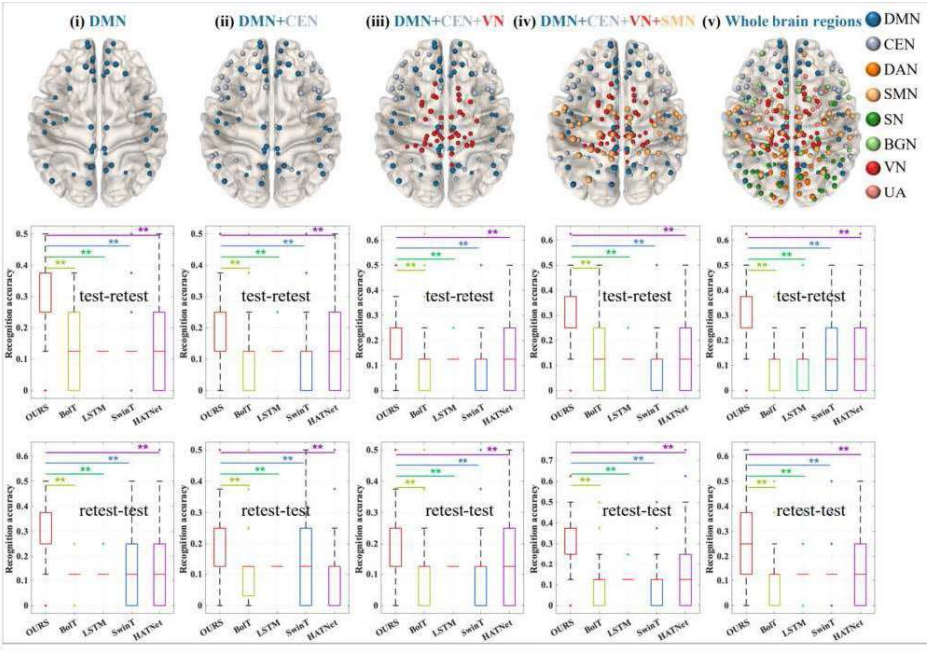

Figure 2: The task recognition accuracy with respective to network size. The task recognition of test-retest and retest-test scenario are shown in the middle and bottom, where '*' denotes the significant difference ($p<0.0001$).

Conclusions: We bring attention to a critical issue of model replicability in consistently linking dynamic neural activity with cognition and behaviors. Upon identifying the prominent obstacle of limited generalizability within existing deep models used in fMRI research, we present a practical solution to address the replicability issue using a novel cross-attention transformer for test-retest scans of multi-session fMRI data, indicating great applicability of our data-driven approach in various neuroscience studies.

References

1. Price, C. J. (2018). "The evolution of cognitive models: From neuropsychology to neuroimaging and back." Cortex 107: 37-49.
2. Thomas, A., C. Ré and R. Poldrack (2022). "Self-supervised learning of brain dynamics from broad neuroimaging data." Advances in Neural Information Processing Systems 35: 21255-21269.
3. Bedel, H. A., I. Sivgin, O. Dalmaz, S. U. Dar and T. Çukur (2023). "BolT: Fused window transformers for fMRI time series analysis." Medical Image Analysis 88: 102841.
4. Hochreiter, S. and J. Schmidhuber (1997). "Long short-term memory." Neural computation 9(8): 1735-1780.
5. Liu, Z., Y. Lin, Y. Cao, H. Hu, Y. Wei, Z. Zhang, S. Lin and B. Guo (2021). Swin transformer: Hierarchical vision transformer using shifted windows. Proceedings of the IEEE/CVF international conference on computer vision.
6. Mehta, S., X. Lu, D. Weaver, J. G. Elmore, H. Hajishirzi and L. Shapiro (2020). "Hatnet: an end-to-end holistic attention network for diagnosis of breast biopsy images." arXiv preprint arXiv:2007.13007.
7. Barch, D. M., G. C. Burgess, M. P. Harms, S. E. Petersen, B. L. Schlaggar, M. Corbetta, M. F. Glasser, S. Curtiss, S. Dixit and C. Feldt (2013). "Function in the human connectome: task-fMRI and individual differences in behavior." Neuroimage 80: 169-189.
8. Vaswani, A., N. Shazeer, N. Parmar, J. Uszkoreit, L. Jones, A. N. Gomez, Ł. Kaiser and I. Polosukhin (2017). "Attention is all you need." Advances in neural information processing systems 30.

Poster No 1395

BrainGET: Decoding Brain Dynamic Functional Connectivity Implicated in ADHD Subtypes

Deepank Girish[1], Yi Hao Chan[1], Jing Xia[1], Sukrit Gupta[2], Jagath Rajapakse[1]

[1]School of Computer Science and Engineering, Nanyang Technological University, Singapore, Singapore, [2]Department of Computer Science and Engineering, Indian Institute of Technology, Ropar, India

Introduction: Subtype-specific differences in functional connectivity (FC) have been well-documented for ADHD[2]. Recent studies have revealed strong associations between dynamic FC (dFC) changes and behavioral/cognitive functions[7,9]. While static FC has been thoroughly investigated in this regard, more needs to be done to study the subtype-specific changes in dFC. We propose BrainGET (Graph neural network Ensembles with Transformers) architecture to capture different extents of spatiotemporal relationships in dFC. BrainGET outperforms state-of-the-art models in ADHD detection and GNNExplainer was used on BrainGET to generate potential subtype-specific biomarkers from the ADHD-200 dataset.

Methods: ADHD-200 contains rs-fMRI scans from 279 individuals diagnosed with ADHD and 488 age-matched typical controls, collected from 4 sites: NI, NYU, OHSU and PKU. Also, there are 3 subtypes of ADHD: Hyperactive-Impulsive, Inattentive and Combined (Figure 1c). dFC matrices were generated using a sliding window approach and used as inputs to our proposed model. BrainGET integrates Graph Convolutional Network (GCN) and Graph Isomorphism Network (GIN) in an ensemble framework, then uses Transformers to capture temporal dynamic patterns (Figure 1a). GCN and GIN differ in how node information is spatially aggregated, while Transformers provide an effective way of capturing temporal dynamics from FC. Using an ensemble allows the model to learn the optimal way of combining these spatiotemporal representations.

Results: We compared BrainGET's site-specific classification performance (healthy vs ADHD) to current state-of-the-art dFC models based on GNNs and Transformer architectures, including: DGCN[8], ST-GCN[3] and STAGIN[4] (Figure 1b). Our model was statistically significant (with paired t-test p-value < 0.05) and outperformed existing methods due to the combined expressive power of GCN and GIN. For model explainability, attention scores were used to find salient sliding windows from both GCN and GIN component of BrainGET, for each subtype across all 4 sites. We subsequently applied GNNExplainer to generate saliency scores which reveal the contribution of each node to the classification task. Saliency scores derived from the GCN and GIN components were combined using the same weights as utilized in the ensemble of classification predictions. Decoding was done for each site, but analysis and figures exclude site NI due to small sample size. We found that the connection between insula and extra-nuclear is most salient for both sites NYU and OHSU (Figure 2). Notably, it is not present in PKU, possibly due to different races (Western vs Chinese). Additionally, its presence in both combined and inattentive subtypes and absence in hyperactive subtype suggests that it could be an FC feature specific to the inattentive subtype. While the combined and inattentive subtypes have distinct salient connections, the involvement of insula and extra-nuclear regions, known for their role in consciousness and cognitive functions within the brain, aligns with findings from prior ADHD studies[1,5]. When saliency scores are consolidated at the level of brain modules, we find significant similarities between the combined and inattentive subtypes (with all p-values < 0.05): Person's r = 0.97 for NYU, r = 0.84 for OHSU and r = 0.71 for PKU.

Correlations between combined and hyperactive subtypes were moderate (r = 0.45 for NYU, r = 0.73 for OHSU), correlation between inattentive and hyperactive subtypes were even lower.

Conclusions: Put together, our results from decoding BrainGET suggest that the combined and inattentive subtypes share significant similarities in dFC (in particular, connections between insular and extra-nuclear regions), both at the level of ROIs and brain modules. This could suggest that combined subtypes are dominated by inattentive traits, or that dFC does not differentiate these clinically derived subtypes.

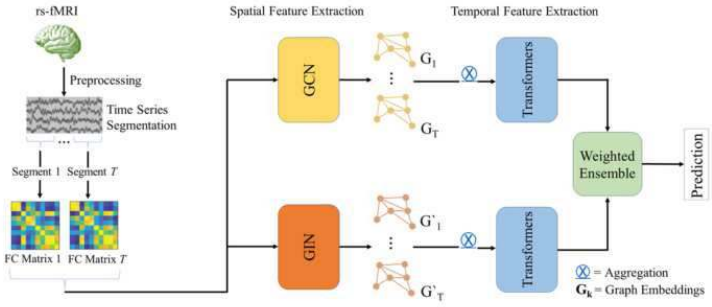

(a)

Models	Sites			
	NI	NYU	OHSU	PKU
DGCN	60.00 ± 6.32*	61.00 ± 2.00*	67.23 ± 3.71	65.13 ± 3.84*
STGCN	62.00 ± 11.66*	57.50 ± 3.54*	66.81 ± 2.89*	69.74 ± 2.99
STAGIN-GARO	56.00 ± 8.00*	58.50 ± 1.22*	62.13 ± 5.11*	66.15 ± 5.23*
STAGIN-SERO	72.00 ± 17.20	60.25 ± 4.14*	62.13 ± 6.37*	65.64 ± 4.76*
BrainGET	**76.00 ± 4.90**	**67.75 ± 1.46**	**71.06 ± 2.89**	**71.79 ± 1.62**

(b)

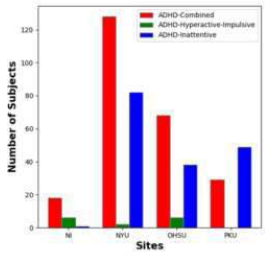

(c)

Figure 1: (a) Illustration of BrainGET. Following recommended practices [6, 10], dFC matrices were constructed by segmenting BOLD signals into overlapping windows of length 60s and stride 1s. Power atlas was used to identify 264 diverse regions of interest. Functional connectivity matrices were computed by determining the Pearson correlation between mean activation timeseries for each ROI pair. These matrices were provided as input to the GCN and GIN components for spatial feature extraction. Resulting graph embeddings were aggregated and fed into Transformers for temporal feature extraction. Predictions from GCN and GIN are then ensembled using weighted grid search (b) Comparison of model accuracies for individual ADHD sites. '*' next to the results indicates significance (p-value < 0.05). (c) Frequency distribution of subjects in all subtypes across each site.

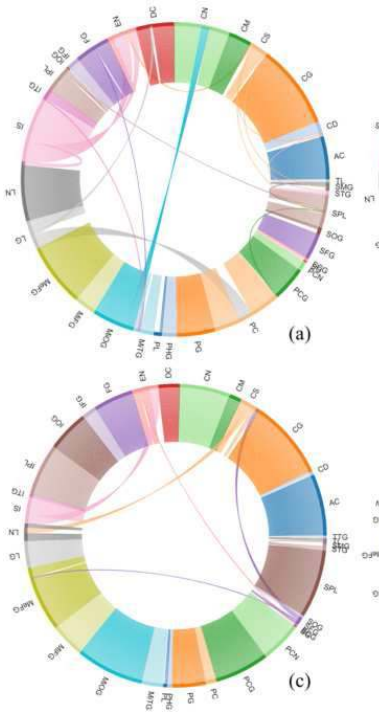

AC: Anterior Cingulate
CD: Caudate
CG: Cingulate G
CS: Claustrum
CM: Culmen
CN: Cuneus
DC: Declive
EN: Extra-Nuclear
FG: Fusiform G
IFG: Inf. Frontal G
IOG: Inf. Occipital G
IPL: Inf. Parietal Lobule
ITG: Inf. Temporal G
IS: Insula
LN: Lentiform Nucleus
LG: Lingual G
MeFG: Medial Frontal G
MiFG: Mid Frontal G
MOG: Mid Occipital G
MTG: Mid Temporal G
PL: Paracentral Lobule
PHG: Parahippocampal G
PG: Postcentral G
PC: Posterior Cingulate
PCG: Precentral G
PCN: Precuneus
SG: Sub-Gyral
SCG: Subcallosal G
SFG: Sup. Frontal G
SOG: Sup. Occipital G
SPL: Sup. Parietal Lobule
STG: Sup. Temporal G
SMG: Supramarginal G
TL: Thalamus
TTG: Trans. Temporal G

Figure 2: To view salient ROI connections, chord diagrams were plotted for combined and inattentive subtypes, respectively, for site NYU {(a), (b)} and OHSU {(c), (d)}. Due to space constraints, only two chord diagrams from these two sites are included.

References

1. Fateh, A. A. (2022). Abnormal insular dynamic functional connectivity and its relation to social dysfunctioning in children with attention deficit/hyperactivity disorder. Frontiers in Neuroscience, 16, 890596.
2. Firouzabadi, F. D. (2022). Neuroimaging in attention-deficit/hyperactivity disorder: recent advances. American Journal of Roentgenology, 218(2), 321-332.

3. Gadgil, S. (2020). Spatio-temporal graph convolution for resting-state fmri analysis. In Medical Image Computing and Computer Assisted Intervention–MICCAI 2020: 23rd International Conference, Lima, Peru, October 4–8, 2020, Proceedings, Part VII 23 (pp. 528-538). Springer International Publishing.
4. Kim, B. H. (2021). Learning dynamic graph representation of brain connectome with spatio-temporal attention. Advances in Neural Information Processing Systems, 34, 4314-4327.
5. Kim, S. (2021). Machine-learning-based diagnosis of drug-naive adult patients with attention-deficit hyperactivity disorder using mismatch negativity. Translational Psychiatry, 11(1), 484.
6. Leonardi, N. (2015). On spurious and real fluctuations of dynamic functional connectivity during rest. Neuroimage, 104, 430-436.
7. Luo, L. (2023). Patterns of brain dynamic functional connectivity are linked with attention-deficit/hyperactivity disorder-related behavioral and cognitive dimensions. Psychological Medicine, 1-12.
8. Manessi, F. (2020). Dynamic graph convolutional networks. Pattern Recognition, 97, 107000.
9. Zhu, Z. (2023). Dynamic functional connectivity changes of resting-state brain network in attention-deficit/hyperactivity disorder. Behavioural Brain Research, 437, 114121.
10. Zhang, H. (2017). Test-retest reliability of “high-order” functional connectivity in young healthy adults. Frontiers in neuroscience, 11, 439.

Poster No 1396

Brain age pre-training for prediction of Alzheimer’s disease diagnosis and progression

Trevor Wei Kiat Tan[1,2,3,4,5], Kim-Ngan Nguyen[1,2], Chen Zhang[1,2,4,5], Ru Kong[1,2,4,5], Susan Cheng[1,2,3,4], Fang Ji[1,2,4], Joanna Su Xian Chong[1,2,4], Eddie Jun Yi Chong[6,7], Narayanaswamy Venketasubramanian[8], Christopher Chen[6,7,9], Juan Helen Zhou[1,2,3,4], B. T. Thomas Yeo[1,2,3,4,5]

[1]Centre for Sleep and Cognition, Yong Loo Lin School of Medicine, National University of Singapore, Singapore, Singapore, [2]Centre for Translational MR Research, Yong Loo Lin School of Medicine, National University of Singapore, Singapore, Singapore, [3]Integrative Sciences and Engineering Programme (ISEP), National University of Singapore, Singapore, Singapore, [4]Department of Electrical and Computer Engineering, National University of Singapore, Singapore, Singapore, [5]N.1 Institute for Health & Institute for Digital Medicine (WisDM), National University of Singapore, Singapore, Singapore, [6]Memory, Aging and Cognition Centre, National University Health System, Singapore, Singapore, [7]Department of Psychological Medicine, Yong Loo Lin School of Medicine, National University of Singapore, Singapore, Singapore, [8]Raffles Neuroscience Centre, Raffles Hospital, Singapore, Singapore, [9]Department of Pharmacology, Yong Loo Lin School of Medicine, National University of Singapore, Singapore, Singapore

Introduction: An individual’s brain age, predicted by a machine learning algorithm using structural MRI, holds vital clinical importance. Brain age higher than chronological age is linked to cognitive decline[1], mortality[2], and brain disorders[3]. Age data is widely available across MRI datasets. Therein lies a theoretical advantage in training brain age models on larger and diverse datasets and applying these pre-trained brain age models for downstream prediction on smaller clinical samples via transfer learning[4]. We aim to investigate if pre-trained brain age models outperform models trained-from-scratch to diagnose Alzheimer’s disease (AD) and predict mild cognitively impaired (MCI) progression to AD.

Methods: The study employed three datasets – Alzheimer’s Disease Neuroimaging Initiative (ADNI), Australian Imaging, Biomarkers and Lifestyle (AIBL) study, and Singapore Memory Aging and Cognition Centre (MACC) Harmonization cohort – for AD diagnosis and MCI progression tasks. Both tasks involved binary classification and used the same nested cross-validation method. Models were compared using Area Under the Curve (AUC) on test set and resampled t-tests with FDR correction. No participant overlap occurred between the two tasks. Models shared a common network architecture with a pre-trained brain age model[4]. Feature-extracted pre-trained models processed structural MRI and generated 64-dimensional features per participant, which were used for logistic regression label prediction[4]. Finetuned models retrained all layers and replaced the last age prediction layer with a binary prediction layer. AD diagnosis distinguished between AD and non-cognitively impaired (NCI) individuals, using 856 ADNI, 156 AIBL, and 260 MACC participants. Three models were compared – trained-from-scratch model (Direct-scratch), feature-extracted brain age pre-trained model (Indirect-brainage), and finetuned brain age pre-trained model (Indirect-brainage-finetune), with training + validation set sizes ranging from 50 to 997. Indirect-brainage and Indirect-brainage-finetune were initialized with a state-of-the-art pre-trained brain age model[4]. MCI progression distinguished stable from progressive MCI, using 478 ADNI, 20 AIBL, and 78 MACC participants. Two models were compared – feature-extracted Indirect-brainage-finetune (Indirect-brainage-finetune-AD), and feature-extracted Direct-scratch (Direct-AD), with training + validation set sizes ranging from 50 to 448.

Results: Figure 1 shows the relationship between the model’s AD diagnosis test AUC and the training + validation set sizes for three models – Indirect-brainage, Indirect-brainage-finetune, and Direct-scratch. Direct-scratch outperformed Indirect-brainage significantly from size 400 or greater up to the largest size of 997. However, there were no significant differences between Direct-scratch and Indirect-brainage-finetune across all training and validation set sizes. Figure 2 shows the

relationship between the model's MCI progression test AUC and the training + validation set sizes for two models – Indirect-brainage-finetune-AD and Direct-AD. Notably, there were no significant differences in test AUCs between the two models across all training and validation set sizes.

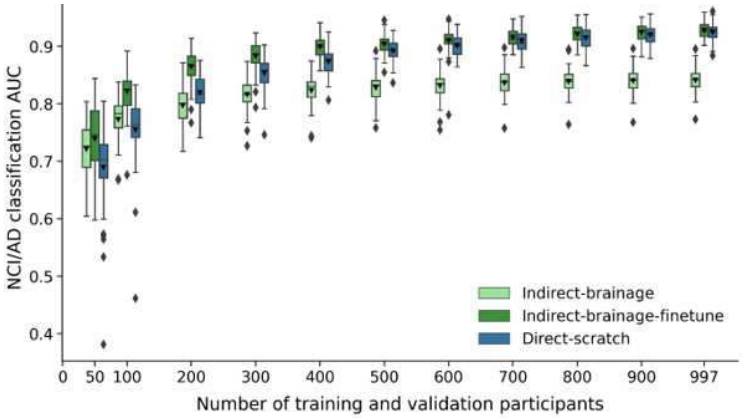

Figure 1. AD diagnosis prediction performance (AUC) of 3 models – feature-extracted brain age pre-trained model (Indirect-brainage), finetuned brain age pre-trained model (Indirect-brainage-finetune), and trained-from-scratch model (Direct-scratch) – across different numbers of training and validation participants. Box plots show test performance across 50 random repeats of train-validation split. Black horizontal line is the median, triangle is the mean, black diamond is the outliers, and whiskers represent 1.5 times the interquartile range.

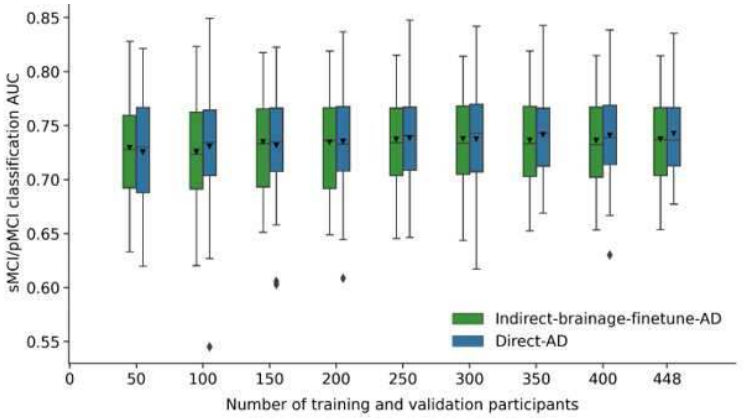

Figure 2. MCI progression prediction performance (AUC) of 2 models – feature-extracted Indirect-brainage-finetune (Indirect-brainage-finetune-AD) and feature-extracted Direct-scratch (Direct-AD) – across different numbers of training and validation participants. Box plots show test performance across 50 random repeats of train-validation split. Black horizontal line is the median, triangle is the mean, black diamond is the outliers, and whiskers represent 1.5 times the interquartile range.

Conclusions: For AD diagnosis, finetuning the pre-trained brain age model significantly improves prediction versus feature extracting the pre-trained brain age model. Interestingly, a model trained-from-scratch significantly outperforms a feature extracted pre-trained brain age model at a training and validation sample size equal to 400 or greater. Hence, for smaller sample sizes (less than 400), using the less computationally intensive feature extraction from the pre-trained model is more beneficial than training a model from scratch. For MCI progression, there is no significant difference in performance between brain age pre-training versus random initialization, when both models feature-extracted AD diagnosis weights, from 50 to 448 sample sizes.

References

1. Cole, J. H., S. J. Ritchie, M. E. Bastin, M. C. Valdes Hernandez, S. Munoz Maniega, N. Royle, J. Corley, A. Pattie, S. E. Harris, Q. Zhang, N. R. Wray, P. Redmond, R. E. Marioni, J. M. Starr, S. R. Cox, J. M. Wardlaw, D. J. Sharp and I. J. Deary (2018). "Brain age predicts mortality." Mol Psychiatry 23(5): 1385-1392.
2. Elliott, M. L., D. W. Belsky, A. R. Knodt, D. Ireland, T. R. Melzer, R. Poulton, S. Ramrakha, A. Caspi, T. E. Moffitt and A. R. Hariri (2021). "Brain-age in midlife is associated with accelerated biological aging and cognitive decline in a longitudinal birth cohort." Mol Psychiatry 26(8): 3829-3838.

3. Kaufmann, T., D. van der Meer, N. T. Doan, E. Schwarz, M. J. Lund, I. Agartz, D. Alnaes, D. M. Barch, R. Baur-Streubel, A. Bertolino, F. Bettella, M. K. Beyer, E. Boen, S. Borgwardt, C. L. Brandt, J. Buitelaar, E. G. Celius, S. Cervenka, A. Conzelmann, A. Cordova-Palomera, A. M. Dale, D. J. F. de Quervain, P. Di Carlo, S. Djurovic, E. S. Dorum, S. Eisenacher, T. Elvsashagen, T. Espeseth, H. Fatouros-Bergman, L. Flyckt, B. Franke, O. Frei, B. Haatveit, A. K. Haberg, H. F. Harbo, C. A. Hartman, D. Heslenfeld, P. J. Hoekstra, E. A. Hogestol, T. L. Jernigan, R. Jonassen, E. G. Jonsson, P. Karolinska Schizophrenia, P. Kirsch, I. Kloszewska, K. K. Kolskar, N. I. Landro, S. Le Hellard, K. P. Lesch, S. Lovestone, A. Lundervold, A. J. Lundervold, L. A. Maglanoc, U. F. Malt, P. Mecocci, I. Melle, A. Meyer-Lindenberg, T. Moberget, L. B. Norbom, J. E. Nordvik, L. Nyberg, J. Oosterlaan, M. Papalino, A. Papassotiropoulos, P. Pauli, G. Pergola, K. Persson, G. Richard, J. Rokicki, A. M. Sanders, G. Selbaek, A. A. Shadrin, O. B. Smeland, H. Soininen, P. Sowa, V. M. Steen, M. Tsolaki, K. M. Ulrichsen, B. Vellas, L. Wang, E. Westman, G. C. Ziegler, M. Zink, O. A. Andreassen and L. T. Westlye (2019). “Common brain disorders are associated with heritable patterns of apparent aging of the brain.” Nat Neurosci 22(10): 1617-1623.
4. Leonardsen, E. H., H. Peng, T. Kaufmann, I. Agartz, O. A. Andreassen, E. G. Celius, T. Espeseth, H. F. Harbo, E. A. Hogestol, A. M. Lange, A. F. Marquand, D. Vidal-Pineiro, J. M. Roe, G. Selbaek, O. Sorensen, S. M. Smith, L. T. Westlye, T. Wolfers and Y. Wang (2022). “Deep neural networks learn general and clinically relevant representations of the ageing brain.” Neuroimage 256: 119210.

Poster No 1397

Adapted 3D deep learning model for Parkinson’s disease classification based on white matter changes

Hyewon Shin[1], Yong Jeong[1]

[1]Korea Advanced Institute of Science & Technology, Daejeon, Republic of Korea

Introduction: Parkinson’s disease (PD) is the world’s second most common neurodegenerative disease, caused by dopaminergic neuronal loss in the substantia nigra due to the deposition of misfolded α-synuclein. As α-synuclein pathology has been suggested to cause early axonal changes that later result in neuronal degeneration, multiple previous studies have shown that diffusion tensor imaging (DTI), as an in vivo imaging technique, is capable of characterizing early detectable white matter (WM) changes in PD. However, another recent study suggested that DTI-based analyses may not be best suited for PD classification, as their binary support vector machine (bSVM) and multiple kernel learning (MKL) model demonstrated low accuracy. Recent advancements in the field of deep learning have given rise to models such as ResNet, designed specifically for image classification, with specialized convolutional layers and residual connections that handle grid-like data in a more efficient manner without the need for manual feature engineering. Therefore, we wondered whether we would be able to generate a DTI-based PD classification model demonstrating high classification accuracy if the machine learning technique itself was deeper and able to learn more complex baseline features. In this study, we generated a novel 3D deep learning classification model with a whole brain fractional anisotropy (FA) map input to classify Parkinson’s disease patients from healthy controls with comparable accuracy to other recent state-of-the-art classification models.

Methods: 625 healthy control (age, 61.4 ± 11.3; female, 37.3%) and 1402 cognitively unimpaired PD patient (age, 63.4 ± 9.4; female, 34.8%) data were selected from the PPMI database for training, validating and testing our model at a 7:2:1 ratio. The DTI and T1-weighted images were preprocessed using MRtrix3, FMRIB Software Library (FSL) and Advanced Normalization Tools (ANTs). The response function, estimating the signal expected in each voxel, was returned for each subject using the Dhollander algorithm. Using the returned response functions, we estimated the fiber orientation distributions (FODs) for each voxel, where the response function was used as a kernel in a contained spherical deconvolution operation. Using these FODs, we were able to estimate the fractional anisotropy (FA) values in each voxel. The returned 3D FA brain map acted as the input into the proposed 3D ResNet-34 PD classification model composed of novel skip connection structures in tandem with SE blocks. Pre-trained 2D ResNet-34 was converted into 3D by duplicating the 2D filters into the third dimension, and transfer learning was employed to reduce training time. Other layers were adjusted to match the 3D filters. Furthermore, the Taguchi method was employed to optimize the performance and improve the robustness of the model.

Architecture of the proposed 3D ResNet

Results: Our proposed model demonstrates a validation accuracy of 99.74% and a validation loss of 0.0418. Moreover, when evaluated on the test data set, the model demonstrated an accuracy of 95.35% and an AUC value of 0.98. Compared to most recent studies, which exhibit a range of accuracies between 49.4% and 98.2%, our model shows high accuracy, precision and recall. Furthermore, the model holds its own merits over other state-of-the-art models with higher classification accuracy in that it does not require multi-modal imaging data and manual feature extraction, which can easily increase computational cost and information loss.

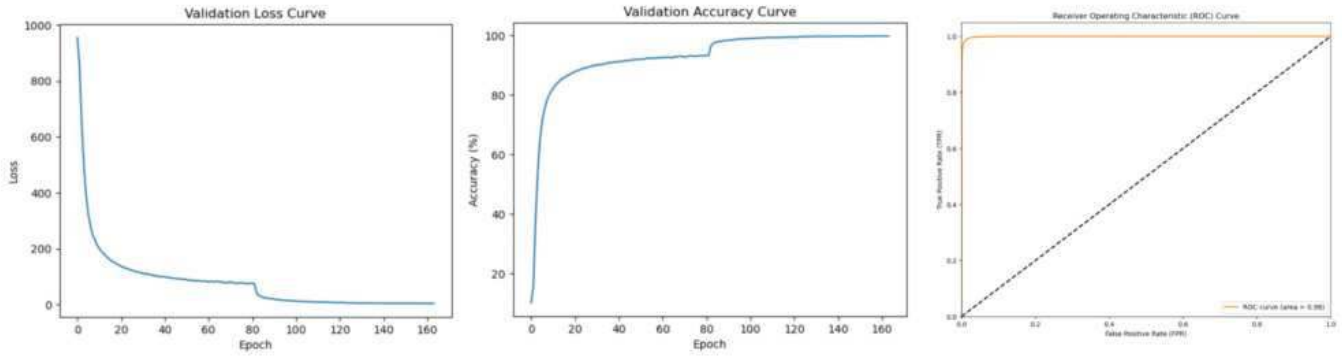

Conclusions: We propose a novel 3D deep learning PD classification model with an accuracy that can compete against other state-of-the-art models. The main difference this model holds is its lack of need for manual feature extraction and multi-modal analysis to raise model accuracy. Furthermore, the proposed model has a strong advantage in that it can be applied to any other task with a 3D input, extending its value to characterizing other pathological changes and accommodating other imaging modalities.

References
1. Alexander, A. L. (2020), 'A machine learning-based classification approach on Parkinson's disease diffusion tensor imaging datasets', Neurological Research and Practice, 4(1), 3.
2. Dhollander, T. (2019), 'Improved white matter response function estimation for 3-tissue constrained spherical deconvolution', Proceedings of the 27th annual meeting of the International Society of Magnetic Resonance in Medicine, 555.
3. Ebrahimi, A. (2020), 'Introducing transfer learning to 3D ResNet-18 for Alzheimer's disease detection on MRI images', 2020 35th International Conference on Image and Vision Computing New Zealand (IVCNZ). Wellington, New Zealand, 2020, pp. 1-6.
4. Gatti, G. (2023), 'Machine learning for the classification of Alzheimer's disease and its prodromal stage using brain diffusion tensor imaging data: A systematic review', Processes, 8(9), 1071.
5. Ghahremani, A. A. (2016), 'Diffusion tensor imaging in Parkinson's disease: Review and meta-analysis', Journal of Neurological Sciences, 367, 213-222.
6. Jenkinson, M. (2012), 'FSL', NeuroImage, 62(2), 782-790.
7. Marek, K. (2018), 'The Parkinson's progressions marker initiative (PPMI) - establishing a PD biomarker cohort', Annals of clinical and translational neurology, 5(12), 1460-1477.
8. Sarwinda, D. (2021), 'Deep learning in image classification using residual network (ResNet) variants for detection of colorectal cancer', Procedia Computer Science, 179(2021), 423-431.
9. Shih, Y. (2023), 'Recent advancements in using diffusion tensor imaging to study white matter alterations in Parkinson's disease: A mini review', Frontiers in Aging Neuroscience, 14, 1018017.
10. Tournier, J. D. (2012), 'Diffusion tensor imaging and beyond', Nature methods, 9(6), 632-641.
11. Vyas, T. (2022), 'Deep learning-based scheme to diagnose Parkinson's disease', Expert Systems, 39(6), e12739.

Poster No 1398

Predicting Mental and Neurological Illnesses Using Cerebellar Heterogeneity

Milin Kim[1], Nitin Sharma[2], Esten Leonardsen[3], Saige Rutherford[4], Geir Selbæk[5], Karin Persson[5], Nils Eiel Steen[6], Olav Smeland[7], Torill Ueland[8], Geneviève Richard[7], Aikaterina Manoli[9], Sofie Valk[9], Christian Beckmann[10], Andre Marquand[11], Ole Andreassen[12], Lars Westlye[13], Thomas Wolfers[14], Torgeir Moberget[15]

[1]Norwegian Centre for Mental Disorders Research (NORMENT),Oslo University Hospital & Institute of Cli, Oslo, Oslo, [2]University of Tübingen;German Center for Mental Health (DZPG), Tübingen, Germany, [3]NORMENT; University of Oslo, Oslo, Norway, [4]Radboud University, Nijmegen, Netherlands, [5]Oslo University Hospital; The Norwegian National Centre for Ageing and Health, Oslo, Norway, [6]NORMENT, Division of Mental Health and Addiction, Oslo University Hospital & University of Oslo, Oslo, Norway, [7]Norwegian Centre for Mental Disorders Research (NORMENT), Oslo, Norway, [8]Norwegian Centre for Mental Disorders Research (NORMENT);University of Oslo, Oslo, Norway, [9]Max Planck Institute for Human Cognitive and Brain Sciences, Leipzig, Germany, [10]Donders Institute for Brain, Cognition, and Behavior, Radboud University Nijmegen, Nijmegen, NL, Nijmegen, Netherlands, [11]Radboud University Nijmegen, Nijmegen, Gelderland, [12]NORMENT, Oslo, Norway, [13]Norwegian Centre for Mental Disorders Research (NORMENT), Oslo University Hospital, Oslo, Norway, [14]Laboratory for Mental Health Mapping, University of Tübingen, Tübingen, BW, [15]Norwegian Centre for Mental Disorders Research (NORMENT); OsloMet, Oslo, Norway

Introduction: The cerebellum has been associated not only with motor coordination but also with cognitive and emotional processing, extending its relevance to a broad spectrum of clinical conditions. As the case-control model overlooks individual-level variability, normative models have been used to map normative development and aging across the lifespan. The normative model is analogous to a paediatric growth chart used to examine how individuals develop and age. Therefore, we predicted mental and neurological illnesses, including autism spectrum disorder (ASD), mild cognitive impairment (MCI), Alzheimer's disease (AD), bipolar disorder (BD), and schizophrenia (SZ), using the cerebellar lobular and voxel-wise normative modelling features. By assessing the predictive performance of the machine learning models, we investigated the impact of various feature categories.

Methods: We employed cerebellar volume and voxel-wise normative models that were introduced in (Kim et al., 2023) which trained on more than 27k individuals across 132 scanning sites, with an age range spanning from 3 to 85 years. The test set comprised more than 26k individuals without a diagnosis, along with clinical sets of 1,757 (Figure 1A). The cerebellar volume normative model utilised ACAPULCO (Han et al., 2020) algorithm, a convolutional neural network-based algorithm that divides the cerebellum into 28 lobules and voxel-wise model used SUIT (Spatially Unbiased Infratentorial Toolbox) (Diedrichsen et al., 2009) toolbox (Figure 1B). The spatial precision normative models enabled integration with existing cerebellar atlases, including 28 anatomical cerebellar regions, 10 regions of interest from the multi-domain task battery (MDTB) (King et al., 2019), and 17 regions of interest from resting-state connectivity (Buckner et al., 2011; Yeo et al., 2011). Here, we developed different machine learning models using raw scores, median and percentage of extreme deviation (threshold at $|z| > 1.96$) from the normative model mapped onto existing atlases as features (Figure 1C). Deviation score assess how an individuals deviate from individuals without diagnosis at each lobule or voxel in the cerebellum. We assessed the diagnostic accuracy using the

area under the receiver operating characteristic curve (ROAUC) with matched samples of the sites and age, addressing the imbalanced dataset with the synthetic minority oversampling technique (SMOTE) (Chawla et al., 2002) which were compared using 1000 permutations (Figure 1D). The models were explained by employing Shapley Additive Explanations to underscore the influence of each individual feature.

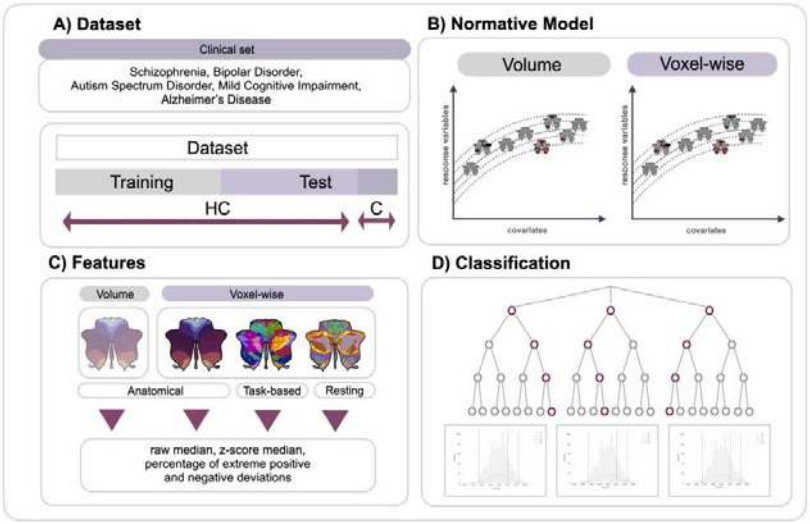

Results: In our investigation, the voxel-wise models yielded slightly higher ROAUC performance compared to volumetric models (Figure 2A). The ROAUC values that surpassed chance levels are displayed in the figure. In the voxel-wise models, methods that used extreme negative percentage of deviations as features outperformed extreme positive percentage of deviations in the all three atlases. Notably, ASD, MCI and SCZ model predictions were better than BD and AD. Shapley Additive Explanation (SHAP) showed that regions important for predictions, where Figure 2B displays the extreme deviation of SHAP values.

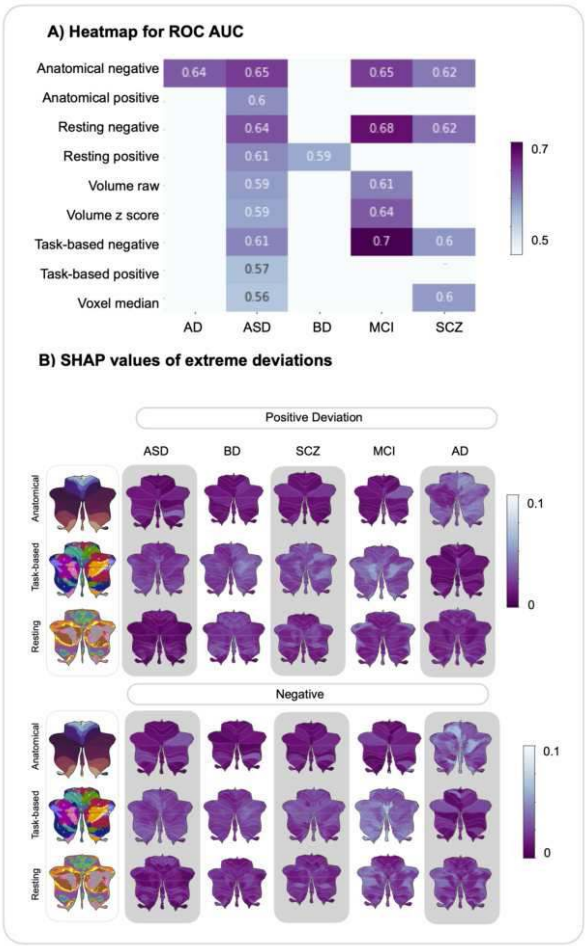

Conclusions: We discovered that voxel-wise models that utilize percentage of extreme negative deviation exhibited superior performance in classifying mental and neurological disorders, while across atlases showed similar performance. We demonstrated the advantages of implementing normative modelling features in the classification. This underscores the constraints posed by anatomical boundaries of the cerebellum and highlights the importance of employing a functional map of the cerebellum.

References

1. Buckner, R. L., et al. (2011). 'The organization of the human cerebellum estimated by intrinsic functional connectivity', Journal of Neurophysiology, vol.106, no. 5, pp. 2322–2345.
2. Chawla, N. V., et al. (2002). 'SMOTE: Synthetic Minority Over-sampling Technique', Journal of Artificial Intelligence Research, vol.16, pp 321–357.
3. Diedrichsen, J., et al. (2009). 'A probabilistic MR atlas of the human cerebellum', NeuroImage, vol. 46, no. 1, pp. 39–46.
4. Han, S., et al. (2020). 'Automatic cerebellum anatomical parcellation using U-Net with locally constrained optimization', NeuroImage, vol. 218, no. 116819.
5. Kim, M., et al. (2023). 'Mapping Cerebellar Anatomical Heterogeneity in Mental and Neurological Illnesses', bioRxiv, 2023.11.18.567647.
6. King, M., et al. (2019). 'Functional boundaries in the human cerebellum revealed by a multi-domain task battery', Nature Neuroscience, vol. 22, no. 8, pp. 1371–1378.
7. Yeo, B. T. T., et al.(2011). 'The organization of the human cerebral cortex estimated by intrinsic functional connectivity', Journal of Neurophysiology, vol. 106, no. 3, pp.125–1165

Poster No 1399

Multi-modal predictors of fMRI-identified brain states

Karl-Heinz Nenning[1], Arielle Tambini[1], Eduardo Gonzalez-Moreira[1], Ting Xu[2], Takuya Ito[3], Francisco Castellanos[4], Stanley Colcombe[1], Alexandre Franco[1], Michael Milham[2]

[1]Nathan Kline Institute, Orangeburg, NY, [2]Child Mind Institute, New York, NY, [3]IBM Research, Yorktown Heights, NY, [4]NYU Grossman School of Medicine, New York, NY

Introduction: Human behavior and attentional focus vary over time. Functional magnetic resonance imaging (fMRI) is well-suited to track associated dynamic and spatial patterns of widespread network interactions, referred to as brain states[1]. Previous work has shown that fMRI-identified brain states are related to fluctuations in ongoing behavior and may be promising markers of psychiatric disorders[2,3]. However, practical challenges of high-quality fMRI data collection (extensive infrastructure, cost, challenges for patient populations), especially at large scales, fundamentally limit its utility. In contrast, pupillometry or electroencephalography (EEG) are readily available less expensive methods that are better suited for large-scale data collection and clinical applications. Here, we examine the utility of non-fMRI-based signals (pupillometry, EEG) to characterize and predict fMRI-identified brain states to bridge the gap between sensitive fMRI markers and more accessible physiological measures.

Methods: We studied an openly available dataset that includes the simultaneous collection of fMRI, EEG, eye tracking, and other physiological measures[4]. Data from 22 individuals were acquired across two sessions while participants performed multiple tasks including resting-state, flickering checkerboard, and naturalistic movie viewing paradigms, allowing us to characterize brain states associated with activity across stimulus-driven task conditions and task-free states. Co-activation pattern (CAP) analysis[6] was used to characterize fMRI-identified brain states across task conditions. We first examined whether the strength of each CAP (i.e. graded measure of brain state) cross-correlated reliably with non-fMRI signals (i.e. pupil diameter, PD) at varying temporal lags. We next adapted a previously introduced regression framework to establish pupillometry and EEG predictors of time-varying fMRI-identified brain states[5]. The fMRI-identified CAP strength was used as a target in the regression framework, and for each time-point, non-fMRI features within a preceding time-window were used to train the coefficients of the prediction model. We performed cross-subject prediction (i.e. leave one participant out) to test the generalizability of non-fMRI predictors, and quantified performance with Pearson's correlation between predicted and actual data.

Results: Temporal clustering of the fMRI data yielded 4 pairs of CAPs, comprising distinct modes of time-varying brain states: one CAP strongly weighted the visual network, another reflected internal vs. external focus (differentially weighting the default mode vs. dorsal attention network), and others weighted frontoparietal networks. Preliminary results of the cross-subject regression framework revealed that PD was predictive for visual CAPs during the checkerboard stimulus ($r=0.3$) and the internal-focus CAP during movie watching ($r=0.25$), but less reliable during rest ($r<0.05$ for all CAPs). Preliminary results using single electrode EEG prediction revealed reliable predictive performance ($r>0.5$) for all tasks and CAPs. Preliminary

analyses indicated that the electrodes associated with CAP-specific spatial patterns exhibited the most reliable predictions, demonstrating the feasibility of the approach.

Conclusions: Our preliminary findings suggest the feasibility of bridging the gap between sensitive fMRI markers of dynamic brain states and more readily scalable physiological measures such as EEG and pupillometry. A generalizable model could have practical implications, enhancing the value of more accessible physiological measures. Further research is necessary to identify the most sensitive non-fMRI features and their optimal predictive potential.

References

1. Greene, AS (2023), 'Why is everyone talking about brain state?', Trends in Neurosciences, vol. 46, pp. 508–524.
2. Marshall, E (2020), 'Coactivation pattern analysis reveals altered salience network dynamics in children with autism spectrum disorder', Network Neuroscience, vol. 4, pp. 1219–1234.
3. Cai, W (2021), 'Latent brain state dynamics distinguish behavioral variability, impaired decision-making, and inattention', Molecular Psychiatry, vol. 26, pp. 4944–4957.
4. Telesford, QK (2023), 'An open-access dataset of naturalistic viewing using simultaneous EEG-fMRI', Scientific Data, vol. 10, pp. 1–13.
5. Meir-Hasson, Y, (2014), 'An EEG Finger-Print of fMRI deep regional activation', Neuroimage, vol. 102, pp. 128-141
6. Liu, X, (2018), 'Co-activation patterns in resting-state fMRI signals', Neuroimage, vol. 180, pp. 485-494

Poster No 1400

A Robust Pipeline For Personalised Localisation of Brain Regions Using Image Quality Transfer

Ying-Qiu Zheng[1], Harith Akram[2], Stephen Smith[1], Saad Jbabdi[3]

[1]University of Oxford, Oxford, Oxfordshire, [2]UCL Queen Square Institute of Neurology, London, UK, [3]Oxford University, Oxford, United Kingdom

Introduction: Accurate identification and localisation of brain regions in individual subjects is increasingly important in both neuroscience research and clinical practice. In functional neurosurgery, e.g. deep brain stimulation, targeting precision is essential for symptom relief in various neurological and psychiatric disorders. However, this task is hampered by the lack of distinct contrast for many target brain structures on conventional medical images and significant variability in individual brain anatomies. A common practice is to rely on standardised atlases, but this often fails to account for inter-individual variations[1-3]. Advancements in neuroimaging have enabled brain region localisation in individual brains. For instance, a popular approach is the use of connectivity-based functional localisation with tractography or resting-state connectivity, alongside prior knowledge of a region's connectional fingerprint. This however requires high-quality diffusion/functional MRI data, limiting application in clinical settings with scan-time constraints. To address this challenge, we developed LOCALISE, a tool that enables individualised delineation of brain regions. The main purpose of this tool is to enable connectivity-based localisation in low-quality datasets. Using Image Quality Transfer (IQT) techniques[9-10], LOCALISE transfers anatomical information from large-scale high-quality MRI (e.g. HCP data) enabling functional localisation on clinical-quality data. Here, we focus on the ventral intermediate nucleus of the thalamus (Vim), a key DBS target for the treatment of tremor in Parkinson's patients, to demonstrate LOCALISE's capabilities, with ongoing work to incorporate more brain structures.

Methods: Localising Vim illustrates the idea behind LOCALISE. In theory, Vim can be found using literature-based connectional information, namely the connections to M1 and the contralateral Cerebellum. However, these connections cannot be robustly extracted. Instead, LOCALISE creates a large number of more "robust" connectional features, and learns to segment Vim using these features and the high-quality prior-based segmentation as a target "ground truth". This mapping is then used on low-quality data where the direct prior-based method fails. To train LOCALISE for Vim, we used high-quality diffusion MRI data from the Human Connectome Project (HCP) to generate Vim locations and trained an IQT model[10] to locate Vim in surrogate low-quality datasets based on their connectivity profiles. The segmentation model employs a Conditional Random Field (CRF)[11] to map high-quality Vim labels to low-quality features. This CRF model is optimised to maximise the likelihood of correct HQ-Vim label assignments based on voxel-wise connectivity profiles. The trained model was then applied to left-out low-quality subjects and evaluated against their high-quality counterparts.

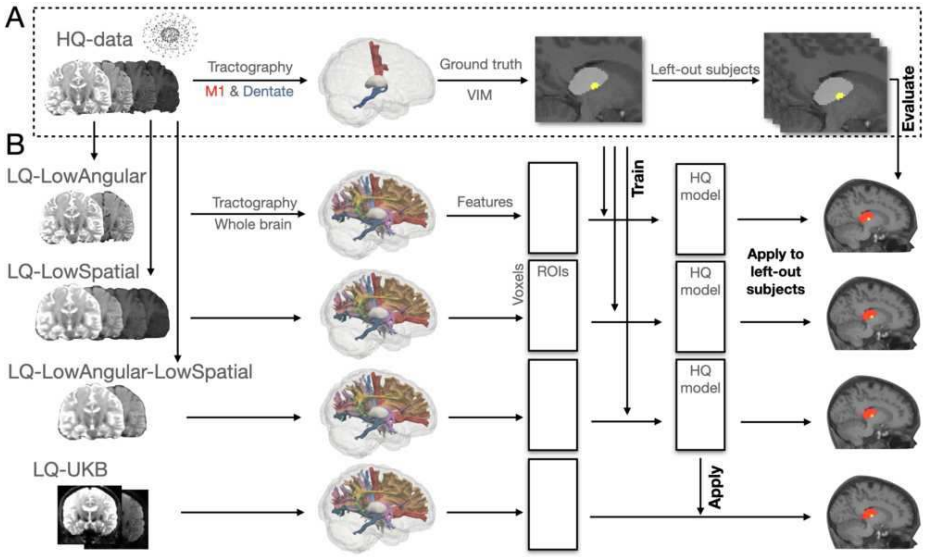

Figure 1. Illustration of the workflow of LOCALISE, using the Vim as an example. (A) First, the HQ diffusion data were used to create "ground truth" Vim within the thalamic masks, based on its white matter connectivity with M1 and contralateral cerebellum. (B) Next, surrogate low-quality diffusion datasets were created by corrupting the HQ datasets. The HQ-augmentation model was trained with the HCP HQ "ground truth" Vim as target labels and an extended set of HCP low-quality connectivity profiles as input features. The trained model was applied to unseen low-quality datasets (surrogate low-quality HCP and UK Biobank diffusion data) to generate Vim predictions, and evaluated against the corresponding HQ "ground truth".

Results: Using Vim localisation as an example, LOCALISE's accuracy was evaluated using the Dice coefficient and centroid displacement, the latter a measure of distance between the centroids of predicted and actual clusters. LOCALISE outperformed two established methods, the (original, simple) connectivity-driven and atlas-based approach, on HCP surrogate low-quality datasets, showing higher overlap with high-quality "ground truth" and greater reliability across varying data quality and scanning sessions. Notably, when applied to UK Biobank low-quality datasets, LOCALISE, trained on HCP data, generalised effectively, surpassing alternative methods in Vim localisation.

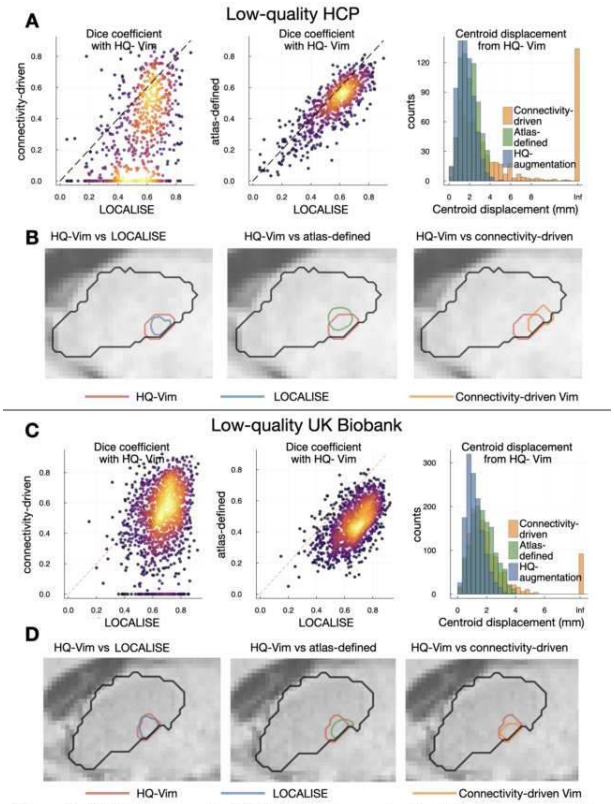

Figure 2. (A) On low-quality HCP data, when using the HQ-Vim as ground truth, LOCALISE gives higher Dice coefficient and smaller centroid displacement with the HQ-Vim, than the atlas-defined Vim (green) and the low-quality connectivity-driven Vim (orange). (B) Example contours yielded by each approach. (C) and (D). Equivalent plots of (A) and (B), on low-quality UK Biobank subjects.

Conclusions: LOCALISE offers robust localisation of brain regions even when using clinical-standard data, and has the potential to enhance targeting accuracy in neurosurgical procedures. Its adaptability to diverse data conditions makes it a valuable tool in settings where high-quality MRI is unavailable or inappropriate for certain cohorts. The tool can be found in https://git.fmrib.ox.ac.uk/yqzheng1/python-localise.

References

1. Finn, Emily S., et al. "Functional connectome fingerprinting: identifying individuals using patterns of brain connectivity." Nature neuroscience 18.11 (2015): 1664-1671.
2. Johansen-Berg, Heidi, et al. "Functional–anatomical validation and individual variation of diffusion tractography-based segmentation of the human thalamus." Cerebral cortex 15.1 (2005): 31-39.
3. Morel, Anne, Michel Magnin, and Daniel Jeanmonod. "Multiarchitectonic and stereotactic atlas of the human thalamus." Journal of Comparative Neurology 387.4 (1997): 588-630.
4. Akram, Harith, et al. "Connectivity derived thalamic segmentation in deep brain stimulation for tremor." NeuroImage: Clinical 18 (2018): 130-142.
5. Ferreira, Francisca, et al. "Ventralis intermedius nucleus anatomical variability assessment by MRI structural connectivity." NeuroImage 238 (2021): 118231.
6. Bertino, Salvatore, et al. "Ventral intermediate nucleus structural connectivity-derived segmentation: anatomical reliability and variability." Neuroimage 243 (2021): 118519.
7. Bridge, Holly, Stuart Clare, and Kristine Krug. "Delineating extrastriate visual area MT (V5) using cortical myeloarchitecture." Neuroimage 93 (2014): 231-236.
8. Glasser, Matthew F., and David C. Van Essen. "Mapping human cortical areas in vivo based on myelin content as revealed by T1-and T2-weighted MRI." Journal of neuroscience 31.32 (2011): 11597-11616.
9. Alexander, Daniel C., et al. "Image quality transfer and applications in diffusion MRI." NeuroImage 152 (2017): 283-298.
10. Zheng, Ying-Qiu, et al. "A Transfer Learning Approach to Localising a Deep Brain Stimulation Target." International Conference on Medical Image Computing and Computer-Assisted Intervention. Cham: Springer Nature Switzerland, 2023.
11. Zheng, Shuai, et al. "Conditional random fields as recurrent neural networks." Proceedings of the IEEE international conference on computer vision. 2015.

Poster No 1401

Enhancing Alzheimer's disease prediction using genetic-guided brain volumetric phenotype network

Yonghyun Nam[1], Jakob Woerner[1], Sang-Hyuk Jung[1], Erica Suh[1], Haochang Shou[1], Li Shen[1], Dokyoon Kim[1]

[1]Department of Biostatistics, Epidemiology and Informatics, University of Pennsylvania, Philadelphia, PA

Introduction: Genetic predispositions related to brain volumetric phenotypes are known to be associated with complex brain-related traits, including Alzheimer's disease (AD), which often involves significant brain volume reduction. Recent genome-wide association studies (GWASs) have shown that brain imaging-derived phenotypes (IDP) are phenotypically and genetically associated with AD. However, existing AD risk prediction models, primarily based on conventional polygenic risk scores (PRSs), are limited in capturing the complex relationships between IDPs and AD. To address these limitations, we have developed a network-based risk scoring model to enhance AD risk prediction ability.

Methods: We propose the BrainNetScore, a novel AD risk scoring model that quantifies genetic impacts of associations among multiple brain IDPs and AD incidence. First, a brain connectivity network was constructed using genetic correlations from the UK Biobank GWAS summary statistics across 96 regional brain volume IDPs. Subsequently, this network was expanded into a heterogenous BrainNet graph, comprising 96 IDPs and their associated 12,043 common variants (SNPs), by attaching significant SNPs (P-value < 5e-8) to each brain IDP. The set of SNPs in BrainNet were then used to obtain individual genotype information from independent cohorts, such as the Alzheimer's Disease Neuroimaging Initiative (ADNI). Next, label propagation algorithms were applied to generate individualized predicted scores for each IDP, leveraging genetic correlations and SNP effect directions. To provide a comprehensive view of risk factors with respect to AD, logistic regression was utilized to aggregate the predicted scores for the IDPs, denoting these aggregated scores as BrainNetScore.

Results: To build the BrainNet, we obtained the GWAS summary statistics of 96 brain volume IDPs for UK biobank European participants downloaded from the Brain Imaging Genetics Knowledge Portal (Big-KP). Individual genotype data for 914 samples (550 AD cases and 364 cognitive normal controls) were collected from ADNI and ADNI-WGS-2 with ADSP Follow-Up Study after excluding samples involved in International Genomics of Alzheimer's Project (IGAP) consortium. To demonstrate the utility of BrainNetScore in predicting AD status compared to conventional risk models, PRSs, as a baseline model, were calculated using pruning and thresholding (PRS P+T, P-value threshold as 1e-6) with GWAS summary statistics from IGAP. We assessed the predictive performance of three models: a singleton scoring model, an additive model incorporating covariates (sex, age, and APOE), and a combined model integrating PRS and BrainNetScore. Across 10-fold cross-validation, the combined PRS + BrainNetScore model yielded an average AUC of 0.684 ± 0.034, surpassing both the PRS only model (0.595 ± 0.075) and the BrainNetScore only model (0.666 ± 0.029). Models with sex as a covariate further enhanced the predictive

robustness of the combined model (0.684 ± 0.030). Additionally, when integrating APOE genotypes into the combined model, the predictive accuracy further increased (0.778 ± 0.043), suggesting the significant role of genetic factors in AD risk assessment (Figure 1).

Conclusions: The study demonstrates the enhanced predictive ability of the BrainNetScore model for AD risk, particularly when combined with conventional PRSs. These findings underscore the value of incorporating network-based approaches and comprehensive genetic information in improving AD risk prediction models. The enhanced predictive capability of the combined model shows promise for personalized medicine and early intervention strategies in AD and brain-related traits. Future research should focus on expanding the model's applicability to a wider range of populations.

Figure 1. Performance Comparison in Predicting Alzheimer's Disease Across Various Risk Scoring Models: All models were evaluated using the ADNI cohort (comprising 550 AD cases and 364 cognitively normal controls). Summary statistics from IGAP were employed, with the APOE region excluded from PRS calculations. The experiments were conducted using 10-fold cross-validation.

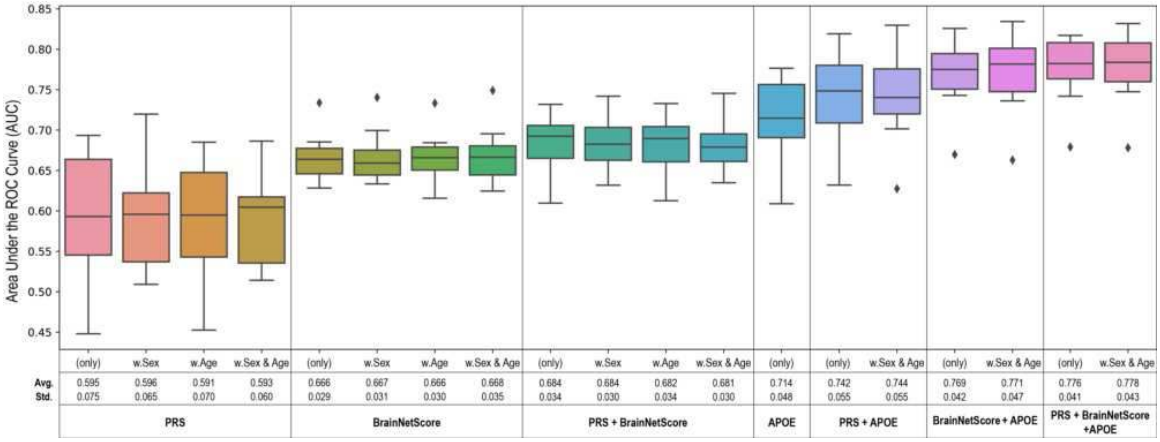

References

1. Nam, Y. (2022), 'netCRS: Network-based comorbidity risk score for prediction of myocardial infarction using biobank-scaled PheWAS data', Pacific Symposium on Biocomputing, vol. 27, pp. 325-336.
2. Smith, S.M. (2021). 'An expanded set of genome-wide association studies of brain imaging phenotypes in UK Biobank', Nature Neuroscience, vol. 24, pp. 737–745.
3. Song, Z. (2022), 'Graph-Based Semi-Supervised Learning: A Comprehensive Review', IEEE Transactions on Neural Networks and Learning Systems, vol. 34, no. 11, pp. 8174-8194.
4. Suh, Erica H. (2023), 'An interpretable Alzheimer's disease oligogenic risk score informed by neuroimaging biomarkers improves risk prediction and stratification', Frontiers in Aging Neuroscience, 15
5. Zhao, B. (2019). 'Genome-wide association analysis of 19,629 individuals identifies variants influencing regional brain volumes and refines their genetic co-architecture with cognitive and mental health traits', Nature Genetics, vol. 51, pp. 1637–1644.

Poster No 1402

Unsupervised Learning for Lesion Detection on 7T Brain MRI in Patients with Focal Epilepsy

Soumen Ghosh[1,2], Viktor Vegh[1,2], John Phamnguyen[1,3], Shahrzad Moinian[1,2], David Reutens[1,3]

[1]Centre for Advanced Imaging, The University of Queensland, Brisbane, Australia, [2]ARC Centre for Innovation in Biomedical Imaging Technology, The University of Queensland, Brisbane, Australia, [3]Royal Brisbane and Women's Hospital, Brisbane, Australia

Introduction: The localization of a focal epileptogenic lesion on MRI by visual inspection is often challenging and even when a lesion is identified its delineation using current approaches can be incomplete. These considerations motivated the development of automated methods for lesion identification based on machine learning approaches.

Methods: The study was approved by the Human Research Ethics Committee Queensland (HREC/17/QRBW/284), and focal epilepsy patients were recruited from the Epilepsy Clinic at the Royal Brisbane Women's Hospital (Brisbane, Australia). MRI scans were performed in-house at the Centre for Advanced Imaging, The University of Queensland. 3D GRE-MRI flow compensated scans were obtained using a 7T ultra-high field whole-body MRI research scanner (Siemens Healthcare, Erlangen, Germany) equipped with a single channel transmit and 32 channel receive head coil (Nova Medical, Wilmington, USA) using voxel size = 0.75 × 0.75 × 0.75 mm3. MP2RAGE data with the same resolution were also acquired. 7T MRI scans of the brain were acquired in patients with focal epilepsy and in healthy controls. Pre-processing of the T1 and T2-weighted images comprised skull stripping using SPM (Version 7.4) followed by the creation of an FSL brain mask (Version 6.0.7) and

registration to the MNI 1 mm3 brain template using MIPAV (Version 10.0.0). A one-class support vector machine (oc-SVM) was the constructed. Figure 1 shows two basic building blocks: unsupervised learning-based feature representation and anomaly detection. The first block extracts a latent representation of the patch from brain MRI using a Siamese autoencoder consisting of convolution and deconvolution layers. We implemented the state-of-the-art (SOA) method,1 and two machine learning methods, all of which use images patches as the input: • SOA: 2D patch-based autoencoder with input size 15×15×2 comprising two 15×15 obtained from T1 and T2-weighted MRI. • 2D patch-based autoencoder: Same as SOA with static (i.e., epoch independent) regularization incorporated into the loss function. • 2.5D patch-based autoencoder: SOA with static regularization and increased the input patch dimension to 15×15×6. Here, T1 and T2-weighted MRI patches are added from the other two orthogonal dimensions to increase the number of patches at the input from 2 to 6. In this case the autoencoder is able to extract information based on 3D brain information. The anomaly detection module employs an oc-SVM trained using the 64-entry feature vector extracted from either the SOA, 2D and 2.5D Siamese autoencoders. An oc-SVM model was trained and tested for each image voxel coordinate. Training utilised data from 62 healthy subjects by taking patches from two different healthy subjects at the same time. Data from 5 epilepsy patients were used for testing. The output was a score map of abnormal voxels. Model performance was evaluated by comparing the score map with the ground truth MRI, delineated on MRI by an expert neurologist aided by clinical findings, SPECT, and PET images. Lesion detection accuracy was calculated using Positive Predicted Value (PPV), Dice Index Score (DSC) and Jaccard Similarity Index between the predicted lesion and Ground Truth.

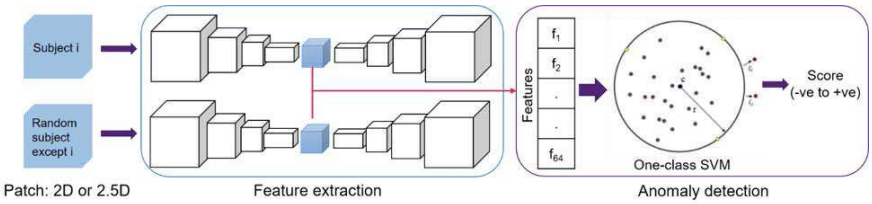

Figure 1 Proposed machine learning framework for brain anomaly detection. The proposed framework used unsupervised deep learning network for feature extraction and one-class SVM for outlier detection

Patient	GT Volume	PDGT Ratio			Sensitivity			Specificity			NPV			PPV			DSC (F1 Score)			JACCARD		
		SOA	2D	2.5D	SOA	2D	2.5D	SOA	2D	2.5D	SOA	2D	2.5D	SOA	2D	2.5D	SOA	2D	2.5D	SOA	2D	2.5D
1	33217	0.41	0.44	0.47	23.77	32.23	36.79	66.81	76.68	80.16	30.97	36.68	39.36	58.32	72.97	78.36	33.77	44.71	50.07	20.32	28.79	33.39
3	10788	0.85	0.89	1.05	54.69	46.26	56.1	83.06	76.03	73.23	76.77	71.84	75.44	64.17	51.69	53.23	59.05	48.82	54.63	41.89	32.3	37.58
4	42879	0.7	0.63	0.69	49.53	45.51	55.21	76.26	80.06	84.56	56.68	55.98	62.04	70.68	72.5	80.51	58.25	55.92	65.5	41.09	38.81	48.56
5	392	3.97	1.34	1.23	88.27	73.98	85.46	85.94	97.27	98.28	99.38	98.8	99.33	22.24	55.24	69.36	35.52	63.25	76.57	21.6	46.25	62.04

Table 1 Performance of ML model for lesion detection compared to ground truth. The PDGT ratio represents the similarity between the predicted lesion and ground truth volume (the closer to 1 the higher the similarity).

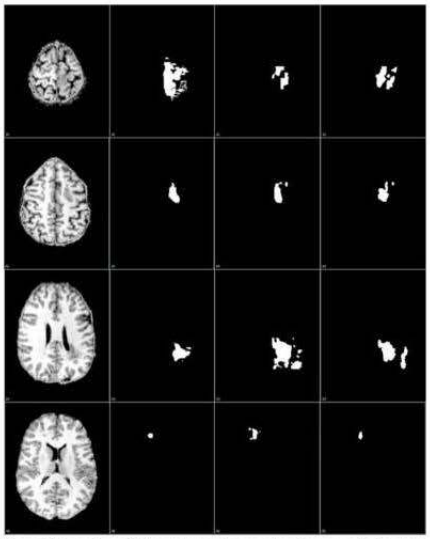

Figure 2: Comparison of lesion detected by our method, paper method and the ground truth. From left to right, MP2RAGE of a focal epilepsy patient, Ground Truth, lesion detected by paper method and lesion detected by proposed method. Subject ids from top to bottom sequentially P03, P07, P09, and P10

Results: All models were tested on five patients, and all models detected a lesion in four patients. For the four positive lesion patients, Figure 2 depicts the 7T brain MRI, the ground truth, and lesions identified by the SOA and 2D implementations. Lesion detection accuracy for the four patients is summarized in Table 1. Generally, the 2.5D model outperformed the 2D implementation and the SOA method.

Conclusions: The proposed 2.5D lesion detection model may provide an automated way to identify MRI-positive focal epilepsy lesions using T1 and T2 weighted MRI.

References
1. Alaverdyan, Z. (2020), 'Regularized siamese neural network for unsupervised outlier detection on brain multiparametric magnetic resonance imaging: application to epilepsy lesion screening'. Medical image analysis, 60, 101618.

Poster No 1403

Revealing distinct neuroanatomical subtypes of Major depression disorder and Schizophrenia

Yinghan Zhu[1], Norihide Maikusa[1], Kiyoto Kasai[1], Shinsuke Koike[1]

[1]The University of Tokyo, Tokyo, Tokyo

Introduction: Prior neuroimaging studies primarily focused on investigating neuroanatomical abnormalities in mental disorders such as major depression disorder (MDD) or schizophrenia (SCZ) use binary case-control approach.Brain structural abnormalities such as cortical thinning and subcortical volume increasing were reported in MDD or SCZ compare to heathy controls (HCs). We investigated neuroanatomical subtypes in multi-disorder, multi-site multi-protocol, using semi-supervised machine learning methods heterogeneity through discriminative analysis (Varol et al., 2017) to discover variations of anatomical alterations within disorders.

Methods: T1-weighted structural brain MRI scans from patients with MDD (n=544), SCZ (n= 176), and 1,819 HCs, were obtained from 9 sites. Regional cortical thickness (CT), surface area (SA) and subcortical volumes (SV) served as features in building the classifier differentiating disorder subtypes from HCs. We used traveling subjects dataset to harmonize measures of CT, SA and SV data. Next, we fitted general addictive models to only the HC data (n=1148) to estimate non-linear effects of age and sex for every structural feature; then we applied the fitted GAMs to obtain non-linear age- and sex-corrected features. Individuals those who were younger than 65 years old (MDD, n=445; SCZ, n=158) and HC (n=599) data served as training, test, and external validation datasets.

Results: Two distinct neuroanatomical subtypes were found for MDD and SCZ(Figure 1). In differentiating Subtype 1 or subtype 2 from HCs, the accuracy of each classifier was higher than those built for disorder without subtypes (MDD subtype1 vs HCs 79%; MDD subtype2 vs HCs 76%; MDD vs HCs 67%; SCZ subtype1 vs HCs 83%; SCZ subtype2 vs HCs 86%; SCZ vs HCs 75%). Indicating that by identifying subtypes of MDD and SCZ improved the performance in differentiating those from HCs.

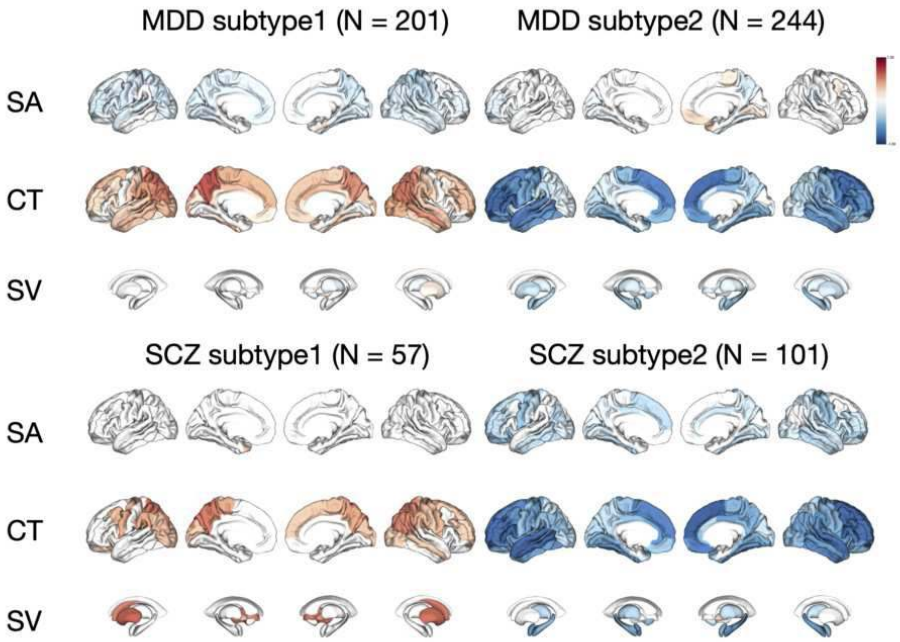

Conclusions: Discovering of neuroanatomical subtypes of MDD and SCZ may be helpful to identify their prognosis and underlying neuropathological processes. Future prospective studies are required about whether the classifier could be actually helpful in the clinical settings.

References
1. Varol E. (2017), 'HYDRA: revealing heterogeneity of imaging and genetic patterns through a multiple max-margin discriminative analysis framework', Alzheimer's Disease Neuroimaging I, NeuroImage, 145: 346–64.

Poster No 1404

Junifer and Julearn: From Neuroimaging to Machine Learning models without expert-level coding skills

Federico Raimondo[1,2], Synchon Mandal[1,2], Sami Hamdan[1,2], Shammi More[1,2], Leonard Sasse[1,2,3], Vera Komeyer[1,2,4], Amir Omidvarnia[1,2], Simon Eickhoff[1,2], Kaustubh Patil[1,2]

[1]Institute of Neuroscience and Medicine (INM-7: Brain and Behaviour), Research Centre Jülich, Jülich, Germany, [2]Institute of Systems Neuroscience, Heinrich Heine University Düsseldorf, Düsseldorf, Germany, [3]Max Planck School of Cognition, Leipzig, Germany, [4]Department of Biology, Faculty of Mathematics and Natural Sciences, Heinrich-Heine-University Düsseldorf, Düsseldorf, Germany

Introduction: Thanks to big data and computational power, the study of brain-cognition relationships using neuroimaging and machine learning (ML) has gained significant popularity[1]. Importantly, decisions in data processing[2] and predictive modeling[3] strongly impact the results. Also, misconceptions about ML procedures can distort or invalidate findings[4], hence escalating the neuroimaging reproducibility crisis[5]. These decisions and implementations can become increasingly complex, posing challenges for early-career researchers: they require proficiency in diverse skills to deal with large-scale datasets, algorithms, and complex ML set-ups, while they also require domain-specific knowledge for experiment design and interpretation. To mitigate these issues, we introduce two complementary instruments: Junifer, a feature-extraction tool that does not require coding, and Julearn, an easy-to-use ML library. These tools aim to create a bridge between preprocessed neuroimaging data and ML-based analysis by emphasizing ease-of-use and maintainability.

Methods: ML-based neuroimaging analysis entails four steps: 1) preprocessing (e.g. using FreeSurfer, fMRIPrep, CAT, AFNI, ANTS, SPM, etc), 2) feature extraction, 3) ML model building and benchmarking, and 4) post-hoc model analysis (e.g. evaluate features importance)[6]. All steps entail technical and conceptual challenges. However, steps 2 and 3 are more vulnerable due to the complexity of the required code or scripts. We here propose to facilitate step 2 with Junifer, and step 3 with Julearn. Junifer (https://juaml.github.io/junifer) is a no-code tool that allows parametrizing each step of a feature extraction pipeline in a text file, using the simple YAML syntax specification. By specifying the dataset (or its structure) and a list of markers to compute, the user can easily compute all the features required for their ML models. And with a just a few more lines of text, all the processing can be done in computational clusters. Among Junifer's most prominent features are a vast list of built-in datasets, parcellations, masks and markers, as well as processing in native and standard spaces (various MNI). Feature extraction is transparent and reproducible, as the full pipeline configuration is stored within each output file. Julearn (https://juaml.github.io/julearn) is created for building and evaluating ML models. Built on top of the highly influential scikit-learn[7], Julearn offers a robust interface to build complex ML pipelines in a user-friendly way suitable also for novice programmers. It allows users to evaluate and compare ML models in a CV-consistent manner, minimizing the risks of leakage and overestimation of results. Further features include neuroimaging specific models, corrected statistical test for ML models' comparisons[9], interactive results visualization, and inspection tools to link to post-hoc analysis.

Results: To exemplify, we aimed at evaluating the performance of a ML-model to predict chronological age from cortical and subcortical functional connectivity (FC) in native space. The 34-lines long text file allows us to compute the FC for all the participants and resting state recordings (N=4800) in the HCP-YA dataset, combining a cortical and a subcortical parcellation (Figure 1-A). With 42 more lines of Python code, we can evaluate the performance of the neuroimaging specific Connectome-Based Predictive Modelling (CBPM)[8]-based linear regression model, using nested cross-validation and hyperparameter tuning (Figure 1-B).

Conclusions: Junifer and Julearn enable researchers to easily and correctly bridge neuroimaging and ML models. Junifer provides the tools to process large-scale neuroimaging datasets and extract tabular features for ML applications. Julearn allows users to build and compare ML models from any tabular dataset minimizing the code complexity, lowering the coding skills required to perform advanced ML-based analysis.

A) Junifer YAML

```yaml
workdir: /tmp

datagrabber:
  kind: DataladHCP1200
  tasks:
    - REST1
    - REST2
  ica_fix: true

preprocess:
  - kind: BOLDWarper
    reference: T1w

markers:
  - kind: FunctionalConnectivityParcels
    name: fc-parcels-schaefer400-tian_native
    parcellation:
      - Schaefer400x17
      - TianxS2x3TxMNI6thgeneration
    cor_method: correlation
    cor_method_params:
      empirical: true

storage:
  kind: HDF5FeatureStorage
  uri: ../junifer_storage/fc-parcels-schaefer400-tian/native.hdf5

queue:
  jobname: HCP_FC_ShaeferTian
  kind: HTCondor
  env:
    kind: conda
    name: junifer
  mem: 20G
```

Dataset Defintion: HCP1200 Only REST1 and REST2 Use ICA+FIX data

Warp to T1w (native) space

Compute FC

Merge parcellations

FC parametrization

HDF5 File with results

HPC Configuration

B) Julearn Python code

```python
from sklearn.model_selection import RepeatedKFold
from julearn.pipeline import PipelineCreator
from julearn import run_cross_validation
from junifer.storage import HDF5FeatureStorage
import pandas as pd

# Read data from junifer output
storage = HDF5FeatureStorage("fc-parcels-schaefer400-tian/native.hdf5")
df_data = storage.read_df("BOLD_fc-parcels-schaefer400-tian_native")
features = [x for x in df_data.columns if "~" in x]
# Average across runs
df_data = df_data.groupby("subject")[features].mean()
# Add demographic data (including age)
df_demographics = pd.read_csv("demographics.csv")
df_data = df_data.join(df_demographics)

# Define CBPM model
cbpm_pipeline = PipelineCreator(problem_type="regression")
cbpm_pipeline.add(
    step="cbpm", significance_threshold=[0.01, 0.05, 0.1],
    corr_sign="posneg"
)
cbpm_pipeline.add(step="linreg")

# Set-up cross-validation
cv = RepeatedKFold(n_splits=10, n_repeats=10, random_state=10)
scoring = ["neg_mean_absolute_error", "r2", "r_corr"]
X = [r".*\~.*"]
y = "age"
X_types = {"continuous": r".*\~.*"}

# Run cross-validation
scores, final_estimator, inspector = run_cross_validation(
    model=cbpm_pipeline, data=df_data, X=X, y=y, cv=cv, scoring=scoring,
    return_estimator="all", return_inspector=True, X_types=X_types,
)
# Save results
scores.to_csv("scores.csv")

# Get fold-wise predictions and save
predictions = inspector.folds.predict()
predictions.to_csv("predictions.csv")
```

Figure 1: Text and code required to evaluate the performance of an age prediction model from cortical and subcortical functional connectivity using the HCP-YA S1200 release. The Junifer YAML (left) is used to extract functional connectivity from all the participants. The Junifer Python code (right) is used to estimate the performance of an age prediction model using CBPM and a linear regression, using nested cross-validation for hyperparameter tuning.

References

1. J. Wu, J. Li, S. B. Eickhoff, D. Scheinost, and S. Genon, 'The challenges and prospects of brain-based prediction of behaviour', Nat Hum Behav, vol. 7, no. 8, Art. no. 8, Aug. 2023, doi: 10.1038/s41562-023-01670-1.
2. G. Antonopoulos, S. More, F. Raimondo, S. B. Eickhoff, F. Hoffstaedter, and K. R. Patil, 'A systematic comparison of VBM pipelines and their application to age prediction', NeuroImage, vol. 279, p. 120292, Oct. 2023, doi: 10.1016/j.neuroimage.2023.120292.
3. S. More et al., 'Brain-age prediction: A systematic comparison of machine learning workflows', Neuroimage, vol. 270, p. 119947, Apr. 2023, doi: 10.1016/j.neuroimage.2023.119947.
4. L. Sasse et al., 'On Leakage in Machine Learning Pipelines'. arXiv, Nov. 07, 2023. doi: 10.48550/arXiv.2311.04179.
5. K. J. Gorgolewski and R. A. Poldrack, 'A Practical Guide for Improving Transparency and Reproducibility in Neuroimaging Research', PLOS Biology, vol. 14, no. 7, p. e1002506, Jul. 2016, doi: 10.1371/journal.pbio.1002506.
6. S. M. Lundberg and S.-I. Lee, 'A Unified Approach to Interpreting Model Predictions', in Advances in Neural Information Processing Systems, I. Guyon, U. V. Luxburg, S. Bengio, H. Wallach, R. Fergus, S. Vishwanathan, and R. Garnett, Eds., Curran Associates, Inc., 2017. [Online]. Available: https://proceedings.neurips.cc/paper_files/paper/2017/file/8a20a8621978632d76c43dfd28b67767-Paper.pdf
7. F. Pedregosa et al., 'Scikit-learn: Machine Learning in Python', Journal of Machine Learning Research, vol. 12, pp. 2825–2830, 2012, doi: 10.1007/s13398-014-0173-7.2.
8. X. Shen et al., 'Using connectome-based predictive modeling to predict individual behavior from brain connectivity', Nat Protoc, vol. 12, no. 3, pp. 506–518, Mar. 2017, doi: 10.1038/nprot.2016.178.
9. C. Nadeau and Y. Bengio, 'Inference for the Generalization Error', Machine Learning, vol. 52, no. 3, pp. 239–281, Sep. 2003, doi: 10.1023/A:1024068626366.

Poster No 1405

Structure-function coupling of the brain using Graph Neural Network

Yeongjun Park[1], Mansu Kim[2], Bo-yong Park[3,4,5]

[1]Department of Computer Engineering, Inha University, Incheon, Republic of Korea, [2]Graduate School of Artificial Intelligence, Gwangju Institute of Science and Technology, Gwangju, Republic of Korea, [3]Department of Data Science, Inha Unversity, Incheon, Republic of Korea, [4]Department of Statistics and Data Science, Inha Unversity, Incheon, Republic of Korea, [5]Center for Neuroscience Imaging Research, Institute for Basic Science, Suwon, Republic of Korea

Introduction: One of the core assumptions in neuroscience is that brain structure and function are strongly intertwined. Previous neuroimaging studies proposed methods for predicting functional connectivity from structural connectivity

information based on eigenvector decomposition approaches[1] and neural network-based techniques[2]. However, the predictive performance has not been optimized at an individual subject level. In this work, we propose a model that integrates eigenvector decomposition and graph neural network (GNN) methodologies, which appropriately infers relationships of the latent features embedded based on the graph structure among different brain regions[3].

Methods: We obtained preprocessed diffusion-weighted imaging (DWI) and resting-state functional magnetic resonance imaging (rs-fMRI) of 974 young, healthy subjects from the Human Connectome Project database (age = 28.76 years; 54.93% female)[4,5]. We constructed the structural connectivity via diffusion tractography and built the functional connectivity by calculating inter-regional correlations of functional time series, and the matrices were mapped onto the Schaefer atlas with 200 parcels[6]. We estimated the low-dimensional representations of the structural connectivity (i.e., structural gradients) using nonlinear dimensionality reduction techniques, and used these gradients for predicting the functional connectivity matrix. We built a prediction model using GNN, composed of three graph attention network (GAT) layers and one fully connected layer[7], to predict the functional connectivity matrix from the structural connectivity matrix (Fig. 1). The parameters of GAT layers were set as follows: the number of output channels = 30; the number of heads = 2. We randomly divided the data into training (n = 624), validation (n = 155), and test datasets (n = 195). The model was trained using the training data and validated using the validation dataset. The performance of the model was assessed using the test dataset based on the Pearson correlation between the upper triangular elements of the original and predicted matrices. Additionally, we re-performed the above processes based on the five-fold cross-validation instead of the holdout validation approach.

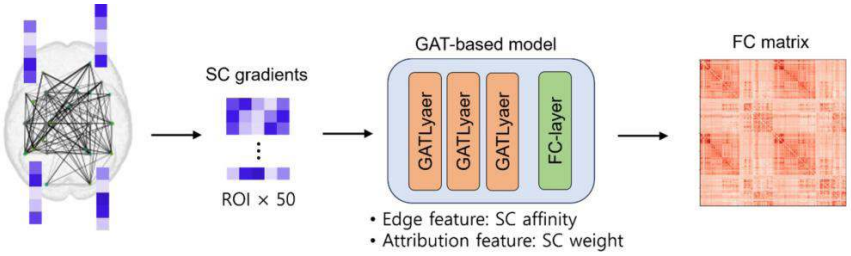

Fig. 1 Pipeline of the proposed graph attention network-based model. Our model predicts functional connectivity (FC) matrix from structural connectivity (SC) gradients Abbreviation: ROI, region of interest; GAT, graph attention networks

Results: Our model showed high performance in predicting functional connectivity at an individual level. The mean ± standard deviation correlation coefficients were 0.843 ± 0.037 across individuals. It outperformed previous approaches based on the Riemannian optimization approach, which showed a performance of 0.776 ± 0.052[1], as well as the previous deep learning-based approach, which showed 0.55 ± 0.1[2]. When we performed the five-fold cross-validation, the performance was 0.843 ± 0.003 across the cross-validation folds, and it outperformed the Riemannian optimization approach based on the three-fold cross-validation (0.775 ± 0.049).

Conclusions: In this study, we proposed an integrated model for predicting the functional connectivity matrix from the structural connectome information. We confirmed that the proposed model outperformed previous state-of-the-art methods. Our approach may provide a new direction in structure-function coupling studies in neuroscience.

References

1. B. T. Thomas Yeo, "The organization of the human cerebral cortex estimated by intrinsic functional connectivity," J Neurophysiol, vol. 106, no. 3, pp. 1125–1165, Sep. 2011, doi: 10.1152/jn.00338.2011.
2. D. C. Van Essen, "The WU-Minn Human Connectome Project: An overview," Neuroimage, vol. 80, pp. 62–79, Oct. 2013, doi: 10.1016/j.neuroimage.2013.05.041.
3. J. Zhou, "Graph neural networks: A review of methods and applications," AI Open, vol. 1. Elsevier B.V., pp. 57–81, Jan. 01, 2020. doi: 10.1016/j.aiopen.2021.01.001.
4. M. F. Glasser, "The minimal preprocessing pipelines for the Human Connectome Project," Neuroimage, vol. 80, pp. 105–124, Oct. 2013, doi: 10.1016/j.neuroimage.2013.04.127.
5. O. Benkarim, "A Riemannian approach to predicting brain function from the structural connectome," Neuroimage, vol. 257, Aug. 2022, doi: 10.1016/j.neuroimage.2022.119299.
6. P. Veličković, "Graph Attention Networks," Oct. 2017, [Online]. Available: http://arxiv.org/abs/1710.10903
7. T. Sarwar, "Structure-function coupling in the human connectome: A machine learning approach," Neuroimage, vol. 226, Feb. 2021, doi: 10.1016/j.neuroimage.2020.117609.

Acknowledgements

This study was funded by the National Research Foundation of Korea (NRF-2021R1F1A1052303; NRF-2022R1A5A7033499), Institute for Information and Communications Technology Planning and Evaluation (IITP) funded by the Korea Government (MSIT) (No. 2022-0-00448, Deep Total Recall: Continual Learning for Human-Like Recall of Artificial Neural Networks; No. RS-2022-00155915, Artificial Intelligence Convergence Innovation Human Resources Development (Inha University); No. 2021-0-02068, Artificial Intelligence Innovation Hub), and Institute for Basic Science (IBS-R015-D1).

Poster No 1406

Human functional connectome fingerprinting using resting-state dynamic functional connectivity

Amin Ghaffari[1], Yufei Zhao[1], Jason Langley[1], Xu Chen[1], Xiaoping Hu[1]

[1]*University of California, Riverside, Riverside, CA*

Introduction: Resting-state functional connectivity (FC) networks have distinct, personalized connectivity patterns that could act as a unique fingerprint for individual identification (Kazeminejad, A. (2019)). Prior work on functional connectome fingerprinting relied on static FC patterns and considered a single functional connectivity map across the whole data collection session for subjects for individual identification (Finn, E.S. (2015)). However, the brain is a dynamic system that switches between multiple metastable states rather than staying in a single state (Fox, M.D. (2005)), and each of the metastable states could represent a different FC map that has unique information for each individual. Based on this understanding, incorporating dynamic FC information may improve identification accuracy in FC fingerprinting.

Methods: In this paper, we use resting state data from the Human Connectome Project (HCP) with a sample size of 100 subjects to evaluate the performance of our dynamic states-based brain fingerprinting method. Regions of Interest (ROIs) are extracted based on the 268-node functional parcellation map of (Shen, X. (2013)). Using the time series of each ROI and a sliding time window of 20 time points, we develop a framework for the analysis of dynamic functional connectivity of the subjects and corresponding individualization. Initially, at each time window, we calculate the Pearson correlation coefficients between pairs of regions and obtain the functional connectivity maps. By subtracting the mean of all of the FC maps across all subjects and time windows, we obtain the demeaned version of FC networks. We consider each brain to go into 3 dominant connectivity states within the scan session, and utilize the K-Means clustering methods twice to obtain these states. To achieve this, first, we apply a data reduction technique on the FC maps in which we sum all correlation coefficients for each ROI and call that the correlation strengths (Ou, J. (2013)). Then, we perform K-Means (K=30) clustering on correlation strengths and calculate the centers of clusters for each individual. Next, we place all of those clusters' centers from all subjects into a pool of correlation strengths and acquire the main dominant states by computing the 3 main cluster centers. By calculating the correlations between each individual's correlation strength at each time window with the dominant brain states, we obtain the average representation of the 3 states for each subject. Finally, by normalizing and concatenation of those representations, we achieve a final vectorized representation for the individuals, and using the Pearson correlation coefficient between these vectors, we identify subjects' scans from the rest of the group.

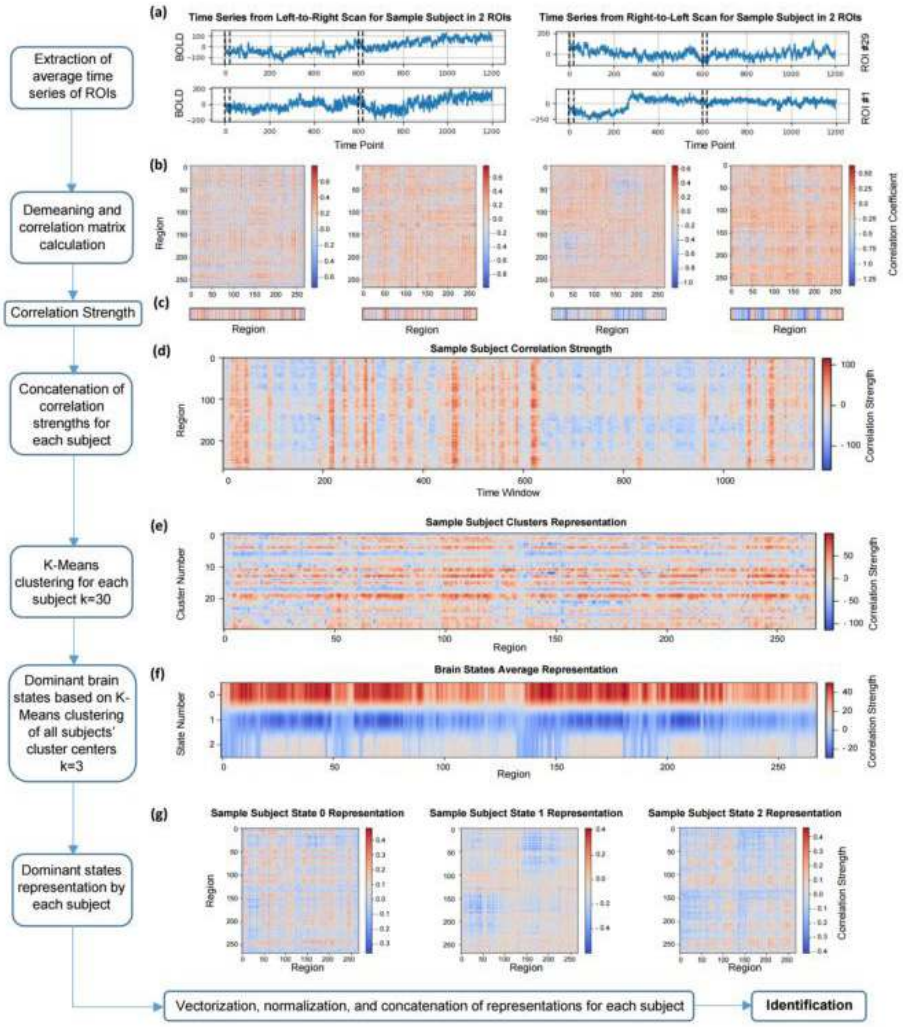

Figure 1. The proposed pipeline for functional connectome fingerprinting: (a) Visualization of the time series of a sample subject extracted from two random ROIs of the 268-node parcellation map. The time series on the left are acquired from a subject in the HCP dataset with Left-to-Right phase encoding direction, whereas the ones on the right are obtained with Right-to-Left phase encoding direction. **(b)** Demeaned correlation matrices for the time windows indicated by black dashed lines in part (a). **(c)** Correlation strength vectors of the correlation matrices of part (b) by summing all the values within each column for each region. **(d)** Illustration of correlation strengths of all the time windows for the sample subject. **(e)** Visualization of cluster centers extracted from the subject-level K-Means clustering (K=30) for the sample subject. **(f)** Dominant brain states: Cluster centers extracted from the group-level K-Means clustering (K=3). **(g)** Average representation of the dominant states by the sample subject. Next, the matrices are vectorized, normalized, and concatenated for each subject, and identification is performed based on these vectors.

Results: Our results demonstrate a notable enhancement in identification accuracy with dynamic states-based fingerprinting. More specifically, incorporating dynamic functional connectivity patterns for identification resulted in an accuracy of 100% when identifying day 2 scans based on day 1 data, and 98% when identifying day 1 scans using day 2 data, surpassing the performances based on the whole-brain static functional connectome, which is below 95% (Finn, E.S. (2015)).

Conclusions: Our results indicate that for more accurate individualization of the human functional brain map, it is beneficial to consider the effects of dynamics in the resting state network. Considering the average functional connectivity map reduces the differentiation power between subjects and is associated with more misidentified samples because it neglects the inherent dynamics of the functional connectivity pattern of the brain. In contrast, looking at representations of different brain states by each subject has a better "fingerprinting" ability and therefore is a better method of identification.

References

1. Finn, E.S. (2015), 'Functional connectome fingerprinting: identifying individuals using patterns of brain connectivity' Nature neuroscience, vol. 18, no. 11, pp. 1664-1671.
2. Fox, M.D. (2005), 'The human brain is intrinsically organized into dynamic, anticorrelated functional networks' Proceedings of the National Academy of Sciences, vol. 102, no. 27, pp. 9673-9678.
3. Kazeminejad, A. (2019), 'Topological properties of resting-state fMRI functional networks improve machine learning-based autism classification', Frontiers in neuroscience, vol. 12, p. 1018.
4. Ou, J. (2013), 'Modeling brain functional dynamics via hidden Markov models' in 2013 6th International IEEE/EMBS Conference on Neural Engineering (NER), pp. 569-572.
5. Shen, X. (2013), 'Groupwise whole-brain parcellation from resting-state fMRI data for network node identification' Neuroimage, vol. 82, pp. 403-415.

Poster No 1407

Deep neural networks predict future overweight/obesity and obesity-related major psychiatric disorde

Heehwan Wang[1], Yoonjung Joo[2], Eun-Ji Lee[1], Bo Gyeom Kim[1], Gakyung Kim[1], Jiook Cha[3]

[1]Seoul National University, Seoul, Other, [2]Sungkyunkwan University, Seoul, Other, [3]Seoul National University, Seoul, Seoul

Introduction: Childhood overweight/obesity is a global health issue affecting life-long risks for chronic diseases and mental health. Although the role of the brain in the development of overweight/obesity is well recognized, the potential of the brain as a predictor for future childhood overweight/obesity remains unclear. We hypothesize that the brain structure can accurately predict whether children become overweight/obese within 1 and 2 years via deep neural networks.

Methods: We used brain structural MRI data and behavioral assessment data of 11,316 children (ages 9 to 10 years) from the Adolescent Brain Cognitive Development (ABCD) study. We calculated Body Mass Index standard deviation score (BMI-sds) of children based on the Grwoth Chart released by the Center for Disease Control and Prevention, used for an index of weight status at the baseline year. We respectively assigned children who were in the normal weight status at the baseline year but became overweight/obese and excessively gained weight (the change of BMI-sds > 0.2) within 1-year follow-up and 2-year follow-up to become overweight within 1 year and become overweight within 2 years group. If children did not satisfy those requirements, they were assigned to still normal group. We employed transfer learning approach to predict future overweight/obesity. We pre-trained deep neural networks to predict BMI-sds at the baseline year from brain structure MRI at the baseline year and respectively fine-tuned them to predict whether children become overweight/obesity within 1-year follow-up and 2-year follow-up based on brain structure MRI at the baseline year. Furthermore, we employed explainable AI (XAI) algorithms to investigate brain structures attributing to deep neural networks' predictions, i.e., the combination of SmoothGrad and Integrated Gradients. Using XAI-driven attribution scores, we performed clustering analysis and statistical analyses to test the difference in polygenic risk and the development of behavioral problems between children who became overweight/obese. To investigate the utility of deep neural networks and transfer learning approach, we fine-tuned those pre-trained model, learned to predict BMI-sds at the baseline year from brain structure MRI at the baseline year, to predict the diagnoses of major psychiatric disorders which are frequently comorbid with obesity, such as Major Depressive Disorder and Anxiety disorders.

Results: Our results showed that deep neural networks accurately predict current weight status (R2 = 0.49 ± 0.01; Mean Squared Error = 1.97 ± 0.06) and transfer learning approach significantly improved future overweight/obesity prediction within 1 year (ACC = 0.64 ± 0.03; AUROC = 0.70 ± 0.02) and 2 years (ACC = 0.61 ± 0.01; AUROC = 0.66 ± 0.03). When investigating brain structures attributing to the prediction of current weight status and future overweight/obesity, we found the brain stem, the pituitary gland, the cerebellum, various temporal lobe regions, and the amygdala were important for deep neural network's prediction. Additonally, XAI-driven the amygdala subnuclei attribution scores for future overweight/obesity revealed individual differences in the development of CBCL anxiety problem (Cohen's d = 0.14, FDR corrected p value < 0.05). One step further, we investigated the potential of pre-trained deep neural networks for current weight status by demonstrating significant improvements in classifying current diagnoses of major psychiatric disorders frequently comorbid with obesity, such as Major Depressive Disorder (ACC = 0.60 ± 0.04; AUROC = 0.67 ± 0.05).

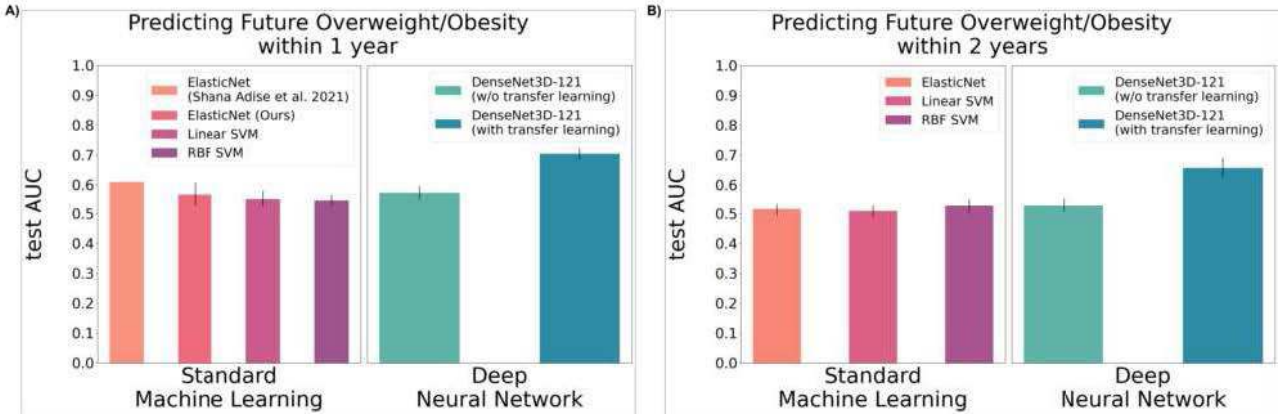

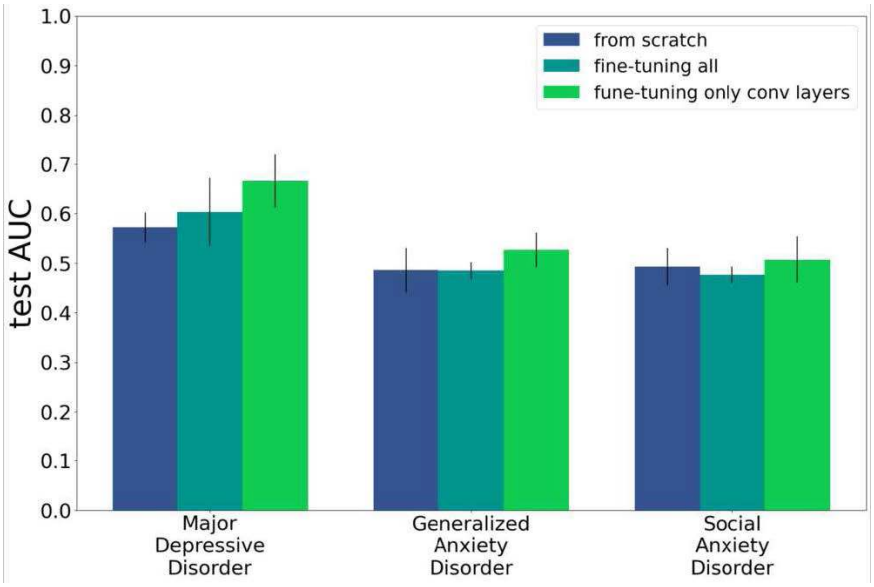

Conclusions: We showed the utility of deep neural networks and transfer learning approach in early detection of childhood overweight/obesity. Using XAI algorithms, we revealed the individual differences in the development of anxiety problems. One step further, we also demonstrated the potential of our novel transfer learning approach in psychiatric research.

References

1. Geserick, M. et al (2018). Acceleration of BMI in Early Childhood and Risk of Sustained Obesity. N. Engl. J. Med. 379, 1303–1312 .
2. Freemark, M (2010). Pediatric Obesity: Etiology, Pathogenesis, and Treatment. (Springer Science & Business Media)

Poster No 1408

Predictability of phenotype information from functional connectivity in large imaging datasets

Jessica Dafflon[1], Dustin Moraczewski[1], Eric Earl[1], Gabriel Loewinger[1], Patrick McClure[2], Adam Thomas[1], Francisco Pereira[1]

[1]National Institute of Mental Health, Bethesda, MD, [2]Naval Postgraduate School, Monterey, CA

Introduction: One of the ultimate objectives of neuroimaging research is to create predictive models that can reveal the connection between patterns of functional connectivity and observable characteristics or behavior, often called phenotypes. Previous studies have shown that models trained to predict behavioral features from the individual's functional connectivity have modest to poor performance[1,2,5]. One possible reason is that brain-behavior models have focused on meticulously chosen individual phenotypes scrutinized in isolation. Previous research has shown predicting latent phenotypes, i.e., a decomposition from the phenotypes obtained using dimensionality reduction algorithms, can yield better performance than predicting individual phenotypes[5]. The results were, however, mainly evaluated on one dataset. To address this gap, we compare the predictive performance obtained from untransformed phenotypes and latent phenotypes, and also assess the model's performance with and without regressing out covariates.

Methods: We analyzed the reliability and predictability of phenotypes and latent phenotypes components within two large neuroimaging datasets, the Human Connectome Project (HCP; N=964; development set N=856; test set N=108)[6] and the Philadelphia Neurodevelopmental Cohort (PNC; N=973; development set N=864; test set N=109)[4]. We chose phenotypes that span behavioral domains of cognition and personality. We extracted corresponding singular value decomposition (SVD) representations of these phenotypes, and assessed if the latent phenotypes are more predictable than the original phenotype variables. For the prediction experiments, we used a Ridge regression model, estimating result variability over 100 bootstrap samples. We also assessed the impact of regressing out age and sex and their squared interaction from the phenotypes and how these impacted the prediction performance. Additionally, we explore how removing unreliable phenotypic information from the targets of the training data changes the model's performance and evaluate if there is a significant change in predictive performance using a critical difference analysis[3].

Results: If not accounted for, the covariates can inflate the prediction results; this is particularly visible, in the relation between the phenotypic variable "strength unadjusted" and sex in the HCP dataset (r=0.6 before; r=0.1 after adjustment). Even after accounting for the covariates, prediction performance is low in both datasets. To assess if latent phenotypes were more

predictable than individual phenotypes, we computed the SVD of the phenotypes on both datasets. Remarkably, we observed that only the loadings of the first 4-6 SVD components obtained from the phenotypes were reliably identified when the same experiment was repeated on different splits of the same dataset (Fig 1). Finally, we examine how removing unreliable phenotypic (cutoff 30/100 in our reliability analysis) information from the targets of the training data changes the model's performance. We observed that reconstructing the phenotypes using only the first five components achieved a very similar performance as using all components, indicating that most of the information relevant to prediction is present in the first components and the remaining can be filtered out without harm to the predictive performance (Fig 2).

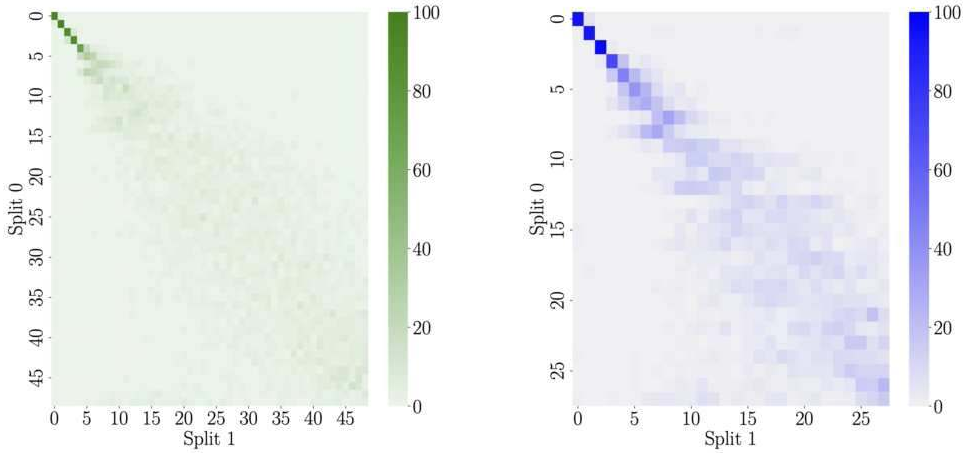

Figure1: Latent phenotypes reliability for both datasets HCP (in green) and PNC (in blue). The loadings of the first 5 SVD components were reliable (HCP - 1st: 96/100; 2nd: 96/100; 3rd: 89/100; 4th: 89/100; 5th: 32/100) and (PNC - 1st: 94/100; 2nd: 93/100; 3rd: 97/100; 4th: 46/100; 5th: 38/100) of the 100 permuted repetitions. The colorbar represents the number of times the component loadings could be matched between SVDs from each half of the dataset over the 100 repetitions (i.e., the darker the color means that the component was more often identified as having the highest correlation). The results show all the components that explain 95% of the variance.

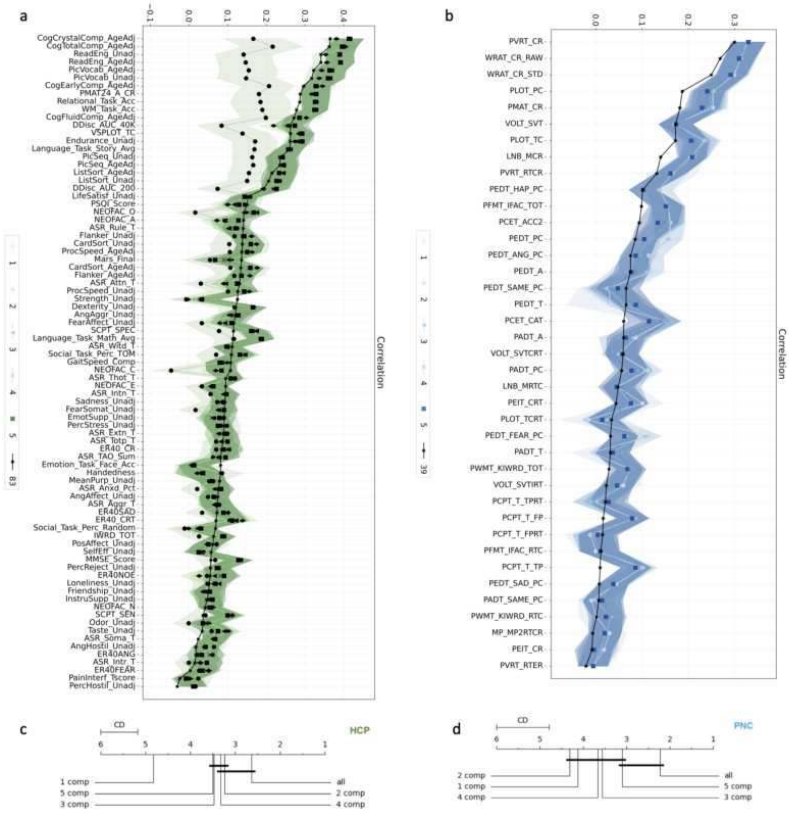

Figure2: Predictability of phenotype variables in the test set, quantified by the correlation between predictions and true values, for HCP (a) and PNC (b). Each plot has six prediction curves, each corresponding to the performance of a model trained using reconstructions of the phenotype measures using the first 1 through 5 components obtained from the SVD, as well as all of them. The data points and connecting lines depict the mean prediction performance, and the shaded regions represent its standard deviation across multiple resamplings. Critical difference diagrams for the HCP (c) and PNC (d), showcase if there is a significant difference in the model's performance when using all components or a fraction of them. For the HCP data, there was no significant difference in the model's performance when using 2, 4, or all components. For the PNC dataset, there was no significant difference when using all or 5 components. A look-up table for the phenotype acronyms is provided here (https://bit.ly/ohbm2024tables).

Conclusions: If not accounted for, covariates can inflate the performance of predictive models. We observed that apart from the first latent phenotypes the remainder were not reliably identified over repetitions of the same dataset. Highlighting the fact that most of the predictive information is present in the first components, we showed that removing the remaining components did not significantly impact the model's performance (Fig 2). In summary, our study sheds light on the intricate relationship between resting state functional connectivity, predictability, and reliability of phenotypic information.

References

1. Chen, J (2023), 'Relationship between prediction accuracy and feature importance reliability: An empirical and theoretical study', NeuroImage, vol. 274, pp. 120115, https://doi.org/10.1016/j.neuroimage.2023.120115
2. Bertolero, M (2020), 'Deep Neural Networks Carve the Brain at its Joints', arxiv, https://doi.org/10.48550/arXiv.2002.08891
3. Demsar. J (2006), 'Statistical comparisons of classifiers over multiple data sets', The Journal of Machine learning research, vol. 7, p. 1-30, https://www.jmlr.org/papers/volume7/demsar06a/demsar06a.pdf
4. Gur, R. C (2010), 'A cognitive neuroscience-based computerized battery for efficient measurement of individual differences: standardization and initial construct validation', Journal of neuroscience methods, vol. 187, p. 254–262, https://doi.org/10.1016/j.jneumeth.2009.11.017
5. Ooi, L (2022), 'Comparison of individualized behavioral predictions across anatomical, diffusion and functional connectivity MRI', NeuroImage, vol. 263, p. 119636, https://doi.org/10.1016/j.neuroimage.2022.119636
6. Van Essen, D. C. (2012), 'The human connectome project: a data acquisition perspective'. Neuroimage, vol. 62, no. 4, p. 2222-2231, https://doi.org/10.1016/j.neuroimage.2012.02.018

Poster No 1409

Disentangled Representation Learning for Capturing Individualized Atrophy of Alzheimer's Disease

Zhuangzhuang Li[1], Yibao Sun[1], Kun Zhao[1], Yong Liu[1]

[1]School of Artificial Intelligence, Beijing University of Posts and Telecommunications, Beijing, China

Introduction: Alzheimer's disease (AD) is a highly heterogeneous neurodegenerative disease, characterized by cognitive decline, irreversible memory loss, psychiatric symptoms, and brain atrophy. Capturing individualized pathological changes from healthy controls (HC) to AD is critical for early diagnosis and targeted treatment. However, existing studies focus on the group averages, assuming homogeneity between AD patients. We proposed a novel deep disentangled generative model (DDGM) for capturing individualized neuroanatomical alterations. The proposed method disentangles AD into "realistic" healthy counterfactual images and residual maps. The residual map can localize hypothetical abnormalities within a normal brain image that may cause it to be diagnosed with AD.

Methods: DDGM is composed of two encoder-decoder branches and a decoder branch. One encoder-decoder branch generates pseudo-healthy images by adversarial training, and the other is for synthetic disease residual maps. The decoder branch is for facilitating the training process. From Fig.1B, we can see that an input image can synthesize a realistic pseudo-healthy image, reconstruct the input image, and produce a residual map. The residual map indicates the underlying abnormal changes with disease progression.

Results: Preserving the healthiness and subject identity of pseudo-healthy images for medical image translation tasks is important. The biological validity of synthetic pseudo-healthy images was evaluated by longitudinal data (HC convert to AD) from the ADNI database. We calculated the structural similarity index (SSIM) between synthetic pseudo-healthy images and longitudinal HC images to guarantee healthiness when AD images are fed into DDGM. The generated pseudo-healthy images and longitudinal HC images have a similar image structure (SSIM: 89.98% ± 0.04, Fig. 1C). To preserve the subject identity, we computed the SSIM values between synthetic pseudo-healthy images and original images across the testing subjects. The mean SSIM values between synthetic HC images produced by AD and longitudinal HC images are 98.04% ± 0.13. The generated HC images and original HC images have a similar image structure (SSIM: 98.71% ± 0.20, Fig. 1D) when HC images are fed into DDGM. The residual maps generated by DDGM can reflect the brain atrophy patterns of AD individuals. Finally, we used the ADNI dataset to explore the brain atrophy patterns of each condition in the human brain, such as HC, PMCI, SMCI, and AD. As shown in Fig. 1E, it is observed that AD, PMCI, SMCI, and HC showed an increasing trend of brain atrophy. The regions with the most severe gray matter atrophy were found in the hippocampus, amygdala, and part of the temporal lobe regions by AD abnormal residual maps.

Conclusions: We proposed a novel DRL-based model for capturing individualized neuroanatomical alterations. The proposed model can synthesize realistic healthy counterfactual images and produce saliency residual maps to indicate the underlying abnormal regions for interpretation. The saliency residual maps can help neurologists to understand the changes in disease progression. We believe that our proposed method will open new avenues for improving individualized diagnosis and the development of precision medicine for clinical intervention.

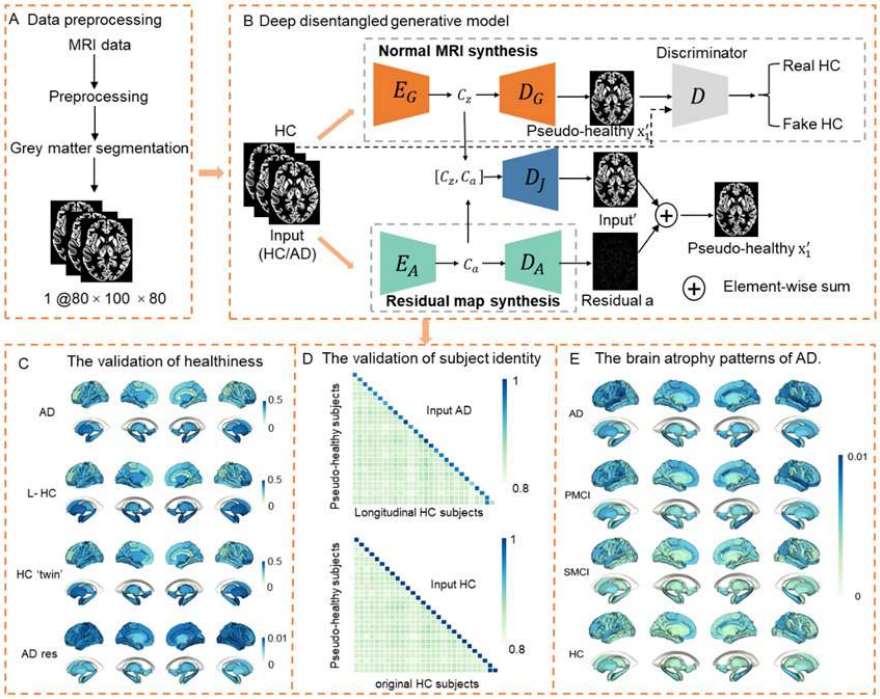

Location: https://files.aievolution.com/prd/hbm2401/abstracts/abs_2362/.png

References

1. K. Oh (2023), "Learn-Explain-Reinforce: Counterfactual Reasoning and its Guidance to Reinforce an Alzheimer's Disease Diagnosis Model," IEEE TRANSACTIONS ON PATTERN ANALYSIS AND MACHINE INTELLIGENCE, vol. 45, no. 4, pp. 4843-4857, Apr 2023, doi: 10.1109/TPAMI.2022.3197845.
2. K. Zhao (2023), "A neuroimaging biomarker for Individual Brain-Related Abnormalities In Neurodegeneration (IBRAIN): a cross-sectional study," EClinicalMedicine, vol. 65, 2023, doi: 10.1016/j.eclinm.2023.102276.
3. F. Yi (2023), "Identifying underlying patterns in Alzheimer's disease trajectory: a deep learning approach and Mendelian randomization analysis," EClinicalMedicine, vol. 64, p. 102247, Oct 2023, doi: 10.1016/j.eclinm.2023.102247.
4. M. Habes (2020), "Disentangling Heterogeneity in Alzheimer's Disease and Related Dementias Using Data-Driven Methods," Biological Psychiatry, vol. 88, no. 1, pp. 70-82, Jul 1 2020, doi: 10.1016/j.biopsych.2020.01.016.
5. S. Verdi (2021) "Beyond the average patient: how neuroimaging models can address heterogeneity in dementia," Brain, vol. 144, no. 10, pp. 2946-2953, Nov 29 2021, doi: 10.1093/brain/awab165.

Poster No 1410

Enhanced Functional Connectivity Representation by Contrastive Learning for Brain Disease Diagnosis

Wonsik Jung[1], Heung-Il Suk[1]

[1]Korea University, Seoul, Republic of Korea

Introduction: Deep learning models utilizing resting-state functional magnetic resonance imaging (rs-fMRI) have been widely used for diagnosing psychiatric conditions like major depressive disorder (MDD) and autism spectrum disorder (ASD). However, the high costs of data collection and the inherent complex, high-dimensional nature of rs-fMRI data limits its availability, affecting both the statistical power and generalizability of these models in clinical settings[1]. To overcome these issues, existing studies focus on two main strategies: i) data augmentation and ii) transfer learning. The objective of this work is to introduce a novel framework combining multi-view region masking with a self-supervised learning approach, leveraging these strategies to enhance the diagnosis and analysis of brain disorders.

Methods: As depicted in Figure 1(a), our proposed framework is structured into two phases: i) the pretext model, which serves as the backbone network using an autoencoder (AE)-based architecture. This model is designed to learn enriched functional representation through functional connectivity (FC) from unlabeled fMRI data and ii) a fine-tuning model trained on labeled (unseen) fMRI data for brain disorder-specific tasks. To be specific, for the pretext model, we employ a random ROI-level masking strategy[2] to augment the FC matrices and then feed into the shared networks for inter-regional relation learning in a self-supervised learning manner. Henceforth, this model undergoes fine-tuning to refine functional representation for brain disorder-specific diagnosis and analysis.

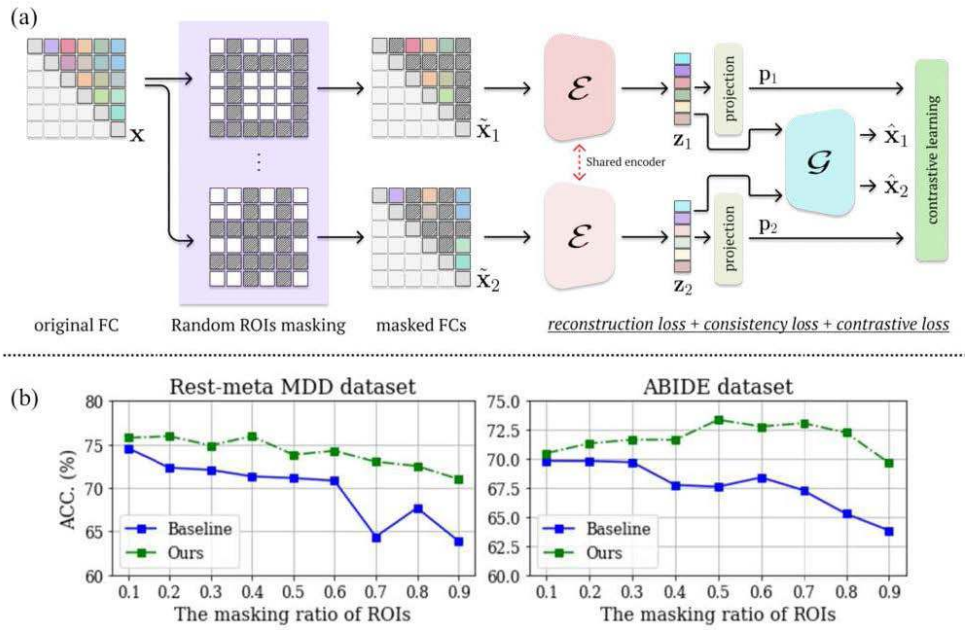

Results: We compared our proposed framework with AE-based approaches[2] and state-of-the-art methods[6,7,8]. Our method achieved superior results in 5-fold cross-validation, with an average accuracy of 73.38% (±3.01) and an AUC of 0.778 (±0.045) on the ABIDE dataset, and similarly, an accuracy of 75.95% (±2.64) and an AUC of 0.830 (±0.035) on the REST-MDD dataset, surpassing all competing methods. Furthermore, to validate the generalizability of our approach, we implemented an ablation study, which involved altering the ratio of random ROI-level masking (as shown in Figure 1(b)) and conducting cross-site classification. Lastly, we applied layer-wise relevance propagation[9] to obtain insights into the interconnections across multi-institutional datasets. As depicted in Figure 2, we observed statistically significant representative regions between groups, colored red for $p<0.05$ (SOG.L, MOG.L, SPG.R, ANG.R, PCUN.L, PCUN.R, PAL.R, CRBL6.R, IFGoperc.L), yellow for $p<0.01$ (SMA.R, OLF.R, REC.R, ACG.L, ACG.R, HIP.L, CAL.L, FFG.L, SMG.R, CRBL9.L), and green for $p<0.001$ (MFG.R, PAL.L). Notably, among them, specific regions (e.g., the superior occipital gyrus (SOG), middle occipital gyrus (MOG), superior parietal gyrus (SPG), angular gyrus (ANG), precuneus (PCUN), hippocampus (HIP), anterior cingulate gyrus (ACG), middle frontal gyrus (MFG)) have been confirmed to be associated with autism.

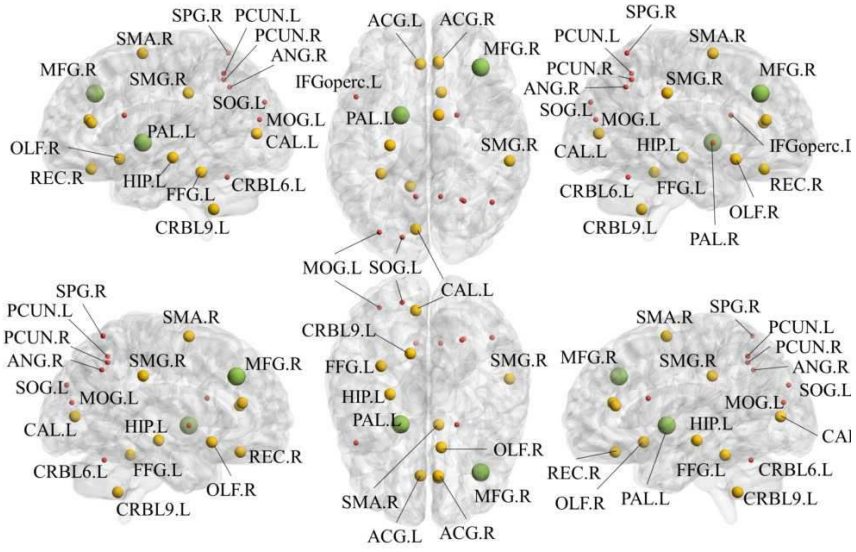

Conclusions: We introduce a novel deep learning framework for diagnosing psychiatric disorders using fMRI, effectively addressing the challenges of high data collection costs and data complexity. Our framework, integrating multi-view region masking with self-supervised learning, consists of a two-phase approach: an AE-based model for training from unlabeled data and a fine-tuning model for specific brain disorders. Through extensive experiments conducted on two multi-institutional datasets, our method demonstrated the superiority of accuracy and generalizability compared to comparative methods, with layer-wise relevance propagation providing further insights into critical brain regions for diagnosis.

References
1. Grady, C.L., et al., (2021), 'Influence of Sample Size and Analytic Approach on Stability and Interpretation of Brain-behavior Correlations in Task-related fMRI Data', Human Brain Mapping, vol. 42, no. 1, pp. 204-219.
2. Jung, W., et al., (2021), 'Inter-Regional High-Level Relation Learning From Functional Connectivity via Self-Supervision', Medical Image Computing and Computer Assisted Intervention–MICCAI 2021: 24th International Conference.
3. Di Martino, A., et al., (2014), 'The Autism Brain Imaging Data Exchange: Towards a Large-Scale Evaluation of the Intrinsic Brain Architecture in Autism', Molecular Psychiatry, Vo. 19 no. 6, pp. 659-667.
4. Yan, C.-G., et al., (2019), 'Reduced Default Mode Network Functional Connectivity in Patients With Recurrent Major Depressive Disorder', Proceedings of the National Academy of Sciences, vol. 116 no. 18, pp. 9078-9083.
5. Tzourio-Mazoyer, N., et al., (2002), 'Automated Anatomical Labeling of Activations in Spm Using a Macroscopic Anatomical Parcellation of the Mni MRI Single-Subject Brain', Neuroimage, vol. 15, no. 1, pp. 273-289.
6. Eslami, T., et al., (2019), 'ASD-Diagnet: A Hybrid Learning Approach for Detection of Autism Spectrum Disorder Using fMRI Data', Frontiers in Neuroinformatics, vol. 13, no. 70.
7. Kawahara, J., et al. (2017), 'BrainNetCNN: Convolutional Neural Networks for Brain Networks; Towards Predicting Neurodevelopment', NeuroImage, vol. 146, pp. 1038-1049.
8. Kan, X., et al. (2022), 'Brain Network Transformer', Advances in Neural Information Processing Systems, vol. 35, pp. 25586-25599.
9. Montavon, G., et al., (2017), 'Explaining Nonlinear Classification Decisions with Deep Taylor Decomposition', Pattern Recognition, vol. 65, pp. 211-222.

Acknowledgements
This research was supported by the National Research Foundation of Korea (NRF) grant funded by the Korea government (No. 2022R1A4A1033856).

Poster No 1411

Classification of Deep Brain Stimulation states in Parkinson's disease using functional MRI

Dimitra Kiakou[1,2], Karsten Mueller[2,1], Pavel Filip[1,3], Andrej Lasica[1], Filip Růžička[1], Dušan Urgošík[4], Kristína Burdová[1], Robert Jech[1,4]

[1]Department of Neurology, Charles University, [1]st Faculty of Medicine and General University Hospital, Prague, Czech Republic, [2]Max Planck Institute for Human Cognitive and Brain Sciences, Leipzig, Sachsen, Germany, [3]Center for Magnetic Resonance Research (CMRR), University of Minnesota, Minneapolis, MN, United States, [4]Na Homolce Hospital, Prague, Czech Republic

Introduction: Deep brain stimulation (DBS) in the sub-thalamic nucleus (STN-DBS) is an effective treatment for Parkinson's disease (PD), however, the precise mechanisms are not yet well established. Recent studies have investigated the effects of DBS in brain networks (Lamoš et al., 2023; Arévalo Sáenz et al., 2022; Accolla et al., 2016), but limited research involved machine learning with post-operative magnetic resonance imaging (MRI) (Peralta et al., 2021). Therefore, the characterization of STN-DBS connectivity alterations using functional MRI may reveal therapeutic markers and improve our understanding of DBS in PD. Thus, this study aimed to differentiate the STN-DBS ON and OFF states using machine learning and identify the brain patterns contributed to the classification in PD patients.

Methods: A total of 104 patients with advanced type of PD (34 females, age 59.5±7.9 years, disease duration 15.1±6.3 years) were recruited. Resting state functional MRI (rs-fMRI) was acquired in two sessions in the STN-DBS ON and OFF state. Data pre-processing included realignment, unwarping, slice-time correction, normalization, and spatial filtering with Gaussian kernel of 10 mm. White matter, cerebrospinal fluid, and the translational and rotational parameters from head movements were regressed out and a high-pass filter with a cutoff frequency of 0.01 Hz was applied. Thereafter, global correlation (GCOR) and eigenvector centrality (EC) maps were estimated using rs-fMRI for each participant and each session resulting 208 network maps respectively. All above analyses were conducted using CONN toolbox, SPM12, and LIPSIA software package. To determine characteristic features of the STN-DBS ON and OFF states, we implemented Leave One Group Out Cross Validation (LOGOCV) classification (each group corresponds to one subject), to predict the ON and OFF connectivity of an individual subject. Support Vector Machines (SVM) classification with Radial Basis Function kernel was performed on the vectorized, masked network maps in Python (v. 3.10). In each iteration, the classifier was trained in 206 samples and tested in two images acquired from the same subject. Furthermore, we applied Random Forest (RF) and Linear Discriminant Analysis (LDA) classification as alternative approaches for the categorization of the two states. Since the input data were high dimensional, we utilized the Python feature selection approach, SelectKBest with the score function f_classif, to extract the best K features based on univariate statistical tests. We explored the values of K in the range of 1000 till maximum number of voxels in intervals of 2000. Finally, the models performance was evaluated on the average classification accuracies across iterations.

Results: SVM outperformed RF and LDA reaching a high accuracy of 82.69% with GCOR robustly across several K values (Figure 1). LDA achieved slightly lower, while RF had the poorest performance with prominent fluctuation (Figure 1).

Classification based on EC maps presented analogous results with maximum accuracy 80.29% using SVM. All algorithms were improved with dimensionality reduction independently of the input maps. To identify and visualize the contributing features to the SVM classification the minimum K voxels required were retrieved and reshaped back to the three-dimensional brain for both GCOR (K = 33000) and EC (K = 27000) (Figure 2). The mask is estimated as the intersection of features (voxels) selected at each iteration of LOGOCV SVM classification with SelectKBest (Figure 2).

Conclusions: SVM classification accurately differentiated the STN-DBS ON and OFF states and revealed specific brain patterns with predominant area the temporal lobe. GCOR and EC maps exhibited equivalent classification accuracy with significantly overlapping selected regions. The selected attributes that detected brain connectivity modifications in STN-DBS may present an essential signature for refining DBS in PD.

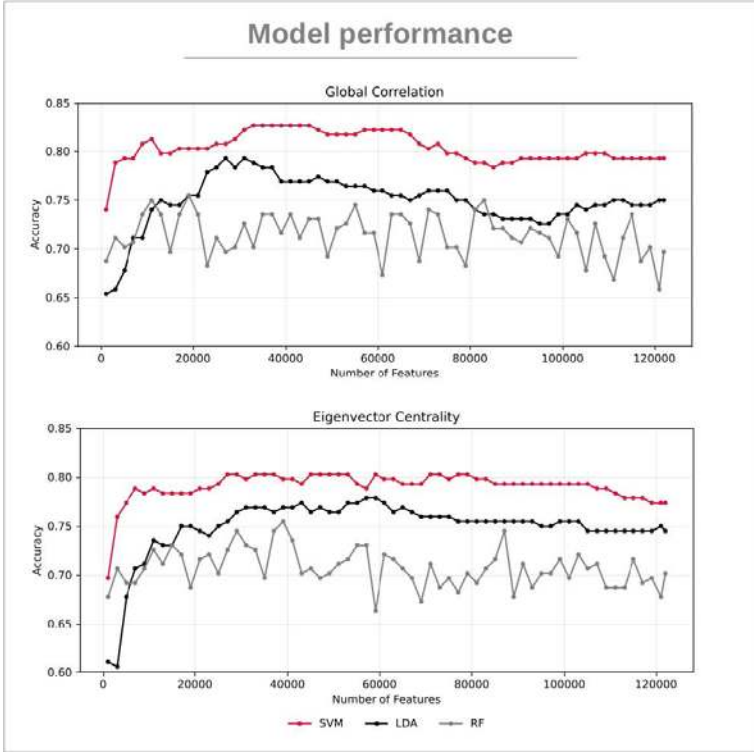

References
1. Accolla, E.A. et al. (2016) 'Brain networks modulated by subthalamic nucleus deep brain stimulation', Brain, 139(9), pp. 2503–2515. doi:10.1093/brain/aww182.
2. Arévalo Sáenz, A. et al. (2022) 'Estimulación cerebral profunda en la enfermedad de parkinson: Análisis de la anisotropía fraccional cerebral en Pacientes Intervenidos Mediante estimulación cerebral profunda', Revista de Neurología, 74(04), p. 125. doi:10.33588/rn.7404.2021196.
3. Lamoš, M. et al. (2023) 'The effect of deep brain stimulation in parkinson's disease reflected in EEG microstates', npj Parkinson's Disease, 9(1). doi:10.1038/s41531-023-00508-x.
4. Peralta, M., Jannin, P. and Baxter, J.S.H. (2021) 'Machine learning in Deep brain stimulation: A systematic review', Artificial Intelligence in Medicine, 122, p. 102198. doi:10.1016/j.artmed.2021.102198.

Acknowledgements
Supported by a grant of the National Institute for Neurological Research, Czech Republic, Programme EXCELES (ID project No. LX22NPO5107) and the Charles University: Cooperatio Program in Neuroscience.

Poster No 1412

Predicting Cognitive Abilities with Graph Signal Processing Metrics

Mikkel Schöttner[1], Thomas Bolton[2], Jagruti Patel[3], Patric Hagmann[2]

[1]University of Lausanne, Lausanne, Vaud, [2]Department of Radiology, Lausanne University Hospital and University of Lausanne (CHUV-UNIL), Lausanne, Switzerland, [3]CHUV, Zurich, Not Specified

Introduction: Predicting behavior from neuroimaging data comes with the prospects of selecting an optimal treatment, detecting mental illness at an early stage, or forecasting cognitive development (Wu et al., 2023). As a notable example, cognitive features have been predicted from functional connectivity (FC) through kernel ridge regression (KRR) (He et al., 2020). However, KRR does not allow direct inference about which brain networks drive the prediction, as it uses the whole feature vector for training. Graph signal processing (GSP) is a multimodal framework that expresses functional brain time series in terms of a basis of connectome harmonics that contrast structural brain features across spatial frequencies (Huang et al., 2018) . Advanced GSP measures like the structural decoupling index (SDI) (Preti & Van De Ville, 2019) enable efficient fingerprinting (Griffa et al., 2022), and might prove useful for behavioral prediction as well. Here, we explore how GSP metrics, combined with an elastic-net regression scheme, compare to the FC/KRR approach in predicting a factor reflective of cognition. We also pinpoint optimal parameter choices for this task.

Methods: We used 847 subjects from the Human Connectome Project (HCP) dataset (Van Essen et al., 2012). As a predictive target, we chose one of four factors that optimally summarize the behavioral variables from the HCP dataset (Schöttner et al., 2022): cognition. For each subject, using T1-weighted and diffusion-weighted imaging data, deterministic fiber tracking was performed with Connectome Mapper 3 (Tourbier et al., 2022), and a structural connectivity (SC) matrix was created using the Lausanne 2018 atlas (Cammoun et al., 2012) at scale 3 (R=274 regions) with normalized fiber density as edge weight. Resting-state functional magnetic resonance imaging (fMRI) data were detrended, regressed for six motion parameters and their derivatives, and parcellated using the same atlas. Finally, the regional time series were z-scored. Two GSP features were computed: the SDI, which measures how much the functional signals are constrained by the underlying structural connectivity (higher values = less constrained) (Preti & Van De Ville, 2019), and the power spectral density (PSD) of the fMRI signals across spatial frequencies. As graph shift operator (GSO, the quantity that connectome harmonics are derived from), we compared the normalized Laplacian and the modularity matrix (Petrovic et al., 2020). For the SDI, a cutoff frequency separating low and high frequencies must be chosen. This can involve (1) a half-half split (i.e., cutting at R/2), (2) choosing the frequency that splits cumulative PSD in half for each time point (individual cumulative sum), (3) using the mode over time points (cumulative sum), or (4) following (2) on the mean PSD spectrum over time (mean cumulative sum). For prediction, an elastic-net regression was evaluated using nested cross-validation with 10 repeated random splits in the inner and outer loops, placing members of the same family in the same split. As a measure of prediction accuracy, we considered the coefficient of determination (R^2). The same evaluation scheme was used for FC/KRR as a baseline.

Results: Both PSD and SDI yielded a median predictive performance close to the baseline with the right parameters (Fig. 1A). In terms of GSO, the normalized Laplacian seemed to work better for PSD and the modularity matrix for the SDI, for which splitting the signal by half was also the optimal choice. Fig. 1B shows the absolute values of the beta coefficients mapped to the brain surface for the best-performing model using the SDI. The largest coefficients were in the left and right superior parietal cortex, and the right inferior parietal cortex.

Conclusions: GSP-derived metrics enable similar predictive performance as FC to predict a factor reflective of cognition, with the added benefit of allowing the direct investigation of what regional features drive the prediction in the case of the SDI.

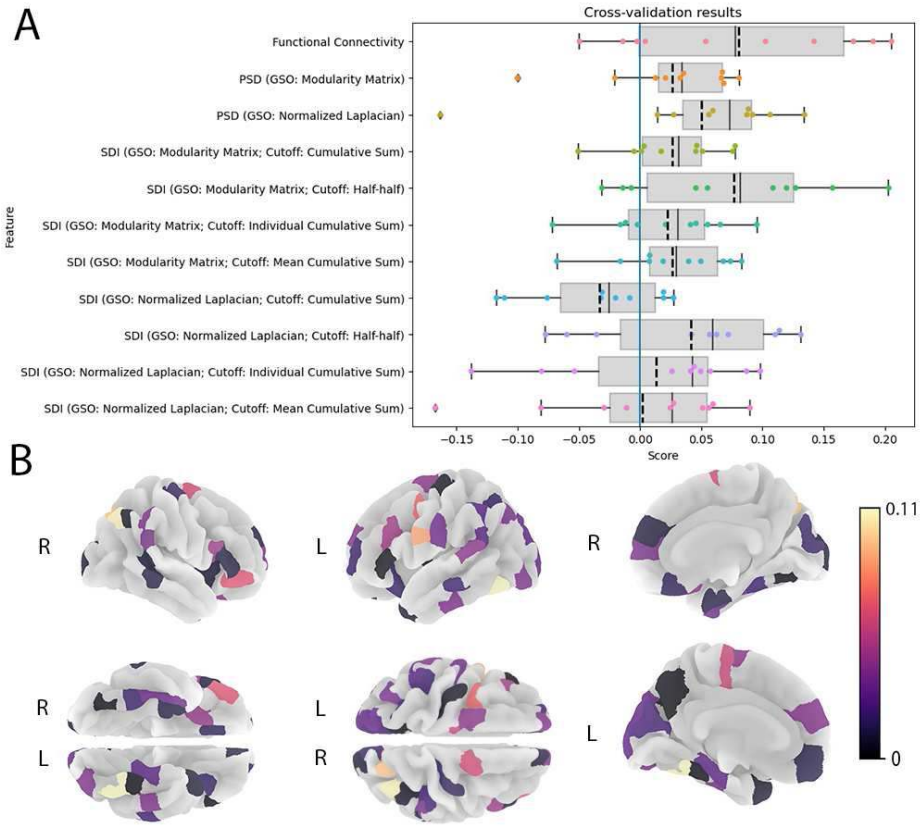

References

1. Cammoun, L. (2012). Mapping the human connectome at multiple scales with diffusion spectrum MRI. Journal of Neuroscience Methods, 203(2), 386–397.
2. Griffa, A. (2022). Brain structure-function coupling provides signatures for task decoding and individual fingerprinting. NeuroImage, 250, 118970.
3. He, T. (2020). Deep neural networks and kernel regression achieve comparable accuracies for functional connectivity prediction of behavior and demographics. NeuroImage, 206, 116276
4. Huang, W., Bolton, T. A. W. (2018). A Graph Signal Processing Perspective on Functional Brain Imaging. Proceedings of the IEEE, 106(5), 868–885.
5. Petrovic, M. (2020). Community-Aware Graph Signal Processing: Modularity Defines New Ways of Processing Graph Signals. IEEE Signal Processing Magazine, 37(6), 150–159.
6. Preti, M. G. (2019). Decoupling of brain function from structure reveals regional behavioral specialization in humans. Nature Communications, 10(1), Article 1.
7. Schöttner, M. (2022, June 19). Domains of Behavior and Psychopathology Derived via Factor Analysis. Annual Meeting of the Organization for Human Brain Mapping. Annual Meeting of the Organization for Human Brain Mapping, Glasgow, United Kingdom.
8. Tourbier, S. (2022). Connectome Mapper 3: A Flexible and Open-Source Pipeline Software for Multiscale Multimodal Human Connectome Mapping. Journal of Open Source Software, 7(74), 4248.
9. Van Essen, D. C. (2012). The Human Connectome Project: A data acquisition perspective. NeuroImage, 62(4), 2222–2231.
10. Wu, J. (2023). The challenges and prospects of brain-based prediction of behaviour. Nature Human Behaviour, 7(8), Article 8.

Poster No 1413

Predictive Coding Theory Inspired Brain Informer Model for Deciphering Mental States Across Subjects

Zi-Han Wang[1,2], Chao-Gan Yan[3]

[1]Institute of Psychology, Chinese Academy of Sciences, Beijing, Beijing, [2]Department of Psychology, University of Chinese Academy of Sciences, Beijing, China, [3]Institute of Psychology, Chinese Academy of Sciences, Beijing, Beijing

Introduction: Decoding the mental states of the brain across diverse subjects through neural activity using non-invasive resting-state functional magnetic resonance imaging (fMRI) has always been a challenging task. Inspired by the predictive coding theory (Eslami 2018; Friston 2018; Ryskin 2023), which bears a resemblance to the way the large-scale language models, such as GPT-4, generate coherent text by predicting the next word when processing text, we proposed a mental state classification model based on the spatial-temporal Brain Informer. Our model simulates the brain's cognitive prediction

process by continuously predicting fMRI trajectories and deciphers mental states across diverse subjects based on a multi-task learning model.

Methods: In this work, we utilized 4 datasets. The CoRR dataset (Zuo 2014) comprises the rest fMRI data from 450 subjects. The Rumination dataset (Chen 2020) includes the fMRI of 41 healthy participants guided by a rumination paradigm in 4 mental states: resting, autobiographical memory, rumination, and distraction (Figure 1A). The Rumination_Suzhou dataset (Jia 2023) involves fMRI from 57 healthy subjects and 62 Major Depressive Disorder (MDD) patients during the rumination task. We also employed the DIRECT phase II dataset (Chen 2023), which contains data from 1216 healthy participants, 1502 MDD patients, 205 Bipolar Disorder (BD) patients, and 314 Schizophrenia (SCZ) patients. Our Brain Informer model (Figure 1B), a Transformer-based time series forecaster using Prob Attention (Zhou 2021), learns time series information for multi-step predictions. We enhanced Informer with a spatial Attention Map to understand interactions between brain regions. The model was pretrained on the CoRR dataset for predicting fMRI time series. We then employed multi-task learning, fine-tuning the model with the Rumination dataset, concurrently handling fMRI time series prediction and mental state decoding as parallel tasks. Subsequently, we validated its cross-subject decoding capability with an independent Rumination_Suzhou dataset. Finally, we used the DIRECT phase II dataset to examine predictive patterns in different patient groups during resting states, aiming to understand the relationship between mental states and mental disorders.

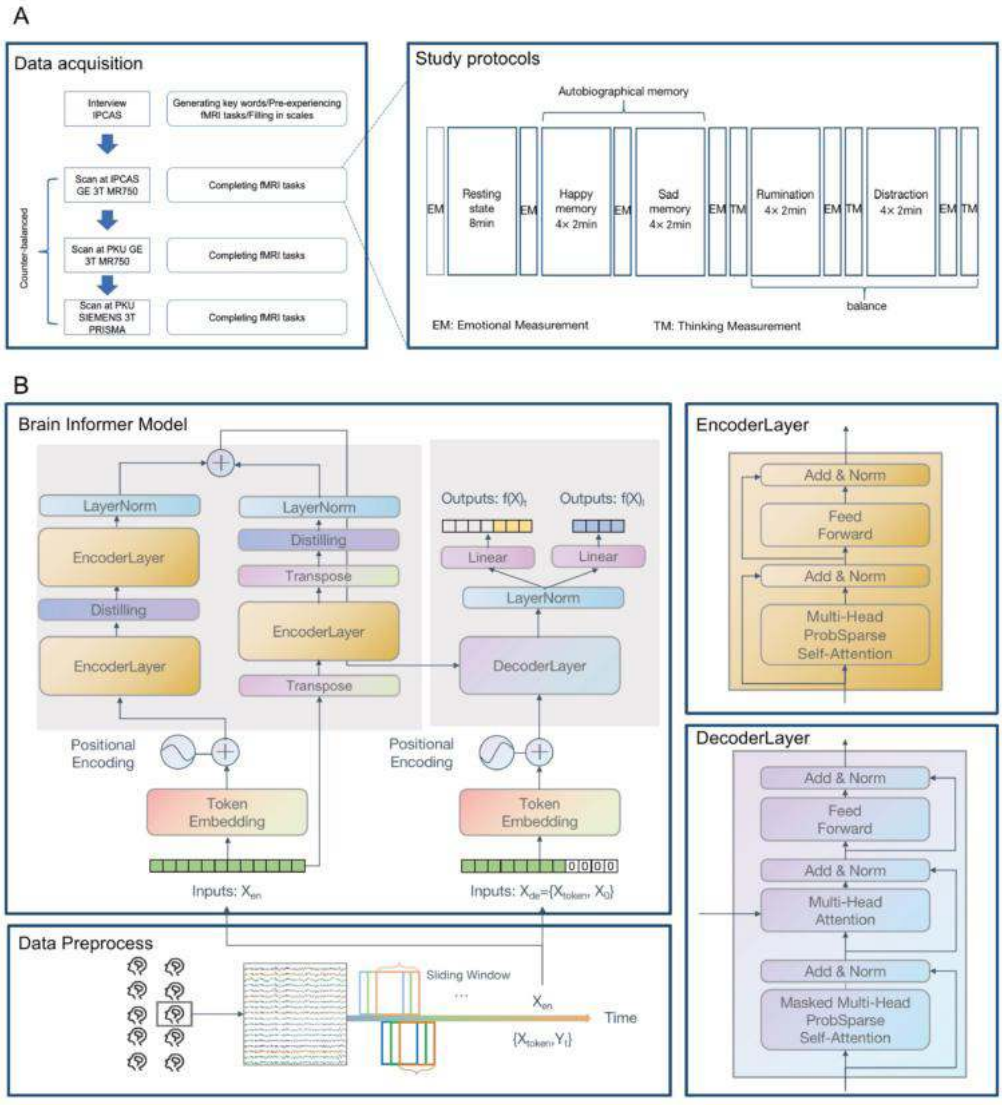

A) Rumination data acquisition and study protocols. We first asked participants to generate keywords that would recall autobiographical memories based on prompted questions. Each participant then completed the same task on 3 different scanners separately. Participants were first required to perform an 8-minute resting-state scan. Then 8 minutes of happy autobiographical memories were performed based on the 4 sets of positive and negative keywords prompted. This was followed by 8 minutes of rumination and 8 minutes of distraction based on the prompts, with the order of rumination and Distraction being balanced across participants. B) Flow diagram of the Brain Informer model. The data is first preprocessed using a time window. Then sending to the Informer-sc model which consists of two parts. The left side of the image shows the Encoder of the joint spatial Attention and temporal Attention. The right side of the image shows the Decoder that outputs both the predicted time series and the category labels.

Results: Experimental results indicate that our model competently predicts fMRI time series (Figure 2A). Incorporating a classification task into the model enables the differentiation of mental states, while also improving the prediction of fMRI time series (Figure 2D). Additionally, integrating spatial attention helps capture interactions between brain regions in the fMRI time series, benefiting both prediction and classification tasks (Figure 2C, 2D). To demonstrate the model's capability for cross-subject mental state classification, we tested on a wholly independent dataset (Figure 2E, 2F). The prediction correlation reached 69.10%, the accuracy for time segments classification reached 71.72%, and the cross-subject classification accuracy rose to 82.47%, which substantiates its generalizability and robustness. Under the validation of a big dataset, we found that patients with depression exhibit more autobiographical memory and rumination behaviors (Figure 2B). This discovery confirms previous research findings. Using our model to classify the mental states of participants can, to some extent, assist in the diagnosis of mental diseases.

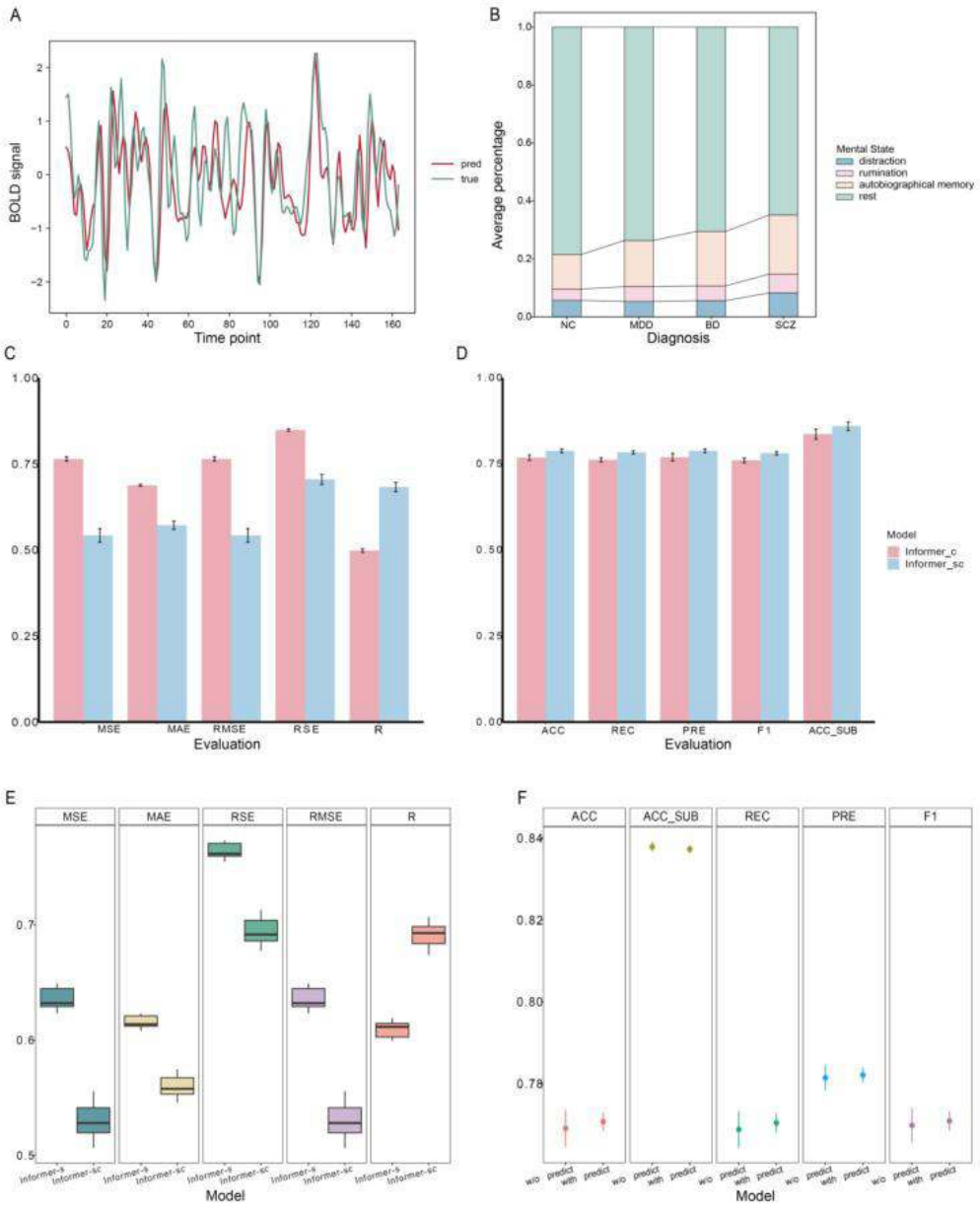

A) The prediction results of the model at the first point. B) The proportion of healthy controls, MDD, BD, and SCZ patients in the DIRECT II dataset predicted to be in various mental states during rest state. C) A performance comparison of predictive performance between the Informer-c model (without spatial attention) and the Informer-sc model (with spatial attention). D) A performance comparative analysis of mental state classification performance between Informer-c and the Informer-sc. E) A performance comparison of predictive task performance between Informer-s (only prediction) and Informer-sc (prediction and classification) on the Rumination_Suzhou dataset. F) A performance comparison on the Rumination_Suzhou dataset for the classification task, contrasting Informer-sc (with predict) when it includes the predictive task versus when it doesn't (w/o predict).

Conclusions: We developed a predictive coding-based fMRI classification model, akin to language models like GPT-4, for decoding brain mental states. It successfully predicts fMRI time series, and classifies mental states, aided by spatial attention mechanisms. Validated with the independent dataset, our model manifested appreciable generalization performance for practical application. Our study links rumination, memory, and MDD, showing more memory and rumination in depression. Future work aims to enhance its capabilities using larger datasets and detailed emotional and linguistic decoding.

References
1. Chen X et al. (2020). The subsystem mechanism of default mode network underlying rumination: A reproducible neuroimaging study. NeuroImage, 221, 117185.
2. Chen X et al. (2023). The Complexity of Functional Connectivity Profiles of the Subgenual Anterior Cingulate Cortex and Dorsal Lateral Prefrontal Cortex in Major Depressive Disorder: A DIRECT Consortium Study (p. 2023.03.09.531726). bioRxiv.
3. Eslami S A et al. (2018). Neural scene representation and rendering. Science, 360(6394), 1204–1210.
4. Friston K. (2018). Does predictive coding have a future? Nature Neuroscience, 21(8), 1019–1021.
5. Jia F-N et al. (2023). Aberrant degree centrality profiles during rumination in major depressive disorder. Human Brain Mapping.
6. Ryskin et al. (2023). Prediction during language comprehension: what is next? Trends in Cognitive Sciences, 27(11),1032-1052.
7. Zhou H et al. (2021). Informer: Beyond Efficient Transformer for Long Sequence Time-Series Forecasting. In Proceedings of the AAAI conference on artificial intelligence 35(12), 11106-11115.
8. Zuo X-N et al. (2014). An open science resource for establishing reliability and reproducibility in functional connectomics. Scientific Data, 1(1), Article 1.

Poster No 1414

AutoML-based model agnostic neuroimaging approach for improved Alzheimer's disease classification

Maitrei Kohli[1], Pedro Da Costa[2], Robert Leech[2], James Cole[1]

[1]Centre of Medical Image Computing, Department of Computer Science, University College London, London, United Kingdom, [2]Institute of Psychiatry, Psychology & Neuroscience, King's College London, London, United Kingdom

Introduction: Classification of individual-level disease stage in Alzheimer's disease (AD) is key for stratification of patients in clinical trials. Machine learning (ML) methods can make patient-specific predictions of disease stage using neuroimaging data. While the goals of these translational models are clear, the details of the analytic processing and modelling are not. This has caused conflicting results, with inconsistent methods, arbitrary processing steps and false positives due to small sample sizes[1,2]. We propose a novel neuroimaging analysis approach based on automated machine learning (autoML) for predictive classification of individual-level AD stage. We hypothesize that our AutoML-based approach will remove experimenter bias, eliminate arbitrary analytic choices, and improve predictive accuracy for clinically relevant outcomes.

Methods: AutoML-multiverse framework Our innovative AutoML-Multiverse framework, building on prior work[3,4] efficiently searches a prediction space formed from thousands of ML pipelines. It distills high-dimensional data to a low-dimension configuration space that can be efficiently sampled using Bayesian Optimisation. Instead of identifying a single best pipeline, this approach constructs fully data-driven ensembles, combining complementary information from different pipelines to improve predictions. For our initial analyses, we leveraged a configuration space crafted from 20,000 ML pipeline instances across 64 OpenML datasets, as per[3], and initiated our test dataset's interaction with the pre-existing autoML-system with a warm start. Objective and Analysis Our primary aim was stratification across three diagnostic categories: (i) Cognitively normal (CN) vs. Alzheimer's disease (AD); (ii) AD vs. mild cognitive impairment (MCI) vs. CN; and (iii) distinguishing stable MCI (sMCI) from fast progressive (pMCI). We compared our autoML framework against nine separate ML models and a stacked ensemble of these models. Each task was run twice: first with only neuroimaging features and secondly with only age, sex, and MMSE scores. Data We used volumetric data extracted from T1-weighted structural MRI (sMRI) scans and clinical data sourced from the Alzheimer's Disease Neuroimaging Initiative (ADNI) dataset. Volumetric features were ventricles, hippocampus, whole-brain, entorhinal, fusiform, and mid-temporal regions. Data were ICV corrected and standard scaled. We had n = 606 (303 CN and 303 AD) for task 1, n = 1930 (760 CN, 867 MCI, and 303 AD) for task 2, and n = 369 (224 sMCI and 145 pMCI) for task 3.

Results: The results are depicted in Figure 1 using the holdout test dataset. Standalone ML models demonstrated limited predictive capability, while the stacked ensemble model exhibits a marginal performance improvement compared to individual models. The autoML ensemble models consistently performed with higher accuracy across the tasks. Additionally, our findings highlight the utility of neuroimaging (sMRI) data, particularly in differentiating sMCI from pMCI, with the autoML ensemble 73% accuracy in discriminating between these categories. This emphasizes the clinical relevance of leveraging sMRI-based methodologies, providing valuable insights for precise stratification in clinical settings.

	sMRI features only			Age, sex, and MMSE only		
	ML models	Stacked ensemble	AutoML	ML models	Stacked ensemble	AutoML
AD vs CN	81%- 88%	88%	88% {12}	84.8%-96.9%	96.8%	**98.3% {3}**
AD vs MCI vs CN	45.2%-52%	59.7%	**64.9% {5}**	54.7%-66.8%	66.8%	**67.4% {6}**
sMCI vs pMCI	60.6%-68.7%	69.0%	**73.1% {7}**	50%-60.5%	62.3%	**68.1% {9}**

The numbers in curly { } brackets in each AutoML column signify the number of pipelines (out of 20,000) selected in fully data-driven way to compose the ensemble of pipelines.

ML models include: Logistic Regression; K-nearest neighbours; Gaussian naïve bayes; multi-layer perceptron; decision tree; support vector machine; Adaboost; random forest; and extreme gradient boosting classifiers.

Figure 1: A comparative evaluation of standard ML models, stacked ensemble model, and autoML based on percentage balanced accuracy across three tasks: (1) distinguishing cognitively normal (CN) from Alzheimer's disease (AD); (2) discerning CN, mild cognitive impairment (MCI), and AD; and (3) stratifying stable MCI (sMCI) against fast progressive MCI (pMCI).

Conclusions: The preliminary results yield three insights: firstly, autoML ensemble exhibit superior predictive capabilities compared to individual pipelines, highlighting their efficacy in predictive modelling. Secondly, the autoML-multiverse approach, assembling ensembles of pipelines in a data-driven manner, circumvents biases and arbitrary decision-making. Thirdly, the integration of neuroimaging with autoML emerges as a potent and clinically relevant tool, particularly evident in tasks such as distinguishing slow and fast progressors, suggesting potential applicability in future clinical trials. These initial results are promising, encouraging rigorous further analysis and experimentation to affirm their robustness and generalisability.

References

1. Botvinik-Nezer, R. (2020), 'Variability in the analysis of a single neuroimaging dataset by many teams. Nature 582, 84–88.
2. Marek, S. (2022), 'Reproducible brain-wide association studies require thousands of individuals'. Nature. 603(7902):654–60.
3. Da Costa, P.F. (2023), 'BUILDING A DATA-DRIVEN CONFIGURATION SPACE FOR AUTOMATED MACHINE LEARNING'. A PREPRINT.
4. Dafflon J, F. (2022), 'A guided multiverse study of neuroimaging analyses'. Nat Commun 13, 3758. https://doi.org/10.1038/s41467-022-31347-8

Poster No 1415

Investigating survival in ALS patients using machine learning and Deformation-Based Morphometry

Isabelle Lajoie[1], Sanjay Kalra[2], Mahsa Dadar[3]

[1]McGill University, Montréal, QC, [2]University of Alberta, Edmonton, Alberta, [3]McGill University, Montreal, QC

Introduction: Amyotrophic lateral sclerosis (ALS) is a neurodegenerative disorder with no known cure, leading to progressive loss of motor function and ultimately the death of the patient. Relationships between brain-related changes in ALS, symptoms and survival outcomes remain unknown. Deformation-based morphometry (DBM) is an MRI-based technique that can quantify regional atrophy (Ashburner, 1998). Here, we used DBM to localize cross-sectional and longitudinal disease-related brain changes and investigate whether ALS-specific brain changes detected by DBM can improve the performance of machine learning survival models.

Methods: Data includes T1-weighted and clinical assessments of 192 ALS patients and 163 healthy controls from the Canadian ALS Neuroimaging Consortium (CALSNIC) study (Kalra, 2020) acquired longitudinally across multiple centers. 104 ALS patients were classified as either short (N=42) or long (N=61) survivors based on the time between disease onset and outcomes (within or more than 24 months). Survival outcome was defined as death or requirement of permanent assisted ventilation for at least 22 hours. All T1-weighted MRIs were preprocessed and quality controlled. DBM maps were obtained by computing the Jacobian determinant of the estimated non-linear deformation fields to the ICBM152 template (Fonov, 2009). DBM values greater than one indicate localized expansion whereas values smaller than one indicate atrophy. To investigate the disease-related brain changes, age and sex were regressed out from the voxel-wise DBM maps of ALS patients based on the estimates of matched controls (Dadar M, 2020). A voxel-wise linear mixed-effects (LME) model was then employed with intercept and follow-up time as variables of interest to evaluate cross-sectional and longitudinal brain changes, respectively.

Patients' ID and scanner site were included as categorical random variables. To investigate cross-sectional differences between short and long survival, an additional LME was employed with a categorical fixed variable contrasting survival groups. All results were corrected for multiple comparisons using False Discovery Rate with a threshold of 0.05. To assess how much the DBM features contribute to prognostic accuracy, the features that were significant predictors of survival in Cox univariate analysis were first identified from an initial set of features comprising 1064 regional DBM values (from Schaefer (Glen, 2021), Allen (Hawrylycz, 2012) and JHU (Wakana, 2007) atlases) and 14 clinical features. A logistic regression model was trained and tested on i) regional DBM features, ii) clinical features, and iii) clinical and DBM features combined. Nested cross-validation was employed for hyperparameters optimization and evaluation of performance generalization.

Results: Figure 1.A shows significant cross-sectional bilateral atrophy in the motor cortex, the corticospinal tract (CST), along with an overall pattern of ventricular enlargement in ALS. Figure 1.B shows additional longitudinal changes in the somatomotor region as well as ventricular and sulcal enlargement. Figure 1.C and 1.D show cross-sectional changes in short and long survival groups, respectively, with more atrophy (such as in CST and corpus callosum) and ventricular enlargement observed in short survival. Figure 1.E shows that a portion of the corpus callosum is significantly more atrophied when comparing short to long survivors. Figure 2 shows mean area under the curve (AUC) and mean accuracy (ACC) for the respective set of features: A) AUC=0.86±0.14;ACC=81±10%, B) AUC=0.77±0.17; ACC=67±14% and C) AUC=0.84±0.14;ACC=80±16%. The results demonstrate that the regional DBM features enhance the accuracy of survival prediction and reduce result variability.

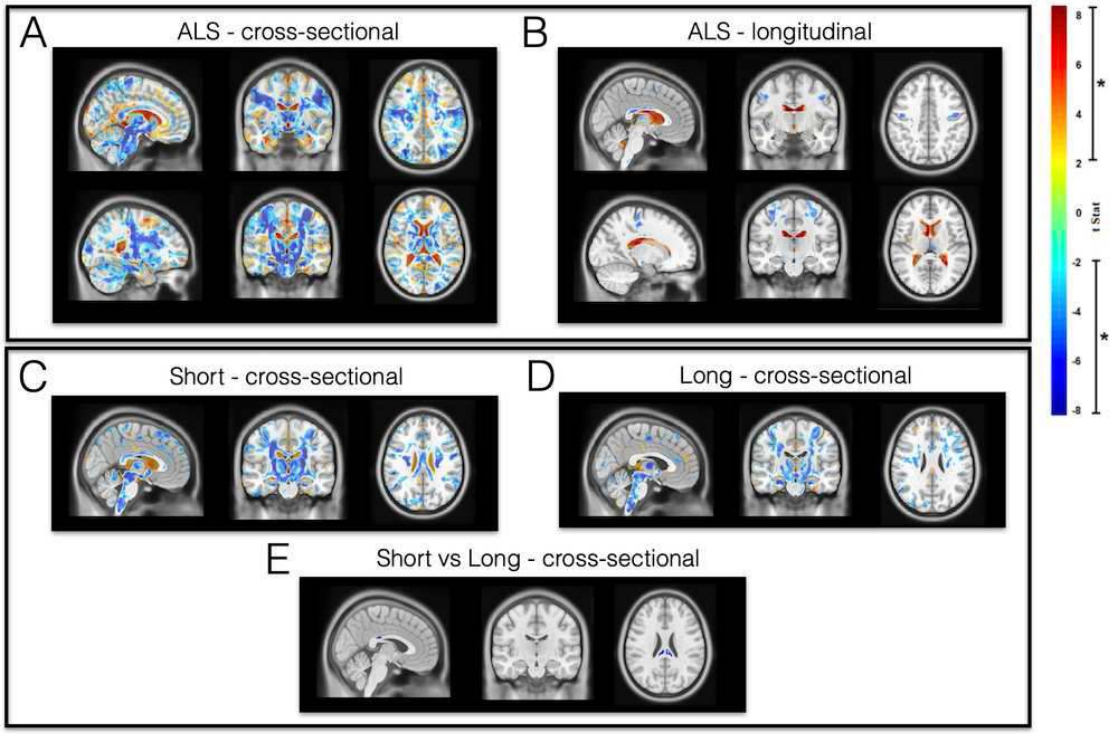

Fig. 1 Voxel-wise changes in ALS. Sagittal, coronal and axial slices showing the t-statistic maps reflecting the significant brain volume changes in ALS (corrected for sex and age) at baseline (A) and over time (B). Short (C) and long (D) survivors are also displayed, along with the short versus long comparison (E). Warm colours indicate enlargement (e.g. ventricular and sulcal regions) and cold colours indicate atrophy.

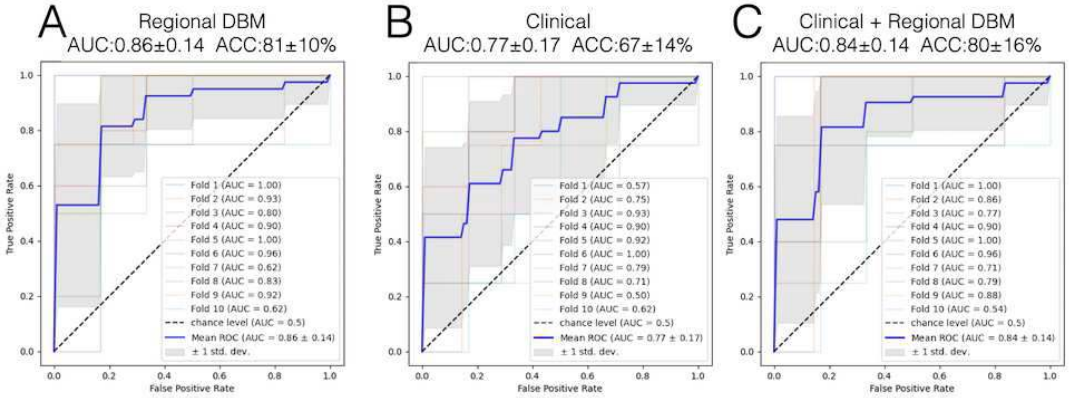

Fig. 2 - Logistic Regression survival performance. Receiver operating characteristic (ROC) curve and area under the curve (AUC) at each fold employing A) regional DBM features; B) clinical features; C) both clinical and regional DBM features. The corresponding mean AUC and mean accuracy (ACC) are provided above each graph. The ROC curve illustrates the trade-off between the true positive rate (sensitivity) and the false positive rate (1 - specificity) at various classification thresholds. An AUC of 0.5 indicates random guessing, while an AUC of 1.0 indicates perfect classification performance.

Conclusions: This study supports the utility of DBM features in localizing brain volume changes in ALS and improving prognostic accuracy, offering a deeper understanding of the mechanisms underlying disease progression, survival, and clinical disability.

References

1. Ashburner, J. (1998), 'Identifying global anatomical differences: deformation-based morphometry' Human Brain Mapping, 6:348-357
2. Dadar, M. (2020), 'Cerebral atrophy in amyotrophic lateral sclerosis parallels the pathological distribution of TDP43', Brain communication, vol. 2,2 fcaa061
3. Fonov, V. (2009), 'Unbiased nonlin- ear average age-appropriate brain templates from birth to adult-hood', Neuroimage; 47: S102
4. Glen, D. (2021), 'Schaefer-Yeo-AFNI-2021 Atlases: Improved ROIs with AFNI+SUMA Processing', Organization for Human Brain Mapping, Poster 1672
5. Hawrylycz M., (2012), 'An anatomically comprehensive atlas of the adult human brain transcriptome', Nature, 489: 391-399
6. Kalra, S. (2020), 'The Canadian ALS Neuroimaging Consortium (CALSNIC) - a multicentre platform for standardized imaging and clinical studies in ALS', MedRxiv
7. Wakana, S. (2007), 'Reproducibility of quantitative tractography methods applied to cerebral white matter', NeuroImage, 36:630-644

Poster No 1416

Brain-based classification of 17 diagnostic groups in the UK Biobank

Ty Easley[1], Lexi (Xiaoke) Luo[1], Kayla Hannon[1], Petra Lenzini[1], Janine Bijsterbosch[1]

[1]Washington University in Saint Louis, Saint Louis, MO

Introduction: Many studies have trained machine learning classifiers on features derived from non-invasive structural and/or functional neuroimaging data to differentiate between cases and healthy controls in a range of diseases[1]. However, the vast majority of published diagnostic classification efforts are single-disease studies performed in disease-specific cohorts. As such, a comprehensive analysis across diseases in population data is lacking. This work uses the UK Biobank (UKB) dataset to systematically compare brain-based classification models across 17 different ICD-10 diagnostic groups.

Methods: The 17 ICD-10 diagnostic groups were derived from Chapter V (mental and behavioral disorders) and Chapter VI (diseases of the nervous system) of the ICD-10 at two different levels of the hierarchy depending on sample size. Only ICD-10 diagnostic groups with N≥125 case participants were included, resulting in 17 diagnostic groups (see x-axis in Fig. 1). In total, this work included N=5,861 unique cases, each with healthy controls matched on sex, age, and resting state head motion out of a pool of UKB individuals with no ICD-10 labels in either Chapter V or VI. Random forest classification models with rigorous shuffle-splits[2] were adopted to predict case versus control labels separately for each diagnostic group, while estimating stability as well as accuracy of case-control classifications. In addition to the separate diagnosis-specific case-control classifications, we performed a multiclass classification. Multiple separate classification models were trained using 20 different feature sets comprising either neuroimaging or socio-demographic features. Neuroimaging features were derived from both structural (surface and volume) and resting-state functional data (network amplitudes and functional connectivity). Diagnostic classification accuracies were benchmarked against age classification (oldest vs. youngest) from the same feature sets and against additional classifier types (K-nearest neighbors and linear support vector machine). Statistical significance of classification was computed as the empirical probability of classifying above chance accuracy (0.5).

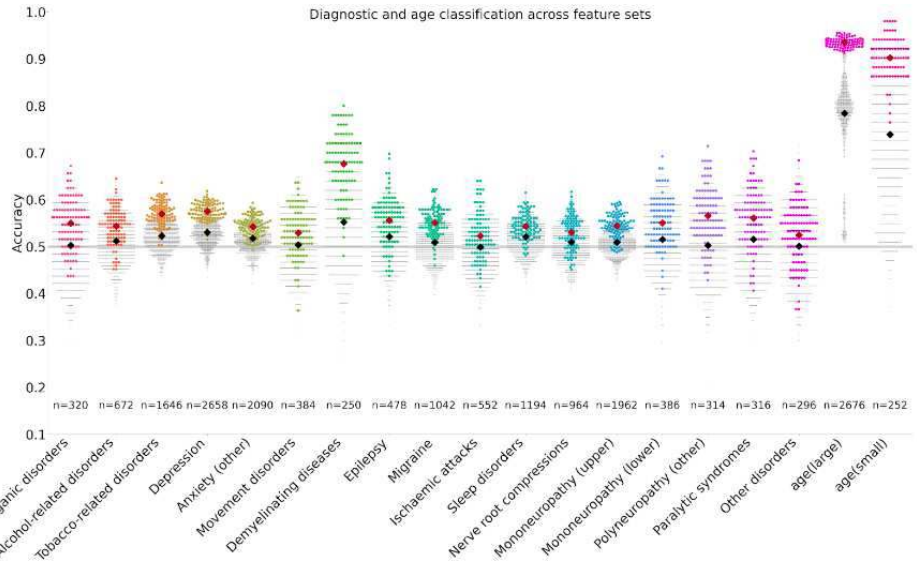

Figure 1. Summary of classification accuracy distributions across all 17 diagnostic groups for structural, functional, and sociodemographic classification features. In each classification group's swarm plot, the accuracy distribution of the best-performing feature is shown in color; the rest are shown in gray. Of the diagnostic groups, only the depression group (N=2,692) was classified significantly above chance after multiple comparison correction. Depression was significantly classified by sociodemographic features and three functional MRI features (full network connectivity matrices for the Schaefer parcellation, full network connectivity matrices for ICA parcellation at rank 150, and at rank and 300). Benchmark results for age (youngest versus oldest) classifications in both a large (matching the largest diagnostic group) and small (matching the smallest diagnostic group) group are shown on the right, and approximate an upper bound on diagnostic classification accuracy in terms of effect size vs. sample size.

Results: Structural neuroimaging data features failed to classify 16 out of 17 diagnostic groups significantly more accurately than chance (p ≳ 0.25); only the Demyelinating diseases ICD-10 diagnostic group (G35-37) was classified significantly above chance (=0.63, p=0.013, n=248). After incorporating functional neuroimaging and sociodemographic feature sets into classification, only the Depression ICD-10 diagnostic group (F32) was classified significantly above chance (=0.58, p=3.5e-3, n=2692) after correcting for multiple comparisons (Fig. 1). Both sociodemographic and functional neuroimaging features significantly classified patients in the Depression (F32) group, but prediction accuracies still remained low. Multiclass classification accuracies were low for all but the largest class sizes (Fig. 2a), and true positive rate was nearly deterministically predicted by class size (R2(pseudo)=0.989, p=6.14e-12; Fig. 2b). As a contrasting benchmark, age classification showed high accuracy in both large (=0.94, p=1.4e-66, n=2676) and small (=0.90, p=1.3e-15, n=246) sample sizes.

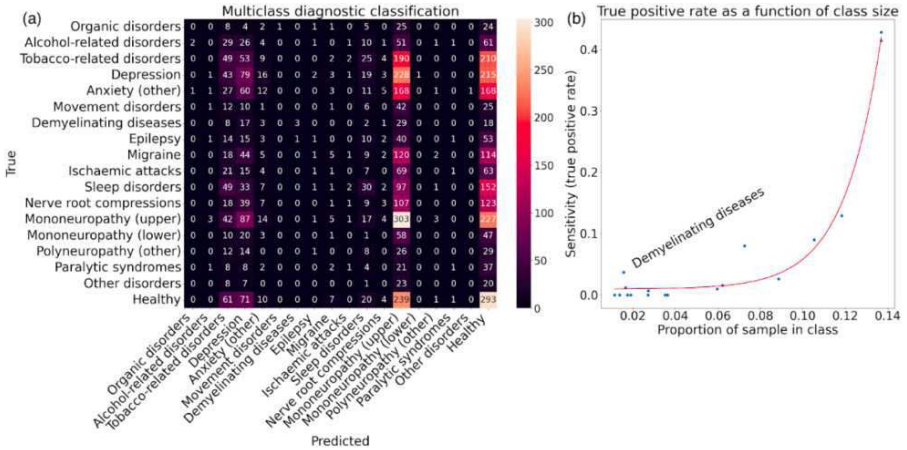

Figure 2. (a) Confusion matrix of the multiclass classification for all 17 ICD-10 diagnostic groups along with healthy controls. Most subjects are misclassified into one of the two largest groups. (b) Plot of sensitivity (true positive rate) vs. proportional group size with exponential curve of best fit. The exponential curve fits well ($R^2_{(pseudo)}$=0.989). The "Demyelinating diseases" group (G35-37) has a large proportional residual; this is consistent with its larger classification effect size in comparison to other groups.

Conclusions: We showed that most ICD-10 diagnostic groups were not classified above chance from neuroimaging or sociodemographic features in the UK Biobank. In particular, our findings shed light on the limited validity of the ICD-10 diagnostic ontology. Consistent with other research pointing to the limited reliability of diagnostic coding systems including the ICD-10[3] and DSM-V[4,5], we demonstrate that these labels are suboptimal clinical targets for machine learning models and may impede meaningful biomarker discovery[6,7]. Our findings highlight the importance of sample size and effect size of drivers of diagnostic classification accuracy, and provide an important benchmark for future work in the UKB and beyond.

References

1. B. Rashid, V. Calhoun, Towards a brain-based predictome of mental illness. Hum. Brain Mapp. 41, 3468–3535 (2020).
2. K. Dadi, et al., Population modeling with machine learning can enhance measures of mental health. Gigascience 10 (2021).
3. J. Stausberg, N. Lehmann, D. Kaczmarek, M. Stein, Reliability of diagnoses coding with ICD-10. Int. J. Med. Inform. 77, 50–57 (2008).
4. S. A. Shankman, et al., Reliability and validity of severity dimensions of psychopathology assessed using the Structured Clinical Interview for DSM-5 (SCID). Int. J. Methods Psychiatr. Res. 27 (2018).
5. D. A. Regier, et al., DSM-5 field trials in the United States and Canada, Part II: test-retest reliability of selected categorical diagnoses. Am. J. Psychiatry 170, 59–70 (2013).
6. A. Nikolaidis, et al., Suboptimal phenotypic reliability impedes reproducible human neuroscience. bioRxiv, 2022.07.22.501193 (2022).
7. M. Gell, et al., The Burden of Reliability: How Measurement Noise Limits Brain-Behaviour Predictions. bioRxiv, 2023.02.09.527898 (2023).

Poster No 1417

Inference of structural alterations in AD from resting-state EEG and whole-brain network model

Yunier Pieur-Coloma[1], Felipe Torres[1], Mónica Otero Ferreiro[2,1], Alejandro Weinstein[1], Wael El-Deredy[1,3,4]

[1]Brain Dynamics Laboratory, Universidad de Valparaíso, Valparaíso, Chile, [2]Universidad San Sebastián, Santiago de Chile, Chile, [3]ValgrAI: Valencian Graduate School and Research Network of Artificial Intelligence, Valencia, Spain, [4]Department of Electronic Engineering, School of Engineering, Universitat de València, Valencia, Spain

Introduction: Alzheimer's disease (AD) causes 60-80% of dementia cases and is the most common neurodegenerative disorder (Zheng et al., 2023; Miltiadous et al., 2023). Identifying AD using non-invasive neuroimaging methods like electroencephalogram (EEG) requires selecting distinctive features. Zheng et al., 2023, found differences in spectrum features, complexity, and synchronization in resting-state EEG (rsEEG) of AD in contrast to Control subjects. Here, we relate these dynamic features to biophysical parameters in a whole-brain Kuramoto model.

Methods: We fit each subject EEG spectrum to a point in the model's parameter space by correlating the EEG spectrum with model spectra. We calculate spectra using Welch's method with a Hann window of 5 seconds, achieving a frequency resolution of 0.2 Hz. We correlate the spatial average spectrum in the frequency range from 0.5 Hz to 44 Hz. EEG recordings: We use recordings from AD and control subjects provided by Miltiadous et al. 2023. The EEG recordings were collected using 19 electrodes while the subjects had their eyes closed. Each record lasted around 13.5 minutes at a sampling rate of 500 Hz. They removed artifacts and filtered the signal between 0.5 Hz and 45 Hz. We removed the EEG's aperiodic component by multiplying by f^∝, where∝ is the logarithmic slope of the average spectrum between 1 Hz and 35 Hz. Model: We use a whole-brain model that consists of a network of delayed Kuramoto oscillators with coupling corresponding to an anatomical brain atlas. The used atlas is the Automated Anatomical Atlas with 90 regions, and we employed 40 Hz as the intrinsic frequency for all the oscillators (Cabral et al., 2014). Our simulations last 200 seconds for each set of parameters with a time step of 1 × 10^-3 s. In addition, Miltiadous et al. 2023 also performed a cognitive and neuropsychological assessment. They employed the Mini-Mental State Examination (MMSE) (Creavin et al., 2016). Starting at 30 points, as lower the MMSE score, the more severe the cognitive decline. The MMSE score for the AD group was 17.75±4.5 and for the control group was 30. The point of best correlation between rsEEG and model spectra corresponds to a value of global coupling K and mean delay MD in the parameters space. For each pair of {K, MD} also corresponds a value of spectral entropy (SE) and Kuramoto Order Parameter (KOP). SE is a metric of metastability of the model signals dependent on the spectrum, while KOP is a metric of global synchrony.

Results: The results show the distributions of structural connectivity parameters from 36 AD subjects and 29 Control subjects across corresponding spectral entropy values. AD subjects exhibit lower K [3.77 SD(1.39)] than Control subjects [4.74 SD(1.08)] (Wilcoxon rank-sum test, *p<0.01). However, both groups exhibit similar MD [AD: 22.5 ms SD(5.42); Control: 20.37 ms SD(4.58)]. The structural connectivity parameters of AD subjects correspond to lower metastability (p>0.09) and synchrony (*p<0.01) than the Control subjects. These findings align with Zheng et al., 2023, using the same database. No significant correlation was found between K, MD, SE, or KOP and MMSE scores for AD subjects. This was expected as in the Control group all K, MD, SE, and KOP values correspond to MMSE = 30.

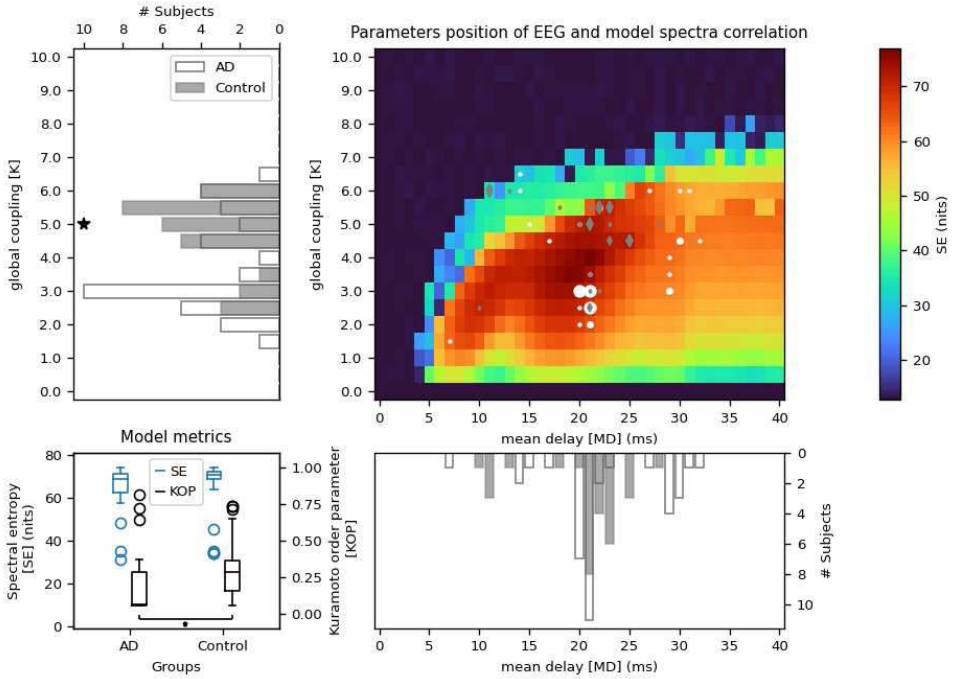

Conclusions: The spectrum, synchrony, and metastability of AD rsEEG differ from Control. We provide quantitative metrics of the dynamic features by correlating the EEG's average spectrum with spectra from a whole-brain model. Fitting with the model, we also extract structural connectivity features, aligning with literature findings of connection loss in AD subjects. In addition, Control subjects show less spread in the parameter space, and there are no AD subjects fitting close to the average point {K = 4.74, MD = 20.37 ms}. Therefore, we propose that fitting far from that point suggests a requirement for diagnosing brain disorders. Additional research is necessary to establish the extent of deviation from that point.

References

1. Cabral, J., Luckhoo, H., Woolrich, M., Joensson, M., Mohseni, H., Baker, A., Kringelbach, M. L., & Deco, G. (2014). Exploring mechanisms of spontaneous functional connectivity in MEG: How delayed network interactions lead to structured amplitude envelopes of band-pass filtered oscillations. NeuroImage, 90, 423–435. https://doi.org/10.1016/j.neuroimage.2013.11.047
2. Creavin ST, Wisniewski S, Noel-Storr AH, Trevelyan CM, Hampton T, Rayment D, Thom VM, Nash KJ, El-hamoui H, Milligan R, Patel AS, Tsivos DV, Wing T, Phillips E, Kellman SM, Shackleton HL, Singleton GF, Neale
3. BE, Watton ME, Cullum S. (2016). Mini-Mental State Examination (MMSE) for the detection of dementia in clinically unevaluated people aged 65 and over in community and primary care populations. Cochrane Database Syst Rev. doi: 10.1002/14651858.CD011145.pub2.
4. Miltiadous, A., Tzimourta, K.D., Afrantou, T., Ioannidis, P., Grigoriadis, N., Tsalikakis, D.G., Angelidis, P., Tsipouras, M.G., Glavas, E., Giannakeas, N. & Tzallas, A. (2023). A Dataset of Scalp EEG Recordings of Alzheimer's Disease, Frontotemporal Dementia and Healthy Subjects from Routine EEG. Data, 8, 95. https://doi.org/10.3390/data8060095
5. Zheng, X., Wang, B., Liu, H., Wu, W., Sun, J., Fang, W., ... & Chen, S. S. C. (2023). Diagnosis of Alzheimer's disease via resting-state EEG: integration of spectrum, complexity, and synchronization signal features. Frontiers in Aging Neuroscience, 15.

Poster No 1418

Using Interpretable Deep Learning to Predict Age with Cortico-Hippocampal Functional Connectivity

Yifei Sun[1], Marshall Dalton[2,3], Fernando Calamante[1,3,4], Jinglei Lv[1,3]

[1]School of Biomedical Engineering, The University of Sydney, Sydney, New South Wales, [2]School of Psychology, The University of Sydney, Sydney, New South Wales, [3]Brain and Mind Center, The University of Sydney, Sydney, New South Wales, Australia, [4]Sydney Imaging, The University of Sydney, Sydney, New South Wales, Australia

Introduction: Exploring healthy brain aging sets a baseline to understand aging related brain diseases and can help develop targeted interventions. Among various brain circuits, cortico-hippocampal connectivity is reported to be associated with age-related cognitive decline (Dennis et al. 2014). However, the impact of aging on the cortico-hippocampal connectivity requires more research. Our study uses convolutional neural networks (CNN) to predict age with the seed-based cortico-hippocampal functional connectivity (FC). We also generated saliency maps of CNN on the cortex to explain the regional variability of contribution to age prediction.

Methods: We used the minimally preprocessed (Glasser et al. 2013) resting-state functional magnetic resonance imaging (rs-fMRI) data from the Human Connectome Project Aging dataset (Bookheimer et al. 2019) (720 subjects, aged 36-100 years). After applying spatial smoothing and temporal filtering, we calculated the seed-based cortico-hippocampal FC. To test our method specificity, we divided the hippocampus into anterior and posterior seeds and computed two additional sets of FC maps. We trained three 3D CNN models to predict age with the same architecture to minimize the mean absolute error (MAE) using the whole, anterior, and posterior hippocampal cortical FC, respectively. 5-fold cross-validation was used to avoid overfitting. We then used Layer Class Activation Mapping (LayerCAM) (Jiang et al. 2021) to interpret models and identify age-predictive brain regions by generating high-resolution saliency maps. We also explored differences between the anterior and posterior hippocampal FC models through one-way t-test on saliency maps.

Results: CNN models predicted age with MAEs of 6.9, 7.1, and 6.8 years for whole, anterior, and posterior hippocampal FC, respectively. Peak prediction accuracy (MAE of 4.4 years) was observed in subjects aged 55-60 (Fig. 1A). While another study, focusing on a narrow age range (40-69), achieved a prediction MAE of 4.8 years using whole brain FC matrices (He et al. 2020), our study involves a wider age span and whole brain voxel-wise hippocampal FC for finer spatial resolution. The mean saliency map from the whole hippocampal cortical FC based model (Fig. 1B) presents hotter (redder) regions with higher contribution of the connectivity to the prediction, e.g. precuneus, retrosplenial cortex, and occipital lobe. These areas align with known aging relevant regions. The precuneus is vulnerable to Alzheimer's disease (AD) (Zhang et al. 2021) and hippocampal-retrosplenial cortex FC relates to tau accumulation in the medial parietal region (Ziontz et al. 2021). The occipital lobe atrophy was also found in healthy old adults (Harrison et al. 2019). Mean saliency maps from anterior and posterior hippocampal cortical FC models (Fig. 2A-B)) show distinct patterns. One-way t-tests identify significant differences (Fig. 2C-D, z-score>1.645). Specifically, FCs between the anterior hippocampus and lateral occipital cortex, precuneus, and medial prefrontal cortex were more influential on age prediction than their posterior hippocampus connections. Conversely, posterior hippocampal FC with medial occipital and posterior parahippocampal had a greater prediction effect. These disparities may due to different functional roles of the anterior and posterior hippocampus (Moser et al.1998), and aging may differently affect anterior and posterior FC.

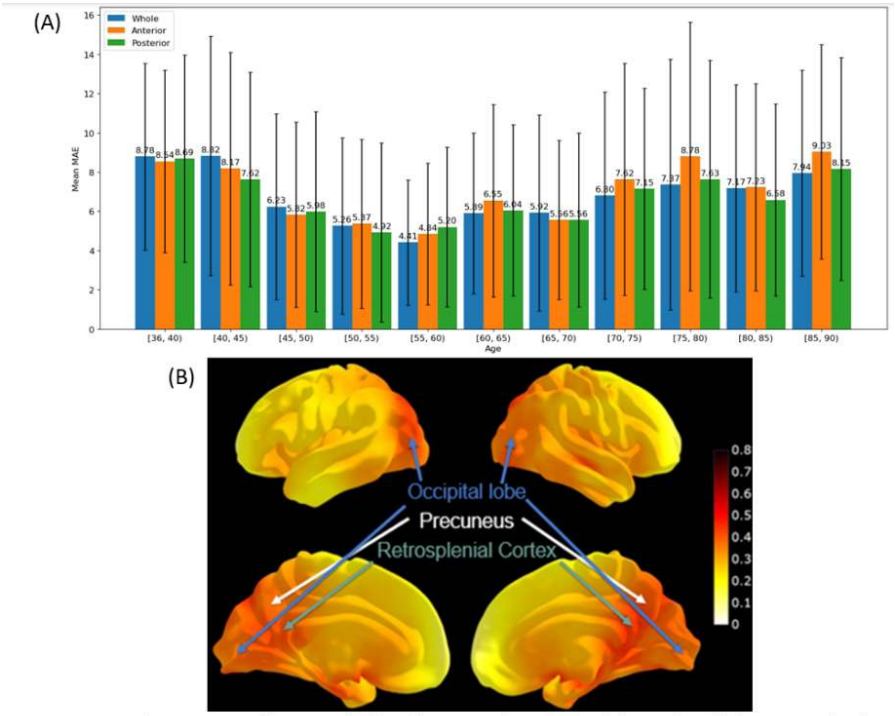

Fig. 1 Age prediction error of our method and mean saliency map (A) Barplot of the mean absolute error (MAE) for each 5-year group for three models, where blue bars are based on the model using whole hippocampal cortical functional connectivity (FC). The orange and green ones are based on models using the anterior and posterior hippocampal cortical FC, respectively. A lower MAE means a smaller prediction error. The height of the bars are MAE values. Lines on top of bars represent the standard deviation. (B) Mean saliency map for the model based on whole hippocampal FC. Higher values indicate higher salience (i.e. higher contribution to the age prediction model). The occipital lobe, precuneus, and retrosplenial cortex are indicated by arrows.

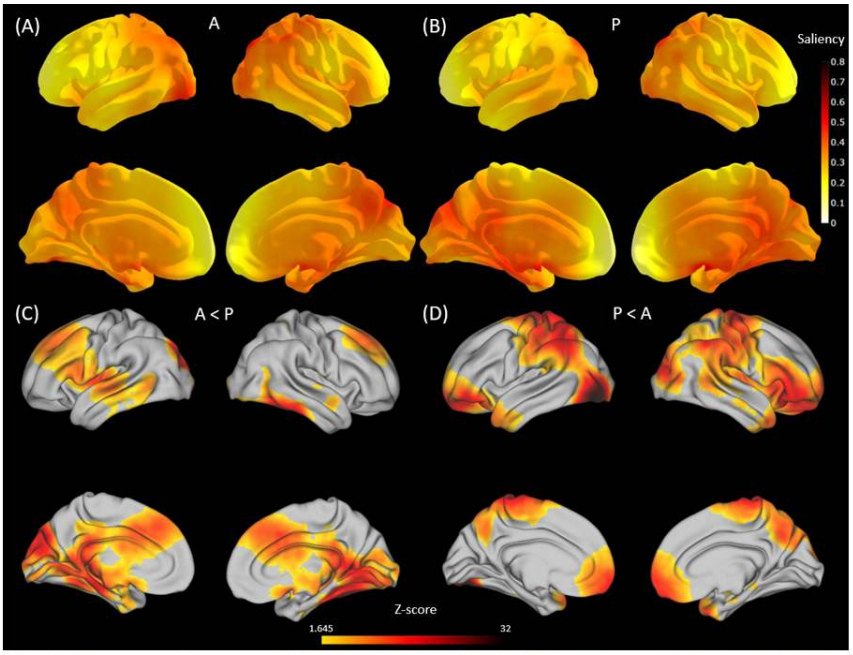

Fig. 2 Comparing the mean saliency maps for models using anterior (A) and posterior (P) hippocampal cortical functional connectivity (FC). (A) The mean saliency map of the model using hippocampalA-cortical FC. (B) The mean saliency map of the model using hippocampalP-cortical FC. Higher values mean higher saliencies. (C, D) Z-scores of two one-way t-tests between individual saliency maps based on models using anterior and posterior hippocampal cortical FC, thresholded at 1.645. Higher z-score values indicate more significant differences. (C) Regions that have significantly stronger contribution in the model using hippocampalP-cortical FC than in the model using hippocampalA-cortical FC. (D) Regions that have significantly stronger contribution in the model using hippocampalA-cortical FC than in the model using hippocampalP-cortical FC.

Conclusions: We trained a 3D CNN model that can predict age using cortico-hippocampal FC, with LayerCAM to aid interpretation. Key regions impacting predictions are consistent with brain regions known to be affected during aging. Further fine-grain analysis showed differences in the contributions from anterior and posterior hippocampal FC to age prediction, indicating our method's specificity to hippocampal subregions. Future efforts will aim to enhancing performance, validate results, and explore clinical applications.

References

1. Bookheimer, S. Y., D. H. Salat, M. Terpstra, B. M. Ances, D. M. Barch, R. L. Buckner, G. C. Burgess, S. W. Curtiss, M. Diaz-Santos and J. S. Elam (2019). "The lifespan human connectome project in aging: an overview." Neuroimage 185: 335-348.
2. Dennis, E. L. and P. M. Thompson (2014). "Functional brain connectivity using fMRI in aging and Alzheimer's disease." Neuropsychology review 24: 49-62.
3. Glasser, M. F., S. N. Sotiropoulos, J. A. Wilson, T. S. Coalson, B. Fischl, J. L. Andersson, J. Xu, S. Jbabdi, M. Webster and J. R. Polimeni (2013). "The minimal preprocessing pipelines for the Human Connectome Project." Neuroimage 80: 105-124.
4. Harrison, T. M., R. La Joie, A. Maass, S. L. Baker, K. Swinnerton, L. Fenton, T. J. Mellinger, L. Edwards, J. Pham and B. L. Miller (2019). "Longitudinal tau accumulation and atrophy in aging and alzheimer disease." Annals of neurology 85(2): 229-240.
5. He, T., R. Kong, A. J. Holmes, M. Nguyen, M. R. Sabuncu, S. B. Eickhoff, D. Bzdok, J. Feng and B. T. Yeo (2020). "Deep neural networks and kernel regression achieve comparable accuracies for functional connectivity prediction of behavior and demographics." NeuroImage 206: 116276.
6. Jiang, P.-T., C.-B. Zhang, Q. Hou, M.-M. Cheng and Y. Wei (2021). "Layercam: Exploring hierarchical class activation maps for localization." IEEE Transactions on Image Processing 30: 5875-5888.
7. Moser, M. B. and E. I. Moser (1998). "Functional differentiation in the hippocampus." Hippocampus 8(6): 608-619.
8. Zhang, K., H. Mizuma, X. Zhang, K. Takahashi, C. Jin, F. Song, Y. Gao, Y. Kanayama, Y. Wu and Y. Li (2021). "PET imaging of neural activity, β-amyloid, and tau in normal brain aging." European Journal of Nuclear Medicine and Molecular Imaging: 1-13.
9. Ziontz, J., J. N. Adams, T. M. Harrison, S. L. Baker and W. J. Jagust (2021). "Hippocampal connectivity with retrosplenial cortex is linked to neocortical tau accumulation and memory function." Journal of Neuroscience 41(42): 8839-8847.

Poster No 1419

Exploration of brain-based prediction of early developmental outcomes using deep learning

Haitao Chen[1,2], Jonathan Stubblefield[3], Xiuzhen Huang[4,3], Emil Cornea[5], John Gilmore[5], Wei Gao[1,2]

[1]Biomedical Imaging Research Institute (BIRI), Cedars-Sinai Medical Center, Los Angeles, CA, [2]Department of Bioengineering, University of California at Los Angeles, Los Angeles, CA, [3]Department of Computer Science, Arkansas State University, Jonesboro, AR, [4]Department of Computational Biomedicine, Cedars-Sinai Medical Center, Los Angeles, CA, [5]Departments of Psychiatry, University of North Carolina Chapel Hill, Chapel Hill, NC

Introduction: One major goal of developmental neuroimaging research is to build imaging-based models to predict later developmental outcomes so we can identify risks at the earliest timepoint for better intervention. In this study, we aimed at exploring the possibility of predicting 1-/2-year Mullen composite and 4-year IQ scores from earlier/concurrent resting-state functional connectivity maps during the first four years of life using deep learning approaches, specifically AlexNet-based 3D convolutional neural networks[1].

Methods: 623 subjects from the Early Brain Development Study (EBDS, 587 with 1-year Mullen composite (MCOMP_1) score, 479 with 2-year Mullen composite (MCOMP_2) score and 364 with 4-year IQ score(IQ_4)) with successful resting-state functional MRI (rsfMRI) scans on at least one of the four timepoints (i.e., three-week (MCOMP_1: n=347; MCOMP_2: n=274; IQ_4: n=229), one-year (MCOMP_1: n=348; MCOMP_2: n=269; IQ_4: n=202), two-year (MCOMP_1: n=256; MCOMP_2: n=244; IQ_4: n=167) and four-year (MCOMP_1: n=138; MCOMP_2: n=135; IQ_4: n=125)) were retrospectively identified and included in this study. All rsfMRI datasets underwent standard preprocessing including global signal regression and scrubbing for motion correction. All datasets were registered to the same two-year-old template space for analysis[2]. Ten seed-based functional-connectivity (FC) maps[3] were generated from preprocessed rsfMRI BOLD signals for each age group and served as the input for prediction of later behavioral outcomes (1-year/2-year Mullen composite or 4-year IQ) separately. Behavioral outcomes were classified into 3 classes: High class (score>mean+std), Low class (score<mean-std) and Middle class (the rest). Each task group was split into 3 parts with balanced demographics, where two-thirds of the sample served as training set and one-third served as testing set. AlexNet-based 3D convolutional neural network (Figure 1) was then trained on the training set using default hyperparameters (batch size=16, learning rate=.001) for 400 epochs for the classification task, and then evaluated on the testing set. Specifically, this model was adapted from AlexNet structure[1], where several convolutional layers with batch normalization layers, ReLU activations and max pooling layers were followed by flatten layer and several fully connected dense layers with dropouts.

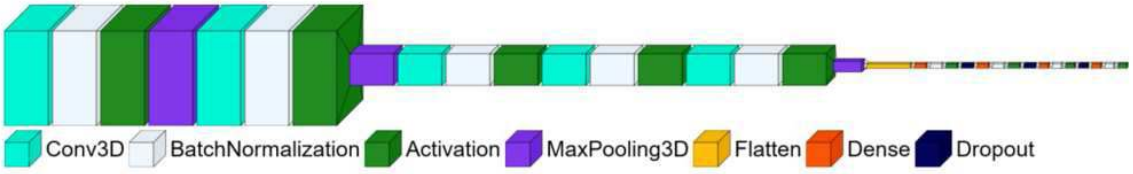

Figure 1. 3D AlexNet-based convolutional neural network model structure used in this study.

Results: Among all prediction tasks (neonates/one-year-olds FC for MCOMP_1, neonates/one-year-olds/two-year-olds FC for MCOMP_2, neonates/one-year-olds/two-year-olds/four-year-olds FC for IQ_4) using ten brain functional-connectivity networks separately, four classification tasks showed relatively strong prediction power (testing set balanced accuracy >= 0.60 and/or AUC >= 0.60): visual-two brain network in neonates predicted 1-year Mullen composite score, sensory-motor brain network in neonates predicted 2-year Mullen composite score, visual-three brain network in two-year-olds correlated 2-year Mullen composite score, and visual-two brain network in two-year-olds predicted 4-year IQ score. Detailed training/testing curve, confusion matrices and testing metrics are shown in Figure 2 for these four classification tasks. Note that Low and High classes were combined as Outlier class only in calculating testing metrics to obtain more cases in Outlier class.

Classification tasks	Training-testing curve	Testing confusion matrix	Testing balanced accuracy	Testing AUC	Testing sensitivity of Middle class	Testing specificity of Middle class
Visual-two brain network in neonates predicted 1-year Mullen composite score	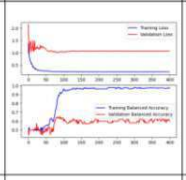	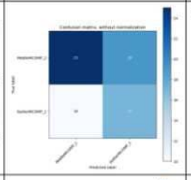	0.60	0.61	0.57	0.63
Sensory-motor brain network in neonates predicted 2-year Mullen composite score	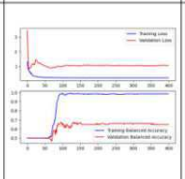	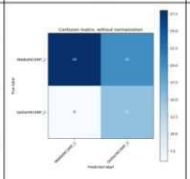	0.65	0.73	0.58	0.71
Visual-three brain network in two-year-olds correlated 2-year Mullen composite score	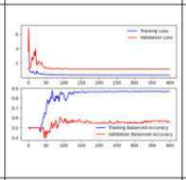	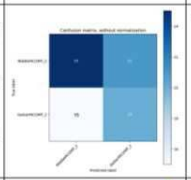	0.56	0.60	0.54	0.57
Visual-two brain network in two-year-olds predicted 4-year IQ score	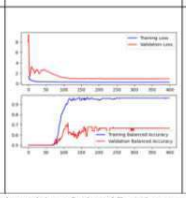	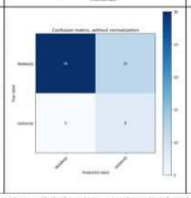	0.66	0.63	0.71	0.62

Figure 2. Result Table of classification tasks which showed relatively strong prediction power (testing balanced accuracy >= 0.60 or testing AUC >= 0.60). Here, balanced accuracy was calculated as the mean of recall across all classes; AUC was the area under the receiver operating characteristic (ROC) curve; sensitivity of Middle class was basically the recall of Middle class (the number of truly detected Middles divided by the number of real Middles), and specificity of Middle class was the recall of Outlier class (the number of truly detected Outliers divided by the number of real Outliers). In this binary case, the balanced accuracy equaled to the mean of sensitivity of Middle class and specificity of Middle class.

Conclusions: This study explored the possibility of predicting later behavioral scores from earlier/concurrent fMRI-based functional-connectivity maps using 3D convolutional neural networks. The preliminary results showed reasonable prediction power of visual / sensory motor functional-connectivity maps, revealing the potential of predicting later IQ / behavioral capabilities from earlier/concurrent brain functional-connectivity topologies in first years of life. Future steps may include adapting deep learning model and employing other models like graph neural networks[4] to explore if better prediction can be achieved beyond the shape and topology of functional network maps.

References

1. Krizhevsky, A., Sutskever, I., & Hinton, G. E. (2012). ImageNet Classification with Deep Convolutional Neural Networks. Advances in Neural Information Processing Systems, 25. http://code.google.com/p/cuda-convnet/
2. Shi, F., Yap, P.-T., Wu, G., Jia, H., Gilmore, J. H., Lin, W., & Shen, D. (2011). Infant Brain Atlases from Neonates to 1- and 2-Year-Olds. PLoS ONE, 6(4), e18746. https://doi.org/10.1371/journal.pone.0018746
3. Smith, S. M., Fox, P. M. T., Miller, K. L., Glahn, D. C., Fox, P. M. T., Mackay, C. E., Filippini, N., Watkins, K. E., Toro, R., Laird, A. R., & Beckmann, C. F. (2009). Correspondence of the brain's functional architecture during activation and rest. Proceedings of the National Academy of Sciences of the United States of America, 106(31), 13040–13045. https://doi.org/10.1073/pnas.0905267106
4. Wu, Z., Pan, S., Chen, F., Long, G., Zhang, C., & Yu, P. S. (2021). A Comprehensive Survey on Graph Neural Networks. IEEE Transactions on Neural Networks and Learning Systems, 32(1), 4–24. https://doi.org/10.1109/TNNLS.2020.2978386

Poster No 1420

EEG-based VR Cybersickness Detection Using Domain Adversarial Deep Learning Model

Wooseok Hyung[1], Jung-Hwan Kim[1], Hyunsub Kim[1], Chang-Hwan Im[1]

[1]Hanyang University, Seoul, Republic of Korea

Introduction: Virtual reality (VR)-induced cybersickness can cause negative effects like dizziness, nausea, and vomiting. Since these effects can be a barrier to some users wearing a VR head-mounted display (HMD) headset, detecting VR-induced cybersickness is becoming an important issue in the popularization of VR services. In this study, we propose a deep learning (DL) architecture for improved EEG-based cybersickness detection in a VR environment.

Methods: Thirty-five participants (19 males, 16 females, 20 to 35 years old) with normal or corrected-to-normal vision were recruited for this study. Each participant watched 360-degree, 15-minute VR rollercoaster video once, while wearing VR-HMD headset. The video consisted of three stages, each lasting five minutes. In the first stage, VR rollercoaster moves slowly and statically, causing little or no cybersickness. In the second and third stages, VR rollercoaster moves faster and more dynamically to cause cybersickness intentionally. EEG signal was measured from 32 electrodes with a 2,048Hz sampling frequency. For EEG signal preprocessing, 512Hz-downsampling, 4-55Hz third-order Butterworth bandpass filtering, and common average referencing were applied. The preprocessed signal was segmented by a 2-second window with 1-second sliding. First stage was categorized as 'non-cybersickness', second and third stages as 'cybersickness' for binary classification. Simulator sickness questionnaire (SSQ)[1] was used before and after the experiment to monitor the participant's cybersickness triggered by the video. Three participants were excluded from the analyses due to low SSQ difference, and four participants were excluded due to bad EEG signal quality. For the subject-independent cybersickness classification, we propose a model to classify cybersickness robust to subjects, and compared the performance with conventional deep learning models. In our proposed architecture, feature extractor from TSception[2] extracts temporal and spatial features, and the classifier determines cybersickness based on the features. Subject discriminator from Domain Adversarial Neural Network (DANN)[3] was trained adversarially to the subject domain by gradient reversal, making feature extractor extract subject-irrelevant features.

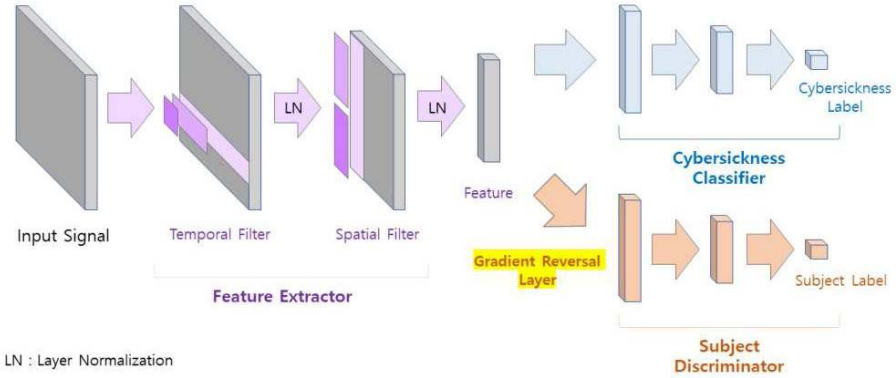

Results: To verify the performance of the subject-independent model, leave-one-subject-out cross-validation of the proposed model and an existing EEG-based classification model was conducted. Proposed model outperforms other existing EEG-based classification models in terms of accuracy and F1-score, and that the proposed model shows fewer instances of poor performance comparing to conventional models.

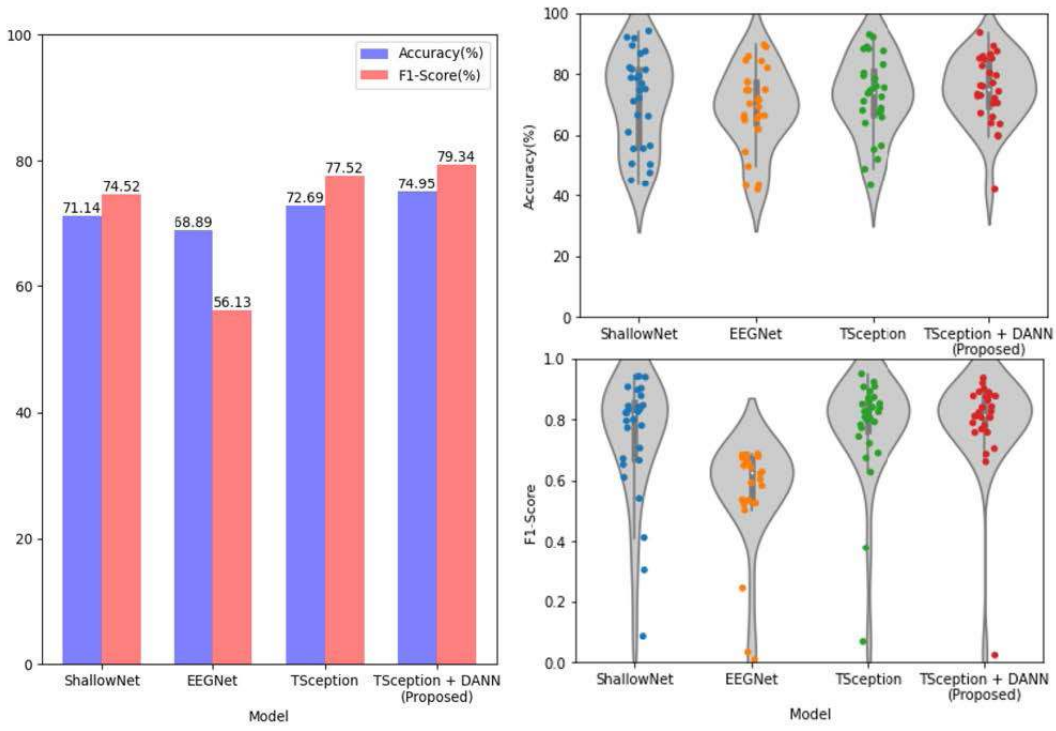

Conclusions: In this study, we proposed a subject-independent DL model for EEG-based cybersickness classification in VR environment. Discriminator was used and trained subject adversarially in this model to train feature extractor robust to subject. The proposed model showed highest accuracy and F1-score compared to the established models.

References
1. Kennedy, R.S., et al. (1993), "Simulator sickness questionnaire: An enhanced method for quantifying simulator sickness." The international journal of aviation psychology 3.3, pp. 203-220
2. Ding, Y., et al. (2023), "TSception: Capturing Temporal Dynamics and Spatial Asymmetry From EEG for Emotion Recognition," in IEEE Transactions on Affective Computing, vol. 14, no. 3, pp. 2238-2250
3. Ganin, Y., et al. (2016), "Domain-adversarial training of neural networks." The journal of machine learning research 17.1, pp. 2096-2030.

Poster No 1421

Predicting Individual Cognitive Functions through Integrated Structural-Functional Connectivity

Eunku Bae[1], Kwangsun Yoo[2], Song E Kim[3], Chang-hyun Park[3], Hyang Woon Lee[3]

[1]Ewha Womans University, Seoul, [2]Sungkyunkwan University, Seoul, Korea, Republic of, [3]Ewha Womans University, Seoul, Korea, Republic of

Introduction: Investigating the delicate interplay between structural and functional brain connectivity (structure-function coupling) is crucial to understand individual differences in cognitive and behavioral capacities. Building on this premise, our research aimed to develop MRI-based predictive models, with a special emphasis on the integration of structural and functional brain connectivity patterns derived from MRI data. This model is designed to predict individual cognitive functions, considering the variances in cognitive traits not only among individuals but also across different socio-demographic factors, including sex, education, and racial differences. The resulting model is tailored for enhanced prediction accuracy within specific populations, providing a novel approach to cognitive function prediction in the realm of structural and functional brain connectivity studies.

Methods: The study involved 191 healthy subjects aged 17 to 80 years old, who underwent both structural and functional MRI, alongside a battery of neuropsychological tests including executive functions, verbal and spatial memory. For structural MRI analysis, high resolution 3-dimensional T1 MR images with the FreeSurfer 6.0 was utilized to quantify cortical thickness and volumes. Functional connectivity was analyzed to extract salient features for developing predictive models using the Connectome-based Predictive Modeling (CPM) framework[1]. This process included creating individual connectivity matrices[2], selecting features for modeling, and building a predictive model for validation on new subjects.

Results: We measured multivariate brain connectivity models based on both structural and functional MRI and evaluated them for various cognitive variables among subjects to predict the individual cognitive capacities. The predictive model based on structural and functional MRI dataset showed distinctive patterns as substantial efficacy in forecasting individual cognitive functions. Notably, feature selection varied across different cognitive tests, suggesting a specific link between brain networks and specific cognitive functions.

Conclusions: Our study demonstrates the potential of employing integrated brain structural and functional connectivity models to predict individual cognitive levels. Furthermore, it underscores the prospect of developing normative models capable of distinguishing between healthy individuals and patients as we recruit more subjects with certain neuropsychiatric diseases, thereby providing a comprehensive tool for assessing cognitive functions. This approach highlights the utility of population-specific models in the realm of cognitive function prediction and brain connectivity research.

References
1. Shen X et al. Using connectome-based predictive modeling to predict individual behavior from brain connectivity. Nat. Protoc 12, 506–518 (2017). [PubMed: 28182017]
2. Yoo, K., Rosenberg, M.D., Kwon, Y.H. et al. A brain-based general measure of attention. Nat Hum Behav 6, 782–795 (2022)

Acknowledgements
This study is supported by the National Research Foundation of Korea (NRF) (No.2020R1A2C2013216, 2019M3C1B8090803, 2019M3C1B8090802, and RS-2023-00265524), Institute of Information & Communication Technology Planning & Evaluation (IITP) grant (No. RS-2022-00155966) by the Korea government (MSIT), and BK21-plus FOUR and Artificial Intelligence Convergence Innovation Human Resources Development programs of Ewha Womans University.

Poster No 1422

Graph neural networks for MDD classification using functional and structural MRIs

Jiwon Lee[1], Ye-Eun Kim[2], Mikhail Votinov[3], Lisa Wagels[4], Ute Habel[5], Sun-Young Kim[6], Munseob Lee[7], Han-Gue Jo[6]

[1]Kunsan National University, Gunsan-si, Jeollabuk-do, [2]Kunsan National University, Kunsan, Jeollabuk do, [3]Institute of Neuroscience and Medicine (INM-10), Research Centre Jülich, Jülich, Germany, [4]RWTH Aachen University Hospital, Aachen, Germany, [5]Department of Psychiatry, Psychotherapy and Psychosomatics, RWTH Aachen University Hospital, Aachen, North Rhine-Westphalia, [6]Kunsan National University, Gunsan, Jeollabuk-do, [7]Electronics and Communication Research Institute (ETRI), Deajeon, Deajeon

Introduction: Graph neural network (GNN), a deep learning-based method known for their effectiveness in analyzing graph-structured data, is inherently suitable for the examination of the complex brain network[1]. GNN can operate on non-Euclidean domains, employing convolutions on graphs by leveraging input node features and the relationships between nodes to produce novel features. Recent studies showed that GNN is suitable for analyzing the connectome of functional magnetic resonance imaging (MRI) and can identify the functional network alteration of major depressive disorder (MDD) patients[2,3]. However, previous GNN studies mainly focus on the brain network derived from one modality, either functional imaging or structural imaging[4-6], potentially leading to the observed shortcomings in model accuracy. In this current study, both functional and structural MRIs are combined and analyzed for MDD classification. Specifically, GNN models were formulated to leverage various types of node attributes derived from functional MRI, structural MRI, or their combination. These distinct node features were performed using graph convolutional network (GCN) and graph attention network (GAT) models.

Methods: GCN and GAT underwent training for classification using resting-state functional and structural MRI scans from a cohort of 775 participants (153 with MDD and 622 healthy controls)[7]. For constructing the graph, a whole-brain functional connectivity matrix was utilized, representing Fisher transformed correlation coefficients among BOLD time series across 100 atlas-based Schaefer's cortical brain regions[8]. Node features were characterized in three ways: i) a nodal functional connectivity vector comprising 100 node features derived from functional MRI, ii) six structural parameters encompassing grey matter volume, fractal dimension, gyrification, Toro GI20, sulcal depth, and thickness extracted from structural MRI, or iii) a combination of both resulting in 106 node features. The fitting procedure and evaluation of predictive models were carried out using a 5-fold cross-validation technique.

Results: The performance of GNN models was highly depend on the node feature type. GCN and GAT achieved the highest accuracies (73.23%±0.04 and 77.65%±0.05, respectively) when the node features were combined with both functional and structural MRI data. Node features with functional MRI alone showed accuracies of 64.84%±0.02 and 75.27%±0.03 for GCN and GAT, respectively. Node features only with structural MRI exhibited the lowest performance, with accuracies of 62.26%±0.06 and 52.35%±0.07 for GCN and GAT, respectively. The impact of the number of GNN layers and hyperparameters was also tested, but it did not change the effect of the node feature type.

Conclusions: This study explored the application value of using both brain functional and structural information in modeling GNN and differentiating patients with MDD from healthy controls. Our proposed multi-modal method achieved prediction results of 77% on a large-sample dataset. These findings highlighted the benefits of incorporating structural information into functional MRI in the development of GNN model for classifying MDD brain networks. Notably, GAT demonstrated better performance compared to the GCN, revealing that within GAT – a model that operates attention mechanism to address important nodes in a neighborhood – the impact of node feature types was relatively diminished. This observation suggests for the integration of functional and structural information, not solely in node features but also about designing the graph architecture in a way that facilitates the fusion of both types of information.

References

1. Zhou, Jie, et al. "Graph neural networks: A review of methods and applications." AI open 1 (2020): 57-81.
2. Qin, Kun, et al. "Using graph convolutional network to characterize individuals with major depressive disorder across multiple imaging sites." EBioMedicine 78 (2022).
3. Venkatapathy, Sujitha, et al. "Ensemble graph neural network model for classification of major depressive disorder using whole-brain functional connectivity." Frontiers in Psychiatry 14 (2023): 1125339.
4. Zhang, Hao, et al. "Classification of brain disorders in rs-fMRI via local-to-global graph neural networks." IEEE Transactions on Medical Imaging 42.2 (2022): 444-455.
5. Gao, Jingjing, et al. "Brain age prediction using the graph neural network based on resting-state functional MRI in Alzheimer's disease." Frontiers in Neuroscience 17 (2023).
6. Subaramya, S., et al. "Graph Neural Network based Alzheimer's Disease Classification using Structural Brain Network." 2022 22nd International Conference on Advances in ICT for Emerging Regions (ICTer). IEEE, 2022.
7. Tanaka, Saori C., et al. "A multi-site, multi-disorder resting-state magnetic resonance image database." Scientific data 8.1 (2021): 227.
8. Schaefer, Alexander, et al. "Local-global parcellation of the human cerebral cortex from intrinsic functional connectivity MRI." Cerebral cortex 28.9 (2018): 3095-3114.

Poster No 1423

Unsupervised anomaly detection and segmentation in brain MRI: a comparative study

Junhyeok Lee[1], Won Hee Lee[1]

[1]Kyung Hee University, Yongin

Introduction: Unsupervised anomaly detection (UAD) plays a crucial role in identifying anomalies by learning the distribution of normal data without relying on labeled anomalies. These methods are widely used in various industries, including manufacturing damage detection, financial fraud detection, cyber intrusion, and medical diagnosis (Chandola et al., 2009). A previous study showed the effectiveness of UAD algorithms in detecting chronic infarction, suggesting their potential for brain MRI applications (van Hespen et al., 2021). However, limited research exists on the performance of UAD algorithms in the context of brain tumor detection and segmentation (Baur et al., 2021). To address this gap, this study aims to conduct a comprehensive evaluation of various UAD algorithms specifically for brain tumor detection and segmentation.

Methods: We used T2-weighted MRI data from two different datasets: 272 patients diagnosed with glioma from the multimodal brain tumor segmentation challenge 2020 (BraTS2020; age range 19 – 87 years) and 252 healthy individuals from the Cambridge Centre for Ageing and Neuroscience (Cam-CAN; 126 females; age range 18 – 88 years). We compared the performance of seven UAD methods on anomaly detection and segmentation. These methods included memory bank approach CFA (Lee et al., 2022), the reconstruction-based method DRAEM (Zavrtanik et al., 2021), the patch distribution-based method PaDiM (Defard et al., 2021), the normalizing flow-based methods CS-Flow (Rudolph et al., 2022), and FastFlow (Yu et al., 2021), and the knowledge distillation-based methods STFPM (Wang et al., 2021), and RD4AD (Deng et al., 2021). To assess the performance of these UAD methods, we used the area under the receiver operator curve (AUC) at image-level for anomaly detection and pixel-level for segmentation.

Results: Figure 1 displays the performance of various UAD methods for anomaly detection and segmentation in brain MRI. The normalizing flow-based models (CS-Flow and FastFlow) achieved the highest detection performance (image-level AUC = 99.47 – 99.78). However, these methods showed the lowest segmentation performance (pixel-level AUC = 81.47 – 83.18) and led to an increased rate of false positives in segmentation tasks (Figure 2a). STFPM and DRAEM, while having the lower detection performance (image-level AUC = 87.51 – 88.55; pixel-level AUC = 96.35 – 96.43), had better segmentation performance compared to the flow-based models. FastFlow, CS-Flow, DRAEM, STFPM showed a substantial performance gap between detection and segmentation, with differences ranging from 7.80 to 18.31. In contrast, RD4AD and CFA exhibited a small difference between detection and segmentation performance ranging from 1.82 to 2.06. RD4AD and CFA achieved superior segmentation performance (pixel-level AUC = 97.67 – 98.18). However, we found that RD4AD and STFPM had a tendency to misidentify the lateral ventricle areas in normal samples as abnormal regions (Figure 2b).

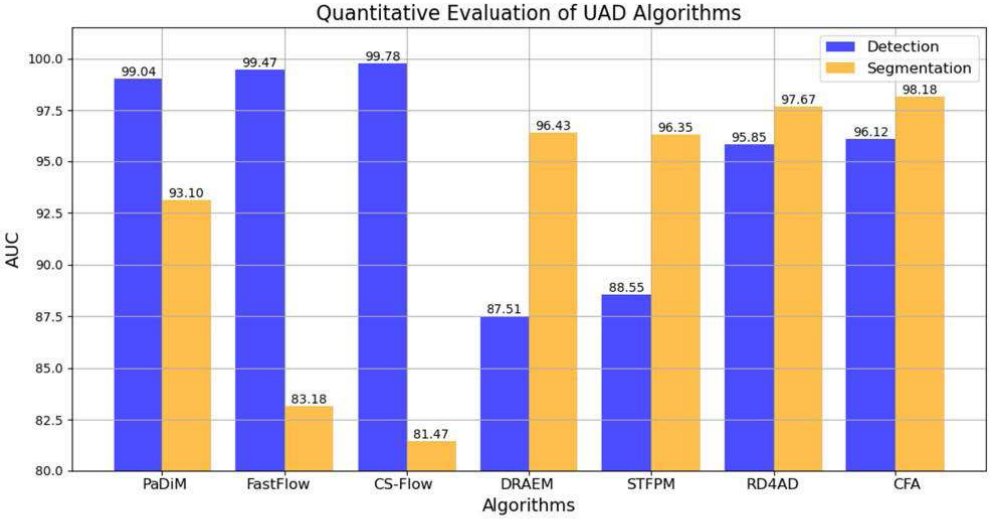

Figure 1. Quantitative evaluation results of various unsupervised anomaly detection algorithms for anomaly detection and segmentation.

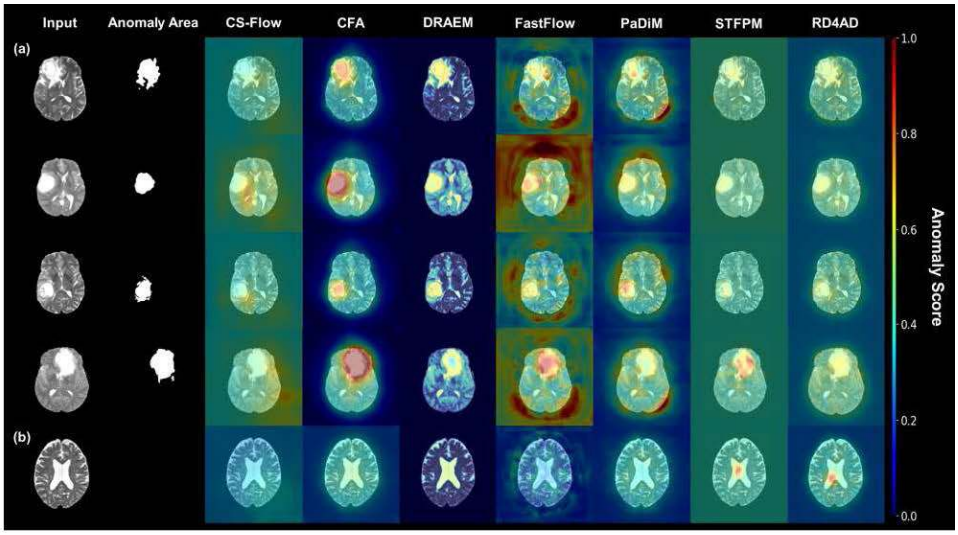

Figure 2 . Anomaly score maps generated by various unsupervised anomaly detection algorithms for qualitative comparison for (a) patients with glioma and (b) a healthy individual.

Conclusions: Our comparative evaluation of various UAD methods for brain MRI reveal their potential applicability. Our results indicate that UAD methods can be adapted for brain anomaly detection and segmentation, while emphasizing the need for optimal model tuning and refinement to improve the performance of the UAD methods. Moreover, the experimental results indicate the potential for improved UAD performance by improving the model's understanding of normal anatomical structures with similar intensities to abnormal regions in MRI scans. Incorporating anatomical information into the learning process may be a key strategy for achieving enhanced performance, offering more reliable support in the clinical diagnosis and monitoring of brain pathologies.

References

1. Chandola. (2009). Anomaly detection: A survey. ACM computing surveys (CSUR), 41(3), 1-58.
2. van Hespen. (2021). An anomaly detection approach to identify chronic brain infarcts on MRI. Scientific Reports, 11(1), 7714.
3. Baur. (2021). Autoencoders for unsupervised anomaly segmentation in brain MR images: a comparative study. Medical Image Analysis, 69, 101952.
4. Lee. (2022). Cfa: Coupled-hypersphere-based feature adaptation for target-oriented anomaly localization. IEEE Access, 10, 78446-78454.
5. Zavrtanik. (2021). Draem-a discriminatively trained reconstruction embedding for surface anomaly detection. In Proceedings of the IEEE/CVF International Conference on Computer Vision (pp. 8330-8339).
6. Defard. (2021, January). Padim: a patch distribution modeling framework for anomaly detection and localization. In International Conference on Pattern Recognition (pp. 475-489). Cham: Springer International Publishing.
7. Rudolph. (2022). Fully convolutional cross-scale-flows for image-based defect detection. In Proceedings of the IEEE/CVF Winter Conference on Applications of Computer Vision (pp. 1088-1097).
8. Yu. (2021). Fastflow: Unsupervised anomaly detection and localization via 2d normalizing flows. arXiv preprint arXiv:2111.07677.
9. Wang. (2021). Student-teacher feature pyramid matching for anomaly detection. arXiv preprint arXiv:2103.04257.
10. Deng. (2022). Anomaly detection via reverse distillation from one-class embedding. In Proceedings of the IEEE/CVF Conference on Computer Vision and Pattern Recognition (pp. 9737-9746).

Poster No 1424

Exploring the Predictive Value of Structural Covariance Networks for the Diagnosis of Schizophrenia

Clara Vetter[1,2,3,4], Annika Bender[5], Dominic Dwyer[6], Anne Ruef[7], Lana Kambeitz-Ilankovic[8], Linda Antonucci[9], Stephan Ruhrmann[8], Joseph Kambeitz[10], Anita Riecher-Rössler[11], Rachel Upthegrove[12], Raimo K. Salokangas[13], Jarmo Hietala[13], Christos Pantelis[14], Rebecca Lencer[15], Eva Meisenzahl[16], Stephen J. Wood[17], Paolo Brambilla[18], Stefan Borgwardt[19], Peter Falkai[7], Alessandro Bertolino[20], Daniel Rückert[21], Nikolaos Koutsouleris[7,22,23]

[1]Max Planck Institute of Psychiatry, Munich, Germany, [2]Department of Psychiatry and Psychotherapy, Ludwig-Maximilian University, Munich, Germany, [3]Munich Center of Machine Learning (MCML), Munich, Germany, [4]Helmholtz Association - Munich School for Data Science (MUDS), Munich, Germany, [5]Department of Psychiatry and Psychotherapy, Ludwig Maximilian University, Munich, Bavaria, [6]Orygen, the National Centre of Excellence for Youth Mental Health, Melbourne, Victoria, [7]Department of Psychiatry and Psychotherapy, LMU University Hospital, LMU Munich, Munich, Germany, [8]University of Cologne, Cologne, Germany, [9]University of Bari Aldo Moro, Milan, Italy, [10]Department of Psychiatry and Psychotherapy,

University of Cologne, Cologne, Germany, [11]Faculty of Medicine, University of Basel, Basel, Basel, [12]Institute of Mental Health, University of Birmingham, Birmingham, United Kingdom, [13]Department of Psychiatry, University of Turku, Turku, Finland, [14]Melbourne Neuropsychiatry Centre, Carlton, Victoria, [15]Institute for Translational Psychiatry, University Münster, Münster, Germany, [16]Department of Psychiatry and Psychotherapy, Medical Faculty, Heinrich Heine University, Düsseldorf, Germany, [17]Centre for Youth Mental Health, University of Melbourne, Melbourne, Australia, [18]Department of Neurosciences and Mental Health, Fondazione IRCCS Ca' Granda Ospedale Maggiore Policli, Milan, Italy, [19]Department of Psychiatry and Psychotherapy, University of Lübeck, Lübeck, Germany, [20]Department of Basic Medical Science, Neuroscience and Sense Organs, University of Bari Aldo Moro, Bari, Bari, [21]Technical University Munich, Munich, Germany, [22]Max Planck Institute for Psychiatry, Munich, Germany, [23]Department of Psychosis Studies, Institute of Psychiatry, Psychology & Neuroscience, King's College London, London, United Kingdom

Introduction: Structural Covariance Networks (SCNs), reflecting coordinated neurodevelopmental processes, offer insights into brain reorganization associated with aging and diseases such as schizophrenia. Despite group-level alterations in SCNs among patients, individual-level analysis has been hindered by a lack of established methods. This study addresses this gap by comparing two individual SCN computation methods using structural MRI-derived gray matter volumes (GMV) for the classification of schizophrenia.

Methods: In this study, we investigated the predictive value of two single-subject SCN computation methods derived from regional gray matter volumes (GMV) measured by structural MRI for classifying patients with schizophrenia within a sample comprising patients and healthy controls (NPAT = 154, NHC = 366). The first SCN method leveraged a reference sample (N = 627) and quantified a single subject's contribution to the reference group's SCN. The second approach defined a subject's SCN from the single image using a symmetric version of KL divergence. To assess the additional predictive value of SCNs compared to regional GMV, we employed a stepwise analysis using linear support vector machines within a nested cross-validation framework. Initially, each modality (the two SCNs and regional GMV) was separately analyzed. Subsequently, we evaluated their complementary predictive value through stacked generalization. To address various model design choices, we systematically varied the granularity of the cortical parcellation atlas used (100 vs. 200 parcels), the feature dimensionality reduction technique employed (LASSO-regularization vs. principal component analysis (PCA)), and, for the two SCN modalities, the type of network features used (pairwise structural covariance, i.e., SCN edges, vs. network summary metrics). This resulted in a total of 28 models, all externally validated in an independent sample (NPAT = 71, NHC =74). For the best-performing model in each modality, global model explainability analyses were conducted to identify the most contributing features. Additionally, derived risk scores were analyzed for their differential relationships with clinical variables.

Results: Machine learning models trained separately on individual SCNs and regional GMV demonstrated consistent classification capability for distinguishing patients with schizophrenia from healthy controls, regardless of cortical parcellations and dimensionality reduction techniques. Among the unimodal models, the LASSO-regularized model trained on the edges of reference-sample-SCNs, computed using the 200-parcel cortical atlas, achieved the highest balanced accuracy (BAC) in the discovery sample (67.03%). Notably, this model outperformed all other unimodal SCN-based models but did not surpass the performance of LASSO-regularized regional GMV models. Decisions in regional GMV models were driven by the somatomotor network, default mode, frontoparietal control, visual, and limbic networks. In SCN-based models, discriminative pairwise structural covariance primarily involved the ventral attention, default mode, frontoparietal control, visual, and somatomotor networks. Stacked generalization revealed that combining SCN modalities and regional GMV significantly improved model performance compared to models trained on individual modalities alone (BAC = 69.96%). Similarly, the highest external validation performance was observed in the multimodal, stacked model using principal component analysis for dimensionality reduction (BAC = 67.10%). No associations were found between models' decision scores and the clinical variables assessed.

Conclusions: In conclusion, individual SCNs, whether derived from normative samples or KL-divergence, contribute valuable information for schizophrenia classification beyond regional GMV. However, the study did not establish direct links between the identified structural information and clinical phenotypes.

References

1. Saggar, M., Hosseini, S. H., Bruno, J. L., Quintin, E. M., Raman, M. M., Kesler, S. R., & Reiss, A. L. (2015). Estimating individual contribution from group-based structural correlation networks. Neuroimage, 120, 274-284.
2. Kong, X. Z., Liu, Z., Huang, L., Wang, X., Yang, Z., Zhou, G., ... & Liu, J. (2015). Mapping individual brain networks using statistical similarity in regional morphology from MRI. PloS one, 10(11), e0141840.

Poster No 1425

Predicting individual differences from task-evoked effective connectivity

Shufei Zhang[1,2], Kyesam Jung[1,2], Robert Langner[1,2], Esther Florin[3], Simon Eickhoff[1,2], Oleksandr Popovych[1,2]

[1]Institute of Neuroscience and Medicine, Brain and Behaviour (INM-7), Research Centre Jülich, Germany, Jülich, Nordrhein-Westfalen, [2]Institute of Systems Neuroscience, Medical Faculty and University Hospital, Heinrich Heine University, Düsseldorf, Nordrhein-Westfalen, [3]Institute of Clinical Neuroscience and Medical Psychology, Medical Faculty and University Hospital, Heinrich Heine University Düsseldorf, Germany

Introduction: In the research field of predicting individual behavior and phenotypes from functional magnetic resonance imaging (fMRI) data, recent studies[1,2] have demonstrated that task-evoked functional connectivity (FC) may perform better at predicting individual traits as compared to resting-state FC. However, it remains largely unknown whether task-modulated and intrinsic effective connectivity (EC) that allows for causal inferences on the brain possess distinct properties in predicting individual behavior, which we explored in this study. We investigated this issue for a variety of data-processing conditions involving different designs of the general linear model (GLM), applications of Bayesian model reduction (BMR) and self-connectivity (SC)[3,4] as well as for a few cross-validation (CV) schemes, whose impact on the EC-based prediction of behavioral scores has been underexplored in the literature yet. In this study we therefore considered task-evoked EC as calculated by dynamic causal modeling (DCM)[5] for the machine-learning prediction of individual reaction time (RT) in the stimulus-response compatibility (SRC) task[6] and age.

Methods: Task-evoked EC during performance of the SRC task was calculated by DCM from the task fMRI data for 271 subjects (123 females, 18-85 years old, mean age: 52.6 ± 16.5 years) recruited from the subject pool of the 1000BRAINS project[7]. The parameters of intrinsic EC (I-EC, matrix A of DCM) and task-modulated EC (M-EC, matrix B of DCM) of individual subjects were used in a least absolute shrinkage and selection operator (LASSO) regression to predict RT and age in training sets and test sets of unseen subjects (Fig. 1). The features were selected based on the results of the group-level and behavior-related Parametric Empirical Bayes (PEB) analyses for the training sets. We considered several conditions that were assumed to influence predictive performance: cross-validation schemes of 5-fold, 10-fold, or leave-one-out CV (LOOCV), event-related vs. block-based GLM designs, application of BMR and self-connectivity (SC). In addition, we compared prediction results with those of the full task-evoked and task-residual FC patterns.

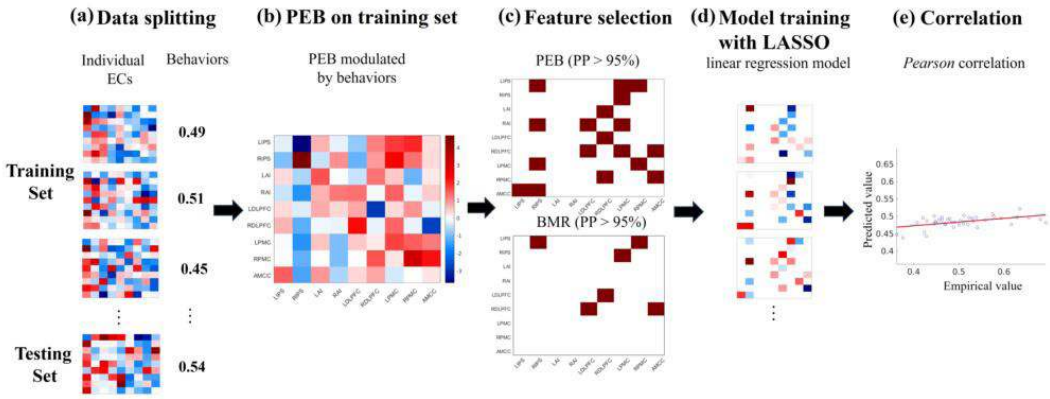

Results: We observed differences in predictive performance (correlation between empirical and predicted behavioral scores) between I-EC and M-EC, as well as between event-related (trial-based) and block-based GLM designs (Fig. 2). There were few differences in prediction accuracy across different CV schemes (but see LOOCV in Fig. 2), and with respect to the application of BMR and SC. For the 5-fold CV, we found statistically significant prediction results for the event-related GLM design, but not for the block-based GLM. For the event-related GLM, M-EC outperformed I-EC in RT prediction ($r = 0.26$ vs $r = 0.09$, Cohen's $d = 3.17$), but was somewhat less effective in age prediction ($r = 0.22$ vs $r = 0.28$, Cohen's $d = 1.09$). The considered task-evoked and task-residual FC patterns showed higher prediction accuracy for age than EC ($r = 0.34/0.37$ vs. 0.28) but were behind task-evoked EC in predicting RT ($r = 0.13/0.22$ vs. 0.26).

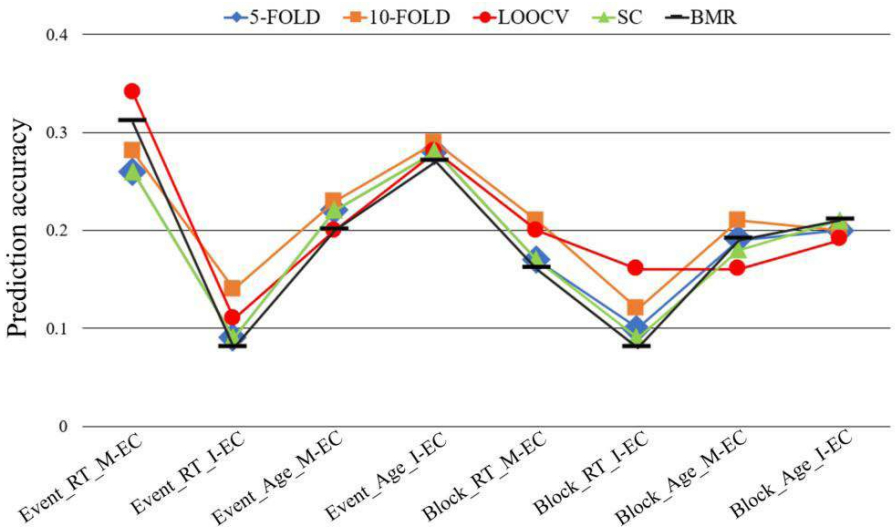

Conclusions: Our results showed that task-modulated and intrinsic EC may capture different behavioral attributes, where M-EC showed higher predictive accuracy for individual RT than I-EC, but I-EC was better predictive of individual age than M-EC. The predictive performance was notably affected by the choice of GLM design for task-fMRI data modeling, and using the event-related GLM design may improve the predictive accuracy for individual RT and age. The selection of EC types for predicting individual differences and the choice of the optimal data processing during DCM estimation of EC should thus be made with care, where our results may guide further research on employing task-evoked EC for the prediction of individual behavior.

References

1. Greene, A.S., et al., Task-induced brain state manipulation improves prediction of individual traits. Nature Communications, 2018. 9(1): p. 2807.
2. Zhao, W., et al., Task fMRI paradigms may capture more behaviorally relevant information than resting-state functional connectivity. NeuroImage, 2023. 270: p. 119946.
3. Friston, K.J., et al., Bayesian model reduction and empirical Bayes for group (DCM) studies. NeuroImage, 2016. 128: p. 413-431.
4. Snyder, A.D., et al., Dynamic Causal Modeling Self-Connectivity Findings in the Functional Magnetic Resonance Imaging Neuropsychiatric Literature. Frontiers in Neuroscience, 2021. 15.
5. Friston, K.J., L. Harrison, and W. Penny, Dynamic causal modelling. NeuroImage, 2003. 19(4): p. 1273-1302.
6. Fitts, P.M. and R.L. Deininger, S-R compatibility: correspondence among paired elements within stimulus and response codes. J Exp Psychol, 1954. 48(6): p. 483-92.
7. Caspers, S., et al., Studying variability in human brain aging in a population-based German cohort—rationale and design of 1000BRAINS. Frontiers in Aging Neuroscience, 2014. 6: p. 149-162.

Poster No 1426

Diagnosis-informed neuro-subtyping of autism spectrum disorder

Zehua Chen[1], Peilun Song[1], Yaping Wang[1], Xiujuan Geng[2]

[1]Zhengzhou University, Zhengzhou, [2]The Chinese University of Hong Kong, Hong Kong

Introduction: Autism Spectrum Disorder (ASD) is a complex neurodevelopmental disorder with heterogeneous symptoms and neurobiological features, which becomes a major hindrance on accurate diagnosis and treatment[6]. Clustering ASD subjects into subtypes with more consistent neural features in each group has practical implications to overcome these obstacles. However, existing findings of neural-subtyping are preliminary and diverse. Moreover, it is unclear whether the degree of deviation from the normal population can be used for ASD subtyping. We aimed to investigate reliable ASD subtypes by clustering methods utilizing diagnosis labels and functional connectivity (FC) as neural features[4].

Methods: Datasets used in this study were from ABIDE I & II, consisting of 1877 subjects including 1030 healthy controls and 847 ASD subjects. Data was the preprocessed following the standard processing pipeline. The FC was estimated followed by Fisher transform between pairs of 116 regions defined by AAL. To reduce the effect caused by non-ASD factors, age, sex and site information were regressed out before sending FC values for clustering. We first conducted dimension reduction based on two types of methods. One is an orthogonal extension of projective non-negative matrix factorization (OPNNMF), a data-driven method for extracting biologically interpretable and reproducible feature representations[8]. The other approach

is based on depicting FC profiles on a network level, i.e., computing the within- and between-network connectivities instead of ROI-based FC[3]. A total of 78 network-level connectivites (12 within- and 66 between-network FCs) were used. After feature reduction, we performed both semi-supervised, HeterogeneitY through DiscRiminative Analysis (HYDRA), and unsupervised k-means clustering for comparison. When conducting HYDRA, both the input features and diagnostic labels (controls or ASD) were used to detect multiple SVM classifiers for hyperplanes to separate the disease samples from controls, and meanwhile assist in assigning each disease sample to a different cluster. Therefore, a total of four approaches were carried out: OPNNMF feature reduction and HYDRA clustering; OPNNMF and k-means; network-based feature reduction and HYDRA; and network-based reduction and k-means. Two cluster validity indices Silhouette Coefficient (SC) and Calinski-Harabasz (CH) were used for performance validation[1]. SC calculates the pairwise difference between the inter- and intra-cluster distances[7]. CH is the ratio of all inter-cluster dispersion to the sum of the intra-cluster dispersion[2]. To evaluate the reliability, we conducted clustering 100 times. Under each repetition, 90% of subjects were randomly stratified for clustering. The adjusted rand index (ARI)[5] and label accuracy (ACC) were used to evaluate the reliability across 100 times. ARI quantifies the similarity between different clustering results. ACC measures label consistency of clustering results across each iteration.

Results: The number of components for OPNNMF was searched from 1 to 1877 by a stepsize of 5. The number of clusters was looped from 2 to 8. Our experimental results show that, the optimal value of the number of components with OPNNMF was 1195 (Fig.1 (a) & (b)). Two clusters show the best performance under all 4 clustering approaches (Fig.1 (c)-(f)). OPNNMF together with HYDRA produced the best performance out of the 4 methods. The average clustering accuracy was above 90% under the semi-supervised method. We further examined the FC matrices under each approach. All methods generated distinct FC patterns for each cluster (Fig.2). Feature reduction with OPNNMF produced similar sub-group FC patterns regardless of the clustering methods.

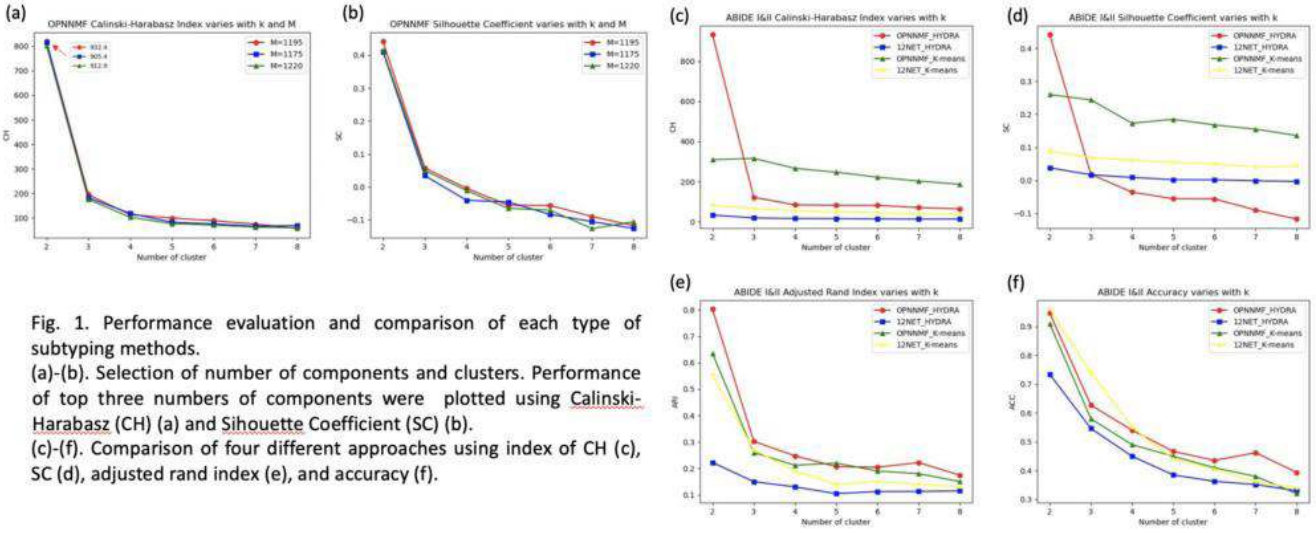

Fig. 1. Performance evaluation and comparison of each type of subtyping methods.
(a)-(b). Selection of number of components and clusters. Performance of top three numbers of components were plotted using Calinski-Harabasz (CH) (a) and Sihouette Coefficient (SC) (b).
(c)-(f). Comparison of four different approaches using index of CH (c), SC (d), adjusted rand index (e), and accuracy (f).

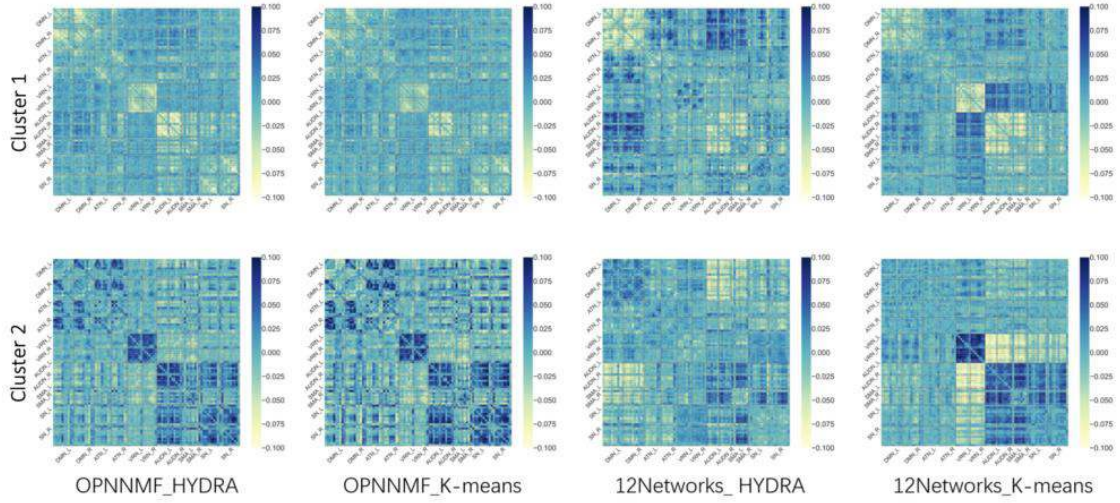

Fig. 2. Average functional connectivity matrices across two subtypes after four different clustering methods.

Conclusions: With a large cohort of ASD subjects, our results show that diagnosis-informed subtyping method performed better in terms of generating more distinct and reliable subtypes compared to unsupervised methods.

References
1. Arbelaitz, O., (2013), 'An extensive comparative study of cluster validity indices', Pattern Recognition: The Journal of the Pattern Recognition Society, vol. 46, no.1.
2. Caliński, T., (1974), 'A dendrite method for cluster analysis', Communications in Statistics, pp. 1-27.
3. Han, S., et al. (2019), 'The distinguishing intrinsic brain circuitry in treatment-naieve first episode schizophrenia: Ensemble learning classification', Neurocomputing, 365 (Nov.6), pp. 44-53 .
4. Hong, S.J., et al. (2019), 'Atypical functional connectome hierarchy in autism', Nat Commun. 2019 Mar 4;10(1):1022.
5. Hubert, L., (1985), 'Comparing partitions', J. Classif, vol. 2, no. 1, pp. 193-218.
6. Lombardo, M.V., et al. (2019), 'Big data approaches to decomposing heterogeneity across the autism spectrum'. Mol Psychiatry. 2019 Oct;24(10):1435-1450.
7. Rousseeuw, P.J., (1984), 'Silhouettes: A Graphical Aid to the Interpretation and Validation of Cluster Analysis', Journal of Computational and Applied Mathematics, pp. 53-65
8. Wen, J., et al. (2021), 'Multi-scale semi-supervised clustering of brain images: deriving disease subtypes', Medical Image Analysis.

Poster No 1427

Confound-free hand grip strength prediction: Synergy of advanced machine learning and neuroimaging

Vera Komeyer[1,2,3], Simon Eickhoff[1,2], Jan Kasper[1,2], Christian Grefkes[4,5], Kaustubh Patil[1,2], Federico Raimondo[1,2]

[1]Institute of Systems Neuroscience, Medical Faculty, Heinrich-Heine University Düsseldorf, Duesseldorf, Germany, [2]Institute of Neuroscience and Medicine (INM-7: Brain and Behaviour), Research Center Juelich, Juelich, Germany, [3]Department of Biology, Faculty of Mathematics and Natural Sciences, Heinrich-Heine-University Duesseldorf, Duesseldorf, Germany, [4]Department of Neurology, University Hospital Frankfurt, Goethe University Frankfurt, Frankfurt am Main, Germany, [5]Department of Neurology, University Hospital Cologne and Medical Faculty, University Cologne, Cologne, Germany

Introduction: Hand grip strength (HGS) not only reflects overall strength, but is also closely related to physical disability, cognitive decline and mortality[2,8,5]. Recognized by the WHO as a key marker for vitality in aging populations[1], HGS is a cost-efficient and reliable measure in clinical practice. Despite its ubiquity, the neural mechanisms governing HGS remain unclear. Our study systematically developed and evaluated the combination of neuroimaging-derived features with machine learning models to predict HGS. The aim was to identify models that are solely driven by brain information free from confounding factors such as sex, age and body composition, of which particularly sex but als age strongly correlates with HGS. Such confound-free models are essential to shed light on the neural basis of HGS.

Methods: We predicted HGS from 9 feature categories in the UK Biobank[3] (N = 22554-33136) including gray matter volume (GMV)[10], functional fALFF, LCOR, GCOR[7] (each 1088 ROIs), cortical thickness, white surface area, white matter hyperintensity (WMH) with PSMD[4], gray white contrast and a collection of 6 white matter microstructural characteristics (Fractional Anisotropy (FA), Mean Diffusivity (MD), free water volume fraction (ISOVF), orientation dispersion index (OD), intra-cellular volume fraction (ICVF), diffusion tensor mode (MO)). For each of the 9 categories 80% data were used to train seven algorithms in a 5-fold (nested) cross validation (CV) (Fig. 1A). Features were univariately, linearly adjusted for six confounder setups (Fig. 1B) in a CV-consistent manner. A final model was trained on the entire training data for out of sample (OOS) predictions on 20% held-out test data. Because of the particularly high influence of sex on linear predictions but less on non-linear predictions (Fig. 1B), we additionally classified sex with a XGBoost classifier with and without linear sex-adjustment to investigate the residual non-linear sex information after confound removal. The same analyses were performed on sex-split data. Six most successful sex-split and age-regressed models underwent SHAP analysis[6] to investigate relevant features for successful models.

Results: The sex-mixed sample analysis identified GMV, white surface, fALFF and white matter as most predictive features (Fig. 1B). Predictability decreased noticeably when adjusting for sex and age, but didn't drop further when removing more confounders (Fig. 1B). Non-linear algorithms performed better than linear ones in the sex-age-adjusted scenario (Fig. 1B purple vs. blue). Classifying sex with and without linear removal of sex suggests that non-linear algorithm superiority is driven by residual non-linear sex information in the features (Fig. 1C). Nonetheless, non-linear approaches also showed superior performance in "sex-split" models, even after controlling for age (Fig. 1D). GMV, fALFF and white matter were most resilient for this very stringent confounder control (Fig. 1D). For these three feature categories XGBoost excelled other non-linear algorithms, leading to the six (3 per sex) best models: r(m)GMV = 0.18, r(f)GMV = 0.20; r(m)fALFF = 0.18, r(f)fALFF = 0.23; r(m) WM = 0.21, r(f)WM = 0.23 (Fig. 1F). Interpretative SHAP analyses suggested GMV's importance in anterior globus pallidus (Fig.

2A, B) and microstructural characteristics of sensory input bundles to the thalamus and thalamo-cortical tracts (Fig. 2E, F) as neural correlates for successful, confound-free HGS predictions.

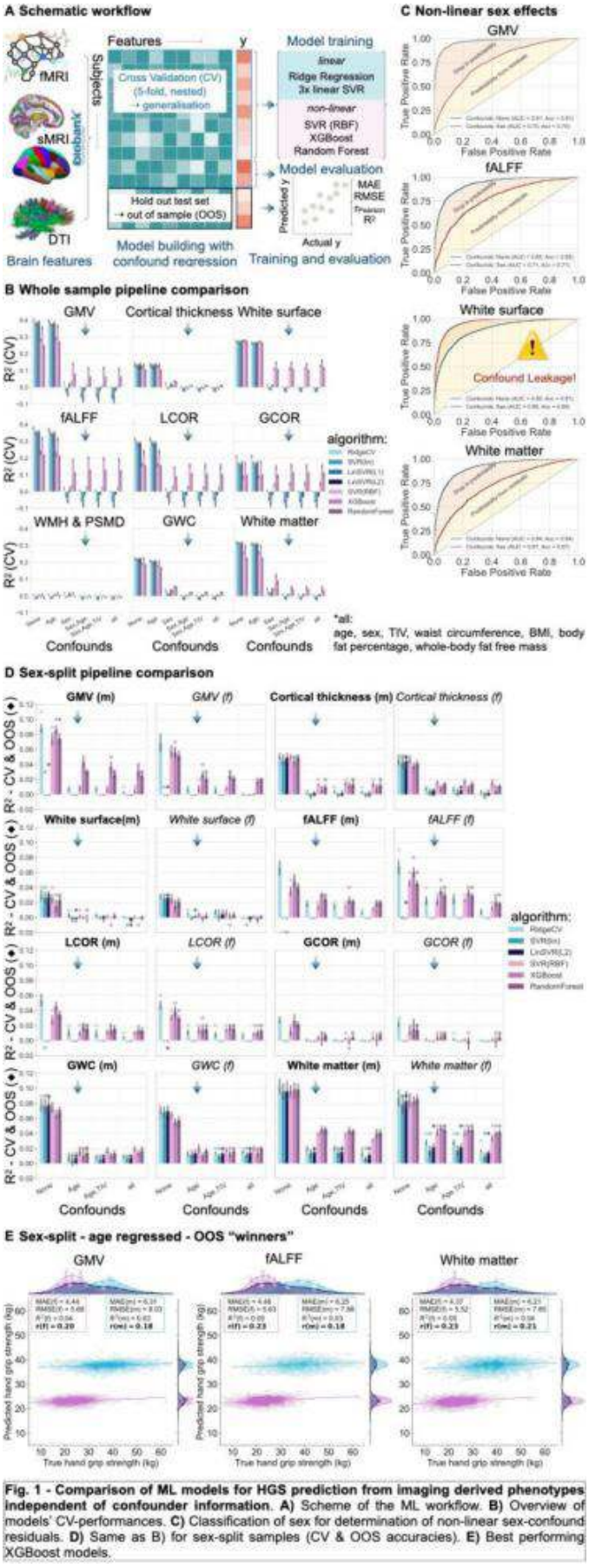

Fig. 1 - Comparison of ML models for HGS prediction from imaging derived phenotypes independent of confounder information. A) Scheme of the ML workflow. **B)** Overview of models' CV-performances. **C)** Classification of sex for determination of non-linear sex-confound residuals. **D)** Same as B) for sex-split samples (CV & OOS accuracies). **E)** Best performing XGBoost models.

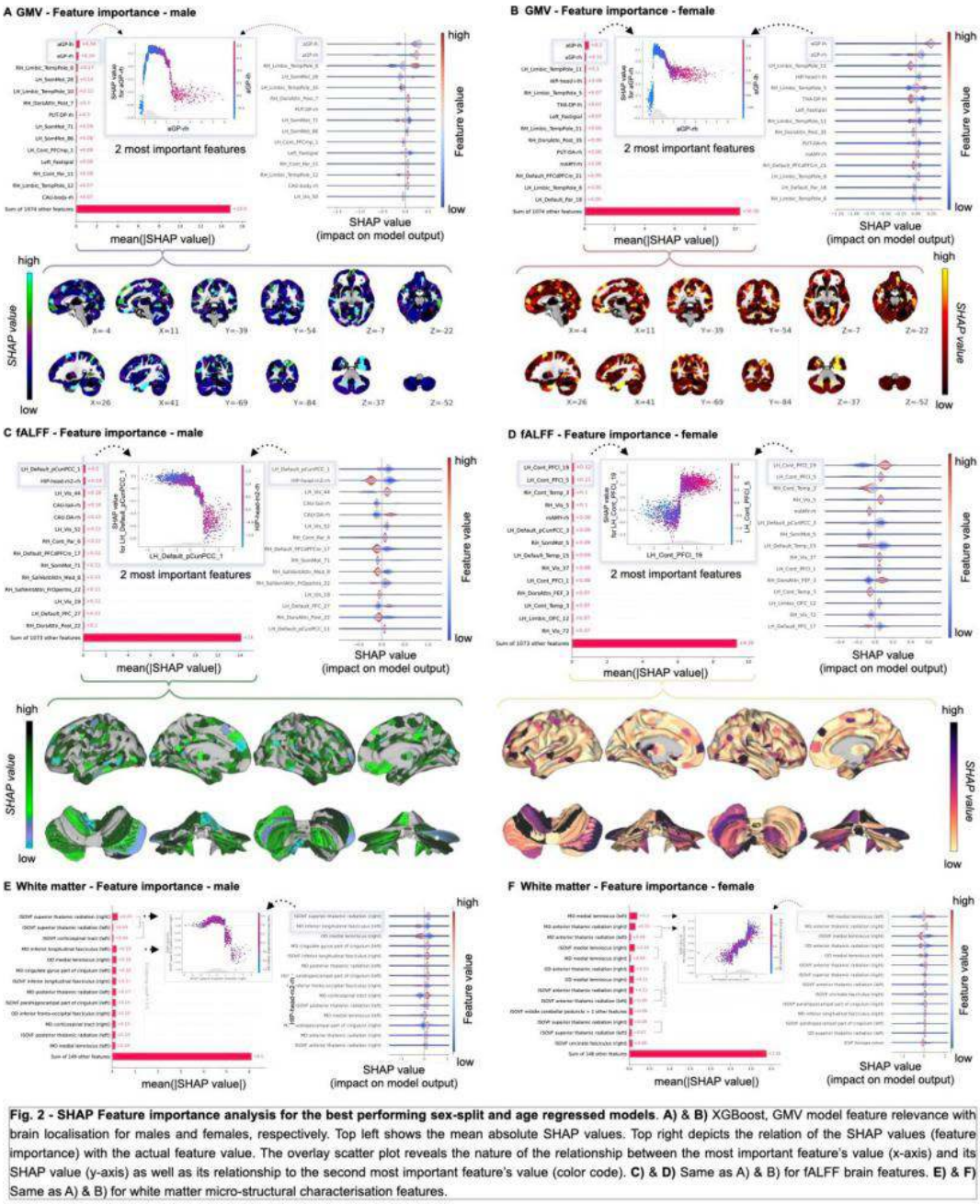

Fig. 2 - SHAP Feature importance analysis for the best performing sex-split and age regressed models. A) & B) XGBoost, GMV model feature relevance with brain localisation for males and females, respectively. Top left shows the mean absolute SHAP values. Top right depicts the relation of the SHAP values (feature importance) with the actual feature value. The overlay scatter plot reveals the nature of the relationship between the most important feature's value (x-axis) and its SHAP value (y-axis) as well as its relationship to the second most important feature's value (color code). **C) & D)** Same as A) & B) for fALFF brain features. **E) & F)** Same as A) & B) for white matter micro-structural characterisation features.

Conclusions: Our exhaustive evaluation of ML models and features from diverse MRI modalities identified six effective models for predicting HGS under stringent confounding constraints. Such strict constraints allow us to conclude that the successful models rely on neural information independent of any sex and linear age signal in the features. Further investigations will delve into feature collinearities and the intricate interplay of feature modalities to gain a better understanding of the underlying biology.

References

1. Afable, S. B. (2022), 'Normative values of hand grip strength of older Filipinos aged 60 to 85 years', Aging Health Research, vol. 2, no. 4, p. 100108.
2. Alfaro-Acha, A. (2006), 'Handgrip strength and cognitive decline in older Mexican Americans', The Journals of GerontologySeries A Biological Sciences and Medical Sciences, vol. 61, no. 8, pp. 859–865.
3. Alfaro-Almagro, F. (2018), 'Image processing and Quality Control for the first 10,000 brain imaging datasets from UK Biobank', NeuroImage, vol. 166, pp. 400–424, doi: 10.1016/j.neuroimage.2017.10.034.
4. Baykara, E. (2016), 'A novel imaging marker for small vessel disease based on skeletonization of white matter tracts and diffusion histograms', Annals of Neurology, vol. 80, no. 4, pp. 581–592.
5. Leong, D. P. (2015), 'Prognostic value of grip strength: findings from the Prospective Urban Rural Epidemiology (PURE) study', The Lancet, vol. 386, no. 9990, pp. 266–273.
6. Lundberg, S. M. (2017), 'A unified approach to interpreting model predictions', Advances in Neural Information Processing Systems, vol. 30.

7. Omidvarnia, A. (2023), 'Is resting state fMRI better than individual characteristics at predicting cognition?', BioRxiv Preprint Server For Biology, pp. 2023–02.
8. Rantanen, T. (1999), 'Midlife hand grip strength as a predictor of old age disability', JAMA The Journal of the American Medical Association, vol. 281, no. 6, pp. 558–560.
9. Wagner, A. S. (2022), 'FAIRly big: A framework for computationally reproducible processing of large-scale data', Nature Scientific Data, vol. 9, no. 80, p. 25.

Poster No 1428

Decoding Neuronal Dynamics: Chaotic Deep Learning for Major Depressive Disorder Classification

Yi-Ju Lee[1,2]

[1]Institute of Statistical Science, Academia Sinica, Taipei City, Taiwan, [2]Smart Healthcare Project, Academia Sinica, Taipei City, Taiwan

Introduction: Navigating the intricacies of Major Depressive Disorder (MDD) proves challenging due to its roots in diverse neurotransmitters, neural circuits, and hormonal systems, making reliance on subjective self-reported symptoms for diagnosis difficult. In the realms of physical statistics, artificial intelligence (AI), and medical research, the amalgamation of complexity science emerges as a robust avenue for extracting vital health insights from intricate medical data, particularly within psychiatry. Innovations such as ChaosNet, an AI model rooted in chaos theory, show promise in faithfully simulating human neuronal firing patterns at a network scale. Concurrently, power law scaling serves to quantify the complexity of brain signal dynamics. In this research, leveraging fMRI data, we aim to scrutinize classification models for MDD diagnosis, integrating the concept of complex systems at different stages of the model analysis process. This comprehensive approach seeks to advance MDD diagnosis by embracing a holistic perspective grounded in the principles of complex systems.

Methods: Participants with structural and fMRI images, demographic and clinical data were selected from the Strategic Research Program for Brain Sciences (SRPBS) cohort. Brain imaging data of 400 age and sex-matched, right-handed MDD patients (age mean = 40.21 ± 7.35; male = 49.5%) and 400 health adults (age mean = 39.46 ± 8.01) were retrieved. The functional images were pre-processed. The power-law scaling of brain activity of each voxel was extracted and transformed into a heatmap for model training. The images were split randomly in the ratio of 8:1:1 for the training, testing, and validation data set. We use ChaosNet and DenseNet 121 as model backbone, and they were trained using Python 3.8 for 500 epochs with 1 Nvidia DGX A100 (40G) GPU.

Results: In contrast to using typical fMRI BOLD signal as input to DenseNet 121, our result has suggested that the complexity-transformed image data with ChaosNet show significant decreased training time from 48.3 hours to 1.12 hours with similar classification results. In the best-performing model, the average testing accuracy is 92.3. We also identified the key brain regions that is related to MDD, such as prefrontal cortex, hippocampus and amygdala. under Bonferroni correction.

Conclusions: This study presents robust biological evidence surpassing previous methods in identifying MDD. We employ signal complexity within chaotic-based models to detect abnormal brain activities in MDD patients, necessitating expertise in statistical science, computer science, and neurosciences. The observed alterations in pathological hemodynamics in MDD suggest a significant loss of brain signal complexity, potentially contributing to precise clinical diagnosis. Our approach harnesses the unique properties of chaotic neurons, proving more efficient than alternative models. The future work will require exploring the integration of genetic data to subtype MDD patients, aiming to enhance our understanding of this complex disorder.

References

1. Balakrishnan, H. N, (2019). 'ChaosNet: A chaos based artificial neural network architecture for classification.', Chaos: An Interdisciplinary Journal of Nonlinear Science, vol. 29, pp.11.
2. Chen, Q., Bi (2022). 'Regional amplitude abnormities in the major depressive disorder: A resting-state fMRI study and support vector machine analysis. Journal of affective disorders', vol. 308, pp. 1-9.
3. Lee, Yi-Ju (2021), 'Alteration of power law scaling of spontaneous brain activity in schizophrenia.' Schizophrenia Research, vol. 238, pp. 10-19.
4. Mousavian, M., (2021). 'Depression detection from sMRI and rs-fMRI images using machine learning.' Journal of Intelligent Information Systems, vol. 57, pp. 395-418.

Poster No 1429

Stacking models of brain dynamics improves prediction of subject traits in fMRI

Ben Griffin[1], Christine Ahrends[2], Fidel Alfaro Almagro[3], Mark Woolrich[4], Stephen Smith[4], Diego Vidaurre[5]

[1]Oxford University, Oxford, Oxford, [2]Aarhus University, Aarhus, Aarhus, [3]WiN FMRIB - University of Oxford, Oxford, Oxfordshire, [4]University of Oxford, Oxford, Oxfordshire, [5]Aarhus University, Aarhus, Aarhus C

Introduction: Beyond structural and static brain measures, brain dynamics can add important information when investigating individual cognitive traits[1]. One way to look at dynamics is through the Hidden Markov Model (HMM), a probabilistic model of temporal dynamics of functional connectivity, which can be combined with machine learning models to generate subject-specific trait predictions[1]. However, there are two potential sources of variability in these predictions. First, the run-to-run variability (e.g., due to different initialisations)[2]; and second, the choice of hyperparameters (e.g., number of HMM states). We propose an approach that leverages this variability to improve prediction accuracy by combining information from different models and runs. We implement a stacked generalisation scheme[3,4] that combines predictions from multiple models of brain dynamics to accomplish two goals: (i) produce robust predictions across multiple cognitive traits; (ii) improve prediction accuracy by combining predictions created by HMMs with varying hyperparameters.

Methods: We aimed to predict cognitive traits for subjects in the Human Connectome Project (HCP)[5] and UK Biobank[6] datasets using models based on their resting-state fMRI functional connectivity dynamics. To achieve this, we used a group-level HMM on surface-based node timeseries concatenated across all subjects, which were generated using 25-dimensional group-ICA surface maps[1,7]. Subsequently, subject-specific HMM parameters were "dual-estimated" using the parameters obtained from the group-level HMM, which involved generating subject-specific state-time courses, from which subject-specific HMM parameters were inferred[1]. We then used the Fisher kernel method, a mathematically principled way of combining generative models (here, the HMM) with discriminative methods (here, kernel ridge regression)[8]. This method operates directly on the Riemannian manifold of the HMM parameters, capturing the natural geometry of the HMM. We are able to construct a The method constructs a subject-by-subject matrix that quantifies the similarities between subjects by examining how the HMM likelihood function varies locally with respect to the subjects' HMM parameters. This entire process was repeated 100 times; applying the HMM 50 times with fixed hyperparameters but different random initialisations (to investigate the HMM run-to-run variability) and 50 times with varying hyperparameters (to investigate hyperparameter selection variability). Separately for each group-level HMM, Fisher kernels were computed and used with kernel ridge regression to produce subject-specific predictions, which were subsequently combined using stacking[3].

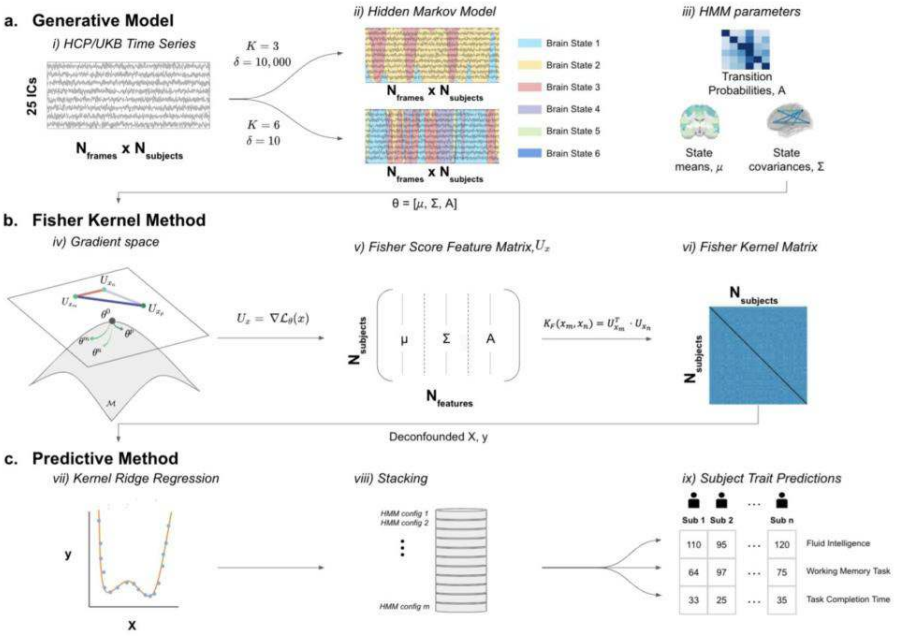

Figure 1: *Procedure for predicting subject traits from resting-state fMRI (rfMRI) timeseries. (a) Generative Model.* (i) HMMs are trained on the rfMRI timeseries in groupICA parcellations with 25 ICs concatenated across subjects. (ii) Different HMM hyperparameters lead to different models of brain dynamics. (iii) The HMM is described by a set of model parameters (θ). (b) Fisher Kernel Method. (iv) Fisher scores are generated for each subject's parameter set by taking the derivative of the log-likelihood with respect to each parameter. (v) The Fisher scores are vectorised for each subject and combined to form the Fisher score feature matrix. (vi) We then construct the practical Fisher kernel from all subjects' Fisher scores to form the Fisher kernel matrix. (c) Predictive Method. (vii) The Fisher kernel matrix is used in a kernel ridge regression model to predict subject traits. (viii) This process is repeated for multiple HMMs independently and combined using stacking. (ix) This last step is carried out independently to predict multiple cognitive traits.

Results: By combining predictions generated using the Fisher kernel method from group-level HMMs, we achieve our first goal (i) of producing a robust prediction across traits. Furthermore, by varying the hyperparameters of the HMM, our second goal (ii) of improving prediction accuracy is achieved. The diversity created by varying the HMM hyperparameters enabled distinct yet complementary predictions to be generated, and stacking resulted in boosting the prediction accuracy. Stacking performs particularly well when, for a given trait, certain predictions are much better than the remaining predictions (e.g., see Figure 2b 'Pic_Vocab_Unadj').

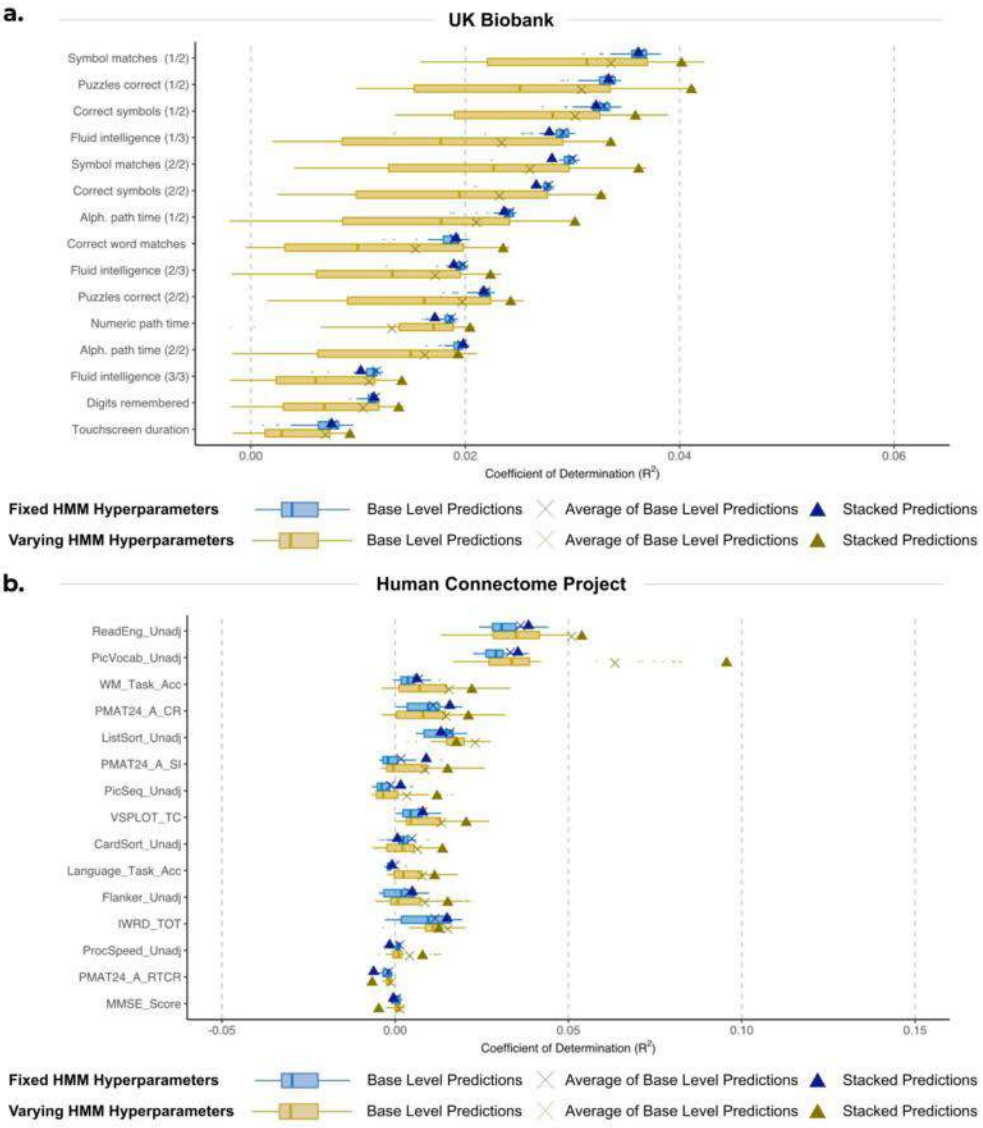

Figure 2: *Comparison of performance for base-level predictions and stacking predictions from HMMs with varying hyperparameters against HMMs with fixed hyperparameters.* Performance of stacking across subject traits for (a) UKB and (b) HCP. Boxplots show the R^2 scores between observed subject traits and base-level predictions generated from 50 HMMs. These are compared to the R^2 scores when we combine the base-level predictions by taking the average of them (×) and by stacking (▲). Blue represents the results of using HMMs with fixed hyperparameters and yellow represents HMMs with varying model hyperparameters.

Conclusions: For predictions to be useful (e.g., in a clinical setting), we require that they are both robust and accurate. We used the Fisher kernel method, leveraging the natural geometry of the HMM, to generated accurate predictions. To enhance robustness and accuracy further, we employed stacking, combining predictions from different HMM configurations that captured distinct patterns in the data. Looking forward, stacking predictions opens up avenues for integrating a wider variety of data or models, for example combining predictions from different brain imaging modalities, or static functional connectivity and structural information.

References

1. Vidaurre, Diego (2021). "Behavioural relevance of spontaneous, transient brain network interactions in fMRI". In: NeuroImage 229, p. 117713.
2. Vidaurre, Diego (2019). "Stable between-subject statistical inference from unstable within-subject functional connectivity estimates". In: Human brain mapping 40.4, pp. 1234–1243.

3. Wolpert, David H (1992). “Stacked generalization”. In: Neural networks 5.2, pp. 241–259.
4. Engemann, Denis A (2020). “Combining magnetoencephalography with magnetic resonance imaging enhances learning of surrogate biomarkers”. In: Elife 9, e54055.
5. Van Essen, David C (2013). “The WU-Minn human connectome project: an overview”. In: Neuroimage 80, pp. 62–79.
6. Sudlow (2015). “UK biobank: an open access resource for identifying the causes of a wide range of complex diseases of middle and old age”. In: PLoS medicine 12.3, e1001779.
7. Vidaurre (2017). “Brain network dynamics are hierarchically organized in time”. In: Proceedings of the National Academy of Sciences 114.48, pp. 12827–12832.
8. Jaakkola (1998). “Exploiting generative models in discriminative classifiers”. In: Advances in neural information processing systems 11.

Poster No 1430

Computer-Aided Diagnosis and Treatment for Hemorrhagic Stroke

Minyue Liu[1], Hengyuan Ma[2], Jiawei Zhang[2], Tianye Jia[2]

[1]Fudan University, Shanghai, Shanghai, [2]Fudan University, Shanghai, Shanghai

Introduction: Hemorrhagic stroke is a disease caused by the sudden rupture of a cerebral aneurysm or leakage due to weakened blood vessels, leading to disturbances in cerebral blood circulation. In patients with vascular diseases, various factors can induce narrowing, occlusion, or rupture of cerebral arteries, resulting in acute cerebral hemorrhage. (Caplan et al, 2023) Clinically, this manifests as temporary or permanent symptoms and signs of brain dysfunction.Hemorrhagic stroke onset is rapid, progression is rapid, and prognosis is poor, with a mortality rate as high as 45-50% during the acute phase. About 80% of patients will leave behind significant neurological dysfunction, bringing a heavy health and financial burden to society and the patients’ families.(Thakur et al, 2022)Therefore, it is of significant clinical importance to identify the risk factors of hemorrhagic stroke, integrate imaging characteristics, clinical patient information, and clinical treatment plans to precisely predict patient prognosis and optimize clinical decisions accordingly.

Methods: The aim of this study was to utilize clinical information and imaging data from stroke patients to analyze and predict the expansion of hematomas and the progression of edema, and to reveal the correlation between treatment modalities and the degree of patient recovery.We acquired 100 CT images from the hospital, in which they were patients with the different stage of stroke with clinical data.Initially, we applied the Naive Bayes method to predict the expansion of hematomas. Concurrently, a dual-exponential model was employed to model the temporal evolution of brain edema volume in patients, serving as the basis for patient classification.The time constant in the model reflected the time-course characteristics of the two edema mechanisms, which was corroborated by clinical data.We applied grouping as a prior for non-parametric probability inference, and further discussed the correlation between different treatment modalities and edema volume groups.Additionally, we utilized ordered logistic regression to predict the clinical prognosis within 90 days based on patient population-level clinical data and initial and follow-up imaging data.Finally, we employed the LIME method for personalized clinical prognostic factor analysis, obtaining an ordering of prognostic key factors applicable to individual patients.

Results: The average accuracy of our model on the validation set just with the clinical data is 0.7400, with a standard deviation of 0.3040, indicating that our model possesses a certain degree of generalization capability.After learning, the accuracy of our model on the training set is 0.91.By integrating the model with clinical data, it was discovered that the edema in the mild group was predominantly caused by cytotoxic edema, while the edema in the moderate and severe groups was primarily due to secondary vasogenic edema. Additionally, it was found that incorporating follow-up imaging data could reduce the prediction error by 30% on the validation set, and provided conclusions consistent with existing literature and testable new clinical recommendations.

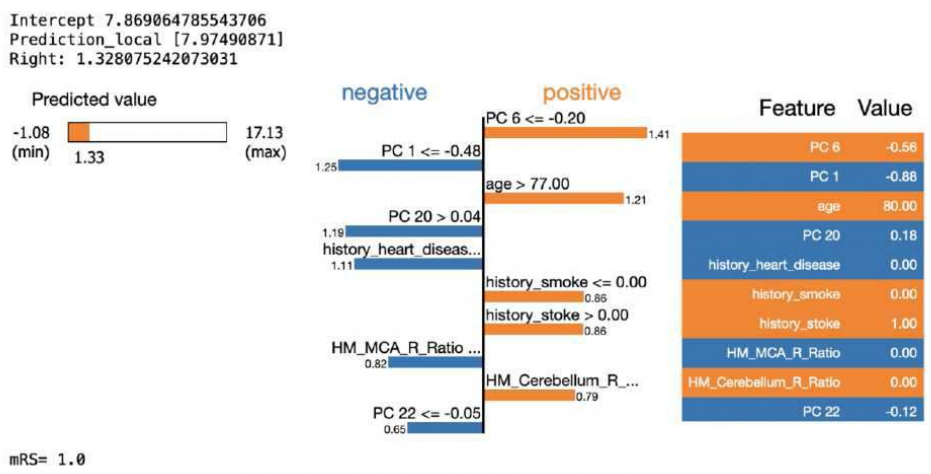

Fig 1. Predictive variable explanation with LIME method for rms classification by training set individual sub010

Conclusions: In our statistical prediction at the group level, certain clinical and imaging information significantly affect the 90-day mRS scores of stroke patients.However, the specific impact of each factor and the prioritization of their importance vary from individual to individual.Therefore, it is imperative to utilize big data to train statistical models at the group level and then employ the LIME method for personalized analysis at the individual level. Such an approach is essential for the prediction and diagnosis of mRS. After training the model using big data, employing personalized and interpretative methods such as the LIME method for precision medicine is also a future trend in the development of medical artificial intelligence.

References

1. Caplan, L. R., Simon, R. P., & Hassani, S. . (2023). Cerebrovascular disease—stroke. Neurobiology of Brain Disorders (Second Edition), 457-476.
2. Thakur, A., Bhanot, S., & Mishra, S. N. . (2022). Early diagnosis of ischemia stroke using neural network.

Poster No 1431

Magnetic resonance-based eye tracking can detect subject arousal state

Rongjie Hu[1], Jie Liang[1], Yiwen Ding[2], Shuang Jian[2], Xiuwen Wu[1], Yanming Wang[1], Zhen Liang[2], Bensheng Qiu[1], Xiaoxiao Wang[1]

[1]University of Science and Technology of China, Hefei, China, [2]Anhui Medical University, Hefei, China

Introduction: Eye movements directly reflect human thoughts and play key roles in cognitive researches (Klein & Ettinger, 2019). fMRI combined with eye tracking provide a window into brain cognition and disease diagnosis (LaConte, Glielmi, Heberlein, & Hu, 2007). However, conventional eye tracking methods reliant on MRI-compatible equipment are expensive and intricate. Frey et al. designed an exciting CNN model 'DeepMReye' which performed camera-free eye tracking (Frey, Nau, & Doeller, 2021). But DeepMReye and our previous work (Wu et al., 2023) operate at interval of time of repetition (TR, in seconds), unable to fast eye movements such as blink and saccade. Therefore, we propose an eye-movement deep learning prediction pipeline, MRGazerII, which reads in fMRI slices and reports the eye movements at the interval of tens of milliseconds.

Methods: Our study employed data from the Human Connectome Project (HCP) 7T Movie release (Van Essen et al., 2013), in which subjects watched four movies with eye tracking (416 fMRI runs from 158 subjects). The eye balls were segmented by a binary morphology method, and the intermediate 6-layer slices of the eye balls were fed into the deep model. The model comprised a ResNet-CBAM backbone, a Transformer encoder and a fully connected layer for outputting slice-level eye movements (Fig 1a). Cross-individual 5-fold cross-validation was executed. Preprocessing procedures, including artifact removal, registration, and regression of 12 motion parameters and signals in ventricles (Jo, Saad, Simmons, Milbury, & Cox, 2010), were applied to HCP 7T Rest1 dataset. Poudel, Innes, Bones, Watts, and Jones (2014) has found the arousal state was correlated with long blink, thus, the subjects with eye tracking data (N=131) were separated into the high arousal group (long blink proportion < 5%, N=73) and low arousal group (long blink proportion > 5%, N=58, Fig 2a). Schaefer et al. (2017) 300 parcellations were then used to generate functional connectivity (FC). FCs-based behavioral prediction was also applied for predicting subjects list sorting score. In the feature selection step, Pearson correlation was performed between each edge and list sorting score across subjects in the training set, with top 3000 FCs being selected. Principal component analysis

reduced the selected 3000 FCs in training set to 30 dimensions. Linear support vector machine (SVM) regression was used for prediction, with 10-fold cross validation. Beyond training and validating in all the subjects, we trained and validated the behavior prediction in high arousal group, then tested it in the low arousal group, and vice versal.

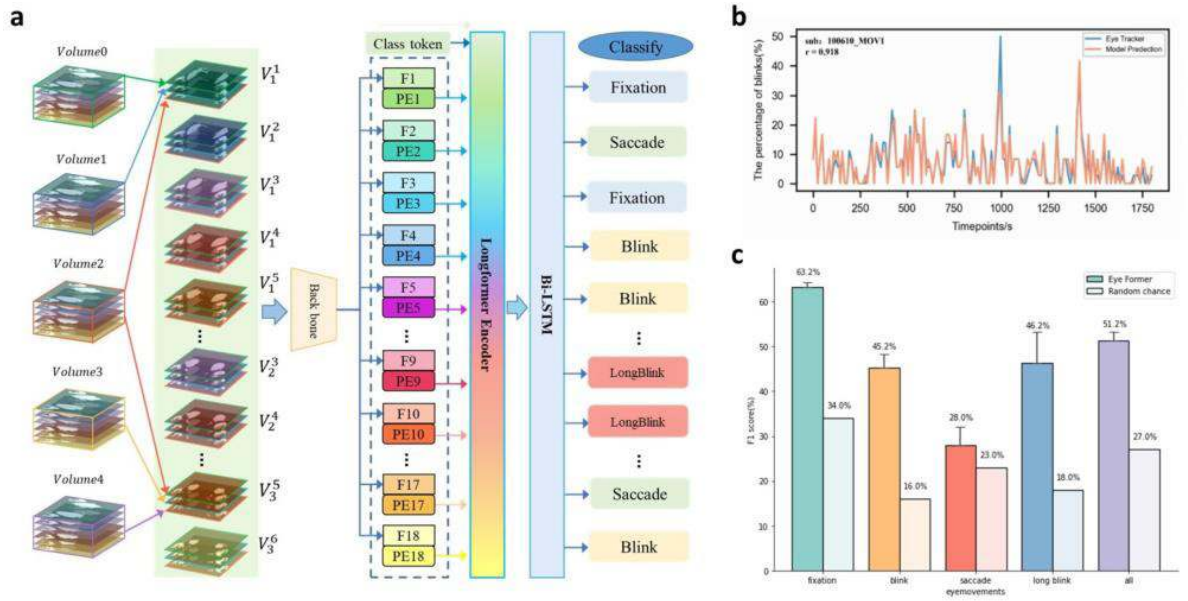

Fig 1. Model for eye movement time series classification (a), a sample illustration (b) and the model's performance (c).

Results: The proposed model achieves an f1-score of 51.2% in classifying eye movements with f1-scores of 63%, 45%, 28% and 43% for the fixation, blink, saccade and long blink respectively, surpassing the chance level (Fig 1c). Cross-dataset testing (training on HCP 7T Movie and Wu et al. (2023)'s dataset, testing on Zhang and Naya (2022)'s) reports an averaged accuracy of 38.0% (chance level at 26.0%). FC analysis reveals significantly reduced FCs in the high arousal group compared to the low arousal group (FDR corrected $p < 0.01$, Fig 2d). The FC-based behavior prediction achieves a Pearson's r=0.26 using data from all subjects. While training and validating on the high arousal group, the r increases to 0.38, but fails in the low arousal group (r<0.1). Training and validating on the low arousal group resulting in r=0.42, but fails in the high arousal group (r<0.1).

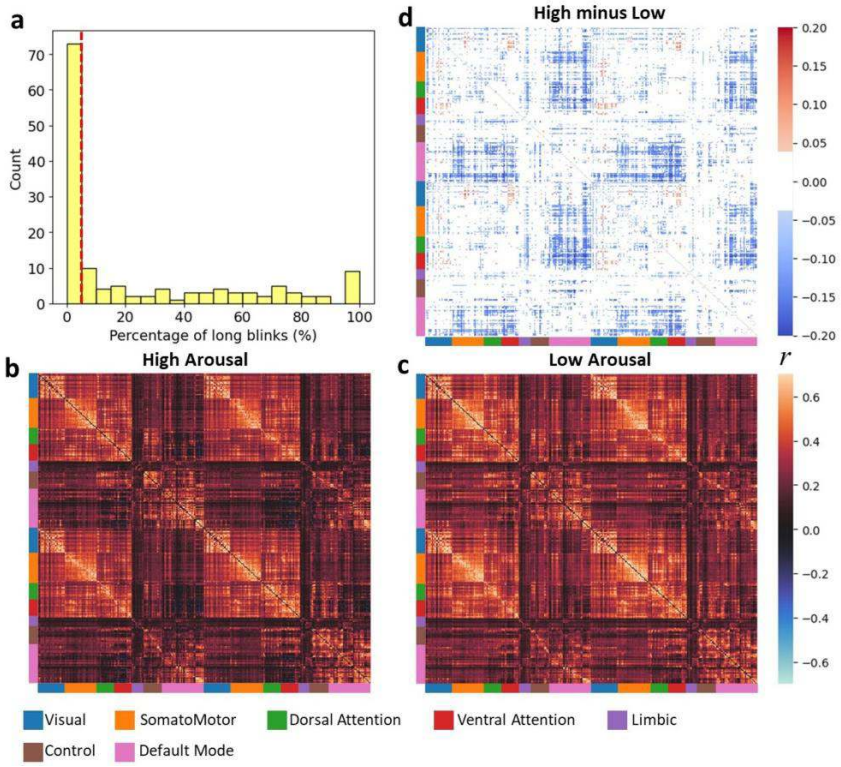

Fig 2. The histogram of proportion of long blinks (a); the FC of high arousal group (b) and low arousal group (c); group difference (d).

Conclusions: The proposed method, MRGazerII, can predict fixation, blink, long blink, saccade and fixation point in an acceptable accuracy at a fine interval of tens of milliseconds from fMRI data, both across individual and datasets. Eye movement based arousal grouping shows that the brain–phenotype model trained in one arousal state fails on another arousal state. This study underscores the indispensable role of eye tracking in understanding fMRI data and introduces MRGazerII as a solution.

References

1. Frey, M., Nau, M., & Doeller, C. F. (2021). Magnetic resonance-based eye tracking using deep neural networks. Nat Neurosci, 24(12), 1772-1779. doi:10.1038/s41593-021-00947-w
2. Jo, H. J., Saad, Z. S., Simmons, W. K., Milbury, L. A., & Cox, R. W. (2010). Mapping sources of correlation in resting state FMRI, with artifact detection and removal. Neuroimage, 52(2), 571-582. doi:https://doi.org/10.1016/j.neuroimage.2010.04.246
3. Klein, C., & Ettinger, U. (2019). Eye movement research: An introduction to its scientific foundations and applications: Springer Nature.
4. LaConte, S., Glielmi, C., Heberlein, K., & Hu, X. (2007). Verifying visual fixation to improve fMRI with predictive eye estimation regression (PEER). Paper presented at the Proc. Intl. Soc. Magn. Reson. Med.
5. Poudel, G. R., Innes, C. R. H., Bones, P. J., Watts, R., & Jones, R. D. (2014). Losing the struggle to stay awake: Divergent thalamic and cortical activity during microsleeps. Human Brain Mapping, 35(1), 257-269. doi:10.1002/hbm.22178
6. Schaefer, A., Kong, R., Gordon, E. M., Laumann, T. O., Zuo, X.-N., Holmes, A. J., . . . Yeo, B. T. T. (2017). Local-Global Parcellation of the Human Cerebral Cortex from Intrinsic Functional Connectivity MRI. Cereb Cortex, 28(9), 3095-3114. doi:10.1093/cercor/bhx179
7. Van Essen, D. C., Smith, S. M., Barch, D. M., Behrens, T. E. J., Yacoub, E., Ugurbil, K., & Consortium, W. U.-M. H. (2013). The WU-Minn Human Connectome Project: An overview. Neuroimage, 80, 62-79. doi:10.1016/j.neuroimage.2013.05.041
8. Wu, X., Hu, R., Liang, J., Wang, Y., Qiu, B., & Wang, X. (2023). MRGazer: Decoding Eye Gaze Points from Functional Magnetic Resonance Imaging in Individual Space. arXiv. doi:10.48550/arXiv.2311.13372
9. Zhang, B., & Naya, Y. (2022). A dataset of human fMRI/MEG experiments with eye tracking for spatial memory research using virtual reality. Data in Brief, 43, 108380. doi:https://doi.org/10.1016/j.dib.2022.108380

Poster No 1432

Stacking pre-trained classifiers across subjects improves fMRI task decoding accuracy

Himanshu Aggarwal[1], Bertrand Thirion[1]

[1]INRIA Saclay, France, Palaiseau, Ile-de-France

Introduction: Decoding refers to the process of inferring the stimuli from an individual's brain signals. In the context of task fMRI, high-dimensional voxel-wise BOLD activation patterns are used as features to decode the stimuli presented to the subject during the task. Imaging sessions are constrained by the time and resources available to researchers, resulting in a limited number of samples per subject. This leads to a suboptimal feature-to-instance ratio, causing low decoding accuracy. Many such small fMRI datasets are publicly available but hard to use due to their small sample sizes and domain-specific nature. Therefore, there is a need for methods that can leverage these data and can be used to efficiently transfer learning across subjects, tasks, and cohorts (Gu et al. 2022). In this study, we test a stacking approach for transfer learning across subjects within four small cohorts with a few trials of a given task.

Methods: In a conventional decoding setting, a classifier is trained to learn the mapping between stimuli labels and features in the voxel space. Here, we present a stacking approach where we train a classifier to learn the mapping between true stimuli labels and the stimuli predictions from classifiers pre-trained on other subjects' voxel-space features (Figure 1). This converts a high-dimensional problem (where the number of features is the number of voxels) to a low-dimensional one (where the number of features is one minus the number of subjects in the cohort). We compare the stacking approach against the conventional one in four different cohorts and tasks: BOLD5000 (Chang et al. 2019), Forrest (Hanke et al. 2015), Neuromod (Bellec and Boyle 2019), and RSVP (Pinho et al. 2020). We use trial-by-trial GLM parameter maps from each of these tasks. Each of these datasets has about 4-6 classes of stimuli to be decoded and hence has similar decoding complexity. We also compare the two decoding settings across two different feature spaces - full voxel space and 1024 modes of the DiFuMo atlas (Dadi et al. 2020) and use two different classifiers for decoding - linear SVC and random forest (Pedregosa et al. 2011). Within each cohort, we vary the size of the training set in increments of 10% of the samples available for each subject and always test the trained model on 10% of the samples.

Figure 1: Stacking involves (top) pre-training separate classifiers for each of N-1 subjects and then (bottom) training a final classifier to learn the mapping between each of their predictions and the true labels for Nth subject.

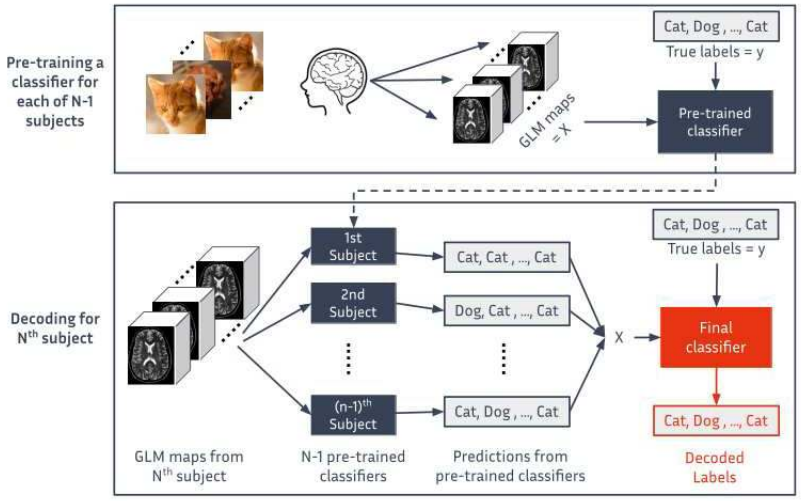

Results: As can be seen in Figure 2 (a), the stacking approach achieves the highest average accuracy within three (Neuromod, Forrest, and RSVP) of the four cohorts. For the Neuromod dataset, the best-performing scenario at an average accuracy of 80% is that of the stacking approach using the full voxel space and linear SVC classifier (Figure 2 (a)). For this dataset, we also see a maximum average gain (accuracy of stacking - accuracy of conventional setting) ranging between 15-22% (Figure 2 (b) and (c)). In contrast, for BOLD5000 (having only 3 subjects), the stacking approach performs worse than the conventional one across all classification scenarios.

Figure 2:

(a) Average decoding accuracies from stacking and conventional approach when using different features and classifiers

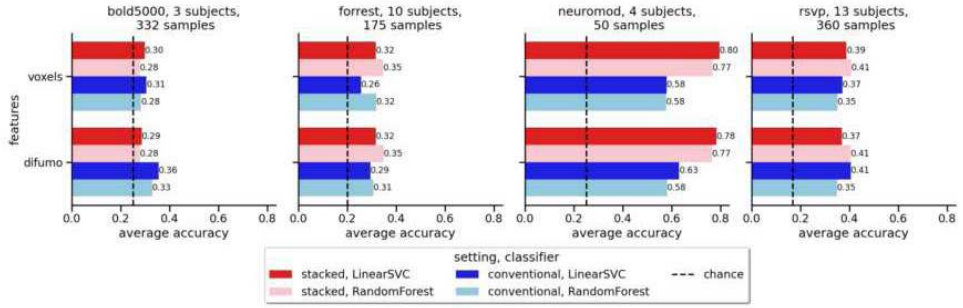

(b) Decoding accuracy across training sizes when using all voxels as features

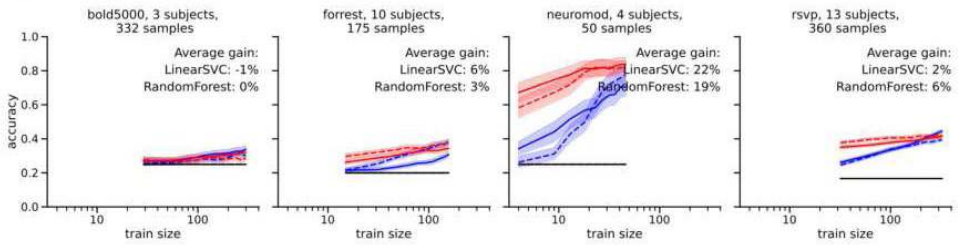

(c) Decoding accuracy across training sizes when using 1024 dimensions from DiFuMo atlas as features

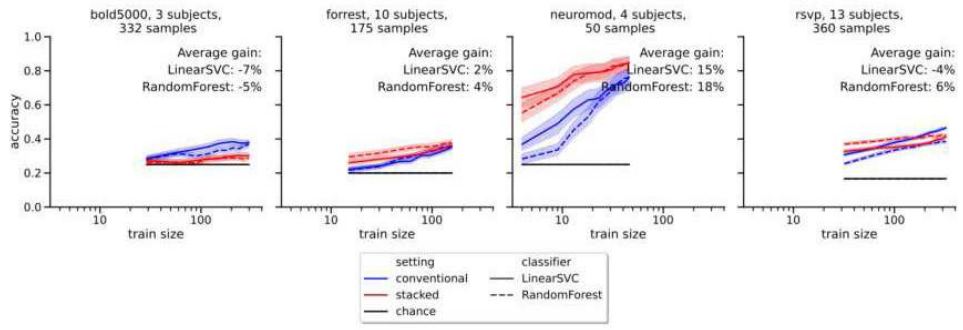

Conclusions: The stacking approach presented in this study improves decoding performance, specifically in small training samples. This demonstrates a direct application for cohorts with small samples (like Neuromod). Since the final classifier in this method encounters a low dimensional feature space (one minus the number of subjects), the performance can be further improved by using a random forest classifier instead of linear SVC. This is especially true for relatively larger cohorts (like Forrest and RSVP). While the stacking approach works as well on reduced data (as with the DiFuMo approach), the benefits are less clear in the latter case, given that overfitting risks are lower. Finally, if the number of subjects in the cohort is too low, the method performs worse than conventional, as observed in BOLD5000. Overall, this suggests that off-the-shelf classifiers can chart the space of cognitive domains, which calls for a generalization of this approach across datasets.

References

1. Bellec, Pierre, and Julie Boyle. 2019. "Bridging the Gap between Perception and Action: The Case for Neuroimaging, AI and Video Games." PsyArXiv. https://doi.org/10.31234/osf.io/3epws.
2. Chang, Nadine, John A. Pyles, Austin Marcus, Abhinav Gupta, Michael J. Tarr, and Elissa M. Aminoff. 2019. "BOLD5000, a Public fMRI Dataset While Viewing 5000 Visual Images." Scientific Data 6 (1): 49. https://doi.org/10.1038/s41597-019-0052-3.
3. Dadi, Kamalaker, Gaël Varoquaux, Antonia Machlouzarides-Shalit, Krzysztof J. Gorgolewski, Demian Wassermann, Bertrand Thirion, and Arthur Mensch. 2020. "Fine-Grain Atlases of Functional Modes for fMRI Analysis." NeuroImage 221 (November): 117126. https://doi.org/10.1016/j.neuroimage.2020.117126.
4. Gu, Zijin, Keith Jamison, Mert Sabuncu, and Amy Kuceyeski. 2022. "Personalized Visual Encoding Model Construction with Small Data." Communications Biology 5 (1): 1–12. https://doi.org/10.1038/s42003-022-04347-z.
5. Hanke, Michael, Richard Dinga, Christian Häusler, J. Swaroop Guntupalli, Michael Casey, Falko R. Kaule, and Jörg Stadler. 2015. "High-Resolution 7-Tesla fMRI Data on the Perception of Musical Genres – an Extension to the Studyforrest Dataset." F1000Research. https://doi.org/10.12688/f1000research.6679.1.
6. Pedregosa, Fabian, Gael Varoquaux, Alexandre Gramfort, Vincent Michel, Bertrand Thirion, Olivier Grisel, Mathieu Blondel, et al. 2011. "Scikit-Learn: Machine Learning in Python." The Journal of Machine Learning Research 12: 2825--2830. https://www.jmlr.org/papers/volume12/pedregosa11a/pedregosa11a.pdf.
7. Pinho, Ana Luísa, Alexis Amadon, Baptiste Gauthier, Nicolas Clairis, André Knops, Sarah Genon, Elvis Dohmatob, et al. 2020. "Individual Brain Charting Dataset Extension, Second Release of High-Resolution fMRI Data for Cognitive Mapping." Scientific Data 7 (1): 353. https://doi.org/10.1038/s41597-020-00670-4.

Poster No 1433

Multimodal connectivity-based graph transformer networks and its application to sex classification

Hye Won Park[1], Won Hee Lee[1]

[1]Kyung Hee University, Yongin, Republic of Korea

Introduction: The integration of multimodal brain imaging data and the use of graph-based approaches have emerged as powerful tools for gaining deep insights into the complex relationships and topological characteristics of brain connectivity[1,2]. The combination of structural connectivity (SC) derived from diffusion tensor imaging (DTI) and functional connectivity (FC) obtained from functional MRI (fMRI) provides a comprehensive representation of brain connectivity, encompassing both the physical connections between brain regions and their dynamic interactions[3]. By analyzing these modalities in conjunction, researchers can uncover brain patterns that may be obscured when examining each modality in isolation. In this context, we propose a new method that leverages a graph transformer network (GTN) to fuse multimodal connectivity information, and evaluate its performance on sex classification. We also identify important nodes to provide insights into the roles of specific brain regions in the sex classification task.

Methods: We used SC and resting-state FC data of 753 healthy individuals derived from the Human Connectome Project (HCP)[4,5]. Cortical regions were defined based on the 400-region Schaefer parcellation[6]. SC was computed using fiber tractography and a log transformation of stream counts was applied. FC was generated using Pearson's correlation of fMRI signals between regions of interest (ROIs). Figure 1(a) shows the pipeline of the proposed model. For each subject, both SC and FC graphs were created, where rows and columns represent nodes and their features, respectively. The edges were derived from Euclidean distances between ROI pairs of MNI 152 centroid coordinates. A Gaussian kernel was employed to distances, retaining the top 1% of connections. Both graphs were trained with the graph transformer[7], followed by batch normalization and parametric ReLU. To fuse graphs, we combined the nodes of two graphs using learnable weights (θ_1 and θ_2) using weighted summation. The edges and their features in a fusion graph were trained using XGBoost (Figure 1(b)). SHAP[8] was employed to assess feature importance, retaining the top 1% of connections. Edge features were defined by concatenating the filtered SC, FC, and centroid distances. After applying adjacency dropout, the GTN updated node features considering edge features. Concatenating pooling was applied to merge features from all nodes, followed by sex classification using fully connected layers. Salient nodes were identified using GNNExplainer[9]. The model was evaluated using a 10-fold cross-validation and compared to single modality-based GTN models.

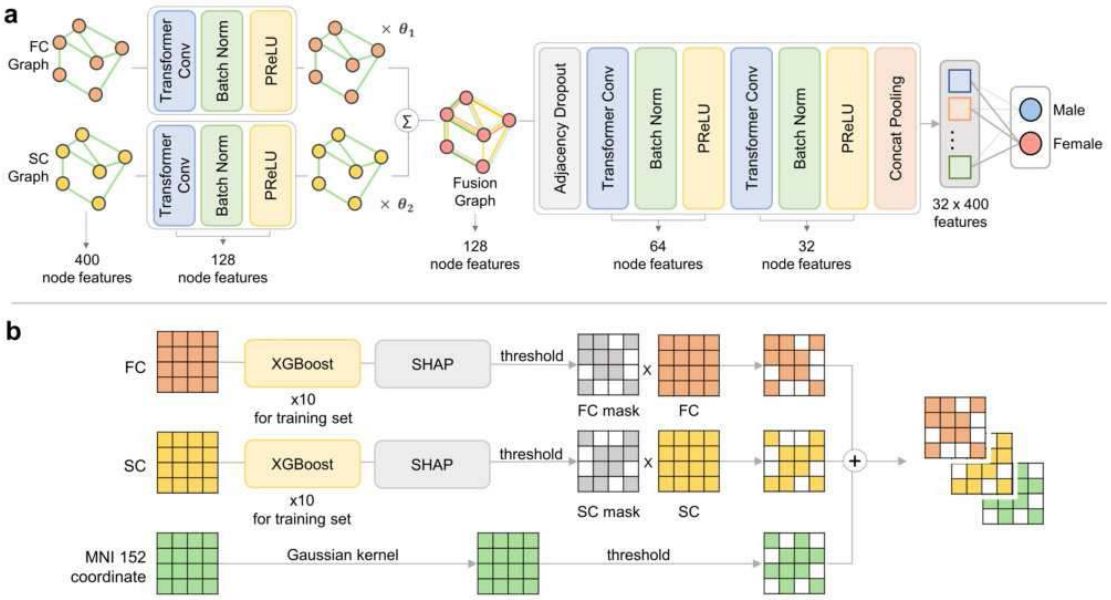

Figure 1. (a) An overview of our GTN-based classification framework. In the first graph transformer layer, edges are represented as binary values derived from MNI 152 coordinates distances. The entire model is trained in a single backpropagation. (b) The workflow for computing edge features of fusion graph. XGBoost was trained using vectorized upper triangular entries of each connectivity. The 10-fold cross-validation strategy is applied exclusively to the training set for training and evaluating XGBoost, and SHAP values are calculated. Three-dimensional features are used to define the edges of fusion graph.

Results: Our proposed multimodal connectivity model shows superior performance compared to the single modality model (Figure 2(a)). The average accuracy of our model reached 95.76%, outperforming both the single SC (88.71%) and the single FC model (90.04%). Figure 2(b) shows the top 10 brain regions contributing to the sex classification. The most salient regions in the fusion model included the left temporal, the left inferior parietal lobule, and the left temporal pole for SC, and the left temporal, the left lateral prefrontal cortex, and the left inferior parietal lobule for FC. These findings indicate the significance of integrating information from both SC and FC modalities, as different regions contribute uniquely to the sex classification task in each modality.

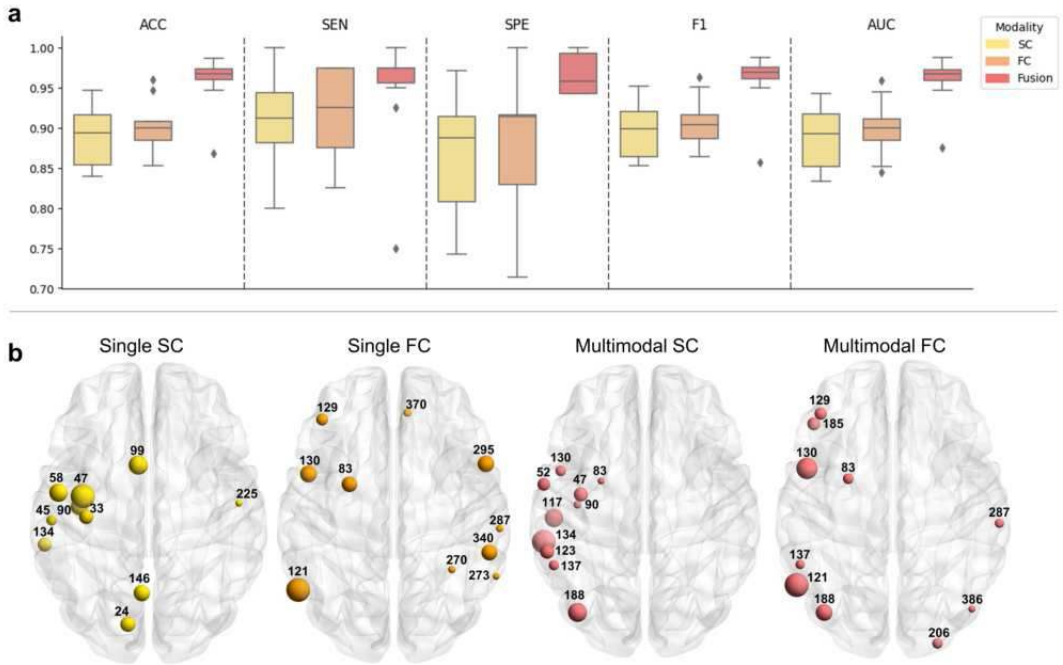

Figure 2. (a) Comparison of classification performance between our proposed multi-modal fusion model and single modality models. Abbreviations: ACC, Accuracy; SEN, Sensitivity; SPE, Specificity; AUC, Area Under the Curve. (b) The top 10 salient brain regions. The numbers indicate the indices of the Schaefer 400 atlas, and the size of spheres represents their importance.

Conclusions: We proposed a new GTN-based multimodal fusion model that effectively integrates the FC and SC modalities to capture complex brain connectivity patterns. Our proposed model achieved high accuracy in the sex classification task and provided interpretable insights into the key brain regions contributing to the model's decisions. This study contributes to advancing our understanding of brain connectivity and lays the groundwork for future studies aiming to enhance the robustness and interpretability of models in neuroimaging research.

References

1. Calhoun, V. D., Sui, J. (2016). 'Multimodal fusion of brain imaging data: a key to finding the missing link (s) in complex mental illness', Biological psychiatry: cognitive neuroscience and neuroimaging, vol. 1, no.3, pp. 230-244.
2. Sporns, O. (2022). 'Graph theory methods: applications in brain networks', Dialogues in clinical neuroscience, vol., pp.
3. Zhu, D., Zhang, T., Jiang, X., Hu, X., Chen, H., Yang, N., Lv, J., Han, J., Guo, L., Liu, T. (2014). 'Fusing DTI and fMRI data: a survey of methods and applications', NeuroImage, vol. 102, pp. 184-191.
4. Van Essen, D. C., Smith, S. M., Barch, D. M., Behrens, T. E., Yacoub, E., Ugurbil, K., Consortium, W.-M. H. (2013). 'The WU-Minn human connectome project: an overview', NeuroImage, vol. 80, pp. 62-79.
5. Ooi, L. Q. R., Chen, J., Zhang, S., Kong, R., Tam, A., Li, J., Dhamala, E., Zhou, J. H., Holmes, A. J., Yeo, B. T. (2022). 'Comparison of individualized behavioral predictions across anatomical, diffusion and functional connectivity MRI', NeuroImage, vol. 263, pp. 119636.
6. Schaefer, A., Kong, R., Gordon, E. M., Laumann, T. O., Zuo, X.-N., Holmes, A. J., Eickhoff, S. B., Yeo, B. T. (2018). 'Local-global parcellation of the human cerebral cortex from intrinsic functional connectivity MRI', Cerebral cortex, vol. 28, no.9, pp. 3095-3114.
7. Shi, Y., Huang, Z., Feng, S., Zhong, H., Wang, W., Sun, Y. (2020). 'Masked label prediction: Unified message passing model for semi-supervised classification', arXiv preprint arXiv:2009.03509, vol., pp.
8. Lundberg, S. M., Lee, S.-I. (2017). 'A unified approach to interpreting model predictions', Advances in neural information processing systems, vol. 30, pp.
9. Ying, Z., Bourgeois, D., You, J., Zitnik, M., Leskovec, J. (2019). 'Gnnexplainer: Generating explanations for graph neural networks', Advances in neural information processing systems, vol. 32, pp.

Poster No 1434

Explainable Graph Neural Network on Imaging Genetics for Schizophrenia Classification

Badhan Mazumder[1], Vince Calhoun[2], Dong Hye Ye[1]

[1]Georgia State University, Atlanta, GA, [2]GSU/GATech/Emory, Decatur, GA

Introduction: Investigation into the brain's structure and functional connections could provide vital insights into neuropsychiatric disorders like schizophrenia (SZ). Genetic markers, such as single nucleotide polymorphisms (SNP), are known to play a significant role in identifying SZ patients due to their strong heritability. In this study an explainable graph neural network (GNN) framework is introduced to classify SZ patients. By obtaining rich data embeddings from multimodal graph-structured data formed with the subject-wise functional network connectivity (FNC) obtained from resting-state fMRI (rs-fMRI), structural connectivity (SC) derived from diffusion magnetic resonance imaging (dMRI), and SNPs. Experimental outcomes showed that in contrast to unimodal methods, our multimodal approach notably enhanced the classification of SZ patients against healthy controls (HC).

Methods: Data preprocessing Subject-specific FNC matrices were obtained via the Neuromark pipeline[1]. To derive SC matrices, we computed diffusion tensors with dtifit (FSL)[2], followed by deterministic tractography generation of the whole brain using track (CAMINO)[3]. To create a compatible atlas in local space, firstly we performed inverted spatial normalization to the NeuroMark atlas[1], then warped the native fractional anisotropy map onto the standard MNI space. Finally, we isolated the streams passing through each pair of atlas ROIs and counted them individually. Proposed method As depicted in Figure 1, we constructed graph structure data where the edges were formed by applying a k-nearest neighbors (KNN) graph on subject-specific SC to consider crucial connections only. Since a large fraction of SNP data is unrelated to SZ, we employed a subset of 4943 SNPs, that by the findings of the psychiatric genomic consortium have been observed for SZ risk[4]. A 1-D convolutional neural network (CNN) followed by layer-wise relevance propagation (LRP)[5] was applied to identify the top 100 SZ-linked SNPs. Then the corresponding FNC matrix was concatenated with the selected SNPs and employed as node features. After that, we input the multimodal graph data to our GNN framework that includes 5 graph convolution (GCN)[6] layers, a global mean pooling layer followed by a linear layer, and a softmax for classification. Additionally, to explain, we employed GNNExplainner[7] to identify the important edges of the graph which were highly significant for SZ classification.

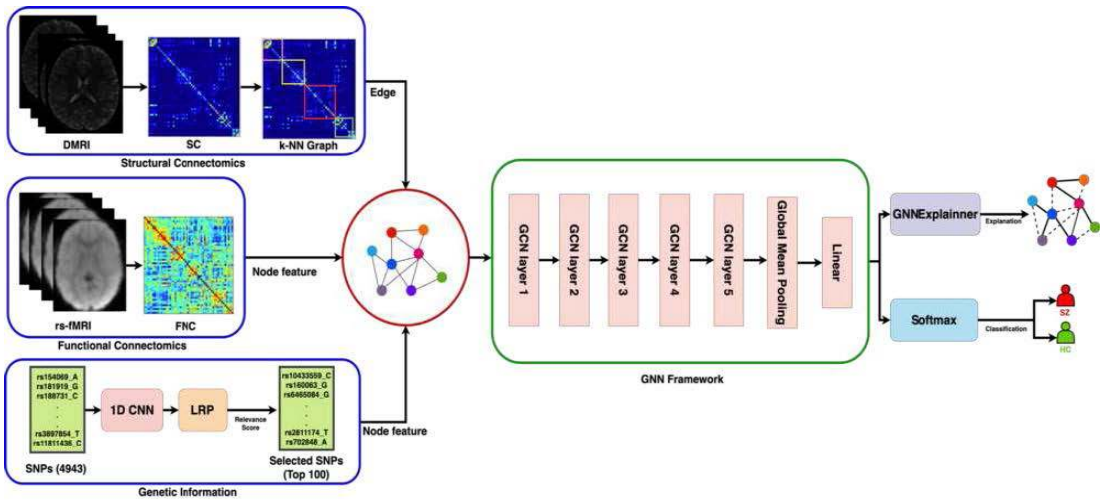

Figure 1. Overview of proposed method

Results: For validation, we utilized a subset (Total:165; SZ:93, HC:72) of the Function Biomedical Informatics Research Network (FBIRN)[8] dataset with 80:20 training-testing split ratio. We evaluated using 5-fold cross-validation against 3 different indices: accuracy, precision, and f1-score. For the k-NN graph on SC, different k values (3, 5, 10, and 20) were utilized. Among them, k=10 resulted in the highest performance. Results shown in Figure 2a indicate that compared with the unimodal (SC and FNC separately) model the multimodal (SC+FNC) model was giving higher performance which improved to 73.38% (accuracy), 75.10% (precision) and 72.79% (f1-score) when SNP was also considered. As shown in Figure 2b, from our generated explanations for SZ patients, we found significance in default mode (DMN), visual (VSN), and cognitive-control (CON) network which is consistent with the clinical findings. We also conducted a group analysis using a 2-sample T-test ($p<0.05$) in-between generated explanations for HC and SZ and depicted the finding in Figure 2c which also indicates the same networks.

Methods (Modality-wise)	Accuracy	Precision	f1-score
GCN (SC)	52.05±8.65	55.89±10.34	49.98±8.25
GCN (FNC)	64.99±3.63	68.89±4.67	64.10±3.44
GCN (SC-FNC)	69.14±4.69	70.64±5.36	68.25±4.96
GCN (SC-SNP)	63.67±1.87	64.99±1.98	63.32±1.81
GCN (SC-FNC-SNP) [proposed]	**73.38±4.07**	**75.10±4.12**	**72.79±4.36**

(a)

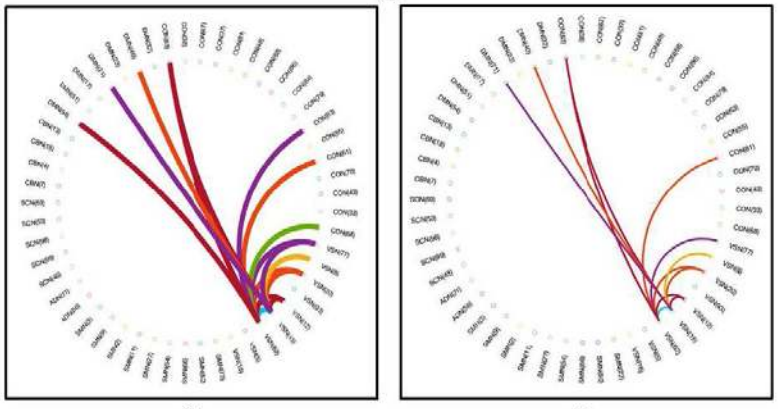

(b) **(c)**

Figure 2. (a) Comparison of classification in both unimodal and multimodal configuration. [Unit: %] (Mean ± Standard Deviation). **(b)** Visualization of GNNExplainer generated important structural connections among subcortical (SCN), auditory (ADN), sensorimotor (SMN), visual (VSN), congnitive-control (CON), default mode (DMN), and cerebellum (CBN) network for one representative SZ patient from test dataset. **(c)** Visualization of 2-sample T-test outcome for group analysis between SZ and HC using GNNExplainer generated important structural connections.

Conclusions: We presented an explainable GNN framework that incorporates structural-functional connectomics and genetic information simultaneously, to improve SZ classification and interpret potential structural biomarkers. Obtained experimental findings showed improved performance gain in comparison to unimodal set-up which provides evidence of the robustness of our multimodal approach.

References
1. Du, Yuhui, Zening Fu, Jing Sui, Shuang Gao, Ying Xing, Dongdong Lin, Mustafa Salman et al. "NeuroMark: An automated and adaptive ICA based pipeline to identify reproducible fMRI markers of brain disorders." NeuroImage: Clinical 28 (2020): 102375.
2. Woolrich, Mark W., Saad Jbabdi, Brian Patenaude, Michael Chappell, Salima Makni, Timothy Behrens, Christian Beckmann, Mark Jenkinson, and Stephen M. Smith. "Bayesian analysis of neuroimaging data in FSL." Neuroimage 45, no. 1 (2009): S173-S186.
3. Alexander, D. C., K. Seunarine, S. Nedjati-Gilani, M. G. Hall, G. J. Parker, Y. Bai, and P. J. Cook. "Camino: Open-source diffusion-MRI reconstruction and processing." In Proceedings of the 14th Scientific Meeting of the International Society for Magnetic Resonance in Medicine (ISMRM), Seattle, WA, USA, pp. 6-12. 2006.
4. Yu, Hongkun, Thomas Florian, Vince Calhoun, and Dong Hye Ye. "Deep Learning From Imaging Genetics for Schizophrenia Classification." In 2022 IEEE International Conference on Image Processing (ICIP), pp. 3291-3295. IEEE, 2022.
5. Bach, Sebastian, Alexander Binder, Grégoire Montavon, Frederick Klauschen, Klaus-Robert Müller, and Wojciech Samek. "On pixel-wise explanations for non-linear classifier decisions by layer-wise relevance propagation." PloS one 10, no. 7 (2015): e0130140.
6. Kipf, Thomas N., and Max Welling. "Semi-supervised classification with graph convolutional networks." arXiv preprint arXiv:1609.02907 (2016).
7. Ying, Zhitao, Dylan Bourgeois, Jiaxuan You, Marinka Zitnik, and Jure Leskovec. "Gnnexplainer: Generating explanations for graph neural networks." Advances in neural information processing systems 32 (2019).
8. Keator, David B., Theo GM van Erp, Jessica A. Turner, Gary H. Glover, Bryon A. Mueller, Thomas T. Liu, James T. Voyvodic et al. "The function biomedical informatics research network data repository." Neuroimage 124 (2016): 1074-1079.

Poster No 1435

Heterogeneity and Brain Age in Depression: A HYDRA-Based Investigation of Lifestyle Exposures

Nicole Sanford[1], Yuetong Yu[1], Sophia Frangou[1]

[1]University of British Columbia, Vancouver, British Columbia

Introduction: Major depression is intricately linked to brain health, with depressive episodes potentially contributing to accelerated brain aging (Schiweck et al., 2020; Simon et al., 2023). Further, lifestyle factors such as diet and physical exercise may contribute to psychiatric and neurological wellbeing, although relationships are complex (Lopresti et al., 2013). The present study aimed to identify comprehensive profiles distinguishing adults with a history of depression with respect to modifiable risk factors and brain age.

Methods: The sample comprised adults from the UK Biobank (ages 44-82 years). Brain age gap estimates (brainAGE; Cole & Franke, 2017) were computed from 3T structural MRI data using support vector regression to predict biological brain age from regional cortical thicknesses, cortical surface areas, and subcortical volumes. Heterogeneity Through Discriminative Analysis (HYDRA; Varol et al., 2017) was used to identify clusters of individuals with a history of depression (n = 896; 305 males) compared to a non-psychiatric control group (n = 36,206; 17,232 males) based on 224 features encompassing diet and nutrition, alcohol use, smoking history, pastimes, relationship quality, physical exercise, and fitness, with sex and age included as covariates. The resulting clusters were compared on brainAGE and mood-related psychopathology. All group differences were identified following false discovery rate correction ($p < .05$).

Results: HYDRA identified four clusters (n = 253, 178, 315, and 150, respectively) which were differentiated by 39 variables comprising social support and activities, physical exercise, fitness, smoking history, alcohol use, dietary patterns, nutritional supplements, computer and TV use, sleep quality, and outdoor exposure. These clusters varied in mood-related psychopathology but not in brainAGE. Cluster 1 exhibited the lowest psychopathology and was characterized by relatively strong social support and activities, frequent physical exercise, low BMI, high grip strength, varied diet, low computer usage, and low insomnia as compared to the other three clusters. In contrast, Cluster 3 exhibited the greatest psychopathology and was characterized by relatively low social support and activities, minimal physical exercise, high BMI, high meat and salt intake, low fruit and vegetable intake, high computer and TV use, frequent insomnia, and minimal outdoor exposure.

Conclusions: This study underscores the potential of comprehensive interventions that could positively impact mental health. The uniformity in brainAGE among the identified clusters suggests that certain key aspects of neurological health may be resilient across individuals with varying lifestyle exposures and depressive histories. Further investigations in longitudinal cohorts are needed to determine how these relationships may evolve with clinical progression and medication exposure.

References
1. Cole, J.H. (2017), 'Predicting age using neuroimaging: Innovative brain ageing biomarkers', Trends in Neurosciences, vol. 40, pp. 681-690.
2. Lopresti, A.L. (2013), 'A review of lifestyle factors that contribute to important pathways associated with major depression: diet, sleep and exercise', Journal of Affective Disorders, vol. 148, pp. 12-27.
3. Schiweck, C. (2020), 'Depression and suicidality: A link to premature T helper cell aging and increased Th17 cells', Brain, Behavior, and Immunity, vol. 87, pp. 603–609.

4. Simon, M.S. (2023), 'Premature T cell aging in major depression: A double hit by the state of disease and cytomegalovirus infection', Brain, Behavior, & Immunity - Health, vol. 29, pp. 100608.
5. Varol, E. (2017), 'HYDRA: Revealing heterogeneity of imaging and genetic patterns through a multiple max-margin discriminative analysis framework', NeuroImage, vol. 145, Pt B, pp. 346–364.

Poster No 1436

Skullstripping anatomical MRIs in AFNI using volumetric deep learning network: Preliminary results

Yamuna Narayana Swamy[1], Patrick McClure[2], Richard Reynolds[3], Francisco Pereira[3], Paul Taylor[3]

[1]Scientific and Statistical Computing Core, NIMH, NIH, USA, [2]Naval Postgraduate School, Monterey, CA, [3]National Institute of Mental Health, Bethesda, MD

Introduction: Identifying the brain within an anatomical MRI (i.e., skullstripping or brain extraction) is a standard step in many neuroimaging analysis pipelines. While it is generally easy to tell by eye which voxels belong to the brain and which do not, it is surprisingly difficult to automate. There are existing tools that do this well for good quality data with standard characteristics, but the challenge is to perform this task robustly across variations in physiology, cortical thickness, or other individual features, as well as the many types of noise or image distortions such as ringing, noise, dropout, and brightness inhomogeneity. In this work we demonstrate a new 3D skullstripping tool in AFNI[1] using a volumetric, convolutional neural network (V-net) that can estimate detailed brain masks for raw-to-minimally processed human anatomical datasets.

Methods: A V-net is a volumetric neural network that is particularly suited to whole brain classification due to its in-built 3D convolutional kernel. Milletari et. al.[2] applied a V-net to MRI volumes for prostate segmentation, and Bontempi et al.[3] used a modified version for brain tissue classification. Here, we adopt this framework as a starting point for skullstripping, using a larger number of layers to perform a 2-channel classification problem: to identify "brain" and "non-brain". The architecture contains both a volumetric down-sampling path and a volumetric up-sampling path. We implemented V-net in Python using PyTorch[4]. We trained it end to end to predict binary masks from T1-weighted (T1w) anatomical MRI volumes, using Sorensen-Dice loss[5]. The training dataset masks were created by using FreeSurfer[6] on good quality T1w volumes. To increase robustness and generalizability of the V-net, we augmented the training data by using AFNI to derive volumes with the following characteristics: Gibbs ringing, gain inhomogeneity, zipper noise, strong shading and affine transforms. The output of the V-net is a softmax layer, which provides a probability map of voxels belonging to foreground or background; specifically, it is a two channel volumetric segmentation corresponding to brain and the non-brain. The training and testing data were T1w volumes (1mm isotropic voxels) from across 8 sites on 3 continents with a large age range (8-70 yrs) and different 3T scanner types[7]. Here, the network was trained for 100 epochs on 131 original plus 72 augmented datasets, and tested on 38 datasets.

Results: Most skullstripping algorithms perform well in the "core" brain region, i.e., away from the boundary. In our evaluations, we have computed the performance metrics around the brain edge where algorithms vary the most, defining an "inner" and "outer" rim, using AFNI's 3dDepthMap (Fig 1a). The true positive rate (TPR) was computed in the inner rim (Fig 1b), and the true negative rate (TNR) was computed for the outer rim (Fig 1c). In both cases, the typical V-net results closely match the initial mask datasets. Visually checking example subjects, we can see multiple cases where differences are due to the V-net providing more accurate masks to the underlying anatomy than FreeSurfer (Fig 2), e.g., see the arrows in Fig 2a. The V-net performs well in identifying the brain region in a dataset having considerable ringing artifacts (Fig 2b).

Figure 1.a

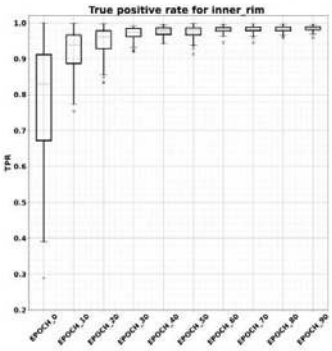

Figure 1.b

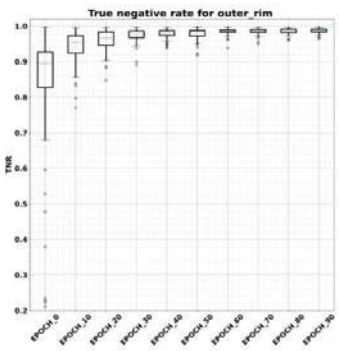

Figure 1.c

Figure 1. (a) A full "rim" region (red overlay) is shown around a ground truth brain mask (white underlay) for an example subject, in axial, sagittal and coronal views. The "inner rim" is where the two masks overlap, and the "outer rim" is the rim region surrounding the brain mask. **(b)** The plot shows boxplots of the true positive rates within the inner rim region for the training group across epochs. **(c)** The plot shows boxplots of the true negative rate (increasing TNR means increasing agreement) for the outer rim region for the training group across epochs.

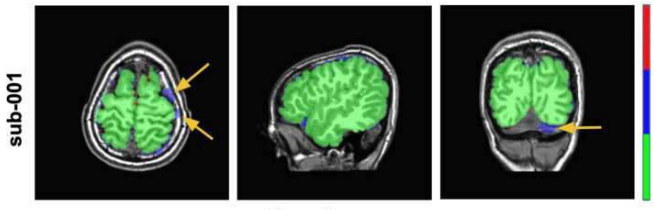

Figure 2.a

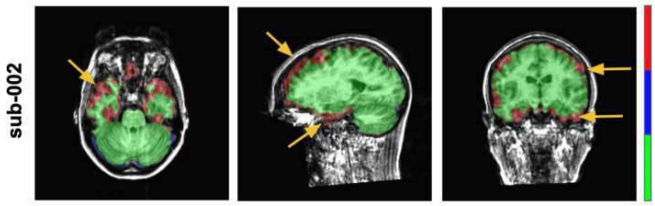

Figure 2.b

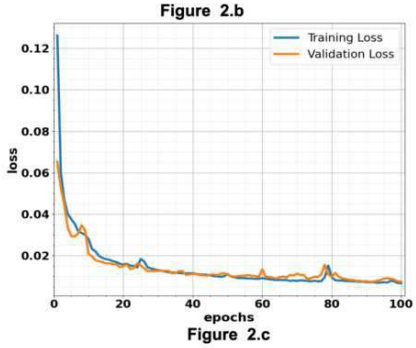

Figure 2.c

Figure 2. (a & b) Example cases of the similarities and differences between the Freesurfer and V-net predicted masks for a given T1w anatomical input (shown as underlay in axial, sagittal and coronal views). Green regions show where the two masks overlap/agree, while blue shows FreeSurfer-only regions and red shows V-net only ones. While general agreement is high, results differ in several places around finer features around the boundary, particularly for sub-002 whose dataset contains notable ringing. **(b)** Plot shows the average loss value across groups in training and validation phases over many epochs.

Conclusions: The preliminary results are encouraging for this architecture to classify the brain from anatomical MRI volumes. Even with a small training dataset, the V-net shows high accuracy for standard datasets, and also shows some advantages over traditional skullstripping approaches in cases of lower data quality, such as ringing. In future work we plan to expand the training dataset size, as well as augmented sample size and variety. Finally, we also plan to expand the application to multiclass (e.g., tissue) classification[8].

References

1. Cox RW. (1996) AFNI: 'Software for analysis and visualization of functional magnetic resonance neuroimage'. Computers and Biomedical Research, 29:162-173.
2. Fausto Milletari et al.,(2016), "V-Net : Fully Convolutional Neural Networks for Volumetric Medical Image Segmentation", Fourth International Conference on 3D Vision (3DV)
3. D. Bontempi et al.,(2020), "CEREBRUM: a fast and fully-volumetric convolutional Encoder-decodeR for weakly-supervised sEgmentation of BRain strUctures from out-of-the-scanner MRI" Med. Image Anal., 62 (2020)
4. Paszke, A. et al.,(2019), PyTorch: An Imperative Style, High-Performance Deep Learning Library. In Advances in Neural Information Processing Systems 32. Curran Associates, Inc., pp. 8024–8035.
5. Dice L.,(1945), Measures of the amount of ecologic association between species. Ecology, 26:207–302
6. Fischl B, et al. "Whole brain segmentation: automated labeling of neuroanatomical structures in the human brain." Neuron vol. 33,3 (2002): 341-55. doi:10.1016/s0896-6273(02)00569-x
7. Taylor PA, Glen DR, Reynolds RC, Basavaraj A, Moraczewski D, Etzel JA. (May 2023), Editorial: Demonstrating quality control (QC) procedures in fMRI., Frontiers in Neuroscience.
8. McClure P, Rho N, Lee JA, Kaczmarzyk JR, Zheng CY, Ghosh SS, Nielson DM, Thomas AG, Bandettini P, Pereira F (2019) "Knowing what you know in brain segmentation using Bayesian deep neural networks". Frontiers in neuroinformatics.

Poster No 1437

Surface-based Middle-Fusion Attention model for Early Alzheimer's Disease Diagnosis

Quan Duong[1], Jin Kyu Gahm[1]

[1]Pusan National University, Busan, Busan

Introduction: Surface-based analysis offers many advantages for early Alzheimer's disease diagnosis. Cortical surface representaion helps analyzing cortical atrophy patterns through quantifiable metrics such as cortical thickness, sulci depth and curvature. It also reveals regional changes in cortical functions by analyzing the PET standardized uptake value ratio. Many studies deployed graph convolutional neural network to extract features from cortical surface. However, they did not achieve state-of-the-art results, possibly due to suboptimal GCNN or not incorporating multimodal features. In this study, we propose a new middle-fusion attention model that effectively leveragings multimodal cortical surface features derived from T1w MRI and FDG PET. The proposed model achieves high performances on the ADNI1, ADNI2 & ADNI3 dataset.

Methods: 1. Data Acquisition: We acquired publicly available ADNI1 datasets from the Alzheimer's disease neuroimaging initiative (ADNI). Baseline FDG PET scans were acquired for ADNI1, Amyloid PET and Tau PET for ADNI2&3 along with T1w MRI that was taken no more than two months prior. The acquired ADNI1 dataset consists of 101 CN, 208 MCI and 84 AD. ADNI2 & ADNI3 datasets comprises 258 CN, 159 MCI and 55 AD. 2. Data Preprocessing: We used FreeSurfer on T1w MRI to reconstruct cortical surface representation and generate cortical structure related metrics including cortical thickness, sulci depth and curvature. Subsequently, we employed PETSurfer on PET images as follows: registering to anatomical space, perform partial volume correction, compute SUVR and sampling SUVR onto the cortical surface. Finally, we resampled cortical thickness, sulci depth, curvature and PET SUVR onto a sixth-ordered icosphere and extract non-overlapping triangular patches. 3. Model Architecture: We designed middle-fusion attention model for effectively analyzing multimodal cortical features. The model consists of two stages: Modality-specific analysis and Inter-modality analysis. The first stage analyzes extract features from each modality through self-attention mechanism. Then features extracted from each modality are fed into the second stage, where cross-attention is performed to extract inter-modality relationship. The outputs of the second stage are concatenated and analyzed by a classifier to produce class probabilities.

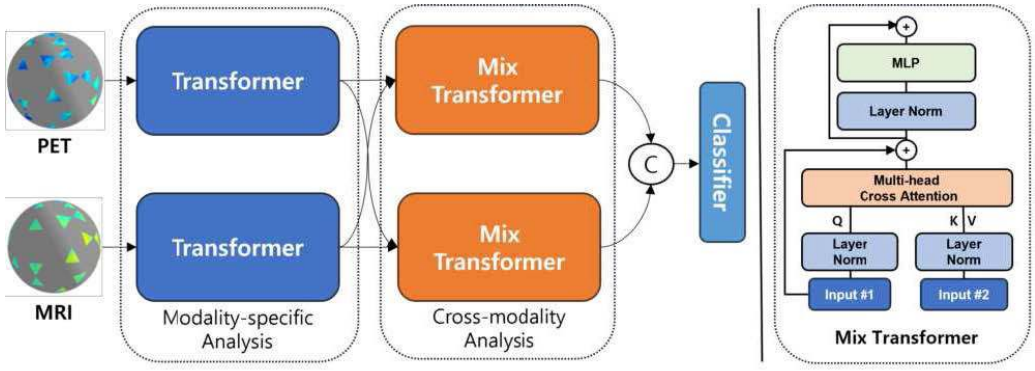

Figure 1. The proposed middle-fusion attention model. The model comprises two stages. The first stage extracts modality-specific features using self-attention operation. The second stages performs cross-modality analysis by employing cross-attention mechanism.

Results: We evaluated the proposed model using 5-fold stratified cross-validation. Area under the ROC curve was used as the evaluation metric. For ADNI1 dataset, the model achieved 97% AUC and 81% AUC on AD diagnosis (CN vs. AD) and early AD diagnosis (CN vs. MCI), respectively. For ADNI2 & ADNI3 datasets, the model scored 95% AUC on AD diagnosis and 79% AUC on early AD diagnosis.

Conclusions: We developed a new middle-fusion attention model for early AD diagnosis. The proposed model is capable of leveraging multimodal cortical features, demonstrated by high performances on both AD diagnosis and early AD diagnosis across ADNI1, ADNI2 & ADNI3 datasets.

References

1. A. Dosovitskiy et al., "An Image is Worth 16x16 Words: Transformers for Image Recognition at Scale," p.arXiv:2010.11929.
2. B. Fischl, "FreeSurfer," Neuroimage, vol. 62, no. 2, pp. 774-81, Aug 15 2012
3. D. N. Greve, "Different partial volume correction methods lead to different conclusions: an 18F-FDG-PET study of
4. aging," Neuroimage, vol. 132, pp. 334-343, 2016
5. D. N. Greve, "Cortical surface-based analysis reduces bias and variance in kinetic modeling of brain PET data,"Neuroimage, vol. 92, pp. 225-236, 2014.
6. Petersen, Ronald Carl, et al. "Alzheimer's disease neuroimaging initiative (ADNI): clinical characterization." Neurology 74.3 (2010): 201-209.

Poster No 1438

Language Activation from Naturalistic fMRI Time Series using Machine Learning

Elaine Kuan[1,2], Viktor Vegh[1,2], John Phamnguyen[1,3], Kieran O'Brien[4], Amanda Hammond[4], David Reutens[1,2,3]

[1]Centre for Advanced Imaging, The University of Queensland, QLD, Australia, [2]ARC Training Centre for Innovation in Biomedical Imaging Technology, The University of Queensland, QLD, Australia, [3]Royal Brisbane and Women's Hospital, QLD, Australia, [4]Siemens Healthineers, QLD, Australia

Introduction: Naturalistic fMRI can overcome some limitations of traditional task-based fMRI. Due to the dynamic nature of the naturalistic stimulus, task regressors are difficult to define, which pose a challenge for conventional General Linear Model (GLM) analysis. Data driven methods, namely machine learning (ML), may provide an alternative solution as they are successful in decoding fMRI data. The aim of this study is to investigate the use of Rotation Forest (RotF) (Rodriguez et al, 2006) in classifying areas of language activation from naturalistic fMRI time series data, and to identify the segments of the naturalistic fMRI time series contributing mostly to the classification achieved by RotF.

Methods: Twenty healthy controls completed language tasks including sentence completion (SC) and watched a 15-minute in-house created video made up of segments of a quiz show with advertisements. Gradient Echo Planar Imaging (EPI) fMRI data for each paradigm were acquired using the following parameters: matrix size = 64 x 64 x 42, TR = 2s, TE = 30ms and voxel size 3 x 3 x 3 mm^3. The raw EPI data were pre-processed using the SPM12 software according to the following steps: slice timing correction, realignment of volumes, co-registration and smoothing. Voxel-wise fMRI time series of the SC task were modelled with GLM (Friston et al., 1994) to obtain binarized activation maps at $p < 0.001$ uncorrected. Voxel-wise naturalistic fMRI time-series (frames 0 to 440) from 14 participants were extracted and labelled based on SC activation maps. Whilst we have evaluated a range of classification methods, here we provide results for Rotation Forest (RotF). The number of samples to be used for training was experimentally evaluated, resulting in 4872 single voxel time series samples. Similarly, voxel-wise time series data from six participants formed the test set, resulting in around 60,000 samples from fMRI images of each participant. The RotF based activation maps were first reconstructed and then compared with SC activation maps of each test participant. The Area Under the Curve (AUC) and Euclidean Distance (ED) between language activation peaks were evaluated. Sequential Forward Feature Elimination (SFFE) (Ferri et al.,1994) was performed 10 times on the trained RotF model using a 2-fold cross validation. The top five frames were labelled with ones while the remaining frames were labelled with zeros to produce a frame importance metric over the naturalistic fMRI time series. Addition of the importance metrics over repeated runs produced an overall frame importance for the naturalistic time series data.

Results: From Fig. 1, we deduce that the RotF method is successful at capturing fronto-temporal and temporal activation associated with language, but is not as successful in capturing Supplementary Motor Area (SMA) activation. Occipital activation, expected for a visual stimulus but not for language activation, can also be observed in all test participants using RotF applied to the naturalistic fMRI time series. Notably, HC20 had limited activation in general but occipital activation was still present, which is expected due to the visual nature of the naturalistic stimulus. The mean whole-brain AUC and mean ED across all test participants were 0.83 and 5.4mm, respectively. From Fig. 2, we observe that over 10 runs of SFFE, there are

spikes in the waveform that concentrate between the first two advertisement blocks (frames 202 to 367), indicating that the naturalistic fMRI time series within those time points are important for the classification performed by RotF.

Conclusions: With its success in identifying language activation corresponding to SC activation, RotF can potentially be used to identify language activation from naturalistic fMRI data. The application of SFFE further enhances the use of RotF, in allowing informative time points within the naturalistic fMRI time series to be identified, which can be translated to the stimulus to facilitate stimulus designs.

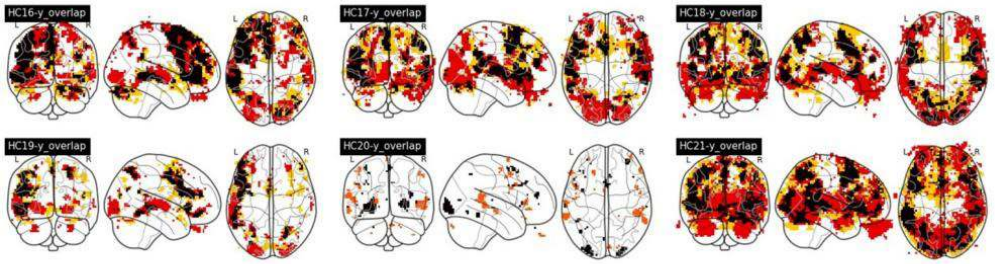

Figure 1: The overlap between SC activation and RotF activation for six test participants (Black – overlap, Yellow – SC activation, Red – RotF activation)

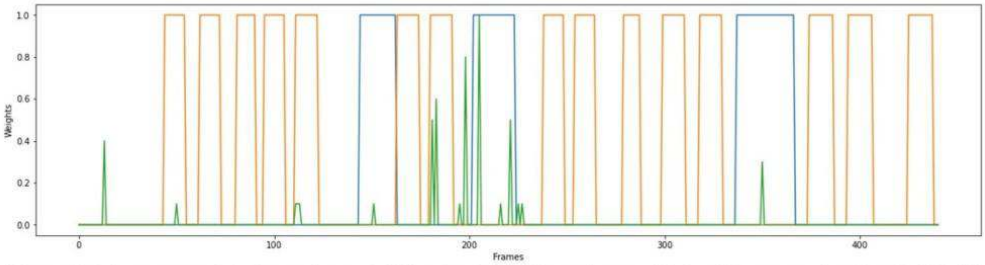

Figure 2: The green plot shows the weighting for frame importance obtained from running the SFFE 10 times. The blue blocks show the frames corresponding to advertisement segments and the orange blocks are the frames over which questions are shown during the quiz show (i.e., in the naturalistic stimulus).

References

1. Friston, K. J., Holmes, A. P., Worsley, K. J., Poline, J. P., Frith, C. D., Frackowiak, R. S. (1994). Statistical parametric maps in functional imaging: a general linear approach. Human brain mapping, vol. 2, no. 4, pp.189-210.
2. Rodriguez, J. J., Kuncheva, L. I., & Alonso, C. J. (2006). Rotation forest: A new classifier ensemble method. IEEE transactions on pattern analysis and machine intelligence, vol. 28, no. 10, pp.1619-1630.
3. Ferri, F. J., Pudil, P., Hatef, M., & Kittler, J. (1994). Comparative study of techniques for large-scale feature selection. In Machine intelligence and pattern recognition, vol. 16, pp. 403-413.

Poster No 1439

Classification of migraine with aura based on grey matter structure within the visual networks

David Niddam[1], Kuan-Lin Lai[2], Shuu-Jiun Wang[2]

[1]National Yang Ming Chiao Tung University, Taipei, Taiwan, [2]Taipei Veterans General Hospital, Taipei, Taiwan

Introduction: Migraine auras are transient neurological symptoms that typically occur before a headache attack. The occipital cortex is thought to have a pivotal role in the initiation of visual auras, as cortical spreading depression, the mechanism underlying visual auras, arises within this region (Hadjikhani et al., 2001). Interictal changes in resting-state functional connectivity and grey matter structure within the occipital cortex has also been observed in migraine with visual auras (Karsan et al., 2023; Niddam et al., 2016). Previous neuroimaging studies on migraine auras have primarily used mass-univariate analyses in which each voxel is considered as a spatially independent unit. Multivariate pattern analysis is a complementary approach in which information contained jointly among multiple voxels is taken into account at once. Multivariate pattern classification can identify distributed patterns of voxels which can be used to differentiate groups of participants and to make predictions about diagnoses at the individual level. Since the occipital cortex is involved in the generation of visual aura and may exhibit altered interictal grey matter structure and functional connectivity, we hypothesized that grey matter within the functionally defined resting-state visual networks contains discriminative information that can be used to differentiate migraine patients with visual auras (MA) from migraine patients without visual auras (MO) and healthy controls (HC).

Methods: Structural and functional resting-state MRI images were obtained from 50 MA patients, 50 MO patients and 50 HCs. All patients were in the interictal state and had low-frequency episodic migraine. Independent component analysis with 40 components was first used in each of the three groups to identify the functional visual networks (see Figure). The resulting images were thresholded and binarized. These binarized images were then used to constrain the structural images. The masked images entered a multivariate analysis in which Gaussian process classification was used to generate pair-wise models (see Figure). The performance of the models was indexed by the balanced accuracy (BA) and the area under the receiver operating characteristic curve (AUC). Generalizability was assessed by 5-fold cross-validation and non-parametric permutation tests were used to estimate significance levels. Only results passing a false discovery rate corrected threshold for the multiple models set up were considered significant.

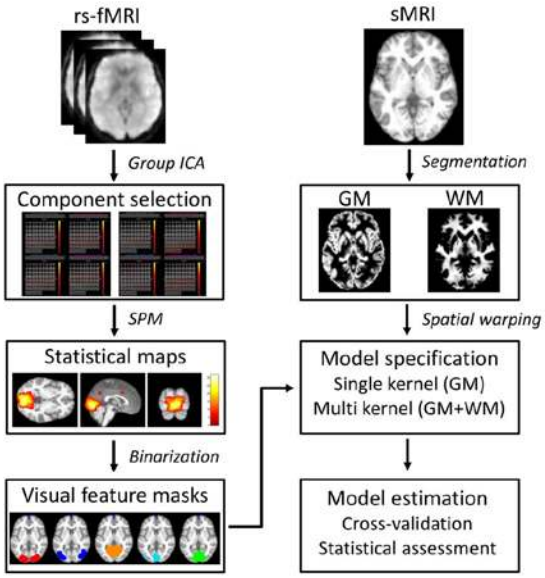

Results: Five functional networks were identified within the occipital cortex. Of these, one corresponded to the occipital visual network and one corresponded to the lateral visual network (Laird et al., 2011). The remaining 3 networks covered the anterior and the posterior dorsal and ventral medial visual networks (Laird et al., 2011). The multivariate pattern of grey matter voxels within the ventral medial visual network contained significant information related to the MA diagnosis (MA vs. HC: BA=78% [P<0.001]; AUC=0.84 [P<0.001]; MA vs. MO: BA=71% [P<0.001]; AUC=0.73 [P=0.003]). Grey matter voxels with the anterior medial visual network also contained significant information related to the MA diagnosis, albeit less significant (MA vs. HC: BA=67% [P=0.004]; AUC=0.70 [P=0.005]; MA vs. MO: BA=68% [P=0.001]; AUC=0.79 [P<0.001]).

Conclusions: Migraine with visual aura is characterized by multivariate patterns of grey matter changes within the medial visual cortex that have discriminative power and may reflect pathological mechanisms. The medial visual cortex is known to processes simple visual stimuli, both static and moving (Laird et al., 2011). This is congruent with common symptoms associated with visual aura.

References

1. Hadjikhani, N. (2001) 'Mechanisms of migraine aura revealed by functional MRI in human visual cortex', Proceedings of the National Academy of Sciences, vol. 98, pp. 4687-92.
2. Karsan, N. (2023) 'Evaluating migraine with typical aura with neuroimaging. Frontiers in Human Neuroscience, vol. 17, pp. 1112790.
3. Laird, A.R. (2011), 'Behavioral interpretations of intrinsic connectivity networks', Journal of Cognitive Neuroscience, vol. 23, pp. 4022-37.
4. Niddam, D.M. (2016) 'Reduced functional connectivity between salience and visual networks in migraine with aura', Cephalalgia, vol. 36, pp. 53-66.

Poster No 1440

Geometric constraints on individual brain function: a deep learning approach

Mehul Gajwani[1], Zachary Zendarski[1], Stuart Oldham[2], Trang Cao[1], Mehrtash Harandi[1], James Pang[1], Alex Fornito[1]

[1]Monash University, Melbourne, Victoria, [2]Murdoch Children's Research Institute, Melbourne, Victoria

Introduction: Brain structure necessarily constrains brain function, but correlations between structural connectivity (SC; as measured by streamline count from diffusion MRI) and functional connectivity (FC; as measured by pairwise correlation of

resting-state BOLD-fMRI time-series) are relatively modest. Deep learning models can reveal a tighter relationship, predicting FC from SC with a reasonable degree of accuracy (e.g. Pearson's r = 0.55 ± 0.1 for individuals and r = 0.9 ± 0.1 for group average estimates) (Sarwar et al., 2021). Recent work (Pang et al., 2023) has shown that brain geometry may contain at least as much information about function as structural connectivity. Specifically, linear combinations of the eigenmodes of cortical surface geometry are capable of reconstructing group-averaged FC (e.g. group r = 0.7 when using 50 modes). Here, we move beyond these linear models to evaluate the relative performance of SC and cortical geometry in predicting FC through deep learning.

Methods: We used structural, functional, and diffusion MRI data from the Human Connectome Project as previously described (Glasser et al., 2013; Oldham & Ball, 2023; Pang et al., 2023). Cortical surface meshes, SC, and FC matrices passed quality control in 967 participants; hence, we used 767 were used for training, 100 for validation, and 100 for testing. We used a fully-connected feed-forward neural network (Fig. 1B) developed in (Sarwar et al., 2021) with vectorized input to test three competing models using different input data from individuals (Fig. 1). The input of the first model input is the upper triangle of the SC matrix with 100 nodes (Fig. 1A). The input of the second model is the parcellated (Schaefer et al., 2018) first 50 geometric eigenmodes (GM) calculated in fsLR-32k space as previously described (Pang et al., 2023) (Fig. 1D and E). Finally, the input of the third model is 50 connectome eigenmodes (CM) (Naze et al., 2021) generated from the graph Laplacian of the SC matrix . After training (Fig. 1C and F), one run of each model was selected by matching the model inter-prediction similarity to the empirical distribution of similarity between individuals' FC.

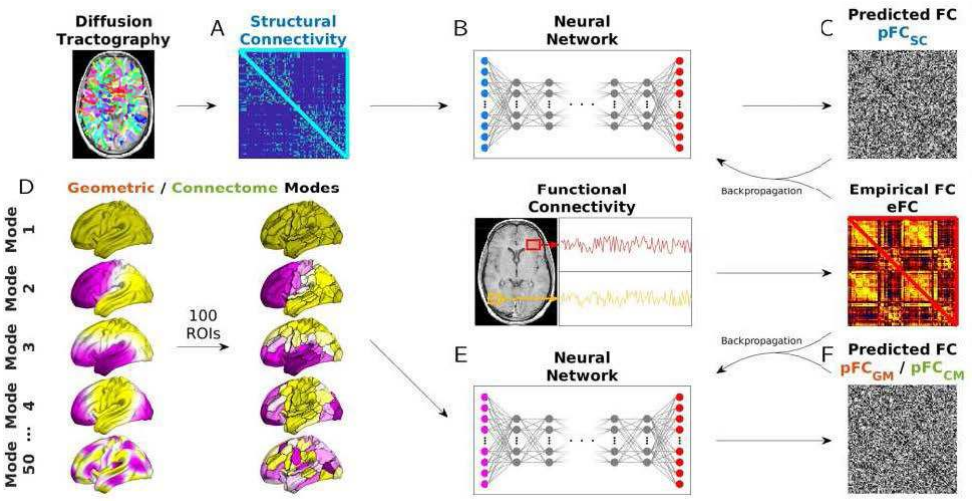

Figure 1: Machine learning methods used to compare structural connectivity, geometric eigenmodes, and connectome eigenmodes. (A-C) Structural connectivity is derived for each individual and used as the input to a fully-connected feed forward neural network, which is trained to predict functional connectivity for each individual. (D) For each individual, geometric modes are derived from the cortical surface and then parcellated to 100 nodes. Connectome modes are also derived from the SC matrix of each individual. (E-F) Modes are used as input to a neural network with the same architecture as (B), and again trained to predict functional connectivity. Abbreviations: eFC, empirical functional connectivity; pFC, predicted functional connectivity; SC, structural connectivity; GM, geometric eigenmodes; CM, connectome eigenmodes.

Results: Model accuracy was assessed using Pearson correlation. Group level estimates were generated by averaging model predicted FC (pFC) across individuals and comparing it to the average empirical FC (eFC) across the same individuals. Across 100 individuals in the test set, the resulting correlations between the group pFC and eFC are r = 0.98 for the SC model, r = 0.99 for the GM model, and r = 0.99 for the CM model (Fig. 2A). Furthermore, all models accurately predict the group average even when using test sets with fewer individuals (Fig. 2B). At the individual level, the models reconstruct individual FC matrices more accurately than the previous state-of-the-art(Sarwar et al., 2021): SC r = 0.63 ± 0.19; GM r = 0.64 ± 0.15; CM r = 0.65 ± 0.17. Results from five example individuals are shown in Fig. 2C. Models generally replicate large-scale patterns of FC, and individuals with erroneous reconstructions vary between models. Finally, paired-samples ANOVA showed no significant difference between the predictive accuracy of each model across 100 test individuals.

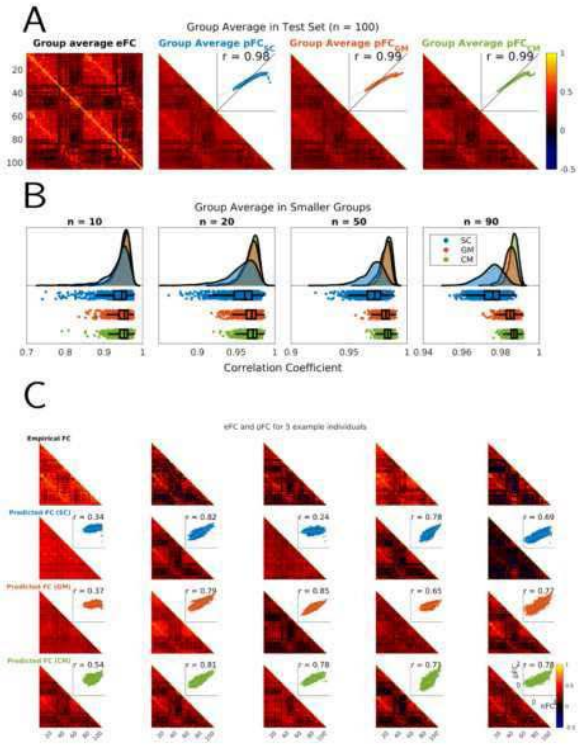

Figure 2: Group- and individual-level results for the structural connectivity, geometric eigenmode, and connectome eigenmode models. (A) Group average predictions across all 100 participants in the test set. Group average eFC was generated by averaging eFC across all individuals. Similarly, group average pFC for each model was generated by averaging pFC across all individuals. Inset, correlation between eFC and pFC for each model (each point represents one edge). (B) Group average predictions from randomly sampled subgroups of the test set. Each point represents one subgroup of n subjects. (C) Examples of eFC and model predictions from 5 example individuals in the test set. Abbreviations: eFC, empirical functional connectivity; pFC, predicted functional connectivity; SC, structural connectivity; GM, geometric eigenmodes; CM, connectome eigenmodes.

Conclusions: Overall, we demonstrate that structural connectivity, geometric eigenmodes, and connectome eigenmodes can reconstruct functional connectivity with comparable accuracy. Notably, the geometric eigenmodes do not directly measure any information pertaining to inter-regional connectivity; instead, they represent local variations in shape and carry an implicit distance-dependence between points that is captured by an exponential-decay rule that is known to dominate many features of cortical organization. Together, these findings suggest that cortical geometry is as informative of large-scale brain functional connectivity as inter-regional structural connectivity.

References

1. Glasser, M. F. (2013). 'The minimal preprocessing pipelines for the Human Connectome Project'. NeuroImage, 80, 105–124. https://doi.org/10.1016/j.neuroimage.2013.04.127
2. Naze, S. (2021). 'Robustness of connectome harmonics to local gray matter and long-range white matter connectivity changes'. NeuroImage, 224, 117364. https://doi.org/10.1016/j.neuroimage.2020.117364
3. Oldham, S. (2023). 'A phylogenetically-conserved axis of thalamocortical connectivity in the human brain'. Nature Communications, 14(1), Article 1. https://doi.org/10.1038/s41467-023-41722-8
4. Pang, J. C. (2023). 'Geometric constraints on human brain function'. Nature, 1–9. https://doi.org/10.1038/s41586-023-06098-1
5. Sarwar, T. (2021). 'Structure-function coupling in the human connectome: A machine learning approach'. NeuroImage, 226, 117609. https://doi.org/10.1016/j.neuroimage.2020.117609
6. Schaefer, A. (2018). 'Local-Global Parcellation of the Human Cerebral Cortex from Intrinsic Functional Connectivity MRI'. Cerebral Cortex, 28(9), 3095–3114. https://doi.org/10.1093/cercor/bhx179

Poster No 1441

Machine learning-based fMRI feature extraction of major depressive disorders

Ye-Eun Kim[1], Jiwon Lee[2], Mikhail Votinov[3], Lisa Wagels[4], Ute Habel[5], Sun-Young Kim[6], Munseob Lee[7], Han-Gue Jo[6]

[1]Kunsan National University, Kunsan, Jeollabuk do, [2]Kunsan National University, Gunsan-si, Jeollabuk-do, [3]Institute of Neuroscience and Medicine (INM-10), Research Centre Jülich, Jülich, Germany, [4]RWTH Aachen University Hospital, Aachen, Germany, [5]Department of Psychiatry, Psychotherapy and Psychosomatics, RWTH Aachen University Hospital, Aachen, North Rhine-Westphalia, [6]Kunsan National University, Gunsan, Jeollabuk-do, [7]Electronics and Communication Research Institute (ETRI), Deajeon, Deajeon

Introduction: Literature has demonstrated the applicability of graph neural network (GNN) in analyzing the connectome derived from functional magnetic resonance imaging (fMRI), particularly in identifying alterations within the functional networks of major depressive disorder (MDD)[1,2]. Building upon these findings, the current study employs a data-driven machine learning approach with GNNs to uncover the fundamental features characterizing the functional brain network of MDD.

Methods: Resting-state functional MRI scans from a dataset of 821 MDDs were used to train a GNN model[3]. For constructing the graph, a whole-brain functional connectivity matrix was utilized, representing Fisher transformed correlation coefficients among BOLD time series across 160 Dosenbachs' atlas-based cortical brain regions[4]. Since default mode network frequently reported to be different in MDD[5], thirty-four regions of them were taken to represent default mode network within the matrix. The establishment of edges was achieved through the application of a k-nearest neighbors (KNN) algorithm, with the node feature set as a vector reflecting nodal functional connectivity. To decode the fundamental features characterizing the MDD brain network, a graph autoencoder (GAE) framework[6] was employed. GAE operates through unsupervised learning on graph-structured data, utilizing a variational autoencoder to model the latent space as a lower-dimensional vector, serving as a representation of the input dataset. Once the GAE model was trained, the connections within the input matrix significantly influencing the latent vector were identified.

Results: Figure 1 illustrates the GAE architecture with seven fully-connected (FC) layers in the encoding phase, and three FC layers and four graph convolutional network (GCN) layers in the decoding phase. The first step involved training the GAE to derive the low-dimensional representation vector Z for the provided brain networks. This training process aimed to minimize the disparity between the input X and its corresponding output X'. Upon testing the training loss across various latent dimensions, it was found that eight dimensions yielded the lowest training loss. Subsequently, the investigation focused on identifying the top salient connections contributing to the latent vector of the trained GAE. By altering the connectivity strength of each input X ij, the variations in the latent vector concerning specific connections between brain regions i and j were inferred. The assessment involved calculating the average squared variance (MSE) between the latent vectors encoded by the input X and those encoded by X ij . These MSE values were then sorted, revealing the connections with higher MSE values, indicating a more substantial impact on the latent space. Essentially, these connections signify significant features that could characterize the given input X. Figure 2 demonstrates this sorting process. It revealed a cluster of three connections above 0.175 MSE (ventromedial prefrontal cortex and left superior frontal gyrus, medial prefrontal cortex and posterior cingulate cortex, and medial prefrontal cortex and left inferior temporal gyrus), which are the top features potentially characterizing the brain networks associated with MDD.

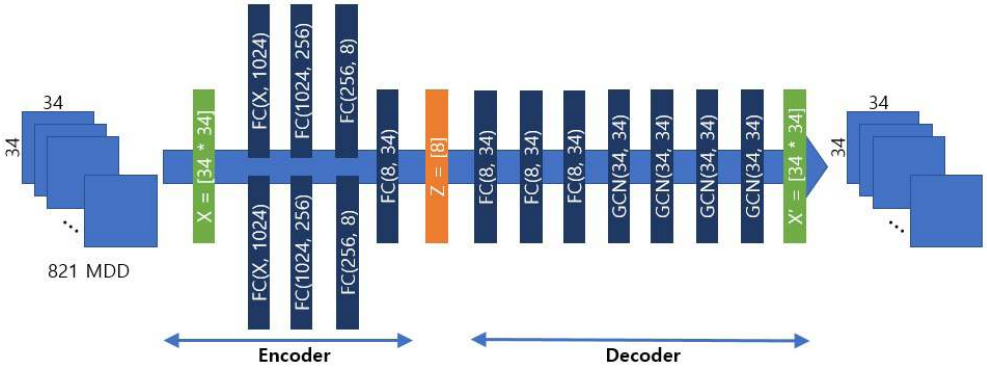

Figure 1 . The architecture of graph auto encoder. Abbreviations: GCN, graph convolutional network; FC, fullyconnected layer; Z, latent vector; MDD, major depressive disorder.

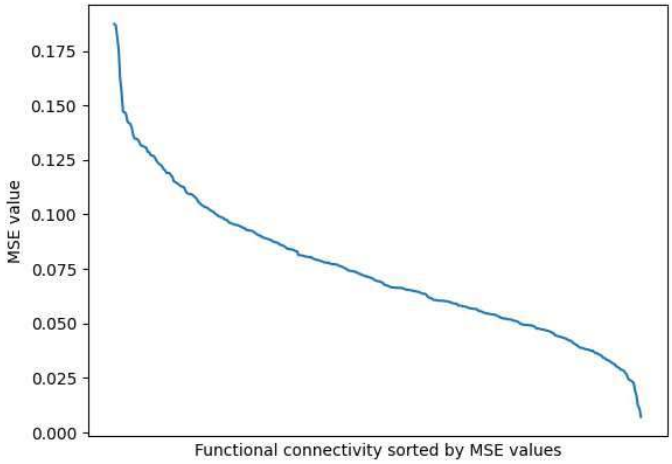

Figure 2 . MSE sorted functional connectivity. The higher the MSE values implies the higher impact on the latent vector Z of the trained GAE.

Conclusions: This study employed a data-driven GNN approach to identify the fundamental features characterizing the brain networks associated with MDD. Utilizing the autoencoder method, GAE model was trained to minimize training loss, allowing the latent vector to serve as a concise representation of the MDD brain networks. Based on data-driven analysis of a large dataset related to MDD, these findings indicate potential brain biomarkers that could be pivotal in clinical diagnosis and formulating treatment plans for psychiatric disorders.

References

1. Qin, K., Lei, D., Pinaya, W. H., Pan, N., Li, W., Zhu, Z., ... & Gong, Q. (2022). Using graph convolutional network to characterize individuals with major depressive disorder across multiple imaging sites. EBioMedicine, 78.
2. Venkatapathy, S., Votinov, M., Wagels, L., Kim, S., Lee, M., Habel, U., ... & Jo, H. G. (2023). Ensemble graph neural network model for classification of major depressive disorder using whole-brain functional connectivity. Frontiers in Psychiatry, 14, 1125339.
3. Yan, C. G., Chen, X., Li, L., Castellanos, F. X., Bai, T. J., Bo, Q. J., ... & Zang, Y. F. (2019). Reduced default mode network functional connectivity in patients with recurrent major depressive disorder. Proceedings of the National Academy of Sciences, 116(18), 9078-9083.
4. Dosenbach, N. U., Nardos, B., Cohen, A. L., Fair, D. A., Power, J. D., Church, J. A., ... & Schlaggar, B. L. (2010). Prediction of individual brain maturity using fMRI. Science, 329(5997), 1358-1361.
5. Kaiser, R. H., Andrews-Hanna, J. R., Wager, T. D., & Pizzagalli, D. A. (2015). Large-scale network dysfunction in major depressive disorder: a meta-analysis of resting-state functional connectivity. JAMA psychiatry, 72(6), 603-611.
6. Liu, M., Zhang, Z., & Dunson, D. B. (2021). Graph auto-encoding brain networks with applications to analyzing large-scale brain imaging datasets. Neuroimage, 245, 118750.

Poster No 1442

Whole-brain fMRI Pattern Extractor: 3D Variational Autoencoder for Sensorimotor Classification

Ji-Hye Lim[1], Jong-Hwan Lee[2], Hyun-Chul Kim[1]

[1]Kyungpook National University, Daegu, Korea, Republic of, [2]Korea University, Seoul, Korea, Republic of

Introduction: By extracting representation features from whole-brain fMRI datasets and inputting them into machine learning models, it is possible to alleviate an overfitting issue in fMRI classification tasks. Since the complex brain patterns occurring in the brain are not derived from a single cause but from multiple factors, it is desirable to use 3D Variational Autoencoder (3D-VAE) that can well explain non-linearity[1]. We hypothesize that Gaussian sampling in the latent space of 3D-VAE can produce a diverse array of plausible brain activity patterns, potentially improving classification task performance. Thus, this study aims to explore if features derived from 3D-VAE improve performance in four sensorimotor classification tasks.

Methods: Twelve right-handed male individuals (age = 25.0 ± 2.0 years) participated in four sensorimotor tasks: auditory attention, left-hand clenching, right-hand clenching, and visual stimulation. Each activity began with a 30-second period of focusing on a cross, followed by three task blocks of 20 seconds each, interspersed with 20-second periods of cross-fixation. The fMRI data were processed using a standardized protocol in SPM[2]. Task-specific volumes (repetition time = 2 s; 30 volumes for each task; totaling 1,440 volumes across all participants) were subsequently prepared for a four-category classification task. For extracting representation features from the whole-brain fMRI data, we employed a 3D-VAE model. Subsequently, we carried out four sensorimotor classification tasks to verify the robustness of these representations using a Multi-Layer Perceptron (MLP) classifier (including two hidden layers). The classification performance was assessed for leave-one-subject-

out CV (LOOCV). More specifically, the training dataset was used to develop a 3D-VAE model featuring a 3D Convolutional Neural Network (3D-CNN), included in both encoder and decoder components. This model was designed to extract latent representations in lower-dimensional space. In particular, the representations used the z latent calculated through the reparameterization trick for backpropagation. The representation features derived from the training dataset were used to train a MLP classifier, while features from the test dataset were used to evaluate the classification performance. Also, we visualized the reconstructed fMRI pattern using the Decoder of the 3D-VAE to explore features related to the task, further enhancing implementation of the pattern captured by the model.

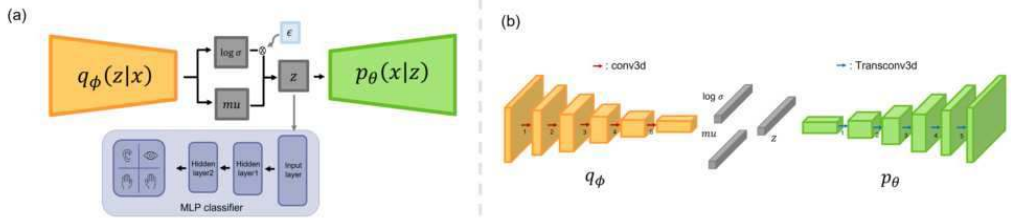

Figure 1. 3D Variational Autoencoder model architecture. (a) 3D fMRI data is the input of Encoder q_ϕ. The output of encoder mu, log σ, are reparametrized with the white noise ϵ. Extracting representation vector z is reconstructed by decoder p_θ. Finally, classification is performed using a Multi-layer Perception with the extracted representation. (b) The encoder q_ϕ and the decoder p_θ include four 3D convolution layers, each performing batch normalization. The input shape for fMRI is 1 × 54 × 64 × 46, and the output shapes of the feature maps in the encoder q_ϕ are 8 × 52 × 62 × 44, 16 × 26 × 31 × 22, 32 × 24 × 29 × 20, 64 × 12 × 15 × 10, and 128 × 10 × 13 × 8. The latent dimension of the representation is set to 256. In the decoder p_θ, the output shapes of the feature maps are 128 × 10 × 13 × 8, 64 × 12 × 15 × 10, 32 × 24 × 29 × 20, 16 × 26 × 31 × 22, 8 × 26 × 31 × 22, and 1 × 54 × 64 × 46.

Results: We observed that the 3D-VAE, featuring encoder network with convolution layers of 5 and a latent space dimensions of 256, achieved a mean error rate achieved 1.81±1.66 %, using LOOCV. This represents a decrease of 0.29% in the error rate compared to the LOOCV of a 3D-CNN using whole brain data without extracting representation using 3D-VAE[2]. Visualizing the representations extracted from each test subject with t-distributed stochastic neighbor embedding in LOOCV demonstrated effective subject identification and task-specific clustering within subjects. Furthermore, the decoded fMRI patterns based on the employed representations revealed brain patterns specific to the sensorimotor tasks.

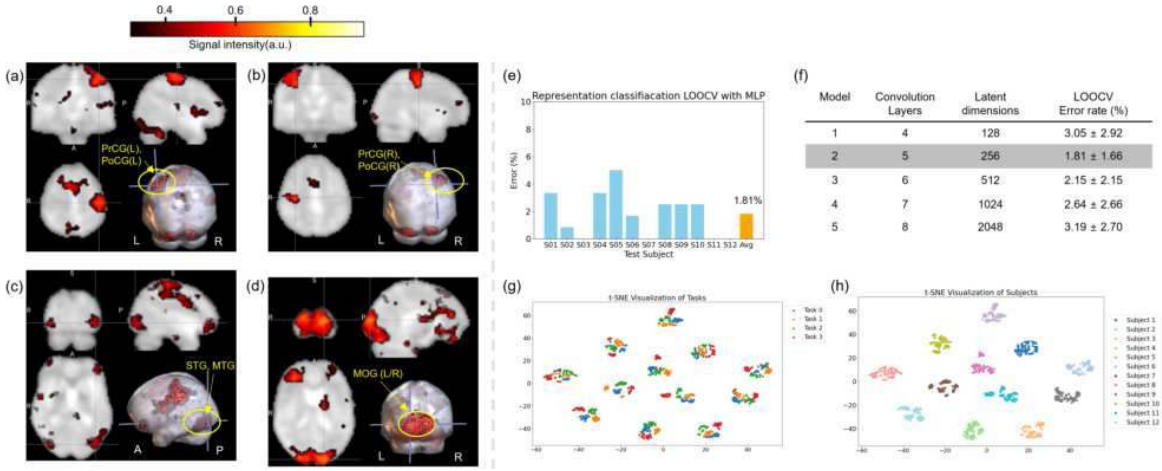

Model	Convolution Layers	Latent dimensions	LOOCV Error rate (%)
1	4	128	3.05 ± 2.92
2	5	256	1.81 ± 1.66
3	6	512	2.15 ± 2.15
4	7	1024	2.64 ± 2.66
5	8	2048	3.19 ± 2.70

Figure 2. Visualization of reconstructed fMRI patten using the Decoder of the 3D-VAE. (a) RH, right-hand clenching (b) LH, left-hand clenching (c) AD, auditory attention (d) VS, visual stimulus; PrCG, precentral gyrus; PoCG, postcentral gyrus; STG, superior temporal gyrus; MTG, middle temporal gyrus; MOG, middle occipital gyrus. 3D-VAE representations. (e) LOOCV, Leave-One-Out-Cross-Validation, Representation classification LOOCV Error rate about MLP. (f) 3D-VAE convolution layer and latent dimensions experiment. Baseline is marked in gray. (g) t-SNE for four tasks. (h) t-SNE for twelve subjects.

Conclusions: We discovered that the 3D-VAE can extract crucial representations in a lower latent space from the whole-brain, and these representations have demonstrated enhanced performance in the classification of four sensorimotor tasks. Future work is warranted to investigate the efficacy of the proposed approach in different classification tasks (e.g., working memory, emotion, social, language, gambling, relational) using Human Connectome Project datasets.

References

1. Acknowledgment: This work was supported by the National Research Foundation of Korea(NRF) grant funded by the Korea government(MSIT) (No. RS-2022-00166735 & No. RS-2023-00218987).
2. References
3. Kim, J. H., Zhang, Y., Han, K., Wen, Z., Choi, M., & Liu, Z. (2021). Representation learning of resting state fMRI with variational autoencoder. NeuroImage, 241, 118423.
4. Vu, H., Kim, H. C., Jung, M., & Lee, J. H. (2020). fMRI volume classification using a 3D convolutional neural network robust to shifted and scaled neuronal activations. NeuroImage, 223, 117328.

Poster No 1443

Graph machine learning-based classification of PTSD using verbal memory task-based fMRI

Shin-Eui Park[1], Yeong-Jae Jeon[2,3], Kyungmin Nam[4], Alex Bhogal[4], Hyeon-Man Baek[2,3], Jong-Il Park[5], Jong-Chul Yang[5]

[1]Gachon University, Incheon, Incheon, [2]Lee Gil Ya Cancer & Diabetes Institute, Gachon University, Incheon, Korea, Republic of, [3]Department of Health Sciences and Technology, GAIHST, Gachon University, Incheon, Korea, Republic of, [4]Centre for Image Sciences, Department of High Field MR, University Medical Centre Utrecth, Utrech, The Netherlands, [5]Department of Psychiatry, Jeonuk National University Medical School, Jeonju, Jeonbuk

Introduction: This study aims to develop a classification model to distinguish between individuals with Post-Traumatic Stress Disorder(PTSD) and healthy controls(HC). Utilizing memory task-based fMRI data, we can seek to identify distinctive patterns in brain activity that can serve as markers for the classification of PTSD and HC individuals. The objective is to contribute to the development of a reliable and objective method for differentiating between individuals with PTSD and those without utilizing graph machine learning algorithm, potentially enhancing diagnostic precision and informing targeted interventions.

Methods: 23 healthy controls and 13 individuals diagnosed with PTSD underwent verbal memory task fMRI scans (Fig. 1.a). Graph analysis was conducted using the CONN-fMRI FC toolbox (version 21a)[1], in conjunction with SPM12 software. Graph matrices, featuring 164 nodes as Regions of Interest (ROI), were constructed, and a connectivity matrix was derived through ROI-to-ROI correlations[2]. Following the acquisition of the connectivity matrix, thresholding was applied to eliminate less relevant information, resulting in an adjacency matrix as part of the preprocessing. Subsequently, low-dimensional features (specifically, 10 features) were extracted from functional brain connectivity networks using the “graph2vec” graph embedding technique[3]. Our classification approach involved employing RandomForest, XGBoost, Support Vector Classifier (SVC), Gaussian Naïve Bayes (Gaussian NB), and k-Nearest Neighbors (KNN) models to identify PTSD-related brain networks based on the aforementioned low-dimensional features (Fig. 1.b). Classification results were compared against the ground-truth to derive classification accuracy. To ensure robust prediction accuracy, we employed k-fold cross-validation with k=5.

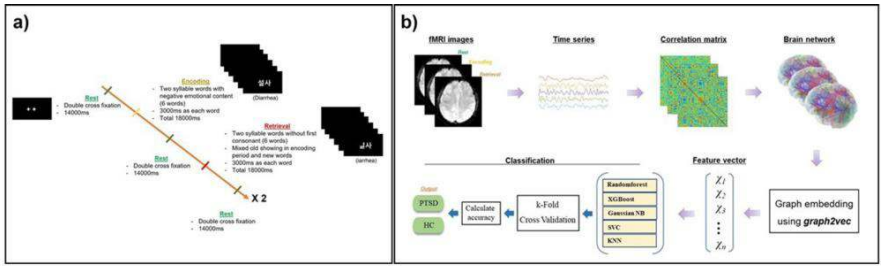

Figure 1. Activation paradigm depicting the memory task involving unpleasant words during each encoding period. Sequential presentation of six distinct two-syllable words, each appearing once (a). Subsequently, during the retrieval period, both the previously presented words from the encoding period and new words, lacking the first consonant, were randomly presented. The schematic representation of the feature extraction and pattern classification procedure is illustrated in (b).

Results: Figure 2 illustrates the classification accuracy achieved across the rest, encoding, and retrieval datasets. In the rest dataset, XGBoost exhibited the highest performance with a 73% classification accuracy at the 0.05 threshold level, while Gaussian NB and KNN models achieved a comparable accuracy of 73% at the 0.15 threshold level. For the encoding dataset, XGBoost demonstrated the most effective classification performance, achieving a 75% accuracy at the 0.25 threshold level. Finally, in the retrieval dataset, Gaussian NB emerged as the best-performing model, attaining a 70% classification accuracy at the 0.45 threshold level.

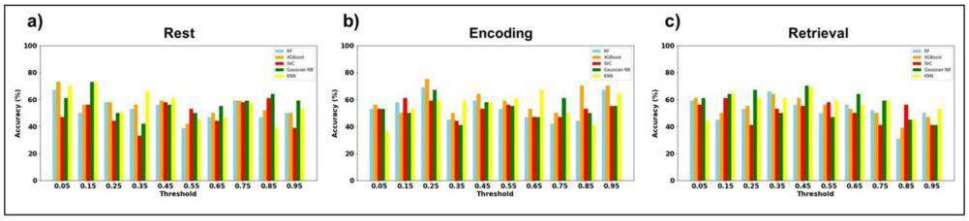

Figure 2. Classification accuracy assessed through k-fold cross-validation (n_splits=5) employing Random Forest (RF), XGBoost, Support Vector Classifier (SVC), Gaussian Naïve Bayes (Gaussian NB), and K-Nearest Neighbor (KNN) models. The results are presented for the Rest (a), Encoding (b), and Retrieval (c) blocks. The horizontal axis represents the threshold level of the connectivity matrix before graph embedding.

Conclusions: This study distinguishes itself from prior machine learning-based classification studies because we utilize memory tasks in the fMRI dataset for PTSD. While most machine learning studies[4,5] rely on resting-state fMRI due to its stability and sufficient scan time, our approach focuses on understanding how the brain functions during memory tasks, enabling us to capture more sensitive brain activation during the memory process. Notably, verbal memory impairment is a prominent feature in PTSD[6,7]. Focusing on memory tasks helps us identify unique patterns associated with memory in people with PTSD. Our study is the first to use memory task-based fMRI along with graph machine learning algorithms to identify PTSD. The different brain functional network patterns observed during memory tasks provide valuable insights for clinical understanding and identification of PTSD. In our results, XGBoost demonstrated strong performance in both the rest and encoding datasets, indicating its ability to effectively capture complex patterns associated with PTSD. On the other hand, Gaussian NB was outstanding in the retrieval dataset, highlighting its proficiency, particularly in the memory recall process. The result that different models succeeded in various datasets highlights importance of customizing machine learning methods for specific memory processing in PTSD. This comprehensive approach, incorporating memory tasks and graph machine learning, contributes to a detailed understanding of PTSD's neural correlates and its identification.

References

1. Morfini F, (2023), 'Functional connectivity MRI quality control procedures in CONN', Front Neurosci. vol. 17:1092125.
2. Achard S, (2007), 'Efficiency and cost of economical brain functional networks', PLoS Comput Biol. vol. 3, no.2:e17.
3. A. Narayanan, (2017), 'graph2vec: Learning Distributed Representations of Graphs', arXiv:1707.05005v1.
4. Khosla M, (2019), 'Machine learning in resting-state fMRI analysis. Magn Reson Imaging', vol. 64, pp. 101-121.
5. Santana CP, (2022), 'rs-fMRI and machine learning for ASD diagnosis: a systematic review and meta-analysis', Sci Rep, vol. 12, no. 1,6030.
6. Brownlow JA, (2014), 'Relationships of posttraumatic stress symptoms and sleep measures to cognitive performance in young-adult African Americans', J Trauma Stress. vol. 27, no. 2, pp. 217-223.
7. Samuelson KW, (2011), Post-traumatic stress disorder and declarative memory functioning: a review. Dialogues Clin Neurosci. vol. 13, no. 3, pp. 346-351.

Poster No 1444

Cortical Simplicial Complex Neural Networks for Alzheimer's Disease Classification

Zhiyang Li[1], Seung-Yeon Son[1], Jae-Eun Choi[1], Jong-Min Lee[1,2,3]

[1]Department of Artificial Intelligence, Hanyang University, Seoul, Korea, Republic of, [2]Department of Electronic Engineering, Hanyang University, Seoul, Korea, Republic of, [3]Department of Biomedical Engineering, Hanyang University, Seoul, Korea, Republic of

Introduction: Alzheimer's disease (AD) is a progressive and irreversible neurodegenerative disease. Early and accurate diagnosis is considered crucial for intervention as treatment. There have been many 3D volumetric analysis study using CNN models[6] on the regular voxel data structure and have been able to achieve impressive classification result. However, the intrinsic topology of the cerebral cortex is hard to preserve in such methods. On the other hand, the surface-based analysis mainly takes advantage of the geometry of the highly folded and curved cerebral cortex on the non-Euclidean space. Several works use Graph Convolutional Neural Networks[3,5] or specialized Spherical Convolutional layers[2,4] on the cortical surface mesh. Contrast to those works where they model the local one-ring patch vertices in each layer, we propose to model extended higher-order neighborhoods using Simplicial Neural Networks on the cortical surface mesh. To our knowledge, this is the first work that model cortical surface mesh as a simplicial complex that uses Simplicial Neural Networks for Alzheimer's Disease classification. We show how one can model the cortical surface mesh as a simplicial complex and utilize the Message Passing Simplicial Networks on the surface in the next section.

Methods: Given a cortical surface mesh, contrary to model it as a Graph G=(V,E), where V and E present the set of nodes and edges, we model the surface mesh as a Simplicial Complex K on the set of vertices. Where $\sigma=\{v_0,v_1,\ldots,v_k\}\in K$ is a k-dimensional simplex with k+1 cardinality. In this work, it is apparent we can model vertices as 0-simplices, edges as 1-simplices and triangles as 2-simplices. Under such simplicial complex and with the information of connection of 0-simplicies from cortical surface file, we can subsequently calculate Boundary matrices that describes the incident relations between simplices. Given every cortical surface mesh have the same connection, only one set of boundary matrices is needed for surface mesh with 40962 nodes. But since our method also models the cortical surface with different levels of discrete icosahedron meshes, a set of boundary matrices is also precomputed from mesh with 10242 nodes to icosahedron with 42 nodes. After precomputing the boundary matrices and Laplacian matrices that required for message passing simplicial layer[1], the cortical surface simplicial complex can be used to learn our classification network. Figure shows one branch of our network that process each hemisphere cortical surface simplicial complex. Where we use cortical thickness as our node feature, the feature is then transfer to higher dimension by using our STEM layer using Reparametrized Convolutional Layer[4].

We simply define the 1-simplces and 2-simplices feature as interpolation of their boundary nodes. Then we sequentially update the feature of each simplices to finally get a new set of 0-simplex features. After several layers of message passing simplicial layers and down sampling layers, we concatenate the global averaged feature for each hemisphere and sent it to the classifier layer.

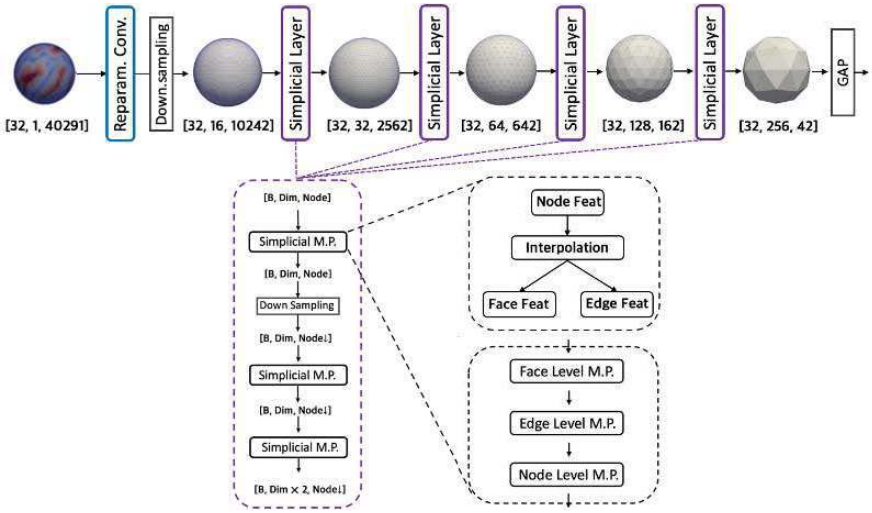

Figure: Network branch for each side of the hemisphere

Results: We conduct our experiment of AD classification using ADNI1 dataset. More specifically, after preprocessing and quality control, 225 normal control and 184 AD subjects were selected. Under the setting of stratified 5-fold cross validation. Our model achieves 90.24% accuracy with 85.40% sensitivity and 94.46% specificity. The training time for our model with 30 epoch is under 8 minutes.

Conclusions: We propose to model the cortical surface as simplicial complex and introduce a deep learning algorithm to classify Alzheimer's Disease with T1w data. Using ADNI1 dataset for the classification task, we show the effectiveness of such approach, and the potential of further using more sophisticated networks to achieve better results on surface-based analysis.

References

1. Bodnar, C. 'Weisfeiler and Lehman Go Topological: Message Passing Simplicial Networks'. (2021). Proceedings of Machine Learning Research.
2. Fenqiang Z. 'Spherical U-Net on Cortical Surfaces: Methods and Applications'. (2019). Information Processing in Medical Imaging.
3. Gopinath K. 'Learnable pooling in graph convolutional networks for brain surface analysis'. (2022). IEEE Transactions on pattern analysis and machine intelligence.
4. Jiang C. 'Spherical CNNs on unstructured grids'. (2019). International Conference on Learning Representations.
5. Liu, C. (2021). 'Fast vertex-based graph convolutional neural network and its application to brain images'. Neurocomputing.
6. Wen, J. (2020). 'Convolutional neural networks for classification of Alzheimer's disease: Overview and reproducible evaluation'. Medical Image Analysis.

Poster No 1445

Predicting post-stroke functional deficits through structural disconnection mapping

Ardalan Aarabi[1], Maedeh Khalilian[1], Martine Roussel[1], Olivier Godefroy[1]

[1]*University of Picardy Jules Verne, Amiens, Picardie*

Introduction: Post-stroke deficits arise from both localized structural damage at the injury site and widespread network dysfunction caused by structural disconnection (Salvalaggio, 2020; Siegel, 2016). Recent research has leveraged alterations in functional and structural connectivity derived from lesions to predict behavioral deficits, accounting for 40–60% of variability in acute-stage stroke patients' functional scores[2]. In this study, we assessed the predictive power of lesion-derived structural network features, derived from structural disconnection, for predicting post-stroke motor, executive and processing speed deficits in stroke patients at the chronic stage.

Methods: Structural imaging and clinical data from 340 stroke patients (aged 63.9±10.5 years) included in the GRECogVASC study cohort, who were experiencing motor, executive function, and/or processing speed deficits, were acquired six months post-stroke at Amiens University Hospital (Barbay, 2018). Lesions for each patient were manually segmented on 3D T1w images, normalized into the MNI152 template, and binarized to generate lesion masks. For post-stroke deficit prediction,

structural features were extracted from structural disconnection maps. To this end, a probabilistic structural disconnection map was first generated for each patient using streamlines passing through the patient's lesion mask, estimated by fiber tracking from diffusion-weighted imaging data of over 400 healthy controls (62.87 ± 13.47 years) from the Cambridge Centre for Ageing and Neuroscience repository (CamCAN, Stage 2) (Taylor, 2017). In the probabilistic maps, each voxel represented a disconnection probability (0 to 1) based on the number of healthy subjects showing a disconnection in that voxel (Thiebaut de Schotten, 2011). Additionally, a connectivity matrix was initially constructed for each healthy subject based on the number of streamlines connecting parcels using a high-resolution parcellation atlas with 1133 regions. Then, for each patient, fibers passing through the patient's lesion were removed from the connectivity matrices of all healthy subjects and averaged to generate a group lesion-derived structural connectivity matrix for the patient. Finally, two graph metrics (degree and clustering coefficient) were calculated for each group connectivity matrix using graph analysis. Subsequently, each feature, including the lesion mask, probabilistic maps binarized at probability thresholds of 0.1, 0.3 and 0.5, lesion-derived group connectivity matrices, as well as nodal degree and clustering coefficient, underwent decomposition by PCA. The principal components explaining 99% of variance were then input into the ridge regression model using leave-one-out cross-validation across patients to predict post-stroke deficits in motor, executive function, and processing speed.

Results: Our research indicated that lesion patterns, structural disconnection maps, and lesion-derived changes in structural connection strengths outperformed connectome-based features derived from brain networks. Optimal predictions for left/right motor scores (R2: 0.92 and 0.69) and processing speed scores (R2: 0.6) were achieved using the probabilistic structural disconnection map binarized at a probability threshold of 0.5. For executive function deficits, the most effective prediction was obtained by combining the probabilistic structural disconnection map binarized at probabilities of 0.1, 0.3, and 0.5, resulting in an R2 of 0.64.

Conclusions: Our results indicate that although structural and functional connectivity can predict behaviors, they do not consistently surpass lesion-based models. Our study also revealed that models incorporating lesion-induced alterations in structural connection strengths slightly outperformed the lesion mask in predicting deficits. Structural disconnection patterns exhibited similar predictive capabilities to lesion masks, likely due to the alignment of structural disconnection patterns with the damage caused by the lesion.

References

1. Salvalaggio, A. (2020). Post-stroke deficit prediction from lesion and indirect structural and functional disconnection. Brain, 143(7), 2173-2188. doi:10.1093/brain/awaa156
2. Siegel, J. S. (2016). Disruptions of network connectivity predict impairment in multiple behavioral domains after stroke. Proc Natl Acad Sci U S A, 113(30), E4367-4376. doi:10.1073/pnas.1521083113
3. Barbay, M. (2018). Prevalence of Poststroke Neurocognitive Disorders Using National Institute of Neurological Disorders and Stroke-Canadian Stroke Network, VASCOG Criteria (Vascular Behavioral and Cognitive Disorders), and Optimized Criteria of Cognitive Deficit. Stroke, 49(5), 1141-1147.
4. Taylor, J. R. (2017). The Cambridge Centre for Ageing and Neuroscience (Cam-CAN) data repository: Structural and functional MRI, MEG, and cognitive data from a cross-sectional adult lifespan sample. Neuroimage, 144(Pt B), 262-269.
5. Thiebaut de Schotten, M. (2011). Atlasing location, asymmetry and inter-subject variability of white matter tracts in the human brain with MR diffusion tractography. Neuroimage, 54(1), 49-59.

Poster No 1446

Generality evaluation of meta-matching models for cognitive function prediction with small datasets

Minjae Kim[1], Juhyuk Han[1], Won Hee Lee[1]

[1]Kyung Hee University, Yongin, Republic of Korea

Introduction: There is a growing interest in leveraging resting-state functional connectivity (RSFC) data derived from resting-state functional MRI to predict non-imaging phenotypes[1]. The introduction of the meta-matching framework has extended this paradigm to predicting non-imaging phenotypes such as cognitive functioning[2]. The meta-matching framework operates under the assumption that most phenotypes are interconnected rather than independent, aiming to transfer predictive models from large datasets (e.g., UK Biobank) to smaller ones (e.g., HCP). However, the efficacy of meta-matching models trained on small datasets remains unexplored. To address this gap, we assess the generality of meta-matching models trained with RSFC and 58 non-imaging phenotypes within small HCP datasets[3] for predicting individual cognitive measures across two independent datasets.

Methods: The training meta-set comprised 750 HCP subjects, each with 400 × 400 RSFCs based on the 400-region Schaefer parcellation and 58 phenotypes[3,4]. To assess the generality of meta-matching models for predicting cognitive measures, we used two independent datasets: 418 subjects from the Amsterdam Open MRI Collection (AOMIC)[5] and 116 subjects from

the Consortium for Neuropsychiatric Phenomics (CNP)[6]. Each test meta-set included 400 × 400 RSFC matrix and cognitive measure for each subject. We used the Raven's sum score for AOMIC and global cognitive function obtained from the first principal component across 24 cognitive measures for CNP[7]. Four existing models were tested using the meta-matching approach: (1) kernel ridge regression (KRR); (2) deep neural network (DNN) comprising four convolutional layers; (3) advanced fine-tuning where the weights of the last two layers of the DNN was fine-tuned; (4) advanced stacking with KRR, selecting a node with the highest coefficient of determination (COD) for the phenotypes based on the DNN, and training KRR with the selected node. We further evaluated three models: (5) advanced stacking with support vector regression (SVR), where SVR with a Gaussian kernel was trained for the selected node; (6) deep graph convolutional network (DGCNN) consisting of four graph convolutional layers and 1 pooling operator[8]; (7) graph convolutional network (GCN) consisting of three graph convolutional layers[9]. Using the meta-matching approach, each model was trained with the HCP RSFC data to predict 58 phenotypes. The COD was computed between the predicted phenotypes from the trained model and cognitive measures in a subset of the test meta-set (AOMIC or CNP). The node with the highest COD was identified as the most influential in predicting cognitive function within the given meta-set. Subsequently, the remaining RSFC data from a different test meta-set was fed into the trained models, and then cognitive function prediction was made exclusively for the previously identified influential node. The Pearson's correlation between the true and predicted score was calculated to evaluate the model's generalization. We conducted this procedure 50 times and correlations with the true cognitive score were averaged across 50 repetitions (Figure 1).

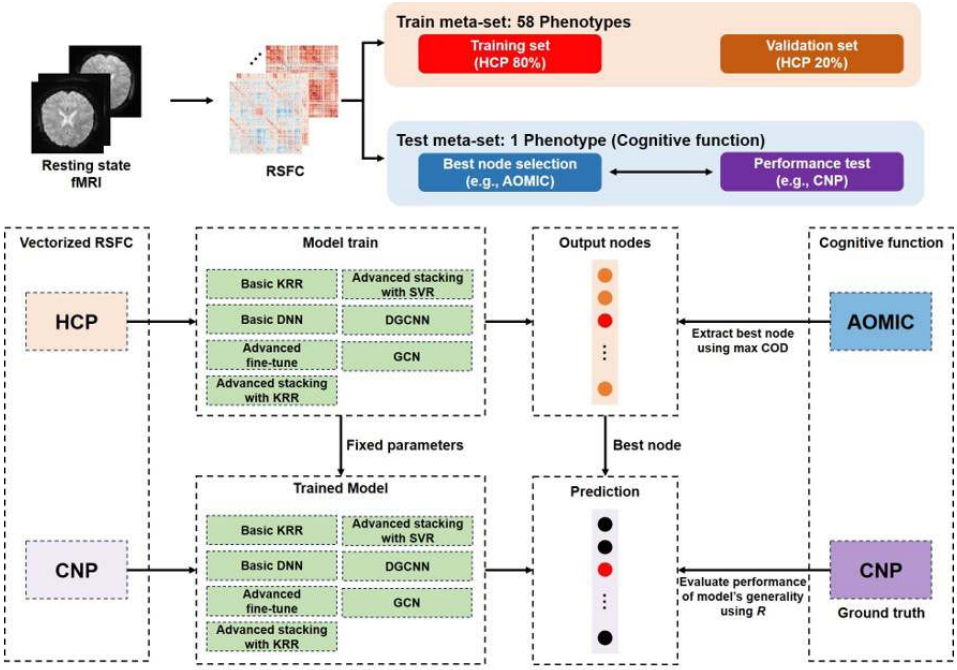

Figure 1. Overview of the meta-matching framework. The HCP dataset is used as a training meta-set comprising 750 healthy individuals and 58 non-imaging phenotypes. The test meta-set is subdivided into two subsets: one subset is used for extracting the node with the highest COD between model-generated phenotypes and cognitive function in a subset of the test meta-set (AOMIC/CNP). This other is used for inputting the identified node into the model trained on the remaining subset of the test meta-set (CNP/AOMIC). Then, the Pearson's correlation is computed between the predicted and true cognitive scores to quantify the generalization performance. We trained the meta-matching model on the HCP dataset and evaluated prediction accuracy on the other, resulting in two pairs of generalization evaluations for both AOMIC and CNP datasets.

Results: The predictive ability of RSFC for cognitive function was compared across seven models within the meta-matching method on the AOMIC and CNP datasets (Figure 2). Overall, the GCN model provided better performance compared to the other models on both datasets. Specifically, it improved generalization performance by an average correlation of 0.11 on the CNP compared to KRR ($t = 6.40$, $p < 0.05$).

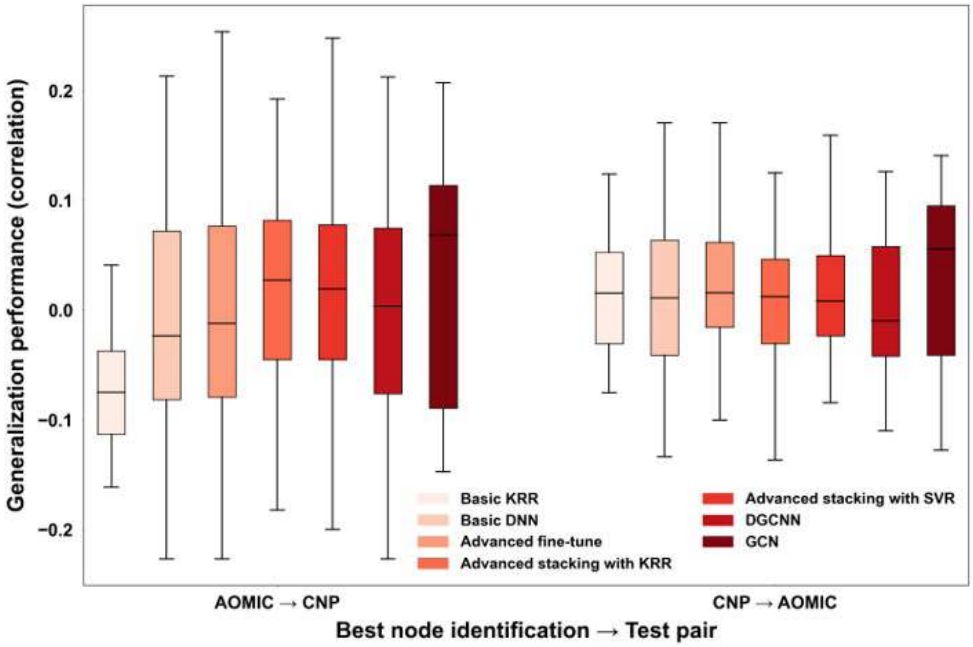

Conclusions: This study investigated the predictive ability of RSFC for cognitive function using seven different models trained on the HCP dataset within the meta-matching framework. Our GCN model demonstrated superior generalizability across healthy individuals (AOMIC) and individuals with psychiatric illness (CNP), suggesting that it can be used in clinical settings to assess cognitive function and inform treatment decisions.

References

1. He, T., Kong, R., Holmes, A.J., Nguyen, M., Sabuncu, M.R., Eickhoff, S.B., Bzdok, D., Feng, J., Yeo, B.T. (2020). Deep neural networks and kernel regression achieve comparable accuracies for functional connectivity prediction of behavior and demographics. NeuroImage, 206, 116276.
2. He, T., An, L., Chen, P., Chen, J., Feng, J., Bzdok, D., Holmes, A.J., Eickhoff, S.B., Yeo, B.T. (2022). Meta-matching as a simple framework to translate phenotypic predictive models from big to small data. Nature neuroscience, 25(6), 795-804.
3. Ooi, L.Q.R., Chen, J., Zhang, S., Kong, R., Tam, A., Li, J., Dhamala, E., Zhou, J.H., Yeo, B.T. (2022). Comparison of individualized behavioral predictions across anatomical, diffusion and functional connectivity MRI. NeuroImage, 263, 119636.
4. Van Essen, D.C., Smith, S.M., Barch, D.M., Behrens, T.E., Yacoub, E., Ugurbil, K., Wu-Minn HCP Consortium. (2013). The WU-Minn human connectome project: an overview. NeuroImage, 80, 62-79.
5. Snoek, L., van der Miesen, M.M., Beemsterboer, T., Van Der Leij, A., Eigenhuis, A., Steven Scholte, H. (2021). The Amsterdam Open MRI Collection, a set of multimodal MRI datasets for individual difference analyses. Scientific data, 8(1), 85.
6. Poldrack, R.A., Congdon, E., Triplett, W., Gorgolewski, K.J., Karlsgodt, K.H., Mumford, J.A., Sabb, F.W., Freimer, N.B., London, E.D., Cannon, T.D., Bilder, R.M. (2016). A phenome-wide examination of neural and cognitive function. Scientific data, 3(1), 1-12.
7. Chopra, S., Dhamala, E., Lawhead, C., Ricard, J., Orchard, E., An, L., Chen, P., Wulan, N., Levi, P., Moses, J., Chen, L., Kumar, P., Rubenstein, A., Aquino, K., Fornito, A., Harpaz-Rotem, I., Germine, L., Baker, J.T., Yeo, B.T., Holmes, A. (2022). Reliable and generalizable brain-based predictions of cognitive functioning across common psychiatric illness. medRxiv, 2022-12.
8. Zhang, M., Cui, Z., Neumann, M., Chen, Y. (2018). An End-to-End Deep Learning Architecture for Graph Classification. Proceedings of the AAAI Conference on Artificial Intelligence, 32(1).
9. Kipf, T.N., Welling, M. (2016). Semi-Supervised Classification with Graph Convolutional Networks. ArXiv, abs/1609.02907

Poster No 1447

Generalization performance of sex classification models to multiple datasets

Lisa Wiersch[1,2], Patrick Friedrich[1,2], Sami Hamdan[1,2], Vera Komeyer[1,2], Felix Hoffstaedter[1,2], Kaustubh Patil[1,2], Simon Eickhoff[1,2], Susanne Weis[1,2]

[1]Institute of Systems Neuroscience, Heinrich Heine University Düsseldorf, Düsseldorf, Germany, [2]Institute of Neuroscience and Medicine (INM-7), Research Centre Jülich, Jülich, Germany

Introduction: Machine Learning (ML) methods are a powerful tool increasingly applied for studying phenotypes based on neuroimaging data. Knowing to what extent the choice of training samples influences the generalizability of ML-models is crucial to achieve most accurate model performance in across-sample predictions. The present study investigates the influence of the choice of sample for sex classification analyses based on resting-state functional connectivity (RSFC) in a variety of cohorts differing in sample size, age range and imaging quality.

Methods: We employed samples from four different independent cohorts: HCP (N = 878, age range = 22-37, mean age: 28.49;[1]), GSP (N = 854, age range = 21-35, mean age: 22.92;[2]), eNKI (N = 190, age range = 20-83, mean age: 46.02;[3]) and 1000Brains (N = 1000, age range = 21-85, mean age: 61.18;[4]). For each sample, we included healthy subjects aged 20 years or older with a similar number of men and women who were matched for age. Sex classification models were trained on the data of each of the four cohorts individually and a compound sample comprising 75% data of all four samples (N = 2190, age range = 20-85, mean age: 40.10). Following the parcelwise approach by Weis et al. (2020;[5]), we trained sex classifiers on the parcelwise RSFC profile of 436 parcels individually resulting in five sets of parcelwise Classifiers (pwCs;[6]). Each of the classification models was trained with a Support Vector Machine Classifier implemented in Julearn[7]. All five pwCs were applied on test samples derived from the four original samples. In addition, out-of-sample performance of all pwCs was evaluated on data extracted from the AOMIC dataset (N = 370, age range: 20-26, mean age: 22.50) which was not included in training any of the pwCs.

Results: For pwCs trained on single samples, pwC HCP demonstrated highest mean cross-validation (CV) accuracy averaged across all 436 parcels (figure 1a). However, pwC HCP showed lowest generalization in across-sample predictions with mean accuracies ranging between 52% (eNKI) and 55% (1000Brains). In contrast, pwC GSP, pwC eNKI and pwC 1000Brains achieved lower mean CV accuracies than pwC HCP but higher generalization performance for across-sample predictions (figure 1a). Highest classifying parcels per model application were consistently located in the temporal lobe, inferior parietal lobule, posterior cingulate gyrus and inferior frontal gyrus (figure 2a). Except for pwC HCP, pwC compound achieved higher mean CV and generalization performance than pwCs trained on single samples: Mean accuracies in across-sample predictions ranged between 61% (HCP test sample) and 65% (GSP test sample, figure 1b) with up to 83% accuracy (eNKI test sample, figure 2b). Highest classifying parcels were located in similar regions as for pwCs trained on single samples (figure 2b). Likewise, pwC compound also showed highest generalization performance for the out-of-sample prediction of the AOMIC sample with a mean accuracy of 59% (figure 1c) with highest classifying parcels - up to 69% - being located in the inferior parietal lobule, inferior frontal gyrus and posterior cingulate gyrus (figure 2c).

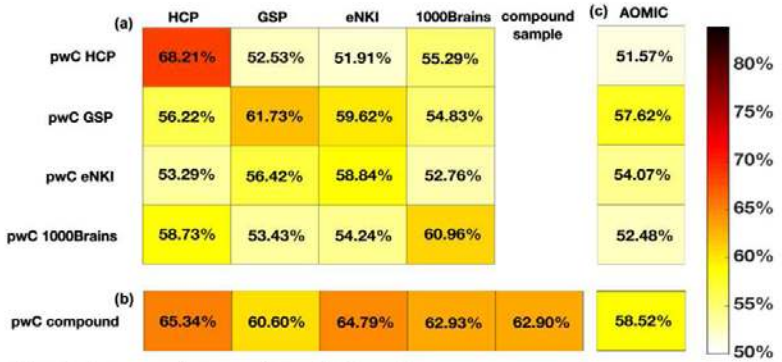

Figure 1. Mean accuracies averaged over all 436 parcels
(a) Mean accuracies for CV and across-sample predictions of pwCs trained on single samples
(b) Mean accuracies for CV and across-sample predictons of pwC trained on the compound sample
(c) Mean accuracies for model application to the independent AOMIC sample

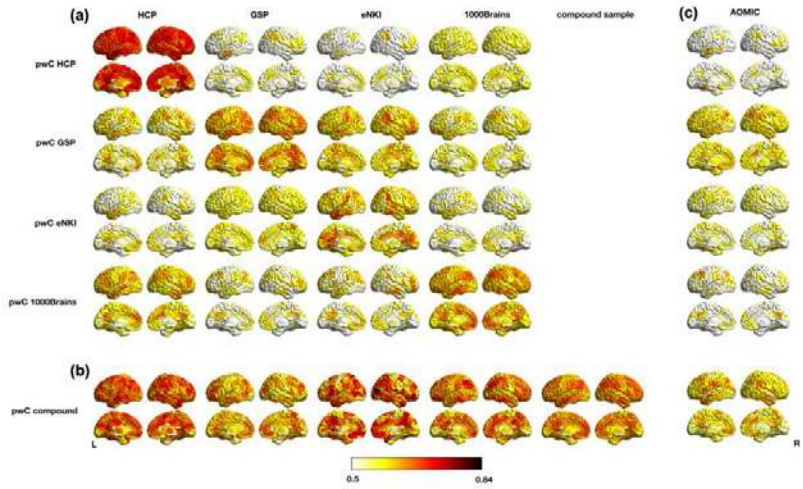

Figure 1. Accuracy maps representing the spatial distribution of parcelwise sex classification accuracies across the brain
(a) Accuracy maps for CV and across-sample predictions of pwCs trained on single samples
(b) Accuracy maps for CV and across-sample predictons of pwC trained on the compound sample
(c) Accuracy maps for model application to the independent AOMIC sample

Conclusions: The present results showed that classifiers trained on single samples generalized well for some, but not all, test samples. Specifically, classifiers trained on one sample performed well on a certain other sample, and vice versa as e.g. HCP & 1000Brains as well as eNKI & GSP. In contrast, pwC trained on the compound sample outperformed single sample trained classifiers in classification accuracy. This was not only the case for the test samples, parts of which were used to train pwC compound, but also for the independent AOMIC sample. Overall, the aggregation of multiple samples for training sex classification models resulted in superior generalization performance which could be attributed to the high sample size but also the heterogeneous data composition of pwC compound.

References

1. Caspers, S., Moebus, S., Lux, S., Pundt, N., Schutz, H., Muhleisen, T. W., . . . Amunts, K. (2014). Studying variability in human brain aging in a population-based German cohort-rationale and design of 1000BRAINS. Front Aging Neurosci, 6, 149. doi:10.3389/fnagi.2014.00149
2. Hamdan, S., More, S., Sasse, L., Komeyer, V., Patil, K. R., & Raimondo, F. . (2023). Julearn: an easy-to-use library for leakage-free evaluation and inspection of ML models. arXiv preprint arXiv:2310.12568.
3. Holmes, A. J., Hollinshead, M. O., O'Keefe, T. M., Petrov, V. I., Fariello, G. R., Wald, L. L., . . . Buckner, R. L. (2015). Brain Genomics Superstruct Project initial data release with structural, functional, and behavioral measures. Sci Data, 2, 150031. doi:10.1038/sdata.2015.31
4. Nooner, K. B., Colcombe, S. J., Tobe, R. H., Mennes, M., Benedict, M. M., Moreno, A. L., . . . Milham, M. P. (2012). The NKI-Rockland Sample: A Model for Accelerating the Pace of Discovery Science in Psychiatry. Frontiers in neuroscience, 6, 152. doi:10.3389/fnins.2012.00152
5. Van Essen, D. C., Smith, S. M., Barch, D. M., Behrens, T. E., Yacoub, E., Ugurbil, K., & Consortium, W. U.-M. H. (2013). The WU-Minn Human Connectome Project: an overview. NeuroImage, 80, 62-79. doi:10.1016/j.neuroimage.2013.05.041
6. Weis, S., Patil, K. R., Hoffstaedter, F., Nostro, A., Yeo, B. T. T., & Eickhoff, S. B. (2020). Sex Classification by Resting State Brain Connectivity. Cereb Cortex, 30(2), 824-835. doi:10.1093/cercor/bhz129
7. Wiersch, L., Friedrich, P., Hamdan, S., Komeyer, V., Hoffstaedter, F., Patil, K. R., ... & Weis, S. (2023). Sex classification from functional brain connectivity: Generalization to multiple datasets. bioRxiv, 2023-08.

Poster No 1448

Variability of brain-age estimates in MS within and between three different MR scanners

Lonneke Bos[1], David Van Nederpelt[1], James Cole[2], Hugo Vrenken[1], Eva Strijbis[3], Bastiaan Moraal[1], Joost Kuijer[1], Bernard Uitdehaag[1], Alle Meije Wink[1], Frederik Barkhof[1], Bas Jasperse[1]

[1]Amsterdam University Medical Centre, Amsterdam, Netherlands, [2]University College London, London, London, [3]Department of Neurology, MS Center Amsterdam, Amsterdam Neuroscience, Amsterdam UMC, Amsterdam, Netherlands

Introduction: Neurodegenerative processes due to normal aging change the macroscopic structure of the brain, which are similar to brain changes observed in neurodegenerative brain diseases. "Accelerated" aging of the brain is therefore regarded as a marker of disease-related neurodegeneration. Recent deep and machine learning techniques trained on aging healthy subjects estimate the subjects age from standard brain MRI scans. By subtracting the person's true age from this estimated brain-age the brain predicted age difference (brain-PAD) is acquired. Brain-PAD is related to clinical and radiological evidence of disease severity in multiple sclerosis (MS). Previous research showed that people with MS (pwMS) have a brain-PAD of 7.3 ± 0.8 (SD) years, on average. The intra- and inter-scanner reliability of brain-PAD estimation is currently unknown and is important for interpreting brain-PAD and for clinical implementation. The aim of this project is to investigate within-scanner repeatability and between-scanner reproducibility of brain-PAD using three different brain-age models and same-day scan-rescan imaging on three different scanners.

Methods: For 30 pwMS and 10 age and sex-matched HC (mean age 44.2 ± 11.7 years and 39.2 ± 12.9 years, respectively), MS with EDSS range: 0.0–6.5, 3D T1-weighted MRI scans were acquired on a GE Discovery MR750 (3T), a Siemens Sola (1.5T) and a Siemens Vida (3T) scanner (AMS2 dataset). Each person was scanned twice on all scanners in one day. Brain-PAD was determined using the MIDI model (DenseNet121), the brainageR model (Gaussian Process Regression) and DeepBrainNet (inception-resnetv2). Repeatability and reproducibility were assessed using intraclass correlation coefficient (ICC, ICC absolute agreement within-scanner and ICC consistency between-scanners). Another way to measure repeatability and reproducibility was the smallest detectable change (SDC).

Results: Within-scanner repeatability was excellent (ICC>0.93) for all three models for both HC and pwMS (see Fig 1.A). Within-scanner repeatability was better for HC (SDC range 1.56 - 3.06 years) than for pwMS (SDC range 2.63 – 4.08 years) (see Table 1.A) for all three models. Between-scanner ICC for brainageR and the MIDI model was good to excellent (>0.85), for both HC and pwMS. For DeepBrainNet the ICC between-scanners was between 0.15 and 0.32 when the GE was compared with the Sola or the Vida, but was >0.92 for comparison between the Sola and the Vida (see Fig 1.B). Between-scanner SDC for the MIDI model was 5.06 years for HC and 5.73 years for pwMS. Between-scanner SDC for brainageR between 6.50 years for

HC and 6.86 years for pwMS. Between-scanner consistency was lower for the brainageR model for GE vs Sola, than for GE vs Vida. For DeepBrainNet the SDC between-scanners was 24.27 years for HC and 22.08 years for pwMS (see Table 1.B). Between-scanner consistency was lower for the brainageR model when comparing the Sola (1.5T) with the 3T scanners. This might be due to the lower signal to noise ratio as a result of the lower field strength. Differences in scanner characteristics and imaging protocols cause an imbalance of within-scanner repeatability and between-scanner reproducibility. Model fine-tuning could minimize discrepancies without sacrificing one for the other. The SDC within-scanner is clinically acceptable, whereas the SDC between-scanners is too large to detect the increase of brain-age for pwMS. This makes it difficult to use brain-age prediction on an individual level to predict disease progression.

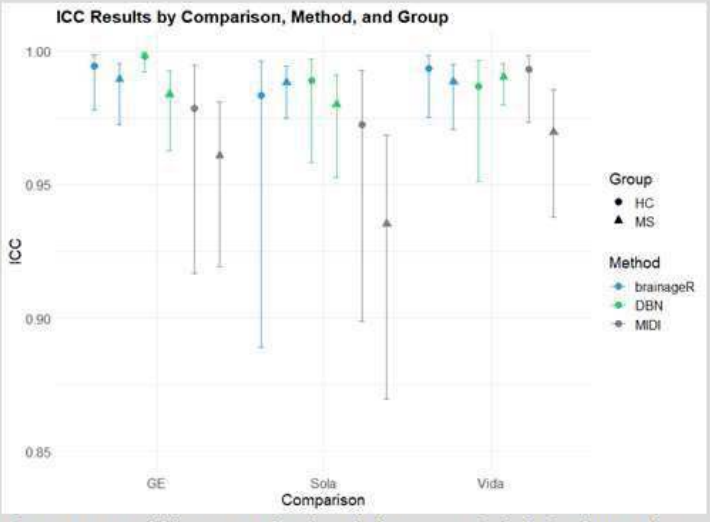

Figure 1.A ICC within-scanner for three brain-age methods for both HC and pwMS

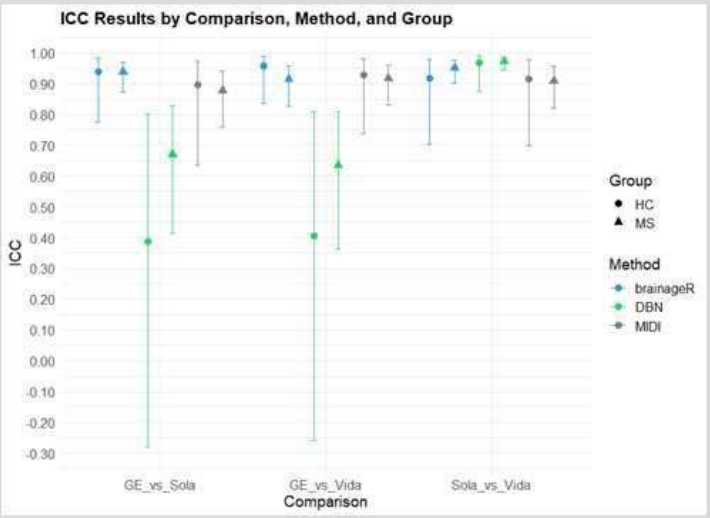

Figure 1.B ICC between-scanner for three brain-age methods for both HC and pwMS

TABLE 1.A SDC within-scanner analyses, for HC and pwMS

SDC within-scanner, for HC and pwMS		
	SDC HC [years]	SDC MS [years]
brainageR	3,06	4,08
MIDI	2,22	3,48
DBN	1,56	2,63

TABLE 1.B SDC between-scanner analyses, for HC and pwMS

SDC between-scanner, for HC and pwMS		
	SDC HC [years]	SDC MS [years]
brainageR	6,50	6,86
MIDI	5,06	5,72
DBN	24,27	22,08

Conclusions: Within-scanner reproducibility was excellent for all brain-PAD models for both HC and pwMS. The brainageR model was most robust between-scanners, while DeepBrainNet was most robust within-scanners. The MIDI model showed overall the best results for repeatability and reproducibility. While within-scanner repeatability showed promising results, caution is warranted in determining brain-age across different scanners.

References
1. Cole, J. H. (2020), "Longitudinal assessment of multiple sclerosis with the brain-age paradigm." Annals of neurology, 88(1), 93-105.
2. Wood, D. A. (2022), "Accurate brain-age models for routine clinical MRI examinations." Neuroimage, 249, 118871.
3. Bashyam, V. M. (2020), MRI signatures of brain age and disease over the lifespan based on a deep brain network and 14 468 individuals worldwide. Brain, 143(7), 2312-2324.
4. Biondo, F. (2021), "Brain-age predicts subsequent dementia in memory clinic patients." medRxiv, 2021-04.

Poster No 1449

Improving stroke recovery prediction by estimating subject information from population disconnectome

Patrik Bey[1], Kiret Dhindsa[2], Michael Schirner[2], Jan Feldheim[3], Marlene Bönstrup[4], Robert Schulz[3], Bastian Cheng[3], Götz Thomalla[3], Christian Gerloff[3]

[1]Berlin Institute of Health at Charité, Berlin, Berlin, [2]Berlin Institute of Health, Berlin, Berlin, [3]Universitätsklinikum Hamburg-Eppendorf, Hamburg, Hamburg, [4]Universitätsklinikum Leipzig, Leipzig, Sachsen

Introduction: The detrimental impact of stroke on motor function depends on various factors, from lesion topology and location to alterations in both functional and structural connectivity[1,2]. Reliable biomarkers for predicting recovery remain an ongoing challenge, particularly during the acute phase after stroke[3]. Population-based disconnectomes capture lesion impact on connectivity, relate to brain function[4] and have been shown to enable prediction of clinical scores with moderate accuracy[1,5–7]. Here we provide proof-of-concept enhancing this approach. We approximated patient information from disconnectomes, constructed from healthy controls, using a regression model and consequently improved machine learning classification of recovery without the need for individual disconnectomes. This is of particular interest as the clinical context of stroke severely restricts data availability, reducing the capacity to create individual disconnectomes. We show that our framework can use limited data to predict metrics for new patients, recovering some classification accuracy driven by individual variability, thus salvaging direct clinical applicability.

Methods: We used previously processed[8] MRI data from 20 stroke patients[9] and corresponding clinical scores including Barthel, ARAT, MRS and NIHSS. Severity of motor deficit was defined via an aggregate of all scores, computed as the ratio of maximum possible severity. Patient data was acquired 3-5 days (acute) and 85-95 days (subacute) post stroke onset. All patients were assigned a recovery class (good, medium, bad) according to longitudinal motor recovery (Figure 1 (A)). Individual lesion disconnectomes were created by extracting white matter streamlines intersecting the lesion volume. Each subject's brain parcellation was then used to create the disconnectome . We repeated this approach using data of 15 healthy controls from the same cohort[9], after transferring each patient's lesion mask into control subject brain. The resulting disconnectomes were averaged to create a population-based disconnectome for each patient (Figure 1 (B)). A total of eight network measures were computed describing complementary properties of the disconnectome: degree, strength, centrality, assortativity, clustering coefficient, density as well as skewness and kurtosis of the degree distribution[10]. Those measures were used as input to a non-linear support vector machine (SVM) to perform three-way classification using leave-one-out cross validation (LOOCV). A linear regression was fitted to map the population disconnectome to the individual network metrics of each patient. The fitted model was then used to estimate network measures for previously unseen data. Finally, the predicted metrics were used as input to the SVM classification framework to investigate differential information based on these estimates of subject specificity.

Results: Both disconnectomes and corresponding network measures show distinct patterns and distributions between individual and population-based data (Figure 1 (B, D)). The classification showed a strong performance using individual disconnectome information (F1 score: 0.75) (Figure 1 (C)). Population-based information resulted in a reduced performance (F1 score: 0.55). Using the regression-based estimates as input features resulted in an increased performance (F1 score: 0.65) while retaining population-based disconnectomes as the basis.

Conclusions: We first showed that individual disconnectomes provide a higher level of information with regards to prediction of motor-deficit recovery compared to population-based approaches. Critically we could further show that by enhancing population-based disconnectome information, improvement of recovery prediction was significant. Future research can

expand upon this work by integrating such estimates of subject variability in recovery predictions and in whole brain modelling for stroke, e.g. using TheVirtualBrain, investigating recovery mechanisms.

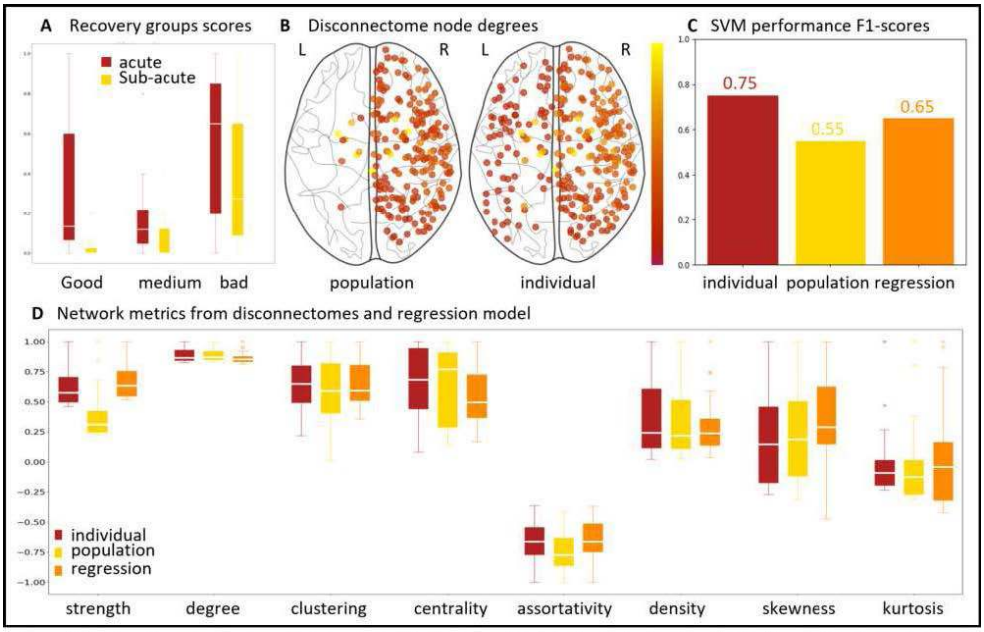

Figure 1 *(**A**) Severity scores for recovery groups for acute and subacute state. Boxplots show the distribution of clinical severity for all four included clinical tests (Barthel, ARAT, MRS and NIHSS). (**B**) Node degrees of averaged population based and individual lesion disconnectomes of all included stroke patients (left hemisphere strokes were mapped into right hemisphere for visualization). The individual disconnectomes show a higher integration of contralesional hemisphere connections which has been shown to be related to stroke recovery. (**C**) Machine learning based recovery prediction is driven by subject variability showing the highest performance (F1: 0.75) of the SVM for individual disconnectome based features. Regression-based estimates still provide a high performance for the three-class problem (F1: 0.65) while only population-based measures deliver a slightly above chance performance (F1: 0.55) indicating the lowest level of subject specificity. (**D**) Network measures computed for individual disconnectomes, population based disconnectomes and estimated via the fitted regression model. For visualization all values were normalized.*

References

1. Bey, P. et al. Lesion aware automated processing pipeline for multimodal neuroimaging stroke data and The Virtual Brain (TVB). bioRxiv (2023) doi:10.1101/2023.08.28.555078.
2. Bowren, M. et al. Post-stroke outcomes predicted from multivariate lesion-behaviour and lesion network mapping. Brain 145, 1338–1353 (2022).
3. Bullmore, E. & Sporns, O. Complex brain networks: Graph theoretical analysis of structural and functional systems. Nat. Rev. Neurosci. 10, 186–198 (2009).
4. Forkel, S. J. & Catani, M. Lesion mapping in acute stroke aphasia and its implications for recovery. Neuropsychologia 115, 88–100 (2018).
5. Jimenez-Marin, A. et al. Multimodal and multidomain lesion network mapping enhances prediction of sensorimotor behavior in stroke patients. Sci. Rep. 12, 22400 (2022).
6. Pini, L. et al. A novel stroke lesion network mapping approach: improved accuracy yet still low deficit prediction. Brain Communications 3, (2021).
7. Schlemm, E. et al. Structural brain networks and functional motor outcome after stroke—a prospective cohort study. Brain Communications 2, 1–13 (2020).
8. Siegel, J. S., Shulman, G. L. & Corbetta, M. Measuring functional connectivity in stroke: Approaches and considerations. J. Cereb. Blood Flow Metab. 37, 2665–2678 (2017).
9. Talozzi, L. et al. Latent disconnectome prediction of long-term cognitive-behavioural symptoms in stroke. Brain (2023) doi:10.1093/brain/awad013.
10. Thiebaut de Schotten, M., Foulon, C. & Nachev, P. Brain disconnections link structural connectivity with function and behaviour. Nat. Commun. 11, (2020).

Poster No 1450

Using Neurotransmitter Vulnerability to Discriminate Schizophrenia Patients from Healthy Controls

Lisa Hahn[1,2], Florian Raabe[1], Daniel Keeser[1,3], Moritz Rossner[1,4], John Fanning[1,2], Clara Vetter[1], Alkomiet Hasan[5], Peter Falkai[1], Nikolaos Koutsouleris[1,2,6]

[1]Department of Psychiatry and Psychotherapy, Ludwig-Maximilian University, Munich, Germany, [2]Max-Planck Institute of Psychiatry, Munich, Germany, [3]Clinical Radiology, Ludwig-Maximilian University, Munich, Germany, [4]Systasy Bioscience GmbH, Munich, Germany, [5]Department of Psychiatry, Psychotherapy and Psychosomatics, Medical Faculty, University of Augsburg, Ausgburg, Germany, [6]Institute of Psychiatry, Psychology and Neurosciences, King's College London, London, United Kingdom

Introduction: Aside to common psychotic symptoms such as hallucinations, delusions and disorganized thinking, schizophrenia (SCZ) is characterized by structural alterations such as volume reductions in the temporal, frontal, and parietal lobes. Here, we evaluated if the co-localization of these alterations with the distribution of specific neurotransmitter systems, i.e. an indication of neurotransmitter vulnerability) can be utilized to discriminate SCZ patients from healthy controls (HC).

Methods: Maps of grey matter volume (GMV) were derived from T1-weighted structural magnetic resonance imaging for 445 SCZ patients (mean age = 34.0 ± 11.3, 103 females) and 416 HC (mean age = 33.5 ± 11.3, 108 females) from the Multimodal Imaging in Chronic Schizophrenia Study (MIMICSS; part of the PsyCourse study), the Center for Biomedical Research Excellence (COBRE; part of the COIN study) cohort, Mind Clinical Imaging Consortium (MCIC; part of the COIN study) cohort, the UCLA Consortium for Neuropsychiatric Phenomics LA5c Study, and the Munich cohort (internal dataset). Two linear classifiers utilizing a leave-site-out cross-validation (CV) design (CV1: 10x5, CV2: 1x10) for the discrimination of SCZ patients and HC were created. The preprocessing steps computed within the CV framework included offset correction using the global mean, correction for age and sex using partial correlations, the model-specific feature computation, and standardization. The model-specific features either entailed whole-brain correlation coefficients between GMV and 29 nuclear-imaging derived neurotransmitter maps (e.g., receptor and transporter density) from a healthy volunteer population computed using the JuSpace toolbox or 29 eigenvariates computed using principal component analysis (PCA) as a control model.

Results: The first classifier (using whole-brain correlation coefficients) discriminated SCZ from HC with a balanced accuracy of 64.1 % and area under the curve of 0.68 (sensitivity = 64.7 %, specificity = 63.6 %). The control classifier (using PCA eigenvariates) performed similarly, discriminating SCZ from HC with a balanced accuracy of 66.4 % and area under the curve of 0.72 (sensitivity = 75.2 %, specificity = 57.5 %).

Conclusions: SCZ patients were distinguishable from HC based on the association of structural alterations with specific neurotransmitter systems. These findings suggest that this indication of neurotransmitter vulnerability might serve as a diagnostic biomarker.

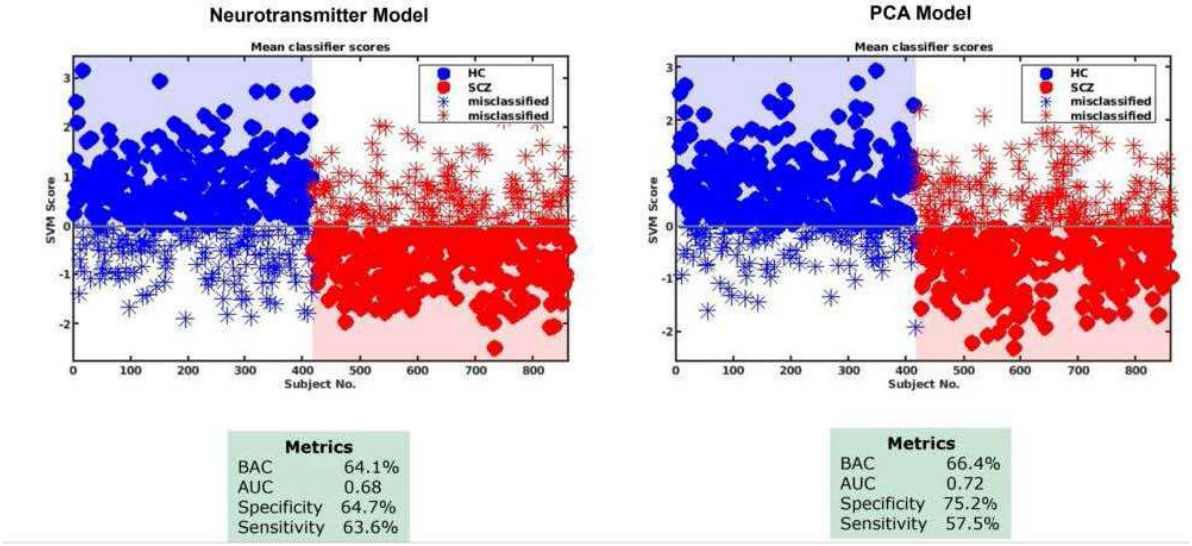

References

1. Aine, C. J., Bockholt, H. J., Bustillo, J. R., Cañive, J. M., Caprihan, A., Gasparovic, C., ... & Calhoun, V. D. (2017). Multimodal neuroimaging in schizophrenia: description and dissemination. Neuroinformatics, 15, 343-364.
2. Budde, M., Anderson-Schmidt, H., Gade, K., Reich-Erkelenz, D., Adorjan, K., Kalman, J. L., ... & Heilbronner, U. (2019). A longitudinal approach to biological psychiatric research: The PsyCourse study. American Journal of Medical Genetics Part B: Neuropsychiatric Genetics, 180(2), 89-102.
3. Dukart, J., Holiga, S., Rullmann, M., Lanzenberger, R., Hawkins, P. C., Mehta, M. A., ... & Eickhoff, S. B. (2021). JuSpace: A tool for spatial correlation analyses of magnetic resonance imaging data with nuclear imaging derived neurotransmitter maps (Vol. 42, No. 3, pp. 555-566). Hoboken, USA: John Wiley & Sons, Inc..
4. Gollub, R. L., Shoemaker, J. M., King, M. D., White, T., Ehrlich, S., Sponheim, S. R., ... & Andreasen, N. C. (2013). The MCIC collection: a shared repository of multi-modal, multi-site brain image data from a clinical investigation of schizophrenia. Neuroinformatics, 11, 367-388
5. Gorgolewski, K. J., Durnez, J., & Poldrack, R. A. (2017). Preprocessed consortium for neuropsychiatric phenomics dataset. F1000Research, 6.
6. Lieberman, J. A., & First, M. B. (2018). Psychotic disorders. New England Journal of Medicine, 379(3), 270-280.

Poster No 1451

A transformer-based meta-matching stacking method improves prediction accuracy of fluid intelligence

Juhyuk Han[1], Minjae Kim[2], Won Hee Lee[3]

[1]KyungHee University, Gyeonggi-do, Republic of Korea, Korea, Republic of, [2]Kyung Hee University, Yong-in, Yong-in, [3]KyungHee University, Yonginsi, Yonginsi

Introduction: The proliferation of datasets integrating both imaging and non-imagining phenotypes has provided a rich resource for advancing predictive modeling in neuroscience. The meta-matching framework has emerged as a promising avenue, offering the potential to harness models trained on large-scale datasets for predicting non-imaging phenotypes within smaller datasets[1]. Despite its promise, the conventional application of the meta-matching framework to a single modality has revealed limitations, particularly in integrating and exploiting information from diverse modalities. To address this gap, we propose a new stacking approach, termed multimodal transformer stacking, which incorporates self-attention[2] to extract meaningful patterns and relationships across multiple modalities, advancing its potential for accurate predictions of non-imaging phenotypes.

Methods: We used 58 non-imaging phenotypes and multimodal imaging features of 750 subjects from the HCP dataset[3]. We computed a new set of structural features derived from the same HCP participants, namely morphometric inverse divergence networks (MIND)[4] and morphometric similarity networks[5]. We used 16 diffusion features derived from diffusion MRI and 6 functional features derived from each task and resting-state fMRI scan. Details about the imaging features derived from T1-weighted, diffusion, and functional MRI scans can be found elsewhere[3]. We divided the data into the training meta-set with 600 participants and 57 phenotypes, and test meta-set with 150 participants and fluid intelligence selected as the target phenotype. We subdivided the test meta-set into a K-shot sample set (n = 100) and a test set (n = 50). We initiated our approach with the advanced stacking method using each imaging feature. In this process, the nodes with the highest coefficient of determination (COD) from the basic deep neural network were selected. A kernel ridge regression was trained on a K-shot sample set using the predictions for the chosen nodes. Across diverse imaging features, we identified those yielding high performance in a test set. These were integrated into the multimodal transformer stacking. Predictions from the five imaging features were concatenated to form a multimodal feature matrix. This matrix entered into a transformer encoder to learn relationships among the phenotypes through self-attention across predicted phenotypes from multiple modalities. The resulting matrix was employed to predict fluid intelligence through a dense layer. The process was repeated 50 times, and the correlations and CODs with the true score were averaged over these 50 repetitions. Our approach was compared against existing methods[1].

Results: Traditional advanced stacking methods resulted in better performance for predicting fluid intelligence, when using MIND ($r = 0.09$), TBSS axial diffusivity ($r = 0.22$), tractography axial diffusivity ($r = 0.19$), resting-state ($r= 0.29$) and working memory fMRI features ($r = 0.37$). These were further used as features for the multimodal transformer stacking. Our results demonstrate that multimodal transformer stacking ($r = 0.41$) outperforms both stacking average and traditional advanced stacking of individual features (r: $t = 3.13 – 11.11$, $p < 0.05$; COD: $t = 3.12 – 9.77$, $p < 0.05$) (Figure 2). This suggests that the transformer encoder's ability to capture long-range dependencies and relationships among phenotypes from different modalities contributes to improved predictive performance.

Conclusions: We proposed a new stacking strategy for integrating information from diverse imaging modalities to improve the prediction of fluid intelligence. Stacking average averages the predictions from individual models, which may not fully account for the interactions and relationships between the modalities. Our proposed approach has the potential to learn more complex relationships between the features and capture more subtle patterns and interactions for improved prediction of cognitive functioning.

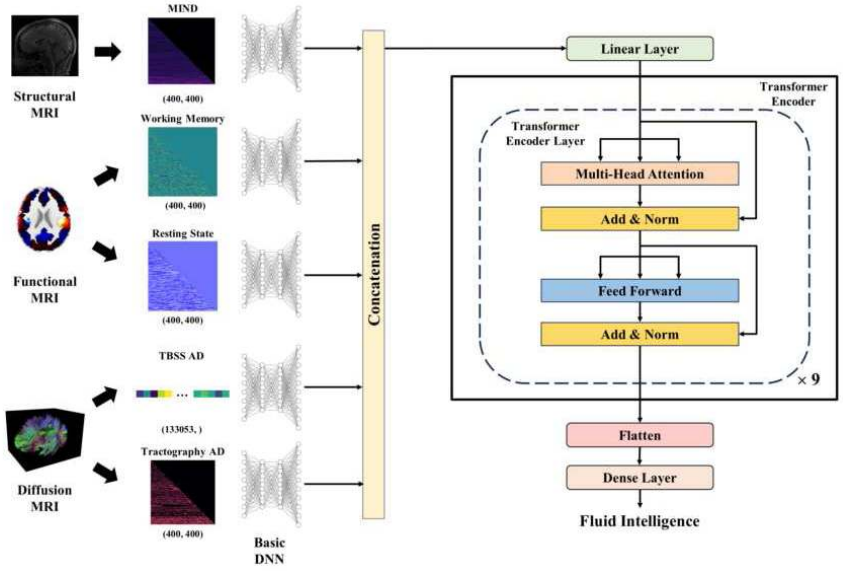

Figure 1. Workflow for multimodal transformer stacking. Imaging features with optimal performance for each modality are selected. These include MIND, working memory functional connectivity, resting-state functional connectivity, TBSS axial diffusivity. Each selected imaging feature generates prediction using a basic deep neural network. Predictions from the selected imaging features are concatenated along the appropriate axis to create a multimodal feature matrix. This matrix is input into a transformer encoder, which learns relationships among phenotypes through self-attention across predictions from multiple modalities. The output from the transformer encoder is processed through a dense layer to predict fluid intelligence.

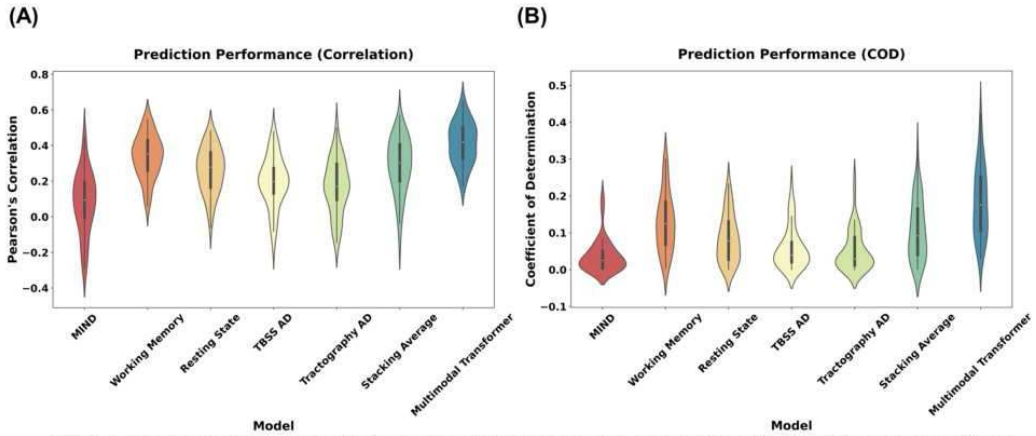

Figure 2. Violin plots for (a) Pearson's correlation and (b) coefficient of determination, illustrating the performance of the conventional advanced stacking, stacking average (averaging predictions of advanced stacking), and multimodal transformer across five imaging features: MIND, working memory functional connectivity, resting state functional connectivity, TBSS axial diffusivity, tractography axial diffusivity.

References

1. He, T., An, L., Chen, P., Chen, J., Feng, J., Bzdok, D., Holmes, A. J., Eickhoff, S. B., & Yeo, B. T. (2022). 'Meta-matching as a simple framework to translate phenotypic predictive models from big to small data', Nature neuroscience, vol. 25, no.6, pp. 795-804.=
2. Bahdanau, D., Cho, K., & Bengio, Y. (2014). 'Neural machine translation by jointly learning to align and translate', arXiv preprint arXiv:1409.0473, vol., pp.
3. Ooi, L. Q. R., Chen, J., Zhang, S., Kong, R., Tam, A., Li, J., Dhamala, E., Zhou, J. H., Holmes, A. J., & Yeo, B. T. (2022). 'Comparison of individualized behavioral predictions across anatomical, diffusion and functional connectivity MRI', Neuroimage, vol. 263, pp. 119636.
4. Sebenius, I., Seidlitz, J., Warrier, V., Bethlehem, R. A., Alexander-Bloch, A., Mallard, T. T., Garcia, R. R., Bullmore, E. T., & Morgan, S. E. (2023). 'Robust estimation of cortical similarity networks from brain MRI', Nature neuroscience, vol. 26, no.8, pp. 1461-1471.
5. Seidlitz, J., Váša, F., Shinn, M., Romero-Garcia, R., Whitaker, K. J., Vértes, P. E., Wagstyl, K., Reardon, P. K., Clasen, L., & Liu, S. (2018). 'Morphometric similarity networks detect microscale cortical organization and predict inter-individual cognitive variation', Neuron, vol. 97, no.1, pp. 231-247. e237.
6. Schaefer, A., Kong, R., Gordon, E. M., Laumann, T. O., Zuo, X.-N., Holmes, A. J., Eickhoff, S. B., & Yeo, B. T. (2018). 'Local-global parcellation of the human cerebral cortex from intrinsic functional connectivity MRI', Cerebral cortex, vol. 28, no.9, pp. 3095-3114.V
7. Vaswani, A., Shazeer, N., Parmar, N., Uszkoreit, J., Jones, L., Gomez, A. N., Kaiser, Ł., & Polosukhin, I. (2017). 'Attention is all you need', Advances in neural information processing systems, vol. 30, pp.

Poster No 1452

DL joint-fusion model with explanation shows the interplay between sMRI and fMRI in the study of ASD

Francesca Lizzi[1], Sara Saponaro[2], Giacomo Serra[3], Francesca Mainas[4], Piernicola Oliva[4], Alessia Giuliano[5], Sara Calderoni[6], Alessandra Retico[7]

[1]Pisa Division of National Institute for Nuclear Physics (INFN), pisa, Italy, [2]Pisa Division of National Institute for Nuclear Physics (INFN), Pisa, Italy, [3]National Institute of Nuclear Physics (INFN), Cagliari, Italy, [4]National Institute of Nuclear Physics (INFN), Cagliari, Italy, [5]Unit of Medical Physics, Pisa University Hospital "Azienda Ospedaliero-Universitaria Pisana", Pisa, Italy, [6]Developmental Psychiatry Unit – IRCCS Stella Maris Foundation, Pisa, Italy, [7]National Institute of Nuclear Physics (INFN), Pisa, Italy

Introduction: The development of multi-modal models that used data from different modalities has the potential to advance precision medicine. Combining data from multiple modalities allows the extraction of more comprehensive and complementary information, resulting in the creation of better-performing models. Additionally, this approach reveals important relationships that may cannot be detected when relying on a single modality. In this work, we develop a joint fusion deep learning (DL) model to combine harmonized structural and functional MRI features trained to discriminate subjects with Autism Spectrum Disorders (ASD) with respect to typically developing controls (TD). Additionally, we implement the SHapley Additive exPlanations (SHAP) explainability framework to identify the most significant features contributing to the classification of ASD subjects.

Methods: We analyzed both structural and functional MRI brain scans publicly available within the ABIDE I and II data collections[2,3]. We considered 1383 male subjects with age between 5 and 40 years, including 680 subjects with ASD and 703 TD from 35 different acquisition sites. Due to the multisite nature of the dataset, we separately harmonized the Freesurfer structural features and the functional connectivity measures using the NeuroHarmonize package[4] as reported in[5]. The ASD vs. TD classification was carried out with a DL model, consisting in a feature dimensionality reduction neural network (FR-NN) and a classification neural network (C-NN). The FR-NN generates a fixed-length feature representation for each data modality. Specifically, we implemented the joint fusion approach[1], which propagates the loss back to the FR-NN during training, allowing the creation of informative feature representations for each data modality. Additionally, we implemented single data modality-based models to assess the potential enhancement offered by using a multimodal model. The single-modality models exclusively considered either structural or connectivity features and utilized similar neural networks for classification. The models were training for 150 epochs, applying standard deep learning techniques to mitigate overfitting. The performance was evaluated by computing the Area under the Receiver Operating Characteristic curve (AUC) within a nested 10-fold cross-validation, preserving the matching proportions of ASD and TD diagnoses. To identify the most significant features able to discriminate between ASD and TD subjects, we selected features with scores exceeding the 99th percentile among those determined by SHAP as important. Additionally, we quantified the effect size of the ASD vs. TD group difference using Cohen's d coefficient.

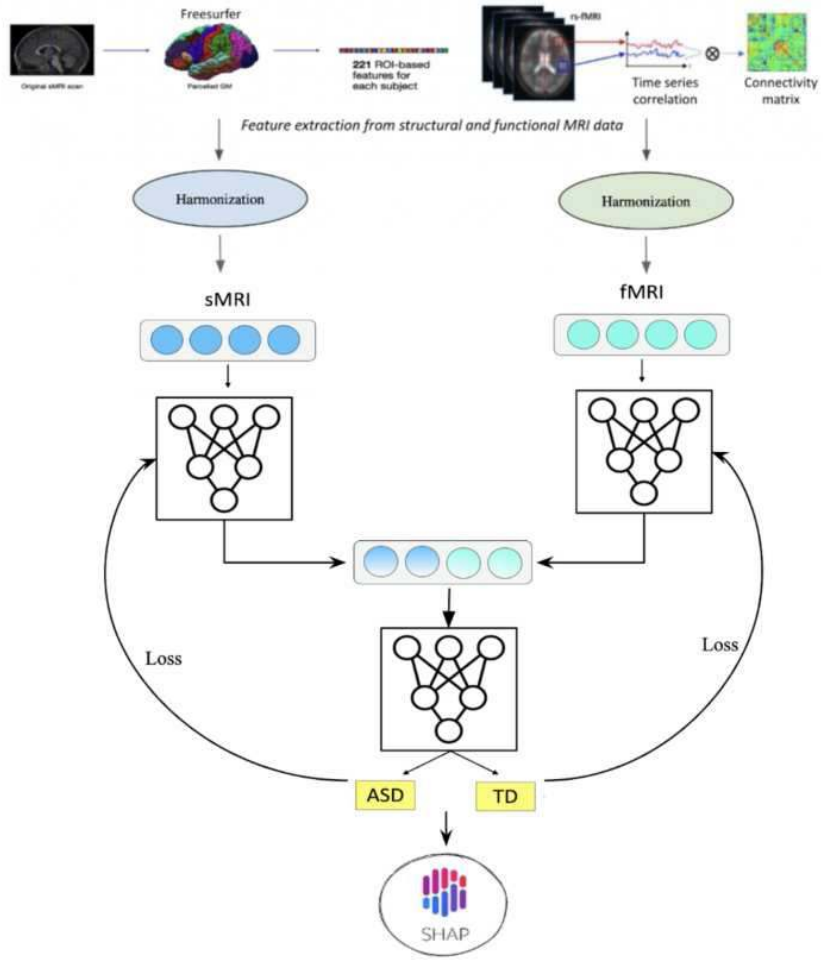

Work pipeline. The Freesurfer segmentation software allows the computation of 221 structural brain features from structural MRI data, whereas the C-PAC pipeline has been implemented to compute the functional connectivity maps between different brain areas based on the Pearson correlation between the time series. The model contains a feature-reduction neural network and a classification neural network. The main advantage of this strategy is that the loss is propagated back to the FR-NN during the training (black arrows). The solid blue and cyan circles represent a starting feature set, while the shaded circles represent the fixed-length feature vectors extracted from all modalities.

Results: The AUC values of 0.66±0.05 and of 0.76±0.04 were obtained in the ASD vs. TD discrimination when only structural or functional features are considered, respectively. The joint fusion approach resulted in an AUC of 0.78±0.04. The features identified as crucial in discriminating between ASD and TD subjects primarily originated from functional MRI data. Additionally, we observed a pattern of reduced long-range inter-hemispheric connectivity and increased intra-hemispheric connectivity in ASD subjects compared to TDs. Finally, the set of features identified as the most important for the two-class discrimination supports the idea that brain changes tend to occur in individuals with ASD in regions belonging to the Default Mode Network and to the Social Brain.

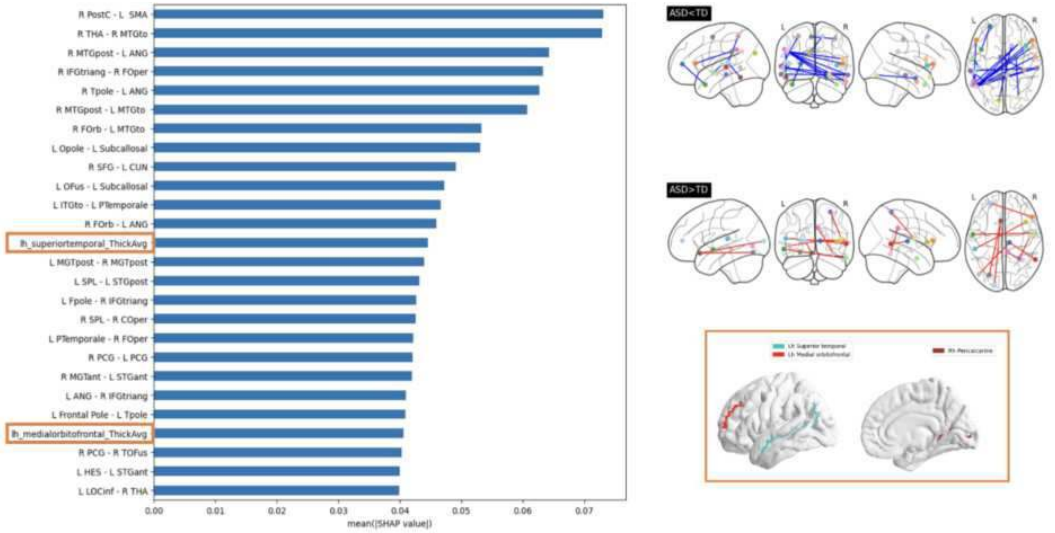

Most important features in ASD classification. The most important features in the ASD vs. TD discrimination is reported in the box plot. The over-connectivity (in red) and under-connectivity (in blue) patterns are shown. In the orange box the structural brain regions whose features were identified as relevant are highlighted.

Conclusions: Our results demonstrate that the DL-based joint fusion approach outperforms the other ones as it efficiently exploits the complementary information related to the ASD diagnosis contained in sMRI and rs-fMRI images. Furthermore, this work suggests that multi-modality DL models are promising tools for identifying potential neuroimaging biomarkers of neurodevelopmental disorders. Acknowledgments: FAIR-AIM project (POR FSE 2014-2020) and PNRR - M4C2 - PE “FAIR - Future Artificial Intelligence Research”

Poster No 1453

Divide and Conquer: Improving Brain Age Predictions through Contrastive Pre-Training

Maximilian Konowski[1], Ramona Leenings[1], Jan Ernsting[2], Nils Winter[3], Lukas Fisch[4], Daniel Emden[4], Carlotta Barkhau[4], Susanne Meinert[5], Elisabeth Leehr[6], Xiaoyi Jiang[7], Udo Dannlowski[4], Tim Hahn[4]

[1]University of Münster, Münster, North Rhine Westphalia, [2]University of Münster, Münster, NRW, [3]University of Münster, Münster, North-Rhine Westphalia, [4]Institute for Translational Psychiatry, Münster, North Rhine Westphalia, [5]Institute for Translational Psychiatry, Münster, Germany, [6]Institute for Translational Psychiatry, University of Münster, Münster, North Rhine-Westphalia, [7]University of Münster, Münster, Northrine-Westphaila

Introduction: Brain Age models learn to derive the chronological age of healthy subjects from brain structure represented in T1-weighted MR images or derivatives thereof. The difference between predicted and chronological age, called brain age gap (BAG), has been used as a marker for atypical neurodegeneration and has shown significant salience in the context of different psychiatric conditions and lifestyle factors (Cole 2019, Bittner 2021, Wrigglesworth 2021, Hahn 2022, Blake 2023). Yet, prevalent imbalances in age distributions-e.g. an over representation of younger individuals-can introduce challenges to the training. A brain age model might benefit from disproportionately generating age predictions for larger age groups, as this statistically optimizes the loss function during training. Consequently, the BAG distributions among different age groups could vary significantly: The inherent meaning of a BAG of e.g. +2 years might have a training-induced shift in meaning across the age continuum. Artificially balancing the dataset by undersampling over-represented age groups, however, risks the loss of crucial information and variance that could be valuable for the learning process. To mitigate the negative effects of a skewed age distribution, we test a pre-training strategy. Specifically, we utilize samples from over-represented age groups to impart a structural understanding of MRI images to a deep learning model before fine-tuning it on a balanced dataset for chronological age prediction.

Methods: We loosely lean on Chaitanya et al. (2021) and implement a self-supervised pre-training with two focus points: First, we use a context restoration task to foster an understanding of the MRI-inherent data structure. Second, we use a contrastive

loss to encourage an understanding of fine granular inter-individual differences. As our backbone, we utilize a 3D ResNet10 architecture implemented in PyTorch. We train and evaluate three brain age models, for which we obtained a total of n=8911 cat12-preprocessed T1-MRI scans from healthy control subjects (Gaser, https://neuro-jena.github.io/cat/; MACS cohort: Vogelbacher et al., 2018; publicly available studies curated by Fisch et al. 2023). For evaluation, we randomly select 5 samples from each age bin to form a balanced test set Xtest (n=260). The first brain age model was trained on the unbalanced dataset Xtrain(n=8651) to serve as benchmark performance. Second, we pre-train a model with samples from over-represented age groups Xpretrain (n=7080), before we fine tune it to age prediction with an age-balanced data subset Xfine-tune (n=1571). Third, we train a randomly initialized model on the downsampled fine-tuning set only. Finally, we use the model's predictions to calculate the brain age gap (BAG) for the test set and compare the BAG distributions per age group.

Results: Compared to the benchmark model, the fine-tuned model exhibited accelerated convergence and yielded superior results on the balanced test set (MAE of 9.9 to 4.68 years), despite utilizing only a fraction of the available data, see figure 1. Although the benchmark model exhibited promising performance on a validation set during training (MAE of 3.68), its performance notably deteriorated when assessed on the balanced test set. Notably, age predictions from the fine-tuned model exhibited a more uniform distribution, contrasting the benchmark model's implicit bias towards the skewed training data distribution. Consequently, the range of the BAGs of the benchmark model differs substantially over different age groups, potentially confounding later statistical analysis. Remarkably, the pre-trained model showed only slight improvements against a model trained on the fine-tuning dataset, only.

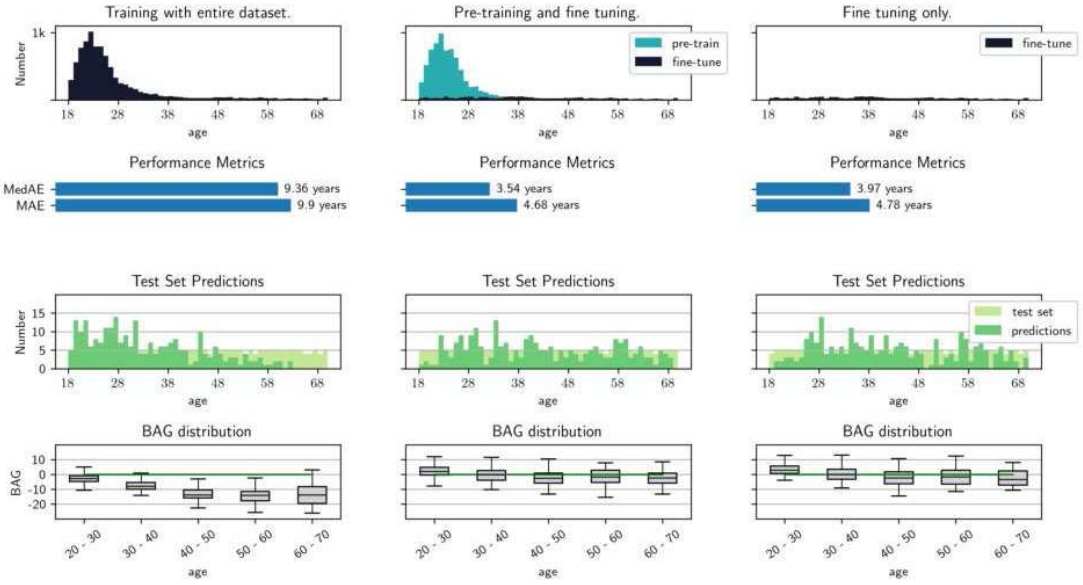

Conclusions: Our findings emphasize the nuanced relationship between data volume and bias, as well as the relevance of a carefully curated dataset. In the future, we aim to explore pre-training strategies which are specifically tailored to the brain age learning objective.

References

1. Bittner, N. (2021), 'When your brain looks older than expected: combined lifestyle risk and BrainAGE', Brain Structure and Function, vol. 226, pp. 621–645.
2. Blake, K. V. (2023), 'Advanced brain ageing in adult psychopathology: A systematic review and meta-analysis of structural MRI studies', Journal of Psychiatric Research, vol. 157, pp. 180–191.
3. Chaitanya, K. (2020), 'Contrastive learning of global and local features for medical image segmentation with limited annotations', Advances in neural information processing systems, vol. 33, pp. 12546-12558.
4. Fisch, L. (2023), 'Deepbet: Fast brain extraction of T1-weighted MRI using Convolutional Neural Networks', arXiv preprint arXiv:2308.07003
5. Hahn, T. (2022), 'An uncertainty-aware, shareable, and transparent neural network architecture for brain-age modeling'. Science advances, vol. 8, no. 1, p. eabg9471.
6. Vogelbacher, C. (2018), 'The Marburg-Münster Affective Disorders Cohort Study (MACS): a quality assurance protocol for MR neuroimaging data', Neuroimage, vol. 172, pp. 450-460
7. Wrigglesworth, J. (2021), 'Factors associated with brain ageing - a systematic review', BMC Neurology, vol. 21, no. 1, p. 312.

Poster No 1454

Deep Generative Anomaly Detection for Structural Anomalies in Fetal Brain with Ventriculomegaly

Sungmin You[1,2], Carlos Simon Amador Izaguirre[1], Seungyoon Jeong[1,2], Hyukjin Yun[1,2,3], Ellen Grant[1,4,5], Kiho Im[1,2,3]

[1]Fetal Neonatal Neuroimaging and Developmental Science Center, Boston Children's Hospital, Boston, MA, [2]Division of Newborn Medicine, Boston Children's Hospital, Harvard Medical School, Boston, MA, [3]Department of Pediatrics, Harvard Medical School, Boston, MA, [4]Fetal Neonatal Neuroimaging and Developmental Science Center, Boston Children's Hospital, Harvard Medical School, Boston, MA, [5]Department of Radiology, Boston Children's Hospital, Harvard Medical School, Boston, MA

Introduction: Fetal ventriculomegaly (VM) means the enlargement of the cerebral ventricles diagnosed in utero and occurs in up to 2 per 1000 births. (Pisapia, Sinha, Zarnow, Johnson, & Heuer, 2017) The potential effects of VM on neurodevelopment can be variable depending on the severity from little impact to developmental delays, motor skill challenges, and intellectual disabilities.(Chervenak et al., 1984; Weichert et al., 2010) Early diagnosis of VM using fetal MRI is essential for the better identification of etiology and guidance of prognosis. (Pisapia et al., 2017) This study proposes a deep generative anomaly detection model for the diagnosis of VM based on structural anomalies in fetal brain MRI.

Methods: This study was approved by the local Institutional Review Board at Boston Children's Hospital. For the training and test of the proposed model, 151 typically developing (TD) fetuses (gestational weeks [GW]: 31.3±4.0, range: 22.0-38.7; sex: 69/49/28 [male/female/unknown]) and 46 fetuses with VM (GW: 29.8±4.5, range: 20.2-38.0; sex: 33/11/2) were included in this study. The TD subjects were divided into training-testing groups, which resulted in 121 subjects for the training set and 30 subjects for the test set while all VM subjects were used only for the test. We used our pipeline for fetal MRI processing which has been validated in several studies (Yun et al., 2022) including brain masking, non-uniformity correction, and slice-to-volume registration (Kuklisova-Murgasova, Quaghebeur, Rutherford, Hajnal, & Schnabel, 2012) to preprocess the fetal MRIs. We extracted 30 center slices on each view for training and testing after cropping them to different sizes according to their view, sagittal 158×126, coronal 110×126, and axial 110×158. We normalize the intensities of images with min-max normalization. Our anomaly detection model is based on the variational autoencoder (VAE) (Kingma & Welling, 2013) composed of four convolutional blocks on the encoder and decoder. [Figure 1] The proposed model was trained for each view during 2000 epochs with the Adam optimizer with a learning rate of 1e-4 and the mean squared error loss. For the evaluation, the averaged pixel-wise mean absolute error between the input and reconstruction was used to compute the anomaly score for each image. We performed the area under the receiver operating characteristic(AUROC) analysis to confirm the feasibility of classification between TD and VM. We extracted the center slice as a representative image of a volume and performed the Mann-Whitney U-test to compare the distribution of anomaly scores between groups.

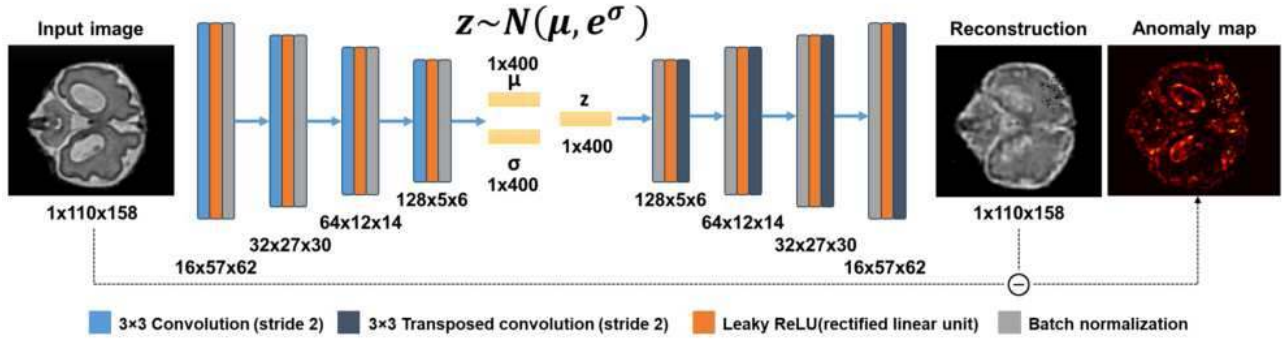

Figure 1. Overview of the variational autoencoder for anomaly detection in fetal MRI

Results: Our proposed model showed 0.836 from the AUROC analysis on the test set using the sagittal view. Furthermore, the Mann-Whitney showed statistically significant higher anomaly scores ($p<0.001$) in the VM than in TD with the sagittal view, where an elevation of anomaly scores distribution in the VM than the TD is observed. [Figure2]

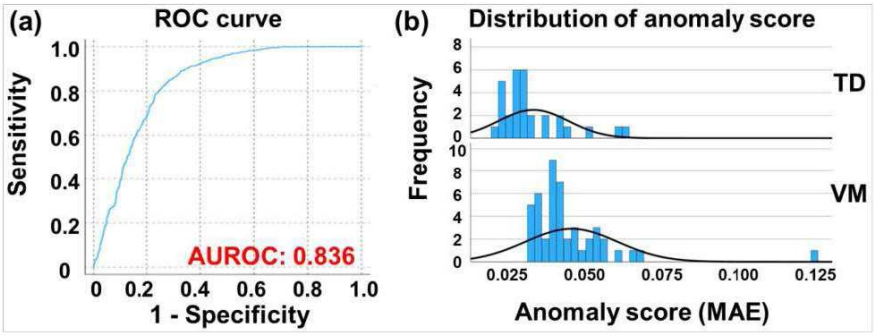

Figure 2. (a) AUROC analysis for the sagittal view model; (b) Comparison of anomaly score distribution from the sagittal slide between TD and VM

Conclusions: Our VAE-based anomaly detection model for diagnosing fetal VM on MRI showed an AUROC of 0.836 in the sagittal view. This demonstrates the potential of the anomaly detection model for the accurate prenatal detection of VM, which can aid in understanding VM's etiology and improving prognosis guidance. For a future study, including other views and developing a framework for aggregating slice-wise results into volume-level predictions will further enhance the diagnostic power. This model can also be used for detecting and diagnosing other various neurodevelopmental disorders in utero.

References

1. Chervenak, F., Ment, L., Mcclure, M., Duncan, C., Hobbins, J., Scott, D., & Berkowitz, R. (1984). Outcome of fetal ventriculomegaly. The Lancet, 324(8396), 179-181.
2. Kingma, D. P., & Welling, M. (2013). Auto-encoding variational bayes. arXiv preprint arXiv:1312.6114.
3. Kuklisova-Murgasova, M., Quaghebeur, G., Rutherford, M. A., Hajnal, J. V., & Schnabel, J. A. (2012). Reconstruction of fetal brain MRI with intensity matching and complete outlier removal. Med Image Anal, 16(8), 1550-1564. doi:10.1016/j.media.2012.07.004
4. Pisapia, J. M., Sinha, S., Zarnow, D. M., Johnson, M. P., & Heuer, G. G. (2017). Fetal ventriculomegaly: diagnosis, treatment, and future directions. Child's Nervous System, 33, 1113-1123.
5. Weichert, J., Hartge, D., Krapp, M., Germer, U., Gembruch, U., & Axt-Fliedner, R. (2010). Prevalence, characteristics and perinatal outcome of fetal ventriculomegaly in 29,000 pregnancies followed at a single institution. Fetal diagnosis and therapy, 27(3), 142-148.
6. Yun, H. J., Lee, H. J., Lee, J. Y., Tarui, T., Rollins, C. K., Ortinau, C. M., . . . Im, K. (2022). Quantification of sulcal emergence timing and its variability in early fetal life: Hemispheric asymmetry and sex difference. Neuroimage, 263, 119629. doi:10.1016/j.neuroimage.2022.119629

Poster No 1455

Leveraging periodic activation functions in deep neural network to predict fMRI signals from EEG

Yamin Li[1], Ange Lou[1], Shiyu Wang[1], Catie Chang[1]

[1]*Vanderbilt University, Nashville, TN*

Introduction: fMRI has been an irreplaceable neuroimaging modality but is limited by hemodynamic blurring, high cost, and incompatibility with metal implants[1]. Complementary to fMRI, EEG directly records cortical electrical activity at high temporal resolution, but has limited spatial resolution and limited sensitivity to deep subcortical brain structures. The ability to obtain fMRI information from EEG would enable cost-effective, naturalistic imaging across a wider set of brain regions. Further, beyond augmenting the capabilities of EEG, cross-modality models would facilitate the interpretation of fMRI signals. However, as both EEG and fMRI are high-dimensional and prone to noise and artifacts, it is currently still challenging to model fMRI from EEG. To address this challenge, here we aimed to construct a novel deep learning framework to reconstruct fMRI signals directly from EEG data.

Methods: Simultaneous "Eyes Open – Eyes Closed" EEG-fMRI data from 8 subjects were used in this analysis (EEG: 30channels; fMRI: TR=1.95s for first 4 subjects and TR = 2s for the last 4; resolution=3mm isotropic; duration=5min per subject, data and preprocessing details see in[2]). fMRI ROI signals were extracted using the Harvard-Oxford structural atlas[3] and interpolated to 100 Hz. EEG was downsampled to the same sampling rate, and shifted by 6 seconds to approximate the time delay of the HRF[4]. In our analysis, we trained subject-specific models given the potentially unique response properties of individuals. The preprocessed data for each subject were divided into training and testing sets in a ratio of 4:1. The training samples with a window length of 20.48 seconds were randomly sampled from the 4-minute training time course. Our model comprises two main components: 1) sinusoidal representation network (SIREN) blocks and 2) feature encoder and decoder blocks. Inspired by[5], the input is first passed to SIREN, a framework that leverages the periodic activation function in each layer of a multilayer perceptron for spatial filtering and frequency-related feature extraction. The output of SIREN is sent into

a subsequent encoder-decoder to recover the fMRI signals. Each encoder block has a down-sampling operation to increase the receptive field while retaining important information. The decoder comprises the same symmetric building blocks and up-samples the latent space features to produce the fMRI signal of a certain ROI. The model optimizes the linear combination of the mean squared error loss and the correlation loss: Loss=L_mse+αL_corr. The prediction performance is evaluated by calculating the Pearson correlation between predicted ROI signals and the ground truth.

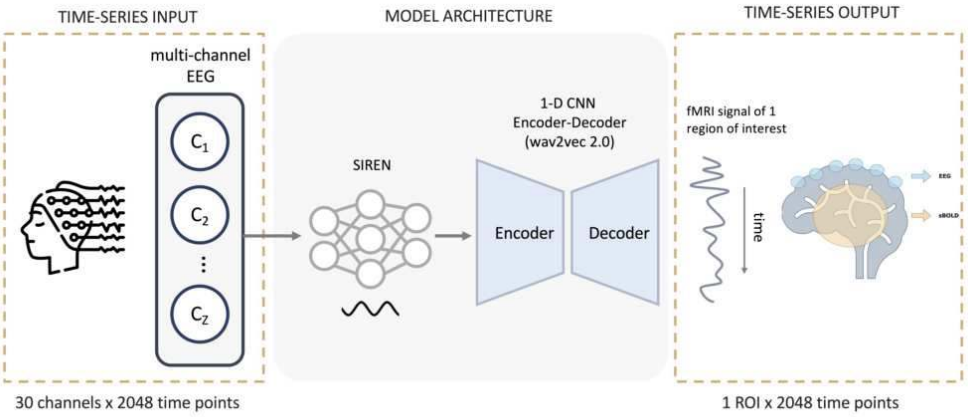

Fig. 1 Research pipeline and model architecture

Results: We observe a reasonable agreement between the actual and predicted ROI fMRI traces in subcortical regions. The corresponding attribution topographies mainly emphasize the motor cortex which is consistent with the functional role of basal ganglia and the presence of corresponding interconnections leading to motor cortical areas[6]. Overall, as shown in Fig. 2(C), our model outperforms the current state-of-the-art deep learning model that was designed for the same task[4].

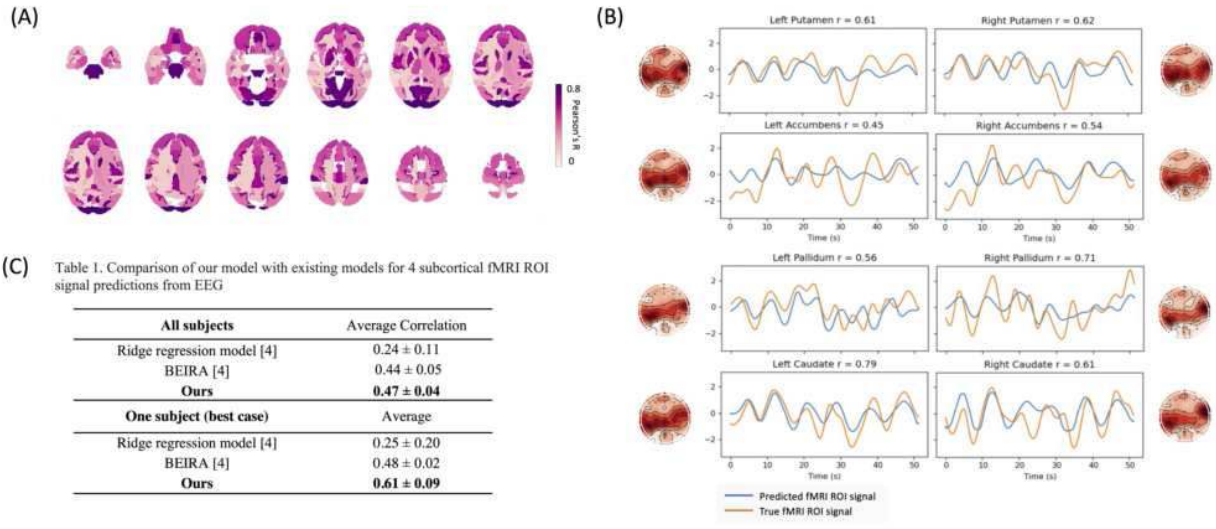

(C) Table 1. Comparison of our model with existing models for 4 subcortical fMRI ROI signal predictions from EEG

All subjects	Average Correlation
Ridge regression model [4]	0.24 ± 0.11
BEIRA [4]	0.44 ± 0.05
Ours	**0.47 ± 0.04**
One subject (best case)	Average
Ridge regression model [4]	0.25 ± 0.20
BEIRA [4]	0.48 ± 0.02
Ours	**0.61 ± 0.09**

Fig. 2 (A) The correlations between predicted signal and ground truth in various brain regions from one subject (best case). **(B)** The prediction result and attribution topographies of deep brain regions from one subject (best case). **(C)** Tables of correlations between true and predicted signals, averaged across 4 deep brain ROIs.

Conclusions: Our proposed model successfully reconstructs fMRI signals from EEG time series without explicit feature engineering and improves the prediction accuracy compared with existing models. This work contributes a novel framework that leverages periodic activation functions in deep neural networks to learn representations of functional neuroimaging data. As we only train our model on the "eyes-open-eyes-closed" data on healthy control and the prediction performances might vary on different datasets, future work would try to assess performance on different task conditions and patient populations.

References

1. Chang, C. and Chen, J. E. (2021), 'Multimodal EEG-fMRI: Advancing insight into large-scale human brain dynamics' Current opinion in biomedical engineering, vol. 18, p. 100279.
2. van der Meer, J. et al. (2016), 'Eyes Open - Eyes Closed' EEG/fMRI data set including dedicated 'Carbon Wire Loop' motion detection channels,' Data in brief, vol. 7, pp. 990–994.
3. Desikan, R. S. et al.(2006), 'An automated labeling system for subdividing the human cerebral cortex on MRI scans into gyral based regions of interest,' Neuroimage, vol. 31, no. 3, pp. 968–980.

4. Kovalev, A., Mikheev, I., and Ossadtchi, A.(2022), 'fMRI from EEG is only Deep Learning away: the use of interpretable DL to unravel EEG-fMRI relationships,', preprint.
5. Sitzmann, V. et al. (2020), "Implicit neural representations with periodic activation functions," Advances in neural information processing systems, vol. 2020-Decem.
6. Purves, D. et al. (2001), Neuroscience 2nd edition. glutamate receptors in chapter 7.

Poster No 1456

Usage of Different Brain Atlases on Comprehensive Training Procedure Using Basic MLP Structure

Jo-Hsin Shih[1], Po-Hsien Lee[2], Zhitong John Wang[3], Changwei Wu[3], Ai-Ling Hsu[4]

[1]Department of Artificial Intelligence, Chang Gung University, Taoyuan, Taiwan, [2]School of Medicine, Taipei Medical University, Taipei, Taiwan, [3]Graduate Institute of Mind, Brain and Consciousness, Taipei Medical University, New Taipei, Taiwan, [4]Department of Psychiatry, Chang Gung Memorial Hospital at Linkou, Taoyuan, Taiwan

Introduction: Major depressive disorder (MDD) is a prevalent and severe mental illness, posing a high risk of disability worldwide (Whiteford et al., 2013). Characterized by impairments in mood and cognitive functioning, MDD has been associated with malfunctions of brain networks, as measured by resting-state functional magnetic resonance imaging (rs-fMRI) (Kaiser et al., 2015). The growing availability of large-scale rs-fMRI datasets focusing on MDD has enabled the development of various deep-learning models in differentiating MDD patients from controls (Qin et al., 2022; Venkatapathy et al., 2023). Among these models, the mandatory selection of a parcellation atlas for feature extraction may affect the resulting accuracy; however, there is a lack of studies investigating its impact on model performances. In this work, we tested the hypothesis that models trained with the rs-fMRI parcellated atlas would achieve the highest performance as compared to those trained with other atlases generated from structural or task-based origins.

Methods: The rs-fMRI scans of 498 subjects (256 MDD patients vs. 242 controls) from the Rest-meta-MDD consortium (Chen, X. et al., 2022) were analyzed to assess the impact of using commonly adopted whole-brain atlases on model accuracy. Given the inhomogeneous confounding factors in the consortium collected from 25 sites, data from a single site (site 20) of 533 subjects, all acquired on a 3T scanner (Siemens Tim Trio), were specifically chosen. Additional inclusion criteria included (1) preprocessed data parcellated using four atlases, i.e., AAL (Tzourio-Mazoyer et al., 2002), Dosenbach (Dosenbach et al., 2010), Craddock (Craddock et al., 2012), and Power (Power et al., 2011) atlases; and (2) subjects aged between 21 to 70 years. Next, the functional connectivities of each atlas were calculated using Pearson correlation. Considering that the complexity of deep-learning architectures often determines its learning capability, models were trained using the simple two-layer architecture of multi-layer perceptron with 32 and 16 neurons in each layer. To prevent information leakage that potentially inflates model accuracy, the models were trained on 80% of the data using BRAPH (Mite et. al 2017). The parameters were validated on 10% of the data, and the accuracy was tested on the remaining 10% of the data. Additionally, the settings for model training included the use of Adam optimizer, L2 regularization, a dropout rate of zero, a batch size of 32, 20 epochs, and a loss function of cross entropy. Moreover, models were repeatedly trained using a 30-time resample approach to statistically assess the impact of atlas utilization on model accuracy. This assessment was conducted using an ANOVA and post-hoc tests with a p-value < 0.05 being considered statistically significant.

Results: During training, every model achieved an accuracy over 80% (in the training dataset) within 5 epochs and reached 100% in 20 epochs. Figure 1 shows the model accuracies on the testing dataset, presenting the mean and standard error of the mean across 30 repetitions. Moreover, an ANOVA test showed a significant difference in accuracy among models trained with data parcellated by 4 atlases at $F(3, 116) = 2.93$, $p < 0.036$. Post-hoc Tukey HSD tests were conducted for pairwise comparisons. Notably, the accuracy between the model trained by Craddock and Power atlases was found to be significantly different ($p < 0.05$).

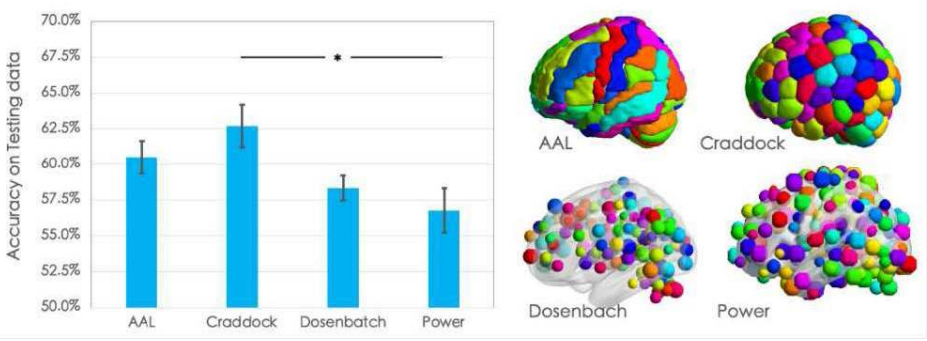

Conclusions: This study investigated the effect of data parcellation using four different atlases on the accuracies of deep-learning models. By employing a 30-time resampling method on the dataset, we demonstrated that the data parcellated using rs-fMRI-based atlas (Craddock) resulted in a higher model accuracy compared to data parcellated using task-fMRI-based atlas (Power).

References

1. Whiteford, H. A. et al. (2013), 'Global burden of disease attributable to mental and substance use disorders: findings from the Global Burden of Disease Study', The lancet, vol. 382, pp. 1575-1586.
2. Kaiser, R. H. et al. (2015), 'Large-scale network dysfunction in major depressive disorder: a meta-analysis of resting-state functional connectivity', vol. 72, pp. 603-611.
3. Qin, K. et al. (2022), ' Using graph convolutional network to characterize individuals with major depressive disorder across multiple imaging sites ', EBioMedicine, vol. 78
4. Venkatapathy, S. et al. (2023), 'Ensemble graph neural network model for classification of major depressive disorder using whole-brain functional connectivity', Frontiers in Psychiatry, vol. 14
5. Chen, X. et al. (2002), 'The DIRECT consortium and the REST-meta-MDD project: towards neuroimaging biomarkers of major depressive disorder', Psychoradiology, vol. 2, pp. 32-42.
6. Tzourio-Mazoyer. et al. (2002), 'Automated anatomical labeling of activations in SPM using a macroscopic anatomical parcellation of the MNI MRI single-subject brain', Neuroimage, vol. 15, pp. 273-289.
7. Craddock, R. C. et al. (2012), 'A whole brain fMRI atlas generated via spatially constrained spectral clustering', Human brain mapping, vol. 33, pp.1914-1928.
8. Dosenbach, N. U. et al. (2010), 'Prediction of individual brain maturity using fMRI', Science, vol. 329, pp. 1358-1361.
9. Power, J. D. et al. (2011), 'Functional network organization of the human brain', Neuron, vol. 72, pp. 665-678.
10. Mijalkov, M. et al. (2017), 'BRAPH: a graph theory software for the analysis of brain connectivity', PloS one, vol. 12

Poster No 1457

Scalable and accessible normative modelling for cross-cultural generalizability in neuropsychiatry

Pieter Barkema[1], Saige Rutherford[2], Christian Beckmann[3], Andre Marquand[4]

[1]Queen Square Institute of Neurology, University College London, London, United Kingdom, [2]Radboud University, Nijmegen, Netherlands, [3]Donders Institute for Brain, Cognition, and Behavior, Radboud University Nijmegen, Nijmegen, NL, Nijmegen, Netherlands, [4]Radboud University Nijmegen, Nijmegen, Gelderland

Introduction: The study of individual variability through normative modelling has recently shown to have great potential for understanding the mysterious neurobiology of mental disorders (A. F. Marquand et al., 2019; Rutherford et al., 2023). Accurate modeling of variability across the lifespan, however, requires processing of neuroimaging data from tens of thousands of participants, large amounts of compute power to estimate models, and labour and expertise to implement, which provides a barrier for many users of these models. To address these issues, we recently introduced PCNportal (https://pcnportal.dccn.nl/), allowing free and online access to pre-estimated normative models, requiring no compute power, code or domain expertise (Barkema et al., 2023) – using the well-validated PCNtoolkit library as a modelling backend (A. Marquand et al., 2021). We demonstrate this framework and provide a showcase application to evaluate the global usefulness of PCNportal in context of cross-ethnical generalizability. A key feature of PCNportal is how easily models can be added and accessed across the world. On PCNportal's launch we provided access to normative models for cortical thickness and brain volume, and now expand our repertoire to include models trained on resting-state fMRI data using multiple parcellations, and additional models for cortical thickness, surface area and cerebellar volume. Can these models, however, generalize to cohorts of different ethnic backgrounds? The largest neuroimaging cohorts available are strongly biased towards white ethnicity, such as UK Biobank, ABCD and HCP (Fry et al., 2017; Ricard et al., 2023), and several studies suggest that bias may confound studies (Chee et al., 2011; Tang et al., 2018). We test cross-ethnical generalizability of one ethnically biased model by applying it to an East Asian cohort.

Methods: Data We use the SRPBS-database (Tanaka et al., 2021), containing structural MRI data of 150 Image-Derived Phenotypes (IDPs) for 993 patients and 1421 controls from fourteen collection sites in Japan. We split the data into an adaptation and test set (50/50) ensuring an equal split for each collection site. Model We use a Bayesian Linear Regression (BLR) model trained on average cortical thickness measures from 58,836 data points from 82 sites (Rutherford et al., 2022) – a model with white ethnical bias. Importantly, this model is hosted on PCNportal and was similarly used in Barkema et al (2023). Analysis We analyze the deviations in cortical thickness and compare between the schizophrenia group (N=68) and the control group (N=468). We apply our biased model to obtain individualized deviation scores, modelling age, sex and sites as covariates.

Results: We investigated cross-ethnical generalizability of PCNportal by applying an ethnically biased model to a predominantly East Asian cohort, with a good model fit (Figure 1). We tested whether absolute deviation scores are greater in

the schizophrenia group than the control group by using a one-sided Wilcoxon rank sums test and found a significant effect (statistic=2.383, pvalue=0.009). This analysis replicates a well-established finding and shows that models have the potential to generalize to other ethnic groups, despite having a dangerous ethnic training bias.

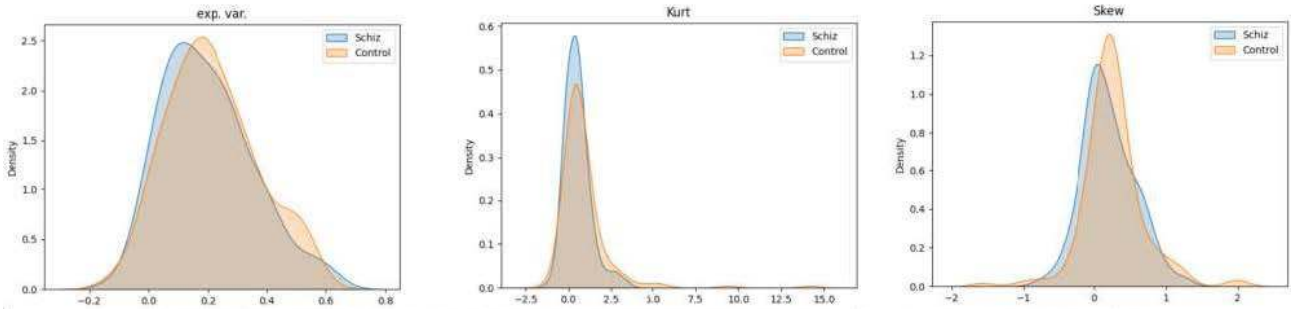

The explained variance of the adapted model (left), and the kurtosis and skew of the deviation scores (middle and right) per group. The plots demonstrate a good model fit after adaptation.

Conclusions: We showcase the PCNportal tool for online normative modelling of neuroimaging data. We release four extra normative models, trained on fMRI resting-state data, cerebellar volume or average thickness. We also bring attention to an important issue of easy global access by illustrating cross-ethnical generalizability. We replicate a well-established effect of cortical thickness abnormalities in schizophrenia, in a cohort of primarily East Asian ethnicity. We hope this analysis inspires other cross-ethnical generalizability initiatives. PCNportal can tackle ethnical neuroimaging bias through facilitating global model and data contributions, aiming to build a more inclusive future in neuropsychiatric precision medicine.

References

1. Barkema, P. (2023). Predictive Clinical Neuroscience Portal (PCNportal): Instant online access to research-grade normative models for clinical neuroscientists. [Version 2; peer review: 2 approved]. Wellcome Open Research, 8(326). https://doi.org/10.12688/wellcomeopenres.19591.2
2. Chee, M. W. L. (2011). Brain structure in young and old East Asians and Westerners: Comparisons of structural volume and cortical thickness. Journal of Cognitive Neuroscience, 23(5), 1065–1079. https://doi.org/10.1162/jocn.2010.21513
3. Fry, A. (2017). Comparison of Sociodemographic and Health-Related Characteristics of UK Biobank Participants With Those of the General Population. American Journal of Epidemiology, 186(9), 1026–1034. https://doi.org/10.1093/aje/kwx246
4. Marquand, A. F. (2019). Conceptualizing mental disorders as deviations from normative functioning. Molecular Psychiatry, 24(10), 1415–1424. https://doi.org/10.1038/s41380-019-0441-1
5. Marquand, A. (2021). PCNToolkit. Zenodo. https://doi.org/10.5281/ZENODO.5207839
6. Ricard, J. A. (2023). Confronting racially exclusionary practices in the acquisition and analyses of neuroimaging data. Nature Neuroscience, 26(1), 4–11. https://doi.org/10.1038/s41593-022-01218-y
7. Rutherford, S. (2023). Evidence for embracing normative modeling. ELife, 12, e85082. https://doi.org/10.7554/eLife.85082
8. Rutherford, S. (2022). Charting brain growth and aging at high spatial precision. ELife, 11, e72904. https://doi.org/10.7554/eLife.72904
9. Tanaka, S. C. (2021). A multi-site, multi-disorder resting-state magnetic resonance image database. Scientific Data, 8(1), 227. https://doi.org/10.1038/s41597-021-01004-8
10. Tang, Y. (2018). Brain structure differences between Chinese and Caucasian cohorts: A comprehensive morphometry study. Human Brain Mapping, 39(5), 2147–2155. https://doi.org/10.1002/hbm.23994

Poster No 1458

Shape matters: Unsupervised Exploration of Glioblastoma Imaging Survival Predictors

Martha Foltyn-Dumitru[1], Mustafa Mahmutoglu[1], Felix Sahm[1], Wolfgang Wick[1], Martin Bendszus[1], Philipp Vollmuth[1], Marianne Schell[1]

[1]Heidelberg University Hospital, Heidelberg, Germany

Introduction: Within glioblastoma research, conventional metrics such as 2D/3D tumor size measurements have long served as reliable prognostic indicators. However, the complete prognostic potential of sophisticated structural parameters, particularly morphological radiomics, remains to be thoroughly explored. This investigation delves into a clustering technique on morphological radiomics along with tumor volume to unveil distinct glioblastoma phenotypes, assessing their prognostic impact on overall survival (OS).

Methods: A retrospective study included 436 glioblastoma patients (2009-2020) from Heidelberg University Hospital. Data were split into training and test datasets (80:20 ratio), with external validation using the UCSF glioma dataset including 397 patients (Calabrese et al., 2022). MRI acquisition involved 3D T1-weighted imaging (pre/post contrast administration), axial 2D FLAIR, and T2-weighted imaging. Automated tumor segmentation was performed using a variant of HD-GLIO (Isensee et al., 2019; Kickingereder et al., 2019). PyRadiomics facilitated the radiomic feature extraction of nine morphological radiomic

features from the tumor (van Griethuysen et al., 2017), and the total tumor volume was ascertained. Threshold determination for morphological radiomic features and tumor volume involved hierarchical Bayesian modeling within a Cox proportional hazards framework for OS (Chen et al., 2014; Fang et al., 2017). Parameters were binarized according to their respective thresholds. Subsequently, a Gower distance was computed using these binarized parameters, serving as the foundational metric for subsequent partition around medoids (PAM) clustering (Hennig, 2023; Maechler et al., 2022). Cluster robustness was quantitatively appraised using the Jaccard index across 500 bootstrap iterations. Survival rates were visualized using Kaplan-Meier curves and tested for significance by log-rank test. Univariate and multivariate Cox regression models, adjusted for clinical covariates, explored cluster and tumor volume impact on OS. Discriminative ability was evaluated using the concordance probability (C index) and Akaike information criterion (AIC). ANOVA compared C indices for embedded models, and the evidence ratio from AIC assessed differences between non-embedded models.

Results: PAM clustering identified two clusters with the highest silhouette coefficient (width=0.44) and high stability (Jaccard index: 0.94 for cluster 1, 0.89 for cluster 2). Cluster composition analysis showed distinct patterns: Cluster 1 (n=233) had a higher proportion of patients with higher Sphericity and Elongation, while Cluster 2 (n=115) had a higher proportion of patients with higher Maximum 3D Diameter, Surface Area, Axis Lengths, and tumor volume ($p<0.001$ for each). OS differed significantly between clusters: Cluster 1 showed median OS of 18.8, 23.8, and 20.1 months in the training, test, and UCSF datasets, respectively, whereas Cluster 2 showed 11.7, 11.4, and 13.7 months ($p<0.003$ for all; Figure 1). Univariate Cox regression linked cluster affiliation with OS (HR=2.25, p=0.003, C index=0.625) in the test dataset. Multivariate Cox regression showed improved performance with cluster affiliation over clinical data alone (C index 0.67 vs. 0.59, p=0.003) and further enhanced predictive accuracy with preoperative ECOG status (C index=0.68, p=0.005). Cluster-based models outperformed the models with tumor volume alone (evidence ratio 5.16-5.37; Table 1).

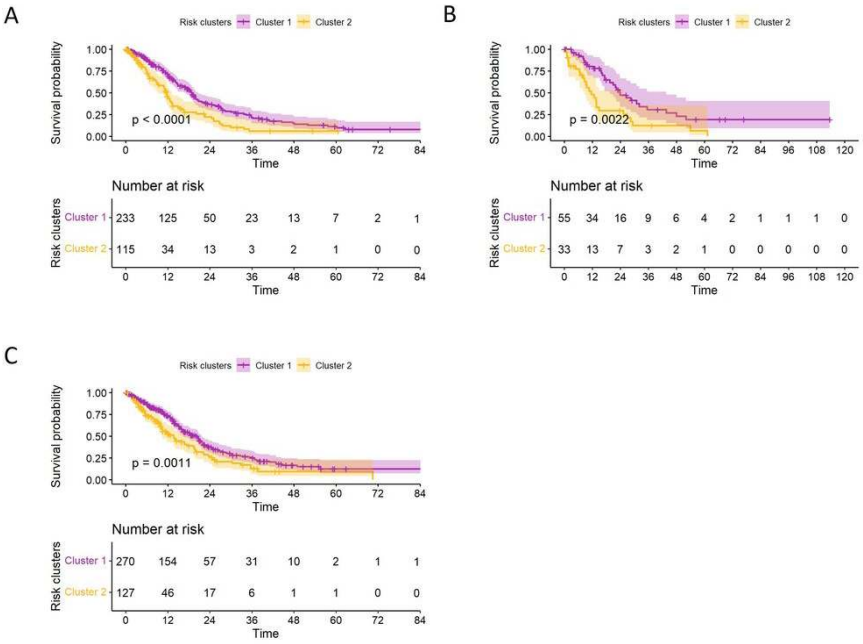

Models	Parameter	HR, 95% CI	p-value	C index	AIC
Model 1: Cluster (univariate)	Cluster 2	2.25, 1.32-3.84	**0.003***	0.624	385.21
Model 2a: Cluster + Sex + Age	Cluster 2 Sex w Age	2.27, 1.33-3.87 1.00, 0.57-1.72 1.01, 0.99-1.04	**0.003*** 0.973 0.354	0.671	388.56
Model 2b: Sex + Age	Sex w Age	0.98, 0.56-1.70 1.01, 0.99,1,04	0.943 0.380	0.592	395.09
Model 2c: Tumor volume + Sex + Age	Tumor volume Sex w Age	1.01, 1.00-1.01 1.21, 0.67-2.17 1.02, 0.99-1.04	**0.018*** 0.527 0.230	0.641	391.84
Model 3a: Cluster + Sex + Age + ECOG	Cluster Sex w Age ECOG = 2	2.20, 1.28-3.78 1.02, 0.58-1.78 1.01, 0.99-1.04 0.09, 0.01-0.80	**0.004*** 0.947 0.368 **0.031***	0.676	387.95
Model 3b: Sex + Age + ECOG	Sex w Age ECOG = 2	1.01, 0.58-1.76 1.01, 0.99-1.04 0.06, 0.01-0.52	0.971 0.397 **0.011***	0.608	393.64
Model 3c: Tumor volume + Sex + Age + ECOG	Tumor volume Sex w Age ECOG = 2	1.01, 1-00-1.01 1.23, 0.68-2.20 1.02, 0.99-1.04 0.09, 0.01-0.85	**0.03*** 0.497 0.250 **0.035***	0.640	391.31

Conclusions: Data-driven clustering reveals clinically relevant imaging phenotypes. This underscores the enhanced prognostic value achieved by combining morphological radiomics with tumor size, emphasizing the superiority of this integrated approach over relying solely on tumor size when predicting survival outcomes in glioblastoma patients.

References

1. Calabrese, E., Villanueva-Meyer, J. E., Rudie, J. D., Rauschecker, A. M., Baid, U., Bakas, S., Cha, S., Mongan, J. T., & Hess, C. P. (2022). The University of California San Francisco Preoperative Diffuse Glioma MRI Dataset. Radiol Artif Intell, 4(6), e220058. https://doi.org/10.1148/ryai.220058
2. Chen, B. E., Jiang, W., & Tu, D. (2014). A hierarchical Bayes model for biomarker subset effects in clinical trials. Computational Statistics & Data Analysis, 71, 324-334. https://doi.org/https://doi.org/10.1016/j.csda.2013.05.015
3. Fang, T., Mackillop, W., Jiang, W., Hildesheim, A., Wacholder, S., & Chen, B. E. (2017). A Bayesian method for risk window estimation with application to HPV vaccine trial. Computational Statistics and Data Analysis.
4. Hennig, C. (2023). fpc: Flexible Procedures for Clustering. In https://www.unibo.it/sitoweb/christian.hennig/en/
5. Isensee, F., Schell, M., Pflueger, I., Brugnara, G., Bonekamp, D., Neuberger, U., Wick, A., Schlemmer, H. P., Heiland, S., Wick, W., Bendszus, M., Maier-Hein, K. H., & Kickingereder, P. (2019). Automated brain extraction of multisequence MRI using artificial neural networks. Hum Brain Mapp, 40(17), 4952-4964. https://doi.org/10.1002/hbm.24750
6. Kickingereder, P., Isensee, F., Tursunova, I., Petersen, J., Neuberger, U., Bonekamp, D., Brugnara, G., Schell, M., Kessler, T., Foltyn, M., Harting, I., Sahm, F., Prager, M., Nowosielski, M., Wick, A., Nolden, M., Radbruch, A., Debus, J., Schlemmer, H. P., . . . Maier-Hein, K. H. (2019). Automated quantitative tumour response assessment of MRI in neuro-oncology with artificial neural networks: a multicentre, retrospective study. Lancet Oncol, 20(5), 728-740. https://doi.org/10.1016/s1470-2045(19)30098-1
7. Maechler, M., Rousseeuw, P., Struyf, A., & Hubert, M. (2022). cluster: "Finding Groups in Data": Cluster Analysis Extended Rousseeuw et al. In https://svn.r-project.org/R-packages/trunk/cluster/
8. van Griethuysen, J. J. M., Fedorov, A., Parmar, C., Hosny, A., Aucoin, N., Narayan, V., Beets-Tan, R. G. H., Fillion-Robin, J. C., Pieper, S., & Aerts, H. (2017). Computational Radiomics System to Decode the Radiographic Phenotype. Cancer Res, 77(21), e104-e107. https://doi.org/10.1158/0008-5472.CAN-17-0339

Poster No 1459

Explainable AI for High-Dimensional Neuroimaging Data

Julia Kropiunig[1], Øystein Sørensen[1]

[1]*Centre for Lifespan Changes in Brain and Cognition, Department of Psychology, University of Oslo, Oslo, Norway*

Introduction: The availability of masses of neuroimaging data has given rise to increased use of machine learning techniques for their analysis. These models are usually complex and therefore not easily interpretable by humans. However, it is crucial to explain and interpret those seemingly incomprehensible "black box" models, both for scientific and regulatory reasons. Model interpretability has two aspects to it trying to either focus on individual level explanations or global model behaviour, often referred to as local and global interpretability (Covert et al., 2021). Explainable AI methods are still at the early stages of their development, even more so if the feature space of the machine learning application is very high-dimensional and/or features are highly correlated. The following work discusses several interpretability methods - local as well as global - in the context of correlated features in a high-dimensional feature space and shows their application on tabular neuroimaging data.

Methods: We used magnetic resonance imaging (MRI) data from the UK Biobank (https://www.ukbiobank.ac.uk), including 44164 participants between the ages of 40 and 70 (mean=55.09, standard deviation (SD)=7.56) at recruitment having both a T1-weighted MRI scan and neuropsychological test scores for fluid intelligence (mean=7.61, SD=2.06). Two machine learning models using the tree ensemble gradient boosting library XGBoost (Chen and Guestrin, 2016) were trained to firstly predict age and secondly fluid intelligence from subcortical volumes (ASEG) and parcellations of the white surface using the Desikan-Killiany-Tourville atlas (285 features in total) on a 75:25 training-test set split using a grid parameter search on tree depth, L1-regularization, L2-regularization and learning rate. On both trained models global and local interpretability methods were applied and compared. For individual prediction explanations well-established model-agnostic interpretability methods such as LIME (Ribeiro et al., 2016) and Shapley values (Lundberg and Lee, 2017; Shapley, 1953) as well as state-of-the-art improvements to the Shapley values accounting for feature correlations (Aas et al., 2021; Jullum et al., 2021) were applied and compared. Global interpretability methods used included partial dependence plots (PDPs) (Greenwell, 2017) and global feature importance measure using Shapley values, SAGE (Covert et al., 2020).

Results: The model predicting fluid intelligence was able to establish a weak connection between the response and the brain measures with RMSE = 2.00, MAE = 1.61 on the test dataset whereas the model trying to predict brain age could establish decent predictive power with RMSE = 4.49 and MAE = 3.60. We could assert that PDPs could not give discernible insights into global model behavior due to small effects and high feature correlations and are clearly surpassed by feature importance measures. In the plot Shapley values according to Aas et al. (2021) and Jullum et al. (2021) accounting for correlations among features for the model predicting age are visualized. Since computational efforts increase with increasing feature space

dimensions the brain areas were grouped together into 28 theoretically plausible groups. Shapley values for a specific observation try to quantify how much a feature/group of features contributes to a specific prediction. Thus, it can be observed that the specific instances of Accumbens, Caudate and Amygdala lead to the addition of multiple years to the mean age whereas the values for Thalamus and Putamen take off years from the prediction. The prediction can be assembled by adding all the positive and negative contributions to the mean age.

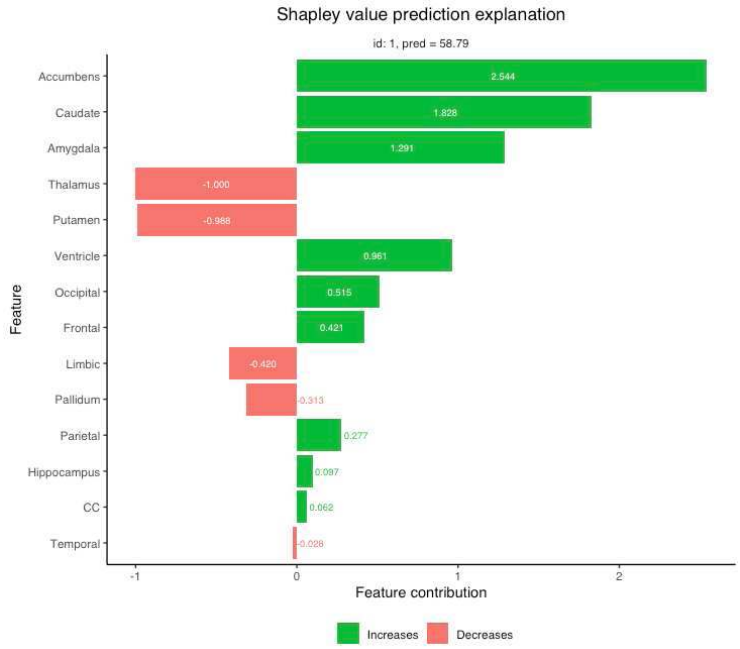

Age prediction explanation for one participant from the test set

Conclusions: Shapley values seemed to give good local explanations but have a computational bottleneck that becomes apparent when looking at a high-dimensional feature space, even more so in combination with a huge sample size leading to the well-known trade-off between accuracy and computation time.

References

1. Aas, K., Jullum, M., and Løland, A. (2021). Explaining individual predictions when features are dependent: More accurate approximations to Shapley values. Artificial Intelligence, 298:103502.
2. Chen, T. and Guestrin, C. (2016). XGBoost: A Scalable Tree Boosting System. In Proceedings of the 22nd ACM SIGKDD International Conference on Knowledge Discovery and Data Mining, pages 785–794, San Francisco California USA. ACM.
3. Covert, I., Lundberg, S., and Lee, S.-I. (2020). Understanding Global Feature Contributions With Additive Importance Measures. arXiv:2004.00668 [cs, stat].
4. Covert, I., Lundberg, S., and Lee, S.-I. (2021). Explaining by removing: A unified framework for model explanation. Journal of Machine Learning Research, 22(209):1–90.
5. Greenwell, M., B. (2017). pdp: An R Package for Constructing Partial Dependence Plots. The R Journal, 9(1):421.
6. Jullum, M., Redelmeier, A., and Aas, K. (2021). group Shapley: Efficient prediction explanation with Shapley values for feature groups. Publisher: arXiv Version Number: 1.
7. Lundberg, S. and Lee, S.-I. (2017). A Unified Approach to Interpreting Model Predictions.
8. arXiv:1705.07874 [cs, stat].
9. Ribeiro, M. T., Singh, S., and Guestrin, C. (2016). "Why Should I Trust You?": Explaining the
10. Predictions of Any Classifier. arXiv:1602.04938 [cs, stat].
11. Shapley, L. S. (1953). A value for n-person games. Publisher: Princeton University Press Princeton.

Poster No 1460

Identifying food cue-induced activity pattern for obesity and normal–weight individuals via LSTM

Zaichen La[1,2], Guanya Li[1,2], Wenchao Zhang[1,2], Yang Hu[1,2], Jingyuan Li[1,2], Weibin Ji[1,2], Mengshan Li[1,2], Huiling Zhou[1,2], Yonghuan Feng[1,2], Zhao Yan[1,2], Yi Zhang[1,2]

[1]Center for Brain Imaging, School of Life Science and Technology, Xidian University, Xi'an, Shaanxi 710126, China, [2]International Joint Research Center for Advanced Medical Imaging and Intelligent Diagnosis and Treatment & Xi'an Key Laboratory of Intelligent Sensing and Regulation of trans-Scale Life Information, School of Life Science and Technology, Xidian University, Xi'an, Shaanxi 710126, China

Introduction: Growing evidence indicates individuals with obesity exhibit hyperactive brain responses to high–caloric food cues in regions involved in food reward processing[1]. The enhanced sensitivity of the reward circuitry is associated with higher food craving[2–4], and it is also accompanied by impaired function of the executive control circuitry, which is an important cause of excessive eating[5]. Most neuroimaging studies focused on altered functional activity in certain brain regions. However, it is still poorly unclear whether the whole-brain activity pattern of visual perception in food energy density in obese patients is different from normal weight individuals. With the application of artificial neural network methods in the field of neuroimaging, it provides a new way to understand the brain functional activity pattern from a higher dimension.

Methods: fMRI task with high– (HiCal) and low–caloric (LoCal) food cues was employed to investigate brain responses to visual perception in food energy density cues in 155 individuals with obesity (OB) and 105 normal–weight controls (NW). Based on Brainnetome Atlas, the time series of 246 brain functional regions were extracted under the stimulation of HiCal and LoCal food pictures. Thus, the 1D Convolution operations (conv1D) and the long short-term memory block (LSTM) were utilized to measure the time sequence information. The attention mechanism was further employed to recognize the significative features from the aforementioned information, which were used to construct HiCal/LoCal food cue-induced activity pattern for OB and NW group respectively via 5-fold cross-validation (Fig. 1A). The importance of features in different brain regions were accessed by the shap interpreter. In order to identify the meaningful brain regions related to activity patterns of OB and NW, test data from OB (NW) were further cross-tested by the NW (OB) classifier (Fig. 1B).

Results: Based on the brain functional activity signals, the proposed model can effectively distinguish the HiCal/LoCal food cue–induced functional activity patterns from OB to NW group, and the accuracy of the OB model (90.96%) is significantly higher than NW model (83.92%) ($t = 5.42$, $P < 0.001$). Cross–testing showed lower accuracy of NW data tested in the OB model (OB model➔NW data: 78.84%) than in the NW model($t = -3.92$, $P < 0.001$) and lower accuracy of OB data tested in the NW model (NW model➔OB data: 83.12%) than in the NW model($t = -7.86$, $P < 0.001$), however there was no significant difference between the accuracy of OB and NW data tested in the NW model ($t = 0.45$, $P = 0.66$, Fig. 1C). Feature importance analysis showed that the top 20% of important features of the NW model (including dorsolateral prefrontal cortex, hippocampal gyrus, parahippocampal gyrus, Lingual_R, Fusiform_R, Frontal_Mid_Orb_L, Frontal_Sup_Medial_L and so on) were significantly different with the OB model (including insula, nucleus accumbens, orbitofrontal cortex, Lingual, Cuneus_R, Fusiform, Calcarine_R, Precuneus_L, Cingulum_Ant_R, Putamen, Frontal_Sup_Orb, Frontal_Sup_Medial, Occipital_Inf, Occipital_Mid_L cortex and so on, Fig. 2A). There was a high degree of overlap between the top 50% of important brain regions of the NW and OB model.

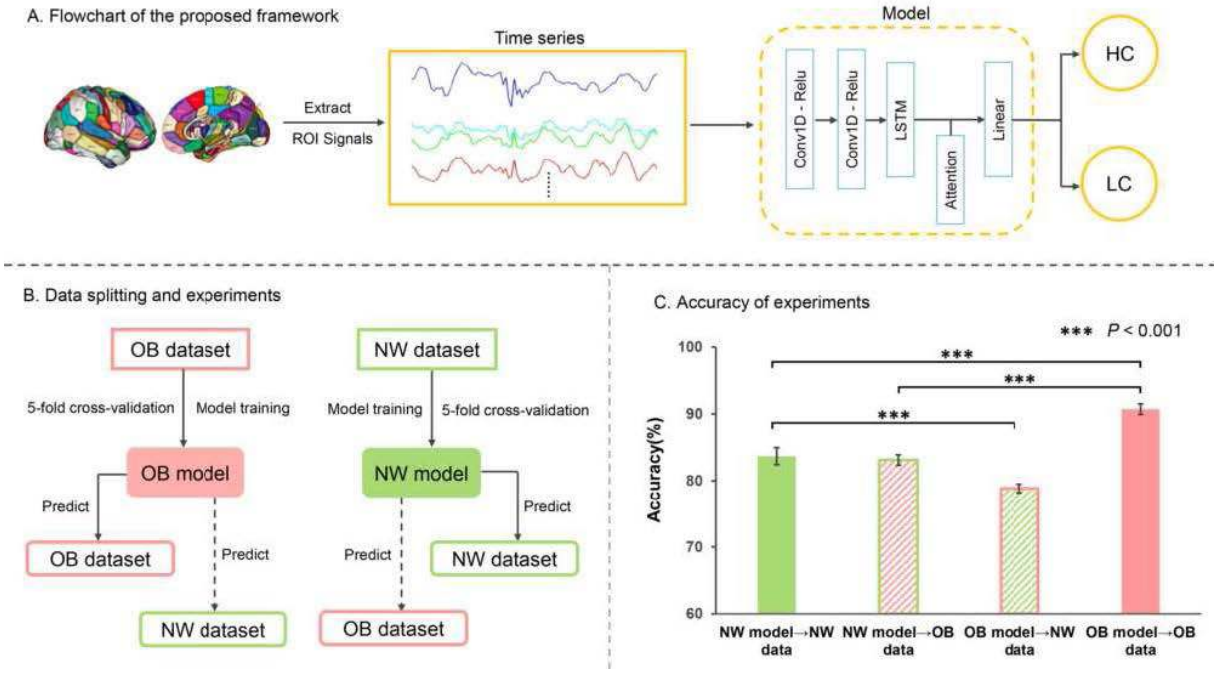

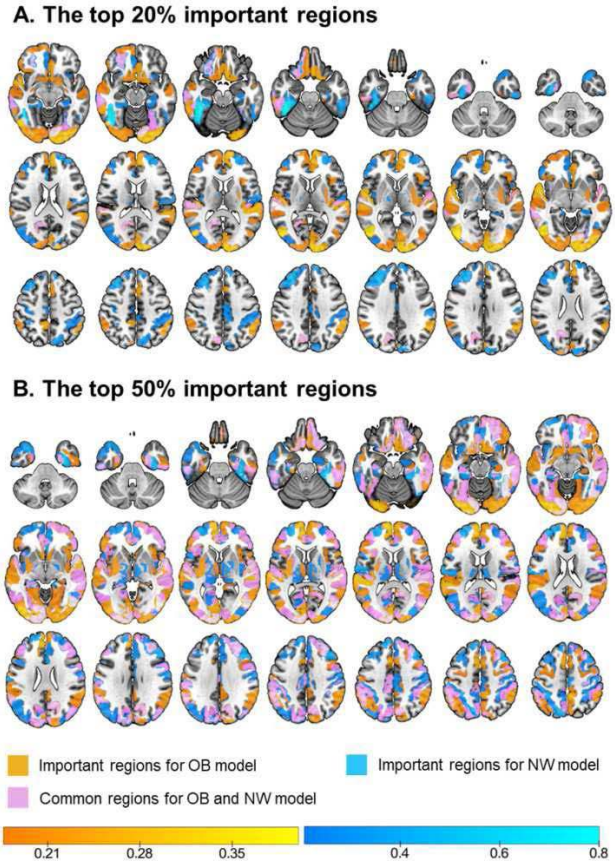

Conclusions: These findings indicate that the important role of the memory and executive control circuits in the food energy density perception in NW, while the insula, nucleus accumbens and the orbitofrontal gyrus, Calcarine_R, Lingual, Cuneus_R and Occipital_Inf_R in OB group enhance the brain perception of food energy density.

References

1. Li, Guanya et al. "Resting activity of the hippocampus and amygdala in obese individuals predicts their response to food cues." Addiction biology vol. 26,3 (2021): e12974. doi:10.1111/adb.12974
2. Dunigan, Anna I, and Aaron G Roseberry. "Actions of feeding-related peptides on the mesolimbic dopamine system in regulation of natural and drug rewards." Addiction neuroscience vol. 2 (2022): 100011. doi:10.1016/j.addicn.2022.100011
3. Alsiö, Johan et al. "Feed-forward mechanisms: addiction-like behavioral and molecular adaptations in overeating." Frontiers in neuroendocrinology vol. 33,2 (2012): 127-39. doi:10.1016/j.yfrne.2012.01.002
4. McCutcheon, James Edgar. "The role of dopamine in the pursuit of nutritional value." Physiology & behavior vol. 152,Pt B (2015): 408-15. doi:10.1016/j.physbeh.2015.05.003
5. Gunstad, John et al. "Cognitive dysfunction is a risk factor for overeating and obesity." The American psychologist vol. 75,2 (2020): 219-234. doi:10.1037/amp0000585

Poster No 1461

Time Domain Classification for Brain-Computer Interface Based Problems

Aiden Rushbrooke[1], Jason Lines[1], Thomas Kinna[1], Anthony Bagnall[2], Saber Sami[1]

[1]University of East Anglia, Norwich, Norfolk, [2]University of Southampton, Southampton, Hampshire

Introduction: Electroencephalographic (EEG) data classification is a ubiquitous task across various disciplines. This task is of particular significance in Brain Computer Interfacing (BCI) enabling direct communication between the brain and external devices. Despite the prevalence of EEG classification many of the current popular approaches use standard classifiers rather than algorithms designed to explicitly exploit information within the time domain. These time series classification (TSC) methods have been shown to perform better than standard approaches such as deep learning on a range of time series machine learning tasks and problem domains[1]. We explore the application of TSC algorithms to BCI based EEG classification problems and highlight their potential to enhance performance and interpretability compared to conventional classification techniques.

Methods: Classifier Selection: For our experimental TSC framework we used the recent Random Convolutional Kernel Transform (ROCKET) algorithm[2]. A large number of random convolutions are used to transform the data, which is then used to train a ridge regression classifier. The main advantage of ROCKET methods are that they are fast and achieve accuracy comparable to state of the art approaches. To enhance BCI efficiency, we explored an adaptation of ROCKET known as MINI-ROCKET[3]. This was selected for its increased speed and deterministic nature. In order to provide a comparison between TSC and traditional methods we employed Support Vector Machine (SVM), Random Forest, and K-Nearest Neighbors (KNN), chosen for their wide applicability in EEG data classification[4]. Datasets: Five BCI datasets were used to compare performance. The first was a novel dataset for a BCI benchmark experiment where 28 participants were asked to press a button when a stimulus appears on a screen. The data was recorded at 1000Hz with 32 EEG channels. Each participant completed 40 button presses, spaced 1.5 second apart. Each participant also recorded resting state data. To form the BCI experiment 1 second segments around each press were taken, starting 200ms before the initial stimulus. This dataset, whilst not currently publicly available, will be released on timeseriesclassification.com in the future. The other 4 datasets were formed from a larger existing BCI motor data collection[5,6] (see table 1). Experimental Design: A leave-one-out strategy was used to reduce the risk of bias caused by a train test split. The model is trained on all but one participant, who is used to evaluate performance. This is then repeated on a new model for each participant, and average accuracy calculated. The experiments were run using the Aeon toolkit.

Results: The results of the experiments are displayed in the tables below, with average accuracy shown in Table 1 and average time taken to fit a model in Table 2. For all classifiers except for SVM, prediction speed was around 1ms. Overall Mini-ROCKET was the best performing classifier in terms of accuracy. Unsurprisingly KNN, whilst being the fastest classifier used, performed much worse than the rest. A time-accuracy plot for the ButtonPress dataset is shown in Figure 2a. From this we can clearly see that the two best performing are MINI-ROCKET and Random Forest. We also tested reducing the training size of the ButtonPress dataset with the two best classifiers, the results of which are shown in Figure 2b. The results show even with a low number of instances, MINI-ROCKET performs well, and outperforms Random Forest at all points.

Dataset	MINI-ROCKET	SVM	Random Forest	KNN
ButtonPress	0.915	0.890	0.872	0.613
OpenCloseFist	0.752	0.747	0.70	0.580
ImaginedOpenCloseFist	0.765	0.759	0.720	0.611
HandFootMovement	0.684	0.676	0.630	0.573
ImaginedHandFootMovement	0.680	0.681	0.643	0.602

(a) Accuracy scores for 5 BCI datasets for both TSC and traditional methods

Dataset	MINI-ROCKET	SVM	Random Forest	KNN
ButtonPress	35.7	354.2	24.3	0.12
OpenCloseFist	98.8	2665.5	65.7	0.25
ImaginedOpenCloseFist	104.2	2211.4	67.9	0.23
HandFootMovement	90.5	2850.5	65.0	0.41
ImaginedHandFootMovement	103.1	2838.9	74.0	0.40

(b) Average time taken to fit each classifier in seconds

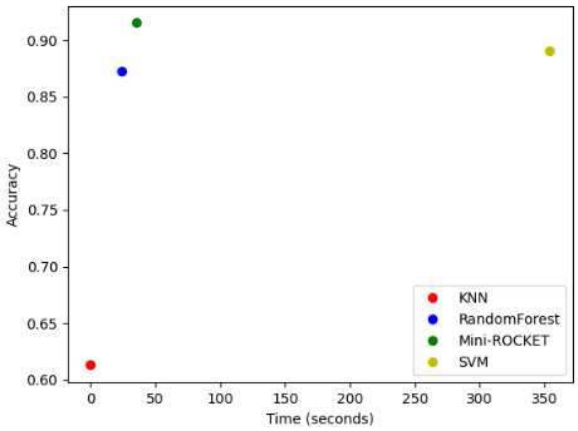

(a) Time-Accuracy comparison for each classifier with the ButtonPress dataset

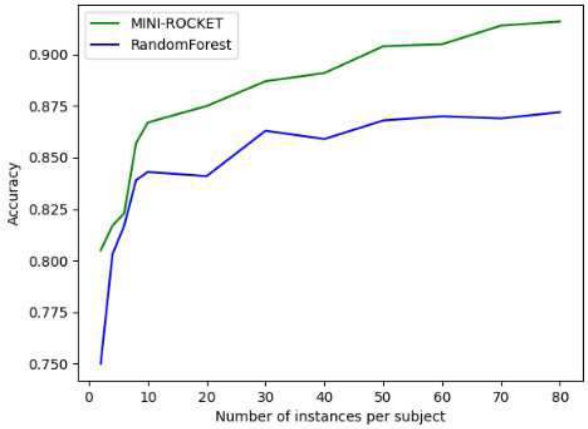

(b) Accuracy for MINI-ROCKET with a variable number of button press instances per subject used the train the model for the ButtonPress dataset.

Fig. 2: Graphs showing further investigation into the ButtonPress dataset

Conclusions: Our experiments show that TSC methods have potential when applied to BCI problems, achieving high accuracy whilst needing little pre-processing or prior knowledge. The speed of models such as those based on ROCKET could be used for real time BCI classification experiments. Further work would be to expand both the range of datasets and models to evaluate the generalisable nature of TSC methods to real-time BCI adaptations and test their potential for clinical usage.

References

1. A. Bagnall, J. Lines, A. Bostrom, J. Large, and E. Keogh (2017). The great time series classification bake off: a review and experimental evaluation of recent algorithmic advances. Data Mining and Knowledge Discovery, 31(3):606–
2. Angus Dempster, Francois Petitjean, and Geoffrey Webb(2020). ROCKET: Exceptionally fast and accurate time series classification using random convolutional kernels. Data Mining and Knowledge Discovery, 34:1454–1495.
3. Angus Dempster, D Schmidt, and Geoffrey Webb (2021). Minirocket: A very fast (almost) deterministic transform for time series classification. In proceedings of the 27th ACM SIGKDD International Conference on Knowledge Discovery and Data Mining.
4. Fabien Lotte, Laurent Bougrain, Andrzej Cichocki, Maureen Clerc, Marco Congedo, Alain Rakotomamonjy, and Florian Yger (2018). A review of classification algorithms for eeg-based brain-computer interfaces: A 10-year update. Journal of Neural Engineering, 15, 02.
5. G. Schalk, D.J. McFarland, T. Hinterberger, N. Birbaumer, and J.R. Wolpaw (2004). Bci2000: a general-purpose brain-computer interface (bci) system. IEEE Transactions on Biomedical Engineering, 51(6):1034–1043.
6. Gerwin Schalk, Dennis J McFarland, Thilo Hinterberger, Niels Birbaumer, and Jonathan R Wolpaw (2022). “eeg motor movement/ imagery dataset”.

Poster No 1462

Power and reproducibility in the external validation of brain-phenotype predictions

Matthew Rosenblatt[1], Link Tejavibulya[1], Chris Camp[1], Rongtao Jiang[2], Margaret Westwater[2], Stephanie Noble[3], Dustin Scheinost[1]

[1]Yale University, New Haven, CT, [2]Yale School of Medicine, New Haven, CT, [3]Northeastern University, Boston, MA

Introduction: Identifying reproducible and generalizable brain-phenotype associations is a central goal of neuroimaging. Consistent with this goal, prediction frameworks evaluate brain-phenotype models in unseen data. Most prediction studies train and evaluate a model in the same dataset. However, external validation, or the evaluation of a model in an external dataset, provides a better assessment of robustness and generalizability[1], and it may improve reproducibility. Yet, the statistical power of such studies has not been investigated. Here, we ran over 60 million simulations across several datasets, phenotypes, and sample sizes to better understand how the sizes of the training and external datasets affect statistical power.

Methods: We used resting-state fMRI data from the Adolescent Brain Cognitive Development (ABCD) Study[2] (N=7822-7969), the Healthy Brain Network (HBN) Dataset[3] (N=1024-1201), the Human Connectome Project Development (HCPD) Dataset[4] (N=424-605), and the Philadelphia Neurodevelopmental Cohort (PNC) Dataset[5,6] (N=1119-1126). Resting-state functional connectomes were formed using the Shen 268 atlas[7]. We performed external validation, where a model was developed in one dataset and applied to the other three datasets. Ridge regression models[8] with 1% feature selection were trained to predict age, attention problems, and matrix reasoning from functional connectivity. We subsampled the training and external datasets at various sample sizes (Figure 1) to determine how sample size affects external validation performance (Pearson's r). We defined the "ground truth" prediction performance as the performance when using the full training and external datasets. The fraction of significant simulation results was calculated. This fraction was considered power for models with a significant ground truth effect and false positive rate for models with an insignificant ground truth effect (Figure 1). Among the significant prediction results, effect size inflation was calculated as the difference between the observed performance and the ground truth performance (Figure 2). We further compared our simulation results to the median sample sizes of external validation studies in the field (training sample: n=129; external sample: n=108)[1].

Results: Increasing the external sample size increased the power consistent with theoretical curves, and decreasing the size of the training dataset negatively offset the power curve (Figure 1). For sample sizes similar to the median in the field, the power ranged from 99.11-100.00% for age, 5.47-8.35% for attention problems, and 5.24-72.74% for matrix reasoning. For insignificant ground truth effects, the false positive rate was highest for large external samples and small training samples. Effect size inflation was greatest in weaker predictions and smallest in strong predictions, such as age (Figure 2). For the weakest predictive models, the training dataset size made little difference in effect size inflation, likely because effect size inflation is a consequence of low power based on the external sample size. For stronger models (e.g., age), we saw a greater effect of training size. There was little to no inflation, but smaller training sizes produced worse predictions. For sample sizes comparable to the median in the field, the median inflation rates ranged from Δr of -0.12 to -0.05 for age, 0.10 to 0.20 for attention problems, and -0.17 to 0.21 for matrix reasoning, where negative inflation means deflation.

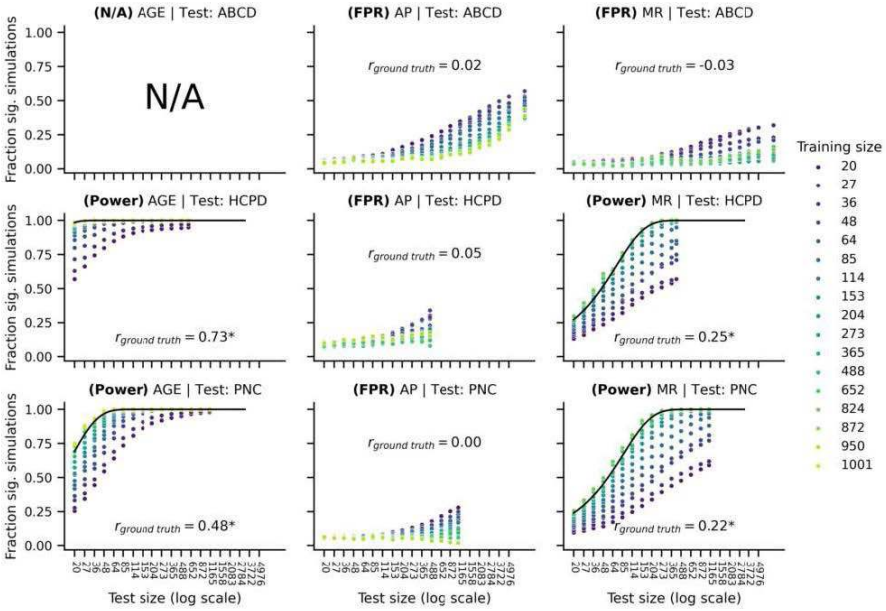

Figure 1. Power and false positive rates for cross-dataset predictions, training in HBN and testing in ABCD (top row), HCPD (middle row), or PNC (bottom row) for prediction of age (left column), attention problems (middle column), or matrix reasoning (right column). The blue lines represent theoretical power assuming a known ground truth performance. The panel with N/A means that data were not included in this study. Similar results were observed for training in the ABCD, HCPD, and PNC datasets, but are not displayed in this abstract. AP: attention problems, MR: matrix reasoning.

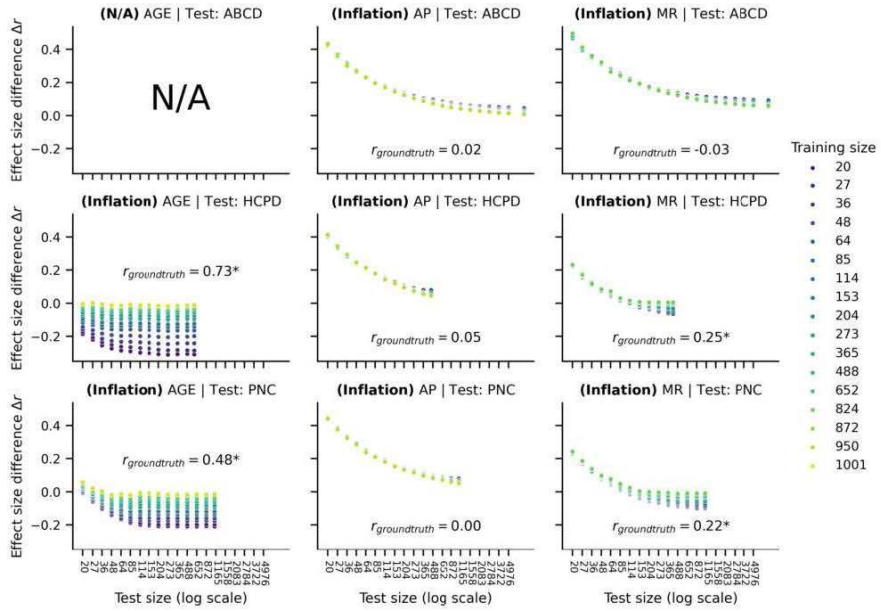

Figure 2. Median effect size inflation for cross-dataset predictions, training in HBN and testing in ABCD (top row), HCPD (middle row), or PNC (bottom row) for prediction of age (left column), attention (middle column), or matrix reasoning (right column). Panels with N/A mean that data were not available. Similar results were observed for training in the ABCD, HCPD, and PNC datasets, but are not displayed in this abstract. AP: attention problems, MR: matrix reasoning.

Conclusions: For attention problems and matrix reasoning, typical sample sizes for external validation in the field are underpowered. Relatedly, due to low power and publication bias, effect sizes may be overestimated for certain phenotypes. External validation is expected to become more widespread as the field confronts reproducibility challenges (9), and this work provides a starting point for understanding the sample sizes needed to power external validation studies adequately.

References

1. Yeung, A. W. K., More, S., Wu, J. & Eickhoff, S. B (2022). Reporting details of neuroimaging studies on individual traits prediction: A literature survey. Neuroimage 256, 119275.
2. Casey, B. J. et al (2018). The Adolescent Brain Cognitive Development (ABCD) study: Imaging acquisition across 21 sites. Dev. Cogn. Neurosci. 32, 43–54.

3. Alexander, L. M. et al (2017). An open resource for transdiagnostic research in pediatric mental health and learning disorders. Sci Data 4, 170181.
4. Somerville, L. H. et al (2018). The Lifespan Human Connectome Project in Development: A large-scale study of brain connectivity development in 5-21 year olds. Neuroimage 183, 456–468.
5. Satterthwaite, T. D. et al (2014). Neuroimaging of the Philadelphia neurodevelopmental cohort. Neuroimage 86, 544–553.
6. Satterthwaite, T. D. et al (2016). The Philadelphia Neurodevelopmental Cohort: A publicly available resource for the study of normal and abnormal brain development in youth. Neuroimage 124, 1115–1119.
7. Shen, X., Tokoglu, F., Papademetris, X. & Constable, R. T (2013). Groupwise whole-brain parcellation from resting-state fMRI data for network node identification. Neuroimage 82, 403–415.
8. Pedregosa, F. et al (2011). Scikit-learn: Machine learning in Python. The Journal of machine Learning research 12, 2825–2830.
9. Marek, S. et al (2022). Reproducible brain-wide association studies require thousands of individuals. Nature 605, E11.

Poster No 1463

The effects of data leakage on connectome-based machine learning models

Matthew Rosenblatt[1], Link Tejavibulya[1], Rongtao Jiang[1], Stephanie Noble[2], Dustin Scheinost[1]

[1]Yale University, New Haven, CT, [2]Northeastern University, Boston, MA

Introduction: Understanding individual differences in brain-behavior relationships is a central goal of neuroscience. As such, machine learning approaches using neuroimaging data, such as functional connectivity, have grown increasingly popular in predicting numerous phenotypes. The reproducibility of such studies is hindered by data leakage, where information about the test data is introduced into the model during training[1]. Although leakage is never a correct practice, quantifying the effects of leakage in neuroimaging data is important due to its pervasiveness. Here, we evaluate the effects of leakage on functional connectome-based machine learning in four large datasets for the prediction of three phenotypes.

Methods: We obtained resting-state fMRI data from the Adolescent Brain Cognitive Development (ABCD) Study[2] (N=7822-7969), the Healthy Brain Network (HBN) Dataset[3] (N=1024-1201), the Human Connectome Project Development (HCPD) Dataset[4] (N=424-605), and the Philadelphia Neurodevelopmental Cohort (PNC) Dataset[5,6] (N=1119-1126). Resting-state functional connectomes were formed using the Shen 268 atlas[7]. Throughout this work, we predicted age, attention problems, and matrix reasoning from functional connectivity using ridge regression[8] with 5-fold cross-validation. We evaluated a gold standard model, which included covariate regression, site correction, and feature selection within the cross-validation scheme and was split accounting for family structure. We also evaluated four other categories of models. First, several alternative analysis choices that do not contain leakage were included as a reference point, such as omitting site correction, covariate regression, or both. Second, feature leakage involves selecting features in the combined training/test data instead of only in the training data. Third, covariate-related forms of leakage in this study included correcting for site differences and performing covariate regression in the combined training and test data (i.e., outside the cross-validation folds). Fourth, subject-level leakage was evaluated in the forms of family leakage and repeated subjects leakage. For family leakage, the family structure of the data was ignored, where leakage may occur if one family member is in the training set and another in the test set. For subject leakage, a percentage of the participants were randomly repeated in the dataset, mimicking the possible mishandling of repeated measurements datasets.

Results: We first analyzed leakage in HCPD and found that leaky feature selection and subject leakage (20%) most inflated performance, but leaky covariate regression deflated performance (Figure 1). Other forms of leakage, including family leakage and leaky site correction, had little to no effect on performance (Figure 1). Results were similar when considering all the datasets, where leaky feature selection (Δr=0.03-0.52, $\Delta q2$=0.01-0.47) and subject leakage (20%) (Δr=0.06-0.29, $\Delta q2$=0.03-0.24) led to the greatest performance inflation (Figure 2). Notably, weaker baseline models were more affected by feature leakage. Leaky covariate regression was the only form of leakage that consistently deflated performance (Δr=-0.09-0.00, $\Delta q2$=-0.17-0.00). Family leakage (Δr=0.00-0.02, $\Delta q2$=0.00) and leaky site correction (Δr=-0.01-0.00, $\Delta q2$=-0.01-0.01) had little effect. We repeated the analyses with support vector regression[8] and connectome-based predictive models[9] and saw similar results.

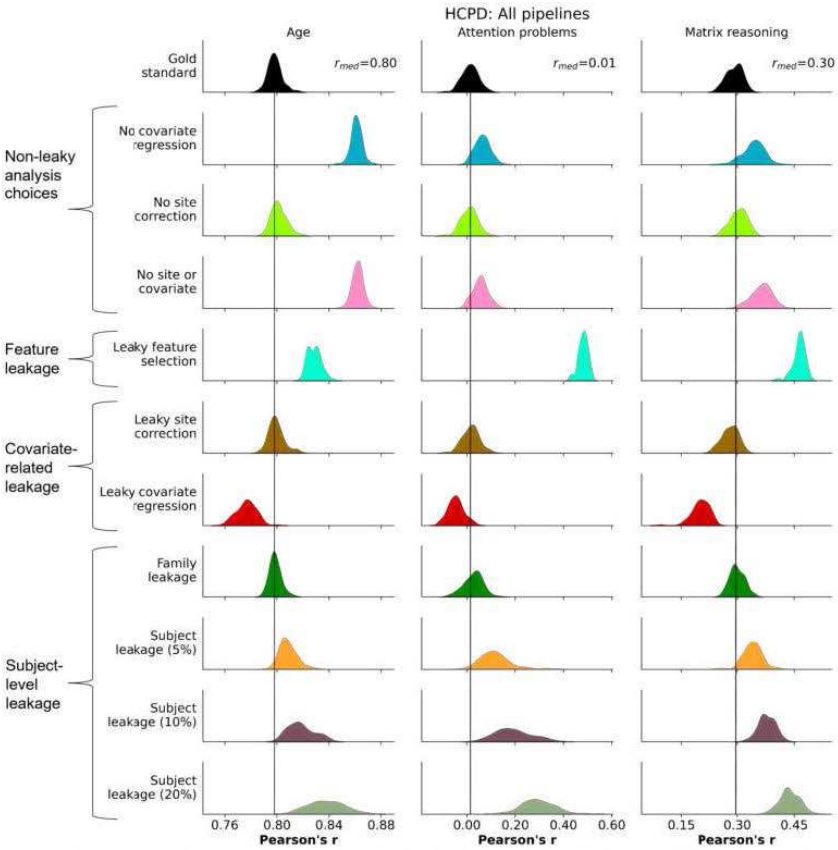

Figure 1. Evaluation of leakage in HCPD with a metric of Pearson's *r* between the predicted and observed values. Rows represent different leakage types, and columns show different phenotypes. The black bar represents the median performance of the "gold standard" models across random iterations, and the histograms show prediction performance across 100 iterations of 5-fold cross-validation. In each iteration, performance was assessed using ridge regression with 5% feature selection and a grid search for the L2 regularization parameter. In general, leaky feature selection and subject leakage (20%) most inflated performance, while leaky covariate regression deflated performance.

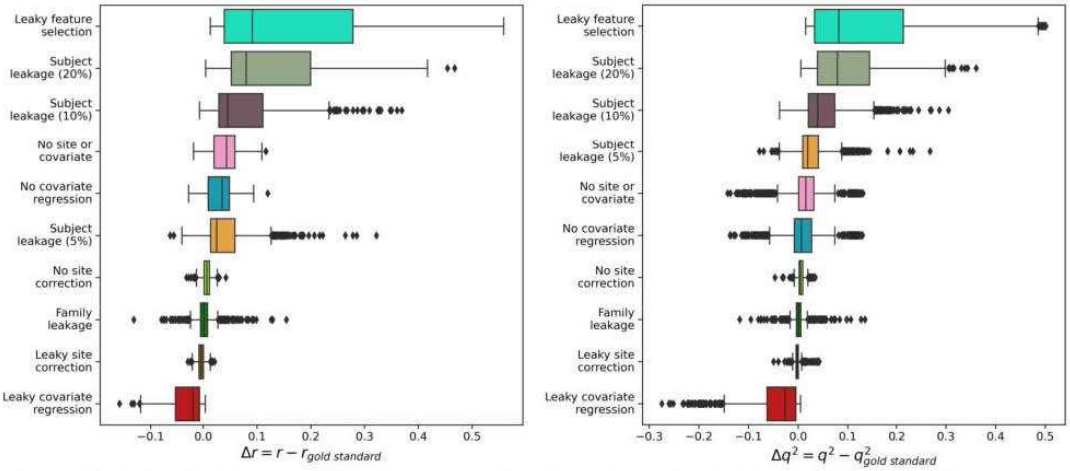

Figure 2. Evaluation of performance differences between all pipelines and the gold standard pipeline across all four datasets and three phenotypes for Pearson's *r* (left) and prediction R^2 (q^2) (right). For each of *r* and q^2, the plots are ranked from the most inflated performance (top) to the most deflated performance (bottom).

Conclusions: Concerns about reproducibility in machine learning can be partially attributed to leakage[1]. Some forms of leakage greatly affected the results. But, other types did not affect predictions, which means that published results with these forms of leakage likely remain valid. Since the effects of leakage vary greatly, the best practice remains to avoid data leakage altogether through the careful development and sharing of code, alternative validation strategies (lock box[10], external validation), and model information sheets[1].

References
1. Kapoor, S. & Narayanan, A (2023). Leakage and the reproducibility crisis in machine-learning-based science. Patterns 4, 100804.
2. Casey, B. J. et al (2018). The Adolescent Brain Cognitive Development (ABCD) study: Imaging acquisition across 21 sites. Dev. Cogn. Neurosci. 32, 43–54.
3. Alexander, L. M. et al (2017). An open resource for transdiagnostic research in pediatric mental health and learning disorders. Sci Data 4, 170181.
4. Somerville, L. H. et al (2018). The Lifespan Human Connectome Project in Development: A large-scale study of brain connectivity development in 5-21 year olds. Neuroimage 183, 456–468.
5. Satterthwaite, T. D. et al (2014). Neuroimaging of the Philadelphia neurodevelopmental cohort. Neuroimage 86, 544–553.
6. Satterthwaite, T. D. et al (2016). The Philadelphia Neurodevelopmental Cohort: A publicly available resource for the study of normal and abnormal brain development in youth. Neuroimage 124, 1115–1119.
7. Shen, X., Tokoglu, F., Papademetris, X. & Constable, R. T. (2013). Groupwise whole-brain parcellation from resting-state fMRI data for network node identification. Neuroimage 82, 403–415.
8. Pedregosa, F. et al (2011). Scikit-learn: Machine learning in Python. The Journal of machine Learning research 12, 2825–2830.
9. Shen, X. et al (2017). Using connectome-based predictive modeling to predict individual behavior from brain connectivity. Nat. Protoc. 12, 506–518.
10. Hosseini, M. et al (2020). I tried a bunch of things: The dangers of unexpected overfitting in classification of brain data. Neurosci. Biobehav. Rev. 119, 456–467.

Poster No 1464

Association between DBM-derived Atrophy Patterns and Cognition in Frontotemporal Dementia Variants

Amelie Metz[1], Yashar Zeighami[2], Simon Ducharme[3], Sylvia Villeneuve[4], Mahsa Dadar[5]

[1]McGill University, Montreal, Quebec, [2]Douglas Research Centre, Montreal, Quebec, [3]McGill University, Montreal, ., [4]Brain Imaging Centre, Douglas Institute Research Centre, Montreal, Qc, [5]McGill University, Montreal, QC

Introduction: Frontotemporal Dementia (FTD) is a prevalent form of early-onset dementia characterized by progressive neurodegeneration[1,2]. It encompasses a group of heterogeneous neuropathological disorders, including behavioral variant frontotemporal dementia (bvFTD), nonfluent variant primary progressive aphasia (nfvPPA), and semantic variant primary progressive aphasia (svPPA), each exhibiting distinct symptoms. BvFTD initially presents with abnormal behavior, changes in personality, and reduced executive control while in primary progressive aphasias, cognitive deficits predominantly manifest themselves in distinct skills within the language domain[3]. Previous magnetic-resonance imaging (MRI) studies have highlighted atrophy patterns in specific brain regions corresponding to symptom manifestations[2] but few have validated these findings using deformation-based morphometry (DBM)[4-7] which offers increased sensitivity to subtle local differences in structural image contrasts compared to traditional methods. Here, we tested whether DBM-derived brain atrophy patterns in the core variants of FTD are associated with severity of cognitive impairment and whether this relationship differs between the phenotypic subtypes.

Methods: A total of 136 patients (70 bvFTD, 36 svPPA, 30 nfvPPA) and 133 cognitively unimpaired controls from the frontotemporal lobar degeneration neuroimaging initiative (FTLDNI) database underwent high-resolution brain MRI and clinical, neuropsychological examination. Cognitive measures included global cognition, language, memory and executive functions. DBM values[4] were calculated as an estimation of regional cortical and subcortical atrophy. Atlas-based associations between DBM values and performance across different cognitive tests were assessed using partial least squares (PLS)[8,9]. We then applied linear regression models to discern the group differences regarding the relationship between atrophy and cognitive decline in the three FTD variants. Lastly, we assessed whether the combination of neural and behavioral patterns in the latent variables identified in the PLS analysis could be used as features in a machine learning model to predict FTD subtypes in patients.

Results: PLS revealed three significant latent variables (LV) that combined accounted for over 85% (42.98%, 35.60%, and 6.97% respectively, permuted p-values<0.01) of the shared covariance between cognitive and brain atrophy measures. It identified neural networks whose collective atrophy was associated with the clinical phenotype (Fig.1). The atrophy pattern included left-hemispheric subcortical structures (LV-I), left temporal and bilateral subcortical areas (LV-II), and frontal and right subcortical regions (LV-III). Brain scores were significantly related to behavioral scores in all LVs in that subjects with greater expression of the respective brain pattern had greater impairment in most cognitive measures included in the LV (LV-I: R2=0.37, p=0.0, LV-II: R2=0.77, p=0.0, LV-III: R2=0.43, p=0.0). In LV-II, the brain pattern had a higher impact on cognition in bvFTD whereby the atrophy pattern was related to higher performance in language tests and lower scores in executive function (bvFTD vs nfvPPA tStat=-2.48 p=0.01, bvFTD vs svPPA tStat=3.52 p=0.0). In LV-II, subjects with svPPA showed higher performance in the included cognitive scores (vs bvFTD tStat=-5.20 p=0.0, vs nfvPPA tStat=-6.21 p=0.0), whereas subjects

with nfvPPA had higher scores in LV-III compared to bvFTD (tStat=3.06 p=0.0, Fig.2). Individual variation in the atrophy and behavioral patterns predicted classification of patients into FTD subtypes with an accuracy of 75.09%.

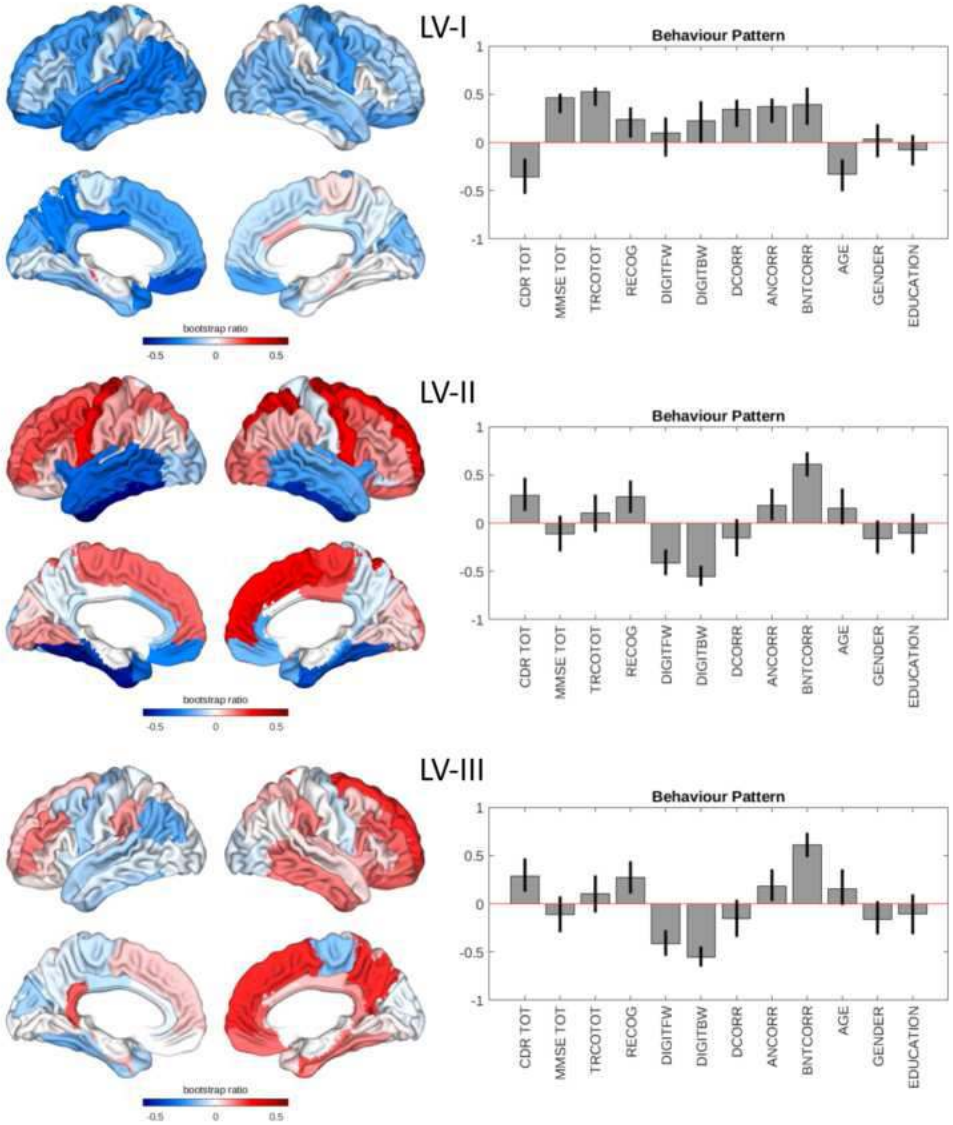

Figure 1. Latent variables (LV-I - III) obtained from the PLS analysis. Left panels: Brain pattern bootstrap ratios in MNI space; right panels: Pattern of demographic and cognitive test scores. The effect size estimates are derived from SVD analysis and the Confidence Intervals (CI) are calculated by bootstrapping, hence the CI are not necessarily symmetrical.

CDRTOT = total CDR score; MMSETOT = total MMSE score; TRCOTOT = CVLT total items remembered; RECOG = CVLT total items recognized; DIGITFW = forward digit span; DIGITBW = backward digit span; DCORR = phonological verbal fluency score; ANCORR = semantic verbal fluency score; BNTCORR = total BNT score.

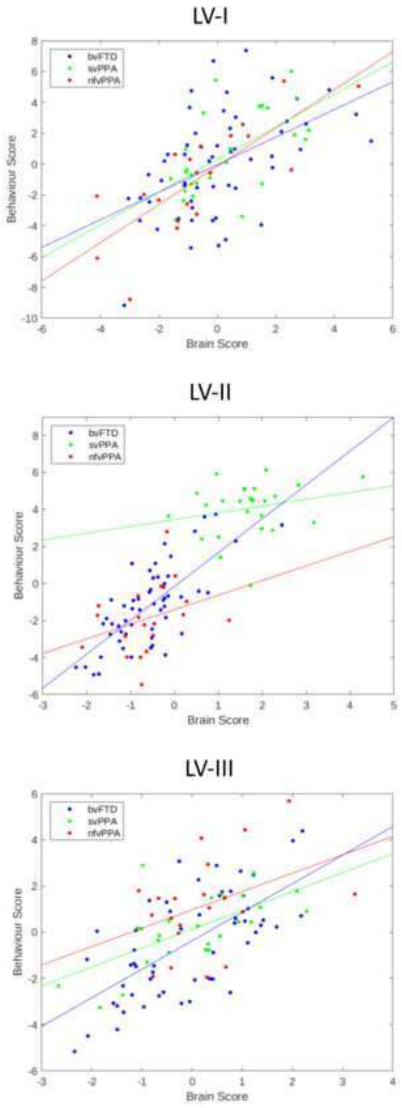

Figure 2. Individual patients' brain versus behavioral PLS score and group differences between FTD variants in LV-I (top), LV-II (middle), LV-III (bottom).

bvFTD = behavioral variant FTD (blue); svFTD = semantic variant primary progressive aphasia (green); nfvFTD = nonfluent variant primary progressive aphasia (red)

Conclusions: Findings in this study demonstrate a robust mapping between neurodegeneration as estimated by DBM values and the cognitive manifestations of FTD variants. The combination of DBM and multivariate statistical methods could potentially serve as an imaging biomarker for early disease severity assessment and phenotyping in FTD.

References

1. Bang, J. (2015). Frontotemporal dementia. The Lancet, 386(10004), 1672–1682.
2. Cardenas, V. A. (2007). Deformation-Based Morphometry Reveals Brain Atrophy in Frontotemporal Dementia.
3. Gorno-Tempini, M. L. (2011). Classification of primary progressive aphasia and its variants. Neurology, 76(11), 1006–1014.
4. Olney, N. T. (2017). Frontotemporal Dementia. Neurologic Clinics, 35(2), 339–374.
5. Manera, A. L. (2019). Deformation based morphometry study of longitudinal MRI changes in behavioral variant frontotemporal dementia. NeuroImage: Clinical, 24, 102079.
6. McIntosh, A. R. (2004). Partial least squares analysis of neuroimaging data: Applications and advances. NeuroImage, 23 Suppl 1, S250-263.
7. Shafiei, G. (2023). Network structure and transcriptomic vulnerability shape atrophy in frontotemporal dementia. Brain, 146(1), 321–336.
8. Wisse, L. E. M. (2021). Cross-sectional and longitudinal medial temporal lobe subregional atrophy patterns in semantic variant primary progressive aphasia. Neurobiology of Aging, 98, 231–241.
9. Zeighami, Y. (2019). A clinical-anatomical signature of Parkinson's disease identified with partial least squares and magnetic resonance imaging. NeuroImage, 190, 69–78.

Poster No 1465

Structural Brain Abnormalities of Childhood Trauma: An ENIGMA Transdiagnostic Mega-Analysis Sutdy

Haley Wang[1], Zhen-Qi Liu[2], Lauren Salminen[3], Rajendra Morey[4], Lianne Schmaal[5], Laura Han[5], Elena Pozzi[5], ENIGMA MDD Working Group[6], ENIGMA PTSD Working Group[6], Tiffany Ho[1]

[1]UCLA, Los Angeles, CA, [2]McGill University, Montreal, Quebec, [3]University of Southern California, Los Angeles, CA, [4]Duke University, Durham, NC, [5]University of Melbourne, Melbourne, Australia, [6]ENIGMA, International, International

Introduction: Early life adversity (ELA), including abuse and neglect, is strongly linked to stress-related mental disorders, such as major depressive disorder (MDD) and post-traumatic stress disorder (PTSD). Neuroimaging studies showed that individuals with more severe ELA have lower cortical thickness (CT), lower surface area (SA), and smaller subcortical volumes (SV). Case-control studies reported similar neuroanatomical abnormalities in MDD and PTSD, yet the extent to which MDD or PTSD-related brain alterations are attributable to ELA remains uncertain. Furthermore, neuroimaging studies of ELA showed heterogeneous effect sizes, and the regional distribution of structural brain abnormalities associated with ELA has been inconsistent. Here, we address these gaps by pooling together structural neuroimaging data from 25 international cohorts via the ENIGMA-MDD and PTSD Working Groups and leveraging data-driven methods to test whether neuroanatomical features (CT, SA, and SV) predict the severity of ELA.

Methods: Of the included 3,668 subjects (mean age=35.1; age range: 8.3-73.7 years), 2027 (55.3%) were female. This study included 2,263 healthy control (HC) subjects, 890 MDD patients, and 515 PTSD patients. T1w structural MRI data were processed using harmonized FreeSurfer quality assurance protocols with neuroCombat to correct for site and scanner effects across cohorts. ELA severity was measured by the Childhood Trauma Questionnaire (CTQ). We examined diagnostic group differences in regional CT, SA, and SV, controlling for age, sex, and intracranial volume, correcting for multiple tests. Using Partial Least Square (PLS) correlation, we extracted latent components (LCs) that maximize covariance between the neuroanatomical features and CTQ scores across all subjects. Additionally, seven machine learning (ML) models (linear, tree-based, support vector regression, and ensemble methods) were trained on the neuroimaging data to assess top neural features contributing to predictions of ELA severity (i.e., the CTQ total and subscale scores separately) across all subjects.

Results: The PTSD group had significantly higher total CTQ scores compared to the HC ($d=1.47$; $p<.001$) and MDD ($d=0.73$; $p<.001$) groups, with HC being lower than the MDD group ($d=-0.64$; $p<.001$). Compared with HC, MDD group exhibited widespread lower CT measures, with the largest effect sizes seen in the bilateral supramarginal, fusiform, and middle temporal regions ($q<.05$). MDD group also showed lower SA in the right superior temporal sulcus and bilateral superior temporal sulcus regions ($q<.05$). However, no differences in SV were observed. No structural brain measure differences were found between the PTSD as compared with the HC or MDD groups. Transdiagnostic PLS analyses revealed significant but weak LCs linking CT and SA with total CTQ ($p<.001$; $r=.07$), neglect ($p<.001$; $r=.06$), and abuse ($p<.001$; $r=.06$). No LCs were found correlating SV with CTQ scores. Consistent with the PLS analyses, all ML algorithms failed to predict CTQ scores based on neuroanatomical features reliably.

Conclusions: Consistent with prior work, we found that MDD is associated with lower CT and SA in the supramarginal, fusiform, and middle temporal regions compared to HC, whereas PTSD showed no detectable neuroanatomical differences from MDD or HC after multiple tests correction. Interestingly, ELA severity did not correlate with the variances in macroscale neuroanatomical features transdiagnostically. Together, our results suggest that factors other than ELA, perhaps later environmental influences, may play a significant role in brain development and the neurophenotypes of MDD and PTSD. One possible interpretation is that ELA does not play an outsized role in shaping brain morphometry by adulthood and that these effects are more prominent during childhood and adolescence. To test this formulation, future work will include separate analyses for children, adolescents, and adults, within the inherent limitations of these consortia data.

References

1. Fortin, J.-P., Cullen, N., Sheline, Y.I., Taylor, W.D., Aselcioglu, I., Cook, P.A., Adams, P., Cooper, C., Fava, M., McGrath, P.J., et al. (2018). Harmonization of cortical thickness measurements across scanners and sites. Neuroimage 167, 104–120.
2. Frodl, T., Reinhold, E., Koutsouleris, N., Reiser, M., and Meisenzahl, E.M. (2010). Interaction of childhood stress with hippocampus and prefrontal cortex volume reduction in major depression. J. Psychiatr. Res. 44, 799–807.
3. Jenness, J.L., Peverill, M., Miller, A.B., Heleniak, C., Robertson, M.M., Sambrook, K.A., Sheridan, M.A., and McLaughlin, K.A. (2021). Alterations in neural circuits underlying emotion regulation following child maltreatment: a mechanism underlying trauma-related psychopathology. Psychol. Med. 51, 1880–1889.
4. McLaughlin, K.A., Greif Green, J., Gruber, M.J., Sampson, N.A., Zaslavsky, A.M., and Kessler, R.C. (2012). Childhood adversities and first onset of psychiatric disorders in a national sample of US adolescents. Arch. Gen. Psychiatry 69, 1151–1160.
5. Schmaal, L., Pozzi, E., C Ho, T., van Velzen, L.S., Veer, I.M., Opel, N., Van Someren, E.J.W., Han, L.K.M., Aftanas, L., Aleman, A., et al. (2020). ENIGMA MDD: seven years of global neuroimaging studies of major depression through worldwide data sharing. Transl. Psychiatry 10, 172.

6. Schmaal, L., Veltman, D.J., van Erp, T.G.M., Sämann, P.G., Frodl, T., Jahanshad, N., Loehrer, E., Tiemeier, H., Hofman, A., Niessen, W.J., et al. (2016). Subcortical brain alterations in major depressive disorder: findings from the ENIGMA Major Depressive Disorder working group. Mol. Psychiatry 21, 806–812.
7. Sun, D., Rakesh, G., Clarke-Rubright, E.K., Haswell, C.C., Logue, M.W., O'Leary, E.N., Cotton, A.S., Xie, H., Dennis, E.L., Jahanshad, N., et al. (2022). Remodeling of the Cortical Structural Connectome in Posttraumatic Stress Disorder: Results From the ENIGMA-PGC Posttraumatic Stress Disorder Consortium. Biol Psychiatry Cogn Neurosci Neuroimaging 7, 935–948.
8. Teicher, M.H., Samson, J.A., Anderson, C.M., and Ohashi, K. (2016). The effects of childhood maltreatment on brain structure, function and connectivity. Nat. Rev. Neurosci. 17, 652–666.

Poster No 1466

A Novel Graph Convolutional Network for Predicting Cognitive Deficits in Very Preterm Infants

Hailong Li[1,2], Junqi Wang[1], Zhiyuan Li[1,2], Kim Cecil[1,2], Mekibib Altaye[1,2], Jonathan Dillman[1,2], Nehal Parikh[1,2], Lili He[1,2]

[1]Cincinnati Children's Hospital Medical Center, Cincinnati, OH, [2]University of Cincinnati, Cincinnati, OH

Introduction: Very preterm (VPT) infants (born at or less than 32 weeks gestational age) are at high risk for adverse cognitive deficits.(Linsell et al. 2018) Given the known benefits of early interventions, accurate prediction soon after birth are urgently needed for at-risk VPT infants. Several studies have applied the brain structural connectome (SC) derived from diffusion tensor imaging (DTI) to predict cognitive deficits. (Kawahara et al. 2017; He et al. 2021; Girault et al. 2019) However, none of these models are specifically designed for graph-structured data, and thus, potentially miss certain topological information conveyed in the brain SC. In this work, we developed graph convolutional network (GCN) models (Kipf and Welling 2016) to learn the SC acquired at term-equivalent age as a graph for early prediction of cognitive deficits at 2 years corrected age in VPT infants. The supervised contrastive learning (SCL) technique(Khosla et al. 2020) is applied to mitigate the impacts of the data scarcity problem. We hypothesize that SCL will enhance GCN models for early prediction of cognitive deficits in VPT infants using the SC.

Methods: This IRB-approved study utilized a regional VPT infant cohort from Cincinnati Infant Neurodevelopment Early Prediction Study (CINEPS) that includes a total of 393 VPT infants. DTI and T2-weighted MRI data were acquired on 3T MRI scanner (Philips Ingenia) for all infants between 39- and 44-weeks postmenstrual age. VPT infants received standardized Bayley Scales of Infant and Toddler Development, Third Edition (Bayley-III) during the 2-year corrected age follow-up visit. We dichotomize the subjects into high-risk (≤85) and low-risk (>85) groups for developing long-term cognitive deficits. We preprocessed MRI data using the developing Human Connectome project (dHCP) processing pipeline (Bastiani et al. 2019). We used the dHCP neonatal brain atlas to define 82 ROIs, and considered the mean fractional anisotropy over all fiber tracts between the two brain ROIs as the structural connectivity (i.e., edges) of each SC. This results in an adjacency matrix with a size of 82 × 82. An overview is illustrated in Figure 1. We first augment a given subject's brain SC into multiple ones via a random edge perturbation approach. (Figure 1(A)) The newly generated samples are assigned with the same class label as the original subjects. Next, we trained a graph encoder and an embedding projector to accomplish a pretext contrasting "pull-push" task, which repeatedly pulls together a random subject (i.e., the anchor) and subjects of the same class as the anchor, and pushes apart the anchor and subjects of different classes. (Figure 1(B)) Finally, we develop a GCN model for predicting the risk of cognitive deficits by reusing the pre-trained graph encoder. Figure 1(C) We used a stratified random split strategy to separate subjects into training (60%), validation (20%), and testing (20%) sets. We compared our SCL-GCN model with multiple peer competing models (Kipf and Welling 2016; Hoffer and Ailon 2015; Chen et al. 2020; He et al. 2020). We calculated accuracy, sensitivity, specificity, and area under the receiver operating characteristic curve (AUC).

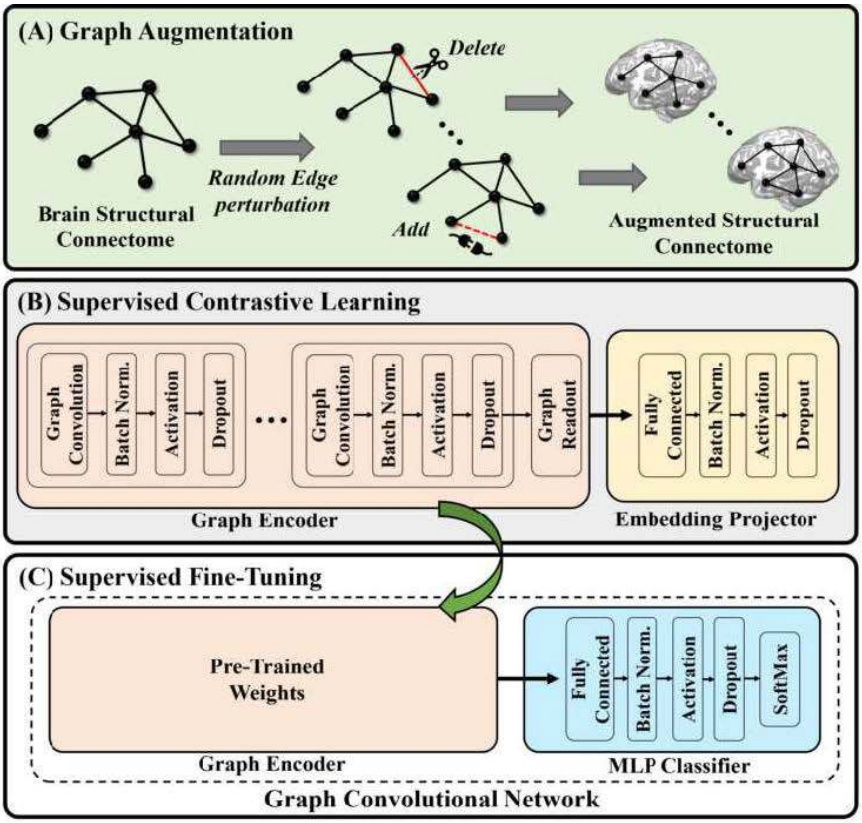

Figure 1. Overview of the early prediction study of cognitive deficits using Supervised Contrastive Learning (SCL) Graph Convolutional Network (GCN) models. (A) Graph Augmentation – Each brain SC is randomly transformed into k augmented SCs using an edge perturbation strategy, resulting in a total of M original and augmented subjects. (B) Supervised Contrastive Learning – Both graph encoder and embedding projector are pre-trained using a SCL technique for a pretext contrasting "pull-push" task, which pull together a random subject (a.k.a., the anchor) and subjects of the same class as the anchor and push apart the anchor and subjects of different classes. (C) Supervised Fine-Tuning – A GCN model is built by appending a multi-layer perceptron (MLP) classifier to the pre-trained graph encoder from previous stage. It is then fine-tuned using a typical supervised learning algorithm for the real downstream classification task (i.e., neurodevelopmental deficits prediction). This is equivalent to finding a hyperplane boundary that is able to separate subjects of different classes in the graph embedding space.

Results: After data exclusion, we have a total of 282 VPT infants (gestational age at birth 29.2 ± 2.5 weeks, 142 (50.4%) male) with cognitive assessment. The proposed SCL-GCN model achieved a mean AUC of 0.75 on cognitive deficit prediction, significantly higher than Triplet-GCN (0.73, $p<0.001$) and GCN (0.70, $p<0.001$). (Table 1) Our SCL-GCN model also achieved 73.1%, 65.9%, and 76.9% on accuracy, sensitivity, and specificity, respectively.

Table 2. Prediction performance of various models for risk of cognitive deficits using the brain SC data.

Models	Accuracy (%)	Sensitivity (%)	Specificity (%)	AUC
MLP	63.2 ± 3.9	65.1 ± 5.3	62.2 ± 4.9	0.64 ± 0.04
CNN	64.9 ± 4.1	65.0 ± 4.9	64.8 ± 5.1	0.67 ± 0.04
GCN	67.4 ± 4.0	71.2 ± 4.3	64.9 ± 4.8	0.70 ± 0.04
Triplet-GCN	70.2 ± 3.5	65.0 ± 4.1	72.8 ± 4.6	0.73 ± 0.03
SCL-GCN	73.1 ± 3.4	65.9 ± 4.1	76.9 ± 4.5	0.75 ± 0.03

Multi-Layer Perceptron (MLP); Convolutional Neural Network (CNN); Graph Convolutional Network (GCN); Supervised Contrastive Learning (SCL); area under the receiver operating characteristic curve (AUC)

Conclusions: In a large cohort of VPT infants, we demonstrated that the SCL-GCN model achieved a mean AUC of 0.75 for predicting cognitive deficits. Our results support our hypothesis that the SCL technique is able to enhance the GCN model in our prediction tasks. We also demonstrated that the proposed model outperformed several competing models.

References

1. Bastiani, M., J. L. Andersson, L. Cordero-Grande, M. Murgasova, J. Hutter, A. N. Price, A. Makropoulos, S. P. Fitzgibbon, E. Hughes and D. Rueckert (2019). "Automated processing pipeline for neonatal diffusion MRI in the developing Human Connectome Project." NeuroImage 185: 750-763.
2. Chen, M., H. Li, J. Wang, W. Yuan, M. Altaye, N. A. Parikh and L. He (2020). "Early Prediction of Cognitive Deficit in Very Preterm Infants Using Brain Structural Connectome With Transfer Learning Enhanced Deep Convolutional Neural Networks." Front Neurosci 14: 858.
3. Girault, J. B., B. C. Munsell, D. Puechmaille, B. D. Goldman, J. C. Prieto, M. Styner and J. H. Gilmore (2019). "White matter connectomes at birth accurately predict cognitive abilities at age 2." NeuroImage 192: 145-155.
4. He, L., H. Li, M. Chen, J. Wang, M. Altaye, J. R. Dillman and N. A. Parikh (2021). "Deep Multimodal Learning From MRI and Clinical Data for Early Prediction of Neurodevelopmental Deficits in Very Preterm Infants." Front Neurosci 15: 753033.
5. He, L., H. Li, J. Wang, M. Chen, E. Gozdas, J. R. Dillman and N. A. Parikh (2020). "A multi-task, multi-stage deep transfer learning model for early prediction of neurodevelopment in very preterm infants." Sci Rep 10(1): 15072.
6. Hoffer, E. and N. Ailon (2015). Deep metric learning using triplet network. Similarity-Based Pattern Recognition: Third International Workshop, SIMBAD 2015, Copenhagen, Denmark, October 12-14, 2015. Proceedings 3, Springer.
7. Kawahara, J., C. J. Brown, S. P. Miller, B. G. Booth, V. Chau, R. E. Grunau, J. G. Zwicker and G. Hamarneh (2017). "BrainNetCNN: Convolutional neural networks for brain networks; towards predicting neurodevelopment." Neuroimage 146: 1038-1049.
8. Khosla, P., P. Teterwak, C. Wang, A. Sarna, Y. Tian, P. Isola, A. Maschinot, C. Liu and D. Krishnan (2020). "Supervised contrastive learning." Advances in neural information processing systems 33: 18661-18673.
9. Kipf, T. N. and M. Welling (2016). "Semi-supervised classification with graph convolutional networks." arXiv preprint arXiv:.02907.
10. Linsell, L., S. Johnson, D. Wolke, H. O'Reilly, J. K. Morris, J. J. Kurinczuk and N. Marlow (2018). "Cognitive trajectories from infancy to early adulthood following birth before 26 weeks of gestation: a prospective, population-based cohort study." Arch Dis Child 103(4): 363-370.

Poster No 1467

More Robust MRI Preprocessing Yields More Accurate and Generalizable Age Predictions

Reza Rajabli[1], Mahdie Soltaninejad[1], Sofia Fernandez Lozano[1], Neda Shafiee[1], Vladimir Fonov[1], Danilo Bzdok[1], D Louis Collins[1]

[1]McConnell Brain Imaging Centre, Montreal Neurological Institute, McGill University, Montreal, Quebec

Introduction: Deep learning approaches have revolutionized the way various patterns are found in different data settings. The vast number of trainable parameters in deep models make them capable of capturing complex patterns. However, this comes at the expense of their considerable appetite for data. Since these are high variance models, they risk being overtrained if the sample size is not sufficient, which is often the case in medical datasets. For example, training a model on Magnetic Resonance Images (MRIs) to predict a diagnostic/prognostic label, the number of available images can be at most in the order of 100K, significantly less than the 14M samples of ImageNet. Consequently, it is vital to implement measures that ensure the generalizability of medical image deep learning models. A noteworthy approach is to reduce the number of trainable parameters with shallower models. The Simple Fully Convolutional Network (SFCN) [Peng 2021] is one such successful example incorporated into the SFCN-Reg architecture [Leonardsen 2022] to build a generalizable brain age model. Leonardsen et al. trained their model on ~53K MRIs (from multiple studies) reporting a mean absolute error (MAE) of 2.47 years on the internal test and 3.90 years on average on external test images from other studies. While they are one of few who tested their model externally and reported one of the lowest prediction errors, the disparity between internal and external test results raises the question of the model's ability to generalize to future brain scans and maintain high accuracy. We hypothesized that enhanced MR preprocessing could address this issue and lead to a reduction in external test error.

Methods: We downloaded 39,676 images from the UK Biobank (UKBB) dataset (version 49190) and applied the following preprocessing steps to each image: 1) brain extraction using SynthStrip [Hoopes 2022], 2) intensity normalization through histogram matching [Shah 2011], 3) denoising with adaptive non-linear means [Manjón 2010], 4) N4 bias field correction [Tustison 2010], 5) repeating step 2, and 6) affine registration to the MNI152 nonlinear symmetric template using ANTs [Avants 2014]. Next, we manually inspected all preprocessed images, and eliminated 1,975 (~5%) as failed, mostly due to either corrupted brain masks or failed registration. Then, we re-implemented the SFCN-Reg architecture with identical hyperparameters as detailed in [Leonardsen 2022], training it on 33,724 randomly subsampled MRIs from the preprocessed images. Finally, we assessed the trained model internally using ~1K MRIs not seen during training from the UKBB and externally (out of domain) on baseline visit scans of cognitively healthy subjects in the ADNI, AIBL, and OASIS3 datasets that underwent the same preprocessing steps and quality control procedures as the UKBB MRIs.

Results: After training our model, we identified the epoch with the best validation error and proceeded to assess its generalizability. To have a better understanding of the model's reliability and robustness, we calculated the mean and standard deviation for the MAE using bootstrapping by randomly selecting 100 subjects 10 times from each test set. The MAE for predictions on the internal test set (UKBB) was 2.22±0.17 years, and for external tests (ADNI, AIBL, and OASIS3), the MAE results were 3.45±0.28, 3.64±0.26 and 2.82±0.18, respectively (Figs 1-A, 1-B, 1-C, and 1-D).

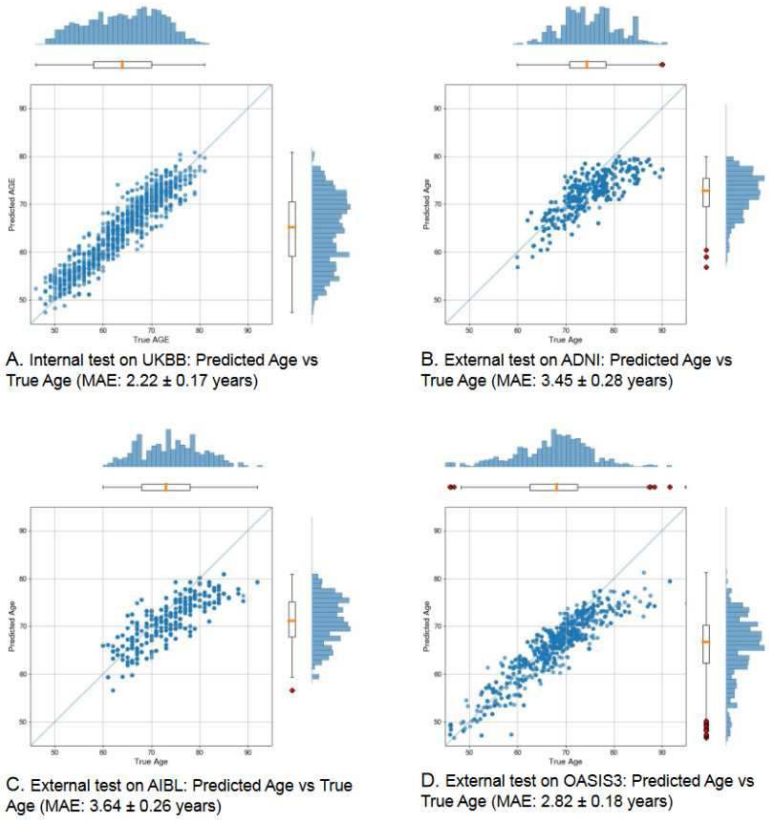

Fig 1. Performance of our trained model on different datasets. None of the samples from the test sets were introduced to the model during the training phase.

Conclusions: Since SFCN-Reg was originally trained and tested on approximately ~53K MRIs (3-95 years) from multiple datasets, a direct comparison poses challenges. Nevertheless, we trained the SFCN-Reg on a smaller dataset with narrower age range (45-82 years) while maintaining the hyperparameters consistent with the original paper (Table 1). The experiments demonstrate that a more robust preprocessing pipeline, compared to simpler alternatives used by Leonardson, enhances the generalizability of shallower models.

	Test	Internal	External			
Model	Dataset	UKBB	ADNI	AIBL	OASIS3	Average
SFCN-Reg (Leonardsen 2022)		2.47 yrs	5.25 yrs	4.35 yrs	-	3.90[1] yrs
SFCN-Reg + More Robust Preprocessing Pipeline (Ours)		2.22 ± 0.17 yrs	3.45 ± 0.28 yrs	3.64 ± 0.26 yrs	2.82 ± 0.18 yrs	3.31 yrs

Table 1. Performance comparison of SFCN-Reg and SFCN-Reg + More Robust Preprocessing Pipeline. Reported numbers are mean absolute errors measured in years.
[1] The external test average for the original SFCN-Reg (Leonardsen 2022) includes test results on IXI and the Norwegian Cognitive NeuroGenetics Sample.

References

1. Avants, B. B. (2009). Advanced normalization tools (ANTS). Insight j, 2(365), 1-35.
2. Hoopes, A. (2022). SynthStrip: Skull-stripping for any brain image. NeuroImage, 260, 119474.
3. Leonardsen, E. H. (2022). Deep neural networks learn general and clinically relevant representations of the ageing brain. NeuroImage, 256, 119210.
4. Manjón, J. V. (2010). Adaptive non-local means denoising of MR images with spatially varying noise levels. Journal of Magnetic Resonance Imaging, 31(1), 192-203.
5. Peng, H. (2021). Accurate brain age prediction with lightweight deep neural networks. Medical image analysis, 68, 101871.
6. Shah, M. (2011). Evaluating intensity normalization on MRIs of human brain with multiple sclerosis. Medical image analysis, 15(2), 267-282.
7. Tustison, N. J. (2010). N4ITK: improved N3 bias correction. IEEE transactions on medical imaging, 29(6), 1310-1320.

Poster No 1468

Reliability and robustness in static and dynamic FC predictions

Christine Ahrends[1], Mark Woolrich[2], Diego Vidaurre[3]

[1]Aarhus University, Aarhus, Aarhus, [2]University of Oxford, Oxford, Oxfordshire, [3]Aarhus University, Aarhus, Aarhus C

Introduction: Predicting individual traits from brain measures is a major goal in modern neuroscience. Many studies aim to use either time-averaged (static) or time-varying (dynamic) estimates of functional connectivity (FC) for these predictions. While the focus of this work is mainly to increase prediction accuracy, it is crucial to consider the reliability and robustness of different approaches[1]. This is particularly important if we want to be able to meaningfully interpret model errors, such as to estimate brain age[2]. For instance, a model may predict accurately in some cases but make excessive errors in other cases (poor reliability), or predict generally well, but predict poorly when the training set contains outliers (poor robustness). We here compare a range of different methods using either time-averaged or time-varying estimates of FC in terms of reliability and robustness.

Methods: We use the Human Connectome Project (HCP) S1200 dataset[3], where we estimate FC on resting-state fMRI and predict individual cognitive traits. We then compare four methods using time-averaged FC and seven methods using time-varying FC for the prediction. For time-averaged FC, we use two variants of an Elastic Net model[4], one in Euclidean and one in Riemannian space[5], a Selected Edges model where relevant edges of the time-averaged FC matrices are first selected and then used as predictors[6], and a model based on Kullback-Leibler (KL) divergence[7]. For time-varying FC prediction, we use a Hidden Markov Model[8] and construct seven different kernels from it using different projections of the individual-level parameters[9]. We use kernel ridge regression for the kernel-based models and ridge regression for the other models. All models use nested 10-fold cross validation (CV), and folds are constructed accounting for family structure in the dataset. We compare the methods using two criteria: reliability and robustness. To assess reliability, we compute the normalised maximum absolute errors. This indicates whether the single largest error in the predicted values exceeds the range of the original variable by orders of magnitude. To assess robustness, we run each model 100 times, each time randomising CV folds, i.e., randomising which combinations of subjects the model is trained and which subjects the model is tested on. We then consider the standard deviation across prediction accuracies across these 100 iterations, where low standard deviation indicates high robustness.

Results: In the time-averaged FC models, all but the KL divergence-based model have high reliability and robustness. In the time-varying FC models, the linear kernels are generally more reliable and robust than the Gaussian kernels, with the linear naïve normalised kernel and the linear Fisher kernel performing significantly better than other kernels. The models based on KL divergence (both time-averaged and time-varying FC) were overall the most problematic ones, both in terms of reliability and robustness. Comparing the time-averaged and the time-varying FC models, the better models perform similarly in terms of reliability, but the time-varying FC models outperform the time-averaged FC models in terms of robustness. These models also have a higher prediction accuracy than the time-averaged FC models.

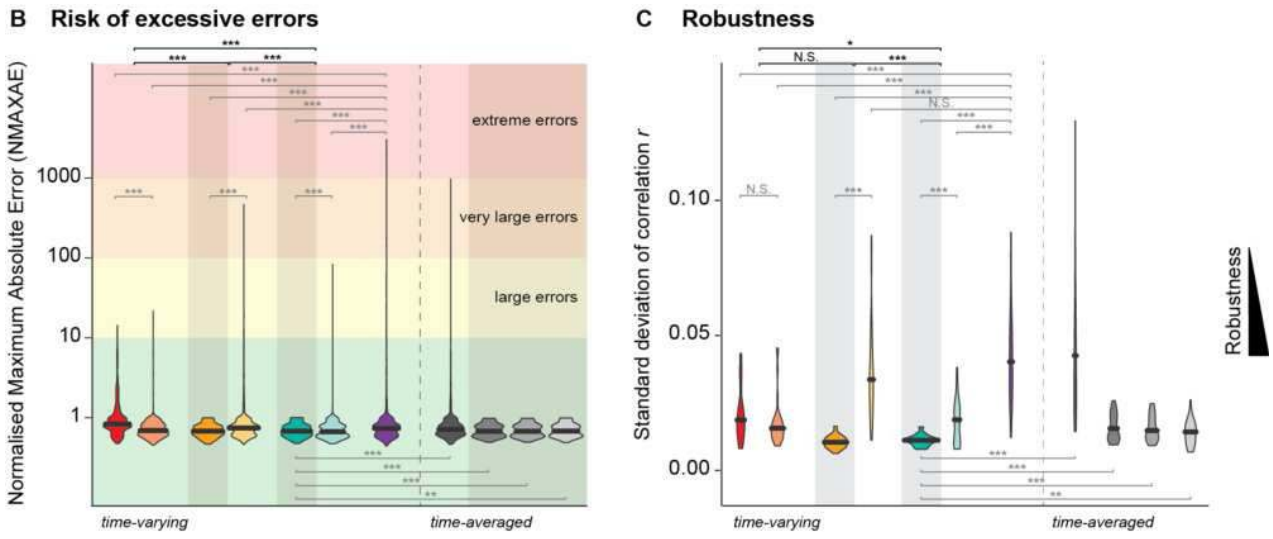

Conclusions: We here proposed an approach to assess reliability and robustness, two important criteria for studies aiming to predict individual traits from FC. We showed that the best-performing methods in terms of reliability and robustness are the Elastic Net and the Selected Edges approach for time-averaged FC and the linear naïve normalised and linear Fisher kernel

for time-varying FC. Overall, the time-varying FC models outperformed the time-averaged FC models. By considering not only prediction accuracy, but also the models' reliability and robustness, we may be able to move further towards interpreting model errors and using predictive models based on FC in clinical contexts.

References

1. Varoquaux, G., (2017), 'Assessing and tuning brain decoders: Cross-validation, caveats, and guidelines', Neuroimage, 145, pp. 166-179.
2. Cole, J. H. (2017), 'Predicting Age Using Neuroimaging: Innovative Brain Ageing Biomarkers', Trends Neurosci., 40(12), pp. 681-690.
3. Van Essen, D. C. (2012), 'The Human Connectome Project: a data acquisition perspective', Neuroimage, 62(4), pp. 2222-2231.
4. Zou, H. (2005), 'Regularization and Variable Selection Via the Elastic Net', J. R. Stat. Soc. Series B Stat. Methodol., 67(2), pp. 301-320.
5. Barachant, A. (2013), 'Classification of covariance matrices using a Riemannian-based kernel for BCI applications', Neurocomputing, 112, pp. 172-178.
6. Rosenberg, M. D. (2016), 'A neuromarker of sustained attention from whole-brain functional connectivity', Nat. Neurosci., 19(1), pp. 165-171.
7. Vidaurre, D. (2021), 'Behavioural relevance of spontaneous, transient brain network interactions in fMRI', Neuroimage, 229, 117713.
8. Vidaurre, D. (2017), 'Brain network dynamics are hierarchically organized in time', Proc. Natl. Acad. Sci. U.S.A., 114(48), pp. 12827-12832.
9. Ahrends, C. (2023), 'Predicting individual traits from model of brain dynamics using the Fisher kernel', bioRxiv. 2023.03.02.530638.

Poster No 1469

Deep convolutional neural networks can discriminate pain from other aversive states in EEG data

Alyson Champagne[1], Mathilda Buschmann[2], Mathieu Roy[3], Michel-Pierre Coll[1]

[1]Laval University, Québec, Quebec, [2]Universität Osnabrück, Osnabrück, Germany, [3]McGill University, Montreal, Quebec

Introduction: Pain is experienced differently by each person, depending on their previous experiences, emotions and mood. In research contexts, pain is assessed by scales or verbal reports, measures with several limitations (Smith et al., 2016). Thus, the scientific community has invested considerable effort in creating pain biomarkers based on brain activity (Davis et al., 2020; Wager et al., 2013) recorded by electroencephalography (EEG; Mari et al., 2022) that could provide a complementary way of measuring pain. However, these attempts are limited by the use of univariate analyses that do not utilize the rich multivariate nature of EEG signals and the lack of adequate control conditions (Mari et al., 2022). Here, we collected EEG data while individuals experienced various levels of pain and other aversive control stimulations. The aim of this study was to assess the sensitivity and specificity of various machine learning algorithms applied to EEG data to discriminate between pain and other aversive states within and across individuals.

Methods: EEG data (64 channels, Brain Vision Acticap) was collected from 65 healthy individuals (39 females, mean age: 24.2 +/- 6.14) under three conditions: resting state (five minutes), experiencing tonic thermal pain for eight minutes, or listening to an unpleasant auditory stimulus for eight minutes. Twenty-two of the participants were tested using a different EEG system of the same model in a different location. These participants served as the test sample. During all tasks except resting, participants first experienced the stimulation passively and then experienced it a second time while providing a continuous intensity or unpleasantness rating using a visual analog scale. We preprocessed EEG data using a semi-automated approach, with steps including bandpass and powerline noise filtering, removal of bad channels and artifactual independent components and rejection of bad trials (Jas et al., 2017; Pion-Tonachini, Kreutz-Delgado & Makeig, 2019). The continuous recordings in each condition were split into 4-second epochs with no overlap, and classifiers were applied to sensor space data to attempt to classify these epochs according to their pain condition (pain vs no pain) in the training sample (n = 43). We compared the performance of a random forest classifier, a shallow convolutional neural network (CNN) and a deep CNN (Schirrmeister et al., 2017). Nested cross-validation was used to optimize hyperparameters and perform model comparisons. Within-participant accuracy was assessed using 10-fold cross-validation in each participant of the training sample, and between-participant accuracy was assessed in the independent test sample (n = 22).

Results: In line with previous research using machine learning on EEG (Engemann et al., 2022), the shallow CNN showed the best classification performance compared to the deep CNN and random forest classifier. The accuracy of the shallow CNN was significantly above chance (0.5) for the classification performed within participants (mean cross-validation balanced accuracy = 0.68 +/- 0.09, range: 0.54-0.90; Figure 1A). Between participants, classification performed in the independent test sample led to a drastically lower accuracy but still significantly above chance (mean balanced accuracy = 0.56 +/- 0.07, range: 0.42-0.73; Figure 1B).

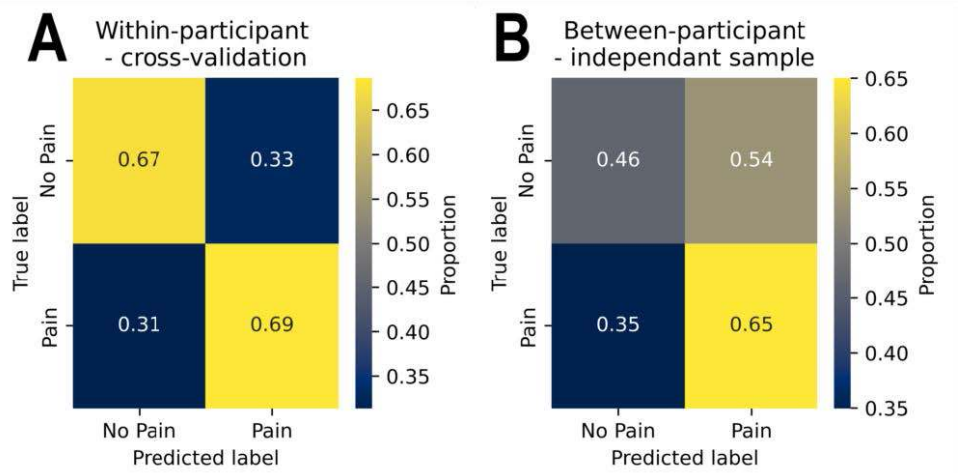

Figure 1. (A) Confusion matrix associated with the shallow convolutional neural network (CNN) classification model evaluated through cross-validation with within-participant data. **(B)** Confusion matrix associated with the shallow CNN classification model evaluated on an independant sample with between-participant data.

Conclusions: Our results confirm the ability of convolutional models to distinguish EEG signals associated with experimental pain from those associated with other aversive conditions across individuals. However, considerable work remains necessary to improve the performance of the models and establish the best approach to identify and measure pain using EEG signals. Our future work will aim to create a large open database of EEG pain recordings to provide the community with adequate data to test different approaches to reach this goal.

References

1. Davis, K. D., Aghaeepour, N., Ahn, A. H., Angst, M. S., Borsook, D., Brenton, A., Burczynski, M. E., Crean, C., Edwards, R., Gaudilliere, B., Hergenroeder, G. W., Iadarola, M. J., Iyengar, S., Jiang, Y., Kong, J. T., Mackey, S., Saab, C. Y., Sang, C. N., Scholz, J., Segerdahl, M., … Pelleymounter, M. A. (2020), 'Discovery and validation of biomarkers to aid the development of safe and effective pain therapeutics: challenges and opportunities', Nature reviews. Neurology, vol. 16, pp. 381–400.
2. Engemann, D. A., Mellot, A., Höchenberger, R., Banville, H., Sabbagh, D., Gemein, L., Ball, T., & Gramfort, A. (2022), 'A reusable benchmark of brain-age prediction from M/EEG resting-state signals', NeuroImage, vol. 262, 119521.
3. Jas, M., Engemann, D. A., Bekhti, Y., Raimondo, F., & Gramfort, A. (2017), 'Autoreject: Automated artifact rejection for MEG and EEG data', NeuroImage, vol. 159, pp. 417-429.
4. Mari, T., Henderson, J., Maden, M., Nevitt, S., Duarte, R., & Fallon, N. (2022), 'Systematic review of the effectiveness of machine learning algorithms for classifying pain intensity, phenotype or treatment outcomes using electroencephalogram data', The Journal of Pain, vol. 23, 349–369.
5. Pion-Tonachini, L., Kreutz-Delgado, K., & Makeig, S. (2019), 'ICLabel: An automated electroencephalographic independent component classifier, dataset, and website', NeuroImage, vol. 198, pp. 181–197.
6. Schirrmeister, R. T., Springenberg, J. T., Fiederer, L. D. J., Glasstetter, M., Eggensperger, K., Tangermann, M., Hutter, F., Burgard, W., & Ball, T. (2017), 'Deep learning with convolutional neural networks for EEG decoding and visualization', Human brain mapping, vol. 38, 5391-5420.
7. Smith, S. M., Amtmann, D., Askew, R. L., Gewandter, J. S., Hunsinger, M., Jensen, M. P., McDermott, M. P., Patel, K. V., Williams, M., Bacci, E. D., Burke, L. B., Chambers, C. T., Cooper, S. A., Cowan, P., Desjardins, P., Etropolski, M., Farrar, J. T., Gilron, I., Huang, I. Z., Katz, M., … Dworkin, R. H. (2016), 'Pain intensity rating training: results from an exploratory study of the ACTTION PROTECCT system', Pain, vol. 157, pp. 1056–1064.
8. Wager, T. D., Atlas, L. Y., Lindquist, M. A., Roy, M., Woo, C.-W., & Kross, E. (2013), 'An fMRI-based neurologic signature of physical pain', New England Journal of Medicine, vol. 368, pp. 1388–1397.

Poster No 1470

Computational modeling of MEG event-related beta oscillations during auditory verb generation

Minarose Ismail[1], Davide Momi[2], Zheng Wang[3], Cathy Barr[4], Randy McIntosh[5], John Griffiths[6], Darren Kadis[4]

[1]University of Toronto, Toronto, Ontario, [2]CAMH, Toronto, Ontario, [3]Centre for Addiction and Mental Health, Toronto, Ontario, [4]Hospital for Sick Children, Toronto, Ontario, [5]Simon Fraser University, Vancouver, BC, [6]Centre for Addiction and Mental Health, Toronto, MT

Introduction: Lateralization of low beta (13-23Hz) event-related desynchrony (ERD) and synchrony (ERS) during verb generation in MEG provides a robust assay of language hemispheric dominance[1]. In young children, low beta ERD and ERS are observed bilaterally, with lateralization emerging in early adolescence[2,3]. These task-related oscillatory changes could serve as neural signatures of language network maturation, as well as its potential for plasticity. However, the neural mechanisms

underlying lateralization remain unclear. Exploring the emergence of macro-scale brain activity from anatomical network structure and micro-scale neuronal dynamics using biologically inspired neurocomputational models holds promise in addressing this gap.

Methods: Individual connectome-based neural mass models were constructed for 10 healthy adolescents (15-18 years old) using the Jansen-Rit model[4] and individual structural connectivity matrices derived from multi-shell diffusion-weighted MRI tractography, segmented with the Shen 200-node atlas[5] . The auditory event was parameterized as a 40ms square-wave stimulus injected bilaterally into neural masses representing left and right Heschl's gyri. This model was used to fit trial-averaged MEG time series representing the early (-100-400ms) auditory evoked response in a verb generation task using the Whole-Brain Modelling in PyTorch (WhoBPyt)[6] library, estimating local and global coupling parameters. For each individual, two sets of models were created: a verb model fitted with verb generation trials data, and a noise model fitted with speech-shaped noise trials data. These models were then used to simulate 1200ms epochs, and power spectral densities (PSDs) were computed using Welch's method for the 700-1200ms time window that, critically, was not used for fitting. Simulated and empirical PSDs in left and right frontal ROIs were then averaged across subjects and compared.

Results: Brain network models for verb and noise conditions accurately captured auditory evoked field topographies at both the group average and the individual subject level (Figure 1). Interestingly, these early auditory-evoked models were also able to accurately predict the out-of-sample late (700-1200ms) effect of a left-lateralized low beta ERD and a right-lateralized low beta ERS (Figure 2). Consistent with empirical data, averaged PSDs from left frontal ROIs in the verb models correctly predicted a decrease in beta power relative to the noise models (ERD), while averaged PSDs of the right frontal ROIs predicted the observed increase in beta power relative to the noise models (ERS).

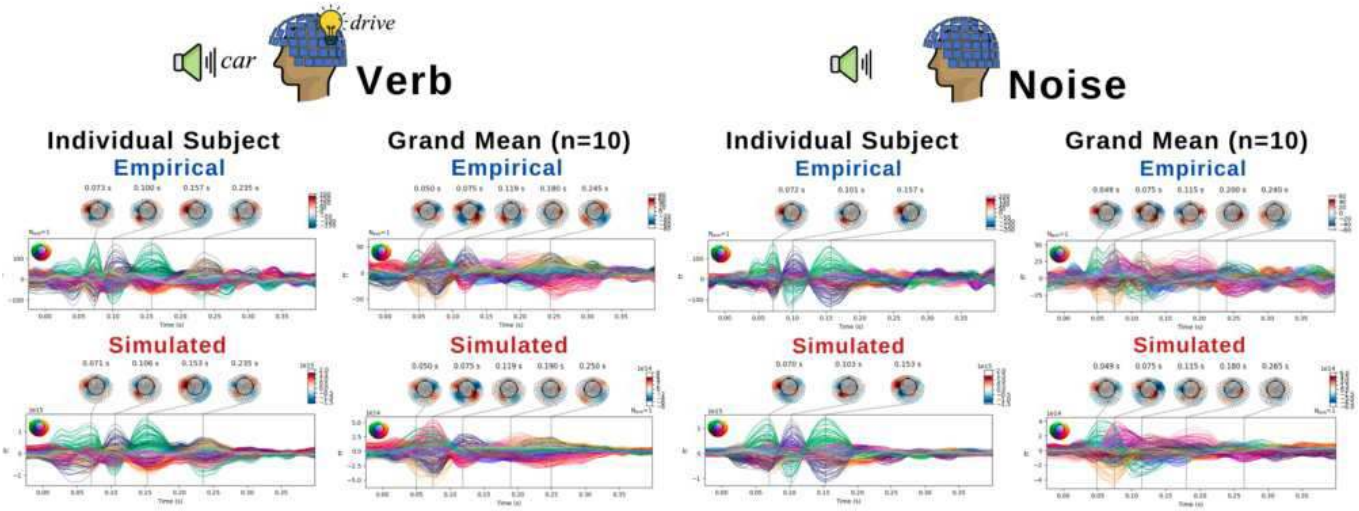

Figure 1. Empirical (upper row) and simulated (lower row) evoked butterfly plots with sensor topographies for an individual representative subject and the grand mean across all subjects for verb generation (left) and noise (right) trial modelling. Model-generated magnetoencephalography (MEG) time series and sensor topographies show a robust recovery of individual and average across subjects empirical auditory evoked fields.

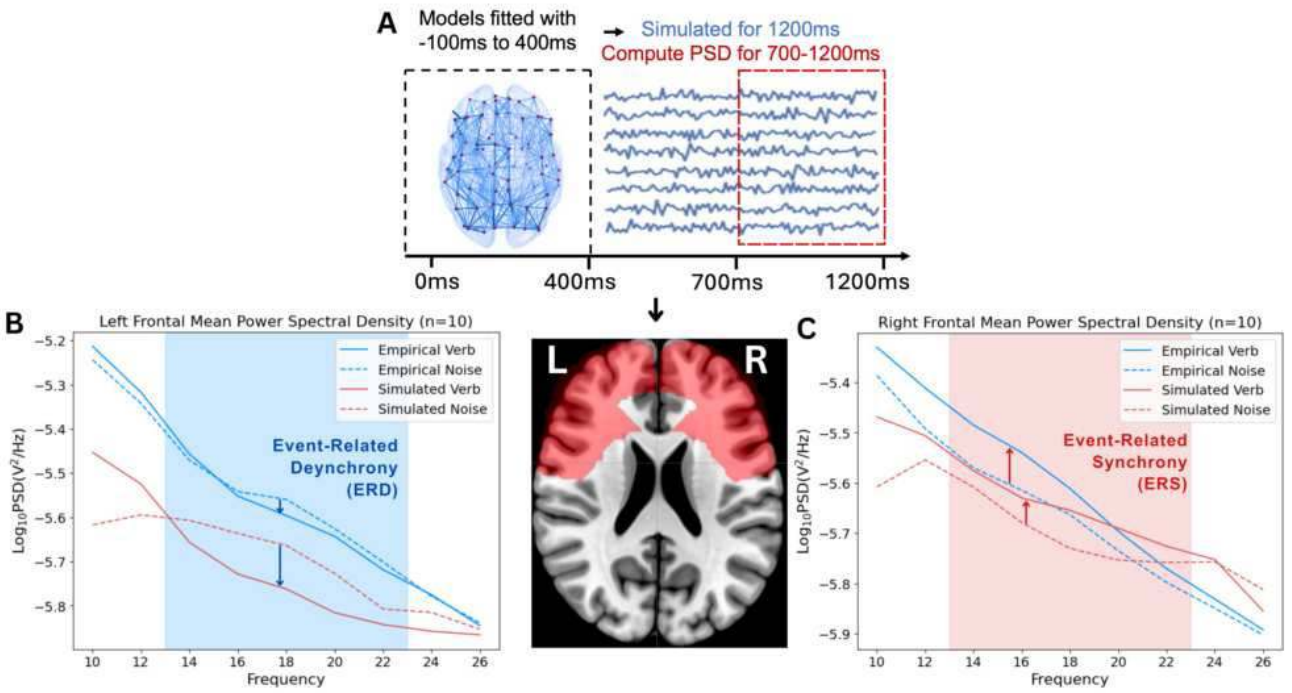

Figure 2. Individual models fitted with early auditory MEG predict left-lateralized event-related desynchrony (ERD) and right-lateralized event-related synchrony (ERS) consistent with empirical data. **(A)** Fitted verb and noise models were simulated for 1200 ms and power spectral densities (PSDs) were computed using Welch's method for the 700-1200 ms windows in the left and right frontal parcels. **(B)** Average PSDs of simulated verb trials (blue line) in the left frontal parcels across subjects demonstrate a decrease in low beta power (13-23 Hz; shaded blue) relative to simulated noise trials (blue dashed line), as observed in the empirical PSDs of verb and noise trials (red). **(C)** Average PSDs of simulated verb trials (blue line) in the left frontal parcels across subjects demonstrate an increase in low beta power (13-23 Hz; shaded red) relative to simulated noise trials (blue dashed line), as observed in the empirical PSDs of verb and noise trials (red).

Conclusions: We present the first individualized whole-brain model of auditory verb generation, demonstrating validity by reproducing the temporal dynamics of sensory-evoked activity, and its potential in predicting the lateralization of late oscillatory responses within higher-order language regions. Importantly, the model replicated late (700-1200ms) induced spectral effects after only being fit on early (-100-400ms) evoked response time series. Our findings suggests that language lateralization is encoded in the interaction between the structure and the dynamics of early sensory responses to language stimuli.

References

1. Sharma, V. V., & Kadis, D. S. (2024). 'A powerful metric for expressive language lateralization in MEG'. Neuroscience Letters, 818, 137539. https://doi.org/10.1016/j.neulet.2023.137539.
2. Sharma, V., Vannest, J., Greiner, H.M., Fujiwara, H., Tenney, J.R., Williamson, B. J., Kadis, D.S. (2021). 'Beta synchrony for expressive language lateralizes to right hemisphere in development', Scientific Reports 11, 3949. https://doi.org/10.1038/s41598-021- 83373-z.
3. Kadis, D. S., Pang, E. W., Mills, T., Taylor, M. J., McAndrews, M. P., & Smith, M. L. (2011). 'Characterizing the normal developmental trajectory of expressive language lateralization using magnetoencephalography'. Journal of the International Neuropsychological Society, 17(5). doi:10.1017/S1355617711000932.
4. Jansen, B. H., & Rit, V. G. (1995). 'Biological Cybernetics Electroencephalogram and visual evoked potential generation in a mathematical model of coupled cortical columns'. Biol. Cybern, 73. https://doi.org/10.1007/BF00199471.
5. Griffiths, J. D., Wang, Z., Ather, S. H., Momi, D., Rich, S., Diaconescu, A., McIntosh, A. R., & Shen, K. (2022). 'Deep Learning-Based Parameter Estimation for Neurophysiological Models of Neuroimaging Data', bioRxiv. https://doi.org/10.1101/2022.05.19.492664
6. Shen X, Tokoglu F, Papademetris X, Constable RT. (2013) 'Groupwise whole-brain parcellation from resting-state fMRI data for network node identification'. Neuroimage, 82. https://doi.org/10.1016/j.neuroimage.2013.05.081.

Poster No 1471

Classification of infant fNIRS data improves prediction of cognitive development 18 months later

Sumin Byun[1], Benjamin Zinszer[1]

[1]*Swarthmore College, Philadelphia, PA*

Introduction: Recent studies in Dhaka, Bangladesh have identified correlations between developmental risk factors (e.g., family conflict) and fNIRS responses of infants and toddlers in a passive social cognition task (Perdue et al., 2019; Pirazzoli et al., 2022). A key goal of such work is prediction: the ability to identify children most likely to experience adverse

developmental outcomes months or years later. Behavioral measures offer one source of predictive power, but differences in neural responses can provide insight on processes that are not yet behaviorally realized, like language production or motor skills. We analyzed longitudinal data from 29 infants previously reported in these studies and asked whether multivariate analyses of fNIRS collected at 6 months old could enhance prediction of the children's behavioral outcomes at 24 months.

Methods: All children were assessed on Mullen Scale of Early Learning (Mullen, 1995). Each child completed a passive social cognition task (Lloyd-Fox et al., 2007, 2009) with fNIRS imaging over bilateral frontal, temporal and parietal regions. In this task, children saw images of vehicles and videos of a woman in three conditions: silent, paired with vocal sounds (laughing, coughing, etc.), and paired with nonvocal sounds (a fan, water, etc.). We co-registered each child's data to a 10-20 based scalp parcellation (Magee et al., 2023) and computed median HbO and HbR responses for each condition in the window 5-8 s (baseline 0-2 s). Multi-parcel response patterns for each child were Spearman-correlated with their same-age cohort (n-fold cross-validation) for pairwise classification of the four conditions (Emberson et al., 2018; Zinszer et al., 2023). We entered these six classification accuracies and five Mullen subscores from each child's first visit (6 m.o.) into a binomial regression to predict their membership in the lower third of Mullen scores at their second visit (24 m.o.).

Results: Predictions of Mullen scores at 24 m.o. based on 6 m.o. Mullen subscores (AUC=0.76) were significantly improved by the inclusion of the 6 m.o. fNIRS data (AUC=0.88, likelihood ratio=8.60, p=0.003). ROC curves for these predictions are depicted in the figure. Among fNIRS predictors, the visual social contrast (accuracy of Silent Videos vs. Cars) was the strongest predictor. A model including only this predictor alongside Mullen subscores also improved predictions relative to the Mullen data only (AUC=0.82, likelihood ratio=4.84, p=0.028).

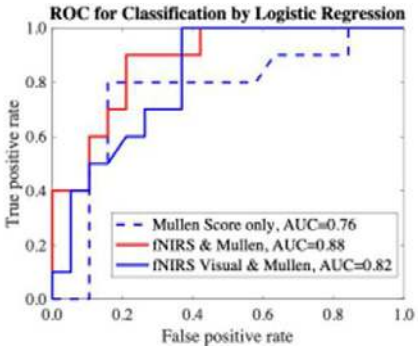

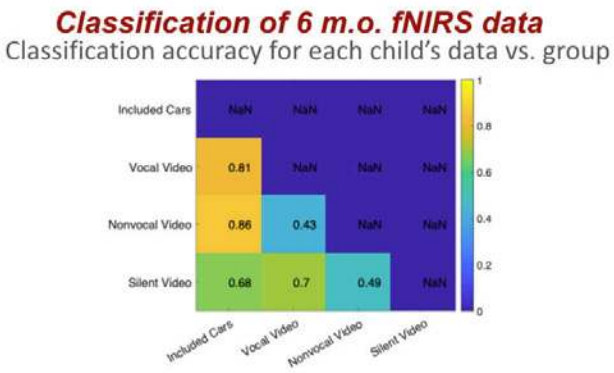

Conclusions: Including fNIRS data from a single subject-level classification test of visual stimuli (cars vs. faces) significantly improved predictions beyond the information provided by behavioral testing. Individual differences in this kind of visual processing may underlie later differences in socially relevant outcomes, such as language acquisition.

References

1. Emberson, L. L. (2017), 'Decoding the infant mind: Multivariate pattern analysis (MVPA) using fNIRS', PloS ONE, 12(4), e0172500. https://doi.org/10.1371/journal.pone.0172500
2. Lloyd-Fox, S. (2009), 'Social perception in infancy: A near infrared spectroscopy study', Child Development, 80(4), 986–999. https://doi.org/10.1111/j.1467–8624.2009.01312.x.
3. Magee, A. L. (2023), 'Scalp-based parcellation for longitudinal fNIRS studies' In Diffuse Optical Spectroscopy and Imaging IX,12628, 32-34. http://dx.doi.org/10.1117/12.2670765
4. Perdue, K. L. (2019), 'Using functional near-infrared spectroscopy to assess social information processing in poor urban Bangladeshi infants and toddlers' Developmental Science, 22(5), e12839. https://doi.org/10.1111/desc.12839
5. Pirazzoli, L. (2022), 'Association of psychosocial adversity and social information processing in children raised in a low-resource setting: an fNIRS study' Developmental Cognitive Neuroscience, 56, 101125. https://doi.org/10.1016/j.dcn.2022.101125
6. Zinszer, B. D. (2023), 'Multivariate fNIRS response patterns to social information are increasingly discriminable from six to sixty months of age', PsyArXiv. Preprint under review. https://psyarxiv.com/zmrkn

Poster No 1472

Cross-Modal Synthesis of Functional Network Connectivity and Magnetic Resonance Imaging Data

Reihaneh Hassanzadeh[1], Vince Calhoun[2]

[1]Georgia Institute of Technology, Atlanta, GA, [2]GSU/GATech/Emory, Decatur, GA

Introduction: Brain disorders such as Alzheimer's disease (AD) can be characterized by brain imaging methods such as structural MRI (sMRI) and functional MRI (fMRI). While providing several modalities, many imaging datasets may have missing modalities for many subjects. This missing modality issue limits multi-modal analysis, where all the modalities of a subject are needed. Hence, we study the possibility of the challenging cross-modality transition task where sMRI images are transformed into fMRI images and vice versa. More specifically, we utilized generative deep learning methods to generate sMRI from functional network connectivity (FNC), which are feature maps extracted from fMRI, and FNC from sMRI. Our results show that our generative deep learning approach can generate samples close to the real images.

Methods: We studied 982 subjects from the Alzheimer's Disease Neuroimaging Initiative (ADNI) dataset. Among the 982 subjects, 305 of them have both of the modalities (i.e., sMRI and FNC), 920 have an sMRI image, and 413 subjects have FNC maps. Furthermore, FNC is a correlation map that is measured as follows: We applied a spatially constrained group ICA to the data to extract 53 time courses and then computed the Pearson correlation between the time courses to form FNC. For the generative model, we used cycle GAN[1] while adapting to transforming 1D flattened FNC maps to 3D-sMRI images and vice versa. For translating 3D-sMRI images to 1D-FNC maps, we used 3D-CNN layers to learn spatial information in the sMRI images and transform them into FNC features using fully connected layers.

Results: Figure 1 shows the real sMRI and generated sMRI by the GAN model, which is averaged across all AD samples and controls (CN). According to the figure, the GAN model could effectively generate samples that resemble sMRI while it used FNC information. Moreover, comparing the AD to CN samples, the generated samples could show the AD patterns, i.e., brain atrophy, similar to the pattern in the real data. Furthermore, Figure 2 shows the averaged FNC maps for real and generated samples. According to the figure, the model could learn the general FNC structure while transforming sMRI images into FNC maps and generating realistic FNC maps. Comparing AD to CN suggests that some of the reduced connectivity in the AD group was captured by the model while generating the FNC maps, such as the connectivity between sensory-motor (SM) and subcortical (SC) networks and the connectivity between SM and cerebellum (CB) networks.

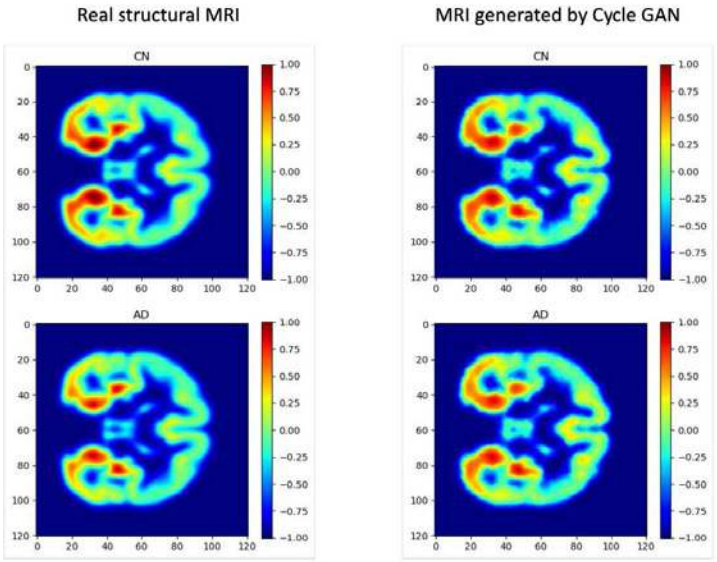

Figure 1. Real and Generated sMRI: AD vs. CN

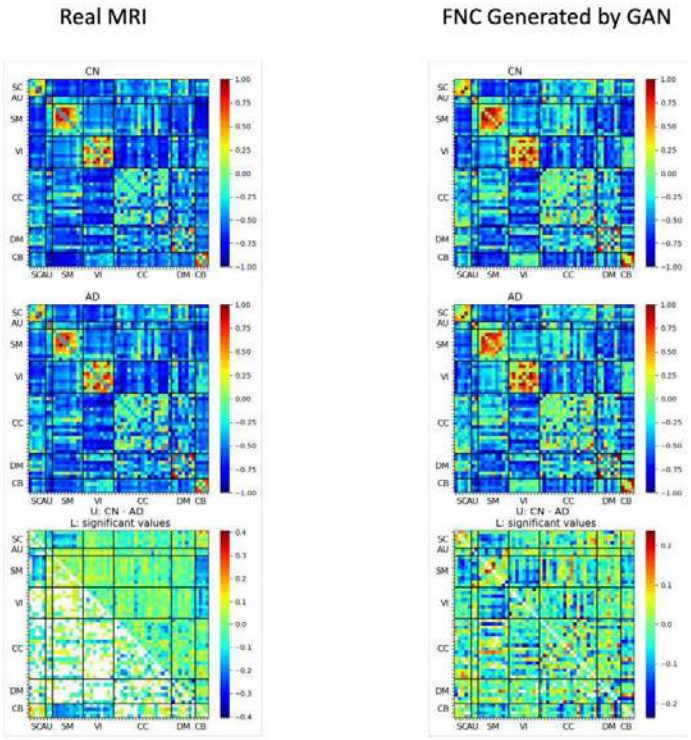

Figure 2. Real and Generated FNC: AD vs. CN

Conclusions: In summary, our study demonstrates the effective use of generative deep learning models, specifically cycle GANs, to translate structural MRI to functional network connectivity data and vice versa. We analyzed the ADNI database and could successfully generate realistic sMRI images from FNC maps and vice versa, capturing key pathological features of Alzheimer's disease. This achievement addresses the challenge of missing modalities in brain imaging datasets. It opens new paths for enhanced multi-modal analysis in neuroscience research, particularly in understanding and diagnosing neurodegenerative diseases like Alzheimer's.

References

1. Zhu, J.Y., Park, T., Isola, P. and Efros, A.A., 2017. Unpaired image-to-image translation using cycle-consistent adversarial networks. In Proceedings of the IEEE international conference on computer vision (pp. 2223-2232).

Poster No 1473

Can Critical Behaviour Change Windows Successfully Predict Physical Activity Engagement in Aging?

Nagashree Thovinakere[1], Sue-Jin Lin[2], Robert Baumeister[2], Yasser Iturria Medina[3], Maiya Geddes[2]

[1]McGill University, Westmount, Quebec, [2]McGill University, Montreal, QC, [3]McGill University, Montreal, Quebec

Introduction: Physical activity is a crucial modifiable factor in preventing cognitive decline and dementia[1]. Lifestyle changes following a new cardiovascular disease diagnosis provide an opportunity for improved health outcomes[2]. However, successful behaviour change remains challenging, necessitating a deeper understanding of neurobiological mechanisms. This study aims to identify functional brain features predicting successful behaviour change (increased physical activity) among older adults with new diagnosis of a cardiovascular risk factor.

Methods: Methods: We analyzed baseline resting-state functional magnetic resonance imaging (rs-fMRI) data in a subsample from the UK Biobank, a large population longitudinal cohort (n=295; mean age = 63.13 years ± 7.5; cognitively normal). Brain imaging was obtained at baseline, and physical activity data was obtained for two time-points: Baseline and follow up after 5 years. Participants met the following inclusion criteria: 1) reported a new diagnosis of a cardiovascular risk factor (i.e., hypertension, type II diabetes, dyslipidemia, cardiac angina or myocardial infarction) between baseline and follow-up, and 2) did not meet the World Health Organization recommended 150 minutes/week of moderate-to-vigorous physical activity (MVPA) at baseline, 3) age >= 60, cognitively unimpaired. Self-reported MVPA were recorded using the Lifetime Total Physical Activity Questionnaire. Demographic variables including age, sex, years of education, and socioeconomic status were

included as covariates of non-interest. To assess whether baseline rs-fMRI connectivity predicts future change in physical activity behaviour, we used a Random Forest Classifier. Preprocessed rs-fMRI data from the UK Biobank was used as the input for these analyses. The Schaefer 2018 atlas was used to parcellate the brain, with 400 regions of interest (ROIs) and 7 rs fMRI networks. The analysis followed a nested cross-validation approach with 5 inner loop resampling and 10fold outer loop cross-validation to prevent overfitting. Our machine learning pipeline involved: 1) feature reduction using grid search, 2) hyperparameter selection and tuning within the inner loop, and 3) model building with the best cost value for each fold in outer loop cross-validation. Model performance, averaged across all 10folds in the outer loop, was assessed using two metrics-accuracy and Receiver Operating Characteristic (ROC) curves. The significance of accuracy was determined through a permutation test, repeating 1000 times to establish the null distribution. The post-hoc analysis involved extracting weights for all features from the best estimator, ranking the absolute values of coefficients, and selecting the top 30 features.

Results: Results: Our prediction model delivered a highly accurate performance with mean accuracy (0.80 ± 0.05) and Area Under Curve (0.78 ± 0.08) in predicting future behavior change (≥150 min/week MVPA at follow-up). The frontal operculum/ insula node in the Salience Ventral Attention Network emerged as the most critical predictor. Enhanced between-network connectivity, particularly between visual and somatomotor networks and transmodal brain networks (Default Mode and Salience) was associated with successful behaviour change.

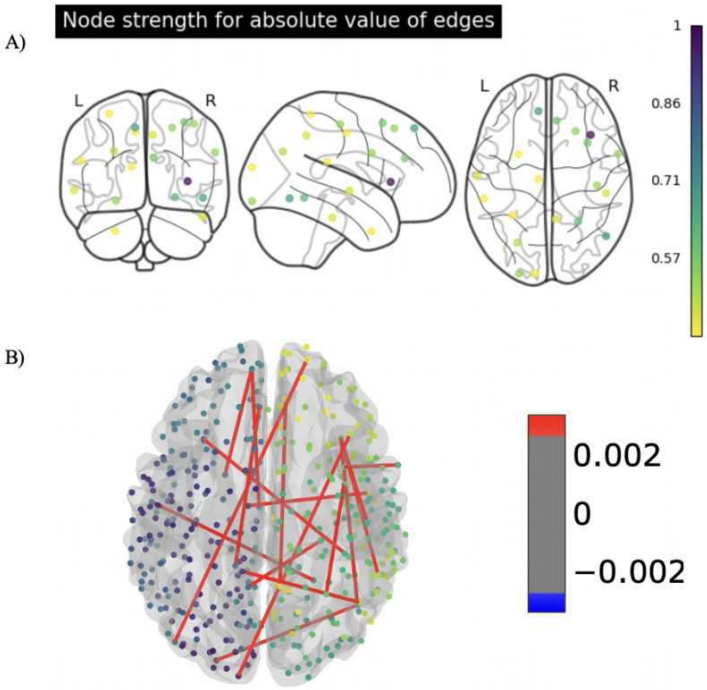

Figure 1. Important Functional Features. A) Anatomical map of the nodes that were most important to the prediction model. Greater node strength indicates greater aggregated connectivity strength for all connections corresponding to the node. B) Functional Connectome map demonstrating the between-network connections for all the important nodes.

Conclusions: The finding that functional network differentiation supports successful physical activity behaviour aligns with recent findings suggesting a shift in overall network activity balance during external versus internally guided decision-making. Notably, localized activity within unimodal networks supports cognition reliant on immediate perceptual input, while greater segregation of unimodal from transmodal networks supports internally oriented processing, including self-referential processes5. Speculatively, this suggests that functional segregation may sustain long-term engagement in physical activity.

References

1. Buckley, R. F.(2017), 'Functional Network Integrity Presages Cognitive Decline in Preclinical Alzheimer Disease', Neurology, vol. 89, no. 1, pp. 29–37.
2. Duckworth, A. L. (2020), 'Behavior Change', Organizational Behavior and Human Decision Processes, vol. 161, pp. 39–49.
3. Gallen, C. L. (2019), 'Brain Modularity: A Biomarker of Intervention-Related Plasticity', Trends in Cognitive Sciences, vol. 23, no. 4, pp. 293–304.
4. Harvey, J. (2013), 'Prevalence of Sedentary Behavior in Older Adults: A Systematic Review', International Journal of Environmental Research and Public Health, vol. 10, no. 12, pp. 6645–6661.
5. Murphy, C. (2019), 'Modes of Operation: A Topographic Neural Gradient Supporting Stimulus-Dependent and Independent Cognition', NeuroImage, vol. 186, pp. 487–496.

Poster No 1474

Towards personalized multimodal lesion mapping of temporal lobe epilepsy: a multisite validation

Judy Chen[1], Jessica Royer[1], Oualid Benkarim[2], Alexander Ngo[2], Ella Sahlas[3], Sara Larivière[4], Raúl Rodriguez-Cruces[2], Ke Xie[3], Yifei Weng[5], Jordan DeKraker[6], Andrea Bernasconi[1], Neda Bernasconi[1], Dewi Schrader[7], Zhiqiang Zhang[8], Luis Concha[9], Boris Bernhardt[2]

[1]Montreal Neurological Institute and Hospital, Montreal, QC, [2]Montreal Neurological Institute and Hospital, Montreal, Quebec, [3]McGill University, Montreal, Quebec, [4]Brigham and Women's Hospital, Portsmouth, NH, [5]Nanjing University, Nanjing, Nanjing, [6]McGill University, Montreal, Canada, [7]University of British Columbia, Vancouver, BC, [8]Jinling Hospital, the First School of Clinical Medicine, Southern Medical University, Nanjing, Jiangsu, [9]Universidad Nacional Autonoma de Mexico, Queretaro

Introduction: Drug-resistant epilepsy affects over 20 million people worldwide, and a majority of these patients are diagnosed with temporal lobe epilepsy (TLE)[1]. Diagnostic methods to lateralize the lesion for surgical resection remains a challenge due to the heterogeneity in clinical phenotypes. Past work leveraging MRI to individually characterize patients and lateralize their pathology has been promising but remains limited to a single modality and/or single site[2]. Here, we leverage our open-source image processing and analysis tools to: 1) map the distribution of patient-specific alterations in neocortical and hippocampal subregions from structural (T1w) and diffusion (DTI) scans across three sites; 2) evaluate the efficacy of these features to lateralize patients in a machine learning framework.

Methods: Participants. We studied 388 individuals aggregated from 3 independent sites. Our cohort comprised 123 TLE patients (61 females; mean±SD: 32.4±11.1 years; 57 left-sided focus) and 265 healthy individuals (94 female; mean±SD age: 29.0±9.6 years). All participants underwent 3T T1-weighted (T1w) and diffusion MRI scans. The Nanjing cohort consists of 122 healthy controls (HCs) and 70 TLE patients; EpiC cohort consists of 32 HCs and 18 TLE patients; and MNI cohort consists of 111 HCs and 35 TLE patients. Image processing and analysis. Multimodal imaging data were processed using micapipe_v0.2.03 and hippunfold_v1.3.04. Post-processing using z-brains (https://github.com/MICA-MNI/z-brains) involved z-scoring surface based features in the neocortex and hippocampus of each patient against their site-matched healthy controls while controlling for age and sex in fsLR 64k vertex space and 5k hippocampal space. Right-TLE patients were flipped to reflect ipsilateral and contralateral regions with respect to seizure focus. Significantly altered vertices were defined at |z| 1.96 and the probability of each vertex being altered across the patient cohort was mapped across three features: cortical thickness (CT), fractional anisotropy (FA), and apparent diffusion coefficient (ADC). Logistic regression (LR) and support vector machine (SVM) algorithms were trained with 10-fold cross validation on 5k fsLR vertex-wise neocortical and hippocampal data to lateralize the seizure focus in TLE.

Results: Proportion maps. The temporal lobe demonstrated the highest proportion of neocortical alterations across all features (thickness, FA, and ADC), and were most pronounced with ADC, reaching over 40% (F1A). However, mean proportion of each region parsed through the Desikan-killiany atlas revealed high neocortical variability remains even in the best performing feature (ADC) as no specific region was altered in more than 50% of patients. Hippocampal maps showed moderate atrophy, subtle FA decreases, and highly pronounced ADC signal (F1A). An anterior-posterior gradient was most prominent across the ADC feature and somewhat noticeable in the hippocampal atrophy patterns. Site-specific alteration proportion maps for both neocortex and hippocampus demonstrated preservation of the overall neocortical alteration patterns across sites (F2B). Lateralization performance. Classifiers trained on hippocampal data vastly outperformed those on neocortical data, achieving the highest accuracy score of 85.4% (logistic regression on ADC) as compared to the maximum accuracy score of 70.8% (logistic regression on ADC & FA). Overall highest accuracy score of 87.1% was SVM trained on ADC&CT neocortical and hippocampal data.

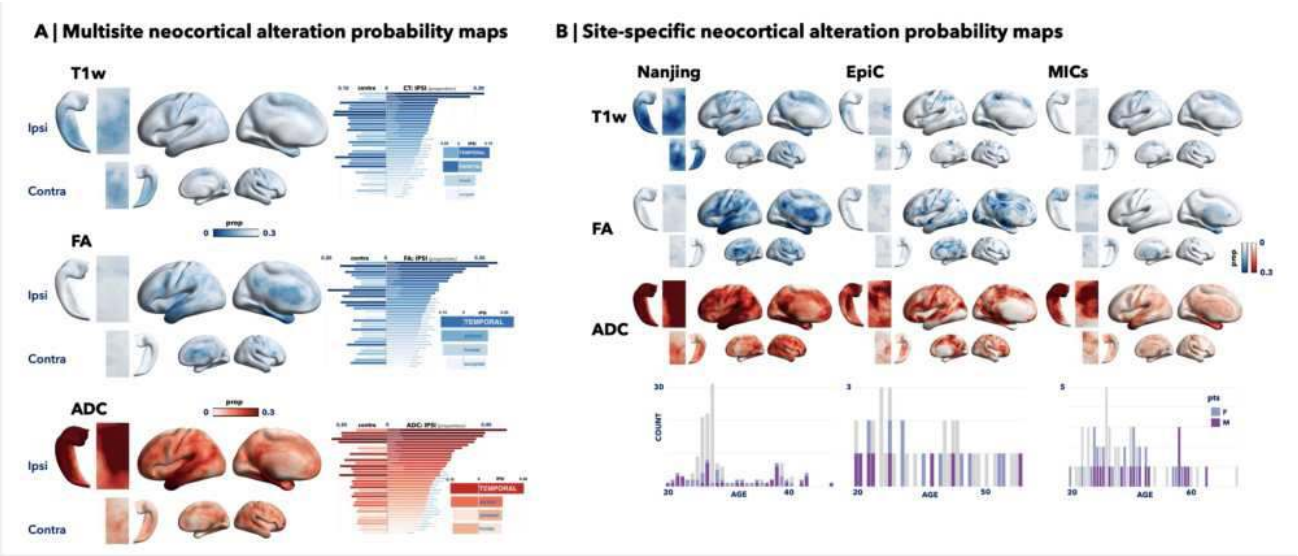

Figure 1. Mapping neocortical alteration probability maps. A | Hippocampal alteration maps show moderately distributed hippocampal atrophy, subtle FA decreases, and highly pronounced ADC signal.

	CORTEX & HIPPOCAMPUS							HIPPOCAMPUS							CORTEX						
FEATURE	ADC	CT	FA	**ADC CT**	ADC FA	FA CT	ADC FA CT	**ADC**	FA	CT	**ADC CT**	ADC FA	FA CT	ADC FA CT	**ADC**	FA	CT	**ADC CT**	ADC FA	FA CT	ADC FA CT
LR	81.4	77.9	73.4	**86.2**	83.8	78.0	83.7	**85.4**	66.0	82.8	85.3	82.1	79.6	84.7	67.5	**70.7**	63.2	68.2	63.3	61.5	81.4
SVM	84.6	81.2	66.0	**87.1**	82.2	73.3	84.7	84.5	66.9	82.9	**84.7**	84.6	83.1	83.8	61.0	63.2	**69.9**	60.8	58.5	62.4	84.6

Figure 1. Lateralization accuracy scores of machine learning algorithms trained on neocortical and hippocampal data.

Conclusions: MRI phenotypes among patients are too variable to rely on single modality for accurate lesion lateralization. It is possible to accurately lateralize TLE patients using personalized lesion mapping techniques with machine learning classification models. We present here a multisite validation of this technique, achieving a maximum accuracy score of 87.1%.

References

1. Sander et al., 1996. J Neurol Neurosurg Psychiatry, 61(5):433–443.
2. Sone et al., 2021. Front Neurosci, 10.3389/fnins.2021.684825.
3. Cruces, R et al., 2022 NeuroImage, 10.1016/j.neuroimage.2022.119612.
4. DeKraker, J et al., 2022 eLife, 10.7554/eLife.77945.

Poster No 1475

AI&ML in MRI for the lateralization of temporal lobe epilepsy: a systematic review and meta-analysis

Judy Chen[1], Natalie Chen[2], Yigu Zhou[3], Sienna Armstrong[4], Lorenzo Caciagli[5], Andrea Bernasconi[1], Neda Bernasconi[1], Boris Bernhardt[6]

[1]Montreal Neurological Institute and Hospital, Montreal, QC, [2]University of Toronto, Toronto, ON, [3]Montreal Neurological Institute, Montreal, Quebec, [4]McGill University, Montreal, QC, [5]University of Bern, Bern, Bern, [6]Montreal Neurological Institute and Hospital, Montreal, Quebec

Introduction: Accurate lateralization of temporal lobe epilepsy (TLE) is critical for drug-resistant patients undergoing surgery but is often difficult to achieve due to conflicting evidence in presurgical work-up.[1] Artificial intelligence (AI) and machine learning (ML) methods have been increasingly leveraged to analyze brain magnetic resonance imaging (MRI) for this purpose, but their true accuracy and effectiveness in supporting clinical decision making remains unclear.[2] The aim of this meta-analysis was to synthesize current AI/ML models used in MRI and assess their performance in lateralizing TLE.

Methods: MEDLINE and Embase databases were searched for original research articles and yielded 2606 publications after removing duplicates. Studies were included if they used any AI/ML model trained on (but not limited to) MRI images to

classify laterality and reported any evaluation metric (sensitivity/specificity, AUC under ROC, or total accuracy score). Articles were excluded if they were conference abstracts without a full-text publication or had a patient cohort of n<10. Information regarding the publication (year, first author), MRI (Tesla, modality), AI/ML algorithm (model type, input), demographics (patient/control cohort size, sex, epilepsy duration, age of onset, lesion laterality), and algorithm performance metrics (training and test cohort: Sn/Sp, AUC, accuracy score) was extracted from all articles. The risk of bias of each included study was independently assessed by two reviewers using the Prediction model Risk Of Bias Assessment Tool (PROBAST) tool.[3]

Results: Abstract and title screening yielded 328 publications, and 51 studies were included. The majority of studies reported an accuracy score (n=29) and were thus included for the meta-analysis; 1440 TLE patients in total (left-sided = 761; mean +/- SD age: 35.4 +/- 5.2, age of onset: 16.3+/-4.6). The accuracy scores in relation to year of study publication, MRI modality, and size of cohort show increasing publications after 2015 with larger cohort sizes and more multimodal MRI used (Fig 2A). The ML algorithms include support vector machine (n=16), any type of discriminant analysis (n=10), logistic regression (n=1), random forest (n=1), and k-means clustering (n=1). Preliminary analyses show that the overall accuracy of AI/ML methods to lateralize patients is 91% (95% CI 87-93%) (Fig 2A). Influence diagnostic plots show general concordance between studies across several influence measures (Fig 2B). Leave-one-out meta-analysis also show highly concordant effect sizes, demonstrating robust accuracies across different modalities and AI/ML algorithms (Fig 2B).

Conclusions: AI/ML methods are highly accurate in lateralizing temporal lobe epilepsy (TLE). They have an overall accuracy rate of over 90%, with highly consistent and robust results across various study designs and algorithm types. AI/ML on multimodal MRI images can be a powerful aid for the presurgical assessment of drug-resistant TLE patients.

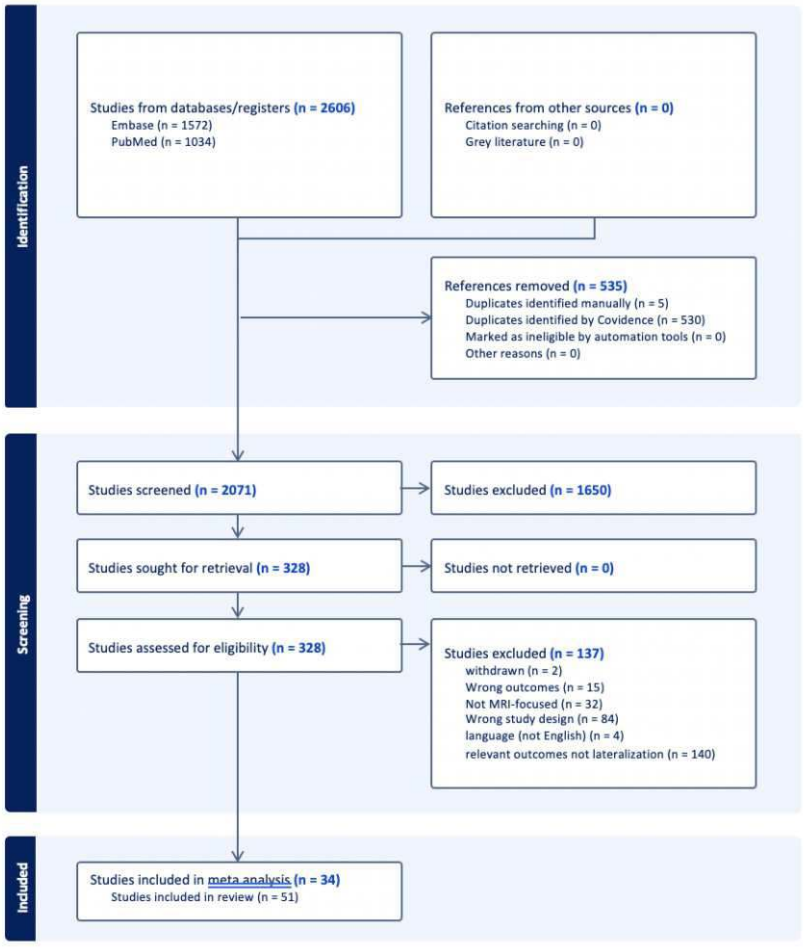

Figure 1. PRISMA reporting. MEDLINE and Embase databases were searched for original research articles that yielded 2606 publications after removing duplicates.

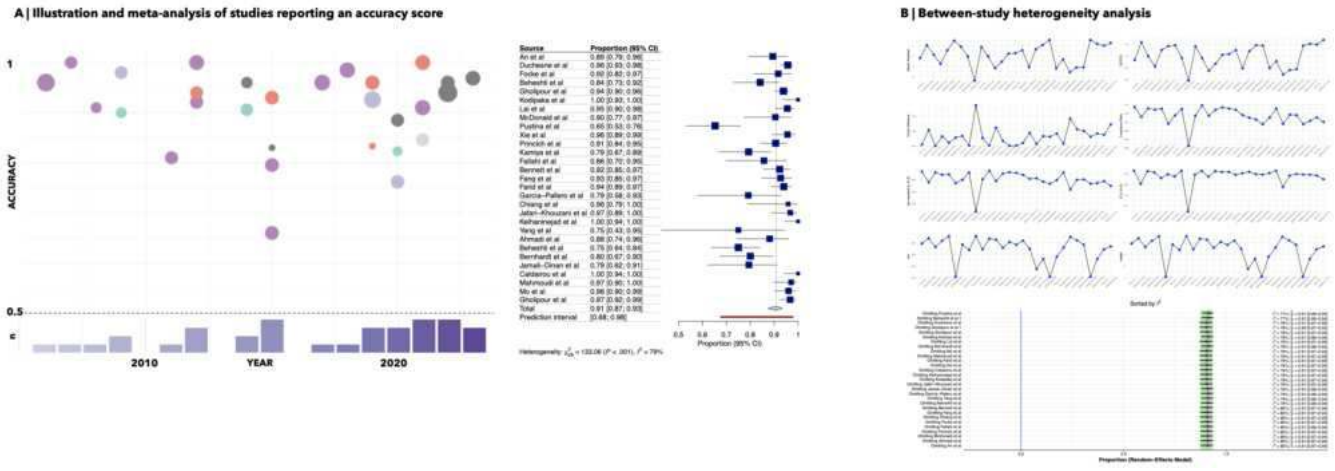

Figure 2. Meta-analysis and evaluation of heterogeneity.

References

1. Anyanwu, et al. "Diagnosis and Surgical Treatment of Drug Resistant Epilepsy." Brain Sci. 2018. 8(4):49
2. Cendes, et al. "Artificial Intelligence Applications in the Imaging of Epilepsy and its Comorbidities: Present and Future" Epilepsy Currents 2022. 22(2):91-96
3. Wolff, Robert F., et al. "PROBAST: a tool to assess the risk of bias and applicability of prediction model studies." Annals of internal medicine 170.1 (2019): 51-58.

Poster No 1477

State descriptions drive predictions of individual cognitive traits from time-varying FC

Christine Ahrends[1], Mark Woolrich[2], Diego Vidaurre[3]

[1]Aarhus University, Aarhus, Aarhus, [2]University of Oxford, Oxford, Oxfordshire, [3]Aarhus University, Aarhus, Aarhus C

Introduction: Observing a person's behaviour over time is how we understand the individual's personality, cognitive traits, or psychiatric condition. The same should apply at the brain level, where we may be able to gain crucial insights by observing the patterns in which brain activity unfolds over time. Recent approaches allow predicting individual traits, such as age or cognitive traits, from time-varying or dynamic functional connectivity (FC). However, it is still unclear which aspects of this spatiotemporal level of description best characterise subject differences or predict individual traits. Time-varying or dynamic FC is represented using models of varying complexity (Lurie et al., 2019) that are estimated from modalities such as functional MRI or MEG. The parameters of these models describe different aspects of dynamic FC: In a state-based model, for instance, this may be the connectivity strength between nodes in the network of a transient FC state, or the transition probabilities between all states. By interrogating these parameters, we may be able to understand which aspects of dynamic FC are unique to an individual and related to their specific traits and which aspects are common between individuals.

Methods: We here use resting-state fMRI data and behavioural measures of cognitive traits from 1,001 subjects from the Human Connectome Project (HCP) (van Essen et al., 2013). We use a Hidden Markov Model (HMM) to describe time-varying FC in the group of subjects (Vidaurre et al., 2017). We then estimate individual-level parameters of the HMM and construct from them the Fisher kernel (Jaakkola et al., 1999; Jaakkola & Haussler, 1998; Ahrends et al., 2023). The Fisher kernel is a mathematically principled approach for using a generative probabilistic model like the HMM in a prediction model or classifier. The HMM parameters can be categorised into two types: parameters related to the transitions between states and parameters related to the state descriptions (i.e., connectivity strength between brain regions). To test the influence of the different types of parameters, we construct three different kernels: one using all parameters, one using only transition parameters, one using only state descriptions. We then predict individual cognitive traits separately from each of these kernels and compare their prediction accuracies.

Results: We found that state description parameters were the most relevant features for the Fisher kernel predictions in all cognitive traits. Both the full kernel and the kernel containing only state parameters predicted cognitive traits at high accuracy. The prediction accuracy was significantly reduced when state features were removed, while removing transition features had no significant effect. One reason for the dominance of state parameters may simply be that the state parameters outnumber the other parameters. However, reducing the number of state parameters to match the number of other parameters did not

significantly affect accuracy. This indicates that the content of the state descriptions is more relevant for the prediction of cognitive traits than information about state transitions.

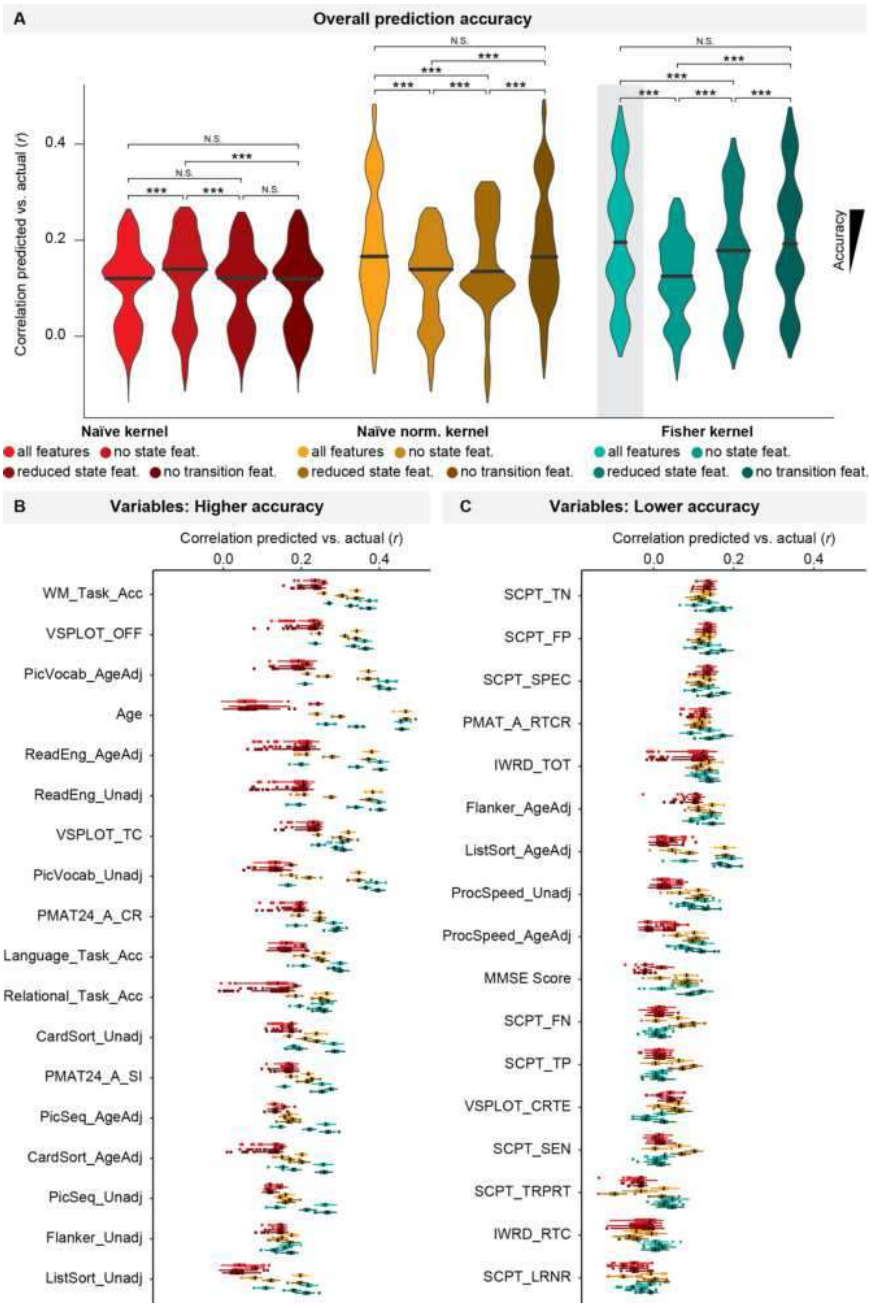

Conclusions: Cognitive traits can be accurately predicted from time-varying FC using the HMM-Fisher kernel approach. We here showed that descriptions of transient FC states are highly predictive of individual cognitive traits, whereas state transitions carry little information about individuals. This suggests that differences between individuals in cognitive traits are linked to changes in connection strengths within resting-state functional networks.

References

1. Ahrends, C. (2023), 'Predicting individual traits from model of brain dynamics using the Fisher kernel', bioRxiv. 2023.03.02.530638.
2. Jaakkola, T. (1999), 'Using the Fisher kernel method to detect remote protein homologies', Proc Int Conf Intell Syst Mol Biol, pp. 149-158.
3. Jaakkola, T. (1998), 'Exploiting Generative Models in Discriminative Classifiers', NIPS, 11, pp. 487-493.
4. Lurie, D. (2019), 'Questions and controversies in the study of time-varying functional connectivity in resting fMRI', Netw. Neurosci., 4(1), pp. 30-69.
5. Vidaurre, D. (2017), 'Brain network dynamics are hierarchically organized in time', Proc Natl Acad Sci U S A, 114(48), pp. 12827-12832.
6. Van Essen, D. C. (2013), 'The WU-Minn Human Connectome Project: an overview', Neuroimage, 80, pp. 62-79.

Poster No 1478

Generalization of Brain-Behavior Predictions to Unharmonized Data Towards Real-World Applications

Brendan Adkinson[1], Matthew Rosenblatt[2], Javid Dadashkarimi[2], Link Tejavibulya[2], Dustin Scheinost[2]

[1]Yale School of Medicine, New Haven, CT, [2]Yale University, New Haven, CT

Introduction: Despite the significant attention devoted to power, reproducibility, and generalizability, only a minority of neuroimaging studies undertake external validation. Compounding this issue, there is a notable lack of focus on external validation under real-world conditions wherein—unlike research settings—imaging and phenotypic data are largely unharmonized across sites. Neuroimaging research studies, by design, remove the between-site variations that future clinical applications will demand. Only by including multiple datasets with different imaging parameters, patient demographics, and choice of clinical instruments can the true effect sizes of predictive models be evaluated. Therefore, it is imperative to assess whether predictions can survive generalization across diverse dataset features. In this work, we use advanced methodological approaches to achieve generalization of predictive models across three markedly unharmonized samples.

Methods: Data from the Philadelphia Neurodevelopmental Cohort (PNC, n=1294, ages 8-21), Healthy Brain Network (HBN, n=1110, ages 6-17), and Human Connectome Project in Development (HCPD, n=428, ages 8-22) were used to generate connectome-based predictive models (CPM) of language abilities and executive function. PCA-derived 'latent' measures of each cognitive construct were created from 23 individual tasks. Resting-state and task-fMRI data were collected on 3T Siemens Tim Trio (HBN and PNC) and 3T Siemens Prisma (HBN and HCPD) scanners. Imaging data (motion < 0.20mm) were processed using BioImage Suite. Whole-brain functional connectivity matrices were created using the Shen 268x268 atlas. Connectomes were combined across rest and task runs within each dataset. Within-dataset models were trained with 10-fold cross-validation. Both within-dataset and externally-validated models were evaluated with Pearson's r, representing the correspondence between predicted versus observed values. Significance testing was performed via permutation testing.

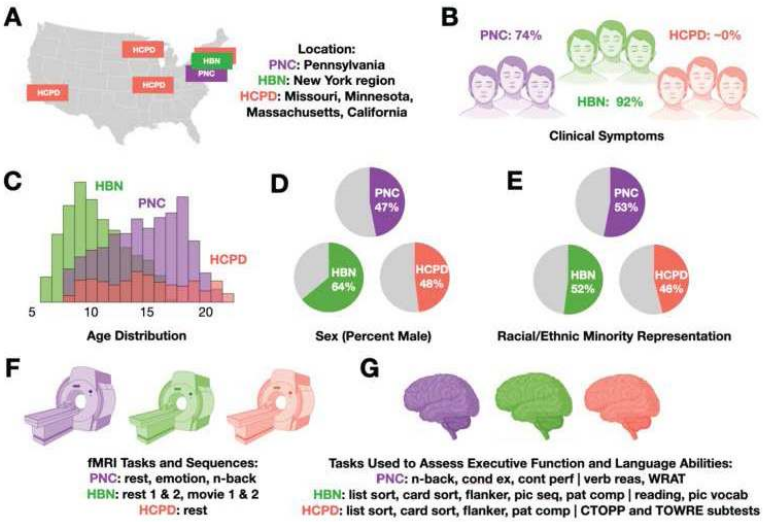

Figure 1. Differences across the PNC, HBN, and HCPD datasets. The Philadelphia Neurodevelopmental Cohort (PNC), Healthy Brain Network (HBN), and Human Connectome Project in Development (HCDP) datasets exhibit a notable lack of harmonization across recruitment geography (A), participant clinical symptom burden (B), age distribution (C), sex (D), racial and ethnic minority representation (E), fMRI tasks and sequences (F), and measures used to assess language abilities and executive function (G).

Results: CPM successfully predicted language abilities (PNC: r=0.50, p<0.01, q2=0.24, MSE=1.05; HBN: r=0.27, p<0.01, q2=0.06, MSE=4.42; HCPD: r=0.22, p<0.01, q2=0.01, MSE=1.47) and executive function (PNC: r=0.39, p<0.01, q2=0.14, MSE=1.17; HBN: r=0.17, p<0.01, q2=0.02, MSE=2.03; HCPD: r=0.17, p=0.02, q2=-0.01, MSE=1.98) within each dataset. The addition of covariates into models yielded similar results for age, sex, race, socioeconomic status, head motion, and clinical symptom burden. Training models in one dataset and testing in another yielded significant predictions across all six dataset pairings for both language abilities (range of r=0.13 to 0.35, all p<0.001) and executive function (range of r=0.1 to 0.28, all p<0.001).

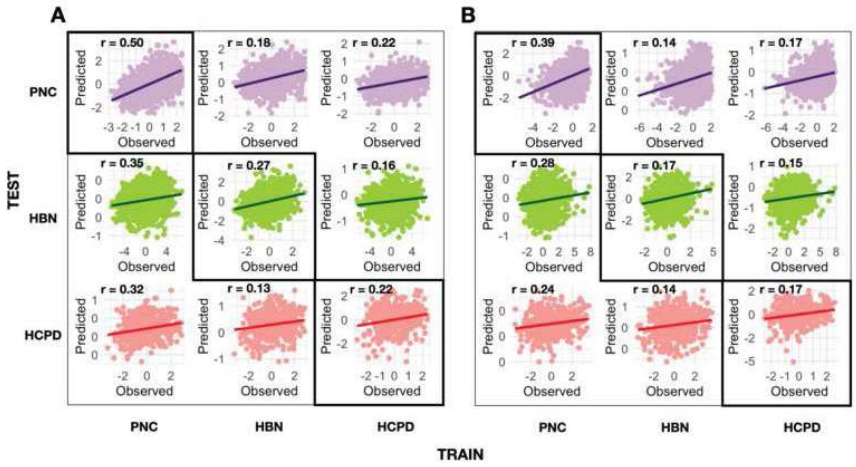

Figure 2. Connectome-based predictive model performance within and across datasets. Scatter plots of model performance across PNC (purple), HBN (green), and HCPD (red) for language abilities (A) and executive function (B). Pearson's r values represent the correspondence between predicted versus observed 1st principal component values. Bolded diagonals show within-dataset predictions. Each circle represents data for an individual participant.

Conclusions: PNC, HBN, and HCPD are characterized by a high degree of inter-dataset heterogeneity, encompassing substantial variations in participant demographics such as age, sex, and race, as well as geographic distribution and clinical symptom burdens. Further diversifying these datasets is a notable lack of harmonization in imaging acquisition parameters, fMRI tasks, and behavioral paradigms employed to assess language abilities and executive function. We demonstrate that robust and reproducible brain-behavior associations can indeed be realized across such diverse dataset features, which are inherent to future clinical applications. Our results were achieved by employing state-of-the-field methodological approaches including the combination of multiple connectomes, harmonization of behavioral measures via PCA, and preservation of participant data (e.g., use of behavioral data from 6745 PNC and 1281 HBN participants without imaging data to derive principal components). This work provides a critical foundation for future work to test the generalizability of brain-behavior predictions to clinical settings. Furthermore, our findings contribute to the ongoing discourse surrounding the requisite sample sizes for reproducible brain-behavior association studies.

References

1. Rosenblatt, M., Tejavibulya, L., Camp, C. C., Jiang, R., Westwater, M. L., Noble, S., & Scheinost, D. (2023), 'Power and reproducibility in the external validation of brain-phenotype predictions', bioRxiv : the preprint server for biology, 2023.10.25.563971.
2. Alexander, L., Escalera, J., Ai, L. et al. (2017), 'An open resource for transdiagnostic research in pediatric mental health and learning disorders', Sci Data, vol. 4, 170181.
3. Satterthwaite, T. D., Connolly, J. J., Ruparel, K., Calkins, M. E., Jackson, C., Elliott, M. A., Roalf, D. R., Hopson, R., Prabhakaran, K., Behr, M., Qiu, H., Mentch, F. D., Chiavacci, R., Sleiman, P. M. A., Gur, R. C., Hakonarson, H., & Gur, R. E. (2016), 'The Philadelphia Neurodevelopmental Cohort: A publicly available resource for the study of normal and abnormal brain development in youth', NeuroImage, vol. 124, Pt B, pp. 1115–1119.
4. Somerville, L. H., Bookheimer, S. Y., Buckner, R. L., Burgess, G. C., Curtiss, S. W., Dapretto, M., Elam, J. S., Gaffrey, M. S., Harms, M. P., Hodge, C., Kandala, S., Kastman, E. K., Nichols, T. E., Schlaggar, B. L., Smith, S. M., Thomas, K. M., Yacoub, E., Van Essen, D. C., & Barch, D. M. (2018), 'The Lifespan Human Connectome Project in Development: A large-scale study of brain connectivity development in 5-21 year olds', NeuroImage, vol. 183, pp. 456–468.
5. Shen, X., Finn, E., Scheinost, D. et al. (2017), 'Using connectome-based predictive modeling to predict individual behavior from brain connectivity', Nat Protoc, vol. 12, pp. 506–518.
6. Gao, S., Greene, A. S., Constable, R. T., & Scheinost, D. (2019), 'Combining multiple connectomes improves predictive modeling of phenotypic measures', NeuroImage, vol. 201, 116038.
7. Marek, S., Tervo-Clemmens, B., Calabro, F.J. et al. (2022), 'Reproducible brain-wide association studies require thousands of individuals', Nature, vol. 603, pp. 654–660.

Poster No 1479

A Deep Learning Approach for Consciousness Level Assessment in Sleep Stages: An Case framework Study

Yong Liu[1], Gan Huang[2], Jinfei Tian[3], Yao Wang[4], Kin Cheung Lee[5], Junling Gao[6]

[1]Department of Critical Care Medicine, Shenzhen Hospital of Southern Medical, shenzhen, shenzhen, [2]Shen Zhen University, Shenzhen, AK, [3]Department of Critical Care Medicine, Shenzhen Hospital of Southern Medical, Shenzhen, AR, [4]The University of Hong Kong, Hong Kong, AZ, [5]The University of Hong Kong, Hong Kong, Hong Kong, [6]The University of Hong Kong, Hong Kong, AS

Introduction: Consciousness level assessment in clinical settings often relies on the Glasgow Coma Scale, which tends to be arbitrary. Additional information from EEG data could provide more objectivity. With this in mind, Lee et al. developed an explainable consciousness index (ECI) using deep learning methods. This study applies the ECI and the associated deep learning algorithm to sleep EEG data to assess its ability to categorize different sleep stages, each assumed to represent different levels of consciousness.

Methods: The ECI method, employing deep learning and the Layer-Wise Relevance Propagation (LRP) toolbox, was used to categorize overnight sleep EEG data. The C4 channel was selected, as previous studies have indicated that parietal EEG is likely related to consciousness activities. Sleep stages were labeled by clinicians for each 30-second EEG segment. The EEG data were first preprocessed by filtering at 0.1-45 Hz. Corrupted segments were replaced with adjacent EEG data, as independent component analysis could not be applied to single-channel EEG data or those with limited channels.

Figure 1. Framework of ECI categorization to sleep EEG data

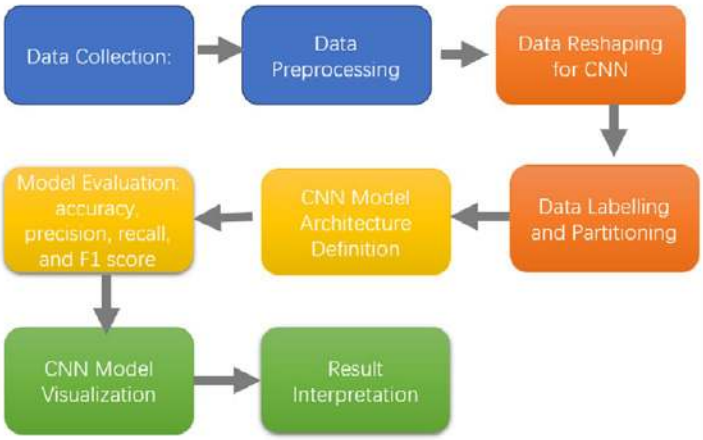

Results: The data processing procedure was as follows: Consciousness levels for the stages of wakefulness, rapid-eye-movement, N1, N2, and N3 were arbitrarily assigned values of 1, 0.6, 0.4, 0.3, and 0.2, respectively. The adapted ECI deep learning algorithm was then used to calculate the consciousness level for each 30-second stage. A correlation analysis was performed on the results from the clinical labels and the ECI-calculated results, yielding a correlation coefficient (r) of -0.199. When corrupted EEG segments were not replaced with adjacent EEG data, the correlation dropped to -0.132.

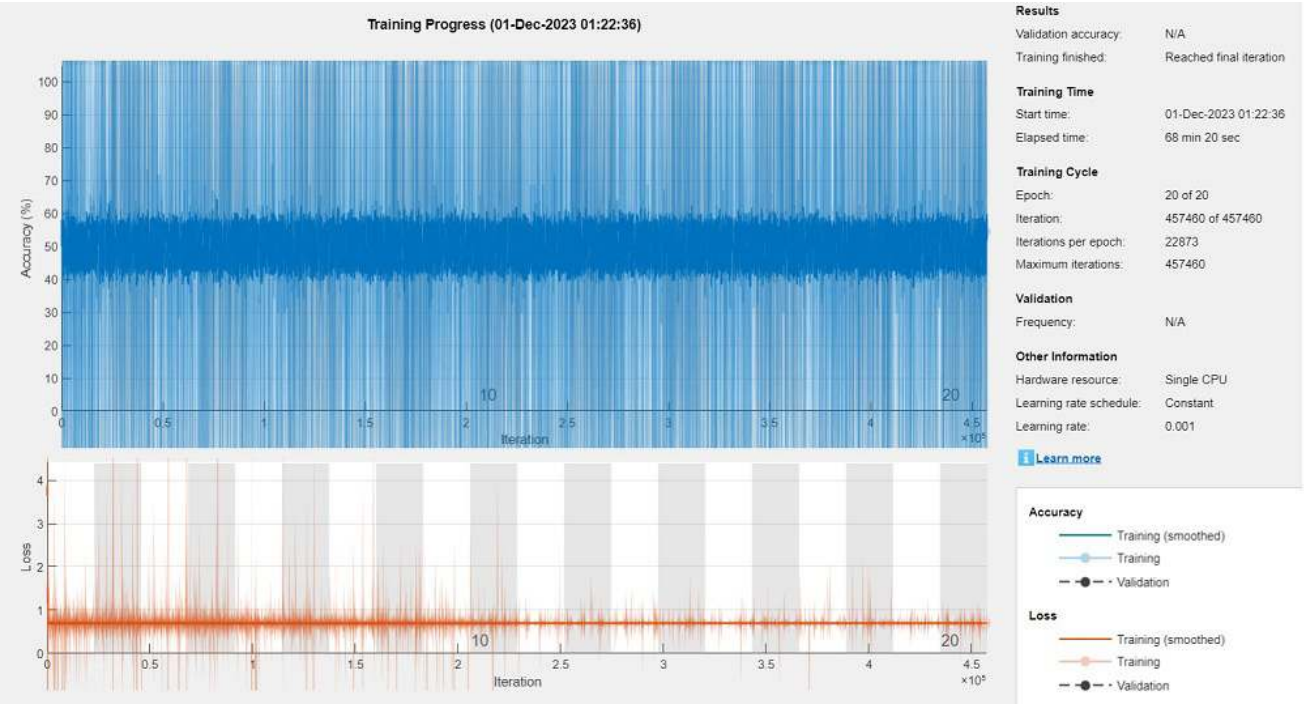

Conclusions: The application of the ECI algorithm to single-channel sleep data was not as effective as desired. This could be due to the lack of spatial information in single or limited-channel EEG data from ordinary sleep, which may weaken the ECI algorithm's ability to categorize consciousness levels. Additionally, the consciousness levels in sleep stages may not align directly with those seen in clinical conditions, such as the comparison between wakefulness and coma. Clinicians can often observe sleep and wakefulness even in coma patients. Corrupted EEG data may contain movement information, and additional information from heart rate, breathing rate, and body movement could be analyzed by the ECI algorithm, potentially improving its applicability to sleep data.

References

1. Lee, Minji, Sanz, Leandro R. D., Barra, Alice, Wolff, Audrey, Nieminen, Jaakko O., Boly, Melanie, Rosanova, Mario, Casarotto, Silvia, Bodart, Olivier, Annen, Jitka, Thibaut, Aurore, Panda, Rajanikant, Bonhomme, Vincent, Massimini, Marcello, Tononi, Giulio, Laureys, Steven, Gosseries, Olivia, & Seong-Whan Lee. (2022). Quantifying arousal and awareness in altered states of consciousness using interpretable deep learning. Nature Communications, 13, Article 1064.
2. Wong, GoonFui, Rui Sun, Jordana Adler, Kwok Wah Yeung, Song Yu, and Junling Gao. 2022. "Loving-kindness meditation (LKM) modulates brain-heart connection: An EEG case study." Frontiers in Human Neuroscience 16. https://doi.org/10.3389/fnhum.2022.891377.

Poster No 1480

Experience-dependent plasticity in fMRI: an investigation using linear regression models & VideoMAE

Katrina Portelli[1], Simon Dahan[1], Yourong Guo[2], Anderson Winkler[3], Logan Williams[1], Emma Robinson[1]

[1]King's College London, London, London, [2]King's College London, London, London, [3]University of Texas Rio Grande Valley, Brownsville, TX

Introduction: Self-supervision algorithms that approximate neural processing of speech offer potential for data-driven hypotheses of sensory processing and model-free extraction of spatio-temporal features from complex stimuli[1,3,4]. We take this approach to investigate experience-dependent changes in brain activity following repeated movie watching, using data from the Human Connectome Project (HCP). We use a vision transformer to construct a latent encoding of movie frames that predict neural responses to movie stimuli. Following validation, we use this model to identify areas whose activity changes with repeated exposure to the same movies.

Methods: Functional magnetic resonance imaging (fMRI) data was obtained from the HCP 7T release[9]. 184 participants were scanned while passively viewing a series of movie clips, acquired in up to four separate sessions. At the end of each session, the same test-retest movie clip was presented. We limited analyses to participants who had completed four runs of interest (n = 172). fMRI responses were projected from volume to the cortical surface space and aligned using MSMAll[2,7].

Movie frames were encoded using a video masked autoencoder (VideoMAE)[8], pre-trained on the Kinetics400 movie dataset[4]. Spatio-temporal activations were extracted from segments of 3-second movie clips. These activations were linearly regressed against brain activity from the central time point of each clip. A ridge regression model was trained for each subject, regularised with Thikonov penalties, accounting for temporal lag using the approach of[3]. Training data consisted of fMRI compiled from all sessions, excluding the test-retest clips. The linear model's performance was assessed for each session by generating correlation maps at the vertex level (fig.1b), using Pearson correlation between the predicted and actual time series in response to the test-retest clip. Correlation values were averaged across the 360 regions of the HCP multimodal parcellations, propagated to individuals as described in[2]. Correlations were then compared across sessions using repeated measures permutation analysis of linear models (PALM) corrected for multiple comparisons.

Results: Here we focus on fMRI responses from scanning sessions 1 and 4. We first assessed correlations between the linear regression model's predicted fMRI timeseries and the actual fMRI timeseries from session 1. Significant correlations were found in 87 and 91 parcels in the left and right hemispheres, respectively (fig.1c). These areas functionally fall within the dorsal and ventral visual streams, auditory association areas and frontal regions related to decision-making and reward. Comparing correlation coefficients in the significant parcels from session 1 to the same parcels in session 4 revealed significant decreases in prediction accuracy (fig.2). These decreases were observed in 88 parcels (44/87 in the left and 44/91 in the right hemisphere). Specifically, parcels in the left and right superior and inferior temporal cortex, frontal opercular cortex, orbitofrontal cortex, posterior cingulate cortex and the MT+ cortex. Activity in these cortices has been linked to the processing of dynamic visual stimuli[5]. In a subset of parcels, lateralisation of changes in accuracy was observed. Parcels specific to the right hemisphere included the premotor eye field, retrosplenial cortex, area PFm, area LO3 and visual area 8. In contrast to the left hemisphere, prediction accuracy in the right early visual areas V2 V3, was not significantly different between sessions.

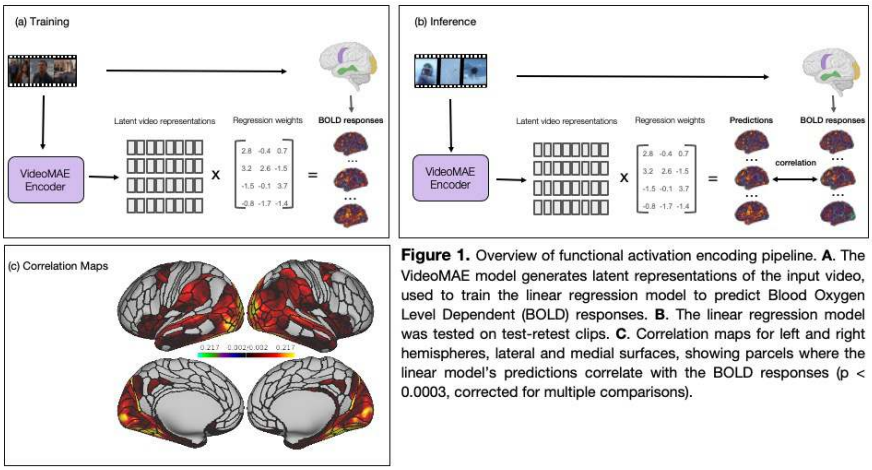

Figure 1. Overview of functional activation encoding pipeline. **A**. The VideoMAE model generates latent representations of the input video, used to train the linear regression model to predict Blood Oxygen Level Dependent (BOLD) responses. **B**. The linear regression model was tested on test-retest clips. **C**. Correlation maps for left and right hemispheres, lateral and medial surfaces, showing parcels where the linear model's predictions correlate with the BOLD responses ($p < 0.0003$, corrected for multiple comparisons).

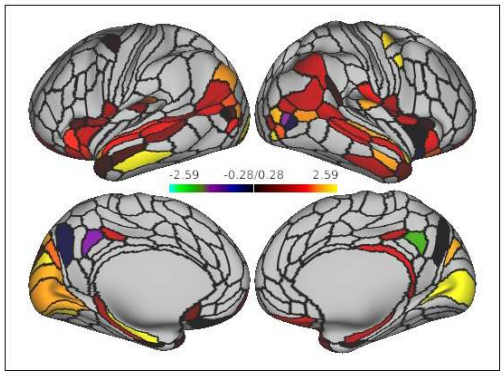

Figure 2. Effect of scanning session on predictive accuracy. Depicted are parcels that show a significant group-wise difference between session 1 and session 4 at $p_{mcfwe} < 0.05$. Colour bars show T-values.

Conclusions: We show videoMAE-derived features reliably predicted neural responses to movie clips in visual processing areas. Repeat exposure to movie stimuli was associated with a change in prediction accuracy in a subset of these areas, demonstrating the potential of these models for identifying areas undergoing experience-dependent neural plasticity, thereby advancing our mechanistic understanding of sensory processing.

References
1. Caucheteux, C., Gramfort, A. & King, JR (2023). Evidence of a predictive coding hierarchy in the human brain listening to speech. Nature Human Behaviour 7, 430–441.
2. Glasser, M.F., Coalson, T., Robinson, E. et al. (2016). A multi-modal parcellation of human cerebral cortex. Nature 536, 171–178.
3. Huth, A., de Heer, W., Griffiths, T. et al.(2016). Natural speech reveals the semantic maps that tile human cerebral cortex. Nature 532, 453–458
4. Kay, W., Carreira, J., Simonyan, K. et al. (2017). The kinetics human action video dataset. arXiv preprint arXiv:1705.06950.
5. Lahnakoski, J.M., Salmi, J., Jaaskelainen, I.P. et al. (2012). Stimulus-Related Independent Component and VoxelWise Analysis of Human Brain Activity during Free Viewing of a Feature Film. PLoS ONE 7(4): e35215.
6. Millet, J., Caucheteux, C., Orhan P. et al. (2022). Toward a realistic model of speech processing in the brain with self-supervised learning. arXiv preprint arXiv:2206.01685.
7. Robinson, E., Garcia, K., Glasser, M.F. et al. (2018). Multimodal Surface Matching with Higher-Order Smoothness Constraints. NeuroImage, 167, 453–465.
8. Tong, Z., Song, Y., Wang, J., & Wang, L. (2022). VideoMae: Masked autoencoders are data-efficient learners for self-supervised video pre-training. Advances in neural information processing systems, 35, 10078-10093.
9. Van Essen, D.C., Smith, S.M., Barch, D.M., Behrens, T.E., Yacoub, E., and Ugurbil, K. (2013). The WU-Minn human connectome project: an overview. Neuroimage 80, 62–79.

Poster No 1481

Multimodal Ensemble Deep Learning for Mental Disorder Classification Using Neuroimaging Data

Hooman Rokham[1], Haleh Falakshahi[2], Vince Calhoun[3]

[1]Georgia Institue of Technology, Atlanta, GA, [2]Georgia Institute of Technology, Atlanta, GA, [3]GSU/GATech/Emory, Decatur, GA

Introduction: The intricate exploration of brain functional mechanisms within mood and mental disorders remains a formidable undertaking. Existing challenges in the categorization of psychosis, characterized by issues like heterogeneity, lack of validity, and the constraints of unbalanced, small sample sizes, further compound the complexity of unraveling and recognizing essential biological features associated with these disorders. This study addresses these challenges by implementing a sophisticated multimodal ensemble deep learning approach. The primary objective is to perform a four-way classification task for the diagnosis of individual subjects, utilizing a comprehensive dataset that incorporates both structural and resting-state functional MRI data. This innovative methodology spans across three diverse datasets, fostering a more nuanced and insightful understanding of the intricate interplay between brain function and psychiatric disorders.

Methods: In this investigation, we scrutinized the structural and resting-state functional MRI data of a cohort comprising 1520 subjects, encompassing 566 normal controls, 234 with bipolar disorder, 249 with schizoaffective disorder, and 473 with schizophrenia from three distinct datasets-FBIRN, B-SNIP1, and B-SNIP2. The preprocessing steps involved slice timing and rigid body head motion correction, followed by registration to the standard Montreal Neurological Institute (MNI) and subsequent smoothing. Subsequently, a fully automated Neuromark ICA pipeline (Du et al., 2020) was employed on the preprocessed data, extracting 53 intrinsic connectivity networks (ICNs) from seven different domain regions. Subject-specific functional networks and associated time-courses (TC) were then extracted. Following this, we utilized a fully convolutional neural network (CNN) architecture as the foundational model for fMRI data and a 3D convolutional neural network for structural MRI (sMRI) data. Our proposed multimodal ensemble deep learning method was assessed for its ability to glean features from time courses and gray matter images using undersampling technique in conjunction with repeated cross-validation. By adopting this approach, each individual subject appeared in different test sets, facilitating evaluation and classification using models trained with distinct randomly generated training sets. The labeling assigned to each test sample was determined based on the maximum averaged probabilities obtained from the individual base models for each class.

Results: Results demonstrates that the ensemble deep learning approach surpasses the performance of the base deep CNN models in handling both structural and functional MRI data. This enhancement is particularly evident in a performance boost of 0.11 for sMRI data and 0.13 for fMRI data. Furthermore, employing data fusion techniques and an ensemble approach elevates the overall accuracy to 0.61, accompanied by an area under the curve (AUC) of 0.83. Notably, statistical examinations of group differences in gray matter and functional connectivity data, coupled with post-classification analysis, reveal that misclassified subjects exhibit more pronounced distinctions within their respective groups compared to others predicted by the model.

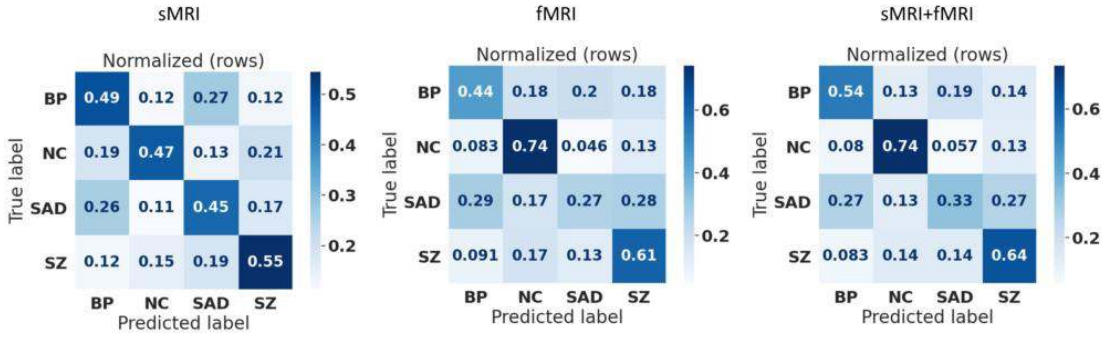

Fig. Unimodal and multimodal confision matrices of ensemble method.

Conclusions: In summary, we have introduced a multimodal ensemble deep learning method for the classification of mood and psychosis disorders. The findings indicate that amalgamating individual base models as ensemble deep learning methods outperforms a single CNN. Additionally, the multimodal ensemble method further enhances performance. The results suggest that multimodal ensemble deep learning methods exhibit robustness to label noise and demonstrate superior performance in the presence of noisy and heterogeneous data, as compared to single deep learning models. Moreover, the ensemble deep learning method exhibits improved performance, especially in scenarios with small sample sizes, such as in small neuroimaging datasets within the field of psychiatry.

References

1. Du, Y., Fu, Z., Sui, J., Gao, S., Xing, Y., Lin, D., . . . Calhoun, V. D. (2020). NeuroMark: An automated and adaptive ICA based pipeline to identify reproducible fMRI markers of brain disorders. NeuroImage: Clinical, 28, 2213-1582.

Poster No 1482

Using Manifold Learning to Uncover the Embedded Brain and Implications for Mental Health in Youth

Erica Busch[1], May Conley[1], Arielle Baskin-Sommers[1]

[1]Yale University, New Haven, CT

Introduction: Advancing the study of biosocial transactions, which considers the interplay between youth and environment, is essential to improving our understanding of how information processing and neural differences contribute to the formation and maintenance of mental health problems. To move the study of biosocial transactions beyond what we have achieved so far (e.g., a complex account of contexts and behaviors without understanding the neurobiological embedding within these transactions), we need to find ways of studying the complex, transactional relationships between neurocognitive functioning and the social world (Viding et al. 2023). Manifold learning techniques can discover and highlight latent structure from high-dimensional, noisy biomedical data, such as fMRI. Here, we develop and apply a novel manifold learning technique to capture the interplay between various environmental factors, neuroimaging data, and mental health outcomes in youth.

Methods: We used data from 5,245 9–10 year old youth enrolled in the Adolescent Brain and Cognitive Development StudySM (ABCD Study®) Data Release 4.0 to ask how brain activation during an emotional n-back task and measures of environmental adversity interact and reflect emotional and behavioral problems. We extracted activation patterns from parcels including the amygdala and the executive control network during cognitive processing (i.e., the contrast of 2-back vs. 0-back and of emotional and neutral task blocks) (Conley et al. 2023). fMRI activation maps contain high levels of noise and intersubject variance. Recent work shows that manifold learning unveils meaningful structure from biomedical data (Moon et al. 2019) and fMRI activity (Huang & Busch et al. 2022). Explicitly modeling additional signals like temporal dynamics in the manifold calculation improves insight into the geometry of fMRI activity and its relation to behavior (Busch et al. 2023). We modified the manifold learning method T-PHATE, designed for fMRI timeseries, to combine multivariate environmental features with neural manifold geometry to embed youth brain data in a latent space via approach we call “Feature PHATE (F-PHATE)” (Fig. 1). We then used the coordinates embedded coordinates of each participants’ data to predict their Child Behavior Checklist (CBCL) total problem, externalizing, and internalizing scores. We benchmarked prediction using F-PHATE embeddings against embeddings in a standard embedding model without the environmental features (PHATE) and from the full voxel-resolution data.

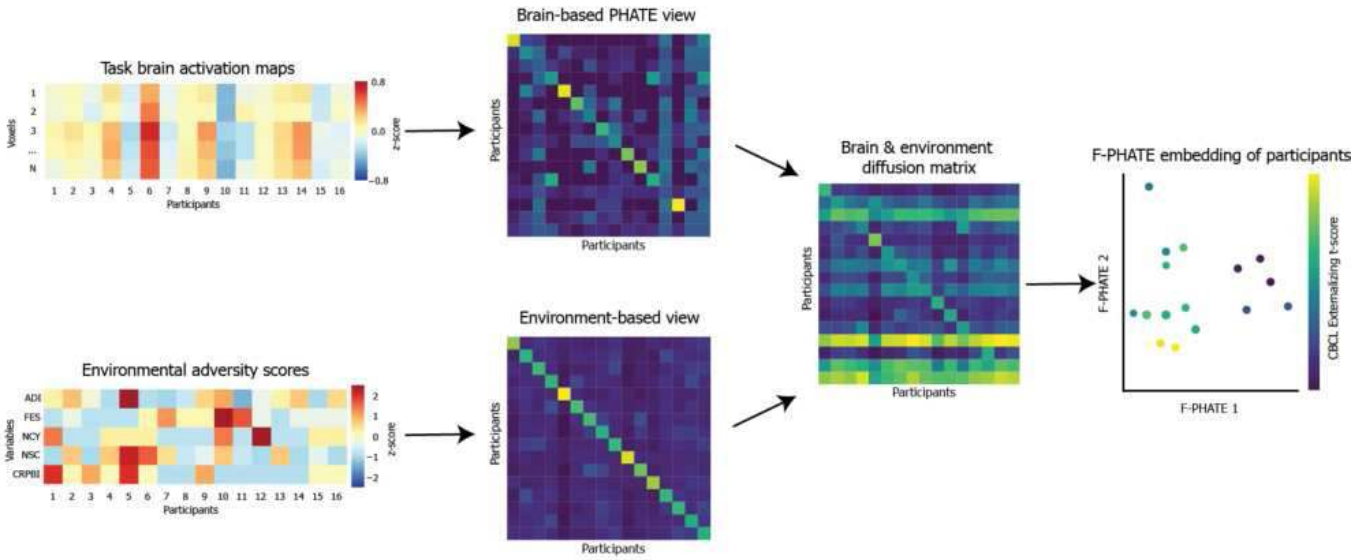

Figure 1: Feature-PHATE procedure. The F-PHATE uses a multi-view manifold learning approach to combine neural activation data with non-neural features hypothesized to modulate or lend latent structure to a neurobiological process. In the first view, we extract multivariate voxel activation patterns from participants performing an n-back task and apply the manifold learning algorithm PHATE to build a participants x participants diffusion matrix, which highlights local and global geometric structure in the neural data across participants. In the second view, we include features (here, measures of environmental adversity) for the same participants, and compute an affinity matrix representing the similarity between participants along these environmental dimensions (using a Euclidean similarity metric). The affinity matrix is normalized to represent transitional probabilities. The two views (capturing the PHATE manifold geometry and the similarity of environmental experience) are combined into a dual-diffusion operator, which jointly represents neural and environmental information, and embedded into a low-dimensional space via metric multi-dimensional scaling (m-MDS). Here, we visualize two dimensions and show in a sample of eight participants how the embedding space reveals clusters of participants with similar externalizing symptomatology.
Variable key: ADI = reshist_addr1_adi_perc ; FES = fes_y_ss_fc ; NCY: neighborhood_crime_y ; NSC: nsc_p_ss_mean_3_items ; CRPBI: crpbi_y_ss_caregiver

Results: First, we validated that embeddings with standard PHATE captured cognitive processing by predicting n-back performance. Linear regression trained on PHATE embeddings significantly outperformed those trained on the full voxel resolution data (amygdala and control network, Fig 2A). Next, we predicted CBCL scores from PHATE and F-PHATE embeddings, and the voxel resolution data for comparison (Fig. 2B). In the amygdala, neither PHATE embeddings nor voxel resolution data predict CBCL externalizing (Fig 2C) or internalizing scores (Fig 2D), though the PHATE embedding does predict total problem scores. PHATE embeddings of the executive control network predict both total problem and externalizing scores (but not internalizing scores) better than the voxel data. With the addition of environment information, prediction performance for F-PHATE exceeds that of either standard PHATE or the voxel data.

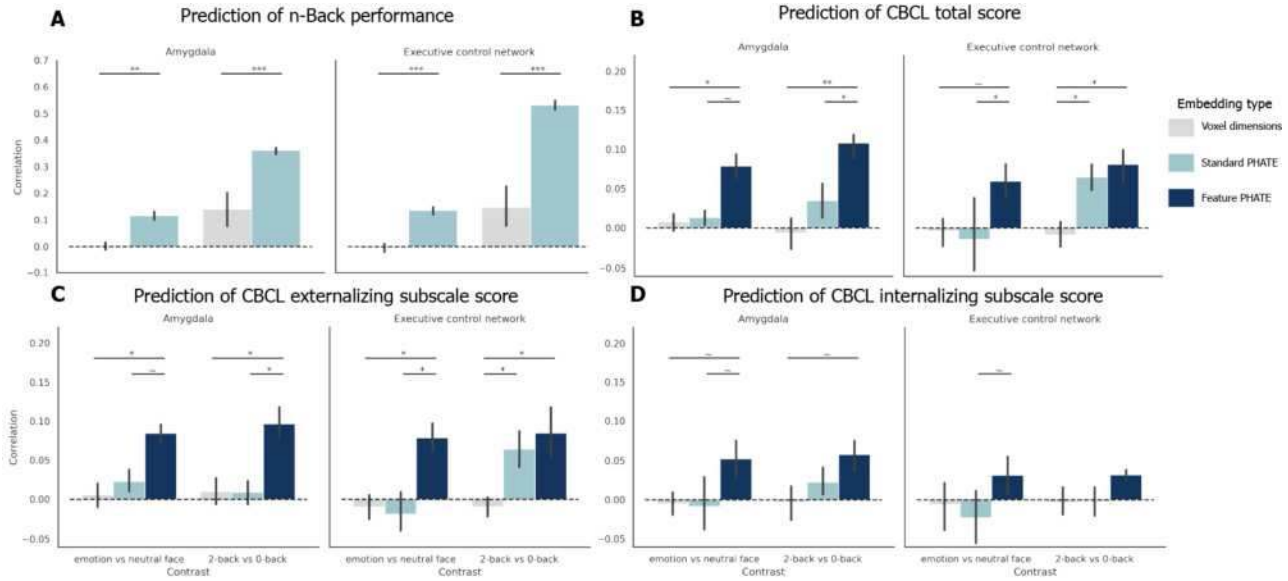

Figure 2: Prediction results. Prediction of n-Back performance (A), CBCL total score (B), CBCL externalizing (C) and internalizing subscales (D) from brain data in amygdala (left plot) and executive control netowrk (right plot). X-axis shows two different linear contrasts: n-back blocks with emotion versus neutral faces and the contrast of 2-back and 0-back blocks. Prediction was performed with a linear regression trained and scored with 5-fold cross validation. Embeddings using standard PHATE and F-PHATE were all 20 dimensions. Significance of difference in prediction accuracy between two embedding types was assessed with a Fisher's r to z transformation.
~ $p < 0.1$; * $p < 0.05$; ** $p < 0.01$; *** $p < 0.001$

Conclusions: We present a manifold-learning approach to incorporating environmental or other information in a low-dimensional embedding space. Embedding participants into a joint neural-and-environmental manifold uncovered latent

structure predictive of broad emotional and social problems and externalizing behavior. This work holds important implications for understanding the relationship between biosocial transactions and mental health.

References

1. Busch, Erica L., Jessie Huang, Andrew Benz, Tom Wallenstein, Guillaume Lajoie, Guy Wolf, Smita Krishnaswamy, and Nicholas B. Turk-Browne. 2023. "Multi-View Manifold Learning of Human Brain-State Trajectories." Nature Computational Science, March, 1–14. https://doi.org/10.1038/s43588-023-00419-0.
2. Conley, May I., Kristina M. Rapuano, Callie Benson-Williams, Monica D. Rosenberg, Richard Watts, Cassandra Bell, BJ Casey, and Arielle Baskin-Sommers. 2023. "Executive Network Activation Moderates the Association between Neighborhood Threats and Externalizing Behavior in Youth." Research on Child and Adolescent Psychopathology 51 (6): 789–803. https://doi.org/10.1007/s10802-022-01003-2.
3. Huang, Jessie, Erica Busch, Tom Wallenstein, Michal Gerasimiuk, Andrew Benz, Guillaume Lajoie, Guy Wolf, Nicholas Turk-Browne, and Smita Krishnaswamy. 2022. "Learning Shared Neural Manifolds from Multi-Subject FMRI Data." In 2022 IEEE 32nd International Workshop on Machine Learning for Signal Processing (MLSP), 01–06. https://doi.org/10.1109/MLSP55214.2022.9943383.
4. Moon, Kevin R., David van Dijk, Zheng Wang, Scott Gigante, Daniel B. Burkhardt, William S. Chen, Kristina Yim, et al. 2019. "Visualizing Structure and Transitions in High-Dimensional Biological Data." Nature Biotechnology 37 (12): 1482–92. https://doi.org/10.1038/s41587-019-0336-3.
5. Viding, Essi, Eamon McCrory, Arielle Baskin-Sommers, Stephane De Brito, and Paul Frick. 2023. "An 'Embedded Brain' Approach to Understanding Antisocial Behaviour." Trends in Cognitive Sciences 0 (0). https://doi.org/10.1016/j.tics.2023.08.013.

Poster No 1483

Perception similarity enhances visual encoding of natural scenes in the human brain

Yuduo Zhang[1,2], Zhang Jing[1], Siyang Li[1], Weiyang Shi[1], Yongfu Hao[1], Zhang Yu[1], Tianzi Jiang[3]

[1]Zhejiang Lab, Hangzhou, China, [2]Shanxi University, Taiyuan, China, [3]Brainnetome Center, Institute of Automation, Chinese Academy of Sciences, Beijing, China

Introduction: The integration of brain responses with artificial neural network (ANN) models has opened new avenues for understanding the neural basis of cognitive functions. This study introduces an innovative encoding approach using the dreamsim_Openclip model, leveraging the joint mechanism of image-text alignment and perceptual similarity training. By employing advanced spatial and layer attention mechanisms, the proposed model not only achieve state-of-the-art encoding performance in the cortex, but also provides novel insights into the receptive field mapping and hierarchical structure of visual coding. This work marks a substantial advancement in bridging the fields of artificial intelligence and neuroscience, particularly in the realms of visual processing and scene comprehension.

Methods: We used 7T-fMRI dataset of the Natural Scenes Dataset (Allen 2021), when participants viewed 10,000 different natural scene images collected from Coco (Lin 2014). Image-wise brain response were estimated by using fmriprep and GLMsingle (Prince 2022) and then projected onto the fsaverage cortical surface. We utilized the pretrained dreamsim-openclip model (Fu 2023) to extract latent features of each scene image. This model is adept at encoding multimodal information, encompassing both objects and captions through text-image contrastive learning, and capturing the semantic relationships between objects through human perceptual similarity tasks of image triplets. To predict the neural response of each vertex in the cerebral cortex, we integrated latent features from multiple layers of openclip using a 1x1 convolution, followed by the application of spatial (196-dimensional) and layer (12-dimensional) attention mechanisms. The spatial attention specifically targets capturing the retinotopic mapping of the visual cortex, while the layer attention mechanism reflects the hierarchy of visual coding. Based on the spatial attention map, the angle and eccentricity of each cortical vertex can be estimated and subsequently compared with the actual population receptive field (pRF) parameters provided by the dataset.

Results: State-of-art encoding performance in the visual cortex was achieved by using the dreamsim-openclip model (Fig 1B), with a maximum prediction accuracy as 0.86. Medium encoding accuracy was observed in the prefrontal and parietal regions. Additionally, the receptive field mapping derived from the spatial attention map of each vertex highly resembled the actual pRF map (Fig 1C). The layer attention map aligns with the hierarchical structure of visual coding (Fig 1E), demonstrating low-layer representations predominantly for early visual areas (e.g., V1), middle-layer representations for higher visual areas including V4, and high-layer representations for higher-order areas in the dorsal and ventral streams. We observed that the proposed encoding model exhibited superior performance compared to other models, such as dreamsim-dino, particularly in high-order cognitive areas beyond the visual cortex (Fig 2A). Notably, this enhanced performance was evident in regions including the lateral and medial prefrontal cortex, as well as the superior parietal and temporal cortex. However, no significant improvement was detected in the early visual cortex, encompassing areas V1 to V3.

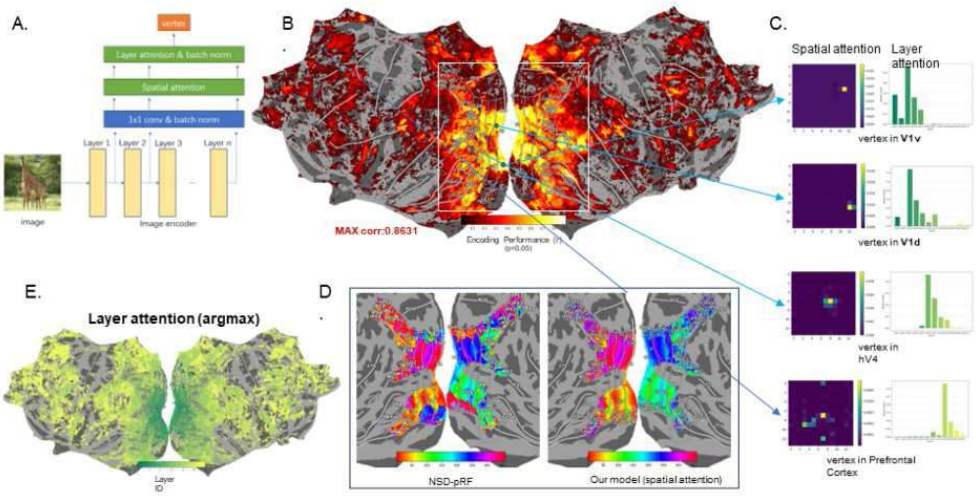

Figure 1. (A). Architecture of the encoding model using spatial and layer attention mechanisms. (B). Encoding performance of dreamsim-openclip model, evaluated by using Person correlation coeffection. (C). Examples of spatial attention and layer attention for vertices in early and high visual areas. (D). Receptive field mapping derived from the spatial attention map resembled the actual pRF map angles. (E). Layer attention captured the hierarchical structural of visual coding across the cortex.

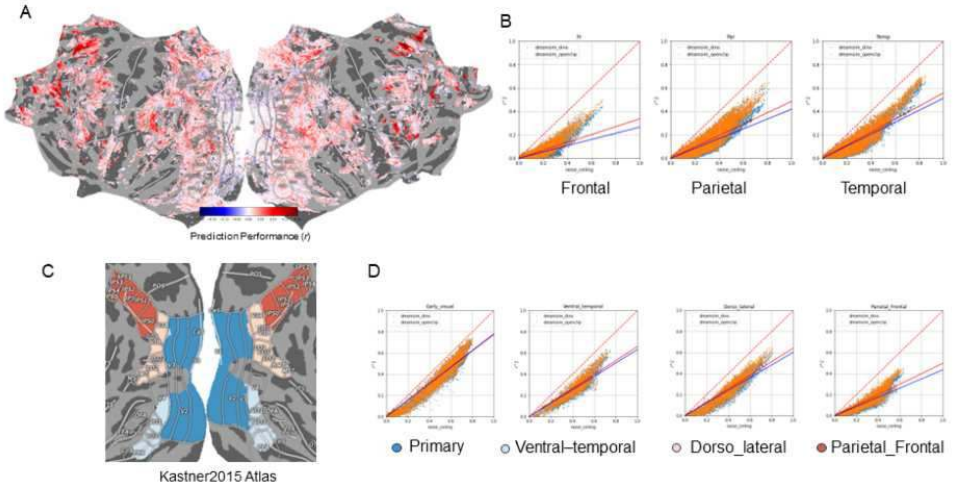

Figure 2. (A). Model comparison (dreamsim_Openclip > dreamsim_Dino). (B). Dreamsim-Openclip exhibited significant improvement in the high-order cognitive areas, particularly in the frontal and parietal lobes. (C).Dreamsim_Openclip demonstrated competitive performance in early visual cortex (V1-V3), but showed enhanced performance in high-order areas in the frontal, parietal and temporal cortex.

Conclusions: Our study employed the pre-trained dreamsim_Openclip model to encode neural responses to natural scenes across the entire cortex. Leveraging a joint mechanism of image-text alignment with perceptual similarity training, the proposed model achieved state-of-the-art encoding performance in the visual cortex, and demonstrated enhanced performance in high-order cognitive areas, particularly within prefrontal regions. Furthermore, the model effectively captured the receptive field mapping and the hierarchical structure of visual coding, utilizing both spatial and layer attention mechanisms.

References

1. Allen, E. J., St-Yves, G., Wu, Y., Breedlove, J. L., Prince, J. S., Dowdle, L. T., ... & Kay, K. (2022), A massive 7T fMRI dataset to bridge cognitive neuroscience and artificial intelligence. Nature neuroscience, 25(1), 116-126.
2. Prince, J. S., Charest, I., Kurzawski, J. W., Pyles, J. A., Tarr, M. J., & Kay, K. N. (2022). Improving the accuracy of single-trial fMRI response estimates using GLMsingle. Elife, 11, e77599.
3. Lin, T. Y., Maire, M., Belongie, S., Hays, J., Perona, P., Ramanan, D., ... & Zitnick, C. L. (2014), Microsoft coco: Common objects in context. In Computer Vision–ECCV 2014: 13th European Conference, Zurich, Switzerland, September 6-12, 2014, Proceedings, Part V 13 (pp. 740-755). Springer International Publishing.
4. Fu, S., Tamir, N., Sundaram, S., Chai, L., Zhang, R., Dekel, T., & Isola, P. (2023), DreamSim: Learning New Dimensions of Human Visual Similarity using Synthetic Data. arXiv preprint arXiv:2306.09344.

Poster No 1484

Head motion does not drive success of dynamical classification approaches for fMRI

Grace Huckins[1], David Glahn[2], Russell Poldrack[3]

[1]Stanford University, Stanford, CA, [2]Department of Psychiatry, Harvard Medical School, Boston, MA, [3]Stanford University, Palo Alto, CA

Introduction: Historically, analysis of resting-state fMRI has largely focused on static measures like functional connectivity. In contrast, dynamical approaches remain underexplored, but they do present challenges. In particular, head motion in the scanner introduces artifacts that can exert a strong effect on the results of analyses[3], but throwing out high-motion volumes would disrupt the dynamical structure of the data. In work presented at OHBM 2023, we demonstrated that a dynamical, hidden Markov model-based approach can successfully classify resting-state fMRI data and achieve higher accuracy than static approaches. Those previous analyses, however, did not account for the fact that head motion differences may have been driving classification performance. In the current study, we establish that the success of dynamical classification methods is not driven by head motion artifacts. Additionally, we apply our dynamical classification approach to a problem where head motion is a particular concern: classifying resting-state fMRI data according to psychiatric diagnosis.

Methods: All of the experiments in this study used the same HMM-based dynamical classification approach, which is detailed in Figure 1. For the first portion of this study, we used data from the MyConnectome dataset, which includes dozens of resting-state scans from a single individual. Data were preprocessed as in[1]. We previously demonstrated that dynamical classification can distinguish runs where the subject had and had not ingested caffeine; for that study, high-motion volumes were censored and censored volumes were reconstructed using linear interpolation. To test the impact of interpolation on model performance, we generated two versions of the MyConnectome data-one containing only the continuous sequences of low head-motion volumes, and the other containing interpolated sequences. Dynamical classification performance was evaluated using the SSM Python package. The second portion of this study used a dataset including individuals with and without a diagnosis of psychosis[2]. Data were preprocessed using fMRIPrep and XCP_D, and high-motion volumes were removed and reconstructed using linear interpolation. Dynamical classification of the psychosis data was performed using the Dynamax Python package, which implements the same models as the SSM packing using Jax and is therefore significantly faster (but cannot handle ragged sequences).

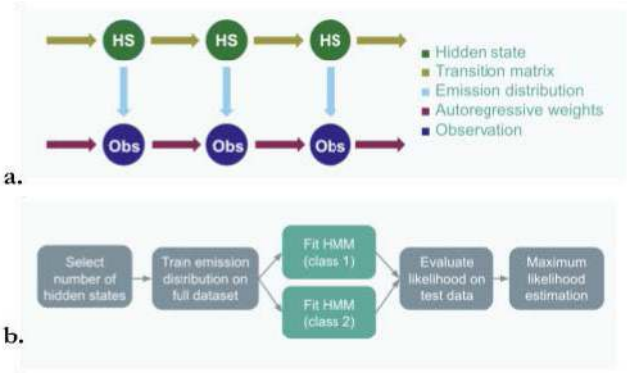

Figure 1: The classification approach. **a.** A graphical representation of the hidden Markov models used throughout this study. Models with a Gaussian emission distribution simply lack the burgundy autoregressive weights. **b.** The classification scheme. Emission distributions and autoregressive weights were first fit on the entire dataset; then, transition matrices were fine-tuned for each of the two classes of the training data. Labels were assigned to test data based on the hidden Markov model under which the data had the highest log likelihood.

Results: As shown in Fig 2a, linear interpolation over censored volumes appears to have had no effect on classification performance. Across a wide range of hidden states, MyConnectome classification performance was virtually identical, whether or not head motion had been fully censored or subject to interpolation. In both cases, performance was significantly higher than the chance level of 50%, despite the fact that the amount of data had been significantly limited by censoring high-motion volumes. In contrast, Fig 2b demonstrates that neither the dynamical classification approach nor a baseline approach, which applied linear SVM to functional connectivity matrices, was able to achieve above-chance performance in distinguishing individuals with psychosis from healthy controls.

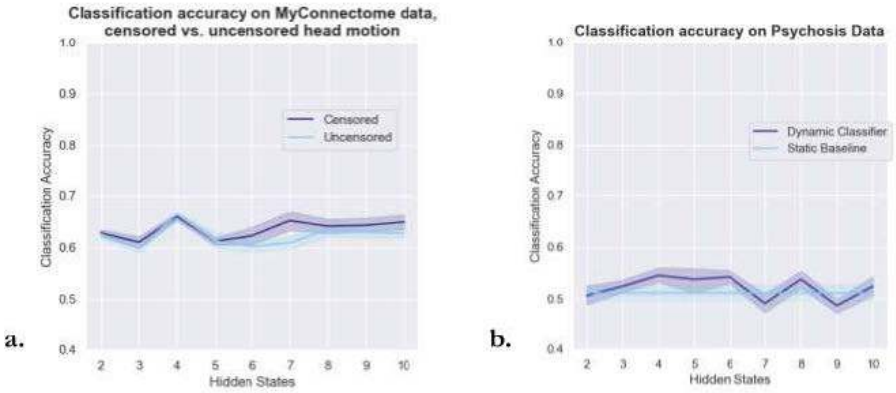

Figure 2: **a.** Classification results for the head motion analysis. For both the censored and uncensored datasets, a diagonal Gaussian emission model was used. **b.** Classification results for the psychosis dataset. The dynamic classifier used had an autoregressive emission model; the static baseline model was a support vector machine applied to the functional connectivity matrices from each participant.

Conclusions: This study shows that the success of dynamical classification on MyConnectome rsfMRI data is not driven by differences in head motion between classes. Completely eliminating high head motion volumes from the dataset had no effect on classification performance. This HMM-based classification strategy is thus a robust and effective method for classifying rsfMRI data, and its high performance indicates that examining whole-brain dynamics in resting-state data may be a fruitful path forward for the field.Additionally, the fact that the dynamical approach was unable to distinguish two groups who differed in their head motion frequency (people with psychosis and healthy controls) provides further evidence that the success of dynamical classification is not driven by head motion.

References

1. Lauman, T.O. (2015), "Functional System and Areal Organization of a Highly Sampled Individual Human Brain," Neuron, vol. 87, no. 3, pp. 657-70.
2. Rodrigue, A.L. (2021), "Searching for Imaging Biomarkers of Psychotic Dysconnectivity," Biological Psychiatry: Cognitive Neuroscience and Neuroimaging, vol. 6, no. 12, 1135-1144.
3. Van Dijk, K.R.A. (2012), "The influence of head motion on intrinsic functional connectivity MRI," NeuroImage, vol. 59, no. 1, pp. 431-438.

Poster No 1485

Thumbs up or down: Simple quality assessment tool for physiological signals

Roza Bayrak[1], Richard Song[1], Ruogi Yang[1], Catie Chang[1]

[1]*Vanderbilt University, Nashville, TN*

Introduction: Functional MRI measures the BOLD signal as a proxy for neural activity. The BOLD signal is based on changes in blood oxygenation, and therefore is modulated by peripheral physiological factors such as breathing and heart rate in addition to neural activity. While traditionally regarded as noise, systemic physiological processes are frequently shown to be linked with cognitive processes and may contribute valuable information to fMRI studies. Recognizing this, neuroimaging research increasingly draws upon concurrent recordings of peripheral physiology to enhance fMRI analysis. However, the usefulness of physiological data is contingent upon the quality of the recordings as well as expertise in data handling, which can vary significantly. To address this critical gap, we devised a simple tool for assessing the quality of peripheral physiological recordings. This deep-learning based tool not only ensures data integrity but could describe data quality issues and suggest steps for fixing the data, thereby promising to improve the accuracy and reliability of downstream research. The code and data used in this abstract are publicly available.

Methods: Classification Tool: A simple classification pipeline is developed to assess the quality of raw physiological measures (Fig. 1, left), focusing on respiration and cardiac waveforms. Here, we use the data from the HCP Young Adult cohort. Physiological signals in this dataset were collected using a pulse oximeter and a respiration belt, sampled at 400 Hz. These raw waveforms were downsampled by a factor of 4, temporally normalized (zero mean, unit variance) and provided to the neural networks. The network is composed of stacked 1D CNNs (Convolutional Neural Networks) with decreasing feature map sizes at each layer. The models are trained using a learning rate of 0.0001 and a batch size of 2, employing Adam as the optimizer and binary cross-entropy as the loss function. The dataset is divided into training and test sets, employing rotating

partitions in a 5-fold cross-validation framework. To prevent overfitting, an early stopping criterion is applied based on the performance on the validation set. Link to repo: github.com/neurdylab/physio_qa_dl Annotation Tool: To train our supervised neural networks, we labeled the physiological signals using an in-house annotation tool (github.com/neurdylab/physio_qa_manual), consisting of a matlab-based GUI that enables fast annotations of physiological signals. The tool (1) takes in raw recordings, (2) passes them through initial quality checkpoints (i.e. detecting empty files, clipping), (3) plots full length raw time series, and finally (4) provides the rater (annotater) with visual information for quality inspection and annotation (Fig 1, right). Since manual annotations are cumbersome, we aim to build a fully automated quality assurance method. However, manually assessing the quality of labels is vital in this initial stage to ensure the accuracy of our models.

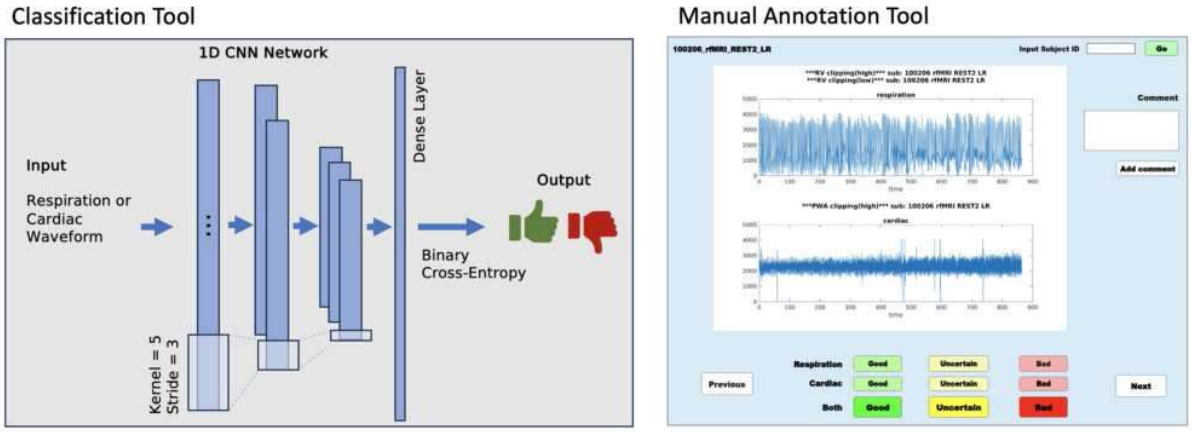

Results: The models were able to classify the quality of respiration data with 83.35 ± 1.01% and cardiac data with 88.49 ± 1.42% accuracy.

Conclusions: Here, we provide a simple thumbs up / thumbs down tool that can save several hours of manually vetting physiological recordings. While the current study focuses on respiration and cardiac data, the CNN models may in the future be easily trained to handle different physiological metrics, such as eye tracking and end-tidal CO2. We envision that in future iterations, the tool can be further developed by adding new modules to (1) generate text-based reports detailing specific reasons for why the quality check for a given recording has failed and whether it is fixable (e.g., if a recording is partly usable, or if a simple interpolation algorithm could fix the problem), (2) provide suggestions for fixing the data, and (3) apply the suggested fix and return the corrected data.

Poster No 1486

Unraveling Alzheimer's Disease Heterogeneity: A Comparative Analysis Using HYDRA and CHIMERA

Zhaoqi An[1], Aristeidis Sotiras[2], Brian Gordon[3]

[1]Washington University in St. Louis, Saint Louis, MO, [2]Washington University in St Louis, St Louis, MO, [3]Washington University School of Medicine, Saint Louis, MO

Introduction: Alzheimer's Disease can present with heterogenous neurodegenerative patterns. In order to optimize clinical trials and personalized medicine, the identification and characterization of diverse pathological brain patterns associated with AD have become paramount. Optimal approaches to identify such heterogeneity are unknown.

Methods: The present study employed two distinct clustering approaches, namely HYDRA and CHIMERA, to delineate the spatial pattern of brain atrophy attributable to AD. Methods were applied to MRI scans from the Open Access Series of Imaging Studies (OASIS-4) project. HYDRA uses a convex polytope formed by multiple linear hyperplanes that correspond to various pathological patterns, capturing disease subtypes. CHIMERA assesses the pathological transition by transforming NC distribution to separate transformations matching the disease distribution. While both identify spatial patterns, the distinction lies in HYDRA's discriminative analysis of disease subtypes and CHIMERA's generative nature on disease progression through distribution matching.

Results: Both approaches identified two patterns, or subtypes (Figure 1) with similar CDR results (Figure 2). Preliminary analyses revealed distinct spatial patterns of brain atrophy associated with AD subtypes. The patterns, illustrated in Figure 1, showcase fluctuating regions of atrophy in volumes across the brain. All subtypes demonstrate marked atrophy within the medial temporal areas, notably the hippocampus. Disparities are evident when assessing subtypes: Subtype-2 across both

methods shows pronounced variations in regions such as superior frontal, middle temporal, parietal cortex, and precuneus, areas paramount in AD pathology. Conversely, HYDRA's Subtype-1 highlights subtle differences in temporal cortex relative to its Subtype-2. CHIMERA's Subtype-1, while mirroring its Subtype-2 pattern, is less intensified, suggesting an earlier AD stage. Collectively, these patterns concur with recognized AD neuropathological trajectories, pinpointing regions initially impacted in progression. In addition, an in-depth exploration of subsequent analysis including a longitudinal data evaluation to observe the progression of these patterns over time and the amyloid biomarker's role and its correlation with the identified patterns is slated for later investigation.

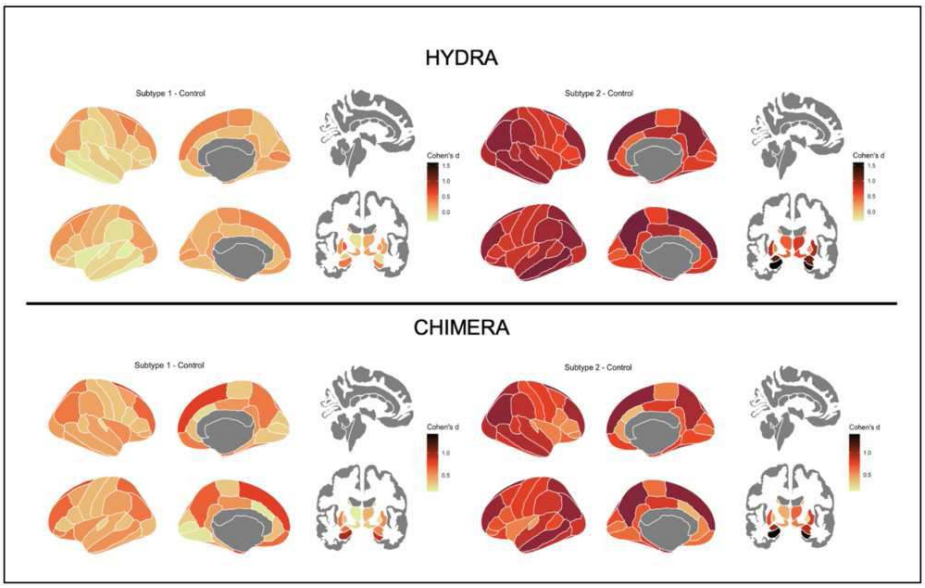

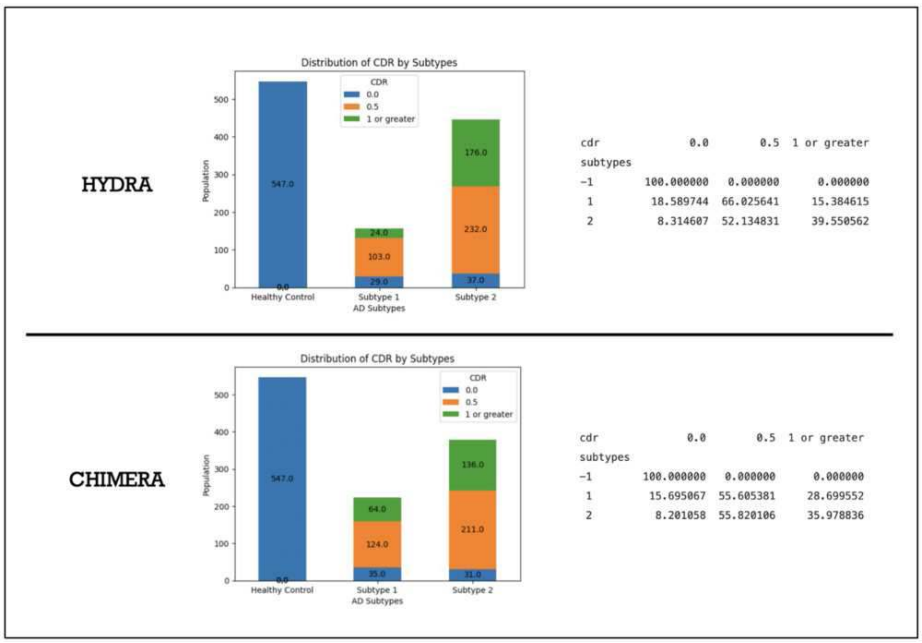

Conclusions: Our findings demonstrate data-driven approaches to derive clinically meaningful patterns of neurodegeneration. A parallel evaluation of both approaches accentuates the robustness of clustering techniques, revealing consistent and overlapping insights into the intricate pathological landscapes of AD. This convergence in findings bolsters confidence in the reliability of such analytical tools in AD research.

References

1. Varol, E. (2017), 'HYDRA: Revealing heterogeneity of imaging and genetic patterns through a multiple max-margin discriminative analysis framework', NeuroImage, 145(Pt B), 346–364.
2. Dong, A.(2016), 'CHIMERA: Clustering of Heterogeneous Disease Effects via Distribution Matching of Imaging Patterns', IEEE transactions on medical imaging, 35(2), 612–621.

Poster No 1487

Situating edge time series within the generalized linear model framework

Richard Betzel[1], Haily Merritt[1], Amanda Mejia[1]

[1]*Indiana University, Bloomington, IN*

Introduction: Functional connectivity (FC) is typically modeled as a linear correlation between time courses recorded at distinct locations in the brain. Recent work has shown that static FC can be transformed into "edge time series" (eTS; Figure 1a), revealing framewise fluctuations in connections' weights (Zamani Esfahlani et al 2020; Figure 1b). To date, eTS have largely been interpreted in terms of time-varying FC. Here, however, we show that eTS can also be interpreted through a statistical lens. Namely, the derivation of the eTS between regions i and j is identical to the interaction term in a standard linear model (Figure 1c). Here, we exploit this link to build linear models in which we explain time-varying behavior using both activations and edge time series (their interaction). For this abstract, we focus on calcium imaging recordings made in larval zebrafish (Chen et al 2018).

Methods: Consider the z-scored activity time series from region i, zi. We can calculate the edge time series between regions i and j as rij = zi*zj, where * denotes element-wise multiplication. The element rij(t)=zi(t)zj(t) corresponds to the instantaneous co-fluctuation between regions i and j at time t. In statistics, it is common to explain a variable y as a linear combination of predictors x1, x2, x3, and so on. It is also common to include interactions between predictors as x1*x2. Note that if x1 and x2 are z-scored, then the interaction between predictors 1 and 2 is calculated identically to their eTS. Here, we models of the following form to explain some time-varying behavior, y: y = βizi + βjzj + βijzi*zj + β0 + ε. We fit models of this type for every pair of regions, ij, and calculate t-statistics for each regression coefficient, including βij. If we find that βij is statistically significant, i.e. that there is a significant interaction between i and j, then we can also conclude that the time-varying edge between i and j--the edge time series--carries unique explanatory power not carried by the activities of regions i and j alone. We applied this framework to calcium imaging recordings of N=18 larval zebrafish. Neurons were assigned to one of 164± 39 parcels (defined at the single-subject level and were functionally homogeneous and spatially co-localized) and mean time courses derived for each parcel. Though unable to move freely, the animals engaged in fictive spontaneous behavior, including swimming (left/turns turns and forward movements decoded from motor neuron outputs) and eye movements.

Results: Across animals, we found robust evidence that eTS explained time-varying behavior at a level above and beyond that of activations alone (see Figure 2 for results from a representative animal). We found that, across behavioral measures, 24.4%±21.3% of edges exhibited statistically significant effects (FDR corrected at q=0.01; mean adjusted p-value of 0.0025). We found evidence supporting the hypothesis that the same or similar sets of edges are significantly associated with multiple distinct behavioral measures and that significant edges share a common neuroanatomical substrate, favoring the rhombencephalon.

Conclusions: In summary, our findings suggest that edges, above and beyond activations alone, carry meaningful information about time-varying behavioral measures. These findings suggest that dynamic coupling between groups of neurons--rather than reflecting stochastic fluctuations--may be neurobiologically meaningful and challenge the view that FC is purely time-invariant.

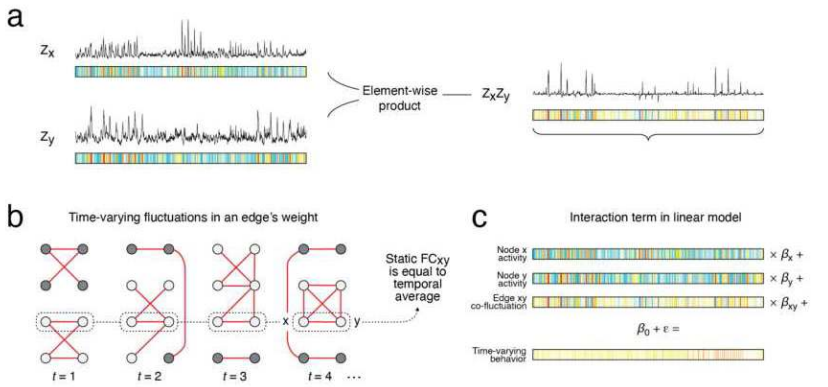

Figure 1. (a) Edge time series are calculated by z-scoring two activation time series, shown here for regions x and y, and calculating their element-wise product. (b) Historically, the edge time time series has been interpreted as a measure of time-varying connectivity, with the additional caveat that the edge time series is also an exact temporal decomposition of FC (its mean across time is equal to FC). (c) However, we can also interpret edge time series in the context of linear models. Namely, edge time series are calculated identically to the "interaction term," thereby placing edge time series on firmer theoretical ground.

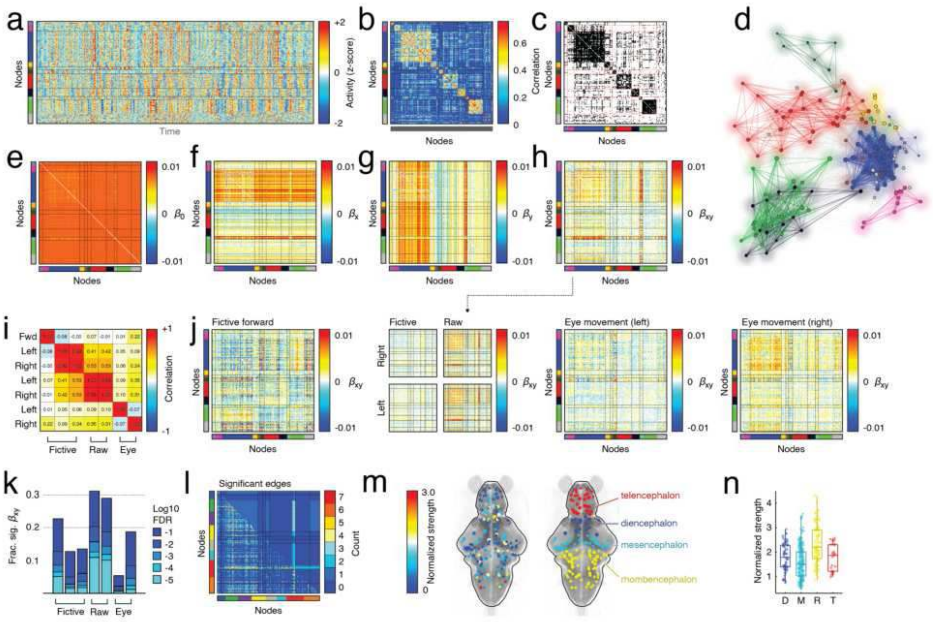

Figure 2. Application of edge time series data to representative zebrafish. (a) Activity time series from a single animal. All time series are z-scored. (b) Unthresholded correlation matrix. (c) Thresholded correlation matrix. (d) Force directed layout of thresholded network; node color corresponds to module label. Panels e-h show regression coefficients for single task (raw right turns). Panel h shows the interaction term, i.e. the coefficients fit to edge time series. (i) Correlation of interaction term matrices across measures. (j) All interaction term matrices. (k) Fraction of edges (interactions) that were significant at varying statistical cutoffs. (l) Number of behavioral measures for which each edge was statistically significant. (m) Mean number of statistically significant behaviors associated with edges incident upon nodes. (n) Mean values aggregated by anatomical division (D = diencephalon; M = mesencephalon; R = rhombencephalon; T = telencephalon).

References

1. Zamani Esfahlani, F., Jo, Y., Faskowitz, J., Byrge, L., Kennedy, D. P., Sporns, O., & Betzel, R. F. (2020). High-amplitude cofluctuations in cortical activity drive functional connectivity. Proceedings of the National Academy of Sciences, 117(45), 28393-28401.
2. Chen, X., Mu, Y., Hu, Y., Kuan, A. T., Nikitchenko, M., Randlett, O., ... & Ahrens, M. B. (2018). Brain-wide organization of neuronal activity and convergent sensorimotor transformations in larval zebrafish. Neuron, 100(4), 876-890.

Poster No 1488

Dynamic Modulation of Information Flow from Occipitotemporal Cortex According to Cognitive Demands

Vicky He[1,2], Bahman Tahayori[1], David Vaughan[1,2], Graeme Jackson[1,2], David Abbott[1,2], Chris Tailby[1,2], for the Australian Epilepsy Project Investigators[1]

[1]The Florey Institute of Neuroscience and Mental Health, Melbourne, Australia, [2]University of Melbourne, Melbourne, Australia

Introduction: Neurobiological models of cognition hold that the degree to which information flows between different brain areas is modulated as a function of cognitive demands (Park and Friston 2013). Psychophysiological interaction analysis (PPI) is a regression-based method for evaluating such modulations in functional magnetic resonance imaging (fMRI) data (Friston et al. 1997). Here we applied PPI to investigate the task dependent modulation of connectivity from the ventral occipitotemporal cortex (vOT, also known as the Visual Word Form Area) during execution of a language task (pseudoword rhyming) versus a visuospatial task. We hypothesised that there will be reweighting of information flow from vOT according to task demand. More specifically, the vOT will interact more strongly with perisylvian language areas during pseudoword rhyming than during visual pattern matching.

Methods: Ninety-four Australian Epilepsy Project (AEP) participants completed a block design fMRI task contrasting rhyming blocks (whether two visually presented pseudowords would rhyme if pronounced aloud) against pattern matching blocks (whether two patterns composed of forward and backslashes matched). First level analysis was applied using the iBrain Toolbox (Abbott and Jackson 2001) with SPM12 (Ashburner et al. 2021). The PPI regression includes the main effect of task, the main effect of the seed (vOT) time course, the interaction between the two, and nuisance regressors. The PPI was

implemented using the gPPI (generalised PPI) toolbox (McLaren et al. 2012), which incorporates a deconvolution procedure in forming the interaction (Gitelman et al. 2003). Given some debate around whether mean centring the task regressor in the interaction term is necessary (see Di, Reynolds, and Biswal 2017; 'NITRC: Generalized PPI Toolbox: Task Time Course Not Mean-Centered' n.d.) we modified the code in the toolbox to carry out PPI both with and without (default setting) mean-centring. Finally, we carried out a systematic search on papers that used PPI from 2018 to 2022 to examine whether mean-centring has become the standard in the field.

Results: Figure 1a shows the SPM-t map of the group level analysis on the interaction term with recommended mean-centring. As hypothesised, the vOT connects more strongly with classical language areas (left inferior frontal gyrus and superior temporal sulcus) during the rhyming task. On the other hand, there is greater connectivity between the vOT and the right intraparietal sulcus in the visuospatial task. Figure 1b shows the results without mean-centring, where there is extensive interaction with a peak at the seed location. This indicates a misspecification of the model, as the seed should not appear significant in the interaction (because the main effect of the seed is already included in the regression). Through the systematic search, we found that most papers do not include sufficient information about how the PPI model is implemented, with a number of published figures showing interaction effects within the seed region suggesting model misspecification.

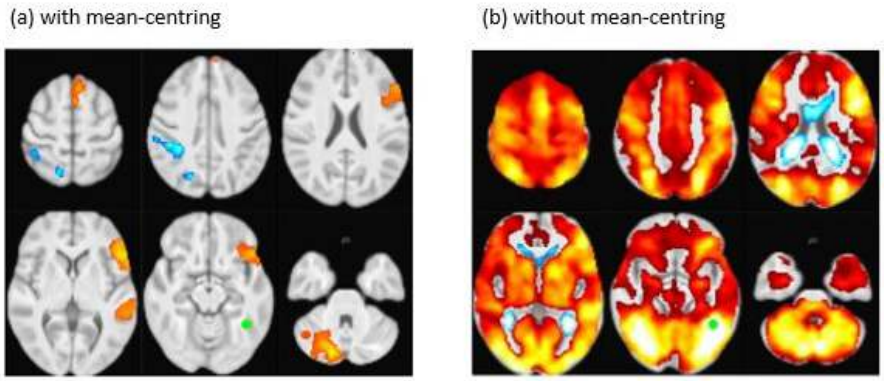

Figure 1. One sample t-test showing positive interactions (hot colours) and negative interactions (cool colours). vOT seed location shown in green. Left hemisphere on the right side. FWE cluster correct $p < 0.025$ for each t-test (positive and negative interactions). (a) Results obtained with mean-centring the task regressor, confirming hypothesised dynamic modulation of regional interactions with the seed. (b) Results obtained without mean-centring, showing widespread spurious interactions including with the seed itself, confirming the model is misspecified.

Conclusions: Our findings utilising the mean-centred PPI method are consistent with the idea of dynamic modulation of information flow according to cognitive demands (Park and Friston 2013). Using comparable visual stimuli as input, connectivity from left vOT was increased to key language areas during a linguistic task, but to visuospatial processing areas of the right hemisphere during visuospatial judgments. These findings are consistent with models of the reading system (Sandak et al. 2004) and language (Hickok and Poeppel 2007). Furthermore, we support the observations of Di and colleagues (Di, Reynolds, and Biswal 2017), that with deconvolution, it is essential for the task regressor to be mean centred to avoid spurious results.

References

1. Abbott D.F. (2011), 'The iBrain(TM) Analysis Toolbox for SPM', Proceedings of the 17th Annual Meeting of the Organisation for Human Brain Mapping, Quebec City, Canada. 364 WTh [See also https://florey.edu.au/iBrain]
2. Ashburner, J. (2021), 'SPM12 Manual', October
3. Di, X. (2017), 'Imperfect (de)Convolution May Introduce Spurious Psychophysiological Interactions and How to Avoid It', Human Brain Mapping, vol. 38, no. 4, pp. 1723-1740
4. Friston, K. J. (1997), 'Psychophysiological and Modulatory Interactions in Neuroimaging', NeuroImage, vol. 6, no. 3, pp. 218-229
5. Gitelman, D.R. (2003), 'Modeling Regional and Psychophysiologic Interactions in fMRI: The Importance of Hemodynamic Deconvolution', NeuroImage, vol. 19, no. 1, pp. 200-207
6. Hickok, G. (2007), 'The Cortical Organization of Speech Processing', Nature Reviews Neuroscience, vol. 8, no. 5, pp. 393-402
7. 'JISCMail - SPM Archives'. n.d. Accessed 7 November 2023. https://www.jiscmail.ac.uk/cgi-bin/webadmin?A2=spm;ddcb0ac1.1403
8. McLaren, D.G. (2012), 'A Generalized Form of Context-Dependent Psychophysiological Interactions (gPPI): A Comparison to Standard Approaches', NeuroImage, vol. 61, no. 4, pp. 1277-1286
9. Park, H. (2013), 'Structural and Functional Brain Networks: From Connections to Cognition', Science, vol. 342, no. 6158, pp. 1238411
10. Sandak, R.W. (2004), 'The Neurobiological Basis of Skilled and Impaired Reading: Recent Findings and New Directions', Scientific Studies of Reading, vol. 8, no. 3, pp. 273-292

Poster No 1489

A Connectome Generative Model with Dynamic Axon Growth

Yuanzhe Liu[1], Caio Seguin[2], Richard Betzel[3], Danyal Akarca[4], Maria Di Biase[1], Andrew Zalesky[1]

[1]The University of Melbourne, Melbourne, Victoria, [2]Department of Psychological and Brain Sciences, Indiana University, Bloomington, IN, [3]Indiana University, Bloomington, IN, [4]University of Cambridge, Cambridge, England

Introduction: Connectome generative models provide insight into the wiring mechanisms underpinning connectome topology[1,2]. However, current generative models do not account for the dynamics of axonal growth, limiting their biological interpretability. The aims of this study are threefold: i) to build a connectome generative model that incorporates dynamic axon growth, ii) to develop a method that optimizes model parameters for individual connectomes, and iii) to test if the model can generate brain-like networks and white matter fiber bundles.

Methods: The cerebral volume is modelled as a 2D circle, with the circumference and the internal space representing brain gray and white matter, respectively. The circumference is randomly parcellated to represent the 84 regions in Desikan-Killiany atlas, otherwise known as nodes (Fig. 1a). Simulated axons are uniformly seeded at random along the circumference. Each axon propagates step-by-step within the circle, and the direction of propagation is dynamically updated based on a combined attractive force exerted by each node (Fig. 1a-1b). The attractive forces represent axon guiding cues that decay as a function of distance between the node exerting the force and the axon's growth tip. An axon terminates when its tip encounters the circle circumference, forming a connection between its origin and intersection with the circle (Fig. 1c). Generated networks are constructed by counting the number of axons interconnecting each pair of nodes (Fig. 1d-1e). Two key model parameters control network topology: The force decay parameter β, and the axon growth length of each extending step L. Using an extensive grid search, we first examined how generated network topology, in terms of small-worldness and modularity, varied with respect to parameters. Next, we mapped structural connectomes for 1064 participants of the Human Connectome Project (HCP) and fitted model parameters to individual connectomes by minimizing the difference in above-mentioned topological measures, between empirical and generated networks. Finally, we generated networks with fitted parameters and tested if the generated networks recapitulate connectomic properties that the parameters were not optimized for.

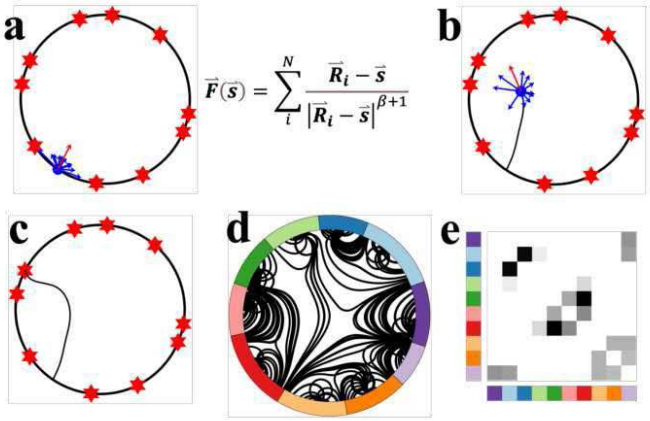

Figure 1.An illustrative example of the generative process governing axonal growth and network formation. a) The model is formulated on a circle, with the circumference and the internal space representing brain gray and white matter, respectively. Node centers (red hexagram) are randomly sampled on the circumference to parcellate the circumference into regions. This example parcellates 10 nodes for an illustrative purpose, where we use 84 nodes in the study to match the number of brain regions in Desikan-Killiany atlas. An example axon (blue dot) is randomly seeded on the circumference, perceiving attractive force from all nodes (blue arrows) and propagating in the direction of the net force (red arrow). The force $\vec{F}$ that an axon tip located at position $\vec{s}$ perceived is computed according to the function, where N is the total number of nodes, R_i stands for the coordinate of node i, and β controls for the power-law decay of attractive force as a function of the distance between the axon's tip and each node. **b)** The axon propagates in a step-by-step manner. The attractive force experienced by the axon tip is updated at each propagation step to ensure nodes becoming closer to the tip exert greater force, while nodes becoming further from the tip exert less force. As a result, the axon gradually steers its path during the propagation. **c)** The simulated axon forms a connection when its tip reaches a point on the circular circumference. **d)** Multiple axons are generated, giving rise to structures resembling axonal fiber bundles. Both endpoints of axons are assigned to the nearest node (colored patches) to construct a network. **e)** The generated network is represented using a weighted, undirected connectivity matrix.

Results: Within the parameter space evaluated, generated networks were consistently characterized by a small-world and modular organization. Despite this, variations in model parameters altered the strengths of small-worldness and modularity in a continuous manner, such that increasing β and/or decreasing L resulted in stronger clustering and small-worldness, longer characteristic path length, and weaker modularity. By minimizing the small-world and modular disparity between empirical and generated networks, we optimized model parameters of connectomes mapped for HCP participants (Fig. 2a). The networks generated with our model not only displayed brain-like small-worldness and modularity, but also recapitulated several properties characterizing empirical connectomes that the parameters were not optimized for (Fig. 2b). Specifically, generated networks showed realistic axonal fascicle structures (i.e. short-range U-fibers and long-range bundles), negatively correlated connection weight and distance[5,7], strong long-range connections that deviated from the exponential distance rule[6], lognormally distributed connection weights[5], and scale-free degree distributions[3,4].

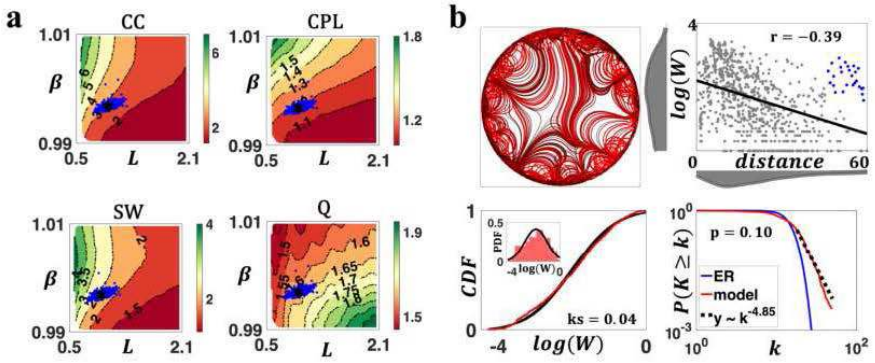

Figure 2. The model recapitulates a diverse array of topological features characteristic of nervous systems. a) The model generated small-world and modular networks. Contour plots displayed the weighted network average clustering coefficient (CC), characteristic path length (CPL), small-worldness (SW), and modularity (Q) of generated networks. All measures were normalized to the null networks, such that a value larger than 1 means the property is stronger in model networks. Blue dots represented the model parameters fitted to 1,064 HCP individual connectomes that quantitatively minimized the small-world and modular disparity between empirical and generated networks. The black hexagram represented the group average parameters for the HCP population. **b)** The group average parameters generated networks with connectomic properties that they were not optimized for. **Top left** – Realistic axonal projections resembling U-fibers and white-matter fascicles. Each curve represented the axonal trajectory connecting a pair of nodes and was color-coded using a black-red spectrum (red representing stronger connections). Axonal projections were organized into bundles at a distance from their origins and were defasciculated before reaching their targets. **Top right** – Negative associations between connection weights (W) and Euclidean distances between nodes, displayed in a scatter plot with histograms. Blue dots represented strong long-range connections that deviated from the exponential distance rule (EDR, which stipulates that the connection weights change as an exponential function of Euclidean distances). **Bottom left** – Lognormally distributed connection weights. Connection weights spanned four orders of magnitude and were best described as a lognormal distribution. The main figure and inset displayed the cumulative density function (CDF) and probability density function (PDF) of the connection weight distribution (red) and fitted lognormal distribution (black), respectively. The lognormal fit had a Kolmogorov-Smirnov (KS) statistic of 0.04 (average across 50 generated networks), significantly smaller than alternative fits (gamma, normal, and exponential distributions, all $p<0.05$). **Bottom right** – Degree (k) distributions in generated network (model, red), compared to Erdos Renyl random networks (ER, blue), and scale-free fit (black dotted line). The significance of scale-free was evaluated using the method developed by Clauset et al. (2009). In brief, a population of networks were considered scale-free if their median p-value given by the test was larger than or equal to 0.1. The median p-value in 1,000 networks generated by our model (with HCP average parameters; 300 nodes were used to avoid bias caused by finite network size) was marginally above the threshold, thus scale-free was deemed plausible.

Conclusions: The present study developed a connectome generative model that features dynamic axon outgrowth. The model recapitulated a diverse array of topological features characteristic of nervous systems, at the connection, node, and network levels. A parameter inference approach was proposed, enabling parameter optimization for individual connectomes. Overall, our work enables generation of connectomes in silico that are weighted, spatially embedded, and feature axonal trajectories that appear biologically realistic.

References

1. Akarca, D. (2023). "A weighted generative model of the human connectome." bioRxiv: 2023.2006. 2023.546237.
2. Betzel, R. F. (2016). "Generative models of the human connectome." Neuroimage 124: 1054-1064.
3. Broido, A. D. (2019). "Scale-free networks are rare." Nature communications 10(1): 1017.
4. Clauset, A. (2009). "Power-law distributions in empirical data." SIAM review 51(4): 661-703.
5. Ercsey-Ravasz, M. (2013). "A predictive network model of cerebral cortical connectivity based on a distance rule." Neuron 80(1): 184-197.
6. Roberts, J. A. (2016). "The contribution of geometry to the human connectome." Neuroimage 124: 379-393.
7. Song, H. F. (2014). "Spatial embedding of structural similarity in the cerebral cortex." Proceedings of the National Academy of Sciences 111(46): 16580-16585.

Poster No 1490

Can function be predicted from structure at individual level?

Lars Smolders[1,2], Wouter De Baene[3], Geert-Jan Rutten[1], Remco Hofstad[2], Luc Florack[2]

[1]Elisabeth-Tweesteden Hospital, Tilburg, Netherlands, [2]Eindhoven University of Technology, Eindhoven, Netherlands, [3]Tilburg University, Tilburg, Netherlands

Introduction: Understanding how anatomical connections give rise to functional interactions in the brain is a major goal in neuroscience. These ideas have been conceptualized in terms of networks of connections between Regions Of Interest (ROIs), where anatomical white-matter connections are represented by Structural Connectivity (SC) and functional interactions by Functional Connectivity (FC). Recently, several studies have attempted predicting FC from SC at individual level using machine learning methods. If successful, this could have significant benefits for clinical applications. Three such studies (Benkarim et al., 2022; Neudorf et al., 2022; Sarwar et al., 2021) show promising results on large data sets, making them attractive for further development. We examined these studies in detail, to determine whether the models indeed represent meaningful individual-level mappings of SC to FC.

Methods: See Figure 1 for a summary. On the data set used in the three studies, comprising MRI images of 1000 Human Connectome Project (HCP) subjects, we calculated SC and empirical FC (eFC) in the same way as Sarwar et al. Briefly, we calculated SC as the streamline count from whole-brain tractography on diffusion-weighted MRI between each ROI pair and calculated FC as the Pearson correlation coefficient between the resting-state fMRI activity of each ROI pair. We used ROIs from the Desikan-Killiany and Schaefer 200 parcel atlas. Using a 10-fold cross-validation workflow, we compared the performance of the presented models to the group average eFC of each training fold (avg-eFC) and to avg-eFC with random noise added to artificially introduce inter-individual differences. We also reproduced analyses demonstrating additional usefulness of predicted FC (pFC) from the authors' models: predicting cognitive performance from pFC (Sarwar et al., 2021), analyzing predictive power of pFC for network centrality measures in eFC (Neudorf et al., 2022) and analyzing differences in performance across Yeo's 7 networks (Benkarim et al., 2022).

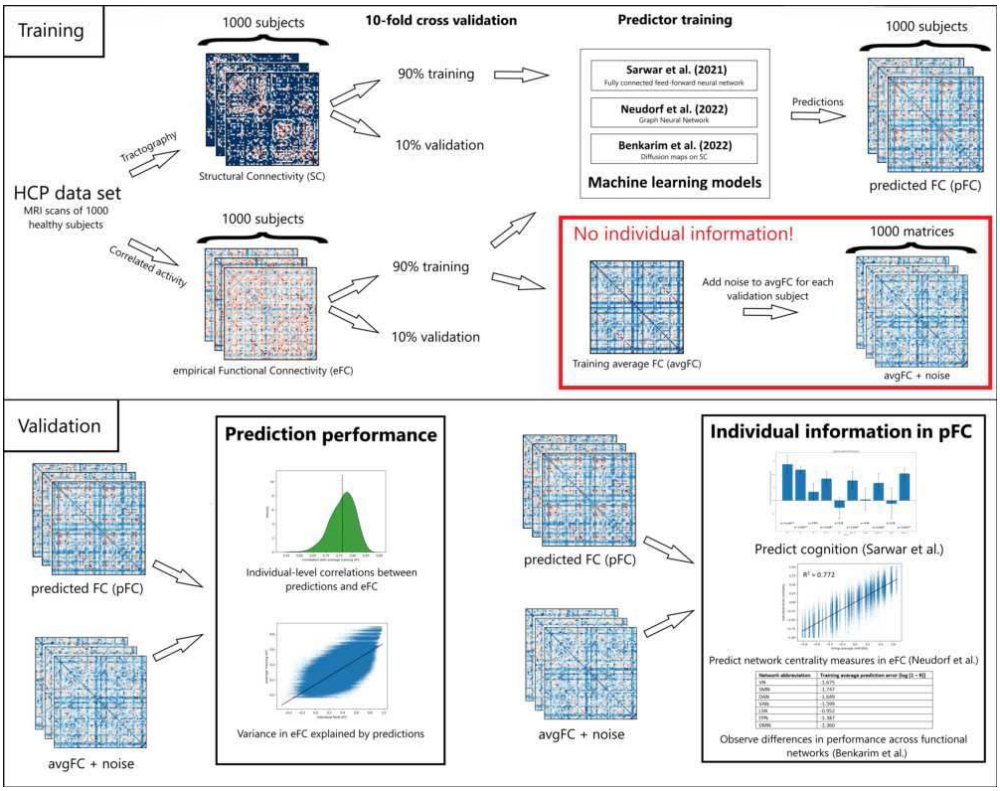

Results: Sarwar et al. reported (on Supplementary data) an average individual-level eFC-pFC correlation of 0.7 and showed that pFC was not a group average by reporting an average inter-pFC correlation of 0.7. These values were reproduced by avg-eFC plus noise tuned to 0.1 standard deviation (Figure 2a). A correlation between predicted and actual cognitive score of 0.29 using pFC with SC regressed out was presented. When reproduced by us, we found a correlation of 0.19. Avg-eFC plus noise with SC regressed out achieved a correlation of 0.20. Neudorf et al. showed that pFC explained 56% of variance in eFC at individual level. Avg-eFC explained 55% of variance (Figure 2b). They also showed that centrality measures of pFC explain

81%, 55% and 55% of variance in degree, eigenvector and PageRank centrality respectively. However, Avg-eFC explains 77%, 76% and 77% of variance in these measures. Benkarim et al. presented an average individual-level eFC-pFC correlation of 0.775. Avg-eFC achieved 0.762 (Figure 2c). Finally, differences in performance found by Benkarim et al., i.e. lower performance in default, frontoparietal and limbic networks, were also reproduced by avg-eFC.

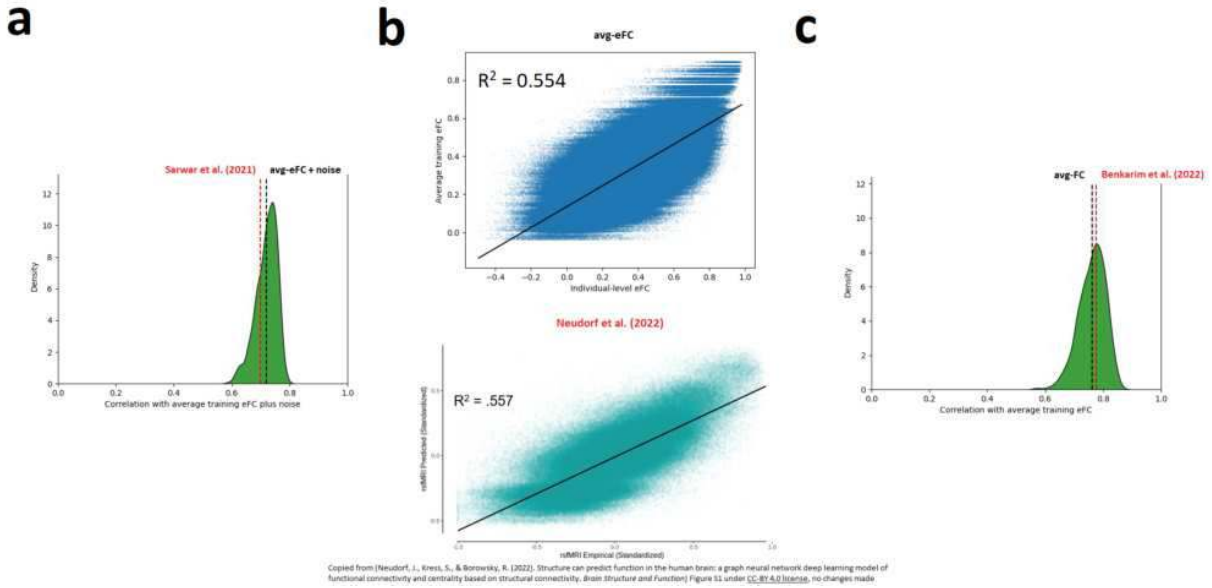

Figure 2: comparison of results from the group average training eFC with the results of a) Sarwar et al. b) Neudorf et al. c) Benkarim et al. Bottom plot in b) copied from Neudorf et al. (2022)

Conclusions: We conclude that we cannot ascertain that the models as presented in the three studies represent a meaningful mapping from SC to FC. Firstly, the reported predictive performances do not exceed the performance of avg-eFC. Secondly, analyses into additional usefulness were reproduced by replacing pFC with the avg-eFC plus noise. Although it appears that current methods fail to find a meaningful mapping from SC to FC, we are convinced that this line of work should be continued, taking care to ensure that trained models do not converge to the group average. We believe that taking a step back and re-assessing the construction of SC and FC may yield more informative versions of both, and thus improve the chances of finding a meaningful mapping from structure to function at individual level.

References

1. Benkarim, O. (2022), 'A Riemannian approach to predicting brain function from the structural connectome', NeuroImage, vol.257
2. Neudorf, J. (2022), 'Structure can predict function in the human brain: a graph neural network deep learning model of functional connectivity and centrality based on structural connectivity', Brain Structure and Function, vol. 227, no. 1, pp. 331-343
3. Sarwar, T. (2021), 'Structure-function coupling in the human connectome: A machine learning approach', NeuroImage, vol. 226

Poster No 1491

Does the rich club control brain state transitions? A network control theoretical investigation

Alina Podschun[1], Richard Betzel[2], Sebastian Markett[3]

[1]Humboldt-Universität zu Berlin, Berlin, Germany, [2]Indiana University, Bloomington, IN, [3]Humboldt-Universtität zu Berlin, Berlin, Germany

Introduction: The brain seamlessly transitions between functionally relevant patterns of activity, often referred to as "brain states." Extensive research indicates that the underlying dynamics of these processes are linked to the structural connectome of the brain (Cole et al., 2016). The rich club-a network comprising densely interconnected brain regions-emerges as particularly pivotal for efficient integration of information (van den Heuvel & Sporns, 2011). Disruption of its organizational integrity results in an increase in energetic cost during transitions between brain states (Betzel et al., 2016), prompting some to designate its regions as potential control centers (Gu et al., 2014). In contrast, compelling evidence also underscores the significance of peripheral, sparsely connected regions in governing control processes (Betzel et al., 2016; Senden et al., 2018). In this study, we systematically delved into the specific role played by the rich club in overseeing transitions between behaviorally constrained brain states. Leveraging a network control theoretical (NCT) framework and openly available data

from the Human Connectome Project (HCP), our investigation sought to elucidate potential control functions carried out by the rich club.

Methods: Analyses were grounded in individually reconstructed FA-weighted, undirected structural brain networks, constructed using the CATO pipeline (de Lange et al., 2023) and Lausanne sub-parcellation (219 ROI) of the Desikan Killiany atlas (Cammoun et al., 2021). Brain states were delineated using preprocessed contrasts from all seven tasks provided by the HCP. Individual rich clubs for each subject were identified based on the maximal normalized rich club coefficient (Riedel et al., 2022). On average, 21 regions (9.69%) of an individual's nodes were categorized as rich club members. The group-level rich club definition was consequently established by selecting the top-ranking 9.69% of nodes across subjects-those consistently identified as rich club members. For the analysis of brain state stability and energetic cost of brain state transitions, we applied an optimal control framework (see Braun and colleagues, 2021). Linear approximations were used to represent brain state dynamics. The rich club's control contribution was assessed by excluding group-level rich club nodes from a matrix of potential control regions, preventing them from influencing brain state dynamics. Results were compared to a spin-test-based null model (Váša et al., 2018), where a size-matched set of random nodes was excluded instead. Statistical comparisons were conducted using repeated measures ANOVA.

Results: Figure 1 shows an overview of constituent regions of the group-level rich club. When these regions were excluded from the matrix of control nodes, the impact on control metrics was significantly less pronounced compared to excluding a size-matched set of random regions (see Figure 2). Brain state stability consistently remained higher when rich club nodes were excluded (all $p < 0.01$), and the energy required for transitioning between brain states was higher when excluding random regions than when excluding the rich club (all $p < 0.01$). These findings suggest that, contrary to expectations, the rich club consistently contributed less to the stabilization of brain states and the energetic control of state transitions than would be anticipated by chance.

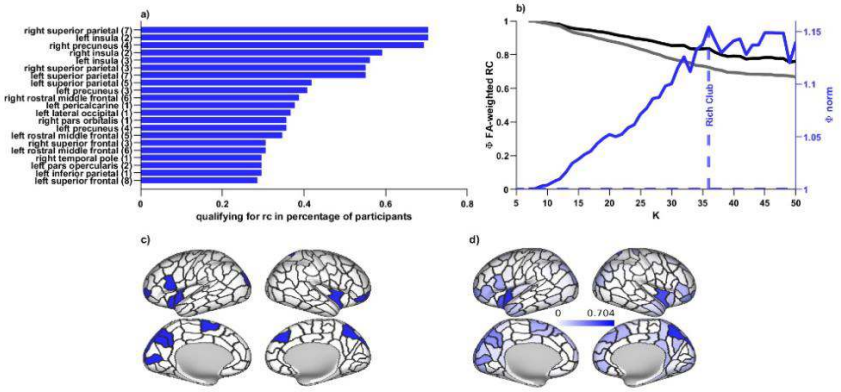

Figure 1. **Visualizations of the concept of rich-clubness and our group-level rich club.**
a) regions qualifying for the group-level rich club and the corresponding relative frequency with which a region is assigned rich club membership on an individual level
b) exemplary empirical (black), randomized (grey) and normalized (blue) rich club curves in relation to nodal degree level k. The rich club regime starting at kmax(Φnorm), that is, all regions with a nodal degree greater than kmax(Φnorm) are considered rich club members. Curves are based on a group-level connectome and included merely for visualization
c) Projection of the 21 group-level rich club members onto an inflated map of the cortical surface (blue). Shown in black are border-lines of group-level definitions of the ROI as defined in the Lausanne atlas.
d) Interindividual variation: Projections of the relative frequency with which a certain region is assigned rich club membership on an individual level. The more saturated the color, the higher the frequency.

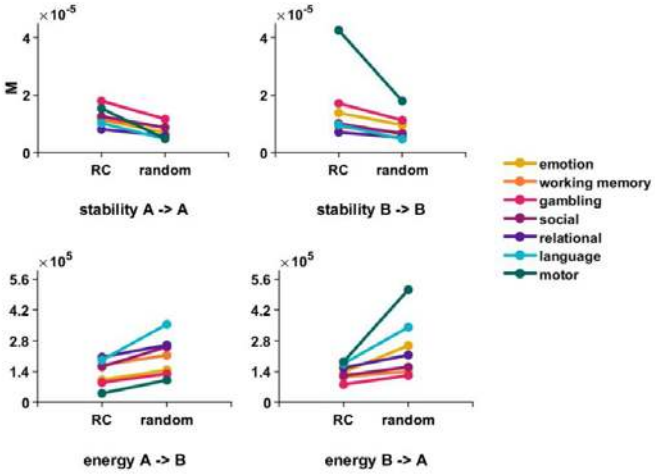

Figure 2. **Results of repeated measures ANOVA comparing exclusion of rich club (RC) and exclusion of a size-matched set of random regions. Displayed are mean NCT values across individuals, and for each measure. A brain state was always less stable when excluding random regions from the control matrix than when excluding the rich club. Additionally, when excluding random regions, more energy was needed to traverse between brain states than when excluding the rich club. All differences between exclusion of the rich club vs. random regions are significant for all tasks, with all $p < 0.01$.**

Conclusions: In excluding rich club nodes as controllers within the optimal control energy framework, we consistently observed less pronounced impacts on control measures compared to the exclusion of random regions. Our findings challenge the notion of the rich club as a potential control center in the human brain, indicating that its influence on controlling brain state dynamics is less significant than previously believed. Instead, our results underscore the critical role of weakly connected peripheral nodes in efficiently controlling the brain's activity landscape.

References

1. Betzel, R. F. et al. (2016), 'Optimally controlling the human connectome: The role of network topology', Scientific Reports, vol. 6, no. 1, 30770. https://doi.org/10.1038/srep30770
2. Braun, U. et al. (2021), 'Brain network dynamics during working memory are modulated by dopamine and diminished in schizophrenia', Nature Communications, vol. 12, no. 1, pp. 3478. https://doi.org/10.1038/s41467-021-23694-9
3. Cammoun, L. et al. (2012), 'Mapping the human connectome at multiple scales with diffusion spectrum MRI,' Journal of Neuroscience Methods, vol. 203, no. 2, pp. 386–397. https://doi.org/10.1016/j.jneumeth.2011.09.031
4. Cole, M. W. et al. (2016), 'Activity flow over resting-state networks shapes cognitive task activations', Nature Neuroscience, vol. 19, no. 12, pp. 1718–1726. https://doi.org/10.1038/nn.4406
5. de Lange, S. C. et al. (2023), 'Structural and functional connectivity reconstruction with CATO - A Connectivity Analysis Toolbox', vol. 273, pp. 120108. https://doi.org/10.1016/j.neuroimage.2023.120108
6. Gu, S. et al. (2015), 'Controllability of structural brain networks', Nature Communications, vol. 6, no. 1, pp. 8414. https://doi.org/10.1038/ncomms9414
7. Riedel, L. et al. (2022), 'Trajectory of rich club properties in structural brain networks', Human Brain Mapping, vol. 43, no. 14, pp. 4239–4253. https://doi.org/10.1002/hbm.25950
8. Senden, M. et al. (2018), 'Task-related effective connectivity reveals that the cortical rich club gates cortex-wide communication', Human Brain Mapping, vol. 39, no. 3, pp. 1246–1262. https://doi.org/10.1002/hbm.23913
9. van den Heuvel, M. P. et al. (2011), 'Rich-Club Organization of the Human Connectome', The Journal of Neuroscience, vol 31, no. 44, pp. 15775–15786. https://doi.org/10.1523/JNEUROSCI.3539-11.2011
10. Váša, F. et al. (2018), 'Adolescent Tuning of Association Cortex in Human Structural Brain Networks', Cerebral Cortex, vol. 28, no. 1, pp. 281–294. https://doi.org/10.1093/cercor/bhx249

Poster No 1492

Network control theory (NCT) for neuroscientists: a Python-based protocol

Linden Parkes[1], Jason Kim[2], Julia Brynildsen[3], Matthew Cieslak[3], Sydney Covitz[4], Raquel Gur[3], Ruben Gur[3], Fabio Pasqualetti[5], Russell Shinohara[3], Jennifer Stiso[3], Dale Zhou[5], Theodore Satterthwaite[3], Dani Bassett[3]

[1]Rutgers University, Philadelphia, PA, [2]Cornell University, Ithaca, NY, [3]UPenn, Philadelphia, PA, [4]Stanford, Palo Alto, CA, [5]University of California, Riverside, CA

Introduction: Network neuroscience is principally concerned with studying the connectome, the complete description of the brain's connectivity. This connectome is encoded as a graph of nodes interconnected by edges that can be defined across multiple scales, species, and modalities[1]. The connectome gives rise to complex topology, including hubs, modules, small-

worldness, and core-periphery structure[2]. Understanding how this topology shapes and constrains the brain's rich repertoire of dynamics is a central goal of network neuroscience. Network control theory (NCT) provides an approach to studying these neural dynamics that yields insights into how they emerge from the topology of the underlying structural connectome. Here, NCT assumes that inter-nodal communication follows a linear model of diffusion, where activity from one set of nodes spreads across the network over time along a series of fronts[2]. Then, upon this dynamical system, NCT models a set of external control signals that are designed to guide these diffusing activity patterns towards a chosen target state (i.e., a user-defined pattern of neural activity). These control signals are found by minimizing the total magnitude of their input over a given time horizon; that is, they are designed to achieve a state transition with the lowest amount of control energy. Once modeled, these control signals can be examined to determine to what extent, and how, they were constrained by topology, thus allowing researchers to study how the connectome can be leveraged to control dynamics. To facilitate the application of NCT to neuroscience research, we developed a protocol accompanied by a Python-based software package called nctpy (https://github.com/BassettLab/nctpy).

Methods: Our protocol (Fig. 1) guides researchers through the process of modeling dynamics on a structural connectome, defining a state transition, computing the control signals and the associated state trajectory (i.e., simulated neural activity), as well as integrating control signals to compute control energy. We also include tools for deploying null network models, which enable researchers to examine which topological features affect their model outputs. We tested our protocol on an undirected connectome representing interregional structural connectivity in the group-averaged (n=253) human brain[3]. Using nctpy, we computed the control signals required to transition the brain between two activity states; one characterized by activity concentrated in the visual cortex (vis; Fig. 2A, left), and the other characterized by activity in the default mode network (DMN; Fig. 2A, right). These states were extracted from clustering of resting-state fMRI timeseries[4]. Next, we integrated these control signals over time, and summed those outputs over brain regions, to obtain control energy. We computed control energy for the vis-to-DMN transition as well as the reverse DMN-to-vis transition.

Results: We found that control energy was 24% higher for the vis-to-DMN transition (energy=2676) compared to the DMN-to-vis transition (energy=2154), suggesting that the latter transition was easier to complete. Next, we tested these energies against a null network model that preserved both the spatial embedding and the strength sequence of the nodes[5]. We found that energy for both the vis-to-DMN (Fig. 2D) and the DMN-to-vis (Fig. 2E) transitions were lower than expected relative to their respective nulls, indicating that the energy associated with these transitions was not explained by a combination of spatial embedding and nodes' strength. This result suggests that these transitions were supported by higher-order topology.

Conclusions: nctpy provides intuitive tools for performing NCT analysis on connectomes. Users can define their own state transitions, interrogate the corresponding control signals, summarize those signals into control energy, and examine to what extent their results are explained by different aspects of topology.

	Step	Description	Python code / function

System	Select time system	Select whether linear dynamics will be modeled as a *continuous*-time or a *discrete*-time system	`system='continuous'`
			or
			`system='discrete'`

	Normalize structural connectome	Prepare connectome for modeling dynamics according to the selected time system	`A_norm = matrix_normalization(A, system, c=1)`

Control task	Define initial and target states	Define initial and target states using two patterns of brain activity. These states can be extracted from empirical data as shown in Fig. 2	`# initial state`
			`x0 = [vector of node activity]`
			`# target state`
			`xf = [vector of node activity]`
			
			`# normalize states`
			`x0 = normalize_state(x0)`
			`xf = normalize_state(xf)`

	Define control nodes	Control nodes are the nodes for which control signals will be generated. These nodes can be assigned weights which determine their influence over system dynamics. Here, we use uniform weights	`# uniform full control set. all nodes are control nodes and all control nodes are assigned equal control weight`
			`n_nodes = A.shape[0]`
			`B = np.eye(n_nodes)`

	Define time horizon	This will determine how long the dynamical model will run. Higher values correspond to longer running models. Units are arbitrary	`# set time horizon` `T = 1`
Compute model outputs	Compute control inputs (u) and state trajectory (x)	This is the primary function of the protocol. This function will generate the *control signals*, one for each control node	`# get x and u` `x, u, n_err = get_control_inputs(A_norm, T, B, x0, xf, system)`

	Compute control energy	Integrate *control signals* over time and sum over control nodes to get *control energy*	`# integrate control inputs to get control energy`
			`node_energy = integrate_u(u)`
			
			`# summarize nodal energy`
			`energy = np.sum(node_energy)`

Figure 1: Python functions from *nctpy* that comprise our protocol. Our protocol consists of several functions from *nctpy*. We color-coded our protocol into a series of stages that cover (i) defining the system, (ii) defining the control task, and (iii) computing the model outputs. Executing the above protocol requires a structural connectome stored as an $N \times N$ adjacency matrix in variable `A`. N represents the number of nodes. Additionally, our protocol assumes that users can provide their own initial and target states (`x0`, `xf`), each comprising node-level patterns of neural activity stored as $N \times 1$ vectors.

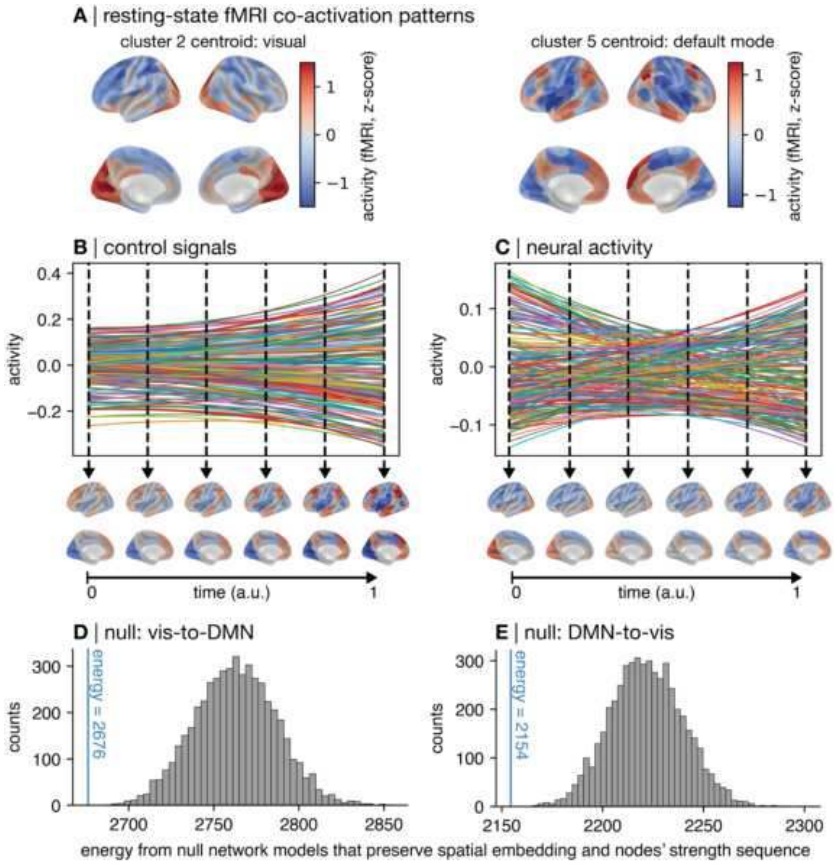

Figure 2: The *control energy* associated with transitioning between the visual cortex and the default mode network leverages higher-order connectome topology. We applied K-means clustering to resting-state fMRI time-series to extract patterns of co-activation. These patterns were used as brain states for network control theory (NCT) analysis. **A**, resting-state fMRI clusters representing activity concentrated in the visual system (left) and the default mode network (DMN, right). *Control signals* (***u***) and neural activity (***x***) were modeled for transitioning from the visual state to the DMN state (vis-to-DMN) and back again (DMN-to-vis). **B**, *control signals* for the vis-to-DMN transition visualized using line plots (top) as well as on the cortical surface for select time points (bottom). **C**, state trajectory (neural activity) for the vis-to-DMN transition visualized using line plots (top) as well as on the cortical surface for select time points (bottom). The *control signals* and the state trajectory for the DMN-to-vis transition are not shown. We integrated these *control signals* over time, and summed those outputs over brain regions, to obtain *control energy*. Next, we tested this energy against a null network model. Briefly, our null network model generates empirical null distributions of *control energy* by randomly rewiring the connectome 10,000 times. Within each rewired connectome, both the spatial embedding of the nodes as well as their strength sequence are preserved. **D**, *control energy* for the vis-to-DMN transition plotted against its corresponding null distribution. **E**, *control energy* for the DMN-to-vis transition plotted against its corresponding null distribution. We found that *control energy* was 24% higher for the vis-to-DMN transition compared to the DMN-to-vis transition. This result suggests that the DMN-to-vis transition was easier to complete. We also found that both estimates of *control energy* were lower than expected relative to their respective nulls. This result suggests that higher-order topology was responsible for enabling both state transitions.

References

1. Bassett DS, Sporns O (2017): Network neuroscience. Nat Neurosci 20: 353–364.
2. Fornito A, Zalesky A, Bullmore ET (2016): Fundamentals of Brain Network Analysis. Elsevier/Academic Press.
3. Satterthwaite TD, Elliott MA, Ruparel K, Loughead J, Prabhakaran K, Calkins ME, et al. (2014): Neuroimaging of the Philadelphia Neurodevelopmental Cohort. NeuroImage 86: 544–553.
4. Cornblath EJ, Ashourvan A, Kim JZ, Betzel RF, Ciric R, Adebimpe A, et al. (2020): Temporal sequences of brain activity at rest are constrained by white matter structure and modulated by cognitive demands. Commun Biol 3: 261.
5. Roberts JA, Perry A, Lord AR, Roberts G, Mitchell PB, Smith RE, et al. (2016): The contribution of geometry to the human connectome. NeuroImage 124: 379–393.

Poster No 1493

Intrinsic Phase-Coupled Variations of Global Signal in Human Resting State Functional Connectivity

Theodore LaGrow[1], Harrison Watters[2], Nmachi Anumba[3], Lauren Daley[3], Vaibhavi Itkyal[3], Lisa Meyer-Baese[3], Wen-Ju Pan[3], Shella Keilholz[3]

[1]Georgia Institute of Technology, Atlanta, GA, [2]Emory University, Decatur, GA, [3]Georgia Institute of Technology and Emory University, Atlanta, GA

Introduction: This study explores the complex relationship between global signal (GS) and organization of brain states derived by co-activation patterns (CAPs) in human resting-state fMRI data, highlighting the intrinsic phase-coupled relationship between brain states and GS. While CAPs are beneficial in analysis (Bolton et al. 2020; Liu et al. 2018), their effectiveness is influenced by methodological choices such as seed regions and clustering methods (Liu et al. 2018; Iraji et al. 2022). Our focus is on CAPs' correlation with the GS, typically considered a nuisance but shown indicative of brain dynamics (Gutierrez-Barragan et al. 2019; Bolt et al. 2022). Extending previous rodent studies (Gutierrez-Barragan et al. 2019), we assess these relationships using two human datasets to include a broader range of clinical data. This approach facilitates understanding the GS's role in brain function, particularly in different age groups, underscoring its potential in exploring neuropathological and clinical contexts.

Methods: This study uses two datasets: (1) HCP (Van Essen et al. 2013) consisting of 20 subjects (10F/10M; 4 scans/subject; 80 scans total; avg. age 29.6±3.8) at TR=0.72s; and (2) ADNI (Mueller et al. 2005) consisting of 4 normal cognitive subjects (2F/2M; 16/14 scans; 30 scans total, avg. age 71.5±4.3) at TR=3.0s. Preprocessing follows the standard C-PAC pipeline (Craddock et al. 2013) to best remove non-neuronal noise. Both datasets are parcellated with the Brainnetome atlas (Fan et al. 2016). For HCP, the dataset was bandpass filtered with the Slow-5 range (0.01-0.027 Hz) for specific replication. CAPs analysis followed standard protocol where the top 15% of the DMN was utilized for the HCP data (Liu et al. 2018; Iraji et al. 2022). For ADNI, the dataset was bandpass filtered with Infraslow range (0.01-0.1 Hz). Further, 100% of the dataset was used for CAPs analysis for the ADNI dataset, feasibility demonstrated by Maltbie et al. 2022, to demonstrate the intrinsic nature of the phase-coupled brain states. An ANOVA analysis was performed to test the separability of the brain states to instantaneous phase (Hilbert transform) of the GS

Results: We find similar variations in the number of brain states for both datasets observing at least two distinct phase-coupled brain states. Understanding GS is usually linked to noise distribution needing removal, organization of nonuniform brain state groups phase-coupled with GS furthers the utility of GS in fMRI analysis. Replicating Gutierrez et al.'s approach, we first examined brain states with 6 components, k=6. By visual inspection, we can a see distinct separation of the GS phase. Fig 1 shows the replication of functional brain states and the relationship to the GS phase with at least two distinct phase-coupled brain state groups of the GS (ANVOA 3-way test: $p<1.40973e-17$). Fig 2 extends this work and validates two distinct phase-coupled brain state groups with the GS utilizing the Infraslow signal (ANOVA 2-way: $p<0.1278$; ANOVA 3-way: $p<2.57435e-07$). These results further our investigation extending to clinical populations. Noting several brain states group at specific GS phases in both rodents and humans, we simplified the analysis by considering 2 brain states, k=2. The separation of these states is highlighted by a clear distinction in the absolute phase values of the GS. Finally, with 3 brain states, k=3, and post ANOVA we confirm the separation of functional brain states based on the phase of the GS. The separation of unique phase-couple brain states into 2 groups is significant for both datasets, however there is less separation for the clinical population. There is clear evidence of separation validating this signal of brain states is intrinsic phase-coupled to the GS.

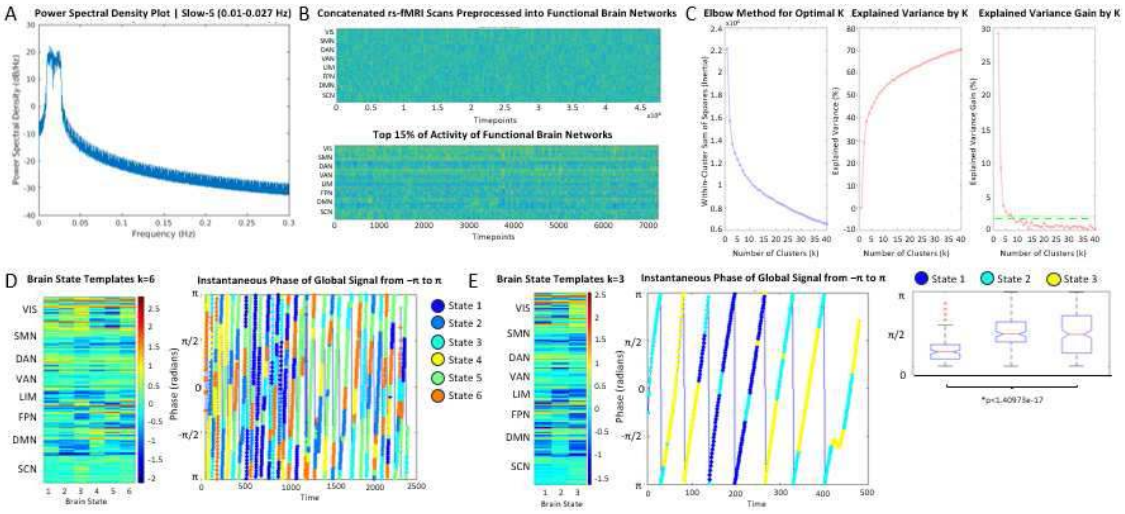

Figure 1: *Global Signal Phase-Coupled Brain States Demonstration in Human rs-fMRI with HCP dataset.* (A) Power spectral density plot of preprocessed data within the Slow-5 band for replication of Gutierrez-Barragan et al. 2019. (B) (top) Concatenated preprocessed data used in study. (bottom) For full CAP replication, only top 15% of the signal correlated with the DMN is used. Signal is organized into functional brain networks defined by the Brainnetome Atlas (Fan et al. 2016) over time. (C) (left) Inertia calculated for elbow method by varying number of k; (middle) explained variance by choice of k; (right) explained variance gained by choice of k where green dashed lined indicates a threshold of 1%, threshold indicated a choice surrounding k=6; (D) (left) Demonstration of each brain state template based on functional connectivity network. (right) Functional brain state GS phase-coupled demonstration with k=6. (E) (left) Demonstration of each brain state template based on functional connectivity network; (middle) Functional brain state GS phase-coupled demonstration with k=3; (right) ANOVA tests demonstrate there are at least two well-separated parts of the GS (3-way: p<1.40973e-17).

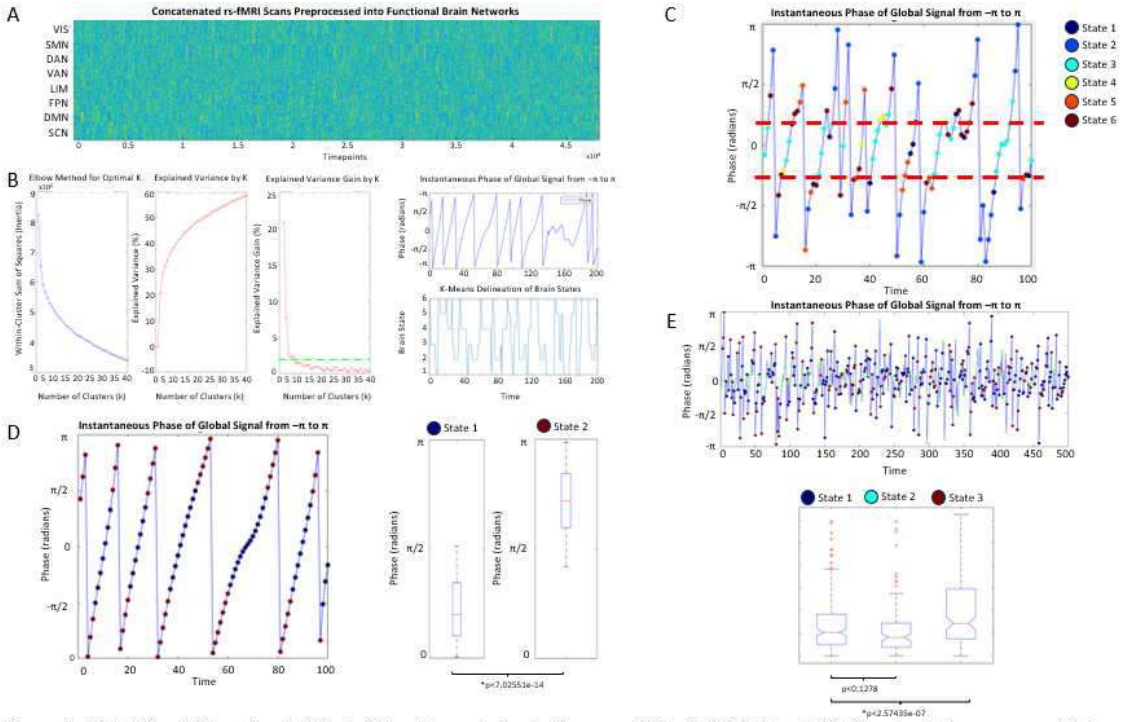

Figure 2: *Global Signal Phase-Coupled Brain States Demonstration in Human rs-fMRI with ADNI dataset.* (A) Concatenated preprocessed data used in study. Signal is organized into functional brain networks defined by the Brainnetome Atlas (Fan et al. 2016) over time. (B)-(E) replicate findings in Gutierrez-Barragan et al. 2019 with human rs-fMRI data at various choices of the number of brain states. Previously shown in rodent models, this is the first demonstration of separation of global signal in human data. (B)-(C) Demonstration of replication with functional brain states of k=6 (mirroring the number of brain states from Gutierrez-Barragan et al. 2019). (D) From left to right: inertia calculated for elbow method by varying number of k; explained variance by choice of k; explained variance gained by choice of k where green dashed lined indicates a threshold of 1%, threshold indicated a choice surrounding k=6; (top) instantaneous phase of global signal; (bottom) estimated functional brain state at each time point. (C) Functional brain state global signal phase-coupled demonstration with k=6. Red dashed lines indicate a clear separation of phase-coupled brain states. (D) Demonstration of functional brain states of k=2, for the simplest delineation of signal. Shown as boxplots, the absolute value of the phase of global signal of each state is well separated (2-way: p<7.02551e-14). (E) With functional brain states of k=3, further analysis of separation of functional brain states to global signal phase. The ANOVA tests demonstrate there are at least two well-separated parts of the GS (2-way: p<0.1278; 3-way: p<2.57435e-07). The GS signal a prime candidate to investigate neuropathological and clinical data.

Conclusions: Our study both replicates previous findings from rodents to clinical populations and reveals new insights into the phase-coupled relationship in human rs-fMRI data, emphasizing the need for further GS analysis across clinical cohorts.

References

1. Bolt, T., Nomi, J.S., Bzdok, D., Salas, J.A., Chang, C., Thomas Yeo, B.T., Uddin, L.Q. and Keilholz, S.D. (2022). A parsimonious description of global functional brain organization in three spatiotemporal patterns. Nature neuroscience, 25(8), pp.1093-1103.

2. Bolton, T.A., Tuleasca, C., Wotruba, D., Rey, G., Dhanis, H., Gauthier, B., Delavari, F., Morgenroth, E., Gaviria, J., Blondiaux, E. and Smigielski, L. (2020). TbCAPs: A toolbox for co-activation pattern analysis. Neuroimage, 211, p.116621.
3. Craddock, C., Sikka, S., Cheung, B., Khanuja, R., Ghosh, S.S., Yan, C., Li, Q., Lurie, D., Vogelstein, J., Burns, R. and Colcombe, S., 2013. Towards automated analysis of connectomes: The configurable pipeline for the analysis of connectomes (c-pac). Front Neuroinform, 42(10.3389).
4. Fan, L., Li, H., Zhuo, J., Zhang, Y., Wang, J., Chen, L., ... & Jiang, T. (2016). The human brainnetome atlas: a new brain atlas based on connectional architecture. Cerebral cortex, 26(8), 3508-3526.
5. Gutierrez-Barragan, D., Basson, M. A., Panzeri, S., & Gozzi, A. (2019). Infraslow state fluctuations govern spontaneous fMRI network dynamics. Current Biology, 29(14), 2295-2306.
6. Iraji, A., Faghiri, A., Fu, Z., Kochunov, P., Adhikari, B.M., Belger, A., Ford, J.M., McEwen, S., Mathalon, D.H., Pearlson, G.D. and Potkin, S.G. (2022). Moving beyond the 'CAP'of the Iceberg: Intrinsic connectivity networks in fMRI are continuously engaging and overlapping. Neuroimage, 251, p.119013.
7. Maltbie, E., Yousefi, B., Zhang, X., Kashyap, A. and Keilholz, S., 2022. Comparison of Resting-State Functional MRI Methods for Characterizing Brain Dynamics. Frontiers in Neural Circuits, 16, p.681544.
8. Mueller, S.G., Weiner, M.W., Thal, L.J., Petersen, R.C., Jack, C., Jagust, W., Trojanowski, J.Q., Toga, A.W. and Beckett, L., 2005. The Alzheimer's disease neuroimaging initiative. Neuroimaging Clinics, 15(4), pp.869-877.
9. Van Essen, D.C., Smith, S.M., Barch, D.M., Behrens, T.E., Yacoub, E., Ugurbil, K. and Wu-Minn HCP Consortium, 2013. The WU-Minn human connectome project: an overview. Neuroimage, 80, pp.62-79.
10. Zhang, N., Chang, C., & Duyn, J. H. (2018). Co-activation patterns in resting-state fMRI signals. Neuroimage, 180, 485-494.

Poster No 1494

Postoperative limbic functional connectivity predicts 5-year BMI in children with craniopharyngioma

Jennapher Lingo VanGilder[1], Paul VanGilder[1], Nicholas Phillips[1], Jinsoo Uh[1], Thomas Merchant[1]

[1]St. Jude Children's Research Hospital, Memphis, TN

Introduction: Children treated for craniopharyngioma, a brain tumor associated with the hypothalamic-pituitary axis, are at-risk for developing severe obesity. Studies have shown that the extent of hypothalamic involvement by tumor is linked to body mass index (BMI) (Klages et al. 2022), and our preliminary work suggests that the integrity of the fornix, a white matter tract that emerges from the hypothalamus, is associated with BMI in children five years after treatment. Functional MRI studies report that obesity is associated with abnormal activation of prefrontal (i.e., inhibitory control) and limbic (i.e., reward processing) cortices (Berridge et al. 2010). These reports implicate limbic structure and function in BMI regulation, yet the neural substrate underlying poor BMI trajectories in children treated for craniopharyngioma remains unknown. The purpose of this study was to evaluate the extent that postoperative fornix integrity impacts neural networks associated with long-term BMI. We hypothesized that greater functional connectivity between limbic and prefrontal brain regions would predict lower BMI at a 5-year follow-up visit.

Methods: Thirty-eight children (mean±SD age=12.99±3.54 years, female=18) underwent MRI after surgery but prior to radiotherapy (54 Gy [RBE]). DWI data were collected using a 1.5T Siemens scanner: b-value = 1 ms/μm2 with 12 directions and one b=0 image; four scans were collected to increase the signal-to-noise ratio. Raw images were preprocessed to reduce noise and the DTI model was applied to quantify FA in each voxel. A region of interest (ROI) approach was used to quantify fornix FA for each patient. Resting state fMRI images were acquired on a Siemens 3T scanner: TR=2.01 s, TE=30 ms, flip angle=90°, slice thickness=3.5 mm, and nslice=32. We performed a functional connectivity (FC) analysis using a seed-based approach with the CONN toolbox. Whole-brain correlation maps for each patient were calculated between 166 ROIs using the AAL atlas 3 (Rolls et al. 2020). A general linear model assessed whether ROI-ROI connectivity strength was correlated with the fornix FA value for each patient (FDR-corrected $p<0.05$). BMI was collected 5 years after radiotherapy and the age- and sex-specific z-score was calculated using normative values. Simple linear regression evaluated the relationship between 5-year BMI z-score and FC values for ROI pairs that were significantly correlated with fornix integrity.

Results: Whole-brain analyses revealed that the connectivity between 31 ROI pairs were associated with fornix FA after FDR-correction. Among these, the FC between three pairs of brain regions were negatively associated with 5-year BMI z-scores, i.e., greater connectivity predicted lower BMI at 5-year follow-up. The connectivity pairs were the right putamen and middle cingulate (β=-1.58, p=0.05), the right supplementary motor area and pallidum (β=-1.94, p=0.02), and the right supplementary motor area and putamen (β=-1.50, p=0.02) (Fig. 1). A schematic of the connectivity between prefrontal and limbic brain regions associated with fornix integrity and BMI at 5-year follow-up is shown in Fig. 2.

Conclusions: Our findings suggest that children with better postoperative fornix integrity have greater connectivity between neural regions in the prefrontal (i.e., cognitive control) and limbic (i.e., reward processing) networks. These findings align with previous literature that report greater activation of brain regions associated with cognitive control (e.g., the cingulate and supplementary motor area (Aron 2011)), are linked to suppressed activation of brain regions associated with reward processing

(e.g., pallidum and putamen (Berridge 2010)), and regulation of food consumption (Farr et al. 2016). Our results suggest that conservative treatment approaches should be considered to preserve the integrity of limbic anatomy to reduce the risk of developing obesity later in life. Future work will evaluate if surgical approach impacts postoperative limbic anatomy.

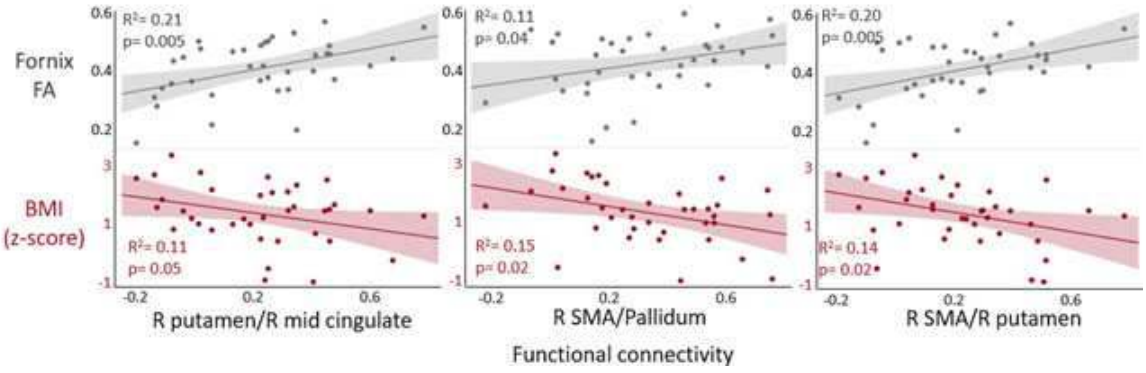

Fig. The connectivity between limbic and prefrontal networks is associated with fornix fractional anisotropy (FA, in gray) and five-year BMI z-score (in red). SMA=supplementary motor area.

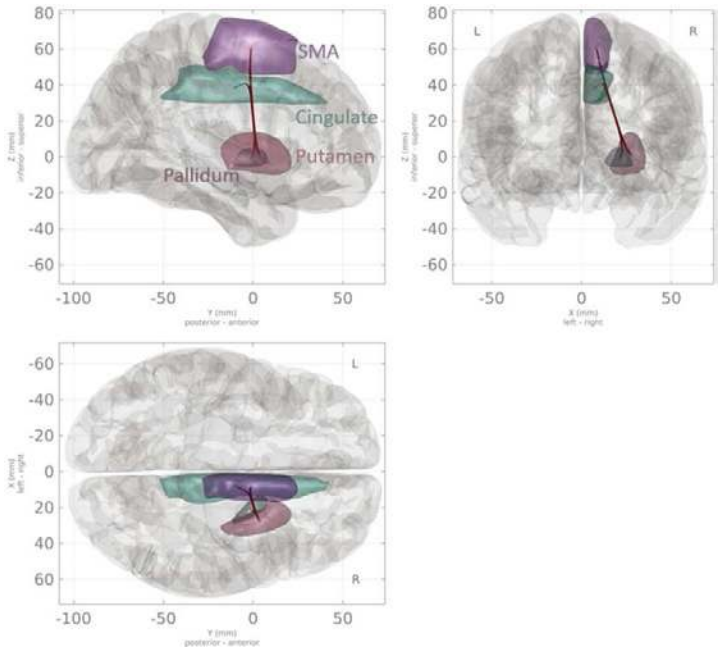

Fig. Right, coronal, and axial glass brain views of connectivity between prefrontal and limbic brain regions associated with fornix integrity and BMI 5 years after treatment. SMA=supplementary motor area

References

1. Aron, A.R. (2011), 'From Reactive to Proactive and Selective Control: Developing a Richer Model for Stopping Inappropriate Responses', Society of Biological Psychiatry, vol. 69, no. 12, pp. 55–68
2. Berridge K.C. (2010), 'The tempted brain eats: Pleasure and desire circuits in obesity and eating disorders', Brain Research, vol. 1350, pp. 43-64
3. Farr, O.M. (2016), 'Central nervous system regulation of eating: Insights from human brain imaging', Metabolism, vol. 65, no. 5, pp. 699-713
4. Klages K.L. (2022), 'Health-related quality of life, obesity, fragmented sleep, fatigue, and psychosocial problems among youth with craniopharyngioma', Psycho-Oncology, vol. 31, no. 5, pp. 779-787
5. Rolls E.T. (2020), 'Automated anatomical labelling atlas 3', NeuroImage, vol. 206, no. 116189, pp. 1053-8119

Poster No 1495

Gray and white matter functional organization and their individual variabilities in normal aging

Chenye Shen[1], Chenlu Ma[2], Chaoqiang Liu[1], Nanguang Chen[1], Anqi Qiu[1,3,4]

[1]Department of Biomedical Engineering, National University of Singapore, Singapore, Singapore, [2]Department of Chinese Language and Literature, Fudan University, Shanghai, China, [3]Department of Health Technology and Informatics, Hong Kong Polytechnic University, Kowloon, Hong Kong, [4]Department of Biomedical Engineering, Johns Hopkins University, Baltimore, MD

Introduction: The normal aging brain experiences a progressive deterioration in brain function, impacting cognition (Hedden et al. 2004). Recent studies reveal that brain function is embedded in a large-scale functional organization. While prior studies focused on gray matter (GM) functional organization in the cortex (Margulies et al. 2016), cerebellum (Guell et al. 2018), and subcortex (Tian et al. 2020), emerging evidence underscores the importance of BOLD signals in white matter (WM) (Peer et al. 2017). A recent study uncovered WM and GM function organization interaction in neurodevelopment (Zhu et al. 2023). This study explores the interplay between GM and WM functional organization in a normal aging population, hypothesizing that WM functional organization alterations align with GM changes and are linked to cognitive performance.

Methods: This study leveraged demographic, cognitive function tests, disease diagnosis, and brain imaging data (T1 and rs-fMRI) from the UK Biobank. We excluded participants with cancers, neurological or cardiovascular diseases, resulting in a normal aging population (N=23,051, age=44~82 years). T1 and rs-fMRI data were preprocessed in FreeSurfer and FSL. Cortical GM and WM functional organizations were identified using methods from (Zhu et al. 2023). Group-level GM and WM masks were first generated based on T1 segmentation (Peer et al. 2017), and GM and WM functional gradients were computed separately through the decomposition of corresponding functional connectivity (FC) (Margulies et al. 2016). Cortical GM was parcellated into 7 networks (Yeo et al. 2011). The WM functional networks were identified by assessing the voxel's highest FC strength with GM, associating the WM network with the functional role of its corresponding GM counterpart. We assessed the individual variability of each gradient by calculating the Euclidian distance between individual and group-averaged gradient space. The age-related individual variability changes were investigated using linear regression. We also assessed its cognitive relevance, covarying for age, sex, and education.

Results: Figure 1 illustrates GM and WM functional gradients. The first GM gradient explained 20.6% of cortical GM FC variance, with limbic (Lim) and default mode network (DMN) anchoring the transmodal pole and visual (Vis) and sensorimotor (SM) networks at the unimodal end (Fig. 1a). The second GM gradient, accounting for 16.8% of variance, was situated between Vis and SM networks (Fig. 1b). The first two WM gradients, contributing 18.0% and 14.5% to cortical WM FC variance, exhibited a reciprocal mirror ordering, wherein the first WM gradient resembled the second GM gradient, and vice versa (Fig. 1c,d). This suggests that different tissues may preferentially support specific aspects of brain functional organization. Figure 2 depicts the associations of individual variabilities in gradients with age (Fig. 2a) and six domains of cognitive function (Fig. 2b). It highlights that the ability to capture age and cognitive information was more pronounced in the individual variabilities observed in GM gradients compared to WM, and in the unimodal-transmodal axis compared to the Vis-SM axis. This aligns with fMRI's known sensitivity to GM signals (Gawryluk et al. 2014) and unimodal-transmodal axis' ability to capture diverse brain properties (Bernhardt et al. 2022). The greatest relevance of individual variability to age and cognition at the transmodal end is observed in DMN for GM and Lim for WM, indicating non-uniformities in brain organization (Sydnor et al. 2021).

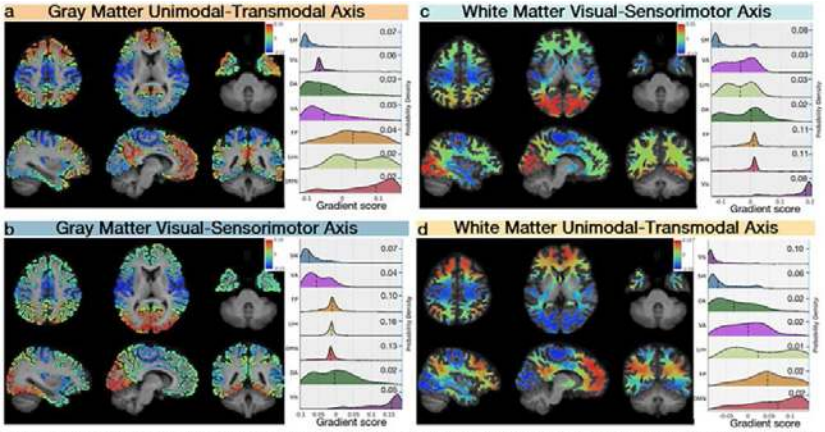

Figure 1. The brain cortical gray matter and white matter functional organization in the normal aging population. (a-b) illustrate the first two gray matter functional gradients, and (c-d) show the first two white matter functional gradients. The left panel presents gradient patterns in the volume space, and the right panel displays the distribution of gradient values within each functional network.
Abbreviations: SM, sensorimotor network; Vis, visual network; DA, dorsal attention network; VA, ventral attention network; FP, frontoparietal network; Lim, limbic network; DMN, default mode network.

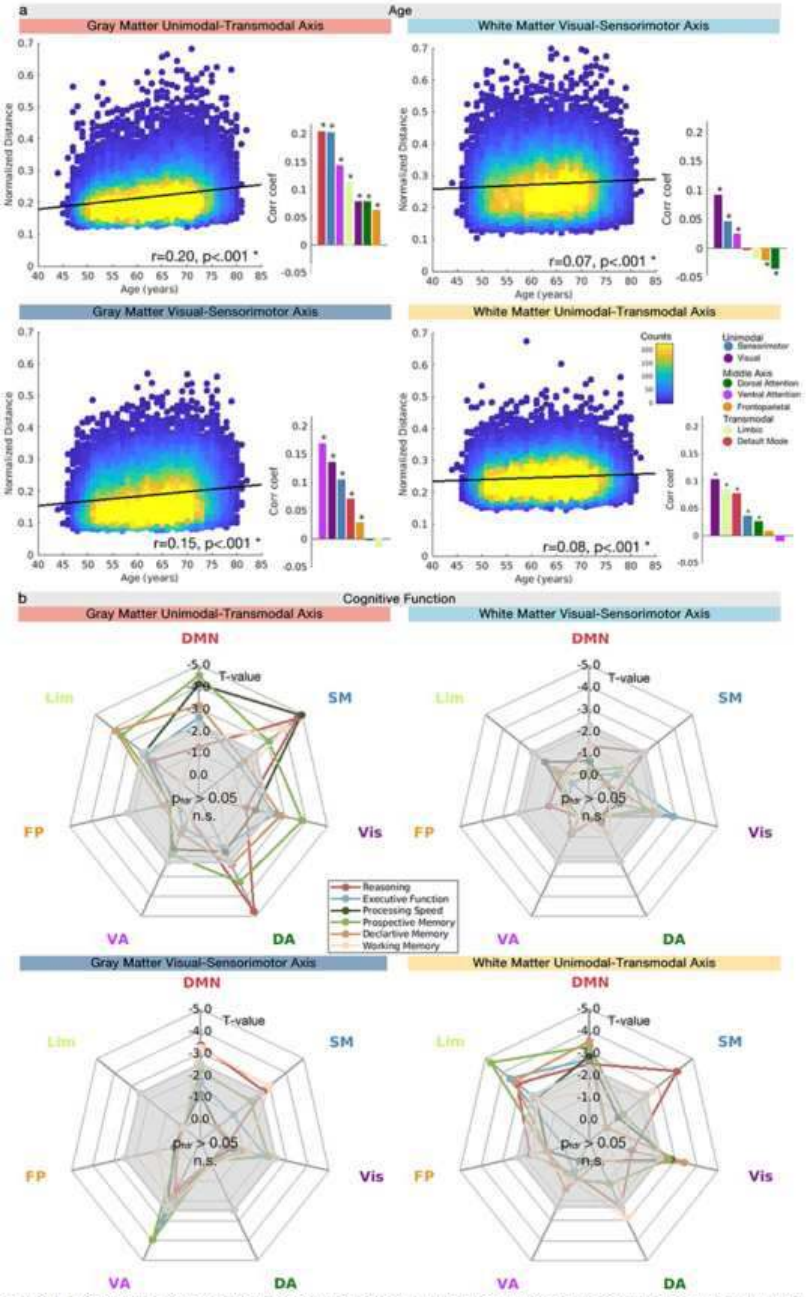

Figure 2. The individual variabilities of brain cortical gray matter and white matter functional organization and their age and cognition relevance in the normal aging population. (a) illustrates correlations between age and individual variability for each gradient. Individual variability is quantified by the average Euclidean distance of all voxels between an individual's and the group-averaged gradient space, normalized by the group-averaged gradient range for comparability across axes. The scatter plot in the left panel depicts the relationship between age and individual variability of the entire axis, with dot colors indicating participant count. The right panel presents Pearson's correlation coefficients between age and individual variability in each functional network. P values are false discovery rate-corrected. *corrected $p < 0.01$. (b) demonstrates t-values indicating associations between six domains of cognitive score and individual variabilities in gradients at network level, while controlling for age, sex, and education. Cognitive function test scores are transformed to reflect better performance as higher scores. P values are false discovery rate-corrected at a significance level of 0.05. Associations within the middle gray regions are non-significant.
Abbreviations: SM, sensorimotor network; Vis, visual network; DA, dorsal attention network; VA, ventral attention network; FP, frontoparietal network; Lim, limbic network; DMN, default mode network.

Conclusions: This study delineated WM functional organization in normal aging, revealing a close alignment with GM functional organization. The functional organization of GM and WM proves effective in capturing age and cognition information in different networks. This work sheds light on future studies investigating WM functional organization and its role in aging.

References

1. Bernhardt, B. C., et al. (2022). "Gradients in brain organization." Neuroimage 251: 118987.
2. Gawryluk, J. R., et al. (2014). "Does functional MRI detect activation in white matter? A review of emerging evidence, issues, and future directions." Frontier Neuroscience 8: 239.
3. Guell, X., et al. (2018). "Functional gradients of the cerebellum." Elife 7.
4. Hedden, T. and J. D. Gabrieli (2004). "Insights into the ageing mind: a view from cognitive neuroscience." Nature Reviews Neuroscience 5(2): 87-96.

5. Margulies, D. S., et al. (2016). “Situating the default-mode network along a principal gradient of macroscale cortical organization.” Proceedings of the National Academy of Sciences of the United States of America 113(44): 12574-12579.
6. Peer, M., et al. (2017). “Evidence for Functional Networks within the Human Brain’s White Matter.” The Journal of Neuroscience 37(27): 6394-6407.
7. Sydnor, V. J., et al. (2021). “Neurodevelopment of the association cortices: Patterns, mechanisms, and implications for psychopathology.” Neuron 109(18): 2820-2846.
8. Tian, Y., et al. (2020). “Topographic organization of the human subcortex unveiled with functional connectivity gradients.” Nature Neuroscience 23(11): 1421-1432.
9. Yeo, B. T., et al. (2011). “The organization of the human cerebral cortex estimated by intrinsic functional connectivity.” Journal of Neurophysiology 106(3): 1125-1165.
10. Zhu, J., et al. (2023). “White matter functional gradients and their formation in adolescence.” Cerebral Cortex 33(21): 10770-10783.

Poster No 1496

Human Cerebral Cortex Organization Estimated by Functional PET-FDG “Metabolic Connectivity”

Penghui Du[1,2], Sean Coursey[2,3], Ting Xu[4], Hsiao-Ying Wey[2,5], Jonathan Polimeni[2,5,6], Quanying Liu[1], Jingyuan Chen[2,5]

[1]Department of Biomedical Engineering, Southern University of Science and Technology, Shenzhen, Guangdong, China, [2]Athinoula A. Martinos Center for Biomedical Imaging, Massachusetts General Hospital, Charlestown, MA, USA, [3]College of Science, Northeastern University, Boston, MA, USA, [4]Child Mind Institute, New York, NY, USA, [5]Department of Radiology, Harvard Medical School, Boston, MA, USA, [6]Harvard-MIT Division of Health Sciences and Technology, Massachusetts Institute of Technology, Cambridge, MA, USA

Introduction: The recent development of high-temporal resolution functional PET (fPET) introduces an emerging focus on “metabolic connectivity (MC)”[1-3], providing a complementary perspective to the hemodynamic-based “functional connectivity (FC)” assessed by fMRI[4-6]. In this study, we applied a connectivity gradient-based analytical scheme on a resting-state simultaneous fPET-fMRI dataset, aiming to characterize the detailed cortical organization of fPET-derived MC and understand how it differs from the fMRI-derived functional network structures.

Methods: The publicly available Monash rsPET-MR dataset[7] was utilized for this study. A group of 26 healthy young adults each underwent a 95-minute simultaneous BOLD-fMRI (TR=2450 ms, 3×3x3 mm3 voxels) and constant-infusion FDG-PET scan (2.09x2.09x2.03 mm3 nominal voxels, 16 s per frame) while resting with their eyes open. As summarized in Figure 1a, we first estimated four types of connectivity metrics: a) FC, temporal synchrony of instantaneous fMRI fluctuations; b) MC, temporal synchrony of instantaneous fPET fluctuations; c) metabolic covariance (MCov), across-subject covariance of the static PET-FDG measures1; and d) ALFF connectivity (ALFF-C), temporal synchrony of fMRI amplitude of low-frequency fluctuations (ALFF), using a time-windowed measure (width=34.3s, step=9.8s), motivated by established link between ALFF and glucose metabolism[8]. After obtaining these four connectivity metrics, we quantified region-specific connectivity gradients following an analytical pipeline in previous study[5], with larger gradients suggesting more rapidly changing connectivity patterns. Then a watershed algorithm was applied to identify potential boundaries between different brain regions. Finally, we derived multiple parcels from the boundary maps, and grouped them into separate networks using the Louvain community detection algorithm[9].

Results: As illustrated in Fig. 1b, MC exhibited modest consistency of local gradients and boundaries with other metrics. At the network level (parcellation), we identified a prominent fronto-parietal component and an inferior temporal-occipital component in MC that deviated from the fMRI-derived FC and ALFF-C networks. Similar networks were also observed in MCov despite the dissociation of MC and Mcov in the connectivity profile. We then applied high-pass and low-pass filtering to the fPET data with a cutoff at 1/300 Hz (5 minutes) (Fig. 2). While both contributed to the local features, the global organization of MC was primarily driven by low-frequency components. Although high-frequency components also exhibited connectivity patterns and networks, they were noisy and resembled patterns derived from random noise. Surprisingly, we also noticed considerable across-subject consistency of the fPET time-activity curves (TACs). As shown in Fig. 2, both local and global features of group-averaged TACs to some extent resembled those derived from the individual data (Fig 2b). Synchronized fPET TACs across subjects may potentially stem from similar scanning experience coupled to experimental design, or from misspecification of baseline fPET TACs that have specific spatial signatures[10].

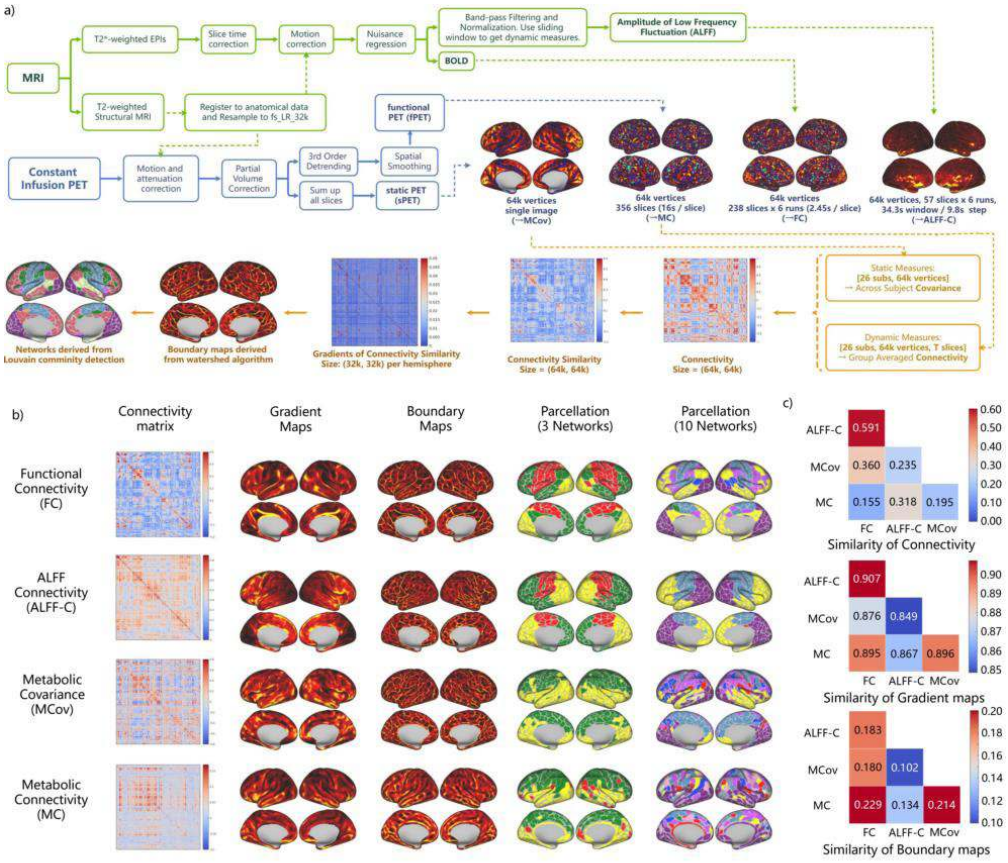

Figure 1. a) Flow chart of fMRI and PET data processing and the connectivity gradient-based parcellation. All data were resampled to the standard fs_LR_32k surface space. For dynamic connectivity metrics ("FC", "MC", and "ALFF-C"), patterns of temporal correlations were averaged across subjects; and for static connectivity metric ("MCov"), across-subject covariance of the static PET data was calculated, as described in the main text. **b)** Summary of cortical organization estimated by different connectivity metrics. "Connectivity matrices" were calculated based on the Glasser 2016 multi-modal atlas, and exhibited patterns consistent with previous studies (Jamadar et al., 2021); "Gradient maps" show the local gradient map of connectivity similarity averaged across all vertices, with yellow color indicating rapidly changing connectivity patterns; and "Boundary Maps" show the edge-detection results, with yellow lines indicating potential boundaries separating different brain regions. Cortical "parcellation" results at two different network levels are shown. **c)** Similarity of connectivity, gradient maps, and boundary maps across different connectivity metrics, estimated at the region-of-interest level (Glasser et al., 2016) and quantified using the Spearman's correlation coefficients.

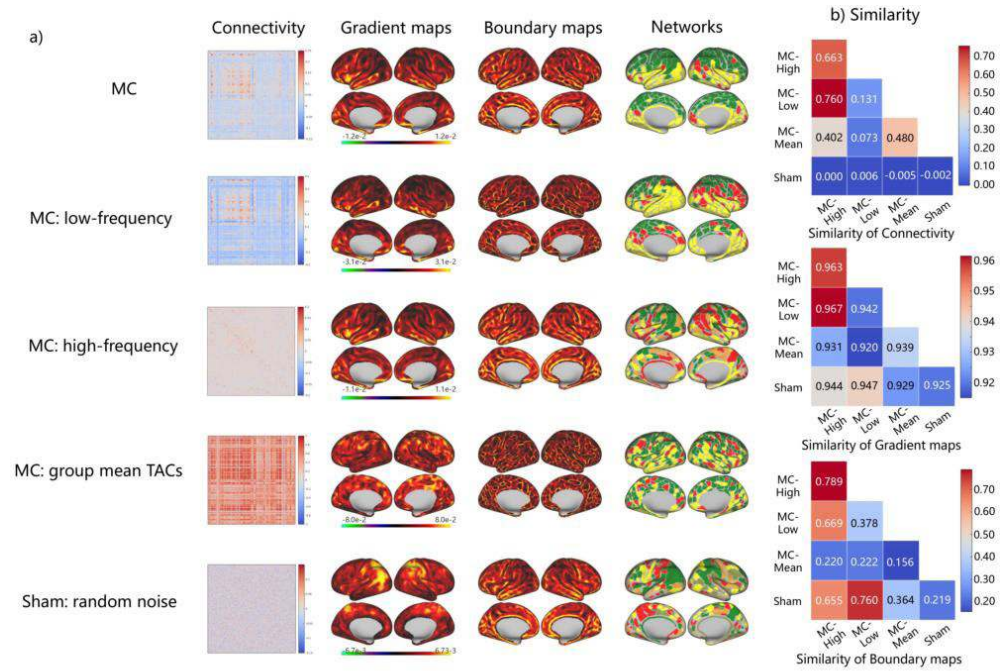

Figure 2. a) Across-frequency dependence and across-subject consistency of the metabolic connectivity results. "MC: low-frequency": temporal synchrony of low-frequency components (≥5min) of instantaneous fPET fluctuations; "MC: high-frequency": temporal synchrony of high-frequency components (<5min) of instantaneous fPET fluctuations; "MC: group mean TACs": temporal synchrony of smoothed group-average fPET time-activity curves. To test the influence of cortical geometry and spatial smoothing on local gradient estimates, the results of a sham dataset, simulated by random noise, are also shown at the bottom ("Sham: random noise"). Note that while random noise resulted in spatially varying connectivity gradients, demonstrating a bias imposed by cortical anatomy and data processing, the effect size is small—the scales of sham gradients and boundary maps are significantly lower than other measures. **b)** Similarity of connectivity, gradient maps, and boundary maps across different preprocessing schemes, estimated at the region-of-interest level (Glasser et al., 2016) and quantified using the Spearman's correlation coefficients.

Conclusions: In this study, we explored cortical organization using fPET-based MC. We found that while MC shares some local gradient and parcellation similarities with FC, the overall MC networks deviated from conventional FC-based networks. Our results also suggested that the metabolic networks were dominated by low-frequency components (≥5min) and were partially driven by surprisingly synchronized fPET dynamics across subjects. We corroborate previous MC findings that fPET sheds complementary insights into the cerebral functional architecture; additionally, we highlight the complexity of interpreting the fPET-based MC and a need for examining the specific signal mechanisms in future studies.

References

1. Jamadar S D, Ward P G D, Liang E X, et al. Metabolic and hemodynamic resting-state connectivity of the human brain: a high-temporal resolution simultaneous BOLD-fMRI and FDG-fPET multimodality study[J]. Cerebral Cortex, 2021, 31(6): 2855-2867.
2. Yakushev, I., Drzezga, A. and Habeck, C., 2017. Metabolic connectivity: methods and applications. Current opinion in neurology, 30(6), pp.677-685.
3. Di, X. and Biswal, and Alzheimer's Disease Neuroimaging Initiative, B.B., 2012. Metabolic brain covariant networks as revealed by FDG-PET with reference to resting-state fMRI networks. Brain connectivity, 2(5), pp.275-283.
4. Yeo B T T, Krienen F M, Sepulcre J, et al. The organization of the human cerebral cortex estimated by intrinsic functional connectivity[J]. Journal of neurophysiology, 2011.
5. Gordon E M, Laumann T O, Adeyemo B, et al. Generation and evaluation of a cortical area parcellation from resting-state correlations[J]. Cerebral cortex, 2016, 26(1): 288-303.
6. Schaefer A, Kong R, Gordon E M, et al. Local-global parcellation of the human cerebral cortex from intrinsic functional connectivity MRI[J]. Cerebral cortex, 2018, 28(9): 3095-3114.
7. Jamadar S D, Ward P G D, Close T G, et al. Simultaneous BOLD-fMRI and constant infusion FDG-PET data of the resting human brain[J]. Scientific data, 2020, 7(1): 363.
8. Aiello M, Salvatore E, Cachia A, et al. Relationship between simultaneously acquired resting-state regional cerebral glucose metabolism and functional MRI: a PET/MR hybrid scanner study[J]. Neuroimage, 2015, 113: 111-121.
9. Blondel V D, Guillaume J L, Lambiotte R, et al. Fast unfolding of communities in large networks[J]. Journal of statistical mechanics: theory and experiment, 2008, 2008(10): P10008.
10. Coursey S, Hartung GA, Polimeni JR, Chen JE. Bias of Metabolic (De)activations Introduced by Polynomial Detrending of fPET-FDG Data. OHBM, 2023

Poster No 1497

Normative Measures Harmonization for Pathway Dependent Connectivity Measures in Multiple Sclerosis

Mark Lowe[1], Ajay Nemani[1], Xuemei Huang[2], Katherine Koenig[1]

[1]The Cleveland Clinic, Cleveland, OH, [2]Cleveland Clinic, Cleveland, OH

Introduction: We recently validated a statistically straightforward, connectivity-based metric as a marker for multiple sclerosis (MS) disease status and progression[1]. This metric is composed of pathway-dependent structural and functional connectivity measures and normalized using values derived from sex- and age-matched healthy controls (HC). The stability and robustness of this metric depends on having a stable HC distribution from which to derive normative values. The applicability of the metric depends on ensuring that the measures are not biased by the measurement systems used to collect functional and structural connectivity data. In this study, we apply a harmonization procedure intended to produce device-independent normative values using data obtained from a multi-MRI scanner platform dataset known as the Cleveland Clinic Brain Study (CCBS)[2].

Methods: The structural and functional connectivity index (SFCI) is calculated using resting state functional connectivity (rsfMRI) and diffusion-based structural connectivity (DTI). In this study, we use rsfMRI and DTI data acquired by the CCBS, a lifespan study of older healthy adults[2]. Data for this study are produced on two MRI scanners at Cleveland Clinic, a Siemens Skyra 3T and a Siemens Prisma 3T MRI. We selected two sets of 10 age- and sex-matched subjects from each scanner. The same protocol is run on both scanners, so any biases are device-dependent and not protocol-dependent. Identical processing pipelines were performed on all data. Structural connectivity was taken to be mean pathway-dependent radial diffusivity and functional connectivity was taken to be the z-score-converted Pearson correlation of seed regions at the endpoints of the desired pathways. Details of the SFCI and calculation of component measures is described in Koenig et al.[1]. ComBat data harmonization[3,4] is a popular batch correction tool that removes inter-site variability while preserving inherent biological variability. We applied harmonization separately to the structural and functional connectivity results. ComBat was applied with default parameters using the three underlying pathways described above as features across subjects. The SFCI was then recalculated on these harmonized data.

Results: Paired t-tests between original SFCI and ComBat harmonized SFCI showed no significant differences. Figure 1 shows a comparison of the harmonized results on component and combined metrics. Comparison of Figures 1c and 1d show that ComBat is effective at removing scanner-dependent effects such that norms can be calculated across data acquired from

both scanners, resulting in normalization that is equivalent to using within-scanner normalization (1d). Figure 2 shows the SFCI calculated for each of the 20 subjects, with each column representing a different calculation method for the normative values used for z-scoring. Column 1 uses unharmonized values normed across both scanners. Column 2 uses unharmonized values normed separately for each scanner. Column 3 uses norms calculated using harmonized data across all scanners. The fact that there is very little difference between SFCI calculated in columns 2 and 3 indicates that harmonization has effectively removed scanner-dependent biases from the pooled calculation.

Conclusions: ComBat is increasingly utilized in imaging studies because of its wide availability and effectiveness at removing site- or system-dependent biases from multi-platform studies. Here, we demonstrate that ComBat can be used in a combined DTI and rsfMRI context to effectively remove scanner biases. Using harmonized versions of our metrics, we can take advantage of a very large pooled dataset to produce stable normative values for SFCI calculation in individual MS patients. By incorporating more platforms, the goal would be to produce norms that would be applicable to connectivity measures obtained on any MRI scanner.

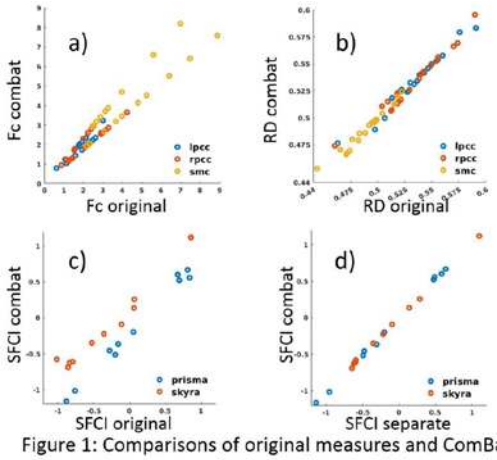

Figure 1: Comparisons of original measures and ComBat corrected measures. a) rsfMRI, b) Radial diffusivity, c) SFCI using norms from pooled data across scanners, and d) SFCI with ComBat pooled vs. SFCI with norms calculated within scanner

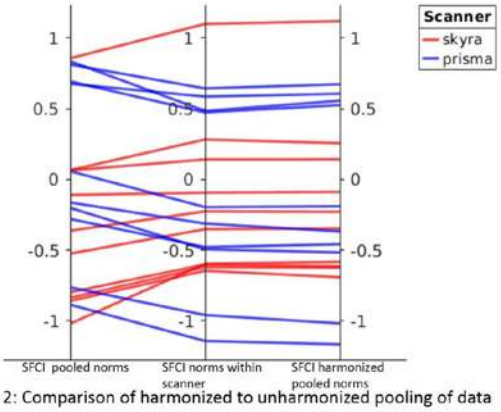

Figure 2: Comparison of harmonized to unharmonized pooling of data for norming. Column 1 is SFCI calculated using unharmonized data from both scanners. Column 2 is SFCI calculated using norms produced within the scanner used for the individual measurement. Column 3 is SFCI calculated using harmonized data pooled across both scanners.

References

1. Koenig, K.A., et al., Evaluation of a connectivity-based imaging metric that reflects functional decline in Multiple Sclerosis. PLoS One, 2021. 16(6): p. e0251338.
2. Available from: https://my.clevelandclinic.org/departments/neurological/research-innovations/brain-study.
3. Fortin, J.-P., et al., Harmonization of multi-site diffusion tensor imaging data. NeuroImage, 2017. 161: p. 149-170.
4. Johnson, W.E., C. Li, and A. Rabinovic, Adjusting batch effects in microarray expression data using empirical Bayes methods. Biostatistics, 2006. 8(1): p. 118-127.

Poster No 1499

Linking structural and effective connectivity to explain motor recovery after stroke

Valerie Wiemer[1,2], Theresa Paul[1,2], Lukas Hensel[1], Matthew Cieslak[3], Caroline Tscherpel[4], Christian Grefkes[4], Scott Grafton[5], Gereon Fink[1,2], Lukas Volz[1]

[1]Medical Faculty, University of Cologne, and Department of Neurology, University Hospital Cologne, Cologne, Germany, [2]Institute of Neuroscience and Medicine, Cognitive Neuroscience (INM-3), Research Centre Juelich, Juelich, Germany, [3]Department of Psychiatry, Perelman School of Medicine, University of Pennsylvania, Philadelphia, PA, [4]Department of Neurology, University Hospital Frankfurt, Goethe University Frankfurt, Frankfurt am Main, Germany, [5]Department of Psychological & Brain Sciences, University of California, Santa Barbara, CA

Introduction: While motor recovery after stroke is thought to arise from functional reorganization of the motor network, the underlying mechanisms remain poorly understood (Grefkes & Fink, 2020). Structural cortico-cortical motor network connectivity assessed via diffusion MRI (dMRI) has recently been shown to be strongly associated with distinct aspects of motor control after stroke, highlighting that undamaged fiber tracts may serve as a structural reserve to enable reorganization and recovery (Paul et al., 2023a). However, it remains unclear whether and how the structural reserve of the motor network allows changes in information integration that may help to compensate for motor impairment. To address this critical question, we assessed dMRI-based structural and fMRI-based effective connectivity within a cortical motor network to characterize structure-function relationships of motor network reorganization in chronic stroke patients.

Methods: Structural motor network connectivity was quantified using a novel approach combining diffusion spectrum imaging and compartment-wise analysis of anisotropy (Volz et al., 2018; Paul et al., 2023b). In the same cohort of chronic stroke patients (N=23), the modulation of effective motor network connectivity underlying the control of finger-tapping movements with the paretic hand was assessed using dynamic causal modeling (DCM). Spearman correlations between tractwise anisotropy and DCM coupling parameters were computed to test for structural and effective connectivity associations. Motor impairment was quantified via finger-tapping frequency during the fMRI task, the Motricity Index Arm Score reflecting basal motor control, and the Action Research Arm Test indicating complex motor control. Associations between multimodal motor network connectivity and impairment were assessed via Spearman correlations and multiple linear backward regressions. Finally, subgroup analyses were performed to disentangle the relationship between motor network connectivity and recovery from the acute to chronic phase after stroke (substantial vs. non-substantial recovery).

Results: Besides the expected excitatory influences from premotor areas onto the ipsilesional primary motor cortex (M1), DCM results revealed a significant pathophysiological excitatory influence from ipsi- to contralesional M1 during paretic hand movements. No significant correlations between structural and effective connectivity were observed at the group level. While structural connectivity was highly indicative of motor impairment after stroke, effective connectivity showed no association with motor impairment. However, when combining structural and effective connectivity estimates as predictors in the regression models, we were able to meaningfully increase the explained variance for all outcome variables (all $R2>74\%$, $adj.R2>61\%$, $P<.003$). Notably, subgroup analyses revealed differential results for structure-function relationships concerning motor recovery: In contrast to substantially recovered patients, non-substantially recovered patients showed a negative association for the contra- to ipsilesional M1 connection, indicating recovery-dependent network alterations after stroke.

Conclusions: We here provide the first integration of structural and task-related effective cortical motor network connectivity in chronic stroke patients. Our results support the notion that interhemispheric cortical routes may support motor control and emphasize that the cortical structural reserve may facilitate functional reorganization after stroke. In particular, interhemispheric excitatory input from the ipsi- to the contralesional hemisphere may help to access undamaged contralesional descending fiber pathways, offering new insights into conflicting views on the functional role of contralesional M1. The high behavioral variance explained by a combination of structural and effective connectivity underlines their potential as future biomarkers for motor recovery after stroke.

References

1. Grefkes, C. (2020), 'Recovery from stroke: current concepts and future perspectives', Neurological research and practice, 2(1), 1-10
2. Paul, T. (2023a) 'Interhemispheric structural connectivity underlies motor recovery after stroke', Annals of Neurology, 94(4), 785-797
3. Paul, T., (2023b) 'The role of corticospinal and extrapyramidal pathways in motor impairment after stroke', Brain Communications, 5(1), fcac301
4. Volz, L. J., (2018) 'A probabilistic atlas of fiber crossings for variability reduction of anisotropy measures', Brain Structure and Function, 223, 635-651

Poster No 1500

Second-order instantaneous causal analysis of spontaneous MEG

Yongjie Zhu[1], Lauri Parkkonen[2], Aapo Hyvärinen[1]

[1]Department of Computer Science, University of Helsinki, Helsinki, Finland, [2]Department of Neuroscience and Biomedical Engineering, Aalto University, Espoo, Finland

Introduction: Despite decades of research, discovering instantaneous causal relationships from observational brain imaging data, such as spontaneous MEG and fMRI, remains a difficult problem. Popular methods, such as Granger Causality (GC)[1] and Non-Gaussian Structural Equation Models (e.g., linear non-gaussian acyclic model, LiNGAM)[2], either fall short in handling complex aspects of neuroimaging data such as contemporaneous effects or the data is not non-Gaussian enough.

Methods: Here we propose a model with instantaneous causality and temporally dependent variables, both of which are very empirically plausible in neuroimaging data. Then, we propose a method to estimate such causal models based on a pairwise approach inspired by[3]. The method is based on likelihood ratio with a connection to mutual information computed from second-order statistics between the residual and data variables to construct a simple decision criterion. Since the method is based on second-order statistics, we call it Second-Order Causal (SOC) analysis. To estimate the whole causal connectivity networks of n variables (or nodes), we apply a two-stage approach that is well-known in the literature[3,4]. The L1-penalized inverse covariance (graphical lasso estimator) was used to estimate which nodes are connected, and then the proposed pairwise method was used to estimate the causal directions for each pair of connected nodes. We first applied the proposed method to simulated data generated according to the generative causal models. Then, we applied it to a resting-state MEG dataset from the CamCAN repository[5] (650 healthy subjects) with a split-half analysis to examine the consistency as well as to a brain age prediction task to show the usefulness. Specifically, the parcelled cortical MEG data was separated and reduced into 15 sources with nonlinear independent component analysis (NICA)[6]. The energies of NICA sources were computed and resampled into a sampling frequency of 1 Hz. Regarding the consistency analysis of the causal whole networks, we reported the consistency of the L1-penalized precision matrix and consistency of the causal methods (e.g., SOC, GC and pairwise LiNGAM (pwLiNGAM)[3]), and the consistency of the two-stage methods combining the two.

Results: The simulations (Fig. 1A-D) confirm that the SOC method is able to estimate the proposed model with instantaneous causality and time-dependent variables when the true regressor does not have the same autocorrelation as the noise. Compared with GC, SOC performs better, especially in cases where the number of time points is typically quite small and limited. Moreover, pwLiNGAM[3] is unable to work when the autocorrelated variables are generated with Gaussian innovations. When applied on CamCAN data, the method gives consistent results across intra- and inter-subject in a split-half test (correlation between two halves for each subject or group) when estimating causal directionalities (Fig.1 E-J). The SOC method gives significantly better inter- and intra-subject results than GC and pwLiNGAM methods. Fig. 2A shows the resulting causal connectivity networks, with the influences significant at a 5% level. One can see that the connections tend to be strong between sources, which are close to each other. Fig. 2B-C shows better performance in a brain age prediction task as well.

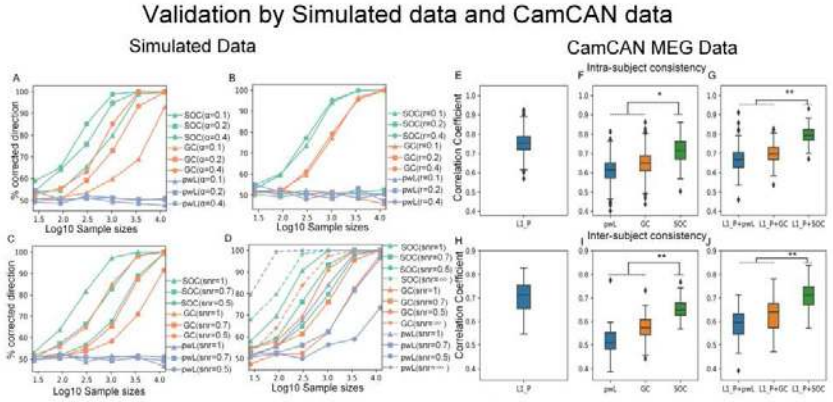

Fig.1 Results from simulated and real MEG data (SOC: Second-Order Causality; GC: Granger Causality; pwL: pairwise linear non-Gaussian acyclic model (LiNGAM)) [3]. Percentage of directions found correctly among all connections estimated to exist (A-D). **A**. Impact of the regression coefficients in the true model, indicating the larger the regression coefficient α (essentially the correlation coefficient) in the true model, the easier it makes the correct decision; **B**. Impact the autocorrelation in the regressor variables. One can see the method failed with $r = 0.2$ since the variable had the same autocorrelations as the noise variable in the true causal model; **C**. Adding observational noise in variables. Gaussian innovations in AR model and with Gaussian observational noises, indicating that the lower the signal-to-noise ratio (SNR), the more difficult it is to determine the causal direction for both SOC and GC; the pwLiNGAM still failed in these cases with Gaussian innovations since all the variables are Gaussian; **D**. Laplace innovations in AR model and with Gaussian observational noises. One can see when using Laplace innovations to generate the data and without Gaussian observational noises (or SNR is typically high), the pwLiNGAM works best (Figure 1D dotted lines).
Intra- and inter-subject consistency analysis of split-half tests ($p < 0.01$ *, $p < 0.001$ **, Wilcoxon signed-rank test with FDR correction) on MEG data. **E&H**: Consistency of L1-penalted precision matrix (cross-validated graphical lasso). **F&I**: Consistency of causal methods alone. **G&J**: consistency of two-stage approaches.

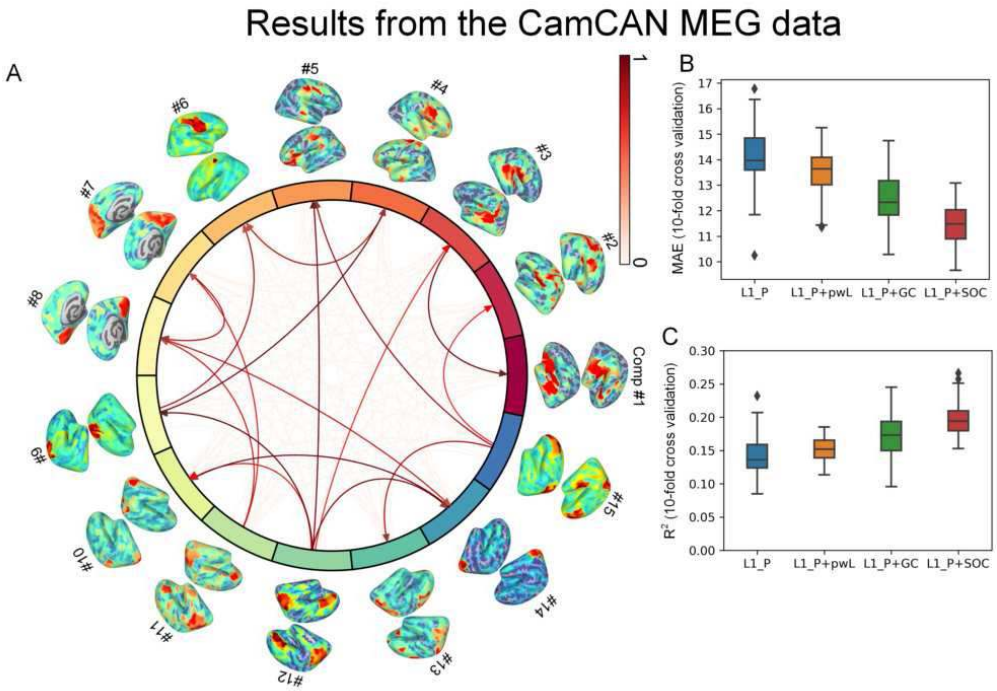

Fig.2. **A**: Effective (or causal/directed) connectivity networks derived from the concatenated MEG sources across the whole subjects. The top 5% connections are demonstrated and the arrow represents the causal direction. **B-C**: Brain age prediction using the effective connectivity features (Precision: L1-panalty precision matrix; pwLiNGAM: pairwise LiNGAM; Granger: standard Granger Causality and SOC: the proposed second-order causal discovery method). Generalization performance was assessed by 10-fold cross-validation. **B**). The MAE years (smaller is better) and **C**). the R2 score (bigger is better) were compared for different methods.

Conclusions: We presented a model and corresponding estimation method for instantaneous causal discovery in time-dependent variables based on second-order blind source separation methods. Since the method exploits only autocorrelations of the variables and not non-Gaussianity, it could be particularly useful for time-dependent brain imaging data such as fMRI, or energies of E/MEG data, which follow practically instantaneous causal relationships as above, due to the slow temporal scale of the measurement system.

References

1. Seth, A. K., Barrett, A. B., & Barnett, L. (2015). Granger causality analysis in neuroscience and neuroimaging. Journal of Neuroscience, 35(8), 3293-3297.
2. Shimizu, S., Hoyer, P. O., Hyvärinen, A., Kerminen, A., & Jordan, M. (2006). A linear non-Gaussian acyclic model for causal discovery. Journal of Machine Learning Research, 7(10).
3. Hyvärinen, A., & Smith, S. M. (2013). Pairwise likelihood ratios for estimation of non-Gaussian structural equation models. The Journal of Machine Learning Research, 14(1), 111-152.
4. Hyvärinen, A., Zhang, K., Shimizu, S., & Hoyer, P. O. (2010). Estimation of a structural vector autoregression model using non-gaussianity. Journal of Machine Learning Research, 11(5).
5. Taylor, J. R., Williams, N., Cusack, R., Auer, T., Shafto, M. A., Dixon, M., ... & Henson, R. N. (2017). The Cambridge Centre for Ageing and Neuroscience (Cam-CAN) data repository: Structural and functional MRI, MEG, and cognitive data from a cross-sectional adult lifespan sample. neuroimage, 144, 262-269.
6. Zhu, Y., Parviainen, T., Heinilä, E., Parkkonen, L., & Hyvärinen, A. (2023). Unsupervised representation learning of spontaneous MEG data with nonlinear ICA. NeuroImage, 274, 120142.

Poster No 1501

Statistical Link Prediction for Temporal Networks with Epilepsy MEG Data

Jaehee Kim[1], Heaji Lee[1]

[1]*Duksung Women's University, Seoul, Seoul*

Introduction: Networks have become a fundamental approach to understanding systems of interacting objects, unifying the study of diverse phenomena, including biological organisms and human brain systems. With the rise of large-scale temporal networks, such as social and neuroimaging networks, temporal link prediction has become an interesting issue. Brain neuroimaging network data are dynamic or temporal networks where entities and relationships appear, disappear, strengthen, and weaken over time. Nodes and their relationships represent links and entities. Each link contains information on the time when it is active and other possible characteristics. The evolutionary behavior of temporal networks got the attention of interest. As adding or removing new links or edges over time leads to network evolution, learning the evolutionary behavior of networks is directly related to the link prediction problem. Different types of edges represent different relationships, including connectivity and similarity among nodes. Adopting a specific definition of edges can fundamentally alter how we analyze and interpret a brain network. Temporal link prediction (TLP) is a classic yet challenging inference task on dynamic graphs, which predicts possible future linkage based on historical topology. The predicted future topology can be used to support some advanced applications on real-world systems (e.g., resource pre-allocation) for better system performance or information. It aims to predict possible linkages in specific future time steps based on the observed historical topology, essential in revealing brain systems' dynamic nature.

Methods: We develop a link prediction method based on a stochastic block model as a probabilistic approach and another method based on the exponentially weighted moving average for node centrality as a time series approach combined with the neighbor similarity. We apply the proposed methods to MEG data for temporal link prediction. Link prediction aims to estimate the evolving likelihood of the existence of a link in a given network based on observed information in the network's evolving process. We apply our method to the epilepsy patients' magnetoencephalography (MEG) data on 72 ROIs collected at Seoul National University Hospital (SNUH). The dataset contained MEG data from 44 mesial temporal lobe epilepsy (mTLE) with hippocampal sclerosis (HS) patients who underwent epilepsy surgery between 2005 and 2011. Temporal link predictions are made and compared with the similarity-based methods such as CN (common neighbor), AA (Adamic-Adar), Jacard index and PA (preferential attachment).

Results: Static and temporal link prediction is done with epilepsy MEG data. We compare link prediction for the temporal MEG network data with the proposed methods. Table 1 shows the comparison results (omitted), for example. Figure 1 reveals the link prediction networks at the next time-point via the proposed method using node centrality and common neighbors for exemplary subject in each group. We further demonstrate the utility of our proposed methodology via simulation studies. Our methods perform reasonably well for the MEG network link prediction.

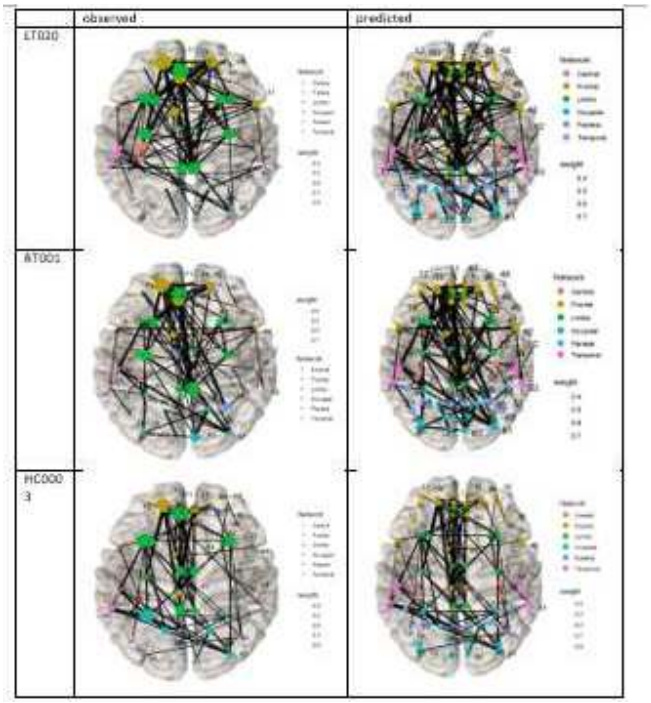

Conclusions: Networks have become increasingly important to model complex brain systems with interacting elements such as links. Link prediction aims to infer the behavior of the network link formation process by predicting missed or future relationships based on currently observed connections. It has become an attractive study area since it allows us to predict how networks will evolve. Network neuroscience explorations can benefit from edge-centric perspectives.

References

1. Adamic, L. A., & Adar, E. (2003) Friends and neighbors on the web. Social networks, 25(3), 211-230.
2. Bullmore, E. & Sporns, O. (2009) Complex brain networks: graph theoretical analysis of structural and functional systems. Nature reviews
3. Divakaran, A., & Mohan, A. (2020) Temporal link prediction: A survey. New Generation Computing, 38, 213-258.
4. Katz, L. (1953) A new status index derived from sociometric analysis. Psychometrika 18(1), 39–43.
5. Kossinets, G. (2006) Effects of missing data in social networks. Soc. Netw. 28(3), 247–268.
6. Liu, W., Lü, L. (2010) Link prediction based on local random walk. EPL (Europhysics Letters) 89(5), 58007.
7. Lü, L., Jin, C.H., Zhou, T. (2009) Similarity index based on local paths for link prediction of complex networks. Phys. Rev. E 80(4), 046122.
8. Lü, L., & Zhou, T. (2011). Link prediction in complex networks: A survey. Physica A: statistical mechanics and its applications, 390(6), 1150-1170.
9. Thompson, W. H., Brantefors, P. & Fransson, P. (2017). From static to temporal network theory: Applications to functional brain connectivity. Network Neuroscience, 1(2), 69-99.
10. Zhu, B., & Xia, Y. (2015) An information-theoretic model for link prediction in complex networks. Scientific reports, 5(1), 13707.

Poster No 1503

The macroscale routing mechanism of structural brain connectivity related to body mass index

ChaeYeon Kim[1], Yeongjun Park[2], Jong Young Namgung[1], Yunseo Park[1], Bo-yong Park[1,3,4]

[1]Department of Data Science, Inha University, Incheon, Republic of Korea, [2]Department of Computer Engineering, Inha University, Incheon, Republic of Korea, [3]Department of Statistics and Data Science, Inha University, Incheon, Republic of Korea, [4]Center for Neuroscience Imaging and Research, Institute for Basic Science, Suwon, Republic of Korea

Introduction: Previous neuroimaging studies observed that morphological and functional activity patterns are associated with body mass index (BMI) [1], [2]. However, most studies focused on identifying regional abnormalities in gray matter volume and functional activation according to BMI [3], and how the network communication altered is relatively underinvestigated. In this study, we aimed to identify the link between the network-level communication mechanisms and BMI using a measure of network routing.

Methods: We studied T1-weighted structural magnetic resonance imaging (MRI) and diffusion MRI data from the S1200 release of the Human Connectome Project (HCP) database [4]. Among 1,206 subjects, we excluded participants who were genetically related (i.e., twins) and had a family history of mental illness and history of drug ingestion, resulting in 290 participants (mean ± standard deviation age = 28.3 ± 3.9 years, 51% female). The MRI data were preprocessed using the HCP minimal preprocessing pipeline [5]. Navigation efficiency was calculated from structural connectivity using the Brain Connectivity Toolbox to assess network communication ability. This measure estimates the signal propagation efficiency of a given brain region to reach the target region based on the greedy routing algorithm [6]. While controlling for age and sex, we assessed the association between navigation efficiency and BMI. The significance of the association was assessed based on the 1,000 spin permutation tests to adjust for the spatial autocorrelation [7] and further corrected for multiple comparisons using a false discovery rate (FDR) [8]. To examine neurobiological aspects, we linked the BMI-navigation efficiency association map to the neurotransmitter distribution maps of serotonin and dopamine, where the significance was assessed using 1,000 spin permutations [7] and FDR correction [8]. In addition, we identified gene lists associated with the BMI-navigation efficiency association map using the post-mortem gene expression data provided by the Allen Human Brain Atlas (AHBA) using the abagen toolbox (https://github.com/rmarkello/abagen) [9]. Significances were assessed using Fisher's exact test and FDR [8]. We compared the identified gene lists with cell-specific genes and calculated the overlap ratio of how many genes expressed for BMI-navigation efficiency associations were included in each cell-type–specific gene set.

Results: We found significant positive associations between BMI and navigation efficiency in the sensory, reward, and executive control-related brain regions. Specifically, ventrolateral and dorsolateral prefrontal ($r = 0.279$, $pFDR < 0.001$), somatomotor ($r = 0.279$, $pFDR < 0.001$), visual ($r = 0.299$, $pFDR < 0.001$), medial temporal ($r = 0.220$, $pFDR < 0.001$), and inferior parietal cortices ($r = 0.273$, $pFDR < 0.001$), as well as the accumbens ($r = 0.170$, $pFDR = 0.004$) and thalamus ($r = 0.181$, $pFDR = 0.002$) showed significant effects (Fig. 1A). The associations with the neurotransmitter maps exhibited significant correlations with the D1 ($r = 0.148$, $pFDR = 0.01$), 5HT2a ($r = 0.154$, $pFDR = 0.008$), and 5HT1a ($r = 0.178$, $pFDR = 0.002$) receptors (Fig. 1B). The genes associated with the BMI-navigation efficiency association map were more highly overlapped with excitatory (2.31 ± 0.87%) and inhibitory neurons (1.47 ± 0.89%) (Fig. C).

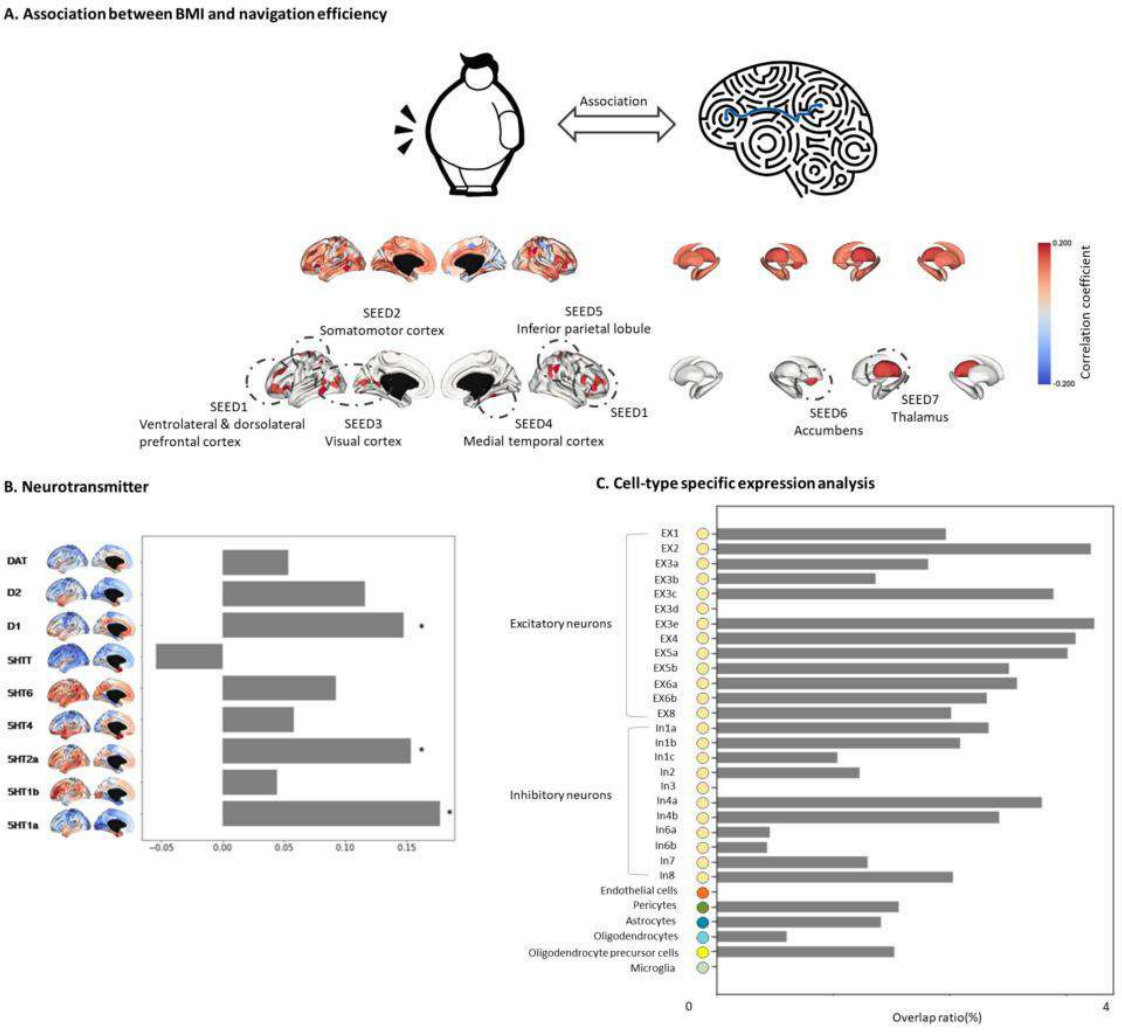

Fig. 1 | Alterations in navigation efficiency according to body mass index (BMI). (A) We describe a schema of the association between BMI and navigation efficiency (top). The association effects of the whole brain (middle) and the regions that showed significant effects are visualized on brain surfaces (bottom). **(B)** Spatial correlations between the BMI-navigation efficiency association map and neurotransmitter distributions are performed. The correlation coefficients are reported with bar plots, and the asterisks indicate significant associations (FDR < 0.05). **(C)** The overlap ratio between the genes associated with BMI-navigation efficiency association map and cell-type specific genes are shown.

Conclusions: We studied network routing mechanisms related to BMI and associated with the neurotransmitter and transcriptomic data. Our findings provide potential links for understanding the network-level mechanisms of the brain related to the variations in BMI.

References

1. Donofry, S.D., Stillman, C.M., Erickson, K.I., 2020. A review of the relationship between eating behavior, obesity and functional brain network organization. Soc Cogn Affect Neurosci. https://doi.org/10.1093/scan/nsz085
2. Kenny, P.J., 2011. Reward Mechanisms in Obesity: New Insights and Future Directions. Neuron. https://doi.org/10.1016/j.neuron.2011.02.016
3. Shott, M.E., Cornier, M.A., Mittal, V.A., Pryor, T.L., Orr, J.M., Brown, M.S., Frank, G.K.W., 2015. Orbitofrontal cortex volume and brain reward response in obesity. Int J Obes 39, 214–221. https://doi.org/10.1038/ijo.2014.121
4. Van Essen, D.C., Smith, S.M., Barch, D.M., Behrens, T.E.J., Yacoub, E., Ugurbil, K., 2013. The WU-Minn Human Connectome Project: An overview. Neuroimage 80, 62–79. https://doi.org/10.1016/j.neuroimage.2013.05.041
5. Glasser, M.F., Sotiropoulos, S.N., Wilson, J.A., Coalson, T.S., Fischl, B., Andersson, J.L., Xu, J., Jbabdi, S., Webster, M., Polimeni, J.R., Van Essen, D.C., Jenkinson, M., 2013. The minimal preprocessing pipelines for the Human Connectome Project. Neuroimage 80, 105–124. https://doi.org/10.1016/j.neuroimage.2013.04.127
6. Seguin, C., Van Den Heuvel, M.P., Zalesky, A., 2018a. Navigation of brain networks. Proc Natl Acad Sci U S A 115, 6297–6302. https://doi.org/10.1073/PNAS.1801351115/SUPPL_FILE/PNAS.1801351115.SAPP.PDF
7. Alexander-Bloch, A.F., Shou, H., Liu, S., Satterthwaite, T.D., Glahn, D.C., Shinohara, R.T., Vandekar, S.N., Raznahan, A., 2018. On testing for spatial correspondence between maps of human brain structure and function. Neuroimage 178, 540–551. https://doi.org/10.1016/j.neuroimage.2018.05.070
8. Benjamini, Y., Hochberg, Y., 1995. Controlling the False Discovery Rate: A Practical and Powerful Approach to Multiple Testing. Journal of the Royal Statistical Society: Series B (Methodological) 57, 289–300. https://doi.org/10.1111/J.2517-6161.1995.TB02031.X
9. Markello, R.D., Arnatkeviciute, A., Poline, J.-B., Fulcher, B.D., Fornito, A., Misic, B., n.d. Standardizing workflows in imaging transcriptomics with the abagen toolbox. https://doi.org/10.7554/eLife

Poster No 1504

Shifts in structural connectome manifolds in patients with migraine

Eunchan Noh[1], Yeongjun Park[2], Yurim Jang[3], Jong Young Namgung[4], Mi Ji Lee[5,6], Bo-yong Park[4,7,8]

[1]College of Medicine, Inha University, Incheon, Republic of Korea, [2]Department of Computer Engineering, Inha University, Incheon, Republic of Korea, [3]Artificial Intelligence Convergence Research Center, Inha University, Incheon, Republic of Korea, [4]Department of Data Science, Inha University, Incheon, Republic of Korea, [5]Department of Neurology, Seoul National University Hospital, Seoul, Republic of Korea, [6]Department of Neurology, Seoul National University College of Medicine, Seoul, Republic of Korea, [7]Department of Statistics and Data Science, Inha University, Incheon, Republic of Korea, [8]Center for Neuroscience Imaging Research, Institute for Basic Science, Suwon, Republic of Korea

Introduction: Migraine is a neurological condition showing a phase of headache often accompanied by vomiting and sensitivity to sound or light[1]. Prior research based on functional magnetic resonance imaging (fMRI) found alterations in functional connectivity in patients with migraine[2,3], but structural connectome alterations have not been fully investigated. In this study, we aimed to identify alterations in structural connectome organization in patients with migraine using manifold learning techniques that project high-dimensional data onto the low-dimensional manifold space.

Methods: We obtained T1-weighted and diffusion MRI of 47 migraine patients (age = 34.3 ± 8.3, 74.5% female) and 41 healthy controls (age = 35.2 ± 7.7, 75.6% female). The T1-weighted data were preprocessed using a FuNP surface-based pipeline[4], and diffusion MRI data were preprocessed using MRtrix3[5]. The neuronal streamlines were estimated using probabilistic tractography, and the structural connectivity matrix was constructed based on the sub-parcellation of the Desikan-Killiany atlas divided into 300 regions[6]. Low-dimensional eigenvectors were estimated by a nonlinear dimensionality reduction technique - diffusion map embedding. Individual eigenvectors were aligned to a template eigenvector, which was generated from the group representative matrix computed using distance-dependent thresholding[7]. We defined the manifold eccentricity feature by calculating the Euclidean distance between each data point and the center of the data on the manifold space[8] (Fig. 1). The differences in the manifold eccentricity between patients with migraine and healthy controls were estimated using an independent samples t-test while controlling for age and sex. The multiple comparisons across brain regions were corrected using a false discovery rate (FDR) < 0.05. The between-group differences in subcortical connectivity were assessed using the degree values of the subcortico-cortical connectivity.

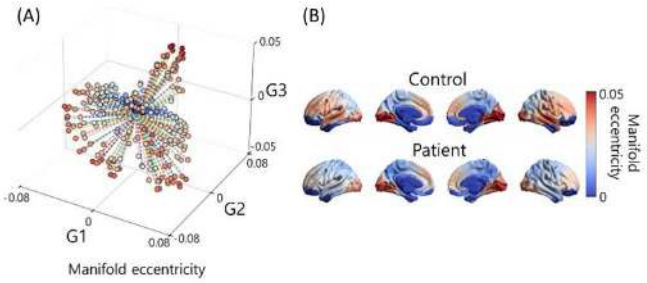

Fig. 1 Manifold eccentricity. (A) Schema of the manifold eccentricity. **(B)** Group-averaged manifold eccentricity of control and patient groups.

Results: We found significant shifts in the manifold eccentricity in the orbitofrontal cortex, temporal pole, and somatomotor regions. The largest effect was observed in the limbic areas when we summarized the statistics according to seven functional networks and four cortical hierarchical levels (Fig. 2A). Additionally, significant shifts in degree values of the subcortico-cortical connectivity were observed in the caudate, amygdala, thalamus, and accumbens (Fig. 2B).

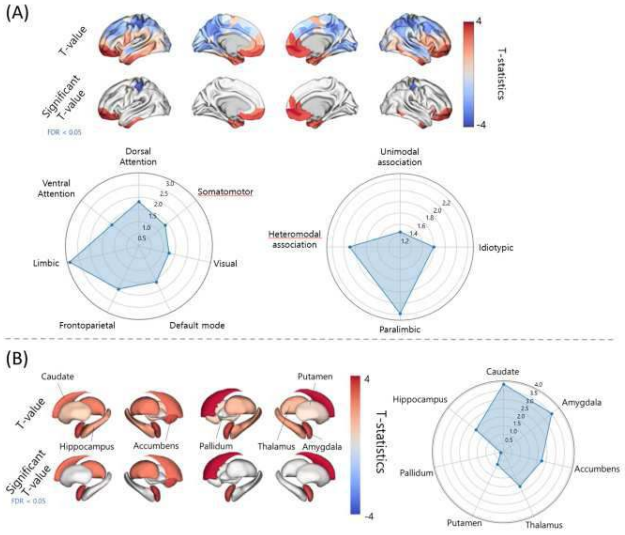

Fig. 2 Between-group differences in manifold eccentricity and subcortico-cortical degree values. **(A)** T-statistic values of the whole brain and the regions showed significant effects are shown on the brain surfaces. We summarized the statistics according to functional networks and cortical hierarchical levels. **(B)** Between-group differences in subcortico-cortical degree values.

Conclusions: Leveraging manifold learning techniques, we found that patients with migraine show shifts in structural connectome organization, particularly in the limbic and amygdala-caudate systems. Our findings may provide a clue for understanding the large-scale brain organization in migraine. Funds: This research was supported by the National Research Foundation of Korea (NRF2020R1A2B5B01001826; NRF-2021R1F1A1052303; NRF2022R1A5A7033499), Institute for Information and Communications Technology Planning and Evaluation (IITP) funded by the Korea Government (MSIT) (No. 2022-0-00448, Deep Total Recall: Continuous Learning for Human-Like Recall of Artificial Neural Networks; No. RS-2022-, Artificial Intelligence Convergence Innovation Human Resources Development. 2022-0-00448, Deep Total Recall: Continuous Learning for Human-Like Recall of Artificial Neural Networks; No. RS-2022-00155915, Artificial Intelligence Convergence Innovation Human Resources Development (Inha University); No. RS-2022R1A5A7033499, Institute for Information and Communications Technology Planning and Evaluation (IITP) funded by the Korean Government (MSIT) (No. RS-2022R1A5A7033499) 021-0-02068, Artificial Intelligence Innovation Hub), Institute for Basic Science (IBSR015-D1), and the Korea Medical Device Development Fund grant funded by the Korean government (the Ministry of Science and ICT, the Ministry of Trade, Industry and Energy, the Ministry of Health & Welfare, the Ministry of Food and Drug Safety) (Project number: RS-2023-00229484).

References

1. Bo-yong Park et al. (2019), 'FuNP (Fusion of Neuroimaging Preprocessing) Pipelines: A Fully Automated Preprocessing Software for Functional Magnetic Resonance Imaging', Frontiers in Neuroinformatics, vol. 13
2. Bo-yong Park et al. (2021), 'An expanding manifold in transmodal regions characterizes adolescent reconfiguration of structural connectome organization', eLife, vol. 10, e64694
3. Colombo B. et al. (2015), 'Resting-state fMRI functional connectivity: a new perspective to evaluate pain modulation in migraine?', Neurological Sciences, vol. 36, pp.41–45
4. Desikan RS et al. (2006), 'An automated labeling system for subdividing the human cerebral cortex on MRI scans into gyral based regions of interest.', Neuroimage, vol. 31, no. 3, pp. 968-80
5. J-Donald Tournier et al. (2019), 'MRtrix3: A fast, flexible and open software framework for medical image processing and visualization', Neuroimage, vol. 202, e116137
6. Lee CH et al. (2023), 'Whole-brain functional gradients reveal cortical and subcortical alterations in patients with episodic migraine.', Human Brain Mapping, vol. 44, no. 6, pp. 2224-2233
7. Richard F. Betzel et al. (2019), 'Distance-dependent consensus thresholds for generating group-representative structural brain networks', Network Neuroscience, vol. 3, no. 2, pp. 457-496
8. Walter K. (2022), 'What Is Migraine?', JAMA, vol. 327, no. 1, p. 93

Poster No 1505

Validation of Krakencoder's ability to predict cognition and demographics across lifespan datasets

Qinxin Wang[1], Keith Jamison[2], Amy Kuceyeski[2]

[1]Cornell university, Ithaca, NY, [2]Weill Cornell Medicine, New York City, NY

Introduction: Krakencoder is a simultaneous, multi-atlas, multi-modality brain connectivity set of encoding models that addresses the challenge of integrating diverse brain connectivity types that each carry unique information and possible noise (Jamison OHBM 2023). Its architecture includes a set of encoders and decoders designed to transform one connectivity type into another through the shared latent representation (See Figure 1). It was trained on resting-state functional and white-matter structural connectivity data from 700 healthy young adults in the Human Connectome Project (HCP-YA), optimizing for reconstruction accuracy and within-subject similarity in latent-space. Building on recent studies that demonstrated the effectiveness of kernel regression models for predicting demographics from brain connectomes (Li 2019, Ooi 2022), we trained kernel regression or classification models to predict sex, age and cognition. Using held-out subjects from HCP-YA, as well as two out-of-sample datasets, we compared the predictions of subject demographics from latent representations and the raw brain connectivity data, demonstrating Krakencoder's generalizability to data with diverse subjects and acquisition parameters.

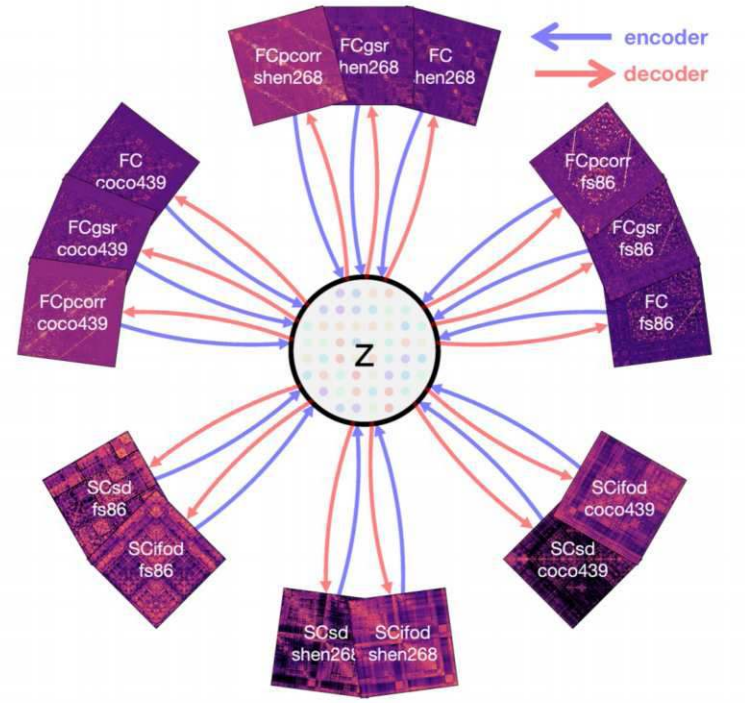

Figure 1: Krakencoder architecture. Krakencoder is an encoding model that addresses the challenge of integrating diverse brain connectivity types. This architecture includes a set of encoders and decoders designed to transform one connectivity type into another through the shared latent space. Z represents the low-dimensional structure latent space embodying crucial collective information in all connectivity variations, allowing for reconstruction and translation. The 15 input matrices include three parcellations (86, 268, and 439 regions), three common functional connectivity (FC) metrics (Pearson correlation, Pearson correlation with global signal regression, and regularized partial correlation), and two structural connectivity (SC) approaches (volume-normalized streamline counts from deterministic and probabilistic tractography).

Methods: Our study utilized three datasets from the Human Connectome Project, drawn from individuals across the lifespan, including young adults (HCP-YA, 22-37), developing individuals (HCP-D, 8-22), and an aging population (HCP-A, 36-86). Beyond age differences, the HCP D/A acquisitions are approximately half the length of HCP-YA. All datasets include three parcellations (86, 268, and 439 regions), three common functional connectivity (FC) metrics (Pearson correlation, Pearson correlation with global signal regression, and regularized partial correlation), and two structural connectivity (SC) approaches (streamline counts from deterministic and probabilistic tractography), yielding 15 total connectivity types. For Krakencoder, our predictions use the mean latent vectors across FC flavors, SC flavors, or both SC and FC for each subject. For the raw data, we use the mean cosine similarity matrices for FC, SC, or SC and FC. We employed cross-validation in fitting and testing the models, ensuring that family groups are not split.

Results: The analysis of held-out HCP-YA subjects reveals that predictions from Krakencoder's latent representations generally outperform raw connectome data, though raw FC predicts age better than latent FC. FC latent space predicts cognition better than SC latent space. SC latent space better predicts age, and both predict sex with accuracy > 93%. The combination of FC and SC consistently yields high predictive performance for all three variables, outperforming or at least matching the better-performing individual modality. For out-of-sample HCP-D/A datasets, latent representations perform comparably to raw data. Latent was better in sex prediction but worse in age prediction, with minor differences in cognition prediction. Within latent representations, SC outperforms FC in predicting age, while FC is more predictive of sex and cognition. Combined connectivities also maintain relatively high performance.

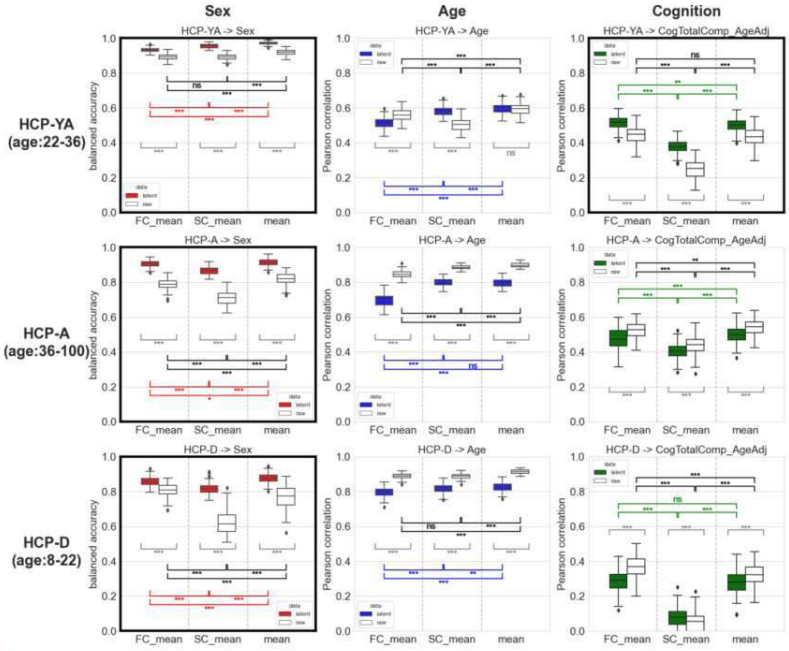

Figure 2: Comparisons between demographic predictions from latent representations and the raw data across three distinct datasets. Balanced accuracy is employed as the performance metric for sex prediction, while Pearson correlation is used for age and cognition prediction. The four highlighted subplots show the datasets and demographic variables where latent representations consistently outperform the raw data. *FC_mean*: predictions based on the average 128-dimensional latent vector for 9 FC flavors for each subject, or the average cosine similarity matrix for 9 FC flavors from raw data. *SC_mean*: predictions based on the average of 6 SC latent vectors, or 6 SC raw data cosine similarity matrices. mean: predictions based on the average of FC_mean and SC_mean. Bars denote significant differences between each pair of inputs, where 'ns' signifies not significant, 'ns' represents 'not significant', '*' represents $p < 0.05$, '**' for $p < 0.01$, and '***' for $p < 0.001$, all being adjusted using the same correction.

Conclusions: Krakencoder effectively reduces the high dimensionality of raw data (677,870 dimensions) into low-dimensional vectors (128 dimensions) within the latent space, facilitating an integrated and aligned representation across diverse modalities. The resulting latent representations largely preserve the predictive properties inherent in the raw data, as evidenced by the marginal disparities in their predictive performances observed in our results. Although Krakencoder was originally trained on the HCP-YA dataset, it exhibits strong generalizability when applied to the HCP-A&D datasets, despite differences in data acquisition methods and substantial variations in the age distribution of subjects. This robust performance across distinct datasets underscores Krakencoder's generalizability and versatile applicability.

References

1. Jamison KW.(2023),'Krakencoder: A simultaneous multi-atlas, multi-modality brain connectivity encoding model', 2023 OHBM Annual Meeting, Montreal, QC.
2. Li J.(2019),'Global signal regression strengthens association between resting-state functional connectivity and behavior', Neuroimage. 2019 Aug 1;196:126-141.
3. Ooi LQR.(2022), 'Comparison of individualized behavioral predictions across anatomical, diffusion and functional connectivity MRI', Neuroimage. 2022 Nov;263:119636.

Organization for Human Brain Mapping

Advancing Understanding of the Human Brain

ORGANIZATION FOR HUMAN BRAIN MAPPING

www.humanbrainmapping.org

1935 County Road B2 W, Ste 165
Roseville, MN 55113
info@humanbrainmapping.org
952-641-2294